SCHOLARLY PUBLICATIONS

A CURRENT AWARENESS BULLETIN
OF RESEARCH OUTPUT

@DTU

(110th Edition)

FEBRUARY 2022

BY: CENTRAL LIBRARY

DELHI TECHNOLOGICAL UNIVERSITY
(FORMERLY *DELHI COLLEGE OF ENGINEERING)*
GOVT. OF N.C.T. OF DELHI
SHAHBAD DAULATPUR, MAIN BAWANA ROAD
DELHI 110042

PREFACE

This is the **One Hundred Tenth** Issue of Current Awareness Bulletin started by Delhi Technological University, Central Library. The aim of the bulletin is to compile, preserve and disseminate information published by the faculty, students and alumni for mutual benefits. The bulletin also aims to propagate the intellectual contribution of Delhi Technological University (DTU) as a whole to the academia.

The bulletin contains information resources available in the internet in the form of articles, reports, presentations published in international journals, websites, etc. by the faculty and students of DTU. The publications of faculty and student which are not covered in this bulletin may be because of the reason that the full text either was not accessible or could not be searched by the search engine used by the library for this purpose.

The learned faculty and students are requested to provide their uncovered publications to the library either through email or in CD, etc. to make the bulletin more comprehensive.

This issue contains the information published during **February, 2022**. The arrangement of the contents is alphabetical. The full text of the article which is either subscribed by the university or available in the web is provided in this bulletin.

Central Library

CONTENTS

1. A BILEVEL GAME MODEL FOR ASCERTAINING COMPETITIVE TARGET PRICES FOR A BUYER IN NEGOTIATION WITH MULTIPLE SUPPLIERS, ***6.Akhilesh Kumar***, ***3.Anjana Gupta*** and Aparna Mehra, Applied Physics, DTU

2. A general Multilevel Polygonal Space Vector Generation scheme with reduced switching for the inverter and harmonic suppression using a switched-capacitive filter for the full modulation range, ***8.1.Rahul Dewani***, K.Gopakumar, Umanand Loganathan and Subhashish Bhattacharya, Electronics, DTU

3. A GENERALIZED BOHR-ROGOSINSKI PHENOMENON, ***6.KAMALJEET GANGANIA*** AND ***3.S. SIVAPRASAD KUMAR***, Applied Mathematics, DTU

4. A Novel Analytical Approach for Optimal Integration of Renewable Energy Sources in Distribution Systems, ***3.Prem Prakash***, ***3.Duli Chand Meena***, Hasmat Malik, Majed A. Alotaibi and Irfan Ahmad Khan, Electrical, DTU

5. A Novel methodology for planning of charging infrastructure in the scenario of high EV penetration, Mandhir Kumar Verma, Vivekananda Mukherjee, ***3.Vinod Kumar Yadav*** and Santosh Ghosh, Electrical, DTU

6. An Energy-Efficient High CSNR XNOR and Accumulation Scheme For BNN, Dinesh Kushwaha, Ashish Joshi, ***3.C. I. Kumar***, Neha Gupta, Sandeep Miryala, Rajiv Joshi, Sudeb Dasgupta and Anand Bulusu, Electrical, DTU

7. Analytical study on properties of concrete materials incorporating recycled aggregates from construction & demolition waste, ***6.Shanko Ayele Abera***, Civil, DTU

8. Catalytic Performance of Cow-Dung Sludge in Water Treatment Mitigation and Conversion of Ammonia Nitrogen into Nitrate, ***6.Lokesh Kumar***, ***3.Jaigopal Sharma*** and ***3.Raminder Kaur***, Chemistry and Biotechnology, DTU

9. CFD Study of Flow Characteristics and Pressure Distribution on Re-Entrant Wing Faces of L-Shape Buildings, ***6.Arun Kumar*** and ***3.Ritu Raj***, Civil, DTU

10. CNFMD: Convolutional Network-based Face Mask Detection, ***8.Saksham Checker***, Applied Physics, DTU

11. CNTFET based Transmission Gate Diffusion Input Logic (C-TGDI) design, ***6.Neetika Yadav***, ***3.Neeta Pandey*** and ***3.Deva Nand***, Electronics, DTU

12. ConRec: malware classification using convolutional recurrence, ***8.Abhishek Mallik***, ***8.Anavi Khetarpal*** and ***3.Sanjay Kumar***, CSE, DTU

13. Coordinated Allocation of Electric Vehicle Charging Stations and Capacitors in Distribution Network, ***6.Mohd Bilal***, ***6.Astitva Kumar*** and ***3.Mohammad Rizwan***, Electrical, DTU

14. CSR: A community based spreaders ranking algorithm for influencemaximization in social networks, ***3.Sanjay Kumar***, ***8.Aaryan Gupta*** and ***8.Inder Khatri***, CSE and Applied Mathematics, DTU

15. Defect predictionmodel using transfer learning, ***3.Ruchika Malhotra*** and ***3.Shweta Meena***, Software Engineering, DTU

16. Design of PSO-tuned FOPI & Smith predictor controller for nonlinear polymer electrolyte membrane fuel cell, Swati Singha, Vijay Kumar Tayal, Hemender Pal Singh, and ***3.Vinod Kumar Yadav***, Electrical, DTU

17. Detection of Cotton Plant Disease for Fast Monitoring Using Enhanced Deep Learning Technique, ***7.Himani Bhatheja*** and ***3.N. Jayanthi***, Electronics, DTU

18. Effect of Load Frequency and Amplitude of Displacement on Soft Rock Joints under Cyclic Shear loads, S. M. Mahdi Niktabar, K. Seshagiri Rao, ***3.Amit Kumar Shrivastava*** and Jiří Ščučka, Civil, DTU

19. Effect of Multipass FSP on Si-rich TIG Welded Joint of Dissimilar Aluminum Alloys AA8011-H14 and AA5083-H321: EBSD and Microstructural Evolutions, Abdellah Nait Salah, ***6.Sipokazi Mabua***, ***6.Husain Mehdi***, Velaphi Msomi, Mohammed Kaddami and Prabhujit Mohapatra, Mechanical, DTU

20. Estimation of crack growth on rails under the combined influence of thermo-mechanical loading due to the sliding of wheel, ***6.Aakash D Bansal***, ***3.Atul Kumar Agrawal*** and ***3.Vikas Rastogi***, Mechanical, DTU

21. Evaluation of Municipal Solid Waste Management Scenarios using Multi-Criteria Decision Making under Fuzzy Environment, Aakash Gaur, Harshita Prakash, Kuwar Anand, ***3.Girish Kumar*** and Athar Hussain, Mechanial, DTU
22. Experimental and theoretical investigation into surface roughness and residual stress using ball end magnetorheological finishing, ***6.Anand Sharma*** and ***3.Mahendra Singh Niranjan***, Mechanical, DTU
23. Experimental Investigation on Machinability and Geometric Tolerance in Die-Sinking EDM of Microholes and Channels, ***6.S. Vidya***, ***3.R. Wattal*** and P. V. Rao, Mechanical, DTU
24. Exploring intergenerational differences in technology-oriented ethical behavior, ***6.Shivangi Verma*** and ***3.Naval Garg***, USME, DTU
25. FPGA-based Pipelined LSTM accelerator with Approximate matrix multiplication technique, ***8.Aniket Chaudhary***, ***8.Arun Kumar***, ***8.Ayush Srivastava*** and ***3.Kriti Suneja***, Electronics, DTU
26. Human Activity Recognition Using LongShort-Term Memory, ***8.1.Vibhor Vimal***, ***8.1.Anshuman Singh*** and ***3.Priyanka Meel***, IT, DTU
27. Implementation of Soft Computing Techniques to Evade Partial Shading Effects for PV Based Off-Grid System, Ashish Grover, Anita Khosla, ***3.Dheeraj Joshi*** and Vrince Vimal, Electrical, DTU
28. Improving document representation using KPCA and clustered word embeddings, ***8.Aakansha Gupta*** and ***3.Rahul Katarya***, CSE, DTU
29. Influence of Source Electrode Metal Work Function on Polar Gate Prompted Source Hole Plasma in Arsenide/Antimonide Tunneling Interfaced Junctionless TFET, ***6.Samriti Sharma*** and ***3.Rishu Chaujar***, Applied Physics, DTU
30. Intelligent Energy Management System for a Smart Home Integrated with Renewable Energy Resources, Arjun Baliyan, Isaka J. Mwakitalima, Majid Jamil and ***3.M. Rizwan***, Electrical, DTU
31. Intra-Block Correlation Based Reversible Data Hiding in Encrypted Images Using Parametric Binary Tree Labeling, Arun Kumar Rai, Neeraj Kumar, ***3.Rajeev Kumar***, Hari Om, Satish Chand and Ki-Hyun Jung, CSE, DTU
32. Investigation of fresh, mechanical, and impact resistance properties of rubberized concrete, ***6.Rahul Kumar***, ***6.Manvendra Verma*** and ***3.Nirendra Dev***, Civil, DTU
33. IOT BASED NON-CONTACT FUEL LEVEL MONITORING, ***8.Abhishek Singh***, Mechanical, DTU

34. Layered Double Hydroxide Nanomaterials: Biomedical Applications, Current Status and Challenges, Ritika Sharma, Bhawna, Sanjeev Kumar, ***3.Poonam Singh***, Akanksha Gupta and Vinod Kumar, Applied Chemistry, DTU

35. LBECR: load balanced, efficient clustering and routing protocol for sustainable internet of things in smart cities, ***3.Pawan Singh Mehra***, CSE, DTU

36. Leaf senescence and its regulation with phytohormones and essential elements: An overview, ***7.Shatrupa Singh***, ***6.Madhulika Singh***, ***3.Sanskriti Bisht*** and ***3.Jai Gopal Sharma***, Biotechnology, DTU

37. Link prediction in complex networks using node centrality and light gradient boosting machine, ***3.Sanjay Kumar***, ***8.Abhishek Mallik*** and B. S. Panda, CSE, DTU

38. Low Power Swing Restoration Circuit Reduce Threshold Voltages of SRAMs Improve Read & Write Operations, ***3.Vinod Kumar*** & ***3.Ram Murti Rawat***, CSE, DTU

39. Minor tropical fruits as a potential source of bioactive and functional foods, Tanmay Sarkar, Molla Salauddin, Arpita Roy, ***8.Nikita Sharma***, ***8.Apoorva Sharma***, ***8.Saanya Yadav***, ***8.Vaishnavi Jha***, Maksim Rebezov, Mars Khayrullin, Muthu Thiruvengadam, Ill-Min Chung, Mohammad Ali Shariati & Jesus Simal-Gandara, Biotechnology, DTU

40. MODELING FOR THE ENERGY POTENTIAL OF BIOGAS POWER PLANTS IN NATIONAL CAPITAL TERRITORY, ***7.Rohit Agrawal*** and ***3.S.K. Singh***, Environmental, DTU

41. Optimizable face detection and tracking model with occlusion resolution for high quality videos, ***7.Akshay Mool***, ***3.J. Panda*** and ***3.Kapil Sharma***, IT & Electronics, DTU

42. Optimization of long-term storage stability of Kusum biodiesel using herbal anti-oxidant, Harveer Singh Pali, Abhishek Sharma, ***3.Naveen Kumar*** and Yashvir Singh, Mechanical, DTU

43. Positive reframing as a mediator between gratitude and technostress amongst Indian students during the COVID-19 pandemic, ***3.Naval Garg***, ***6.Shivangi Verma*** and Jason Timothy Palframan, USME, DTU

44. Realizing high thermoelectric performance in p-type RbZn4P3 Zintl compound: a first-principles investigation, , Ramesh Kumar and ***3.Mukhtiyar Singh***, Applied Physics, DTU

45. Response of Tall Building with Different Side Ratio under the Effect of Wind Load, ***6.PAYAL DEVI***, ***6.RAHUL KUMARMEENA*** and ***3.RITU RAJ***, Civil, DTU

46. Role of Bioactive Glass materials in Beyond Bone Regeneration, ***3.Deenan Santhiya***, Applied Chemistry, DTU

47. Role of socioemotional wealth (SEW) in the internationalization of family firms, ***6.Apoorva Jain*** and ***3.Sonal Thukral*** and Justin Paul, DSM, DTU

48. Sensitivity Analysis of Biomolecule Nanocavity Immobilization in a Dielectric Modulated Triple-Hybrid Metal Gate-All-Around Junctionless NWFET Biosensor for Detecting Various Diseases, ***6.Mekonnen Getnet*** and ***3.Rishu Chaujar***, Applied Physics, DTU

49. State and Parameter Estimation of Non-Uniform Transmission Line Using Kronecker Product Based Modeling, ***6.Amit Kumar Gautam***, ***3.Sudipta Majumdar*** and Harish Parthasarthy, Electronics, DTU

50. State-of-Art Review of Traffic Light Synchronization for Intelligent Vehicles: Current Status, Challenges, and Emerging Trends, ***6.Ishu Tomar***, ***3.Indu Sreedevi*** and ***3.Neeta Pandey***, Electronics, DTU

51. State-of-the-Art Applications of GraphConvolutional Neural Networks, ***8.Rajat Singh***, ***8.Sanchit Bathla*** and ***3.Priyanka Meel***, IT, DTU

52. Structural and color tunable properties in Sm3+/Eu3+- doped Ca3Bi(PO4)3 phosphor for solar cell and w-LED applications, ***7.Mukesh K. Sahu*** and ***3.M. Jayasimhadri***, Applied Physics, DTU

53. Sustainable supply chain risk mitigation: a mixed method approach, Madhukar Chhimwal, ***3.Saurabh Agrawal*** and ***3.Girish Kumar***, Mechanical, DTU

54. Therapeutic applications of mesenchymal cells derived from human placenta A comprehensive meta-review, ***8.Ritika Luthra***, ***8.Saanya Yadav*** and ***3.Smita Rastogi Verma***, Biotechnology, DTU

55. Thermodynamic analysis of sensible heat storage based double pass hybrid solar air heater with and without reflector, OM PRAKASH, ***3.ANIL KUMAR*** and VINOD LAGURI, Mechanical and Environment, DTU

56. Uncovering the geometrical aspects of intramolecular hydrogen bond in meta-benziporphodimethenes through molecular tailoring approach, ***6.Deepali Ahluwalia***, ***3.Anil Kumar***, ***3.Sudhir G. Warkar***, Milind M. Deshmukh and Arijit Bag, Applied Chemistry, DTU

1. *Vice Chancellor*
2. *Pro Vice Chancellor*
3. *Faculty*
4. *Teaching-cum-Research Fellow*
5. *Asst. Librarian*
6. *Research Scholar*
7. *PG Scholar*
8. *Undergraduate Student*

1.1. *Ex Vice chancellor*
2.1. *Ex Pro Vice Chancellor*
3.1. *Ex Faculty*
4.1. *Alumni*
5.1 *Others*
6.1. *Ex Research Scholar*
7.1. *Ex PG Scholar*
8.1. *Ex Undergraduate Student*

RAIRO-Oper. Res. 56 (2022) 293–330
https://doi.org/10.1051/ro/2021185

RAIRO Operations Research
www.rairo-ro.org

A BILEVEL GAME MODEL FOR ASCERTAINING COMPETITIVE TARGET PRICES FOR A BUYER IN NEGOTIATION WITH MULTIPLE SUPPLIERS

Akhilesh Kumar[1,2,*], Anjana Gupta[1], and Aparna Mehra[3]

Abstract. In this paper, a decision-support is developed for a strategic problem of identifying target prices for the single buyer to negotiate with multiple suppliers to achieve common goal of maintaining sustained business environment. For this purpose, oligopolistic-competitive equilibrium prices of suppliers are suggested to be considered as target prices. The problem of identifying these prices is modeled as a multi-leader-single-follower bilevel programming problem involving linear constraints and bilinear objective functions. Herein, the multiple suppliers are considered leaders competing in a Nash game to maximize individual profits, and the buyer is a follower responding with demand-order allocations to minimize the total procurement-cost. Profit of each supplier is formulated on assessing respective operational cost to fulfill demand-orders by integrating aggregate-production-distribution-planning mechanism into the problem. A genetic-algorithm-based technique is designed in general for solving large-scale instances of the variant of bilevel programming problems with multiple leaders and single follower, and the same is applied to solve the modeled problem. The developed decision support is appropriately demonstrated on the data of a leading FMCG manufacturing firm, which manufactures goods through multiple sourcing.

Mathematics Subject Classification. 90C33, 90C59, 91B50.

Received January 26, 2021. Accepted December 16, 2021.

1. Introduction

Suppliers compete on prices to attract a competitive demand share from their buyer, in an oligopolistic-monopsony market, for maximizing their profits. On the other side, the buyer intends to minimize the overall procurement cost for receiving a regular supply of required products. To purse this objective, the buyer seeks to exploit the competition between suppliers and therefore negotiates with them to lower down the prices. The status of being a sole buyer of an oligopolistic-monopsony market provides a bargaining power to entice suppliers with a larger share of demand-order in exchange for lowering the prices. In our problem, the buyer's overall demand is less than the combined output capacities of all the suppliers. In this situation, the buyer's bargaining power gets further increased, and therefore suppliers are forced to renegotiate prices for obtaining

Keywords. Competitive target prices, price negotiations, bilevel programming, multi-leader-single-follower bilevel game, aggregate-production-distribution-planning, genetic algorithm.

[1] Department of Applied Mathematics, Delhi Technological University, Bawana Road, Rohini, Delhi 110042, India.
[2] Department of Mathematics, Arignar Anna Government Arts & Science College, Karaikal, Puducherry 609602, India.
[3] Department of Mathematics, Indian Institute of Technology Delhi, Hauz Khas, New Delhi 110016, India.
*Corresponding author: akhilesh.maths@gmail.com

© The authors. Published by EDP Sciences, ROADEF, SMAI 2022

This is an Open Access article distributed under the terms of the Creative Commons Attribution License (https://creativecommons.org/licenses/by/4.0), which permits unrestricted use, distribution, and reproduction in any medium, provided the original work is properly cited.

demand-orders. In such a scenario, the buyer can adopt an opportunistic discriminatory approach for negotiation with suppliers to reduce the procurement cost to a minimum. Some of the suppliers' prices negotiated in this manner may be well below a point where all the suppliers would have agreed upon due to complete awareness of competition in the discussed business environment. It develops a dissonance among such suppliers, and a tendency of non-cooperation with the buyer starts emerging among suppliers [58]. This antipathy adversely affects the buyer-supplier relationship [40,68,78,84], which, in turn impacts performance of their supply chain detrimentally [93]. On the other hand, if the buyer's price-negotiations with suppliers settle at a point above an equilibrium point of suppliers' oligopolistic competition, the buyer's financial interests are adversely affected, incurring a potentially higher procurement cost. If suppliers resist lowering the prices towards the equilibrium point, it compels the buyer to look for alternative sourcing arrangements as a long-term initiative to intensify the competition among suppliers. This remedial action by the buyer results in reducing the supplier's bargaining power and their demand-shares in the future, resulting in reduced profit in the long run.

The aggrieved stakeholders on either side of the considered market situation have an adverse action space that can thwart from maintaining a sustained and continuous business environment. Accordingly, the outcome of price-negotiations should ensure long term gains through sustained and continuous replenishment of products for the buyer *vis-à-vis* short-term gains through opportunistic discrimination in price negotiation. Similarly, each supplier should prefer getting sustained and continuous replenishment orders from the buyer, *vis-à-vis* creating an adverse action space that may affect their business prospects. Therefore, it is imperative to identify prices for the business deal to achieve common goal while pursuing parallel individual objectives. Consequently, it is appropriate for the stakeholders at both sides to settle at equilibrium prices of suppliers' oligopolistic competition.

Identifying suppliers' oligopolistic competitive equilibrium prices as target prices for negotiation imposes the competition among suppliers up to their individual production-distribution capabilities, and cost-efficiencies. As a result, the negotiated prices leave no space for any opportunistic discrimination on the buyer's part and protect her/his financial interests as well. As these target prices for negotiation are based only on suppliers' competitive capabilities, we appropriately term these as *competitive target prices*. Further, in case the price-negotiations with some supplier(s) settle significantly away from these prices, it indicates that negotiations have not resulted purely due to a fair competition among suppliers.

The oligopolistic-monopsony market ecosystem with the situation described above is common in many sectors. It can emerge because of localization of the market of suppliers due to transportation cost efficiencies. Whenever a manufacturing firm comes up with a new product, which involves a completely new technology, the market situation emerging with its suppliers who associate for providing required components refers to oligopolistic-monopsony market ecosystem. Another example of this market ecosystem is observed in case of sole manufactures of non-substitutable products when they need to procure components or raw material from their suppliers for the execution of manufacturing process. This situation is prevalent in case of specialized products, for example, in case of luxury cars. A particular example for getting more insight can be discussed in context of Indian Railways. Indian Railways is the only organization providing railway travel services within India and for providing these services it manufactures train coaches at its own factories situated at multiple locations within India. For this manufacturing it requires multiple electrical equipments with specific technical requirements, which are fulfilled by a limited number of specialized suppliers. This makes the Indian Railways a single buyer for these specific products, thereby positioning the market system as a monopsony from the buyer's side, and oligopoly from the suppliers' side.

Although, multiple examples of the discussed market ecosystem are observed in many sectors, but to the best of our knowledge, the problem of identifying target prices for negotiations among the buyer and suppliers is not studied in the literature.

In this paper, we develop a decision support for identifying competitive target prices for the buyer's negotiations with multiple suppliers in the oligopolistic-monopsony market. We model the problem of identifying the competitive target prices as a multi-leader-single-follower (MLSF) bilevel programming problem. The model formulated as MLSF bilevel programming problem involves linear constraints and bilinear objective functions.

The model involves integer variables for capturing an actual practice of supply chain where demand orders, production and logistic quantities take integral values. For formulating the action-and-reaction mechanism of price-negotiations in our bilevel programming model, we consider suppliers as leaders and the buyer as a follower. This is based on the chronology of communication among them *viz*, suppliers making the first move by offering the price quotes to the buyer, whereas the buyer responding to those in terms of the demand-order allocation. The price-competition among the group of suppliers for receiving maximum profitable demand shares from the buyer leads to a game situation among these suppliers, thereby making it appropriate to model the problem as an MLSF bilevel programming problem. In the oligopolistic competition among suppliers, the assessment of price offers by the buyer requires an integrated planning, as the total cost of fulfilling demand-orders is related to different operating costs of production and distribution. Therefore, for assessing total operating costs and production-and-logistics capacity constraints of each supplier it is compelling to embed the aggregate-production-distribution-planning (APDP) of suppliers in the formulation of our model. The optimal demand-order allocation problem from the point of view of buyer is woven as the follower's reaction mechanism in the formulation of the model. By considering all the essential factors highlighted above in design of the model, a solution of the problem thus formulated represents competitive target prices.

The structure of modeled problem corresponds to a specific type of MLSF bilevel programming problem which involves linear constraints and bilinear objective functions at both levels. Direct methods existing in the literature have been experienced as incapable of handling the large-scale instance of the modeled problem with practical data taken from industry. In this situation, first a nested GA based solution method is suggested for solving generic problems of the specified type of bilevel programming problems. Then, a modification is further suggested in the solution algorithm to capture a peculiar interdependence of variables of the modeled problem. Finally, the proposed model and the solution method are then illustrated on a data set of an FMCG sector firm concerned about optimality of the procurement cost of ingredients required for manufacturing its products in an environment discussed above.

The paper is organized as follows. Section 2 presents literature review. Section 3 describes the problem, its assumptions and formulation as an MLSF bilevel game model. Section 4 describes the GA-based solution methodology proposed for solving the discussed problem. Section 5 demonstrates an experimental study of a manufacturing firm and analysis of the results obtained through the formulation and algorithm. Managerial implications of adopting the suggested approach and utilizing the proposed decision-support are listed in Section 6. Section 7 concludes the paper with the scope of the research work.

2. Literature review

2.1. Price setting and negotiation pricing problems

From the perspective of a supplier, problems of optimal price-setting (including high and low pricing strategies), flexible pricing (like market segmentation), differential pricing, price skimming, penetration pricing, and revenue management based pricing are studied in literature and reviewed by Dolgui and Proth [32]. The pricing problem, when demand is influenced by prices to maximize the turnover, is modeled as a bilevel programming problem by Labbé *et al.* [57], and implemented on a toll setting problem. Dempe and Zemkoho [27] use non-smooth analysis to design Karush–Kuhn–Tucker (KKT) type optimality conditions, which preserve essential data in the traffic assignment problem. Some other studies which model the toll price-setting problems include [18, 29, 46, 105]. Kumar *et al.* [55] studied a strategic pricing problem in a non-competitive environment from a small-scale supplier, coherently discerning operational capacities before quoting the prices to the buyer. A monograph by Nagle and Müller [79] is appropriate to refer to the basics of pricing, price competition, and price negotiations. A survey on price setting problems modeled as bilevel programming problems is provided by Labbé and Violin [56].

Negotiation pricing problems attempt to identify the prices where both seller and buyer mutually agree as beneficial price. The research on devising a mechanism for price negotiation seems limited and evolving, with

some of research developments in this field to name (*e.g.*, [14, 37, 42, 75, 87, 97, 98]). None of the framework in existing studies match our situation.

2.2. Supplier selection and order allocation

The supplier selection is a crucial strategic decision-making process for the procurement of the required products or the raw material. The primary literature on it begins with the work of Dickson [30]. The next accompanying vital decision is on the order allocation under multiple sourcing. Gaballa [38] and Jayaraman *et al.* [52] developed decision support for the order allocation problem to minimize the total procurement cost. The prevalent use of just-in-time approach for inventory procurement resulted in the recommendation of multiple factors for supplier selection [59, 92, 102]. Several researchers investigated the order allocation in concurrence with supplier selection [10, 80, 96]. The supplier selection and order allocation issues have been modeled as multi-objective decision-making problems also [4, 25, 90]. One can refer to the recent literature review by Aouadni *et al.* [3] on supplier selection and order allocation techniques.

2.3. Operational planning problems

Planning of various tasks to fulfill the demand of end-users over a short-term horizon is termed as operational planning under the supply chain management [72]. Production planning in regular-time, over-time, and outsourcing (in each plant in each period), shipping volumes from the production facility or stack buffers to warehouses, shipping volumes from warehouses and stack buffers directly to end-users, inventory of finished products in warehouses at each period, is categorized as aggregate production-distribution planning (APDP) [36]. The literature in the field of APDP problems is extensive and classified into seven categories [36]. Some of the significant contributions worth citing in APDP are [35, 64, 65, 85]. Recent research developments in operational planning include [74, 81].

2.4. MLSF bilevel game problem

In certain business planning situations, the decision-makers are often unable to realize their decisions independently but forced to act according to a specific hierarchy. The programming problem formulated to solve this situation is a multilevel programming problem with a case as a bilevel programming problem involving a leader and a follower. A leader is the decision-maker who can take an independent position in analyzing and using the reaction of the dependent decision-maker, and the latter one is the follower. For the theoretical development, algorithms, and applications of bilevel programming, one can refer to excellent texts [6, 16, 26]. One can refer to Sinha *et al.* [91] for a detailed review of classical and evolutionary algorithms and several applications of bilevel optimization. Multilevel decision-making problems, including applications into the supply chain, are reviewed by Lu *et al.* [69]. Some of the issues in supply chain planning and management are studied using the bilevel programming framework (*e.g.*, [5, 88, 99]).

MLSF bilevel games are categorized as a variant of bilevel programming problems, which involve multiple competing leaders and each one needs to incorporate the response of their common follower in their decision making. Some interesting practical problems have been modeled using this bilevel-game framework (*e.g.*, [45, 46, 89]). Theoretical developments are suggested in the literature for solving such problem by reformulating them using stationarity conditions [51, 60]. The suggested solution methodologies in the literature solve the multi-leader-common-follower (MLCF) bilevel game problems in terms of strong-stationary points [60] and strong-stationary equilibrium points [51]. Leyffer and Munson [60] suggested a direct method for obtaining strong-stationary points by solving a nonlinear programming problem derived from strong-stationarity conditions by posing complementarity conditions as the objective function to be minimized to zero. The authors demonstrated the proposed approach through numerical experiments on randomly generated small-scale and medium-scale electricity market problems involving 150 constraints and 160 variables. Hori and Fukushima [51] proposed a Gauss-Seidel method for numerical convergence to a strong-stationary equilibrium point, which

involves solving a penalty-based quadratic optimization problem in each of the iterations. Five examples, involving a maximum of 12 variables and less than 10 constraints, are presented to demonstrate the process. An extensive literature review of methodologies for solving MLCF bilevel game problems has indicated that none of the methods have been tested on large-scale problems involving more than 160 variables and 150 constraints. Moreover, no algorithm is developed for solving an MLCF bilevel game problem involving integer variables.

2.5. Genetic algorithms approaches

Genetic algorithms are bio-inspired artificially intelligent random search algorithms, which are developed due to seminal works of pioneers Holland [50] and Goldberg [43]. Initial development of GA encodes chromosomes as binary strings and thus is called Binary Coded GA (BCGA). The real coded GA (RCGA) [20,70], which encodes chromosomes as strings of real numbers has been found superior to BCGA in terms of efficiency of exploration and against challenges like Hamming Cliff [44, 104]. Contributions towards further development improved the efficiency and acceptance of RCGA [34, 86]. Eventually, several researchers have employed RCGA for solving numerical optimization problems involving continuous variables [21,34,48,49,77,100,104]. Due to the capability of solving majority of complex NP-hard real-world large scale optimization problems, RCGA has been used in almost every area of practical application (*e.g.*, [7, 8, 19, 71, 94, 95]). Later, an Integer Coded GA (ICGA) was developed to solve integer or mixed integer programming problems. Crossover and mutation operators have specifically been developed for ICGA [1,19,22–24,82]. One can refer to Mirjalili [76] for rudimentary prelude and a bird's-eye review on developments of GA. Some standard problems of supply chain planning and management, which are NP-hard, are solved using GA and its variants [35, 41, 67]. GA and its other variants are extensively used in supplier selection problems [28, 31, 66, 106].

Evolutionary approaches for solving the bilevel programming problems are studied separately from those developed for solving general optimization problems due to the special structure of the bilevel problems. Moreover, due to the same reason, evolutionary approaches have been developed in the literature for specific variants of the bilevel programming problems. Pricing problems modeled in the bilevel programming framework have also been solved using GA [33, 103], and a similar artificially intelligent algorithm *viz.*, particle search optimization algorithm [39]. GA based evolutionary algorithms have been used to solve some special classes of bilevel programming problems [9, 11, 15, 47, 54, 55, 61, 63, 101, 107]. Among the evolutionary algorithms developed for solving bilevel programming problems, those based on nested approach are effectively used over those developed for solving general optimization problem. In this approach, only the leader(s) variables are encoded and explored randomly, while the respective values of follower's variables are obtained directly by solving follower(s) problem after passing the values of leader's variables as parameters. Therefore, the nested GA for bilevel programming problems focuses on developing the reaction mechanism for the follower(s) problem in response to the given values of leader's variables and formulating the fitness function. Algorithms developed under this approach for solving some particular cases of bilevel programming problems can be referred in the literature [2, 12, 13, 54, 62, 73, 107, 108]. But none of the studies have considered solving a bilevel programming problem involving integer variables particularly at followers' level.

In this backdrop, we are now ready to present our problem statement, model formulation, and the associated theoretical developments. In subsequent sections we present an algorithm developed for solving the formulated model and its illustration on a real-life case.

3. Bilevel game for ascertaining competitive target prices

3.1. Problem description

The negotiation process among buyer and suppliers is considered in the following setup.

– A buyer has already identified a set of suppliers based on their production and logistic infrastructural capacities and the quality standards of both products and services.

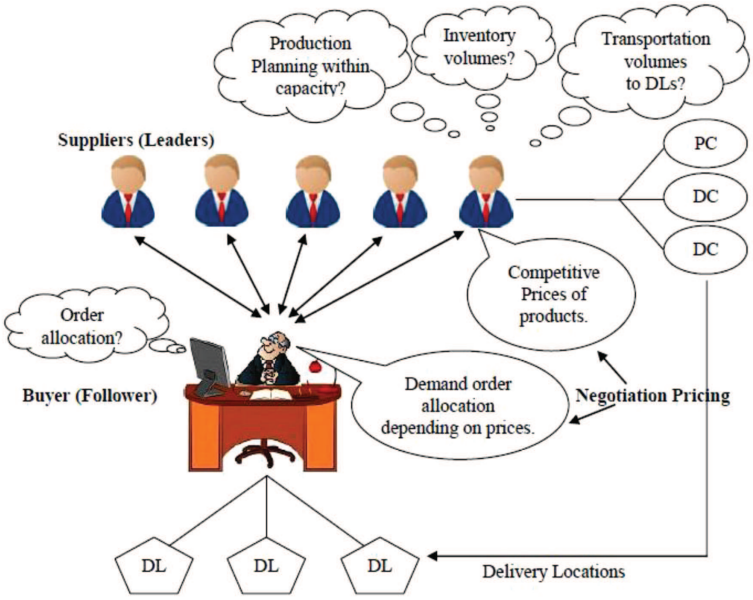


FIGURE 1. Depiction of structure.

- Each of these suppliers can produce some or all the required products and deliver them at various locations of the buyer.
- Considering the supply capacities of all the suppliers the total requirements of the buyer for various products can be fulfilled in each period.
- This setup is considered for a pre-defined planning horizon fixed by suppliers and the buyer together. The planning horizon is further divided into multiple time intervals, called periods[1].

The buyer wishes to negotiate on prices with these suppliers before entering into a new agreement. At this stage, suppliers have opportunity to review and agree on the prices of the goods considering production-and-logistics costs over the planning period and competition from the other suppliers. We consider the business setup where the suppliers bear the cost of on-time delivery at various delivery locations. It compels the suppliers to assess their transportation cost, inventory cost, and production cost in pricing while negotiating with the buyer.

The price-negotiation process of the buyer with each supplier begins with the supplier's offer on the prices of the products. The buyer tries to negotiate with each supplier to lower the prices of the products by offering a greater proportion of the demand-order. The supplier rethinks on the profit while discerning the production-distribution costs and reviews the competition from those suppliers who deal with the buyer in these products particularly. The supplier then agrees for these prices or tries to negotiate further with the buyer. The process of price negotiation gets over once the supplier and the buyer arrive at the final prices. Figure 1 provides a schema for the discussed negotiation process. We develop a model for the buyer to identify competitive target prices for negotiations with a relatively competitive group of suppliers.

[1]The planning horizon is identified as that time duration by which the actual realization of various costs is expected to remain same as per the assessments. The planning horizon can be any duration, for example a month, quarter, or a year and can be discretized into multiple periods, say weeks, fortnights, or months, respectively, depending on replenishment frequencies of various suppliers.

3.2. Basic assumptions of the model

- Any alternative modes or business options will have an adverse impact on the overall business prospects of stakeholders of either side. This consideration for an oligopolistic-monopsony market compels all the stakeholder of the market to discipline themselves for the stability of the market ecosystem.
- The buyer has a knowledge of production and logistic resources and infrastructure of each supplier, to assess an aggregate-production-distribution plan on behalf of the later for any given demand order allocation[2]. This enables the buyer to have an idea of production-distribution capacities and cost efficiencies of suppliers which are required as inputs of our model.
- Each supplier may deal in some or all products among those required by the buyer. This is assumed to consider a more general situation in which different suppliers deal in subsets of the set of all products required by the buyer.
- Each product is homogenous in form, quality, quantity, size, across various suppliers dealing in that product. This is assumed to consider the perfect substitutability of the products of various suppliers which keeps only the price as a decision-variable for competition among suppliers.
- The prices of products are to be negotiated for a fixed time horizon which is discretized into equal subintervals. These subintervals are termed as periods. The demand orders are to be allocated to various suppliers for the delivery of products at each delivery location, during every period of planning horizon.
- The number of periods, into which the planning horizon be discretized, is considered to be the same for all the suppliers. This assumption is considered for reducing the complexity of the model formulation, which would otherwise be involved by considering it to be different for different suppliers. The same can be practically achieved by considering the length of each period as least common multiple of replenishment frequencies of various suppliers.
- Each supplier has a single production center with no capacity to store any inventory over a period. This is an assumption considered to capture into the model the actual practice observed generally about the production-distribution setups of manufacturers in B2B markets.
- All or some part of products manufactured in any period can be transported directly to various delivery locations of the buyer. In general, the products are transported first from the production center to distribution centers for inventory and cross-docking, and from there transported to the different delivery locations. This transportation arrangement of each supplier is depicted in Figure 2. This arrangement of transportation is considered for capturing into the model the most general provisions of transportation arrangements.
- The distribution centers can store each product that the supplier is dealing in. Likewise, all delivery locations can accommodate all types of products.
- Suppliers are aware of the production-distribution capacities of their competitors through their market intelligence. This practical assumption on competitive awareness of suppliers is considered to capture in our model the competency of negotiators from each supplier which enables them to estimate that up to what their counterparts can lower their price offers. Such an assumption is required as a basic consideration from the game theory that players in a game opt only for their best strategy.
- Suppliers' possible cost fluctuations are taken into consideration during the estimation of parameters. Assuming this makes it possible to consider the parameters as fixed numbers any not fuzzy, as fuzziness will further complicate the model to a very high level of complexity.
- The cost (per unit) of the products by the suppliers is estimated by including all direct and indirect expenses, if any. This relieves from the hassle of considering the fixed costs of production or distribution separately in the APDP part of the model responsible for computing the total cost of supply incurred to each supplier.
- No significant changes in technology and business environment are expected during the planning horizon which may impact the costs drastically. This assumption is made for considering the parameter values taken in our model to beat par with their estimates during the planning horizon. As the planning horizon is of short-term this assumption is realized most of the times apart from some exceptional unprecedented incidences.

[2]Such an assumption is practical in view of the assessment by the buyer during the supplier selection process.

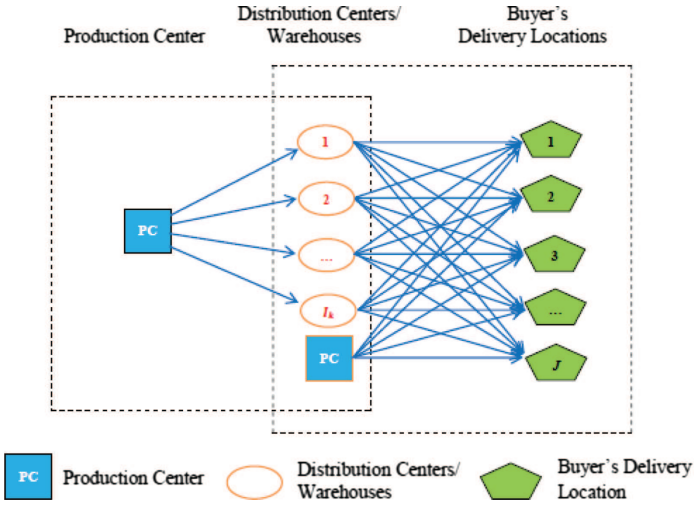


FIGURE 2. Production and distribution structure.

- The variance between the forecasted demand and actual demand for the required products shall be negligible at the buyers end during the planning horizon. Since the planning horizon is short-term, it is reasonable to assume that the buyer can forecast demand encompassing fluctuations in it.
- The buyer knows the price for each supplier below which the supplier would no longer be able to bargain. These prices are identified through break-even prices of suppliers and can be estimated by the buyer during the supplier assessment made during the supplier selection process.
- Discounts or differential pricing are not provisioned in our model. This is assumed for preventing the formulation of our model from including binary integer variables, as they will complicate the model from solution point of view.

3.3. Model formulation

Price quotes from suppliers are a requisition for computing the demand shares by the buyer, which in turn is a requirement for each supplier to assess the profit to be earned as a result. This is a perplexed problem involving action-and-reaction among suppliers and the buyer. The bilevel programming framework is appropriate to model this situation, which terms the action takers as leaders and reaction givers as followers. According to this terminology of bilevel programming, we identify in our problem the suppliers as leaders and the buyer as follower. As there are multiple leaders (suppliers) and single follower (buyer) in the addressed situation, therefore the formulation of model corresponds to a MLSF bilevel programming problem.

Suppliers decide on best price offers, and thereupon prepare the aggregate-production-distribution-plan based on the demand shares received from the buyer in response to the offered prices. Depending on individual resources and surmised prices of other suppliers, each supplier tries to decide on such price offers which can provide appropriate demand allocations from the buyer for achieving the maximum total profit over the planning horizon. This suggests considering the prices and production distribution arrangements of suppliers as leaders variables, whereas the demand allocation decisions as followers variables. Formulating this model of price competition among suppliers thereby requires embedding the APDP problem at leaders' level while posing the demand allocation problem of the supplier at follower's level.

With this basic structure of the model introduced here, the nomenclature of indices, parameters and decision-variables is detailed below, followed by an explanation of components of the model.

3.3.1. Nomenclature

The indices, parameters, and variables used to mathematically formulate our model are listed below. Here, production center of a supplier is termed as "PC". A warehouse/distribution center, which is used for storing the inventory and for cross-docking the in-supply of consignment to out-supply for various delivery locations of the buyer, is termed as "DC". Delivery location of the buyer is denoted as "DL". Prices are discussed in the official currency of the Republic of India, the Indian Rupee, with currency code INR.

Indices and sets	
K	Number of suppliers; $k = 1, 2, \ldots, K$
N	Number of different type of products; $n = 1, 2, \ldots, N$
J	Number of Buyer's Delivery Locations (DLs); $j = 1, 2, \ldots, J$
T	Number of periods in the planning horizon; $t = 1, 2, \ldots, T$
N_k	Set of indices of the products that the supplier k deals in ($N_k \subseteq \{1, 2, \ldots, N\}$); $n_k \in N_k$
I_k	Number of Distribution Centers of the supplier k; $i_k = 1, 2, \ldots, I_k$ $i_k = 0$ stands for the PC of the supplier k, to act as a source to transport products to directly to DLs.
Leaders' parameters and variables (This is practically interpreted as break-even price of the supplier for a product.)	
Parameters	
lp_{kn_kj}	Minimum reservation price of product n_k from supplier k for its demand at buyer's DL j (INR/unit)[3]
Lp_{kn_kj}	Maximum reservation price of product n_k from supplier k for its demand at buyer's DL j (INR/unit)
a_{kn_kt}	Regular time production cost of product n_k for supplier k in period t (INR/unit)
b_{kn_kt}	Overtime production cost of product n_k for supplier k in period t (INR/unit)
r_{kn_kt}	Machine-hours required by supplier k for production of per unit of product n in period t
$tcp_{kn_ki_kt}$	Cost of transportation of product n_k from PC to DC i_k of supplier k in period t (INR/unit)
$tc_{kn_ki_kjt}$	Cost of transportation of product n_k from DC i_k of supplier k to buyer's DL j in period t (INR/unit)
$d_{kn_ki_kt}$	Inventory carrying cost of product n_k at DC i_k of supplier k in period t (INR/unit)
v_n	Space occupied by per unit of product n_k(cu-ft/unit)
MR_{kt}	Maximum regular machine-hours (man-hours) available with supplier k in period t
M_{kt}	Maximum total machine-hours (man-hours) available with supplier k in period t
V_{i_kt}	Maximum space available in DC i_k of supplier k in period t (cu-ft)
Variables	
z_{L_k}	Gross profit of supplier k
p_{kn_kj}	Per unit price of product n_k from supplier k for its demand at DL j (INR/unit)
Q_{kn_kt}	Regular time production volume of product n_k of supplier k in period t (units)
O_{kn_kt}	Overtime production volume of product n_k of supplier k in period t (units)
$\mathrm{SS}_{kn_ki_kt}$	Inventory level (safety stock) of product n_k at DC i_k of supplier k in period t (units)
$I_{kn_ki_kt}$	Consignment volume of product n_k to be sent from PC to DC i_k of the supplier k in period t (units)
$x_{kn_ki_kjt}$	Consignment volume of product n_k from DC i_k of supplier k to buyer's DL j in period t
Follower's parameters and variables	
Parameters	
z_F	Total cost of procurement and holding products at various DLs (INR/unit)
D_{jnt}	Total forecasted demand of product n at buyer's DL j in period t (units)
My_{kn_k}	Maximum purchase volume of product n_k from supplier k in any period
VF_j	Maximum inventory carrying space at DL j of the buyer (cu-ft)
Variables	
y_{kn_kjt}	Number of units of product n_k to be purchased from supplier k for DL j in period t

[3]This is practically interpreted as break-even price of the supplier for a product.

The mathematical model (Price-BLP) for ascertaining competitive target prices using the MLSF bilevel programming framework can be summarized as follows.

3.3.2. Suppliers' optimization problem

Objective function

For each supplier ($k = 1, 2, \ldots, K$), the objective is to maximize the total profit through the decision on values of price variables (p_{kn_kj}) for each product $n_k \in N_k$ and each delivery location $j = 1, 2, \ldots, J$, and thereupon values of variables of production, inventory, and transportation ($Q_{kn_kj}, O_{kn_kj}, \mathrm{SS}_{kn_ki_kt}, I_{kn_ki_kt}, x_{kn_ki_kjt}$) based on the demand shares received as a response to the prices quoted by all the suppliers. The objective function is given as following.

$$\begin{aligned}\text{Max } z_{L_k} = \sum_{t=1}^{T}\sum_{n_k\in N_k}\sum_{j=1}^{J} p_{kn_kj}y_{kn_kjt} - \Bigg\{\sum_{t=1}^{T}\sum_{n_k\in N_k}(a_{kn_kt}Q_{kn_kt} + b_{kn_kt}O_{kn_kt}) \\ + \Bigg(\sum_{t=1}^{T}\sum_{n_k\in N_k}\sum_{i_k=1}^{I_k} d_{kn_ki_kt}\mathrm{SS}_{kn_ki_kt} + \sum_{t=1}^{T}\sum_{n_k\in N_k}\sum_{i=1}^{I} tcp_{kn_ki_kt}I_{kn_ki_kt} \\ + \sum_{t=1}^{T}\sum_{n_k\in N_k}\sum_{i=0}^{I}\sum_{j=1}^{J} tc_{kn_ki_kjt}x_{kn_ki_kjt}\Bigg)\Bigg\}. \end{aligned} \tag{3.1}$$

Price bounds

The prices are speculated within bounds; lower bounds are the minimum prices acceptable to the supplier emerging due to their cost efficiencies, whereas the upper bounds are enforced through the competition imposed by the other suppliers. Lower bounds on these prices are termed as minimum reservation prices and upper bounds as maximum reservation prices.

$$lp_{kn_kj} \le p_{kn_kj} \le Lp_{kn_kj}, \qquad \forall n_k, \forall j. \tag{3.2}$$

Regular time production hours

The production volumes for various products are restricted by the regular time production hours.

$$\sum_{n_k\in N_k} r_{kn_kt}Q_{kn_kt} \le \mathrm{MR}_{kt}, \qquad \forall t. \tag{3.3}$$

Total production hours

The total production volumes obtainable through the provisions of overtime engagement of labor/machines along with the regular time production are also restricted by the total available production hours.

$$\sum_{n_k\in N_k} r_{kn_kt}(Q_{kn_kt} + O_{kn_kt}) \le M_{kt}, \qquad \forall t. \tag{3.4}$$

Inventory balancing constraints

The demand orders received for each product are fulfilled through the total production volumes together with the available inventory volumes maintained in the previous period while maintaining required inventory volumes for the current period.

$$Q_{kn_kt} + O_{kn_kt} + \sum_{i_k=1}^{I_k}\mathrm{SS}_{kn_ki_k(t-1)} - \sum_{i_k=1}^{I_k}\mathrm{SS}_{kn_ki_kt} = \sum_{j=1}^{J} y_{kn_kjt}, \qquad \forall n_k, \forall t. \tag{3.5}$$

Space constraints at DC

At any period, the consignment volumes of various products to be received at each DC ($I_{kn_k i_k t}$) along with the products already available there as inventory maintained during the previous period ($\mathrm{SS}_{kn_k i_k (t-1)}$) should be capacitated in the available space at the DC.

$$\sum_{n_k \in N_k} v_n \big(I_{kn_k i_k t} + \mathrm{SS}_{kn_k i_k (t-1)} \big) \leq V_{i_k t}, \qquad \forall t, \forall i_k. \tag{3.6}$$

Transport plan for delivery at each DL

For each period, the consignment volumes of various products from PC to DC(s), from DC(s) to DLs, and directly from PC to DLs are to be planned to fulfill the demand of each DL for each product. Following three constraints govern this requirement. First two of the following constraints describe the transportation plan from DC(s) to DLs, whereas the third one describes transportation plan directly from PC to DLs.

$$\sum_{i=0}^{I} x_{kn_k i_k j t} \geq y_{kn_k j t}, \qquad \forall j, \forall n_k, \forall t, \tag{3.7}$$

$$\sum_{j=1}^{J} x_{kn_k i_k j t} \leq I_{kn_k i_k t} + \mathrm{SS}_{kn_k i_k (t-1)} - \mathrm{SS}_{kn_k i_k t}, \qquad \forall i_k \neq 0, \forall n_k, \forall t, \tag{3.8}$$

$$\sum_{j=1}^{J} x_{kn_k 0 j t} = Q_{kn_k t} + O_{kn_k t} - \sum_{i_k=1}^{I_k} I_{kn_k i_k t}, \qquad i_k = 0, \forall n_k, \forall t. \tag{3.9}$$

3.3.3. Buyer's optimization problem

Based on the price quotations received from various suppliers, the buyer solves the cost optimal demand allocation problem.

Objective function

The buyer decides on allocating demand shares ($y_{kn_k j t}$) corresponding to the received price quotes ($p_{kn_k j}$) from each supplier for various products for minimum total procurement cost.

$$\text{Min } z_F = \sum_{k=1}^{K} \sum_{j=1}^{J} \sum_{n_k \in N_k} \sum_{t=1}^{T} p_{kn_k j} y_{kn_k j t}. \tag{3.10}$$

Constraint on maximum purchase volumes

The total of purchase volumes of each product over all DLs is restricted by a maximum value in any period by each supplier. Such restrictions are pre-decided by the suppliers due to the potential of their production line or sometimes the supplier managing business with multiple buyers.

$$\sum_{j=1}^{J} y_{kn_k j t} \leq M y_{kn_k}, \qquad \forall k, \forall n_k, \forall t. \tag{3.11}$$

Constraint on maximum purchase volumes

The total of purchase volumes of each product for each period from various suppliers must meet the demand of each DL.

$$\sum_{k=1}^{K} y_{kn_k j t} = D_{jnt}, \qquad \forall j, \forall n_k, \forall t. \tag{3.12}$$

Space constraint

The total of purchase volumes of all the products from various suppliers at each DL should be up to maximum inventory carrying capacity of the DL, for each period.

$$\sum_{k=1}^{K} \sum_{n_k \in N_k} v_n y_{kn_kjt} \leq \mathrm{VF}_j, \qquad \forall j, \forall t. \tag{3.13}$$

3.3.4. Price-negotiation problem in a MLSF bilevel game framework

The MLSF bilevel game problem for obtaining competitive target prices is described below as (Price-BLP), considering suppliers as leaders and the buyer as follower. The problem formulated to determine values of variables $\{\{p_{kn_kj}\}, \{Q_{kn_kt}\}, \{O_{kn_kt}\}, \{\mathrm{SS}_{kn_ki_kt}\}, \{I_{kn_ki_kt}\}, \{x_{kn_ki_kjt}\} : n_k, i_k, j, t\}$ for each supplier $(k = 1, 2, \ldots, K)$ and respective demand allocations $\{y_{kn_kjt} : n_k, j, t, k\}$ for the buyer.

(Price-BLP)

$$\begin{aligned}(\mathrm{LDMP} - k)\ \mathrm{Max}\ z_{L_k} = {} & \sum_{t=1}^{T} \sum_{n_k \in N_k} \sum_{j=1}^{J} p_{kn_kj} y_{kn_kjt} - \left\{ \sum_{t=1}^{T} \sum_{n_k \in N_k} (a_{kn_kt} Q_{kn_kt} + b_{kn_kt} O_{kn_kt}) \right. \\ & + \left(\sum_{t=1}^{T} \sum_{n_k \in N_k} \sum_{i_k=1}^{I_k} d_{kn_ki_kt} \mathrm{SS}_{kn_ki_kt} + \sum_{t=1}^{T} \sum_{n_k \in N_k} \sum_{i=1}^{I} tcp_{kn_ki_kt} I_{kn_ki_kt} \right. \\ & \left. \left. + \sum_{t=1}^{T} \sum_{n_k \in N_k} \sum_{i=0}^{I} \sum_{j=1}^{J} tc_{kn_ki_kjt} x_{kn_ki_kjt} \right) \right\}\end{aligned}$$

subject to

$$\begin{aligned}
& lp_{kn_kj} \leq p_{kn_kj} \leq Lp_{kn_kj}, && \forall n_k, \forall j, \\
& \sum_{n_k \in N_k} r_{kn_kt} Q_{kn_kt} \leq \mathrm{MR}_{kt}, && \forall t, \\
& \sum_{n_k \in N_k} r_{kn_kt} (Q_{kn_kt} + O_{kn_kt}) \leq M_{kt}, && \forall t, \\
& Q_{kn_kt} + O_{kn_kt} + \sum_{i_k=1}^{I_k} \mathrm{SS}_{kn_ki_k(t-1)} - \sum_{i_k=1}^{I_k} \mathrm{SS}_{kn_ki_kt} = \sum_{j=1}^{J} y_{kn_kjt}, && \forall n_k, \forall t, \\
& \sum_{n_k \in N_k} v_n \left(I_{kn_ki_kt} + \mathrm{SS}_{kn_ki_k(t-1)} \right) \leq V_{i_kt}, && \forall t, \forall i_k, \\
& \sum_{i=0}^{I} x_{kn_ki_kjt} \geq y_{kn_kjt}, && \forall j, \forall n_k, \forall t, \\
& \sum_{j=1}^{J} x_{kn_ki_kjt} \leq I_{kn_ki_kt} + \mathrm{SS}_{kn_ki_k(t-1)} - \mathrm{SS}_{kn_ki_kt}, && \forall i_k \neq 0, \forall n_k, \forall t, \\
& \sum_{j=1}^{J} x_{kn_k0jt} = Q_{kn_kt} + O_{kn_kt} - \sum_{i_k=1}^{I_k} I_{kn_ki_kt}, && i_k = 0, \forall n_k, \forall t, \\
& p_{kn_kj}, Q_{kn_kt}, O_{kn_kt}, I_{kn_ki_kt}, \mathrm{SS}_{kn_ki_kt}, x_{kn_ki_kjt} \geq 0, && \forall n_k, \forall i_k, \forall j, \forall k, \forall t, \\
& Q_{kn_kt}, O_{kn_kt}, I_{kn_ki_kt}, \mathrm{SS}_{kn_ki_kt}, x_{kn_ki_kjt} \text{ are integer variables}, && \forall n_k, \forall i_k, \forall j, \forall k, \forall t;
\end{aligned}$$

where, $\{y_{kn_kjt} : k, n_k, j, t\}$ is rational response obtained from following problem

$$\text{(FDMP) Min } z_F = \sum_{k=1}^{K}\sum_{j=1}^{J}\sum_{n_k\in N_k}\sum_{t=1}^{T} p_{kn_kj}y_{kn_kjt}$$

subject to

$$\sum_{j=1}^{J} y_{kn_kjt} \le My_{kn_k}, \qquad \forall k, \forall n_k, \forall t,$$

$$\sum_{k=1}^{K} y_{kn_kjt} = D_{jnt}, \qquad \forall j, \forall n_k, \forall t,$$

$$\sum_{k=1}^{K}\sum_{n_k\in N_k} v_n y_{kn_kjt} \le \mathrm{VF}_j, \qquad \forall j, \forall t,$$

$$y_{kn_kjt} \ge 0, \qquad \forall j, \forall n_k, \forall k, \forall t,$$

$$y_{kn_kjt} \text{ are integer variables}, \qquad \forall j, \forall n_k, \forall k, \forall t.$$

Here, it is noted that all the constraints of the MLSF bilevel game problem modeled above are linear and objective functions of leaders and follower are bilinear. With this niceness of linearity in constraints and bilinearity of objective functions involved in the model, a challenge is to handle integer variables. In the next section, we concentrate on solving a MLCF bilevel programming problem with the special properties noted above.

4. Solution methodology

In the model formulated above, the variables $Q_{kn_kt}, O_{kn_kt}, I_{kn_ki_kt}, \mathrm{SS}_{kn_ki_kt}, x_{kn_ki_kjt}$ and y_{kn_kjt} are considered to have integer values, only for realizing the actual practices of industry. But no direct or evolutionary method is available in the literature for solving a MLSF bilevel programming problem which particularly involves integer variables. In this situation, a possible approach is to relax the integer restriction on these variables and then try to solve the equivalent MLSF bilevel programming problem by applying any of the state-of-the-art approaches by Leyffer and Munson [60] and Hori and Fukushima [51]. We attempted to solve an instance of our practical problem, for which the data was obtained from a manufacturing firm by following this scheme. This instance of the modeled problem involves a total of 1000 variables (760 of leaders' and 240 of the follower). The equivalent nonlinear optimization problems formulated by following the referred approaches could not converge even to a local optimal solution after long hours of computation on computers. From this experience it is evident that direct methods based on the theoretical approaches suggested in literature turn out to be incapable of handling large scale MLSF bilevel game problems. Therefore, it is compelling to adopt some evolutionary search technique for solving a large instance of our problem.

Although, as mentioned in the literature review, evolutionary algorithms are developed specifically for some variants of the bilevel programming problems, even then we made a sincere attempt for solving the considered instance of MLSF bilevel programming problem using the general GA. Also, we attempted to apply integer-coded GA [24] for solving our original problem with integer restriction on variables imposed again. Both the GA approaches also failed to converge to even a feasible solution of the problem. This impels us to develop an algorithm capable of handling large scale MLSF bilevel game problems to obtain strong-stationary points.

In this situation, we propose solution method for solving MLSF bilevel game problems involving integer variables and having the specific structure as involved in our model, *viz.* linear constraints, and bilinear objective functions at both levels. The proposed solution method is based on nested GA approach and uses some theoretical concepts from of Leyffer and Munson approach [60] particularly for devising fitness function. We express below

a general MLSF bilevel programming problem with linear constraints and bilinear objective functions at both levels followed by a discussion on appropriately structuring theoretical concepts for developing a nested GA based solution method.

(MLSF-BL-BLP)

$$
\begin{aligned}
&(\text{LDMP}-i)\ \min_{u_i \geq 0}\ f_i(u_i, v)\\
&\quad \text{subject to}\\
&\qquad g_i(u_i, v) \geq 0,\\
&\qquad G_i(u_i, v) = 0,\\
&\qquad \text{where, } v \text{ is optimal response of the follower corresponding to the leaders' variables, } u = \{u_i : i = 1, 2, \ \ldots, k\},\\
&(\text{FDMP})\ \min_{w}\ b(u,\ w)\\
&\quad \text{subject to}\\
&\qquad c(u, w) \geq 0,\\
&\qquad w \geq 0\\
&\qquad \text{Here, constraints } g_i(u_i, v) \geq 0, G_i(u_i, v) \geq 0, \text{ and } c(u, v) \geq 0 \text{ are considered as linear and objective functions } f_i(u_i, v) \text{ and } b(u, v) \text{ are bilinear in the sense that functions } f_i \text{ and } b \text{ are linear in the variable } v \text{ for when } u \text{ is considered as parameter and } \textit{vice-versa.}
\end{aligned}
\tag{4.1}
$$

Here, $(\text{LDMP}-i)$ is optimization problem of leader $i(i = 1, 2, \ldots, k)$, in which the follower's optimization problem (FDMP) is incorporated as a constraint.

A MLSF bilevel programming problem is solved by obtaining strong stationary points [60], or further by obtaining strong stationary Nash-equilibrium points[4], if one such exists [51]. We have developed nested GA based solution method for obtaining strong stationarity points by using some theoretical concepts from the penalty based approach of Leyffer and Munson [60] (explained in Appendix A). The theoretical development in connection with features of the problem (MLSF-BL-BLP) that enables designing the nested GA based solution methodology for it is outlined below.

4.1. Structuring theoretical concepts to design nested GA based solution method for solving (MLSF-BL-BLP)

A nested GA based solution method for any bilevel programming problem principally requires devising the reaction mechanism of follower's (followers') problem, corresponding to a given value of leader's variables, and formulating the fitness function. In the following subsections, we explain devising the reaction mechanism and formulating the fitness function of chromosomes through a typical structuring of the theoretical concepts taken from penalty based approach [60].

4.1.1. Devising the reaction mechanism for the proposed nested GA

For the considered specific structure of the MLSF bilevel programming problem (MLSF-BL-BLP), the follower decision problem is a linear programming problem (LPP) or a mixed integer linear programming problem (MILPP) parameterized in the leader's variables u. We put forward exploring values of leaders' variables u in

[4]If a strong stationary point is obtained, then one can further test whether it is a strong stationary Nash-equilibrium point, following the procedure remarked in Appendix C.

$i=1$				$i=2$				...		$i=k$			
$j=1$	$j=2$	...	$j=r_1$	$j=1$	$j=2$	...	$j=r_2$	...	...	$j=1$	$j=2$	...	$j=r_k$
u_{11}	u_{12}	...	u_{1R}	u_{21}	u_{22}	...	u_{2r_2}	...	...	u_{k1}	u_{k2}	...	u_{kr_k}

FIGURE 3. Chromosome structure.

GA, through their encoding as a chromosome, while obtaining the corresponding follower's responses (values of follower's variable v) by directly solving the parameterized LPP/MILPP with the chromosome values supplied as parameter u. Accordingly, for any chromosome representing the value u^* of leaders' variables u, the reaction of the follower, say v^*, can be obtained. This gives (u^*, v^*) as a feasible solution of the MLSF bilevel programming problem with considered specific structure. Devising such a reaction mechanism for nested GA gives an advantage over general GA that every chromosome corresponds to a feasible solution of (MLSF-BL-BLP), thereby the exploration remains in the feasible region throughout all the generations of GA.

Remark 4.1. As we are developing a heuristic search algorithm, it is acceptable to relax the integer condition from follower's variables, if there is any, and then solve the equivalent parameterized LPP instead of MILPP for approximating the follower's response. This privilege of obtaining approximate values of follower's responses is justified because by the heuristic approach anyways obtain an approximate solution of the problem. The approximate real values of the variables (originally integer restricted) can be rounded-off eventually. Relaxing the integer conditions and then rounding-off the approximated real value of the obtained solution is justified by Joseph *et al.* [53] for obtaining near optimal solutions.

4.1.2. Using theoretical developments for formulating the fitness function of nested GA

A feasible solution (u^*, v^*), obtained by the procedure suggested above, can further be tested for strong stationary point by adopting the procedure detailed in Appendix B. For this purpose, we need to solve the LPP $(\text{Para} - \text{LP})$ by substituting the values (u^*, v^*) as parameters and check the optimal value. Referring to the result in Appendix B, if the optimal value is zero, then (u^*, v^*) represents a strong stationary point of the considered MLSF bilevel programming problem. Therefore, for a chromosome representing a feasible solution (u^*, v^*) of (MLSF-BL-BLP), we define the fitness value as the objective function value c_{pp} of the LPP $(\text{Para} - \text{LP})$ with values of (u^*, v^*) substituted as parameters.

The objective function value of $(\text{Para} - \text{LP})$ is always non-negative for any feasible solution. Therefore, for guiding the algorithm towards a chromosome representing strong stationary point (*i.e.*, fitness value 0) it is appropriate to identify a chromosome as better fit than another on the smaller value of fitness function.

With this background, the minute details of the proposed algorithm are provided in the following subsection.

4.2. Nested GA for solving (MLSF-BL-BLP)

GA components used in our algorithm are presented below followed by their assembly into the algorithm presented through a pseudocode.

4.2.1. Chromosome encoding

For leaders' variables $u = \{u_i : i = 1, 2, \ldots, k\}$, where each $u_i = \{u_{i1}, u_{i2}, \ldots, u_{ir_i}\}$, the chromosomes of the population are encoded as an array of length equal to the number of all the leaders' variables indicating the values $\{u_i : i = 1, 2, \ldots, k\}$. A general chromosome structure used in the implementation of the algorithm is shown in Figure 3.

4.2.2. Initialization

The following GA parameters are used in the proposed algorithm: population size *popsize*; number of generations G; current generation g, $(g = 1, 2, \ldots, G)$; crossover rate *pc*; mutation rate *pm*; location parameter a and scaling parameter $b > 0$ for Laplace crossover; index of power mutation p.

4.2.3. Incorporating follower's reaction and fitness evaluation

Follower's reaction and inputs for (Para – LP): for each chromosome in population (which corresponds to leaders' variables u), problem (FDMP) is solved. The optimal response v thus obtained is supplied along with u for testing the feasibility of each chromosome (LDMP – k) of (MLSF-BL-BLP). Through this complete information about (u, v), the values of variables s and t_i are calculated using relations referred in (A.7e) and (A.7g).

Fitness evaluation: for each chromosome, with its value $u = \{u_i : i = 1, 2, \ldots, k\}$ and obtained values v, s, $t_i : i = 1, 2, \ldots, k$, the problem (Para – LP) is solved. Corresponding value of the objective function C_{penalty} is considered as the fitness value of that chromosome.

4.2.4. Genetic operators

Selection operator: tournament selection operator is used to choose relatively fit chromosome. A tournament selection mechanism, (with size 2), is adopted for selecting chromosomes with better fitness. For guiding the search of the algorithm towards strong stationary points, a chromosome with smaller fitness value is considered to have better fitness that the other.

Crossover operator: we use a single point crossover for a chromosome, Laplace crossover (LX) operator with the probability *pc* [24]. The same is explained in [54].

Mutation operator: the mutation is performed on a chromosome with the probability *pm* using the power mutation (PM) operator [24]. The same is explained in [54].

We note that LX and the PM operators do not disturb feasibility of chromosomes in terms of reservation price bounds in problem (LDMP – k).

4.2.5. Updating the new population

The new population obtained from the parent population P^g is adopted to be a population of the next generation P^{g+1} only if it's maximum fitness value, in comparison to the maximum fitness value of the previous generation, does not decrease. Otherwise, the population P^g is preserved as population P^{g+1} for regenerating the next generation.

4.2.6. Termination criterion

The execution of the algorithm is terminated after the completion of pre-defined maximum number of generations G. The value of G may be tuned by observing stability in the fitness value through various combinations of GA parameters.

Finally, the steps involved in the proposed GA are summarized below through a pseudocode presented in Algorithms 1 and 2. Algorithms 1 and 2, collectively represent a nested type of GA, with Algorithm 2 performing as a subprogram of the main program given by Algorithm 1. Here, Algorithm 2 is responsible for evaluating optimal reaction of the follower corresponding to leaders' potential actions represented by each chromosome of the population (nested action), and thereby determining the fitness values of chromosomes.

Algorithm 1: Nested GA for solving (MLSF-BL-BLP).

Data: Input data and GA parameters
$g \leftarrow 0$;
Initialize population (values of LDMs' variables $u_i : i = 1, 2, \ldots, k$);
Evaluate fitness of population members (along with corresponding response v) (using Algorithm 2);
while $g < G$ **do**
  Tournament selection (retaining best-fit chromosome);
  Generate new individuals through extended Laplace Crossover and Power Mutation.
  Evaluation fitness of population members (along with corresponding response v) (using Algorithm 2);
  Update new population for next generation.
  $g \leftarrow g + 1$;
  Select best-fit chromosome of the new generation (along with corresponding response v);
end
Return best-fit chromosome (along with corresponding response v) over all generations

Algorithm 2: Fitness evaluation of population members – for (MLSF-BL-BLP).

Input: GA population of chromosomes
for $i \leftarrow 1$ **to** *Pop_size* **do**
  Substitute values of LDM variables $u_i : i = 1, 2, \ldots, k$ (represented by chromosome) in (FDMP) to solve the follower's relaxed LPP for obtaining v;
  Round-off values of v to the closest integers;
  Obtain $s = h(u, v)$ and $t_i = g_i(u_i, v)$;
  Solve (Para – LP) by supplying values of u, v, s, t_i.
  Evaluate the fitness value as objective function value of (Para – LP);
end
Output: Fitness values of all chromosomes of the population (along with corresponding response v)

Going back to solve our model (Price-BLP), a particular problem in the class of (MLSF-BL-BLP) problems, a specific interdependence among leader's variables can be noticed. Some modifications in the proposed algorithm are suggested further in the following subsection to capture this interdependence of variables for solving particularly the modeled problem (Price-BLP).

4.3. Modifications in the proposed algorithm for solving (Price-BLP)

As in the problem (Price-BLP), the values of Leaders' price variables ($\{p_{kn_kj} : k, n_k, j\}$) decide the demand allocations $\{y_{kn_kjt} : k, n_k, j, t\}$ by the follower, and thereafter the values of production-and-distribution planning variables ($Q_{kn_kj}, O_{kn_kj}, \mathrm{SS}_{kn_ki_kt}, I_{kn_ki_kt}, x_{kn_ki_kjt} : k, n_k, i_k, j, t$) can be obtained, depending on these demand allocations. This interdependence of one part of leader's variables with other gives a specific structure to the bilevel programming problem (Price-BLP). A problem-specific minor modification is thus presented below for the proposed GA for solving particularly the problem (Price-BLP) for capturing this interdependence and thereby maintaining feasibility during the GA exploration.

We encode the chromosomes as a row vector of values corresponding to leaders' price variables (p_{kn_kj}) only, with each value ranging in the interval $[lp_{kn_kj}, Lp_{kn_kj}]$ for $k = 1, 2, \ldots, K$, $n_k = 1, 2, \ldots, N_k$, $j = 1, 2, \ldots, J$. Values of the rest of leaders' variables are obtained during the fitness evaluation. For the values of leaders' prices $\{p_{kn_kj} : k, n_k, j\}$ generated as a chromosome, we first evaluate the optimal response of the follower $\{y_{kn_kjt} : k, n_k, j, t\}$ by solving (FDMP) as a parameterized LPP in price variables $\{p_{kn_kj} : k, n_k, j\}$. Thereby, $(\mathrm{LDMP} - k)$ is solved to obtain $Q_{kn_kt}, O_{kn_kt}, \mathrm{SS}_{kn_ki_kt}, I_{kn_ki_kt}, x_{kn_ki_kjt} : k, n_k, i_k, j, t$ for each leader k, by solving a LPP parameterized in variables $\{y_{kn_kjt} : k, n_k, j, t\}$.

The concatenated vector values for $\{p_{kn_kj}, Q_{kn_kj}, O_{kn_kj}, \mathrm{SS}_{kn_ki_kt}, I_{kn_ki_kt}, x_{kn_ki_kjt}, y_{kn_kjt} : k, n_k, i_k, j, t\}$ thus becomes a feasible solution of (Price-BLP), in concurrence with a feasible solution (u, v) of the general game problem (MLSF-BL-BLP).

Due to the sequential dependence of follower's variables y_{kn_kjt} on leader's prices p_{kn_kj}, and in turn, of other variables of leaders $Q_{kn_kj}, O_{kn_kj}, \mathrm{SS}_{kn_ki_kt}, I_{kn_ki_kt}, x_{kn_ki_kjt}$ on y_{kn_kjt}, these modifications suggested above are appropriate for any chromosome to represent a feasible solution of (Price-BLP) problem. As, on the contrary, if we encode all the variables of leaders $p_{kn_kj}, Q_{kn_kj}, O_{kn_kj}, \mathrm{SS}_{kn_ki_kt}, I_{kn_ki_kt}, x_{kn_ki_kjt}$ as chromosomes, then the issue of infeasibility of values for $Q_{kn_kj}, O_{kn_kj}, \mathrm{SS}_{kn_ki_kt}, I_{kn_ki_kt}, x_{kn_ki_kjt}$ in connection with the values of p_{kn_kj} (through the responses y_{kn_kjt} calculated as usual by solving (FDMP)) will be of a concern. This manifests the appropriateness of modifications suggested in the proposed GA for the specific bilevel programming problem (Price-BLP) in hand.

The algorithm modified for the problem (Price-BLP) is summarized through the following pseudocode.

Algorithm 3: Modified nested GA for (Price-BLP).

Data: Input data and GA parameters
$g \leftarrow 0$;
Initialize population (values of LDMs' variables $p_{kn_kj} : k, n_k, j$);
Evaluate fitness of population members (along with complete vectors of u and v) (using Algorithm 4);
while $g < G$ **do**
  Tournament selection (retaining best-fit chromosome);
  Generate new individuals through extended Laplace Crossover and Power Mutation;
  Evaluate fitness of population members (along with complete vectors of u and v) (using Algorithm 4);
  update new population for next generation;
  $g \leftarrow g + 1$;
  Select best-fit chromosome of the new generation (along with complete vector of u and v, as obtained in Algorithm 4);
end
Return best-fit chromosome (along with complete vectors of u and v) over all the generations

Algorithm 4: Fitness evaluation of population members – for (Price-BLP).

Input: GA population of chromosomes
for $i \leftarrow 1$ **to** *Pop_size.* **do**
  Substitute LDM prices p_{kn_kj} (represented by chromosome) in (FDMP) to solve the follower's relaxed LPP for obtaining y_{kn_kjt};
  Round-off values of y_{kn_kjt} to the closest integer;
  For each leader k, solve (LDMP $-$ k) to obtain Q_{kn_kt}, O_{kn_kt}, $\mathrm{SS}_{kn_ki_kt}$, $I_{kn_ki_kt}$, $x_{kn_ki_kjt}$
  Obtain s and t_i following the rule $s = h(u, v)$ and $t_i = g_i(u_i, v)$ with
  $u = \{p_{kn_kj}, Q_{kn_kj}, O_{kn_kj}, \mathrm{SS}_{kn_ki_kt}, I_{kn_ki_kt}, x_{kn_ki_kjt}, y_{kn_kjt}\}$ and $v = \{y_{kn_kjt}\}$;
  Solve (Para – LP) with values of u, v, s, t_i supplied as parameters;
  Evaluate the fitness value as objective function value of (Para – LP);
end
Output: Fitness values of all chromosomes of the population (along with complete vectors of u and v)

5. An experimental study from a manufacturing firm

5.1. Relevant information about the firm

The formulation of our model is inspired by a scenario of a leading manufacturing firm of the fast-moving consumer goods (FMCG) sector. The firm has 5 production plants in the southern region of the Republic of India. Each of its production plants manufactures certain finished products, which require 5 ingredients of varied

TABLE 1. Supplier's profile (products and DCs).

	Supplier (k)						
	1	2	3	4	5	6	7
Product sets (N_k)	{1}	{2, 3}	{1}	{4}	{2, 3}	{1, 4}	{2, 3, 4}
Number of DC(s) (I_k)	2	1	1	0	1	2	2

quantities over each week, depending upon the production plan. A production plan is prepared for a block of 4 weeks. The requirement arises for procuring different amounts of ingredients for each of the manufacturing plants by suppliers over each week. These ingredients are procured from a total of 8 suppliers who deal with some or all these ingredients. The buyer has already identified these suppliers through various quality and potential parameters. Further, as the buyer and suppliers are at economies of scale in the present environment of localized buying and selling, therefore the ecosystem for purchasing of these ingredients pertains to an oligopolistic-monopsony market. As most of the required components involve frequently fluctuating production costs to vary over each month, the price-quotes must be invited from the suppliers. Based on their price-quotes, the demand allocation is done to these suppliers to supply the ingredients over the planning horizon of 4 weeks.

For its financial planning, the firm is concerned about assessing the total budget allocated for the procurement of ingredients before the invitation of price quotes from suppliers. More importantly, the firm is also keen to observe whether its suppliers are competing for price quotes or having a co-operative game to settle at some higher prices. The latter situation may result in a dominance of its suppliers over the buyer. In such a case, the buyer firm would need to consider more suppliers for selection and demand order allocation to induce more competition to the existing suppliers. A manufacturer is vigilant for performing such analysis in pursuit of minimizing procurement cost, which comes as a significant component of production cost. At the same time, the firm is a production giant with a high brand value in the market of its finished products. Another priority concern of such a firm at this point of time is supplier integration to strengthen its inbound supply chain. In this line of thought, the firm is open to suggesting that any of its suppliers adjust the price quotes to avoid their opportunity losses for the same demand order allocation in case of raised prices. Further, through a prior assessment of prices, the firm would be better prepared to manage its inbound supply chain to be snag-free by allocating demand orders to its suppliers. As the concerns of this manufacturing firm match the theme of our framework therefore a case data from this firm is taken-up our study.

5.2. Data input

Henceforth, the manufacturing firm is the buyer, whereas the ingredients to be procured from its suppliers are products. Out of the five, one product is patent with a specific supplier, and the supplier can supply this product only, so there is no competition. We consider the remaining 4 products to be provided by 7 suppliers. Each of the seven suppliers has a single production center (PC) and a different number of distribution centers/warehouses for inventory storage as well as for cross-docking of shipments of products for transportation from PC to delivery location(s) DL(s). For reference, the products, suppliers, and their DC(s), and DLs numbered with corresponding indices.

The 4th product is a volatile product in a liquid state and is transported only through special containers, so neither its cross-docking nor maintaining inventory is considered practically feasible. This specification of the structural setup can easily be incorporated into the modeling by not defining any variable against the product for inventory and transportation to DC(s) for all suppliers dealing in this product. The details of suppliers dealing in products and other data relevant to the problem is tabulated in Tables 1–9.

TABLE 2. Forecasted demands of products at each DL for each time period.

D_{jnt}	DL (j)																			
	1				2				3				4				5			
Product	Time period (t)				Time period (t)				Time period (t)				Time period (t)				Time period (t)			
(n)	1	2	3	4	1	2	3	4	1	2	3	4	1	2	3	4	1	2	3	4
1	150	75	100	75	125	100	75	50	75	75	50	50	75	50	75	50	200	100	120	80
2	75	75	75	75	75	75	75	50	75	50	75	25	75	75	50	25	100	100	80	50
3	125	125	100	50	100	75	75	75	100	75	50	50	80	80	100	15	130	130	90	90
4	50	75	75	50	50	75	75	25	75	75	50	0	60	60	80	0	80	80	80	60

TABLE 3. Reservation prices and maximum purchase volumes.

		Supplier (k)											
		1	2		3	4	5		6		7		
	DL	n_1	n_2		n_3	n_4	n_5		n_6		n_7		
	(j)	1	2	3	1	4	2	3	1	4	2	3	4
lp_{kn_kj}	1	25 700	5560	5550	31 000	89 600	4750	4695	24 250	90 050	5790	6010	92 700
	2	25 800	5660	5700	31 100	89 300	4850	4795	24 100	89 800	6040	6260	92 800
	3	25 950	5810	5450	31 175	89 700	5000	4945	24 200	89 350	6365	6585	92 875
	4	25 950	5560	5050	30 300	91 000	5000	4945	24 350	89 600	6340	6560	92 000
	5	25 600	5160	4850	29 800	90 600	4650	4595	24 250	89 850	5640	5860	91 500
Lp_{kn_kj}	1	28 700	5700	5700	32 900	94 500	5100	4900	27 700	92 500	6250	6350	97 400
	2	28 800	5800	5850	33 000	94 200	5200	5000	27 550	92 250	6500	6600	97 500
	3	28 950	5950	5600	33 075	94 600	5350	5150	27 650	91 800	6825	6925	97 575
	4	28 950	5700	5200	32 200	95 900	5350	5150	27 800	92 050	6800	6900	96 700
	5	28 600	5300	5000	31 700	95 500	5000	4800	27 700	92 300	6100	6200	96 200
My_{kn_k}		175	350	430	225	175	275	350	250	100	300	300	100

TABLE 4. Production costs – regular-time and overtime (INR per unit), and machine-hours required for production (hours per unit).

	Product	Supplier (k)						
	(n)	1	2	3	4	5	6	7
a_{kn_kt}	1	20 000	–	21 000	–	–	20 500	–
	2	–	3600	–	–	3500	–	3400
	3	–	3500	–	–	3450	–	3600
	4	–	–	–	81 000	–	80 500	83 000
b_{kn_kt}	1	20 200	–	21 200	–	–	20 700	–
	2	–	3650	–	–	3550	–	3450
	3	–	3550	–	–	3500	–	3650
	4	–	–	–	82 000	–	81 500	84 000
r_{kn_kt}	1	0.75	0.5	0.75	–	–	0.75	–
	2	–	0.5	–	–	0.5	–	0.33
	3	–	–	–	–	0.5	–	0.33
	4	–	–	–	1.5	–	1.5	1.25

TABLE 5. Maximum machine-hours available regular-time and total (including overtime).

	Supplier (k)						
	1	2	3	4	5	6	7
MR_{kt}	168	144	168	168	288	336	456
M_{kt}	168	168	168	168	336	336	504

TABLE 6. Transportation costs from PC to DC(s) and costs of inventory at DC(s) (INR per unit), maximum space available at DC(s).

k	n_k	i_k	$tcp_{kn_ki_kt}$	$d_{kn_ki_kt}$	V_{i_kt}
1	1	1	1200	10	4000
		2	900	10	6000
2	2	1	1000	10	4000
	3	1	1000	10	
3	1	1	6500	10	6000
5	2	1	400	9	4000
	3	1	400	9	
6	1	1	900	10	5000
		2	600	10	5000
7	2	1	850	10	4000
		2	950	10	4000
	3	1	850	10	
		2	950	10	

TABLE 7. Costs of transportation from PC or DC(s) to DLs (As all the suppliers in the problem have DCs not more than 2, due to this fact the costs of transportation have been listed in a single table only. But this doesn't mean that all the suppliers have same DCs. It is simply an enumeration of DCs. They own or hire for their individual warehouses which are located even at different places).

$tc_{kn_ki_kjt}$		$i_k = 0$					$i_k = 1$					$i_k = 2$				
Supplier	Product	DL (j)					DL (j)					DL (j)				
(k)	(n_k)	1	2	3	4	5	1	2	3	4	5	1	2	3	4	5
1	1	1000	1100	1250	1000	850	500	600	750	750	400	750	800	900	700	400
2	2	500	600	750	750	400	600	700	850	600	200	–	–	–	–	–
	3	500	600	750	750	400	600	700	850	600	200	–	–	–	–	–
3	1	5500	5000	4800	5500	6500	1400	1500	1575	700	200	–	–	–	–	–
4	4	500	200	600	1900	1500	–	–	–	–	–	–	–	–	–	–
5	2	900	1000	1000	1000	400	500	600	750	750	400	–	–	–	–	–
	3	900	1000	1000	1000	400	500	600	750	750	400	–	–	–	–	–
6	1	1500	1250	800	1050	1300	500	600	750	750	400	1100	950	200	1200	1100
	4	1500	1250	800	1050	1300	–	–	–	–	–	–	–	–	–	–
7	2	1400	1500	1575	700	200	600	800	1150	1550	850	1100	1350	1675	1650	950
	3	1400	1500	1575	700	200	600	800	1150	1550	850	1100	1350	1675	1650	950
	4	1400	1500	1575	700	200	–	–	–	–	–	–	–	–	–	–

TABLE 8. Space occupied per tonne (in sq. ft).

v_n	Product (n)			
	1	2	3	4
	8	8	8	12.5

TABLE 9. Maximum inventory carrying space at DLs of the buyer (This accounts for the capacity to accommodate all the products except product 4, which needs to be stored in a separately installed container (at each DL) having storage capacity which is more sufficient to accommodate the demand for each period.) (sq. ft).

VF_j	DL (j)				
	1	2	3	4	5
	8000	8000	4000	5500	6000

5.3. Implementation of GA

The (Price-BLP) problem modeled as a MLSF game, discussed in context of manufacturing firm with the input data tabulated above is solved using the modified algorithm proposed in the Section 4.3. The program is coded in MATLAB 2019a. The parameters of Laplace crossover and power mutation along with population size (*Pop_size*) are tuned for various combinations of probabilities of crossover, mutation, and tournament selection. The best found are $Pop_size = 20$, $a = 0$, $b = 0.15$, $p = 1$ or 10. We set the maximum number of generations to 1000 after tuning the parameters for attainment of the best fitness value equal to zeros for strong stationary point. For each combination of parameters (Tab. 10), we performed a set of 10 experiments of GA. Table 10 tabulates the relative error of the best solutions obtained for each combination of parameters against the ideal fitness value zero in comparison with the arithmetic mean of the best fitness values of various combinations. Figure 4 shows the variation in the best fitness attained in various generations of a GA run. Among 240 solutions generated (24 combinations with 10 runs each) for (Price-BLP), 22 strong-stationary points (fitness value = 0) were obtained. The arithmetic mean of total procurement cost of the buyer corresponding to these 22 instances of prices (corresponding the strong-stationarity points) is INR 166 844 775, with a standard deviation of 266 396.83, giving coefficient of variation 0.16%. This indicates parity among all the 22 strong-stationarity points from buyer's perspective, in terms of the total procurement cost. The desired fitness value zero (for strong-stationarity points) is attained for the runs of 18 out of 24 combinations of GA parameters, whereas for rest of the combinations there no improvement in fitness value for more than last 300 generations.

5.4. Analysis of the results of computation

The strong-stationarity point with the total procurement cost closest to the arithmetic mean of all the 22 ones obtained from our computation is detailed as following. Table 11 shows the competitive target prices to settle negotiations with each of suppliers for various products they deal in and deliver at each of 5 DLs. As a response to these prices, the consequent demand allocations from the buyer are tabulated in Table 12. The consequent total procurement cost of the buyer in this instance is assessed as INR 166 871 150. The accompanying part of the results comprising of respective aggregate-production-distribution plans for each of 7 suppliers are presented through Tables D.1–D.20 in Appendix D. It is noted that the inventory volumes for all the suppliers at each of their warehouses are obtained as zeros for all products during each period, indicating the availability of a cost-wise efficient production and distribution setup at suppliers ends. It adds an advantage to the suppliers owing to multiple operational challenges of warehousing and inventory management.

TABLE 10. Error analysis for different combinations of parameters in GA; those giving strong-stationary points highlighted in bold.

pt	*pc*	*pm*	*p*	Fitness value	Relative error
0.8	0.7	0.001	1	**0**	0
0.8	0.7	0.001	10	6263	0.920
0.8	0.7	0.005	1	**0**	0
0.8	0.7	0.005	10	**0**	0
0.8	0.8	0.001	1	**0**	0
0.8	0.8	0.001	10	12780	1.877
0.8	0.8	0.005	1	**0**	0
0.8	0.8	0.005	10	**0**	0
0.8	0.9	0.001	1	**0**	0
0.8	0.9	0.001	10	1145	0.168
0.8	0.9	0.005	1	3500	0.514
0.8	0.9	0.005	10	**0**	0
0.9	0.7	0.001	1	**0**	0
0.9	0.7	0.001	10	3500	0. 514
0.9	0.7	0.005	1	**0**	0
0.9	0.7	0.005	10	**0**	0
0.9	0.8	0.001	1	**0**	0
0.9	0.8	0.001	10	**0**	0
0.9	0.8	0.005	1	**0**	0
0.9	0.8	0.005	10	**0**	0
0.9	0.9	0.001	1	197	0.029
0.9	0.9	0.001	10	**0**	0
0.9	0.9	0.005	1	**0**	0
0.9	0.9	0.005	10	**0**	0

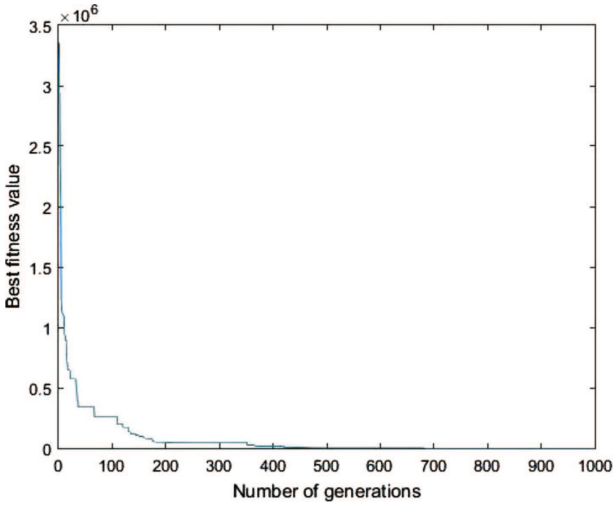


FIGURE 4. Best fitness value *vs.* Generation of a solution.

TABLE 11. Suppliers' prices (competitive target prices) p_{kn_kj} (INR per tonne),

Supplier (k)	Product (n_k)	DL (j)				
		1	2	3	4	5
1	1	28 700	25 800	25 950	28 950	28 599.92
2	2	5560	5560	5950	5560	5160
	3	5689.914	5850	5450	5050	4850
3	1	32 899.92	33 000	31 175	30 300	29 800
4	4	89 600	94 200	93 504.25	91 000	90 600
5	2	4750	4850	5000	5000	4650
	3	4695	4795	4945	5150	4595
6	1	24 250	27 550	24 200	24 350	24 250
	4	92 499.98	89 800	89 350	92 050	93292.56
7	2	6250	6499.984	6824.942	6800	6100
	3	6350	6599.426	6925	6882.551	6200
	4	92 707.78	92 800	92 875	96 700	91 500

Remark 5.1. Further testing of the 22 strong-stationarity points for strong-stationarity Nash-equilibrium point is not being taken-up for the following reasons.

(1) There is parity among all the obtained strong-stationarity points in terms of total procurement cost of the buyer (the problem being studied from buyer's perspective only).
(2) The decision-makers of the discussed firm (buyer here) confirmed the efficacy of the results obtained so far in the context of total procurement cost assessed corresponding to competitive prices obtained corresponding to all the 22 strong-stationarity points when compared with the actual costs incurred. From the perspective of business management, this indicates that for the buyer a scope of further negotiation on prices was there without any compromise on the cooperative relation with suppliers.
(3) Thus, even if the buyer would have considered the target prices as any one of those obtained corresponding to these strong-stationarity points, and negotiated the same with suppliers, then the objective of strategic pricing discussed in Section 1, would be satisfactorily achieved.
(4) Over that, theoretically, there is no surety of obtaining a strong-stationarity Nash-equilibrium point, and the question of its existence remaining unconfirmed.

The competitive target prices depicted in Table 11 are a set of prices at which the suppliers can settle during negotiations due to a fair competition among them. Further, if the negotiations are settled at these prices, then the demand orders from the buyer is listed in Table 12. Let us try to have an insight of these results in connection with the production and distribution efficiencies of the suppliers. For product 1, the competition is between suppliers 1, 3, and 6, and the demand order allocation for this product seems distributed among them specific to DLs. Demand order for DL 1 is allocated completely to the supplier 6, completely to supplier 1 for DL 2, for DL 3 distributed between suppliers 1 and 6, and for DL 4 and DL 5 completely to supplier 6 and supplier 3, respectively. This allocation of demand orders is clearly reflected to the prices listed in Table 11. This competition of their prices is evidently due to their cost efficiencies. For example, per unit production costs (regular and overtime) for product 1 are lower for supplier 1 and 6 in comparison to supplier 3 (*c.f.*, Tab. 4). Further, it is evident from the reservation prices of these suppliers given in Table 3 that supplier 3 cannot compete with other suppliers except for DL 5, that too up to some extent only. Thereby with its lowest quote it gets almost a complete share of demand order for delivery at DL 5. Similarly from Tables 11 and 12, it can be observed that for the products 2 and 3 the supplier 5, due to its lowest prices, gets more demand orders than suppliers 2 and 7.

TABLE 12. Buyer's Demand allocation y_{kn_kjt} (number of tonnes to be purchased)

		DL (j)																			
		1				2				3				4				5			
Supplier	Product	Time period (t)				Time period (t)				Time period (t)				Time period (t)				Time period (t)			
(k)	(n_k)	1	2	3	4	1	2	3	4	1	2	3	4	1	2	3	4	1	2	3	4
1	1	0	0	0	0	125	100	75	50	50	0	25	25	0	0	0	0	0	0	0	0
2	2	0	0	0	0	0	0	0	0	0	0	0	0	25	0	0	0	100	100	80	0
	3	0	0	0	0	0	0	0	0	0	0	0	0	80	80	100	15	105	55	0	0
3	1	0	0	0	0	0	0	0	0	0	0	0	0	0	0	0	0	200	100	120	30
4	4	50	75	75	50	0	0	0	0	0	0	0	0	60	60	80	0	65	40	20	60
5	2	75	75	75	75	75	75	75	50	75	50	75	25	50	75	50	25	0	0	0	50
	3	125	125	100	50	100	75	75	75	100	75	50	50	0	0	0	0	25	75	90	90
6	1	150	75	100	75	0	0	0	0	25	75	25	25	75	50	75	50	0	0	0	50
	4	0	0	0	0	25	25	50	25	75	75	50	0	0	0	0	0	0	0	0	0
7	2	0	0	0	0	0	0	0	0	0	0	0	0	0	0	0	0	0	0	0	0
	3	0	0	0	0	0	0	0	0	0	0	0	0	0	0	0	0	0	0	0	0
	4	0	0	0	0	25	50	25	0	0	0	0	0	0	0	0	0	15	40	60	0

Further, even though supplier 7 has better cost competencies of production and distribution for products 2 and 3 (*c.f.*, Tabs. 4 and 7), still the prices for supplier 7 for these products, listed in Table 11, are higher than those of suppliers 2 and 5. Consequently, no demand orders would be allocated to supplier 7 for these products, as reflected in Table 12. Whereas supplier 7 is observed to compete quite well with suppliers 4 and 6 for product 4 to receive a substantial demand share. This indicates that supplier 7 is more interested in dealings product 4, which is costlier in comparison to products 2 and 3. This market insight of supplier 7 seems clear from the reservation prices (given in Tab. 4) as noted here. Minimum reservation prices (lp_{kn_kj}) of products 2 and 3 are higher for supplier 7 in comparison of other suppliers. This restricts the negotiations for products 2 and 3 up to a limit and allows the supplier 7 to negotiate better on product 4.

A significant conclusion comes out from these observations that although the model is being discussed from the buyer's point of view, still the suppliers hold self-control over lowering their prices in the competitive environment. As the considered problem addresses a complex market structure with multiple factors included, accordingly many more similar observations can be made by looking into the results while connecting them with the input data. To summarize, the overall results of computation presented in this section evince the accomplishment of the proposed method to handle a large-scale instance of our problem.

6. Managerial implications

Negotiations handled transparently using this decision support system will portray the buyer's intention of creating constructive competition and non-indulgence into opportunistic discrimination with the motive of minimizing procurement cost. Similarly it will ensure that the suppliers arrive at a settlement price for supply which have adequate margin of safety with regard to their profitability. Thus, the use of developed decision support will ensure that there is no opportunistic discrimination from the buyer by exploiting the bargaining power as a single buyer. On the contrary, with the negotiations settled at prices suggested by the decision support the suppliers too cannot reap enormous surplus profits defying the competition. Hence, this model helps to arrive at that satisficing point of demand and supply which will be logically beneficial for both buyers and sellers in the discussed market situation.

In all, the decision support system developed for our study will help in creating healthy entrepreneurial platform in which the business interests of the buyer and sellers are protected. Eventually, such a business relationship with the suppliers inculcates a support behavior in them which proves to be helpful in combating sudden unforeseen contingency situations in the future. The use of this decision support system can help even in reducing the lengthy negotiation and communication time span, as the target prices ascertained by the model can be used as consensus base prices for fixing the deal.

The proposed model can be appropriately used by any buyer firm which is concerned for minimizing the total procurement costs by creating a healthy competition among its suppliers through a non-cooperative game for their price quotes. The scope of application of our model is listed below.

(1) The model can be used by government authorities for assessment of competitive prices for the tenders invited for the purchase of required material. An indication can be obtained about the existing suppliers for any possible cartels, as these practices are prevalently found among those who supply products to government organizations.
(2) In case of the setup of strategic business units by the suppliers dealing in multiple products, our model is capable of catering such a scenario due to consideration of transportation cost as product dependent.
(3) This model can be used by non-trading and non-manufacturing organizations like Universities, hospitals which procure a sizable proportion of purchases locally.
(4) The situation of suppliers having multiple production centers can also be catered through simple extension of our model by merely introducing additional index for the production centers.

Major challenges of study

Exact assessment of suppliers' operational parameters is a major challenge. Technical expertise at managerial level is a major requirement for an effective use of this model.

7. Conclusions

This work is first of its kind to mathematically address the problem of ascertaining competitive target prices for the buyer of an oligopolistic-monopsony market to negotiate with suppliers in line with a balanced approach of safeguarding the financial interests of each supply-chain partner. The problem is formulated as an MLSF bilinear bilevel game model, featuring suppliers as leaders and the buyer as a follower, as it fits naturally to the problem. Annexing suppliers' operational planning with the bilevel game problem of price-setting enables the buyer to assess the capacities of suppliers for fulfilling the demand-orders. Faced with lack of solution methodologies to handle large-scale instances, a GA-based method is proposed to solve a general MLSF bilevel game problem with bilinear objectives and linear constraints. Further, a modification to the proposed algorithm is suggested to solve the bilevel game problem having a specific dependence structure among variables at leaders' level, as present in our proposed model. The decision support developed is finally illustrated by a study on an FMCG manufacturing firm's procurement setup having similar concerns.

An interesting future research direction is to specifically design an algorithm for handling MLCF bilevel programming problems with integer variables in a large-scale situation. Another challenging potential problem can be addressed for the case of differential pricing. Similar problems may be studied for other market setups, for example, where multiple buyers also compete to fulfill their demands-orders.

Appendix A. Penalty approach [60]

Theoretical developments of the penalty approach [60] for solving the general MLSF bilevel programming problem (MLSF-BLP) given in (4.1) is explained below.

(MLSF-BLP)

$$
\begin{array}{l}
(\mathrm{LDMP}-i)\ \min\limits_{u_i \geq 0}\ f_i(u_i, v) \\
\qquad \text{subject to} \\
\qquad\qquad g_i(u_i, v) \geq 0, \\
\qquad\qquad G_i(u_i, v) = 0, \\
\qquad\qquad \text{where, } v \text{ is optimal response of the follower corresponding} \\
\qquad\qquad \text{to the leaders' variables, } u = \{u_i : i = 1, 2, \ldots, k\}, \\
\quad (\mathrm{FDMP})\ \min\limits_{w}\ b(u, w) \\
\qquad \text{subject to} \\
\qquad\qquad c(u, w) \geq 0, \\
\qquad\qquad w \geq 0.
\end{array}
\tag{A.1}
$$

Observation: The MLSF bilevel programming problem with linear constraints and bilinear objective functions (MLSF-BL-BLP) is a particular case of the general problem (MLSF-BLP), with all the notations taken appropriately as same. Therefore, the penalty approach [60] explained here for the general problem can directly be referred in the discussion in Section 4 with notations $f_i, g_i, G_i, b, c, w, u, v$ symbolizing same functions and variables at both places.

Definition A.1. If, for any given vector $u = \{u_i : i = 1, 2, \ldots, k\}$, y is an optimal solution of (FDMP) in (MLSF-BLP), such that the vector (u, v) satisfy constraints $g_i(u_i, v) \geq 0$ and $G_i(u_i, v) = 0, (i = 1, 2, \ldots, k)$, then (u, v) is a *feasible solution* of (MLSF-BLP).

For the (MLSF-BLP) problem described above, the penalty approach is described in following the steps.

Step 1. The KKT equivalent of (FDMP) (in w)

$$0 \leq w \perp \nabla_w b(u, w) - \nabla_w c(u, w) z \geq 0 \tag{A.2a}$$

$$0 \leq z \perp c(u, w) \geq 0. \tag{A.2b}$$

Step 2: (a) Redefining y as $v = (w, z)$, and defining

$$h(u, v) = \begin{bmatrix} \nabla_w b(u, w) - \nabla_w c(u, w) z \\ c(u, w) \end{bmatrix}. \tag{A.3}$$

(b) Introducing slack variables s, the conditions become

$$h(u, v) - s = 0 \tag{A.4a}$$

$$0 \leq v \perp s \geq 0. \tag{A.4b}$$

Step 3. Incorporating the conditions reduces (MLSF-BLP) to the following Equilibrium Problem with Equilibrium Constraints (EPEC).
For each leader $i = 1, 2, \ldots, k$

$$
\begin{array}{l}
\min\limits_{u_i \geq 0}\ f_i(u_i, v) \\
\text{subject to} \\
\qquad g_i(u_i, v) \geq 0, \\
\qquad G_i(u_i, v) = 0,
\end{array}
$$

$$h(u,v) - s = 0,$$
$$0 \le v \perp s \ge 0.$$

The above EPEC is rewritten as following.

$$\left.\begin{array}{ll} \text{(SLNG) min} & f_i(u_i,v) \\ \text{subject to} & \\ & -g_i(u_i,v) \le 0, \\ & G_i(u_i,v) = 0, \\ & s - h(u,v) = 0, \\ & -u_i \le 0, \\ & -v \le 0, \\ & -s \le 0, \\ & Vs \le 0. \end{array}\right\} \tag{A.5}$$

(Here, $V = \text{diag}(v_1, v_2, \ldots, v_r)$.)

Step 4. A desired solution to (SLNG) is a solution of the following strong-stationarity conditions

$$\nabla_{x_i} f_i(u_i,v) - \lambda_i' \nabla_{x_i} g_i(u_i,v) - \nu_i' \nabla_{x_i} G_i(u_i,v) - \mu_i' \nabla_{x_i} h(u_i,v) - \chi_i = 0 \tag{A.6a}$$
$$\nabla_y f_i(u_i,v) - \lambda_i' \nabla_y g_i(u_i,v) - \nu_i' \nabla_y G_i(u_i,v) - \mu_i' \nabla_y h(u_i,v) - \psi_i + S\xi_i = 0 \tag{A.6b}$$
$$\mu_i' \nabla_s (s - h(u,v)) - \sigma_i' \nabla_s (s) - \xi_i' \nabla_s (Vs) = 0 \tag{A.6c}$$
$$0 \le g_i(u_i,v) \perp \lambda_i \ge 0 \tag{A.6d}$$
$$G_i(u_i,v) = 0 \tag{A.6e}$$
$$h(u,v) - s = 0 \tag{A.6f}$$
$$0 \le u_i \perp \chi_i \ge 0 \tag{A.6g}$$
$$0 \le v \perp \psi_i \ge 0 \tag{A.6h}$$
$$0 \le s \perp \sigma_i \ge 0 \tag{A.6i}$$
$$0 \le -Vs \perp \xi_i \ge 0. \tag{A.6j}$$

(Here, $S = \text{diag}(s_1, s_2, \ldots, s_r)$.)

Definition A.2. A feasible solution (u, v) of (MLSF-BLP) is called a *strong-stationarity point* if there exist multipliers λ_i, χ_i, ψ_i, σ_i, ξ_i, ν_i, μ_i which satisfy strong-stationarity conditions (A.6).

Step 5. Among the strong-stationarity conditions written above, as (A.6d), (A.6g)–(A.6j) are complementarity conditions, therefore the process of solving the system of conditions (A.6) can be eased out by solving instead the following nonlinear programming problem. If an optimal solution of (A.7) gives the objective function value zero *i.e.*, $C_{\text{penalty}} = 0$, then that optimal solution satisfies the strong-stationarity conditions (A.6).

$$\text{(Pen-NLP) min } C_{\text{penalty}} = \sum_{i=1}^{k} (u_i' \chi_i + t_i' \lambda_i + v' \psi_i + s' \sigma_i) + v' s \tag{A.7a}$$

subject to

$$\nabla_{u_i} f_i(u_i,v) - \lambda_i' \nabla_{u_i} g_i(u_i,v) - \nu_i' \nabla_{u_i} G_i(u_i,v) - \mu_i' \nabla_{u_i} h(u_i,v) - \chi_i = 0, \qquad \forall i = 1,2,\ldots,k, \tag{A.7b}$$
$$\nabla_v f_i(u_i,v) - \lambda_i' \nabla_v g_i(u_i,v) - \nu_i' \nabla_v G_i(u_i,v) - \mu_i' \nabla_v h(u_i,v) - \psi_i + S\xi_i = 0, \quad \forall i = 1,2,\ldots,k, \tag{A.7c}$$
$$\mu_i - \sigma_i + \text{V}\xi_i = 0, \qquad \forall i = 1,2,\ldots,k, \tag{A.7d}$$

$$-g_i(u_i, v) + t_i = 0, \qquad \forall i = 1, 2, \ldots, k, \tag{A.7e}$$

$$G_i(u_i, v) = 0, \qquad \forall i = 1, 2, \ldots, k, \tag{A.7f}$$

$$h(u, v) - s = 0, \tag{A.7g}$$

$$u_i \geq 0, v \geq 0, s \geq 0, t_i \geq 0, \lambda_i \geq 0, \chi_i \geq 0, \psi_i \geq 0, \sigma_i \geq 0, \xi_i \geq 0, \tag{A.7h}$$

$$\nu_i, \mu_i \text{ unrestricted in sign.} \tag{A.7i}$$

(Here, $V = \operatorname{diag}(v_1, v_2, \ldots, v_r)$.)

Result. If $(u^*, v^*, s^*, t_i^*, \lambda_i^*, \chi_i^*, \psi_i^*, \sigma_i^*, \xi_i^*, \nu_i^*, \mu_i^*)$ is a local solution of (A.7) with $C_{\text{penalty}} = 0$, then (u^*, v^*) is a strong-stationary point of (MLSF-BLP).

Thus for testing a feasible solution (u^*, v^*) of (MLSF-BLP)to be a strong-stationary point, it is sufficient to solve the (Pen-NLP) parameterized in $(u, v) = (u^*, v^*)$ for optimal values of s, t_i, λ_i, χ_i, ψ_i, σ_i, ξ_i, ν_i, μ_i and check whether the objective function value $C_{\text{penalty}} = 0$.

Appendix B. A special case of (MLSF-BLP)

We now discuss a special case of (MLSF-BLP) and observe a practical method to test the strong-stationarity for a feasible solution of this special case.

If in (MLSF-BLP) the upper level constraint functions g_i, G_i are linear in (u, v), lower level constraints c are linear in (u, w); and upper level objective functions f_i are bilinear in (u_i, v), lower level objective is bilinear in (u, w), then for a feasible solution (u^*, v^*) of (MLSF-BLP) the optimization problem (A.7) becomes a linear programming problem in variables λ_i, $\chi_i, \psi_i, \sigma_i, \xi_i, \nu_i, \mu_i$, and parameterized in corresponding values u, v, s, t_i.

Reason: because, for a given feasible solution (u^*, v^*), the values of s can be obtained using (A.7g), say it as s^*. Also, then the values of S and V become known as $S = \operatorname{diag}(s_1, s_2, \ldots, s_r)$ and $V = \operatorname{diag}(v_1, v_2, \ldots, v_r)$. Further, the non-negativity of t_i can be tested using the condition (A.7e), say it as t_i^*.

Thus, for testing a feasible solution (u^*, v^*) of this special case of (MLSF-BLP) to be a stationary point, it reduces to:

(1) obtain values of t_i^* and s^* using (A.7e) and (A.7g), respectively, such that $s^* \perp v^*$, test check for non-negativity conditions, then
(2) solve the linear programming problem (Para-LP) given in (B.1) parameterized in (u^*, v^*, s^*, t_i^*), for $\lambda_i, \chi_i, \psi_i, \sigma_i, \xi_i, \nu_i, \mu_i$, and then
(3) check the objective function value $C_{pp} = 0$ for an optimal solution.

$$\text{(Para-LP)} \quad \min_{\lambda_i, \chi_i, \psi_i, \sigma_i, \xi_i, \nu_i, \mu_i} \; C_{pp} = \sum_{i=1}^{k} (u_i^{*\prime} \chi_i + t_i^{*\prime} \lambda_i + v^{*\prime} \psi_i + s^{*\prime} \sigma_i)$$

subject to

$$\nabla_{u_i} f_i(u_i^*, v^*) - \lambda_i' \nabla_{u_i} g_i(u_i^*, v^*) - \nu_i' \nabla_{u_i} G_i(u_i^*, v^*) - \mu_i' \nabla_{u_i} h(u_i^*, v^*) - \chi_i = 0, \qquad \forall i = 1, 2, \ldots, k,$$

$$\nabla_v f_i(u_i^*, v^*) - \lambda_i' \nabla_v g_i(u_i^*, v^*) - \nu_i' \nabla_v G_i(u_i^*, v^*) - \mu_i' \nabla_v h(u_i^*, v^*) - \psi_i + S^* \xi_i = 0, \qquad \forall i = 1, 2, \ldots, k,$$

$$\mu_i - \sigma_i + V^* \xi_i = 0, \qquad \forall i = 1, 2, \ldots, k,$$

$$\lambda_i \geq 0, \chi_i \geq 0, \psi_i \geq 0, \sigma_i \geq 0, \xi_i \geq 0,$$

$$\nu_i, \mu_i \text{ unrestricted in sign.} \tag{B.1}$$

Appendix C. Theoretical development for solving special case of (MLSF-BLP)

For the special case of (MLSF-BLP) discussed above, if a vector values for the variable u is chosen randomly, then the lower-level problem (FDMP) in (4.1) becomes a linear programming problem (LPP) in variables w, parametrized in the values of u. This LPP can be easily solved for obtaining an optimal solution v. And therefore, the corresponding vector of values for (u, v) would satisfy the KKT conditions (A.2). Accordingly, the vector of values for the variable s can be obtained using (A.7g) (same as (A.4)). Further, the values of each variable t_i can be obtained using (A.7e) and tested for non-negativity. If, through all these computations a vector of values for (u, v) is obtained which satisfies the testing criteria just discussed, then it is a feasible solution of (MLSF-BLP). Then for the obtained values of (u, v, s, t_i) the (Para-LP) can be solved for an optimal solution. If the objective function value $C_{pp} = 0$, then we get (u, v) as a strong stationary point of (MLSP-BLP).

Through this discussion it is learnt that if we randomly generate a vector of values for leaders' variables u, we can obtain follower's reaction v and test for strong-stationary point of this special case of (MLSP-BLP). Thus, if we use a real-coded GA by coding the chromosomes as vectors of values for u, obtain corresponding values for v, and take the fitness value of each chromosome as objective function value C_{pp} to be computed by the above procedure, then we can achieve a stationary-point in some generation obtained through reproduction operators of GA. A GA-based approach is proposed in Section 4 for solving the special case of (MLSF-BLP) which involves linear constraints and bilinear objective functions.

Based on above discussion, a GA based approach, for solving a MLSF game involving linear constraints and bilinear objective functions, is proposed in Section 4.

Remark: a strong-stationarity point (u^*, v^*) for $u^* = \{u_i^* : i = 1, 2, \ldots, k\}$, thus obtained can further be tested for a strong-stationary Nash-equilibrium point of the (MLSF-BLP) by repeatedly solving single-leader-single-follower bilevel programming problems for each leader given by:

$$
\begin{aligned}
&\left(\text{LDMP} - i^{-1}\right) \min_{u_i \geq 0} \; f_i(u_i, v) \\
&\qquad \text{subject to} \\
&\qquad\qquad g_i(u_i, v) \geq 0, \\
&\qquad\qquad G_i(u_i, v) = 0, \\
&\qquad\qquad \text{where, } v \text{ is optimal response of the follower corresponding to above values of } u_i \text{ and keeping values of other leaders' variables fixed as } u_{\bar{i}} = u_{\bar{i}}^* : \bar{i} = 1, 2, \ldots, k, \bar{i} \neq i, \\
&\text{(FDMP)} \min_{w} \; b(u, w) \\
&\qquad \text{subject to} \\
&\qquad\qquad c(u, w) \geq 0 \\
&\qquad\qquad w \geq 0.
\end{aligned}
\tag{C.1}
$$

For solving such a problem having large number of variables, it further requires a heuristic algorithm. One such algorithm is proposed by Kumar *et al.* [55].

Appendix D. Complementary results

Table D.1. Production volumes (regular-time and over-time): Supplier 1.

		Time period (t)			
		1	2	3	4
Q_{kn_kt}	$n_k = 1$	175	100	100	75
O_{kn_kt}	$n_k = 1$	0	0	0	0

TABLE D.2. Consignment volumes from PC to DC(s): Supplier 1.

$I_{kn_ki_kt}$	Time period (t)			
DC (i_k)	1	2	3	4
1	0	0	0	0
2	0	0	0	0

TABLE D.3. Transportation volumes from PC to DC(s): Supplier 1 ($n_k = 1$).

$x_{kn_ki_kjt}$	DC (i_k)											
	0				1				2			
DL	Time period (t)				Time period (t)				Time period (t)			
(j)	1	2	3	4	1	2	3	4	1	2	3	4
1	0	0	0	0	0	0	0	0	0	0	0	0
2	125	100	75	50	0	0	0	0	0	0	0	0
3	50	0	25	25	0	0	0	0	0	0	0	0
4	0	0	0	0	0	0	0	0	0	0	0	0
5	0	0	0	0	0	0	0	0	0	0	0	0

TABLE D.4. Production volumes (regular-time and over-time): Supplier 2.

		Time period (t)			
	Product (n_k)	1	2	3	4
Q_{kn_kt}	1	103	100	80	0
	2	185	135	100	15
O_{kn_kt}	1	22	0	0	0
	2	0	0	0	0

TABLE D.5. Consignment volumes from PC to DC(s): Supplier 2 (DC: $i_k = 1$).

$I_{kn_ki_kt}$	Time period (t)			
Product (n_k)	1	2	3	4
2	0	0	0	0
3	0	0	0	0

TABLE D.6. Transportation volumes from PC to DC(s): Supplier 2.

$x_{kn_ki_kjt}$		$i_k = 0$				$i_k = 1$			
Product	DL	Time period (t)				Time period (t)			
(n_k)	(j)	1	2	3	4	1	2	3	4
2	1	0	0	0	0	0	0	0	0
	2	0	0	0	0	0	0	0	0
	3	0	0	0	0	0	0	0	0
	4	25	0	0	0	0	0	0	0
	5	100	100	80	0	0	0	0	0
3	1	0	0	0	0	0	0	0	0
	2	0	0	0	0	0	0	0	0
	3	0	0	0	0	0	0	0	0
	4	80	80	100	15	0	0	0	0
	5	105	55	0	0	0	0	0	0

TABLE D.7. Production volumes (regular-time and over-time): Supplier 3.

		Time period (t)			
	Product (n_k)	1	2	3	4
Q_{kn_kt}	1	200	100	120	30
O_{kn_kt}	1	0	0	0	0

TABLE D.8. Consignment volumes from PC to DC(s) ($I_{kn_ki_kt}$; $n_3 = 1,\ i_3 = 1$): Supplier 3.

Time period (t)			
1	2	3	4
0	0	0	0

TABLE D.9. Transportation volumes from PC to DC(s) ($n_3 = 1$): Supplier 3.

$x_{kn_ki_kjt}$	$i_k = 0$				$i_k = 1$			
DL	Time period (t)				Time period (t)			
(j)	1	2	3	4	1	2	3	4
1	0	0	0	0	0	0	0	0
2	0	0	0	0	0	0	0	0
3	0	0	0	0	0	0	0	0
4	0	0	0	0	0	0	0	0
5	200	100	120	30	0	0	0	0

TABLE D.10. Production volumes (regular-time and over-time) ($n_k = 5$): Supplier 4.

	Time period (t)			
	1	2	3	4
Q_{kn_kt}	175	175	175	110
O_{kn_kt}	0	0	0	0

TABLE D.11. Transportation volumes from PC to DC(s) ($i_k = 0,\ n_k = 5$): Supplier 4.

	Time period (t)			
DL (j)	1	2	3	4
1	50	75	75	50
2	0	0	0	0
3	0	0	0	0
4	60	60	80	0
5	65	40	20	60

TABLE D.12. Production volumes (regular-time and over-time): Supplier 5.

		Time period (t)			
		1	2	3	4
Q_{kn_kt}	$n_k = 2$	226	226	261	225
	$n_k = 3$	350	350	315	265
O_{kn_kt}	$n_k = 2$	49	49	14	0
	$n_k = 3$	0	0	0	0

TABLE D.13. Consignment volumes from PC to DC(s): Supplier 5.

	Time period (t)			
	1	2	3	4
$n_k = 2, i_k = 1$	0	0	0	0
$n_k = 3, i_k = 1$	0	0	0	0

TABLE D.14. Transportation volumes from PC to DC(s): Supplier 5.

$x_{kn_ki_kjt}$		$i_k = 0$				$i_k = 1$			
	DL	Time period (t)				Time period (t)			
	(j)	1	2	3	4	1	2	3	4
$n_k = 2$	1	75	75	75	75	0	0	0	0
	2	75	75	75	50	0	0	0	0
	3	75	50	75	25	0	0	0	0
	4	50	75	50	25	0	0	0	0
	5	0	0	0	50	0	0	0	0
$n_k = 3$	1	125	125	100	50	0	0	0	0
	2	100	75	75	75	0	0	0	0
	3	100	75	50	50	0	0	0	0
	4	0	0	0	0	0	0	0	0
	5	25	75	90	90	0	0	0	0

TABLE D.15. Production volumes (regular-time and over-time): Supplier 6.

	Product	Time period (t)			
	(n_k)	1	2	3	4
Q_{kn_kt}	1	250	200	200	200
	5	100	100	100	25
O_{kn_kt}	1	0	0	0	0
	5	0	0	0	0

TABLE D.16. Consignment volumes from PC to DC(s): Supplier 6.

$I_{kn_k i_k t}$	Time period (t)			
	1	2	3	4
$n_k = 2, i_k = 1$	150	75	100	75
$n_k = 3, i_k = 1$	0	0	0	0

TABLE D.17. Transportation volumes from PC to DC(s): Supplier 6

$x_{kn_k i_k jt}$		DC (i_k)											
		0				1				2			
Product	DL	Time period (t)				Time period (t)				Time period (t)			
(n_k)	(j)	1	2	3	4	1	2	3	4	1	2	3	4
1	1	0	0	0	0	150	75	100	75	0	0	0	0
	2	0	0	0	0	0	0	0	0	0	0	0	0
	3	25	75	25	25	0	0	0	0	0	0	0	0
	4	75	50	75	50	0	0	0	0	0	0	0	0
	5	0	0	0	50	0	0	0	0	0	0	0	0
5	1	0	0	0	0	–	–	–	–	–	–	–	–
	2	25	25	50	25	–	–	–	–	–	–	–	–
	3	75	75	50	0	–	–	–	–	–	–	–	–
	4	0	0	0	0	–	–	–	–	–	–	–	–
	5	0	0	0	0	–	–	–	–	–	–	–	–

TABLE D.18. Production volumes (regular-time and over-time): Supplier 7.

	Product (n_k)	Time period (t)			
		1	2	3	4
$Q_{kn_k t}$	1	0	0	0	0
	3	0	0	0	0
	5	40	90	85	0
$O_{kn_k t}$	1	0	0	0	0
	3	0	0	0	0
	5	0	0	0	0

TABLE D.19. Consignment volumes from PC to DC(s) ($I_{kn_k i_k t}$): Supplier 7.

Product (n_k)	DC (i_k)	Time period (t)			
		1	2	3	4
2	1	0	0	0	0
	2	0	0	0	0
3	1	0	0	0	0
	2	0	0	0	0

TABLE D.20. Transportation volumes from PC to DC(s): Supplier 7.

$x_{kn_k i_k jt}$		DC (i_k)											
		0				1				2			
Product	DL	Time period (t)				Time period (t)				Time period (t)			
(n_k)	(j)	1	2	3	4	1	2	3	4	1	2	3	4
1	1	0	0	0	0	0	0	0	0	0	0	0	0
	2	0	0	0	0	0	0	0	0	0	0	0	0
	3	0	0	0	0	0	0	0	0	0	0	0	0
	4	0	0	0	0	0	0	0	0	0	0	0	0
	5	0	0	0	0	0	0	0	0	0	0	0	0
3	1	0	0	0	0	0	0	0	0	0	0	0	0
	2	0	0	0	0	0	0	0	0	0	0	0	0
	3	0	0	0	0	0	0	0	0	0	0	0	0
	4	0	0	0	0	0	0	0	0	0	0	0	0
	5	0	0	0	0	0	0	0	0	0	0	0	0
5	1	0	0	0	0	–	–	–	–	–	–	–	–
	2	25	50	25	0	–	–	–	–	–	–	–	–
	3	0	0	0	0	–	–	–	–	–	–	–	–
	4	0	0	0	0	–	–	–	–	–	–	–	–
	5	15	40	60	0	–	–	–	–	–	–	–	–

Acknowledgements. Authors are extremely thankful to the Editor-in-Chief, Associate Editor, and the anonymous referees for their critical suggestions to improve the paper. Authors deeply acknowledge valuable technical inputs from Dr. Manoj Pillai, Department of Commerce, and Mr. Nimain Charan Swain, Department of Economics, Arignar Anna Government Arts & Science College, Karaikal, U.T. of Puducherry, India. Authors are thankful to Mr. Sudhir K. Varma for help on insight of the data structures used for the empirical analysis.

REFERENCES

[1] N. Amjady and A. Shirzadi, Unit commitment using a new integer coded genetic algorithm. *Eur. Trans. Electr. Power* **19** (2009) 1161–1176.

[2] J.S. Angelo and H.J.C. Barbosa, A study on the use of heuristics to solve a bilevel programming problem. *Int. Trans. Oper. Res.* **22** (2015) 861–882.

[3] S. Aouadni, I. Aouadni and A. Rebaï, A systematic review on supplier selection and order allocation problems. *J. Ind. Eng. Int.* **15** (2019) 267–289.

[4] A.H. Azadnia, M.Z.M. Saman and K.Y. Wong, Sustainable supplier selection and order lot-sizing: an integrated multi-objective decision-making process. *Int. J. Prod. Res.* **53** (2015) 383–408.

[5] G. Barbarosoglu and D. Özgür, Hierarchical design of an integrated production and 2-echelon distribution system. *Eur. J. Oper. Res.* **118** (1999) 464–484.

[6] J.F. Bard, Practical Bilevel Optimization: Algorithms and Applications Nonconvex Optimization and its Applications. Springer, USA (1998).

[7] S. Baskar, P. Subbaraj and M.V.C. Rao, Hybrid real coded genetic algorithm solution to economic dispatch problem. *Comput. Electr. Eng.* **29** (2003) 407–419.

[8] A. Blanco, M. Delgado and M.C. Pegalajar, A real-coded genetic algorithm for training recurrent neural networks. *Neural Networks* **14** (2001) 93–105.

[9] L. Brotcorne, M. Labbe, P. Marcotte and G. Savard, A bilevel model for toll optimization on a multicommodity transportation network. *Transp. Sci.* **35** (2001) 345–358.

[10] F.P. Buffa and W.M. Jackson, A goal programming model for purchase planning. *J. Purchasing Mater. Manage.* **19** (1983) 27–34.

[11] H.I. Calvete, C. Galé and P.M. Mateo, A new approach for solving linear bilevel problems using genetic algorithms. *Eur. J. Oper. Res.* **188** (2008) 14–28.

[12] H.I. Calvete, C. Galé and M.J. Oliveros, Bilevel model for production-distribution planning solved by using ant colony optimization. *Comput. Oper. Res.* **38** (2011) 320–327.

[13] J.F. Camacho-Vallejo, R. Muñoz-Sánchez and J.L. González-Velarde, A heuristic algorithm for a supply chain's production-distribution planning. *Comput. Oper. Res.* **61** (2015) 110–121.

[14] L.H. Chen and F. Sen Kang, Integrated inventory models considering the two-level trade credit policy and a price-negotiation scheme *Eur. J. Oper. Res.* **205** (2010) 47–58.
[15] B. Colson, P. Marcotte and G. Savard, A trust-region method for nonlinear bilevel programming: algorithm and computational experience. *Comput. Optim. App.* **30** (2005) 211–227.
[16] B. Colson, P. Marcotte and G. Savard, An overview of bilevel optimization. *Ann. Oper. Res.* **153** (2007) 235–256.
[17] Competition Commission of India, Provisions relating to cartels, Competition Act, 2002. Competition Commission of India (2002) https://www.cci.gov.in/advocacy-booklets.
[18] B. Crevier, J.F. Cordeau and G. Savard, Integrated operations planning and revenue management for rail freight transportation. *Transp. Res. Part B Methodol.* **46** (2012) 100–119.
[19] I.G. Damousis, A.G. Bakirtzis and P.S. Dokopoulos, Network-constrained economic dispatch using real-coded genetic algorithm. *IEEE Trans. Power Syst.* **18** (2003) 198–205.
[20] L. Davis, Adapting operator probabilities in genetic algorithms. In: *Proceedings of the Third International Conference on Genetic Algorithms. Morgan Kaufmann Publishers Inc., San Francisco, CA, USA* (1989) 61–69.
[21] L. Davis, Handbook of Genetic Algorithms. Van Nostrand Reinhold, New York (1991).
[22] K. Deep and M. Thakur, A new crossover operator for real coded genetic algorithms. *Appl. Math. Comput.* **188** (2007) 895–912.
[23] K. Deep and M. Thakur, A new mutation operator for real coded genetic algorithms. *Appl. Math. Comput.* **193** (2007) 211–230.
[24] K. Deep, K.P. Singh, M.L. Kansal and C. Mohan, A real coded genetic algorithm for solving integer and mixed integer optimization problems. *Appl. Math. Comput.* **212** (2009) 505–518.
[25] E.A. Demirtas and Ö. Üstün, An integrated multiobjective decision making process for supplier selection and order allocation. *Omega* **36** (2008) 76–90.
[26] S. Dempe, Foundations of Bilevel Programming, 1st edition. Springer, US (2002).
[27] S. Dempe and A.B. Zemkoho, Bilevel road pricing: theoretical analysis and optimality conditions. *Ann. Oper. Res.* **196** (2012) 223–240.
[28] S. Deng, R. Aydin, C.K. Kwong and Y. Huang, Integrated product line design and supplier selection: a multi-objective optimization paradigm. *Comput. Ind. Eng.* **70** (2014) 150–158.
[29] S. Dewez, M. Labbe, P. Marcotte and G. Savard, New formulations and valid inequalities for a bilevel pricing problem. *Oper. Res. Lett.* **36** (2008) 141–149.
[30] G.W. Dickson, An analysis of vendor selection systems and decisions. *J. Purchasing* **2** (1966) 5–17.
[31] H. Ding, L. Benyoucef and X. Xie, A simulation-optimization approach using genetic search for supplier selection. In: *Proceedings of the 2003 International Conference on Machine Learning and Cybernetics (IEEE Cat No03EX693)* (2003) 1260–1267.
[32] A. Dolgui and J.-M. Proth, Pricing strategies and models. *Ann. Rev. Control* **34** (2010) 101–110.
[33] J.P. Dussault, P. Marcotte, S. Roch and G. Savard, A smoothing heuristic for a bilevel pricing problem. *Eur. J. Oper. Res.* **174** (2006) 1396–1413.
[34] L.J. Eshelman and J.D. Schaffer, Real-coded genetic algorithms and interval-schemata. *Found. Genet. Algorithms* **2** (1993) 187–202.
[35] B. Fahimnia, L. Luong and R. Marian, Genetic algorithm optimisation of an integrated aggregate production-distribution plan in supply chains. *Int. J. Prod. Res.* **50** (2012) 81–96.
[36] B. Fahimnia, R.Z. Farahani, R. Marian and L. Luong, A review and critique on integrated production-distribution planning models and techniques. *J. Manuf. Syst.* **32** (2013) 1–19.
[37] X. Fu, X.J. Zeng, X. Luo, D. Wang, D. Xu and Q.L. Fan, Designing an intelligent decision support system for effective negotiation pricing: a systematic and learning approach. *Decis. Support Syst.* **96** (2017) 49–66.
[38] A.A. Gaballa, Minimum cost allocation of tenders. *J. Oper. Res. Soc.* **25** (1974) 389–398.
[39] Y. Gao, G. Zhang, J. Lu and H.M. Wee, Particle swarm optimization for bi-level pricing problems in supply chains. *J. Global Optim.* **51** (2011) 245–254.
[40] C.J. Gelderman, J. Semeijn and M. Verhappen, Buyer opportunism in strategic supplier relationships: triggers, manifestations and consequences. *J. Purchasing Supply Manage.* **26** (2020) 100581.
[41] M. Gen and A. Syarif, Hybrid genetic algorithm for multi-time period production/distribution planning. *Comput. Ind. Eng.* **48** (2005) 799–809.
[42] B.C. Giri and T. Maiti, Supply chain model with price- and trade credit-sensitive demand under two-level permissible delay in payments. *Int. J. Syst. Sci.* **44** (2013) 937–948.
[43] D.E. Goldberg, Genetic Algorithms in Search, Optimization and Machine Learning, 1st edition. Addison-Wesley Longman Publishing Co., Inc., USA (1989).
[44] D.E. Goldberg, Real-coded genetic algorithms, virtual alphabets, and blocking. *Complex Syst.* **5** (1991) 139–167.
[45] H. Haghighat and S.W. Kennedy, A bilevel approach to operational decision making of a distribution company in competitive environments. *IEEE Trans. Power Syst.* **27** (2012) 1797–1807.
[46] H. Haghighat, H. Seifi and A.R. Kian, Pay-as-bid versus marginal pricing: the role of suppliers strategic behavior. *Int. J. Electr. Power Energy Syst.* **42** (2012) 350–358.
[47] S.R. Hejazi, A. Memariani, G. Jahanshahloo and M.M. Sepehri, Linear bilevel programming solution by genetic algorithm. *Comput. Oper. Res.* **29** (2002) 1913–1925.

[48] F. Herrera, E. Herrera-viedma, M. Lozano and J.L. Verdegay, Fuzzy tools to improve genetic algorithms. In: *Proc of the Second European Congress on Intelligent Techniques and Soft Computing* (1994) 1532–1539.
[49] F. Herrera, M. Lozano and J.L. Verdegay, Tuning fuzzy logic controllers by genetic algorithms. *Int. J. Approximate Reasoning* **12** (1995) 299–315.
[50] J.H. Holland, Adaptation in Natural and Artificial Systems. MIT Press, Cambridge, MA, USA (1975).
[51] A. Hori and M. Fukushima, Gauss–Seidel method for multi-leader-follower games. *J. Optim. Theory App.* **180** (2019) 651–670.
[52] V. Jayaraman, R. Srivastava and W.C. Benton, Supplier selection and order quantity allocation: a comprehensive model. *J. Supply Chain Manage.* **35** (1999) 50–58.
[53] A. Joseph, S.I. Gass and N.A. Bryson, Nearness and bound relationships between an integer-programming problem and its relaxed linear-programming problem. *J. Optim. Theory App.* **98** (1998) 55–63.
[54] A. Kumar, A. Gupta and A. Mehra, A bilevel programming model for operative decisions on special trains: an Indian Railways perspective. *J. Rail Transp. Planning Manage.* **8** (2018) 184–206.
[55] A. Kumar, A. Gupta and A. Mehra, A bilevel programming model for a cohesive decision-making on strategic pricing and production distribution planning for a small-scale supplier. *Int. Game Theory Rev.* **22** (2020) 2040009.
[56] M. Labbé and A. Violin, Bilevel programming and price setting problems. *Ann. Oper. Res.* **240** (2016) 141–169.
[57] M. Labbe, P. Marcotte and G. Savard, A bilevel model of taxation and its application to optimal highway pricing. *Manage. Sci.* **44** (1998) 1608–1622.
[58] L. Lai, H.R. Bowles and L. Babcock, Social costs of setting high aspirations in competitive negotiation. *Negotiation Conflict Manage. Res.* **6** (2013) 1–12.
[59] L.R. Lamberson, D. Diederich and J. Wuori, Quantitative vendor evaluation. *J. Purchasing Mater. Manage.* **12** (1976) 19–28.
[60] S. Leyffer and T. Munson, Solving multi-leader-common-follower games. *Optim. Methods Softw.* **25** (2010) 601–623.
[61] H. Li and L. Fang, An evolutionary algorithm for solving bilevel programming problems using duality conditions. *Math. Prob. Eng.* **2012** (2012) 1–14.
[62] H. Li and Y. Wang, A hybrid genetic algorithm for solving nonlinear bilevel programming problems based on the simplex method. In: *Proceedings – Third International Conference on Natural Computation, ICNC 2007. Vol. 4* (2007) 91–95.
[63] H. Li, L. Zhang and Y.C. Jiao, Solution for integer linear bilevel programming problems using orthogonal genetic algorithm. *J. Syst. Eng. Electron.* **25** (2014) 443–451.
[64] T.-F. Liang, Fuzzy multi-objective production/distribution planning decisions with multi-product and multi-time period in a supply chain. *Comput. Ind. Eng.* **55** (2008) 676–694.
[65] T.-F. Liang and H.-W. Cheng, Application of fuzzy sets to manufacturing/distribution planning decisions with multi-product and multi-time period in supply chains. *Expert Syst. App.* **36** (2009) 3367–3377.
[66] Z. Liao and J. Rittscher, A multi-objective supplier selection model under stochastic demand conditions. *Int. J. Prod. Econ.* **105** (2007) 150–159.
[67] X. Liu and H. Liu, A logistics production-distribution scheme based on intelligent computing. *Comput. Modell. New Technol.* **18** (2014) 1332–1336.
[68] Y. Liu, C. Su, Y. Li and T. Liu, Managing opportunism in a developing interfirm relationship: the interrelationship of calculative and loyalty commitment. *Ind. Marketing Manage.* **39** (2010) 844–852.
[69] J. Lu, J. Han, Y. Hu and G. Zhang, Multilevel decision-making: a survey. *Inf. Sci.* **346, 347** (2016) 463–487.
[70] C.B. Lucasius and G. Kateman, Application of genetic algorithms in chemometrics. In: *Proceedings of the Third International Conference on Genetic Algorithms*, edited by J.D. Schaffer. Morgan Kaufmann Publishers, San Mateo (1989) 170–176.
[71] A.K. Maiti, A.K. Bhunia and M. Maiti, An application of real-coded genetic algorithm (RCGA) for mixed integer non-linear programming in two-storage multi-item inventory model with discount policy. *Appl. Math. Comput.* **183** (2006) 903–915.
[72] R. Manzini, M. Gamberi and A. Regattieri, Applying mixed integer programming to the design of a distribution logistic network. *Int. J. Ind. Eng. Theory App. Pract.* **13** (2006) 207–218.
[73] R. Mathieu, L. Pittard and G. Anandalingam, Genetic algorithm based approach to bi-level linear programming. *RAIRO-Oper. Res.* **28** (1994) 1–21.
[74] A. Megahed and M. Goetschalckx, A modeling framework and local search solution methodology for a production-distribution problem with supplier selection and time-aggregated quantity discounts. *Appl. Math. Modell.* **68** (2019) 198–218.
[75] F. Meng, B. Kazemtabrizi, X.J. Zeng and C. Dent, An optimal differential pricing in smart grid based on customer segmentation. In: *2017 IEEE PES Innovative Smart Grid Technologies Conference Europe, ISGT-Europe 2017 – Proceedings. 2018–January* (2017) 1–6, DOI: 10.1109/ISGTEurope.2017.8260255.
[76] S. Mirjalili, Genetic algorithm. *Stud. Comput. Intell.* **780** (2019) 43–55.
[77] H. Mühlenbein and D. Schlierkamp-Voosen, Predictive models for the breeder genetic algorithm I. Continuous parameter optimization. *Evol. Comput.* **1** (1993) 25–49.
[78] T. Mysen, G. Svensson and J.M. Payan, The key role of opportunism in business relationships. *Marketing Intell. Planning* **29** (2011) 436–449.
[79] T.T. Nagle and G. Müller, The Strategy and Tactics of Pricing: A Guide to Growing More Profitably, 6th edition. Taylor & Francis, Routledge (2018).
[80] R. Narasimhan, S. Talluri and D. Mendez, Supplier evaluation and rationalization via data envelopment analysis: an empirical examination. *J. Supply Chain Manage.* **37** (2001) 28–37.
[81] Y. Nemati and M.H. Alavidoost, A fuzzy bi-objective MILP approach to integrate sales, production, distribution and procurement planning in a FMCG supply chain. *Soft Comput.* **23** (2019) 4871–4890.
[82] A. Norouzi, A. Zolfaghari, A.H. Minuchehr and F. Khoshahval, An enhanced integer coded genetic algorithm to optimize PWRs. *Prog. Nucl. Energy* **53** (2011) 449–456.

[83] S.S. Padhi and P.K.J. Mohapatra, Detection of collusion in government procurement auctions. *J. Purchasing Supply Manage.* **17** (2011) 207–221.
[84] A.K. Paswan, T. Hirunyawipada and P. Iyer, Opportunism, governance structure and relational norms: an interactive perspective. *J. Bus. Res.* **77** (2017) 131–139.
[85] B. Raa, W. Dullaert and E.H. Aghezzaf, A matheuristic for aggregate production-distribution planning with mould sharing. *Int. J. Prod. Econ.* **145** (2013) 29–37.
[86] N.J. Radcliffe, Equivalence class analysis of genetic algorithms. *Complex Syst.* **5** (1991) 183–205.
[87] R. Rajavel, S.K. Ravichandran and G.R. Kanagachidambaresan, Agent-based cloud service negotiation architecture using similarity grouping approach. *Int. J. Wavelets, Multiresolution Inf. Process.* **18** (2020) 1941015.
[88] E. Roghanian, S.J. Sadjadi and M.B. Aryanezhad, A probabilistic bi-level linear multi-objective programming problem to supply chain planning. *Appl. Math. Comput.* **188** (2007) 786–800.
[89] C. Ruiz, A.J. Conejo and Y. Smeers, Equilibria in an oligopolistic electricity pool with stepwise offer curves. *IEEE Trans. Power Syst.* **27** (2012) 752–761.
[90] J. Scott, W. Ho, P.K. Dey and S. Talluri, A decision support system for supplier selection and order allocation in stochastic, multi-stakeholder and multi-criteria environments. *Int. J. Prod. Econ.* **166** (2015) 226–237.
[91] A. Sinha, P. Malo and K. Deb, A review on bilevel optimization: from classical to evolutionary approaches and applications. *IEEE Trans. Evol. Comput.* **22** (2018) 276–295.
[92] R.E. Spekman, Strategic supplier selection: understanding long-term buyer relationships. *Bus. Horizons* **31** (1988) 75–81.
[93] C. Steinle, H. Schiele and T. Bohnenkamp, Does supplier opportunism lead to buyer opportunism? A social capital perspective. *J. Bus. Ind. Marketing* **35** (2019) 362–384.
[94] P. Subbaraj and P.N. Rajnarayanan, Optimal reactive power dispatch using self-adaptive real coded genetic algorithm. *Electr. Power Syst. Res.* **79** (2009) 374–381.
[95] L. Sun, Y. Zhang and C. Jiang, A matrix real-coded genetic algorithm to the unit commitment problem. *Electr. Power Syst. Res.* **76** (2006) 716–728.
[96] S. Talluri and R. Narasimhan, A methodology for strategic sourcing. *Eur. J. Oper. Res.* **154** (2004) 236–250.
[97] B. Teixeira, T. Pinto, F. Silva, G. Santos, I. Praça and Z. Vale, Multi-agent decision support tool to enable interoperability among heterogeneous energy systems. *Appl. Sci. (Switzerland)* **8** (2018) 328.
[98] A. Thangam, Optimal price discounting and lot-sizing policies for perishable items in a supply chain under advance payment scheme and two-echelon trade credits. *Int. J. Prod. Econ.* **139** (2012) 459–472.
[99] D.J. Thomas and P.M. Griffin, Coordinated supply chain management. *Eur. J. Oper. Res.* **94** (1996) 1–15.
[100] G.A. Vignaux and Z. Michalewicz, A genetic algorithm for the linear transportation problem. *IEEE Trans. Syst. Man Cybern.* **21** (1991) 445–452.
[101] Y. Wang, Y.C. Jiao and H. Li, An evolutionary algorithm for solving nonlinear bilevel programming based on a new constraint-handeling scheme. *IEEE Trans. Syst. Man Cybern. Part C: App. Rev.* **35** (2005) 221–232.
[102] C.A. Weber, J.R. Current and W.C. Benton, Vendor selection criteria and methods. *Eur. J. Oper. Res.* **50** (1991) 2–18.
[103] H.M. Wee, M.C. Lee, P.C. Yang and R.L. Chung, Bi-level vendor–buyer strategies for a time-varying product price. *Appl. Math. Comput.* **219** (2013) 9670–9680.
[104] A.H. Wright, Genetic algorithms for real parameter optimization. In: Foundations of Genetic Algorithms (1991) 205–218.
[105] H. Yang, X. Zhang and Q. Meng, Modeling private highways in networks with entry-exit based toll charges. *Transp. Res. Part B Methodol.* **38** (2004) 191–213.
[106] P.C. Yang, H.M. Wee, S. Pai and Y.F. Tseng, Solving a stochastic demand multi-product supplier selection model with service level and budget constraints using genetic algorithm. *Expert Syst. App.* **38** (2011) 14773–14777.
[107] Y. Yin, Genetic-algorithms-based approach for bilevel programming models. *J. Transp. Eng.* **126** (2000) 115–119.
[108] X. Zhu, Q. Yu and X. Wang, A hybrid differential evolution algorithm for solving nonlinear bilevel programming with linear constraints. In: *Proceedings of the 5th IEEE International Conference on Cognitive Informatics, ICCI 2006.* Vol. 1 (2006) 126–131.

Subscribe to Open (S2O)
A fair and sustainable open access model

This journal is currently published in open access under a Subscribe-to-Open model (S2O). S2O is a transformative model that aims to move subscription journals to open access. Open access is the free, immediate, online availability of research articles combined with the rights to use these articles fully in the digital environment. We are thankful to our subscribers and sponsors for making it possible to publish this journal in open access, free of charge for authors.

Please help to maintain this journal in open access!

Check that your library subscribes to the journal, or make a personal donation to the S2O programme, by contacting subscribers@edpsciences.org

More information, including a list of sponsors and a financial transparency report, available at: https://www.edpsciences.org/en/maths-s2o-programme

This article has been accepted for publication in a future issue of this journal, but has not been fully edited. Content may change prior to final publication. Citation information: DOI 10.1109/TPEL.2022.3152497, IEEE Transactions on Power Electronics

A general Multilevel Polygonal Space Vector Generation scheme with reduced switching for the inverter and harmonic suppression using a switched-capacitive filter for the full modulation range

Rahul Dewani, *Student Member*, K.Gopakumar, *Fellow, IEEE*, Umanand Loganathan, Subhashish Bhattacharya, *Fellow, IEEE*

***Abstract*—In this work, a general multilevel polygonal space vector generation scheme is proposed for Open End Induction Motor (OEIM) drive schemes, fed with any conventional multilevel inverter with active DC link supply on one end, and a low voltage capacitor fed inverter working as a switched capacitive filter at the other end. The main power delivery primary inverter provides active power for motoring operation, and the capacitor fed secondary switched capacitive filter suppresses lower order harmonics by forming polygonal space vector structures of 36, 42, 48, etc. sides. In the general modulation scheme proposed here, the primary inverter is visualized as a combination of sub-hexagons. Two sub-hexagons of primary inverter are modulated in pseudo 6-step mode of operation to generate the desired fundamental component to drive the induction motor load. The primary inverter also generates undesirable lower order harmonics due to low switching per cycle in primary inverter. The secondary inverter is used as a switched capacitive filter to suppress the lower order harmonics of the 5^th, 7^{th}, 11^th, 13^{th}, ... order by forming polygonal switching vectors with sides greater than 6, like 36, 42, 48. The general scheme proposed here, is verified for a 3-level primary inverter fed with active DC link of V_{dc} and 6-level secondary inverter fed with a capacitive supply balanced at nearly $1/3^{rd}$ of the DC link voltage ($0.39V_{dc}$).**

***Index Terms*—Flying Capacitor, harmonic suppression, Induction Motor drives, polygonal Space Vector Structure, multilevel inverters, pulse width modulation(PWM).**

I. Introduction

INDUCTION motor drives are ubiquitous in industrial applications. Induction Motors (IM) are the preferred choice in industrial applications due to their simple and rugged construction. However, the optimal control of IM for variable speed applications is challenging and a topic of active research.

The Multi-Level Inverter (MLI) topologies [1]–[11] are widely used for induction motor drive schemes. The multi-level IM drives, give stepped waveforms for the motor phase voltages with low Total Harmonic Distortion (THD) [1], [3], and low dV/dt [2]. The advantages of multi-level drives are often accompanied by significant disadvantages. The conventional multi-level IM drive solutions, often employ multiple power supplies [1], [4], [6]. Multiple power supplies impose additional hardware requirements for the drive scheme, and make the regeneration operation of the IM drive difficult. At the same time, the multiple levels (steps in phase voltage waveform) are available, only at the extreme speed range. As the speed of operation decreases, the number of levels (and the number of steps in phase voltage), also reduces [5], [7]. So to attain the same harmonic performance, the number of switching per cycle needs to be increased at low modulation index.

Another performance limitation of the MLI drive schemes is the generation of lower order harmonics at the extreme speed range [1], [4]. Conventional MLI has a hexagonal Space Vector Structure (SVS). At the base speed of operation, the inverter operates in 6-step mode operation, switching only at the vertices of the hexagonal SVS. This generates the 6-step waveform for the phase voltage, which has 5^{th} and 7^{th} order lower order harmonics.

In this paper, a general polygonal SVS scheme [12]–[15] is proposed, which generates higher sided polygons with sides more than 6 (e.g. 30, 36, 42, etc.). As the number of sides of the polygon is increased, more and more lower order harmonics are suppressed in the phase voltage [12], [15].

The proposed IM drive scheme comprises of an Open-End Induction Motor (OEIM), fed with main power delivery inverter on one side, and a switched capacitive filter on the other side, which generates polygonal SVS with sides more than 6 for harmonic suppression. The main power delivery primary inverter provides active power for motoring operation [16], and the secondary switched capacitive filter is used to

Manuscript received December 1, 2021; accepted February 8, 2022.

Rahul Dewani, K.Gopakumar, and Umanand Loganathan are with the Department of Electronic Systems Engineering, Indian Institute of Science, Bangalore-560012, India. (email: rahuldewani@iisc.ac.in; kgopa@iisc.ac.in; lums@iisc.ac.in).

Subhashish Bhattacharya is with the NSF FREEDM Systems Engineering Research Center, North Carolina State University, Raleigh, NC 27606 USA. (email: sbhatta4@ncsu.edu).

0885-8993 (c) 2021 IEEE. Personal use is permitted, but republication/redistribution requires IEEE permission. See http://www.ieee.org/publications_standards/publications/rights/index.html for more information.
Authorized licensed use limited to: DELHI TECHNICAL UNIV. Downloaded on February 24,2022 at 07:02:49 UTC from IEEE Xplore. Restrictions apply.

This article has been accepted for publication in a future issue of this journal, but has not been fully edited. Content may change prior to final publication. Citation information: DOI 10.1109/TPEL.2022.3152497, IEEE Transactions on Power Electronics

generate a dense polygonal SVS for suppression of lower order harmonics. The salient features of the proposed drive scheme are as follows:

1) The main power delivery inverter (primary inverter) can be any conventional multi-level inverter structure fed with an active DC link supply.
2) The main power delivery inverter switches only at the vertices of sub-hexagons in primary SVS, in pseudo 6-step mode of operation.
3) The main power delivery inverter (operating in pseudo 6-step mode of operation) has low switching per cycle for the entire modulation range.
4) The low switching frequency in primary inverter generates lower order harmonics of 5^{th}, 7^{th}, 11^{th}, 13^{th}, etc. The secondary inverter suppresses lower order harmonics by generating the appropriate polygonal sides of more than six. Thus, the secondary inverter is acting acting as a switched capacitive filter.
5) The superposition of primary and secondary inverters generates polygonal SVS for suppression of harmonics. The suppression of lower order harmonics depends on the polygonal sides generated during PWM of the secondary inverter. Thus, by generating higher sided polygon by switching secondary inverter appropriately, more and more harmonics can be suppressed for better harmonic performance.

The proposed scheme is implemented for polygons with various sides of the form $6k$ like 30, 36, 42, etc. In general, any MLI topology could have been used as the main power delivery inverter. For the experimental verification, a 3-level flying capacitor [17], [18] inverter topology is used as the main power delivery inverter. The primary inverter (the 3-level inverter in this work) operates with low switching frequency throughout the modulation range, unlike a conventional multilevel inverter operation. The advantages of polygonal SVS are available throughout the modulation range. The generation of polygonal SVS is explained and presented with hardware results.

In any PWM cycle, the reference vector is sampled by the controller. The sampling period depends on the number of polygonal sides one wishes to generate. Once the reference vector is sampled, it's amplitude and phase are known. With the location of the reference vector known, it can be determined between which two sub-hexagons of primary SVS, the tip of the reference vector lies. The reference space vector is generated by switched averaging the two sub-hexagons of primary SVS.

In a conventional PWM, the adjacent vertices of sub-hexagons are switched, such that during a PWM period itself, the adjacent vectors are switched averaged to generate the average vector from inverter, which coincides with the reference vector. But in the present work, instead of going for a continuous PWM switching, the two adjacent sub-hexagons (between which the tip of the sampled reference vector lies) are switched in pseudo 6-step mode of operation, such that the fundamental of the pseudo 6-step mode of operation with be same as sampled reference space vector in a fundamental cycle. For example, when the inverter is in 6-step mode of operation, the fundamental component of $0.637V_{dc}$ is generated in a fundamental cycle, and not switch-averaged in a PWM cycle (V_{dc} is the length of the 6-step vectors).

As explained before, due to the pseudo 6-step mode of operation in primary inverter, the tip of the reference vector and the primary inverter vector will not coincide in a PWM cycle generating an error vectors. However, in a fundamental cycle, the fundamental components of primary inverter and reference vector coincide. The error is computed by taking the difference of sampled reference vector and primary inverter sub-hexagonal vector and switched by the secondary inverter, which suppresses the harmonics by acting as switched capacitive filter. The harmonic suppression depends on the number of sides of the polygonal reference vectors. For example, by generating 12 sided reference vectors, 5^{th} and 7^{th} order harmonics are suppressed, and by generating a 42-sided polygon, all harmonics upto 39^{th} order are suppressed.

The PWM scheme is explained in detail below for any multilevel inverter used as primary inverter and the secondary inverter acting as switched capacitive filter.

II. General PWM modulation scheme

The general power circuit topology for the proposed polygonal PWM switching scheme is shown in Fig.1. Two inverters, primary inverter and secondary inverter, feed the OEIM from either side in this scheme. The primary inverter used as the main power delivery inverter is fed with a DC link supply to provide active power for motoring operation. The secondary inverter is used only for suppression of lower order harmonics, and does not contribute any active power. Hence, the secondary inverter is fed with a capacitive supply. Any conventional multilevel inverter scheme can be employed for the primary and secondary inverters, as the modulation scheme for polygonal SVS generation is general in nature.

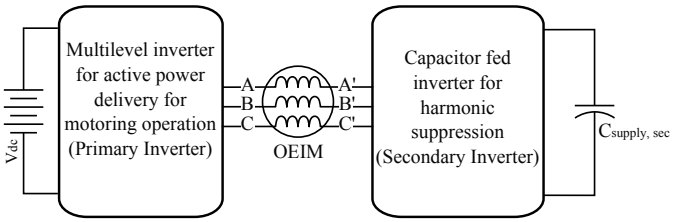


Fig. 1. General schematic of multilevel inverter fed open-end induction motor drive scheme for the polygonal voltage vector generation.

The primary inverter fed with active dc link supply is switched in pseudo 6-step mode of operation, generating lower order harmonics. The harmonics generated by the primary inverter are suppressed by using the low-voltage secondary inverter as switched-capacitive filter. The superposition of the primary and secondary inverter SVS forms a polygonal SVS devoid of lower order harmonics. The general modulation scheme that can be applied to any multi-level inverter topology is presented below. To explain the PWM algorithm better, an example is also presented at each step.

0885-8993 (c) 2021 IEEE. Personal use is permitted, but republication/redistribution requires IEEE permission. See http://www.ieee.org/publications_standards/publications/rights/index.html for more information.
Authorized licensed use limited to: DELHI TECHNICAL UNIV. Downloaded on February 24,2022 at 07:02:49 UTC from IEEE Xplore. Restrictions apply.

This article has been accepted for publication in a future issue of this journal, but has not been fully edited. Content may change prior to final publication. Citation information: DOI 10.1109/TPEL.2022.3152497, IEEE Transactions on Power Electronics

1) Identify all the sub-hexagons in the primary inverter space vector structure along with the corresponding fundamental component of phase voltage, and radii of sub-hexagons generated in 6-step mode of operation for the sub-hexagons. A circular trajectory is presented for each of the sub-hexagons, that generates the same fundamental component for the three phase voltages, as the sub-hexagon operating in 6-step mode of operation, without any harmonics. The radius of the corresponding circular trajectory is marked as the radius for sub-hexagons. For a sub-hexagon of length kV_{dc} operating in 6-step mode of operation, the fundamental component of phase voltage is $0.637kV_{dc}$, and the radius is $0.956kV_{dc}$.
Example: For the example of a 3-level inverter used as primary inverter, the three sub-hexagons along with their fundamental phase voltages and radii (A_{hex-1} to A_{hex-3}) are shown in Fig.2.

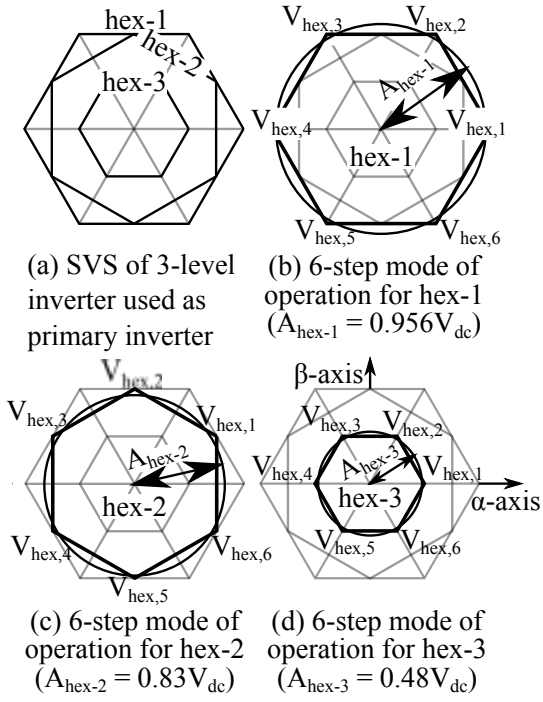


Fig. 2. Sub-hexagons of the 3-level SVS used as primary inverter.

The radii and fundamental components of sub-hexagons, are obtained (presented in Table.I) and stored in the digital platform (DSP/FPGA) that is used for the implementation of the polygonal PWM switching scheme.

2) The location of the sampled reference space vector, $A_{ref}\angle\theta_{ref}$, where A_{ref} is the amplitude and θ_{ref} is the phase of the sampled space vector with respect to $\alpha-$axis (Fig.2 (d)), is obtained for the PWM switching cycle from the control loop. The amplitude of the space vector, A_{ref}, is compared with the radii of the sub-hexagons (presented in Table.I), to obtain the adjacent sub-hexagons (outer hexagon and inner hexagon), between which the tip of the reference vector lies. The outer and inner hexagons are switch-averaged over a fundamental cycle to generate the fundamental amplitude of A_{ref}.

TABLE I
PRIMARY INVERTER SUB-HEXAGONS ALONG WITH THE CORRESPONDING FUNDAMENTAL COMPONENTS.

Hexagon	Fundamental component of phase voltage	Radius of polygon
Hex-1 (radius = V_{dc})	$V_{phase,max}$ $(= 0.637V_{dc})$	$A_{hex-1} = 0.956V_{dc}$
Hex-2 (radius = $0.87V_{dc}$)	$0.866V_{phase,max}$ $(= 0.552V_{dc})$	$A_{hex-2} = 0.828V_{dc}$
Hex-3 (radius = $0.5V_{dc}$)	$0.5V_{phase,max}$ $(= 0.319V_{dc})$	$A_{hex-3} = 0.478V_{dc}$
Hex-4 (radius = 0)	0	$A_{hex-4} = 0$

A fourth hexagon, Hex-4 is visualized for PWM operation at low modulation index.

Example: The sampled reference space vector along with the primary inverter 3-level SVS is shown in Fig.3 (a). The reference amplitude of A_{ref} is compared with the radii of the sub-hexagons: A_{hex-1}, A_{hex-2}, A_{hex-3} and A_{hex-4} in Table.I, to find between which two sub-hexagons (the outer and inner sub-hexagon), the tip of the reference vector lies.

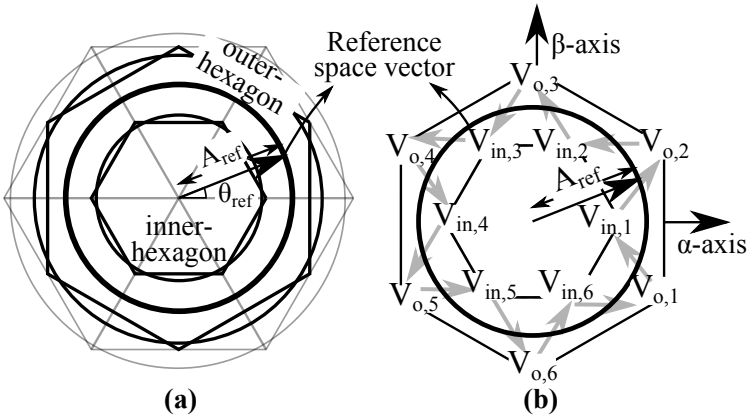


Fig. 3. (a) Primary inverter 3-level SVS sub-hexagons along with sampled reference space vector of amplitude A_{ref} and phase θ_{ref}. (b) The primary inverter switching vector trajectory marked with arrows.

The pseudo code for this step is added below:

$Pseudo$-code for 3-level SVS:
$if(A_{hex-2} \leq A_{ref} \leq A_{hex-1})$
$\quad outer - hexagon = hex - 1$
$\quad inner - hexagon = hex - 2$
else-$if(A_{hex-3} \leq A_{ref} \leq A_{hex-2})$
$\quad outer - hexagon = hex - 2$
$\quad inner - hexagon = hex - 3$
else-$if(A_{hex-4} \leq A_{ref} \leq A_{hex-3})$
$\quad outer - hexagon = hex - 3$
$\quad inner - hexagon = hex - 4$
end

With the outer and inner hexagons (between which the tip of the reference vector lies) determined, all the vectors to

0885-8993 (c) 2021 IEEE. Personal use is permitted, but republication/redistribution requires IEEE permission. See http://www.ieee.org/publications_standards/publications/rights/index.html for more information.
Authorized licensed use limited to: DELHI TECHNICAL UNIV. Downloaded on February 24,2022 at 07:02:49 UTC from IEEE Xplore. Restrictions apply.

This article has been accepted for publication in a future issue of this journal, but has not been fully edited. Content may change prior to final publication. Citation information: DOI 10.1109/TPEL.2022.3152497, IEEE Transactions on Power Electronics

be used for the primary inverter PWM can be obtained in this step. For example, for $A_{ref} = 0.6V_{dc}$, the outer and inner hexagons are determined to be $hex-2$ and $hex-3$, as shown in Fig.3 (a).

The outer and inner sub-hexagons are shown in Fig.3(b) along with the reference space vector circle of amplitude A_{ref}. The outer hexagonal vectors are marked from $\overrightarrow{V_{o,1}}$, to $\overrightarrow{V_{o,6}}$; whereas, the inner hexagonal vectors are marked from $\overrightarrow{V_{in,1}}$, to $\overrightarrow{V_{in,6}}$ in Fig.3(b). The outer and inner sub-hexagons are switch-averaged over a fundamental cycle, by operating them in pseudo 6-step mode of operation. In pseudo 6-step mode of operation, each of the 6 outer vectors is switched for equal time duration of T_{outer} in a fundamental cycle. Similarly, each of the 6 inner vectors is switched for equal time duration of T_{inner}. The switching sequence can be realized by following the switching vector trajectory marked with arrows in Fig.3(b). The switching sequence starts with the $\vec{V}_{in,1}$ vector from inner sub-hexagon (hex-3) for T_{in} duration, followed by the $\vec{V}_{o,2}$ vector from outer sub-hexagon (hex-2) for T_{out} duration. The vectors from inner and outer hexagons are switched alternatingly over a fundamental cycle. The switching sequence of vectors highlighted with arrows in Fig.3(b) is as follows: $\vec{V}_{in,1} \rightarrow \vec{V}_{o,2} \rightarrow \vec{V}_{in,2} \rightarrow \vec{V}_{o,3} \rightarrow \vec{V}_{in,3} \rightarrow \vec{V}_{o,4} \rightarrow \vec{V}_{in,4} \rightarrow \vec{V}_{o,5} \rightarrow \vec{V}_{in,5} \rightarrow \vec{V}_{o,6} \rightarrow \vec{V}_{in,6} \rightarrow \vec{V}_{o,1} \rightarrow \vec{V}_{in,1}$, and so on.

3) In this step, the durations for which the inner and outer vectors are switched are calculated. The reference space vector circle of radius A_{ref} is generated by switched-averaging of the inner and outer hexagonal vectors in a fundamental cycle. Thus, the durations can be calculated using the volt-second relations used for switched-averaging of the outer and inner sub-hexagons.

The durations for which the inner and outer vectors are switched are represented as angular durations here. The space vector covers an angular duration of 360^o over a fundamental time period T, of motor operation. The angular durations of the inner and outer hexagonal vectors are θ_{inner} and θ_{outer} each. Thus, θ_{inner} is the angular duration for which the switching vector remains stationary at one of the inner hexagonal vectors, as the reference vector moves continuously over a fundamental period of 360^o. Similarly, θ_{outer} is the active angular duration for which the switching vector remains stationary at one of the outer hexagonal vectors. The angular duration of the inner and outer hexagonal vectors can be related with the corresponding time durations as,

$$\theta_{outer} = T_{out}.\frac{360^o}{T}$$
$$\theta_{innner} = T_{in}.\frac{360^o}{T}$$

The sum of angular durations of the 6 outer and the 6 inner hexagonal vectors should add up to, 360^o, the fundamental period of motor operation,

$$\begin{aligned} \implies 6\theta_{outer} + 6\theta_{inner} &= 360^o \\ \implies \theta_{outer} + \theta_{inner} &= 60^o \end{aligned} \quad (1)$$

The phase duration of θ_{outer} and θ_{inner} can be expressed in terms of the duty ratios of outer hexagon, β and inner hexagon, $(1-\beta)$, where $0 \leq \beta \leq 1$, as,

$$\begin{aligned} \implies \theta_{outer} &= 60^o\beta \\ \implies \theta_{inner} &= 60^o(1-\beta) \end{aligned} \quad (2)$$

From the harmonic analysis, the fundamental component for pseudo 6-step mode of operation of the outer and inner sub-hexagons can be derived in as,

$$A_{ref} = A_{hex-outer}2sin(\frac{\beta\pi}{6}) + A_{hex-inner}2sin(\frac{(1-\beta)\pi}{6})$$

The non-linear terms in the above relation, $2sin(\frac{\beta\pi}{6})$ and $2sin(\frac{(1-\beta)\pi}{6})$, are plotted in Fig.4 with their linear counterparts.

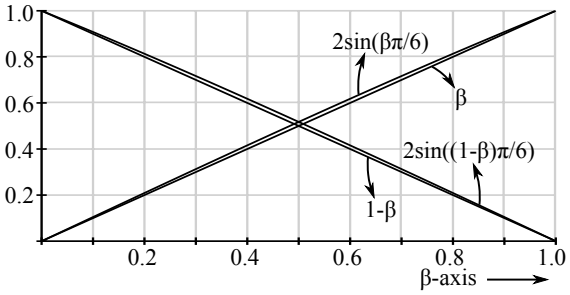


Fig. 4. The non-linear terms $2sin(\frac{\beta\pi}{6})$ and $2sin(\frac{(1-\beta)\pi}{6})$ along with their linear counterparts.

Since the non-linear terms have small deviation from their linear counterparts ($< 1.5\%$), they are approximated as the linearized terms in above relation. The value of β can be calculated from the linearized relationship as,

$$\begin{aligned} A_{ref} &= A_{hex-outer}\beta + A_{hex-inner}(1-\beta) \\ \beta &= \frac{A_{ref} - A_{hex-inner}}{A_{hex-outer} - A_{hex-inner}} \end{aligned} \quad (3)$$

Where, $A_{hex-outer}$ and $A_{hex-inner}$ are the fundamental components of the space vector for 6-step mode of operation of outer and inner hexagons, respectively.

Example: Consider the sampled reference space vector of amplitude $A_{ref} = 0.6V_{dc}$ and phase $\theta_{ref} = 15^o$ (refer Fig.5). The outer and inner sub-hexagons for this example can be determined to be hex-2 and hex-3, respectively (refer Table.I). β is determined from Equation.3 as,

$$\begin{aligned} \beta &= \frac{A_{ref} - A_{hex-inner}}{A_{hex-outer} - A_{hex-inner}} \\ \implies \beta &= \frac{0.6V_{dc} - 0.478V_{dc}}{0.828V_{dc} - 0.478V_{dc}} \\ \implies \beta &= 0.35 \end{aligned} \quad (4)$$

Based on the value of β in Equation.4,the values of θ_{inner} and θ_{outer} are calculated as,

0885-8993 (c) 2021 IEEE. Personal use is permitted, but republication/redistribution requires IEEE permission. See http://www.ieee.org/publications_standards/publications/rights/index.html for more information.
Authorized licensed use limited to: DELHI TECHNICAL UNIV. Downloaded on February 24,2022 at 07:02:49 UTC from IEEE Xplore. Restrictions apply.

This article has been accepted for publication in a future issue of this journal, but has not been fully edited. Content may change prior to final publication. Citation information: DOI 10.1109/TPEL.2022.3152497, IEEE Transactions on Power Electronics

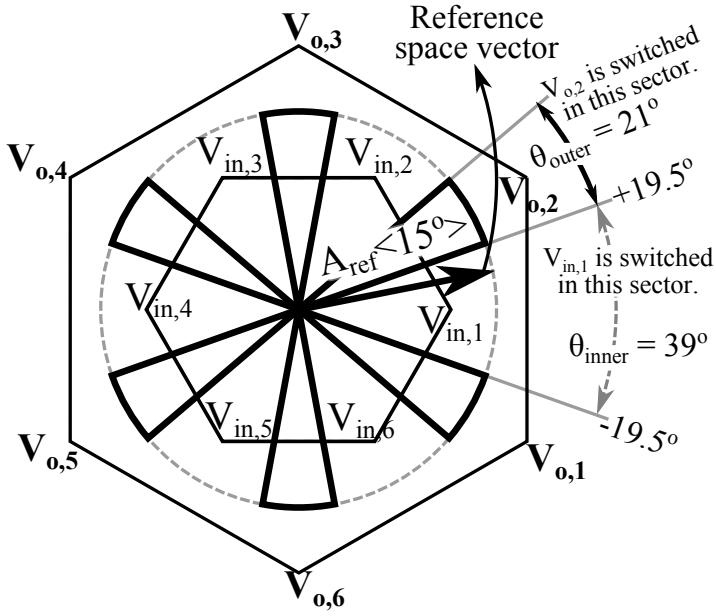


Fig. 5. The reference space vector circle, split into 12 sectors of angular durations of $\theta_{inner} = 39^o$ (thin lines) and $\theta_{outer} = 21^o$ (thick lines), for the example of $A_{ref} = 0.6V_{dc}$ and $\theta_{ref} = 15^o$

$$\begin{aligned} & \theta_{outer} = 60^o * 0.35 \\ \implies & \theta_{outer} = 21^o \\ & \theta_{inner} = 60^o * (1 - 0.35) \\ \implies & \theta_{inner} = 39^o \end{aligned} \tag{5}$$

The reference space vector circle along with the angular durations for inner and outer hexagonal vectors is shown in Fig.5. The angular durations of inner vectors is marked with thin lines and that of outer vectors with thick lines.

4) By obtaining β in step.3, the angular durations of each of the inner and outer hexagonal vectors to be applied in a fundamental period are determined. The primary inverter space vector to be switched for the PWM cycle can be determined by comparing the reference phase θ_{ref}, with the angular durations of inner (θ_{inner}) and outer (θ_{outer}) hexagonal vectors.

Example: The selection of primary vector for the PWM cycle for the example of $A_{ref} = 0.6V_{dc}$ and $\theta_{ref} = 15^o$ is illustrated in Fig.5. Here, the entire reference circle is split into 12 sectors (6 sectors corresponding to inner hexagonal vectors are shown with thin lines; whereas the remaining 6 sectors corresponding to outer hexagonal vectors are shown with thick lines). The six sectors corresponding to inner hexagonal vectors are of duration $\theta_{inner} = 39^o$ each. The 39^o duration sectors are centered at the inner hexagonal vectors. For example, for the inner hexagonal vector $V_{in,1} = V_{dc}/2\angle 0^o$, the sector starts at -19.5^o and ends at $+19.5^o$, covering a total angular duration of 39^o. Similarly, the 6-sectors corresponding to outer hexagonal vectors are of duration $\theta_{outer} = 21^o$ and centered at outer hexagonal vectors as illustrated in Fig.5. It can be observed that the sampled reference space vector lies in the sector corresponding to inner hexagonal vector $V_{in,1}$ for the example of $A_{ref} = 0.6V_{dc}$ and $\theta_{ref} = 15^o$. Thus, vector $V_{in,1}$ is switched from the primary inverter for the PWM switching cycle considered in this example. A pseudo-code to implement the aforementioned algorithm for 60^o sector is presented below:

Pseudo-code for 3-level SVS for 60^o duration:

$if(0 \leq \theta_{ref} \leq \frac{\theta_{inner}}{2})$

$\quad \vec{V}_{pri} = \vec{V}_{in,1} \qquad [0^o \text{ to } 19.5^o \text{sector}]$

else-$if(\frac{\theta_{inner}}{2} \leq \theta_{ref} \leq \frac{\theta_{inner}}{2} + \theta_{outer})$

$\quad \vec{V}_{pri} = \vec{V}_{o,2} \qquad [19.5^o \text{ to } 19.5^o + 21^o \text{sector}]$

else-$if(\frac{\theta_{inner}}{2} + \theta_{outer} \leq \theta_{ref} \leq 60^o)$

$\quad \vec{V}_{pri} = \vec{V}_{in,2} \qquad [19.5^o + 21^o \text{ to } 60^o \text{sector}]$

end

For the reference space vector location shown in Fig.5, the tip of the reference vector is within the sector corresponding to inner vector $\vec{V}_{in,1}$ (sector marked with thin line). As the reference vector moves along this region, vector $\vec{V}_{in,1}$ will be switched for a duration of $\theta_{inner} = 39^o$ (for $-19.5^o \leq \theta_{ref} \leq +19.5^o$). As the sampled reference space vector switches to the next region corresponding to outer vector $\vec{V}_{o,2}$ (marked with thick line), the corresponding vector $\vec{V}_{o,2}$ will be switched for a duration of $\theta_{outer} = 21^o$, and so on.

5) The reference space vector, $\vec{V}_{sv,ref} = A_{ref}\angle\theta_{ref}$ is generated by the superposition of the primary and secondary inverter space vectors.

$$\vec{V}_{sv,ref} = \vec{V}_{pri} + \vec{V}_{sec} \tag{6}$$

In this step, the secondary inverter space vector is determined using the above relationship. $\vec{V}_{sv,ref} = A_{ref}\angle\theta_{ref}$ is obtained from the controller as explained in step.2, and $\vec{V}_{pri}$, the primary sub-hexagonal vector, is determined from the pseudo-code in step.4,

$$\begin{aligned} \vec{V}_{sec} &= \vec{V}_{sv,ref} - \vec{V}_{pri} \\ &= A_{ref}\angle\theta_{ref} - \vec{V}_{pri} \end{aligned} \tag{7}$$

The above relation can be used to determine the α-β components of the secondary space vector as,

$$\begin{aligned} V_{sec,\alpha} &= A_{ref} cos\theta_{ref} - V_{pri,\alpha} \\ V_{sec,\beta} &= A_{ref} sin\theta_{ref} - V_{pri,\beta} \end{aligned} \tag{8}$$

The α-β components are then used to find the references for the three phases of secondary inverter as,

$$\begin{aligned} V_{sec,A-ref} &= \frac{2}{3} V_{sec,\alpha} \\ V_{sec,B-ref} &= \frac{-V_{sec,\alpha}}{3} + \frac{V_{sec,\beta}}{\sqrt{3}} \\ V_{sec,C-ref} &= \frac{-V_{sec,\alpha}}{3} - \frac{V_{sec,\beta}}{\sqrt{3}} \end{aligned} \tag{9}$$

0885-8993 (c) 2021 IEEE. Personal use is permitted, but republication/redistribution requires IEEE permission. See http://www.ieee.org/publications_standards/publications/rights/index.html for more information.
Authorized licensed use limited to: DELHI TECHNICAL UNIV. Downloaded on February 24,2022 at 07:02:49 UTC from IEEE Xplore. Restrictions apply.

This article has been accepted for publication in a future issue of this journal, but has not been fully edited. Content may change prior to final publication. Citation information: DOI 10.1109/TPEL.2022.3152497, IEEE Transactions on Power Electronics

The nearest levels of the secondary multilevel inverter can be switched for appropriate durations to generate the reference voltage in switch-averaged sense. The secondary inverter modulation is explained in further detail in [16].

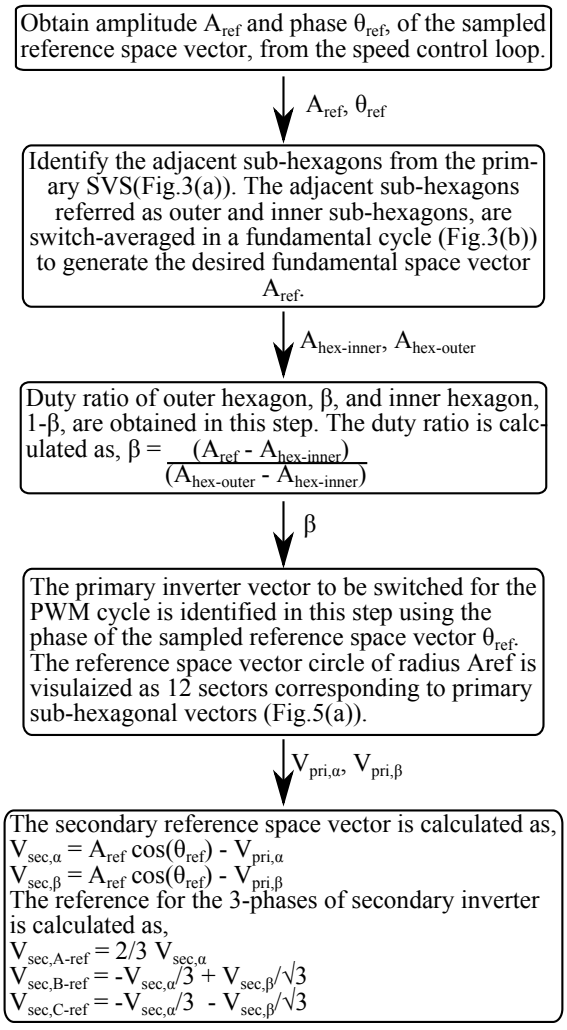


Fig. 6. The switching cycle algorithm for PWM modulation of primary and secondary inverters.

The switching cycle algorithm for the PWM modulation of primary and secondary inverters is summarized in the flow chart presented in Fig.6.

III. Power Circuit Topology

The power circuit topology used for experimental verification of the general polygonal PWM switching algorithm is shown in Fig.7. The primary and secondary inverters are connected to the open-end Induction Motor (OEIM) on either side. The primary inverter, fed with an active DC link supply of V_{dc}, provides all of the active power for motoring operation. The secondary inverter is a capacitor fed 2-level stage (balanced at a nominal voltage of $0.39V_{dc}$ [16]), connected to a H-bridge stage balanced at $0.13V_{dc}$. The secondary inverter absorbs the reactive power generated by the primary inverter resulting in suppression of lower order harmonics in

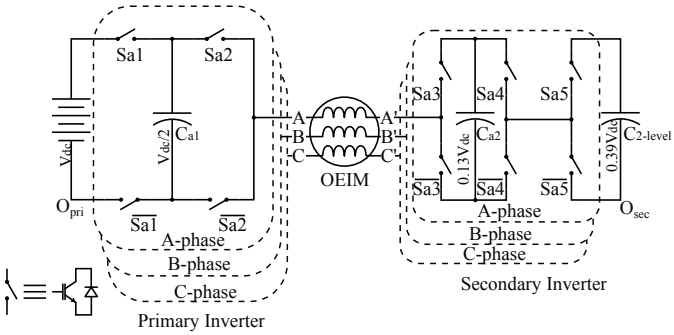


Fig. 7. Power Circuit Topology for experimental verification: A 3-level primary inverter and capacitor fed 6-level secondary inverter feeding an open-end induction motor drive.

motor phase voltage. The proposed general polygonal PWM switching scheme offers the advantages of the low switching in the primary inverter and suppression of lower order harmonics throughout the modulation range.

Here, the primary is a 3-level topology. The sub-hexagons of the primary inverter are operated in pseudo 6-step mode of operation. The amplitude of the sampled reference space vector is generated by switched-averaging of sub-hexagons over a fundamental cycle of operation. As a result, the main power delivery primary inverter operating with the full DC link voltage, is operated at low switching frequency. The secondary inverter operating at lower voltages ($0.39V_{dc}$) is switched at higher frequencies to suppress the harmonics generated by the primary inverter. The secondary inverter switching vectors are superimposed with the primary inverter space vectors to generate the polygonal SVS vectors. Thus, by increasing the secondary inverter switching, a denser polygonal SVS with improved harmonic profile can be generated.

The primary inverter capacitors are balanced using the pole voltage redundancies. The secondary inverter H-bridge stage capacitors are balanced in a switching cycle time. The secondary inverter supply capacitor suppresses the harmonic power generated by the primary inverter as explained in [19]. Hence, the secondary inverter supply capacitor is balanced by using the power relations of the primary inverter, motor load and secondary inverter.

IV. Capacitor Balancing Scheme

The capacitor balancing scheme for the capacitor feeding the secondary inverter in the general polygonal PWM switching scheme is presented in this section. The balancing scheme exploits the power relations of the primary inverter, motor load and secondary inverter. The block diagram for the proposed balancing scheme is shown in Fig.9.

The general polygonal PWM switching algorithm explained in section.II is used to generate the PWM for the primary inverter. The sampled reference space vector location is used to determine the primary inverter space vector, $\vec{V}_{pri}$, to be switched in the PWM switching cycle. In the secondary inverter capacitor balancing scheme, the primary inverter PWM is not disturbed.

0885-8993 (c) 2021 IEEE. Personal use is permitted, but republication/redistribution requires IEEE permission. See http://www.ieee.org/publications_standards/publications/rights/index.html for more information.
Authorized licensed use limited to: DELHI TECHNICAL UNIV. Downloaded on February 24,2022 at 07:02:49 UTC from IEEE Xplore. Restrictions apply.

This article has been accepted for publication in a future issue of this journal, but has not been fully edited. Content may change prior to final publication. Citation information: DOI 10.1109/TPEL.2022.3152497, IEEE Transactions on Power Electronics

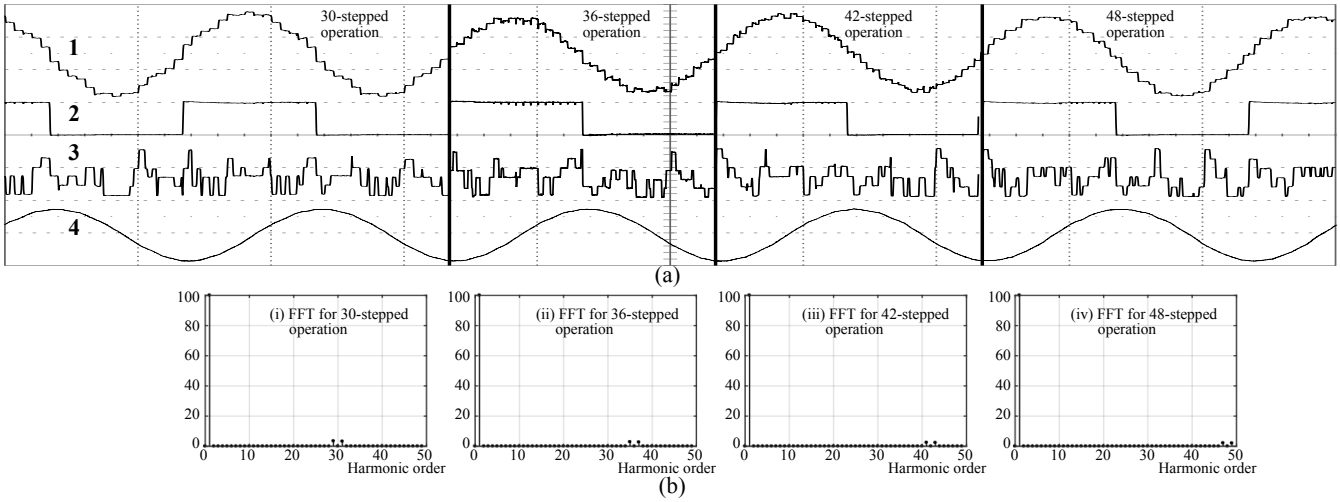


Fig. 8. **(a)** Experimental steady-state results for 50Hz operation. Traces: (1) Motor phase voltage (100V/div), (2) Primary inverter pole voltage (200V/div), (3) Secondary inverter pole voltage (100V/div), (4) Motor phase current (5A/div). **(b)** FFT results of phase voltage for polygonal modulation scheme.

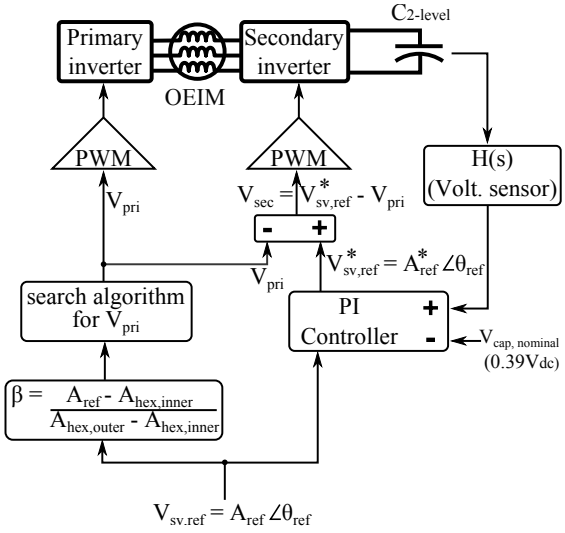


Fig. 9. Functional Block Diagram of the capacitor balancing scheme.

In the ideal case, when the secondary inverter supply capacitor is balanced at it's nominal voltage, the secondary inverter PWM is generated by the relation $\vec{V}_{sec} = A_{ref}\angle\theta_{ref} - \vec{V}_{pri}$, as explained in section.II, step.5. In the algorithm of section.II, the fundamental space vector generated by primary inverter is delivered to the motor load entirely. As a result, the secondary inverter does not participate in power transfer. The power drawn from main power delivery primary inverter is delivered to the motor load entirely.

$$P_{sec} = P_{pri} - P_{OEIM}$$
$$P_{pri} = P_{OEIM} \implies P_{sec} = 0$$

Where, P_{sec}, P_{pri} and P_{OEIM} are the power delivered to secondary inverter, power drawn from primary inverter, and power delivered to OEIM.

Due to circuit non-idealities, the secondary inverter supply capacitor may deviate from it's nominal voltage. For example, consider the capacitor is discharged below it's nominal voltage. To charge the capacitor, the power delivered to motor load is momentarily reduced by a small fraction ($< 5\%$), and supplied to the secondary inverter to charge the supply capacitor.

$$P_{sec} = P_{pri} - P_{OEIM}$$
$$P_{OEIM} < P_{pri} \implies P_{sec} > 0$$

As shown in Fig.9, the secondary inverter capacitor voltage is compared with it's nominal voltage and fed to a $PI-$controller. The PI controller modifies the motor phase voltage A^*_{ref} to reduce the power delivered to motor load momentarily. The primary inverter PWM is not disturbed in the proposed capacitor balancing scheme.

The power circuit topology also has FC stage in primary inverter and H-bridge stage capacitors in secondary inverter, which need capacitor balancing schemes. The FC stage capacitors are balanced using the pole voltage redundancies as explained in [17], [18]. The H-bridge stage capacitors are balanced using a switching cycle capacitor balancing scheme, first proposed in [16]. The work in [16] has presents a balancing scheme that takes advantage of space vector redundancies in the secondary inverter topology.

V. Implementation and Results

A 2-kW, 415-V, 4-pole Open End Induction Motor (OEIM) is used to validate the proposed drive scheme in Field Oriented Control (FOC) operation. The general polygonal PWM switching algorithm is implemented in the TMS320F28334 DSP platform for ease of debugging. The TMS320F28334 DSP platform offers advanced features such as Floating Point Unit (FPU) hardware capabilities which facilitate the implementation of the proposed scheme. The switching state for the primary and secondary inverter vectors is found out in the DSP and communicated to the FPGA (Xilinx Spartan-XC3S200).

0885-8993 (c) 2021 IEEE. Personal use is permitted, but republication/redistribution requires IEEE permission. See http://www.ieee.org/publications_standards/publications/rights/index.html for more information.
Authorized licensed use limited to: DELHI TECHNICAL UNIV. Downloaded on February 24,2022 at 07:02:49 UTC from IEEE Xplore. Restrictions apply.

This article has been accepted for publication in a future issue of this journal, but has not been fully edited. Content may change prior to final publication. Citation information: DOI 10.1109/TPEL.2022.3152497, IEEE Transactions on Power Electronics

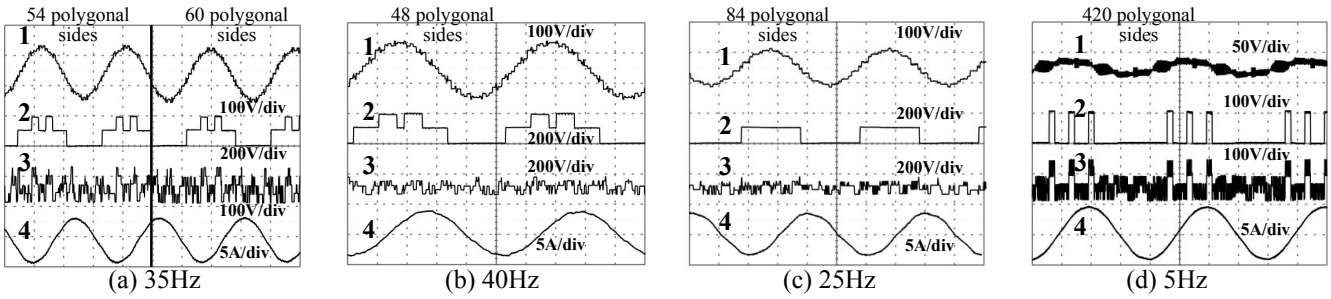


Fig. 10. Experimental steady-state results. Traces: (1) Motor phase voltage, (2) Primary inverter pole voltage, (3) Secondary inverter pole voltage, (4) Motor phase current.

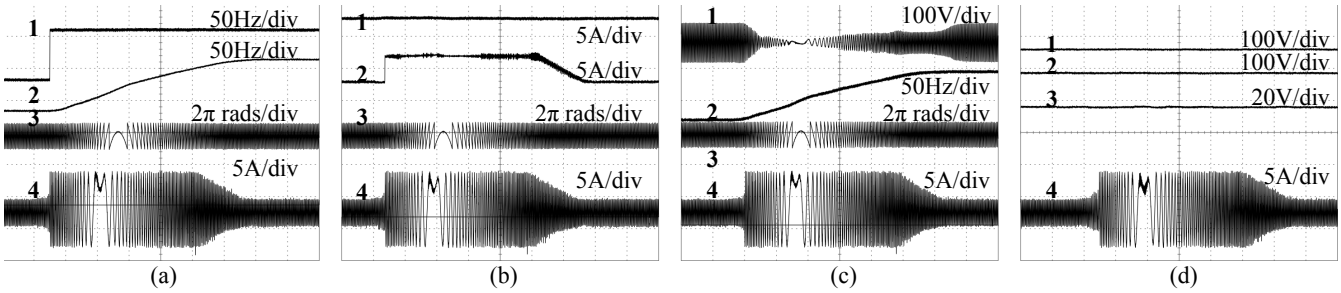


Fig. 11. Experimental results for speed reversal from -30Hz to 30Hz under Field Oriented Control: **(a)** Traces: (1) Motor speed reference, (2) Motor speed, (3) Rotor flux angle ρ, (4) Motor phase current; **(b)** Traces: (1) d-axis component of phase current, (2) q-axis component of phase current, (3) Rotor flux angle ρ, (4) Motor phase current; **(c)** Traces: (1) Motor phase voltage, (2) Motor speed, (3) Rotor flux angle ρ, (4) Motor phase current; **(d)** Traces: (1) FC stage capacitor voltage, (2) secondary supply capacitor voltage, (3) CHB stage capacitor voltage, (4) Motor phase current.

The timings corresponding to the vectors are stored in the compare registers of the ePWM peripheral in DSP. The PWM output pins in DSP are connected to the FPGA for PWM modulation. The FPGA generates the necessary gating signals for gate drivers of the inverters.

The experiment is performed with Vdc = 200 V. The capacitor voltage balancing schemes are implemented in DSP. The capacitor voltages of FC, secondary 2-level, and H-bridge stages are maintained at 100V, 78V ($= 0.39V_{dc}$), and 26V ($= 0.13V_{dc}$), respectively. The capacitors used for the FC, 2-level stage and H-bridge stage are 4400uF each, so as to keep the voltage ripples within a tolerance band. SKM75GB12T4 half-bridge modules are used to realize inverter switches.

A. Steady-State Results

The experimental results for steady state are shown in Fig.8 and Fig.10. The waveforms are presented for: (1) Motor phase voltage, (2) Primary inverter pole-voltage, (3) Secondary inverter pole voltage, and (4) Motor phase current. In Fig.8(a), the steady state results at base speed (50Hz) of operation of the induction motor are presented. At the base speed of operation, the primary inverter is operated in 6-step mode of operation, resulting in maximum phase voltage. Using the general polygonal PWM switching scheme proposed in this work, the motor is operated in 30-stepped mode of operation for 30-sided polygonal PWM switching. Thereafter, by modifying the PWM of secondary inverter alone, denser polygonal switching (for 36-sided, 42-sided and 48-sided) is generated. As denser polygonal switching is generated, the harmonic performance of the inverter improves, as shown in the FFT plots in Fig.8(b).

To generate a denser polygon, the secondary inverter switching per cycle is increased. To keep the secondary inverter switching frequency nearly constant, the switching per cycle is increased at lower frequency of operation. At 50Hz, a 42-sided polygonal PWM switching, results in 2.1KHz switching frequency for secondary inverter. Similarly, at 35Hz, a 60-sided polygonal PWM switching, results in 2.1KHz switching frequency for secondary inverter. In Fig.10 the steady state results for 35Hz operation are presented, as the phase voltage goes from 54-stepped operation to 60-stepped operation. The results for steady state operation at 40Hz, 25Hz, and 5Hz operation are also shown in Fig.10.

B. Transient Results

The dynamic performance of the proposed drive scheme under Field Oriented Control (FOC) [20] is verified for speed reversal from -30Hz to 30Hz. The experimental results are presented in Fig.11. In Fig.11(a), the speed reference, the motor speed, rotor flux angle ρ, and motor phase current are presented. The motor phase current increases to provide the necessary torque for fast dynamic response. Fig.11(b) shows the $d-q$ axis components of the motor phase current. The torque producing component increases in response to the change in speed reference. The phase voltage during speed reversal is presented in Fig.11(c), and the capacitor voltages for FC, 2-level and H-bridge stages are shown in Fig.11(d). The capacitors are balanced close to their nominal voltages during the transient operation.

0885-8993 (c) 2021 IEEE. Personal use is permitted, but republication/redistribution requires IEEE permission. See http://www.ieee.org/publications_standards/publications/rights/index.html for more information.
Authorized licensed use limited to: DELHI TECHNICAL UNIV. Downloaded on February 24,2022 at 07:02:49 UTC from IEEE Xplore. Restrictions apply.

This article has been accepted for publication in a future issue of this journal, but has not been fully edited. Content may change prior to final publication. Citation information: DOI 10.1109/TPEL.2022.3152497, IEEE Transactions on Power Electronics

VI. Conclusion

The polygonal space vector structure based PWM modulation techniques reported in literature offer a wide range of advantages over conventional MLI topologies. The works proposed in literature, have introduced various power circuit topologies, specific to each polygonal space vector structure generation. In this work, the general structure of power circuit topology is identified and the general polygonal space vector structure modulation scheme is proposed. The open-end induction motor is fed with a main power delivery primary inverter and a secondary inverter acting as a switched capacitive filter. Using the same secondary switched capacitive filter, any conventional multilevel inverter can be used as main power delivery primary inverter. The main power delivery inverter is visualized as a combination of sub-hexagons. The primary inverter can be switched along the vertices of sub-hexagons operated in pseudo 6-step mode of operation with low switching per cycle for the main power delivery inverter. The lower order harmonics generated by the primary inverter are suppressed by a secondary inverter, acting as a switched capacitive filter. The order of harmonic suppression depends on the sides of polygon one generates. The proposed scheme is verified for a 3-level primary inverter and 6-level secondary inverter topology. In the power circuit topology used here, polygonal space vector structure from 30-sides to 48-sides, are generated at the base speed of operation and presented in hardware results. As the fundamental frequency of operation is reduced, polygonal space vector structures with more number of sides can be generated to maintain constant switching frequency in the secondary inverter. The general algorithm for polygonal space vector modulation scheme is verified for the proposed power circuit with detailed experimental results.

References

[1] S. Kouro, M. Malinowski, K. Gopakumar, J. Pou, L. G. Franquelo, B. Wu, J. Rodriguez, M. A. Pérez, and J. I. Leon, "Recent advances and industrial applications of multilevel converters," *IEEE Transactions on Industrial Electronics*, vol. 57, no. 8, pp. 2553–2580, 2010.

[2] A. K. Rathore, J. Holtz, and T. Boller, "Synchronous optimal pulsewidth modulation for low-switching-frequency control of medium-voltage multilevel inverters," *IEEE Transactions on Industrial Electronics*, vol. 57, no. 7, pp. 2374–2381, 2010.

[3] V. S. S. P. K. Hari and G. Narayanan, "Space-vector-based hybrid pwm technique to reduce peak-to-peak torque ripple in induction motor drives," *IEEE Transactions on Industry Applications*, vol. 52, no. 2, pp. 1489–1499, 2016.

[4] A. Edpuganti and A. K. Rathore, "A survey of low switching frequency modulation techniques for medium-voltage multilevel converters," *IEEE Transactions on Industry Applications*, vol. 51, no. 5, pp. 4212–4228, 2015.

[5] A. A. Khan, U. A. Khan, H. F. Ahmed, H. Cha, and S. Ahmed, "Improved npc inverters without short-circuit and dead-time issues," *IEEE Transactions on Power Electronics*, vol. 37, no. 2, pp. 2180–2190, 2022.

[6] A. Edpuganti and A. K. Rathore, "Optimal low switching frequency pulsewidth modulation of nine-level cascade inverter," *IEEE Transactions on Power Electronics*, vol. 30, no. 1, pp. 482–495, 2015.

[7] J. Azurza Anderson, G. Zulauf, P. Papamanolis, S. Hobi, S. Miric, and J. W.Kolar, "Three levels are not enough: Scaling laws for multilevel converters in ac/dc applications," *IEEE Transactions on Power Electronics*, vol. 36, no. 4, pp. 3967–3986, 2021.

[8] P. Bhatnagar, A. K. Singh, K. K. Gupta, and Y. P. Siwakoti, "A switched-capacitors-based 13-level inverter," *IEEE Transactions on Power Electronics*, vol. 37, no. 1, pp. 644–658, 2022.

[9] H. Azeem, S. Yellasiri, V. Jammala, B. S. Naik, and A. K. Panda, "A fuzzy logic based switching methodology for a cascaded h-bridge multilevel inverter," *IEEE Transactions on Power Electronics*, vol. 34, no. 10, pp. 9360–9364, 2019.

[10] Z. Ni, A. Abuelnaga, and M. Narimani, "A novel high-performance predictive control formulation for multilevel inverters," *IEEE Transactions on Power Electronics*, vol. 35, no. 11, pp. 11 533–11 543, 2020.

[11] V. Anand and V. Singh, "A 13-level switched-capacitor multilevel inverter with single dc source," *IEEE Journal of Emerging and Selected Topics in Power Electronics*, pp. 1–1, 2021.

[12] R. R, M. Ghosh Majumder, R. Dewani, K. Gopakumar, U. Loganathan, W. Jarzyna, and L. G. Franquelo, "A very high resolution 30-sided space vector generation from a single dc-link for induction motor drives," *IEEE Transactions on Industrial Electronics*, pp. 1–1, 2021.

[13] M. Boby, S. Pramanick, R. S. Kaarthik, A. Rahul S., K. Gopakumar, and L. Umanand, "Fifth- and seventh-order harmonic elimination with multilevel dodecagonal voltage space vector structure for im drive using a single dc source for the full speed range," *IEEE Transactions on Power Electronics*, vol. 32, no. 1, pp. 60–68, 2017.

[14] K. Mohapatra, K. Gopakumar, V. Somasekhar, and L. Umanand, "A harmonic elimination and suppression scheme for an open-end winding induction motor drive," *IEEE Transactions on Industrial Electronics*, vol. 50, no. 6, pp. 1187–1198, 2003.

[15] R. Dewani, M. G. Majumder, R. R., K. Gopakumar, L. Umanand, D. Zieliski, and W. Jarzyna, "Generation of 42-sided polygonal voltage space vector structure for suppression of lower order harmonics in im drive applications," in *2020 IEEE 29th International Symposium on Industrial Electronics (ISIE)*, pp. 313–318, 2020.

[16] R. Dewani, R. R, K. Gopakumar, U. Loganathan, D. Zielinski, and L. G.Franquelo, "Suppression of lower order harmonics for the full modulation range for a two-level inverter-fed im drive with a switched-capacitive filter technique forming a 42-sided voltage space vector structure," *IEEE Transactions on Industrial Electronics*, vol. 68, no. 8, pp. 6701–6709, 2021.

[17] R. Dewani, M. G. Majumder, R. R., K. Gopakumar, L. Umanand, D. Zieliski, and W. Jarzyna, "Generation of 42-sided polygonal voltage space vector structure for suppression of lower order harmonics in im drive applications," pp.313–318, 2020.

[18] M. Escalante, J.-C. Vannier, and A. Arzande, "Flying capacitor multilevel inverters and dtc motor drive applications," *IEEE Transactions on Industrial Electronics*, vol. 49, no. 4, pp. 809–815, 2002.

[19] R. Dewani, K. Gopakumar, L. Umanand, and S. Bhattacharya, "Suppression of lower order harmonics by switched-capacitive filtering using polygonal space vector structures and capacitor sizing for induction motor drive applications," in *IECON 2021 - 47th Annual Conference of the IEEE Industrial Electronics Society*, pp. 1–6, 2021.

[20] K. Upamanyu, C. Ameta, and G. Narayanan, "Simplified input voltage sensorless vector control for pwm rectifiers," *IEEE Transactions on Industry Applications*, vol. 56, DOI10.1109/TIA.2020.2992955, no. 4, pp. 4051–4060, 2020.



Rahul Dewani (Student Member, IEEE) received the B.Tech. degree in electronics engineering from Delhi Technological University, New Delhi, India, in 2014, and the M.Tech. degree (sponsored by Texas Instruments) in analog VLSI Design from the VLSI Design Tools and Technology program, Indian Institute of Technology, New Delhi, in 2016. He is currently working toward the Ph.D. degree in Power Electronics with the Department of Electronic Systems Engineering, Indian Institute of Science, Bengaluru, India.

He was with the buck converter design team, Texas Instruments, Bangalore, India, in 2016, and RF IC design group, Aura Semiconductor, Bangalore, from 2016 to 2018. His research interests include induction motor drive applications, DC-DC converters, and IC design solutions for power electronics applications.

0885-8993 (c) 2021 IEEE. Personal use is permitted, but republication/redistribution requires IEEE permission. See http://www.ieee.org/publications_standards/publications/rights/index.html for more information.
Authorized licensed use limited to: DELHI TECHNICAL UNIV. Downloaded on February 24,2022 at 07:02:49 UTC from IEEE Xplore. Restrictions apply.

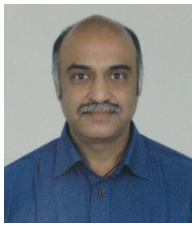
This article has been accepted for publication in a future issue of this journal, but has not been fully edited. Content may change prior to final publication. Citation information: DOI 10.1109/TPEL.2022.3152497, IEEE Transactions on Power Electronics



K. Gopakumar (Fellow, IEEE) received the B.E., M.Sc. (Engg.), and Ph.D. degrees from the Indian Institute of Science, Bangalore, India, in 1980, 1984, and 1994, respectively, all in electrical engineering.

He was with the Indian Space Research Organization, Bangalore, from 1984 to 1987. He is currently a Professor with the Department of Electronic Systems Engineering, Indian Institute of Science. His research interests include pulsewidth modulation converters and high-power drives.

Dr. Gopakumar is a Fellow of Institution of Electrical and Telecommunication Engineers, India, and the Indian National Academy of Engineers. He is currently a Co-Editor-in-Chief of the IEEE TRANSACTION ON INDUSTRIAL ELECTRONICS and also a Distinguished Lecturer of the IEEE Industrial Electronics Society. He is also the recipient of the Eugene Mittelmann Outstanding Research Achievement Award in 2019.



Umanand Loganathan received the bachelor's degree in electronics and communication from Bangalore University, Bangalore, India, in 1987, and the M.Tech. degree in electronics design and the doctoral degree in control of high performance induction motor drives from the Indian Institute of Science, Bangalore, India, in 1989 and 1996, respectively.

He is an Associate Professor with the Department of Electronics Systems Engineering, Indian Institute of Science. His major research interests include photovoltaic system design, bond graph modeling of power electronic systems, high-performance control of induction motors, designing for reliability, and hybrid electric vehicles.



Subhashish Bhattacharya (Fellow, IEEE) received the B.E. degree from the Indian Institute of Technology Roorkee, Roorkee, India, the M.E. degree from the Indian Institute of Science, Bengaluru, India, in 1988 and the Ph.D. degree from the University of Wisconsin, Madison, Madison, WI, USA, in 2003, all in electrical engineering.

He was with the FACTS and Power Quality Division, Westinghouse/Siemens Power T&D, during 1998-2005. In August 2005, he joined the Department of Electrical and Computer Engineering, NC State University, Raleigh, NC, USA, where he is currently the Duke Energy Distinguished Professor in electrical and computer engineering, and also a Founding Faculty Member of NSF FREEDM Systems Center and DOE Power America Institute. A part of his Ph.D. research on active power filters was commercialized by York Corporation for air-conditioner chillers. His research interests include solid-state transformers, MV power converters, FACTS, utility applications, high-frequency magnetics, and power-conversion applications of SiC devices.

0885-8993 (c) 2021 IEEE. Personal use is permitted, but republication/redistribution requires IEEE permission. See http://www.ieee.org/publications_standards/publications/rights/index.html for more information.
Authorized licensed use limited to: DELHI TECHNICAL UNIV. Downloaded on February 24,2022 at 07:02:49 UTC from IEEE Xplore. Restrictions apply.

arXiv:2202.02560v1 [math.CV] 5 Feb 2022

A GENERALIZED BOHR-ROGOSINSKI PHENOMENON

KAMALJEET GANGANIA AND S. SIVAPRASAD KUMAR

Abstract. In this paper, we generalize the Bohr-Rogosinski sum for the Ma-Minda classes of starlike and convex functions. Also the phenomenon is studied for the classes of starlike functions with respect to symmetric points and conjugate points along with their convex cases. Further, the connection between the derived results and the known ones are established with the suitable examples.

2010 AMS Subject Classification. Primary 30C45, 30C50, Secondary 30C80.
Keywords and Phrases. Subordination, Radius problem, Bohr Radius, Bohr-Rogosinski radius.

1. Introduction

Let $\mathcal{A}$ denote the class of analytic functions of the form $f(z) = z + \sum_{k=2}^{\infty} a_k z^k$ in the open unit disk $\mathbb{D} := \{z : |z| < 1\}$. We denote by $\mathcal{S}$, the subclass of $\mathcal{A}$ of univalent functions. Using subordination [18], Ma and Minda [17] (also see [13]) introduced the unified class of univalent starlike and convex functions defined as follows:

$$\mathcal{S}^*(\psi) := \left\{ f \in \mathcal{A} : \frac{zf'(z)}{f(z)} \prec \psi(z) \right\}$$

and

$$\mathcal{C}(\psi) := \left\{ f \in \mathcal{A} : 1 + \frac{zf''(z)}{f'(z)} \prec \psi(z) \right\},$$

where ψ is univalent, analytic and sarlike with respect to 1 with $\Re\psi(z) > 0$, $\psi'(0) > 0$, $\psi(0) = 1$ and $\psi(\mathbb{D})$ is symmetric about real axis. Note that $\psi \in \mathcal{P}$, the class of Carathéodory functions. Also when $\psi(z) = (1+z)/(1-z)$, $\mathcal{S}^*(\psi)$ and $\mathcal{C}(\psi)$ reduce to the standard classes $\mathcal{S}^*$ and $\mathcal{C}$ of univalent starlike and convex functions respectively.

In GFT, radius problems have a long and glorious history that continues to this day, see the recent articles [9, 10, 12, 13, 15]. In 1914, Harald Bohr [8] proved a significant radius problem for the absolute power series:

K. Gangania thanks to University Grant Commission, New-Delhi, India for providing Research Fellowship under UGC-Ref. No.:1051/(CSIR-UGC NET JUNE 2017).

Theorem 1.1 (Bohr's Theorem, [8]). *Let $g(z) = \sum_{k=0}^{\infty} a_k z^k$ be an analytic function in $\mathbb{D}$ and $|g(z)| < 1$ for all $z \in \mathbb{D}$, then*

$$\sum_{k=0}^{\infty} |a_k||z|^k \leq 1, \quad for \quad |z| \leq \frac{1}{3}.$$

In analogy with Bohr's Theorem, there is also the notion of Rogosinski radius, however a little is known about Rogosinski radius (also see [16, 25, 26]) as compared to Bohr radius, which is defined as follows:

Theorem 1.2 (Rogosinski Theorem). *If $g(z) = \sum_{k=0}^{\infty} b_k z^k$ with $|g(z)| < 1$, then for every $N \geq 1$, we have*

$$\left|\sum_{k=0}^{N-1} b_k z^k\right| \leq 1, \quad for \quad |z| \leq \frac{1}{2}.$$

The radius $1/2$ is called the Rogosinski radius.

Recently, Kumar and Sahoo [29] obtained the generalized classical Bohr's Theorem for functions satisfying $\Re(f)(z) \leq 1$. Also see, Kayumov et al.[28].

Theorem 1.3. [29, Theorem 2.2] *Let $\{\nu_k(r)\}_{k=0}^{\infty}$ be a sequence of non-negative continuous functions in $[0, 1)$ such that the series*

$$\nu_0(r) + \sum_{k=1}^{\infty} \nu_k(r)$$

converges locally uniformly with respect to $r \in [0, 1)$. Let $f(z) = \sum_{n=0}^{\infty} a_n z^n$ with $\Re f(z) \leq 1$ and $p \in (0, 1]$. If

$$\nu_0(r) > \frac{2(1 + r^m)}{p(1 - r^m)} \sum_{k=1}^{\infty} \nu_k(r).$$

Then the following sharp inequality holds:

$$|f(z^m)|\nu_0(r) + \sum_{k=1}^{\infty} |a_k|\nu_k(r) \leq \nu_0(r) \quad for\ all \quad |z| = r \leq R_1,$$

where R_1 is the minimal postive root of the equation:

$$\nu_0(r) = \frac{2(1 + r^m)}{p(1 - r^m)} \sum_{k=1}^{\infty} \nu_k(r).$$

In case when

$$\nu_0(r) < \frac{2(1 + r^m)}{p(1 - r^m)} \sum_{k=1}^{\infty} \nu_k(r)$$

in some interval $(R_1, R_1 + \epsilon)$, then the number R_1 can not be improved.

If we choose $\nu_k(r) = r^k$ in Theorem 1.3, we get Theorem 1.1. At this juncture, it is natural to pose the following problem:

Problem 1.4. Can we establish the analogue of Theorem1.3 for the Ma-Minda classes $\mathcal{S}^*(\psi)$ and $\mathcal{C}(\psi)$?

In context of the above problem and Muhanna [19], we now describe the notion of generalized Bohr-Rogosinski phenomenon here below, in terms of subordination, following the recent development as seen in [28, 29, 30].

Definition 1.5. Let $f(z)=\sum_{k=0}^{\infty}a_kz^k$ and $g(z)=\sum_{k=0}^{\infty}b_kz^k$ are analytic in $\mathbb{D}$. Let $d(f(0),\partial\Omega)$ denotes the Euclidean distance between $f(0)$ and the boundary of $\Omega=f(\mathbb{D})$. For a fixed f, consider a class of analytic functions

$$S(f):=\{g:g\prec f\}$$

or equivalently,

$$S(\Omega):=\{g:g(z)\in\Omega\}.$$

Then we say $S(f)$ satisfies the *Generalized Bohr-Rogosinski phenomenon*, if there exists a constant $r_0\in(0,1]$ such that

$$\mathcal{P}(r,g,f)+\sum_{k=1}^{\infty}|b_k|\phi_k(r)\leq d(f(0),\partial\Omega),$$

holds for all $|z|=r\leq r_0$, where

(1) $\mathcal{P}(r,g,f)$ represent some function of r or certain proper combination of moduli of g, f and their derivatives.
(2) $\{\phi_k(r)\}$ be a sequence of non-negative continuous functions in $[0,1)$ such that the series of the form

$$p_0\phi_0(r)+\sum_{k=1}^{\infty}p_k\phi_k(r)$$

converges locally uniformly with respect to $r\in[0,1)$, where p_k depends on the function f and provide bounds for b_k.

For $\mathcal{P}(r,g,f)=|g(z)|$, $\phi_k(r)=r^k$ $(k\geq N)$ and 0 otherwise in the Definition 1.5 gives the quantity considered by Kayumov et al. [11], which is known as the Bohr-Rogosinski sum, given by

$$|g(z)|+\sum_{k=N}^{\infty}|b_k||z|^k,\quad |z|=r.$$

The link between the Bohr-Rogosinski and Bohr phenomenon can be noticed, if we replace $|g(z)|$ by $g(0)$ with $N=1$. We also refer the readers to see [1, 4]. Now we see that the family $S(f)$ has Bohr-Rogosinski phenomenon provided there exists $r_N^f\in(0,1]$ such that the inequality:

$$|g(z)|+\sum_{k=N}^{\infty}|b_k||z|^k\leq|f(0)|+d(f(0),\partial\Omega)$$

holds for $|z|=r\leq r_N^f$. The largest such r_N^f is called the Bohr-Rogosinski radius.

In case when the function f is normalized, then Kumar and Gangania [31] considered the class

Definition 1.6. Let $f \in \mathcal{S}^*(\psi)$ or $\mathcal{C}(\psi)$ be fixed. Then the class of subordinants functions g is defined as:

$$S_f(\psi) := \left\{ g(z) = \sum_{k=1}^{\infty} b_k z^k : g \prec f \right\}.$$

and studied the Bohr-Rogosinski phenomenon for the class of analytic subordinants $S_f(\psi)$:

The class $S_f(\psi)$ has a Bohr-Rogosinski phenomenon, if there exists an $0 < r_0 \leq 1$ such that

$$|g(z^m)| + \sum_{k=N}^{\infty} |b_k||z|^k \leq d(f(0), \partial\Omega)$$

for $|z| = r \leq r_0$, where $m, N \in \mathbb{N}$, $\Omega = f(\mathbb{D})$ and $d(f(0), \partial\Omega)$ denotes the Euclidean distance between $f(0)$ and the boundary of Ω.

Theorem 1.7. [31, Theorem 2.3, Page no. 7] *Let $f_0(z)$ be given by the equation* (3.9) *and $f(z) = z + \sum_{n=2}^{\infty} a_n z^n \in \mathcal{S}^*(\psi)$. Assume $f_0(z) = z + \sum_{n=2}^{\infty} t_n z^n$ and $\hat{f}_0(r) = r + \sum_{n=2}^{\infty} |t_n| r^n$. If $g \in S_f(\psi)$. Then*

$$|g(z^m)| + \sum_{k=N}^{\infty} |b_k||z|^k \leq d(0, \partial\Omega)$$

holds for $|z| = r_b \leq \min\{\frac{1}{3}, r_0\}$, where $m, N \in \mathbb{N}$, $\Omega = f(\mathbb{D})$ and r_0 is the unique positive root of the equation:

$$\hat{f}_0(r^m) + \hat{f}_0(r) - p_{\hat{f}_0}(r) = -f_0(-1),$$

where

$$p_{\hat{f}_0}(r) = \begin{cases} 0, & N = 1; \\ r, & N = 2; \\ r + \sum_{n=2}^{N-1} |t_n| r^n, & N \geq 3. \end{cases}$$

The result is sharp when $r_b = r_0$ and $t_n > 0$.

For the class $\mathcal{C}(\psi)$, see [31, Theorem 2.13, page no. 12]. In context of the above, also see [11, 1, 4, 6].

The Bohr Operator

$$M_r(f) = \sum_{n=0}^{\infty} |a_n||z^n| = \sum_{n=0}^{\infty} |a_n| r^n$$

for the analytic functions $f(z) = \sum_{n=0}^{\infty} a_n z^n$ was used by Paulsen and Singh [23] to provide a simple proof of the Bohr's Theorem 1.1 and extended it to the Banach algebras (for the basic important discussion, see [22, 23]). Later, Muhanna et al. [22] used this operator to obtain some new Bohr type of inequalities for the k-th section $\sum_{n=0}^{k} a_n z^n$ and also obtain simple proofs of the known results.

Gangania and Kumar [31] considered the basic operator for f, given by:

$$M_r^N(f) = \sum_{n=N}^{\infty} |a_n||z^n| = \sum_{n=N}^{\infty} |a_n| r^n,$$

and thus the following observations hold for $|z| = r$ for each $z \in \mathbb{D}$

(*i*) $M_r^N(f) \geq 0$, and $M_r^N(f) = 0$ if and only if $f \equiv 0$
(*ii*) $M_r^N(f+g) \leq M_r^N(f) + M_r^N(g)$
(*iii*) $M_r^N(\alpha f) = |\alpha| M_r^N(f)$ for $\alpha \in \mathbb{C}$
(*iv*) $M_r^N(f.g) \leq M_r^N(f).M_r^N(g)$
(*v*) $M_r^N(1) = 1$.

For the above properties in terms of the sequence $\{\nu_n(r)\}_{n=0}^{\infty}$, see [24, Lemma 1]. Using this operator, a simple proof of [6, Lemma 1] was achieved by Gangania and Kumar [31] to settle the Bohr-Rogosinski Phenomenon for the classes $\mathcal{S}^*(\psi)$ and $\mathcal{C}(\psi)$, which in terms of interim k-th section $f_k(z) := \sum_{n=N}^{k} a_n z^n$ is as follows:

Lemma 1.1. [31] *let $f(z) = \sum_{n=0}^{\infty} a_n z^n$ and $g(z) = \sum_{k=0}^{\infty} b_k z^k$ be analytic in $\mathbb{D}$ and $g \prec f$, then*

$$M_r^N(g_k) \leq M_r^N(f_k) \tag{1.1}$$

for all $|z| = r \leq 1/3$ and $k, N \in \mathbb{N}$.

when $N = 1$ and $k \to \infty$, the lemma was obtained by Bhowmik and Das [6]. Various interesting applications of this lemma can be seen in [31, 6, 37, 9, 13].

While we establish the Bohr-type inequalities for the general class $\mathcal{S}^*(\psi)$ or $\mathcal{C}(\psi)$, the main difficulty that we come across is the unavailability of the sharp coefficients bounds. Here, we require use of the Lemma 1.1 or its proper modifications. Interestingly, the Lemma 1.1 also implies that if $f \prec g$, then within the disk $|z| \leq 1/3$, we have $|a_n| \leq |b_n|$ for all $n \in \mathbb{N} \cup \{0\}$, where b_n are the coefficients of the function g in Lemma 1.1. Further, this readily gives the following:

Lemma 1.2. *Let $f(z) = \sum_{n=0}^{\infty} a_n z^n$ and $g(z) = \sum_{n=0}^{\infty} b_n z^n$ be analytic in $\mathbb{D}$. Let $\{\nu_k(r)\}_{k=0}^{\infty}$ be a sequence of non-negative functions, continuous in $[0,1)$ such that the series*

$$\sum_{n=0}^{\infty} |b_n| \nu_k(r)$$

converges locally uniformly with respect to $r \in [0,1)$. If $g \prec f$, then

$$\sum_{n=0}^{\infty} |a_n| \nu_n(r) \leq \sum_{n=0}^{\infty} |b_n| \nu_n(r)$$

for all $|z| = r \leq \frac{1}{3}$.

For a different version of the Lemma 1.2 with the conditions $\nu_{m+n}(r) \leq \nu_m(r)\nu_n(r)$ and $\nu_0(r) = 1$, see [24, Theorem 3].

A function $f \in \mathcal{A}$ is in the class $\mathcal{K}$ of close-to-convex if $\Re(zf'(z)/g(z)) > 0$, where $g \in \mathcal{S}^*$. In 2004, Ravichandran studied the amalgamated treatment for the classes of starlike and convex functions with respect to the symmetric points for the growth and distortion theorems:

Definition 1.8. [34] A function $f \in \mathcal{A}$ is in the class $\mathcal{S}_s^*(\psi)$ and $\mathcal{C}_s(\psi)$ if it satisfy $zf'(z)/h(z) \prec \psi(z)$ and $(zf'(z))'/h'(z) \prec \psi(z)$ respectively, where $2h(z) = f(z) - f(-z)$.

Now if we take $h(z) = f(z) + \overline{f(\bar{z})}$ in Definition 1.8, we obtain the classes $\mathcal{S}_c^*(\psi)$ and $\mathcal{C}_c^*(\psi)$ of starlike and convex functions with respect to conjugate points, respectively. For the choice $h(z) = f(z) - \overline{f(-\bar{z})}$, we have the classes $\mathcal{S}_{sc}^*(\psi)$ and $\mathcal{C}_{sc}^*(\psi)$ of starlike and convex functions with respect to the symmetric conjugate points, respectively. See [34].

Motivated, by the class $\mathcal{S}_s^*((1+z)/(1-z))$ [32], Gao and Zhou [33] studied the class $\mathcal{K}_s$ of close-to-convex functions f, which is characterized as:

$$\Re\left(\frac{z^2 f'(z)}{g(z)g(-z)}\right) > 0,$$

where g is some starlike function of order $1/2$. In view of the Definition 1.8, the generalized class $\mathcal{K}_s(\psi)$ was studied by Cho et al. [36] and Wang et al. [35].

In this paper, we positively answer the Problem 1.4 in Section 2 for the class $\mathcal{S}^*(\psi)$. In Section 3, we study the Bohr-Rogosinski phenomenon for the classes $\mathcal{S}_s^*(\psi)$, $\mathcal{S}_c^*(\psi)$, $\mathcal{S}_{sc}^*(\psi)$ and corresponding convex classes. For convenience, we denote $\hat{f}(z) = \sum_{n=0}^{\infty} |a_n| z^n$, whenever $f(z) = \sum_{n=0}^{\infty} a_n z^n$.

2. Generalized Bohr's sum for Ma-Minda starlike functions

We here solve the Problem 1.4. But as we do not have sharp coefficient's bound for each a_n for the given class in general. Thus to solve it, we need the following:

Lemma 2.1. *The families $\mathcal{S}^*(\psi)$ and $\mathcal{C}(\psi)$ are normal and compact.*

Proof. From Montel's Theorem [27], we see that the class $\mathcal{S}^*(\psi)$ is a normal family. Now let us prove that $\mathcal{S}^*(\psi)$ is compact. Let $\{f_n\}_{n\in\mathbb{N}}$ be a sequence of functions from $\mathcal{S}^*(\psi)$. Suppose that $\{f_n\}$ be convergent. Then it is well-known that

$$\lim_{n\to\infty} f_n := f \in \mathcal{S}.$$

We show that $f \in \mathcal{S}^*(\psi)$. If possible, suppose that there exists a nonzero point $z_0 \in \mathbb{D}$ such that

$$g(z_0) \notin \psi(\mathbb{D}),$$

where $g(z) = zf'(z)/f(z)$. Note that the corresponding sequence $\{g_n\}$ converges to g, where $g_n(z) = zf_n'(z)/f_n(z)$. Now let

$$\epsilon = dist(g(z_0), \partial\psi(\mathbb{D})).$$

Then the open ball

$$B(g(z_0), \epsilon) \not\subset \psi(\mathbb{D}).$$

Since $g_n \to g$, in particular, $g_n(z_0) \to g(z_0)$. There exists $n(\epsilon) \in \mathbb{N}$ such that

$$g_n(z_0) \in B(g(z_0), \epsilon), \quad \forall n \geq n(\epsilon),$$

which implies

$$g_n(z_0) \notin \psi(\mathbb{D}), \quad \forall n \geq n(\epsilon).$$

But as $f_n \in \mathcal{S}^*(\psi)$,

$$g_n(z_0) = \frac{z_0 f_n'(z_0)}{f_n(z_0)} \in \psi(\mathbb{D}), \quad \forall n.$$

Hence, we must have $f \in \mathcal{S}^*(\psi)$, that means the family $\mathcal{S}^*(\psi)$ is compact. With the similar arguments, it is easy to see that the family $\mathcal{C}(\psi)$ is also compact. □

Remark 2.1. (*Existence of sharp coefficients Bounds)* Let us consider the real-valued functional $\mathcal{J}$ defined on $\mathcal{S}^*(\psi)$ as

$$\mathcal{J}(f) = \max\{|a_n|\} \quad \textit{for every} \quad f \in \mathcal{S}^*(\psi),$$

where n is fixed and $f(z) = z + \sum_{n=2}^{\infty} a_n z^n$. From Lemma 2.1, $\mathcal{S}^*(\psi)$ is normal and compact. Further, since $\mathcal{S}^*(\psi) \subseteq \mathcal{S}^*$, we have $|a_n| \leq n$, that means $\mathcal{J}$ is a bounded functional. Hence, following the discussion in the Goodman's Book [27, page no. 44-45], we conclude that

$$\mathcal{J}(f) = \max\{|a_n|\} \quad \textit{exists in the family} \quad \mathcal{S}^*(\psi).$$

Thus, let us say that

$$\max_{f \in \mathcal{S}^*(\psi)} \{|a_n|\} := M(n)$$

for each $n \in \mathbb{N}$. For instance, $M(n) = n$ for the class of univalent starlike functions. For the Janowski starlike functions, it is given by [5, Theorem 3].

We can now state our result in a general setting whose complement is Theorem 2.3:

Theorem 2.1. *Let $\{\phi_n(r)\}_{n=1}^{\infty}$ be a sequence of non-negative continuous functions in $(0,1)$ such that the series*

$$\phi_1(r) + \sum_{n=2}^{\infty} M(n)\phi_n(r)$$

converges locally uniformly with respect to each $r \in [0,1)$. If for $\beta \in [0,1]$

$$\beta f_0'(r^m) + (1-\beta) f_0(r^m) + \sum_{n=1}^{\infty} M(n)\phi_n(r) < -f_0(-1). \tag{2.1}$$

and the function $f(z) = z + \sum_{n=2}^{\infty} a_n z^n \in \mathcal{S}^*(\psi)$. Then the following inequality

$$\beta |f'(z^m)| + (1-\beta)|f(z^m)| + \sum_{n=1}^{\infty} |a_n|\phi_n(r) \leq d(0, \partial\Omega)$$

holds for $|z| = r \leq r_0$, *where* $m \in \mathbb{N}$, $\Omega = f(\mathbb{D})$ *and* r_0 *is the smallest positive root of the equation:*

$$\beta f_0'(r^m) + (1-\beta) f_0(r^m) + \sum_{n=1}^{\infty} M(n)\phi_n(r) = -f_0(-1), \tag{2.2}$$

where $M(1) = 1$ *and*

$$f_0(z) = z \exp \int_0^z \frac{\psi(t) - 1}{t} dt.$$

In case when f_0 *or it's rotation serves as an extremal for the coefficient's bounds* $M(n)$, *then the radius* r_0 *is sharp.*

Proof. From Lemma 2.1 and Remark 2.1, we see that: (a) $\mathcal{J}$ is a bounded real valued continuous functional, (b) $\mathcal{S}^*(\psi)$ is a normal family, and (c) $\mathcal{S}^*(\psi)$ is a compact family in $\mathbb{D}$. Thus, the sharp bounds for each a_n exists. In view of Remark 2.1, we have

$$|a_n| \leq M(n),$$

which yields that

$$\sum_{n=1}^{\infty} |a_n| \phi_n(r) \leq \sum_{n=1}^{\infty} M(n)\phi_n(r). \tag{2.3}$$

The Koebe-radius for the functions in $\mathcal{S}^*(\psi)$ satisfies

$$d(0, \partial f(\mathbb{D})) \geq -f_0(-1). \tag{2.4}$$

Now combining it with the growth and distortion theorems [17], and using the condition 2.1, the inequalities (2.3) and (2.4) gives

$$\begin{aligned} \beta|f'(z^m)| + (1-\beta)|f(z^m)| + \sum_{n=1}^{\infty} |a_n|\phi_n(r) & \\ \leq \beta f_0'(r^m) + (1-\beta) f_0(r^m) + \sum_{n=1}^{\infty} M(n)\phi_n(r) & \\ \leq d(0, \partial\Omega), & \end{aligned}$$

which holds in $|z| = r \leq r_0$, where r_0 is the minimal positive root of the equation (2.2). Existence of the root r_0 follows from the Intermediate value theorem for continuous function in $(0, 1)$. To see the sharpness case, let us consider the function

$$f_0(z) = z \exp \int_0^z \frac{\psi(t) - 1}{t} dt.$$

such that it's Taylor series coefficients $a_n(f_0)$ satisfies $|a_n(f_0)| = M(n)$. For this function we have

$$d(0, \partial f(\mathbb{D})) = -f_0(-1),$$

and the following equality holds for $|z| = r_0$:

$$\beta f_0'(r^m) + (1-\beta) f_0(r^m) + \sum_{n=1}^{\infty} M(n)\phi_n(r) = d(0, \partial f(\mathbb{D})),$$

and therefore, if f_0 is extremal for each coefficient's bound, then the radius r_0 can not be improved. □

Question 2.2. What if we do not have $M(n)$?

For such cases, the following result complements Theorem 2.1:

Theorem 2.3. *Let $\{\phi_n(r)\}_{n=1}^{\infty}$ be a non-negative sequence of continuous functions in $[0,1]$ such that*

$$\phi_1(r) + \sum_{n=2}^{\infty} \left| \frac{f_0^{(n)}(0)}{n!} \right| \phi_n(r)$$

converges locally uniformly with respect to each $r \in [0,1)$. If

$$\beta |f'(z^m)| + (1-\beta)|f(z^m)| + \phi_1(r) + \sum_{n=2}^{\infty} \left| \frac{f_0^{(n)}(0)}{n!} \right| \phi_n(r) < -f_0(-1)$$

and $f(z) = z + \sum_{n=2}^{\infty} a_n z^n \in \mathcal{S}^*(\psi)$. Then

$$\beta |f'(z^m)| + (1-\beta)|f(z^m)| + \sum_{n=1}^{\infty} |a_n| \phi_n(r) \leq d(0, \partial\Omega) \tag{2.5}$$

holds for $|z| = r \leq r_b = \{1/3, r_0\}$, where $m \in \mathbb{N}$, $\Omega = f(\mathbb{D})$ and r_0 is the smallest positive root of the equation:

$$\beta f_0'(r^m) + (1-\beta) f_0(r^m) + \sum_{n=2}^{\infty} \left| \frac{f_0^{(n)}(0)}{n!} \right| \phi_n(r) = -f_0(-1) - \phi_1(r),$$

where

$$f_0(z) = z \exp \int_0^z \frac{\psi(t) - 1}{t} dt.$$

Moreover, the inequality (2.5) also holds for the class $S_f(\psi)$ in $|z| = r \leq r_b$. When $r_b = r_0$, then the radius is best possible.

Proof. Since $f \in \mathcal{S}^*(\psi)$, it is known that

$$\frac{f(z)}{z} \prec \frac{f_0(z)}{z}.$$

Applying Lemma 1.1, we see that

$$\sum_{n=N}^{m} |a_n||z|^n \leq \sum_{k=N}^{m} \left| \frac{f_0^k(0)}{k!} \right| |z|^k \quad \text{for} \quad |z| = r \leq \frac{1}{3}.$$

Now choosing $N = m$, we conclude that

$$|a_n| \leq \left| \frac{f_0^n(0)}{n!} \right|$$

holds for each n with in the disk $|z| = r \leq 1/3$. Hence, it suffices to see

$$\begin{aligned}
&\beta|f'(z^m)| + (1-\beta)|f(z^m)| + \sum_{n=1}^{\infty} |a_n|\phi_n(r) \\
\leq\ & \beta|f_0'(z^m)| + (1-\beta)|f_0(z^m)| + \phi_1(r) + \sum_{n=2}^{\infty} \left|\frac{f_0^{(n)}(0)}{n!}\right| \phi_n(r) \\
\leq\ & -f_0(-1) \\
\leq\ & d(0, \partial\Omega),
\end{aligned}$$

holds in $|z| = r \leq \{r_0, 1/3\}$. If $r_0 \leq 1/3$, then equatity case can be seen for the function $f = f_0$, whenever Taylor coefficients of ψ are postive. □

Remark 2.2.
(1) By taking $\phi_n(r) = r^n$ in Theorem 2.3 give [14, Theorem 5.1], and [37, Theorem 3.1] for the choice $g = f$ with Taylor coefficients of ψ being postive.
(2) Taking $\phi_n = r^n$ for $n \geq N$ and 0 elsewhere in Theorem 2.3 yields [31, Theorem 5, Corollary 3].

Let us discuss the generalized Bohr-Rogosinski phenomenon for the celebrated Janowski class of univalent starlike functions. For simplicity, write $\mathcal{S}^*((1+Dz)/(1+Ez)) \equiv \mathcal{S}[D, E]$, where $-1 \leq E < D \leq 1$.

Corollary 2.4. *Let $\{\phi_n(r)\}_{n=1}^{\infty}$ be a sequence of non-negative continuous functions in $(0, 1)$ such that the series*

$$\phi_1(r) + \sum_{n=2}^{\infty} \prod_{k=0}^{n-2} \frac{|E - D + Ek|}{k+1} \phi_n(r)$$

converges locally uniformly with respect to each $r \in [0, 1)$. If for $\beta \in [0, 1]$

$$\beta f_0'(r^m) + (1-\beta) f_0(r^m) + \sum_{n=1}^{\infty} |a_n(f_0)|\phi_n(r) < -f_0(-1). \tag{2.6}$$

and the function $f(z) = z + \sum_{n=2}^{\infty} a_n z^n \in \mathcal{S}[D, E]$. Then the following sharp inequality

$$\beta|f'(z^m)| + (1-\beta)|f(z^m)| + \sum_{n=1}^{\infty} |a_n|\phi_n(r) \leq d(0, \partial\Omega) \tag{2.7}$$

holds for $|z| = r \leq r_0$, where $m \in \mathbb{N}$, $\Omega = f(\mathbb{D})$ and r_0 is the minimal positive root of the equations:
If $E \neq 0$

$$\begin{aligned}
&\beta(1+Dr^m)(1+Er^m)^{\frac{D-2E}{E}} + (1-\beta)r^m(1+Er^m)^{\frac{D-E}{E}} \\
&+ \sum_{n=2}^{\infty} \prod_{k=0}^{n-2} \frac{|E - D + Ek|}{k+1} \phi_n(r) = (1-E)^{\frac{D-E}{E}} - \phi_1(r),
\end{aligned}$$

and if $E = 0$

$$e^{Dr^m}(\beta + (1 - \beta(1 - D))r^m) + \sum_{n=2}^{\infty} \prod_{k=0}^{n-2} \frac{D}{k+1} \phi_n(r) = e^{-D} - \phi_1(r),$$

where

$$f_0(z) = \begin{cases} z(1 + Ez)^{\frac{D-E}{E}}, & E \neq 0; \\ ze^{Dz}, & E = 0. \end{cases} \tag{2.8}$$

The radius r_0 *can not be improved.*

Proof. Let $f(z) = z + \sum_{n=2}^{\infty} a_n z^n \in \mathcal{S}[D, E]$. Then for $n \geq 2$, [5, Theorem 3] states that:

$$|a_n| \leq \prod_{k=0}^{n-2} \frac{|E - D + Ek|}{k+1} = M(n),$$

where the function f_0 given by (2.8) gives equality. The result now follows by Theorem 2.1. □

Remark 2.3. Taking $m \to \infty$ and $\beta = 0$ in Corollary 2.4 yields: If

$$\sum_{n=1}^{\infty} |a_n(f_0)| \phi_n(r) < -f_0(-1).$$

Then the sharp inequality

$$\sum_{n=1}^{\infty} |a_n| \phi_n(r) \leq d(0, \partial\Omega)$$

holds for $|z| = r \leq r_0$, where $m \in \mathbb{N}$, $\Omega = f(\mathbb{D})$ and r_0 is the minimal positive root of the equations:
If $E \neq 0$

$$\sum_{n=2}^{\infty} \prod_{k=0}^{n-2} \frac{|E - D + Ek|}{k+1} \phi_n(r) = (1 - E)^{\frac{D-E}{E}} - \phi_1(r),$$

and if $E = 0$

$$\sum_{n=2}^{\infty} \prod_{k=0}^{n-2} \frac{D}{k+1} \phi_n(r) = e^{-D} - \phi_1(r),$$

where f_0 is given in (2.8).

In Corollary 2.4, putting $D = 1 - 2\alpha$ and $E = -1$, where $0 \leq \alpha < 1$, we get the result for the class of univalent starlike functions of order α, that is, $\mathcal{S}^*(\alpha)$:

Corollary 2.5. *Let* $\{\phi_n(r)\}_{n=1}^{\infty}$ *be a sequence of non-negative continuous functions in* $(0, 1)$ *such that the series*

$$\phi_1(r) + \sum_{n=2}^{\infty} \prod_{k=0}^{n-2} \frac{k + 2(1 - \alpha)}{k+1} \phi_n(r)$$

converges locally uniformly with respect to each $r \in [0,1)$. *If for* $\beta \in [0,1]$

$$\frac{\beta(1+(1-2\alpha)r^m)}{(1-r^m)^{2(1-\alpha)+1}} + \frac{(1-\beta)r^m}{(1-r^m)^{2(1-\alpha)}} + \sum_{n=2}^{\infty}\prod_{k=0}^{n-2}\frac{k+2(1-\alpha)}{k+1}\phi_n(r) < \frac{1}{4^{1-\alpha}} - \phi_1(r).$$

and $f(z) = z + \sum_{n=2}^{\infty} a_n z^n \in \mathcal{S}^*(\alpha)$. *Then the sharp inequality* (2.7) *holds for* $|z| = r \le r_0$, *where* $m \in \mathbb{N}$, $\Omega = f(\mathbb{D})$ *and* r_0 *is the minimal positive root of the equations:*

$$\frac{\beta(1+(1-2\alpha)r^m)}{(1-r^m)^{2(1-\alpha)+1}} + \frac{(1-\beta)r^m}{(1-r^m)^{2(1-\alpha)}} + \sum_{n=2}^{\infty}\prod_{k=0}^{n-2}\frac{k+2(1-\alpha)}{k+1}\phi_n(r) = \frac{1}{4^{1-\alpha}} - \phi_1(r).$$

The radius r_0 *is sharp.*

Putting $\alpha = 0$ in Corollary 2.5, we get the following:

Corollary 2.6. *Let the sequence* $\{\phi_n(r)\}_{n=1}^{\infty}$ *satisfy the hypothesis of Corollary 2.5 with* $\alpha = 0$. *If* $f(z) = z + \sum_{n=2}^{\infty} a_n z^n \in \mathcal{S}^*$. *Then the inequality* (2.7) *holds for* $|z| = r \le r_0$, *where* $m, N \in \mathbb{N}$, $\Omega = f(\mathbb{D})$ *and* r_0 *is the smallest positive root of the equations:*

$$\frac{\beta(1+r^m)}{(1-r^m)^3} + \frac{(1-\beta)r^m}{(1-r^m)^2} + \sum_{n=1}^{\infty} n\phi_n(r) = \frac{1}{4}.$$

The radius r_0 *is sharp.*

The following series of examples discuss the choices of sequence $\phi_n(r)$:

Example 2.7. *Let us consider* $\phi_n(r) = 0$ *for* $1 \le n \le N$, *and* $\phi_n(r) = r^n$ *for* $n \ge N$ *in Corollary 2.4. Then the following sharp inequality*

$$\beta|f'(z^m)| + (1-\beta)|f(z^m)| + \sum_{n=N}^{\infty}|a_n|r^n \le d(0,\partial\Omega)$$

holds for $|z| = r \le R_{m,\beta,N}$, *where* $m, N \in \mathbb{N}$, $\Omega = f(\mathbb{D})$ *and* $R_{m,\beta,N}$ *is the unique positive root of the equations:*
If $E \neq 0$

$$\beta(1+Dr^m)(1+Er^m)^{\frac{D-2E}{E}} + (1-\beta)r^m(1+Er^m)^{\frac{D-E}{E}} + \sum_{n=N}^{\infty}\prod_{k=0}^{N-2}\frac{|E-D+Ek|}{k+1}r^n = (1-E)^{\frac{D-E}{E}},$$

and if $E = 0$

$$e^{Dr^m}(\beta + (1-\beta(1-D))r^m) + \sum_{n=2}^{\infty}\prod_{k=0}^{n-2}\frac{D}{k+1}\phi_n(r) = e^{-D}.$$

Example 2.8. *Taking $\phi_{2n-1}(r) = 0$ and $\phi_{2n}(r) = r^{2n}$ in Corollary 2.5 yields*

$$\beta|f'(z^m)| + (1-\beta)|f(z^m)| + \sum_{n=1}^{\infty} |a_{2n}| r^{2n} \leq d(0, \partial\Omega)$$

which holds for $|z| = r \leq R_{m,\beta,\alpha}$, where $m \in \mathbb{N}$, $\beta[0,1]$, $\Omega = f(\mathbb{D})$ and $R_{m,\beta,\alpha}$ is the unique positive root of the equations:

$$\frac{\beta(1+(1-2\alpha)r^m)}{(1-r^m)^{2(1-\alpha)+1}} + \frac{(1-\beta)r^m}{(1-r^m)^{2(1-\alpha)}} + \sum_{n=1}^{\infty} \prod_{k=0}^{2(n-1)} \frac{k+2(1-\alpha)}{k+1} r^{2n} = \frac{1}{4^{1-\alpha}}.$$

The radius is sharp.

Example 2.9. *Letting $\phi_{2n}(r) = 0$ and $\phi_{2n-1}(r) = r^{2n-1}$ in Corollary 2.6 gives the following sharp inequality*

$$\beta|f'(z^m)| + (1-\beta)|f(z^m)| + \sum_{n=1}^{\infty} |a_{2n-1}| r^{2n-1} \leq d(0, \partial\Omega)$$

in $|z| = r \leq R_{m,\beta}$ where $m \in \mathbb{N}$, $\beta[0,1]$, $\Omega = f(\mathbb{D})$ and $R_{m,\beta}$ is the unique positive root of the equations:

$$\frac{\beta(1+r^m)}{(1-r^m)^{2+1}} + \frac{(1-\beta)r^m}{(1-r^m)^2} + \frac{r(1+r^2)}{(1-r^2)^2} = \frac{1}{4}.$$

The radius is sharp.

3. Bohr-Rogosinski sum for starlike and convex functions with respect to conjugate and symmetric points

Definition 3.1. Let us consider the subclass of close-to-convex univalent functions given by

$$\mathcal{K}_s(\psi) = \left\{ f \in \mathcal{A} : -\frac{z^2 f'(z)}{h(z)h(-z)} \prec \psi(z) \right\}$$

for some $h \in \mathcal{S}^*(1/2)$.

Theorem 3.2. *Let $f \in \mathcal{K}_s(\psi)$ and $\Omega = f(\mathbb{D})$. If $g \in S_f(\psi)$. Then*

$$|g(z^m)| + \sum_{k=N}^{\infty} |b_k||z|^k \leq d(0, \partial\Omega) \tag{3.1}$$

holds for $|z| = r_b \leq \min\{\frac{1}{3}, r_0\}$, where $m, N \in \mathbb{N}$ and r_0 is the minimal positive root of the equation:

$$\int_0^{r^m} \frac{\psi(t)}{1-t^2} + R^N(r) = \int_0^1 \frac{\psi(-t)}{1+t^2} dt, \tag{3.2}$$

where

$$R^N(r) = \int_0^r \frac{M_t^N(\psi) t^{2N}}{t^2(1-t^2)} dt \quad \text{and} \quad f_0(z) = \int_0^z \frac{\psi(t)}{1-t^2} dt.$$

Proof. Let $g(z) = \sum_{k=1}^{\infty} b_k z^k \prec f(z)$. Then by Lemma 1.1, for $r \leq 1/3$

$$\sum_{k=N}^{\infty} |b_k| r^k \leq \sum_{n=N}^{\infty} |a_n| r^n = \sum_{n=N}^{\infty} \frac{|\tilde{b}_n|}{n} r^n, \tag{3.3}$$

where $\tilde{b}_n$ are the power series coefficient of $\tilde{G}(z)$ defined below. From Definition 3.1, we have

$$zf'(z) = G(z)\psi(\omega(z)) =: \tilde{G}(z),$$

where

$$G(z) = \frac{-h(z)h(-z)}{z} =: z + \sum_{n=2}^{\infty} h_{2n-1} z^{2n-1},$$

which is an odd starlike function. Now a simple integration gives that

$$f(z) = \int_0^z \frac{G(t)\psi(\omega(t))}{t} dt.$$

For $f \in \mathcal{A}$, let us consider the operator

$$M_r^N(f) = \sum_{n=N}^{\infty} |a_n||z^n| = \sum_{n=N}^{\infty} |a_n| r^n.$$

Then

$$M_r^N(\tilde{G}) \leq M_r^N(G).M_r^N(\psi \circ \omega). \tag{3.4}$$

Since $\psi \circ \omega \prec \psi$, we get

$$M_r^N(\psi \circ \omega) \leq M_r^N(\psi), \quad \text{for} \quad r \leq 1/3. \tag{3.5}$$

It is known that odd starlike functions statisfies $|h_{2n-1}| \leq 1$. Thus

$$M_r^N(G) \leq \sum_{n=N}^{\infty} r^{2n-1} = \frac{1}{r}\left(\frac{r^{2N}}{1-r^2}\right). \tag{3.6}$$

Now combining the inequalities (3.3), (3.4), (3.5) and (3.6), the following sequence of inequalities holds for $r \leq 1/3$:

$$\begin{aligned} \sum_{k=N}^{\infty} |b_k| r^k &\leq \sum_{n=N}^{\infty} \frac{|\tilde{b}_n|}{n} r^n = \int_0^r \frac{M_t^N(\tilde{G})}{t} dt \\ &\leq \int_0^r \frac{M_t^N(G).M_t^N(\psi \circ \omega)}{t} dt \\ &\leq \int_0^r \frac{M_t^N(\psi) t^{2N}}{t^2(1-t^2)} dt := R^N(r). \end{aligned} \tag{3.7}$$

Since, also see growth theorem in [36, Theorem 2, page no. 4],

$$|g(z)| = |f(\omega(z))| \leq \max_{|z|=r} |f(|z| \leq r)| \leq \int_0^r \frac{\psi(t)}{1-t^2} dt = f_0(r),$$

it follows that

$$|g(z^m)| \leq f(r^m) \leq \hat{f}_0(r^m), \quad \text{where} \quad f_0(z) = \int_0^z \frac{\psi(t)}{1-t^2} dt. \tag{3.8}$$

Finally, note that

$$d(0,\Omega) \geq \int_0^1 \frac{\psi(-t)}{1+t^2}dt.$$

Hence, from (3.7) and (3.8), we get

$$|g(z^m)| + \sum_{k=N}^{\infty} |b_k||z|^k \leq d(0,\partial\Omega)$$

for $|z| = r \leq r_b = \{1/3, r_0\}$, where $r_0 \in (0,1)$ is the minimal root of the equation (3.2). Existence of the root follows by Intermediate value theorem in the interval $[0,1]$. □

Remark 3.1. Taking $m \to \infty$ and $N = 1$, then Theorem 3.2 reduces to [38, Theorem 2.2].

Corollary 3.3. *If $f \in \mathcal{K}_s(\psi)$ and $\Omega = f(\mathbb{D})$. Then*

$$|f(z^m)| + \sum_{n=N}^{\infty} |a_n||z|^n \leq d(0,\partial\Omega)$$

holds for $|z| = r_b \leq \min\{\frac{1}{3}, r_0\}$, where $m, N \in \mathbb{N}$ and r_0 is the minimal positive root of the equation:

$$\int_0^{r^m} \frac{\psi(t)}{1-t^2} + R^N(r) = \int_0^1 \frac{\psi(-t)}{1+t^2}dt,$$

where

$$R^N(r) = \int_0^r \frac{M_t^N(\psi)t^{2N}}{t^2(1-t^2)}dt \quad \text{and} \quad f_0(z) = \int_0^z \frac{\psi(t)}{1-t^2}.$$

Definition 3.4. The class of starlike functions with respect to conjugate points given by

$$\mathcal{S}_c^*(\psi) = \left\{ f \in \mathcal{A} : \frac{zf'(z)}{f(z) + \overline{f(\bar{z})}} \prec \psi(z) \right\}.$$

Lemma 3.1. ([17]) *Let $f \in \mathcal{S}^*(\psi)$ and $|z_0| = r < 1$. Then $f(z)/z \prec f_0(z)/z$ and*

$$-f_0(-r) \leq |f(z_0)| \leq f_0(r).$$

Equality holds for some $z_0 \neq 0$ if and only if f is a rotation of f_0, where

$$f_0(z) = z\exp\int_0^z \frac{\psi(t)-1}{t}dt. \tag{3.9}$$

Theorem 3.5. *Let h_ψ be given by* (3.9) *and $f(z) = z + \sum_{n=2}^{\infty} a_n z^n \in \mathcal{S}_c^*(\psi)$. If $g \in S_f(\psi)$. Then*

$$|g(z^m)| + \sum_{k=N}^{\infty} |b_k||z|^k \leq d(0,\partial\Omega) \tag{3.10}$$

holds for $|z| = r_b \leq \min\{\frac{1}{3}, r_0\}$, where $m, N \in \mathbb{N}$, $\Omega = f(\mathbb{D})$ and r_0 is the unique positive root of the equation:

$$h_\psi(r^m) + R^N(r) + h_\psi(-1) = 0, \tag{3.11}$$

where

$$R^N(r) = \int_0^r \frac{M_t^N(h_\psi).M_t^N(\psi)}{t}dt$$

The result is sharp when $r_b = r_0$ *and* $t_n > 0$.

Proof. Since the function $G(z) = (f(z)+\overline{f(\bar{z})})/2$ belongs to $\mathcal{S}^*(\psi)$. Therefore, by Lemma [17] we have

$$\frac{G(z)}{z} \prec \frac{h_\psi(z)}{z},$$

which using Lemma 1.1 yields

$$M_r^N(G) \leq M_r^N(h_\psi) \quad \text{for} \quad r \leq \frac{1}{3}. \tag{3.12}$$

From Definition 3.4, we get $zf'(z) = G(z)\psi(\omega(z))$ which after integration gives

$$f(z) = \int_0^z \frac{G(t)\psi(\omega(t))}{t}dt. \tag{3.13}$$

Since $\psi \circ \omega \prec \psi$,

$$M_r^N(\psi \circ \omega) \leq M_r^N(\psi) \quad \text{for} \quad r \leq \frac{1}{3}. \tag{3.14}$$

Thus, combining (3.12), (3.13) and (3.14), we see that

$$\begin{aligned}\sum_{k=N}^{\infty} |b_k||z|^k = M_r^N(g) &\leq M_r^N(f)\\ &= \int_0^r \frac{M_t^N(G)M_t^N(\psi \circ \omega)}{t}dt\\ &\leq \int_0^r \frac{M_t^N(h_\psi)M_t^N(\psi)}{t}dt =: R^N(r),\end{aligned}$$

holds for $r \leq 1/3$. Also, using Maximum-principle of modulus and growth theorem [34], $g \prec f$ implies that

$$|g(|z| \leq r)| = |f(\omega(|z| \leq r))| \leq \max_{|z|=r} |f(|z| \leq r)| = h_\psi(r),$$

which yields

$$|g(z^m)| \leq h_\psi(r^m).$$

Finally, note that

$$d(0, \Omega) \geq -h_\psi(-1).$$

Hence,

$$|g(z^m)| + \sum_{k=N}^{\infty} |b_k||z|^k \leq d(0, \partial\Omega)$$

holds for $|z| \leq \{1/3, r_0\}$, where r_0 is the root of the equation (3.11). The existence of the root follows by Intermediate value theorem for continuous function in $[0, 1]$. For the sharpness, note that for the function h_ψ

$$d(0, \Omega) = -h_\psi(-1)$$

such that if $r_b = r_0$, then for the choice $g = f = h_\psi$:

$$|h_\psi(z^m)| + \sum_{n=N}^{\infty} |t_n||z|^n = d(0, \partial\Omega)$$

holds for $|z| = r_b$ with $t_n > 0$, where $h_\psi(z) = z + \sum_{n=2}^{\infty} t_n z^n$ as given in (3.9). □

Remark 3.2. Let $\psi(z) = (1+z)/(1-z)$, then Theorem 3.5 reduces to [11, Theorem 6].

The following result is explicitly for the class $\mathcal{S}_c^*(\psi)$.

Corollary 3.6. *Let $f(z) = z + \sum_{n=2}^{\infty} a_n z^n \in \mathcal{S}_c^*(\psi)$. Then*

$$|f(z^m)| + \sum_{n=N}^{\infty} |a_n||z|^n \leq d(0, \partial\Omega) \tag{3.15}$$

holds for $|z| = r_b \leq \min\{\frac{1}{3}, r_0\}$, where $m, N \in \mathbb{N}$, $\Omega = f(\mathbb{D})$ and r_0 is the unique positive root of the equation:

$$h_\psi(r^m) + R^N(r) + h_\psi(-1) = 0,$$

where

$$R^N(r) = \int_0^r \frac{M_t^N(h_\psi).M_t^N(\psi)}{t} dt$$

and h_ψ be given by (3.9). *The result is sharp when $r_b = r_0$ and $t_n > 0$.*

Remark 3.3. Taking $m \to \infty$ and $N = 1$ in Theorem 3.5 and Corollary 3.6 establish the Bohr phenonmenon for the classes $S_f(\psi)$ and $\mathcal{S}_c^*(\psi)$, respectively given in [38, Lemma 2.12] and [38, Theorem 2.9].

To proceed further, we need to recall the following fundamental result:

Lemma 3.2. [17] *Let $f \in \mathcal{C}(\psi)$. Then $zf''(z)/f'(z) \prec zl_0''(z)/l_0'(z)$ and $f'(z) \prec l_0'(z)$. Also, for $|z| = r$ we have*

$$-l_0(-r) \leq |f(z)| \leq l_0(r),$$

where

$$1 + zl_0''(z)/l_0'(z) = \psi(z). \tag{3.16}$$

Definition 3.7. The class of convex functions with respect to conjugate points given by

$$\mathcal{C}_c(\psi) = \left\{ f \in \mathcal{A} : \frac{(zf'(z))'}{(f(z) + \overline{f(\bar{z})})'} \prec \psi(z) \right\}.$$

Theorem 3.8. *Let $f(z) = z + \sum_{n=2}^{\infty} a_n z^n \in \mathcal{C}_c(\psi)$. If $g \in S_f(\psi)$. Then*

$$|g(z^m)| + \sum_{k=N}^{\infty} |b_k||z|^k \leq d(0, \partial\Omega)$$

holds for $|z| = r_b \leq \min\{\frac{1}{3}, r_0\}$, *where* $m, N \in \mathbb{N}$, $\Omega = f(\mathbb{D})$ *and* r_0 *is the minimal positive root of the equation:*

$$k_\psi(r^m) + R^N(r) + k_\psi(-1) = 0, \tag{3.17}$$

where

$$R^N(r) = \int_0^r \frac{1}{s} \int_0^s M_t^N(k'_\psi).M_t^N(\psi)dtds,$$

and $k_\psi(z) = z + \sum_{n=2}^{\infty} l_n z^n$ *is given by* (3.16). *The result is sharp when* $r_b = r_0$ *and* $l_n > 0$.

Proof. Consider the function

$$G(z) = \frac{f(z) + \overline{f(\bar{z})}}{2}.$$

Then $G \in \mathcal{C}(\psi)$. Now from Definition 3.7, we see that

$$(zf'(z))' = G'(z)\psi(\omega(z)). \tag{3.18}$$

This gives

$$f(z) = \int_0^z \frac{1}{y} \int_0^y G'(t)\psi(\omega(t))dtdy. \tag{3.19}$$

As $G' \prec k'_\psi$, see Lemma 3.2, it follows using Lemma 1.1 that

$$M_r^N(G') \leq M_r^N(k'_\psi) \quad \text{for} \quad r \leq \frac{1}{3}. \tag{3.20}$$

Hence, using (3.18), (3.19) and (3.20)

$$\begin{aligned} |g(z^m)| + M_r^N(f) &\leq k_\psi(r^m) + \int_0^r \frac{1}{y} \int_0^y M_t^N(G')M_t^N(\psi \circ \omega)dtdy \\ &\leq k_\psi(r^m) + \int_0^r \frac{1}{y} \int_0^y M_t^N(k'_\psi)M_t^N(\psi)dtdy \\ &\leq -k_\psi(-1) \\ &\leq d(0, \partial\Omega), \end{aligned}$$

holds for $|z| = r \leq r_b = \{1/3, r_0\}$, where r_0 is minimal root of the equation (3.17). The existence of $0 < r_0 < 1$ can be seen by Intermediate value theorem for continuous function in $[0, 1]$. The case of equality

$$|g(z^m)| + \sum_{k=N}^{\infty} |b_k||z|^k = d(0, \partial\Omega)$$

follows with the choice $g = f = k_\psi$, whenever $r_b = r_0$ and $l_n > 0$. □

Corollary 3.9. *If* $f(z) = z + \sum_{n=2}^{\infty} a_n z^n \in \mathcal{C}_c(\psi)$. *Then*

$$|f(z^m)| + \sum_{k=N}^{\infty} |a_n||z|^n \leq d(0, \partial\Omega)$$

holds for $|z| = r_b \leq \min\{\frac{1}{3}, r_0\}$, *where* $m, N \in \mathbb{N}$, $\Omega = f(\mathbb{D})$ *and* r_0 *is the minimal positive root of the equation:*

$$k_\psi(r^m) + R^N(r) + k_\psi(-1) = 0,$$

where

$$R^N(r) = \int_0^r \frac{1}{s} \int_0^s M_t^N(k'_\psi).M_t^N(\psi)dtds.$$

The result is sharp when $r_b = r_0$ *and* $l_n > 0$.

Remark 3.4. Taking $m \to \infty$ and $N = 1$ in Corollary 3.9 gives [38, Theorem 2.23].

Definition 3.10. The class of convex function with respect to symmetric points is given by

$$\mathcal{C}_s(\psi) = \left\{ f \in \mathcal{A} : \frac{2(zf'(z))'}{f'(z) + f'(-z)} \prec \psi(z) \right\}.$$

Now, we omit the details of the proof as it works on the similar lines discussed in the above theorems.

Theorem 3.11. *Let* $k_\psi(z) = z + \sum_{n=2}^{\infty} l_n z^n$ *be given by* (3.16) *and* $f(z) = z + \sum_{n=2}^{\infty} a_n z^n \in \mathcal{C}_s(\psi)$. *If* $g \in S_f(\psi)$. *Then*

$$|g(z^m)| + \sum_{k=N}^{\infty} |b_k||z|^k \leq d(0, \partial\Omega)$$

holds for $|z| = r_b \leq \min\{\frac{1}{3}, r_0\}$, *where* $m, N \in \mathbb{N}$, $\Omega = f(\mathbb{D})$ *and* r_0 *is the unique positive root of the equation:*

$$\int_0^r \frac{1}{s} \int_0^s \psi(t)(k'_\psi(t^2))^{1/2}dtds + R^N(r) = \int_0^1 \frac{1}{s} \int_0^s \psi(-t)(k'_\psi(-t^2))^{1/2}dtds,$$

where $K'(z) = (k'_\psi(z^2))^{1/2}$ *and*

$$R^N(r) = \int_0^r \frac{1}{s} \int_0^s M_t^N(K').M_t^N(\psi)dtds.$$

The result is sharp when $r_b = r_0$ *and* $l_n > 0$.

Corollary 3.12. *If* $f(z) = z + \sum_{n=2}^{\infty} a_n z^n \in \mathcal{C}_s(\psi)$. *Then*

$$|f(z^m)| + \sum_{k=N}^{\infty} |a_n||z|^n \leq d(0, \partial\Omega)$$

holds for $|z| = r_b \leq \min\{\frac{1}{3}, r_0\}$, *where* $m, N \in \mathbb{N}$, $\Omega = f(\mathbb{D})$ *and* r_0 *is as given in Theorem 3.11. The result is sharp when* $r_b = r_0$ *and* $l_n > 0$.

Remark 3.5. Taking $m \to \infty$ and $N = 1$ in Corollary 3.12 gives [38, Theorem 2.25].

Conflict of interest

The authors declare that they have no conflict of interest.

References

[1] L. Aizenberg, Remarks on the Bohr and Rogosinski phenomena for power series, Anal. Math. Phys. **2** (2012), no. 1, 69–78.

[2] R. M. Ali, R. W. Barnard and A. Yu. Solynin, A note on Bohr's phenomenon for power series, J. Math. Anal. Appl. **449** (2017), no. 1, 154–167.

[3] R. M. Ali, N. K. Jain and V. Ravichandran, Bohr radius for classes of analytic functions, Results Math. **74** (2019), no. 4, Paper No. 179, 13 pp.

[4] S. A. Alkhaleefah, I. R. Kayumov and S. Ponnusamy, Bohr-Rogosinski inequalities for bounded analytic functions, Lobachevskii J. Math. **41** (2020), no. 11, 2110–2119.

[5] M. K. Aouf, On a class of p-valent starlike functions of order α, Internat. J. Math. Math. Sci. **10** (1987), no. 4, 733–744.

[6] B. Bhowmik and N. Das, Bohr phenomenon for subordinating families of certain univalent functions, J. Math. Anal. Appl. **462** (2018), no. 2, 1087–1098.

[7] H. P. Boas and D. Khavinson, Bohr's power series theorem in several variables, Proc. Amer. Math. Soc. **125** (1997), no. 10, 2975–2979.

[8] H. Bohr, A Theorem Concerning Power Series, Proc. London Math. Soc. (2) **13** (1914), 1–5.

[9] K. Gangania and S. S. Kumar, On Certain Generalizations of $\mathcal{S}^*(\psi)$, Comput. Methods Funct. Theory (2021), https://doi.org/10.1007/s40315-021-00386-5. arXiv:2007.06069v1

[10] W. Janowski, Extremal problems for a family of functions with positive real part and for some related families, Ann. Polon. Math. **23** (1970/71), 159–177.

[11] I. R. Kayumov, D. M. Khammatova and S. Ponnusamy, Bohr-Rogosinski phenomenon for analytic functions and Cesáro operators, J. Math. Anal. Appl. **496** (2021), no. 2, 124824, 17 pp.

[12] S. S. Kumar and G. Kamaljeet, A cardioid domain and starlike functions, Anal. Math. Phys. **11** (2021), no. 2, 54.

[13] S. S. Kumar and G. Kamaljeet, On Geometrical Properties of Certain Analytic functions, Iran. J. Sci. Technol. Trans. A Sci. (2020), https://doi.org/10.1007/s40995-021-01116-1

[14] S. S. Kumar and G. Kamaljeet, On Certain Generalizations of $\mathcal{S}^*(\psi)$, (2020), arXiv:2007.06069v1

[15] S. S. Kumar and G. Kamaljeet, $\mathcal{S}^*(\psi)$ and $\mathcal{C}(\psi)$-radii for some special functions, (2020), arXiv:2008.13499v1

[16] E. Landau and D. Gaier, *Darstellung und Begründung einiger neuerer Ergebnisse der Funktionentheorie*, third edition, Springer-Verlag, Berlin, 1986.

[17] W. C. Ma and D. Minda, A unified treatment of some special classes of univalent functions, in *Proceedings of the Conference on Complex Analysis (Tianjin, 1992)*, 157–169, Conf. Proc. Lecture Notes Anal., I, Int. Press, Cambridge, MA.

[18] S. S. Miller and P. T. Mocanu, *Differential subordinations*, Monographs and Textbooks in Pure and Applied Mathematics, 225, Marcel Dekker, Inc., New York, 2000.

[19] Y. A. Muhanna, Bohr's phenomenon in subordination and bounded harmonic classes, Complex Var. Elliptic Equ. **55** (2010), no. 11, 1071–1078.

[20] Y. Abu Muhanna and R. M. Ali, Bohr's phenomenon for analytic functions into the exterior of a compact convex body, J. Math. Anal. Appl. **379** (2011), no. 2, 512–517.

[21] Y. Abu Muhanna, R. M. Ali, Z. C. Ng and S. F. M. Hasni, Bohr radius for subordinating families of analytic functions and bounded harmonic mappings, J. Math. Anal. Appl. **420** (2014), no. 1, 124–136.

[22] Y. Abu Muhanna, R. M. Ali and S. K. Lee, The Bohr operator on analytic functions and sections, J. Math. Anal. Appl. **496** (2021), no. 2, 124837, 11 pp.

[23] V.I. Paulsen, D. Singh, A simple proof of Bohr's inequality, https://www .math .uh .edu / vern /bohrconf .pdf.

[24] S. Ponnusamy, R. Vijayakumar anf K. J. Wriths, Modifications of Bohr's inequality in various settings, 2021, arXiv:2104.05920v1

[25] W. Rogosinski, Über Bildschranken bei Potenzreihen und ihren Abschnitten, Math. Z. **17** (1923), no. 1, 260–276.

[26] I. Schur, G. Szegö, Über die Abschnitte einer im Einheitskreise beschränkten Potenzreihe, Sitz.ber. Preuss. Akad. Wiss. Berl. Phys.-Math. Kl. (1925) 545–560.

[27] A. W. Goodman, *Univalent functions. Vol. II*, Mariner Publishing Co., Inc., Tampa, FL, 1983.

[28] I.R. Kayumov, D.M. Khammatova and S. Ponnusamy, The Bohr inequality for the generalized Césaro averaging operators, Preprint, arXiv:2104.01550v1

[29] S. Kumar and S.K. Sahoo, A Generalization of the Bohr-Rogosinski Sum, Priprint, arXiv:2106.06502v1

[30] R.Y. Lin, M.S. Liu and S. Ponnusamy, Generalization of Bohr-type inequality in analytic functions, Priprint, arXiv:2106.11158

[31] K. Gangania, and S. S. Kumar, Bohr-Rogosinski phenomenon for $\mathcal{S}^*(\psi)$ and $\mathcal{C}(\psi)$. Mediterranean Journal of Mathematics (To Appear). https://arxiv.org/abs/2105.08684v1.

[32] K. Sakaguchi, On a certain univalent mapping, J. Math. Soc. Jpn., **11** (1959), 72–75.

[33] C. Gao and S. Zhou, On a class of analytic functions related to the starlike functions, Kayungpook Math. J., **45** (2005), 123–130.

[34] V. Ravichandran, Starlike and convex functions with respect to conjugate points, Acta Math. Acad. Peaedagog. Nyhazi, **20** (2004), 31–37

[35] Z. Wang, C. Gao and S. Yuan, On certain subclass of close-to-convex functions, Acta Math Acad Paedagog Nyházi (N. S.), **22** (2006), 171–177. (electronic)

[36] N.E. Cho, O.S. Kwon and V. Ravichandran, Coefficient, distortion and growth inequalities for certain close-to-convex functions, J. Inequal. Appl., **2011** (2011), 100.

[37] H. Hamada, Bohr phenomenon for analytic functions subordinate to starlike or convex functions, J. Math. Anal. Appl., **499** (2021), no. 1,, Art. 125019.

[38] V. Allu and H. Halder, Bohr phenomenon for certain close-to-convex analytic functions, Comput. Methods Funct. Theory (2021). https://doi.org/10.1007/s40315-021-00412-6

Department of Applied Mathematics, Delhi Technological University, Delhi–110042, India

Email address: gangania.m1991@gmail.com

Department of Applied Mathematics, Delhi Technological University, Delhi–110042, India

Email address: spkumar@dce.ac.in

energies

MDPI

Article

A Novel Analytical Approach for Optimal Integration of Renewable Energy Sources in Distribution Systems

Prem Prakash [1], Duli Chand Meena [1], Hasmat Malik [2,*], Majed A. Alotaibi [3,*] and Irfan Ahmad Khan [4]

[1] Electrical Engineering Department, Delhi Technological University, Shahbad Daulatpur, Main Bawana Road, Delhi 110042, India; ppyadav1974@gmail.com (P.P.); dcmeena@dce.ac.in (D.C.M.)
[2] BEARS, University Town, NUS Campus, Singapore 138602, Singapore
[3] Department of Electrical Engineering, College of Engineering, King Saud University, Riyadh 114211, Saudi Arabia
[4] Clean and Resilient Energy Systems (CARES) Lab, Electrical and Computer Engineering Department, Texas A&M University, Galveston, TX 77553, USA; irfankhan@tamu.edu
* Correspondence: hasmat.malik@gmail.com (H.M.); majedalotaibi@ksu.edu.sa (M.A.A.)

Abstract: The present research article focuses on an analytically based method for the optimal allocation and sizing of a renewable energy source (RES) capable of injecting both active and reactive powers in the distribution network. The placement of distributed generation (DG) in the distribution network reduces the magnitude of branch current in between the reference bus and the bus where DG is to be installed. Due to this, system power loss decreases significantly. The proposed method considers different levels of load in addition to peak load demand. The goal of the developed method is to minimize system losses by optimal DG allocations. In the proposed method, the optimum size of the DG is obtained on the basis of maximum loss saving criterion. For the execution of proposed method, only a base case load flow solution is required. The developed method has been tested on IEEE 69-bus and 33-bus radial distribution networks. On the basis of obtained results, it has been realized that the developed method is more capable of diminishing system energy losses.

Keywords: analytical approach; distributed generations; optimum sizing and siting; radial distribution network; renewable energy sources; renewable energy source

check for updates

Citation: Prakash, P.; Meena, D.C.; Malik, H.; Alotaibi, M.A.; Khan, I.A. A Novel Analytical Approach for Optimal Integration of Renewable Energy Sources in Distribution Systems. *Energies* **2022**, *15*, 1341. https://doi.org/10.3390/en15041341

Academic Editor: Abu-Siada Ahmed

Received: 3 January 2022
Accepted: 5 February 2022
Published: 12 February 2022

Publisher's Note: MDPI stays neutral with regard to jurisdictional claims in published maps and institutional affiliations.

Copyright: © 2022 by the authors. Licensee MDPI, Basel, Switzerland. This article is an open access article distributed under the terms and conditions of the Creative Commons Attribution (CC BY) license (https://creativecommons.org/licenses/by/4.0/).

1. Introduction

Exponential increase in electricity demand, continuous depletion of conventional power resources, environmental issues, uncertainties related to fuel prices and advances in DG technologies have motivated the power system planner to use small-scale generation units. A small-scale, electrical power generation unit is termed as DG. Further, DGs can be defined as the electricity-generating systems which are connected to customer side of the meter or load directly [1].

Moreover, DGs are beneficial when these DGs are integrated in the existing distribution network if allocation and sizing is performed in a strategic mode. Optimal sizing and siting of DG resources leads to decreased system power, energy loss along with system cost, and also enhances system bus voltage considerably. Further, optimally placed and sized DGs improve the voltage stability margin, loadability, quality of power and system reliability [1–28]. Moreover, DGs are driven by renewable energy sources and have the property of low emission of greenhouse gases (GHG) which are mainly responsible for global warming [1,4,13,15–18,22,23,26].

Non-optimally placed and sized DGs give rise to upsurges in system energy and power loss, increase system cost and enhance the profile of voltage in various load buses. Consequently, system performance deteriorates [4,13,18,19]. Therefore, optimum siting and sizing of DG units is a significant aspect and needs to be further investigated.

Many researchers investigated optimum sizing and siting of DGs as an objective to reduce system power and energy loss [2–27], voltage profile enhancement [2–8,10,18,19]. References [8,15,17,19,23,25,26] have addressed the betterment of the voltage stability margin (VSM), loadability of the system and system energy loss reduction as a single and multi-objective. Further, [2–4,6–10] have developed analytical methods for optimum siting and sizing of DG. References [5,24] addressed mixed integer non-linear programming (MINLP)-based methods, authors of [5,8,15,16,19,22,25] highlighted index-based methods, and evolutionary algorithms (EA) techniques have been applied by [11,18] for the solution and development of formulations. Reference [20] addressed the improvement of system reliability with the placement of DG.

In [2], authors have developed a technique based on an exact loss formula for the optimization of DG sizes and placement; authors derived analytical method-based formulations for the minimization of system power loss. Authors also examined the effect of DG size on system loss. References [3,4] developed a methodology for the optimal siting and sizing of renewable energy sources (RES) to decrease system active power loss on analytical method-based expressions. Wang and Nehrir [6] highlighted an analytically based technique for the siting of a single DG unit injecting real power into the system for mesh and radial distribution networks to reduce system losses. The authors considered different types of loads, but the optimum size of DG was not considered. The authors of [7] developed a loss sensitivity index based on analytical expressions and eliminate the need of the formation of a Jacobin matrix for optimum size and location of a single DG unit to minimize system power loss.

Hung and Mithulananthan [8] extended the similar technique as in [10] to the optimal installation of multiple DG units to reduce system power loss. In [9] authors have applied analytical formulations for optimal capacity and installation of renewable DGs to reduce the power loss of systems using a combination of time-varying load and different outputs from DG units. Further, Hung et al. [10] developed an improved analytical (IA)-based method for the optimum sizing and installation of different types of single DG units for loss reduction. In [11] authors have proposed a method for the optimal integration of non-dispatchable DG; the method is based on evolutionary programming. Hung et al. [12] applied an analytical formulation based on the multi-objective index for solar photovoltaic-based DGs for minimizing energy loss and the improvement of system voltage stability with time-varying load. Kansal et al. [14] highlighted the classification of different types of DGs which are operated by a non-conventional energy source such as biomass, solar and wind to decrease power loss via the optimal placement and sizing of DG. Murty and Kumar [15,16] proposed a new index method based on the power loss sensitivity factor and power stability for the optimal siting of DG units to reduce the energy loss cost of systems. In [17] authors have highlighted an analytically based method for optimum capacity and integration of both non-dispatchable and dispatchable DGs to minimize the system loss. Esmaili [18,19] addressed a method for optimum sizing and siting of DG to enhance system voltage stability and reduce system loss. Tah and Das [21] proposed new analytical formulations for optimal siting and sizing of DG for the minimization of system loss. Aman et al. [22,26] and Al Abri et al. [23] proposed a power stability index-based methodology for the optimum siting of DGs to reduce network power loss and enhance the voltage of bus. Ochoa and Harrison [25] addressed a new method for the optimal siting and sizing of DG to reduce energy loss of system. Mehta et al. [27] proposed a technique which is based on analytical formulations for the optimal selection, size and installation of different categories of DGs using the voltage sensitivity index method. Tawfeek et al. [28] proposed an exact loss formula based the analytical technique for the optimal allocation of DG and compared the results with PSO-based optimization techniques. The data of IEEE bus systems under investigation in the present study has been taken from [24]

In the proposed technique, system energy loss and energy loss saving formulations with DG and without DG have been derived in terms of *D* matrix. The process of formation of *D* matrix has been explained in Appendix A. Further, in earlier research papers, only

peak load demand has been considered. Additionally, in the present study, three different levels of load demand have been considered. Moreover, as per available literature, the majority of the power system planners have developed expressions of DGs on exact loss formula-based analytical derivations [2,7–10,15,28] which are applicable for multiple and single DG unit(s) sizing and placement. The exact loss formula-based methodology requires the formation and calculation of an admittance (Y_{BUS}) matrix for solution of load flow equations which is a time-consuming process.

Moreover, due to the high R/X ratio and negligible shunt admittance of distribution lines, the conventional method of load flow, i.e., the Newton-Raphson and Gauss-Seidel methods, are not very suitable because of the convergence problem of these techniques. In the proposed paper the backward–forward sweep (BFS)-based method for load flow solution has been applied. The BFS-based method does not require the formation of a (Y_{BUS}) matrix, therefore the method has an excellent convergence property [2–5,7,9]. The present research article aims to estimate the optimal sizes and locations of DGs so that system energy losses could be reduced.

Further, the methods which appeared in the literature are suitable for passive networks; in such circuits a voltage issue is exposed due to variation in load demand. Therefore, in the present study, load demand is considered in different load levels.

Basically, the addition of DG units in distribution network changes the power flow which in turn changes the magnitude of branch current components (active and reactive); due to this system power losses are reduced. The candidate bus for DG placement are obtained on the basis of maximum loss saving criterion.

Furthermore, the developed technique needs solutions of base case load flow only for small as well as larger networks. The present technique has been applied to IEEE 69-bus and 33-bus and 85-bus radial distribution systems. Further, the results obtained by the present developed method are immensely encouraging for system energy loss minimization and the enhancement of system voltage profile view point.

In the proposed method, type 2 DGs have been considered for placement. This category of DG injects powers, i.e., active power and reactive power. In [18] authors proposed a bifurcation-based method to place the optimum number of DGs by finding the vulnerable buses, and these buses are found on the basis of voltage stability criteria. Beside the above explanation, a summary of the related work is represented in Table A1.

In the above-mentioned literature review, it is clear that very few authors addressed the analytical-based method, which is described in the present research article. In the present method, expressions of the optimum capacity of DGs are derived on the basis of maximum loss saving criterion. In the proposed method, sequence of buses is found on the basis of maximum power loss saving. The suitability of the proposed method is also checked and matching with available literature. Therefore, the current method is a novel analytically based method for the optimum capacity and integration of DGs (single as well as multiple DG units) in a distribution system. The computation time of the proposed method is very low, i.e., 10 s to 12 s, as it does not require the solution and formation of a Jacobian matrix.

The present paper is arranged in 5 sections: Section 2 describes the proposed methodology and mathematical formulation. Section 3 explains the algorithm for a solution, and Section 4 highlights the discussions along with results. Lastly, Section 5 describes conclusions and represents Appendix A.

2. Proposed Methodology and Mathematical Formulation

The following assumptions are made to the mathematical formulations of the developed analytically based method:

- The system under consideration is balanced, radial and fed by a substation.
- Voltage of all nodes is close to 1 p.u.
- The Shunt admittances of lines are negligible.
- Bus loads are modeled as a constant power load.

- The maximum capacity of DG for various test systems does not exceed the total connected load.
- The present paper investigates the optimal placement and sizing of such DG which is capable of delivering both active and reactive power. The flow diagram of the proposed approach is shown in Figure 1.

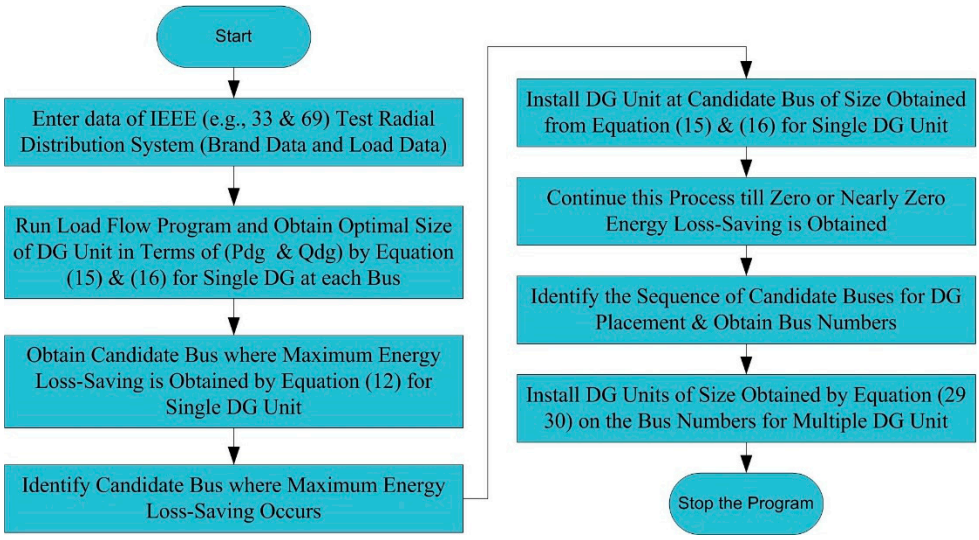


Figure 1. Proposed Approach for Optimal Integration of Renewable Energy Sources in Distribution Systems.

2.1. Mathematical Formulations for Single DG Unit

Let us assume an 'n' bus test system of radial nature. Figure 2 represents the single line diagram. In this diagram it is assumed that I_i is the current of ith branch. Further, $(P_{Li} + jQ_{Li})$ is the load at ith bus and $(P_i + jQ_i)$ power flow at the sending end of the ith branch. In these abbreviations, P_L denotes the active power component of the load, and Q_L denotes the reactive power component of the load power.

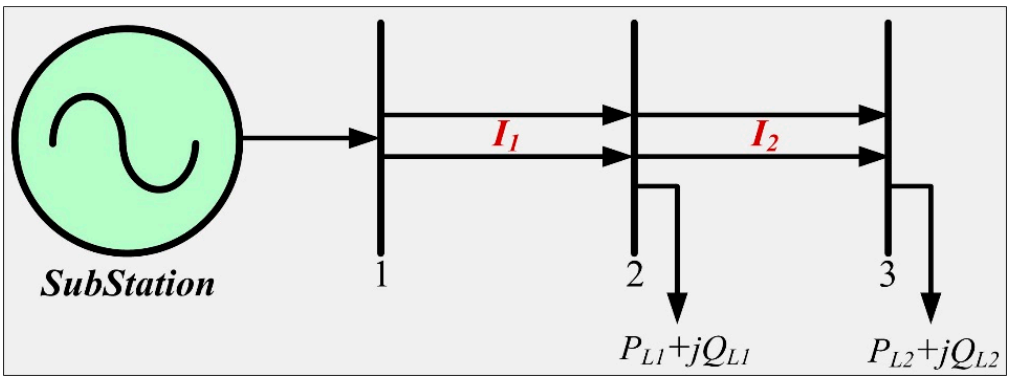


Figure 2. Single line diagram for n-bus test radial distribution network.

Expression for phasor current in ith branch has been expressed as

$$I_i = \frac{P_i - jQ_i}{V_i^*} \tag{1}$$

where, V_i^* is the conjugate of phasor voltage at bus i, as it is assumed that the voltage magnitude at different buses remains closed to 1.0 p.u. after DG integration, therefore the magnitude of current I_i in ith branch can be approximated as

$$I_i \approx P_i - jQ_i \tag{2}$$

In the present paper, three different load levels (50%, 70% and 100%) with reference to system peak load have been considered. The yearly load duration curve is depicted in Figure 3. The current in various branches is computed by load flow analysis for each load level. Therefore, the magnitude of I_i as given by (2) is calculated as:

$$|I_i| = \sqrt{P_i^2 + Q_i^2} \tag{3}$$

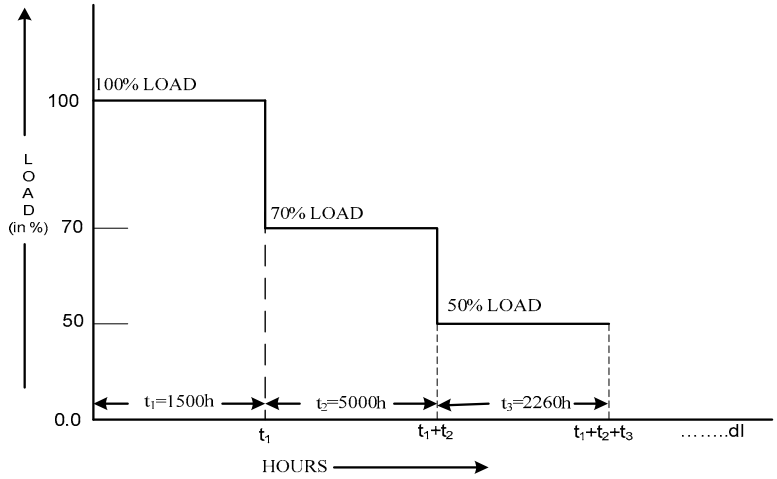


Figure 3. Load duration curve for different load levels.

The total energy loss for different load levels and durations is calculated in an equation and its description is given as follows:

$$\begin{aligned} EL = & \sum_{i=1}^{n-1} \left(I_i^1\right)^2 R_i t_1 + \sum_{i=1}^{n-1} \left(I_i^2\right)^2 R_i t_2 + \ldots + \sum_{i=1}^{n-1} \left(I_i^{dl}\right)^2 R_i t_{dl} \\ EL = & \sum_{s=1}^{dl} \sum_{i=1}^{n-1} \left|I_i^s\right|^2 R_i t_s \end{aligned} \tag{4}$$

Here, n is the number of nodes of the system, EL is the system energy loss, R_i is the resistance of the ith branch of the system, dl denotes the number of various levels of load, t_s represents the corresponding duration of the 'sth' load levels and I_i^s is the current in the ith branch during the sth load level. The value of EL has been calculated on the basis of (5) using the value of $\left|I_i^s\right|$ from (3)

$$EL = \sum_{s=1}^{3} \sum_{i=1}^{n-1} \left\{ \left(P_i^s\right)^2 + \left(Q_i^s\right)^2 \right\} R_i t_s \tag{5}$$

Here, P_i^s & Q_i^s is the injected active and reactive component of power at ith bus for sth load level.

Now, suppose a DG unit is sited at the kth bus of the considered system as depicted in Figure 4; because of the placement of DG units at the kth bus, the current changes in those branches which are in between bus 1 and bus k. While the current magnitude in the leftover branches remains the same.

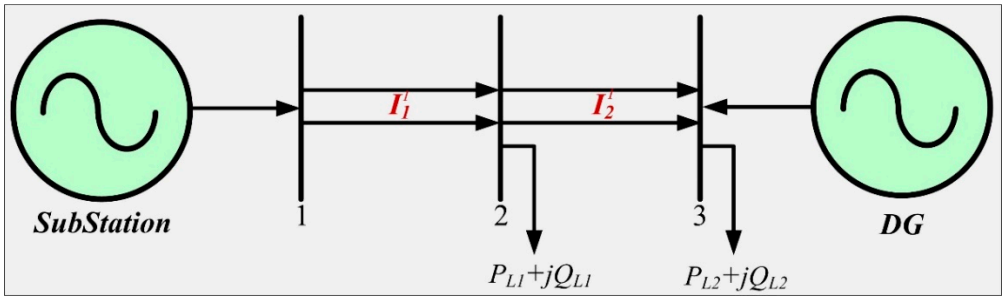


Figure 4. Single line diagram for n-bus test radial distribution network with DG.

The I_i^N represents the magnitude of phasor current in *i*th branch after DG integration and $\left(P_i^N + jQ_i^N\right)$ represent the active component and reactive components of injected power at *i*th bus after DG placement. The expression for I_i^N after DG placement is given by (6)

$$I_i^N = I_i - D_i I_{dg} \tag{6}$$

where I_{dg} is the phasor current injected by DG unit and D_i is the matrix which contains binary values given as $D_i = \begin{cases} 1 \text{ if } i\text{th branch in between } k\text{th bus} \\ 0 \text{ otherwise} \end{cases}$

The phasor current supplied by DG can be given as

$$I_{dg} = \frac{P_{dg} - jQ_{dg}}{V_i^*} \tag{7}$$

Here P_{dg} and Q_{dg} are the components of active and reactive power injected from DG, or basically, it is the optimal capacity of the DG unit. In the present methodology it is assumed that the voltage magnitude at different buses is close to 1.0 p.u., therefore the current injected by the DG unit, i.e., I_{dg}, can be approximated as (8)

$$I_{dg} \approx P_{dg} - jQ_{dg} \tag{8}$$

Using (6) and (8) I_i^N is expressed in Equation (9) whose description is given below:

$$I_i^N \approx \left(P_i - D_i P_{dg}\right) - j\left(Q_i - D_i Q_{dg}\right) \tag{9}$$

2.2. System Energy Loss Due to the Placement of a Single DG Unit

Due to the allocation of DG in the distribution system the current in network branches is changed; therefore, the system losses are also changed. Hence system energy losses after DG placement can be given as:

$$EL^N = \sum_{s=1}^{dl} \sum_{i=1}^{n-1} \left|I_i^N\right|^2 R_i t_s \tag{10}$$

where EL^N is system energy loss after the placement of DG.

Substituting the values of $\left|I_i^N\right|$ from (9), the Equation (10) reduces to

$$EL^N = \sum_{s=1}^{dl} \sum_{i=1}^{n-1} \left\{ \left(P_i^s - D_i P_{dg}\right)^2 + \left(Q_i^s - D_i Q_{dg}\right)^2 \right\} R_i t_s \tag{11}$$

Here P_i^s & Q_i^s are the real and reactive powers of the ith branch for different load levels. Using (5) and (11) for energy loss savings of the system after DG placement

$$\begin{aligned} S_E &= EL - EL^N \\ S_E &= \sum_{s=1}^{dl}\sum_{i=1}^{n-1}\left\{\left(P_i^s\right)^2 + \left(Q_i^s\right)^2 - \left(P_i^s - D_i P_{dg}\right)^2 - \left(Q_i^s - D_i Q_{dg}\right)^2\right\} R_i t_s \text{ or} \\ S_E &= \sum_{s=1}^{dl}\sum_{i=1}^{n-1}\left\{2D_i P_i^s P_{dg} + 2D_i Q_i^s Q_{dg} - \left(D_i P_{dg}\right)^2 - \left(D_i Q_{dg}\right)^2\right\} R_i t_s \end{aligned} \tag{12}$$

For maximum energy loss saving, partial differentiation of Equation (12) with respects to P_{dg} and Q_{dg} should be zero as

$$\frac{\partial S_E}{\partial P_{dg}} = \sum_{s=1}^{dl}\sum_{i=1}^{n-1}\left\{2D_i P_i^s - 2D_i^2 P_{dg}\right\} R_i t_s = 0 \tag{13}$$

$$\frac{\partial S_E}{\partial Q_{dg}} = \sum_{s=1}^{dl}\sum_{i=1}^{n-1}\left\{2D_i Q_i^s - 2D_i^2 Q_{dg}\right\} R_i t_s = 0 \tag{14}$$

Solving (13) and (14) for P_{dg} and Q_{dg}, respectively

$$P_{dg} = \frac{\sum_{s=1}^{dl}\sum_{i=1}^{n-1} D_i P_i^s R_i t_s}{\sum_{s=1}^{dl}\sum_{i=1}^{n-1} D_i^2 R_i t_s} \tag{15}$$

$$Q_{dg} = \frac{\sum_{s=1}^{dl}\sum_{i=1}^{n-1} D_i Q_i^s R_i t_s}{\sum_{s=1}^{dl}\sum_{i=1}^{n-1} D_i^2 R_i t_s} \tag{16}$$

The final optimum size of DG will be as

$$S_{dg} = P_{dg} + jQ_{dg} \tag{17}$$

And the optimum power factor of the DG unit is given as

$$OPF_{dg} = \frac{P_{dg}}{\sqrt{P_{dg}^2 + Q_{dg}^2}} \tag{18}$$

2.3. Formulation for System Energy Loss by Placement of Multiple DG Units

The present section is similar to the previous section, which is developed for the single DG placement of the present study. For the installation of multiple DG units, m is the number of DG units to be placed in an n-bus distribution network. The placement of DGs at various nodes changes the magnitude of the current in system branches; hence, the new current in the ith branch is expressed as $I_i^N = I_i - \sum_{j=1}^{m} D_{ij} I_{dg}^j$; where I_{dg}^j is the phasor current injected from jth DG. Further, D_{ij} is given as

$$D_{ij} = \begin{cases} 1 \text{ if } i\text{thbranch in between bus 1 and } j\text{thbus} \\ 0 \text{ otherwise} \end{cases}$$

The phasor current supplied by *j*th DG is similar to (7). By considering different load levels, the energy losses after placement of m DGs in the system can be given as

$$EL^{new} = \sum_{s=1}^{dl}\sum_{i=1}^{n-1}\left[\left(\left\{P_i^s - \sum_{j=1}^{m} D_{ij}P_{dg}^j\right\}^2 + \left\{Q_i^s - \sum_{j=1}^{m} D_{ij}Q_{dg}^j\right\}^2\right)\right]R_i t_s \tag{19}$$

where EL^{new} is the energy losses in the system after installation of m DG units in the system, using (5) and (19) the net energy loss saving after multiple DG placements can be given as: $S_{EN} = EL - EL^{new}$

$$S_{EN} = \sum_{s=1}^{dl}\sum_{i=1}^{n-1}\left[-\sum_{j=1}^{m} D_{ij}^2\left(P_{dg}^j\right)^2 + 2\sum_{j=1}^{m} D_{ij}P_i^s\left(P_{dg}^j\right) - \sum_{j=1}^{m} D_{ij}^2\left(Q_{dg}^j\right)^2 + 2\sum_{j=1}^{m} D_{ij}Q_i^s\left(Q_{dg}^j\right)\right]R_i t_s \tag{20}$$

Maximum loss saving of energy of system is obtained with installation of multiple DGs by taking the partial derivative of S_{EN} with respect to P_{dg}^j & Q_{dg}^j, j = 1 to m and equating to zero as

$$\left.\begin{array}{l} \frac{\partial S_{EN}}{\partial P_{dg}^1} = 0 \\ \frac{\partial S_{EN}}{\partial Q_{dg}^1} = 0 \\ . \\ . \\ \frac{\partial S_{EN}}{\partial P_{dg}^m} = 0 \\ \frac{\partial S_{EN}}{\partial Q_{dg}^m} = 0 \end{array}\right\} \tag{21}$$

Differentiating (20), partially w.r.t P_{dg}^j & Q_{dg}^j and equating as zero are represented as follows

$$\frac{\partial S_{EN}}{\partial P_{dg}^j} = \sum_{s=1}^{dl}\sum_{i=1}^{n-1}\left[2\sum_{j=1}^{m} D_{ij}\left(P_i^s - D_{ij}P_{dg}\right)\right]R_i t_s \tag{22}$$

$$\frac{\partial S_{EN}}{\partial Q_{dg}^j} = \sum_{s=1}^{dl}\sum_{i=1}^{n-1}\left[2\sum_{j=1}^{m} D_{ij}\left(Q_i^s - D_{ij}Q_{dg}\right)\right]R_i t_s \tag{23}$$

Equation (21) provides a set of 2m linear equations, out of which m are as (22) and rest equations are as (23). These 2m equations can be expressed in the form of a matrix as:

$$[A]_{m\times m}.\left[P_{dg}\right]_{m\times 1} = [B]_{m\times 1} \tag{24}$$

$$[A]_{m\times m}.\left[Q_{dg}\right]_{m\times 1} = [C]_{m\times 1} \tag{25}$$

$[P_{dg}]$ and $[Q_{dg}]$ are vectors, which represent the active and reactive power components injected from DG. A is a matrix of size $m \times m$. B and C are the column vectors containing m elements. The elements of matrices A, B and C can be determined as

$$A_{xy} = \sum_{s=1}^{dl}\sum_{i=1}^{n-1} D_{ix}D_{iy}R_i t_s \tag{26}$$

$$B_x = \sum_{s=1}^{dl}\sum_{i=1}^{n-1} D_{ix}P_i^s R_i t_s \tag{27}$$

$$C_x = \sum_{s=1}^{dl}\sum_{i=1}^{n-1} D_{ix}Q_i^s R_i t_s \tag{28}$$

where A_{xy} represents $(x, y)^{th}$ element of matrix A. B_x and C_x are the xth element of matrix B and C respectively. Further, $[P_{dg}]$ and $[Q_{dg}]$ can be expressed as

$$\left[P_{dg}\right] = [A]^{-1}_{m\times m}.[B]_{m\times 1} \tag{29}$$

$$\left[Q_{dg}\right] = [A]^{-1}_{m\times m}.[C]_{m\times 1} \tag{30}$$

By solving (26) and (27), the optimum size and power factor of jth DG can be calculated as

$$S^j_{dg} = P^j_{dg} + jQ^j_{dg} \tag{31}$$

$$OPF^j_{dg} = \frac{P^j_{dg}}{\sqrt{P^j_{dg} + jQ^j_{dg}}} \tag{32}$$

where Equation (32) is the optimal power factor of DG unit.

The different equations from (1) to (32) are derived by the proposed technique. The base of these derivations is energy loss savings (subtraction of system energy loss with DG from system energy loss without DG). Differentiating Equation (12) partially with respect to P_{dg} and Q_{dg}, respectively, and equate the equation so obtained in order to obtain the optimum capacity of DG by proposed analytical technique for single DG. Differentiating Equation (20) partially with respect to P_{dg} and Q_{dg}, respectively, and equate the equation so obtained in order to obtain the optimum capacity of DG by the proposed analytical technique for multiple DG. All these equations so obtained are described in different equations from Equations (13) and (14) for single DG and (22) and (23) for multiple DG.

3. Algorithm for Solution

The formulations which are described in Sections 2.1 and 2.2 are applied to find the expressions for the optimal size of DG unit. Further, the proposed method is tested on IEEE 69-bus and 33-bus test radial distribution networks, respectively. In the proposed method 'm' numbers of DG units are to be placed in an n-bus network. Therefore, there are ${}^{n}c_{m}$ probable combinations for different buses. These possible combinations become very large in the case of $m << n$, hence computationally it is very difficult to analyze all combinations [3]. Therefore, the following steps are taken to compute the optimum sizing and bus where DG is to be placed for the purpose of the reduction of the loss of system energy in the test radial distribution network. The flow chart of the proposed algorithm is depicted in Figure 5. The required data is taken from [24].

Step 1: Read corresponding system data such as (line data, load data, load levels and duration) and run load flow program for base case using BFS-based method, and evaluate the active and reactive component of the powers and current in different branches along with sending end voltage.

Step 2: Set counter at $i = 0$ for bus number and $T_{dg} = 0$ for DG size.

Step 3: Determine DG size and corresponding loss savings by using (17) and (12), respectively, at each bus except the root bus.

Step 4: Increase DG counter, $i = i + 1$; and DG size $T_{dg} = T_{dg} + |S_{dg}|$.

Step 5: Check $T_{dg} \leq$ Total peak load of the system. If yes, go to step 3; otherwise, go to step 7.

Step 6: Categorize the node number and corresponding DG size where maximum loss saving occurs; this bus number serves as a candidate bus for DG placement.

Step 7: Install DG unit of size obtained from step 6 at the candidate bus which is obtained from step 6 and continue the process till negative or zero loss saving, and thus obtain the sequence of candidate buses

Step 8: For multi-DG placement, use the sequence of buses which is obtained from step 7, and install DG units of the size calculated by (31) and (19) and perform load flow analysis to determine system energy loss and voltage profile.

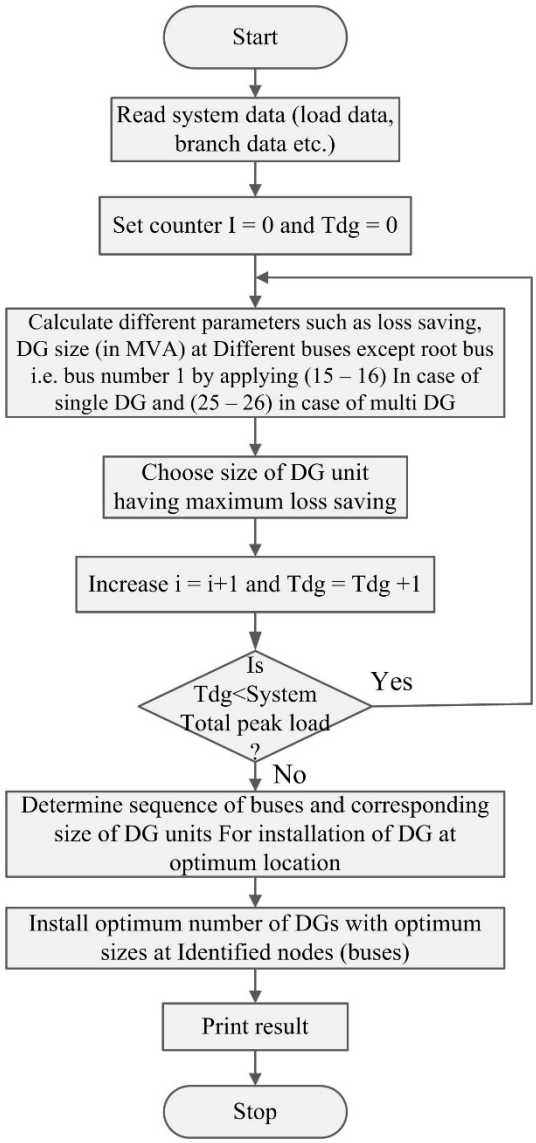


Figure 5. Flowchart for the placement of multiple DG in the radial distribution system.

4. Results and Discussion

In this section IEEE 69-bus and 33-bus radial, networks are considered for testing the developed technique. The method under consideration has been implemented in MATLAB environment to determine the optimum allocation and sizing of DGs. In proposed method the DG units which are capable to inject active and reactive both are considered for placement in the distribution system.

In the proposed method, the sequence of candidate bus for DG placement is identified on the basis of the power loss saving criterion. Further, the bus which has highest power loss saving is considered for DG placement and this process will continue till zero or nearly zero power loss saving is obtained. Therefore, in figures number 7 to 11, the power loss saving has appeared.

The details of simulation results are presented in Tables A2–A4. These tables are given in Appendix A at the end of this manuscript.

4.1. IEEE 69-Bus Test Radial Distribution System

The Figure 6 is used for the representation of a single-line diagram of the IEEE 69-bus test radial distribution network. This system has a total peak load of (3.80219 + *j*2.69460) MVA. This given yearly load of the system is divided into three levels. Furthermore,

active and reactive components of energy loss due to the branch current are obtained as 93.22 MWh, and 41.86 MVARh, respectively, for the base case, i.e., without DG from load flow solutions.

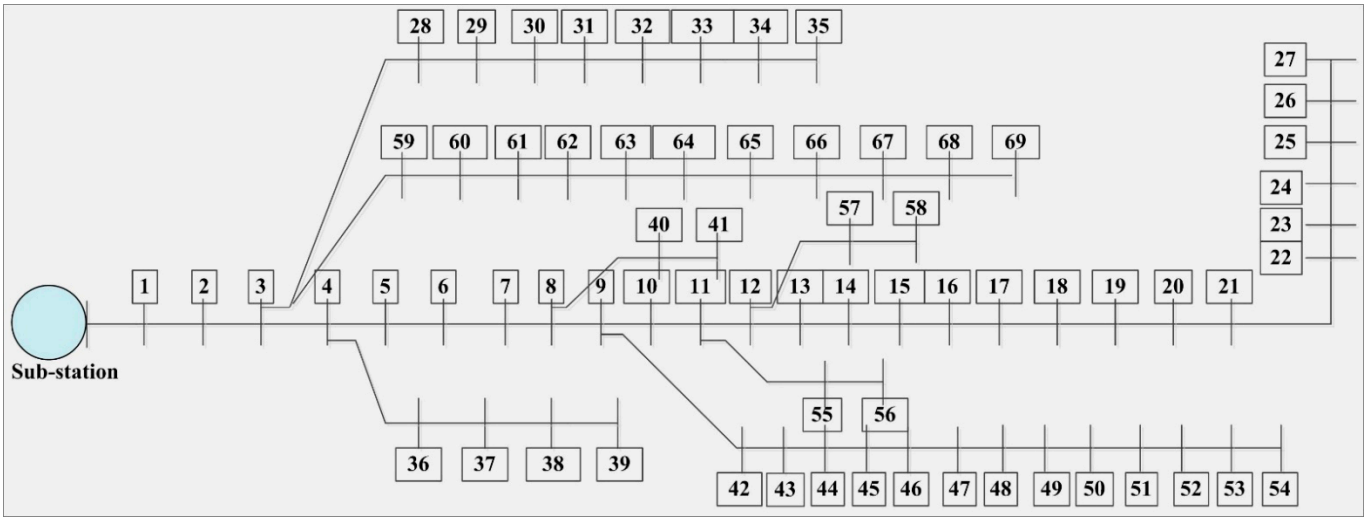


Figure 6. Single line diagram for IEEE 69-bus test radial distribution system.

Initially, optimum sizing of DGs and corresponding saving of energy loss at different buses has been determined by (17) and (12), respectively. Further, Figure 7 shows the active energy loss savings followed by optimum size of DGs (in MVA) and along with power factors of these DGs at various nodes for IEEE 69-bus network. Moreover, as is evident from Figure 7, the maximum saving of energy loss is 77.1758 MWh which occurs at node 50, and the corresponding DG size is of (0.4093 + *j*0.3041) MVA at the same bus number 50.

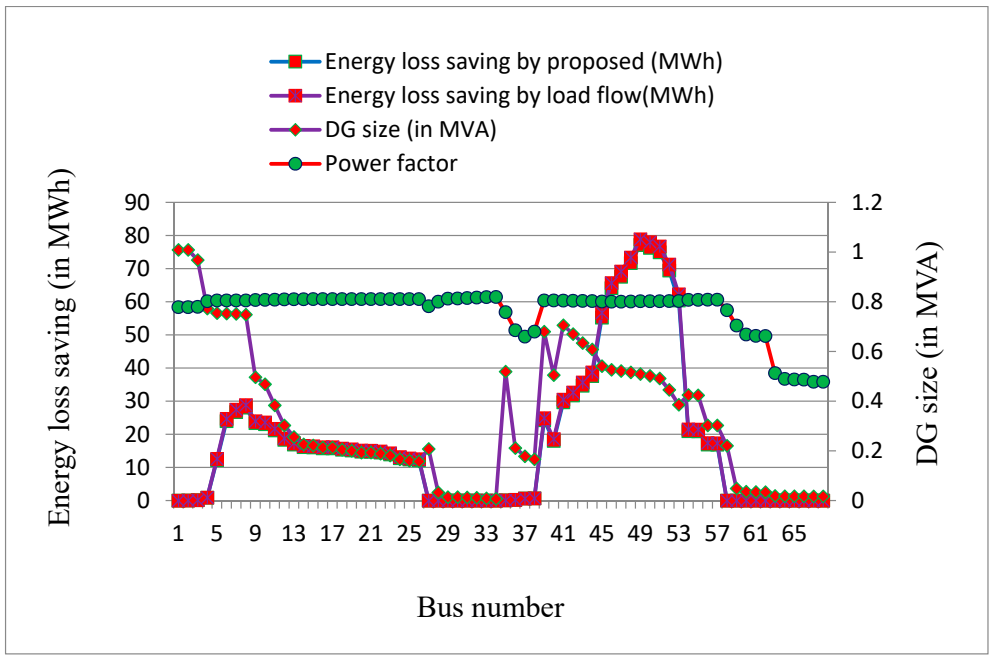


Figure 7. Optimum DG size (in MVA) and active energy loss saving (in MWh) by proposed method and load flow method at the different bus for 69-bus radial distribution system.

Therefore, install a DG unit of size (0.4093 + *j*0.3041) MVA at bus number 50 and run the load flow program in order to obtain the next bus for DG placement. In this process a maximum energy loss saving of 6.644186 MWh is observed at bus number 17 and its

corresponding DG size (0.1128 + *j*0.0804) MVA at bus number 17 as it is shown in Figure 8. Therefore, bus number 17 serves as the candidate bus for the second DG unit placement. In this process, the 84.70% of real power loss reduction is observed. To search other buses for DG placement, this process will remain to continue till zero power loss saving is achieved. In these series two buses, 50 and 17, are identified for DG installation.

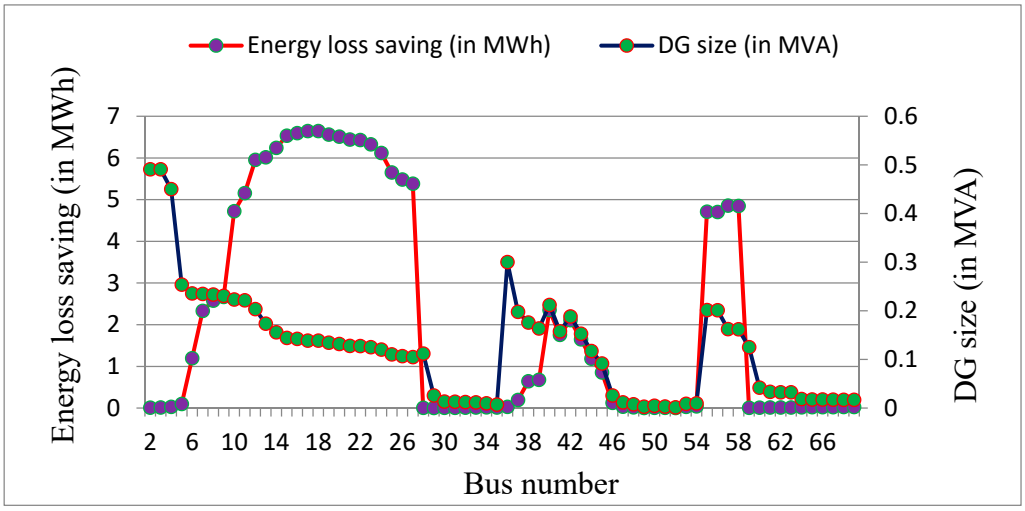


Figure 8. Loss savings of active energy component with subsequent size of DGs (in MVA) for different nodes for first iteration with DG placed at node 50 for IEEE 69-bus system.

Moreover, DGs of size (0.4093 + *j*0.3041) MVA and (0.1128 + *j*0.0804) MVA are placed at bus number 50 and 17, and results are depicted in Figure 9. From Table A2, the energy loss saving of 6.62 MWh is observed after placing a DG of the above-mentioned size at bus numbers 50 and 17. Further, bus number 11 is observed as the candidate bus whose size is (0.066318 + *j*0.048861) MVA. In this process the method reduces the system power loss by 91.84% as is evident from Table A2. The total size of the DG units is (0.6221 + *j*0.3845) MVA, which is less than that of system peak load. Additionally, the proposed method keeps on continuing to find the DG size and candidate bus for a third DG unit. Now three DG units of sizes (0.4093 + *j*0.3041) MVA, (0.1128 + *j*0.0804) MVA and (0.066318 + *j*0.048861) MVA obtained from the above process are placed at buses 50, 17 and 11, respectively. It is observed from Figure 10 that maximum energy loss savings occurs at bus 39 with a corresponding DG of size (0.1098 + *j*0.1195) MVA, the value of the maximum loss savings at bus 39 is 0.666570 MWh. Moreover, in this iteration, the system energy loss is reduced by 92.61%. In the fourth iteration, the total size of DG becomes (0.6326 + *j*0.5040) MVA which is less than that of the total load on the system. In these iterations the 50, 17, 11 and 39 buses are identified as optimal buses for DG placement and corresponding DG sizes. These buses are (0.4093 + *j*0.3041) MVA, (0.1128 + *j*0.0804) MVA, (0.066318 + *j*0.048861) MVA and (0.1098 + *j*0.1195) MVA, respectively.

Finally, Figure 11 provides the information that is for four DG units of the size mentioned above, the maximum energy loss saving is on bus 50. Further, it is noticed that the maximum energy loss saving was obtained on node 50 in the first iteration. Therefore, the procedure is converged, and in this whole process, the sequence of buses for DG placement obtained is 50, 17, 11 and 39, and the system energy loss reduces by 93.25%. Finally, the total DG size becomes (0.698232 + *j*0.552889) MVA, which is less than that total load on the system. The detail of these results is presented in Table A2.

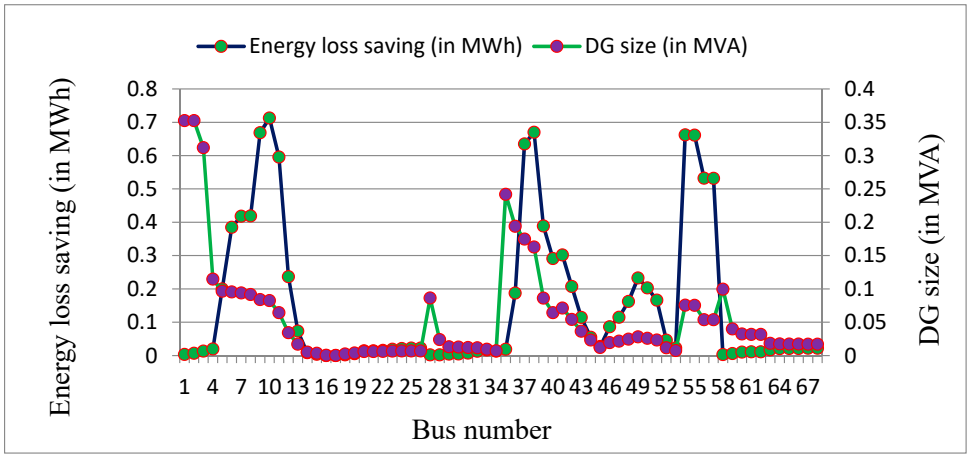


Figure 9. Loss saving of active energy component with corresponding sizes of DGs (in MVA) at different nodes for the second iteration when DGs are placed at nodes 3 and 6 for IEEE 69-bus system.

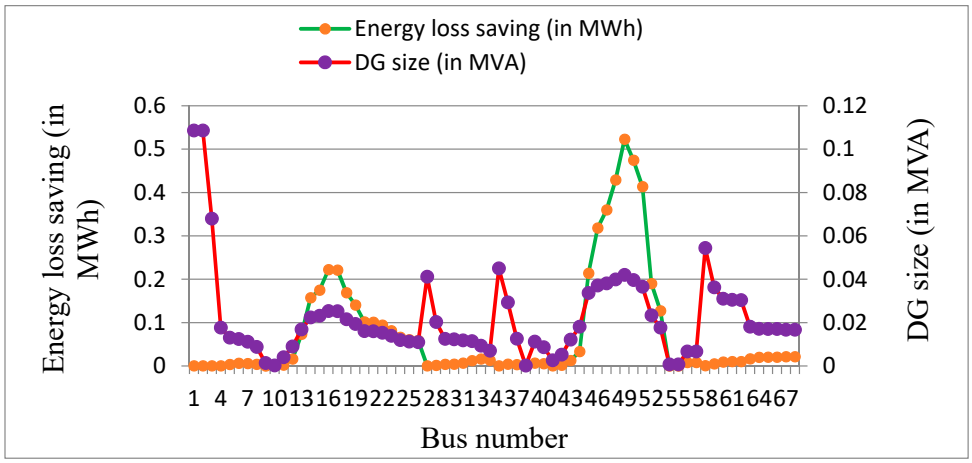


Figure 10. Loss saving of active energy components with the subsequent size of DGs (in MVA) for different nodes for the third iteration with DGs placed at nodes 50, 17 and 11 for IEEE 69-bus system.

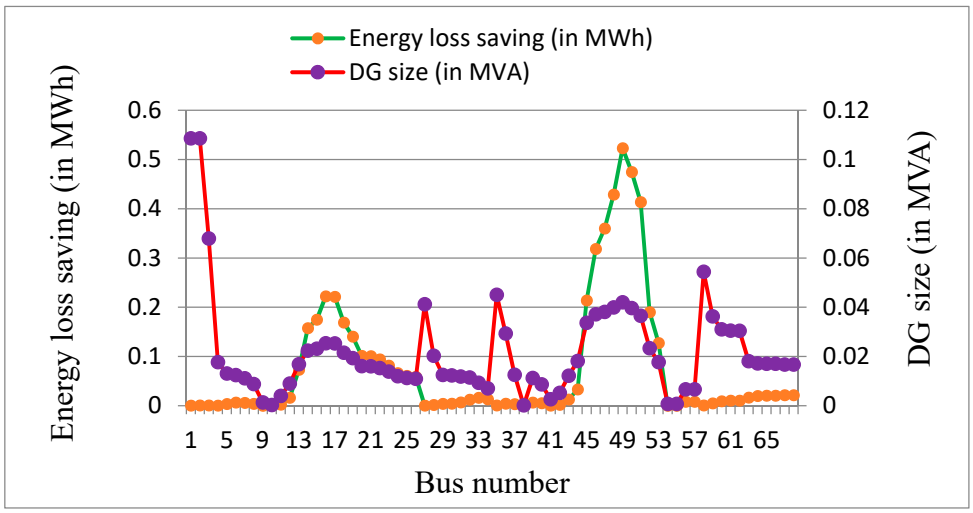


Figure 11. Loss savings of active energy components with subsequent sizes of DGs (in MVA) for different nodes for the fourth iteration with DG placed at nodes 50, 17, 11 and 39 for IEEE 69-bus system.

Additionally, for siting of multiple units of DG in IEEE 69-bus system size and locations of DGs has been determined by the method which is described in Section 2.3. In this process, the sequence of candidate buses for DG placement is the same as was determined in the preceding section as per this, the sequence of buses is 11, 17, 39 and 50 and the corresponding sizes are (0.115766 + *j*0.083357) MVA, (0.083643 + *j*0.059049) MVA, (0.109937 + *j*0.119590) MVA and (0.375638 + *j*0.280022) MVA, respectively. The system active component of energy loss without DG and with DG becomes 93.22 MWh and 5.36 MWh, respectively.

Figure 12 represents the profile of bus voltage for the IEEE 69-bus system with and without DG for various load levels. From this figure it is noticed that the allocation of DG improved system bus voltage significantly. Further, a maximum and minimum value of voltage with and without DG for various load levels ise presented in Table A4.

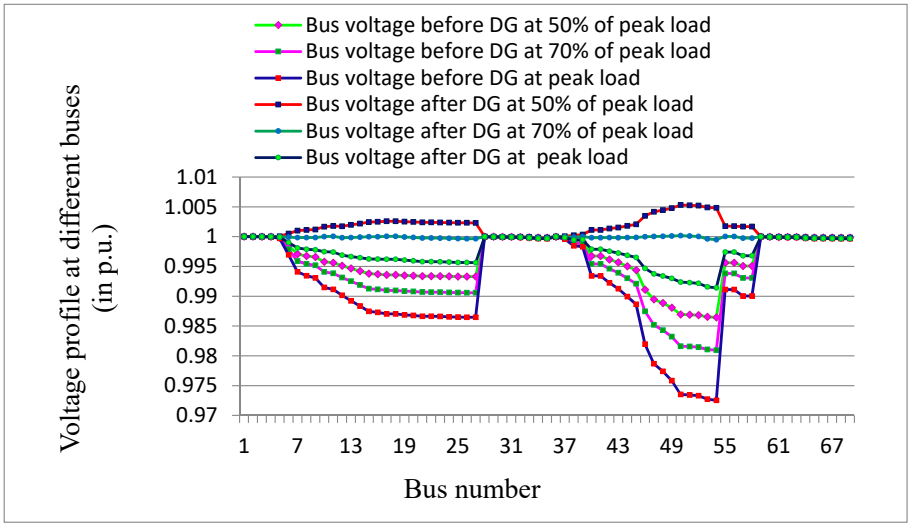


Figure 12. Voltage profile of IEEE 69-bus radial distribution network at different load levels before and after placement of DG unit.

4.2. IEEE 33-Bus Test Distribution Network

Figure 13 shows the single line diagram of 12.66 kV, 1 MVA IEEE 33-bus radial distribution network having a load of (3.715 + *j*2.300) MVA. System total energy losses in the form of real and reactive components without DG are 884.95 MWh and 589.77 MVARh, respectively.

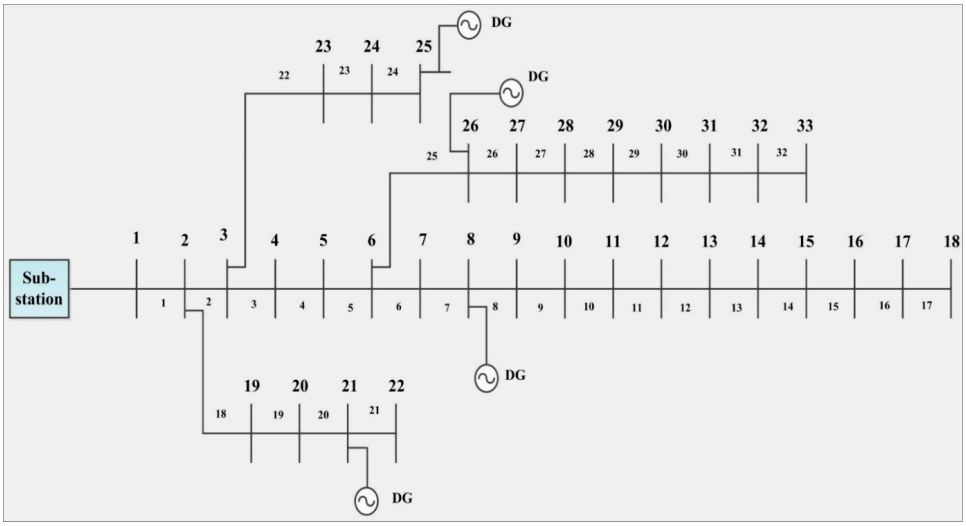


Figure 13. IEEE 33-bus test distribution system.

Firstly, the optimum sizes of individual DG units and the corresponding energy loss savings of these DG units have been calculated by developed formulation using Equations (17) and (12). Figure 13 represents the optimum power factor and size of the DG units (in MVA) and the consequent active loss saving (in kW) at various nodes for the IEEE 33-bus system. From Figure 14 the maximum active power loss saving (130.71 kW) occurs at bus 6, and the corresponding DG size (1.772 + *j*1.220) MVA at the same bus. Therefore, bus 6 serves as a candidate bus for DG placement. Placing a DG unit of size (1.772 + *j*1.220) MVA at bus 6 provides a maximum loss savings of 60.78 kW at node 31 shown in Figure 15, and the next optimum size of DG unit is (0.295 + *j*0.314) MVA at node 31. In this process system, energy loss is reduced by 66.22%. In second iteration, bus 31 becomes a candidate node for DG installation. Further, a second DG unit of (0.295 + *j*0.314) MVA is installed at node 31 gives rise to the maximum energy loss of 35.48 MWh along with DG unit of (0.445 + *j*178) MVA at bus 25 as it is depicted in Figure 16. Moreover, the system loss reduces by 73.21%.

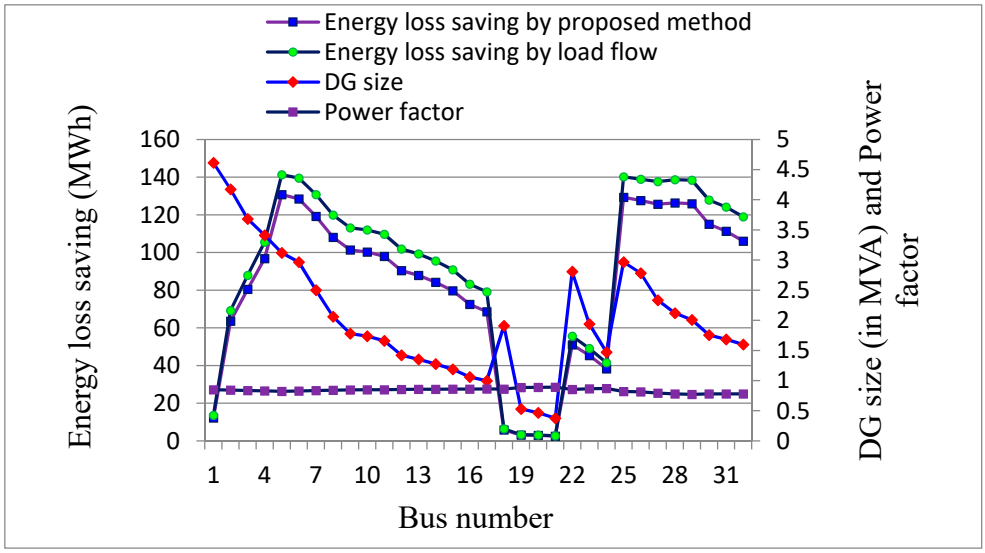


Figure 14. DG units' size (in MVA), power factor and energy loss saving (in MWh) at various nodes for the IEEE 33-bus radial distribution system.

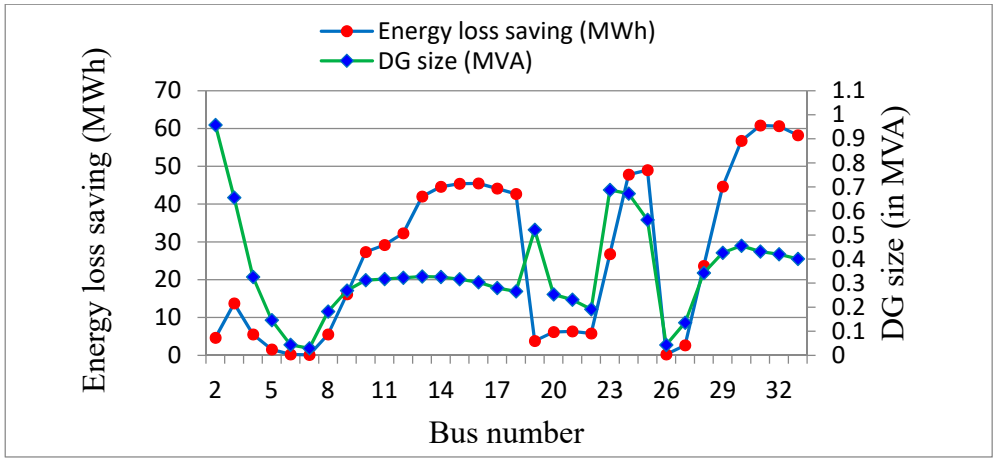


Figure 15. Optimal DG size (in MVA) and corresponding energy loss saving (in MWh) with DG at node 6 for various nodes for the IEEE 33-bus system.

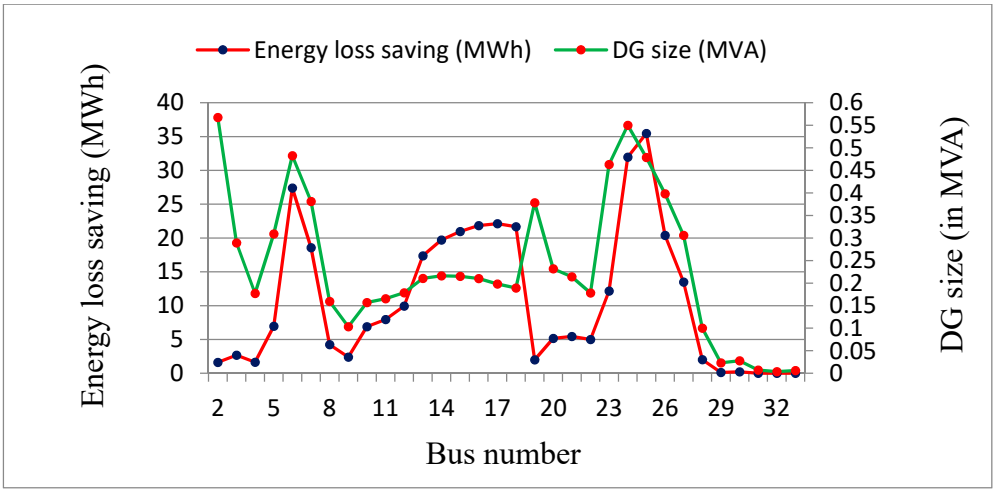


Figure 16. DG sizes (in MVA) with DG placed at nodes 6 and 31 and corresponding energy loss saving (in MWh).

Furthermore, a third DG unit of (0.445 + *j*178) MVA installed at node 25 gives a maximum loss savings of 26.14 kW further at node 6 along with a DG of (−0.460 − *j*0.394) MVA at the same node as is shown in Figure 17. Further, it is observed that first –ve sized DG is on bus 6, which is identical to the bus which was obtained in the very first iteration. Further, it is important to mention that initially the DG at bus 6 was oversized. Further, to obtain the optimal size of DG unit at bus 6 by subtracting (−0.460 − *j*0.394) MVA from the initially obtained size, i.e., (1.772 + *j*1.220) MVA, therefore, the optimum size of DG unit at bus 6 is (1.312 + *j*0.826) MVA. Thus, the identified sequence of candidate buses for DG placement is 6, 31 and 25. In this process, the system loss is reduced by 82.12%.

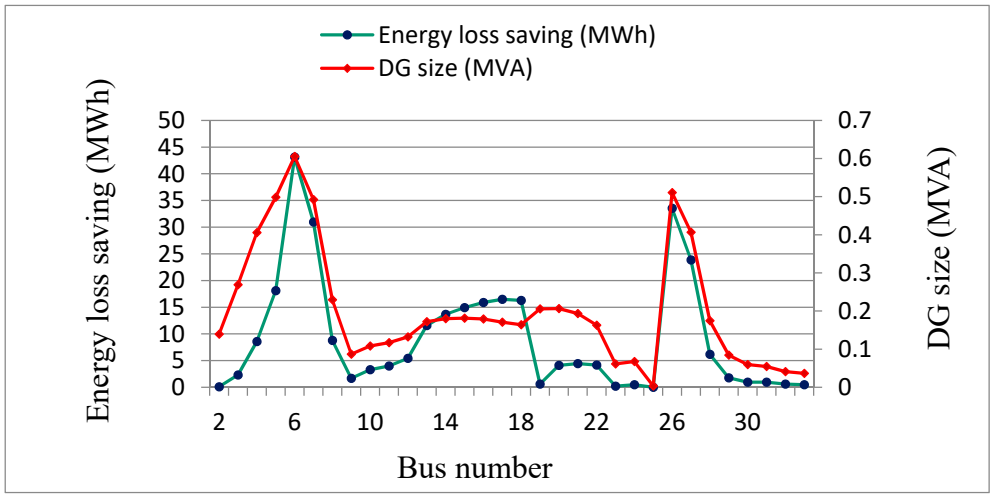


Figure 17. DG sizes (in MVA) and energy loss saving (in MWh) with DG units are placed at nodes 6, 31 and 25 for IEEE 33-bus system.

The method described under sub-section C of section II of this study has been applied for the installation of multiple DGs in IEEE 33-bus network. Equations (19) and (28) have been applied to determine the net energy loss savings and optimum sizes of DG units, respectively. Further, DG units having sizes of (1.141 + *j*0.643) MVA, (0.482 + *j*0.505) MVA and (0.551 + *j*0.267) MVA are placed at the identified buses 6, 31 and 25, respectively, provide system energy loss reduction from 884.95 MWh to 144.38 MWh with 83.69%. Moreover, the placement of the above-mentioned sizes of DGs at the respective places, i.e., the 6, 31 and 25 number buses, gives rise to energy loss savings of 740.57 MWh.

In this entire process, the system energy losses get reduced from 884.95 MWh to 298.98 MWh with 66.22% in case of the methodology of single DG placement. Further, in case of the multiple DG placement methodology, three DG units are placed at identified buses, these are 6, 31 and 25 of sizes mentioned above, the active energy losses of the system reduced from 884.95 MWh to 144.38 MWh with 83.69%.

The detailed results of IEEE 33-bus system with respect to DG sizes, energy loss saving and percentage of energy loss reduction have been presented in Table A3.

Figure 18 shows the profile of system voltage of IEEE 33-bus system without and with DG unit installation for three load levels it is noticed from this figure that voltage profile of system enhanced significantly. On the basis of these results it is concluded that branch current is reduced due to the installation of DG in the network, and as a consequence, the system voltage profile gets improved. Further, the maximum and minimum values of bus voltage without and with DG for the three load levels is presented in Table A4. From this table it is noticed that the minimum voltage (0.9582 p.u.) appears at bus 18 in the base case, i.e., without DG placement, and this value of voltage is increased up to 0.9936 p.u. for 50% load, and the same pattern is observed for other load profilis, i.e., 75% and 100% load. Table A5 represents the comparison of different results obtained by the proposed method and the results achieved by other methods which are available in the literature. On the basis of obtained results, it is found that the power loss saving capability is more as compared to other methods in the case of a 33-bus radial distribution system. Size of DG is also less as compared to other methods. It is also observed from Table A5 that the optimal locations of DGs by the proposed method are also similar to other available methods for 33-bus and 69-bus test radial distribution systems. Therefore, this phenomenon proves the suitability of this proposed method. Further, Table A6 represents the description of data with respect to different load levels and durations which is considered in the proposed method.

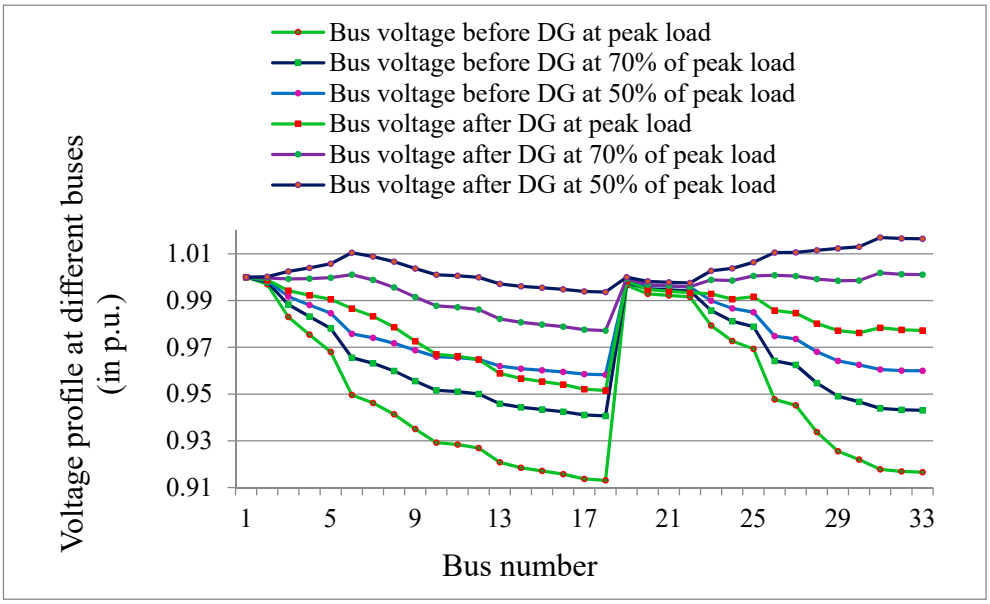


Figure 18. Bus voltage for IEEE 33-bus system for various load levels before and after DG placement at different bus.

5. Conclusions

The objective of the present research article is to decrease system energy loss with optimum sizing and placement of DG by applying an analytically based method. There is no need oof the formation and computation of the admittance matrix in the developed method. The present technique is intended to identify the order of buses to DG installation by process of maximum energy loss saving of real components of energy. The developed method is valid for multiple DGs along with single DG in test radial distribution systems.

Moreover, this developed method is more advantageous over the other method because it requires only a few power flow solutions in order to find out the optimum DG size even for larger networks. The developed modus operandi is applied on an IEEE 69-bus and 33-bus network. The simulation results obtained by the present developed approach are compared with the other methods which are discussed in literature, and it is established that the energy loss reduction capability of the proposed method is more as compared to other methods. The basic and foremost objective of present study is to minimize energy loss and to obtain the optimum position of DG placement and hence, improvement in voltage profile.

Author Contributions: Conceptualization, H.M.; Data curation, P.P., D.C.M., H.M. and I.A.K.; Formal analysis, P.P., D.C.M., H.M., M.A.A. and I.A.K.; Funding acquisition, P.P., H.M., M.A.A. and I.A.K.; Investigation, P.P. and H.M.; Methodology, P.P., D.C.M., H.M., M.A.A. and I.A.K.; Project administration, D.C.M., H.M. and M.A.A.; Resources, P.P., H.M., M.A.A. and I.A.K.; Software, P.P. and D.C.M.; Supervision, D.C.M. and I.A.K.; Visualization, P.P., D.C.M. and M.A.A.; Writing—original draft, P.P., H.M., M.A.A. and I.A.K.; Writing—review & editing, M.A.A. All authors have read and agreed to the published version of the manuscript.

Funding: The authors extend their appreciation to the Researchers Supporting Project at King Saud University, Riyadh, Saudi Arabia, for funding this research work through the project number RSP-2021/278.

Institutional Review Board Statement: Not applicable.

Informed Consent Statement: Not applicable.

Data Availability Statement: Not applicable.

Acknowledgments: The authors would like to acknowledge the support from King Saud University, Saudi Arabia. The authors would like to acknowledge the support from Intelligent Prognostic Private Limited Delhi, India Researcher's Supporting Project.

Conflicts of Interest: The authors declare no conflict of interest.

Appendix A

The following procedure is adopted for the formation of a D matrix for multiple DG allocation. Suppose four DG units are to be installed at buses 8, 21, 25 and 26 in an IEEE 33-bus system. Here m is total number of DG units which are to be placed. Therefore, $m = 4$ and the set of branches β_j containing the branches between bus j where DG is to be installed, and source bus is given as

$m = 4$,
$\beta_8 = \{1, 2, 3, 4, 5, 6, 7\}$
$\beta_{21} = \{1, 18, 19, 20\}$
$\beta_{25} = \{1, 2, 22, 23, 24\}$
$\beta_{26} = \{1, 2, 3, 4, 5, 25\}$

Let DG is placed at bus no. 8 (β_8), due to this magnitude of current is changed in the branches 1, 2, 3, 4, 5, 6, 7 only and current in other branches remains same. DG is placed at bus no. 21 (β_{21}), due to this magnitude of current is changed in the branches 1, 18, 19, 20 only and current in other branches remains same. DG is placed at bus no. 25 (β_{25}), due to this magnitude of current is changed in the branches 1, 2, 22, 23, 24 only and current in other branches remains same. DG is placed at bus no. 26 (β_{26}), due to this magnitude of current is changed in the branches 1, 2, 3, 4, 5, 25 only and current in other branches remains same.

The matrix D^T has an order of $m \times n - 1$, where m is 4 that is DG units' number which are is to be placed, and $n - 1$ is 32 that is a number of branches that is a column vector of D^T matrix. Therefore, the elements of the first row oof the D^T matrix will be 1 at columns (1, 2, 3, 4, 5, 6, 7) and the remaining elements in same row are 0. Similarly, the elements of the second row will be 1 at columns (1, 18, 19, 20), and elements of other columns in the

same row are 0. The elements of the third row will be 1 at columns (1, 2, 22, 23, 24) and the elements of the other columns are 0 in third row. Finally, the elements of the fourth row will be 1 at columns (1, 2, 3, 4, 5, 25), and elements of the other columns are 0 in the fourth row.

The rows of the above matrix represent buses of the network while columns of the matrix represent branches of the matrix respectively. In the present case, D^T is of order ($m \times n - 1$ or 4×32) matrix in same way D_{ij} can be determined for n number of DG.

Table A1. Summary of the related work.

Reference Number and Year of Publication	Type of Application	Main Contribution and Characteristics	Analyzed Method/Remarks	Recommended System/Similarity with Current Approach
[1], 2001, [13], 2016, [24],1995	Investigated the impact of penetration level of DG in distribution network	Addressed the transient stability and static performance of large system by considering penetration of DG	Addressed different issues and challenges related to DG placement in distribution system	No similarity
[2], 2006, [3], 2014, [4], 2015, [5], 2014, [6], 2004, [7], 2009, [8], 2013, [9], 2013, [10], 2010, [17], 2014, [21], 2016	All these research paper applied an Analytical method for optimal sizing and siting of DG in distribution system	Investigation of optimal sizing and siting of DG on the basis of loss sensitivity factor and equivalent current injection based analytical methods. The objective functions are optimized by PSO and ELF-absed Technique. In some references the sensitivity of loss factor is applied to minimize the search space.	Authors described an analytical based method for optimum size and location of DG to minimize the total power loss of the system without using Jacobian matrix. The proposed methods are implemented on IEEE 33-bus and 69-bus radial distribution system	Analytical based is addressed which is not using admittance or Jacobian matrix. But in the current method, the analytical-based method is described by using load flow method solutions
[11], 2013	Evolutionary based technique for optimal placement of (wind and solar) based DG in distribution network	Sensitivity indexed based Evolutionary optimization technique is used to optimal placement and sizing of non-dispatchable DG	The proposed technique is applied on IEEE 69-bus distribution network and sensitivity indexed is considered to limit the search space	No similarity
[12], 2014	New multi-objective index (IMO) based method for integration of SPV	An analytical based expressions are derived to for optimal sizing of SPV based	Authors investigate an analytical based method for optimal integration of SPV based DG along with BES (battery energy storage system). The proposed method is applied on IEEE 33-bus distribution system	No similarity
[14], 2013	PSO based optimization technique	Authors investigate the PSO based optimization technique for optimal sizing and siting of different types of DGs in distribution ystem	The objective of proposed method is to minimize the system power loss by considering placement of different types of DGs. The methodology is tested on IEEE 33-bus and 69-bus radial distribution system	No similarity
[15], 2015	Novel power loss sensitivity and power stability index (PSI) based method	Authors describe comparison of Novel Power Loss Sensitivity, Power Stability Index (PSI), further voltage stability index (VSI) methods for optimal location and sizing of DG in radial distribution network.	The optimal location and sizing of DG is performed by considering load growth. The proposed technique is tested on IEEE 12-bus, modified 12-bus, 69-bus and 85-bus test systems.	No similarity

Table A1. *Cont.*

Reference Number and Year of Publication	Type of Application	Main Contribution and Characteristics	Analyzed Method/Remarks	Recommended System/Similarity with Current Approach
[16], 2013	Comparison of different novel techniques for optimal sizing and siting of DG	Authors investigate the comparison of different techniques like combined power loss sensitivity, index vector, voltage sensitivity index and modified novel method for optimal sizing and siting of DG	The objective of proposed method to improve system voltage profile and minimize system power loss. The proposed method is applied on IEEE 33-bus and 69-bus radial distribution system	No similarity
[18], 2014	Identification of vulnerable buses for DG placement by bifurcation based method	Placement of optimal number DGs in order maintain system voltage within permissible limit by bifurcation method	The global optimization of optimal number of DGs is found on the basis of dynamic programming search method. The proposed method is applied on 34-bus distribution network	No similarity
[19], 2013	Multi-objective based nonlinear programming (NLP) based method	Optimum sizing and siting of DG in distribution system is performed by NLP based method. The objective of proposed method to improve voltage stability	A fuzzy logic based method by selecting appropriate weight factors is applied to obtain the desired objectives	No similarity
[20], 2006	Application of GA based optimization technique	Authors applied GA technique for optimum sizing and siting of DG to enhance system reliability, system voltage and minimize system losses	The proposed method is demonstrated on standard IEEE test radial distribution network	No similarity
[22], 2012	Indexed based method for DG placement and results are compared by Golden Section Search (GSS)	Authors proposed a new analytical based index (PSI) algorithm for DG placement and sizing in distribution system	The proposed technique is applied on 12-bus, modified 12-bus and 69-bus distribution networks.	No similarity
[23], 2013	MINLP based technique for optimal sizing and siting of DG	Authors proposed a methodology for improving voltage profile and voltage stability margin	The objective of proposed method is to improve VSM and method is tested on standard IEEE test radial distribution system	No similarity
[25], 2011	AC optimal power flow based method	Authors investigate AC optimal power flow (OPF) for optimal penetration of DG to minimize system loss	Optimal penetration and placement of DG using multi-period AC OPF based method. Proposed method is tested on U.K. based distribution network	No similarity
[26], 2013, [28]—2018	PSO based optimization technique	PSO based optimization technique is applied for optimal placement and sizing of DG in distribution system	The objective of proposed method is to minimize of power loss and maximization of voltage stability. The method is tested on 12-bus, 30-bus, 33-bus, 41-bus and 69-bus test distribution system	No similarity
[27], 2018	Selection and integration of best DG in distribution system	Author addressed the impact of reactive power on voltage stability and penetration level by analytical based method	The various indices are evaluated by modal analysis method. The proposed method is tested on 33-bus and 136-bus distribution network	No similarity

Table A2. Summary of the simulation results for IEEE 69-bus radial distribution network.

S.No.	Network Condition	Real Energy Loss (MWh)	Number of DG	Node(s) for DG Placement	Size of DG ($P_{dg} + jQ_{dg}$) MVA	Size of DG (in MVA)	Optimum DG Power Factor	Loss Saving (MWh)	Active Energy Loss Reduction in (%)
1.	Without DG	93.22	-	-	-	-	-	-	-
2.	0.409 + *j*0.304 MVA, DG placed at bus 50	77.18	1	50	0.409 + *j*0.304	0.510	0.8025	14.55	84.39
3.	0.409 + *j*0.304 MVA DG placed at bus 50 and 0.113 + *j*0.080 MVA DG placed at bus 17	7.62	2	50 17	0.409 + *j*0.304 0.113 + *j*0.080	0.139	0.8162	6.64	91.84
4.	0.409 + *j*0.304 MVA DG placed at bus 50, 0.113 + *j*0.080 MVA DG placed at bus 17, and 0.066 + *j*0.048 MVA DG at bus 11	6.88	3	50 17 11	0.409 + *j*0.304 0.113 + *j*0.0800.066 + *j*0.048	0.082	0.8087	0.713	92.61
5.	0.409 + *j*0.304 MVA DG placed at bus 50, 0.113 + *j*0.080 MVA DG placed at bus 17, 0.066 + *j*0.048 MVA DG at bus 11, and 0.110 + *j*0.120 MVA DG at bus 39	6.21	4	50 17 11 39	0.409 + *j*0.304 0.113 + *j*0.0800.066 + *j*0.0480.110 + *j*0.120	0.162	0.6757	0.667	93.32
6.	Base case	93.22	-	-	-	-	-	-	-
7.	0.116 + *j*0.083 MVA, DG at bus 11, 0.084 + *j*0.059 MVA DG at bus 17, 0.110 + *j*0.120 MVA DG at bus 39 and 0.376 + *j*0.280 MVA DG at bus 50	93.22	4	11 17 39 50	0.116 + *j*0.083 0.084 + *j*0.059 0.110 + *j*0.120 0.376 + *j*0.280	0.1427 0.1024 0.1624 0.4685	0.8115 0.8169 0.6768 0.8017	5.36	94.22

Table A3. Summary of simulation results for IEEE 33-bus network.

S.No.	Network Condition	Real Energy Loss (MWh)	Number of DG	Node(s) Where DG Is Placed	Size of DG ($P_{dg} + jQ_{dg}$) MVA	Optimum Power Factor of DG	Loss Saving (in MWh)	Real Energy Loss Reduction in (%)
1.	Without DG	884.95	-	-	-	-	-	-
2.	1.772 + *j*1.220 MVA DG placed at bus 6	298.98	1	6	1.772 + *j*1.220	0.8237	544.34	66.22
3.	1.772 +*j*1.220 MVA DG placed at bus 6 and 0.295 + *j*0.314 MVA DG placed at bus 31	237.11	2	6 31	1.772 + *j*1.220 0.295 + *j*0.314	0.8237 0.6847	60.78	73.21
4.	1.772 + *j*1.220 MVA, DG placed at bus 6, 0.295 + *j*0.314 MVA, DG placed at bus 31, and 0.444 + *j*0.179 MVA DG placed at bus 25	158.27	3	6 31 25	1.772 + *j*1.220 0.295 + *j*0.314 0.444 + *j*0.179	0.8237 0.6847 0.9275	35.48	82.12
	Multi-DG (Three-DGs of following size are placed at a time in 6, 25, 31)							
5.	Base case	884.95	-	-	-	-	-	-
6.	1.141 + *j*0.643 MVA, 0.8712 PF lag DG at bus 6, 0.482 + *j*0.505 MVA DG at bus 31 and 0.551 + *j*0.267 MVA, 0.9 PF lag DG placed at bus 25	884.95	3	6 31 25	1.141 + *j*0.643 0.482 + *j*0.505 0.551 + *j*0.267	0.8712 0.6903 0.9000	144.38	83.69

Table A4. Maximum and minimum value of voltage for IEEE 69-bus and IEEE 33-bus network before and after dg placement.

System Type	Maximum and Minimum Bus Voltage before DG						Maximum and Minimum Bus Voltage after DG					
	50% of Peak Load		70% of Peak Load		100% of Peak Load		50% of Peak Load		70% of Peak Load		100% of Peak Load	
	Minimum Voltage (in p.u.) Bus	Maximum Voltage (in p.u.) Bus	Minimum Voltage (in p.u.) Bus	Maximum Voltage (in p.u.) Bus	Minimum Voltage (in p.u.) Bus	Maximum Voltage (in p.u.) Bus	Minimum Voltage (in p.u.) Bus	Maximum Voltage (in p.u.) Bus	Minimum Voltage (in p.u.) Bus	Maximum Voltage (in p.u.) Bus	Minimum Voltage (in p.u.) Bus	Maximum Voltage (in p.u.) Bus
69-bus	0.9864 54	1.0000 1	0.9809 54	1.0000 1	0.9725 54	1.0000 1	0.9998 69	1.0053 50	0.9995 54	1.0002 51	0.9914 54	1.0000 1
33-bus	0.9582 18	1.0000 1	0.9407 18	1.0000 1	0.9131 18	1.0000 1	0.9936 18	1.017 31	0.9771 18	1.0019 31	0.9515 18	1.0 1

Table A5. Comparison of results by different methods for IEEE 69-bus and 33-bus radial distribution system.

System	Parameters	Murty and Kumar [15]		Naik and Khatod [3]		Viral and Khatod [4]	Proposed Technique
69-bus	Optimum bus	-		-		3	3
	DG size	1.85 MW UPF, 2.20 MVA, 0.9 PF lag		2.22 MVA, 0.82 PF lag		-	0.73 MVA, 0.8033 PF lag
	Loss saving (in percentage)	87.59 at 0.9 PF lag		89.39 at 0.82 PF lag		-	94.25 at 0.8033 PF lag
33-bus	Optimum bus	50		50		50	50
	DG size	2.5 MVA at UPF	3.01 MVA 0.9 PF lag	2.48 MVA UPF	3.01 MVA at 0.85 PF lag	2.969 MVA, 0.8180 PF lag	3.121 MVA, 0.8231PF lag
	Loss saving (in percentage)	47.32	66.39	48.65	69.55	33.88	83.69

Table A6. Data for load level and load duration.

Load level (in the percentage of peak load)	100	70	50
Time interval (in hours)	1500	5000	2260

References

1. Ackermann, T.; Andersson, G.; Söder, L. Distributed generation: A definition. *Electr. Power Syst. Res.* **2001**, *57*, 195–204. [CrossRef]
2. Acharya, N.; Mahat, P.; Mithulananthan, N. An analytical approach for DG allocation in primary distribution network. *Int. J. Electr. Power Energy Syst.* **2006**, *28*, 669–678. [CrossRef]
3. Naik, S.N.G.; Khatod, D.K.; Sharma, M.P. Analytical approach for optimal siting and sizing of distributed generation in radial distribution networks. *IET Gener. Transm. Distrib.* **2015**, *9*, 209–220. [CrossRef]
4. Viral, R.; Khatod, D. An analytical approach for sizing and siting of DGs in balanced radial distribution networks for loss minimization. *Int. J. Electr. Power Energy Syst.* **2015**, *67*, 191–201. [CrossRef]
5. Kaur, S.; Kumbhar, G.; Sharma, J. A MINLP technique for optimal placement of multiple DG units in distribution systems. *Int. J. Electr. Power Energy Syst.* **2014**, *63*, 609–617. [CrossRef]
6. Wang, C.; Nehrir, M. Analytical approaches for optimal placement of distributed generation sources in power systems. *IEEE Trans. Power Syst.* **2005**, *19*, 2068–2076. [CrossRef]
7. Gözel, T.; Hocaoglu, M.H. An analytical method for the sizing and siting of distributed generators in radial systems. *Electr. Power Syst. Res.* **2009**, *79*, 912–918. [CrossRef]
8. Hung, D.Q.; Mithulananthan, N. Multiple Distributed Generator Placement in Primary Distribution Networks for Loss Reduction. *IEEE Trans. Ind. Electron.* **2011**, *60*, 1700–1708. [CrossRef]
9. Hung, D.Q.; Mithulananthan, N.; Bansal, R. Analytical strategies for renewable distributed generation integration considering energy loss minimization. *Appl. Energy* **2013**, *105*, 75–85. [CrossRef]
10. Hung, D.Q.; Mithulananthan, N.; Bansal, R. Analytical Expressions for DG Allocation in Primary Distribution Networks. *IEEE Trans. Energy Convers.* **2010**, *25*, 814–820. [CrossRef]
11. Khatod, D.K.; Pant, V.; Sharma, J. Evolutionary programming based optimal placement of renewable distributed generators. *IEEE Trans. Power Syst.* **2012**, *28*, 683–695. [CrossRef]

12. Hung, D.Q.; Mithulananthan, N.; Bansal, R. Integration of PV and BES units in commercial distribution systems considering energy loss and voltage stability. *Appl. Energy* **2014**, *113*, 1162–1170. [CrossRef]
13. Prakash, P.; Khatod, D.K. Optimal sizing and siting techniques for distributed generation in distribution systems: A review. *Renew. Sustain. Energy Rev.* **2016**, *57*, 111–130. [CrossRef]
14. Kansal, S.; Kumar, V.; Tyagi, B. Optimal placement of different type of DG sources in distribution networks. *Int. J. Electr. Power Energy Syst.* **2013**, *53*, 752–760. [CrossRef]
15. Murty, V.; Kumar, A. Optimal placement of DG in radial distribution systems based on new voltage stability index under load growth. *Int. J. Electr. Power Energy Syst.* **2015**, *69*, 246–256. [CrossRef]
16. Murthy, V.; Kumar, A. Comparison of optimal DG allocation methods in radial distribution systems based on sensitivity approaches. *Int. J. Electr. Power Energy Syst.* **2013**, *53*, 450–467. [CrossRef]
17. Hung, D.Q.; Mithulananthan, N.; Lee, K.Y. Optimal placement of dispatchable and nondispatchable renewable DG units in distribution networks for minimizing energy loss. *Int. J. Electr. Power Energy Syst.* **2013**, *55*, 179–186. [CrossRef]
18. Esmaili, M.; Firozjaee, E.C.; Shayanfar, H.A. Optimal placement of distributed generations considering voltage stability and power losses with observing voltage-related constraints. *Appl. Energy* **2014**, *113*, 1252–1260. [CrossRef]
19. Esmaili, M. Placement of minimum distributed generation units observing power losses and voltage stability with network constraints. *IET Gener. Transm. Distrib.* **2013**, *7*, 813–821. [CrossRef]
20. Borges, C.L.T.; Falcão, D.M. Optimal distributed generation allocation for reliability, losses, and voltage improvement. *Int. J. Electr. Power Energy Syst.* **2006**, *28*, 413–420. [CrossRef]
21. Tah, A.; Das, D. Novel analytical method for the placement and sizing of distributed generation unit on distribution networks with and without considering P and PQV buses. *Int. J. Electr. Power Energy Syst.* **2016**, *78*, 401–413. [CrossRef]
22. Aman, M.; Jasmon, G.; Mokhlis, H.; Bakar, A. Optimal placement and sizing of a DG based on a new power stability index and line losses. *Int. J. Electr. Power Energy Syst.* **2012**, *43*, 1296–1304. [CrossRef]
23. Al Abri, R.S.; El-Saadany, E.F.; Atwa, Y.M. Optimal Placement and Sizing Method to Improve the Voltage Stability Margin in a Distribution System Using Distributed Generation. *IEEE Trans. Power Syst.* **2012**, *28*, 326–334. [CrossRef]
24. Das, D.; Kothari, D.; Kalam, A. Simple and efficient method for load flow solution of radial distribution networks. *Int. J. Electr. Power Energy Syst.* **1995**, *17*, 335–346. [CrossRef]
25. Ochoa, L.; Harrison, G. Minimizing Energy Losses: Optimal Accommodation and Smart Operation of Renewable Distributed Generation. *IEEE Trans. Power Syst.* **2010**, *26*, 198–205. [CrossRef]
26. Aman, M.; Jasmon, G.; Bakar, A.; Mokhlis, H. A new approach for optimum DG placement and sizing based on voltage stability maximization and minimization of power losses. *Energy Convers. Manag.* **2013**, *70*, 202–210. [CrossRef]
27. Mehta, P.; Bhatt, P.; Pandya, V. Optimal selection of distributed generating units and its placement for voltage stability enhancement and energy loss minimization. *Ain Shams Eng. J.* **2018**, *9*, 187–201. [CrossRef]
28. Tawfeek, T.S.; Ahmed, A.; Hasan, S. Analytical and particle swarm optimization algorithms for optimal allocation of four different distributed generation types in radial distribution networks. *Energy Procedia* **2018**, *153*, 86–94. [CrossRef]

Research Square

Preprints are preliminary reports that have not undergone peer review.
They should not be considered conclusive, used to inform clinical practice,
or referenced by the media as validated information.

A Novel methodology for planning of charging infrastructure in the scenario of high EV penetration

Mandhir Kumar Verma (mandhirverma@gmail.com)
Indian Institute of Technology Dhanbad https://orcid.org/0000-0002-1573-108X
Vivekananda Mukherjee
Indian Institute of Technology Dhanbad
Vinod Kumar Yadav
Delhi Technological University
Santosh Ghosh
Kirloskar Brothers Pune

Research Article

Keywords: Distribution network expansion planning (DNEP), electric busses (EBs), electric vehicles (EVs), Host charging station (HCS), response surface methodology (RSM)

Posted Date: February 14th, 2022

DOI: https://doi.org/10.21203/rs.3.rs-874556/v1

License: This work is licensed under a Creative Commons Attribution 4.0 International License.
Read Full License

A Novel methodology for planning of charging infrastructure in the scenario of high EV penetration

Mandhir Kumar Verma[1,*], Vivekananda Mukherjee[1], Vinod Kumar Yadav[2] and Santosh Ghosh[3]

[1]Department of Electrical Engineering, Indian Institute of Technology, Dhanbad, Jharkhand, India
[2]Department of Electrical Engineering, Delhi Technological University, Delhi, India
[3]Corporate R&D Department, Kirloskar Brothers Limited, Pune, India

Abstract
This article presents a novel methodology for distribution network expansion planning (DNEP) considering the inclusion of electric vehicles (EV), especially, electric bus (EB) charging loads. The proposed methodology addresses network congestion through an optimum time of charging, cost optimization, new charging infrastructure, and minimization of losses under a set of technical and physical constraints, which represents practical uncertainties. Along with load flow analysis, selection of the number of ports and technology at the host charging station is obtained through the application of response surface methodology. The proposed methodology provides a coordinated planning for the development of EB charging station infrastructure that takes into account the effects of both the power dispersion framework and transportation framework. The effectiveness of the proposed methodology is investigated by applying it on 69-node IEEE modified distribution test system considering three charging technologies viz. fast charging, ultra-fast charging, and battery swapping. The results of the proposed model are compared with the direct statistical method and it revealed that the right selection of technology for EB charging and the right planning of the charging infrastructure can effectively optimize the cost of EV charging infrastructure and thereby catalyze the decarbonization of the transportation sector.

Keywords- Distribution network expansion planning (DNEP); electric busses (EBs); electric vehicles (EVs); Host charging station (HCS); response surface methodology (RSM)

*Corresponding author.
Tel.: +918448615745
E-mail: mandhirverma@gmail.com (Mandhir Kumar Verma)
ORCID id: 0000-0002-1573-108X

1. Introduction

Electric vehicles (EVs), along with their charging infrastructures, are being deployed at a fast pace by city administrations across the globe to curb greenhouse gas emissions and reverse climate change. However, without proper planning, the introduction of a large number of charging stations will put an additional burden on the grid and thereby impact grid reliability. The optimal location of charging stations to ensure uninterrupted service of public transport and impact on the distribution system thereof are matters of great concern to the energy planners and the policymakers today. Charging station (CS) zones will require meticulous and innovative distribution network expansion planning (DNEP) to meet the additional demand due to the increased number of EVs, especially electric busses (EBs) (Xiang et al. 2019). EBs consume considerably higher energy than personal cars, and unplanned penetration of EBs will increase the losses, voltage drop, and overload the distribution network, which will eventually impact the system reliability and power supply quality (Gomez and Morcos 2002). Past studies show that, without adequate focus on DNEP, even a low penetration rate of EBs may lead to distribution transformer overloading (Li and Bai 2011), overshooting of peak load demand (Shao et al. 2009), and higher power losses (Hadley and Tsvetkova 2009). While planning for the charging infrastructure for the EB fleet, three vital strategic elements are essential to consider: where, when, and how to charge the EBs. Literature reveals that the optimal location of charging stations would improve the EB productivity and deliver unwavering quality and intensity of supply (Zhao et al. 2011), which will eventually encourage consumers to opt for this new mode of transport (Karfopoulos and Hatziargyriou 2013, Dong et al. 2018). Hence it is important to adopt smart charging technologies and positioning and scheduling of charging stations based on real-time data. The distance between the charging stations needs to be strategically maintained so that the EV users are not stressed over the possibility of a loss of energy in transit as well, and make the charging stations' location progressively sensible and predictable in the real world.

Much comparisons of planning strategies have been made by the researchers in the past. Zhao et al. 2020 compared over 20 research works related to the charging station planning, and the review of the past research shows that none of them considered integration of various types of charging technology, particularly for electric buses. Zeb et al. 2020 have compared normal and fast charging technologies with ultra-fast charging technology (UFCT) utilizing PSO technique. It has been shown that UFCT, when used along with photovoltaic generation, is more beneficial in all technical aspects as compared to normal and fast charging technologies. Complexity of planning of distribution network and changing infrastructure increses with consideration of renewable energy integration, as energy yield of those are intermittent and unpredictable (Ghosh and Yadav 2021, Yadav et al. 2021). A review on

UFCT has also been done by Wang et al. 2021, which presents the impact of UFCT on battery life and grid. Along with the optimal setup of the charging station, (Nicolaides et al. 2019) compared the heating effects of diesel vs. electric while using the opportunity charging approach. No doubt that the electrification of any public transport route will yield more profit in the long run than conventional diesel buses. Battapothula 2019 has handled the burden on the distribution grid due to fast charging station load by optimally placing distributed generators in the system. While doing charging station planning, the most important factors considered are location, required load (which in turn depends upon the number and types of chargers), and investment (Chen *et al*. 2020).

Presently, load modeling based investigation and control methodologies are mainly adopted by the researchers to address the issues discussed above, *viz*. traffic simulation software (Galus et al. 2012), demographic model (Bessa and Matos 2013), parking generation rate model (Zhang et al. 2014), fuzzy logic system (Jingwei et al. 2014), Monte-Carlo technique (Yang et al. 2015), trip chain hypothesis (Tang and Wang 2016), Markov chain hypothesis (Wei et al. 2016), and dynamic traffic flow model (Xiang et al. 2016). Zhang et al. (2019) studied the location of charging stations for EVs and built a charging station location model based on the improved whale optimization algorithm. Most of the works found on charging stations and EVs have been brought up with meta-heuristic techniques. While considering several design parameters and output responses for measuring the relative performance of the units, continuous refinements have been performed by the researchers by creating and collaborating various effective ranking methodologies for DNEP under uncertainty (Ghosh et al. 2017, Verma et al. 2016, 2019).

However, traditionally, DNEP is evaluated and executed through static techniques. In the present work, an innovative, dynamic evaluation and optimization technique was employed for siting and sizing of host charging station (HCS), based on response surface methodology (RSM) introduced by Box and Wilson 1951. The proposed methodology reconnoiters the relationships between innumerable critical design parameters and multiple response variables. Though numerous response variables increase the complexity because what is optimal for one response may not be so for the others, this problem can be subdued by reducing the variability of a single response (Khuri and Mukhopadhyay 2010).
RSM is an optimization tool which was initially introduced to advance information factors for obtaining maximum yield reaction parameters of any vitality change frameworks. However, due to its versatility and efficiency, its application has been extended to a wide and diverse field of research. While considering design parameters as battery capacity, PV size, and wind turbine rotor swept area, Ekren and Ekren (2008) optimized the hybrid system cost with RSM. Hasanien and Muyeen (2013) obtained the design parameters for the cascaded controller of the power conversion system unit using the Taguchi method, which was then verified by RSM and the genetic algorithm collaboration approach under the grid fault conditions. RSM has also been applied in the field of EV for optimization of charging infrastructure design (Bayram et al. 2013) in the past. The authors of this work proposed an effective scheme for optimization of charging procedure, which also increased the profitability of the CS operators. RSM has been applied in the field of machine design as well. The shape of the rotor slots of the EV induction motor was optimized by Jeon et al. (2011), in which the authors reported that the dynamic characteristics of the machine obtained through the application of RSM are most suited to EV. RSM has been reported to be effective in voltage stability analysis in power distribution system planning problems (Haesen et al. 2009, Wang et al. 2019 and Ren et al. 2016) as well. Two categories of RSMs, viz. the 2nd order polynomial and the Kriging method, were applied to evaluate reliability and efficiency in transformer cooling system design optimization (Zhang et al. 2018). To manage the vulnerability of sustainable dispersed generators and the burden under fault conditions of the power distribution system, an assistance rebuilding technique dependent on stochastic RSM is proposed in Wang et al. (2019).

In the present work, a methodology for quantifying the optimal dispatch and charging of EBs is proposed considering three technologies: viz. fast charging technology (FCT), ultra-fast charging technology (UFCT), and battery swapping technology (BST) through the application of RSM as an optimization tool. A comparative analysis of these technologies is carried out while keeping economy, time of utilization, and infrastructure in mind, along with other technical and non-technical objectives and constraints. The proposed methodology removed decision-makers' subjectivity in weight assignment to the set of near-optimal solutions and relied on the statistical method, which is well proven in other fields of research. The main contributions of this paper are the following.

(a) A novel methodology is proposed for DNEP for the inclusion of charging stations for EBs, considering both technical and commercial aspects of planning. The placement and the sizing of HCS, along with the number of charging ports (CPs) at each HCS, are considered to be the objective functions of the proposed methodology.
(b) Comparative analysis of the multiple near-optimal solutions is carried out against a set of criteria, including power losses, voltage deviations, and setup expenses.
(c) RSM is employed in the present work for obtaining the most optimal solutions from a set of near-optimal solutions.

The rationale behind the choice of RSM in the present work as the optimization tool is as below.

1. RSM enables solving multi-objective optimization problem.
2. Most of the other techniques provide one of the best solutions from a set of feasible solutions, whereas RSM precisely provides of the optimal solution, which may or may not be the same present in the search space.
3. RSM provides accurate results under probabilistic analysis (Wang et al. 2019).

Therefore, to handle different design variables, the RSM model built with the help oforthogonal arrays, is advantageous for obtaining the optimal solution (Hasanien 2013), and hence RSM is employed in the present work as an optimization tool.

After this introductory section, the rest of the article is organized as follows. Section 2 presents problem formulation comprising of assumptions, objectives, and constraints. Section 3 describes the EB specifications and battery charging optional technologies considered in the present work. The methodology is discussed in Section 4. Results and discussions are presented in Section 5. Finally, Section 6 delineates the conclusions of the present work.

Nomenclature

Indices

b	For spare battery
f	For feeder section
i	For electric bus (EB)
k	For host charging station (HCS)
l, L	For network line
m	For charging ports (CP)
n	For network nodes
N	For number of technology ports
t	For time

Sets

T	Set of time intervals
ψ_{NW2}	Set of new wirings
ψ_{B1}, ψ_{B2}	Set of primary network branches (existing and proposed)
ψ_{SS1}, ψ_{SS2}	Set of substations (existing and planned)
ψ_{F1}	Set of the feeder of system
ψ_{N1}, ψ_{N2}	Set of number of bus substation nodes (existing and planned)

Variables and parameters:

C_{SB}^{UP}	Spare battery unit price
C_{RA}^{UP}	Swapping robotic arm unit price
C_{SH}^{sub}	Cost of selected heads falling under government subsidy scheme
CC_{HCS}^{k}	Capital costs for the k^{th} HCS
CRS_z	Customer reliability of service at load point z
CP_{F}^{UP}	Unit price of fast ports
CP_{BS}^{UP}	Unit price of ultra-fast ports
CP_{UF}^{UP}	Unit price of battery swapping ports
C_{USEI}, $C_{USEI,kW}$	Upstream electrical infrastructure total cost and per kW cost
C_{CSC}, $C_{CSC,kW}$	Charging system component total cost and per kW cost
d	Difference of number of CP considered for every charging technology at each step
EC	Energy charges as per State electricity regulatory commission's notification
$E_{tot,n}$	Total energy delivered to n^{th} node over the period
E_i^{rat}	Rated capacity of the i^{th} EB battery
$I_{l,t}$	Current of line l at time t
$I_{n,t}{}^{*}$	Current difference between two adjacent lines at time t
I_f^{Low}, I_f^{Up}	Lower and upper bound of current magnitudes at feeder section f
L_{HCSO}^{k}	Operational load of HCS k
$L_{FC}^{k}, L_{UFC}^{k}, L_{BS}^{k}$	Load for all FCT, UFCT, and BST ports at HCS k
$L_{FC}^{cap}, L_{UFC}^{cap}, L_{BS}^{cap}$	Load capacity of each FCT, UFCT, and BST ports at HCS k
MCB_i	Maximum capacity of the battery of the i^{th} EB
N	Maximum number of technology ports of any one technology out of the three considered that can be installed at HCS
N_{LP2}	Maximum number of new connected load points
N_{FCP}^{k}	Proposed number of fast charging ports at k^{th} HCS
N_{UFCP}^{k}	Proposed number of ultra-fast charging ports at k^{th} HCS
N_{BSP}^{k}	Proposed number of battery swapping ports (slow charging) at k^{th} HCS
N_{SB}^{k}	Proposed number of spare batteries (for battery swapping) at k^{th} HCS
N_{RA}^{k}	Proposed number of swapping robotic arm at k^{th} HCS
N_{CP1}	Number of active CP
N_{mth}	Number of days in a month
N_{Br1}, N_{Br2}	Number of primary network branches (existing and proposed)
N_{SS1}, N_{SS2}	Number of substations (existing and planned)
P_{EBm}	Power delivered to EB connected at the m^{th} CP
PR, PR_{kW}	Total power required at HCS, in kW
P_{EB_m}	Power demand of EB at m^{th} CP
P_{max}	Maximum charging power
r_o	Discount rate offered by the state government
RC_i^{exp}	Expected residual charge (RC) of the i^{th} EB
$RC_{i,t}$	Real-time battery refresh charging of the i^{th} EB at time t
RCB_m	Residual charge in EB (in kWh) connected at m^{th} CP
R_l	Resistance of line l
$S_{n,t}$	Load at node n at time t

$S_{min,n,t}$, $S_{max,n,t}$	Minimum and maximum allowable load at node n at time t
$S_{b,f,ss}$, $S_{b,f,ss}^{max}$	Power (and max power) flow in branch b of the network feeder f at substation ss
S_i	Initial state of EB with a full charge and at first stop of the route
S_{i+}, S_{k+}	State of EB during one-way trip of first/next round
S_j	State of EB at last stop of one-way trip of the first round
S_{j+}, S_{l+}	State of EB during the returning trip of first/next round
T_{FCP}^c	Charging times taken by FCT port for an SOC of 90%
T_{UFCP}^c	Charging times taken by UFCT port for an SOC of 80%
T_{BSP}^c	Charging times taken by BST port for an SOC of 100%
T_{FC}, T_{UFC}, T_{BS}	Time periods of the day for which each FCT, UFCT and BST port utilized
T_{FCBL}, T_{UFCBL}, T_{BSBL}	Useful time span of spare battery charged with: FCT port, UFCT port and BST port respectively
$TLL_{TX_{init}}$, $TLL_{TX_{max}}$	Initial and maximum thermal loading limits of distribution network transformer
$TLL_{L_{init}}$, $TLL_{L_{max}}$	Initial and maximum thermal loading limits of distribution network line
T_P	Time horizon of planning
T_{OH}	Outage hours of load node
$V_{n,t}$	Voltage at node n at time t
$V_{init,m}$	Initial voltage at m^{th} CP with no EB connected
$V_{min,m}$, $V_{max,m}$	Minimum and maximum voltage at the m^{th} CP when an EB is connected.
W^{bkW}	Rated power of the battery in kW
W^{bkWt}	Rated capacity of the battery in kWh
x	Available area of substations for expansion.
x_m	Status of EB connection with m^{th} CP
X_t^b	Energy in the battery in time interval t
X_t^{b-}	Power to the battery in time interval t
Δ	Power incremental limit by which the charging rate can vary in kW
μ_{mm}, μ_{mp}	Sensitivity of voltage at m^{th} CP due to EB power demanded at the m^{th} CP and the p^{th} CP, respectively in V/kW.
δ_m	Sensitivities of the distribution network transformer to power demand of EB at m^{th} CP in kVA/kW
β_m	Sensitivities of the distribution network line to power demand of EB at m^{th} CP in kVA/kW
η_c	Charging efficiency

2. Problem formulation

The main objective of the present work is to derive the placement (location) and sizing (number and capacity of charging ports) of HCS, considering several economic, technical, and non-technical objective functions, under physical and capacity constraints.. Also several parameters are considered based on the socio-economic characteristics of the region under study (city of Delhi, India in this case) to increase the feasibility of the solution. The complete methodology adopted in the present work is delineated in in Figure 1. In order to make the problem formulation closer to the real-world scenario, in the present work, the parameters and constraints of the city of Delhi, India, are considered. For the present case (i.e., the city of Delhi), the Government of Delhi (GoD) has planned the induction of 1000 EBs and identified six locations for constructing the parent charging stations (PCSs), which will facilitate parking and charging the EBs overnight by normal charging mode. For ensuring equal distribution charging load, about 166 EBs are allotted to each PCS. Further, each PCS will cater to several sub-PCSs (e.g., Rohini PCS is planned to have four sub-PCSs), and, hence, each sub-PCS will be catering to about 40-45 EBs. The schedule and route of plying of EBs are considered to be the same as that of the presently running busses on compressed natural gas (CNG). Practically length of all the routes are greater than 50 km, and each busses are required to ply to and fro (from the PCS to the end of the route) at least twice per day. The stoppage time (or idle time) is considered as ten seconds for embarkation and /disembarkation of commuters at bus stops, stoppages at traffic signals, and stoppages on-road due to congestion. The maximum speed of the chosen EBs is considered to be 75 km/h, and the maximum distance which can be covered by those is considered to be 151 km per charge (full)[1]. Hence, the EB running at any specific route will require midway charging to ensure uninterrupted service to the commuters. Normal charging will require more than two hours for re-charge, which will not be a feasible option of charging while the EBs are in transit.

In the proposed solution, a different mode of charging is considered for different times of the day. The EBs shall be charged at their PCS in normal mode and leave the PCS in a fully charged condition. For refresh charging while plying between the PCS and the final stop, the EBs are considered to halt at HCSs and get charged by either FCT, UFCT, or BST. For all EBs as well as for BST spare battery units, the Li-ion battery is considered for the present case.

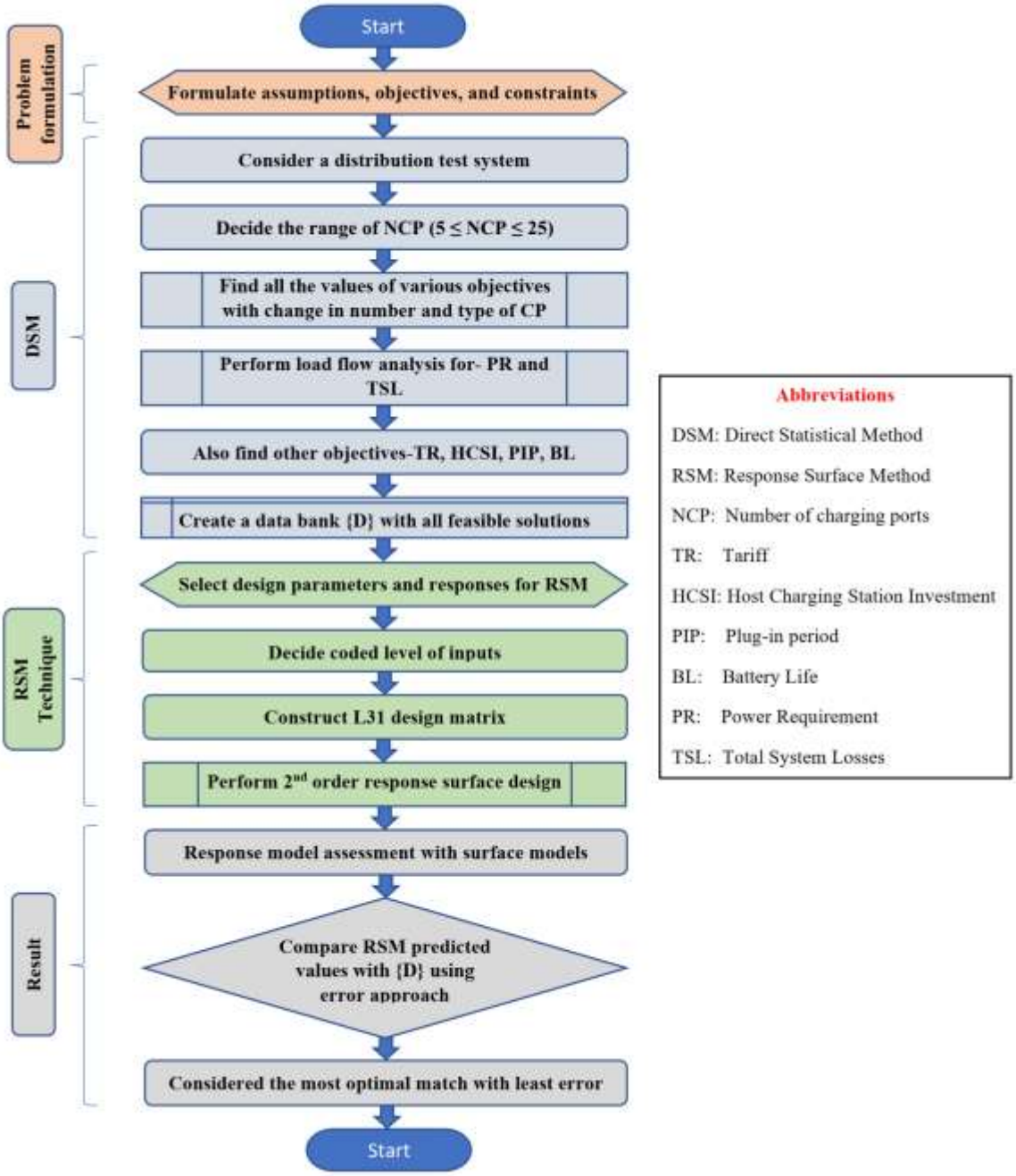


Fig. 1 Flow chart of the entire methodology.

2.1 Assumptions

Assumptions on some of the parameters are made regarding the optimization model, information on which are not available in the public domain. These assumptions may vary as per the discretion of the planner, for studies on different cities based on the priorities and objectives to be achieved, equality, and inequality constraints for keeping the pool of solutions under bounded conditions. While considering the overall cost, capital cost for extra batteries and setup cost for HCS is assumed in the present work, as detailed information on the same could not be found. The cost of land required for setting up the charging stations is not considered while estimating the overall cost. It is assumed that excess land available with city public transport authorities shall be used for setting up the charging stations. The EB battery charging process is considered to be a continuous,i.e., without any voltage fluctuation and power cut, until the charging state of up to 85% capacity is reached. It is also considered that every EB will get seven hours in the night for a full normal charge, and it will leave PCS with full SOC.

Each fast and ultra-fast charging point is considered to be equipped with smart metering and load control capability. EBs cannot deliver power back to the grid, so the bi-directional flow of electricity is not considered. The EBs battery capacity utilization depends directly upon the actual distance traveled. A safety margin charge reserve is kept for every EB to deal with all odds against running out the power capacity.

DC chargers are considered instead of AC ones, as in case of AC chargers, high power rectifiers will be required to be installed in EB, which will consume additional space and will increase the cost of EB. Battery swapping technology consists of a charging system (done with normal charging technology (NCT)) and a robotic swapping mechanism. The charging of spare batteries can be done on-station as well as off-station. Off-station charging may be done to take advantage of the lower tariff in case of space scarcity.

The charging process of spare batteries is considered to be a continuous and cyclical process (24 hours). The spare batteries will get charged by NCT in 6-7 hours, whereas the swapping process will take place in around 5 minutes duration. While the EBs will

get charged overnight by NCT at PCS, charging of spare battery packs will happen at HCS. The side-swapping method is considered in the present work for BST operation. Considering one swapping per hour, every HCS must have a minimum of 8 spare charged batteries, and further, if the number of ports is greater than 5, then the number of spare batteries must be equal to the thrice number of ports available at that particular HCS.

2.2 Objectives

This section describes various technical and non-technical objectives taken into consideration for optimizing the charging of EBs with optimal DNEP.

(a) *HCS investment (HCSI):* The first objective function considered for the optimization model of DNEP is to minimize the total investment for each type of HCS, as noted in (1)

$$min\ HCSI = (N_{FCP}^{k} CP_{F}^{UP} + N_{UFCP}^{k} CP_{UF}^{UP} + N_{BSP}^{k} CP_{BS}^{UP} + CC_{HCS}^{k} + N_{SB}^{k} C_{SB}^{UP} + N_{RA}^{k} C_{RA}^{UP} - r_o C_{SH}^{sub}) \quad (1)$$

Where the terms used can be explained with the following equations ((2) - (5)):

$$CC_{HCS}^{k} = C_{USEI} + C_{CSC} \quad (2)$$

$$C_{USEI} = C_{USEI,kW} \times PR_{kW} \quad (3)$$

$$C_{CSC} = C_{CSC,kW} \times PR_{kW} \quad (4)$$

$$C_{SH,sub} = N_{FCP}^{k}\ CP_{F}^{UP} + N_{UFCP}^{k} CP_{UF}^{UP} + N_{BSP}^{k} CP_{BS}^{UP} + N_{RA}^{k} C_{RA}^{UP} + C_{CSC} \quad (5)$$

The first, second, and third terms in (1) represent charging ports cost of the fast, ultra-fast, and battery swapping technologies, respectively. The fourth term represents capital cost, the fifth and sixth terms represent spare battery cost and robotic arm cost, respectively, and the last term represents the subsidy provided by the Government of India (GoI). All N represent various ports quantities.

(b) *Number of Charging Points (NCP):* As per the GoI guidelines for setting up EV charging infrastructure (under Faster Adoption and Manufacturing of Electric Vehicles (FAME) India Scheme, phase-II), a minimum of five chargers of any one or combination of slow and FCT is mandatory (TGOI 2019, DHI FAME-II 2019). In the present work, all the NCPs are considered to be a combination of BST, FCT, and UFCT based ports. Because of space constraints in the city, the maximum NCP is considered as 25. The number of configurations is a function of N, and may be obtained using (6)

$$CP = \frac{N+1}{2}[2a + Nd] \quad (6)$$

where, a is the initial number of CP considered for any charging technology (i.e., one for all the cases and a minimum of 3).

(c) *Plug-in period (PIP):* The plug-in period is considered as the average time taken by each EBs in the queue to get charged in a scenario when all the charging points in an HCS are occupied (in use). Plug-in-period is governed by (7).

$$PIP = \frac{N_{FCP}^{k} \times T_{FCP}^{c} + N_{UFCP}^{k} \times T_{UFCP}^{c} + N_{BSP}^{k} \times T_{BSP}^{c}}{N_{FCP}^{k} + N_{UFCP}^{k} + N_{BSP}^{k}} \quad (7)$$

(d) *Battery Life (BL):* Battery life is considered as 'long' for normal charging. While quantifying battery life, the ambient temperature conditions and driving style of drivers are not considered. Literature reveals that as compared to uncontrolled charging, controlled normal charging yields 15.8% more battery life (Jafari et al. 2018). Accordingly, the governing equation for average battery life (BL) calculation may be represented by (8).

$$BL = \frac{N_{FCP}^{k} \times T_{FCBL} + N_{UFCP}^{k} \times T_{UFCBL} + N_{BSP}^{k} \times T_{BSBL}}{N_{FCP}^{k} + N_{UFCP}^{k} + N_{BSP}^{k}} \quad (8)$$

As the sensitivity of the voltage level has a negative correlation with the proximity of additional load to the transformer (Richardson et al. 2012), EBs connected closer to the transformer will get charged at a higher rate, especially in a radial distribution network. To balance the load on the distribution network for maximizing its capacity utilization, the charging rate of each EB must be optimized to maximize the energy delivery to all connected EBs at all times. So, to rank batteries with a low residual charge in battery (RCB), while assuming that the RCB of each EB is known at the commencement of individual optimization time step (a short time interval of 15 min is assumed), the function for maximization of energy delivery to all EBs is expressed as in (9).

$$\mathcal{F} = \sum_{i=1}^{N_{CP1}} 1 - \left(\frac{RCB_m}{MCB_m}\right) P_{EBm} x_m \quad (9)$$

This energy delivery optimization will ultimately impact the battery life in the long run; hence, (9) is also considered as the objective for achieving longer battery life. Here, x_m which denotes status of EB connection with CP will be '0' when not connected and is '1' when connected. Hence this energy delivery to all EBs is considered as integral part of BL.

(e) *Power requirement (PR):* Total PR (including operational power required for each HCS) is governed by (10).

$$PR = L_{FC}^{k} + L_{BS}^{k} + L_{UFC}^{k} + L_{HCSO}^{k} \quad (10)$$

(f) *Total system losses (TSL):* The loss minimization (Verma et al. 2019) is expressed by (11).

$$P_{Loss,min} = \sum_{\substack{t-1 \\ t \in T}}^{T} \sum_{l=1}^{L} R_l I_{l,t}^2 \Bigg\} \quad (11)$$

(g) *Tariff (TR):* The tariff fluctuate as per the power demand. The demand depands upon type and number of carging ports. Tariff calculations per month is governed by (12)

$$TR = [(L_{FC}^{k} \times T_{FC}) + (L_{UFC}^{k} \times T_{UFC}) + (L_{BS}^{k} \times T_{BS}) + (L_{HCSO}^{k} \times 24)] N_{mth} \times EC \quad (12)$$

where

$$L_{FC}^{k} = N_{FCP}^{k} \times L_{FC}^{cap} \quad (13)$$

$$L_{UFC}^{k} = N_{UFCP}^{k} \times L_{UFC}^{cap} \quad (14)$$

$$L_{BS}^{k} = N_{BSP}^{k} \times L_{BS}^{cap} \quad (15)$$

2.3 Constraints

At each time interval, the objective functions described in subsection 2.2, can be optimized (minimized or maximized) subject to certain constraints. To obtain optimal values of system losses, power flow, thermal loading and optimal EB charging, the following constraints are considered in the present work.

(a) The energy storing system constraints are described as follows. The boundation on the power supply to the battery in any time interval (which cannot exceed the rated charging power) is expressed by (16).

$$X_t^{b-} \leq W^{bkW} \qquad \forall t \in T \quad (16)$$

$$X_t^{b} \leq W^{bkWt} \qquad \forall t \in T \quad (17)$$

$$(P_{EBm}^{t-1} - \Delta) \leq P_{EBm}^{t} \leq (P_{EBm}^{t-1} + \Delta) \quad (18)$$

Moreover, the boundation on the energy stored in the battery in any time interval (which cannot exceed the rated capacity) is expressed by (17). A charging rate variation constraint is also imposed by (18) keeping in mind the present battery technology (Hadley and Tsvetkova 2009).

(b) The constraints related to minimum loss are expressed by (19)-(23):

$$S_{n,t} = V_{n,t}(I_{n,t})^{*} \quad (19)$$

where,

$$I_{n,t} = I_{l,t} - I_{l+1,t} \quad (20)$$

$s.t.$

$$S_{n,t} \geq S_{min,n,t} \quad (21)$$

$$S_{n,t} \leq S_{max,n,t} \quad (22)$$

$$\sum_{t} S_{n,t} = E_{tot,n} \quad (23)$$

(c) The constraint for maintaining voltage level and deviation (V_{dev}) within allocated limits can be summarized as in (24) and (25).

$$V_{min,m} \leq \left[V_{init,m} + \mu_{mm} P_{EB,m} + \sum_{p=1}^{N} \mu_{mp} P_{EB,j} \right] \leq V_{max,m} \Bigg\} \quad (24)$$

$$m \forall N, m \neq p$$

$$V_{dev} = \left[\frac{V_{min,m} - V_{max,i}}{2.V_{init,m}} \right].100\% \quad (25)$$

(d) Branch current flow constraints are expressed as (26).

$$I_f^{Low} \leq I_f \leq I_f^{Up} \quad (26)$$

(e) Operational radiality of the distribution network is imposed by (27), which will ensured that the basic rules are obeyed in the planning model (Zhang et al. 2014),

$$\sum_{i \in \psi_{NW2}} N_{Br2} = N_{LP2} - \sum_{s2 \in \psi_{SS2}} N_{SS2} \quad (27)$$

(f) The thermal loading constraints for distribution network transformers and lines are summarized as in (28) and (29).

$$TLL_{TX_{init}} + \sum_{k=1}^{N} \delta_m P_{EB_m} \leq TLL_{TX_{max}} \qquad k \forall N \quad (28)$$

$$TLL_{L_{init}} + \sum_{k=1}^{N} \beta_m P_{EB_m} \leq TLL_{L_{max}} \qquad k \forall N \quad (29)$$

(g) Power flow capacity constraints can be quantified by (30).

$$\left| S_{b,f,ss} \right| \leq S_{b,f,ss}^{max} \Bigg\} \quad (30)$$

$$b \in \psi_{B1},$$

$$f \in \psi_{F1},$$

$$ss \in \psi_{N1}, \psi_{N2}$$

(h) Reliability constraints are expressed by (31) and (32). Here, (31) ensures that service reliability remains in upper and lower allowable values and power shortage rate reliability is expressed by (32).

$$CRS_z^{min} \leq CRS_z \leq CRS_z^{max} \quad (31)$$

$$CRS_z = 1 - \frac{T_{OH}}{T_P} \quad (32)$$

(i) During DNEP for charging EBs, constraints on charging station are given by (33), which also ensures that at least five new charging points (term N_{CP2}) can be added to the existing station.

$$\sum_{t=1}^{T} \sum_{ss=1}^{N_{SS1}} x_{m,t,ss} \leq N_{CP2} \quad \forall j \in \psi_{SS1}, \psi_{SS2} \quad (33)$$

(j) The proposed HCSs will exclusively serve the EBs, which will have to be commercially viable and, hence, the least plug-in-period (PIP) is to be ensured to avoid loss of revenue due to waiting time. Hence, a PIP constraint is imposed on every HCS to achieve the financial sustainability of the EB operation, which can be mathematically expressed by (34).

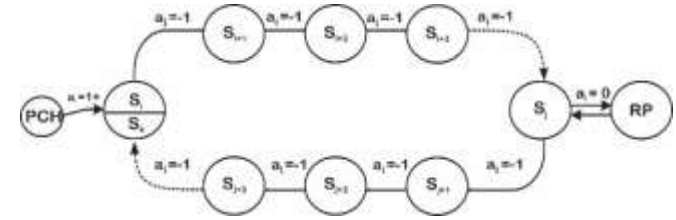
$$T_{i,t}^{min} \leq PIP \leq 50 \quad (34)$$

where the minimum duration needed to plug in EB to achieve desirable charging requirements ($T_{i,t}^{min}$), which can be mathematically defined as:

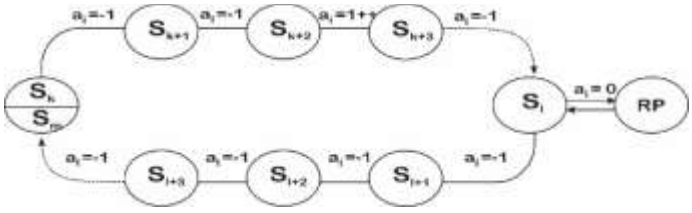
$$T_{i,t}^{min} = \begin{cases} \dfrac{E_i^{rat}\left(RC_i^{exp} - RC_{i,t}\right)}{\eta_c . P_{max}} & RC_{i,t} < RC_i^{exp} \\ 0 & RC_{i,t} \geq RC_i^{exp} \end{cases} \quad (35)$$

3. EBs charging: *when, where, and how*?

It is considered that the location of the HCS on each route should be such that the EBs reaching the HCS shall have SOC of 10 to 20%, and 80 to 85% while leaving. This is so because the EBs must reach the HCS before complete drain-out and will leave the HCS before 100% SOC as the last 20% of charging is slow and require more time as compared to the time taken to reach 20% to 80% SOC.



(a)



(b)

Fig. 2 Charging and discharging state alteration process of EB (a) First round trip of the day (b) Next consecutive rounds

The charging and discharging state alteration process of EB is shown in Figure 2, in which the terms shown outside the circle have the following interpretations:

$a_i = -1$ represents the driving state of i^{th} EB,
$a_i = 0$ represents ideal state of i^{th} EB,
$a_i = 1+$ normal charging or fast charging of i^{th} EB at PCS
$a_i = 1++$ ultra-fast charging or battery swapping of i^{th} EB at HCS

4. Methodology

In the present work a 69-node IEEE modified distribution test system (Savier and Das 2007) is considered to evaluate the effect of EBs' charging on the power quality and reliability. The reconfigured system is modified by utilizing tie switches based on the fuzzy multi-objective approach.

The single line diagram of the 69-node IEEE modified distribution test system, as shown in Figure 3, has 68 branches with normally closed switches without any tie lines. The current carrying capacity of branches 1-9 is 400 A, of branches 25, 40, 49-51, 53-59, 61-65 is 300 A, and for the rest of the branches are 200 A. The system base voltage and MVA are assumed at 12.66 kV and 100 MVA, respectively. The rest of the section is divided into three parts describing design parameters, output responses, and the methodology used.

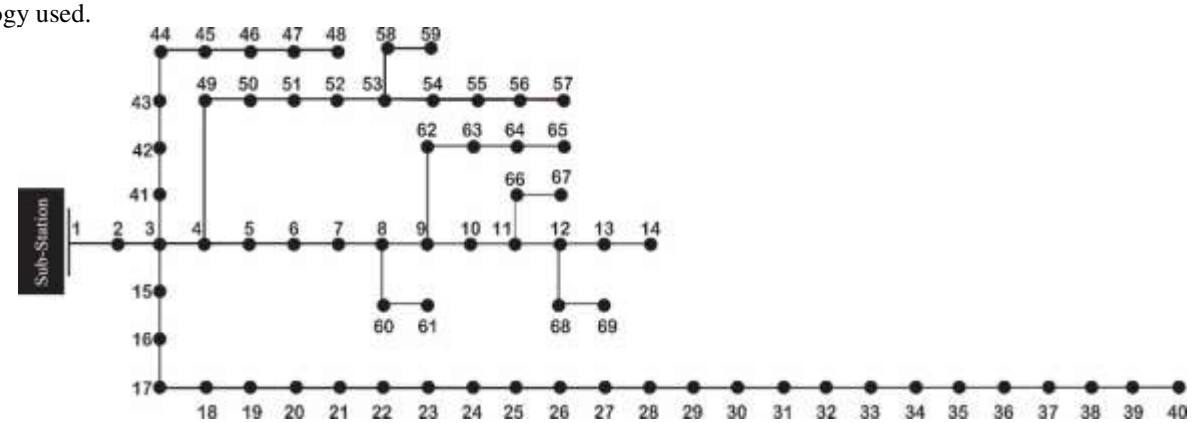


Fig. 3 Single-line diagram of 69-node IEEE modified distribution test system

4.1 Direct Statistical Method (DSM)

For producing the pool of feasible solutions, direct statistical method is utilized. The computational region for optimizing the sitting and sizing of HCS is based upon seven objectives. To strengthen the mathematical modelling of various objectives, the considerations are explained below.

(a) *Host charging station investment (HCSI):* Creating apposite FCT infrastructure is the key for speedy electrification of the bus fleet. However, the following two concerns are typically cited as crucial issues – minimization of the cost of the FCT infrastructure and up-gradation of power system for coordinating the charging load. HCSI is one of the design parameters for the present work. Main terms are considered in (1), and their further classifications are given in (2) - (5)). The capital cost for setting up HCS in India is calculated based on the data given in Table 1.

Table 1 Bifurcation of the HCS establishment capital cost

Investment Head	Unit Price (₹ M)	Ref.
BST port (20 kW)	0.24	TGOI (2019), DHI FAME-II (2019)
FCT port (50 kW)	0.725	TGOI (2019), DHI FAME-II (2019)
UFCT port (450 kW)	1.5	TGOI (2019), DHI FAME-II (2019)
DRDO Li-ion spare battery	0.5	TET (2015)
Subsidy provided by GOI[2]	70%	TGOI (2019), DHI FAME-II (2019)
Capital investment		
Upstream electrical infra (per kW)	0.005476	Pillai et. al. (2018)
Charging system component cost (per kW)	0.017982	Pillai et. al. (2018)

Three swapping robotic arms are considered for each HCS configuration. An exchange rate of ₹ 74 per USD is considered while calculating the capital cost.

(b) *The number of charging points (NCP):* Table 2 shows the number of configurations of charging ports at HCS formed due to various charging technologies (as per (6)), which sum up to 3241 configurations. For example, if the total charging ports to be installed at an HCS are 6 (BST, FCT, and UFCT based ports), the second row (No. of configurations) presents total permutation and combinations of 6 ports.

Table 2 Number of configurations of charging ports

N (Number of charging ports)	5	6	7	8	9	10	11	12	13	14	15
No. of configurations	21	28	36	45	55	66	78	91	105	120	136
N (Number of charging ports)	16	17	18	19	20	21	22	23	24	25	
No. of configurations	153	171	190	210	231	253	276	300	325	351	

(c) *Plug-in-period (PIP):* PIP is calculated by considering that, for a particular CP configuration, all types of CPs are occupied, and the next EB in the queue will require an average time of all types of CP duration (expressed in (7)). The charging time is considered as 5, 15, and 120 minutes for BST, UFCT, and FCT, respectively (An et al. 2019). In the case of battery swapping, the charging time will be the same as normal charging. However, the time which is considered in the present work is that time which the EB will consume in the swapping process.

(d) *Battery life (BL):* Battery life is considered 'long' for normal charging. Accordingly, the governing equation for average BL, the expression may be represented by (8), and for economic consideration, (8) must be maximized.

(e) *Power requirement (PR):* Total power required (including operational power required) for each HCS is governed by (10). The whole planning revolves around the power required for charging EBs in a minimum time frame. Hence, this response is maximized during optimization compared to other DNEP problems, where the planner targets to minimize this response.

(f) *Total System losses (TSL):* The fundamental objective and constraint equations for total system losses are described in (11) and (19)-(23), respectively, and the calculations are carried out by performing load flow analysis on 69-node IEEE modified distribution test system (see Figure 3) in MATLAB R2017a environment. It is obvious that the minimization of TSL is targeted in the present work.

(g) *Tariff (TR):* Delhi electricity regulatory commission has introduced a separate energy tariff (substantially lower than industrial tariff) for EV charging stations, which are ₹ 4/kWh for charging from HT network and ₹ 4.5/kWh for charging from LT network (DERC 2019). There are no fixed monthly charges applicable as well. The same is considered in the present work. Tariff calculations per month is governed by (12). UFCT port utilization-based consumption is considered 4 hours for up to 10 ports, 3 hours for 10-20 ports, and 2 hours for more than 20 ports. A 20 kW of continuous (for all-day) load is considered for the rest of the power consumed in HCS. As per the guidelines of the Ministry of Power, GOI (GoI-MoP 2018), for normal charging (as well as for battery swapping), 15 kW (model- Bharat DC-001) charger and, for fast charging, 50 kW (CHAdeMO) charger is considered for each charging port. The off-board DC chargers for ultra-fast charging is considered as super-chargers having 450 kW capacity (Muratori et al. 2019). From a total of 3241 configurations, the maximum and minimum values of the seven objectives are summarized in Table 3.

Table 3 Summary of calculated results with DSM

	Indexing (Config.)	Charging ports				HCS	TR	BL	PR	TSL	PIP
		No of FCT Ports	No of UFCT Ports	No of BST Ports	NCP						
Lowest value	1	05	05	05	05	04.43	0.432	4.210	00.12	0.1903	05.00
Highest Value	3241	25	25	25	25	134.04	4.482	5.000	11.27	0.6991	50.00

4.2 The optimization model: RSM

Response surface methodology (RSM) is an optimization technique used to acquire the exact models of the design parameters in terms of response factors in the wake of recognizing their relative commitment, utilizing the Taguchi technique. The strategy for steepest ascent/descent can be successfully used to recognize the ideal estimations of the responses.

RSM addresses a diverse set of queries, for example:

(a) How is a specific output influenced by a given arrangement of information factors over some predetermined area of interest?
(b) To what extent, the information sources are to be controlled to give an item, fulfilling required details.
(c) What estimations of design parameters will yield the greatest for an appropriate response, and what is the idea of response surface near the most extreme?

If the output is very much displayed by a direct capacity of the autonomous factors, at that point, the approximating capacity is the first-order model. If there is a curvature in the framework, at that point, a polynomial of a higher degree must be utilized, for example, the second-order model. This model would almost certainly be valuable as a guess to the genuine response surface in generally smaller sections. The second-order model is generally utilized in RSM for the following reasons:

(a) The second-order model is truly adaptable. It can take on a wide assortment of practical structures, so it will regularly function admirably as a guess to the genuine response surface.
(b) Utilizing the technique for least squares, it is easy to evaluate the parameters in the second-order model.

There is significant handy experience as well as literature available, showing that second-order models function admirably in taking care of genuine response surface issues (Haesen et al. 2009, Ren et al. 2016, Wang et al. 2019). The relationship between a response (y) and of the set of associated design parameters ($x_1, x_2, \dots, x_k$) can be mathematically expressed as in (36).

$$y = \beta f'(x) + \varepsilon \tag{36}$$

And, for a second-order model, it is expressed as in (37)-(38).

$$y = \beta_o + \sum_{i=1}^{k} \beta_i x_i + \sum\sum_{i<j} \beta_{ij} x_i x_j + \sum_{i=0}^{k} \beta_{ii} x_i^2 + \varepsilon \tag{37}$$

$$\left.\begin{aligned} & s.t. \\ & p = 1 + 2k + \frac{1}{2}k(k-1) \\ & \frac{1}{n}\sum_{u=1}^{n} x_{ui} = 0 \\ & \frac{1}{n}\sum_{u=1}^{n} x_{ui}^2 = 1 \\ & i = 1,2,\dots,k \\ & u = 1,2,\dots,n \end{aligned}\right\} \tag{38}$$

where $x = x_1, x_2, \dots, x_k$, and $f'(x)$ is a vector function of elements p which consists of powers and cross-products of powers of x up to a certain degree represented by the positive integer d , β is a vector of p unknown constant coefficients (parameters), ε is random error in the experimental result, n is number of experiments and x_{ui} is the u^{th} setting of the i^{th} control variable. Here, $u = 1,2,\dots,n$.

Central composite design (CCD): One of the most popular second-order designs, CCD consists of three constituent parts (Khuri and Mukhopadhyay 2010). The first one is a factorial portion, which consists of 2^k factorial design whose factors' levels are coded as $-1, 1$. The second one is an axial portion consisting of $2k$ points arranged so that two points are picked on the hub of each design parameter at a distance of α from the design center. And the third segment is n_o center focuses. So, the total number of design points in a CCD may be evaluated by (39).

$$n = 2^k + 2k + n_o \tag{39}$$

Taguchi's approach: The design parameters of any process can be classified as control parameters (which are easy to control) and the noise parameters (which are difficult to control). The noise factors are the reason behind numerous output responses. The fundamental point of parameter configuration is to decide the settings of the control factors for which the procedure reaction is robust to the inconstancy in the framework brought about by the noise factors. To accomplish this objective, Genichi Taguchi advocated the use of crossed arrays by crossing an orthogonal array of control variables (internal array) with an orthogonal array of noise variables (external array) (Khuri and Mukhopadhyay 2010). Taguchi identified three specific goals (minimize, maximize, or achieve the target value of the response) in a process and defined them with a signal-to-noise ratio (S/N). This S/N performance criteria (considering both processes mean and variance) can be expressed as:

$$\left.\begin{aligned} Minimize\ S/N\colon\ -10log\left[\frac{1}{n}\sum_{i=0}^{n} y_i^2\right] \\ Maximize\ S/N\colon\ -10log\left[\frac{1}{n}\sum_{i=0}^{n}\frac{1}{y_i^2}\right] \\ Target\ S/N\colon\ -10log\left[\sum_{i=0}^{n}\frac{s^2}{\bar{y}_i^2}\right] \end{aligned}\right\} \quad (40)$$

where $\bar{y}$ and s^2 are the sample mean and variance, respectively.

4.2.1 Design parameters and responses

As per the Taguchi's approach, for the mathematical modeling of the 2nd order RSM methodology, design parameters are considered as: *number of charging points (NCP), the investment required for setting up HCS (HCSI), energy tariffs (TR), and plug-in-period (PIP).* The objective of the proposed charging strategy is to find the optimal location of charging stations along the plying route such that the total travel time, including driving time from current location to destination HCS, waiting and charging time at HCS and the charging cost are minimized while capacities of the HCSs are fully utilized. To achieve the above objective, the responses considered are: *power requirement (PR), total system losses (TSL), and battery life (BL).*

4.2.2 Mathematical modeling

The second order model for responses PR, TSL, and BL are recognized from the optimal sizing of HCS response achieved by considering CCD given in Table 4. The central value of design parameters for the sizing of HCS conforming to code '0′ are the optimum design parameters for the sizing of HCS obtained from Taguchi's multi-objective optimization methodology. Here, the coded values for CCD at diverse levels are $-2, -1, 0, 1,$ and 2.

Table 4 Coded level of design parameters for sizing of HCS and their values

Input parameters	Symbol	Coded Levels				
		-2	-1	0	1	2
No. of charging points	NCP	5	10	15	20	25
HCS investment	HCSI	4.43	26.59	48.75	80.01	134.04
Tariff	TR	0.432	1.908	2.736	3.339	4.482
Plug-in period	PIP	5	15	25	35	50

The outcomes acquired from C++ code composed for sizing of HCS and in the wake of executing CCD were expressed in Table 5 as RSM L31 design matrix.

Table 5 L31 design Matrix

Exp. Run	NCP	HCSI (million ₹)	TR (million ₹)	PIP (min)	PR (MW)	TSL (MW)	BL (Yr)
1	20	80.01	3.339	35	16.73	0.828339	4.01
2	15	48.75	2.736	25	3.76	0.256164	4.58
3	15	48.75	2.736	25	3.76	0.256164	4.58
4	15	48.75	4.482	25	9.12	0.526806	4.37
5	20	26.59	3.339	15	5.29	0.370335	4.68
6	10	26.59	3.339	15	0.79	0.217092	4.91
7	20	80.01	3.339	15	9.79	0.523569	4.45
8	10	26.59	1.908	35	2.57	0.357344	4.94
9	10	26.59	3.339	15	0.79	0.217092	4.91
10	15	48.75	2.736	5	0.12	0.190318	5
11	15	48.75	2.736	25	3.76	0.256164	4.58
12	15	48.75	0.432	25	0.12	0.190318	5
13	10	80.01	1.908	35	7.07	0.510578	4.71
14	15	48.75	2.736	25	3.76	0.256164	4.58
15	15	48.75	2.736	50	11.27	0.699134	4.21
16	20	80.01	1.908	15	4.63	0.359051	4.92
17	10	80.01	3.339	35	12.23	0.675096	4.24

18	5	48.75	2.736	25	0.12	0.190318	5
19	10	80.01	3.339	15	5.29	0.370326	4.68
20	15	4.43	2.736	25	0.12	0.190318	5
21	15	134.04	2.736	25	11.27	0.699134	4.21
22	10	26.59	3.339	35	7.73	0.521862	4.47
23	15	48.75	2.736	25	3.76	0.256164	4.58
24	15	48.75	2.736	25	3.76	0.256164	4.58
25	20	26.59	1.908	35	7.07	0.510587	4.71
26	20	80.01	1.908	35	11.57	0.663821	4.48
27	20	26.59	3.339	35	12.23	0.675105	4.24
28	10	80.01	1.908	15	0.13	0.205808	5
29	15	48.75	2.736	25	3.76	0.256164	4.58
30	20	26.59	1.908	15	0.13	0.205817	5
31	25	48.75	2.736	25	11.27	0.699134	4.21

The design matrix was created with the assistance of MINITAB 17, comprising of a full factorial plan including 31 most appropriate combinations. Analysis of variance (AOV) was utilized to break down the model and foresee the noteworthiness of every parameter considered for the examination, and the aftereffect of the created models are shown in Tables 6-8.

Table 6 Analysis of Variance for BL developed under RSM model

	Battery Life				
Source	DF	Adj SS	Adj MS	F-Value	P-Value
Regression	4	2.57190	0.64297	65.91	0.000
NCP	1	0.45028	0.45028	46.15	0.000
HCSI (million ₹)	1	0.44693	0.44693	45.81	0.000
TR (million ₹)	1	0.94568	0.94568	96.93	0.000
PIP (Min.)	1	1.02313	1.02313	104.87	0.000
Error	26	0.25366	0.00976		
Lack-of-Fit	19	0.25366	0.01335		
Pure Error	7	0.00000	0.00000		
Total	30	2.82555			

Table 7 Analysis of Variance for TSL developed under RSM model

	Total System Losses				
Source	DF	Adj SS	Adj MS	F-Value	P-Value
Regression	4	1.00950	0.252375	32.43	0.000
NCP	1	0.20446	0.204455	26.28	0.000
HCSI (million ₹)	1	0.24243	0.242433	31.16	0.000
TR (million ₹)	1	0.15912	0.159118	20.45	0.000
PIP (Min.)	1	0.48819	0.488193	62.74	0.000
Error	26	0.20231	0.007781		
Lack-of-Fit	19	0.20231	0.010648		
Pure Error	7	0.00000	0.000000		
Total	30	1.21181			

Table 8 Analysis of Variance for PR developed under RSM model

	Power Required				
Source	DF	Adj SS	Adj MS	F-Value	P-Value
Regression	4	594.717	148.679	80.18	0.000
NCP	1	135.758	135.758	73.21	0.000
HCSI (million ₹)	1	144.131	144.131	77.72	0.000
TR (million ₹)	1	132.191	132.191	71.29	0.000
PIP (Min.)	1	240.880	240.880	129.90	0.000
Error	26	48.214	1.854		
Lack-of-Fit	19	48.214	2.538		
Pure Error	7	0.000	0.000		
Total	30	642.931			

Additionally, the regression conditions for each response are given as under by (Eqs. (41)-(43)).

$$Power\ Requirement\ (MW) = -9.2 - 0.426\,NCP + 0.0442\,HCSI + 0.25\,TR + 0.135\,PIP + 0.0279\,NCP \times NCP + 0.000128\,HCSI \times HCSI + 0.496\,TR \times TR + 0.00284\,PIP \times PIP + 0.00021\,NCP \times HCSI + 0.009\,NCP \times TR + 0.00124\,NCP \times PIP + 0.0034\,HCSI \times TR + 0.00050\,HCSI \times PIP - 0.0089\,TR \times PIP \quad (41)$$

$$Total\ System\ Losses\ (MW) = 0.183 - 0.0471\,NCP - 0.00014\,HCSI - 0.041\,TR - 0.0009\,PIP + 0.002268\,NCP \times NCP + 0.000032\,HCSI \times HCSI + 0.0345\,TR \times TR + 0.000322\,PIP \times PIP - 0.000024\,NCP \times HCSI - 0.00028\,NCP \times TR - 0.000008\,NCP \times PIP - 0.000124\,HCSI \times TR + 0.000012\,HCSI \times PIP - 0.00098\,TR \times PIP \quad (42)$$

$$Battery\ Life\ (Years) = 6.089 - 0.0200\,NCP - 0.00145\,HCSI - 0.109\,TR - 0.0193\,PIP + 0.000386\,NCP \times NCP + 0.000016\,HCSI \times HCSI + 0.0000\,TR \times TR + 0.000165\,PIP \times PIP - 0.000055\,NCP \times HCSI - 0.00346\,NCP \times TR - 0.000255\,NCP \times PIP - 0.00112\,HCSI \times TR - 0.000053\,HCSI \times PIP - 0.00087\,TR \times PIP \quad (43)$$

The genuine issues need enhancement with various responses of intrigue. The present work embraces procedures, for example, plotting surface plots for each response with two design parameters while keeping the other two at hold; constrained enhancement and attractive quality methodology. The present work utilizes RSM-based quality methodology for doing enhancement of measuring of HCS parameters (BL, TSL, and PR) for choosing the optimal number of charging technology ports for EB load. The streamlining investigation is done by utilizing MINITAB 17 software, where each response is changed to dimensionless desirability significance (DDS), and its worth ranges between $0 \leq DDS \leq 1$. These qualities show that $DDS = 0$ represents a totally unsuitable reaction while $DDS = 1$ represents progressively attractive reactions. The condition of desirability is given for both bigger-the-better (BTB) and smaller-the-better (STB) kinds of reaction, which are mathematically expressed as:

$$DDS_{BTB} = \begin{cases} \left|\frac{y - LDL}{UDL - LDL}\right|^{s} & LDL \leq y \leq UDL \\ 0, & y < LDL \\ 1, & y > UDL \end{cases} \quad (44)$$

$$DDS_{STB} = \begin{cases} \left|\frac{y - LDL}{a - LDL}\right|^{t} & a \leq y \leq UDL \\ 0, & y > UDL \end{cases} \quad (45)$$

where s and t are the shape constants exponents, LDL and UDL are lower and upper design limits ('a' is the lowest conceivable incentive for response y). After getting the most appropriate combinations according to the design matrix, AOV was calculated, which offers the numerical data about the p-value. The p-value is characterized as the option in contrast to the elimination points to give the littlest degree of significance at which the invalid speculation would be dismissed. The greatest estimation of p is taken as 0.05, and the $p - values > 0.05$ are considered unimportant.

To check suitability of the created model for the acquired data, the S-value is calculated from the regression analysis for each response BL, TSL, and PR, which are 0.0988, 0.0882, and 1.3618 respectively, which are the lowest. R^2value for the three responses are 91.02%, 83.31%, and 92.5%, respectively, and R^2 (adj)-values are 89.64%, 80.74% and 91.35% respectively. These values indicate that the applied model fits well with the acquired data.

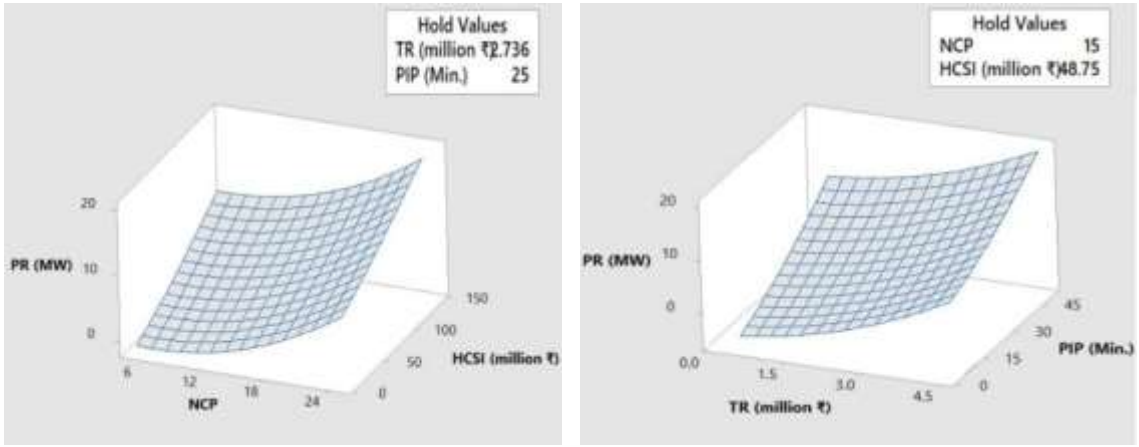
5. Results and discussion

After performing load flow analysis on 69-node IEEE modified distribution test system in MATLAB R2017a environment and financial analysis on considered configurations for optimal siting of HCS, the results for optimal sizing of HCS using RSM are carried out in the present work. The following sub-sections present the results of the above analysis, i.e., the calculated results of the impact of design parameters (NCP, HCSI, TR, and PIP) on output responses (PR, TSL, and BL) of the optimization process with RSM and, finally, the results obtained from RSM are verified with those of the calculated results. The results are depicted with the help of surface plots for output responses. These surface plots relate one response with two design parameters (out of four) at a time while keeping the rest of the two design parameters constant. These hold values are the central value of the CCD Table. As per Table 2, after calculation, a total of 3241 responses are obtained, whose summary is presented in Table 3.

The optimized location for sitting of HCS comes out to be nodes 17, 18, or 19. In the following subsections, the results obtained from RSM are discussed.

5.1 Effect of design parameters on power requirement (PR)

Figure 4 presents the surface plots of variation in PR with the change in various design parameters.



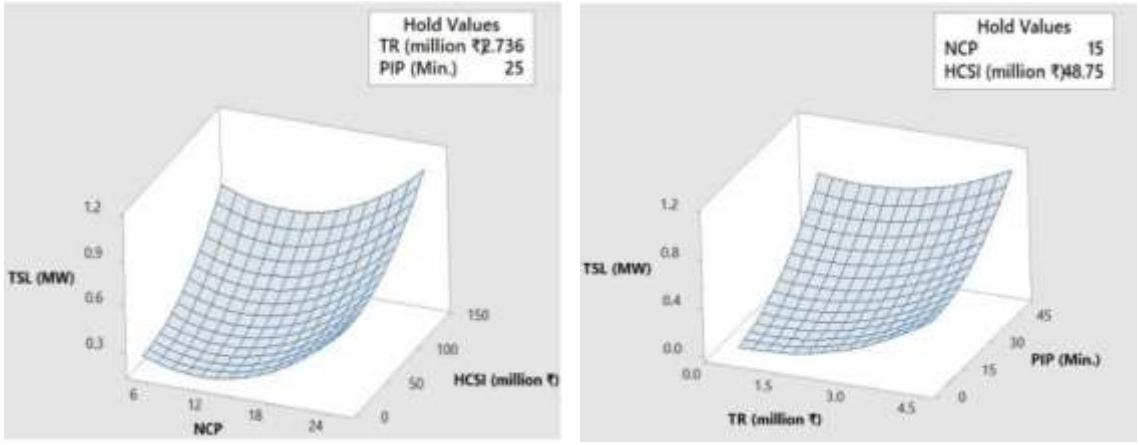
(a) (b)

Fig. 4 Surface plot of response PR versus design parameters (a) PR versus HCSI and NCP, (b) PR versus PIP and TR

Figure 4**a** represents the effect of NCP and HCSI on PR while keeping TR and PIP at hold values of ₹ 2.736 million and 25 min, respectively, which shows that PR increases with an increase in NCP as well as HCSI. Initially, the change in PR is gradual with the variation of NCP as in the beginning; the charging ports configurations are based on BST ports. BST ports require less power for operation as compared to that of the other two technologies. After NCP reaches a value of 12, the variation in PR increases exponentially because, for a higher value of NCP, the FCT and the UFCT ports dominate over BST ports. It can also be seen from Figure 3a that the PR varies almost linearly with HCSI. Figure 4**b** shows the effect of TR and PIP on PR while HCSI and NCP are kept at hold (₹ 48.75 M and 15, respectively). It is evident from the curve that there is an exponential increase in PR with the increase in PIP since, as compared to BST ports, an increase in FCT and UFCT ports will sharply increase PR, and also will take more plug-in time due to their charging characteristics. Similar relations are obtained when the combinations of design parameters are changes. The trends show that PR has an almost linear and increasing relationship with all four design parameters. This indicates how the power requirement for various technology ports will increase with an increase in all four design parameters.

5.2 Effect of design parameters on total system losses

Figure 5 depicts the effect on TSL with variation in design parameters. Figure 5**a** shows the variation of TSL with NCP and HCSI while keeping the other two design parameters constant (hold). The trend shows a slight reduction in TSL initially and then a considerable increase in losses as NCP increases further. This tendency is validated by the fact that in the beginning, the number of BST ports is less, the FCT and UFCT ports dominate, and hence the PR increases exponentially. Later, with changing configurations, the number of BST ports increases (hence the number of the FCT and UFCT ports decrease), while the PR decreases. The required investment increases when the number of FCT and UFCT ports increases. Along with the investment, losses increase as well, as they consume bulk power, whereas the BST requires normal power for long-duration charging of spare battery packs. The plug-in period also increases with higher penetration of these two technologies and, hence, after a slight dip in losses initially, those increase with an increase in PIP (Figure 5**b**). These sub-plots clearly show that TSL value increases with an increase in TR and attains a peak value when all the ports considered are of UFCT type while HCSI and PIP are kept at hold. Total system losses have the same trend as that of power requirement, and that is because those have a positive correlation.



(a) (b)

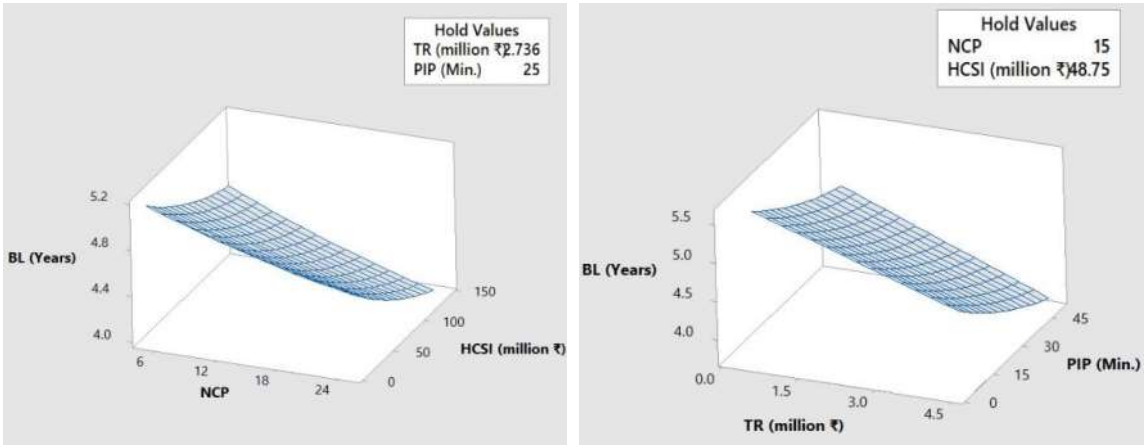
Fig. 5 Surface plot of response TSL versus design parameters (a) TSL versus HCSI and NCP (b) TSL versus PIP and TR

5.3 Effect of design parameters on battery life

Figure 6 shows the graphical plot of BL with the change in various design parameters. It may be noted from Figure 6**a** that BL value monotonously decreases with an increase in both NCP and HCSI, from an initial peak value, and attains minimum value at maximum NCP and HCSI. The reason behind this nature of the plot is that BL is maximum in the case of BST and minimum in the rest of the two charging technology. The same trend is noted for the variation of BL with PIP (Figure 6**b**). Although there is no direct relation of

TR with BL, even though indirectly, the BL decreases with an increase in TR. It may be concluded from the results that except for BST ports, all other fast chargers will decrease the life of the battery, whether it is a spare one; or the one mounted on EBs.

The battery life is observed to decrease with an increase in PIP and with more usage, apart from an increase in the number of FCT or UFCT ports. It is high initially for all the cases because the initial port configuration consists of BST ports which charge spare battery packs with least charging power and in a maximum allowable time frame.



(a) (b)

Fig. 6 Surface plot of response BL versus design parameters (a) BL versus HCSI and NCP, (b) BL versus PIP and TR

5.4 Optimization reaction

The present study primarily focuses on optimizing the sitting and sizing of HCS through the application of the RSM technique. The results obtained through the analysis are summarized in Figure 7.

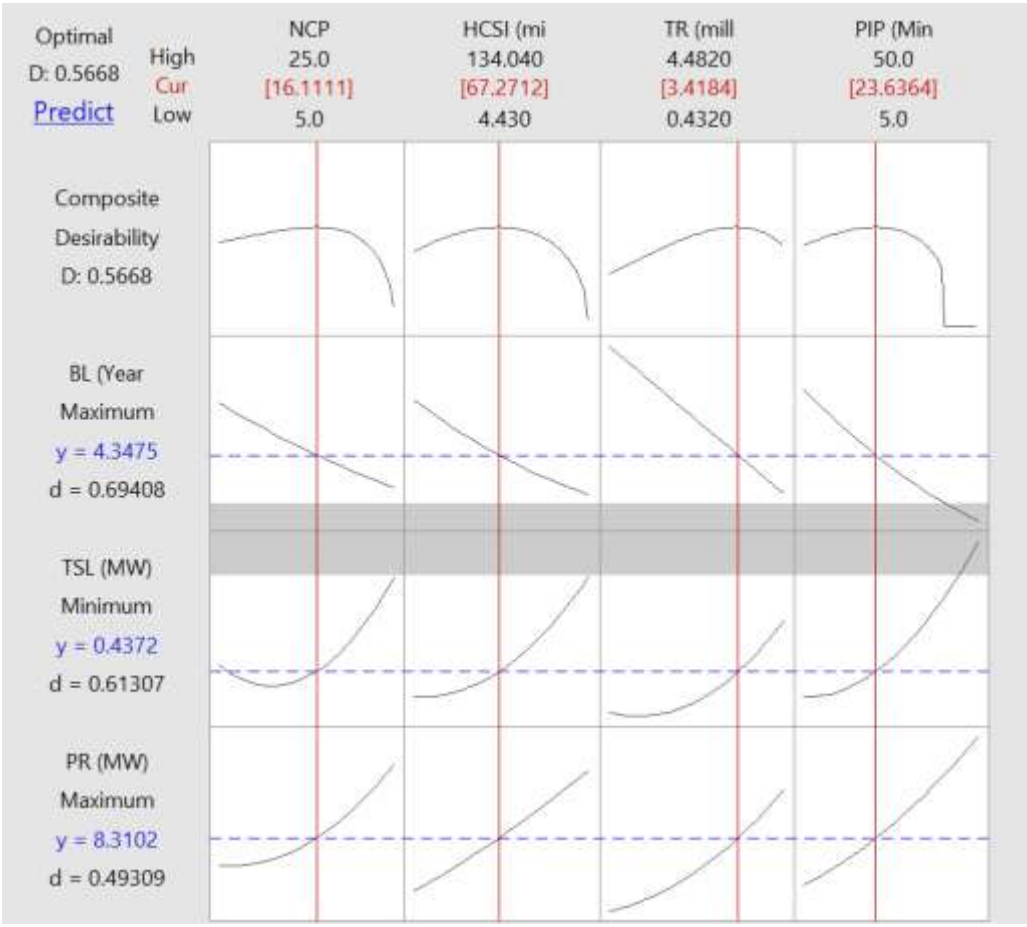


Fig. 7 RSM optimizer plot

Optimum values obtained for various input design parameters are NCP of 16.11 numbers, HCSI of ₹ 67.2712 M, TR of ₹ 3.4184 M, PIP of 23.6364 minutes, and the optimum values of output responses obtained are PR of 8.3102 MW, TSL of 0.4372 MW, and BL of 4.3475 years.

5.5 Validation of results

The results obtained from RSM are compared with the responses attained from the DSM calculations, and the closest ones are shown in Table 9. Table 10 presents results justification with percentage variation to the optimized design parameters and output response values obtained from the RSM optimizer.

Table 9 Closest responses attained from calculated result to RSM

	Design Parameters							Output Responses		
Index	No. of FCT ports	No. of UFCT Ports	No. of BST ports	Input-1 NCP	Input-2 HCSI (M ₹)	Input-3 TR (M ₹)	Input-4 PIP (min)	Output-1 PR (MW)	Output-2 TSL (MW)	Output-3 BL (Yr)
HCS-846	3	4	9	16	67.1192	3.35	24.38	8.11	0.4308	4.50625

Table 10 Validation test of RSM optimize results with calculated values

Design parameters	Notation	Units	Predicted (RSM)	Actual Calculated (DSM)	% Variation
No. of CP	NCP		16	16	0
HCS investment	HCSI	M ₹	67.2712	67.1192	-0.23
Tariff	TR	M ₹	3.4184	3.35	-2.06
Plug-in period	PIP	min	23.6364	24.38	+3.04
Output responses					
Power requirement	PR	MW	8.3102	8.11	-2.46
Total system losses	TSL	MW	0.4372	0.4308	-1.49
Battery life	BL	Yr	4.3475	4.50625	+3.52

The % variation for the optimal sitting and sizing of HCS response parameters PR (MW), TSL (MW), BL (Yr) are 2.46%, 1.49%, and 3.52%, respectively, and all are well within limits. This indicates that RSM methodology can be adopted for the prediction of best-suited HCS sizing input parameters for optimized performance responses. Out of a total of 3241 calculated responses, the closest and optimal solution provided by RSM is of 16 charging ports (consist of 3 FCT ports, 4 UFCT ports, and 9 BST ports). The best location for the optimal sitting of HCS comes out to be at nodes 17, 18, and 19 (see Figure 8) with a minimum voltage of 0.921 p.u. at node 57.

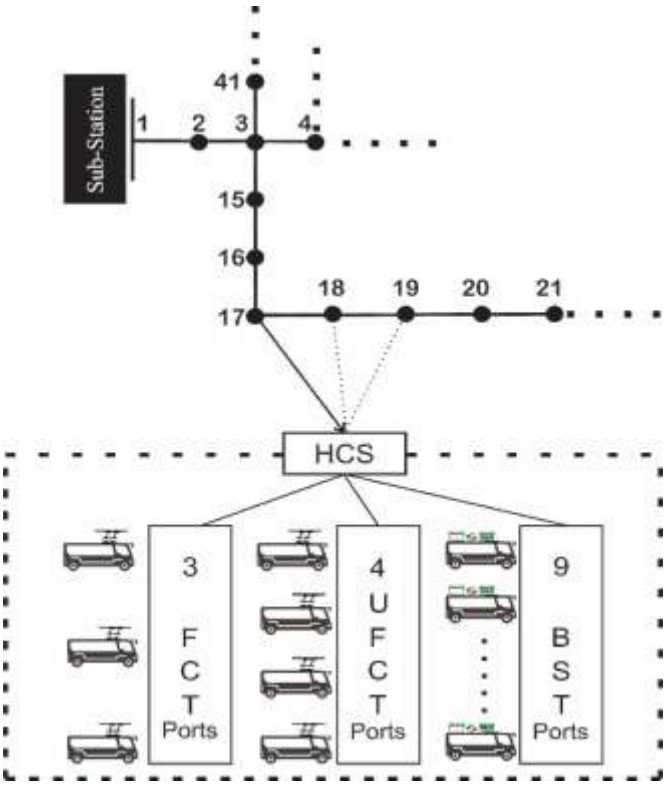


Fig. 8 Best possible node connection of purposed HCS

6. Conclusion

Faster adoption of EVs and EBs will help the global community deal with environmental pollution and climate change. However, this will also put additional stress on the distribution network. Hence, DNEP will be of paramount importance as the penetration of EVs

and EBs increases. A novel technique is proposed in this paper for solving the DNEP problem, considering the integration of parent and host charging stations. In the proposed model, various parameters such as number charging port, types of charging technology, and power requirements are optimized under the predetermined constraints of voltage fluctuation, minimization of losses, and plug-in-period. It can be concluded from the analysis that BST is the most efficient option in all considered charging ports categories' permutations and combinations. However, under practical constraints, when a combination of technologies is to be used, an entwined network of a low number of FCT and UFCT with maximum counts of BST emerges to be best suited. Out of a total of 3241 calculated responses, the closest and optimal solution provided by RSM is of 16 charging ports (consist of 3 FCT ports, 4 UFCT ports, and 9 BST ports). The best location for the optimal sitting of HCS comes out to be at nodes 17, 18, and 19 with a minimum voltage of 0.921 p.u. at node 57.

The methodology can be implemented considering the projected requirement to meet future demand. By keeping two out of four design parameters non-variable (fixed at mid-point value), the methodology presents the variation of each response with the other two variable design parameters. The results provide a vast field of choices to the HCS planner to choose and prioritize design parameters. As a case study, data of the city of Delhi, India, is used in the present work. The proposed methodology can help the planner to prioritize and integrate a significant number of charging points of different technologies into the distribution network without adversely affecting its reliability, stability, and performance.

As a scope of future work, the proposed model can be further improved by considering the following.

(a) Re-compute a fresh power assignment profile during the day itself, considering the personal and commercial EV charging at night.
(b) In highly polluted cities like New Delhi, India, to reduce the impact on the environment further, the power generation for charging stations may be from renewable energy sources.
(c) The spare capacity of the HCS can be utilized for private and commercial EV charging.
(d) The temperature variation factor has not been considered in the present work, which can be included in future work.

Compliance with ethical standards

Conflict of interest The authors declare that they have no conflict of interest.

Ethical approval The article does not contain any studies with human participants or animals performed by any of the authors.

References

An K, Jing W, Kim I (2019) Battery-swapping facility planning for electric buses with local charging systems. International Journal of Sustainable Transportation 13:1-13 https://doi.org/10.1080/15568318.2019.1573939

Box GEP, Wilson KB (1951) On the Experimental Attainment of Optimum Conditions. Journal of the Royal Statistical Society 13(1):1-45 https://www.jstor.org/stable/2983966

Bessa RJ, Matos MA (2013) Global against divided optimization for the participation of an EV aggregator in the day-ahead electricity market Part II: numerical analysis. Electrical Power System Research 95:319-329 https://doi.org/10.1016/j.epsr.2012.08.013

Bayram IS, Michailidis G, Devetsikiotis M, Granelli F (2013) Electric Power Allocation in a Network of Fast Charging Stations. IEEE Journal on Selected Areas in Communications 31(7):1235-1246 https://doi.org/10.1109/JSAC.2013.130707

Battapothula G, Yammani C, Maheswarapu S (2019) Multi-objective simultaneous optimal planning of electrical vehicle fast charging stations and DGs in distribution system. J. Mod. Power Syst. Clean Energy 7:923-34. https://doi.org/10.1007/s40565-018-0493-2

Chen T et al. (2020) A review on electric vehicle charging infrastructure development in the UK. Journal of Modern Power Systems and Clean Energy 8(2):193-205. 10.35833/MPCE.2018.000374

Dong X, Mu Y, Xu X et al. (2018) A charging pricing strategy of electric vehicle fast charging stations for the voltage control of electricity distribution networks. Applied Energy 225:857-868 https://doi.org/10.1016/j.apenergy.2018.05.042

DERC (Delhi Electricity Regulatory Commission) 2019. "Press Note for Electricity Tariff For FY 2019-20". Accessed 16 October 2019. http://www.derc.gov.in/Press_Release/Press_Release_31.07.2019/Press_release.pdf

DHI FAME-II (Department of Heavy Industry- Faster Adoption and Manufacturing of Electric Vehicles in India Phase II) 2019. "Expression of interest inviting proposals for availing incentives under Fame India scheme phase II for deployment of EV charging infrastructure within cities." Accessed 12 September 2019. https://dhi.nic.in/writereaddata/UploadFile/Revised-%20Expression%20of%20Interest.pdf

Ekren O, Ekren BY (2008) Size optimization of a PV/wind hybrid energy conversion system with battery storage using response surface methodology. Applied Energy 85(11):1086-1101. https://doi.org/10.1016/j.apenergy.2008.02.016

Gomez J, Morcos M (2002) Impact of EV Battery Chargers on the Power Quality of Distribution Systems. IEEE Power Engineering Review 22(10):63 https://doi.org/10.1109/TPWRD.2003.813873

Galus MD, Waraich RA, Noembrini F et al. (2012) Integrating power systems, transport systems and vehicle technology for electric mobility impact assessment and efficient control. IEEE Transections on Smart Grid 3(2):934-949. https://doi.org/10.1109/TSG.2012.2190628

Ghosh S, Yadav VK, Mehta G, Birajdar R (2017) Evaluation of Indian power sector reform strategies and improvement direction though DEA. IEEE Power & Energy Society General Meeting, Chicago, IL, 2017, pp. 1-5.

Ghosh S, Yadav R (2021) Future of Photovoltaic Technologies: A Comprehensive Review, Sustainable Energy Technologies and Assessments 47:101410. https://doi.org/10.1016/j.seta.2021.101410.

GoI-MoP (Government of India-Ministry of Power) 2018. "Charging Infrastructure for Electric Vehicles-Guidelines and Standards – reg." Accessed 31 October 2019. https://powermin.nic.in/sites/default/files/webform/notices/scan0016%20%281%29.pdf

Haesen E, Bastiaensen C, Driesen J, Belmans R (2009) A probabilistic formulation of load margins in power systems with stochastic generation. IEEE Transactions on Power Systems 24(2):951-958. https://doi.org/10.1109/TPWRS.2009.2016525

Hadley SW, Tsvetkova AA (2009) Potential impacts of plug-in hybrid electric vehicles on regional power generation. The Electricity Journal 22(10):56-68. https://doi.org/10.1016/j.tej.2009.10.011
Hasanien HM, Muyeen SM (2013) A Taguchi Approach for Optimum Design of Proportional-Integral Controllers in Cascaded Control Scheme. IEEE Transactions on Power Systems 28(2):1636-1644 https://doi.org/10.1109/TPWRS.2012.2224385
Jeon K, Chung T, Hahn S (2011) NEMA class a slot shape optimization of induction motor for electric vehicle using response surface method. International Conference on Electrical Machines and Systems, Beijing, 2011, 1-4. https://doi.org/10.1109/ICEMS.2011.6073692
Jingwei Y, Diansheng L, Shuang Y, Shiyu H (2014) Charging Load Forecasting for Electric Vehicles Based on Fuzzy Inference. Communications in Computer and Information Science, Springer 484:585-594. https://doi.org/10.1007/978-3-662-45643-9_62
Jafari M, Gauchia A, Zhao S, Zhang K, Gauchia L (2018) Electric Vehicle Battery Cycle Aging Evaluation in Real-World Daily Driving and Vehicle-to-Grid Services. IEEE Transactions on Transportation Electrification 4(1):122-134 https://doi.org/10.1109/TTE.2017.2764320
Khuri AI, Mukhopadhyay S (2010) Response surface methodology. Wires Computational Statistics 2(2):128-149 https://doi.org/10.1002/wics.73
Karfopoulos EL, Hatziargyriou ND (2013) A multi-agent system for controlled charging of a large population of electric vehicles. IEEE Transections on Power Systems 28(2):1196-1204 https://doi.org/10.1109/TPWRS.2012.2211624
Li H, Bai X (2011) Impacts of electric vehicles charging on distribution grid. Automation of Electric Power Systems 35(17):38-43
Muratori M, Elgqvist E, Cutler D, et al. (2019) Technology solutions to mitigate electricity cost for electric vehicle DC fast charging. Applied Energy 242:415-423 https://doi.org/10.1016/j.apenergy.2019.03.061
Nicolaides D et al. (2019) Technoeconomic analysis of charging and heating options for an electric bus service in London. IEEE Transactions on Transportation Electrification 5(3):769-781. 10.1109/TTE.2019.2934356
Pillai RK, Suri R, Kundu S, Singh H, Roy SS, Dhuri S (2018) Electric Vehicle Charging Stations Business Models for India. India Smart Grid Forum (ISGF) White Paper 1-15. accessed 15 August 2019 http://www.indiasmartgrid.org/reports/ISGF_White_Paper_-_EVSE_Business_Models_for_India.pdf
Richardson P, Flynn D, Keane A (2012) Optimal charging of electric vehicles in low-voltage distribution systems. IEEE Transactions on Power System 27(1):268-279. https://doi.org/10.1109/TPWRS.2011.2158247
Ren Z, Li W, Billinton R, Yan W (2016) Probabilistic Power Flow Analysis Based on the Stochastic Response Surface Method. IEEE Transactions on Power Systems 31(3):2307-2315. https://doi.org/10.1109/TPWRS.2015.2461159
Savier JS, Das D (2007) Impact of network reconfiguration on loss allocation of radial distribution systems. IEEE Transactions on Power Delivery 22(4):2473-2480. https://doi.org/10.1109/TPWRD.2007.905370
Shao S, Pipattanasomporn M, Rahman S (2009) Challenges of PHEV penetration to the residential distribution network. Power & Energy Society General Meeting (PESGM'2009), Calgary AB Canada, 1-8. https://doi.org/10.1109/PES.2009.5275806
TET (The Economics Times) (2015). “Rs 10-crore electric bus pilot in final leg; PM to gift two to ferry MPs.” Accessed 1 June 2019. https://economictimes.indiatimes.com/industry/transportation/rs-10-crore-electric-bus-pilot-in-final-leg-pm-to-gift-two-to-ferry-mps/articleshow/50235921.cms?from=mdr.
Tang D, Wang P (2016) Probabilistic modeling of nodal charging demand based on spatial-temporal dynamics of moving electric vehicles. IEEE Transections on Smart Grid 7(2):627-636. https://doi.org/10.1109/TSG.2015.2437415
TGOI (The Gazette of India). 2019. “Scheme for Faster Adoption and Manufacturing of Electric Vehicles in India Phase II (FAME India Phase II).” Part II, Section 3, Sub-section (ii). India: Department of Heavy Industry. https://dhi.nic.in/writereaddata/UploadFile/DHI_FAMEII_Gazette.pdf
Verma MK, Mukherjee V, Yadav VK, (2016) Greenfield distribution network expansion strategy with hierarchical GA and MCDEA under uncertainty. Electrical Power and Energy Systems 79:245-252. https://doi.org/10.1016/j.ijepes.2016.01.004
Verma, MK, Yadav, VK, Mukherjee, V, Ghosh, S (2019) A Multi-criteria Approach for Distribution Network Expansion Through Pooled MCDEA and Shannon Entropy. International Journal of Emerging Electric Power Systems 20(4):245-252. https://doi.org/10.1515/ijeeps-2019-0043
Wang Y, Chiang H, Wang T (2013) A two-stage method for assessment of voltage stability in power system with renewable energy. In: IEEE Electrical Power and Energy Conference, pp 1-6. https://doi.org/10.1109/EPEC.2013.6802933
Wei X, Lin L, Yue X, et al. (2016) Optimal allocation for charging piles in multi-areas considering charging load forecasting based on Markov chain. In: China International Conference on Electricity Distribution (CICED), Xi'an, pp 1-7. https://doi.org/10.1109/CICED.2016.7576277
Wang F, Xiao X, Sun Q, et al. (2019) Service restoration for distribution network with DGs based on stochastic response surface method. International Journal of Electrical Power and Energy Systems 107:557-568. https://doi.org/10.1016/j.ijepes.2018.12.015
Wang L et al. (2021) Grid impact of electric vehicle fast charging stations: trends, standards, issues and mitigation measures - an overview. IEEE Open Journal of Power Electronics 2:56-74. 10.1109/OJPEL.2021.3054601
Xiang Y, Liu J, Tang S et al. (2016) A traffic flow-based planning strategy for optimal siting and sizing of charging stations. In: Asia-Pacific Power and Energy Engineering Conf (APPEEC), Brisbane, Australia, pp 1-5. https://doi.org/10.1109/APPEEC.2015.7380895
Xiang Y, Hu S, Liu Y, Zhang X, Liu J (2019) Electric vehicles in smart grid: a survey on charging load modelling. IET Smart Grid 2(1):25-33. https://doi.org/10.1049/iet-stg.2018.0053
Yadav AS, Yadav VK, Mukherjee V, Ghosh S (2021) Performance Investigation of Different Bypass Diode Topology Based SDK-PV Arrays Under Partial Shading Conditions. In: Favorskaya M., Mekhilef S., Pandey R., Singh N. (eds) Innovations in Electrical and Electronic Engineering. Lecture Notes in Electrical Engineering, vol. 661, pp. 261-270. Springer, Singapore. https://doi.org/10.1007/978-981-15-4692-1_20.
Yang B, Wang L, Liao C, et al. (2015) Charging load calculation method of large-scale electric vehicles with coupling characteristics. Automation of Electric Power Systems 39(22):76-82

Zhao J, Wen F, Yang A, et al. (2011) Impacts of electric vehicles on power systems as well as the associated dispatching and control problem. Automation of Electric Power Systems 35(14):2-10

Zhang H, Hu Z, Song Y, et al. (2014) A prediction method for electric vehicle charging load considering spatial and temporal distribution. Automation of Electric Power Systems 38(1):13-20

Zhang Y, Ho SL, Fu W (2018) Applying Response Surface Method to Oil-Immersed Transformer Cooling System for Design Optimization. IEEE Transactions on Magnetics 54(11):1-5. https://doi.org/10.1109/TMAG.2018.2840337

Zhang H, Tang L, Yang C, Lan S (2019) Locating electric vehicle charging stations with service capacity using the improved whale optimization algorithm. Advanced Engineering Informatics 41:1-14. https://doi.org/10.1016/j.aei.2019.02.006

Zhao Y et al. (2020) Deployment of the electric vehicle charging station considering existing competitors. IEEE Transactions on Smart Grid 11(5): 4236-4248. 10.1109/TSG.2020.2991232

Zeb M Z et al. (2020) Optimal placement of electric vehicle charging stations in the active distribution network. IEEE Access 8:68124-34. 10.1109/ACCESS.2020.2984127

Foot Notes:

[1]For the present case, Tata Starbus Ultra Electric 9/12 EV, 41 seaters electric bus (manufactured by Tata Motors, India) having PMAC traction motor of 145 kW power, has been considered. The time taken to get fully charged by NCT is 7 hours, and by FCT is 2 hours, 15 minutes with UFCT and 5 minutes with BST.

[2]A subsidy of 70% earmarked by GoI on electrical vehicle supply equipment includes chargers, cable, smart metering, energy meter, breakers, etc. The upstream electrical infrastructure investment (which also includes transformers) is not included under this subsidy. As of now, there is no clarity on subsidy on spare batteries for the swapping process.

This article has been accepted for publication in a future issue of this journal, but has not been fully edited. Content may change prior to final publication. Citation information: DOI 10.1109/TCSII.2022.3149818, IEEE Transactions on Circuits and Systems II: Express Briefs

An Energy-Efficient High CSNR XNOR and Accumulation Scheme For BNN

Dinesh Kushwaha, Ashish Joshi, *Member, IEEE,* C. I. Kumar, Neha Gupta, Sandeep Miryala, *Senior Member, IEEE,* Rajiv Joshi, *Fellow, IEEE,* Sudeb Dasgupta, Anand Bulusu

***Abstract*—In this brief, we present an energy-efficient and high compute signal-to-noise ratio (CSNR) XNOR and accumulation (XAC) scheme for binary neural networks (BNNs). Transmission gates achieve a large compute signal margin (CSM) and high CSNR for accurate XAC operation. The 10T1C XNOR SRAM bit-cell performs the in-memory XAC operation without pre-charging the larger bitline capacitances and significantly reducing energy consumption per XAC operation. The validation of the proposed XAC scheme is done through the post-layout simulations in 65nm CMOS technology with V_{DD} of 1 V. The achieved 1 ns of latency and 2.36 fJ of energy consumption per XAC operation are (7.2×, 7.2×) and (2×, 1.31×) lower than state-of-the-art digital and analog compute in-memory (CIM) XAC schemes respectively. The proposed XAC design achieves 8.6× improvement in figure-of-merit (FoM), over prior state-of-the-art. Moreover, (σ/μ) average of 0.2% from Monte Carlo simulations show that proposed XAC scheme is robust against systematic mismatch and process variations.**

***Index Terms*—Accuracy, accumulation, artificial intelligence (AI), compute signal margin (CSM), compute signal to noise ratio (CSNR), energy-efficiency, latency, neuron, SRAM.**

I. Introduction

COMPUTE IN-MEMORY (CIM) architecture is a promising solution to overcome the limitation of Von-Neumann architecture for AI/ML applications [1]. Several dedicated CIM architectures are developed to accelerate Machine learning (ML) algorithms like convolutional neural networks (CNNs) for edge device applications [2]–[17]. The ML algorithms have computation complexity and require high storage area [3]. They consume enormous power when run on hardware [1]. The challenge is to run ML algorithms such as CNN on low-power devices like edge devices. A possible solution is to reduce the computational cost by converting floating-point weights and activation to binary (±1). A binary neural network (BNN) was reported in [4]. The BNN reduces the required storage and computation complexity by replacing multiplication and accumulation (MAC) operation in ML algorithms with bitwise binary XNOR and accumulation (XAC) operation [5]. Hence, SRAM-based CIM architectures for BNN implementation have gained significant attention among researchers in recent years [6]. Due to the feasibility of implementation, CIM architectures using complementary metal-oxide-semiconductor (CMOS) SRAMs have become an attractive choice for various AI/ML applications [7]–[17]. The XAC operation is energy-efficient for low-bit precision computation [1]. In prior work, SRAM-based CIM architectures for BNN implementation were categorized as digital CIM and analog CIM. Digital CIM provides a large-signal margin and high CSNR at the cost of more significant area overhead, high latency, and high energy consumption [17]. The cause is XNOR logic gates and Full-adder circuits are used for XAC operation, and both are physically separated. The analog CIM benefits include less latency, a smaller area, lower energy consumption at the cost of a small signal-margin, and less CSNR [6]–[8]. The small CSNR reduces the computation accuracy of XAC operations. In this work, our primary focus is to solve circuit design challenges associated with analog CIM, especially signal-margin, latency, and energy consumption per XAC. Many SRAM-based analog CIM schemes have been proposed in recent years for inference tasks [1]–[3]. In these schemes, additional transistors are added to standard 6T SRAM bit-cells to perform in-memory XAC operations for BNN. But they suffer from read-disturb issues, small signal-margin, and low CSNR, thus reducing computation accuracy [1]–[3]. In prior works [1] and [6], source/drain terminal of pass transistors are directly connected to the storage nodes of SRAM bit-cell, which will create a read-disturb issue when multiple rows are asserted. They also suffer from small CSNR due to leakage. In [2], a 12T XNOR SRAM bit-cell has transistors driving strength dependent resistive divider network for XAC operations. It has the limitation of small signal-margin and less CSNR due to process variations. Similarly, [3] also has a small signal margin and low CSNR due to a V_{th} drop across the NMOS pass transistor during the XAC

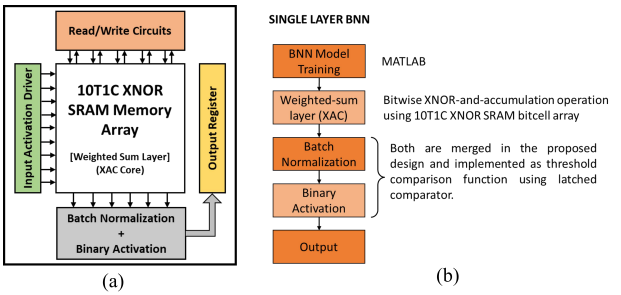


Fig. 1. (a) A functional block diagram to implement BNN using the proposed XAC scheme. (b) Operation flowchart of single layer BNN.

Dinesh Kushwaha, Neha Gupta, Sudeb Dasgupta and Anand Bulusu are with the Department of Electronics and Communication Engineering, Indian Institute of Technology Roorkee, Roorkee, Uttarakhand 247667 India (e-mail: dkushwaha1@ec.iitr.ac.in; anand.bulusu@ece.iitr.ac.in)

Ashish Joshi is with Intel Technology India Pvt. Ltd., Bangalore, Karnataka 560103 India.

Indra Kumar Chaudhary is with the Department of Electrical Engineering, Delhi Technological University, Delhi 110042 India.

Sandeep Miryala is with Brookhaven National Laboratory, Upton, NY 11973 USA.

Rajiv V. Joshi is with Thomas J. Watson Research Center, Yorktown Heights, NY 10598 USA.

1549-7747 (c) 2021 IEEE. Personal use is permitted, but republication/redistribution requires IEEE permission. See http://www.ieee.org/publications_standards/publications/rights/index.html for more information.
Authorized licensed use limited to: DELHI TECHNICAL UNIV. Downloaded on February 15,2022 at 10:02:05 UTC from IEEE Xplore. Restrictions apply.

This article has been accepted for publication in a future issue of this journal, but has not been fully edited. Content may change prior to final publication. Citation information: DOI 10.1109/TCSII.2022.3149818, IEEE Transactions on Circuits and Systems II: Express Briefs

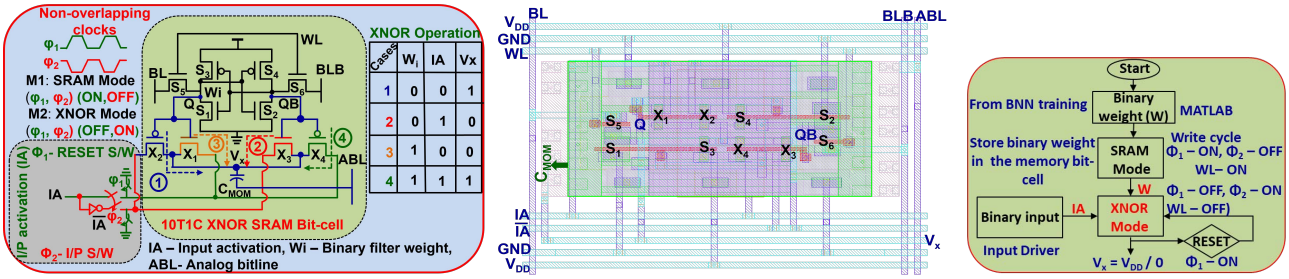


Fig. 2. Proposed XAC scheme for in-memory computation in BNN. (a) Schematic of 10T1C XNOR SRAM bit-cell with its different operating modes, SRAM (M1) and XAC (M2) at different input/output cases. (b) Layout of the bit-cell. The MOM capacitor is laid on top of the SRAM cell hence no additional area is required. (c) Flowchart of CIM binary XNOR operation in 10T1C SRAM bit-cell.

operation.

The design challenges such as read-disturb issue, reduced signal-margin, and CSNR are significant for analog CIM. In this paper, a novel CIM XAC scheme based on 10T1C XNOR SRAM bit-cell is proposed to handle these design challenges. A functional block diagram to implement BNN using the proposed XAC scheme and the flowchart are shown in Fig. 1. The primary objective is to design energy-efficient, fast and robust XAC core. The major contributions and novel attributes of this work are as follows:

- A transmission gates-based novel XAC scheme provides high compute signal margin (CSM) and high CSNR.
- Gate input connected transmission gates solve the problem of read-disturb
- The design does not requires an explicit pre-charge of bitline, which reduces energy consumption per XAC operation.
- The XAC operation is performed in single clock cycle to reduce latency.
- The proposed XAC design is free from capacitive coupling (gate-to-source/drain) error because transmission gate cancels the charge injection.
- The capacitive 10T1C XNOR SRAM bitcell avoids static current flow which reduces the power consumption.
- On-resistance of transmission gate is relatively independent of voltage across the computation capacitor during the XAC operation. This helps to achieve robust XAC scheme against process, voltage and temperature (PVT) variations.
- Transmission gate followed by capacitive coupling provides reduced transient delay for XAC operation.

This brief is organized as follows: Section II presents the proposed CIM XAC scheme using 10T1C XNOR SRAM bit-cell and its operation modes. Section III explains the implementation of single-layer binary neural networks using the proposed CIM XAC scheme. Section IV presents simulation results and discussion. Section V concludes the proposed work.

II. Proposed CIM XAC Scheme using 10T1C XNOR SRAM bitcell and its Operation

The proposed XAC scheme using 10T1C XNOR SRAM bit-cell and its modes of operation (M1 - SRAM mode,

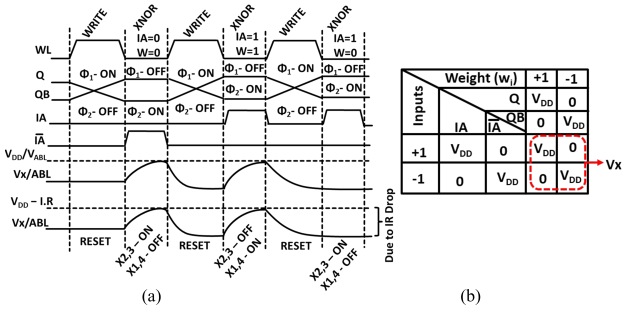


Fig. 3. (a) Simulation waveform for SRAM and XNOR mode of operation with ON/OFF conditions of switches and MOSFETs. IR drop is due to parasitic resistance of the interconnect lines. (b) Operating conditions of proposed design for XAC operation.

M2 - XNOR mode) are shown in Fig. 2(a). This bit-cell topology was reported in our previous work [18]. The cell has a standard 6T SRAM cell (S_1-S_6) and two decoupled read ports (X_1, X_2) and (X_3, X_4), which are implemented using transmission gates for in-memory XAC operation. The inherent benefit of transmission gate is large voltage swing, high speed, low resistance, lesser charge injection error and voltage independent ON resistance. The metal-oxide-metal (MOM) capacitor is used to sample the output results of the XAC operation. It provides capacitive coupling of V_x to analog bitline (ABL) for accumulation operation when multiple rows are asserted. The advantage of transmission gates is high signal margin for high compute SNR and inference accuracy. The MOM capacitor provides good matching characteristics and less sensitivity to process variations and noise. The capacitive divider circuit provides a more robust and power-efficient XAC operation than the resistive divider circuit used by [2]. The MOM capacitor laid on top of the SRAM bit-cell requires no area overhead as in [1]. The value of the MOM capacitor designed using the metal layers (M3-M4) in 65nm CMOS (STMicroelectronics) technology is 3.38 fF. The 10T1C XNOR SRAM cell is designed with a minimum sized device because there are no design constraints on devices for bit-cell stability due to decoupled read and write ports. The layout of the 10T1C XNOR SRAM bit-cell is shown in Fig. 2(b). The cell area is 2.64 μm^2. The 10T1C XNOR SRAM cell operates in two modes. The first mode of operation (ϕ_1 - ON, ϕ_2 - OFF, and WL - ON) is standard SRAM mode (write cycle), in which binary filter weight (W_i) is stored inside the memory bit-cell. The second mode of operation (ϕ_1 - OFF, ϕ_2

1549-7747 (c) 2021 IEEE. Personal use is permitted, but republication/redistribution requires IEEE permission. See http://www.ieee.org/publications_standards/publications/rights/index.html for more information.
Authorized licensed use limited to: DELHI TECHNICAL UNIV. Downloaded on February 15,2022 at 10:02:05 UTC from IEEE Xplore. Restrictions apply.

This article has been accepted for publication in a future issue of this journal, but has not been fully edited. Content may change prior to final publication. Citation information: DOI 10.1109/TCSII.2022.3149818, IEEE Transactions on Circuits and Systems II: Express Briefs

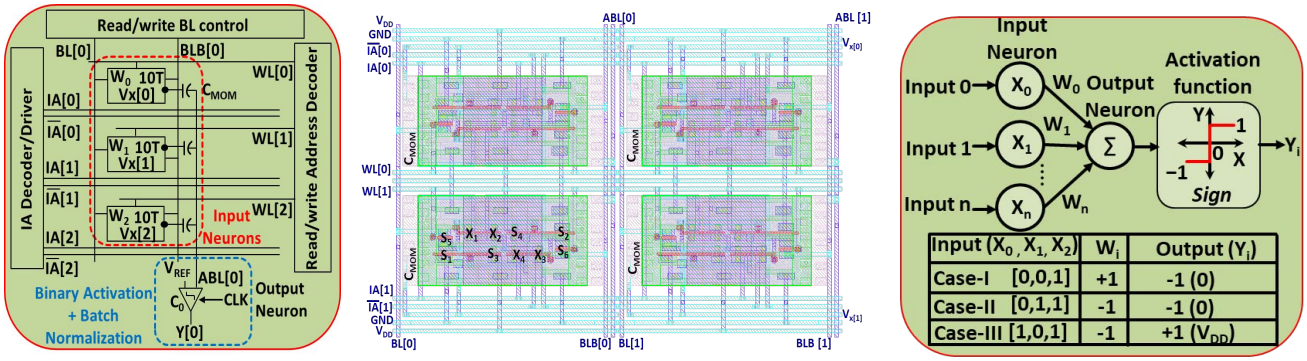


Fig. 4. (a) The CIM architecture of single layer BNN. The XAC operation implementation using 10T1C XNOR SRAM bit-cell. The single-layer BNN has three input neurons and one output neuron to validate the functionality and scalability of the proposed 10T1C XNOR SRAM bit-cell (this architecture is scalable for larger size BNN). (b) A 2×2 array level layout of 10T1C XNOR SRAM bit-cell with all metals shows horizontal and vertical routing. (c) Single layer BNN with binary activation function. Three test cases are considered to train and test single layer BNN on MATLAB.

- ON, and WL - OFF) is binary XNOR. In this mode, input activation and their complement (IA and $\overline{IA}$) are applied to input read ports of 10T1C XNOR SRAM bit-cell. The stored filter weight (W_i) is accessed through the transmission gates. The transmission gates are controlled (ON/OFF) by the logic state (Q and QB) of the stored weight inside the bit-cell. The XNOR operation conditions for input activation (IA) and store binary filter weight (W_i) for the cases (1 to 4) along with the ON paths of the transistors to charge the MOM capacitor are shown in Fig. 2(a). For the cases (1 and 4), shown in the truth table in Fig. 2(a), XNOR output is high. The node V_x is charged up to (V_{DD} = 1 V), then the voltage on V_x is coupled to the analog bitline (ABL). For the remaining two cases (2 and 3), the XNOR output is low, and the node V_x is discharged to 0 V. The CIM binary XNOR operation flow-chart in 10T1C XNOR SRAM bit-cell is presented in Fig. 2(c). The simulation waveform of the XNOR operation and its operating conditions is illustrated in Fig. 3(a) and (b) respectively. It is worth noting that the proposed XNOR 10T SRAM cell is more energy-efficient than previously reported works because pre-charging of bitline (BL) is not required for the XAC operation. The proposed XAC scheme is based on capacitive divider network with no static current flow to reduce power consumption. The computation capacitor (C_{MOM}) entirely isolates the bitcell from the ABL, hence no leakage path is present from ABL to GND. We have also performed static and dynamic stability analyses of the 10T1C SRAM bit-cell. The static noise margins (SNM): hold SNM (HSNM), read SNM (RSNM), write SNM (WSNM) and compute static noise margin (CSNM) are 265mV, 128mV, 384mV, and 267mV, respectively, at 1 V supply voltage. The measured noise voltage at cell storage nodes is 24 mV due to gate-to-drain capacitive coupling during the XAC operation, which is 5× lower as compared to static noise margins. The dynamic write margin is 150 ps for a successful write operation. At array level implementation, the current-resistance (IR) drop is a problem in long interconnect lines. Due to IR drop, the available voltage range is less than V_{DD} for XAC operation, as shown in Fig. 3(a). For correct digital output of XAC, the minimum voltage difference between two consecutive XAC voltages must be greater than the offset of the readout circuit.

III. A CIM Architecture of Single Layer BNN using Proposed XAC Scheme

We have designed a CIM architecture of single layer BNN with three input neurons and one output neuron to prove the scalability and functionality of the proposed XAC scheme for BNN, as shown in Fig. 4(a). We have trained and tested a single layer BNN in MATLAB for three test cases (Case-I, Case-II, and Case-III), as mentioned in Fig. 4(c). The inputs (X_i) and outputs (Y_i) have 3b and 1b resolution, respectively. The optimized real value filter weights (W_0, W_1, W_2) obtained through the BNN model training for the test cases-I, II, and III are 8.8608, -1.5689, and -4.3384, respectively. At the same time, the corresponding predicted output levels from the trained model are 0.0129, 0.0027, and 0.9893. For the BNN, real value weights (8.8608, -1.5689, and -4.3384) are converted into a binary equivalent using the *sign* activation function as shown in Fig. 4(c). In this work, batch normalization is combined with binary activation function in a single threshold comparison step where the accumulated analog voltage at ABL (V_{ABL}) is compared with reference voltage (V_{REF}) of the comparator as shown in Fig. 4(a). The binary equivalent filter weights are (+1, -1, -1). The filter weights are stored in column-wise format. The binary filter weights +1 and -1 are stored as logic 1 (V_{DD}) and logic 0 (GND) in the memory bit-cell. The architecture also contains a read/write control block to set the BL voltage values during the SRAM write mode and the input activation decoder/driver to apply the IAs for CIM mode. The address row and column decoders activate rows/columns during the SRAM and XNOR modes. The accumulation of XNOR outputs of two or more memory bit-cells is performed through capacitive coupling in a selected column. The resultant voltage is accumulated on analog bitline ABL. Finally, a latched comparator (C_0) is used as a readout circuit to sense analog voltage on ABL corresponding to the XAC result and generate the final digital output (Y). Fig. 4(b) shows the 2×2 array level layout of 10T1C XNOR SRAM bit-cell to show scalability of the proposed XAC scheme. This work considers a single column to describe the proposed XAC scheme, but it is scalable for large BNN implementation.

1549-7747 (c) 2021 IEEE. Personal use is permitted, but republication/redistribution requires IEEE permission. See http://www.ieee.org/publications_standards/publications/rights/index.html for more information.
Authorized licensed use limited to: DELHI TECHNICAL UNIV. Downloaded on February 15,2022 at 10:02:05 UTC from IEEE Xplore. Restrictions apply.

This article has been accepted for publication in a future issue of this journal, but has not been fully edited. Content may change prior to final publication. Citation information: DOI 10.1109/TCSII.2022.3149818, IEEE Transactions on Circuits and Systems II: Express Briefs

IV. Simulation Results and Performance Parameters

A. Post-layout Simulation results of CIM BNN architecture

All simulations are performed using HSPICE in a 65nm CMOS (STMicroelectronics) process design kit (PDK) where the operating voltage is (V_{DD} = 1 V). In order to incorporate array level impact on performance parameters, the lumped capacitors equivalent to 256×64 array are included in the test setup. Fig. 4(a) shows a column of single layer BNN CIM architecture to explain binary XAC operation with three input neurons and one output neuron. Binary input activations (IA_0, IA_1, IA_2) are applied to three input neurons and multiply with corresponding filter weights (W_0, W_1, W_2) to perform the CIM XAC operation. The output result of XNOR operation would be high (V_{DD}) if input activation (IA) and stored filter weight (W) have the same sign otherwise low (0).

The input test cases, stored filter weights, and corresponding XAC output results are summarized in Table I. After completing the XAC operation, the resultant output voltage on ABL is passed through a comparator to get the final output level (Y_0). In this work, latched comparator is used as a readout circuit to provide binary output level depending on the polarity of ($V_{ABL} - V_{REF}$) as shown in Fig. 5(a). The comparator reference voltage is 0.5 V, and the DC offset voltage is 12 mV at 1 V supply voltage. The XAC Simulation results for test cases (I, II, and III) are shown in Fig. 5(b).

B. Performance parameters of CIM XAC schemes for BNN

We have calculated critical performance metrics such as energy consumption, latency, and CSNR for XAC operation. The comparison of XAC schemes has been made between the proposed work and previously reported results [1]–[3], [17]. We have also performed process variation analysis on the XAC output voltage (V_x).

1) Energy consumption and latency per XAC operation: Energy efficiency is the primary benchmark to evaluate the performance of a CIM architecture, and it depends on energy consumption to execute XAC operations. The proposed XAC scheme eliminates larger bitline capacitances for XAC operation pre-charging, thus reducing energy consumption. In this work, energy consumption per XAC operation is 2.36 fJ at 1 V supply voltage. The proposed XAC scheme using 10T1C is 7.2× and 1.31× times more energy-efficient than digital CIM [17] and analog CIM [1] XAC schemes. The latency for the XAC operation is also a crucial parameter to define the throughput of the CIM architecture. The latency is reduced because the XAC operation is performed within the memory in single clock cycle. The latency of the proposed XAC scheme is 1 ns, which is 7.2× and 2× lower than digital CIM [17] and previous analog CIM [1] XAC schemes. The comparison of energy consumption and latency per XAC is summarized in Table II.

2) Process variation analysis on XAC output voltage (V_x): Process variations affect the driving strength of the transistors and disturb the charging and discharging rate of the capacitor during the XAC operation. It reduces the signal margin and produces an error in XAC output results. We have analyzed the effect of process variation on XAC output voltage (V_x) of the proposed SRAM cell, as shown in Fig. 6(a). The comparison of normalized standard deviation (σ/μ)% in V_x for [1]–[3] and proposed work is shown in Fig. 6(b). This result average (σ/μ) = 0.2% indicates that the proposed XAC scheme is more robust against the process variations than previously reported works. The standard deviation in XAC output voltage for proposed work and previously reported work is summarized in Table II.

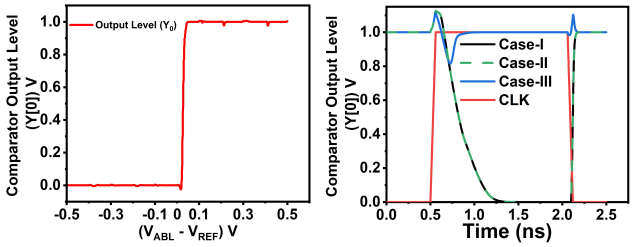


Fig. 5. (a) Input-output characteristics of a latched comparator to generate binary output (Yi). (b) Post-layout simulation result of CIM XAC operation for BNN architecture with three input neurons and one output neuron for different test cases summarized in Table I. Positive and negative XAC results are equivalent to V_{DD} and 0 respectively.

TABLE I
Binary Test Input Cases and Stored Binary Filter Weights for the Validation of the Proposed CIM XAC Schemes for BNN

Binary Weights (W_i)	Case I	Case II	Case III
W_0 = +1	IA_0 = -1	IA_0 = -1	IA_0 = +1
W_1 = -1	IA_1 = -1	IA_1 = +1	IA_1 = -1
W_2 = -1	IA_2 = +1	IA_2 = +1	IA_2 = +1
Binary XAC results (Y_0)	-1+1-1 = -1 (0)	-1-1-1 = -3 (0)	+1+1-1 = +1 (V_{DD})

3) Signal margin and compute SNR (CSNR): Signal margin is strongly related to CSNR and computation accuracy. In previously reported works [1]–[3], CIM XAC schemes suffer from small signal margins due to pass gate (NMOS/PMOS) based implementation and process variations. The proposed XAC scheme based on transmission gates achieves a high signal margin and high compute SNR due to elimination of leakage. The CSNR of the XAC operation is represented by (1).

$$\text{CSNR} = \frac{(CSM)^2}{(\sigma_x)^2} \qquad \text{CSM} = \frac{V_{DD}C_{MOM}}{C_{MOM} + C_{ABL}} \tag{1}$$

where CSM is compute signal margin and σ_x is standard deviation in V_x. The comparison of CSNR for proposed work and previously reported results is shown in Fig. 6(c). We also compare the Figure of merit (FoM), defined as follows:

$$\text{FoM} = \frac{Energy\text{-}Efficiency \times CSNR}{Bitcell\ Area} \tag{2}$$

The comparison of FoM is presented in Fig. 6(d).

V. Conclusion

In this paper, a robust and energy-efficient XAC scheme for BNN is presented. The scheme supports parallel multi-bit CIM XAC operation without pre-charging the bit lines. The MOM capacitor and accumulation through the capacitive coupling has enabled less sensitivity to process variation. The proposed CIM XAC scheme provides a high signal margin and high CSNR. Transmission gate followed by capacitive coupling

1549-7747 (c) 2021 IEEE. Personal use is permitted, but republication/redistribution requires IEEE permission. See http://www.ieee.org/publications_standards/publications/rights/index.html for more information.
Authorized licensed use limited to: DELHI TECHNICAL UNIV. Downloaded on February 15,2022 at 10:02:05 UTC from IEEE Xplore. Restrictions apply.

This article has been accepted for publication in a future issue of this journal, but has not been fully edited. Content may change prior to final publication. Citation information: DOI 10.1109/TCSII.2022.3149818, IEEE Transactions on Circuits and Systems II: Express Briefs

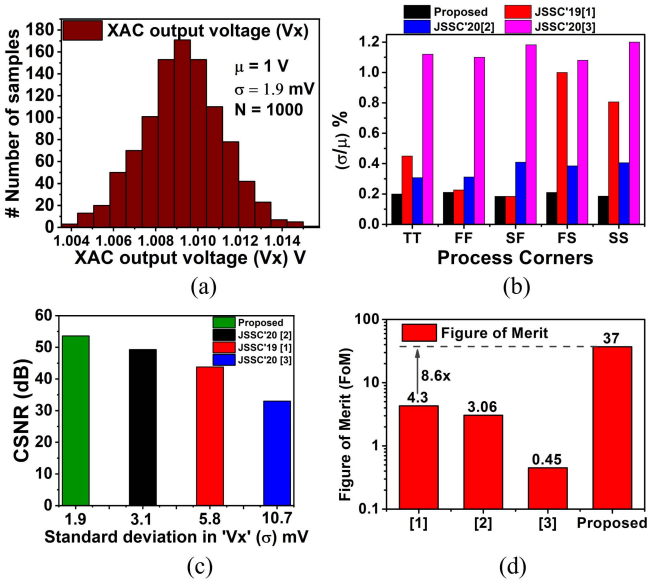


Fig. 6. Comparison of XAC schemes (a) Monte Carlo simulation (1000 samples) for XAC output voltage (Vx) in the proposed work, mean value is 1 V, and sigma value is 1.9 mV. (b) Normalized standard deviation in percentage of XAC output voltage (Vx), 25°C. (c) CSNR. (d) Figure of merit.

TABLE II
COMPARISON OF CIM XAC SCHEMES FOR BNN IN 65NM CMOS PDK.

Parameters	[2]	[3]	[17]	Charge-Domain Compute* (Post Layout Simulations)	Proposed Work (Post Layout Simulations)
Technology	65nm	65nm	65nm	65nm (STM)	65nm (STM)
Bitcell Type	12T SRAM	8T1C SRAM	XNOR Gate, Adders	8T1C SRAM	10T1C SRAM
Supply Voltage (V)	1	1	0.8	1	1
Energy Consumption per XAC (fJ)	7.2**	1.48**	17	3.1	2.36
Latency per XAC (ns)	0.8	20	7.2	2	1
Standard Deviation in Vx (mV)	3.1	10.7	NA	5.8	1.9
Cell Area (μm^2)	3.9	2.9	10.53	1.8	2.64
FoM	3.06	0.45	NA	4.3	37

* XAC scheme from [1]. We have calculated the performance parameter using the same simulation setup and technology same as the proposed work.
** Estimated from reported TOPS/W

provides reduced transient delay for XAC operation. The XAC operation is performed in single clock cycle to reduce latency. This XAC scheme has been validated using post-layout simulations in a standard 65nm CMOS (STMicroelectronics) PDK. At 1 V of V_{DD}, the energy consumption per XAC operation is 2.36 fJ, and latency is 1 ns. The achieved energy consumption and latency are (7.2× and 7.2×) lesser than digital and (1.31× and 2×) lesser than analog state-of-the-art CIM XAC schemes, respectively. The proposed XAC scheme achieved 8.6× higher FoM than prior work.

REFERENCES

[1] H. Valavi, P. J. Ramadge, E. Nestler and N. Verma, "A 64-Tile 2.4-Mb In-Memory-Computing CNN Accelerator Employing Charge-Domain Compute," in *IEEE Journal of Solid-State Circuits*, vol. 54, no. 6, pp. 1789-1799, June 2019, doi: 10.1109/JSSC.2019.2899730.

[2] S. Yin, Z. Jiang, J. Seo and M. Seok, "XNOR-SRAM: In-Memory Computing SRAM Macro for Binary/Ternary Deep Neural Networks," in *IEEE Journal of Solid-State Circuits*, vol. 55, no. 6, pp. 1733-1743, June 2020, doi: 10.1109/JSSC.2019.2963616.

[3] Z. Jiang, S. Yin, J. Seo and M. Seok, "C3SRAM: An In-Memory-Computing SRAM Macro Based on Robust Capacitive Coupling Computing Mechanism," in *IEEE Journal of Solid-State Circuits*, vol. 55, no. 7, pp. 1888-1897, July 2020, doi: 10.1109/JSSC.2020.2992886.

[4] M. Rastegari, V. Ordonez, J. Redmon, and A. Farhadi, "XNOR-Net: ImageNet classification using binary convolutional neural networks," *In proceedings Eur. Conf. Comput. Vis. (ECCV)*, 2016.

[5] S. Yin, Z. Jiang, M. Kim, T. Gupta, M. Seok, and J. Seo, "Vesti: Energy-Efficient In-Memory Computing Accelerator for Deep Neural Networks," *IEEE Transactions on Very Large-Scale Integration (VLSI) Systems*, vol. 28, no. 1, pp. 48-61, Jan. 2020.

[6] X. Si et al., "A Dual-Split 6T SRAM-Based Computing-in-Memory Unit-Macro with Fully Parallel Product-Sum Operation for Binarized DNN Edge Processors," *IEEE Transactions on Circuits and Systems I: Regular Papers*, vol. 66, no. 11, pp. 4172-4185, Nov. 2019

[7] A. Agrawal et al., "Xcel-RAM: Accelerating Binary Neural Networks in High-Throughput SRAM Compute Arrays," *IEEE Transactions on Circuits and Systems I: Regular Papers*, vol. 66, no. 8, pp. 3064-3076, Aug. 2019.

[8] A. Biswas and A. P. Chandrakasan, Conv-RAM: An energy-efficient SRAM with embedded convolution computation for low-power CNN-based machine learning applications, *in Proceedings IEEE International Solid-State Circuits Conference - (ISSCC)*, San Francisco, CA, 2018.

[9] H. Zhang, Y. Shu, W. Jiang, Z. Yin, W. Zhao, and Y. Ha, "A 55nm, 0.4V 5526-TOPS/W Compute-in-Memory Binarized CNN Accelerator for AIoT Applications," *in IEEE Transactions on Circuits and Systems II: Express Briefs*, vol. 68, no. 5, pp. 1695-1699, May 2021.

[10] X. Si et al., "15.5 A 28nm 64Kb 6T SRAM Computing-in-Memory Macro with 8b MAC Operation for AI Edge Chips," *2020 IEEE International Solid-State Circuits Conference - (ISSCC)*, 2020, pp. 246-248, doi: 10.1109/ISSCC19947.2020.9062995.

[11] X. Si et al., "24.5 A Twin-8T SRAM Computation-In-Memory Macro for Multiple-Bit CNN-Based Machine Learning," *2019 IEEE International Solid-State Circuits Conference - (ISSCC)*, 2019, pp. 396-398, doi: 10.1109/ISSCC.2019.8662392.

[12] J. Yang et al., "24.4 Sandwich-RAM: An Energy-Efficient In-Memory BWN Architecture with Pulse-Width Modulation," *in Proceedings IEEE International Solid-State Circuits Conference - (ISSCC)*, San Francisco, CA, USA, 2019.

[13] S. Liu, H. Zhu, C. Chen, L. Zhang, and C. Richard Shi, "XNORAM: A Networks with Flexible Dataflow Mapping," *in proceedings 2nd IEEE International Conference on Artificial Intelligence Circuits and Systems (AICAS)*, Genova, Italy, 2020.

[14] J. Zhang, Z. Wang, and N. Verma, "In-Memory Computation of a Machine- Learning Classifier in a Standard 6T SRAM Array," *IEEE Journal of Solid-State Circuits*, vol. 52, no. 4, pp. 915-924, April 2017.

[15] M. Kang, S. Lim, S. Gonugondla, and N. R. Shanbhag, "An In-Memory VLSI Architecture for Convolutional Neural Networks," *IEEE Journal on Emerging and Selected Topics in Circuits and Systems*, vol. 8, no. 3, pp. 494-505, Sept. 2018

[16] X. Si et al., "15.5 A 28nm 64Kb 6T SRAM Computing-in-Memory Macro with 8b MAC Operation for AI Edge Chips," *in Proceedings IEEE International Solid-State Circuits Conference - (ISSCC)*, San Francisco, CA, USA, 2020.

[17] H. Kim, T. Yoo, T. T. -H. Kim and B. Kim, "Colonnade: A Reconfigurable SRAM-Based Digital Bit-Serial Compute-In-Memory Macro for Processing Neural Networks," *in IEEE Journal of Solid-State Circuits*, vol. 56, no. 7, pp. 2221-2233, July 2021.

[18] Dinesh Kushwaha, Indra Kumar Chaudhry, Sudeb Dasgupta, Rajiv Joshi, Anand Bulusu "An Energy-Efficient and Robust 10T SRAM cell for In-memory computation" *IBM IEEE CAS/EDS AI Compute Symposium (AICS)*,2020.

1549-7747 (c) 2021 IEEE. Personal use is permitted, but republication/redistribution requires IEEE permission. See http://www.ieee.org/publications_standards/publications/rights/index.html for more information.
Authorized licensed use limited to: DELHI TECHNICAL UNIV. Downloaded on February 15,2022 at 10:02:05 UTC from IEEE Xplore. Restrictions apply.

Materials Today: Proceedings xxx (xxxx) xxx

Contents lists available at ScienceDirect

Materials Today: Proceedings

journal homepage: www.elsevier.com/locate/matpr

Analytical study on properties of concrete materials incorporating recycled aggregates from construction and demolition waste

Shanko Ayele Abera

Department of Construction Technology and Management, Dilla University, Ethiopia
Department of Civil Engineering, Delhi Technological University, India

ARTICLE INFO

Article history:
Available online xxxx

Keywords:
Performance behavior
Waste management
Physical properties
Construction and demolition waste
Recycling
Reuse

ABSTRACT

The concrete materials' fundamental behavior has significant effects on performance characteristics and their general nature. The current study analyzes recycled aggregate materials' basic properties from construction and demolition waste and identifies drawbacks while using excessive amounts. The volume of recycled aggregate materials used to replace natural aggregate materials in concrete production ranged from 0% to 100% to evaluate the suitability range in the current study. Evaluations have been done on the fundamental properties such as workability and strength performance of concrete materials for the M20 mix design, ranging from 0% to 100% replacement of recycled and natural aggregate material. While doing practical tests using various replacement rates, the conventional aggregate materials outperformed the concrete materials that incorporate recycled aggregate materials from construction and demolition debris. Based on the results obtained on investigations, a reduction in performance has been observed in almost all the basic properties of the concrete materials that contain recycled aggregate materials. Hence, most of the basic properties have been impacted by the increasing amount of recycled aggregate materials. So, it is not recommended to use recycled aggregate materials in excessive volume only to save materials. Of course, these materials' utilization will help us create a waste-free environment and have economic benefits. Still, the negative impacts must also be considered while using such materials in structural and foundation works.
Copyright © 2022 Elsevier Ltd. All rights reserved.
Selection and peer-review under responsibility of the scientific committee of the International Conference on Smart and Sustainable Developments in Materials, Manufacturing and Energy Engineering.

1. Introduction

Construction and Demolition (C&D) debris is a widely produced waste material throughout the construction, repairing, renovation, and demolition of various structures of civil engineering projects across the world. In the last two and three decades, C&D debris is considering the recycling process, and some approaches to reuse such waste materials for construction purposes have been tried a lot. Due to rapid economic changes and increasing population, the C&D waste generation is overgrowing compared to the last two and three decades. This situation put it a negative impact on the environment as well as economic development. The condition worsens when the construction industry recycles and utilizes C&D waste in a negligible amount [33].

Currently, recovery and utilization of C & C&D waste have become increasing because of its apparent durability, ready availability, and economical. This increasing utilization, in its turn, has consistently decreased the volume of C&D debris. Every day, tons of C&D trash are unexploited. In inner-city areas, waste production had estimated the amount to roughly 2.5 tons daily. C&D waste substantially subsidizes the growing manufacture of solid waste worldwide, especially in developing countries, with only approximately 30%, and less of such debris is only subjected to recycling [1].

The discarding of Construction and Demolition debris can be a source for many problems that damage any society because natural processes cannot degrade most of these materials into usable materials. The use of C&D debris is a significant problem-solving in landfills and grants adversative possessions on environmental issues. Thus, there should be the best mechanism to turn this C&D debris into recycled aggregate materials see Fig. 1) that can be standard to produce concrete materials for different purposes [2].

E-mail address: shagenet2002@gmail.com

https://doi.org/10.1016/j.matpr.2022.01.191
2214-7853/Copyright © 2022 Elsevier Ltd. All rights reserved.
Selection and peer-review under responsibility of the scientific committee of the International Conference on Smart and Sustainable Developments in Materials, Manufacturing and Energy Engineering.

Please cite this article as: Shanko Ayele Abera, Analytical study on properties of concrete materials incorporating recycled aggregates from construction and demolition waste, Materials Today: Proceedings, https://doi.org/10.1016/j.matpr.2022.01.191



Fig. 1. Recycled aggregate materials from C&D debris. Source: http://www.prolandscapermagazine.com.

Recycled concrete aggregate (RCA) and Recycled aggregate (RA) from C&D debris can be utilized as coarse and fine aggregate material substitutes in concrete material and other applications. Recycled concrete aggregate is a significant construction and civil and construction engineering project [5]. RCA is a type of concrete manufactured from concrete material waste during C&D waste recycling. It contains an intensifying agent, which increases the mix's capacity while providing other potentials, such as reducing dead load [11].

When recycling C&D debris, it is evident that it has drawbacks. Accumulations of C&D debris can occupy many spaces. If not engaged in recycling works as fast as possible, the damped debris can cause another challenge for many who spend a long time around the recycling sites. In natural hazards like the landslide and earthquake, the damped C&D trash can cause fatal problems to society [6]. So, it is better to recycle or remove the C&D wastes without dumping them for a long time. As a directive, all responsible bodies have to minimize or eliminate C&D debris to minimize social and environmental impacts.

2. Methods and materials

The current study focuses on how recycled aggregate material can be produced using various mix designs of Construction and Demolition (C&D) debris recycled aggregate as replacements for Natural aggregate materials (NA). This process confirmed that the desired densities and strength criteria were attained, and hence, it can be used as a replacement material for natural aggregate materials at various substitution levels [8]. Investigations on the concrete materials' fundamental performance behavior that incorporate recycled aggregate materials from C&D debris have been done to determine the recycled materials' aptness in different civil engineering projects [4].

2.1. Mix design of concrete materials

Indian standard [15] was used to guide sample-making in the current investigation. Mix design for sample production is according to Indian standards, as mentioned in the text. The traditional strength of 20 N/mm^2 in 28 days should be achieved in the mix design of 1:0.75:1.5, recommended again by Indian standards [16]. A similar water-cement ratio (w/c) (see Table 1) had been applied for the recycled aggregate (at various substitution rates) and conventional aggregate materials [35].

2.2. Production of recycled aggregates and recycled concrete aggregates from C&D debris

The shape of the resulting C&D debris got further reshaping procedure to make it suitable for utilization. Before crushing, the C&D waste recycled aggregates (RAs) diameter was varied depending on its demolition procedures. The first type of Recycled aggregates (RAs), manufactured from mixed C&D waste material, was sent to the wet segregation process and maintained for reuse [7]. The second type of recycled aggregate, known as Recycled concrete aggregate (RCA), which directly sent to the dry segregation process for reshaping and is also used in concrete material [13].

A recycled aggregate material manufactured from C&D waste goes through laboratory tests to determine its general character. The obtained results are analyzed using standard techniques. The second type of recycled aggregate, recycled concrete aggregate (RCA), is preferred over recycled aggregate materials produced from mixed C&D wastes [9]. The performance is also showing the difference between these two products. While in recycling and recovery C&D debris, some new technologies and advanced approaches must be practiced. This technological advancement makes easy the production and recycling process for recycled aggregate materials [15].

Table 1
Mix design sample for concrete production from recycled aggregate materials (M20).

Parameters	NA (0%)	RA-1 (15%)	RA-2 (30%)	RA-3 (45%)
W/C (%)	0.5	0.5	0.5	0.5
Cement (kg/m^3)	360	360	360	360
Water (kg/m^3)	180	180	180	180
FA (kg/m^3)	270	270	270	270
CA (kg/m^3)	540	459	378	297
RA (kg/m^3)	0	81	162	243

2.3. Proposed utilization areas of recycled aggregate and recycled concrete aggregate

The recycled aggregate materials produced from mixed construction waste and recycled concrete aggregate materials made from demolished concrete debris are used in different civil engineering projects [17]. It can be used in bare cement concrete up to 25% replacement of coarse aggregate and 20% replacement for reinforced cement concrete [28]. It is possible to utilize recycled aggregates in lean concrete for 100% replacement for natural aggregate materials (see Table 2).

In the reinforced concrete, the recycled aggregate can be used up to 20% substitution for natural aggregate, and the grade of the concrete is limited to the M25 category only [17]. It is also limited to M15 grade concrete in lean concrete to be produced using recycled aggregate materials from C&D debris [20]. According to this Indian standard, using recycled aggregate materials from C&D scrap beyond the specified limits can bring severe damage to the structure, and it has problems with overall work. The strength issue that becomes questionable is that this standard is not applied correctly [12].

Some of the utilization areas proposed (see Fig. 2) for recycled aggregate materials from C&D waste are: Park sitting benches, pre-fabricated interior walls, tree planting, electric poles, and other many activities that don't need high strength of concrete can be a suitable area for the utilization of recycled aggregate materials from C&D wastes. As revealed in Table 1, recycled aggregate materials from mixed construction waste can only be used in lean concrete. It is not permitted to use these materials in Plain cement concrete (PCC) and Reinforced cement concrete (RCC) [17].

The maximum utilization of Recycled Aggregate materials manufactured from C&D waste is mentioned above (see Table 2). The data is the permissible limit for using recycled aggregate materials according to the Indian standard [17]. The current study then investigates the substitution of these the so-called recycled aggregate materials from C&D debris with virgin aggregate materials in various replacement rates in M20 mix design concrete to evaluate its performance so that it can be utilized in real civil and construction projects [22].

3. Results and discussions

3.1. Aggregate impact value (AIV)

Aggregate impact value is measured using an abrasion resistance test for the aggregates produced from C&D debris. It is the capacity of the aggregate materials that can resist the potential loads that are applied on it through various time intervals. The investigation on the outcome of Construction and Demolition

Table 2
Shows the allowable utilization percentage. Source: IS:383-2016.

No	Type of recycled aggregate materials	Maximum utilisation, %		
		Plain cement concrete	Reinforced cement concrete	Lean concrete (less than M15 grade)
1	Coarse Aggregate materials			
	RCA(Coarse)	25%	20% (only up to M25 Grade)	100%
	RA	0%	0%	100%
2	Fine Aggregate materials			
	RCA(Fine)	25%	20% (only up to M25 Grade)	100%

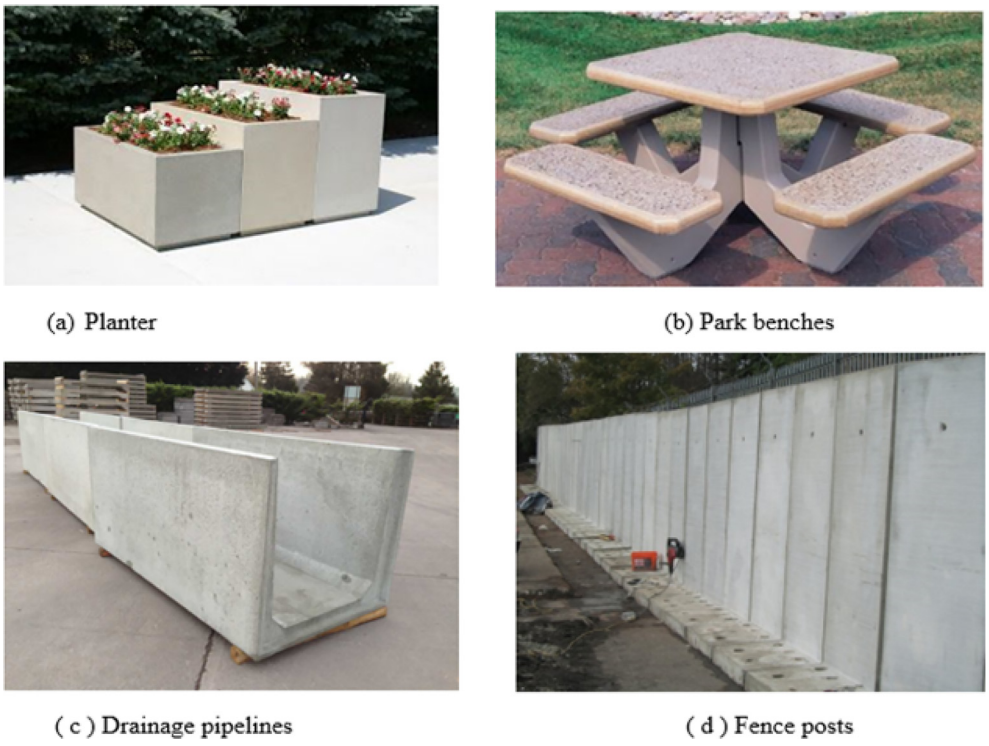


Fig. 2. Suggestive utilization area for recycled aggregate from C&D debris.

Table 3
Aggregate impact values of three different substitution rates of recycled aggregate materials from C&D debris.

Weight	RA-1	RA-2	RA-3	NA
(W_1 g)	212.45	242.58	262.42	334
(W_2 g)	51.24	56.43	62.62	82.26
AIV = (W_2/W_1) * 100	24.11	23.27	23.86	25.22

debris recycled aggregate materials (RA and RCA) and the natural aggregates protracted to evaluate the aggregate impact value (AIV) (see Table 3 and Fig. 3). The laboratory investigations were done for this specific parameter as per the Indian standard [14,13].

The results of the Aggregate impact value of C&D debris recycled aggregate material and natural aggregate material in the current investigation were compared to each other to identify the best options of substitution rate. The AIV of the conventional aggregate material was higher than recycled aggregate material [21]. Different weights (W1 and W2) were used to calculate aggregate impact values (see Table 3).

3.2. The aggregate crushing value (ACV)

The Aggregate Crushing Value of recycled aggregate materials is an essential part of evaluating the concrete strength. So, determining the performance of the different substitution rates of C&D waste recycled aggregate and conventional aggregate is vital because of their indeterminate strength. The Aggregate crushing value test has been done according is to Indian standards [14,13]. The C&D debris recycled aggregate materials and natural aggregate materials can pass through a 14.0 mm sieve for sample making and a 10.0 mm sieve used for application and investigation purposes [33].

The aggregate crushing value was done in the laboratory, and the results are compared to the conventional aggregate materials. The natural aggregate crushing value was more significant than C&D waste recycled aggregate materials [23]. The result showed that the natural aggregate material was weaker than its C&D waste counterparts because a substantial aggregate crushing quantity essentially equates to fragile material. Thus, the C&D waste recycled aggregate material (see Fig. 4) used in this investigation was well-thought-out, with a reasonable substitution rate for the conventional aggregates.

3.3. Relative density and water absorption behavior test for aggregate material

The specific gravity of recycled aggregate materials and their water absorption behavior was tested by following recommended procedures. The water absorption behavior of the various replacement percentages of recycled and conventional aggregate suggests the amounts of water used in the concrete material. The Indian standard [18] is used in this specific section as a guideline for applications. The results obtained in investigations are recorded in the table below, and there is variation in each test result based on its replacement percentage [29]. Recycled aggregates with 15% of the replacement amount have a nearly related performance to the conventional aggregate materials [41]. As shown in the results (see Table 4 and Fig. 5), the specific gravity and the apparent specific gravity of recycled aggregate materials are similar. However, recycled aggregate materials have higher water absorption than conventional materials [30].

3.4. Bulk density and moisture content of recycled aggregate materials

The bulk density and moisture contents (see Fig. 6) are another essential behavior of recycled aggregate materials manufactured from C&D debris. As seen in the figure below, the rise in recycled aggregate materials' moisture content increases the aggregate materials' specific gravity Marzena et al. [24].

3.5. Compressive strength test for M20 concrete

The performance of concrete materials containing 0% to 100% of recycled aggregate materials and recycled concrete aggregate materials from C&D waste was tested after 7 and 28 days (see Tables 5, 6, and 7). The maximum strength was achieved for the concrete mix with 30% recycled aggregate material replacements for coarse and fine aggregate materials [35]. The lowermost compressive strength found for the sample mix with a total substitution of recycled aggregate material from C&D debris will reduce concrete materials' strength when an increase in replacement amount [25]. The test results for 7 and 28 days are displayed on the tables (see Tables 5, 6, and 7). Variations in the results show that the more substituted amount of recycled aggregate material to the conventional aggregate weakens the Strength of Concrete. It also reduces the workability of C&D recycled aggregate material [38].

The investigations reveal that the substitution amount of recycled aggregate materials and recycled concrete aggregate materials used in excess amounts reduces compressive strength and flexural strength of recycled materials from C & C&D wastes. The continuous decline of strength behavior is observed in both 7- and 28-day strength tests (see Tables 5, 6, and 7) [26]. Recycled aggregate materials from concrete wastes are more durable than recycled aggregate materials from mixed C&D debris. So, it is more suitable to use recycled concrete aggregate materials in various places to replace natural aggregate materials [31]. When recycled aggregate

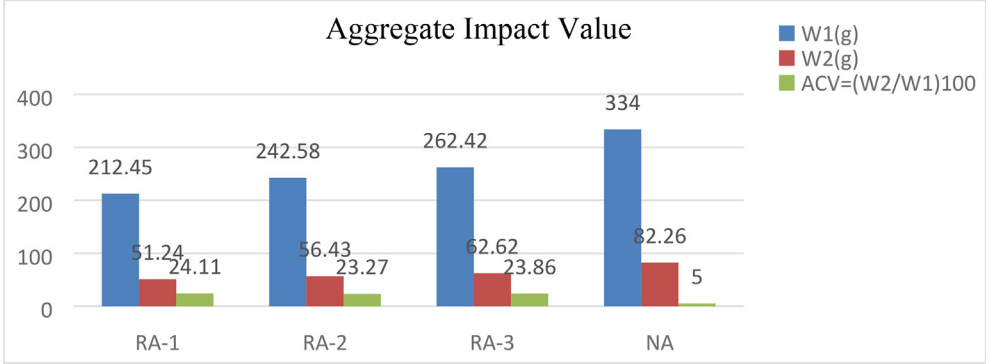


Fig. 3. Aggregate impact values of recycled aggregates in different replacement rates.



Fig. 4. Manufacturing of recycled aggregates from C&D debris. Source: Shukla [3].

Table 4
Physical properties of the recycled aggregate materials for 15% substitution rate.

Properties	RA-1	RA-2	RA-3	NA
Specific gravity (%)	1.02	1.12	1.14	2.58
Apparent specific gravity (%)	1.02	1.12	1.15	2.89
Water absorption (%)	3.21	3.64	4.26	2.78
Moisture content (%)	1.68	1.72	1.78	1.52

materials and recycled aggregate materials are produced massively, it has many important factors. It reduces C&D debris and saves nature by lowering natural aggregate consumption. It also enables the sustainability of construction materials [27].

3.6. Workability (Slump) test for M20 concrete

As the ratio for substituting recycled aggregate materials from C&D debris tends to increase, it also has adverse implications of the concrete materials' workability behavior that contained recycled aggregate materials instead of natural aggregates. These conditions were observed in the tables below (see Tables 8, 9, and 10). Compared to concrete materials produced from natural aggregate materials, the workability directly increases for the concrete materials that incorporate recycled aggregate materials [36]. Hence, it comes to the weakest concrete on 100% replacement [42]. The laboratory investigations for every mix design included in the tables have been conducted based on Indian standards for M20 grade concrete as indicated on the supportive figure (see Fig. 7).

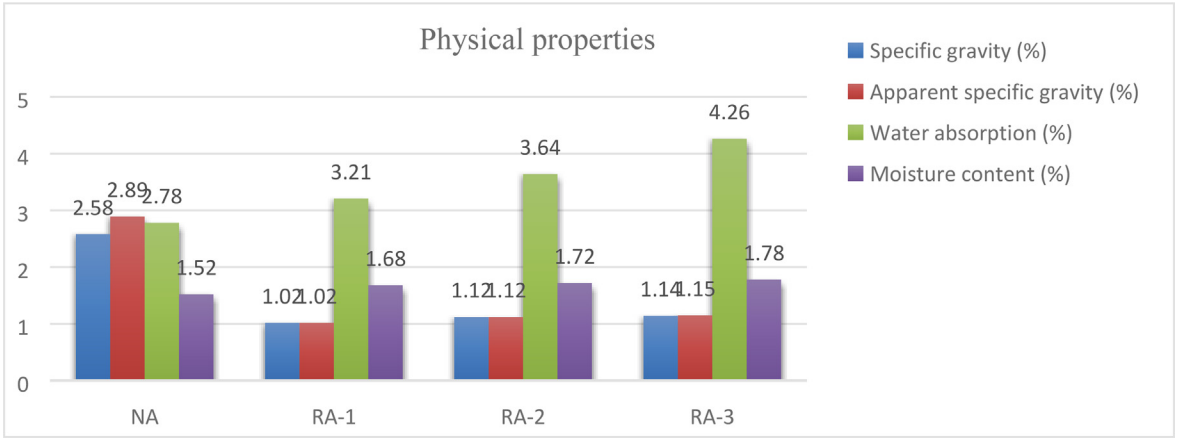


Fig. 5. Specific gravity, apparent specific gravity, and water absorptions for 15% substitution rate.

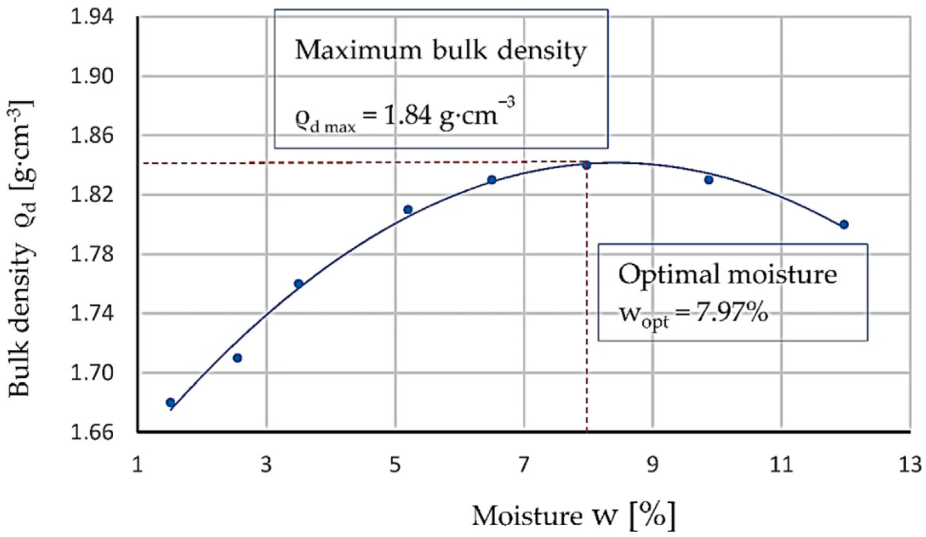


Fig. 6. Bulk density and moisture of the article relationships. Source: Marzena et al. [24].

Table 5
Compressive strength of mix design for M20 concrete (fine aggregate replacements).

Mix no	Coarse aggregate		Fine aggregate	Compressive strength in N/mm^2	
	Natural aggregate	Replacement with recycled aggregate	Natural aggregate	7 days	28 days
$M20_{(P)}$	100%	0%	100%	**13.50**	**20.00**
$M20_{(1)}$	90%	10%	≫	**13.12**	**19.72**
$M20_{(2)}$	80%	20%	≫	**11.96**	**19.47**
$M20_{(3)}$	70%	30%	≫	**11.08**	**19.34**
$M20_{(4)}$	60%	40%	≫	**10.24**	**19.19**
$M20_{(5)}$	50%	50%	≫	**10.01**	**18.75**
$M20_{(6)}$	40%	60%	≫	**9.63**	**18.42**
$M20_{(7)}$	30%	70%	≫	**8.84**	**18.13**
$M20_{(8)}$	20%	80%	≫	**8.24**	**17.72**
$M20_{(9)}$	10%	90%	≫	**8.04**	**17.26**
$M20_{(10)}$	0%	100%	≫	**7.79**	**16.14**

Table 6
Compressive strength of mix design for M20 concrete (coarse aggregate replacements).

Mix no	Coarse aggregate		Fine aggregate	Compressive strength in N/mm^2	
	Natural aggregate	Replacement with recycled aggregate	Natural aggregate	7 days	28 days
$M20_{(P)}$	100%	0%	100%	**13.50**	**20.00**
$M20_{(1)}$	90%	10%	≫	**13.12**	**19.72**
$M20_{(2)}$	80%	20%	≫	**11.96**	**19.47**
$M20_{(3)}$	70%	30%	≫	**11.08**	**19.34**
$M20_{(4)}$	60%	40%	≫	**10.24**	**19.19**
$M20_{(5)}$	50%	50%	≫	**10.01**	**18.75**
$M20_{(6)}$	40%	60%	≫	**9.63**	**18.42**
$M20_{(7)}$	30%	70%	≫	**8.84**	**18.13**
$M20_{(8)}$	20%	80%	≫	**8.24**	**17.72**
$M20_{(9)}$	10%	90%	≫	**8.04**	**17.26**
$M20_{(10)}$	0%	100%	≫	**7.79**	**16.14**

Comparisons were made according to standards that have been applied to this specific investigation [13].

3.7. Compaction factor test of Mix design for M20 concrete

Compaction factor tests have been done after incorporating various substitution rates for concrete materials from recycled aggregate materials recycled from C&D debris. All the results are recorded (see Tables 11, 12, and 13). According to some investigations and standards, the compaction factor for concrete material should be considered normal and acceptable in the range of 0.7–0.95 [37]. The replacement ranges from 40% to 60% for coarse and fine aggregate, shows that the value lies on ranges that can be accepted according to the standards, but this result may vary while using admixtures in a mix-design [39]. So, the increase of the substitution rate of recycled aggregate materials from C&D debris significantly impacts the concrete materials' compaction factor that incorporates recycled aggregate materials [32].

Table 7
Compressive strength of mix design for M20 concrete (coarse and fine aggregate replacements).

Mix no	Coarse aggregate		Fine aggregate		Compressive strength in N/mm^2	
	Natural aggregate	Replacement with recycled aggregate	Natural aggregate	Replacement with recycled aggregate	7 days	28 days
$M20_{(P)}$	100%	0%	100%	0%	**13.50**	**20.00**
$M20_{(1)}$	90%	10%	90%	10%	**13.02**	**19.05**
$M20_{(2)}$	80%	20%	80%	20%	**12.26**	**18.47**
$M20_{(3)}$	70%	30%	70%	30%	**11.34**	**18.15**
$M20_{(4)}$	60%	40%	60%	40%	**10.54**	**17.71**
$M20_{(5)}$	50%	50%	50%	50%	**9.75**	**17.25**
$M20_{(6)}$	40%	60%	40%	60%	**9.34**	**16.42**
$M20_{(7)}$	30%	70%	30%	70%	**8.87**	**16.13**
$M20_{(8)}$	20%	80%	20%	80%	**8.54**	**15.72**
$M20_{(9)}$	10%	90%	10%	90%	**8.08**	**15.26**
$M20_{(10)}$	0%	100%	0%	100%	**7.63**	**14.84**

Table 8
Workability (slump test) of mix design for M20 concrete (fine aggregate replacements)

Mix no	Coarse aggregate	Fine aggregate		Workability (Slump test in mm)
	Natural aggregate	Replacement with recycled aggregate	Natural aggregate	
$M20_{(P)}$	100%	0%	100%	**25.05**
$M20_{(1)}$	≫	10%	90%	**26.12**
$M20_{(2)}$	≫	20%	80%	**27.25**
$M20_{(3)}$	≫	30%	70%	**28.51**
$M20_{(4)}$	≫	40%	60%	**29.75**
$M20_{(5)}$	≫	50%	50%	**30.26**
$M20_{(6)}$	≫	60%	40%	**32.64**
$M20_{(7)}$	≫	70%	30%	**34.56**
$M20_{(8)}$	≫	80%	20%	**36.37**
$M20_{(9)}$	≫	90%	10%	**39.52**
$M20_{(10)}$	≫	100%	0%	**42.24**

Table 9
Workability (slump test) of mix design for M20 concrete (coarse aggregate replacements).

Mix no	Coarse aggregate		Fine aggregate	Workability (Slump test in mm)
	Natural aggregate	Replacement with recycled aggregate	Natural aggregate	
$M20_{(P)}$	100%	0%	100%	**25.05**
$M20_{(1)}$	90%	10%	≫	**26.32**
$M20_{(2)}$	80%	20%	≫	**28.85**
$M20_{(3)}$	70%	30%	≫	**29.51**
$M20_{(4)}$	60%	40%	≫	**30.75**
$M20_{(5)}$	50%	50%	≫	**31.26**
$M20_{(6)}$	40%	60%	≫	**33.04**
$M20_{(7)}$	30%	70%	≫	**35.43**
$M20_{(8)}$	20%	80%	≫	**37.34**
$M20_{(9)}$	10%	90%	≫	**39.48**
$M20_{(10)}$	0%	100%	≫	**43.01**

Table 10
Workability (slump test) of mix design for M20 concrete (coarse and fine aggregate replacements).

Mix no	Coarse aggregate		Fine aggregate		Workability (slump test in mm)
	Natural aggregate	Replacement with recycled aggregate	Natural aggregate	Replacement with recycled aggregate	
$M20_{(P)}$	100%	0%	100%	0%	**25.05**
$M20_{(1)}$	90%	10%	90%	10%	**28.12**
$M20_{(2)}$	80%	20%	80%	20%	**31.25**
$M20_{(3)}$	70%	30%	70%	30%	**34.51**
$M20_{(4)}$	60%	40%	60%	40%	**37.75**
$M20_{(5)}$	50%	50%	50%	50%	**39.26**
$M20_{(6)}$	40%	60%	40%	60%	**41.64**
$M20_{(7)}$	30%	70%	30%	70%	**43.56**
$M20_{(8)}$	20%	80%	20%	80%	**45.37**
$M20_{(9)}$	10%	90%	10%	90%	**47.52**
$M20_{(10)}$	0%	100%	0%	100%	**49.24**

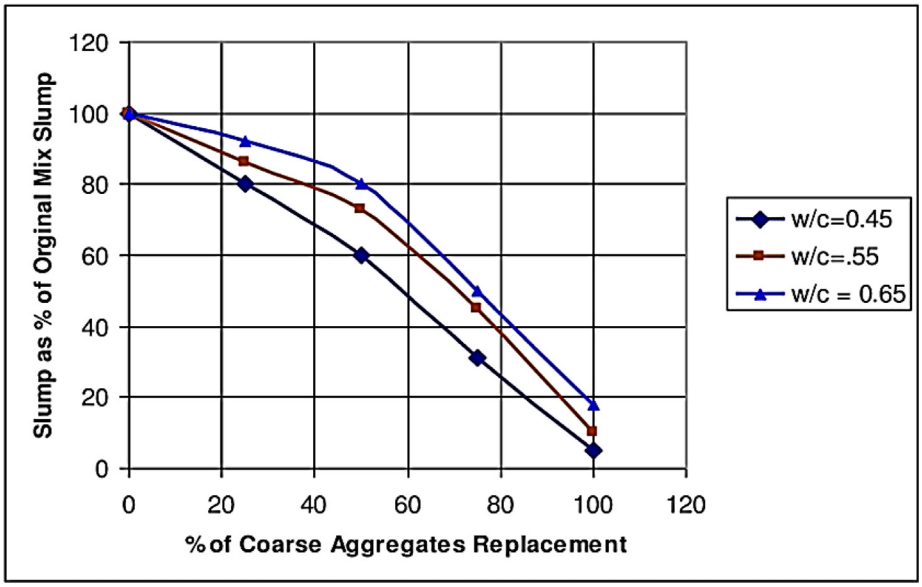


Fig. 7. Workability (slump test) for recycled aggregate materials. Source: Hisham et al. [10].

Table 11
Compaction factor test of mix design for M20 concrete (fine aggregate replacements).

Mix no	Coarse aggregate	Fine aggregate		Compaction factor test
	Natural aggregate	Replacement with recycled aggregate	Natural aggregate	
$M20_{(P)}$	100%	0%	100%	**0.92**
$M20_{(1)}$	≫	10%	90%	**0.89**
$M20_{(2)}$	≫	20%	80%	**0.86**
$M20_{(3)}$	≫	30%	70%	**0.82**
$M20_{(4)}$	≫	40%	60%	**0.77**
$M20_{(5)}$	≫	50%	50%	**0.69**
$M20_{(6)}$	≫	60%	40%	**0.65**
$M20_{(7)}$	≫	70%	30%	**0.62**
$M20_{(8)}$	≫	80%	20%	**0.59**
$M20_{(9)}$	≫	90%	10%	**0.55**
$M20_{(10)}$	≫	100%	0%	**0.51**

Note: (P), Parental mix-100% natural aggregate materials.

Table 12
Compaction factor test of mix design for M20 concrete (coarse aggregate replacements).

Mix no	Coarse aggregate		Fine aggregate	Compaction factor test
	Natural aggregate	Replacement with recycled aggregate	Natural aggregate	
$M20_{(P)}$	100%	0%	100%	**0.92**
$M20_{(1)}$	90%	10%	≫	**0.88**
$M20_{(2)}$	80%	20%	≫	**0.85**
$M20_{(3)}$	70%	30%	≫	**0.81**
$M20_{(4)}$	60%	40%	≫	**0.77**
$M20_{(5)}$	50%	50%	≫	**0.73**
$M20_{(6)}$	40%	60%	≫	**0.69**
$M20_{(7)}$	30%	70%	≫	**0.65**
$M20_{(8)}$	20%	80%	≫	**0.61**
$M20_{(9)}$	10%	90%	≫	**0.56**
$M20_{(10)}$	0%	100%	≫	**0.50**

3.8. Permeability test of Mix design for M20 concrete

Permeability tests were done for sample cubes produced incorporating recycled aggregate materials from C&D debris to substitute for natural aggregate materials (see Tables 14, 15, and 16). The M20 grade concrete's relative permeability produced by applying recycled aggregate materials as a replacement has been included as an illustration (see Figs. 8, 9, and 10). These properties of concrete materials produced from recycled aggregate materials of C&D waste have a significant impact on the concrete materials' performance. The values decrease with the increase in the replacement rate for the natural aggregate materials [34].

The permeability of the concrete materials (see Table 14 and Fig. 9) shows that the increasing replacement rate of recycled aggregate materials in concrete production reduces the permeability of the concrete materials. Hence this will end with negative

Table 13
Compaction factor test of mix design for M20 concrete (coarse and fine aggregate replacements).

Mix no	Coarse aggregate		Fine aggregate		Compaction factor test
	Natural aggregate	Replacement with recycled aggregate	Natural aggregate	Replacement with recycled aggregate	
$M20_{(P)}$	100%	0%	100%	0%	**0.91**
$M20_{(1)}$	90%	10%	90%	10%	**0.86**
$M20_{(2)}$	80%	20%	80%	20%	**0.81**
$M20_{(3)}$	70%	30%	70%	30%	**0.75**
$M20_{(4)}$	60%	40%	60%	40%	**0.70**
$M20_{(5)}$	50%	50%	50%	50%	**0.65**
$M20_{(6)}$	40%	60%	40%	60%	**0.60**
$M20_{(7)}$	30%	70%	30%	70%	**0.55**
$M20_{(8)}$	20%	80%	20%	80%	**0.51**
$M20_{(9)}$	10%	90%	10%	90%	**0.47**
$M20_{(10)}$	0%	100%	0%	100%	**0.42**

Table 14
Permeability test of mix design for M20 concrete (fine aggregate replacements).

Mix no	Coarse aggregate	Fine aggregate		Permeability test		
	Natural aggregate	Replacement with recycled aggregate	Natural aggregate	K (m/s) $\times 10^{-12}$		Avg. K (m/s) $\times 10^{-12}$
$M20_{(P)}$	100%	0%	100%	**24.02**	**23.54**	**23.78**
$M20_{(1)}$	≫	10%	90%	**23.21**	**22.37**	**22.79**
$M20_{(2)}$	≫	20%	80%	**22.12**	**21.14**	**21.63**
$M20_{(3)}$	≫	30%	70%	**20.96**	**20.18**	**20.57**
$M20_{(4)}$	≫	40%	60%	**19.73**	**19.95**	**19.84**
$M20_{(5)}$	≫	50%	50%	**18.25**	**18.21**	**18.23**
$M20_{(6)}$	≫	60%	40%	**17.63**	**17.55**	**17.59**
$M20_{(7)}$	≫	70%	30%	**16.26**	**16.68**	**16.47**
$M20_{(8)}$	≫	80%	20%	**15.36**	**15.74**	**15.55**
$M20_{(9)}$	≫	90%	10%	**14.98**	**14.34**	**14.66**
$M20_{(10)}$	≫	100%	0%	**13.23**	**13.91**	**13.57**

Table 15
Permeability test of mix design for M20 concrete (coarse aggregate replacements).

Mix no	Coarse aggregate		Fine aggregate	Permeability test		
	Natural aggregate	Replacement with recycled aggregate	Natural aggregate	K (m/s) $\times 10^{-12}$		Avg. K (m/s) $\times 10^{-12}$
$M20_{(P)}$	100%	0%	100%	**24.52**	**25.34**	**24.93**
$M20_{(1)}$	90%	10%	≫	**23.10**	**24.19**	**23.64**
$M20_{(2)}$	80%	20%	≫	**22.92**	**23.44**	**23.18**
$M20_{(3)}$	70%	30%	≫	**20.26**	**21.88**	**21.07**
$M20_{(4)}$	60%	40%	≫	**19.73**	**20.74**	**20.23**
$M20_{(5)}$	50%	50%	≫	**19.31**	**20.21**	**19.76**
$M20_{(6)}$	40%	60%	≫	**18.66**	**19.54**	**19.10**
$M20_{(7)}$	30%	70%	≫	**17.96**	**18.68**	**18.32**
$M20_{(8)}$	20%	80%	≫	**16.26**	**17.74**	**17.00**
$M20_{(9)}$	10%	90%	≫	**15.46**	**16.36**	**15.91**
$M20_{(10)}$	0%	100%	≫	**14.45**	**15.23**	**14.84**

Table 16
Permeability test of mix design for M20 concrete (coarse and fine aggregate replacements).

Mix no	Coarse aggregate		Fine aggregate		Permeability test		
	Natural aggregate	Replacement with recycled aggregate	Natural aggregate	Replacement with recycled aggregate	K (m/s) $\times 10^{-12}$		Avg. K (m/s) $\times 10^{-12}$
$M20_{(P)}$	100%	0%	100%	0%	**24.02**	**23.54**	**23.78**
$M20_{(1)}$	90%	10%	90%	10%	**23.21**	**22.37**	**22.79**
$M20_{(2)}$	80%	20%	80%	20%	**22.12**	**21.14**	**21.63**
$M20_{(3)}$	70%	30%	70%	30%	**20.96**	**20.18**	**20.57**
$M20_{(4)}$	60%	40%	60%	40%	**19.73**	**19.95**	**19.84**
$M20_{(5)}$	50%	50%	50%	50%	**18.25**	**18.21**	**18.23**
$M20_{(6)}$	40%	60%	40%	60%	**17.63**	**17.55**	**17.59**
$M20_{(7)}$	30%	70%	30%	70%	**16.26**	**16.68**	**16.47**
$M20_{(8)}$	20%	80%	20%	80%	**15.36**	**15.74**	**15.55**
$M20_{(9)}$	10%	90%	10%	90%	**14.98**	**14.34**	**14.66**
$M20_{(10)}$	0%	100%	0%	100%	**13.23**	**13.91**	**13.57**

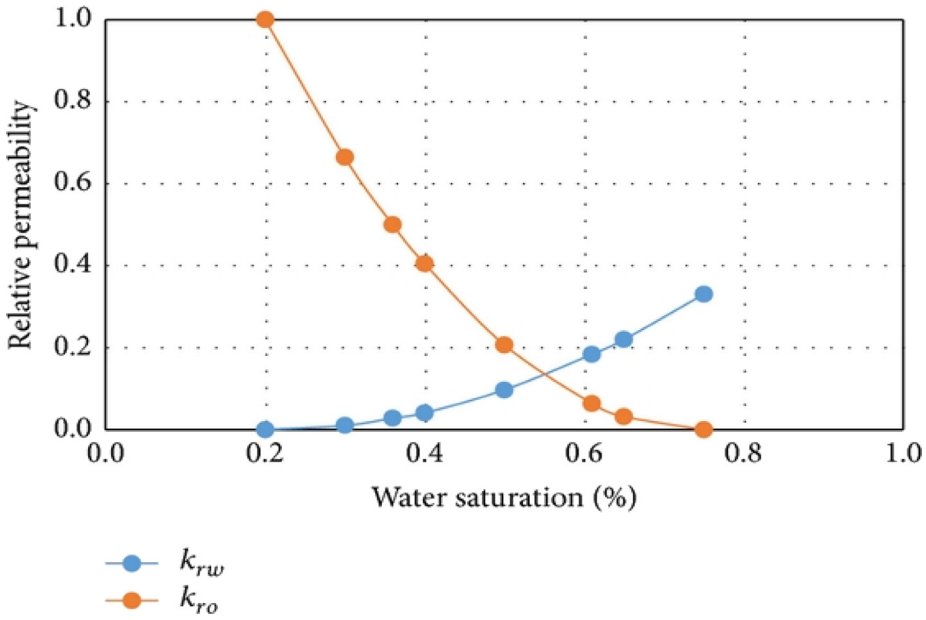


Fig. 8. Relativity permeability of recycled aggregate materials. Source: Jeong and Lee [19].

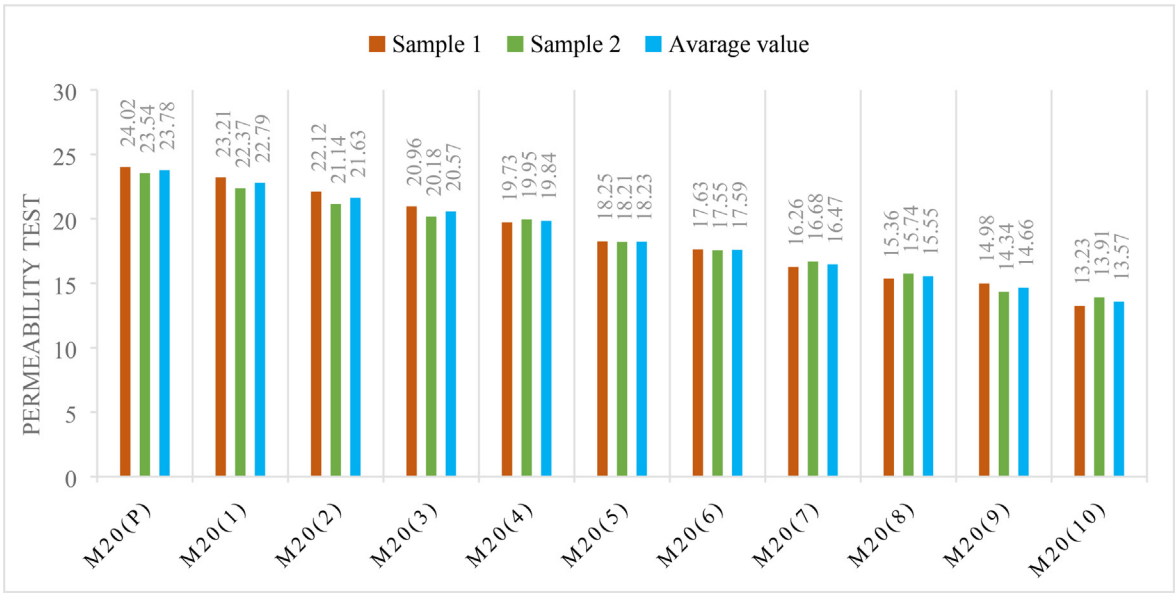


Fig. 9. Permeability tests for recycled aggregate concrete materials.

impacts on the behavior of the concrete materials and cause significant failure in the area where we can use these recycled aggregate materials [40,43].

4. Conclusions

All the intended laboratory investigations have been done on concrete materials containing recycled aggregate materials produced from C&D waste. Using these materials is recommended based on studies that it is possible to utilize them in works other than high strength demanding areas. As a finding, recycled aggregate materials can be used in low-rise buildings and mainly on the road to replace natural aggregate materials. Substitutions of recycled aggregate materials to the conventional material are permissible to some extent. If it exceeds the limits, it creates various impacts on concrete strength properties, and hence, the material will be of low quality. This situation can create severe problems with structures. Recycling and reusing C&D debris have various benefits to society. It creates job opportunities for a group of people and also brings positive impacts on environmental conditions. According to the current investigations, the following main findings were observed;

- The performance of the concrete material produced from C&D debris was reduced with the increasing volume of recycled aggregate material substitution. It gives better workability to the concrete material, reducing a substitution volume of natural aggregate materials.
- The manufacturing of recycled concrete aggregate (RCA) was done through the dry segregation process, and this creates lots

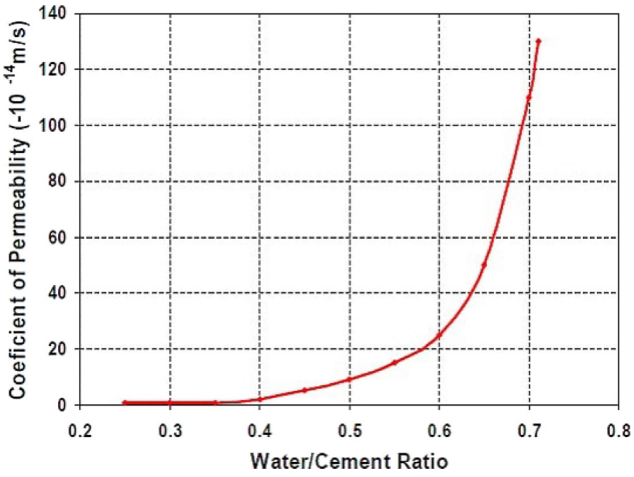


Fig. 10. Coefficient of permeability for recycled aggregate materials. Source: http://www.thecontractor.org.

of dust materials produced during the process. These particles have negative impacts on the society that resides near or around the recycling plants. So, it needs careful placement of the recycling plants.

- As a result, tiny particles need other protection not to bring a severe problem to the inhabitants. As an alternative, the wet process should be an alternative approach to remove the dust particles.
- The recycled aggregate materials from C&D debris have higher workability and water absorption behavior than conventional aggregate materials. This situation increases the acceptability of these materials in road construction and some parking areas where the surface water stays for a long time.
- Recycled aggregate materials manufactured from C&D debris are an environmentally friendly means to remove C&D waste. It also improves the nation's economy if applied widely and adequately. All the concrete materials' performance behavior is affected by the substitution rate for coarse and fine aggregate materials and needs precautions while reusing them.

5. Declarations

5.1. Data availability

Data for this research is included in the manuscript.

Funding

This research received no external funding. The researcher has covered all the financial issues.

Declaration of Competing Interest

The author declares that they have no known competing financial interests or personal relationships that could have appeared to influence the work reported in this paper.

Acknowledgments

The author would like to thank all the concrete laboratory assistants of the Civil Engineering Department, Delhi Technological University, for their valuable initiatives during practical laboratory works that were part of the current research work. Moreover, we would like to thank all who facilitated site visits at Burari C&D waste recycling plants, Delhi.

References

[1] A.M. Mustafa Al Bakri et al.,. Effects of HDPE C&D waste aggregate on the properties of concrete, J. Asian Sci. Res. 1(7) (2011) 340–345.
[2] M.W. Ashraf, Z.E. Hossam, E. Magda, H.O. Samir, Recycled construction and concrete demolition waste as aggregate for structural concrete, HBRC J. (2013), https://doi.org/10.1016/j.hbrcj.2013.08.007.
[3] Awanish Shukla, Application of CNC Waste with Recycled Aggregate in the Concrete Mix, A Project at Indian Concrete Institute, 2013.
[4] V.S. Babu, A.K. Mullick, K.K. Jain, P.K. Singh, Strength and durability characteristics of high-strength concrete with recycled aggregate-influence of processing, J. Sust. Cem.-Based Mater. 4 (1) (2015) 54–71, https://doi.org/10.1080/21650373.2014.976777.
[5] C. Clark, J. Jambeck, T. Townsend, A review of construction and demolition debris regulations in the United States, Crit. Rev. Environ. Sci. Technol. 36 (2) (2006) 141–186.
[6] F.U.A. Shaikh, H.L. Nguyen, Properties of concrete containing recycled construction and demolition wastes as coarse aggregates, J. Sust. Cem.-Based Mater. 2 (3–4) (2013) 204–217, https://doi.org/10.1080/21650373.2013.833861.
[7] Gagan, A. Sumit, Recycled aggregates: a sustainable solution of construction and demolished waste, OSR J. Mech. Civil Eng. (IOSR-JMCE) e-ISSN: 2278-1684, p-ISSN: 2320-334X, 2015, pp. 58–63.
[8] G. Ganesh Prabhu, Jung Hwan Hyun, Yun Yong Kim, Effects of foundry sand as a fine aggregate in concrete production, Constr. Build. Mater. (2014).
[9] G.C. Mays, R.A. Barnes, The performance of recycled aggregate concrete structures in service, Struct. Eng. 69(20) (1991) 351–361.
[10] Hisham Qasrawi, Iqbal Marie, Hasan Tantawi, Use of recycled concrete rubbles as coarse aggregate in concrete, in: Conference: Proceedings of the 5th Jordanian International Civil Engineering Conference at Amman, Jordan, 2012.
[11] http://www.prolandscapermagazine.com.
[12] http://www.thecontractor.org.
[13] IS 2386 – (Part 4), Methods of Test for Aggregates for concrete materials, Mechanical Properties, 1963 (Reaffirmed, 2002).
[14] IS 2386 (Part 3), Methods of Test for Aggregates for Pavement materials art 3, 1963 (Reaffirmed 2002).
[15] IS 516, Method of Tests for Strength of Concrete, 1959 [CED 2: Cement and Concrete].
[16] IS: 10262, Guidelines for Pavement Mix Design Proportioning, 2009.
[17] IS 383-2016: Coarse and Fine Aggregate-Specification.
[18] IS 1124, Method of test for determination of water absorption, apparent specific gravity, and porosity of natural building stones, 1974 [CED 6: Stones].
[19] M. Jeong, K. Lee, Simulation study on miscibility effect of CO2/solvent injection for enhanced oil recovery at non-isothermal conditions, Math. Probl. Eng. (2016).
[20] J. de Brito, N. Saikia, Recycled Aggregate in Concrete, Springer Science and Business Media LLC., 2013.
[21] M. Berra, G. Ferrara, Standard weight and total-recycled high strength concrete, a comparative experimental study, in: Proc. of High-Strength Concrete. 2d Int. Symp., ACI, SP-121, 1990, pp. 701–733.
[22] M. Chakradhara Rao, S.K. Bhattacharyya, S.V. Barai, Systematic Approach of Characterization and Behaviour of Recycled Aggregate Concrete, Springer Science and Business Media LLC., 2019.
[23] Manas Ranjan Senapati, C&D waste from thermal power plants-waste management and overview, Curr. Sci.100-20 (2011) 1791–94.
[24] Marzena Karpinska, Beata Grzyl, Marek Pszczola, Adam Kristowski, The application of granulated expanded glass aggregate with cement grout as an alternative solution for sub-grade and frost-protection sub-base layer in road construction, Materials 12 (2019) 3528. doi:10.3390/ma12213528.
[25] P.K. Mehta, P.J.M. Monteiro, Pavement – Microstructure, Properties, and Materials, The Indian Concrete Institute, Chennai, India, 2006.
[26] M. Yeheyis, M. Kasun Hewage, S. Alam, C. Eskicioglu, R. Sadiq, An overview of construction and demolition waste management in Canada: a lifecycle analysis approach to sustainability, Clean Technol. Environ. Policy (2012).
[27] Niyazi Ugur Kockal, Turan Ozturan, The durability of recycled pavements with recycled C&D waste aggregates, Constr. Build. Mater. 25 (2011) 1430–1438.
[28] F. Özalp, D.Y. Halit, K. Mustafa, K. Ömer, Ş. Aylin, The effects of recycled aggregates from construction and demolition waste on the mechanical and permeability properties of paving stones, curbs, and concrete pipes, Constr. Build. Mater. (2016), https://doi.org/10.1016/j.conbuildmat.2016.01.030.
[29] K. Parisi, A. Michele, F. Dias, M.P. Kulakowski, P.G. Luciana, Waste generated in high-rise buildings construction: a quantification model based on multiple statistical regression, Waste Manage. (2015), https://doi.org/10.1016/j.wasman.2015.01.043.
[30] P. Ghisellini, M. Ripa, S. Ulgiati, Exploring environmental and economic costs and benefits of a circular economy approach to the construction and demolition sector. Literature reviews, J. Clean. Prod. (2018).
[31] I. Pérez, J. Gallego, M. Toledano, Construction and Demolition Debris in Hot Mix Asphalt, Geo-Hunan International Conference in 2009, 2009, doi:10.1061/41043(350)19.
[32] P. Priyadharshini, Experimental Study on Cold Bonded C&D Waste Aggregates, 2, 2011, ISSN 0976-4399.

[33] R. Islam, T.H. Nazifa, A. Yuniarto, A.S.M. Shanawaz Uddin, S. Salmiati, S. Shahid, An empirical study of construction and demolition waste generation and implication of recycling, Waste Manage. 95 (2019) 10–21.
[34] H. Rosario, P. Pérez, L. Garach, J. Ordóñez, Use of Recycled Construction and Demolition Waste Aggregate for Road Course Surfacing, 2012. <http://dx.doi.org/10.1061/(ASCE)TE.1943-5436.0000320>.
[35] R. Jin, B.o. Li, T. Zhou, D. Wanatowski, P. Piroozfar, An empirical study of perceptions towards construction and demolition waste recycling and reuse in China, Resour. Conserv. Recycl. 126 (2017) 86–98.
[36] T.-S. Seo, M.-S. Lee, Experimental study on tensile creep of coarse recycled aggregate concrete, Int. J. Concr. Struct. Mater. 9 (3) (2015) 337–343, https://doi.org/10.1007/s40069-015-0105-8.
[37] R. Siddique et al., Use of recycled C&D in concrete: a review, Waste Manage. 28 (10) (2008) 1835–1852.
[38] C.W. Tang, H.J. Chen, S.Y. Wang, J. Spaulding, Production of recycled aggregate using reservoir sediments for concrete and masonry, Cem. Concr. Compos. 33 (2) (2010) 292–300, https://doi.org/10.1016/j.cemconcomp.2010.10.008.
[39] T. Townsend, T. Tolaymat, K. Leo, J. Jambeck, Heavy metals in recovered fines from construction and demolition debris recycling facilities in Florida, Sci. Total Environ. 332 (1–3) (2004) 1–11.
[40] W. Tangchirapat, R. Buranasing, C. Jaturapitakkul, Use of high fineness of fly ash to improve properties of recycled aggregate concrete, J. Mater. Civil Eng. 22 (6) (2010) 565–571, https://doi.org/10.1061/(ASCE)MT.1943-5533.0000054.
[41] Y.-C. Jang, Effect of waste depth on leachate quality from laboratory construction and demolition debris landfills, Environ. Eng. Sci. (2003).
[42] Zhao Youcai, Huang Sheng, Recycling Technologies and Pollution Potential for Contaminated Construction and Demolition Waste in Recycling Processes, Elsevier BV, 2017.
[43] M. Zhiming, T. Qin, Y. Dingyi, B. Guangzhong, Durability Studies on the Recycled Aggregate Concrete in China over the Past Decade: A Review, 2019. <https://doi.org/10.1155/2019/4073130>.

sustainability

MDPI

Article

Catalytic Performance of Cow-Dung Sludge in Water Treatment Mitigation and Conversion of Ammonia Nitrogen into Nitrate

Lokesh Kumar [1,*], Jaigopal Sharma [2] and Raminder Kaur [3,*]

[1] Department of Applied Chemistry, Delhi Technological University, Delhi 110042, India
[2] Department of Biotechnology, Delhi Technological University, Delhi 110042, India; sharmajaigopal@yahoo.com
[3] Department of Polymer Science and Chemical Technology, Delhi Technological University, Delhi 110042, India
* Correspondence: lokeshdjb@gmail.com (L.K.); raminderkaur@dce.ac.in (R.K.); Tel.: +91-9818863285 (L.K.); +91-9717212152 (R.K.)

Abstract: The present research study was performed to find a solution for the mitigation of ammonia nitrogen in municipally treated sewage effluent (MTSE) using two natural bio-resources. One was composted cow-dung sludge that had catalytic enzymes and nitrifying bacterial mass, and the second was *Yucca* extract (a desert plant). MTSE samples put in one-liter beakers/jars having initial ammonia nitrogen content of 34.78 mg/L, when treated with 0.0 g/L (control Sample), 1 g/L, 5 g/L (cowdung) and 10 mg/L, 50 mg/L (*Yucca* extract), respectively, reported depletion of ammonia nitrogen to about 0.00 mg/L ammonia (NH_3) as N. It (NH_3) transformed to 17.8, 0.18, 0.09, 18.65, and 18.85 mg/L nitrite asN. Ammonia converted to 21.8, 110.1, 133.5, 20.5, 20.8 mg/L nitrate asNO_3, respectively. After eight days of treatment, the jar test apparatus reported the results at 35 rounds per minute (RPM) and a temperature of 32 °C. It was found that digested cowdung acted catalytically in eliminating the ammonia nitrogen by converting it to nitrate in a short period of nearly eight days, leading to almost 100% ammonia conversion.

Keywords: municipal sewage; biological treatment; ammonia nitrogen; cow-dung sludge; *yucca* extract

check for updates

Citation: Kumar, L.; Sharma, J.; Kaur, R. Catalytic Performance of Cow-Dung Sludge in Water Treatment Mitigation and Conversion of Ammonia Nitrogen into Nitrate. *Sustainability* **2022**, *14*, 2183. https://doi.org/10.3390/su14042183

Academic Editors: Sanjeev Kumar Prajapati, Halis Simsek and Silvia Fiore

Received: 31 December 2021
Accepted: 8 February 2022
Published: 14 February 2022

Publisher's Note: MDPI stays neutral with regard to jurisdictional claims in published maps and institutional affiliations.

Copyright: © 2022 by the authors. Licensee MDPI, Basel, Switzerland. This article is an open access article distributed under the terms and conditions of the Creative Commons Attribution (CC BY) license (https://creativecommons.org/licenses/by/4.0/).

1. Introduction

Today, globally, drinking water sources have either been polluted or are under continuous threat of contamination by wastewater intrusion. Ammonia pollution in water has become a significant concern for environmentalists, chemists, and biologists due to the health hazards. There is a necessity for an appropriate technology that can accelerate nitrification by which ammonia nitrogen can be converted to stable compounds such that its adverse effects could be neutralized. Mere aeration in wastewater for biological stabilization of biological oxygen demand (BOD) and nitrification takes an extended time [1,2]. The elevated nitrogen concentrations in the surface waters have primarily resulted from modern agricultural practices, mainly due to nitrogen fertilizers [3–5]. However, the nitrogen discharge from the point sources, such as sewage treatment plants and industries, also contributes significantly to riverine nitrogen loading. Ammonia exists in the water in both organic and inorganic nitrogen. Organic nitrogen (ON) includes a wide variety of compounds derived from natural and anthropogenic sources. The natural sources are principally nitrogenous end products of biological metabolism. Agricultural fertilizers also aid in the anthropogenic cause of organic nitrogen. Many bacteria, such as species of *Nitrosomonas*, possess the enzymeurease, which catalyzes the conversion of urea to in organic nitrogen (IN) forms, like Ammonia>(NH_3) orammoniumion (NH_4^+), that further oxidize to nitrite by the process of nitrification [6–8]. The wastewater rich in ammonia nitrogen harms the environment significantly as the ammonia nitrogen may inhibit natural nitrification, cause water hypoxia, result in fish poisoning, and decrease the water purifica-

tion capacity [4,5,8]. Composted cowdung was studied to analyze its catalysis properties in accelerating nitrification.

2. Ammonia Nitrogen in the Water and Discharge Limit

Ammonia nitrogen exists in water in two forms, free or unionized ammonia (NH_3) and ionized ammonium (NH_4^+) [9], and both these forms are pH and temperature dependent [10]. In aqueous ammonia solutions, the un-ionized ammonia exists in equilibrium with the ammonium and hydroxide ions [10]. Central Pollution Control Board (CPCB), a statutory organization of the Indian Government, has amended its discharge standards for sewage under the Water (Prevention and Control of Pollution) Act, 1974, vide order No. A-10014/43/06-MON/709 dated 21 April 2015, and further proceedings of the 199th Board meeting held on the 8 September 2015. The new standard for ammonia nitrogen in the treated sewage has stipulated that it is not more than 5mg/L and that total nitrogen is not more than 10mg/L. Previously the standard values for ammonia nitrogen were limited to the extent of 50 mg/L and that of total nitrogen or total Kjeldahl nitrogen 100 mg/L [11].

3. Available Techniques and Demerits on Mass-Scale Treatment

There are many techniques for removing ammonia nitrogen from waste water, such as nitrification–denitrification, ammonia stripping, ion exchange, zeolite process, breakpoint chlorination, and algae ponds. Still, none are free from the operational complications [1,12–16]. Moreover, the available techniques are not feasible for large water masses, as are required by municipal sewage disposal works in large cities [17–21]. Secondary treated sewage effluents require treatment so that the ammonia nitrogen can be converted into nitrate without any limitations/demerits of the process. In some cases, the growth of algae is also a problem. The ammonia nitrogen contributes to the development of the algal bloom in the presence of bluish-white light, as it accumulates in the algae's moiety. The algal growth increases the pH of the water. It produces cyanotoxins [22]. When disinfected with chlorine, it creates a problem of filter bed choking in the water treatment utilities and hinders the water treatment process by making coagulants ineffective at water treatment plants. Higher pH of water (>8.2), as sometimes faced at municipal waterworks of Delhi (India), creates hindrance in the conventional water treatment processes, as it makes the chlorine ineffective. Furthermore, the coagulant poly aluminum chloride is inefficient at higher pH [23].

4. Focus on New Research: Catalytic Effect of Cow-Dung Sludge

The present studies have been conducted to combat the ammonia nitrogen in the secondary treated municipal sewage water by using a desert plant extract, *Yucca* schidigera, and cowdung. However, *Yucca* extract has been reported in some previous studies for its capability of removing ammonia nitrogen from the water [24–27]. The experimental studies conducted using the cowdung on treated sewage yielded better results for combating the ammonia nitrogen and have shown its potential to be applied in real life for large masses of wastewater. In addition to cowdung, Blue-buck dung and Buffalo dung, both fresh and digested, were also employed for the studies on removing ammonia nitrogen, but the digested cowdung was found to be effective.

5. CowDung as a Bioresource of Catalytic Enzymes and Nitrifying Bacterial Mass

The cowdung has been used successfully in previous studies for industrial wastewater treatment for combating heavy metals, pharmaceuticals, pesticides, and petrochemicals [28–32]. cowdung harbors a rich microbial diversity, containing different bacteria, protozoa, and yeast. Godambe and Fulekar [32] separated the species of bacteria: *Enterobacter cloacae*, *Pseudomonas pseudoalcaligenes*, *Archromobacter* sp., *Aeromonashydrophila*, *Bacillus pumilis* belonging to the genus of *Pseudomonas* sp., *Escherichia* sp., *Staphylococcus* sp., *Aeromonas* sp., *Bacillus* sp., *Enterobacter* sp. and yeast *Rhizopus* sp. In addition toprotozoa and yeasts (*Saccharomyces* and

Candida), a beneficial bacterial mass of *Citrobacterkoseri*, *Enterobacteraerogenes*, *Escherichia coli*, *Klebsiella oxytoca*, *Klebsiella pneumonia*, *Kluyvera* spp., *Morgarellamorganii*, *Pasteurella* spp., *Providenciaalcaligenes*, *Providenciastuartii*, and *Bacillus* spp., *Corynebacterium* spp., and *Lactobacillus* spp. are present in cowdung [31,33]. Randhawa and Kullar (2011) found that the indigenous Indian cowdung contains more calcium, phosphorus, zinc, and copper than the cross-breed cowdung. Teo and Teoh (2011) studied five different isolates from the cowdung. They found that all isolates were positive for the presence of esterase and esterase lipase. All strains were able to produce protease, esterase, and esterase lipase. The protease is an enzyme that catalyzes proteolysis, which breaks down the proteins to their respective amino acids. Furthermore, they have a variety of applications, mainly in the detergent and food industries. Esterase and esterase lipase belonging to the hydrolase enzymes split esters into acids and alcohols, as was observed in a chemical reaction of the hydrolysis process involving the addition of water molecules [34]. Cowdung, containing a diverse group of microorganisms such as *Acinetobacter*, *Bacillus*, *Pseudomonas*, *Serratia*, and *Alcaligenes* spp., makes them suitable for microbial degradation of the pollutants [29,35,36]. The cowdung slurry maintained in the ratio of 1:10 or 1:25 can degrade the rural, urban, and hospital wastes, including oil spillage, to five essential elements [31].

Quaraishi et al. (2018) evaluated the performance of the cowdung as microbial inoculums in industrial wastewater treatment and found a significant reduction in chemical oxygen demand (COD). They observed a 45.7, 62.3 and 84.04% reduction on the 5th, 10th, and 15th day of treatment. The bacterial mass found in the cowdung offers practical bioremediation for treating hydrocarbon-benzene. In a study, benzene was degraded entirely from 50 and 100 mg/L concentration after 96 and 144 h, respectively, whereas for 200 mg/L, about 99 percent degradation was observed after 240 and for 400 mg/L up to 69.2% degradation observed. As per the study of Godambe and Fulekar, cowdung possesses a huge microbial load, Table 1 [32].

Table 1. Characteristics of Cow Dung.

Microbial Enumeration of the cow dung Sample	
Parameters	Results
Total viable count	2.29×10^8 cell/ml
Total Fungal count	1.16×10^7 cell/ml
Yeast count	7.5×10^6 cfu/ml
Physico-Chemical Characterization of a Cow Dung Sample	
pH	7.3
Dissolved Oxygen	6.4 mg/L
Temperature	25.9 °C
% Organic Carbon	0.67%
Biological Oxygen Demand	19.83 mg/L
Chemical Oxygen Demand	195.2 mg/L
Phosphorous	0.23 mg/L
Sulphate	38.5 mg/L

The bold from the title it's important because it distinguishes between microbial and physico-chemical properties.

The cow dung consortium (bacteria, fungi, and actinomycetes) has also helped degrade phenol ranging from 100 to 1000 mg/L Table 2. The phenolic toxicant is converted to nutrients, biomass, and CO_2 via biodegradation through their intermediates. Thus, cow dungcan potentially beused in the petrochemical and chemical industries, generating waste-containing phenol compounds [31,37].

However, there are no reports of cow dung being used in wastewater treatment specifically to combat ammonia nitrogen. India'sgovernment provides enormous funds on Scientific Validation and Research on Panchgavya (a concoction of cowdung, cow urine, milk, curd, and ghee). The present research presents a comparative study of *Yucca* extract and cow dung use for ammonia combat in wastewater.

Table 2. Degradation of phenol with cow-dung slurry.

Concentration of Phenol	Degradation %	Time Duration
100 mg/L	98.59	24 h
250 mg/L	99.4	72 h
500 mg/L	99.6	96 h
1000 mg/L	Not degraded	up-to 168 h

However, there are no reports of cow dung being used in wastewater treatment specifically to combat ammonia nitrogen. India'sgovernment provides enormous funds on Scientific Validation and Research on Panchgavya (a concoction of cowdung, cow urine, milk, curd, and ghee). The present research presents a comparative study of *Yucca* extract and cow dung use for ammonia combat in wastewater.

6. Materials and Methods

6.1. Collection of Samples and Testing

The 25 L, secondary treated sewage effluent samples were collected from Sewage Disposal Works (SDW), Delhi, India. This SDW treats about 40 MGD municipal sewage using the activated sludge method. The collected sample was immediately tested for the initial parametric values of ammonia nitrogen, nitrite, nitrate, pH value, total dissolved solids, electrical conductivity, temperature, etc. The ammonia nitrogen, nitrite, and nitrate tests were performed on Eppendorf Bio Spectrometer model 2019 (Eppendorf AG, Hamburg, Germany). The ammonia nitrogen was tested as per the Nesslerization method, 4500-NH_3 C, Nitrite by 4500-NO_2^- B, and Nitrate by 4500-NO_3^- B, prescribed in the standard methods for the examination of water and waste water [38]. The pH values, total dissolved solids, and electrical conductivity were measured by a Hach HQ 440 d Multi Ion Analyser, Loveland. Colorado, United State The authors prepared standard solutions for ammonia nitrogen, nitrite, and nitrate tests designed from analytical-grade reagents for calibration purposes.

6.2. Preparation of Yucca Extract

Yucca schidigera, a desert plant, was collected from the Forest Research Institute, Dehradun, Uttrakhand State, India. The Yucca plant's stem (about 250 g) was cut and chopped with a knife into small pieces. Then, the chopped pieces were ground in a grinder mixture, dried in the open sun for three days, and again dropped to make a fine powder. This Yucca powder was sieved through a 150-mesh sieve and stored in an airtight container. In the present study, the *Yucca* extract was used in the form of a solution. *Yucca* solution was prepared by mixing and dissolving 50 g of *Yucca* powder in 700 mL distilled water in a 1 L beaker, stirred on jar test apparatus for seven days (about 250 mL water wasevaporated in the air) so that its contents could dissolve well, filtered through ordinary filter paper and made up to 500 mL with distilled water in a measuring flask. Thus, 1 mL of *Yucca* extract produces 100 mg solution.

6.3. Preparation of Indian Cow Dung

The cow dung was collected locally from a heap dumped by a farmer in a village of Delhi. The age of the cow-dung pile was about one year old. The digested wet dark-brown colored cow dung, about 500 g, was taken from a depth of 6 inches inside the heap in a clean glass bottle. Collected cow dung was ready to be used. A total of 1 g of cow dung was weighed in an electronic balance three times and poured into three different beakers containing 1 L of municipally treated sewage effluent (MTSE) in each. The experiments were performed in triplicate, and the average of all was taken for calculation purposes. Similarly, other operations were performed with a higher amount of cow-dung sludge (2–5 g).

6.4. Experimental Setup and Oxidation of Ammonia Nitrogen

The jar test apparatus (Figure 1) was used to observe the biomass's effectiveness (*Yucca* extract and cow dung) with a stirring speed of 35 RPM. The experiments were carried out in triplicate for more precise results. Because of the jar test apparatus's limitations, the triplicate samples were treated separately because it had only a six-beaker arrangement. The reported results are the final valid values extracted after several experiments under varying experimental conditions. The collected MTSE were taken into the six one-liter beakers.

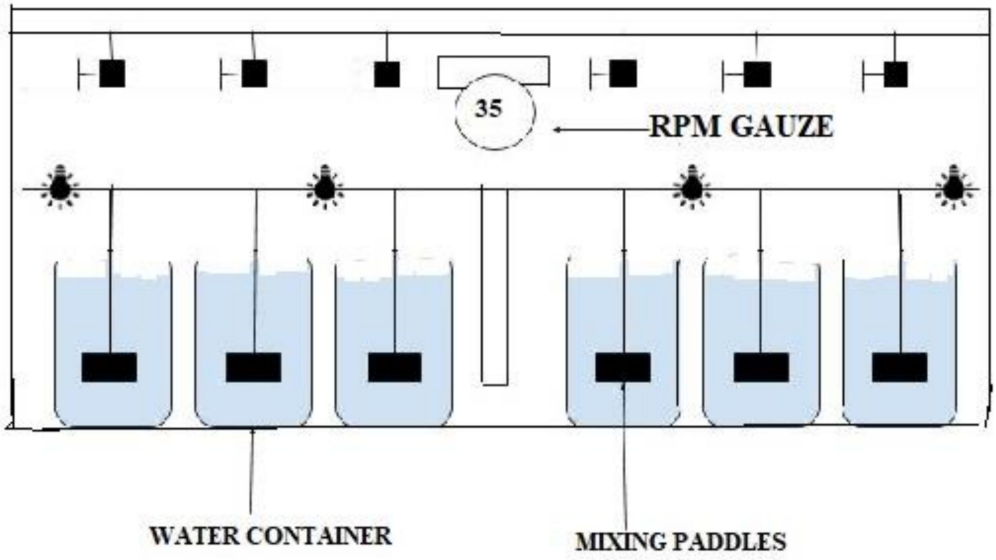


Figure 1. Experimental Setup—Jar Test Apparatus.

Parameters for ammonia nitrogen, nitrite, nitrate, pH, electrical conductivity, total dissolved solids, color, odor, and temperature were tested immediately in the laboratory after sample collection. We kept beakers 1 and 2 for reference. Beaker 1 served as a control to measure the amount of water evaporated during the experiment. Beaker 2 served as a control to measure the change in parameters naturally. We added 1and 5 g of cow dung into the beakers 3 and 4 while 0.1 and 0.5 mL of *Yucca* extract was added to beakers 5 and 6, respectively. Four 15-watt tungsten bulbs were hung over the jar test apparatus to illuminate the system round the clock. The stirrers of the equipment are set at 35 RPM. Every 48 h, a 100 mL sample was taken from the jars numbered from 2 to 6 and tested for changes in parameters. We used the content of beaker 1for measuring the quantity of water evaporated during the processing period of 48 (2 days), 96 (4 days), 144 (6 days), and 192 (8 days) h, respectively.

7. Results and Discussions

Initially, *Yucca* schidigera extract was used with varying concentrations in the presence and absence of lights. We measured initial levels ofammonia nitrogen and other parameters of MTSE, and the experiments were performed at room temperature with pristine samples. It was observed that, even with multiple experimental studies using the different dosages of *Yucca* extract, there was no significant difference in the concentration of ammonia nitrogen, nitrite, and nitrate with the control sample. Instead, the ammonia nitrogen found increased in the *Yucca* extract dosed samples after the 8th day. An increase in ammonia content indicated that the *Yucca* extract started fermenting after the 6th day. The *Yucca* extract did not help combat ammonia nitrogen in municipal sewage water. After this, the experiments were conducted using the excreta of the bovine animals such asBlue-buck, Buffalo, and Cow, as a potential bioresource to combat the ammonia nitrogen from wastewater. Among all these, the cow dung was found most effective against removing ammonia nitrogen. As per the previously reported studies, the cow dung was very effective against reducing the

effluent's chemical oxygen demand (COD) [30]. COD is the amount of oxygen required to stabilize organic and inorganic (ammonia and nitrite) pollutants in water under heat and acidic conditions, using a highly oxidizing agent, potassium dichromate, corrected for the influence of chloride. The cow dung, in this case, acted as a bio-catalyst.

7.1. Biological Oxidation of Ammonia Nitrogen

We experimented with digested cow dung, and it was found that catalytical enzymes and nitrifying bacteria present in cow dung reduced ammonia significantly. The results of the present study aredepicted in Figure 1, wherein an initial amount of 34.780 mg/L ammonia nitrogen (as NH_3) in municipally treated sewage effluent (MTSE)was reduced to 23.210 (in control sample), 22.590 (with 1g/L cow dung), 18.390 mg/L (with five g/L cow dung), 23.580 mg/L (with 10mg/L *Yucca* extract) and 24.705 mg/L (with 50 mg/L *Yucca* extract) in 48 h or the 2nd day of the process at 32°C temperature and 35 RPM. In 96 h, or the 4th day of the experimental set-up, ammonia nitrogen was reduced to 2.040, 0.960, 1.390, 2.735 and 7.135 mg/L, respectively. In 144 h, or the 6th day, ammonia nitrogen was reduced to 0.032, 0.00, 0.00, 0.036 and 0.154 mg/L. In 192 h, or the 8th day, ammonia nitrogen had been reduced to 0.00, 0.00, 0.00, 0.00 and 0.88 mg/L, respectively (Figure 2).

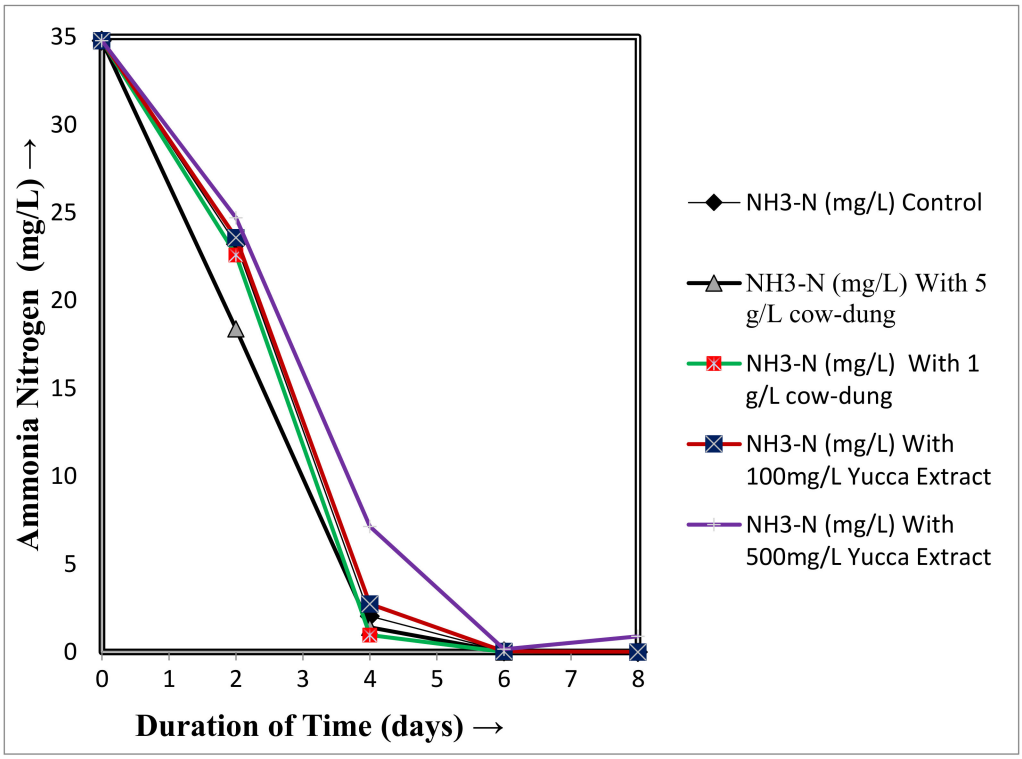


Figure 2. Biological Oxidation of Ammonia Nitrogen. (In Control, with Cow Dung and *Yucca* extract).

7.2. Biological Oxidation of Nitrite to Nitrate

Figure 2 shows the oxidation of nitrite (NO_2) into nitrate (NO_3). The initial content of ammonia nitrogen in municipally treated sewage effluent (MTSE) is converted to nitrite and nitrate simultaneously. The conversion of ammonia into nitrite and nitrate in biological oxidation is a continuous process. Experimental study explored that the effluent with aninitial amount of 34.789 mg/L ammonia nitrogen and 0.150 mg/L nitrite nitrogen has converted or oxidized to 0.210 mg/L (in blank), 2.880 mg/L (with 1 g/L cow dung), 3.265 mg/L (with 5 g/L cow dung), 0.545 mg/L (with 10 mg/L *Yucca* extract) and 0.575 mg/L (with 50 mg/L *Yucca* extract) into nitrite (NO_2)in 48 h, or the 2nd day of the process, at 32 °C temperature and 35 RPM. In 96 h, or the 4th day of the experimental set-up, ammonia nitrogen oxidized

to 11.70, 16.15, 11.45, 13.525 and 9.60 mg/L nitrite (NO_2), respectively. In 144 h, or the 6th day, ammonia nitrogen was converted to nitrite (which further kept oxidizing to nitrate) as 14.70, 8.80, 0.30, 15.525 and 14.375 mg/L. In 192 h, or the 8th day, ammonia nitrogen oxidized to 17.80, 0.18, 0.09, 18.65 and 18.85 mg/L nitrite (NO_2), respectively (Figure 3).

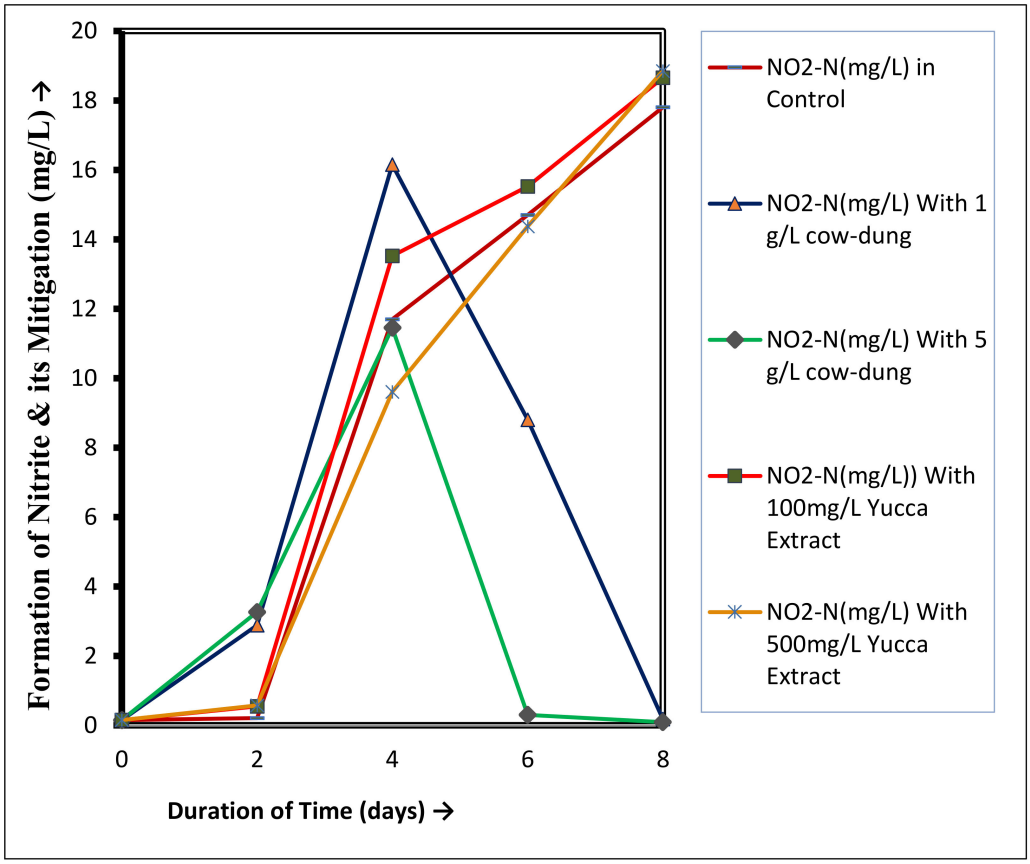


Figure 3. Formation of nitrite nitrogen during oxidation of ammonia nitrogen (in control, with cow dung and *Yucca* extract).

7.3. Oxidation of Nitrite (NO_2) into Nitrate (NO_3)

Ammonia nitrogen is readily converted to nitrite biologically, but its further oxidation to nitrate (a stable form) is typical. It has been observed that the oxidation of nitrite into nitrate is recalcitrant. Cow dung accelerated the process of nitrification. Figure 4 shows that theinitial amount of 34.789 mg/L ammonia nitrogen and 0.45 mg/L nitrate as NO_3 converted or oxidized to 2.25 mg/L (In blank), 3.80 mg/L (with 1 g/L cow dung), 11.70 mg/L (with 5 g/L cow dung), 1.60 mg/L (with 10 mg/L *Yucca* extract) and 2.35 mg/L (with 50 mg/L *Yucca* extract) into nitrate (NO_3)in 48 h, or the 2nd day of the process, at 32 °C temperature and 35 RPM. In 96 h, or the 4th day of the experimental set-up, ammonia nitrogen oxidized to 12.90, 22.25, 59.30, 11.75 and 8.05 mg/L nitrate (NO_3), respectively. In 144 h, or the 6th day, ammonia nitrogen was converted to nitrate as 16.60, 67.30, 109.0, 17.80 and 17.0 mg/L. In 192 h, or the 8th day, ammonia nitrogen oxidized to 21.80, 110.10, 133.5, 20.50 and 20.80 mg/L nitrate (NO_3), respectively (Figure 4).

The ammonia nitrogen is completely converted to its final and stable product nitrate in 6 to 8 days, depending on the amount of cow dungused. However, the samples' total dissolved solids have been found to increase due to water evaporation during ammonia nitrogen oxidation. Because of evaporation, there was 5.7, 10.2, 15.7 and 21.9% water loss on the 2nd, 4th, 6th, and 8th day of the experimental process.

We also determined the effect of the cow dung and *Yucca* extract dosing on different parameters such as ammonia, nitrite, nitrate, pH, electrical conductivity, and Total Dissolved

Solids (TDS). We found both light and temperature to affect ammonia removal significantly. During the initial experimental studies, it has been seen that, in the absence of light and at a low temperature (below 30 °C), the nitrite (intermediate product) could not be converted to nitrate substantially. In some cases, intense white light illuminated by LED bulbs resulted in algal growth. The development of algae in the samples hindered the conversion of nitrite into nitrate, increased high pH to about ten, and algae grew out into large masses. However, the total dissolved solids decreased substantially. The tungsten bulbs were found fit for illuminations, as they did not support the algal formation in the samples.

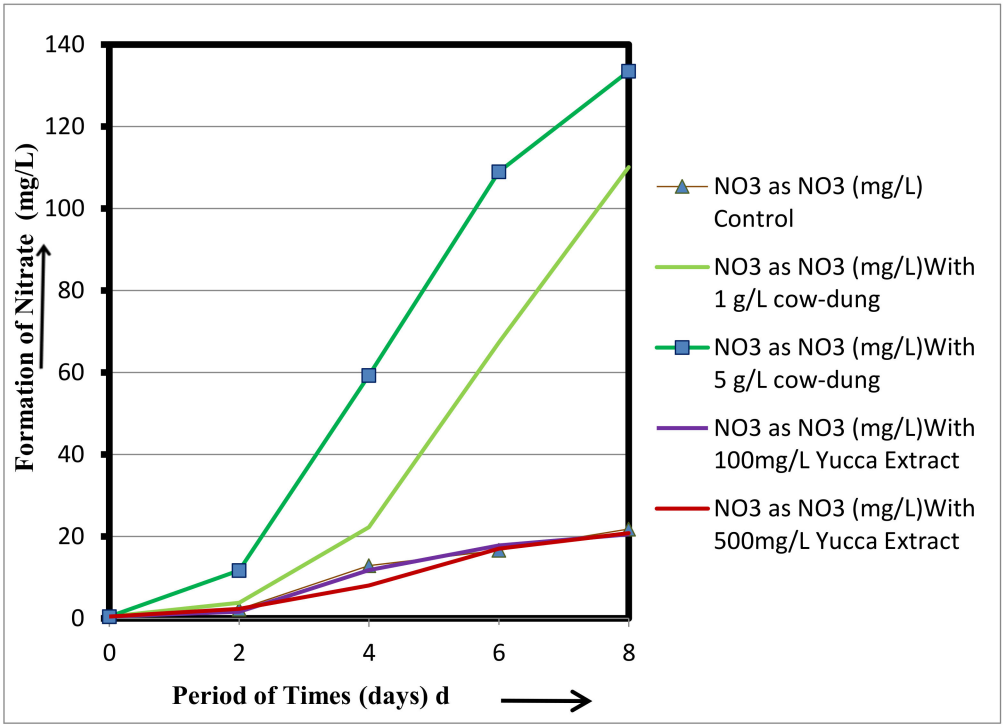


Figure 4. Conversion of ammonia nitrogen into nitrate (in control, with cow dung and *Yucca* extract).

The conversion of ammonia nitrogen into the stable nitrate form is a very typical mechanism. In general practice, the treated effluent's mechanical stirring oxidizes the ammonia nitrogen to nitrite in the presence of nitrifying bacteria and natural oxidation. However, nitrite is also as harmful as ammonia regarding the production of disinfection by-products. In the present experimental study, the conversion of ammonia nitrogen into nitrite and nitrite into nitrate is simultaneous. However, the cow dung (digested) contributes to adding an insignificantly small amount of ammonia nitrogen to the samples. This negligible amount has not been counted for the sake of convenience. The authors analyzed the exact maximum amount of nitrite and nitrate formation.

Based on the current experimental studies, the addition of the cow dung and a few additional modifications in the existing conventional sewage treatment plants' existing infrastructure can give better final effluent quality, free from ammonia nitrogen and nitrite pollution. The proposed design of a modified sewage treatment plant working on the activated sludge process has been suggested in Figure 5, including tertiary treatment units. Here, Hydraulic Retention Time (HRT) in the Flocculator chamber with RPM 35 is eight days for the biological oxidation of ammonia nitrogen (NH_3-N into nitrate (NO_3)).

Cow dung is abundantly available in India. Using cow dung as a bio-resource in wastewater treatment plants is safe and environmentally friendly because cow dung and cow urine are used to treat several human diseases in Indian herbal and natural treatment systems [39–41]. Activated sludge from the final settling tank has to take to feed the aeration

tank. It would be required to maintain a temperature of 32 to 38 °C of the mesophilic temperature range as microbiological activities are more prominent at higher temperatures.

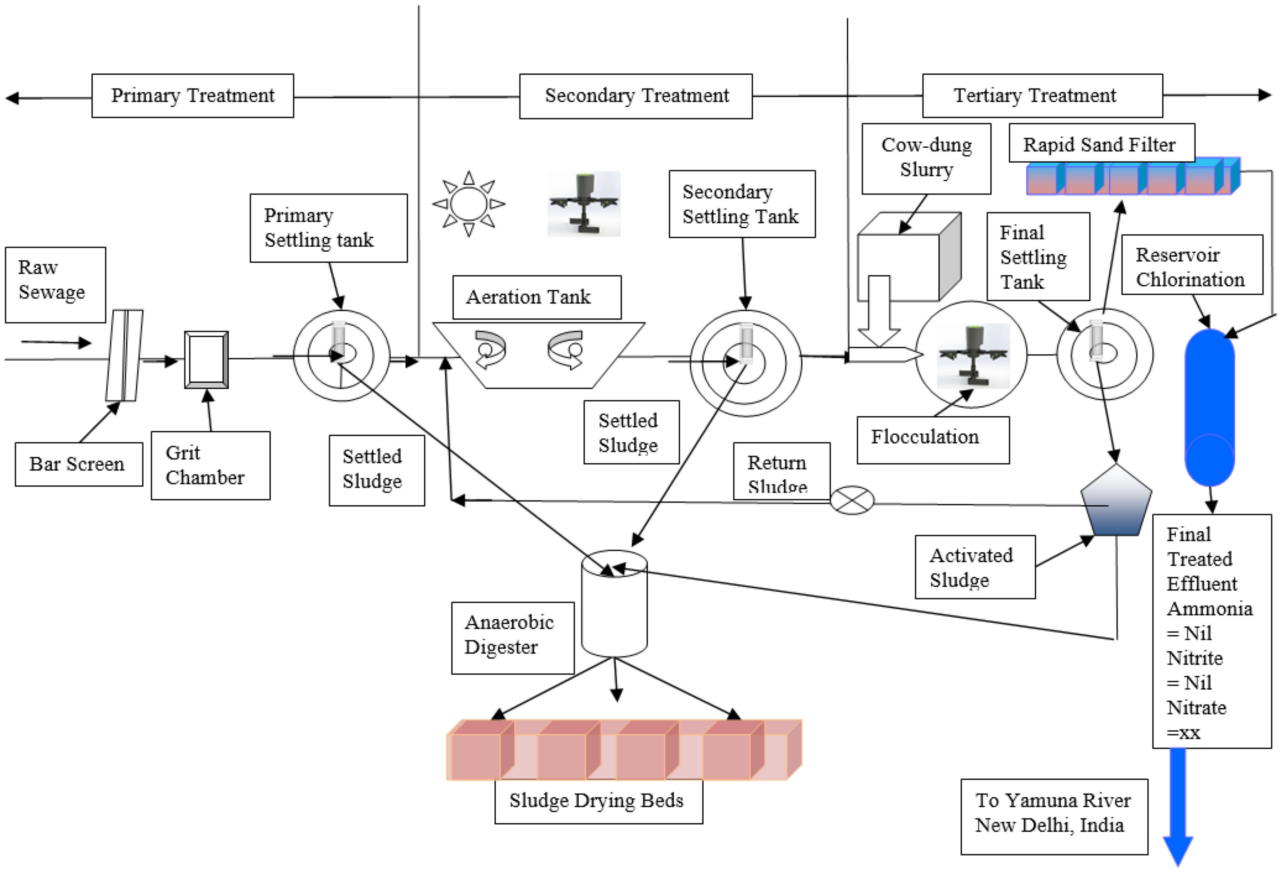


Figure 5. Proposed Sewage Treatment Plant with Biological Tertiary Treatment Units.

Cow dung has successfully proved to play an important role in wastewater treatment. Even cow dung ash has been found active in water disinfection [42]. The dried powder form of cow dung is also helpful as a green adsorbent material to remove carcinogenic and heavy metal water pollutants [28,43]. FAO, 1998 mentioned that cow dung and cow urine possess complex degrading substances [44].

8. Conclusions

The digested cow dung is an excellent biological remedy for the complete treatment of wastewater for combating ammonia nitrogen. The worldwide water scarcity can be mitigated by reusing properly treated municipal sewage and industrial effluents to augment water resources and a circular economy. In the current study, 1gcow dung has transformed 34.78 mg/L ammonia nitrogen in a municipally treated sewage effluent to 110.1 mg/L nitrate on the 8th day under aerobic conditions and a temperature of 32 °C performed with jar test apparatus at 35 RPM. At the same experimental conditions, the higher amount of cow dung of 5 mg/L mitigated ammonia nitrogen rapidly and yielded 133.5 mg/L nitrates. Most importantly, cow dung proved to be capable of transforming to the extent of 99.4% an intermediate product nitrite, as hazardous as ammonia. The presence of numerous microbiological organisms and biocatalysts in cow dung makes it a faster and more efficient way to treat ammonia nitrogen-contaminated wastewater. Secondly, cow dung may be rich in *Nitrosospira*, *Nitrosomonas*, *Nitrospira*, and *Nitrobacter*, which may assist in converting ammonia nitrogen to nitrite and nitrate. Cow dung can also be an excellent bio-resource for the biological treatment of sewage effluent, municipal, hospital, pharmaceutical, and industrial solid/ liquid wastes. For further research, a case study is recommended in the

existing activated sludge plant (SDW) using digested cow-dung slurry to study ammonia nitrogen conversion at the aeration chamber so that the present research can be utilized in real-life projects.

Author Contributions: Execution of experimental work and preparation of standard solutions and reagents, L.K.; Conceptualization, R.K.; Formal analysis, R.K.; Writing manuscript, R.K.; Corresponding R.K. and J.S.; Supervision, R.K.; Writing—review and editing, L.K.; Proposing experimental setup, J.S.; Interpreting results, J.S.; Supervising analytical work, J.S.; Providing instruments, J.S. All authors have read and agreed to the published version of the manuscript.

Funding: No Funding was provided for this research work.

Informed Consent Statement: Not Applicable.

Data Availability Statement: The datasets generated during and analyzed during the current study are available from the corresponding author on reasonable request.

Acknowledgments: We are thankful to Delhi Technological University for providing us with the necessary facilities to conduct these studies.

Conflicts of Interest: The authors declare that they have no known competing financial interests or personal relationships that could have influenced the work reported in this paper. There are no conflict of interest.

References

1. Lawson, C.E.; Lücker, S. Complete ammonia oxidation: An important control on nitrification in engineered ecosystems? *Curr. Opin. Biotechnol.* **2018**, *50*, 158–165. [CrossRef] [PubMed]
2. Kumar, L.; Kaur, R.; Sharma, J. The efficiency of zeolites in water treatment for combating ammonia – An experimental study on Yamuna River water & treated sewage effluents. *Inorg. Chem. Commun.* **2021**, *134*, 108978.
3. Grady, C.P.L.; Daigger, G.T.; Love, N.G.; Filipe, C.D.M. *Biological Wastewater Treatment*, 3rd ed.; CRC Press: Boca Raton, FL, USA, 2011; ISBN 9781420009637.
4. Spellman, F.R. *Handbook of Water and Wastewater Treatment Plant Operations*; CRC Press: Boca Raton, FL, USA, 2003; ISBN 0471084980.
5. Gray, N.F. *Biology of Wastewater Treatment*, 2nd ed.; Imperial College Press: London, UK; University of Dublin: Dublin, Ireland, 2004; ISBN 1-86094-328-4/1-86094-332-2.
6. Chen, G.H.; van Loosdrecht, M.C.; Ekama, G.A.; Brdjanovic, D. (Eds.) *Biological Wastewater Treatment Principles, Modelling and Design*; IWA Publishing: London, UK, 2008; ISBN 9781843391883.
7. Spellman, F.R. *Mathematics Manual for Water and Wastewater Treatment Plant Operators*; American Water Works Association: Denver, CO, USA, 2004; ISBN 1566706750.
8. Gerardi, M.H. *Wastewater Microbiology: Nitrification and Denitrification in the Activated Sludge Process*; John Wiley & Sons: New York, NY, USA, 2002; ISBN 9780471065081.
9. EPA. *Ambient Water Quality Criteria for Endosulfan*; EPA: Washington, DC, USA, 1980.
10. Emerson, K.; Russo, R.C.; Lund, R.E.; Thurston, R.V. Aqueous Ammonia Equilibrium Calculations: Effect of pH and Temperature. *J. Fish. Res. Board Can.* **1975**, *32*, 2379–2383. [CrossRef]
11. The Environment (Protection) Rules. General standards for discharge of environment pollutants: Effluent. *Gaz. Notif. MoEF* **1986**, *2*, 545–560.
12. EPA. *Wastewater Technology Fact Sheet—Ammonia Stripping (EPA 832-F-00-019)*; EPA: Washington, DC, USA, 2000; pp. 1–7.
13. De la Noue, J.; de Pauw, N. The potential of microalgal biotechnology: A review of production and uses of microalgae. *Biotechnol. Adv.* **1988**, *6*, 725–770. [CrossRef]
14. Prajapati, J.C.; Syed, H.S.; Chauhan, J. Removal of ammonia from wastewater by ion exchange technology. *Int. J. Innov. Res. Technol.* **2014**, *1*, 6–11.
15. Margeta, K.; Zabukovec, N.; Siljeg, M.; Farkas, A. Natural Zeolites in Water Treatment—How Effective is Their Use. *Water Treat.* **2013**, *5*, 81–112.
16. Mitch, W.A.; Sedlak, D.L. Formation of N-nitrosodimethylamine (NDMA) from dimethylamine during chlorination. *Environ. Sci. Technol.* **2002**, *36*, 588–595. [CrossRef]
17. Siciliano, A.; Curcio, G.M.; Limonti, C. Experimental analysis and modeling of nitrate removal through zero-valent magnesium particles. *Water* **2019**, *11*, 1276. [CrossRef]
18. Keerio, H.A.; Bae, W.; Park, J.; Kim, M. Substrate uptake, loss, and reserve in ammonia-oxidizing bacteria (AOB) under different substrate availabilities. *Process Biochem.* **2020**, *91*, 303–310. [CrossRef]
19. Keerio, H.A.; Bae, W. Experimental investigation of substrate shock and environmental ammonium concentration on the stability of ammonia-oxidizing bacteria (AOB). *Water* **2020**, *12*, 223. [CrossRef]

20. Ramavandi, B.; Mortazavi, S.B.; Moussavi, G.; Khoshgard, A.; Jahangiri, M. Experimental investigation of the chemical reduction of nitrate ion in aqueous solution by Mg/Cu bimetallic particles. *React. Kinet. Mech. Catal.* **2011**, *102*, 313–329. [CrossRef]
21. Ahmadi, M.; Rahmani, H.; Ramavandi, B.; Kakavandi, B. Removal of nitrate from aqueous solution using activated carbon modified with Fenton reagents. *Desalination Water Treat.* **2017**, *76*, 265–275. [CrossRef]
22. Kumar, L. Study of double breakpoints during chlorination of river Yamuna water, Delhi, India. *Int. J. Water Resour. Environ. Eng.* **2013**, *5*, 370–379. [CrossRef]
23. Environmental Protection Agency. *Water Treatment Manuals: Coagulation, Flocculation & Clarification*; EPA: Washington, DC, USA, 2002; ISBN 1840950900.
24. Cheeke, P.R.; Piacente, S.; Oleszek, W. Anti-inflammatory and anti-arthritic effects of yucca schidigera: A review. *J. Inflamm.* **2006**, *3*, 2–8. [CrossRef]
25. Santacruz-Reyes, R.A.; Chien, Y.H. Efficacy of Yucca schidigera extract for ammonia reduction in freshwater: Effectiveness analysis and empirical modeling approach. *Aquaculture* **2009**, *297*, 106–111. [CrossRef]
26. Yu, X.; Dimitriou, E.; Konstantinos, S.; Markogianni, V.; Politi, D. EFFECTS of yucca shidigera extract on the reduction of ammonia concentration in lake Koumoundourou. *J. Ecol. Eng.* **2015**, *16*, 1–7. [CrossRef]
27. Santacruz-Reyes, R.A.; Chien, Y.H. Yucca schidigera extract—A bioresource for the reduction of ammonia from mariculture. *Bioresour. Technol.* **2010**, *101*, 5652–5657. [CrossRef]
28. Barot, N.S.; Bagla, H.K. Eco-friendly waste water treatment by cow dung powder (Adsorption studies of Cr(III), Cr(VI) and Cd(II) using tracer technique). *Desalination Water Treat.* **2012**, *38*, 104–113. [CrossRef]
29. Umanu, G.; Nwachukwu, S.C.U.; Olasode, O.K. Effects of Cow Dung on Microbial Degradation of Motor Oil in Lagoon Water. *Glob. J. Bio-Sci. Biotechnol.* **2013**, *2*, 542–548.
30. Quraishi, T.; Kenekar, A.; Ranadive, P.; Kamath, G. Evaluation of Performance of cow dung as Microbial Inoculum in Industrial Wastewater Treatment and its Environmental Implications. *Indian J. Sci. Technol.* **2018**, *11*, 1–7. [CrossRef]
31. Randhawa, G.K.; Kullar, J.S. Bioremediation of Pharmaceuticals, Pesticides, and Petrochemicals with Gomeya/Cow Dung. *ISRN Pharmacol.* **2011**, *2011*, 362459. [CrossRef] [PubMed]
32. Tanvi Godambe, M.H.F. Cow dung Bacteria offer an Effective Bioremediation for Hydrocarbon-Benzene. *Int. J. Biotechnol. Trends Technol.* **2016**, *6*, 13–20.
33. Sawant, A.A.; Hegde, N.V.; Straley, B.A.; Donaldson, S.C.; Love, B.C.; Knabel, S.J.; Jayarao, B.M. Antimicrobial-resistant enteric bacteria from dairy cattle. *Appl. Environ. Microbiol.* **2007**, *73*, 156–163. [CrossRef] [PubMed]
34. Marler, L.; Allen, S.; Siders, J. Rapid enzymatic characterization of clinically encountered anaerobic bacteria with the API ZYM system. *Eur. J. Clin. Microbiol.* **1984**, *3*, 294–300. [CrossRef] [PubMed]
35. Adebusoye, S.A.; Ilori, M.O.; Amund, O.O.; Teniola, O.D.; Olatope, S.O. Microbial degradation of petroleum hydrocarbons in a polluted tropical stream. *World J. Microbiol. Biotechnol.* **2007**, *23*, 1149–1159. [CrossRef]
36. Akinde, S.B.; Obire, O. Aerobic heterotrophic bacteria and petroleum-utilizing bacteria from cow dung and poultry manure. *World J. Microbiol. Biotechnol.* **2008**, *24*, 1999–2002. [CrossRef]
37. Singh, D.; Fulekar, M. Bioremediation of phenol using microbial consortium in bioreactor. *Innov. Rom. Food Biotechnol.* **2007**, *1*, 31–36.
38. APHA; AWWA. *Standard Methods for the Examination of Water and Wastewater*; American Public Health Association: Washington, DC, USA, 2005.
39. Gulhane, H.; Nakanekar, A.; Mahakal, N.; Bhople, S.; Salunke, A. Gomutra (Cow Urine): A Multidimensional Drug Review Article. *Int. J. Res. Ayurveda Pharm.* **2017**, *8*, 1–6. [CrossRef]
40. Dhama, K.; Rathore, R.; Chauhan, R.S.; Tomar, S. Panchgavya (Cowpathy): An Overview. *Int. J. Cow Sci.* **2005**, *1*, 1–17.
41. Munshi, S.K.; Roy, J.; Noor, R. Microbiological investigation and determination of the antimicrobial potential of cow dung samples. *Stamford J. Microbiol.* **2018**, *8*, 34–37. [CrossRef]
42. Thakare, A.; Ahmad, M.; Pande, K.; Metkari, S.; Engineering, C.; College, D.Y.P. Purification of Water by using Cow Dung Ash. *Int. J. Eng. Technol.* **2019**, *6*, 393–397.
43. Ojedokun, A.T.; Bello, O.S. Sequestering heavy metals from wastewater using cow dung. *Water Resour. Ind.* **2016**, *13*, 7–13. [CrossRef]
44. Verma, L. *Indigenous Technology Knowledge for Watershed Management in Upper North-West Himalayas of India (PWMTA, 1998)*; FAO (UN): Kathmandu, Nepal, 1998.

ResearchGate

See discussions, stats, and author profiles for this publication at: https://www.researchgate.net/publication/358140263

CFD Study of Flow Characteristics and Pressure Distribution on Re-Entrant Wing Faces of L-Shape Buildings

Article *in* Civil Engineering and Architecture · January 2022

DOI: 10.13189/cea.2022.100125

CITATIONS
0

READS
55

2 authors:



Arun Kumar
Delhi Technological University
2 PUBLICATIONS **3** CITATIONS
SEE PROFILE



Ritu Raj Ahirwar
Delhi Technological University
22 PUBLICATIONS **55** CITATIONS
SEE PROFILE

Some of the authors of this publication are also working on these related projects:

Wind effects on tall buildings View project

Study of edge configuration on the response of tall buildings under wind load. View project

All content following this page was uploaded by Ritu Raj Ahirwar on 27 January 2022.

The user has requested enhancement of the downloaded file.

Civil Engineering and Architecture 10(1): 289-304, 2022 http://www.hrpub.org
DOI: 10.13189/cea.2022.100125

CFD Study of Flow Characteristics and Pressure Distribution on Re-Entrant Wing Faces of L-Shape Buildings

Arun Kumar*, Ritu Raj

Department of Civil Engineering, Delhi Technological University (DTU), India

Received September 23, 2021; Revised December 22, 2021; Accepted January 16, 2022

Cite This Paper in the following Citation Styles

(a): *[1] Arun Kumar, Ritu Raj , "CFD Study of Flow Characteristics and Pressure Distribution on Re-Entrant Wing Faces of L-Shape Buildings," Civil Engineering and Architecture, Vol. 10, No. 1, pp. 289-304, 2022. DOI: 10.13189/cea.2022.100125.*

(b): *Arun Kumar, Ritu Raj (2022). CFD Study of Flow Characteristics and Pressure Distribution on Re-Entrant Wing Faces of L-Shape Buildings. Civil Engineering and Architecture, 10(1), 289-304. DOI: 10.13189/cea.2022.100125.*

Copyright©2022 by authors, all rights reserved. Authors agree that this article remains permanently open access under the terms of the Creative Commons Attribution License 4.0 International License

Abstract The purpose of this research is to investigate the wind flow pattern and pressure distributions on the re-entrant wing facades of an irregular L-cross sectional shape model over the range of wind incidence angles. Computational simulation with ANSYS (CFX) solver has been used for the study on model of the building of cross-sectional area 300m^2 and height 50m at a length scale of 1:100. ANSYS (CFX) is a finite element modelling CFD program of pressure-based solver technology suitable for low Mach No. (Ma) fluid flow. Homogeneous flow of steady wind with gustiness of 5% turbulence in boundary layer of atmosphere is taken for the study. Investigation has been conducted for a range of wind angle of attack from 0° to 180° @ 15° interval. The findings were confirmed by examining similar wind flow on a rectangular model of same cross-sectional area and height under same boundary conditions as applied to L shape model. The results were compared with the values given in various international wind design codes/standards. For a better understanding of the flow characteristics around the L shape model in terms of flow stagnation, flow separation, creation of wakes & vortices and reattachment of flow; illustrations of flow patterns around the model for certain specific wind incidence angles are presented. On the basis of study of surface pressure generated on the model envelope, coefficient of pressure on the re-entrant corner faces has been discussed. The pressure on these wing faces has been found critical between 75° & 180° wind incident angles.

Keywords Wind Pressure Coefficients, ANSYS (CFX); L-plan Shape, Standard k-ε Model

1. Introduction

With the rising use of new façade assemblies and unique shapes in the design of high-rise buildings, a precise description of wind action and its interaction with building shape is essential for a rational structural design approach. While considerable study has been done on regular cross-sectional shape buildings, on the basis of which many international wind design codes have been formulated, few research studies have been found on irregular-shape buildings.

A general estimation of magnitude of wind pressure on surfaces of a bluff body is the mean pressure coefficient (C_{Pe}) , which is pressure normalised by upwind velocity/dynamic pressure $\left(\frac{1}{2}\rho u^2\right)$ at roof height, where ρ is density of air and u is mean wind velocity at roof height. It is a dimensionless measure independent of the velocity of flow. However, it depends on the shape and size of the bluff body for a similar wind flow characteristic. The oblique wind also causes a varied wind flow pattern around the body, as well as varying impact pressure on the surfaces themselves.

Baines [1] was the first to represent the influence of wind pressure distribution and flow pattern on tall

buildings. Positive pressure on the windward surface and negative pressures on the side surfaces, top and rear surface of a square-shape building were intuitively depicted as the contour of the mean wind pressure. Data for designing such simple-shaped buildings are available in various international codes/standards. But more complex tall buildings have necessitated study of the effect of wind on such buildings through available experimental research in wind tunnels. Computational simulations and field measurements on full scale buildings have also been conducted by other researchers. Various researchers have published their study publications on the topic of the wind effect on irregular-shape tall buildings. Distribution of pressure on various surfaces was observed to be different from that of cube-shape model. Mendis et al. [2] investigated the interference effect and also along and across wind impacts for high rise buildings, using wind tunnel testing and CFD. The experimental and analytical results were found to be within the acceptable limit of 20 percent to 25 percent. Fu et al. [3] published field measurements of boundary layer wind parameters for two super tall buildings across open country terrain and urban terrain. Full scale measurements were compared to wind tunnel test data and the results were found to be within acceptable range (20% - 25%). Tanaka et al. [4] used wind tunnel measurements to show the aerodynamic properties of different irregular cross-sectional shaped high-rise buildings. Amin and Ahuja [5] studied effect of various side ratios ranging from 0.25 to 4 on a rectangular model of similar area and height. The negative pressure on the side and downwind faces of the building is reported to be affected by wind incidence angles and side ratios. The wind pressure on the building faces is substantially affected by the cross-sectional shapes of the building, according to Kushal et al. [6]. The computational investigation of distribution of pressure on faces of tall building of square cross-section under three wind incidence angles is presented by Chakraborty and Dalui [7] using ANSYS (Fluent) solver. ANSYS (Fluent) is a finite volume modelling based CFD program having facility of customizable tools for study of complex fluid flow. Three wind incidence angles 0°, 30° and 45° were investigated and discussed by them. Through wind tunnel tests at various wind angles, Bhattacharyya et al. [8] investigated the distribution of pressure on the surfaces of an E- shape tall building. Chakraborty et al. [9] discussed result of wind effect on a plus shape tall building model conducted through wind tunnel study and simulation as well and; compared with the results for 0° and 45° wind angles. Differences in coefficient of pressure between CFD study and wind tunnel study were found to be within the acceptable range. Kheyari and Dalui [10] used CFD to investigate the wind forces on a high-rise building under interference effects. Roy and Bairagi [11] evaluated the pressure and velocity fluctuation of wind around stepped high-rise building with rectangular, square and triangular shapes placed one above another. Mukherjee and Bairagi [12] studied the pressure and velocity distribution of wind around N shape tall building. Bairagi and Dalui [13] examined distribution of pressure on square tall building having a reduced offset of 20% at half the height of building and a reduced offset of 10% at one third height and two third height of building, each. For a 100 percent blockage condition, Pal S. et al. [14] assessed the interference effect of square and remodeled triangular shape buildings of equal plan area. The shape and orientation of interfering building are shown to have a significant role on pressure and force generated on main building. Through open circuit boundary layer experiments, Raj, Ritu, and Ahuja, A.K. [15] compared plus shape rigid high-rise building models of varying wing lengths with a square model having same cross-sectional area. It was reported that shear force at base, torque about the two vertical planes and about the plan depend on wind incidence angles as well as the wing lengths in plus shape buildings. Raj, Ritu, et al. [16] used ANSYS (CFX) solver to simulate H shape high-rise building model in isolated and interfering condition using the same shape model at various positions. In an open wind tunnel Pal S. et al. [17] studied wind generated mutual interference effect on twin square and fish shape tall building models placed at a distance of 0.1H (H being height of the model) with various combinations of orientation between forward-facing and back-facing and presented induced pressure and base shear on the models. S.K. Nagar et al. [18] evaluated the coefficient of pressure and interference factor for different interfering situations of square and H shape tall buildings of same floor area and discovered that H shape building is under more pressure than the square building. Kumar A, Raj R [19] studied pressure distribution on an irregular octagonal (oval) shape building using ANSYS (CFX) for varied wind incidence angles. It was reported that the flow characteristics is influenced by side ratio of the building and that inclined surfaces of the building are subjected to high pressure gradient.

Despite the fact that L shape is a highly typical arrangement, most of studies on such plan-shaped buildings have been limited to conventional wind directions. Stathopoulos T. [20] has examined the wind induced pressure for L shape of low-rise model through computational method for normal wind direction. The results between computational and experimental study were reported to be with good agreement between the two. Gomes et al. [21] used a wind tunnel test as well as CFD to evaluate wind pressure distribution on the facades of L and U shape buildings of identical height. They compared the results from a cube of same dimension and height and found different pressure distributions on the models than those of single cube. Amin and Ahuja [22] investigated pressure distribution on various sides of L and T shape tall buildings for varied wind angles in a wind tunnel test. The cross-sectional shape of the buildings was revealed to play

an important role in pressure distribution, particularly on the re-entrant wing side.

The pressure distribution on re-entrant faces depends on the respective lateral dimension (width of the faces) and height of the building. The influence of wind incidence angles on pressure distribution on faces of a L shape model (figure 1) of equal re-entrant wing faces for a prototype building of 50 m height and 300 sqm floor area have been investigated in the present study using a standard k-ε turbulent model on ANSYS (CFX) solver.

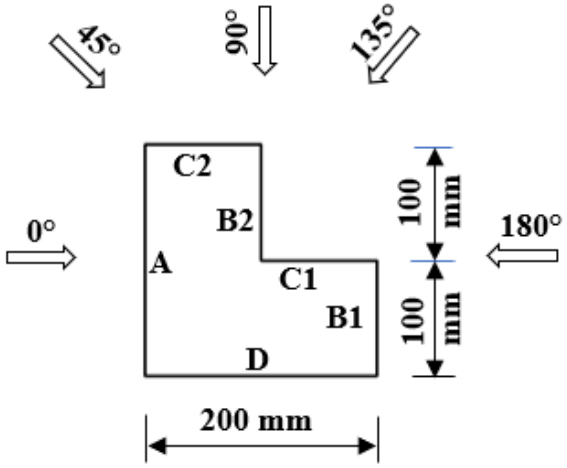


Figure 1. L Shape Model

2. Numerical Analysis

Navier-Stokes equations of (a) Continuity and (b) Momentum which governs the pressure and velocity in three-dimensional unsteady fluid flow are expressed as:

(a) Continuity equation

$$\frac{\delta u}{\delta x}+\frac{\delta v}{\delta y}+\frac{\delta w}{\delta Z}=0 \quad (1)$$

(b) Momentum Equation

X - Momentum

$$\rho\left(\frac{\delta u}{\delta t}+u\frac{\delta u}{\delta x}+v\frac{\delta u}{\delta y}+w\frac{\delta u}{\delta z}\right)=$$

$$=(-)\frac{\delta \rho}{\delta x}+\rho g_x+\mu\left(\frac{\delta^2 u}{\delta x^2}+\frac{\delta^2 u}{\delta y^2}+\frac{\delta^2 u}{\delta z^2}\right) \quad (2)$$

Y - Momentum

$$\rho\left(\frac{\delta v}{\delta t}+u\frac{\delta v}{\delta x}+v\frac{\delta v}{\delta y}+w\frac{\delta v}{\delta z}\right)=$$

$$=(-)\frac{\delta \rho}{\delta y}+\rho g_y+\mu\left(\frac{\delta^2 v}{\delta x^2}+\frac{\delta^2 v}{\delta y^2}+\frac{\delta^2 v}{\delta z^2}\right) \quad (3)$$

And Z – Momentum

$$\rho\left(\frac{\delta w}{\delta t}+u\frac{\delta w}{\delta x}+v\frac{\delta w}{\delta y}+w\frac{\delta w}{\delta z}\right)=$$

$$=(-)\frac{\delta \rho}{\delta z}+\rho g_z+\mu\left(\frac{\delta^2 w}{\delta x^2}+\frac{\delta^2 w}{\delta y^2}+\frac{\delta^2 w}{\delta z^2}\right) \quad (4)$$

Where ρ is density and g's are sum of body forces in the respective directions. Rest symbols are carrying usual meanings.

In computational fluid dynamics (CFD), wind simulation is created in virtual wind tunnel called domain within which model is kept alike as in the wind tunnel experiment. CFD models try to resolve the fluid flow around any bluff body, as specified by the aforementioned Navier-Stokes Equations, by modelling the flow at continuous finite grid locations. Researchers have created a number of mathematical models to define the flow properties and the influence of turbulence in the fluid flow. To replicate the near-real scenario that occurs in nature, a number of models have been developed. However, no model for determining the precise characteristics of turbulent flow has yet been developed. k-epsilon (k- ε) model is the most common among them for CFD study of wind flow on buildings. The actual k-ε turbulent model comprises several unmeasurable variable quantities and unknowns. This model has been further simplified (standard k- ε turbulence model) in which turbulence is described by two partial differential energy equations- Turbulence Kinetic Energy (k) and; dissipation of turbulence kinetic energy called the Turbulent Eddy Dissipation (ε). It is the simplest model, requiring the input of only the initial boundary conditions to the solver. Fluid shear, friction, buoyancy, and tiny eddies contribute to the Turbulent Kinetic Energy equation. Mathematically, it is defined as the mean kinetic energy per unit mass of eddies having dimension [L2T2]. Physically, the Turbulence Kinetic Energy is the Root Mean Square (RMS) velocity fluctuations. Turbulence Kinetic energy is converted to turbulent energy, which dissipates (Turbulent Eddy Dissipation, ε) at the Kolmogorov micro scale by viscous forces, resulting in heat production. Dimension of Turbulent Eddy Dissipation, ε is [L^2T^3] i.e., Turbulent Kinetic Energy per unit time. The energy equations are as follows.

(c) Turbulence Kinetic Energy

$$\frac{\delta(\rho k)}{\delta t}+\frac{\delta}{\delta x_i}(\rho u_i k)=\frac{\delta}{\delta x_j}\left(\frac{\mu_t}{\sigma_k}.\frac{\delta k}{\delta x_j}\right)+2\mu_t.E_{ij}.E_{ij}-\rho\varepsilon \quad (5)$$

(d) Turbulence Eddy Dissipation

$$\frac{\delta(\rho\varepsilon)}{\delta t}+\frac{\delta}{\delta x_i}(\rho u_i \varepsilon)=\frac{\delta}{\delta x_j}\left(\frac{\mu_t}{\sigma_\varepsilon}.\frac{\partial \varepsilon}{\partial x_j}\right)+$$

$$+\frac{\varepsilon}{k}C_{\varepsilon 1}.2\mu_t.E_{ij}.E_{ij}-C_{\varepsilon 2}\rho\frac{\varepsilon^2}{k} \quad (6)$$

Where, u_i is velocity component in respective directions.

E_{ij} is rate of deformation i.e., strain rate.

μ_t is Eddy Viscosity and is represented as $\mu_t=C_\mu\rho\frac{k^2}{\varepsilon}$

$\sigma_k, \sigma_\varepsilon, C_{\varepsilon 1}$ and $C_{\varepsilon 2}$ are adjustable constants. Values of these constants have been determined after multiple iterations of data fitting for a variety of turbulent flows as;

$$C_\mu = 0.09, \quad \sigma_k = 1.00, \quad \sigma_\varepsilon = 1.3, \quad C_{\varepsilon 1} = 1.44 \ \ and \ \ C_{\varepsilon 2} = 1.92$$

3. Mean Velocity Characteristics

Wind does not flow evenly in nature. Due to friction generated by vegetation and structures at ground level, wind speed increases as height from the earth increases in a semi empirical relationship. As a result, the wind flow encountered in high-rise buildings is not constant along the height of building. The vertical distribution of horizontal mean wind flow is defined by the following empirical equations.

1) Parabolic Law:

$$u = u_{Ref}\sqrt{\frac{Z+22}{Z_{Ref}+22}} \tag{7}$$

Where, u_{Ref} is the reference wind speed in m/s

Z_{Ref} is the reference height usually taken as 10 m above ground.

u is longitudinal wind velocity (time averaged) at height Z above ground.

2) Power Law:

$$u = u_{Ref}\left(\frac{Z}{Z_{Ref}}\right)^{\alpha} \tag{8}$$

Where, value of α depends upon terrain category.

This is an upgraded formula over Parabolic Law. It is generally used for its simplicity. But it does not provide correct results in the bottom 10 m of ABL.

3) Logarithmic Law:

$$u = \frac{1}{k}u_0 L_n\left(\frac{Z-Z_d}{Z_0}\right) \tag{9}$$

Where, k is Von Karman Constant = 0.4

u_0 is Friction Velocity represented as $u_0 = \sqrt{\frac{\tau_w}{\rho}}$, τ_w is wall shear stress and is represented as $\tau_w = \mu\left(\frac{du}{dy}\right)_{y=0}$ and; ρ is density of air.

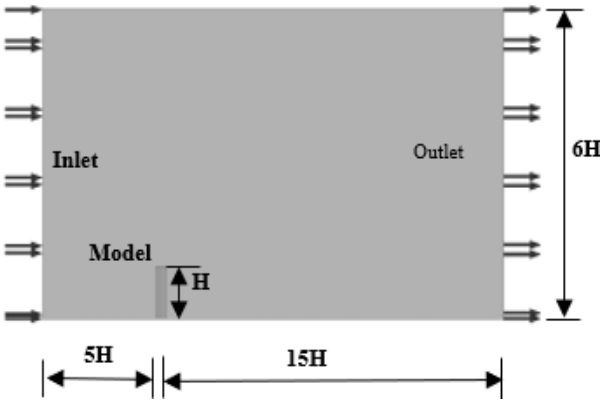
Z_0 is aerodynamic roughness length which is a surface roughness parameter.

Z_d is the height of zero wind speed achieved above the ground.

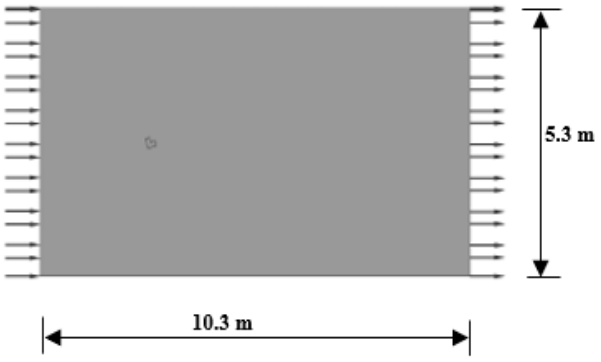
In the bottom 10 meters of the earth are covered by the Logarithmic Law for the vertical distribution of horizontal mean wind speeds.

4. Model and Computational Domain

For computational simulation model is positioned inside a computational domain which is equivalent to a wind tunnel. The dimensions of the domain are created large enough to eliminate fluid stream reflections so that any unusual fluid pressure adjacent to and on the model is avoided and; the blockage ratio remains below 3 %. At the same time, it is ensured that during the simulation, velocity variations, uplift forces, backwash and vortex formations in the wake zone are adequately formed. The domain size should also not be too large, since this would need greater number of grid elements for analysis, which will take longer time and demand more processing power for the solution to converge. In the current investigation recommendations of Revuz, J. et al. [23] have been adopted for the purpose. The domain inlet wall, side walls and the domain roof wall are kept at a distance of five times the height of the model from the respective faces of the model. The distance of domain outlet from the model leeward face is fixed at fifteen times the height of the model in order to produce a realistic wake and vortex behind the model. The domain length, L = 10.3 m, width, B = 5.3 m and height, H = 3.0 m created and model built with a scale of 1:100 positioned inside the domain is shown in figure 2. Homogeneous steady wind flow under atmospheric boundary layer at the inlet using power law wind profile with roughness coefficient, α = 0.143 for terrain category-II [as per IS: 875 (Part 3): 2015] has been adopted. The gustiness effect is achieved by providing 5% turbulence intensity. 0.63 m/s uniform flow of wind velocity at the roof height of the model is attained. Figure 3 depicts the obtained velocity profile at the inlet.



(a) Elevation



(b) Plan

Figure 2. Schemetic Diagram of Domain

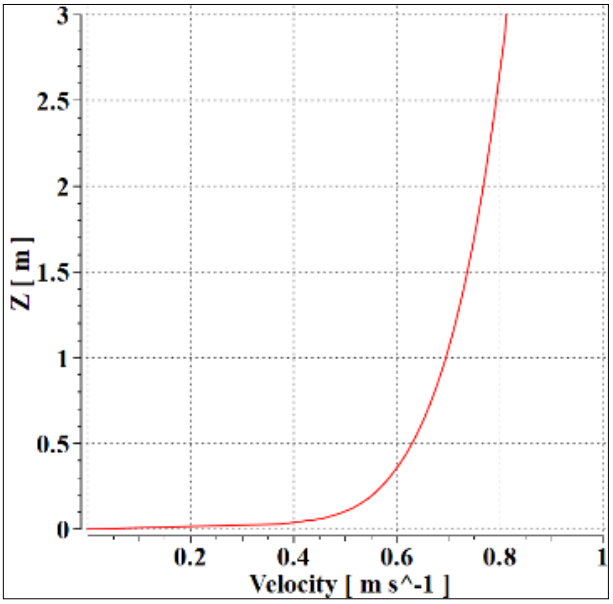


Figure 3. Velocity Profile

table 1 and are within acceptable limits, particularly for the upwind and downwind faces. Due to the anisotropic nature of turbulence and eddy viscosity, some larger discrepancies appeared on the side faces, whereas isotropic nature of boundary condition is used in the simulation. The numerical simulation, however, has caught the primary flow features, addressed later, which justifies the approach for further research on the L-plan shape model.

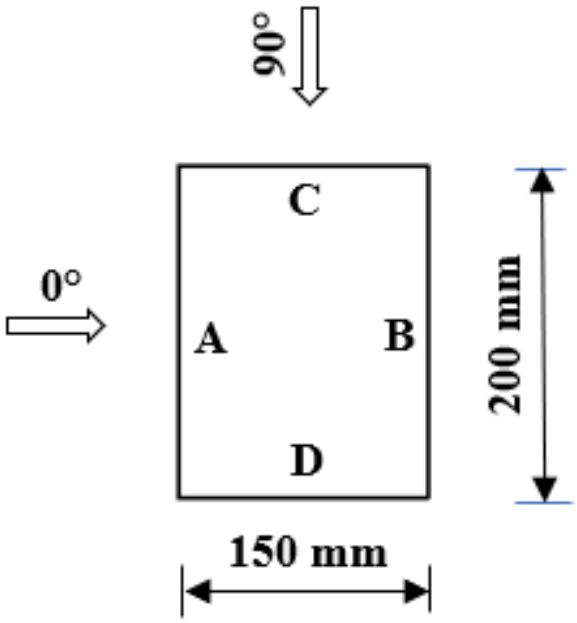


Figure 4. Rectangular Shape Model

5. Validation

Figure 4 shows a rectangular plan model having same area in plan and same height as the L-plan shape model. Simulation results on this model under the same wind flow and boundary conditions were used to test the validity of the numerical technique investigated. The findings of the coefficient of pressure on the rectangular plan shape model faces were matched with several international codes/standards. The results are shown in

Table 1. Comparison of C_{Pe} on Faces of Rectangular Model

As per	Wind Angle	C_{Pe} Face A	C_{Pe} Face B	C_{Pe} Face C	C_{Pe} Face D
ANSYX (CFX)	0°	+0.68	-0.28	-0.48	-0.48
	90°	-0.43	-0.44	0.71	-0.23
IS: 875 (Part 3): 2015	0°	+0.8	- 0.25	-0.8	-0.8
	90°	-0.8	-0.8	0.8	-0.25
ASCE/SEI 7-10	0°	+0.8	-0.5	-0.7	-0.7
	90°	-0.7	-0.7	0.8	-0.5
AS/NZS- 1170.2 (2002)	0°	+0.8	-0.5	-0.65	-0.65
	90°	-0.65	-0.65	0.8	-0.5
EN: 1991-1-4	0°	0.8	-0.55	-0.8	-0.8
	90°	-0.8	-08	0.8	-0.55
BS: 6399-2	0°	0.76	-0.5	-0.8	-0.8
	90°	-0.8	-0.8	0.76	-0.5

6. Computational Grid, Boundary Conditions

Discretized grid of computational domain and the model have a significant impact on the result of the simulation. The grid resolution is set to precisely capture crucial physical flow parameters on the model surfaces, flow separations, vortices generated and reattachment of flow etc. The faces of the model have been discretized at a finer level than the volume of domain, since our focus is to scan the model precisely. CFD gives good results if discretization is done with finer cell elements. However, when the cell numbers are increased in number computational duration are also increased, which may require more computational resources [24]. Hence, a tradeoff between the two is maintained. Various attempts of meshing techniques and boundary conditions were explored during the present study. By using the option of automatic method in the global setting, final meshing of domain volume with maximum element size of 90 mm was adopted. From the local setting on domain ground surface maximum element size was kept as 40 mm, and model walls & roof as 20 mm. Smooth inflation is applied to the model such that the domain grid meets the model walls orthogonally, allowing for a smooth simulation transition on the surfaces. Figure 5 depicts meshing. The total number of nodes produced is around 465000 and the number of elements is 2550000. The domain walls except ground and the model roof were defined as free slip walls ($\tau_{wall} = 0; u_{wall} = 0$), where τ_{wall} is representing fluid shear stress on wall and u_{wall} is representing component of fluid velocity normal to the wall. This means, component of fluid velocity parallel to wall has a predetermined value, which is computable. But, component of velocity normal to wall as well as fluid shear on wall, are both zero. The model faces and the domain ground were specified as no slip walls ($u_{wall} = 0$), which means component of fluid velocity at the boundary of wall is zero and the wall is not moving i.e., wall velocity is also zero. To obtain different angle of attack of wind, model was rotated about its mass center of gravity, keeping the model boundary and flow parameters unchanged.

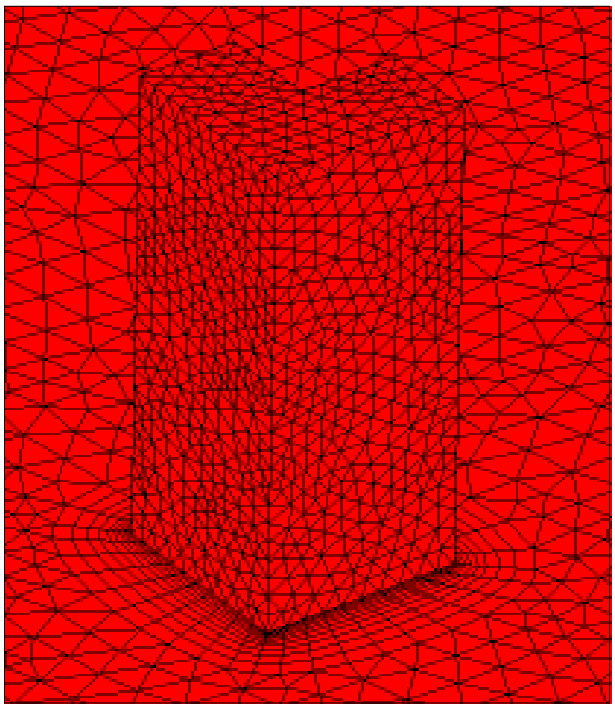


Figure 5. Meshing

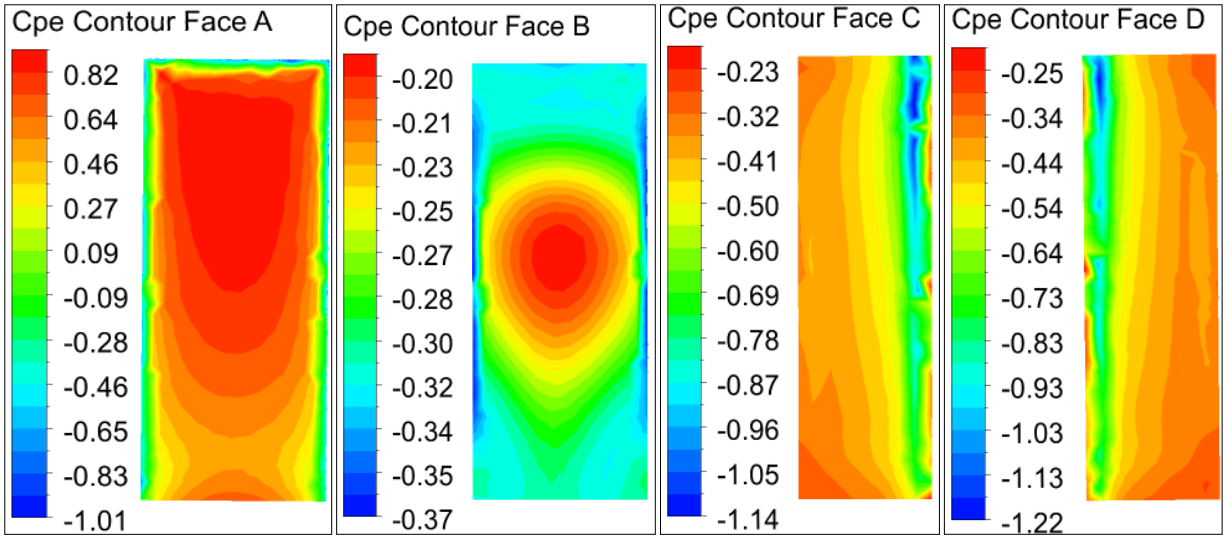


Figure 6 (a). C_{Pe} Contour on Faces of Rectangular Model for 0° Wind Angle

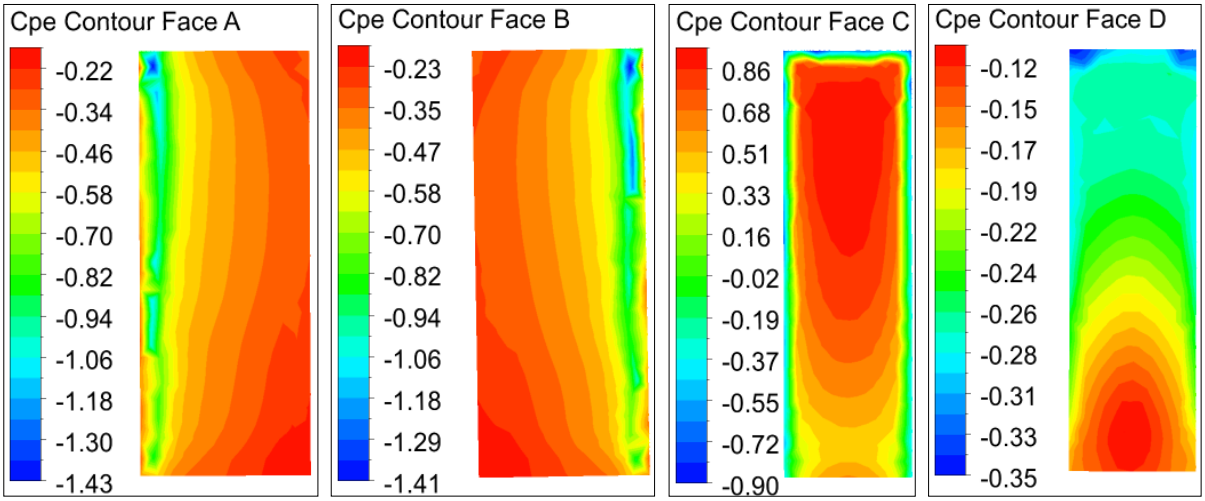
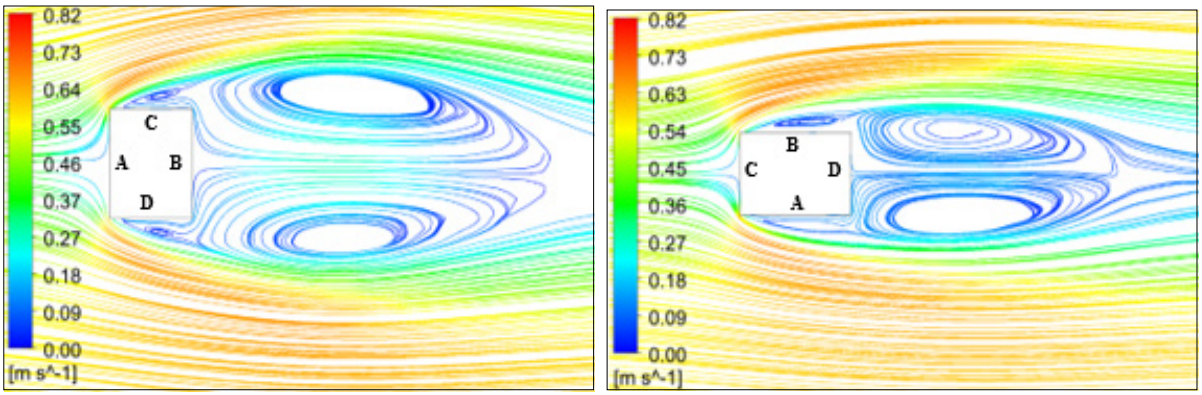


Figure 6 (b). C_{Pe} Contour on Faces of Rectangular Model for 90° Wind Angle



(a) 0° Wind Angle (b) 90° Wind Angle

Figure 7. Streamlines at Mid Height of Rectangular Model

7. Result and Discussion

7.1. Rectangular Model

Figure 6 (a) and (b) shows the mean pressure coefficients for the rectangular model for the two orthogonal wind directions. The mean pressure coefficients are positive at the stagnation points on the respective windward faces of wind orientation (face A for 0° wind angle & face C for 90° wind angle). The maximum values are in the upper heights of the respective windward faces and symmetrical from the vertical center line. Due to an increase in wind velocity along the height, the pressure distribution also increases along height. The flow separation takes place from the leading edges where wind flows sharply away at high speed. The pressure decreases creating negative pressure or suction pressure on side faces and roof. The leeward faces (face B for 0° wind angle & face D for 90° wind angle) are under almost uniform suction as expected. However, the pattern of the suction pressure distribution for both wind directions is different. For 0° wind angle suction is the minimum at the center of the leeward face whereas for 90° wind angle, it is at the lower height of the leeward face. This is due to difference in intensity of horizontal and vertical vorticity generated in the wake region on account of different side ratio. The wake area on the leeward face for 0° wind angle & 90° wind angle can be seen in figure 7 (a) and (b).

7.2. L-Plan Shape Model

Coefficients of pressure on the faces of L-plan shaped model have been shown in figure 8 (a) to (m) for extended range of wind incident angles from 0° to 180° @ 15°. Following are the overall features and observed pressure distribution on these faces.

At 0°, the wind flow around the model is very similar to that of the rectangular model in the windward region. But the flow pattern is totally different in the leeward region. Unsymmetrical vortices, figure 9 (a), are formed behind the model with a smaller vortex in the L cavity behind face B2, whereas in the rectangular model two similar vortices are formed, figure 7 (a), behind the model. The upwind face A is subjected to similar positive mean coefficient of pressure of 0.68/0.69 for both the models - rectangular and L-plan shaped respectively. The remaining faces are under negative pressure.

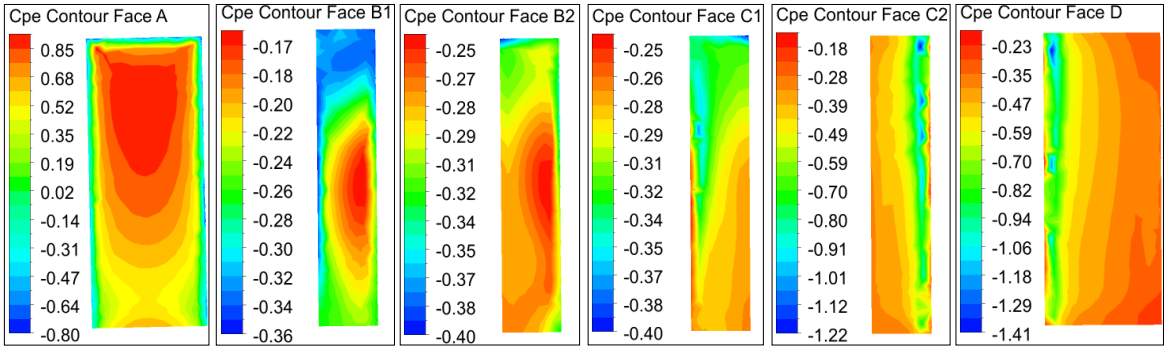


Figure 8 (a). C_{Pe} Contour on Faces for 0° Wind Angle

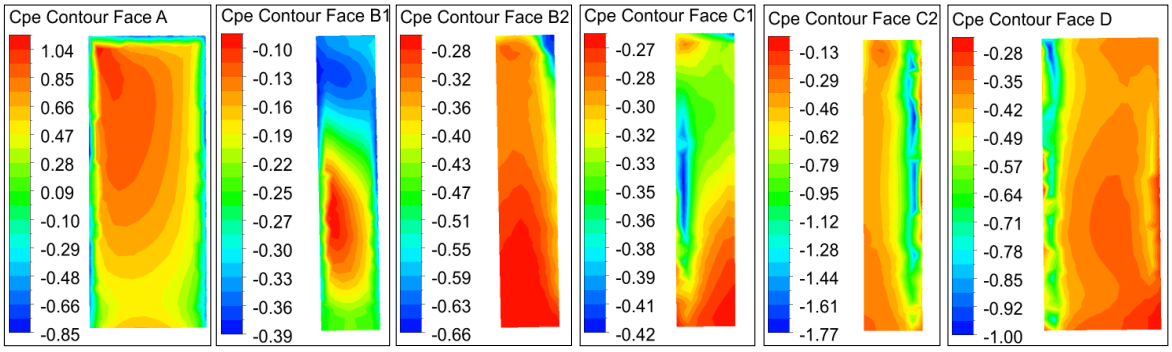


Figure 8 (b). C_{Pe} Contour on Faces for 15° Wind Angle

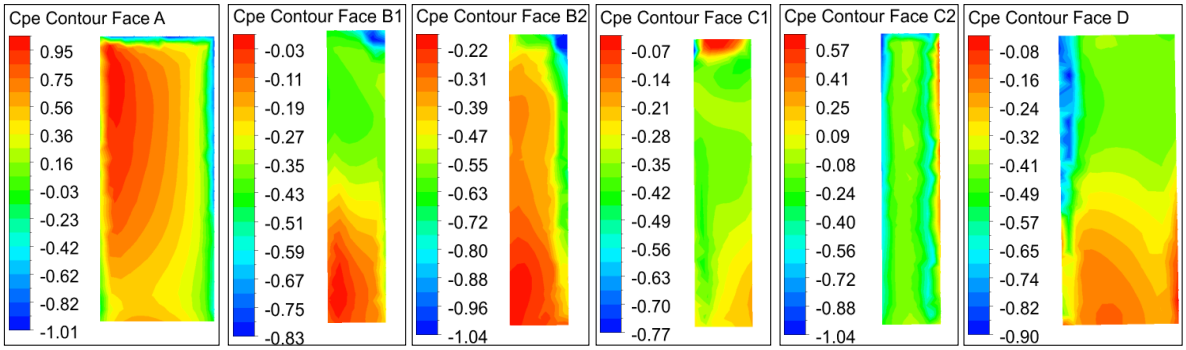


Figure 8 (c). C_{Pe} Contour on Faces for 30° Wind Angle

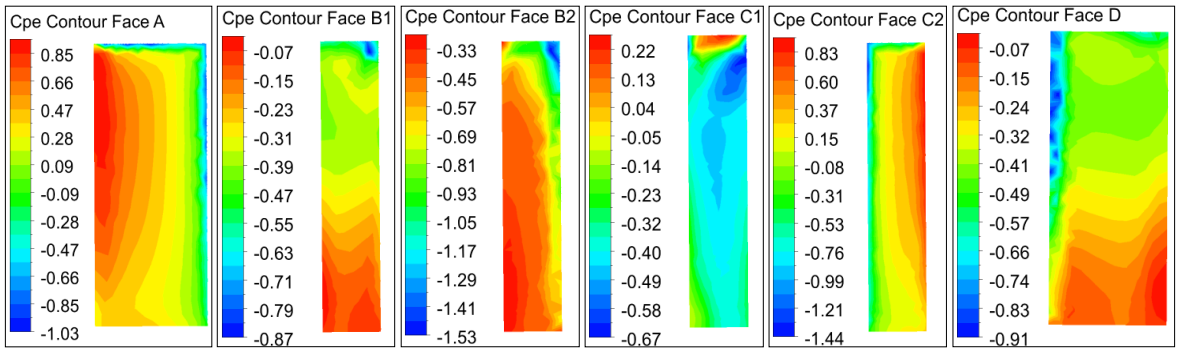


Figure 8 (d). C_{Pe} Contour on Faces for 45° Wind Angle

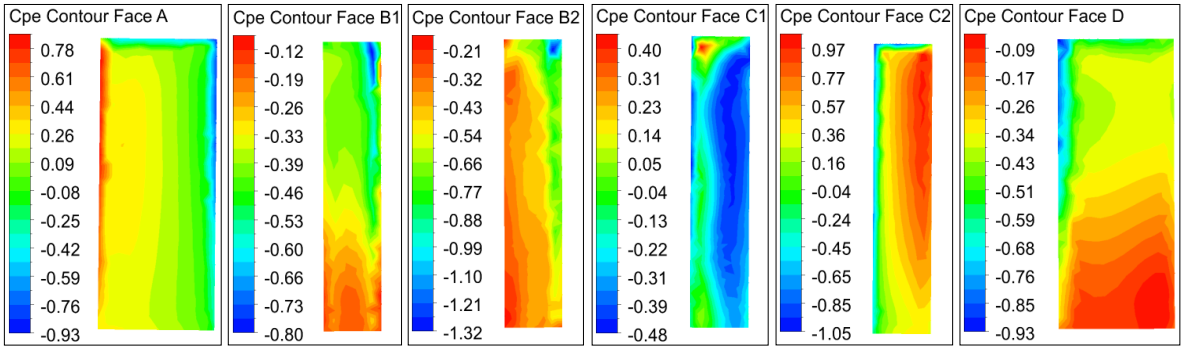


Figure 8 (e). C_{Pe} Contour on Faces for 60° Wind Angle

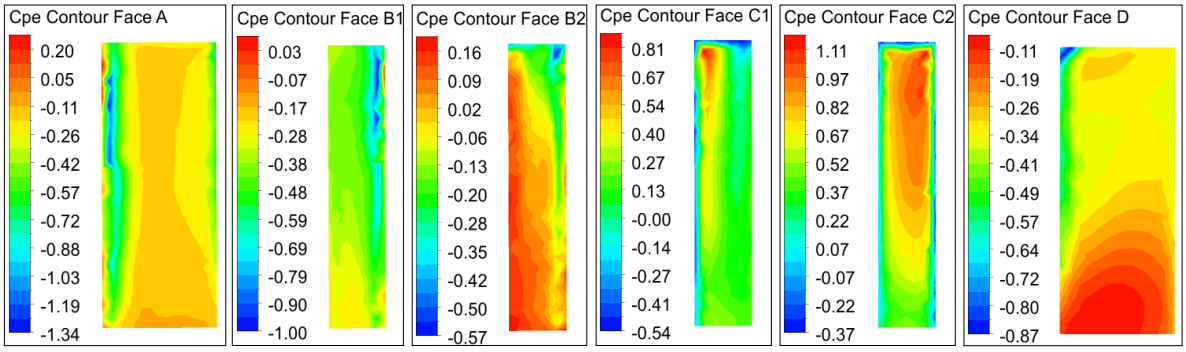


Figure 8 (f). C_{Pe} Contour on Faces for 75° Wind Angle

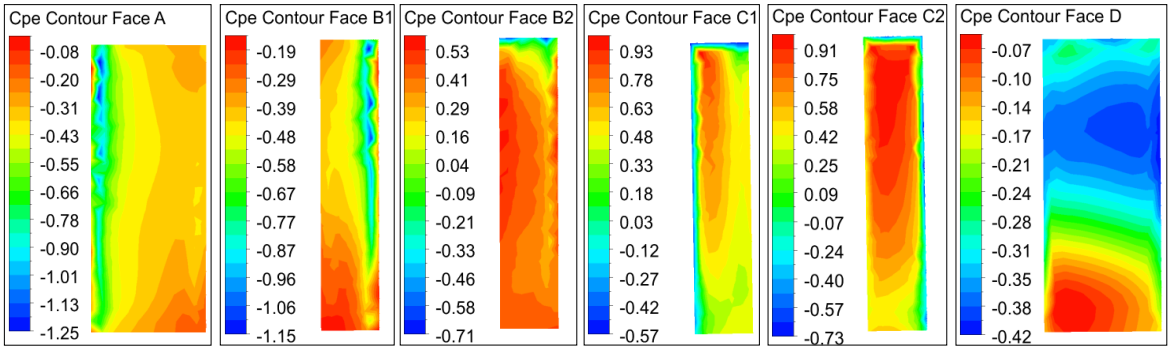


Figure 8 (g). C_{Pe} Contour on Faces for 90° Wind Angle

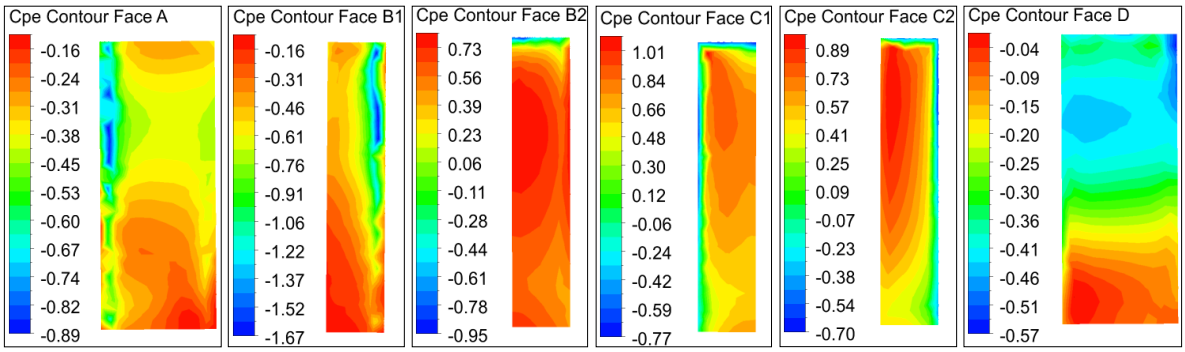


Figure 8 (h). C_{Pe} Contour on Faces for 105° Wind Angle

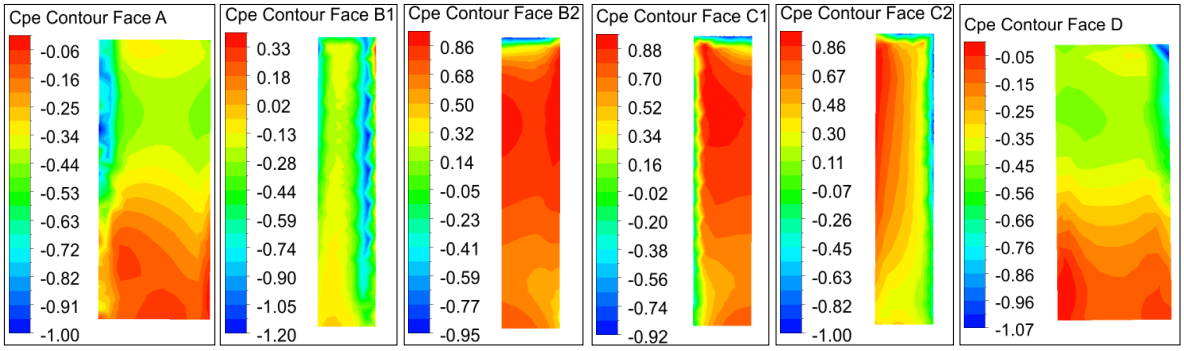


Figure 8 (i). C_{Pe} Contour on Faces for 120° Wind Angle

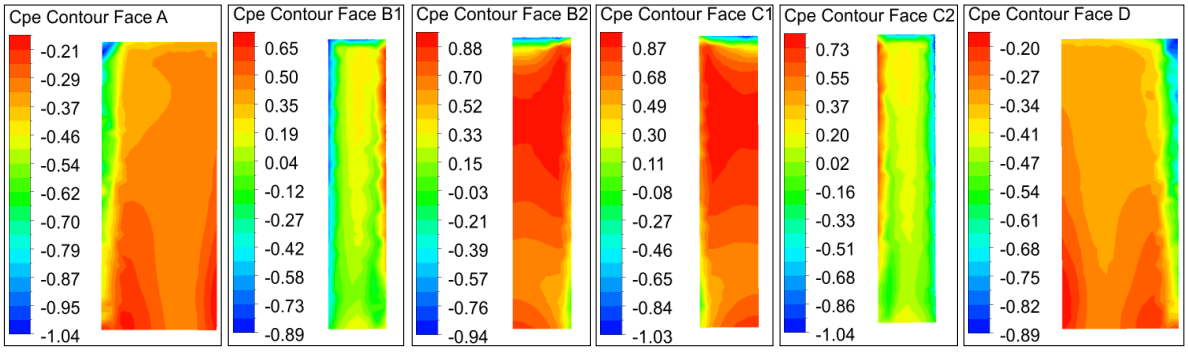


Figure 8 (j). C_{Pe} Contour on Faces for 135° Wind Angle

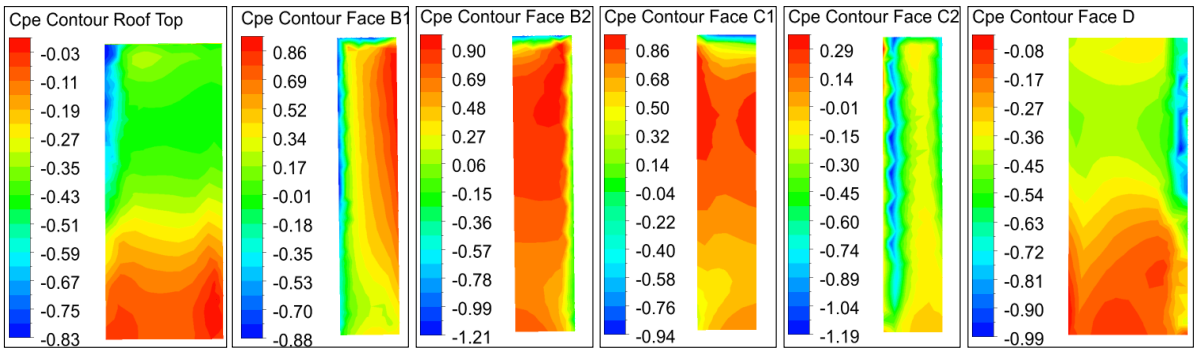


Figure 8 (k). C_{Pe} Contour on Faces for 150° Wind Angle

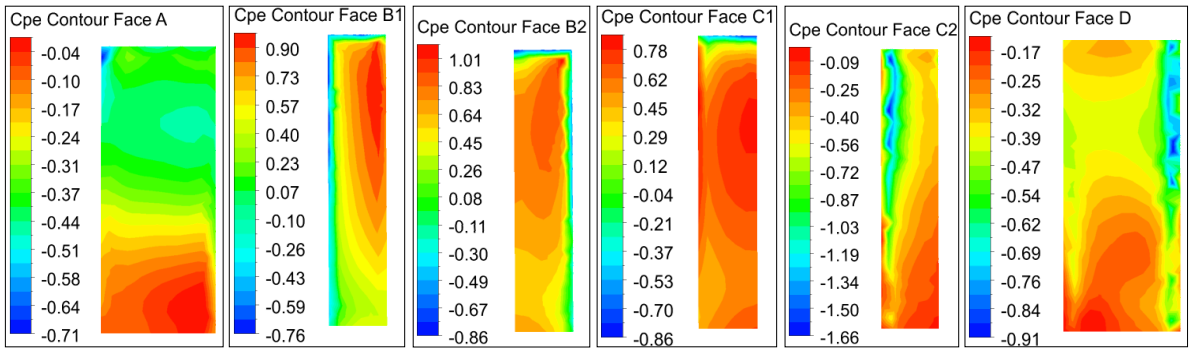


Figure 8 (l). C_{Pe} Contour on Faces for 165° Wind Angle

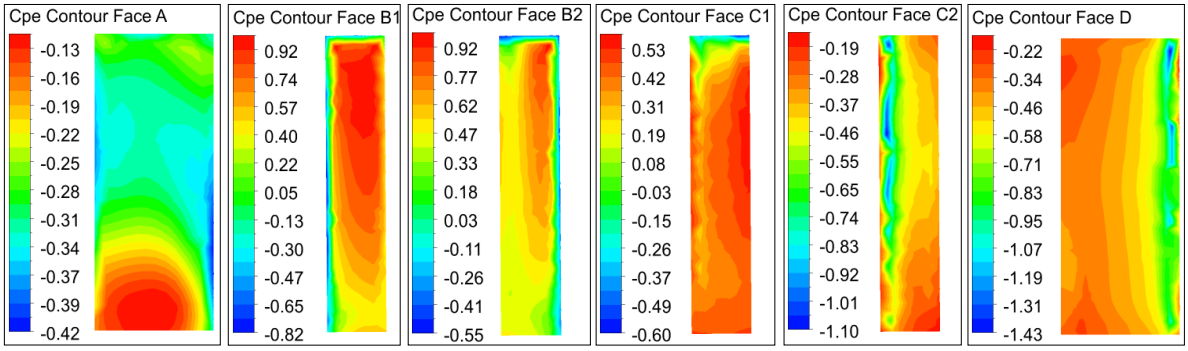
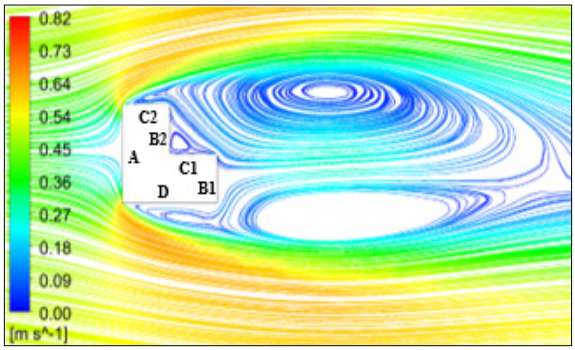
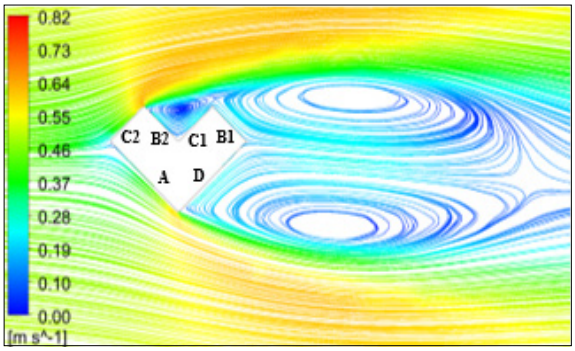


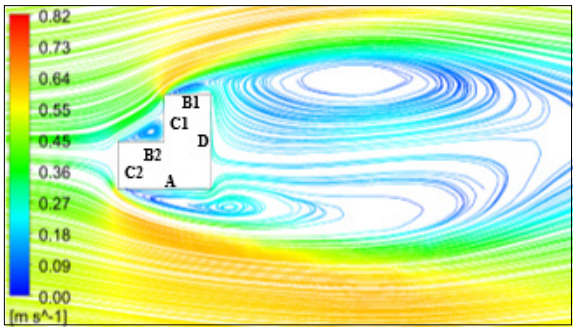
Figure 8 (m). C_{Pe} Contour on Faces for 180° Wind Angle



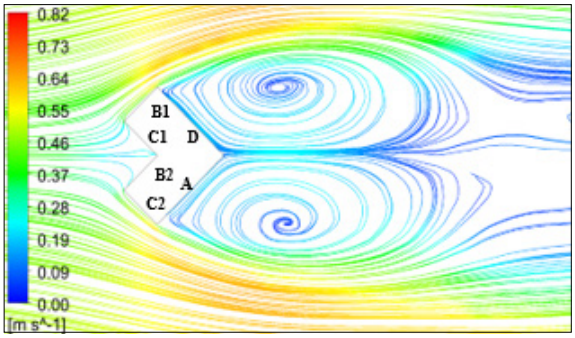
(a): Streamlines at 0° Wind Angle



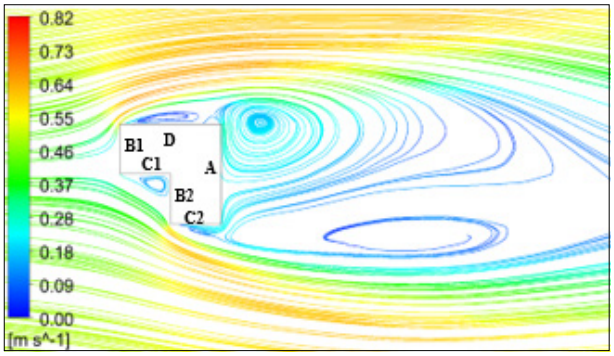
(b): Streamlines at 45° Wind Angle



(c) Streamlines at 90° Wind Angle



(d) Streamlines at 135° Wind Angle



(e) Streamlines at 180° Wind Angle

Figure 9. Streamlines L-Plan Shaped Model

Between wind incident angles of 0° and 60°, the inner faces B2 and C1 are under the wake. region, figure 9 (a) and (b), and hence coefficient of pressure on these faces are negative. Peak negative pressure coefficient (-1.50) occurs at wind incident angle of 45° on face B2. At wind incident angle of 75° the inner part near the re-entrant

corner of face C1 is subjected to suction due to formation of vortex in the region, but the outer part is subjected to positive pressure as the wind hits that region directly after separating from the outer edge of the wing face B2. Highly fluctuating pressure exists on both the inner faces B2 and C1 at wind incident 75°, figure 8 (f).

At 90° wind angle the inner faces B2 and C1 are subjected to positive pressure, figure 9 (c). On the inner part of face C1, positive pressure exits due to direct impact of wind. However, at the leading-edge suction occurs from where the wind separates. On face B2 the pressure is positive on its entire extent due to stagnation of flow at the re-entrant corner and recirculation of air from face C1. At wind incident angles between 105° and 135° the inner faces B2 and C1 are subjected to high wind pressure at the re-entrant corner. Variation of mean C_{Pe} with wind incident angles has been drawn in figure 10. At an angle of 135° a large area of stagnation occurs at the re-entrant corner. The size of this area of stagnation depends upon the height and the relative dimension of the wing faces B2 and C1. Under uniform dimension of the wing faces, the area of this stagnation zone increases with the increase in the height [25]. This is owing to the fact that the flow has a tendency to contour the sides rather than flow into the cavity. Greater the wing length of face B2, higher the blockage and hence greater the positive pressure on the wing face C1. It is a unique characteristic of L-plan shape building.

At wind incident angle greater than 135° face B1 starts experiencing positive pressure. As the wind incident angle increases, the positive pressure on face B1 increases. Peak negative coefficient of pressure on face B1 is observed to be – 1.67 at 105° wind angle. At an angle of 75° both the wing faces B2 and C1 are experiencing positive pressure and continue to be positive owing to the re-entrant corner effect. On face C2 suction occurs at 150° wind angle and continues to be up to 180° wind angle. However, peak negative coefficient of pressure is observed on face C2 to be -1.77 at 15° wind angle.

At 180° wind incident angle both the upwind faces B1 and B2 are subjected to positive pressure. But the pressure distribution is not symmetrical about the vertical center line of the faces, figure 8 (m), unlike in the case of rectangular model. The pressure increases from the left edge of face B1 towards its right edge i.e., towards the re-entrant corner of wing faces B2 and C1. This can be credited to blockage of air flow by the wing face B2 and stagnation of wind at the re-entrant corner. On face B2 positive pressure also exists being the windward face except at the leading edges from where flow separation takes place. The pressure increases along the height due to increase in wind velocity along the height. The phenomenon also affects the wing face C1 and positive pressure exits on its entire extent unlike in the rectangular model where suction occurs on the side faces. Due to separation of wind from the leading edges, the side faces D and C2 are subjected to suction pressure progressively increasing from the near edge to the far edge. The downwind face is subjected to suction. It can be observed that the effect of recirculation on the face is not symmetrical, figure 9 (e), unlike in the rectangular model.

The influence of wind incident angles on the wing faces B2 and C1 is shown in figure 11 in terms of central vertical C_{Pe} variations on faces. For clarity and understanding few wind incident angles are shown. It is observed that the pressure values on these faces are having a great influence of wind angles. It is noticed that there is little variation on suction along height whereas the positive pressure coefficient increases with height. The maximum value of C_{Pe} is found to be above the height of 0.8 Z where Z is the height of the model.

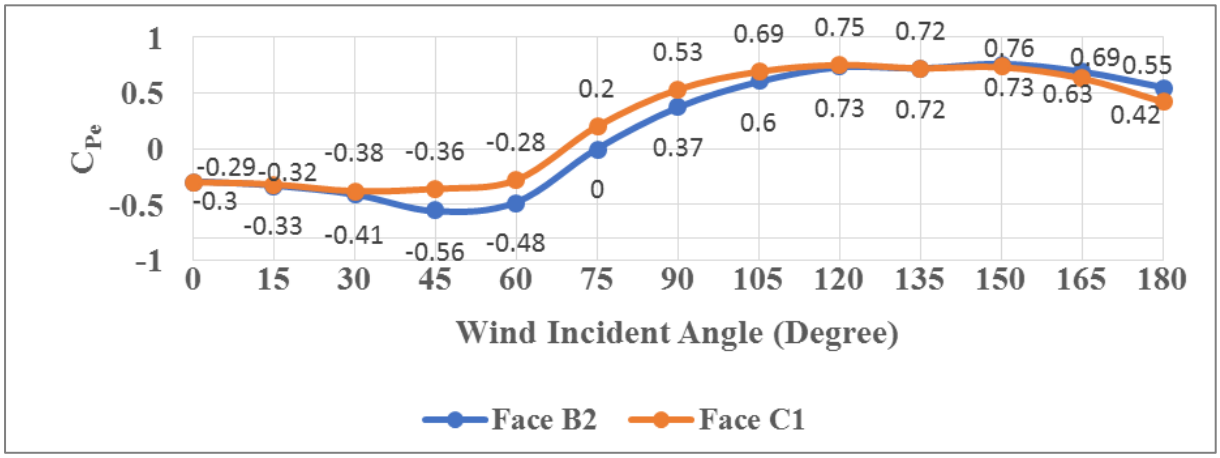
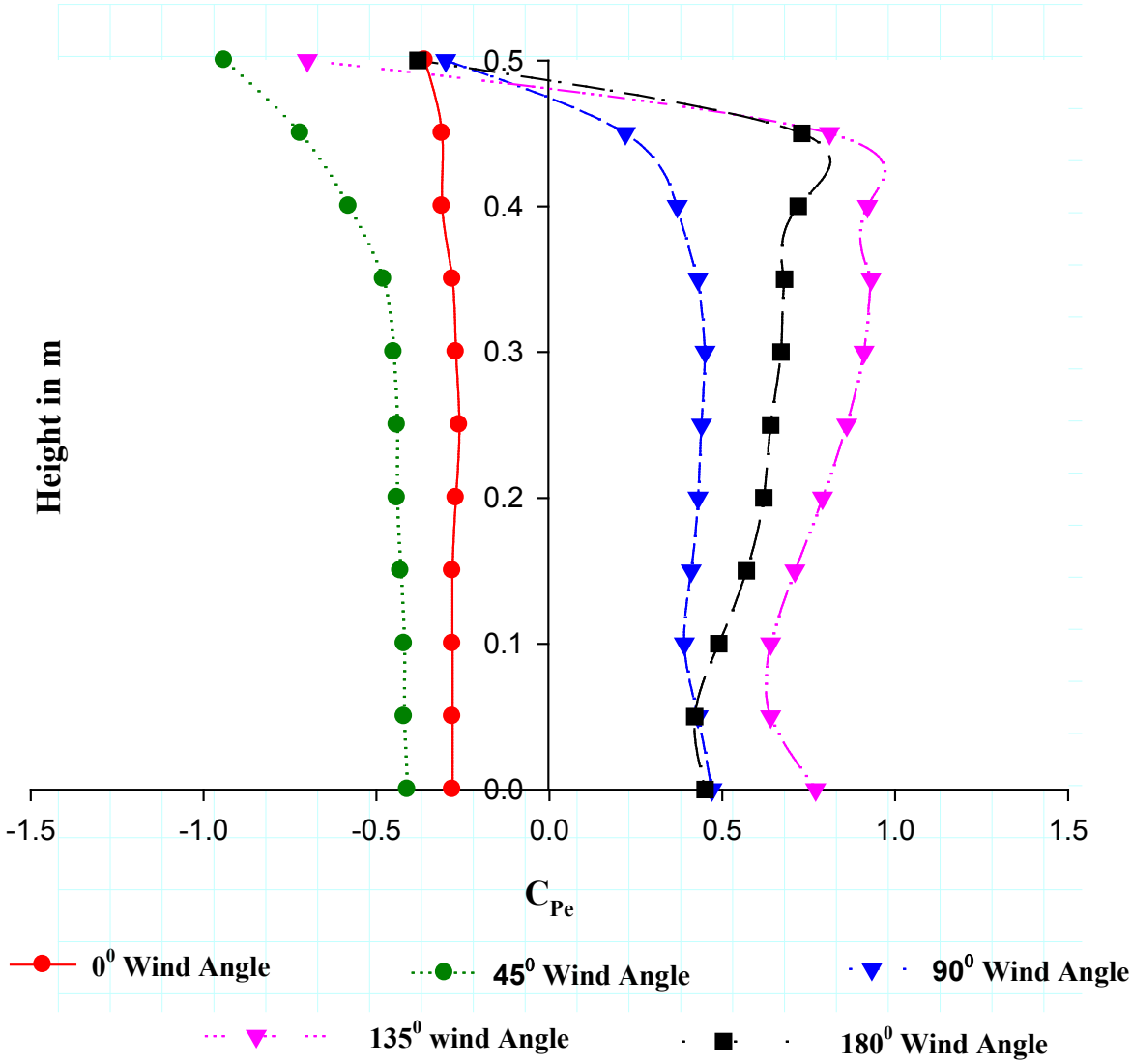
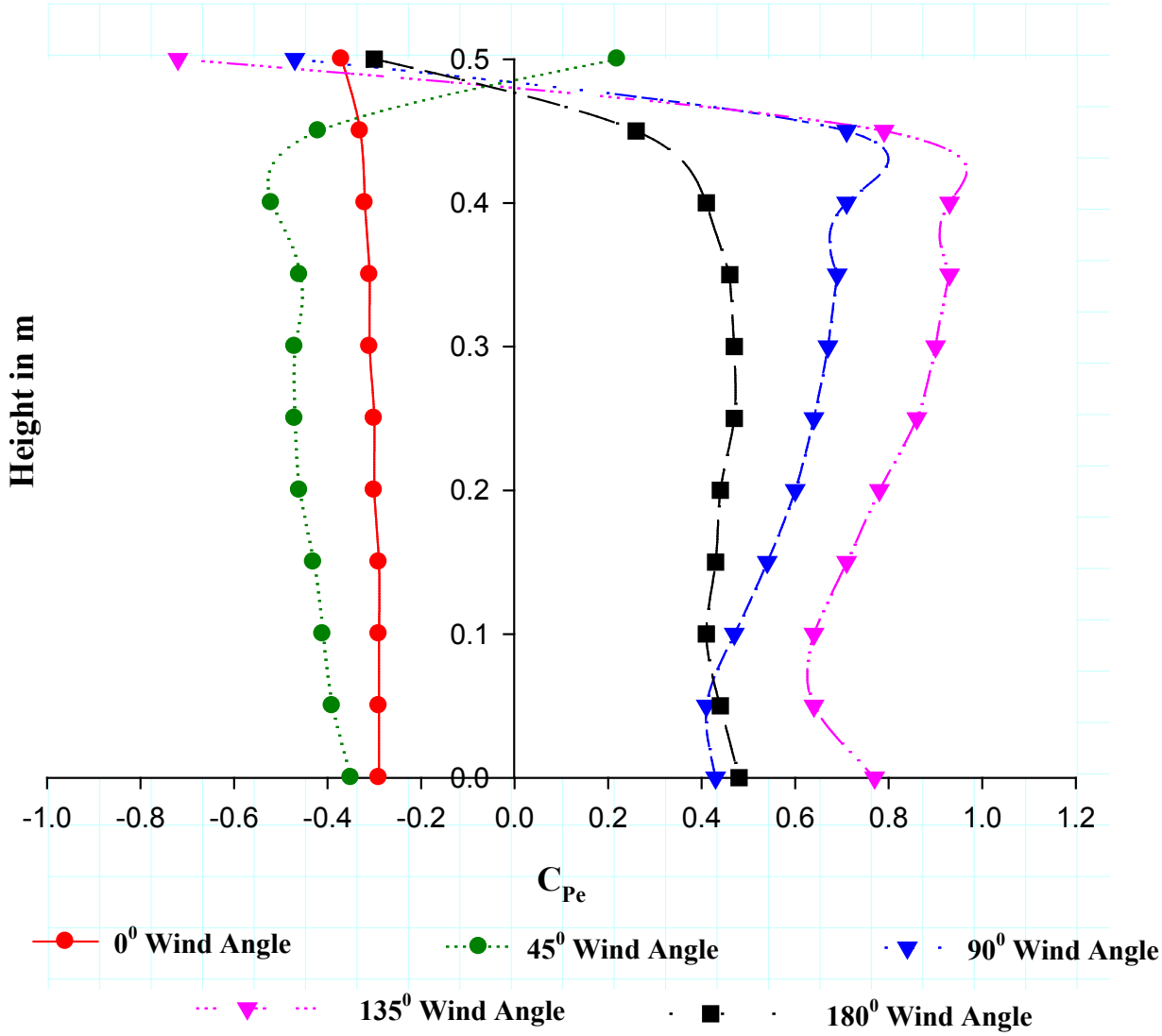


Figure 10. Variation of Mean C_{Pe} with wind angles on the re-entrant faces B2 and C1

Wind flow patterns for certain wind incident angles are shown in figure 9 (a) to (e). Flow separation and vortices can be seen from the flow patterns. It is observed that the vortices are not symmetrical as in the case of rectangular model, figure 7. Small vortex is created within the re-entrant corner for different wind angles other than where wind is directly hitting the corner (viz 135° wind angle). Streamlines along the central vertical plane for different wind incidence angles are shown in figure 12. The creation of upstream vortex near ground due to down wash of wind after hitting the windward face, flow separation from the leading edges, recirculation cavity at roof and vortex on the downstream side of the model can be visualized. It is noticed that the pattern and intensity of vortices created for different wind angles are different. Major difference is found between 'before 90°' wind incident angles and 'after 90°' wind incident angles. At 45° wind incident angle the recirculation cavity at roof does not appear.

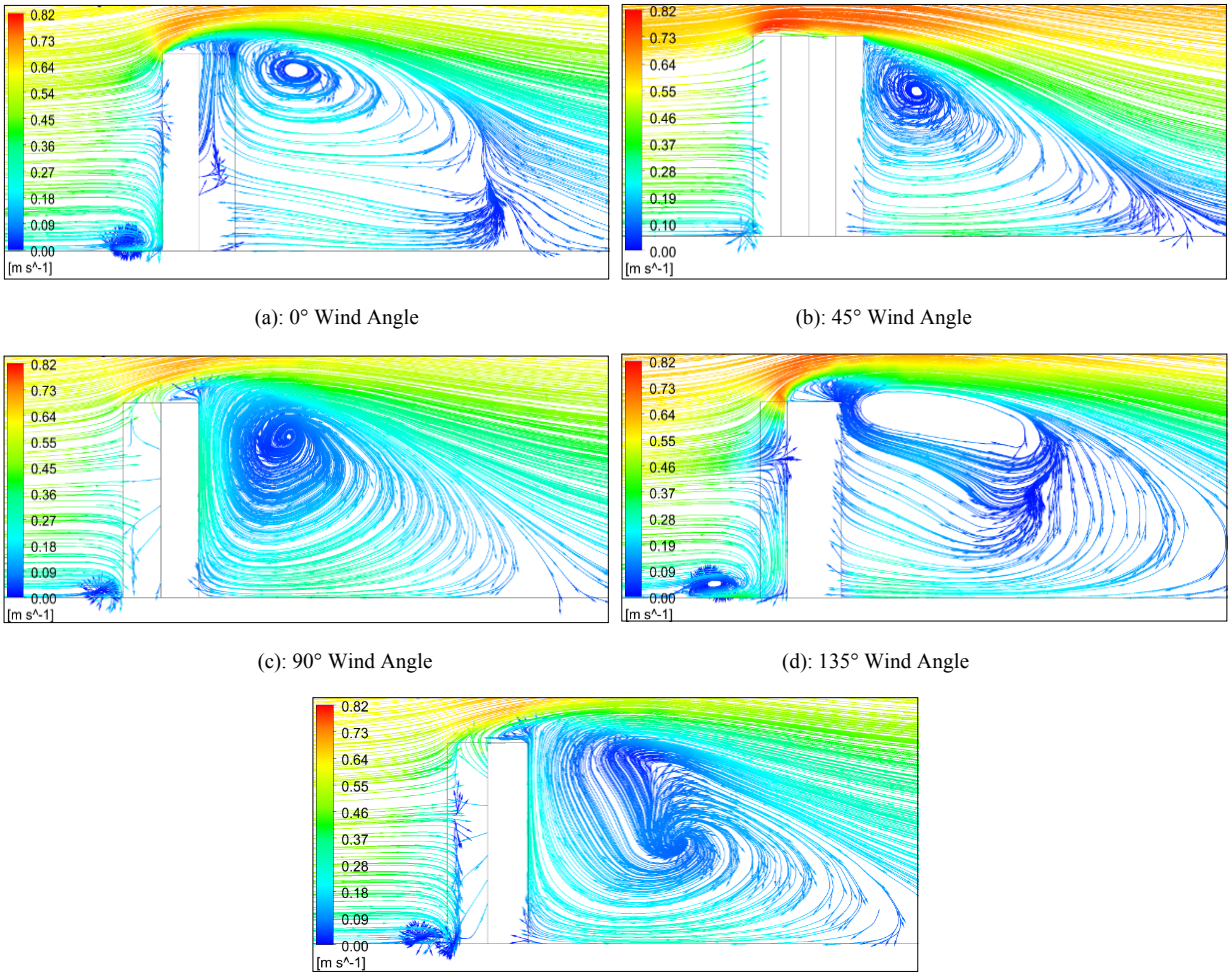


(a) Face B2



(b) Face C1

Figure 11. Variation of C_{Pe} Central Vertical on Face B2 and Face C1 with Wind Angle



(a): 0° Wind Angle

(b): 45° Wind Angle

(c): 90° Wind Angle

(d): 135° Wind Angle

(e): 180° Wind Angle

Figure 12. Streamlines along Wind Central on Vertical L-Plan Shaped Model

8. Conclusions

The present study shows that the wind incident angle has significant impact on the L shape building. For wind incident angles ranging 0° to 60° the re-entrant wing faces experience homogeneous suction pressure. Upon further increase of the wind incident angles between 75° to 180°, the pressure on the re-entrant wing faces increases due to stagnation of air. This is the unique characteristic of L shape buildings which plays an important role in design of cladding systems on re-entrant faces. The height of the building and the relative length dimensions of the wing faces play an important role in producing pressure on the wing faces.

Result of numerical simulation with standard k- ε model showed a good agreement in case of normal wind incident angle. However, some differences cannot be ruled out for other directions of wind angles due to the non-isometric unsteady three-dimensional flow behavior of wind. Denser mesh arrangement in the particular flow region and improved modelling for mapping the three-dimensional non isometric unsteady flow could enhance the quality of results. Nevertheless, the results obtained can provide useful information about wind pressure on re-entrant wing faces of L shape buildings for practical engineering calculations.

REFERENCES

[1] Baines W. D., "Effect of Velocity Distribution on Wind Loads on a Tall Building," 1952.

[2] Mohotti D., Mendis P., and Ngo Y. D., "Application of Computational Fluid Dynamics (CFD) in Predicting the Wind Loads on Tall Buildings - A Case study," in *23rd Australasian Conference of the Mechanics of Structures ma Materials (ACMSM23)*, Dec. 2014, pp. 1–6.

[3] Fu J. Y., Li Q. S., Wu J. R., Xiao Y. Q., and Song L. L., "Field measurements of boundary layer wind characteristics and wind-induced responses of super-tall buildings," *Journal of Wind Engineering and Industrial Aerodynamics*, vol. 96, no. 8–9, pp. 1332–1358, Aug. 2008, doi: 10.1016/j.jweia.2008.03.004.

[4] Tanaka H, Tamura Y, Ohtake K, Nakai M, Kim YC, and Bandi E K, "Experimental Investigation of Aerodynamic Forces and Wind Pressure Acting on Tall Buildings with Various Unconventional Configuration," *Journal of Wind Engineering and Industrial Aerodynamics*, vol. 107–108, pp. 179–191, 2013.

[5] Amin J.A and Ahuja A.K, "Effects of Side Ratio on Wind Induced Pressure Distribution on Rectangular Buildings," *Hindawi Publishing Corporation, J Struct*, pp. 1–12, 2013. doi: dx.doi.org/10.1155/2013/176739.

[6] Kushal T, Ahuja A.K, and Chakrabarti A, "An Experimental Investigation of Wind Pressure Developed in Tall Buildings for Different Plan Shape," *Int. J Innov Res Studies*, vol. 1, no. 12, pp. 605–614, 2013.

[7] Chakraborty S and Dalui S K, "Numerical Study of Surface Pressure on Square Plan Shape Tall Building," in *Symposium on sustainable infrastructure development (SID)*, Feb. 2013, pp. 252–258.

[8] Bhattacharyya B, Dalui S.K, and Ahuja A.K, "Wind Induced Pressure on 'E' Plan Shaped Tall Buildings," *Jordon J Civil Eng*, vol. 8, no. 2, pp. 120–134, 2014.

[9] Chakraborty S., Dalui S. K., and Ahuja A. K., "Experimental Investigation of Surface Pressure on '+' Plan Shape Tall Building," *Jordan Journal of Civil Engineering*, vol. 8, no. 3, pp. 251–261, 2014.

[10] Kheyari P. and Dalui S.K., "Estimation of Wind Load on a Tall Building under Interference Effect," *Jordon J Civil Eng*, vol. 9, no. 1, pp. 84–101, 2014.

[11] Roy K., and Bairagi A. K., "Wind Pressure and Velocity Around Stepped Unsymmetrical Plan Shape Tall Building Using CFD Simulation—A Case Study," in *Asian J. Civil Eng. (BHRC) 17*, 2016, vol. BHRC, no. 17, pp. 1055–1075.

[12] Mukherjee A., and. Bairagi A. K., "Wind Pressure and Velocity Pattern Around 'N' Plan Shape Tall Building- A Case Study," in *Asian J. Civil Eng*, 2017, pp. 1241–1258.

[13] Bairagi A.K., and Dalui S.K., "Distribution of Wind Pressure Around Different Shape Tall Building," *Advances in Structures, System and Material*, pp. 31–38, 2020.

[14] Pal S., and Ritu Raj, "Evaluation of Wind Induced Interference Effects on Shape Remodeled Tall Buildings," *Arabian Journal for Science and Engineering (Online Publication)*, 2021.

[15] Ritu Raj and Ahuja. A.K., "Wind Loads on Cross Shape Tall Buildings," *JAIR*, vol. 2, no. 2, 2013.

[16] Ritu Raj, Rana T., Anchalia, and Khola U., "Numerical Study of Wind Excited Action on H Plan-Shaped Tall Building," *International Journal of Emerging Technologies*, vol. 11, no. 3, pp. 591–605, 2020.

[17] Pal S., Ritu Raj, and Anbukumar S., "Comparative Study of Wind Induced Mutual Interference Effects on Square and Fish-plan Shape Tall Buildings," *Sadhana (Indian Academy of Science)*, pp. 46–86, 2021.

[18] Nagar S. K., Ritu Raj, and Dev N., "Experimental study of wind-induced pressures on tall buildings of different shapes," *Wind and Structure*, vol. 31, no. 5, pp. 441–453, 2020.

[19] Kumar A., and Ritu Raj, "Study of pressure distribution on an irregular octagonal plan oval-shape building using cfd," *Civil Engineering Journal (Iran)*, vol. 7, no. 10, pp. 1787–1805, Oct. 2021, doi: 10.28991/cej-2021-03091760.

[20] Stathopoulos T., "Numerical Simulation of Wind-induced Pressure on Buildings of Various Geometries," *J. Wind Engg. Indus. Aerodynam*, vol. 46 & 47, pp. 419–430, 1993.

[21] Gomes M. G., Moret Rodrigues A., and Mendes P., "Experimental and numerical study of wind pressures on irregular-plan shapes," *Journal of Wind Engineering and Industrial Aerodynamics*, vol. 93, no. 10, pp. 741–756, 2005, doi: 10.1016/j.jweia.2005.08.008.

[22] Amin J.A and Ahuja A.K, "Experimental Study of Wind-induced Pressure on Buildings of Various Geometries," *Industrial Journal of Engineering Science and Technology*, vol. 3, no. 5, pp. 1–19, 2011.

[23] Revuz J, Hargraves D. M, and Owen J.S., "On the Domain Size for the Steady State CFD Modelling of a Tall Building," *Wind Structure*, vol. 15, no. 4, pp. 313–329, 2012.

[24] Franke J., et al., "Impact of wind and storm on city life and built environment," *Recommendation on the use of CFD in Wind Engineering. In: COST action C14*, vol. Version 1.0, pp. 1–12, 2004.

[25] Cook N. J., *The Designer's Guide to Wind Loading of Building Structures. Part 2: Static Structures*. London: Butterworths Press, 1985.

View publication stats

ResearchGate

See discussions, stats, and author profiles for this publication at: https://www.researchgate.net/publication/358637307

CNFMD: Convolutional Network-based Face Mask Detection

Article · February 2022

DOI: 10.30574/wjarr.2022.13.2.0142

CITATIONS
0

READS
3

1 author:



Saksham Checker
Delhi Technological University
2 PUBLICATIONS **0** CITATIONS

SEE PROFILE

All content following this page was uploaded by Saksham Checker on 16 February 2022.

The user has requested enhancement of the downloaded file.

World Journal of Advanced Research and Reviews
eISSN: 2581-9615 CODEN (USA): WJARAI
Cross Ref DOI: 10.30574/wjarr
Journal homepage: https://wjarr.com/

(RESEARCH ARTICLE)

Check for updates

CNFMD: Convolutional Network-based Face Mask Detection

Saksham Checker *

Student, Department of Applied Physics, Delhi Technological University, New Delhi, India.

World Journal of Advanced Research and Reviews, 2022, 13(02), 232–238

Publication history: Received on 07 January 2022; revised on 09 Februay 2022; accepted on 11 Februay 2022

Article DOI: https://doi.org/10.30574/wjarr.2022.13.2.0142

Abstract

After the rise of the coronavirus, every country has made a compulsion on wearing face masks in public places. Even though a few countries have reached a good number of vaccinations to date, the human body is still not immune to the new variants of the virus. It will take a few more years till everyone becomes mask-free. Thus, authorities need a system to keep a proper check on the discipline whether everyone is wearing a mask in a public place or not. This paper proposes a model with 99.5% accuracy which can be deployed and thus can monitor public places. This will help the authorities to control the spread of the virus. The model proposed is a fast model which took only 38.03 seconds on average per epoch while training. Using the Kaggle dataset, the CNFMD model is trained and tested. The dataset, pre-split into three parts is used from training, validation as well as testing of the model.

Keywords: Machine Learning; Deep Learning; COVID-19; Face Mask

1. Introduction

Face masks have become a need for human life after the breakout of SARS-Cov2 also knows as the Coronavirus. Virus and Bacteria transmission can be prevented with the use of face masks along with social distancing, and proper sanitation [1]. Many studies thus suggest that during transportation, one must wear a mask to prevent the transmission of disease from themselves to others and vice-versa [1]. Studies suggest that the COVID-19 can spread with immediate contact between two people (nearly 6 feet). It can also spread to people who do not have symptoms [2]. Further, many reasons show that the virus could be air-borne, making Face Masks a must for everyone while traveling or working [3].

Face mask detection has become the latest field of study such that it can be assured that people are wearing face masks in public areas. This paper proposes a new CNFMD model to detect whether a person is wearing a face mask or not. For training the model, a dataset having around twelve thousand images is used divided into three parts-train, validation, and test [4].

In this paper, section 2 summarizes the previous work done by other authors in the field of face mask detection. Section 3 and section 4 give the proposed methodology and experimental results of the model which are all concluded in section 5.

2. Related Works

Since the outbreak of the virus, many pieces of research have been carried out to detect face masks and have also been applied to assure that the spread of the virus is limited reducing the number of cases as well as deaths among the people.

* Corresponding author: Saksham Checker
Student, Department of Applied Physics, Delhi Technological University, New Delhi, India.

Copyright © 2022 Author(s) retain the copyright of this article. This article is published under the terms of the Creative Commons Attribution Liscense 4.0.

The letter [1], shows a case study when a patient can infect 39 passengers during bus travel of 2 hours and 10 minutes whereas in a mini-bus, the patient can affect 14 other passengers for 50 minutes because the patient was not wearing a mask. The authors also refer to the study where 65.7% of healthcare workers agree that face masks can prevent the transmission of the virus.

Further, the study [2] proposed a residual network(ResNet) for extracting features, followed by classic machine learning techniques like SVM, Decision trees, and ensemble to detect the face masks. The researchers removed the last layer of ResNet and replaced it with three Machine learning classification layers. They used three datasets, RMFD, SMFD, and LFW where the dataset was split into train, validation, and testing as 70%, 10%, and 20% respectively. They also explained the Machine learning Layers which were applied in detail. Their proposed hybrid work achieved 99.64% accuracy using SVM on the RMFD dataset, whereas 99.49% and 100% accuracy on SMFD and LFW datasets.

A real-time study, SSDMNV2 [5] proposed a face mask detection model where the DNN module of OpenCV was used with ResNet-10 as the backbone. Further, the pre-trained model of MobileNetV2 was used to predict. They used an artificially created dataset by Prajna Bhandary. They explain the building of the MobileNetV2 model layer by layer. Their proposed model had a better F-1 score compared to the ResNet model. While detection of Faces using OpenCV DNN, it was established on the Single Shot Multi-box detector which has two versions- CaffeImplementation and Original TensorFlow Implementation.

The authors of [6] proposed an object detection method, which combined the one-stage and two-stage detectors. They thus worked on cropping facial areas which can be used in their proposed model. The ResNet-50 pre-trained model was fine-tuned by the researchers to check the performance. They used the images available at Kaggle to train and test their model. The train, test, and validation set was split up into a 64:40:16 ratio. They compared their model to AlexNet and MobileNet pre-trained models.

The latest study, [7], proposed a two-stage model. The first stage had the Face detector system where RGB image was taken as an input and a few pre-trained models were tested to detect the faces of people within the images. These models were trained on big datasets. Introducing stage two, which had the Face mask classifier. The detected faces from stage one were used in three known classification models- MobileNetV2, DenseNet121, and NASNet. After training, the best model was turned out to be the NASNetMobile model with 99.45% test accuracy.

Using the TensorFlow and Keras algorithms applied on datasets collected from Kaggle, authors of [8] proposed a system for face mask detection. They used 3918 images which were divided into two parts, with masks, and without masks. For classification, they implemented MobileNet and OpenCV. Their dataset had 3918 images which trained and tested the model.

3. Proposed Methodology

To predict if a person is wearing a mask or not, a proper dataset of faces with and without a mask was used. The dataset was thus used to train the proposed CNFMD model. This section explains the contents of the dataset, the building blocks of the CNFMD model, and also the algorithm of the model proposed.

3.1. Dataset used

As there has been only a year and a half since the outbreak of the virus and the importance of masks to stay protected from the deadly virus, there are not many datasets available compared to other fields of studies. The dataset published on Kaggle [4] is used to train and test our model.

The dataset consists of a total of 11,792 images as shown in Figure 1. The images are pre-divided in the dataset with 10000 images equally divided into the two-class labels – WithMask and WithoutMask, in the train set, 992 images in the test set with 483 as WithMask and 509 as WithoutMask, and the last set, Validation, having 800 images equally divided in the two labels. The images in all the sets are real-life images such that the model thus formed can be used in the future.

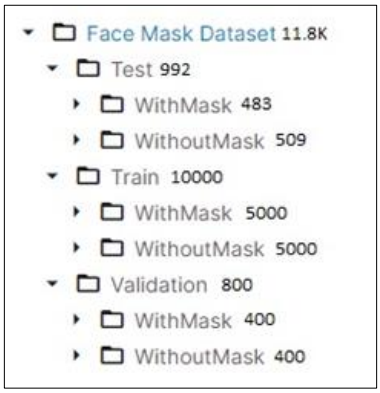


Figure 1 Data Directory

Figure 2 shows the WithMask images from the Train dataset, whereas Figure 3 shows WithoutMask images from the same dataset. It can be observed that there are images from different shapes

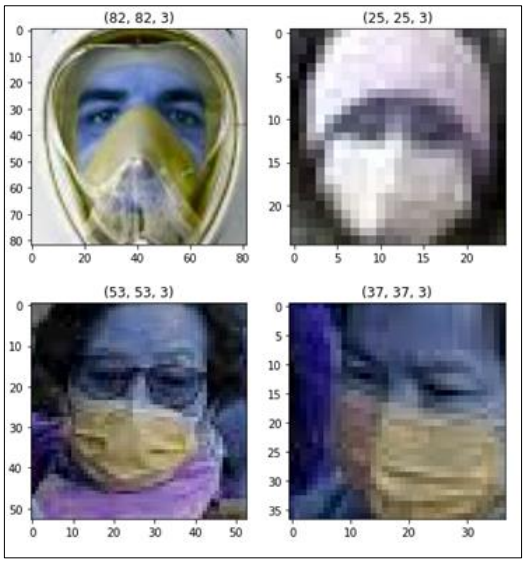


Figure 2 With Mask Images

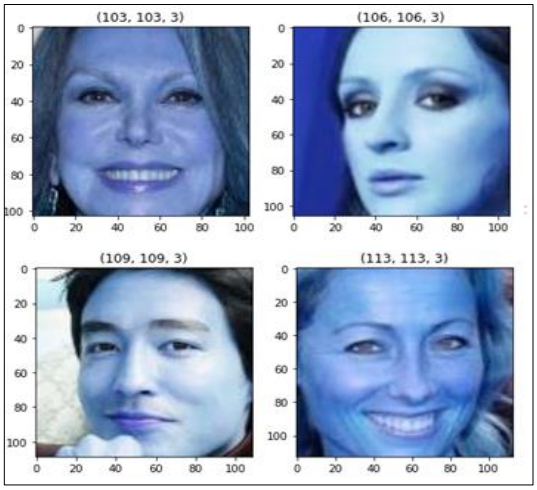


Figure 3 Without Mask Images

3.2. Building Blocks of CNFMD

3.2.1. Convolutional Layer

This is the fundamental block of CNN networks. Convolution is a combination of two functions to get a new function. Features are generated from an image using this layer. Figure 3 shows how the convolution process is done. The generated feature maps are thus processed further. Equation 1 shows the function with A being input matrix, and B as kernel to give output C [5][9][10].

$$C(T) = (A \times B)(x) = \int_{-\infty}^{\infty} A(T) \times B(T - x) \times dT \quad (1)$$

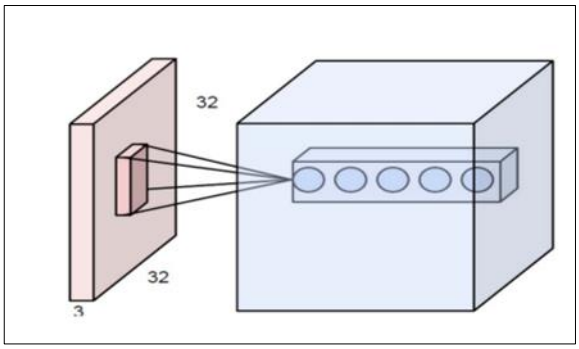


Figure 4 Convolutional Process

3.2.2. Non-Linear Layer

These layers follow the convolutional layers and are known as activation functions. In the CNFMD, ReLU activation is applied and is represented in Equation 2 [5][10].

$$ReLU: f(x) = \max(0, x) \quad (2)$$

3.2.3. Pooling Layer

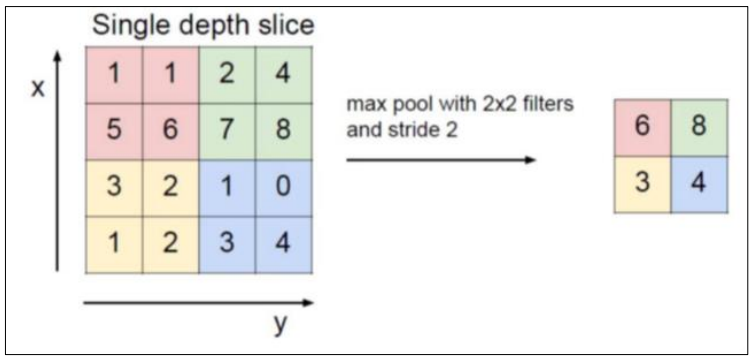


Figure 5 Max Pooling Process

Pooling works on the concept of down-sampling. It reduces the complexity of further layers. It can be compared to the process of reducing the resolution in images. Several filters are not affected by the pooling methods. MaxPooling is the most common type and it is the one that is applied in the proposed CNFMD model. Figure 5 shows the process of Maxpooling with 2x2 filters and stride as 2 [10] [5].

3.2.4. Data Augmentation

In data augmentations, images are applied with a few techniques to generate a larger dataset from the given one and thus for getting a better model for the problem [11]. In this study, augmentation techniques used are - rescale, rotation_range , width_shift_range , height_shift_range, shear_range , zoom_range and horizontal_flip.

3.2.5. Model Visualization

Using the layers mentioned above, the CNFMD model is formulated as shown in figure 6 below. The model takes an input of shape 82,82,3 and at the output, classifies the image as WithMask or WithoutMask image.

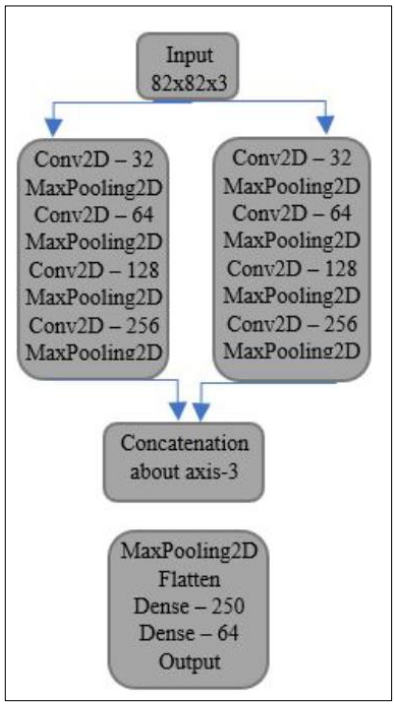


Figure 6 Model Design

With the generated model and defined layers, a final algorithm is thus proposed mentioned as algorithm 1.

ALGORITHM: Pre-processing and Training on Dataset

INPUT: Images along with their pixel values.

OUTPUT: Trained Model

- **STEP 1:** Loading images from the train folder.
- **STEP 2:** Load labels from the folder.
- **STEP 3:** Process the images, i.e., resizing, normalization of images.
- **STEP 4:** Perform Data augmentation and split the data into training and validation batches.
- **STEP 5:** Train the formulated CNFMD model on training batches.
- **STEP 6:** Save the model for the future.

4. Experimental Results

The generated model was trained on Kaggle Notebook Kernel having 13 GB of RAM and 16 GB of GPU memory. The images were loaded using the ImageDatagen where data augmentation was also done, for train dataset as follows- rescale=1. / 255, rotation_range = 10, width_shift_range = 0.2, height_shift_range = 0.2, shear_range = 0.2, zoom_range = 0.2. Whereas, test and validation set was just rescaled with 1./255.

The model was thus compiled using Adam as an optimizer. Metrics used to check the performance were Accuracy (Equation 3) and Binary cross-entropy /Log loss (Equation 4).

$$Accuracy = \frac{(TP+TN)}{(TP+TN+FP+FN)} \quad (3)$$

$$\log loss = -\frac{1}{N}\sum_{i=1}^{N} -(\log(p_i)) \quad (4)$$

Here, TP is True Positive, FP is False Positive, TN is True Negative and FP is False Negative from equation 3 and N is the number of data entries, and p_i is corrected probability.

The model was trained with 50 epochs. It took a total time of 1904 seconds with an average of 38.08 seconds per epoch. As seen in figures 7 and 8 model accuracy for both Train and Validation increased and Loss was decreased. Table 1 shows the experimental results of the model after 50 epochs

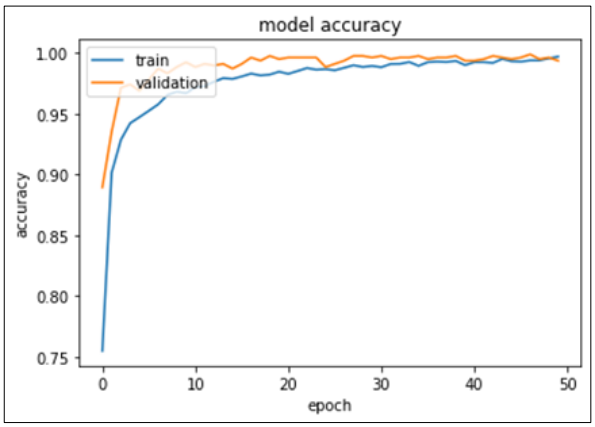


Figure 7 Model Accuracy

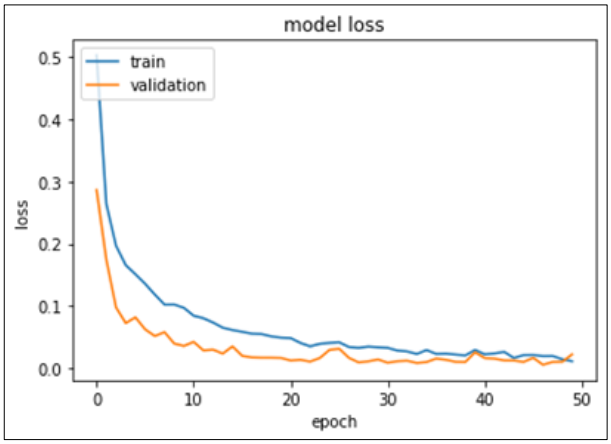


Figure 8 Model Loss

Table 1 Experimental results of CNFMD model

SN.	Dataset	Accuracy	Loss
1	Train	0.9970	0.0106
2	Validation	0.9935	0.0221
3	Test	0.9950	0.0262

5. Conclusion

As face masks will be an important part of human life for the next few years, authorities can use these models for real-time tracking of people without wearing masks and could educate them with the same. It was observed that the CNFMD

model gave good accuracy and minimal log loss on all three datasets. Test accuracy was turned out to be 99.50% which is very good on a real-life dataset

In the future, face recognition with face masks can be implemented and this model can be deployed using real-time cameras and thus can be used in public places. The research can further be broadened to detect people with face masks not worn properly.

Compliance with ethical standards

Acknowledgments

There is no external funding or institution involved in this study.

Statement of informed consent

The study doesn't include any work that requires consent.

References

[1] X. Liu and S. Zhang, "COVID-19: Face masks and human-to-human transmission," *Influenza Other Respi. Viruses*. 2020; 14(4): 472–473.

[2] M Loey, G Manogaran, MHN Taha, NEM Khalifa. "A hybrid deep transfer learning model with machine learning methods for face mask detection in the era of the COVID-19 pandemic," *Meas. J. Int. Meas. Confed.* July 2020; 167: 108288.

[3] T Greenhalgh, JL Jimenez, KA Prather, Z Tufekci, D Fisman, R Schooley. "Ten scientific reasons in support of airborne transmission of SARS-CoV-2," *Lancet*. 2021; 397: 10285 1603–1605.

[4] A Jangra, "Face Mask Detection ~12K Images Dataset." 2020, [Online].

[5] P Nagrath, R Jain, A Madan, R Arora, P Kataria, J Hemanth. "SSDMNV2: A real time DNN-based face mask detection system using single shot multibox detector and MobileNetV2," *Sustain. Cities Soc.* Mar. 2021; 66: 102692.

[6] S Sethi, M Kathuria, T Kaushik. "Face mask detection using deep learning: An approach to reduce risk of Coronavirus spread," *J. Biomed. Inform.* September 2020; 120; 103848.

[7] A Chavda, J Dsouza, S Badgujar, A Damani. "Multi-Stage CNN Architecture for Face Mask Detection," *2021 6th Int. Conf. Converg. Technol. I2CT. 2021*; 1–8.

[8] K Suresh, MB Palangappa, S Bhuvan. "Face Mask Detection by using Optimistic Convolutional Neural Network," *Proc. 6th Int. Conf. Inven. Comput. Technol. ICICT.* 2021; 1084–1089.

[9] Y Li *et al.* "Robust detection for network intrusion of industrial IoT based on multi-CNN fusion," *Meas. J. Int. Meas. Confed.* 2020; 154: 107450.

[10] S Albawi, TA Mohammed, S Al-Zawi. "Understanding of a convolutional neural network," *Proc. 2017 Int. Conf. Eng. Technol. ICET. 2017*, 2018-Janua, 1–6.

[11] C Shorten, TM Khoshgoftaar. "A survey on Image Data Augmentation for Deep Learning," *J. Big Data*. 2019; 6(1).

View publication stats

2021 5th International Conference on Electrical, Electronics, Communication, Computer Technologies and Optimization Techniques (ICEECCOT) 10-11, December 2021

2021 5th International Conference on Electrical, Electronics, Communication, Computer Technologies and Optimization Techniques (ICEECCOT) | 978-1-6654-3272-6/21/$31.00 ©2021 IEEE | DOI: 10.1109/ICEECCOT52851.2021.9707944

CNTFET based Transmission Gate Diffusion Input Logic (C-TGDI) design

Neetika Yadav a,b
a.*Department of Electronics and Communication Engineering, Delhi Technological University*,
Delhi, 110042, India
b.*Amity Institute of Space Science and Technology, Sector 125,*
Noida 201303, India
yadav.neetika92@gmail.com

Neeta Pandey
Department of Electronics and Communication Engineering, Delhi Technological University,
Delhi, 110042, India
n66pandey@rediffmail.com

Deva Nand
Department of Electronics and Communication Engineering, Delhi Technological University,
Delhi, 110042, India
devkamboj07@gmail.com

***Abstract*— This paper proposes Transmission Gate Diffusion Input (TGDI) based design using Carbon Nano tube Field Effect Transistors (CNTFETs). The performance of proposed design is analyzed for 2-input gates, 2:1 multiplexer(MUX), 1-bit full adder and 2-bit Ripple Carry Adder (RCA) in terms of delay, power and Power Delay Product (PDP). Simulative investigation is done at 32nm using HSPICE tool and comparison of performance of the proposed with GDI based CNTFET counterparts. Analysis of result shows that TGDI based CNTFET circuits offer benefits of less power and delay resulting in reduction of overall PDP in comparison with GDI based CNTFET circuits. A maximum PDP reduction of 77.23% and 81.92% for 2-input gates and multiplexer is achieved using the proposed approach respectively as compared to their GDI counterparts. Corresponding values are 67.79% and 21.35% for a 1-bit full adder and 2-bit RCA circuit respectively.**

Keywords— Adder, CNTFET, GDI, TGDI

I. INTRODUCTION

Technology scaling is one of the most effective methods for enhancing efficiency of digital circuits, however this poses multiple challenges in Complementary Metal Oxide Semiconductor (CMOS) based designs[1].Scaling silicon transistors like MOSFET causes a slew of issues, such as increased current leakage, reduced gate control, short channel effects and a rise in power consumption[2].As a consequence, researchers are considering new digital circuit design technologies and logic styles. Quantum Dot Cellular Automata (QCA) [3-4],Multi Gate Field Effect Transistor (MUGFET) [5],Single Electron Transistor (SET) [6]and CNTFETs[7-19] are some of the emerging new technologies. Out of these, CNTFET has been considered as a suitable alternative for conventional MOSFET as it offers electrical characteristics such as low-resistivity, high electron mobility, high current density, long electron mean-free paths and high thermal conductivity[7-10]. CNTFETs exhibit great similarity with traditional CMOS devices in terms of operating principle and device structure[10-11]. A wide range of logic styles have been implemented in CNTFET like CMOS[12], Complementary Pass Logic (CPL)[13], CNTFET based domino[14-15], Transmission Gate- Carbon Nanotube Field Effect Transistor (TG-CNFET)[16-17] and found to have better Power Delay Product (PDP) as compared to conventional MOS [12-17].

Recently Gate Diffusion Input (GDI) logic style is implemented using CNTFETs which offers benefits of low power and high-speed[18-19].For specific input combinations, output swing is decreased in GDI logic. To solve this problem, an additional buffer stage is required, which increases power consumption[18-19]. To overcome these disadvantages, a new design based on transmission gates using CNTFETs is presented in this contribution. This design uses CNTFETs based transmission gates to modify GDI based design. The proposed novel design is referred to as C-TGDI.

The paper is divided into four sections: overview of CNTFET and TGDI is given in section 2. Section 3 elaborates the proposed CNTFET based TGDI design. In section 4, simulation results for 2-input gates, 2:1MUX , full adder and 2-bit Ripple Carry Adder (RCA) are stated. The conclusion of this contribution is placed in section 5.

II. OVERVIEW OF CNTFET AND GDI

A carbon nanotube (CNT) is a rolled-up sheet of graphite which is wrapped around a vector, which is referred to as Chirality vector, determined by (n,m) indices[20].Based on the number of cylinders present, a CNT can be classified as Single Walled Carbon nanotube (SWCNT) or Multi Walled Carbon nanotube (MWCNT)[20].Depending on the chirality vector, a single-walled carbon nanotube (SWCNT) can be metallic or semiconducting[9].The SWCNT is conducting if the expression n-m evaluates to 3i (i € Z), else it is semiconducting[9-10].The channel in CNFETs is made up of semiconducting SWCNTs. The chirality vector and diameter of the CNT determine the CNTFET's threshold voltage (V_{th}), given by equation 1[20] below:

$$Vth = \frac{0.43}{DCNT(nm)} (1)\ [20]$$

where DCNT is the diameter of CNT in nm

A CNTFET based GDI cell is shown in Fig.1, it consists of three inputs- G, P and N and one output, OUT. G node is the gate input for PCNT and NCNT, P node is PCNT's source input, and N node is NCNT's source input. The drain

Authorized licensed use limited to: DELHI TECHNICAL UNIV. Downloaded on February 24,2022 at 06:55:31 UTC from IEEE Xplore. Restrictions apply.

terminals of PCNT and NCNT are connected to get the output, OUT.

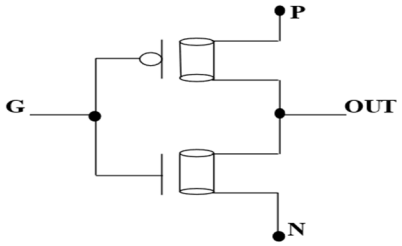


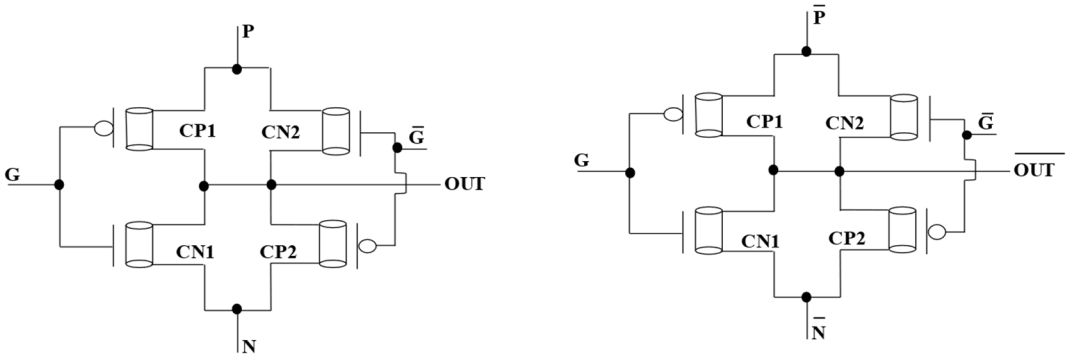
Fig.1. *CNTFET based GDI cell*

This cell is used to get various logic functions by applying different inputs to G, P and N[18].The GDI approach is useful for constructing low-power and fast circuits using only two transistors[19]. However, this logic suffers from problem of low output voltage swing. Because GDI only employs a single NMOS or PMOS transistor while charging or discharging, switching speed degrades significantly.

III. PROPOSED CNTFET BASED TGDI DESIGN

The proposed CNTFET based TGDI cell is shown in Fig.2 with or without complementary outputs. CNTFET based TGDI cell without complementary outputs is shown in Fig.2(a),it consists of G, $\overline{G}$, P and N as inputs. Each CNTFET transistor of GDI cell is replaced with two CNTFETs to get TGDI structure. G and $\overline{G}$ are common gate inputs of transistors (CP1,CN1) and (CP2,CN2) respectively. Source of transistor CP1 and drain of transistor CN2 are connected together to get input, P. Similarly, source of CN1 and drain of CP2 are connected to get input, N.By applying different inputs to G,$\overline{G}$, P and N, this cell is used to get various logic functions as tabulated in table 1.Complementary output of a given logic function can be obtained by taking complementary inputs G,$\overline{G}$, $\overline{P}$ and $\overline{N}$ as shown in Fig.2(b).

A C-TGDI based AND gate with inputs A and B is shown in Fig.3 with P input as ground (GND), N input as B and input G as A.Consider the case when input A and B are HIGH, the lower half of C-TGDI AND gate is on, which leads to charging of output node, OUT to logic HIGH. Similarly, the output node is discharged to LOW when input A and B are LOW as the upper half of C-TGDI cell becomes on.



(a) (b)

Fig. 2. (a) *C-TGDI cell*(b) *C-TGDI cell with complementary outputs*

TABLE I. TRUTH TABLE OF C-TGDI CELL

N	P	G	GBAR	OUT	FUNCTION
0	B	A	A’	A’B	F1
B	1	A	A’	A’+B	F2
1	B	A	A’	A+B	OR
B	0	A	A’	AB	AND
C	B	A	A’	A’B+AC	MUX

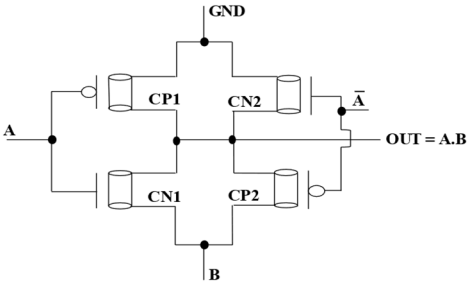


Fig.3. *C-TGDI based AND gate*

Authorized licensed use limited to: DELHI TECHNICAL UNIV. Downloaded on February 24,2022 at 06:55:31 UTC from IEEE Xplore. Restrictions apply.

IV. SIMULATION RESULTS

The two input gates, 2:1 MUX , 1-bit full adder and 2-bit RCA are simulated using CNTFET based GDI and proposed C-TGDI based technique using Stanford 32nm model for CNTFETs with 1fF load capacitance. HSPICE tool is used for simulation at 0.9 V supply voltage with CNT diameter of 1.487 nm for all CNTFETs.Values of delay, average power and PDP are obtained for all the circuits. This section consists of two subsections. Various logic functions results are discussed in one subsection while the implementation of 1-bit full adder and 2-bit RCA is demonstrated and analysed in another subsection.

A. LOGIC FUNCTIONS

The delay, average power and PDP values for 2-input gates- AND, OR, ABARB, ABARPLUSB, XOR and 2:1 MUX are tabulated in table 2. As observed from table 1, the proposed C-TGDI approach is beneficial for reducing the circuit's delay, power and PDP. For 2-input gates, the proposed technique has PDP reduction up to 77.23% and for 2:1 MUX, corresponding value is 81.92%.

B.1-BIT FULL ADDER AND 2-BIT RCA

The schematic of the implemented 1-bit full adder circuit and 2-bit RCA is shown in Figs.4 and 5 respectively.The 1-bit full adder circuit has inputs- A, B and Cin and outputs as Carry and Sum. The 2-bit RCA has 2-bit inputs A(A1,A0) and B (B1,B0) and S0, S1, C_{out} as outputs. S0 and S1 input represent LSB and MSB bits of sum output and C_{out} denotes carry output , as demonstrated in Fig.5.The values of delay, power and PDP for GDI based 1-bit full adder and 2-bit RCA designwith complementary outputs and the proposed C-TGDI designs are tabulated in table 3 . Using the proposed approach, PDP reduction of 67.79% and 21.35% for a 1-bit full adder and 2-bit RCA circuit respectively is achieved.

The percentage PDP reduction achieved for 2-input gates, 2:1 MUX, 1-bit full adder and 2-bit RCA circuits using the proposed novel design is shown in Fig.6.As demonstrated in Fig.6, a maximum PDP reduction of 81.92% and minimum PDP reduction of 12.35% is obtained using the C-TGDI design, which proves the efficacy of the proposed work.

TABLE II. DELAY, POWERAND PDP VALUES FOR 2-INPUT

	DELAY(ps)		POWER (uW)		PDP (aJ)	
	GDI	C-TGDI	GDI	C-TGDI	GDI	C-TGDI
AND	0.93	0.57	50.7	52	46.9	29.48
OR	0.94	0.58	50.5	52.1	47.62	30.01
ABARB	0.52	0.45	110	28.9	56.98	12.98
ABARPLUSB	0.51	0.45	51.3	51.2	26.11	22.89
XOR	0.9	0.56	45.6	44.9	41.04	25.05
MUX	0.68	0.4	116.2	35.3	78.9	14.26

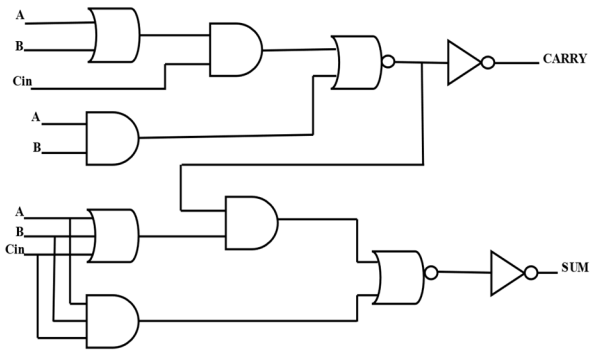


Fig. 4. *Schematic of1-bit full-adder [21]*

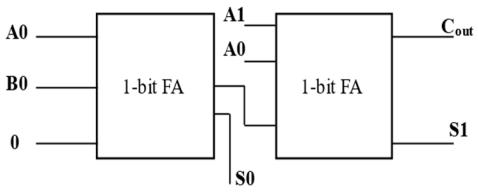


Fig. 5. *Schematic of2-bit RCA [22]*

Authorized licensed use limited to: DELHI TECHNICAL UNIV. Downloaded on February 24,2022 at 06:55:31 UTC from IEEE Xplore. Restrictions apply.

TABLE III. DELAYS, POWERAND PDP VALUES FOR 1-BIT FULL ADDER AND 2-BIT RCA

	1-bit Full Adder		2-bit RCA	
	GDI	C-TGDI	GDI	C-TGDI
DELAY(ps)	31.85	6.82	44.3	6.43
POWER (uW)	2.34	3.52	2.27	12.3
PDP (aJ)	74.53	24.01	100.56	79.09

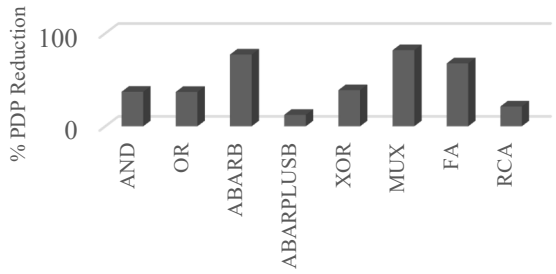


Fig. 6. *Percentage PDP reduction achieved for 2-input gates, 2:1 MUX, 1-bit full adder and 2-bit RCA*

V. CONCLUSION

A new technique based onTGDI using CNTFETs, referred to as C-TGDI is proposed in this contribution. The C-TGDI based design uses transmission gates for better performance in terms of delay, power and PDP. The proposed design is effective in reducing power, delay and PDP for various logic functions, 1-bit full adder and 2-bit RCA as indicated by simulation results. The percentage PDP reduction varies from 12.35 % to 81.92% for different circuits as compared to corresponding CNTFET based GDI circuits. It can be concluded that the presented work can be used for designing low power and high-speed circuits.

REFERENCES

[1] X. Jiang, Digitally-assisted analog and analog-assisted digital IC design. Cambridge, England: Cambridge University Press, 2015.

[2] A. Pal, Low-Power VLSI Circuits and Systems. New Delhi, India: Springer, 2016.

[3] H. Cho and E. E. Swartzlander, "Adder Designs and Analyses for Quantum-Dot Cellular Automata," IEEE Trans. Nanotechnol., vol. 6, no. 3, pp. 374–383, 2007.

[4] K. S S and K. Narasimha, "Quantum dot cellular automata (QCA) design for the realization of basic logic gates," International Conference on Electrical, Electronics, Communication, Computer, and Optimization Techniques (ICEECCOT), pp. 314–317, 2017.

[5] V. Subramanian, "Multiple gate field-effect transistors for future CMOS technologies," IETE Tech. Rev., vol. 27, no. 6, p. 446, 2010.

[6] S. Kanjanachuchai and S. Panyakeow, "Beyond CMOS: single-electron transistors,"IEEE International Conference on Industrial Technology, vol. 2, pp. 1219–1222, 2003.

[7] W. Hoenlein et al., "Carbon Nanotube Applications in Microelectronics," IEEE trans. compon. packag. technol., vol. 27, no. 4, pp. 629–634, 2004.

[8] M. L. P. Tan, G. Lentaris, and G. Amaratunga Aj, "Device and circuit-level performance of carbon nanotube field-effect transistor with benchmarking against a nano-MOSFET," Nanoscale Res. Lett., vol. 7, no. 1, p. 467, 2012.

[9] D. Kumar, A. K. Dadoria, and T. K. Gupta, "Carbon NanoTube based logic gates structure for low power consumption at nano-scaled era,"6th International Conference - Cloud System and Big Data Engineering (Confluence), pp. 675–679, 2016.

[10] S. K. Sinha, K. Kumar, and S. Chaudhury, "CNTFET: The emerging post-CMOS device," International Conference on Signal Processing and Communication (ICSC), pp. 372–374, 2013.

[11] A. Raychowdhury and K. Roy, "Carbon nanotube electronics: Design of high-performance and low-power digital circuits," IEEE Trans. Circuits Syst. I Regul. Pap., vol. 54, no. 11, pp. 2391–2401, 2007.

[12] L. Ding et al., "CMOS-based carbon nanotube pass-transistor logic integrated circuits," Nat. Commun., vol. 3, no. 1, p. 677, 2012.

[13] I. Hussain, A. Singh, and S. Chaudhury, "A review on the effects of technology on CMOS and CPL logic style on performance, speed and power dissipation,"IEEE Electron Devices Kolkata Conference (EDKCON), 2018.

[14] V. K. Sharma, "CNTFET circuit-based wide fan-in domino logic for low power applications," J. Circuits Syst. Comput., p. 2250036, 2021.

[15] S. Garg, T. K. Gupta, and A. K. Pandey, "A 4:1 Multiplexer using dual chirality CNTFET-based domino logic in nano-scale technology," Int. J. Electron., vol. 107, no. 4, pp. 513–541, 2020.

[16] S. Das, S. Bhattacharya, and D. Das, "Design of digital logic circuits using carbon nanotube field effect transistors", International Journal of Soft Computing and Engineering (IJSCE), vol.1, pp. 173-178, 2011.

[17] S. Das, S. Bhattacharya, and D. Das, "Design of Transmission Gate Logic Circuits using Carbon Nanotube Field Effect Transistors," Proc. National conference on Advanced Communication Systems and Design Techniques, 2011.

Authorized licensed use limited to: DELHI TECHNICAL UNIV. Downloaded on February 24,2022 at 06:55:31 UTC from IEEE Xplore. Restrictions apply.

[18] H. M. N. Ahmad, M. S. Islam, K. M. Jameel, A. R. Ochi, and R. Hafiz, "Performance study of 12-CNTFET and GDI CNTFET based full adder in HSPICE," International Conference on Advances in Engineering & Technology Research (ICAETR), 2014.

[19] P. Tyagi, S. K. Singh, and P. Dua, "Gate diffusion input based 10-T CNTFET power efficient full adder," Recent Adv. Electr. Electron. Eng., vol. 14, no. 4, pp. 415–427, 2021.

[20] V. Prasadand D. Das, "A Review on MOSFET-Like CNTFETs," Sci. Technol. J., vol. 4, no. 2, pp. 124–129, 2016.

[21] S.-M. Kang and Y. Leblebici, CMOS Digital Integrated Circuits: Analysis and Design, 2nd ed. London, England: McGraw-Hill Education, 1999.

[22] K. Miettinen, P. Neittaanmaki, M. M. Makela, and J. Periaux, Evolutionary algorithms in engineering and computer science, John Wiley & Sons, 2008.

Authorized licensed use limited to: DELHI TECHNICAL UNIV. Downloaded on February 24,2022 at 06:55:31 UTC from IEEE Xplore. Restrictions apply.

Journal of Computer Virology and Hacking Techniques
https://doi.org/10.1007/s11416-022-00416-3

ORIGINAL PAPER



ConRec: malware classification using convolutional recurrence

Abhishek Mallik[1] · **Anavi Khetarpal**[1] · **Sanjay Kumar**[1]

Received: 29 May 2021 / Accepted: 17 January 2022
© The Author(s), under exclusive licence to Springer-Verlag France SAS, part of Springer Nature 2022

Abstract
Today, the extensive reliae on technology has exposed us to a constant threat of sophisticated malware attacks. Various automated malware production techniques have evolved, some of which reuse specific segments of existing malware to produce new malware, making malware detection challenging. In this paper, we propose a Convolutional Recurrence based malware classification technique that exploits the visual recurrences in the grayscale images of the malware samples belonging to the same malware families. Firstly, we convert the malware samples into grayscale images to capture the structural similarities from the malware samples using a Convolutional Neural Network architecture. Then we perform data augmentation to counter the effects of high data imbalance and reduce the class bias, such that training on that dataset would generate a more generalized framework. The augmented dataset is then passed through a VGG16 based feature extractor to extract the visual outliers amongst the malware families. Now, the extracted features are processed by passing them through two stacked BiLSTM layers. The outputs generated by the BiLSTM layers and the VGG16 layer are then merged to perform the final classification of the malware sample into its malware family. The model's performance is further improved by using proper hyperparameter tuning. We compare the performance of our algorithm against several baseline methods and some contemporary state-of-the-art methods for visual malware detection by utilizing two benchmarked datasets. The obtained experimental results reveal the utility and efficacy of our proposed malware family classification technique.

Keywords Malware classification · Malware visualization · Visual recurrence · Convolutional neural network · Recurrent neural network

1 Introduction

In recent years, with the boom in multimedia technologies, internet services, and their accessibility, we heavily rely on various electronic gadgets for almost all of our daily needs. Nowadays, the internet has deep access to both our social as well as professional lives. This arouses the question of secure internet access, and with the recent rampant spread of malware, it has become a rather critical question. By definition, "Malware is any software intentionally designed to cause damage to a computer, server, client, or computer network" [1]. It can conform to a script, an executable, a segment of specific software, or any other software program. Malware can be classified as Ransomware, Viruses, Worms, Trojans, Bots, and other malicious programs. Many multimedia tools and devices are infested by several malicious files and software that hinder the performance of these gadgets severely [2].

The process of detecting and thereby classifying malware is called Malware Analysis. Labeling malware as benign or malign formulates the detection part. If found malign, the labeling of the detected malware into its appropriate family comes under the classification part of malware analysis. Traditionally, Malware analysis is performed using static analysis, dynamic analysis, or a hybrid static and dynamic analysis approach [3]. Static analysis is usually carried out by parsing the executable and extracting features and signatures that ultimately help research. A pattern like string signatures, byte sequences, various API calls made are used for static analysis. These identified signatures paired with machine learning techniques have given excellent results [4]. Static analysis mostly succumbs to the problem of code obfusca-

✉ Sanjay Kumar
sanjay.kumar@dtu.ac.in

Abhishek Mallik
abhishekmallik265@gmail.com

Anavi Khetarpal
anavikhetarpal@gmail.com

[1] Department of Computer Science and Engineering, Delhi Technological University Main Bawana Road, New Delhi 110042, India

Published online: 09 February 2022

tion. On the other hand, dynamic analysis runs the executable file in a sandboxed environment to monitor its behavior. Various system calls, instructions executed, and registers accessed by the executable are scrutinized for dynamic malware analysis. It stands better to the code obfuscation problem than static analysis. These techniques of analysis are very cumbersome in terms of time and resource efficiency. And with rapidly changing signatures of malware, these conventional techniques are often not very accurate. Apart from the static and dynamic methods of malware analysis, various deep learning techniques [5,6] coupled with data extracted from static and dynamic analysis to generate a hybrid tool for malware analysis are also used. There are also visualization-based techniques wherein malware samples are visualized and then analyzing these images for textures, patterns, and signatures to perform malware analysis [7]. Various automated malware production techniques reuse specific segments of existing malware to produce new malware. Certain segments of this newly generated malware are further used to generate newer malware. This process goes on and on. As a result, different copies of malware that are yet similar in their structural patterns are generated. This structural pattern similarity can be exploited to classify different malware variants into their respective families.

This paper aims to exploit this structural recurrence available in the visual representations of the malware samples belonging to the same malware family. Initially, we convert the malicious files into their corresponding grayscale images. It is often the case that the number of such malicious files belonging to each malware family isn't the same and is highly unbalanced. So we perform image augmentation to balance the number of samples belonging to each malware family. These augmented images then constitute a well-balanced dataset. These visual malware samples are passed through a hybrid deep learning architecture, ConRec (Convolutional Recurrence). The first segment of ConRec consists of a VGG16 based feature extractor to explore convolutional outliers and similarities amongst the malware families. These extracted features are then passed into two stacked BiLSTM layers to process these features further. The features extracted from VGG16 architecture and the processed features from the BiLSTM architecture are then combined and fed into stacked dense layers to classify the malware sample into its corresponding malware family. This merging of outputs performs global feature exploration and feature exploitation in the visual malware sample. The performance of the model is further enhanced by proper hyperparameter tuning. We evaluate our model's performance on two benchmarked malware datasets. The results are also compared against several baseline machine learning and deep learning methods and also against some contemporary visual malware classification techniques. The primary contributions of our work can be summarised as follows:

(i) We introduce a hybrid malware detection model comprising a VGG16 extractor and stacked BiLSTM layers exploiting and exploring the structural recurrence in visual representations of malware samples belonging to the same malware family.
(ii) By merging the extracted features from the VGG16 architecture and the processed features from BiLSTM layers, we perform a global feature exploration and extracted feature exploitation for malware classification.
(iii) An end-to-end unified framework is proposed to analyze the grayscale malware representation obtained from the binary malware executable file and classify it into its respective malware family class.
(iv) We perform an extensive experimental analysis of our proposed approach for malware detection using standard evaluation metrics evaluated on two publicly available benchmarked datasets. The obtained results show that our proposed approach outperforms most of the existing state-of-the-art methods by a considerable margin.

The rest of the paper is organized as follows. In Sect. 2, the literature review of the work already done in this domain is presented. In Sect. 3, the proposed malware analysis technique is discussed in detail. Section 4 discusses the dataset and evaluation metrics used in this study. The experimental results performed are illustrated in Sect. 5. Finally, Sect. 6 concludes the paper along with the future scope of the work.

2 Related work

The proliferation of malware has gained much attention in the literature, and an increasing number of researchers have been exploring this field. The recent advancements in machine learning and deep learning techniques have proved their mantle in solving real-world problems like malware classification, image classification, medical image analysis, predicting customer churn [18–20]. This section presents a consolidated summary of the various scholarly works previously carried out in the domain of malware analysis. We discuss the existing novel methods for malware detection and classification techniques on multiple datasets. According to Singh et al. [21], most of the work used in production can broadly be categorized as signature-based or anomaly-based malware detection systems. The signature-based systems comprise a unique code segment present in the malicious binary executable file or the files infected by malware. Although this system is fast and has high accuracy, it fails to detect previously unseen malware signatures. The malware signature database needs to be updated regularly and manually, which is a very tedious task. On the other hand, within

an anomaly-based system, expressly permitted protocols to make up a database. If the software deviates from these predefined protocols, it is labeled as malicious. This approach is highly effective in detecting unseen malware; however, it raises a false alarm way too often.

A malware behavior visualization technique was used by Zainudeen et al. [8] in their study, where they collected the behavioral characteristics of malware in a virtual environment and then converted the collected characteristics into a color image. Through their experiments, they were able to achieve accuracies ranging from 95.92% to 98%. Trinius et al. [9] used a malware treemap and a thread graph visualization to develop a novel dynamic malware detection tool. The malicious behavior was observed in a sandboxed environment. Jae et al. [10] followed the approach of using an image similarity matrix through static visualization by using opcode sequences to generate image matrices along with computing similarity using selective area matching. Their approach gave a 98% similarity rate. Similar to the previous work, Eul et al. [11] presented an entropy graph-based system to achieve a better similarity rate in their study. They first transformed the executable files to grayscale images, after which they generated entropy graphs, obtaining similarity rates. Their approach managed a similarity rate of 97.9%. Another malware detection model using SURF descriptor was given by Ban et al. [12]. They extracted local features from each malware image and computed the similarity through a Local Sensitivity Hashing (LSH) scheme, obtaining a classification accuracy of 85%. Natraj et al. [13] made use of the Malimg dataset. They first converted an executable code into a grayscale image and then used a GIST descriptor to extract global features from the generated images. The nearest neighbor classifier was employed to classify the malware variants into their respective families. Their approach achieved a classification accuracy of 97.4%. Similar to the previously mentioned approach, Aziz et al. [14] also used a GIST descriptor to extract global features from the visual representations of the malware variants. They then used a feed-forward artificial neural network to achieve a classification accuracy of 96.3%. Using a Random Forest classifier as a classification tool and the GIST descriptor for the feature extraction purpose, researchers Kosmidis et al. [16] achieved an accuracy of 91.6%. Barath et al. [15] performed a study using a Principal Component Analysis (PCA) for extracting global features and then employed a nearest neighbor classifier to classify the malware variants. They claimed that their approach had a classification accuracy of 96%. Agarap et al. [17] used the Malimg dataset [13] for their study. In their work, they proposed a deep learning-based approach for malware detection. To better understand the comparative study, they employed three models, namely, CNN-SVM, GRU-SVM, and MLP-SVM. They achieved the maximum classification accuracy of 84.92% with the GRU-SVM model.

Singh et al. [21] identified malware by using a deep convolutional-based system by experimenting using two models, a deep CNN model and ResNet-50. But instead of directly using grayscale images from the Malimg dataset, they first converted it into a color image and then used it for classification. Their applied approach gave a classification accuracy of 98.10%. Zhu et al. [22] propose a novel deep learning-based approach to detect malware straightforwardly from the information streams of android applications. They achieved a high f1 score of 95.05%. Cui et al. [24] presented a novel deep learning-based approach for malware classification by handling the dataset imbalance problem using the bat algorithm and using a convolutional neural network (CNN) for the classification task. Vinayakumar et al. [25] put forward a more scalable deep learning-based framework using the same setup. Naeem et al. [26] used local and global patterns of malware images along with SVM and KNN to achieve an accuracy of 98.0%. They improved their performance slightly by using Combined local and global malware features [27,28] along with a deep convolutional neural network to achieve an accuracy of 98.18%. Nisa et al. [29] used segmentation-based fractal texture analysis along with deep convolutional neural network-based feature extractor and deep CNN-based models (Alexnet and Inception v3) for final classification to achieve an accuracy of 99.3%. Researchers Ren et al. [30] proposed two different visualization methods for visualizing malware based on n-gram features of a byte sequence. The Markov dot plot technique visualizes bi-gram features along with the statistical data of byte sequences. In contrast, the space-filling curve mapping technique uses fractal curves for visualizing only the one-gram features of the same. Tuncer et al. [31] presented a byte-code-based malware recognition method consisting of feature extraction with the proposed local neighborhood binary pattern. Feature selection and concatenation were carried out using neighborhood component analysis, after which feature reduction and classification took place using principal component analysis and linear discriminant analysis, respectively.

A unified framework that incorporated both static as well as dynamic nature of a malicious file for malware classification was given by Anderson et al. [32]. They utilized kernels to place similarity metrics onto every distinct view and then employed multiple kernel learning, ultimately yielding a high classification accuracy. Researchers Dahl et al. [33] used random projections for feature selection in large-scale malware and then used this architecture to train multiple neural network systems. They also compare the performance of neural networks with that of logistic regression for the task of classifying multi-class malware. Zhang et al. [34] proposed a semantic-based classification approach to classify android malware via the use of a dependency graph. They extracted

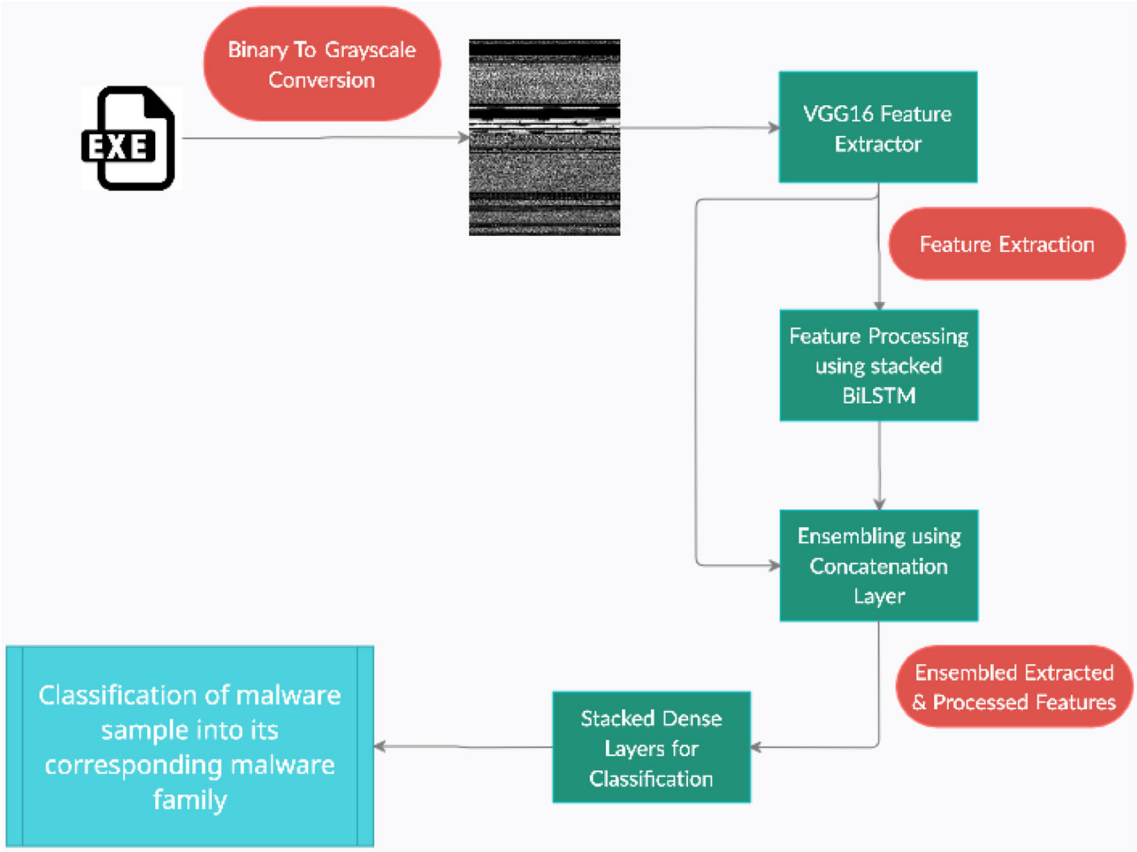


Fig. 1 Model architecture of proposed work ConRec

an API dependency graph and introduced graph similarity metrics to construct feature sets to uncover homogeneous application behaviors. Echo state networks and recurrent neural networks were used by Pascanu et al. [35] to extract the malware features, which are then passed through a malware classifier to make malware classification. Garcia et al. [36] used a random forest-based classifier to perform malware classification on visual representations of malware samples. The model was evaluated using a 10-fold cross-validation procedure and obtained an accuracy of 0.9562. Moshiri et al. [37] performed dynamic malware analysis by using information theory and machine learning. They generated a malware data repository for training a classifier and then used it to predict the malware family of test samples. First and second-order statistical texture features of visual representations of malware samples are utilized by Verma et al. [38] for feature extraction. They further used an ensemble learning model for making the final classification. Word2vec architecture was used by Cakir et al. [39] to perform feature extraction by representing the malware by their opcodes.

A CNN-based architecture was used by Kalash et al. [40] to perform malware classification. They first converted malware binaries into their corresponding grayscale images, followed by training a CNN for classification. Gibert et al. [41] in their work, put forward a file agnostic deep learning-based approach for malware classification. Their techniques were assessed on two datasets, namely, the Microsoft Malware Classification Challenge and the MaIIMG. They also carried out a comparative study of the image-based machine learning methods for classifying malware and found that their approach had outperformed other existing ones. Semantics-preserving syntactic code transformations and a CNN-based architecture were employed by Marastoni et al. [42]. They designed two models, a bi-directional long short-term memory and a convolutional neural network, and then trained them on images taken from the generated dataset. Bhodia et al. [43] employed transfer learning for detecting as well as classifying malware based on image analysis. They converted executable files into images and then used deep learning models for image recognition. Prajapati et al. [44] also made the use of image features; however, they use a more diverse dataset and use multiple neural networking techniques such as vanilla recurrent neural networks, multilayer perceptrons, etc. They also experiment with a complex model which combines both GRU and LSTM. Yajamanam et al. [45] analyze, test, and implement malware scores based on image features called gist descriptors. In addition to this, they explore the robustness of the gist-based technique when applied to

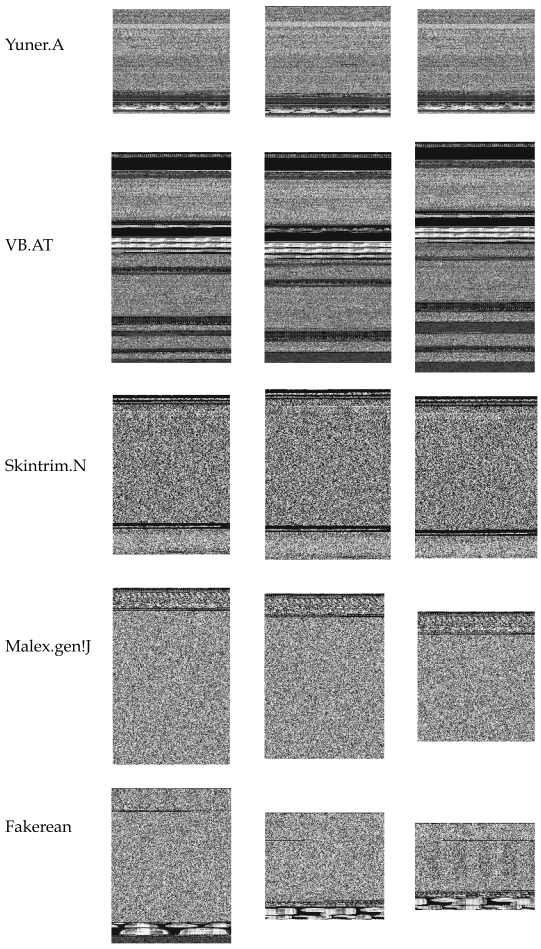


Fig. 2 Grayscale images of malware samples belonging to different malware families in Malimg dataset

malware and compare it with deep learning techniques for image-based malware classification. Vasan et al. [46] presented an ensemble CNN-based architecture for malware classification. Their results demonstrate over 98% and 99% accuracy for packed and unpacked malware, respectively. A convolutional neural networks (CNN) and extreme learning machines (ELM) based framework for malware classification was proposed by Jain et al. [47]. They claimed that ELMs and CNN's perform well when trained on one-dimensional data and two-dimensional data.

3 Proposed work

This section presents a detailed description of our proposed work. We convert the malicious samples belonging to each malware family into their grayscale visual representations. We exploit the Convolution Recurrence (ConRec), i.e., the repeating visual characteristics in the visual representations of malware samples belonging to the same malware families. We perform image augmentation to the visible dataset to handle the vast variations in the number of malware samples belonging to each malware family. This well-labeled dataset is then passed onto a VGG16 based feature extractor. The extracted features are then passed through two stacked BiLSTM layers for feature processing. The features extracted from the VGG16 features and the processed features from the BiLSTM are then ensembled together to achieve a sense of feature exploration and feature exploitation. This curated feature set is then used for classifying the malware samples into their corresponding families. Figure 1 shows the model architecture of our proposed model, ConRec. Our proposed work consists of six phases: Visual Representation of Malware, Augmenting the Samples, Feature Extraction, Feature Processing, Ensembling the features, and Classifying and Hyperparameter Tuning. They are described as follows:

3.1 Visual representation of malware

For this study, we convert various malware samples into their corresponding visual representations. The binary information provided by the malware variants is converted into 8-bit vector representations to obtain a 2D matrix, which is then used to generate a grayscale image in the range [0,255], with 0 being black and 255 being white. The final image captures various DLLs, API calls, and other segments of the malware file. The width of the generated images was kept constant at 256 pixels across the malware variants, while the height of the images varied according to the file size. Figures 2 and 3 shows the images generated by converting the malicious files into their visual representations. It can be seen that the images belonging to the same malware families share the same visual texture, while those belonging to different malware families have a different texture. It can also be seen that the width of the images is kept the same while the height of the malware samples varies. A convolutional neural network architecture requires input images of fixed dimensions and the images obtained by us are of varying dimensions. To overcome this issue, we resize all the images to 224×224 dimensions. This helps us obtain an uniformity in the dataset and the images can be fed to a pre-defined CNN architecture.

3.2 Augmenting the samples

The number of samples belonging to different malware families varies greatly, thus making the dataset unbalanced. This is very well observed in the real-life datasets chosen by us. We can see that for the Malimg dataset (Table 2, we have 2949 Allaple.A samples while only 80 Skintrim.N malware samples. Also, for the BIG 2015 dataset (Table 3), we see that there are 2942 Kelihos_ver3 samples while only 42 Simda malware samples. Hence, we observe a high data imbalance in the chosen Malimg and the BIG 2015 malware datasets.

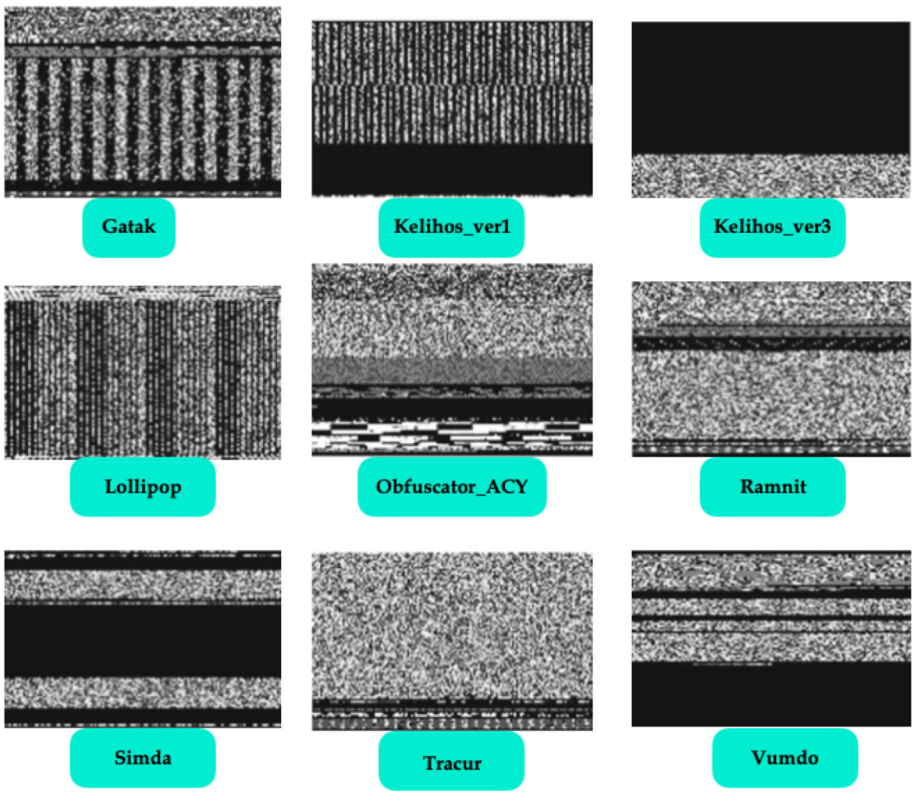


Fig. 3 Grayscale images of malware samples belonging to different malware families in BIG 2015 dataset

We perform image augmentation on the malware samples belonging to each malware family as a regularization technique to counter the effects of class bias and to obtain a more generalised framework. Through image augmentation, the number of samples is increased by generating newer samples for training the model by following several techniques like rotating the original image to a certain degree, by shifting the image through a particular value, and finally by horizontally and vertically flipping the original image. Fig. 4, shows the image augmentation techniques performed on a malware sample belonging to the fakerean family. Figure 4(a) shows the original image for a fakerean malware variant, while Fig. 4(b) shows the shifted image. Figure 4(c) and (d) show the images rotated by 45 degrees anticlockwise and clockwise respectively. While the Fig. 4(e) and (f) depict the horizontally and vertically flipped images, respectively. These image augmentation techniques are in agreement with some of the recent malware detection papers [29,48,49]. The augmentation techniques help the model to avoid over-fitting on a particular structural pattern and provide us a generalised model.

3.3 Feature extraction

Feature extraction is the process of selecting the features that uniquely characterize an image deterministically and is amongst the most critical steps in the approach of any deep learning technique. For our model, ConRec, we employ a pruned VGG16 architecture [23] for feature extraction. VGG16 is one of the best benchmarked *"imagenet"* models used for image classification. VGG16 has 16 weight layers which help in extracting vital information from the images. However, by constantly improving the depth of the VGG16 architecture, it suffers from a vanishing gradient problem. Hence, instead of using VGG16 directly for the classification task, we use it for extracting the features of the images. Figure 5 illustrates the pruned VGG16 architecture that we have used for the task of feature extraction. We only use the convolutional layers and the max-pooling layers to extract the features. This extracts essential features from the entire image globally, thereby performing a convolutional exploration in the image.

3.4 Feature processing

The extracted features from VGG16 architecture are then fed into two stacked Bidirectional Long Short Term Memory (BiLSTM) layers. The BiLSTM layers process these extracted features and enhance them to reveal latent characteristics of the structural identities in the malware samples. The quality of BiLSTM to process the inputs sequentially is crucial for processing the derived features of an image. Moreover, since BiLSTM takes the input data from beginning to end and end to beginning, it helps process the extracted fea-

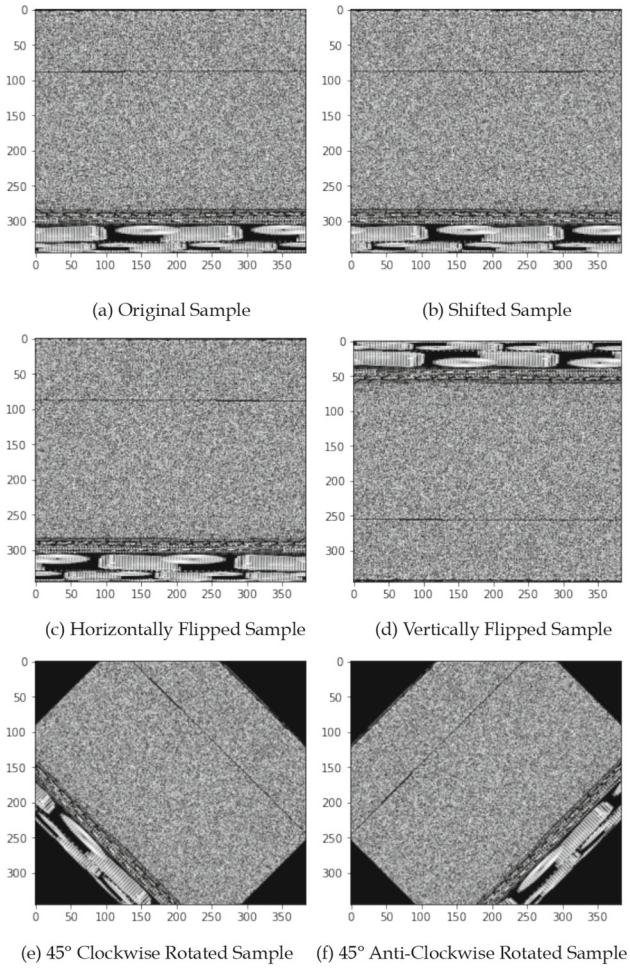


Fig. 4 Some examples of image augmentation for a Fakerean malware variant

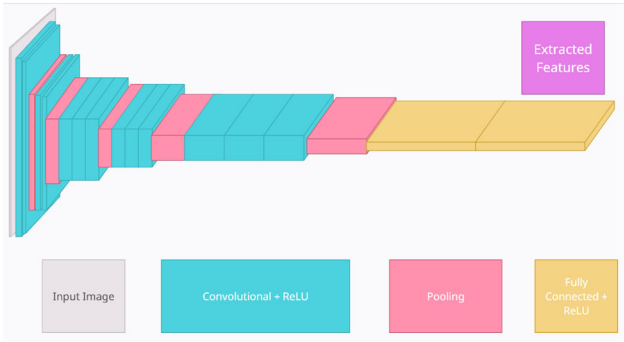


Fig. 5 Pruned VGG16 architecture used for feature extraction

tures better. This helps in correctly exploiting the extracted features. In our model, we utilize two stacked BiLSTM layers. The first layer outputs a sequence of all obtained outputs, while the second layer outputs only the last obtained output.

Table 1 Hyperparameters for ConRec

Hyperparameter	Description or value
Number of VGG16 Feature extractor	1
Number of BiLSTM layers	2
Number of Dense layers	2
Dropout rate	0.25
Recurrent dropout rate	0.20
Optimizer	SGD (lr = 1e–4, momentum = 0.9)
Activation function	ReLu and Softmax
Loss function	Categorical-crossentropy
Number of epochs	30
Callbacks	ReduceLROnPlateau

3.5 Ensembling the features and classifying

The features extracted from the VGG16 architecture and the processed features obtained from the BiLSTM layers are further ensembled to get a sense of feature exploration and exploitation. The extarcted convolutional features of VGG16 are further accounted for by the sequential dependencies by the BiLSTM layers. This helps in generating a more ad-hoc feature set for capturing the structural details in a better manner. The features are ensembled by concatenating them alongside. These ensembled features are then passed through two stacked dense layers for the final classification task.

3.6 Hyperparameter tuning

Hyperparameters attribute to the design technicality of a model's architecture. Formally speaking, model parameters that specify the architectural details of a machine learning model are known as hyperparameters. These hyperparameters have a profound impact on a deep learning model's performance. The process of choosing the appropriate values for the hyperparameters of a model is known as hyperparameter tuning. For performing hyperparameter tuning, we use Random Search. Random search is a hyperparameter tuning technique wherein we define a search space of various hyperparameter values and then we iterate over random combinations from amongst these values [50]. The optimal hyperparameters are selected based on the accuracy value achieved by those hyperparameters. For our experiments, we tried different values of Dropout rate, Recurrent dropout rate, Optimizer, Learning rate, etc. The reason for using the random search is that the chances of finding the optimal parameters are relatively higher with the random search technique. The reason behind this can be understood by the notion that the random search pattern enables the model to

Table 2 Distribution of malware samples amongst the 25 malware families in the Malimg dataset

No.	Class	Family Name	Number of variants
1	Dialer	Adialer.C	122
2	Backdoor	Agent.FYI	116
3	Worm	Allaple.A	2949
4	Worm	Allaple.L	1591
5	Trojan	Alueron.gen!J	198
6	Worm:AutoIT	Autorun.K	106
7	Trojan	C2Lop.P	146
8	Trojan	C2Lop.gen!G	200
9	Dialer	Dialplatform.B	177
10	Trojan Downloader	Dontovo.A	162
11	Rogue	Fakerean	381
12	Dialer	Instantaccess	431
13	PWS	Lolyda.AA1	213
14	PWS	Lolyda.AA2	184
15	PWS	Lolyda.AA3	123
16	PWS	Lolyda.AT	159
17	Trojan	Male.gen!J	136
18	Trojan Downloader	Obfuscator.AD	142
19	Backdoor	Rbot!gen	158
20	Trojan	Skintrim.N	80
21	Trojan Downloader	Swizzor.gen!E	128
22	Trojan Downloader	Swizzor.gen!I	132
23	Worm	VB.AT	408
24	Trojan Downloader	Wintrim.BX	97
25	Worm	Yuner.A	800

be trained on optimal parameters without any aliasing. Table 1 tabulates the hyperparameters chosen by us for our experimental analysis from a list of plausible values. As can be seen in Table 1, we employ a VGG16 feature extractor, two stacked BiLSTM layers, and two Dense layers. The VGG16 is used with the default 'imagenet' weights. The values for dropouts and recurrent dropouts for both the BiLSTM layers are 0.25 and 0.20, respectively. The optimizer used while compiling the model is Stochastic Gradient Descent (SGD) with a learning rate of 1e–4 and momentum equals 0.9. The activation function employed in the first dense layer is ReLu while that used for the second layer is Softmax. Since this is a multi-class classification problem, hence the loss function used to monitor the loss is Categorical-crossentropy. As the training loss stabilized at around 30 epochs, therefore, the model was run for 30 epochs. The callback method used in our technique is ReduceLROnPlateau, which diminishes the model's learning rate when the monitored metric, which in this case is validation accuracy, fails to improve after a fixed number of iterations.

4 Dataset and evaluation metrics

This section presents the description of the dataset which we use to test the performance of our proposed model. It also lists the various evaluation metrics used by us to quantify the performance of our approach.

4.1 Dataset description

We used two benchmarked datasets for our study. The detailed description of these datasets is listed below:

(i) **Malimg dataset**
The Malimg dataset was introduced by Nataraj et al. [13] in their work. The dataset consists of 9339 visual representations of malware variants belonging to 25 different malware families. Some of the malware families present in the dataset are: Adialer.C, Allueron.gen!J, Dialplatform.B, Obfuscator.AD, etc. The distribution of malware samples amongst the 25 malware families is presented in Table 2. Based on Table 2, we see that there are about 2949 Allaple.A samples while there are just 80 Rbot!gen

Table 3 Distribution of malware samples amongst the 9 malware families in the BIG 2015 dataset

No.	Malware Family	Number of variants
1	Ramnit	1541
2	Lollipop	2478
3	Kelihos_ver3	2942
4	Vundo	475
5	Simda	42
6	Tracur	751
7	Kelihos_ver1	398
8	Obfuscator.ACY	1228
9	Gatak	1013

Table 4 Comparison of various deep convolutional neural networks for feature extraction on the Malimg dataset

Models	Training Accuracy(%)	Testing Accuracy(%)
VGG16	98.92	95.51
Xception	93.92	93.37
InceptionV3	96.79	91.76
DenseNet201	98.74	94.65
NasNetLarge	95.45	95.45
MobileNetV2	91.67	94.58

Table 5 Comparison of various deep convolutional neural networks for feature extraction on the BIG dataset

Models	Training Accuracy(%)	Testing Accuracy(%)
VGG16	95.48	87.27
Xception	97.57	93.16
InceptionV3	93.72	87.06
DenseNet201	96.81	90.05
NasNetLarge	87.12	93.07
MobileNetV2	86.90	89.93

samples. This shows the huge data imbalance in the malimg dataset.

(ii) **BIG 2015 dataset**
This dataset was provided by Microsoft as part of the Big Data Innovators Gathering (BIG 2015) Anti-Malware Prediction Challenge. It contains 21741 malware samples, 10868 for training and 10873 for testing. For every sample in the dataset, we have hexadecimal representation of malware's binary content and its corresponding assembly file. However, the labels are present for only the training dataset. There are 9 classes of malware in this dataset. The distribution of malware samples amongst the 9 malware classes is given in Tab. 3. From Tab. 3, we can also see that there are about 2941 Kelihos_ver3 samples while there are just 42 Simda samples. It shows that there is high data imbalance in the BIG 2015 dataset.

4.2 Evaluation metrics

For the evaluation of performance of our proposed model, we compute several standard classification based evaluation metrics. The description of those metrics is given below:

(i) Accuracy:
It represents the ratio of total number of data points classified correctly to the total number of data points. Mathematically, it can be expressed as follows:

$$Accuracy = \frac{TP + TN}{TP + TN + FP + FN} \tag{1}$$

(ii) Precision:
It represents the fraction of positive classifications made that were actually positive. Mathematically, it can be represented as follows:

$$Precision = \frac{TP}{TP + FP} \tag{2}$$

(iii) Recall:
It represents the fraction of positive samples that were actually classified as positive. More formally it is represented as follows:

$$Recall = \frac{TP}{TP + FP} \tag{3}$$

(iv) F1 Score:
F1 Score is representative of the existent balance between precision and recall. In mathematical terms, it is represented as follows:

$$F1\ Score = \frac{2 * Precision * Recall}{Precision + Recall} \tag{4}$$

Here,

True positive (TP) - Correctly identified
False positive (FP) - Incorrectly identified
True negative (TN) - Correctly rejected
False negative (FN) - Incorrectly rejected

5 Experimental results and analysis

This section consolidates the intensive experimental analysis of our proposed model ConRec and establishes its utility as

Table 6 Performance comparison of proposed ConRec framework with augmented samples as well as without augmented samples against various baseline Machine Learning models used on the Malimg dataset

Models	Accuracy(%)	Precision(%)	Recall(%)	F1 score(%)
Logistic Regression	75.65	97.03	52.61	68.23
K-means Clustering	79.25	79.25	79.25	79.25
Multinomial Naive Bayes	70.12	95.14	62.03	75.10
KNN	82.61	78.81	96.62	86.81
Decision Trees	84.67	84.67	84.67	84.67
Random Forest	88.65	88.46	88.75	88.59
SVM	89.84	89.84	89.84	89.84
ConRec (without augmentation)	95.61	98.63	85.32	91.47
ConRec (with augmentation)	99.56	82.80	95.40	88.65

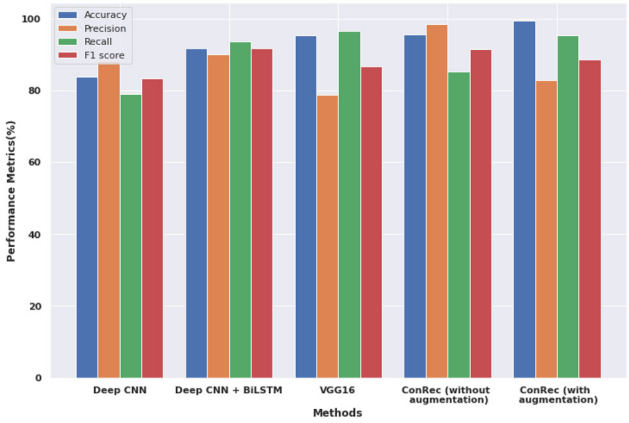


Fig. 6 Performance comparison of proposed ConRec framework with augmented samples as well as without augmented samples against various baseline deep learning models on the Malimg dataset

a malware family classification tool. The experimentations are carried out on the datasets described in Sect. 4.1. The dataset is divided in the ratio of 80:20 to have 80% of the dataset for the training purpose while 20% of the dataset for testing the model. The dataset split ratio is chosen to avoid the over-fitting and the under-fitting problem associated with various deep learning models. Several machine learning techniques like Support Vector Machines (SVM), K nearest neighbors (KNN), and decision trees, etc., are used as baseline methods to demonstrate a more comparative study. Also, various deep learning-based approaches like a deep convolutional neural network (DCNN), a DCNN and BiLSTM hybrid model, and a VGG16 architecture are used. The performance of ConRec is also compared with some of the recently proposed models available in the literature. We also present classification results without performing data augmentation to grasp the utility of data augmentation better. A detailed study is also performed by us to better understand the suitability of VGG16 as a feature extractor. The evaluation metrics mentioned in Sect. 4.2 are calculated for both the datasets and all the methods and techniques. We present below the experimental analysis of the proposed method and various considered methods on each dataset.

5.1 VGG16 as the feature extractor

One of the important tasks of our approach is to extract relevant features from our grayscale malware images. To achieve this, we try a variety of deep convolutional neural networks like VGG16, Xception, InceptionV3, DenseNet201, NasNetLarge, and MobileNetV2. The results obtained for the Malimg dataset are represented in Table 4 while those for the BIG 2015 dataset are represented in Table 5. We can clearly see that VGG16 is the best performer for feature extraction from grayscale malware images. This suggests that VGG16 would be an optimal feature extractor for our methodology to classify malware samples into their respective malware families. This forms the notion for using a VGG16 architecture as the feature extractor.

5.2 Results on Malimg dataset

This section illustrates the experimental results obtained for the Malimg dataset. We perform a performance comparison of ConRec with several machine learning models as baselines. Table 6 lists the results obtained for the machine learning baselines on the Malimg dataset. The results for ConRec are evaluated with data augmentation as well as without data augmentation. As can be seen from the result that ConRec outperforms all the other baseline machine learning models for the malware classification task. This is well justified because the machine learning models cannot capture the non-linear convolutional features of the malware samples appropriately. We also test our approach against several deep learning-based classifiers. Figure 6 shows the results of our proposed framework ConRec with data augmentation and without data augmentation in contrast to various deep learning models for classifying the malware into their respective families. From Table 6 and Fig. 6 show that the proposed approach performs better with data augmentation. This can

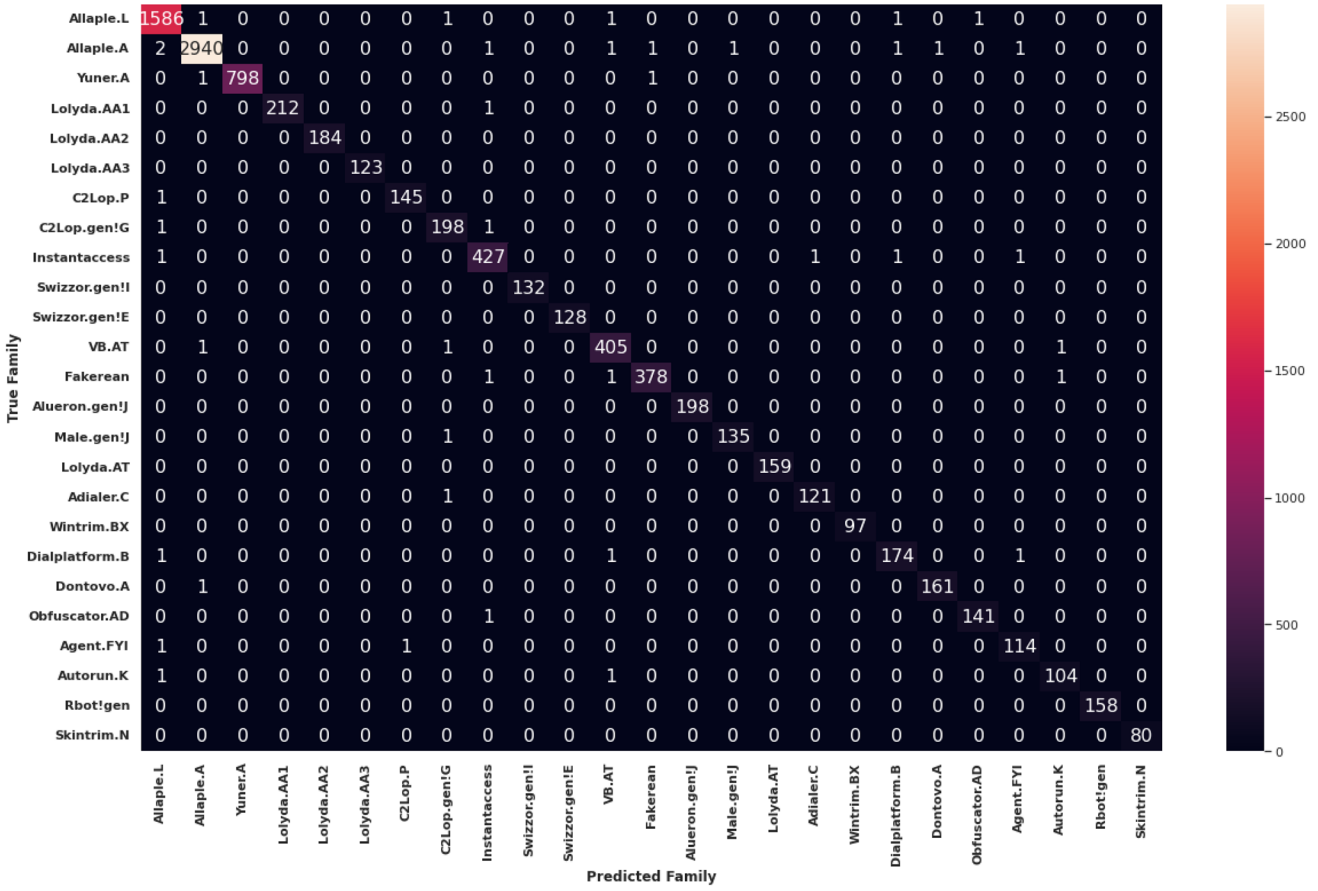


Fig. 7 Confusion matrix of ConRec on the Malimg dataset showing the number of classifications made by our proposed framework ConRec into various families

be attributed to the reduction of bias of the classifier towards a particular family existent in larger numbers. It is well evident from the results that ConRec outperforms the chosen deep learning baselines as well. The deep learning models still are a better performer than the machine learning baselines. This can be attributed to the convolution-specific architecture of these deep learning models. Even with improved performance, these models still fall short of the proposed model, ConRec. The confusion matrix shown in Fig. 7 provides a clearer picture of the classification errors for the various classes as achieved by our proposed work, ConRec. This confusion matrix shows that our model performs only a few misclassifications that are minimal compared to the correct classifications performed by it. Also, Table 7 indicates the number of malware samples that are correctly classified. This reinforces the results for the confusion matrix.

5.3 Results on BIG 2015 dataset

This section presents the results of the extensive experimentations performed on the BIG 2015 dataset. Our proposed model's performance is compared against several chosen machine learning and deep learning baselines. The chosen machine learning baselines are Logistic Regression, K-means Clustering, Multinomial Naive Bayes, KNN, Decision Trees, Random Forest, and SVM. The deep learning baselines chosen are Deep CNN, Deep CNN + BiLSTM, and a VGG16 based classifier. Table 8 tabulates the results obtained for the machine learning baselines, while Fig. 8 presents the results computed for the deep learning-based baselines. The comparison is made with the proposed ConRec framework with and without data augmentation. As is visible from these results that our proposed method, ConRec, outperforms the machine learning and deep learning-based baselines by a substantial margin. Table 8 and Fig. 8 also show that the results obtained by ConRec with augmentation are better than those obtained without augmentation. This can be attributed to the framework generalisation achieved by data augmentation which helps in generalising the framework for various families instead of just particularising it for the family existing in abundance. This justifies our choice of introducing data augmentation in our proposed work. The

Table 7 Family wise performance of our model on the Malimg dataset

Family	No. of correctly classified sample
Allaple.L	1586
Allaple.A	2940
Yuner.A	798
Lolyda.AA1	212
Lolyda.AA2	184
Lolyda.AA3	123
C2Lop.P	145
C2Lop.gen!G	198
Instantaccess	427
Swizzor.gen!I	132
Swizzor.gen!E	128
VB.AT	405
Fakerean	378
Alueron.gen!J	198
Male.gen!J	135
Lolyda.AT	159
Adialer.C	121
Wintrim.BX	97
Dialplatform.B	174
Dontovo.A	161
Obfuscator.AD	141
Agent.FYI	114
Autorun.K	104
Rbot!gen	158
Skintrim.N	80

confusion matrix obtained by us while making classifications for the BIG 2015 dataset is presented in Fig. 9. It shows how minutely our proposed model, ConRec misclassifies the malware variant of the BIG 2015 dataset. It also corroborates the performance standards of our work. Also, Tab. 9 shows the number of malware samples which are correctly classified. This supports the results of our confusion matrix.

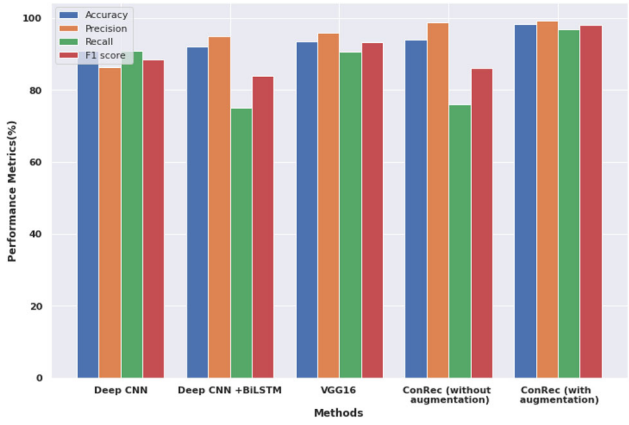


Fig. 8 Performance comparison of proposed ConRec framework with augmented samples as well as without augmented samples against various baseline Deep Learning models on BIG 2015 dataset

5.4 Combined dataset

This section presents the accuracy, precision, recall, and F1 Score results obtained for the combined samples of both datasets. Fig. 10 represents the same. The results for ConRec are calculated with and without data augmentation. As we can see, the performance achieved is slightly inferior compared to the results obtained for individual datasets. This can be understood as the malware samples belonging to the two datasets are of different families. But still, the results obtained by our proposed framework ConRec are quite promising as all the performance metrics reach a value of about 90%. This shows the utility of our proposed ConRec as a generalized framework for malware detection.

Table 8 Performance comparison of proposed ConRec framework with augmented samples as well as without augmented samples against various baseline Machine Learning models used on the BIG 2015 dataset

Models	Accuracy(%)	Precision(%)	Recall(%)	F1 score(%)
Logistic Regression	59.01	56.80	59.01	57.88
K-means Clustering	50.94	50.94	50.94	50.93
Multinomial Naive Bayes	69.69	71.72	69.69	70.69
KNN	77.28	78.88	77.28	78.01
Decision Trees	83.57	83.29	83.71	83.49
Random Forest	87.22	76.07	87.22	81.27
SVM	90.41	90.53	90.41	90.47
ConRec (without augmentation)	93.92	98.90	76.02	85.98
ConRec (with augmentation)	98.36	99.40	96.88	98.12

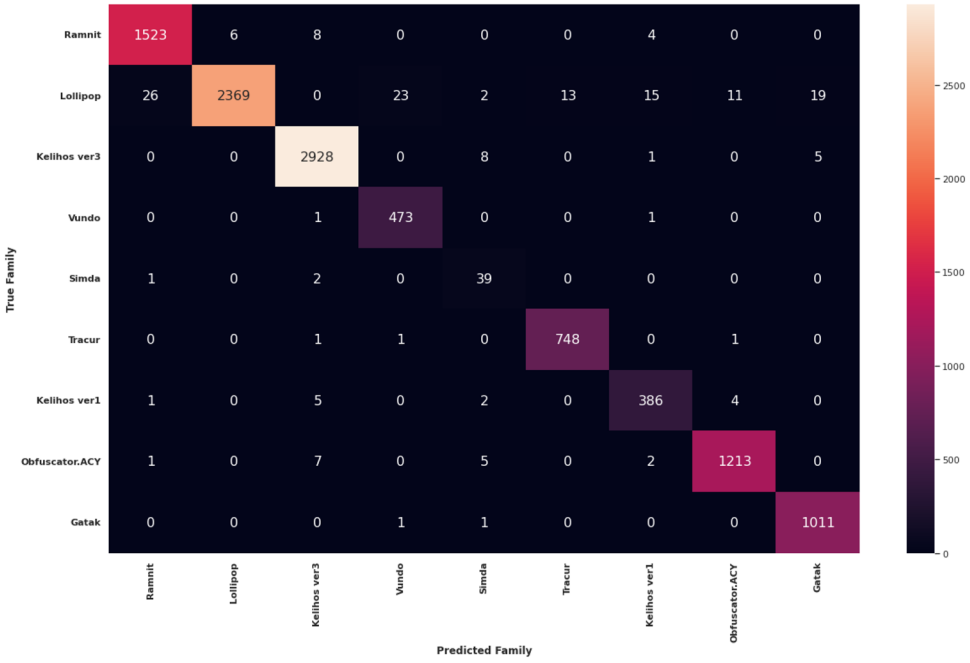


Fig. 9 Confusion matrix of ConRec on the BIG 2015 dataset showing the number of classifications made by our proposed framework ConRec into various families

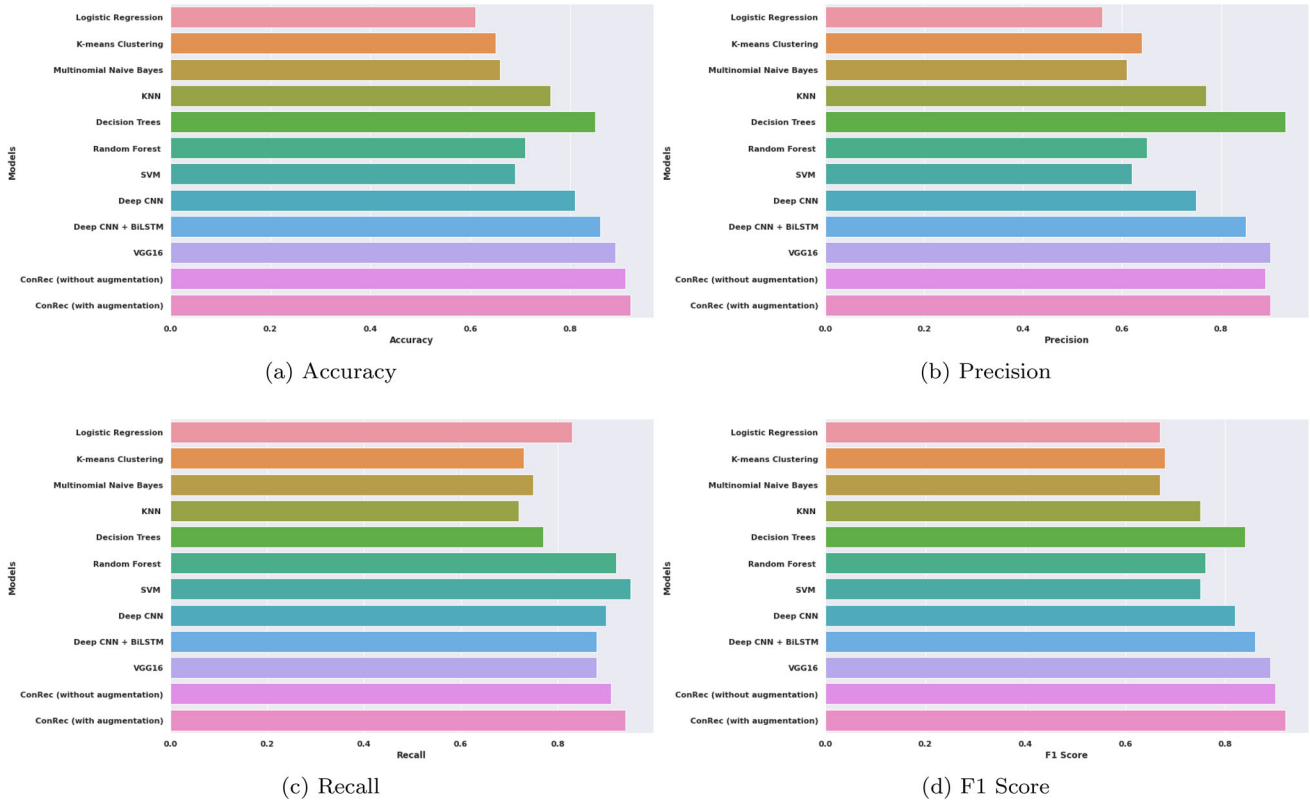
Table 9 Family wise performance of our model on the BIG 2015 dataset

Family	No. of correctly classified sample
Ramnit	1523
Lollipop	2369
Kelihos_ver3	2928
Vundo	473
Simda	39
Tracur	748
Kelihos_ver1	386
Obfuscator.ACY	1213
Gatak	1011

5.5 Comparison with existing approaches

In this section, we compared the performance of our model with the existing popular methods and techniques of malware classifications. Table 10 tabulates the various state-of-the-art techniques for malware classification proposed by the researchers over the years as compared to the results obtained by ConRec with and without data augmentation. It also presents the features used and the classification techniques adopted by the researchers, along with the dataset used and achieved accuracy in percentage.

For the GIST features on the Malimg dataset, [13,40] the accuracy is quite good even with a simple machine learning classifier. Thus confirming that it is an efficient feature extractor. However, the achieved performance is still a bit less as compared to our proposed approach. The features extracted based on texture also perform well for malware classification [36,38]. The technique of using ad-hoc feature extraction [26,27,29,31,42] provides exemplary performance as the features are extracted specific to the task of malware classification. These extracted features paired with several different classifiers still lag behind our proposed approach ConRec. For our study, we used VGG16 based feature extraction. Therefore, we also compared its performance with deep learning [39] and CNN [6,21,24,41,46,47] based feature extraction techniques. It is evident that the our proposed approach is better in terms of accuracy. Even when the extracted features by deep learning or CNN techniques are combined with several sophisticated and complex deep learning classifiers, our proposed approach ConRec still outperforms them by a considerable margin. As is evident from the results depicted in Tab. 10 and the above discussion that our proposed model, ConRec, clearly surpasses the contemporary and the existing state-of-the-art models in terms of accuracy. It is also clear that our choice of using VGG16 as a feature extractor and using BiLSTM as a feature processor is reasonably optimal. The performance comparison of our proposed method shows its excellent capability of classifying malware into their respective families. Moreover, the feature extraction and feature processing technique used by us also proves to be highly effective when compared against the various chosen baselines and the existing state-of-the-art methods. The exemplary performance of our model can also be attributed to the ensembling of the extracted and processed features, which give a sense of global feature exploration and feature exploitation. All the results mentioned above validate



(a) Accuracy (b) Precision

(c) Recall (d) F1 Score

Fig. 10 (**a**)–(**d**) The accuracy, precision, recall and F1 score calculated for various malware detection framework evaluated on the combined samples of both the datasets

the performance of our proposed model, ConRec, for the task of Malware detection and classification, thereby strengthening its claim as an effective malware analysis tool.

6 Conclusion

Nowadays, malware is infesting many multimedia tools and devices and is constantly adapting to malware detection tools. Therefore, malware detection is an ever-evolving heuristic to make the malware detection tools more and more sophisticated in spotting malware software. In this paper, we proposed a model named ConRec for Malware detection, which relies on Convolutional Recurrence (ConRec) in the visual representations of malware variants belonging to the same malware family. Our proposed model relies on using grayscale images generated from malware binaries. These generated images are then passed through a phase of data augmentation to obtain a well-balanced dataset. This dataset is then fed into a VGG16 feature extractor. Two stacked BiLSTM layers then process the extracted features. The extracted and processed features are then ensembled, thereby performing global feature exploration and feature exploitation. These ensembled features form an ad-hoc feature set, capturing the structural details of malware samples efficiently. This feature set is then passed into stacked dense layers to classify malware samples into their corresponding malware families. We conducted extensive experimentations on two benchmarked datasets and calculated various performance metrics. To get a sense of a more profound comparative study, we compared our model's performance with several machine learning and deep learning models and some of the existing state-of-the-art methods in the related literature. This work could further be enhanced by representing the malware samples as colored images instead of plain grayscale images. Moreover, our model is tested on an already existing database of known malware. This approach can further be extended to previously unseen malware samples, packed or obfuscated malware samples.

Table 10 Performance comparison of proposed ConRec framework with augmented samples as well as without augmented samples against various contemporary methods in literature based on accuracy (%)

Authors	Datasets	Features	Techniques	Accuracy(%)
Natraj et al. [13]	Malimg	GIST features	K nearest neighbours	97.18
Garcia [36]	Malimg	Texture features	Random forests	95.26
Barath et al. [15]	BIG 2015	CNN based features	KNN techniques	96.6
Verma et al. [38]	Malimg	first & second order texture feature	Ensemble learning	98.58
Cakir et al. [39]	BIG 2015	Deep learning based features	Gradient boosting	96.0
Kalash et al. [40]	Malimg	GIST Feature	CNN	98.5
Singh et al. [21]	Malimg	CNN based features	ResNet-50	98.10
Gilbert et al. [41]	Malimg,	CNN based features	CNN	93.9
	BIG 2015			97.5
Cui et al. [24]	Malimg	CNN based features	CNN	97.6
Naeem et al. [26]	Malimg	Local and Global Malware Pattern (LGMP) Feature	SVM, KNN	98.0
Naeem et al. [27]	Malimg	Combined Local & Global Malware (CLGM) Features	DCNN	98.18
Nisa et al. [29]	Malimg	Fused SFTA & deep network features	DCNN (Alexnet, Inception v3)	99.3
Vasan et al. [6]	Malimg	Colored images based features	CNN	98.82
Vasan et al. [46]	Malimg	CNN based feature	Ensemble of CNNs	99.50
Jain et al. [47]	Malimg	CNN based features	CNN	95.7
Tuncer et al. [31]	Malimg	Local neighborhood binary pattern	LDA	89.4
Marastoni et al. [42]	Malimg,	Code Obfuscation	CNN	98.3
	BIG 2015			92.0
ConRec (without augmentation)	Malimg,	VGG16	VGG16 + BiLSTM	95.61
	BIG 2015			93.92
ConRec (with augmentation)	Malimg,	VGG16	VGG16 + BiLSTM	99.56
	BIG 2015			98.36

Funding (nformation that explains whether and by whom the research was supported.

Availability of data and materials Not applicable.

Code availability (software application or custom code) Not applicable.

Declarations

Conflicts of interest/Competing interests (Include appropriate disclosures)- Authors declare that they have no conflict of interests.

Authors' contributions (optional: please review the submission guidelines from the journal whether statements are mandatory)

Humans and animals. Additional declarations for articles in life science journals that report the results of studies involving humans and/or animals.

Ethics approval (include appropriate approvals or waivers) Not applicable.

Consent to participate (include appropriate statements) Not applicable.

Consent for publication (include appropriate statements) Authors declare to provide Consent for publication to journal.

References

1. Sikorski, Michael, Honig, Andrew: Practical Malware Analysis: The Hands-On Guide to Dissecting Malicious Software, 1st edn. No Starch Press, USA (2012)
2. Ye, Y., Li, T., Adjeroh, D., Iyengar, S.S.: A survey on malware detection using data mining techniques. ACM Comput. Surveys (CSUR). **50**(3), 1–40 (2017)
3. Damodaran, A., Di Troia, F., Visaggio, C.A., Austin, T.H., Stamp, M.: A comparison of static, dynamic, and hybrid analysis for malware detection. J. Comput. Virol. Hacking Tech. **13**(1), 1–2 (2017)
4. Shabtai, A., Moskovitch, R., Elovic,i Y., Glezer, C.: Detection of malicious code by applying machine learning classifiers on static features: A state-of-the-art survey, Information Security Tech. Report **14**(1), 16–29 (2009)
5. Kancherla Mukkamala, K. S.: Image visualization based malware detection. In: Proceedings of the 2013 IEEE Symposium on Computational Intelligence in Cyber Security (CICS), Singapore, pp. 40–44 (2013)
6. Vasan, D., Alazab, M., Wassan, S., Naeem, H., Safaei, B., Zheng, Q.: IMCFN: Image-based malware classification using fine-tuned convolutional neural network architecture. Comput. Netw **171**, 107138 (2020)
7. Wagner, M., Fischer, F., Luh, R., Haberson, A., Rind, A., Keim, D. A., Aigner, W.: A Survey of Visualization Systems for Malware Analysis. EuroVis (2015)
8. Shaid, S.Z., Maarof, M.A.: Malware behaviour visualization. J. Teknologi **70**(5), 25–33 (2014)
9. Trinius, P., Holz, T., Gobel, J., Freiling, F. C.: Visual analysis of malware behavior using treemaps and thread graphs. In: Proceedings of 6th International Workshop on Visualization for Cyber Security, pp. 33–38 (2009)
10. Jae, H.L., KyoungSoo, H., Eul, G. I.: Malware analysis method using visualization of binary files. In: Proceedings of 2013 ACM Conference on Research in Adaptive and Convergent Systems, pp. 317–321 (2013)
11. Eul, G.I., KyoungSoo, H., Jae, H.L., Boojoong, K.: Malware analysis using visualized images and entropy graphs. Int. J. Inform. Secur. **14**, 1–14 (2014)
12. Ban, X., Chen, L., Hu, W., Wu, Q.:Malware variant detection using similarity search over content fingerprint. In: Proceedings of the IEEE Conference on Control and Decision, pp. 5334–5339 (2014)
13. Nataraj, L., Karthikeyan, S., Jacob, G., Manjunath, B.: Malware images: visualization and automatic classification. In: Proceedings of the 8th International Symposium on Visualization for Cyber Security, pp. 1–7 (2011)
14. Aziz, M., Anita, P.: Malware class recognition using image processing techniques. In: Proceedings of the IEEE Conference on Data Management, Analytics and Innovation, (ICDMAI), pp. 76–80 (2017)
15. Barath, N. N., Ouboti, D. B., Temesguen, M. K.:Pattern recognition algorithms for Malware classification. In: Proceedings of the IEEE Conference of Aerospace and Electronics, pp. 338–342 (2016)
16. Kosmidis, K., Kalloniatis, C.:Machine Learning and Images for Malware detection and classification. In: Proceedings of the 21st Pan-Hellenic Conference on Informatics, pp. 1–6 (2017)
17. Agarap, A. F., Pepito, F. J. :Towards building an intelligent anti-malware system: a deep learning approach using Support Vector Machine (SVM) for Malware classification. arXiv preprint arXiv:1801.00318 (2017)
18. Bhowmik, A., Kumar, S. Bhat, N.: Evolution of automatic visual description techniques-a methodological survey. In: Multimedia Tools and Applications, pp. 1–45 (2021)
19. Bhowmik, A., Kumar, S., Bhat, N.: Eye disease prediction from optical coherence tomography images with transfer learning. In: International Conference on Engineering Applications of Neural Networks, pp. 104–114 (2019)
20. Kumar, S., Kumar, M.: Predicting customer churn using artificial neural network. In: International Conference on Engineering Applications of Neural Networks, pp. 299-306 (2019)
21. Singh, A., Handa, A., Kumar, N., Shukla, S. K.:Malware classification using image representation. In: Cyber Security Cryptography and Machine Learning, pp. 75–92 (2017)
22. Zhu, D., Jin, H., Yang, Y., Wu. D., Chen, W.:DeepFlow: Deep learning-based malware detection by mining Android application for abnormal usage of sensitive data. In: Proceedings of the 2017 IEEE Symposium on Computers and Communications (ISCC), pp. 438–443 (2017)
23. Simonyan, K., Zisserman, A. : Very Deep Convolutional Networks for Large-Scale Image Recognition. arXiv:1409.1556 (2014)
24. Cui, Z., Xue, F., Cai, X., Cao, Y., Wang, G., Chen, J.: Detection of malicious code variants based on deep learning. IEEE Trans. Ind. Inform. **14**(7), 3187–96 (2018)
25. Vinayakumar, R., Alazab, M., Soman, K.P., Poornachandran, P., Venkatraman, S.: Robust intelligent malware detection using deep learning. IEEE Access **7**, 46717–46738 (2019)
26. Naeem, H., Guo, B., Naeem, M.R., Ullah, F., Aldabbas, H., Javed, M.S.: Identification of malicious code variants based on image visualization. Comput. Electr. Eng. **76**, 225–237 (2019)
27. Naeem, H.: Detection of malicious activities in internet of things environment based on binary visualization and machine intelligence. Wireless Personal Commun. **108**(4), 2609–29 (2019)
28. Kumar, S., Kumar, M: A study on the image detection using convolution neural networks and TenserFlow. In: 2018 International Conference on Inventive Research in Computing Applications (ICIRCA), IEEE, pp. 1080–1083 (2018)
29. Nisa, M., Shah, J.H., Kanwal, S., Raza, M., Khan, M.A., Damaševičius, R., Blažauskas, T.: Hybrid malware classification method using segmentation-based fractal texture analysis and deep convolution neural network features. Appl. Sci. **10**(14), 4966 (2020)
30. Ren, Z., Chen, G., Lu, W.: Malware visualization methods based on deep convolution neural networks. Multimedia Tools Appl. **16**, 1–9 (2020)
31. Tuncer, T., Ertam, F., Dogan, S.: Automated malware recognition method based on local neighborhood binary pattern. Multimedia Tools Appl. **79**(37), 27815–32 (2020)
32. Anderson. B., Storlie, C. Improving malware classification: bridging the static/dynamic gap. In: Proceedings of the 5th ACM Workshop on Security and Artificial Intelligence, pp. 3–14 (2012)
33. Dahl, G. E., Stokes, J. W., Deng, L., Yu, D.: Large-scale malware classification using random projections and neural networks. In: Proceedings of the IEEE International Conference on Acoustics, Speech and Signal Processing (ICASSP), pp. 26–31 (2013)
34. Zhang, M., Duan, Y., Yin, H., Zhao, Z.:Semantics-aware android malware classification using weighted contextual api dependency graphs. In: Proceedings of the ACM SIGSAC Conference on Computer and Communications Security, pp. 1105–1116 (2014)
35. Pascanu, R.; Stokes, J.W.; Sanossian, H.; Marinescu, M.; Thomas, A. Malware classification with recurrent networks. In: Proceedings of the 2015 IEEE International Conference on Acoustics, Speech and Signal Processing (ICASSP), Brisbane, QLD, Australia, pp. 7–24 (2015)
36. Garcia, F. C., Muga, F. P. Random forest for malware classification. arXiv preprint arXiv:1609.07770 (2016)
37. Moshiri, E., Abdullah, A.B., Azlina, R., Raja, B., Muda, Z.: Malware classification framework for dynamic analysis using information theory. Indian J. Sci. Technol. **10**, 1–10 (2017)
38. Liu, L., Wang, B., Yu, B., Zhong, Q.: Automatic malware classification and new malware detection using machine learning. Front. Inform. Technol. Electr. Eng. **18**(9), 1336–47 (2017)

39. Cakir, B., Dogdu, E.:Malware classification using deep learning methods. In: Proceedings of the ACM Southeast Conference (ACMSE) Association for Computing Machinery, pp. 1–5 (2019)
40. Kalash, M., Rochan, M., Mohammed, N., Bruce, N. D. B., Wang, Y., Iqbal, F.: Malware Classification with Deep Convolutional Neural Networks. In: Proceedings of the 2018 9th IFIP International Conference on New Technologies, Mobility and Security (NTMS), pp. 1–5 (2018)
41. Gibert, L.D., Mateu, P.C., Planes, C.J., Vicens, R.: Using convolutional neural networks for classification of malware represented as images. J. Comput. Virol. Hacking Tech. **15**, 15–28 (2019)
42. Marastoni, N., Giacobazzi, R., Dalla, P. M.: Data augmentation and transfer learning to classify malware images in a deep learning context. J. Comput. Virol. Hack. Tech. 1–9 (2021)
43. Bhodia N, Prajapati P, Di Troia F, Stamp M. Transfer learning for image-based malware classification. arXiv preprint arXiv:1903.11551. 2019 Jan 21
44. Prajapati P, Stamp M. An empirical analysis of image-based learning techniques for malware classification. In: Malware Analysis Using Artificial Intelligence and Deep Learning 2021, pp. 411–435. Springer, Cham (2021)
45. Yajamanam, S., Selvin, V. R., Di Troia, F., Stamp, M.: Deep Learning versus Gist Descriptors for Image-based Malware Classification. InIcissp, pp. 553–561 (2018)
46. Vasan, D., Alazab, M., Wassan, S., Safaei, B., Zheng, Q.: Image-Based malware classification using ensemble of CNN architectures (IMCEC). Comput. Secur. **92**, 101748 (2020)
47. Jain, M., Andreopoulos, W., Stamp, M.: Convolutional neural networks and extreme learning machines for malware classification. J. Comput. Virol. Hacking Tech. **16**(3), 229–44 (2020)
48. Vasan, D., Alazab, M., Wassan, S., Naeem, H., Safaei, B., Zheng, Q.: IMCFN: image-based malware classification using fine-tuned convolutional neural network architecture. Comput. Networks. **22**(171), 107138 (2020)
49. Lad, S. S., Adamuthe, A.C. Malware classification with improved convolutional neural network model. Int. J. Comput. Network Inform. Secur. **12**(6) (2020)
50. Bergstra, J., Bengio, Y.: Random search for hyper-parameter optimization. J. Mach. Learn. Res. **13**(2) (2012)

Publisher's Note Springer Nature remains neutral with regard to jurisdictional claims in published maps and institutional affiliations.

2021 IEEE 2nd International Conference on Electrical Power and Energy Systems (ICEPES)
MANIT, Bhopal, India. Dec 10-11, 2021

Coordinated Allocation of Electric Vehicle Charging Stations and Capacitors in Distribution Network

Mohd Bilal
Department of Electrical Engineering
Delhi Technological University
New Delhi, India
bilal.zhcet01@gmail.com

Astitva Kumar
Department of Electrical Engineering
Delhi Technological University
New Delhi, India
astitvakumar.27@gmail.com

Mohammad Rizwan
Department of Electrical Engineering
Delhi Technological University
New Delhi, India
rizwan@dce.ac.in

2021 IEEE 2nd International Conference On Electrical Power and Energy Systems (ICEPES) | 978-1-6654-0236-1/21/$31.00 ©2021 IEEE | DOI: 10.1109/ICEPES52894.2021.9699775

***Abstract*— Greenhouse gas emissions from internal combustion engines-based transport sector are a major source of concern in large cities. Electric vehicles (EVs) adoption at a worldwide scale is seen as a possible solution to mitigate global warming and security of energy supply. Charging stations (CS) are an obligatory requirement to meet the energy demand of EVs. Because of the incorrect location and size of the CS, other technical issues arise, such as fluctuations in voltage levels and abrupt increase in system's loss. The efficient allocation of CS and capacitors (CAP) is presented in this research work to sustain voltage profile and reduce losses in electrical grid networks. In this work, the aim of minimizing power loss is considered along with some constraints such as power balance equations, voltage limits, and thermal limits. The meta-heuristic-based optimization algorithm i.e., GWO is employed to handle the objective functions. This proposed technique is tested on East Delta Network (EDN) consisting of 30 buses. The results show how optimal CS and CAP planning affects system's loss and voltage levels in standard electrical networks. The superiority of the recommended technique is established when the acquired results are compared to that of PSO,**

Keywords*— Optimization approach, Electric vehicle, Charging station, Distribution system

I. INTRODUCTION

Greenhouse gas emissions from fossil fuel vehicles is one of most difficult challenges which are faced by metropolitan cities. One of the most successful options for electrical stability and reduction in carbon content is to accelerate the worldwide utilization of 30 million electric vehicles (EVs) by 2030 [1]. If current trends continue, EVs will replace 62% of commercial vehicles by 2050. Versatile fuels, ease, safe charging, excellent performance, and a 40%–60% decline in fossil fuel dependency are all big advantages of EVs [2]. Charging stations (CS) are an essential prerequisite for supplying the increased quantity of EVs around the globe. For a sustainable flow, the CS delivers electrical energy from a power source to EV terminals via communication facilities. In addition, houses, offices, personal fleet services, and government platforms may be suitable locations for CS installation. The allotment of CS will pose new problems for grid network if technicalities are not accounted during the preparation phase. Academia and government agencies are working together to ensure that CS in electric systems is properly planned [3]. The impact of integrated CS on the power networks in terms of losses and voltage regulation has been examined in recent studies.

Numerous researches reported on the siting and sizing of CS united to the standard distribution network. A variety of nature-inspired approaches have been used to address the CS placement issue. Concerning this, the authors carried out a descriptive assessment to determine the best way to plan CS in transmission and distribution grids [4]. The IEEE 123 grid network is used as a standard framework to determine the best CS position by implementing a modified primal-dual interior point algorithm (MPDIPA) [5]. A detailed survey based on machine learning methodologies is conducted for anticipating EV charging patterns [6]. In [7], parking lots are allocated using a genetic algorithm in electrical network. CS have been optimally sited in Allahabad's distribution network using a hybrid optimization strategy that combines GA and particle swarm optimization (PSO) [8]. Jaya optimization method is considered for optimally allocating the CS by minimalizing the operating cost, installation cost and grid losses [9]. An efficient planning for placing electric vehicle charging station (EVCS) in various well-known places of South Delhi, India is presented [10]. A hybrid solution of CSO and TLBO is used for the allocation of CS taking into account various financial and grid operational problems [11]. The optimum location for an electric vehicle parking lot in Beijing's district has been identified to minimize total cost and system's losses [12]. The HGWOPSO hybrid technique is described for the joint placement of EVCS and DG in electrical network while keeping the system's reliability in mind [13]. A novel approach called demand side management is used for the assignment of CS in electric power systems. A meta-heuristic technique i.e., PSO for the CS and Distributed Generations (DGs) planning in unbalanced distribution network is applied [14]. The installation of EVCS in an integrated distribution and road infrastructure is achieved in [15]. To account for EV uncertainties, the 2m point estimation method is applied. In addition, the approaches of differential evolution (DE) and Harris Hawks optimization (HHO) are used to tackle the optimization problem.

As a result of CS integration into electric systems, technical problems, such as voltage deterioration and increased power loss, may arise. Earlier planning analyses haven't looked the positive consequences of CAPs for reducing losses and improving voltage profiles when inserting CS into system. Capacitor placement in the radial power network provide a number of advantages, including decreased energy losses and power factor compensation etc. The direct search based algorithm to figure out the capacity and location of fixed as well as switched capacitors is demonstrated in a grid network while reducing power loss and increasing energy savings [16]. The artificial bee colony technique for the determination of best site for the capacitor allocation is illustrated. Researchers presented a two-step technique for determining the best capacitor position and size in a distribution network [17]. A novel technique for proper EVCS siting is developed, focusing on congestion

Authorized licensed use limited to: DELHI TECHNICAL UNIV. Downloaded on February 10,2022 at 10:16:12 UTC from IEEE Xplore. Restrictions apply.

management and reactive power compensation to assign parking lots and capacitors. For the best parking lot size, a biogeography-based optimization strategy was examined [18].

The major goal of this investigation is to allocate CS and capacitors in a radial distribution system at the same time. This plan is aimed at reducing power loss while improving the voltage profile. In this current work, EVCS have been assigned to EDN system consisting of 30 buses. In addition, the objective functions are solved using GWO, a new intelligent optimization method. Comparison of the obtained findings with other algorithms such as PSO validates the performance of the chosen optimization approach.

II. PROBLEM FORMULATION

EVCS implementation at the correct location is critical for EV users and power providers. Because all electric range is limited, EVs must be recharged frequently throughout a journey. CS is commonly used as a high load that causes increased power loss when improperly installed in the grid network. As a result, the optimal siting of CS is required for a slight rise in system losses. The influence of introducing CS into the grid network is mitigated by installing capacitors, which lessen power losses and reinforce the voltage levels.

A. Modeling of CS load

CSs serve as supplementary load for the electrical network. When CS is integrated into the power system, the overall load in the system can be estimated as follows [15]:

$$T_{load} = \sum_{bs=1}^{N_{bus}} P_{avail,bs} + P_{EVCS}^{bs} \quad (1)$$

Where, T_{load} indicates the overall load, N_{bus} is the total number of nodes, $P_{avail,bs}$ denotes the previously connected load at bs^{th}bus and P_{EVCS}^{bs} is EVCS load connected to bs^{th} bus.

The added load for the EVCS will be applied only to the bus on which it is mounted.

B. Modeling of capacitor integrated to distribution network

The following is a mathematical model for integrating capacitors into a distribution network. The integration of CS and capacitor to the electrical power network is represented in Fig.1.

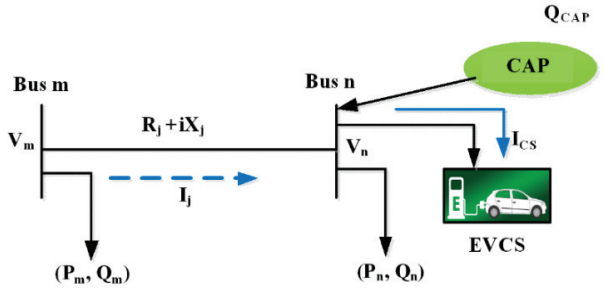


Fig.1. Interpretation of integrated CS and capacitor in distribution network

The actual and reactive power loss in the branch joining the m and n buses are estimated using the following formula:

$$P_{loss}(m,n) = \frac{(P_n^2+Q_n^2)}{|V_n|^2} \times R_j \quad (2)$$

$$Q_{loss}(m,n) = \frac{(P_n^2+Q_n^2)}{|V_n|^2} \times X_j \quad (3)$$

The total active power loss, $P_{T,loss}$, can be determined by adding the separate power losses of all distribution lines, and is expressed as follows:

$$P_{T,loss} = \sum_{j=1}^{N_{br}} P_{loss,j}\,(m,n) \quad (4)$$

$$P_{T,loss}^{cap} = R_j \times \frac{(P_n^2+Q_n^2)}{|V_n|^2} + \frac{Q_{cap}^2 - 2\times Q_n \times Q_{cap}}{|V_n|^2} \times R_j \quad (5)$$

$$\text{Energy loss reduction} = K_{ep} \times \left(P_{T,loss} - P_{T,loss}^{cap}\right) \times T \quad (6)$$

$$\text{Total capacitor cost} = \frac{K_c \times Q_{cap(total)}}{life\ expectancy}\ \$\ per\ year \quad (7)$$

where, V_m and V_n are the voltages at bus m and n respectively, δ_m and δ_n are the voltage angle at bus m and n respectively, I_j is the branch current, Z_j is the branch impedance, P_{loss} and Q_{loss} are active and reactive power loss respectively, $P_{T,loss}$ is the total active power loss, K_{ep} is the amount of energy paid per kWh, K_c is the purchasing cost of capacitor, N_{br} and N_{bus} indicates the number of branches (lines) and buses (nodes) in the distribution network.

C. Technical Constraints

The objective functions are evaluated with the following restrictions.

1) Power balance constraints:

The restrictions associated with load flow analysis can be indicated as given below

$$P^{substation} = \sum_{j=1}^{N_{br}} P_{loss}^{j}(m,n) + \sum_{bs=1}^{N_{bus}} P_{avail,bs} + P_{EVCS}^{bs} \quad (8)$$

$$Q^{substation} + \sum_{bs=1}^{N_{bus}} Q^{cap}(bs) = \sum_{j=1}^{N_{br}} Q_{loss}^{j}(m,n) + \sum_{bs=1}^{N_{bus}} Q_{avail,bs} \quad (9)$$

2) Voltage restrictions:

The value of the voltage on every bus must be within certain limits.

$$V_{bs}^{min} \le \mathrm{V}\,(bs) \le V_{bs}^{max} \qquad bs = 1,2,3 \ldots N_{bus} \quad (10)$$

Where, V_{bs}^{min} is the minimum voltage, V_{bs}^{max} is maximum voltage and V (bs) is voltage at bs^{th} bus.

3) Transmission line restriction:

The active power flow in every branch (line) should be less than the line's maximum permitted capacity.

$$S_{Lp} \le S_{Lp}^{max} \quad (11)$$

Where, S_{Lp}^{max} is the maximum permissible capacity of branch number p.

4) Quantity of capacitor used:

The goal of this constraint is to reduce the quantity of capacitor placements. As a result, the number of installed capacitors N^{cap} must be less than or equal to the overall number of capacitors $N^{cap}(max)$.

$$N^{cap} \le N^{cap}(max) \quad (12)$$

5) Sizing of capacitor:

Authorized licensed use limited to: DELHI TECHNICAL UNIV. Downloaded on February 10,2022 at 10:16:12 UTC from IEEE Xplore. Restrictions apply.

The injected reactive power i.e., Q_{cap} should lie within $Q_{cap}(min)$ and $Q_{cap}(max)$.

$$Q_{cap}(min) \le Q_{cap} \le Q_{cap}(max) \quad (13)$$

III. OPTIMIZATION TECHNIQUE APPLIED

A. Description of GWO

S. Mirjalili and Lewis [19] in 2014 suggested a new intelligent technique named Grey Wolf Optimizer (GWO). These wolves tend to survive in packs of 5 to 12 individuals. They adhere to a dominating social structure, with alphas (α) and betas (β) occupying the first and second levels, respectively. α and β are followed by delta (δ) wolves. The omega (ω), the pack's lowest level wolves, serve as a scapegoat.

The social hierarchy of GWO, surrounding, and chasing prey are all important steps in the mathematical modelling of GWO. The collaboration and interaction among grey wolves provide optimum solution in minimum time. This algorithm works on simple principle characterized by fast convergence rate, high precision and provides proper balance between both exploration and exploitation capability.

The steps adapted to govern encircling and hunting mechanism of proposed GWO algorithm are as follows:

1) Encircling Prey

The encirclement of prey is the first step in the hunting process. The stages of encircling are defined in [19] as follows:

$$\overrightarrow{M} = \left|\overrightarrow{C} . \overrightarrow{Z_p}(t) - \overrightarrow{Z}(t)\right| \quad (14)$$

$$\overrightarrow{Z}(t+1) = \overrightarrow{Z_p}(t) - \overrightarrow{N} . \overrightarrow{M} \quad (15)$$

where t specifies the iteration, $\vec{N}$ and $\vec{C}$ denotes the coefficient vectors, $\vec{Z}$ and $\overrightarrow{Z_P}$ are the position vector of prey and grey wolf respectively.

$$\overrightarrow{N} = 2n . \overrightarrow{r_1} - \overrightarrow{a} \quad (16)$$

$$\overrightarrow{C} = 2 . \overrightarrow{r_2} \quad (17)$$

$$a = 2 - t * \frac{2}{\text{maximum iteration}} \quad (18)$$

where r_1 and r_2 are random numbers with values in the range of 0 and 1, and the magnitude of a declines linearly from two to zero during the iterations.

2) Hunting Prey

It is assumed that, α, β and δ and have appropriate detail regarding the location of the scavengers in order to mathematically replicate the hunting mechanism of grey wolves. The best solutions so far are, α, β and δ, while the remaining of the search agents upgrade their location after every iterative process based on the best position of the first three wolves. The mathematical expressions which are created in this context are described below [19]

$$\overrightarrow{M_\alpha} = \left|\overrightarrow{C} . \overrightarrow{Z_\alpha} - \overrightarrow{Z}(t)\right| \quad (19)$$

$$\overrightarrow{M_\beta} = \left|\overrightarrow{C} . \overrightarrow{Z_\beta} - \vec{Z}(t)\right| \quad (20)$$

$$\overrightarrow{M_\delta} = \left|\overrightarrow{C} . \overrightarrow{Z_\delta} - \overrightarrow{Z}(t)\right| \quad (21)$$

$$\overrightarrow{Z_1} = \overrightarrow{Z_\alpha} - \overrightarrow{N} . \overrightarrow{M_\alpha} \quad (22)$$

$$\overrightarrow{Z_2} = \overrightarrow{Z_\beta} - \overrightarrow{N} . \overrightarrow{M_\beta} \quad (23)$$

$$\overrightarrow{Z_3} = \overrightarrow{Z_\delta} - \overrightarrow{N} . \overrightarrow{M_\delta} \quad (24)$$

$$\overrightarrow{Z}(t+1) = \frac{\overrightarrow{Z_1} + \overrightarrow{Z_2} + \overrightarrow{Z_3}}{2} \quad (25)$$

The exploration ability of the GWO symbolizes the grey wolf's search process, whereas the exploitation ability depicts the grey wolf's attacking phase. The detailed explanation of GWO algorithm can be understand with the help of flow chart portrayed in Fig. 2.

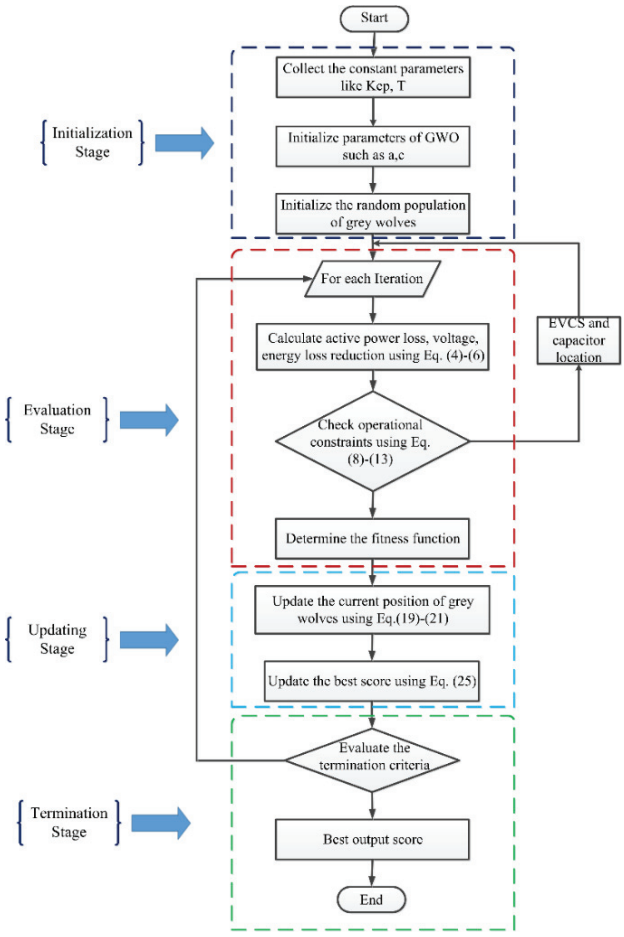


Fig. 2. Step by step diagram of the GWO technique for the EVCS and capacitor allocation

IV. SIMULATION RESULTS AND DISCUSSIONS

A detailed diagram of the EDN 30 bus distribution power system with 3 EVCS and 2 capacitors are displayed in Fig. 3. There are 30 nodes and 29 branches in the EDN 30 bus distribution network. The system may run at a maximum of 100 kVA and 12.66 kV. It has a total reactive power load of 14248.26 kVAr and a total actual power load of 22483.25 kW. Each outlet requires 50 kW, and CS are considered to have 30 charging outlets. As a result, CS can charge 30 EVs at once. In the distribution network, the optimal number of CS must be put at the ideal bus. Because the installation of CS increases the network's active power loss. As a result, capacitors are strategically located to mitigate for CS losses. The direct approach-based load flow analysis is performed to compute the system losses. It is assumed that charging power

Authorized licensed use limited to: DELHI TECHNICAL UNIV. Downloaded on February 10,2022 at 10:16:12 UTC from IEEE Xplore. Restrictions apply.

of 15 kW is provided to charge the EVs batteries. GWO is employed to optimize the objective functions.

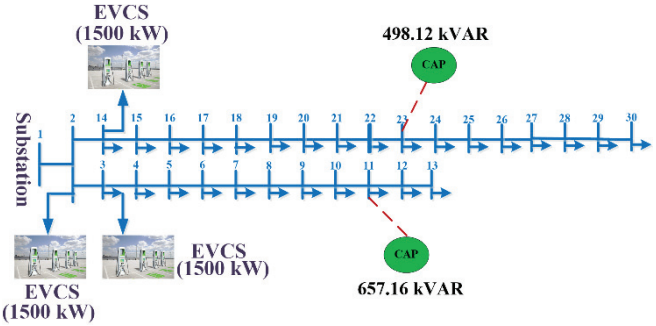


Fig. 3. Line diagram of EDN system with three EVCS and two capacitors

According to the EDN radial distribution scheme, the loads are coupled at different nodes. The additional load created by EV charging in CS is taken into account at the node where the CS is being assigned.

The MATLAB (R2015a) programming language is used to execute this research work, which is installed on a machine with an Intel i3 at 2.3 GHz and 2 GB RAM.

The total number of feasible capacitor placement places is assumed to be two for the EDN 30-bus networks. On every bus, the voltage constraint is between 0.95 and 1.05 p.u. The maximal limit of active power flow is set at 5000 kW. Bus 1 is a substation bus for the 30-bus system with a constant voltage of 1 p.u., hence EVCS and capacitor are unlikely to be found there. In addition, the amount of reactive power to be supplied for compensation is chosen between 150 and 1200 kVAr.

TABLE I. INPUT PARAMETERS NEEDED FOR THE CALCULATION OF ENERGY LOSS REDUCTION [20]

Parameter	Value	Unit
Cost of energy paid per kWh ($\mathbf{K_{ep}}$)	0.06	$/kWh
Hours per year (T)	8760	Hours
Cost of purchase of capacitor per kVAr ($\mathbf{K_c}$)	5	$/kVAr
Life expectancy	10	years

The suggested algorithm's quality and performance have been verified on a 30-bus standard system with the objective of lowering active power loss and enhancing savings. The proposed methodology emphasizes on the ideal placement of CS, considering the 100% penetration of EVs, and then capacitors are deployed to offset the additional losses caused by CS incorporation and therefore boost the robustness of electrical network. The parameters considered for the computation of active power losses and energy loss cost are mentioned in Table I.

To analyze the active power losses, a direct approach method for load flow analysis is used at first, yielding a result of 598.19 kW. The minimum voltage is 0.9112 p.u., and the highest voltage is 0.9942 p.u. in this situation. The yearly cost of energy loss for 598.19 kW is 314408.66 $. The best nodes for CS placement, according to the proposed method, are nodes 2, 3 and 14, which result in least power losses 624.29 kW, 634.49 kW and 642.53 kW respectively. Although CS are positioned near the substation bus, the results show that the optimal CS placement approach increases power loss and disrupts the voltage profile in

TABLE II. COMPARATIVE ANALYSIS OF RESULTS ATTAINED USING GWO AND PSO FOR EDN-BUS SYSTEM

Parameter	Base Case	EVCS and capacitor placement	
		GWO	PSO
Active power losses (kW)	598.19	557.12	562.34
Reactive power losses (kVAr)	268.35	250.98	253.15
Optimal nodes for EVCS	–	2, 3, 14	2, 3, 14
Total number of EVs	–	100	100
Optimal nodes for capacitor	–	11, 23	15, 29
Capacitor sizes (kVAr)	–	657.16, 498.12	782.19, 543.56
Total kVAr	–	1155.28	1325.75
Energy loss cost ($)	314408.66	292822.27	295565.91
% loss reduction in energy loss cost	–	6.82	5.99
Total capacitor cost ($)	–	577.64	662.87

electrical networks. Capacitors are located near to CS and the end of lines in order to enhance the voltage level and loss by giving some reactive power. In this regard, Table II shows the best position and capacities of CS and capacitors using the suggested approach, as well as comparisons with PSO. When capacitors with ratings of 657.16, and 498.12 kVAr are put at ideal nodes 11, 23 respectively, active power loss drops to 557.12 kW, down from 598.19 kW in the base scenario, resulting in a 6.82 percent reduction in yearly energy loss cost. The 15th bus has a minimum voltage of 0.9515 p.u., which is within the voltage restriction limit. In this article, the suggested GWO reduces annual energy loss costs by 6.82 percent, which is better than PSO, which reduce losses by 5.99 percent. In addition, as compared to PSO, the cost of installing capacitors with GWO is low, as indicated in Table II.

The preceding analysis establishes the superiority of the GWO algorithm over the PSO algorithm. Table II shows a comparison of the obtained results utilizing the suggested method vs PSO for the EDN 30-bus system.

Fig. 4. depicts the voltage profile of a 30-bus system after the EVCS and capacitor have been placed optimally. The installation of the capacitor improves the voltage profile. As a result, the suggested GWO technique is successful in sustaining the 30-bus distribution system's healthy voltage profile.

After adding CS and capacitor, Fig. 5. displays the flow of active power in all lines of the 30-bus distribution system. Due to an increase EVCS loading, the active power flow increases, however it is regulated by placing capacitors at appropriate nodes and maintaining it within permitted limits.

When the capacitors are not installed, the system losses are 624.29 kW, 634.49 kW and 642.53 kW respectively. Active power losses decrease as the number of capacitors grows.

Authorized licensed use limited to: DELHI TECHNICAL UNIV. Downloaded on February 10,2022 at 10:16:12 UTC from IEEE Xplore. Restrictions apply.

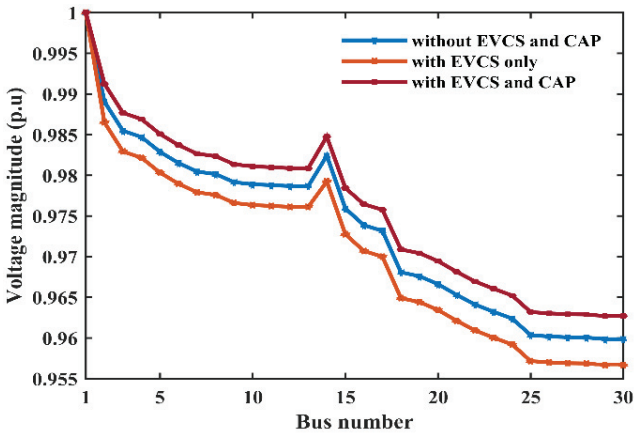


Fig. 4. Voltage profile of EDN bus system after placing EVCS and capacitors

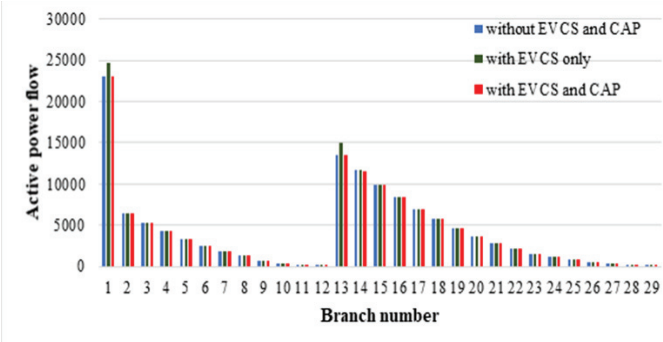


Fig. 5. Effect of placing EVCS and capacitors on active power flow

Furthermore, Fig. 6. depicts the fluctuation in power losses when the EVCS and capacitor are integrated. It's easy to see how power losses decrease as the number of capacitors grows. However, increasing the capacitors reduces power loss only somewhat, and it also poses cost concerns.

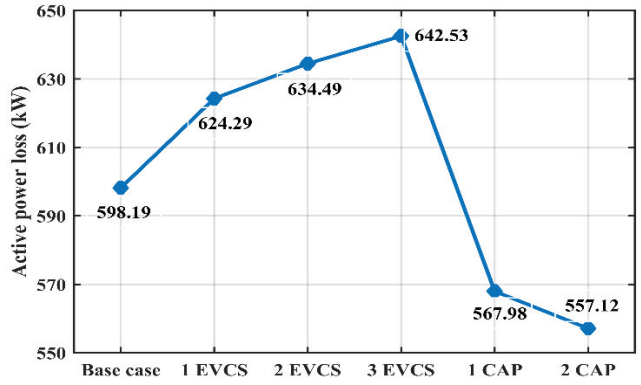


Fig. 6. Variation in power losses after the placement of EVCS and capacitors

As that of active power losses, capacitor placement also reduces the reactive power loss as shown in Fig. 7. The base case reactive power loss was 268.35 kVAr. It reduced to 250.98 kVAr after placing two capacitors. The varying behavior of reactive power losses is displayed in Fig. 7.

By comparing the findings of GWO to those of PSO, the efficacy of GWO may be confirmed. Fig. 8. shows the response of the GWO and PSO. It is revealed that the suggested algorithm has high convergence toward the global optimum than PSO.

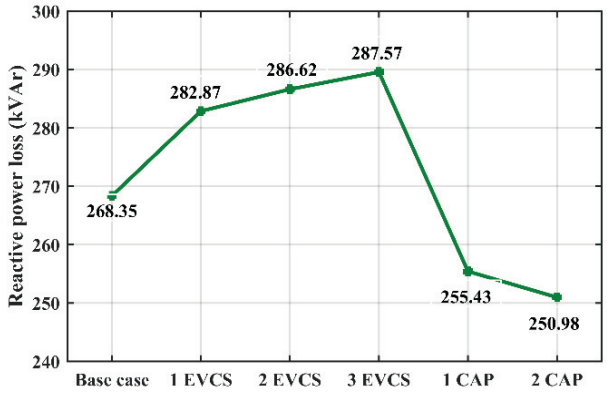


Fig. 7. Effect of placing EVCS and capacitors on reactive power losses

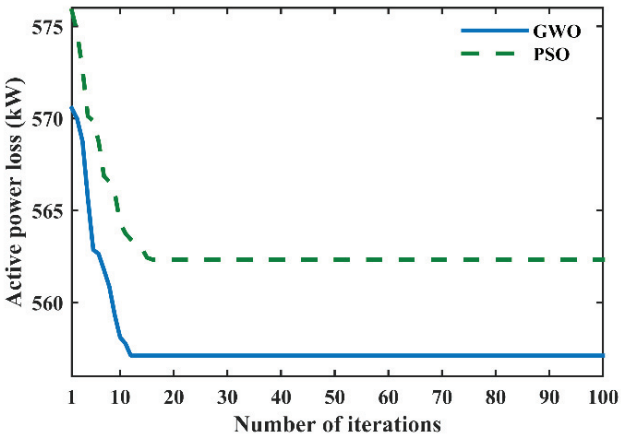


Fig. 8. Response of GWO and PSO for EDN system

V. CONCLUSION

This research is done to reduce active power losses while maximizing the savings after determining the optimum location and size of EVCS and CAP using GWO. The findings show that optimal EVCS planning increases system losses and lowers voltage in grid networks. It is also shown that the capacitors installation lessens the losses of the system and enhance the voltage levels. The anticipated technique is applied on EDN system which comprise of 30 buses. The efficiency of the GWO approach is validated by comparing the research findings to those of the traditional PSO method. Furthermore, power loss minimization must not be the primary goal. Energy loss reduction is calculated in this work as one of the objectives.

The intended study effort can be pushed even farther after reconfiguring the distribution system following the addition of EVCS to reduce losses and improve voltage levels. It is also possible to analyze the allocation of distributed generations in a radial network with EVCS. These are the unmet research questions that can be investigated in future research.

REFERENCES

[1] Global EV Outlook 2013—Understanding the Electric Vehicle Landscape to 2020, "International Energy Agency, Clean Energy Ministerial, and Electric Vehicles Initiative," pp. 14–15, 2013.

[2] S. Pazouki, A. Mohsenzadeh, M.-R. Haghifam, and S. Ardalan, "Simultaneous Allocation of Charging Stations and Capacitors in Distribution Networks Improving Voltage and Power Loss," *Can. J. Electr. Comput. Eng.*, vol. 38, no. 2, pp. 100–105, 2015, doi: 10.1109/CJECE.2014.2377653.

Authorized licensed use limited to: DELHI TECHNICAL UNIV. Downloaded on February 10,2022 at 10:16:12 UTC from IEEE Xplore. Restrictions apply.

[3] Sekyung Han, Soohee Han, and K. Sezaki, "Development of an Optimal Vehicle-to-Grid Aggregator for Frequency Regulation," *IEEE Trans. Smart Grid*, vol. 1, no. 1, pp. 65–72, Jun. 2010, doi: 10.1109/TSG.2010.2045163.

[4] M. Bilal and M. Rizwan, "Electric vehicles in a smart grid: a comprehensive survey on optimal location of charging station," *IET Smart Grid*, vol. 3, no. 3, pp. 267–279, Jun. 2020, doi: 10.1049/iet-stg.2019.0220.

[5] Z. Liu, F. Wen, and G. Ledwich, "Optimal Planning of Electric-Vehicle Charging Stations in Distribution Systems," *IEEE Trans. Power Deliv.*, vol. 28, no. 1, pp. 102–110, Jan. 2013, doi: 10.1109/TPWRD.2012.2223489.

[6] S. Shahriar, A. R. Al-Ali, A. H. Osman, S. Dhou, and M. Nijim, "Machine Learning Approaches for EV Charging Behavior: A Review," *IEEE Access*, vol. 8, pp. 168980–168993, 2020, doi: 10.1109/ACCESS.2020.3023388.

[7] M. Moradijoz, M. Parsa Moghaddam, M. R. Haghifam, and E. Alishahi, "A multi-objective optimization problem for allocating parking lots in a distribution network," *Int. J. Electr. Power Energy Syst.*, vol. 46, pp. 115–122, Mar. 2013, doi: 10.1016/j.ijepes.2012.10.041.

[8] A. Awasthi, K. Venkitusamy, S. Padmanaban, R. Selvamuthukumaran, F. Blaabjerg, and A. K. Singh, "Optimal planning of electric vehicle charging station at the distribution system using hybrid optimization algorithm," *Energy*, vol. 133, no. 6, pp. 70–78, Aug. 2017, doi: 10.1016/j.energy.2017.05.094.

[9] B. Ajit, KM and Suresh, "Optimal placement of electric vehicle charging station using jaya algorithm," *Recent Adv. power Syst.*, pp. 259–266, 2020.

[10] M. Bilal and M. Rizwan, "Intelligent Algorithm based Efficient Planning of Electric Vehicle Charging Station: A Case Study of Metropolitan City of India," *Sci. Iran.*, pp. 0–0, Aug. 2021, doi: 10.24200/sci.2021.57433.5238.

[11] S. Deb, K. Kalita, X.-Z. Gao, K. Tammi, and P. Mahanta, "Optimal placement of charging stations using CSO-TLBO algorithm," in *2017 Third International Conference on Research in Computational Intelligence and Communication Networks (ICRCICN)*, Nov. 2017, pp. 84–89, doi: 10.1109/ICRCICN.2017.8234486.

[12] Y. Zhang, Q. Zhang, A. Farnoosh, S. Chen, and Y. Li, "GIS-Based Multi-Objective Particle Swarm Optimization of charging stations for electric vehicles," *Energy*, vol. 169, pp. 844–853, Feb. 2019, doi: 10.1016/j.energy.2018.12.062.

[13] M. Bilal, M. Rizwan, I. Alsaidan, and F. M. Almasoudi, "AI-based Approach for Optimal Placement of EVCS and DG with Reliability Analysis," *IEEE Access*, pp. 1–1, 2021, doi: 10.1109/ACCESS.2021.3125135.

[14] M. S. K. Reddy and K. Selvajyothi, "Optimal placement of electric vehicle charging station for unbalanced radial distribution systems," *Energy Sources, Part A Recover. Util. Environ. Eff.*, pp. 1–15, Feb. 2020, doi: 10.1080/15567036.2020.1731017.

[15] A. Pal, A. Bhattacharya, and A. K. Chakraborty, "Allocation of electric vehicle charging station considering uncertainties," *Sustain. Energy, Grids Networks*, vol. 25, no. 6, p. 100422, Mar. 2021, doi: 10.1016/j.segan.2020.100422.

[16] M. Ramalinga Raju, K. V. S. Ramachandra Murthy, and K. Ravindra, "Direct search algorithm for capacitive compensation in radial distribution systems," *Int. J. Electr. Power Energy Syst.*, vol. 42, no. 1, pp. 24–30, Nov. 2012, doi: 10.1016/j.ijepes.2012.03.006.

[17] A. A. El-Fergany and A. Y. Abdelaziz, "Capacitor placement for net saving maximization and system stability enhancement in distribution networks using artificial bee colony-based approach," *Int. J. Electr. Power Energy Syst.*, vol. 54, no. 6, pp. 235–243, Jan. 2014, doi: 10.1016/j.ijepes.2013.07.015.

[18] S. Sachan and M. H. Amini, "Optimal allocation of EV charging spots along with capacitors in smart distribution network for congestion management," *Int. Trans. Electr. Energy Syst.*, vol. 30, no. 9, pp. 1–14, Sep. 2020, doi: 10.1002/2050-7038.12507.

[19] S. Mirjalili, S. M. Mirjalili, and A. Lewis, "Grey Wolf Optimizer," *Adv. Eng. Softw.*, vol. 69, no. 6, pp. 46–61, Mar. 2014, doi: 10.1016/j.advengsoft.2013.12.007.

[20] S. K. Injeti, V. K. Thunuguntla, and M. Shareef, "Optimal allocation of capacitor banks in radial distribution systems for minimization of real power loss and maximization of network savings using bio-inspired optimization algorithms," *Int. J. Electr. Power Energy Syst.*, vol. 69, pp. 441–455, Jul. 2015, doi: 10.1016/j.ijepes.2015.01.040.

Authorized licensed use limited to: DELHI TECHNICAL UNIV. Downloaded on February 10,2022 at 10:16:12 UTC from IEEE Xplore. Restrictions apply.

World Wide Web
https://doi.org/10.1007/s11280-021-00996-y

CSR: A community based spreaders ranking algorithm for influence maximization in social networks

Sanjay Kumar[1] · **Aaryan Gupta**[2] · **Inder Khatri**[2]

Received: 4 March 2021 / Revised: 11 September 2021 / Accepted: 22 December 2021
© The Author(s), under exclusive licence to Springer Science+Business Media, LLC, part of Springer Nature 2022

Abstract

Online social networks have become a consistent part of our day-to-day life. They virtually connect people around the world and serve as ideal platforms for interactions, sharing of information, ideas, and products. Influence maximization (IM) is the problem of maximizing the reach of an idea or an opinion in a network by shortlisting the most influential nodes in the respective network, which are further used as seed nodes to spread the information in the rest of the network. It is a problem of great relevance in today's world because of its real life applicability in the business. Numerous methods have been proposed in the literature to rank the nodes according to their spreading ability and certain other characteristics. In this paper, we propose a novel method to solve the problem of influence maximization named Communities based Spreader Ranking (CSR), which is based on the notions of communities and bridge nodes. It identifies bridge nodes as influential nodes based on three concepts: community diversity, community modularity, and community density. Community diversity is used to identify bridge nodes and the rest two are used to identify significant communities. Extensive experimentation validation on various datasets using popular information diffusion models demonstrates that the proposed method delivers proficient results compared to numerous previously known contemporary influence maximization methods.

Keywords Complex networks · Community structure · Influence maximization · Information diffusion · Online Social Networks(OSNs)

This article belongs to the Topical Collection: *Special Issue on Computational Aspects of Network Science*
Guest Editors: Apostolos N. Papadopoulos and Richard Chbeir

✉ Sanjay Kumar
sanjay.kumar@dtu.ac.in

Aaryan Gupta
aryan227227@gmail.com

Inder Khatri
inderkhatri999@gmail.com

[1] Department of Computer Science and Engineering, Delhi Technological University, Main Bawana Road, New Delhi, 110042, India

[2] Department of Applied Mathematics, Delhi Technological University, Main Bawana Road, New Delhi, 110042, India

Published online: 10 February 2022

1 Introduction

Complex network analysis is the study of the structural and dynamical aspects of complex networks. It is found to be useful in many real-world problems and has become one of the hot topics in the industry and academia because of its increasing relevance and applications [16, 19]. Complex network based systems like social networks, biological networks, citation networks are some of the areas where complex network analysis could be advantageous. In these systems, the entities could be represented as nodes and the relationship between them as edges, e.g. in a citation network, the publications are the nodes, whereas the citation is its edges. In online social network graphs, individual's accounts are nodes, while the link like friendship or follow-follower between two nodes forms the edge. Usually, these real-life networks are scale-free and follow power-law degree distribution which makes their behavior unpredictable. Therefore, a proper and comprehensive study is required to achieve desirable results on these networks for any specific network analysis task like influence maximization, link prediction, community detection.

Online social networks (OSNs) facilitate an efficient way for users to interact and share their ideas with each other. With the internet revolution, the upsurge in the number of users of OSNs has provided the marketing professionals a new approach of advertisement, which is found to be more effective and cheaper than the traditional approaches [18, 25]. This new approach through OSNs has gained a lot of popularity and is known as the 'viral marketing' [9, 42]. The reason behind their effectiveness is word-of-mouth [15], as listening to a suggestion from a known person is always more effective than any other advertisement method. The advertisers influence the buyers by targeting some of the influential people who have the capability of persuading society into trying the product. Hence, the concept of viral marketing has led to the formation of the idea of influence maximization [31].

Influence Maximisation (IM) is the problem of identifying a set of k potential nodes whose influence spread over the whole network is maximum amid any union of k users where k is a small positive constant. The aim is to maximise the spread of the opinion and increase the number of nodes influenced [20]. Formally IM problem can be considered as : $G(V, E)$ where V is the the set of nodes, E is the set of edges, k is the budget and IM problem refers to shortlisting a set of k nodes such that it maximises the influence spread. Mathematically, it can be presented as shown below.

$$S = \arg\max \sigma(S) \; where \; S \subset V, |S| = k \tag{1}$$

The initial step of IM is to choose spreader nodes, but due to the limitation of resources and budget, the number of seed nodes should be significantly limited in comparison to the whole population. In addition, every node in a network has its own spreading capability depending upon its locality and links within the networks. Hence, to achieve maximum influence in the network, it becomes necessary to choose the appropriate set of seed nodes while taking care of the limitation on the number of selections and influence capability of each node. The next step of IM is to compute the spread of influence originating from the chosen seed nodes by utilising an information propagation model. The presence of community structure is relatively frequent in complex networks like social networks. Community detection can provide more insights into the network structure and further can be employed to accelerate the spread of information.

In this paper, we introduce a spreader ranking algorithm for influence maximization using the notion of community structure and community bridge nodes in the network. A community bridge is a node connecting distinct components of a network. In the proposed method, a bridge node with maximum influence on distinct communities is tried

to be identified in order to maximize the spread of information. We formulate three measures to identify an influential node, namely community diversity, community modularity, and community density, discussed in detail in the following sections. We utilize two popular methods of influence maximization models, namely, independent cascade (IC) and Susceptible-infected-recovered (SIR), to perform the information dissemination originating from the selected seed nodes. Our method has demonstrated excellent results over a variety of datasets when compared on several performance metrics. Our major contribution is summarised as below:

1. We propose a novel approach, community based spreaders ranking (CSR) to identify influential nodes in a social network based on the notion of communities and bridge nodes.
2. We formulate three characteristics to utilize communities and bridge nodes to their fullest to identify the seed nodes: community diversity, community modularity, and community density.
3. We evaluate and test the performance of the proposed algorithm using eight complex real-life networks of varying size, complexity and applicability to achieve commendable results.

The rest of the paper is organized as follows. Section 2 presents related work. Section 3 discusses some preliminary concepts relevant to this study. In Section 4, we present the proposed algorithm in detail. Section 5 depicts the datasets and evaluation metrics used in this paper. Section 6 describes extensive results performed to reveal the effectiveness of the proposed algorithm. Finally, Section 7 concludes our study.

2 Related Work

Numerous approaches are available in the literature to find the influential nodes. These approaches can be broadly categorized into descriptive approaches [2], diffusion process based approaches, statistical and stochastic approaches, topological measures based approaches, data mining, and machine learning approach [40]. Among all of these, topological-based approaches have been observed to be most effective and time-saving [23]. In topological-based approaches, nodes are selected on the basis of ranking done by a predefined centrality measure. These centrality measures are designed to focus on some specific topological properties suitable for selecting influential nodes. In literature, various topological measures based spreader ranking algorithms are introduced based on local, semi-local, and global features of nodes with certain limitations and consistency in performance issues. Global centrality measures look for the relation of the node with the rest of the nodes in the network and the best node is selected on the basis of global properties like closeness centrality, betweenness centrality, k-shell centrality, etc. In contrast, the local centrality measure focuses on the links with the nearby locality to choose the best initial spreaders.

In Degree Centrality [12], the nodes with maximum number of links are chosen as the best spreaders. It is a local measure to assess the importance of a node. Generally, local measures are simple and effective on small dataset. However, local measure ignore the topological position of other nodes and may not produce good results in a large-scale network. Betweenness centrality [11] is the fraction of shortest paths between all pair of nodes passing through a given node. Closeness Centrality [37] calculates a node's closeness to other nodes of a graph. Usually, the global measures like Betweenness and Closeness centrality produce good results but require high time complexity. In Eigenvector [5] Centrality,

ranking is done on the basis of importance of the neighbors of a node. If a node is connected to the influential nodes then the node is itself considered a important node. Pagerank [7] is a method to rank the web pages which is used by Google. In page rank, every page's scoring depends on the probability of being browsed. A node is considered as an influential node according to Pagerank, if it is connected to the nodes which are important nodes. k-shell Centrality [22] is a centrality measure that assign a shell value to each node and argues that a node lying in the core of the network is more important for spreading the information. One of the major drawback of k-shell centrality is its inability to differentiate between the spreading capability of two nodes with same k-shell values. To overcome this problem the concept of neighbourhood coreness [1] was introduced and neighbourhood coreness centrality of a node is equal to the sum of the k-shell value of its direct neighbor nodes. Entropy centrality [43] uses the concept of entropy to get the nodes having uniform distribution of the influential nodes in its neighborhood. Gravity Centrality [35] is based on the classical theory of the Gravity. Here the k-shell index of a node is considered as mass and the shortest path distance between the nodes is considered as distance. LID [41] centrality gives ranking on the basis of the local structural properties around the central node and considers the quasilocal information.

In recent years, some greedy based algorithms [20, 30, 33] are introduced for ranking spreader nodes which employ sub-modularity and monotony of the independent cascade (IC) model along with Monte Carlo simulations to improve the overall performance. In general, the greedy based are slow due to a huge number of simulations and require high time.

Recently, many community structures based spreader ranking algorithms are introduced with better results [6, 26]. Such algorithms argue that information spread can occur faster in a community because of dense connection between the nodes of a community. Some popular community structure based algorithms are Community Finding Influential Node (CFIN), Community-based Approach for Opinion Maximization(CAOM), Gateway Local Ranking(GLR), etc. In GLR [38], after dividing the graph into communities, local cores and gateway nodes are selected for each community. The nodes are ranked as influential spreaders on the basis of their shortest paths to the local cores and the gateway nodes. In CAOM method [17], firstly the whole network is divided into communities, and the significant communities are selected among them. Then the candidate nodes are selected from each community using one-hop measure and from the candidate nodes, seed nodes are selected by eliminating nodes producing overlapping influence. CFIN [21] follows a similar approach to the CAOM, here the candidate nodes are selected using the degree centrality and further the seed nodes are selected using the clustering coefficient measure.

Most of the existing community structure based works focussed on the core nodes present in each community based on specific parameters like degree and the shortest path to find influential spreader nodes. However, the proposed work focuses on bridge nodes between different communities and parameters like community density and community modularity parameters, as introduced by us, to find the influential spreader nodes. We argue that a core node plays a crucial role within a community. However, on the other hand, a bridge node connects different communities, which results in spreading information in more than one community. Hence, the proposed algorithm aims at spreading the information to a maximum number of nodes in the entire network instead of just spreading within some significant communities. Also, other existing community structure based spreader ranking algorithm either gives equal importance to each community or prioritize these communities based on the number of nodes present in that community. However, our method introduces the notion of community density parameter, which measures the connectivity of nodes within

a community, and communities are ranked based on community density parameters along with the number of nodes present in each community.

3 Preliminaries

3.1 Community structure

A community is a subset of a graph with nodes that are supposed to have more interaction with each other than the rest of the nodes. It is a structure of eminent uses in complex networks. Community detection in complex networks is one of the widely studied problem [10, 24]. In real-life, a community can be considered a group of people living in the same area, same age group, having the same profession, lying in the same financial state, facing the same problems, etc. Usually, the nodes within a community are much densely linked to each other than other parts of the network. Therefore, the information diffusion within the community is fast and effective compared to the other parts of the network.

3.2 Bridge nodes

Bridge nodes can be defined as the nodes connecting different groups in a network. These nodes act as a bridge between different groups, and therefore, they have more control over the flow of information than other regular nodes in the graph. Bridge nodes make the propagation of information over different parts easier, and hence they are considered good influential.

3.3 Information propagation model

The propagation of the information in the complex network is identical to the epidemic spreading [8, 32]. A propagation model captures the stochastic process for spreading information on the network. The process of propagation of information continues until no active node is left. This paper employs two well-known information diffusion models, namely, independent cascade (IC) and susceptible-infected-recovered (SIR) model.

3.3.1 Susceptible-Infected-Recovered (SIR) model

In SIR model [39], each node has three conditions: susceptible, infected and recovered. Some nodes are selected in the beginning as infected nodes, and susceptible nodes are infected by infected nodes when they interact, and further recovered nodes are the ones that have recovered after being infected once. Infected nodes infect their neighboring nodes with a probability of λ, and Infected nodes recover with a probability of β. Such models are used to model the spread of diseases. SIR model is used to measure the spreading ability of initially infected nodes or what influence does a node impart on the rest of the network. The sum of infected and recovered nodes is the total impact of the nodes infected in the beginning.

3.3.2 Independent Cascade (IC) model

In IC model [14], nodes can be divided into two categories: active or infected and non-active or susceptible nodes. Some nodes are selected in the beginning as active or infected

nodes, and non-active or susceptible nodes are infected by actives nodes on interaction. It is assumed that once a node is infected, it can't be recovered. Infected nodes infect their neighbors with a probability γ. IC models can be used to imitate the spread of information. IC model measures the spreading ability of a node by calculating the total number of active nodes at the end of the simulations triggered due to the influence of that particular node. A node is said to be more influential if it causes more nodes to become active at the end of the information diffusion process.

4 Proposed algorithm

In this section, we discuss the proposed **Community based Spreaders Ranking (CSR)** algorithm to rank the nodes of the network based on their spreading capability for influence maximization. Most of the existing community structure based spreader ranking algorithm identified core node as influential nodes on the basis of certain parameters. Whereas, CSR identifies community bridge nodes as influential nodes. Core nodes are such nodes which play a crucial role in spreading information to other members within the same community. However, the community bridge nodes are such nodes which are connected to more than one community and plays a bridging role in information propagation between the members of different communities. By considering bridge nodes as influential nodes instead of a core nodes, we are trying to reach as many nodes as possible in the entire network. They have a reasonable control over the flow of information to different parts of the network, and hence, the information introduced to these, reaches as many nodes as possible in the whole network. Hence, a bridge node reaches more than one community, whereas a core node can spread only in one community. Therefore with respect to a given single community, a bridge node may not prove to be more influential than a core node but with respect to the entire network, a bridge node is certainly more influential when compared to the core nodes.

The proposed methodology begins by identifying communities present in the graph using Louvain's algorithm [3]. Louvain's algorithm is based on greedy optimization technique which helps in its faster convergence and hence makes it efficient. First, smaller communities are found by optimizing modularity locally on all nodes, then each small community is grouped into one node, and the first step is repeated. Further the bridge nodes, connected to distinct communities of a network are identified using the concept of community diversity. According to this, a node would be scored higher if it has connections to distinct communities, or we can say it is connected to more communities. Since considering only the connections with the communities seems a very naive approach for finding the influential nodes, it also considers the significance of communities with which the bridge node is connect by using the concepts of Community modularity and Community density. Community modularity draws attention towards the size of the community whereas community density draws attention towards the intra-connectivity of nodes within community. The expression of the proposed algorithm is based on the concepts of community diversity, community modularity, and community density discussed in detail below.

4.1 Community diversity

The community diversity of a node depends on its connections with different communities in the network. The community diversity of a node can be formally defined as the measure of the probability of finding a certain community in the neighborhood of a node. It is directly proportional to the number of different communities a node is connected to and the number

of links with each one of them. The more the number of communities a node connects to, the more its community diversity score is. Community diversity ensures to mark a node as influential if and only if it is a bridge node. It can be computed as shown in Eq. 2 where CDv_i is the community diversity value of i^{th} node, CDv_{ic} is the contribution of c^{th} community in Community Diversity of i^{th} node and P_{ic} represents the probability of finding the i^{th} node's neighbour in c^{th} community. Further, this probability can be calculated as shown in Eq. 3 where η_{in} represents number of nodes in c^{th} community in the neighbourhood of node i and η_i represents number of nodes in the neighbourhood of node i.

$$CDv_i = -\sum_{c=1}^{comm} CDv_{ic} = -\sum_{c=1}^{comm} P_{ic} * log(P_{ic}) \tag{2}$$

$$P_{ic} = \frac{\eta_{ic}}{\eta_i} \tag{3}$$

Community diversity is a relative score depicting the variety of communities in the neighborhood of a node. As discussed in Section 4, it is multiplied by the degree of the node to compensate for the effect of division by achieving an absolute score.

The working concept of community diversity can be easily understood by applying the measure on Figure 1. It could be observed in the graph that node v_5 and v_{16} are the community bridge nodes. They have connections to more than one community. Node v_{16} is connected to more communities along with the more evenly distributed connections to those communities when compared to the node v_5. It could be interpreted that node v_5 is somewhat more of a core node to the community C_1, limiting its reach and hence making it a less preferable seed node. When the community diversity score for both the node v_5 and v_{16} is calculated as shown below. Here, node v_{16} is given a higher score indicating the efficiency of the community diversity measure.

$v_5 : -6 * (2/6 * log(2/6) + 4/6 * log(4/6)) = 1.65860754566$

$v_{16} : -6 * (2/6 * log(2/6) + 3/6 * log(3/6) + 1/6 * log(1/6)) = 2.63548374681$

4.2 Community modularity

In real-life networks, communities often vary a lot in the number of nodes. When the Jazz network is passed through Louvain's algorithm, it is divided into four communities with the size of 62,42,34, and 60. Similarly, the Dolphin network is divided into five communities with communities' size 8,17,12,18 and 7. Community modularity brings the significance of a community into consideration while computing the influence of a community on the whole network. More the nodes in the community, more the influence on the whole network. It can be understood that the impact of the spread of an opinion or information in a community will depend a lot on the size of the community which is influenced by it. With the variation in the size of communities, their contribution to the total spread will also vary. Therefore, the influence of a community in the community diversity formula is weighted by the community modularity factor. Community modularity can be defined as the measure of a community's size or spreading the information when compared to the size of the entire network. The primary motivation behind community modularity is determining the importance of a particular community for spreading information compared to the whole network . It is computed as shown in the Eq. 4 where CM_c is community modularity for c^{th} community, ν_c represents the number of nodes in c^{th} community and ν represents the number of nodes in the graph.

$$CM_c = \frac{\nu_c}{\nu} \tag{4}$$

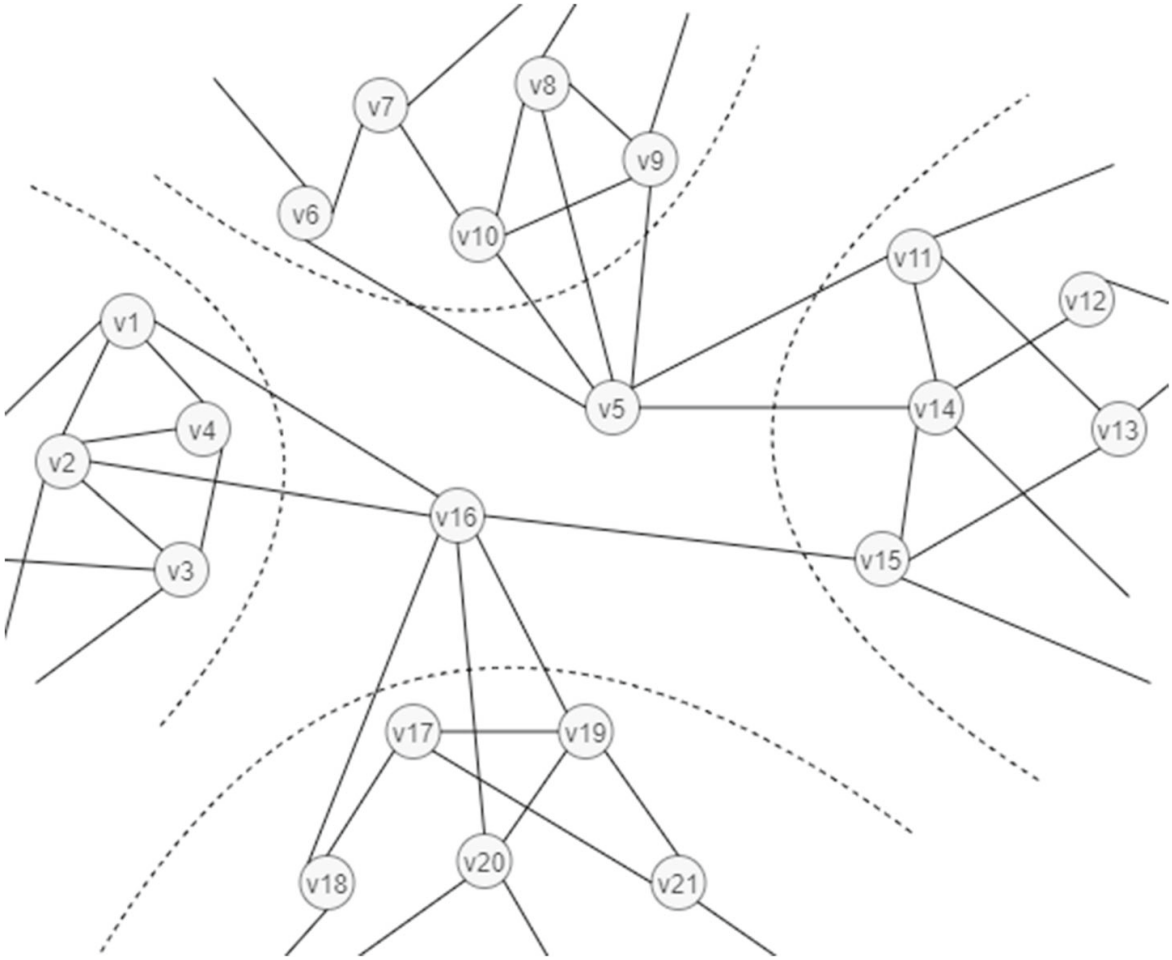


Figure 1 Toy networks consisting of different number of Communities. (a) node v_5 connected with two communities. (b) node v_{16} connected with three communities

As shown in Eq. 4, community modularity is computed by computing the ratio of size of the community in comparison to the whole network. It is figured out by calculating the proportion of a network held by a community. It will help us understand what proportion of the network will be influenced if the community is influenced.

4.3 Community density

The variation in the level of connectivity within the communities play an important role in deciding if a community is significant. This factor considers the rate at which a community would be influenced once it is introduced to an opinion. If the density of a community is large then the average degree of constituting nodes would be also large. Hence, each influenced node in community can influence more number of nodes. Therefore, the concept of community density plays an important role in our proposed work. Community density can be formally defined as the measure of intra- connectivity of nodes within a community and how that community is closer to a complete sub-graph possible due to the nodes present in that particular community. It is computed as shown in the Eq. 5 where CDn_c is the Community Density for c^{th} community, ϵ_c denotes the number of edges in the community c and ϵ denotes maximum number of edges that are possible in that community.

$$CD_c = \frac{\epsilon_c}{\epsilon} \tag{5}$$

Density or connectivity of a network is computed by checking how many edges exist between nodes of a community. To make it a relative term, number of edges present in a community are divided by the number of edges present in a possible complete sub-graph using nodes of that particular community. By complete sub-graph, we mean the concept of complete graph possible due to nodes present in that community, which provides an ideal community configuration for transmission of information where all nodes of a community would be influenced even if a single node of the community is influenced as there exist an edge between each pair of nodes of the community. This factor helps in deducing how well connected or dense a community is? How efficiently an information would spread in a community, once introduced in it?

4.4 Community based Spreader Ranking score (CSR)

Thus by uniting the above mentioned characteristics of communities and understanding their roles in identifying influential seed nodes. We can define the formula for CSR score for any i^{th} node through the Eq. 6, where $Deg(i)$ is the degree of node i and $comm$ is the set of communities to which the given node i is connected.

$$CSR(i) = Deg(i) \times (1 + \sum_{c=1}^{comm} CDv_{ic} \times CM_c \times CDn_c) \tag{6}$$

For each community in $comm$, the product of CDv_{ic}, CM_c and CDn_c is calculated and further the product is summed over the $comm$. This gives us the weighted Community diversity which incorporates the significance of communities connected to the bridge node. We consider multiplication instead of addition for CM, CDn, CDv because we weigh each characteristic equally. In this case, if a node has relatively less value of any particular component than overall, it gets a relatively lower CSR score. The obtained expression of weighted community diversity is further multiplied by the node's degree to get the absolute value of a node's influencing power. This factor brings into consideration the impact of several connections with each community as more the number of connections, more the influence on the community. Suppose there is more than one bridge node between two communities. In that case, the algorithm will prefer the bridge node with more degree and evenly distributed connections with the other connected communities. Such bridge nodes achieve a higher CSR score according to the proposed algorithm. Hence, the bridge node with a higher CSR score should be selected. Further, Eq. 6 can be expanded by using Eqs. 2, 3, 4 and 5 as follows:

$$CSR(i) = Deg(i) \times (1 + \sum_{c=1}^{comm} \frac{\eta_{ic}}{\eta_i} \times log(\frac{\eta_{ic}}{\eta_i}) \times (\frac{v_c}{v}) \times (\frac{\epsilon_c}{\epsilon})) \tag{7}$$

Finally, based on the calculated CSR score of all the nodes, we can select top k nodes as the seed nodes. These seed nodes intend to be influential spreaders and play crucial role to achieve influence maximization in the network.

The algorithm to find community diversity as depicted in Algorithm 1, represents the contribution of community c in the community diversity score of a node v i.e. CDv_{vc} as required in Eq. 6. In this Algorithm, a variable to store the finally computed score is initialised in line 1, named as $value$. In line 3, the number of neighbouring nodes of each node is calculated and the probability of finding v's neighbouring node in c^{th} community is calculated in lines 4 and 5. This probability is further used to calculate the value of expression $-p*log(p)$ in line 6, where p is the computed probability. The final value of the contribution of community c in the community diversity score of a node v is returned in line 8.

Algorithm 1 Community diversity.

Input: $v : Node\ whose\ community\ diversity\ is\ to\ be\ found$
$c : Community\ whose\ contribution\ is\ to\ be\ found\ in\ community\ diversity\ of\ node\ v$
$G = (V, E)$, where $n = \|V\|, e = \|E\|$
$Communities$ {c1,c2....cm} : $partitioned\ using\ Louvain\ Algorithm$
Output: $Community_Diversity$
1: $value \leftarrow 0$
2: **for** $nb \in \{Neighbours\ of\ node\ v\}$ **do**
3: $neigh_len \leftarrow number\ of\ neighbours\ of\ v$
4: $neigh_com_len \leftarrow number\ of\ neighbours\ with\ Communities(nb) == c$
5: $ratio \leftarrow \frac{neigh_com_len}{neigh_len}$
6: $value \leftarrow -ratio * log(ratio)$
7: **end for**
8: $CDv(i, c) = value$
9: **return** $CDv(i, c)$

Algorithm 2 Community based spreader ranking.

Input: $G = (V, E)$, where $n = \|V\|, e = \|E\|$
Output: CSR
1: $Communities$ {c1,c2....cm} $\leftarrow$ $partitioned\ using\ Louvain\ Algorithm$
2: $CSR \leftarrow \{\}$
3: $CM(c) \leftarrow \{\}$
4: $CDn(c) \leftarrow \{\}$
5: **for** $c \in$ {c1,c2....cm} **do**
6: $CM \leftarrow Community\ Modularity\ of\ community\ c\ using\ Eq.\ 4$
7: $CDn \leftarrow Community\ Density\ of\ community\ c\ using\ Eq.\ 5$
8: **end for**
9: **for** $i \in$ {1,2....n} **do**
10: $CSR(i) \leftarrow\ CSR\ score\ for\ node\ i\ using\ Eq.\ 6$
11: **end for**
12: **return** CSR

In the algorithm to find the CSR score as depicted in Algorithm 2, from line 1-4 the variables are initialised. From lines 5-8, Community Modularity and Community Density is computed for each and every community as shown in Eqs. 4 and 5. Further, from lines 9-12 CSR score is computed for each and every node as shown in Eq. 6.

5 Dataset and performance metrics

5.1 Dataset

In order to show the effectiveness of the CSR model, it is tested on different real-world network datasets. The types of datasets used are peer-to-peer networks, i.e., a group of computers linked together with equal responsibilities and permissions to process data, Collaboration networks, i.e., an alliance of autonomous people and organizations, who share resources such as data and connectivity via a certain network. Social networks bring

like-minded individuals in touch with each other using websites and web-based applications. Technological Networks, i.e., where users use data systems to deliver and manage e-resources over a computer network.

In this paper, eight datasets have been used in total, varying in their size, nature, density, and applications. Out of eight datasets, one dataset, namely p2p-Gnutella30 [36], is a Internet peer-to-peer network. four networks namely CA-CondMat [28], CA-AstroPh [29], CA-GrQc [29], jazz [13] are collaboration networks and two networks i.e. soc-hamsters [27], dolphins [34] are social networks and one technological network PGP [4]. Statistical properties, i.e., the number of nodes, edges, Clustering Coefficient, the density of graph, maximum and average degrees of each of the datasets, have been listed in the table. The β_{th} denotes the rate of infection for the information spread. We need to suitably choose the rate of infection (β_{th}) in SIR and activation probability (p_{uv}) in the IC model, which decides the rate at which an infected or active node infects or influences its neighbors. In the literature, most of the IM algorithms have considered the rate of infection as an epidemic threshold which is calculated as

$$\beta_{th} = \frac{\sum_{i=1}^{n} d_i}{\sum_{i=1}^{n} (d_i)^2} \tag{8}$$

where d_i denote the degree of node v_i. Hence, the value β_{th} for a dataset is equal to the average degree of the nodes divided by the square of the average degree of the nodes.

p2p-Gnutella30 is a sequence of snapshots of the Gnutella peer-to-peer file-sharing network from August 2002, where hosts in the Gnutella network topology are represented as nodes, and connections between the Gnutella hosts are represented as edges. The CA-Condmat (Condense Matter Physics) dataset, CA-AstroPh (Astro Physics) dataset, and CA-GR-QC (General Relativity and Quantum Cosmology) dataset consist of authors as nodes, and they are connected by edges they have co-authored a research paper with each other. PGP stands for Pretty Good Privacy which is a communication network with encryptions. Dolphins presents undirected social connections between 62 dolphins in a community living off Doubtful Sound, New Zealand. Soc-Hamster is a Network of friendships and family links between users of the website http://www.hamsterster.com.Jazz is a collaboration network of Jazz musicians. A node represents a musician, and they are connected by an edge if they have played together in a band. The data was collected in 2003.

Louvain's algorithm was applied over all of these datasets, and the resulting number of communities with their quantitative properties i.e. community modularity and qualitative properties i.e. community density have been mentioned in the Table 2.

5.2 Performance metrics

To validate the effectiveness of the proposed algorithm, we use various performance metrics, as discussed below.

5.2.1 Infection scale

The infection scale measure represents the scale at which nodes get infected and further gets recovered. Some nodes are initially infected known as seed nodes to spread the influence. A diffusion model is used to reckon the total number of nodes affected by the spread of information. Seed nodes are selected in a SIR model initially which infects its neighbouring

nodes with a probability of λ and recovers the already infected nodes with a probability of β. The recovered node no longer acts like a seed node therefore stops infecting other nodes. The scale is the summation of the number of infected and recovered nodes at a particular timestamp. The graph initially increases significantly but after sometime varies comparatively less because of increased number of recovered nodes

5.2.2 Final Infected spread or active nodes

The influence spread measure represents the final measure of infection scale or final measure of total number of nodes infected by the initially infected nodes. Final infected scale in SIR includes the ratio of total number of nodes which received information at the end of the process to the total number of nodes in the network. As mentioned earlier, Iin SIR models nodes gets infected with a probability λ and gets recovered after infection with a probability β whereas in an IC model susceptible get infected by a probability γ , from the nodes infected initially. In IC models, active nodes are the nodes that are finally infected at the end of the propogation.

5.2.3 Time

The time taken by the proposed method in ranking the nodes on the basis of their spreading ability has been also considered in order to compare it with other methods. The time consumption of all the centralities were computed on the Google's Colab platform with 12 GB Ram and Tesla T4 GPU.

6 Experimental results and analysis

In this section, we present the experimental results performed for the proposed method and reveal its utility on real-life networks. We performed the investigation on eight datasets of diverse sizes and properties as listed in Table 1 and using all the performance measures described in Section 5. We compared the performance of the proposed method with some popular and recent methods of IM, namely Extended Neighbourhood Coreness(ENC) [1], Eigenvector(EVC) [5], Gravity Centrality(GC) [35], GLR [38], Entropy Centrality(EC) [43] and LID [41]. We considered β value of each dataset as listed in Table 1. We utilized the stochastic SIR model to calculate the infection scale ($F(t)$) and final infected scale ($F(t_c)$)

Table 1 Brief statistical descriptions of the different datasets where CC is the clustering coefficients

S.No.	Dataset	Nodes (n)	Edges (m)	d_{max}	d_{avg}	β_{th}	CC
1	Dolphins	62	159	12	5	0.1469	0.2589
2	Jazz	198	2,742	100	27	0.0258	0.6174
3	Hamsterster	2,400	16,600	273	13	0.0235	0.5375
4	GrQc	5,247	14,488	81	6	0.0592	0.5296
5	PGP	10,638	24,301	205	4	0.0529	0.2659
6	AstroPh	18,777	1,98,054	504	22	0.0152	0.6305
7	CondMat	23,133	93,439	279	8	0.0453	0.6334
8	Gnutella30	36,686	88,331	55	4	0.0872	0.0063

as a function of time (t) and further utilized IC model to calculate active nodes ($F(I_c)$)). We executed the SIR and IC simulation 100 times, and the results are averaged over the total number of times for each performance measure. The experiments are conducted for the different fractions of initial spreaders, and influence is propagated using SIR and IC information diffusion models.

6.1 Final infected scale in SIR model

The final infected scale is one of the most important metrics used to judge the performance of the initial spreaders selection method in the SIR propagation model. It represents the fraction of the final number of nodes that are infected at the end of the diffusion process for a given fraction of spreaders. Here, the final infection scale is calculated for a different scale of spreaders fraction to analyze the efficiency over the variation in the initial seed nodes' number. We elect the bridge nodes, which is spreader nodes, fraction in the range of 0.005, 0.01, 0.015, 0.02, 0.025,0.03, 0.035, 0.04 for networks containing nodes more than 2000.We choose the spreaders fraction in the range of 0.005, 0.01, 0.015, 0.02, 0.025, 0.03, 0.035, 0.04 for networks containing nodes more than 2000 and for network with nodes less than 2000 spreaders fraction are 0.05, 0.06, 0.07, 0.08, 0.09, 0.10. To achieve a fair comparison, we have selected spreader nodes from each dataset which is bridge nodes in our method and core nodes in case of other methods according to the above mentioned spreader fractions. e.g. in case of jazz dataset which have 198 nodes, for 0.05 i.e. 5% of spreader fraction it will be 10 bridge nodes. Finally, the graph is plotted between Final Infected Scale and spreaders fraction for the proposed method and other comparing methods. The results are obtained over 100 independent simulations on the SIR model. Figure 2 shows the graph of the Final infected scale for all the datasets. It is evident from the result that all the methods' final infected scale increases with an increase in the spreaders fraction. On analyzing AstroPh, Condmat, and Hamsterster closely, it can be observed that CSR performed better than LID with a very marginal distance till 0.025 value of spreader fraction. After this fraction it performed better than all the methods present. In all the rest datasets, the obtained results depicted that the proposed CSR algorithm performed quite well and outperformed all other methods considered in the comparison.

6.2 Active nodes in IC model

Similar to the final infected scale in the SIR model, active nodes are the total number of activated nodes at the end of the spreading process in the IC propagation model. The active nodes at the end of a spreading process highly depend upon the seed nodes selected initially as the spreaders nodes; therefore, it is one of the distinguishing metrics in the performance evaluation of the initial spreaders ranking method. Active nodes corresponding to the different initial spreaders are calculated and are plotted as shown in Figure 3. The spreaders fractions are the same as taken in the SIR propagation model i.e. 0.005, 0.01, 0.015, 0.02, 0.025, 0.03, 0.035, 0.04 for networks containing nodes more than 2000 and for network with nodes less than 2000 spreaders fraction are 0.05, 0.06, 0.07, 0.08, 0.09, 0.10. It is evident from the result that the active nodes in the IC model of all the methods increase with the increase in spreaders fraction. The varied performance pattern was observed for each method in each dataset. The proposed methodology outperformed all the comparing methods for all the spreader fractions in Dolphins, Gnutella30, jazz, and GrQc. It performed the best for most of the spreader fractions in AstroPh, PGP, CondMat, and Hamsterster. Hence, the Proposed method performed quite well and has outperformed the other methods.

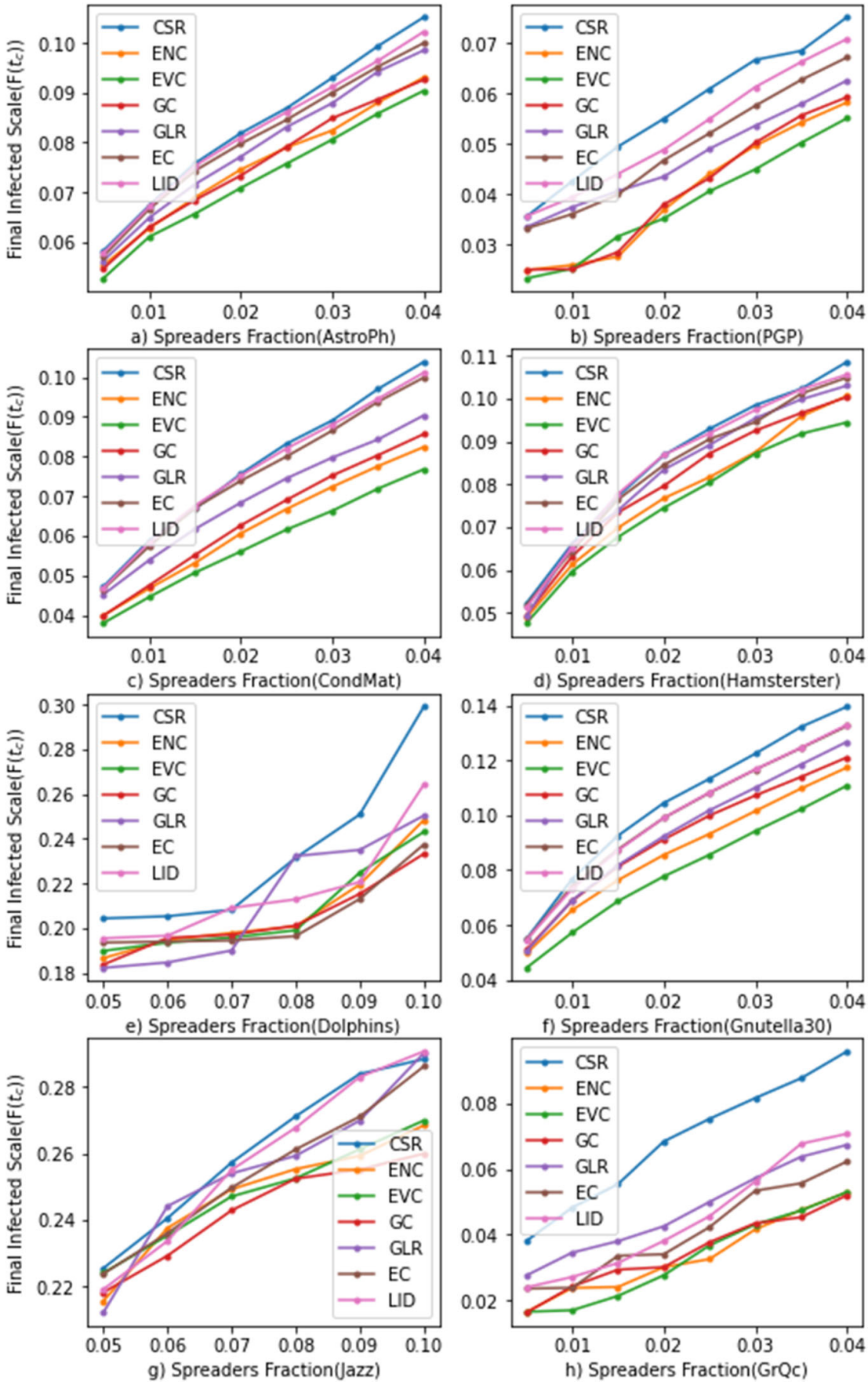


Figure 2 Final infected scale with respect to spreader fractions using SIR model on eight different real networks- a) AstroPh b) PGP c) CondMat d) Hamsterster e) Dolphins f) Gnutella30 g) Jazz h) GrQc. The results are obtained over 100 independent simulations of SIR model

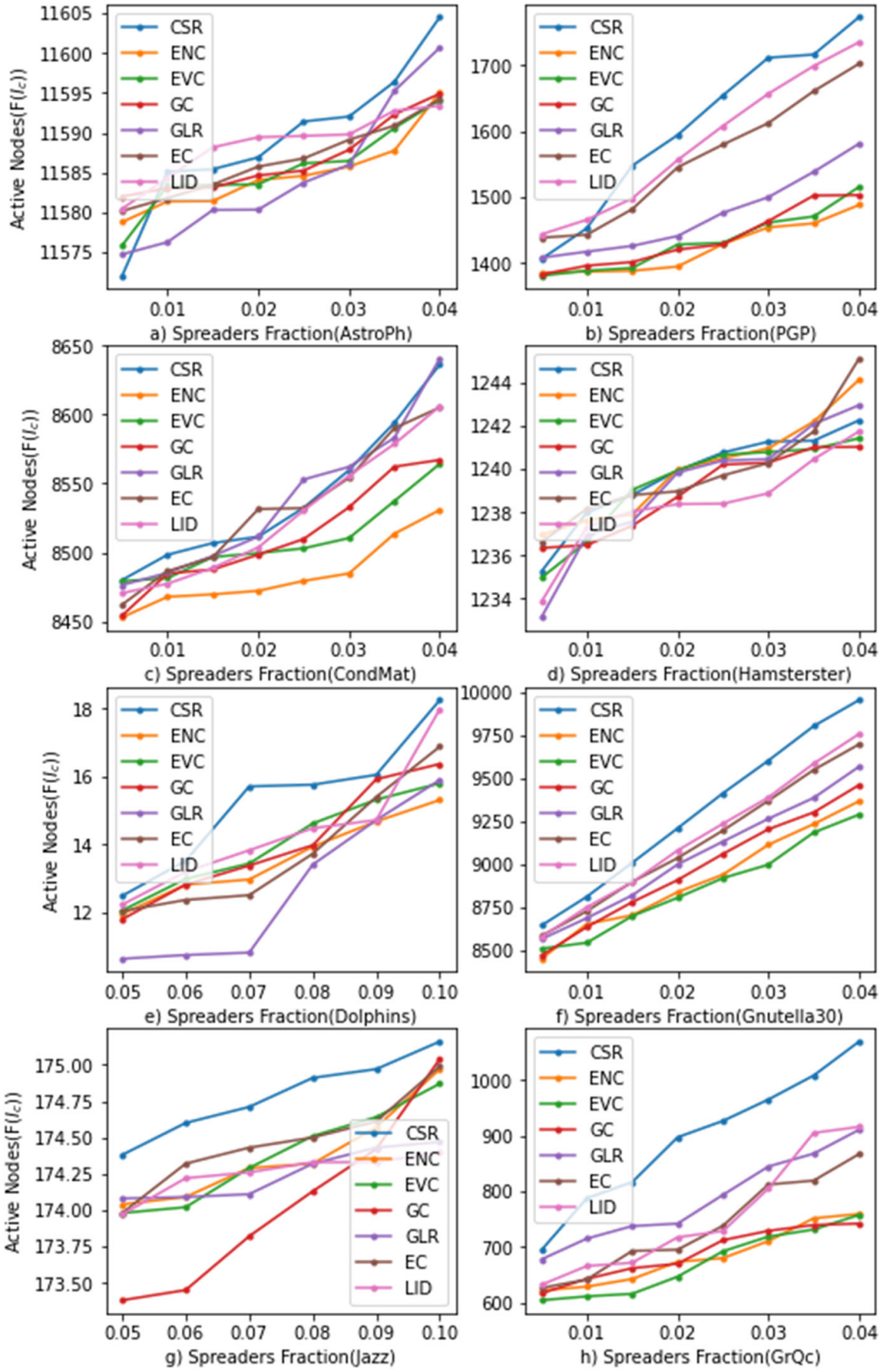


Figure 3 Number of active nodes with respect to spreader fraction using IC model on eight different real networks- a) AstroPh b) PGP c) CondMat d) Hamsterster e) Dolphins f) Gnutella30 g) Jazz h) GrQc. The results are obtained over 100 independent simulations of IC model

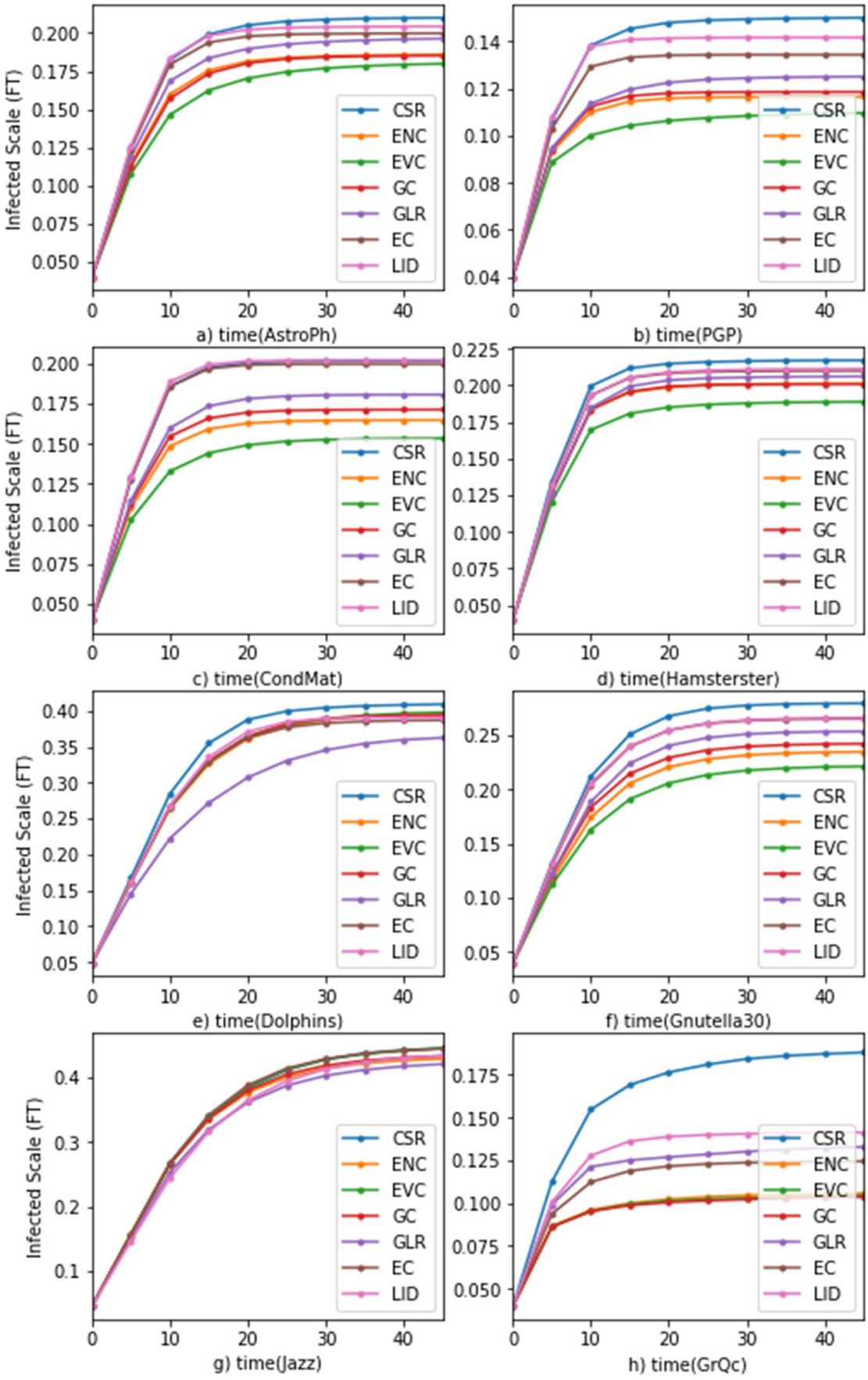


Figure 4 Infection scale at different timestamps for each dataset by taking fraction of 0.03 nodes as influential nodes for a) AstroPh b) PGP c) CondMat d) Hamsterster f) Gnutella30 h) GrQc and fraction of 0.06 nodes for e) Dolphins g) Jazz. The results are obtained over 100 independent simulations of SIR model

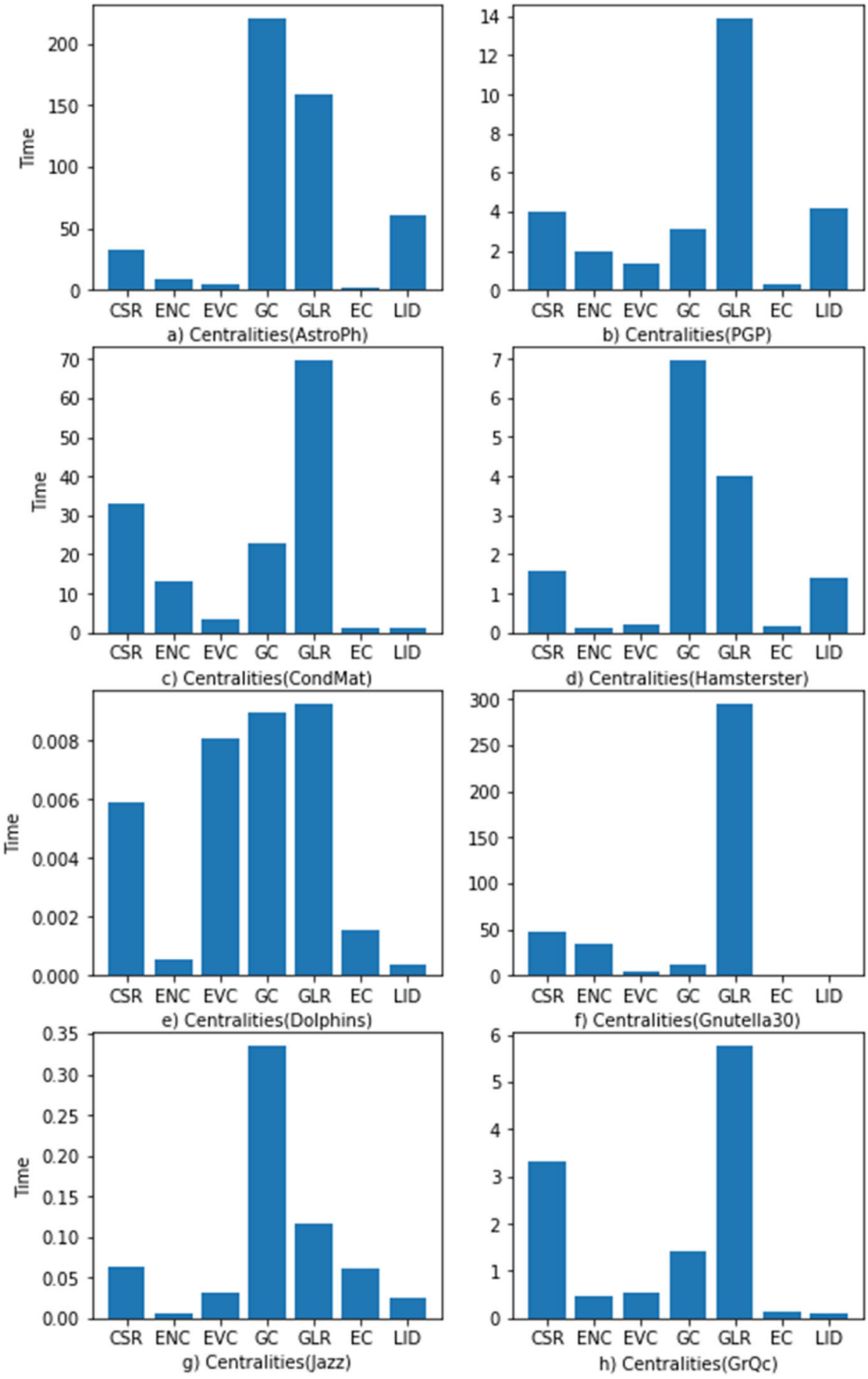


Figure 5 (a)-(j) The actual running time to generate the ranking list of nodes under different methods for a) AstroPh b) PGP c) CondMat d) Hamsterster e) Dolphins f) Gnutella30 g) Jazz h) GrQc .The x-axis shows the the different methodologies and y-axis shows the running time

Table 2 Brief qualitative and quantitative descriptions of the communities formed in different datasets where Com. is Communities

S.No.	Dataset	No. of Com.	Avg Com. Density	Avg Com. Modularity
1	Dolphins	5	0.3462	12.4
2	Jazz	4	0.4061	49.5
3	Hamsterster	169	0.8967	14.35
4	GrQc	396	0.8113	13.25
5	PGP	104	0.1602	102.28
6	AstroPh	324	0.8589	57.95
7	CondMat	626	0.8497	36.95
8	Gnutella30	58	0.1675	632.51

6.3 Infection scale

The plot of the Infection scale is shown in Figure 4. In the infection scale, the fraction of influenced nodes is plotted against each timestamp, i.e., from 0s to 40s and above. We have used the SIR model for comparing the infection scale and have averaged the result over 100 simulations. The number of initial spreaders was chosen to be the fraction of 0.03 of the total spreaders for datasets above 2000 nodes, i.e., AstroPh, PGP, Hamsterster, Gnutella30, CondMat, and GrQc, and 0.06 of the total dataset for datasets below 2000 nodes, i.e., jazz and dolphins. The value of infection rate for each dataset is taken as β shown in Table 1. It is evident from the result that the Infection scale in the SIR model for all the methods increases with an increase in time stamp. It can be concluded that the proposed method has shown better results on the infection scale when compared with other methods on all the datasets. Where LID and CSR performed the best with marginal differences on the CondMat dataset, EC and CSR performed best on the jazz dataset with comparable results. Hence, the proposed method performed well and has outperformed when compared to the other methods.

6.4 Execution time

We also compared CSR with other methods on the basis of the absolute execution time required to rank the nodes in accordance with their spreading ability. As it can be seen in Figure 5, we analyzed it on all the eight datasets as listed in Table 2. It is evident from the results that the proposed CSR method is faster than GLR and GC Centrality measures, comparable to LID, and slower than ENC, EVC, and EC. On observing the actual execution time taken by CSR for the generation of the ranked list, it can be concluded that the proposed methodology is relatively more efficient in most cases. According to the results obtained in all the performance metrics, i.e., Final Infected Scale, Active nodes, Infection Scale, and execution time, The proposed method of Community Spreader based Ranking (CSR) for influence maximization performed better than many well-known and recently published methods.

7 Conclusion

Ranking nodes of the network based on their spreading capabilities is one of the prominent research topics in network science. In this paper, we introduced a novel method, namely

Communities based Spreader Ranking (CSR), to rank the spreader nodes based on the notion of community structure and some associated features. The approach seeks to select a bridge node as a seed node by computing its influence on the whole network using three community based features, namely community diversity, community modularity, and community density. We performed the investigation on eight real-life datasets of diverse sizes, nature, and applications based on the various performance metrics. We utilized IC and SIR information diffusion models to calculate the different performance metrics. The results obtained reveal that the proposed CSR method outperformed other popular methods of IM.

References

1. Bae, J., Kim, S.: Identifying and ranking influential spreaders in complex networks by neighborhood coreness. Phys. A: Stat. Mech. Appl. **395**, 549–559 (2014)
2. Bamakan, S.M.H., Nurgaliev, I., Qu, Q.: Opinion leader detection: a methodological review. Expert Syst. Appl. **115**, 200–222 (2018)
3. Blondel, V.D., Guillaume, J.L., Lambiotte, R., Lefebvre, E.: Fast unfolding of communities in large networks. J Stat. Mech: Theo. Exp. **2008**(10), P10008 (2008)
4. Boguná, M., Pastor-Satorras, R., Díaz-Guilera, A., Arenas, A.: Models of social networks based on social distance attachment. Phys. Rev. E **70**(5), 056122 (2004)
5. Bonacich, P.: Some unique properties of eigenvector centrality. Soc. Net. **29**(4), 555–64 (2007)
6. Bozorgi, A., Samet, S., Kwisthout, J., Wareham, T.: Community-based influence maximization in social networks under a competitive linear threshold model. Knowl. Based Syst. **134**, 149–58 (2017)
7. Brin, S., Page, L.: Reprint of: the anatomy of a large-scale hypertextual web search engine. Comput. Net **56**(18), 3825–3833 (2012)
8. Chen, W., Lakshmanan, L.V., Castillo, C.: Information and influence propagation in social networks. Synthesis Lectures on Data Management **5**(4), 1–177 (2013)
9. Domingos, P., Richardson, M.: Mining the network value of customers. In: Proceedings of the seventh ACM SIGKDD international conference on knowledge discovery and data mining, pp.57–66 (2001)
10. Fortunato, S.: Community detection in graphs. Phys. Rep. **486**(3-5), 75–174 (2010)
11. Freeman, L.C.: A set of measures of centrality based on betweenness. Sociometry pp.35–41 (1977)
12. Freeman, L.C.: Centrality in social networks conceptual clarification. Soc. Net. **1**(3), 215–239 (1978)
13. Gleiser, P.M., Danon, L.: Community structure in jazz. Adv. Complex Syst **6**(04), 565–573 (2003)
14. Goldenberg, J., Libai, B., Muller, E.: Using complex systems analysis to advance marketing theory development: Modeling heterogeneity effects on new product growth through stochastic cellular automata. Acad. Mark. Sci. Rev. **9**(3), 1–18 (2001)
15. Goldenberg, J., Libai, B., Muller, E.: Talk of the network: a complex systems look at the underlying process of word-of-mouth. Mark. lett **12**(3), 211–223 (2001)
16. Havlin, S., Kenett, D.Y., Ben-Jacob, E., Bunde, A., Cohen, R., Hermann, H., Kantelhardt, J.W., Kertész, J., Kirkpatrick, S., Kurths, J., Portugali, J.: Challenges in network science: Applications to infrastructures, climate, social systems and economics. Eur. Phys. J Spec. Top **214**(1), 273–293 (2012)
17. He, Q., Wang, X., Mao, F., Lv, J., Cai Y Huang, M., Xu, Q.: CAOM: A community-based approach to tackle opinion maximization for social networks. Inform. Sci. **513**, 252–269 (2019)
18. Heidemann, J., Klier, M., Probst, F.: Online social networks: a survey of a global phenomenon. Comput. Net. **56**(18), 3866–3878 (2012)
19. Jia-sheng, W., Xiao-ping, W., Bo, Y., Jiang-wei, G.: Improved method of node importance evaluation based on node contraction in complex networks. Procedia Engineering **15**, 1600–1604 (2011)
20. Kempe, D., Kleinberg, J., Tardos, É.: Maximizing the spread of influence through a social network. In: Proceedings of the ninth ACM SIGKDD international conference on Knowledge discovery and data mining, pp 137–146 (2003)
21. Khomami, M.M.D., Rezvanian, A., Meybodi, M., Bagheri, A.: CFIN: A community-based algorithm for finding influential nodes in complex social networks. The Journal of Supercomputing, pp.1–30 (2020)
22. Kitsak, M., Gallos, L.K., Havlin, S., Liljeros, F., Muchnik, L., Stanley, H.E., Makse, H.A.: Identification of influential spreaders in complex networks. Nat. Phys **6**(11), 888–893 (2010)
23. Kumar, S., Lohia, D., Pratap, D., Krishna, A., Panda, B.S.: MDER: Modified degree with exclusion ratio algorithm for influence maximisation in social networks. Computing. 1–24 (2021)

24. Kumar, S., Panda, B.S., Aggarwal, D.: Community detection in complex networks using network embedding and gravitational search algorithm. J Intell Inf. Syst. **57**, 51–72 (2020)
25. Kumar, S., Saini, M., Goel, M., Panda, B.S.: Modeling information diffusion in online social networks using a modified forest-fire model. J Intell. Inf. Syst **56**(2), 355–77 (2020)
26. Kumar, S., Singhla, L., Jindal, K., Grover, K., Panda, B.S.: IM-ELPR: Influence Maximization in social networks using label propagation based community structure, Applied Intelligence. pp 1–19 (2021)
27. Kunegis, J.: KONECT: the Koblenz network collection. In: WWW 2013 Companion–Proceedings of the 22nd International Conference on World Wide Web (2013)
28. Leskovec J, Kleinberg J, Faloutsos C: Graph evolution: Densification and shrinking diameters. ACM transactions on Knowledge Discovery from Data (TKDD) **1**(1), 2–es (2007)
29. Leskovec, J., Kleinberg, J., Faloutsos, C.: Graph evolution: densification and shrinking diameters. ACM Trans Knowledge Discov Data. 1 (2006)
30. Leskovec, J., Krause, A., Guestrin, C., Faloutsos, C., VanBriesen, J., Glance, N.: Cost-effective outbreak detection in networks. In: Proceedings of the 13th ACM SIGKDD international conference on Knowledge discovery and data mining, pp 420–429 (2007)
31. Li, Y., Fan, J., Wang, Y., Tan, K.L.: Influence maximization on social graphs: a survey. IEEE Trans. Knowl. Data Eng. **30**(10), 1852–1872 (2018)
32. Li, M., Wang, X., Gao, Z.hang.S.: A survey on information diffusion in online social networks: Models and methods. Information **8**(4), 118 (2017)
33. Liu, W., Chen, X., Jeon, B., Chen, L., Chen, B.: Influence maximization on signed networks under independent cascade model. Appl. Intell. **49**(3), 912–28 (2019). Mar 15
34. Lusseau, D., Schneider, K., Boisseau, O.J., Haase, P., Slooten, E., Dawson, S.M.: The bottlenose dolphin community of Doubtful Sound features a large proportion of long-lasting associations. Behav. Ecol. Sociobiol. **54**(4), 396–405 (2003)
35. Ma, L.L., Ma, C., Zhang, H.F., Wang, B.H.: Identifying influential spreaders in complex networks based on gravity formula. Phys. A: Stat. Mech. Appl. **451**, 205–212 (2016)
36. Matei, R., Iamnitchi, A., Foster, P.: Mapping the gnutella network. IEEE Internet Computing **6**(1), 50–57 (2002)
37. Okamoto, K., Chen, W., Li, X.Y.: Ranking of Closeness Centrality for Large-Scale Social Networks. In: International Workshop on Frontiers in Algorithmics, (Pp. 186-195) Springer, Berlin, Heidelberg (2008)
38. Salavati, C., Abdollahpouri, A., Manbari, Z.: Ranking nodes in complex networks based on local structure and improving closeness centrality. Neurocomputing **336**, 36–45 (2018)
39. Satsuma, J., Willox, R., Ramani, A., Grammaticos, B., Carstea, A.S.: Extending the SIR epidemic model. Phys. A: Stat. Mech. Appl. **336**(3-4), 369–75 (2004)
40. Valente, T.W., Pumpuang, P.: Identifying opinionlLeaders to promote behavior change. Health Educ. Behav. **34**(6), 881–896 (2008)
41. Wen, T., Deng, Y.: Identification of influencers in complex networks by local information dimensionality. Inform. Sci. **512**, 549–562 (2019)
42. Yang, J., Yao, C., Ma, W., Chen, G.: A study of the spreading scheme for viral marketing based on a complex network model. Phys. A: Stat. Mech. Appl **389**(4), 859–870 (2010)
43. Zareie, A., Sheikhahmadi, A., Fatemi, A.: Influential nodes ranking in complex networks: an entropy-based approach. Chaos, Solitons & Fractal **104**, 485–494 (2017)

Publisher's note Springer Nature remains neutral with regard to jurisdictional claims in published maps and institutional affiliations.

Soft Computing
https://doi.org/10.1007/s00500-022-06846-x

DATA ANALYTICS AND MACHINE LEARNIN

Defect prediction model using transfer learning

Ruchika Malhotra[1] · **Shweta Meena**[1]

Accepted: 26 January 2022
© The Author(s), under exclusive licence to Springer-Verlag GmbH Germany, part of Springer Nature 2022

Abstract
Software defect prediction (SDP) plays an important role in new research areas of software engineering. Cross-project defect prediction (CPDP) technique achieved success for prediction of defects in innovating projects having lack of data. In this study, we have developed predictive models using different machine learning algorithms. Two approaches for DP were discussed in this study. One approach is heterogeneous defect prediction (HDP), and another approach is within-project defect prediction (WPDP). We have used different projects in HDP. The metrics matching analyzer is used for identifying matching metrics across different projects. The concept of transfer learning helps to improve DP by using HDP. HDP takes one project for training and testing against another project. We have shown the best machine learning algorithm for the DP model. The DP helps us in identifying defects before its delivery to the customer. To achieve our goal, we have taken twelve datasets from NASA and PROMISE repository. The machine learning algorithms are compared using statistical tests. The performance of the developed prediction model has been evaluated using area under curve performance measure

Keywords Software defect prediction · Transfer learning · Heterogeneous defect prediction · Machine learning · Statistical test

1 Introduction

In software engineering field, DP is one of the important research topic. In the last few years, DP is exhaustively studied Nam et al. (2018). SDP aims to detect defect prone modules at different levels, such as functions, classes, and files. It improves software quality, reduces cost, and development time. It helps in software quality assurance in terms of software development effort, software testing, or code review. It plays a significant role when an organization has limited resources. Over the past few years, researchers have developed various methods for DP at an early stage.

Transfer learning is a new research area for transferring knowledge across different projects. The concept of transfer learning is to learn some knowledge while solving some problems and apply that knowledge to a similar problem. Transfer learning states that the knowledge extracted or learned from the existing code can be applied to the innovative system. In this study, transfer learning concept has been used for DP. Transfer learning is used when we have a projects of similar nature. The concept of transfer learning is used in this study such that the model is trained on one dataset which can be also termed as pre-trained model (PTM). Now, the PTM is used to test another project of similar characteristics. In this study, feature-based transfer learning is used such that the two training and testing dataset have a similar features to some extent. In order to select the matching features, we have used algorithm for selection of matching pairs out of all the features for development of prediction model. Transfer learning is used to obtain generalized and unbiased results.

Nowadays, researchers, software experts, and academicians are working beyond WPDP. Moreover, in the upcoming years, the systems are designed with innovative ideas and techniques. The larger part of existing codes is used for the designing of innovative systems. However, using the existing code, which is designed by different people with different techniques, was difficult to understand by other people. Thus, the concept of transfer learning has emerged.

Data on various projects have been collected for prediction model development. These software data consist of different types of software metrics and label such as defective or non-defective. Software metrics are defined as a quantitative measure; these metrics are a descriptive analysis of software

✉ Shweta Meena
shweta82336@gmail.com

Ruchika Malhotra
ruchikamalhotra2004@yahoo.com

[1] Department of Software Engineering,
Delhi Technological University, Delhi, India

Published online: 22 February 2022

data. There are various types of software metrics. The most commonly used software metrics for DP are Halstead metrics, complexity metrics, and software process metrics Nam et al. (2018). The label indicates the presence of a defect in the project's data. Labels are used for the indication of defect presence.

The proposed models for DP are designed for WPDP and HDP. In WPDP, training and testing of model have been on the same project. Each instance in WPDP represents particular module of a project. The presence of labels corresponding to each instance whether the module is defective or not, i.e., defect proneness tendency of a project is present in the column of a project dataset. In WPDP, the prediction model is trained on some part of Project X, and testing of the prediction model is done on some part of Project X.

However, WPDP has various limitations. WPDP cannot be used when we have to make a DP for completely new projects. In some other cases also, when different people were working on the same project for a longer duration, then many changes are introduced in the code. With the help of the previous code, we cannot predict the defect for a newer version or with new changes in the code. To overcome this issue, researchers and academicians have started exploring cross-project defect prediction (CPDP). CPDP takes two different projects for training and testing. In CPDP, Project A can be used for training, and Project B can be used for testing. In this way, CPDP can be used for projects having lack of historical data. Till now, most of the researchers and academician have explored CPDP for the projects that have the same software metric; that limits the CPDP. Thus, HDP Nam et al. (2018) approach has been proposed. HDP allows prediction between two projects if they use different metrics.

There are various limitations of CPDP Nam et al. (2018). The open-source, available datasets consist of different metric sets. In heterogeneous data, all the projects have completely different metrics. For example, the datasets of the AEEEM group consist of 61 software metrics and the NASA dataset in the PROMISE repository consist of 31 software metrics. The common metrics between NASA and AEEEM dataset are LOC.

There exist various studies in the literature based on cross-project validation Malhotra and Bansal (2014); Malhotra (2015); He et al. (2012). However, most of the authors have not developed models for generalized results. Thus, to achieve generalized results, we have developed a predictive model for DP using different machine learning algorithms across different projects.

In this paper, we have analyzed the HDP approach for DP across various projects with different metrics suite. Thus, using HDP, researchers or experts can develop other prediction models to predict defects. HDP finds the matching metrics having same distribution from source (Project A) to target (Project B) dataset. For effective knowledge transfer, we have also demonstrated the size of a source and target dataset. To achieve our aim of improving the model for DP using heterogeneous metrics, we have formulated the research questions. The research questions are as follows: RQ1: Does the feature selection necessary for WPDP? RQ2: How does WPDP models perform using tenfold cross-validation? RQ3: Which machine learning algorithm performs best for HDP using transfer learning? RQ4: How does HDP models perform using tenfold cross-validation in comparison with WPDP?

The contribution of this paper is to analyze, experiment, and assess the empirical evidence regarding (1) the importance of feature selection for WPDP, (2) performance capability of machine learning techniques for HDP, (3) predictive performance capability of HDP and WPDP in comparison with tenfold cross-validation, (4) the applicability of cross-project defect prediction. DP models are developed using different machine learning algorithms to produce generalized results using transfer learning. The organization of the paper is as follows: Sect. 2 of this paper summarizes the exiting studies related to transfer learning, and SDP. Section 3 of this paper summarizes the types of variables and dataset used in this study. The research approach is discussed in Sect. 4. In Sect. 5 is presented the discussion based on the experimental results obtained in this study. The threats to validity are discussed in Section 6. Conclusion is discussed in Section 7.

2 Related work

The existing experiments and studies completed for DP and transfer learning are discussed in this section.

2.1 Transfer learning

The definition of transfer learning has been provided Pan and Yang (2010) in the literature. The definition of transfer learning is as follows: "Given a source domain D(s) and learning task T(s), a target domain D(t) and learning task T(t), transfer learning aims to improve the learning of the target predictive function f(a) in $D(t)$ using the knowledge in $D(s)$ and $T(s)$, where $D(s) = D(t)$, or $T(s) = T(t)$"Pan and Yang (2010). Hence, transfer learning is defined as establishing a relationship between two different problems. We solve one problem, and the knowledge gained from one problem can be used for solving another problem. Thus, transfer learning is used for knowledge transfer/transferring knowledge. Various types Pan and Yang (2010) of transfer learning are defined in the literature [5]. Instance transfer provides crucial data

to build a model in the target domain. Feature representation transfers the synthesized data in the form of examples for developing prediction models. Parameter transfer provides specific terms related to parameters for existing models. Relational transfer defines the relationship between terms specific to some relation in the source and target domain.

It has been specified when to use which type of transfer learning Pan and Yang (2010) in the study. The categorization of transfer learning types is based on feature space. As per the existing study Pan and Yang (2010), transfer learning is categorized into two categories, i.e., heterogeneous and homogeneous transfer learning. The feature space of source and target domain consists of different attributes in heterogeneous transfer learning. The features need to be transformed to reduce the gap between data distributions. The feature space of source and target domain consists of similar attributes in homogeneous transfer learning. Homogeneous transfer learning aims to reduce the gap between source and target data distribution. In the existing literature, heterogeneous transfer learning is divided into symmetric and asymmetric transformation. Symmetric distribution defines a common latent space for both training and testing features. Asymmetric transformation modifies the alignment of training and testing features to create common space for functions. The three types of transfer learning are discussed below Pan and Yang (2010).

2.2 Inductive transfer learning

In this setting, the target and source task is different from each other, irrespective of the source and target domains. The target domain consists of labeled data. Depending on data label (labeled and non-labeled) in the source domain, the inductive transfer learning is further divided into two categories. In the first category, the availability of labeled data is large in the source domain. This case is similar to a multi-task learning setting. Inductive transfer learning provides better performance in the target task by transferring knowledge from the source task, while multi-task learning learns both source and target tasks concurrently. In the second category, the labeled data are not available to us in the source domain. This category is similar to a self-taught learning. In self-taught learning, the source information cannot be indirectly used for the target domain.

2.3 Transductive transfer learning

In transductive transfer learning, source and target domains are different, while the source and target tasks are similar to each other. The availability of labeled data is in the source domain, while there are unlabeled data in the target domain.

2.4 Unsupervised transfer learning

In unsupervised transfer learning, the target task is not similar to source task, but they are related to each other in terms of some features. Unlabeled data present in the source and target domain.

The different types of transfer learning are given in Figure 1. Areas related to each transfer learning are also discussed. In Figure 2, the transfer learning types are summarized with each transfer learning approach.

2.5 Related work on DP

There are many studies that predict defects using predictive modeling. However, we referred only those studies that are related to DP using transfer learning. Most of the studies have shown the differentiation among CPDP and WPDP. Most of the researchers have studied CPDP Canfora et al. (2013); Ma et al. (2012); Nam et al. (2013); Panichella et al. (2014); Rahman et al. (2012); Ryu et al. (2017); Turhan et al. (2009); Zhang et al. (2015); Zimmermann et al. (2009). In the study proposed by Nam et al. Nam et al. (2018), it has been shown that how HDP can be used for creating generalized models for DP. Several studies exist in which the effectiveness of cross-project validation has been investigated. The study has been proposed by Nam et al. Nam et al. (2018) in which the defects are identified in cross-projects with the help of transfer learning. For transferring knowledge across two different projects, the object-oriented metrics are selected as features. In the existing studies, it has been specified to establish the correlation between selected metrics for knowledge transfer. The matching metrics can be obtained by using different metrics matching analyzer. The metrics among source and target dataset should be matched. Spearman's correlation coefficient method is used to compute similarity measure between source and target metrics pair.

In the study proposed by Ma et al. Ma et al. (2012), the author proposed a transfer learning algorithm using Naive Bayes machine learning algorithm known as transfer Naive Bayes (TNB) for CPDP. Here, the main focus is on instance-based transfer learning. TNB algorithm has executed some appropriate steps to transfer the information relevant to test data. In the first step, the collection of information related to the target dataset has been done. In the second step, the comparison has been performed between the test and target data. In the last step, a predictive model is developed based on weighted training data. Hence, the author has concluded that TNB gives the best performance for test data in comparison with other nearest neighbors. Ma et al. Ma et al. (2012) stated that the nearest neighbor filter technique is used, when the prediction model is developed using source instances, and the target instances are predicted based on nearest neighbor source instances.

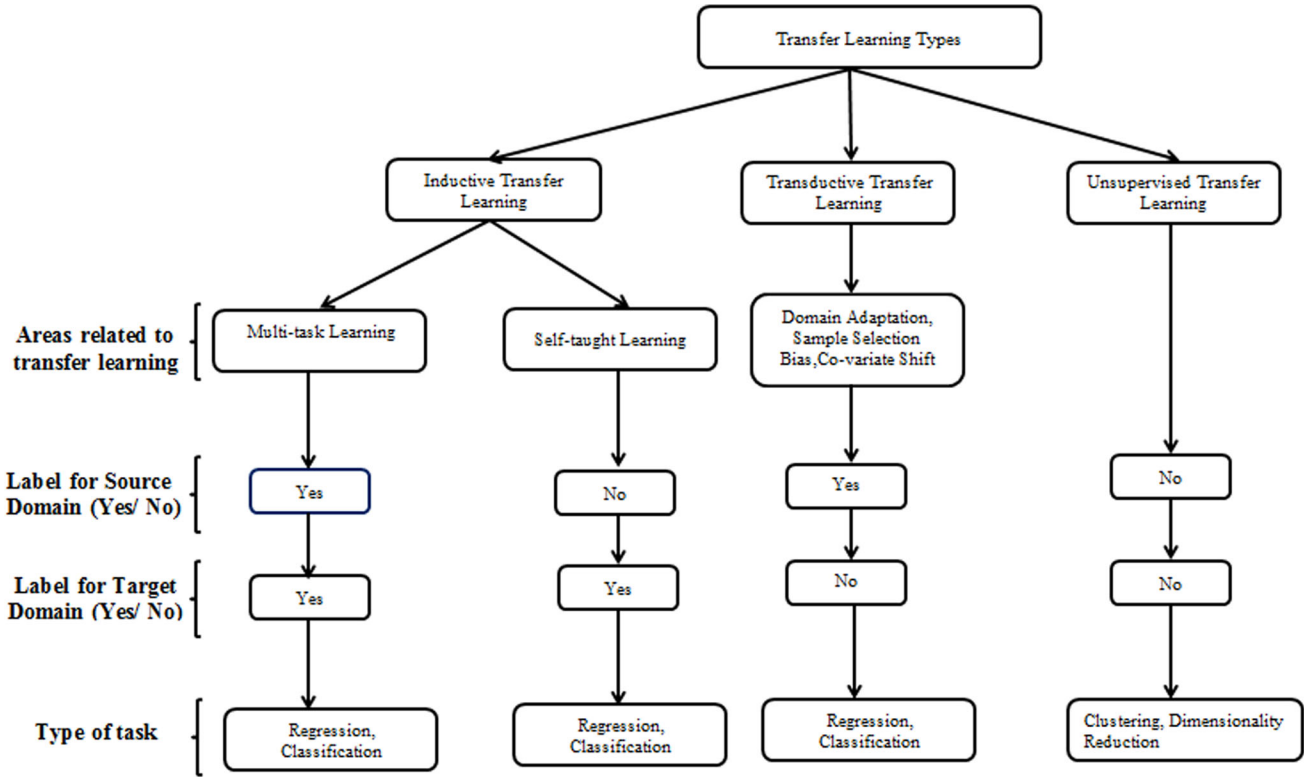


Fig. 1 Types of transfer learning

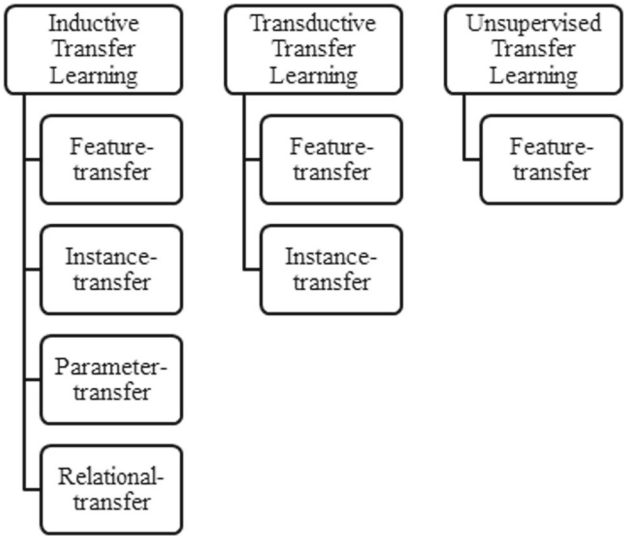


Fig. 2 Transfer learning types corresponding to transfer learning approach

The study given by Turhan et al. Turhan et al. (2009) used feature-based transfer learning for CPDP. In the study given by He et al. He et al. (2012), DP is done based on the features of a project. The author has explained that when the training data are not sufficient, feature-based transfer learning helps to train a model for predicting target project defects.

In the study given by Chen and Ding Kamei and Shihab (2016), the learning methods have been decided on the basis of domain adaptation technology. It is divided into feature-based and instance-based transfer learning. Feature-based transfer refers to dataset at a lower dimension to minimize differences between learning domains. Instance-based transfer learning assigns different weights to the instances depending on the instance in the target domain to establish the role of the model. This study presents a cross-project SDP method based on transfer learning called NTrA.

In the study given by Yu at al. Yuand et al. (2017), it has been analyzed that building a prediction model on sufficient historical data does not result in a better prediction model. The CPDP approach has been proposed by the lack of historical data. The developed CPDP model made prediction on the dataset of another project.

3 Dataset used

This section describes the types of variables and dataset used in this study. The two types of variables are used to conduct this study such as independent and dependent variable.

Table 1 Summary of defect datasets for twelve projects

Group	Dataset Name	Number of instances		Number of metrics	Prediction Granularity
		All	Defective(%)		
MORPH	ant-1.7	724	166 (22.93%)	20	Class
	CM1	498	49 (9.84%)	21	
	KC1	2109	326 (15.46%)	21	
	KC2	522	107 (20.50%)	21	
	KC3	194	36 (18.56%)	39	
NASA	MC1	1988	46 (2.31%)	38	Function
	MC2	125	44 (35.20%)	39	
	MW1	253	27 (10.67%)	37	
	PC1	1109	77 (6.94%)	21	
	PC2	745	16 (2.15%)	36	
	PC3	1077	134 (12.44%)	37	
	PC4	1458	178 (12.21%)	37	

3.1 Independent variable

The datasets are collected from NASA and MORPH group. Dataset consists of independent variables, such as software metrics and process metrics. These variables are required for the training of a model and to complete the predictive model task. These software metrics consist of McCabe's cyclomatic metrics, CK metrics, and other object-oriented metrics. In this study, we have used eleven datasets of NASA and one dataset of the MORPH group. All of these datasets have a different number of independent variables. These software metrics are characterized based on different measures such as cohesion, inheritance, coupling, the complexity of a dataset, and LOC of a particular software.

3.2 Dependent variable

The datasets used in this study have one dependent variable, i.e., the label for presence and absence of a defect. This variable is categorical, and it defines the presence of defect either by using True or False and Yes or No in the dataset file.

In this study, we have used publicly available datasets on Github. Table 1 summarizes all the datasets used in this study. We have used datasets of two groups: One is of NASA and another one MORPH. These datasets have different metrics, and they also differ from each other in terms of function and class level granularity. We have conducted experiment used 12 datasets. Each of these datasets has different metrics. We have also presented the prediction granularity of these datasets in Table 1. NASA contains confidential datasets from NASA software company Nam et al. (2018).

The MORPH group comprise of defect datasets; these datasets are for various free open-source software projects used in various studies Nam et al. (2018). There are total 21 features in the MORPH group dataset. The first 20 features are metrics, and the last feature defines a label for defective and non-defective instances.

4 Research approach

The MORPH group comprise of defect datasets; these datasets are of different open-source software projects used in various studies Nam et al. (2018). There are total 21 features in the MORPH group dataset. The first 20 features are metrics, and the last feature defines a label for defective and non-defective instances. In this study, we have discussed HDP with different datasets of two different groups. In HDP, we have considered two different datasets: One is source dataset, and another one is the target dataset, with different metrics. The instance is represented by a tuple of a dataset, and metrics are represented by an attribute of a dataset. The last attribute of a dataset represents a label for the presence and absence of defects. In Figure 3, we have presented the framework for HDP. In the first step, we have selected source (X) and target project (Y). The source and target dataset has a different metrics set. In the second step, we have selected metrics from both the projects. We have selected equal number of metrics from source and target dataset. In the next level, we find matching metrics for the target dataset into the source dataset. The matching metrics in the source and target dataset are found based on the similarity among them. The metrics matching has been done with the help of a correlation analyzer. At the end of this process, we have a set of matched metrics from source and target dataset. The matched source dataset has been trained using different machine learning algorithms. This step results in a prediction model that can be further used for predicting labels of the target dataset.

The WPDP is explained in Figure 4. WPDP considers a single project data due to lack of traditional data. In WPDP,

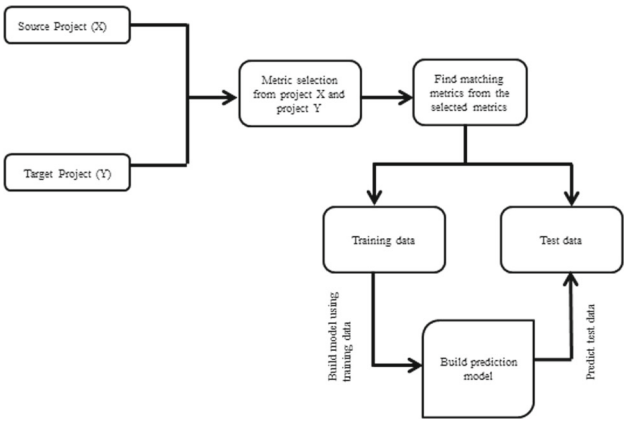


Fig. 3 Framework for heterogeneous defect prediction

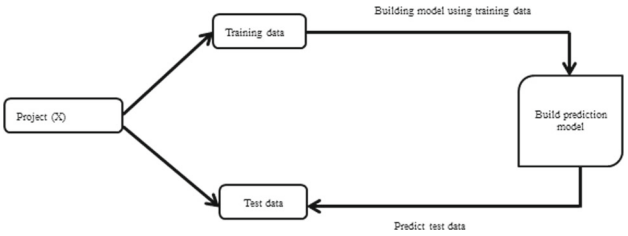


Fig. 4 Framework for within project defect prediction

we have divided a dataset in two different parts. One part of a dataset is training data, and another part is testing data. In the second step, it builds a model for the training data, and it uses that model for predicting labels of test data. In the next subsections, we have explained the approach in more detail.

4.1 Data collection

In this study, we have collected data from an open-source repository. NASA and MORPH group dataset is used in this study. The dataset collected from these groups has different projects and different attributes. These datasets consist of various software metrics. Software metrics provided in these studies are considered as independent variable. Each software metric provided with some numerical value corresponding to each module of a project. The last column corresponding to each module of a project provides a label for defect proneness. The defect proneness attribute is considered as an dependent variable.

4.2 Developing a prediction model

In this study, various machine learning algorithms were used. The machine learning algorithms used in this study such as logistic regression (LR), random forest (RF), hybrid voting (HV), multilayer perceptron (MLP), AdaBoost (ADB), and decision tree (DT). These machine learning algorithms have been discussed below:

1. LR:- LR is named after a function called as sigmoid function. This function is interpreted by an S-shaped curve that takes a real-valued number and maps it to values in the range of 0 and 1, but it should not be at the extreme points. The coefficients of the LR algorithm are determined from training data.
2. RF:- The name of this technique itself specifies that it consists of various decision trees. These individual decision trees operate as groups, i.e., ensemble. In this technique, each of the RF predicts an output class label, and the class having majority counts represents a model's prediction. RF provides an understandable model for researchers and academician. This algorithm is robust to noisy and missing values of the dataset.
3. HV:- In the HV technique, various machine learning algorithms are combined to build a prediction model.
4. MLP:- This technique consists of multiple perceptrons. This algorithm focuses on creating robust algorithms and uses those algorithms for building a prediction model. The neural network can learn the training data representation easily, and it easily predicts the label of the output variable. These networks can learn the mapping function, and they are proved as a global algorithm. The predictive capability of the neural networks comes from the hierarchical or multilayered structure of the networks. It takes different features of input data over various scales and groups them into high-order features.
5. ADB:- This classifier also makes a prediction. It is similar to the RF classifier. It applies multiple decision trees to individual samples, and it takes a combination of these predictions from each decision tree or majority trees in the classification problem. Each DT contributes a significant amount to the final prediction.
6. DT:- This technique works on the divide-and-conquer concept. It uses a heuristic approach known as recursive partitioning. This approach is based on the divide-and-conquer problem. It divides the original dataset into small groups, which are repeatedly split into even smaller groups. It solves each subproblem. In the end, the solution of all subproblems combined to produce solution to the actual problem. DT is easy to apply and easy for development of prediction models. It is not based on any assumption. It has no effect of outliers.

4.3 Cross-validation method

Cross-validation is a technique used for model evaluation by partitioning the given dataset into two parts Malhotra (2015). One part is for training, and another part is testing data. The data are divided into respective ratio and proportion using cross-validation method. The model is trained using training dataset. The prediction model is used for making predictions of testing data. The division of dataset into training

and testing dataset depends on the type of cross-validation method used Kohavi (1995). There exist three types of cross-validation methods, such as hold-out validation, K-fold cross-validation, and leave-one-out cross-validation. We have used K-fold cross-validation in this study. Due to the limitations of input data/lack of input data, we have used K-fold cross-validation in this study.

In K-fold cross-validation, the dataset is divided into K different parts. For training the model, we use K-1 parts, and the remaining part is used for testing. In this study, the value of K is considered as 10. In tenfold cross-validation, the complete dataset is partitioned into ten parts, and each part is of equal size. Nine parts are randomly selected for training, while the remaining part, i.e., the tenth part, is used as a validation set. This process iterates for ten times. In the end, the results of each iteration would be combined. K-fold cross-validation method is mostly used by researchers/academician and professionals in empirical studies Forman and Scholz (2010).

4.4 Performance metrics

There exist various performance metrics/measures. These metrics/measures are used to evaluate and analyze the performance of different machine learning algorithms. Different performance metrics exist for classification and regression problems. The selection of performance metrics/measures is very crucial. The performance metrics used for classification problems are confusion matrix, accuracy, precision, recall or sensitivity, specificity, F-score, and area under the curve (AUC) receiver operating characteristics (ROC) curve Bekkar et al. (2013). In this study, we have used the AUC-ROC performance metric. It helps in identifying the goodness of a developed prediction model. AUC-ROC curve is represented with a curve between recall and specificity. The value of AUC lies from 0 to 1. Depending on the AUC values, we can predict how good or bad the developed model Bekkar et al. (2013). The significance of AUC corresponding to 0, 0.5, and 1 has been represented in equation (1) given below.

$$AUC = \begin{cases} 0, \ the\ developed\ model\ wrongly\ classifies\ output\ class \\ 0.5, \ no\ discrimination\ between\ output\ classes \\ 1, \ the\ developed\ model\ perfectly\ classifies\ output\ class \end{cases} \quad (1)$$

4.5 Statistical test

In this study, we have used statistical test for validation of results. The statistical test is used to check if there is any significant difference between the machine learning techniques used in this study. For independent groups, Friedman test is used. The data can be selected randomly from any distribution for the Friedman test Malhotra (2015). This test does not consider any assumption; i.e., it is a nonparametric test. With the help of these, we have checked if there is any significant difference among the performance of machine learning algorithms used for HDP. In the first step, we have designed two hypotheses: the null hypothesis H_o and the alternate hypothesis H_a. In the second step, we have obtained p-value at a significant level of 0.05. The null hypothesis is accepted if the p-value > 0.05. An alternate hypothesis is accepted if the p-value ≤ 0.05. The pairwise comparison of the post hoc analysis is done using Wilcoxon signed-rank test Benavoli et al. (2016). We have also used Wilcoxon signed-rank test to analyze the results statistically. However, it is used to compare repeated measurements Taheri and Hesamian (2013).

5 Experimental results and discussion

In this section, we have addressed the answers to the research questions designed in this paper. The results for the comparison of HDP and WPDP are presented in this section.

5.1 RQ1: Does the feature selection necessary for WPDP?

We have applied various feature selection techniques for selection of features from different projects. In this study, Chi-square method and recursive feature elimination (RFE) method were used feature selection. We have observed that prediction model does not work efficiently after applying feature elimination method. Moreover, the large number of features is reduced and irrelevant features are removed using feature selection technique. With feature selection techniques, we got AUC values near 0.5. AUC value of 0.5 does not make correct predictions. We have performed experiment without feature selection techniques. Based on the observation, the prediction model provided efficient result using feature selection technique. Hence, it is concluded that feature selection techniques are not necessary for WPDP.

5.2 RQ2: How does WPDP models perform using tenfold cross-validation?

We have used different machine learning algorithms to develop these predictive models. For WPDP, the AUC values are computed using different machine learning algorithms and tenfold cross-validation method. The values for 12

Table 2 AUC values for WPDP

Source dataset	Target dataset	LR	RF	HV	MLP	ADB	DT	Average AUC value
ant-1.7	ant-1.7	0.76	0.83	0.82	0.73	0.82	0.72	0.78
CM1	CM1	0.47	0.73	0.65	0.42	0.62	0.58	0.58
KC1	KC1	0.55	0.79	0.73	0.6	0.76	0.74	0.70
KC2	KC2	0.63	0.82	0.76	0.53	0.76	0.66	0.69
KC3	KC3	0.55	0.76	0.73	0.49	0.63	0.62	0.63
MC1	MC1	0.4	0.9	0.78	0.48	0.83	0.71	0.68
MC2	MC2	0.7	0.71	0.77	0.62	0.63	0.59	0.67
MW1	MW1	0.72	0.71	0.74	0.32	0.67	0.59	0.63
PC1	PC1	0.61	0.83	0.77	0.48	0.79	0.75	0.71
PC1	PC1	0.61	0.83	0.77	0.48	0.79	0.75	0.71
PC2	PC2	0.52	0.81	0.71	0.21	0.77	0.59	0.60
PC3	PC3	0.66	0.83	0.79	0.57	0.77	0.74	0.73
PC4	PC4	0.76	0.92	0.9	0.71	0.91	0.88	0.85

datasets used for WPDP are shown in Table 2. In this study, all the machine leaning techniques performed significantly different based on the mathematical interpretation.

From the results obtained for WPDP, we have observed that RF technique performs better than LR, HV, MLP, ADB, DT technique. RF works better for building a prediction model for WPDP as it takes a combination of individual trees. RF provides a binary classification of data points, but it also provides the probabilities for each instance belong to defective and non-defective label. From the observation, the AUC value improved for all datasets. In some of the datasets, LR and HV also performed efficient. Further, we have statistically identified the best machine learning algorithms for WPDP.

5.3 RQ3: Which machine learning algorithm performs best for HDP using transfer learning?

To answer this research question, statistical test has been used. We have designed two hypotheses such as H_o and H_a.
$\mathbf{H}_o$: There is no statistical difference between six machine learning algorithms
$\mathbf{H}_a$: There is a statistical difference between six machine learning algorithms
Friedman test for testing the above hypothesis. The statistical test is used at a significance level of 0.05. The p-value obtained is 0.00 in this case. The value of Friedman's statistics is computed as 210.9. Hence, the p-value is less than 0.05; we reject H_o and accept H_a. In Figure 5, the Friedman mean rank corresponding to machine learning algorithms is presented. We have observed that the mean rank of RF is highest, i.e., 4.92. It implies that RF performs efficiently in comparison with other algorithms used in this study. ADB has the second-highest mean rank, i.e., 4.05, which implies that after RF, ADB is best performing machine learning algorithm

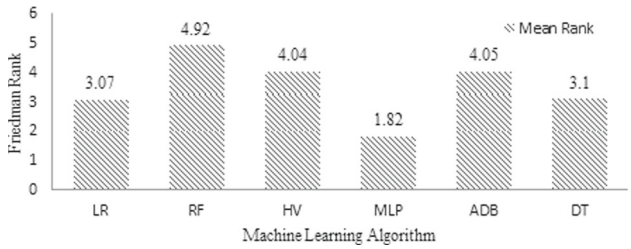


Fig. 5 Friedman mean rank for machine learning algorithm

for HDP. We have also performed Wilcoxon signed-rank test to check the statistical difference among all the algorithms. The Wilcoxon signed-rank test is used to check if any statistical difference exists or not. The hypothesis testing is performed at 0.05 significance level. The p-value provided by Wilcoxon signed-rank test is 0.000. The computed p-value is less than the significance level. Thus, there is a statistical difference among the performance of machine learning algorithms. Hence, alternate hypothesis is accepted.

5.4 RQ4: How does HDP models perform using tenfold cross-validation in comparison with WPDP?

To answer this RQ, we have experimented on twelve different datasets. In HDP, the source and target dataset is different. This experiment has been observed at different cutoff_threshold for metrics matching. The metrics matching has been done by Spearman's correlation coefficient analyzer. In this analyzer, we have performed experiments by taking different threshold values, e.g., cutoff_threshold= 0.1, 0.05, 0.3, 0.9. We have observed in this analyzer. By changing the threshold to more than 0.05, it does not perform well. So, we have set the threshold value to 0.05. Twelve different datasets are used as a target datasets, for

Table 3 AUC values for HDP (Source dataset:- 11 different datasets, Target dataset:- ant-1.7)

Source dataset	Target dataset	LR	RF	HV	MLP	ADB	DT	Average AUC value
CM1	ant-1.7	0.67	0.71	0.69	0.57	0.72	0.67	0.67
KC1	ant-1.7	0.69	0.73	0.67	0.68	0.7	0.69	0.69
KC2	ant-1.7	0.68	0.72	0.67	0.58	0.67	0.7	0.67
KC3	ant-1.7	0.71	0.75	0.72	0.47	0.68	0.66	0.67
MC1	ant-1.7	0.61	0.72	0.66	0.54	0.69	0.66	0.65
MC2	ant-1.7	0.68	0.67	0.66	0.56	0.59	0.54	0.62
MW1	ant-1.7	0.65	0.63	0.64	0.56	0.61	0.6	0.62
PC1	ant-1.7	0.66	0.75	0.71	0.57	0.72	0.71	0.69
PC2	ant-1.7	0.68	0.73	0.7	0.62	0.72	0.69	0.69
PC3	ant-1.7	0.64	0.73	0.66	0.54	0.66	0.66	0.65
PC4	ant-1.7	0.63	0.73	0.67	0.56	0.71	0.69	0.67

Table 4 AUC values for HDP (Source dataset:- 10 different datasets, Target dataset:- CM1)

Source dataset	Target dataset	LR	RF	HV	MLP	ADB	DT	Average AUC value
ant-1.7	CM1	0.64	0.67	0.68	0.6	0.62	0.6	0.64
KC1	CM1	0.6	0.64	0.65	0.6	0.67	0.65	0.64
KC2	CM1	0.59	0.68	0.66	0.56	0.63	0.6	0.62
KC3	CM1	0.54	0.48	0.58	0.64	0.67	0.46	0.56
MC1	CM1	0.54	0.66	0.6	0.59	0.66	0.61	0.61
MW1	CM1	0.56	0.59	0.62	0.61	0.65	0.61	0.61
PC1	CM1	0.62	0.71	0.63	0.5	0.69	0.59	0.62
PC2	CM1	0.57	0.6	0.6	0.52	0.64	0.54	0.58
PC3	CM1	0.58	0.68	0.63	0.49	0.65	0.61	0.61
PC4	CM1	0.55	0.71	0.6	0.49	0.7	0.49	0.59

Table 5 AUC values for HDP (Source dataset:- 11 different datasets, Target dataset:- KC1)

Source dataset	Target dataset	LR	RF	HV	MLP	ADB	DT	Average AUC value
ant-1.7	KC1	0.68	0.76	0.69	0.75	0.74	0.68	0.72
CM1	KC1	0.64	0.69	0.65	0.61	0.71	0.65	0.66
KC2	KC1	0.61	0.77	0.72	0.57	0.76	0.69	0.69
KC3	KC1	0.71	0.71	0.72	0.6	0.78	0.72	0.71
MC1	KC1	0.59	0.75	0.69	0.62	0.75	0.73	0.69
MC2	KC1	0.54	0.69	0.69	0.51	0.63	0.65	0.62
MW1	KC1	0.64	0.74	0.71	0.56	0.68	0.64	0.66
PC1	KC1	0.67	0.75	0.68	0.62	0.72	0.74	0.7
PC2	KC1	0.68	0.73	0.72	0.61	0.74	0.68	0.69
PC3	KC1	0.62	0.74	0.71	0.55	0.74	0.69	0.68
PC4	KC1	0.62	0.75	0.7	0.62	0.74	0.75	0.7

which we have executed our experiment iteratively, by setting different source and target dataset in each iteration. In Tables (3, 4, 5, 6, 7, 8, 9, 10, 11, 12, 13, 14) are presented the AUC values corresponding to the machine learning algorithms used. The pairwise combination of the source and target dataset is presented separately in Tables (3, 4, 5, 6, 7, 8, 9, 10, 11, 12, 13, 14).

Transfer learning concept helps us in developing a generalized model. Generalized DP model can be easily developed for industry or academic purpose. The software quality also improves with the generalized prediction model. We have used existing software knowledge for building purpose. We can remove the ambiguities in the new projects by using the existed project's knowledge, patterns, design. It improves the maintainability and understandability of a software. It would

Table 6 AUC values for HDP (Source dataset:- 11 different datasets, Target dataset:- KC2)

Source dataset	Target dataset	LR	RF	HV	MLP	ADB	DT	Average AUC value
ant-1.7	KC2	0.79	0.82	0.8	0.76	0.78	0.68	0.77
CM1	KC2	0.71	0.79	0.75	0.7	0.8	0.67	0.74
KC1	KC2	0.73	0.81	0.81	0.69	0.77	0.69	0.75
KC3	KC2	0.76	0.82	0.79	0.6	0.8	0.79	0.76
MC1	KC2	0.63	0.79	0.76	0.65	0.76	0.68	0.71
MC2	KC2	0.8	0.76	0.78	0.63	0.74	0.67	0.73
MW1	KC2	0.75	0.79	0.75	0.6	0.67	0.64	0.7
PC1	KC2	0.72	0.79	0.8	0.68	0.76	0.74	0.75
PC2	KC2	0.78	0.79	0.79	0.7	0.75	0.75	0.76
PC3	KC2	0.72	0.8	0.77	0.67	0.77	0.75	0.75
PC4	KC2	0.74	0.79	0.77	0.64	0.77	0.66	0.73

Table 7 AUC values for HDP (Source dataset:- 11 different datasets, Target dataset:- KC3)

Source dataset	Target dataset	LR	RF	HV	MLP	ADB	DT	Average AUC value
ant-1.7	KC3	0.78	0.84	0.79	0.8	0.77	0.74	0.79
CM1	KC3	0.54	0.58	0.6	0.5	0.47	0.58	0.55
KC1	KC3	0.56	0.61	0.58	0.45	0.45	0.44	0.52
KC2	KC3	0.63	0.64	0.65	0.49	0.6	0.51	0.59
MC1	KC3	0.59	0.62	0.64	0.48	0.56	0.55	0.57
MC2	KC3	0.51	0.57	0.46	0.39	0.52	0.49	0.49
MW1	KC3	0.66	0.63	0.6	0.51	0.69	0.42	0.59
PC1	KC3	0.66	0.6	0.64	0.46	0.59	0.53	0.58
PC2	KC3	0.63	0.57	0.66	0.56	0.55	0.46	0.57
PC3	KC3	0.46	0.54	0.52	0.51	0.58	0.52	0.52
PC4	KC3	0.59	0.52	0.56	0.6	0.56	0.52	0.56

Table 8 AUC values for HDP (Source dataset:- 9 different datasets, Target dataset:- MC1)

Source dataset	Target dataset	LR	RF	HV	MLP	ADB	DT	Average AUC value
ant-1.7	MC1	0.62	0.74	0.62	0.52	0.56	0.54	0.6
CM1	MC1	0.5	0.6	0.59	0.35	0.59	0.56	0.53
KC1	MC1	0.5	0.62	0.62	0.54	0.61	0.67	0.59
KC2	MC1	0.5	0.52	0.59	0.41	0.5	0.5	0.5
MW1	MC1	0.62	0.64	0.55	0.53	0.61	0.52	0.58
PC1	MC1	0.41	0.42	0.51	0.42	0.49	0.51	0.46
PC2	MC1	0.53	0.47	0.5	0.55	0.47	0.56	0.51
PC3	MC1	0.58	0.62	0.62	0.59	0.59	0.46	0.58
PC4	MC1	0.54	0.65	0.64	0.55	0.61	0.65	0.61

be easy to use prediction model for end-users. The feature-based transfer learning method is used in this study. The computed results of this study were compared with existing studies also. AUC values for RF in HDP and WPDP are 0.673 and 0.803 in this study. However, the AUC values for RF in HDP and WPDP in existing studies are 0.640 and 0.732. The AUC values for DT in HDP and WPDP are 0.617 and 0.681 in this study. However, the AUC values for DT and WPDP in existing studies are 0.568 and 0.598. Hence, the computed AUC values indicated that RF and DT performed better for HDP and WPDP based on the experiment performed in this study.

The feature-based transfer learning method is used for HDP. We have selected equal feature count from source and target projects, through which the DP knowledge is transferred for testing of target project. We have performed metrics matching from the selected features using Spearman's correlation coefficient. Based on the correlation coefficient among these features, we selected metrics for training and test data. The prediction model is developed using one project dataset

Table 9 AUC values for HDP (Source dataset:- 11 different datasets, Target dataset:- MC2)

Source dataset	Target dataset	LR	RF	HV	MLP	ADB	DT	Average AUC value
ant-1.7	MC2	0.61	0.46	0.54	0.49	0.46	0.57	0.52
CM1	MC2	0.67	0.68	0.66	0.57	0.67	0.56	0.64
KC1	MC2	0.78	0.76	0.77	0.64	0.81	0.72	0.75
KC2	MC2	0.7	0.71	0.74	0.56	0.61	0.7	0.67
KC3	MC2	0.61	0.66	0.57	0.48	0.59	0.61	0.59
MC1	MC2	0.67	0.59	0.62	0.49	0.57	0.54	0.58
MW1	MC2	0.61	0.52	0.64	0.5	0.56	0.48	0.55
PC1	MC2	0.66	0.56	0.61	0.59	0.55	0.57	0.59
PC2	MC2	0.65	0.57	0.64	0.49	0.46	0.57	0.56
PC3	MC2	0.58	0.57	0.55	0.51	0.57	0.55	0.56
PC4	MC2	0.56	0.56	0.56	0.48	0.6	0.42	0.53

Table 10 AUC values for HDP (Source dataset:- 11 different datasets, Target dataset:- MW1)

Source dataset	Target dataset	LR	RF	HV	MLP	ADB	DT	Average AUC value
ant-1.7	MW1	0.56	0.63	0.56	0.52	0.57	0.51	0.56
CM1	MW1	0.56	0.68	0.62	0.53	0.55	0.55	0.58
KC1	MW1	0.54	0.66	0.6	0.47	0.56	0.56	0.57
KC2	MW1	0.62	0.61	0.66	0.44	0.53	0.43	0.55
KC3	MW1	0.64	0.52	0.46	0.51	0.39	0.48	0.5
MC1	MW1	0.63	0.55	0.6	0.57	0.57	0.5	0.57
MC2	MW1	0.36	0.52	0.57	0.52	0.34	0.68	0.5
PC1	MW1	0.6	0.6	0.6	0.44	0.56	0.54	0.56
PC2	MW1	0.64	0.68	0.64	0.54	0.53	0.6	0.61
PC3	MW1	0.69	0.67	0.71	0.54	0.59	0.47	0.61
PC4	MW1	0.55	0.54	0.55	0.56	0.46	0.57	0.54

Table 11 AUC values for HDP (Source dataset:- 10 different datasets, Target dataset:- PC1)

Source dataset	Target dataset	LR	RF	HV	MLP	ADB	DT	Average AUC value
ant-1.7	PC1	0.66	0.67	0.62	0.59	0.61	0.47	0.6
CM1	PC1	0.43	0.64	0.6	0.4	0.57	0.51	0.53
KC1	PC1	0.57	0.72	0.67	0.59	0.78	0.74	0.68
KC2	PC1	0.66	0.7	0.59	0.51	0.6	0.53	0.6
KC3	PC1	0.68	0.73	0.76	0.42	0.74	0.63	0.66
MC1	PC1	0.53	0.59	0.56	0.53	0.63	0.66	0.58
MW1	PC1	0.69	0.64	0.68	0.69	0.6	0.62	0.65
PC2	PC1	0.61	0.6	0.65	0.53	0.66	0.49	0.59
PC3	PC1	0.55	0.69	0.63	0.56	0.72	0.67	0.64
PC4	PC1	0.56	0.69	0.64	0.48	0.6	0.57	0.59

for training, and we use that model for the prediction of labels in test data. In this manner, we have transferred the feature-based knowledge from source and target projects to build a prediction model

In order to analyze the effectiveness of HDP, we have performed hypotheses testing. Hypothesis testing is performed using Friedman test. These hypotheses are designed based on effectiveness of HDP and WPDP using RF machine learning algorithm.

$\mathbf{H}_o$: HDP performs better than WDP for RF

$\mathbf{H}_a$: WDP performs better than HDP for RF

The Friedman test is used for testing the above hypothesis. The statistical test is performed at a 0.05 significance level. The obtained p-value is 0.001. The value of Friedman's

Table 12 AUC values for HDP (Source dataset:- 8 different datasets, Target dataset:- PC2)

Source dataset	Target dataset	LR	RF	HV	MLP	ADB	DT	Average AUC value
ant-1.7	PC2	0.6	0.48	0.51	0.42	0.66	0.58	0.54
CM1	PC2	0.4	0.57	0.49	0.63	0.55	0.66	0.55
KC1	PC2	0.58	0.7	0.73	0.5	0.48	0.6	0.6
KC2	PC2	0.28	0.65	0.4	0.42	0.4	0.41	0.43
MC1	PC2	0.6	0.64	0.59	0.63	0.53	0.5	0.58
PC1	PC2	0.67	0.58	0.64	0.49	0.52	0.6	0.58
PC3	PC2	0.48	0.5	0.49	0.45	0.49	0.56	0.5
PC4	PC2	0.39	0.58	0.45	0.46	0.51	0.48	0.48

Table 13 AUC values for HDP (Source dataset:- 11 different datasets, Target dataset:- PC3)

Source dataset	Target dataset	LR	RF	HV	MLP	ADB	DT	Average AUC value
ant-1.7	PC3	0.66	0.75	0.67	0.65	0.73	0.67	0.69
CM1	PC3	0.57	0.76	0.69	0.58	0.69	0.66	0.66
KC1	PC3	0.56	0.74	0.65	0.59	0.71	0.69	0.66
KC2	PC3	0.6	0.71	0.68	0.58	0.71	0.69	0.66
KC3	PC3	0.45	0.67	0.62	0.42	0.77	0.65	0.6
MC1	PC3	0.63	0.74	0.69	0.61	0.75	0.73	0.69
MC2	PC3	0.67	0.84	0.76	0.46	0.87	0.77	0.73
MW1	PC3	0.63	0.65	0.61	0.37	0.69	0.54	0.58
PC1	PC3	0.62	0.77	0.72	0.55	0.74	0.72	0.69
PC2	PC3	0.78	0.76	0.72	0.6	0.72	0.62	0.7
PC4	PC3	0.6	0.76	0.68	0.48	0.74	0.74	0.67

Table 14 AUC values for HDP (Source dataset:- 11 different datasets, Target dataset:- PC4)

Source dataset	Target dataset	LR	RF	HV	MLP	ADB	DT	Average AUC value
ant-1.7	PC4	0.72	0.89	0.82	0.73	0.91	0.82	0.82
CM1	PC4	0.63	0.7	0.66	0.53	0.68	0.69	0.65
KC1	PC4	0.49	0.74	0.64	0.53	0.73	0.74	0.65
KC2	PC4	0.57	0.85	0.75	0.47	0.84	0.8	0.71
KC3	PC4	0.51	0.6	0.53	0.48	0.7	0.7	0.59
MC1	PC4	0.54	0.74	0.64	0.55	0.74	0.73	0.66
MC2	PC4	0.59	0.57	0.57	0.46	0.68	0.76	0.61
MW1	PC4	0.35	0.62	0.43	0.42	0.76	0.53	0.52
PC1	PC4	0.5	0.74	0.68	0.49	0.73	0.7	0.64
PC2	PC4	0.64	0.79	0.71	0.51	0.7	0.69	0.67
PC3	PC4	0.58	0.9	0.83	0.62	0.89	0.87	0.78

statistics is computed as 12.0. Hence, the p-value is less than 0.05. Therefore, we reject H_o and accept H_a. Table 15 represents the Friedman mean rank for HDP and WPDP corresponding to RF machine learning algorithm. It is observed that the mean rank of WPDP is highest, i.e., 2.00. Hence, RF performed efficiently for WPDP.

Table 15 Friedman mean rank for DP methods using RF

DP Method	Mean rank
RF for HDP	1.00
RF for WPDP	2.00

6 Threats to validity

In this study, the dataset size is not very large. Moreover, this experiment should be performed for large datasets. In such a case, this study might result in conclusion validity. Different data processing or engineering activities such as feature reduction, dealing with outliers, and scaling are not considered in this study. For mitigating this threat, we should use different feature reduction and data preprocessing techniques. It should be done in such a way that the conclusion should not vary significantly.

The relationship between the independent and dependent variables used in this study has not accounted for using a specific experiment. Moreover, the experiment should be conducted to establish a constant relationship between specific measures. However, the conduction of such experiments is difficult. Hence, this study might result in internal validity. The dataset collected from the software repository may contain some noisy data. The noisy data provide irrelevant information. Moreover, the studies should remove noisy data before experimentation.

This study does not consider the programmer's capability or other human factors to explore the relationship between independent and dependent variables. The academician, experts, and researchers knowledge have been accounted for the relationship between independent and dependent variables. Moreover, the study should analyze the effect of researchers, experts, domain-knowledge experts, and professionals on the cause–effect relationship between variables. However, it is difficult to collect datasets for evaluating such relationships. In such case, it might result in internal validity.

There is no threshold value defined for software metrics. Therefore, the results of the experiment on different threshold values lead to bias. Thus, this study leads to construct validity. Threshold values have a subjective nature. Moreover, the significance of the results should be increased. This threat can be mitigated by validating the results over other threshold values.

The datasets used in this study are having a small size. It affects the results of generalizability. The datasets evaluated in this study are extracted from a specific software repository. Thus, the results are biased for other datasets. It leads to external validity for this study. Hence, a large dataset should be evaluated by considering the generalization of results and applications of this study. Moreover, the industry sized dataset should be evaluated. It would provide more generalized results. The results are specific to only specified dependent variables, such as defect proneness. The results should be generalized. Moreover, it should explore other dependent variables also, such as change prediction, maintenance, and reliability.

7 Conclusion

The datasets used in this study contain projects developed in various languages such as C, Java, and C++. To analyze the capability of DP techniques, we have used twelve datasets of two different groups, named as NASA and MORPH. We have conducted various experiments in this study. In the experimental procedure, firstly, we have developed a predictive model for predicting defects using different machine learning algorithms and tenfold cross-validation for WPDP. In the next experiment, we have developed a predictive model using different machine learning algorithms and tenfold cross-validation methods for HDP. We have observed that the size of the source dataset should be larger than 23%. We have explored that WPDP performs better than HDP. However, due to the presence of historical data in WPDP, it provides a better result. In this way, it would be helpful to identify the defect in the early stage before its delivery to end-users. In the end, we have tested the hypothesis using the Friedman test. The designed hypothesis is to evaluate the significant difference between machine learning algorithms for HDP. The result of Friedman test proves that there is a significant difference among all the machine learning algorithms used in this study. With our observation on Friedman's mean ranks, RF performs best for HDP in our experiments. The hypothesis testing has been performed to analyze the performance of RF in WPDP and HDP. Thus, RF performs best out of all the six machine learning algorithms used in this study. In future work, we try to integrate the instance-based transfer learning method. Moreover, we test this experiment with large datasets with different techniques. We also investigate the effect of transfer learning on change prediction models with different datasets.

Acknowledgements This research is not supported under any funding.

Funding Authors certify that no funding has been received for the conduct of this study and preparation of this manuscript.

Data Availability Enquiries about data availability should be directed to the authors.

Declarations

Conflict of interest The authors declare that they have no conflict of interest.

Ethical approval This article does not contain any studies with human participants or animals performed by any of the authors.

References

Bekkar M, Djemaa HK, Alitouche TA (2013) Evaluation measures for models assessment over imbalanced data sets. J Info Eng Applicat 3(10):1–13

Benavoli A, Corani G, Mangili F (2016) Should we really use post-hoc tests based on mean-ranks? J Machine Learn Res 7(1):152–161

Bird C, Nagappan N, Murphy B, Gall H, Devanbu P(2011)"Don't touch my code!: examining the effects of ownership on software quality,"In ACM SIGSOFT Symposium and the european conference on foundations of software engineering, pp. 4–14

Bowes D, Hall T, Petric J (2018) Software defect prediction: do different classifiers find the same defects? Softw Qual J 26:525–552

Canfora G, De Lucia A, Di Penta M, Oliveto R, Panichella A, Panichella S(2013) "Multi-objective Cross-Project Defect Prediction,"In 2013 IEEE International Conference on Software Testing, Verification and Validation, pp. 252–261

Cao Q, Sun Q, Cao Q, Tan H(2015) "Software defect prediction via transfer learning based neural network,"2015 First international conference on reliability systems engineering (ICRSE), pp. 1–10

Caruana R (1997) Multitask Learning. Machine Learn 28:41–75

Forman G, Scholz M (2010) Apples-to-apples in cross-validation studies: pitfalls in classifier performance measurement. ACM SIGKDD Explorat Newslett 12(1):49–57

He Z, Shu F, Yang Y, Li M, Wang Q (2012) An investigation on the feasibility of cross-project defect prediction. Automat Soft Eng 19(2):167–199

Jing X, Wu F, Dong X, Qi F, Xu B(2015) "Heterogeneous cross-company defect prediction by unified metric representation and CCA-based transfer learning,"In Proceedings of the joint meeting on foundations of software engineering, association for computing machinery, pp. 496–507

Kamei Y, Shihab E(2016) "Defect prediction: accomplishments and future challenges,"2016 IEEE 23rd International conference on software analysis, evolution, and reengineering (SANER), pp. 33–45

Kohavi R (1995) A study of cross-validation and bootstrap for accuracy estimation and model selection. In Ijcai 14(2):1137–1145

Krishna R, Menzies T (2019) Bellwethers: a baseline method for transfer learning. IEEE Trans Softw Eng 45(11):1081–1105

Lessmann S, Baesens B, Mues C, Pietsch S (2008) Benchmarking classification models for software defect prediction: a proposed framework and novel findings. IEEE Trans Softw Eng 34(4):485–496

Liu X, Liu Z, Wang G, Cai Z, Zhang H (2018) Ensemble transfer learning algorithm. IEEE. Access 6:2389–2396

Long M, Wang J, Ding G, Pan SJ, Yu PS (2014) Adaptation regularization: a general framework for transfer learning. IEEE Trans Knowl Data Eng 26(5):1076–1089

Long M, Wang J, Sun J, Yu PS (2015) Domain invariant transfer kernel learning. IEEE Trans Knowl Data Eng 27(6):1519–1532

Ma Y, Luo G, Zeng X, Chen A (2012) Transfer learning for cross-company software defect prediction. Info Softw Tech 54(3):248–256

Malhotra R (2015) Empirical research in software engineering concepts, analysis and applications. CRC Press, Florida

Malhotra R, Bansal A. J(2014) "Cross project change prediction using open source projects,"2014 International conference on advances in computing, communications and informatics (ICACCI), 2014, pp. 201–207

Nam J, Fu W, Kim S, Menzies T, Tan L (2018) Heterogeneous defect prediction. IEEE Trans Soft Eng 44(9):874–896

Nam J, Pan S. J, Kim S(2013) "Transfer defect learning,"International conference on software engineering (ICSE), pp. 382–391

Pan SJ, Yang Q (2010) A survey on transfer learning. IEEE Trans Knowl Data Eng 22(10):1345–1359

Pan W, Liu M, Ming Z (2016) Transf Learn Heterogen One-Class Collaborat Filter. IEEE Intell Sys 31(4):43–49

Panichella A, Oliveto R, De Lucia A(2014) "Cross-project defect prediction models: L'union fait la force,"In Software maintenance, reengineering and reverse engineering (CSMR-WCRE), 2014 Software Evolution Week - IEEE conference, pp. 164–173

Pan S. J, Kwok J. T, Yang Q(2008) Transfer learning via Dimensionality Reduction. In Proceedings of the 23rd national conference on Artificial intelligence - Volume 2 (AAAI'08), AAAI Press, pp. 677–82

Peters F, Menzies T(2012) "Privacy and utility for defect prediction: experiments with MORPH,"2012 34th International conference on software engineering (ICSE), pp. 189–199

Qing H, Biwen L, Beijun S, Xia Y (2015) "Cross-project software defect prediction using feature-based transfer learning,"In: Asia-pacific symposium on internetware. ACM, New York, USA, pp 74–82

Rahman F, Posnett D, Devanbu P(2012) "Recalling the "imprecision"of cross-project defect prediction,"In International symposium on the foundations of software engineering, pp 1–11

Ryu D, Jang J, Baik J (2017) A transfer cost-sensitive boosting approach for cross-project defect prediction. Softw Qual J 25(1):235–272

Taheri SM, Hesamian G (2013) A generalization of the Wilcoxon signed-rank test and its applications. Stat Paper 54(2):457–470

Tantithamthavorn C, McIntosh S, Hassan AE, Matsumoto K (2017) An empirical comparison of model validation techniques for defect prediction models. IEEE Trans Softw Eng 43(1):1–18

Turhan B, Menzies T, Bener AB, Di Stefano J (2009) On the relative value of cross-company and within-company data for defect prediction. Empir Softw Eng 14:540–578

Xu Y et al (2017) A unified framework for metric transfer learning. IEEE Trans Knowl Data Eng 29(6):1158–1171

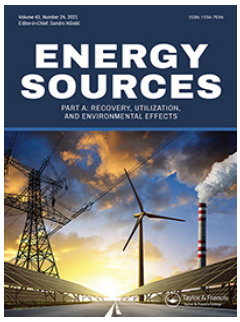
Yan S, Shen B, Mo W, Li N(2017) "Transfer Learning for Cross-Platform Software Crowdsourcing Recommendation,"2017 24th Asia-Pacific software engineering conference (APSEC), pp. 269–278

Yuand Q, Jiang S, Zhang Y (2017) A feature matching and transfer approach for cross-company defect prediction. J Sys Softw 132:366–378

Zhang Y, Lo D, Xia X, Sun J(2015) "An empirical study of classifier combination for cross-project defect prediction,"2015 IEEE 39th Annual computer software and applications conference, pp. 264–269

Zimmermann T, Nagappan N, Gall H, Giger E, Murphy B(2009) "Cross-project defect prediction: a large scale experiment on data vs. domain vs. process,"In Proceedings of the 7th joint meeting of the european software engineering conference and the ACM SIGSOFT symposium on The foundations of software engineering (ESEC/FSE'09), pp. 91–100

Publisher's Note Springer Nature remains neutral with regard to jurisdictional claims in published maps and institutional affiliations.



Energy Sources, Part A: Recovery, Utilization, and Environmental Effects

ISSN: (Print) (Online) Journal homepage: https://www.tandfonline.com/loi/ueso20

Design of PSO-tuned FOPI & Smith predictor controller for nonlinear polymer electrolyte membrane fuel cell

Swati Singh, Vijay Kumar Tayal, Hemender Pal Singh & Vinod Kumar Yadav

To cite this article: Swati Singh, Vijay Kumar Tayal, Hemender Pal Singh & Vinod Kumar Yadav (2022): Design of PSO-tuned FOPI & Smith predictor controller for nonlinear polymer electrolyte membrane fuel cell, Energy Sources, Part A: Recovery, Utilization, and Environmental Effects, DOI: 10.1080/15567036.2022.2025954

To link to this article: https://doi.org/10.1080/15567036.2022.2025954

Published online: 10 Feb 2022.

Submit your article to this journal

Article views: 8

View related articles

View Crossmark data

Full Terms & Conditions of access and use can be found at
https://www.tandfonline.com/action/journalInformation?journalCode=ueso20

ENERGY SOURCES, PART A: RECOVERY, UTILIZATION, AND ENVIRONMENTAL EFFECTS
https://doi.org/10.1080/15567036.2022.2025954

Taylor & Francis
Taylor & Francis Group

Check for updates

Design of PSO-tuned FOPI & Smith predictor controller for nonlinear polymer electrolyte membrane fuel cell

Swati Singh[a], Vijay Kumar Tayal[a], Hemender Pal Singh[a], and Vinod Kumar Yadav[b]

[a]Electrical and Electronics Engineering Department, Amity School of Engineering & Technology, Noida, India; [b]Electrical Engineering Department, Delhi Technological University, Delhi, India

ABSTRACT

The polymer electrolyte membrane (PEM) fuel cell or proton exchange membrane fuel cell (PEMFC) has sparked a lot of interest in renewable electricity generation due to high efficiency, quick start up time, and low operating temperature. However, they exhibit highly nonlinear behavior with degraded power quality under uncertain input conditions. The hydrogen, oxygen, and air feed determine the PEMFC system's performance. Controlling the manifold pressure at the cathode side is essential in preventing the problem of oxygen starvation. In this paper, a nonlinear dynamic model of the PEMFC is considered to control the supply manifold pressure. The performance of the nonlinear PEMFC with various classical controllers (PI, PD, PID, and PID with filter derivative), Smithpredictor, and Fractional Order PI (FOPI) controllers are compared. The optimization of classical controllers is performed by PID tuner. On the other hand, Smith predictor and FOPI controller are tuned by artificial intelligence technique, namely, Particle Swarm Optimization (PSO). The FOPI controller is also tuned with Genetic Algorithm (GA). The PEMFC output is compared in terms of performance evaluation parameters, i.e. settling time, overshoot, and steady state error. The computer simulations suggest that in comparison with GA-FOPI [settling time (t_s) = 1.374 s, overshoot (M_p) = 18.452%, steady state error (e_{ss}) = 0.1%] and PSO-Smith predictor (t_s = 1.262 s, M_p = 5.581%, e_{ss} = 0%), the PSO-FOPI controller results in much better settling time (t_s = 1.008 s), overshoot (M_p = 2.577%), and steady state error (e_{ss} = 0%). Thus, PSO-optimized FOPI controller with nonlinear PEMFC outperforms the classical, PSO-Smith predictor, and GA-FOPI control schemes.

ARTICLE HISTORY
Received 30 July 2021
Revised 27 December 2021
Accepted 29 December 2021

KEYWORDS
Proton electrolyte membrane (PEM) fuel cell (FC); proportional-integral-derivative (PID) controller; PID-controller with filter derivative (PIDF); fractional order (FO) proportional integral (PI) controller; particle swarm optimization (PSO); settling time (t_s); overshoot (M_p); steady state error (e_{ss})

1. Introduction

With excellent reliability, negligible contamination, low operating temperature, and a wide range of applications, the PEM fuel cell is one of the finest power generating systems to make hydrogen energy commercially viable (Daud, Rosli, Majlan, Hamid and Mohamed 2017). They are useful for a variety of applications due to their short start time, strong ratio of power and weight, and high power density. PEMFCs (Eini and Rakhtala 2014) are commonly utilized in transportation infrastructure like automobiles, buses, and aviation. However, the quality of output of a PEMFC is affected by the inner electrochemical reactions and problems like variable cell voltage, fuel starvation, and nonlinearities. Oxygen starvation is one of the major challenges for a FC system. When the load rapidly changes, then the stack current of the fuel cell increases. Thus, it requires more power. To meet the rise in power demand, equivalent chemical reactions should be increased by utilizing additional oxygen or air supply on the cathode side, which is given by a supply manifold from the compressor. Therefore, at the cathode end, required supply manifold pressure should be maintained which necessitates the control of the manifold pressure.

CONTACT Swati Singh singh.swati2703@gmail.com Electrical and Electronics Engineering Department, Amity School of Engineering & Technology, Noida, India; Vijay Kumar Tayal vktayal@amity.edu Electrical and Electronics Engineering Department, Amity School of Engineering & Technology, Noida, India

© 2022 Taylor & Francis Group, LLC

Several strategies have been suggested in the literature to enhance the quality of power generated by PEMFCs. A nonlinear design predictive control (NMPC) method is developed to utilize air flow rate (Gruber, Bordons, and Oliva 2012). This is done to sustain the oxygen excess ratio in a desired value and thus increasing safety and enhancing the system performance. A nonlinear dynamic model is created for PEM fuel cell system, to construct control mechanism, by implementing linearization approach (Na, Gou, and Diong 2007). This is done to refine the transient response of the PEMFC system. To be able to offer good servo control, nonlinear model for PEMFC system is proposed (Bedi et al. 2007). The regulation of the FC system to maintain a sufficient level of oxygen partial pressure in the cathode side, during rapid variations in the current, is studied using model-based control techniques (Grujicic et al. 2004). A feedback linearization controller is developed to control oxygen level for the van compressor in a PEMFC system (Chen et al. 2018). Granular function based Fuzzy PID control has been employed to maintain the excess oxygen ratio in PEM fuel cells (Tang et al. 2021). To regulate oxygen deprivation and fuel-cell stack degradation, a hybrid fuzzy-PID controller is designed for a proton exchange membrane fuel cell (PEMFC) system (Baroud, Benalia, and Ocampo-Martinez 2016). The fuel-cell based technology is integrated with the grid by using a Fuzzy PID (FPID) approach to manage the inverter's triggering circuitry (Khubchandani et al. 2016). Other control techniques like neural network control, model predictive control, robust control, intelligent control consists of fuzzy logic control, self-adaptive control, composite control, and sliding mode control can be employed for prevention of oxygen starvation in PEM fuel cells.

The structure of Smith predictor controller was developed to eliminate the delay effect from closed-loop designs (Abe and Yamanaka 2003). This controller is similar to IMC (Internal Model Control) that enables the plant model to cancel the delayed behavior of the plant. An outer loop of Smith predictor controller corrects the impacts of load disruption and modeling inaccuracy (Hang 2009). The Smith predictor responds more quickly and yields in less over-shoot. As Smith predictor eliminates time delay, thus it increases system stability. It can also be employed for high-order systems with perceived dead time and operations with strong nonminimum phase dynamics. To improve the system's performance and resilience, a Smith predictor control is developed. This is accomplished by limiting the impact of design factors such as shifting time delay and fluctuating system time constant (More and Lakhekar 2017).

FOPI controller has extra degree of freedom which makes it better in contrast to classical controllers. A PSO optimized FO-PID controller is proposed for voltage module compensation. FOPI controller is designed for modeling of the first order plus time delay (FOPDT) system (Baruah, Majhi, and Mahanta 2019; Wang, Luo, and Chen 2009). A FOPI controller is developled for linearly unstable system where transfer function of open loop is compared with fractional order transfer function whose closed loop response is always stable (Bhisrkar, Vyawahare, and Tare 2014; Singh, Tayal, Singh, Yadav 2021). PEM fuel cell is used in power electric vehicles, unmanned aerial vehicle (UAV), and mobile robots. These applications are driven by brushless DC motor which, on other hand, is controlled by MSA (Moth Swarm Algorithm) optimized FOPI controller (Yigit and Celik 2020). The FOPI controller has the benefit of contributing to system robustness by achieving better damping properties during parameter fluctuations. With the implementation of fractional controllers, the performance of the system gets improved and it becomes more robust. With extra tuning parameters, the complexity of tuning the fractional order controller increases (Petchinathan, Valarmathi, and Radhakrishnan 2017). This issue can be easily resolved by employing an AI technique for the optimization of the controller. The merits of FOPI controller over powers the problem associated with it. In this paper, PSO-based FOPI controller is developed for controlling supply manifold pressure of a PEMFC system.

A performance analysis is being carried out for controlling irregular flow rate of hydrogen by employing fuzzy control scheme (Pangaribowo, Utomo, Bakar and Khaerudini 2020). A control-oriented composite dynamic model is developed under real-world operating circumstances to predict the effects of PEM hydration kinetics on the output characteristics of commercially available high-power integrated PEMFC systems (Penga et al. 2020). The LMBP (Leven-Berg-Marquardt BP)

algorithm neural network is built up easily to simulate the complicated nonlinear PEMFC system with a high modeling frequency (Tao, Guang-yi, and Xin-jian 2005). For a PEM fuel cell, globally linearizing controller (GLC) and nonlinear multivariate sliding-mode controller (SMC) are designed (Sankar et al. 2017). The PID tuner approach is adopted to enhance the system performance (time responsiveness) and robustness (stability margins) of a dc motor (Yadav and Tayal 2018).

To simulate the PEMFC system's nonlinear characteristics, a nonlinear approach based on a Neural Network Auto-regressive model with eXogenous inputs (NNARX) is used (Cheng et al. 2015). Loading uncertainty is used to design a P-I-D controller for an integrated AFC (Alkali Fuel Cell) system (Dwivedi and Tayal 2017). A PSO-PID based MPPT (Maximum Power Point Tracker) is developed for PEM fuel cells, and its performance is collated with Perturb & Observation (P&O) and sliding mode approaches (Ahmadi, Abdi and Kakavand 2017). For controlling the voltage of the PEM Fuel Cell, PSO-PID controller is designed (Farhadi and Sojoudi 2014). For the generation of power by a PEMFC system, an FSBB converter is used to construct a DC/DC controlled voltage module (Qi et al. 2020). FACTS controller helps in congestion management for deregulation problem and increases the total available transfer capability (Arora, Tayal, and Singh 2017). Low solution accuracy, sluggish convergence, and poor local searching capabilities are some of the drawbacks of the typical Grey Wolf Optimization (GWO) method. (Singh 2020; Wen, Dongquan, and Songjin 2015). The various algorithms like Moth-Flame Optimization (MFO), Constant Modulus Algorithm (CMA), and Adaptive guided differential evolution algorithm (AGDE) have limitation of slow convergence time which limits the usefulness of the algorithm in a dynamic environment (Gao et al. 2012; Mohamed and Mohamed 2019; Nwalozie et al. 2012; Shehab et al. 2020). This affects the performance of the system. While on other hand PSO has fast convergence time and based on the present position in particle space and the related velocity vector, the variables can take on any value (Shabir and Singla 2016). PSO requires less number of parameters and thus it can handle complexity very well (Almeida and Leite 2019). PSO is easier to implement than other heuristic techniques, and it is a very efficient global search algorithm due to its small computing time (Selvi and Umarani 2010). There are no overlapping or mutation calculations in PSO. The particle's speed can be used to do the search (Lee and Park 2006). To select the most suitable parameters of a PEM fuel cell, an enhanced variant of the Archimedes optimization algorithm (AOA) named I-AOA is developed (Houssein et al. 2021). AOA is a revolutionary optimization technique that was presented to solve real-world issues. It depicts how the applied force behaves when an item is partially or entirely submerged in a fluid.

The genetic algorithm (GA) is a probabilistic global search method based on Darwinian natural selection and evolution concepts (Bhatt, Agarwal, and Chakraborty 2016). GA approach isnot entirely random. They infer the direction of search using statistical and historical data to arrive at the best or near-best solution to the problem. PID controllers, which are deployed for managing PEMFC system, were proposed (Chen, Tzeng, and Chen 2010). They used GeneticAlgorithm (GA) to boost PEMFC intermittent and steady-state performance. The Genetic Algorithm is a slow method which can not find a precise solution each time. A multi-objective genetic algorithm (MOGA) is employed to optimize the controller gains of PID controller for the voltage regulation of fuel cell (Qin et al. 2019). The limitation of GA is its large computational time. GA belongs to the nondeterministic class of algorithm. The optimal solution obtained from GA may vary each time while running the algorithm for similar input data (Liu, Chen, and Huang 2015). In Ant Colony Optimization Technique, the probability distribution can change for each iteration and have uncertain time for convergence. The search space in Artificial Bee Colony (ABC) algorithm is limited by initial solution and thus it abandons poor solution for the system. In contrast to GA and ACO artificial intelligence techniques, PSO algorithm is easily implemented with higher probability and efficiency to find the global optima. Further, PSO technique offers fast convergence time, robust, less computation, coherent in solving problems and very few parameters to adjust.

In order to enhance the performance of nonlinear PEMFC system by regulating the supply manifold pressure, the design of PI, PID, PIDF, Smith predictor and PSO tuned FOPI controllers is presented in this paper. The FOPI controller is also optimized by GA technique to reflect the efficacy of PSO-FOPI controller. In contrast to GA tuned FOPI controller, PSO-FOPI controller is far better and shows remarkable improvement in the performance. The PSO-FOPI controller is best suited amongst classical controller, PSO-Smith predictor and GA-FOPI controller. This paper is organized in ten main sections. The PEMFC system's functioning and system dynamics are explained in Section 2. Control schemes implemented are detailed in Section 3. The PID tuner which is used to tune classical controllers is explained in Section 4. The operation and Simulink model of the proposed controllers Smith predictor and FOPI are elaborated in Section 5 and 6, respectively. In Sections 7 and 8, the optimization techniques Genetic Algorithm and Particle-Swarm-Optimization (PSO) Techniques are discussed, respectively, which are used to tune the proposed controller parameters. The outcomes of the simulation are illustrated in Section 9, while the conclusions are discussed in Section 10.

2. Proton exchange membrane fuel cell (PEMFC)

The structure of PEMFC system is described in Figure 1, including three primary loops (oxygen, hydrogen, and thermal). The system is made up of various parts such as PEMFC stack, humidifier, pumps, air compressor, radiator, and heat exchangers. These components are present for the flow valves, cooling circuit, and controllers. Prior to entering the stack, compressed air is cooled and humidified before being delivered into the cathode. A control valve controls the flow of pressurized hydrogen from the storage tank into the anode. Because the stack is not in dead-end mode, the fuel concentration is retained. The fuel which is not in the use at the exhaust of the anode is re-circulated back into the input stream through a recirculation pump. This allows the fuel to get moistened.

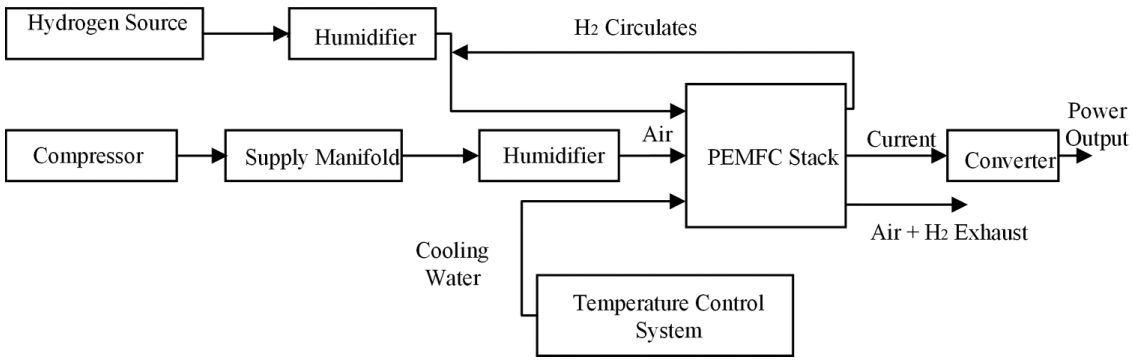


Figure 1. Block diagram for PEM fuel cell.

2.1 PEM Fuel Cell- Electrochemical Model

To evaluate voltage output (V_{FC}) of the fuel cell, the implementation of steady-state electrochemical model can be done (Li et al. 2014). The value of V_{FC} can be expressed by Eq.(1)

$$V_{FC} = E_N - (\eta_{ohmic} + \eta_c + \eta_a) \tag{1}$$

where ohmic over voltage (η_{ohmic}), concentration over voltage (η_c), and activation over voltage (η_a) are detailed in Eqs.(2–4), respectively,

$$\eta_{ohmic} = I[R_e + R_m] \tag{2}$$

$$\eta_c = -b \ln\left(1 - \frac{J}{J_{\max}}\right) \tag{3}$$

$$\eta_a = -[\xi_1 + \xi_2 T_s + \xi_3 T_s \ln(C_{O_2}) + \xi_4 T_s \ln(I)] \tag{4}$$

The voltage of the PEM fuel cell in an open circuit is symbolized by the Nernst potential. The Nernst equation establishes a relation among the potential of an electrochemical cell, temperature, the quotient of reaction, and the standard cell potential. The Nernst equation is helpful even in non-standard conditions for evaluating the potential of electrochemical cells. It is mathematically given by Eq. (5)

$$E_N = \frac{\Delta G_e}{2F} + \frac{\Delta S}{2F}(T_s - T_r) + \frac{RT_s}{2F}\left(\ln\left(\rho_{H_2}\right)\right) + \frac{1}{2}\left(\ln\left(\rho_{O_2}\right)\right) \tag{5}$$

2.2 Cathode Pressure Model and Pressure Model for Anode

The pressure at the cathode in the FC is evaluated by Eq. (6)

$$P_c = \rho_{O_2} + \rho_q + P_{vap,c} \tag{6}$$

where Eqs. (7)–(9) outline the oxygen's partial pressure, q species partial pressure, and atmospheric pressure, respectively.

$$\rho_{O_2} = \frac{1/K_{O_2}}{1 + \tau_{O_2} s}\left(0.21 F_{in,c} - F_{O_2}\right) \tag{7}$$

$$\rho_q = \frac{1/K_q}{1 + \tau_q s} 0.79 F_{in,c} \tag{8}$$

$$P_{vap} = \frac{1/K_{vap,c}}{1 + \tau_{vap,c} s} \frac{P_{vap,c}}{P_c - P_{vap,c}} F_{in,c} \tag{9}$$

The anode pressure in the fuel cell is given by Eq. (10)

$$P_a = \rho_{H_2} + P_{vap,a} \tag{10}$$

The values of the hydrogens' partial pressure and ambient pressure at anode side are defined in Eqs. (11) and (12), respectively,

$$\rho_{H_2} = \frac{1/K_{H_2}}{1 + \tau_{H_2} s}\left(F_{in,a} - F_{H_2}\right) \tag{11}$$

$$P_{vap,a} = \frac{1/K_{vap,a}}{1 + \tau_{vap,a} s} \frac{P_{vap,a}}{P_a - P_{vap,a}} F_{in,a} \tag{12}$$

2.3 Thermal Model for PEMFC

There is a generation of heat due to energy loss. The heat is dissipated in the locations where the relevant losses occur. This heat is then removed from the cell by conducting through the bipolar plates. After this, it is circulated to the air and cooling liquid, through convection. By assuming temperature of bipolar plate to be constant and considering stack as a lumped model of capacitance, the conduction phenomena inside the plate are neglected. The temperature, T_s, of a FC is expressed, by Eq. (13)

$$\frac{dT_s}{dt} = \frac{1}{M_{FC} \times c_P}\left[Q_{loss} + m_{cl} \times c_{P,cl}(T_1 - T_2) - k_{cell} \times (T_s - T_{atm})\right] \tag{13}$$

2.4 Air Supply Model of Fuel Cell

A motor-driven compressor, a fuel injection system, and a humidifier create the air supply system. The heat exchanger (cooler) of the compressor cools the compressed air before it is supplied into the fuel injection system to achieve the desired temperature. Equation(14) may be used to evaluate how the motor and compressor's dynamic behavior is represented:

$$J_E \frac{d\omega_{cp}}{dt} = \tau_m - \tau_{cp} \tag{14}$$

The motor torque τ_m is given in Eq. (15)

$$\tau_m = \eta_m \frac{k_\tau}{R_M}\left(V_m - k_v \omega_{cp}\right) \tag{15}$$

Constants are obtained from Eqs. (1–15), and the entire model of the air feed system is represented in Eq. (16)

$$x = [\rho_{O_2}\ \rho_{N_2}\ \omega_{cp}\ P_{sm}] = [x_1\ x_2\ x_3\ x_4] \tag{16}$$

Here, the output of the system is P_{sm},which is the supply manifold pressure. Thus, pressure at x_4 is to be controlled. The model parameters of the PEMFC system are detailed in Table 1.

The PEMFCs are naturally nonlinear. The linear models are just approximated from the original nonlinear equations (Bei, Woon, and Bill 2010). By implementing linear system techniques, the developed model is beneficial for the analysis of transient response and designing of controller. Application of partially linearized model of PEMFC is done when first-order dynamics is used for the modeling of the partial pressures of the oxygen, water, and hydrogen in the fuel cell. This paper comprises transfer function which is approximated to the first-order system by taking time delay into account so as to ease the analysis part. Thus, the dynamic model of a nonlinear PEM fuel cell is approximated (Divi, Sonawane, and Das 2018) and is expressed in Eq. (17)

$$G_p(s) = \frac{1252e^{-0.1562s}}{0.3551s + 1} \tag{17}$$

3. Control Strategy

PEMFCs have been a long-term goal because of their great efficiency and environmental benefits. Nonlinearities, uncontrolled voltage, and fuel starvation, on the other hand, diminish the system's performance. This paper designs different controllers viz. classical controllers (PI, PID, and PID controller with filter derivative), GA-based FOPI, PSO-Smith predictor, and PSO-tuned FO-PI controller for the performance improvement of nonlinear PEM fuel cell.

3.1 Proportional (P) Integral (I) Controller

A PI controller has a feedback loop where calculation of an error signal is done by comparing a system's output to its set point. Nonintegrating processes are defined as any process containing same set of inputs and disturbances, eventually returns to the same output. These processes require PI controller. The transfer function of a PI controller is represented in Eq. (18), where K_P and K_I are designations of proportional gain and integral gain, respectively,

Table 1. PEMFC model parameters.

Parameter	Unit	Description
V_{FC}	V	Voltage of fuel cell
η_{ohmic}	V	Ohmic overvoltage
η_a	V	Activation overvoltage
η_c	V	Concentration overpotential
E_N	V	Open circuit voltage of fuel cell
I	A	Current of fuel cell
R_e	Ω	Electron flow resistance
R_m	Ω	Proton flow resistance
b	-	Parametric coefficient
J	mA/cm^2	Current density
J_{max}	mA/cm^2	Maximum current density,
ξ_1,ξ_2,ξ_3,ξ_4		Parametric coefficients
T_s	K	Fuel cell stack temperature
ΔG_e	J/mol	Gibbs energy
ΔS	J/mol	Change of the entropy
T_r	K	Reference temperature
F	C/mol	Faraday's constant
R	J/(mol K)	Gas constant, 8.314
ρ_{H_2},ρ_{O_2}	Pa	Partial pressures of hydrogen and oxygen, respectively
P_c,P_a	Pa	Cathode and anode pressure, respectively
ρ_q	Pa	Partial pressure of q species
$P_{vap,c},P_{vap,a}$	Pa	Partial pressure of vapors at cathode and anode end, respectively
K_{O_2}, K_q,$K_{vap,c}$, $K_{vap,a}$,K_{H_2}	kmol/(atm s)	Molar constant of the exit valve of O_2, q series, vapor (cathode, anode), and H_2, respectively
F_{O_2},F_{H_2}	kmol/s	Oxygen & hydrogen molar flow rate consumed by fuel cell, respectively
$F_{in,c},F_{in,a}$	kmol/s	Cathode and anode inlet molar flow rates, respectively
τ_q, τ_{O_2},τ_{H_2}, $\tau_{vap,c},\tau_{vap,a}$	s	Time constant of q species, O_2, H_2, and vapor (cathode and anode), respectively
M_{FC}	kg	Overall mass of fuel cell
c_P	J/(kg K)	Overall fuel cell specific heat equivalence
Q_{loss}	-	Per cell heat dissipation
m_{cl}	kg/s	Flow rate of cooling water
$c_{P,cl}$	J/(kg K)	Cooling water's equivalent specific heat
T_1,T_2	K	Temperatures of the cooling water at the inlet and exit
k_{cell}	W/K	Natural convection coefficient
T_{atm}	K	Environmental temperature
J_E	kg m^2	Inertia of compressor and motor
ω_{cp}	rad/s	Rotational speed of compressor
τ_m	Nm	Motor torque
τ_{cp}	Nm	Compressor torque
η_m	%	Motor mechanical efficiency
k_τ	Nm/A	Motor torque constant
R_M	Ω	Motor resistance
V_m	V	Control voltage of compressor
k_v	V/(rad/s)	Motor electromotive constant

$$G(s) = K_P + \frac{K_I}{s} = K_I\left(\frac{K_P}{K_I} + \frac{1}{s}\right) \tag{18}$$

The P controller enhances system reaction time while lowers the system stability and steady-state error (e_{ss}) (Yu, Wang, and Liu 2019). P controller, on the other hand, is unable to minimize e_{ss} to zero. The impact of the I controller in removing e_{ss} is better than that of the P controller, although it reduces system stability. Consequently with the P and I controller's performance, the PI controller can minimize steady state error. Figure 2 depicts the PI controller's block diagram.

3.2 PID Controller

When the control error is substantial, the proportional action in a PID controller achieves the usual operation of raising the control variable (Dormido and Visioli 2014). The derivative action is based on expected future values of the error signal and hence has a high potential for increasing control

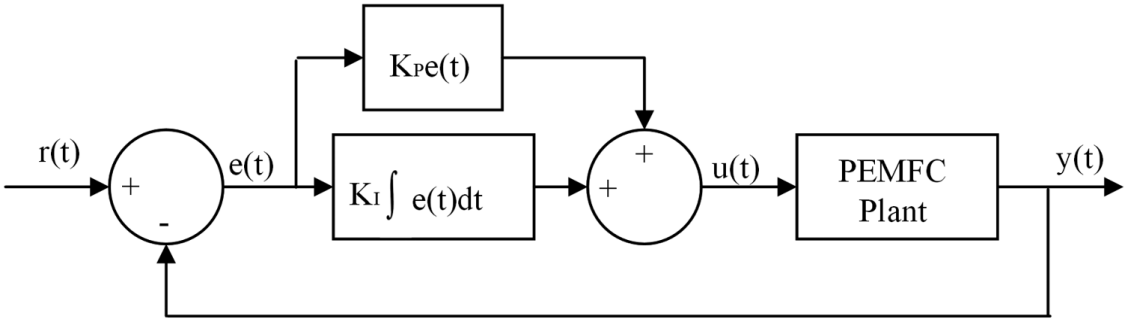


Figure 2. Block diagram of PI controller.

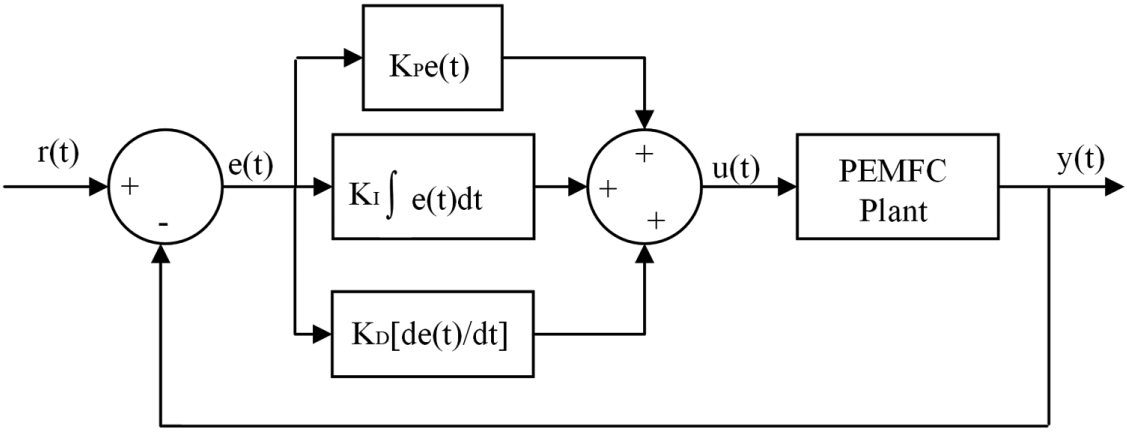


Figure 3. Block diagram of PID controller.

performance since it can forecast and counteract an inaccurate control error trend. The P-I-D controller has the effective control dynamics, including minimal steady-state error, rapid responsiveness (short rising time), no oscillations, and more stability. To avoid overshoot and oscillations in the system's output response, a derivative gain component must be included to the PI controller. The block diagram of PID controller is depicted in Figure 3.

The P-I-D controller has the benefit of being able to handle higher-order operations with more than one energy storage. As seen in Eq. (19), the PID controller's output u(t) may be written in terms of the input e(t), and the controller's transfer function is provided in Eq. (20):

$$u(t) = \left[e(t) + T_d \frac{de(t)}{dt} + \frac{1}{T_i}\int_0^t e(\tau)d\tau\right] \tag{19}$$

$$G(s) = K_P\left(1 + T_d s + \frac{1}{T_i s}\right) \tag{20}$$

where K_P, T_d, and T_i indicate proportional gain, derivative time, and integral time, respectively.

3.3 PID Controller with Filter Derivative (PIDF)

While using PID controllers, mainly two problems are stated: (i) By including derivative term in PID controller, sometimes, the reference input has sharp corners which results in restrictive size control of the input to the plant; (ii) the derivative term causes high frequency noise in the plant (Sahu, Sekhar, and Panda 2015). The presence of these two issues creates difficulties in installing PID controllers and so the derivative element is frequently switched off in industries. But, due to the benefits offered by

derivative action, specifically its 'predictive capability,' it is not turned off. Therefore, the solution for above two problems is to be obtained, for which, a first-order filter is kept at the derivative term. Hence, the controller is known as PID controller with filter derivative (PIDF). The transfer function of PIDF controller in equated in Eq. (21)

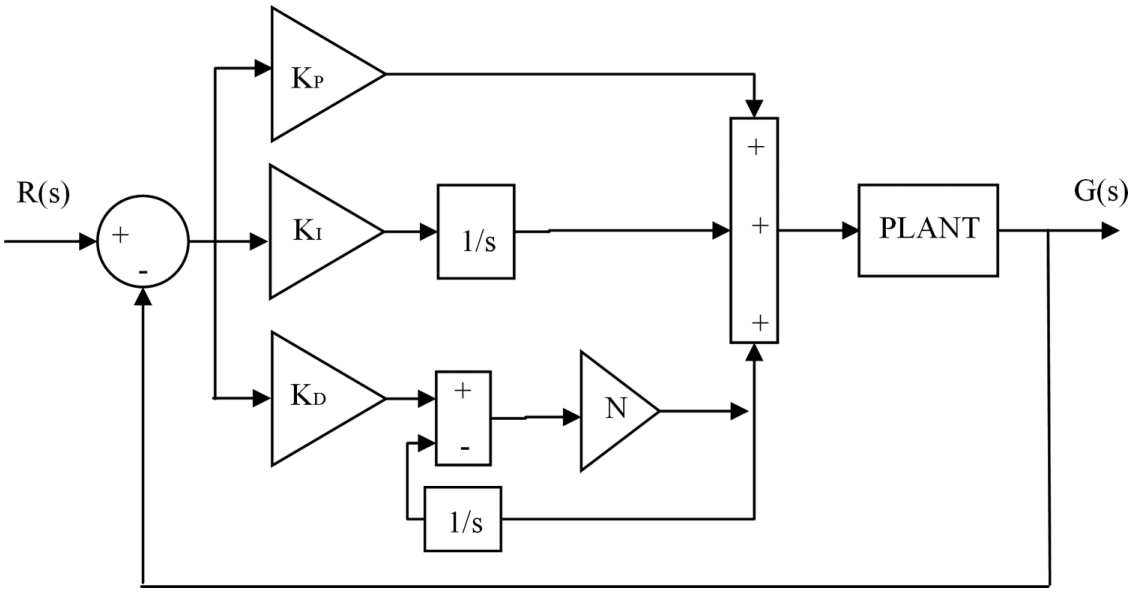


Figure 4. Block diagram of PIDF controller.

$$G(s) = K_P + \frac{K_i}{s} + K_D \frac{Ns}{N+s} \tag{21}$$

where derivative filter coefficient is designated as N. Block diagram of PIDF controller is depicted in Figure 4.

4.PID Tuner for the Optimization of PI, PID and PIDF Controller

The PID tuner is used to optimize the controller gains (K_P, K_D, and K_I) of the PI, PID, and PIDF controllers in this work. In MATLAB, the PID tuner GUI (Graphical User Interface) is provided. It is used to automatically optimize the controllers such as PI, P, PID, PID with filter, PD, and 2 DOF PID.

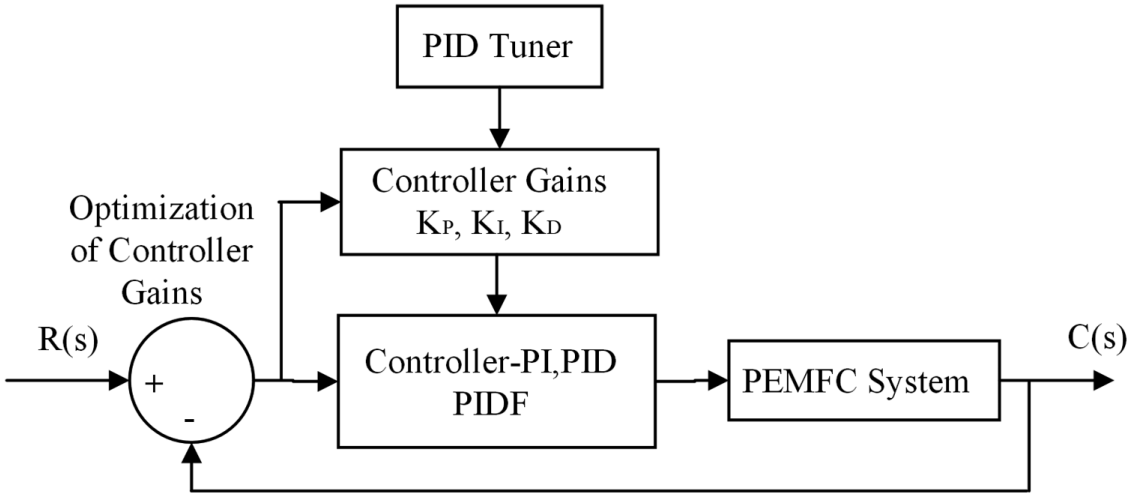


Figure 5. Controllers-PI, PID and PIDF.

For single input and single output systems, it maintains the equilibrium between performance and robustness. To adjust loop bandwidth and phase margin, the controller's performance is enhanced. The tuning time is minimal with the PID tuner. When the PID tuner is used to tune the controller, it updates the design to emphasize reference tracking or disturbance rejection, depending on the requirements of the application. The PID tuner adjusts the controller gains in real time to achieve the desired performance. The PID tuner algorithm selects a crossover frequency to achieve a 60-degree phase margin. With each change in steady state and transient response, the PID tuner computes new PID gains every time. PID tuner balances disturbance rejection with reference tracking to provide the appropriate robustness. Figure 5 outlines the tuning of PI, PID, and PIDF controller with PID Tuner.

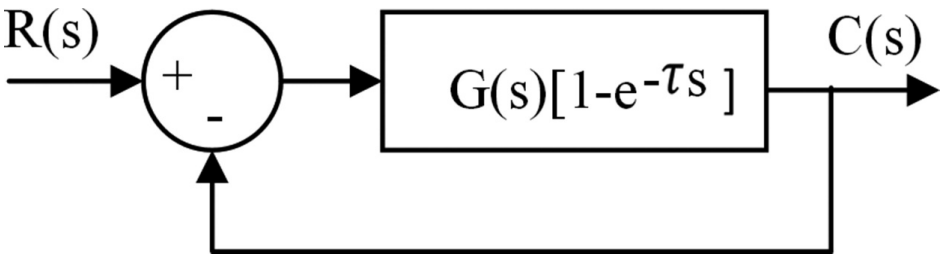


Figure 6. Closed loop control system with delay.

5. Smith Predictor

The Smith predictor is a design-based controller that works well for long-dead-time processes (GnanaMuruga and Senthilkumar 2014). It features an inner loop with a primary controller that can be constructed quickly and easily without requiring any dead time. The Smith predictor is used in the construction of a controller for a plant that has a time delay or a time delay approximation. It works with a closed-loop control system. The effects of load interruption and model inaccuracy are addressed by an outer loop. The Smith predictor can be utilized for processes with significant nonminimum phase dynamics and high-order systems with apparent dead time. In control systems, the Smith predictor is frequently used as delay compensation device. For both minor and significant delays, this strategy can be employed. In the Smith predictor, the delay component from system's closed loop is to be removed (Mirzal 2017). It is done as the systems' stability is hampered with the delay component. Thus, the stability is enhanced by removing delay from the closed loop. In general, the closed loop response with delay is presented in Figure 6.

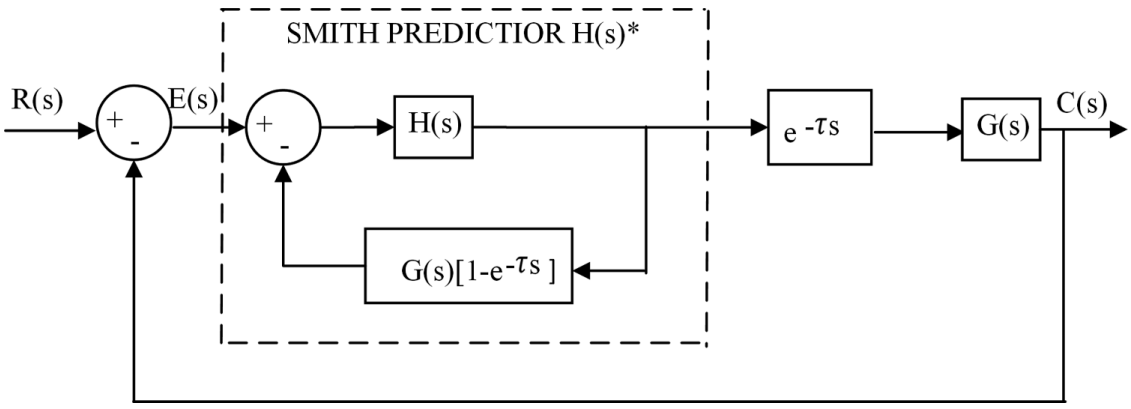


Figure 7. Structure of Smith predictor for delay compensation.

The first order plus time delay system investigated in this work has the following transfer function as shown in Eq. (21):

$$G(s) = \frac{e^{-\tau s}}{1 + ks} \tag{22}$$

The Smith predictor's structure (shown in Figure 6) is separated into two components: the primary controller H(s) and the predictor structure. Typically, the controller H(s) is a PID, but it can also be a higher-order controller.

From Figure 7, the value of H(s)* can be defined as detailed in Eq. (23) and the systems' output is detailed in Eq. (24).

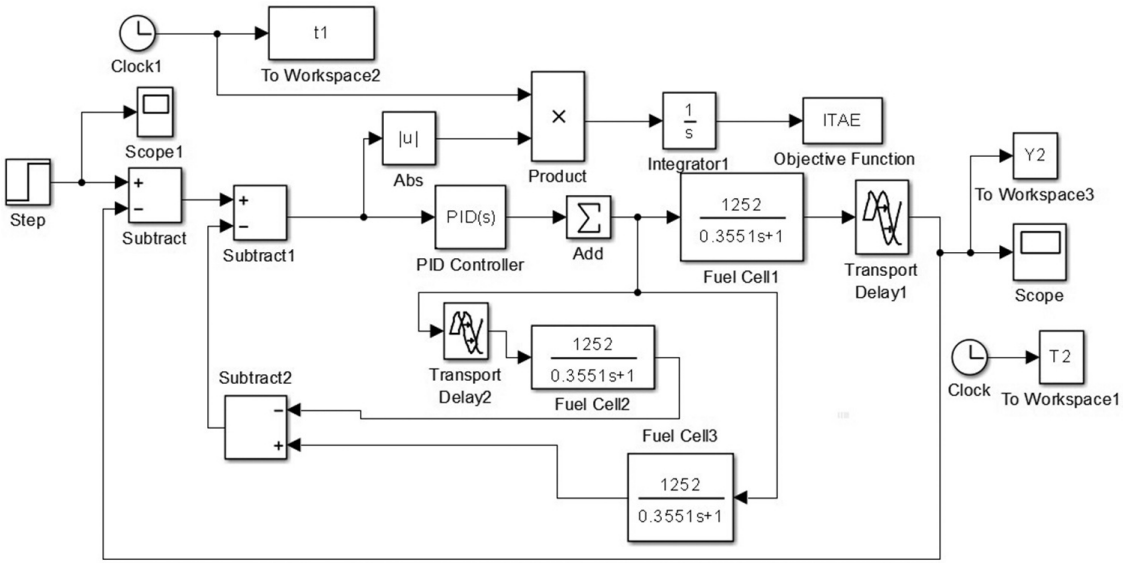


Figure 8. Simulink model for fuel cell with Smith predictor.

$$\frac{N(s)}{E(s)} = H(s)* = \frac{H(s)}{1 + H(s)G(s)(1 - e^{-\tau s})} \tag{23}$$

$$\frac{C(s)}{R(s)} = \frac{H(s) * G(s)e^{-\tau s}}{1 + H(s)^{*}G(s)e^{-\tau s}} = \frac{H(s)G(s)}{1 + H(s)G(s)}e^{-\tau s} \tag{24}$$

The Simulink model incorporated in this work is depicted in Figure 8.

Smith predictor has basically three fundamental properties:

(a) Compensation of Dead Time: This means that dead time is no longer included in the closed loop characteristic equation.
(b) For variations in the set-point, the predictor's feedback signal predicts the output of the system; however, this is not the case for disturbances.
(c) The structure of the Smith predictor implicitly factorizes the plant into two components: H(s), which can be invertible for some instances and $e^{-\tau s}$, which is noninvertible owing to dead time.

6. Fractional Order (FO) Proportional Integral (PI) Controller

Fractional order controllers are the generalization of classical controllers having greater flexibility in the modeling of the system. The FOPID controller is a fractional calculus-based extension of the traditional PID controller. The F-O controllers have better response in contrast to the classical order integer controllers. Fractional order differential equations are used to elucidate these control systems. Differential equations of fractional order could better model varied materials than integer order. For noninteger order basic operators, a generalized illustration of differentiation and integration is denoted as ${}_{\alpha}D_t^x$ where α and t are limits for an operator and $x \in \Re$ (Rajesh 2019).This integrator-differential operator is elucidated in Eq. (25)

$$ {}_bD_t^p f(t) = \begin{cases} \frac{dp}{dt^p}\Re(p) > 0 \\ 1\Re(p) > 0 \\ \int_a^t (d\gamma)^{-p}\Re(p) > 0 \end{cases} \tag{25} $$

As FOPI controller is of higher order in contrast to integer-order (IO) proportional-integral (PI) controller, the approximation of PI controller is the main step of FOPI controller's discretization (Keek, Loh, and Chong 2018). In this paper, the simplicity and Euler's gamma function (Faieghi and Nemati 2011) are defined by incorporating Riemann-Liouville (RL) definition, Eq. (26).

$$ {}_bD_t^p f(t) = \frac{1}{\Gamma(c-p)}\left(\frac{d}{dt}\right)^c \int_b^t \frac{f(\gamma)}{(t-\gamma)^{p-c+1}} d\gamma \tag{26} $$

Equation (27) gives the Riemann–Lioville Laplace transform definition.

$$ L_d\left\{{}_0D_t^p f(t); s\right\} = s^p(Lf(t)) - \sum_{t=0}^{(n-1)} s^l\left[{}_0D_t^{p-l-1} f(t)\right]_{t=0} \tag{27} $$

Several definitions are available for fractional order derivatives, the most common definition which is known as Caputo Derivative (Palaniyappan et al. 2018) is expressed in Eq. (28) and its Laplace transform is outlined in Eq. (29)

$$ {}_bD_t^p f(t) = \frac{1}{\Gamma(c-p)}\left(\frac{d}{dt}\right)^c \int_b^t \frac{f^c(\gamma)}{(t-\gamma)^{p-c+1}} d\gamma \tag{28} $$

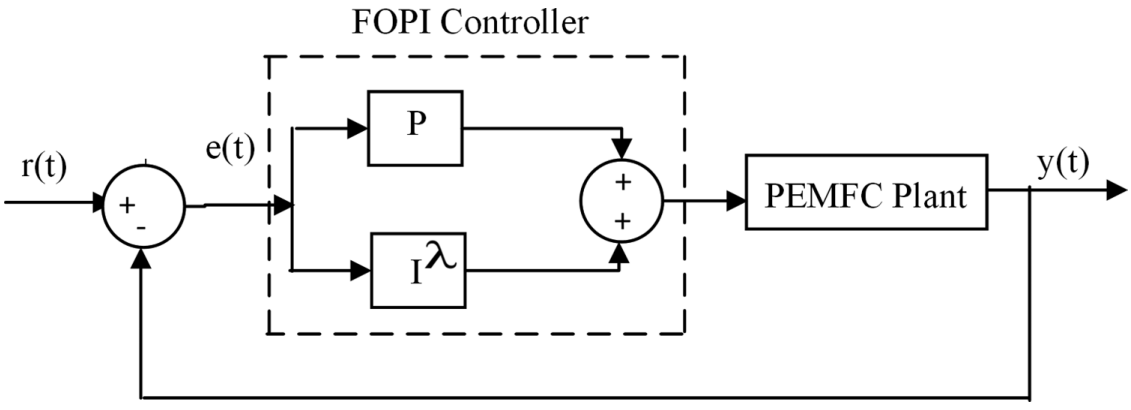


Figure 9. Block diagram of FOPI controller.

$$L\{{}_0D_t^p f(t);s\} = s^p(Lf(t)) - \sum_{t=0}^{(n-1)} s^{(p-l-1)} f^{'}(0) \tag{29}$$

The output of the FOPI controller is thus provided by Eq. (30) in discrete form,

$$u(r) = K_P e(r) + K_I \left(\sum_{r=0}^{r_f} \left[\Gamma(\lambda+1) e(r) \times \Delta t(r)^{\lambda} \right] \right) \tag{30}$$

where Γ denotes the gamma function and it is defined in Eq. (31)

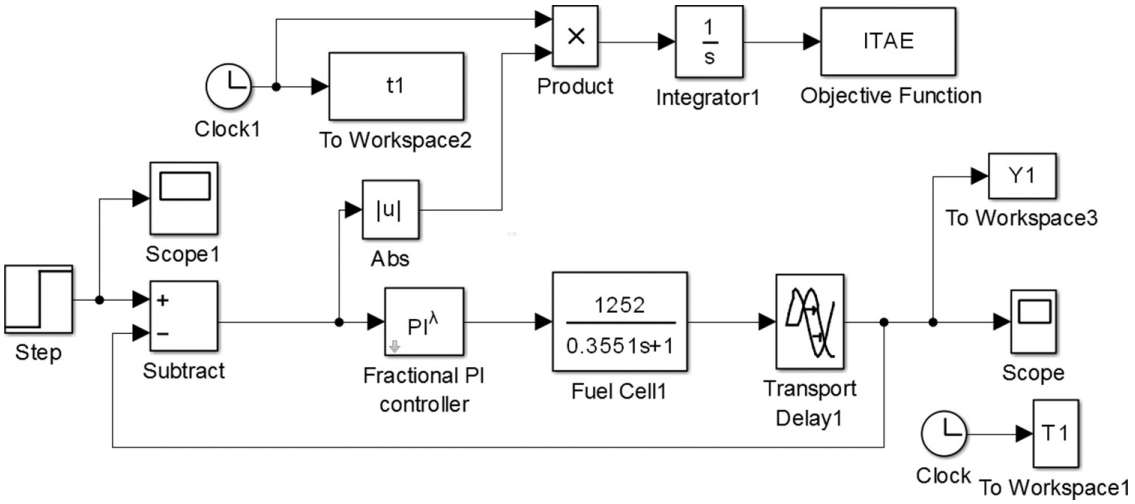


Figure 10. Simulink model for PSO-FOPI controller.

$$\Gamma(n) = \int_0^{\infty} e^{-x} x^{n-1} dx \tag{31}$$

The PI^{λ} controller outperforms the integer-order PI controller in controlling the system as it has one extra tuning parameter. Fractional-order (FO) controllers are more flexible, robust and are less sensitive to changes of parameter. The FOPI controller's block diagram is shown in Figure 9, and its transfer function (Podlubny 1999) is detailed in Eq. (32)

$$G(s) = K_P + K_I s^{-\lambda} \tag{32}$$

Figure 10 represents the Simulink model of PSO-FOPI controller.

7.Genetic Algorithm For the Optimization of FOPI Controller

The genetic algorithm (GA) is a natural selection-inspired optimization method. It is a population-based search method that employs the survival of the fittest principle. Genetic Algorithm generalizes the problem space as a population of people and then iteratively produce generations in order to find the fittest one. GA transforms a population of low-quality individuals into a high-quality population, with each individual representing a solution to the problem. A fitness function

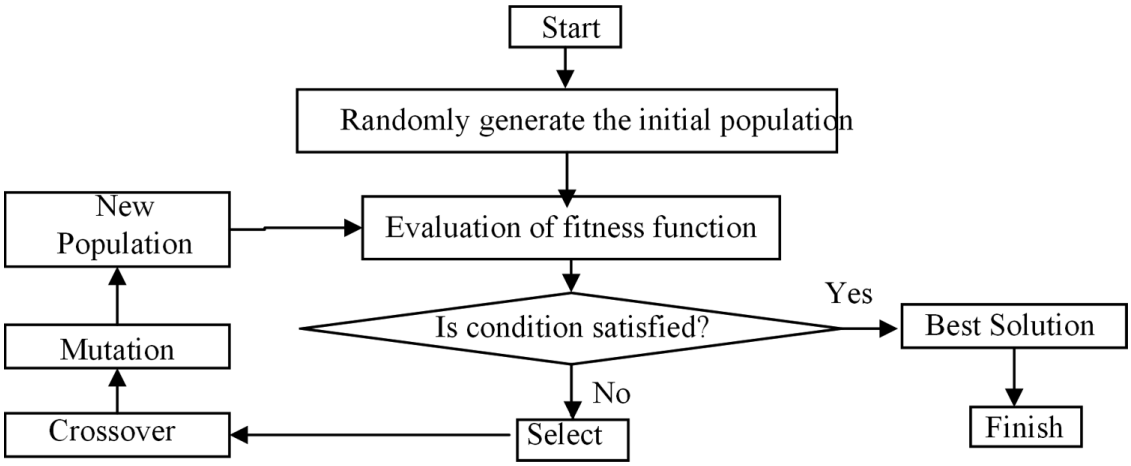


Figure11. Flowchart for the process of GA technique.

Table 2. GA parameters.

S.No.	Parameters	Value
1.	No. of variable	3
2.	Lower bound	[0 0 0]
3.	Upper bound	[0.25 0.25 1.5]
4.	Population size	50
5.	Iterations	40
6.	Tournament size	4

is a numerical representation of how well each rule adapts to a given environment. It is used to assess its quality. The method begins with a randomly created population of individuals. The steps are shown in Figure 11. The following is the procedure for utilizing GA to find the best solution to a problem: (a) in a chromosome, the search parameters are encoded as binary strings; (b) this method is performed at random to generate N initial species (strings); (c) based on the solution circumstances, the fitness function is created. The production process is chosen from species with high fitness values; and (d) to complete one generation of GA, the crossover and mutation processes are computed.

In this work, existing technique GA is used to optimize the FOPI controller. The GA parameters considered in Optimization Toolbox are detailed in Table 2.

8.Particle Swarm Optimization Algorithm for the Tuning of Smith Predictor & FOPI Controller

PSO is initiated with a collection of random solution known as swarms (Kennedy and Eberhart 1995; Tayal and Lather 2015). Each possible solution, referred as particle, moves across the problem space at the same speed as the current optimal particles and updates generations to look for optima. PSO is a population of candidate solutions that iteratively tries to optimize a problem space to enhance an individual solution. Figure 12 shows the process involved in the PSO algorithm.

The individual particles or solutions move about in the search space using a basic particle location and velocity computation. Each particle's mobility is limited by its local optimum location. These particles move toward the optimal position within a search space after changing their position and velocity. The entire particle inside a search space does this procedure, and it goes to the global best place.The population is randomly initialized in the PSO approach, with each particle having a velocity $v_i(t)$ and a position $x_i(t)$ in relation to an objective. The main loop then evaluates each particle and

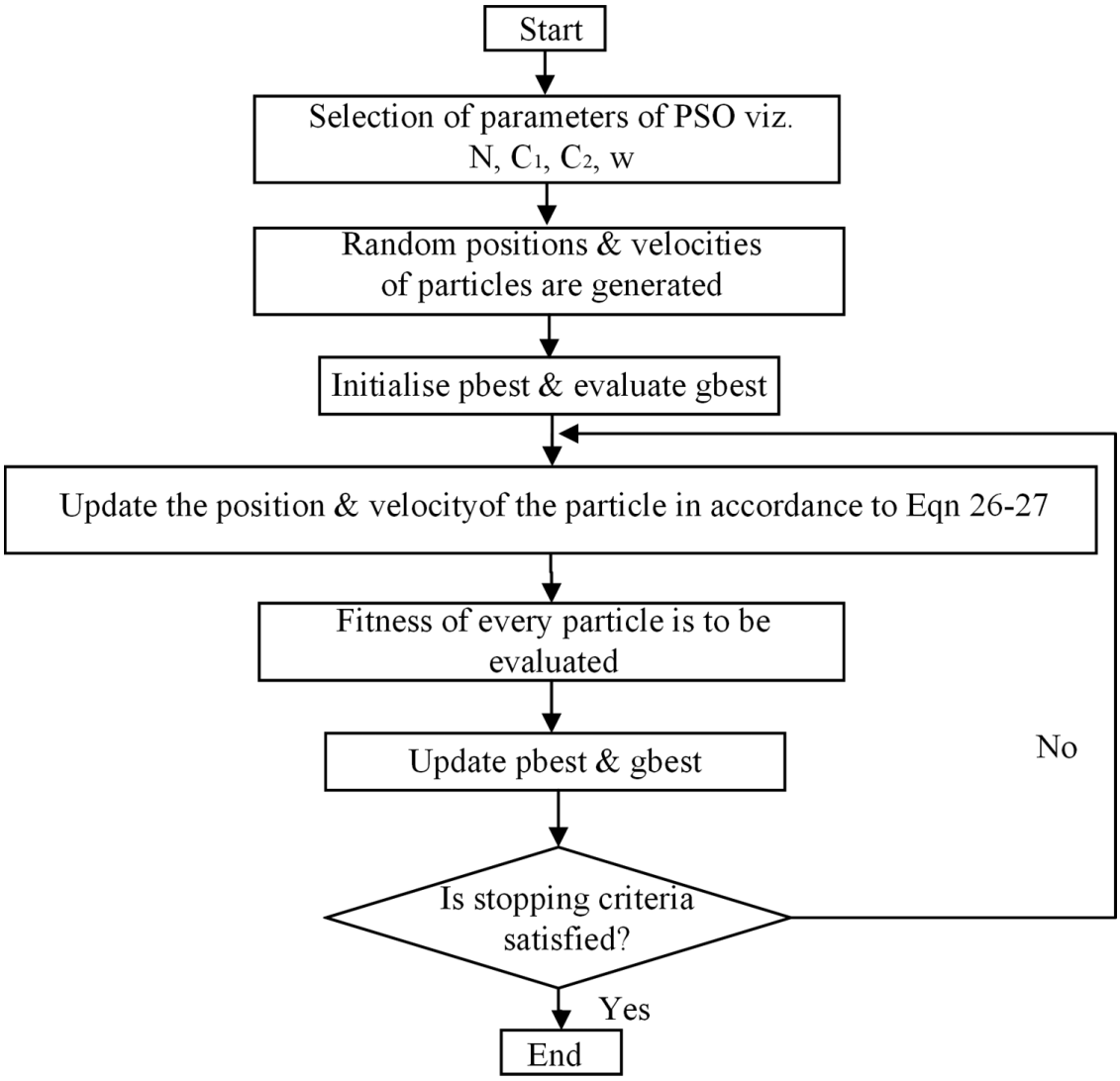


Figure 12. Flowchart of PSO technique.

updates $x_i(t)$ and $v_i(t)$ in each iteration (Long et al. 2020). The new position of the particle is compared to the prior best local location $P_i(t)$. The value of the best local position is updated if the new position is better than the prior best local position. Finally, the new position is also compared with the best global position $g(t)$. The closest to a target is $g(t)$, and if the new particle location is superior to global position, the best global position's value is modified. Equations (33) and (–34) outline the updated position and velocity, respectively.

$$P_{ij}(t+1) = V_{ij}(t+1) + P_{ij}(t) \tag{33}$$

$$V_{ij}(t+1) = \xi V_{ij}(t) + R_{1j}c_1\left(p_{ij}(l) - x_{ij}(t)\right) + R_{2j}c_2\left(g_{ij}(t) - x_{ij}(t)\right) \tag{34}$$

where inertia constant 'ξ' is added to enhance the particles ability to jump out of the local extremum. 'ξ' is given in Eq. (35):

$$\xi = \xi_{\max} - \frac{(\xi_{\max} - \xi_{\min})t}{T_{\max}} \tag{35}$$

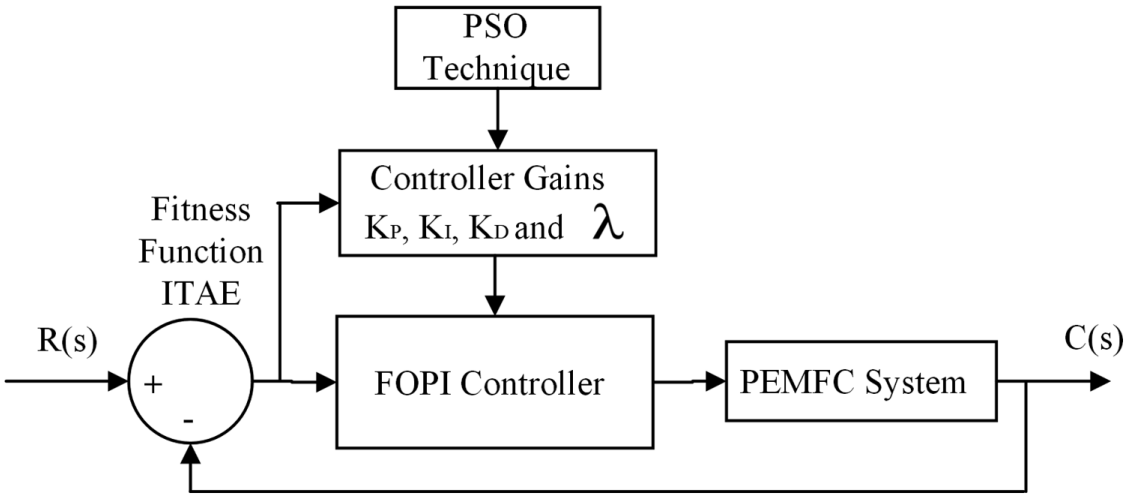


Figure 13. Smith predictor and FOPI controller with PSO.

Table 3. PSO parameters.

S.No.	PSO parameter	Values
1	Accelerating factor,C_1	2
2	Accelerating factor,C_2	2
3	Inertial weight, w	0.9
4	Population size	60

ξ_{min} and ξ_{max} are the minimum and maximum inertia coefficients, respectively, while, t and T_{max} are present iterations and maximum iterations, respectively. The effect of the particle's experiential information is determined by the acceleration constants C_1 and C_2 in the PSO algorithm. When the number of iterations changes, the values of C_1 and C_2 dynamically change and become highly nonlinear.

In this work, PSO algorithm optimizes the controller gains of the FOPI and Smith predictor controllers. Figure 13 depicts the FOPI and Smith predictor controller with PSO technique and Table 3 shows the parameters of PSO algorithm used in this work.

The fitness function is a single figure of merit used to indicate the closeness of solution achieved by PSO algorithm with optimal solution. In this work, ITAE (Integral time absolute error) is used as objective function and is mathematically represented by Eq. (36)

$$ITAE = \int_0^{T(s)} t|e(t)|dt \tag{36}$$

The PSO is one of the most effective methods for dealing with nonsmooth complex optimization problems. It is a derivative-free methodology, like other heuristic optimization techniques. In comparison to other empirical optimization approaches, PSO has a simple idea and code implementation. As compared to other competing heuristic optimization methods, PSO has a small number of parameters, comprising just an inertia weight factor and two acceleration coefficients. In addition, in contrast to other metaheuristics, the influence of parameters on the outcomes is thought to be less sensitive.

9.Simulation Results

In this work, uncertainty is considered in nonlinear PEMFC input (Figure 14). To judge the effectiveness of the classical controllers (PI, PID, PIDF), GA-FOPI, PSO-FOPI, and PSO-Smith predictor controller for controlling manifold pressure at cathode side of PEMFC system, the step disturbance is created at

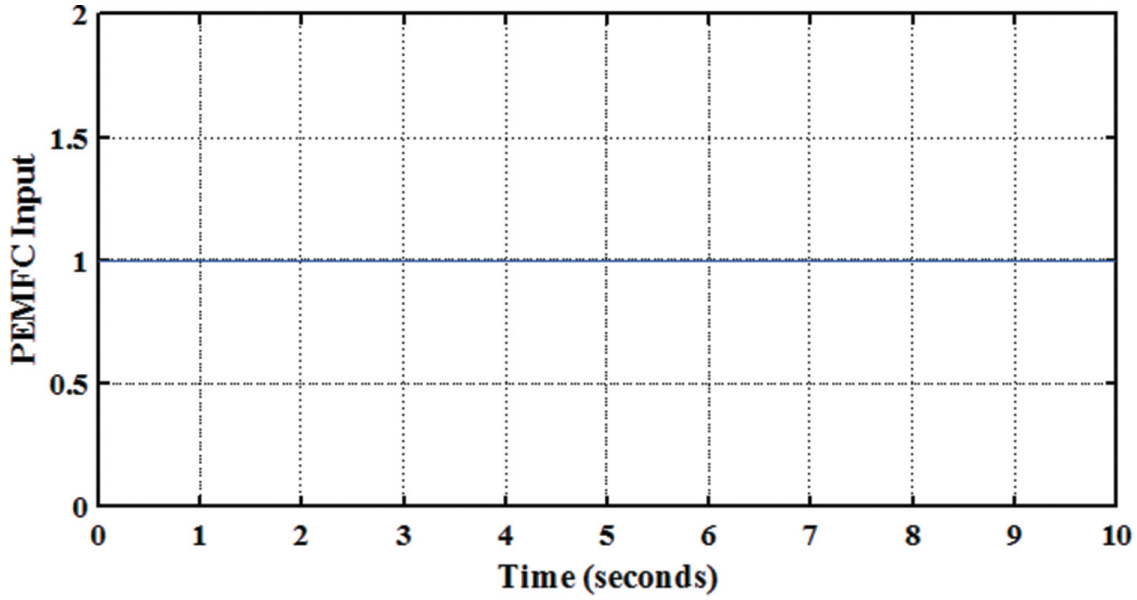


Figure 14. PEMFC input.

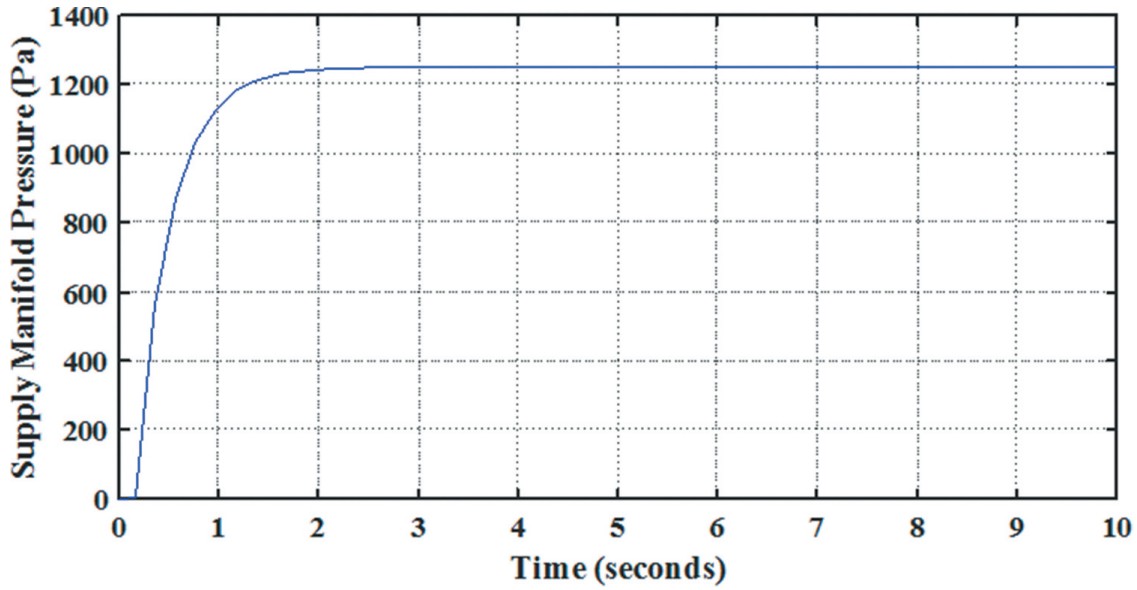


Figure 15. PEMFC output without controller.

Table 4. Controller parameters.

	Controller parameters			
Type of controller	K_p	K_i	K_d	λ
PI	0.00109	0.00281	NA	NA
PID	0.00161	0.00287	2.49e-05	NA
PIDF	0.00179	0.00358	7.5e-05	NA
GA-FOPI	0.0014	0.0033	NA	1.0073
PSO-Smith predictor	0.00151	0.01290	6.02e-04	NA
PSO-FOPI	0.00120	0.00250	NA	1.05700

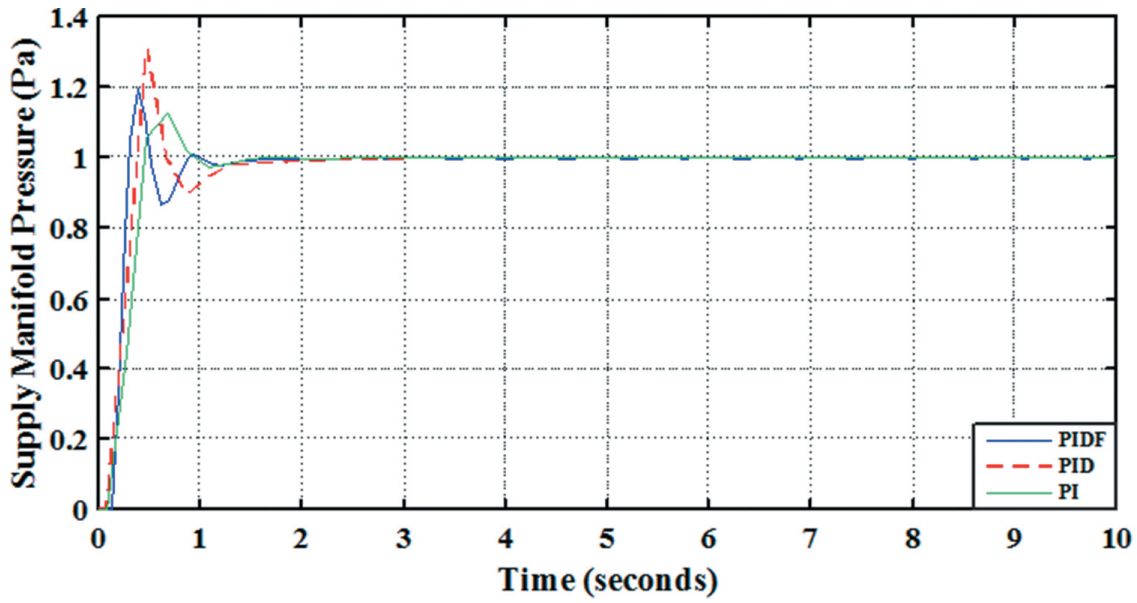


Figure 16. PEMFC output with (a) PIDF controller, (b) PID controller, and (c) PI controller.

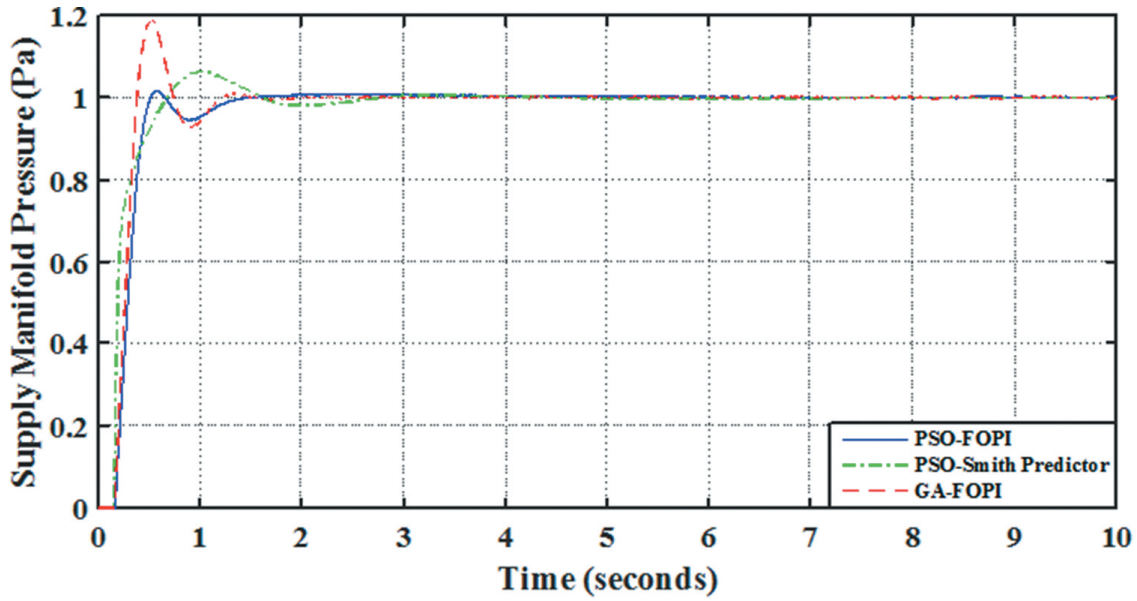


Figure 17. PEMFC output with (a) PSO-FOPI controller, (b) PSO-Smith predictor controller, and (c) GA-FOPI controller.

Table 5. Comparison of PEMFC output with various controllers.

		Type of controller					
Parameters	Without controller	PI	PID	PIDF	GA-FOPI	PSO-Smith predictor	PSO-FOPI
Settling time (s)	1.414	1.496	1.449	1.290	1.374	1.262	1.008
Overshoot (%)	0.498	8.152	30.921	19.880	18.452	5.581	2.577
Steady state error (%)	$1.25*10^5$	0	0	0	0.1	0	0

t = 0 s. In the absence of a controller, the PEMFC system's output is shown in Figure 15. The values of various controller parameters K_p, K_i, K_d and order of integration (λ), obtained after optimization are detailed in Table 4.

The outputs of PEM Fuel Cell with classical controllers (PI, PID, and PID controller with filter derivative) are plotted in one graph (Figure 16) while the output with GA-FOPI, PSO-FOPI, and PSO-Smith predictor controllers is combined in one plot (Figure 17). The system performance in terms of settling time, overshoot, and steady state error is summarized in Table 5. It has been observed that the steady state error is very high ($1.25*10^5$%), when the system does not possess any controller. The steady state error is completely eliminated with PI, PID, PIDF, PSO-FOPI, and Smith predictor controllers while a negligible amount (0.1%) of steady state error exists when the system is controlled with GA tuned FOPI controller. With PID, PIDF, and GA-FOPI controllers, the overshoot values (30.921%, 19.880%, and 18.452%, respectively) are quite high. On other hand, the overshoots obtained are in tolerance limit with PI (8.152%), PSO-Smith predictor (5.581%) and PSO-FOPI (2.577%) controllers respectively. With the proposed PSO-FOPI controller the value of settling time is least and has improved to 1.008 s. Table 5 shows that the PSO-FOPI controller significantly reduces the values of performance metrics such as settling time, overshoot, and steady state error. The PEMFC system exhibits best performance with PSO-FOPI controller in comparison with classical, PSO-Smith predictor controllers, and GA-FOPI controller.

10.Conclusion

A PEM fuel cell is a complex nonlinear system. Its major issue is to deal with oxygen starvation which can be done by controlling manifold supply pressure. This paper utilizes classical controllers (PI, PID, PIDF), PSO tuned Smith predictor, GA-FOPI controllers, and PSO-FOPI controllers to regulate the manifold pressure. In the absence of any controller, nonlinear PEM fuel cell system is sluggish with very high steady state error. The steady state error becomes zero with all controllers. With classical controllers and GA-FOPI controller, the overshoot obtained is very high. The performance parameters viz. settling time, steady state error and overshoot are reduced with the implementation of PSO-Smith predictor and PSO-FOPI controllers. The overshoot has been remarkably improved by employing PSO-FOPI controller. The simulation results indicate that the PSO-FOPI controller surpasses other existing approaches such as classical controllers (PI, PID, and PIDF), GA-FOPI, and PSO based Smith predictor Controller for nonlinear PEMFC systems. In the future, the fractional order controller can be used to control the stack voltage of the PEMFC system. Furthermore, it is possible to optimize the controller by using other artificial techniques, viz. Firefly Algorithm, Cuckoo Search Method and Grey Wolf Optimization Algorithm. Other control techniques like neural network control, model predictive control, robust control, intelligent control consists of fuzzy logic control, self-adaptive control, composite control, and sliding mode control can be employed for prevention of oxygen starvation in PEM fuel cells.

Disclosure statement

No potential conflict of interest was reported by the author(s).

Notes on contributors

Swati Singh is research scholar at Amity School of Engineering & Technology, Noida. Her interests includes controller design and renewable energy systems.

Vijay Kumar Tayal received his M.Tech and Ph.D. from NIT, Kurukshetra. He is currently an Associate Professor at Amity School of Engineering and Technology (ASET), Noida, in the Department of Electrical and Electronics Engineering. His research interests are Robust, Fuzzy Controller Design and intelligent controller design.

Hemender Pal Singh received his Ph.D. degree from Rohilkhand University Bareilly, UP. Presently he is Professor and Head, Department of Electrical & Electronics Engineering at Amity School of Engineering & Technology (ASET), Noida. His research interests are Optical Communication, and Instrumentation Systems.

Vinod Kumar Yadav received his Ph.D. from Indian Institute of Technology, Roorkee, Uttarakhand. He is currently Professor in Department of Electrical Engineering at Delhi Technological University, New Delhi.

References

Abe, N., and K. Yamanaka. 2003. Smith Predictor control and internal model control - a tutorial, SICE 2003 Annual Conference (IEEE Cat. No. 03TH8734) Fukui, Japan, 2:1383–87.

Ahmadi, S., S. H. Abdi, and M. Kakavand. 2017. Maximum power point tracking of a proton exchange membrane fuel cell system using PSO-PID controller, science direct. *Elsevier* 42:20430–43. doi:10.1016/j.ijhydene.2017.06.208.

Almeida, B. S. G., and V. C. Leite. 2019. Particle swarm optimization: A powerful technique for solving engineering problems, swarm intelligence - recent advances. *New Perspectives and Applications*. doi:10.5772/intechopen.89633.

Arora, R., V. K. Tayal, and H. P. Singh. 2017. Series FACTS controllers for power oscillations damping of power system, 2017 recent developments in control. *Automation & Power Engineering (RDCAPE)* 245–50. doi:10.1109/RDCAPE.2017.8358275.

Baroud, Z., A. Benalia, and C. Ocampo-Martinez. 2016. Air flow regulation in fuel cells: An efficient design of hybrid fuzzy-PID control, electrotehnica, electronica. *Automatica (EEA)* 64 (4):28–32.

Baruah, G., S. Majhi, and C. Mahanta. 2019. Design of FOPI controller for time delay systems and its experimental validation. *International Journal Automation and Computing* 16 (3):310–28. doi:10.1007/s11633-018-1165-4.

Bedi, P. S., R. N. Methekar, S. C. Patwardhan, V. Prasad, and R. D. Gudi. 2007. Nonlinear internal model control of pem fuel cell, 8th International IFAC Symposium on Dynamics and Control of Process Systems Proceedings Cancun, Mexico, 3:101–06. doi:10.3182/20070606-3-mx-2915.00135

Bei, B. G., K. N. Woon, and D. Bill. 2010. *Fuel Cells*. 1st ed. Boca Raton: Taylor & Francis & Group.

Bhatt, P., N. Agarwal, and U. K. Chakraborty. 2016. Parameter optimization of PEMFC with genetic algorithm. *New Mathematics and Natural Computation* 13 (3):241–49. doi:10.1142/s1793005716500162.

Bhisrkar, K. K., V. A. Vyawahare, and A. V. Tare. 2014. Design of Fractional-order PI controller for linear unstable systems, 2014 IEEE Students' Conference on Electrical, Electronics and Computer Science Bhopal, India, 1–6, doi: 10.1109/SCEECS.2014.6804523.

Chen, H. C., S. Y. Tzeng, and P. H. Chen. 2010. Optimization design of PID controllers for PEMFC with reformer using genetic algorithm, Proceedings of the Ninth International Conference on Machine Learning and Cybernetics Qingdao, 2990–95. doi:10.1109/ICMLC.2010.5580735.

Chen, J., Z. Liu, F. Wang, Q. Ouyang, and H. Su. 2018. Optimal oxygen excess ratio control for PEM fuel cells. *IEEE Transactions on Control Systems Technology* 26 (5):1711–21. doi:10.1109/TCST.2017.2723343.

Cheng, S. J., T. J. Chang, K. H. Tan, and S. L. Kuo. 2015. Nonlinear modeling of the PEMFC based on NNARX approach, world academy of science. *Engineering and Technology International Journal of Computer and Information Engineering* 9 (5):1211–15. doi:10.5281/zenodo.1105835.

Daud, W. R. W., R. E. Rosli, E. H. Majlan, S. A. A. Hamid, and R. Mohamed. 2014. PEM fuel cell system control: A review, renewable energy. *An International Journal* 113:620–38. doi:10.1016/j.renene.2017.06.027.

Divi, S., S. H. Sonawane, and S. Das. 2018. Uncertainty analysis of transfer function of proton exchange membrane fuel cell and design of PI/PID controller for supply manifold pressure control. *Indian Chemical Engineer* 1–15. doi:10.1080/00194506.2018.1510794.

Dormido, S., and A. Visioli. 2014. PID control. *Encyclopedia of Systems and Control"* 1–11. doi:10.1007/978-1-4471-5102-9_245-1.

Dwivedi, Y., and V. K. Tayal. 2017. Dynamic stability improvement of alkali fuel cell integrated system using PSO optimized PID control design, IEEE International Conference on Recent Developments in Control, Automation & Power Engineering (RDCAPE), Amity University, Noida, India, 499–504. doi:10.1109/RDCAPE.2017.8358322.

Eini, R., and S. M. Rakhtala. 2014. Nonlinear modeling of a PEM fuel cell system; a practical study with experimental validation. *International Journal of Mechatronics, Electrical and Computer Technology* 4 (10):1272–96.

Faieghi, M. R., and A. Nemati. 2011. On Fractional-Order PID Design. In *Applications of MATLAB in Science & Technology*, Chapter 13, (InTech):273–292. doi: 10.5772/22657.

Farhadi, P., and T. Sojoudi. 2014. PEMFC voltage control using PSO-tuned-PID controller, Proceedings of the 2014 IEEE NW Russia Young Researchers in Electrical and Electronic Engineering Conference, St. Petersburg, Russia. 32–35.

Gao, H., W. Rao, H. Anping, T. Yuanfen, and L. Zhibiao. 2012. New dual-mode CMA equalizer. *Physics Procedia* 25:1973–79. doi:10.1016/j.phpro.2012.03.337.

GnanaMuruga, M., and A. Senthilkumar. 2014. Smith predictor for control of the process with long dead time. *International Journal of Engineering Research & Technology (IJERT)* 2(6): 81–85.

Gruber, J. K., C. Bordons, and A. Oliva. 2012. Nonlinear MPC for the airflow in a PEM fuel cell using a Volterra series model. *Control Engineering Practice* 20 (2):205–17. doi:10.1016/j.conengprac.2011.10.014.

Grujicic, M., K. M. Chittajallu, E. H. Law, and J. T. Pukrushpan. 2004. Model based strategies in the dynamic interaction of air supply and fuel cell. *Proceedings of the I MECH E Part A Journal of Power and Energy* 218 (7):487–99. doi:10.1243/0957650042456999.

Hang, C. C. 2009. *Control systems, robotics, and automation* –, Vol. II-Smith Predictor and Its Modifications. - EOLSS Publications.

Houssein, E., B. E. Helmy, H. Rezk, and A. M. Nassef. 2021. An enhanced Archimedes optimization algorithm based on Local escaping operator and Orthogonal learning for PEM fuel cell parameter identification. *Engineering Applications of Artificial Intelligence* 103:104309–31. doi:10.1016/j.engappai.2021.104309.

Keek, J. S., S. L. Loh, and S. H. Chong. 2018. Fractional-order proportional-Integral (FOPI) controller for mecanum-wheeled robot (MWR) in path-tracking control. *International Journal of Mechanical Engineering and Technology (IJMET)* 9 (11):325–37.

Kennedy, J., and R. Eberhart. 1995. Particle swarm optimization In Proceedings of IEEE International Conference on Neural Networks (Perth, Australia) (IEEE Service Center, Piscataway, NJ 1942–48. doi:10.1109/ICNN.1995.488968.

Khubchandani, V., K. Pandey, V. K. Tayal, and S. K. Sinha. 2016. PEM fuel cell integration with using Fuzzy PID technique, 2016 IEEE 1st International Conference on Power Electronics, Intelligent Control and Energy Systems (ICPEICES), Delhi, India, 1–4. doi:10.1109/ICPEICES.2016.7853450.

Lee, K. Y., and J. B. Park. 2006. Application of particle swarm optimization to economic dispatch problem: Advantages and disadvantages, 2006 IEEE PES Power Systems Conference and Exposition PSCE, Atlanta, GA, USA, 188–92. doi: 10.1109/PSCE.2006.296295.

Li, C. H., X. P. Ji, Q. J. Zeng, Y. L. Wang, and X. D. Wu. 2014. Modeling and performance analysis of a PEM fuel cell system, unifying electrical engineering and electronics engineering. *Lecture Notes in Electrical Engineering* 943–51. doi:10.1007/978-1-4614-4981-2_102.

Liu, Y.-H., J.-H. Chen, and J.-W. Huang. 2015. A review of maximum power point tracking techniques for use in partially shaded conditions. *Renewable and Sustainable Energy Reviews* 41:436–53. doi:10.1016/j.rser.2014.08.038.

Long, Z., Z. Jiang, C. Wang, Y. Jin, Z. Cao, and Y. Lia. 2020. Novel approach to control of piezo-transducer in microelectronics packaging: PSO-PID and editing trajectory optimization. *IEEE Transactions On Components, Packaging And Manufacturing Technology* 10 (5):795–805. doi:10.1109/TCPMT.2020.2984701.

Mirzal, A. 2017. Delay compensation using the smith predictor: A brief review with numerical examples. *International Journal of Computer-aided Mechanical Design and Implementation* 3 (1):1–8. doi:10.21742/ijcmdi.2017.3.1.01.

Mohamed, A. K., and A. W. Mohamed. 2019. Real-parameter unconstrained optimization based on enhanced AGDE algorithm. *Studies in Computational Intelligence* 801:431–50. doi:10.1007/978-3-030-02357-7_21.

More, A., and G. Lakhekar. 2017. Non-linear predictive terminal sliding mode control based cascade control for interconnected system. *International Journal of Industrial Electronics and Electrical Engineering (IJIEEE)* 5 (6):29–35.

Na, W. K., B. Gou, and B. Diong. 2007. Nonlinear control of PEM fuel cells by exact linearization. *IEEE Transactions On Industry Applications* 43 (6):1426–32. doi:10.1109/TIA.2007.908193.

Nwalozie, G. C., V. N. Okorogu, K. C. Umeh, and C. D. Oraetue. 2012. Performance analysis of constant modulus algorithm (CMA) blind adaptive algorithm for smart antennas in a W-CDMA network. *International Journal of Engineering Science and Innovative Technology (IJESIT)* 1 (2):246–54.

Palaniyappan, T. K., V. Yadav, V. K. Tayal, and P. Choudekar. 2018. PID control design for a temperature control system, International Conference on Power Energy, Environment and Intelligent Control (PEEIC), Greater Noida, India, 632–37. doi: 10.1109/PEEIC.2018.8665469

Pangaribowo, T., W. Utomo, and A.A. Bakar, Khaerudini, D.S. 2020. Modeling of control system for hydrogen and oxygen gas flow into PEMFC based on load demand by using fuzzy controller. *International Journal of Advanced Trends in Computer Science and Engineering* 9 (1):606–11. doi:10.30534/ijatcse/2020/8491.42020.

Penga, F., L. Renb, Y. Zhaob, and L. Li. 2020. Hybrid dynamic modeling-based membrane hydration analysis for the commercial high-power integrated PEMFC systems considering water transport equivalent. *Energy Conversion & Management* 205:1–19. doi:10.1016/j.enconman.2019.112385.

Petchinathan, G., K. Valarmathi, and T. K. Radhakrishnan. 2017. Optimal tuning of fractional order PI controller using particle swarm optimization for pH process. *International Journal of Applied Engineering Research* 12 (1).

Podlubny, I. 1999. *Fractional differential equations*. USA: Academic Press.

Qi, Z., J. Tang, J. Pei, and L. Shan. 2020. Fractional controller design of a DC-DC Converter for PEMFC. *IEEE Access* 8:120134–44. doi:10.1109/ACCESS.2020.3005439.

Qin, Y., G. Zhao, Q. Hua, L. Sun, and S. Nag. 2019. Multiobjective genetic algorithm-based optimization of PID controller parameters for fuel cell voltage and fuel utilization, sustainability, MDPI. *Open Access Journal* 11 (12):1–20. doi:10.3390/su11123290.

Rajesh, R. 2019. Optimal tuning of FOPID controller based on PSO algorithm with reference model for a single conical tank system. *SN Applied Sciences* 1 (7):1–14. doi:10.1007/s42452-019-0754-3.

Sahu, R. K., G. T. C. Sekhar, and S. Panda. 2015. DE optimized fuzzy PID controller with derivative filter for LFC of multi-source power system in deregulated environment. *Ain Shams Engineering Journal* 6 (2):511–30. doi:10.1016/j.asej.2014.12.009.

Sankar, K., N. Thakre, S. M. Singh, and A. K. Jana. 2017. Sliding mode observer based nonlinear control of a PEMFC integrated with a methanol reformer. *Energy* 139:1126–43. doi:10.1016/j.energy.2017.08.028.

Selvi, V., and D. R. Umarani. 2010. Comparative analysis of ant colony and particle swarm optimization techniques. *International Journal Computer Applications* 5 (4):1–6. doi:10.5120/908-1286.

Shabir, S., and R. Singla. 2016. A comparative study of genetic algorithm and the particle swarm optimization. *International Journal of Electrical Engineering* 9 (2):215–23.

Shehab, M., L. Abualigah, H. A. AlHamad, H. M. Alabool, M. Alshinwan, and A. M. Khasawneh. 2020. Moth–flame optimization algorithm: Variants and applications. *Neural Computing and Applications* 32 (14):9859–84. doi:10.1007/s00521-019-04570-6.

Singh, N. 2020. A modified variant of grey wolf optimizer. *Scientia Iranica* 27 (3):1450–66. doi:10.24200/SCI.2018.50122.1523.

Singh, Swati, Tayal, Vijay Kumar, Singh, Hemender Pal, and Yadav, Vinod Kumar 2021 Performance Analysıs Of Proton Exchange Membrane Fuel Cell (PEMFC) Wıth PI And FOPI Controllers National Conference on Renewable Energy & Sustainable Environment 28-29 August 2020 211–219 NIT, Kurukshetra, India doi:10.1007/978-981-16-1186-5_17

Tang, X., C. Wang, Y. Hu, Z. Liu, and F. Li. 2021. Adaptive fuzzy PID based on granular function for proton exchange membrane fuel cell oxygen excess ratio control. *Energies* 14 (4):1140. doi:10.3390/en14041140.

Tao, S., C. Guang-yi, and Z. Xin-jian. 2005. Nonlinear modeling of PEMFC based on neural networks identification. *Journal of Zhejiang University-SCIENCE A* 6 (5):365–70. doi:10.1631/jzus.2005.A0365.

Tayal, V. K., and J. S. Lather. 2015. PSO based robust Fuzzy power system stabilizer design for single machine infinite bus system, Annual IEEE India Conference (INDICON) New Delhi, India, 1–6. doi: 10.1109/INDICON.2015.7443821

Wang, C., Y. Luo, and Y. Chen. 2009. Fractional order proportional integral (FOPI) and [proportional integral] (FO[PI]) controller designs for first order plus time delay (FOPTD) systems, 2009 Chinese Control and Decision Conference Guilin, China, 329–34. doi: 10.1109/CCDC.2009.5195105

Wen, L., Z. Dongquan, and X. Songjin. 2015. Improved grey wolf optimization algorithm for constrained optimization problem. *Journal of Computer Applications* 35 (9):2590–95. doi:10.11772/j.1001-9081.2015.09.2590.

Yadav, V., and V. K. Tayal. 2018. Optimal controller design for a DC motor using PID tuner, 2018 International Conference on Power Energy, Environment and Intelligent Control (PEEIC), Greater Noida, India, 442–45. doi: 10.1109/PEEIC.2018.8665658.

Yigit, T., and H. Celik. 2020. Speed controlling of the PEM fuel cell powered BLDC motor with FOPI optimized by MSA. *International Journal of Hydrogen Energy* 45 (60):35097–107. doi:10.1016/j.ijhydene.2020.04.091.

Yu, C. L., T. C. Wang, and C. Y. Liu. 2019. Numerical investigation on the influence of the type of PI controller combined with MAAP code on the steady-state performance of a nuclear power plant. *Nuclear Engineering and Design* 343:248–56. doi:10.1016/j.nucengdes.2019.01.004.

2021 5th International Conference on Electrical, Electronics, Communication, Computer Technologies and Optimization Techniques (ICEECCOT) 10-11, December 2021

2021 5th International Conference on Electrical, Electronics, Communication, Computer Technologies and Optimization Techniques (ICEECCOT) | 978-1-6654-3272-6/21/$31.00 ©2021 IEEE | DOI: 10.1109/ICEECCOT52851.2021.9708045

Detection of Cotton Plant Disease for Fast Monitoring Using Enhanced Deep Learning Technique

Himani Bhatheja
Department of Electronics and Communication
Delhi Technological University (DTU)
Delhi, India
himani.bhatheja09@gmail.com

N. Jayanthi
Department of Electronics and Communication
Delhi Technological University (DTU)
Delhi, India
njayanthi@dce.ac.in

***Abstract*—Disease detection in agriculture has become very crucial in today's deteriorating climatic conditions. Cotton production plays a significant part in our country's economic growth for being a major cotton producer in the world. Monitoring the large cotton fields manually becomes a tiresome activity for farmers. To leverage advancements in technology, deep learning and image processing techniques are being used to detect diseases in crops at the onset before time and thus preventing them from further harm. In this work, we have done analysis of transfer learning techniques for disease detection and proposed a sequential deep convolutional neural network for accurately classifying fresh and diseased plants. The proposed model gives better accuracy and performs much faster than pre-trained models like VGG16, ResNet50, and ResNet152V2. So, monitoring of large fields can be done using the proposed model for faster diagnosis and treatment for better production.**

Keywords— Deep Learning, Transfer Learning, ResNet model, VGG16, Deep Convolutional Neural Networks, Disease Detection

I. INTRODUCTION

Agriculture is a very important part of any country's growth and economy, so it becomes very important to consider the quality of crop production and supervise the crop growth. Cotton production is of vital importance to India because of being one of the largest producers in the world accounting to almost 26% of the entire cotton production [17]. Cotton crops can suffer from several diseases like Cercospora, Bacterial blight, Ascochyta blight, and Target spot. Thus, identifying these diseases at an early time becomes crucial for farmers to produce a healthy productive harvest and removing the infected plants before they are ruined. Therefore, modern technologies for detection of plant diseases are being used to help farmers in monitoring of crops. One such technique is Deep Learning. It is more hierarchically complex and abstracted than machine learning.

For feasible agriculture, technological advancements can be leveraged for automating detection of diseases. There are several factors that can affect the crop's health, such as moisture, pathogens, temperature invariability, strong winds, soil quality etc. The input dataset, which is used in our research work, therefore, has images from open fields of cotton crop with varying background, size and sunlight conditions. Also, the dataset has plant images as well as leaf images to classify the diseased crop and fresh crop.

This research work intends to utilize Deep convolutional neural network which is built from scratch by adding convolutional layers and compares it with well renowned pre-trained CNN architecture ResNet50, VGG16 and ResNet152V2 for classification of diseased cotton plant images. The method of using pre-trained deep CNN neural network for a new set of problem and feature extraction with changing final layers is known as Transfer Learning.

Transfer Learning technique is essentially a sum of Convolutional neural networks designed, which is actually giving state-of-the-art algorithm to classify different kinds of images. Every year ImageNet Classification competition is held where people design a new convolutional neural network to classify different images of 1000s of objects. Then, the one with the highest accuracy will be given the price money and will be treated as the state-of-the-art model. Some of the really good algorithms that are designed and are used for classification problem are as follows: Xception, VGG 16, VGG 19, ResNet50, ResNet101, InceptionV3, ResNet152V2, Inception-ResNetV2, MobileNet, EfficientNet, DenseNet. The proposed work consists of analysis of two ResNet architecture models, VGG16 and a Deep CNN which is built using sequential layers. Cotton disease dataset is used for the training purpose and insights drawn from implementation of these models and testing them on unseen data are given in the end.

In this paper, a summary of related work done before will be given in the form of Literature review in Section 2. The transfer learning methods, image pre-processing work and deep convolutional neural network overview will be provided in Section 3. The experimental results obtained from implementation followed by conclusive comments and summary are given in Section 4 and 5.

II. LITERATURE REVIEW

A research paper [1] that develops an Apple Leaf Diseases Classifier in real time uses a combination of deep-CNNs by proposing the GoogLeNet Inception network along with Alex Precursor and Cascade Inception architecture to perform the classification of diseased apple leaves dataset. This paper also gives a comparative analysis between their own model and previously advanced models like SVM, back propagation (BP) Neural Net, ResNet-20, AlexNet and VGG

Authorized licensed use limited to: DELHI TECHNICAL UNIV. Downloaded on February 24,2022 at 06:56:01 UTC from IEEE Xplore. Restrictions apply.

Network 16. The metrics that were used in this paper were accuracy, performance, convergence rate and the computational resources that are required. These architectures were tested on the basis of above stated metrics. The dataset used was Apple Leaf Disease Dataset (ALDD), and these criteria were tested on the dataset that comprised of nearly 1053 images. The built classifier was tested on the dataset and accuracy for that came out to be 97.62%

In paper [9], the authors used VGG16 and ResNet50 as transfer learning models and compared them with Multi-layered Convolutional Neural Network (MCNN) on Potato, tomato and corn plant images. The PlantVillage dataset was used for collecting the data and the classification was done for tomato, potato and corn. Out of the three, MCNN was 93.70% accurate, VGG16 had 98.30% accuracy and ResNet50 attained highest accuracy of 98.70%.

Geetharamani G. et al. [10] proposed a novel method to detect plant leaf disease which also included six kinds of data augmentation techniques like noise injection, gamma correction, principal component analysis color augmentation, scaling, rotation and flip. The performance of proposed model was rigorously compared with different machine learning algorithms. Training was done on Plant leaves dataset and the proposed deep CNN model achieved accuracy of 96.46% for classification of 38 different classes.

Jian-hua ZHANG et al. in [2] used automated segmentation model including active gradient and local information to enhance performance of segmentation of images of cotton leaves. The model used could segment the cotton leaves with uneven lighting, shadow, leaf disease spot blur, staggered condition, unclear diseased leaf edges, adhesive diseased leaf and complex background. A comparative analysis for all seven types of images was conducted between Geodesic Active Contour (GAC) algorithm, Local Binary Fitting (LBF) algorithm, Chan-Vese (C-V) algorithm and the proposed algorithm. The advantages of this model include accuracy in segmentation and running time in processing 7 types of diseased cotton leaves images.

In [13], the authors introduced EfficientNet deep CNN model for disease detection in plant leaves which was also compared with other state-of-the-art convolutional neural network models using transfer learning technique. Both the original dataset and augmented dataset of PlantVillage dataset were fed to these models for training. While using transfer learning, all the layers of these pre-trained models were used for training purpose. The EfficientNet B4 model achieved highest accuracy amongst other models for augmented image dataset with 99.91%, and the EfficientNet B5 performed well for original dataset with accuracy of 99.91%.

Rafael Faria Caldeira et al. [15] used deep neural network models ResNet50 and GoogleNet for transfer learning on Cotton leaves dataset. Testing of four traditional machine learning models such as Support Vector Machine (SVM), Hybrid Neuro-Fuzzy networks (NFC), Artificial neural network (ANN) and Closest k-neighbors (KNN) was done in comparison to new transfer learning models. The deep CNN based transfer learning models performed with 25% more precision than machine learning algorithms. Among the CNN based models, ResNet50 performed better than GoogleNet, although the technical difference of performance was insignificant according to authors.

Zhenping Qiang et al. [16] proposed fine tuning based Inception V3 transfer learning method on PlantVillage dataset. They obtained results for various batch sizes and learning rate that best suited the detection. The base model layers were frozen and three-layer neural network layer added from bottleneck node to perform fine-tuning. They obtained a highest test set precision of 93% for batch size 100 and learning rate 0.01.

III. METHODOLOGY

To use the most efficient technique for detection of cotton plant diseases, two approaches were used, first was to building a deep convolutional neural network from scratch and second was using state-of-the-art architectures as feature extractors by means of transfer learning.

A. Dataset Collection and pre-processing

As the cotton plant is majorly grown in areas of Western India like Gujarat, Maharashtra and Karnataka, so to collect the images of cotton plants we referred the internet. The dataset was taken from the Cotton Disease database with images of healthy cotton plants and leaves, and diseased cotton plants and leaves. The Fig. 1 describes the different types of input images in the dataset. Diseases like white spots, bacterial blight, leaf sucking and chewing pests, grey mildew, Myrothecium leaf spot, Cercospora leaf spot, etc. affect the cotton crops adversely.

This dataset has examples of leaf sucking pests such as Aphids - affected plants in the diseased cotton plants class, and white spots on leaves in the diseased leaves class – which happens because of excessive use of herbicides and pesticides which can affect cotton production and even death in plants. Fresh plant and leaves images are present in the cotton fresh plant and cotton fresh leaves categories. In fig. 1, the first image is of diseased leaf with white spots on it, the second image is of a diseased plant which is suffering from leaf sucking pest, the third one is of a fresh leaf and last one is of a fresh plant with no diseases.

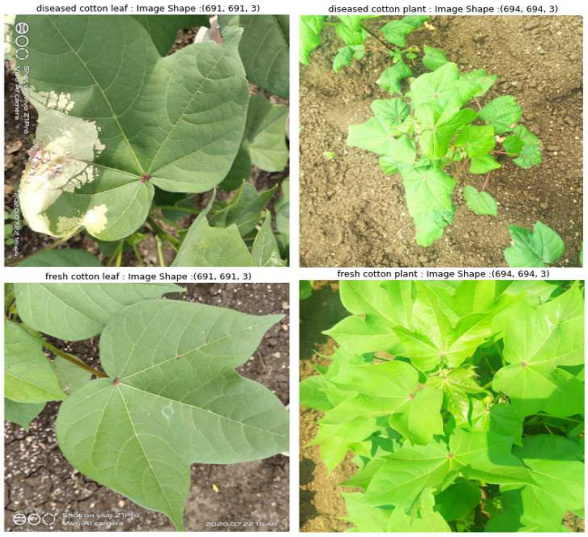


Fig. 1. *Sample images from the dataset*

Authorized licensed use limited to: DELHI TECHNICAL UNIV. Downloaded on February 24,2022 at 06:56:01 UTC from IEEE Xplore. Restrictions apply.

To increase the training efficiency of the model, we implemented data augmentation techniques on training set for generating extra images from existing input images by rescaling, rotating, shifting width, shifting height, and applying zoom, shear and horizontal flip. On validation set and test set, only scaling and resizing of images is done to maintain uniformity in the dataset.

B. *Disease Detection Model for Cotton Plant*

In this research work, we have opted two paths: first one is using pre-trained architectures as feature extractors and changing the last layers to make use of transfer learning, second one is by developing a deep convolutional neural network by adding different convolutional, batch normalizing, pooling, fully connected/dense and flatten layers.

- Transfer Learning – VGG16, ResNet50 and ResNet152V2 are some of the state-of-the-art models that give excellent performance in classification. Use of weights that are pre-trained from ImageNet is done and a flatten layer along with dense layer and softmax activation with 4 output neurons are added instead of fully connected layers of these models.
- Deep-Convolutional Neural Network – A multilayer deep network has been designed and proposed for more accurate and faster implementation. The architectural details of the model can be seen in figure 2. The model has 4 convolutional layers with activation function as 'ReLU', 5 batch normalization layers, 4 max pooling layers, 5 drop-out layers, a flatten layer, a dense layer with ReLU activation and a final fully connected layer with softmax activation and size 4 for output categories. The input image is of dimensions 224 * 224 * 3 and is given to the first layer which has 32 filters and kernel size 3. It is followed by a batch normalization layer, a max pooling layer with pooling size (3,3) and a dropout layer with rate 0.25. These layers are repeated 3 times with change in filter size of convolutional layer to 64 and then, max pooling size of (2,2). After the 4th dropout layer, a flatten layer is added to provide the output from dropout layer to the next layer. It is followed by dense/fully connected layer, batch normalization layer and then 5th dropout layer with rate 0.25. Then final fully connected layer is added having softmax activation because of multi-classification problem.

The learning rate for deep-CNN model was determined using an analysis of base model of deep-CNN using loss and epochs using adam optimizer, batch size 32 and 40 epochs. Upon analysis, it was observed that the loss was increasing after the lr of 0.001. So, we changed the learning rate to 0.001 to train using the same Adam optimizer, 32 batch size and 30 epochs.

C. *Implementation Setup*

For Implementation, Windows 10 PC with 64-bit Operating system was used. The model training was done using 12 GB NVIDIA Tesla K80 GPU. The software tools used are Keras 2.2.6, Tensorflow 1.13.0, Matplotlib 3.4.1 and Python 3.8.2. For performing experiments, we used Google Colab and Jupyter Notebooks.

IV. RESULTS

The proposed networks are tested on 106 images from test set using the methodologies described earlier. The plot of accuracy and loss for VGG16, ResNet50 and ResNet152V2 are shown in Fig. 3, 4 and 5 respectively. Table I depict the results according to different metrics. After 10 epochs, the performance of ResNet152-V2 was best among others, but the results were under-trained, so we increased epochs to 30 and then the proposed model accuracy achieved very good training and validation accuracies.

The fig. 6 depicts that the training and validation accuracy of the proposed model is increasing as the number of epochs is increasing. This indicates that our model is neither over-fitting nor under-fitting. Also, the training and validation accuracies achieved are comparable to the pre-trained models' accuracies. Not only that, the execution time for implementing the deep-CNN model is lesser by 50% in comparison to the other transfer learning methods used.

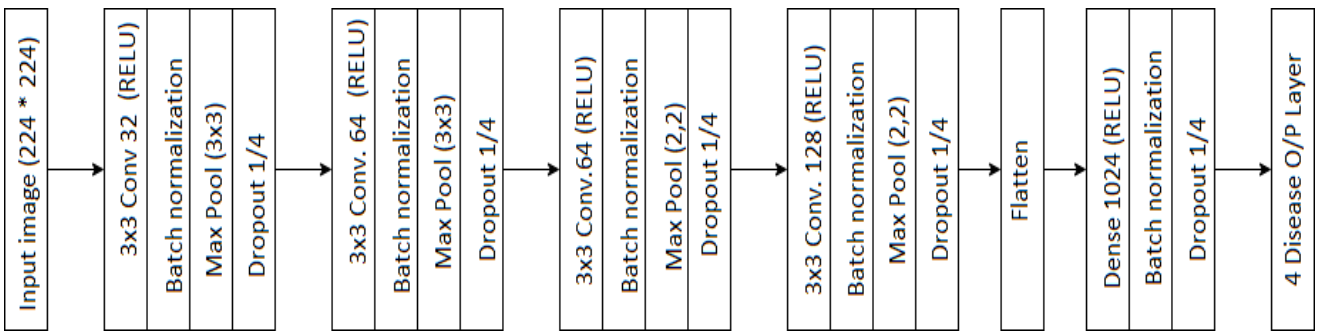


Fig. 2. *Proposed model architecture*

Authorized licensed use limited to: DELHI TECHNICAL UNIV. Downloaded on February 24,2022 at 06:56:01 UTC from IEEE Xplore. Restrictions apply.

TABLE I. RESULTS

Model specifications			10 epochs		30 epochs			
Model	Layers	Params	Training Acc.	Validation Acc.	Training Acc.	Validation Acc.	Test Accuracy	Time (in sec)
VGG	16	138.35M	95.54%	94.34%	99.33%	97.17%	96.04%	2515
ResNet	50	25.63M	64.22%	64.43%	72.53%	83.00%	71.70%	2402
ResNet	152	60.38M	95.69%	95.26%	99.08%	96.05%	98.01%	2748
Proposed	**6**	**4.8M**	**65.09%**	**43.75%**	**94.52%**	**96.88%**	**98.11%**	**1079**

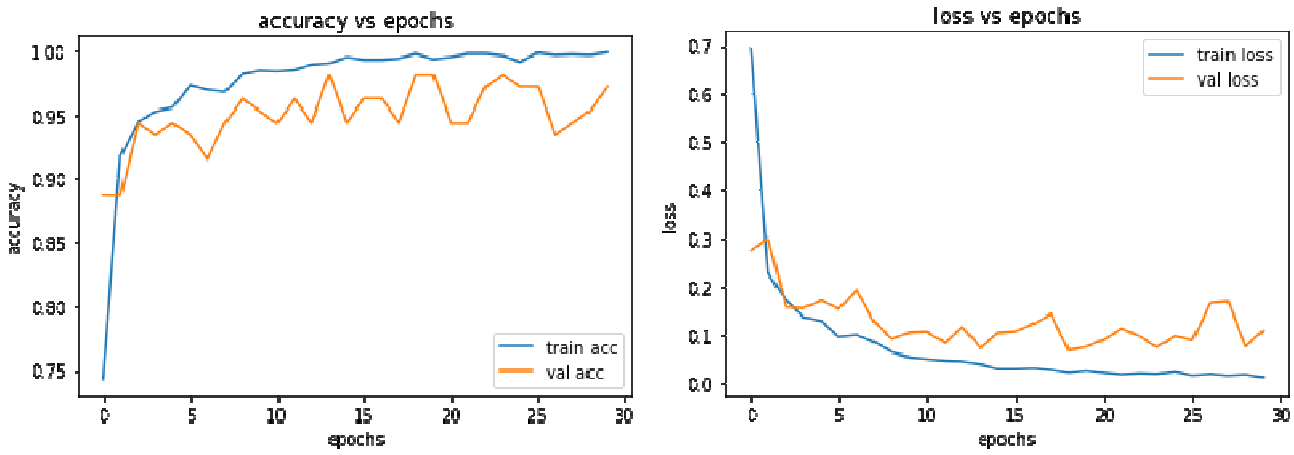


Fig. 3. *Accuracy versus epochs and in the right loss versus epochs analysis of VGG16*

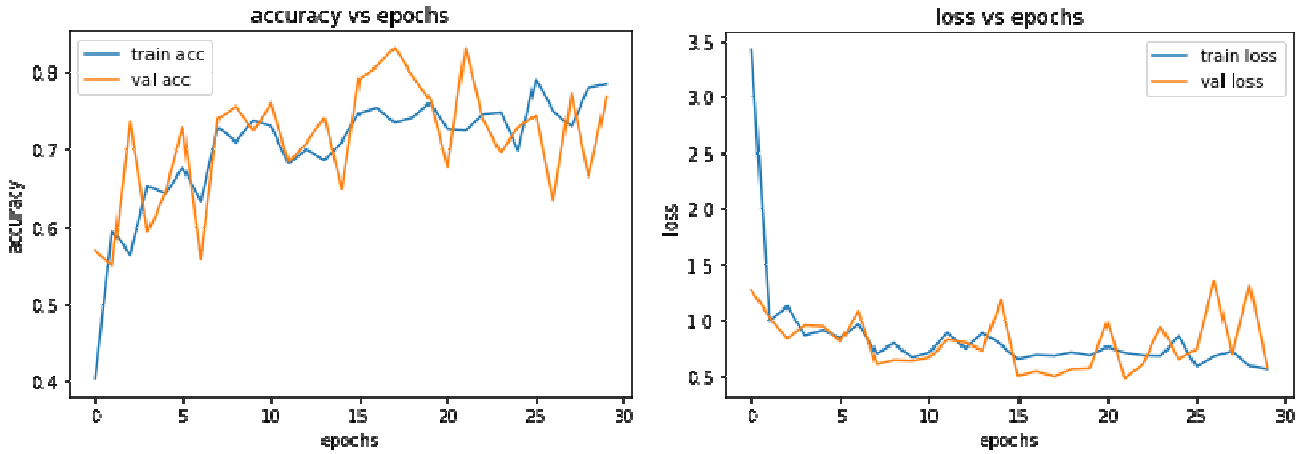


Fig. 4. *Accuracy versus epochs and in the right loss versus epochs analysis of ResNet50*

From Table 1, it can be seen that large parameters are causing the execution time to be higher for transfer learning models. The deep CNN model has only significant number of parameters for the problem statement and therefore result in less computational time.

Authorized licensed use limited to: DELHI TECHNICAL UNIV. Downloaded on February 24,2022 at 06:56:01 UTC from IEEE Xplore. Restrictions apply.

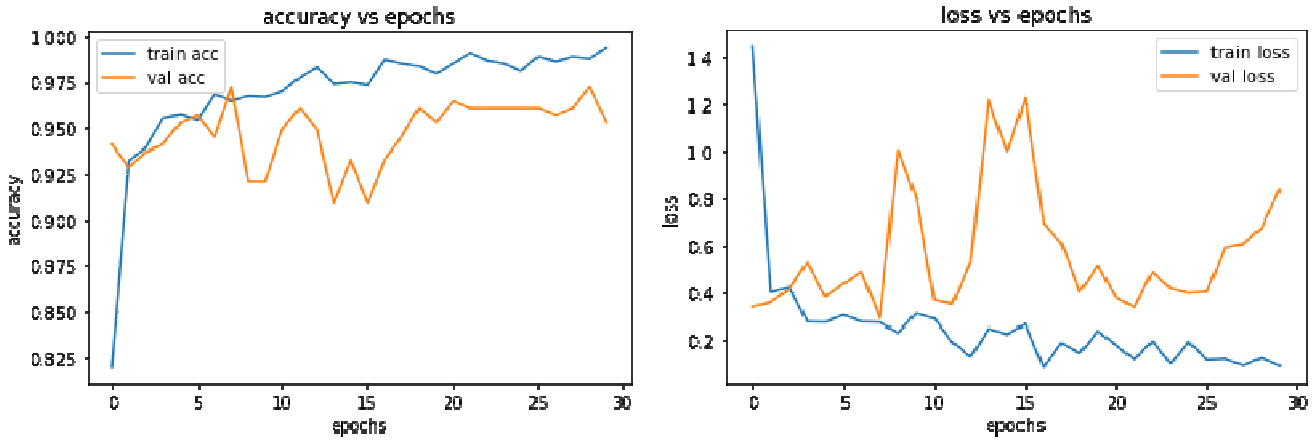


Fig. 5. *Accuracy versus epochs and in the right loss versus epochs analysis of ResNet152V2*

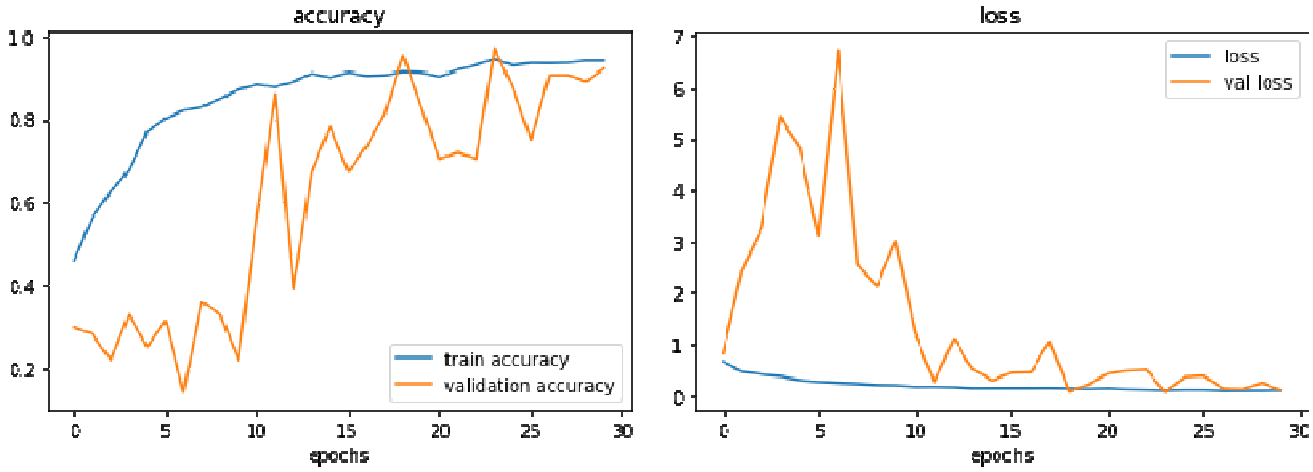


Fig. 6. *Accuracy versus epochs and in the right loss versus Epochs analysis of proposed model*

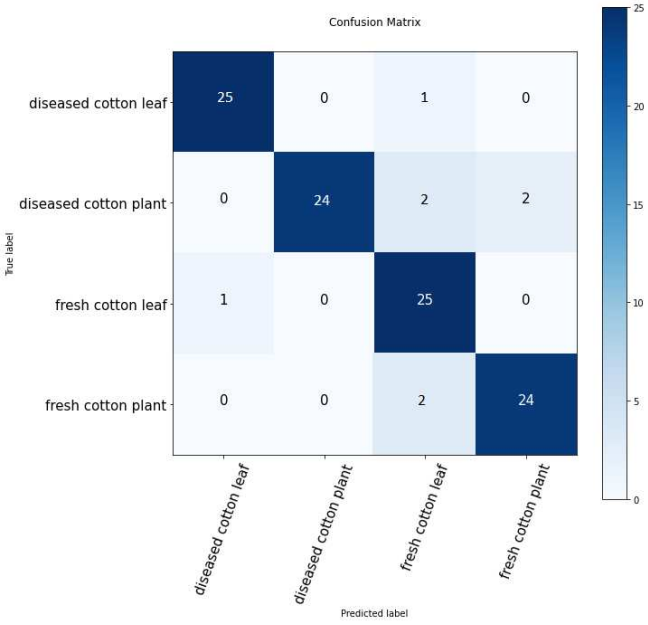


Fig. 7. *Confusion matrix using proposed model*

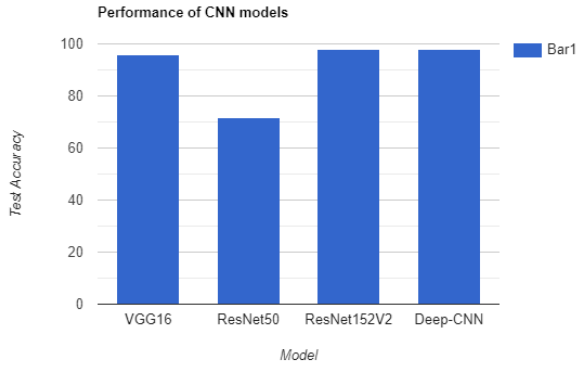


Fig. 8. *Performance of all CNN models with respect to test accuracy*

The confusion matrix is also drawn for analysis of accuracy of our model in fig. 7. The correct detections for all classes were 98 and incorrect were 8. The test accuracy comparison of all these sequential structure-based models is given in fig. 8 which shows that the testing accuracy of ResNet152V2 and proposed model is nearly equal. But as evident from the above discussion, the proposed model is faster than all the other models by more than 50%.

Authorized licensed use limited to: DELHI TECHNICAL UNIV. Downloaded on February 24,2022 at 06:56:01 UTC from IEEE Xplore. Restrictions apply.

V. CONCLUSION

Cotton plants production is vital for our country's economy and therefore preventing the diseases in cotton plants can help manyfold in the production of cotton-based products. Therefore, automated detection of diseases can help farmers in producing highly efficient crops. Transfer learning has been gaining popularity for detection of diseases, but this technique is susceptible to over-fitting. Therefore, we have done a comparison of transfer learning using pre-trained models which are based on sequential layers with our own proposed sequential deep-CNN model. We have detected diseases like Aphids which are leaf sucking pests and white spots on leaves. Experimental results depicted that the proposed model performed well on unseen data and gave better test accuracy of 98.11% compared to transfer learning techniques like 96.04% for VGG16, 71.70% for ResNet50 and 98.01% for ResNet152V2. The time in execution of proposed model is significantly reduced along with increase in accuracy.

Further, we are planning to implement the proposed detection model on different types of diseases other than described in this work. We plan to collect more dataset samples on different types of cotton diseases and improve the performance of our model.

REFERENCES

[1] P. Jiang, Y. Chen, B. Liu, D. He and C. Liang, "Real-Time Detection of Apple Leaf Diseases Using Deep Learning Approach Based on Improved Convolutional Neural Networks", *IEEE Access*, vol. 7, pp. 59069-59080, 2019.

[2] J. ZHANG, F. KONG, J. WU, S. HAN and Z. ZHAI, "Automatic image segmentation method for cotton leaves with disease under natural environment", *Journal of Integrative Agriculture*, vol. 17, no. 8, pp. 1800-1814, 2018.

[3] H. -T. Thai, N. -Y. Tran-Van and K. -H. Le, "Artificial Cognition for Early Leaf Disease Detection using Vision Transformers," *2021 International Conference on Advanced Technologies for Communications*, 2021, pp. 33-38, doi: 10.1109\ATC52653.2021.9598303

[4] E. Too, L. Yujian, S. Njuki and L. Yingchun, "A comparative study of fine-tuning deep learning models for plant disease identification", *Computers and Electronics in Agriculture*, volume 161, pp. 272-279, 2019.

[5] de Castro Megías A.I. et al. (2021) Applications of Sensing for Disease Detection. In: Kerry R., Escolà A. (eds) Sensing Approaches for Precision Agriculture. Progress in Precision Agriculture. Springer, Cham.

[6] G. Wang, Y. Sun and J. Wang, "Automatic Image-Based Plant Disease Severity Estimation Using Deep Learning", *Computational Intelligence and Neuroscience*, vol. 2017, pp. 1-8, 2017. doi: 10.1155/2017/2917536.

[7] M. Tan and Q. Le, "EfficientNet: Rethinking Model Scaling for Convolutional Neural Networks", *Proceedings of the 36th International Conference on Machine Learning*, PMLR 97:6105-6114, 2019

[8] C. Szegedy, V. Vanhoucke, S. Ioffe, J. Shlens and Z. Wojna, "Rethinking the Inception Architecture for Computer Vision," in *2016 IEEE Conference on Computer Vision and Pattern Recognition (CVPR)*, Las Vegas, NV, USA, 2016 pp. 2818-2826. doi: 10.1109/CVPR.2016.308

[9] M. S. Arshad, U. A. Rehman and M. M. Fraz, "Plant Disease Identification Using Transfer Learning," *2021 International Conference on Digital Futures and Transformative Technologies*, 2021, pp. 1-5.

[10] G. G. and A. J., "Identification of plant leaf diseases using a nine-layer deep convolutional neural network", *Computers & Electrical Engineering*, volume 76, pp. 323-338, 2019. doi: 10.1016/j.compeleceng.2019.04.011.

[11] V. Dhaka et al., "A Survey of Deep Convolutional Neural Networks Applied for Prediction of Plant Leaf Diseases", *Sensors*, vol. 21, no. 14, p. 4749, 2021. doi: 10.3390/s21144749.

[12] M. Agarwal, A. Singh, S. Arjaria, A. Sinha and S. Gupta, "ToLeD: Tomato Leaf Disease Detection using Convolution Neural Network", *Procedia Computer Science*, vol. 167, pp. 293-301, 2020. doi: 10.1016/j.procs.2020.03.225.

[13] Ü. Atila, M. Uçar, K. Akyol and E. Uçar, "Plant leaf disease classification using EfficientNet deep learning model", *Ecological Informatics*, vol. 61, p. 101182, 2021. doi: 10.1016/j.ecoinf.2020.101182.

[14] K. Ferentinos, "Deep learning models for plant disease detection and diagnosis", *Computers and Electronics in Agriculture*, vol. 145, pp. 311-318, 2018. doi: 10.1016/j.compag.2018.01.009.

[15] R. Caldeira, W. Santiago and B. Teruel, "Identification of Cotton Leaf Lesions Using Deep Learning Techniques", *Sensors*, vol. 21, no. 9, p. 3169, 2021. doi: 10.3390/s21093169.

[16] Z. Qiang, L. He, F. Dai, "Identification of Plant Leaf Diseases Based on Inception V3 Transfer Learning and Fine-Tuning", *Wang G., El Saddik A., Lai X., Martinez Perez G., Choo KK. (eds) Smart City and Informatization. iSCI 2019, Communications in Computer and Information Science*, vol. 1122. Springer, Singapore, 2019.

[17] https://cotcorp.org.in/national_cotton.aspx?AspxAutoDetectCookieSupport=1.

Authorized licensed use limited to: DELHI TECHNICAL UNIV. Downloaded on February 24,2022 at 06:56:01 UTC from IEEE Xplore. Restrictions apply.

Research Square

Preprints are preliminary reports that have not undergone peer review.
They should not be considered conclusive, used to inform clinical practice,
or referenced by the media as validated information.

Effect of Load Frequency and Amplitude of Displacement on Soft Rock Joints under Cyclic Shear loads

S.M.Mahdi Niktabar (mahdi.niktabar@ugn.cas.cz)
ÚGN AV ČR: Ustav geoniky Akademie ved Ceske republiky https://orcid.org/0000-0002-1723-3375
K. Seshagiri Rao
Indian Institute of Technology Delhi
Amit Kumar Shrivastava
Delhi Technological University
Jiří Ščučka
ÚGN AV ČR: Ustav geoniky Akademie ved Ceske republiky

Research Article

Keywords: Rock joints, Cyclic shear load, Frequency of load, Displacement amplitude, Shear mechanism

Posted Date: February 11th, 2022

DOI: https://doi.org/10.21203/rs.3.rs-1256859/v1

License: This work is licensed under a Creative Commons Attribution 4.0 International License.
Read Full License

Effect of Load Frequency and Amplitude of Displacement on Soft Rock Joints under Cyclic Shear loads

S. M. Mahdi Niktabar[1,*], K. Seshagiri Rao[2], Amit Kumar Shrivastava[3], Jiří Ščučka[1]

[1]Department of Laboratory Research on Geomaterials, Institute of Geonics of the Czech Academy of Sciences, Ostrava, Czech Republic
[2]Department of Civil Engineering, Indian Institute of Technology Delhi, India
[3]Department of Civil Engineering, Delhi Technological University, India

Acknowledgments:

The financial support from Indian Institute of Technology Delhi is greatly appreciated

Abstract

A series of cyclic shear tests was conducted on soft synthetic rock joints with 30°- 30° asperities. Large scale shear apparatus was used in the experiments to investigate effects of shear load frequency and amplitude of displacement on the joint behaviour. Varying load frequencies (0.01, 0.05 and 0.1 Hz,) and displacement amplitudes (±4, ±6, and ±8 mm) for three different normal stresses (0.1, 0.5 and 1 MPa) were applied. The results indicated that the first peak shear stress on the joint is significantly influenced by the frequency of cyclic shear load and subsequent peaks of shear stress are largely influenced by the amplitude of displacement. Reduction in peak shear stress at higher frequency of load is greater than the reduction at lower frequency of load under cyclic movements. Shear mechanism on the joint asperities at low normal stress demonstrate asperity diminishing does not depend on load direction at high frequency. Whereas,

---

*Corresponding Author
1. Department of laboratory research on geomaterials, Institute of Geonics of the Czech Academy of Sciences, Czech Republic, Ostrava
Email address: Mahdi.Niktabar@ugn.cas.cz
Postal address: Studentska 1768, 708 00 Ostrava-Poruba,

at low frequency of loads, it depends on direction of starting cyclic shear load. Low amplitude of displacement has no effect on asperity deformation under cyclic loads. As the amplitude rises, the diminishing of asperities increases significantly. Shear mechanism and asperity diminishing at low normal stress is similar for the both higher amplitude of displacement and lower frequency of load. Comparison of shear strength envelopes indicated an opposite behaviour of the joint at varying load frequencies and displacement amplitudes.

Key words: Rock joints; Cyclic shear load; Frequency of load; Displacement amplitude; Shear mechanism;

1. Introduction

Earthquakes and other seismic activities (due to excavation in mining or underground structures) distribute dynamic loads on rock masses. These dynamic loads can lead to number of cyclic shear movements with different frequencies and amplitudes of displacement along the joints in the rock mass. Hence, shear resistance of the joints can change under cyclic loads and affect the rock mass stability. Study of cyclic shear behaviour of jointed rocks under different dynamic parameters plays an important role for analysis, design and safety of rock structures.

Shear behaviour of rock joints was investigated with different shear velocity under monotonic loads. Results of experiments indicate that shear resistance increases with increasing shear velocity (Schneider 1977; Gillette et al. 1983; Barla et al. 1990; Barbero et al. 1996 and Hencher 1981). However, other results show that shear resistance decreases with increasing shear velocity (Jafari et al. 2003; Mirzaghorbanali et al. 2014; Tang et al. 2016). No velocity dependency was reported by Hassani and Scoble (1985) for shear resistance in sandstone (0.012–0.180 mm/min).

Crawford and Curran (1981) and Atapour and Moosavi (2014) observed different shear behaviour on natural and artificial joints in soft and hard rocks. The results indicate that the shear resistance of real joint increases with increasing shear velocity on soft rocks (up to critical shear displacement rate) but it declines for hard rocks. However, the opposite shear behaviour was observed for artificial joints. Thus, the shear resistance under different shear velocity is probably influenced by the type of rocks and joints.

Most studies on cyclic shear loads were conducted under constant frequency and amplitude of displacement as presented by Hutson and Dowding (1990), Qiu et al. (1993), Huang et al. (1993), Jing et al. (1993), Homand-Etienne et al. (1999), Lee et al. (2001), Ferrero et al. (2010), Nemcik et al. (2013), and Niktabar et al. (2017). As the seismic events can occur at different distances from the rock mass, it is also necessary to study the behaviour of rock joints at different shear load frequencies and amplitudes of displacement (Ramulu et al. 2009, Yang et al. 2019 and Gomez et al. 2020).

Variation of shear displacement on rock joints under cyclic load was investigated by Jafari et al. (2003). They observed second-order asperities were demolished on rock joints with low amplitude of displacement. At high loading amplitude both first and second-order asperities diminished. Similar joint degradation was observed by Ferrero et al. (2010). Damage of joint asperities at lower shear amplitudes was smaller compared to the higher amplitudes. Nguyen (2013) studied the behaviour of jointed rocks under cyclic shear loading with different frequencies (dynamic condition). The results show that the peak shear stress under this condition is 30% greater than that under static condition. Nemcik et al. (2013) investigated influence of initial normal stress and number of shear cycles on the joints under constant normal stiffness. Results indicate that with increasing initial normal stress, the influence of shear rate is not

significant under this condition. Insignificant effect of shear rate on peak shear stress with increasing number of cycles was observed. The shear stress, normal stress and normal displacement for rock joints (infilled) under constant normal stiffness was increased with increasing shear rate as presented by Guansheng et al. (2020). Wu et al. (2019) conducted cyclic shear load on bolted rock joints for small and large displacements. When displacement was large; the shear strength reduction of bolted joints was comparable to the unbolted joint. However, for small displacement, the rock bolt had minor effect on the shear strengths.

Soft rock joints or weathered joints usually have a low shear resistance (Richards 1975; Barton and Choubey 1977; Dearman 1978; Ram and Basu 2019) and it is the main reason of rock mass failure (Nkpadobi 2015; Yan et. al 2019). Regarding cyclic shear loads, deterioration of joint asperities is faster as the number of cycle increases. Hence, in this study a series of cyclic shear tests was conducted on simulated soft rock joints with varying load frequency and amplitude of displacement to investigate effects of these dynamic parameters on shear behaviour of the joints. There is a lack of information in shear mechanism on soft (or weathered) rock joints under cyclic shear loads.

2. Experimental Methodology

2.1 Preparation of Specimens

In order to model soft rock or weathered joints, plaster of Paris has been selected as model material. The test specimens with synthetic joints were prepared by casting the plaster into special steel moulds. The plaster paste with water-powder ratio of 0.6 was mixed for 2 minutes and then poured into the moulds with inside dimensions of 299 × 299 × 85 mm, placed on a vibrating table. An aluminium plate with 30°- 30° asperity was placed on the bottom of each mould before pouring the paste. Inside of the mould and surface of the asperity plate were

lubricated with oil for easy removal of the specimen without breaking the asperities. The paste in the moulds was vibrated for 30 seconds to remove the air bubbles from the material (Fig. 1a). The hardened specimens were removed from the moulds after 60 minutes and then left for 20 days at laboratory temperature for the air curing (Fig. 1b). The test specimens with joint asperity angles of 30°- 30° were formed.The hardened plaster, having the uniaxial compressive strength of 6 MPa, is suitable for simulating the mechanical behaviour of joints in weathered or soft rocks like siltstone, claystone, shale, coal and rock salt. Tangent modulus, Poisson ratio, cohesion and intact friction angle of specimens are 2.45 GPa, 0.27, 0.72 MPa and 51.3° respectively.

Fig. 1 [Near here]

2.2 Shear Machine and Testing Procedure

Automatic static and cyclic shear testing machine (Niktabar et al. 2018) was utilized in this experiments (Fig. 2). The shear machine is a large scale apparatus and it is combination of the four main units, including frame and loading unit (1), hydraulic power pack (2), data acquisition (3), and cooling unit (4). The size of each shear box is 300 mm × 300 mm × 448 mm. Maximum capacities of normal and horizontal load cells are 500 kN and 1000 kN, respectively. Calibration of the load cells and linear variation displacement transducers (LVTD) was conducted before the experiment. Software automatically collects data during the shear loading. This apparatus has capability to carry out cyclic shear tests (Fig. 3) on jointed rocks under different frequencies (f_s) and displacement amplitudes (a_s).

A series of cyclic shear tests were performed on soft rock joints under varying frequencies (0.01, 0.05 and 0.1 Hz) by keeping amplitude of displacement constant (±8mm). Another series of tests were conducted under varying displacement amplitudes (±4, ±6 and ±8 mm) while keeping frequency of shear loads constant (0.01 Hz). Three different normal stresses (P= 0.1, 0.5 and 1 MPa) and thirty shear loading cycles were applied for each shear test. The tests were conducted

based on shear displacement control and constant normal load condition (normal stiffness was kept zero). Shear test parameters are presented in Table 1.

Fig. 2 and Fig. 3 [Near here]

Table 1 [Near here]

3. Results and Discussion

3.1 Effect of Cyclic Shear Load Frequency on the Joint

Test results for different shear load frequencies at the normal stress of 0.1 MPa are presented in Fig. 4. The graphs show shear stress and normal displacement (dilation) vs. horizontal displacement. With increasing frequency of cyclic shear load from 0.01 Hz to 0.05 Hz, first peak shear stress of the joint was increased from 0.34 MPa to 0.42 MPa (23%). When frequency increased from 0.01 Hz to 0.1 Hz, peak shear stress increased from 0.34 MPa to 0.48 MPa (41%) (Table 2; Fig. 4a, b, c), i.e. shear strength on the joints increases with rising shear load frequency. However, with increasing number of cycles (N>2), the influence of frequency was insignificant on the joint (Fig. 6a, b, and c). The maximum difference of peak shear stress was observed between the first and the second cycles (Table 2). With increasing frequency of shear load, the difference of peak shear stress between the first and the last cycle (N=30) increased. It was 59%, 64% and 67% for shear frequencies of 0.01, 0.05 and 0.1 Hz respectively (Table 2). These results demonstrate that the reduction of shear strength at higher frequency (0.1 Hz) was greater than the reduction at lower frequency (0.01 Hz) under cyclic movements (Fig. 6a, b, and c).

Angle of slope for the post peak shear stress increases (negatively) as the load frequency increases. It is clear for the first cycle (Fig. 4a, b, c; Fig.13a, b, c in appendix), but it was not observed for subsequent cycles.

Joint with low shear frequency (0.01 Hz) was under compression (positive normal displacement) after several cycles (Fig. 4d). But joint with high frequency of shear load (0.1 Hz) could dilate

(negative normal displacement) even at the last cycle (Fig. 4f), i.e. compression of joint asperities was more significant at lower shear frequency under cyclic loads.

Peak dilation of the joint vs. number of cycles for different shear load frequencies is illustrated in Fig. 7a, b, c. For low frequency (0.01 Hz), the peak joint dilation at forward movement (+8mm) was higher than at backward movement (-8mm) for the first cycle. This difference was 33.4% (Fig. 7a). However, the difference of peak joint dilation between forward and backward movements decreases gradually and it was equal after several cycles (N=22).

Fig. 4[Near here]

Table 2 [Near here]

With increasing frequency of cyclic shear load to 0.05 and 0.1 Hz, the difference of peak joint dilation between forward and backward movements was decreased to 20.1% and 1.2% for the first cycle (Fig. 7b and c). With increasing frequency of shear load, peak joint dilation between forward and backward movements became equal for the first cycle (Fig. 7c). As the number of cycles increased, the peak dilation decreased with the same rate for the both movements. This joint behaviour shows that the shear mechanism is different at high and low frequency of cyclic loads. Asperity diminishing on the both slopes was equal at high frequency of load (Fig. 8b), because there was no sufficient time to deform second slopes of the asperities. Hence, the peak dilation was the same in the both forward and backward movement. At low frequency of load, asperity diminishing on the both slopes was unequal (Fig. 8a), because there was a sufficient time to deform second slopes of the asperities (significant deformation was observed during the backward movements). Therefore, the peak dilation was different in forward and backward movements. It can be stated that the shear mechanism on the joint at high load frequency does not depend on load direction. However, at low frequency, the shear mechanism depends on direction of starting movement of cyclic load. As the normal stress increases (0.5 and 1 MPa) on

the joint, the joint behaviour has changed due to significant degradation of asperities at the first cycle (Figs. 12 and 13 in appendix). After few cycles, the joint behvaiour was same as a planar joint behaviour because of complete demolishing of asperities.

3.2 Effect of Cyclic Shear Displacement on the Joint

Shear test results for different amplitude of displacement at the normal stress of 0.1 MPa are presented in Fig. 5. The graphs show shear stress and normal displacement (dilation) vs. horizontal displacement. Peak shear stress on the joint was constant as the number of shear cycles increased for amplitude of ±4 mm (Fig. 5a), i.e. number of cycles was not effective on peak shear stress at low level of amplitude (Table 3). With increasing displacement amplitude to ±6mm (Fig. 5b), peak shear stress started to decrease as the number of shear cycles increased. This reduction for peak shear stress was more significant when shear amplitude was ± 8mm (Fig. 5c). The peak shear stress decreased by 33% and 57% for ±6mm and ±8mm amplitudes at thirty cycles.

Fig. 5[Near here]

Table 3 [Near here]

Peak shear stress vs. number of cycles is demonstrated for different amplitudes of displacement in Fig.6d, e and f. The peak shear stress was equal for varying shear amplitudes at the first cycle (N=1), but it was different for subsequent cycles.Joint was under compression at low shear amplitude (± 4mm) during all cycles (Fig.5d). When the amplitude increased (±6 and ± 8mm), significant dilation was observed on the joint (Fig. 5e and f). Due to diminishing of asperities, this dilation was declined as the number of cycles increased.

Fig. 6 and Fig. 7 [Near here]

Comparison between the graphs in Fig. 6 shows that frequency of load (Fig. 6a, b and c) has significant effect on the first peak shear stress. However, for different displacement amplitudes

(Fig. 6d, e and f), the first peak shear stress was similar and significant difference of peak shear stress was observed for subsequent cycles.

Peak joint dilation vs. number of cycles for different displacement amplitude is demonstrated in Fig. 7 (d, e and f). According to the graphs, peak dilation values at forward and backward movements are equal at low displacement amplitude (±4 mm; Fig. 7d) for thirty cycles. With increasing amplitude (±6 mm) the difference of peak dilation between both movements appeared and it was 14.9% for the first cycle (Fig. 7e). For the amplitude of ±8 mm, the difference of peak dilation was increased by 33.4% for the same cycle. This difference decreases gradually with increasing number of cycles (Fig. 7f).

Shear mechanism at low displacement amplitude was sliding only (Fig. 9a) without diminishing the asperities; hence, direction of movements (forward or backward) has no effect on asperities degradation. However, at high amplitude (±8 mm), the shear mechanism depends on direction of starting movement of cyclic load (Fig. 9b). Asperity diminishing for high displacement amplitude was significant in the second slope of asperity which was involved in the cyclic shear.

Shear mechanism and asperity diminishing were similar for the both higher amplitude of displacement (Fig. 9b) and lower frequency of load (Fig. 8a). It is because of grater diminishing on the second slopes of asperities during cyclic movements. Hence, failure on rock joint is more expected in opposite to the direction of starting movement of cyclic load.

Fig. 8 and Fig. 9 [Near here]

Specimens were removed from the shear box to observe the effect of displacement amplitude (±4, ±6 and ±8 mm) on the joint surface (Fig. 10). In case of joint with low displacement amplitude (±4 mm), most of the asperities remained intact after cyclic shear test. With increasing amplitude (±6 mm), degradation of asperities was observed. For high displacement amplitude (±8mm), the degradation of asperities was significant.

Fig. 10 [Near here]

3.3 Shear Strength Envelope for Cyclic Shear Load

Joints under cyclic shear load exhibit double peak shear stress for each cycle, i.e. one peak at the forward movement and another peak at the backward movement. Shear strength envelopes for different shear load frequencies and displacement amplitudes at forward and backward movements are presented in Fig. 11. The envelopes were plotted based on peak shear stress values in Figs. 4 and 5 (P = 0.1 MPa) and Figs. 12-15 (P = 0.5 and 1 MPa) in appendix.

At the first cycle, shear strength envelope was curvilinear (Fig. 11a) and it rose with increasing load frequency (from 0.01 to 0.1 Hz). The envelope was greater for the first forward movement compared to the first backward movement. For the backward movement the effect of frequency was negligible. For subsequent cycles, the envelope was linear (relatively) and no significant change was observed as the load frequency increased (Fig. 11b and c; Fig. 16a-c in appendix).

Shear strength envelope was equal for varying displacement amplitudes (±4, ±6, and ±8 mm) at the first forward movement (Fig. 11d). However, it was different for the first backward movement. For subsequent cycles, this difference between the envelopes was significant (Fig. 11e and f; Fig. 16d-f in appendix).

The opposite effect of load frequency and displacement amplitude was observed on the joint by comparing the envelopes. Shear strength envelope for varying frequencies was different at the first forward movement and it started to be similar from the first backward movement. However, shear strength envelope for varying amplitude was similar at the first forward movement and it started to be different from the first backward movement.

Fig. 11 [Near here]

4. Conclusions

A series of cyclic shear tests was conducted on soft synthetic rock joints. Varying load frequencies and displacement amplitudes for three different normal stresses were applied. Based on the experimental results, the following conclusions can be obtained:

1) The first peak shear stress on the joint is significantly influenced by the frequency of cyclic shear load and subsequent peaks of shear stress are largely influenced by the amplitude of displacement. Reduction in peak shear stress for higher frequency of load is greater than the reduction for lower frequency of load under cyclic movements.

2) Diminishing of asperities on the joint is equal at high frequency of shear loads under low normal stress for the both directions (forward and backward movements), i.e. shear mechanism on the joint asperities does not depend on load direction at high frequency. But at low frequency of loads, diminishing of asperities is unequal, i.e. shear mechanism depends on direction of starting cyclic shear load.

3) Low amplitude of displacement has no effect on asperities degradation under cyclic loads. Only sliding is dominating on the joint. As the amplitude rises, the diminishing of asperities increases significantly.

4) Shear mechanism and asperity diminishing is similar for the both higher amplitude of displacement and lower frequency of load at low normal stress. It is because of grater diminishing on the second slopes of asperities during cyclic movements. In consequence, failure on a rock joint is more expected in opposite to the direction of starting movement of cyclic load.

5) The joint exhibits an opposite behaviour at varying load frequencies and displacement amplitudes. Shear strength envelope for varying frequencies is different at the first forward movement and it starts to be similar from the first backward movement. Shear strength envelope

for varying amplitude is similar at the first forward movement and it starts to be different from the first backward movement.

References

Atapour H, Moosavi M (2014) The influence of shearing velocity on shear behavior of artificial joints. Rock Mech Rock Eng 47(1):1745–61. https://doi.org/10.1007/s00603-013-0481-9

Barbero M, Barla G, Zaninetti A (1996) Dynamic shear strength of rock joints subjected to impulse loading. Int J Rock Mech Min Sci 33(2):141–151. https://doi.org/10.1016/0148-9062(95)00049-6

Barla G, Barbero M, Scavia C, Zaninetti A (1990) Direct shear testing of single joints under dynamic loading. In: Barton N, Stephansson O (eds) Rock Joints, Balkema, Rotterdam, pp 447–454.

Barton N, Choubey V (1977) The shear strength of rock joints in theory and practice. Rock Mech 10(1):1–54. https://doi.org/10.1007/BF01261801

Crawford AM, Curran JH (1981) The influence of shearing velocity on the frictional resistance of rock discontinuities. Int J Rock Mech Min Sci 18(1):505–515. https://doi.org/10.1016/0148-9062(81)90514-3

Dearman WR, Baynes FJ, Irfan TY (1978) Engineering grading of weathered granite. Eng Geol 12: 345–374. https://doi.org/10.1016/0013-7952(78)90018-2

Ferrero AM, Migliazza MR, Tebaldi G (2010) Development of a new experimental apparatus for the study of the mechanical behaviour of a rock discontinuity under monotonic and cyclic loads. Rock Mech Rock Eng 43(6):685-695. https://doi.org/10.1007/s00603-010-0111-8

Gillette DR, Sture S, Ko HK, Gould M, Scott G (1983) Dynamic behavior of rock joints. Proceedings of the 24th US Symposium on Rock Mechanics, Texas, pp 163–79.

Guansheng H, Hongwen J, Yujing J, Richeng L, Jiangyu W (2020) Effect of cyclic loading on the shear behaviours of both unfilled and infilled rough rock joints under constant normal stiffness conditions. Rock Mech Rock Eng 53(1):31–57. https://doi.org/10.1007/s00603-019-01866-w

Hassani FP, Scoble M J (1985) Frictional mechanism and properties of rock discontinuities. Proceedings of the Symposium on Fundamental of Rock Joints, Bjorkliden, pp 185–196

Hencher SR (1981) Friction parameters for the design of rock slopes to withstand earthquake loading. Proceedings of the Conference in Dams and Earthquake, pp 79–87. https://doi.org/10.1680/dae.01237.0012

Homand-Etienne F, Lefeˆvre F, Belem T, Souley M (1999) Rock joints behaviour under cyclic direct shear tests. Proceedings of the 37th US Symposium on Rock Mechanics, Colorado pp 399–406

Huang X, Haimson B, Plesha ME, Qiu X (1993) An Investigation of the Mechanics of Rock Joints. Int J Rock Mech Min Sci 30(3): 257–269. https://doi.org/10.1016/0148-9062(93)92729-A

Hutson RW, Dowding CH (1990) Joint asperity degradation during cyclic shear. In J Rock Mech Min Sci 27(2):109–119. https://doi.org/10.1016/0148-9062(90)94859-R

Yang J, Cai J, Yao C, Li P, Jiang Q, Zhou C (2019) Comparative study of tunnel blast-induced vibration on tunnel surfaces and inside surrounding rock. Rock Mech Rock Eng 52(11):4747–4761. https://doi.org/10.1007/s00603-019-01875-9.

Jafari MK, Hosseini Amini K, Pellet F, Boulon M, Buzzi O (2003) Evaluation of shear strength of rock joints subjected to cyclic loading. Int J Soil Dyn Earth Eng 23(7):619–630. https://doi:10.1016/S0267-7261(03)00063-0

Jing L, Stephansson O, Nordlund E, (1993) Study of rock joints under cyclic loading conditions Rock Mech Rock Eng 26(3):215–232. https://doi.org/10.1007/BF01040116

Lee HS, Park YJ, Cho TF, You KH (2001) Influence of asperity degradation on the mechanical behavior of rough rock joints under cyclic shear loading. Int J Rock Mech Min Sci 38(7):967–980. https://doi.org/10.1016/S1365-1609(01)00060-0

Mirzaghorbanali A, Nemcik J, Aziz N (2014) Effects of shear rate on cyclic loading shear behaviour of rock joints under constant normal stiffness conditions. Rock Mech Rock Eng 47(5): 1931–1938. https://doi.org/10.1007/s00603-013-0453-0

Nemcik j, Mirzaghorbanali A, Aziz N (2013). An elasto-plastic constitutive model for rock joints under cyclic loading and constant normal stiffness. Geotech Geol Eng 32(2):321–335 https://doi.org/10.1007/s10706-013-9716-5.

Niktabar SMM, Rao KS, Shrivastava AK (2017) Effect of rock joint roughness on its cyclic shear behavior. Rock Mech Geotech Eng 9(6):1071–1084. https://doi.org/10.1016/j.jrmge.2017.09.001

Niktabar SMM, Rao KS, Shrivastava AK (2018) Automatic static and cyclic shear testing machine under constant normal stiffness boundary conditions. Geotech Testing J 41(3):508–525. https://doi.org/10.1520/GTJ20170083.

Nguyen VM (2013) Static and dynamic behaviour of joints in schistose rock. Dissertation, University of Bergakademie Freiberg

Nkpadobi JI, Raj JK, Ng TF (2015) Failure mechanisms in weathered meta-sedimentary rocks Environ Earth Sci 73:4405–4418. https://doi.org/10.1007/s12665-014-3725-4

Qiu X, Plesha ME, Huang X, Haimson B (1993) An investigation of the mechanics of rock joints. Part II—analytical investigation. Int J Rock Mech Min Sci 30:271–287. https://doi.org/10.1016/0148-9062(93)92730-E.

Richards LR (1975) Shear strength of joints in weathered rocks. Dissertation, Imperial College of Science and Technology

Ram BK, Basu A (2019) Shear behavior of unfilled-planar quartzitic rock joints with reference to weathering grade of joint surfaces. Rock Mech Rock Eng 52:4113–4121. https://doi.org/10.1007/s00603-019-01815-7.

Ramulu M, Chakraborty A, Sitharam T (2009) Damage assessment of basaltic rock mass due to repeated blasting in a railway tunnelling project—a case study. Tunn Undergr Space Technol 24(2):208–221. https://doi:10.1016/j.tust.2008.08.002

Schneider HJ (1977) The time dependence of friction of rock joints. Bull Eng Geol Environ 16:235–239.

Tang ZC, Wong LNY (2016) Influences of normal loading rate and shear velocity on the shear behavior of artificial rock joints. Rock Mech Rock Eng 49(6):2165–2172. https://doi.org/10.1007/s00603-015-0822-y

Wu XZ, Jiang YJ, Gong B, Guan ZC, Deng T (2019) Shear performance of rock joint reinforced by fully encapsulated rock bolt under cyclic loading condition. Rock Mech Rock Eng 52:2681–2690 https://doi.org/10.1007/s00603-018-1698-4.

Yan X, Xu B, Zhang L. et al. (2019) Mechanism analysis of a landslide in highly weathered volcanic rocks of Niushoushan Hill in Nanjing. Environ Earth Sci 78:676. https://doi.org/10.1007/s12665-019-8705-2

Statements and Declarations

There are no conflicts of interest to declare and we believe that the manuscript and the study, none of them violate journal's policies. All authors have seen the manuscript and they have approved its submission to your journal.

Figures

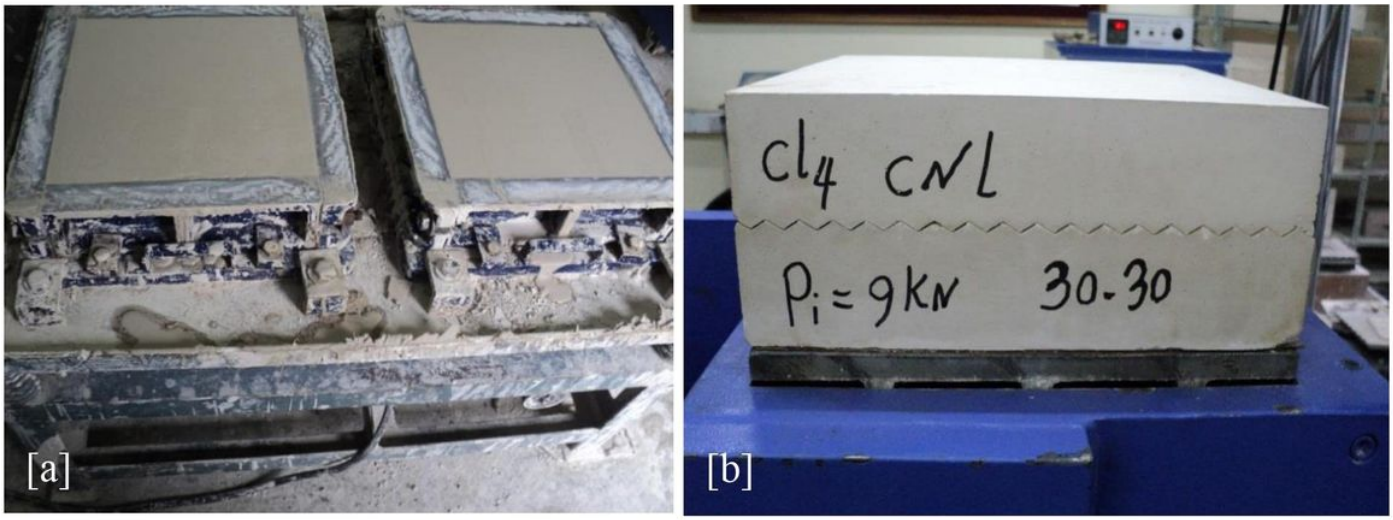


Fig. 1 Moulds fixed on the vibration table during specimen preparation (a) and prepared 30°- 30° joint asperity (b)

Figure 1

Please See image above for figure legend.

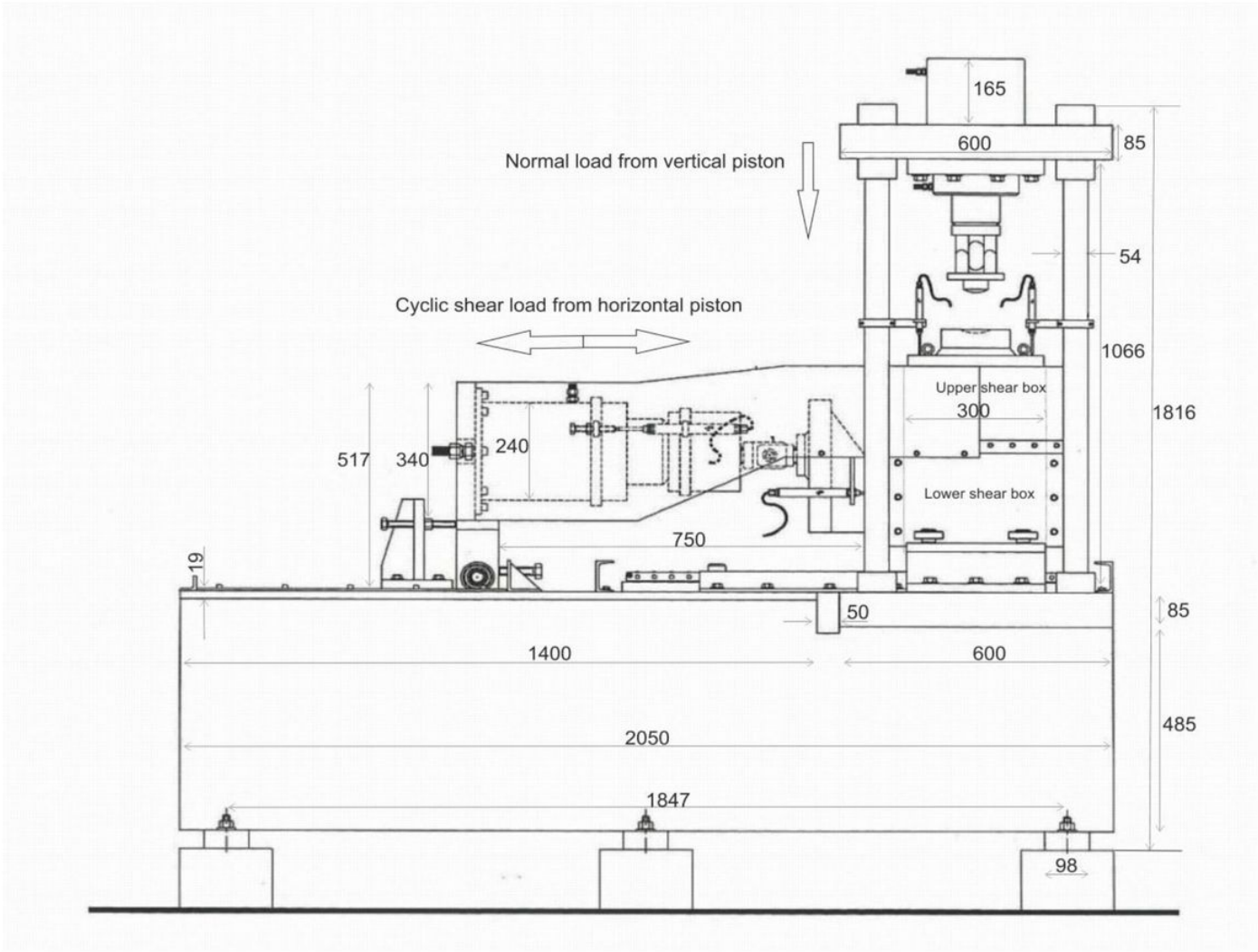


Fig. 2 Diagrams of the large scale shear testing machine (all dimensions in mm)

Figure 2

Please See image above for figure legend.

Figure 3

Please See image above for figure legend.

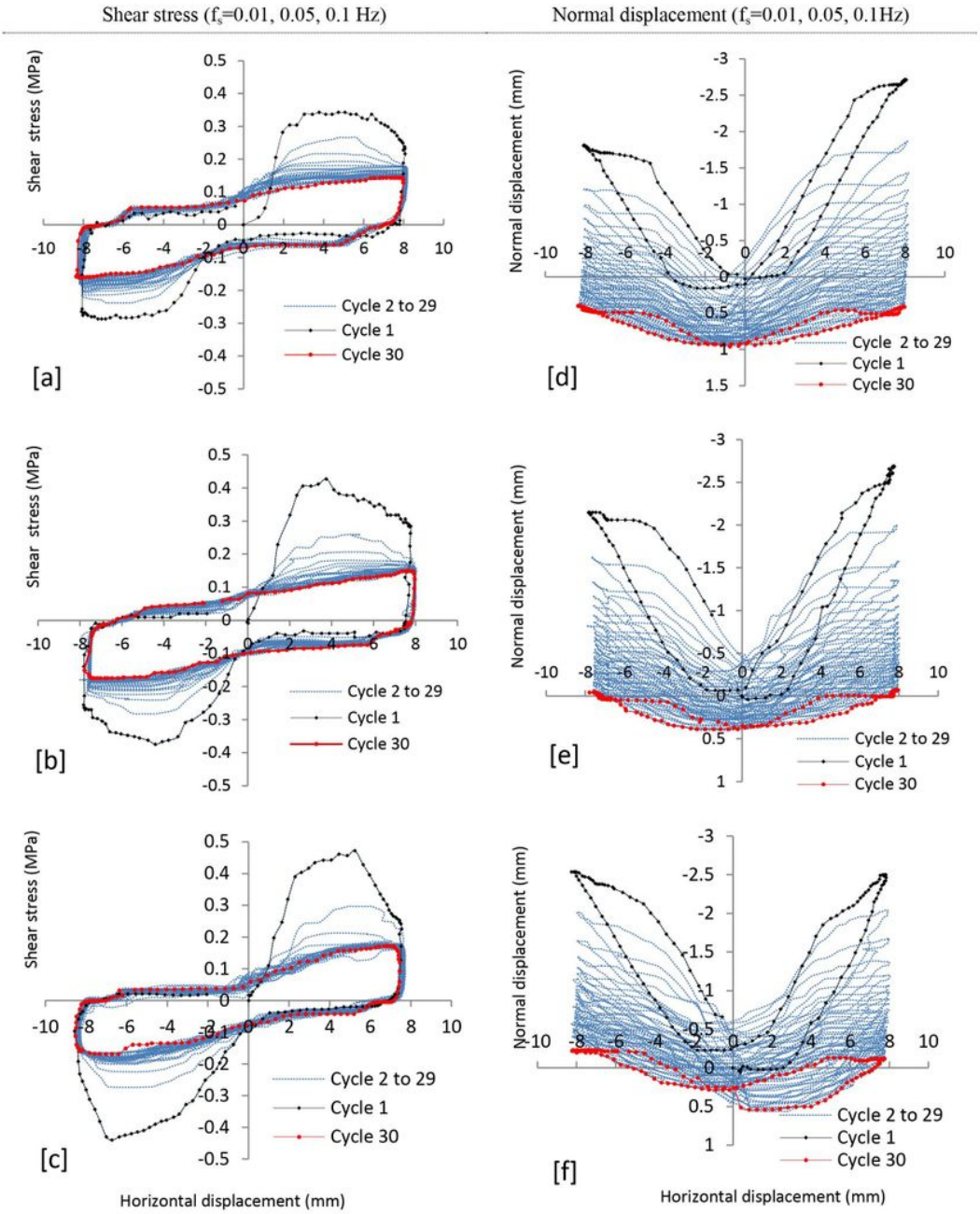


Fig. 4 Shear stress and normal displacement vs. horizontal displacement of the joint for cyclic shear load with different frequencies, f_s=0.01, 0.05 and 0.1 Hz respectively (P=0.1 MPa)

Figure 4

Please See image above for figure legend.

Figure 5

Please See image above for figure legend.

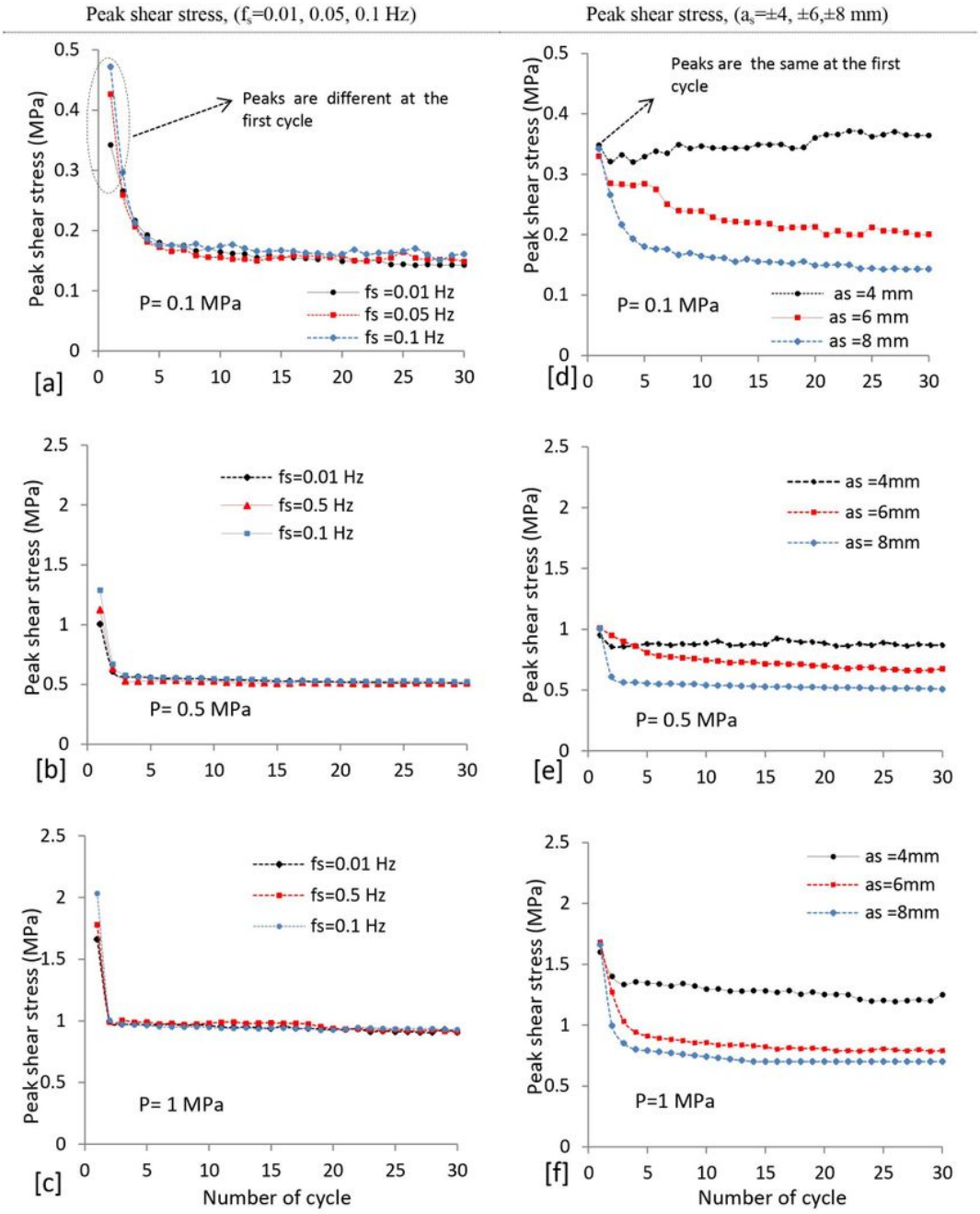


Fig. 6 Peak shear stress vs. number of cycles under varying load frequencies (f_s=0.01, 0.05, 0.1 Hz) and amplitudes of displacement (a_s=±4, ±6, ±8 mm) on the joint for P=0.1, 0.5 and 1 MPa respectively

Figure 6

Please See image above for figure legend.

Figure 7

Please See image above for figure legend.

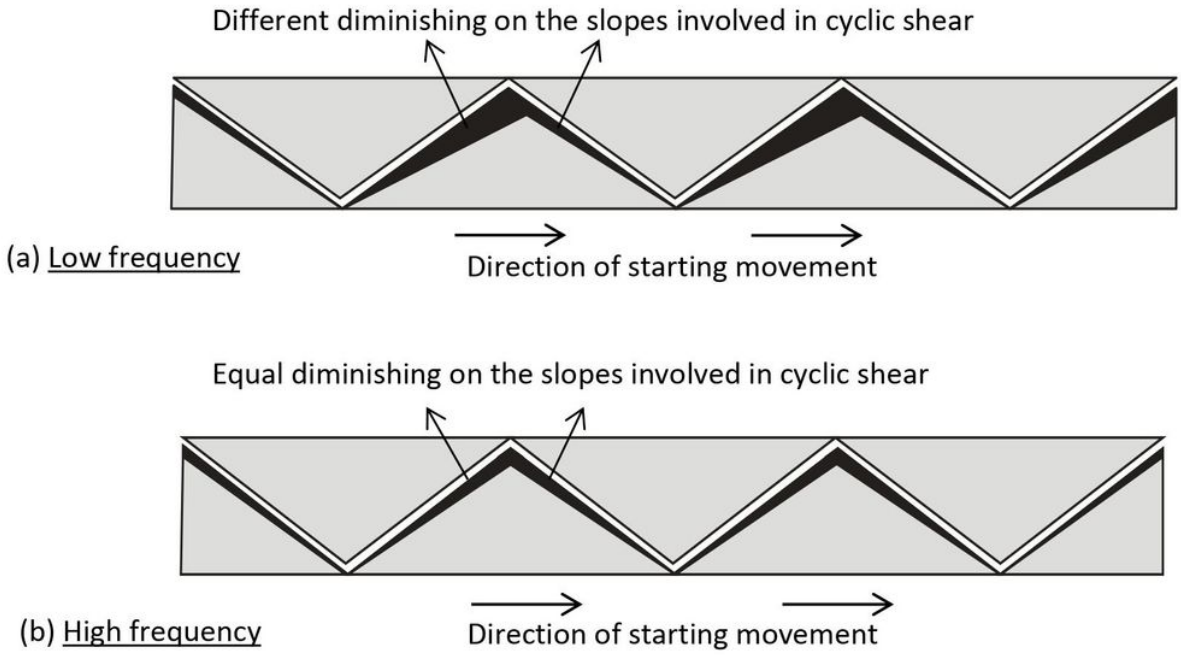


Fig. 8 Asperity diminishing on the joint for low (a) and high (b) shear load frequency under cyclic movements (P = 0.1 MPa)

Figure 8

Please See image above for figure legend.

Figure 9

Please See image above for figure legend.

Figure 10

Please See image above for figure legend.

Figure 11

Please See image above for figure legend.

Supplementary Files

This is a list of supplementary files associated with this preprint. Click to download.

- Table13.pdf
- AppendixFig.14.pdf
- AppendixFig.15.pdf
- AppendixFig.16.pdf
- Appendix.Fig12.pdf
- Appendix.Fig.13.pdf

Silicon
https://doi.org/10.1007/s12633-022-01717-4

ORIGINAL PAPER

Effect of Multipass FSP on Si-rich TIG Welded Joint of Dissimilar Aluminum Alloys AA8011-H14 and AA5083-H321: EBSD and Microstructural Evolutions

Abdellah Nait Salah[1,2] · Sipokazi Mabua[2,3] · Husain Mehdi[3,4] · Velaphi Msomi[4] · Mohammed Kaddami[4] · Prabhujit Mohapatra[4]

Received: 2 January 2022 / Accepted: 24 January 2022
© Springer Nature B.V. 2022

Abstract
In this analysis, friction stir processing (FSP) was applied to the Si rich TIG welded joint to study the influence of multi-pass FSP (MPFSP) on microstructure, hardness and tensile properties. The TIG welding defects (coarse grain structure, porosity, microvoids, and solidification cracking) were eliminated, and the grain size of the TIG welded joint was decreased. As the FSP passes increases, the coarse eutectic Mg_2Si and $Al_{13}Fe_4$ phases are converted into small phases. The coarse and elongated dendrite structure of the TIG welded joint was decreased after one FSP pass. The homogenization or modification of the primary α-Al exists in the TIG weldment was continuously improved as the TIG + FSP pass increased. The SZ of TIG + 3 pass FSP showed ultrafine grains of 3.42 µm compared to other welded specimens. The average ultimate tensile strength (UTS) of the TIG welded joint with filler ER4043 was observed to be 79.82 MPa, whereas the UTS of TIG + 1 pass FSP, TIG + 2 pass FSP, and TIG + 3 pass FSP was 97.87 MPa, 120.36 MPa, and 126.92 MPa respectively.

Keywords Friction stir processing · Tensile strength · Microstructure · Microhardness

1 Introduction

Aluminum alloys are versatile materials used in structural components, automotive parts, maritime components, and aerospace parts [1–3] because they have better formability, high toughness, good corrosion resistance and high specific strength. Furthermore, the mechanical properties of aluminum alloys can be improved by natural or artificial aging and solution treatment. There are various aluminum alloys available on the market depending upon alloying elements. These aluminum alloys possess different mechanical, electrical, and chemical properties with diverse industrial applications. Recently, AA5083, containing Al–Mg, and AA8011 containing Al–Fe, has emerged as the basic structural aluminum alloy in modern engineering applications. AA5083 is used in pressure vessels, drilling rigs, shipbuilding, railroad cars, etc., whereas AA8011 is used in transportation and construction work [4, 5]. Various nanoparticles were employed during friction stir processing to enhance the mechanical properties, microstructure, and wear behavior of the base metal [6–8]. The Al–Mg and Al–Fe-based alloys AA5083-H321 and AA8011-H14 have excellent corrosion resistance, moderate strength, and high ductility [9]. The fusion welding of aluminum alloys presents a prodigious challenge for investigators. Tungsten inert gas (TIG) welding is an appropriate technique for aluminum alloy welding, and it has wide application in various industries [10]. The defects observed in TIG welded joints are high residual stress, solidification shrinkage, coarse grain structure, aluminum oxide, and micro-cracks [11]. Various conventional/unconventional welding processes, i.e., laser-TIG hybrid welding [12, 13], laser beam welding [14], TIG welding [15], friction stir welding (FSW) [16], TIG + FSP welding [17–20],

✉ Husain Mehdi
husainmehdi4u@gmail.com

1 Faculty of Science and Technology, Laboratory "Physical Chemistry of Processes and Materials", Hassan First University of Settat, Settat, Morocco

2 Mechanical Engineering Department, Cape Peninsula University of Technology, P.O. Box 1906, Bellville 7535, South Africa

3 Department of Mechanical Engineering, Delhi Technological University, Delhi, India

4 School of Advanced Sciences, VIT University, Vellore, India

Published online: 12 February 2022

Table 1 Chemical composition of AA5083 and AA8011

BM	Si	Fe	Cu	Mn	Mg	Cr	Ti	Zn	Al
AA5083	0.139	0.153	0.010	0.649	4.339	0.040	0.011	0.013	Bal
AA8011	0.421	1.119	0.106	0.549	0.326	0.027	0.015	0.079	Bal
ER4043	5.2	0.74	0.25	0.04	0.04	0.01	0.15	0.1	Bal

have been applied to join aluminum alloys. Among these processes, the TIG welding process is commonly employed for aluminum alloys in terms of economy and utility. In TIG welding process, penetration occurs in the weldment and it may increase as the heat input increases. Due to high heat input, the coarse grains, formation of porosity, and wide heat affected zone were observed, which depreciate the UTS of the weldment. Numerous works have been published to improve the UTS and grains structure of the TIG welded aluminum alloy joints, i.e., using welding flux to rise the penetration [21], taking double side TIG welding to remove porosities, optimizing the welding process parameters [22, 23], post or preheat treatment to enhance the grain structure of the welded region [24, 25]. Conversely, in many cases, the joint efficiency of the weldment was found to be lesser than the parent material due to the unlike grain structure between the welded joints and the parent metals. The brittle interdendritic structure was observed due to re-solidification and eutectic melting of the fusion zone (FZ), which affects the hardness, ductility, and UTS [26, 27]. To remove these defects, FSW/FSP was introduced in 1991 at the Welding Institute in the U.K. by Wayne Thomas [28]. Friction stir processing (FSP) makes the material undergo severe plastic deformation, leading to a homogenous refined microstructure via stirring and frictional heat during processing [29]. During this process, a rotating tool comprising of a tool pin enters into the base plate and moves in the welding direction with constant tool rotational speed. The base metal in front of the tool pin transmits backward because linear motion and tool pin rotation are subjected to forging and extrusion under a high strain rate. Hence, the FSPed zone exhibited increased tensile properties and fatigue life of the processed region due to the enhancement of microstructure [30, 31]. There is no melting point of metal during FSP, which effectively avoids defects such as thermal cracks and porosities that are generated during the melting and solidification of the metal. FSP is a microstructure modification technique that eliminates the defects in the existing base plate and enhances the tensile properties and hardness value of the base metal. Low welding speeds with high tool rotational speeds (TRS) were used to fabricate the dissimilar aluminum alloys AA2219 and AA5083 and observed defect-free joints with 97% joint efficiency [32]. The non-heat-treatable alloy AA5083 has the highest strength, but it is not recommended for use in temperatures above 70° C. This alloy retains exceptional strength after welding compared to other aluminum alloys

Table 2 Mechanical properties of the alloys

BM	UTS (MPa)	Strain (%)	Hardness (HV)
AA5083	320.891	27.9	91.373
AA8011	93.07	39.1	31.820

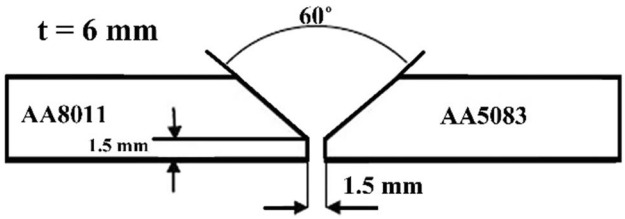


Fig. 1 Design and dimension of V groove

[33]. The tensile properties and grain structure of the dissimilar welded joints of AA8011/AA6082 were enhanced by submerging friction stir processing and results revealed that the grain size decreased compared to base metal and FSWed joints [34]. Most of the research scholars have analyzed that all these techniques enhance the material strength but decrease their ductility because large defect volumes develop after deformation, resulting in premature plastic instability and little strain hardening [35–38]. Very limited work has been done on the FSWed joints of AA5083 and AA8011. During this study, the focus was made on the effect of FSP on the tensile properties, microhardness and grain structure of the TIG welded joints.

2 Materials and Method

The aluminum alloy grades used were AA5083-H321 and AA8011-H14, with a plate thickness of 6 mm. The chemical composition and mechanical properties of the base materials were predetermined prior to the study, refer to Tables 1 and 2 respectively. The said materials were cut into dimensions of 250 × 52 mm to accommodate the bed of the FSP fixture/jig. The dissimilar cuts of the plates were prepared into a single v-groove as depicted in Fig. 1. The JavWeld pulsed TIG welding machine was used to fabricate the TIG welds. The parameters used for the TIG and TIG + FSP welding process are shown in Table 3. Three TIG- welded plates were produced, one to be kept as is and the other two to

Table 3 TIG and TIG + FSP welding parameters

Parameter	
Filler wire	AA4043
Wire diameter (mm)	2.5
Shielding gas	Argon
Welding current (Amps)	120
Gas flowrate (L/min)	25
Welding speed (mm/min)	40
Voltage (V)	35
Tool rotational speed (rpm)	1450
Too traverse speed (mm-min^{-1})	105

be used later for FSP. The fabricated TIG-welded plate is presented in Fig. 2b.

Figure 2c shows the milling machine, LAGUN FU.1-LA model, that was used for FSP. The square FSP tool was used for the processing of the TIG welds. Figure 3 show the FSP tool profile. The dimensions of the tool included a tool shoulder diameter of 20 mm, a tool pin length of 5.6 mm, and a 7 mm tool pin diameter. It should be noted that two different material positioning were taken into consideration during the FSP of the TIG welds. Figure 2e shows TIG + FSP welds. The produced TIG and TIG + FSP plates were cut for different tests, including XRD, microstructure electron backscatter diffraction (EBSD), microhardness, and tensile tests. Prior XRD chemical composition of the produced weld was analyzed using the Belec compact port. The Motic AE2000 metallurgical light optical microscope was used for microstructural examination. The grain orientation, grain size, and grain boundary structure were examined by the EBSD process. The samples for EBSD analysis were electro polished at 15 V for 35–40 s at 25 °C in a mixed solution of 30% HNO_3 + 70% CH_3OH, and then examined. The microstructure grain sizes were measured using the Image J software, adapting the line intercept method as described in the ASTME112-12 standard. Prior to the examination, the specimens were metallurgical prepared and etched using sodium hydroxide and modified Keller agents. The composition of the NaOH included the 2 g of NaOH and 100 ml of distilled water, while the modified Kellers consisted of 10 ml of HNO_3, 1.5 ml HCl, 1 ml of HF, and 87.5 ml of H_2O. The microhardness was measured using the Innova Test Falcon 500 Vickers hardness testing machine, and the ASTME384-11 standard. A mass of 0.3 kg, a 1 mm spacing between points, and a single line was used. A total of 20 indentations were measured from base metal to weld ceneter. The

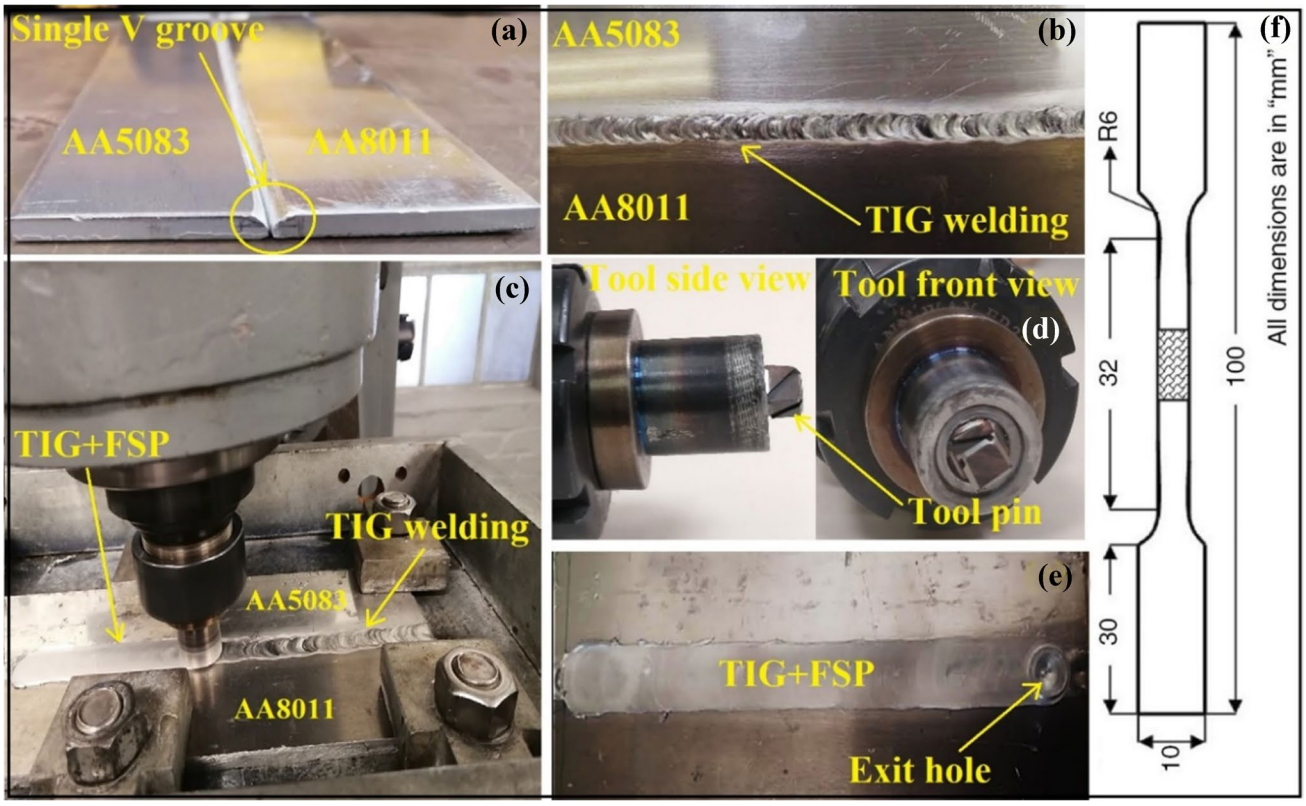


Fig. 2 Experimental process of TIG and TIG + FSP welded joints, (**a**) V groove of 60° for TIG welding, (**b**) TIG weldment with filler ER4043, (**c**) TIG + FSP process, (**d**) tool used during FSP, (**e**) TIG + FSP welded joint, (**f**) tensile sub test specimen

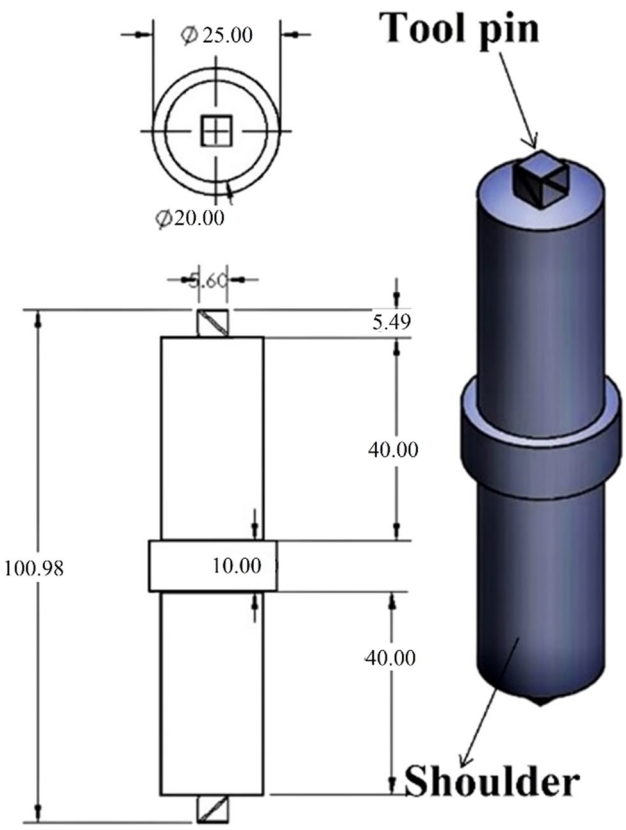


Fig. 3 Design and dimension of FSP tool

Hounsfield 50 K machine was used for tensile testing. The tensile testing was conducted with reference to the ASTM E8M-04 standard as shown in 1f.

3 Microstructural observation

3.1 Microstructural characterization of TIG and TIG + FSP welded joints

The optical images of the cross-section of the TIG weldment of AA5083 and AA8011 is shown in Fig. 4, and it was noticed that welding parameters, controlling the intermetallic distribution, and heat input have a prominent role in the broadening of grain size and partially melted zone (PMZ) [39, 40]. As the heat input increases, the size of the PMZ flares away, and the grain structure coarsens [41]. This results in poor UTS and a decrease in sample hardness in the weld fusion zone. Image J software was used to examine the grain structure of the different welded zones. The microstructure of the base metal (AA8011 and AA5083) was obtained by optical and SEM observation. The average grain size of the AA8011 and AA5083 exhibits 114 µm and 98 µm respectively (Table 4).

The microstructure of different zones of TIG-welded joints of AA5083 and AA8011 is revealed in Fig. 4, which exhibits the microstructures of the fusion zone and weld zone. The fusion zone is a semi-molten region between the HAZ and WZ that preserves severe inhomogeneity physical and chemical properties, which reveals the transition tissue i.e., discontinuous banded structure. The microstructure of HAZ was illustrated in Fig. 4c, which revealed elongated and coarse grains formed by rolling. The grains dissemination in the HAZ is non-uniform and the grains were elongated and coarsened compared to the fusion zone. Most strengthening phases in the HAZ might be reduced by re-dissolution because of the rapid cooling and high temperature during the TIG welding.

The optical macrostructure of TIG + FSP with different zones SZ, and TMAZ is illustrated in Fig. 5. The sharp interface was observed between the TMAZ and SZ on the advancing side (AS) and uncertain on the retreating side (RS), which demonstrates that the advancing side has some larger gradients of temperature and strain [42, 43]. The slop of the interface between the TMAZ and SZ was larger on the RS, which may be attributed to the different material flows on both sides [44]. The TMAZ region experienced weaker deformation, and heating effects than the SZ, and partial recrystallization and dynamic recovery took place at TMAZ. Hence, elongated deformation and equiaxed DRX grains were observed in the TMAZ region. The grain size of the TIG + 1FSP, TIG + 2FSP, and TIG + 3FSP joints at the SZ exhibits 10.85 µm, 6.95 µm, and 3.42 µm respectively, which reveals that the microstructure in the SZ may have refined for increased strain by applying the FSP. During FSP, the coarse eutectic Mg_2Si precipitates dissolved completely into the AMC, forming a stronger diverse structure than the TIG weldment of AA5083 and AA8011. Friction stir processing is comprising heat generation and intense material flow obtaining from plastic deformation and frictional heat generated between the base plate and FSP tool [45]. The SZ reveals the basin-like bottom region shown in the dotted line. The microstructure of the TIG + FSP joints exhibits a defect-free region and observed homogenous and fine grain structure in the SZ, as shown in Fig. 6b-d.

Figure 7a reveals the high magnification SEM image of the TIG-weldment at the fusion zone and observed Mg_2Si precipitates at the grain boundaries. This intermetallic compound is commonly generated in aluminum alloys. Due to grain growth caused by input heat, the average grain size of the FZ and HAZ was 19.52 µm and 24.85 µm, respectively, which was less than that of the parent metals AA5083 and AA8011. The fusion zone's microstructure was characterized by globular primary α-Al and precipitated Mg_2Si, where α particles were found along the grain boundaries. The HAZ observed a larger thermal cycle than the fusion zone experiencing lesser α-Al particles in the HAZ and few

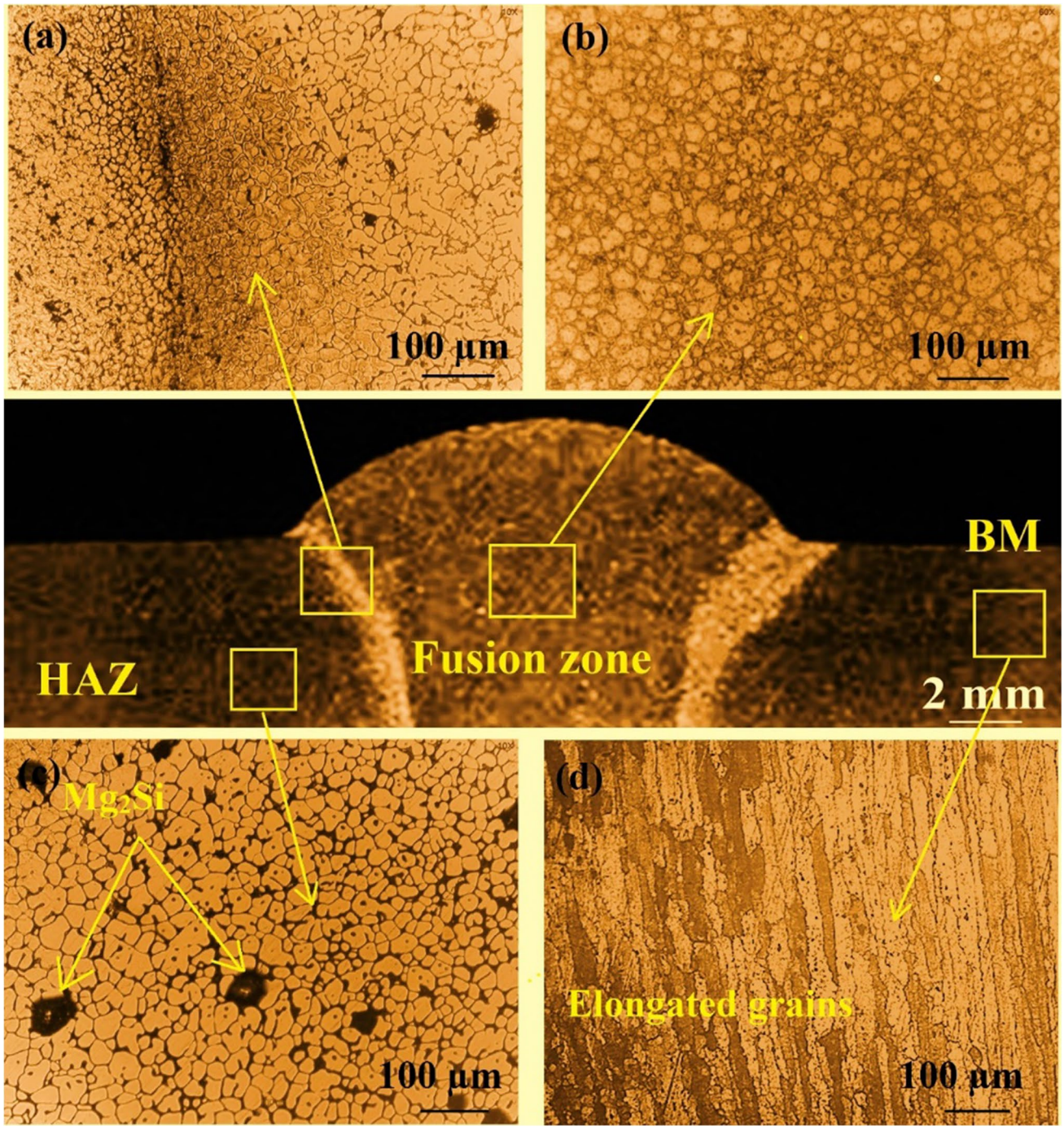


Fig. 4 TIG welded joint of AA5083 and AA8011 with filler ER4043, (**a**) different zone of TIG welding, (**b**) HAZ region, (**c**) fusion zone, (**d**) welding zone

α-particles precipitated out at grain boundary. The HAZ and fusion zone reveal different microstructures compared to base metals. Moreover, microspores of different diameters were generated in the fusion zone. The back surface was unable to be preserved by the shielding gas, whereas the top surface of the melting pool was preserved in the TIG welding process. Therefore, the air quickly entered the melting pool through the gap between the two plates. Due to the comparatively low cooling rate of the TIG welding process, hydrogen cannot have separated from the melting pool, which creates pores in the fusion zone, resulting in the formation of microfractures around the pores [46, 47].

The homogenization or modification of the primary α-Al exists in the TIG weldment of AA8011 and AA5083 was

Table 4 Mechanical properties of the TIG and TIG + FSP welded joints of AA5083 and AA8011

Materials	UTS (MPa)	Joint efficiency (%)	Strain (%)	Hardness (HV)	Grain size (μm)	Fractured location
AA5083	320.89	-	27.92	91 ± 2	98	-
AA8011	93.07	-	39.1	31 ± 3	114	-
TIG	79.82	85.76	24.95	52 ± 4	19.52	HAZ
TIG + 1 FSP pass	97.87	105.15	21.89	60 ± 2	10.85	TMAZ
TIG + 2 FSP pass	120.36	129.32	26.52	64 ± 4	6.95	Base material (AA8011)
TIG + 3 FSP pass	126.92	136.37	29.41	68 ± 3	3.42	Base material (AA8011)

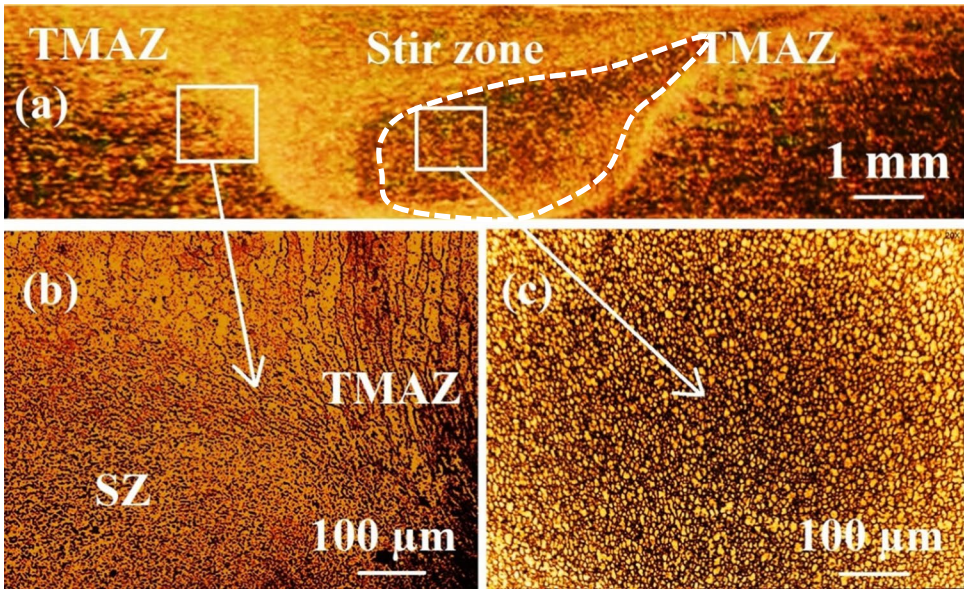


Fig. 5 Different zone of TIG + FSP welded joint

continuously improved as the TIG + FSP pass increased. The coarse and elongated dendrite structure of the TIG welded joint was decreased after one FSP pass, as shown in Fig. 7b. Due to the enhancement of material mixing and dispersion, the eutectic Mg_2Si precipitates were further decimated. The area fraction of the fine and equiaxed grains increases as the TIG + FSP pass increases, demonstrating a direct correlation between particle dispersion and FSP passes due to the reduction of eutectic Mg_2Si precipitates [48]. After the 3rd FSP pass, the coarse and elongated grain structure was completely converted into the fine and equiaxed microstructure illustrated in Fig. 7d. During multipass FSP, an incessant kind of strain was observed, leading to the breakdown of coarse and elongated grains, drastically reducing the grain size of the TIG + FSP welded joints of AA5083 and AA8011. Moreover, the MPFSP boosted the DRX mechanism and found fine grain structures [49]. A eutectic Mg_2Si precipitates with less formability than the parent material and is concerted within the grain boundaries observed in TIG welded joints (see Fig. 7a). The material flow was tough, and most precipitates remained at grain boundaries. They move near the SZ as an increment of FSP passes on the TIG weldment, observing more uniform dissemination and fewer clusters of eutectic Mg_2Si precipitates (Fig. 7b-d).

3.2 EDX analysis of TIG and TIG + FSP welded joints

Figure 8 reveals the energy-dispersive x-ray spectroscopy (EDX) of TIG-weldment of AA5083 and AA8011, and TIG + 3 pass FSP, where the atomic percentages of aluminum and silicon in the SZ and fusion zone were higher than the other elements. In TIG weldment, the percentage of Al is highest (91.82), Si is second highest (4.25%), and Mg is the third highest (3.12%). The alloying elements were uniformly diffused in TIG + 3pass FSP at the SZ. The alloying elements Mg, and Si generates the precipitates, and this precipitation intensity disseminated after one pass FSP, which enhanced the mechanical properties of the processed zone [50], the XRD study is shown in Fig. 11 verified this finding. The EDX was used in map scanning mode on the marked area of TIG and TIG + FSP weldment illustrated in Figs. 9 and 10 to analyze the distribution of the elements between

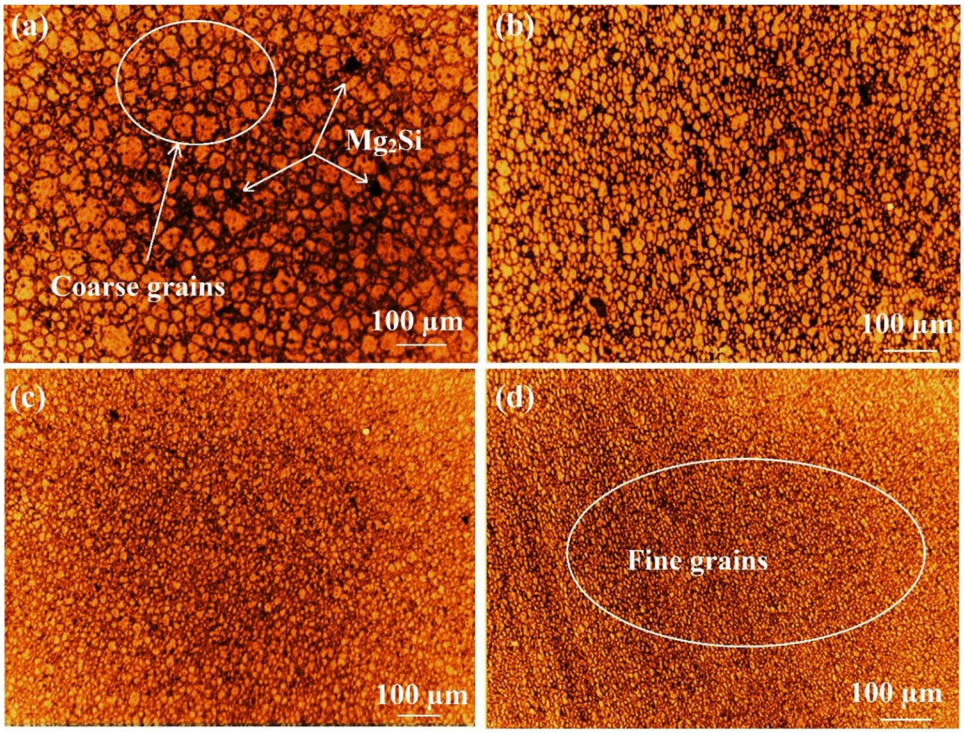


Fig. 6 TIG + FSP welded joint of AA5083 and AA8011, **a** HAZ of TIG + 1 FSP, **b** SZ of TIG + 1FSP, **c** SZ of TIG + 2FSP, **d** SZ of TIG + 3FSP

the different locations. In the fusion zone and the SZ, the primary elements are distributed. The aluminum content on the grain boundaries is lower than that within the grains. Figure 10 reveals that major alloying elements were more evenly disseminated in the SZ after the 3rd pass FSP compared to the TIG weldment.

3.3 XRD analysis

XRD (BRUKER D8 ADVANCE) was employed to phase identify the TIG and TIG + FSP welded joints Cukα radiation at 1.518 Å, illustrated in Fig. 11. Due to the unique d-spacing for each material, the conversion of the diffraction peaks to d spacing allows for the identification of the metal. The XRD peak of Mg_2Si revealed the disparately visible that confirmed the successful fabrication of TIG, and TIG + FSP welded joint with filler ER4043. The considerable presence of peaks corresponding to any other compound (except Al, Si, Mg_2Si, and $Al_{13}Fe_4$) was not observed in the XRD diagram, which showed the thermodynamic stability of Mg2Si, $Al_{13}Fe_4$. The phase identification of the TIG and TIG + FSP welded joints of AA5083 and AA8011 is illustrated in Fig. 11. Four major phases (Al, Si, Mg_2Si, and $Al_{13}Fe_4$) were detected in welded joints. The intensity of Mg_2Si, $Al_{13}Fe_4$ was reduced as the FSP pass increased from 1 to 3 passes. The penetration depth of TIG and TIG + FSP welded joints were evaluated by $\tau = \cos\psi 2\ \mu.\ \mathrm{Sin}\theta$ [51], where θ is the Bragg peak, μ is the coefficient of linear absorption, ψ is the tilt angle, and τ is the depth of mean penetration. The hardness values of the TIG + FSPed zone was influenced by strain hardening, precipitate formation, and boundary energy [52]. Figure 11 reveals no unfavorable reaction ensues between the dissimilar aluminum alloys AA5083 and AA8011. The phase intensity decreases as the FSP pass increases [53]. As the FSP passes increases, the coarse eutectic Mg_2Si and $Al_{13}Fe_4$ phases are converted into small phases. The microstructure of the TIG + FSP region enhanced the variation of temperature in the stir zone, which improved the UTS. The effect of grain size on the precipitates, dislocation density, and solid solution was insignificant [54, 55]. Precipitate advancement comprises the dissolution, coarsening, and nucleation of the precipitate. In the FSP region, magnesium and silicon form strong precipitates of Mg_2Si, due to the precipitate of Mg_2Si. The TIG + FSP's hardness depends on the precipitate formation, strain hardening, and boundary energy.

The nucleation rate can be calculated as [56].

$$I = I0\exp\left[-\left(\frac{A_0}{RT}\right)^3\left(\frac{1}{\ln\overline{C}/C_e}\right)^2\right]\exp\left(-\frac{Q_d}{RT}\right) \quad (1)$$

The dissolution of precipitates may be written as

$$v = \frac{\overline{C} - C_i D}{C_p - C_i r} \quad (2)$$

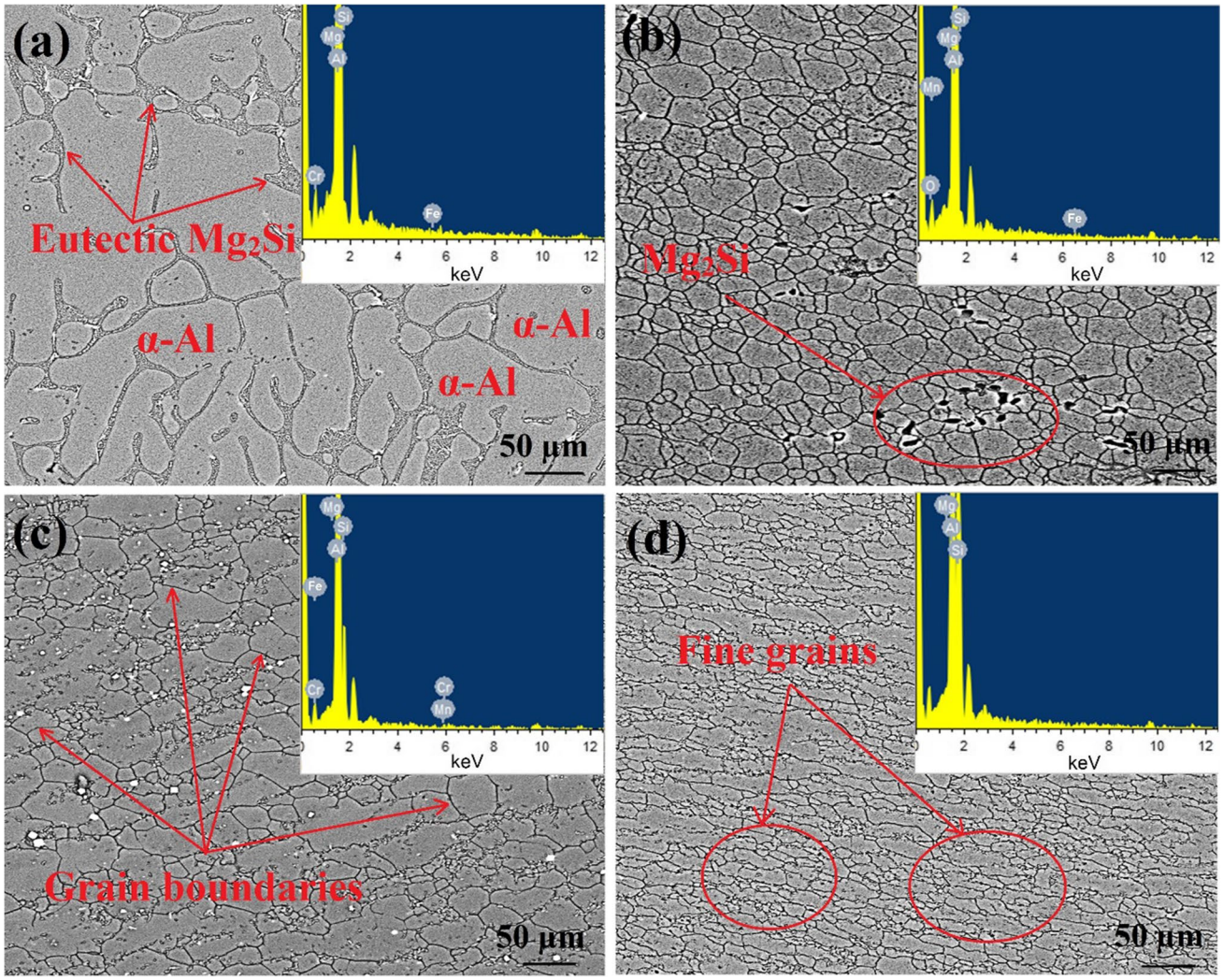


Fig. 7 SEM images of TIG and TIG + FSP welded joint, (**a**) TIG welded joint, (**b**) SZ of TIG + 1FSP, (**c**) SZ of TIG + 2FSP, (**d**) SZ of TIG + 3FSP

C_i can be calculated as following [57].

$$C_i = C_e \exp\left(\frac{2\gamma V_m}{rRT}\right) \tag{3}$$

The involvement to the yield strength (YS) from the hardening precipitates can be written as

$$\sigma_P = \frac{M}{b\bar{r}}\left(2\beta Gb^2\right)^{-1/2}\left(\frac{3f}{2\pi}\right)^{1/2}\left(\frac{\sum_i N_i F_i}{\sum_i N_i}\right)^{3/2} \tag{4}$$

$$F_i = 2\beta Gb^2\left(\frac{r_i}{r_c}\right) \tag{5}$$

When $r_i = r_c$ then $F_i = 2\beta Gb^2$
So, the YS can be evaluated as

$$\sigma_{ss} = k_{Fe}C_{Cu}{}^{2/3} + k_{Si}C_{Si}{}^{2/3} + k_{Mg}C_{Mg}{}^{2/3} \tag{6}$$

where.

R	8.314 J/K/mol.
Q_d	130kJ/mol.
A_0	Energy barrier for nucleation (16.22 kJ/mol).
r	Particle radius.
C_p	Concentration of element.
I_0	9.66×10^{34} s/m^3.
C_i	Concentration of solute.
Q_d	130 kJ/mol.
$\bar{r}$	Mean particle radius.
M	3.1 (Taylor factor).
b	2.84×10^{-10}.
Vm	3.95×10^{-5} m^3/mol.
k_{Mg}	Concentration of Mg.

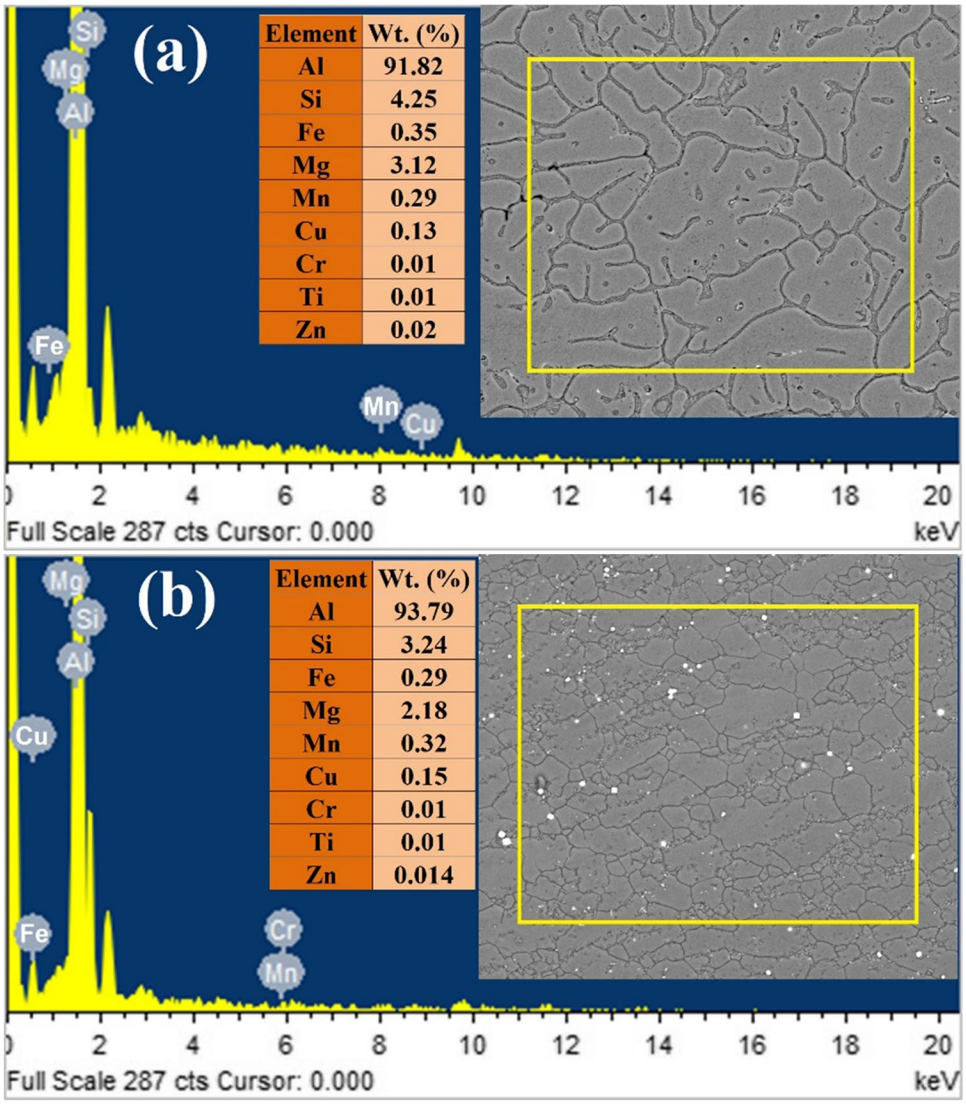


Fig. 8 EDS analysis, (**a**) TIG welded joint, (**b**) TIG + FSP welded joint

γ	Particle interface energy (0.2).
C_e	Equilibrium solute content in the matrix.
D	Diffusion coefficient.
C_{Cu}	Scaling factor of Cu.
F_i	Particle radius' function.
r_i	Particle radius.
$\bar{C}$	Mean solute content in the matrix.
N_i	Density number of the particles.
k_{Si}	Concentration of Si.
C_{Si}	Scaling factor of Si.
f	Volume fraction.
G	2.7×10^{-10} N/m^3.
β	Dissolution line tension (0.36).
C_{Mg}	Scaling factor of Mg.
k_{Cu}	Concentration of Cu.
r_c	Critical radius.

3.4 EBSD analysis of TIG and TIG + FSP welded joints

Figure 12 represents the EBSD diagram of the TIG and TIG+FSP weldments of AA5083 and A8011. The grain colors demonstrate the various grain orientations and crystallographic axes. The high angle grain boundaries (3-15°) and low angle grain boundaries (less than 15°) were marked in red and yellow color in the EBSD map. During FSP, the material flows in different fashions on the RS and the AS [58, 59]. The microstructure of the SZ was found systematically at the center and on the RS (3 mm from the center) and AS (3 mm from the center) sides. The transition from the AZ to the parent material through TMAZ and HAZ was also observed. The MPFSP refined the grain size of the TIG weldment. The amount of grain refinement is very significant, and the final grain size after FSP depends on the tool

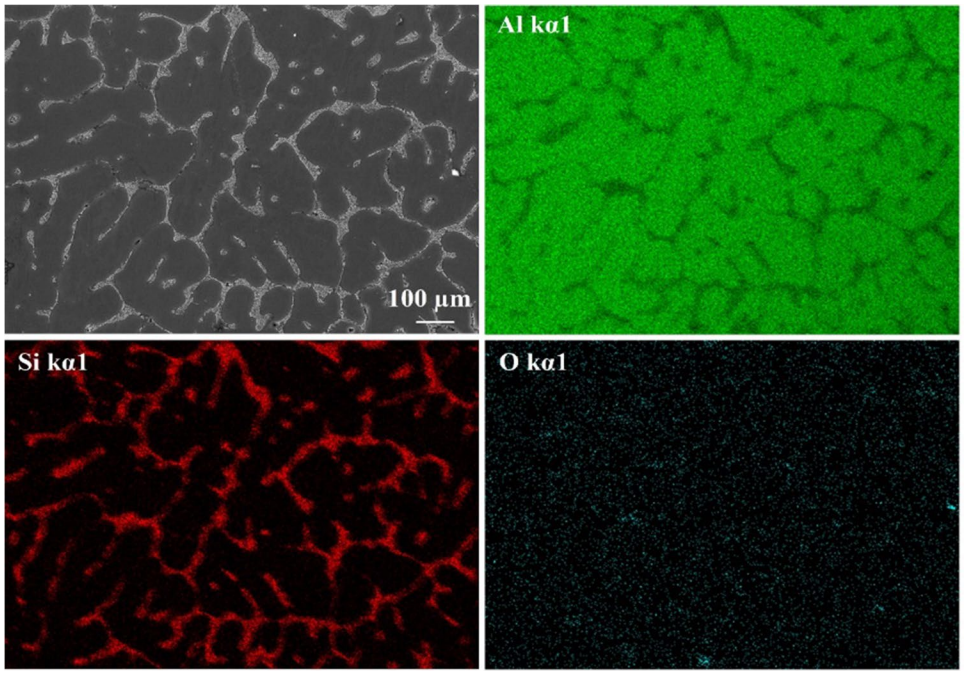


Fig. 9 Elemental mapping of TIG welded joint

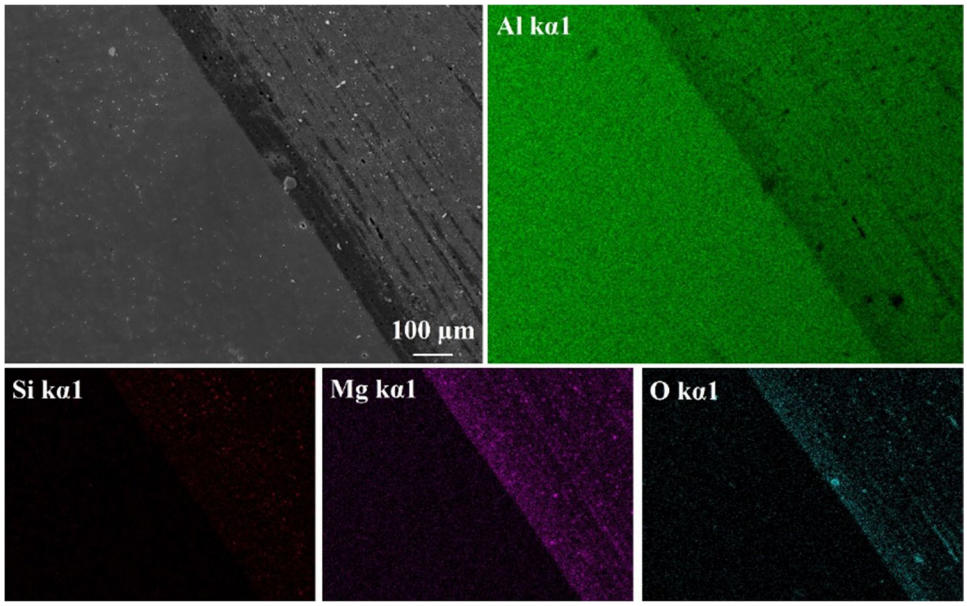


Fig. 10 Elemental mapping of TIG + FSP welded joint

geometry and processing parameters rather than the grain refinement occurring by the DRX. Apart from the coarse and inhomogeneous structure of the TIG welded joint, progressive DRX was observed as the FSP pass increased from one to three. The uniform color mixing in the TIG+FSP reveals the grain refinement, effective inter-metal mixing, and particle distribution. The microstructure modification and degree of grain reduction during TIG+FSP include acceleration flow, material preheating, deceleration flow, and high-velocity flow, which were attributed to continuous and discontinuous DRX, respectively [60, 61]. During deceleration, strain reversal induced grain modification was promoted. Figure 12b-d reveals the grain dissemination from the EBSD map of the TIG + FSP welded joint. As the FSP increased, the TIG+FSP composite's grain size was changed to be assisted by particle-induced pinning. The TIG+FSP welded joints observed higher DRX; this occurrence was attributed to the growth of the different nucleation sites and consequently decreasing the grain size within the SZ [62]. A frictional temperature of 0.55 to 0.75 times the melting point was observed for FSP composites for all the specimens. The temperature variation of each zone is shown

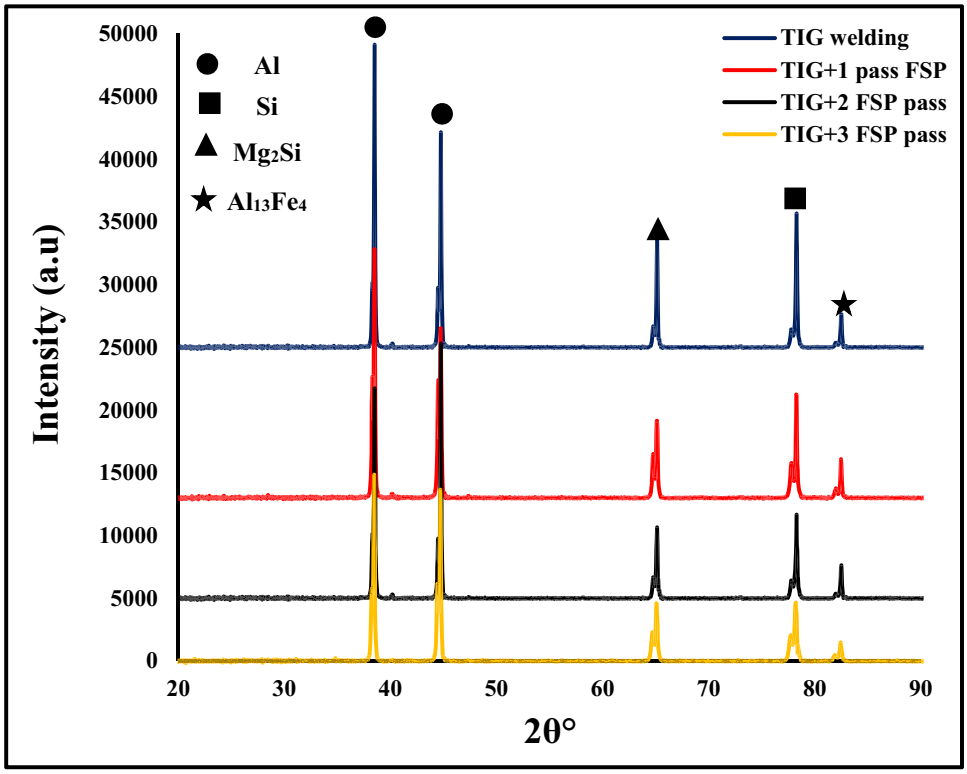


Fig. 11 XRD analysis of TIG and TIG + FSP welded joints of AA5083 and AA8011

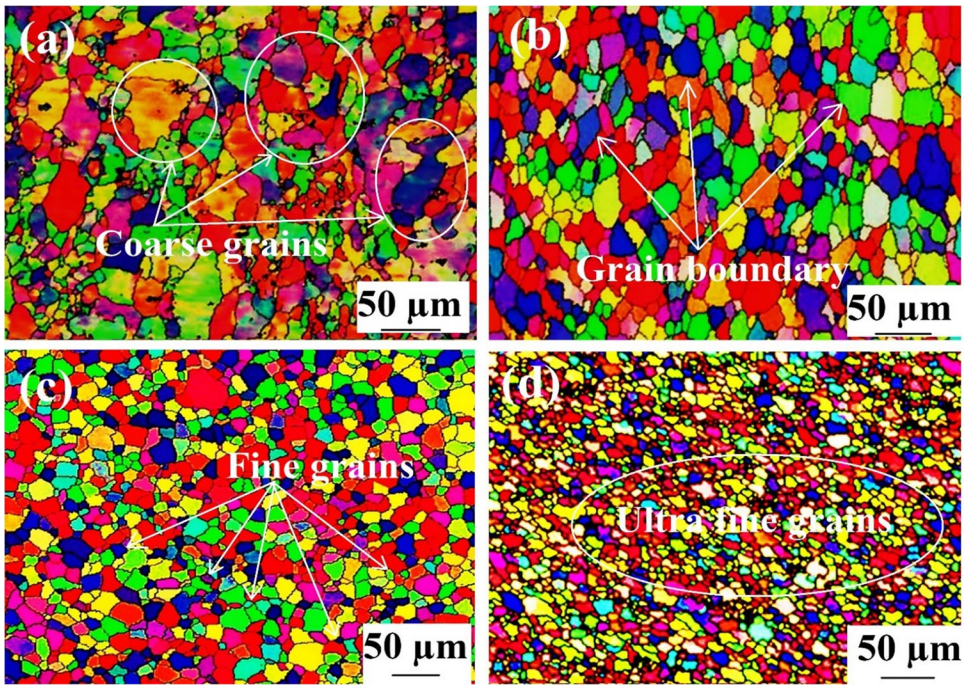


Fig. 12 EBSD image of welded joints of AA5083 and AA8011, (**a**) TIG welded joint, (**b**) TIG + 1pass FSP, (**c**) TIG + 2pass FSP, (**d**) TIG + 3pass FSP

in Table 5. Average grain size of 10.85 µm was observed in a single FSP pass that generates the fine and equiaxed grain structures illustrated in Fig. 12a. As the FSP passes increase, the grain modification occurs, and we observe an average grain size of 6.95 µm and 3.42 µm after 2 passes and 3 passes, respectively. The fine and equiaxed grain size of the composite MPFSP is correlated to DRX, followed by grain growth. The interaction between dislocations and reinforcement particles may lead to a higher density of stored dislocations [63, 64]. The fine grains contain a large

Table 5 Temperature ranges of TIG + FSP at different zones

Position	AA8011		SZ	AA5083	
	HAZ	TMAZ		TMAZ	HAZ
Temperature range (°C)	355–370	390–415	430–445	405–425	375–390

fraction of HAGBs, which reveals that a high fraction of LAGBs in the base metal was converted into HAGBs after FSP. The precipitation sequence in aluminum alloys was observed during MPFSP [27, 65]. The maximum grain size of the TIG + FSP weldment is about 1.5 to 2.5 times larger than the average grain size. The average grain size of the TIG+1 pass FSP, TIG+2 pass FSP, and TIG+3 pass FSP was around 10.85 µm, 6.95 µm, and 3.42 µm respectively. During TIG+FSP, severe plastic deformation and high temperatures will support the DRX [66]. Since HAGBs are more stable than LAGBs in AMCs, a high proportion of the HAGBs could contribute to the thermal stability of the TIG+FSP welded joints.

3.5 Tensile strength

The UTS of TIG and TIG + FSP welded joints of AA5083 and AA8011 was analyzed by universal testing machine. The fracture in the TIG weldments occurred in the HAZ because this region is the weakest among all zones. The TIG + 1 FSP pass specimen fractured at the TMAZ region, whereas the TIG + 2 FSP pass and TIG + 3 FSP pass specimens fractured at the base metal (AA8011), an indication of the increased UTS of the TIG + FSP joints due to the lack of a low hardiness region and the strengthened SZ. To investigate the exact UTS of the TIG + FSP weldment, the tensile specimens were cut along the FSP direction. The stress–strain diagram of the different processes reveals in Fig. 13.

The equiaxed and fine-grain structures with a large fraction of HAGBs obtained by TIG+FSP welded joints have a momentous influence on the UTS. The enhancement of the UTS of TIG+ FSP was primarily attributed to the significant grain modification. Furthermore, an enormous HAGBs fraction illustrates that enormous misorientation exists between the neighboring grains, which offers additional obstruction and increases the resistance against grain boundaries interrupted by dislocation, resulting in grain boundary strengthening [67, 68]. Moreover, the 2nd phase crystals with homogenous dissemination act as dominant barriers to dislocation motion, increasing the TIG+FSP region's UTS [69]. The grain refinement helps to enhance the compatibility of neighboring grains and thus improves the percentage strain. The uniform dissemination of the fine 2nd phase crystals was responsible for the enhancement of the percentage strain. The base metal (AA5083 and AA8011) exhibits a UTS of 320.89 MPa and 93.07 MPa, while the % strain is 27.9 and 39.1 respectively. Due to welding defects and coarse grain structure in the FZ, the TIG welded joints reveal a minimum UTS of 79.82 MPa. After FSP on TIG weldment, the UTS and % strain increased. A maximum UTS of 126.92 MPa was observed in TIG+3pass FSP illustrated in Table 4. Due to the significant grain refinement and

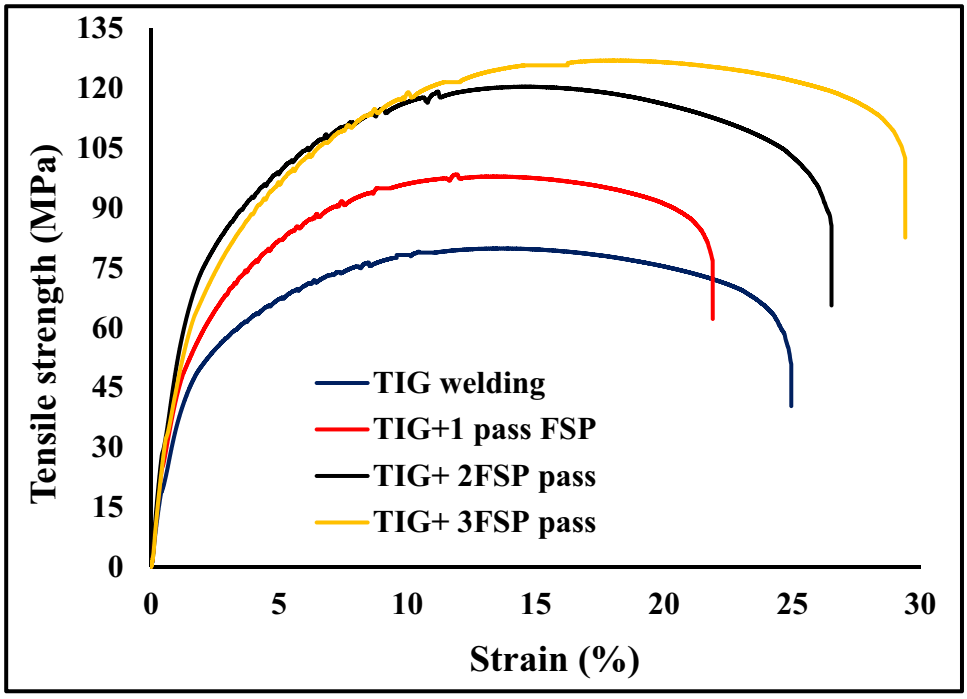


Fig. 13 Stress strain diagram of TIG and TIG + FSP welded joint of AA5083 and AA8011

dissolution of coarse Mg_2Si, and $Al_{13}Fe_4$ phases. Moreover, the dissolution of coarse Mg_2Si and $Al_{13}Fe_4$ phases can significantly decrease the crack's growth rate and enhance the ductility of TIG+FSP welded joints.

3.6 Microhardness of TIG and TIG + FSP welded joints

The hardness distribution profile of TIG and TIG+FSP weldments of AA5083 and AA8011 is illustrated in Fig. 14. The microhardness variation may be related to the microstructure of the welded region. The variations in the hardness values show the non-uniformity of grain structures. The grain structure or grain size may be the dominating factor in determining the hardness value, but it is not the only one. Temperature distribution, strain rate, and particle density seem to affect the hardness of the welded region [70]. The decrease in temperature causes an increase in strain hardening. As a result, smaller grain size, as well as strain rate at low temperature-induced strain hardening of the TIG+FSP, welded joints. In TIG welded joints, the HAZ region exhibits the lowest hardness due to the combined mixture of ER4043 and base metal in the TIG welded region. The hardness distribution pattern for TIG + FSP welded joints was similar to that of TIG-welded joints but different from that of TIG-welded joints. The inhomogeneity of microhardness in the SZ is due to inadequate material flow engendered by the FSP tool [71]. As per the Hall-Petch correlation, the fine grain structure was observed to have a higher hardness at room temperature. A large fluctuation was seen in the TIG weldments compared to the TIG + FSP welded joints. This is due to the TIG joints' being composed of coarse Mg_2Si and $Al_{13}Fe_4$ precipitating intermetallic phases. The α-Al phase weaker than the Mg_2Si, and $Al_{13}Fe_4$ phases, has an enormous volume fraction. The hardness value would be lower if the indenter was placed near the primary α-Al phase rather than the Mg_2Si phase in the opposite condition, the hardness value was observed to be high.

The hardness value of the TIG weldment was lower than the TIG+FSP weldments. The average hardness value of TIG weldment at the FZ was observed to be 52 HV, whereas the hardness value at the SZ of TIG + FSP welded joints of 1 pass, 2 passes, and 3 passes were found to be 60.3 HV, 64.8 HV, and 68 HV, respectively. Along with grain coarsening, the strengthening phase coarsens and partially dissolves in the HAZ, resulting in a steady fall in hardness in the HAZ. Most precipitates were found to dissolve in the TMAZ region [72]. With the Sharpe grain size gradient and high-stress concentration, the occurrence of the worst tensile properties was observed in the TMAZ region. The fracture at the TMAZ region can have occurred due to the heat effect, non-uniform microstructure, and distortion. It was also found that the dissolution and defects of the precipitate were created by inadequate heat input, which had a deleterious effect on the performance of welded joints [73]. So, the TIG+FSP welded joint with the finest tensile properties was observed with adequate heat input with the 3rd FSP pass.

3.7 Fractography

The fracture surface of the TIG and TIG + FSP welded joints (Fig. 15) of AA5083 and AA8011 was analyzed under SEM. In tensile specimens, the shear plane of 45° (approximately) to the tensile axis is observed along the peripheral of the test specimens [74, 75]. The cup cone fracture was observed in the TIG + FSP welded joints. The fracture surface of TIG and TIG + FSP welded joints characterized by the cleavage facets, tear ridges, deep dimples

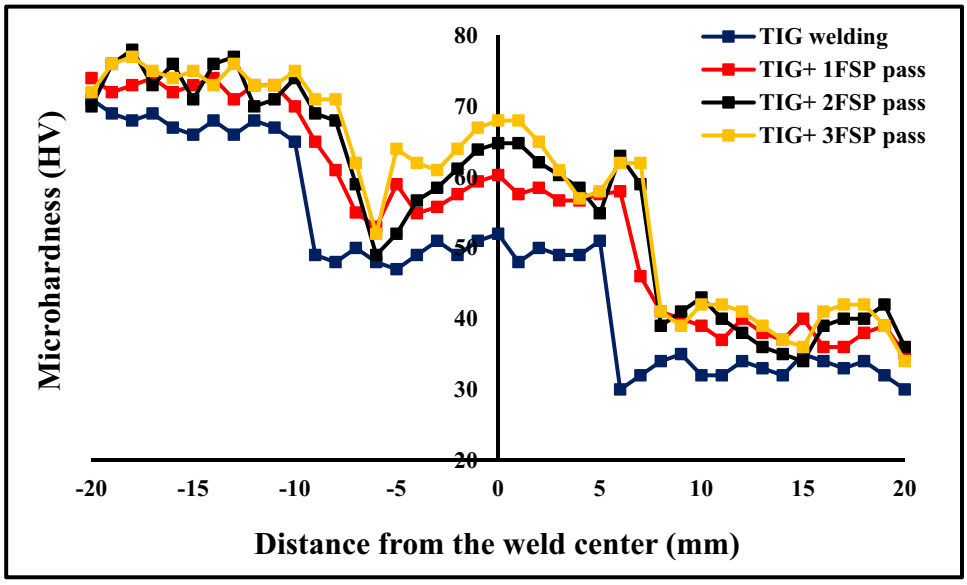


Fig. 14 Hardness distribution profile of TIG and TIG + FSP welded joints of AA5083 and AA8011

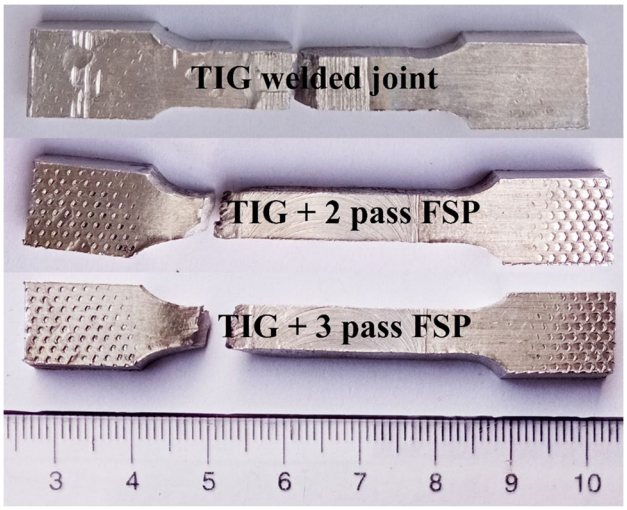


Fig. 15 Fractured specimens of TIG and TIG + FSP

and ductile dimples as shown in Fig. 16. TIG welded joint consisted deep dimples resulting from the microvoids coalescence with cleavage facets. The large area of fine and ductile dimples was observed in the TIG + 3 pass FSP, whereas ductile dimples with tear ridge, and cleavage facets was observed in the TIG + 1 pass FSP and 2 pass FSP. In TIG + 1 pass FSP, the particles were redistributed and refined. Because the redistribution removes the dendritic structure to a greater extent, inter-dendritic crack propagation was prevented and the cracks were disseminated through the aluminum base. The heat input and the TRS were observed to have a linear correlation, which affects the joint's efficiency. When the TRS increases, heat input also increases, which influences the grain size of SZ. However, as the heat input increased, the grain size of the HAZ also increased, resulting in a reduction in tensile properties. This phenomenon encouraged the fracture to occur in the HAZ region in TIG + 1 pass FSP [76, 77]. Meanwhile, the aluminum base zone was ductile. The dissemination of cracks through the aluminum base led to improved ductility. This leads to the formation of micro dimples in the ruptured surface was observed in the TIG + FSP welded joints shown in Fig. 16. The ruptured interface with cleavage and dimples was the foremost reason for the fraction. Figure 16 reveals a network of fine dimples in TIG + 2 pass FSP and TIG + 3 pass FSP, indicating a ductile failure. Conversely, a distinct difference in the size of the dimples may be observed between the TIG and TIG + FSP welded joints. Large voids and dimples were easily visible in the TIG welded joint shown in Fig. 16a, whereas fine and more uniform-sized dimples in the TIG + 3 pass FSP were observed as compared to the TIG welded joint.

4 Conclusions

The tensile properties and microstructural evaluation of TIG and TIG + FSP of dissimilar aluminum alloys of AA8011 and AA5083 were successfully carried out and the following conclusions were made.

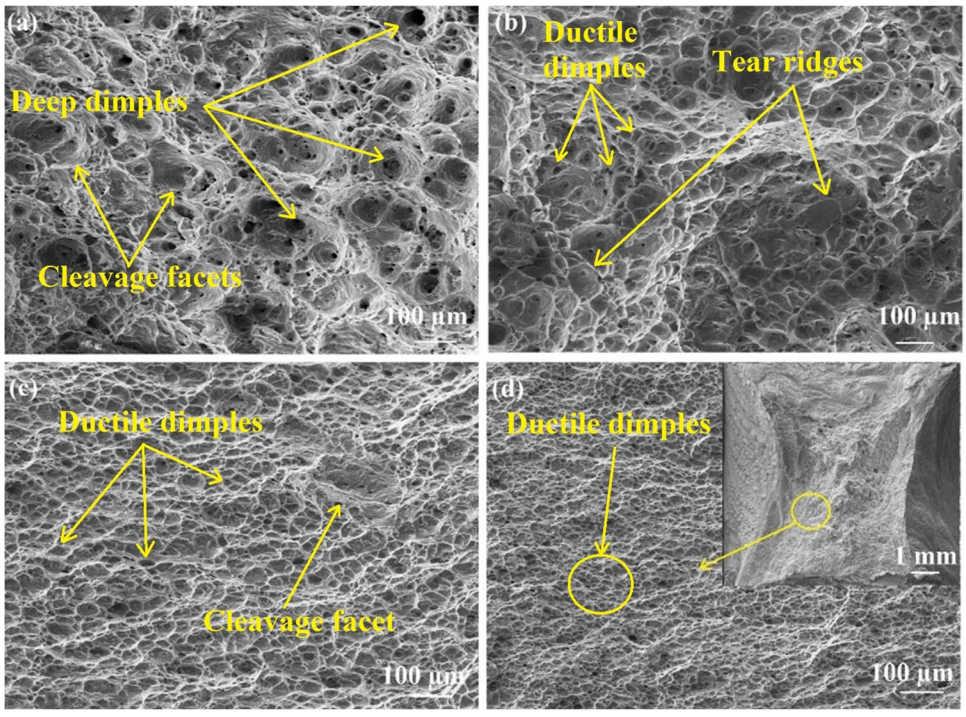


Fig. 16 Fractography images of welded joint of AA5083 and AA8011, (**a**) TIG welded joint, (**b**) TIG + 1pass FSP, (**c**) TIG + 2pass FSP, (**d**) TIG + 3pass FSP

- The multipass FSP was employed on Si-rich TIG welded joint of AA5083 and AA8011. The TIG welding defects were eliminated, and the grain size of the TIG welded joint was decreased. As the FSP passes increases, the coarse eutectic Mg_2Si and $Al_{13}Fe_4$ phases are converted into small phases.
- The homogenization or modification of the primary α-Al exists in the TIG weldment was continuously improved as the TIG + FSP pass increased. The coarse and elongated dendrite structure of the TIG welded joint was decreased as the FSP passes increased.
- Due to the enhancement of material mixing and dispersion, the eutectic Mg_2Si precipitates were further decimated. The TIG + FSP welded joints observed higher DRX; this occurrence was attributed to the growth of the different nucleation sites and consequently decreasing the grain size within the SZ.
- The fine and equiaxed grain size of the composite MPFSP is correlated to DRX, followed by grain growth. The interaction between dislocations and reinforcement particles may lead to a higher density of stored dislocations. The fine grains contain a large fraction of HAGBs, which reveals that a high fraction of LAGBs in the base metal was converted into HAGBs after FSP.
- The average UTS of the TIG welded joint with filler ER4043 was observed to be 79.82 MPa, whereas the UTS of TIG + 1 pass FSP, TIG + 2 pass FSP, and TIG + 3 pass FSP was 97.87 MPa, 120.36 MPa, and 126.92 MPa respectively. The average grain size of the TIG + 1 pass FSP, TIG + 2 pass FSP, and TIG + 3 pass FSP was around 10.85 µm, 6.95 µm, and 3.42 µm respectively.
- During TIG + FSP, severe plastic deformation and high temperatures will support the DRX. Since HAGBs are more stable than LAGBs in AMCs, a high proportion of the HAGBs could contribute to the thermal stability of the TIG + FSP welded joints.

Acknowledgements The authors would like to express heartfelt thanks to Department of Mechanical engineering, Cape Peninsula University of Technology, South Africa for providing the experimental setup and their corresponding labs for supporting this work.

Author contributions Abdellah Nait Salah: Data curation, Writing-original draft preparation.

Sipokazi Mabua, and Velaphi Msomi: Conceived and planned the experiments, and carried out the experiments.

Husain Mehdi: Paper writing, and reviewing.

Mohammed Kaddami: Reviewing and editing.

Prabhujit Mohapatra: Editing and Visualization.

Data Availability Not applicable.

Declarations

Conflict of Interest Authors declare no conflict of interest.

Compliance with ethical standards The authors have declared that no competing interests exist.

Consent to participate Not applicable.

Consent for Publication Not applicable.

References

1. Mishra RS, Ma ZY, Charit I (2003) Friction stir processing: a novel technique for fabrication of surface composite. Mater. Sci. Eng. A 341(1–2):307–310
2. Husain M, Mishra RS (2021) Effect of multi-pass friction stir processing and SiC nanoparticles on microstructure and mechanical properties of AA6082-T6. Adv Ind Manuf Eng 3:100062. https://doi.org/10.1016/j.aime.2021.100062
3. Husain Mehdi, R.S. Mishra, Study of the influence of friction stir processing on tungsten inert gas welding of different aluminum alloy. SN Appl. Sci. 1, 712 (2019). https://doi.org/10.1007/s42452-019-0712-00.
4. Fayomi J, Popoola API, Popoola OM, Fayomi OSI, Ajenifuja E (2021) Response evaluation of AA8011 with nano ZrB2 inclusion for multifunctional applications: Considering its thermal, electrical, and corrosion properties. Journal of Alloys and Compounds 853:157197
5. Huang Chuanjun, Zhixiong Wu, Huang Rongjin, Wang Wei, Li Laifeng (2017) Mechanical properties of AA5083 in different tempers at low temperatures. IOP Conf. Series: Materials Science and Engineering 279:012002
6. Saini N, Pandey C (2018) Dheerendra Kumar Dwivedi, Ductilizing of cast hypereutectic Al–17%Si alloy by friction stir processing. Proceedings of the Institution of Mechanical Engineers, Part E: Journal of Process Mechanical Engineering 232(6):696–701
7. Saini N, Pandey C, Thapliyal S et al (2018) Mechanical Properties and Wear Behavior of Zn and MoS2 Reinforced Surface Composite Al- Si Alloys Using Friction Stir Processing. SILICON 10:1979–1990
8. Deepan M, Pandey C, Saini N et al (2017) Estimation of strength and wear properties of Mg/SiC nanocomposite fabricated through FSP route. J Braz Soc Mech Sci Eng 39:4613–4622
9. Fayomi J, Popoola API, Popoola OM, Oladijo OP, Fayomi OSI (2019) Tribological and microstructural investigation of hybrid AA8011/ZrB2-Si3N4 nanomaterials for service life improvement. Results Phys. 14:102469
10. Li Quan Wu, Ai-ping Zhao Yue, Guo-qing Wang, Dong-yang Yan, Hui-qiang Wu (2015) Fracture behavior of double-pass TIG welded 2219–T8 aluminum alloy joints under transverse tensile test [J]. Transactions of Nonferrous Metals Society of China 25(6):1794–1803
11. Takhti S, Reihanian M, Ashrafi A (2015) Microstructure characterization and mechanical properties of gas tungsten arc welded cast A356 alloy. Trans Nonferrous Met Soc China 25(7):2137–2146. https://doi.org/10.1016/S1003-6326(15)63825-0
12. Chen YB, Lei ZL, Li LQ, Wu L (2006) Experimental study on welding characteristics of CO2 laser TIG hybrid welding process. Sci Technol Weld Joining 11(4):403–411
13. Song G, Luo Z (2011) the influence of laser pulse waveform on laser–TIG hybrid welding of AZ31B magnesium alloy. Opt Lasers Eng 49(1):82–88

14. A. El-Batahgy and M. Kutsuna, "Laser beam welding of AA5052, AA5083, and AA6061 aluminum alloys, Advances in Materials Science and Engineering, 2009, 1–9. https://doi.org/10.1155/2009/974182.
15. Verma Rajesh P, Pandey KN, Sharma Yogesh (2015) Effect of ER4043 and ER5356 filler wire on mechanical properties and microstructure of dissimilar aluminium alloys, 5083-O and 6061–T6 joint, welded by the metal inert gas welding. Proceedings of the Institution of Mechanical Engineers, Part B: Journal of Engineering Manufacture 229(6):1021–1028
16. Elanchezhian C, VijayaRamnath B, Venkatesan P, Sathish S, Vignesh T, Siddharth RV, Vinay B, Gopinath K (2014) Parameter Optimization of Friction Stir Welding of AA8011–6062. Procedia Engineering 97:775–782
17. Mehdi Husain, Mishra RS (2021) Microstructure and mechanical characterization of TIG-welded joint of AA6061 and AA7075 by friction stir processing. Proceedings of the Institution of Mechanical Engineers, Part L: Journal of Materials: Design and Applications 235(11):2531–2546
18. Mehdi Husain, Mishra RS (2020) Influence of friction stir processing on weld temperature distribution and mechanical properties of TIG welded joint of AA6061 and AA7075. Transactions of the Indian Institute of Metals 73:1773–1788
19. Mehdi Husain, Mishra RS (2020) Effect of Friction Stir Processing on Microstructure and Mechanical Properties of TIG Welded Joint of AA6061 and AA7075. Metallography, Microstructure, and Analysis 9:403–418
20. Mehdi Husain, Mishra RS (2020) Investigation of mechanical properties and heat transfer of welded joint of AA6061 and AA7075 using TIG+FSP welding approach. Journal of Advanced Joining Processes 1:100003
21. Takhti S, Reihanian M, Ashrafi A (2015) Microstructure characterization and mechanical properties of gas tungsten arc welded cast A356 alloy. Trans Nonferrous Met Soc China 25:2137–2146
22. Chen Y-B, Miao Y-G, Li L-Q, Lin Wu (2009) Joint performance of laser-TIG double-side welded 5A06 aluminum alloy. Transactions of Nonferrous Metals Society of China 19(1):26–31
23. Chen Y-B, Miao Y-G, Li L-Q, Lin Wu (2008) Arc characteristics of laser-TIG double-side welding. Sci Technol Weld Joining 13(5):438–444
24. Shen J, Xu N (2012) Effect of preheat on TIG welding of AZ61 magnesium alloy. Int J Miner Metall Mater 19:360–363
25. Ramana Venkat, Yelamasetti Balram, Vardhan Vishnu (2021) Study on weldability and effect of post heat treatment on mechanical and metallurgical properties of dissimilar AA 2025, AA 5083 and AA7075 GTAW weld joints. Materials today proceedings 46(1):878–882
26. Husain Mehdi RS (2021) Mishra, Effect of Friction Stir Processing on Mechanical Properties and Wear Resistance of Tungsten Inert Gas Welded Joint of Dissimilar Aluminum Alloys. Journal of Material Engineering and Performance 30:1926–1937
27. Su JQ, Nelson TW, Mishra R, Mahoney M (2003) Microstructural investigation of friction stir welded 7050–T651 aluminium. Acta Mater 51:713–729
28. Thomas WM, Nicholas ED, Needham JC, Murch MG, Temple-Smith P, Dawes CJ (1991) Friction stir butt welding. International Patent Application No. PCT/GB92/02203; 1991. G.B. Patent Application No. 9125978.8
29. Mishra RS, Ma ZY (2005) Friction stir welding and processing. Mater Sci Eng R Rep 50:1–78
30. A Nait Salah, Husain Mehdi, Arshad Mehmood, Abdul Wahab Hashmi, Chandrabhanu Malla, Ravi Kumar, Optimization of process parameters of friction stir welded joints of dissimilar aluminum alloys AA3003 and AA6061 by RSM, materials today proceedings, 2021, https://doi.org/10.1016/j.matpr.2021.10.288.
31. Sadoun AM, Wagih A, Fathy A, Essa ARS (2019) Effect of tool pin side area ratio on temperature distribution in friction stir welding. Results in Physics 15:102814
32. Mastanaiah P (2016) Abhay Sharma G, Madhusudhan Reddy, Dissimilar Friction Stir Welds in AA2219-AA5083 AluminiumAlloys: Effect of Process Parameters on Material Inter-Mixing. Defect Formation, and Mechanical Properties, Trans Indian Inst Met 69(7):1397–1415
33. Taban E, Kaluc E (2006) Microstructural and mechanical properties of double-sided MIG, TIG and friction stir welded 5083–H321 aluminium alloy. Kovove Mater 44:25–33
34. Mabuwa S, Msomi V (2020) The impact of submerged friction stir processing on the friction stir welded dissimilar joints. Mater. Res. Express 7:096513
35. Singh D, Rao PN, Jayaganthan R (2013) Effect of Deformation Temperature on Mechanical Properties of Ultrafine Grained Al – Mg Alloys Processed by Rolling. Mater Des 50:646–655
36. Lee YB, Shin DH, Park KT, Nam WJ (2004) Effect of Annealing Temperature on Microstructures and Mechanical Properties of a 5083 Al Alloy Deformed at Cryogenic Temperature. Scr Mater 51(4):355–359
37. Ma ZY (2008) Friction stir processing technology: a review. Metall Mater Trans A 39:642–658. https://doi.org/10.1007/s11661-007-9459-0
38. Su JQ, Nelson TW, Sterling CJ (2006) Grain Refinement of Aluminum Alloys by Friction Stir Processing. Philos Mag 86(1):1–24
39. Rastkerdar E, Shamanian M, Saatchi A (2013) Taguchi optimization of pulsed currentGTA welding parameters for improved corrosion resistance of 5083 aluminumwelds. J Mater Eng Perform 22(4):1149–1160
40. Liu Y et al (2012) Microstructure and mechanical properties of aluminum 5083weldments by gas tungsten arc and gas metal arc welding. Mater Sci Eng A 549:7–13
41. Guo Y et al (2018) An investigation on plasma-MIG hybrid welding of 5083 aluminum alloy. Int J Adv Manuf Technol 98(5–8):14331440
42. Wang J, Zhou D, Xie L, Li X, Lu Y, Bai Z, Zhou J (2021) Effect of multi-pass friction stir processing on microstructures and mechanical behaviors of as-cast 2A14 aluminum alloy. J Mater Eng Perform 30:3033–3043
43. Chen Y, Ding H, Cai Z, Zhao J, Li J (2016) Effect of initial base metal temper on microstructure and mechanical properties of friction stir processed Al-7B04 alloy Mater. Sci Eng A 650:396–403
44. Wang J, Yang K, Zhou D, Xie L, Lu Y, Li X (2021) Investigation on the microstructures and mechanical properties of friction stir processed 2A14 aluminum alloy fabricated by different initial precipitation states, The Int. J. Adv. Manuf. Technol. 116:3549–60
45. He XC, Gu FS, Ball A (2014) A review of numerical analysis of friction stir welding. Prog Mater Sci 65:1–66
46. Liu LM, Song G, Liang GL, Wang JF (2005) Mater Sci Eng A 390:76–80
47. Duan S, Matsuda K, Zou Y, Wang T (2019) Influence of two-stage ageing process and Cu additions on conductive Al alloys based on AA 6063. Materials Research Express 6:106509
48. Barmouz M, BesharatiGivi MK, Seyfi J (2011) On the role of processing parameters in producing Cu/SiC metal matrix composites via friction stir processing: investigating microstructure, microhardness, wear and tensile behavior. Mater. Charact. 62:108–117
49. Barmouz M, BesharatiGivi MK (2011) Fabrication of in situ Cu/SiC composites using multi-pass friction stir processing: evaluation of microstructural, porosity, mechanical and electrical behavior. Compos. Part A 42(10):1445–1453
50. Su P, Gerlich A, North TH, Bendzsak GJ (2013) Material flow during friction stir spot welding. Sci Technol Weld Joining 11(1):61–71
51. Zhang Z, Chen DL (2006) Consideration of Orowan strengthening effect in particulate-reinforced metal matrix nanocomposites: A model for predicting their yield strength Author links open overlay panel. Scripta Materialia 54(7):1321–1326

52. Chang CI, Lee CJ, Huang JC (2004) Relationship between grain size and Zener-Holloman parameter during friction stir processing in AZ31 Mg alloys. Scripta Mater 51:509–514
53. Oladijo OP, Venter AM, Cornish LA, Sacks N (2012) X-ray diffraction measurement of residual stress in WC-Co thermally sprayed coatings onto metal substrates. Surf Coat Techno 206:4725–4729
54. Paidar M (2019) Olatunji Oladimeji Ojo, Hamid Reza Ezatpour, Influence of multi-pass FSP on the microstructure, mechanical properties and tribological characterization of Al/B C composite fabricated by accumulative roll bonding (ARB). Surf Coat Technol 361:159–169
55. Pandey Chandan, AnojGiri MM (2016) Mahapatra, Evolution of phases in P91 steel in various heat treatment conditions and their effect on microstructure stability and mechanical properties. Materials Science & Engineering A 664:58–74
56. Simar A, Brechet Y, Meester BD, Denquin A, Gallais C, Pardoen T (2012) Integrated Modeling of Friction Stir Welding of 6xxx Series Al Alloys: Process Microstructure and Properties. Prog Mater Sci 57:95–183
57. Zhang Z, Wan ZY, Lindgren LE, Tan ZJ, Zhou X (2017) The Simulation of Precipitation Evolutions and Mechanical Properties in Friction Stir Welding with Post Weld Heat Treatments. J Mater Eng Perform 26:5731–5740
58. McNelley TR, Swaminathan S, Su JQ (2008) Recrystallization mechanisms during friction stir welding/processing of aluminum alloys. Scripta Mater 58:349–354
59. Seidel TU, Reynolds AP (2001) Visualization of the material flow in AA2195 friction-stir welds using a marker insert technique. Metall Mater Trans A 32:2879–2884
60. Srivastava M, Rathee S, Siddiquee AN (2019) Investigation on the Effects of Silicon Carbide and Cooling Medium during Multi-Pass FSP of Al-Mg/ SiC Surface Composites. SILICON 11:2149–2157
61. Mehdi H, Mishra RS (2021) Consequence of reinforced SiC particles on microstructural and mechanical properties of AA6061 surface composites by multi-pass FSP. J Adhes Sci Technol. https://doi.org/10.1080/01694243.2021.1964846
62. Moradi MM, Aval HJ, Jamaati R, Amirkhanlou S, Ji S (2018) Microstructure and texture evolution of friction stir welded dissimilar aluminum alloys: AA2024 and AA6061. J Manuf Process 32:1–10
63. Liu XC, Sun YF, Nagira T, Ushioda K, Fujii H (2019) Evaluation of dynamic development of grain structure during friction stir welding of pure copper using a quasi in situ method. J Mater Sci Technol 35:1412–1421
64. Barmouz M, BesharatiGivi MK (2011) Fabrication of in situ Cu/SiC composites using multi-pass friction stir processing: evaluation of microstructural, porosity, mechanical and electrical behavior. Compos. Part A Appl. Sci. Manuf. 42:1445–1453
65. Lang P, Povoden-Karadeniz E, Falahati A, Kozeschnik E (2014) Simulation of the effect of composition on the precipitation in 6xxx Al alloys during continuous-heating DSC. J. Alloys Compd. 612:443–449
66. Liu FC, Ma ZY (2010) Contribution of grain boundary sliding in low-temperature superplasticity of ultrafine-grained aluminum alloys. Scr Mater 62:125–128
67. Paidar M, Asgari A, Ojo OO, Saberi A (2018) Mechanical properties and wear behavior of AA5182/WC nanocomposite fabricated by friction stir welding at different tool traverse speeds. J Mater Eng Perfor 27:1714–1724
68. Sharma DK, Patel V, Badheka V, Mehta K, Upadhyay G (2019) Fabrication of hybrid surface composites AA6061/(B4 C+MoS) via friction stir processing. J Tribolo 141(5):52201–52210
69. Husain Mehdi, R.S. Mishra, An experimental analysis and optimization of process parameters of AA6061 and AA7075 welded joint by TIG+FSP welding using RSM, Advances in Materials and Processing Technologies, 2020, https://doi.org/10.1080/2374068X.2020.1829952.
70. Tariq M, Khan I, Hussain G, Farooq U (2019) Microstructure and micro-hardness analysis of friction stir welded bi-layered laminated aluminum sheets. International Journal of Lightweight Materials and Manufacture 2(2):123–130
71. Patel VV, BadhekaVand Kumar A (2017) Effect of polygonal pin profiles on friction stir processed superplasticity of AA7075 alloy. J. Mater. Process. Technol. 240:68–76
72. Qin H, Zhang Hand WuH (2015) The evolution of precipitation and microstructure in friction stir welded 2195–T8 Al–Li alloy Mater. Sci. Eng. A 626:322–329
73. Chaurasia PK, Pandey C, Giri A, Saini N, Mahapatra MM (2018) a comparative study of residual stress and mechanical properties for fsw and tig weld on structural steel. Arch Metall Mater 63:1019–1029
74. Pandey C, Saini N (2017) Manas Mohan Mahapatra, Pradeep Kumar, Study of the fracture surface morphology of impact and tensile tested cast and forged (C&F) Grade 91 steel at room temperature for different heat treatment regimes. Eng Fail Anal 71:131–147
75. ChandanPandey MM, Mahapatra Pradeep Kumar, Prakash Kumar N, Saini J.G. Thakare (2019) Study on effect of double austenitization treatment on fracture morphology tensile tested nuclear grade P92 steel. Engineering Failure Analysis 96:158–167
76. Msomi Velaphi, Mabuwa Sipokazi (2020) Analysis of material positioning towards microstructure of the friction stir processed AA1050/AA6082 dissimilar joint. Advances in Industrial and Manufacturing Engineering 1:100002
77. Orłowska Marta, Brynk Tomasz, Hütter Andreas, Enzinger Norbert, Olejnik Lech, Lewandowska Małgorzata (2020) Similar and dissimilar welds of ultrafine grained aluminium obtained by friction stir welding. Materials Science and Engineering: A 777:139076

Publisher's Note Springer Nature remains neutral with regard to jurisdictional claims in published maps and institutional affiliations.

Estimation of crack growth on rails under the combined influence of thermo-mechanical loading due to the sliding of wheel

DOI : 10.36909/jer.14917

Aakash D Bansal*, Atul Kumar Agrawal, Vikas Rastogi

Mechanical Engineering Department, Delhi Technological University, Delhi, 110042, India.

*Email: aakashdbansal17@gmail.com; Corresponding Author.

ABSTRACT

Development and growth of surface and subsurface cracks on rail profile is one of the major reasons for deterioration of rails near the halting zones. Rail tracks are subjected to combination of thermal loads during the sliding motion of the wheel while braking and structural load due to the weight of the vehicle. In this paper, an FEA model is been developed to study and analyze the effect of coupled thermo-mechanical load during braking on contact stress and contact area at the rail-wheel interface. Both elastic and elasto-plastic FEA models are used and compared with analytical Hertzian approach to accurately predict rail-wheel contact parameters. A synthetic loading spectrum is proposed to simulate the combination of thermal and thermo-mechanical loading cycles on the rail during braking of vehicle. The loading cycle is used to predict the growth of previously present flaws using Modified Paris Law and Generalized Frost-Dugdale approach. It has been found that elasto-plastic FEA is inclined to predict lesser contact stresses than the elastic FEA or Hertzian model. Furthermore, shape of the contact patch for elasto-plastic FEA is observed to be unsymmetrical in the rolling direction unlike the elliptical contact area in elastic FEA approach. Macro scale initial cracks having length more than 2 mm are also realized to grow faster than their smaller counterparts under the combined effect of thermal and mechanical loads.

Key words: Contact Mechanics; Finite Element Modeling; Hertz contact; Stop Braking; Abaqus; Dynamic-Explicit; Plasticity.

INTRODUCTION

Railways is the most popular means of transportation and is recognized for its cost effectiveness and ride comfort when compared with other means of transportation. However, wear and damage of rails can substantially influence the service life and passenger's comfort. Rails have a service life of 8-10 years and are typically condemned due to worn out profiles. Altering of rail profile is impacted by the heat produced at the rail-wheel interface during the motion of wheel over the rail. In addition to it, the contact pressure due to the vertical load acting from the wagon contributes significantly to the wear and life of rails.

Thermal loading may result on the wheel surface from the application of the brakes. This temperature on the wheel in further addition to the heat generated due to the friction between the contacting bodies is conducted to the rail surface. The localized interaction at the contacting surface can be additionally complicated by the continuous variation in interface pressure distribution, heat generation, temperature and wear at the contact surface.

The effect of temperature and rolling contact of the wheel on the rail have been studied separately by authors previously. Taciroglu et. al. suggests that degradation of track components occurs over time due to repeated rail-wheel contact. The problem of contact in rail-wheel application is mostly addressed either analytically or by numerical methods. The analytical approach to solve rail-wheel contact can be typically categorized into: i) Normal contact problem and ii) Tangential contact. Various contact models in the above two categories have been developed over the years to successfully estimate contact stresses, size of contact patch and creepages. The class of Contact Models which assumes the surfaces in contact to exhibit elastic behavior only along with smooth contact and no friction in between the contacting surfaces comes under the category of Hertzian Models. These Hertzian Models have later evolved into Semi- Hertzian (Ayasse et. al. 2005}, Multi- Hertzian (Piotrowski et. al., 2005) or Non- Hertzian Approaches (Kalker et. al., 1993) but none of them can match the

relative ease of computation of contact parameters offered by the Hertzian Approach. The pressure distribution assumed by Hertz is a semi-ellipsoid normal pressure curve exerting pressure over both the surfaces in contact. Hertzian theory though computationally inexpensive, is based upon assumptions which are tended to get violated while estimating actual contact parameters during rail-wheel contact. For example, bodies in contact may tend to show plastic behavior and laws of plastic ratcheting will come into the play. That is why, FEA and other numerical integration techniques involving simple direct formulation into rail–wheel contact problems are favored by railway engineers and researchers to verify their results by equating them to their actual life determined over the past years. Murat et. al. and Yaylaci et. al. suggests that FEA can be an efficient alternative method to the analytical solutions. The FE approach is further categorized into assumption of elastic material properties or elasto-plastic material properties for the rail. Sladowsky et. al. assumed elastic rail and wheel material and solved the contact problem for static and quasi-static loading to determine distribution of contact zone for various rail and wheel geometries. Zhao et. al. studied the problem for both normal and tangential contacts in elastic rail and found good agreement between the FE results and analytical Hertzian approach. Tigdemir et. al. modeled wheel-snow interaction using Explicit FEA package. Assumption of elastic rail material properties gives unrealistically high stresses and eventually may lead to errors in calculation of fatigue life of the rail and wheel. For this reason, authors have looked into the prospect of assuming elasto-plastic rail material. Johansson et. al. simulated dynamic rail-wheel interaction for a single wheel pass assuming plastic material properties in rail to study the effect of vehicle running conditions. Kubin et. al. developed a 2-D FE model with elasto-plastic rail properties which accounts for roughness of the contact surfaces. Toumi et. al. studied 3-D FE frictional wheel-rail rolling contact in an elasto-plastic rail for explicit, implicit quasi-static and implicit moderate energy dissipation schemes. While authors have studied the problem of rail-wheel contact in detail, research on the combination of thermal and mechanical load and its effect on contact characteristics has

been limited. Wu et. al. developed a 2-D FE model to study the thermo-elasto-plastic deformation in material during sliding of wheel. K D Vo et. al. coupled thermal and mechanical loads in a 3-D FE model and evaluated the contribution of thermal effects and plasticity on contact characteristics. The studies however had the following limitations: 1) The material properties were considered independent of the temperature which is not the case for wheel-rail material, 2) Presence of wheel is simplified by means of a moving heat load over the rail surface which only establish full-slip contact and thus partial-slip conditions were ignored. Based on this knowledge, it can be understood that a new method for estimation of rail-wheel simulation under a combination of thermal and mechanical load is required.

The current study offers advantage of evaluating contact characteristics on the rail surface under the combined effect of thermal and mechanical loading while considering temperature dependent elastic and elasto-plastic material properties. The 3-D dynamic model will help in establishing variation in contact parameters when vehicle is in running conditions. The proposed research further aims at comparing the effect of elastic and elasto-plastic material behavior on the rail-wheel contact conditions. The contact parameters thus obtained as a result of assuming elasto-plastic material behavior will then be used to determine fatigue life of rail having an existing initial crack under the combined effect of thermo-mechanical loading.

FINITE ELEMENT METHOD

A 3-D elastic–plastic FE model is used in the present study to reproduce the motion of wheel over the rail. In the present study, rail-wheel contact is considered flexible-to-flexible as both surfaces are deformable. The wheel and rail geometry considered are 920 mm and UIC 60 as per standard used by Freight wagons and tracks respectively in Indian Railways as shown in Figure 1.

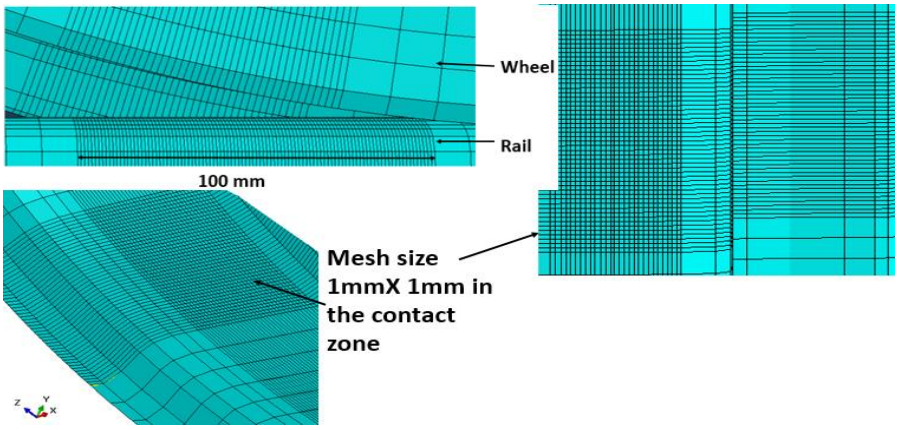


Figure 1 Meshed model of rail and wheel.

The geometries should be assembled carefully in the *Assembly* module such that the wheel is resting vertically on the rail. The contact characteristics are obliged to change in accordance with the relative position of wheel and rail. The problem of Rail-wheel interaction in FEA on account of variation of contact forces, is significantly non-linear in nature and thus is highly dependent on the mesh size and shape in the contact region. The model is meshed with 351,732 C3D8T brick elements which are capable to calculate trilinear displacement and temperature in a coupled temperature-displacement analysis. The size of the mesh in the contact region is taken to be 1mm*1mm to systematize results for all the simulation cases. Appropriate mesh convergence analysis is performed to suggest that the results in the contact region are estimated under minimal influence of mesh size.

Kinematic contact constraint which actively predicts and corrects the contact characteristics after every time increment is created between the contacting surfaces. The coefficient of friction between the interacting surfaces is assumed to be 0.3. The wheel bore surface is connected to the *Inertial Mass* of the wagon by means of a *Tied Constraint*. An initial rotation and translation which is kept constant over the simulation time is further applied on the wheel. Simulation time was kept 0.1 second in due accordance with Courant stability condition. Keeping time step small in an *Explicit* analysis assures convergence and inclusion of all the vibration modes in the FEA result. In contrast, analytical estimation by means of Hertzian Approach ignores the vibration of the structure and the continua excited by the motion of the

wheel on the rail. Therefore, for the purpose of correct comparison between the analytical and FEA results, rail should be supported by a rigid foundation by means of *Rigid Body constraint*. The total load acting on the rail consists of mass of the wheel which is 1000 kg and a fragment of the vehicle mass. The wheel is assumed to be of elastic in nature and the rail surface is modeled with elasto-plastic material behavior as shown in Table 1 (Srivastava et. al., 2017). The properties used to exhibit thermal behavior of the rail steel is shown in Table 2.

Table 1 Mechanical Elastic and Elasto-plastic properties of Rail and Wheel Steel

Temperature (^oC)	**Young's Modulus (MPa)**	**Poisson's ratio**	**Yield Strength (MPa)**	**Kinematic Hardness Parameter, C_1 (MPa)**	**γ_1**
20	180	0.2841	540	20800	26
100	180	0.2865	540	19600	25.4
200	180	0.2902	540	18000	24
300	175	0.2940	540	16000	27.7
400	170	0.2985	540	13900	34

Table 2 Thermal properties of Rail and Wheel Steel (Srivastava et. al., 2017)

Temperature (^oC)	**Thermal Conductivity (W/m ^oC)**	**Coefficient of Thermal Expansion (X $10^{-6}K^{-1}$)**	**Specific Heat (J/kg ^oC)**
20	47.1	11.72	468.6
100	47.1	12.2	490.7
200	45	12.8	527.2
300	43	13.4	565.9

QUALITATIVE HEAT TRANSFER ANALYSIS

Simulations of wheel passing over a point on the rail are performed using Abaqus CAE. When the wheel crosses the predefined point on the rail during braking, the sliding action produces high temperature on the wheel as well as the rail surface. As a consequence of this thermal load which is acting in combination with mechanical load of the vehicle, the material of rail undergoes plastic deformation and a dent remains after the first passage of the wheel. Every following passage of wheels from that point onward during the course of braking will then partly impact on a deformed surface of the rail.

SYNTHETIC LOADING SPECTRUM

In this paper, the multi-physics phenomenon concerning both mechanical and thermal analysis are coupled simultaneously to allow for estimation of life of rail. Total stress acting on the rail is a combined outcome of the thermal stresses induced in the rail due to the sliding of wheel and structural stresses originated due to the axle load on the wheel. The resultant stress produced due to the combination of thermal and mechanical loading will then be used to estimate stress intensity factor. As a part of this study, it is further assumed that a point on the rail surface will be under the effect of thermal load only until the wheel passes over it, at which point it will be under the combined effect of both thermo-structural loads. Stress intensity factor will then serve as an input to estimate fatigue crack growth. Number of cycles for a crack to grow from an initial length to a final length will be eventually determined using modified Paris Law and Generalised Frost-Dugdale approach as discussed in Appendix-I.

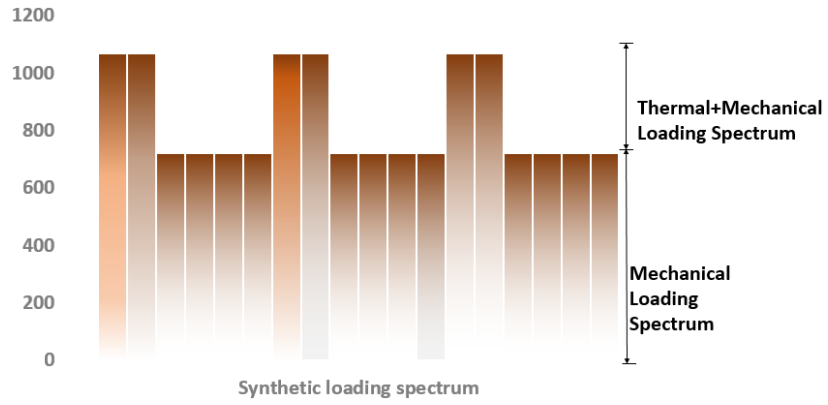


Figure 2 Synthetic Loading Spectrum

In this case, the train assumed initially running at an initial velocity brakes while entering the platform. Braking action will result in increasing sliding motion at the rail-wheel interface. Synthetic method (Peng et. al., 2012) assumes that thermal loading is acting for M cycles beginning from the instant braking is initiated as shown in Equations (1-2). Mechanical loading will act only when there is contact between the points of stress estimation on the rail and the wheel. Assuming N cycles of mechanical loading such that N<M. All the cycles in thermal loading spectrum are divided into M/N equal parts whereas in mechanical loading spectrum divided into N parts.

$$\sigma_i^{Synthetical} = \sigma_j^{Mechanical} + \sigma_k^{Thermal} \in i = k : k = (j-1)\frac{M}{N} + 1 \qquad (1)$$

$$\sigma_i^{Synthetical} = \sigma_k^{Thermal} \in i \neq k \quad (2)$$

Synthetic loading spectrum adds the thermal and mechanical stress magnitudes at same cycle while keeping the rest of the values unchanged as shown in Figure 2.

RESULTS AND DISCUSSIONS

All the FE simulations were performed using 3.2 GHz Intel® Core TM I78700 workstations. In this section, results from variation of load using Hertzian approach and FEA approach are discussed. The vertical normal force on the wheel due to the axle is varied from 70 kN to 130 kN to envelope the variation of loads carried by all types of passenger and freight wagons used by Indian Railways. The contact pressure and contact area are observed to be increasing with an increase in the axle load of the vehicle as shown in Figure 3(a) and Figure 3(b). For a *Dynamic Explicit* analysis, the appropriateness of the simulation response can be evaluated by use of *Energy Balance* Equation 3.

ALLWK=ALLIE+ALLKE+ALLVD (3)

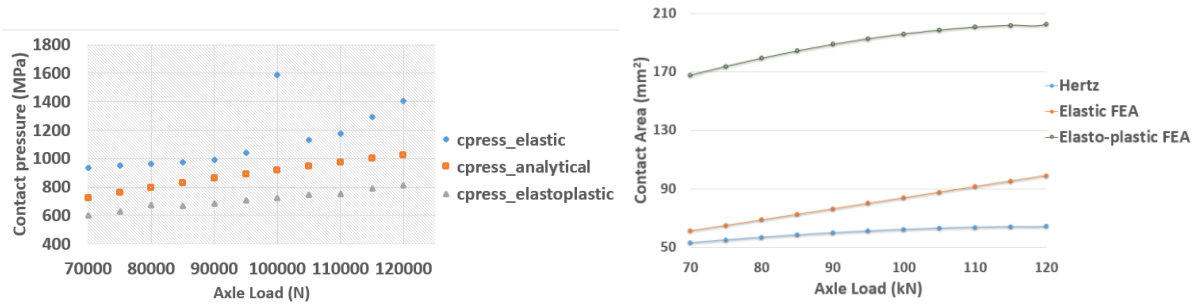


Figure 3 Variation of a) contact pressure b) contact area at rail-wheel interface with axle load

The plots comparing external work of applied forces for the whole model and algebraic sum of the Internal Energy, Kinetic Energy and Viscous Dissipation Energy of the model for elastic material response can be seen in Figure 4. The closeness of the two curves throughout simulation time suggests that the energy equilibrium is satisfied. It is observed that results from elasto-plastic FEA differs notably from Hertzian or elastic FEA formulations and agrees with the data from field trials and experiments. A valid explanation for this behavior is the increase in contact area size at the rail-wheel interface while using the elasto-plastic FEA. The contact area is no longer elliptical as shown in Figure 5 and symmetric as found during

Hertzian or elastic FEA approach, instead has a conicity in the rolling direction. Distribution of Contact Pressure and Von Mises stress on the rail surface can be seen in Figure 6(a) and Figure 6(b) respectively. Variation of contact area over the course of simulation of wheel on the rail assuming elastic material properties for both rail and wheel is shown in Figure 7. It can be seen that the contact area keeps on varying throughout the simulated motion of the wheel owing to the non-linearity in contact and asymmetric wheel profile geometry. These continuous fluctuations in the contact simulations are termed as *Contact Chattering* and are largely observed in the coarse mesh region. Contact pressure and contact area results from various approaches used in this paper are found in agreement with Toumi et. al. In addition to it, distribution of plastic strain across the transverse and longitudinal directions of rolling can be seen in Figure 8(a) and Figure 8(b) respectively.

INFLUENCE OF TEMPERATURE

Heating of the rail material leads to thermo-mechanical fatigue and generation of white brittle etching layer which increases the possibility of crack initiations and growth. Therefore, an indirect coupled thermo-elasto-plastic FEA approach is employed to evaluate the effect of motion of the wheel on the contact pressure and temperature of the rail. This approach is applied in two stages: firstly, the estimation of temperature distribution profile on the rail surface during the simulated movement of wheel over the rail surface, and secondly combining the thermal load on the rail surface with the structural load to determine displacement, strains and stress field on the rail surface. The maximum temperature on the rail surface as shown in Figure 9 due to the sliding motion of wheel is found to be 227^{o}C which is significantly lower than the critical temperature of steel (approximately 730^{o}C) required for phase transformation. Free convection to environment is assumed to model natural convection of air using standard correlations to simulate heat dissipation from the rail surface.

FATIGUE LIFE ESTIMATION

Modified Paris law suggests that number of cycles required for a crack to grow is a function of initial crack length. As a part of this study, various initial crack sizes are taken to study the

life of rails near platforms and stations in Indian Railways. A 24 coach Indian Railways passenger train as shown in Figure 10 consist of 96 wheels for each rail. Assuming each wheel imparts uniform heat to the rail surface while braking, a total of 96 coupled thermo-structural loading cycles will be experienced by a point on the rail for every passenger train coming to a halt at the junction. In this article, we have considered the number of trains terminating and halting at New Delhi Railway Station, having 16 platforms where an average of 225 trains terminates and stops on a daily basis. It is further assumed that each platform invites same number of trains and each train has same number of coaches. Standard calculations imply that each rail surface may thus live through approximately 500,000 loading cycles of thermal and coupled thermo-structural loads every year. Initial flaws are typically categorized on the basis of their length as: i) micro-cracks (less than 0.5mm) ii) small cracks (size varying from 1mm to 2 mm) and iii) large cracks (size greater than 2mm). Variation of final crack size as a function of initial crack length and number of loading cycles can be seen in Figure 11(a), Figure 11(b) and Figure 11(c) respectively.

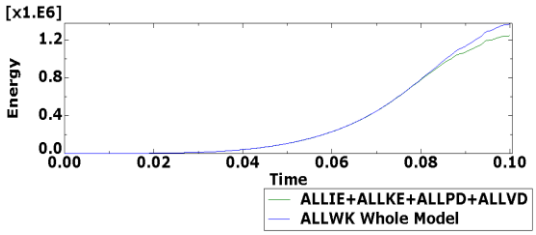


Figure 4 Energy balance plots for the whole model for elastic material behavior.

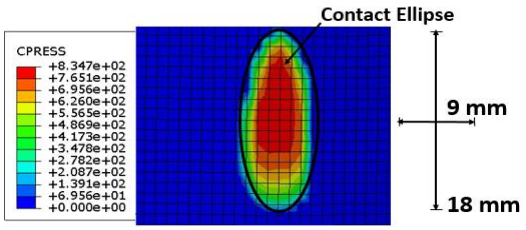


Figure 5 Shape and size of contact patch assuming elasto-plastic rail material properties.

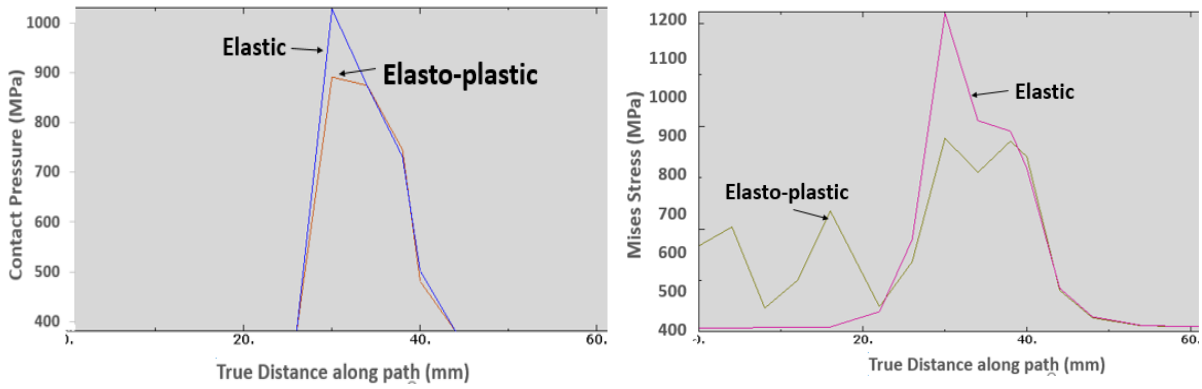


Figure 6 Variation of a) contact pressure b) Stress distribution along longitudinal direction of

travel for elastic and elasto-plastic materials

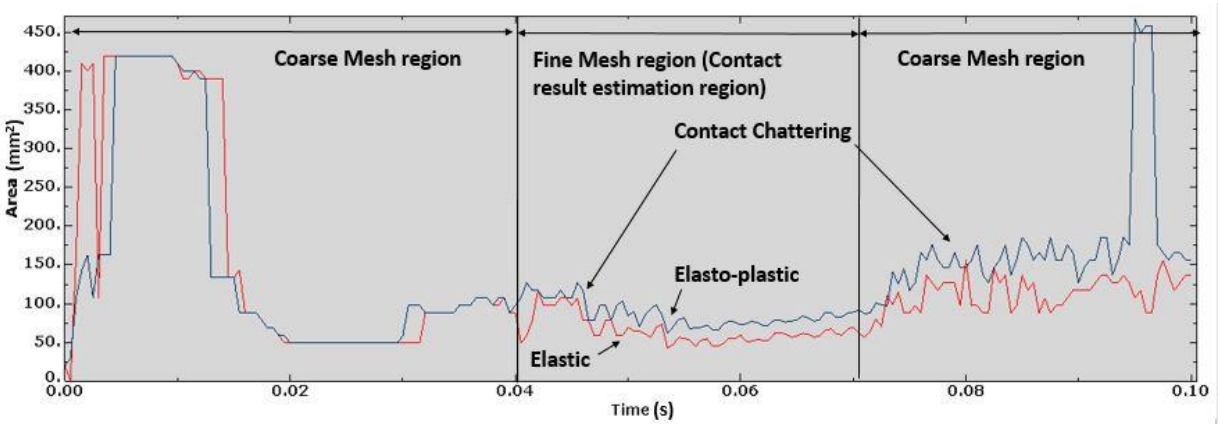


Figure 7 Variation of contact area at rail-wheel interface during the course of simulation

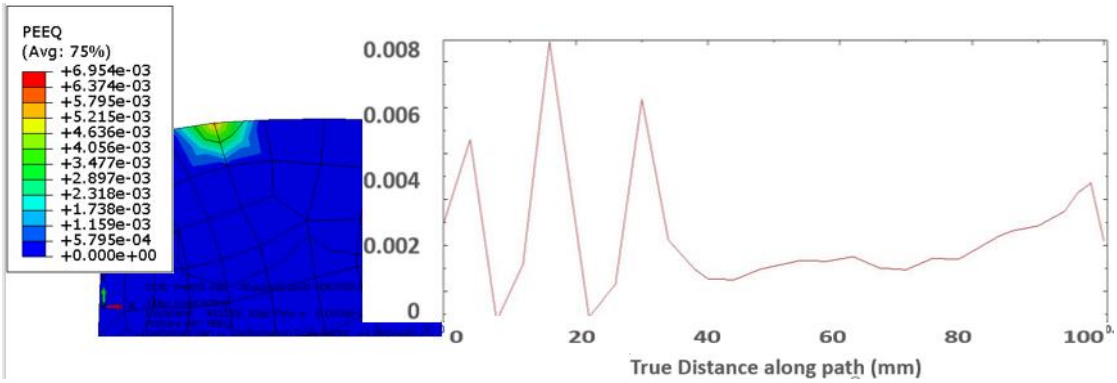


Figure 8 Equivalent plastic strain distribution on rail across a) cross-section of rail b) longitudinal direction of travel

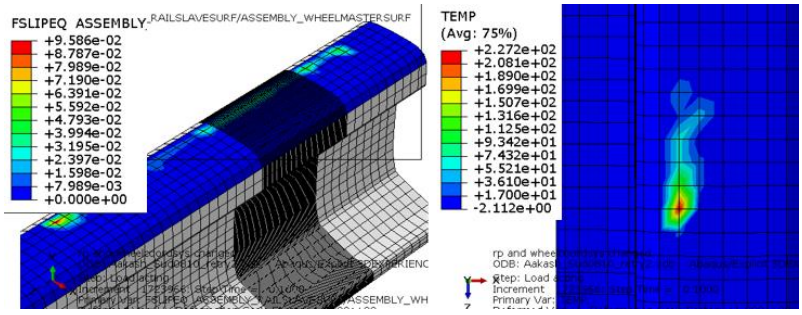


Figure 9 Temperature distribution on the rail during the sliding motion of wheel

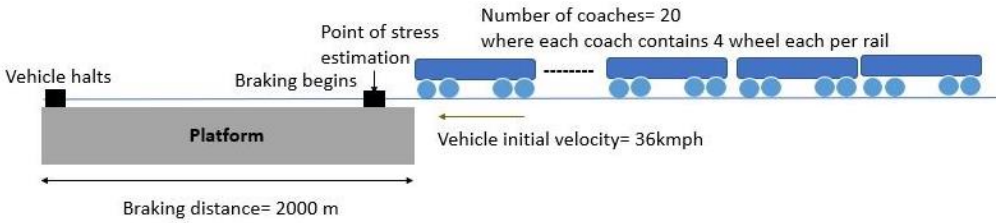


Figure 10 Schematic sketch of the passage of bogie over a point on the rail

CONCLUSION

It is observed that the normal contact solution considering elastic material properties in FEA model is in a good agreement with the Hertzian approach. It can also be seen that while considering elasto-plastic material properties in rail, both Von Mises stress and contact pressure reduced significantly. The elasto-plastic contact pressure is 1.25 and 1.75 times lesser than the analytical Hertzian and Elastic FEA approach respectively. The contact area is found to be larger and shape of contact patch in elasto-plastic FEA is not uniformly elliptical as determined with elastic FEA and Hertzian approach, instead has a conicity in the direction of travel. An indirect coupled thermo-mechanical approach is used to study the effect of temperature on the existing crack growth during the sliding motion of the wheel during braking. The analysis revealed that major cracks having initial length more than 2mm are very critical and require frequent attention and maintenance. It is to be noted here that simulations in this article are performed considering a uniform deceleration rate of 0.5 m/s^2 of vehicle. An increase in rate of deceleration can further increase the temperature on the rail surface and can consequently increase the rate of crack growth. The presented model discusses the impact of considering elasto-plastic material properties for assessing contact parameters at the rail-wheel interface. It further highlights the importance of temperature generated on the rail surface during the sliding motion of the wheel and its effect on the growth of cracks present on the contact surface.

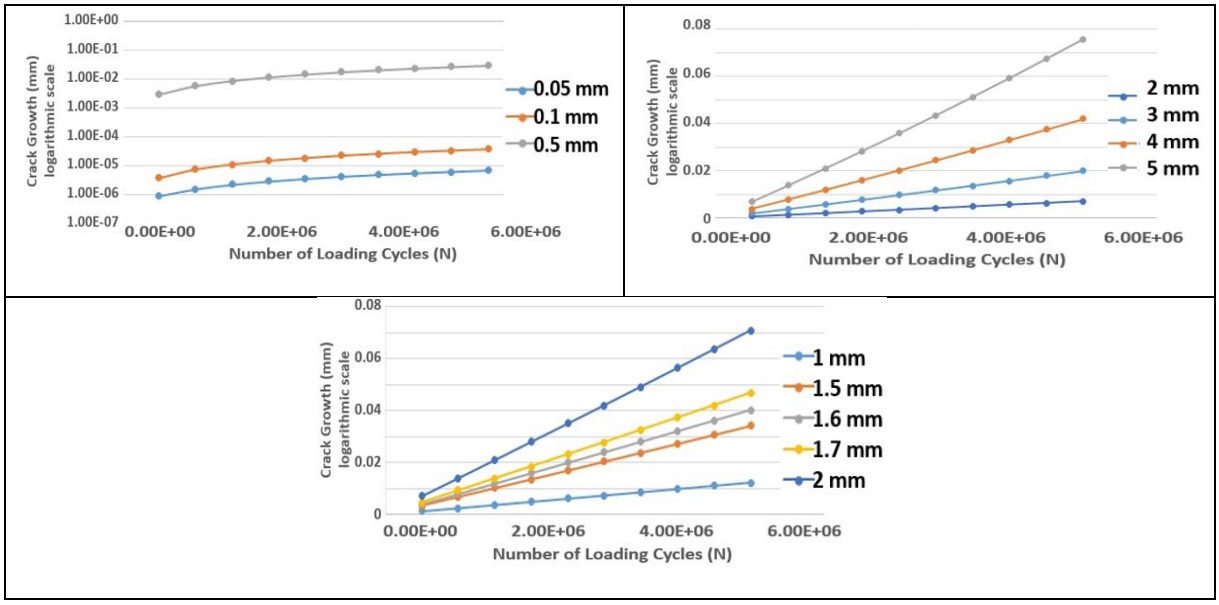


Figure 11 Comparison of a) micro b) small c) macro/large scale crack growth

REFERENCES

Taciroglu, M. V., Karasahin, M., Tigdemir, M. & Isiker, H., 2020. Fractal analysis of high speed rail geometry data: A case study of Ankara-Eskisehir high speed rail. Measurement.165: 108120-108134.

Ayasse, J. B., & Chollet, H., 2005. Determination of the wheel rail contact patch in semi-Hertzian conditions. Vehicle System Dynamics, 43(3), 161–172.

Piotrowski, J., & Chollet, H., 2005. Wheel-rail contact models for vehicle system dynamics including multi-point contact. Vehicle System Dynamics, 43(6–7), 455–483.

Kalker J. J. & Johnson K. L., 1993. Three-dimensional elastic bodies in rolling contact. Solid mechanics and its applications, Springer-Science+ Business Media B.V.

Murat, Y., & Mehmet, A., 2020. Finite element modeling of contact between an elastic layer and two elastic quarter planes. Computers and Concrete, 26(2), 107–114.

Murat, Y., Terzi, C. & Mehmet, A., 2019. Numerical analysis of the receding contact problem of two bonded layers resting on an elastic half plane. Structural Engineering and Mechanics, 72(6), 775–783.

Sladkowski, A., & Sitarz, M. 2005. Analysis of wheel-rail interaction using FE software. Wear,

258(7–8), 1217–1223.

Zhao, X., & Li, Z. 2011. The solution of frictional wheel-rail rolling contact with a 3D transient finite element model: Validation and error analysis. Wear, 271(1–2), 444–452.

Mesut, T., Mahyar, J. & Mehmet, C. B., 2018. Numerical modeling of wheel on the snow. International Journal of Engineering and Applied Sciences, 10(2), 64–72.

Johansson, A., Pålsson, B., Ekh, M., Nielsen, J. C. O., Ander, M. K. A., Brouzoulis, J. & Kassa, E., 2011. Simulation of wheel-rail contact and damage in switches & crossings. Wear, 271(1–2), 472–481.

Kubin, W. K., Pletz, M., Daves, W. & Scheriau, S., 2013. A new roughness parameter to evaluate the near-surface deformation in dry rolling/sliding contact. Tribology International, 67, 132–139.

Toumi, M., Chollet, H., & Yin, H. 2016. Finite element analysis of the frictional wheel-rail rolling contact using explicit and implicit methods. Wear, 366–367, 157–166.

Wu, L., Wen, Z., Li, W. & Jin, X., 2011. Thermo-elastic-plastic finite element analysis of wheel/rail sliding contact. Wear, 271(1–2), 437–443.

Vo, K. D., Tieu, A. K., Zhu, H. T. & Kosasih, P. B., 2015. The influence of high temperature due to high adhesion condition on rail damage. Wear, 330-33, 571–580.

Srivastava, J. P., Sarkar, P. K., Meesala, V. R. K. & Ranjan, V., 2017. Rolling contact fatigue life of rail for different slip conditions. Latin American Journal of Solids and Structures, 14(12), 2243–2264.

Peng, D., Jones, R., Constable, T., Lingamanaik, S. N. & Chen, B. K., 2012. The tool for assessing the damage tolerance of railway wheel under service conditions. Theoretical and Applied Fracture Mechanics, 57(1), 1–13.

APPENDIX-1

Generalized Frost Dugdale approach suggests that stress intensity factor, K and crack growth can be given by:

$$\Delta K = K_{max} - K_{min} = F\sqrt{\pi a}(\sigma_{max} - \sigma_{min}) \quad (4)$$

where ΔK is the change on stress intensity factor, a_i is the initial crack length and F is the

finite element correction factor given by:

$$F = F_e + (F_s - F_e)e^{-\alpha_d(\frac{a}{\rho})} \quad (5)$$

where F_e and F_s are Stress Intensity Boundary Correction Factor and

$$F_e = [M_1 + M_2(\frac{a}{t})^2 + M_3(\frac{a}{t})^4]gf_\phi f_w \quad (6)$$

$$M_1 = 1 \qquad M_2 = \frac{0.05}{0.11+(a/c^*)^{1.5}} \qquad M_3 = \frac{0.29}{(0.23+(a/c^*)^{1.5}} \quad (7)$$

where M_1, M_2, M_3 are Applied Bending Moment

$$\text{Curve Fitting function, } g = 1 - [\frac{(\frac{a}{t})^4(2.6-2(\frac{a}{t}))^{t/2}}{(1+4(a/c^*)}]\cos\phi \quad (8)$$

$$\text{Angular function from elliptical crack solution, } f_\phi = [(\frac{a}{c^*})^2\cos^2\phi + \sin^2\phi]^{0.25} \quad (9)$$

Modified Paris law suggests that,

$$\frac{da}{dN} = C.a^{(1-\epsilon/2)}.(\Delta K^\eta.K_{max}^{1-\eta})^\epsilon = A.(\Delta\sigma)^\eta(\pi a)^{\eta/2}.\alpha^\eta \quad (10)$$

where the material properties assumed for crack growth rate are ε=3, η=1 and C=3.38E-12 m/cycle. Value of constant A also varies with initial crack size as:

$$A = C.a^{(1-\frac{\epsilon}{2})} \quad (11)$$

Integrating the above equation, we get the analytical formula for calculating number of loading cycles required for a crack to grow from an initial size of a_i to a final size of a_f

$$N_f = \int_0^{N_f} dN = \int_{a_i}^{a_f} \frac{da}{A(\Delta\sigma)^\eta(\pi a)^{\eta/2}\alpha^\eta} = \frac{1}{A(\Delta\sigma)^\eta(\pi)^{\eta/2}}\int_{a_i}^{a_f}\frac{da}{(\alpha)^\eta(a)^{\eta/2}} = \frac{1}{A(\Delta\sigma)^\eta(\pi)^{\eta/2}(\alpha)^\eta}\int_{a_i}^{a_f}\frac{da}{(a)^{\eta/2}}$$

$$N_f = \frac{a_f^{\frac{-\eta}{2}+1} - a_i^{\frac{-\eta}{2}+1}}{((-\frac{\eta}{2}+1)A(\Delta\sigma)^\eta(\pi)^{\frac{\eta}{2}}(\alpha^\eta)} \quad (13)$$

Process Integration and Optimization for Sustainability
https://doi.org/10.1007/s41660-021-00215-1

ORIGINAL RESEARCH PAPER

Evaluation of Municipal Solid Waste Management Scenarios using Multi-Criteria Decision Making under Fuzzy Environment

Aakash Gaur[1] · Harshita Prakash[1] · Kuwar Anand[1] · Girish Kumar[2] · Athar Hussain[1]

Received: 10 November 2020 / Revised: 14 November 2021 / Accepted: 30 November 2021
© The Author(s), under exclusive licence to Springer Nature Singapore Pte Ltd. 2022

Abstract

Treatment of municipal solid waste in India is facing a grave crisis, where merely 25% of waste is treated per day. There is a desperate need for efficient as well as compatible options for the proper management of solid waste, which otherwise causes not only health problems but also creates social trouble. Therefore, there is a requirement of determining suitable treatment technology for respective waste material among its available options. In this study, various commonly used municipal solid waste management techniques are identified, investigated, and further different criteria are selected to evaluate them. Eight solid waste management scenarios are formed using core municipal solid waste management techniques such as landfill, incineration, biomethanation, composting, recycling and reuse, and aerobic digestion. The scenarios are evaluated using nine criteria, which are classified into four major categories as environmental, social, financial, and profitable criteria. The criteria are finalized, and their weights are determined by utilizing the data collected as per the opinions of the experts from relevant domains and weighted using the Fuzzy Analytic Hierarchy Process (Fuzzy AHP) technique. The data is collected by way of questionnaires for various solid waste management techniques. Then, a Multi-Criteria Decision Making (MCDM) method, namely the Fuzzy Technique for Order Preferences by Similarity to Ideal Solutions (Fuzzy TOPSIS) approach is applied for ranking of the different treatment waste management scenarios. The result of this study shows that 40% Biomethanation + 60% Landfill is the best scenario among the available methodologies of solid waste management. This study would help in determining the suitable treatment technology for Municipal Solid Waste (MSW) material. All stakeholders including civic organizations, government bodies, society as a whole, would be able to understand the various techniques and tools used in the study and hence make judgments.

Keywords Municipal solid waste · Fuzzy · Analytic Hierarchy Process · Technique for Order Preferences by Similarity to Ideal Solutions · Biomethanation · Landfill · Composting · Aerobic digestion · Incineration

Introduction

Municipal Solid Waste (MSW) is an unavoidable by-product of human civilization. Earlier, municipal waste consisted mainly of biodegradable composition and hence did not create many problems for society. With the increase in the rate of urbanization, the content of plastics and inorganic packaging materials in municipal wastes has also increased substantially. The increased population is generating an enormous quantity of solid waste. This results in the excessive amassing of solid waste in an urban environment, which creates a severe threat. In the present situation, the discarding of trash at the landfill site or uncontrolled discarding is the ultimate fate of most of the solid residues (Hussain and Aggarwal 2016). In addition, most of the world's cities do not have any processing facilities and are experiencing unplanned urban sprawl.

The quantum of solid waste generated and its management primarily depends upon the population, composition, and economic growth of an area. It also depends on the efficiency of the reuse and recycling systems and gets affected by the change in seasons. Due to the variation in characteristics and quantity of the generated solid waste, the management of solid waste in terms of handling and disposal is of significant concern. In addition, management proves to be

✉ Girish Kumar
girish.kumar154@gmail.com

[1] Department of Civil Engineering, Netaji Subhas University of Technology, West Campus, Delhi 110073, India

[2] Department of Mechanical Engineering, Delhi Technological University, Delhi 110042, India

Published online: 02 February 2022

more challenging in an economically and environmentally feasible manner. It has also been reported that the waste generated by a highly urbanized country or wealthier community produces solid waste with high inorganic composition. This can be compared with less urbanized countries like India, having people with middle-income groups producing solid waste composition with high organic matter content in between 40 and 85% (Coban et al. 2018). The average value of organic matter content in India, as reported by the World Bank, is found to be 64% as compared to 28% in high-income countries (Hoornweg and Bhada-Tata 2012). The amount of MSW generation in developed countries is higher than that of the developing countries. MSW generation is about 0.3–0.7 kg/capita-day and about 0.5–1.5 kg/capita-day in less developed cities and rapidly developing cities, respectively (Imura et al. 2005). The Indian capital, Delhi, is generating about 7000 tonnes/day of MSW and is estimated to rise to 17,000–25,000 tonnes/day by the year 2021. This condition is almost the same for all the metropolitan cities in the country. About 70–80% of generated MSW is collected, and the rest remains unattended on streets or in small open dumps (Talyan et al. 2008).

The present study has proposed two main contributions to confine this existing problem of managing the MSW. First, the analysis of Solid Waste Management (SWM) problems is carried out by comprehensively studying the waste composition and waste management methodologies, and then the scenarios are formulated. Secondly, these scenarios are evaluated from all perspectives including economical, technical, environmental, and social, using Multi-Criteria Decision Making (MCDM) techniques. The result obtained by the MCDM technique is appropriate based upon the actual practical outline of waste management. On the other hand, solid waste treatment methodologies used in this study involve selecting disposal scenarios alternatives that are comprehensive in terms of covering several treatment technologies. The present study has a comparatively larger domain, which can be implemented on the other developing countries producing a high proportion of organic waste.

Literature Review

In the past few years, various studies focusing on developing a model on municipal SWM were conducted. The studies suggested that MCDM for the solution of SWM proves to be very useful in identifying suitable SWM methods. For computational and mathematical equations, the traditional AHP method is more suitable than other methods (Saaty 1980). AHP involves the approach that consists of independently evaluating the various aspects against each other and then laying out the hierarchical results as contrived by Saaty (2008). But this method received criticism as it becomes ineffective in application to ambiguous decision problems which does not involve any numerical comparison data but instead through linguistic inputs, used by the real world which are vague and uncertain (Javanbarg et al. 2012). The use of the fuzzy set theory allows incorporating unquantifiable, incomplete, and partially known information into the decision model (Duran et al. 2008). Fuzzy set theory is concerned mainly with unclear human thoughts and perception, which is used to deal with the problem quantitatively (Beskese et al. 2014). Therefore, the fuzzy set theory is unified with the traditional AHP, which uses the principles of disintegration, set wise comparison for the beneficial and effective analysis of data (Taylan et al. 2014).

A fuzzy number is a generalization of a regular, real number in the sense that it does not refer to one single value but rather to a connected set of possible values, where each possible value has its weight between 0 and 1 (Dijkman et al. 1983). Zadeh (1965) initiated the idea of fuzzy sets. According to Zadeh, a fuzzy set is a group of objects with a spectrum of a set of membership. The concept of inclusion, union, intersection, complement, etc., is enlarged to fuzzy sets. Bellman and Zadeh (1970) evolved a general theory of decision-making in a fuzzy environment and put forward the notion of maximizing decision.

A study based on the assessment of different technologies for managing yard waste in India was performed using AHP that considered composting, incineration, landfills, anaerobic digestion, pelletization-gasification, and pelletization-pyrolysis. Four criteria namely environmental, economic, technical, and socio-political were considered for evaluation (Thengane 2019). Results showed that the most promising technology was pelletization-gasification followed by pelletization-pyrolysis.

"TOPSIS" is an acronym for 'Technique for Order of Preference by Similarity to Ideal Solution' is a multi-criteria decision-making method, initially advanced by Hwang and Yoon (1981). Later Yoon in 1987 and Hwang et al. (1993) modified it. It is based on the remunerative aggregation that examines a set of alternatives by classifying the weights for each criterion, assigning the scores to each criterion and calculating the geometric distance between every alternative and the ideal alternative. It works on the fact that the geometric distance should be least from the Positive Ideal Solution (PIS) (Assari 2012) and longest from the Negative Ideal Solution (NIS) for the selected alternative (Beikkhakhian et al. 2015; Taylan et al. 2014).

In the TOPSIS method, the data is collected in the form of crisp values. To remove the vagueness and uncertainty from the evaluations and judgment, Fuzzy TOPSIS was developed by Chen in 2000 to solve the MCDM problem in the fuzzy environment (Lima et al. 2014). The areas where Fuzzy TOPSIS have been used are Health issues (Muhlbacher et al. 2015), location decisions (Kumar et al. 2019), social issues (Verheyden & L Moor 2015), problems related to

environmental concern (Molinos et al. 2015), economic issues (Cobuloglu and Buyuktahtakin 2015; Piltan & Sowlati 2016) and mass customization challenges (Dwivedi et al. 2021).

Jovanovic et al. (2016) suggested an approach to select an optimal MSW management system based on the MCDM method for the Kragujevac city in the Republic of Serbia. In their study, two techniques of Multi-Attribute Decision Making (MADM) consisting of Simple Additive Weighting method (SAW) and Technique for Order of Preferences by Similarity to Ideal Solution (TOPSIS) were used for the comparison of waste management strategies. Rahimi et al. (2020) used fuzzy MCDM and Geographic Information System (GIS) techniques to select landfill sites in an environmentally critical area of Mahallat city, Iran. The study comprises fourteen effective criteria-categorized into three groups including environmental, economic and social criteria. Fuzzy Best–Worst Method (BWM) was used to obtain weights of criteria and the maps were generated using GIS for spatial analysis. Respective sites were ranked using the MULTIMOORA method. Behzad et al. (2020) evaluated the current waste management system in the Nordic countries. The comparison was drawn using BWM combined with evaluation based on the distance from the average solution. Further, sensitivity analysis was done that proved Sweden's waste management performance is dominant in the Nordic region. Makan et al. (2013) derived alternative schemes for MSW management and analyzed them using the Preference Ranking Organisation Method for Enrichment Evaluation (PROMETHEE) in Morocco. Analytic Network Process (ANP) and Decision-Making Trial and Evaluation Laboratory (DEMATEL) were the MCDM tools used by the expert group to determine valid and beneficial solutions regarding municipal solid waste management in Metro Manila (Tseng 2008). Ekmekçioğlu et al. (2010) proposed a modified fuzzy TOPSIS methodology to evaluate a suitable solid waste management site in Çatalca, a rural district in Istanbul, Turkey. The use of Fuzzy pairwise comparison matrices of the Analytic Hierarchy Process (AHP) was recommended to determine the weights of the selection criteria. Chabuk et al. (2019) proposed landfill site selection criteria for an arid area named Babylon Governorate, which is located in the middle region of Iraq by using selected fifteen of the essential criteria for their study. The MCDM methods were applied for the suitable weight for each criterion using methods of AHP and Ratio Scale Weighing (RSW). Roy et al. (2018) presented an extended TOPSIS methodology in the Indian context for the disposal of MSW with methods evaluated under some fixed criteria by the experts based on the credibility theory.

Chaudhary et al. (2017) used the fuzzy MCDM technique for landfill site selection for Allahabad city (Kareli, Chandpur Salori, Phaphamau) and reported the study area Kareli was ranked first among the selected sites. A similar approach was used for modeling landfill site selection in Mumbai (Kharat et al. 2016a, b). Khan and Farooqi. (2012) prioritize the municipal SWM factors in India using the Fuzzy AHP method. The study focuses on the importance of the segregation of waste at its origin into recyclables and compostable matter. Khan and Faisal (2008) evaluated three alternative integrated waste disposal scenarios for India comprising landfill, composting and incineration by using ANP. The problem of waste management was assessed in Thiruvananthapuram, Kerala, for the local self-government body. A clear preference for community Biomethanation emerged with the next preference for community vermicomposting using AHP and Simple Additive Weighting (SAW) (Thampi and Rao 2015).

Kharat et al. (2016a, b) evaluated six methods of solid waste management using Delphi and AHP considering social, economic, technical, and environmental criteria for India. Among the six methods comprising bio-methanation, RDF-combustion, pyrolysis, incineration and landfilling, composting was reported to be the most appropriate MSW management technique. The present study is carried out with a different approach. In general, simple treatment methods are not performed; rather a combination of several methods is practiced. Thus, analysis is carried out by considering scenarios comprising of desired combinations of waste management techniques, which are based on the waste composition, studies of various organizations, past works of literature and researches. Further, the scenarios generated are finalized in consultation with domain experts. The use of fuzzy AHP and fuzzy TOPSIS instead of the conventional AHP and TOPSIS method allowed the Decision Makers to handle decision problems more effectively that are uncertain and vague which do not comprise crisp numerical inputs. It can be assessed that the work carried out by Ekmekçioğlu et al. (2010) and Coban et al. (2018) have used scenario-based evaluation for managing the solid waste of a city. This study can be well compared with the studies being carried out by various researchers and investigators discussed above.

Methodology

This section comprises four different parts namely; List of Symbols, fuzzy AHP method, fuzzy TOPSIS method and Methodology Procedure. The fuzzy AHP method is applied to calculate the weights of each criterion, and the fuzzy TOPSIS method is employed to rank the most suitable scenarios.

List of Symbols.

{A}: Comparison Matrix used in Fuzzy AHP.

l, m, n: First, Second and Third Components of the Fuzzy Scale values which are converted from the linguistic response.

a_{ij}: Elements of Matrix.

r_i: Geometric Mean.

$\otimes$: fuzzy multiplication symbol.
$\oplus$: fuzzy addition symbol.
w_i: Fuzzy weight.
W_p: Importance of weight of p^{th} criteria.
w_p: Weight of criteria considered.
X_{ij}: Fuzzy ratings of location (i) with respect to each criterion (j).
a_{ij},b_{ij},c_{ij}: Elements of each column in Combined Decision Matrix.
R_{ij}: Normalized Fuzzy Decision Matrix.
c_j*: Benefit Criteria.
a_j^-: Cost Criteria.
w_j: weights of criteria obtained from AHP.
V_{ij}: Weighted Normalized Fuzzy Decision Matrix.
A1 and A2: Arbitrary fuzzy matrix.
A*: Fuzzy Positive Ideal Solution (FPIS).
A^-: Fuzzy Negative Ideal Solution (FNIS).
v_j*: Maximum value of the third component in each column of Weighted Normalized Fuzzy Decision Matrix.
v_{ij3}: Third component in each column of weighted normalized fuzzy decision matrix.
v_{ij1}: First component in each column of Weighted Normalized fuzzy Decision Matrix.
v_j^-: Minimum value of the first component in each column of Weighted Normalized Fuzzy Decision Matrix.
d: distance from each alternative to FPIS and FNIS.
d_i*: Summation of all values of i^{th} row (i = 1, 2, ….,8) of Table 1
d_i^-: Summation of all values of i^{th} row (i = 1, 2, ….,8) of Table 2
CC_i: Closeness Coefficient of each option.

Fuzzy AHP method

In this study, the Triangular Fuzzy Numbers (TFNs) are used to convert the variables into an analytical form (fuzzy sets), which is further transformed into crisp values. The triangular fuzzy membership functions are used because of their simple implementation and precise evaluation. The nature of inputs is well computed by a chosen membership function. The relevance of considered attributes or the relative pair-wise comparison was done by following certain mathematical operations, which consist of using a definite scale from 1 to 9. The linguistic scales and fuzzy triangle were made as per Table 3 and Fig. 1.

The stepwise procedure of fuzzy AHP is detailed below:

Step—I

MATRIX {A} is formulated from the fuzzy set numbers used for the individual criteria. The derived variables are then replaced by the respective fuzzy scale, as given by matrix **{A}**.

Table 1 Distance to FPIS

	C1	C2	C3	C4	C5	C6	C7	C8	C9	d_i^*
S1	0.1072	0.0664	0.0172	0.0475	0.0351	0.0355	0.0000	0.0413	0.0926	0.4430
S2	0.0887	0.0551	0.0217	0.0396	0.0351	0.0296	0.0270	0.0304	0.0915	0.4186
S3	0.0068	0.0067	0.0413	0.0030	0.0351	0.0296	0.0016	0.0144	0.0094	0.1479
S4	0.0000	0.0090	0.0362	0.0393	0.0422	0.0296	0.0269	0.0000	0.0000	0.1832
S5	0.0888	0.0067	0.0192	0.0394	0.0351	0.0296	0.0016	0.0133	0.0915	0.3252
S6	0.0887	0.0000	0.0362	0.0030	0.0351	0.0296	0.0026	0.0133	0.0908	0.2993
S7	0.0891	0.0551	0.0328	0.0396	0.0000	0.0000	0.0016	0.0348	0.0917	0.3447
S8	0.0890	0.0556	0.0000	0.0000	0.0351	0.0296	0.0324	0.0304	0.0917	0.3640

Table 2 Distance to FNIS

	C1	C2	C3	C4	C5	C6	C7	C8	C9	d_i^-
S1	0.0000	0.0000	0.0266	0.0000	0.0071	0.0060	0.0324	0.0000	0.0000	0.0721
S2	0.0200	0.0114	0.0230	0.0080	0.0073	0.0013	0.0056	0.0161	0.0091	0.1019
S3	0.1065	0.0651	0.0000	0.0473	0.0073	0.0018	0.0323	0.0289	0.0918	0.3811
S4	0.1072	0.0648	0.0158	0.0092	0.0000	0.0018	0.0059	0.0413	0.0926	0.3389
S5	0.0192	0.0651	0.0246	0.0085	0.0072	0.0025	0.0323	0.0318	0.0091	0.2002
S6	0.0200	0.0664	0.0158	0.0473	0.0072	0.0008	0.0322	0.0318	0.0183	0.2398
S7	0.0182	0.0114	0.0192	0.0080	0.0422	0.0296	0.0323	0.0183	0.0068	0.1860
S8	0.0186	0.0108	0.0413	0.0475	0.0072	0.0000	0.0000	0.0161	0.0068	0.1485

Table 3 Pairwise comparison scale of the study

Fuzzy number	Importance	Triangular fuzzy scale
1	Equally important	(1,1,1)
3	Moderately important	(1,3,5)
5	Highly important	(3,5,7)
7	Very highly important	(5,7,9)
9	Absolutely important	(7,9,9)

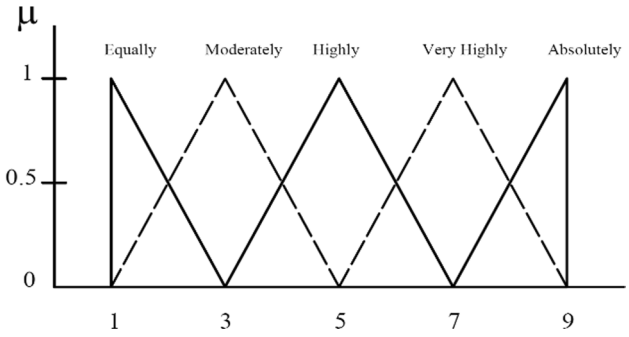


Fig. 1 Triangular fuzzy scale adopted for the study

$$\mathbf{MATRIX\{A\}} = \left[1 \cdots a_{1m} \vdots \ddots \vdots a_{m1} \cdots 1\right] = \left[1 \cdots 1/a_{1m} \vdots \ddots \vdots 1/a_{m1} \cdots 1\right] \tag{1}$$

In this,

$$a_{ij=}\langle for\forall < jfor\forall = jfor\forall > j\rangle \tag{2}$$

$$a_{ij=}\langle for\forall < jfor\forall = jfor\forall > j\rangle$$

Step—II

A group of responses is collected from various domains, which result in varying decision matrices. Therefore, an aggregate matrix is constructed by the geometric mean technique (3) which satisfies each response of the decision-makers. ⊗ is a fuzzy multiplication symbol and ⊕ fuzzy addition symbol respectively. The fuzzy weight matrix is derived by using Buckley's Method as given by Kahraman and Cebi (2009). The geometric mean value of the matrix row is evaluated, and then the derived values are multiplied accordingly by the fuzzy relative matrix, given by Eq. (4).

$$r_i = \sqrt[n]{\{a_{i1} \otimes \ldots \ldots a_{ij} \cdots \otimes \ldots .a_{in}\}} \forall_i = 1, 2, 3, 4, 5 \ldots .n \tag{3}$$

$$w_i = r_i \otimes (r_1 \oplus r_2 \oplus r_3 \ldots \ldots \cdots \oplus r_n)^{-1} \forall_i = 1, 2, 3 \ldots \ldots .n \tag{4}$$

Step—III

Following the calculations of fuzzy weights, the fuzzy numbers are converted to crisp values using the centroid method. It is the most common method for defuzzification (Opricovic and Tzeng 2004). After the defuzzification of elements is completed, normalization is carried out. These two processes can be applied concurrently, as shown in Eq. (5)

$$W_p = \frac{w_p}{\sum_{i=1}^{n} w_i} \tag{5}$$

where the importance of the weight of p^{th} criteria is W_p, a crisp number and 'i' is the number of the criteria.

Fuzzy TOPSIS method

The fuzzy scale as shown in Table 4 is used to evaluate various scenarios related to the nine criteria.

The steps involved in Fuzzy TOPSIS are:

Step I

Get a Combined Decision Matrix by using Eq. (6). The Fuzzy ratings of location (i) with respect to each criterion (j) is given by $X_{ij} = (a_{ij}, b_{ij}, c_{ij})$.

Where $a_{ij} = \min_k\{a^k_{ij}\}, b_{ij} = 1/k\sum^k_{k=1} b^k_{ij}$,

$$c_{ij} = max_k\left\{c^k{}_{ij}\right\} \tag{6}$$

Step II

Obtain the Normalized Fuzzy Decision Matrix R_{ij}:

For Benefit Criteria:

$$R_{ij} = \left(a_{ij}/c_j^*, b_{ij}/c_j^*, c_{ij}/c_j^*\right), where c_j^* = max_i\left\{c_{ij}\right\} \tag{7}$$

For Cost criteria:

$$R_{ij} = \left(a_j^-/c_{ij}, a_j^-/b_{ij}, a_j^-/a_{ij}\right), where a_j^- = min_i\{aij\} \tag{8}$$

Table 4 Triangular fuzzy scale for responses

Triangular fuzzy scale	Responses
(1,1,1)	Very low
(1,3,5)	Low
(3,5,7)	Moderate
(5,7,9)	High
(7,9,9)	Very high

Step III

Multiply Normalized Fuzzy Decision Matrix R_{ij} with weights w_j of evaluation criteria obtained from AHP to get the Weighted Normalized Fuzzy Decision Matrix V_{ij}:

$$V_{ij} = R_{ij}{}^* w_j \tag{9}$$

$$A_1 \otimes A_2 = (a_1, b_1, c_1) \otimes (a_2, b_2, c_2) = \left(a_1{}^* a_2, b_1{}^* b_2, c_1{}^* c_2\right) \tag{10}$$

Step IV

Compute Fuzzy Positive Ideal Solution (FPIS) and Fuzzy Negative Ideal Solution (FNIS):

$$A^* = \left(v_1{}^*, v_2{}^*, \ldots\ldots v_n{}^*\right), v_j{}^* = max_i\left\{v_{ij3}\right\} \tag{11}$$

$$A^- = \left(v_1{}^-, v_2{}^- \ldots\ldots v_n{}^-\right), v_j{}^- = min_i\left\{v_{ij1}\right\} \tag{12}$$

Step V

Calculate the distance 'd' from each alternative to the FPIS and to FNIS:

$$d(x,y) = \left[\frac{1}{3}\left\{\left(a_1 - a_2\right)^2 + \left(b_1 - b_2\right)^2 + \left(c_1 - c_2\right)^2\right\}\right]^{0.5} \tag{13}$$

Step VI

Compute the distance d_i^* and d_i^- of each option from the FPIS and FNIS:

$$d_j^* = \sum_{j=1}^{n} d\left(v_{ij}, v_j^*\right) \tag{14}$$

$$d_j^- = \sum_{j=1}^{n} d\left(v_{ij}, v_j^-\right) \tag{15}$$

Step VII

Compute Closeness Coefficient CC_i of each option to rank the options in decreasing order of CC_i values

$$CC_i = d_i^-/\left(d_i^- + d_i^*\right) \tag{16}$$

The above methodology of Multi-Criteria Decision Making (Fuzzy TOPSIS and Fuzzy AHP) can be extensively used in different areas where the collection

of numerical data points is not possible and there is no concrete solution to the particular problem having several criteria. For implementing the above methodology, the information in the form of linguistic variables is gathered and it is converted into a fuzzy number, which is further processed to obtain the final ranking/priority of the alternatives. The unique forms of fuzzy numbers, which include triangular and trapezoidal fuzzy numbers, can be used to illustrate the vagueness of the input constants related to the specific subject.

Methodology Procedure

Stepwise procedure for the methodology is presented below:

Step 1

Various solid waste management methods that are in practice are shortlisted. Out of these SWM methods, suitable scenarios are formulated.

Step 2

According to the context of SWM, numerous criteria are considered for the evaluation of scenarios. Out of which most suitable criteria are selected with the help of domain experts.

Step 3

Considering the selected criteria and scenarios, a questionnaire is prepared with suitable options ranging from "extremely important" to "not at all important" to weigh the criterion. The questionnaire is used to obtain the responses from domain experts.

Step 4

Fuzzy AHP: A pair-wise comparison matrix is constructed based on the responses obtained from experts. This matrix is used to derive the weights for each criterion by using the Fuzzy AHP procedure detailed in this section.

Step 5

Fuzzy TOPSIS: After the fuzzy AHP analysis, ranks are assigned to the scenarios using the fuzzy TOPSIS method as per the procedure discussed in the "Fuzzy TOPSIS" sub-section.

Case Illustration

This section illustrates the work done in this study. At present, concern about the management of municipal solid waste is important, especially for a country with the second-largest population (India). There is a need to determine the best suitable Solid Waste Management (SWM) technique, which is feasible, reliable and practical. Hence, this study comes intending to identify the most appropriate (SWM) using Multi-criteria Decision Making. The information obtained through questionnaires included uncertainty and vagueness because of the incomplete data, impreciseness of human judgments. Hence, to overcome this constraint, fuzzy AHP is implemented. Fuzzy AHP assigns weights to the criteria used to evaluate the alternative solutions. For the linguistic assessment of solid waste management scenarios, the Fuzzy Technique for Order Preferences by Similarity to Ideal Solutions (Fuzzy TOPSIS) is used, which gives preferential order to the respective scenarios. TOPSIS is more preferred for SWM analysis, which belongs to a 'distance-based approach' (Coban et al. 2018). Therefore, Fuzzy AHP and Fuzzy TOPSIS have been opted for a comprehensive analysis of the selected scenarios. The set of results obtained from the investigation gives the ranking to the Solid waste management scenario. In line with the procedure mentioned in the methodology, the outputs obtained from the study are as follows:

Step 1

Solid Waste Management Scenarios The various MSW treatment methods such as composting, incineration, refuse-derived fuel, reusing, recycling, Biomethanation, landfilling, anaerobic degradation, etc. are being practiced worldwide. In this study, the six most widely adopted MSW treatment methodologies in India were identified. These methodologies include Landfill (LF), Aerobic Digestion (AD), Biomethanation (BM), Composting (C), Recycling and Reuse (RE) and Incineration (IN).

The eight scenarios were modeled using the information gathered from the National Solid Waste Association of India, a professional body advocating and promoting sustainable management of solid waste. Municipal Solid Waste composition details were examined thoroughly from the Central Pollution Control Board (CPCB), which is undertaken, by the Ministry of Environment, Forest and Climate Change, Government of India. According to the CPCB, the organic fraction was 40% on average, regarding the average constituent of MSW composition. Incinerable, recyclable and inert waste was 25%, 10%, and 25%, respectively. The above data aided in figuring out the combination percentage of MSW methodologies and the past literature from various sources were considered to form scenarios. Further, the generated

scenarios were finalized in consultation with domain experts. The description of the various scenarios is as follows:

Scenario 1 (S1) In this scenario, all the waste goes to landfills. Only 10% of solid municipal waste is disposed of by the scientific method of landfilling where an organized collection of waste and leveling the compacted waste by using the mechanical method is carried out (Sharholy et al. 2008). It is the simplest and economical method, which is used for disposing of all kinds of waste.

Scenario 2 (S2) This scenario takes into account the segregation process of waste into organic biodegradable and inorganic dry waste. Organic waste is treated by aerobic digestion. In aerobic digestion, mesophilic bacteria oxidize the waste, which produces carbon dioxide and heat along with water. When the temperature rises to 45°, thermophilic bacteria dominate and oxidize the maximum organic matter of the waste. The whole process takes about 3–4 months (Obeta 2005). The remaining residual inorganic waste goes to recycling units or is dumped in landfills, depending upon the feasibility**.**

Scenario 3 (S3) In this scenario, Biomethanation treats about 40% of the organic waste. It produces biogas and manure by the microbial action in the absence of air and rejected waste goes to landfill. The screened and shredded solid waste is mixed with the raw sewage and then stored in the airtight digester for 30 days. Produced gas such as H_2S and SO_2 is removed with moisture, and the remaining clean gas is used as fuel.

Scenario 4 (S4) This scenario considers the recycling process, where the separated dry waste is transformed into potentially useful material. Organic waste is treated by composting, and then leftovers go to landfills.

Scenario 5 (S5) This scenario is similar to that of the above-mentioned scenario number 4; the only difference is that the remaining waste is incinerated instead of disposing it into the landfills. Incineration is the burning of waste, notably the burning of hazardous solid and liquid waste of hospitals. Thermal pyrolysis is another such method carried out in an oxygen-free environment that initiates destructive distillation.

Scenario 6 (S6) This scenario consists of solid waste management using composting, incineration, recycling, as well as landfilling.

Scenario 7 (S7) This scenario constitutes 50% of the waste taken for landfilling and the remaining 50% of waste is incinerated.

Scenario 8 (S8) In this scenario, all the waste is managed by using the incineration process. The method of Refuse-Derived Fuel (RDF) is also practiced where the mixture of higher concentrations of combustible material is segregated and processed as RDF. The produced RDF waste possesses high Gross Calorific Values (GCVs) ranging between 14.6 and 40.2 kJ/g. The plastic possesses significantly high calorific values of 33.6 ± 0.5 kJ/g, 40.2 ± 1.0 kJ/g, and 28.6 ± 0.4 kJ/g for non-packaging hard plastics, packaging foils, and packaging polyethylene terephthalate (PET), respectively (Nam-Chol et al. 2017).

All the scenarios considered for evaluations in this study are summarized in Table 5.

Step 2

Criteria for Evaluation This section discusses the criteria used for evaluating municipal solid waste management scenarios. Numerous criteria affecting MSW management scenarios were identified, out of which nine most relevant criteria were selected. These criteria were shortlisted based on the past literature and the opinion of domain experts. Haaren (2009) considered five criteria to find out the best technology for SWM by Multi-Criteria Analysis (MCA), namely, environmental impact, cost, land area requirement, odor control, and feedstock flexibility. In this study, two environmental criteria including health risk and environmental impact were also considered to provide more authentic results. Three types of financial-based criteria were also included; namely, Transportation Cost, Maintenance Cost, and Initial Investment Cost. The financial criteria depict the fund, which has to be spent to establish the respective waste management scenario. In addition to these essential criteria, two profit-based criteria were also considered, which include the Output from processed MSW and Internal Rate of Return (IRR). The profitable criteria depict the monetary gain generated from the scenarios after processing the solid waste.

The criteria used in this study are equivocal, with no exact data to evaluate MSW treatment scenarios. Hence, a questionnaire was developed, filled by experts from the field on a five-point scale described in the methodology section.

Table 5 MSW management scenarios

S no	Scenarios	Code
1	100%LF	S1
2	40% AD + 60% LF	S2
3	40% BM + 60%LF	S3
4	40%C + 10%RE + 50%LF	S4
5	10%RE + 40%C + 50% IN	S5
6	40% C + 10% RE + 25%IN + 25%LF	S6
7	50%LF + 50%IN	S7
8	100%IN	S8

Table 6 Evaluation criteria used in the study

Category	Criteria	Code
Environmental criteria	Environmental impacts	C_1
	Health risks	C_2
Social criteria	Odour control	C_3
	Land area requirement	C_4
Financial criteria	Transportation Cost	C_5
	Initial Investment Cost	C_6
	Maintenance Cost	C_7
Profitable criteria	Output from processed MSW	C_8
	Internal Rate of Return (IRR)	C_9

A brief description of the nine criteria used in this study is as follows:

1. **Environmental Impacts**
2. This criterion includes the possible threats that may cause to the environment, atmosphere resulting from municipal solid waste management activities. It can also be referred to as vulnerability to the environment in waste management.
3. **Health Risks**
4. Handling and management of municipal solid waste can cause a lot of harm, and many kinds of infectious and chronic diseases. However, the unorganized sector comprising of explicitly waste workers and rag pickers are the most vulnerable victims to such infectious ailments.
5. **Odor Control**
6. Odor consisting of H_2S creates social nuisance all around the area and hence it is observed as a criterion for evaluating scenarios. The odor also affects the materials and damages the instruments, equipment and other components.
7. **Land Area Requirement**
8. It refers to the total land area available or required for all the activities on the waste management and disposal of the same.
9. **Transportation Cost**
10. It includes the total cost to be incurred for transporting solid waste while handling, managing, and ultimately disposing at the site.
11. **Initial Investment cost**
12. It involves costs related to the construction and setting up of a solid waste management scenario.
13. **Maintenance Cost**
14. The total cost occurring in various activities, including the payment of wages to workers involved in the system, payment of electricity bills and other miscellaneous expenditures incurred in the overall management of the solid waste, are part of maintenance cost.
15. **Output from Processed MSW**
16. It includes the energy and useful by-products generated, including high calorific value products and methane gas formed during Incineration and composting respectively.
17. **Internal Rate of Return (IRR)**
18. IRR is the discount rate at which the present value of cost is equal to the present value of the benefits. It is a rate of return at which the Net Present Value (NPV) is equal to zero. IRR gives a number by which the economic viability of the technique can be determined (Hussain and Aggarwal 2016).

The criteria have been designated by codes C_1, C_2, C_3, C_4, C_5, C_6, C_7, C_8, C_9, respectively, as shown in Table 6 below:

According to the present context of SWM, various criteria were considered for the evaluation of scenarios. Out of which nine most suitable criteria were selected with the help of field experts.

Step 3

The questionnaire was designed as per step-3 of the procedure of methodology. Responses given by the respective academicians, other professionals involved in the management of the civic body and pollution regulatory agency were collected. The Decision Makers (DM) were chosen such that every aspect of solid waste management is covered while collecting the necessary information required. The decision-makers were selected from industrial as well as academic backgrounds, which helped in obtaining optimum results in the outcome of this study. The judgments of the four decision-makers are utilized to carry out the analysis. Table 7 gives the details of the decision-makers.

Table 7 Decision makers (DM) profile

S. no	Background	Designation	Experience	Organization
1	Industry	Deputy Director	> 18 years	National Productivity Council, New Delhi-110003
2	Industry	Executive Engineer	> 20 years	Delhi Pollution Control Committee, Civil Lines, Delhi-110054
3	Academic	Professor	> 22 years	MNIT Jaipur-302017, Rajasthan
4	Academic	Professor	> 24 years	Jamia Millia Islamia, New Delhi-110025

Step 4

Fuzzy AHP: A pair-wise comparison matrix is constructed based on the responses obtained from experts. This matrix is further used to derive the weights for each criterion by using Fuzzy AHP. The pairwise comparison matrix obtained from each of the four Decision Makers (DM) involving all the nine criteria is shown in Tables 8, 9, 10, 11, GM (L), GM (M) and GM (N) in Table 6 are the Geometric Mean which is used to calculate the fuzzy weights W (L), W (M) and W (N) respectively.

The final weightage of each criterion is obtained by taking the arithmetic mean of all the obtained weights as

Table 8 Pairwise Comparison Matrix- DM 1 with different criteria and obtained weights

	C1			C2			C3			C4			C5			C6			C7			C8			C9			GM(L)	GM(M)	GM(N)	W(L)	W(M)	W(N)	WEIGHTS
C1	1	1	1	1	1	1	3	5	7	1	3	5	1	1	1	3	5	7	1	3	5	1	3	5	1	3	5	1.28	2.33	3.15	0.19	0.21	0.19	**0.20**
C2	1	1	1	1	1	1	3	5	7	1	3	5	1	1	1	3	5	7	1	3	5	1	3	5	1	3	5	1.28	2.33	3.15	0.19	0.21	0.19	**0.20**
C3	0.14	0.2	0.33	0.14	0.2	0.33	1	1	1	0.2	0.33	1	0.14	0.2	0.33	1	1	1	0.2	0.33	1	0.2	0.33	1	0.2	0.33	1	0.25	0.36	0.69	0.04	0.03	0.04	**0.04**
C4	0.2	0.33	1	0.2	0.33	1	1	3	5	1	1	1	0.2	0.33	1	1	3	5	1	1	1	1	1	1	1	1	1	0.58	0.88	1.43	0.09	0.08	0.09	**0.08**
C5	1	1	1	1	1	1	3	5	7	1	3	5	1	1	1	3	5	7	1	3	5	1	3	5	1	3	5	1.28	2.33	3.15	0.19	0.21	0.19	**0.20**
C6	0.14	0.2	0.33	0.14	0.2	0.33	1	1	1	0.2	0.33	1	0.14	0.2	0.33	1	1	1	0.2	0.33	1	0.2	0.33	1	0.2	0.33	1	0.25	0.36	0.69	0.04	0.03	0.04	**0.04**
C7	0.2	0.33	1	0.2	0.33	1	1	3	5	1	1	1	0.2	0.33	1	1	3	5	1	1	1	1	1	1	1	1	1	0.58	0.88	1.43	0.09	0.08	0.09	**0.08**
C8	0.2	0.33	1	0.2	0.33	1	1	3	5	1	1	1	0.2	0.33	1	1	3	5	1	1	1	1	1	1	1	1	1	0.58	0.88	1.43	0.09	0.08	0.09	**0.08**
C9	0.2	0.33	1	0.2	0.33	1	1	3	5	1	1	1	0.2	0.33	1	1	3	5	1	1	1	1	1	1	1	1	1	0.58	0.88	1.43	0.09	0.08	0.09	**0.08**
																											SUM	6.68	11.23	16.56	1.00	1.00	1.00	1.00

Table 9 Pairwise Comparison Matrix- DM 2 with different criteria and obtained weights

	C1			C2			C3			C4			C5			C6			C7			C8			C9			GM(L)	GM(M)	GM(N)	W(L)	W(M)	W(N)	WEIGHTS
C1	1	1	1	3	5	7	1	3	5	1	3	5	3	5	7	1	3	5	3	5	7	3	5	7	3	5	7	1.84	3.53	5.04	0.27	0.31	0.30	**0.30**
C2	0.14	0.2	0.33	1	1	1	0.2	0.33	1	0.2	0.33	1	1	1	1	0.2	0.33	1	1	1	1	1	1	1	1	1	1	0.47	0.58	0.88	0.07	0.05	0.05	**0.06**
C3	0.2	0.33	1	1	3	5	1	1	1	1	1	1	1	3	5	1	1	1	1	3	5	1	3	5	1	3	5	0.84	1.63	2.45	0.12	0.14	0.15	**0.14**
C4	0.2	0.33	1	1	3	5	1	1	1	1	1	1	1	3	5	1	1	1	1	3	5	1	3	5	1	3	5	0.84	1.63	2.45	0.12	0.14	0.15	**0.14**
C5	0.14	0.2	0.33	1	1	1	0.2	0.33	1	0.2	0.33	1	1	1	1	0.2	0.33	1	1	1	1	1	1	1	1	1	1	0.47	0.58	0.88	0.07	0.05	0.05	**0.06**
C6	0.2	0.33	1	1	3	5	1	1	1	1	1	1	1	3	5	1	1	1	1	3	5	1	3	5	1	3	5	0.84	1.63	2.45	0.12	0.14	0.15	**0.14**
C7	0.14	0.2	0.33	1	1	1	0.2	0.33	1	0.2	0.33	1	1	1	1	0.2	0.33	1	1	1	1	1	1	1	1	1	1	0.47	0.58	0.88	0.07	0.05	0.05	**0.06**
C8	0.14	0.2	0.33	1	1	1	0.2	0.33	1	0.2	0.33	1	1	1	1	0.2	0.33	1	1	1	1	1	1	1	1	1	1	0.47	0.58	0.88	0.07	0.05	0.05	**0.06**
C9	0.14	0.2	0.33	1	1	1	0.2	0.33	1	0.2	0.33	1	1	1	1	0.2	0.33	1	1	1	1	1	1	1	1	1	1	0.47	0.58	0.88	0.07	0.05	0.05	**0.06**
																											SUM	6.70	11.30	16.80	1.00	1.00	1.00	1.00

Table 10 Pairwise Comparison Matrix- DM 3 with different criteria and obtained weights

	C1			C2			C3			C4			C5			C6			C7			C8			C9			GM(L)	GM(M)	GM(N)	W(L)	W(M)	W(N)	WEIGHTS
C1	1	1	1	1	3	5	1	3	5	1	3	5	5	7	9	3	5	7	1	3	5	1	1	1	1	3	5	1.35	2.73	3.87	0.19	0.24	0.24	**0.22**
C2	0.2	0.33	1	1	1	1	1	1	1	1	1	1	3	5	7	1	3	5	1	1	1	0.2	0.33	1	1	1	1	0.79	1.06	1.48	0.11	0.09	0.09	**0.10**
C3	0.2	0.33	1	1	1	1	1	1	1	1	1	1	3	5	7	1	3	5	1	1	1	0.2	0.33	1	1	1	1	0.79	1.06	1.48	0.11	0.09	0.09	**0.10**
C4	0.2	0.33	1	1	1	1	1	1	1	1	1	1	3	5	7	1	3	5	1	1	1	0.2	0.33	1	1	1	1	0.79	1.06	1.48	0.11	0.09	0.09	**0.10**
C5	0.11	0.14	0.2	0.14	0.2	0.33	0.14	0.2	0.33	0.14	0.2	0.33	1	1	1	0.2	0.33	1	0.14	0.2	0.33	0.11	0.14	0.2	0.14	0.2	0.33	0.17	0.23	0.38	0.02	0.02	0.02	**0.02**
C6	0.14	0.2	0.33	0.2	0.33	1	0.2	0.33	1	0.2	0.33	1	1	3	5	1	1	1	0.2	0.33	1	0.14	0.2	0.33	0.2	0.33	1	0.26	0.43	0.93	0.04	0.04	0.06	**0.04**
C7	0.2	0.33	1	1	1	1	1	1	1	1	1	1	3	5	7	1	3	5	1	1	1	0.2	0.33	1	1	1	1	0.79	1.06	1.48	0.11	0.09	0.09	**0.10**
C8	1	1	1	1	3	5	1	3	5	1	3	5	5	7	9	3	5	7	1	3	5	1	1	1	1	3	5	1.35	2.73	3.87	0.19	0.24	0.24	**0.22**
C9	0.2	0.33	1	1	1	1	1	1	1	1	1	1	3	5	7	1	3	5	1	1	1	0.2	0.33	1	1	1	1	0.79	1.06	1.48	0.11	0.09	0.09	**0.10**
																											SUM	7.09	11.41	16.48	1.00	1.00	1.00	1.00

Table 11 Pairwise Comparison Matrix- DM 4 with different criteria and obtained weights

	C1			C2			C3			C4			C5			C6			C7			C8			C9		
S1	5	9	9	5	7.5	9	3	6.5	9	5	8	9	3	6.5	9	5	7	9	1	4.5	7	1	2.5	9	1	2	7
S2	3	5.5	9	3	5.5	9	3	5.5	9	3	6.5	9	3	5.5	9	3	6.5	9	3	5.5	9	1	5	9	1	4	7
S3	1	5.5	9	1	4	7	1	4.5	7	1	5.5	9	3	5.5	9	3	6	9	1	5	9	3	6.5	9	3	5	7
S4	1	4.5	7	1	4.5	7	1	5	9	3	5	7	5	7	9	3	6	9	3	5	7	5	7.5	9	3	5.5	9
S5	3	6	9	1	4	7	3	6	9	3	5.5	9	3	6	9	3	5.5	9	1	5	9	3	7	9	1	4	7
S6	3	5.5	9	1	3	7	1	5	9	1	5.5	9	3	6	9	3	7	9	1	6	9	3	7	9	1	5.5	9
S7	3	7	9	3	5.5	9	1	6	9	3	6.5	9	1	5.5	9	1	6	9	1	5	9	1	4.5	7	1	3.5	7
S8	3	6.5	9	3	6.5	9	5	7.5	9	1	4.5	7	3	6	9	3	8	9	5	7	9	1	5	9	1	3.5	7

summarized in Table 10 along with a pairwise comparison matrix of each of the decision-makers. A perusal of the data summarized in Table 12 indicates that the decision matrix obtained in different criteria is being converted into average values. The highest weightage value of 0.2297 indicates that while management of solid waste, the environmental impacts need to be considered on priority followed by health risks. However, the results also indicate that cost is given the least preference as compared to odor control, land area requirement and outputs in processing the waste.

From the results obtained from fuzzy AHP, Environmental Impacts (C1) is the most important criteria as solid waste affects the environment through soil contamination, water contamination and releases various greenhouse gases due to burning and decomposing leads to climate contamination. The flora and fauna are also severely affected as their natural habitat is polluted. The collection and segregation of solid waste impact the health of workers engaged in waste management as well as the people living around the dump yards. Thus, harmful chemicals and gases produced to attract attention to the Health Risks (C2) and Odour Control (C3) as the second and third most important criteria respectively.

Step 5

Fuzzy TOPSIS: After the fuzzy AHP analysis, ranks were given to the scenarios using the fuzzy TOPSIS method. As per the procedure discussed previously, Tables 13, 14, 15, 16 shows the responses given by the decision-makers converted to fuzzy numbers. Tables 17 and 18 illustrate the combined decision matrix and normalized decision matrix obtained respectively. Table 19 illustrates the weighted normalized decision matrix which accounts for the weight of each criterion obtained using fuzzy AHP.

Finally, the ranks for each of the municipal solid waste management scenarios were obtained. Table 20 shows the rank of each scenario arranged in preferential order.

Result and Discussion

This section discusses the results obtained in this study. Rank 1 is designated to scenario S3 and thus it stands out as the best scenario to treat Municipal Solid Waste. The agro-based industries as well as the waste from households in developing countries have high organic content, which is treated efficiently by the process of Biomethanation. Biogas and nutrient-enriched manure are the product of Biomethanation. Biogas consists mainly of methane used to produce electricity in small towns whereas; manure is substantially used in organic farming**.** Landfill practices are more desired than incineration due to the lack of necessary infrastructure and monetary resources and the high amount of wet and organic waste is hard to incinerate, producing toxic gases. The development of scientific landfills should be encouraged to tackle the air, land and water pollution caused by

Table 12 Final weights of criteria with decision matrices obtained in the present study

Criteria	DM 1	DM 2	DM 3	DM 4	Final weights
Environment impacts	0.1963	0.2957	0.2218	0.2052	**0.2297**
Health risks	0.1963	0.0580	0.0980	0.2052	**0.1394**
Odor control	0.0372	0.1381	0.0980	0.2052	**0.1196**
Land area requirement	0.0842	0.1381	0.0980	0.0880	**0.1021**
Transportation cost	0.1963	0.0580	0.0225	0.0880	**0.0912**
Initial investment cost	0.0372	0.1381	0.0438	0.0880	**0.0768**
Maintenance cost	0.0842	0.0580	0.0980	0.0389	**0.0698**
Output from processed MSW	0.0842	0.0580	0.2218	0.0389	**0.1007**
Internal Rate of Return (IRR)	0.0842	0.0580	0.0980	0.0429	**0.0708**

Table 13 Responses by DM 1

	C1			**C2**			**C3**			**C4**			**C5**			**C6**			**C7**			**C8**			**C9**		
S1	7	9	9	7	9	9	3	5	7	5	7	9	5	7	9	5	7	9	3	5	7	5	7	9	1	1	1
S2	3	5	7	5	7	9	3	5	7	5	7	9	5	7	9	5	7	9	5	7	9	5	7	9	3	5	7
S3	5	7	9	3	5	7	1	3	5	5	7	9	5	7	9	5	7	9	5	7	9	5	7	9	3	5	7
S4	3	5	7	3	5	7	3	5	7	3	5	7	5	7	9	5	7	9	3	5	7	5	7	9	5	7	9
S5	3	5	7	3	5	7	5	7	9	3	5	7	5	7	9	5	7	9	5	7	9	3	5	7	3	5	7
S6	3	5	7	3	5	7	5	7	9	5	7	9	5	7	9	5	7	9	5	7	9	3	5	7	3	5	7
S7	5	7	9	5	7	9	3	5	7	5	7	9	5	7	9	5	7	9	5	7	9	1	3	5	1	3	5
S8	5	7	9	5	7	9	5	7	9	3	5	7	5	7	9	7	9	9	5	7	9	1	3	5	1	3	5

Table 14 Responses by DM 2

	C1			C2			C3			C4			C5			C6			C7			C8			C9		
S1	7	9	9	5	7	9	5	7	9	7	9	9	3	5	7	5	7	9	3	5	7	1	1	1	3	5	7
S2	5	7	9	3	5	7	3	5	7	5	7	9	3	5	7	5	7	9	3	5	7	3	5	7	3	5	7
S3	5	7	9	3	5	7	3	5	7	5	7	9	3	5	7	3	5	7	3	5	7	3	5	7	3	5	7
S4	3	5	7	3	5	7	3	5	7	3	5	7	5	7	9	5	7	9	3	5	7	5	7	9	3	5	7
S5	7	9	9	3	5	7	3	5	7	5	7	9	3	5	7	3	5	7	5	7	9	5	7	9	1	1	1
S6	5	7	9	1	3	5	1	3	5	3	5	7	3	5	7	3	5	7	7	9	9	7	9	9	1	3	5
S7	3	5	7	3	5	7	1	3	5	3	5	7	1	3	5	1	3	5	1	3	5	3	5	7	1	3	5
S8	5	7	9	5	7	9	5	7	9	3	5	7	5	7	9	7	9	9	5	7	9	1	3	5	1	3	5

Table 15 Responses by DM 3

	C1			C2			C3			C4			C5			C6			C7			C8			C9		
S1	7	9	9	5	7	9	5	7	9	7	9	9	5	7	9	5	7	9	1	3	5	1	1	1	1	1	1
S2	3	5	7	3	5	7	3	5	7	5	7	9	3	5	7	5	7	9	3	5	7	3	5	7	1	3	5
S3	3	5	7	1	3	5	3	5	7	3	5	7	3	5	7	3	5	7	3	5	7	5	7	9	3	5	7
S4	1	3	5	1	3	5	1	3	5	3	5	7	5	7	9	3	5	7	3	5	7	7	9	9	3	5	7
S5	3	5	7	1	3	5	3	5	7	3	5	7	5	7	9	3	5	7	1	3	5	7	9	9	3	5	7
S6	3	5	7	1	1	1	1	3	5	5	7	9	5	7	9	7	9	9	1	3	5	5	7	9	5	7	9
S7	7	9	9	3	5	7	7	9	9	7	9	9	3	5	7	5	7	9	3	5	7	3	5	7	1	3	5
S8	5	7	9	5	7	9	5	7	9	3	5	7	3	5	7	3	5	7	5	7	9	5	7	9	1	3	5

Table 16 Responses by DM 4

	C1			C2			C3			C4			C5			C6			C7			C8			C9		
S1	7	9	9	5	7	9	5	7	9	5	7	9	5	7	9	5	7	9	3	5	7	1	1	1	1	1	1
S2	3	5	7	3	5	7	5	7	9	3	5	7	3	5	7	3	5	7	3	5	7	1	3	5	1	3	5
S3	1	3	5	1	3	5	3	5	7	1	3	5	3	5	7	5	7	9	1	3	5	5	7	9	3	5	7
S4	3	5	7	3	5	7	5	7	9	3	5	7	5	7	9	3	5	7	3	5	7	5	7	9	3	5	7
S5	3	5	7	1	3	5	5	7	9	3	5	7	3	5	7	3	5	7	1	3	5	5	7	9	3	5	7
S6	3	5	7	1	3	5	5	7	9	1	3	5	3	5	7	5	7	9	3	5	7	5	7	9	5	7	9
S7	5	7	9	3	5	7	5	7	9	3	5	7	5	7	9	5	7	9	3	5	7	3	5	7	3	5	7
S8	3	5	7	3	5	7	7	9	9	1	3	5	3	5	7	7	9	9	5	7	9	5	7	9	3	5	7

Table 17 Combined decision matrix

	C1			C2			C3			C4			C5			C6			C7			C8			C9		
S1	5	9	9	5	7.5	9	3	6.5	9	5	8	9	3	6.5	9	5	7	9	1	4.5	7	1	2.5	9	1	2	7
S2	3	5.5	9	3	5.5	9	3	5.5	9	3	6.5	9	3	5.5	9	3	6.5	9	3	5.5	9	1	5	9	1	4	7
S3	1	5.5	9	1	4	7	1	4.5	7	1	5.5	9	3	5.5	9	3	6	9	1	5	9	3	6.5	9	3	5	7
S4	1	4.5	7	1	4.5	7	1	5	9	3	5	7	5	7	9	3	6	9	3	5	7	5	7.5	9	3	5.5	9
S5	3	6	9	1	4	7	3	6	9	3	5.5	9	3	6	9	3	5.5	9	1	5	9	3	7	9	1	4	7
S6	3	5.5	9	1	3	7	1	5	9	1	5.5	9	3	6	9	3	7	9	1	6	9	3	7	9	1	5.5	9
S7	3	7	9	3	5.5	9	1	6	9	3	6.5	9	1	5.5	9	1	6	9	1	5	9	1	4.5	7	1	3.5	7
S8	3	6.5	9	3	6.5	9	5	7.5	9	1	4.5	7	3	6	9	3	8	9	5	7	9	1	5	9	1	3.5	7

Table 18 Normalized decision matrix

	C1			C2			C3			C4			C5			C6			C7			C8			C9		
S1	0.11	0.11	0.2	0.11	0.13	0.2	0.33	0.72	1	0.11	0.13	0.2	0.11	0.15	0.33	0.11	0.14	0.2	0.14	0.22	1	0.11	0.28	1	0.11	0.22	0.78
S2	0.11	0.18	0.33	0.11	0.18	0.33	0.33	0.61	1	0.11	0.15	0.33	0.11	0.18	0.33	0.11	0.15	0.33	0.11	0.18	0.33	0.11	0.56	1	0.11	0.44	0.78
S3	0.11	0.18	1	0.14	0.25	1	0.11	0.5	0.78	0.11	0.18	1	0.11	0.18	0.33	0.11	0.17	0.33	0.11	0.2	1	0.33	0.72	1	0.33	0.56	0.78
S4	0.14	0.22	1	0.14	0.22	1	0.11	0.56	1	0.14	0.2	0.33	0.11	0.14	0.2	0.11	0.17	0.33	0.14	0.2	0.33	0.56	0.83	1	0.33	0.61	1
S5	0.11	0.17	0.33	0.14	0.25	1	0.33	0.67	1	0.11	0.18	0.33	0.11	0.17	0.33	0.11	0.18	0.33	0.11	0.2	1	0.33	0.78	1	0.11	0.44	0.78
S6	0.11	0.18	0.33	0.14	0.33	1	0.11	0.56	1	0.11	0.18	1	0.11	0.17	0.33	0.11	0.14	0.33	0.11	0.17	1	0.33	0.78	1	0.11	0.61	1
S7	0.11	0.14	0.33	0.11	0.18	0.33	0.11	0.67	1	0.11	0.15	0.33	0.11	0.18	1	0.11	0.17	1	0.11	0.2	1	0.11	0.5	0.78	0.11	0.39	0.78
S8	0.11	0.15	0.33	0.11	0.15	0.33	0.56	0.83	1	0.14	0.22	1	0.11	0.17	0.33	0.11	0.13	0.33	0.11	0.14	0.2	0.11	0.56	1	0.11	0.39	0.78

Table 19 Weighted normalized decision matrix

Weights	0.2297			0.1394			0.1196			0.1021			0.0912			0.0768			0.0698			0.1007			0.0708		
	C1			C2			C3			C4			C5			C6			C7			C8			C9		
S1	0.03	0.03	0.05	0.02	0.02	0.03	0.04	0.09	0.12	0.01	0.01	0.02	0.01	0.01	0.03	0.01	0.01	0.02	0.01	0.02	0.07	0.01	0.03	0.10	0.08	0.02	0.06
S2	0.03	0.04	0.08	0.02	0.03	0.05	0.04	0.07	0.12	0.01	0.02	0.03	0.01	0.02	0.03	0.01	0.01	0.03	0.01	0.01	0.02	0.01	0.06	0.10	0.08	0.03	0.06
S3	0.03	0.04	0.23	0.02	0.03	0.14	0.01	0.06	0.09	0.01	0.02	0.10	0.01	0.02	0.03	0.01	0.01	0.03	0.01	0.01	0.07	0.03	0.07	0.10	0.24	0.04	0.06
S4	0.03	0.05	0.23	0.02	0.03	0.14	0.01	0.07	0.12	0.01	0.02	0.03	0.01	0.01	0.02	0.01	0.01	0.03	0.01	0.01	0.02	0.06	0.08	0.10	0.24	0.04	0.07
S5	0.03	0.04	0.08	0.02	0.03	0.14	0.04	0.08	0.12	0.01	0.02	0.03	0.01	0.02	0.03	0.01	0.01	0.03	0.01	0.01	0.07	0.03	0.08	0.10	0.08	0.03	0.06
S6	0.03	0.04	0.08	0.02	0.05	0.14	0.01	0.07	0.12	0.01	0.02	0.10	0.01	0.02	0.03	0.01	0.01	0.03	0.01	0.01	0.07	0.03	0.08	0.10	0.08	0.04	0.07
S7	0.03	0.03	0.08	0.02	0.03	0.05	0.01	0.08	0.12	0.01	0.02	0.03	0.01	0.02	0.09	0.01	0.01	0.08	0.01	0.01	0.07	0.01	0.05	0.08	0.08	0.03	0.06
S8	0.03	0.04	0.08	0.02	0.02	0.05	0.07	0.10	0.12	0.01	0.02	0.10	0.01	0.02	0.03	0.01	0.01	0.03	0.01	0.01	0.01	0.01	0.06	0.10	0.08	0.03	0.06
A*	0.03	0.05	0.23	0.02	0.05	0.14	0.07	0.10	0.12	0.01	0.02	0.10	0.01	0.02	0.09	0.01	0.01	0.08	0.01	0.02	0.07	0.06	0.08	0.10	0.24	0.04	0.07
A-	0.03	0.03	0.05	0.02	0.02	0.03	0.01	0.06	0.09	0.01	0.01	0.02	0.01	0.01	0.02	0.01	0.01	0.03	0.01	0.01	0.01	0.01	0.03	0.10	0.08	0.02	0.06

Table 20 Ranks of scenarios

Scenarios	CODE	d^*_i	d^-_i	CC_i	Rank
40% BM + 60%LF	S3	0.1479	0.3811	0.7204	**1**
40%C + 10%RE + 50%LF	S4	0.1832	0.3389	0.6491	**2**
40% C + 10% RE + 25%IN + 25%LF	S6	0.2993	0.2398	0.4448	**3**
10%RE + 40%C + 50% IN	S5	0.3252	0.2002	0.3810	**4**
50%LF + 50%IN	S7	0.3447	0.1860	0.3505	**5**
100%IN	S8	0.3640	0.1485	0.2897	**6**
40% AD + 60% LF	S2	0.4186	0.1019	0.1958	**7**
100%LF	S1	0.4430	0.0721	0.1401	**8**

huge waste dumps in landfills. Scenario, S4 and S6 share the second and third ranks respectively, which highlight the fact that recycling should also be practiced, which is a premier method of treating inorganic waste. Rag pickers are seen on streets collecting waste such as plastics, cardboards, metal waste and other non-biodegradable waste, which they sell to recycling units and earn some money. However, this method of managing waste is harmful as it risks their health. Although incineration is less practiced (scenarios 6, 5, 7 and 8), it is used to dispose of hospital waste, sanitary napkins, cardboard, paper and other waste, which have high calorific value. Ashes produced can be used in construction and the generated heat can be used in making electricity. Stakeholders can implement anyone from the top-ranked three scenarios (S3, S4 and S6) for the cities producing similar waste characteristics. Scenarios ranked last (scenario 7, 8, 2 and 1), consist mainly of incineration and landfill that are not solely efficient methods of waste management. Recycling of inorganic and composting of organic waste should be done to reduce the consumption of fresh raw material and to recover waste in the form of nutrients and energy.

Biomethanation and composting are distinct methods from socio-economic and environmental viewpoints, as all the top favored scenarios by the analysis (S3, S4, and S6) involve this method. Determining the relevant organic waste percentage and devoting the resources toward obtaining the targeted composting rate is the major issue. Biomethanation is gaining importance at considerable amounts but very few local government bodies initiate this technology due to high capital investment. However, the by-product of Biomethanation can compensate for the initial financing. The municipalities should actively plan for improving the waste

collection techniques and should encourage people to dispose of organic and inorganic waste separately so that the treatment of waste is done specifically.

The alternative scenarios incorporated in this study are coincidental with the current integrated solid waste management process in India. The ongoing applications are in organization with scenarios 3, 4 and 6, which were also justified by MCDM methods in the study. The proposed methodology may be replicated for the other developing/developed countries. However, results may differ from country to country. More and different types of scenarios can be generated for evaluation specific to the respective country.

Conclusion

The problem of managing municipal solid waste is growing tremendously. Production of waste is increased by blooming industrialization and increment in living standards. Even though the management of this issue needs sophisticated analytical techniques, the professionals from the operation management domain have paid little attention to the problem so far.

Among various municipal SWM studies that involve MCDM methodology as a solution approach, this study projects out in the following perspective. Firstly, the methodology used involves selecting disposal scenario alternatives that are comprehensive in terms of covering several treatment technologies, which were categorized under eight scenarios. The consideration of scenarios suggests being more practical and relevant for the diverse waste composition which includes organic, inorganic and recyclable. Secondly, the conventional AHP and TOPSIS methods are quantitative techniques that do not allow the Decision Makers to handle decision problems that are ambiguous and do not comprise crisp numerical inputs. The formulated questionnaire gathers the feedback from the domain experts in the linguistic form, which is more appropriate in context to this study. Therefore, Fuzzy AHP and Fuzzy TOPSIS use these linguistic variables to describe the subjective judgment of the decision-maker quantitatively to rank the scenarios.

The present study is limited to the treatment of municipal solid waste, but it can also be extended to radioactive waste, hazardous waste, industrial waste and electronic waste. The composition of waste differs from region to region such as tourist spot which comprises more plastic and food packaging waste. Rural areas are majorly comprised of biodegradable wet waste. Therefore, a region-specific analysis can be conducted to determine the suitable waste management technology. A separate analysis on liquid and gaseous waste can also be performed which contributes to water and air pollution respectively.

This study is a modest endeavor to demonstrate different ways to manage the SWM problem of a developing country. It represents the various opportunities incorporated in approaching this problem from a quantitative perspective through the implementation of MCDM methods.

Supplementary Information The online version contains supplementary material available at https://doi.org/10.1007/s41660-021-00215-1.

Data availability The datasets generated during and/or analyzed during the current study are available from the corresponding author on reasonable request.

Declarations

Conflict of interest The authors declare no competing interests.

References

A Assari 2012 Role of public participation in sustainability of historical city: usage of TOPSIS method Indian J Sci Technol 5 3 1 6

M Behzad S Hashemkhani Zolfani D Pamucar M Behzad 2020 A comparative assessment of solid waste management performance in the Nordic countries based on BWM-EDAS Journal of Cleaner Production 266 122008

Y Beikkhakhian M Javanmardi M Karbasian B Khayambashi 2015 The application of the ISM model in evaluating agile suppliers selection criteria and ranking suppliers using fuzzy TOPSIS-AHP methods Experts Systems with Applications 42 15–16 6224 6236

R Bellman L Zadeh 1970 Decision-making in a Fuzzy environment. Manage Sci 17(4) B-141–B-164

A Beskese H Demir H Ozcan H Okten 2014 Landfill site selection using fuzzy AHP and fuzzy TOPSIS: a case study for Istanbul Environmental Earth Sciences 73 7 3513 3521

A Chabuk N Al-Ansari H Hussain J Laue A Hazim S Knutsson R Pusch 2019 Landfill sites selection using MCDM and comparing method of change detection for Babylon Governorate Iraq Environmental Science and Pollution Research 26 35 35325 35339

S Chaudhary, NR Rawal A Husain 2017 A fuzzy analytical hierarchy process approach for landfill site selection: a case study in Allahabad City, India 1118–1122

A Coban I Ertis N Cavdaroglu 2018 Municipal solid waste management via multi-criteria decision-making methods: a case study in Istanbul, Turkey J Clean Prod 180 159 167

HI Cobuloglu IE Buyuktahtakin 2015 A stochastic multi-criteria decision analysis for sustainable biomass crop selection Expert Syst Appl 42 15–16 6065 6074

JG Dijkman H Haeringen van SJ Lange de 1983 Fuzzy numbers J Math Anal Appl 92 2 301 341

O Duran J Aguilo 2008 Computer-aided machine-tool selection based on a Fuzzy-AHP approach Expert Syst Appl 34 3 1787 1794

PK Dwivedi G Kumar RC Singh 2021 Challenges for mass customization in Industry 4.0 environment: an analysis using fuzzy TOPSIS approach. In: Kumar A., Pal A., Kachhwaha S.S., Jain P.K. (eds) Recent Advances in Mechanical Engineering. Lecture Notes in Mechanical Engineering. Springer, Singapore, 1079–1089

M Ekmekçioğlu T Kaya C Kahraman 2010 Fuzzy multi-criteria disposal method and site selection for municipal solid waste Waste Manage 30 8–9 1729 1736

D Hoornweg P Bhada-Tata 2012 What a waste: a global review of solid, Washington, DC 20433 USA: Urban Development & Local Government Unit World Bank

A Hussain K Aggarwal 2016 Solid waste management in India, MTech Dissertation, School of Engineering, Gautam Buddha University, Greater Noida, Uttar Pradesh, India

C Hwang Y Lai T Liu 1993 A new approach for multiple objective decision making Computers and Operational Research 20 8 889 899

CL Hwang K Yoon 1981 Multiple attribute decision making methods and applications. Berlin: Heidelberg: Springer- Verlag

H Imura S Yedla H Shirakawa MA Memon 2005 Urban environmental issues and trends in Asia — an overview Int Rev Environ Strateg 5 35

M Javanbarg C Scawthorn J Kiyono B Shahbodaghkhan 2012 Fuzzy AHP-based multi-criteria decision-making systems using particle swarm optimization Expert Syst Appl 39 960 966

S Jovanovic S Savic N Jovicic G Boskovic Z Djordjevic 2016 Using multi-criteria decision making for selection of the optimal strategy for municipal solid waste management Waste Manage Res 34 9 884 895

C Kahraman S Cebi 2009 A new multi-attribute decision-making method: hierarchical fuzzy axiomatic design Expert SystAppl 36 3 4848 4861

S Khan I Farooqi 2012 Prioritising municipal solid waste management factors in India using Fuzzy analytic hierarchy process Int J Environment and Waste Management 10 4 423 440

S Khan M Faisal 2008 An analytic network process model for municipal solid waste disposal options Waste Manage 28 9 1500 1508

M Kharat S Kamble R Raut S Kamble S Dhume 2016 Modeling landfill site selection using an integrated fuzzy MCDM approach. Modeling Earth Syst Environ 2(2)

MG Kharat RD Raut SS Kamble SJ Kamble 2016b The application of DELPHI and AHP method in environmentally conscious solid waste treatment and disposal technology selection Manag Environ Qual 27 4 427 440

A Kumar H Kashyap H Malhotra K Rawat G Kumar U Soni 2019 Preferential selection of locations for installing CCTV using fuzzy TOPSIS approach: A case study for North Delhi. Twelfth International Conference on Contemporary Computing (IC3), Noida, India, 1–7

F Lima Junior L Osiro L Carpinetti 2014 A comparison between Fuzzy AHP and Fuzzy TOPSIS methods to supplier selection Appl Soft Comput 21 194 209

A Makan 2013 Multi-criteria decision aid approach for the selection of the best compromise management scheme for the treatment of municipal solid waste in Morocco Int J Environment and Waste Management 12 3 300 317

M Molinos-Senante T Gomez R Caballero F Hernandez-Sancho R Sala-Garrido 2015 Assessment of wastewater treatment alternatives for small communities: an analytic network process approach Sci Total Environ 532 676 687

A Muhlbacher A Kaczynshi 2015 Making good decisions in healthcare with multi-criteria decision analysis: the use, current research and future development of MCDA. Appl Health Econ Health Policy 1–12

O Nam-Chol W Kim 2017 Investigation of characterization of municipal solid waste for refused-derived fuel, a case study. Energy Sources, Part A: Recovery, Utilisation, and Environmental Effects, 1–8

S Opricovic GH Tzeng 2004 Compromise solution by MCDM methods: a comparative analysis of VIKOR and TOPSIS Eur J Oper Res 156 2 445 455

M Piltan T Sowlati 2016 A multi-criteria decision support model for evaluating the performance of partnerships Expert System with Applications 45 373 384

S Rahimi A Hafezalkotob S Monavari A Hafezalkotob R Rahimi 2020 Sustainable landfill site selection for municipal solid waste based on a hybrid decision-making approach: Fuzzy group BWM-MULTIMOORA-GIS Journal of Cleaner Production 248 119186

Rob van Haaren (2009): Large sale aerobic composting of source-separated organic waste: a comparative study of environmental impacts, costs, and contextual effects, New York

Roy J, Adhikary K and Kar S (2018) Credibilistic TOPSIS model for evaluation and selection of municipal solid waste disposal methods. Advances in Waste Management, 243–261

TL Saaty 1980 The analytic hierarchy process: planning, priority setting, resource allocation McGraw New York

Saaty TL (2008) Decision making with the analytic hierarchy process, Int. J. Services Sciences, 1(1)

M Sharholy K Ahmad G Mahmood 2008 Trivedi R (2008) Municipal solid waste management in Indian cities — a review Waste Manage 28 2 459 467

V Talyan R Dahiya T Sreekrishnan 2008 State of municipal solid waste management in Delhi, the capital of India Waste Manage 28 7 1276 1287

O Taylan A Bafail R Abdulaal M Kabli 2014 Construction project selection and risk assessment by fuzzy AHP and fuzzy TOPSIS methodologies Appl Soft Comput 17 105 116

A Thampi B Rao 2015 Application of multi-criteria decision-making tools for technology choice in treatment and disposal of municipal solid waste for local self government bodies—a case study of Kerala, India The Journal of Solid Waste Technology and Management 41 1 84 95

SK Thengane 2019 Assessment of different technologies for managing yard waste using analytic hierarchy process Process Integr Optim Sustain 3 255 272

M Tseng 2008 Application of ANP and DEMATEL to evaluate the decision-making of municipal solid waste management in Metro Manila Environ Monit Assess 156 1–4 181 197

J Obeta Ugwuanyi 2005 Effect of digestion temperature and pH on treatment efficiency and evolution of volatile fatty acids during thermophilic aerobic digestion of model high strength agricultural waste Biores Technol 96 6 707 719

T Verheyden L Moor 2015 Multi-criteria decision analysis: methods to define and evaluate socially responsible investments Int J Manag Decis Mak 14 1 44 65

B Vucijak S Kurtagic I Silajdzic 2016 Multicriteria decision making in selecting best solid waste management scenario: a municipal case study from Bosnia and Herzegovina J Clean Prod 130 166 174

K Yoon 1987 A reconciliation among discrete compromise situations J Oper Res Soc 38 3 277 286

L Zadeh 1965 Fuzzy sets Inf Control 8 3 338 353

Publisher's Note Springer Nature remains neutral with regard to jurisdictional claims in published maps and institutional affiliations.

Experimental and theoretical investigation into surface roughness and residual stress using ball end magnetorheological finishing

DOI : 10.36909/jer.14281

Anand Sharma*, Mahendra Singh Niranjan*

**Department of Mechanical Engineering, Delhi Technological University, Delhi, India*

Corresponding Author: doc.asharma@yahoo.in

ABSTRACT

The generation of residual stresses by grinding process on the surface for a soft material results in poor performance and diminished life. In this paper, grinding-induced residual stresses is addressed and an attempt is made to relieve these residual stresses while achieving nano level surface finish using ball end magnetorheological finishing (BEMRF) process. BEMRF is a recently developed process that is effectively used to for fine figuring and polishing of a variety of magnetic and non-magnetic materials. In our present work we will demonstrate the relieving of residual stresses and reduction in surface roughness generated after surface grinding of Aluminium 7075 workpiece using BEMRF process. The impact of various BEMRF variables on reduction in surface roughness and residual stresses are discussed statistically and graphically. Residual stresses of workpiece surfaces have been measured by using portable X-ray residual stress analyzer. Significant process parameters affecting the residual stresses during polishing of workpiece are obtained using Analysis of variance (ANOVA) and F-test. It has been observed that reduction in residual stress is achieved along with nano level surface finish on aluminium workpiece surface using BEMRF technique.

Keywords: Residual stress; nanofinishing; magnetorheological; aluminium; ANOVA

INTRODUCTION

In this age of new industrialization revolution, there is a high demand for both nano products and macro products with high surface finish and strength (Li, 2020). Arun et al., 2021; Mahadik et al., 2020 & Qiu, 2021 discussed various applications of nano products in the field of biomedical and solar cells. However, development of gigantic Airbus A380 mostly with aluminium alloy confirms that this material possesses properties like high hardness, toughness, strength to weight ratio values etc. that are required in today's advanced industries. While achieving the best out of the aluminium alloys sometimes unwanted residual stresses are generated on the workpiece surface which leads to sub-surface damage resulting in part distortion. Brinksmeier (2007) observed that the various types of material processing methods, complex component design and

manufacturing techniques causes high residual stresses to be induced in the workpiece surface resulting in part distortion. Sim (2010) described that every year millions of Euros are spent trying to improve the quality of parts or components specially in aerospace industries by removing or avoiding such distortions. Ghosh (2021) mentioned in the article that even sometimes while polishing of workpiece, some amount of residual stresses is induced on workpiece surfaces leading to alteration in inter-planar spacing which directly influences the reflectivity and refraction index of polished product to be used in optical applications. Tyagi (2002) investigated the effect of residual stress on the optical properties of cadmium iodide films. The results showed that the residual stress was increased nonlinearly with thickness of the film and temperature of the treatment whereas a linear decrement in residual stress was observed with substrate temperature. Yi (2011) theoretically and experimentally explained the controlling of compression molding process through proper cooling in order to control the residual stresses which affects the glass properties. Sugano (1987) experimentally showed that an unwanted compressive residual stress of 60 MPa was induced during the diamond turning of aluminium alloy which resulted in sub-surface damage. Residual stresses are generally undesirable stresses that are developed in a workpiece after machining. Upon removal of such unwanted stresses can enhance the functional behavior and efficiency of machined components.

Being one of the most popular machining methods for hard materials the grinding process directly influences the operational properties of the workpiece such as fatigue strength, abrasive and corrosion resistance etc while creating a new surface of the workpiece. Achieving favourable surface integrity while obtaining high productivity during grinding process leads to a serious damage to the surface layer. Due to the high importance of grinding process, various investigations have been made to find a compromise between high productivity and favourable surface layer. Some approaches are analytical in nature which are based on the mathematical calculations of temperature distribution in the workpiece helping in the estimation of microhardness, residual stresses, microstructure etc. Kruszynski (1991) analytically analyzed the damage to the surface layer of the metal by grinding process through creation of residual stress keeping a close view of thermal aspects of grinding. It was concluded that the new proposed grinding parameter combining depth of cut, work speed and wheel speed have better control on the surface integrity during industrial practice. Tönshoff (1992) modeled and simulated the grinding energy and force models during grinding process. Also, kinematic and energetic processes were taken into consideration for temperature and surface integrity models. Brinksmeier (1987) established a model signifying that the generation of residual stresses depends on the machining parameters and selection of grinding wheel. Other approaches are purely experimental aiming at discovering the

best possible relationship between grinding and surface quality parameters. Zhejun (1989) investigated the surface integrity of grinding of hardened bearing steel. Results showed that the compressive residual stresses and harmful tensile residual stresses are formed when cubic boron-nitride wheels and aluminium oxide wheels are used respectively. Robinson (2010) measured residual stress distribution in 7449 aluminium alloy through neutron diffraction and deep hole drilling. Results of the neutron diffraction showed that a large amount of tensile residual stresses were formed at the centre of the quenched forging which was balanced by a compressive residual stress on surface region. Jomaa (2014) investigated the surface finish and development of residual stresses during orthogonal cutting of AA7075-T651 alloy under dry conditions. Results showed that with increase in cutting speed the residual stresses were tensile on surface. Lambropoulos (2001) demonstrated the issue of grinding-induced stresses and deformation in commercial Si wafers and removal of these stresses using non-conventional magnetorheological finishing (MRF) method. The results showed that by MRF polishing 90-95% of the residual stresses are relieved. Arrasmith (2001) introduced compressive surface stress by lapping 100mm diameter silicon wafer with different alumina abrasive particles and subsequently polished using magnetorheological finishing technique for relieving of induced stresses. Results showed that MRF technique successfully removed the surface grinding force for silicon wafer lapped with 5μm alumina abrasives.

Aluminium alloys are extensively used in semi-conductor manufacturing, specific purpose telescopes, optical systems and sensors, micro-electronic devices and at an enormous extent for conduction through wires. Koul (2011) made diamond cut aluminum based mirrors to be used as light collector in a specific telescope at Hanle, a high altitude astronomical site in India. Jaecklin (1994) experimentally observed the optical properties such as surface reflectivity and scattering characteristics of aluminum based micro mirrors along with two other materials such as single-crystal silicon and polycrystalline silicon and their mechanical properties. Results showed that the mirrors made of aluminum had higher surface reflectivity. Ahn (2004) polished aluminium surface through chemical mechanical polishing process which is increasingly used for developing MEMS using silica based slurry. However, apart from the properties mentioned above possessed by aluminium alloys they are also very ductile, malleable and poorly resistant to scratching behaviour which hinders the aim of achieving nano level surface finish. Chiu (2003) mentioned that it is a challenge to obtain good structural planarity and minimum surface scratching during chemical mechanical polishing of aluminum due to its soft nature. Considering low resistivity to scratching of aluminium, it becomes difficult to achieve nano level surface finish without damaging the surface integrity using conventional finishing processes. Vahdati (2008) found that various

finishing constraints such as finishing tool rotation, duration of finishing, type of abrasives, distance between magnetic tool & workpiece, lubricant used and finishing forces acting on the workipece can influence the removal rate of material and finish of the surface. Khan (2019) observed that the fluid composition especially the abrasive mesh size is an important parameter for finishing soft material like copper. Zhong (2003) found conventional process like turning of workpiece through single-point diamond also known as SPDT to be an efficient method to attain nanometric finish on soft materials such as copper, aluminium etc. but it is difficult to control the finishing forces.

Keeping in view the limitation of conventional finishing processes, various non-conventional finishing methods like magnetorheological fluid finishing (MRF), magnetorheological abrasive flow finishing (MRAFF), Chemo-mechanical magnetorheological finishing (CMMRF) etc. have been developed which controls the finishing forces using magnetic field to attain high surface finish. Jacobs (1995) described MRF process for finishing of optical components. Experimental results demonstrated that this process can be used to finish both spheres and aspheres optical glasses.

Golini (1997) experimentally finished a variety of spherical, flat, aspheres optical materials with two different machine configurations through MRF process. Results showed that the MRF process is highly capable of finishing optical materials, correcting figure errors without leaving any sub-surface damage to the workpiece.

Jha (2004) developed MRAFF process for finishing of complex internal geometries. To observe the performance of the process, surface roughness of stainless steel workpieces was referred as main output response. Magnetic flux density was varied from 0 to 0.574 Tesla to study the variation in surface roughness. Results showed that the surface roughness was reduced from 0.49μm to 0.34μm when the magnetic flux density value was fixed at 0 and 0.575 Tesla respectively. Also, at higher magnetic flux density the depths of grinding marks were reduced.

Jain (2010) made an effort in designing a finishing process (CMMRF) which combines the advantageous features of chemical mechanical polishing (CMP) and MRF for achieving nano level surface finish of silicon blanks with minimum surface damage and high material removal rate. Silicon blanks were polished in four stages with MR fluid containing silicon carbide, cerium oxide abrasives and magnetic particles mixed in water and oil base. It was observed that surface finish of 4.8Å was obtained through this process.

The limitations of finishing restricted geometries such as convex, curved in, plane and aspherical due to the constraint in relative motion of workpiece and finishing tool, were surpassed by developing BEMRF process a recently advanced version of MRF method. Singh (2012)

validated the BEMRF process developed by finishing EN31 and copper workpieces experimentally and simulating the magnetic flux density between the tool and workpiece. It was demonstrated that the performance of the newly developed process depends on magnetic nature of the workpiece, working gap and magnetizing current as EN31 workpiece obtained a surface finish of 70nm whereas surface finish of copper workpiece reached to a value of 102nm. Simulation of magnetic flux showed that the shape and size of the ball-end finishing spot varied with the working gap at particular magnetic current. Sharma (2019) critically reviewed MRF, MRAFF, CMMRF, BEMRF finishing process and concluded that BEMRF process is an effective process to obtain high level of surface finish on variety of work pieces. Sharma (2020) reviewed in detail the BEMRF process and concluded that this process can be effectively used for finishing of both magnetic and non-magnetic materials.

It has been observed from the past studies that the reduction of surface roughness and residual stress induced on aluminium alloy after grinding are rarely discussed. In this paper, high surface irregularity and residual stresses induced by grinding in the aluminium 7075 surface and subsequent polishing by BEMRF process resulting in reduction of residual stresses and surface roughness is discussed. Maloney (2016) observed that the ball end magnetorheological finishing (BEMRF) process based on smart fluids have an ability to control the finishing forces which enables it to finish 3D surfaces to nanometer levels without imposing surface or sub-surface damage to the finished component. This process is capable of finishing and polishing a variety of materials, either magnetic materials like diverse alloys of steel etc., or nonmagnetic materials such as glass, silicon, aluminum, copper, etc. Singh (2012) finished fused silica glass workpiece using computer numerically controlled BEMRF process for achieving nanometric level surface finish without sub-surface damage. A minimum of 0.14nm arithmetical mean roughness was obtained after finishing four times for 30 minutes each. Deep scratches on the workpiece surface were also observed when the applied magnetizing current was at a level of 4 amperes in first experiment. However, the magnetizing current was reduced to 2.4 amperes which resulted in much improved surface quality. Saraswathamma (2015) experimentally observed the effect of tool rotational speed, gap between the tool and workpiece and magnetizing current on surface roughness of silicon wafer during BEMRF process. Obtained results exhibited that on increasing the working gap decreases the surface finish whereas an increase in magnetizing current increases the surface finish of the silicon wafer. Also, surface finish decreased with increase in tool rotation at higher working gap. Khan (2018) finished non-magnetic copper workpiece through BEMRF process and simulated the magnetic flux density between the workpiece and the finishing tool which was then verified experimentally. Optimized MR fluid was also synthesized to obtained best results during

finishing of copper workpiece. It was observed that the magnetic flux density between the tool and the workpiece was significantly increased from 0.35 to 0.85 Tesla when copper was placed above a permanent magnet for creating two opposite magnetic poles which lacked before the introduction of permanent magnet due to copper being non-magnetic in nature.

The setup of BEMRF included vertically oriented MR finishing tool driven by servo motor comprising of cylindrically shaped inner core (made of iron), an outer core oriented concentrically to each other and electromagnetic coil (Figure 1(a)). The designing of electromagnet coil is done keeping in view to attain magnetic flux density not less than ~0.8 T at the MR finishing tool tip and is surrounded by copper tube through which chilled water is circulated to maintain the setup at a suitable temperature. The delivery of MR fluid was controlled by a delivery pump from the storage tank (funnel shape) to the tool tip. Figure 1(b) represents the development of a nearly ball shaped highly viscous MR fluid at the tool tip. As soon the MR fluid reaches the tip of the finishing tool, the magnetic CI particles present in the MR fluid aligns themselves along the magnetic field flow direction. The viscosity of the MR fluid is controlled or varied by regulating the power supply or current hence controlling the magnetic field strength.

The effectiveness of BEMRF process is highly affected by the magnitude and distribution of the magnetic flux density around the finishing region. Kansal (2018) invested during BEMRF of diamagnetic material the tip of the tool acts as a single pole and due to lack of opposite magnetic pole the deviation of magnetic flux lines take place which reduces the magnetic strength resulting in low material removal rate. In order to avoid the deviation of magnetic flux lines, a permanent magnet was placed under the workpiece so as to direct the magnetic flux through the non-magnetic material.

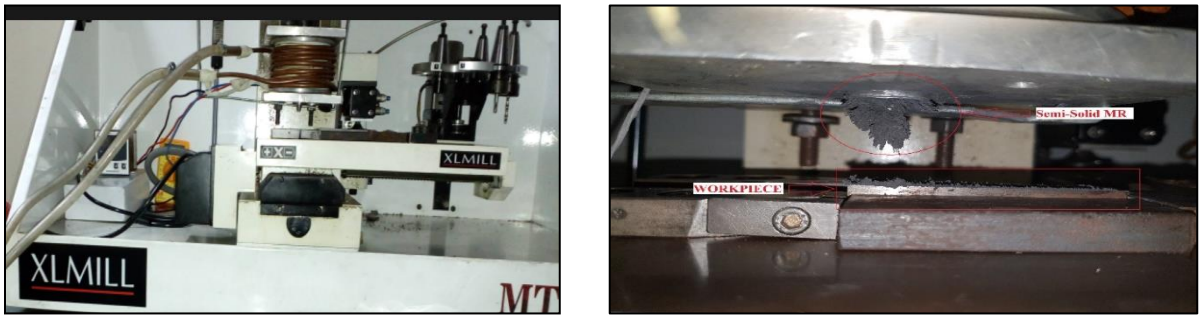
EXPERIMENTATION

In the present study, the effect of BEMRF input process parameters viz. magnetizing current (V_M), tool rotation (T_R) and working gap (W_X) on percentage surface roughness reduction (%SRR) and percentage reduction in residual stresses (%RRS) has been discussed. Table 1 presents the levels of the selected input parameters based on the preliminary experiments conducted and the parameters to be kept constant. Initial and final surface roughness values of workpiece were measured at five places using Mitutoyo Surftest SJ-301 before and after finishing through BEMRF process. Residual stresses initially induced after grinding procedure in aluminium 7075 workpieces and final residual stresses after BEMRF were measured using X-Ray residual stress analyzer. The residual stresses can be measured efficiently by detecting the full Debye ring data from a single incident X-ray angle.

According to Box-Behnken design technique, 17 experiments had to be conducted varying the input process parameters at three different levels. The experiments were conducted on 3-axis CNC BEMRF setup as shown in figure 1(a). Table 2 indicates the run order for performing of experiments, initial and final values of surface roughness and residual stresses and output responses i.e. percentage reduction in surface roughness (%SRR) and residual stresses (%RRS) for each specimen.

Table 1. Levels and ranges of selected process parameters

Process parameter	Units	Levels			Static Parameters	Description
		I	II	III		
Magnetizing Current (V_M)	amp	1.5	2.5	3.5	Feed Rate	5 mm/min
Tool rotation (T_R)	rpm	300	500	700		
Working gap (W_X)	mm	0.5	1.5	2.5		



(a) (b)

Figure 1. (a) setup of BEMRF tool and (b) semi-solid MR ball formation

Table 2. Design of experiments and output responses

Input Process Parameters					Initial Surface Roughness	Final Surface Roughness	Output Response 1	Initial Residual Stress	Final Residual Stress	Output Response 2
Std Order	Run Order	V_M	T_R	W_X	SR_i (nm)	SR_f (nm)	%SRR	RS_i (MPa)	RS_f (MPa)	% RRS
1	15	1.5	300	1.5	825	491	40.48	124	55	55.7
2	3	3.5	300	1.5	873	410	53.04	122	21	82.8
3	7	1.5	700	1.5	825	499	39.52	130	29	77.8
4	14	3.5	700	1.5	844	468	44.55	140	10	92.8
5	12	1.5	500	0.5	828	493	40.46	140	28	80
6	8	3.5	500	0.5	888	455	48.76	140	13	90.7
7	1	1.5	500	2.5	844	468	44.55	116	46	60.7
8	17	3.5	500	2.5	888	410	53.83	140	20	85.7
9	6	2.5	300	0.5	865	453	47.63	140	28	80
10	13	2.5	700	0.5	825	499	39.52	124	16	87.1
11	4	2.5	300	2.5	889	455	48.81	142	55	61.4
12	9	2.5	700	2.5	868	482	44.47	122	21	82.8
13	16	2.5	500	1.5	828	451	45.53	142	34	76.1
14	2	2.5	500	1.5	892	485	45.63	119	28	76.4
15	5	2.5	500	1.5	895	467	45.14	124	30	75.8

16	11	2.5	500	1.5	863	461	46.58	130	29	77.8
17	10	2.5	500	1.5	865	466	46.13	119	28	76.4

Legend: VM = magnetizing current, TR = tool rotation, WX = working gap, %SRR = Percentage surface roughness reduction and %RRS = percentage reduction in residual stresses

OUTCOME AND DISCUSSION

Surface roughness and residual stress information is noted at an increment of 10mm for each specimen surface, thus an average of total 5 readings were collected for each workpiece. Percentage surface roughness reduction (%SRR) and residual stress (%RRS) is calculated by equation 1 and 2 respectively.

$$\%SRR = \frac{Initial\ Surface\ Roughness - Final\ Surface\ Roughness}{Initial\ Surface\ Roughness} \times 100 \quad \textbf{(1)}$$

$$\%RRS = \frac{Initial\ Residual\ Stress - Final\ Residual\ Stress}{Initial\ Residual\ Stress} \times 100 \quad \textbf{(2)}$$

Firstly, fitness of the obtained statistical data is to be found i.e. how well the observed data fits with the expected data.

Surface Roughness of Al 7075

Quadratic model was recommended by Design Expert 6.0.8 software for percentage reduction in surface roughness. Table 3 shows the significant parameters or terms. F-value of the model 129.3567 and the corresponding p-value which is less than 0.001 as shown in table 3 indicates that the quadratic model is significant.

An empirical relationship (Equation (3)) between the output response i.e. percentage reduction in surface roughness and input process parameters is acquired after eliminating the non-significant parameters. This equation can be used for obtaining maximum reduction in surface roughness while BEMRF of Al 7075 material by predicting optimal values of input process parameters.

$$\%SRR = 46.13 + 4.50125 * V_M - 2.84625 * T_R + 1.8925 * W_X - 1.635 * T_R^2 + 0.6875 * W_X^2 - 2.1025 * V_M * T_R + 0.94 * T_R * W_X \quad \textbf{(3)}$$

Table 3. ANOVA table for %SRR after eliminating non-significant parameters

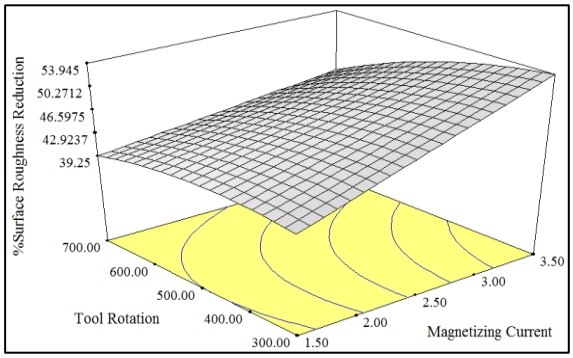
Source	Sum of Squares	Degree of Freedom	Mean Square	F Value	Prob > F	
Model	289.5628	7	41.366	129.3567	< 0.0001	Significant
V_M	162.09	1	162.09	506.8745	< 0.0001	Significant
T_R	64.80911	1	64.809	202.6657	< 0.0001	Significant
W_X	28.65245	1	28.652	89.59957	< 0.0001	Significant
T_R^2	11.28695	1	11.287	35.29562	0.0002	Significant
W_X^2	1.99566	1	1.9957	6.240662	0.0340	Significant
$V_M \times T_R$	17.68203	1	17.682	55.29377	< 0.0001	Significant
$T_R \times W_X$	3.5344	1	3.5344	11.05248	0.0089	Significant
Residual	2.87805	9	0.3198			
Lack of Fit	2.02697	5	0.4054	1.905316	0.2760	Not Significant

Pure Error	0.85108	4	0.2128
Cor Total	292.4408	16	

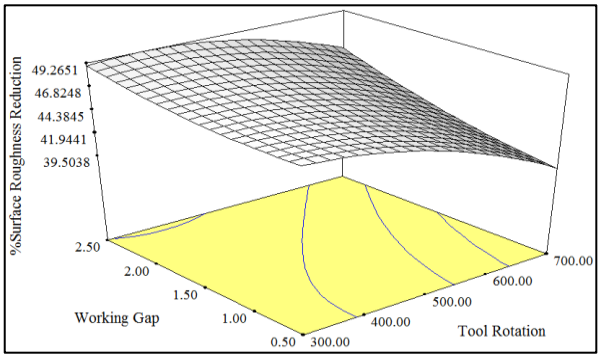
Standard Deviation = 0.565494, R^2 = 0.990159, Adjusted R^2 = 0.982504, Predicted R^2 = 0.946623, Mean = 45.68412, Coefficient of Variance = 1.23784, PRESS = 15.60952, Adequate Precision = 37.88097

Interaction graph of V_M and T_R on %SRR as shown in figure 2(a) clearly explains that %SRR attains a maximum value of 53.94% when V_M is kept at highest level of 3.5A and T_R at lowest value of 300 rpm, keeping W_X constant at 1.5 mm. This is due to the reason that at high level of magnetizing current the normal forces and tangential forces increases which shears more amount of material from the workpiece surface resulting in improved surface finish. On the other hand, a minimum of 39.25% reduction in surface roughness is attained at lowest value (1.5 A) of V_M and highest value (700 rpm) of T_R. This drastic decline in %SRR is due to the fact that at large rotational speed of the tool the quantity of abrasives interacting with workpiece surface through same working gap increases leading to an increase in indentation force. This increase in indentation force results in decrease in surface finish of the workpiece surface.

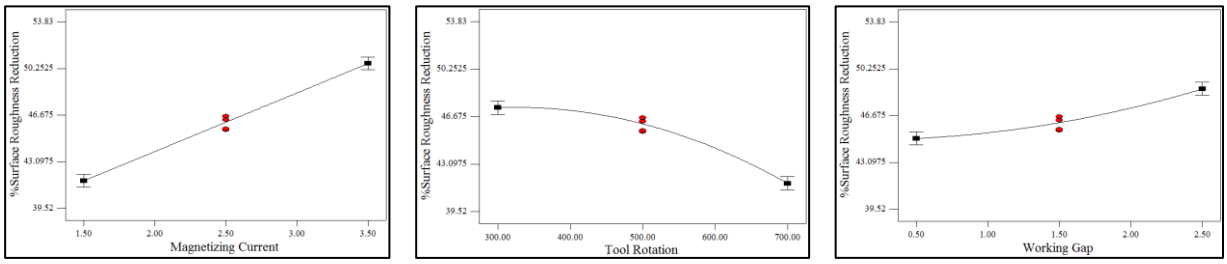
Combined effect of T_R and W_X on %RRS as represented in figure 2(b) shows that %SRR value increased from 39.5% to 45.17% on increasing W_X from 0.5 to 2.5 mm while keeping T_R at 700 rpm. A significant jump in %SRR value is seen due to the reason that at low W_X more volume of finishing fluid is squeezed between the tip of tool and finishing surface at same tool rotational speed thereby increasing the normal and tangential forces on the surface of the workpiece resulting in poor surface finish. Furthermore, magnetization intensity increases at smaller working gap leading to generation of deep abrasions thus increasing surface roughness. It is also observed that %SRR value further increased to 48.98% from 45.17% once tool rotation value is decreased to 300 rpm, working gap constant at 2.5 mm.



(a)



(b)



(c) (d) (e)

Figure 2. (a) Interaction graph of V_M & T_R on %SRR, (b) Interaction graph of T_R & W_X on %SRR, (c) Individual effect of V_M on %SRR, (d) Individual effect of T_R on %SRR and (e) Individual effect of W_X on %SRR

Figure 2 (d, e, f) represents the individual impact of magnetizing current, tool rotation and working gap on %SRR respectively. The same slant as the interaction graph was followed by the individual effect plot, which showed that an increase in V_M and W_X increased the %SRR while an increase in T_R reduced %SRR due to the reasons quoted above. Surface finish is an important constraint to assess the materials functional performance. Ghosh (2018) concluded that the optical materials to be utilised in optical industries are expected to acquire nanometric finish without any surface or sub-surface damage.

Residual Stress on Al 7075

Figure 3 represents the residual stresses on aluminium 7075 workpiece obtained after BEMRF process keeping magnetizing current, tool rotation and working gap at 1.5 mm, 3.5 amp, 700 rpm respectively. A maximum of 92.8 percentage reduction in residual stress is obtained at above mentioned parametric values. Table 4 shows the significant parameters or terms. F-value of the model 133.6858 and the corresponding p-value which is less than 0.001 as shown in table 4 indicates that the quadratic model is significant.

An empirical relationship (Equation (4)) between the output response i.e. percentage reduction in residual stress and input process parameters is acquired after eliminating the non-significant parameters. This equation can be used for obtaining maximum reduction in residual stress while BEMRF of Al7075 material by predicting optimal values of input process parameters.

$$\%RRS = 75.88888889 + 9.45 * V_M + 7.65 * T_R - 5.95 * W_X + 2.586111111 * C^2 - 1.925 * V_M * T_R + 3.875 * V_M * W_X + 3.425 * T_R * W_X \quad \textbf{(4)}$$

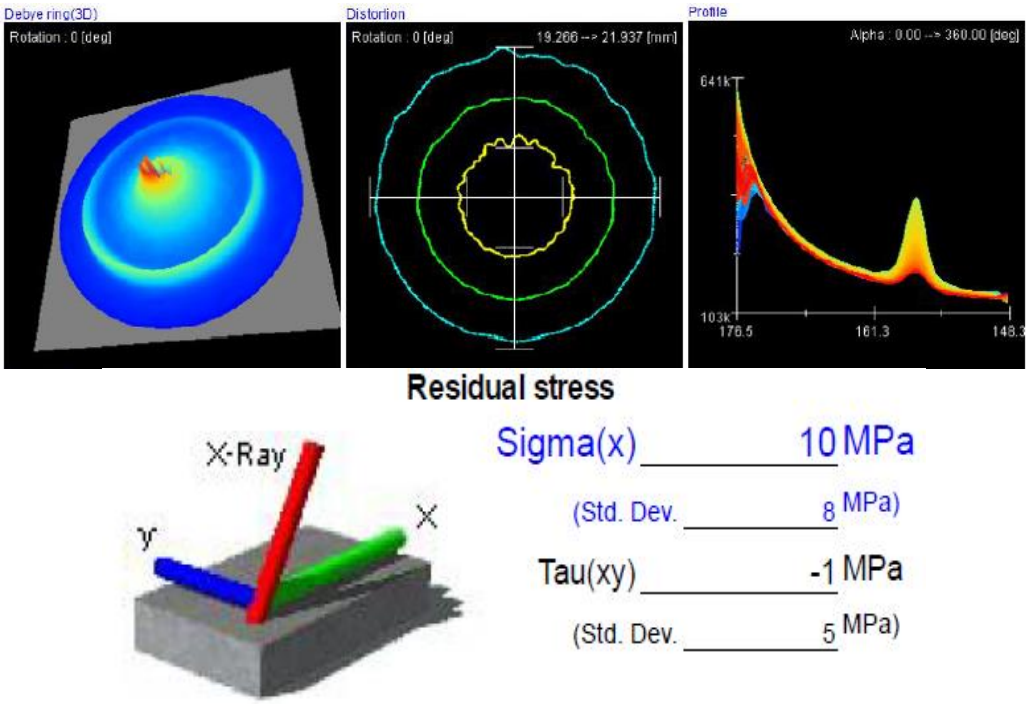


Figure 3. Residual stress on aluminium 7075 workpiece after BEMRF

Table 4. ANOVA table for %RRS after eliminating non-significant parameters

Source	Sum of Squares	Degree of Freedom	Mean Square	F Value	Prob > F	
Model	1646.11	7	235.159	133.6858	< 0.0001	Significant
V_M	756.605	1	756.605	430.123	< 0.0001	Significant
T_R	459.045	1	459.045	260.9629	< 0.0001	Significant
W_X	278.480	1	278.480	158.3133	< 0.0001	Significant
W_X^2	13.1358	1	13.1358	7.467592	0.0231	Significant
$V_M \times T_R$	36.6025	1	36.6025	20.80819	0.0014	Significant
$V_M \times W_X$	51.1225	1	51.1225	29.06267	0.0004	Significant
$T_R \times W_X$	51.1225	1	51.1225	29.06267	0.0004	Significant
Residual	15.8314	9	1.75904			
Lack of Fit	12.8914	5	2.57828	3.507861	0.1239	Not Significant
Pure Error	2.94000	4	0.73500			
Cor Total	1661.95	16				

Standard Deviation = 1.326289, R^2 = 0.990474, Adjusted R^2 = 0.983065, Predicted R^2 = 0.946557, Mean = 77.61765, Coefficient of Variance = 1.70875, PRESS = 88.8201, Adequate Precision = 38.02

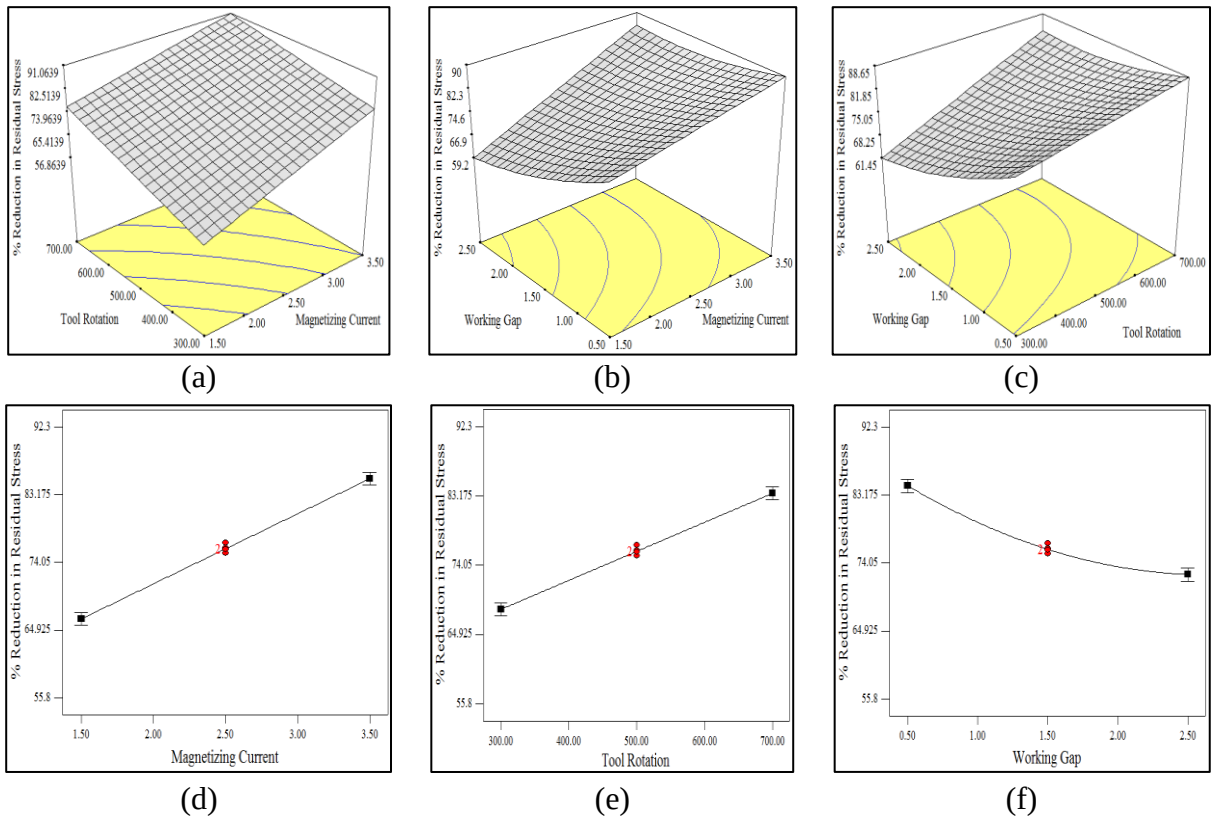


Figure 4. (a) Interaction graph of V_M and T_R on %RRS, (b) Interaction graph of V_M and W_X on %RRS, (c) Interaction graph of T_R and W_X on %RRS, (d) Individual effect of V_M on %RRS, (e) Individual effect of W_X on %RRS

Combined effect of T_R and W_X on %RRS as represented in figure 4(c) shows that %RRS value reduced from 80.2% to 61.45% on increasing W_X from 0.5 to 2.5 mm while keeping T_R at 300 rpm. Whereas, on increasing T_R from 300 to 700 rpm and keeping W_X constant at 2.5 mm, the percentage reduction in residual stress drastically increased to a high value of 83.6%. On the other hand, keeping T_R at maximum value of 700 rpm and reducing W_X to the lowest value of 0.5 mm results in increase of percentage reduction in residual stress to a value of 88.65%. It was observed that with a surge in tool rotation and simultaneous decrement in working gap, the residual stress increases as the workpiece experiences shear and Hertzian stress owing to the vibrations with the abrasive particles.

Figure 4 (d, e, f) shows the individual impact of V_M, T_R and W_X on %RRS. The same slant as the interaction graph was followed by the individual effect plot, which showed that an increase in V_M and T_R increased the %RRS while an increase in W_X reduced the %RRS.

OUTPUT RESPONSE OPTIMIZATION

Derringer (1980) introduced a desirability function approach that was applied to optimize the response to the output i.e. percentage surface reduction (%SRR) and percentage reduction in residual stress (%RRS). In this approach, the measured properties of each predicted response where d ranges between 0 and 1 are assigned a dimensionless desirability value (d). Montgomery

(2001) described that if the desirability function reaches a value of 0 it refers to an unacceptable response and if d = 1 then the answer is exactly to the destination. As the desirability of the corresponding response increases the value of d increases. In the present work, the scenario considered is larger the better rate of cutting. The equation given below is used to transform the response into a dimensionless function di.

$$d_i = \begin{cases} 0 & Xi < Bi \\ (Xi - Bi/Hi - Bi)^w & Bi \leq Mi \leq Hi \\ 1 & Bi > Hi \end{cases} \quad \textbf{(5)}$$

where Bi = Lower response limit, Mi = Upper response limit, Hi = Response goal value. B and M are selected in RSM according to the mathematical.

Optimization Steps:

- Finding the desirability response value
- Optimizing desirability function and detecting the best possible response value

Table 5 shows the top 10 solutions achieved using desirability method after response optimization. A highest desirability value of 0.95 is obtained after optimization which means that maximum percentage reduction in surface roughness and residual stress value can be obtained at V_M = 3.5 amp, T_R = 300 rpm and W_X = 0.5 mm while finishing of aluminium 7075 through BEMRF process.

Table 5. Top 10 predicted solutions using desirability method

Solution Number	Magnetizing Current	Tool Rotation	Working Gap	% Surface Roughness Reduction	% Reduction in Residual Stress	Desirability	
1	**3.50**	**300.00**	**0.50**	**53.680**	**89.6249**	**0.951226**	**Selected**
2	**3.49**	**300.01**	**0.50**	**53.615**	**89.5343**	**0.947760**	**Selected**
3	3.50	300.02	0.53	53.669	89.3828	0.947468	
4	3.50	311.46	0.50	53.524	89.6808	0.946769	
5	3.41	300.04	0.50	53.091	88.8078	0.919958	
6	3.50	300.00	0.79	53.615	87.0794	0.912754	
7	3.50	487.43	2.50	53.457	85.4392	0.883565	
8	3.50	495.32	2.50	53.304	85.7601	0.883439	
9	3.50	502.38	2.50	53.163	86.0465	0.883097	
10	3.50	471.75	2.50	53.745	84.8023	0.883041	

In order to check the above solutions a confirmatory experiment was conducted for solution no. 1 and 2. The values of the input process parameters in table 5 are rounded to the nearest integer

value and the results of the confirmatory experiments mentioned in table 6 indicates that less than 2% of error was obtained. These results confirm excellent reproducibility of the favorable solutions obtained after the optimization.

Table 6. Confirmatory experiments

Solution Number	Magnetizing Current	Tool Rotation	Working Gap	Predicted		Actual		Error %	Error %
				%RRS	%SRR	%RRS	%SRR	%RRS	%SRR
1	3.50	300	0.5	89.6249	53.680	90.7811	54.2329	-1.29	-1.03
2	3.50	300	0.5	89.5343	53.615	89.6686	53.7544	-0.15	-0.26

CONCLUSION

This research work explores the minimization of surface roughness and residual stresses induced after grinding process on Al 7075 workpiece surface through polishing using BEMRF process. The effects of input constraints viz. magnetizing current, tool rotation and working gap were studied through variation in percentage surface roughness reduction (%SRR) and percentage reduction in residual stresses (%RRS). Desirability approach was used to carry out the optimization of %SRR and %RRS through design expert software. From this study, following conclusions are drawn.

- All the input process parameters had a significant effect on both the output responses viz. percentage surface roughness reduction and percentage reduction in residual stress during the BEMRF process.
- Although according to ANOVA table, combined impact of magnetizing current and tool rotation and collective effect of tool rotation and working gap on percentage surface roughness reduction was found to be significant.
- It was found that the %SRR increased from 41.63% to 50.63% when magnetizing current value was increased from 1.5 A to 3.5 A keeping tool rotation and working gap constant at 500 rpm and 1.5 mm respectively.
- Results also showed that the percentage reduction in surface roughness decreased to 41.65% from 47.34% when tool rotation increased to highest level of 700 rpm.
- Although according to ANOVA table, effect of W_X was found to be significant on %SRR but only 3.78% increase was observed when W_X was increased from 0.5 to 2.5 mm.
- Also, combined impact of magnetizing current and tool rotation, magnetizing current and working gap and tool rotation and working gap on percentage reduction in residual stress was found to be significant.

- Results showed that the % reduction in residual stress value elevated from 60.44 to 85.34% when magnetizing current was increased from 1.5 to 3.5 amp.
- It was observed that on increasing tool rotation from 300 to 700 rpm, the percentage reduction in residual stress value was increased to 83.54% from 68.24%.
- Results also showed that on increasing working gap to the highest level (2.5 mm) the percentage reduction in residual stressed decreased to 72.53% from 84.43%.

FUTURE SCOPE

There are various areas of future research depending on the current mentioned technique. Some of the areas to engage in are nano level finishing of nanocomposite materials (Qi et al., 2021; Wu et al. 2021 & Wu et al. 2020), ceramics (Sun et al. 2021) and also comparing two or more nano level finishing techniques like MRAFF, CMMRF etc.

REFERENCES

Ahn, Y., Yoon, J. Y., Baek, C. W., & Kim, Y. K., 2004. Chemical mechanical polishing by colloidal silica-based slurry for micro-scratch reduction. *Wear*, *257*(7-8), 785-789., https://doi.org/10.1016/j.wear.2004.03.020.

Arrasmith, S. R., Jacobs, S. D., Lambropoulos, J. C., Maltsev, A., Golini, D., & Kordonski, W. I., 2001, December. Use of magnetorheological finishing (MRF) to relieve residual stress and subsurface damage on lapped semiconductor silicon wafers. In *Optical manufacturing and testing IV* (Vol. 4451, pp. 286-294). International Society for Optics and Photonics.

Arun, A., Malrautu, P., Laha, A., & Ramakrishna, S., 2021. Gelatin Nanofibers in Drug Delivery Systems and Tissue Engineering. *Engineered Science*, *16*, 71-81.

Brinksmeier, E., 1987. A model for the development of residual stresses in grinding. In *Advances in Surface Treatments* (pp. 173-189). Pergamon.

Brinksmeier, E., Sölter, J., & Grote, C., 2007. Distortion engineering–identification of causes for dimensional and form deviations of bearing rings. *CIRP annals*, *56*(1), 109-112.

Chiu, S. Y., Wang, Y. L., Liu, C. P., Lan, J. K., Ay, C., Feng, M. S., ... & Dai, B. T., 2003. The application of electrochemical metrologies for investigating chemical mechanical polishing of Al with a Ti barrier layer. *Materials chemistry and physics*, *82*(2), 444-451., https://doi.org/10.1016/S0254-0584(03)00312-2.

Derringer, G., & Suich, R., 1980. Simultaneous optimization of several response variables. *Journal of quality technology*, *12*(4), 214-219.

Ghosh, G., Sidpara, A., & Bandyopadhyay, P. P., 2018. Fabrication of optical components by ultraprecision finishing processes. In *Micro and Precision Manufacturing* (pp. 87-119). Springer, Cham.

Ghosh, G., Sidpara, A., & Bandyopadhyay, P. P., 2021. Experimental and theoretical investigation into surface roughness and residual stress in magnetorheological finishing of OFHC copper. *Journal of Materials Processing Technology*, *288*, 116899.

Golini, D., Jacobs, S. D., Kordonski, W. I., & Dumas, P., 1997, July. Precision optics fabrication using magnetorheological finishing. In *Advanced Materials for Optics and Precision Structures: A Critical Review* (Vol. 10289, p. 102890H). International Society for Optics and Photonics

Jacobs, S. D., Golini, D., Hsu, Y., Puchebner, B. E., Strafford, D., Prokhorov, I. V., ... & Kordonski, W. I., 1995. Magnetorheological finishing: a deterministic process for optics manufacturing. In *International Conference on Optical Fabrication and Testing* (Vol. 2576, pp. 372-383). International Society for Optics and Photonics

Jaecklin, V. P., Linder, C., Brugger, J., De Rooij, N. F., Moret, J. M., & Vuilleumier, R., 1994. Mechanical and optical properties of surface micromachined torsional mirrors in silicon, polysilicon and aluminum. *Sensors and Actuators A: Physical*, *43*(1-3), 269-275., https://doi.org/10.1016/0924-4247(93)00699-5.

Jain, V. K., Ranjan, P., Suri, V. K., & Komanduri, R., 2010. Chemo-mechanical magneto-rheological finishing (CMMRF) of silicon for microelectronics applications. *CIRP Annals-Manufacturing Technology*, *59*(1), 323-328

Jha, S., & Jain, V. K., 2004. Design and development of the magnetorheological abrasive flow finishing (MRAFF) process. International Journal of Machine Tools and Manufacture, 44(10), 1019-1029

Jomaa, W., Songmene, V., & Bocher, P., 2014. Surface finish and residual stresses induced by orthogonal dry machining of AA7075-T651. Materials, 7(3), 1603-1624.

Kansal, H., Singh, A. K., & Grover, V., 2018. Magnetorheological nano-finishing of diamagnetic material using permanent magnets tool. *Precision Engineering*, *51*, 30-39.

Khan, D. A., & Jha, S., 2018. Synthesis of polishing fluid and novel approach for nanofinishing of copper using ball-end magnetorheological finishing process. *Materials and Manufacturing Processes*, *33*(11), 1150-1159

Khan, D. A., & Jha, S., 2019. Selection of optimum polishing fluid composition for ball end magnetorheological finishing (BEMRF) of copper. The International Journal of Advanced Manufacturing Technology, 100(5-8), 1093-1103.

Kruszynski, B. W., & Van Luttervelt, C. A., 1991. An attempt to predict residual stresses in grinding of metals with the aid of a new grinding parameter. *CIRP annals*, *40*(1), 335-337.

Lambropoulos, J. C., Arrasmith, S. R., Jacobs, S. D., & Golini, D., 2001, December. Manufacturing-induced residual stresses in optical glasses and crystals: Example of residual stress relief by magnetorheological finishing (MRF) in commercial silicon wafers. In *Optical Manufacturing and Testing IV* (Vol. 4451, pp. 181-190). International Society for Optics and Photonics.

Li, Q.Y., Hao, Q., Zhu, T., & Zebarjadi, M., 2020. Nanostructured and heterostructured 2D materials for thermoelectrics. *Engineered Science*, 13, 24-50.

Mahadik, S.A., Patil, A., Pathan, H.M., Salunke-Gawali, S., & Butcher, R.J., 2020. Thionaphthoquinones as Photosensitizers for TiO2 Nanorods and ZnO Nanograin Based Dye-sensitized Solar Cells: Effect of Nanostructures on Charge Transport and Photovoltaic Performance. *Engineered Science*, *14*, 46-58.

Maloney, C., Lormeau, J. P., & Dumas, P., 2016, June. Improving low, mid and high-spatial frequency errors on advanced aspherical and freeform optics with MRF. In *Third European Seminar on Precision Optics Manufacturing* (Vol. 10009, p. 100090R). International Society for Optics and Photonics.

Montgomery, D.C., 2001. Design and Analysis of Experiments, John Wiley & Sons Inc. New York.

Qi, G., Liu, Y., Chen, L., Xie, P., Pan, D., Shi, Z., ... & Guo, Z., 2021. Lightweight Fe3C@ Fe/C nanocomposites derived from wasted cornstalks with high-efficiency microwave absorption and ultrathin thickness. *Advanced Composites and Hybrid Materials*, *4*(4), 1226-1238.

Qiu, Y., Xu, M., Li, Q., Huang, R., & Wang, J., 2021. A high-temperature near-perfect solar selective absorber combining tungsten nanohole and nanoshuriken arrays. *ES Energy & Environment*, *13*, 77-90.

RKoul, R., AMitra, A., & VChitnis, T., 2011. An update on the design and implementation of the MACE gamma-ray telescope. In *International Cosmic Ray Conference* (Vol. 9, p. 106)., https://doi.org/10.7529/ICRC2011/V09/0803.

Robinson, J. S., Hossain, S., Truman, C. E., Paradowska, A. M., Hughes, D. J., Wimpory, R. C., & Fox, M. E., 2010. Residual stress in 7449 aluminium alloy forgings. *Materials Science and Engineering: A*, *527*(10-11), 2603-2612.

Saraswathamma, K., Jha, S., & Rao, P. V., 2015. Experimental investigation into ball end magnetorheological finishing of silicon. *Precision Engineering*, *42*, 218-223.

Sharma, A., & Niranjan, M.S., 2019. Magnetorheological Fluid Finishing of Soft Materials: A Critical Review. International journal of advanced production and industrial engineering, Vol 4 (1), 48-55.

Sharma, A., Vaish, A. & Sharma, A., 2020. Detailed Review of Ball End Magnetorheological Fluid Finishing Process. WSEAS TRANSACTIONS on HEAT and MASS TRANSFER, Vol 15, 163-173.

Sim, W. M., 2010. Challenges of residual stress and part distortion in the civil airframe industry. *International Journal of Microstructure and Materials Properties*, *5*(4-5), 446-455.

Singh, A. K., Jha, S., & Pandey, P. M., 2012. Magnetorheological ball end finishing process. *Materials and Manufacturing Processes*, *27*(4), 389-394.

Singh, A. K., Jha, S., & Pandey, P. M., 2012. Nanofinishing of fused silica glass using ball-end magnetorheological finishing tool. *Materials and Manufacturing Processes*, *27*(10), 1139-1144.

Sugano, T., Takeuchi, K., Goto, T., Yoshida, Y., Ikawa, N., 1987. Diamond turning of an aluminum alloy for mirror. CIRP Ann. Manuf. Technol. 36 (1), 17–20.

Sun, Z., Huang, X., Xia, A., Yan, Z., & Qian, L., 2021. Tunable Bandwidth of Negative Permittivity from Graphene-Silicon Carbide Ceramics. *Engineered Science*, *16*, 19-25.

Tönshoff, H. K., Peters, J., Inasaki, I., & Paul, T., 1992. Modelling and simulation of grinding processes. *CIRP annals*, *41*(2), 677-688.

Tyagi, P., & Vedeshwar, A. G., 2002. Effect of residual stress on the optical properties of CdI 2 films. *Physical Review B*, *66*(7), 075422.

Vahdati, M., & Shokuhfar, A., 2008. A trend toward abrasive nano finishing of plane surfaces with magnetic field energy. Materialwissenschaft und Werkstofftechnik, 39(2), 167-170.

Wu, H., Zhong, Y., Tang, Y., Huang, Y., Liu, G., Sun, W., ... & Guo, Z. 2021. Precise regulation of weakly negative permittivity in CaCu3Ti4O12 metacomposites by synergistic effects of carbon nanotubes and grapheme. *Advanced Composites and Hybrid Materials*, 1-12.

Wu, N., Du, W., Hu, Q., & Jiang, S.V.Q., 2020. Recent development in fabrication of Co nanostructures and their carbon nanocomposites for electromagnetic wave absorption. *Engineered Science*, *13*(13), 11-23.

Yi, A. Y., Tao, B., Klocke, F., Dambon, O., & Wang, F., 2011. Residual stresses in glass after molding and its influence on optical properties. *Procedia Engineering*, *19*, 402-406

Zhejun, Y., Zhonghui, H., & Kobayashi, A., 1989. Surface integrity of grinding of bearing steel GCr15 with CBN wheels. *CIRP annals*, *38*(1), 553-556.
Zhong, Z.W., Lu, Y.G., 2003. Fractal roughness structure of diamond-turned copper mirrors. Mater. Manuf. Process. 18 (2), 219–227.

MĀPAN-Journal of Metrology Society of India
https://doi.org/10.1007/s12647-022-00532-x

ORIGINAL PAPER

Experimental Investigation on Machinability and Geometric Tolerance in Die-Sinking EDM of Microholes and Channels

S. Vidya[1,3]*, R. Wattal[1] and P. V. Rao[2]

[1]Department of Mechanical Engineering, Delhi Technological University, New Delhi, India

[2]Department of Mechanical Engineering, Indian Institute of Technology, New Delhi, India

[3]Department of Mechanical Engineering, Galgotias University, Greater Noida, Uttar Pradesh, India

Received: 01 November 2021 / Accepted: 11 January 2022

© Metrology Society of India 2022

Abstract: Die-sinking electrical discharge machining (EDM) technology integrated with short electronic pulsed electrical discharge and CNC-controlled positioning along with precise movement of tool electrode enables it to produce microscale geometries of different contours. The present investigation starts with the small area EDM machining of microholes and channels over EN-24 alloy steel with an unshaped cylindrical electrode of 400 μm diameter. Further, these machined features are critically analysed through optical microscopy, profile projector and SEM (scanning electron microscope) to assess the performance and capabilities of EDM machining in terms of dimensional accuracy, shape error, geometric tolerance, material removal rate and tool wear rate. Energy-dispersive X-ray (EDX) analysis is carried out for the machined surfaces to examine the presence of elements at their surface. The experimental results reveal that the microholes machined by die-sinking have better dimensional accuracy as compared to the microchannels. In terms of MRR and TWR, microchannels have higher material removal rate and lesser tool wear due to the presence of larger discharge area. On the basis of calculated values, the microholes have roundness error of 46.33 μm and the microchannels have straightness tolerance of 13.51 μm. In a nutshell, on the basis of experimental results, it can be revealed that die-sinking EDM integrated with advanced technologies is capable for producing microstructures under optimum operating conditions.

Keywords: EDM; Holes; Channels; Tolerance; SEM; EDX

1. Introduction

Electrical discharge machining (EDM) has become a prominent tool for fabrication of microscale structures, components, devices and microelectro-mechanical systems with high-precision and finer-dimensional tolerances in wide variety of applications in industries. The integration of die-sinking EDM with CNC-controlled positioning stages and short electronic pulses enhances its machining capability and makes capable to produce precise and dimensionally controlled microstructures at small values of machining parameters. In EDM, material removal occurs by a series of discharges between the work and tool electrode. The important feature of contactless machining irrespective of hardness, strength and toughness of workpiece material makes EDM an important tool for advanced machining.

In EDM, most of the researchers reported the large area machining of holes over different work materials, utilization of different electrode materials and optimization of process parameters, but limited or no studies have been carried out to perform small area machining of holes and channels using die-sinking EDM. However, researchers have explored machining of holes, channels and geometries of different shapes in micro-EDM. In context to EDM, optimization of EDM drilling parameters was performed by Maradia et al. [1] using E-smeshing technique. It was reported that the length of electrode influences drilling time and electrode wear considerably, while there is less effect on material removal rate. Electrode dressing and pulse duration had no considerable effect on MRR, while discharge current put high impact on the rate of material removal and peak current had influence over the rate of electrode wear. On the same ground, researchers carried

*Corresponding author, E-mail: skvrsm@gmail.com

Published online: 31 January 2022

out a comparative investigation on performance of hybrid EDM by using brass, copper and copper tungsten electrodes during the drilling of Inconel 718 [2]. It was concluded that highest MRR was achieved in case of brass electrode followed by copper and then copper tungsten electrode at all selected current values, while the wear rate of electrode is the lowest in case of copper tungsten electrode followed by brass and then copper electrode. In terms of surface finish, the quality of machined surface is better in case of copper and brass electrodes as compared to copper tungsten electrodes. In an approach towards improving process performance of EDM, Kliuev et al. [3] combined drilling and shaping of cooling holes with diffusers in turbine blades using same electrode in a single process and reported that the rate of material removal got improved and electrode wear rate got decreased by 20%. There was also decrease in recast layer and surface roughness after utilization of this combined process of drilling and shaping. To report the effects of dielectrics on the machining performance of EDM, Li et al. [4] selected four different dielectric fluids during drilling of nickel alloy and examined the performance of EDM with reference to surface integrity. It was reported that the formation of recast layer is minimum in case of kerosene as dielectric fluid as compared to water-based dielectric, emulsion and de-ionized water. In order to present the influence of dielectrics in EDM, researchers have carried out studies in variants of EDM also [5–8]. Process of curved EDM was put into existence by Meshram et al. [9] for producing curvature channel. After carrying out optimization, it was concluded that the machining efficiency gets improved using this technique in case of solid as well as hollow electrodes. Central composite design technique was employed by Dikshit et al. [10] for optimization of parameters in the die-sinking EDM machining of Inconel 625. It was stated that MRR and surface roughness increase with pulse-on-time, while there was little influence of pulse-off-time on MRR. The confirmation results were concluded on the experimental as well as predicted values. In correspondence to improve EDM capabilities, Shabgard et al. [11] proposed a finite element model of ultrasonic-assisted EDM process to analyse its electrothermal process and investigated the influence of ultrasonic vibrations of tool on the performance measures. They reported that the plasma flushing efficiency gets improved and the extent of recast layer formation decreases after the application of ultrasonic vibrations. In order to improve the flushing and debris removal system in deep-hole EDM drilling, Tanjilul et al. [12] presented the debris removal system comprising of simultaneous flushing and vacuum-assisted system. It was reported that there was improvement in the time of drilling as well as surface roughness of the produced hole which was also investigated through development of computational fluid dynamics model. The utilization of microlevel variant of EDM known as micro-EDM was also done by several researchers in machining of microholes and channels using various electrode materials of tool as well as work [13–18]. Several studies also report the exploitation of technologies to enhance the micro-EDM performance in drilling of microholes [19–24]. In reference to tolerance analysis, volumes of research have been carried out to evaluate roundness, flatness, straightness, etc., utilizing various approaches [25–27].

On the basis of reviews carried out, it can be concluded that most of the literature in die-sinking EDM dealt with the production of macroholes and parametric optimization utilizing variations in tool and work materials and dielectric medium. But, very limited studies have been carried out to investigate the machining capabilities of die-sinking EDM in producing holes as well as channels on microscale using cylindrical electrode. In this paper, authors look into the machining performance of die-sinking electrical discharge machine in fabrication of microholes and channels and micromachining capabilities of die-sinking EDM are assessed on the basis of the analysis of dimensional accuracy, geometric tolerances, material removal rate, rate of tool wear and elemental characterization.

2. Experimental Details

XPERT-1 series of EDM machining centre of Electronica Machine Tools was selected for carrying out the research experiments which has an integration of CNC precise controlled axes movements and e-pulse 50 CNC power supply unit aiding in the production of complex structures of microscale involving comprehensive tool path trajectories. The material chosen as a work material was EN-24

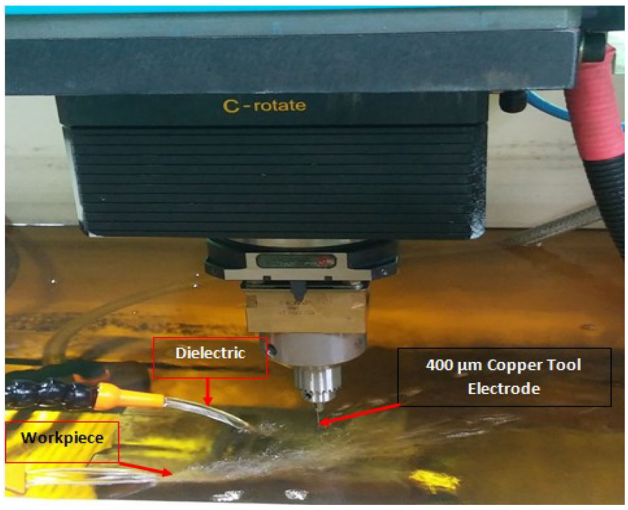


Fig. 1 Die-sinking EDM machining setup

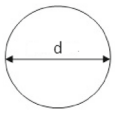
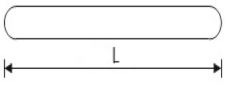
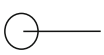
alloy steel, while 400-µm cylindrical electrode of copper was selected as tool material. Figure 1 represents the set-up employed for EDM machining. The dielectric used here is EDM oil—IPOL SEO 450. The tool electrode was mounted onto the spindle, and the workpiece was mounted over the *X*–*Y* positioning table. The diameter of electrode was taken as reference diameter, and the machining of microholes and channels was carried out by the CNC-controlled tool trajectory at chosen parameters listed in Table 1. Table 2 shows the dimensions and tool paths adopted in micromachining. There were three microholes and channels were fabricated to ensure the precision and the average value of the performance measures was noted for analysis.

The machined cavities were analysed under an Olympus optical microscope (magnification of 5 ×, 10 ×, 20 ×, 50 × and 100 ×), Nikon profile projector (least count of 0.001 mm/1 min of arc) and scanning electron microscope (Hitachi, SEM, model: S-3000 N) having magnification up to 100,000 × to examine their dimensional accuracy, shape error, recast layer formation and geometric tolerances. EDS analysis of microholes and channels was also conducted to depict the presence of elements at the machined surface.

Table 1 Parameters selected for machining

Parameters	Values
Pulse-on time	5 µs
Pulse-off time	16 µs
Pulse current	1 A
Gap voltage	75 V
Feed rate	450 µm/s
Polarity	Tool electrode (+ ve)

Table 2 Dimensions of geometries to be made

Geometry	Reference dimensions	Tool paths
 Circular	d = 400 µm depth = 2000 µm	
 Channel	W = 400 µm L = 2000 µm depth = 2000 µm	

3. Results and Discussion

Figure 2 portrays the images of microholes and channels machined in die-sinking EDM obtained through optical microscope. The machined samples were decisively examined to assess the EDM machinability on various measures like dimensional accuracy, shape error, geometric tolerance, recast layer formation and elemental characterization.

3.1. Dimensional Accuracy and Shape Error

Profile projector having least count of 0.001 mm/1 min of arc was used for analysing the dimensions of the microscopic images of cavities. The value of measured dimensions and standard deviations with respect to reference dimensions is listed in Table 3. On the basis of calculated dimensions, it is clear that the circular microholes are consistent in dimensions having the lowest standard deviation of 9, whereas the microchannels are relatively poor in terms of dimensional control with standard deviation of 20.84 and 43.02 along width and length, respectively. The reasons behind this can be attributed that in case of holes, the tool advancement is along Z-axis only, while in case of channels, there is movement of tool along both *Z*- and *X*-axes at the same time. Due to this, there is continuous change in the position of spark discharge leading to instability and jumping of discharges. Apart from the primary discharge occurring at the front of the tool electrode, the secondary discharge takes place at the side of the electrode due to improper flushing at the depth of the cavities which is pivotal influencer for instable spark gap, short circuiting, spark jumping, overcuts and recast layer formation. From Table 3, it can be noted that the dimensions of the machined cavities are larger than the proposed dimensions which represents overcut error. From Fig. 2, it is reported that due to the occurrence of side discharges, there is presence of burrs at the cavity edges, and in case of microchannels, there is lacking of sharp corners at the corners (corner error) necessitating the requirements of secondary finishing operations.

3.2. Geometric Tolerance Estimation

Geometric tolerances are used to control the shape and form of a component more precisely. They are used only when the shape or form has a particular function and errors would result in poor performance. Geometrical tolerances are applied in addition to dimensional tolerances. Geometric tolerances specify the maximum variation that is allowed in form or position from true geometry. To specify the geometric tolerances, reference features—planes, lines, or surfaces can be established. According to ISO 1101, "A

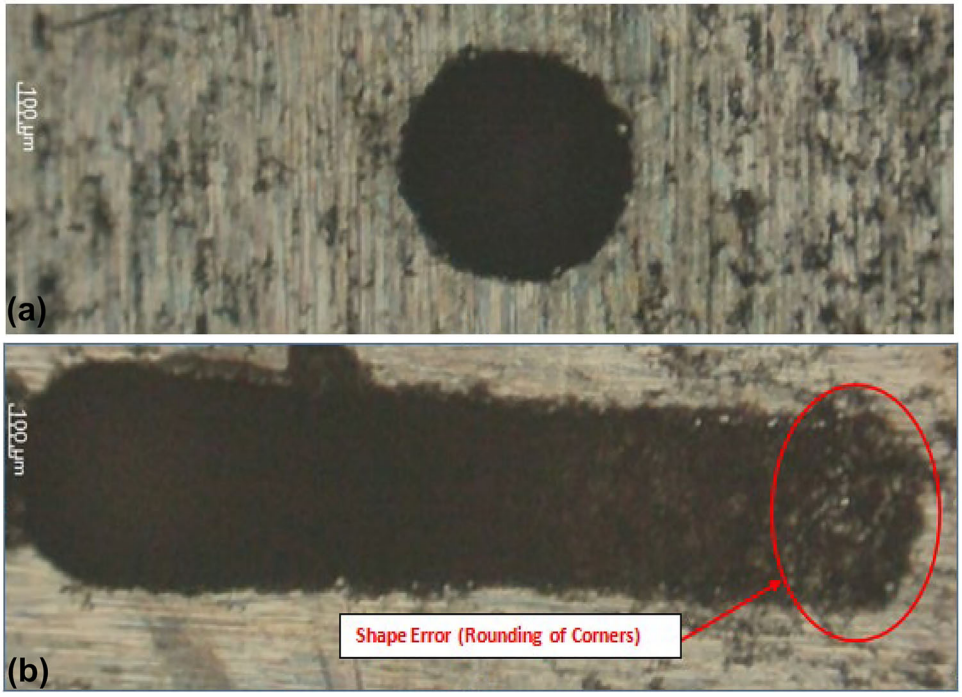


Fig. 2 Microscopic images (5X) of **a** microholes, **b** microchannels

Table 3 Dimensional error for microholes and microchannels

Geometries	Reference dimension (μm)	Measured dimensions (μm)				Standard deviations (S.D)
		1	2	3	Mean error	
Circular	400	469	460	451	60	9
Channels	400	437	451	478	34.33	20.84
	2000	2097	2087	2018	67.33	43.02

geometrical tolerance applied to a feature defines the tolerance zone within which that feature shall be contained".

3.2.1. Out of Roundness (for Circular Geometries)

Roundness error can be defined by means of least square circle (LSC), minimum zone circle (MZC), minimum circumscribed circle (MCC) and maximum inscribed circle (MIC). In this paper, MZC approach has been employed to evaluate the roundness error. In MZC method, two circles are used as reference for measuring the roundness error (Fig. 3). One circle is drawn outside the roundness profile just as to enclose the whole of it, and the other circle is drawn inside the roundness profile such that it just inscribes the profile.

For this, four tangent points are identified (two on the maximum circle and two on the minimum circle). The identification of tangent points is initiated by determination of two or three vertices over maximum as well as minimum circle, and this process is repeated until the two concentric circles drawn contain all points. Finally, the roundness error is calculated difference of diameters of maximum circle (d_1) and minimum circle (d_2).

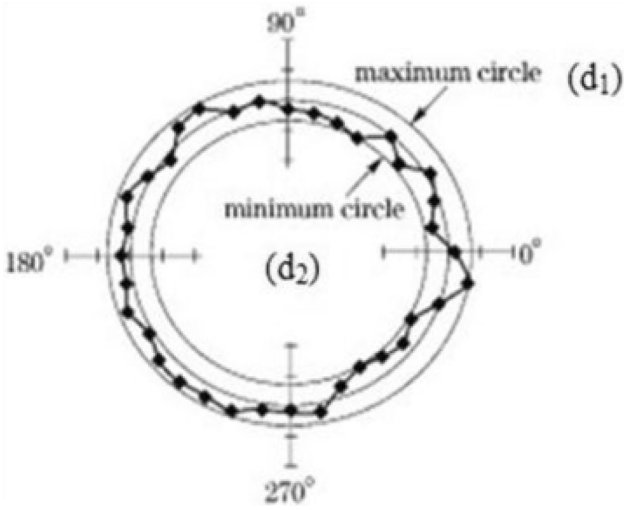


Fig. 3 Minimum zone circle (MZC) method to find roundness error [28]

Table 4 Roundness Error of microholes

Geometry	Roundness error (μm)	Average roundness error (μm)
Micro hole 1	45	46.33
Micro hole 2	41	
Micro hole 3	53	

The error of three circular microholes is calculated separately, and average value is considered (Table 4). Therefore, the roundness error of circular microholes was estimated as 46.33 μm.

3.2.2. *Straightness (for Microchannels)*

Straightness is the condition where an element of a surface or an axis is a straight line specifying a tolerance zone within which the considered element or axis must lie [29].

For straightness, the assessment line is:

$$y = y_0 + l_0 x \tag{1}$$

The deviation can be expressed in the form of:

$$e_i = y_i - (y_0 + l_0 x_i) \tag{2}$$

The least square (LS) solutions are given as:

$$l_0 = \frac{(N\sum x_i y_i) - \sum x_i \sum y_i}{(N\sum x_i^2) - (\sum x_i^2)} \tag{3}$$

$$y_0 = \frac{(\sum y_i - l_0 \sum x_i)}{N} \tag{4}$$

Straightness tolerance:

$$h_{\text{straightness}} = \frac{|e_{\text{MAX}(+)}| + |e_{\text{MAX}(-)}|}{\sqrt{1 + l_0^2}} \tag{5}$$

Three microchannels of length 2000 micron were produced in patterned form using die-sinking EDM. After obtaining their microscopic views, dimension at ten different locations each 200 μm apart (fixed interval of *X*) is measured through Olympus Analysis Five software to obtain measurement data (*Y* coordinates). Figure 4 portrays the steps involved in analysing microscopic images in Olympus Analysis Five software.

Table 5 Straightness Tolerance of microchannels

Geometry	Straightness tolerance (μm)	Average straightness tolerance (μm)
Microchannel 1	16.58	a13.51
Microchannel 2	9.57	
Microchannel 3	14.39	

The straightness tolerance is calculated using the above procedures listed by Eqs. (1), (2), (3), (4) and (5). The straightness tolerance of each microchannel is calculated separately, and then, their average value is reported in Table 5.

So, the average straightness tolerance of microchannel was estimated as 13.51 μm.

From the calculated value of roundness of microholes and straightness of microchannels, it can be stated that the geometries produced are of good quality in terms of tolerance.

3.3. Material Removal Rate and Tool Wear Rate (MRR and TWR)

The performance measures MRR and TWR are evaluated by determining the volumetric material removal from workpiece and tool electrode, respectively. In case of holes, calculation of MRR is determined by keeping in account of the total machining area, average depth of the machined cavity and the machining time, while in case of channels, calculation of material removal rate is based on the average length and width of machined channel, average depth and machining time. The value of MRR and TWR is calculated for each geometry, and average value is reported. Figure 5 presents the graphical representation of average values of MRR and TWR for microholes and channels. From Fig. 5, it is evident that the material removal rate is more as well as tool wear rate is lesser in case of microchannels as compared to microholes. This can be attributed to the reason that in case of microholes, there is tool movement in *Z*-axis only, i.e. discharge area is limited, and due to greater

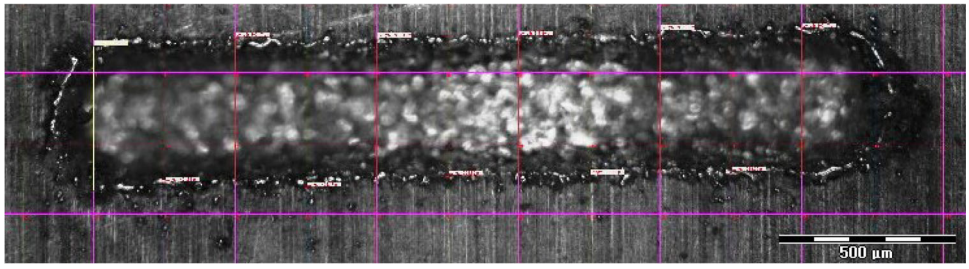


Fig. 4 Olympus Analysis Five software analysis process of microchannels

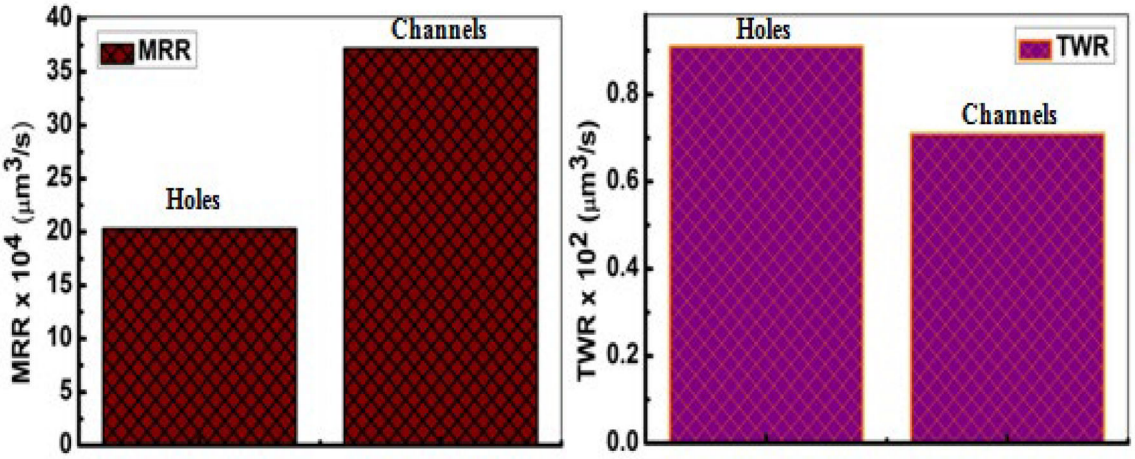


Fig. 5 Data representing higher MRR and lower TWR in microchannels

extent of side discharge at depth, there is more tool wear and lesser MRR, whereas, in case of machining of microchannels, the discharge area is larger leading to lesser extent of side discharges resulting in lesser wear rate of tool and higher rate of material removal [22].

3.4. Surface Characteristics and Elemental Characterization

Due to the improper flushing of molten particles at the depth, the secondary discharges take place due to which the material gets re-deposited and forms a white layer over the surface called as recast layer. During the course of cooling of these re-deposited materials, the contained gases escape which results in the formation of pockmarks, voids and debris particles. Recast layer formation also results in the generation of residual stress on the surface resulting in formation of microcracks. However, the formation of recast layer was lesser because machining has been carried out at lesser value of parameters as an attempt of micro-machining in die-sinking EDM. Hence, the formation of microcracks was also negligible. But, if comparison is done among the machined geometries in our case, the extent of recast layer formation is greater at the edges of the cavities as compared to the bottom due to the side discharges (Fig. 6).

Energy-dispersive X-ray (EDX) technique was employed to study the presence of elements on the machined surface of cavities. Figure 7 represents EDX spectrogram of microholes and channels and their relative proportions by percentage of weight. From Fig. 6, it can be stated clearly that there is deposition of tool material

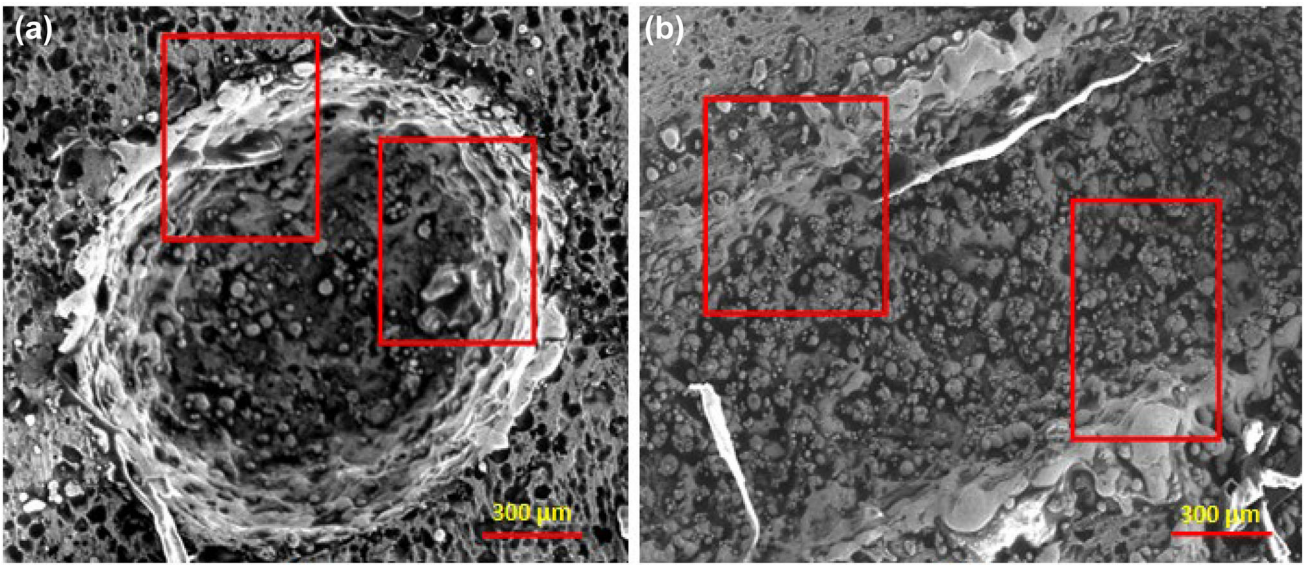


Fig. 6 SEM micrographs of cavity representing recast layer formation: **a** microhole, **b** microchannel

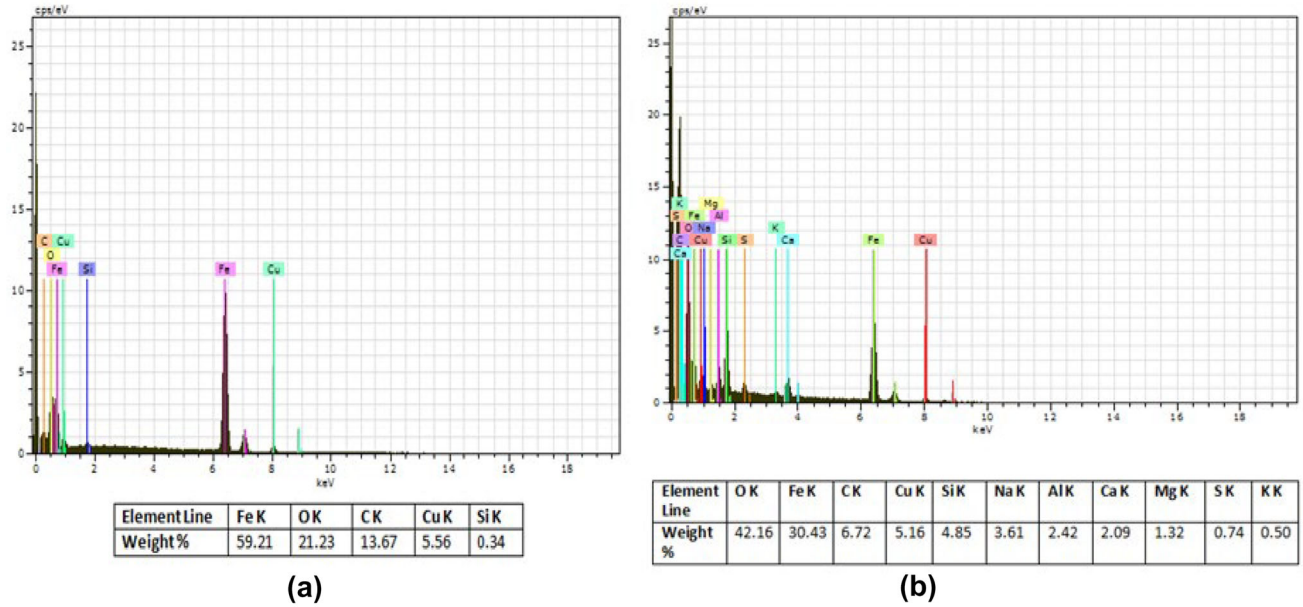


Fig. 7 EDX analysis of machined surface of **a** microhole, **b** microchannel

copper on the surfaces of the cavities because of the local evaporation of the metal at the surface and a little of electrode material due to thermal flux. It was also found that during the electrical discharge and handling of dielectric as well as from the environment, various foreign elements like oxygen, silicon, sodium, etc., also got accumulated on the surface of the cavities. It may be also due to the presence of impurities in the work and tool material.

4. Conclusions

The production of microholes and channels over EN-24 alloy steel by employing cylindrical electrode in die-sinking EDM was carried out and assessed for its machinability and forms tolerances. The process involved movement of circular tool in Z- and X-axes simultaneously without tool rotation unlike in micro-EDM. The machinability was analysed in terms of dimensional accuracy, corner error, material removal rate, tool electrode wear rate and surface characteristics, while tolerance was evaluated in the form of roundness and straightness. Based on the experimental analysis, the following conclusions are drawn:

- The presence of stochastic secondary discharge, change in discharge position and combined effect of ion bombardment and thermomechanical waves lead to overcut, rounding of corners as well as tool wear which cannot be ignored in EDM machining.
- Geometric tolerance greatly affects the performance and lifetime of the mechanical parts. The value of roundness error achieved by MZC and straightness tolerance by least square method complies with ISO and ANSI standards.
- In correspondence to the geometric tolerance achieved, it is found that the produced cavities are of good quality having fine tolerance, i.e. the microholes have very less roundness error and the microchannels are almost straight.
- Since the discharge area is more in case of channel machining, the extent of occurrence of side discharge is lower and hence the tool wear rate is lesser and rate of material removal rate is greater in case of channels. It is reported that the calculated values of MRR are 20.30×10^4 $\mu m^3/s$ and 37.20×10^4 $\mu m^3/s$ for microholes and microchannels, respectively, whereas the calculated values of TWR are found to be 0.91×10^2 and 0.71×10^2, respectively.
- Critical examination of machined surface features marked the existence of recast layer which was greater at the edges of cavities. EDX analysis marks the presence of eroded tool particles along with the foreign materials.

In an attempt to evaluate the micromachining capabilities of die-sinking EDM and present promising research, authors propose to explore further to exploit the technological advancements in die-sinking EDM to be able to assist in the development of macro- and microscale functional systems. The scope of research also exists in the development and utilization of micromeasurement techniques, mathematical and computational techniques of tolerance analysis for enhancing the reliability and precision of the results.

Funding The authors declare that they have no funding source.

Availability of Data and Materials Not applicable.

Declarations

Conflict of interest The authors declare that they have no conflict of interest.

Ethical Approval and Consent to Participate Not applicable.

Consent to Publish Not applicable.

References

[1] U. Maradia, A. Benavoli, M. Boccadoro, C. Bonesana, M. Klyuev, M. Zaffalon, L. Gambardella and K. Wegenerc, EDM Drilling Optimisation Using Stochastic Techniques. Procedia CIRP, *67* (2018) 350–355.

[2] A. Ahmed, M. Tanjilul, M. Rahman et al., Ultrafast Drilling of Inconel 718 Using Hybrid EDM with Different Electrode Materials. Int. J. Adv. Manuf. Technol., *106* (2020) 2281–2294. https://doi.org/10.1007/s00170-019-04769-w.

[3] M. Kliuev, M. Boccadoro, R. Perez, W. Dal Bó, J. Stirnimann, F. Kuster and K. Wegener, EDM Drilling and Shaping of Cooling Holes in Inconel 718 Turbine Blades. Procedia CIRP, *42* (2016) 322–327.

[4] C. Li, X. Xu, Y. Li, H. Tong, S. Ding, Q. Kong, L. Zhao and J. Ding, Effects of Dielectric Fluids on Surface Integrity for the Recast Layer in High Speed EDM Drilling of Nickel Alloy. J. Alloys Compd. (2019). https://doi.org/10.1016/j.jallcom.2018.12.283.

[5] S. Chakraborty, S. Mitra and D. Bose, Performance Characterization of Powder Mixed Wire Electrical Discharge Machining Technique for Processing of Ti_6Al_4V Alloy. Proc. Inst. Mech. Eng. Part E J. Process Mech. Eng. (2021). https://doi.org/10.1177/09544089211060722.

[6] V. Kumar, K.K. Jangra and V. Kumar, An Experimental Study on Trim Cutting Operation Using Metal Powder Mixed Dielectric in WEDM of Nimonic-90. Int. J. Ind. Eng. Comput., *7* (2016) 135–146.

[7] S. Patel, D. Thesiya and R. Avadhoot, Aluminium Powder Mixed Rotary Electric Discharge Machining (PMEDM) on Inconel 718. Australas. J. Eng., *16* (2018) 21–30.

[8] C. Prakash, H.K. Kansal, B.S. Pabla et al., Experimental Investigations in Powder Mixed Electric Discharge Machining of Ti-35Nb-7Ta-5Zrβ-Titanium Alloy. Mater. Manuf. Proc., *32* (2016) 274–285.

[9] D.B. Meshram and Y.M. Puri, Optimized Curved Electrical Discharge Machining-Based Curvature Channel. J. Braz. Soc. Mech. Sci. Eng., *42* (2020) 82. https://doi.org/10.1007/s40430-019-2162-4.

[10] M.K. Dikshit, J. Anand, D. Narayan and S. Jindal, Machining Characteristics and Optimization of Process Parameters in Die-Sinking EDM of Inconel 625. J. Braz. Soc. Mech. Sci. Eng., *41* (2019) 302. https://doi.org/10.1007/s404300191809-5.

[11] M.R. Shabgard, A. Gholipoor and M. Mohammadpourfard, Numerical and Experimental Study of the Effects of Ultrasonic Vibrations of Tool on Machining Characteristics of EDM Process. Int. J. Adv. Manuf. Technol., *96* (2018) 2657–2669. https://doi.org/10.1007/s00170-017-1487-3.

[12] M. Tanjilul, A. Ahmed, A.S. Kumar and M. Rahman, A Study on EDM Debris Particle Size and Flushing Mechanism for Efficient Debris Removal in EDM-Drilling of Inconel 718. J. Mater. Process. Technol. (2010). https://doi.org/10.1016/j.jmatprotec.2017.12.016.

[13] G. D'Urso, G. Maccarini and C. Ravasio, Influence of Electrode Material in Micro-EDM Drilling of Stainless Steel and Tungsten Carbide. Int. J. Adv. Manuf. Technol., *85* (2016) 2013–2025. https://doi.org/10.1007/s00170-015-7010-9.

[14] L. Raju and S.S. Hiremath, Machining and Characterization of Micro-Channels Generated on Phosphor Bronze Using μ-EDM. J. Adv. Manuf. Syst., *19* (2020) 87–106. https://doi.org/10.1142/S0219686720500055.

[15] A. Schubert, H. Zeidler, M. Hahn, M. Hackert-Oschätzchen and J. Schneider, Micro-EDM Milling of Electrically Nonconducting Zirconia Ceramics. Procedia CIRP, *6* (2013) 297–302. https://doi.org/10.1016/j.procir.2013.03.026.

[16] M.P. Jahan, Y.S. Wong and M. Rahman, A Study on the Fine-Finish Die-Sinking Micro-EDM of Tungsten Carbide Using Different Electrode Materials. J. Mater. Process. Technol., *209* (2009) 3956–3967. https://doi.org/10.1016/j.jmatprotec.2008.09.015.

[17] O. Yilmaz and M.A. Okka, Effect of Single and Multi-channel Electrodes Application on EDM Fast Hole Drilling Performance. Int. J. Adv. Manuf. Technol., *51* (2010) 185–194. https://doi.org/10.1007/s00170-010-2625-3.

[18] A.A. Khan, Electrode Wear and Material Removal Rate During EDM of Aluminum and Mild Steel Using Copper and Brass Electrodes. Int. J. Adv. Manuf. Technol., *39* (2008) 482–487. https://doi.org/10.1007/s00170-007-1241-3.

[19] M. Bellotti, J. Qian and D. Reynaerts, Enhancement of the Micro-EDM Process for Drilling Through-Holes. Procedia CIRP, *68* (2018) 610–615.

[20] Y. Feng, Y. Guo, Z. Ling and X. Zhang, Micro-holes EDM of Superalloy Inconel 718 Based on a Magnetic Suspension Spindle System. Int. J. Adv. Manuf. Technol., *101* (2019) 2015–2026. https://doi.org/10.1007/s00170-018-3075-6.

[21] G. Karthikeyan, A.K. Garg, J. Ramkumar and S. Dhamodaran, A Microscopic Investigation of Machining Behaviour in l-ED-Milling Process. J. Manuf. Process., *14* (2012) 297–306.

[22] S. Vidya, Vijay, S. Barman, A. Chebolu, Nagahanumaiah and A.K. Das, Effects of Different Cavity Geometries on Machining Performance in Micro-Electrical Discharge Milling. ASME J. Micro Nano-Manuf., *3* (2015) 011007. https://doi.org/10.1115/1.4029275.

[23] S. Kar and P.K. Patowari, Experimental Investigation of Machinability and Surface Characteristics in Microelectrical Discharge Milling of Titanium, Stainless Steel and Copper. Arab. J. Sci. Eng., *44* (2019) 7843–7858. https://doi.org/10.1007/s13369-019-03918-3.

[24] K. Khanafer, A. Eltaggaz, I. Deiab et al., Toward Sustainable Micro-drilling of Inconel 718 Superalloy Using MQL-Nanofluid. Int. J. Adv. Manuf. Technol., *107* (2020) 3459–3469. https://doi.org/10.1007/s00170-020-05112-4.

[25] D. Liu, P. Zheng, M. Cao, H. Yin, Y. Xu and L. Zhang, A New Method of Roundness Error Evaluation Based on Twin Support Vector Machines. Meas. Sci. Technol., *32* (2021) 075008.

[26] Y. Arezki, Investigation of Minimum Zone Assessment Methods for Aspheric Shapes. Precis. Eng. (2018). https://doi.org/10.1016/j.precisioneng.2018.01.008.

[27] A. Rossi, M. Antonetti, M. Barloscio and M. Lanzetta, Fast Genetic Algorithm for Roundness Evaluation by the Minimum Zone Tolerance (MZT) Method. Measurement, *44* (2011) 1243–1252. https://doi.org/10.1016/j.measurement.2011.03.031.

[28] J. Li, Z. Zhi-jing, W.U. Wei-ren, J. Xin and J. De-gang, Roundness Error Evaluation by Minimum Zone Circle via Microscope Inspection. J. Beijing Inst. Technol., *22* (2013) 185–190.

[29] N. Hanumaiah and B. Ravi, Rapid Tooling Form Accuracy Estimation Using Region Elimination Adaptive Search Based Sampling Technique. Rapid Prototyp. J., *13* (2007) 182–190.

Publisher's Note Springer Nature remains neutral with regard to jurisdictional claims in published maps and institutional affiliations.

The current issue and full text archive of this journal is available on Emerald Insight at:
https://www.emerald.com/insight/0368-492X.htm

Exploring intergenerational differences in technology-oriented ethical behavior

Shivangi Verma and Naval Garg
Delhi Technological University, Delhi, India

Received 21 September 2021
Revised 7 December 2021
Accepted 12 January 2022

Abstract

Purpose – The proliferation of information technology (IT) and IT-enabled devices has brought various challenges for modern organizations. These challenges are aggravated by the fact that the employees of different generations have a varying degree of expertise and ethical orientation regarding technology. This study has two primary objectives to have an in-depth understanding of technology-related ethical behavior of a diverse workforce. First, it aims to develop a valid and reliable scale to measure technology-oriented ethical behavior. Second, it investigates variations in technology-oriented ethical behavior among Generation X (pre-millennial), Generation Y (millennial) and Generation Z (post-millennial) using the scale.

Design/methodology/approach – The study is conducted in two steps. The first step, a techno-ethical scale, is developed with the help of the six steps of scale development proposed by Churchill (1979). These steps include exploratory factor analysis (EFA), confirmatory factor analysis (CFA), reliability analysis (composite reliability) and validity analysis (convergent and divergent validity). In the second step, intergenerational variation in different factors of technology-oriented ethical behavior among generation X, Y and Z employees is explored with the help of ANOVA and mean plots.

Findings – The study suggests a four-dimensional techno-ethical scale comprising fourteen statements. These four dimensions of the scale are the invasion of the right of privacy, defamation, self-enrichment and loafing during office hours. The scale is reported to have adequate reliability and validity estimates. Results also recommend statistically significant variations in all four dimensions of technology-oriented ethical behavior among pre-millennial, millennial and post-millennial. Also, except for self-enrichment, the mean values progressively increase from pre-millennial to post-millennial. Even for self-enrichment, the mean value is highest for post-millennial.

Originality/value – This study is one of the pioneer studies that explore ethical orientation towards technology usage of three generations of employees.

Keywords Pre-millennial, Millennial, Post-millennial, Intergenerational difference, Technology-oriented behavior

Paper type Research paper

Introduction

The contemporary workplace witnesses a peculiar challenge of management of the diverse workforce. Although diversity brings diverse perspectives to the table, it constantly tests the HR manager to collaborate values and aspirations of people of different gender, caste, creed, nationality, cultures and generations. Previous researchers have well researched and documented the generation-based variations in various organizational factors. Rudolph and Zacher (2015) reported different generations' work values and career priorities. Westerman and Yamamura (2007) found a lower level of job satisfaction among baby boomers than generation X and Y. Other researchers also reported significant intergenerational variation across a variety of work behaviors like work values (Bennett *et al.*, 2012; Smola and Sutton, 2002; Yogamalar and Samuel, 2016), work ethics and motivation (Soto and Lugo, 2013; Zemke *et al.*, 2000; Olson and Brescher, 2011), learning orientation (D'Amato and Herzfeldt, 2008), psychological empowerment and flexibility (Toro *et al.*, 2019), use of influence tactics (Landry, 2009) intention to leave the job (Benson and Brown, 2011) and narcissism (Trzesniewski and Donnellan, 2010). These differences have a significant effect on the successful implementation of HR policies and practices of an organization.

Kybernetes
© Emerald Publishing Limited
0368-492X
DOI 10.1108/K-09-2021-0897

The proliferation of information technology (IT) and IT-enabled devices brought specific challenges for the modern organizations that employ people of all generations. One such challenging issue is the different technology usage and expertise levels across different generations. Several researchers, including Purcell *et al.* (2012) and Zickuhr and Madden (2012), have highlighted significant differences in IT usage across different generations. Although these studies vary in sample, methodology and design, they unanimously conclude generation-based differences. Studies have posited that age-based obstacles might prohibit older generations from taking full advantage of digital avenues for communication. Older adults may be less familiar with the nuances of newer digital forms of interaction (Comunello *et al.*, 2017).

Now, similar to technology usage, research has also reported considerable variations in ethical ideologies and ethical orientation among generations (Zabel *et al.*, 2017; Weber and Urick, 2017). Now, when IT has become an indispensable part of human life, it is imperative to understand the techno-ethical orientation of different age cohorts. Although few studies conducted by Boyd (2010) and Wright *et al.* (2014) tried to explore techno-ethical orientation based on generational differences, literature still lacks a systematic comparative study of pre-millennial, millennial and post-millennial, especially in the Indian context. Such explorations are highly desirable in an age where diverse generations work under a common roof. HR managers find it challenging to implement a uniform code of conduct in their respective organizations. Thus, learning more about this unexplored area becomes necessary, which will serve as an essential thrust for corporate HR policymakers to strategize and implement policies accordingly.

The extensive survey of the existing literature reveals two major research gaps in these domains. First, it reveals the scarcity of a scale that could measure technology-oriented ethical behavior of the employees. Thus, this study develops a valid and reliable techno-ethical scale using wide range of statistical tools like exploratory factor analysis (EFA) and confirmatory factor analysis (CFA). The study offers a four-dimensional scale to measure techno-ethical orientation of an individuals. The four dimensions of the scale are infringement of right to privacy, defamation, self-enrichment and loafing during office time. Second, available literature highlights lack of studies exploring the technology-oriented ethical behavior among Generation X (pre-millennial), Generation Y (millennial) and Generation Z (post-millennial). Accordingly, the present study explores generation-based variations across four dimensions of techno-ethical scale using ANOVA.

Theoretical framework

Defining generations

Becker (1992) defined a generation as "a clustering of birth cohorts that are marked by a specific historic location, common traits at an individual level (life courses, value orientations, and behavioral patterns) and at a system level (size and composition, generational culture and generational organizations)" (p. 23). It may also be referred to as an "aggregate of all people born over roughly the span of a phase of life who share a common location in history and, hence, a common collective persona" (Strauss and Howe, 1997, p. 61). The basis of these and other definitions is the generational cohort theory developed by Mannheim (1952). The theory states that people of a generation experience the same economic, political, environmental and social events. Thus, they develop similar values, attitudes, habits and behaviors (Inglehart, 1977). The generational cohort theory identifies two pivotal aspects that form the basis of the formation of a generation: generational context and generational unit. Generational contexts are the resemblance of experience of similar social, technological, economical and political events by people of same generation. Such similar experience leads to development of informal cooperation and collaborations among people of same generation (Ng and Parry,

2016). McMullin *et al.* (2007) argue that the variations in people's attitudes and values of different generations result from important economic, political and social events they witness during their childhood. This explanation resembles the "critical period" concept for learning societal values and aspiration studies by developmental psychologists (Schuman and Scott, 1989).

As such, the differentiation of generations is done on the basis of birth years. Generation X was born between the 1960 and 1980s (Gordinier, 2008). Today, Generation X enjoys prominent positions in work organizations. They are the decision-makers and are generally in their late-career. Generation Y's birth years range from the early 1980s to the mid-1990s, i.e. until 1996 (Horovitz, 2012). The people of this generation are trying to consolidate their position in the workplace. Generation Z is the cohort of people born from 1996 onwards (Dimock, 2019). This generation has started to enter the labor market with enthusiasm and energy. Some of them are keen to start their ventures. A notable change can be seen in the generational distribution in 2020, wherein Gen Y constitutes 35%, Gen X 33%, Boomers 18% and Gen Z 11% in the global workforce (Abdullah *et al.*, 2021). Modern-day workplace is also referred as multigenerational workforce, as they house employees from different generational cohort (Hisel, 2020; Lang, 2020).

Ethical and techno-ethical orientation

Ethics may be defined as "guidelines to influence human behavior in a manner intended to protect and fulfill the rights of individuals in a society"(Marshall, 1999, p. 82). In other words, ethics is a "systematic approach to understand, analyze and distinguish between the matters of right and wrong, good or bad, admirable and deplorable as they relate to the well-being of and the relationships among sentient beings" (Rich, 2013, p. 4). In a nutshell, it includes a code of conduct of how to behave in a society. And, ethical orientation is one's internal inclination towards ethical paradigms like deontology or ontology (Sullivan and Kymlicka, 2007). One's orientation towards moral values like honesty, utilitarianism, etc. influences decision-making (Burton-Jones and Hubona, 2005). Understanding ethical orientation is a prerequisite for judging one's choice for ethical or unethical behavior (Garg and Sarkar, 2020).

The term "techno-ethics" was first coined by Bunge (1977), who advocated the development of ethical and moral theories to deal with unique challenges posed by the rapid growth of IT. According to Galvan (2001), techno-ethics is the "total of ideas that bring into evidence a system of ethical reference that justifies that profound dimension of technology as a central element in the attainment of a finalized perfection of man." In other words, techno-ethics is an interdisciplinary field that deals with all the ethical aspects of technology (Martin and Roberts, 2021). Techno-ethics provides a perfect amalgamation of technology and ethics as socially embedded enterprises. It focuses on identifying the ethical use of technology and preventing misuse of technology. Also, it tends to explore universal principles that guide technological advancement and its application for the benefit of society (Luppicini, 2009a). Techno-ethics essentially ensures tickle down of benefits of technology to last rung of the society.

Generational differences in technology-oriented ethical behavior

The intergenerational differences in techno-ethical orientations are theoretically premised in generational theory (Mannheim, 1952), the uses and gratification theory (Katz *et al.*, 1974) and the technology acceptance theory (Davis *et al.*, 1989; Venkatesh *et al.*, 2003). The generational theory states that the age cohort that experiences and remembers the same social and political event develops similar values, attitudes and expectations. Clark (2017) maintained that generational differences dictate how each person can and will learn. The three generations (generation X, Y and Z) have witnessed different stages of technological advancement, especially in India. The Indians of Generation X did not have the luxury of IT

and IT-enabled devices in childhood and adulthood. Even in professional organizations, they either worked manually or through simple manual machines like typewriters. They witnessed an IT revolution in the workplace only in their late-career with the bombardment of sophisticated and complex hardware and software. Through liberalization, privatization and globalization in 1991, Indian opened its doors for technology (Ravan, 2014). Thus, Generation Y encountered IT-enabled devices in late adulthood or at the early career stage. The Gen Yers are also the most technologically learned and well-educated cohorts (Cekada, 2012).

Generation Z is the most privileged cohort that understands and cherishes advanced technologies from their childhood. These post-millennials are much benefitted from technology because computers and the Internet have become a part of their educational environment whereby all students are taught how to use sophisticated tools of information technologies. Technology is an integral part of post-millennials life (Pásztor and Bak, 2020). Pre-millennial and millennials are the ones who later adopted the technology (Doyle and Goldingay, 2012). Seemiller *et al.* (2019) reported that Gen Xers are not technological novices because many of them exhibit behavior similar to younger generations in their social media usage and smart phones. Both Gen Xers and Zers have different communication preferences as the latter are more interested in texting than writing emails. Thus, since pre-millennial are less tech-savvy, they are more likely to have rigid and dogmatic techno-ethical orientation in comparison to younger generation. Younger generation does not hesitate to deviate from established ethical standards (Martin and Roberts, 2021). Millennial ethical mindset fluctuates between self-gratification and societal benefits (Boyd, 2010). While pre-millennial emphasizes need fulfillment in ethical ways, the focus of post-millennial is on self-enrichment with little concern for ethical or unethical behavior (Boyd, 2010).

The use and gratification theory explains the relationship between psychological motives and technology use and behaviors. According to the theory, one selects and uses technology in a goal-directed manner to achieve gratifications and fulfill its needs. And researchers like Magsamen-Conrad *et al.* (2015) reported significant variances in the way different age cohorts use technology. Generational cohort influences usage and engagement with technology. Generation X generally chooses technology to perform works that are manually too complex or difficult. They do not use technology for entertainment of fun. Generation Yers are "looking for active, alive, open and informal workplaces that offer the latest technology" (Cushing, 2020). Like Generation Yers, Gen Z prefers using the Internet to communicate with others because of their interest in the new technology. Individuals of Gen Z can typically be located where the advantages of being hooked up to the Internet are available (Kirchmayer and Fratricova, 2020). Concerning the impact of technologies on the workplace networks, Lanier (2017) indicates that the inclusion of necessary online communication tools and technologically competent managers leads to a high level of satisfaction and motivation among Generation Z employees. They use technology for nearly everything. There life is incomplete without technology. Thus, different usage pattern is poised to bring different ethical orientation towards technology.

Although generation-based ethical positions are well researched, the studies to investigate techno-ethical orientation are scarce. The scarcity of such studies in the Indian context is evident from the fact that a validated and well-accepted scale to measure techno-ethical orientation is not available. Thus, the present study tends to develop a validated techno-ethical scale in the study's first phase. And in the second phase, this scale is used to evaluate differences in the technology-oriented behavior of pre-millennial, millennial and post-millennial.

Research methodology

Scale development

Churchill (1979) suggested six steps of scale development, i.e. specification of the domain of the construct, generation and classification of items through experience survey, initial data

collection and purification through a pilot study and expert reviews, data collection, EFA and CFA.

Step 1: Specification of the domain of the construct: The first step requires finalization of definition of the concept. The concept definition facilitates identification of measures of the construct. Accordingly, techno-ethical orientation is defined as relational orientation to technology and human activity concerned with all ethical aspects of technology within a society shaped by technology (adapted from Luppicini, 2009b).

Step 2: Generation and classification of items: Experience survey method was employed to gage which items to be included or excluded for the generation and classification of items. The experience survey was conducted among the employees of educational institutions and professional organizations for their opinion, beliefs and feelings about the usage of technology by various generations and how technology has shaped the ethical orientation. The sample items of the experience survey were "please indicate the extent to which you experience that technology has taken over the control of your life" (on a scale of 1 = strongly agree, to 5 = strongly disagree), and "technology seems user-friendly to me." Based on this survey, 27 statements have been formulated that try to capture the techno-ethical orientation of the individuals.

Step 3: Initial data collection and purification: The 27 statements were subjected to a pilot study on a small sample of 33 respondents. Afterward, an expert committee consisting of research scholars working in ethics, human-technology interaction, corporate social responsibility and academicians from 3 colleges were presented with the draft questionnaire. Based on extensive discussions of the panel, seven statements that appeared irrelevant were omitted. After modifications, the final questionnaire consisted of 20 statements.

Step 4: Data collection: Now, data were collected using twenty-item modified questionnaire. The employees engaged in different industries were approached either through emails or through personal visits using convenience sampling. Employees engaged in any professional organization were presented with the questionnaire. As many as 425 people were approached, but only 350 respondents returned the questionnaire. Out of these 350 questionnaires, 48 were discarded for incomplete or negligently filled (Meade and Craig, 2012). Among the pool of 302 responses, 58 participants belong to the pre-millennial group, 111 participants from the millennial group and 133 respondents from the post-millennial group. Among the pre-millennial cohort, 36.8% were male, and 36.2% were female. From the millennial group, 40.5% were male; 57.7% were female, and 1.8% were the third gender.

Similarly, the post-millennial group consists of 56.4% males and 43.6% females. Based on industry-wise distribution, in the millennial cohort, 50% of the respondents belong to the education industry, followed by 11% from the information and technology industry. Similarly, 36% of pre-millennial were from education industry followed by 24% from manufacturing and 12% from information and technology sector. For post-millennial, almost half of the respondents, i.e. 59%, were from the education industry, followed by 25% from the finance and insurance sectors. The sample items of the questionnaire were "sharing confidential information with others on social media" and "using instant messaging apps during work hours," rated on a five-point rating scale ranging from 1 (most unethical) to 5 (most ethical).

Step 5: EFA: EFA was employed using principal component analysis and varimax rotation using IBM SPSS 25. Prior to EFA, Kaiser-Meyer-Olkin (KMO) measure of

sampling adequacy and Bartlett's test of sphericity were applied to assess the data's suitability for factor analysis. Finally, 20 statements were subjected to factor analysis using principal component analysis. Application of principal component analysis is recommended because of its use when no prior theory or model exists (Gorsuch, 1997). Moreover, varimax rotation was applied because it makes interpretable clusters by maximizing the dispersion of loadings (Field, 2009) and provides consistent utility. Six statements were discarded for low factor loading. The remaining fourteen statements yielded four latent variables (see Table 1). The four factors have a cumulative value of 58.646% in explaining the total variance in the data. And these factors are described as four dimensions of technology-oriented ethical behavior. These four dimensions are as follows.

F1: Infringement of the right of privacy: This involves statements that encompass creating hindrance in the matter of confidential information and also interference into other's privacy. Statements such as "Reading and forwarding emails of others without their consent," "sending files with virus intentionally," and "Not giving due credits to someone for providing assignment-related material" are included in this factor. The factor could explain the 30.161% variance.

F2: Self–enrichment: Statements that deal with using an organization's material for personal benefits or gains were covered under this factor, with 11.962% of the variance. Examples include making a personal copy of a rented movie, copying software from the organization for personal use and using workplace organizations to play games online.

F3: Defamation: Statements intended to harm someone by criticizing them on the Internet were covered under this factor and explain 9.207% of the total variance. It involves labeling the organization or workplace.

F4: Loafing during work hours: This factor comprises four statements and constitutes 7.317% of the total variance in the EFA analysis. Loafing, i.e. using instant messaging apps during work hours, is evident in this factor extraction. It involves having fun during office work instead of doing productive work.

Step 6: CFA: CFA helps examine the link between observed and latent variables based on the underlying theoretical constructs (Hair *et al.*, 2014). Statistics associated with the default model were discouraging and indicated poor model fit. Value of χ^2 ($\chi^2 = 734.816$) and other indexes such GFI, *p*-close and RMSEA showed that the default model does not fit well as the values of these parameters are not in line with the cut-off values suggested by Hu and Bentler (1999) and Ullman (2001). Since model did not fit well, it required certain modifications. The following steps are followed for model modifications (Harrington, 2009; Simon *et al.*, 2010): (1) check the regression loadings of observed variables on unobserved variables, (2) look out for modification indices (MI) and (3) examine the standardized residual covariance. Based on the modification steps mentioned above, final model highlights RMSEA came out as 0.098, CMIN/df = 3.839, GFI has a value of 0.895,

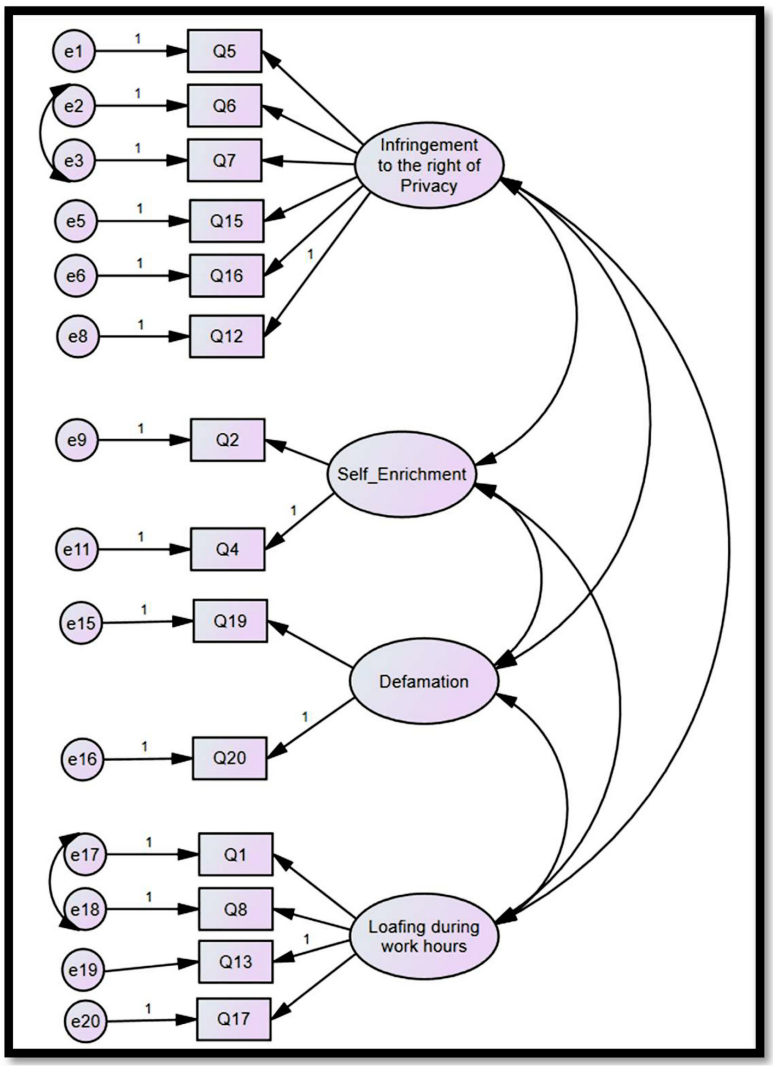
Table 1. Results of factor analysis

Factors	Eigen values	% of variance
F1 – infringement of the right of privacy	6.032	30.161
F2 – self-enrichment	2.392	11.962
F3 – defamation	1.841	9.207
F4 – loafing during work hours	1.463	7.317

Source(s): Primary data

TLI = 0.790, CFI = 0.841 and *p* close is 0.000. Now, all values show a good model fit except TLI, *p*-close, RMSEA. Figure 1 depicts a well-fitted theoretical model for measuring techno-ethical orientation in the Indian context. And this scale comprises 14 statements now. After CFA, reliability and validity testing was done.

The scale's reliability was accessed using composite reliability estimates, whose values should be greater than 0.70 to support good reliability (Hair *et al.*, 2010). Table 2 reports that all four dimensions of technology-oriented behavior are reliable. Now, convergent validity is calculated with the help of average variance extracted (AVE). As a rule of thumb, the AVE of 0.50 or higher was promising and indicated an adequate level of convergent validity (Fornell and Larcker, 1981). Table 2 reported AVE values of all four extracted factors. Also, the AVE values (highlighted in bold and placed diagonally in Table 3) are more significant than the squared inter-correlation of the constructs. It confirms the discriminant validity of the scale (Fornell and Larcker, 1981). These results suggest that four-dimensional techno-ethical scale is both reliable and valid.



Source(s): Primary Data

Figure 1.
Final CFA model

Intergenerational differences in technology-oriented ethical behavior

Tables 4 and 5 describe intergenerational variations of four factors of the technology-oriented behavior of pre-millennial, millennial and post-millennial. Table 4 observes that except for self-enrichment; mean values progressively increase from pre-millennial to post-millennial. Even for the self-enrichment factor, the mean value (mean = 2.97) is maximum for post-millennial. Figure 2a–d graphically depicts the same. It indicates that younger generations are relatively more open to infringement of the right to privacy, self-enrichment, defamation and loafing during office hours. The younger generation considers these actions as more ethical than their previous generations. Table 5 reports statistically significant variations in four factors of technology-oriented behavior among pre-millennial, millennial and post-millennial (all p value < 0.05). These results suggest that there exist significant variation in technology-oriented ethical behavior among employees of different generations. It simple words, pre-millennial, millennial and post-millennial employees have different ethical orientation towards technology.

Discussion and conclusion

The present study offers two significant findings. First, the study provides four-dimensional techno-ethical scale in the context of the use of technology in the workplace. These dimensions are infringement of the right of privacy, self-enrichment, defamation and loafing during work hours. Second, the study suggests significantly different technology-oriented ethical behavior among generations X, Y and Z. The findings state that older generations consider these traditional organizational taboos more ethical than younger generations. It indicates a shift towards acceptance and tolerance of more liberal techno-ethical policies. For inference, loafing at the workplace is generally seen as unethical by the HR manager and management. But post-millennial perceive such workplace behavior as more ethical and acceptable than millennial and pre-millennial. These findings are in alignment with the concept of "weisure" time, which considers work and leisure as one and same (Meister and Willyerd, 2010). This indicates that for digital generations, the division between labor and leisure will increasingly blur in the quest for a work-life balance. Similarly, self-enrichment (use of organizational resources for personal gains) is seen more unethical by older

Table 2. Composite reliability and average variance extracted for each factor

Factor	Composite reliability	AVE
Infringement of the right of privacy	1.120	0.554
Self-enrichment	0.760	0.615
Defamation	0.765	0.620
Loafing during work hours	0.709	0.584

Source(s): Primary data

Table 3. Discriminant validity of extracted factors

Factors	Factor 1	Factor 2	Factor 3	Factor 4
Infringement of the right of privacy	*0.554*			
Self-enrichment	0.064	*0.615*		
Defamation	0.150	0.087	*0.620*	
Loafing during work hours	0.084	0.028	0.046	*0.584*

Source(s): Primary data

Factors		*N*	Mean	SD
Infringement of the right to privacy	Pre-millennial	58	1.39	0.452
	Millennial	110	1.54	0.429
	Post-millennial	131	1.88	0.741
Self-enrichment	Pre-millennial	58	2.32	0.814
	Millennial	110	2.11	0.991
	Post-millennial	131	2.97	0.923
Defamation	Pre-millennial	58	1.90	0.827
	Millennial	110	1.91	0.649
	Post-millennial	131	2.26	1.121
Loafing during work hours	Pre-millennial	58	1.82	0.614
	Millennial	110	2.26	0.616
	Post-millennial	131	2.32	0.633

Source(s): Primary data

Table 4. Descriptive statistics for each factor according to generations

Factors		SS	df	MS	*F*	Sig.
Infringement of the right of privacy	Between groups	14.7	2	7.355	20.87	0.000*
	Within groups	104.2	296	0.352		
	Total	119.0	298			
Self-enrichment	Between groups	40.5	2	20.29	25.11	0.000*
	Within groups	239.2	296	0.808		
	Total	279.8	298			
Defamation	Between groups	9.15	2	4.577	5.165	0.006*
	Within groups	262.3	296	0.886		
	Total	271.4	298			
Loafing during work hours	Between groups	16.2	2	8.116	20.87	0.000*
	Within groups	115.0	296	0.389		
	Total	131.2	298			

Source(s): Primary data, *Sig at 05, SS- Sum of Squares, MS- Mean Square, Df- Degree of freedom

Table 5. Results of one-way ANOVA

generation. Younger generation find it quite acceptable. And it is considered as a routine affair by younger employees.

This shifting ethical paradigm poses a new challenge for modern-day HR managers. They need to bring about necessary and desirable changes in organizational ethical philosophy and policies to accommodate the new ethical positioning of a new generation of employees. Although more research is required, there is a clear trend towards new normal techno-ethics in the workplace. The new normal paradigm of techno-ethics necessitates more liberal and generous ethical policies towards using technology at the office. The survival of an organization requires reshaping and redefining its policies and strategies accordingly. There seems to be a need of changing both organizational culture and activities to accommodate changing attitude and behavior of upcoming new generation workforce.

Although, to the best of our knowledge, no previous study has investigated the technology-related ethical behavior of three generations, inferences of generation-based technology usage variations are reported in earlier studies. The millennial cohort usually utilizes technologies for entertainment and hedonic purposes. And pre-millennials rely on technologies for utilitarian purposes and information search (Calvo-Porral and Pesqueira-Sanchez, 2019). Millennials or Generation Y is more inclined to adapt to the new cyber environment than Generation X (Gafni and Geri, 2013). Members of Gen Y are considered harbingers for changing technology (Abdullah *et al.*, 2021). Peek *et al.* (2014) concluded that

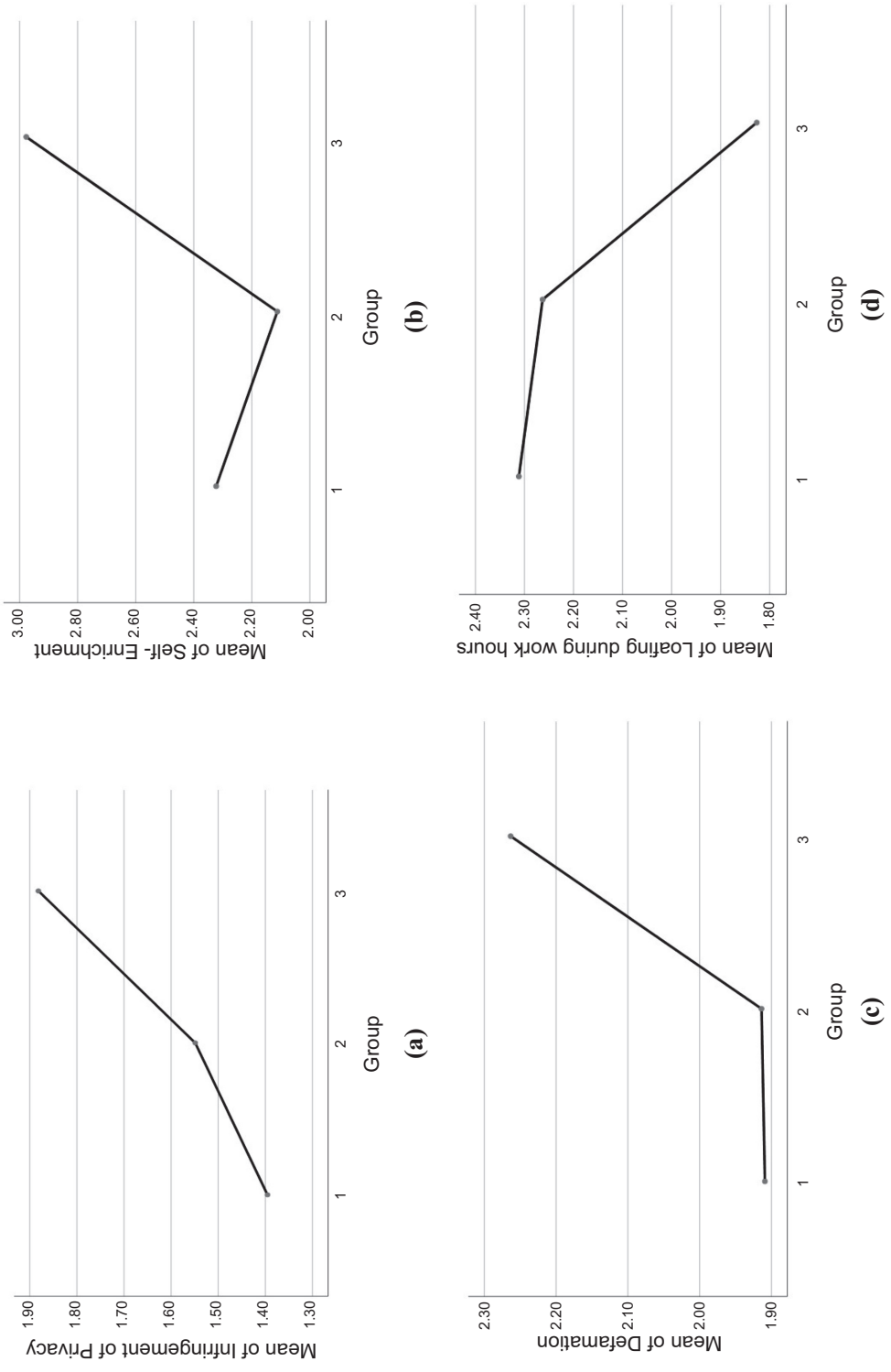


Figure 2.
Means plot for
(a) "infringement of the right of privacy",
(b) "self-enrichment",
(c) "defamation",
(d) "loafing during work hours"

limited usability, fear of technology and no control over activation and de-activation of technology are few reasons which restrict the use of technology for limited purposes by the older generation. Other researchers, including Purcell *et al.* (2012), van der Kaay and Young (2012), also claimed that the younger generation has a more liberal and positive attitude towards technology than the older population. The findings are also in line with the generational difference in emotional reactions to emerging technologies. Pre-millennials expect simple interfaces for technology use and experience anxiety while using Internet-enabled devices (Czaja, 2006; Rosenthal, 2008; Shedletsky, 2006), whereas the Generation X population likes sophisticated devices because of their exposure and adaptability with the Internet and Internet-enabled modern devices.

Theoretical implications

There are several significant theoretical contributions of the present study. First, the study offers a reliable and valid scale to measure the technology-oriented behavior of employees. The scale is posed to help future researchers to expand the knowledge horizon of ethical studies. Second, the study provides an insight into intergenerational variations of three generations, i.e. pre-millennials, millennials and post-millennials. The majority of previous studies are restricted to compare the ethical positioning of two generations only. Third, the present study inspires a way to look at the shifting of ethical positioning of younger generations. Instead of labeling post-millennials as unethical, the present study initiates a debate of ethical repositioning in the light of technology bombardment. Ethical values change with the time and this study proposes a discussion on ethical reorientation.

Fourth, the findings of this study made a significant contribution to existing theories in several ways. One of the prominent models referred to as "Igbaria's model" posited that perceived fun and perceived usefulness influences behavior (computer usage) and attitude towards new technology acceptance or rejection (Igbaria *et al.*, 1994). Consistent with this view, millennials and post-millennials of this study perceive technology as useful and fun compared to their counterparts. Therefore, their technology-oriented behavior is shaped by these motivators. The results presented in this study further strengthened the unified theory of acceptance and use of technology (UTAUT) (Venkatesh *et al.*, 2003). According to UTAUT, age and experience moderate the impact of usage intention and behavior. With age, individuals require more assistance in operating new technology due to higher levels of computer anxiety and fear of change. The findings of this study also lend an indirect support through suggesting that older generation is relatively less flexible for ethical repositioning.

Lastly, the results of the study offer empirical evidence of generational theory in a non-western context. The majority of generational theories were developed in the western background. The findings of the current study provide empirical evidences to these theories in non-western context too, which leads to cross-cultural validation of these theories.

Practical implications

This study makes several practical implications for modern organizations that house employees of all three generations. It is being argued that existing organizational policies and HRM practices have been drafted by pre-millennials (Ng and Parry, 2016). And, thus the aspirations and concerns of younger generations are yet to be fully integrated into these policies and practices. The same is also true for the firm's ethical policy regarding the use of technology in the workplace. The findings of the present study suggest that younger generation have relatively liberal view regarding ethical use of technology. The younger generations have already started to demand the freedom to use technology at the office. Thus, it is suggested that organizational techno-ethical policies may be revised in light of changing technology usage, norms and the associated attitude of the new generation workforce. New

policy may keep zero tolerance approach towards universal unethical practices like infringement of right to privacy, defamation, etc. At the same, such a newly devised policy may adapt more open and liberal approach towards limited self-enrichment or social loafing. It will help achieve a delicate balance of ethical aspirations of different generations. Such policy revision also requires separate training program for older and younger generations to enhance their tolerance and acceptance towards each other's ethical orientation.

The new generation employees will play a pivotal role in decision-making in the next five to ten years. Shortly Gen Z will represent almost 30% of the world population and 25% of the global workforce (Gomez *et al.*, 2018). Acknowledging the future roles of today's Generation Z, HR managers may have to use different innovative mechanisms to help them realize importance of techno-ethical orientation. Sensitive training, experience sharing sessions with victim of defamation, didactic decision-making, etc. may prove very helpful in attracting younger employees' attention towards dark side of the unethical use of technology. In a nutshell, the present study offers two major practical suggestions. First, it recommends revision in ethical policies of the company to accommodate opinions and attitudes of younger generations. Second, it suggests training and learning sessions for younger employees to help them realize danger of too flexible ethical approach.

Limitations, direction for future researchers and conclusion

It is acknowledged that there are limitations in using a questionnaire as the sole method for data collection in this study. Study in one culture also limits the generalization of findings in other cultures. The sample size was not equal for each cohort because of the removal of many outliers. Future studies investigating the role of other relevant factors using interviews or longitudinal studies can provide a comprehensive idea of how technology use has changed over generations and what the future holds for the next generation. Face to Face interviews will provide immense information necessary for our understanding of factors influencing the digital divide or techno-ethical orientation with technology usage. Future studies might explore the social environment, experience, gender and ethical judgment that impact the techno-ethical orientation of people. The use of moral dilemmas or scenarios will examine the broader implication of technology and ethics interrelation.

References

Abdullah, M., Ali, O. and Alias, R.B. (2021). "Generational differences in values and attitudes within the workplace generational differences in values and attitudes within workplace", Vol. 57 No. February, pp. 1496-1503.

Becker, H.A. (1992), "A pattern of generations and its consequences", in *Dynamics of Cohort and Generations Research*, Thesis Publishers, Amsterdam, p. 38.

Bennett, J., Pitt, M. and Price, S. (2012), "Understanding the impact of generational issues in the workplace", *Facilities*, Vol. 30, pp. 278-288.

Benson, J. and Brown, M. (2011), "Generational differences at work: do they matter?", *The International Journal of Human Resource Management*, Vol. 22 No. 9, pp. 1843-1865.

Boyd, D. (2010), "Ethical determinants for generations X and Y", *Journal of Business Ethics*, Vol. 93 No. 3, pp. 465-469, doi: 10.1007/s10551-009-0233-7.

Bunge, M. (1977), "Towards a technoethics", *The Monist*, Vol. 60 No. 1, pp. 96-107.

Burton-Jones, A. and Hubona, G.S. (2005), "Individual differences and usage behavior: revisiting a technology acceptance model assumption", *Data Base for Advances in Information Systems*, Vol. 36 No. 2, pp. 58-77, doi: 10.1145/1066149.1066155.

Calvo-Porral, C. and Pesqueira-Sanchez, R. (2019), "Generational differences in technology behaviour: comparing millennials and Generation X", *Kybernetes*, Vol. 49 No. 11, pp. 2755-2772, doi: 10.1108/K-09-2019-0598.

Cekada, T.L. (2012), "Training a multigeneration workgorce: understanding key needs & learning sytles", *Professional Safety*, March, Vol. 57 No. 3, pp. 40-44, available at: http://www.hhs.iup.edu/cekadat/safe644tlc/Links/Mod5_Week9_Cekada_multigen.pdf.

Churchill, G.A. (1979), "A paradigm for developing better measures of marketing constructs", *Journal of Marketing Research*, Vol. 16 No. 1, pp. 64-73, doi: 10.2307/3150876.

Clark, K.R. (2017), "Managing multiple generations in the workplace", *Radiologic Technology*, Am Soc Radiol Tech, Vol. 88 No. 4, pp. 379-396.

Comunello, F., Fernández Ardèvol, M., Mulargia, S. and Belotti, F. (2017), "Women, youth and everything else: age-based and gendered stereotypes in relation to digital technology among elderly Italian mobile phone users", *Media, Culture and Society*, Vol. 39 No. 6, pp. 798-815, doi: 10.1177/0163443716674363.

Cushing, G.M. (2020), "Multi-generational workforce strategies for 21st century managers", *Dissertation Abstracts International Section A: Humanities and Social Sciences*, Vol. 81 Nos 5-A, pp. 1-97, available at: http://search.ebscohost.com/login.aspx?direct=true&db=psyh&AN=2020-04052-231&site=ehost-live.

Czaja, S.J. (2006), "Technology and older adults: designing for accessibility and usability", in *Eighth International ACM SIGACCESS Conference on Computers and Accessibility, ASSETS 2006*, doi: 10.1145/1168987.1168988.

Davis, F.D., Bagozzi, R.P. and Warshaw, P.R. (1989), "User acceptance of computer technology: a comparison of two theoretical models", *Management Science*, INFORMS, Vol. 35 No. 8, pp. 982-1003.

Dimock, M. (2019), "Defining generations: where Millennials end and Generation Z begins", *Fact Tank: News in the Numbers*, available at: https://www.pewresearch.org/fact-tank/2019/01/17/where-millennials-end-and-generation-z-begins/.

Doyle, C. and Goldingay, S. (2012), "The rise of the 'silver surfer': online social networking and social inclusion for older adults", *Journal of Social Inclusion*, Vol. 3 No. 2, pp. 40-54, doi: 10.36251/josi.54.

D'Amato, A. and Herzfeldt, R. (2008), "Learning orientation, organizational commitment and talent retention across generations: a study of European managers", *Journal of Managerial Psychology*, Vol. 23 No. 8, pp. 929-953, doi: 10.1108/02683940810904402.

Field, A. (2009), "Exploring assumptions", *Discovering Statistics Using SPSS*, Sage Publications, London, doi: 10.1111/insr.12011_21.

Fornell, C. and Larcker, D.F. (1981), "Evaluating structural equation models with unobservable variables and measurement error", *Journal of Marketing Research*, Vol. 18 No. 1, pp. 39-50, doi: 10.2307/3151312.

Gafni, R. and Geri, N. (2013), "Generation Y versus generation X: differences in smartphone adaptation", in *Proceedings of the 8th Chais Conference on Innovation and Learning Technologies*, pp. 18-23, available at: http://www.openu.ac.il/innovation/chais2013/download/b1_4.pdf.

Galvan, J.M. (2001), "Technoethics: acceptability and social integration of artificial creatures", in *Presented at Humanoids – A Techno-Ontological Approach*, 21 Novembre 2001, Waseda University, Tokyo.

Garg, N. and Sarkar, A. (2020), "Vitality among university students: exploring the role of gratitude and resilience", *Journal of Organizational Effectiveness: People and Performance*, Vol. 7 No. 3, doi: 10.1108/JOEPP-03-2020-0041.

Gomez, K., Tiffany, M., Kimberly, B., Sapp, K., Brown, A. and Santner, K. (2018), "Welcome to generation z - 1", available at: https://www2.deloitte.com/us/en/pages/consumer-business/articles/understanding-generation-z-in-the-workplace.html#.

Gordinier, J. (2008), *X Saves the World: How Generation X Got the Shaft but Can Still Keep Everything from Sucking*, Penguin.

Gorsuch, R.L. (1997), "Exploratory factor analysis: its role in item analysis", *Journal of Personality Assessment*, Vol. 68 No. 3, pp. 532-560, doi: 10.1207/s15327752jpa6803_5.

Hair, J.F., Black, W.C., Babin, B.J. and Anderson, R.E. (2010), *Multivariate Data Analysis: A Global Perspective*, Pearson Custom Library.

Hair, J.F., Black, W.C., Babin, B.J. and Anderson, R.E. (2014), *Multivariate Data Analysis*, 7th ed., Prentice-Hall, doi: 10.1038/259433b0.

Harrington, D. (2009), *Confirmatory Factor Analysis*, Oxford University Press, New York, doi: 10.1093/acprof:oso/9780195339888.001.0001.

Hisel, M.E. (2020), "Measuring work engagement in a multigenerational nursing workforce", *Journal of Nursing Management*, Wiley Online Library, Vol. 28 No. 2, pp. 294-305.

Horovitz, B. (2012), "After Gen X, Millennials, what should the next generation be called? – USATODAY.com", *USA Today*, available at: https://abcnews.go.com/Business/gen-millennials-generation/story?id=16275187#:~:text=Last%20July%2C%20TRU%20sent%20all,and%20defined%20the%20next%20generation.

Hu, L.T. and Bentler, P.M. (1999), "Cut-off criteria for fit indexes in covariance structure analysis: conventional criteria versus new alternatives", *Structural Equation Modeling*, Lawrence Erlbaum Associate, doi: 10.1080/10705519909540118.

Igbaria, M., Schiffman, S.J. and Wieckowski, T.J. (1994), "The respective roles of perceived usefulness and perceived fun in the acceptance of microcomputer technology", *Behaviour and Information Technology*, Vol. 13 No. 6, pp. 349-361, doi: 10.1080/01449299408914616.

Inglehart, R. (1977), "Changing values and skills among western publics", *The Silent Revolution: Changing Values and Political Styles Among Western Publics*, Princeton University Press, New Jersey, doi: 10.2307/j.ctt13x18ck.5.

Katz, E., Blumler, J.G. and Gurevitch, M. (1974), *Uses and Gratification Theory Research*, American Association for Public Opinion Research.

Kirchmayer, Z. and Fratricova, J. (2020), "What motivates generation Z at work? Insights into motivation drivers of business students in Slovakia", *Innovation Management and Education Excellence through Vision*, Milan.

Landry, D.J. (2009), *Effects of Generational and Gender Differences on the Use of Influence Tactics*, Capella University, Michigan.

Lang, A.R. (2020), *A Phenomenological Study of the Practices Millennial Supervisors Report Using with Baby Boomer Subordinates*, Creighton University, Nebraska.

Lanier, K. (2017), "5 things HR professionals need to know about Generation Z: thought leadersshare their views on the HR profession and its direction for the future", *Strategic HRReview*, Vol. 16 No. 6, pp. 288-290.

Luppicini, R. (2009a), "Handbook of research on technoethics", *Choice Reviews Online*, Vol. 46 No. 6, pp. 1-19, doi: 10.5860/choice.46-2996.

Luppicini, R. (2009b), "Technoethical inquiry: from technological systems to society", *Global Media Journal – Canadian Edition*, Vol. 2 No. 1, pp. 5-21.

Magsamen-Conrad, K., Upadhyaya, S., Joa, C.Y. and Dowd, J. (2015), "Bridging the divide: using UTAUT to predict multigenerational tablet adoption practices", *Computers in Human Behavior*, pp. 186-196, doi: 10.1016/j.chb.2015.03.032.

Mannheim, K. (1952), "The sociological problem of generation", *Essays on the Sociology of Knowledge*, Routledge, Oxon.

Marshall, K.P. (1999), "Has technology introduced new ethical problems?", *Journal of Business Ethics*, Vol. 19, pp. 81-90, doi: 10.1023/A:1006154023743.

Martin, G. and Roberts, S. (2021), "Exploring legacies of the baby boomers in the twenty-first century", *The Sociological Review*, SAGE Publications, London, Vol. 69 No. 4, doi: 00380261211006326.

McMullin, J.A., Duerden Comeau, T. and Jovic, E. (2007), "Generational affinities and discourses of difference: a case study of highly skilled information technology workers", *British Journal of Sociology*, Vol. 58 No. 2, pp. 297-316, doi: 10.1111/j.1468-4446.2007.00152.x.

Meade, A.W. and Craig, S.B. (2012), "Identifying careless responses in survey data", *Psychological Methods*, Vol. 17 No. 3, pp. 437-455, doi: 10.1037/a0028085.

Meister, J.C. and Willyerd, K. (2010), "Mentoring millennials", *Harvard Business Review*, Vol. 88 No. 5, pp. 68-72.

Ng, E.S. and Parry, E. (2016), "Multigenerational research in human resource management", *Research in Personnel and Human Resources Management*, Emerald Group Publishing, Bingley, doi: 10.1108/S0742-730120160000034008.

Olson, P. and Brescher, H. (2011), "The power of 4. The four generations: who they are", *Journal of Business and Management Studies*, Vol. 1 No. 2, pp. 1-13.

Pásztor, J. and Bak, G. (2020), "Digital divide: a technological generation gap", in *Management, Enterprise and Benchmarking in the 21st Century*, Óbuda University Keleti Károly Faculty of Economics, pp. 158-168.

Peek, S.T.M., Wouters, E.J.M., van Hoof, J., Luijkx, K.G., Boeije, H.R. and Vrijhoef, H.J.M. (2014), "Factors influencing acceptance of technology for aging in place: a systematic review", *International Journal of Medical Informatics*, Vol. 83 No. 4, pp. 235-248, doi: 10.1016/j.ijmedinf.2014.01.004.

Purcell, K., Brenner, J. and Rainie, L. (2012), *Search Engine Use 2012*, Pew Research Center, Washington.

Ravan, S.V. (2014), "Impact of LPG on Indian economy", *Prime International Research Journal*, Vol. 1 No. 4, pp. 21-33.

Rich, K.L. (2013), "Introduction to ethics", *Nursing Ethics: Across the Curriculum and into Practice*, Jones & Bartlett Publishers, Massachusetts, p. 1.

Rosenthal, R.L. (2008), "Older computer-literate women: their motivations, obstacles, and paths to success", *Educational Gerontology*, Vol. 34 No. 7, pp. 610-626, doi: 10.1080/03601270801949427.

Rudolph, C.W. and Zacher, H. (2015), "Intergenerational perceptions and conflicts in multi-age and multigenerational work environments", *Facing the Challenges of a Multi-Age Workforce: A Use-Inspired Approach*, Routledge/Taylor & Francis Group, doi: 10.4324/9780203776322.

Schuman, H. and Scott, J. (1989), "Generations and collective memories", *American Sociological Review*, Vol. 54 No. 3, pp. 359-381, doi: 10.2307/2095611.

Seemiller, C., Grace, M., Dal Bo Campagnolo, P., Mara Da Rosa Alves, I. and Severo De Borba, G. (2019), "How generation Z college students prefer to learn: a comparison of US and Brazil students", *Journal of Educational Research and Practice*, Vol. 9 No. 1, p. 25.

Shedletsky, L. (2006), "Internet training for older adult learners: an intergenerational mentoring approach", *LLI Review*, available at: https://www.academia.edu/25839001/Internet_Training_for_Older_Adult_Learners_An_Intergenerational_Mentoring_Approach.

Simon, D., Kriston, L., Loh, A., Spies, C., Scheibler, F., Wills, C. and Härter, M. (2010), "Confirmatory factor analysis and recommendations for improvement of the Autonomy-Preference-Index (API)", *Health Expectations*, Vol. 13 No. 3, pp. 234-243, doi: 10.1111/j.1369-7625.2009.00584.x.

Smola, K.W. and Sutton, C.D. (2002), "Generational differences: revisiting generational work values for the new millennium", *Journal of Organizational Behavior*, Vol. 23 No. 4, pp. 363-382, doi: 10.1002/job.147.

Soto, M. and Lugo, M.V. (2013), *Multigenerational Differences in the Puerto Rican Workforce*, North American Business Press.

Straus, W. and Howe, N. (1997), *The Fourth Turning: An American Prophecy*, Broadway Books, New York.

Sullivan, W.M. and Kymlicka, W. (2007), "The globalization of ethics: religious and secular perspectives", *The Globalization of Ethics: Religious and Secular Perspectives*, Cambridge University Press, Cambridge, doi: 10.1017/CBO9780511498701.

Toro, I.S.D., Labrador-Fernández, J. and De Nicolás, V.L. (2019), "Generational diversity in the workplace: psychological empowerment and flexibility in Spanish companies", *Frontiers in Psychology*, Vol. 10, doi: 10.3389/fpsyg.2019.01953.

Trzesniewski, K.H. and Donnellan, M.B. (2010), "Rethinking "generation me": a study of cohort effects from 1976–2006", *Perspectives on Psychological Science*, Vol. 5 No. 1, pp. 58-75, doi: 10.1177/1745691609356789.

Ullman, J.B. (2001), "Structural equation modeling", in Tabachnick, B.G. and Fidell, L.S. (Eds), *Using Multivariate Statistics*, 4th ed., Allyn & Bacon, Needham Heights, MA.

van der Kaay, C.D. and Young, W.H. (2012), "Age-related differences in technology usage among community college faculty", *Community College Journal of Research and Practice*, pp. 570-579, doi: 10.1080/10668920903054865.

Venkatesh, V., Morris, M.G., Davis, G.B. and Davis, F.D. (2003), "A unified theory of acceptance and use of technology", *MIS Quarterly*, Vol. 27 No. 3, pp. 425-478.

Weber, J. and Urick, M.J. (2017), "Examining the millennials' ethical profile: assessing demographic variations in their personal value orientations", *Business and Society Review*, Vol. 122 No. 4, pp. 469-506.

Westerman, J.W. and Yamamura, J.H. (2007), *Generational Preferences for Work Environment Fit: Effects on Employee Outcomes*, Career Development International.

Wright, E., Marvel, J.E. and DesMarteau, K. (2014), "Exploring millennials: a surprising inconsistency in making ethical decisions", *Journal of Academic and Business Ethics*, Vol. 9, pp. 1-14, available at: https://proxy.lib.utc.edu/login?url=http://search.proquest.com/docview/1658213133?accountid=14767%5Cnhttp://grlinker.coalliance.org/grlinker/grl000122/grl-UTC.cgi?method=grlResolveArticle&atitle=Exploring+millennials:+A+surprising+inconsistency+in+making+.

Yogamalar, I. and Samuel, A.A. (2016), "Shared values and organizational citizenship behavior of generational cohorts: a review and future directions", *Management - Journal of Contemporary Management Issues*, Vol. 21 No. 2, pp. 249-271.

Zabel, K.L., Biermeier-Hanson, B.B.J., Baltes, B.B., Early, B.J. and Shepard, A. (2017), "Generational differences in work ethic: fact or fiction?", *Journal of Business and Psychology*, Springer US, Vol. 32 No. 3, pp. 301-315.

Zemke, R., Raines, C. and Filipczak, B. (2000), *Generations at Work: Managing the Clash of Veterans, Boomers, Xers. And Nexters in Your Workplace Chapter 6: Where Mixed Generations Work Well Together*, AMACOM, New York.

Zickuhr, K. and Madden, M. (2012), *Older Adults and Internet Use (Pew Research Center Report)*, Pew, Washington.

Further reading

Babalola, M.T., Bligh, M.C., Ogunfowora, B., Guo, L. and Garba, O.A. (2019), "The mind is willing, but the situation constrains: why and when leader conscientiousness relates to ethical leadership", *Journal of Business Ethics*, Vol. 155 No. 1, pp. 75-89, doi: 10.1007/s10551-017-3524-4.

Bejtkovsky, J. (2016), "The employees of baby boomers generation, generation X, generation Y and generation Z in selected Czech corporations as conceivers of development and competitiveness in their corporation", *Journal of Competitiveness*, Vol. 8 No. 4, pp. 105-123, doi: 10.7441/joc.2016.04.07.

Bonfadelli, H. (2002), "The Internet and knowledge gaps: a theoretical and empirical investigation", *European Journal of Communication*, Vol. 17 No. 1, doi: 10.1177/0267323102017001607.

Bucic, T., Harris, J. and Arli, D. (2012), "Ethical consumers among the millennials: a cross-national study", *Journal of Business Ethics*, Vol. 110 No. 1, pp. 113-131, doi: 10.1007/s10551-011-1151-z.

Calvo-Porral, C., Pesqueira-Sanchez, R. and Faiña Medín, A. (2019), "A clustered-based categorization of millennials in their technology behavior", *International Journal of Human-Computer Interaction*, Vol. 35 No. 5, doi: 10.1080/10447318.2018.1451429.

Chan, C. and Ananthram, S. (2020), "A neo-institutional perspective on ethical decision-making", *Asia Pacific Journal of Management*, Vol. 37 No. 1, pp. 227-262, doi: 10.1007/s10490-018-9576-x.

Eweje, G. and Brunton, M. (2010), "Ethical perceptions of business students in a New Zealand university: do gender, age and work experience matter?", *Business Ethics*, Vol. 19 No. 1, pp. 95-111, doi: 10.1111/j.1467-8608.2009.01581.x.

Latif, K.F. (2018), *The Development and Validation of Stakeholder-Based Scale for Measuring University Social Responsibility (USR)*, Social Indicators Research.

Okros, A. (n.d), Alan Okros.

Quan-Haase, A., Williams, C., Kicevski, M., Elueze, I. and Wellman, B. (2018), "Dividing the grey divide: deconstructing myths about older adults' online activities, skills, and attitudes", *American Behavioral Scientist*, Vol. 62 No. 9, pp. 1207-1228, doi: 10.1177/0002764218777572.

Sauser, W.I., Jr. (2013), "Empowering leaders to craft organizational cultures of character: conceptual framework and examples", *Journal of Leadership, Accountability & Ethics*, Vol. 10 No. 1, pp. 14-27.

Schumacker, R.E. and Lomax, R.G. (2004), "A beginner's guide to structural equation modeling", *Technometrics*, doi: 10.1198/tech.2005.s328, available at: https://www.taylorfrancis.com/books/mono/10.4324/9780203851319/beginner-guide-structural-equation-modeling-randall-schumacker-richard-lomax.

Supervisor, M.G. and Hughes, C. (2019), *An Exploratory Study of Managers' Perceptions of Millennials in the Workplace and the Introduction of Workplace Initiatives to Retain Millennials*, National College of Ireland, Ireland.

Van Volkom, M., Stapley, J. and Amaturo, V. (2014), "Revisiting the digital divide: generational differences in technology use in everyday life", *North American Journal of Psychology*, Vol. 16 No. 3, pp. 557-574.

VanMeter, R.A., Grisaffe, D.B., Chonko, L.B. and Roberts, J.A. (2013), "Generation Y's ethical ideology and its potential workplace implications", *Journal of Business Ethics*, Vol. 117 No. 1, pp. 93-109, doi: 10.1007/s10551-012-1505-1.

Corresponding author
Naval Garg can be contacted at: naval.garg@dtu.ac.in

For instructions on how to order reprints of this article, please visit our website:
www.emeraldgrouppublishing.com/licensing/reprints.htm
Or contact us for further details: **permissions@emeraldinsight.com**

2021 5th International Conference on Electrical, Electronics, Communication, Computer Technologies and Optimization Techniques (ICEECCOT) 10-11, December 2021

2021 5th International Conference on Electrical, Electronics, Communication, Computer Technologies and Optimization Techniques (ICEECCOT) | 978-1-6654-3272-6/21/$31.00 ©2021 IEEE | DOI: 10.1109/ICEECCOT52851.2021.9707941

FPGA-based Pipelined LSTM accelerator with Approximate matrix multiplication technique

Aniket Chaudhary
Electronics and Communication
Delhi Technological University
Delhi, India
aniketchaudhary979539@gmail.com

Arun Kumar
Electronics and Communication
Delhi Technological University
Delhi, India
arunkumar.06185@gmail.com

Ayush Srivastava
Electronics and Communication
Delhi Technological University
Delhi, India
ayushsrivastavakv8@gmail.com

Kriti Suneja
Electronics and Communication
Delhi Technological University
Delhi, India
kritisuneja@dtu.ac.in

***Abstract*—In recent times Long Short-Term Memory (LSTM) which is a type of artificial neural network, is being extensively used in real-time applications such as voice recognition, handwriting recognition, detection of human action, etc. In this paper,an implementation of the LSTM Accelerator on FPGA is presented where a fast approximate matrix multiplication technique is employed to reduce the delay encountered in calculations of the 4 layers of the LSTM network. The structure is implemented as a 5-stage pipeline to provide overlapped execution. The results presented highlight that the architecture proposed achieves higher performance through overlapped execution of different stages in an LSTM network, as compared to the non-pipelined design using DSP multipliers. The proposed architecture is implemented using Verilog HDL and Artix-7 xc7a100t3cgs324 is used as a target FPGAin Xilinx ISE Design Suite 14.7.**

Keywords—Field Programmable Gate Array (FPGA), Long Short-Term Memory (LSTM) layer, Approximate computing.

I. INTRODUCTION

Artificial Neural Networks (ANNs) or simply neural networks are modeled to match the capability of the human brain to provide machines with the abilities(for example) to interact with the environment and process real-time data, to recognize real-life objects to provide resultsthat were previously impossible to achieve with a computer without these networks. Neural networks of the like of Convolutional Neural Networks (CNNs) and Recurrent Neural Networks (RNNs) are widely employed for the analysis and manipulation of images, videos, etc. However, for sequential data like audio sequences, languages, handwriting, etc. these networks run into a problem of short-term memory. This happens because the gradient vanishes after a short time and the persistence of data in sequential data makes it necessary that the long-term relations between them should be remembered. Though RNNs solve this problem of long-term dependencies in the data, LSTM offers more accuracy and greater performance. They do this by implementing feedback connections in contrast to the feed forward structure of most of the ANNs. Hence, LSTMs are better at solving various Natural Language Processing (NLP) problems. Recent work proposed in [1] presents a flexible pipelined architecture of LSTM. Sepp and Schmidhuber [2] in 1997 first proposed the LSTM architecture, then Gers and Schmidhuber introduced an additional functionality of forget gate in the structure[3] in 1999.Further advancements include the introduction of direct connections from between memory cells and gates called peepholes by Gers et al[4] in 2000, then in 2014,Kyunghyun Cho et al proposed a different but somewhat similar structure called Gated Recurrent Unit (GRU)[5]. Problems like script recognition [6],[7], translation of languages (as used in many AI assistants) [8] are efficiently solved by these networks with greater accuracy and speed. LSTMs employed in the text-to-speech conversion (like Amazon's Polly) yields effective results. A chain-like structure of recurring modules is displayed by all RNNs. LSTMs also have this chain-like form comprising four interconnected layers. The basic structure of LSTM is presented in Figure 1.

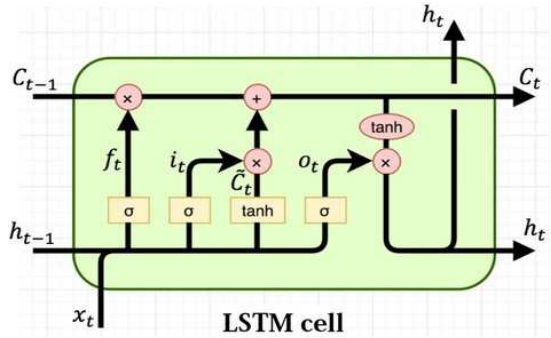


Fig. 1. *LSTM cell having four gates [9], here we considerg,as* $\hat{c}_t$.

Authorized licensed use limited to: DELHI TECHNICAL UNIV. Downloaded on February 23,2022 at 10:35:51 UTC from IEEE Xplore. Restrictions apply.

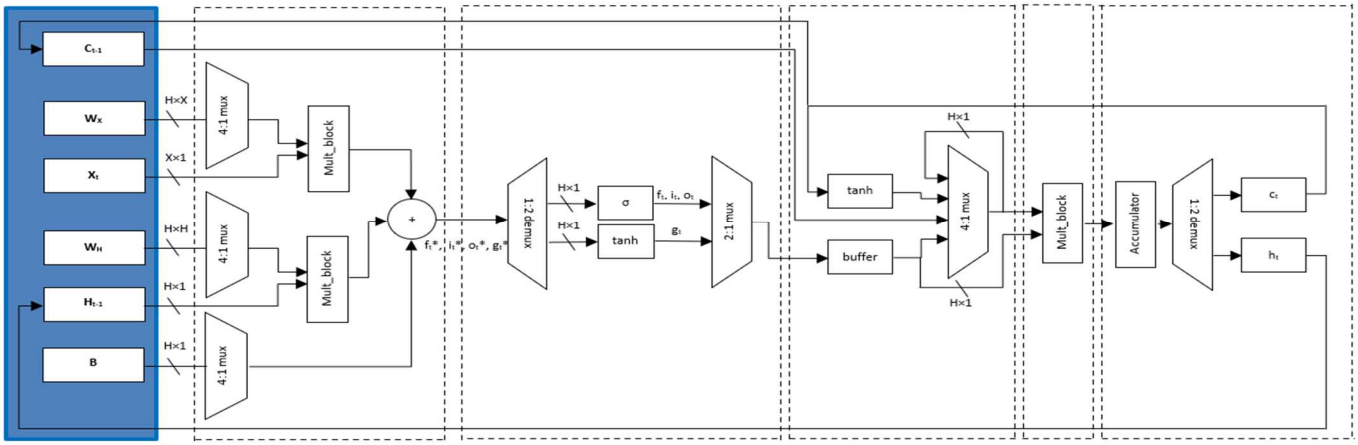


Fig. 2. *Proposed architecture of 5 stage pipelined implementation of LSTM accelerator*

Implementation cost, power consumption, and inefficiency to provide real-time results limit the use of CPU and GPU-based LSTM networks for embedded applications.Various software implementation of LSTMs has been proposed but the current focus is on hardware implementation for efficient computation because the inherent structure of LSTMs makes it difficult to incorporate computational parallelism in CPUs and GPUs.FPGAs offer much greater flexibility and programmability to implement various computations in an overlapped fashion, thus providing a significant increase in performance and throughput while having less power consumption. Works involving hybrid structures like a combination of hardware and software [10] are also proposed. Cloud intensive specific hardware like Google's tensor processing unit provide higher performance, less consumption of power but as these are cloud-based services, they have greater latency. In FPGAs, the availability of on-chip memory counters the effect of large delays encountered in using off-chip memories. But the same feature limits the amount of parallelization, as the limited amount of data could be stored in on-chip memory.

The remaining paper is organized as follows. Section 2 contains three sub sections, section A provides an overview of the general structure of LSTM layer, section B give a background about approximate matrix multiplication, and section C provides details of the proposed architecture. Section 3 presents related works; section 4 presents results and section 5 concludes the paper.

II. Background

A. Basic LSTM structure

In figure 1, each connecting line is an n-bit vector. The pink circles in the block represent point wise operations such as additions, multiplications. The yellow rectangles represent the activation functions that calculate the value of each layer. Merging lines denotes concatenation and diverging ones denotes copying. Peepholes can also be added to the structure, but we synthesized a structure without them. Predominantly, LSTM consisted of a single layer, but more layers could be stacked to make the model deeper. A LSTMcell consists of modules called gates which are used to regulate the state of the LSTM cell. The LSTM cell can be explained in the form of four layers. First layer, which accumulates previous outputs (i.e., c_{t-1}, h_{t-1}) and also the present input (i.e., x_t), second layer which regulates which information to be remembered and which should be forgotten, in this layer value of 1 is provided to completely keep the corresponding modification and a value of 0 is provided to completely forget the same, third layer which decides what updated data to be stored as the state of the cell(c_t), and the final layer applies the outputs of previous layers to activation function blocks to get a value between 1 and 0 for sigmoid activation and value between 1 and -1 for tanh activation. The mapped-out layers are as follows:

$$f_t = sig(f_t^*) = sig(W_{fx}x_t + W_{fh}h_{t-1} + b_f) \quad (1)$$
$$o_t = sig(o_t^*) = sig(W_{ox}x_t + W_{oh}h_{t-1} + b_o) \quad (2)$$
$$i_t = sig(i_t^*) = sig(W_{ix}x_t + W_{ih}h_{t-1} + b_i) \quad \text{(iii)}$$
$$g_t = \tanh(g_t^*) = \tanh(W_{gx}x_t + W_{gh}h_{t-1} + b_g) \quad \text{(iv)}$$
$$c_t = f_t \odot c_{t-1} + i_t \odot g_t \quad (5)$$
$$h_t = o_t \odot \tanh(c_t) \quad (6)$$

where tanh and sigmoid (sig; symbolically 'σ') are the activation functions and ⊙denote the pointwise multiplication operation. A first-order approximation technique ($ax+b$) or any other polynomial approximation can be employed to realize activation functions with less hardware resource and latency. W and b are the matrices for storing weight and bias vector respectively. Gates *f, i, o, and g*are called forget gate, input gate, output gate, and candidate cell respectively. Size of x is taken to be $X\times1$ and that of *h, b, c* is taken as $H\times1$ each ,correspondingly the sizes of matrices for weightW_x and $W_h$are$H\times X$ and $H\times H$ respectively.

B. Fast Approximate Matrix Multiplier

In figure 2 *Mult_block*(a basic block in figure 2) is a fast approximate matrix multiplier which is presented byArun et al in[11]. In the approximate matrix multiplier *AND* gates are used to generate the partial products. After that, partial products are divided into two parts, MSB part is known as accurate part and LSB part is known as inaccurate part. In the inaccurate part approximation is used where instead of using full adders or half adders to compress the partial products, the partial products are bitwise- *ORed*.

Now to obtain the final product of the numbers we have to add the partial products but we have used Dadda reduction

Authorized licensed use limited to: DELHI TECHNICAL UNIV. Downloaded on February 23,2022 at 10:35:51 UTC from IEEE Xplore. Restrictions apply.

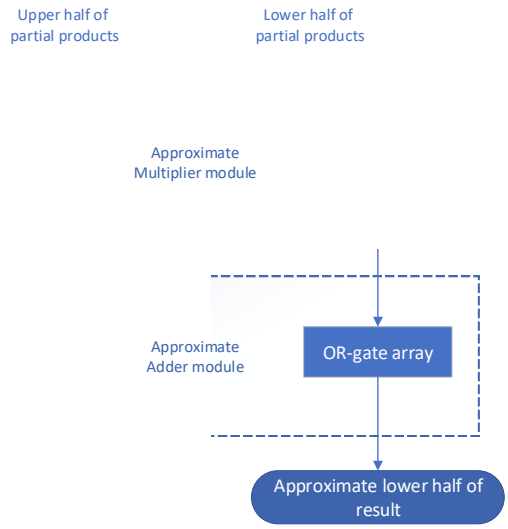


Fig. 3. *The basic workflow of approximate matrix multiplier proposed in [11].*

technique instead. Unlike Wallace multiplier, which utilized as possible as many full adders and half adders on each step for partial product reduction. Dadda multiplier utilizes the minimum number of full adders and half adders on each step for partial product, thus giving a uniform number of elements on each row after reduction. This reduction is what we are referring to as Dadda reduction. So, on the accurate part Dadda reduction is applied to reduce the number of adders and finally the reduced partial product of different terms is added using Carry Save Ahead Adder and result of multiplication is obtained.

C. Proposed Architecture

Figure 2 shows the proposed architecture implemented as a 5 staged pipeline. The input vector (x_t) for training data, weight matrices (W_x,W_h*and* b), previous cell data (c_{t-1}) and

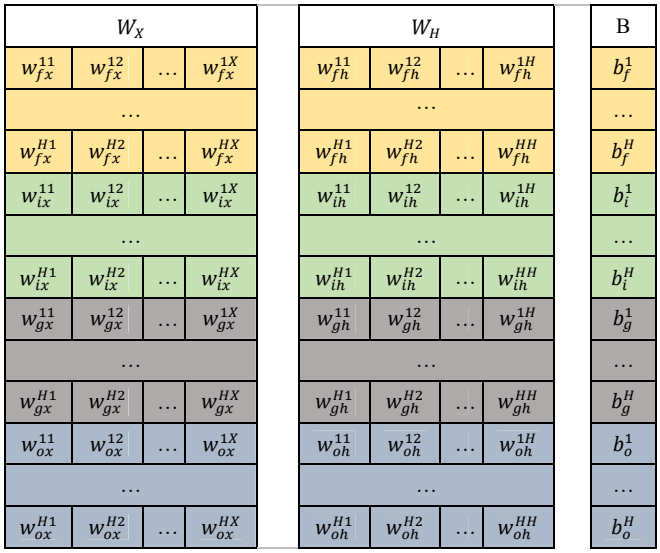


Fig. 4. *Storage pattern for weight matrices and bias vectors in memory where each element is of n-bit.*

previous cell output (h_{t-1}) are stored in memory indicated by the blue box in figure 2. Figure4 illustrates the storage pattern of weight matrices and bias vectors.

The first stage of the pipeline calculates f_t^*, i_t^*, g_t^* and o_t^* by matrix multiplication and addition. In this stage, two *Mult_block* are synthesized for *(H×X)*(X×1)* dimensional and *(H×H)*(H×1)* dimensional matrix multiplication. The multiplication blocks are a modified form of approximate matrix multiplication with DADDA reduction technique as proposed in [11]. For the addition of the outputs of multiplication blocks and the bias vector we have tried a combination of different adders, but the delay obtained on using the default adders of the FPGA device was the lowest. The 4 to 1 multiplexor select one of the four weight and bias matrices to calculate each of f_t^*, i_t^*, g_t^* and o_t^*after every clock cycle. Second stage computes the value of f_t, i_t, g_t and o_t. In this stage H number of sigmoid and tanh modules are synthesized to simultaneously compute the value of all the Helements of each of the equations*(i)-(iv)*. For the calculation of sigmoid and tanh we have used the first-order approximation presented in the paper [12].

This calculation yields an approximation error of ±0.005 while providing less resource utilization and less delay. The third stage consists of a *buffer*, H instances of tanh module, and a 4 to 1 multiplexor to direct the result of the second stage to the fourth stage for the computation of dot product indicated in equations (v) and (vi). As the values of f_t, i_t, g_t and o_t are available after one clock cycle each and the computation of equation (v) requires $i_t$and g_t so there is a need to store the value of i_t for which the *buffer* module is synthesized. The fourth stage is a multiplication module that computes the dot product for equation (v) and (vi). And the last stage consists of an accumulator and a multiplexor to direct the results.

The bit width of each element is n-bits, and the data is represented in fixed point representation. We have chosen 8-bit signed representation of each element and taken sizes H and X as 2, 4 and 6 to do a comparative analysis. After multiplication the data is truncated to 8 bits and to avoid overflow, we have made proper corrections for the most significant bit of the results.

III. Related Work

One of the primary endeavors of implementing LSTM on hardware to surpass implementations of software was proposed in[13]. The activation functions were computed using polynomial approximation, and the vector multiplication module was built by utilizing multiple multipliers in such a way that some performance was sacrificed in order to reduce the number of DSP slices needed. [14] examined how to implement LSTM in the real world by optimizing computing performance and communication requirements to speed up the inference process. Data dispatcher (communication with AXI4Lite bus), FPGA (LSTM layer), DDR3 DRAM (for storing input vectors, output vectors, and other parameters), AXI4Lite bus (for on-chip connections), UART, and MicroBlaze for initialization were all utilized in this paper. [15] suggested a power-saving and optimized architecture based on tiled vector multiplication, a binary adder tree, and overlapped computation and data access. [15] utilized a combination of ARM processors (as system controllers) and FPGAs in their architecture. DMA manages the input and output processes, BRAMs are used for storage, and the accelerator is modelled using an FPGA. [15] is further improved in [16] to include

Authorized licensed use limited to: DELHI TECHNICAL UNIV. Downloaded on February 23,2022 at 10:35:51 UTC from IEEE Xplore. Restrictions apply.

sparse LSTM layers that require less storage and are more power efficient than ARM Cortex-A9 CPUs.

The paper in [17] proposes a customizable architecture that allows for the adjustment of different hardware parameters to balance the design's power, area, and speed, resulting in a small and configurable design. [18] suggested a unique architecture based on low-power approximation multipliers and a two-level controller design for synchronization of variable clock cycle multiplications, resulting in considerably lower latency. In contrast to single-core accelerators, [19] implements model level parallelism. The capacity to execute many activities concurrently or divide the work of one job amongst two cores is an advantage of this architecture. This work improves throughput while lowering latency. Pruning to produce organized sparse features for hardware efficient purposes using permutation block diagonal mask matrix is presented in [20] as a way to reduce the LSTM inference phase, which helps achieve energy efficiency. The focus of this research was on reducing the LSTM layer's computational operations.

The work in [21] proposes multilevel storage and multiple processing engines for vector-matrix multiplication in order to construct LSTM, which delivers 10.9 GOP/s.In [22], a low-energy LSTM is built in a small-scale FPGA for the regression of microwave sensor data.[23] suggests using a blocked batching approach to reuse LSTM weights retrieved from external memory.This study achieves 20.8 GOPs/W, which is among the highest for architectures that store weights in external memory.

The paper in [24] proposes a design that eliminates duplication in LSTM gate computations, lowering latency[25] focuses on column-wise matrix multiplication to decrease data dependencies and improve throughput; this work differs from the traditional method of row multiplication. [26] presented an innovative LSTM accelerator architecture for FPGA and ASIC that exhibits complete parallelism, in which two basic computing patterns are combined into a single computing kernel that simultaneously executes all functions of the function unit. While this design has low latency, it requires more RAM to attain the same level of parallelism. However, none of these efforts provided the user with a level of parallelism freedom. Because the LSTM layer being implemented here is based on [27] but without peepholes, a modified layer can be implemented in a pipelined manner, similar to the work proposed in [28], which substantiates the LSTM layer with a stacked memory layer that stores the entire output sequence from the last LSTM cell rather than just the output value as in a basic LSTM cell.

TABLE I. COMPARISON OF FREQUENCY OF OPERATION OF PROPOSED LSTM CELL AND STANDARD LSTM CELL.

MATRIX SIZE	Frequency (in MHz)	
	Standard LSTM	*Proposed LSTM*
2x2	91.68	252.752
4x4	62.73	224.182
6x6	55.54	207.992

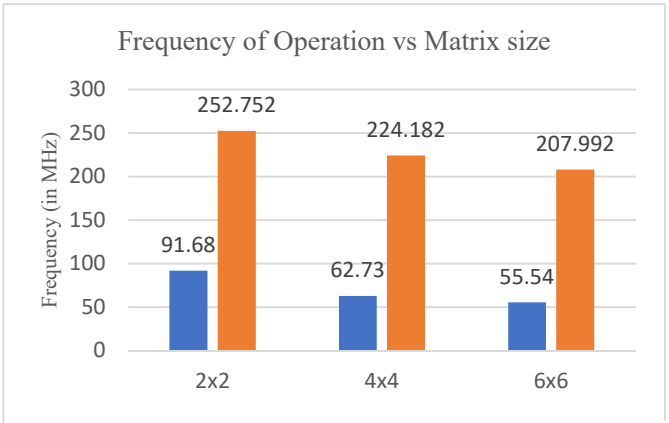


Fig. 5. *Frequency of Operation Vs Matrix size comparison bar-graph.*

IV. RESULTS AND ANALYSIS

Implementation of 8-bit with *2x2, 4x4,* and *6x6* matrix size LSTM is done using Verilog HDL with and without the use of the approximate matrix multiplier proposed in [11]. Performance is compared with the help of the maximum frequency of operation of each design. It was verified that the proposed design has more than double the frequency of operation as compared to previous work on LSTM.

V. CONCLUSION

In this paper, we proposed a novel architecture of implementing LSTM on FPGA which provided greater speed than the standard one. The paper begins with a brief overview of LSTM networks highlighting their importance and applications. Earlier works implemented LSTMs on CPUs but the complexity of computations involved makes it imperative to make use ofF PGA which has inherent ability to optimize pipelined execution. Although, constraints like resources, memory etc. presents some difficulty to implement a deep neural network. Given all of these, recent works have show cased improved efficiency as compared to their software counterparts on GPUs or CPUs.

REFERENCES

[1] E. Bank-Tavakoli, S. A. Ghsemzadeh, M. Kamal, A. Afzali-Kusha and M. Pedram, "POLAR: A pipelined/Overlapped FPGA-based LSTM Accelerator," in *IEEE Transactions on Very Large-Scale Integration (VLSI) Systems,* vol.28, no. 3, pp. 838-842, March 2020.

[2] S. Hochreiter and J. Schmidhuber, "Long Short-Term Memory," *in Neural Computation,* vol. 9, no. 8, pp. 1735-1780, 15 Nov. 1997

[3] F. A. Gers, J. Schmidhuber and F. Cummins, "Learning to forget: continual prediction with LSTM," *1999 Ninth International Conference on Artificial Neural Networks ICANN 99. (Conf. Publ. No. 470),* 1999, pp. 850-855 vol.2

[4]F. A. Gers and J. Schmidhuber, "Recurrent nets that time and count," *Proceedings of the IEEE-INNS-ENNS International Joint Conference on Neural Networks. IJCNN 2000. Neural Computing: New Challenges and Perspectives for the New Millennium,* 2000, pp. 189-194 vol.3

[5]Cho, Kyunghyun; van Merrienboer, Bart; Gulcehre, Caglar; Bahdanau, Dzmitry; Bougares, Fethi; Schwenk, Holger; Bengio, Yoshua (2014). "Learning Phrase Representations using RNN Encoder-Decoder for Statistical Machine Translation,"10.3115/v1/D14-1179.

[6]Märgner, Volker; Abed, Haikal El (July 2009). "ICDAR 2009 Arabic Handwriting Recognition Competition," *2009 10th International Conference on Document Analysis and Recognition:* 1383–1387.

[7] E. Grosicki and H. El Abed, "Icdar 2009 handwriting recognition competition," July 2009, pp. 1398–1402.

[8] Wu, Yonghui& Schuster, Mike & Chen, Zhifeng& Le, Quoc &Macherey, Wolfgang &Krikun, Maxim & Cao, Yuan & Gao, Qin &Macherey, Klaus &Klingner, Jeff & Shah, Apurva & Johnson,

Authorized licensed use limited to: DELHI TECHNICAL UNIV. Downloaded on February 23,2022 at 10:35:51 UTC from IEEE Xplore. Restrictions apply.

Melvin & Liu, Xiaobing& Kaiser, ukasz& Gouws, Stephan & Kato, Yoshikiyo& Kudo, Taku&Kazawa, Hideto& Dean, Jeffrey. (2016),"Google's Neural Machine Translation System: Bridging the Gap between Human and Machine Translation."

[9] S. Varsamopoulos, K. Bertels and C. G. Almudever, "Comparing Neural Network Based Decoders for the Surface Code," *in IEEE Transactions on Computers,* vol. 69, no. 2, pp. 300-311, 1 Feb. 2020

[10] Y. Guan, Z. Yuan, G. Sun and J. Cong, "FPGA-based accelerator for long short-term memory recurrent neural networks," *2017 22nd Asia and South Pacific Design Automation Conference (ASP-DAC),* 2017, pp. 629-634.

[11] A. Kumar, A. Ansari, A. Srivastava and K. Suneja, "Fast Approximate Matrix Multiplier based on Dadda Reduction and Carry Save Ahead Adder," *2021 7th International Conference on Advanced Computing and Communication Systems (ICACCS), 2021, pp. 1058-1061.*

[12] SyahrulanuarNgah and R. A. Bakar, "Sigmoid Function Implementation using the unequal segmentation of Differential Lookup Table and Second Order Nonlinear Function," *Journal of Telecommunication, Electronics and Computer Engineering, 2017, vol. 9, pp. 2-8.*

[13] J. C. Ferreira and J. Fonseca, "An FPGA implementation of a long short-term memory neural network," *2016 International Conference on ReConFigurable Computing and FPGAs (ReConFig)*, 2016, pp. 1-8.

[14] Y. Zhang et al., "Implementation and Optimization of the Accelerator Based on FPGA Hardware for LSTM Network," *2017 IEEE International Symposium on Parallel and Distributed Processing with Applications and 2017 IEEE International Conference on Ubiquitous Computing and Communications (ISPA/IUCC), 2017*, pp. 614-621.

[15] Y. Zhang et al., "A Power-Efficient Accelerator Based on FPGAs for LSTM Network," *2017 IEEE International Conference on Cluster Computing (CLUSTER),* 2017, pp. 629-630.

[16] K. Chen, L. Huang, M. Li, X. Zeng and Y. Fan, "A Compact and Configurable Long Short-Term Memory Neural Network Hardware Architecture," *2018 25th IEEE International Conference on Image Processing (ICIP), 2018,* pp. 4168-4172

[17] E. Azari and S. Vrudhula, "An Energy-Efficient Reconfigurable LSTM Accelerator for Natural Language Processing," *2019 IEEE International Conference on Big Data (Big Data), 2019*, pp. 4450-4459

[18] L. Peng, W. Shi, J. Zhang and S. Irving, "Exploiting Model-Level Parallelism in Recurrent Neural Network Accelerators," *2019 IEEE 13th International Symposium on Embedded Multicore/Many-core Systems-on-Chip (MCSoC)*, 2019, pp. 241-248.

[19] Y. Zheng, H. Yang, Z. Huang, T. Li and Y. Jia, "A High Energy-Efficiency FPGA-Based LSTM Accelerator Architecture Design by Structured Pruning and Normalized Linear Quantization," *2019 International Conference on Field-Programmable Technology (ICFPT),* 2019, pp. 271-274

[20] W. Zhang, F. Ge, C. Cui, Y. Yang, F. Zhou and N. Wu, "Design and Implementation of LSTM Accelerator Based on FPGA,"*2020 IEEE 20th International Conference on Communication Technology (ICCT),* 2020, pp. 1675-1679.

[21] U. Yoshimura, T. Inoue, A. Tsuchiya and K. kishine, "Implementation of Low Energy LSTM with Parallel and Pipelined Algorithm in small-scale FPGA,"*2021 International Conference on Electronics, Information and Communication (ICEIC),* 2021, pp. 1-4.

[22] Que, Zhiqiang& Zhu, Yongxin& Fan, Hongxiang& Meng, Jiuxi&Niu, Xinyu&Luk, Wayne, *"Mapping Large LSTMs to FPGAs with Weight Reuse,"* Journal of Signal Processing Systems, 2020.

[23] Que, Z., et al.,"Efficient Weight Reuse for Large LSTMs,"*In30th international conference on application-specific systems, architectures and processors (ASAP). IEEE*, 2019.

[24] Que, Z., et al.,"Real-time Anomaly Detection for Flight Testing using AutoEncoder and LSTM,"*inInternational conference on field-programmable technology (FPT). IEEE*, 2019.

[25] X. Zhang, W. Jiang and J. Hu, "Achieving Full Parallelism in LSTM via a Unified Accelerator Design,"*2020 IEEE 38th International Conference on Computer Design (ICCD),* 2020, pp. 469-477.

[26] H. Xu *et al.,* "Modified LSTM with Memory Layer for Power Grid Signal Classification,"*2020 IEEE 4th Conference on Energy Internet and Energy System Integration (E12),* 2020, pp. 3693-3697.

[27] K. Greff, R. K. Srivastava, J. Koutník, B. R. Steunebrink, and J. Schmidhuber, "LSTM: A search space odyssey," *IEEE Trans. Neural Netw. Learn. Syst*., vol. 28, no. 10, pp. 2222–2232, Oct. 2017.

[28] S. Han, J. Kang, H. Mao, Y. Hu, X. Li, Y. Li, D. Xie, H. Luo, S. Yao, and Y. Wang, "Ese: Efficient speech recognition engine with sparse lstm on fpga," *in Proceedings of the International Symposium on Field-Programmable Gate Arrays (FPGA). ACM*, 2017, pp. 75–84.

Authorized licensed use limited to: DELHI TECHNICAL UNIV. Downloaded on February 23,2022 at 10:35:51 UTC from IEEE Xplore. Restrictions apply.

ResearchGate

See discussions, stats, and author profiles for this publication at: https://www.researchgate.net/publication/351016562

Human Activity Recognition Using Long Short-Term Memory

Chapter · April 2021

DOI: 10.1007/978-981-33-4501-0_57

CITATIONS
0

READS
6

3 authors, including:



Priyanka Meel
Delhi Technological University
35 PUBLICATIONS **166** CITATIONS

SEE PROFILE

Some of the authors of this publication are also working on these related projects:

Fake News and Rumour Detection View project

All content following this page was uploaded by Priyanka Meel on 14 January 2022.

The user has requested enhancement of the downloaded file.

Springer Link

Human Activity Recognition Using Long Short-Term Memory

Proceedings of 6th International Conference on Recent Trends in Computing pp 613-623 | Cite as

- Vibhor Vimal (1) Email author (vibhorvimal5598@gmail.com)
- Anshuman Singh (1)
- Priyanka Meel (1)

1. Department of Information Technology, Delhi Technological University, , New Delhi, India

Conference paper
First Online: 21 April 2021

- 49 Downloads

Part of the Lecture Notes in Networks and Systems book series (LNNS, volume 177)

Abstract

The aim of this project is to perform human activity recognition using recurrent neural networks by long short-term memory. Human activity recognition involves dividing the accelerometer input sequences into well-defined movements. The project uses tensor flow which is a math library that performs programming tasks across a wide range of objectives. Recurrent neural networks are a type of artificial neural network that are designed to identify patterns in data sequences. The project uses deep learning architecture. The problem of long-term dependencies is solved using a long short-term memory mechanism of recurrent neural networks, also known as LSTM. The advantage of using LSTM for the model is that it can learn directly from the time series data. The project also develops an Android application to study the real-life application of the model by directly using data from the accelerometer in the device. Additionally, a GUI was also developed to display the results.

Keywords

Activity recognition Recurrent neural network LSTM Accelerometer Android

This is a preview of subscription content, log in to check access.

References

1. Jiang W, Yin Z (2015) Human activity recognition using wearable sensors by deep convolutional neural networks. In: Proceedings of the 23rd ACM

international conference on multimedia (MM '15), ACM, New York, NY, USA, pp 1307–1310
Google Scholar (https://scholar.google.com/scholar?q=Jiang%20W%2C%20Yin%20Z%20%282015%29%20Human%20activity%20recognition%20using%20wearable%20sensors%20by%20deep%20convolutional%20neural%20networks.%20In%3A%20Proceedings%20of%20the%2023rd%20ACM%20international%20conference%20on%20multimedia%20%28MM%20%E2%80%9915%29%2C%20ACM%2C%20New%20York%2C%20NY%2C%20USA%2C%20pp%201307%E2%80%931310)

2. Alsheikh MA, Selim A, Niyato D, Doyle L, Lin S, Tan H-P (2016) Deep activity recognition models with triaxial accelerometers. In: Proceedings of the AAAI workshops, Phoenix, Az, USA, Feb 2016
Google Scholar (https://scholar.google.com/scholar?q=Alsheikh%20MA%2C%20Selim%20A%2C%20Niyato%20D%2C%20Doyle%20L%2C%20Lin%20S%2C%20Tan%20H-P%20%282016%29%20Deep%20activity%20recognition%20models%20with%20triaxial%20accelerometers.%20In%3A%20Proceedings%20of%20the%20AAAI%20workshops%2C%20Phoenix%2C%20Az%2C%20USA%2C%20Feb%202016)

3. Hammerla NY, Halloran S, Plotz T (2016) Deep, convolutional, and recurrent models for human activity recognition using wearables. In: Proceedings of the 25th international joint conference on artificial intelligence (IJCAI '16)
Google Scholar (https://scholar.google.com/scholar?q=Hammerla%20NY%2C%20Halloran%20S%2C%20Plotz%20T%20%282016%29%20Deep%2C%20convolutional%2C%20and%20recurrent%20models%20for%20human%20activity%20recognition%20using%20wearables.%20In%3A%20Proceedings%20of%20the%2025th%20international%20joint%20conference%20on%20artificial%20intelligence%20%28IJCAI%20%E2%80%9916%29)

4. Milenkoski M, Trivodaliev K, Kalajdziski S, Jovanov M, Stojkoska BR (2018) Real time human activity recognition on smartphones using LSTM networks. In: MIPRO 2018
Google Scholar (https://scholar.google.com/scholar?q=Milenkoski%20M%2C%20Trivodaliev%20K%2C%20Kalajdziski%20S%2C%20Jovanov%20M%2C%20Stojkoska%20BR%20%282018%29%20Real%20time%20human%20activity%20recognition%20on%20smartphones%20using%20LSTM%20networks.%20In%3A%20MIPRO%202018)

5. Hochreiter S, Schmidhuber J (1997) Long short-term memory. Neural Comput 9(8):1735–1780
CrossRef (https://doi.org/10.1162/neco.1997.9.8.1735)
Google Scholar (http://scholar.google.com/scholar_lookup?title=Long%20short-term%20memory&author=S.%20Hochreiter&author=J.%20Schmidhuber&journal=Neural%20Comput&volume=9&issue=8&pages=1735-1780&publication_year=1997)

6. Gers FA, Schmidhuber J, Cummins F (2000) Learning to forget: continual prediction with LSTM. Neural Comput **12**(10):2451–2471
Google Scholar (https://scholar.google.com/scholar?q=Gers%20FA%2C%20Schmidhuber%20J%2C%20Cummins%20F%20%282000%29%20Learning%20to%20forget%3A%20continual%20prediction%20with%20LSTM.%20Neural%20Comput%2012%2810%29%3A2451%E2%80%932471)

7. Abadi M, Barham P, Chen J, Chen Z, Davis A, Dean J, Devin M et al (2016) TensorFlow: a system for large-scale machine learning. In: OSDI, vol 16, pp 265–283
Google Scholar (https://scholar.google.com/scholar?q=Abadi%20M%2C%20Barham%20P%2C%20Chen%20J%2C%20Chen%20Z%2C%20Davis%20A%2C%20Dean%20J%2C%20Devin%20M%20et%20al%20%282016%29%20TensorFlow%3A%20a%20system%20for%20large-scale%20machine%20learning.%20In%3A%20OSDI%2C%20vol%2016%2C%20pp%20265%E2%80%93283)

8. Android Developers (n.d.) Retrieved 24 May 2019, from https://developer.android.com/ (https://developer.android.com/)

Copyright information

© Springer Nature Singapore Pte Ltd. 2021

About this paper

Cite this paper as:

Vimal V., Singh A., Meel P. (2021) Human Activity Recognition Using Long Short-Term Memory. In: Mahapatra R.P., Panigrahi B.K., Kaushik B.K., Roy S. (eds) Proceedings of 6th International Conference on Recent Trends in Computing. Lecture Notes in Networks and Systems, vol 177. Springer, Singapore. https://doi.org/10.1007/978-981-33-4501-0_57

- First Online 21 April 2021
- DOI https://doi.org/10.1007/978-981-33-4501-0_57
- Publisher Name Springer, Singapore
- Print ISBN 978-981-33-4500-3
- Online ISBN 978-981-33-4501-0
- eBook Packages Intelligent Technologies and Robotics Intelligent Technologies and Robotics (R0)

- Buy this book on publisher's site
- Reprints and Permissions

Personalised recommendations

SPRINGER NATURE

© 2020 Springer Nature Switzerland AG. Part of Springer Nature.

Not logged in Delhi Technological University (2000607895) - Convener, UGC-Infonet Digital Library Consortium (3000132959) - INDEST-AICTE-Level III (3000168247) - Information and Library Network (INFLIBNET) Centre (3994475188) 14.139.251.100

Implementation of Soft Computing Techniques to Evade Partial Shading Effects for PV Based Off-Grid System

Ashish Grover & Anita Khosla
MRIU,Faridabad. Haryana, India
ashishgrover.fet@mriu.edu.in,
anitakhosla.fet@mriu.edu.in

Dheeraj Joshi
Delhi Technological University,
Delhi, India
Email: ee.dheeraj@gmail.com

Vrince Vimal, SMIEEE
Graphic Era Hill University
Dehradun U.K.,India
vvimal@ec.iitr.ac.in

2021 13th IEEE PES Asia Pacific Power & Energy Engineering Conference (APPEEC) | 978-1-6654-4878-9/21/$31.00 ©2021 IEEE | DOI: 10.1109/APPEEC50844.2021.9687716

***Abstract*—Awareness regarding the clean environment and increased demand for energy encourages generating power from natural sources. Among all the renewable sources available, generation from solar technology is rapidly growing to meet the energy requirements for various applications due to its ubiquity, sustainability, and plenty of availability. According to the global PV market, 594 GW capacity of PV was installed worldwide in 2019 by replacing the conventional source-based generation plants. However, the main challenge involved in PV generation is to evaluate the Maximum power from the available tracking techniques. Another major complication in the solar array is the non-uniformity of radiations on the PV panel, which descends its performance and is termed partial shading. The partial shading effect on PV Array gives subsequent power loss. The consequences of shading effects are multiple peaks in P-V characteristics that are not deluded using a conventional method such as P & O or Incremental conductance methods. The paper presents ways to overcome the partial shading effect, which involves reconfiguring PV panels and reducing the power disparity evolutionary algorithm particle swarm optimization (PSO) to attain P-V Curves' peak power point**

***Index Terms*—Solar Energy,Energy Harvesting, MPPT, PSO, Partial shading, off-grid.**

I. Introduction

Solar energy generation through photovoltaic (PV) technology leads to the most promising clean energy generation. PV generation is in demand as it is environment-friendly, abundantly available, and economically optimum, due to which numerous applications of PV cells are available [1], [2]. Electric power generated from PV cells is DC in nature. Therefore it is required to convert unidirectional power generated from PV panels into alternating power at the suitable frequency for feeding the loads. Thus, Power converters are interfaced with PV systems tied to grids. Power generated from PV systems has to be delivered to different loads through grids via inverters. The major problem in integrating a PV system with a grid is the performance curves of the load corresponding to the solar array [3]. The crossover point on the I-V curves of the photovoltaic array provides the maxima of the power, which is not stable most of the time. The maximum power point techniques are being implemented to obtain the regular and maximum power point (MPP) on the I-V curve. Priorly, to achieve the MPP, the modeling of the PV array is done for measurements of irradiance and temperature. Several software's are available to calculate different parameters such as irradiance and temperature as manual calculations are not feasible [4]. Therefore, these computing techniques are based on designing the algorithm to get the maximum power from the PV system. The continuous research in this area has proposed many algorithms.

The MPPT techniques are deployed to attain peak power from the solar panel according to the defined location for different characteristics of PV panels. The interface between the load and module is done through DC-DC converter which performs the function to transfer power from panel to load [1]. To obtain load matching and extreme powerpoint, the duty cycle is varied within the defined range.

After the fixation of Maxima of power, another issue was taken into account to reduce the partial shadings due to non-uniform sun radiations on the panel. Therefore, research explicitly reconfigures PV panels and algorithm development using intelligent technique Particle swarm optimization to decrease power disparity.

II. MODELING OF PV CELL AND ITS CHARACTERISTICS

A photovoltaic cell is a photoactive P-N junction diode that converts solar energy into electrical energy. To increase the generated power, several PV cells are connected in series and parallel and are known as PV cell Panels. The light energy absorbed by the free electrons in semiconductors excites free electrons to jump from the low energy band to the high energy band [2]. The illumination of PV cell creates more electron-hole pairs, and p-n junction behaves like short-circuited, and the electric current starts flowing the circuit [3].

A. PV Array Modelling

The characteristics of PV cells can be analyzed using the single diode equivalent circuit shown in figure 1. The ideal PV cell I-V characteristics can be examined in MATLAB using basic equations of the semiconductors [4], [5].

$$I_{ph} = [I_{sc} + k_i(T - 298)] \times I_r/1000 \quad (1)$$

Authorized licensed use limited to: DELHI TECHNICAL UNIV. Downloaded on February 10,2022 at 10:24:16 UTC from IEEE Xplore. Restrictions apply.

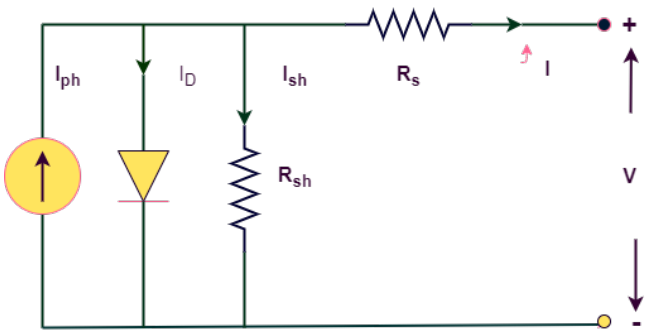


Fig. 1. PV cell equivalent circuit.

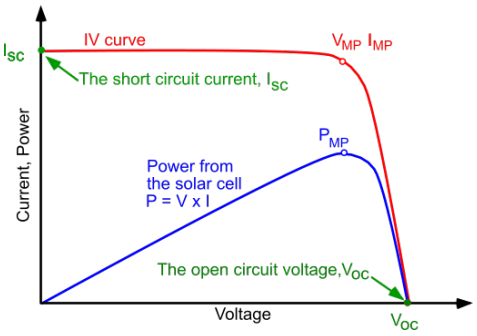


Fig. 2. V-I Characteristics of PV cell

where, I_{ph} is photo current (A); I_{sc} is short circuit current (A); k_i is short circuit current of the cell at $25°C$ and $1000W/m^2$; T is operating temprature (K);I_r is solar irradiation (W/m^2).

PV cell reverse saturation current I_{rs}:

$$I_{rs} = I_{sc}/[e^{(qV_{oc}/N_s nkT)} - 1] \quad (2)$$

where, $q = 1.6 \times 10^{-19}$;V_{oc} is open circuit voltage (V); N_s represents number of cells connected in series; n is ideality factor of diode; $k = 1.3805 \times 10^{-23}$ J/K (Boltzmann's constant).

PV cells are the integration of series and parallel combinations of cells [6], [7]. To increase the voltage, cells are connected in series, and to improve the current, the cells are connected in parallel. The equivalent circuit shown in Fig. 1 is of an ideal PV cell with series resistance R_s and parallel resistance R_{sh} where I :

$$I = I_{pv} - I_0[e^{(V+IR_s/V_t.a)} - 1] - V + I\,R_s/R_{sh} \quad (3)$$

where, $V_t = N_s nkT/q$ is thermal voltage of N_s cells connected in series. V is terminal voltage. The ideality factor a is defined as the measure of ideal characteristics of the PV module depending on type of material and technology used.

B. PV Array Characteristics

PV cell, array, or module I-V characteristics provide the solar power conversion's energy conversion capability and efficiency. The characteristics are described as solar radiation that hits the PV module, controls the current (I), and the rise in temperature on the cell reduces the voltage (V). Therefore, the I-V characteristics of a solar cell represent the current and voltage relationship for existing irradiance and temperature conditions, which provides information regarding the optimal peak power [8]. For I-V characteristics, it is always suggested for commercial use to keep the value of series resistance Rs to be very low and the parallel resistance R_{sh} to be high compared to the forward resistance of the diode [9]. The Characteristics define the open-circuit voltage (VOC), short circuit current (ISC) at Maximum Power Point (MPP) for the given temperature, and values of irradiance shown in figure 2.

III. MPPT Techniques for Partially Shaded PV System

MPPT helps improve the PV array's efficiency, which depends on the radiations of sun falling on the PV Module, temperature, and the electrical load characteristics connected to the System. MPPT devices or techniques are integrated through a power electronic converter system used to convert the voltage and current to a required value after filtration and regulation to drive different applications such as power grids, batteries, and motors. Many research articles published about MPPT techniques for PV systems with even irradiance. Although there are many conventional methods such as P& O, Incremental Conductance and fractional open circuit voltage have been addressed to track the peak point[10]. The P & O method is observed to be the most simple and widely used technique. In PV applications, Artificial Intelligence techniques, mainly fuzzy logic, ANN-based MPPT, have also been implemented, which helps solve time dependence and fast-tracking time for exchanging reference voltage [11]. Gradually the paradigm of research changes towards the effect of partial shadings (PS). The PV modules constitute series and Parallel combinations to form a PV array [12], [13]. Experiments were done on PV systems with prognostic shading effect drawn enormous attention to conquest the global peak point from multiple power peaks curves. The conventional MPPT approaches may not be a triumph to attain a global peak due to shading. Fuzzy logic and ANN techniques are active mechanisms to reach the peak power output for in-homogeneous radiations.

A. Dodging Algorithm to mitigate shading effect

Dodging Algorithm to mitigate shading effect In the configuration of PV array , the panels connected in series render with constant current however cells under shading effect got reverse biased which indeed reverse the polarity of power and thereby reduction in power output and its conversion efficacy.An illustrative PV array with shading is shown in fig. Reconfiguration of PV modules are adept to mitigate the PS issues in PV system. Various configurations which are mainly used are series, parallel, series-parallel and total cross tied configuration(TCT) in figure 3.

The Proposed dodging algorithm introduces the intelligent control to diminish the shading effect. The arrangement of

Authorized licensed use limited to: DELHI TECHNICAL UNIV. Downloaded on February 10,2022 at 10:24:16 UTC from IEEE Xplore. Restrictions apply.

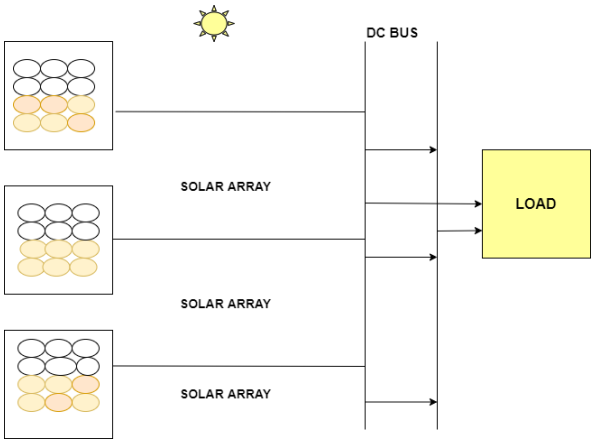


Fig. 3. Typical Shaded PV System

TABLE I
SWITCHING ALGORITHM FOR PV PANELS.

Case	US1	US2	US3	UM1	UM2	UM3	LM1	LM2	LM3	LS1	LS2	LS3	Expected Output
A(1)	0	1	1	0	1	1	0	1	1	0	1	1	56.32V, 1.043A
A(2)	0	1	1	0	1	1	1	0	1	1	0	1	56.32V, 1.043A
A(3)	0	1	1	0	1	1	1	1	0	1	1	0	56.32V, 1.043A
A(4)	1	0	1	1	0	1	0	1	1	0	1	1	56.32V, 1.043A
A(5)	1	0	1	1	0	1	1	0	1	1	0	1	56.32V, 1.043A
A(6)	1	0	1	1	0	1	1	1	0	1	1	0	56.32V, 1.043A
A(7)	1	1	0	1	1	0	0	1	1	0	1	1	56.32V, 1.043A
A(8)	1	1	0	1	1	0	1	0	1	1	0	1	56.32V, 1.043A
A(9)	1	1	0	1	1	0	1	1	0	1	1	1	56.32V, 1.043A
B	1	1	1	1	1	1	1	1	1	1	1	1	56.32V, 1.043A

PV cells will evade the impact of shading and provide the desired output voltage and current. The panels are systematically placed to reform the array. The upper panels are symbolized by $\boldsymbol{U} = [U_1, U_2, U_3 \ldots U_n]$ and are connected to a positive terminal. The single positive terminal is taken from the combination of upper panels .M is a single big panel in the center to avoid the shade consequence, and lower panels are represented by set $\boldsymbol{L} = [L_1, L_2, L3 \ldots L_n]$ and single negative terminal will be taken from combined lower panels.

Total Voltage at the output terminal is given by:

$$V = \sum V_n \tag{4}$$

where, n = 1,2,3... (Number of panels)

However, Voltage across upper panels is as follows:

$$V_1 = \sum V_{n1} \tag{5}$$

where n = 1,2,3...(Number of panels)
The voltage across middle row:

$$V_2 = V_2 \tag{6}$$

The voltage across the lower row:

$$V_3 = \sum V3_n \tag{7}$$

The output current of the system is calculated using the equation:

$$I = \sum I_{1n} = \sum I_{2n} = \sum I_{3n} \tag{8}$$

where, n =1,2,3.....

The investigational analysis is performed on 100W PV system using a dodging algorithm for constant power load at a reference current of 1 amp to get desired output voltage. The switching operations elude the shaded panel and provide the continuous power output. For the uniform irradiations, all switches are in process, and maximum output can be extracted. Correspondingly, any combinations can be framed for the required power, and the flow diagram shows the operational logic of the Dodging algorithm. The TCT configuration is used to examine the PV panel's performance for 100 W(10*10 W) in MATLAB Software with a connected load of 32 Ohms. The algorithm provides the constant power output for constant power applications. The comparative results that output Power obtained using TCT configuration is 48.6W without dodging algorithm, and with dodging algorithm, it gives a power output of 58.7W under shading conditions [14].

B. Particle Swarm optimization based MPPT Technique

In recent past years, swarm intelligence (SI) has gained enormous attention because of its simple and efficient search mechanism [15], [16], [17], [18], [19]. The maximum power point trackers are used to track the extreme potential power for PV panels. However, due to PS conditions, the conventional methods get trapped to local maxima through these trackers. Therefore, to obtain a fast response and to achieve a global peak intelligent technique has been deployed to a PV off-grid and an on-grid system. In this paper, Particle swarm optimization (PSO) for an off-grid Photovoltaic system is proposed to get faster and more accurate tracking time with peak power Points . The PSO was developed by Eberhart and Kennedy in 1995 [20]. It's an Artificial Intelligence technique used to find the approximate solutions for extremely difficult numeric maximization and Minimization problems. The algorithm can optimize the multidimensional equations with a high convergence rate. The PSO is based on significant parameter i: e population size. According to the optimization problem, the population size is assumed to design the PSO algorithm. To decrease the convergence time, generally, population size is taken as a minimum.

The PSO is called as Swarm of particles. In which each particle act as an entrant solution in search space. The hypothetical graph is plotted in search space with initial velocity seeded to the particles and communication channel within the particles [21].

A Group of random particles is used to initialize the PSO and then searches for the finest solution by upgrading the compeers. The best two values are evaluated according to the optimum criteria after each step. The first fitness obtained is called 'pbest' (Position best), and its value is stored in search space. The second best is found with intercommunication with different particles for the whole population and is stored

Authorized licensed use limited to: DELHI TECHNICAL UNIV. Downloaded on February 10,2022 at 10:24:16 UTC from IEEE Xplore. Restrictions apply.

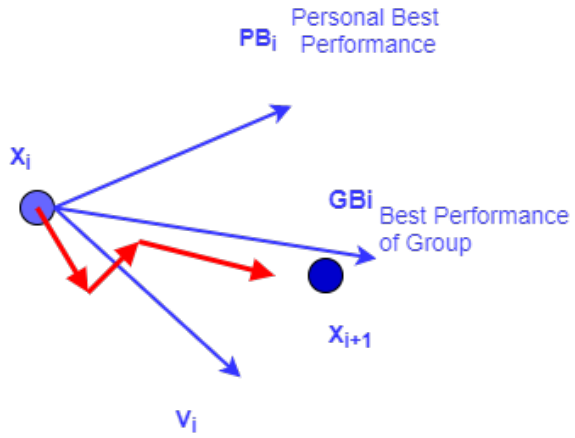


Fig. 4. Particle Search Space diagram for PSO.

TABLE II
ELECTRICAL PARAMETERS FOR PV OFF-GRID SYSTEM

Maximum power point (MPP)	650W
Maximum voltage (VPP)	150 V
Maximum power current (IPP)	8A
Short circuit current (Isc)	8.5A
Open circuit voltage (Voc)	191V

'gbest' (Global best). When a particle takes part of the population as its topological neighbors, the second-best value is a local best and is called 'lbest'. Neighborhood space and reduce the susceptibility of PSO to falling into local minima, but slow down convergence speed [12].

Typical PSO equations can be written as follows:

$$V_j^{k+1} = wv_j^k + c_1 r_1 \left(p_{bestj} - p_j^k\right) + c_2 r_2 \left(g_{best} - p_j^k\right) \quad (9)$$

$$P_j^{k+1} = p_j^k + v_j^{k+1} \quad (10)$$

Power tracking is a difficult task in a PV system under irradiance shading conditions. Out of multiple peaks, one global peak is to be traced from P-V curves. This paper aims to improve the maximum operational point with three particles and nonlinear inertia weight using PSO-based MPPT.

The nonlinear inertia weight to be considered for PSO is given by the following equation:

$$w_k = w_{k-1} \times e^{(-k/k_{\max})} \quad (11)$$

Where, k is the number of iteration and k_{max} is the maximum iteration number. W_{k-1} is inertia weight at$k-1^{th}$ iteration.

The change in solar radiations reactivate the dynamic tracking algorithm and initialize the algorithm to obtain a new

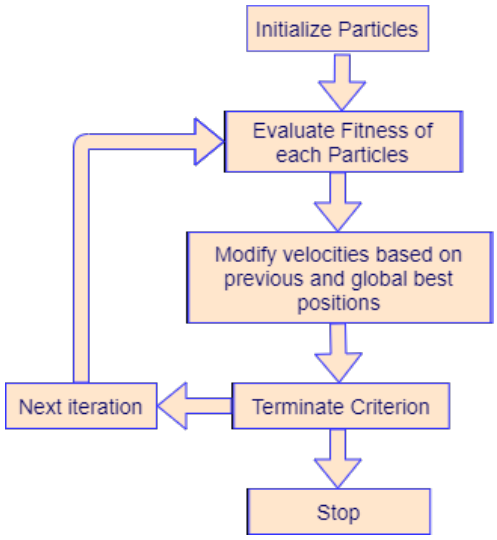


Fig. 5. Flow diagram PSO Algorithm

TABLE III
ELECTRICAL PARAMETERS FOR SIMULATION

Number of Particles	3
Maximum number of iterations	300
C_{max}	0.8
C_{min}	0.1
$C_{initial}$	0.8
r_1	1
r_2	1

MPP. The execution must satisfy the following condition for reinitializing the algorithm:

$$\frac{|P_{pv} - P_{pv,old}|}{P_{pv,old}} \geq \triangle P \quad (12)$$

Where $\triangle P$ value is taken as 0.1. Electrical parameters of PV module is given in table 2 and Parameters for simulation of PSO algorithm in MATLAB software given in table 3 .

IV. SIMULATION AND RESULTS

The PV system is developed with three modules, and it is connected to the resistive load via a boost converter. The cell modeling is explained with single diode equivalent circuit-related equations that are already constructed in this work. The simulation results are shown for Standard test conditions(STC) for PSC various Irradiance values using the PSO algorithm. Waveforms for nonlinear decreasing inertia weights are shown for duty Cycle, PWM Pulses, Voltage in volts, current(mA), PV Power(Watts) and Output power(watts) shown in results Fig. 6 to Fig. 13.

Fig. 6 shows the duty cycle to be fed to boost converter, which the PSO MPPT controller generates. The Duty ratio

Authorized licensed use limited to: DELHI TECHNICAL UNIV. Downloaded on February 10,2022 at 10:24:16 UTC from IEEE Xplore. Restrictions apply.

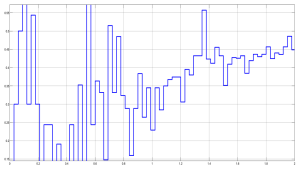


Fig. 6. Duty Cycle for Boost Converter.

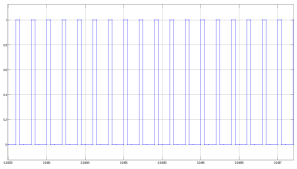


Fig. 7. Pulses Generator using PWM Technique.

varies from 0.4 to 0.7. The pulses generated by the PWM technique with a switching frequency of 50kHz is given to the DC-DC converter shown in fig.7. The MOSFET based boost converter is used for obtaining the simulation results shows the output current of 3.5amps and voltage of 198V.

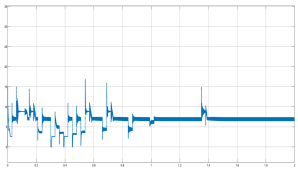


Fig. 8. Current Waveform for PV Array IPV(A).

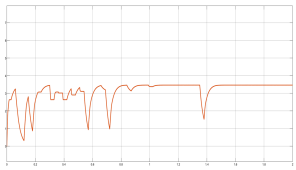


Fig. 9. Output Current Waveform using PSO Io(A).

Fig. 8 shows the current PV array, and Fig. 9 shows the output current using the PSO MPPT controller. Similarly, Fig. 10 & Fig. 11 display voltage waveforms for PV array and output voltage after PSO. Fig. 12 and Fig. 13 gives the maximum power attain with a magnitude of 637.7 volts across the PV array.

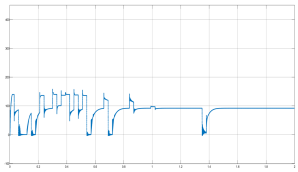


Fig. 10. Voltage Waveform for PV Array VPV(V).

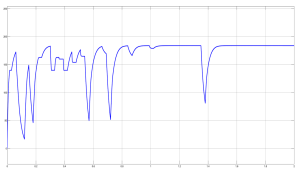


Fig. 11. Output Voltage Waveform using PSO Vo(V).

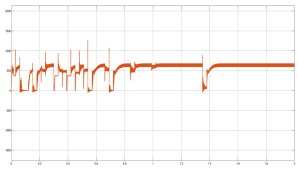


Fig. 12. Power Waveform for PV array ,Ppv(W).

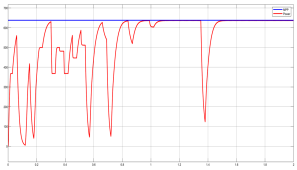


Fig. 13. Output Power Waveform using PSO Po(W).

The experimental results show that to trigger the PV system; the duty cycle is varied from 0.4 to 0.7 using PSO. The implementation of this technique delivers a high rate of early convergence with a tracking time of 0.5 secs and a setting time of 1.5 secs for various partial shading conditions. The proposed methods provide one global peak point for different solar irradiance, ranging from 500 to 1000 given to solar panels shown in figure 14. The experimental study successfully detects the partial shading conditions and reinitializes the MPPT process. The results show that the PSO-based MPPT algorithm provides high efficiency in tracking the global Maximum Power Point(GMPP).

V. Conclusion

The papers present two algorithms-based techniques to evade Partial Shading effects in PV-based off-grid systems. In the first section, the dodging algorithm for reconfiguring PV panels has been established to avoid the partial shading Conditions (PSC), resulting in increased PV array efficiency. Further, in the second section, a PSO-based MPPT controller with nonlinear inertia weight generates the global maximum power point for multiple peaks due to PSC with high convergence speed. In the future, this work can be extended with hardware enactment using the DSP board.

References

[1] S. B. Thanikanti, P. Jothi Kumar, and R. Natarajan, "A comprehensive review on solar pv maximum power point tracking techniques," *Renewable and Sustainable Energy Reviews*, vol. 67, 01 2017.

[2] J. Enslin, M. Wolf, D. Snyman, and W. Swiegers, "Integrated photovoltaic maximum power point tracking converter," *Industrial Electronics, IEEE Transactions on*, vol. 44, pp. 769 – 773, 01 1998.

[3] J. Appelbaum, "The quality of load matching in a direct-coupling photovoltaic system," *Power Engineering Review, IEEE*, vol. PER-7, pp. 27 – 28, 01 1988.

[4] A. Podder, N. Roy, and H. Pota, "Mppt methods for solar pv systems: A critical review based on tracking nature," *IET Renewable Power Generation*, vol. 13, 04 2019.

[5] R. B. Bollipo, S. Mikkili, and P. K. Bonthagorla, "Hybrid, optimal, intelligent and classical pv mppt techniques: A review," *CSEE Journal of Power and Energy Systems*, vol. 7, no. 1, pp. 9–33, 2021.

[6] R. Faranda and S. Leva, "Energy comparison of mppt techniques for pv systems," *J. Electromagn. Anal. Appl.*, vol. 3, 01 2008.

[7] ——, "Energy comparison of mppt techniques for pv systems," *J. Electromagn. Anal. Appl.*, vol. 3, 01 2008.

[8] H. Basha and C. Rani, "Different conventional and soft computing mppt techniques for solar pv systems with high step-up boost converters: A comprehensive analysis," *Energies*, vol. 13, p. 371, 01 2020.

[9] P. R. Satpathy, S. Panda, A. Mahmoud, and R. Sharma, "Optimal design and performance survey of a 100kwp grid-connected pv plant for installation near the top ranked green city of india," in *2021 1st Odisha International Conference on Electrical Power Engineering, Communication and Computing Technology(ODICON)*, 2021, pp. 1–6.

[10] A. Podder, N. Roy, and H. Pota, "Mppt methods for solar pv systems: A critical review based on tracking nature," *IET Renewable Power Generation*, vol. 13, 04 2019.

[11] A. Mirza, Q. Ling, M. Y. Javed, and M. Mansoor, "Novel mppt techniques for photovoltaic systems under uniform irradiance and partial shading," *Solar Energy*, vol. 184, pp. 628–648, 05 2019.

[12] M. Kermadi, Z. Salam, J. Ahmed, and E. M. Berkouk, "An effective hybrid maximum power point tracker of photovoltaic arrays for complex partial shading conditions," *IEEE Transactions on Industrial Electronics*, vol. 66, no. 9, pp. 6990–7000, 2019.

[13] A. Kishor, M. Chandra, and P. Singh, *An Astute Artificial Bee Colony Algorithm*, 02 2017, pp. 153–162.

[14] M. Lasheen and M. Abdel-Salam, "Maximum power point tracking using hill climbing and anfis techniques for pv applications: A review and a novel hybrid approach," *Energy Conversion and Management*, vol. 171, pp. 1002–1019, 09 2018.

[15] B. Nautiyal et al, "Improved salp swarm algorithm with mutation schemes for solving global optimization and engineering problems." *Engineering with computer*, 2021.

Authorized licensed use limited to: DELHI TECHNICAL UNIV. Downloaded on February 10,2022 at 10:24:16 UTC from IEEE Xplore. Restrictions apply.

[16] A. Khosla, G. Leena, and M. Soni, "Interval type-2 fuzzy logic controller to control the velocity and angle of inverted pendulum," *International Journal of Intelligent Systems and Applications*, vol. 6, pp. 44–51, 06 2014.
[17] A. Kishor, M. Chandra, and P. Singh, *An Astute Artificial Bee Colony Algorithm*, 02 2017, pp. 153–162.
[18] J. Prakash, P. Singh, and A. Kishor, "Integrating fitness predator optimizer with multi-objective pso for dynamic partitional clustering," *Progress in Artificial Intelligence*, vol. 8, 07 2018.
[19] A. Kishor and R. Niyogi, "Multi-objective load balancing in distributed computing environment: an evolutionary computing approach," 03 2020, pp. 170–175.
[20] J. Kennedy and R. Eberhart, "Particle swarm optimization," in *Proceedings of ICNN'95 - International Conference on Neural Networks*, vol. 4, 1995, pp. 1942–1948 vol.4.
[21] S. Salman, X. Ai, and Z. WU, "Design of a p-and-o algorithm based mppt charge controller for a stand-alone 200w pv system," *Protection and Control of Modern Power Systems*, vol. 3, 12 2018.

Authorized licensed use limited to: DELHI TECHNICAL UNIV. Downloaded on February 10,2022 at 10:24:16 UTC from IEEE Xplore. Restrictions apply.

2021 5th International Conference on Electrical, Electronics, Communication, Computer Technologies and Optimization Techniques (ICEECCOT) 10-11, December 2021

2021 5th International Conference on Electrical, Electronics, Communication, Computer Technologies and Optimization Techniques (ICEECCOT) | 978-1-6654-3272-6/21/$31.00 ©2021 IEEE | DOI: 10.1109/ICEECCOT52851.2021.9707915

Improving document representation using KPCA and clustered word embeddings

Aakansha Gupta
Department of Computer Science and Engineering
Delhi Technological University
Delhi, India
aakanshagupta.74@gmail.com

Rahul Katarya
Department of Computer Science and Engineering
Delhi Technological University
Delhi, India
rahuldtu@gmail.com

***Abstract*—Text mining approaches have shown to be an efficient way to examine publicly available online information on a variety of topics. However, because of the lack of context, online texts are difficult to represent. Word embedding techniques, such as word2vec, capture semantic relationships between words particularly well when trained on large text collections; but they fail when trained on small datasets. This paper proposes a document representation method based on word clusters. In this approach, Word embeddings created by word2vec are supplemented with morphological information collected from kernel principal component analysis (KPCA) computed on word similarity. After running KPCA, a spherical k-means algorithm is applied, with centroid representing the topic of that cluster. Next, the document is vectorized using the frequencies of these clusters. The proposed approach successfully includes the effects of semantically and morphologically related terms on document proximity through these data-driven notions. When combined with an appropriate weighting system, the proposed approach enables improved document representation and interpretability of the resulted document vectors.**

Keywords—clustering, document representation, KPCA, skip-gram, weighting scheme

I. INTRODUCTION

Online textual data has gradually become a key source for data analysis as the relevance of unstructured data has grown [1]. The most fundamental and critical stage in extracting intriguing patterns and insights from them is document representation. Raw documents must be converted into numerical vectors that capture the distinguishing features of each document before using various machine learning and data mining approaches. If these document vectors can retain documents and their distinguishing properties in close proximity, subsequent text mining algorithms will be able to mine more accurate and significant hidden information within data. Traditional methods for the representation of documents include bag-of-words, vector space models (VSM), word2vec, and doc2vec based approaches [2] [3] [4]. For decades, these approaches have been shown to be useful in addressing different text mining jobs [5]. Although these methods are simple and robust, they cannot explain the semantics of the document. Also, approaches based on bag-of-words or VSM, on the other hand, suffer from excessive dimensionality and sparsity, rendering traditional distance measures inefficient in reflecting the correct vicinity between the texts [6].

Furthermore, these approaches are based on the assumption that the document consists of independent words. However, semantically and morphologically related words generally represent comparable information in the document. As a result, this independence between words may negatively influence capturing proximity between document vectors. As a result, text mining models built using either the bag-of-words or VSM approaches may fail to capture the correct distinctions between sparse and high dimensional vectors. Although different dimensionality reduction strategies [7,8] exist, they lack the inherent interpretability of the aforementioned approaches.

Word2vec is a popular word embedding that captures the semantic relationships between words [9]. However, Word2vec requires huge text corpora with billions of words to learn high-quality embeddings and still fails to generate high-quality vector representations for less frequent or unknown words. Although fastText [10] improves the results by incorporating morphological information, it still fails in many cases. This is particularly evident in the news domain, where frequently new words such as names occur over time which, in turn, impacts the performance of downstream applications. In this research, we, therefore, propose an alternative approach which not only makes use of morphological information but also performs well when trained on smaller datasets or domains with rapidly changing vocabulary.

Our method is based on the distributed representation to represent word vectors, which can be an alternative to mainstream technologies and is primarily based on the original count. Next, the distributed word embedding is enriched with morphological information using KPCA (Brito et al., 2017). Semantically and morphologically related keywords are grouped into a common concept by clustering distributed representations of words created using word2vec and KPCA, integrating the influence of semantically and morphologically similar words on proximity between the documents. The frequency of these clusters is then used to represent document vectors. This article evaluated the proposed method by performing document classification on several datasets. We evaluated the proposed method's document representation performance to average word2vec, doc2vec, latent semantic analysis (LSA) [12], fastText, the bag-of-words, and tf-idf weighted word embedding clusters.

The remainder of this paper is organized as follows. Section II delves into the related work. Section III discusses the proposed approach for document representation. Section IV shows the experiments and results of the proposed approach to support its representation efficiency and interpretability. Section V concludes with a recommendation for further work.

Authorized licensed use limited to: DELHI TECHNICAL UNIV. Downloaded on February 24,2022 at 07:00:07 UTC from IEEE Xplore. Restrictions apply.

II. Related work

Document representation is frequently discussed in the literature as a method for text mining. As a result, many document representation approaches for analyzing textual data have been developed. Most of the existing work uses the bag-of-words and VSM with tf-idf [13],[14]. Despite widespread acceptance among practitioners, these methods have some drawbacks. The bag-of-words and VSM produce a high-dimensional and considerably sparse data representation, impacting document classification and clustering performance [6] [15]. Although document vectors created by these techniques may be easily understood due to understandable features, they do not provide any insight into semantic relations between words [16].

To overcome the limitation of high dimensionality, various embedding techniques such as LSA [7] have been examined for the reduction of input dimensionality in data analysis. These matrix decomposition-based approaches, based on singular value decomposition, discover orthogonal basis by decomposing the term-document matrix, which may be considered artificial concepts. Even though they have high representation efficacy, the document matrix decomposition fails to capture non-linear semantic associations between the words. [17] presented an LSA-based system that tries to group terms that are significantly associated with most occurred words in the stream. The resulting cluster represents the most popular topics. LSA-based approaches make it possible to discover latent meanings in texts. Despite its effectiveness in reducing dimensionality, LSA has several drawbacks, including difficulties understanding the result and a high computational cost.

Similarly, methods based on random indexing were proposed for representing document vectors [18]. In these approaches, each context inside a document is assigned randomly generated index vectors, thereby generating initial vector representations, resulting in dimensionality reduction of document vectors. Though the word vectors are generated randomly, semantic relationships between words are not taken into account when constructing the document vectors. As a result, semantically and contextually different words can incorrectly correlate to a single topic. Moreover, topically identical texts with differing sentence patterns and word choices will produce distinct document vectors.

Other techniques utilize ontologies for enrichment; for example, [18] clustered hashtags semantically by the unsupervised approach to find the major topics in textual data. In terms of the semantic data treatment, ontology-based techniques have produced superior outcomes [19]. However, these approaches need external information, and their effectiveness is dependent on the availability of domains.

On the other hand, word embedding such as word2vec and doc2vec has been used as an effective solution to document representation. Although the doc2vec method generates low-dimensional vectors while effectively preserving proximity information, the interpretability suffers since the meanings underlying each feature are ineffable. Whereas word2vec tends to capture the semantic relationship between words, it ignores morphology.

III. Proposed method

The main purpose of the proposed method is to produce word vectors representation in an embedded space so that semantic and morphologic relations between words are preserved. The flowchart of the proposed is shown in Fig. 1. Initially, KPCA is implemented on words in the vocabulary. Then, we computed the KPCA of out-of-vocabulary words. Next, we use word2vec skip-gram model and similar morphological words from KPCA embeddings word vectors from documents to train word vectors. Using KPCA based skip-gram model, the word vectors are trained in a non-linear, morphologically, and semantically informed space to anticipate a subsequent word in a document. As a result, word vectors with similar contexts are embedded in close spatial space. After embedding word vectors in a close semantic space, they are grouped into a single cluster.

Because word2vec optimizes the cross-product of the word vectors, cosine distance was chosen as a suitable measure for evaluating semantic space distances between embedding vectors and the context vectors and grouping adjacent word vectors into a common context. As a result, the spherical k-means(SKM) [20] method is used to cluster the resulted word vectors. SKM clustering, like k-means, allocates every data point to the nearest cluster and then iteratively updates the centroid. In spherical k-means, the clustering distance measure is cosine similarity. After successful clustering of word embeddings, each cluster would have words with similar meanings or contexts.

In the conventional vector representations methods, the features are represented by the different words of the vocabulary. In the proposed approach, the word clusters obtained after clustering the word embedding create our new features; consequently, reducing the total number of features to the total words clusters. Thus, the proposed method lowers the dimensions of vector representations, resulting in a new tf-idf based on word clusters. Next, we apply cluster frequency-inverse document frequency (cf-idf) to our new features to highlight their discriminative topics while removing the influence of often occurring but non-discriminative topics using (1):

$$cf - idf_{c_i,d_j} = cf_{c_i,d_j} \times \log \frac{|D|}{|\{d \in D; c_i \in d\}|} \quad (1)$$

Our approach not only reduces the dimensionality issue but is also able to generate more intuitive and interpretable document vectors become since each concept cluster comprises semantically and morphologically related phrases.

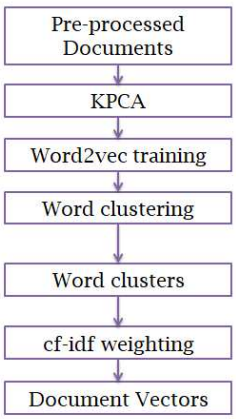


Fig.1 *Flowchart of the proposed approach*

Authorized licensed use limited to: DELHI TECHNICAL UNIV. Downloaded on February 24,2022 at 07:00:07 UTC from IEEE Xplore. Restrictions apply.

IV. Experiments and Results

Several experiments are carried out to assess the feasibility and performance of our method. The performance of the proposed method is compared against the traditional document representation methods such as average word2vec, doc2vec, LSA, fastText, the bag-of-words, and tf-idf weighted word embedding clusters.

To evaluate the performance of the proposed method, we have used two publicly datasets, i.e., 20Newsgroup and Reuters R52.

A. Effect of Word vector dimension

When dealing with word vector representation, the number of dimensions is always specified to learn the vector representation. Therefore, it is critical to analyze the effect of the number of vector dimensions on the clustering performance. We use F1-score to evaluate the quality of the obtained results. As shown in Tables I–II, The performance of the several document representation methods concerning dimensions of the vector representations is calculated using an F1-score. For a fixed dimension, the proposed model has the maximum F1-score among document representation models trained with varied numbers of clusters,*k,* ranging from 50 to 500. It was observed that the proposed approach showed poor performance with the low dimensions, i.e., with 50 and 100 dimensions, and the highest F1-score was observed for 150 and 200 dimensions. As can be seen from Table I and Table II, the proposed method has outperformed all the other document representation techniques in terms of F1-score for both datasets. However, vector representation from word2vec+k-means+tf-idf has shown high representation efficacy for the Reuters R52 dataset depending on the choice of embedding dimensions. Moreover, the performance of the proposed method is robust for various dimensions representing the influence of retaining the semantic and morphological information in word embeddings with a suitable weighting scheme that captures the well-defined characteristics. Other methods such as word2vec and bag-of-words consider words as the fundamental unit for document representation.

TABLE I. F1-score with respect to the number of dimensions for the 20 Newsgroup dataset

	Dimensions									
	50	***100***	***150***	***200***	***250***	***300***	***350***	***400***	***450***	***500***
average word2vec	56.36	37.26	65.64	64.74	63.26	64.74	63.36	64.4	62.66	62.73
Doc2Vec	54.73	66.64	73.15	66.64	66.27	73.25	56.73	72.84	56.74	64.83
LSA	64.64	64.74	73.4	64.74	67.63	53.64	73.6	63.72	64.85	46.73
fastText	65.47	65.54	73.12	63.72	66.22	73.82	73.78	63.72	67.23	67.35
word2vec+k-means+tf-idf	61.45	69	70.34	**71.84**	69.26	63.73	59.73	71.83	**70.82**	71.27
Proposed	**73.74**	**75.35**	**75.43**	70.35	**75.23**	**74.26**	**74.82**	**73.26**	63.73	**74.23**
Bag-of-words	62.28									

B. TABLE I. *F1-score with respect to the number of dimensions for the 20Newsgroup dataset* ***Error! Not a valid link.*** *Effect of changing the number of word clusters,k*

As the new features for the document representation are the word clusters, we also conduct an experiment to show the effect of changing the number of word clusters,*k*, on the F1-score. Table III summarises the results. For both the data sets, *k*=100 has generated the maximum value for the F1-score and 500 dimensions have the lowest values. This might be connected to cluster fragmentation and merging challenges. The influence of this parameter can be more noticeable with larger data sets.

TABLE II. F1-score with respect to the number of dimensions for Reuters R52

	Dimensions									
	50	***100***	***150***	***200***	***250***	***300***	***350***	***400***	***450***	***500***
average word2vec	53.87	43.75	48.19	58.31	57.53	56.31	57.58	58.31	57.21	57.25
Doc2Vec	56.69	55.39	57.10	54.23	52.53	54.60	52.48	53.43	53.35	54.59
LSA	55.26	53.12	57.13	53.31	55.84	52.43	52.83	54.23	53.37	48.77
fastText	57.84	56.67	65.65	67.67	**65.68**	67.73	56.56	66.66	67.88	62.57
word2vec+k-means+tf-idf	63.31	54.32	62.68	**69.02**	64.12	66.11	59.07	**67.63**	**59.07**	**63.36**
Proposed	**64.08**	**64.94**	**69.98**	64.64	64.87	**69.36**	**68.65**	62.83	57.78	63.34
Bag-of-words	54.65									

TTABLE III. F1-score of the proposed method with respect to the number of clusters

	k	**F1-score**
20Newsgroup	50	0.78
	100	0.875
	200	0.847
	500	0.733
Reuters R52	50	0.845
	100	0.865
	200	0.834
	500	0.767

V. Conclusion

This paper proposes a document vector representation method, considering the semantic and morphological similarity between words in a non-linear vector space. The proposed approach employs feature clusters as the foundation for encoding document vectors, capturing real aspects of the texts more effectively. The proposed approach shows a good result in proving high-quality document vector representation compared to existing methods. Future work can examine the effects of various clustering and mixing methods on the quality of the generated topics.

References

[1] K. Keswani, I. Das, B. Shrivastava, A. Gupta, R. Katarya, LDA Based model for mining textual features from financial news articles, in: Proc. - IEEE 2020 2nd Int. Conf. Adv. Comput. Commun. Control Networking, ICACCCN 2020, Institute of Electrical and Electronics

Authorized licensed use limited to: DELHI TECHNICAL UNIV. Downloaded on February 24,2022 at 07:00:07 UTC from IEEE Xplore. Restrictions apply.

Engineers Inc., 2020: pp. 43–48. https://doi.org/10.1109/ICACCCN51052.2020.9362882.

[2] D.J. P. P., Expedient Information Retrieval System for Web Pages Using the Natural Language Modeling, J. Artif. Intell. Capsul. Networks. 2 (2020) 100–110. https://doi.org/10.36548/jaicn.2020.2.003.

[3] S.K. Putri, A. Amalia, E.B. Nababan, O.S. Sitompul, Bahasa Indonesia pre-trained word vector generation using word2vec for computer and information technology field, in: J. Phys. Conf. Ser., IOP Publishing, 2021: p. 12007. https://doi.org/10.1088/1742-6596/1898/1/012007.

[4] D. Kim, D. Seo, S. Cho, P. Kang, Multi-co-training for document classification using various document representations: TF–IDF, LDA, and Doc2Vec, Inf. Sci. (Ny). 477 (2019) 15–29. https://doi.org/10.1016/j.ins.2018.10.006.

[5] A. Onan, Sentiment analysis on product reviews based on weighted word embeddings and deep neural networks, in: Concurr. Comput., 2020. https://doi.org/10.1002/cpe.5909.

[6] R.S.O. Rossi Rafael Geraldeli, Generating Features from Textual Documents Through Association Rules, ENIA Encontro Nac. Inteligência Artif. 01 (2011) 311–322. http://sites.labic.icmc.usp.br/feature/enia/Enia-RossiRezende-v2.pdf (accessed October 18, 2021).

[7] S. Ayesha, M.K. Hanif, R. Talib, Overview and comparative study of dimensionality reduction techniques for high dimensional data, Inf. Fusion. 59 (2020) 44–58. https://doi.org/10.1016/j.inffus.2020.01.005.

[8] W. Pindah, S. Nordin, A. Seman, M.S. Mohamed Said, Review of dimensionality reduction techniques using clustering algorithm in reconstruction of gene regulatory networks, in: I4CT 2015 - 2015 2nd Int. Conf. Comput. Commun. Control Technol. Art Proceeding, Institute of Electrical and Electronics Engineers Inc., 2015: pp. 172–176. https://doi.org/10.1109/I4CT.2015.7219560.

[9] T. Mikolov, K. Chen, G. Corrado, J. Dean, Efficient estimation of word representations in vector space, in: 1st Int. Conf. Learn. Represent. ICLR 2013 - Work. Track Proc., International Conference on Learning Representations, ICLR, 2013. https://arxiv.org/abs/1301.3781v3 (accessed October 17, 2021).

[10] P. Bojanowski, E. Grave, A. Joulin, T. Mikolov, Enriching Word Vectors with Subword Information, Trans. Assoc. Comput. Linguist. 5 (2017) 135–146. https://doi.org/10.1162/tacl_a_00051.

[11] E. Brito, R. Sifa, C. Bauckhage, KPCA embeddings: An unsupervised approach to learn vector representations of finite domain sequences: A use case for words and DNA sequences, in: CEUR Workshop Proc., 2017: pp. 87–96. https://code.google.com/archive/p/word2vec (accessed October 17, 2021).

[12] S. Deerwester, S.T. Dumais, G.W. Furnas, T.K. Landauer, R. Harshman, Indexing by latent semantic analysis, J. Am. Soc. Inf. Sci. 41 (1990) 391–407. https://doi.org/10.1002/(SICI)1097-4571(199009)41:6<391::AID-ASI1>3.0.CO;2-9.

[13] M.P. Naik, H.B. Prajapati, V.K. Dabhi, A survey on semantic document clustering, in: Proc. 2015 IEEE Int. Conf. Electr. Comput. Commun. Technol. ICECCT 2015, Institute of Electrical and Electronics Engineers Inc., 2015. https://doi.org/10.1109/ICECCT.2015.7226036.

[14] J. Vosecky, D. Jiang, K.W.T. Leung, W. Ng, Dynamic multi-faceted topic discovery in twitter, in: Int. Conf. Inf. Knowl. Manag. Proc., 2013: pp. 879–884. https://doi.org/10.1145/2505515.2505593.

[15] M. Fraj, M.A. Ben Hajkacem, N. Essoussi, A Novel Tweets Clustering Method using Word Embeddings, in: Proc. IEEE/ACS Int. Conf. Comput. Syst. Appl. AICCSA, IEEE Computer Society, 2019. https://doi.org/10.1109/AICCSA.2018.8612816.

[16] U. Scaiella, P. Ferragina, A. Marino, M. Ciaramita, Topical clustering of search results, in: WSDM 2012 - Proc. 5th ACM Int. Conf. Web Search Data Min., 2012: pp. 223–232. https://doi.org/10.1145/2124295.2124324.

[17] M. Mathioudakis, N. Koudas, TwitterMonitor: Trend detection over the twitter stream, in: Proc. ACM SIGMOD Int. Conf. Manag. Data, 2010: pp. 1155–1157. https://doi.org/10.1145/1807167.1807306.

[18] P. Kanerva, J. Kristofersson, A. Holst, Random indexing of text samples for latent semantic analysis, Proc. 22nd Annu. Conf. Cogn. Sci. Soc. 1036 (2000) 16429–16429. http://citeseerx.ist.psu.edu/viewdoc/download?doi=10.1.1.4.6523&rep=rep1&type=pdf (accessed October 18, 2021).

[19] B. Zhong, H. Li, H. Luo, J. Zhou, W. Fang, X. Xing, Ontology-Based Semantic Modeling of Knowledge in Construction: Classification and Identification of Hazards Implied in Images, J. Constr. Eng. Manag. 146 (2020) 04020013. https://doi.org/10.1061/(asce)co.1943-7862.0001767.

[20] I.S. Dhillon, D.S. Modha, Concept decompositions for large sparse text data using clustering, Mach. Learn. 42 (2001) 143–175. https://doi.org/10.1023/A:1007612920971.

Authorized licensed use limited to: DELHI TECHNICAL UNIV. Downloaded on February 24,2022 at 07:00:07 UTC from IEEE Xplore. Restrictions apply.

Journal of Micromechanics and Microengineering

ACCEPTED MANUSCRIPT

Influence of Source Electrode Metal Work Function on Polar Gate Prompted Source Hole Plasma in Arsenide/Antimonide Tunneling Interfaced Junctionless TFET.

To cite this article before publication: Samriti Sharma *et al* 2022 *J. Micromech. Microeng.* in press https://doi.org/10.1088/1361-6439/ac516f

Manuscript version: Accepted Manuscript

Accepted Manuscript is "the version of the article accepted for publication including all changes made as a result of the peer review process, and which may also include the addition to the article by IOP Publishing of a header, an article ID, a cover sheet and/or an 'Accepted Manuscript' watermark, but excluding any other editing, typesetting or other changes made by IOP Publishing and/or its licensors"

This Accepted Manuscript is **© 2022 IOP Publishing Ltd**.

During the embargo period (the 12 month period from the publication of the Version of Record of this article), the Accepted Manuscript is fully protected by copyright and cannot be reused or reposted elsewhere.
As the Version of Record of this article is going to be / has been published on a subscription basis, this Accepted Manuscript is available for reuse under a CC BY-NC-ND 3.0 licence after the 12 month embargo period.

After the embargo period, everyone is permitted to use copy and redistribute this article for non-commercial purposes only, provided that they adhere to all the terms of the licence https://creativecommons.org/licences/by-nc-nd/3.0

Although reasonable endeavours have been taken to obtain all necessary permissions from third parties to include their copyrighted content within this article, their full citation and copyright line may not be present in this Accepted Manuscript version. Before using any content from this article, please refer to the Version of Record on IOPscience once published for full citation and copyright details, as permissions will likely be required. All third party content is fully copyright protected, unless specifically stated otherwise in the figure caption in the Version of Record.

View the article online for updates and enhancements.

This content was downloaded from IP address 14.139.251.100 on 10/02/2022 at 10:23

Influence of Source Electrode Metal Work Function on Polar Gate Prompted Source Hole Plasma in Arsenide/Antimonide Tunneling Interfaced Junctionless TFET.

Samriti Sharma [a], Rishu Chaujar [a,*]

[a] *Department of Applied Physics, Delhi Technological University, Delhi, India*

Abstract

Numerous studies have explored the impact of control gate and polar gate on the retention of hole and electron charge plasma to induce the source and channel region polarity in junctionless tunnel field effect transistor (JLTFET). However, polar gate is not the only one responsible for the retention of hole plasma in the p^+ prompted source but the hole plasma near the interface of source electrode metal and p^+ prompted source (SEM/S) is influenced by the choice of source electrode metal work function too. This paper features a comprehensive investigation of the mutual significance of PG and SEM work function on p^+ prompted source to study key analog characteristics of arsenide/antimonide tunneling interfaced hetero-material JLTFET (HJLTFET), which is unexplored in the literature otherwise. We have considered three metals – W (4.55 eV), Mo (4.65 eV), and Pd (5.3 eV) as the source electrodes in HJLTFET. For source electrode metal work function lesser than p^+ prompted source (W and Mo), the Schottky contact is formed by the depletion of hole plasma near source electrode metal and p^+ prompted source interface. This results in the immediate current inhibition at source to channel interface caused by an undesired movement of electrons en route to the Schottky interface. The Schottky tunneling phenomenon is considered by implementing the Universal Schottky Tunneling model to study the underestimated drain current of HJLTFET. However, the Universal Schottky Tunneling model becomes inconsequential for source electrode metal work function higher than p^+ prompted source (Pd) as hole plasma is preserved by the ohmic contact formation.

Keywords: Arsenide; Hole plasma; Junctionless TFET; Source electrode metal; Universal Schottky Tunneling

* Corresponding author.

E-mail addresses: sharmasmriti_phd2k18@dtu.ac.in (S.Sharma), Chaujar.rishu@dtu.ac.in (R. Chaujar).

Accepted Manuscript

1. Introduction

The fast-growing need of next generation devices in artificial intelligence, cloud computing, low power and high-speed modern communication systems, and internet of things has led the research community to explore new innovative ideas at the sub 20 nm technology node like never before. The high operation speed, improved functionality and enhanced packing density are the results of continuous downscaling of CMOS technology. However, it results in various critical challenges like high leakage current, high static power dissipation and short channel effects [1-7]. Other modern electronic devices like MOSFET, HEMT, HBT, and negative capacitance filed effect transistors (FETs) show degraded performance at sub 20 nm technology node despite being widely used in modern communication systems. The alternative to such issues can be the device having steeper swing and lower leakage current. Tunnel field effect transistor (TFET) is amongst the most promising devices to fill these gaps along with improved performance pertaining to steeper swing and lower leakage current. It overcomes the prime issue of thermionic limit of 60 mV/decade (MOSFET) owing to the band-to-band tunneling (BTBT) of carriers rather than thermionic emission in MOSFET [4-8]. However, inferior ON current (I_{ON}) is still a snag for the TFET devices. Moreover, the development of extremely thin doping junctions using highly doped source and drain region is one of the major obstacles owing to the increased thermal expenses for hybrid thermal annealing and ion implantation [8-9]. Along with that, random dopant fluctuations are also generated due to the highly doped source and drain regions [10]. Therefore, to eradicate the junction constraint and simplify the fabrication complexity, junctionless FETs were introduced based on charge plasma concept. The fundamental basis of charge plasma is to utilize gates having different work functions to induce the source and channel region polarity [8]. Thus, junctionless TFETs have given a new outlook to the electronic industry by merging the advantages of TFET (steeper swing) and JLFET (high I_{ON}) [11-17].

Many researchers have paid attention to analyze the performance characteristics of JLTFET by exploring the impact of control gate (CG) and polar gate (PG) work functions. However, the depletion of hole plasma by the work function of source electrode metal (SEM) at the interface of SEM and p^+ prompted source region (SEM/S) has not been given due importance [11-16, 18-20]. The depletion of hole plasma gives rise to a Schottky interface at the SEM/S interface, which is implemented through the universal Schottky tunneling mechanism

Accepted Manuscript

(UST) at the SEM/S interface. The ignorance of UST at the SEM/S interface leads to underrated performance of the device. In this work, we have given due attention to the UST at the SEM/S interface by selecting appropriate source electrode metal work function. To take into account the Schottky tunneling at the SEM/S interface, an in-depth attention has been laid upon incorporating the Universal Schottky Tunneling model (UST) in our present work, which has been overlooked by many researchers before [8-9, 11, 16]. Fig. 1 represents the grid sites near the Schottky contact, which signifies the localized tunneling generation rates of electrons. In UST mechanism, the tunneling current is calculated across these grid sites within a specified distance of the electrode. Eq. 1 describe the calculation of tunneling current component as follows [18-19, 21]:

$$J_T = \frac{A^* T_L}{K} \int_E^{\infty} \Gamma(E') \ln\left[\frac{1+f_s(E')}{1+f_m(E')}\right] dE' \quad (1)$$

$$G_T = \frac{1}{q} \nabla J_T \quad (2)$$

Where, J_T is the tunneling current density, A^* is the effective Richardson's coefficient, T_L is the lattice temperature, $I(E')$ is the tunneling probability, $f_s(E')$ and $f_m(E')$ are the Maxwell-Boltzmann distribution functions in the semiconductor and metal and E' is the carrier energy. G_T is the localized tunnelling rate.

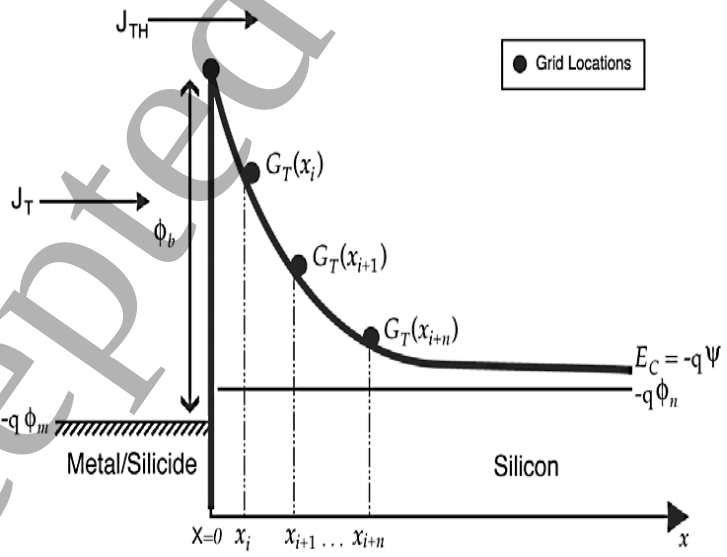


Fig. 1. The universal Schottky tunnelling mechanism representing the local tunnelling generation rate at the metal/semiconductor interface [21].

Accepted Manuscript

The total current density across the Schottky barrier is the sum of thermionic emission component and tunnelling component as shown in Fig. 1. Eq. 3 represents the mathematical expression for total current density across the Schottky barrier:

$$J_{TOT} = J_T + J_{TH} \quad (3)$$

Where J_{TOT} is the total current density and J_{TH} is the thermionic emission component. For lower Schottky barrier height, the thermionic emission of the carriers over the barrier increases leading to enhancement in the thermionic emission component of current. In that case the tunnelling current density is reduced. However, the tunnelling current comes into play only if the tunnelling width is lower than 10 nm [18].

We utilized the binary/ternary compound semiconducting hetero-material based hetero-junctionless TFET (HJLTFET) using InAs/AlGaSb with Al mole fraction of 0.15 (our previously published work [17]). In present work, for the first time, metals with different work functions as the source electrode have been implemented to study the significance of SE metals on the analog characteristics of HJLTFET. The presented work may be helpful to study various underrated physical effects of JLTFETs in regards to ohmic and schottky contacts. It may put the research of junctionless devices in the right direction owing to the hole plasma depletion consideration at the SEM/S interface, which has been overlooked before. Our article is framed into five parts. First part presents the details of literature review and the introduction of the presented work. Second part describes the details of device structure, parametric details and device material information. Third part explains

Table 1
Device Parameters

Parameter	Symbol	Value
Channel Length	L_G	20 nm
Doping Concentration	N_D	$1 \times 10^{19} cm^{-3}$
Oxide thickness	T_{OX}	2 nm
Isolation thickness	L_{Gap}	2 nm
CG work Function	ϕ_{CG}	4.5 eV
PG Work Function	ϕ_{PG}	5.93 eV
Spacer Length	L_{Spr}	2 nm

Accepted Manuscript

the simulation models, methodology, calibration and the fabrication process flow of our device. The results and detailed discussion are presented in part four. The summary of the presented work is concluded in part five of the paper.

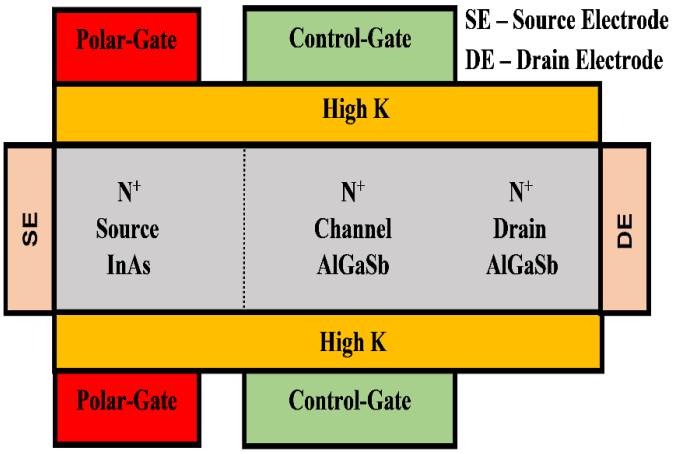
2. Device Structure

The schematic device architecture of our proposed device HJLTFET is presented in Fig. 2(a). The optimization of Al mole fraction in AlGaSb used in channel region is already presented in [17]. The doping concentration of the source and channel region is kept uniform at 1×10^{19} cm^{-3}. The thickness of the semiconductor body is 3 nm. The other device design parameters are framed in Table 1. A polarity gate PG with work function 5.93 eV is implemented over the source region to prompt the (hole plasma) p^+ source. The CG with work function of 4.5 eV is implemented over the channel region to prompt the electron plasma. The 2 nm thick high k dielectric material (HfO_2) is applied to insulate the gate electrodes from the source and channel semiconductor material. To study the impact of metal work function in the source electrode, we employed three metals viz. tungsten (W, 4.55 eV), Molybdenum (Mo, 4.75 eV), and palladium (Pd, 5.3 eV) [20]. The ON state and OFF state corresponds to V_{GS} = 1.5 V, V_{DS} = 1.5 V and V_{GS} = 0.0 V, V_{DS} = 1.5 V, respectively.

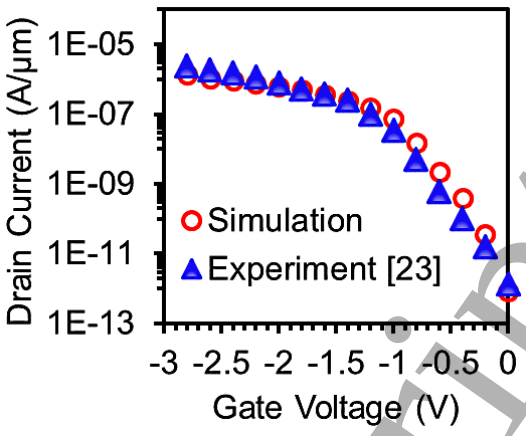
3. Simulation Methodology

The simulation modeling and physics based numerical calculations are performed using Silvaco-ATLAS TCAD tool [21]. To implement the device physics, various physical models have been applied like Fermi Dirac statistics, Band gap narrowing model (BGN), CVT model (Lombardi) to understand the significance of concentration, electric field, and temperature associated mobility, and Hansch quantum confinement (QC) model [22]. To emulate the physics related to the electron density, hole density, and trapped electron density in the conduction band, valence band, and forbidden gap, respectively, we have incorporated SRH (trap assisted recombination) and Auger recombination models in our device to include minority recombination effects with carrier lifetime (TAUP0 = 1×10^{-7} s). The trap assisted tunneling dominates the SRH recombination process

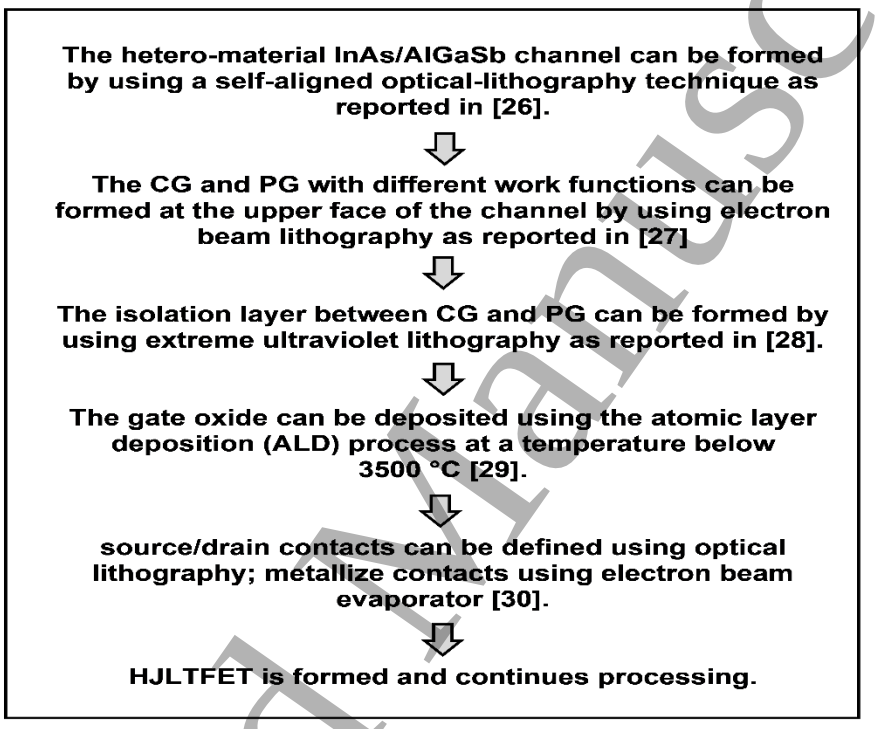
Accepted Manuscript



(a)



(b)



(c)

Fig. 2. (a) Device schematic architecture of HJLTFET, (b) Calibration plot, and (c) Fabrication process flow of proposed HJLTFET.

and reduces the carrier lifetimes near the strong electric field regions, which affects the leakage current of the device. Therefore, we have applied the TAT model in our device.

To inculcate the source/channel (S/C) arsenide/antimonide interface tunneling and to define the electric field along the whole tunneling area, non-local BTBT model is used by generating a quantum tunneling meshing around the S/C interface. The calibration of the simulation models and parameters being used in our device has

Accepted Manuscript

been validated with the information extracted from a fabrication-based research work [23] by maintaining the device biasing settings precisely the same as that of the published results stated in [23]. Fig. 2(b) illustrates the calibration of the transfer characteristics obtained from the extracted data of the experimental work and our simulations. It validates all the model parameters due to the close propinquity of the compared results. To account for the gate leakage impact on SS in HJLTFET, we have implemented the Fowler-Nordheim (FN) model in our simulations. The FN model calculates the tunneling current due to the tunnelling of electrons from the semiconductor fermi level into the oxide conduction band. This is caused by the high electric field across the oxide. Each electrode-oxide and oxide-semiconductor interface is divided into discrete segments and for each oxide-semiconductor segment, the Fowler-Nordheim current is calculated. Which is further added to the electrode-oxide boundary. Table 2 represents the model parameters for HJLTFET simulations. To consider the quantum mechanical effects of thin body semiconductor, we have invoked the drift-diffusion mode-space method (DD_MS). This model solves the 1D transport equations in each sub-band and quasi-fermi levels are extracted.

Table 2
FN Model Parameters [21]

Parameter	Value
A_{FN}	1.82×10^{-7}
B_{FN}	1.90×10^{8}
A_{FH}	1.82×10^{-7}
B_{FH}	1.90×10^{8}

The currents and bulk carrier densities are calculated by summating over all sub-bands. It captures quantum effects in transverse direction along with other models for band-to-band tunnelling, mobility and recombination. To inculcate the impact of interface trap charges and band tailing in our device, the interface charges are uniformly distributed with trap charge density fixed at $N_f = 1\times10^{12}$ cm^{-2} for semiconductor/semiconductor and semiconductor/oxide interfaces (S/S and S/O interface) based on earlier reported simulation and experimental data involving the hot carrier/radiation/process damages [24-25]. The polarity and position of interface charge is specified using the INTERFACE statement [21]. The prime focus of the work is to include the impact of SE metal work function on the device performance. For that purpose, we evoked the UST model in case of

Accepted Manuscript

designing the HJLTFET having SE metal work function lower than the p^+ (hole plasma) prompted source region. Moreover, the results obtained are also compared with HJLTFET after the exclusion of UST model, to study the variation of result characteristics with the inclusion and exclusion of UST model. The SE metal work function lower than p^+ prompted source region gives rise to the Schottky tunneling at the SEM/S interface, which is taken into account by the implementation of UST model. Such aspect of HJLTFET devices have not been considered in former studies to the best of our knowledge. Fig. 2 (c) illustrates the fabrication process flow chart of the proposed HJLTFET.

4. Results and Discussion

In this section, a thorough investigation of the impact of three SE metal work functions on the analog characteristics of InAs/AlGaSb based HJLTFET has been carried out.

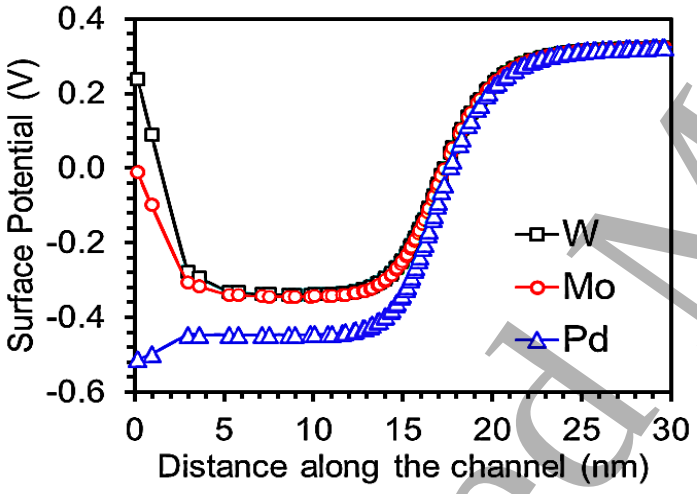


Fig. 3. Surface potential variation along the channel direction for three SE metals at thermal equilibrium state.

Fig. 3 illustrates the variation of surface potential along the channel direction for no biasing condition (thermal equilibrium state, V_{GS} = 0.0 V, V_{DS} = 0.0 V) for three SE metal work functions. For SEMs, W and Mo having work function lesser than p^+ prompted source, the hole plasma induced by the PG nearby the SEM/S interface gets depleted by the surface potential. However, for the larger work function metal Pd, the hole plasma at the SEM/S interface is retained by the PG (Fig. 3). Such variation of surface potential with respect to the different SE metal work function shows synchronization with the already existing theories [31]. Fig. 4 (a-c) displays the

Accepted Manuscript

disparity of energy band profile along the channel direction at thermal equilibrium for three SE metal work functions. We have calculated the energy band profile of HJLTFET by considering the cutline across the whole channel length (along the x-direction) 1 nm below the channel surface. In Fig. 4(a), the depletion of hole plasma near the SEM/S interface for W and Mo gives rise to Schottky contact due to the SEM work function lesser than p^+ prompted source. Whereas the higher work function SE metal, Pd gives rise to ohmic contact owing to the preservation of hole plasma. In Fig. 4(b), for W and Mo SEs, the source region is no longer p^+ type at the SEM/S interface.

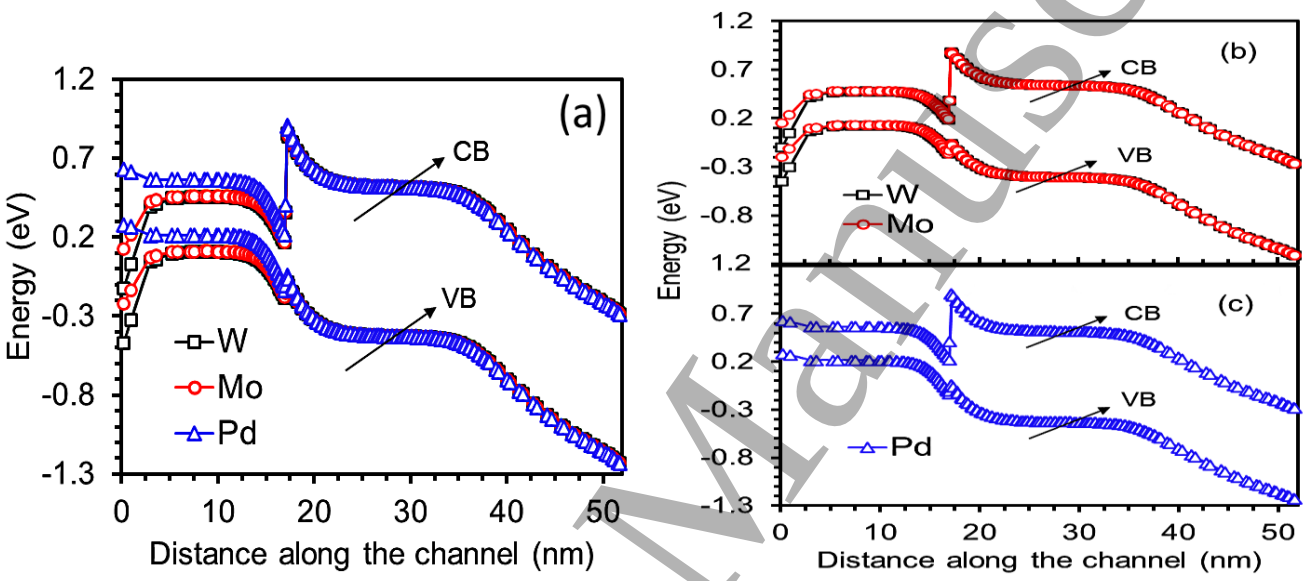


Fig. 4. (a) Energy band profile of HJLTFET for three SE metals at thermal equilibrium state, (b) Formation of Schottky interface at W and Mo SE/Source interface, and (c) Formation of ohmic contact for Pd SE.

The depletion of hole plasma leads to reduction of effective carrier conduction as the electrons attain higher probability to move towards the SE. Thus, the electrons available for tunneling across the S/C interface reduces (Fig. 4b). However, the hole plasma is preserved for SEM work function higher than p^+ prompted source (for Pd), maintaining the electron movement only towards the S/C interface. Thus, the effective carrier conduction remains unaltered for Pd SE metal (Fig. 4c). It confirms that along with PG, the choice of SEM work function is equally responsible for the induction of hole plasma in the source region of HJLTFET. A detailed theory regarding the transformation of metal contact from ohmic to Schottky by choosing appropriate work functions

Accepted Manuscript

has been developed in [20]. However, the transformation of metal contacts from ohmic to Schottky for hetero-material junctionless TFETs leads to new aspects for the research community and mobile industry.

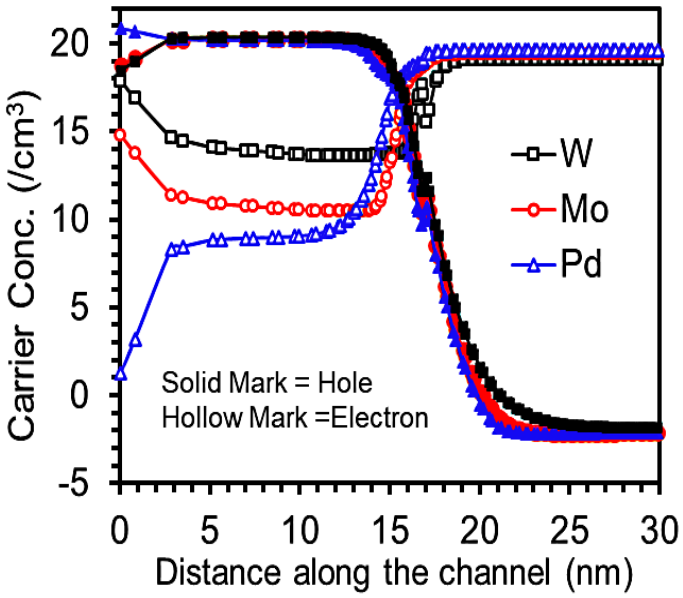


Fig. 5. ON state electron and hole concentration along the channel direction for three SE metals.

Fig. 5 illustrates the electron/hole concentration of carriers along the channel length for three SE metals. As stated before, in Fig. 4(a-b) regarding the electrons moving towards the SE region for W and Mo SE metals, a similar phenomenon has been observed regarding the carrier concentration in Fig. 5. The electron concertation increases greatly as compared to the hole concentration near the SE region for W and Mo metals confirming the movability of electrons in the direction of SE. This declines the tunneling of electrons across the S/C interface and hence the BTBT rate of HJLTFET is diminished for W and Mo SE metals (Fig. 6a). Therefore, the overall conduction of HJLTFET is also hampered owing to the lowered BTBT rate. Since number of electrons available for tunneling across the S/C interface has declined, the drain current of HJLTFET also reduces for W and Mo SEs. For Pd SE, the absence of Schottky interface at the SEM/S interface leads to the highest electron BTBT rate. There is only one way movability of electrons from source to channel region through S/C interface leading to numerous electrons available for effective conduction of HJLTFET (Fig. 6a). As mentioned before, the W and Mo SEs exhibit the Schottky tunneling at the SEM/S interface. Therefore, the

Accepted Manuscript

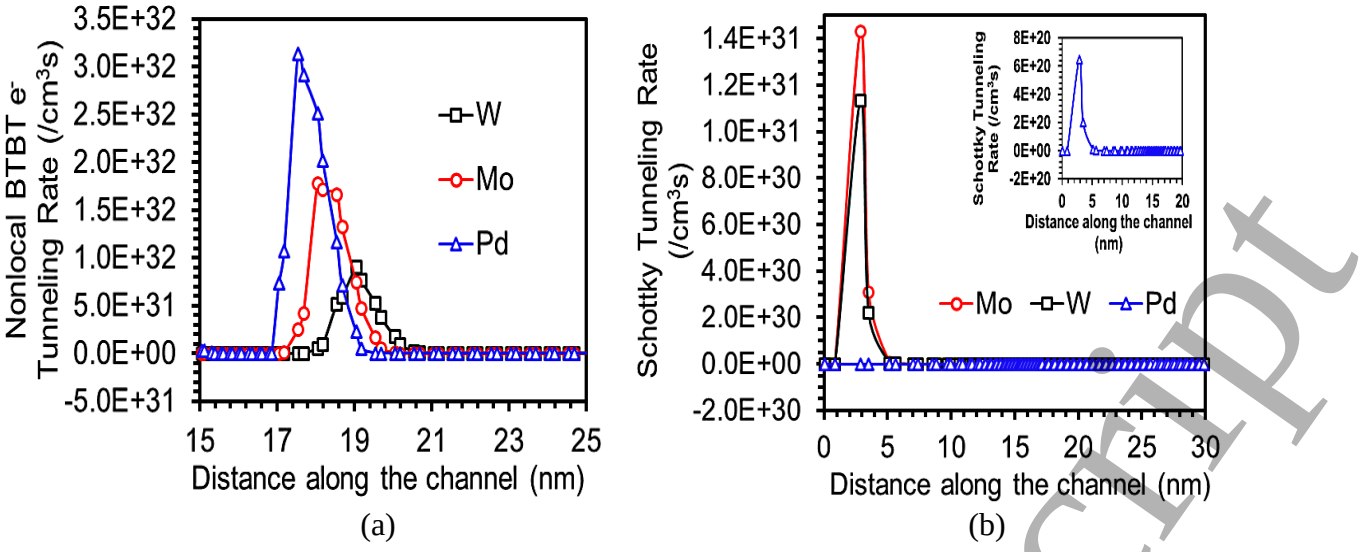


Fig. 6. (a) Band to band tunneling rate at S/C interface and (b) Schottky tunneling rate at SEM/S interface for different SE metals

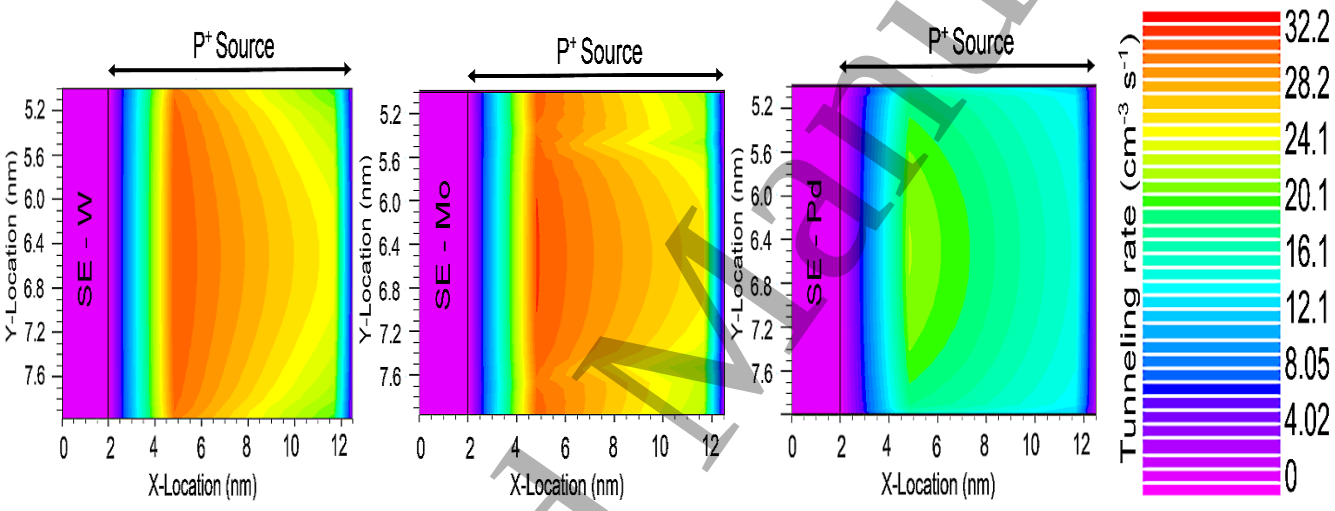


Fig. 7. ON state level curve (contour) of Schottky tunneling rate (log scale) of HJLTFET for (a) W, (b) Mo, and (c) Pd.

UST model need to be implemented to emulate the accurate device physics regarding the tunneling phenomenon at the SEM/S interface.

Fig. 6(b) displays the Schottky tunneling rate of electrons at the SEM/S interface for all three metal SEs – W, Mo, and Pd. The comparison of contour plot of Schottky tunneling is also illustrated in Fig. 7. The Schottky tunneling for W is lower than Mo. The reason behind lower Schottky tunneling of W is the larger Schottky

Accepted Manuscript

potential barrier, whereas Mo SE attains lower Schottky potential barrier height (Fig. 3) and width leading to enhanced Schottky tunneling rate (Fig. 6b). The Schottky tunneling rate for Pd SE is almost negligible owing to higher SE work function than p^+ prompted source. This is because of the non-existence of Schottky interface at the SEM/S interface of Pd SE. Therefore, the UST model has no influence on the performance of Pd SE. The contour plots of the three aforementioned SE metals show similar variation in Fig. 7. Here, the Mo SE (Fig. 7b) leads to significantly higher Schottky tunneling rate than W SE (Fig. 7a) at the SEM/S interface, whereas the Schottky tunneling rate of Pd SE is diminished (Fig. 7c).

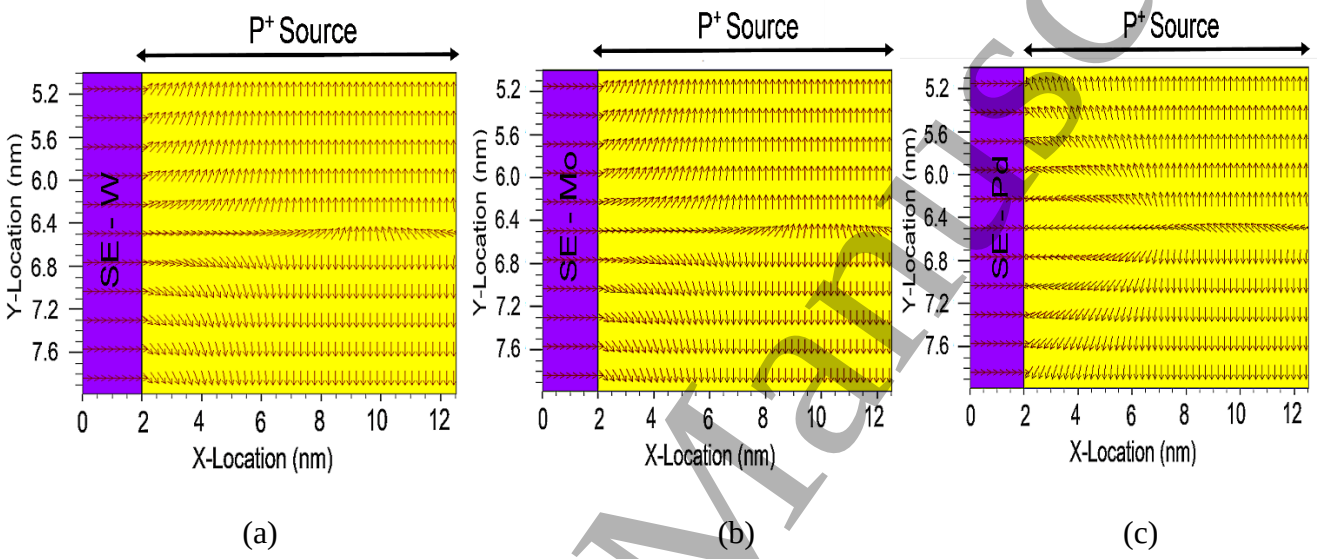


Fig. 8. ON State electric field vector illustration of HJLTFET for (a) W, (b) Mo, and (c) Pd.

Fig. 8(a-b) illustrates the vector representation of the electric field direction of HJLTFET for three SE metal work functions under the ON state. We have displayed the electric field vector representation in the hole plasma depleted region near the SEM/S interface. Since the direction of electric field is opposite to the direction of flow of electrons, therefore the movability of electrons from source to channel is defined by the electric field vector. It helps to outline the impact of SEM work function on the formation of Schottky tunneling interface at the SEM/S interface of HJLTFET. For W and Mo SEs, the movability of electrons is more in the direction of SE forming the Schottky interface (Fig. 8a-b). This is due to the hole plasma depletion at the SEM/S interface and hence the current conduction is abstained in the channel region (Fig. 8a-b), whereas, the electric filed vector shows only one way movability of electrons from source to channel vanishing the Schottky contact formation

Accepted Manuscript

at the SEM/S interface of Pd SE. Hence, the current conduction remains immune for Pd SE, due to ohmic contact formation at SEM/S interface (Fig. 8c).

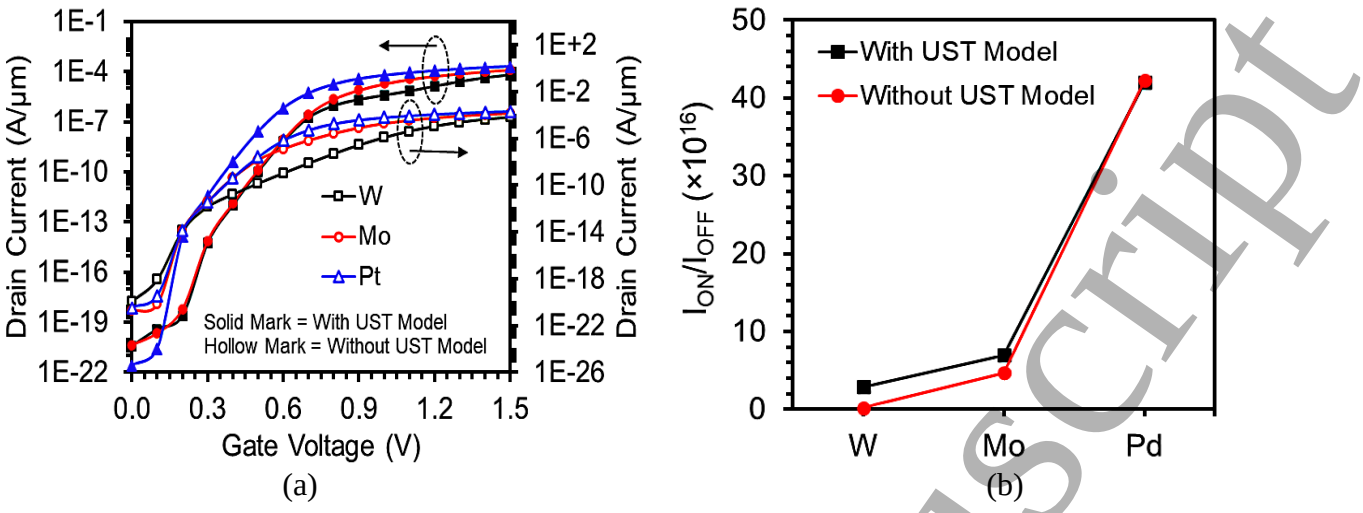


Fig. 9. (a) Transfer characteristics and (b) current switching ratio (I_{ON}/I_{OFF}) of HJLTFET for three SE metals.

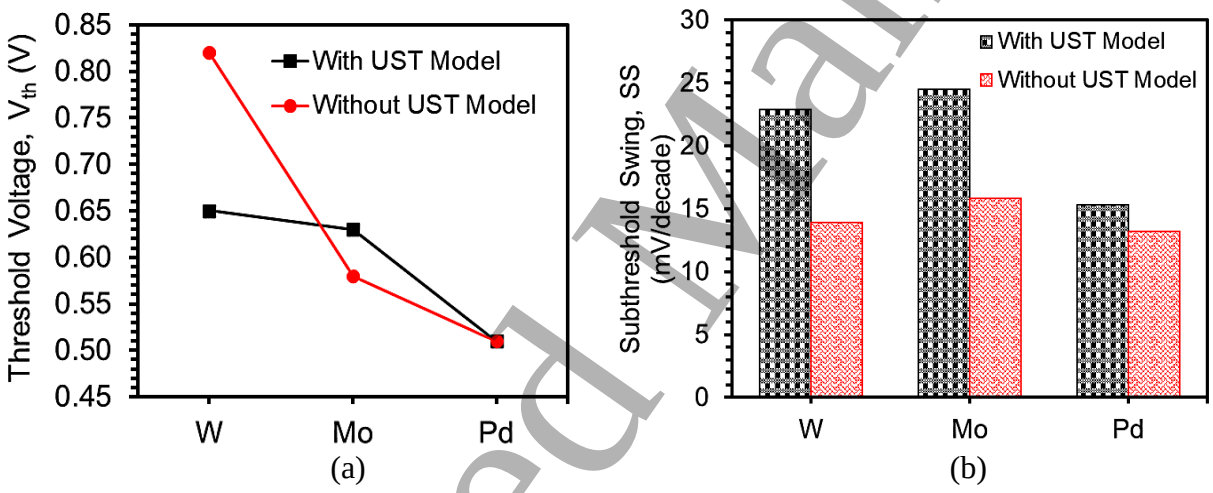


Fig. 10. Impact of SE metal work function on (a) Threshold voltage and (b) SS of HJLTFET.

To illustrate the impact of inclusion and exclusion of UST model in the SE-HJLTFET device physics, we have plotted the transfer characteristics of HJLTFET for three aforementioned SE metal work functions (W, Mo, and Pd) in Fig. 9(a). For the both inclusion and exclusion of UST model, the results show major variation for SEM work functions lesser than the p^+ prompted source region (W and Mo). On the implementation of UST model, the Schottky tunneling is taken into account due to the depleted hole plasma at the SEM/S interface. This Schottky tunneling gives precise calculations of the drain current, which is overlooked without the

Accepted Manuscript

implementation of UST model. There is no variation of transfer characteristics in Pd SE with or without the UST model. The reason behind this is the formation of ohmic contact by Pd SE with the p^+ prompted source and hence the hole plasma is preserved by the PG. Therefore, role of UST becomes meaningless for Pd SE so the drain current remains unchanged with or without UST model application. Also, the maximum drain current is obtained for Pd SE, which justifies the above discussion of ohmic contact formation at the Pd SEM/S interface. The result is supported by the highest BTBT rate of electrons at the S/C interface in Pd SE shown in Fig. 6(a). It is inferred that along with BTBT (S/C interface) the Schottky tunneling (SEM/S interface) is equally significant in defining the conduction of HJLTFET. The drain current for W (Mo) is almost 2.44% (1.56%) enhanced on the inclusion of UST model. The significance of SEM work function comes into play only for the ON state. When no gate bias is applied, the wider hetero-material tunneling barrier restricts the flow of electrons across the S/C interface, such that the effect of SE metal diminishes. For the whole simulation process and result parameters extraction, we have kept the work function of CG at a fixed value. So, it is primarily the impact of SE metal work function on the results variation, which describes the role of UST model in formation of Schottky and ohmic contacts.

Further, the impact of UST model has been studied for current switching ratio (I_{ON}/I_{OFF}) of HJLTFET for three SE metals W, Mo, and Pd (Fig. 9b). For SEM work function lesser than p^+ prompted source (W and Mo) there is a noticeable variation of I_{ON}/I_{OFF} with or without UST model. However, for Pd SE having higher work function than p^+ prompted source, there is a negligible variation of I_{ON}/I_{OFF} for both cases. This signifies the importance of the role of SE metal work function being played in the conduction of HJLTFET. The I_{ON}/I_{OFF} ratio of HJLTFET for W (Mo) SE becomes 16 (1.5) times higher on the inclusion of UST model as compared to without UST model case. Fig. 10(a) displays the significance of UST model on the variation of threshold voltage (V_{th}) of HJLTFET for three SE metal work functions. The V_{th} of HJLTFET reduces by 0.79/1.08 times for W/Mo SE with UST model implementation than without the UST model case. This shows the undervalued drain current of HJLTFET (W and Mo) without UST model implementation, whereas, Pd SE preserve the hole plasma in the source region and hence the ohmic contact formed at Pd SEM/S interface shows improved V_{th} in comparison to other two metal SEs. Thus, the comparison of with and without UST model for Pd SE shows no

Accepted Manuscript

variation of V_{th}. Fig. 10(b) shows the comparison of SS for all three SE metal work functions with and without UST model implementation. The variation of SS for Pd SE is marginally increased, whereas the variation is larger in case of other two metal SEs. Fig. 11 illustrates the significance of inclusion and exclusion of FN model on the SS value for three SE metals (W, Mo, and Pd). The variation of SS shows no significant change on the application of FN model. So, there is a negligible effect of gate leakage in HJLTFET.

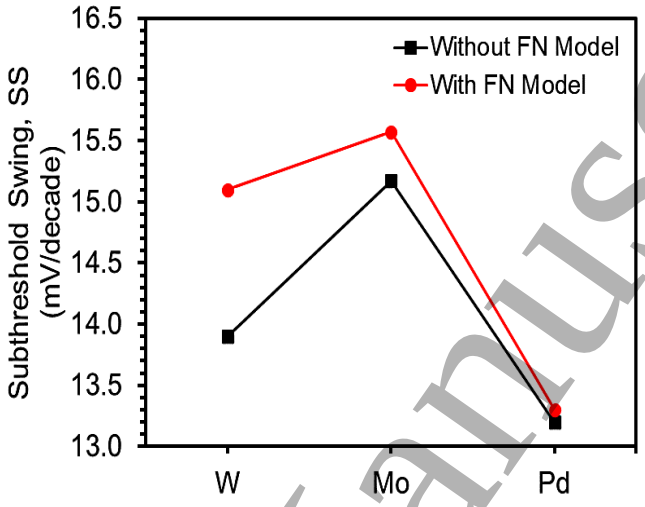


Fig. 11. Impact of inclusion and exclusion of FN model on SS of HJLTFET.

5. Conclusion

This research gives the detailed analysis of the influence of different SE metal work functions in the formation of Schottky and ohmic contacts by including the most important UST model in our proposed hetero-material InAs/AlGaSb based HJLTFET. The role of different SE metal work functions was evaluated with respect to the polarity gate prompted source region of HJLTFET (p^+ source) for analog performance parameters. It is found that the total current conduction of HJLTFET gets hampered with SEM work function lesser than p^+ prompted source as the hole plasma gets depleted near the SEM/S interface. This results in the formation of Schottky contact leading to the undesired electrons' movement towards the SE. The electrons available for BTBT through S/C interface gets reduced in number, hence hampering the effective conduction of HJLTFET (drain current). Thus, inspite of efficient BTBT of electrons at S/C interface, the formation of Schottky contact abstain the

Accepted Manuscript

current conduction of HJLTFET (for W and Mo SE work functions). This signifies the requirement of ohmic contact formation at the SEM/S interface in addition to the sufficient band to band tunneling across the S/C interface. Therefore, the SE work function must be higher than the p^+ prompted source forming the ohmic contact at the SEM/S interface to facilitate the effective current conduction in the n-type HJLTFET. Moreover, the UST model must be implemented during the simulations to include the device physics of the Schottky tunneling at the SEM/S interface, which is overlooked otherwise. However, for the fabrication of HJLTFET, the SE with higher work function than the p^+ prompted source must be preferred to ensure effective device functioning.

References

[1] Chakraborty, S., Mallik, A., Sarkar, C. K., & Rao, V. R. (2007). Impact of halo doping on the subthreshold performance of deep-submicrometer CMOS devices and circuits for ultralow power analog/mixed-signal applications. *IEEE Transactions on Electron Devices*, *54*(2), 241-248.

[2] Choi, W. Y., Park, B. G., Lee, J. D., & Liu, T. J. K. (2007). Tunneling field-effect transistors (TFETs) with subthreshold swing (SS) less than 60 mV/dec. *IEEE Electron Device Letters*, *28*(8), 743-745.

[3] Madan, J., Gupta, R. S., & Chaujar, R. (2017). Mathematical modeling insight of hetero gate dielectric-dual material gate-GAA-tunnel FET for VLSI/analog applications. *Microsystem Technologies*, *23*(9), 4091-4098.

[4] Gupta, A. K., Raman, A., & Kumar, N. (2019). Design and investigation of a novel charge plasma-based core-shell ring-TFET: analog and linearity analysis. *IEEE Transactions on Electron Devices*, *66*(8), 3506-3512.

[5] Djeffal, F., Ferhati, H., & Bentrcia, T. (2016). Improved analog and RF performances of gate-all-around junctionless MOSFET with drain and source extensions. *Superlattices and Microstructures*, *90*, 132-140.

Accepted Manuscript

[6] Madan, J., Gupta, R. S., & Chaujar, R. (2017). Performance investigation of heterogeneous gate dielectric-gate metal engineered–gate all around-tunnel FET for RF applications. *Microsystem Technologies*, *23*(9), 4081-4090.

[7] Colinge, J. P., Lee, C. W., Afzalian, A., Akhavan, N. D., Yan, R., Ferain, I., ... & Murphy, R. (2010). Nanowire transistors without junctions. *Nature nanotechnology*, *5*(3), 225-229.

[8] Basak, S., Asthana, P. K., Goswami, Y., & Ghosh, B. (2015). Leakage current reduction in junctionless tunnel FET using a lightly doped source. *Applied Physics A*, *118*(4), 1527-1533.

[9] Bal, P., Akram, M. W., Mondal, P., & Ghosh, B. (2013). Performance estimation of sub-30 nm junctionless tunnel FET (JLTFET). *Journal of Computational Electronics*, *12*(4), 782-789.

[10] Damrongplasit, N., Kim, S. H., & Liu, T. J. K. (2013). Study of random dopant fluctuation induced variability in the raised-Ge-source TFET. *IEEE electron device letters*, *34*(2), 184-186.

[11] Aghandeh, H., & Ziabari, S. A. S. (2017). Gate engineered heterostructure junctionless TFET with Gaussian doping profile for ambipolar suppression and electrical performance improvement. *Superlattices and Microstructures*, *111*, 103-114.

[12] Vadizadeh, M. (2019). Performance estimation of junctionless field effect diode. *Applied Physics A*, *125*(8), 1-9.

[13] Vadizadeh, M. (2021). Digital Performance Assessment of the Dual-Material Gate GaAs/InAs/Ge Junctionless TFET. *IEEE Transactions on Electron Devices*, *68*(4), 1986-1991.

[14] Asthana, P. K., Ghosh, B., Goswami, Y., & Tripathi, B. M. M. (2014). High-speed and low-power ultradeep-submicrometer III-V heterojunctionless tunnel field-effect transistor. *IEEE Transactions on Electron Devices*, *61*(2), 479-486.

[15] Sharma, S., & Chaujar, R. (2021). Band gap and gate metal engineering of novel hetero-material InAs/GaAs-based JLTFET for improved wireless applications. *Journal of Materials Science: Materials in Electronics*, *32*(3), 3155-3166.

[16] Rajabi, B., & Vadizadeh, M. (2021). Investigation of the impact of mole-fraction on the digital benchmarking parameters as well as sensitivity in Ga X In 1− X As/Ga Y In 1− Y Sb vertical

Accepted Manuscript

heterojunctionless tunneling field effect transistor. *International Journal of Modern Physics B*, 2150161.

[17] Sharma, S., & Chaujar, R. (2021). Performance enhancement in a novel amalgamation of arsenide/antimonide tunneling interface with charge plasma junctionless-TFET. *AEU-International Journal of Electronics and Communications*, *133*, 153669.

[18] Boksteen, B. K. (2010). *A simulation study and analysis of advanced silicon Schottky barrier field effect transistors* (Master's thesis, University of Twente).

[19] Matsuzawa, K., Uchida, K., & Nishiyama, A. (2000). A unified simulation of Schottky and ohmic contacts. *IEEE Transactions on Electron Devices*, *47*(1), 103-108.

[20] Drummond, T. J. (1999). *Work functions of the transition metals and metal silicides* (No. SAND99-0391J). Sandia National Labs., Albuquerque, NM (US); Sandia National Labs., Livermore, CA (US).

[21] ATLAS User's Guide, SILVACO Int., Santa Clara, CA, USA, Version 5.26.1.R, 2018.

[22] Hänsch, W., Vogelsang, T., Kircher, R., & Orlowski, M. (1989). Carrier transport near the Si/SiO2 interface of a MOSFET. *Solid-State Electronics*, *32*(10), 839-849.

[23] Zhao, Y., Wu, C., Huang, Q., Chen, C., Zhu, J., Guo, L., ... & Huang, R. (2017). A Novel Tunnel FET Design Through Adaptive Bandgap Engineering with Constant Sub-Threshold Slope Over 5 Decades of Current and High I_{ON}/I_{OFF} Ratio. *IEEE Electron Device Letters*, *38*(5), 540-543.

[24] Pala, M. G., Esseni, D., & Conzatti, F. (2012, December). Impact of interface traps on the IV curves of InAs tunnel-FETs and MOSFETs: A full quantum study. In *2012 International Electron Devices Meeting* (pp. 6-6). IEEE.

[25] Qiu, Y., Wang, R., Huang, Q., & Huang, R. (2014). A comparative study on the impacts of interface traps on tunneling FET and MOSFET. *IEEE Transactions on Electron Devices*, *61*(5), 1284-1291.

[26] Zhou, G., Lu, Y., Li, R., Zhang, Q., Hwang, W., Liu, Q., ... & Xing, H. (2011, June). Self-aligned InAs/Al 0.45 Ga 0.55 Sb vertical tunnel FETs. In *69th Device Research Conference* (pp. 205-206). IEEE.

[27] Na, K. Y., & Kim, Y. S. (2006). Silicon complementary metal–oxide–semiconductor field-effect transistors with dual work function gate. *Japanese journal of applied physics*, *45*(12R), 9033.

Accepted Manuscript

[28] C.H. Wang, H. Chu, Y.S. Lai, et al., Dual work-function metal gates. US Patent, No. 73 81619B2, Jun. 3, 2008.

[29] Johnson, R. W., Hultqvist, A., & Bent, S. F. (2014). A brief review of atomic layer deposition: from fundamentals to applications. *Materials today*, *17*(5), 236-246.

[30] Brouzet, V., Salem, B., Periwal, P., Rosaz, G., Baron, T., Bassani, F., ... & Ghibaudo, G. (2015). Fabrication and characterization of silicon nanowire pin MOS gated diode for use as p-type tunnel FET. *Applied Physics A*, *121*(3), 1285-1290.

[31] Hueting, R. J., Rajasekharan, B., Salm, C., & Schmitz, J. (2008). The charge plasma PN diode. *IEEE electron device letters*, *29*(12), 1367-1369.

Accepted Manuscript

Hindawi
International Journal of Photoenergy
Volume 2022, Article ID 9607545, 6 pages
https://doi.org/10.1155/2022/9607545

Research Article

Intelligent Energy Management System for a Smart Home Integrated with Renewable Energy Resources

Arjun Baliyan,[1] **Isaka J. Mwakitalima**,[2] **Majid Jamil**,[1] **and M. Rizwan**[3]

[1]*Department of Electrical Engineering, Jamia Millia Islamia, New Delhi 110025, India*
[2]*Department of Electrical and Power Engineering, Mbeya University of Science and Technology, P.O. Box 131, Mbeya, Tanzania*
[3]*Department of Electrical Engineering, Delhi Technological University, Delhi 110042, India*

Correspondence should be addressed to Arjun Baliyan; arjunresearch16@gmail.com

Received 24 October 2021; Revised 21 December 2021; Accepted 19 January 2022; Published 8 February 2022

Academic Editor: Yaxuan Xiong

Copyright © 2022 Arjun Baliyan et al. This is an open access article distributed under the Creative Commons Attribution License, which permits unrestricted use, distribution, and reproduction in any medium, provided the original work is properly cited.

In this paper, an intelligent energy management system for the smart home that combines the solar energy as well as the energy from the battery storage devices has been proposed to reduce the dependency on the power grid and make the system to be more economical. The proposed system manages the energy requirement of the smart home by properly rescheduling and arranging the power flow between the energy storage devices, grid power, and the photovoltaics. The power grid can absorb the excess power from the designed system whenever the load requirement is low, and on the other hand, it can supply the power to the load in case of peak demand. Therefore, in the designed system, a user has the flexibility to sell the extra power for the purpose of revenue. A thorough simulation of the system has been carried out, and the results obtained show the effectiveness of the approach in terms of energy management between the different sources.

1. Introduction

Renewable energy resources (RER) are getting popularity nowadays since they are environmentally friendly and available in abundance. Also, due to the rapid decline in the conventional energy resources, the renewable sources are the best alternative to replace them. A home energy management (HEM) system is basically a system that has been designed with the help of renewable energy resources with an aim to reduce the overall energy consumption. This type of configuration is usually done in order to reduce the electricity bill and manage the peak load demand. Apart from it, the research on converting the power grid into smart grid by combining the already existing grid with the renewable energy resources will further reduce the dependency on the conventional energy resources [1]. In the recent years, research topics focus on home energy management integrated with storage devices and the photovoltaics [2–9]. In [2–5], the authors have considered energy cost minimization as an optimization problem based on the unpredictable behaviour of the output from the renewable energy resources. In [6–8], demand response (DR) programs have been explained for the priority wise rescheduling of the load based on the prediction of renewable energy (RE) output. In [9], the dependence on the battery and its characteristics have been explained and how they can be useful in-home energy management. In [10, 11], the photovoltaic integrated with the home energy management is discussed in detail. Although a lot of discussion on the integration of energy storage units and photovoltaics with the HEM have been explained in the literature [12–14], but still there are certain issues that need to be resolved. For example, how the battery can play an important role in case the power from the solar panel is not sufficient to fed the load and how much benefit the renewable sources of energy can provide in case of peak load demand. This paper resolves one of the such issues by proposing an integration of storage devices and photovoltaics with the HEM that provides surplus power to the grid

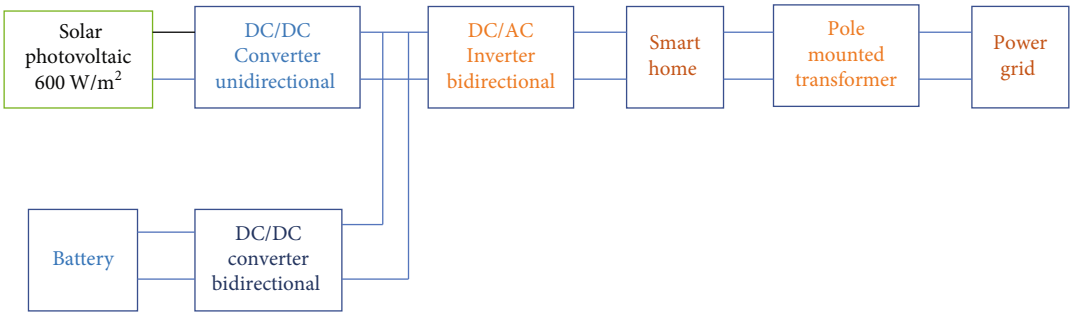


Figure 1: Block diagram of the system.

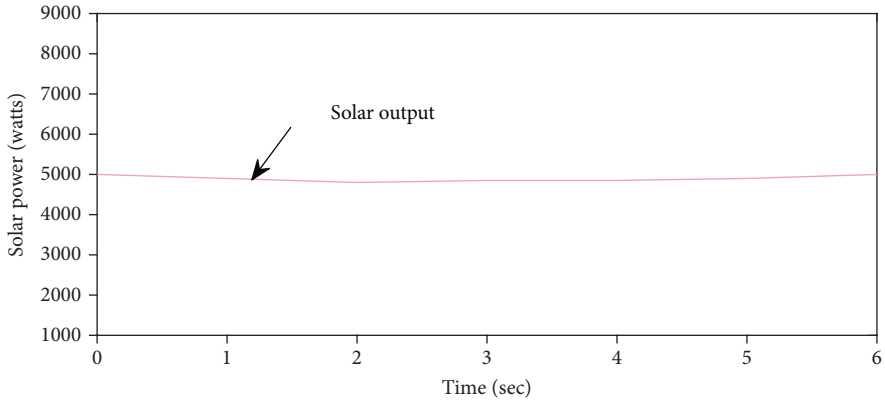


Figure 2: Solar panel output.

Table 1: Battery specifications.

S. no.	Battery parameters	Values
(1)	Nominal voltage	24 V
(2)	Ampere-hour	40 Ah
(3)	State of charge (SOC)	80%
(4)	Fully charged voltage	232.7 V

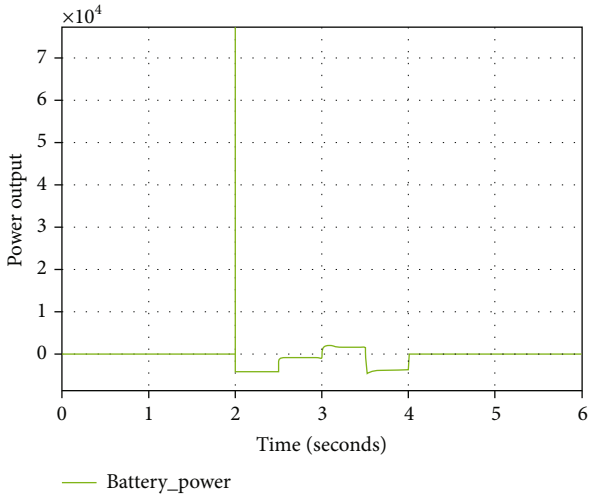


Figure 3: Battery characteristics.

as well as absorb power in case of deficiency. Hence, a perfect balance is maintained to make the system more reliable and economical.

The paper is arranged as per the following sections: Section 2 describes the proposed system, Section 3 explains the obtained simulation results, and Section 4 finally concludes the paper.

2. Simulation Components of Proposed System

This method explains how the existing HEM model can be integrated with the renewable energy resources and the battery storage devices. The block diagram of the above proposed system is given in Figure 1.

Photovoltaics and battery storage devices are working as a complementary power source for a smart home. The rating of photovoltaic system is 5 kW and is described by the current voltage look up table. In order to track the maximum power point, MPPT control algorithm has been used which extracts maximum power under variable system conditions.

2.1. Photovoltaic (PV) System. In this system, PV and the storage device models are developed in order to make the HEM system to operate in integration with the renewable energy resources. To track the maximum power from the solar panel, MPPT technique [15] has been applied which manages the operating point of the array in such a way that

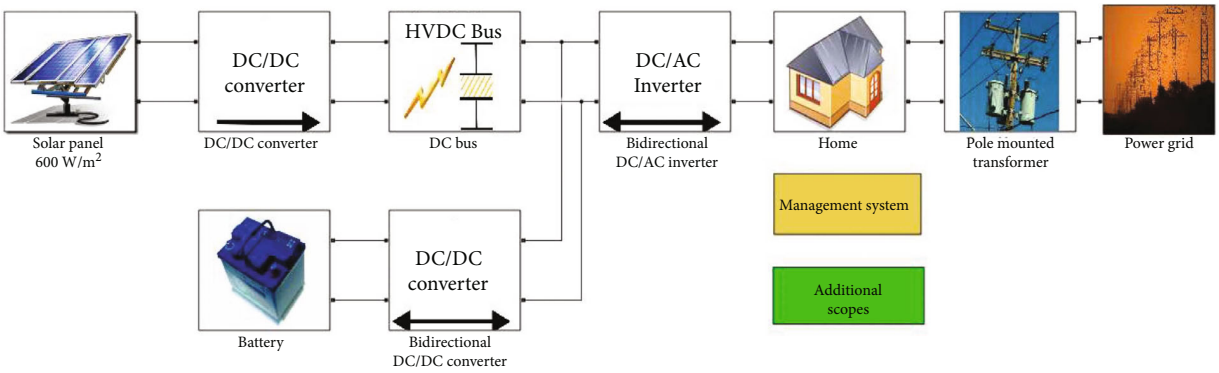


Figure 4: Simulation of the proposed system.

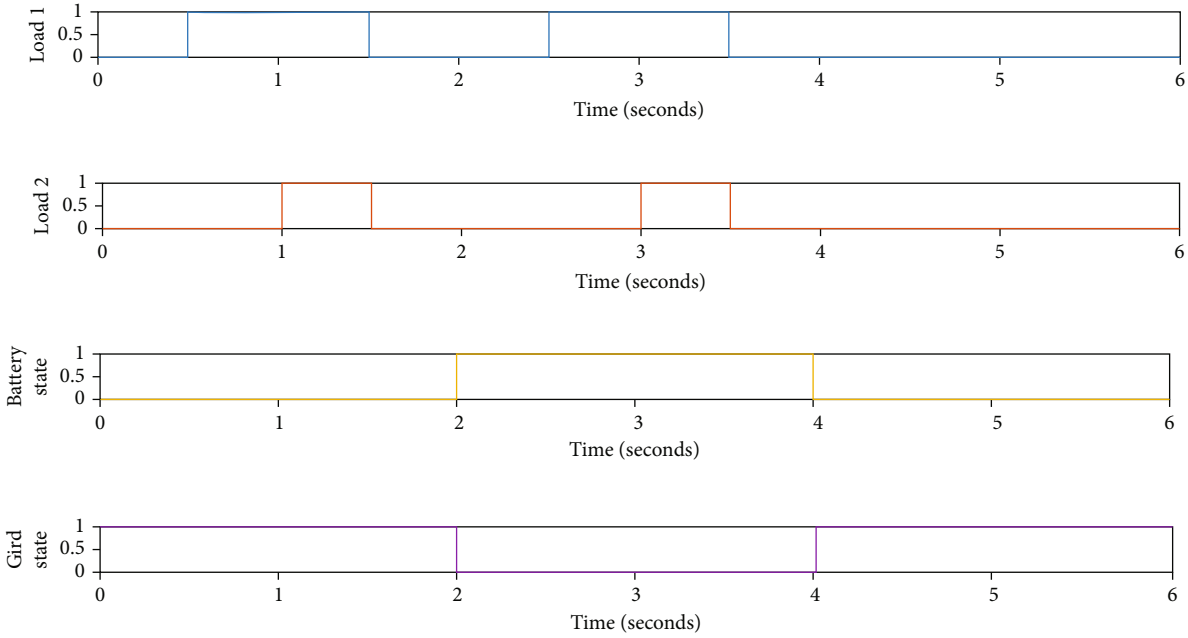


Figure 5: Switching characteristics of loads, battery, and power grid.

it always obtains the maximum power in the different varying conditions.

For photovoltaic system, the energy output or the energy delivered is given by the following

$$E_B = Q\rho_A C_{gt} t\left(1-\delta_p\right)\left(1-\delta_c\right), \quad (1)$$

where Q is the array area in m^2, ρ_A is the average efficiency of an array (%), C_{gt} is the global radiation, T is the time period in secs, δ_p is the PV panel losses (%), and δ_c is the power conditioning losses (%).

And the power absorbed by the grid can be defined as follows:

$$E_{\text{grid}} = E_B * \beta_{\text{inv}} * \beta_{\text{abs}}, \quad (2)$$

where E_B is the energy by PV panel, β_{inv} is the inverter efficiency (%), and β_{abs} is the PV panel energy absorption (%).

Figure 2 shows the output from solar panel which is around 5 kW.

2.2. Battery Characteristics. A 200 V and 40 Ah lithium-ion battery is used as a storage device to provide the power in case of peak load demand. The battery specifications are mentioned in Table 1. The battery is charged and discharged with the help of bidirectional converter that takes power from the solar panel while charging and fed the load when solar panel alone is not enough to feed the total load demand. The battery model that has been used in the paper is explained in [16]. In the proposed system, total loads of 3 kW each are taken, and it was observed that in case when both the loads are ON, the solar panel was not sufficient to provide power, since the total capacity of solar photovoltaic is 5 kW.

The battery output power (W) is shown in Figure 3. It is clear from the figure that from time $t = 0$ to $t = 2$ secs and $t = 4$ sec to $t = 6$ secs the battery is not functioning so the extra power has to be taken from grid for that time instant.

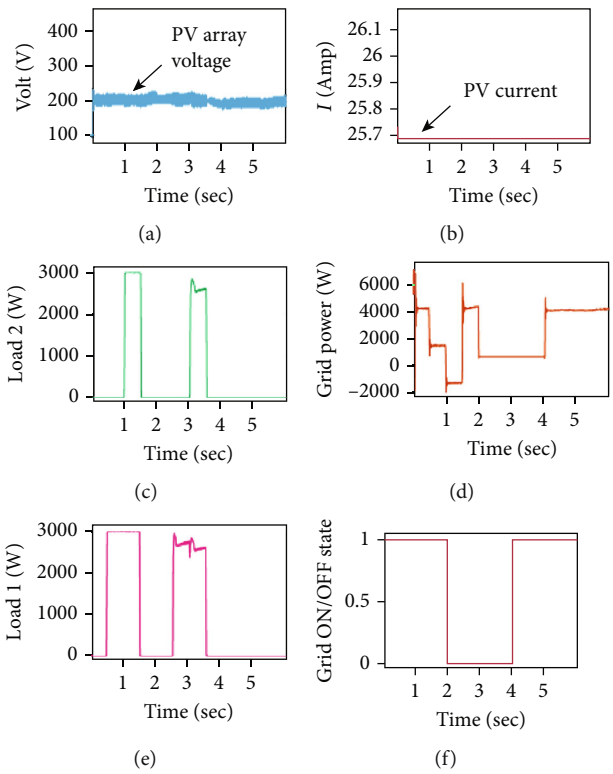


Figure 6: Load, grid, and solar photovoltaic characteristics.

3. Simulation Results

Initially, the battery was not connected to the system, and the loads were also disconnected, so therefore, the total solar power was transferred to the grid. The power generated by the panel was almost constant at 5 kW, and it was obtained by MPPT control algorithm.

Case 1. One of the two loads of 3 kW was turned on, and it was observed that it was consuming more than half of the power produced by the solar panel, and therefore, the excess power is again transferred to the grid.

Case 2. Both the loads are turned on, and the total power demand reaches to 6 kW, so therefore, the solar panel was not sufficient, and hence, the power demand was met by the grid.

Case 3. Now the loads are again disconnected, and the battery is connected which ensures that the total power as the combination of solar energy and storage devices is sufficient to meet the load demand when both the loads are again connected to the system in the same fashion as they were connected.

Figure 4 shows the simulation of the proposed system with renewable sources integrated with the power grid.

From Figure 5, it is clear that initially out of the two loads only one was switched at instant $t = 0.5$ sec and at $t = 1$ secs; both the loads were on, and therefore, the grid has to supply the extra power to meet the load demand. It is also clearly visible that between the time instant $t = 2$ secs to $t = 4$ secs, the battery was delivering the power, and hence, the power delivered by the grid was zero. Figure 6 depicts the photovoltaic, grid power, and the load characteristics.

It can be seen from the figure that at time instant $t = 1$ sec, the total load demand hits 6 kW as clear from Figures 6(c) and 6(e) since the total load adds up at that time instant, but before that, only load 1 was active, and therefore, the grid that was absorbing the surplus power before $t = 1$ sec has to now deliver the power that can be clearly visible from Figure 6(f). But again, at $t = 2$ sec, both the loads are in OFF state, and the battery is now in the on state, so therefore, the power will now be delivered to the grid, and the grid remains in off state. Also, Figure 6(d) shows the continuous power variation that indicates the power absorbed as well as power delivered by the grid for the entire time duration which depends on the changing load conditions. Similarly, Figures 6(a) and 6(b) give the insight of the photovoltaic (PV) voltage and current that is continuously varying according to the solar insolation. Figure 7 depicts the grid power components, solar power that remains almost constant throughout the time period, and load demand.

In the above figure, power delivered from the different renewable energy sources as well as the power absorbed by the load configuration is shown to have a better clarity of the proposed system and how it is able to manage the changing load demand with proper switching between the RER and grid power. In continuation of the above power flow diagram, Figure 7(a) shows the power taken by the grid as well as power supplied in case of changing load conditions

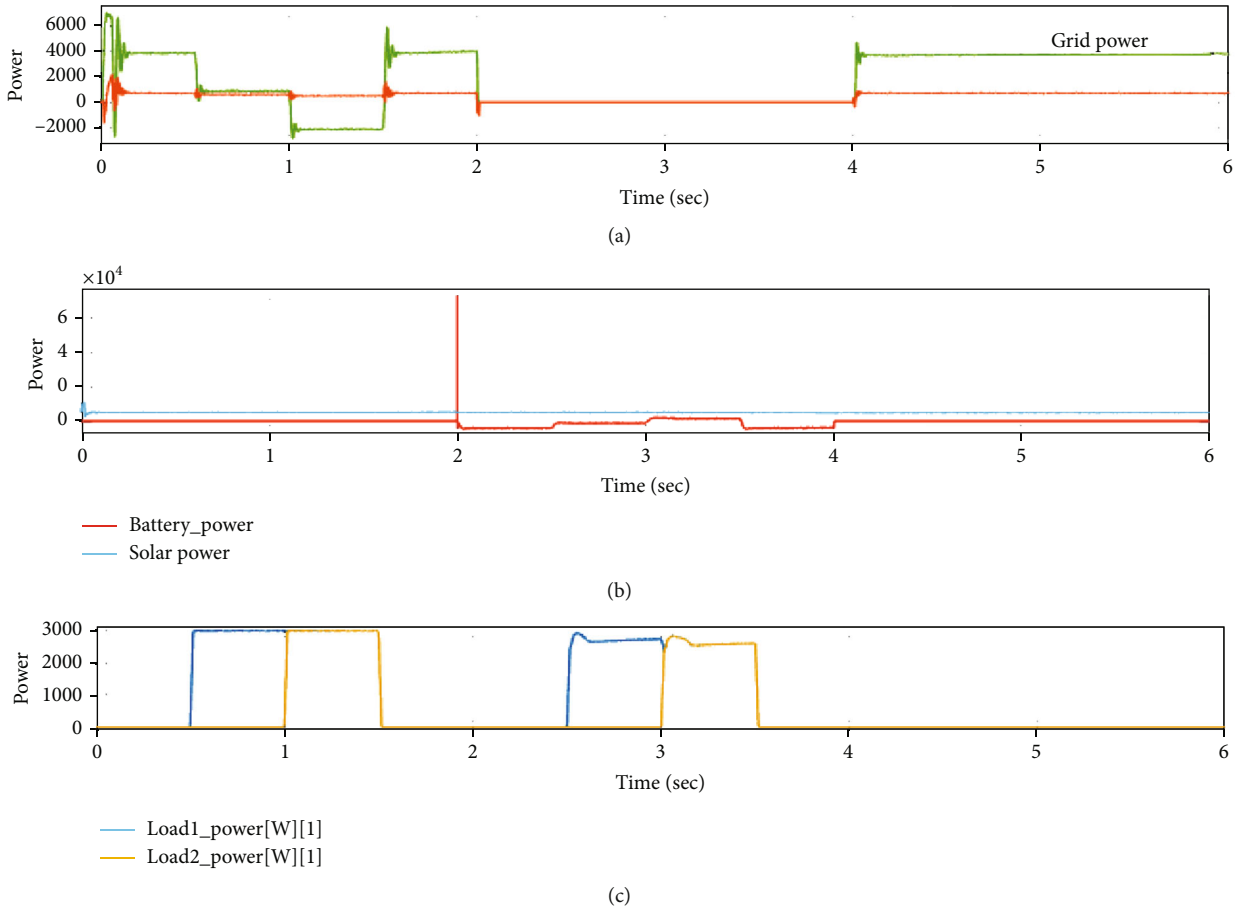


Figure 7: Power flow diagram.

Table 2: System parameters.

S. no	Parameters	Values
(1)	Solar panel	5 kW
(2)	System loads (load 1 and load 2)	6 kW
(3)	Power grid (phase to phase voltage)	66 kV
(4)	Switching frequency	10 kHz
(5)	Reference voltage (V_{dc})	370 V
(6)	Inverter controller gain parameters Tuned with PSO technique	$K_{P1} = 0.01, K_{I1} = 25$ $K_{P2} = 2.5, K_{I2} = 2.5$

and the power availability conditions. Figure 7(b) shows the variation in battery power and the solar power needed to feed the load in case of excess load demand. Similarly, Figure 7(c) illustrates the switching load pattern which clearly shows the maximum and minimum load demand in the entire time duration. The different system parameters and their values are given in Table 2.

4. Conclusion

This paper presents an idea of load management in case of base and peak load demand by integrating the supply with the renewable energy resources. It consists of various energy producing sources that is solar and battery storage devices as well as different energy consuming devices, called loads. Here, the switching between the different energy sources is done for energy management, and the results are shown in MATLAB. It is clear from the above results that the dependency on the grid is minimized, and even the consumer can now provide surplus power to the grid which will ultimately increase the overall revenue. The simulation shows how the HEM integrated with renewable sources is useful for residential load management, and further studies could be done in order to allow HEM to manage the different residential loads with respect to time-of-use pricing.

Data Availability

There is no data taken from any source.

Conflicts of Interest

The authors have no conflicts of interest regarding this article.

References

[1] M. Lissere, T. Sauter, and J. Y. Hung, "Future energy systems: integrating renewable energy sources into the smart power

grid through industrial electronics," *IEEE Industrial Electronics Magazine*, vol. 4, no. 1, pp. 18–37, 2010.

[2] C. Cecati, C. Citro, and P. Siano, "Combined operations of renewable energy systems and responsive demand in a smart grid," *IEEE Transactions on Sustainable Energy*, vol. 2, no. 4, p. 468476, 2011.

[3] Y. Guo, M. Pan, and Y. Fang, "Optimal power management of residential customers in the smart grid," *IEEE Transactions on Parallel and Distributed Systems*, vol. 23, no. 9, pp. 1593–1606, 2012.

[4] H. Wu, M. Shahidehpour, and A. Al-Abdulwahab, "Hourly demand response in day-ahead scheduling for managing the variability of renewable energy," *IET Generation Transmission and Distribution*, vol. 7, no. 3, pp. 226–234, 2013.

[5] Y. Guo, M. Pan, Y. Fang, and P. P. Khargonekar, "Decentralized coordination of energy utilization for residential households in the smart grid," *IEEE Transactions on Smart Grid*, vol. 4, no. 3, pp. 1341–1350, 2013.

[6] A. Papavasiliou and S. S. Oren, "Large-scale integration of deferrable demand and renewable energy sources," *IEEE Transactions on Power Systems*, vol. 29, no. 1, pp. 489–499, 2014.

[7] X. Liu, L. Ivanescu, R. Kang, and M. Maier, "Real-time household load priority scheduling algorithm based on prediction of renewable source availability," *IEEE Transactions on Consumer Electronics*, vol. 58, no. 2, pp. 318–326, 2012.

[8] S. Chen, N. B. Shroff, and P. Sinha, "Heterogeneous delay tolerant task scheduling and energy management in the smart grid with renewable energy," *IEEE Journal on Selected Areas in Communications*, vol. 31, no. 7, pp. 1258–1267, 2013.

[9] J. Byun, I. Hong, and S. Park, "Intelligent cloud home energy management system using household appliance priority-based scheduling based on prediction of renewable energy capability," *IEEE Transactions on Consumer Electronics*, vol. 58, no. 4, p. 11941201, 2012.

[10] P. T. V. B. N. Kumar, S. Suryateja, G. Naveen, M. Singh, and P. Kumar, "Smart home energy management with integration of PV and storage facilities providing grid support," in *2013 IEEE Power & Energy Society General Meeting*, pp. 1–5, Vancouver, BC, Canada, July 2013.

[11] C.-S. Choi, J. I. Lee, and I.-W. Lee, "Complex home energy management system architecture and implementation for green home with Built-in Photovoltaic and motorized blinders," in *2012 International Conference on ICT Convergence (ICTC)*, pp. 295-296, Jeju, Korea (South), Oct 2012.

[12] M. Pipattanasomporn, M. Kuzlu, and S. Rahman, "An algorithm for intelligent home energy management and demand response analysis," *IEEE Transactions on Smart Grid*, vol. 3, no. 4, p. 21662173, 2012.

[13] M. Kuzlu, M. Pipattanasomporn, and S. Rahman, "Hardware demonstration of a home energy management system for demand response applications," *IEEE Transactions on Smart Grid*, vol. 3, no. 4, pp. 1704–1711, 2012.

[14] A. Q. H. Badar and A. Anvari-Moghaddam, "Smart home energy management system – a review," *Advances in Building Energy Research*, vol. 16, no. 1, pp. 1–26, 2020.

[15] L. Xu, R. Cheng, and J. Yang, "A new MPPT technique for fast and efficient tracking under fast varying solar irradiation and load resistance," *International Journal of Photoenergy*, vol. 2020, Article ID 6535372, 18 pages, 2020.

[16] O. Tremblay and L.-A. Dessaint, "Experimental validation of a battery dynamic model for EV applications," *World Electric Vehicle Journal*, vol. 3, 2009.

ACADEMIA
Accelerating the world's research.

Intra-Block Correlation Based Reversible Data Hiding in Encrypted Images Using Parametric Binary Tree Labeling

hari om

Symmetry

Cite this paper

Downloaded from Academia.edu

Get the citation in MLA, APA, or Chicago styles

Related papers

Download a PDF Pack of the best related papers



Reversible Data Hiding in Encrypted color images by Reserving Room before Encryption with L...
Independent IJCEROnline

One-pass lossless data hiding and compression of remote sensing data
alireza liaghat

ALGORITHM FOR ENHANCED IMAGE SECURITY WITH REVERSIBLE DATA HIDING
Saranya M R, Arun K Mohan

symmetry

MDPI

Article

Intra-Block Correlation Based Reversible Data Hiding in Encrypted Images Using Parametric Binary Tree Labeling

Arun Kumar Rai [1], Neeraj Kumar [2], Rajeev Kumar [3], Hari Om [1], Satish Chand [4] and Ki-Hyun Jung [5,*]

[1] Department of Computer Science and Engineering, Indian Institute of Technology (Indian School of Mines), Dhanbad 826004, India; arun.18DP000380@cse.iitism.ac.in (A.K.R.); hari@iitism.ac.in (H.O.)
[2] Department of Electronics and Communication Engineering, Nagarjuna College of Engineering and Technology, Bengaluru 562164, India; neeraj.mohiwal@gmail.com
[3] Department of Computer Science and Engineering, Delhi Technological University, Delhi 110042, India; rajeevkumar@dtu.ac.in
[4] School of Computer and System Sciences, Jawaharlal Nehru University, Delhi 110067, India; schand@mail.jnu.ac.in
[5] Department of Cyber Security, Kyungil University, Kyeongbuk 38424, Korea
* Correspondence: kingjung@kiu.kr or khanny.jung@gmail.com; Tel.: +82-53-600-5626

Abstract: In this paper, a high capacity reversible data hiding technique using a parametric binary tree labeling scheme is proposed. The proposed parametric binary tree labeling scheme is used to label a plaintext image's pixels as two different categories, regular pixels and irregular pixels, through a symmetric or asymmetric process. Regular pixels are only utilized for secret payload embedding whereas irregular pixels are not utilized. The proposed technique efficiently exploits intra-block correlation, based on the prediction mean of the block by symmetry or asymmetry. Further, the proposed method utilizes blocks that are selected for their pixel correlation rather than exploiting all the blocks for secret payload embedding. In addition, the proposed scheme enhances the encryption performance by employing standard encryption techniques, unlike other block based reversible data hiding in encrypted images. Experimental results show that the proposed technique maximizes the embedding rate in comparison to state-of-the-art reversible data hiding in encrypted images, while preserving privacy of the original contents.

Keywords: image encryption; reversible data hiding; parametric binary tree labeling; privacy; intra-block correlation

check for updates

Citation: Rai, A.K.; Kumar, N.; Kumar, R.; Om, H.; Chand, S.; Jung, K.-H. Intra-Block Correlation Based Reversible Data Hiding in Encrypted Images Using Parametric Binary Tree Labeling. *Symmetry* **2021**, *13*, 1072. https://doi.org/10.3390/sym13061072

Academic Editors: Kuo-Hui Yeh and Peng-Yeng Yin

Received: 20 April 2021
Accepted: 7 June 2021
Published: 16 June 2021

Publisher's Note: MDPI stays neutral with regard to jurisdictional claims in published maps and institutional affiliations.

Copyright: © 2021 by the authors. Licensee MDPI, Basel, Switzerland. This article is an open access article distributed under the terms and conditions of the Creative Commons Attribution (CC BY) license (https://creativecommons.org/licenses/by/4.0/).

1. Introduction

Cloud computing is a great technology for remote sharing and accessing of information across the world. It renders a simplistic model for real-time information sharing, accessing, and/or storing on the cloud server [1] on a pay-per-use basis. Due to its simplicity, today, cloud computing services have millions of subscribers who store their public/private data on cloud servers. The cloud servers possess several data storage devices for storing subscribers' data which can be any multimedia data (such as image, video, audio), text data, program data, etc., in any format. To protect against information leakage and maintain confidentiality, subscriber data is first encrypted and then stored on the cloud servers [2]. To manage the cloud services and data storages, and also to control loading–unloading of data between storages for load balancing, the cloud servers makes use of a cloud administrator which attaches some auxiliary information, such as subscriber name, file name, file type, source information, etc., to subscriber's data for its efficient handling without decoding the subscriber data. The auxiliary information is attached secretly by embedding the same in the encrypted subscriber data so that unauthorized access can be prevented without incurring additional storage cost. Since the auxiliary information is cloud management information, it is embedded in a lossless and reversible manner in the subscriber data. For this, there exist several reversible data hiding (RDH) techniques

which have been developed in the past for lossless embedding and recovery of both secret data and subscriber data. Some of the popular RDH techniques are lossless compression based [3–6], difference expansion-based [7], histogram expansion, and prediction error expansion based [8–12] RDH techniques. However, these techniques are only suitable for plaintext data, but not for encrypted data.

In 2008, Puech et al. [13] unveiled an RDH technique for encrypted images (RDHEI). They first encrypted the original image using Advanced Encryption Standard (AES) and then embedded the secret data bits at random locations in each 4×4 by simple substitution. At the receiver end, local standard deviation analysis is performed to reinstate the original image and get back the hidden secret data. After Puech et al.'s technique [9], the RDHEI field has been explored by various researchers [14–36].

Based on the analysis of available RDHEI literature, the RDHEI techniques can be classified into three major categories, namely, vacating room after encryption (VRAE) [12,15,21,22], vacating room by encryption (VRBE) [32,34,35], and reserving room before encryption (RRBE) [23,29–31,33]. The VRAE techniques create vacancies for secret data hiding in encrypted data whereas techniques that fall into the VRBE category create vacancies for secret data hiding during encryption. As far as the RRBE category is concerned, first, a room is reserved in the unencrypted media which is then exploited for embedding the secret data after the media's encryption. Among these three approaches, the VRAE approach offers very limited embedding capacity (EC) because encrypted data provides limited room for secret data hiding as encryption destroys the correlations of subscriber data. Therefore, the cloud administrator is unable to produce many vacancies for secret data embedding in encrypted data. In the VRBE approach, specific encryption tactics are applied to subscriber data, which maintain some correlations in encrypted data. Later, the correlations present in the encrypted data are exploited by the cloud administrator for embedding auxiliary information. Still, this approach does not yield a high EC as spatial redundancy existing in the subscriber data is not fully utilized. However, the RRBE approach is an altogether different approach, in which subscriber data in unencrypted form is exploited to reserve vacancies. This means that, later on, the subscriber data can be encrypted and auxiliary information can be embedded in the encrypted data, by exploiting the redundancy of non-encrypted data due to the reserved vacancies. Thus, the RRBE approach renders higher EC than the VRAE and VRBE approaches.

In RDHEI, the encryption of plain-text data is performed by the subscriber using an encryption key K_e, who then uploads the encrypted data on the cloud server. Next, the cloud administrator performs embedding of auxiliary information using a secret key K_s to transform the encrypted data into marked encrypted data. The marked encrypted data accommodates both subscriber data and auxiliary information in encrypted form, and is stored on the cloud server. At the decoder side, three cases may exist. In the first case, if a user owns both the encryption key K_e and the secret key K_s, he/she can retrieve both subscriber data and auxiliary information. In case only the encryption key K_e or the secret key K_s is possessed by the user then only subscriber data or the auxiliary information can be recovered, respectively. A schematic diagram of the RDHEI approach is shown in Figure 1.

In the literature, some RDHEI techniques have been introduced [14–18] which allow retrieval of auxiliary information only after decryption of marked encrypted data. In other words, auxiliary information can be extracted using a secret key K_s only after performing the decryption using the encryption key K_e. TheseRDHEI techniques are known as non-separable techniques. In [19–35], another variant of RDHEI techniques, i.e., separable RDHEI techniques, was introduced to overcome the limitation of non-separability. These techniques allow separate restoration of subscriber data and extraction of auxiliary information from the marked encrypted information. In other words, an encryption key K_e keeper can perform the decryption process separately without being restricted by the auxiliary information extracting process, and similarly a secret key K_s keeper can perform the auxiliary information extracting process without being restricted by the decryption process.

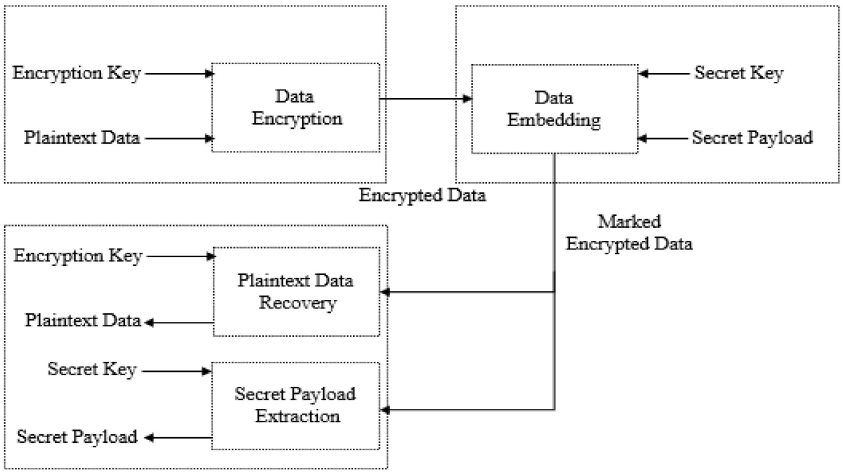


Figure 1. A schematic diagram of RDHEI technique.

In this paper, an intra-block correlation based high capacity RDHEI technique using PBTL is proposed. In the proposed technique, the original image is first partitioned into non-overlapping blocks of a predetermined size (e.g., 4×4) which are then categorized into smooth, moderately complex, and highly complex blocks. Now, prediction errors and residual errors are calculated for pixels of the smooth blocks and moderately complex blocks. Next, the proposed technique applies a stream encryption method (different from Yi et al.'s technique) to the original host image to improve the security of the encrypted subscriber data (or the encrypted host image). The pixels of the encrypted image are then labeled using the PBTL scheme and the calculated prediction and residual errors. Finally, the labelled pixels are exploited to reversibly embed the secret data. Contributions of the proposed RDHEI technique can be summarized as follows:

(1) The proposed work discloses a high capacity RDHEI technique using PBTL. The proposed RDHEI technique first partitions the original image into uniformly sized blocks and then categorizes the image blocks into three categories, i.e., smooth, moderately complex, and highly complex blocks based on the prevalent correlation of each block. This granular classification of the image blocks helps in reserving pixels for efficiently embedding the secret information.
(2) The smooth and moderately complex blocks generally possess high and decent pixel correlation, respectively. Thus, both types of blocks are used for embedding the secret information whereas the highly complex blocks are snubbed in the data embedding process as there is no or minimal correlation.
(3) Further, the proposed technique uses a stream encryption method for encrypting the original image. The stream cipher provides higher security in comparison to block cipher as it completely destroys the correlation of image pixels.
(4) In addition, the proposed technique is a separable RDHEI technique which allows separate recovery and extraction of subscriber data and the secret message in a lossless manner.
(5) Experimental results show that the proposed RDHEI technique has superior embedding performance in comparison to related previous RDHEI techniques while ensuring security of the image contents.

The rest of this paper is structured as follows. Section 2 discusses related separable RDHEI techniques. Section 3 introduces the review of parametric binary tree labeling (PBTL) scheme. The proposed RDHEI technique is discussed in Section 4. Section 5 shows the experimental results and their comparative analysis. Lastly, a conclusion as well as the scope of future works has been drawn for the proposed work.

2. Related Works

In this section, some of the popular RDHEI techniques are briefly reviewed. In 2012, Zhang discussed a separable RDHEI technique [19]. In the separable RDHEI technique [19], the subscriber data (which is an image) is first encrypted using a standard encryption method and then a room/space is reserved for embedding the secret/auxiliary information by compressing three least significant bits (LSBs) of the encrypted data. However, the generated space is sparse in nature which limits the embedding rate. Xiaotian et al. [17] discussed a separable RDHEI technique which outperforms the earlier technique [19]. Dragoi et al. [21] proposed a new separable RDHEI scheme by creating space after the encryption. The main feature of this scheme is the use of a two-stage data hiding process in which the reference pixel is predicted based on the median context value. As far as performance improvement is concerned, the proposed scheme marginally improves embedding capacity in comparison to erstwhile related schemes. In 2018, Dragoi et al. [22] again came up with a new separable RDHEI scheme with color images, where correlation between RGB color planes of a target pixels and its correlation with neighboring pixels are exploited to embed data in a color image. In 2013, Ma et al. unfolded the first RRBE approach based RDHEI technique [23]. The technique partitions the image to get smooth and complex regions. Next, one or more LSBs of complex regions are embedded into the smooth regions using any of the conventional RDH algorithms such as [5–7] to create room in the rough regions. Finally, the reserved room in the encrypted images are filled by auxiliary information. This reservation of space in the complex regions yields a high embedding rate which goes up to 0.5 bit-per-pixel (bpp). Similarly, Zhang et al. reserved room for secret data hiding using the prediction error (PE) based histogram shifting method [18]. In [24], Xu et al. disclosed the calculation of prediction error based on interpolation technique then applied histogram shifting and the difference expansion technique to exploit the prediction error for data hiding. However, only a small improvement in performance was achieved. In [25], Mathew et al. refine the work of Ma et al. [23] by introducing a new pixel intensity variation criterion for classifying image blocks into smooth blocks and rough blocks. However, the work only marginally improves the embedding rate. To further upgrade the embedding rate, Cao et al. [26] discuss a patch-level sparse representation method for RDHEI. The method performs encryption in phases so that the maximum correlation between the image pixels can be maintained in the encrypted image. Additionally, a room is created inside the encrypted image for embedding the secret data. Therefore, the technique archives higher embedding capacity than the erstwhile state-of the art RDHEI techniques. In 2018, Li et al. [27] disclosed a novel RDHEI technique which makes use of combined block permutation and stream cipher for image encryption. Next, prediction errors in nearby pixels are exploited for data hiding. Thus, Li et al.'s technique improves the embedding rate by 0.5 bpp in comparison to the existing related RDHEI techniques, which signifies high embedding capacity.

In literature, it has been observed that a number of techniques [28–31] have been introduced for MSB prediction and then exploiting the MSB for data hiding. In 2018, one such work is proposed by Puteaux et al. [29] in which a simple but powerful high capacity RDHEI technique was discussed. The technique utilizes the correlation with neighboring pixel to predict the reference pixel value and uses a location binary map for marking the prediction errors. Next, the image is encrypted using stream cipher, and embedding of the secret message is done in the MSBs of the encrypted pixels with the help of location binary map. The location binary map helps the receiver in extracting the secret message and in the complete recovery of the original image. However, the MSB prediction technique can only embed up to one bit of the secret message into an encrypted pixel. To overcome this limitation, Puyang et al. [30] discuss a new RDHEI technique which can replace up to two MSBs of an encrypted pixel to significantly improve the embedding capacity without affecting the reversibility. To further improve the EC, Chen et al. [31] makes use of run length encoding (RLE) to compress the binary sequence of MSB data so that a room can be reserved in the image. For optimal compression, the image is first divided into blocks and

then the binary sequence of MSB data is created. Thus, the technique further boosts the embedding rate in comparison to [29,30] without compromising the reversibility.

Yi et al. [32] propounded a headway technique in the separable RDHEI domain using parametric binary tree labeling (PBTL). The host image is first partitioned into blocks of a certain size (either 2×2 or 3×3 pixels) and then calculates prediction errors in neighboring pixels within the block. Next, the host image is encrypted using a block-based encryption method. Based on the prediction errors and PBTL scheme, pixels of the encrypted are labeled which are exploited for embedding the secret information later on. The PBTL-RDHEI is extended by Su et al. [33] by combining the PBTL and absolute moment block truncation coding (AMBTC) for efficiently exploiting the correlation of the host image. Yin et al. [26] used the AMBTC technique for data embedding, although not in the RDHEI domain. Further, it has been observed that the AMBTC technique is a popular lossy compression technique which has been widely used in data hiding [14,36–38]. As far as working method of [33] is concerned, Su et al.'s technique first scrambles and then compresses the host image into triplets in a block-wise manner, where each triplet includes two quantization level (high & low) and a bitmap. Next, the triplets are encrypted in such a way that the correlation between the two quantization levels is retained. The retained correlation is then exploited to create a room for embedding the secret information. Therefore, a compressed marked-encrypted image in the form of AMBTC codes is obtained by the receiver. Since the bits required to represent the AMBTC coded image are lesser, the embedding capacity is also lower than that of Yi et al. [32]. It can be easily stated that Su et al.'s case is one of the earliest methods to utilize AMBTC in the RDHEI domain. In the next section, the parametric binary tree labeling scheme is reviewed in the context of the proposed work.

3. Parametric Binary Tree Labeling Scheme

This Parametric binary tree labelling (PBTL) scheme is first postulated by Yi et al. in 2018 for labelling the pixels of the plaintext image so that the auxiliary information can be efficiently embedded. The plaintext image pixels are represented by 8-bit depth; hence, the seven layers are generated in the parametric binary tree as shown in Figure 2. In the PBTL, each layer has 2^n nodes and each node is represented by n binary bits where $n \in \{1, 2, \ldots, 7\}$ is the layer number. The details regarding the total number of nodes in each layer of the seven-layered PTBL is provided in Table 1.

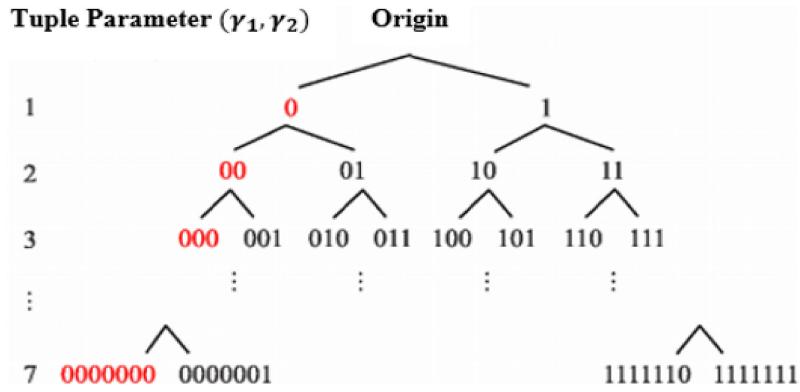


Figure 2. A 7-layered PBTL structure for 8-bit depth plaintext image.

Table 1. Number of nodes in a 7-layered PBTL.

Layer	1	2	3	4	5	6	7
Number of Nodes	2	4	8	16	32	64	128

The nodes at each layer are distributed into two different sets, namely S_1 and S_2, based on a tuple parameter (γ_1, γ_2). The first node of eachlayer is assigned into set S_1 and is labeled by n number of zero bits based on the value of γ_1, where n is the layer number. The number of nodes assigned to set S_2 are determined in accordance to the relation between the tuple parameter $\gamma_1 \wedge \gamma_2$ using Equation (1), defined as follows:

$$N_{\gamma_2} = \begin{cases} 2^{\gamma_2} - 1, \ \gamma_2 \leq \gamma_1 \\ (2^{\gamma_1} - 1) * (2^{\gamma_2 - \gamma_1}), \ \gamma_2 \leq \gamma_1 \end{cases} \quad (1)$$

where N_{γ_2} represents the total number of nodes in the set S_2 and the range of values of the tuple parameter is defined as $1 < \gamma_1, \gamma_2 < 7$. The specific details regarding the number of nodes in set S_2 for each layer of the PBTL based on the different values of $\gamma_1 \wedge \gamma_2$ are provided in Table 2. As per Table 2, if the value of tuple parameter $(\gamma_1, \gamma_2) is (2, 3)$, then number of nodes in set S_2 are 6 as per Equation (1), which are labeled as (111_2), (110_2), (101_2), (100_2), (011_2), and (010_2). Basically, the node labelling in the set S_2 is started from the right-most side to the left side of the PBTL (in accordance with Figure 2) until the N_{γ_2} is not labelled. Further, the first node in set S_1 will be labeled as (000_2).

Table 2. N_{γ_2}-based on $\gamma_1 \wedge \gamma_2$ for 7-layered PBTL.

γ_1	**Number of Nodes (N_{γ_2}) in S_2**						
	γ_2						
	1	**2**	**3**	**4**	**5**	**6**	**7**
1	1	2	4	8	16	32	64
2	1	3	6	12	24	48	96
3	1	3	7	14	28	56	112
4	1	3	7	15	30	60	120
5	1	3	7	15	31	62	122
6	1	3	7	15	31	63	126
7	1	3	7	15	31	63	127

4. The Proposed EPBTL-RDHEI Technique

The proposed High Capacity RDHEI technique is described in two phases, where the subscriber's data encryption and secret payload embedding is done in the first phase, and subscriber's data decryption and extraction of the secret payload is done in the second phase. Usually, subscribers upload their data which can be image, text, video, audio, etc., in encrypted form on the cloud server and a cloud administrator associates secret payload (which also includes auxiliary information) with the encrypted data. Although the proposed technique is equally applicable to all types of data, for simplicity, the plaintext images are considered as subscriber data. The proposed technique is a separable RDHEI technique which allows separate extraction of the hidden message and recovery of the original image at the receiving end. The RDHEI technique first uses an AMBTC based method for classifying the image regions and then uses a PBTL scheme for labelling the pixels. Figure 3 illustrates a framework of the proposed RDHEI technique.

The first phase of the proposed technique performed in five steps. In the first step, the subscriber's image is uniformly partitioned into non-overlapping blocks of a predetermined size and then each block is categorized into as smooth, moderately complex, and highly complex block based on the difference between high and low quantization levels which are calculated using the AMBTC method. In the second step, prediction errors and residual errors are generated based on the difference between pixel and corresponding block's mean. In the third step, the subscriber's image is encrypted using a stream encryption technique. In the fourth step, pixels of the encrypted image are categorized into regular pixels, irregular pixels, base pixels, and special pixels. Then, regular pixels and irregular

pixels are labeled according to the PBTL scheme and thereby labeled encrypted image is obtained. In the final (i.e., fifth) step, the secret payload embedding is done to get the marked encrypted image. The detailed working of each step is discussed in following subsections.

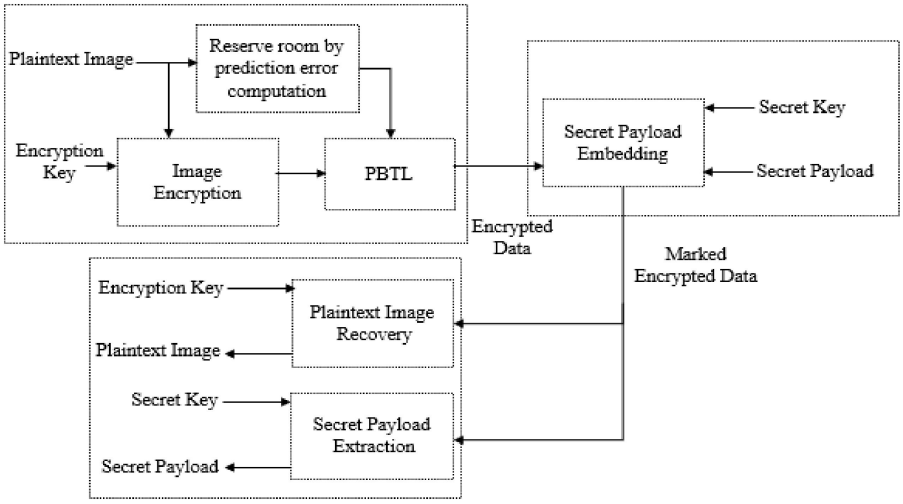


Figure 3. A framework of the proposed EPBTL-RDHEI technique.

4.1. Block Categorization (Step-1)

Initially, the subscriber-provided plaintext image $\mathbb{I}$ of size $N_1 \times N_2$ is partitioned into a number of non-overlapping blocks (P) of size $n_1 \times n_2$ pixels where $P = [N_1/n_1].[N_2/n_2]$. Therefore, each block (B_k) has $n_1 \times n_2$ pixels, such that, $\{x_1, x_2 \ldots . x_{n_1 \times n_2}\}$ if scanned in raster scan manner, where $k \in (1, 2 \ldots P)$. Now, mean (μ) of each block is computed using Equation (2):

$$\mu = \frac{1}{n_1 * n_2} \sum_{i=1}^{n1*n2} (x_i) \tag{2}$$

After computing mean (μ) of each block B_k, a bit-plane (b) of size $n_1 \times n_2$ is formed, where every pixel is represented by either bit '0' or '1' as follows.

$$b_i = \begin{cases} 0 \ if \ x_i < \mu, \\ 1 \qquad else. \end{cases} \tag{3}$$

As per the Equation (3), the pixel x_i of block B_k is represented by '0' if its value is less than mean (μ) of the block, otherwise represented by '1'. Thus, the bit-plane (b) for B_k has $n_1 \times n_2$ bits, meaning every pixel of the block is represented by 1 bit in the bit-plane. Next, two quantization levels, i.e., high quantization level q_0 and low quantization level q_1, are computed using Equations (4) and (5), respectively.

$$q_0 = \frac{1}{b_0} \sum_{x_i \geq \mu} x_i \tag{4}$$

$$q_1 = \frac{1}{b_1} \sum_{x_i < \mu} x_i \tag{5}$$

where b_0 and b_1 represent number of zeros and number of ones, respectively, in b. Thus, the high quantization level (q_0) is calculated by taking the mean of the pixels which have a value greater than the mean of the block. Similarly, the low quantization level (q_1) is computed by taking the mean of the pixels which have a value lower than the mean of the block. Thus, for each image block, a triplet $\{q_0, q_1, b\}$ is obtained.

Next, the image blocks are categorized into smooth, moderately complex, and highly complex block categories based on the difference between q_0 and q_1. More specifically, if the difference between q_0 and q_1 of block B is less than the first user-defined threshold T_s, then the block B is characterized as a smooth block type; if the difference between q_0 and q_1 is greater than or equal to the threshold T_s and less than a second user-defined threshold T_c, then the block B is characterized as moderately complex; and, otherwise, the block B is characterized as a highly complex block. In this step, the number of smooth blocks are counted as P_s, the number of moderately complex blocks are counted as P_m, and the number of high complex blocks are counted as P_h. A smooth block indicates that pixels in the block are high correlated and less distributed. A moderately complex block indicates that pixels in the block are less correlated and moderately distributed. A highly complex block indicates that pixels in the block are uncorrelated (or very little correlated) and highly distributed.

4.2. Computation of Prediction and Residual Errors (Step-2)

Once all the blocks of the plaintext image $\mathbb{I}$ are categorized, then prediction errors and residual errors are computed to reserve room for secret payload embedding as follows:

- If the block (B_k), where $k \in (1, 2 \ldots P)$ is a smooth block, then it indicates that pixels in the block B_k are high correlated and less distributed. Thus, each pixel in smooth block B_k can be best predicted by its mean value μ_k. Prediction error e_i is determined using the difference between the original pixel x_i and the mean value μ_k of the block (B_k) as per Equation (6). It is to be noted that the original pixel value (x_i) can be recovered by adding the μ_k to the corresponding prediction error (e_i) as per Equation (7), at the decoding side.

$$e_i = x_i - \mu_k \tag{6}$$

$$x_i = e_i + \mu_k \tag{7}$$

- If the block (B_k) is a moderately complex block, then it indicates that pixels in B_k are less correlated. In case of a moderately complex block, prediction errors (e_i) and residual errors (r_i) need to be calculated using Equations (8) and (9), respectively. It is to be noted that the original pixel value (x_i) can be recovered using Equation (10), at the decoder side.

$$e_i = \lfloor x_i/2 \rfloor - \lfloor \mu_k/2 \rfloor \tag{8}$$

$$r_i = mod(x_i/2) \tag{9}$$

$$x_i = e_i + r_i + 2 * \mu_k \tag{10}$$

- If the block (B_k) is a highly complex block, then it indicates that that pixels in B_k are uncorrelated (or very less correlated) and highly distributed. Thus, it requires a greater number of bits to represent the errors, and it is suggested that highly complex blocks are not used for secret payload embedding.

4.3. Image Encryption (Step-3)

After calculating the prediction errors and mean values for smooth blocks, and predication errors, residual errors, and mean values for moderately complex blocks, a stream encryption process is performed on the plaintext image $\mathbb{I}$. For this, a pseudo-random matrix $\mathbb{Z}$ of size $N_1 \times N_2$ is generated using an encryption key K_e. Each pixel $x_{i,j}$ of the image $\mathbb{I}$ is converted into an 8-bit binary sequence as $(b_8 b_7 b_6 b_5 b_4 b_3 b_2 b_1)$, where $b \in (0, 1)$ using Equation (11). Similarly, each element $z_{i,j}$ of pseudo-random matrix $\mathbb{R}$ is converted into 8-bit binary sequence using Equation (11).

$$x_{i,j}^k = \left\lfloor x_{i,j}/2^{k-1} \right\rfloor mod(2), k = (1, 2 \ldots 8) \tag{11}$$

Then, bitwise exclusive-or-operation is performed between plaintext image $\mathbb{I}$ and pseudo-random matrix $\mathbb{Z}$ using Equation (12) to encrypt the image.

$$xe_{i,j}^{k} = x_{i,j}^{k} \oplus z_{i,j}^{k} \tag{12}$$

Therefore, an encrypted 8-bit binary sequence for each pixel of the encrypted image is obtained. The binary sequence is converted into decimal form using Equation (13), to obtain an encrypted pixel which in turn helps in getting the encrypted image I^e.

$$xe_{i,j} = \sum_{k=1}^{8} xe_{i,j}^{k} \cdot 2^{k-1} \tag{13}$$

4.4. Pixel Grouping and Labelling Using PBTL (Step-4)

In this step, pixels of the encrypted image $\mathbb{I}^e$ are grouped and then labeled using PBTL structure based on tuple parameter (γ_1, γ_2) as described in Section 3. Firstly, the encrypted pixels of $\mathbb{I}^e$ are grouped into four sets which are special set (x^s), a base set (x^b), a regular set (x^r) and an irregular set (x^i). The special set (x^s) contains special pixels, the base set (x^b) contains base pixels, a regular set (x^r) contains regular pixels, and an irregular set (x^i) contains irregular pixels. Special set (x^s) includes the last pixel xe_{N_1,N_2} and the second last pixel $xe_{N_1-1,\ N_2-1}$ of the encrypted image $\mathbb{I}^e$. However, other locations can also be used in special set (x^s). One of the special pixels is used to indicate block size and other one indicates a tuple parameter (γ_1, γ_2). A base set (x^b) includes all the first encrypted pixel $xe_{1,1}$ of each block, where MSB bit-planes of the base pixels (the first encrypted pixel $xe_{1,1}$) are used to indicate block type that can be smooth, moderately complex, and highly complex. Table 3 illustrates that how the 7th & 8th MSB bit-planes of the encrypted pixel $xe_{1,1}$ is being used to identify block type.

Table 3. Block type identification based on 7th–8th bit-plane of $xe_{1,1}$ of each block B_k.

Bit-Plane of $xe_{1,1}$	**8th Bit-Plane**	**7th & 8th Bit-Planes**	**7th & 8th Bit-Planes**
Bit-Value	0	01	11
Block Type	Smooth block	Moderate complex block	High complex block

Pixels in the regular set (x^r) and irregular set (x^i) are determined in accordance to prediction errors $(e_{i,j})$ calculated using Equation (5) for smooth block and using Equation (7) for moderately complex block. If prediction errors $(e_{i,j})$ of block (B_k) of $\mathbb{I}$ meets the condition mentioned in Equation (13), then the pixel $(xe_{i,j})$ of the encrypted image $\mathbb{I}^e$ is grouped into the regular set (x^r), otherwise, it is grouped into the irregular set (x^i). In this step, the number of regular pixels and irregular pixels in smooth blocks are counted as x_s^r and x_s^i, respectively, and the number of regular pixels and irregular pixels in moderately complex blocks are counted as x_m^r and x_m^i, respectively.

$$\lceil -N_{\gamma_2}/2 \rceil \leq P_e \leq \lceil (N_{\gamma_2} - 1)/2 \rceil \tag{14}$$

After grouping the pixels into four sets, pixels of sets x^r and x^i are labeled using the PBTL scheme. Note that the pixels of highly complex blocks are not labeled as they do not participate in the data embedding process. In x^i, the γ_1-LSB bits of all the pixels are labeled as $(0...0_2)$ as per the PBTL scheme. In x^r, γ_2-LSB bits of all the pixels are labeled using different binary sequences represented by N_{γ_2} sub-categories as per the PBTL scheme. Thus processed, the labeled encrypted image I^l is obtained.

4.5. Secret Payload Embedding (Step-5)

After pixel grouping and pixel labelling process, secret payload embedding process is carried-out in the labeled encrypted image $\mathbb{I}^l$. This step outputs a marked encrypted image $\mathbb{I}^m$ by replacing the (8- γ_2) bits of pixels of x^r by secret payload. The secret payload (S_b) contains two type of data; one is encrypted auxiliary information (A_b) which is provided by cloud administrator and other is overhead (O_b) which is obtained during transforming encrypted image $\mathbb{I}^e$ into labeled encrypted image $\mathbb{I}^l$. To protect the auxiliary information (A_b) from unauthorized access, it is encrypted using a secret key k_s. The overhead (O_b) is required for lossless recovery of original image. The length of the overhead (O_b) is calculated as below:

(a) 16 bits to represent original pixel values of $xe_{N_1-1,\ N_2-1}$ and $xe_{N_1,\ N_2}$.
(b) Total bits (*equal to* $P_s + 2 * P_m + 2 * P_h$) of base set to store original bit values which are used in block types indication.
(c) Total bits (equal to $\gamma_2 * x_s^i + \gamma_2 * x_m^i$) of irregular set to store original replaced bit-planes.
(d) Total bits (equal to $8 * P_s$) to store mean value μ_k of each smooth block.
(e) Total bits (equal to $7 * P_m$) to store mean value $\mu_k/2$ of each complex block.

Now, auxiliary information (A_b) is obtained by reducing overhead (O_b) from the secret payload (S_b) using Equations (15)–(17), and effective embedding rate $ER_{\gamma_1,\ \gamma_2}$ is calculated using Equation (18).

$$A_b = S_b - O_b \tag{15}$$

$$S_b = (8 - \gamma_2) * x^{rs} + (7 - \gamma_2) * x^{rm} \tag{16}$$

$$O_b = (16 + \gamma_2 * x^i + 8 * P_s + 7 * P_m + P + P_m + P_h) \tag{17}$$

$$ER_{\gamma_1,\gamma_2} = \frac{A_b}{N_1 * N_2} = \frac{S_b - O_b}{N_1 * N_2} \tag{18}$$

The second phase of decryption of the original image and data recovery from the marked encrypted image has two steps. The first step is related to extraction of auxiliary information from the marked encrypted and second step is to restore original image from marked encrypted image. Both these steps are mutually exclusive.

4.6. Extraction of Auxiliary Information

At the receiver end, once the marked encrypted image $\mathbb{I}^m$ is received, the extraction process for auxiliary information is started. Initially, the pixels of x^s at locations xe_{N_1-1,N_2-1} and xe_{N_1,N_2} in $\mathbb{I}^m$ are utilized to determine tuple parameter $(\gamma_1,\ \gamma_2)$ and image block size. Then, $\mathbb{I}^m$ is divided into number of non-overlapping blocks as per the determined block size. After this, pixels of x^b in each image block are utilized to determine the type of the image block i.e. the smooth block, moderately complex block and highly complex block as per Table 3. Now, the tuple parameter $(\gamma_1,\ \gamma_2)$ is utilized to determine pixels x_s^r of regular set and pixels x_s^i of irregular set corresponding to smooth blocks, and pixels x_m^r of regular set and pixels x_m^i of irregular set corresponding to moderately complex blocks. Then, secret payload is extracted from (8- γ_2) bit-planes of regular pixels x_s^r of smooth blocks, and also from (8- γ_2) bit-planes of regular pixels x_m^r of moderately complex blocks. Further, residual errors are also extracted from regular pixels x_m^r of moderately complex blocks. Now, from the secret payload, encrypted auxiliary information is obtained by removing overhead as per Equations (15)–(17). Further, encrypted auxiliary information is decrypted by only authorized user which has secret key k_s.

4.7. Recovery of Plaintext Image

Now, recovery process for encrypted auxiliary information is discussed. The overhead information is utilized to recover plaintext image $\mathbb{I}$. Initially, 16 bits of overhead corresponding to $xe_{N_1-1,\ N_2-1}$ and $xe_{N_1,\ N_2}$. are restored on their predetermined position using x^s. Next, original bits (*equal to* $P_s + 2 * P_m + 2 * P_h$) are restored at locations of pixels of base set. Then, subsequent overhead bits equal to length $\gamma_2 * (x_s^i + x_m^i)$ are utilized to restore γ_2-bits of irregular pixels. After this, next overhead bits up to $8 * P_m$ are read to determine mean values of smooth blocks and subsequent overhead bits up to $7 * P_s$ are read to determine mean values of moderately complex blocks. Now, the authorized user which has encryption key K_e can generate the pseudo-random matrix $\mathbb{Z}$ and can obtain the decrypted image using Equations (12) and (13). Now, the user has only original pixel values of first two rows and two columns, which are utilized to recover other pixels of the image. The original pixel values of regular pixels of smooth blocks are obtained by their corresponding mean values stored as $8 * P_s$ overhead bits and prediction errors P_e calculated using Equation (7) from PBTL labeled pixels corresponding to $\gamma_2 - bits$. Similarly, to get original values of regular pixels of moderately complex blocks, mean values stored in next $7 * P_m$ overhead bits and residual errors P_r and prediction errors P_e calculated using Equation (10) from PBTL labeled pixels corresponding to $\gamma_2 - bits$. Now, remaining overhead bits are related to irregular pixels which are restored at their original location based on PBTL labeled pixels corresponding to $\gamma_1 - bits$. Thus, original image is retrieved in lossless manner.

Figure 4 shows an illustrative example of proposed RDHEI technique. The tuple parameter is taken as $(\gamma_1,\ \gamma_2) = (2, 3)$ and block size is taken as 4×4. Figure 4a shows a part of the baboon image of size 12×4. The input image is partitioned into non-overlapping blocks of size 4×4. Now, the blocks are categorized into smooth blocks, moderately complex blocks, and highly complex blocks using their corresponding quantization levels and mean values calculated by Equations (3)–(5), considering first threshold parameter $T_s = 16$ and second threshold parameter $T_c = 32$. The absolute difference between quantization levels $q_0 - q_1$ of the first block is 3, so it is a smooth block. The absolute difference between quantization levels $q_0 - q_1$ of the second block is 29, so it is a moderately complex block. The absolute difference between quantization levels $q_0 - q_1$ of the third block is 32, so it is a highly complex block. Highly complex blocks do not participate in secret payload embedding because pixels in the block are uncorrelated or correlated very little. Thus, only smooth blocks and moderately complex blocks are utilized for data embedding. The mean value of the first block is computed as 190 and the mean value of second block is computed as 103 using Equation (3). In Figure 4b,c, prediction errors are shown for each pixel of the block except for highly complex block. Based on the prediction errors, pixels of special set (x^s), base set (x^b), regular set (x^r) and irregular set (x^i) are determined as shown in Figure 4d. Now, input image is encrypted using stream encryption with encryption key K_e as shown in Figure 4e. Figure 4f shows an 8-bit binary representation of encrypted image. Using the tuple parameter (2,3), labelling bits for each pixel are determined PBTL structure. Pixels of the encrypted image corresponding to regular set (x^r) and irregular set (x^i) are labeled based on predictor errors. Figure 4h shows number of vacancies created in labeled regular pixels for embedding secret payload.

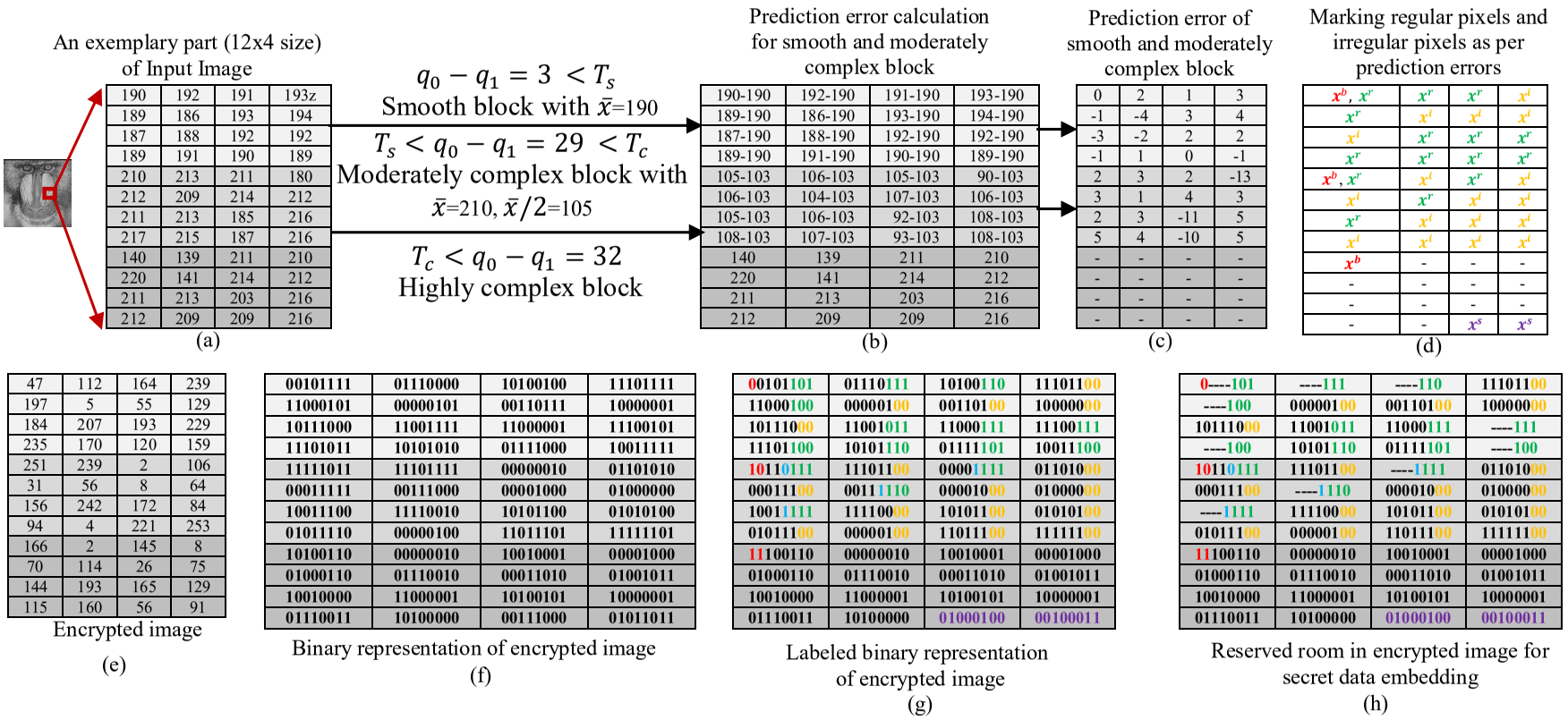


Figure 4. An illustrative example of the proposed scheme. (please resize to the format).

5. Experiment Results and Analysis

In this section, experiment results of the proposed RDHEI technique are discussed and compared with state-of-the-art techniques. To evaluate the performance of the proposed technique, we have taken four test images as shown in Figure 5. The test images are Lena, Airplane, Man, and Baboon, each one of size 512 × 512 with 8-bit depth gray values. The proposed technique has been evaluated using encryption performance and embedding rate. Encryption performance is estimated on two quality parameters, PSNR (peak signal-to-noise ratio) and SSIM (structural similarity), and one security parameter. Embedding rate (ER) basically represents embedding performance, which is measured in terms of bits per pixel (bpp).



(**a**) Lena (**b**) Airplane (**c**) Man (**d**) Baboon

Figure 5. Test images: (**a**) Lena, (**b**) Airplane, (**c**) Man, (**d**) Baboon.

5.1. Encryption Performance of Proposed Technique

In this subsection, encryption performance of the proposed technique is examined by computing pixel distributions of the marked encrypted images. Ideally, it should be uniform for the encrypted data as the encryption process completely destroys correlations present in original data to provide robustness. The proposed technique also provides uniform pixel distribution which is evident from Figure 6a–f, showing histograms of all test images, and Figure 6g–l, showing histograms of marked encrypted images for all the test images. The *X*-axis and *Y*-axis of the histograms represents number of pixels and intensity range (0–255), respectively.

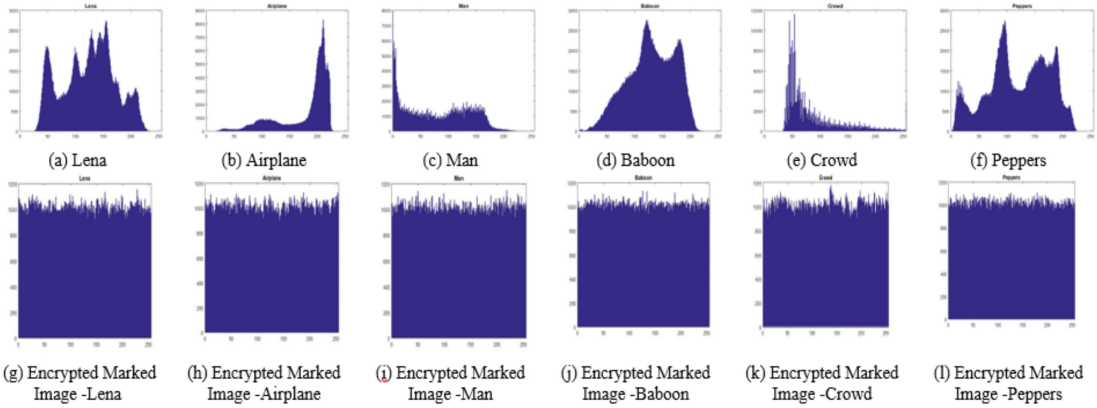


Figure 6. (**a**–**f**) histogram of test images, and (**g**–**l**) histograms of the encrypted marked images.

To further show the encryption performance of proposed technique, PSNR and SSIM values for marked encrypted images corresponding to the original test images are calculated and the results are provided in Table 4. The results are taken by considering tuple parameter (γ_1, γ_2) = (4,4) and block size of 4 × 4 pixels. It is to be noted that the experimental results on other tuple parameter values and block size are also similar. From Table 4, it can be clearly seen that PSNR of each encrypted marked image is very small and the SSIM value is also nearly 0, which indicates that encrypted marked image does not provide any information about the original image and secret payload.

Table 4. PSNR and SSIM values of encrypted marked image.

Test Image	PSNR (dB)	SSIM
Lena	9.2629	0.0203
Airplane	9.0388	0.0355
Man	8.3069	0.0260
Baboon	9.0285	0.0630
Crowd	9.1914	0.0116
Peppers	9.0116	0.0145

Thus, it is validated that the proposed technique provides good encryption performance. Figure 7a–f show the outcomes of different stages of image encryption and secret payload embedding for one of the test images. Figure 7a shows an original Lena image and Figure 7b shows an encrypted Lena image which is encrypted using the encrypted key K_e by employing a standard stream encryption algorithm.

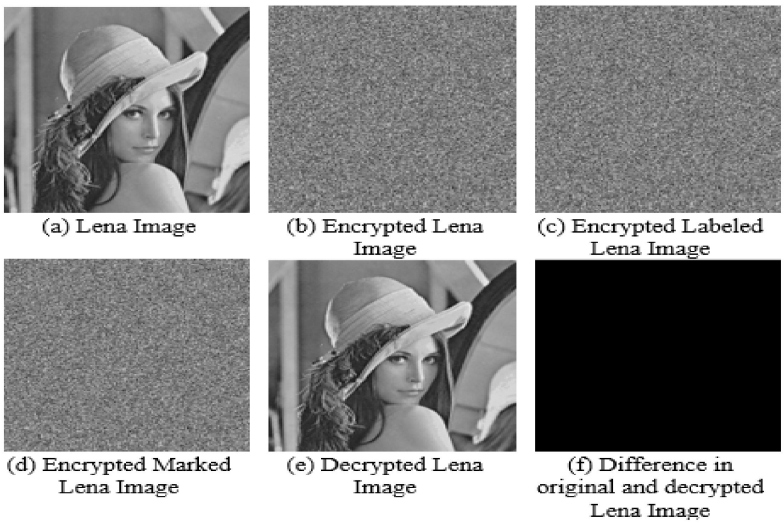


Figure 7. Encryption and decryption of Lena image.

In Figure 7c, an encrypted labeled Lena image is shown and Figure 7d shows a marked encrypted Lena image which includes a secret payload containing the encrypted auxiliary information, encrypted using secret key K_s. In Figure 7e, a decrypted Lena image is shown, which is similar to the original Lena image. In Figure 7f, the difference between Figure 7a,e is seen, showing a black image as all the pixel values are zero. Thus, Figure 7e depicts that the original image is fully recovered as it has PSNR $\rightarrow +\infty$ and SSIM = 1 with respect to the original image.

5.2. Embedding Performance of the Proposed Technique

In this subsection, embedding rate (ER) of the proposed technique is discussed in terms of bpp. The embedding rate has been shown for various values of tuple parameters (γ_1, γ_2 of the PBTL scheme and on different block sizes 4×4, 8×8, 16×16. Further, the thresholds are taken as $T_s = 5$, $T_c = 25$ to categorize image blocks as smooth, moderately complex, and highly complex blocks. Experimental results are provided in Tables 5–8 for test images. From the experimental results, it can be seen that embedding rate is increased, when tuple parameters are also increased up to a limit. Thereafter, embedding rate starts to decrease as tuple parameters are increased. This is because increasing in tuple parameters reduces vacancies for embedding secret data. Further, embedding rate is decreased for parameter γ_2 = 3, 4, 5 when block size is increased and the embedding rate is increased for

parameter γ_2 = 1, 2, 6, 7. The negative values of bpp depict that overhead bits are higher than or approximately equal to reserved room for secret data embedding.

Table 5. Embedding rates of Lena image at different values γ_1 and γ_2 for 4 × 4, 8 × 8, 16 × 16 blocks.

Lena Image, Block Size 4 × 4							
				γ_2			
γ_1	1	2	3	4	5	6	7
1	−0.3802	0.2735	1.2016	1.8779	1.5697	0.7723	−0.085
2	−1.1117	0.5411	1.8115	2.2203	1.6197	0.7736	−0.085
3	−1.8432	0.0459	2.018	2.2900	1.6251	0.7737	−0.085
4	−2.5747	−0.4493	1.8354	2.3141	1.6265	0.7738	−0.085
5	−3.3062	−0.9445	1.6528	2.289	1.6266	0.7737	−0.085
6	−4.0378	−1.4397	1.4701	2.2639	1.6258	0.7737	−0.085
7	−4.7693	−1.9349	1.2875	2.2388	1.6249	0.7737	−0.085
Block Size 8 × 8							
				γ_2			
γ_1	1	2	3	4	5	6	7
1	−0.0894	0.4042	1.1410	1.7434	1.5565	0.8958	0.1655
2	−0.7225	0.5738	1.6104	2.0712	1.6096	0.8983	0.1656
3	−1.3556	0.1291	1.7698	2.1362	1.6177	0.8987	0.1656
4	−1.9887	−0.3156	1.5864	2.1544	1.6197	0.8986	0.1656
5	−2.6218	−0.7603	1.403	2.1244	1.6199	0.8985	0.1656
6	−3.2548	−1.2051	1.2196	2.0944	1.618	0.8986	0.1656
7	−3.8879	−1.6498	1.0362	2.0644	1.6162	0.8985	0.1656
Block Size 16 × 16							
				γ_2			
γ_1	1	2	3	4	5	6	7
1	−0.085	0.2539	0.7632	1.2429	1.189	0.6916	0.1261
2	−0.5862	0.3104	1.0661	1.5345	1.2394	0.6947	0.1263
3	−1.0874	−0.0584	1.1793	1.6044	1.2473	0.6951	0.1264
4	−1.5886	−0.4273	1.0082	1.6205	1.2484	0.695	0.1264
5	−2.0898	−0.7961	0.8371	1.5898	1.2472	0.695	0.1264
6	−2.591	−1.1649	0.666	1.5591	1.2444	0.6949	0.1264
7	−3.0921	−1.5337	0.495	1.5284	1.2415	0.6946	0.1264

Table 6. Embedding rates of Airplane image at different values γ_1 and γ_2 for 4 × 4, 8 × 8, 16 × 16 blocks.

Airplane Image, Block Size 4 × 4							
				γ_2			
γ_1	1	2	3	4	5	6	7
1	0.0450	0.716	1.6555	2.0797	1.6411	0.8698	0.0542
2	−0.6023	1.2755	2.2124	2.3159	1.6763	0.8711	0.0542

Table 6. *Cont.*

Airplane Image, Block Size 4 × 4							
3	−1.2495	0.8933	2.3982	2.3613	1.6808	0.8712	0.0542
4	−1.8968	0.5111	2.2717	2.3693	1.6819	0.8712	0.0542
5	−2.544	0.129	2.1452	2.35	1.6822	0.8712	0.0542
6	−3.1913	−0.2532	2.0187	2.3307	1.6813	0.8712	0.0542
7	−3.8385	−0.6353	1.8922	2.3114	1.6805	0.8712	0.0542
Block Size 8 × 8							
				γ_2			
γ_1	1	2	3	4	5	6	7
1	0.2153	0.7296	1.4998	1.9414	1.6306	0.9878	0.2948
2	−0.3497	1.1507	1.9766	2.1751	1.6671	0.9899	0.2949
3	−0.9147	0.799	2.1473	2.2203	1.6736	0.9902	0.2949
4	−1.4797	0.4472	2.0201	2.2242	1.6749	0.9902	0.2949
5	−2.0447	0.0955	1.8929	2.2018	1.6739	0.9902	0.2949
6	−2.6098	−0.2563	1.7657	2.1794	1.672	0.9902	0.2949
7	−3.1748	−0.6081	1.6385	2.157	1.6701	0.9901	0.2949
Block Size 16 × 16							
				γ_2			
γ_1	1	2	3	4	5	6	7
1	0.1614	0.5260	1.1428	1.5400	1.3086	0.7920	0.2357
2	−0.3015	0.8476	1.5346	1.7483	1.3354	0.7946	0.2359
3	−0.7643	0.5505	1.6901	1.7828	1.3396	0.7947	0.236
4	−1.2271	0.2534	1.5821	1.7851	1.3406	0.7947	0.2361
5	−1.6899	−0.0437	1.4741	1.7664	1.3384	0.7943	0.2361
6	−2.1528	−0.3408	1.3662	1.7478	1.3357	0.794	0.2361
7	−2.6156	−0.6379	1.2582	1.7292	1.333	0.7936	0.2361

Table 7. Embedding rates of Man image at different values γ_1 and γ_2 for 4 × 4, 8 × 8, 16 × 16 blocks.

Man Image, Block Size 4 × 4							
				γ_2			
γ_1	1	2	3	4	5	6	7
1	−0.4069	0.1733	0.9315	1.4777	1.2980	0.5978	−0.2026
2	−1.0968	0.3123	1.3616	1.8139	1.3764	0.6004	−0.2026
3	−1.7867	−0.1722	1.4769	1.8907	1.3885	0.6007	−0.2026
4	−2.4766	−0.6567	1.2620	1.9133	1.3912	0.6007	−0.2026
5	−3.1665	−1.1412	1.0471	1.8714	1.3919	0.6007	−0.2026
6	−3.8565	−1.6256	0.8321	1.8295	1.3902	0.6007	−0.2026
7	−4.5464	−2.1101	0.6172	1.7877	1.3884	0.6007	−0.2026

Table 7. *Cont.*

Block Size 8 × 8							
				γ_2			
γ_1	1	2	3	4	5	6	7
1	−0.1553	0.2655	0.8052	1.2536	1.1992	0.6775	0.0286
2	−0.7307	0.2760	1.0819	1.5326	1.2917	0.6838	0.0287
3	−1.3061	−0.1497	1.1359	1.6029	1.3090	0.6842	0.0287
4	−1.8815	−0.5755	0.9212	1.6142	1.3120	0.6843	0.0287
5	−2.4569	−1.0012	0.7066	1.5595	1.3125	0.6843	0.0287
6	−3.0323	−1.4270	0.4919	1.5048	1.3084	0.6843	0.0287
7	−3.6077	−1.8527	0.2773	1.4502	1.3042	0.6841	0.0287
Block Size 16 × 16							
				γ_2			
γ_1	1	2	3	4	5	6	7
1	−0.1489	0.1368	0.4943	0.8332	0.8754	0.5204	0.0399
2	−0.5902	0.0772	0.6419	1.0590	0.9603	0.5275	0.0402
3	−1.0315	−0.2643	0.6461	1.1145	0.9773	0.5288	0.0402
4	−1.4728	−0.6059	0.4532	1.118	0.9811	0.5290	0.0403
5	−1.9141	−0.9474	0.2602	1.0616	0.9795	0.5289	0.0403
6	−2.3554	−1.2890	0.0673	1.0052	0.9734	0.5287	0.0403
7	−2.7967	−1.6305	−0.1256	0.9488	0.9672	0.5283	0.0403

Table 8. Embedding rates of Baboon at different values γ_1 and γ_2 for 4 × 4, 8 × 8, 16 × 16 blocks.

Baboon Image, Block Size 4 × 4							
				γ_2			
γ_1	1	2	3	4	5	6	7
1	−0.5311	−0.3264	−0.0006	0.4225	0.6605	0.3702	−0.1360
2	−1.0109	−0.4916	0.0785	0.7055	0.8125	0.3801	−0.1360
3	−1.4906	−0.8955	0.0214	0.786	0.8445	0.3810	−0.1360
4	−1.9704	−1.2994	−0.2418	0.7943	0.8536	0.3812	−0.1360
5	−2.4502	−1.7033	−0.505	0.7081	0.8552	0.3813	−0.1360
6	−2.9299	−2.1072	−0.7682	0.6218	0.8490	0.3814	−0.1360
7	−3.4097	−2.5111	−1.0314	0.5356	0.8428	0.3813	−0.1360
Block Size 8 × 8							
				γ_2			
γ_1	1	2	3	4	5	6	7
1	−0.2529	−0.1006	0.1333	0.4396	0.6186	0.4100	0.0215
2	−0.6273	−0.2436	0.1757	0.6395	0.7409	0.4217	0.0216
3	−1.0017	−0.5607	0.1120	0.6929	0.7663	0.4232	0.0216
4	−1.3760	−0.8779	−0.0999	0.6905	0.7723	0.4236	0.0216
5	−1.7504	−1.1951	−0.3117	0.6151	0.7712	0.4237	0.0216

Table 8. *Cont.*

6	−2.1248	−1.5122	−0.5236	0.5397	0.7633	0.4238	0.0216
7	−2.4992	−1.8294	−0.7355	0.4642	0.7553	0.4236	0.0216
Block Size 16 × 16							
				γ_2			
γ_1	1	2	3	4	5	6	7
1	−0.1643	−0.052	0.1171	0.3358	0.4629	0.3089	0.0168
2	−0.4502	−0.1665	0.1343	0.4706	0.5529	0.3198	0.0174
3	−0.7361	−0.4093	0.0777	0.5044	0.5715	0.3212	0.0174
4	−1.0220	−0.6522	−0.0874	0.5004	0.5745	0.3214	0.0174
5	−1.3079	−0.8951	−0.2525	0.4383	0.5720	0.3213	0.0174
6	−1.5937	−1.1379	−0.4176	0.3761	0.5634	0.3210	0.0174
7	−1.8796	−1.3808	−0.5827	0.3140	0.5548	0.3204	0.0174

5.3. Comparison of Results of the Proposed Technique with State of Art Techniques

In this subsection, experimental results of the proposed techniques are compared with related techniques including those of Yi et al. [32], Su et al. [33], Li et al. [27], Puteaux et al. [29], Puyang et al. [30], Chen et al. [31]. Since PBTL was first introduced in the RDHEI domain by Yi et al., the same [24] has been primarily considered for comparison. Su et al.'s [33] technique demonstrates application of AMBTC concept along with PBTL. However, it is a lossy technique where a decrypted image is obtained in compressed form. Since the proposed technique also considers some aspects of AMBTC in block categorization, Su et al.'s [33] technique has also been used to comparatively evaluate the performance. However, the proposed technique is a lossless and fully reversible technique in which both secret payload and original image are retrieved in undistorted form. Additionally, the performance of the proposed technique is evaluated against some of the early high capacity RDHEI techniques, e.g., Li et al. [27], Puteaux et al. [29], Puyang et al. [30], and Chen et al. [31]. Table 9 shows the encryption method of the proposed technique and state-of-art techniques. In comparison to this, Yi et al. [32] retains some pixel correlations in blocks which makes encryption week.

Table 9. Comparison of encryption performance with state-of-art techniques.

Technique	Encryption Method	Preserving Pixel Redundancy
Yi et al. [32]	Block Permutation and block modulation	Yes
Su et al. [33]	Block Scrambling and Stream Encryption	Yes
Li et al. [27]	Block Permutation and Stream Encryption	No
Puteaux et al. [29]	Stream Encryption	No
Puyang et al. [30]	Stream Encryption	No
Chen et al. [31]	Stream Encryption	No
Proposed RDHEI	Stream Encryption	No

For optimal embedding performance, $\gamma_1 = 4$ & $\gamma_2 = 4$ and a block size of 4×4 pixels is considered for the proposed RDHEI technique. The embedding performance is compared with some of the high-capacity state-of-the-art techniques that provide highest embedding

rate. Since Yi et al.'s [32] and Chen et al. [33] have optimal performance at $\gamma_1 = 2$ & $\gamma_2 = 5$ with block size of 3×3 pixels and block size of 4×4 pixels, respectively.

Figure 8 shows the maximal embedding rates of the proposed technique as well as existing RDHEI techniques for all the test images. It clearly shows that proposed technique has highest embedding rate than other techniques. It is also evident from the figure that the proposed scheme provides higher embedding capacity with smooth images like Lena, Airplane, whereas it has lower embedding capacity with complex images such as Baboon.

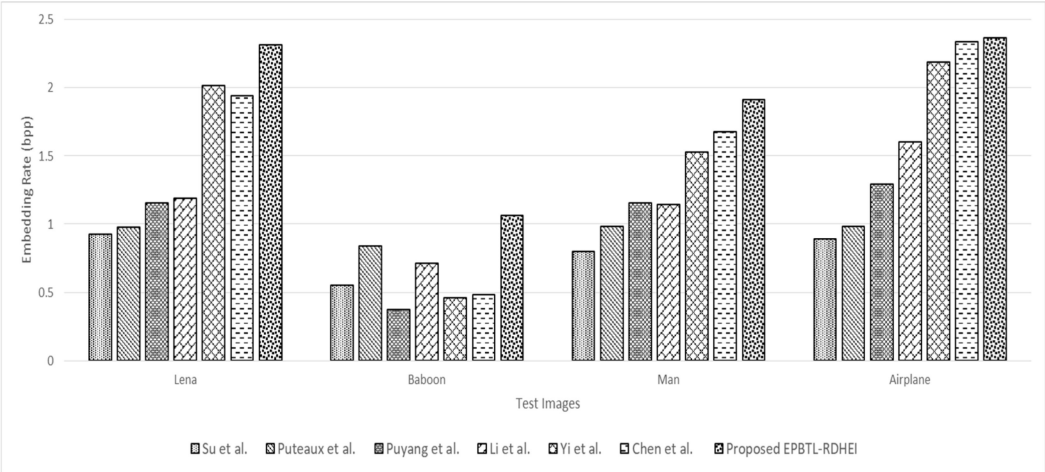


Figure 8. Comparison of embedding rate of the proposed and state-of-art techniques.

6. Conclusions

In this paper, an intra-block correlation based high capacity RDHEI technique using a parametric binary tree labelling scheme has been proposed. In the proposed technique, the cover image was divided into blocks and then the blocks were categorized according to the prevalent correlation through a symmetric or asymmetric process. Next, an adaptive method for reserving the room inside the image was applied, based on the block categories so that a large amount of secret data could be embedded. Further, the proposed RDHEI technique used a stream cipher for encrypting the image contents. Experimental results showed that the proposed RDHEI technique provided the highest embedding rate in comparison to all the aforementioned state-of-the art techniques. Additionally, the proposed method provided a good level of security in encryption process to protect the privacy of the original plaintext image. In future work, compression methods can be explored to further condense the size of prediction errors, and also an improvised AMBTC method may be designed to predict the pixel values more accurately.

Author Contributions: Conceptualization, A.K.R. and N.K.; Methodology, A.K.R. and N.K.; Visualization, R.K.; Writing—A.K.R., N.K.; Writing—review and editing, R.K., H.O., S.C. and K.-H.J. All authors have read and agreed to the published version of the manuscript.

Funding: This research was supported by Brain Pool program funded by the Ministry of Science and ICT through the National Research Foundation of Korea (2019H1D3A1A01101687) and Basic Science Research Program through the National Research Foundation of Korea (NRF) funded by the Ministry of Education (NRF-2018R1D1A1A09081842 and 2021R1I1A3049788).

Conflicts of Interest: The authors declare no conflict of interest.

Abbreviations

The following abbreviations are used in this manuscript:

Symbols	**Meaning**
A_b	auxiliary information
μ	Mean
B_k	Block
b_i	Logic bit value
K_e	Encryption Key
K_s	Secret Key
n	Number of Layers
γ_1, γ_2	Tuple Parameter
S_1, S_2	Two different sets
N_{γ_2}	Total number of nodes in the set S_2
$\mathbb{I}$	plaintext image
I^e	Encrypted image
$N_1 \times N_2$	Image Size
$n_1 \times n_2$	Block Size
O_b	Overhead
p	Number of non-overlapping blocks
q_0, q_1	Quantization values
T_s, T_c	Threshold values
x_i	i-th pixel
x^s	Special set
x^b	Base set
x^r	Regular set
x^i	Irregular set
Abbreviation	**Meaning**
AES	Advanced Encryption Standard
AMBTC	Absolute Moment Block Truncation Coding
BPP	Bit-Per-Pixel
EC	Embedding Capacity
ER	Embedding Rate
LSB	Least Significant Bits
MSB	Maximum Significant Bits
PBTL	Parametric Binary Tree Labeling Scheme
PE	Prediction Error
PSNR	Peak Signal-To-Noise Ratio
RDH	Reversible Data Hiding
RDHEI	Reversible Data Hiding in Encrypted Images
RLE	Run Length Coding
RRBE	Reserving Room Before Encryption
SSIM	Structural Similarity Index
VRAE	Vacating Room After Encryption
VRBE	Vacating Room by Encryption

References

1. Pahl, C.; Brogi, A.; Soldani, J.; Jamshidi, P. A State-of-the-Art Review. *IEEE Trans. Cloud Comput.* **2019**, *7*, 677–692. [CrossRef]
2. Chandramouli, R.; Iorga, M.; Chokhani, S. Cryptographic key management issues and challenges in cloud services. *Secure Cloud Comput.* **2014**, 1–30. [CrossRef]
3. Kumar, R.; Chand, S. A reversible high capacity data hiding scheme using pixel value adjusting feature. *Multimed. Tools Appl.* **2016**, *75*, 241–259. [CrossRef]
4. Lee, C.; Shen, J.; Wu, Y.; Agrawal, S. PVO-based reversible data hiding exploiting two-layer embedding for enhancing image fidelity. *Symmetry* **2020**, *12*, 1164. [CrossRef]
5. Khan, S.; Khan, K.; Arif, A.; Hassaballah, M.; Ali, J.; Ta, Q.; Yu, L. A modulo function-based robust asymmetric variable data hiding using DCT. *Symmetry* **2020**, *12*, 1659. [CrossRef]
6. Kim, S.; Cho, N.I. Hierarchical Prediction and Context Adaptive Coding for Lossless Color Image Compression. *IEEE Trans. Image Process.* **2014**, *23*, 445–449. [CrossRef] [PubMed]

7. Alattar, A.M. Reversible Watermark Using the Difference Expansion of a Generalized Integer Transform. *IEEE Trans. Image Process.* **2004**, *13*, 1147–1156. [CrossRef] [PubMed]
8. Kumar, R.; Jung, K.-H. Enhanced pairwise IPVO-based reversible data hiding scheme using rhombus context. *Inf. Sci.* **2020**, *536*, 101–119. [CrossRef]
9. Wu, H.; Li, X.; Zhao, Y.; Ni, R. Improved reversible data hiding based on PVO and adaptive pairwise embedding. *J. Real-Time Image Process.* **2019**, *16*, 685–695. [CrossRef]
10. Ou, B.; Li, X.; Wang, J. High-fidelity reversible data hiding based on pixel-value-ordering and pairwise prediction-error expansion. *J. Vis. Commun. Image Represent.* **2016**, *39*, 12–23. [CrossRef]
11. Gao, G.; Tong, S.; Xia, Z.; Wu, B.; Xu, L.; Zhao, Z. Reversible data hiding with automatic contrast enhancement for medical images. *Signal Process.* **2021**, *178*, 107817. [CrossRef]
12. Kumar, R.; Jung, K.-H. Robust reversible data hiding scheme based on two-layer embedding strategy. *Inf. Sci.* **2020**, *512*, 96–107. [CrossRef]
13. Puech, W.; Chaumont, M.; Strauss, O. A reversible data hiding method for encrypted images. In Proceedings of the SPIE, San Jose, CA, USA, 18 March 2008; pp. 68191E-1–68191E-9.
14. Bhardwa, J.R.; Aggarwal, A. An improved block based joint reversible data hiding in encrypted images by symmetric cryptosystem. *Pattern Recognit. Lett.* **2020**, *139*, 60–68. [CrossRef]
15. Hong, W.; Chen, T.-S.; Wu, H.-Y. An Improved Reversible Data Hiding in Encrypted Images Using Side Match. *IEEE Signal Process. Lett.* **2012**, *19*, 199–202. [CrossRef]
16. Zhou, J.; Sun, W.; Dong, L.; Liu, X.; Au, O.C.; Tang, Y.Y. Secure Reversible Image Data Hiding Over Encrypted Domain via Key Modulation. *IEEE Trans. Circuits Syst. Video Technol.* **2016**, *26*, 441–452. [CrossRef]
17. Wu, X.; Sun, W. High-capacity reversible data hiding in encrypted images by prediction error. *Signal Process.* **2014**, *104*, 387–400. [CrossRef]
18. Zhang, W.; Ma, K.; Yu, N. Reversibility improved data hiding in encrypted images. *Signal Process.* **2014**, *94*, 118–127. [CrossRef]
19. Zhang, X. Separable Reversible Data Hiding in Encrypted Image. *IEEE Trans. Inf. Forensics Secur.* **2012**, *7*, 826–832. [CrossRef]
20. Kaur, G.; Singh, S.; Rani, R.; Kumar, R.; Malik, A. High-quality reversible data hiding scheme using sorting and enhanced pairwise PEE. *IET Image Process.* **2021**, 1–15. [CrossRef]
21. Dragoi, I.C.; Coanda, H.-G.; Coltuc, D. Improved reversible data hiding in encrypted images based on reserving room after encryption and pixel prediction. In Proceedings of the 25th European Signal Processing Conference (EUSIPCO), Kos Island, Greece, 28 August–2 September 2017; pp. 2186–2190.
22. Dragoi, I.C.; Coltuc, D. Reversible Data Hiding in Encrypted Color Images Based on Vacating Room After Encryption and Pixel Prediction. In Proceedings of the 25th IEEE International Conference on Image Processing (ICIP), Athens, Greece, 7–10 October 2018; pp. 1673–1677.
23. Ma, K.; Zhang, W.; Zhao, X.; Yu, N.; Li, F. Reversible Data Hiding in Encrypted Images by Reserving Room Before Encryption. *IEEE Trans. Inf. Forensics Secur.* **2013**, *8*, 553–562. [CrossRef]
24. Xu, D.; Wang, R. Separable and error-free reversible data hiding in encrypted images. *Signal Process.* **2016**, *123*, 9–21. [CrossRef]
25. Mathew, T.; Wilscy, M. Reversible data hiding in encrypted images by active block exchange and room reservation. In Proceedings of the 2014 International Conference on Contemporary Computing and Informatics (IC3I), Mysore, India, 27–29 November 2014; pp. 839–844.
26. Cao, X.; Du, L.; Wei, X.; Meng, D.; Guo, X. High Capacity Reversible Data Hiding in Encrypted Images by Patch-Level Sparse Representation. *IEEE Trans. Cybern.* **2016**, *46*, 1132–1143. [CrossRef] [PubMed]
27. Li, Q.; Yan, B.; Hui, L.; Chen, N. Separable reversible data hiding in encrypted images with improved security and capacity. *Multi. Tools Apps.* **2018**, *77*, 30749–30768. [CrossRef]
28. Hang, Y.; Wei, T.; Menghan, G.; Shoushun, C. A two-step prediction ADC architecture for integrated low power image sensors. *IEEE Trans. Circuits Syst. I* **2017**, *64*, 50–60.
29. Puteaux, P.; Puech, W. An Efficient MSB Prediction-Based Method for High-Capacity Reversible Data Hiding in Encrypted Images. *IEEE Trans. Inf. Forensics Secur.* **2018**, *13*, 1670–1681. [CrossRef]
30. Puyang, Y.; Yin, Z.; Qian, Z. Reversible Data Hiding in Encrypted Images with Two-MSB Prediction. In Proceedings of the 2018 IEEE International Workshop on Information Forensics and Security (WIFS), Hong Kong, China, 11–13 December 2018; pp. 1–7.
31. Kaimeng, C.; Chang, C.C. High-capacity Reversible Data Hiding in Encrypted Images Based on Extended Run-Length Coding and Block-based MSB Plane Rearrangement. *J. Vis. Commun. Image Represent.* **2019**, *58*, 334–344.
32. Yi, Y.; Zhou, Y. Separable and Reversible Data Hiding in Encrypted Images Using Parametric Binary Tree Labeling. *IEEE Trans. Multimed.* **2019**, *21*, 51–64. [CrossRef]
33. Su, G.-D.; Chang, C.-C.; Lin, C.-C. A High Capacity Reversible Data Hiding in Encrypted AMBTC-Compressed Images. *IEEE Access* **2020**, *8*, 26984–27000. [CrossRef]
34. Yin, Z.; Niu, X.; Zhang, X.; Tang, J.; Luo, B. Reversible data hiding in encrypted AMBTC images. *Multimed. Tools Appl.* **2018**, *77*, 18067–18083. [CrossRef]
35. Yin, Z.; Wang, H.; Zhao, H.; Luo, B.; Zhang, X. Complete separable reversible data hiding in encrypted image. In Proceedings of the 1st International Conference on Cloud Computing and Security, Nanjing, China, 13–15 August 2015; pp. 101–110.

36. Wang, R.; Wu, G.; Wang, Q.; Yuan, L.; Zhang, Z.; Miao, G. Reversible Data Hiding in Encrypted Images Using Median Edge Detector and Two's Complement. *Symmetry* **2021**, *13*, 921. [CrossRef]
37. Kumar, R.; Kim, D.-S.; Jung, K.-H. Enhanced AMBTC based data hiding method using hamming distance and pixel value differencing. *J. Inf. Secur. Appl.* **2019**, *47*, 94–103. [CrossRef]
38. Kim, S. Reversible Data-Hiding Systems with Modified Fluctuation Functions and Reed-Solomon Codes for Encrypted Image Recovery. *Symmetry* **2017**, *9*, 61. [CrossRef]

ResearchGate

See discussions, stats, and author profiles for this publication at: https://www.researchgate.net/publication/358638582

Investigation of fresh, mechanical, and impact resistance properties of rubberized concrete

Conference Paper · January 2022

CITATIONS
0

READS
21

3 authors:



Rahul Kumar
Delhi Technological University
6 PUBLICATIONS **6** CITATIONS
SEE PROFILE



Manvendra Verma
Dr. Akhilesh Das Gupta Institute of Technology and Management
10 PUBLICATIONS **55** CITATIONS
SEE PROFILE



Nirendra Dev
Delhi Technological University
20 PUBLICATIONS **63** CITATIONS
SEE PROFILE

Some of the authors of this publication are also working on these related projects:

behavior of Geopolymer concrete View project

Investigation of behaviour of rubberised concrete View project

All content following this page was uploaded by Rahul Kumar on 16 February 2022.

The user has requested enhancement of the downloaded file.

Investigation of fresh, mechanical, and impact resistance properties of rubberized concrete

Rahul Kumar (Corresponding author), Manvendra Verma, Nirendra Dev
Department of Civil Engineering
Delhi Technological University
Delhi 110042, India.
rahul_phd2k17@dtu.ac.in, mv075415@gmail.com, nirendradev@dce.ac.in

ABSTRACT - Rubberized concrete is ideal for applications that demand additional flexibility. Rubberized concrete provides more flexibility, impact resistance, and a lower unit weight than ordinary concrete. As a partial substitute for fine aggregate in concrete, six waste tire rubber crumb contents (0, 10, 15, 20, 25, and 30 percent) and particle sizes of 0.6-2.36 mm are utilized. Rubberized concrete's fresh, mechanical, and impact resistance characteristics are studied and found that by increasing the amount of rubber crumb in the mix, the fresh and mechanical characteristics are reduced. The energy absorption capacity of rubberized concrete increases with the increase of rubber crumb in concrete. However, the results aren't too concerning, up to a 15% rubber crumb replacement level.

Keywords - *Rubberized concrete; Fresh properties; Mechanical Properties; Energy absorption capacity*

I. Introduction

Over the years, the disposal of waste tires increasing the issue continuously for the environment. Waste Rubber tires have a little scope of being recycled and mostly form a landfill and degrade the environment [1]–[3]. There is an excellent potential for the rubber to be used in concrete, thus saving the area from becoming a landfill, which means eco-friendly. According to previous research, the utilization of rubber shreds in concrete enhanced the property of resistance to acid attack but decreased the compressive strength of RuC (Rubberized concrete) [4]. Due to the ability to absorb impacts, RuC has a better energy absorption capacity than standard concrete [5], [6]. Steel fibers have more negative impacts than polypropylene fibers in RuC [7]. The compressive strength of RuC after treatment with sodium hydroxide is slightly enhanced compared with ordinary concrete [8]. The inclusion of powder rubber in concrete showing better performance in terms of fresh and mechanical properties than rubber crumb, allowing up to 40% rubber replacement [9]. Six levels of rubber fiber (0, 5, 10, 15, 20, and 25%) are used for replacement of FA (Fine aggregate) and three w/c ratios (0.35, 0.45, and 0.55) and two stages of silica fume (5 and 10%) are used as partial replacement of cement. The compressive strength and MOE (Modulus of elasticity) decrease with increasing rubber fiber quantity [10]–[12]. The flexural strength of RuC decreases with increasing the quantity of rubber ash but increases with the increasing content of rubber fiber [13]. Waste tire rubber fiber can be used to increase the impact resistance and ductility of concrete as a recycled material [14]. Crumb rubber as an FA reduces the concrete's compressive strength and abrasion resistance while greatly increasing its energy absorbing capacity [15]. The rubber substitution in concrete increases the damping potential, ductile performance and improves

the energy absorption of self-compacting RuC compared to normal self-compacting concrete [16].

II. Materials and testing

In this study, PPC (Portland pozzolana cement) JK Laxmi pro+, up to 30% replacement by fly ash-based, is used. The compressive strength of PPC is 44 MPa at 28 days. The standard consistency of the cement is obtained at 33%. Sp. Gr. of cement is found to be 2.97. PPC's initial setting time is 90 min, and the final setting time is 155 min. The soundness of PPC is tested by the Le-chatelier method, and cement expansion is noted at 3 mm.

FA in the form of stone dust is procured from a local material shop in Delhi, which falls in zone II with a finesse modulus is 2.75, Sp. Gr. is 2.62, and water absorption is 1.21%. Crushed rock as CA (Coarse aggregate) is also procured from a local material shop in Delhi, which has sp. Gr. of 2.79 at 28°C, water absorption is 0.2%, finesse modulus is 7.29, impact value is 26.3, and Loss Angeles Abrasion Value is 36.

Auramix 400 SP (Superplasticizer) based on polycarboxylate ether-based is used and obtained from Fosroc Chemical (India). SP's Sp Gr (Specific gravity) is 1.09, and P^H Value is 6. SP's optimum dosage and efficiency are determined from the marsh cone apparatus with a nozzle aperture diameter of 8 mm. The optimum dosage of SP is found to be 1.4%.

Rubber crumb is obtained from a local waste tire rubber factory with a particle size of 0.6 mm-2.36 mm. Rubber is a lightweight material because it's Sp. Gr. is 1.07. Rubber crumb is used as a partial replacement of FA. Rubber crumb particles are gained from the waste rubber tire after grinding in a mechanical grinder.

III. Mix Proportion

The concrete mixes are prepared with a w/c ratio of 0.38 and a partial FA replacement by rubber particles with a 0-30% replacement level. The proportion of the mix design for the M40 grade of concrete is shown in Table 1. Machine mixing is adopted for the homogeneity of the concrete. First dry mixing of material is done for 2-3 minutes, then water and SP are mixed with materials. A mechanical vibrator is used for the compaction and uniformity of the concrete.

IV. Testing program

Various tests are performed to find the concrete properties, such as compressive strength, split tensile strength, workability, density, and flexural strength. Three specimens are cast for each testing of concrete. The density of the concrete mixes is measured according to IS code (Indian standard code) [17]. The compressive strength and flexural strength of RuC are tested on a universal testing machine with 2000 tons capacity and an automatic controller with specimen size 150X150X150 mm for compressive strength and 100X100X500 mm [18] for flexural strength and compared with standard concrete. The examination for rebound impact loading is performed on 150 mm cube specimens. A steel ball weighing 300 gm is used to transmit impact energy from a height of 1.0 m to the specimens in the testing. "The initial and final potential energies are denoted by $E_{p,ri,}$ and $E_{p,rf}$ respectively (the subscripts *p, ri*, and *rf* indicate potential energy at initial and final rebound stages, respectively), and can be calculated as follows" [19]:

$$\boldsymbol{E_{p,ri} = mgh_i} \quad (1)$$

$$\boldsymbol{E_{p,rf} = mgh_f} \quad (2)$$

where m = mass of steel ball (0.3 kg), h_i = preliminary height of steel ball (1.0 m), and h_f = height noted after a rebound.

The discrepancy between the final and initial potential energy is used to assess the energy absorption capacity of the concrete specimen $E_{p,r}$.

$$\boldsymbol{E_{p,r} = E_{p,ri} - E_{p,rf}} \quad (3)$$

Table 1 Mix proportion for concrete

Mix no.	Cement (kg/m^3)	Fine aggregate (kg/m^3)	Coarse aggregate (kg/m^3)		Rubber crumb replacement level (wt %)	Rubber crumb (kg/m^3)	w/c ratio	SP (%)	Slump (mm)
			(20 mm)	(10 mm)					
R1	390	666	769.8	513.2	0	0	0.38	1.4	99
R2	390	599.4	769.8	513.2	10	66.6	0.38	1.4	96
R3	390	566.1	769.8	513.2	15	99.9	0.38	1.4	94
R4	390	532.8	769.8	513.2	20	133.2	0.38	1.4	91
R5	390	499.5	769.8	513.2	25	166.5	0.38	1.4	86
R6	390	466.2	769.8	513.2	30	199.8	0.38	1.4	84

V. Results and discussion

A. Workability

At the time of batch mixing, 1.4% SP by the weight of cement is used to maintain the workability of concrete. The slump cone results are shown in Figure 1. The results show that RuC's workability decreases with increasing the quantity of rubber crumbs. The replacement level of rubber crumbs up to 30% can be used with reinforced concrete members, and no need to add extra SP for making the concrete workable. The rubber particles have a rough surface and lead to large undulations in concrete. The greater the rubber content in the mixture, the reduction in the value of the compaction factor would be the higher.

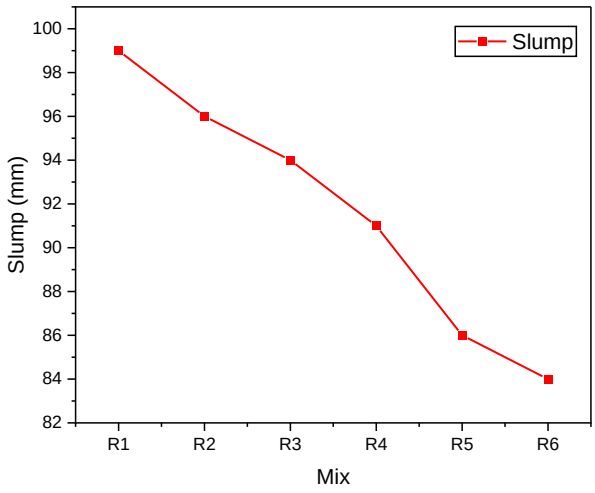


Fig. 1 Results of slump for all mixes

B. Density

The mix's density results are shown in Figure 2. The results show that the density of concrete mixtures decreases with increasing the quantity of rubber crumb in concrete. The rubber crumb has low sp gr than the FA, which is the reason for the decrement pattern in the density of RuC. The sp gr of natural FA is much higher than the waste tire rubber crumb, so the density of RuC will decrease. The appearance of entrapped air on rubber particles' rough surfaces could be another explanation for the decrement in the density of RuC [20], [21].

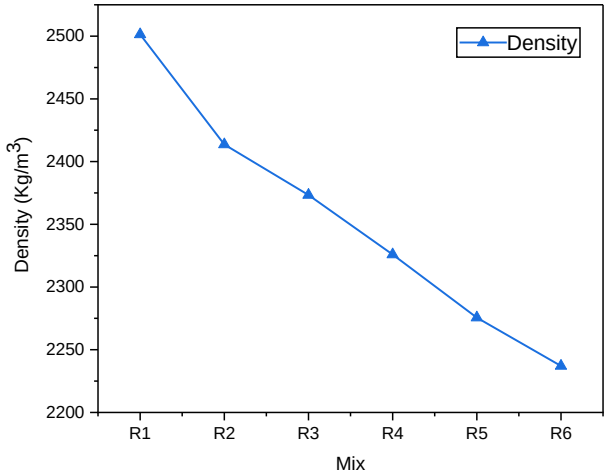


Fig. 2 Density of different mixes

C. Compressive strength

The compressive strength of the concrete mixes at 7, 14, and 28 days after casting is presented in Figure 3. The decrement in the compressive

strength at 15% replacement level of rubber crumb is just 20.36% after 28 days of curing, and the compressive strength of the RuC is 40.12 MPa, which is suitable for the M40 classification. The compressive strength of RuC is not much affected at 15% replacement level of rubber crumb. The low adhesion between the rubber particle and the cement paste reduces the bonding, resulting in a declining trend in compressive strength at all ages. Rubber crumbs are softer and more elastically deformable than the cement matrix around them, indicating that the material stiffness of rubber and cement paste is incompatible. The above factors make it easier for cracks to form at the cement paste and rubber crumb interface, and the cracks' progression speeds up, reducing RuC's compressive strength.

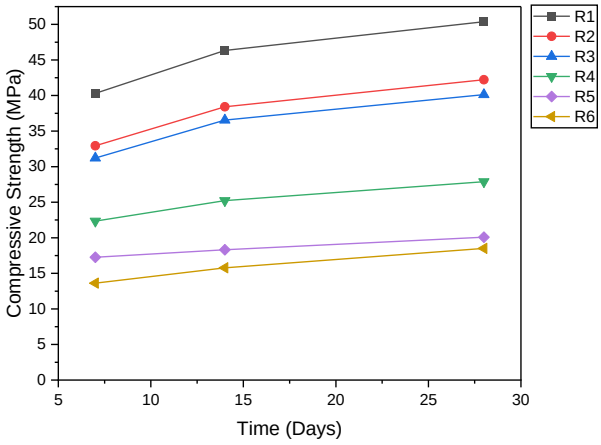


Fig. 3 Compressive strength of standard concrete and RuC

D. Split tensile strength

The split tensile strength results of the concrete mixes at 7, 14, and 28 days after casting are shown in Figure 4. In this study, at 15% replacement level of rubber crumb, the reduction is only 22.48% at 28 days of curing, and the split tensile strength is found to be 3.24 MPa. Due to weak bonding between rubber crumbs and cement, the RuC doesn't bear much tensile load than standard concrete, and the gaps between rubber crumbs and cement become larger quickly. The decrement in split tensile strength is 17-60% at 7-days, and 16-58% at 28 days.

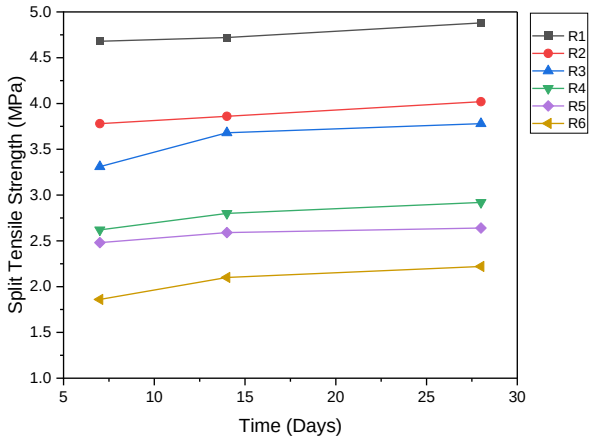


Fig. 4 Split tensile strength of standard concrete and RuC

E. Flexural strength

The flexural strength results of the concrete mixes at 7, 14, and 28 days after casting are shown in Figure 5. In this study, at 15% replacement level of rubber crumb, the reduction is 28% at 28 days of curing, and the flexural strength is found to be 4.00 MPa. The decrement in flexural strength is 18-59% at 7-days and 17-53% at 28 days at replacement level of rubber 0-30%. Since micro-crack forms when the post-peak region is reached and propagates after exceeding this stage in flexural strength testing, cracking may begin before the maximum load is applied.

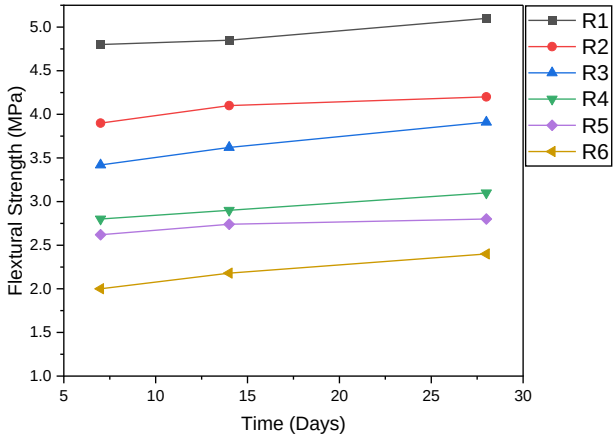


Fig. 5 Flexural strength of standard concrete and RuC

F. Impact resistance by rebound Test

The experimental setup is shown in Fig. 6(a), and Fig. 6(b) illustrates the impact energy absorbed by standard concrete and RuC in the rebound test. Based on the findings, it is discovered that increasing the amount of rubber in concrete increases resistance to the impact of RuC after comparing with standard concrete. The absorbed impact energy by RuC increases from 2.75 to 2.90 J with an entire 30% replacement of FA by rubber crumb in the concrete mix. The absorption of impact energy by the rebound test of the concrete increases from 2.56 to 2.82 J (0 - 10.156) by a 15% replacement level of rubber crumb in the concrete mix. This is a good development for RuC and is useful for the absorption of impact energy due to seismic loading.

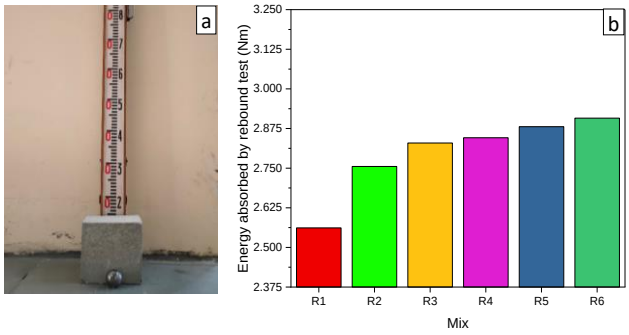


Fig. 6(a) Testing setup of Impact resistance by rebound test (b) Impact energy absorbed by the rebound of standard and RuC mixes

Conclusions

1. As a partial replacement of FA, Rubber crumb can be up to 15% without significant compressive strength loss.
2. The density of RuC decreases with the increasing replacement level and can be considered the semi-light weight of concrete. The density of RuC decreases due to low sp gr of rubber crumb.
3. The concrete's fresh and mechanical properties decrease with increasing the quantity of rubber crumb in concrete.
4. The impact resistance and the energy absorption capacity of the RuC improve when the rubber crumb is added to the concrete. These are the positive results of RuC, and it can absorb the impact energy by the seismic activities.

REFERENCES

[1] O. By, Z. K. Khatib, and F. M. Bayomy, "Rubberized portland cement concrete," *J. Mater. Civ. Eng.*, vol. 11, no. August, pp. 206–213, 1999.

[2] M. Gesoğlu and E. Guneyisi, "Strength development and chloride penetration in rubberized concretes with and without silica fume," *Mater. Struct.*, vol. 40, pp. 953–964, 2007.

[3] T. Uygunoğlu and I. B. Topçu, "The role of scrap rubber particles on the drying shrinkage and mechanical properties of self-consolidating mortars," *Constr. Build. Mater.*, vol. 24, no. 7, pp. 1141–1150, 2010.

[4] T. Gupta, S. Siddique, R. K. Sharma, and S. Chaudhary, "Effect of aggressive environment on durability of concrete containing fibrous rubber shreds and silica fume," *Struct. Concr.*, no. April, pp. 18–23, 2020.

[5] G. Murali, L. Poka, K. Parthiban, M. K. Haridharan, and A. Siva, "Impact Response of Novel Fibre-Reinforced Grouted Aggregate Rubberized Concrete," *Arab. J. Sci. Eng.*, vol. 44, no. 10, pp. 8451–8463, 2019.

[6] R. Kumar and N. Dev, "Assessment of Mechanical and Impact Resistance Properties of Rubberized Concrete After Surface Modification of Rubber Crumb," *Iran. J. Sci. Technol. Trans. Civ. Eng.*, Nov. 2021.

[7] F. Aslani and R. Gedeon, "Experimental investigation into the properties of self-compacting rubberised concrete incorporating polypropylene and steel fibers," *Struct. Concr.*, vol. 20, no. 1, pp. 267–281, 2019.

[8] L. He *et al.*, "Research on the properties of rubber concrete containing surface-modified rubber powders," *J. Build. Eng.*, vol. 35, p. 101991, Mar. 2021.

[9] M. K. Ismail, M. A. A. Sherir, H. Siad, A. A. A. Hassan, and M. Lachemi, "Properties of self-consolidating engineered cementitious composite modified with rubber," *J. Mater. Civ. Eng.*, vol. 30, no. 4, 2018.

[10] T. Gupta, S. Chaudhary, and R. K. Sharma, "Mechanical and durability properties of waste rubber fiber concrete with and without silica fume," *J. Clean. Prod.*, vol. 112, pp. 702–711, 2016.

[11] S. Raffoul, R. Garcia, K. Pilakoutas, M. Guadagnini, and N. F. Medina, "Optimisation of rubberised concrete with high rubber content: An experimental investigation," *Constr. Build. Mater.*, vol. 124, pp. 391–404, 2016.

[12] R. Kumar and N. Dev, "Mechanical and Microstructural Properties of Rubberized Concrete After Surface Modification of Waste Tire Rubber Crumb," *Arab. J. Sci. Eng.*, 2021.

[13] T. Gupta, S. Chaudhary, and R. K. Sharma, "Assessment of mechanical and durability properties of concrete containing waste rubber tire as fine aggregate," *Constr. Build. Mater.*, vol. 73, pp. 562–574, 2014.

[14] T. Gupta, R. K. Sharma, and S. Chaudhary, "Impact resistance of concrete containing waste rubber fiber and silica fume," *Int. J. Impact Eng.*, vol. 83, pp. 76–87, 2015.

[15] E. Ozbay and M. Lachemi, "Compressive strength, abrasion resistance and energy absorption capacity of rubberized concretes with and without slag," *Mater. Struct.*, pp. 1297–1307, 2011.

[16] K. B. Najim and M. R. Hall, "Mechanical and dynamic properties of self-compacting crumb rubber modified concrete," *Constr. Build. Mater.*, vol. 27, no. 1, pp. 521–530, 2012.

[17] IS: 1199 - 1959 Reaffirmed, "Methods of sampling and analysis of concrete," *Indian Stand.*, 2004.

[18] IS: 10086-1982 Reaffirmed, "Specification for moulds for use in tests of cement and concrete," *Indian Stand.*, 2008.

[19] T. Gupta, A. Tiwari, S. Siddique, R. K. Sharma, and S. Chaudhary, "Response assessment under dynamic loading and microstructural investigations of rubberized concrete," *J. Mater. Civ. Eng.*, vol. 29, no. 8, pp. 1–15, 2017.

[20] M. K. Batayneh, I. Marie, and I. Asi, "Promoting the use of crumb rubber concrete in developing countries," *Waste Manag.*, vol. 28, no. 11, pp. 2171–2176, Nov. 2008.

[21] M. M. R. Taha, M. Asce, and M. A. A. El-wahab, "Mechanical , Fracture , and Microstructural Investigations," vol. 20, no. 10, pp. 640–649, 2009.

View publication stats

ResearchGate

See discussions, stats, and author profiles for this publication at: https://www.researchgate.net/publication/358368081

IOT BASED NON-CONTACT FUEL LEVEL MONITORING

Article *in* IARJSET · January 2022

DOI: 10.17148/IARJSET.2022.9128

CITATIONS
0

READS
5

1 author:



Abhishek Singh
Delhi Technological University
2 PUBLICATIONS **0** CITATIONS

SEE PROFILE

Some of the authors of this publication are also working on these related projects:

IOT BASED NON CONTACT FUEL LEVEL MONITORING View project

All content following this page was uploaded by Abhishek Singh on 05 February 2022.

The user has requested enhancement of the downloaded file.

IARJSET ISSN (O) 2393-8021, ISSN (P) 2394-1588

International Advanced Research Journal in Science, Engineering and Technology

Impact Factor 7.105 ⁜ Vol. 9, Issue 1, January 2022

DOI: 10.17148/IARJSET.2022.9128

IOT BASED NON-CONTACT FUEL LEVEL MONITORING

Abhishek Singh

Undergraduate student, Department of Mechanical Engineering Delhi Technological University,

Bawana Road, New Delhi- 110042, India.

Abstract: In recent years, technology has advanced at a breakneck pace, making human existence simpler in a variety of ways. The Internet of Things is widely employed in daily objects, and its popularity is growing by the day. The design and implementation of an IoT and mobile-based vehicle fuel / tank level activities such as real-time fuel/water monitoring are covered in this article. Capacitance is used in the suggested IoT gadget to measure the amount of fuel/water. The driver receives a notification through mobile application when the vehicle's fuel/water reaches a specified level. A capacitive sensor for detecting water level has been created. As can be seen from the impedance (reactance) equation for a capacitor, it often has a high-impedance sensor, especially at low frequencies. In addition, in most cases, a capacitive sensor is a non-contacting device . In this study, copper plates were used to produce a capacitive fuel/water level sensor. The fuel/water level determines the dielectric constant between two plates. As a result, because it is inversely proportional to sensor impedance, it may be utilised to calculate fuel/water level from electrical characteristics. Signal conditioning for the system includes linearization, inverting amplifiers, and rectifier circuits.

Keywords: **ESP32**, **Capacitive sensing, Liquid level monitoring , Android Application.**

1.INTRODUCTION

Internet of Things (IoT) is a system of interconnected computing devices and machines with unique identifiers (UIDs) and the ability to transfer data without human intervention. IOT stands for the Internet of Things, which means they can transfer data between machines and other machines. Liquid storage tanks have been widely used in different industrial facilities and power plants as large-scale fuel and oil storage tanks, as well as small-scale water tanks for residential water and cooling or heating air-conditioning systems. Liquid storage tanks' dynamic characteristics are influenced by their geometry and materials, the types of fluids stored in them, their water level, and the excitation force applied to them.

Capacitive methods are widely utilised to measure various sorts of water levels. The majority of capacitors are built with a set physical structure in mind. However, many circumstances can cause the capacitor's structure to change, and the subsequent change in capacitance can be utilised to detect those changes. Changes in dielectrics alter the distance between the plates as well as their effective area. The different types of liquid level transducers for liquid level measurement in any process industry are designed using liquid properties such as pressure at depth, buoyancy, relative electrical permittivity, electrical and thermal conductivity, liquid surface reflection of sound or light waves, and radiation absorption. For measuring water level, there are two types of capacitive level sensors: contact-type and non-contact-type. In this study, we showed how a capacitive sensor may be developed to inspect the liquid level within any container without interfering with the liquid. We ensured an effective method of inspecting and monitoring liquid levels from outside the container. A significant benefit of the capacitive approach is that it detects the level without involving any insertion into our container.

The system consists of a continuous detecting or transmitting device that assesses the measurement level and transfers the data to a microcontroller. The liquid level indicator displays the height of the liquid contained in the tank's interior using a capacitive sensor. The liquid level is determined by measuring the change in capacitance of the fluid with a capacitive sensor and displaying the results on a display screen (LCD).
This project has now become paramount for vehicle activity. Real-time fuel-filled and fuel usage in automobiles is no longer maintained. When the driver begins filling the tank with petrol, the Capacitive sensor activates and stores data on the mobile application. Some drivers are permitted to drive without first obtaining permission from the owner of the vehicle. At the time, the driver was renting or using the automobile for personal reasons. The suggested vehicle activity monitoring system is dependable, simple to build, and user-friendly, and it continues to monitor via a mobile application.

IARJSET ISSN (O) 2393-8021, ISSN (P) 2394-1588

International Advanced Research Journal in Science, Engineering and Technology

Impact Factor 7.105 ⁜ Vol. 9, Issue 1, January 2022

DOI: 10.17148/IARJSET.2022.9128

2. RELATED WORK

The specific origin of the capacitive water level sensor is unknown, but it appears to date from the beginning of the last decade. A low-cost non-contact-type capacitive approach for conducting liquid level sensing evolved in 2006.The liquid level is connected to qualities such as buoyancy, pressure at depth, relative electrical permittivity, electrical conductivity, thermal conductivity absorption or radiation, liquid surface reflection of sound or light waves, and so on.
Different inferential forms of liquid level transducers, such as float, displacer, pressure sensor, capacitive probe, partly submerged resistance wire probes, and so on, are designed using these liquid qualities. Contact-type liquid level detecting probes, such as floats, displacers, capacitive probes, and others, have the problem that their characteristic characteristics with liquid level may vary owing to physical or chemical reactions between the liquid and the probe material, limiting their life span.
Due to buoyancy, the float travels up and down in them. A magnet in the float activates a reed switch in the stem, which produces a detecting signal (see the figure below).The level metre, however, may not be able to measure liquids with certain viscosities and specific gravities. The float gets stuck easily and does not move. The float float type liquid level switch uses the buoyancy of the liquid to push the float of the magnet up and down, opening and closing the internal reed switch, limiting the minimum liquid level.

The magnetic float level switch has a loose structure and is not easy to clean. The magnet will adsorb impurities in the water and cause scale. The liquid level float switch can only be mounted on the upper or lower side, and the product's functionality is limited by the fixed installation technique. However, there are several electrical equipment, and the tanks are formed strangely.

So we employ a uniform right circular cylinder made of an insulating material such as glass, ceramic, nylon, PVC, and so on as the dielectric of the cylindrical capacitor in this technology to try to remove the faults of the convectional non-contact capacitance type level sensing probe. Three-electrode capacitive liquid level sensor is not only measure the liquid level of the vessel, but also to assess the vessel's gradient state. Identical electrodes are used in a traditional sensor to detect liquid levels in a non-metallic storage tank.



Fig1. Pictures of the foil paper assembled with the container to conduct the performance test.

Plates have ability to store electrical charges. The value of capacitor C obtains from equation where L is the distance between two plates, and ε is dielectric constants of the insulator materials between two plates (which it consists of o ε (permittivity of vacuum) and r ε (relative permittivity))(equation)

$C = \varepsilon (A / L)$ (1)

From equation, the capacitance (C) value is affected by the value of ε , A , and l . Hence, equation 2 , which shows the influence of the variables to sensor's capacitance value, can be derived from equation.

$C = \varepsilon_o \varepsilon_r (A / L)$ (2)

From equation , the capacitance (C) value is affected by the value of A , and l . Hence, equation (2) , which shows the influence of the variables to sensor's capacitance value, can be derived from equation (1).

$$s = \frac{\Delta C}{\Delta A} = \frac{1}{b}\frac{\Delta C}{\Delta x} = \frac{\varepsilon}{l} \quad (3)$$

Because of the level role as the measuring object, the ideal sensor's sensitivity can be written as equation (3) where l represents level of the liquid and b is width of the sensor. It shows the sensitivity of the sensor depends on water level is a constant if the values of ε and l are also constants.

IARJSET ISSN (O) 2393-8021, ISSN (P) 2394-1588

International Advanced Research Journal in Science, Engineering and Technology

Impact Factor 7.105 ⁜ Vol. 9, Issue 1, January 2022

DOI: 10.17148/IARJSET.2022.9128

3. THEORY OF OPERATION

One of the numerous reasons why a owner instals a vehicle monitoring system for his or her long-distance vehicle is to reclaim control over road losses. As a starting step, he or she should concentrate on decreasing fuel waste and detecting route fuel theft efforts. Fuel theft is a risk for unmonitored automobiles, thus keeping an eye on the fuel tank level is crucial for catching thieves in the act. And also I Proposed a strategy for controlling and preventing petrol-pump fraud. When the agent starts filling the vehicle tank with fuel, the Capacitive sensor activates and sends out a sequence of pulses proportionate to the immediate flow rate.

The overall tracking and monitoring system has been integrated with Cloud computing and cloud-based application software. The data is sent to the cloud server via the ES32. The user application also uses GPS to find the user. The evaluated research uses a flow sensor to measure fuel, whereas the suggested system uses an capacitive sensor to measure fuel in tanks of varied sizes.

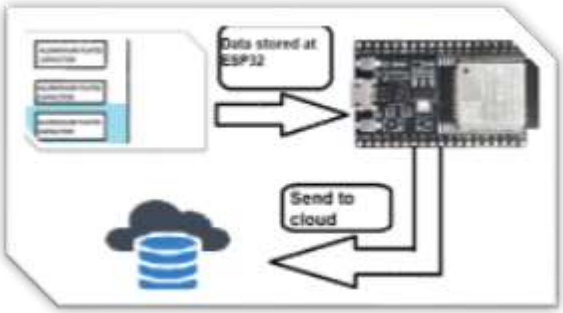


Fig 2.Process flow diagram of the proposed work

3.1 ESP32 MICROCONTROLLERS

ESP32 is a powerful SoC (System on Chip) microcontroller with built-in Wi-Fi 802.11 b/g/n, dual-mode Bluetooth 4.2, and a wide range of peripherals. It is an improved successor to the 8266 chip, especially in terms of the installation of two cores clocked at varying speeds up to 240 MHz in different versions. Apart from these improvements, it also increases the number of GPIO pins from 17 to 36, the number of PWM channels from 16 to 16, and includes 4MB of flash memory.

The Espressif Systems firm created the ESP32 chip, and it presently provides multiple ESP32 variants of the SoC, including the ESP32 Developer Kit, the ESP32 Wrover Kit, which contains an SD card and a 3.2" LCD display, and the ESP32 Azure IoT kit with USB Bridge and other built-in sensors. Other manufacturers, such as SparkFun with its ESP32 Thing DB, WeMoS with its TTGO, D1, Lolin32, and Lolin D32, Adafruid (with Huzzah32), DF Robot (ESP32 FireBeeatle), and many more, occasionally provide decent and sometimes awful clones of these chips.

4. HIGH-LEVEL DESIGN & IMPLEMENTATION DETAILS

Our research into employing capacitive sensing to externally assess the liquid level within a container is split into two parts. To begin, we investigate the usefulness of several capacitive sensor designs in containers composed of various materials. To accomplish so, we analyse several designs for a capacitive sensor in terms of the number, size, and positioning of the electrodes. Surfaces of conductivity in respect to dielectric materials (comprised of the container and the liquid inside it).

Second, we utilise the results of the first investigation to evaluate the usefulness of a certain capacitive sensor design for measuring the amount of liquid medication in a plastic container from the outside. This allows us to see if the data from the first phase can be used to measure a different type of liquid within a different shape and size container.

Aluminium foil was used to create the conductive surfaces. The conductive surfaces were then linked up to esp32 in order to measure the capacitance change when the liquid level in the cup changed. One conductive surface is linked to touch pins. In the circuit, these connections are the signal pin, respectively. To use any of the implemented sensors, we must first configure the signal pin to produce a high voltage while the sensor pin remains low. The electrical charge will then flow into one of the capacitor's conducting surfaces, charging it until the sensor pin and the signal pin are at the same voltage.

IARJSET ISSN (O) 2393-8021, ISSN (P) 2394-1588

International Advanced Research Journal in Science, Engineering and Technology

Impact Factor 7.105 ⁜ Vol. 9, Issue 1, January 2022

DOI: 10.17148/IARJSET.2022.9128

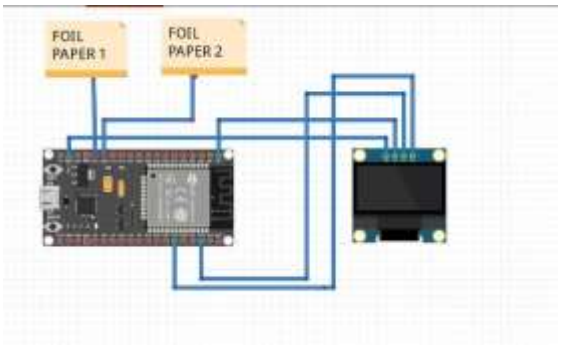
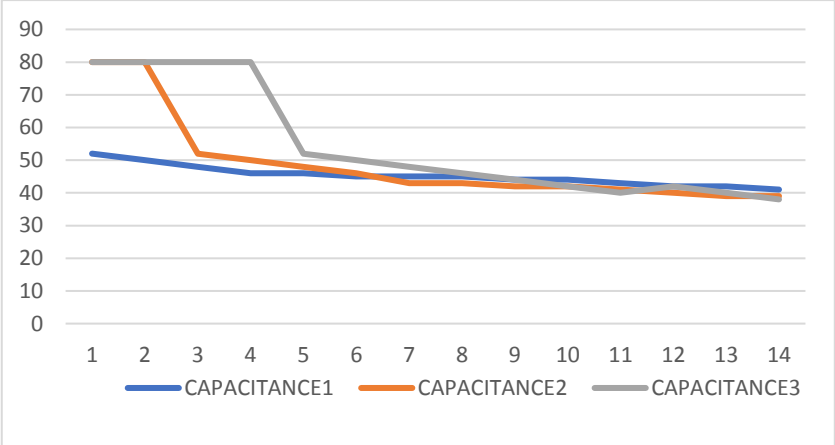


Fig 3.Circuit Diagram

Then, with the signal pin in a low voltage condition, we configure the sensor pin to produce a high voltage. Until the sensor and signal pins attain the same voltage, electrical charge will flow out of the capacitor's conducting surface. The capacitor is effectively charged and then discharged. Upon reaching the critical water level in the tank, an indication is sent through IOT module to the technician in charge for further.

5. RESULT AND DISCUSSION

The test was performed by measuring the water level while filling and emptying the tank. The acquired result depicts the variation in capacitance as the water level changes. On the serial plotter, the curve was noticed. . Figures depict the collected data waveform without and with 100 ml of water, respectively. The time duration of the signal rose as the amount of water in the tank climbed from 0 to 100 ml.



Similarly, measurements for varying levels of water were taken. These measurements were quantitatively analysed using embedded code and the look up table idea. Figure depicts a portion of the data gathered from the experimental setup. To study the behaviour of capacitance change, different sets of measurements were obtained.

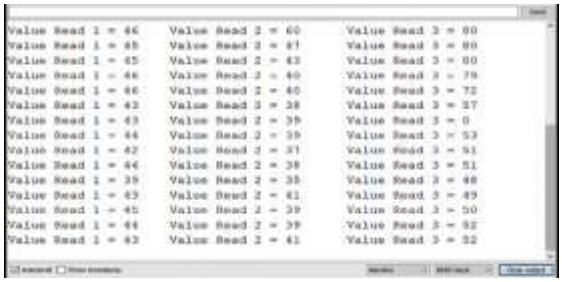


Fig.4 Experimental results of capacitance value measured by increasing the amount of water.

IARJSET ISSN (O) 2393-8021, ISSN (P) 2394-1588

International Advanced Research Journal in Science, Engineering and Technology

Impact Factor 7.105 ⁜ Vol. 9, Issue 1, January 2022

DOI: 10.17148/IARJSET.2022.9128



The current research might be used for a variety of additional experiments. It comprises substance identification in the container as well as level detection for fluids other than water. For example, the dielectric constant of air is 1, that of water is 80, and that of petroleum is 2.2. The acquired data fluctuates as the dielectric constant of the material changes.

5. CONCLUSION

In this paper, we presented the results of a study on designing a capacitive sensor for developing an automatic water level measuring container. The proposed design differs from a traditional capacitive sensor with one pair of electrodes, because it has three pairs of electrodes as the main sensors for measuring the capacitance value of the water level in the tumbler. Without submerging the sensor. It finds widespread use in automobile fuel measuring systems, substance identification, and level detection, among other things. The data from a certain medium is gathered in the lookup table. The usage of lookup tables in software implementation allows for more efficient data analysis. As a result, the sensitivity of this sensor is determined by the medium's and container's dielectric properties.

6.REFERENCES

1. Khaliq S, James SW, Tatam RP. Fiber-optic liquid-level sensor using a long-period grating. Optics Letters 2001; 26(16): 1224.
2. Raatikainena P, Kassamakovb I, Kakanakovb R, Luukkalaa M. Fiber-optic liquid-level sensor. Sens, Actuators, A 2009; 58(2): 685.
3. Baxter, L. Capacitive Sensors Design and Applications, IEEE Press, Piscataway, NJ, USA, 1997.
4. Canbolat, H. (2009). A novel level measurement technique using three capacitive sensors for liquids. Instrumentation and Measurement, IEEE Transactions on, 58(10), 3762-3768.
5. Texas Instrument. (2015, March) Capacitive-Based Liquid Level Sensing Sensor Refecence Design.
6. Alfadhl Yahya Khaled, Samsuzana Abd Aziz, and Fakhrul Zaman Rokhani, "Capacitive Sensor Probe to Assess Frying Oil Degradation," Information Processing in Agrigulture, pp. 142-148, 2015.
7. P. Srivastava, M. Bajaj, and A.S. Rana. IOT based controlling of hybrid energy system using ESP8266. 2018 IEEMA Engineer Infinite Conference (eTechNxT), pp. 1-5, March 2018.
8. R. Gupta, and K. K. Singh. Blynk-based Water Level Monitoring System. Current Trends in Signal Processing, vol. 8, no. 2, pp. 1-3, May 2018.
9. D. Nyce. Tank gauging advances. Fuel Technology amp Management, vol. 7, no. 1, Jan. 1997.
10. K.W. Brown and T.J. Armstrong. Hydrocarbon Inhalation, StatPearls. StatPearls Publishing, June 2019.

© IARJSET This work is licensed under a Creative Commons Attribution 4.0 International License

View publication stats

ResearchGate

See discussions, stats, and author profiles for this publication at: https://www.researchgate.net/publication/353422825

Layered Double Hydroxide Nanomaterials: Biomedical Applications, Current Status, and Challenges

Article *in* Nano LIFE · July 2021

DOI: 10.1142/S1793984421300089

CITATION
1

READS
58

6 authors, including:



Ritika Sharma
University of Delhi
4 PUBLICATIONS **3** CITATIONS
SEE PROFILE



Poonam Singh
Delhi Technological University
16 PUBLICATIONS **19** CITATIONS
SEE PROFILE



Vinod Kumar
Jawaharlal Nehru University
30 PUBLICATIONS **584** CITATIONS
SEE PROFILE

Some of the authors of this publication are also working on these related projects:

Project
Environmental Applications of Composites Based on Layered Double Hydroxides View project

Project
Molecular docking View project

All content following this page was uploaded by Ritika Sharma on 09 February 2022.

The user has requested enhancement of the downloaded file.

Nano LIFE
Vol. 11, No. 3 (2021) 2130008 (20 pages)
© World Scientific Publishing Company
DOI: 10.1142/S1793984421300089

World Scientific
www.worldscientific.com

Layered Double Hydroxide Nanomaterials: Biomedical Applications, Current Status and Challenges

Ritika Sharma*, Bhawna[†,‡], Sanjeev Kumar[†,‡], Poonam Singh[§], Akanksha Gupta[¶,**] and Vinod Kumar[†,‖,††]

*Department of Biochemistry
University of Delhi, New Delhi, India

[†]Department of Chemistry, Kirori Mal College
University of Delhi, New Delhi, India

[‡]Department of Chemistry, University of Delhi
New Delhi, India

[§]Department of Applied Chemistry
Delhi Technological University, New Delhi, India

[¶]Department of Chemistry, Sri Venkateswara College
University of Delhi, New Delhi, India

[‖]Special Centre for Nano Sciences
Jawaharlal Nehru University, New Delhi, India
**akankshachem05@gmail.com
††kumarv@mail.jnu.ac.in

Received 28 April 2021
Accepted 3 July 2021
Published 18 August 2021

Layered double hydroxide nanomaterials (LDH NMs) have been dragging the researchers' attention toward biomedical applications owing to their physiochemical properties, biocompatibility, environmental sensitivity and good cellular uptake mechanisms. Various synthetic methods have been presented in brief. This paper draws attention toward the modification and functionalization of LDH nanostructures for biomedical applications in targeted and controlled drug release, anticancer, bioimaging, bone therapy and regeneration, gene delivery, ophthalmic and antitumor activities. Further, it explains the properties of conjugated LDH NMs which put forward their possibilities to be used in synthesizing the most demanding vaccine for COVID-19 pandemic. Current scenario, challenges and future perspective of LDH NMs have also been discussed.

Keywords: Nanotechnology; nanomedicine; drug delivery; bone therapy; toxicity.

1. Introduction

Over the past few decades, there is currently an increasing interest in layered double hydroxides (LDHs) because of their practical applications in a wide variety of fields i.e., flame retardants, catalysis, adsorption, electrochemical and biomedical

**,††Corresponding authors.

applications. LDH-based nanostructures have a number of benefits over other materials such as ease of synthesis, good stability, rich intercalation chemistry, high drug incorporation capacity, superior cellular uptake behavior over other conventional drug carriers, biocompatibility, etc.[1–3] Nanomedicine is the culmination of applications in nanotechnology along with functionalized nanoparticles (NPs) for diagnosis and treatment of many diseases.[4,5] Among various nanomaterials (NMs), LDHs have drawn lot of interest in the area of biomedicine. LDHs have procured great importance owing to the physicochemical properties which make them appropriate for applications in biomedicine such as carrier for drug delivery, gene therapy, bone targeting, etc.[6–8] Hence, due to the versatile uses, scientists look for the emergence usage of LDH NPs as a substantial area for research.

LDH has a layered brucite-type structure containing MO_6 octahedral where anions are present in between the interlayers [Fig. 1]. LDHs are usually represented using the chemical composition $[M^{2+}_{1-x}M^{3+}x(OH)_2]^{x+}(A^{n-}_{x/n}) \cdot yH_2O$; where M^{2+} (Ca^{2+}, Ni^{2+}, Zn^{2+}, Fe^{2+}, etc.) and M^{3+}(Mn^{3+}, Co^{3+}, Cr^{3+}, Mn^{3+}, La^{3+}, etc.) are bivalent and trivalent metal cations, A^{n-} is the interlamellar or the charge compensating anion of valence n, y signifies the amount of water molecule present in the interlamellar region and x is the ratio $M^{3+}/(M^{2+} + M^{3+})$. The interlayer interactions of LDH NMs are relatively weak and consequently put forth an extraordinary possibility for innovation of strategies that would allow functional modulations without hampering structural attributes. Adjustable interlayer spacing and biocompatibility make them highly desirable NMs for biomedical applications.[8,9]

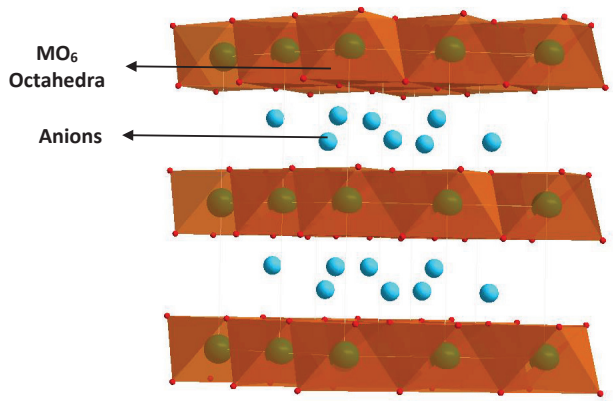


Fig. 1. The schematic structure of LDH.

It possesses a two-dimensional (2D) structure and has emerged as an indispensable class of inorganic NMs with the ability to accommodate large molecules on account of increased surface-to-volume ratio. The divalent metal ion in the structure of LDH, when substituted by the trivalent ion, results in the formation of positively charged sheets, balancing the presence of exchangeable anions such as nitrates, sulfates, etc.[10,11] Such characteristics and their lamellar structure facilitate their use in therapeutic agents, reducing dire side effects, etc. Also, LDH NMs intercalated with therapeutic agents could be released in a prolonged manner, therefore, decreasing the frequency of administered drug.[12] They exhibit exceptional properties such as cost-effectiveness, enhanced biocompatibility, feasible synthesis and lower toxicity, makes them suitable for applications in biomedical field.

Herein, a brief discussion on LDH NMs' synthesis, characteristics, functionalization and their prospective applications in biomedicine has been highlighted. Additionally, an emphasis has been given on the current status and future perspective for development of LDH NPs in the field of biomedicine.

2. Synthesis of LDH NPs

The rationale behind several applications of LDHs in biomedical science is their ease of synthesis. The synthetic method of LDH NPs has broadly been classified into two categories: (1) direct synthesis and (2) indirect synthesis. Direct synthesis can be further classified into several categories: (1) co-precipitation method, (2) urea hydrolysis method, (3) salt-oxide method, (4) sol–gel method, (5) hydrothermal method and (6) electrochemical method. The indirect synthetic method is based on the conventional strategies and is classified into three categories: (1) anion-exchange method, (2) memory effect method and (3) delamination method.[6] Several factors influence the strategy selectivity such as nature of cations making hydroxide layers, anionic interlayers and the desired properties of the final product such as phase purity, degree of crystallinity, particle size and shape, porosity, electronic and optical properties. LDHs have several characteristics such as morphology, crystal structure, size, etc. that account for the selection of synthetic method for preparation. Mostly, solution-phase approaches offer better flexibility and controlled

particle shape over gas phase approaches. Morphologies can be varied owing to subtle changes in the reaction conditions. Few of the most common and facile synthetic methods are discussed here.

2.1. *Co-precipitation method*

It is a frequently used and facile approach to synthesize LDH NMs, involving the addition of alkali to inorganic salt solution at a defined pH followed by precipitation [Fig. 3].[17] In this method, an important factor to be controlled is the ($OH-/M^{2+}/M^{3+}$) molar ratio. Here, hydroxyl anions and corresponding metal ions are mixed with salt of interlayer anions at constant and variable pH value. N_2 gas purging prevents intercalation of carbonate as it has a good affinity for LDH and makes it suitable to intercalate other ions, drugs, etc.[18] In addition, pH plays an important role, as change in pH leads to variable properties including crystallinity, size, specific surface area, etc. for LDH NMs. Along with pH, calcination temperature also has a major effect on particle size. For example, in the facile synthesis of $CoFe_2O_4$ LDH NPs, the measured particles size

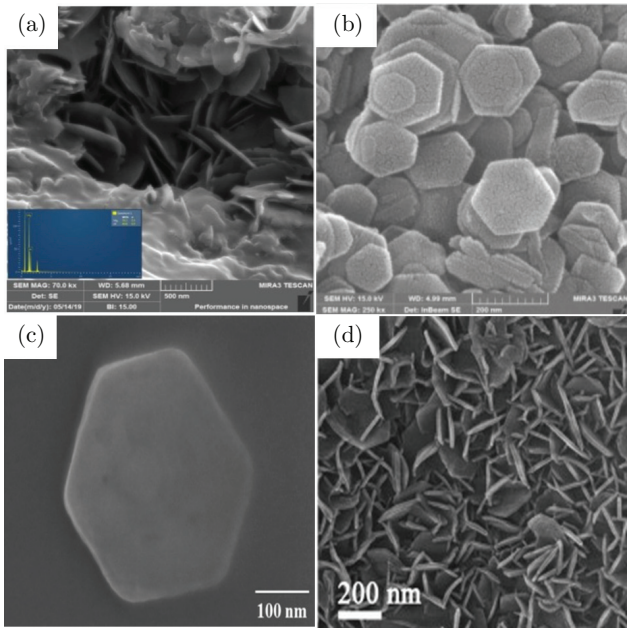


Fig. 2. SEM images of LDHs synthesized via (a) co-precipitation method (Copyright © 2021 Elsevier Ltd. All rights reserved),[13] (b) hydrothermal method (Copyright © 2017 Elsevier Ltd. All rights reserved),[14] (c) sol–gel method (Copyright © 2019 Elsevier Ltd. All rights reserved[15] and (d) reconstruction method (Copyright © 2012 Elsevier Ltd. All rights reserved).[16]

was 44 nm at 800°C and that was increased by 1.1 mm when the temperature reaches 1100°C which further increases linearly with increasing temperature.[19] Abdollahi *et al.* fabricated Mg-Al LDH NPs via co-precipitation technique, where chloride salt of magnesium was dropwise added to the salt of aluminum at constant stirring for a day at room temperature and pH ∼ 12 which was controlled by ammonium solution to get the nano-LDH petal-like morphology [Fig. 2(a)]. Results demonstrate the enhanced structural and antifouling properties.[13]

2.2. *Hydrothermal method*

In hydrothermal method, reactors made of stainless steel lined with Teflon are used. The operation temperature in reactor is generally kept high along with pressure generated by autoclave for long hours to synthesize LDH NMs [Fig. 4].[20,21] Different LDH nanostructures with uniform morphology such as nanosheets, nanofibers, etc. can be formed by this method by changing the reaction conditions. Xu *et al.* investigated the correlation between nano-LDHs' size and treatment conditions such as time, temperature and concentration. Results conclude that particle size could be controlled between 40 nm and 300 nm by adjusting reaction conditions.[22] Likewise, Pourfaraj *et al.* synthesized hexagonal-shaped Mg-Al LDH via hydrothermal method by adding the above-mentioned aqueous slurry to autoclave in oven at 180°C for a day [Fig. 2(b)].[14]

2.3. *Sol–gel method*

A low-cost and energy efficient method named sol–gel is used to synthesize composition controlled LDH [Fig. 5]. It involves room temperature dissolution of inorganic salts or organic compounds in water or solvent and generates high surface mesoporous LDH NPs with enhanced properties.[23] Moreover, the synthetic conditions are controlled in a better way over co-precipitation method and yielded larger surface area LDHs. Further, it provides phase purity, homogeneity and reproducibility of the synthesized nano-LDH.[24] Based on a recent study, Valeikiene *et al.* demonstrated the synthesis of $Mg_{3-x}M_x/Al_1$ LDHs using a complexing agent (glycol and citric acid) where M is transition metal such as Ni, Zn, CO, etc. The synthesized LDH could be implemented in several biomedical applications

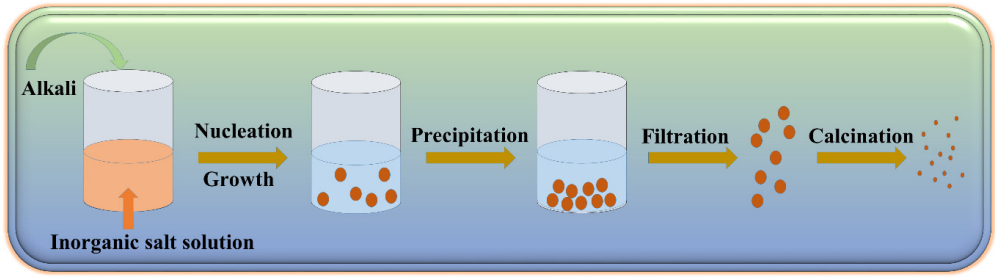


Fig. 3. The schematic diagram of co-precipitation method.

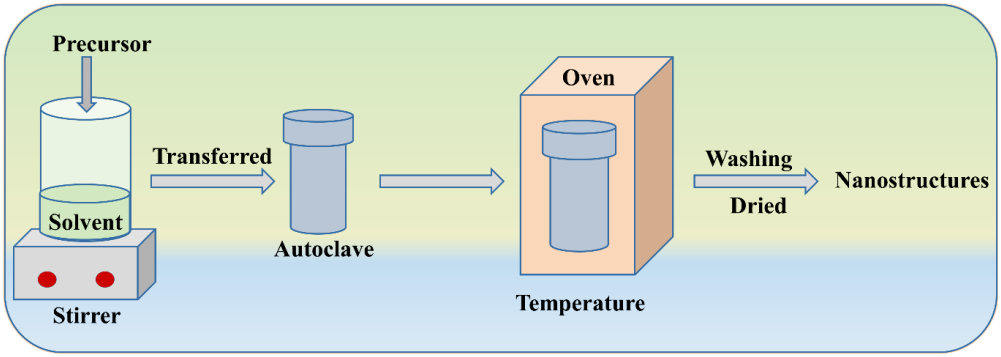


Fig. 4. The schematic diagram of hydrothermal synthetic method.

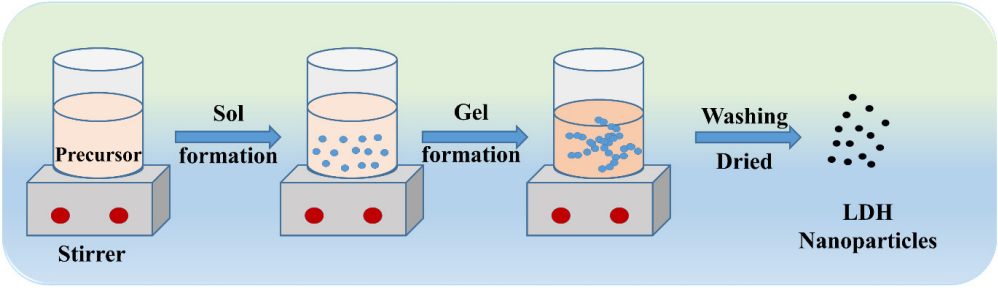


Fig. 5. The schematic diagram of sol–gel method.

and could be used as a progenitor for the development of useful mixed metal oxides NPs. Furthermore, these properties could be explored in developing ultra-thin films and potential role in biological implants, regenerative medicines and biosensors.[24] Vieira *et al.* developed Mg-Al-Ce LDHs via sol–gel method and successfully intercalated corrosion inhibitor $H_2PO_4^-$ anion into the layered structure which showed a promising corrosion protector [Fig. 2(c)].[15]

2.4. *Reconstruction or memory effect method*

Another vital method used for synthesis of LDH is reconstruction or memory effect method. In reconstruction or memory effect method, LDH interlayers undergo a calcination and then mixed with the preferred anion for rehydration and reconstruction of the nano-LDH system with the anion of choice. It allows the possibility of getting back the native shape after calcination followed by

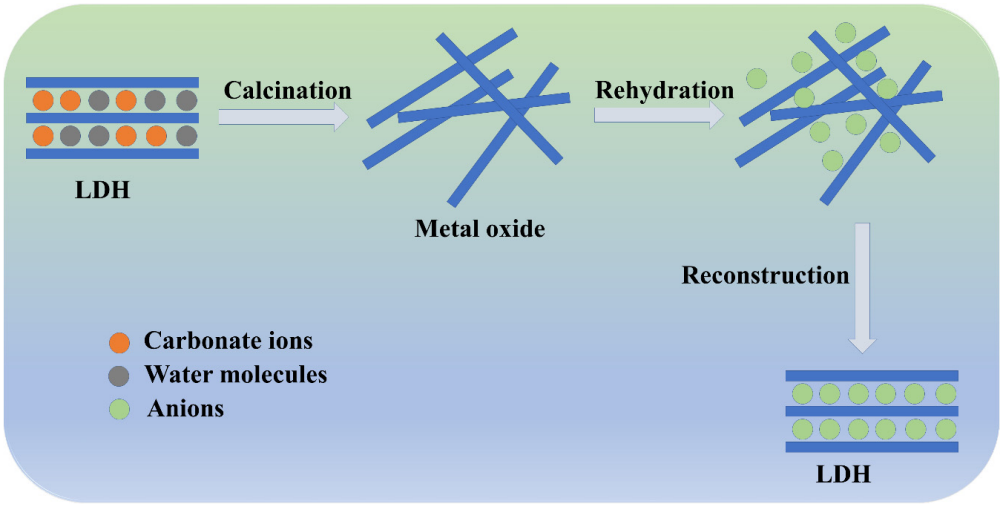


Fig. 6. The schematic diagram of reconstruction method.

rehydration [Fig. 6]. Mansouri *et al.* successfully developed 3D LDH nanostructures to deliver naproxen (an anti-inflammatory drug). They prepared via a solution of magnesium and aluminum chloride in water–ethanol to obtain iridescent crystal. Obtained sample was immersed in naproxen and potassium hydroxide in decarbonated water at room temperature and pH ~ 9 for 12 h. Their results demonstrated the utilization of the synthesized nano-LDH in delivering of naproxen (an anti-inflammatory drug).[25] Kuroda *et al.* synthesized LDH NPs with size ranging from 5 nm to 25 nm having hexagonal shape. In their study, they used tri(hydroxymethyl)aminomethane as a ligand, which was conjugated to the LDH NPs through tridentate linkage. Further, their results demonstrate their prospective utilization in dissolution enhancement.[26] TiO_2/CuMgAl-LDH NPs [Fig. 2(d)] were synthesized through reconstruction method by Lu *et al.*[16]

2.5. *Anion-exchange method*

An indirect method that is widely used for synthesis of nano-LDHs is anion-exchange method. The LDH

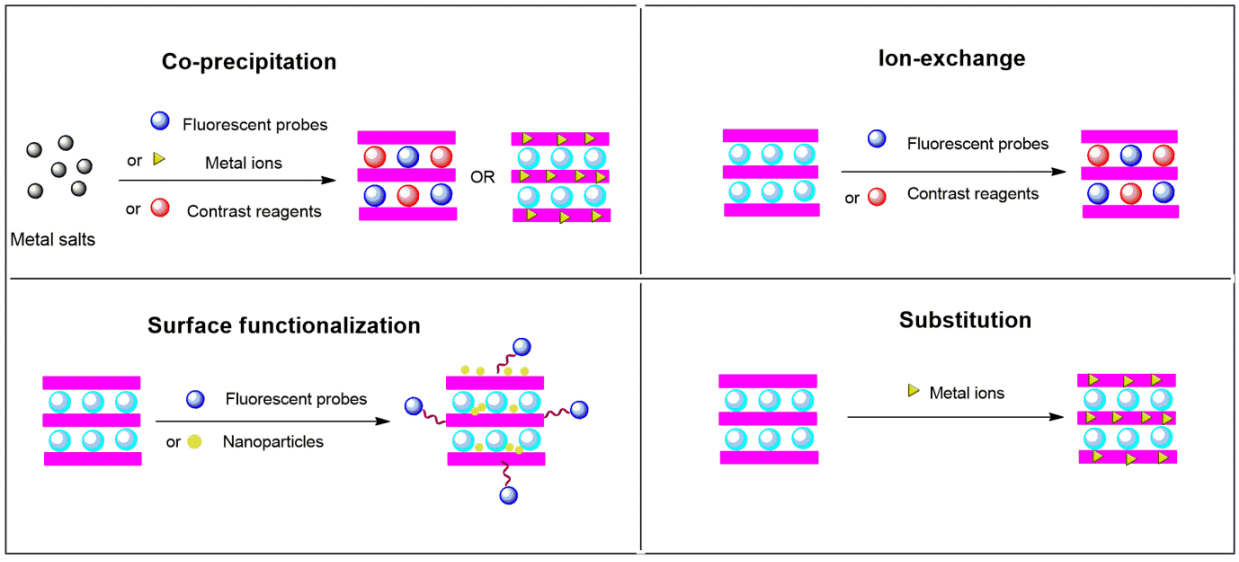


Fig. 7. Synthetic strategies for functionalized LDH nanohybrids — co-precipitation, ion-exchange, surface functionalization and substitution.[30]

synthesized by direct route acts as precursor material for indirect synthesis methods. This indirect process is based on the approach that the layered structure of LDH is extremely prone to anion diffusion and exchange. In this method, first the LDHs are synthesized using direct approach with easily exchangeable anions (hosts). After that, the solutions containing synthesized LDHs and excess of desirable anions are stirred together.[27] The exchange process strongly depends on electrostatic interaction among positively charged LDHs and negatively charged anions. Other factors such as solvent, pH, temperature, etc., play a crucial role in LDH anion-exchange.[28] Hence, this method is useful for drug insertion into LDH NPs, making them suitable for biomedical applications. Cefazolin was successfully intercalated into Zn,Al-nitrate LDH through anion-exchange method under a controlled pH 7 in an inert N_2 atmosphere to decant any CO_2 if present in the reaction medium. Preparation of intercalated compound involves dissolution of sodium salt of cefazolin into a 70:30 ratio of ethanol: water mixture using a ratio of 2:1 for cefazolin: LDH. 37% cefazolin was found incorporated into LDH layers as assessed through PXRD.[29]

Some of the important and commonly used methods for nano-LDH preparation in biomedical applications have also been explained in Fig. 7.

3. Characteristics and Biocompatibility

LDH NMs possess excellent characteristics, making them suitable for perspective role in the field of biomedicine. These properties are flexibility, low toxicity, sensitivity to pH, etc. They are found to have excellent flexibility to be synthesized in various shapes and assist as a target drug carrier. Uptake of LDH inserted drug molecule is based on particle shape. The cellular localization is influenced by the morphological orientation of LDHs, for example, rod-like and sheet-like LDH morphology was successfully targeted to the nucleus and cytoplasm, respectively, in mammalian cell lines.[31,32] Being positively charged, LDH NMs possess high drug loading capacity and therefore, have the efficacy as delivery carrier for genes and antibodies. The size tunability of LDH NMs approaches toward their wide range of biological applications. Flexibility in size has revolutionized nano-LDH in drug delivery and diagnosis. Li *et al.* and Chung *et al.* carried out studies based on the morphological effects of conjugated LDH NMs toward particle uptake[33,34] and differently sized particles are localized differently. Further, Chung *et al.* found that particles sized of 20 nm were localized within the nucleus, while greater-sized particles, i.e., 180 nm were present in the cytoplasm.[34]

Nanomedicine based on LDHs has been explored for pH-responsive imaging and therapeutic treatments. The hydroxide composition of LDH is responsible for their sensitivity to acidic environments. The pH sensitivity along with good biodegradability makes them useful for biomedical applications. Li *et al.* studied pH response of nano-LDHs loaded with ZnPcS8 via co-precipitation method. Photosensitizer formed was assembled based on electrostatic interactions among negative charge on ZnPcS8 and positive charge on LDH. In this study, release of ZnPcS8 from LDH was observed at different pH. At pH 7.4, no specific release was noticed, whereas when pH was dropped to 6.5, significant increase in release was observed and resulting in fluorescence imaging.[35]

Besides their unique properties, one of the most important features is their biodegradability and low toxicity. Bi *et al.* showed their biodegradable behavior as LDH is excreted rapidly and no accumulation is observed. Further, biocompatibility and toxicity were confirmed in rats by intramuscular injection of sterile LDH preparation. There were no signs of inflammation even after 20 days of implantation.[36,37] Kwak *et al.* injected LDH NPs intravenously in rats and showed no side effects. Hence, confirmed their minimal toxicity and biocompatibility by extending their application in biomedical science.[38] Notwithstanding, LDH exhibits some toxic effects, but such effects are less over other NPs such as silica, iron oxide or carbon nanotubes, etc. Evidence suggests that LDH ranging from 100 nm to 200 nm shows low toxicity concerning membrane damage, cell proliferation and inflammation. Intriguingly, the potential of toxicity of several drugs can be diminished on intercalation with LDH.[39]

The bioavailability of the drug can be improved due to pH-dependent solubility and ability for controlled release of drug.[8,40,41] Furthermore, they possess anion-exchange capacity and specific surface area. Also, they own better membrane penetration, ability to reconstitute its original structure in mild conditions, better mechanical strength and could be used as coating materials for implant devices

and opens up a promising field for bioimaging applications.[30,42,43]

4. Current Status

Currently, nanomedicines based on engineered LDHs have emerged as a potential source of diagnostic and therapeutic interventions. Also, the advent of development in nanotheranostic has led to an exploration of several diagnostic probing and imaging modalities. The practical implementation, biosafety and biocompatibility of LDH NPs have demonstrated great potential for further clinical translation and *in vivo* applications in biomedicine. Further, it has been explored as a potential adjuvant alternative due to its inherent properties and slow degradation. Therefore, it can be used for immunotherapeutic applications.[3]

Recently, Muráth *et al.* demonstrated utilization of LDH along with an antioxidant, i.e., ellagic acid (EA). A phenolic compound has low solubility in water, further the surface characteristics of the EA-LDH nanohybrid were enhanced with use of various organic solvents via co-precipitation method and also, exhibited high antioxidant activity. Hence, the potential development of such LDH nanocomposites is suitable for reactive oxygen species (ROS) scavenger during treatment.[44] Additionally, the use of Cu-doped LDH nanomedicine for cancer therapy has emerged as a novel rationale for efficient treatment of combinational cancer and showed least side effects in clinical settings.[45] Not the least, Li *et al.* proposed a model where nanomembrane captive deionization (NMCDI) is suitable for desalinization. They synthesized a hollow Co-MOF@Fe/Co-LDH nanocomposite, thereby, increasing the surface area owing to hollow structure. It has shown to enhance absorption of salt and hence, a promising approach for development of hollow LDH nanocomposites.[46]

As of today, nano-LDH or nanomedicine has been widely utilized in various branches of biosciences. Due to customization of LDH NMs to various shapes and sizes, they are appropriate for a plethora of functions, which they can exhibit. Amid the ongoing pandemic crisis, there is a dire need to develop a potential vaccine candidate against SARS-CoV-2. The hypothesized vaccine development is based on molecular approach.[4] Here, short hairpin RNA (shRNA) molecule possesses the ability to perform gene silencing of viral RNA to block production of viral protein molecules.[47–49] As described later in this paper, a prospective role for molecular vaccine development against SARS-CoV-2 has been hypothesized as a potential vaccine to curb the ongoing pandemic, a need of the hour.[49,50]

Recently, Yu *et al.* developed a nanocomposite of LDH intercalating with peptide nucleic acid (PNA)-DNA hybrids for effective treatment of pancreatic ductal adenocarcinoma (PDAC). These results demonstrate highly effective and selective targeting of mutant sequences, causing suppression of cancer cell proliferation leading to inhibition of pancreatic cancer growth. They showed a highly prospective approach for treatment of PDAC, as it is asymptomatic at initial stages, therefore, poor prognosis would cause malignancy of the tumor and hence surgical abscission is not possible.[51] Liu *et al.* demonstrated a strategy of LDH nanohybrids for application in imaging and cancer nanotheranostics. They developed a pH-sensitive charge reversible LDH nanocomposite coated with polymer as an effective approach to enhance nanotheranostic efficacy by increasing cellular uptake and accumulation of tumor cells. These nanohybrids possess long half-life, i.e., they could circulate in blood stream for a longer duration owing to exposure and re-exposure of therapeutic particle to the tumor cells and causes uptake in acidic environments. Further, high accumulation of these nanohybrids in tumor cells could be seen using magnetic resonance imaging (MRI).[52] Another approach based on cellular uptake and tumor accumulation was demonstrated by Xu *et al.* They modified Cu-LDH NPs with charge-changeable polymer, which could respond to pH changes and thereby improving stability when circulating in blood stream and decreases non-specific uptake. Also, they possess pH-responsive MRI contrast capacity.[53] Dragoi *et al.* developed MnAl-LDH nanosheets with fluorouracil as a nanotheranostic approach for cancer. They prepared the nanosheet via co-precipitation and then the model anticancer drug (fluorouracil) was infused with it via co-precipitation coupled with low suprasaturation or ion-exchange. These results demonstrate a promising approach for cancer theranostics.[54]

5. Functionalization and Biomedical Applications

The efficiency of LDHs in drug delivery systems can be increased by modified or functionalized LDH

NMs, as shown in Table 1, enhancing drug affinity to target sites (organs or tissues), improving dosage stability, etc.[36,55] There are several advanced types of LDHs such as magnetic LDH (MLDH),[7,56,57] doped LDH,[58,59] fluorescent LDH,[60] self-assembled LDH[61] and LDH nanoneedles.[62]

Mg-Al LDH NMs functionalized with 3-dimethyl (methacryloyloxyethyl) ammonium propane sulfonate (DMAPS) through atom transfer radical polymerization (ATRP) method and have shown increased hemocompatibility.[63] Another approach based on surface-functionalized LDH NMs has been

Table 1. Functionalized LDH for biomedical applications.

Functionalized LDH	Application	Ref.
Mg-Al-LDH/DMAPS	Substantially increase hemocompatibility	63
LDH/Folic acid	High efficiency for tumor-targeted delivery	64
Mg-Al-LDH/3-aminopropyl triethoxysilane	Controlled release of ciprofloxacin	65
Zn_2Al/LDH/SDS/GLIB	Improve drug absorption and solubilization	67
Mg-Al-LDH/PEG	Drug delivery and *in vivo* bioimaging	66
SiO_2/LDH/Amine	Enhance efficiency of drug delivery	68
Ca/LDH/ME	Controlled release drug	70
SiO_2/LDH/Mannose	Enhance tumor-targeted siRNA delivery	69
Fe_3O_4/LDH	Efficient drug release at acidic Ph	71
	Tumor-targeted drug delivery	
Au/LDH/Doxorubicin	Apoptosis of cancer cell	72
	Better anticancer activity	
Na/Ca/LDH/Dacarbazine	Improvement in efficacy of anticancer drugs in a pH-dependent manner	73
	High loading capacity, stability and low cytotoxicity of the drug	
Ni-Ti/LDH/Nitinol alloy nanofilm	Selective inhibition of tumor growth and bacterial infection	74
LDH/DNA	Sandwich of DNA-LDH-DNA causes easy penetration	75
	Nonendocytic pathway	
Li-Al/LDH/p53 gene	Efficient gene delivery system for cancer treatment	2
LDH/Mg-Al/Oligo-DNA siRNA mimic	Gene therapy for siRNA interference	76
LDH/Mg-Al/shRNA	Treatment of neurodegenerative diseases	48
	Easily target cell membrane	
LDH/Zn-Al/Cdk9 gene or pCEP4 plasmid	Enhances cellular uptake to C2C12 myoblast cells	77
CMCG-GS-DEXP-LDH	Nanohybrid eye drops	78
	Administration of drug to eye's posterior segment	
Zn-Ti/LDH/Cinnamic acid	Improved stability	79
	Increased UV radiation blocking capacity	
Zn-Ti/LDH/p-amino-benzoic acid	Capability to absorb UV radiation	80
	Produce less amounts of free radical	
LDH/Dysprosium	Reduces water proton relaxation time	81
	An MRI contrast agent	
Gd-LDH/Gadolinium	Improve MRI sensitivity	82
LDH/Au	Improve MRI	82
LDH-plasmid-shRNA	Probable vaccine for COVID-19	49
LDH/PNA-DNA hybrid	Therapy for pancreatic cancer	51
	Selective targeting of intranuclear mutant sequences	
	Promising gene therapy agent	
LDH/Polymer	Increases efficacy of nanotheranostics and imaging	52
	Increases tumor accumulation and cellular uptake of the nanocomposite	
Cu/LDH/Polymer	Enhances cellular uptake and tumor accumulation	53
MnAl/LDH/Fluorouracil	Cancer diagnosis and therapy	54
Ca/Al/LDH/Praziquantel	Increase solubility	83
	Makes the praziquantel-LDH complex thermally stable	
	Increases longevity or shelf life	
Zn/Al/LDH/Carprofen	Increases solubility	84
Zn/Al/Cl/GLIB	Increases solubility	85
	Possess antioxidant activity	

Table 1. (*Continued*)

Functionalized LDH	Application	Ref.
Mg-Al/LDH/Yb	Bone repair material Enhanced osteogenic differentiation	86
Mg-Al/LDH	Bone implants based on LDH Controlled release and better loading capacity of drug Better cytocompatibility	87
Mg-Al/LDH/Risedronate	pH-sensitive behavior Bone tumor therapy	88
LDH/β-TCP	Bone regeneration and tissue engineering Possess osteogenic activity Better biocompatibility and mineralization	89
La-LDH nanohybrid scaffold	Osteoporotic bone regeneration Induce osteogenesis Inhibit osteoclastogenesis	90

shown to enhance efficiency in drug targets. This approach has been utilized to immobilize hydroxy-substituted cisplatin on LDH modified with carboxylate via coordination bonding. Using this approach, LDH NM system has been conjugated with folic acid by Yan *et al.*[64] and showed increased efficiency for targeting tumors and for the development of several types of drug targets.[8,64] Another study demonstrates functionalization of Mg-Al-LDH NMs with 3-aminopropyl triethoxysilane has shown sustainable release of ciprofloxacin in a controlled manner.[65] Also, poly(ethylene glycol) (PEG) functionalization plays significant role in drug-delivering mechanism and *in vivo* bioimaging.[66] Controlled release and improved dissolution rate were observed for Zn_2Al-LDH NPs organomodified with sodium dodecylsulfate (SDS), carrying glibenclamide (GLIB) was depicted by Leão*et al.*[67] Besides functionalization, surface-coated biomolecules are also considered suitable for enhancing LDH efficiency in drug delivery applications. The biomolecules that are suitable for such coating are serum albumin, SiO_2, lipids, etc.[3] An extension has been demonstrated by the use of amine immobilized SiO_2-LDH nanodots to achieve increased efficiency of LDH-mediated drug delivery.[68] Also, immobilization using mannose has significant application in tumor-targeted siRNA delivery.[69] There has been a proposed hypothesis for the potential molecular vaccine candidate for COVID-19 amid the ongoing pandemic.[4] They proposed the use of LDH synthesized via co-precipitation along with Mg:Al (2:1 molar ratio). Followed by plasmid isolation and performed with lentiviral shRNA-plasmid transfected *Escherichia coli* cells, the shRNA-plasmid was intercalated with LDH to form the nanoconjugate.[49]

As shown in Fig. 8, the illustration is depicting the applications of functionalized LDH NPs in biomedical sciences and have been discussed as follows.

5.1. *Drug delivery*

In 1999, bioinorganic nanohybrids were proposed for the first time by Choy *et al.* for their work on LDH NMs' intercalation with DNA. Since the use of LDHs in nanomedicine has received continuous attention in biomedical applications,[91] they are proposed to be suitable carriers for gene and drug-related therapeutic interventions. The positively charged surface of LDH has specific implications in

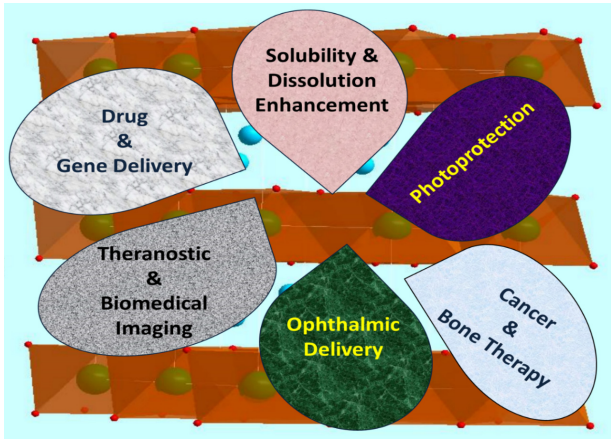


Fig. 8. Representation of various biomedical application of LDHs.

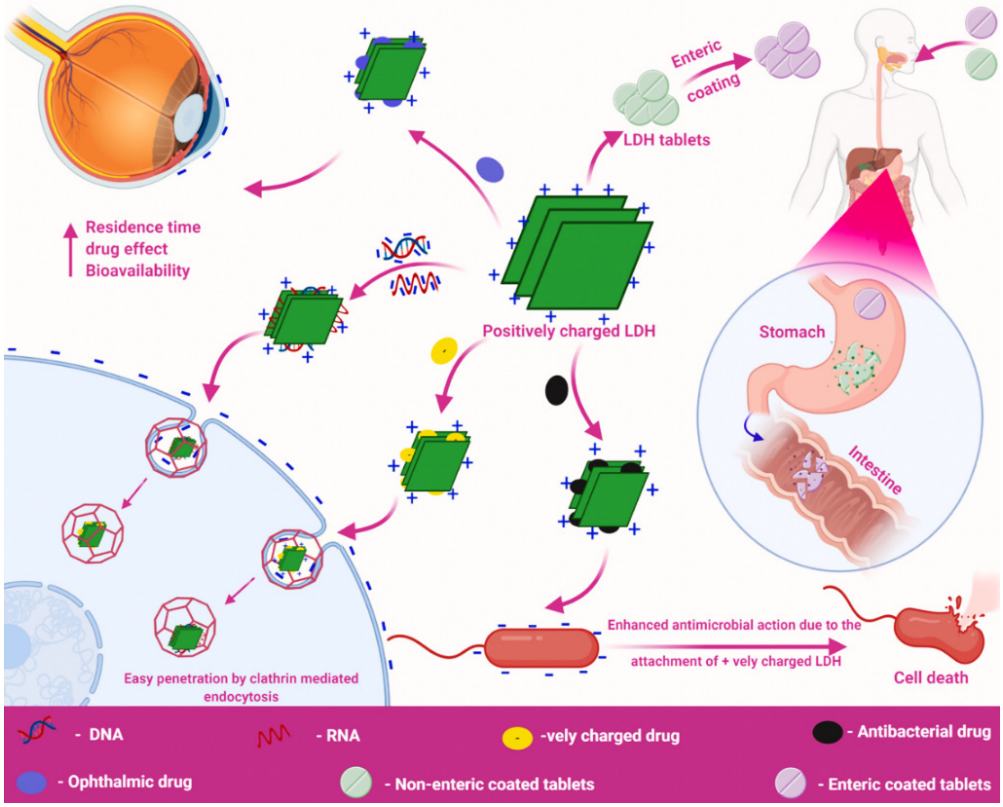


Fig. 9. The effect of the positive charge of LDHs in drug and gene delivery applications (Copyright © 2021 Elsevier Ltd. All rights reserved).[8]

prosperous intervention in drug delivery applications and binding negatively charged DNA/RNA. Also, cornea and conjunctiva being negatively charged can easily get bound with the LDH NM, thereby increasing the time of residence within the eye, as shown in Fig. 9.[12]

One of many investigated applications of LDH NPs in determining cytotoxicity is based on "particle uptake mechanisms". Based on NPs' size, Oh *et al.* developed LDH NPs for the uptake of osteosarcoma cells.[92] In another study by Chung *et al.*, it was revealed that cellular uptake increased with increasing concentration.[34] LDH NPs containing Gd^{3+} ions such as layered gadolinium hydroxide NPs have potent applications for MRI contrast agents and fluorescence imaging purposes.[93] Due to intensive properties suitable for drug delivery such as ion-exchange capacity, high surface area, stable electrochemical properties and carrying net positive charge on their surface, LDH NPs work as delivery carriers in delivering negatively charged drugs. Yan *et al.* found improved blood circulation and increased mice survival with PEGylated LDH.[94] Further, it has been reported that LDH intercalated with antibiotic anions has been reported to show excellent antibiotic properties. For example, Rojas *et al.* intercalated LDH with ibuprofen and studied the influence of different anions changing pH to check the rate of drug release.[95] Without a doubt, LDH molecules have found remarkable efficacy to deliver bioactive moieties such as genes and antibodies. Ladewig *et al.* worked with LDH intercalated siRNA for delivery into mammalian cells.[96] LDH molecules also support the delivery of antibodies into living cells possessing stability. Through electrostatic interactions between differently charged drugs and LDH, Gu *et al.* produced an antibody delivery system to treat atherosclerosis.[97] Many researchers have fabricated nanoconjugates by integrating LDH with other NPs to constitute multiple functions into a single unit. Nanoconjugates of Ag-LDH exhibit excellent antimicrobial behavior against bacteria planktonic.[98] In the same way, magnesium ferrite — LDH has been used for

arthritis therapy.[99] Abniki *et al.* developed a nanohybrid based on Ca-LDH intercalated with mefenamic (ME) acid. It was synthesized via coprecipitation method and their results obtained from *in vitro* studies demonstrate a release of ME anion (an anti-inflammatory drug) in a sustained manner.[70]

5.2. *Cancer therapy*

Nanotechnology had developed a progress toward platforms for early prognosis or therapy of cancer.[100] Anticancer drugs such as 5-Fu and methotrexate (MTX) are intercalated with LDH nanocomposites for cancer treatment. Apart from the distinct characteristics, their endo-lysosomal escape ability and anion-exchange capacity make them a potential candidate as nanocarriers to deliver bioactive molecules.[101,102] Ebadi *et al.* loaded iron oxide NPs with polymer and LDH to deliver anticancer drug sorafenib for liver cancer treatment with minimal side effects.[103] Pooresmaeil *et al.* synthesized LDH (Zn/Al) interacted with carboxymethyl cellulose (CMC) that deliver anticancer 5-Fu drugs via oral for the therapy of colorectal cancer. Moreover, some of the anions in LDH interlayers space are replaced by 5-Fu drug and the drug is bound with LDH layers by electrostatic interactions. The carboxylic acid functional groups in polymer molecules of synthesized nanocomposite-induced pH-sensitive properties that help control drug release.[104] For instance, Li *et al.* synthesized biodegradable magnetic shell LDH nanospheres exhibiting anticancer and antitumor capabilities. These nanospheres further revealed other characteristics such as environmental sensing, biocompatibility, etc.[105] Further, Li *et al.* also synthesized an LDH nanoshell intercalated with carboxylated-doxorubicin (DOX-COOH, an anticancer drug) through anion-exchange intercalation, their results demonstrate anticancer capabilities and showed their potential to subject HeLa cells and HEK 293 cells [Fig. 10].[105]

Wang *et al.* proposed LDH-Gd/Au nanocomposite that delivers a pH-responsive anticancer DOX drug into cancer cells, resulting in the vanishing of cancer cells. The synthesized nanocomposite bounds with DOX via hydrogen bond between hydroxyl functional groups on LDH-Gd surface with carbonyl and hydroxyl functional groups of DOX.[100] Zhao *et al.* proposed LDH@Au to deliver anticancer DOX drugs to reduce tumor cell growth and migration. LDH@Au enhanced the quantity of DOX drugs at the position of the tumor and granted cellular uptake of the drug. Also, LDH@Au-DOX improved inhibition invasion and cell apoptosis as compared to DOX group alone.[72] Also, Hakeem *et al.* demonstrated Mg-Al-LDH nanohybrids conjugated to doxorubicin (Mg-Al-LDH@ DOX) to treat cancer. The nanohybrids released anticancer DOX drugs in an acidic tumor microenvironment. After internalizing nanohybrids in the cancer cells via macropinocytosis and endocytosis, nanohybrids are delivered to lysosomes followed by release of DOX drugs to the nucleus. Furthermore, nanohybrids improved cytotoxicity and cellular uptake toward cancer cells in comparison to DOX alone. Likewise, nanohybrids reduced the growth of tumor cells with reduced cardiotoxicity in comparison to the drug alone *in vivo*.[106]

LDH NMs sensitivity to acidic pH has opened great scope for intervention to cancer therapy. To achieve this, materials responsive to triggers such as pH, temperature, alterations in ionic strength or redox potential have been developed. Drug release by LDH is influenced by factors such as temperature, ionic strength, H_2O_2, etc. Sensitivity of LDHs is in response to H_2O_2 [Fig. 11]. One such intervention is the development of Fe_3O_4-LDH NMs, having the efficiency of drug release under acidic conditions, which helps in accurate drug delivery to the tumor site.[71,107] Another intervention is the development of Na-Ca-LDH intercalated with dacarbazine (a drug for melanoma chemotherapy) prepared via urea hydrolysis possesses better loading capacity, stability and low cytotoxicity. This pH-dependent drug-delivering strategy has shown an improvement in the efficacy of anticancer drugs.[73] Another study demonstrates the fabrication of Ni-Ti-LDH nanofilm on nitinol alloy surface and shows tumor growth and bacterial infection inhibition.[74] Zhao *et al.* developed Mg-Al-LDH via hydrothermal method, mixed with Au nanosol, then doxorubicin was intercalated with LDH-Au nanocomposite. Their results demonstrate better anticancer activity and apoptosis of tumor cells.[72]

5.3. *Gene delivery*

As the LDH NPs possess a positive charge, hence they have the ability to deliver negatively charged molecules such as RNA or DNA. Li *et al.*

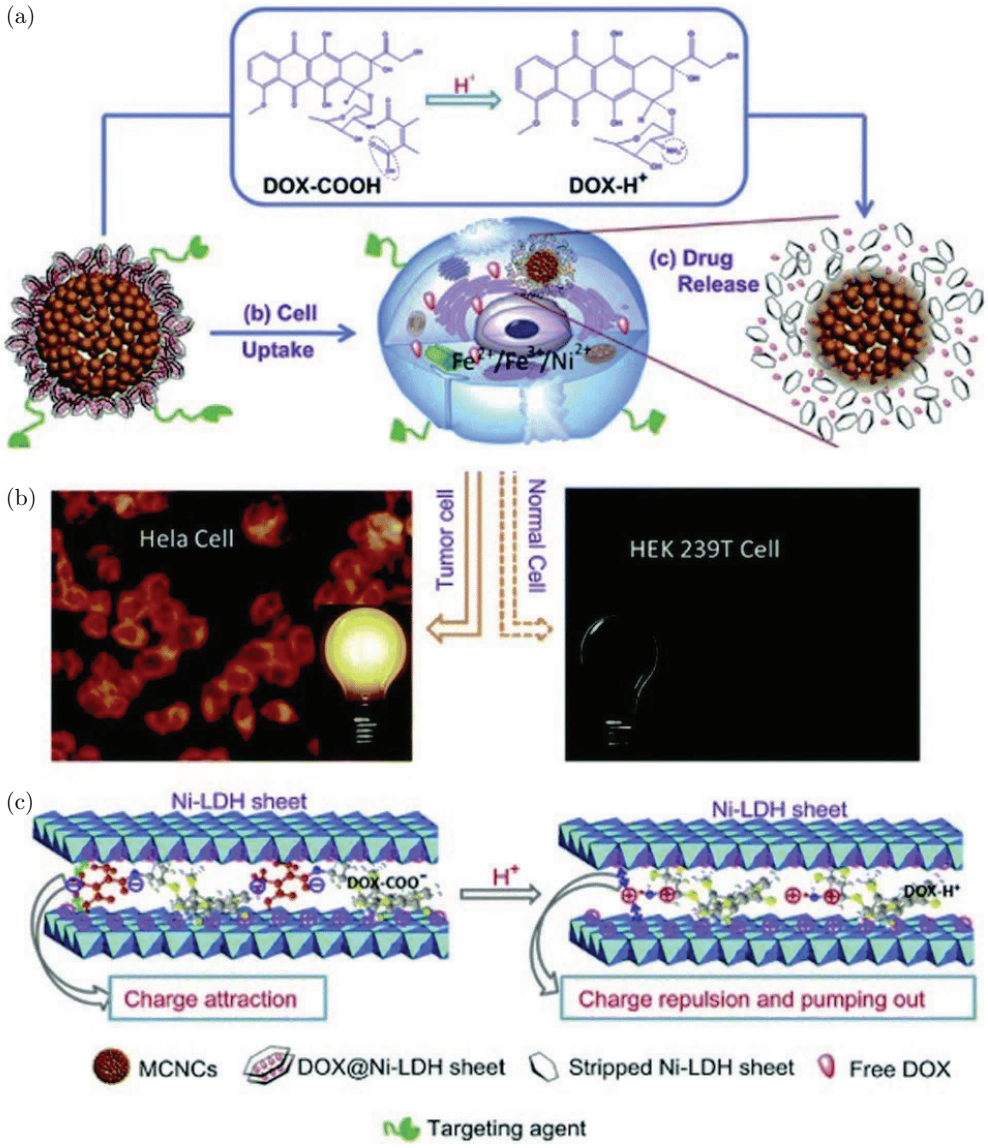


Fig. 10. Schematic representation (a) plausible DOX release mechanism of DOX@MSPs/Ni-LDH-folate in cytoplasm of tumor cells in acidic environments. (b) Fluorescent behavior of HeLa and HEK 293T cells incubated with nanodrugs. (c) Mechanism of pumping positively charged DOX out of the LDH sheets (Copyright © 2013 Elsevier Ltd. All rights reserved).[105]

demonstrated LDH-DNA composite internalized into the plant cells. They revealed that the nanocomposite exists in the sandwich form DNA-LDH-DNA which causes easy penetration and delivery of the gene to its target site.[75] In a recent study, it was investigated that Li-Al-LDH nanovehicles were synthesized via co-precipitation method and effective system for cancer treatment through gene delivery. Bright field TEM and SEM images of show hexagonal shape of LDH NP of dimensions $\sim 74 \pm 4$ nm and LDH-DNA nanocomposite of dimensions 85 ± 3 nm, respectively [Fig. 12].[2] This nanovehicle is intercalated with wild-type p53 gene because, in cancerous conditions, this tumor suppressor gene is either mutated or absent. Hence, the delivery of p53 gene using the nanovehicle system is an effective and promising strategy for treatment of cancer, as it encodes p53 protein, thereby regulating cell cycle, arresting growth or induce apoptosis or programmed cell death and controls proliferation of unwanted cells.

Mg-Al-LDH has applications as a carrier for potential gene delivery. So, the Mg-Al-LDH NPs can be intercalated with siRNA, as demonstrated by

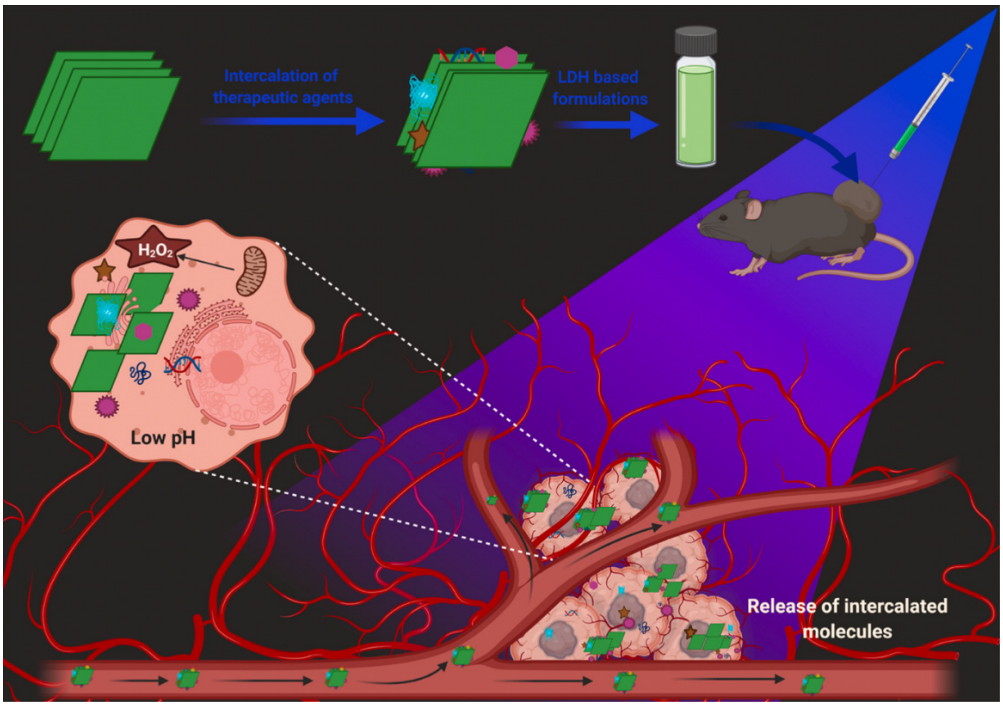


Fig. 11. Schematic representation on the possibility of stimuli-responsive drug delivery at H_2O_2 rich and acidic tumor microenvironment using LDH (Copyright © 2021 Elsevier Ltd. All rights reserved).[8]

Andrea *et al.*, where siRNA delivery to cancerous cells leading to mRNA degradation, and hence the cancer-causing genes are down-regulated. Due to the instability of RNA, a single-stranded antisense oligonucleotide, that is oligo-DNA siRNA mimics were used because of better stability. Further, intercalation of oligo-DNA with Mg-Al-LDH nanocomposite fabricated via co-precipitation method. A promising system for gene delivery as the negatively charged DNA attracts and binds to positively charged Al^{3+} ion (present on the surface of LDH) and the Mg^{2+} ions also binds to the DNA via phosphate backbone.[76] Another strategy was investigated by Acharya *et al.*, as they have devised an Mg-Al-LDH nanocomposite intercalated with shRNA. Their studies reveal that this positively charged system can be easily internalized across membrane of the target cell.[48] Another strategy is based on functionalization of Zn-Al-LDH nanocomposites tightly bounds with pCEP4 plasmid (enhances gene expression). This system is used as a nanocarrier for *cdk9* gene. Their results demonstrate uptake of the Zn-Al-LDH-pCEP4 system into C2C12 myoblast cells.[77]

5.4. *Ophthalmic delivery*

Recent studies on the ocular delivery system based on innovation of nano-LDH have been demonstrated by Wang*et al.* They have explored an organic–inorganic nanohybrid system for delivering dexamethasone disodium phosphate (DEXP). The LDH NM was functionalized with carboxymethyl chitosan-glutathione-glycylsarcosine (CMCG-GS) as in Fig. 13. The results obtained from *in vitro* experiments performed on human conjunctival epithelial cells demonstrate improved nanohybrid permeability, clathrin-mediated endocytosis of nanohybrid eye drops. They further confirmed that conjunctival-scleral route is the pathway intraocular transport of this system and showed an efficient approach for ocular drug delivery.[78]

5.5. *Photoprotection*

LDH can act as a matrix and get intercalated with the organic molecules in the sunscreens, hence preventing the direct contact of those molecules with skin.[108] One such example is the intercalation of cinnamic acid (a UV absorber) with Zn-Ti-LDH producing a synergic effect, resulting in increased

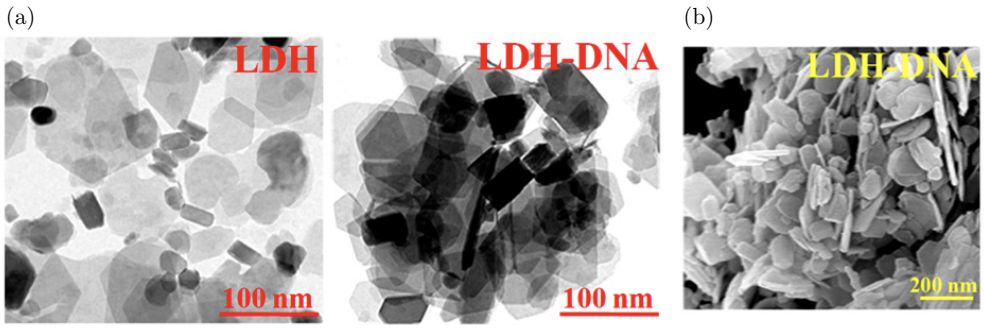


Fig. 12. (a) High-resolution transmission electron microscopic image of hexagonally-shaped LDH and LDH-DNA complex with an average size of 76 nm and 85 nm, respectively; (b) HR-SEM images of LDH-DNA complex showing hexagonal morphology. Reprinted (adapted) with permission from Senapati *et al.*[2] Copyright (2019) American Chemical Society.

blocking capacity of UV radiation and good stability.[79] Likewise, Zn-Ti-LDH intercalated with p-amino-benzoic acid possesses the capability of absorption of UV radiation. They have been shown to produce fewer amounts of free radicals in comparison to other compounds. A similar approach can be utilized to enhance photostability of UV-filter.[8,80]

5.6. *Theranostic and biomedical imaging*

Nanotheranostics is a drug delivery system coupled with a probe that can be used for diagnostic applications. An added advantage of LDH nanocarrier system over other theranostic agents is the ability of the drug delivery system to perform diagnosis. Here, the importance of the LDH nanohybrid system plays an important role.[109,110] Besides, the paramagnetic properties and luminescent properties of the cations intercalated with LDH NPs could be used as a diagnostic approach. Arratia-Quijada *et al.* developed dysprosium metal intercalating with LDH and exhibited theranostic intervention. This nanohybrid was prepared via co-precipitation method and has shown to reduce water proton relaxation time and can also be used as MRI contrast agent.[81] Further, advancements enhancing contrast in MRI studies have shown the development of Gadolinium (Gd)-LDH system via co-precipitation, which can intercalate with the chlorogenic acid (widely used in anticancer applications). Here, Gd is used as a contrast agent and could improve MRI sensitivity. Also, gold (Au) can be absorbed on the surface of LDH, thereby improving MRI.[82]

There have been continuous efforts for improving the performance of noninvasive bioimaging techniques to obtain accurate images for timely diagnosis. LDH, particularly, serve as a nanocontrast agent owing to exchangeable features and distinct 2D crystal structure [Fig. 14].[30,81,111–113]

5.7. *Solubility and dissolution enhancement*

The improvement in solubility and dissolution has been reported using the LDH system in drug delivery and a suitable class of drugs, i.e., BSC class II has been employed because they possess low solubility and high permeability. It is essential that improved solubility would result in better absorption of drugs and significantly increase the drug's bioavailability. A significant limitation associated with poor drug solubility is higher dose administration to demonstrate the required therapeutic effect.[8,55] To overcome this limitation, a study has been conducted, which demonstrates Ca-Al-LDH NP immobilized with praziquantel drug, showing enhanced activation energy. This study suggested that the drug immobilized LDH is thermally stable and yields better longevity or shelf life.[83] Similarly, carprofen (an anti-inflammatory drug) complexed with Zn-Al-LDH via co-precipitation, demonstrating increased solubility of drug and drug-LDH complex.[84] Furthermore, using co-precipitation method, Zn-Al-Cl LDH was intercalated with glibenclamide, exhibiting increased solubility of the complexed drug compared to free drug along with antioxidant activity.[85]

5.8. *Bone therapy and regeneration*

Functionalization of LDH NMs with bisphosphonates for targeting bone. Apart from bone therapy, LDH intervention has been proven as a

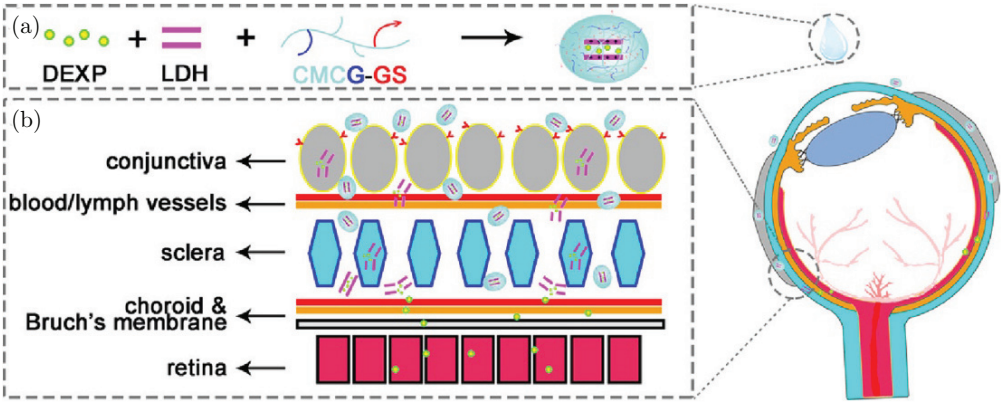


Fig. 13. (a) Schematic design of the multifunctional carboxymethyl chitosan (CS) derivatives-LDH nanohybrids (CMCG-GS-DEXP-LDH); (b) the scheme of drug diffusion routes into the retina for the CMCG-GS-DEXP-LDH nanohybrid eye drops.[78]
Copyright © 2020 Acta Materialia Inc. Published by Elsevier Ltd. All rights reserved.

promising strategy in bone implants for regeneration of bone.[8] Wang *et al.* developed Mg-Al/LDH nanosheets containing Yb and their results demonstrate enhanced osteogenic differentiation. This nanocomposite has ideal properties such as concentration of magnesium is related with bone mass and growth of the osteoblasts and promote osteogenesis. In the entire mechanism of LDH, internalization via endocytosis and magnesium ion release and also degradation of LDH does not lead to any change in pH, hence osteogenicity of the cells would not be influenced.[86] The use of bone implants for bone regeneration is widely used. Yet, the conventional implants such as bioactive ceramic implants have certain limitations, like low drug loading capacity, controlled release of drug is difficult, etc. Due to this, Peng *et al.* showed prospective nano-LDH use as for bone implants. Their results demonstrate that LDH with Mg-Al is suitable for developing bone implants based on LDH via co-precipitation method, as these nanocomposites possess antimicrobial activity, better biocompatibility and low cytotoxicity.[87] Further, Bedoya *et al.* developed an Mg-Al-LDH via co-precipitation method, and intercalated with a bisphosphonate, i.e., risedronate. This nanohybrid is functionalized

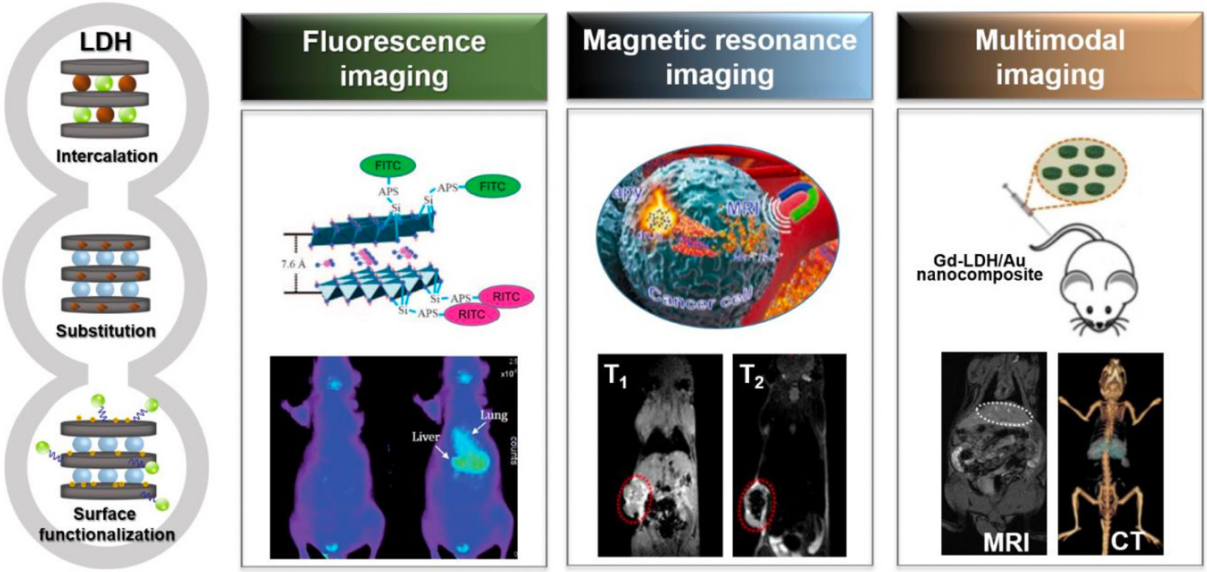


Fig. 14. Schematic overview of functional LDH nanohybrids and their application system; fluorescence imaging, MRI and multimodal imaging.[30]

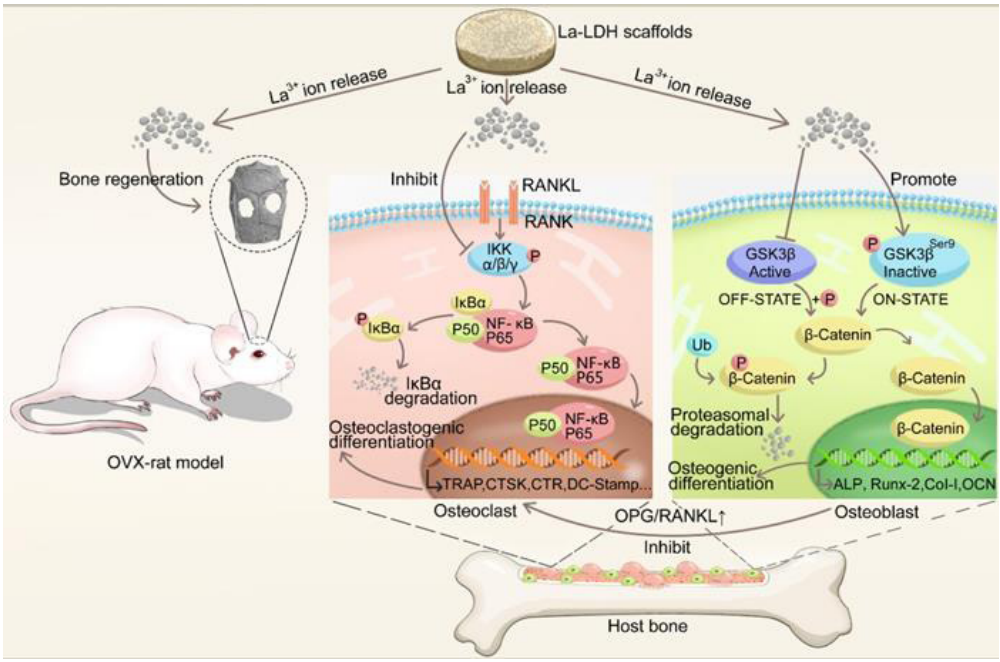


Fig. 15. Schematic overview of biological effects of La-LDH scaffolds. The functional scaffolds promote osteogenic differentiation of rBMSCs-OVX by activating Wnt/β-catenin pathway and suppress RANKL-induced osteoclastogenesis by inhibiting NF-κB signaling pathway.[90]

with minimal interjection, thereby causing insertion of anions within the layers. They demonstrated this nanocomposite possess pH sensitivity characteristics and hence can be used for bone targeting.[88] A strategy based on LDH for bone regeneration was proposed by Eskandari and Shafiei, where they have synthesized a nanocomposite LDH with β-tricalcium phosphate (β-TCP) via co-precipitation method. Their results demonstrate that the nanocomposite possess biocompatible and mineralization characteristics. Further, analysis suggests perspective use of the nanocomposite for bone regeneration and tissue engineering.[89] In a recent study conducted by Chu *et al.*, they have fabricated a lanthanum (La) with LDH nanohybrid via MgAl substitution using freeze-drying method, for its application is regeneration of bone tissue and osteogenic activity. The rationale behind their investigation is to develop a nano-LDH-based scaffold for treatment of bone defects underlying osteoporosis. A rare element, La is used for healing of several bone diseases, as a bioactive element. Here, La was doped with LDH and a nanoscaffold was fabricated using CS as matrix. To reveal the bi-functional activity, *in vivo* studies were conducted on rat bone marrow stromal cells which are ovariectomized (rBMSCs-OVX) and bone marrow-derived macrophages (BMMs) as models. Based on the studies, La-LDH scaffold was able to osteogenesis of rBMSCs-OVX by activation of Wnt/β-catenin signaling pathway (Fig. 15). Besides, it also down-regulated osteoclastogenesis (RANKL suppression) by inhibition of NF-κB signaling pathway. Hence, the La^{3+}-doped LDH nanohybrid has come up as a novel approach for osteoporotic regeneration involving bi-directional role, i.e., in activation of osteogenic activity and inhibition of osteoclastogenesis.[90]

6. Challenges and Future Perspective

Studies on LDH NPs have demonstrated that LDH systems show lower toxicity and enhanced biocompatibility and distribution. Further considerations based on their size, pH dependence, charge distribution and their solubility on exposure to physiological conditions are all responsible for formation of aggregates of LDH NPs and thereby leading to toxicity. Literature has revealed that development of nanocomposites with LDH such as using Mg or Zn and LDH system intercalated with the drug molecule has shown a significant decrease in toxicity and increase in drug specificity and efficacy.[114] Recent advancements have shown that formulation of LDH-based nanocomposites has several

advantages over the conventional drug delivery systems such as enhanced bioavailability, targeted delivery notwithstanding the mode of drug administration, directed distribution, decreases the chances of the accumulation of LDH nanocomposites *in vivo*, etc.[114] A critical consideration for administration of LDH intercalated drugs in the blood stream is the possible formation of LDH nanostructured aggregates due to its electrostatic interaction with the negatively charged biomolecules. To overcome these limitations, research should emphasize on enhancing LDH nanostructure stability and as well as to increase the flexibility of functionalizing LDH surface *in vivo* environment. Due to thickness of the outermost layer of LDH nanostructure, the surface modification is less pliable over other NMs. This could be resolved by the invention of ultra-thin LDH nanostructures.[42] Further, to enhance the reproducibility and desired alterations of LDH over inorganic NMs, continuous synthesis method should be used over conventional ones, as they maintain supersaturation and decreases the residence time period, hence enhancing its reproducibility.[115]

LDH NPs endocytosed into cells have shown to increase efficiency of transfer and no acute toxicity is attributed, making them a prospective candidate for delivery carriers.[116] Further research on nanovehicles response with the biological system is a crucial aspect for increased efficiency of target molecule delivery and circumvent adverse effects. Drugs intercalated with LDH were found difficult for specific targeting because of the presence of ions. One way to overcome such challenges can be achieved by surface modification or alteration of LDH NPs. Further investigations understand the specific interactions between LDH NPs and stem or cancerous cells. Further, the use of combinational nanohybrids with LDH and other NPs could result in stable nanohybrids suitable for biomedical applications.[117] Another major limitation is the LDH sensitivity in acidic environments; hence further investigation is needed in this context. To achieve new properties, LDH can be modulated due to the exchangeable nature of the LDH structure.[8,118] The cationic nature of LDH can be practical for the cellular uptake of nanoconjugates. LDH has the capability to provide resistance from enzyme degradation to shRNA. Hence, the invention of shRNA-intercalated LDH nanoconjugate could be a prospective vaccine strategy for COVID-19.[49,119]

Extensive research is needed to understand intracellular fate and factors responsible for the uptake and toxic response of LDHs. However, there is a dire need to study extensively the toxicity of LDHs in animal models to ascertain safety aspects.[120,121] An inherent limitation associated with the conventional system of drug delivery are high-dosage requirement, drug level in plasma variation and the inefficiency of sustained drug release.[8,122] The nonselectivity of drug delivery at targeted sites using LDH NMs and lack of precision while controlling particle size and distribution limits LDH efficiency in delivering drug targets to the cells. In the recent literature, LDH could be a better choice theranostics for monitoring of diseases, treatment and diagnosis. Therefore, the intervention of LDH in theranostic applications holds a promising alternative for improving the health care system. Last, future research would pave the path of breakthrough advancements in nanomedicine.

7. Conclusion

This paper highlights the properties and functionalization of LDH. Further, it provides updates about the LDH system intervention with a plethora of biomedical applications, challenges, future outlook and the current status. LDH NMs have potent applications in the biomedical field. LDH nanostructures exhibit pH sensitivity, delivery efficiency, size tunability, and other physiochemical properties, which aid their crucial role in bioscience. Researchers have been working on the functionalization of LDHs to enhance their therapeutic activities. Further, the theranostic intervention of the nanohybrid LDHs has provided a new horizon for accurate nanomedicines for the treatment of disease. The recently reported LDH NMs with their therapeutic applications in the biomedical field have been briefly summarized in Table 1. Interacting LDHs with other materials have led to extension of their functions and applications. Additionally, better drug distribution, targeting specific of drug and low accumulation and toxicity makes them a potential candidate for its further utilization and future implications in cellular uptake and drug delivery system. Modified LDHs exhibited attractive behavior in cancer therapy, gene and antibody delivery systems, drug targeting and many more applications in biomedical sciences that needed to

be explored with further research on modifying the LDHs.

Acknowledgments

The authors Bhawna and Sanjeev Kumar thank UGC and CSIR (File No. 08/694(0004)/2018-EMR-I) for the Senior Research Fellowship, respectively.

References

1. S. Senapati, A. K. Mahanta, S. Kumar and P. Maiti, *Signal Transduct. Target. Ther.* **3**, 7 (2018).
2. S. Senapati, T. Sarkar, P. Das and P. Maiti, *Bioconjugate Chem.* **30**, 2544 (2019).
3. Z. Cao, B. Li, L. Sun, L. Li, Z. P. Xu and Z. Gu, *Small Methods* **4**, 1900343 (2020).
4. A. Gupta, S. Kumar, R. Kumar, A. K. Choudhary, K. Kumari, P. Singh and V. Kumar, *ChemistrySelect* **5**, 7521 (2020).
5. K. Vikrant, K.-H. Kim and A. Deep, *Appl. Catal. B, Environ.* **259**, 118025 (2019).
6. J. L. Markman, A. Rekechenetskiy, E. Holler and J. Y. Ljubimova, *Adv. Drug Deliv. Rev.* **65**, 1866 (2013).
7. M. Prasad, U. P. Lambe, B. Brar, I. Shah, J. Manimegalai, K. Ranjan, R. Rao, S. Kumar, S. Mahant, Khurana and S. K., *Biomed. Pharmacother.* **97**, 1521 (2018).
8. V. A. Shirin, R. Sankar, A. P. Johnson, H. Gangadharappa and K. Pramod, *J. Control. Release* **330**, 398 (2021).
9. C. Taviot-Guého, V. Prévot, C. Forano, G. Renaudin, C. Mousty and F. Leroux, *Adv. Funct. Mater.* **28**, 1703868 (2018).
10. H. N. Tran, D. T. Nguyen, G. T. Le, F. Tomul, E. C. Lima, S. H. Woo, A. K. Sarmah, H. Q. Nguyen, P. T. Nguyen and D. D. Nguyen, *J. Hazard. Mater.* **373**, 258 (2019).
11. G. Arrabito, A. Bonasera, G. Prestopino, A. Orsini, A. Mattoccia, E. Martinelli, B. Pignataro and P. G. Medaglia, *Crystals* **9**, 361 (2019).
12. F. Cao, Y. Wang, Q. Ping and Z. Liao, *Int. J. Pharm.* **404**, 250 (2011).
13. E. Abdollahi, A. Heidari, T. Mohammadi, A. A. Asadi and M. A. Tofighy, *Sep. Purif. Technol.* **257**, 117931 (2021).
14. R. Pourfaraj, S. J. Fatemi, S. Y. Kazemi and P. Biparva, *J. Colloid Interface Sci.* **508**, 65 (2017).
15. D. Vieira, D. Sokol, A. Smalenskaite, A. Kareiva, M. Ferreira, J. Vieira and A. Salak, *Surf. Coat. Technol.* **375**, 158 (2019).
16. R. Lu, X. Xu, J. Chang, Y. Zhu, S. Xu and F. Zhang, *Appl. Catal. B, Environ.* **111**, 389 (2012).
17. F. L. Theiss, G. A. Ayoko and R. L. Frost, *Appl. Surf. Sci.* **383**, 200 (2016).
18. R. Rojas, D. Bedoya, C. Vasti and C. Giacomelli, LDH nanoparticles: Synthesis, size control and applications in nanomedicine, *Layered Double Hydroxides (LDHs): Synthesis, Characterization and Applications* (Nova Science Publishers, 2015), pp. 101–120.
19. H. Hamad, M. Abd El-latif, A. Kashyout, W. Sadik and M. Feteha, *Russ. J. Gen. Chem.* **84**, 2031 (2014).
20. X. Wu, B. Li and X. Wen, *J. Nanoparticle Res.* **19**, 131 (2017).
21. X. Zhao, J.-P. Cao, J. Zhao, G.-H. Hu and Z.-M. Dang, *Chem. Phys. Lett.* **605**, 77 (2014).
22. Z. P. Xu, G. Stevenson, C.-Q. Lu and G. Q. Lu, *J. Phys. Chem. B* **110**, 16923 (2006).
23. M. Ahmed and A. Mohamed, *Chemosphere* **174**, 280 (2017).
24. L. Valeikiene, R. Paitian, I. Grigoraviciute-Puroniene, K. Ishikawa and A. Kareiva, *Mater. Chem. Phys.* **237**, 121863 (2019).
25. E. Mansouri, V. Tarhriz, V. Yousefi and A. Dilmaghani, *Adsorption* **26**, 835 (2020).
26. Y. Kuroda, Y. Oka, T. Yasuda, T. Koichi, K. Muramatsu, H. Wada, A. Shimojima and K. Kuroda, *Dalton Trans.* **47**, 12884 (2018).
27. M. Zubair, M. Daud, G. McKay, F. Shehzad and M. A. Al-Harthi, *Appl. Clay Sci.* **143**, 279 (2017).
28. G. Mishra, B. Dash and S. Pandey, *Appl. Clay Sci.* **153**, 172 (2018).
29. S.-J. Ryu, H. Jung, J.-M. Oh, J.-K. Lee and J.-H. Choy, *J. Phys. Chem. Solids* **71**, 685 (2010).
30. W. Jin and D.-H. Park, *Nanomaterials* **9**, 1404 (2019).
31. S. Yan, B. E. Rolfe, B. Zhang, Y. H. Mohammed, W. Gu and Z. P. Xu, *Biomaterials* **35**, 9508 (2014).
32. Z. P. Xu, M. Niebert, K. Porazik, T. L. Walker, H. M. Cooper, A. P. Middelberg, P. P. Gray, P. F. Bartlett and G. Q. M. Lu, *J. Control. Release* **130**, 86 (2008).
33. S. Li, J. Li, C. J. Wang, Q. Wang, M. Z. Cader, J. Lu, D. G. Evans, X. Duan and D. O'Hare, *J. Mater. Chem. B* **1**, 61 (2013).
34. H.-E. Chung, D.-H. Park, J.-H. Choy and S.-J. Choi, *Appl. Clay Sci.* **65**, 24 (2012).
35. X. Li, B.-Y. Zheng, M.-R. Ke, Y. Zhang, J.-D. Huang and J. Yoon, *Theranostics* **7**, 2746 (2017).
36. X. Bi, H. Zhang and L. Dou, *Pharmaceutics* **6**, 298 (2014).
37. V. R. R. Cunha, R. B. De Souza and I. H. J. Koh and V. R. L. Constantino, *Sci. Rep.* **6**, 1 (2016).
38. S.-Y. Kwak, W. M. Kriven, M. A. Wallig and J.-H. Choy, *Biomaterials* **25**, 5995 (2004).

39. A. U. Kura, B. Saifullah, P.-S. Cheah, M. Z. Hussein, N. Azmi and S. Fakurazi, *Nanoscale Res. Lett.* **10**, 1 (2015).
40. Y. Kuthati, R. K. Kankala and C.-H. Lee, *Appl. Clay Sci.* **112**, 100 (2015).
41. B. Saifullah, P. Arulselvan, M. E. El Zowalaty, S. Fakurazi, T. J. Webster, B. M. Geilich and M. Z. Hussein, *Int. J. Nanomed.* **9**, 4749 (2014).
42. L. Yan, S. Gonca, G. Zhu, W. Zhang and X. Chen, *J. Mater. Chem. B* **7**, 5583 (2019).
43. M. Zheng, W. Tao, Y. Zou, O. C. Farokhzad and B. Shi, *Trends Biotechnol.* **36**, 562 (2018).
44. S. Muráth, A. Szerlauth, D. Sebők and I. Szilágyi, *Antioxidants* **9**, 153 (2020).
45. J. Liu, L. Sun, L. Li, R. Zhang and Z. P. Xu, *ACS Appl. Mater. Interfaces* **13**, 7115 (2021).
46. Z. Li, S. Mao, Y. Yang, Z. Sun and R. Zhao, *J. Colloid Interface Sci.* **585**, 85 (2021).
47. R. Acharya, *Mater. Sci. Eng., C* **104**, 109928 (2019).
48. R. Acharya, A. M. Alsharabasy, S. Saha, S. H. Rahaman, A. Bhattacharjee, S. Halder, M. Chakraborty and J. Chakraborty, *J. Drug Deliv. Sci. Technol.* **52**, 500 (2019).
49. R. Acharya, *Med. Hypotheses* **143**, 110084 (2020).
50. M. Tabish, G. Yasin, M. J. Anjum, M. U. Malik, J. Zhao, Q. Yang, S. Manzoor, H. Murtaza and W. Q. Khan, *J. Mater. Res. Technol.* **10**, 390 (2021).
51. Z. Yu, P. Hu, Y. Xu, Q. Bao, D. Ni, C. Wei and J. Shi, *Small* **16**, 1907233 (2020).
52. J. Liu, Y. Wu, C. Fu, B. Li, L. Li, R. Zhang, T. Xu and Z. P. Xu, *Small* **16**, 2002115 (2020).
53. T. Xu, J. Liu, L. Sun, R. Zhang, Z. P. Xu and Q. Sun, *ACS Omega* **6**, 3822 (2021).
54. B. Dragoi, C. M. Uritu, L. Agrigoroaie, D. Lutic, V. Hulea, G. Postole, A. Coroaba and E. Carasevici, *ACS Appl. Nano Mater.* **4**, 2061 (2021).
55. K. Zhang, Z. P. Xu, J. Lu, Z. Y. Tang, H. J. Zhao, D. A. Good and M. Q. Wei, *Int. J. Mol. Sci.* **15**, 7409 (2014).
56. O. Saber, A. Aljaafari, S. Asiri and K. M. Batoo, *Appl. Sci.* **8**, 2099 (2018).
57. J. A. Carrasco, S. Cardona-Serra, J. M. Clemente-Juan, A. Gaita-Arino, G. Abellan and E. Coronado, *Inorg. Chem.* **57**, 2013 (2018).
58. A. Smalenskaite, L. Pavasaryte, T. C. Yang and A. Kareiva, *Materials* **12**, 736 (2019).
59. P. Yaseneva, N. An, M. Finn, N. Tidemann, N. Jose, A. Voutchkova-Kostal and A. Lapkin, *Chem. Eng. J.* **360**, 190 (2019).
60. L. Yan, Y. Wang, J. Li, S. Kalytchuk, A. S. Susha, S. V. Kershaw, F. Yan, A. L. Rogach and X. Chen, *J. Mater. Chem. C* **2**, 4490 (2014).
61. H. Zeng, H. Zhang, L. Deng and Z. Shi, *J. Water Process Eng.* **33**, 101084 (2020).
62. S. Jamil, S. R. Khan, A. R. Alvi, F. Kausar, S. Ali, S. A. Khan, M. Naim, A. Malik and M. R. S. A. Janjua, *Chem. Phys.* **528**, 110530 (2020).
63. H. Hu, X. Wang, S. Xu, W. Yang, F. Xu, J. Shen and C. Mao, *J. Mater. Chem.* **22**, 15362 (2012).
64. L. Yan, W. Chen, X. Zhu, L. Huang, Z. Wang, G. Zhu, V. A. Roy, K. N. Yu, X. Chen, *Chemical Comm.* **49**, 10938 (2013).
65. S. Sohrabnezhad, Z. Poursafar and A. Asadollahi, *Appl. Clay Sci.* **190**, 105586 (2020).
66. L. Yan, M. Zhou, X. Zhang, L. Huang, W. Chen, V. A. Roy, W. Zhang and X. Chen, *ACS Appl. Mater. Interfaces* **9**, 34185 (2017).
67. A. D. Leão, C. Alvarez-Lorenzo and J. L. Soares-Sobrinho, *Colloids Surf. B, Biointerfaces* **193**, 111055 (2020).
68. L. Li, W. Gu, J. Liu, S. Yan and Z. P. Xu, *Nano Res.* **8**, 682 (2015).
69. B. Lakshminarayana, G. Satyanarayana and C. Subrahmanyam, *ACS Omega* **3**, 13065 (2018).
70. M. Abniki, A. Moghimi and F. Azizinejad, *J. Chin. Chem. Soc.* **68**, 343 (2021).
71. N. Shahabadi, M. Razlansari, H. Zhaleh and K. Mansouri, *Mater. Sci. Eng., C* **101**, 472 (2019).
72. H. Zhao and X. Zhang, *Electron. J. Biotechnol.* **32**, 13 (2018).
73. H. Asiabi, Y. Yamini, M. Alipour, M. Shamsayei and S. Hosseinkhani, *Mater. Sci. Eng., C* **97**, 96 (2019).
74. D. Wang, F. Peng, J. Li, Y. Qiao, Q. Li and X. Liu, *Mater. Today* **20**, 238 (2017).
75. Y. Li, W. Bao, H. Wu, J. Wang, Y. Zhang, Y. Wan, D. Cao, D. O'Hare and Q. Wang, *Sci. Bull.* **62**, 686 (2017).
76. K. A. Andrea, L. Wang, A. J. Carrier, M. Campbell, M. Buhariwalla, M. Mutch, S. L. MacQuarrie, C. Bennett, M. Mkandawire and K. Oakes, *Langmuir* **33**, 3926 (2017).
77. P. Yazdani, E. Mansouri, S. Eyvazi, V. Yousefi, H. Kahroba, M. S. Hejazi, A. Mesbahi, V. Tarhriz and M. M. Abolghasemi, *Artif. Cells Nanomed. Biotechnol.* **47**, 436 (2019).
78. Y. Wang, L. Zhou, L. Fang and Cao, *Acta Biomater.* **104**, 104 (2020).
79. Y. Li, L. Tang, X. Ma, X. Wang, W. Zhou and D. Bai, *J. Phys. Chem. Solids* **107**, 62 (2017).
80. Y. Li, L.-P. Tang, W. Zhou and X.-R. Wang, *Chin. Chem. Lett.* **27**, 1495 (2016).
81. J. Arratia-Quijada, C. S. Jiménez, A. Gurinov, A. P. Centeno, I. C. Andrade and G. G. C. Arízaga, *Mater. Sci. Eng., B* **203**, 7 (2016).
82. M. S. Usman, M. Z. Hussein, A. U. Kura, S. Fakurazi and M. J. Masarudin and F. F. A. Saad, *Mater. Chem. Phys.* **240**, 122232 (2020).

83. T. R. R. Timóteo, C. G. de Melo, L. J. de Alencar Danda, L. C. P. B. B. Silva, D. A. F. Fontes, P. C. D. Silva, C. S. B. Aguilera, L. da Paixão Siqueira, L. A. Rolim and P. J. R. Neto, *Appl. Clay Sci.* **180**, 105197 (2019).
84. D. Capsoni, I. Quinzeni, G. Bruni, V. Friuli, L. Maggi and M. Bini, *J. Pharm. Sci.* **107**, 267 (2018).
85. A. D. Leão, V. V. Oliveira, F. A. Marinho, A. G. Wanderley, J. S. Aguiar, T. G. Silva, M. F. Soares and J. L. Soares-Sobrinho, *Appl. Clay Sci.* **181**, 105218 (2019).
86. Y. Wang, X. Mei, Y. Bian, T. Hu, X. Weng, R. Liang and M. Wei, *Nanoscale* **12**, 19075 (2020).
87. F. Peng, D. Wang, D. Zhang, H. Cao and X. Liu, *Appl. Clay Sci.* **165**, 179 (2018).
88. D. A. Bedoya, C. Vasti, R. Rojas and C. E. Giacomelli, *Appl. Clay Sci.* **141**, 257 (2017).
89. N. Eskandari and S. S. Shafiei, *Mol. Biotechnol.* **63**, 477 (2021).
90. M. Chu, Z. Sun, Z. Fan, D. Yu, Y. Mao and Y. Guo, *Theranostics* **11**, 6717 (2021).
91. J.-H. Choy, S.-Y. Kwak, J.-S. Park, Y.-J. Jeong and J. Portier, *J. Am. Chem. Soc.* **121**, 1399 (1999).
92. J. M. Oh, S. J. Choi, G. E. Lee, J. E. Kim and J. H. Choy, *Chem.: Asian J.* **4**, 67 (2009).
93. Y. S. Yoon, B. I. Lee, K. S. Lee, G. H. Im, S. H. Byeon, J. H. Lee and I. S. Lee, *Adv. Funct. Mater.* **19**, 3375 (2009).
94. M. Yan, Z. Zhang, S. Cui, M. Lei, K. Zeng, Y. Liao, W. Chu, Y. Deng and C. Zhao, *Int. J. Nanomed.* **9**, 4867 (2014).
95. R. Rojas, M. Palena, A. Jimenez-Kairuz, R. Manzo and C. Giacomelli, *Appl. Clay Sci.* **62**, 15 (2012).
96. K. Ladewig, M. Niebert, Z. P. Xu, P. P. Gray and G. Q. Lu, *Biomaterials* **31**, 1821 (2010).
97. Z. Gu, B. E. Rolfe, A. C. Thomas, J. H. Campbell, G. M. Lu and Z. P. Xu, *Biomaterials* **32**, 7234 (2011).
98. C. Chen, P. Gunawan, X. W. Lou and R. Xu, *Adv. Funct. Mater.* **22**, 780 (2012).
99. A. N. Ay, B. L. Zumreoglu-Karan, A. Temel and V. Rives, *Inorg. Chem.* **48**, 8871 (2009).
100. L. Wang, H. Xing, S. Zhang, Q. Ren, L. Pan, K. Zhang, W. Bu, X. Zheng, L. Zhou and W. Peng, *Biomaterials* **34**, 3390 (2013).
101. M. Shao, F. Ning, J. Zhao, M. Wei, D. G. Evans and X. Duan, *J. Am. Chem. Soc.* **134**, 1071 (2012).
102. L. Li, W. Gu, J. Chen, W. Chen and Z. P. Xu, *Biomaterials* **35**, 3331 (2014).
103. M. Ebadi, S. Bullo, K. Buskara, M. Z. Hussein, S. Fakurazi and G. Pastorin, *Sci. Rep.* **10**, 1 (2020).
104. M. Pooresmaeil, S. B. Nia and H. Namazi, *Int. J. Biol. Macromol.* **139**, 994 (2019).
105. D. Li, Y.-T. Zhang, M. Yu, J. Guo, D. Chaudhary and C.-C. Wang, *Biomaterials* **34**, 7913 (2013).
106. A. Hakeem, G. Zhan, Q. Xu, T. Yong, X. Yang and L. Gan, *J. Mater. Chem. B* **6**, 5768 (2018).
107. J. Margolesky and C. Singer, *Ther. Adv. Neurol. Disord.* **11**, 1756285617737728 (2018).
108. T. A. D. Silva, T. A. D. Silva, T. G. D. Nascimento, R. E. Yatsuzuka, L. A. M. Grillo and C. B. Dornelas, *Einstein (São Paulo)* **17**, eRW4456 (2019).
109. N. Zhang, Y. Wang, C. Zhang, Y. Fan, D. Li, X. Cao, J. Xia, X. Shi, and R. Guo, *Theranostics* **10**, 2791 (2020).
110. M. S. Usman, M. Z. Hussein, S. Fakurazi and F. F. A. Saad, *Chem. Cent. J.* **11**, 1 (2017).
111. Y. Jung, E. Ji, A. Capasso and G.-H. Lee, *J. Korean Ceram. Soc.* **56**, 24 (2019).
112. A. Viruete, G. G. Carbajal-Arízaga, R. H. Gutiérrez, A. R. O. Camacho and J. Arratia-Quijada, *J. Nanoparticle Res.* **20**, 1 (2018).
113. S. S. Bandgar, H. M. Yadav, S. S. Shirguppikar, M. A. Shinde, R. V. Shejawal, T. V. Kolekar and S. R. Bamane, *J. Korean Ceram. Soc.* **54**, 158 (2017).
114. A. U. Kura, M. Z. Hussein, S. Fakurazi and P. Arulselvan, *Chem. Cent. J.* **8**, 1 (2014).
115. D. Tichit, G. Layrac and C. Gerardin, *Chem. Eng. J.* **369**, 302 (2019).
116. S.-J. Choi and J.-H. Choy, *Nanomedicine* **6**, 803 (2011).
117. K. Charradi, Z. Ahmed, N. Thmaini, P. Aranda, Y. O. Al-Ghamdi, P. Ocon, S. M. Keshk and R. Chtourou, *J. Appl. Polym. Sci.* **138**, 50364 (2021).
118. R. Yang, Y. Gao, J. Wang and Q. Wang, *Dalton Trans.* **43**, 10317 (2014).
119. R. Acharya, M. Chakraborty and J. Chakraborty, *Bull. Mater. Sci.* **43**, 1 (2020).
120. V. Kumar, A. K. Choudhary, P. Kumar and S. Sharma, *Nanosci. Nanotechnol., Asia* **9**, 64 (2019).
121. A. Gupta, S. Kumar and V. Kumar, Challenges for assessing toxicity of nanomaterials, *Biochemical Toxicology: Heavy Metals and Nanomaterials*, Muharrem Ince, Olcay Kaplan Ince and Gabrijel Ondrasek, IntechOpen (2019), pp. 1–21.
122. S. R. Mudshinge, A. B. Deore, S. Patil and C. M. Bhalgat, *Saudi Pharm. J.* **19**, 129 (2011).

View publication stats

Journal of Ambient Intelligence and Humanized Computing
https://doi.org/10.1007/s12652-022-03706-2

ORIGINAL RESEARCH

LBECR: load balanced, efficient clustering and routing protocol for sustainable internet of things in smart cities

Pawan Singh Mehra[1]

Received: 11 August 2020 / Accepted: 10 January 2022
© The Author(s), under exclusive licence to Springer-Verlag GmbH Germany, part of Springer Nature 2022

Abstract
Internet of Things (IoT) has sensor nodes (SNs) in its primitive layer for collecting data from an area of interest. These SNs are powered by a battery which is a significant constraint due to its limited capacity(battery) in ad-hoc IoT networks. Since these SNs are deployed in large numbers forming a network, the network's lifetime is required to be prolonged to serve the objective of deploying the SNs. If the SNs exhaust their energy at par, then the network's lifetime can easily be extended. For achieving an almost equal energy dissipation rate of SNs, the load among the SNs should be balanced. This paper has propounded a load-balanced, efficient clustering and routing (LBECR) protocol for sustainable IoT in smart cities to muddle through this issue. Since in Adhoc IoT networks, the nodes are resource-constrained, with the escalation of input variables in the fuzzy system, the number of rules increases exponentially, leading to more energy dissipation. Therefore we have designed three Fuzzy Inference Systems with minimal inputs for cluster head (CH) selection, formation of clusters and routing of data. The cost to the CH node is considered as one of the parameters of the Fuzzy system as it has a significant impact on the stability period. A fuzzy system is designed for efficient multi-hop routing, conserving a significant amount of network energy. The proposed LBECR protocol is simulated for four different cases and compared with some recent protocols. The obtained experimental results reveal significant improvement with proficiency in balancing the network load by better average energy, delayed death rate of SNs and prolonged lifetime.

Keywords Clustering · Routing · Energy efficiency · Internet of things · Wireless sensor network · Smart cities

1 Introduction

With the rapid advancement in microelectronics, embedded systems and Internet connectivity, IoT is sprawling swiftly to connect many sensors enabled devices. In the past decade, wireless sensors have drastically improved their smartness and usability without human intervention(Jain and Kumar 2020). These tiny sensors communicate among themselves and are capable of self-organising. These sensors collect information from the area of interest and forward it for further processing(Kumaresan and Kalyani 2020; Sethi and Sarangi 2017). The process of sensing, processing and communicating dissipates significant energy of sensor nodes (SNs). For a longer lifetime of the established network, proficient usage of the energy of SNs is required (Lenka et al. 2019; Dwivedi et al. 2020a, b; Haseeb et al. 2020; Yarinezhad and Hashemi 2020). IoT intends to assimilate various conventional and next-generation network technologies to work simultaneously in a mutual infrastructure, which can support diverse ubiquitous applications.With their acceptance and adoption globally, it has necessitated the researchers to address the issues and challenges of implementing IoT-based infrastructure in smart cities. With numerous advancements and improvements, WSN has become one of the favourable, established technologies that can be easily incorporated in an IoT system in terms of Network Layer and Sensing Layer. The sensors in IoT devices establish a network resulting in a WSN assisted IoT. WSN has stepped into our vicinity with several smart applications like remote-controlled systems, home automation, health monitoring etc. (Kumar and Dash 2020; Pirbhulal et al. 2016; Roy and Chandra 2020). Some recent studies have focused on designing low powered WSN for Intelligent Industries and Transportation (Brincat et al. 2019; Kavitha and Vallikannu 2019). In most cases, WSN is set up in an unsupervised

✉ Pawan Singh Mehra
pawansinghmehra@gmail.com

[1] Department of CSE, Delhi Technological University, New Delhi, India

area of interest where replacing or recharging of battery supply is a challenging task once the battery is completely discharged. Prolonged lifetime by efficient utilisation of energy is expected from WSN, which has enticed many academicians and researchers from the diverse domain.

Furthermore, IoT networks resemble Adhoc networks, which can support device to device communication and WiFi-Direct. In such Adhoc type IoT networks, the crucial requirement is the topology management and massive-scale deployment of nodes. Conventionally, a most common approach to topology management is clustering in ad-hoc networks, for example, Wireless Sensor Network (WSN). The clustering method divides the network into groups/clusters for collecting, forwarding data, ensuring service quality, and resource management. Several design commonalities in terms of topology management in Adhoc IoT networks and WSN require data transfer hop by hop. Routing techniques capable of decreasing energy depletion are highly desirable(Mohamed et al. 2018; Rawat and Chauhan 2020; Tanwar et al. 2014). One of the promising approaches is cluster-based routing (Afsar and Tayarani-N 2014; Dabirmoghaddam et al. 2014; Mehra et al. 2018). Each cluster has some member nodes with a coordinator called CH. Members of the cluster pass the information to CH, aggregating it and transferring it to BS for further processing (Gupta et al. 2020). Efficient choice of CH, cluster formation and routing of information are crucial in protracting the network's life expectancy. Therefore, clustering and routing techniques in WSN can presumably be applied in Adhoc IoT networks for topology management without having them design from scratch (Shahraki et al. 2020).

In our proposed work, we have designed a simple architecture for WSN based IoT which can be seen in Fig. 1.

To address the issue of energy-efficient topology management in the network layer of ad-hoc IoT networks, we have proposed a cluster-based routing protocol based on FL, which aims to minimise the network energy expenditure and prolong the lifetime of ad-hoc IoT networks. The integration of fuzzy logic (FL) contributes to the efficient handling of humans' decision-making behaviour by solving the uncertainties. As multiple parameters affect the energy expenditure in SNs, this uncertainty can be handled by FL.

The contributions of the proposed LBECR protocol are enumerated as follows

1. The proposed LBECR protocol is used to balance the network load for a protracted lifetime of the network.
2. A fuzzy inference system (FIS) is designed with influential parameters to select the most appropriate nodes for the CH role.
3. The complete cost that will be borne by an SN if chosen as CH is calculated and fed as one of the parameters to FIS.
4. For the formation of clusters, another FIS is designed to support the decision of non-CH nodes while joining a cluster.
5. For distribution of load while forwarding data to BS, a fuzzy system is designed for efficient multi-hop routing, conserving a significant amount of network energy.
6. The proposed LBECR is simulated and contrasted with recent DFCR (Mazumdar and Om 2018), FBECS (Mehra et al. 2020), I-AREOR (Chithaluru et al. 2020) protocols.

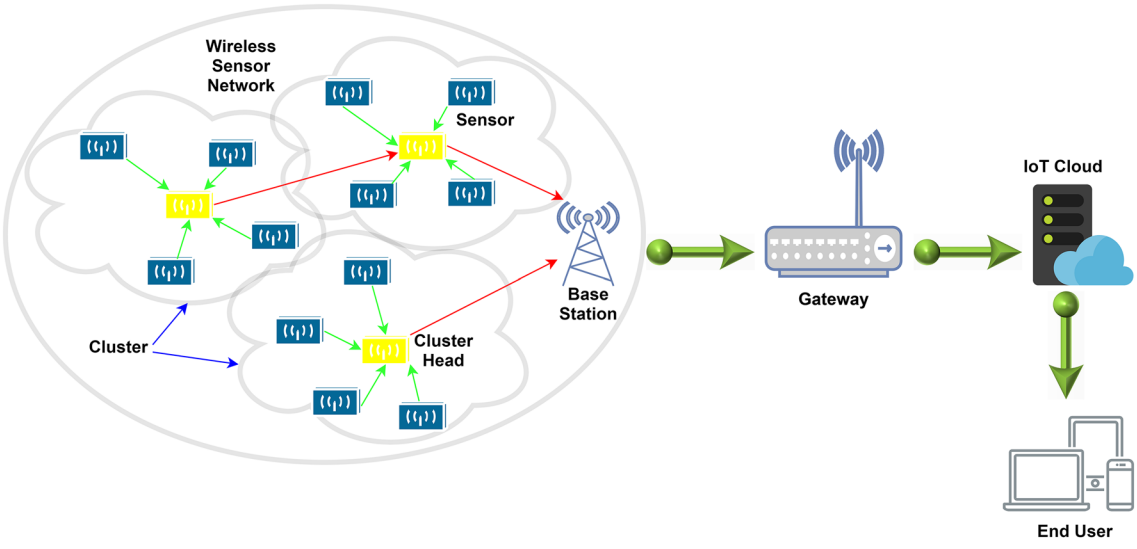


Fig. 1 A simple architecture of WSN based IoT

7. We have designed FIS with minimum and influential inputs as possible so that the energy expenditure of the SNs can be minimised because, with the escalation of input variables, the number of rules is increased exponentially, leading to more dissipation of energy in processing (Alkhawlani and Ayesh 2008; Rattan and Van Cleave 2000).

Section 2 discusses some pertinent work. System models with the energy model, network model and fuzzy model are discussed in Sect. 3. Section 4 describes the proposed LBECR protocol with its different stages. Simulation experiments and result analysis are done in Sect. 5. Section 6 discusses concluding remarks with future directions.

2 Related work

In the past decade, several energy-efficient techniques were proposed for the efficacy of resource-constrained SNs. Most of them are associated with the WSN prototype. Analogous to WSN, SNs in IoT play a crucial part in collecting, transmission and reception of data. Since IoT consists of a massive amount of smart entities connected to the Internet thus, energy conservation is a critical issue in the IoT model. WSNs have been merged with IoT as an integral part (Lazarescu 2016). We have discussed most of the promising clustering solutions for WSNs that can contribute to the IoT with minor modifications if required.

LEACH (Heinzelman et al. 2000) is the first protocol that considered clustering in energy-efficient routing algorithms. The LEACH protocol is proposed to select SNs as CH so that each node gets a chance for becoming a CH. The motivation behind this is that a CH node's energy dissipation rate is enormous compared to the non-CHs SNs; therefore, an SN will not dispel energy by repeatedly becoming a CH. It incorporates uncertainty while choosing the CH, leading to convergence to no CH selection in one round. The first implementation of FL is seen in Gupta et al. (Gupta et al. 2005) for clustering of SNs in WSN. It is proposed as an improvement over LEACH. For the fuzzy system, The inputs considered are remnant energy, centrality and the node degree. However, it is not scalable for the centralised approach. Kim et al. (Kim et al. 2008) propound the CH election mechanism, which relies on Fuzzy reasoning (CHEF). It estimates the probability of the node for acting as CH. The inputs utilise the remnant energy and transmission range to the BS for the fuzzy system during the CH selection, unlike LEACH. The contrast between CHEF and LEACH depicts more enhanced formation of clusters in CHEF than LEACH. An enhanced variant of LEACH is LEACH-FL with FL (Ran et al. 2010). The factors used are the distance of the node from the sink, type of battery used, and node density which differentiates it from the LEACH protocol. The CH selection is a centralised mechanism that is handled by BS like LEACH. It computes the possibility of an SN becoming a CH. The simulation result of LEACH-FL exhibits the reduction of energy dissipation rate over LEACH. The lifespan of LEACH-FL is significantly expanded over LEACH.

Gaur et al. (2015)proposed multi-level smart city architecture and various application domains based on IoT. It focuses on some customised services in the smart city environment by using semantic modelling and Dempster-Shafer theory, along with addressing the uncertainty aspect in the smart city. Shahraki et al. (2020) presented a survey focusing on the study and applicability of WSN clustering techniques in IoT networks. It provides insights into clustering and routing in IoT that provides a broader understanding of the design challenges shedding light on future application modern technologies integrated with IoT. Syed et al. (2021) presented a survey on technologies, practices and challenges in IoT smart cities. The work provides holistic coverage of IoT based Smart city landscapes with the technologies that enable them. A review of prevalent practices and applications is discussed with the encountered challenges with mitigation measures in the deployment of IoT systems. A survey on the fuzzy-based energy-aware protocol in WSN is discussed in (Dwivedi et al. 2020a, b), where the clustering and routing techniques are rigorously compared with the advantages and limitations. NEEF (Dwivedi and Sharma 2020) protocol is proposed for FL based clustering in WSN. It rules out randomness in CH selection by considering primary and secondary factors in the fuzzy system. Each node's probability is computed with fuzzy fitness values, and priority is given to primary factors using arbitrary constants. Significant improvement is seen from experimental results in terms of lifetime, stability period and network energy dissipation.

Memon et al. proposed a fuzzy management system considering the energy efficiency for IoT connected VANET(Memon et al. 2021). Considering the advantages of multi-hop data transmission and clustering, a fuzzy system is designed which contemplates neighbouring nodes, their distance and remnant energy. Effective utilisation of resources with improved Quality of Service can be observed than its comparatives. E-FUCA (Mehra 2021) is proposed for fuzzy-based enhanced clustering and routing for sustainable WSN. The work focus on unequal clustering with the determination of competition radius and rank by using FL. The parameters considered are average distance, residual energy and distance to BS. For determining the chance of CH, CH rank, closeness to CH and count of nodes in CH radius is considered. In the data dissemination stage, it uses next-hop rank, reduced distance to BS and nearness to next-hop as parameters to the fuzzy system for computing the cost. The proposed work significantly extends the lifetime

of the network. MOFCA[37] is proposed for mobile sensor networks, which determines CHs based on range to node and remaining energy. The CH's radius is a critical concern as CH, closer to BS having higher energy levels, can collect and transfer extraneous information. DUCF (Baranidharan and Santhi 2016) is proposed for fuzzy-based clustering systems in WSN. The FL based system contemplates density of node, energy, and nearness to BS as inputs in each round and suitable nodes are considered for the CH role. E-CAFL (Mehra et al. 2019) is proposed as an improvement over CAFL (El Alami and Najid 2017) protocol by eradicating the randomisation of CH by selecting only p% CH in each round. It considers the rank into account for best CH, and member nodes make an intelligent decision using FL to choose the cluster. Simulation experiments rigorously consider adverse environments to prove the efficacy of the proposed work. E-CAFL increases the throughput by 34.54% over CAFL protocol, with a significant increase in the stability period of the network.

A region-based probabilistic clustering is proposed FBECS (Mehra et al. 2020), which incorporates a fuzzy system. The SNs are allocated a probability based on their regions. An eligibility index is computed for each SN during the clustering process. Experimental results reveal the enhancement in the network's lifetime with more information delivered to BS. It encompasses some shortcomings like non-consideration of energy during clustering. Direct relay of data from CH to BS exhausts the energy of the network. DFCR (Mazumdar and Om 2018) is a routing protocol that solves the hotspot problem of WSN by applying an unequal clustering technique. It also reduces the cluster size nearer to the BS. It uses a practical approach for the CH selection and contemplates the relay node for data routing. I-AREOR (Chithaluru et al. 2020) is a clustering protocol proposed for IoT in smart cities. It considers regional density, residual energy and relative distance for CH selection. A dynamic threshold is applied for tentative CHs. Simulation results depict an extended lifetime, but scalability is not considered.

Most of the protocols discussed are using FL either in CH selection or the formation of clusters. Still, they do not consider FL in routing for extending the network lifetime. The parameters used in fuzzy based CH selection are fed in one FIS to get the desired CH. Still, the influence of the parameters is not considered, which can significantly contribute to the extension of the lifetime and stability of the network. In many protocols, cluster formation is based on the greedy choice of non-CH nodes, i.e. non-CH nodes select the nearest CH irrespective of considering the burden of the CH. Fuzzy based selection of next hop with influential parameters may significantly contribute to protracting network lifetime. In the proposed LBECR protocol, we have addressed all the three issues viz CH selection, cluster formation and routing using FL.

3 System model

This section discussed the network model, energy model, and fuzzy model used in the proposed LBECR protocol.

3.1 Network model

In the proposed work, we have considered four cases, as shown in Fig. 2, for validating the scalability, efficiency and applicability in case to case implementation in smart cities. The energy level of the SNs is kept at 0.5 J in all cases. In case 1, we have placed the BS at the centre of the area of interest (AOI), having the size of $100 \times 100 m^2$. The number of SNs deployed are 100. In case 2, the position of BS is similar to case 1, but we have increased the size of AOI, i.e. 200×200 m^2, with the deployment of 200 SNs. In case 3, the location of BS is positioned at a distant place from AOI with the size of 100×100 m^2 having 100 SNs. For case 4, the size of the AOI is increased to 200×200 m^2 with 200 SNs.

Some assumptions are made in the network, which is as follows:

1. The SNs deployment are randomly dispersed in AOI to satisfy the requirements of ad-hoc IoT networks.
2. BS is not having any energy constraint as it will have to perform the resource-intensive task of collecting data for further processing. Also, BS will be located in a position where a direct power supply can be provided.
3. The SNs, once deployed, are immobile as the movement of sensors will be restricted to one location for sensing/monitoring some target points.
4. There is a symmetric communication link between two nodes for easier calculation of energy expenditure.
5. Each SN has only one CH for energy efficiency as more transmission of signals and processing may degrade the network's performance.
6. Link quality indicator (LQI) is used for estimating the distance between two nodes. It can be replaced with GPS enabled device as per the requirement of the application.

3.2 Energy model

In the proposed work, the energy model adopted in (Heinzelman et al. 2000) is employed as shown in Fig. 3

The energy of the network may be depleted in sensing, aggregation, amplification, transmission and reception. Energy dissipations during transmitting (E_{Tx}) and receiving (E_{Rx}) s bits over d distance are given by

$$E_{Tx}(s,d) = \begin{cases} s * E_{elec} + s * \epsilon_{fs} * d^2, & d < d_o \\ s * E_{elec} + s * \epsilon_{mp} * d^4, & d \geq d_o \end{cases} \quad (1)$$

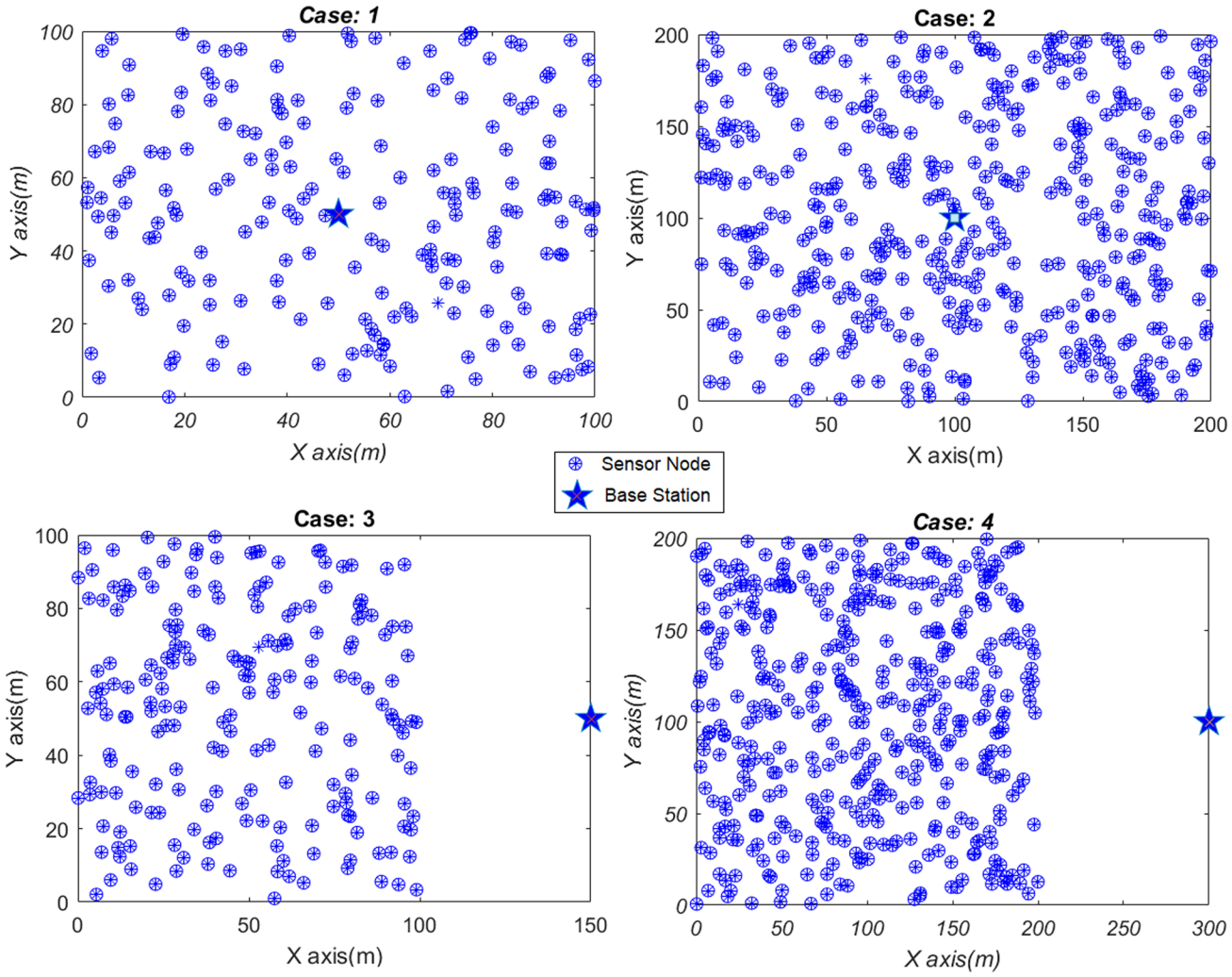


Fig.2 Different cases are considered for the proposed LBECR protocol

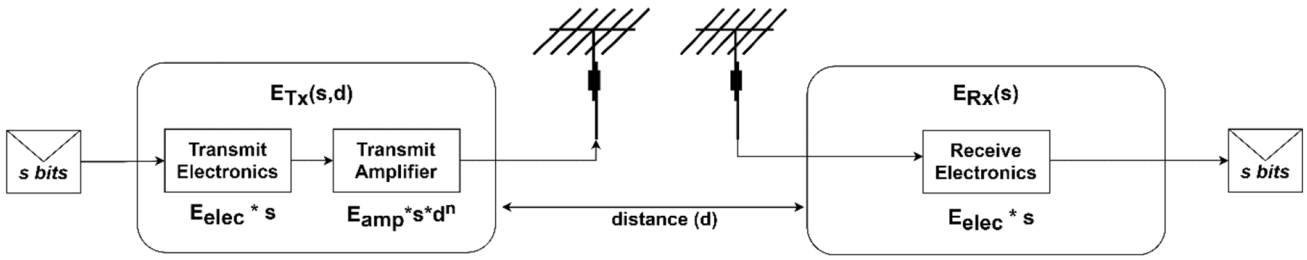


Fig.3 Energy model used in proposed work

$$E_{Rx}(s) = E_{Rx-elec}(s) = s.E_{elec} \tag{2}$$

E_{elec}, $\mathcal{E}_{fs}$ and $\mathcal{E}_{mp}$ is the energy exhausted in electrical components, energy dissipated in free space and energy dissipated in multipath, respectively.

In amplification of signal, energy dissipated (E_{amp}) is calculated by

$$E_{amp} = \begin{cases} \varepsilon_{fs} * d^2, & if \quad d < d_o \\ \varepsilon_{mp} * d^4, & if \quad d \geq d_o \end{cases} \tag{3}$$

d_o is a threshold which determines either free space or multipath model adopted and it can be calculated by

$$d_0 = \sqrt{\frac{\varepsilon_{fs}}{\varepsilon_{mp}}} \tag{4}$$

The communication cost to be borne by a CH in a round is calculated by

$$E_{CH} = n * s\,(E_{DA} + E_{Rx}(s, d(CH, CM)) + E_{amp}) + E_{sens} + E_{Tx}(s, d(BS)) \tag{5}$$

wherein n is the count of cluster members, s is the number of bits, *d(CH, CM)* is the distance between CH and cluster member, E_{DA} is data aggregation energy, E_{sens} is the energy dissipated in sensing, *d(BS)* is the distance between a node to BS.

The total energy drained by a member of a cluster is calculated by

$$E_{CM} = s * (E_{elec} + \varepsilon_{fs} * d_{CH}) \tag{6}$$

wherein d_{CH} is the distance to its CH.

3.3 Fuzzy model

FL is mainly applied for solving the uncertainties involved in any system. For energy efficiency in a network, several overlapping factors like remnant energy, the distance between SN to BS, cost to be borne by CH, the centrality of a node, density of node etc. Thus, FL is appropriate to solve the uncertainty problem of selection of CH, formation of clusters and routing of data as it can amalgam numerous factors dealing with uncertainties for providing better results. Trapezoidal and Triangular Membership Functions (MF) are used for boundary and intermediate variables, respectively, since they provide faster calculation and are simpler to implement. Each MF has a range from 0 to 1, which needs to be satisfied. Other MFs can also be used, like Sigmoid, Bell, Gaussian, etc., but the proposed LBECR protocol has depicted better results with Triangular and Trapezoidal MF.

The Triangular and Trapezoidal MF, which are incorporated in our designed FIS, are given in Eqs. (7) and (8) respectively.

$$f(y;p,q,r) = \max\left(\min\left(\frac{y-p}{q-p}, \frac{r-y}{r-q}\right), 0\right) \tag{7}$$

The parameters p and r set the left and right feet/base of the triangle, respectively, and q sets the peak of the triangle

$$f(y;p,q,r,s) = \max\left(\min\left(\frac{y-p}{q-p}, 1, \frac{s-y}{s-r}\right), 0\right) \tag{8}$$

The feet/base & the shoulders/top points of the trapezoid are located by *p, s* and *q, r,* respectively.

We use the Mamdani Inference method(Mamdani & H., 1977) because of its simplicity and ability to interpret and draw conclusions based on given IF–THEN rules quickly. These rules are of the IF antecedent, THEN consequent, where the antecedent consists of fuzzy input variables connected by logical functions(NOT, AND and OR), and the consequent is a fuzzy output variable.

Consider a p-input 1-output FL system with rules of the form as shown in Eq. 9

$$R^i : \textbf{IF}\, V_1 \,is\, A_1 \,\textbf{AND/ORIF}\, V_2 \,is\, A_2 \,\textbf{AND/OR} \ldots \textbf{IF}\, V_n \,is\, A_n \,\textbf{THEN}\, Y \,is\, Z, \tag{9}$$

where V_1, V_2,….V_n are input linguistic variables and A_1, A_2, … A_n, and Z are linguistic terms for inputs and output, respectively.

For defuzzification, we have used the Centre of Area (COA) method which is most commonly used(El Alami and Najid 2017; Logambigai and Kannan 2016; Nayak and Devulapalli 2016) that can be calculated by Eq. (10)

$$Z* = \frac{\int \mu_A(x)x dx}{\int \mu_A(x) dx} \tag{10}$$

4 Proposed LBECR protocol

In this section, the proposed LBECR protocol is described. It is proposed to extend the span of the first node dead (FND) and the lifetime of the network. Once the SNs are deployed in AOI, the LBECR protocol comes into play. For achieving the objective mentioned above, we have divided the LBECR protocol into rounds. In each round, there are three stages: selection of CH, formation of clusters, and data routing. The subsequent subsections will describe these stages.

4.1 Selection of CH

For the selection of CHs, SNs will broadcast Hello_Msg within its communication range (Rc) so that the nodes in the surrounding area are aware of each other in the vicinity. Each node has to calculate its Eligibility for proclaiming its candidature. We have designed a fuzzy inference system (FIS) that considers two factors of SNs to determine its Eligibility for CH candidature, as depicted in Fig. 4.

Residual energy provides the current battery level of the node, and CH overhead cost estimates the amount of energy that will be dissipated if the SN is chosen as CH. The MFs, along with linguistic variables for the input and output variables, are shown in Fig. 5a–c.

Mamdani Inference system takes two inputs and processes them using designed IF–THEN rules depicted in Table 1.

4.1.1 Illustration of fuzzy rules in Table 1

Consider a node is having an energy level of 0.15 and CH overhead cost is 0.2. From Fig. 5a, b, the linguistic values corresponding to energy level is Deficient and Sufficient, whereas, for CH overhead cost, the linguistic values are Low and Moderate. For these linguistic values, the degree of membership of input variables is to be calculated.

If the value of linguistic variable "Deficient" of Residual energy" is 0.15, on application of Triangular MF we get.

$$f(y;p,q,r) = \max\left(\min\left(\frac{y-p}{q-p}, \frac{r-y}{r-q}\right), 0\right) = 0.25$$

where y = 0.15, p = 0,q = 0,r = 0.2

If the value of linguistic variable "Sufficient" of Residual energy" is 0.15, on application of Triangular MF we get.

$$f(y;p,q,r) = \max\left(\min\left(\frac{y-p}{q-p}, \frac{r-y}{r-q}\right), 0\right) = 0.5$$

where y = 0.15, p = 0.05,q = 0.25,r = 0.45.

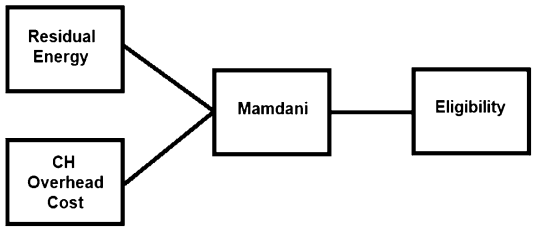


Fig.4 Designed FIS for CH selection

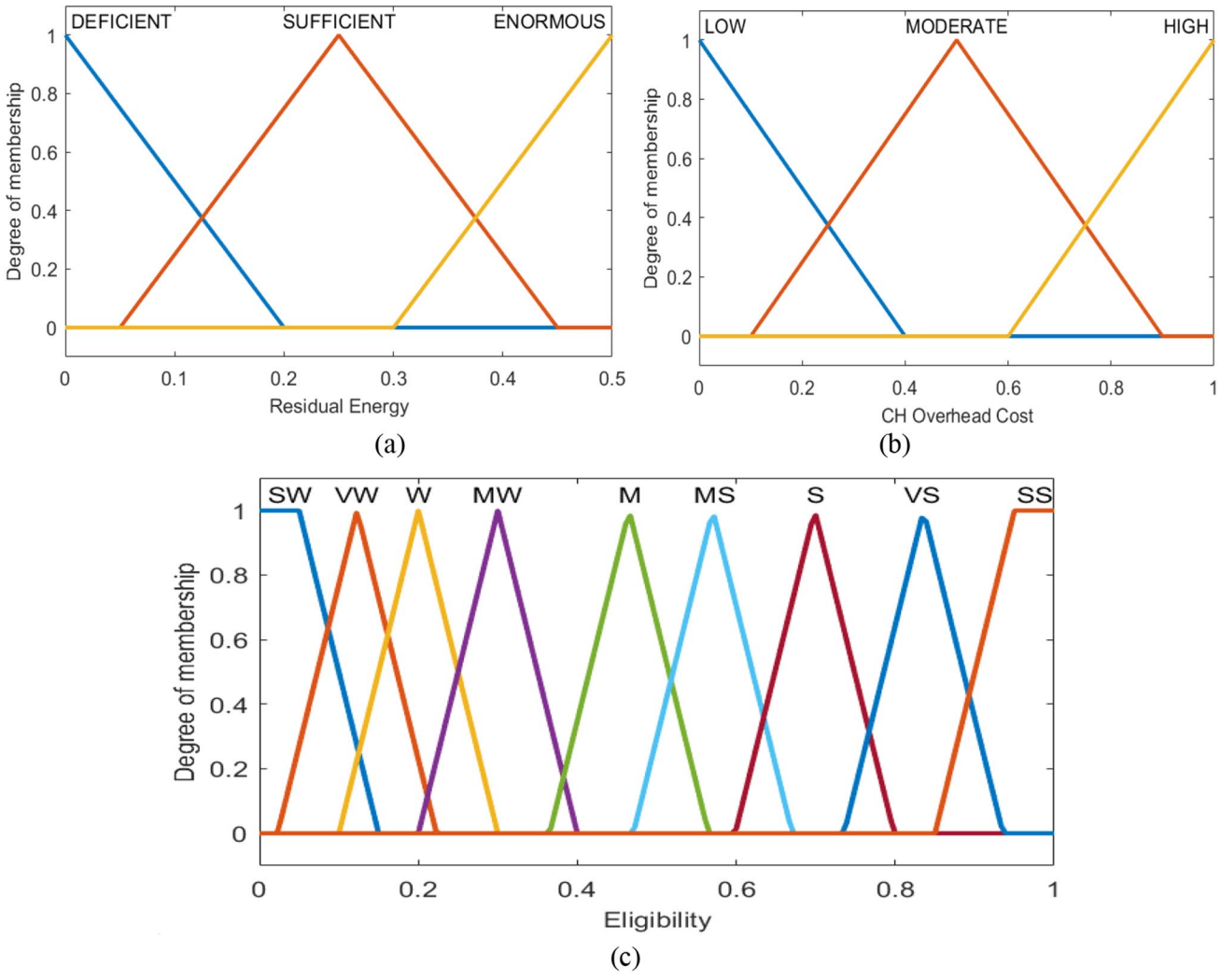


Fig.5 MFs designed for CH selection

Table 1 IF–THEN rules for computing Eligibility

Rule	Residual energy	CH overhead cost	Eligibility
1	Deficient	Low	Weak
2	Deficient	Moderate	Very weak
3	Deficient	High	Super weak
4	Sufficient	Low	Medium strong
5	Sufficient	Moderate	Medium
6	Sufficient	High	Medium weak
7	Enormous	Low	Super strong
8	Enormous	Moderate	Very strong
9	Enormous	High	Strong

If the value of linguistic variable "Low" of CH overhead" is 0.2, on application of Triangular MF we get

$$f(y;p,q,r) = \max\left(\min\left(\frac{y-p}{q-p}, \frac{r-y}{r-q}\right), 0\right) = 0.5$$

where y = 0.2, p = 0,q = 0,r = 0.4

If the value of linguistic variable "Moderate" of CH overhead" is 0.55, on application of Triangular MF we get.

$$f(y;p,q,r) = \max\left(\min\left(\frac{y-p}{q-p}, \frac{r-y}{r-q}\right), 0\right) = 0.25$$

where y = 0.0.2, p = 0.1,q = 0.5,r = 0.9

As per Table 1, the valid rules are as follows.

Rule 1: If Residual Energy is Deficient and CH overhead cost is Low, then Eligibility will be Weak.

Rule 2: If Residual Energy is Deficient and CH overhead cost is Moderate, then Eligibility will be Very Weak.

Rule 4: If Residual Energy is Sufficient and CH overhead cost is Low, then Eligibility will be Medium Strong.

Rule 5: If Residual Energy is Sufficient and CH overhead cost is Moderate, then Eligibility will be Medium.

Applying the values to the fuzzy Rule:

Rule 1: min(0.25,0.5) = 0.25.

Rule 2: min(0.25,0.25) = 0.25.

Rule 4: min(0.5,0.5) = 0.5

Rule 5: min(0.5,0.25) = 0.25.

The maximum value from Rule 1, Rule2, Rule 4 and Rule 5 is 0.5, which is "Medium Strong" for Eligibility as shown in Fig. 5 (c), and the crisp value lies between 0.1 and 0.3. The eligibility index will be 0.456 as the crisp value by applying the COA method.

After the computation of Eligibility, all the SNs broadcast their candidature within the Rc. The SNs will receive each broadcast, and the SN with the highest Eligibility will be selected as CH within that vicinity. For each round, only $p\%$ CHs will be selected. The overall process of selection of CH in the proposed protocol is depicted in Algorithm 1.

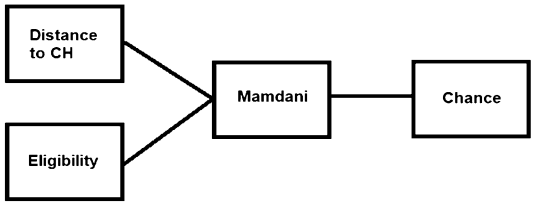


Fig. 6 Designed FIS for CH selection

Algorithm1: Selection of CH

Input: Alive SNs deployed in the AOI
Begin:
GN ← All sensor nodes in AOI.
SN(i) ← Sensor node with i as ID.
Every SN(i) will broadcast a Hello message in Rc
For each SN(i) in GN **do**
  Compute *Eligibility* ←fuzzy(RE,CH overhead cost)
  Broadcast SN(i).Eligibility in Rc
  If CH_Count<$p\%$ **then**
    If SN(i).Eligibility > Rest of the nodes in Rc
      SN(i) becomes CH
      CH_Count ++ \\ Increment the count of CHs
    End If
  End If
End For
Terminate
Output: Set of CHs selected for a round

4.2 Formation of clusters

Once all the CHs are selected, cluster formation needs to be done. In most of the existing protocols, a non-CH node makes a greedy decision for cluster formation by joining the nearest CH node. This may lead to an extraneous burden on an SN, which is already performing a resource-intensive task of CH role (sensing, collecting data from member nodes, data aggregation, and forwarding the aggregated data). To support the decision of non-CH nodes, we have designed FIS as shown in Fig. 6, which considers two inputs to be processed for obtaining chance. These two inputs are distance to the CH and Eligibility (computed during CH selection) of the CH under consideration. The reason for choosing *distance* is that we have to minimise it for preventing energy loss of non- CH nodes, and with the *Eligibility*, we can have some estimation of the burden that CH node can take. All the non-CH nodes have received the broadcast of selected CHs proclaiming their candidature during the CH selection process.

With that broadcast, non-CH nodes will have the distance and Eligibility of all CHs in their vicinity. Now the non-CH

nodes need to take a decision to join the better CH, which can contribute to balancing the load of the network. For supporting this decision, the designed FIS is used. The MFs, along with linguistic variables for the input and output variables, are shown in Fig. 7a–c.

Mamdani Inference system takes two inputs and processes them using designed IF–THEN rules depicted in Table 2.

4.2.1 Illustration of fuzzy rules in Table 2

Consider a node has its Distance to CH as 45, and the Eligibility is 0.45. From Fig. 7a, b, the linguistic values corresponding to Distance to CH is Nearer and Moderate, whereas, for Eligibility, the linguistic values are Good. For these linguistic values, the degree of membership of input variables is to be calculated.

Table 2 IF–THEN rules for computing Chance

Rule	Distance to CH	Eligibility	Chance
1	Nearer	Poor	Medium(M)
2	Nearer	Good	Strong(S)
3	Nearer	Better	Super Strong(SS)
4	Moderate	Poor	Medium Weak(MW)
5	Moderate	Good	Medium Strong(MS)
6	Moderate	Better	Very Strong(VS)
7	Distant	Poor	Super Weak(SW)
8	Distant	Good	Very Weak(VW)
9	Distant	Better	Weak(W)

If the value of linguistic variable "Nearer" of Distance to CH is 45, on application of Triangular MF we get.

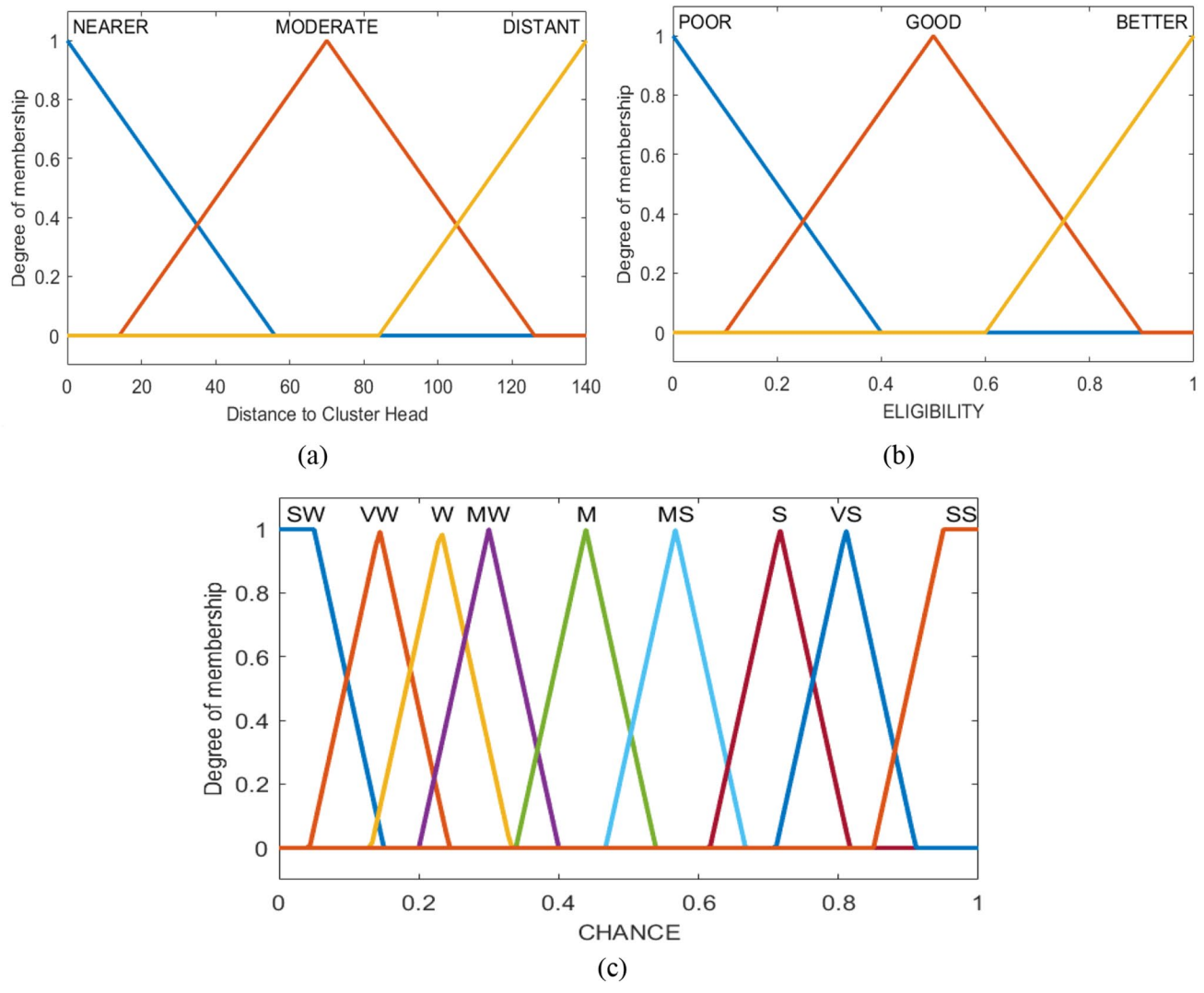


Fig.7 MFs designed for the formation of clusters

$$f(y;p,q,r) = \max\left(\min\left(\frac{y-p}{q-p}, \frac{r-y}{r-q}\right), 0\right) = 0.1964$$

where y = 45, p = 0,q = 0,r = 56.

If the value of linguistic variable "Moderate" of Distance to CH" is 0.45, on application of Triangular MF we get.

$$f(y;p,q,r) = \max\left(\min\left(\frac{y-p}{q-p}, \frac{r-y}{r-q}\right), 0\right) = 0.6226$$

where y = 45, p = 12,q = 65,r = 125.

If the value of linguistic variable "Good" of Eligibility is 0.45, on application of Triangular MF we get.

$$f(y;p,q,r) = \max\left(\min\left(\frac{y-p}{q-p}, \frac{r-y}{r-q}\right), 0\right) = 0.8333$$

where y = 0.45, p = 0.1,q = 0.52,r = 0.92.

As per Table 1, the valid rules are as follows.

Rule 2: If Distance to CH is Nearer and Eligibility is Good, then Chance will be Very Strong.

Rule 5: If Distance to CH is Moderate and Eligibility is Good, then Chance will be Medium Strong.

Applying the values to the fuzzy Rule:

Rule 2: min(0.1964,0.8333) = 0.1964.

Rule 5: min(0.6226,0.8333) = 0.6226.

The maximum value from Rule 2 and Rule 5 is 0.6226 (from Rule 5), which is Medium Strong for Chance, as shown in Fig. 7c, and the crisp value lies between 0.45 and 0.65. The value of the output variable Chance will be 0.642 as the crisp value by applying the COA method.

The non-CH nodes will select the CH with the highest chance and send Join_Req to the CH. In this manner, all the CHs will accept the membership of non-CH nodes and form clusters.

After the formation of clusters, the CH will provide a TDMA slot to each member to collect sensed information. The process of formation of the cluster is depicted in Algorithm 2.

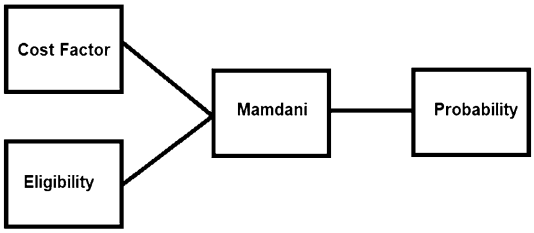


Fig.8 Designed FIS for routing of data

Algorithm2: Cluster formation in LBECR.

Input: Non clustered network

Begin:

GN ← All sensor nodes in AOI.
CHN ← All sensor nodes chosen as CH.
SN (i) ← Sensor node with i as ID.
Every node in CHN will broadcast Join_Req message
For each non CH node in GN **do**
  For each SN(i) in CHN **do**
    Compute *Chance* ←fuzzy(distance to CH, Eligibility)
    Send Join_Ack to SN(i) with the highest Chance
  End for
End For

Terminate

Output : Clustered Network

4.3 Routing of data

Once the CHs have collected the data from their members, they will aggregate the data to minimise the amount of data to be communicated. In most of the protocols, CHs use single-hop for communicating this data to the BS. As discussed earlier, the task of CH is resource-intensive, and if the distance to BS is more extensive, then a large amount of energy will be dissipated by the CH. To minimise the burden of CHs, we have designed FIS, which support the forwarding of data by CHs, as shown in Fig. 8.

There are two inputs, i.e. cost factor and Eligibility (obtained in CH selection) of the node, which are supplied to the FIS for calculating the probability of the next hops. The *cost factor* determines the amount of energy dissipated in processing and forwarding the data to the next-hop or BS. *Eligibility* estimates if the next-hop node can take the burden. The MFs, along with the linguistic variables for the input and output variables, are shown in Fig. 9a–c.

Mamdani Inference system takes two inputs and processes them using designed IF–THEN rules depicted in Table 3.

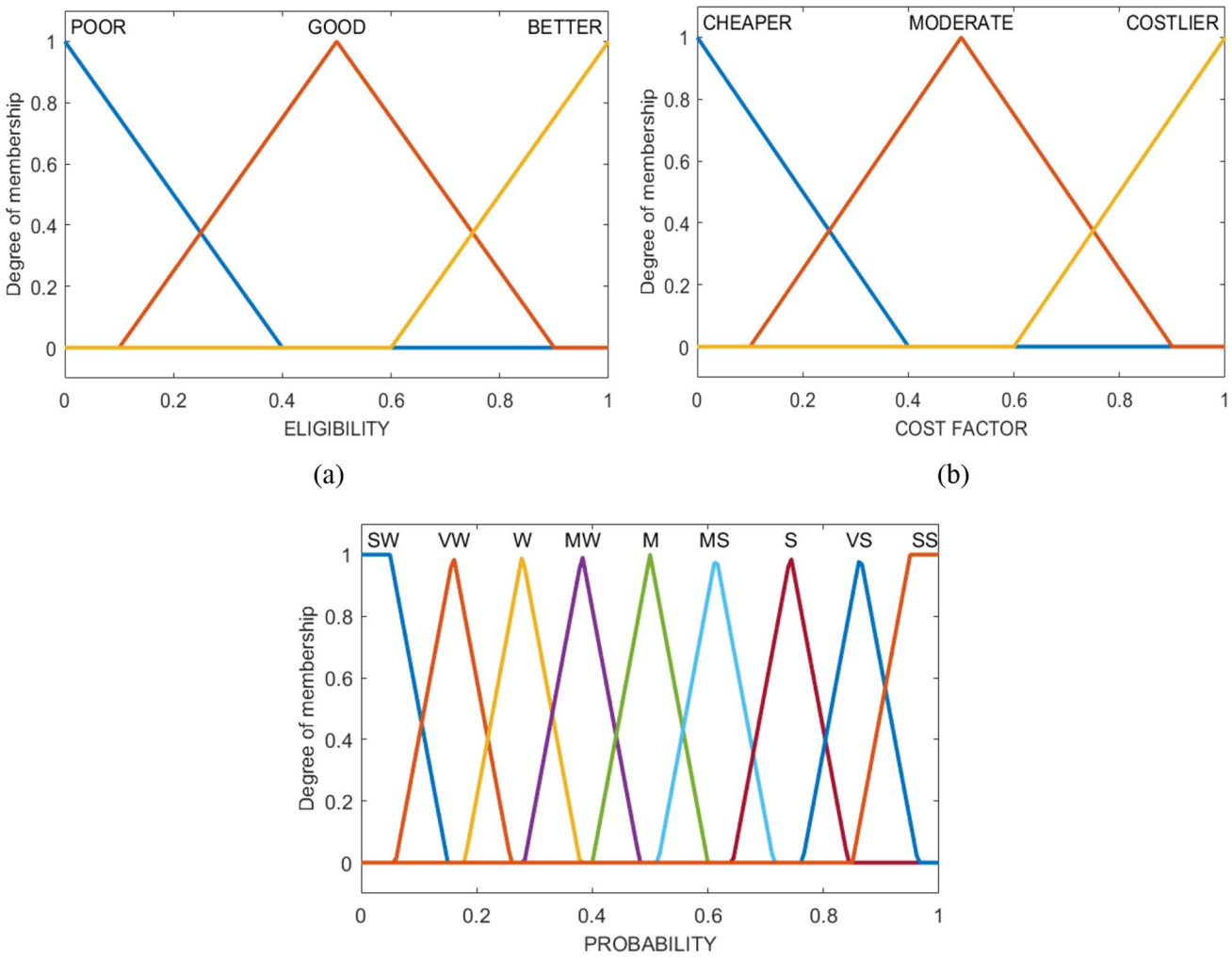


Fig.9 MFs designed for routing of data

Table 3 IF–THEN rules for computing Probability

Rule	Cost factor	Eligibility	Probability
1	Cheaper	Poor	Medium Strong(MS)
2	Cheaper	Good	Very Strong(VS)
3	Cheaper	Better	Super Strong(SS)
4	Moderate	Poor	Medium Weak(MW)
5	Moderate	Good	Very Weak(VW)
6	Moderate	Better	Strong(S)
7	Costlier	Poor	Super Weak(SW)
8	Costlier	Good	Medium(M)
9	Costlier	Better	Weak(W)

4.3.1 Illustration of fuzzy rules in Table 3

Consider a node is having its Eligibility as 0.7 and the Cost Factor as 0.8. From Fig. 9a, b, the linguistic values corresponding to Eligibility is Good and Better, whereas, for Cost Factor, the linguistic values are Moderate and Costlier. For these linguistic values, the degree of membership of input variables is to be calculated.

If the value of linguistic variable "Good" of Cost Factor is 0.8, on application of Triangular MF we get

$$f(y;p,q,r) = \max\left(\min\left(\frac{y-p}{q-p}, \frac{r-y}{r-q}\right), 0\right) = 0.25.$$

where y = 0.8, p = 0.1, q = 0.5, r = 0.9

If the value of linguistic variable "Better" of Cost Factor is 0.8, on application of Triangular MF we get

$$f(y;p,q,r) = \max\left(\min\left(\frac{y-p}{q-p}, \frac{r-y}{r-q}\right), 0\right) = 0.5$$

where y = 0.8, p = 0.6, q = 1, r = 1.

If the value of linguistic variable "Moderate" of Eligibility is 0.7, on application of Triangular MF we get

$$f(y;p,q,r) = \max\left(\min\left(\frac{y-p}{q-p}, \frac{r-y}{r-q}\right), 0\right) = 0.5$$

where y = 0.7, p = 0.1, q = 0.5, r = 0.9

If the value of linguistic variable "Costlier" of Eligibility is 0.7, on application of Triangular MF we get.

$f(y;p,q,r) = \max\left(\min\left(\frac{y-p}{q-p}, \frac{r-y}{r-q}\right), 0\right) = 0.25.$

where y = 0.7, p = 0.6, q = 1, r = 1.

Rule 5: If Cost Factor is Moderate and Eligibility is Good, then probability will be Medium Strong.

Rule 6: If Cost Factor is Moderate and Eligibility is Better, then Probability will be Strong.

Rule 8: If Cost Factor is Costlier and Eligibility is Good, then Probability will be Medium.

Rule 9: If Cost Factor is Costlier and Eligibility is Better, then Probability will be Weak.

Applying the values to the fuzzy Rule 1:

Rule 5: min(0.25,0.5) = 0.25.

Rule 6: min(0.25,0.25) = 0.25.

Rule 8: min(0.5,0.5) = 0.5

Rule 9: min(0.5,0.25) = 0.25.

The maximum value from Rule 5, Rule 6, Rule 8 and Rule 9 are 0.5 (from Rule 8), which is "Medium" for probability as shown in Fig. 9c, and the crisp value lies between 0.4 and 0.6. The value of output variable Probability will be 0.327 as the crisp value by applying the COA method.

The CHs will compute the probability of each node in the next hop and will forward the data to the node with the highest probability.

The process of routing is elaborated in Algorithm 3. In this manner, one round of the proposed LBECR protocol work is completed. The complete process of a round considering the algorithms 1–3 in the proposed LBECR protocol is depicted as a flow chart in Fig. 10.

Algorithm 3: Routing in LBECR.

SNs sense the information from AOI and forward it to CH
CHs collect information and aggregate it
Input : Data ready to be forwarded
Begin:
1 : CHN ← Set of all sensor nodes chosen as CH.
2 : SN(i) ← Sensor node with i as ID.
3 : **For** each SN(i) in CHN **do**
4 : **For** each SN(k) in CHN **do**
5 : Compute *Chance* ←fuzzy(cost factor, Eligibility)
6 : Select CH with maximum *Chance*
7 : Send aggregated data
8 : **End for**
9 : **End For**
Terminate
Output : Data from all CH received by BS

5 Simulation and result analysis

This section discusses the simulation experiments with parameters used in various cases, performance metrics used for comparative study, and analysis.

5.1 Simulation experiment

For evaluating the performance of the LBECR protocol, simulation experiments are conducted extensively in MATLAB for DFCR (Mazumdar and Om 2018), FBECS (Mehra et al. 2020), I-AREOR (Chithaluru et al. 2020) and proposed LBECR and results are obtained. The reason for choosing MATLAB as a simulation tool is that it is easier to conduct simulation, visualise results, and the protocols with which we are comparing our results are also simulated in the same tool. We have considered four cases for validating the scalability, efficiency and applicability in case to case implementation of the proposed work. The different cases are depicted in Table 4.

The operation of the network is divided into rounds. A round is complete if the sensed information from all the SNs is finally received at the BS. A node is deemed dead if it has a battery level less than or equal to zero. The simulation parameters with their values considered in this proposed work are shown in Table 5

5.2 Performance evaluation metrics

For the comparison of the proposed LBECR proposed, we have considered the following metrics.

First node dead (FND) The round number in which the death of one of the deployed SNs occurs in the AOI after the network becomes operational. The span from the first round to FND is very crucial as it ensures that the network is fully operational with all the nodes alive. There is complete reliability on the network in terms of coverage of AOI.

Quarter node dead (QND) The round number in which one-fourth of the deployed SNs in AOI is dead.

Half node dead (HND) The round number up to which half of the SNs in the network is dead.

Lifetime: It depicts the rate of the death of nodes in the network w.r.t the number of rounds.

The average energy of the network This metric depicts the average energy level of the SNs w.r.t. rounds. A network can balance the load if the average energy of the network is at the higher end throughout the lifetime of the network.

The average energy of CHs It shows the average energy level of SNs, which are chosen as CHs. Since clustering is observed to conserve the energy of the network, it is necessary to preferably choose the higher energy level nodes as

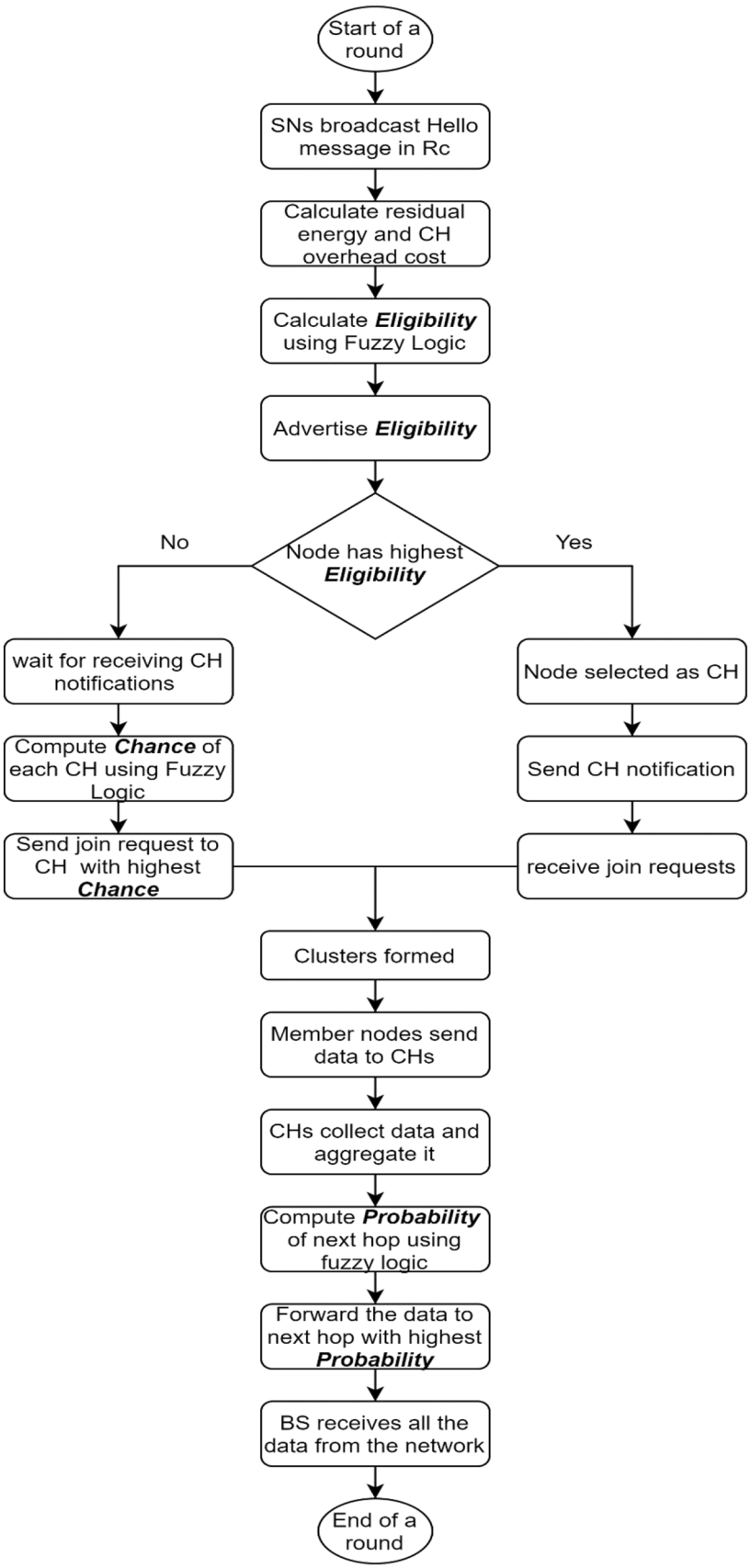


Fig.10 Flowchart depicting one round in the proposed LBECR protocol

Table 4 Different cases are considered in the LBECR protocol

Parameters	Symbol	Case:1	Case:2	Case:3	Case:4
Total SNs in AOI	N	100	200	100	200
Network dimension	$M \times M$	$100 \times 100 m^2$	$200 \times 200 m^2$	$100 \times 100 m^2$	$200 \times 200 m^2$
BS Location	BS	(50,50)	(100,100)	(150,50)	(300,150)

Table 5 Simulation parameters and their values

Parameter	Symbol	Values
Simulator	–	MATLAB
Type of communication	–	Wireless
MAC type	–	IEEE-802.11
Queue type	–	Drop tail priority queue
Energy model	–	First-order
Antenna type	–	Omni-directional
Amplifier energy for multipath	ε_{mp}	$0.0013 pJ/bit/m^4$
Transmission energy	E_{Tx}	50nJ/bit
Reception energy	E_{Rx}	50nJ/bit
Node energy before deployment	E_o	0.5 J
Data packet size	M	4000bits
Energy for data fusion	E_{DA}	5nJ/bit/report
Percentage of CH probability	$p\%$	10%
Electronic circuitry	E_{elec}	50nJ/bit
Maximum rounds	R_{max} $Rmax$	2000
Power dissipation in idle mode	E_{idle}	0.80 mJ/s

Table 6 FND for case 1, case 2, case 3 and case 4

Protocols	Case:1	Case:2	Case:3	Case:4
DFCR(Mazumdar and Om 2018)	480	384	258	80
FBECS(Mehra et al. 2020)	813	751	766	170
I-AREOR(Chithaluru et al. 2020)	878	871	855	819
LBECR(Proposed)	1478	1294	1510	1352

CH because the role of CH is resource-intensive (as discussed above).

Throughput It is the total number of packets delivered to the BS during the network's lifetime.

Average Latency Latency refers to the time taken by a packet to travel from source to destination. Here the average latency shows total latency per round to the number of rounds.

Average Traffic Load per node It shows the average number of packets transmitted/processed by each node during the network lifetime.

5.3 Result analysis

5.3.1 FND

The efficiency of a protocol is considered significant if it can prolong every SNs in the AOI (Smaragdakis et al. 2004). Table 6 depicts the FND of DFCR, FBECS, I-AREOR and proposed LBECR protocol for all the four cases considered in the simulation. We can see that for case 1; the proposed LBECR has shown improvement of 207.91%, 81.79% and 68.33% over DFCR, FBECS and I-AREOR protocol, respectively. Similarly, for case 2, the improvement is 236.97%, 72.30% and 48.56% for DFCR, FBECS and I-AREOR protocol, respectively.

In case 3, LBECR outperforms DFCR, FBECS and I-AREOR protocol by 485.27%, 97.12% and 76.60%, respectively. Likewise, for case 4, enhancement of 1590%, 695.29% and 65.07% can be observed over DFCR, FBECS and I-AREOR protocol, respectively. The reason for the better performance of the proposed LBECR in terms of FND is that during the CH selection, the parameters considered resulted in selecting the best candidates to play the CH role. It also rotated this role and balanced the load of the network.

5.3.2 QND and HND

In the network, if the nodes are depleting energy quickly, resulting in premature failure of the node, then the network may become susceptible to the non-coverage of target points in AOI. To validate the dissipation rate of the nodes are at par in the network, QND and HND are depicted in Fig. 11a–d for all four cases.

In case 1, the proposed LBECR has shown improvement of 149.55%, 90.32%, 52.02% and 131.16%, 87.22%, 47.38% and in case 2, 166.89%,68.07%, 52.06% and 148.84%,71.72%, 50.69% for QND and HND over DFCR, FBECS and I-AREOR protocol respectively. Similarly, the enhancements shown are 204.46%, 90.68%, 81.39% and 161.83%, 79.20%, 68.79% for case 3 and 1505.05%, 706.59%, 66.56% and 964.96%, 329.82%, 71.31% in terms of QND and HND over DFCR, FBECS and I-AREOR protocol.

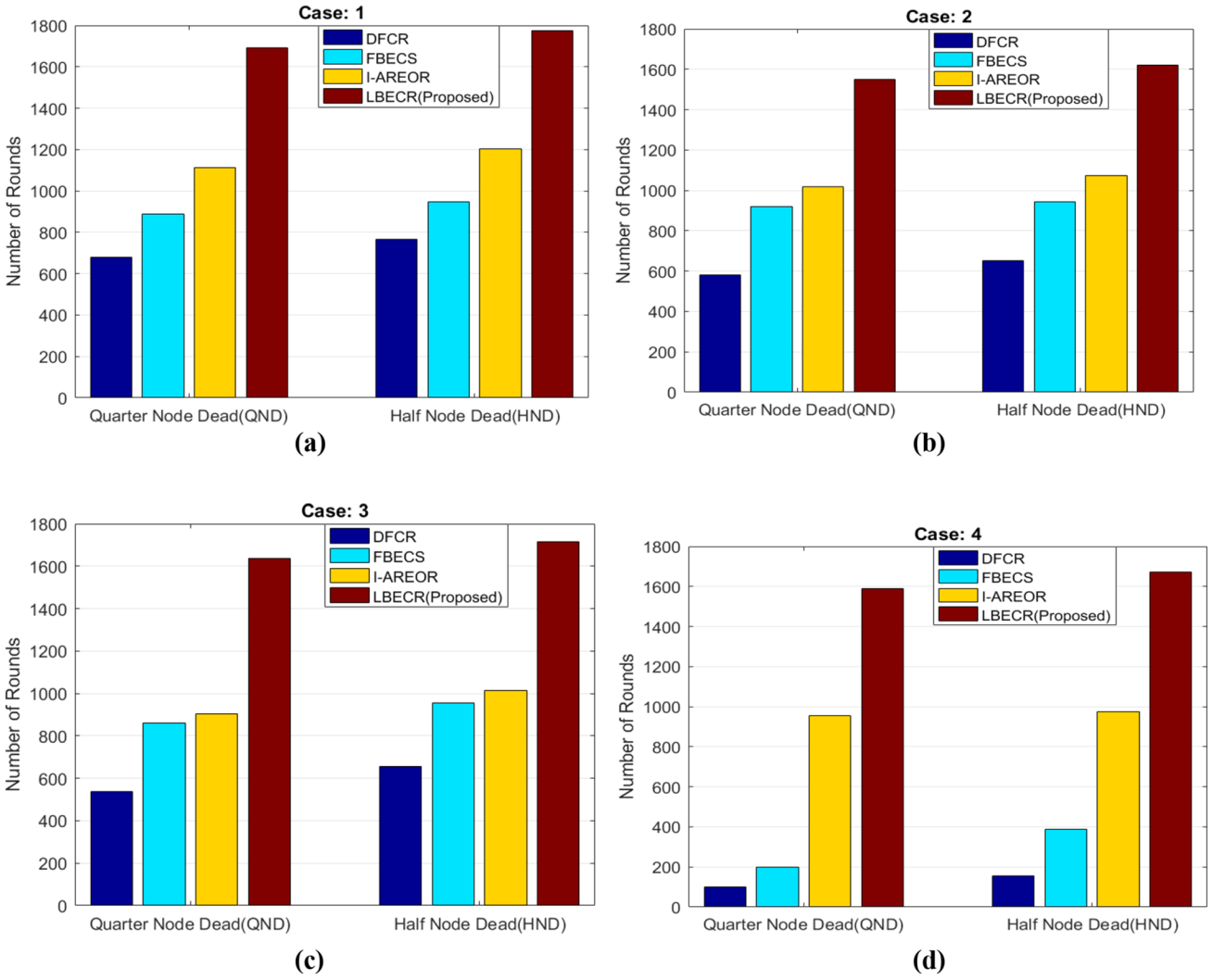


Fig. 11 QND and HND for case 1, case 2, case 3 and case 4

5.3.3 Lifetime

Since the objective of deployment of any network is to prolong its life as much as possible, Fig. 12a–d exhibits the network's lifetime for four cases considered in the simulation. If we talk about the death rate of nodes per round in deployed AOI, then the proposed LBECR protocol has significantly outperformed as compared to DFCR, FBECS and I-AREOR protocol. In all the cases, the proposed LBECR protocol can provide FND greater than 1400 rounds, and the last alive node is sustained up to 1700 rounds. In contrast, in the I-AREOR protocol, the network cannot even survive for 900 rounds with all the nodes alive. In DFCR and FBECS, the performance is abysmal as the load balancing is not achieved in both protocols.

If we carefully observe in all the cases, the lifetime of the DFCR, FBECS and I-AREOR protocol cannot even survive up to the rounds where the death of node begins in LBECR protocol. The reason for achieving this prolonged lifetime is that the network balances the energy dissipation rate of all the nodes in the network. This results in avoiding premature death of the nodes with a prolonged stability period (Smaragdakis et al. 2004).

5.3.4 Average energy of network

The equal distribution of load among the node is necessary to protract the lifetime of the network. If the average energy of the network is higher, then it may be concluded that the nodes are similarly dissipating energy. The average energy of the network is depicted in Fig. 13a–d for all four cases. We can observe from the figure that the energy dissipation rate of the network is meager and consistent as compared to DFCR, FBECS, and I-AREOR protocol either when the BS is at a distant place or when nearby the AOI. The reason for enhanced performance is the efficient cluster formation and

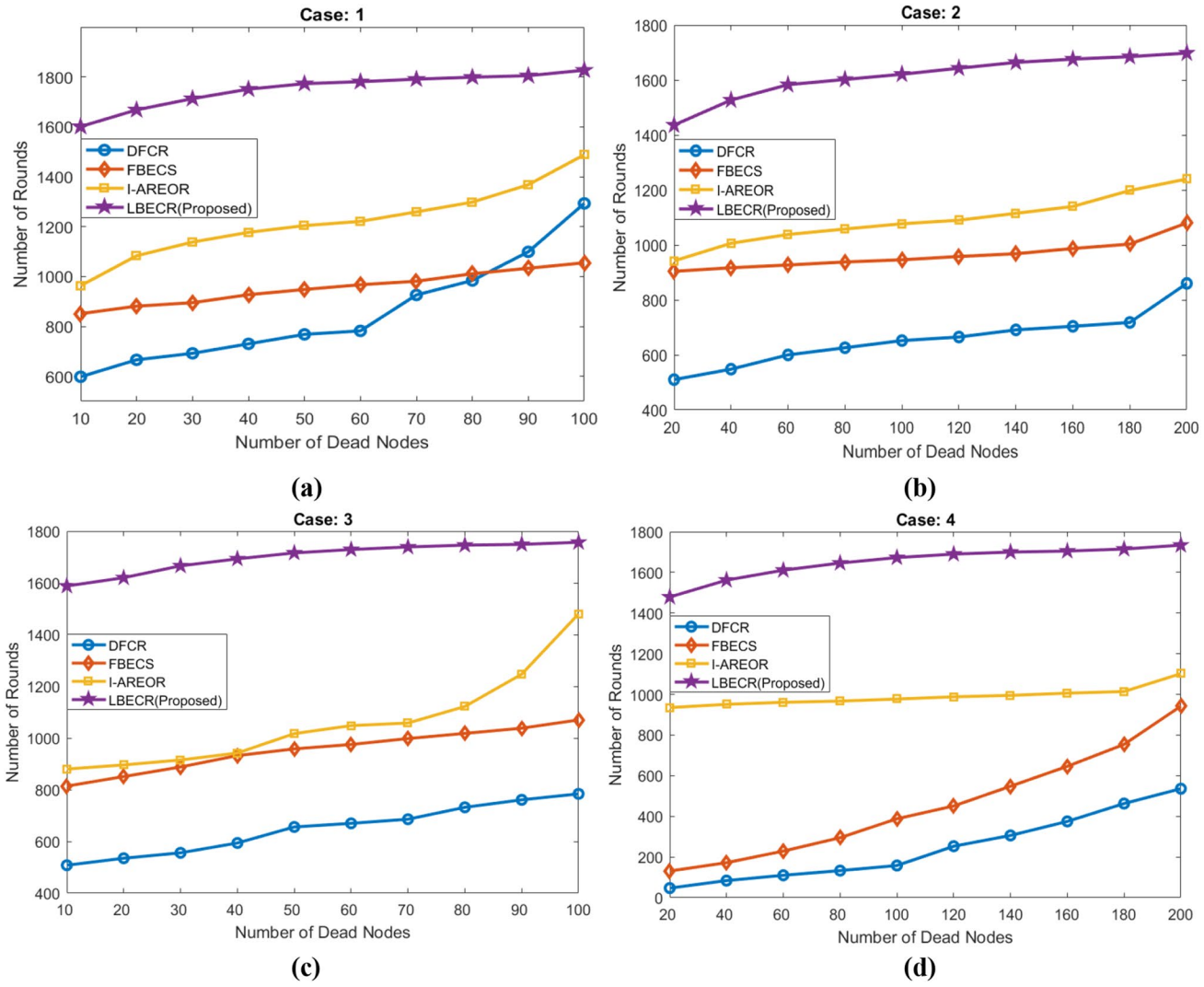


Fig. 12 The lifetime of network for case 1, case 2, case 3 and case 4

routing of data. We have considered the Eligibility and the distance to CH during cluster formation when the non-CH nodes decide to choose their CH. It resulted in the reduction of the burden of the CHs.

In DFCR, cluster radius is determined, and non-CH nodes need to join the CH within that radius; in FBECS, the non-CH nodes join the nearest cluster, which increases the burden of CH if the density is near the CH is high. In I-AREOR, cluster formation is completed by allocating nodes with higher energy density which may lead to premature failure of CH nodes.

5.3.5 Average energy of CHs

The job of a CH is to collect, process and aggregate data from the members and finally forward it to the BS. This job consumes a large amount of power compared to non-CH nodes, which sense and forward data to its CH. As the job is resource-intensive, the network must select the nodes capable of performing this job with a minimum dissipation of energy. Figure 14a–d depicts the average energy of selected CHs in the network. We can observe that the average energy level of CHs in DFCR, FBECS and I-AREOR is comparatively low compared to the LBECR protocol for all four cases. The proposed LBECR protocol has shown better performance because, during the CH selection, we have considered the residual energy and the entire cost incurred if the node is chosen as CH.

5.3.6 Throughput

The network's throughput is determined by the amount of information received by the BS from the network. The number of packets transmitted and received by the BS is

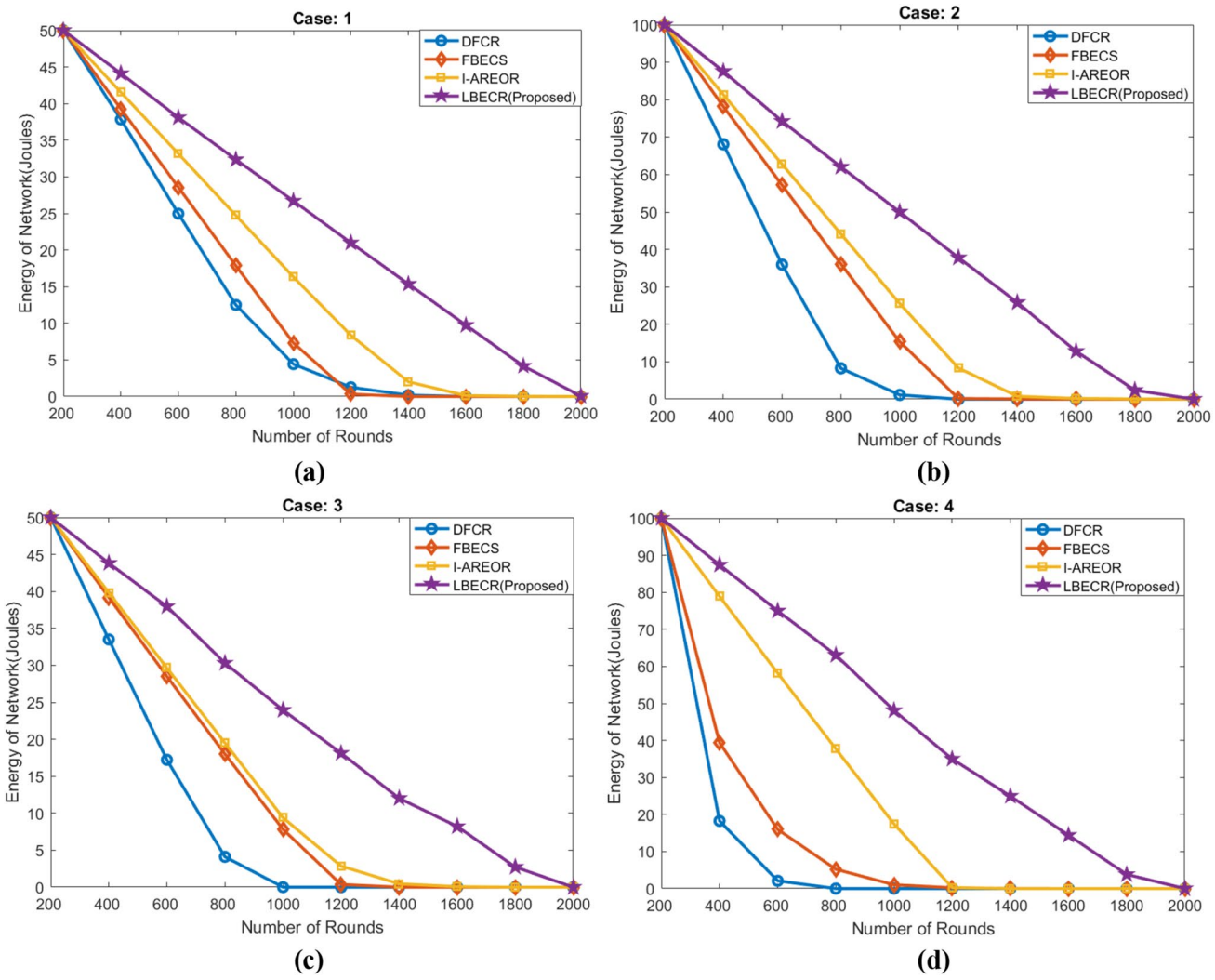


Fig.13 The average energy of network for case 1, case 2, case 3 and case 4

computed for the proposed LBECR, DFCR, FBECS and I-AREOR protocol. As shown in Fig. 15, we have considered the proposed LBECR protocol better than DFCR, FBECS, I-AREOR protocol for all four cases. The reason for the same is that the proposed protocol balances the network load, which in turn increases the network's lifetime.

5.3.7 Average latency

The time interval between the packets transmitted from source and destination determines the latency until it is received. The objective of the network must be to reduce the latency of the network as higher latency may void the purpose of time-critical application. As we can observe from Fig. 16, the proposed LBECR protocol has significantly less latency than DFCR, FBECS and I-AREOR protocols.

5.3.8 Average traffic load per node

We have computed the average traffic load regarding the number of bits transmitted or processed by SNs during their lifetime in the network. From Fig. 17, we can see that the node's average traffic load is comparatively less compared to DFCR, FBECS, I-AREOR protocol. Reduction in average traffic load reduces the energy consumption of the nodes because processing and communication consume significant energy on operating the electronic circuitry. The reason for the reduction in average traffic load is due to the fact that we have considered efficient routing by incorporating FL.

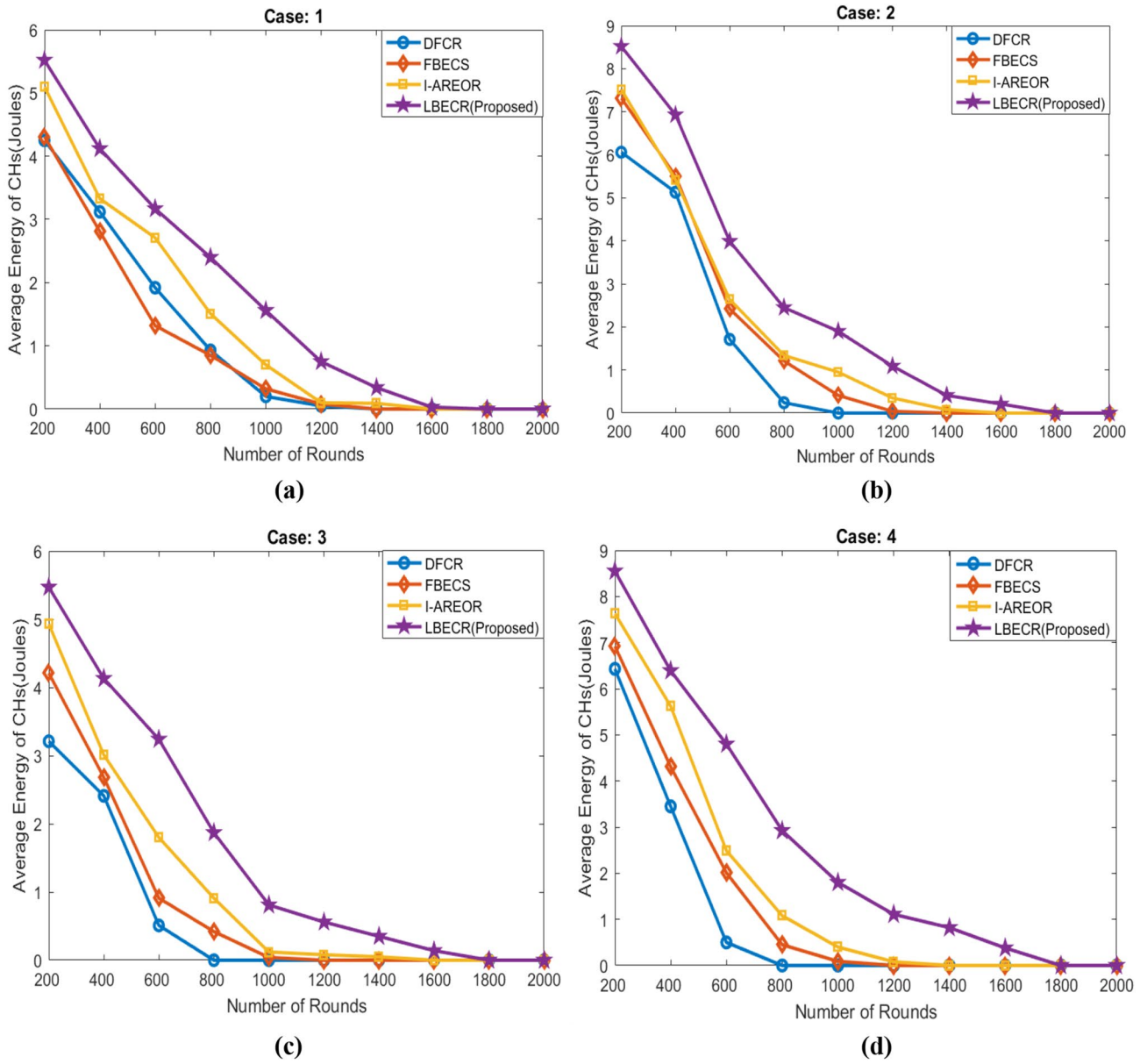


Fig.14 The average energy of CHs for case 1, case 2, case 3 and case 4

5.4 Complexity analysis

5.4.1 Time complexity

For the proposed network, we have deployed a total of n nodes in the network. During the CH selection, every node will compute the Eligibility independently. If we take the worst-case scenario, each SN has to make *(n-1)* comparisons for proclaiming its candidature, as shown in Algorithm 1. For n nodes, there will be *(n-1)* comparisons for CH selection. In cluster formation, non-CH nodes will choose their CHs by making (p_{opt}) comparisons in the worst case, as shown in Algorithm 2. For n nodes, total comparisons will be $n(p_{opt})$. In the routing of data, CH nodes will make p_{opt} comparison for forwarding data to the next hop. In the worst case, it will be $(p_{opt} \times p_{opt})$ as shown in Algorithm 3. Thus, the total operations in the proposed LBECR will be

$$f(n) = n + n(p_{opt}) + (p_{opt} \times p_{opt}) \quad \text{where } p_{opt} < n. \tag{11}$$

Therefore, the time complexity of the proposed work will be $O(n)$.

The comparison of time complexity is shown in Table 7.

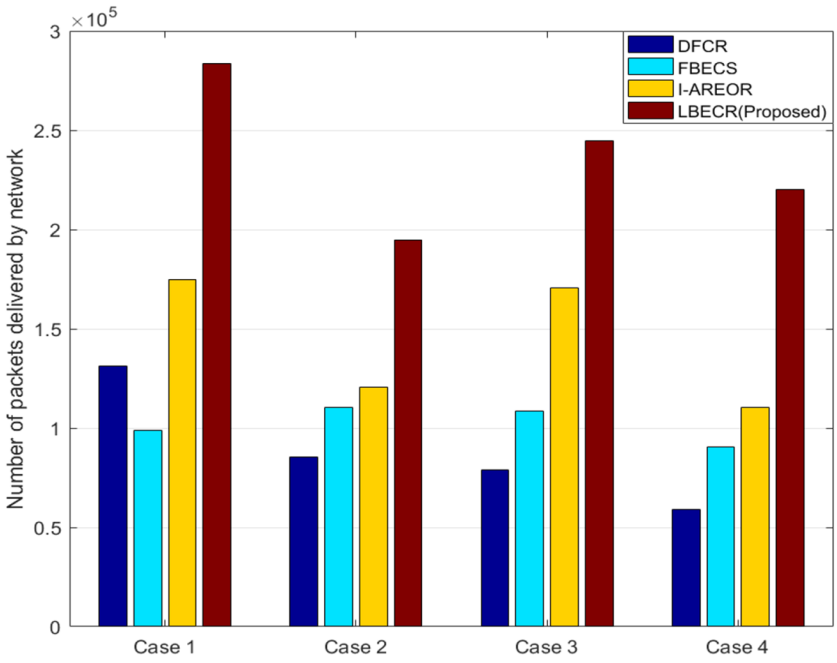


Fig.15 Throughput for case 1, case 2, case 3 and case 4

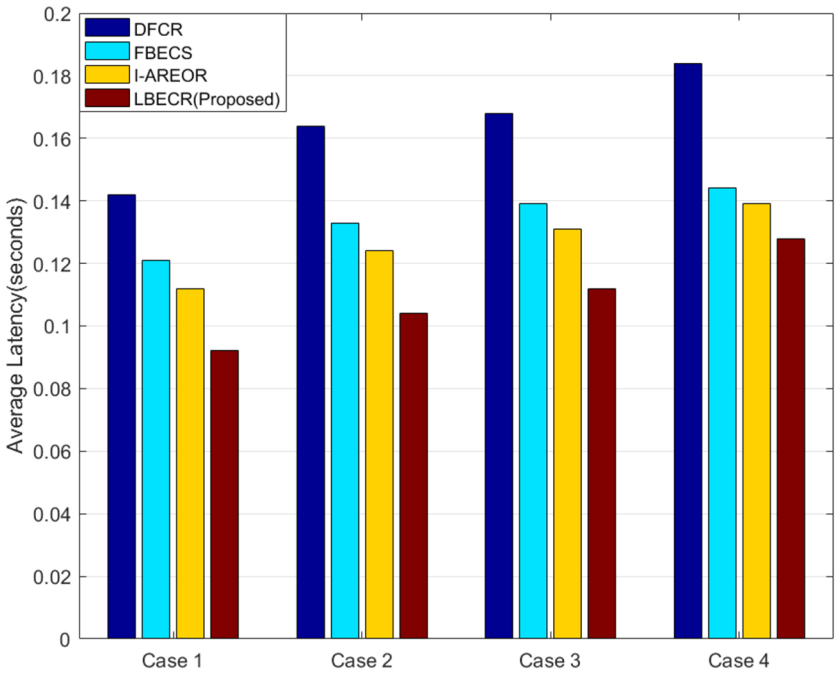


Fig.16 The average latency for case 1, case 2, case 3 and case 4

5.4.2 Message complexity

In each round, During CH selection, every SN will broadcast a Hello message. So total n messages will be broadcast by n nodes. For proclaiming its candidature, so there will n messages in the worst case. There will be total p_{opt} CHs in a round. During cluster formation, every non-CH node will forward a request to join a cluster, resulting in (n- p_{opt}) messages. In routing, p_{opt} CHs will forward the message to the next hop. In the worst case, there will be total p_{opt} messages. Thus, total messages in the proposed LBECR will be

$$g(n) = n + n + \left(n - p_{opt}\right) + p_{opt} = 3n \tag{12}$$

Therefore, the message complexity of the proposed work will be $O(n)$.

The comparison of message complexity is shown in Table 8.

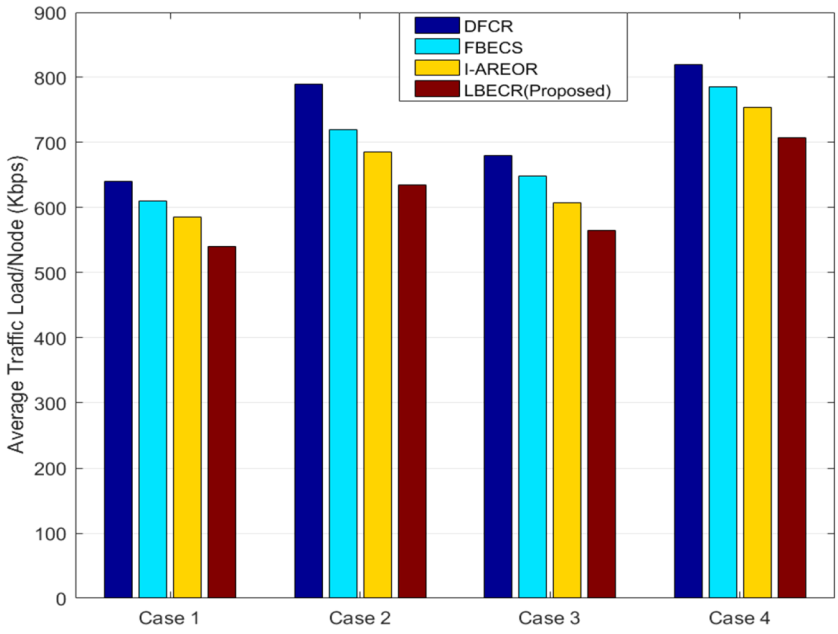


Fig.17 Average traffic load per node for case 1, case 2, case 3 and case 4

Table 7 Comparison of time complexity

Protocols	Time Complexity
DFCR(Mazumdar and Om 2018)	O(n)
FBECS(Mehra et al. 2020)	$O(n^2)$
I-AREOR(Chithaluru et al. 2020)	$O(n^2)$
LBECR(Proposed)	O(n)

Table 8 Comparison of message complexity

Protocols	Message Complexity
DFCR(Mazumdar and Om 2018)	*O(n)*
FBECS(Mehra et al. 2020)	*O(n)*
I-AREOR(Chithaluru et al. 2020)	*O(n)*
LBECR(Proposed)	*O(n)*

5.4.3 Convergence time

Clustering algorithms (CA) can be classified into two categories based on CH convergence time: constant convergence time CA and variable convergence time *CA*. Those algorithms capable of converging completely in a fixed number of iterations, irrespective of the number of devices, are termed constant convergence time CA. Such algorithms follow a localised strategy where the device independently executes the algorithm. The device takes the cluster membership decision based on their state or the state of their neighbours. The algorithms in which there is no fixed number of iterations to decide the clusters are variable convergence CA. The four protocols considered in this work has constant convergence time, as shown in Table 9.

Table 9 Comparison of CH convergence time

Protocols	Convergence time
DFCR(Mazumdar and Om 2018)	*Constant O(1)*
FBECS(Mehra et al. 2020)	*Constant O(1)*
I-AREOR(Chithaluru et al. 2020)	*Constant O(1)*
LBECR(Proposed)	*Constant O(1)*

5.5 Prospective applications of LBECR protocol: a case study

IoT has numerous applications in Smart cities like smart homes, smart agriculture, smart environment monitoring, Smart Health monitoring, Smart homes, Smart Industries, Smart Transport, Smart Infrastructure monitoring, Smart Traffic Management etc. Smart Agriculture requires monitoring of crops and detection of diseases in the plant. In the cities where water is scarce, water levels need to be checked regularly. The temperature, humidity, sunlight need to be monitored for the proper growth of the plant. The fertility of the soil needs to be monitored. Insects and pest detection is also a challenging task for better growth of the agricultural product. Smart Waste management can use IoT by having bins equipped with sensors to inform the authority of the need to empty bins and check if the harmful chemical substance is dumped in bins. It can also monitor the air quality

Table 10 Applicability of Proposed LBECR Protocol

Application	Application requirements									Proposed LBECR applicability
	Power Efficient	Efficient Clustering	Efficient Routing	Load Balancing	Throughput	Mobility of nodes	Scalability	Robustness	Stability	Low Latency	
Smart home	✓	✓	✓	✓	✓	✓	✓	✓	✓	✓	Suitable
Smart environment	✓	✓	✓	✓	✓	-	✓	✓	✓	✓	Highly suitable
Smart industry	✓	✓	✓	✓	✓	✓	✓	✓	✓	✓	Suitable
Smart traffic management	✓	✓	✓	✓	✓	✓	✓	✓	✓	✓	Suitable
Structural infrastructure	✓	✓	✓	✓	✓	-	✓	✓	✓	✓	Highly suitable
Smart Agriculture	✓	✓	✓	✓	✓	-	✓	✓	✓	✓	Highly suitable
Smart waste management	✓	✓	✓	✓	✓	-	✓	✓	✓	✓	Highly suitable
Smart healthcare	✓	✓	✓	✓	✓	✓	✓	✓	✓	✓	Suitable

surrounding the bin. Sewage overflow/blockage can also be monitored. Smart city services include municipal tasks like environmental control, water supply, waste management etc. Smart Health application concerns the facilitation of real-time health monitoring of patients and telehealth services. With the help of sensors placed on the human body externally or internally, the real-time detection of various diseases like heart stroke, epileptic seizures, Parkinson seizure etc., is possible. Smart Industries can contribute to increasing productivity with automation while reducing cost. It can also monitor machine/equipment, ambience, air quality, temperature etc. Traffic problems like congestion, pollution, reduction of public transport cost, emergency ambulance transit, tracking driver behaviour and pattern, nearest parking spot problems are critical issues addressed by smart traffic management. Structural Health Monitoring plays an essential role in ensuring the infrastructure shape and usability for uninterrupted usage by using accelerometers and smart materials. As per the proposed network architecture depicted in Fig. 1, the LBECR protocol can satisfy most smart cities applications, shown in Table 10.

6 Conclusion

Ever since the IoT has entered our day to day life, every device is getting connected with the help of the Internet. Since the efficacy and longevity of the network is a critical issue, researchers all over the world are addressing the issue with their proposed work. This paper has proposed a load-balanced efficient clustering and routing (LBECR) protocol for sustainable IoT in smart cities. We have designed FIS with fewer inputs for CH selection, Cluster formation and routing for reducing the complexity and balancing the energy dissipation rate of SNs. Four cases have been considered in simulation for validating the suitability of LBECR in diverse domains of IoT. Obtained simulation results portray that the proposed work significantly increase the span of FND, which increases the reliability of the network and achieved a longer lifetime than DFCR, FBECS and I-AREOR protocol. In the future, we will apply the Fuzzy Type 2 system for better results because of its ability to handle (large amounts of) uncertainty and combine them to generate an overall model compared to type-1 fuzzy systems. Since mobility is required in most IoT applications, we will consider mobile SNs for the applicability of networks in diverse domains of IoT. Also, we will conduct experiments on real testbeds for a better picture of the protocol.

References

Afsar MM, Tayarani-N MH (2014) Clustering in sensor networks: a literature survey. J Netw Comput Appl 46:198–226. https://doi.org/10.1016/j.jnca.2014.09.005

Alkhawlani M, Ayesh A (2008) Access network selection based on fuzzy logic and genetic algorithms. Adv Artif Intell 793058:12. https://doi.org/10.1155/2008/793058

Baranidharan B, Santhi B (2016) DUCF: distributed load balancing unequal clustering in wireless sensor networks using fuzzy approach. Appl Soft Comput 40:495–506. https://doi.org/10.1016/J.ASOC.2015.11.044

Brincat AA, Pacifici F, Martinaglia S, Mazzola F (2019) The Internet of Things for Intelligent Transportation Systems in Real Smart Cities Scenarios. In: IEEE 5th World Forum on Internet of Things, WF-IoT 2019 - Conference Proceedings, 128–132. https://doi.org/10.1109/WF-IoT.2019.8767247

Chithaluru P, Al-Turjman F, Kumar M, Stephan T (2020) I-AREOR: an energy-balanced clustering protocol for implementing green IoT in smart cities. Sustain Cities Soc 61:102254. https://doi.org/10.1016/j.scs.2020.102254

Dabirmoghaddam A, Ghaderi M, Williamson C (2014) On the optimal randomized clustering in distributed sensor networks. Comput Netw 59:17–32. https://doi.org/10.1016/J.BJP.2013.12.008

Dwivedi AK, Sharma AK (2020) NEEF: a novel energy efficient fuzzy logic based clustering protocol for wireless sensor network. Scalable Comput Pract Exp 21(3):555–568. https://doi.org/10.12694/scpe.v21i3.1749

Dwivedi A, Sharma A, Mehra PS (2020b) Energy-aware routing protocols for wireless sensor network based on fuzzy logic: a 10-years analytical review. EAI Endorsed Trans Energy Web. https://doi.org/10.4108/eai.6-10-2020.166548

Dwivedi AK, Sharma AK, Mehra PS (2020) Energy efficient sensor node deployment scheme for two stage routing protocol of wireless sensor networks assisted iot. ECTI Trans Electr Eng Electron Commun. https://doi.org/10.37936/ecti-eec.2020182.240541

El Alami H, Najid A (2017) Fuzzy logic based clustering algorithm for wireless sensor networks. Int J Fuzzy Syst Appl (IJFSA) 6(4):63–82. https://doi.org/10.4018/IJFSA.2017100105

Gaur A, Scotney B, Parr G, McClean S (2015) Smart City architecture and its applications based on IoT. Procedia Computer Science 52(1):1089–1094. https://doi.org/10.1016/J.PROCS.2015.05.122

Gupta P, Raj P, Tiwari S, Kumari P, Mehra PS (2020) Energy efficient diagonal based clustering protocol in wireless sensor network. SSRN Electron J. https://doi.org/10.2139/ssrn.3565781

Gupta I, Riordan D, Sampalli S (2005) Cluster-Head Election Using Fuzzy Logic for Wireless Sensor Networks. In: 3rd Annual Communication Networks and Services Research Conference (CNSR'05), 255–260. https://doi.org/10.1109/CNSR.2005.27

Haseeb K, Din IU, Almogren A, Islam N (2020) An energy efficient and secure IoT-based WSN framework: an application to smart agriculture. Sensors (switzerland). https://doi.org/10.3390/s20072081

Heinzelman WR, Chandrakasan A, Balakrishnan H (2000) Energy-efficient communication protocol for wireless microsensor networks. In: Proceedings of the 33rd Annual Hawaii International Conference on System Sciences, vol.1, 10. https://doi.org/10.1109/HICSS.2000.926982

Jain K, Kumar A (2020) An energy-efficient prediction model for data aggregation in sensor network. J Ambient Intell Hum Comput 11(11):5205–5216. https://doi.org/10.1007/S12652-020-01833-2

Kavitha BC, Vallikannu R (2019) IoT Based Intelligent Industry Monitoring System. In: 2019 6th International Conference on Signal Processing and Integrated Networks, SPIN 2019, pp 63–65. https://doi.org/10.1109/SPIN.2019.8711597

Kim J, Park S, Han Y, Chung T (2008) CHEF: Cluster Head Election mechanism using Fuzzy logic in Wireless Sensor Networks. In: Proceedings of 10th International Conference on Advanced Communication Technology, pp 654–659. https://doi.org/10.1109/ICACT.2008.4493846

Kumar N, Dash D (2020) Flow based efficient data gathering in wireless sensor network using path-constrained mobile sink. J Ambient Intell Humaniz Comput 11(3):1163–1175. https://doi.org/10.1007/s12652-019-01245-x

Kumaresan K, Kalyani SN (2020) Energy efficient cluster based multilevel hierarchical routing for multi-hop wireless sensor network. J Ambient Intell Humaniz Comput 1:3. https://doi.org/10.1007/s12652-020-01700-0

Lazarescu MT (2016) Wireless sensor networks for the internet of things: Barriers and synergies. In; Components and Services for IoT Platforms: Paving the Way for IoT Standards (pp. 155–186). Springer International Publishing. https://doi.org/10.1007/978-3-319-42304-3_9

Lenka RK, Rath AK, Sharma S (2019) Building reliable routing infrastructure for green IoT network. IEEE Access. https://doi.org/10.1109/ACCESS.2019.2939883

Logambigai R, Kannan A (2016) Fuzzy logic based unequal clustering for wireless sensor networks. Wirel Netw 22(3):945–957. https://doi.org/10.1007/s11276-015-1013-1

Mamdani HE (1977) Application of fuzzy logic to approximate reasoning using linguistic synthesis. IEEE Trans Comput 26(12):1182–1191. https://doi.org/10.1109/TC.1977.1674779

Mazumdar N, Om H (2018) Distributed fuzzy approach to unequal clustering and routing algorithm for wireless sensor networks. Int J Commun Syst 31(12):e3709. https://doi.org/10.1002/dac.3709

Mehra PS (2021) E-FUCA: enhancement in fuzzy unequal clustering and routing for sustainable wireless sensor network. Complex Intell Syst. https://doi.org/10.1007/S40747-021-00392-Z

Mehra PS, Doja MN, Alam B (2019) Enhanced clustering algorithm based on fuzzy logic (E-CAFL) for WSN. Scalable Comput Pract Exp 20(1):41–54. https://doi.org/10.12694/scpe.v20i1.1443

Mehra PS, Doja MN, Alam B (2020) Fuzzy based enhanced cluster head selection (FBECS) for WSN. J King Saud Univ Sci 32(1):390–401. https://doi.org/10.1016/J.JKSUS.2018.04.031

Mehra PS, Doja MN, Alam B (2018) Stable Period Extension for Heterogeneous Model in Wireless Sensor Network. In: Advances in Intelligent Systems and Computing (Vol. 638, pp 479–487). Springer, Singapore. https://doi.org/10.1007/978-981-10-6005-2_48

Memon I, Hasan MK, Shaikh RA, Nebhen J, Bakar KAA, Hossain E, Tunio MH (2021) Energy-efficient fuzzy management system for internet of things connected vehicular Ad Hoc networks. Electronics 10(9):1068. https://doi.org/10.3390/ELECTRONICS10091068

Mohamed RE, Ghanem WR, Khalil AT, Elhoseny M, Sajjad M, Mohamed MA (2018) Energy efficient collaborative proactive routing protocol for wireless sensor network. Comput Netw 142:154–167. https://doi.org/10.1016/J.COMNET.2018.06.010

Nayak P, Devulapalli A (2016) A fuzzy logic-based clustering algorithm for WSN to extend the network lifetime. IEEE Sens J 16(1):137–144. https://doi.org/10.1109/JSEN.2015.2472970

Pirbhulal S, Zhang H, Alahi EM, Ghayvat H, Mukhopadhyay S, Zhang Y-T, Wu W (2016) A novel secure IoT-based smart home automation system using a wireless sensor network. Sensors 17(12):69. https://doi.org/10.3390/s17010069

Ran G, Zhang H, Gong S (2010) Improving on LEACH protocol of wireless sensor networks using fuzzy logic. J Inf Comput Sci 7(3):767–775. https://doi.org/10.1109/SENSORCOMM.2007.21

Rattan KS, Van Cleave D (2000) Design and implementation of a reduced rule fuzzy logic PID controller. In: Annual Conference of the North American Fuzzy Information Processing Society - NAFIPS, pp 465–469. https://doi.org/10.1109/nafips.2000.877475

Rawat P, Chauhan S (2020) Probability based cluster routing protocol for wireless sensor network. J Ambient Intell Humaniz Comput 1:3. https://doi.org/10.1007/s12652-020-02307-1

Roy NR, Chandra P (2020) Threshold sensitive clustering in SEP. Sustain Comput Inform Syst 25:100367. https://doi.org/10.1016/j.suscom.2019.100367

Sethi P, Sarangi SR (2017) Internet of things: architectures, protocols, and applications. J Electr Comput Eng. https://doi.org/10.1155/2017/9324035

Shahraki A, Taherkordi A, Haugen O, Eliassen F (2020) A survey and future directions on clustering: from WSNs to IoT and modern networking paradigms. IEEE Trans Netw Serv Manag. https://doi.org/10.1109/TNSM.2020.3035315

Smaragdakis G, Matta I, Bestavros A (2004) SEP: A Stable Election Protocol for clustered heterogeneous wireless sensor networks

Syed AS, Sierra-Sosa D, Kumar A, Elmaghraby A (2021) IoT in Smart Cities: a survey of technologies, practices and challenges. Smart Cities 4(2):429–475. https://doi.org/10.3390/SMARTCITIES4020024

Tanwar S, Kumar N, Niu J-W (2014) EEMHR: energy-efficient multi-level heterogeneous routing protocol for wireless sensor networks. Int J Commun Syst 27(9):1289–1318. https://doi.org/10.1002/dac.2780

Yarinezhad R, Hashemi SN (2020) A sensor deployment approach for target coverage problem in wireless sensor networks. J Ambient Intell Humaniz Comput 1:3. https://doi.org/10.1007/s12652-020-02195-5

Publisher's Note Springer Nature remains neutral with regard to jurisdictional claims in published maps and institutional affiliations.

World Wide Web
https://doi.org/10.1007/s11280-021-01000-3

Link prediction in complex networks using node centrality and light gradient boosting machine

Sanjay Kumar[1,2] · **Abhishek Mallik**[1] · **B. S. Panda**[2]

Received: 19 February 2021 / Revised: 4 September 2021 / Accepted: 22 December 2021
© The Author(s), under exclusive licence to Springer Science+Business Media, LLC, part of Springer Nature 2022

Abstract

Link prediction is amongst the most crucial tasks in network science and graph data analytics. Given the snapshot of a network at a particular instance of time, the study of link prediction pertains to predicting possible future links amongst the nodes of the networks. It finds applications in recommender systems, traffic prediction in networks, biological interactions, and many others. In this paper, we propose a novel generic approach to link prediction based on using various node centralities and different machine learning classifiers. We utilize some popular and recently introduced node centralities to capture better the network's local, quasi-local and global structure. The value of various node centralities acts as the feature labels for the nodes in the network. The existent and non-existent edge in the network is labeled as positive and negative samples, respectively. The features of the nodes at the end of the edges, along with the positive or negative label, form a well-defined dataset for the task of link prediction. The dataset is then fed into various machine learning classifiers, and the best results are obtained with Light Gradient Boosted Machine (LGBM) classifier. We investigate the performance of the proposed model on multiple real-life networks using various performance metrics and reveal that our approach outperforms many popular and recently proposed link prediction methods.

Keywords Complex networks · Light Gradient Boosted Machine (LGBM) classifier · Link prediction · Node centralities · Online social networks

This article belongs to the Topical Collection: *Special Issue on Computational Aspects of Network Science*
Guest Editors: Apostolos N. Papadopoulos and Richard Chbeir

✉ Sanjay Kumar
sanjay.kumar@dtu.ac.in

Abhishek Mallik
abhishekmallik265@gmail.com

B. S. Panda
bspanda@maths.iitd.ac.in

[1] Department of Computer Science and Engineering, Delhi Technological University, New Delhi-110042, India

[2] Computer Science and Application Group, Department of Mathematics, Indian Institute of Technology Delhi, Hauz Khas, New Delhi-110016, India

Published online: 12 February 2022

1 Introduction

In recent years, the study of complex networks has drawn much attention from researchers of varied communities. Various real-life networks like online social networks, biological networks, transportation networks are examples of complex networks consisting of a large number of nodes or entities and intricate relationships between the nodes [5, 49]. These complex networks give rise to numerous research probems like community detection, influnece maximzation, information diffusion [27, 29]. One of the most sought-after tasks related to complex network analysis is link prediction (LP). It aims at predicting the existence of the links amongst two nodes that are not yet connected but might be connected in the future. Link prediction has been useful for several tasks like suggesting probable friendship links in social networks [50], the possibility of future co-authorship among authors [8], recommendation systems [12] where relevant information of the network users and interactions between them can be extracted from prevailing data that can be useful in making a prediction. Link prediction also helps us apprehend the growth of a network as most real-life networks, like social networks, communication networks grow over time. Over the years, numerous link prediction methods have been proposed in the literature [16, 35]. These techniques can be broadly categorised into similarity based, maximum likelihood based and probabilistic based techniques [28]. Some recent work has also been done by exploring the prospects of machine learning and deep learning techniques [19, 32, 52].

In this paper, we propose a novel approach of link prediction by using a combination of different node centralities to extract the required features for every node followed by machine learning classifiers. We utilize many popular and recent node centrality algorithms, namely Local Interaction Density (LID) [41], Linear Threshold Rank (LTR) [44], betweenness [48], Katz [22], Hubs and Authorities [25] and PageRank [6]. The centralities are chosen so as to better capture the local, quasi-local and global structural details of the entire network. The features are obtained for both the existent as well as non-existent link node pairs or edges. The existent edges form the positive samples while the non-existent egdes form the negative sample. These features along with the corresponding labels for the different node pairs forms a well labeled dataset. The dataset is then passed onto various popular binary machine learning classifiers. The experimentations are carried on several real-life social as well other information networks and various evaluation metrics are utilized to test the adaptability of our proposed approach in different scenarios. The experimental analysis is further accompanied by discussion on the relative feature importance of the different node centralities. This helps in estimating the usefulness of one node centrality over other for link prediction. The main contribution of our work is as follows:

(i) We propose a generic framework for link prediction using node centrality combination and several machine learning classifiers.
(ii) We present a feature importance study to determine the relative impact of the various node centralities chosen for link prediction.
(iii) We perform experiments on several real-life networks of varying size and nature and evaluate multiple performance metrics for several methods of link prediction.
(iv) We reveal that our node centrality based approach paired with LGBM classifier gives the best results through the various investigations performed for the task of link prediction.

The rest of the paper is organized as follows. Section 2 discusses some of the existing research work in link prediction. Section 3 illustrates preliminaries related to link prediction

and various node centrality utilized in this study. Section 4 presents various steps of our proposed approach in detail. Section 5 discusses the datasets and evaluation metrics utilized in this paper for comparing the performance of the proposed method with other existing methods. Section 6 presents the result and analysis of our proposed approach on the chosen networks. It contains the values of evaluated performance metrics and the details about the relative feature importance of our chosen node centralities. Finally, Section 7 concludes our work.

2 Related work

The link prediction problem can mainly predict the existence of new links amongst the nodes of a network based on their properties. Over the years, numerous methods of link prediction have been proposed in the literature, and these methods broadly can be divided into two major categories, namely, feature extraction techniques and feature learning techniques [36]. The feature extraction techniques exploit network features to predict the new links and further can be divided into similarity-based methods and probabilistic-based methods [19]. The feature learning-based method can be split into three categories: graph embedding-based method, and neural network-based method [39].

Similarity-based methods are the most commonly used techniques for link prediction based on the notion nodes tend to form links with other similar nodes. Such methods assign a score s_{uv} between two unconnected nodes u and v. The pair of unconnected nodes with a high value of the score is said to form a link. These methods utilize the topological structure of the network by analyzing specific node pairs. Based on the various features of the nodes, similarity-based methods can be further studied under three categories: local, global, and quasi-local approaches. Local similarity approaches utilize the local information of an edge to compute the similarity matrix. A variety of local feature based algorithms like common neighbors(CN), Adam-Adar (AA) index [1], Jaccard coefficient (JC) [20], preferential attachment (PA) [2], and Salton index [47] have been introduced in the literature. Chen et al. [7] proposed a common neighbors-based link prediction algorithm, known as Friend of a Friend (FOAF), in social networks by performing a personalized survey and a field study. Their works discovered that social network information is primarily helpful in finding known contacts, while similarity-based features were essential in learning new connections. Ibrahim et al. [19] used a multi-domain-based feature extraction technique. They combined the temporal details, community structuring in the graph, and different node centralities for link prediction. Wu et al. [53] proposed a model for link prediction named INILP based on some of the influential node identification metrics. The influential node identification metrics were used based on the common neighbors' criterion for link prediction. In general, these approaches are fast and efficient than nonlocal methods and can be performed in parallel. However, the major drawback of such methods is that they use only local information and restricts the set of the nodes to be linked, which are at a distance of two or more like neighbors of neighbors. In real-life networks, many links are established at distances greater than two in many real-world networks like social networks. The global similarity based approaches utilize the complete topological information of the network to rank similarity between node pairs which are not limited to measuring similarity between nodes up to two distances. Although examining the whole topology of the network gives more flexibility in link prediction analysis, but such methods require high time complexity resulting in being unfeasible for large networks, and their parallelization can be very complex. Global

similarity methods are generally based on two concepts, namely, shortest path and random walk-based techniques. SimRank [21] is a famous global similarity method for link prediction, which relies on the fact that two entities are similar if they are similar to a third entity. Pan et al. [38] proposed a Markov chain model for a random walk-based Random Walk with Restart (RWR) algorithm for link prediction. Quasi-local approaches use more data than local methods and do not require global topological information. Hence, such approaches produce better results, require less time complexity, and have been developed to uncover a balance between local and global measures. The local path index (LPI) [34], local random walks (LRW), and superposed random Walks (SRW) [33] are some common quasi-local approaches.

The probabilistic-based method under feature extraction techniques aim at extracting the underlying structure from the observed network and then predicting the missing links by using the learned model. For a given target network, a probabilistic model attempts to build a target function to establish a model composed of a group of parameters θ, which can best fit the observed data of the target network. Then the probability of the occurrence of a new link (i, j) is estimated by the conditional probability $P(A_{ij} = 1|\theta)$. Probabilistic relational model (PRM) [14], probabilistic entity-relationship model (PERM) [18] and stochastic relational model (SRM) [54] are three popular probabilistic based link prediction methods. Normally, such models works better for dense and directed networks and do not work well for sparse and undirected networks.

Various graph embedding techniques have been explored to perform different data analysis tasks like link prediction on complex networks in recent years. Such techniques represent the graph dataset into low dimensional vector representations preserving the features of nodes and the topological relationship between the nodes. Link prediction studies based on graph embedding methods can be viewed as generative models. Generative algorithms consider the problem of link prediction through an optimization problem maximizing future edge likelihoods [51]. The popular graph embedding techniques based on the idea of random walks utilizing the graph exploration as BFS (breadth-first search) or DFS (depth-first search) are Node2vec [15], Deepwalk [40], and GraphSage [17].

In recent years, some machine learning and deep learning-based approaches have been proposed for link prediction. Leskovec et al. [30] performed a positive and negative link prediction by utilizing the theories of balance and status from social psychology. They used a logistic regression-based machine learning classifier. They divided the positive and negative samples of the dataset in equal proportion for training the classifier to reduce the model's bias towards any particular type of sample. Zhang et al. [55] proposed a Weisfeiler-Lehman based encoding method for subgraphs which preserves the directionality all the while capturing the topological and structural positioning of the nodes. These features are then passed onto a neural network architecture to learn a predictive model, called WLNM, and to make the link predictions. Dai et al. [10] built over the fact that if properly processed, then a link prediction problem can be treated as a classical derivation of the binary classification problem. They achieved an improved performance by considering the AUC value as the optimization function. They used the hinge function as the loss function and constantly reduced the obtained loss by iteratively updating the weight matrix by the stochastic gradient sub-descent method. Qiu et al. [42] proposed the DeepInf model for link prediction. They used a graph autoencoder to compress the graph structurally. Then this compressed feature space is passed into a Graph Convolutional Network (GCN) and Graph Attention Network (GAT) for the final link prediction. Wang et al. [52] proposed a deep convolutional

neural network-based approach for link prediction. Firstly, they implemented a residual neural network and calculated performance metrics for it. The obtained results showed that the residual architecture of the model was inefficient in passing on the information. Then they experimented with dense neural network architecture and obtained improved performance results. Li et al. [32] presented an ensemble learning-based technique for link prediction by combining the logistic regression model and the Xgboost model. Based on the notion of an ensemble model that combines logistic regression and the Xgboost model by exploiting the stacking technology, they propose a new ensemble-model-based link prediction algorithm (EMLP).

There exist various methods of link prediction based on either local, semi-local, or global features of networks and usually suffers from the problems of consistency in their performances over different and large size networks. Also, the machine learning classifier-based link prediction algorithms suffer from dataset imbalance as there are few existent links and many non-existent links. Due to this sparsity of the graph, the dataset formed is highly imbalanced. In general, neural network-based link prediction methods produce good results but demand intensive resources and require more time to complete the executions. Through this work, we intend to propose an approach considering the local, quasi-local and global features of the nodes to capture and exploit the network details and profoundly perform link prediction. The proposed link prediction algorithm uses a Light Gradient Boosting (LGBM) algorithm. It helps in better determining the correlation and relevance of the various node centralities used. Moreover, LGBM also tends to reduce the loss more efficiently and effectively than its peers, which leads to improved results for the link prediction task.

3 Preliminaries

A network can be used to represent various complex relationships and interactions amongst different types of users and entities in a real-life scenario. The users or entities are referred to as nodes or vertices, while the interactions or connections between them can be inferred as links or edges. Consider an undirected and unweighted network represented as a graph $G(V, E)$ with the set of all nodes being represented as V, and the set of links or edges amongst the nodes can be represented as E. Table 1 lists the notation used by us in this paper. If we ignore self-loop and multi edges between a pair of nodes, then the maximum possible edges for a graph (G) can be represented as a universal set (U) as follows.

$$U = \frac{V \times (V-1)}{2} \tag{1}$$

The missing links or the links that will appear shortly can be represented by the set $\bar{E}$ as follows.

$$\bar{E} = \frac{V \times (V-1)}{2} - E \tag{2}$$

Now, we formally define the link prediction problem for an undirected network. Given the network snapshot at timestamp t, the problem of link prediction can be understood as the prediction of the missing links from the set $\bar{E}$, i.e., links that are existing but not yet observed in the current snapshot and will be observed later at the timestamp, $t + \Delta t$.

The connectivity in varied networks may indicate different types of relationships amongst the nodes and can be inferred according to the problem being considered. Node centralities consider the different topological and structural details provided by these connections and indicate which nodes are crucial based on the problem under consideration

Table 1 Various notations used by us throughout the paper

Notation	Description
G	An undirected and unweighted graph
V	Set of nodes in the graph
E	Set of existent edges in the graph
n	Total number of nodes in the graph
U	Maximum possible edges in the graph
$\bar{E}$	The set of non-existent edges in the graph

[26]. The definition of what property to be considered while calling a node central varies across different node centralities. All the node centralities work by assigning an importance score to different nodes based on the definition of centrality being followed. The node centralities considered by us in this study are as follows:

3.1 Local Interaction Density (LID) centrality

Local Interaction Density (LID) [41] centrality assigns an importance score to a node based on the ratio of a number of interacting edges to the number of interacting nodes in a subgraph of the node under consideration. The LID score of a node u in a network can be expressed as,

$$LID(u) = \frac{\mid E_{NB_INT}(u) \mid}{\mid V_{NB_INT}(u) \mid} \tag{3}$$

here, $\mid E_{NB_INT}(u) \mid$ is the number of interactive edges, i.e., the edges which in the subgraph of a node u represent the interaction amongst the nodes in the neighborhood of the node. Similarly, $\mid V_{NB_INT}(u) \mid$ represents the number of nodes that are interacting amongst themselves in the neighborhood of the node under consideration u.

3.2 Linear Threshold Rank (LTR) centrality

Linear Threshold Rank (LTR) [44] centrality is defined for each node as the number of nodes in its neighborhood the node under consideration can influence if it is activated initially. As a whole, it determines to what extent the entire network is centrally structured.

$$LTR(u) = \frac{\mid f(\{u\} \cup neighbors(u))}{n} \tag{4}$$

here, $neighbors(u)$ represents $\{v \in V | (u, v) \in E \vee (v, u) \in E\}$ and f is a labeling function that quantifies how influential each node is. A node $u \in V$ exerts influence over another node $v \in V$ if and only if $(u, v) \in E$. V is the set of nodes while E is the set of edges for the graph under consideration G.

3.3 Betweenness centrality

The betweenness [48] centrality assigns an importance score on the basis of the number of times a node comes in the shortest path between two nodes in the network. It develops on the notion that the node appearing in the shortest path amongst two nodes can act as a bridge amongst the nodes and can significantly influence the information flow between the

two nodes.

$$betweenness(u) = \sum_{i,j=1, i \neq j \neq u}^{n} \frac{\sigma_{ij}(u)}{\sigma_{ij}} \tag{5}$$

here, σ_{ij} represents the number of shortest paths from node i to node j and $\sigma_{ij}(u)$ is the number of shortest path from node i to node j with node u in between them.

3.4 Katz centrality

It was proposed by Leo Katz to measure the relative degree of influence of the nodes in a network [22]. Since the closer nodes tend to bear a larger influence on the node under consideration, a damping factor $\alpha < 1$ was introduced to model this effect. Formally it can be expressed as

$$katz(u) = \sum_{k=1}^{\infty} \sum_{v=1}^{n} \alpha^k (A^k)_{vu} \tag{6}$$

here, A^k represents the power matrix accounting for number of paths of length k amongst the nodes. $(A^k)_{vu}$ represents the number paths of length k starting at node v and ending at node u. With A being the adjacency matrix for the network.

3.5 Hubs and authorities centrality

In a directed graph, nodes can be interpreted slightly differently than in an undirected graph. The node sending out a lot of links can act as a hub, while the nodes receiving a lot of links can act as authorities. This forms the basis of the hyperlink-induced topic search (HITS) algorithm, or hubs and authorities' algorithm [25]. The hubs and authorities values are related as follows:

$$auth(u) = A^T hub(u) \tag{7}$$

$$hub(u) = Aauth(u) \tag{8}$$

here, A represents the adjacency matrix and A^T represents the transpose of the adjacency matrix.

3.6 PageRank centrality

PageRank centrality lies at the core of the Google search engine has become increasingly popular since its inception [6]. It builds on the notion of giving importance to nodes receiving more links from other nodes. Mathematically it can be expressed as,

$$pagerank(u) = \alpha \sum_{v=1}^{n} \frac{pagerank(v)}{degree_v^{out}} + \frac{1-\alpha}{n} \tag{9}$$

here, α is a damping constant similar to that in katz centrality and $degree_v^{out}$ is the outdegree for the node v.

4 Proposed work

This section presents the work proposed by us for the task of link prediction. Our work relies on combining various node centralities to get an optimal mix of node centralities that captures the local structure, global structure, topological features, and relative influence of

one node over the other. These node centralities are then paired with LGBM based machine learning technique to obtain improved performance measures for link prediction. The step wise description of our proposed methodology is presented as follows.

4.1 Feature extraction

To obtain a more generic link prediction algorithm, we consider the network a black box, ignoring the contextual details. This implies that we have no attributes associated with the nodes that can act as possible features for the nodes. This is where node centralities come into play. Irrespective of the context and type of networks under consideration, the node centralities tend to provide crucial information about a node by considering the network structure, the connectivities amongst the nodes, and other topological features of the network. But different node centralities cover various informational aspects of the network. This is indicative of the need to use a combination of these node centralities. For our work, we use node centralities capturing varying domains of the network, namely Local Interaction Density (LID) centrality, Linear Threshold Rank (LTR) centrality, betweenness centrality, Katz centrality, hubs and authorities centrality, and PageRank centrality. The values obtained for the six centrality measures for every node in our network constitute the six different features for each node. These extracted features are then passed on to different machine learning techniques for the task of link prediction at a later phase. The features are calculated over a prior instance of the network to make link predictions on a later instance of the network. This is so justified as in a real-world scenario as well, we make link predictions by using the existing topological details of the network.

4.2 Dataset creation

To apply any supervised machine learning technique, we need a labeled dataset with both positive and negative samples. To achieve this, we create a dataset by using positive samples and negative samples. Here, positive and negative samples represent existent and non-existent edges, respectively. The edges present in the network are existent, and edges that are currently not present in the network and may appear in the near future are non-existent edges. For a complex network represented as an undirected graph $G(V, E)$, E is the set of existent edges, and $\bar{E}$ denotes the set of non-existent edges, which is depicted by (2). The positive samples are given a label of 1, while the negative samples are provided a label of 0. Hence, label 1 represents the presence of edges, while label 0 represents the absence of edges between a pair of nodes. The feature extraction as presented in previous Section 4.1 is done for both types of samples by calculating values of three different node centralities.

Both positive and negative samples in the dataset make it ready for a binary classification task like link prediction. However, real-life networks are often sparse, and the number of connected edges is comparatively less than the number of non-connected edges. Therefore the created dataset may be highly unbalanced. To overcome this problem, we select an equal number of positive edge samples and negative edge samples. This is also in accordance with the work of Leskovec et al. [30]. This gives us a well-balanced dataset having an equal number of positive and negative samples. It also reduces the model's bias towards any particular type of sample. These edge samples are then combined into a single dataset. This dataset is then shuffled so that a randomly picked sample may be positive or negative with equal probability. The shuffled dataset forms the final dataset, D.

4.3 Dividing the dataset

After creating a well-labeled dataset, we need to divide it into two parts: training and testing. The training set is used to train the classifier model, while the testing set is used to evaluate the classifier's performance. We varied the splitting ratio from 50% to 95% in the steps of 5% and observed that the 80:20 split ratio for training and testing the model is optimal. The analysis performed is described in Section 6.1. Therefore, the dataset is divided into an 80:20 ratio using 80% of the dataset as a training set and the remaining 20% of the dataset as the testing set. The choice of dividing the dataset in such a manner is made so that enough data is available for adequately training the classifier but still avoiding overfitting and having enough data spared for optimally testing the classifier's performance.

4.4 Light gradient boosting machine (LGBM)

The dataset generated in the last phase is further passed onto a machine learning classifier to make the link predictions. We try out numerous classifiers like Random forest, Gaussian Naive Bayes, Logistic Regression, K means clustering, K nearest neighbors, Support vector machines and Decision Trees. But to further improve upon the prediction ability of our approach we employ a gradient boosting algorithm [13]. It is an algorithm that combines the weighted outcomes of weak learners to generate a strong learner. For our algorithm, the weak learners are decision trees and the strong learner is an ensemble-based model of these decision trees. For our work we use an implementation of the gradient boosting algorithm known as Light Gradient Boosting Machine (LGBM) [23]. LGBM is a gradient boosting framework that uses decision tree based learning algorithm. The major difference between LGBM and other graident boosting algorithms is that it grows the tree vertically while other algorithms grow the tree horizontally. In simpler words, it can be understood that LGBM grows the decision tree leaf wise while other algorithms grow the tree level wise. LGBM does so by choosing the leaf with the maximum loss. This way LGBM being a leaf-wise algorithm reduces more loss at a faster rate than a level-wise algorithm. Figure 1 shows the leaf-wise tree growth for LGBM. It is the reasoning for us to choose LGBM over other algorithms. Another reason for us to choose LGBM over other contemporary algorithms is that it is faster and uses much less memory to run. It can also be combined with GPU to obtain even faster computations.

We combine LGBM with the node centralities because it can very quickly and efficiently detect correlations and relevance amongst the centralities and further reduce the loss of the algorithm. To obtain a more network-independent link prediction algorithm, we intend to use the values of node centralities as the features of nodes. The value of node centralities provides crucial information about a node by considering the network structure, the connectivities amongst the other nodes, and other topological features of the node. We use six

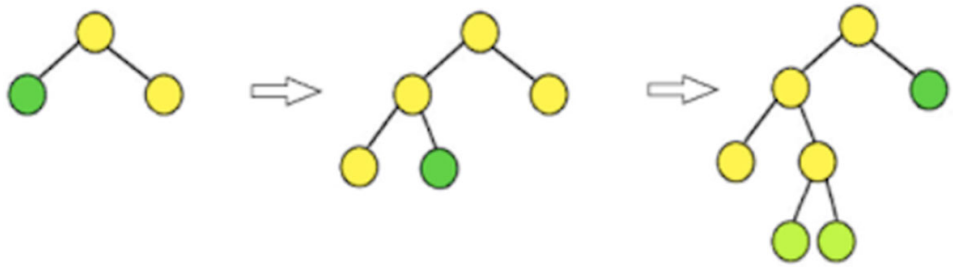


Figure 1 Leaf wise tree growth for LGBM

different node centralities for our work, namely Local Interaction Density (LID) centrality, Linear Threshold Rank (LTR) centrality, betweenness centrality, Katz centrality, hubs and authorities centrality, and PageRank centrality. These diverse node centralities can properly capture the local, quasi-local, and global topological features of the nodes in the network. Figure 2 illustrates our use of node centralities with the LGBM classifier. Here the edge label in the last coulmn represent the existence or non-existence of the links between a pair of nodes, where label 1 means that a link exists while label 0 illustrates that no link exists between the two nodes. Hence, we start by calculating the chosen node centralities for every node in the network as discussed in Section 4.1. The generated dataset of positive and negative samples and curated features as discussed in Section 4.2 are fed into the LGBM model for training and testing. The gradient-based one-side sampling (GOSS) property of the Light Gradient Boosting algorithm helps the classifier to train the data instances with larger gradients while randomly sampling out data instances with lower gradients. This procedure can lead to a more efficient and effective information gain estimation than uniform random sampling, with the same target sampling rate, specifically when the information gain value spans a large range. Also, the Exclusive Feature Bundling (EFB) technique used by the Light Gradient Boosting algorithm helps us to select the most relevant and the least correlated features from the space. This gives us an Exclusive Feature Bundle which reduces the dimensionality for improving the efficiency while maintaining a high level of accuracy.

Figure 3 shows the model architecture of our proposed approach. It visualizes the various steps involved in our approach. The method begins with calculating various node centralities for every node in the given network. This step then generates the feature labels for all the nodes. This processed set of nodes is then passed through a light gradient boosted machine (LGBM) classifier to make the link predictions. Thereby we go on to evaluate the various performance metrics for our approach. We also calculate the relative feature importance of the chosen node centralities for link prediction and the information gain achieved as part of the proposed method compared to some baseline algorithms and recently proposed techniques.

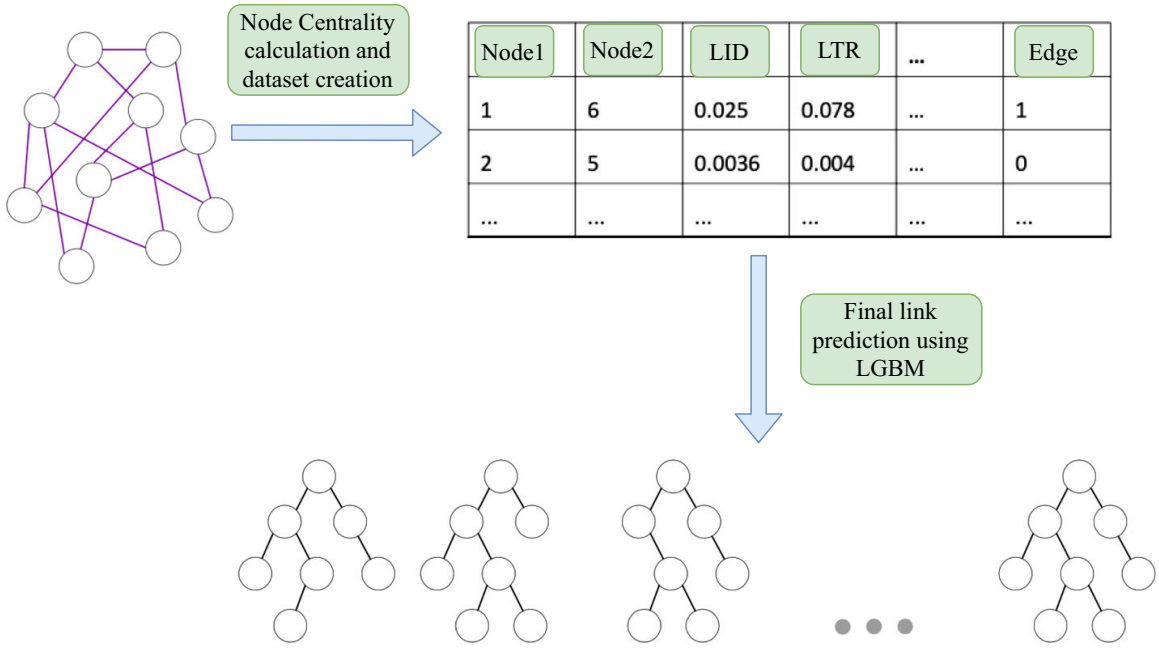


Figure 2 Illustration of use of node centralities with the LGBM classifier

4.5 Hyperparameter tuning

A hyperparameter is a model argument that is used to specify the model's architecture. The process of learning the optimal values of these hyperparameters for a model is known as hyperparameter tuning. For tuning the hyperparameters of our model, we use a randomized grid search [4] based algorithm. The hyperparameters obtained by us are as follows: Bagging fraction as 0.83, feature fraction as 0.1, learning rate as 0.09, maximum depth as 23, number of leaves as 80. These hyperparameters give us the best results for our model for the task of link prediction.

5 Datasets and evaluation metrics

The datasets used and performance metrics considered are discussed as follows.

5.1 Datasets

For our study, we used different real-life datasets belonging to various social and information networks. The datasets used are of varying dimensions and also differ from each other in terms of sparsity. These datasets are chosen to exemplify the applicability and scalability of our proposed algorithm. The various datasets used by us for our study are as follows.

(i) Caltech36 [24]: It is a Facebook friendship graph of the students studying at Caltech, Pasadena. Each node of the graph represents an individual, while the network links represent friendships or social relationships in the network. It has 769 nodes and about 16656 edges. The dataset can be accessed from https://networkrepository.com/socfb-Caltech36.php.

(ii) Fb-Tvshow [46]: It is also a Facebook derived social network that represents the mutual likes amongst different tv show pages on Facebook. The nodes of the network represent the tv show pages, while the edges represent the mutual likes amongst the pages. There are about 3892 nodes and 17260 edges. The dataset can be accessed from https://networkrepository.com/fb-pages-tvshow.php.

(iii) GrQc [31]: GrQc is a co-author collaboration network for the e-print library arXiv. It represents the collaborations between the authors for the papers submitted to General Relativity and Quantum Cosmology category. Here the nodes represent the authors, and the edges represent the existence of co-authorship amongst them. There are 5242 nodes and 14496 edges. The dataset is publicly available at https://snap.stanford.edu/data/ca-GrQc.html.

(iv) DBLP [45]: It is a citation network for the DBLP computer science bibliography. Here each node represents a paper, and each edge represents a citation made amongst the papers. There are 12591 nodes and 49743 edges. The dataset can be obtained from https://networkrepository.com/cit-DBLP.php

(v) Pol [9]:It is a Twitter network presenting the retweet patterns of Twitter users for the weeks leading up to the 2010 U.S. congressional elections. Here nodes represent the Twitter users, and edges represent the retweets made by the users. There are 18470 nodes and 61157 edges for the network. The dataset can be obtained from https://networkrepository.com/rt-pol.php

(vi) Email-EU [31]: It is an email interaction network for a large European research institution. Here nodes represent the users, whereas the edges represent the email

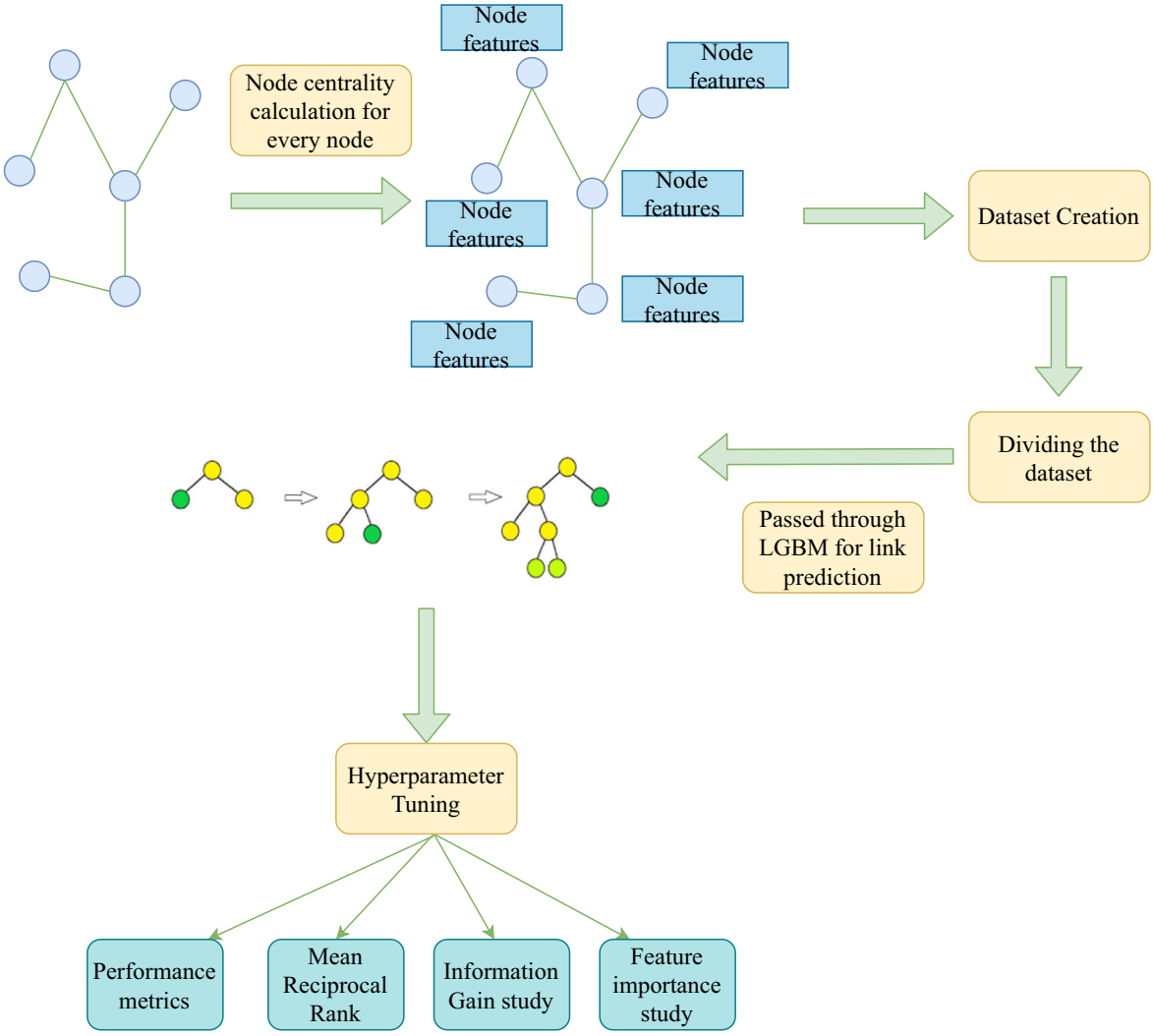


Figure 3 Model architecture for our proposed approach

interactions amongst them. There are 32430 nodes and 54395 edges. The dataset can be accessed from https://networkrepository.com/ia-email-EU.php.

(vii) Epinions [43]: It is a trust-based social network for the customer review platform Epinions. The users of the network decide whom to trust. The nodes represent the users, and the edges represent whether a user trusts another user or not. There are 26588 nodes and 100120 edges in the network. The dataset is available at https://networkrepository.com/rec-epinions.php.

(viii) Higgs [11]: This network represents the spread patterns of the information regarding the discovery of the elusive higgs boson particle on 4^{th} july, 2012. The nodes represent the users and the edges represents the retweet activity between them. There are about 425008 nodes and around 733645 edges in the network. The dataset is available at https://networkrepository.com/rt-higgs.php.

Table 2 presents the brief statistical details of the various social and information networks dataset used. It can be seen that size and complexity vary across the datasets to obtain a more genuine experimental analysis. $\mid V \mid$ and $\mid E \mid$ represents the number of nodes and edges in the network, respectively. $< k >$, $< CC >$ and r represent the average degree, and clustering coefficient respectively.

Table 2 The basic statistical details of the network datasets used

Datasets	$\mid V \mid$	$\mid E \mid$	$< k >$	$< CC >$
Caltech36	769	16656	43	0.409
Fb-Tvshow	3892	17260	8	0.373
GrQc	4158	13422	5	0.529
DBLP	12591	49743	7	0.119
Pol	18470	61157	6	0.059
Email-EU	32430	54395	3	0.112
Epinions	26588	100120	7	0.135
Higgs	425008	733645	3	0.027

5.2 Evaluation metrics

To evaluate our proposed algorithm's performance quantitatively, we use various classical evaluation metrics, namely area under the curve (AUC), precision, recall, and F1 score. We also evaluate the performance of our algorithm with various baseline and existing algorithms of link prediction based on information gain and mean reciprocal rank (MPR) metrics. The mean reciprocal rank (MRR) metric assists us in assessing the performance of our algorithm based on generating an ordered list of plausible links ordered by their likelihood. The information gain study aids us in identifying which of the chosen node centralities is more relevant and important to the task of link prediction. All these evaluation metrics present a clear picture of the predictive performance of various link prediction algorithms. Brief detail about these metrics is given below:

(i) AUC: Area under the receiver operating characteristic curve (AUC) is the area under the graphical plot curve that is used to represent the diagnostic capability of a binary classifier system as its discrimination threshold is varied. The value of AUC varies from 0.0 to 1.0. The higher the value of AUC, the higher the algorithmic accuracy is. For N independent comparisons, if there are N' occurrences of missing links having a higher score and N'' occurrences of missing links and nonexistent links having the same score, the AUC can be defined as,

$$AUC = \frac{N' + 0.5N''}{N} \tag{10}$$

(ii) Precision: Precision is an indicator of the share of positive classifications made that were actually true. Mathematically it can be expressed as

$$Precision = \frac{TP}{TP + FP} \tag{11}$$

(iii) Recall: It is a performance metric, which attempts to implicate what share of actual positives were identified correctly. For a binary classification task, recall can be expressed mathematically as

$$Recall = \frac{TP}{TP + FN} \tag{12}$$

(iv) F1 score: F1 score indicates the balance between precision and recall. Formally speaking, it is the harmonic mean of both precision and recall. Mathematically it is

expressed as

$$F1\ score = \frac{2 * (Precision) * (Recall)}{Precision + Recall} \tag{13}$$

In the above definitions of performance metrics in the context of link prediction, true positive (TP) signifies existent links predicted as existent by the algorithm. False-positive (FP) means non-existent links predicted as existent by the algorithm. Similarly, false negative (FN) implies existent links predicted as non-existent and true negative (TN) indicates non-existent links predicted as non-existent by the algorithm.

5.3 Information gain

The information gain attained by any algorithm represents the increment in the performance metric achieved by the algorithm under consideration for the task being performed as compared to other algorithms. More formally, it can be stated as:

$$\text{Information gain} = \frac{Metric(Proposed) - Metric(Existing)}{Metric(Existing)} \tag{14}$$

Here, $Metric()$ represents the performance metric being evaluated while $Metric(Proposed)$ and $Metric(Existing)$ represents the metric calculated for the algorithm under consideration and the algorithm being compared against, respectively.

5.4 Mean Reciprocal Rank (MRR)

The Mean Reciprocal Rank (MRR) is a metric that is used to evaluate the frameworks that return a list of probable answers which are ranked according to their plausibility. For a query, MRR returns the inverse of the rank of the highest ranked answer for n possible answers. For N queries, the MRR can be defined as follows:

$$\text{MRR} = \frac{1}{N} \sum_{i=1}^{N} \frac{1}{rank_i} \tag{15}$$

Hence, the mean reciprocal rank (MRR) helps us in estimating the capability of the link prediction algorithms to present an ordered list of possible new links. The higher the value of the MRR achieved by the algorithm, better is the likelihood of the predicted links.

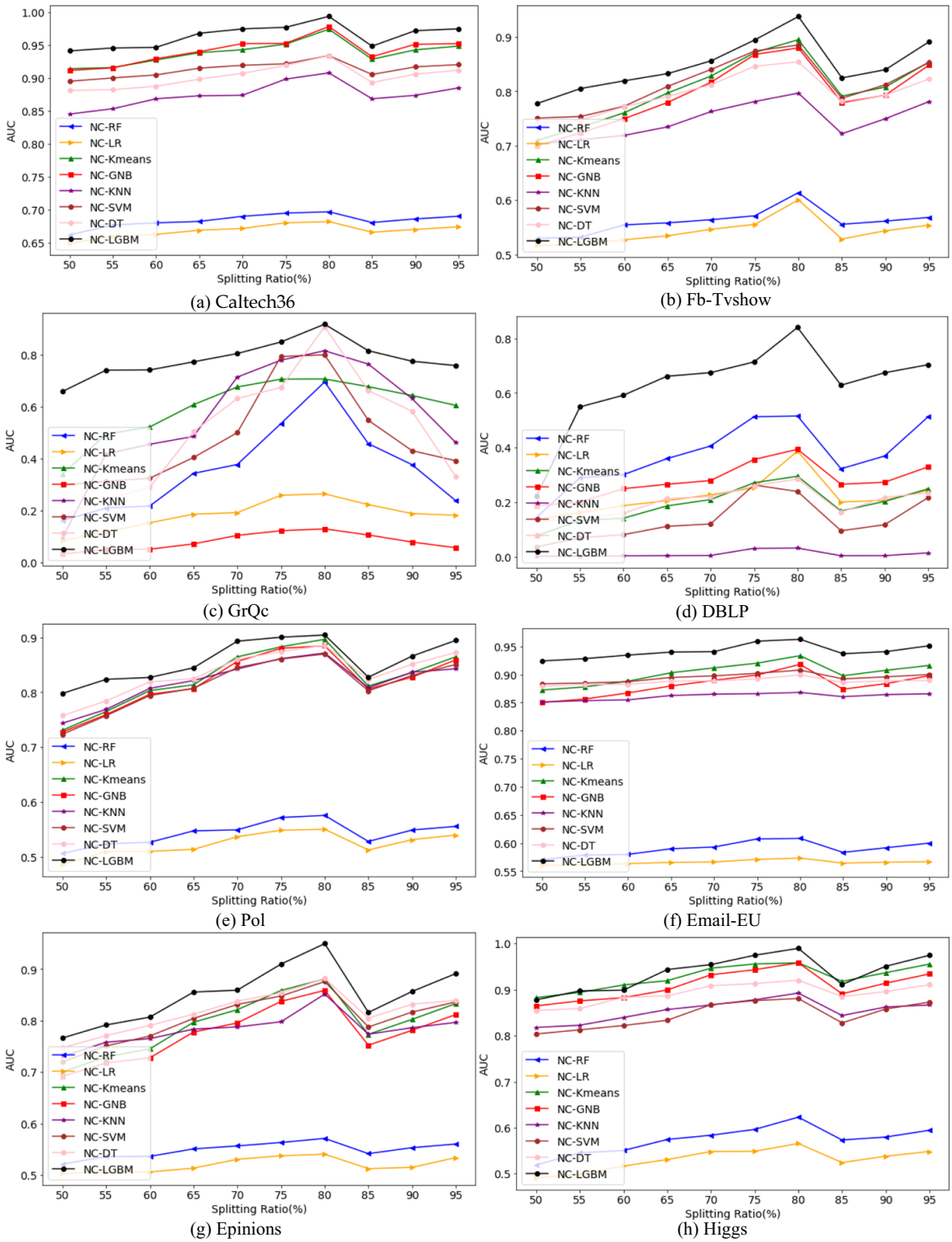
6 Experimental results and analysis

In this section, we present a detailed analysis of the investigation performed by us. For the purpose of our experiments, we split the entire dataset into a ratio of 80:20, which is one of the widely used ratios for training and testing the various machine learning models. We use 80% of the dataset for training purposes, while the remaining 20% of the dataset is used for testing the performance of our model. The choice of dividing the dataset in such a manner is made so that enough data is available for adequately training the classifier but still avoiding overfitting. Moreover, we also present a detailed analysis on the choice of splitting ratio in Section 6.1 to support our split option of 80:20. We also fine-tuned the hyperparameters of the LGBM based proposed framework using randomized grid search. The hyperparameters obtained by us include:- bagging fraction as 0.83, feature fraction as 0.1, learning rate as 0.09, maximum depth as 23, and the number of leaves as 80. We performed fine-tune

of the hyperparameters for the LGBM based proposed framework using randomized grid search. The hyperparameters obtained by us include:- bagging fraction as 0.83, feature fraction as 0.1, learning rate as 0.09, maximum depth as 23, and the number of leaves as 80. The entire code is developed in python programming language. To obtain results on existing techniques, we use several python libraries like sklearn, numpy, pandas, etc., and some publicly available GitHub repositories. We performed simulations on a personal computer with an intel i7 11th generation processor, 16 GB RAM, and RTX 3070 graphics card. To attain the sense of a better comparative study, we compared our proposed algorithm's performance with various classical algorithms for link predictions like Adamic-Adar (AA) [1], Jaccard coefficient (JC) [20], and preferential attachment (PA) [2]. We also used popular network embedding technique, node2vec (N2V) [15] and spectral clustering (SC) [37] technique as baseline algorithms. Along with these baseline algorithms, we also experimented with our extracted node centralities based features as discussed in Section 4.1 with several other machine learning classifiers. Different machine learning classifiers used are Random forest, Logistic regression, Kmeans clustering, Gaussian Naive Bayes, K nearest neighbors, Support vector machine, Decision trees. We add the prefix NC (Node Centrality) to every machine learning classifier to signify that the features passed onto the classifier are node centrality based extracted features. Therefore we named the classifiers as follows: NC-RF (Random Forest), NC-LR (Logistic Regression), NC-Kmeans (Kmeans), NC-GNB (Gaussian NB), NC-KNN (K Nearest Neighbors), NC-SVM (Support vector machine), NC-DT (Decision trees). Apart from this, we also compared our proposed algorithm's performance against some recently proposed methods, namely INILP [53], WLNM [55], DeepInf [42], and EMLP [32], to establish the credibility of our proposed work. We obtained the results of the proposed algorithm along with various comparing algorithms based on multiple performance metrics as presented in Section 5.2 for all the chosen datasets depicted in Table 2. We also present a relative feature importance study of the different node centralities used in the study. We discuss the brief description of the obtained value of multiple evaluation metrics by various considered link prediction methods on each dataset. We also present a relative feature importance study of the different node centralities used.

6.1 Choice of splitting ratio

In this section, we study the optimal ratio in which the dataset should be split for training and testing purposes. To analyze this, we evaluate the performance on AUC metrics for each dataset for various machine learning classifiers like the random forest, logistic regression, etc., and our proposed method. The analysis is performed while varying the value of the splitting ratio from 50% to 95% in the steps of 5%. The obtained results are presented in Figure 4. We can see from Figure 4 that as we increase the splitting ratio, the value of AUC increases across all the datasets and reaches a peak at around 80%. This shows that when the splitting ratio is near 50%, the data is being under-fitted. It means that at a lower splitting ratio, there isn't enough data available for training the dataset, and the applied technique isn't able to properly learn the features of the network. Usually, from these obtained results, it is evident that the AUC performance improves as the split ratio increases from 50% to 80%, and the best result is obtained at 80%. It is also observed that as the splitting ratio goes past 80%, the AUC value drops. This confirms that with an increase in the training data, the data tends to overfit. Hence, the analysis leads us to the conclusion that the dataset can be optimally split in a 80:20 ratio.



(a) Caltech36 (b) Fb-Tvshow

(c) GrQc (d) DBLP

(e) Pol (f) Email-EU

(g) Epinions (h) Higgs

Figure 4 **a**–**h** AUC results obtained for different datasets for various classifiers as the splitting ratio is varied from 50% to 95% in steps of 5%

6.2 Comparative performance study

Here, we compare the performance of our proposed algorithm along with other considered algorithms on each dataset based on multiple evaluation metrics. As most of the link prediction methods are stochastic in nature so we run our experimentations a total of ten times

and then take the average of the obtained results for each evaluation metrics to get a better analysis.

For the Caltech network, Table 3 tabulates the results obtained. It can be clearly seen that in terms of AUC and precision metric our LGBM based approach has outperformed all the baselines and the recently proposed methods. However, in terms of recall and F1 score, random forest classifier in conjunction with chosen node centralities outperformed all the other methods.

Table 4 shows the results obtained for the Fb-Tvshow network. Again for this network also our LGBM based approach is the best performer in terms of AUC and precision while for recall and F1 score WLNM based approach performs best. This can be attributed to the mix of node centralities that we have chosen. It helps our LGBM based model to capture the network details with greater efficiency as compared to other techniques.

It can be interpreted from Table 5 that for the GrQc dataset, the LGBM based approach gives the best results in terms of AUC. Logistic regression, N2V and EMLP give the best results in terms of precision, recall and F1 score respectively. Table 6 illustrates the performance standards obtained on the DBLP citation network. As per AUC metric, LGBM based method is the best performer while for the precision metric, K means based method performs best. In terms of recall and F1 score Jaccard coefficient gives the best outcome. The obtained results for the Pol network can be seen in Table 7. Here, the LGBM based approach tends to be the performer for all the evaluated performance metrics. This can be established by the notion that through LGBM classifier, we are able to ascertain appropriate importance to each of the chosen node centrality. This gives us a balanced and improved results across varying networks with different dimensionalities.

Table 3 Performance comparison of different link prediction methods based on AUC, precision, recall and F1 score metrics for Caltech36 dataset

Models	AUC	Precision	Recall	F1 score
AA	0.897	0.892	0.827	0.829
JC	0.877	0.860	0.649	0.745
PA	0.823	0.805	0.731	0.740
N2V	0.826	0.808	0.843	0.825
SC	0.777	0.795	0.739	0.766
NC-RF	0.903	0.978	**0.978**	**0.978**
NC-LR	0.956	0.986	0.853	0.914
NC-Kmeans	0.358	0.848	0.678	0.753
NC-GNB	0.880	0.978	0.924	0.950
NC-KNN	0.813	0.957	0.971	0.964
NC-SVM	0.868	0.975	0.922	0.948
NC-DT	0.888	0.980	0.922	0.950
EMLP	0.801	0.803	0.808	0.805
INILP	0.917	0.897	0.943	0.918
WLNM	0.796	0.786	0.822	0.804
DeepInf	0.720	0.671	0.810	0.734
NC-LGBM	**0.986**	**0.992**	0.940	0.965

The values in bold signify that a particular entry is maximum in that column

Table 4 Performance comparison of different link prediction methods based on AUC, precision, recall and F1 score metrics for Fb-Tvshow dataset

Models	AUC	Precision	Recall	F1 score
AA	0.839	0.839	0.514	0.679
JC	0.838	0.834	0.645	0.782
PA	0.813	0.834	0.286	0.441
N2V	0.773	0.784	0.739	0.761
SC	0.815	0.795	0.869	0.830
NC-RF	0.877	0.970	0.778	0.863
NC-LR	0.930	0.905	0.769	0.831
NC-Kmeans	0.619	0.936	0.256	0.402
NC-GNB	0.883	0.946	0.813	0.875
NC-KNN	0.841	0.919	0.748	0.825
NC-SVM	0.844	0.867	0.812	0.839
NC-DT	0.862	0.963	0.752	0.845
EMLP	0.904	0.820	0.842	0.831
INILP	0.826	0.808	0.843	0.825
WLNM	0.844	0.910	**0.910**	**0.910**
DeepInf	0.833	0.827	0.827	0.827
NC-LGBM	**0.939**	**0.989**	0.760	0.859

The values in bold signify that a particular entry is maximum in that column

Table 5 Performance comparison of different link prediction methods based on AUC, precision, recall and F1 score metrics for GrQc dataset

Models	AUC	Precision	Recall	F1 score
AA	0.836	0.836	0.674	0.804
JC	0.835	0.832	0.650	0.786
PA	0.805	0.824	0.359	0.520
N2V	0.873	0.873	**0.900**	0.886
SC	0.852	0.852	0.867	0.850
NC-RF	0.848	0.971	0.717	0.825
NC-LR	0.927	**0.986**	0.770	0.865
NC-Kmeans	0.610	0.954	0.232	0.373
NC-GNB	0.870	0.958	0.775	0.857
NC-KNN	0.830	0.922	0.722	0.810
NC-SVM	0.840	0.855	0.819	0.837
NC-DT	0.824	0.955	0.680	0.794
EMLP	0.919	0.901	0.874	**0.916**
INILP	0.827	0.800	0.853	0.826
WLNM	0.873	0.962	0.841	0.870
DeepInf	0.848	0.830	0.862	0.846
NC-LGBM	**0.933**	0.937	0.735	0.824

The values in bold signify that a particular entry is maximum in that column

Table 6 Performance comparison of different link prediction methods based on AUC, precision, recall and F1 score metrics for DBLP dataset

Models	AUC	Precision	Recall	F1 score
AA	0.888	0.983	0.914	0.947
JC	0.794	0.957	**0.971**	**0.964**
PA	0.868	0.979	0.910	0.943
N2V	0.818	0.855	0.782	0.817
SC	0.812	0.820	0.887	0.814
NC-RF	0.808	0.966	0.639	0.769
NC-LR	0.926	0.935	0.704	0.803
NC-Kmeans	0.522	0.964	0.045	0.087
NC-GNB	0.756	0.950	0.541	0.690
NC-KNN	0.856	0.918	0.782	0.845
NC-SVM	0.829	0.934	0.709	0.806
NC-DT	0.790	0.959	0.606	0.743
EMLP	0.840	0.881	0.773	0.824
INILP	0.773	0.784	0.739	0.761
WLNM	0.931	0.944	0.921	0.932
DeepInf	0.820	0.809	0.836	0.822
NC-LGBM	**0.955**	**0.993**	0.675	0.794

The values in bold signify that a particular entry is maximum in that column

Table 7 Performance comparison of different link prediction methods based on AUC, precision, recall and F1 score metrics for Pol dataset

Models	AUC	Precision	Recall	F1 score
AA	0.814	0.705	0.171	0.276
JC	0.727	0.605	0.228	0.331
PA	0.745	0.517	0.582	0.548
N2V	0.789	0.773	0.834	0.803
SC	0.796	0.779	0.816	0.797
NC-RF	0.832	0.972	0.684	0.803
NC-LR	0.948	0.940	0.812	0.871
NC-Kmeans	0.584	0.992	0.169	0.289
NC-GNB	0.770	0.961	0.562	0.710
NC-KNN	0.890	0.939	0.835	0.884
NC-SVM	0.886	0.939	0.826	0.879
NC-DT	0.821	0.974	0.660	0.787
EMLP	0.845	0.882	0.798	0.821
INILP	0.700	0.725	0.725	0.725
WLNM	0.816	0.800	0.842	0.838
DeepInf	0.809	0.836	0.769	0.801
NC-LGBM	**0.965**	**0.998**	**0.850**	**0.918**

The values in bold signify that a particular entry is maximum in that column

Performance evaluation for the Email-EU dataset is presented in Table 8. Our LGBM based approach tends to be the outlier for this network as well in terms of AUC, precision and F1 score while for recall the node centrality based approach paired with Gaussian Naive bayes gives best performance.

The various performance metrics obtained for epinions dataset are shown in Table 9. In terms of AUC the best performer tends to be LGBM based approach while for precision, recall and F1 score, decision trees, SVM and gaussian naive bayes are the best performer. And finally the results obtained for the Higgs dataset are shown in Table 10. For this network as well the best performer tends to be the LGBM based approach in terms of AUC. It can clearly be seen that our proposed method of choosing features as a combination of different node centralities so as to better capture the graph details which is further augmented by using light gradient boosted machine (LGBM) classifier is the best performer. Our proposed approach proves its competitive edge by generating great results in terms of various evaluated performance metrics. The results obtained also show that the our group of chosen node centralities also gives good results when paired with machine learning classifiers other than LGBM like, random forest, logistic regression, k means, etc. Moreover, in terms of AUC, our LGBM based approach tends to be the best performer for all the chosen networks without exception. The consistent and improved performance of our proposed approach can be attributed to the combination of the node centralities chosen by us. These node centralities capture the local, quasi-local and global topologies of the network extensively. LGBM classifier assists in better determining the correlation and relevance of the various node centralities used. Moreover, the gradient-based one side sampling (GOSS) technique used by the LGBM classifier helps it to train the data instances which have higher gradient while randomly sampling out data instances with lower gradient. . This leads to an improved value of information gain estimation compared to the uniformly random sampling

Table 8 Performance comparison of different link prediction methods based on AUC, precision, recall and F1 score metrics for Email-EU dataset

Models	AUC	Precision	Recall	F1 score
AA	0.845	0.718	0.962	0.822
JC	0.618	0.240	0.923	0.382
PA	0.850	0.807	0.881	0.842
N2V	0.917	0.897	0.940	0.918
SC	0.866	0.848	0.894	0.870
NC-RF	0.707	0.994	0.487	0.653
NC-LR	0.915	0.993	0.796	0.883
NC-Kmeans	0.437	0.957	0.827	0.887
NC-GNB	0.833	0.987	**0.993**	0.990
NC-KNN	0.744	0.980	0.988	0.984
NC-SVM	0.835	0.989	0.927	0.957
NC-DT	0.721	0.996	0.491	0.658
EMLP	0.958	0.881	0.903	0.892
INILP	0.854	0.836	0.873	0.854
WLNM	0.947	0.899	0.913	0.906
DeepInf	0.907	0.866	0.957	0.918
NC-LGBM	**0.984**	**0.998**	0.983	**0.991**

The values in bold signify that a particular entry is maximum in that column

Table 9 Performance comparison of different link prediction methods based on AUC, precision, recall and F1 score metrics for Epinions dataset

Models	AUC	Precision	Recall	F1 score
AA	0.818	0.763	0.855	0.806
JC	0.785	0.686	0.855	0.761
PA	0.755	0.526	0.970	0.682
N2V	0.878	0.812	0.947	0.875
SC	0.787	0.785	0.868	0.825
NC-RF	0.861	0.996	0.845	0.915
NC-LR	0.873	0.996	0.631	0.773
NC-Kmeans	0.465	0.977	0.881	0.927
NC-GNB	0.844	0.993	0.991	**0.992**
NC-KNN	0.604	0.983	0.992	0.987
NC-SVM	0.591	0.983	**0.994**	0.988
NC-DT	0.942	**0.997**	0.984	0.991
EMLP	0.836	0.776	0.930	0.846
INILP	0.886	0.873	0.900	0.886
WLNM	0.934	0.955	0.648	0.772
DeepInf	0.822	0.805	0.879	0.875
NC-LGBM	**0.964**	0.989	0.938	0.963

The values in bold signify that a particular entry is maximum in that column

Table 10 Performance comparison of different link prediction methods based on AUC, precision, recall and F1 score metrics for Higgs dataset

Models	AUC	Precision	Recall	F1 score
AA	0.764	0.832	0.879	0.855
JC	0.768	0.620	**0.951**	0.751
PA	0.618	0.299	0.922	0.452
N2V	0.827	0.800	0.853	0.826
SC	0.837	0.879	0.775	0.824
NC-RF	0.663	0.979	0.334	0.498
NC-LR	0.942	0.970	0.807	0.881
NC-Kmeans	0.521	**1.0**	0.043	0.083
NC-GNB	0.837	0.969	0.697	0.810
NC-KNN	0.907	0.981	0.830	**0.899**
NC-SVM	0.904	0.971	0.833	0.897
NC-DT	0.657	0.978	0.321	0.483
EMLP	0.883	0.928	0.830	0.876
INILP	0.818	0.855	0.782	0.817
WLNM	0.772	0.756	0.817	0.785
DeepInf	0.843	0.850	0.827	0.838
NC-LGBM	**0.975**	0.978	0.463	0.629

The values in bold signify that a particular entry is maximum in that column

of other gradient boosting algorithms. The exclusive feature bundling (EFB) technique used by the LGBM classifier also helps it to reduce the dimensionality optimally while maintaining a high level of accuracy. This is achieved by selecting a subset of the feature set which is the most relevant and least correlated.

6.3 Mean Reciprocal Rank (MRR)

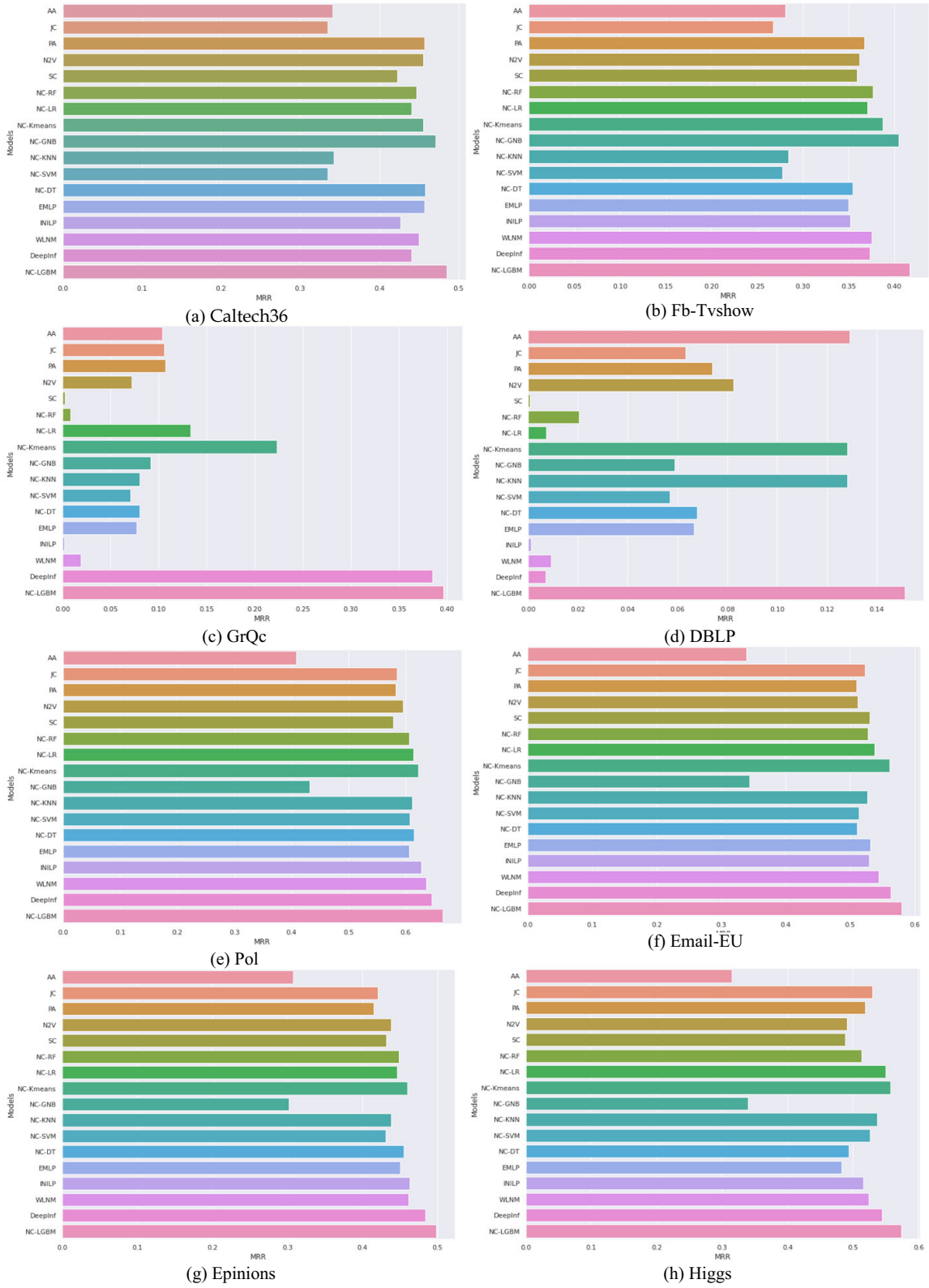
Figure 5 presents the results achieved by our method and other methods considered for comparison based on the value of MRR metrics. The pictorial results where y-axis represents the various methods and x-axis denotes the MPR value obtained by each technique are depicted on all the eight datasets utilized in this study. From the results, it can be seen that for Caltech36, Fb-TvShow, Pol, Email-EU, Epinions and Higgs networks (Figure 5[a, b, e, f, g, & h]), all the methods tend to perform well in terms of the obtained MRR values but our proposed NC-LGBM outperforms all the other methods. While for the GrQc and DBLP networks as in Figure 5[c & d]), the spectral clustering (SC) as well as the INILP method are the worst performers. For these two networks also our proposed method tends to be the best performer.

6.4 Information gain

The information gain obtained by an algorithm represents the relative improvement achieved by any algorithm as compared to the algorithms it is compared against. Table 11 shows the information gain realised by our proposed approach as compared to the best performing baseline algorithm and the best performing methods from the recent literature. As can be clearly seen that the information gain for the proposed approach is immense. This shows that using the combination of chosen node centralities provide our method with additional and crucial information which plays an important role in obtaining an exemplary performance for the task of link prediction.

6.5 Impact of varying the network complexities

In this section, we discuss the impact of varying the complexities of the network on the performance of our proposed approach NC-LGBM. From Tables 3 to 10, we compared the performance of the proposed algorithm against various other baseline and recent methods of link prediction based on the evaluation metrics like AUC, precision, recall, and F1 score. From these tabular results, it can be seen that as the types and size of the network change, our model maintained consistency in the performance and outperformed other methods. For a relatively smaller GrQc, our model obtained an AUC value of 93.3%, while for a larger network like Email-EU, the proposed algorithm obtained an AUC value of 98.4%. Also, for a relatively large Higgs network with 425008 nodes and 733645 edges, our model achieved an AUC value of 97.5%. Hence, we can conclude that as the size of the network increases, the performance of the proposed model is uniform and does not degrade. Table 11 presents a summary of the relative performance gain (in percentage) of the proposed algorithm over best baseline algorithms (as mentioned in 2nd column of the table) and best performing recent methods of link prediction (as mentioned in 3rd column of the table) in terms of AUC value. It is observed from the results in Table 11, for larger networks like Pol and Higgs, the proposed method achieved a relative gain as high as 18.55% against the best baseline. Also, the gain against the best algorithm in the recent literature is 14.2%. This corroborates the efficacy of our proposed algorithm towards larger-sized real-life networks. It proves the usability and adaptability of NC-LGBM to a real-world scenario.



(a) Caltech36 (b) Fb-Tvshow

(c) GrQc (d) DBLP

(e) Pol (f) Email-EU

(g) Epinions (h) Higgs

Figure 5 **a**-**h** MRR results obtained by the proposed method and other methods considered for comparison on each dataset. The x-axis denotes the MPR value, and the y-axis indicates various methods of link prediction

Table 11 Relative gain of proposed approach in terms of AUC against the best baseline and recent literature

Datasets	Against best baseline (%)	Against best recent literature (%)
Caltech36	9.92 (AA)	7.52 (INILP)
Fb-Tvshow	11.91 (AA)	3.87 (EMLP)
GrQc	6.87 (N2V)	1.52 (EMLP)
DBLP	10.02 (PA)	2.58 (WLNM)
Pol	18.55 (AA)	14.20 (EMLP)
Email-EU	7.31 (N2V)	2.71 (EMLP)
Epinions	9.79 (N2V)	3.21 (WLNM)
Higgs	16.49 (SC)	10.42 (EMLP)

6.6 Feature importance

To obtain the relative importance of the different node centralities used, we utilize the CART algorithm [3] for feature importance. Figure 6 shows the relative importance obtained for our proposed algorithm. It is evident from the results that since for none of the features, the relative importance is close to zero. Hence, all the chosen features play an essential role. Moreover, the relative importance of all these features is clearly above 10%. It is also observed that LTR centrality is the most important centrality, closely followed by betweenness and LID centrality in that order. This can easily be understood from the fact that LTR centrality as a whole represents to what extent a network is centrally structured. It also factors in the probable local influence of every node. The betweenness centrality represents the bridging ability of a node for information transfer amongst two nodes. In contrast, the LID centrality represents how well a node is directly connected to most of the nodes in the network. The above discussion concludes that all the centralities chosen by us are equally

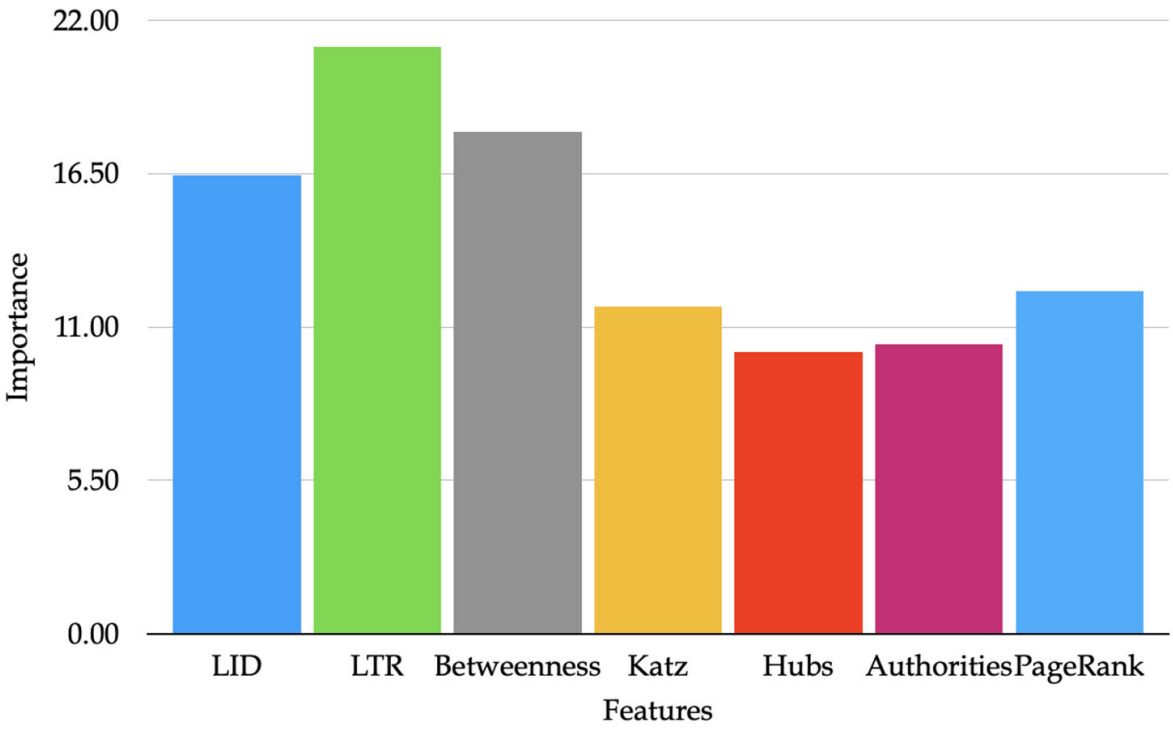


Figure 6 Relative feature importance of the chosen centralities

important towards the task of link prediction and help us reveal different information from across the network.

7 Conclusion

Link prediction is one of the popular research problems in complex network analysis. The problem of link prediction can be inferred as the prediction of the missing links, i.e., links that are existing but are not yet observed and will be observed later. In this paper, we proposed a novel approach of making link predictions using a well-curated combination of node centralities to develop a set of features that can be utilized to make the predictions. These node centralities based features are then passed onto various binary machine learning classifiers. The experimentations were carried out on some real and complex networks, and different performance metrics are calculated. As per the obtained experimental results, it can be interpreted that LGBM based classifier added to the node centralities based features tends to be the best performer. The experimental analysis reveals the superiority of our proposed approach over other popular methods of link prediction. Further, a study to investigate the relative importance of the chosen node centralities for link prediction was also carried out. The study illustrates that all the chosen node centralities are important and present with their own set of information regarding the relative positioning of the node in context. This validates our choice for the chosen node centralities. The future extension of our work can be utilizing deep learning based classifiers along with making an extension towards temporal and dynamic networks.

References

1. Adamic, L.A., Adar, E.: Friends and neighbors on the Web. Soc Netw **25**(3), 211–30 (2003)
2. Barabási, A.L., Albert, R.: Emergence of scaling in random networks. Science **286**(5439), 509–12 (1999)
3. Bel, L., Allard, D., Laurent, J.M., Cheddadi, R., Bar-Hen, A.: CART algorithm for spatial data: application to environmental and ecological data. Comput Stat Data Anal **53**(8), 3082–3093 (2009)
4. Bergstra, J., Bengio, Y.: Random search for hyper-parameter optimization. J Mach Learn Res **13**, 2 (2012)
5. Bonchi, F., Castillo, C., Gionis, A., Jaimes, A.: Social network analysis and mining for business applications. ACM Trans Intell Syst Technol (TIST) **2**(3), 1–37 (2011)
6. Brin, S., Page, L.: The anatomy of a large-scale hypertextual Web search engine. Comput Netw and ISDN Syst **30**(1-7), 107–17 (1998)
7. Chen, J., Geyer, W., Dugan, C., Muller, M., Guy, I.: Make new friends, but keep the old: recommending people on social networking sites. In: Proceedings of the SIGCHI conference on human factors in computing systems, pp 201–210 (2009)
8. Chuan, P.M., Ali, M., Khang, T.D., Dey, N.: Link prediction in co-authorship networks based on hybrid content similarity metric. Appl Intell **48**(8), 2470–2486 (2018)
9. Conover, M.D., Ratkiewicz, J., Francisco, M., Gonçalves, B., Menczer, F., Flammini, A.: Political polarization on Twitter. ICWSM (2011)
10. Dai, C., Chen, L., Li, B.: Network link prediction based on direct optimization of area under curve. Appl Intell **46**(2), 427–437 (2017)
11. De Domenico, M., Lima, A., Mougel, P., Musolesi, M.: The anatomy of a scientific rumor. Sci Rep **3**(1), 1–9 (2013)
12. Eirinaki, M., Gao, J., Varlamis, I., Tserpes, K.: Recommender systems for large-scale social networks: a review of challenges and solutions. Futur Gener Comput Syst **78**(1), 413–418 (2018)
13. Friedman, J.H.: Stochastic gradient boosting. Comput Stat Data Anal **38**(4), 367–78 (2002)
14. Friedman, N., Getoor, L., Koller, D., Pfeffer, A.: Learning probabilistic relational models. In IJCAI **99**, 1300–1309 (1999)

15. Grover, A., Leskovec, J.: node2vec: scalable feature learning for networks. In: Proceedings of the 22nd ACM SIGKDD international conference on Knowledge discovery and data mining, pp 855–864 (2016)
16. Haghani, S., Keyvanpour, M.R.: A systemic analysis of link prediction in social network. Artif Intell Rev **52**(3), 1961–1995 (2019)
17. Hamilton, W.L., Ying, R., Leskovec, J.: Inductive representation learning on large graphs. IN: Proceedings of the 31st International conference on neural information processing systems, pp 1025–1035 (2017)
18. Heckerman, D., Meek, C., Koller, D.: Probabilistic entity-relationship models, PRMs, and plate models. In: Proceedings of the 21st international conference on machine learning. Banff, p 55 (2004)
19. Ibrahim, N.MA., Chen, L.: Link prediction in dynamic social networks by integrating different types of information. Appl Intell **42**(4), 738–750 (2015)
20. Jaccard, P.: Étude comparative de la distribution florale dans une portion des Alpes et des Jura. Bull Soc Vaudoise Sci Nat **37**, 547–79 (1901)
21. Jeh, G., Widom, J.: Simrank: a measure of structural-context similarity. In: Proceedings of the eighth ACM SIGKDD international conference on Knowledge discovery and data mining, pp 538–543 (2002)
22. Katz, L.: A new status index derived from sociometric analysis. Psychometrika **18**(1), 39–43 (1953)
23. Ke, G., Meng, Q., Finley, T., Wang, T., Chen, W., Ma, W., Ye, Q., Liu, T.Y.: Lightgbm: a highly efficient gradient boosting decision tree. Adv Neural Inform Process Syst **30**, 3146–54 (2017)
24. Kelsic, E., Mucha, P., Porter, M.: Comparing community structure to characteristics in online collegiate social networks. SIAM Rev **53,10**, 1137/080734315 (2008)
25. Kleinberg, J.M.: Authoritative sources in a hyperlinked environment. Journal of the ACM (JACM), 46(5) (1999)
26. Kumar, S., Lohia, D., Pratap, D., Krishna, A., Panda, B.S.: MDER: modified degree with exclusion ratio algorithm for influence maximisation in social networks. Computing, 1–24 (2021)
27. Kumar, S., Panda, B.S., Aggarwal, D.: Community detection in complex networks using network embedding and gravitational search algorithm. J Intell Inform Syst **57**, 51–72 (2020)
28. Kumar, A., Singh, S.S., Singh, K., Biswas, B.: Link prediction techniques, applications, and performance: a survey. Physica A: Stat Mech Applic **553**, 124289 (2020)
29. Kumar, S., Singhla, L., Jindal, K., Grover, K., Panda, B.S.: IM-ELPR: influence maximization in social networks using label propagation based community structure. Applied Intelligence, 1–19 (2021)
30. Leskovec, J., Huttenlocher, D., Kleinberg, J.: Predicting positive and negative links in online social networks. In: Proceedings of the 19th international conference on World Wide Web, pp 641–650 (2010)
31. Leskovec, J., Kleinberg, J., Faloutsos, C.: Graph evolution: densification and shrinking diameters. ACM Trans Knowl Discov Data (TKDD) **1**, 1 (2007)
32. Li, K., Tu, L., Chai, L.: Ensemble-model-based link prediction of complex networks. Comput Netw **166**, 106978 (2020)
33. Liu, W., Lü, L.: Link prediction based on local random walk. EPL (Europhysics Letters) **89**(5), 58007 (2010)
34. Lü, L., Jin, C.H., Zhou, T.: Similarity index based on local paths for link prediction of complex networks. Phys Rev E **80**(4), 046122 (2009)
35. Martínez, V., Berzal, F., Cubero, J.C.: A survey of link prediction in complex networks. ACM Comput Surv (CSUR) **49**(4), 1–33 (2016)
36. Mutlu, E.C., Oghaz, T.A.: Review on graph feature learning and feature extraction techniques for link prediction. arXiv:1901.03425 (2019)
37. Ng, A.Y., Jordan, M.I., Weiss, Y.: On spectral clustering: analysis and an algorithm. Adv Neural Inform Process Syst **2**, 849–856 (2002)
38. Pan, J.Y., Yang, H.J., Faloutsos, C., Duygulu, P.: Automatic multimedia cross-modal correlation discovery. In: Proceedings of the tenth ACM SIGKDD international conference on Knowledge discovery and data mining, pp 653–658 (2004)
39. Pandey, B., Bhanodia, P.K., Khamparia, A., Pandey, D.K.: A comprehensive survey of edge prediction in social networks: techniques, parameters and challenges. Exp Syst Applic **124**, 164–81 (2019)
40. Perozzi, B., Al-Rfou, R., Skiena, S.: Deepwalk: online learning of social representations. In: Proceedings of the 20th ACM SIGKDD international conference on Knowledge discovery and data mining, pp 701–710 (2014)
41. Qi, Y., Luo, J.: Prediction of essential proteins based on local interaction density. IEEE/ACM Trans Comput Biol Bioinform **13**(6), 1170–1182 (2015)
42. Qiu, J., Tang, J., Ma, H., Dong, Y., Wang, K., Tang, J.: Deepinf: social influence prediction with deep learning. In: Proceedings of the 24th ACM SIGKDD international conference on knowledge discovery & data mining, pp 2110–2119 (2018)

43. Richardson, M., Agrawal, R., Domingos, P.: Trust management for the semantic Web. In: International semantic Web conference, pp. 351–368. Springer, Berlin (2003)
44. Riquelme, F., Gonzalez-Cantergiani, P., Molinero, X., Serna, M.: Centrality measure in social networks based on linear threshold model. Knowl-Based Syst **140**, 92–102 (2018)
45. Rossi, R., Ahmed, N.: The network data repository with interactive graph analytics and visualization. Proceedings of the AAAI Conference on Artificial Intelligence **29**, 1 (2015)
46. Rozemberczki, B., Davies, R., Sarkar, R., Sutton, C.: Gemsec: graph embedding with self clustering. In: Proceedings of the 2019 IEEE/ACM international conference on advances in social networks analysis and mining, pp 65–72 (2019)
47. Salton, G., McGill, M.J.: Introduction to modern information retrieval. Mcgraw-Hill (1983)
48. Scardoni, G., Petterlini, M., Laudanna, C.: Analyzing biological network parameters with CentiScaPe. Bioinformatics **25**(21), 2857–2859 (2009)
49. Van Mieghem, P.: Performance analysis of complex networks and systems. Cambridge University Press (2014)
50. Wang, Z., Liao, J., Cao, Q., Qi, H., Wang, Z.: Friendbook: a semantic-based friend recommendation system for social networks. IEEE Trans Mobile Comput **14**(3), 538–551 (2014)
51. Wang, H., Wang, J., Wang, J., Zhao, M., Zhang, W., Zhang, F., Xie, X., Guo, M.: Graphgan: graph representation learning with generative adversarial nets. In Proceedings of the AAAI conference on artificial intelligence, vol 32(1) (2018)
52. Wang, W., Wu, L., Huang, Y., Wang, H., Zhu, R.: Link prediction based on deep convolutional neural network. Information **10**(5), 172 (2019)
53. Wu, J., Shen, J., Zhou, B., Zhang, X., Huang, B.: General link prediction with influential node identification. Physica A: Stat Mech Applic **523**, 996–1007 (2019)
54. Yu, K., Chu, W., Yu, S., Tresp, V., Xu, Z.: Stochastic relational models for discriminative link prediction. In NIPS **6**, 1553–1560 (2006)
55. Zhang, M., Chen, Y.: Weisfeiler-Lehman neural machine for link prediction. In: Proceedings of the 23rd ACM SIGKDD international conference on knowledge discovery and data mining, pp 575–583 (2017)

Publisher's note Springer Nature remains neutral with regard to jurisdictional claims in published maps and institutional affiliations.

2021 IEEE International Symposium on Smart Electronic Systems (iSES) | 978-1-7281-8753-2/21/$31.00 ©2021 IEEE | DOI: 10.1109/iSES52644.2021.00018

Low Power Swing Restoration Circuit Reduce Threshold Voltages of SRAMs Improve Read and Write Operations

Vinod Kumar
Department of Computer Science and Engineering
Delhi Technological University
Delhi, India
vinod_k@dtu.ac.in

Ram Murti Rawat
Department of Computer Science and Engineering
Delhi Technological University
Delhi, India
rammurtirawat@dtu.ac.in

***Abstract*— In this paper Swing restoring inverter (SRI), a fast speed and low power circuit technology for VLSI applications that is discussed. In this technology, high speed low power SRAMs circuit performance is achieved by using an SRI to execute threshold voltage reductions and a swing restoring circuit of the latch kind to drive dual node voltages. Cadence Virtuoso schematics tool was used to design an SRI-based SRAM circuit with 130 nm technology for very high speed, low-power VLSI applications.**

This Paper is organized as follows: - I. Introduction II. Related work III. The proposed work IV. Results and discussion and V. Conclusion.

***Keywords-sram; swing restoring inverter; latch type circuit; node voltages; high speed and low-power vlsi technologies*.**

I. INTRODUCTION

Full CMOS is the widely used VLSI circuit design technology today. It has proven appealing because it makes it simple to design stable circuits with high noise margins. However, the ongoing quest for better speed and in recent years, the shortcomings of full CMOS have been brought to the forefront, forcing a number of scholars to propose new logic techniques. Because charge sharing and noise margin concerns of dynamic logic styles cost performance, as well as difficulty in design and design for analysis, many of them have been static techniques.

Pass transistor logic (PTL) uses CMOS inverters to drive the outputs and a complementary output pass transistor logic network to do logic assessment. If a gentle pull-up latch is not employed, this design can result in leakage current via the inverter. To avoid the non-full swing problem, complementary and double pass-transistor logic (CPL and DPL) [3] combines both PMOS and NMOS devices in the pass transistor networks, but it came with the greatest area and greater power downside. As the title implies, the cascade voltage switch logic introduced in [5] is comparable to the differential cascade voltage switch with pass gate (DCVSPG) [4]. In the true and complement logic evaluation trees, however, It introduces a symmetrical logic architecture and improves for logic evaluations. Unfortunately, when employed in a lengthy chain without interim buffering, this logic approach can decrease pull-down performance.

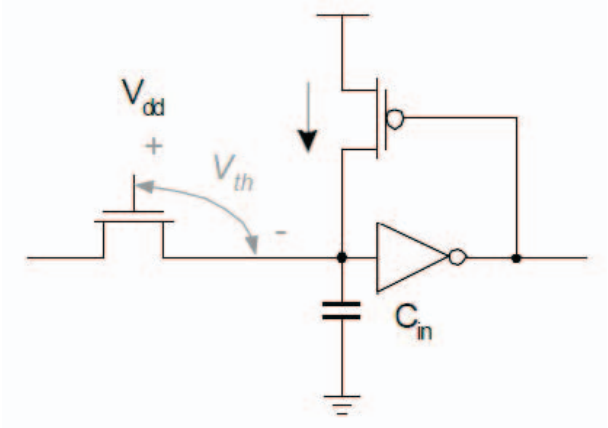


Figure 1. Swing restoring inverter (SRI) Circuit [1] [2].

In this research article, we present a high-speed, low-power solution for addressing these issues.

A. Swing Restoring Inverter

1) Basic Circuit: Figure 1. shows the SRI circuit, which is made up of two basic sections. 1. A pass-transistor logic output made up of CMOS inverters and a CMOS inverter output is connected to the gate input of PMOS logic, as well as a swing-restoring node made up of a single CMOS inverter. There are two sorts of circuit inputs: pass variables attached to logic transistor's drain as well as control variables that are attached to transistor's gate. The SRI has capacity to improve static noise margins in read as well as write operations.

For example, Figure 2. depicts the implementation of a Proposed 8T SRAM Cell. The swing restoration inverter [6] [11] restores the complementing outputs of pass transistor logic to the full swing.

2) SNM Optimization: In presence of DC noise, the SNM assesses the stability of a SNM memory cell . The SNM is the amount of voltage noise needed at the output nodes to flip cell's state. This can be determined using the VTC of the SRAM cell's two cross coupled inverters. The SNM of the SRAM Cell Read and write activities are available when in standby or retain mode. when we plot the

978-1-7281-8753-2/21/$31.00 ©2021 IEEE
DOI 10.1109/iSES52644.2021.00018

Authorized licensed use limited to: DELHI TECHNICAL UNIV. Downloaded on February 15,2022 at 10:02:48 UTC from IEEE Xplore. Restrictions apply.

two cross-coupled inverter's VTC, it yields the SRAM cell's SNM. In order to create a "butterfly curve," in relation to the line y = x, the VTC of one of the inverters is inverted. The SNM is the edge of smaller square fits in the graph's "eye" as demonstrated in Figure 3. [7] [8].

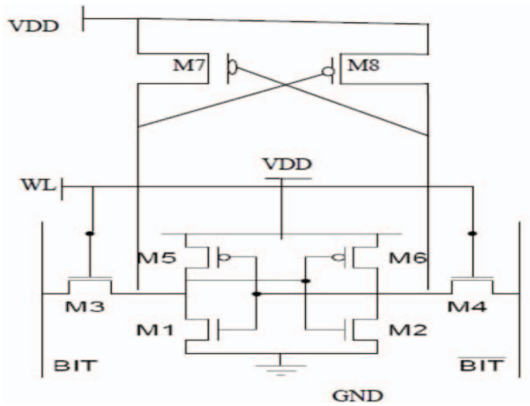


Figure 2. Designed 8T SRAM Cell [6] [11].

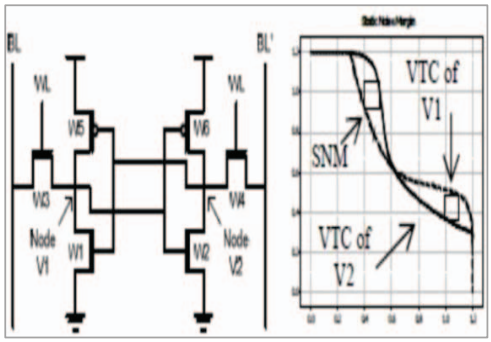


Figure 3. Design of a 6T SRAM cell and sample SNM-the side of the biggest square fitting into the graph [7] [8].

II. Related Work

A. Six Transistor SRAM Cell: During read and write operations in a normal 6T SRAM cell, as displayed in Figure 4. the nodes storing data are accessed directly via the bit lines access transistors. The storage node voltages are accessed between cross coupled inverters during reading, and data is stored at the node voltages during writing. The bit lines are BIT and /BIT, WL stands for word line. The WL controls the access transistors (Pass transistors) to perform read and write operations. Input and output nodes are represented by bit lines. Bit lines access data from SRAM cells during read operations, and bit lines store data during write operations. The minimal transistor length, according to the technology, is 130 nm [9].

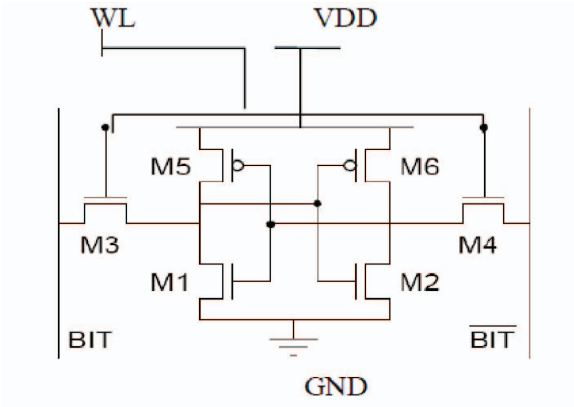


Figure 4. 6T SRAM Cell [9].

B. Standard Eight Transistor SRAM Cell: The read and write operations use various WL and bit lines in the conventional 8T SRAM Cell depicted in Figure 5. Single ended read operations are used in regular 8T SRAM cell, which reduces bit line swing voltages. The RSNM of 8T SRAM cell are much higher than 6T SRAM cell [10].

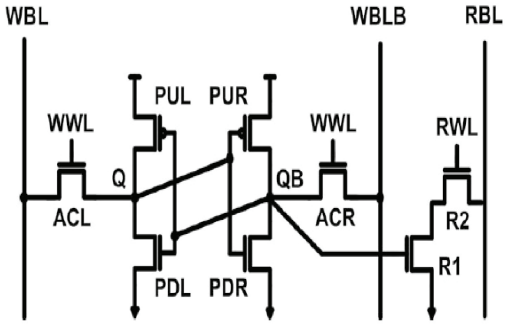


Figure 5. Standard 8T SRAM cell [10].

III. The Proposed Work

A. The cell structure: As illustrated in Figure 2. The Designed SRAM cell has eight transistors: which of 4 NMOS from M1 to M4 and the rest PMOS from M5 to M8. The SRAM cell's internal node is connected to bit lines by two transistors M3 and M4. For data storage, transistors M1, M2, M5, and M6 form a cross-couple arrangement. The M7 and M8 transistors reduce the swing voltages and function as swing restored transistors.

B. Operation of the Cell: In the Designed 8T SRAM cell, a input voltage VDD is given to SRAM in active mode, but a lower supply voltage (VD) is given during standby mode or inactive mode. Because transistor M6 is in the ON state, the drain voltages of M1 and M2 also VD, and with this value of VD less than VDD, the gate leakage currents of M1 and

Authorized licensed use limited to: DELHI TECHNICAL UNIV. Downloaded on February 15,2022 at 10:02:48 UTC from IEEE Xplore. Restrictions apply.

M2 are decreased. Gate leakage currents are determined by the gate-source(gs) and gate-drain(gd) voltages of a transistor, and here these both voltages of M2 and M1 are decreasing. In addition, lowering the drain voltage of transistor M4 reduces gate leakage current. Transistor M3's gate leakage current remains unaltered. The sub-threshold leakage currents in transistor M6 decreased, but not in transistor M2.

In addition, the fall in transistor drain voltage causes to a newly developed sub-threshold leakage current in M4. Making the floating bit lines can help to reduce this sub-threshold leakage current in M4 transistors. As a result, the method described above is effective in lowering transistor gate leakage currents. Figure 2. Shows a designed SRAM cell. Dual Node Voltages with Restoration Circuits Perform node voltage in hold, read, and write operations, as well as other factors like as delay and stability, and compare low-power 6T SRAM cell designs to suggested 8T SRAM cell designs. The comparison shows that the 8T SRAM cell performs better in hold, read, and write mode than the 6T SRAM cell.

IV. RESULT AND DISCUSSIONS

The functionality of the suggested cell is assessed in this part, and a collation is made with the various considered SRAM cell topologies. At the 130 nm technology node, all simulation work was performed on the Cadence Virtuoso environment. Existing topologies, such as 6T SRAM and Standard 8T SRAM cell, are explored for a full analysis. The effect of process variation tolerance (PVT) on several performance measures has also been investigated.

A. Stability: Stability refers to the ability of a cell to endure noise or undesirable cell flipping caused by external disturbances during conducting hold, read and write operations. In the sections below, stability is estimated in the read and write states using RSNM and write trip points, respectively.

1) Read static noise margin (RSNM): It's the term used to define an SRAM cell's read stability. The RSNM is calculated using the butterfly curve approach. SRAM cell's RSNM is defined by the biggest embedded square fit inside the smaller lobe of the curve. The higher the RSNM value, the more stable the cell is while reading its internal storage nodes for stored content.The word-line (wl) is kept active throughout read and write operations to depict the butterfly curve.In comparison to standard 6T SRAM and STANDARD 8T SRAM cells, the proposed cell achieved a greater RSNM.

The fact that the suggested cell's read stability is improved is due to the fact that the BLs are totally segregated from the internal storing nodes Q and Qbar when reading the stored content, resulting in no read disturbance.

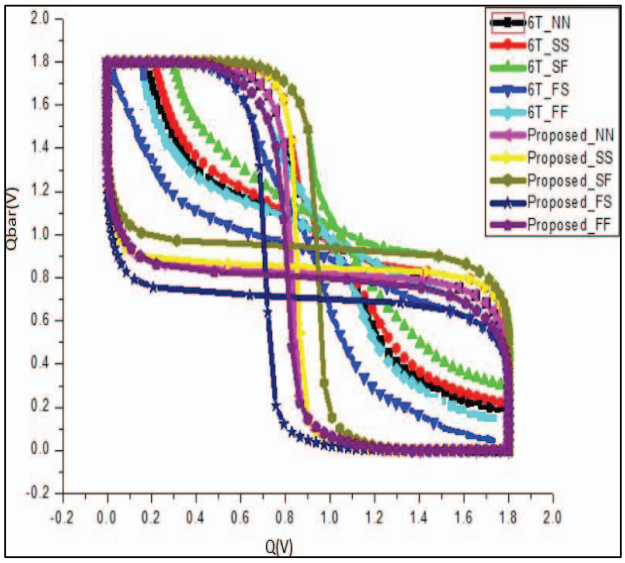


Figure 6. At different processing corners, the butterfly curve of the 6T and the designed cell throughout the read operation.

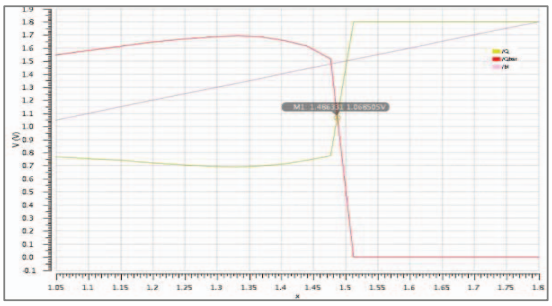
Different SRAM cells' read static noise margins have been investigated. We looked at various process corners, including FF, FS, SF, SS, and NN. Where the first character stands for fast or slow NMOS and similarly the second character stands for fast or slow PMOS. For example FF stands for Fast NMOS and Fast PMOS. The process variation analysis of numerous SRAM cells at different process corners is shown in Figure 6.

2) Write margin (WM): This is a phrase that describes a cell's ability to write at its storage nodes Q and Qbar, or how easily and effectively the cell can do so.

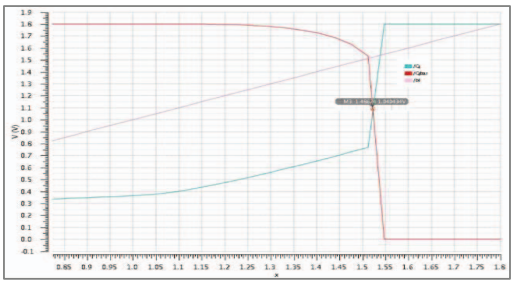
The write trip point and the butterfly curve are two popular ways for estimating writing skill. The biggest square that can be fitted inside the smaller lobe of the curve is examined in the butterfly technique. WL is used to draw the curve for the write process. Sweeping one of the bit lines from GND to VDD and graphing Q Vs Qbar, yields the WTP, which is the point at which each of two storage node flip their contents.

The write trip points for the STANDARD 6T and 8T SRAMs, and planned 8T SRAM are shown in Figures 7 (a), (b), and (c), respectively. The suggested SRAM cell has a write trip point of 417 mV, which is similar to that of a STANDARD 8T SRAM cell, Despite the fact that it 8.36% and 6.9% less than traditional 6T and Standardized 8T SRAM cells, respectively.

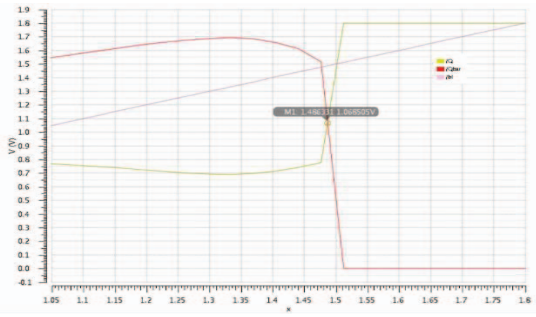
Authorized licensed use limited to: DELHI TECHNICAL UNIV. Downloaded on February 15,2022 at 10:02:48 UTC from IEEE Xplore. Restrictions apply.



(a)



(b)



(c)

Figure 7. various SRAM cells' write trip points (a) 6T SRAM, (b) STANDARD 8T SRAM, and (c) proposed 8T SRAM cell..

V. CONCLUSIONS

Through restoration inverters, a low-power SRAM cell and swing voltages are reduced. Techniques for SRAM are discussed. Also, a new high-speed, low-power Swing Restoring Inverter (SRI) Circuit was suggested and used to create an SRAM cell with 130nm CMOS Technology. The Designed SRAM allows for the creation of a low-power VLSI circuit.

REFERENCES

[1] S. Whitaker, "Pass-transistor networks optimize n-MOS logic", Electronics, September 1983.

[2] V. G. Oklobdžija and B. Duchêne, "Pass-Transistor Dual Value Logic For LowPower CMOS," Proceedings of the 1995 International Symposium on VLSI Technology, Taipei, Taiwan, May 31-June 2nd, 1995.

[3] P.Y.K.Cheung et al., "High Speed Arithmetic Design Using CPL and DPL Logic," Proceedings of the 23rd European Solid-State Circuits Conference, pp.360-3, Sept. 1997.

[4] F.S. Lai, W. Hwang, "Differential Cascode Voltage Switch with the Pass-Gate (DCVSPG) Logic Tree for High Performance CMOS Digital Systems", Proceedings of the 1993 International Symposium on VLSI Technology, Taipei, Taiwan, June 2- 4, 1995.

[5] L.G. Heller, W.R. Griffin, et al, "Cascode Voltage Switch Logic: A Differential CMOS Logic Family", in 1984 Digest of Technical Papers, IEEE International Solid-State Circuits Conference, Vol.27, p.16-17, February 1984.

[6] Parameswar, A., H. Hara, T. Sakurai, "A Swing Restored Pass-Transistor Logic Based Multiply and Accumulate Circuit for Multimedia Applications", Proceedings of the Custom Integrated Circuits Conference, San Diego, California, May 1-4, 1994.

[7] A. Pavlov and Manoj sachdev, CMOS SRAM Circuit Design and parametric Test in Nano- scaled Technologies. Springer 2008.

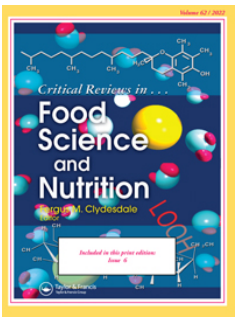
[8] Calhoun, B.H., Chandrakasan, A.P.: Static noise margin variation for sub-threshold SRAM in 65 nm CMOS. IEEE J. Solid-state Circuits 41, 1673-1679 (2006).

[9] Seevinck, "Static-Noise Margin Analysis of MOS SRAM Cells,"IEEE Journal of Solid- State Circuits, SC-22,5 (Oct. 1987),748-754.

[10] Farshad , 8T-SRAM Cell with improved read and write margins in 65 nm CMOS Technology,IFIP AICT 464,PP.95-109,2015.

[11] R. M. Rawat, A Novel Low power and Swing Restoration SRAM Logic Circuit Technique, March 2018, International Journal of Engineering and Technical Research V7(02).

Authorized licensed use limited to: DELHI TECHNICAL UNIV. Downloaded on February 15,2022 at 10:02:48 UTC from IEEE Xplore. Restrictions apply.



Critical Reviews in Food Science and Nutrition

ISSN: (Print) (Online) Journal homepage: https://www.tandfonline.com/loi/bfsn20

Minor tropical fruits as a potential source of bioactive and functional foods

Tanmay Sarkar, Molla Salauddin, Arpita Roy, Nikita Sharma, Apoorva Sharma, Saanya Yadav, Vaishnavi Jha, Maksim Rebezov, Mars Khayrullin, Muthu Thiruvengadam, Ill-Min Chung, Mohammad Ali Shariati & Jesus Simal-Gandara

To cite this article: Tanmay Sarkar, Molla Salauddin, Arpita Roy, Nikita Sharma, Apoorva Sharma, Saanya Yadav, Vaishnavi Jha, Maksim Rebezov, Mars Khayrullin, Muthu Thiruvengadam, Ill-Min Chung, Mohammad Ali Shariati & Jesus Simal-Gandara (2022): Minor tropical fruits as a potential source of bioactive and functional foods, Critical Reviews in Food Science and Nutrition, DOI: 10.1080/10408398.2022.2033953

To link to this article: https://doi.org/10.1080/10408398.2022.2033953

Published online: 14 Feb 2022.

Submit your article to this journal

Article views: 72

View related articles

View Crossmark data

Full Terms & Conditions of access and use can be found at
https://www.tandfonline.com/action/journalInformation?journalCode=bfsn20

CRITICAL REVIEWS IN FOOD SCIENCE AND NUTRITION
https://doi.org/10.1080/10408398.2022.2033953

Taylor & Francis
Taylor & Francis Group

REVIEW

Check for updates

Minor tropical fruits as a potential source of bioactive and functional foods

Tanmay Sarkar[a]*, Molla Salauddin[b]*, Arpita Roy[c]*, Nikita Sharma[d], Apoorva Sharma[d], Saanya Yadav[d], Vaishnavi Jha[d], Maksim Rebezov[e,f,g], Mars Khayrullin[g], Muthu Thiruvengadam[h], Ill-Min Chung[h], Mohammad Ali Shariati[e,g] and Jesus Simal-Gandara[i]

[a]Department of Food Processing Technology, Malda Polytechnic, West Bengal State Council of Technical Education, Malda, India; [b]Department of Food Processing Technology, Mir Madan Mohanlal Govt. Polytechnic, West Bengal State Council of Technical Education, Nadia, India; [c]Department of Biotechnology, School of Engineering and Technology, Sharda University, Greater Noida, India; [d]Department of Biotechnology, Delhi Technological University, Delhi, India; [e]Liaocheng University, Liaocheng, Shandong, China; [f]V. M. Gorbatov Federal Research Center for Food Systems, Moscow, Russian Federation; [g]K.G. Razumovsky Moscow State University of Technologies, and Management (The First Cossack University), Moscow, Russian Federation; [h]Department of Crop Science, College of Sanghuh Life Science, Konkuk University, Seoul, Republic of Korea; [i]Department of Analytical Chemistry and Food Science, Faculty of Science, Universidade de Vigo, Nutrition and Bromatology Group, Ourense, Spain

ABSTRACT

Tropical fruits are defined as fruits that are grown in hot and humid regions within the Tropic of Cancer and Tropic of Capricorn, covering most of the tropical and subtropical areas of Asia, Africa, Central America, South America, the Caribbean and Oceania. Depending on the cultivation area covered, economic value and popularity these tropical fruits are divided into major and minor tropical fruits. There is an annual increment of 3.8% in terms of commercialization of the tropical fruits. In total 26 minor tropical fruits (Kiwifruit, Lutqua, Carambola, Tree Tomato, Elephant apple, Rambutan, Bay berry, Mangosteen, Bhawa, Loquat, Silver berry, Durian, Persimon, Longan, Passion fruit, Water apple, Pulasan, Indian gooseberry, Guava, Lychee, Annona, Pitaya, Sapodilla, Pepino, Jaboticaba, Jackfruit) have been covered in this work. The nutritional composition, phytochemical composition, health benefits, traditional use of these minor tropical fruits and their role in food fortification have been portrayed.

KEYWORDS

Phytochemicals; medicinal properties; nutritional composition; food fortification

Introduction

In recent years concern over healthy diet and nutrition has become a major concern in our food habits and a rapid inclination has been observed toward nature originated healthy foods such as various vegetables, fruits for their rich nutritional profile consists anti-oxidants, minerals, vitamins etc. Fruits are always considered a rich source of nutrient which is beneficial for our health. With rapid globalization, fruits are nowadays used not only as a diet but also in different food product development, cosmetic application, drug development. Tropical fruits are one of the major fruit classes in the fruit kingdom and in a tropical country like India, there is a huge demand for different tropical fruits for various purposes.

Tropical fruits broadly can be classified into two groups – Major tropical fruit and minor tropical fruits. Most tropical and, if climatic limitations allow, subtropical countries produce major tropical fruits, which are generally well known in both local and worldwide markets, and possesses distinct export and production statistics in the global market. The major tropical fruits are characterized by their regular and early production, better shelf life and shipping characteristics, ease of adaptability and cultivation, ease of distribution and propagation of the fruiting plants. While the MTFs are not traded, cultivated and consumed extensively in comparison to the major tropical fruits (Saúco 2013). Their cultivation and consumption are confined within the specific geographical condition, but MTFs are still economically significant in their particular regional markets (Altendorf 2018). Due to healthy dietary preferences, the market opportunities for MTFs in the consumer-driven fruit market is expedited rapidly (Saúco 2013). Pineapple, mango and so on, are major tropical fruits whereas, in minor tropical fruits along with Kiwi-fruit (*Actinidia chinesis*), Lychee (*Litchi chinensis*), Jackfruit (*Artocarpus heterophylus*), Guava (*Psidium guajava*), the lesser-known names are Lutqua (*Baccaurea sapida*), Carambola (*Averrhoa carambola*), Tree Tomato (*Cyphomandra betacea*), Elephant apple (*Dilenia indica*), Rambutan (*Nephelium lappaceum*), Sapodilla (*Manilkara zapota*), Pepino (*Solanum Muricatum*), Mangosteen (*Garcinia mangostana*), Bhawa (*Garcinia cowa*), Loquat (*Eriobotrya japonica*), Silverberry (*Elaeagnus latifolia*), Durian (*Durio zibethinus*), Persimon (*Diospyros kaki*), Longan (*Dimocarpus longan*), Passion (*Passiflora edulis*), Water apple (*Syzygium aqueum*),

CONTACT Jesus Simal-Gandara jsimal@uvigo.es
*Marked author contributed equally.
© 2022 Taylor & Francis Group, LLC

Pulsan (*Nephelium ramboutan*-ake (Labill.) Leenh), Indian gooseberry (*Phyllanthus emblica*), Annona (*Annona cherimola*), Pitaya (*Hylocereus polyrhizus*), Jaboticaba (*Myrciaria jaboticaba*), Bay berry (*Myrica rubra*).

Kiwi-fruit (*Actinidia chinesis*) is a true berry and has furry brownish-green skin. The firm translucent green flesh has numerous edible purple-black seeds embedded around a white center. It is mostly grown in Jammu Kashmir, Himachal Pradesh, Sikkim, Meghalaya, Arunachal Pradesh, Uttar Pradesh, and Kerala (Sanz et al. 2021). Grown in the states of Bihar, Tripura, West Bengal, Uttar Pradesh, Punjab, and Haryana, lychee (*Litchi chinensis*) is one of the well-known tropical fruits across India. Lychee is oval to round, strawberry red in color, and about 25 mm (1 inch) in diameter. The brittle outer covering encloses a translucent white fleshy aril and one large seed (Sarkar, Nayak, and Chakraborty 2018). The jackfruit (*Artocarpus heterophylus*) is the national fruit of Bangladesh and Sri Lanka, and the state fruit of the Indian states of Karnataka, Kerala, and Tamil Nadu. Guavas (*Psidium guajava*) are incredibly delicious and packed with nutrients (Mondal et al. 2013). Guava is low in calories, loaded with fiber, and an excellent addition is that it is the richest food source of vitamin C (Casarotti et al. 2018). Lutqua (*Baccaurea sapida*) is native to the Southeast Asian region and found growing wild as well as under cultivation in Nepal, India, Myanmar, South China, Indo China, Thailand, the Andaman Islands, and Peninsular Malaysia. It is an underutilized fruit species locally known as Kusum (Kermasha et al. 1987). Star fruit – or carambola (*Averrhoa carambola*) is a sweet and sour fruit that has the shape of a five-point star. The skin is edible and the flesh has a mild, sour flavor that makes it popular in several dishes. The star fruit is yellow or green in color. It comes in two main types: a smaller, sour variety and a larger, sweeter one. The star fruit is a decent source of several nutrients – especially fiber and vitamin C (Luan et al. 2021). *Cyphomandra betacea*, commonly known as tamarillo or tree tomato, is a semi-woody, shallow-rooted, sub-tropical evergreen shrub with a treelike form and features large edible tomato-like fruit on plants clothed with large ovate green leaves (Ordóñez et al. 2009). Chalta being its Hindi name, it is commonly called Elephant Apple (*Dilenia indica*), since the delicious chalta fruit is hugely popular amongst the local wild elephants, being widely consumed by them. Its scientific name is *Dillenia indica*. The fruit that is large, oblong and greenish-yellow in color, develops in the autumn and winter seasons (Kamboj, Talukdar, and Banerjee 2019). Rambutan (*Nephelium lappaceum*) is a fruit native to Southeast Asia. The fruit is related to the lychee and longan fruits and has a similar appearance when peeled. Its translucent white flesh has a sweet yet creamy taste and contains a seed in its middle (Mahmood et al. 2018). Mangosteen (*Garcinia mangostana*) is an exotic, tropical fruit with a slightly sweet and sour flavor. It's originally from Southeast Asia but can be found in various tropical regions around the world. The fruit is sometimes referred to as purple mangosteen because of the deep purple color its rind develops when ripe. In contrast, the juicy inner flesh is bright white (Aizat, Ahmad-Hashim, and Syed Jaafar 2019). *Garcinia cowa*/Bhawa is a cousin species of the mangosteen and also bears edible sour fruits (Wahyuni et al. 2017). Loquat (*Eriobotrya japonica*) fruits, also known as Japanese plums, are bright orange ovals. The fruits are about 1-2 inches long and contain large brown seeds. Many people love loquat fruits for their unique tart and sweet flavor (Rai et al. 2020). Silverberries (*Elaeagnus latifolia*) are small fruits that resemble elongated olives. They grow on small shrubs and have smooth, burnt orange-coloured skin covered in small white lenticels or pores. Beneath the thin skin of the Silverberry lies a very juicy inner flesh surrounding a center seed, with a flavor that can be rather tart or acidic. When Silverberries are perfectly ripe, the fruit can be much sweeter. It's popular in Southeast Asia, where it's nicknamed "the king of fruits" (Kar et al. 2019). Durian is very high in nutrients, containing more than most other fruits. However, it also gets a bad rap due to its strong smell. Their orange-coloured fruits called persimmons are known for their sweet, honey-like flavor. The heart-shaped persimmons are astringent, meaning they are very high in plant chemicals called tannins that give the unripe fruit a dry, bitter taste (Conesa et al. 2020). Longan is very round and about the size of a large grape. Beneath the tough, tan shell, you'll find the white flesh of the fruit surrounding a dark seed. This structure is the source of its nickname, dragon's eye. The flesh of the longan fruit resembles that of a grape in taste and texture, but longan has a hint of musk in the flavor (Zhang et al. 2020). Passion fruit is a flowering tropical vine, known as Passiflora, that grows in warm climates, including South America, Australia, South Africa, and India. Passion fruit contains a soft pulp and lots of seeds inside a hard rind. People can eat the seeds and pulp, juice them, or add it to other juices. Passion fruit has recently gained a lot of attention because it is a rich source of powerful antioxidants and may also have other health benefits (He et al. 2020). Water apples are not apples – they are a species of tropical fruit with the botanical name *Syzygium aqueum* (Sobeh et al. 2018). The Pulasan, Nephelium mutabile Blume (family Sapindaceae), is a tropical fruit closely allied to the rambutan and sometimes confused with it. Usually eaten fresh, it is sweeter than the rambutan and lychee, but very rare outside Southeast Asia (Mahmood et al. 2018). Indian gooseberry, or amla, is a fruit tree that grows natively in parts of Asia (Sarkar, Mukherjee, and Chatterjee 2021). It has several culinary and herbal medicine uses, particularly in its native India. The fruit is rich in vitamin C and often purported to have potential antioxidant and heart-health benefits (Rose et al. 2018, Mukherjee, Sarkar, and Chatterjee 2021, Mukherjee, Chatterjee, and Sarkar 2022). Annona fruits are heart-shaped or round. The fruits have a thick brown stem and have an appearance like a pine cone. They are compound fruits, like pineapples, with knobby segments covered in a thin, deep pink or purple skin, most often covered in a light, silvery bloom (Jamkhande, Ajgunde, and Jadge 2017). Pitaya (*Hylocereus polyrhizus*) fruit is cultivated on a large scale in Malaysia. This tropical fruit is a rich source of nutrients as it contains a substantial amount of

polyphenols, betacyanins, four dietary fibers, ascorbic acid, vitamin A, vitamin E, and lycopene (Nurul and Asmah 2014). Jabuticaba is an exotic fruit overpowered with a treasure trove of nutrients that delivers indispensable health benefits. It is also known as the Brazilian grape tree that belongs to the Myrtaceae family (Benvenutti, Zielinski, and Ferreira 2021). The bayberry is best known for its berries, from which wax is derived to make fragrant bayberry candles (Joyce and Sanewski 2010).

Nutritive factors of minor tropical fruits

Fruits have been consistently reported in epidemiological surveys as naturally rich sources of antioxidants, vitamins, minerals that help us to keep our bodies healthy and fit. Consumption of minor tropical fruit (MTF) is clearly increasingly gaining importance due to their sensorial attractiveness and growing recognition of their nutritional and therapeutic values (Pereira-Netto 2018). The MTF is mainly composed of carbohydrates, macro minerals, proteins, and fibers along with vitamins and other bioactive compounds (Table 1).

Carbohydrate

The major component in any tropical fruit is a carbohydrate which is composed of soluble sugars, mainly sucrose, glucose, and fructose along with starch content. As the fruits ripened more the starch content also lowered and it converts into different sugars (Hanhineva et al. 2010). In most of the MTF, sucrose was the major sugar, while in a few of them fructose and glucose were the major sugars. Ripening induces starch degradation and accumulation of soluble sugars, mainly sucrose, glucose, and fructose. The carbohydrate content varies in different MTF. The presence of resistant starch in MTF induces a slow degradation of starch. Resistant starch is a favorable factor to limit non-communicable disorders, mainly obesity and diabetes (Reyniers et al. 2020). It should be taken into account when rating starchy fruit, root, and tuber crops for their nutritional benefits. The amount of carbohydrates in fruits is directly proportional to the amount of energy-providing by the fruits. The carbohydrate content of various MTF is reported in the Table 1 and maximum carbohydrate content is reported in Jaboticaba (90.1%) while the minimum is found in pepino (0.221%).

Fiber

Fibers refer to a group of compounds like non-starch polysaccharides (cellulose, hemicellulose, pectin, and mucilage), lignin, polyphenol propane present in fruit or any plant which the human digestive system cannot be hydrolyzed (Garcia-Amezquita et al. 2018). Compounds like polydextrose, oligosaccharides, resistant starch are also cannot be digested by the human digestive system and though sometimes they act as dietary fiber they are not considered as fiber content. In MTF next to carbohydrate content, fibers content is maximum both in major and minor tropical fruits (Gupta and Pradheep 2020). Fibers are classified into – soluble fibers and insoluble fibers. Fibers have an important role in lipid and carbohydrate metabolism, lowering blood cholesterol, proper gut function as well as it also helps to cures the constipation problem (Carasek and Pawliszyn 2006). The fiber content of various MTF is reported in the Table 1 and maximum fiber content is reported in Jaboticaba (98.2%) while the minimum is found in pulasaan (0.14%).

Minerals

Minerals are defined as micro-nutrients which has a vital role in our body metabolism and immunity system. Fruits and vegetables are considered rich sources of minerals. The MTF are rich in various minerals such as Calcium, magnesium, potassium, sodium etc. which has a very significant role in our body system (Sajib et al. 2014). Mineral deficiency in the human body can be caused due to two reasons – (1) Insufficient intake, (2) Poor absorbance by the body system and thus deficiency resulted in various problems in the human body starting from improper protein synthesis, poor defence against free radicals to enzyme malfunctioning. For proper functioning and activity enzymes needed various minerals as co-factor, in absence of which enzymes got deactivated (Wagner and Elmadfa 2003). Anti-oxidants also needed several minerals for their defence mechanism against free radicals. Malnutrition is a serious problem due to insufficient intake of mineral enriched foods among a larger section of economically back warded people.

Most MTF are good sources of iron (Table 2) which has a vital role in protein synthesis and to cure anemia which is a very common problem in a larger section of females. Zinc is another most important mineral which has been found in bones, muscular structures, cellular components and also as a co-factor of several enzymes that are involved in the metabolism of lipid, carbohydrates and nucleic acids (Pereira-Netto 2018). Magnesium has its role in muscle relaxation and contraction, bone and teeth development. Phosphorus is responsible for cell division, formation of linkage bonds in DNA and RNA chains, ADP and ATP synthesis the main source of body energy (Kumoro, Alhanif, and Wardhani 2020). Calcium is an inevitable part of bone growth and development. Potassium acts as a principal base in blood tissues and acts as a regulator in acid-base balance inside the body system. Sodium has its role in controlling the osmotic pressure of plasma. Selenium deficiency caused higher chances of suffering from cardiovascular diseases (Sajib et al. 2014).

Proteins

The MTF contains a small amount of protein ranging from 3% to 4% of the whole nutrition profile (Pereira-Netto 2018). Such a low amount of protein content of fruits is inadequate

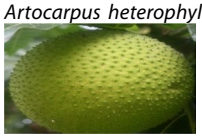
Table 1. Nutritional composition of the minor tropical fruits.

Fruits	Carbohydrate (%)	Protein (%)	Fat (%)	Sugar (%)	Energy (kcal/100 g)	Fiber (%)	References
Kiwifruit *Actinidia chinensis* 	14.23	1.23	0.56	10.98	66.88	2	(Drummond 2013)
Lutqua *Baccaurea sapida* 	81.17	5.43	1.24	–	357.56	3.6	(Pandey, Singh, et al. 2018)
Carambola *Averrhoa Carambo* 	5.6	0.45	0.32	5.04	27.08	0.96	(Tres et al. 2001)
TreeTomato *Cyphomandra betacea* 	87.5	2.5	1.09	3.3	369.81	5.8	(Prohens and Nuez 2011)
Elephant apple *Dillenia indica* 	9.05	0.72	0.592	5	44.408	2.04	(Basumatary et al.)
Rambutan *Nephelium lappaceum* 	23.78	2.04	0.23	–	105.35	0.7	(Mahmood et al. 2018)
Bay berry *Myrica rubra* 	–	27.64	68.18	2.01	–	–	(Cheng et al.)
Mangosteen *Garcinia mangostana* 	17.91	0.41	0.58	–	78.5	1.8	(EL-Meghawry et al. 2019)
Bhawa *Garcinia cowa* 	15.72	4.93	0.49	1.28	87.01	–	(Angami et al. 2020)
Loquat *Eriobotrya japonica* 	43.3	1.4	0.7	–	185.1	1.7	(Pareek 2016)

Table 1. (Continued).

Fruits	Carbohydrate (%)	Protein (%)	Fat (%)	Sugar (%)	Energy (kcal/100 g)	Fiber (%)	References
Silver berry *Elaeagnus latifolia* 	74.34	14.82	1.51	–	370.23	0.7	(Seal 2011)
Durian *Durio zibethinus* 	27.09	1.47	5.33	–	162.21	3.2	(Ho and Bhat 2015)
Persimon *Diospyros kaki* 	55	1.37	–	–	–	2.72	(Kim et al. 2015)
Longan *Dimocarpus longan* 	15.14	1.31	0.1	–	66.7	1.1	(Zhang, Guo, C.T. Ho, et al. 2020)
Passion fruit *Passiflora edulis* 	23.38	2.2	0.7	–	108.62	–	(Kawasoe et al. 2021)
Water apple *Syzygium aqueum* 	8.65	0.43	0.24	–	38.48	1.81	(Lim and Rabeta 2013)
Pulasan *Nephelium ramboutan-ake (Labill.) Leenh* 	12.86	0.82	0.55	–	59.67	0.14	(Lim 2013)
Indian gooseberry *Phyllanthus emblica* 	81.93	4.51	0.46	–	349.9	15.98	(Tewari, Kumar, and Sharma 2019)
Guava *Psidium Guajava* 	17	0.5	0.7	–	76.3	1	(Priya and Joseph)
Lychee *Litchi chinensis* 	15	0.7	0.1	–	63.7	–	(Pareek 2016)

Table 1. (Continued).

Fruits	Carbohydrate (%)	Protein (%)	Fat (%)	Sugar (%)	Energy (kcal/100 g)	Fiber (%)	References
Annona *Annona cherimola* 	21.1	1.96	0.176	–	93.824	5.32	(Gonçalves Albuquerque et al. 2016)
Pitaya *Hylocereus polyrhizus* 	12.97	1.45	–	–	15.05	2.65	(Nurul and Asmah 2014)
Sapodilla *Manilkara zapota* 	24.3	0.6	1	–	108.6	2.6	(Mohd Salleh et al.)
Pepino *Solanum muricatum* 	0.221	0.13	0.002	4.9	1.422	–	(Redgwell and Turner 1986)
Jaboticaba *Myrciaria jaboticaba* 	90.1	5	1.8	–	396.6	38.2	(Inada et al. 2015)
Jackfruit *Artocarpus heterophylus* 	25.4	1.9	0.4	20.6	112.8	1.5	(Goswami and Chacrabati 2016)

to support growth and development. Guava is the highest protein rich among all other fruits and contains about 4.2 g/100 g fresh weight.

Vitamins

Like other micro-nutrients vitamins are also present in a very small amount in minor tropical fruits. Kiwifruits are highly enriched in vitamin c (130.7 mg/100 g) followed by Folate (25 mg/100 g), vitamin A (23 IU) along with Niacin, Riboflavin in very low amounts (He et al. 2019). Lutqua is also a good source of vitamin c (Mann, Satpathy, and Gupta 2016). High amount of vitamin C and vitamin A in carambola contributes to its high anti-oxidant activity which efficiently scavenges reactive oxygen species (ROS) and other free radicals (Lakmal et al. 2021). Elephant apple vitamin profile composed of thiamine/vitamin B1 (0.015 mg/100 g), riboflavin/vitamin B2 (0.525 mg/100 g), niacin/vitamin B3 (0.38 mg/100 g), pantothenic acid/vitamin B5 (0.84 mg/100 g), pyridoxine/vitamin B6 (1.033 mg/100 g), folic acid/vitamin B9 (2.56 mg/100 g) (Seal et al. 2017). Rambutan, longan and lychee are also very good sources of vitamin C and contain 47.83 mg/100 g, 79.23 mg/100 g, 36 mg/100 g of Ascorbic acid respectively (Wall 2006). Total vitamin E content in lychee is 117 µg/100 g (Cabral, Cardoso L de, and Pinheiro-Sant'Ana 2014). Besides vitamin c and vitamin B complex, folate is also an important vitamin that is found in a good amount in minor tropical fruits such as passion (271 µg/100 g), guava (91 µg/100 g), jackfruit (192 µg/100 g), longan (67.8 µg/100 g) (Striegel et al. 2019).

MTFs are a rich source of macro and micronutrients but the detailed composition of the mineral present and the compositional analysis for vitamins are still need to be explored. The free amino acid composition is one of the determining factor for characteristic organoleptic properties of the MTFs, which need to be studied. The other distinguishing characteristics of the MTFs are the lower fat

Table 2. Mineral composition (mg/100g) of the minor tropical fruits.

Fruits	Ca	K	Na	P	Mg	Zn	Cu	Mn	Se	Fe	References
Kiwifruit *Actinidia chinensis*	20	316	3	29	14	0.1	0.147	0.058	0.0031	0.29	(Drummond 2013)
Lutqua *Baccaurea sapida*	23.77	375.37	7.99	–	21.67	0.97	14.33	37.29	–	29.55	(Pandey, Singh, et al. 2018)
Carambola *Averrhoa Carambola*	6.37	167.13	3.8	17.88	12.05	0.49	0.41	0.51	–	0.45	(Muthu et al. 2016)
Tree Tomato *Cyphomandra betacea*	10.3	313	7.1	57.3	21.8	0.2	0.19	0.2	–	0.67	(Prohens and Nuez 2011)
Elephant apple *Dillenia Indica*	122	2.64	0.05	110	37.85	0.5	0.25	0.24	–	0.38	(Goswami and Chacrabati 2016)
Rambutan *Nephelium lappaceum*	8.7	249.4	8.2	18.8	17.2	0.26	0.2	0.38	–	0.56	(Wall 2006)
Bay berry *Myrica rubra*	245.17	780.89	1.27	5.26	371.05	10.48	2.428	7.051	0.032	12.561	(Cheng et al.)
Mangosteen *Garcinia mangostana*	12	48	7	9.21	13	0.21	0.069	0.10	–	0.3	(EL-Meghawry et al. 2019)
Bhawa *Garcinia cowa*	1.436	–	–	–	–	–	–	–	–	1.374	(Sagolsem, Rathi, and Baishya 2021)
Loquat *Eriobotrya japonica*	–	1216	1	126	13	–	–	–	–	–	(Pareek et al. 2014)
Silver berry *Elaeagnus latifolia*	586.04	1358	96.5	–	–	24.8	0.6	2.1	–	17.2	(Seal 2011)
Durian *Durio zibethinus*	199.8	159.42	220.2	–	691.2	4.92	4.92	8.26	–	6.71	(Ho and Bhat 2015)
Persimon *Diospyros kaki*	53.9	631.2	7.8	–	70.9	–		–	–	6.1	(Kim et al. 2015)
Longan *Dimocarpus longan*	–	266	0	21	10	0.05	–	–	–	–	(Zhang, Guo, C.T. Ho, et al. 2020)
Passion fruit *Passiflora edulis*	12	348	28	38	29	0.1	0.086	–	–	1.6	(Corrêa et al. 2016)
Water apple *Syzygium aqueum*	63.6	–	19.6	–	–	2.0	–	3.3	–	3.7	(Lim and Rabeta 2013)
Pulasan *Nephelium ramboutan-ake (Labill.) Leenh*	54	94	6	9	–	–	–	–	–	100	(Lim 2013)
Indian gooseberry *Phyllanthus emblica*	28.06	163.10	1.07	–	78	0.07	0.01	0.03	–	0.68	(Sajib et al. 2014)
Guava *Psidium Guajava*	17	–	–	0.7	–	–	–	–	–	0.4	(Priya and Joseph)
Lychee *Litchi chinensis*	4.9	172.4	6.8	31.1	16.2	0.28	0.23	0.11	0.43	–	(Wall 2006)
Annona *Annona cherimola*	0.6	1.6	1.06	1.8	0.17	0.38	–	–	–	–	(Akomolafe and Ajayi 2015)
Pitaya *Hylocereus polyrhizus*	6.72	437.55	35.63	–	26.4	0.4	–	–	–	0.3	(Nurul and Asmah 2014)
Sapodilla *Manilkara zapota*	180	632	182	–	182	2	0.66	4.96	–	9.49	(Mohd Salleh et al.)
Pepino Solanum muricatum	9.94	41.56	–	35.58	11.7	0.475	0.22	–	–	0.249	(Herraiz et al. 2016)
Jaboticaba *Myrciaria jaboticaba*	27.1	700.7	23.3	75.7	72.3	1.1	0.8	1.1	0.0019	23.7	(Inada et al. 2015)
Jackfruit *Artocarpus heterophylus*	37	407	41	38	27	–	–	–	–	1.1	(Goswami and Chacrabati 2016)

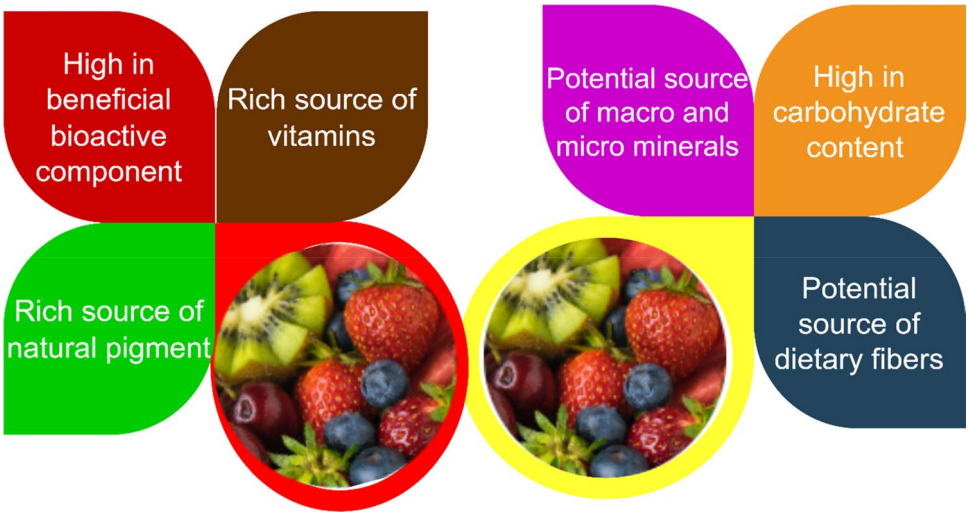


Figure 1. Nutritional and bioactive potential of minor tropical fruits.

content and high sucrose content along with the presence of an adequate amount of fiber (Figure 1).

Bioactive compounds of minor tropical fruits of the Indian subcontinent

Fruit genetic diversity is abundant in the Indian subcontinent. India's climate ranges from moderate to tropical, making it ideal for a wide range of fruit varieties. There are 45 families, 106 genera, and 261 species of edible fruit that are underused and little known (Gupta and Pradheep 2020). Throughout the country, there are several modest and underutilized wild edible tropical fruits (Laldinchhana, Ray, and Pachuau 2020). Plant metabolism is divided into two types: main and secondary metabolic forms (Lattanzio 2013). Lipids, carbohydrates, proteins, and nucleic acids, as well as all necessary components for cell growth and development, are among the main metabolites. Secondary metabolites are chemicals found in particular cells that are only indirectly required for simple respiratory photosynthesis or metabolism but are crucial for a plant's survival (Basheer and Kerem 2015). Bioactive natural compounds are phytochemicals extracted from fruits/food-related products that have always played a key role as innovative therapeutical agents. They have a significant direct and indirect impact on human health, as well as extensive therapeutic characteristics (Karasawa and Mohan 2018).

Polyphenols

Polyphenols are a chemically varied category of secondary metabolites found in plants all over the world (Weber and Passon 2019). Polyphenols are essential components of plants that have a role in color, fragrance, and taste, among other things (Kelly, Kelly, and O'Mahony 2019). Polyphenols are compounds containing one or more hydroxyl groups linked to a phenyl ring. Polyphenols play a critical part in plants' defensive mechanisms against a variety of pathogens as well as herbivores. They are made from tyrosine and phenylalanine (Papuc et al. 2017). Polyphenols are found in larger concentrations in fruit waste, particularly in fruit peel, than in fruit pulp. Fruit peels have a higher antioxidant capacity than fruit pulp, according to studies. Fruit peels contain far more phenolic chemicals than pulp, including carotenoids, anthocyanins, flavonoids, and phenolic acids (Safdar, Kausar, and Nadeem 2017). These include a broad category of bioactive phytochemicals that include flavonoids, stilbenes, phenolic acids, and lignans, among others (Fraga et al. 2019). Phenolic substances can be identified using paper chromatography, high-speed counter-current chromatography, and supercritical fluid chromatography (Khoddami, Wilkes, and Roberts 2013). Studies have suggested that a low intake of polyphenolic compounds, which contains both functional and health-promoting characteristics, may increase the risk of certain illnesses (Swallah et al. 2020). Polyphenols can be extracted from guava's bark (Naseer et al. 2018). Litchi's pulp is a great source of ingesting polyphenols. Phenolic can act as signaling agents or alter cellular signaling pathways during inflammation (Raiola et al. 2014). Polyphenols have an important function in the physical gesture of litchis and are also important nutrients for humans. All sections of the litchi fruit (pericarp, pulp, & seed) contain high levels of phenolic compounds, however, the polyphenol content of litchi pulp, which is the immediately edible element, plays a critical role in guaranteeing nutritional value in our body (Huang et al. 2019). Polyphenols isolated from litchi seeds with 70% or 95% ethanol have high antioxidant activity and can successfully cure diabetes (Jing et al. 2014). Jackfruits' woods can also be used to extract polyphenols (Ranasinghe, Maduwanthi, and Marapana 2019). Polyphenols and actinidin, which are found in kiwifruit, *Elaeagnus latifolia* (Dutta et al. 2018), *Diospyros kaki* (Direito et al. 2021) provide gastrointestinal advantages, such as improved laxation and a reduction in stomach pain, in those who have either constipation or irritable bowel syndrome (Richardson, Ansell, and Drummond 2018). Peel content of rambutan, *Cyphomandra betacea* (Ali Hassan and Abu Bakar 2013), *Passiflora edulis* (He et al. 2020), *Manilkara zapota* (Pravin and Shashikant 2018), *Solanum muricatum*

(Herraiz et al. 2016) and seed extract of rambutan have plenty of polyphenols (Hernández-Hernández et al. 2019). HPLC and spectrophotometric analysis of carambola extracts supported the content of polyphenols and gives a unique taste, color and flavor to the fruit (Khanam et al. 2015). Leaf extract of elephant apple (Kumar Nayak and Rayaguru 2016), *Garcinia cowa* (Ritthiwigrom, Laphookhieo, and Pyne 2013), *Diospyros kaki, Dimocarpus longan* (Zhang et al. 2020), *Syzygium aqueum* (Itam et al. 2021), *Nephelium ramboutan-ake (Labill.) Leenh* (Putri et al. 2021), *Phyllanthus emblica* (Gaire and Subedi 2014), *Psidium Guajava* (Kumar et al. 2021), *Annona cherimola* (Albuquerque et al. 2016), *Hylocereus polyrhizus* (Ramil, Dc. Mendoza, and D. Ramil 2021) had a good amount of phenolic content. Chinese bay berry cultivators also have high phenolic content (Zhang, Zhao, et al. 2015). Xanthones are the major polyphenolic compound available in mangosteen (Rizaldy et al. 2021). Polyphenols in *Eriobotrya japonica* helps in stress conditions (Mogole, Omwoyo, and Mtunzi 2020). Phenols in *Durio zibethinus* have strong vasodilator properties (Saminathan and Doraiswamy 2020). Table 3 represent the bioactive components identified in the minor tropical fruits.

Flavonoids

Polyphenols are divided into two groups: flavonoids and polyphenols. Flavonoids are the most common type of polyphenol. These compounds have a diphenylpropanes structure, which consists of two aromatic rings connected by 3 carbon atoms. Flavonoids have become an essential component in a wide range of nutraceutical, pharmacological, therapeutic, and cosmetic applications. This is due to their ability to control critical cellular enzyme activity as well as their anti-oxidative, anti-inflammatory, anti-mutagenic, and anti-carcinogenic capabilities (Panche, Diwan, and Chandra 2016). Flavonoid structures, which include over 8000 secondary metabolite chemicals, are found all over the place in plants and plant tissues (Kennedy 2014). Based on the number of carbon atoms present and their arrangements, flavonoids can be divided into flavones, flavonols, flavonones, isoflavonoids, neoflavonoids, flavanols, anthocyanins and chalcones, etc (Panche, Diwan, and Chandra 2016). Flavones are found as glucosides in fruits. This group of flavonoids includes luteolin, apigenin, and tangeritin. The polymethoxylated flavones tageretin, nobiletin, and sinensetin are abundant in citrus fruit peels. Flavonoids with a ketone group are known as flavonols. Isoflavones are flavonoids in which the B ring is connected in position 3 of the C ring (Matthies et al. 2008).

Tropical fruits are hub of flavonoids. Flavonoids, notably anthocyanins, and flavanones are the primary bioactive elements of açai fruits. Pro-anthocyanidin groups and trimers, eriodyctiol, taxifoline, and naringenin are the polyphenols found in the most abundance in tamarind (Bressiani et al. 2021). In coconut, 28 phenolic compounds, that includes 12 flavonoids and the rest non-flavonoids have been found (Arivalagan et al. 2018). Five flavones were discovered in the leaves of Jackfruit by Wang et al. (Wang et al. 2017). Litchi is a sweet-tasting tropical or subtropical fruit having a high concentration of flavonoids, proanthocyanidin, and procyanidin in its pericarp (Lv et al. 2015). Indian gooseberry is rich in bioactive compounds, especially flavonoids, which aids in various medicinal activities (Ikram et al. 2021). For some species of kiwifruit, *Actinidia macrosperma* has high flavonoid content, which is useful in the treatment of hypertension (Hettihewa, Hemar, and Rupasinghe 2018). Spectrophotometer analysis of carambola shows the presence of flavonoids in the fruit, and it protects the cell from degradation (Khanam et al. 2015). The flesh and peel of *Cyphomandra betacea, Elaeagnus latifolia* (Dutta et al. 2018), *Dimocarpus longan* (Zhang et al. 2020) have a high amount of flavonoids (Ali Hassan and Abu Bakar 2013). Elephant Apple's sepal also contains a good amount of flavonoids (Kumar Nayak and Rayaguru 2016). Innate pigmentation of rambutan, bay berry (Zhang, Zhao, et al. 2015) is only due to the presence of flavonoids in their husk (Hernández et al. 2017). The pericarp of mangosteen has abundant flavonoids (Rizaldy et al. 2021). 12 flavonoids can be extracted from *Garcinia cowa* (Ritthiwigrom, Laphookhieo, and Pyne 2013). Total flavonoid content for *Eriobotrya japonica* were shown as quercetin equivalent (Mogole, Omwoyo, and Mtunzi 2020). Fruit of *Durio zibethinus* (Saminathan and Doraiswamy 2020), *Diospyros kaki* (Direito et al. 2021), *Passiflora edulis* (He et al. 2020), *Syzygium aqueum* (Itam et al. 2021), *Nephelium ramboutan-ake (Labill.) Leenh* (Putri et al. 2021), *Phyllanthus emblica* (Gaire and Subedi 2014), *Annona cherimola* (Albuquerque et al. 2016), *Hylocereus polyrhizus* (Ramil, Dc. Mendoza, and D. Ramil 2021), *Solanum muricatum* (Herraiz et al. 2016) have antioxidant properties due to presence of flavonoids. Leaf extracts of *Psidium Guajava* give the fruit antibacterial activity (Kumar et al. 2021).

Pigments

Pigments are substances that humans interpret as having color. Natural pigments are responsible for the colors yellow, orange, red, blue, and purple (Choo, Dufossé, and Morales-Oyervides 2021). Chlorophyll, anthocyanins, carotenoids, and betalains are the most frequent plant pigments found in nature (Choo 2018). Alteration in the color and texture of the fruit skin and flesh indicates the fruit's maturation stage. Natural pigments, in addition to their color, have other capabilities and are thus termed bioactive components. One of the most extensively utilized natural colorants in the food business is red. The study of these pigments is motivated by the desire to improve the diet's health benefits (Fernández-López, Fernández-Lledó, and Angosto 2020). Pigments in elephant apple give it a pleasant smell and a colorful appearance (Kumar Nayak and Rayaguru 2016).

Anthocyanins, β-carotene and lycopene are the three abundantly present plant pigments in strawberries, enhancing the antioxidant property of the plant (Šic Žlabur et al. 2020). A mixture of various carotenoids, or carotenoids

Table 3. Bioactive compounds from minor tropical fruits and their method of extraction.

Fruits	Extraction method	Solvent used	Phytochemical identified	Method of estimation (Qualitative/UV-Vis Spectrophotometry/ HPLC/ LCMS/ GCMS)	References
Kiwifruit	Dragendorff's Reagent	Ethyl acetate: Chloroform: Methanol (20:20:10)	Alkaloids	TLC	
	Anisaldehyde sulphuric acid	Acetic acid: Formic acid: Water (100:11:11:26)	Terpenoids	TLC	
	15ml of 3% Boric acid + 5ml of 10% Oxalic acid	Ethyl acetate: Formic acid: Water (8:1:1)	Flavonoids	TLC	
Guava	Headspace Analysis	–	Volatile compound	Gas Chromatography	(Soares et al. 2007)
	Mass Spectrometry	Ammonium hydroxide solution	Quercetin, Gallocatechin (Flavonoids)	Yellow fluorescence	(Sampath Kumar et al. 2021)
Carambola	Alkaline Reagent Test	Sodium hydroxide solution	Isovitexin, norathyriol (Flavonoids)	DPPH	(Soares et al. 2007)
Tree Tomato	DMF	Methanol	PolyPhenols	UV-Vis	(Ammar Altemimi et al. 2017)
Elephant Apple	Alkaline Reagent Test	Sodium hydroxide solution	Flavonoid	DPPH	(Bordoloi and Das 2019)
Rambutan	Dragendorff's Test	Ethyl acetate, Chloroform, Methanol	Alkaloids	TLC	(Kamalanathan and George 2015)
	Shinoda Test	Ethanol	Flavonoids	HPLC	
BayBerry	Rutin equivalents	–	Flavonoids	HPLC	(Zhang, Zhao, et al. 2015)
	Trolox equivalent	ABTS	Anthocyanin	ESI	
Mangosteen	Wagner's Test	Iodine and KI in water	Alkaloid	Mean of inhibition Zone	(Goud, Prasad, and Kumar 2019)
	Shinoda Test	Ethanol	Flavonoids	Mean of inhibition Zone	
Bhawa	Lead Acetate Test	Ethanol	Flavonoids	UV-Vis	(Gulnaz and Savitha 2013)
		Ethanol Hydroxide	Anthocyanin	UV-Vis	
Loquat	Dowd Method	Methanolic solution aluminum chloride	Flavonoids	UV-Vis	(Mogole, Omwoyo, and Mtunzi 2020)
	Folin Ciocalteu method	Sodium carbonate	Polyphenols	Calibration curve	
Silver Berry	Folin–Ciocalteau method	Sodium carbonate	Polyphenols	UV-Vis	(Lachowicz et al. 2019)
Durian	Amyl alcohol layer	0.1-gram Mg powder and 1 mL of concentrated HCl and 2 mL of amyl alcohol	Flavonoids	red or yellow or orange color	(Romatua Aruan et al. 2019)
	Wagner, Dragendorff Test	HCl	Alkaloids	Turbidity check	
Persimmon	UPLC with MS	Methanol	Polyphenols	UPLC-Q-TOF-MS	(Direito et al. 2021)
Longan	Catechin equivalents	*p*-nitrophenyl-α-D-glucopyranoside	Epicatechin, Kaempferol, Quercetin (Flavonoids)	Liquid Chromatography	(Li et al. 2015)
	–		Gallic acid, Ellagic acid, Isoscopoletin (Polyphenols)	HPLC	
Passion Fruit	QuCHERS	–	Polyphenol	UHPLS-MS-MS	(He et al. 2020)
	Quercetin equivalent	–	Flavonoid	Colorimetric Assay	
	Dynamic Headspace	–	Volatile Compound	GC-MS	
Water apple	–	Methanol	Polyphenols	HPLC	(Oszmiański et al. 2018)
Indian Gooseberry	Headspace-solid phase microextraction	–	Volatile Compound	Gas chromatography-mass spectrometry	(Yilmaztekin 2014)
	iron (III) reduction and 1, 1-diphenyl-2-picrylhydrazyl and superoxide anion radical scavenging assays	–	Flavonoid	RP-HPLC coupled with photodiode array detection	(Poltanov et al. 2009)
Pulasan	Extraction of Solvent	Methanol, hexane, and ethyl alcohol	Polyphenol	Infrared Spectroscopy	(Altemimi et al. 2017)
Lychee	Pressurized fluid extraction	*n*-butane	Polyphenol	DPPH	(Paliga et al. 2017)
	Folin–Ciocaulteu method	Sodium carbonate solution	Flavonoid	UV-Vis Spectrophotometer	
Annona	Quantitative Phytochemical Screening	95% Ethanol	Terpenoid, Flavonoid	DPPH	(Ijaiya, Arzika, and Abdulkadir 2014)

Table 3. (Continued).

Fruits	Extraction method	Solvent used	Phytochemical identified	Method of estimation (Qualitative/UV-Vis Spectrophotometry/ HPLC/ LCMS/ GCMS)	References
Pitaya	Ultrasound-assisted extraction	Ethanol	Flavonoid	UV–vis Spectrophotometer	(Bhagya Raj and Dash 2020)
Sapodilla	Folin-Ciocalteu reagent	Sodium carbonate solution	Flavonoid	UV-Vis Spectrophotometer	(Woo et al. 2013)
	Ferric-reducing antioxidant power assay	10 mM tripyridyltriazine (TPTZ) solution, and 20 mM $FeCl_3$ in a ratio of 10:1:1	Terpenoid	UV-Vis Spectrophotometer	
Jabuticaba	Maceration	Ethanol	Polyphenol	HPLC	(Garcia et al. 2019)
Pepino	Aqueous and ethanol extracts	1:10 in sterile phosphate buffered saline	Flavonoid	HPLC	(Herraiz et al. 2016)
	Maceration	Acetone	Terpenoid	HPLC	(Lezoul et al. 2020)
	Solid-liquid extraction	MeOH containing NaF	Polyphenol	HPLC	
Jackfruit	Aqueous acetone, aqueous methanol, and mix solvent	Dichloromethane:methanol::1:1 extract	Flavonoid	UV-VIS spectrophotometer	(Sreeja Devi, Kumar, and Sabu 2021)
	95% ethanol in the soxhlet apparatus	Dichloromethane:methanol::1:1 extract	Terpenoid	UV-VIS spectrophotometer	
	95% ethanol in the soxhlet apparatus	Dichloromethane: methanol: 1:1 extract	Alkaloids	UV-VIS spectrophotometer	

combined with tocopherol or phenolic acid, has simultaneous effects on preventing pathogenic events that produce free radicals that might damage DNA (Bhowmik et al. 2012). Carotenoids, flavonoids, sterols, and tannins are among the phytochemicals found in jackfruit, with amounts changing according to the type. Carotenoids have provitamin A action and are known to help with cancer, inflammation, CVDs, cataracts, and age-related vision problems, among other chronic degenerative disorders. Zeacarotene, carotene-5,6 epoxide, a dicarboxylic carotenoid, and crocetin have been found in jackfruit kernels. According to current studies, all-trans-lutein, all-trans-carotene, all-transneoxanthin, 9-cis-neoxanthin, and 9-cis-vio-laxanthin are the main carotenoids found in jackfruit (Ranasinghe, Maduwanthi, and Marapana 2019). Red pigment can be extracted from the rambutan peel, resulting in a bio-flavonoid complex with a reasonably high purity and good bioactivity (Hernández-Hernández et al. 2019). Various species of Annona plant are known to produce pigments as their bioactive phytochemicals (Bhardwaj et al. 2019). Major pigments present in kiwi fruit include carotenoid and chlorophyll and it is known that chloroplasts of this plant don't get changed to chromoplasts, which is usual in the case of fruit ripening (McGhie and Ainge 2002). Some amount of carotenoid is also found in carambola (Khoo et al. 2011), *Cyphomandra betacea* (Ali Hassan and Abu Bakar 2013), *Diospyros kaki* (Direito et al. 2021) and *Nephelium ramboutan-ake (Labill.) Leenh* (Putri et al. 2021), *Solanum muricatum* (Herraiz et al. 2016) give a unique color to the fruit. Fruit extract of bay berry possesses a high amount of anthocyanin (Zhang, Zhao, et al. 2015). Mangosteen (Rizaldy et al. 2021), *Durio zibethinus* (Saminathan and Doraiswamy 2020), *Dimocarpus longan* (Zhang et al. 2020), *Passiflora edulis* (He et al. 2020), *Psidium Guajava* (Kumar et al. 2021), *Manilkara zapota* (Pravin and Shashikant 2018) possess a good quantity of anthocyanins.

Volatile compounds

Many fruits are found to emit a component that generally vaporizes in thin air and usually leaves a flavor and aroma behind the evaporation. Esters, alcohols, aldehydes, ketones, lactones, terpenoids and apocarotenoids are a few of many volatile compounds that are found in the fruits (El Hadi et al. 2013). There are various methods of profiling done to detect the volatile compounds but many are left undetected as they are produced in trace amounts but the human olfactory response can still counter them. Among the discovery made regarding VCs, the flavor property of its in fruit was discovered first (Maarse 2017). Volatile compounds abundantly found in the fruit include 3-carene, hexanal, trans-2-hexenal, cis-3-hexanol, limonene, α-terpinene and α-terpineol (Swamy Mallappa 2020).

Guava has approximately 34 VCs that were identified from both mature and ripe guava (Pino, Gutierrez, and Rosado 1990). A few years back a research study was conducted where the presence of the volatile compounds was noted at the immature stage, mature and ripped stage by utilizing headspace technique with gas chromatography. Through this, it was found that at the immature stage and a time period before the onset of full maturation generally there predominantly the aldehydes such as (*E*)-2-hexenal and (*Z*)-3-hexenal whereas at the mature stage, esters like *Z*-3-hexenyl acetate and *E*-3-hexenyl acetate and sesquiterpenes caryophyllene, α-humulene and β-bisabollene were present (Soares et al. 2007). Various studies have been conducted to check what happens to VCs if guava is stored under high pressure or are oven-dried. It was found that fresh guava losses its volatile characteristic when dried (Nunes et al. 2016). In lychee few of the predominantly found VCs in lychee are this Hexanoic acid, Octanoic acid, Isobutyl alcohol, 1-Butanol, Ethyl octanoate, Ethyl decanoate, Citronellyl acetate, Citronellol Linalool, Geraniol

cis-Rose oxid etc (Sun et al. 2021). In a study done on free and glycosidically bound VCs, it was concluded that the free one's emitted fresh lychee like aroma whereas the bound ones were odorless (Chyau et al. 2003). Generally, it is said that after fermentation, there is no effect or change occurs in the volatile compounds. However, a study conducted on lychee wine after fermentation by Saccharomyces upon addition of aromatic amino acid does not affect it much but helped intensify the flavor and aroma of lychee (Chen, Chia, and Liu 2014). In BayBerry about 46 VCs are found in bayberry upon fermenting the bayberry and comparing different wines of it by Gas Chromatography and Mass Chromatography. In general terpenes, alcohol, ester, aldehyde, ketones etc volatile compounds were extracted (Cao, Wu, and Weng 2020) A study was conducted to improve the quality of berry juice extracted from the fruit by analyzing the harmful effects of the heat treatment; raw materials addition and long storage time all this was monitored by headspace solid-phase micro extraction coupled with gas chromatography-mass spectrometry (Xu et al. 2014). In Jackfruit with the help of solid-phase micro extraction following gas chromatography-time-of-flight mass spectrometry (GC-TOFMS) following volatile compounds were extracted ethyl isovalerate, 3-methylbutyl acetate, 1-butanol, propyl isovalerate, isobutyl isovalerate, 2-methylbutanol, and butyl isovalerate (Ong et al. 2008). With the help of the adsorption quality of VOCs and the present phosphorene sheet in it, we can easily detect and estimate which jackfruit is of the best quality (Nagarajan, Bhavadharani, and Chandiramouli 2020). A study came suggesting after harvesting of the fruit approximately it took 5 days to start the ripening process and following it 23 VCs were extracted by GS-MS in the same (Ong et al. 2006). In Kiwi-fruit approx. 48 components were discovered where 27 were unique to Kiwifruit only. This was isolated by vacuum distillation and analyzed by gas chromatography (Takeoka et al. 1986). For Lutqua volatile compounds are generally found in trace amounts in most of the fruits and have been responsible for the flavor and aroma of the fruits. A type of fruit has many VCs in it more than 30 that are easily detectable and there are many which lie undetected even with the headspace or distillation method. The fresh fruit of Carambola had been found to have 126 compounds in total and approximately 72 were unique to carambola (Frohlich and Schreier 1989). By HS-SPME-GC-MS methodology in the fruit of Tree Tomato, there were many types of volatile compounds and since it has a high content of vitamins, low calories and iron show medicinal properties (Armando A. Durant, Rodreguez, and Santana 2012). During analysis of slices of elephant apple, there were volatile compounds discovered that might be causing antioxidant properties in the fruit (Smrutimayee Mishra 2021). In the fruit of rambutan after going through GC/MS over 100 volatile compounds were found and among them, 60 had maximum odor activity (Ong, Acree, and Lavin 1998). In mangosteen fruit when fermented with five different stains 36 volatile compounds in it were found by Gas chromatography (Xiao et al. 2015). Eighteen volatile compounds have been identified in a methylene chloride extract of a distilled fraction from loquat fruit and this may be responsible for the fruity-floral flavor of the fruit (Shaw and Wilson 1982). In the durian, 108 volatile compounds were extracted by dichloromethane and analyzed by GC-MS analysis and are responsible for strong fruity smell (Jiang et al. 1998). VCs are mostly present in the mesocarp of the permission and are responsible for its characteristic aroma (Horvat et al. 1991). There are VCs in longan known to heighten the antioxidant properties of the wine (Tandee, Kittiwachana, and Mahatheeranont 2021). The VCs are extracted by the Headspace method and on analysis showed that different VCs helped in different things as some were responsible for the antioxidant activity and some for-odor intensity (Janzantti et al. 2012). Pulasan is generally disregarded but on heating, it was found that most of the fatty acid compounds changed into volatile compounds making it a nutritional snack (Hamid, Yahya, and See 2021). Aroma of the sapodilla fruits is due to VCs but are comparatively less in number than any other fruits (MacLeod and Gonzales de Troconis 1982).Volatile aroma constituents of Pepino fruit were separated by simultaneous distillation and extraction (SDE). They were analyzed by gas chromatography and mass spectrometry (Shiota et al. 1988). By liquid-liquid extraction of the jaboticaba fruit and analysis by GC many VCs were isolated and they were alcohols, terpenes, etc. Mostly terpenes were responsible for the flavor of the fruit (Plagemann et al. 2012).

Alkaloids

Nitrogen-containing compounds are known as alkaloids. It has different types just because of the difference in the position of nitrogen. It could be heterocyclic, non-heterocyclic or simple. Mainly depending upon their biosynthetic pathway they could be classified into terpenoid indole alkaloids, benzylisoquinoline alkaloids, tropane alkaloids, and purine alkaloids (Swamy Mallappa 2020)· Since it is a biological compound, its presence is encountered in fruits also, approximately more than 300 species of plant have this. Namely in families such as Papaveraceae, Ranunculaceae, Solanaceae, and Amaryllidaceae these are found in abundance (Encyclopaedia Britannica, 2018). Some of the tropical fruits with bioactive compounds (alkaloids) are listed below.

Fruit of Morus Alba belonging to the family Moraceae contains nearly 17 pyrrole alkaloid compounds and are most of them were found to show inhibition to pancreatic lipase activity (Kim et al. 2014). A polysaccharide and an alkaloid related to increased macrophage activity were isolated from *M. alba* L. fruit extracts. *M. alba* L. fruit water extracts primarily induced the production of pro-inflammatory substances, in model organisms, via TLR4 in immune cells. Water extracts are effective in pathogen defence and tumor suppression by enhancing macrophage activity. Based on our literature review on the bioactivity of *M. alba* L. fruit extracts, particularly in relation to their immunity enhancement activity, we anticipate that *M. alba*-derived pharmaceuticals will have excellent potential in future medical research (Chang, Koo, and Kim 2021).

From the fruit of the plant Daphniphyllaceae approximately 6 alkaloids were found by using the chemical transformation method where two compounds were new (Toda et al. 1974). The alkaloids derived from this is widely studied nowadays due to their unique biological pathway (Liang et al. 2021). The following alkaloid was determined by using NDMR and mass spectroscopy both are spectroscopic analyses. In green tomatoes, Glycoalkaloids are isolated some of them are solanine, a-tomatine, and dehydrotomatine they are very helpful as they protect the plant from any kind of fungal infection or bacteria attack (Kozukue et al. 2004). 1-methyl-1,2,3,4-tetrahydro-β-carboline may appear in tree-tomato and kiwi. Fruit-occurring tetrahydro-β-carboline alkaloids acted as antioxidants and free radical scavengers in the ABTS assay when compared with ascorbic acid and Trolox. This suggests that tetrahydro-β-carboline alkaloids might act as antioxidants when absorbed and accumulated in the body, contributing to the antioxidant effect of fruit products containing these compounds (Kozukue et al. 2004). In Kiwi-fruit alkaloids are found in roots and shows antitumor, antioxidant, antiviral, detoxifying, antidiuretic, anti-hepatitis and hemostatic activities (Olatunde Yycl and Jianping 2019). Fruit of Carambola were reported to have two new types of alkaloids, that is, tetrahydroisoquinoline having antioxidant properties (Yang et al. 2014). The Tree Tomato has tropane alkaloids in it mostly found in most of the solanaceous family (Bohs 1989). The bark of the elephant apple is blessed with antioxidant activities which are due to the presence of phenolic compounds like alkaloids in its bark (Pandey, Singh, et al. 2018). In the seed, pulp and rind of rambutan alkaloids were found using the gravimetric method proving its consumption helps in maintaining a good lifestyle (Fila et al. 2012). Many of the phenolic content heightens the anti-oxidant properties of Bayberry and one of them is alkaloids and phytic acids (Bhatt, Rawat, and Rawal 2020). During metabolite profiling of the germinating seed of mangosteen, alkaloids were found and held responsible for carbon utilization, seed protection and the middle germination period was increased (Mazlan et al. 2019). There were 33 alkaloids in the leaves, roots and flowers of the loquat and are all contributing to as medicinal ingredients of the fruit (Yunsheng Wang 2021). In silver berry, a unique type of alkaloid is found, that is, beta-carboline (Slywka and Locock 1969). In the durian, the bark had alkaloids that had anti-diabetic activity (Romatua Aruan et al. 2019). The leaves of the permission fruit have alkaloids that are responsible for its antimicrobial activities of it (Ji et al. 2006). The longan fruits by-product are alkaloids and polyphenols widely known to have antioxidant activities, nitrite scavenging activities in simulated gastric fluid and anti-hyperglycemic activities in vitro (Tang, He, et al. 2019). Seed of Pulasan contain alkaloids and steroids and shows antioxidant properties (Hairunisa et al. 2021). The fruit juice of pepino has alkaloids and has antiulcer activity (Nyi Mekar Saptarini 2011). The fruit of sapodilla has alkaloids and no saponin and inhibits the growth of salmonella typhi (Nyi Mekar Saptarini 2011). Alkaloids extracted from tropical fruits hold many antioxidants and medicinal properties.

Terpenoids

Up until now, we have seen that fruits contain many anti-oxidant compounds that show medicinal properties among them is Terpenoids. They are necessarily found in the form of monoterpenes (like limonene, carvone or carveol), diterpenes (including the retinoids), and tetraterpenes (which include all different carotenoids like α- and β-carotene, lutein, lycopene, zeaxanthine and cryptoxanthine) (Wagner and Elmadfa 2003). Earlier terpenoids came into force to specify a name for the hydrocarbons occurring in Turpentine (Dev 1989). These are secondary metabolite found in plant however among all these has the most diverse function and structure (Kim et al. 2021) Bioinformatics tools have been very helpful in the advancement or making the process of synthesis of terpenoids easy and flexible and available to all (Zwenger and Basu 2008). In the fruits of a tropical plant, *Aphanamixis grandifolia* with the combination of a bunch of methods that would be Single-crystal X-ray diffraction studies, the Mosher ester method, $Mo_2(OAc)_4$-induced electronic circular dichroism (ECD) data approximately 12 known and 5 unknown compounds were isolated (Zhang et al. 2013). From the fruits of Vitex *trifolia* L. seven diterpenoids along with 2 new were isolated with the help of an extensive spectroscopic method (Wu et al. 2009). In passion fruit through a biological pathway, a volatile terpenoid is formed via the precursor, that is, nonvolatile and is glycosidic. And was isolated by the method of distillation extraction or capillary method (Wu et al. 2009). Plant antioxidants are composed of a broad variety of different substances like ascorbic acid and tocopherols, polyphenolic compounds, or terpenoids. They perform several important functions in plants and humans (e.g. carotenoids function as accessory pigments for light-harvesting and provide photoprotection and pigmentation in plants). Monoterpenes and diterpenes, which are the main components of essential oils, act as allelopathic agents, attractants in plant–plant or plant–pathogen/herbivore interactions or repellents (Singh and Sharma 2015). A study upon mango extracts showed that biosynthesis of Terpenoids was made easy by utilizing co-factors such as Fe, Mn, Mg ions (Vithana, Singh, and Johnson 2018). Flower of Kiwi-fruit has two volatile terpenes as of now discovered it showed that the both terpenes were responsible for major floral sesquiterpene volatiles observed in both male and female (Nieuwenhuizen et al. 2009). In the leaves of Carambola there are traces of Terpenoids which further is helps in anti-ulcer activities (Pal et al. 2019). In species of tree tomato mostly there are non-terpenoid alcoholic compounds in its fruits and are present in a good amount (Wong and Wong 1997). The anti-leukemiatic potential of leaves, bark, and fruit of elephant apple is due to flavonoids and terpenoids (Khan 2017). When the phytochemical analysis was done of 70% of rambutan seeds had terpenoids as their major component due to which they have the lowest cytotoxic activity (Soeng et al. 2015). Bayberry shows anti-oxidant properties as analyzed by genome sequencing of it and when sis the homology of genes terpenoids were one of the constituents responsible for the same (Ren et al. 2019). The

fruit of mangosteen has terpenoids in the outer part of it, pericarp along with the yellow latex of stem bark (Dorly, Tjitrosemito, and Poerwanto 2008). Cell suspension of loquat has pentacyclic terpenoids in a great number and is a possible candidate for pharmaceutical value (Liu et al. 2016). Leaves of permission have terpenoids and flavonoids that contribute to the treatment of ischemia stroke, angina, internal hemorrhage, hypertension, atherosclerosis and some infectious diseases, and so on (Xie et al. 2015) Peel of longan has terpenoids which has anti-cancerous and anti-bacterial properties against prostate cancer (He et al. 2016). The growth and maturation of jabuticaba are done with the help of terpenoid compounds (Fortes et al. 2011). The predominant aroma volatiles is 3-methyl-3-butenyl acetate and 3-methyl-2-butenyl acetate from the terpenoid pathway in pepino (Contreras et al. 2019). In sapodilla fruit extractant has terpenoid which shows antibacterial properties (Idrus et al. 2019). Terpenoids whenever associated with any fruits have shown a medicinal property.

Researchers have explored the bioactive potential of the MTFs with the aid of different conventional and novel extraction techniques with the different solvent systems, further, the bioactives are quantified with various chromatographic techniques. Though limited evidence is available for the application of different emerging extraction techniques (e.g. ultrasound, microwave, supercritical, pressurized liquid assisted methods) and novel solvent (e.g. deep eutectic solvents) on the bioactive exploration of MTFs. Limited studies are available on the phytochemical potential of the waste part (peel, seeds and non-edible portions) of the MTFs.

Health benefits and medicinal properties of minor tropical fruits of Indian subcontinents

Maybe due to the presence of the beneficial bioactive compounds the minor tropical fruits exhibit immense health benefits (Figure 2).

Anti-oxidants

Kiwifruit is rich in Vitamin C, which is the primary cellular antioxidant and cytoprotector. Compounds like polyphenols which are electron-donating in nature, aromatic in structure cause the antioxidant nature and can be assayed through FRAP (Ferric reducing antioxidant power) (Hunter et al. 2011). It has bioactive compounds like tannins, flavonols and polyphenols that have radical degradation and scavenging abilities (Kim et al. 2020; Hunter et al. 2011). Researchers studied that consumption of kiwifruit juice has the scavenging capability for reactive oxygen species in human plasma and a larger serving linearly correlated with increased plasma antioxidant capability, accompanied with the fact that kiwi fruit can prevent oxidative stress, Lutqua also has antioxidant properties due to the presence of natural compounds like ascorbic acid, curcumin, mannitol, gallic acid, and lipoic acid. This activity can be most favorably be assayed by the DPPH method (Goyal, Middha, and Usha 2020).The phenols present in lutqua help to neutralize as well as absorb the free radicals present (Amudha). Carambola is a wild native fruit grown in the Asian subregion specially India which shows a phenolic content related antioxidant capacity (R^2 = 0.960 positive correlation) (Sharma, Handique, and Devi 2015). The carambola fruit has been isolated and crude extracted to produce sterols and flavone glycosides, whose antioxidant capacity is measured using the DPPH, FRAP assays. It has ethyl acetate and n butanol which show a great result with IC50 values being 90.92 and 124.48 µg/mL, respectively. FRAP showed an ascorbic acid equivalent of 135.64 and 125.12 as well as a positive correlation with phenol and flavonoid content (Cabrini et al. 2011). Tree tomato has a high Vitamin C content occurring in the range of 25–30 mg/100g FW. Vitamin C is a water-soluble, oxygen scavenging, reducing agent. The total oxygen scavenging capacity of tree tomato is multi-fold due to the additional presence of anthocyanins in it (Mutalib et al. 2017). The water and ethanol extract of tree tomato has high antioxidant, scavenging, phenolic and ferric reducing capability with flavonoid concentrations as well. These studies showed a positive correlation between the properties and the chemical constituency (Atiqah, Maisarah, and Asmah 2014). Elephant apple is a fruit found in the northeastern regions of India, with rich nutrient properties and uses as an antimicrobial, antimutagenic and antioxidant activity (Nayak, Rayaguru, and Mishra 2016). It has proanthocyanidin with bioactive traits, assays proved its capability to be antioxidant with high values of oxygen scavenging and FRAP (Fu et al. 2015). The epicarp of Rambutan has an antioxidant effect due to the radical scavenging capacity of phenolic compounds such as flavonoids, polyphenols and tannins (Chingsuwanrote et al. 2016). Phenols are antioxidants due to the redox potentials and can adsorb as well as neutralize the adsorbed nutrients like singlet, triplet oxygen or even peroxide decomposition. The DPPH oxygen scavenging activity was linearly correlated with the increasing concentration of the extract of the fruit (Nethaji et al. 2015). Bayberry has many different cultivars out of which five were studied by and revealed the presence of anthocyanin, flavonols like quercetin and myricetin, phenols like gallic acid and protocatechuic acid, other phenolic acids like vanillic, caffeic, p-coumaric, ferulic acid, and chlorogenic acid. There was a positive relationship between the antioxidant activity and total phenolic, anthocyanins content (Zhou et al. 2009). Its main organic acid is Citric acid positive correlated with the assays (Zhang, Zhao, et al. 2015). Results revealed significant variation in total phenolic and flavonoid contents across populations (Rawat et al. 2011). Mangosteen can control oxidative reactions under in-vitro conditions and comparability with commercially present antioxidants. The oligomeric proanthocyanins are excellent scavengers of reactive oxygen with high ORAC values (Suttirak and Manurakchinakorn 2014). Experiments have shown that extracts of mangosteen have antioxidant characteristics. The pericarp is a source of xanthones and other bioactive substances (Pedraza-Chaverri et al. 2008). The biological activities of the purified compounds from various parts of Bhawa have shown antioxidant properties. The β-carotene-linoleate-model system showed antioxidant

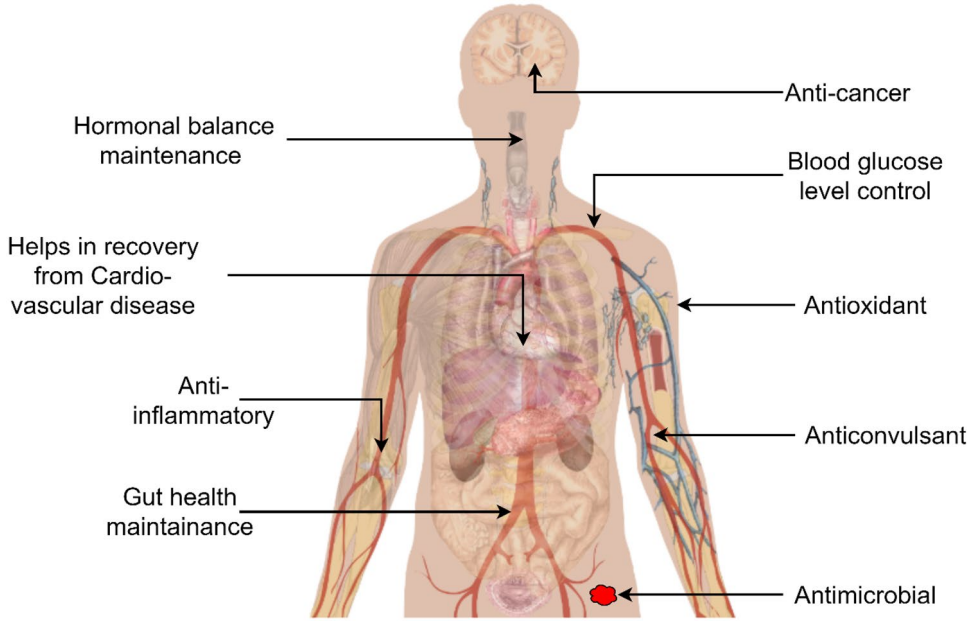


Figure 2. Health benefits of minor tropical fruits.

activity, respectively, however, at lower concentrations, the radical scavenging activity was measured through the DPPH method (Negi, Jayaprakasha, and Jena 2010). Loquats have various phenolic compounds identified in the pulp and peel of the fruit, antioxidant activity being tested by DPPH, FRAP and ABTS assays. The peel is a better antioxidant in nature and co-related with the high phenolic content (Zhang, Zhao, et al. 2015). Silver berry has phytochemicals that are antioxidant with high concentrations of polyphenolic contents, sugars, and vitamin C, as well as linoleic acids. It showed antioxidant nature with better scavenging ability as compared to ascorbic acid at lower as well as higher concentration as well as its ethanol extract showing high superoxide dismutase like activity (Shin, Hong, and Yoon 2008). Durian is an exotic fruit of south-eastern Asia with studied antioxidant activities as well as displayed antioxidant activities against undifferentiated U937 monocyte like cells induced by hydrogen peroxide oxidative stress. It had a suppressive effect on reactive oxygen species formation (Shin, Hong, and Yoon 2008). The leaves and extracts of persimmon are antioxidants with the individual steps of the process affecting the final product (Martínez-Las Heras et al. 2014). Methods such as beta carotene bleaching method, superoxide anion radicals by methanol extract, DPPH radical scavenging confirm the antioxidant capacity of natural source persimmon fruits (Sakanaka, Tachibana, and Okada 2005). The extracts of Longan were studied under DPPH radical scavenging methods, hydroxyl assays and reducing power and showed superior results in the study as compared to synthetic antioxidants (Pan et al. 2008). The logan pericarp also showed reducing activity (Huang et al. 2012). Water apple was studied for its antioxidant activity using β-carotene bleaching and the ABTS radical cation assay resulting in high percentage assays and high antioxidant activity, positively correlated with the bleaching assay. Its leaf extract shows various other pharmacological properties and antioxidant properties in vitro by protecting human keratinocytes (HaCaT cells) against UVA damage, good protection against oxidative stress, free radicals, and could be a good candidate for treating oxidative stress-related diseases (Sobeh et al. 2018). The peels, seeds and leaves of the pulsan have antioxidant nature, positively depicted by DPPH assay with the ethanol extract of leaves having the highest antioxidant activity with the value 20.99 µg/mL (very strong antioxidant), indicating its potential as a source of natural antioxidants (Hairunisa et al. 2021). Indian gooseberry extracts showed 86.4% antioxidant activities when evaluated by the β-carotene bleaching method (Mayachiew and Devahastin 2008). Its actions are a result of its high ascorbic acid content, which acts as a redox buffer reducing and neutralizing reactive oxygen species (Goel and Agarwal 2020). Guava fruit extracts have high amounts of antioxidants with non-peeled fruits having higher total phenol and ascorbic acid content testes successfully by DPPH and FRAP assays (Lim and Tee 2006). In lychee, the presence of compounds like phenols flavonoids and condensed tannins contribute to the antioxidant nature of lychee estimated with Trolox equivalent antioxidant capacity and (DPPH) radical-scavenging assay (Liu et al. 2009). Annona cherimola is an exotic fruit from the Andean highlands in western South America. The fruit skin, flesh and juice have antioxidant capacity confirmed using the oxygen radical absorbance capacity (ORAC) assay, HT-29 (colon cancer) cell line antioxidant uptake in presence of Annona juice (Gupta-Elera et al. 2011). Organic extracts from its pulp have powerful antioxidant and ferric reducing power activities as well as a great decrease in lipid peroxidation and cytoprotective effects against strong oxidants (Barreca et al. 2011). Pitaya peel is rich in betalains, a phenolic compound with antioxidant activity (Mello et al. 2014). Sapodilla pulp and peel has antioxidant activity (Woo et al. 2013), evaluated antioxidant capacity using Ferric Reducing Antioxidant Power

(FRAP) and 1,1-Diphenyl-2-Picrylhydrazyl (DPPH) assays (Murnisyazwani and Rabeta 2019). Pepinos either ripe or unripe have antioxidant activity and are abundant in phenols, flavonoid content. The antioxidant potency is being positively investigated by (DPPH), ABTS, hydroxyl radical scavenging, ferric reducing antioxidant power (FRAP), and lipid peroxidation tests (Sudha et al. 2012). The antioxidant capacity of Jaboticaba is studied in vitro and in vivo models. Phenolic compounds, total anthocyanins, flavonoids and antioxidant capacity (DPPH, FRAP, ABTS, and ORAC assays) (Lenquiste et al. 2015). The jackfruit seed extracts show the percentage inhibition of DPPH radicals (Jagtap et al. 2011). It is an underutilized edible fruit in the tropics and subtropics with phenolic and flavonoid contents and antioxidant properties (Gupta et al. 2011).

Anti-cancer

The presence of various phytocompounds like minerals, caretoinds, oils, nutrients, fibers, polyphenols in subtropical fruits helps in providing various health properties especially when we talk about cancer. Cancer is one of the most abundant and dangerous diseases found in the human race. Scientists are working on various domains and finding different ways to conquer this disease (Pereira-Netto 2018, Kumoro, Alhanif, and Wardhani 2020). Fruit Components specially having polymethoxyflavones are identified to play an important role in the treatment of cancer disease (Li et al. 2009). Researchers found that citrus limonoids which include limonin oxime, obacunone glucoside, limonin, nomilinic acid glucoside have antiproliferative potential against breast cancer line MCF-7. Similarly, there are numerous more phytocompounds present in different plants which exhibit anti-cancer properties (Cirmi et al. 2017, Gyawali and Kim 2014).

Emblic is also known as Indian gooseberry and show various medicinal properties. Aqueous extract of emblic is used in the various treatment of cancer as its extract has the potential of inhibiting the growth of various carcinomas specially for lung cancer and hepatocellular carcinoma (Bhattacharya et al. 2007).

Passion fruit has a high content of bioactive compounds. Ballesteros-vivas investigated the antiproliferative activity of passion fruit against colon cancer cell line HT-29. They showed the potential of passion fruit in blocking HT-29 cells in the S phase of the cell cycle. This was accomplished by inactivating the cancer cell signaling pathway named FAT10 (Ballesteros-Vivas et al. 2020). Another bioactive compound chrysin was analyzed as attenuates the expression of nuclear factor-kB, cyclooxygenase-2 and nuclear antigen which results in regression of cancer cell growth (Kasala et al. 2016). Guava has a very important anticarcinogenic property. Many researchers did various analyses on guava extracts and concluded that quercetin glycosides and guavinosides have the potential to inhibit the cell proliferation of various carcinoma like breast carcinoma, gastric carcinoma and lung carcinoma (Feng et al. 2015). The researcher also worked on guava pulp and demonstrated the anticarcinogenic potential in MCF-7 and MDA-MB-435 cancer cell line. They concluded that guava pulp extracts attenuate the cell viability of cancer cell lines, causing a reduction in cell count at G1 phase of the cell cycle and increased apoptosis (Correa et al. 2020). Sapota exhibits anticancer properties due to the presence of phenolic compounds. Methyol 4-o-galloylchlorogenate extracted from sapota plant is used for examination of cytotoxicity of human colon cancer cells (Alrashood et al. 2020). Methanolic extract of sapota fruit has the potential of inducing apoptosis in B cell leukemia NALM6 and mylogenous leukemia K562 cells (Srivastava et al. 2015). Kiwifruit is highly efficient against carcinogens. It works against cancer by becoming a cytotoxic element for various cancer cells (Lippi and Mattiuzzi 2020). Kiwi has a high quantity of dietary fiber. These fibers help in reducing the occurrence of colon cancer. They contain various antimutagenic components which help in the prevention of mutations in genes that in future can initiate the process of cancer (He et al. 2019). Kiwi fruit has catechin, this compound is responsible for the reduction of toxicity present in anti-cancerous agents. They do this process by narrowing the proliferation of bone marrow. A phytochemical named lutein which is present in the fruit pulp of kiwi helps in attenuating the effect of prostate cancer (el Azab and Mostafa 2021). Loquat is highly recommended for anticancerous activities against various cancer. Loquat leaves show cytotoxic effects against triple-negative breast cancer cell lines, lung carcinoma and cervical cancer (Kang et al. 2006). Oleanolic acid and ursolic acid derived from loquat leaves suppress the proliferation of human lymphoid cancerous cells (Liu, Du, and Yu 2019). Procyanidin oligomers present loquat demonstrates cytotoxic effects against MDA-MB-231 cells line (You et al. 2016). Hydrophilic loquat extracts show anticancer properties against meth-A-fibrosarcoma cells through immunomodulation activity (Alshaker et al. 2011). Apart from this, loquat seed extract shows anti-cancerous effects via inhibition of several migratory cancerous cells of the human breast (Kim and Shin 2009). Research theories revealed that carambola (star fruit) was studied for biotransformation of dihydro-epi-deoxyarteanniun B. 3-α-hydroxydihydro-epideoxyarteannuin mixed with this 7α-hydroxy-dihydro-epideoxyarteannuin B in cell cultures was used on cancerous cell lines. The result demonstrates that Carambola cells have the capacity for reducing the proliferation power of various cells lines like HeLa cells. They inhibit the effects of tumor cells and the inhibitory concentration of 3-α-hydroxydihydro-epideoxyarteannuin and 7α-hydroxy-dihydro-epideoxyarteannuin B was $59.29 \pm 0.99\,\mu mol/mL$ and $40.63 \pm 1.45\,\mu mol/mL$ respectively (Xingyi Li 2012). Elephant apple extract contains botulinic acid which inhibits the growth K562 tumor cells and shows the inhibitory concentration of 1C50 6.25 µg/ml. This acid results in the death of cancerous cells via induction of apoptosis. This fruit is already used on various cancer cell lines like HL60, U937, and K562. They show cytotoxic activities against tumor cells and inhibit their growth. The fruit elephant apple show anti-leukemic activity and it contain a compound known as dimethylbenzene(α)anthracene (DMBA)

which inhibit the growth of melanoma cells (Boparai et al. 2016; Barua, Yasmin, and Buragohain 2018). Pitaya peel has antiproliferative activity against tumor cells which help in the inhibition of tumor growth (Guimarães et al. 2017). Pitaya peels also demonstrate cytotoxic activity against various cancer cells like B cap-37, PC3 and human gastric cancer cell line (Luo et al. 2014). The fruit pulp extract of pitaya is effective against Breast cancer. They decreased the proliferation potential of breast cancer cells and induces apoptosis (Wu et al. 2006). The various kind of passion fruit extracts is examined for anticancerous potential. These extracts are highly cytotoxic specially against HepG2, ADR5000, CCRF-CEM and HCT116 cancer cell lines (Ramírez et al. 2017). Studies revealed that ethanolic extract contains polysaccharides which are responsible for inhibiting the functioning of matrix-metalloprotease (MMP-2) (Puricelli et al. 2003). Yellow passion fruit shows a high inhibition rate thereby increasing the life span. Oral administration of passion fruit extracts inhibits the growth of sarcoma cells (He et al. 2020). Rambutan is a tropical fruit that is majorly cultivated in the southeast part of India. The anticancer activity is examined in methanol extract of rambutan fruit for breast cancer cell lines, HeLa cells and ostecarcoma cancer cells. The results were effective as they inhibited the growth and activity of cancer cells. The seeds and pericarp of rambutan also show their activity toward cancer cells by using DPPH and ABTS radical methods. Studies revealed that methanol extract can be used for drug delivery systems (Perumal et al. 2021; Khaizil, Nik, and Mohd 2017). The pericarp and stem of mangosteen contain α-Mangostin which induces the cell death of D-17 osteosarcoma cells and carcinoma cell lines (Krajarng et al. 2012). Studies revealed that α-Mangostin also induces cell death through caspase-independent apoptosis by releasing endonuclease G from mitochondria (Aisha et al. 2012). It also shows cytotoxic effects against several cancer cell lines. They also cause cell death of the breast cancer cell line via apoptosis. It also decreases the growth of cancer cells and inhibits their further proliferation (Johnson et al. 2012). In vivo experiments were examined by using the leaf extract of silver berry, as a result, the extract showed potential for inhibiting the growth of the human hepatoma Hepg2 cell line. This was in a dose-dependent manner. They were also used for suppressing the H22 hepatoma cells. Methanol extract of silver berry has the potential for improving the pathological observation of tumor tissue (Tehranizadeh, Baratian, and Hosseinzadeh 2016). The peel extract of Durian fruit is used for inhibiting the growth of cancer cells. Durian fruits contain polyphenols which are responsible for inhibiting the proliferative function of the cancer cell. They also help in protecting nitic-oxide in MCF-7 breast cancer cell line (Jayakumar and Kanthimathi 2011, Aziz and Mhd Jalil 2019). Logan fruit pulp contains LPS1 polysaccharide which is responsible for lowering the growth of hepatoma cancer cells. It shows positive effects against it by using a dose-dependent manner. This happens due to the immunomodulatory effect of (1→6)-α-d-glucan (Zhu et al. 2013). Another polysaccharide named LP1, show high antitumor activities against several cancer cell line with an inhibition percentage of 40%, concertation of 40 mg/l (Meng et al. 2014). The extracts of Water apple is used against breast cancer cell line, colon cancer cell lines, lung cancer cell lines and liver cancer cell lines. The methanolic leaf extract has the potential for reducing the functionality of microtubule-associated protein1 light chain 3. It also reduces the expression of beclin telomerase and inhibits the antiapoptotic gene expressions (Mahomoodally et al. 2020). Annona is well-known source for antitumor activity and cytotoxic compounds. The Annona seeds contain annomolin and annocherimolin. These two compounds are responsible for inhibiting the growth of cancer cells. This was examined in breast cancer and prostate cancer (Arun Jyothi et al. 2011). The seed extract of jaboticaba is used for inhibiting the growth of oral carcinoma. The seed extract contains some phenolic compounds which help in reducing the progression of cancer cells. Gallic acid present in jaboticaba fruit show anti-cancer activity. This was examined in prostrate and breast cancer cell lines (Wang, Qu, et al. 2014).

Anti-diabetic

Several tropical fruits have been used as traditional medicine for the treatment of the chronic metabolic disorder, diabetes, correctly justified by the presence of antidiabetic bioactive compounds (Beidokhti and Jäger 2017).

Kiwi fruit has the potential to inhibit the action of alpha amylase which breaks starch into glucose, describing its antidiabetic role (Patel, Padse, and Ingole 2015). This fruit can be consumed by patients suffering from type 2 diabetes mellitus because of its favorable low glycemic index (Satpal et al. 2021). The lutqua leaf has hypoglycemic effect as observed in diabetic rats (induced by alloxan) and reduced the levels up to 50.06% and was comparable with the synthetic drug metfromin (Goyal, Middha, and Usha 2020). The hydroalcoholic extract of leaves of carambola was examined on rats and showed a significant decrease in the levels of fasting glucose (Ferreira et al. 2008). The flavonoid glycosides act as insulin signaling inhibitors and were identified to be potential generators of hypoglycemic effect in hyperglycemic rats, they can reduce the glycogen content with insulin mimicking activity (Cazarolli et al. 2012). Its hypoglycemic effect can be attributed to its high fiber level and other phytocompounds (Lakmal et al. 2021). Tree tomato is rich in phenolic compounds specially chlorogenic acid and shows the health benefit like antidiabetic activities with a reduction in blood glucose levels (Diep, Rush, and Yoo 2020). Tamarillo is also rich in flavonoids with efficient antidiabetic properties. Tree tomato can reduce blood glucose levels in rats with intraperitoneal alloxan-induced diabetes with favorable results of tree tomato as an anti hyperglycemic (Yuliani 2018). This fruit was studied in the diabetic Wistar rats induced by the drug streptozocin and nicotinamide, a significant reduction in blood glucose levels was observed with potential increased secretion of insulin from the cells of islet of Langerhans as well as regeneration of cells (Talukdar et al. 2012). Rambutan fruits also show

a high level of in vivo and in vitro antiglycation activities, streptozotocin-induced diabetes in a mouse model was taken and the rambutan phenolic peel extract helped reduce the fasting blood glucose levels as well as serum levels. The activity of enzymes like superoxide dismutase and glutathione peroxidase was also increased (Ma et al. 2017). Its extract can regenerate functional pancreatic beta cells as well as inhibit carbohydrate hydrolyzing enzymes like alpha-glucosidase and amylase (Palanisamy et al. 2011). It has phenols or volatile constituents that lower glucose levels (Akhtar, Ismail, and Shaari 2017).

Bay berry has Compounds like polyphenols, flavonols and proanthocyanidins. It can reduce fasting glucose levels, increase glucose tolerance levels and insulin sensitivity in diabetic mice as well as decreased levels of leptin, glucagon amd triglycerides which highlighted it potential use as an antidiabetic approach (Liu et al. 2020). Bayberry cultivars with high C-3-Glu and Q-3-Glys have great usage as potential antihyperglycemics (Zhang, Zhao, et al. 2015). The extracts of bayberry leaves can inhibit alpha amylase by interacting with amino acids tyrosine and tryptophan by forming hydrogen and Vander wall bonds (Wang et al. 2020). Mangosteen pericarp has xanthone compounds that recognize and restore the damaged pancreatic beta cells for optimum insulin release. Nano sponges loaded with these compounds were used as an antidiabetic therapeutic with high inhibition of alpha-glucosidase (Usman et al. 2021). The ethanolic extracts of this fruit can lower high blood glucose sugar in streptozotocin-induced diabetic rats (Karim and Tangpong 2018). The leaf extract of bhawa have bioactive compounds that can inhibit alpha-glucosidase enzyme with xanthone derivatives and promotion of glucose consumption by 3T3-L1 cells (Phukhatmuen et al. 2020). The hexane extract of loquat has high alpha-amylase inhibition activity (Mogole, Omwoyo, and Mtunzi 2020). Phytocompound sesquiterpene has been isolated from dried loquat leaves which might have hypoglycemic activity comparable to synthetic drug metformin but acting on different metabolic pathways (Wahjudi et al. 2011). Silver berry fruit is rich in flavonols and ellagitannins with anti-glycation and enzyme inhibition capability (like aldol reductase). Its bioactive compounds can lower the risk of type 2 diabetes as well as obesity (Spínola et al. 2019). The extracts of leaf of durian have flavonoids and steroids with a role in the prevention of diabetes (Aruan et al. 2019). Alloxan induced diabetic rats showed a significant decrease in the level of blood glucose by eating durian fruit (Muhtadi, Primarianti, and Sujono 2015). The studies suggest that the presence of polyphenols in durian are responsible for its antidiabetic properties (Chigurupati 2021). Streptozotocin-induced diabetic rats showed the influence of the phytochemicals from persimmon. It has dietary fibers that reduce lipoproteins and antioxidants with antidiabetic properties (Lee, Chung, and Lee 2006). Longan fruit has a hypoglycemic effect which can inhibit alpha-glucosidase and beta-galactosidase activities. It has phenolic compounds like gallic and ellagic acid (Li et al. 2016). Alloxan induced diabetes in male Wistar rats were treated with passion fruit leaf extract and showed improved glycaemic control and reduce glycation (de Souza et al. 2012). Peel and seeds of passion fruit can reduce oxidative stress in streptozotocin-induced diabetes (Kawasoe et al. 2021). Its leaf extract has protective activity against free radicals, low pro-oxidant nature with inhibition of alpha glycosidase and alpha-amylase, aldol reductase (Palanisamy and Manaharan 2013). This fruit is rich in gallic acid, ellagic acid and corilagin which have antidiabetic effects through their antioxidant and free radical scavenging activities. It can prevent and even prevent hyperglycemia, cardiac complications (D'souza et al. 2014). Guava is phenol rich which contributes to its antihyperglycemic and antihyperlipidemic activities (Díaz-de-Cerio et al. 2016). The polyphenols from guava peel and pulp, seeds were extracted and compared to the control group of diabetic mice suggesting the addition of 200–250 mg/kg of polyphenol extracts as a substitute to the synthetic antidiabetic drugs (Shabbir et al. 2020). Lychee fruit has oligonol which can aid in the health improvement of streptozotocin-induced diabetic rats and improved pancreatic damage (Park and Lee 2018). Oligonol can reduce glucose and insulin levels with a decreased amount of fat content (Liu et al. 2020). The leaves of Annona have antidiabetic properties, its graded doses were given to streptozotocin–nicotinamide induced diabetic rats which revealed a lower plasma glucose level, serum level (Shirwaikar et al. 2004). It can increase the activity of plasma insulin and control diabetes complications (Kaleem et al. 2006). It has a high phenolic content and can be used for the management of diabetes promisingly (Adefegha, Oyeleye, and Oboh 2015). Pitaya extracts are useful for curing aortic stiffness in STZ induced diabetic rats (Joshi and Prabhakar 2020). It can retain insulin longer due to the presence of cAMP phosphodiesterase (Prabhakar and Doble 2011). Phyto compounds obtained from it can reduce blood sugar levels. Ajie et al. have mentioned flavonoid content mediating hypoglycemic action. Thus, proving that pitaya consumption can keep control of diabetes in patients (Joshi and Prabhakar 2020). The seeds, leaves and roots of sapodilla have hypoglycemic activity because of the presence of saponins (Bano and Ahmed 2017). Male Wistar rats showed lower levels of glycemia and insulin through the consumption of sapodilla (Barbalho et al. 2015). Pepino fruit has an inhibitory effect on the enzyme's alpha glycosidase and alpha-amylase with significant antidiabetic activity on animals at 500 mg/kg dose (Orhan et al. 2014). Jaboticaba's polyphenol extract has alpha-glucosidase inhibition with better results than acarbose (Lin et al. 2019). It modulates the insulin signal and glycogen inhibition with glycogen synthase kinase (Benvenutti, Zielinski, and Ferreira 2021). Jackfruit extract has prenylflavonoids, hydroxycinnamic acids and glycosides (BaoMei et al. 2019). These phytocompounds can reduce blood sugar levels and be successful in alloxan-induced diabetic rats as well as Streptozotocin-induced diabetic rats and were comparable to metformin (Asmaliani and Iwo 2016).

Anti-microbial

Subtropical plants like mango, pomegranate, pineapple, papaya, banana, tomato etc are examined to check their

anti-microbial potential. Researchers studied numerous factors and colluded various results which prove that subtropical plants have high anti-microbial potential and can be used against bacteria, microbes and fungi. Methanolic and chloroform extracts of guava leaves show antimicrobial activities against *Pseudomonas aeruginosa, Shigella spp., Escherichia coli and Staphylococcus aureus*. They attenuate the amount of cough as methanolic extract show anti-cough activity. They also suppress the growth of bacteria. Flavonoids like terpinene and pinene are present in the aqueous extract of guava leaves help in suppressing the growth of pathogenic bacteria and are used in cough sirup medicines (Yahaya et al. 2019). Alcohol fruit extract of guava show antimicrobial activities against *Enteroaggregative E coli, Klebsiella, Enterococcus faecalis and S. aureus*. The fruit extract was mixed with 250 ml of 99% methanol (Kabir et al. 2017). Researchers prepared lychee seed extract by using HCl and NaCl and was used to determine the inhibitory effect against pathogenic bacteria. The seed extract contains a higher amount of protein content (Bhat and Al-Daihan 2014). Litchi seed extract also shows antimicrobial effects against *B. substiles, P. aureus, E. coli, Klebsiella pneumoniae, S. aureus*. The seed extract suppresses the growth of bacterial strain and also help in curing the harmful effects caused by these pathogenic bacteria (Zhao et al. 2020). Jackfruit leaf extract has been reported for demonstrating antimicrobial activities against gram-positive and gram-negative bacteria. They also show inhibitory effects against many fungi molds. Cell viability assay, MTT assay, hemolysis assay and agar well disk diffusion assays were used for the investigation of antimicrobial activity of jackfruit (Zhou et al. 2020). The ripe part of jackfruit is used in treating cough caused by rhino virus and in other bacterial diseases. The powder of jackfruit's seed is used in antifungal creams (Vázquez-González, Ragazzo-Sánchez, and Calderón-Santoyo 2020). Many researchers also reported that leave extract and seed extract of jackfruit is used as an alternative to antibiotics against many pathogenic bacteria (Eve et al. 2020). Kiwi fruit show antimicrobial activity against *S.aurues* and *L. monocytogenes*. The flesh polyphenols and peel of kiwifruit help in the inhibition of microbial growth. The concentration of peel was at 100 µg/mL – 13.7 ± 0.4 mm. Researchers found that gram positive bacteria were more inhibited by kiwi fruit in comparison to gram negative bacteria. As gram negative bacteria have a thick out membrane comprised of lipopolysaccharide which enables the entry of phenolic compounds (Alim et al. 2019). Researchers found that Carambola plant extract was highly active against many bacterial strains like - *E. coli, S. aureus, B. substiles, Pseudomonas aeruginosa, Klebsiella pneumoniae, Streptococcus mitis, Proteus vulgaris, Pseudomonas aeruginosa, Salmonella paratyph and S. typhi.* The leaves extract was majorly showing higher antimicrobial effects by inhibiting the growth of bacteria while seed extract was involved in lowering the cell proliferation of various fungus. But they also revealed that crude extract of carambola doesn't show a high effect against *Aspergillus niger* (Majhi, Satapathy, and Mishra 2019). Studies revealed that crude extract of elephant apple in n-hexane was used to determine the antibacterial activates against gram positive and gram-negative bacteria. The best anti-bacterial result was against E. Coli. The researcher took 7 fractions of extract and out of 7, only F fraction was not showing any effect against E. coli. Apart from this, fraction G and fraction D demonstrated the highest antibacterial activity (Bhagyasri et al. 2017). The bark extract of elephant apple was also used to demonstrate antimicrobial properties. N-hexane was mixed with bark extract and Dichlomethane which results in inhibition of microbial growth and as a result majority of the bacterial population couldn't grow further (Boparai et al. 2016b). The study revealed that pitaya peel has methanol which act against bacterial strains. The methanol extract from white flesh pitaya and red flesh pitaya has antimicrobial potential against *S. aureus, S. typhi, Klebsiella sp., P. aureus and Staphylococcus*. The methanolic extract from white pitaya is not much effective against suppressing the growth of bacteria while the extract is taken from red pitaya show a wide range of inhibition. The inhibition zones produced by red pitaya are effective and show high antimicrobial activity. Studies also revealed that pitaya extract can be used in various antimicrobial drugs as they developed frontline antimicrobial response in the human body (Luu et al. 2021, Khalili, Abdullah, and Manaf 2012). The pulp of passion fruit contains antibacterial, antiviral and antifungal properties. The peptide named 2S albumins present in passion fruit seeds show antifungal properties against *Fusarium oxysporum, Candida parapsilosis, Aspergillus fumigatus and Trichoderma harzianum* (Janzantti et al. 2012, Ribeiro et al. 2012). The methanol present in the epicarp of passion fruit has inhibitory effects against gram positive and gram-negative bacteria. They help in inhibiting the growth of bacteria and in some cases, they kill them. The inhibitory concentration ranges from 128 to 1024 µg/ml. This is due to the presence of bioactive compounds like sterols, triterpenes and polyphenols in methanol extract (Dzotam, Touani, and Kuete 2015, Pereira et al. 2019). Many studies have been carried out for validating the antimicrobial potential of Rambutan. Studies revealed that methanol and chloroform extract of rambutan peel extract is highly effective against several microbial strains like *Salmonella typhi, Bacillus cereus, Pseudomonas aeruginosa, Escherichia coli and Staphylococcus aureus* (Thitilertdecha, Teerawutgulrag, and Rakariyatham 2008). These extracts are not highly affected against *P. aeruginosa* but there was a researcher named Thitilertdecha who further took the seeds of Rambutan and tested against *P. aeruginosa* (Tadtong et al. 2011). As a result, the extract was successful in inhibiting the activity of the given strain. A study also reveals that yellow rambutan seeds methanol extract is more effective for inhibiting the activity of bacterial strains (Malini and Maheshkumar 2013). The seed and peel extract of bay berry fruit show microbial action against various microbes by creating a normal inhibition zone of 17.9 mm and 26.9 mm. The bark extract of bay berry is highly effective against microbes and is considered to be a strong anti-microbial specialist. It is also observed that aqueous concentrate shows strong effects against salt water shrimps (Panthari et al. 2012). Mangosteen contains various compounds like γ-mangostin, mangostanin and demethylcalabaxanthone which inhibits the effects of

Mycobacterium tuberculosis. α-Mangostin show its effects against Staphylococcus *aureus* and Enterococci. The methanol extract of mangosteen is used to inhibit the growth of various microbes (Ansori et al. 2020). The methanolic crude extract of silverberry fruits contains anti-microbial potential against E. coli and *S. aureus* (Khan et al. 2016). Leave extract of silver berry has the potential for inhibiting the growth of *Yersinia enterocolitica*. The soft extract of flowering tops is used against different strains of microbes for inhibiting the growth of microbes. It is also used against several fungal species except for *Candida albicans* (Okmen and Turkcan 2013). Durian fruits contain some active compounds which are responsible for inhibiting the microbial activities of several microbes. The research was occurred by using diffusion wells. Apart from this, there was another research study, durian fruit contains a bland zone against microbial species like E. coli. The bland zone was of 12.0 ± 1.00 mm (Basyuni et al. 2019).

Logan seed extract is highly used for inhibiting microbial growth of *S. aureus*, and *P. aeruginosa*. Apart from this, logan fruit contains gallic acid which is also responsible in inhibiting the growth of microbes and it also reduces the microbial activity of bacteria. Ethyl acetate derived from the aerial part of logan fruit has anti-HIV-1 potential (Shahrajabian, Sun, and Cheng 2019). The leave and seed extract of water apple was examined against various gram-positive and negative bacterial strains. It was investigated by using the paper disk diffusion method. The extract is dissolved in DMSO of 10%, as a result, the extract was successful in inhibiting the growth of bacteria (Habisukan et al. 2021). The leaves, flowers and fruit of Annona contain chemical compounds which are responsible for antimicrobial activity. Research studies revealed that leave extract has more antimicrobial functionality in comparison to other extracts. It shows a higher inhibition zone against *E. coli*. Methanolic extract of Annona show the antiviral property (Arun Jyothi et al. 2011). Studies reported that both leaves and bark extract of sapodilla reflects the potential of anti-microbial activities. Compounds like glycosides, flavonoids and terpenoids are responsible for antimicrobial activities. They inhibit the growth of gram positive and gram negetive microbes and reduce microbial activity (Maiyo et al. 2010). Extracts from bark, leaves, stems and flowers of pepino were used to evaluate their potential for antimicrobial activities. They are also used for the treatment of microbial diseases and wounds caused by microbes. Pepino contains terpenes and flavonoids which show anti-microbial properties. Leave extract reduces the growth of gram positive and negative bacteria (Olayemi 2012) Camu-camu juice extract of jaboticaba seed is examined for checking the anti-microbial activity on bacterial strains named: - *Escherichia coli, Staphylococcus aureus and Saccharomyces cerevisiae*. As a result, the extract was more effective against *S. aureus* due to the presence of lipophilic compounds in the extract. Hydro methanolic extract of leaves also represents anti-microbial activities against gram-positive and gram-negative bacteria (Myoda et al. 2010, Macedo-Costa et al. 2009).

Anti-inflammatory

We have already studied numerous medicinal properties of the sub-tropical plant. Some Subtropical plants are evaluated for demonstrating the anti-inflammatory effect. Plants like Mango, tomato, jackfruit, litchi, guava, pineapple, papaya, pomegranate and so on. show anti-inflammatory activity. They reduce the inflammation in the body and blocks certain substances that cause inflammation in the body. Some important plants showing anti-inflammatory effects are described in a subsequent section. Guava extract when mixed with ethyl acetate can stop thymus production and germ infection. It shows anti-viral properties and can enhance the expression of mRNA. The seed extract of guava has the potential for altering the expression of heme oxygenase –1 protein and can be used as an anti-inflammatory agent for skin (Jang et al. 2014). Guava extract when mixed with ethanol show an inhibitory effect and attenuates the manufacturing of nitric oxide and lipopolysaccharides. Thereby suppressing the E2 expression and showing anti-inflammatory power (Díaz-de-Cerio et al. 2017). Leave extract of guava mixed in ethyl acetate can minimize the expression of the antigen. They further stop the production of beta-hexosaminidase in RBL-2H3 cells and attenuate the expression of IL-4 mRNA. Phenols present in guava extract show an anti-inflammatory effect by blocking the expression of inflammatory agents (Felipe do Nascimento et al. 2021). The dose of guava extract is used for the treatment of lung inflammation (Flores et al. 2013). A study reported that litchi seeds contain peptide hydrolysates enzymes that have anti-inflammatory potential activities. The seed extract prepared by various filtration mechanisms was used on RAW macrophage cell and exhibited the downregulatory effect on inducible nitric oxide synthase and IL-6 (Saisavoey et al. 2018). Jackfruit contains polyphenols and flavonoids which show anti-inflammatory effects. They are inhibiting the release of pro-inflammatory cytokines, neutrophils, mast cells and macrophages which result in lowering the inflammation (Ranasinghe, Maduwanthi, and Marapana 2019). Two novel flavonoids named as heteroflavanones A and B was isolated from the root of jackfruit. The anti-inflammatory effect of these flavonoids was evaluated by determining the inhibitory effects on formation and release of pro-inflammatory LPS mediators (Swami et al. 2012). Carambola is also known as Star fruit is considered to have diverse medicinal effects. The leave extract of star fruit demonstrates anti-inflammatory effects. They also reduce ear edema inflammation (Cabrini et al. 2011). Star fruit juices contain flavonoids that attenuate the expression of IL-23 and nitric oxide. They also help in blocking the expression of inflammatory cytokines (Leelarungrayub et al. 2016). Leaves extract of Loquat is highly rich in ursolic acid which are responsible for anti-inflammatory activity. They show their effects on alveolar macrophages (Ge et al. 2009). Loquat seed extracts are mixed with various chemotherapy drugs like 5-fluorouracil which help in the inhibition of mucositis (Takuma et al. 2008). They show their effects in lowering the inflammation caused by various microbes present in hum gut. They help in lowering the increased level

of pro-inflammatory cytokinase like IL-8 and IL-10 which are responsible for cellular inflammation (Lee et al. 2008). Ethyl extract of Elephant apple present in stem bark demonstrates anti- inflammatory effects. Studies show that ethyl acetate extracts show peripheral and central analgesic effects on various animal models. Ethyl extract demonstrates significant activity in chronic inflammation which is induced by mixing formalin and carrageenan in bark extract. It is also used to treat kin inflammation. They also help in healing the wounds caused by wistar rats. Botulinic acid was also examined for anti-inflammatory activity wad its concertation was 107.6 mg/g (Kviecinski et al. 2017, Monirul Islam et al. 2013). Pitaya contains squalene and betalins which has anti-inflammatory potential. Studies revealed that non-encapsulated betalains and encapsulated maltodextrin betalins show anti-inflammatory effects. These are present in pitaya peel extract. The encapsulated betalains have a high anti-inflammatory effect in comparison to non-encapsulated. Betalains encapsulated with maltodextrin pectin show a five to six-fold higher anti-inflammation effect (Rodriguez et al. 2016). The betalains which have a high power of radical scavenging show high effects against neural inflammation through mechanisms like prostaglandins and cholinergic pathways (Eldeen et al. 2020). The anti-inflammatory properties of passion fruits are evaluated through inflammation which is induced by 2,4,6-trinitrobenzenesulphonic acid, substance P, histamine and dextran sodium sulfate (Cazarin et al. 2015). Peel of passion fruit mixed with sodium sulfate attenuates the effect of pro-inflammatory cytokines like IL-12, IL-17 and IL-8. They also decrease the functionality and expression both of MCP-1. The intraperitoneal injection containing polysaccharide extracted from dried passion fruit pulp help in reducing the expression of TNF-alpha and IL-1beta level (Cazarin et al. 2016, Silva et al. 2011). Many experimental studies were carried out to find the anti-inflammatory effects of bay berry in animal models. The ethyl extract of bayberry bark was used against rat paw edema for demonstrating the anti-inflammatory effects. As a result, there was 15-25% inhibition in the rat. The study concluded that flavonoids might be responsible for anti-inflammatory effects (Panthari et al. 2012). The ethanol extract Rambutan peel is used against arthritis induced by collagen by using different dose levels of 100 and 200 mg/g. As a result, the extract reduced inflammation and also induced significant changes in the body like weight loss and paw edema. They also reduce the C-reactive protein. The seeds of Rambutan show both analgesic and anti-inflammatory effects (Kumar et al. 2012). The fruit hull of mangosteen is used against the various treatment of inflammatory diseases. It inhibits the effects of NO and PGE2 and show moderate effects by inhibiting the effects of IL-4. γ-mangostin and α-Mangostin are used for reducing the inflammatory activity of No synthase. Studies revealed that isogarcinol is used for maintaining the anti-inflammatory activities against the arthritis induced by collagen (Tewtrakul, Wattanapiromsakul, and Mahabusarakam 2009, Fu et al. 2014).The aqueous extract of silver berry whole fruit and pericarp was examined against the paw edema. It reduces the formalin in mice. The extract also inhibits the cyclooxygenase enzymes type 1. Results also revealed that the regular use of this extract for the next two weeks reduces the pain of patients suffering with lichen planus (Beigom et al. 2010, Farahbakhsh et al. 2011).

Durian: – The mature Durian fruit was first extracted and the anti-inflammatory function was tested using cell culture U937-activated lipopolysaccharide (LPS). The result was that in the concentration of 0.1 and 0.20 mg/ml of Durian fruit extract can reduce IL-8 release by 23–36%. This shows that Durian fruit skin extract contains anti-inflammatory activity. This anti-inflammatory effect is present due to some bioactive compounds present in various parts of the durian (Chingsuwanrote et al. 2016). Water extract of logan pericarp (WLP) fruit is examined for checking the antimicrobial potential against various bacterial strains. As a result, the extract was successful in inhibiting the lipopolysaccharide-induced nitric oxide which was produced in macrophages. Apart from this, the concentration of Water extract of logan pericarp, (in the range of 100–400 mg/kg) showed inhibiting of paw edema development. It is also responsible for inhibiting the functioning of tumor necrosis factors (Huang et al. 2012). The water apple extract is responsible for anti-inflammatory effects. The leaves extract is also used for anti-inflammatory effects. It is used to inhibit the activity of 5-lipoxygenase (LOX), cyclooxygenase-2(COX-2) and cyclooxygenase-1(COX-1). Studies also revealed that this extract is also used for reducing the level of leukocytes which were responsible for inflammation in rats (Sobeh et al. 2018). The ethanolic and hydroalcoholic extracts Annona have been reported for Anti-inflammatory effects in a mouse model. Annona contains metabolites like arachidonic acid which are involved in anti-inflammatory processes. They also inhibit the mechanisms of COX and LOX (Hamid et al. 2012). The methanolic extract of Sapodilla was used to examine the anti-inflammatory effects in the rat by using rat paw edema test. As a result, methanolic extract decreases the volume of paw edema in the rat. These effects can be caused by flavonoids and tannins. The methanolic extract of pepino was used to examine the anti-inflammatory effects. 500 mg of methanolic fruit extract was used on murine macrophage cell line – RAW 264.7. 20 of µL of a 5 mg/mL MTT solution was used in the cell viability test. As a result, the extract reduces the level of IL-10 and IL-8. It also reduces the inflammatory effects of cytokines (Herraiz et al. 2016). The leaves and peel of Jaboticaba are used for intestinal inflammation and hemoptysis. Apart from this, anthocyanins of jaboticaba are used for reding the inflammation caused by cigarette smoke. Majorly this compound shows its activity toward chronic obstructive pulmonary disease (Dastmalchi et al. 2012).

Cardiovascular effects

Cardiovascular diseases (CVD) are leading all over the world and is becoming a major cause of death. Epidemiological studies revealed that the consumption of fruits in CVD will

attenuate the risk of CVD. Fruits have the potential to prevent CVD and also help in the restoration of heart functioning (Aune et al. 2017). They help in the regulation of lipid metabolism. Maintain blood pressure, suppress thrombosis, provide protection toward vascular endothelium and help in attenuating inflammation (Zhao et al. 2017).

Guava budding leaves extract help in attenuating atherosclerosis. They show their effect on bovine aortal endothelial cells, help in the prevention of low-density lipoprotein and its cytotoxicity, help in delaying the oxidation of low-density lipoprotein (Owen et al. 2007). Budding guava leaves extract acts as an anticoagulant in plasma. They reduce the time of thrombin clotting and inhibit the functioning of antithrombin III (Díaz-de-Cerio et al. 2017). Apart from this, phenolic compounds present in guava juices help in reducing the hypertension effect and thereby keeping the human body away from CVD. They inhibit the functioning of angiotensin-1 and xanthine oxidase (Irondi et al. 2016). Additionally, the fruit and leaf extract of guava help in decreasing the LDL cholesterol thereby raising the level of HDL cholesterol. This help in the reduction of blockage in arteries and veins (Kumari 2016) The blue passion flower, is a rich source of phenolic compounds, amino acid α-alanine and organic acids. A high concentration of flavonoids including isoorientin, orientin, vitexin, saponarin and rutin were also found (el Houda Lezoul et al. 2020). Fruit extract, when tested in swiss albino mice with pilocarpine-induced convulsions, showed anticonvulsant activity by delaying the onset of convulsions and decreasing the duration of clonic convulsions. Reduced oxidative damage, better cognitive function and dose-dependent improvement of cholinergic neurotransmission also evidenced the therapeutic potential (de Souza et al. 2012).

Kiwifruit has potassium and fibers which help in heart diseases. Fibers can reduce cholesterol levels which result in the reduction of heart attack (Duttaroy 2013). Potassium plays a vital role in reducing cardiovascular risk, as kiwi has low sodium quantity and high potassium levels. Potassium helps in the regulation of heart rate by lowering the side effects of sodium (Richardson, Ansell, and Drummond 2018). Kiwi fruit is a rich source of omega-3 fatty acids which help in lowering the effects of coronary heart disease (Bowen, Harris, and Kris-Etherton 2016). Carambola is highly rich in fibers and nutrients which help in lowering the cholesterol levels and bile acids in the human body (Herman-Lara et al. 2014). A study revealed that star fruit fiber concentrate lowers the concentrations of total serum cholesterol and liver lipids. Thereby reducing the chance of hypertension. They also help in reducing the level of myocardial infractions and heart strokes in human beings (Lakmal et al. 2021). The pitaya fruit extract help in lowering the blood lipid level concentration, attenuates the level of liver cholesterol, LDL-cholesterol concentration and total liver cholesterol concentration (Nurul and Asmah 2014). The water pulp extract was examined and as a result, researchers found that it reduces the stiffness of arteries, lowers the risk of atherosclerosis and reduces the risk of a heart attack. Studies demonstrated that diastolic stiffness of rat heart can be reduced through pitaya juice as it is highly rich in carbohydrates (Anand Swarup et al. 2010; Nurul and Asmah 2014). Passion fruit contains ascorbic acid which helps in the prevention of cardiovascular diseases. Ascorbic acid maintains the nervous system which results in the prevention of ischemic heart diseases, congestive heart failure, heart attack, atherosclerosis and hypertension (Leuenberger et al. 2012). Studies also revealed that consumption of passion fruit juice help in the reduction of systolic blood pressure in hypertensive rats (Zhao et al. 2017). Apart from this, intake of passion fruit pulp for 16 weeks improves cardiac functionality and platelet aggregation (Ishihata et al. 2016). Bayberry fruit juice contains components like phenols which lower arterial blood pressure and heart rate. The pulp of bay berry is used in reducing the cholesterol level and also help in atherosclerosis. The leave pulp of bayberry helps in maintaining the level of platelets and improve platelet aggregation. Bayberry fruit extract help in maintaining the heart system and improves the functionality of the cardiovascular system (AlAjmi, Al-Hadiya, and El Tahir 2013). Studies revealed the acute effects of bark extract of rambutan. These extracts were examined on cardiovascular diseases as a result they showed a prolonged cardiovascular response which increases systolic blood pressure, heart rate and MABP (Sukmandari et al. 2017). Studies proved that pericarp extract of mangosteen is used in atherosclerotic rats. As a result, α-Mangostin was used to determine the effects of the antioxidant effects of mangosteen for inhibiting the atherosclerosis process. This study was majorly performed for patients who are at high risk of Framingham (Munandar Zulkifli Ismail et al. 2021). The aqueous extract of silver berry helps in enhancing the flow of coronary arteries, help in maximizing the increase and decrease the velocity of myocardial and also enhance the left ventricular developed pressure. It also helps in improving the lipid profile and reduces the level of plasma triglycerides (Wang, Qu, et al. 2014; Belarbi et al. 2011). Cholesterol is also known as hyperlipidemia is a situation in which the level of blood protein increases. This is due to genetic hereditary or depends on individual diets. Durian has bioactive compounds which are anti-cholesterol in nature. They help in lowering the level of blood protein which are responsible for rising the cholesterol level (Muhtad et al. 2016). Water apples do not contain sodium and cholesterol in excessive amounts. Due to this water apple juice helps in reducing the chances of heart ailment, stroke, atherosclerosis and blood pressure (Sushma, Bhavana, and Padmalatha 2021). The methanolic extract of Annona plant is used for lowering the level of cholesterol. Studies reported that the administration of methanolic extract in a dose-dependent manner helps in reducing the level of triglycerides, LDL-cholesterol and plasma total cholesterol while it also helps in increasing the level of HDL cholesterol. This results in reducing the chances of atherosclerosis (Verma et al. 2011). Sapodilla fruit juice has bioactive compounds which are responsible for lowering the level of cholesterol in the blood. They also augment the level of triglycerides and LDL cholesterol. Sapodilla extract also

helps in reducing the risk of heart attack by keeping the blood pressure in control (Barbalho et al. 2015). Studies revealed that the consumption of freeze peel of jaboticaba helps in increasing the level of HDL and reduces the level of LDL in the blood. Almost 41.7% of HDL was increased when examined in a muse model. They show hypolipidemic activities in the blood (Lenquiste et al. 2012).

Anticonvulsant

Kiwifruit is rich in flavonoids which attribute to its multiple health benefits. The peel of kiwifruit of two species was studied for their hypnotic effects and their oral digestion produced a dose-dependent sleep latency as well as increased sleep duration suggesting its potential use as sleep-inducing on pentobarbital mice (Yang et al. 2013). The extracts of mangosteen from its raw materials have a significant effect on changing the behavior of animals under the swimming test without causing any negative impact under the Porzolt method. It has anti-anxiety effects even in the absence of a depriving effect (Fedorova et al. 2021). Passion fruit has alkaloids that can cause mild sedation as well as relax the nervous system inducing sleep (Vimal and Devaki 2004). Its extracts interact with the benzodiazepine receptors and inhibit the seizure in STR induced mice as well as interacting with inhibitory glycine or NMDA amino acid neurotransmitters (Tripathi 2018). The leaves of water apple have carbohydrates, alkaloids, phytosterols, flavonoids, phenolics and tannins. Its leave showed anticonvulsant activity in both chemically and electrically induced seizures with dose-dependent action in MES and PTZ induced convulsion (Lim and Rabeta 2013). Its extract has benzodiazepine which can bind to the GABAA receptor resulting in its increased receptor activity, inhibition of the action potential generated (Geethu Krishna 2017). The hexane extracts of guava leaves contain sesquiterpenes which have antidepressant activities on the CNS. This fruit is also rich in terpenes such as caryophyllene oxide and beta selinene that could latent the convulsion from leptazol (Meckes et al. 1996). Annona has been used as an anti-anxiety and anticonvulsant traditionally. Annona has alkaloids that have high specific affinities to serotonergic 5HT1A receptors. In mice, aerial parts of Annona were administered during the forced swimming test and confirmed their scope as antidepressants (Martínez-Vázquez and Estrada-Reyes 2014). The bark, leaves extract of the jackfruit have been known to report anticonvulsant properties in swiss mice and provide them protection against maximal electroshock as well as induced seizure with delayed onset of strychnine nitrate caused convulsions. The leaf extracts are more potent than the bark (Prakash 2013). It has a potent effect against neurodegenerative disorders with dose-dependency as well as chemical-induced convulsions (Jain et al. 2009).

Most of the MTFs covered in this review show several health benefits (Table 4). With the presence of various beneficial phytochemicals, and natural pigments the MTFs possess antioxidant, antimicrobial, anti-carcinogenicity, and anti-diabetic effects. Researchers have studied the medicinal potential of these fruits mostly in in-vitro conditions, the diversified medicinal prospects, dose-response study and their in-vivo investigations are yet to be unveiled.

Current status of minor tropical fruits as an ingredient for functional food development

The minor tropical fruits are used in various fields of food industries e.g. dehydrated fruit product formulation, as flavoring and coloring agent, as a preservative and as fortification agent (Figure 3).

Traditional uses

Traditionally, Lutqua has been used largely for medicinal purposes. It may be applied as an anti-phlogistic to treat cellulitis, rheumatoid arthritis. For constipation treatment, the juice of the bark, and seeds are successfully used. In Morang district located in Assam, as snake venom antidote fruit juice is used by the local inhabitants (Khan et al. 2021). Carambola is quite useful in treating several diseases like diabetic nephropathy (DN), arthralgia, vomiting, lithangiuria, coughing and hangovers. In Malaysia, crushed leaves have been used traditionally to control headaches since ages. In the treatment of eczema, fever, and diarrhea, ripe fruit is used in Indian traditional medicine. In traditional Chinese medicine different parts of the tree are used (Binita et al. 2016). Elephant apple may be used to treat stomach illness. It is popular in the state of Assam, India. In different ancient texts, the use of the plant is described. It gives a cooling effect to the body during fever. It also possesses anti-diabetic, anti-inflammatory, analgesic effects (Kamboj, Talukdar, and Banerjee 2019). The leaves of the Rambutan plant are used to get relief from headaches. It has astringency property and decoction of the roots are used in fever treatment (Lim 2013). Bay-berry stem, bark as well as fruit is medicinally very beneficial. It can cure skin problems, ulcers. The plant is used in the treatment of cholera, stomach diseases. It also acts as anti-oxidant agent (Kumnerdkhonkaen et al. 2018). Passion fruit is quite famous in the traditional medicine system; it can be used as a moisturizing agent. Various products like vinegar, beverage, jam, jelly, tea etc have been made with the fruit. In Brazil, juice as a drink is used in the traditional medicinal system (Granato et al. 2011). Water apple as a medicinal plant it has been well utilized in the treatment of several diseases. Mostly its use is found as antibiotics. Its antioxidant activity is due to the presence of phenolic compounds present in it (Sobeh et al. 2018).

Nephelium ramboutan-ake (Labill.) Leenh roots and leaves have anthelmintic properties. Thus traditionally they have been used in fever treatment. Besides this from the dried seed kernel, aromatic oils are also produced (Lim 2013). *Phyllanthus emblica* is extremely popular in the Indian traditional medicinal system. Ayurvedic and Unani medicine systems use this fruit mainly due to its anti-oxidant properties (Golechha et al. 2014). *Psidium Guajava* has been used in folk medicine owing to its antimicrobial and anticancer properties (Goyal, Middha, and Usha 2020). *Each part of*

Table 4. Medicinal properties of the minor tropical fruits.

Fruit	Antioxidant	Anti-cancer	Anti-diabetic	Antimicrobial	Cardiovascular diseases	Anti-inflammatory	References
Guava	AAC 144 ± 60 mg/100g	MTT assay of dH2O. EOH and NH -(51.73 ± 4.31)%, (54.18 ± 9.05)%, and (29.93 ± 3.07)%	200–250 mg/kg.bw of polyphenol extracts of pulp as an alternative to diabetic drugs	1.875 ± 14.43 mg/mL MIC	guava fruit extract: –0.05 mg/ml	50 50 µg/mL	(Oncho, Ejigu, and Urgessa 2021, Lim et al. 2006, Jang et al. 2014, Shabbir et al. 2020, Lok et al. 2020)
Lychee	At 120 lg/ml, the scavenging abilities of DPPH radicals were 94.9%	MTT:-20 to 320 µg/m	–	Inhibitory activity – 15 ± 0.55 mm and 13.5 mg/g seed content	150 µg/mL – lychee extract	5 mg/mL MTT solution (in PBS), 150 µL DMSO	(Punia and Kumar 2021, Emanuele et al. 2018, Wang et al. 2006, Saisavoey et al. 2018)
Jackfruit	(IC50 = 0.6433 ± 0.0029 mg/ml).	50 µg/kg–200 µg/kg	IC 50 is 56,43 %	Inhibition range: – 8.5 +/- 0.5 mm, MIC: – 62.50, MBC: – 250 mg/ml	200 µg/mL – concentration and IC50 – 50%	MEJL – 41%	(Vázquez-González, Ragazzo-Sánchez, and Calderón-Santoyo 2020, Thiruselvi and Durairaj 2018, Zuraidah et al. 2017, Asmaliani and Iwo 2016)
Tree Tomato	(12.17 ± 0.53 µM Fe (II)/g, 3.72 ± 0.20 µM Fe (II)/g)	0.5 mg/mL in PBS	–	MIC less than 0.31 mg/ml	600 mg mL^{-1}- extract concentration	MTT assays:-30 µM	(Chao et al. 2012, Kim et al. 2019, Cha et al. 2017, Noor Atiqah, Maisarah, and Asmah 2014)
Bay Berry	–	9.62 mg/g	IC_{50} value of 3.075 ± 0.073 µg/mL.	200 µL -Extract concentration	MTT :- 20 µl of	DPPH :- 0.1 mM in methanol, 5 mL	(Zhang et al. 2016, Saini et al. 2013, Wang et al. 2019)
Kiwifruit	DPPH: – 191.8 ± 7.2%	Ethane concentration: – 70%, extract concentration: – 50 mg/ml	–	Peel phenol concentration: – 11.4 ± 0.3 mm, 12.6 ± 0.2 mm	Methanolic extract:- 0.1 ml	Inhibitory activity: – 81%, 68%, 63%, 76% against IL-6 and TNF-α	(An et al. 2016, Jung et al. 2005, D'Eliseo et al. 2019)
Loquat	APC- 64.15 to 100 in the peel and from 59.49 to 97.95 in the pulp.	Extract concentration: – 25 to 50µg/ml	α-amylase inhibitory activity of 24% at 1 µg/ml	Minimum inhibitory concentration: – 0.625 µg/mL	–	MTT solution: – 5 mg/ml	(Kim et al. 2009, Zar et al. 2014, Shen et al. 2021)
Pitaya	DPPH: - red peel extract: – 35.85%–54.50 %	IC50: – 0.61 to 0.73 mg mL–1	–	10 g of the extract in 100 mL of DMSO	DAP: – 87.8 ± 1.5 mmHg	BSA: – 28.41–39.52 µg/ml	(Luo et al. 2014, Khalili et al. 2012, Smeriglio et al. 2021, Anand Swarup et al. 2010)
Passion fruit	DPPH: –5-40 µM	–	–	inhibitory concentrations: – 128 to 1024 µg/ml	Passion fruit juice concentration: – 50% (50 g/100 mL)	IC50: – 34.92 µM, NO production decreases	(Sano et al. 2011, Hu et al. 2018, Dzotam et al. 2015, Souza et al. 2012)
Mangosteen	ORAC value (1.7 × 104 µm	Minimum inhibitory concentration (MIC) 6.5 ± 1.0 µg/ml)	MIC 0.9352 ± 0.0856 µM	MIC: – 20 µg/mL	–	–	(Aisha et al. 2012, Tatiya-aphiradee et al. 2016, Usman et al. 2021)
Silver berry	3.62 mM Trolox (TE)/100 g d.m. (FRAP assay), and 5.11 mM TE/100 g d.m. (DPPH assay).	–	-	MIC: – 3250–6500 µg/ml	–	Aqueous extract: – 1000 mg/kg	Okmen and Turkcan 2013, Farahbakhsh et al. 2011)
Durian	–	Fruit extract concentration: – 600 µ g/mL	IC50 values for n-hexane extracts being 9.79 µg/mL	MIC: – 250 µg/ml	Fruit extract: – 500 mg/kg BW	Fruit extract concentration: – 0.20 mg/ml	(Basyuni et al. 2019, Chingsuwanrote et al. 2016, Alkandahri et al. 2021, Aziz and Jalil 2019)

Longan	–	Inhibition percentage: – 40%. Extract concentration: – 40 mg/l	The IC_{50} values of hot water and 50% ethanol ultrasonic extracts against the α-glucosidase were 9.2 and 13.4 mg/mL, and those against the β-galactosidase were 12.9 and 19.7 mg/mL, respectively.	MIC: 64 mg/mL	lipid peroxidation with IC50: – 537.01 ± 42.32 µg/mL	WLP: – 100–400 mg/kg	(Meng et al. 2014, Huang et al. 2012, Farahbakhsh et al. 2011)
Water apple	–	inhibitory activity: – 24.2 ± 2.8 µg/mL	–	DMSO: – 10%	–	IC50 of syzygium aqueum leaves extract: - LOX – 2.5401 ± 0.19 µg/ML, COX-1 7.11 ± 0.43 µg/ML	(Tewtrakul, Wattanapiromsakul, and Mahabusarakam 2009; Basyuni et al. 2019; Yusuf Alkandahri et al. 2021)
Sapodilla	–	dimethyl sulfoxide (DMSO): – 100 μL	–	MIC: – 256 ~ 512 g/ml	Methanolic extract: – 500 mg/kg	ethanolic extracts: – 48.9 %	(Huang et al. 2012; Meng et al. 2014; Sukmandari et al. 2017; Aziz and Jalil 2019)
Pepino	–	DPPH: – 0.1 mM	500 mg/kg dose (27.1%).	MIC: – 10 ± 0.2 – 22 ± 0.3 mg/ml	–	MTT: – 20 µL of a 5 mg/mL	(Herraiz et al. 2016; Paul et al. 2021; Yusuf Alkandahri et al. 2021)
Jaboticaba	–	ethanol DPPH: – 750 μL 0.0025%	IC_{50} of 0.0031 $mg.mL^{-1}$	MIC: – 384.6 µg/ml	DPPH: – 2.5 mL of 0.1 mM	DMSO: – 125 µg/m	(Sravani et al. 2015; Tan, Norhaizan, and Chan 2018; Rummun et al. 2021; Osman et al. 2011)
Lutqua	–	cytotoxic activity: - LC_{50} value 74.2 µg/ml	lowering the blood glucose levels by (50.06%)	MIC 3.20 mg/ml	ethanolic seed extract: – 500 mg/kg	Methanol extract: – 10 mg/kg	(Olayemi 2012; Priya and Chellaram 2014; Wang, Qu, et al. 2014; Souza et al. 2017)
Persimon	–	persimmon calyx- 500 µg/ml showed 31% inhibition in growth	–	DMSO : – 0.5 mL	Gallic acid: – 21.89/± 2.2	chloroform extract: – 200 mg/kg	(Cock and Mohanty 2011; Amin and Nabi 2015; Nesa et al. 2018; de Lima Paula et al. 2021)
Rambutan	–	IC_{50} : 5.42 ± 1.67 µg/ml	Alpha glucosidase (EC_{50}=2.7 µg/mL) and alpha amylase (EC_{50}=70.8 µg/mL),	MIC 2.0 mg/mL	Seed extract - t 19.2 mg/kgbw	Methanol extract – 51.27%	(Park and Lee 2018; Goyal, Middha, and Usha 2020; Bawazeer and Rauf 2021; Sultana Chowdhury 2021)
Bhawa	200 ppm, BHA extract showed 98.0% antioxidant activity	TPTQ: 800 mg/kg of	IC_{50} value 0.5 µM	MIC: 20 µg/mL	methanolic extract: – 1000 mg/kg	Extract concentration: 100 mg/kg	(Park et al. 2008; Jo et al. 2011; Tadtong et al. 2011; Emylia, Snz, and Dasuki 2013; Morshed et al. 2014)

Continued

Table 4. (Continued).

Fruit	Antioxidant	Anti-cancer	Anti-diabetic	Antimicrobial	Cardiovascular diseases	Anti-inflammatory	References
Pulasan	–	IC 50 IC 50 IC 50 Ethanol -IC50:- 20.70 ± 0.49	–	MIC: 312.5 µg/m	–	Methanolic extract: 250 and 500 mg/kg, Inhibition: 41.59 %	(Susilowati et al. 2018; Espirito Santo et al. 2020; Putri et al. 2021),
Annona	–	EtOH :- 500 mg/kg	–	MIC: 128 mg/ml	Methanolic extract: 250 mg/kg	EtOH: 400 mg/kg	(Prasanth et al. 2013; Tatiya-aphiradee et al. 2016; Paul et al. 2017; Wahyuni et al. 2017)
Pepino	The EC_{50} values of ripe ethanolic extract on DPPH radical, reducing power, ferrous ion chelation were obtained to be 2.20, 2.81 respectively.	DPPH: 0.1 mM	–	MIC: 10 ± 0.2 to 22 ± 0.3 mg/ml	–	MTT: – 20 µL of a 5 mg/mL	(Chan et al. 2012; Herraiz et al. 2016; Paul et al. 2021),
Carambola	It has ethyl acetate and n butanol which show a great result with IC50 values being 90.92 and 124.48 µg/mL, respectively.	Carambola fruit extract: – 25 mg/kg/	–	MIC: 15 µg/ml	1000 mg/kg MEACL	IC50value is less than 50 ppm, maximum inhibition of 73 ± 3%	(de Sousa et al. 2010; Okolie, Agu, and Eze 2013; Morshed et al. 2014; Cabral, Cardoso L de, and Pinheiro-Sant'Ana 2014)
Elephant Apple	1.06×10^4 µmol TE/g and ferric reducing antioxidant power of 2320 µmol Fe(II)/g–	IC50: 34.62 ± 5.2 µM against HeLa cells	IC_{50} values 56.77, 63.04, 20 µl of MTT, cells: – 10×10^{-4} cells per 100 µl of media	–	MDIB: 11.09 ± 0.22	–	(Arun Jyothi et al. 2011; Leelarungrayub et al. 2016)
Indian gooseberry	–	Ethanolic extract: - IC_{50} values = 0.12–0.65 mg/mL	–	MIC: – 25-100 µl	fruit powder- 0.1%	hydroalcoholic extract: – 700 mg/kg	(Priya and Chellaram 2014; PK 2014; Aladaileh et al. 2019; Majhi, Satapathy, and Mishra 2019)

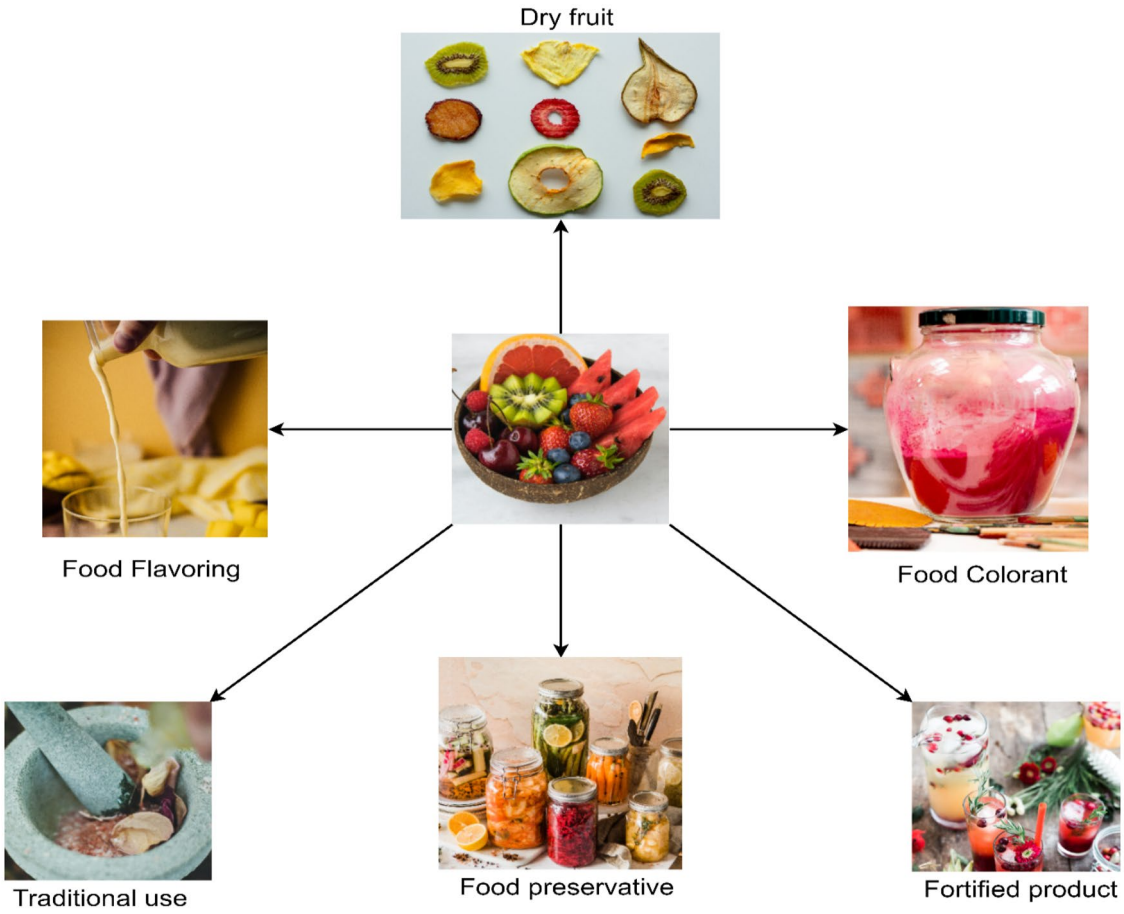


Figure 3. Application of minor tropical fruits in various filed of food industries.

Litchi chinensis is used in a traditional medicinal system like fruits, seeds, pulp, flowers. The phytochemicals present in this plant make it extremely useful for medicinal purposes (Luan et al. 2021). A*nnona cherimola* is quite useful in infection-related diseases like dysentery, ulcer. Traditionally as an antimicrobial agent, this plant is well documented (Sun et al. 2013). *Hylocereus polyrhizus* plant has antioxidant activities thereafter uses are found as anti-diabetic, anti-cancer, immunomodulatory agent (Granato et al. 2011). *Garcinia mangostana* plant has been effectively used in the traditional medicinal system. Due to its antimicrobial nature, it may heal several diseases like dysentery, ulcer. It also possesses anti-inflammatory properties (Krishnaveni and Mirunalini 2010). *Garcinia cowa* has so many medicinal properties like anti-cancer, anti-malarial, anti-inflammatory properties thus this plant is documented in the traditional medicinal system (Daswani, Gholkar, and Birdi 2017). *Eriobotrya japonica* is found in the folk medicine system as it can treat inflammation, cough, diabetes (Pareek et al. 2014). *Elaeagnus latifolia* is found to be used in the traditional medicinal system as it contains several beneficial effects, like diuretic, analgesic in nature (Kilari and Putta 2016). *Durio zibethinus* is acclaimed to be highly useful in the traditional medicinal system. The leaf and root is an ailment to malaria, phlegm, swelling, skin diseases (Coria-Téllez et al. 2018). In the Chinese medicinal system, the plant *Diospyros kaki* is noted. The leaf of the plant is used for the treatment of ischemia stroke, hypertension, angina (Hernawati et al. 2018). *Dimocarpus longan* is well known for several medicinal activities like anti-oxidant, anti-microbial, anti-inflammatory effects (Huang et al. 2012). *Manilkara zapota* is supposed to be an ideal ingredient used in the traditional medicinal system due to its anti-inflammatory, analgesic activity, diuretic properties, the latex content also been used in tooth cavity filling (Ritthiwigrom, Laphookhieo, and Pyne 2013). *Myrciaria jaboticaba* is mentioned in folk medicine as a heal to asthma, cardiovascular treatment, throat inflammation (Tehranizadeh, Baratian, and Hosseinzadeh 2016). Different medicinal properties make different parts of *Artocarpus heterophylus* tree extremely popular in the traditional medicinal system (Husin et al. 2018).

Use as a colorant

Day by day demands for natural colorant in different application is rapidly increasing due to growing safety consciousness about the various detrimental effects of rapidly used low-cost different synthetic colorants (Xie et al. 2015) Natural colorants are derived from various fruits, vegetables and their by-products (Ghosh et al. 2021, Ghosh et al. 2022). More innovative research ideas toward valorization of fruits, vegetables along with their different under-utilized by-products and wastes are one of the key components

toward enhancing the production and exploration of new natural colorants (Huang et al. 2012).

In fruits, the prime source of colorants is the presence of anthocyanin as one of the major natural pigments due to their high color stability and purity (Baskar, Hemalatha, and Muneeshwari 2020). Minor topical fruits are coming out as an excellent source of different pigments (majorly anthocyanin, carotenoids etc.) which seeks the attention of their different possible application in various food application in line with compatibility. In Guava, carotenoids (β- and α- carotene) are identified as major sources of colorants by HPLC-PDA which may be used in different food applications (Patil 2013). For Carambola fruits, researchers have reported the carotenoid content was 22 µg/g fresh weight (Lobo de Andrade et al. 2015). Researchers have reported the use of rambutan peel as a source of natural dye for cotton fabric application (Paramita et al. 2017). Scholars have reported the dyeability and function of silk fabrics using *Myrica Rubra* rind extract (Lee 2018). Basitah reported the application of Natural Dyes from the Fresh Rind of Mangosteen (Basitah 2015). Pigment extract from silver berry has been extensively used as a food colorant in traditional Vietnamese foods (Cortez et al. 2017) Yoo and Shin reported the application of Persimmon peel extract in indigo dyeing as an eco-friendly alternative reductant (Patil 2013). Researchers have analyzed different natural food colorants extracted from Passion fruit (Kawasoe et al. 2021). Functional dye has been developed from Jabuticaba fruit (Beltrão Lessa et al. 2016). Betalain has been from Pitaya for natural food coloring purposes (Naderi et al. 2010).

Use as a flavor enhancer

Flavors are essential commodity foods, cosmetics, perfumeries and phytosanitary products. The characteristic flavor of exotic tropical fruits is one of their most attractive attributes to consumers. Different flavors are generated from different tropical fruits in two ways – 1. Extraction of essential oil by different methods and then essential oil is used for flavor generation, 2. Another interesting way for flavor generation is that different yeast species with high flavoring production potential has been grown over the skin of different tropical fruits which are isolated from the fruit skin and flavors are extracted by following different biotechnological methods.

Researchers have reported the aromatic profile in commercial guava essence and fresh fruit puree extracted with solvent yielded a total of 51 components (Kadam, Kaushik, and Kumar 2012). Passion fruit flavor profile consists of more than 20 essence volatile components which have extensive application in different food applications including bakery, beverages and so on (Le et al. 2018). Researchers have studied carotenoid-derived flavor Precursors from fresh carambola Fruit (Jia et al. 2019). More than 60 flavor compounds have been identified using GC-MS with thermal desorption system (TDS) in Lutqua (Mann, Satpathy, and Gupta 2016). Researchers have used lychee in wine preparation and characterized its flavor profile by using headspace solid-phase microextraction gas chromatography-mass spectrometry combined with headspace gas chromatography-ion mobility spectrometry (Beltrão Lessa et al. 2016). By using Gas chromatography-mass spectrometry (GC-MS) and multidimensional gas chromatography olfactometry (GC/GC-O), researchers have identified and quantified 29 flavor components in kiwi fruit (Jordán et al. 2002). 20 strong aroma volatile compounds in rambutan have been listed which are responsible for "civet-like"-sweaty, spicy, and woody notes generated from rambutan as essence (Ong, Acree, and Lavin 1998). The volatile compounds of durian varieties have been analyzed using headspace solid-phase microextraction (SPME) coupled to fast gas chromatography-mass spectrometry (GC-MS) identified a total of 39 volatile compounds (Muhtadi et al. 2016). Researchers have reported the post-harvest survey of volatile compounds of longon, mangosteen, durian, rambutan, and sapodilla and identified individual tropical fruit's aroma profile by using headspace-solid phase microextraction with the gas chromatography-mass spectrometry technique (Laohakunjit et al. 2007). Volatile flavor compounds of guava and passion fruit have been extracted through comparison and optimization of an internally cooled fiber [cold fiber with polydimethylsiloxane (PDMS) loading] and several commercial solid-phase microextraction (SPME) fibers. It has been found that the cold fiber was the most appropriate fiber to extract volatile compounds (Carasek and Pawliszyn 2006). A study reported innovative research where they have studied the sensory evaluation and consumer acceptability in teenagers about the flavor profile of five tropical fruits - mangosteen, carambola, persimmon and dragon (Stanley, Dietzgen, and Gidley 2009).

Along with the presence of the potential nutraceuticals, various bioactive compounds and the health beneficial effects the MTFs have incredible sensory attributes which make them suitable for functional food and/or food fortification ingredients (Table 5). The above mentioned instances prove the prospect of the MTFs as the agent for nutritional, color, flavor, textural, rheological, and sensory property modification.

Conclusion

MTFs are gaining popularities in terms of commercialization, functional food development, and consumer perspective and mostly consumed as raw fruit. MTFs contain high amount of antioxidants, such as, flavonoids, phenolic acids, ascorbic acids, and other polyphenols. Therefore, it has a great potential to enrich human diets with a large amount of natural antioxidants beneficial to health, thereby avoiding the use of expensive and synthetic antioxidants, and potential hazards, such as toxicity, associated with synthetic dietary supplements. MTFs are produced mainly in the developing countries, thus, it can be concluded that apart from the public health related benefits, it could be beneficial for economic and social development of the MTF producing countries. The 26 MTFs have been discussed in this work are gaining importance financially and modifying the livelihood of the stakeholders associated with the harvesting

Table 5. Application of minor tropical fruits in food industries.

Fruit	Application	Reference
Kiwi-fruit	1. Coagulant activity (in milk product manufacturing). 2. Medicine use-Antioxidant and inhibition of lipid peroxidation, antiproliferative inhibition effect, Anti-inflammatory. 3. Functional food additive-Antimicrobial and antioxidant. 4. Nanocomposite for packaging.	(Tang, He, et al. 2019)
Lutqua	1. Food supplements. 2. Food products development - Jam, juice and wine industries.	(Kermasha et al. 1987)
Carambola	1. Food supplement – to improve the appetite of people. 2. To effectively remedy malarial splenomegaly and food poisoning caused by meat sources. 3. Medicinal uses – to treat diabetes and diabetic nephropathy (DN), chronic paroxysmal headache, as an anti-diarrheal and febrifugal drug.	(Luan et al. 2021)
Tree Tomato	1. Antioxidant supplements. 2. Functional-food products or Ingredients for food processing. 3. Food products development -Preparation of juice, decoction, and maceration. 4. Medicinal uses- Promising Antioxidative and Anticholinesterase Activity.	(Jordán et al. 2002; Ordóñez et al. 2009)
Elephant apple	1. Medicinal uses - fruit pulp is used as tonic and laxative for treatment of chest pain, abdominal disorders mixed with sugar against coughs. It reduces blood pressure and control hypertension problem. 2. Ingredients for food processing - used in curry and fish preparations and often mixed with peanuts or coconut and spices to make ketchups pickled. 3. Therapeutic Benefit in cure of Diabetes and Its associated Complications.	(Kamboj, Talukdar, and Banerjee 2019; Rai et al. 2020)
Rambutan	1. Food products development - juice, marmalade, jam, and jellies. 2. Traditional use- - dried peel of rambutan used in traditional medicine. 3. Medicinal uses – Antioxidant activity, Antimicrobial and antiviral potentials, Anticancer and anti-allergic effects, Anti-obesity effect, Antidiabetic activity, Anti-arthritic activities, Improved cardiovascular response.	(Mahmood et al. 2018)
Bay berry	1. Food products development - Juice and wine and canned, frozen or dried as alternatives to fresh consumption. 2. Traditional use - folk medicines. 3. Medicinal uses - Bayberry extracts contain antioxidants that exhibit bioactivities counteracting inflammation, allergens, diabetes, cancer, bacterial infection, diarrhea and other health issues.	(Joyce and Sanewski 2010; Kumnerdkhonkaen et al. 2018)
Mangosteen	1. Food products development - beverage and jelly from mangosteen rind, mangosteen rind powder, Nano mangosteen tea, mangosteen sirup, 2. Food and functional food products - Functional foods fortified with mangos-teen fruit extract are yogurt, ice cream, chocolate, and lozenges. 3. Animal feed supplementation. 4. Utilization in advanced materials of biomedical benefit. 5. Serve as an appropriate source for AC production. 6. Generation of C-dots for biosensor analysis. 7. Natural dye for fabric and solar cells.	(Aizat, Ahmad-Hashim, and Syed Jaafar 2019)
Bhawa	1. Food products development- food supplements, fortification of pasta with spray dried Bhawa powder, 2. Microencapsulation of fruit extract with whey protein isolate as wall material. 3. Medicinal uses - Anti-inflammatory activity, best source of secondary metabolites, providing flavonoids, phloroglucinols and xanthones.	(Pillai et al. 2012; Wahyuni et al. 2017; Ritthiwigrom, Laphookhieo, and Pyne 2013)
Loquat	1. Food products development – Jelly, juice, wine, canned fruit, dried slices, tofu, cookies, and noodles. 2. Medicinal uses - anti-inflammatory, antitumor, antioxidative, antimutagenic, antidiabetic activity.	(Fröhlich and Schreier 1990; Pareek et al. 2014)
Silver berry	1. Food products development -Juice, jam, ketchup and pickle. 2. Medicinal uses - in combating against kidney dysfunctions, antioxidant.	(Lachowicz et al. 2019; Kar et al. 2019)
Durian	1. Food products development -Noodles, Polysaccharide gel. 2. Medicinal uses – sources of folate, Anti-atherosclerotic activity, Anti-Proliferative Activity, Probiotic Effects, antioxidant activity.	(Ho and Bhat 2015; Chingsuwanrote et al. 2016)
Persimon	1. Persimmon (Peel and Calyx) as a Source for Bio-ethanol Production. 2. Application of persimmon peel extract in indigo dyeing as an eco-friendly alternative reductant. 3. Extraction of bioactive compounds in persimmon for dermatological and cosmetic use. 4. Persimmon hydrolase gene expression and its use in tomato maturation. 5. Food products development -Jam.	(Horvat et al. 1991; Kim et al. 2015)
Longan	1. Antioxidant, immunomodulatory, anti-inflammatory and antitumor activity.	(Zhang, Zhao, et al. 2015)
Passion	1. Medicinal uses-Antioxidant, anti-hypertensive, anti-tumor, antidiabetic, hypolipidemic activities. 2. Antibacterial and antioxidant activity on the preserved meat products.	(Souza et al. 2012; Kawasoe et al. 2021)
Water apple	1. Medicinal uses- Antioxidant, Hepatoprotective, Pain-Killing and Anti-inflammatory Activities.	(Sobeh et al. 2018)
Pulsan	1. Medicinal uses- Anticancer, anti-allergic, anti-obesity, antidiabetic, anti-HIV, antimicrobial, anti-dengue, anti-hypercholesterolemic, and antihyperglycemic effects. 2. Potential Use of Fruit Extract to Protect Skin Keratinocytes from Inflammation. 3. Antioxidant and Neuroprotective Activities. 4. Amla Juice Powder.	(Mahmood et al. 2018)
Guava	1. Food products development - Guava juice, blended RTS beverages, Guava wine, Guava powder, jam, toffee. Cheese, ice cream topping, nectar, Toffee, Guava leather, Guava pectin. 2. Medicinal uses- (a) Gastrointestinal infections; (b) Malaria; (c)Respiratory infections; (d) Oral/dental infections; (e) Skin infections; (f) Diabetes; (g) Cardiovascular/hypertension; (h) Cancer; (i) Malnutrition; (j) Women problems; (k) Pain; (l) Fever; (m) Liver problems; (n) Kidney problems.	(Casarotti et al. 2018; Aziz and Jalil 2019)

(Continued)

Table 5. (Continued).

Fruit	Application	Reference
Lychee	1. Food products development -Litchi Juice, Squash, Sirup, Cordia, Probiotic Litchi based beverage, honey, jelly and wine. 2. Medicinal uses- Hypoglycemic, anticancer, antibacterial, anti-hyperlipidaemic, anti-platelet, anti-tussive, analgesic, antipyretic, hemostatic, diuretic, and antiviral activities.	(Chyau et al. 2003; Sarkar, Nayak, and Chakraborty 2018; Z.S. Tang, He, et al. 2019)
Annona	1. Medicinal uses- Antidiabetic, antimicrobial, antidepressant, anxiolytic, antiviral, antitumor and cytoprotective activity.	(Jamkhande, Ajgunde, and Jadge 2017)
Pitaya	1. Food products development -Food colorant, wine from fruit pulp, betacyanin, jam from fruit peel, fat replacer in ice cream, food packaging and edible coatings. 2. Cosmeceutical Sunscreen Agent. 3. Antioxidant and Photoprotective Properties. 4. Medicinal uses- Retards Alcoholic Liver Disease Progression by Modulating Oxidative Stress and Inflammatory Responses.	(Luo et al. 2014; Guimarães et al. 2017; Joshi and Prabhakar 2020)
Jaboticaba	1. Food products development -Juice. 2. Medicinal uses- Antioxidant, antimicrobial, anti-inflammatory, antidiabetic, anti-obesity, cardioprotective, and antiproliferative 3. Jaboticaba skin flour.	(Plagemanna et al. 2012; Lenquiste et al. 2015)
Jackfruit	1. Food products development -Jam, Jelly, Squash, Pickle. 2. Medicinal uses- Treatment of asthma, prevent ringworm infection, and heal cracking of the feet.	(Goswami and Chacrabati 2016; Ranasinghe, Maduwanthi, and Marapana 2019)

and post-harvest management of the fruits. Out of these 26 MTF, it has been observed that only a few have been explored for their bioactive, and functional food development potential; while most of the MTF are yet to be explored in terms of phytochemical, flavor and sensory profile. The seasonal availability of the MTF may be overcome with proper preservation techniques. Due to the presence of different natural pigments in the MTF, it can be used as a reservoir of natural pigment extraction. Even the in-edible parts of the MTF or the waste generated from these MTF can be used as a source of natural pigment, and bioactive extraction. The MTFs have been studied for their medicinal properties though a very less data is available particularly in this domain. From the nutritional, organoleptic and bioactive potential it is obvious that the MTFs are the hidden treasure in the field of food fortification; though a limited number of regional cuisines are available only with the MTFs.

Future perspective

The peel, seeds and non-edible parts of fruits are generally treated as waste. There are a few or limited studies available on the utilization of the waste part of the MTFs. Further, safety related issues need to be investigated for utilization of the waste generated from the MTFs.

The absorption efficiency, bio-accessibility and bioavailability of the bioactive compounds of the MTFs in the human/animal system needs to be investigated.

It is necessary to investigate the use of the explored phytochemicals from MTFs in many elements of gastrointestinal and food systems in order to understand their release processes and application efficacy.

Exploration for appropriate processing and preservation techniques for the MTFs are pre-requisite to combat the seasonal and limited availabilities of some of the fruits. Simultaneous researches in packaging and transportation requirements are unavoidable to meet the global demand.

For the cost-effective commercial extraction and utilization of phytochemicals, pigments and nutraceuticals from MTFs, novel green technology approaches are necessary.

New technologies and efficient collaborations between academia and industry will be required to ensure the future success of commercialization of the speciality products from MTFS as new and novel therapeutic entities that can make a significant contribution to the treatment of human ailments, and reduction in health care cost.

Limited pieces of evidence are there for MTFs as food fortifying agents, thus multidisciplinary investigation is required in the field of nutrition, food safety, sensory study, toxicity, bioactivity, extraction and chemical exploration.

Acknowledgements

Funding for open access charge: University of Vigo/CISUG

Disclosure statement

All authors have no conflict of interest.

Availability of data and material

All the data used in the manuscript are available in the tables and figures.

Code availability

Not applicable.

Ethics approval

Not applicable.

Consent to participate

All authors has given their full consent to participate.

Consent for publication

All authors has given their full consent for publication.

Funding

The author(s) reported there is no funding associated with the work featured in this article.

ORCID

Tanmay Sarkar http://orcid.org/0000-0003-3869-1604
Maksim Rebezov http://orcid.org/0000-0003-0857-5143
Ill-Min Chung http://orcid.org/0000-0003-4806-0611
Mohammad Ali Shariati http://orcid.org/0000-0001-9376-5771
Jesus Simal-Gandara http://orcid.org/0000-0001-9215-9737

References

Adefegha, S. A., S. I. Oyeleye, and G. Oboh. 2015. Distribution of phenolic contents, antidiabetic potentials, antihypertensive properties, and antioxidative effects of soursop (*Annona muricata* L.) fruit parts *in vitro*. *Biochemistry Research International* 2015:1–8. doi: 10.1155/2015/347673.

Aisha, A. F. A., K. M. Abu-Salah, Z. Ismail, and A. M. S. A. Majid. 2012. In vitro and in vivo anti-colon cancer effects of Garcinia mangostana xanthones extract. *BMC Complementary and Alternative Medicine* 12 (1):104. doi: 10.1186/1472-6882-12-104.

Aizat, W. M., F. H. Ahmad-Hashim, and S. N. Syed Jaafar. 2019. Valorization of mangosteen, "The Queen of Fruits," and new advances in postharvest and in food and engineering applications: A review. *Journal of Advanced Research* 20:61–70. doi: 10.1016/j.jare.2019.05.005.

Akhtar, M. T., S. N. Ismail, and K. Shaari. 2017. Rambutan (*Nephelium lappaceum* L.). *Fruit and Vegetable Phytochemicals*. 1227–1234. doi: 10.1002/9781119158042.ch64.

Akomolafe, S., and O. B. Ajayi. 2015. A comparative study on antioxidant properties, proximate and mineral compositions of the peel and pulp of ripe Annona muricata (L.) fruit. undefined

Aladaileh, S. H., S. A. M. Saghir, K. Murugesu, A. Sadikun, A. Ahmad, G. Kaur, A. M. Mahmoud, and V. Murugaiyah. 2019. Antihyperlipidemic and antioxidant effects of averrhoa carambola extract in high-fat diet-fed rats. *Biomedicines* 7 (3):72. doi: 10.3390/biomedicines7030072.

AlAjmi, M., B. Al-Hadiya, and K. El Tahir. 2013. Pharmacological studies on *Myrica rubra* Sieb et zucc. Effects on the cardiovascular system and platelets. *Drug Research* 63 (9):439–44. doi: 10.1055/s-0033-1348246.

Albuquerque, T. G., F. Santos, A. Sanches-Silva, M. Beatriz Oliveira, A. C. Bento, and H. S. Costa. 2016. Nutritional and phytochemical composition of *Annona cherimola* Mill. fruits and by-products: Potential health benefits. *Food Chemistry* 193:187–95. doi: 10.1016/j.foodchem.2014.06.044.

Ali Hassan, S. H., and M. F. Abu Bakar. 2013. Antioxidative and anticholinesterase activity of *Cyphomandra betacea* fruit. *The Scientific World Journal* 2013:1–7. doi: 10.1155/2013/278071.

Alim, A.,. T. Li, T. Nisar, D. Ren, X. Zhai, Y. Pang, and X. Yang. 2019. Antioxidant, antimicrobial, and antiproliferative activity-based comparative study of peel and flesh polyphenols from *Actinidia chinensis*. *Food & Nutrition Research* 63 (0). doi: 10.29219/fnr.v63.1577.

Alkandahri, M. Y., R. Patala, M. I. Pratiwi, and L. S. Agustina. 2021. Pharmacological studies of *Durio zibethinus*. *A Medicinal Plant Review* 25 (4):640–6.

Alrashood, S. T., A. K. Al-Asmari, A. K. Alotaibi, R. A. Manthiri, S. Rafatullah, R. M. Hasanato, H. A. Khan, K. E. Ibrahim, and A. F. Wali. 2020. Protective effect of lyophilized sapodilla (*Manilkara zapota*) fruit extract against CCl4-induced liver damage in rats. *Saudi Journal of Biological Sciences* 27 (9):2373–9. doi: 10.1016/j.sjbs.2020.05.010.

Alshaker, H. A., N. A. Qinna, F. Qadan, M. Bustami, and K. Z. Matalka. 2011. Eriobotrya japonica hydrophilic extract modulates cytokines in normal tissues, in the tumor of Meth-A-fibrosarcoma bearing mice, and enhances their survival time. *BMC Complementary and Alternative Medicine* 11 (1):9. doi: 10.1186/1472-6882-11-9.

Altemimi, A.,. N. Lakhssassi, A. Baharlouei, D. Watson, and D. Lightfoot. 2017. Phytochemicals: Extraction, isolation, and identification of bioactive compounds from plant extracts. *Plants* 6 (4):42. doi: 10.3390/plants6040042.

Altendorf, S. 2018. Minor tropical fruits mainstreaming a niche market. FAO Food Outlook. 67–73. http://www.fao.org/3/a-I8080e.pdf

Amin, R., and M. N. Nabi. 2015. Evaluation of cytotoxic and antioxidant activity of different fractions of methanolic extract of *Baccaurea ramiflora* (Lour.) fruits. *International Current Pharmaceutical Journal* 4 (6):386–9. doi: 10.3329/icpj.v4i6.23288.

Amiri Tehranizadeh, Z., A. Baratian, and H. Hosseinzadeh. 2016. Russian olive (*Elaeagnus angustifolia*) as a herbal healer. *BioImpacts : Bioimpacts* 6 (3):155–67. doi: 10.15171/bi.2016.22.

Amudha, P. An overview of phytochemical and pharmacological potential of Baccaurea species.

An, X., S. G. Lee, H. Kang, H. J. Heo, Y.-S. Cho, and D.-O. Kim. 2016. Antioxidant and anti-inflammatory effects of various cultivars of kiwi berry (*Actinidia arguta*) on lipopolysaccharide-stimulated RAW 264.7 Cells. *Journal of Microbiology and Biotechnology* 26 (8):1367–74. doi: 10.4014/jmb.1603.03009.

Anand Swarup, K. L., M. A. Sattar, N. A. Abdullah, M. H. Abdulla, I. M. Salman, H. A. Rathore, and E. J. Johns. 2010. Effect of dragon fruit extract on oxidative stress and aortic stiffness in streptozotocin-induced diabetes in rats. *Pharmacognosy Research* 2 (1):31. doi: 10.4103/0974-8490.60582.

Angami, T., L. Wangchu, P. Debnath, P. Sarma, B. Singh, A. K. Singh, S. Singh, B. N. Hazarika, M. C. Singh, and L. Aochen. 2020. Garcinia L.: A gold mine of future therapeutics. *Genetic Resources and Crop Evolution* 68 (1):11–24. doi: 10.1007/s10722-020-01057-5.

Ansori, A. N. M., A. Fadholly, S. Hayaza, R. J. K. Susilo, B. Inayatillah, D. Winarni, and S. A. Husen. 2020. A review on medicinal properties of mangosteen (*Garcinia mangostana* L.). *Research Journal of Pharmacy and Technology* 13 (2):974. doi: 10.5958/0974-360X.2020.00182.1.

Arivalagan, M., T. K. Roy, A. M. Yasmeen, K. C. Pavithra, P. N. Jwala, K. S. Shivasankara, M. R. Manikantan, K. B. Hebbar, and S. R. Kanade. 2018. Extraction of phenolic compounds with antioxidant potential from coconut (*Cocos nucifera* L.) testa and identification of phenolic acids and flavonoids using UPLC coupled with TQD-MS/MS. *LWT* 92:116–26. doi: 10.1016/j.lwt.2018.02.024.

Aruan, D. G. R., T. Barus, G. Haro, R. Siburian, and P. Simanjuntak. 2019. Phytochemical screening and antidiabetic activity of N-hexane, ethyl acetate and water extract from Durian leaves (*Durio zibethinus* L.). *Oriental Journal of Chemistry* 35 (1):487–90. doi: 10.13005/ojc/350166.

Asmaliani, I., and M. I. Iwo. 2016. The effect from methanol extract of jackfruit leaves (Artocarpus heterophyllus Lam) in rheumatoid arthritis rat induced collagen type II. *Der Pharmacia Lettre* 8 (18)

Aune, D., E. Giovannucci, P. Boffetta, L. T. Fadnes, N. Keum, T. Norat, D. C. Greenwood, E. Riboli, L. J. Vatten, and S. Tonstad. 2017. Fruit and vegetable intake and the risk of cardiovascular disease, total cancer and all-cause mortality—a systematic review and dose-response meta-analysis of prospective studies. *International Journal of Epidemiology* 46 (3):1029–56. doi: 10.1093/ije/dyw319.

Atiqah, N. A. A. K. A. M. Maisarah, and R. Asmah. 2014. Comparison of antioxidant properties of tamarillo (*Cyphomandra betacea*), cherry tomato (*Solanumly copersicum* var. cerasiform) and tomato (*Lyopersicon esulentum*). *International Food Research Journal* 21 (6).

Azab, E. F., and H. S. Mostafa. 2021. Phytochemical analysis and antioxidant defense of kiwifruit (*Actinidia deliciosa*) against pancreatic cancer and AAPH-induced RBCs hemolysis. *Food Science and Technology* . doi: 10.1590/fst.06021.

Aziz, N. A. A., and A. M. M. Jalil. 2019. Bioactive Compounds, nutritional value, and potential health benefits of indigenous durian. (*Durio Zibethinus Murr.): A Review. Foods* 8 (3)doi: 10.3390/FOODS8030096.

Aziz, N., and A. Mhd Jalil. 2019. Bioactive compounds, nutritional value, and potential health benefits of indigenous durian (*Durio zibethinus* Murr.). *Foods* 8 (3):96. . doi: 10.3390/foods8030096.

Ballesteros-Vivas, D., G. Alvarez-Rivera, C. León, S. J. Morantes, E. Ibánez, F. Parada-Alfonso, A. Cifuentes, and A. Valdés. 2020. Foodomics evaluation of the anti-proliferative potential of *Passiflora mollissima* seeds. *Food Research International (Ottawa, Ont.)* 130:108938. doi: 10.1016/j.foodres.2019.108938.

Bano, M., and B. Ahmed. 2017. *Manilkara zapota* (L.) P. Royen (Sapodilla): A review. *International Journal of Advance Research, Ideas and Innovations in Technology* 3:1364–71.

BaoMei, L., Q. ShanLian, Z. KaiBin, Z. Shuai, H. JiaMin, and Z. ShaoPing. 2019. Process optimization and in vitro hypoglycemic effect of polyphenols extracted from jaboticaba leaves. *Fujian Journal of Agricultural Sciences* 34 (5):587–94.

Barbalho, S. M., P. C. d S. Bueno, D. S. Delazari, E. L. Guiguer, D. P. Coqueiro, A. C. Araújo, M. d S. S. de Souza, F. M. V. Farinazzi-Machado, C. G. Mendes, and M. Groppo. 2015. Antidiabetic and antilipidemic effects of *Manilkara zapota*. *Journal of Medicinal Food* 18 (3):385–91. doi: 10.1089/jmf.2013.0170.

Barreca, D., G. Laganà, S. Ficarra, E. Tellone, U. Leuzzi, A. Galtieri, and E. Bellocco. 2011. Evaluation of the antioxidant and cytoprotective properties of the exotic fruit *Annona cherimola* Mill. (Annonaceae). *Food Research International* 44 (7):2302–10. doi: 10.1016/j.foodres.2011.02.031.

Barua, C. C., N. Yasmin, and L. Buragohain. 2018. A review update on *Dillenia indica*, its morphology, phytochemistry and pharmacological activity with reference to its anticancer activity. *MOJ Bioequivalence & Bioavailability Research* 5 (5):244–54. doi: 10.15406/mojbb.2018.05.00110.

Basheer, L., and Z. Kerem. 2015. Interactions between CYP3A4 and Dietary Polyphenols. *Oxidative Medicine and Cellular Longevity* 2015:1–15. doi: 10.1155/2015/854015.

Basitah, T. 2015. Extraction, characterization and application of natural dyes from the fresh rind of index colour 5 Mangosteen (*Garcinia mangostana* L.). *International Journal of Chemical and Molecular Engineering* 9 (7):883–6. doi: 10.5281/ZENODO.1108885.

Baskar, M., G. Hemalatha, and P. Muneeshwari. 2020. Traditional and medicinal importance of sapota – Review. *International Journal of Current Microbiology and Applied Sciences* 9 (1):1711–7. doi: 10.20546/ijcmas.2020.901.189.

Basumatary, J., C. B. Khobragade, S. K. Paul, and P. Kumar. Study of physical, optical and biochemical characteristics of elephant apple (*Dillenia indica*) for its utility potential in food processing industries. *Journal of Agricultural Engineering and Food Technology* 3 (1):54–7. http://www.krishisanskriti.org/Publication.html.

Basyuni, M., R. Hayati, M. A. Sihaloho, B. Slamet, Y. Bimantara, T. S. Habsyah, D. S. Hanafiah, and E. Julianti. 2019. Bioinformatics approach of predicted polyprenol reductase in Durian (*Durio zibethinus* Murr.). *IOP Conference Series: Earth and Environmental Science* 305 (1):012036. doi: 10.1088/1755-1315/305/1/012036.

Bawazeer, S., and A. Rauf. 2021. In vivo anti-inflammatory, analgesic, and sedative studies of the extract and naphthoquinone isolated from *Diospyros kaki* (Persimmon). *ACS Omega* 6 (14):9852–6. doi: 10.1021/acsomega.1c00537.

Beidokhti, M. N., and A. K. Jäger. 2017. Review of antidiabetic fruits, vegetables, beverages, oils and spices commonly consumed in the diet. *Journal of Ethnopharmacology* 201:26–41. doi: 10.1016/j.jep.2017.02.031.

Belarbi, M., S. Bendimerad, S. Sour, Z. Soualem, C. Baghdad, S. Hmimed, F. Chemat, and F. Visioli. 2011. Oleaster oil positively modulates plasma lipids in humans. *Journal of Agricultural and Food Chemistry* 59 (16):8667–9. doi: 10.1021/jf201865z.

Beltrão, L. P., F. Jane, G. Da Silva, and P. Roberto Gagliardi. 2016. Functional dye obtained from Jabuticaba Fruit (Myrciaria spp.). doi: 10.7198/S2318-3403201600030073.

Benvenutti, L., A. A. F. Zielinski, and S. R. S. Ferreira. 2021. Jaboticaba (*Myrtaceae cauliflora*) fruit and its by-products: Alternative sources for new foods and functional components. *Trends in Food Science & Technology* 112:118–36. doi: 10.1016/j.tifs.2021.03.044.

Bhagya Raj, G. V. S., and K. K. Dash. 2020. Ultrasound-assisted extraction of phytocompounds from dragon fruit peel: Optimization, kinetics and thermodynamic studies. *Ultrasonics Sonochemistry* 68:105180. doi: 10.1016/j.ultsonch.2020.105180.

Bhagyasri, Y., Goud, S. D., M. Suvarna Ch. and N. Siva Subramania. 2017. A pharmacological review on elephant apple. *World Journal of Pharmacy and Pharmaceutical Sciences* 6 (12):1809–16. doi: 10.20959/wjpps201712-10678.

Bhardwaj, R., S. Pareek, N. A. Sagar, and N. Vyas. 2019. Bioactive compounds of Annona. *In: [Place Unknown]* :1–26. doi: 10.1007/978-3-030-06120-3_5-1.

Bhat, R. S., and S. Al-Daihan. 2014. Antimicrobial activity of *Litchi chinensis* and *Nephelium lappaceum* aqueous seed extracts against some pathogenic bacterial strains. *Journal of King Saud University - Science* 26 (1):79–82. doi: 10.1016/j.jksus.2013.05.007.

Bhatt, I. D., S. Rawat, and R. S. Rawal. 2020. Himalayan bayberries. In: *Nutritional composition and antioxidant properties of fruits and vegetables*, 457–65. Elsevier. doi: 10.1016/B978-0-12-812780-3.00028-3.

Bhattacharya, S., S. R. Chaudhuri, S. Chattopadhyay, and S. K. Bandyopadhyay. 2007. Healing properties of some indian medicinal plants against indomethacin-induced gastric ulceration of rats. *Journal of Clinical Biochemistry and Nutrition* 41 (2):106–14. doi: 10.3164/jcbn.2007015.

Bhowmik, D., K. P. S. Kumar, S. Paswan, and S. Srivastava. 2012. Tomato-A natural medicine and its health benefits. *Phytojournal* 1 (1):33–43.

Binita, S., B. Ajoy, S. Phukan, and B. Singha. 2016. Hypolipidemic activity of *Phyllanthus acidus* leaves in Hypercholesterolemic diet-induced hyperlipidemia in rats. *Scholars Journal of Applied Medical Sciences (SJAMS)* 4 (10B):3648–53. doi: 10.21276/sjams.2016.4.10.21.

Bohs, L. 1989. Ethnobotany of the genus Cyphomandra (Solanaceae). *Economic Botany* 43 (2):143–63. doi: 10.1007/BF02859855.

Boparai, A., J. Niazi, N. Bajwa, and P. A. Singh. 2016. A review update on *Dillenia indica* F. Elongata (MIQ.)MIQ. *Journal of Drug Delivery and Therapeutics* 6 (2). doi: 10.22270/jddt.v6i2.1226.

Bordoloi, B., and S. Das. 2019. Preliminary phytochemical screening and to evaluate anti-oxidant property on root extract of *Dillenia indica* (Elephant Apple). *International Journal of Current Pharmaceutical Research* :128–33. doi: 10.22159/ijcpr.2019v11i4.34957.

Bowen, K. J., W. S. Harris, and P. M. Kris-Etherton. 2016. Omega-3 Fatty Acids and Cardiovascular Disease: Are There Benefits? *Current Treatment Options in Cardiovascular Medicine* 18 (11):69. doi: 10.1007/s11936-016-0487-1.

Bressiani, P. A., G. R. F. De Lima, E. Düsman, and L. T. D. Tonin. 2021. Cytotoxic and antioxidant activities of *Tamarindus indica* pulp extract from Brazil. *Journal of Food Measurement and Characterization* 15 (3):2743–9. doi: 10.1007/s11694-021-00855-4.

Hunter, D., J. Greenwood, J. Zhang, and M. A. Skinner. 2011. Antioxidant and 'natural protective'properties of kiwifruit. *Current Topics in Medicinal Chemistry* 11 (14):1811–20. doi: 10.2174/156802611796235134.

Cabral, T. A., M. Cardoso L de, and H. M. Pinheiro-Sant'Ana. 2014. Chemical composition, vitamins and minerals of a new cultivar of lychee (*Litchi chinensis* cv. Tailandes) grown in Brazil. *Fruits* 69 (6):425–34. doi: 10.1051/fruits/2014031.

Cabrini, D. A., H. H. Moresco, P. Imazu, C. D. d Silva, E. F. Pietrovski, D. A. G. B. Mendes, A. d S. Prudente, M. G. Pizzolatti, I. M. C. Brighente, and M. F. Otuki. 2011. 2011. Analysis of the potential topical anti-inflammatory activity of *Averrhoa carambola* L. in mice. *Evidence-Based Complementary and Alternative Medicine* 2011:1–7. doi: 10.1093/ecam/neq026.

Cao, Y., Z. Wu, and P. Weng. 2020. Comparison of bayberry fermented wine aroma from different cultivars by GC-MS combined with electronic nose analysis. *Food Science & Nutrition* 8 (2):830–40. doi: 10.1002/fsn3.1343.

Carasek, E., and J. Pawliszyn. 2006. Screening of tropical fruit volatile compounds using solid-phase microextraction (SPME) fibers and internally cooled SPME fiber doi: 10.1021/jf0613942.

Casarotti, S. N., T. F. Borgonovi, C. L. F. M. Batista, and A. L. B. Penna. 2018. Guava, orange and passion fruit by-products: Characterization and its impacts on kinetics of acidification and

properties of probiotic fermented products. *LWT* 98:69–76. doi: 10.1016/j.lwt.2018.08.010.

Cazarin, C. B. B., A. Rodriguez-Nogales, F. Algieri, M. P. Utrilla, M. E. Rodríguez-Cabezas, J. Garrido-Mesa, E. Guerra-Hernández, P. A. Braga, C. de, F. G. R. Reyes, et al. 2016. Intestinal anti-inflammatory effects of *Passiflora edulis* peel in the dextran sodium sulphate model of mouse colitis. *Journal of Functional Foods* 26:565–76. doi: 10.1016/j.jff.2016.08.020.

Cazarin, C. B. B., J. K. da Silva, T. C. Colomeu, Â. G. Batista, L. M. M. Meletti, J. A. R. Paschoal, S. Bogusz Junior, P. A. d C. Braga, F. G. R. Reyes, F. Augusto, et al. 2015. Intake of *Passiflora edulis* leaf extract improves antioxidant and anti-inflammatory status in rats with 2,4,6-trinitrobenzenesulphonic acid induced colitis. *Journal of Functional Foods* 17:575–86. doi: 10.1016/j.jff.2015.05.034.

Cazarolli, L. H., V. D. Kappel, D. F. Pereira, H. H. Moresco, I. M. C. Brighente, M. G. Pizzolatti, and F. R. M. B. Silva. 2012. Anti-hyperglycemic action of apigenin-6-C-β-fucopyranoside from *Averrhoa carambola*. *Fitoterapia* 83 (7):1176–83. doi: 10.1016/j.fitote.2012.07.003.

Cha, J. H., W. K. Kim, A. W. Ha, M. H. Kim, and M. J. Chang. 2017. Anti-inflammatory effect of lycopene in SW480 human colorectal cancer cells. *Nutrition Research and Practice* 11 (2):90. doi: 10.4162/nrp.2017.11.2.90.

Chan, C. K., B. H. Goh, M. N. A. Kamarudin, and H. A. Kadir. 2012. Aqueous fraction of *Nephelium ramboutan*-ake rind induces mitochondrial-mediated apoptosis in HT-29 human colorectal adenocarcinoma cells. *Molecules* 17 (6):6633–57. doi: 10.3390/molecules17066658.

Chang, B.-Y., B.-S. Koo, and S.-Y. Kim. 2021. Pharmacological activities for *Morus alba* L., focusing on the immunostimulatory property from the fruit aqueous extract. *Foods* 10 (8):1966. doi: 10.3390/foods10081966.

Chao, M.-W., C.-H. Chen, Y.-L. Chang, C.-M. Teng, and S.-L. Pan. 2012. α-Tomatine-mediated anti-cancer activity in vitro and in vivo through cell cycle- and caspase-independent pathways. *PLoS One.* 7 (9):e44093. doi: 10.1371/journal.pone.0044093.

Chen, D., J. Y. Chia, and S.-Q. Liu. 2014. Impact of addition of aromatic amino acids on non-volatile and volatile compounds in lychee wine fermented with *Saccharomyces cerevisiae* MERIT.ferm. *International Journal of Food Microbiology* 170:12–20. doi: 10.1016/j.ijfoodmicro.2013.10.025.

Cheng, J., X. Ye, J. Chen, D. Liu, and S. Zhou. 2008. Nutritional composition of underutilized bayberry (*Myrica rubra* Sieb. et Zucc.) kernels. *Food Chemistry* 107 (4):1674–80. Analytical Methods. doi: 10.1016/j.foodchem.2007.09.042.

Chigurupati, S. 2021. Antidiabetic and antioxidant potential of *Durio zibethinus* Murr. leaves ethanolic extract. *Indian Journal of Experimental Biology (IJEB)* 59 (02):102–10.

Chingsuwanrote, P., C. Muangnoi, K. Parengam, and S. Tuntipopipat. 2016. Antioxidant and anti-inflammatory activities of durian and rambutan pulp extract. *International Food Research Journal* 23 (3):939–47.

Choo, W. S. 2018. Betalains: Application in functional foods, 1–28. doi: 10.1007/978-3-319-54528-8_38-2.

Choo, W. S., L. Dufossé, and L. Morales-Oyervides. 2021. Editorial: Sustainable production of bioactive pigments. *Frontiers in Sustainable Food Systems* 5. doi: 10.3389/fsufs.2021.674311.

Chyau, C.-C., P.-T. Ko, C.-H. Chang, and J.-L. Mau. 2003. Free and glycosidically bound aroma compounds in lychee (Litchi chinensis Sonn.). *Food Chemistry* 80 (3):387–92. doi: 10.1016/S0308-8146(02)00278-9.

Cirmi, S., A. Maugeri, N. Ferlazzo, S. Gangemi, G. Calapai, U. Schumacher, and M. Navarra. 2017. Anticancer potential of citrus juices and their extracts: A systematic review of both preclinical and clinical studies. *Frontiers in Pharmacology* 8. doi: 10.3389/fphar.2017.00420.

Cock, I. E., and S. Mohanty. 2011. Evaluation of the antibacterial activity and toxicity of *Terminalia ferdinandia* fruit extracts. *Pharmacognosy Journal* 3 (20):72–9. doi: 10.5530/pj.2011.20.14.

Conesa, C.,. N. Laguarda-Miró, P. Fito, and L. Seguí. 2020. Evaluation of persimmon (*Diospyros kaki* Thunb. cv. Rojo Brillante) industrial residue as a source for value added products. *Waste and Biomass Valorization* 11 (7):3749–60. doi: 10.1007/s12649-019-00621-0.

Contreras, C., W. Schwab, M. Mayershofer, I. Morales, M. Gonzalez-Agüero, and B. G. Defilippi. 2019. Study of physiological and quality parameters during development and ripening of pepino (*Solanum muricatum* Aiton) fruit. *Chilean Journal of Agricultural Research* 79 (3):385–95. doi: 10.4067/S0718-58392019000300385.

Coria-Téllez, A. v., E. Montalvo-Gónzalez, E. M. Yahia, and E. N. Obledo-Vázquez. 2018. *Annona muricata*: A comprehensive review on its traditional medicinal uses, phytochemicals, pharmacological activities, mechanisms of action and toxicity. *Arabian Journal of Chemistry* 11 (5):662–91. doi: 10.1016/j.arabjc.2016.01.004.

Correa, M. G., J. S. Couto, B. B. Trindade, J. P. Abreu, V. M. Nakajima, F. L. Oliveira, A. Farah, and A. J. Teodoro. 2020. Antiproliferative effect of guava fruit extracts in MDA-MB-435 and MCF-7 human breast cancer cell lines. *Anais da Academia Brasileira de Ciências* 92 (2). doi: 10.1590/0001-3765202020191500.

Corrêa, R. C. G., R. M. Peralta, C. W. I. Haminiuk, G. M. Maciel, A. Bracht, and I. C. F. R. Ferreira. 2016. The past decade findings related with nutritional composition, bioactive molecules and biotechnological applications of Passiflora spp. (Passion fruit). *Trends in Food Science & Technology* 58:79–95. doi: 10.1016/j.tifs.2016.10.006.

Cortez, R., D. A. Luna-Vital, D. Margulis, and E. Gonzalez de Mejia. 2017. Natural pigments: Stabilization methods of anthocyanins for food applications. *Comprehensive Reviews in Food Science and Food Safety* 16 (1):180–98. doi: 10.1111/1541-4337.12244.

Dastmalchi, K., G. Flores, S.-B. Wu, C. Ma, A. J. Dabo, K. Whalen, K. A. Reynertson, R. F. Foronjy, J. M. D´Armiento, and E. J. Kennelly. 2012. Edible myrciaria vexator fruits: bioactive phenolics for potential COPD therapy. *Bioorganic & Medicinal Chemistry* 20 (14):4549–55. doi: 10.1016/j.bmc.2012.05.013.

Daswani, P. G., M. S. Gholkar, and T. J. Birdi. 2017. *Psidium guajava*: A single plant for multiple health problems of rural Indian population. *Pharmacognosy Reviews* 11 (22):167–74. doi: 10.4103/phrev.phrev_17_17.

de Lima Paula, P.,. A. S. de Oliveira Lemos, L. M. Campos, T. G. Ferreira, T. Freitas de Souza, L. S. Queiroz, M. C. Machado Resende Guedes, M. M. Martins, L. R. Goulart Filho, G. C. Macedo, et al. 2021. Pharmacological investigation of antioxidant and anti-inflammatory activities of leaves and branches extracts from *Plinia cauliflora* (Jaboticaba). *Journal of Ethnopharmacology* 280:114463. doi: 10.1016/j.jep.2021.114463.

de Sousa, O. V., G. D. V. de Vieira, J. R. G. Pinho de, C. H. Yamamoto, and M. S. Alves. 2010. Antinociceptive and anti-inflammatory activities of the ethanol extract of Annona muricata L. leaves in animal models. *International ournal of olecular ciences* 11 (5):2067–78. doi: 10.3390/ijms11052067.

de Souza, C. G., D. M. L. de Andrade, J. B. R. Jordão, R. I. de Ávila, L. L. Borges, B. G. Vaz, M. C. Valadares, E. de Souza Gil, E. C. da Conceição, and M. L. Rocha. 2017. Radical scavenger capacity of jabuticaba fruit (*Myrciaria cauliflora*) and its biological effects in hypertensive rats. *Oxidative Medicine and Cellular Longevity* :1–10. 2017. doi: 10.1155/2017/2383157.

de Souza M da, S. S., S. M. Barbalho, D. C. Damasceno, M. V. C. Rudge, K. E. de Campos, A. C. G. Madi, B. R. Coelho, R. C. Oliveira, R. C. de Melo, and V. C. Donda. 2012. Effects of *Passiflora edulis* (yellow passion) on serum lipids and oxidative stress status of wistar rats. *Journal of Medicinal Food* 15 (1):78–82. doi: 10.1089/jmf.2011.0056.

D'Eliseo, D.,. E. Pannucci, R. Bernini, M. Campo, A. Romani, L. Santi, and F. Velotti. 2019. In vitro studies on anti-inflammatory activities of kiwifruit peel extract in human THP-1 monocytes. *Journal of Ethnopharmacology* 233:41–6. doi: 10.1016/j.jep.2018.12.044.

Dev, S. 1989. Terpenoids. doi: 10.1007/978-3-642-74075-6_19.

Díaz-de-Cerio, E., V. Verardo, A. Gómez-Caravaca, A. Fernández-Gutiérrez, and A. Segura-Carretero. 2017. Health effects of *Psidium guajava* L. Leaves: An overview of the last decade. *International Journal of Molecular Sciences* 18 (4):897. doi: 10.3390/ijms18040897.

Díaz-de-Cerio, E., V. Verardo, A. M. Gómez-Caravaca, A. Fernández-Gutiérrez, and A. Segura-Carretero. 2016. Exploratory Characterization of Phenolic Compounds with Demonstrated Anti-Diabetic Activity in Guava Leaves at Different Oxidation States. *International Journal of Molecular Sciences* 17 (5):699. doi: 10.3390/ijms17050699.

Diep, T. T., E. C. Rush, and M. J. Y. Yoo. 2020. Tamarillo (*Solanum betaceum* Cav.): A review of physicochemical and bioactive properties and potential applications. *Food Reviews International* :1–25. doi: 10.1080/87559129.2020.1804931.

Direito, R., J. Rocha, B. Sepodes, and M. Eduardo-Figueira. 2021. From *Diospyros kaki* L. (Persimmon) phytochemical profile and health impact to new product perspectives and waste valorization. *Nutrients* 13 (9):3283. doi: 10.3390/nu13093283.

Dorly, S., Tjitrosemito, R.Poerwanto. and J. 2008. Secretory duct structure and phytochemistry compounds of yellow latex in mangosteen fruit. *HAYATI Journal of Biosciences* 15 (3):99–104. doi: 10.4308/hjb.15.3.99.

Drummond, L. 2013. The composition and nutritional value of kiwifruit. *Advances in Food and Nutrition Research* 68:33–57. doi: 10.1016/B978-0-12-394294-4.00003-1.

D'souza, J. J., P. P. D'souza, F. Fazal, A. Kumar, H. P. Bhat, and M. S. Baliga. 2014. Anti-diabetic effects of the Indian indigenous fruit *Emblica officinalis* Gaertn: Active constituents and modes of action. *Food & Function* 5 (4):635–44. doi: 10.1039/c3fo60366k.

Durant, A. A., C. Rodreguez, and A. Santana. 2012. Analysis of volatile compounds from *Solanum betaceum* Cav. fruits from Panama by head-space micro extraction. *Records of Natural Products* 7 (1):15–26.

Dutta, I., B. Gogoi, R. Sharma, and H. K. Sharma. 2018. In vitro evaluation of leaves and fruits of *Elaeagnus latifolia* L. for antioxidant and antimicrobial activities. *Asian Journal of Chemistry* 30 (11):2433–6. doi: 10.14233/ajchem.2018.21430.

Duttaroy, A. K. 2013. Cardioprotective properties of kiwifruit :273–82. doi: 10.1016/B978-0-12-394294-4.00015-8.

Dzotam, J. K., F. K. Touani, and V. Kuete. 2015. Antibacterial and antibiotic-modifying activities of three food plants (Xanthosoma mafaffa Lam., Moringa oleifera (L.) Schott and Passiflora edulis Sims) against multidrug-resistant (MDR) Gram-negative bacteria. *BMC Complementary and Alternative Medicine* 16 (1):9. doi: 10.1186/s12906-016-0990-7.

El Hadi, M. A. M., F.-J. Zhang, F.-F. Wu, C.-H. Zhou, and J. Tao. 2013. Advances in fruit aroma volatile research. *Molecules* 18 (7):8200–29. doi: 10.3390/molecules18078200.

el Houda Lezoul, N., M. Belkadi, F. Habibi, and F. Guillén. 2020. Extraction processes with several solvents on total bioactive compounds in different organs of three medicinal plants. *Molecules* 25 (20):4672. doi: 10.3390/molecules25204672.

EL-Meghawry EL-Kenawy, A., H. Hassan Sm, and H.-E. Osman. 2019. Chapter 3.29 -Mangosteen (Garcinia mangostana L.). In. *Nonvitamin and nonmineral nutritional supplement*, 313–9. USA: Academic Press. doi: 10.1016/B978-0-12-812491-8.00045-X.

Emanuele, S., A. Notaro, A. Palumbo Piccionello, A. Maggio, M. Lauricella, A. D'Anneo, C. Cernigliaro, G. Calvaruso, and M. Giuliano. 2018. Sicilian litchi fruit extracts induce autophagy versus apoptosis switch in human colon cancer cells. *Nutrients* 10 (10):1490. doi: 10.3390/nu10101490.

Emylia, K., N. A. Snz, and M. Dasuki. 2013. Preliminary study on antiproliferative activity of methanolic extract of *Nephelium lappaceum* peels towards breast (MDA-MB-231), cervical (HeLa) and osteosarcoma (MG-63) cancer cell lines. *Health and the Environment Journal* 4 (2):66–79.

Espirito Santo, B. L., S., L. F. Santana, W. H. Kato Junior, F. de Araújo, D. Bogo, K. Freitas, R. de Guimarães, et al. 2020. Medicinal potential of Garcinia species and their compounds. *Molecules* 25 (19):4513. doi: 10.3390/molecules25194513.

Eve, A., A. A. Aliero, D. Nalubiri, R. O. Adeyemo, S. A. Akinola, T. Pius, S. Nabaasa, S. Nabukeera, B. Alkali, and I. Ntulume. 2020. In vitro antibacterial activity of crude extracts of *Artocarpus heterophyllus* seeds against selected diarrhoea-causing superbug bacteria. *The Scientific World Journal* 2020:1–11. doi: 10.1155/2020/9813970.

Farahbakhsh, S., S. Arbabian, F. Emami, B. R. Moghadam, H. Ghoshooni, A. Noroozzadeh, H. Sahraei, L. Golmanesh, C. Jalili, and H. Zrdooz. 2011. Inhibition of cyclooxygenase type 1 and 2 enzyme by aqueous extract of *Elaeagnus Angustifolia* in mice. *Basic and Clinical Neuroscience* 2 (2):31–7.

Fedorova, Y. S., P. V. Kulpin, T. V. Kotova, S. V. Denisova, and G. V. Beregovykh. 2021. Research of psychotropic properties of Xanton-containing plants. In: AIP Conference Proceedings. Vol. 2419. AIP Publishing LLC; 50002.

Felipe do Nascimento, K., C. A. Leite Kassuya, M. R. Pereira Cabral, R. I. Carvalho Souza, J. A. Marangoni, R. M. Mussury Franco Silva, D. Alves da Costa Canella, and A. S. Nazari Formagio. 2021. Chemical analysis and antioxidant, anti-inflammatory and toxicological evaluations of the hydromethanolic extract of *Psidium guineense* Swartz leaves. *Journal of Ethnopharmacology* 281:114492. doi: 10.1016/j.jep.2021.114492.

Feng, X., Z. Wang, D. Meng, and X. Li. 2015. Cytotoxic and antioxidant constituents from the leaves of *Psidium guajava*. *Bioorganic & Medicinal Chemistry Letters* 25 (10):2193–8. doi: 10.1016/j.bmcl.2015.03.058.

Fernández-López, J. A., V. Fernández-Lledó, and J. M. Angosto. 2020. New insights into red plant pigments: More than just natural colorants. *RSC Advances* 10 (41):24669–82. doi: 10.1039/D0RA03514A.

Ferreira, E. B., L. C. Fernandes, S. B. Galende, D. A. G. Cortez, and R. B. Bazotte. 2008. Hypoglycemic effect of the hydroalcoholic extract of leaves of *Averrhoa carambola* L. (Oxalidaceae). *Revista Brasileira de Farmacognosia* 18 (3):339–43. doi: 10.1590/S0102-695X2008000300005.

Fila, W. O., J. T. Johnson, P. N. Edem, M. O. Odey, V. S. Ekam, U. Up, and O. E. Eteng. 2012. Comparative anti-nutrients assessment of pulp, seed and rind of rambutan (*Nephelium lappaceum*). *Annals of Biological Research* 3 (11).

Flores, G., K. Dastmalchi, S.-B. Wu, K. Whalen, A. J. Dabo, K. A. Reynertson, R. F. Foronjy, J. M. D'Armiento, and E. J. Kennelly. 2013. Phenolic-rich extract from the Costa Rican guava (*Psidium friedrichsthalianum*) pulp with antioxidant and anti-inflammatory activity. Potential for COPD therapy. *Food Chemistry* 141 (2):889–95. doi: 10.1016/j.foodchem.2013.03.025.

Fortes, G. A. C., S. S. Naves, F. F. F. Godoi, A. R. Duarte, P. H. Ferri, and S. C. Santos. 2011. Assessment of a maturity index in Jabuticaba fruit by the evaluation of phenolic compounds, essential oil components, sugar content and total acidity. *American Journal of Food Technology* 6 (11):974–84. doi: 10.3923/ajft.2011.974.984.

Fraga, C. G., K. D. Croft, D. O. Kennedy, and F. A. Tomás-Barberán. 2019. The effects of polyphenols and other bioactives on human health. *Food & Function* 10 (2):514–28. doi: 10.1039/C8FO01997E.

Frohlich, O., and P. Schreier. 1989. Additional volatile constituents of carambola (*Averrhoa carambola* L.) fruit. *Flavour and Fragrance Journal* 4 (4):177–84. doi: 10.1002/ffj.2730040405.

Fröhlich, O., and P. Schreier. 1990. Volatile constituents of loquat (*Eriobotrya japonica* Lindl.) Fruit. *Journal of Food Science* 55 (1):176–80. doi: 10.1111/j.1365-2621.1990.tb06046.x.

Fu, C., D. Yang, W. Y. E. Peh, S. Lai, X. Feng, and H. Yang. 2015. Structure and antioxidant activities of proanthocyanidins from elephant apple (*Dillenia indica* Linn.).*Journal of Food Science* 80 (10):C2191–C2199. doi: 10.1111/1750-3841.13005.

Fu, Y., H. Zhou, M. Wang, J. Cen, and Q. Wei. 2014. Immune regulation and anti-inflammatory effects of isogarcinol extracted from *Garcinia mangostana* L. against collagen-induced arthritis. *Journal of Agricultural and Food Chemistry* 62 (18):4127–34. doi: 10.1021/jf405790q.

Gaire, B. P., and L. Subedi. 2014. Phytochemistry, pharmacology and medicinal properties of *Phyllanthus emblica* Linn. *Chinese Journal of Integrative Medicine*. doi: 10.1007/s11655-014-1984-2.

Garcia, L. G. C., Silva, F. A. da, Asquieri, E. R. Boas, E. V. de, B. V. Damiani. and C. 2019. Bioactive compounds and antioxidant activity of jabuticaba var. Pingo de mel during its physiological development. *Food Science and Technology* 39 (suppl 2):556–62. doi: 10.1590/fst.25218.

Garcia-Amezquita, L. E., V. Tejada-Ortigoza, O. H. Campanella, and J. Welti-Chanes. 2018. Influence of drying method on the compo-

sition, physicochemical properties, and prebiotic potential of dietary fibre concentrates from fruit peels. *Journal of Food Quality* 2018:1–11. doi: 10.1155/2018/9105237.

Ge, J.-F., T.-Y. Wang, B. Zhao, X.-W. Lv, Y. Jin, L. Peng, S.-C. Yu, and J. Li. 2009. Anti-inflammatory effect of triterpenoic acids of *Eriobotrya japonica* (Thunb.) Lindl. leaf on rat model of chronic bronchitis. *The American Journal of Chinese Medicine* 37 (2):309–21. doi: 10.1142/S0192415X09006862.

Ghosh, S., T. Sarkar, A. Das, and R. Chakraborty. 2021. Micro and nanoencapsulation of natural colors: A holistic view. *Applied Biochemistry and Biotechnology* 193 (11):3787–811. doi: 10.1007/s12010-021-03631-8.

Ghosh, S., T. Sarkar, A. Das, and R. Chakraborty. 2022. Natural colorants from plant pigments and their encapsulation: An emerging window for the food industry. *LWT* 153 (16):112527. doi: 10.1016/j.lwt.2021.112527.

Goel, P., and D. Agarwal. 2020. A strong antioxidant: Ascorbic acid or vitamin C is an active ingredient of Indian Gooseberry (*Emblica officinalis*). *Structure* 4 (5):6.

Golechha, M., V. Sarangal, S. Ojha, J. Bhatia, and D. S. Arya. 2014. Anti-inflammatory effect of *Emblica officinalis* in rodent models of acute and chronic inflammation: Involvement of possible mechanisms. *International Journal of Inflammation* 2014:1–6. doi: 10.1155/2014/178408.

Gonçalves Albuquerque, T., F. Santos, A. Sanches-Silva, M. B. Oliveira, A. C. Bento, and H. S. Costa. 2016. Analytical methods nutritional and phytochemical composition of *Annona cherimola* Mill. fruits and by-products: Potential health benefits. *Food Chemistry* 193:187–95. doi: 10.1016/j.foodchem.2014.06.044.

Goswami, C., and R. Chacrabati. 2016. Chapter 14 - Jackfruit (*Artocarpus heterophylus*). In *Nutritional composition of fruit cultivars*, 317–35. USA: Elsevier, Academic Press. doi: 10.1016/B978-0-12-408117-8.00014-3.

Goud, N., G. Prasad, and S. Kumar. 2019. Phytochemical analysis antibacterial and antioxidant capacity of acetone and methanol pericarp extract of mangosteen. 8:44–7.

Goyal, A. K., S. K. Middha, and T. Usha. 2020. *Baccaurea ramiflora* Lour.: a comprehensive review from traditional usage to pharmacological evidence. *Advances in Traditional Medicine* . doi: 10.1007/s13596-020-00489-9.

Granato, D., I. A. de Castro, F. V. B. W. Piekarski, C. Benincá, and M. L. Masson. 2011. Influence of passion fruit juice on colour stability and sensory acceptability of non-sugar Yacon-based pastes. *Brazilian Archives of Biology and Technology* 54 (1):149–59. doi: 10.1590/S1516-89132011000100020.

Guimarães, D. A. B., D. D. S. De Castro, F. L. de Oliveira, E. M. Nogueira, M. A. M. da, Silva, and A. J. Teodoro. 2017. Pitaya extracts induce growth inhibition and proapoptotic effects on human cell lines of breast cancer via downregulation of estrogen receptor gene expression. *Oxidative Medicine and Cellular Longevity* 2017:1–13. doi: 10.1155/2017/7865073.

Gulnaz, A. R. and G. Savitha. 2013. Phytochemical evaluation of leaf and stem extracts of siddha medicinal plant: Sida cordata. *Journal of Evolution of Medical and Dental Sciences* 2 (15):2514–21. doi: 10.14260/jemds/570.

Gupta, D., S. Mann, A. Sood, and R. K. Gupta. 2011. Phytochemical, nutritional and antioxidant activity evaluation of seeds of jackfruit (*Artocarpus heterophyllus* Lam.). *International Journal of Pharma and Bio Sciences* 2 (4):336–45.

Gupta, S., and K. Pradheep. 2020. Diversity, conservation and use of underutilized and minor fruits in India: An overview. *Acta Horticulturae* 1297 (1297):51–60. doi: 10.17660/ActaHortic.2020.1297.8.

Gupta-Elera, G., A. R. Garrett, A. Martinez, R. A. Robison, and K. L. O'Neill. 2011. The antioxidant properties of the cherimoya (*Annona cherimola*) fruit. *Food Research International* 44 (7):2205–9. doi: 10.1016/j.foodres.2010.10.038.

Gyawali, R., and K. S. Kim. 2014. Anticancer phytochemicals of citrus fruits – A review. *Journal of Animal Research* 4 (1):85. doi: 10.5958/2277-940X.2014.00079.5.

Habisukan, U. H., Elfita, H. Widjajanti, A. Setiawan, and A. R. Kurniawati. 2021. Antioxidant and antimicrobial activity of endophytyc fungi isolated from *Syzygium aqueum* leaves. *Journal of Physics: Conference Series* 1751 (1). doi: 10.1088/1742-6596/1751/1/012059.

Hairunisa, I., I. A. Mentari, T. Julianti, E. R. Wikantyasning, Z. Cholisoh, S. C. Ningsih, and M. R. F. Muslim. 2021. Antioxidant activities in different parts of pulasan (Nephelium mutabile Blume) from East Borneo. *IOP Conference Series: Earth and Environmental Science* 736 (1):012018. doi: 10.1088/1755-1315/736/1/012018.

Hamid, H. A., I. H. Yahya, and C. P. See. 2021. Variability in fat properties, polyphenols and antinutrient contents during fermentation and roasted seed of Pulasan. *Materials Science Forum* 1025:116–21. doi: 10.4028/www.scientific.net/MSF.1025.116.

Hamid, R. A., C. P. Foong, Z. Ahmad, and M. K. Hussain. 2012. Antinociceptive and anti-ulcerogenic activities of the ethanolic extract of *Annona muricata* leaf. *Revista Brasileira de Farmacognosia* 22 (3):630–41. doi: 10.1590/S0102-695X2012005000001.

Hanhineva, K., R. Törrönen, I. Bondia-Pons, J. Pekkinen, M. Kolehmainen, H. Mykkänen, and K. Poutanen. 2010. Impact of dietary polyphenols on carbohydrate metabolism. *International Journal of Molecular Sciences* 11 (4):1365–402. doi: 10.3390/ijms11041365.

He, X., J. Fang, X. Chen, Z. Zhao, Y. Li, Y. Meng, and L. Huang. 2019. *Actinidia chinensis* Planch.: A review of chemistry and pharmacology. *Frontiers in Pharmacology* 10:1236. doi: 10.3389/fphar.2019.01236.

He, X., F. Luan, Y. Yang, Z. Wang, Z. Zhao, J. Fang, M. Wang, M. Zuo, and Y. Li. 2020. Passiflora edulis: An Insight Into Current Researches on Phytochemistry and Pharmacology. *Frontiers in Pharmacology* 11:617. doi: 10.3389/fphar.2020.00617.

He, Y., Z. Du, S. Ma, S. Cheng, S. Jiang, Y. Liu, D. Li, H. Huang, K. Zhang, and X. Zheng. 2016. Biosynthesis, antibacterial activity and anticancer effects against prostate cancer (PC-3) cells of silver nanoparticles using *Dimocarpus longan* Lour. peel extract. *Nanoscale Research Letters* 11 (1):300. doi: 10.1186/s11671-016-1511-9.

Herman-Lara, E., L. I. Elvira-Torales, J. Rodriguez-Miranda, J. G. Torruco-Uco, R. Carmona-García, P. G. Mendoza-García, H. S. García, I. Soto-Rodríguez, E. Sánchez-Valdivieso, and C. E. Martínez-Sánchez. 2014. Impact of micronized starfruit (*Averrhoa carambola* L.) fiber concentrate on lipid metabolism in mice. *International Journal of Food Sciences and Nutrition* 65 (7):862–7. doi: 10.3109/09637486.2014.918590.

Hernández, C., J. Ascacio-Valdés, H. De la Garza, J. Wong-Paz, C. N. Aguilar, G. C. Martínez-Ávila, C. Castro-López, and A. Aguilera-Carbó. 2017. Polyphenolic content, in vitro antioxidant activity and chemical composition of extract from *Nephelium lappaceum* L. (Mexican rambutan) husk. *Asian Pacific Journal of Tropical Medicine* 10 (12):1201–5. doi: 10.1016/j.apjtm.2017.10.030.

Hernández-Hernández, C., C. N. Aguilar, R. Rodríguez-Herrera, A. C. Flores-Gallegos, J. Morlett-Chávez, M. Govea-Salas, and J. A. Ascacio-Valdés. 2019. Rambutan (*Nephelium lappaceum* L.): Nutritional and functional properties. *Trends in Food Science & Technology* 85:201–10. doi: 10.1016/j.tifs.2019.01.018.

Hernawati, N. A. Setiawan, R. Shintawati, and D. Priyandoko. 2018. The role of red dragon fruit peel (*Hylocereus polyrhizus*) to improvement blood lipid levels of hyperlipidaemia male mice. *Journal of Physics: Conference Series* 1013 (1):012167. doi: 10.1088/1742-6596/1013/1/012167.

Herraiz, F., D. Villaño, M. Plazas, S. Vilanova, F. Ferreres, J. Prohens, and D. Moreno. 2016. Phenolic profile and biological activities of the pepino (*Solanum muricatum*) fruit and its wild relative *S. caripense*. *International Journal of Molecular Sciences* 17 (3):394. doi: 10.3390/ijms17030394.

Hettihewa, S., Y. Hemar, and H. Rupasinghe. 2018. Flavonoid-rich extract of actinidia macrosperma (A wild kiwifruit) inhibits angiotensin-converting enzyme in vitro. *Foods* 7 (9):146. doi: 10.3390/foods7090146.

Ho, L.-H., and R. Bhat. 2015. Exploring the potential nutraceutical values of durian (Durio zibethinus L.) â€"An exotic tropical fruit. *Food Chemistry* 168:80–9. doi: 10.1016/j.foodchem.2014.07.020.

Horvat, R. J., S. D. Senter, G. W. Chapman, and J. A. Payne. 1991. Volatile compounds from the mesocarp of persimmons. *Journal of Food Science* 56 (1):262–3. doi: 10.1111/j.1365-2621.1991.tb08027.x.

Hu, Y., L. Jiao, M.-H. Jiang, S. Yin, P. Dong, Z.-M. Zhao, D.-P. Yang, P.-T. Ho, and D.-M. Wang. 2018. A new C-glycosyl flavone and a new neolignan glycoside from *Passiflora edulis* Sims peel. *Natural Product Research* 32 (19):2312–8. doi: 10.1080/14786419.2017.1410809.

Huang, F., Y. Liu, R. Zhang, Y. Bai, L. Dong, L. Liu, X. Jia, G. Wang, and M. Zhang. 2019. Structural characterization and in vitro gastrointestinal digestion and fermentation of litchi polysaccharide. *International Journal of Biological Macromolecules* 140:965–72. doi: 10.1016/j.ijbiomac.2019.08.170.

Huang, G. J., B. Wang, Sen, W. C. Lin, S. S. Huang, C. Y. Lee, M. T. Yen, and M. H. Huang. 2012. Antioxidant and anti-inflammatory properties of longan (*Dimocarpus longan* Lour.) Pericarp. *Evidence-Based Complementary and Alternative Medicine* 2012:1–10. doi: 10.1155/2012/709483.

Husin, N. A., S. Rahman, R. Karunakaran, and S. J. Bhore. 2018. A review on the nutritional, medicinal, molecular and genome attributes of Durian (*Durio zibethinus* L.), the King of fruits in Malaysia. *Bioinformation* 14 (06):265–70. doi: 10.6026/97320630014265.

Idrus, H. H., M. Hatta, A. M. I. Febriza, and V. N. A. Kasim. 2019. Antibacterial activities of sapodilla fruit extract inhibiting *Salmonella typhi* on mice balb/c. *International Journal of Applied Pharmaceutics* :121–6. doi: 10.22159/ijap.2019.v11s5.T0095.

Ijaiya, I. S., S. Arzika, and M. Abdulkadir. 2014. Extraction and phytochemical screening of the root and leave of *Annona senegalesis* (Wild Custad Apple). *Academic Journal of Interdisciplinary Studies*. doi: 10.5901/ajis.2014.v3n7p9.

Ikram, A., W. Khalid, M. Aziz, M. Adnan Arif, R. Prakash Jha, M. Zubair Khalid, C. Fizza, M. Zarnoor Mehmood, M. Haseeb, M. Abdul Rahim, et al. 2021. Nutritional and biochemical composition of amla (*Emblica officinalis*) and its therapeutic impact: A review. *Acta Scientifci Nutritional Health* 5 (2):153–60. doi: 10.31080/ASNH.2020.05.0821.

Inada, K. O. P., A. A. Oliveira, T. B. Revorêdo, A. B. N. Martins, E. C. Q. Lacerda, A. S. Freire, B. F. Braz, R. E. Santelli, A. G. Torres, D. Perrone, et al. 2015. Screening of the chemical composition and occurring antioxidants in jabuticaba (*Myrciaria jaboticaba*) and jussara (*Euterpe edulis*) fruits and their fractions. *Journal of Functional Foods* 17:422–33. doi: 10.1016/j.jff.2015.06.002.

Irondi, E., S. Agboola, G. Oboh, A. Boligon, M. Athayde, and F. Shode. 2016. Guava leaves polyphenolics-rich extract inhibits vital enzymes implicated in gout and hypertension in vitro. *Journal of Intercultural Ethnopharmacology* 5 (2):122–30. doi: 10.5455/jice.20160321115402.

Islam, M., M. S. Pia, R. Sifath-E-Jahan, K. Chowdhury, J. Akter, F. Parvin, N. Akter. and S. 2013. Antidiarrheal activity of *Dillenia indica* bark extract. *Ijpsr* 4 (2):682–8.

Ishihata, A., H. Maruki-Uchida, N. Gotoh, S. Kanno, Y. Aso, S. Togashi, M. Sai, T. Ito, and Y. Katano. 2016. Vascular- and hepato-protective effects of passion fruit seed extract containing piceatannol in chronic high-fat diet-fed rats. *Food & Function* 7 (9):4075–81. doi: 10.1039/C6FO01067A.

Itam, A., M. S. Wati, V. Agustin, N. Sabri, R. A. Jumanah, and M. Efdi. 2021. Comparative study of phytochemical, antioxidant, and cytotoxic activities and phenolic content of *Syzygium aqueum* (Burm. f. Alston f.) extracts growing in West Sumatera Indonesia. *The Scientific World Journal* 2021:1–9. doi: 10.1155/2021/5537597.

Jagtap, U. B., S. R. Waghmare, V. H. Lokhande, P. Suprasanna, and V. A. Bapat. 2011. Preparation and evaluation of antioxidant capacity of Jackfruit (*Artocarpus heterophyllus* Lam.) wine and its protective role against radiation induced DNA damage. *Industrial Crops and Products* 34 (3):1595–601. doi: 10.1016/j.indcrop.2011.05.025.

Jain, A. P., M. V. Tote, N. B. Mahire, V. R. Undale, and A. V. Bhosale. 2009. Evaluation of anticonvulsant activity of methanolic extract of *Artocarpus heterophyllus* Lam.(Moraceae) in mice. *Journal of Pharmacy Research* 2 (6):1004–7.

Jamkhande, P. G., B. R. Ajgunde, and D. R. Jadge. 2017. *Annona cherimola* Mill. (Custard apple): A review on its plant profile, nutritional values, traditional claims and ethnomedicinal properties. *Oriental Pharmacy and Experimental Medicine* 17 (3):189–201. doi: 10.1007/s13596-017-0263-0.

Jang, M., S.-W. Jeong, S. K. Cho, K. S. Ahn, J. H. Lee, D. C. Yang, and J.-C. Kim. 2014. Anti-inflammatory effects of an ethanolic extract of guava (*Psidium guajava* L.) leaves in vitro and in vivo. *Journal of Medicinal Food* 17 (6):678–85. doi: 10.1089/jmf.2013.2936.

Janzantti, N. S., M. S. Macoris, D. S. Garruti, and M. Monteiro. 2012. Influence of the cultivation system in the aroma of the volatile compounds and total antioxidant activity of passion fruit. *LWT - Food Science and Technology* 46 (2):511–8. doi: 10.1016/j.lwt.2011.11.016.

Jayakumar, R., and M. S. Kanthimathi. 2011. Inhibitory effects of fruit extracts on nitric oxide-induced proliferation in MCF-7 cells. *Food Chemistry* 126 (3):956–60. doi: 10.1016/j.foodchem.2010.11.093.

Ji, Z.-P., Su, Y.-Q., Lü, P.-H., and Zhang, C.-L . 2006. Studies on chemical constituents and antimicrobial activities of persimmon leaves. 26(4):87–91. https://www.AiritiLibrary.com/Publication/Index/02532417

Jia, X., D. Yang, Y. Yang, and H. Xie. 2019. Carotenoid-derived flavor precursors from *Averrhoa carambola* fresh fruit. *Molecules* 24 (2):256. doi: 10.3390/molecules24020256.

Jiang, J.,. S. Y. Choo, N. Omar, and N. Ahamad. 1998. GC-MS analysis of volatile compounds in Durian (Durio zibethinus Murr). *Developments in Food Science* 345–52. doi: 10.1016/S0167-4501(98)80058-7.

Jing, Y., L. Huang, W. Lv, H. Tong, L. Song, X. Hu, and R. Yu. 2014. Structural characterization of a novel polysaccharide from pulp tissues of *Litchi chinensis* and its immunomodulatory activity. *Journal of Agricultural and Food Chemistry* 62 (4):902–11. doi: 10.1021/jf404752c.

Jo, K. J., J. M. Lee, S. C. Lee, and H. R. Park. 2011. Anticancer activity of persimmon (*Diospyros kaki* L.) calyx extracts on human cancer cells. *Journal of Medicinal Plants Research* 5 (12).

Johnson, J. J., S. M. Petiwala, D. N. Syed, J. T. Rasmussen, V. M. Adhami, I. A. Siddiqui, A. M. Kohl, and H. Mukhtar. 2012. Mangostin, a xanthone from mangosteen fruit, promotes cell cycle arrest in prostate cancer and decreases xenograft tumor growth. *Carcinogenesis* 33 (2):413–9. doi: 10.1093/carcin/bgr291.

Jordán, M. J., C. A. Margaría, P. E. Shaw, and K. L. Goodner. 2002. Aroma active components in aqueous kiwi fruit essence and kiwi fruit puree by GC-MS and multidimensional GC/GC-O. *Journal of Agricultural and Food Chemistry* 50 (19):5386–90. doi: 10.1021/jf020297f.

Joshi, M., and B. Prabhakar. 2020. Phytoconstituents and pharmaco-therapeutic benefits of pitaya: A wonder fruit. *Journal of Food Biochemistry* 44 (7). doi: 10.1111/jfbc.13260.

Joyce, D., and G. Sanewski. 2010. The commercial potential of red bayberry in Australia. http://www.rirdc.gov.au

Jung, K.-A., T.-C. Song, D. Han, I.-H. Kim, Y.-E. Kim, and C.-H. Lee. 2005. Cardiovascular protective properties of kiwifruit extracts in vitro. *Biological & Pharmaceutical Bulletin* 28 (9):1782–5. doi: 10.1248/bpb.28.1782.

Jyothi, A., J. Venkatesh, K. Chakrapani, and P. R. Rani. 2011. Phytochemical and pharmacological potential of *Annona cherimola*-a review. *International Journal of Phytomedicine* 3 (4):439–47.

Kabir, S., S. M. Jahan, M. M. Hossain, and R. Siddique. 2017. Apple, guava and pineapple fruit extracts as antimicrobial agents against pathogenic bacteria. *American Journal of Microbiological Research* 5 (5):101–6. doi: 10.12691/ajmr-5-5-2.

Kaleem, M., M. Asif, Q. U. Ahmed, and B. Bano. 2006. Antidiabetic and antioxidant activity of *Annona squamosa* extract in streptozotocin-induced diabetic rats. *Singapore Medical Journal* 47 (8):670–5.

Kamalanathan, A., and T. George. 2015. Phytochemical profiling, antioxidant and antimicrobial activity of methanol extract in rambutan fruit (*Nephelium lappacium*) epicarp against the human pathogens.

Kamboj, P., N. C. Talukdar, and S. K. Banerjee. 2019. Therapeutic benefit of *Dillenia indica* in diabetes and its associated complications. *Journal of Diabetes Research* 2019:1–7. doi: 10.1155/2019/4632491.

Kang, S. C., C. M. Lee, H. Choi, J. H. Lee, J. S. Oh, J. H. Kwak, and O. P. Zee. 2006. Evaluation of oriental medicinal herbs for estrogenic and antiproliferative activities. *Phytotherapy Research: PTR* 20 (11):1017–9. doi: 10.1002/ptr.1987.

Kar, P., A. K. Chakraborty, S. Dutta, M. Bhattacharya, T. K. Chaudhuri, and A. Sen. 2019. Fruit juice of silverberry (Elaeagnus) and bayberry (Myrica) may help in combating against kidney dysfunctions. *Clinical Phytoscience* 5 (1):1–9. doi: 10.1186/s40816-019-0117-z.

Karasawa, M. M. G., and C. Mohan. 2018. Fruits as prospective reserves of bioactive compounds: A review. *Natural Products and Bioprospecting* 8 (5):335–46. doi: 10.1007/s13659-018-0186-6.

Karim, N., and J. Tangpong. 2018. Biological properties in relation to health promotion effects of Garcinia mangostana (queen of fruit): A short report. *Journal of Health Research* 32 (5):364–70. doi: 10.1108/JHR-08-2018-043.

Kasala, E. R., L. N. Bodduluru, C. C. Barua, R. M. Madhana, V. Dahiya, M. K. Budhani, R. R. Mallugari, S. R. Maramreddy, and R. Gogoi. 2016. Chemopreventive effect of chrysin, a dietary flavone against benzo(a)pyrene induced lung carcinogenesis in Swiss albino mice. *Pharmacological Reports : PR* 68 (2):310–8. doi: 10.1016/j.pharep.2015.08.014.

Kawasoe, H., M. Wakamatsu, S. Hamada, Y. Arata, K. Nagayoshi, R. Uchida, R. Yamashita, T. Kishita, H. Yamanouchi, Y. Minami, et al. 2021. Analysis of natural colourant extracted from the pericarp of passion fruit. *LWT* 136:110412. doi: 10.1016/j.lwt.2020.110412.

Kelly, N. P., A. L. Kelly, and J. A. O'Mahony. 2019. Strategies for enrichment and purification of polyphenols from fruit-based materials. *Trends in Food Science & Technology* 83:248–58. doi: 10.1016/j.tifs.2018.11.010.

Kennedy, D. O. 2014. Polyphenols and the human brain: plant "secondary metabolite" ecologic roles and endogenous signaling functions drive benefits. *Advances in Nutrition (Nutrition* 5 (5):515–33. doi: 10.3945/an.114.006320.

Kermasha, S., N. N. Barthakur, N. K. Mohan, and N. R. Arnold. 1987. Chemical composition and proposed use of two semi-wild tropical fruits. *Food Chemistry* 26 (4):253–9. doi: 10.1016/0308-8146(87)90068-9.

Khaizil EZ, Nik ASNZ, and Mohd DS. 2017. Preliminary study on anti-proliferative activity of methanolic extract of *Nephelium lappaceum* peels towards breast (MDA-MB-231), cervical (HeLa) and osteosarcoma (MG-63) Cancer Cell. Chemical profiling of Smilax myosotiflora as aphrodisiac agent view pro. (May 2017).

Khalili, A., C. H. E. Abdullah, and A. Manaf. 2012. Antibacterial activity of flesh and peel methanol fractions of red pitaya, white pitaya and papaya on selected food microorganisms. *International Journal of Pharmacy and Pharmaceutical Sciences* 4 (3):185–90.

Khan, A. S. 2017. Trees with anticancer activities. In: *Medicinally important trees*, 55–84. Cham: Springer International Publishing. doi: 10.1007/978-3-319-56777-8_3.

Khan, M. A., T. Ahamad, M. Saquib, M. K. Hussain, and M. F. Khan. 2021. Unmodified household coffee maker assisted extraction and purification of anticancer agents from *Dillenia indica* fruits. *Natural Product Research* 35 (6):984–7. doi: 10.1080/14786419.2019.1608546.

Khan, S. U., A. Khan, A.-H. A. Shah, S. M. Shah, S. Hussain, M. Ayaz, and S. Ayaz. 2016. Heavy metals content, phytochemical composition, antimicrobial and insecticidal evaluation of *Elaeagnus angustifolia*. *Toxicology and Industrial Health* 32 (1):154–61. doi: 10.1177/0748233713498459.

Khanam, Z., K. H. Sam, N. H. B. M. Zakaria, C. H. Ching, and I. U. H. Bhat. 2015. Determination of polyphenolic content, HPLC analyses and DNA cleavage activity of Malaysian *Averrhoa carambola* L. fruit extracts. *Journal of King Saud University - Science* 27 (4):331–7. doi: 10.1016/j.jksus.2015.01.004.

Khoddami, A., M. Wilkes, and T. Roberts. 2013. Techniques for analysis of plant phenolic compounds. *Molecules* 18 (2):2328–75. doi: 10.3390/molecules18022328.

Khoo, H.-E., K. N. Prasad, K.-W. Kong, Y. Jiang, and A. Ismail. 2011. Carotenoids and their isomers: Color pigments in fruits and vegetables. *Molecules* 16 (2):1710–38. doi: 10.3390/molecules16021710.

Kilari, E. K., and S. Putta. 2016. Biological and phytopharmacological descriptions of *Litchi chinensis*. *Pharmacognosy Reviews* 10 (19):60–5. doi: 10.4103/0973-7847.176548.

Kim, D. S., Y. Kwack, J. H. Lee, and C. Chun. 2019. Antimicrobial Activity of various parts of tomato plants varied with different solvent extracts. *The Plant Pathology Journal* 35 (2):149–55. doi: 10.5423/PPJ.OA.07.2018.0132.

Kim, I., J. Lee, S. Kim, J. Cho, S. Dhungana, Y. Lim, and D. Shin. 2015. Exogenous application of natural extracts of persimmon (*Diospyros kaki* Thunb.) can help in maintaining nutritional and mineral composition of dried persimmon. *African Journal of Biotechnology* 13 (22):2231–9. doi: 10.4314/ajb.v13i22.

Kim, M.-S., M.-K. You, D.-Y. Rhuy, Y.-J. Kim, H.-Y. Baek, and H.-A. Kim. 2009. Loquat (*Eriobotrya japonica*) extracts suppress the adhesion, migration and invasion of human breast cancer cell line. *Nutrition Research and Practice* 3 (4):259–64. doi: 10.4162/nrp.2009.3.4.259.

Kim, S., L. van den Broeck, S. Karre, H. Choi, S. A. Christensen, G. Wang, Y. Jo, W. K. Cho, and P. Balint-Kurti. 2021. Analysis of the transcriptomic, metabolomic, and gene regulatory responses to *Puccinia sorghi* in maize. *Molecular Plant Pathology* 22 (4):465–79. doi: 10.1111/mpp.13040.

Kim, S. B., B. Y. Chang, B. Y. Hwang, S. Y. Kim, and M. K. Lee. 2014. Pyrrole alkaloids from the fruits of Morus alba. *Bioorganic & Medicinal Chemistry Letters* 24 (24):5656–9. doi: 10.1016/j.bmcl.2014.10.073.

Kim, S.-H., and T.-Y. Shin. 2009. Anti-inflammatory effect of leaves of *Eriobotrya japonica* correlating with attenuation of p38 MAPK, ERK, and NF-κB activation in mast cells. *Toxicology in Vitro : Vitro* 23 (7):1215–9. doi: 10.1016/j.tiv.2009.07.036.

Kim, Y. M., Y. S. Park, Y.-K. Park, K.-S. Ham, S.-G. Kang, R. M. Shafreen, S. A. Lakshmi, and S. Gorinstein. 2020. Characterization of bioactive ligands with antioxidant properties of kiwifruit and Persimmon cultivars using in vitro and in silico studies. *Applied Sciences* 10 (12):4218. doi: 10.3390/app10124218.

Kozukue, N., J.-S. Han, K.-R. Lee, and M. Friedman. 2004. Dehydrotomatine and α-tomatine content in tomato fruits and vegetative plant tissues. *Journal of Agricultural and Food Chemistry* 52 (7):2079–83. doi: 10.1021/jf0306845.

Krajarng, A., S. Nilwarankoon, S. Suksamrarn, and R. Watanapokasin. 2012. Antiproliferative effect of α-mangostin on canine osteosarcoma cells. *Research in Veterinary Science* 93 (2):788–94. doi: 10.1016/j.rvsc.2012.01.015.

Krishna, G. O. 2017. Evaluation of anticonvulsant and anxiolytic activity of methanolic extract of leaves of *Syzygium aqueum* (Brum. F).

Krishnaveni, M., and S. Mirunalini. 2010. Therapeutic potential of *Phyllanthus emblica* (amla): the ayurvedic wonder. *Journal of Basic and Clinical Physiology and Pharmacology* 21 (1):93–105. doi: 10.1515/JBCPP.2010.21.1.93.

Kumar, M., M. Tomar, R. Amarowicz, V. Saurabh, M. S. Nair, C. Maheshwari, M. Sasi, U. Prajapati, M. Hasan, S. Singh, et al. 2021. Guava (*Psidium guajava* L.) leaves: Nutritional composition, phytochemical profile, and health-promoting bioactivities. *Foods* 10 (4):752. doi: 10.3390/foods10040752.

Kumar Nayak, P., and K. Rayaguru. 2016. Study of physical parameters of elephant apple fruit (*Dillenia indica*): an underutilized fruit of North - Eastern India. *International Journal of Engineering Research & Technology* 5(1):532–5.

Kumar, S., S. Chakravart, G. S. Chiew, T. Subramania, U. Palanisamy, A. Radhakrish, and N. Haleagraha. 2012. Protective effects of *Nephelium lappaceum* rind extract against collagen-induced arthritis in dark agouti rats. *Journal of Biological Sciences* 12 (7):385–92. doi: 10.3923/jbs.2012.385.392.

Kumari, S. 2016. Effect of guava in blood glucose and lipid profile in healthy human subjects: A randomized controlled study. *Journal of Clinical and Diagnostic Research*. doi: 10.7860/JCDR/2016/21291.8425.

Kumnerdkhonkaen, P., S. Saenglee, M. A. Asgar, G. Senawong, K. Khongsukwiwat, and T. Senawong. 2018. Antiproliferative activities and phenolic acid content of water and ethanolic extracts of the powdered formula of *Houttuynia cordata* Thunb. fermented broth and *Phyllanthus emblica* Linn. fruit. *BMC Complementary and Alternative Medicine* 18 (1). doi: 10.1186/s12906-018-2185-x.

Kumoro, A. C., M. Alhanif, and D. H. Wardhani. 2020. A critical review on tropical fruits seeds as prospective sources of nutrition-

al and bioactive compounds for functional foods development: A case of Indonesian exotic fruits. *International Journal of Food Science* 2020:1–15. doi: 10.1155/2020/4051475.

Kviecinski, M. R., David, I. M. B. Fernandes, F. de, S. Correa, M. d R. Clarinda, M. M. Freitas, A. F. Silva, J. da, Gava, M. Müller, S. D, et al. 2017. Healing effect of *Dillenia indica* fruit extracts standardized to betulinic acid on ultraviolet radiation-induced psoriasis-like wounds in rats. *Pharmaceutical Biology* 55 (1):641–8. doi: 10.1080/13880209.2016.1266672.

Lachowicz, S., A. Bieniek, Z. Gil, N. Bielska, and B. Markuszewski. 2019. Phytochemical parameters and antioxidant activity of new cherry silverberry biotypes (*Elaeagnus multiflora* Thunb.). *European Food Research and Technology* 245 (9):1997–2005. doi: 10.1007/s00217-019-03317-w.

Lakmal, K., P. Yasawardene, U. Jayarajah, and S. L. Seneviratne. 2021. Nutritional and medicinal properties of Star fruit (*Averrhoa carambola*): A review. *Food Science & Nutrition* 9 (3):1810–23. doi: 10.1002/fsn3.2135.

Laldinchhana, L. J., S. Ray, and L. Pachuau. 2020. Indian tropical fruits and their bioactive compounds against human diseases. *Plant-derived Bioactives: Chemistry and Mode of Action*:455–94. doi: 10.1007/978-981-15-2361-8_21.

Laohakunjit, N., O. Kerdchoechuen, F. B. Matta, J. L. Silva, and W. E. Holmes. 2007. Postharvest survey of volatile compounds in five tropical fruits using headspace-solid phase microextraction (HS-SPME). *HortScience* 42 (2):309–14. doi: 10.21273/HORTSCI.42.2.309.

Lattanzio V. 2013. Phenolic compounds: Introduction. In: Natural products, 1543–1580. Berlin, Heidelberg: Springer. doi: 10.1007/978-3-642-22144-6_57.

Le, Q.-U., H.-L. Lay, M.-C. Wu, and T. H.-H. Nguyen. 2018. Natural plant colorants widely used in Vietnam traditional food culture. *Journal of Food, Nutrition and Agriculture* :40–6. doi: 10.21839/jfna.2018.v1i1.220.

Lee, C.-H., S.-L. Wu, J.-C. Chen, C.-C. Li, H.-Y. Lo, W.-Y. Cheng, J.-G. Lin, Y.-H. Chang, C.-Y. Hsiang, and T.-Y. Ho. 2008. *Eriobotrya japonica* leaf and its triterpenes inhibited lipopolysaccharide-induced cytokines and inducible enzyme production via the nuclear factor-κB signaling pathway in lung epithelial cells. *The American Journal of Chinese Medicine* 36 (6):1185–98. doi: 10.1142/S0192415X0800651X.

Lee, J. E. 2018. Dyeability and function of silk fabrics using *Myrica rubra* rind extract. *Fashion & Textile Research Journal* 20 (5):608–15. doi: 10.5805/SFTI.2018.20.5.608.

Lee, S.-O., S.-K. Chung, and I.-S. Lee. 2006. The antidiabetic effect of dietary persimmon (*Diospyros kaki* L. cv. Sangjudungsi) peel in streptozotocin-induced diabetic rats. *Journal of Food Science* 71 (3):S293–S298. doi: 10.1111/j.1365-2621.2006.tb15656.x.

Leelarungrayub, J., A. Yankai, D. Pinkaew, R. Puntumetakul, J. J. Laskin, and R. J Bloomer. 2016. A preliminary study on the effects of star fruit consumption on antioxidant and lipid status in elderly Thai individuals. *Clinical Interventions in Aging* Volume 11:1183–92. doi: 10.2147/CIA.S110718.

Lenquiste, S. A., Â. G. Batista, S. Marineli R da, N. R. V. Dragano, and M. R. Maróstica. 2012. Freeze-dried jaboticaba peel added to high-fat diet increases HDL-cholesterol and improves insulin resistance in obese rats. *Food Research International* 49 (1):153–60. doi: 10.1016/j.foodres.2012.07.052.

Lenquiste, S. A., R. da Marineli, S. Moraes, É. A. Dionísio, E. S. de, Brito, and M. R. Maróstica. 2015. Jaboticaba peel and jaboticaba peel aqueous extract shows in vitro and in vivo antioxidant properties in obesity model. *Food Research International* 77:162–70. doi: 10.1016/j.foodres.2015.07.023.

Leuenberger, U. A., L. Linton-Frazier, S. Spilk, and C. Hogeman. 2012. Ascorbic acid attenuates sympathetic activation and endothelial dysfunction induced by short-term intermittent hypoxia in humans. *The FASEB Journal* 26 (S1). doi: 10.1096/fasebj.26.1_supplement.898.6.

Lezoul, N. E. H., M. Belkadi, F. Habibi, and F. Guillén. 2020. Extraction processes with several solvents on total bioactive compounds in different organs of three medicinal plants. *Molecules* 25 (20):4672. doi: 10.3390/molecules25204672.

Li, X. 2012. Biotransformation of dihydro-epi-deoxyarteannuin B by suspension-cultured cells of *Averrhoa carambola*. *African Journal of Biotechnology* 11 (7). doi: 10.5897/AJB11.1187.

Li, L.,. J. Xu, Y. Mu, L. Han, R. Liu, Y. Cai, and X. Huang. 2015. Chemical characterization and anti-hyperglycaemic effects of polyphenol enriched longan (*Dimocarpus longan* Lour.) pericarp extracts. *Journal of Functional Foods* 13:314–22. doi: 10.1016/j.jff.2015.01.006.

Li, P.-H., Y.-W. Lin, W.-C. Lu, J.-M. Hu, and D.-W. Huang. 2016. In vitro hypoglycemic activity of the phenolic compounds in longan fruit (*Dimocarpus longan* var. Fen Ke) shell against α-glucosidase and β-galactosidase. *International Journal of Food Properties* 19 (8):1786–97. doi: 10.1080/10942912.2015.1085398.

Li, S., M.-H. Pan, C.-Y. Lo, D. Tan, Y. Wang, F. Shahidi, and C.-T. Ho. 2009. Chemistry and health effects of polymethoxyflavones and hydroxylated polymethoxyflavones. *Journal of Functional Foods* 1 (1):2–12. doi: 10.1016/j.jff.2008.09.003.

Liang, X., X.-Z. Yang, L. Chen, S. Jiang, Y.-D. Chen, Q.-Y. Deng, X.-G. Chen, and J.-Q. Yuan. 2021. Alkaloids derived from the genus Daphniphyllum. *Medicinal Chemistry Research* 30 (1):1–14. doi: 10.1007/s00044-020-02646-w.

Lim, A. S. L. Rabeta. 2013. Proximate analysis, mineral content and antioxidant capacity of milk apple, malay apple and water apple. *International Food Research Journal* 20 (2):673–9.

Lim, T. K. 2013. Nephelium ramboutan-ake. In: *Edible medicinal and non-medicinal plants*, 75–9. Netherlands: Springer Netherlands. doi: 10.1007/978-94-007-5628-1_13.

Lim, T. T., and J. J. Tee. 2006. Antioxidant properties of guava fruit: Comparison with some local fruits. *Sunway Academic Journal* 3:9–20.

Lin, B., Qiu, S. Zheng, K. Zhang Shuai, Hong, and J. Zhang ShaoPing. 2019. Process optimization and in vitro hypoglycemic effect of polyphenols extracted from jaboticaba leaves. *Fujian Journal of Agricultural Sciences* 34 (5):587–94.

Lippi, G., and C. Mattiuzzi. 2020. Kiwifruit and cancer: An overview of biological evidence. *Nutrition and Cancer* 72 (4):547–53. doi: 10.1080/01635581.2019.1650190.

Liu, P., R. Du, and X. Yu. 2019. Ursolic acid exhibits potent anticancer effects in human metastatic melanoma cancer cells (SK-MEL-24) via apoptosis induction, inhibition of cell migration and invasion, cell cycle arrest, and inhibition of mitogen-activated protein kinase (MAPK)/ERK Sign. *Medical Science Monitor* 25:1283–90. doi: 10.12659/MSM.913069.

Liu, S.-C., J.-T. Lin, C.-K. Wang, H.-Y. Chen, and D.-J. Yang. 2009. Antioxidant properties of various solvent extracts from lychee (*Litchi chinenesis* Sonn.) flowers. *Food Chemistry* 114 (2):577–81. doi: 10.1016/j.foodchem.2008.09.088.

Liu, Y., W. Zhang, C. Xu, and X. Li. 2016. Biological activities of extracts from loquat (*Eriobotrya japonica* Lindl.): A review. *International Journal of Molecular Sciences* 17 (12):1983. doi: 10.3390/ijms17121983.

Liu, Y., X. Zhang, L. Zhan, C. Xu, L. Sun, H. Jiang, C. Sun, and X. Li. 2020. LC-Q-TOF-MS characterization of polyphenols from white bayberry fruit and its antidiabetic effect in KK-Ay mice. *ACS Omega* 5 (28):17839–49. doi: 10.1021/acsomega.0c02759.

Lobo de Andrade, D. M., C. d F. Reis, P. F. d S. Castro, L. L. Borges, N. O. Amaral, I. M. S. Torres, S. G. Rezende, E. d S. Gil, E. Cardoso da Conceição, G. R. Pedrino, et al. 2015. 2015. Vasorelaxant and hypotensive effects of jaboticaba fruit (*Myrciaria cauliflora*) extract in rats. *Evidence-Based Complementary and Alternative Medicine* 2015:1–8. doi: 10.1155/2015/696135.

Lok, B., D. Sandai, H. M. Baharetha, V. Nazari, M. Asif, C. Tan, and A. Majid. 2020. Anticancer effect of *Psidium guajava* (Guava) leaf extracts against colorectal cancer through inhibition of angiogenesis. *Asian Pacific Journal of Tropical Biomedicine* 10 (7):293. doi: 10.4103/2221-1691.284944.

Luan, F., L. Peng, Z. Lei, X. Jia, J. Zou, Y. Yang, X. He, and N. Zeng. 2021. Traditional Uses, Phytochemical Constituents and Pharmacological Properties of Averrhoa carambola L.: A Review. *Frontiers in Pharmacology* 12:1814. doi: 10.3389/fphar.2021.699899.

Luo, H., Y. Cai, Z. Peng, T. Liu, and S. Yang. 2014. Chemical composition and in vitroevaluation of the cytotoxic and antioxidant activities of supercritical carbon dioxide extracts of pitaya (dragon fruit) peel. *Chemistry Central Journal* 8 (1):1. doi: 10.1186/1752-153X-8-1.

Luu, T. T. H., T. L. Le, N. Huynh, and P. Quintela-Alonso. 2021. Dragon fruit: A review of health benefits and nutrients and its sustainable development under climate changes in Vietnam. *Czech Journal of Food Sciences* 39 (No. 2):71–94. doi: 10.17221/139/2020-CJFS.

Lv, Q., F. Luo, X. Zhao, Y. Liu, G. Hu, C. Sun, X. Li, and K. Chen. 2015. Identification of proanthocyanidins from litchi (*Litchi chinensis* Sonn.) Pulp by LC-ESI-Q-TOF-MS and their antioxidant activity. *Plos ONE* 10 (3):e0120480. doi: 10.1371/journal.pone.0120480.

Kadam, D., P. Kaushik, and R. Kumar. 2012. Evaluation of guava products quality. *International Journal of Food Science and Nutrition Engineering* 2 (1):7–11. doi: 10.5923/j.food.20120201.02.

Ma, Q., Y. Guo, L. Sun, and Y. Zhuang. 2017. Anti-diabetic effects of phenolic extract from rambutan peels (*Nephelium lappaceum*) in high-fat diet and streptozotocin-induced diabetic mice. *Nutrients* 9 (8):801. doi: 10.3390/nu9080801.

Maarse, H. 2017. *Volatile compounds in foods and beverages*. Maarse H, editor. Routledge. doi: 10.1201/9780203734285.

Macedo-Costa, M. R., D. N. Diniz, C. M. Carvalho, S. V. Pereira M do, J. V. Pereira, and J. S. Higino. 2009. Eficácia do extrato de *Myrciaria cauliflora* (Mart.) O. Berg. (jabuticabeira) sobre bactérias orais. *Revista Brasileira de Farmacognosia* 19 (2b):565–71. doi: 10.1590/S0102-695X2009000400010.

MacLeod, A. J., and N. Gonzales de Troconis. 1982. Volatile flavor components of sapodilla fruit (*Achras sapota* L). *Journal of Agricultural and Food Chemistry* 30 (3):515–7. doi: 10.1021/jf00111a026.

Mahmood, K., H. Kamilah, A. K. Alias, and F. Ariffin. 2018. Nutritional and therapeutic potentials of rambutan fruit (Nephelium lappaceum L.) and the by-products: A review. *Journal of Food Measurement and Characterization* 12 (3):1556–71. doi: 10.1007/s11694-018-9771-y.

Mahomoodally, M. F., A. Ugurlu, E. J. Llorent-Martínez, M. Nagamootoo, M. C. N. Picot-Allain, M. C. Baloglu, Y. C. Altunoglu, M. Hosenally, and G. Zengin. 2020. *Syzgium coriaceum* Bosser & Guého—An endemic plant potentiates conventional antibiotics, inhibits clinical enzymes and induces apoptosis in breast cancer cells. *Industrial Crops and Products* 143:111948. doi: 10.1016/j.indcrop.2019.111948.

Maiyo, Z. C., R. M. Ngure, J. C. Matasyoh, and R. Chepkorir. 2010. Phytochemical constituents and antimicrobial activity of leaf extracts of three Amaranthus plant species. *African Journal of Biotechnology* 9 (21):3178–82. doi: 10.4314/ajb.v9i21.

Majhi, B., K. B. Satapathy, and S. K. Mishra. 2019. Antimicrobial activity of *Averrhoa carambola* L. leaf extract and its phytochemical analysis. *Research Journal of Pharmacy and Technology* 12 (3):1219. doi: 10.5958/0974-360X.2019.00202.6.

Malini, C., and R. Maheshkumar. 2013. Evaluation of bioactive potential in rambutan fruit (*Nephelium lappaceum*) samples using pathogens. *Rising Research Journal Publication* 3 (3):138–42.

Mann, S., G. Satpathy, and R. K. Gupta. 2016. Evaluation of nutritional and phytochemical profiling of *Baccaurea ramiflora* Lour. syn. Baccaurea sapida (Roxb.) Mull. Arg. fruits. *Indian Journal of Traditional Knowledge* 15 (1):135–42. www.thegoodscentscompany.com

Martínez-Las Heras, R., A. Heredia, M. L. Castelló, and A. Andrés. 2014. Influence of drying method and extraction variables on the antioxidant properties of persimmon leaves. *Food Bioscience* 6:1–8. doi: 10.1016/j.fbio.2014.01.002.

Martínez-Vázquez, M., and R. Estrada-Reyes. 2014. Secondary metabolismin in Annonaceae: Potencial source of drugs. *Revista Brasileira de Fruticultura* 36 (spe1):141–6. doi: 10.1590/S0100-29452014000500017.

Matthies, A., T. Clavel, M. Gütschow, W. Engst, D. Haller, M. Blaut, and A. Braune. 2008. Conversion of daidzein and genistein by an anaerobic bacterium newly isolated from the mouse intestine. *Applied and Environmental Microbiology* 74 (15):4847–52. doi: 10.1128/AEM.00555-08.

Mayachiew, P., and S. Devahastin. 2008. Antimicrobial and antioxidant activities of Indian gooseberry and galangal extracts. *LWT - Food Science and Technology* 41 (7):1153–9. doi: 10.1016/j.lwt.2007.07.019.

Mazlan, O., W. M. Aizat, N. S. Aziz Zuddin, S. N. Baharum, and N. M. Noor. 2019. Metabolite profiling of mangosteen seed germination highlights metabolic changes related to carbon utilization and seed protection. *Scientia Horticulturae* 243:226–34. doi: 10.1016/j.scienta.2018.08.022.

McGhie, T. K., and G. D. Ainge. 2002. Color in fruit of the genus Actinidia: Carotenoid and chlorophyll compositions. *Journal of Agricultural and Food Chemistry* 50 (1):117–21. doi: 10.1021/jf010677l.

Meckes, M.,. F. Calzada, J. Tortoriello, J. L. González, and M. Martínez. 1996. Terpenoids isolated from *Psidium guajava* hexane extract with depressant activity on central nervous system. *Phytotherapy Research* 10 (7):600–3. doi: 10.1002/(SICI)1099-1573(199611)10:7<600::AID-PTR918>3.0.CO;2-7.

Mello, F. R. d., C. Bernardo, C. O. Dias, L. Gonzaga, E. R. Amante, R. Fett, and L. M. B. Candido. 2014. Antioxidant properties, quantification and stability of betalains from pitaya (*Hylocereus undatus*) peel. *Ciência Rural* 45 (2):323–8. doi: 10.1590/0103-8478cr20140548.

Meng, F. Y., Y. L. Ning, J. Qi, Z. He, J. Jie, J. J. Lin, Y. J. Huang, L. F. Sen, and X. H. Li. 2014. Structure and antitumor and immunomodulatory activities of a water-soluble polysaccharide from *Dimocarpus longan* pulp. *International Journal of Molecular Sciences* 15 (3):5140–62. doi: 10.3390/ijms15035140.

Mogole, L., W. Omwoyo, and F. Mtunzi. 2020. Phytochemical screening, anti-oxidant activity and α-amylase inhibition study using different extracts of loquat (*Eriobotrya japonica*) leaves. *Heliyon* 6 (8):e04736. doi: 10.1016/j.heliyon.2020.e04736.

Mondal, C., R. N. Remme, A. A. Mamun, S. Sultana, M. H. Ali, and M. A. Mannan. 2013. Product development from jackfruit (*Artocarpus heterophyllus*) and analysis of nutritional quality of the processed products. *IOSR Journal of Agriculture and Veterinary Science* 4 (1):76–84. doi: 10.9790/2380-0417684.

Morshed, M. T. I., P. R. Dash, F. A. Ripa, T. Foyzun, and M. S. Ali. 2014. Evaluation of pharmacological activities of methanolic extract of *Nephelium lappaceum* L seeds. *International Journal of Pharmacognosy* 1 (10).

Muhtadi, M.,. H. Haryoto, T. Sujono, and A. Suhendi. 2016. Antidiabetic and antihypercholesterolemia activities of rambutan (*Nephelium lappaceum* L.) and durian (*Durio zibethinus* Murr.) fruit peel extracts. *Journal of Applied Pharmaceutical Science* :190–4. doi: 10.7324/JAPS.2016.60427.

Muhtadi, A. U. Primarianti, and T. A. Sujono. 2015. Antidiabetic activity of durian (*Durio zibethinus* Murr.) and Rambutan (*Nephelium lappaceum* L.) Fruit peels in alloxan diabetic rats. *Procedia Food Science* 3:255–61. doi: 10.1016/j.profoo.2015.01.028.

Mukherjee, A., K. Chatterjee, and T. Sarkar. 2022. Entropy-aided assessment of amla (*Emblica officinalis*) quality using principal component analysis. *Biointerface Research in Applied Chemistry* 12 (2):2162–70. doi: http://dx.doi.org/10.33263/BRIAC122.21622170.

Mukherjee, A., T. Sarkar, and K. Chatterjee. 2021. Freshness assessment of Indian gooseberry (*Phyllanthus emblica*) using probabilistic neural network. *Journal of Biosystems Engineering* 46 (4):399–416. doi: 10.1007/s42853-021-00116-8.

Mulye, S. S., A. S. Maurya, S. A. Kamble, P. v Deshmukh, L. S. Yadav, R. K. Mishra, and A. Jain. 2020. Medicinal and phytochemical analysis of alcoholic whole fruit extracts of *Actinidia deliciosa*. *Journal of Scientific Research* 64 (01):179–85. doi: 10.37398/JSR.2020.640126.

Munandar Zulkifli Ismail, A., D. Sargowo, C. Tri Tjahjono, S. Widito, and A. Rizal. 2021. The role of *Garcinia mangostana* pericarp extract as antioxidant to inhibit atherosclerosis process in high risk framingham score patient. *Heart Science Journal* 2 (1):25–9. doi: 10.21776/ub.hsj.2021.002.01.04.

Murnisyazwani, J., and M. S. Rabeta. 2019. Antioxidant and antimicrobial activity of sapodilla (*Manilkara zapota* L.) fresh, juice and bar. *Food Research* 3 (5):400–6.

Mutalib, M. A., A. Rahmat, F. Ali, F. Othman, and R. Ramasamy. 2017. Nutritional compositions and antiproliferative activities of different solvent fractions from ethanol extract of *Cyphomandra betacea* (Tamarillo) Fruit. *The Malaysian Journal of Medical Sciences. Malaysian Journal of Medical Sciences* 24 (5):19–32. doi: 10.21315/mjms2017.24.5.3.

Muthu, N., S. Y. Lee, K. K. Phua, and S. J. Bhore. 2016. Nutritional, medicinal and toxicological attributes of star-fruits (*Averrhoa carambola* L.): A review. *Bioinformation* 12 (12):420–4. doi: 10.6026/97320630012420.

Myoda, T., S. Fujimura, B. J. Park, T. Nagashima, J. Nakagawa, and M. Nishizawa. 2010. Antioxidative and antimicrobial potential of residues of camu-camu juice production. *Journal of Food, Agriculture and Environment* 8 (2):304–7.

Naderi, N.,. F. Stintzing, H. Ghazali, Y. Manap, and S. Jazayeri. 2010. Betalain extraction from *Hylocereus polyrhizus* for natural food coloring purposes. *Journal of the Professional Association for Cactus Development* 12:143–54.

Nagarajan, V., R. K. Bhavadharani, and R. Chandiramouli. 2020. Interaction studies of volatiles from jackfruit on α-phosphorene nanosheet—A DFT outlook. *Structural Chemistry* 31 (5):1851–60. doi: 10.1007/s11224-020-01541-9.

Naseer, S., S. Hussain, N. Naeem, M. Pervaiz, and M. Rahman. 2018. The phytochemistry and medicinal value of *Psidium guajava* (guava). *Clinical Phytoscience* 4 (1):32. doi: 10.1186/s40816-018-0093-8.

Nayak, P. K., K. Rayaguru, and B. K. Mishra. 2016. Study of physical parameters of elephant apple fruit (*Dillenia indica*): An underutilized fruit of North-Eastern India. *Int J Eng Res Technol* 5:532–5.

Negi, P. S., G. K. Jayaprakasha, and B. S. Jena. 2010. Evaluation of antioxidant and antimutagenic activities of the extracts from the fruit rinds of *Garcinia cowa*. *International Journal of Food Properties* 13 (6):1256–65. doi: 10.1080/10942910903050383.

Nesa, M. L., S. M. S. Karim, K. Api, M. M. R. Sarker, M. M. Islam, A. Kabir, M. K. Sarker, K. Nahar, M. Asadujjaman, and M. S. Munir. 2018. Screening of *Baccaurea ramiflora* (Lour.) extracts for cytotoxic, analgesic, anti-inflammatory, neuropharmacological and antidiarrheal activities. *BMC Complementary and Alternative Medicine* 18 (1). doi: 10.1186/s12906-018-2100-5.

Nethaji, R., G. Thooyavan, M. K. Nilla, and K. Ashok. 2015. Phytochemical profiling, antioxidant and antimicrobial activity of methanol extract in rambutan fruit (*Nephelium lappacium*) epicarp against the human pathogens. *International Journal of Current Innovation Research* 1 (9):201–6.

Nieuwenhuizen, N. J., M. Y. Wang, A. J. Matich, S. A. Green, X. Chen, Y.-K. Yauk, L. L. Beuning, D. A. Nagegowda, N. Dudareva, and R. G. Atkinson. 2009. Two terpene synthases are responsible for the major sesquiterpenes emitted from the flowers of kiwifruit (*Actinidia deliciosa*). *Journal of Experimental Botany* 60 (11):3203–19. doi: 10.1093/jxb/erp162.

Nunes, J. C., M. G. Lago, V. N. Castelo-Branco, F. R. Oliveira, A. G. Torres, D. Perrone, and M. Monteiro. 2016. Effect of drying method on volatile compounds, phenolic profile and antioxidant capacity of guava powders. *Food Chemistry* 197:881–90. doi: 10.1016/j.foodchem.2015.11.050.

Nurul, S., and R. Asmah. 2014. Variability in nutritional composition and phytochemical properties of red pitaya (*Hylocereus polyrhizus*) from Malaysia and Australia. undefined.

Nyi Mekar Saptarini, D. 2011. Analyzing antiulcer ratio protection of pepino dulce fruit juice (*Solanum muricatum* Aiton) using mice as an animal experimental model. *Traditional Medicine Journal* 16.

Okmen, G., and O. Turkcan. 2013. A study on antimicrobial, antioxidant and antimutagenic activities of *Elaeagnus angustifolia* L. Leaves. *African Journal of Traditional, Complementary and Alternative Medicines* 11 (1). doi: 10.4314/ajtcam.v11i1.17.

Okolie, N. P., K. Agu, and G. I. Eze. 2013. Protective effect of ethanolic leaf extract of annona muricata linn on some early events in cycas-induced colorectal carcinogenesis in rats. *Journal of Pharmaceutical and Scientific Innovation* 2 (4):14–21. doi: 10.7897/2277-4572.02444.

Olayemi, J. O. 2012. Phytochemical and antimicrobial properties of *Solanum macranthum* Dunal. *African Journal of Biotechnology* 11 (21):4934–7. doi: 10.5897/AJB11.529.

Olatunde Yycl, O., and Y. Jianping. 2019. The progress of chemical constituents isolated from the root of *Actinidia chinensis* planch and their biological activities. *Journal of Biomedical Research and Reviews* 2 (2).

Oncho, D. A., M. C. Ejigu, and O. E. Urgessa. 2021. Phytochemical constituent and antimicrobial properties of guava extracts of east Hararghe of Oromia, Ethiopia. *Clinical Phytoscience* 7 (1):37. doi: 10.1186/s40816-021-00268-2.

Ong, B. T., S. A. H. Nazimah, A. Osman, S. Y. Quek, Y. Y. Voon, D. M. Hashim, P. M. Chew, and Y. W. Kong. 2006. Chemical and flavour changes in jackfruit (*Artocarpus heterophyllus* Lam.) cultivar J3 during ripening. *Postharvest Biology and Technology* 40 (3):279–86. doi: 10.1016/j.postharvbio.2006.01.015.

Ong, B. T., S. A. H. Nazimah, C. P. Tan, H. Mirhosseini, A. Osman, D. Mat Hashim, and G. Rusul. 2008. Analysis of volatile compounds in five jackfruit (*Artocarpus heterophyllus* L.) cultivars using solid-phase microextraction (SPME) and gas chromatography-time-of-flight mass spectrometry (GC-TOFMS). *Journal of Food Composition and Analysis* 21 (5):416–22. doi: 10.1016/j.jfca.2008.03.002.

Ong, P. K. C., T. E. Acree, and E. H. Lavin. 1998. Characterization of volatiles in Rambutan fruit (*Nephelium lappaceum* L.).*Journal of Agricultural and Food Chemistry* 46 (2):611–5. doi: 10.1021/jf970665t.

Ordóñez, R. M., M. L. Cardozo, I. C. Zampini, and M. I. Isla. 2010. Evaluation of antioxidant activity and genotoxicity of alcoholic and aqueous beverages and pomace derived from ripe fruits of *Cyphomandra betacea* Sendt. *Journal of Agricultural and Food Chemistry* 58 (1):331–7. doi: 10.1021/jf9024932.

Orhan, N., D. D. Orhan, M. Aslan, and F. Ergun. 2014. Effect of exotic fruit "Pepino" {*Solanum muricatum* Aiton.) on blood glucose level. *Turkish Journal of Pharmaceutical Sciences* 11 (2).

Osman, M. A., M. A. Aziz, M. R. Habib, M. R. Karim, M. Rezaul, and K. Antimicrobial. 2011. Antimicrobial investigation on *Manilkara zapota* (L.) P. Royen. *International Journal of Drug Development and Research* 3 (1):185–90. https://www.ijddr.in/drug-development/antimicrobial-investigation-on-manilkara-zapota-l-p-royen.php?aid=5545.

Oszmiański, J., S. Lachowicz, E. Gławdel, T. Cebulak, and I. Ochmian. 2018. Determination of phytochemical composition and antioxidant capacity of 22 old apple cultivars grown in Poland. *European Food Research and Technology* 244 (4):647–62. doi: 10.1007/s00217-017-2989-9.

Owen, P. L., T. Matainaho, M. Sirois, and T. Johns. 2007. Endothelial cytoprotection from oxidized LDL by some crude melanesian plant extracts is not related to their antioxidant capacity. *Journal of Biochemical and Molecular Toxicology* 21 (5):231–42. doi: 10.1002/jbt.20186.

Pal, A., S. Kumar Chinnaiyan, A. Mallik, and C. Bhattacharjee. 2019. Anti ulcer activity of leaves of *Averrhoa carambola* Linn. *International Journal of Pharmacological Research* 9 (5).

Palanisamy, U., T. Manaharan, L. L. Teng, A. K. C. Radhakrishnan, T. Subramaniam, and T. Masilamani. 2011. Rambutan rind in the management of hyperglycemia. *Food Research International* 44 (7):2278–82. doi: 10.1016/j.foodres.2011.01.048.

Palanisamy, U. D., and T. Manaharan. 2013. *Syzygium aqueum* leaf extracts for possible antidiabetic treatment. In: International Symposium on Medicinal Plants and Natural Products 1098. [place unknown]; 13–22.

Paliga, M., Z. Novello, R. M. Dallago, J. Scapinello, J. D. Magro, M. di Luccio, M. v Tres, and J. V. Oliveira. 2017. Extraction, chemical characterization and antioxidant activity of *Litchi chinensis* Sonn. and *Avena sativa* L. seeds extracts obtained from pressurized n-butane. *Journal of Food Science and Technology* 54 (3):846–51. doi: 10.1007/s13197-016-2485-4.

Pan, Y., K. Wang, S. Huang, H. Wang, X. Mu, C. He, X. Ji, J. Zhang, and F. Huang. 2008. Antioxidant activity of microwave-assisted

extract of longan (*Dimocarpus Longan* Lour.) peel. *Food Chemistry* 106 (3):1264–70. doi: 10.1016/j.foodchem.2007.07.033.

Panche, A. N., A. D. Diwan, and S. R. Chandra. 2016. Flavonoids: An overview. *Journal of Nutritional Science* 5:47. e. doi: 10.1017/jns.2016.41.

Pandey, S., V. Singh, A. Rao, N. Tiwari, V. Nanda, and V. Pandey. 2018. Antioxidant activity of stem bark of Elephant Apple in different solvents. *Journal of Drug Delivery and Therapeutics* 8 (6-s):311–3.]. doi: 10.22270/jddt.v8i6-s.2250.

Pandey, Y., S. Upadhyay, S. S. Bhatt, L. Sharma, S. Manivannan, and C. Chanbisana. 2018. Nutritional compositions of *Baccaurea sapida* and *Eleaocarpus sikkimnesis* of Sikkim Himalaya. *International Journal of Current Microbiology and Applied Sciences* 7 (2):2101–6. doi: 10.20546/ijcmas.2018.702.250.

Panthari, P.,. Kharkwal Harsha, Kharkwal Harendra, Joshi. and D. D. 2012. *Myrica nagi*: A review on active constituents, biological and therapeutic effects. *International Journal of Pharmacy and Pharmaceutical Sciences* 4 (5):38–42.

Papuc, C., G. V. Goran, C. N. Predescu, V. Nicorescu, and G. Stefan. 2017. Plant polyphenols as antioxidant and antibacterial agents for shelf-life extension of meat and meat products: Classification, structures, sources, and action mechanisms. *Comprehensive Reviews in Food Science and Food Safety* 16 (6):1243–68. doi: 10.1111/1541-4337.12298.

Paramita, V., H. Kusumayanti, W. Rizka Amalia, and S. Nugraheni Setiawati. 2017. Effect of fixative types on the natural dye efficacy of rambutan (*Nephelium lappaceum*) peel extract for the cotton fabric application. *International Journal of Applied Engineering Research* 12:10711–8. http://www.ripublication.com.

Pareek, S. 2016. Chapter 17 - Nutritional and biochemical composition of lychee (*Litchi chinensis* Sonn.) cultivars. In *Nutritional composition of fruit cultivars*, 395–418. doi: 10.1016/B978-0-12-408117-8.00017-9.

Pareek, S., N. Benkeblia, J. Janick, S. Cao, and E. M. Yahia. 2014. Postharvest physiology and technology of loquat (*Eriobotrya japonica* Lindl.) fruit. *Journal of the Science of Food and Agriculture* 94 (8):1495–504. doi: 10.1002/jsfa.6560.

Park, J. H., and H. S. Lee. 2018. In vivo fungicidal properties of *Diospyros kaki*-isolated compound and its analogues. *Applied Biological Chemistry* 61 (4):383–8. doi: 10.1007/s13765-018-0369-1.

Park, Y. S., H. Leontowicz, M. Leontowicz, J. Namiesnik, I. Jesion, and S. Gorinstein. 2008. Nutraceutical value of persimmon (*Diospyros kaki* Thunb.) and its influence on some indices of atherosclerosis in an experiment on rats fed cholesterol-containing diet. *Advances in Horticultural Science* 22. doi: 10.1400/100650.

Patel, I., O. Padse, and Y. Ingole. 2015. Comparative analysis of antioxidant and antidiabetic activity for apple (*Malus domestica*), banana (*Musa paradisiaca*) & kiwi (*Actinidia deliciosa*). In. National Conference "ACGT" 2015:13–4.

Patil, B. S. 2013. Tropical and subtropical fruits : flavors, color, and health benefits. ACS Symposium Series. Oxford University Press, USA, 1–248. doi: http://dx.doi.org/10.13140/RG.2.1.1779.8807.

Paul, P.,. Biswas, P. Dey, D. Saikat, A. S. M. Islam, M. A. Sohel, M. Hossain, R. Mamun, A. Al, Rahman, M. A. Hasan, M. N, et al. 2021. Exhaustive plant profile of "dimocarpus longan lour" with significant phytomedicinal properties: A literature based-review. *Processes* 9 (10):1803. doi: 10.3390/pr9101803.

Paul, S., M. Y. Ali, N. E. N. Rumpa, E. M. Tanvir, M. S. Hossen, M. Saha, N. C. Bhoumik, S. H. Gan, and M. I. Khalil. 2017. Assessment of toxicity and beneficiary effects of *Garcinia pedunculata* on the hematological. *Evidence-Based Complementary and Alternative Medicine* 2017:1–11. doi: 10.1155/2017/4686104.

Pedraza-Chaverri, J., N. Cárdenas-Rodríguez, M. Orozco-Ibarra, and J. M. Pérez-Rojas. 2008. Medicinal properties of mangosteen (*Garcinia mangostana*). *Food and Chemical Toxicology: Toxicology* 46 (10):3227–39. doi: 10.1016/j.fct.2008.07.024.

Pereira, M. G., G. M. Maciel, C. W. I. Haminiuk, F. Bach, F. Hamerski, A. de Paula Scheer, and M. L. Corazza. 2019. Effect of extraction process on composition, antioxidant and antibacterial activity of oil from yellow passion fruit (*Passiflora edulis* Var. Flavicarpa) seeds. *Waste and Biomass Valorization* 10 (9):2611–25. doi: 10.1007/s12649-018-0269-y.

Pereira-Netto, A. B. 2018. Tropical Fruits as natural, exceptionally rich, sources of bioactive compounds. *International Journal of Fruit Science* 18 (3):231–42. doi: 10.1080/15538362.2018.1444532.

Perumal, A., M. S. AlSalhi, S. Kanakarajan, S. Devanesan, R. Selvaraj, and V. Tamizhazhagan. 2021. Phytochemical evaluation and anticancer activity of rambutan (*Nephelium lappaceum*) fruit endocarp extracts against human hepatocellular carcinoma (HepG-2) cells. *Saudi Journal of Biological Sciences* 28 (3):1816–25. doi: 10.1016/j.sjbs.2020.12.027.

Phukhatmuen, P.,. A. Raksat, S. Laphookhieo, R. Charoensup, T. Duangyod, and W. Maneerat. 2020. Bioassay-guided isolation and identification of antidiabetic compounds from Garcinia cowa leaf extract. *Heliyon* 6 (4):e03625. doi: 10.1016/j.heliyon.2020.e03625.

Pillai, D. S., P. Prabhasankar, B. S. Jena, and C. Anandharamakrishnan. 2012. Microencapsulation of garcinia cowa fruit extract and effect of its use on pasta process and quality. *International Journal of Food Properties* 15 (3):590–604. doi: 10.1080/10942912.2010.494756.

Pino, J., S. Gutierrez, and A. Rosado. 1990. Volatile constituents from a guava (*Psidium guajava* L.) natural flavour concentrate. *Food / Nahrung* 34 (3):279–82. doi: 10.1002/food.19900340321.

Pk, University of Rajasthan G. 2014. Chemopreventive and antioxidative effects of averrhoa carambola (Star fruit) extract against diethylnitrosamine induced hepatocarcinogenesis. *Cancer Biology & Treatment* 1 (1):1–7. doi: 10.24966/CBT-7546/100003.

Plagemann, I., U. Krings, R. G. Berger, and M. R. Marostica. 2012. Volatile constituents of jabuticaba (*Myrciaria jaboticaba* (Vell.) O. Berg) fruits. *Journal of Essential Oil Research* 24 (1):45–51. doi: 10.1080/10412905.2012.645651.

Poltanov, E. A., A. N. Shikov, H. J. D. Dorman, O. N. Pozharitskaya, V. G. Makarov, V. P. Tikhonov, and R. Hiltunen. 2009. Chemical and antioxidant evaluation of Indian gooseberry (*emblica officinalis* gaertn., syn. *phyllanthus emblica* L.) supplements. *Phytotherapy Research : PTR* 23 (9):1309–15. doi: 10.1002/ptr.2775.

Prabhakar, P. K., and M. Doble. 2011. Interaction of cinnamic acid derivatives with commercial hypoglycemic drugs on 2-deoxyglucose uptake in 3T3-L1 adipocytes. *Journal of Agricultural and Food Chemistry* 59 (18):9835–44. doi: 10.1021/jf2015717.

Prakash, O. 2013. Antiepileptic potential of bark and leaves of *Artocarpus* heterophyllus Lam.(Jackfruit) against seizures induced by Mes and Strychnine. Nitrate in experimental mice.

Prasanth, N. v., S. P. Rasheed, T. Thomas, S. Joseph, and C. P. Varghese. 2013. Evaluation of in vitro and in vivo anti-inflammatory activity of *Garcinia combogia* L. *International Journal of Pharmacy and Pharmaceutical Sciences* 5(SUPPL. 2).

Pravin P, K., and D. Shashikant C. 2018. Manilkara zapota (L.) royen fruit peel: A phytochemical and pharmacological review. *Systematic Reviews in Pharmacy* 10 (1):11–4. doi: 10.5530/srp.2019.1.2.

Priya, G., and C. Chellaram. 2014. Antiproliferative effect of ethanolic leaf extract of *Solanum trilobatum* on Hep2 cancer cell lines. *Asian Journal of Pharmaceutical and Clinical Research* 7 (2).

Priya M, Joseph B. International journal of pharma and bio sciences review on nutritional, medicinal and pharmacological properties of guava (*Psidium Guajava* Linn.) [Internet]. [accessed 2021 Oct 13]. www.ijpbs.net

Profile, P., and H. Bioactivities. 2021. Guava (*Psidium guajava* L.) leaves. *Nutritional Composition* 1–20.

Prohens, J., and F. Nuez. 2001. The tamarillo (*Cyphomandra betacea*): A review of a promising small fruit crop. *Small Fruits Review* 1 (2):43–68. doi: 10.1300/J301v01n02_06.

Punia, S., and M. Kumar. 2021. Litchi (*Litchi chinenis*) seed: Nutritional profile, bioactivities, and its industrial applications. *Trends in Food Science & Technology* 108:58–70. doi: 10.1016/j.tifs.2020.12.005.

Puricelli, L., I. Dell'Aica, L. Sartor, S. Garbisa, and R. Caniato. 2003. Preliminary evaluation of inhibition of matrix-metalloprotease MMP-2 and MMP-9 by Passiflora edulis and P. foetida aqueous extracts. *Fitoterapia* 74 (3):302–4. doi: 10.1016/S0367-326X(03)00023-6.

Putri, A. S., W. F. Pasedan, I. W. Kusuma, and H. Kuspradini. 2021. Antioxidant and antibacterial activity from three different solvents

of Nephelium ramboutan-ake leaves crude extract. In: Proceedings of the Joint Symposium on Tropical Studies (JSTS-19). Vol. 11. doi: 10.2991/absr.k.210408.003.

Rai, H., S. Upadhyay, A. Sajwan, D. Shuchi, and U. A. Sajwan. 2020. An overview of *Dillenia indica* and their properties. *The Pharma Innovation Journal* 9 (6):41–4. http://www.thepharmajournal.com.

Raiola, A., M. M. Rigano, R. Calafiore, L. Frusciante, and A. Barone. 2014. Enhancing the Health-Promoting Effects of Tomato Fruit for Biofortified Food. *Mediators of Inflammation* 2014:1–16. doi: 10.1155/2014/139873.

Ramil, M. D. I., A. M. Dc. Mendoza, and R. J. D. Ramil. 2021. Assessment on the physicochemical and phytochemical properties, nutritional and heavy metal contents, and antioxidant activities of *Hylocereus polyrhizus* peel from Northern Philippines. *Indian Journal of Science and Technology* 14 (14):1097–104. doi: 10.17485/IJST/v14i14.2286.

Ramírez, V., S. S. Arango, D. Uribe, M. E. Maldonado, and J. Aguillón. 2017. Effect of the ethanolic extract of *Passiflora edulis* F. Flavicarpa leaves on viability, cytotoxicity and apoptosis of colon cancer cell lines. *J Chem Pharm Res* 9 (6):135–9.

Ranasinghe, R. A. S. N., S. D. T. Maduwanthi, and R. A. U. J. Marapana. 2019. Nutritional and health benefits of jackfruit (*Artocarpus heterophyllus* Lam.): A review. *International Journal of Food Science* 2019:1–12. doi: 10.1155/2019/4327183.

Rawat, S., A. Jugran, L. Giri, I. D. Bhatt, and R. S. Rawal. 2011. Assessment of antioxidant properties in fruits of *Myrica esculenta*: A popular wild edible species in Indian Himalayan region. *Evidence-Based Complementary and Alternative Medicine* 2011:1–8. doi: 10.1093/ecam/neq055.

Redgwell, R. J., and N. A. Turner. 1986. Pepino (Solanurn rnun'ca-turn): Chemical composition of ripe fruit. *Journal of the Science of Food and Agriculture* 37 (12):1217–22. doi: 10.1002/jsfa.2740371211.

Ren, H., H. Yu, S. Zhang, S. Liang, X. Zheng, S. Zhang, P. Yao, H. Zheng, and X. Qi. 2019. Genome sequencing provides insights into the evolution and antioxidant activity of Chinese bayberry. *BMC Genomics* 20 (1):458. doi: 10.1186/s12864-019-5818-7.

Reyniers, S., N. Ooms, S. v Gomand, and J. A. Delcour. 2020. What makes starch from potato (*Solanum tuberosum* L.) tubers unique: A review. *Comprehensive Reviews in Food Science and Food Safety* 19 (5):2588–612. doi: 10.1111/1541-4337.12596.

Ribeiro, S. F. F., G. B. Taveira, A. O. Carvalho, G. B. Dias, M. Da Cunha, C. Santa-Catarina, R. Rodrigues, and V. M. Gomes. 2012. Antifungal and other biological activities of two 2S albumin-homologous proteins against pathogenic fungi. *The Protein Journal* 31 (1):59–67. doi: 10.1007/s10930-011-9375-4.

Richardson, D. P., J. Ansell, and L. N. Drummond. 2018. The nutritional and health attributes of kiwifruit: A review. *European Journal of Nutrition* 57 (8):2659–76. doi: 10.1007/s00394-018-1627-z.

Ritthiwigrom, T., S. Laphookhieo, and S. G. Pyne. 2013. Chemical constituents and biological activities of *Garcinia cowa* Roxb. *Maejo International Journal of Science and Technology* 7 (2).

Rizaldy, D., R. Hartati, T. Nadifa, and I. Fidrianny. 2021. Chemical compounds and pharmacological activities of mangosteen (*Garcinia mangostana* L.) – Updated review. *Biointerface Research in Applied Chemistry* 12 (2):2503–16. doi: 10.33263/BRIAC122.25032516.

Rodriguez, E. B., M. L. P. Vidallon, D. J. R. Mendoza, and C. T. Reyes. 2016. Health-promoting bioactivities of betalains from red dragon fruit (*Hylocereus polyrhizus* (Weber) Britton and Rose) peels as affected by carbohydrate encapsulation. *Journal of the Science of Food and Agriculture* 96 (14):4679–89. doi: 10.1002/jsfa.7681.

Romatua Aruan, D. G., T. Barus, G. Haro, R. Siburian, and P. Simanjuntak. 2019. Phytochemical screening and antidiabetic activity of N-hexane, ethyl acetate and water extract from durian leaves (*Durio zibethinus* L.). *Oriental Journal of Chemistry* 35 (1):487–90. doi: 10.13005/ojc/350166.

Rose, K., C. Wan, A. Thomas, N. P. Seeram, and H. Ma. 2018. Phenolic compounds isolated and identified from amla (*Phyllanthus emblica*) juice powder and their antioxidant and neuroprotective activities. *Natural Product Communications* 13 (10):1934578X1801301–11. doi: 10.1177/1934578X1801301019.

Rummun, N., E. Pires, J. McCullagh, T. W. D. Claridge, T. Bahorun, W. W. Li, and V. S. Neergheen. 2021. Methyl gallate – Rich fraction *of Syzygium coriaceum* leaf extract induced cancer cell cytotoxicity via oxidative stress. *South African Journal of Botany* 137:149–58. doi: 10.1016/j.sajb.2020.10.014.

S. Eldeen, I., S. Foong, N. Ismail, and K. Wong. 2020. Regulation of pro-inflammatory enzymes by the dragon fruits from *Hylocereus undatus* (Haworth) and squalene – Its major volatile constituents. *Pharmacognosy Magazine* 16 (68):81. doi: 10.4103/pm.pm_271_19.

Safdar, M. N., T. Kausar, and M. Nadeem. 2017. Comparison of ultrasound and maceration techniques for the extraction of polyphenols from the mango peel. *Journal of Food Processing and Preservation* 41 (4):e13028. doi: 10.1111/jfpp.13028.

Sagolsem, I., S. Rathi, and S. Baishya. 2021. Impact of different drying methods on nutritional quality of *Garcinia cowa* and *Garcinia pedunculata* fruits PD lagiarism etector. *Journal of Environmental Biology* 42 (3):714–9. ¨ . doi: 10.22438/jeb/42/3/MRN-1484.

Saini, R., V. Garg, and K. Dangwal. 2013. Effect of extraction solvents on polyphenolic composition and antioxidant, antiproliferative activities of Himalyan bayberry (*Myrica esculenta*). *Food Science and Biotechnology* 22 (4):887–94. doi: 10.1007/s10068-013-0160-3.

Saisavoey, T., P. Sangtanoo, O. Reamtong, and A. Karnchanatat. 2018. Anti-inflammatory effects of lychee (*Litchi chinensis* Sonn.) seed peptide hydrolysate on RAW 264.7 macrophage cells. *Food Biotechnology* 32 (2):79–94. doi: 10.1080/08905436.2018.1443821.

Sajib, M. A. M., M. M. Hoque, S. Yeasmin, and M. H. A. Khatun. 2014. Minerals and heavy metals concentration in selected tropical fruits of Bangladesh. *International Food Research Journal* 21 (5):1731–6.

Sakanaka, S.,. Y. Tachibana, and Y. Okada. 2005. Preparation and antioxidant properties of extracts of Japanese persimmon leaf tea (kakinoha-cha). *Food Chemistry* 89 (4):569–75. doi: 10.1016/j.foodchem.2004.03.013.

Salleh, M., R. L. Ying, and L. Mousavi. Development of fruit bar using sapodilla (Manilkara *zapota* L). doi: 10.1111/jfpp.12806.

Saminathan, V., and R. Doraiswamy. 2020. Phytochemical analysis, antioxidant and anticancer activities of durian (*Durio zibethinus* Murr.) fruit extract. *Journal of Research in Pharmacy* 24 (6):882–92. doi: 10.35333/JRP.2020.247.

Sampath Kumar, N. S., N. M. Sarbon, S. S. Rana, A. D. Chintagunta, S. Prathibha, S. K. Ingilala, S. P. Jeevan Kumar, B. Sai Anvesh, and V. R. Dirisala. 2021. Extraction of bioactive compounds from *Psidium guajava* leaves and its utilization in preparation of jellies. *AMB Express* 11 (1):36. doi: 10.1186/s13568-021-01194-9.

Sano, S., K. Sugiyama, T. Ito, Y. Katano, and A. Ishihata. 2011. Identification of the strong vasorelaxing substance Scirpusin B, a dimer of piceatannol, from passion fruit (*Passiflora edulis*). *Journal of Agricultural and Food Chemistry* 59 (11):6209–13. doi: 10.1021/jf104959t.

Sanz, V., L. López-Hortas, M. D. Torres, and H. Domínguez. 2021. Trends in kiwifruit and byproducts valorization. *Trends in Food Science & Technology* 107:401–14. doi: 10.1016/j.tifs.2020.11.010.

Sarkar, T., A. Mukherjee, and K. Chatterjee. 2021. Supervised learning aided multiple feature analysis for freshness class detection of indian gooseberry (*Phyllanthus emblica*). *Journal of Institute of Engineers (India): Series A*. doi: 10.1007/s40030-021-00585-2.

Sarkar, T., P. Nayak, and R. Chakraborty. 2018. Litchi (*Litchi chinensis* Sonn.) Products and processing technologies: an Update. *Ambient Science* 5 (01-02, Sp1). doi: 10.21276/ambi.2018.05.1.rv01.

Satpal, D., J. Kaur, V. Bhadariya, and K. Sharma. 2021. Actinidia deliciosa (Kiwi fruit): A comprehensive review on the nutritional composition, health benefits, traditional utilization, and commercialization. *Journal of Food Processing and Preservation* 45 (6):e15588. doi: 10.1111/jfpp.15588.

Saúco, V. G. 2013. Potential of minor tropical fruits to become important fruit crops. *Acta Horticulturae* 975 (975):581–91. doi: 10.17660/ActaHortic.2013.975.74.

Seal, T. 2011. Evaluation of nutritional potential of wild edible plants, traditionally used by the tribal people of Meghalaya State in India. *American Journal of Plant Nutrition and Fertilization Technology* 2 (1):19–26. doi: 10.3923/ajpnft.2012.19.26.

Seal, T., K. Chaudhuri, B. Pillai, and C. Seal. 2017. Water soluble vitamin estimation in five wild edible fruits consumed by the tribal people of north-eastern region in India by high performance liquid chromatography. *International Journal of Chemical Studies* 5 (5).

Shabbir, H., T. Kausar, S. Noreen, H. U. Rehman, A. Hussain, Q. Huang, A. Gani, S. Su, and A. Nawaz. 2020. In vivo screening and antidiabetic potential of polyphenol extracts from guava pulp, seeds and leaves. *Animals* 10 (9):1714. doi: 10.3390/ani10091714.

Shahrajabian, M. H., W. Sun, and Q. Cheng. 2019. Modern pharmacological actions of Longan fruits and their usages in traditional herbal remedies. *Journal of Medicinal Plants Studies* 7 (4):179–85.

Sharma, P. B., P. J. Handique, and H. S. Devi. 2015. Antioxidant properties, physico-chemical characteristics and proximate composition of five wild fruits of Manipur, India. *Journal of Food Science and Technology* 52 (2):894–902. doi: 10.1007/s13197-013-1128-2.

Shaw, P. E., and C. W. Wilson. 1982. Volatile constituents of loquat (Eriobotrya *japonica* Lindl.) fruit. *Journal of Food Science* 47 (5):1743–4. doi: 10.1111/j.1365-2621.1982.tb05028.x.

Shen, Y., C. Chen, N. Cai, R. Yang, J. Chen, İ. Kahramanoğlu, V. Okatan, K. R. R. Rengasamy, and C. Wan. 2021. The antifungal activity of loquat (*Eriobotrya japonica* Lindl.) Leaves Extract against *Penicillium digitatum*. *Frontiers in Nutrition* 8. doi: 10.3389/fnut.2021.663584.

Shin, S.-R., J.-Y. Hong, and K.-Y. Yoon. 2008. Antioxidant properties and total phenolic contents of cherry elaeagnus (*Elaeagnus multiflora* Thunb.) leaf extracts. *Food Science and Biotechnology* 17 (3):608–12.

Shiota, H. Young, V. J. Paterson, and M. Irie. 1988. Volatile aroma constituents of pepino fruit. *Journal of the Science of Food and Agriculture* 43 (4):343–54. doi: 10.1002/jsfa.2740430407.

Shirwaikar, A., K. Rajendran, C. Dinesh Kumar, and R. Bodla. 2004. Antidiabetic activity of aqueous leaf extract of *Annona squamosa* in streptozotocin–nicotinamide type 2 diabetic rats. *Journal of thnopharmacology* 91 (1):171–5. doi: 10.1016/j.jep.2003.12.017.

Šic Žlabur, J., S. Bogdanović, S. Voća, and M. Skendrović Babojelić. 2020. Biological potential of fruit and leaves of strawberry tree (*Arbutus unedo* L.) from Croatia. *Molecules* 25 (21):5102. doi: 10.3390/molecules25215102.

Silva, D. C., A. L. P. Freitas, C. D. S. Pessoa, R. C. M. Paula, J. X. Mesquita, L. K. A. M. Leal, G. A. C. Brito, D. O. Gonçalves, and G. S. B. Viana. 2011. Pectin from *Passiflora edulis* shows anti-inflammatory action as well as hypoglycemic and hypotriglyceridemic properties in diabetic rats. *Journal of edicinal ood* 14 (10):1118–26. doi: 10.1089/jmf.2010.0220.

Singh, B., Sharma. and R. A. 2015. Plant terpenes: efense responses, phylogenetic analysis, regulation and clinical applications. *3 Biotech [Biotech* 5 (2):129–51. doi: 10.1007/s13205-014-0220-2.

Slywka, G. W. A., and R. A. Locock. 1969. Structure of a new beta-carboline alkaloid from *Elaeagnus commutata*, (silverberry or wolf willow). *Tetrahedron Letters* 10 (53):4635–8. doi: 10.1016/S0040-4039(01)88769-4.

Smeriglio, A., C. De Francesco, M. Denaro, and D. Trombetta. 2021. Prickly pear betalain-rich extracts as new promising strategy for intestinal inflammation: plant complex vs. main isolated bioactive compounds. *Frontiers in Pharmacology* 12 (September):1–11. doi: 10.3389/fphar.2021.722398.

S., Mishra, K. R., and P. K. N. 2021. Ultrasound pre-treated osmotic dehydration of elephant apple (*Dillenia indica*) slices. *Journal of Scientific & Industrial Research* 80:17–22.

Soares, F. D., T. Pereira, M. O. Maio Marques, and A. R. Monteiro. 2007. Volatile and non-volatile chemical composition of the white guava fruit (*Psidium guajava*) at different stages of maturity. *Food Chemistry* 100 (1):15–21. doi: 10.1016/j.foodchem.2005.07.061.

Sobeh, M., M. F. Mahmoud, G. Petruk, S. Rezq, M. L. Ashour, F. S. Youssef, A. M. El-Shazly, D. M. Monti, A. B. Abdel-Naim, and M. Wink. 2018. *Syzygium aqueum*: A polyphenol- rich leaf extract exhibits antioxidant, hepatoprotective, pain-killing and anti-inflammatory activities in animal models. *Frontiers in harmacology* 9 (JUN):566. doi: 10.3389/fphar.2018.00566.

Soeng, S.,. E. Evacuasiany, W. Widowati, N. Fauziah, V. Manik, and M. Maesaroh. 2015. Inhibitory potential of rambutan seeds extract and fractions on adipogenesis in 3T3-L1 cell line. *Journal of Experimental and Integrative Medicine* 5 (1):55. doi: 10.5455/jeim.200115.or.120.

Spínola, V., J. Pinto, E. J. Llorent-Martínez, and P. C. Castilho. 2019. Changes in the phenolic compositions of *Elaeagnus umbellata* and *Sambucus lanceolata* after in vitro gastrointestinal digestion and evaluation of their potential anti-diabetic properties. *Food esearch nternational* 122:283–94. doi: 10.1016/j.foodres.2019.04.030.

Sravani, D., K. S. Aarathi, N. S. Kumar, S. Krupanidhi, D. Vijaya Ramu, and T. C. Venkateswarlu. 2015. In vitro anti-inflammatory activity of *Mangifera indica* and *Manilkara zapota* leaf extract. *Research Journal of Pharmacy and Technology* 8 (11):1477. doi: 10.5958/0974-360X.2015.00264.4.

Sreeja Devi, P. S., N. S. Kumar, and K. K. Sabu. 2021. Phytochemical profiling and antioxidant activities of different parts of *Artocarpus heterophyllus* Lam. (Moraceae): A review on current status of knowledge. *Future Journal of Pharmaceutical Sciences* 7 (1):30. doi: 10.1186/s43094-021-00178-7.

Srivastava, M., M. Hegde, K. K. Chiruvella, J. Koroth, S. Bhattacharya, B. Choudhary, and S. C. Raghavan. 2015. Sapodilla plum (*Achras sapota*) induces apoptosis in cancer cell lines and inhibits tumor progression in mice. *Scientific Reports* 4 (1):6147. doi: 10.1038/srep06147.

Stanley, R., Dietzgen, and M. Gidley. 2009. Proceedings of the tropical fruits in human nutrition and health conference 2008.

Striegel, L., Weber, N. Dumler, C. Chebib, S. Netzel, M. E. Sultanbawa, Y. Rychlik. and M. 2019. Promising tropical fruits high in folates. *Foods* 8 (9):363. doi: 10.3390/foods8090363.

Sudha, G., M. Sangeetha Priya, R. B. Indhu Shree, and S. Vadivukkarasi. 2012. Antioxidant activity of ripe and unripe pepino fruit (*Solanum muricatum* Aiton). *Journal of Food Science* 77 (11):C1131–C1135. doi: 10.1111/j.1750-3841.2012.02944.x.

Sukmandari, N. S., G. K. Dash, W. H. W. Jusof, and M. Hanafi. 2017. A review on *Nephelium lappaceum* L. *Research Journal of Pharmacy and Technology* 10 (8):2819–27. doi: 10.5958/0974-360X.2017.00498.X.

Sultana Chowdhury, N. 2021. Traditional and pharmacological reports of the genus baccaurea. A review. *American Journal of Biomedical Science & Research* 11 (6):494–508. doi: 10.34297/AJBSR.2021.11.001683.

Sun, C., H. Huang, C. Xu, X. Li, and K. Chen. 2013. Biological activities of extracts from Chinese bayberry (*Myrica rubra* Sieb. et Zucc.): A review. *Plant Foods for Human Nutrition (Dordrecht, Netherlands)* 68 (2):97–106. doi: 10.1007/s11130-013-0349-x.

Sun, W., M. H. Shahrajabian, H. Shen, and Q. Cheng. 2021. Lychee (*Litchi chinensis* Sonn.), the king of fruits, with both traditional and modern pharmacological health benefits. *Pharmacognosy Communications* 11 (1):22–5. doi: 10.5530/pc.2021.1.5.

Sushma, M., A. Bhavana, and K. Padmalatha. 2021. International journal of modern overview of phytochemistry and pharmacology of syzygium. 5 (4):106–11.

Susilowati, R., M. F. Ibrizah, L. S. Andriani, and K. Nisa. 2018. The potential of rambutan seed extract to reduce risk of cardiovascular disease in diabetes mellitus type 2. doi: 10.2991/amca-18.2018.175.

Suttirak, W., and S. Manurakchinakorn. 2014. In vitro antioxidant properties of mangosteen peel extract. *Journal of ood cience and echnology* 51 (12):3546–58. doi: 10.1007/s13197-012-0887-5.

Swallah, M. S., H. Sun, R. Affoh, H. Fu, and H. Yu. 2020. Antioxidant potential overviews of secondary metabolites (Polyphenols) in fruits. *International Journal of Food Science* 2020:1–8. doi: 10.1155/2020/9081686.

Swami, S. B., N. J. Thakor, P. M. Haldankar, and S. B. Kalse. 2012. Jackfruit and its many functional components as related to human health: A review. *Comprehensive Reviews in Food Science and Food Safety* 11 (6):565–76. doi: 10.1111/j.1541-4337.2012.00210.x.

Swamy Mallappa, K. 2020. *Plant-derived bioactives*. Swamy MK, editor. Singapore: Springer Singapore. doi: 10.1007/978-981-15-2361-8.

Tadtong, S., S. Athikomkulchai, P. Worachanon, P. Chalongpol, P. Chaichanachaichan, and V. Sareedenchai. 2011. Antibacterial activities of rambutan peel extract. *Journal Health Research* 25 (1):35–7.

Taheri, B., J. Anbari, F. Maleki, Z. Boostani, S. Zarghi, and A. Pouralibaba. 2010. Efficacy of *Elaeagnus angustifolia* topical gel in the treatment of symptomatic oral lichen Planus. *Journal of Dental Research, Dental Clinics, Dental Prospects* 4 (1):29–32. doi: 10.5681/joddd.2010.008.

Takeoka, G. R., M. Guntert, R. A. Flath, R. E. Wurz, and W. Jennings. 1986. Volatile constituents of kiwi fruit (*Actinidia chinensis* Planch.). *Journal of Agricultural and Food Chemistry* 34 (3):576–8. doi: 10.1021/jf00069a050.

Takuma, D., S. Guangchen, J. Yokota, A. Hamada, M. Onogawa, S. Yoshioka, M. Kusunose, M. Miyamura, S. Kyotani, and Y. Nishioka. 2008. Effect of *Eriobotrya japonica* seed extract on 5-fluorouracil-induced mucositis in hamsters. *Biological & harmaceutical ulletin* 31 (2):250–4. doi: 10.1248/bpb.31.250.

Talukdar, A., N. Talukdar, S. Deka, and B. J. Sahariah. 2012. *Dillenia indica* (OUTENGA) as anti-diabetic herb found in Assam: A review. *International Journal of harmaceutical ciences and esearch* 3 (8):2482.

Tan, B. L., M. E. Norhaizan, and L. C. Chan. 2018. *Manilkara zapota* (L.) P. Royen leaf water extract induces apoptosis in human hepatocellular carcinoma (HepG2) Cells via ERK1/2/Akt1/JNK1 Signaling Pathways. *Evidence-ased Complementary and Alternative Medicine* 2018 :1–17. doi: 10.1155/2018/7826576.

Tandee, K., S. Kittiwachana, and S. Mahatheeranont. 2021. Antioxidant activities and volatile compounds in longan (*Dimocarpus longan* Lour.) wine produced by incorporating longan seeds. *Food hemistry* 348:128921. doi: 10.1016/j.foodchem.2020.128921.

Tang, Y.-Y., He, X.-M. Sun, J. Li, C.-B. Li, L. Sheng, J.-F. Xin, M. Li, Z.-C. Zheng, F.-J. Liu, G.-M, et al. 2019. Polyphenols and alkaloids in byproducts of longan fruits (*Dimocarpus Longan* Lour.) and their bioactivities. *Molecules* 24 (6):1186. doi: 10.3390/molecules24061186.

Tang, Z. S., X. A. Zeng, M. A. Brennan, Z. Han, D. Niu, and Y. Huo. 2019. Characterization of aroma profile and characteristic aromas during lychee wine fermentation. *Journal of Food Processing and Preservation* 43 (8):e14003. doi: 10.1111/jfpp.14003.

Tatiya-Aphiradee, N., W. Chatuphonprasert, and K. Jarukamjorn. 2016. In vivo antibacterial activity of Garcinia mangostana pericarp extract against methicillin-resistant Staphylococcus aureus in a mouse superficial skin infection model. *Pharmaceutical Biology* 54 (11):2606–15. doi: 10.3109/13880209.2016.1172321.

Tehranizadeh, Z. A., A. Baratian, and H. Hosseinzadeh. 2016. Russian olive (*Elaeagnus angustifolia*) as a herbal healer. *Bioimpacts* 6 (3):155–67. doi: 10.15171/bi.2016.22.

Tewari, R., V. Kumar, and H. K. Sharma. 2019. Physical and chemical characteristics of different cultivars of Indian gooseberry (*Emblica officinalis*). *Journal of ood cience and echnology* 56 (3):1641–8. doi: 10.1007/s13197-019-03595-y.

Tewtrakul, S., C. Wattanapiromsakul, and W. Mahabusarakam. 2009. Effects of compounds from Garcinia mangostana on inflammatory mediators in RAW264.7 macrophage cells. *Journal of thnopharmacology* 121 (3):379–82. doi: 10.1016/j.jep.2008.11.007.

Thiruselvi, M., and B. Durairaj. 2018. In vitro and in vivo antiangiogenic effect of artocarpus heterophyllus seed extract. *Asian Journal of Pharmaceutical and Clinical Research* 11 (9):268–71. doi: 10.22159/ajpcr.2018.v11i9.27488.

Thitilertdecha, N., A. Teerawutgulrag, and N. Rakariyatham. 2008. Antioxidant and antibacterial activities of *Nephelium lappaceum* L. extracts. *LWT - Food Science and Technology* 41 (10):2029–35. doi: 10.1016/j.lwt.2008.01.017.

Toda, M., H. Niwa, H. Irikawa, Y. Hirata, and S. Yamamura. 1974. The alkaloids from the fruits of the plant Daphniphyllaceae. *Tetrahedron* 30 (16):2683–8. doi: 10.1016/S0040-4020(01)97429-0.

Tres, E. N., E. de Madurez, E. De Narain, M. Bora, Holschuh, P. S. Vasconcelos, H. J. Da. and M. A. 2001. Physical and chemical composition of carambola fruit (*Averrhoa carambola* L.) at three stages of maturity composición. *Ciencia y Tecnologia Alimentaria.* 3 (3):144–8.

Tripathi, P. C. 2018. Passion fruit. In: *Horticultural crops of high nutraceutical values*, 245–70. New Delhi: Brillion Publishing.

Usman, F., H. S. Shah, S. Zaib, S. Manee, J. Mudassir, A. Khan, G. E. Batiha, K. M. Abualnaja, D. Alhashmialameer, and I. Khan. 2021. Fabrication and biological assessment of antidiabetic α-mangostin loaded nanosponges: In vitro, in vivo, and in silico studies. *Molecules* 26 (21):6633. doi: 10.3390/molecules26216633.

Vázquez-González, Y., J. A. Ragazzo-Sánchez, and M. Calderón-Santoyo. 2020. Characterization and antifungal activity of jackfruit (*Artocarpus heterophyllus* Lam.) leaf extract obtained using conventional and emerging technologies. *Food hemistry* 330:127211. doi: 10.1016/j.foodchem.2020.127211.

Verma, A. M., A. P. Kumar, R. K. Shekar, K. A. Kumar, and R. R. Chakrapani. 2011. Pharmacological screening of *Annona cherimola* for antihyperlipidemic potential. *Journal of Basic and Clinical Pharmacy* 2 (2):63–9.

Vimal, V.,. and T. Devaki. 2004. Linear furanocoumarin protects rat myocardium against lipidperoxidation and membrane damage during experimental myocardial injury. *Biomedicine & Pharmacotherapy = Biomedecine & Pharmacotherapie* 58 (6-7):393–400. doi: 10.1016/j.biopha.2003.12.007.

Vithana, M. D. K., Z. Singh, and S. K. Johnson. 2018. Levels of terpenoids, mangiferin and phenolic acids in the pulp and peel of ripe mango fruit influenced by pre-harvest spray application of $FeSO_4$ (Fe^{2+}), $MgSO_4$ (Mg^{2+}) and $MnSO_4$ (Mn^{2+}). *Food Chemistry* :71–6. 256. doi: 10.1016/j.foodchem.2018.02.087.

Wagner, K.-H., and I. Elmadfa. 2003. Biological relevance of terpenoids. *Annals of utrition & etabolism* 47 (3-4):95–106. doi: 10.1159/000070030.

Wahjudi, P. N., M. E. Patterson, Q.-Y. Lu, C. J. Li, and W. Lee. 2011. In-vitro tracer-based investigation on the effect of loquat leaves extract toward glucose metabolism using HepG2 cells. *The FASEB Journal* 25 (S1):720–7-720.7. doi: 10.1096/fasebj.25.1_supplement.720.7.

Wahyuni, D. A. Israf Ali, N. H. Lajis, and D. D. 2016. Anti-inflammatory activity of isolated compounds from the Stem Bark of *Garcinia cowa* Roxb. *Pharmacognosy Journal* 9 (1):55–7. doi: 10.5530/pj.2017.1.10.

Wahyuni, L. S. Hui, J. Stanslas, N. H. Lajis, and D. D. 2017. In vivo study of tetraprenyltoluquinone, an anticancer compounds from garcinia cowa roxb. *Journal of Young Pharmacists* 9 (2):296–8. doi: 10.5530/jyp.2017.9.58.

Wall, M. M. 2006. Ascorbic acid and mineral composition of longan (*Dimocarpus longan*), lychee (*Litchi chinensis*) and rambutan (*Nephelium lappaceum*) cultivars grown in Hawaii. *Journal of Food Composition and Analysis* (6-7)19:655–63. doi: 10.1016/j.jfca.2005.12.001.

Wang, B., Qu, H. Ma, J. Sun, X. Wang, D. Zheng, Q. Xing. and D. 2014. Protective effects of *Elaeagnus angustifolia* leaf extract against myocardial ischemia/reperfusion injury in isolated rat heart. *Journal of Chemistry* 2014:1–6. doi: 10.1155/2014/693573.

Wang, M., Chen, J. Ye, X. Liu. and D. 2020. In vitro inhibitory effects of Chinese bayberry (*Myrica rubra* Sieb. et Zucc.) leaves proanthocyanidins on pancreatic α-amylase and their interaction. *Bioorganic Chemistry* 101:104029. doi: 10.1016/j.bioorg.2020.104029.

Wang, M., Y. Liu, R. Pan, R. Wang, S. Ding, W. Dong, G. Sun, J. Ye, and X. Sun. 2019. Protective effects of Myrica rubra flavonoids against hypoxia/reoxygenation-induced cardiomyocyte injury via the regulation of the PI3K/Akt/GSK3β pathway. *International Journal of Molecular Medicine*. doi: 10.3892/ijmm.2019.4131.

Wang, W.-H., Y.-C. Tyan, Z.-S. Chen, C.-G. Lin, M.-H. Yang, S.-S. Yuan, and W.-C. Tsai. 2014. Evaluation of the antioxidant activity and antiproliferative effect of the jaboticaba (*Myrciaria cauliflora*) seed extracts in oral carcinoma cells. *BioMed Research International* 2014:1–7. doi: 10.1155/2014/185946.

Wang, X., S. Yuan, J. Wang, P. Lin, G. Liu, Y. Lu, J. Zhang, W. Wang, and Y. Wei. 2006. Anticancer activity of litchi fruit pericarp extract against human breast cancer in vitro and in vivo. *Toxicology and pplied harmacology* 215 (2):168–78. doi: 10.1016/j.taap.2006.02.004.

Wang, X.-L., X.-X. Di, T. Shen, S.-Q. Wang, and X.-N. Wang. 2017. New phenolic compounds from the leaves of Artocarpus heterophyllus. *Chinese Chemical Letters* 28 (1):37–40. doi: 10.1016/j.cclet.2016.06.024.

Weber, F., and M. Passon. 2019. Characterization and quantification of polyphenols in fruits. In: *Polyphenols in plants*, 111–21. Elsevier. doi: 10.1016/B978-0-12-813768-0.00007-4.

Wong, K. C., and S. N. Wong. 1997. Volatile constituents of *Cyphomandra betacea* Sendtn. *Journal of Essential Oil Research* 9 (3):357–9. doi: 10.1080/10412905.1997.10554261.

Woo, P., H. S. Yim, H. E. Khoo, C. Sia, and Y. K. Ang. 2013. Effects of extraction conditions on antioxidant properties of sapodilla fruit (*Manilkara zapota*). *International Food Research Journal* 20:2065–72.

Wu, J., Zhou, T. Zhang, S. Zhang, X. Xuan. and L. 2009. Cytotoxic terpenoids from the fruits of *Vitex trifolia* L. *Planta Medica* 75 (04):367–70. doi: 10.1055/s-0028-1112211.

Wu, L., Hsu, H.-W. Chen, Y.-C. Chiu, C.-C. Lin, Y.-I. Ho. and J. A. 2006. Antioxidant and antiproliferative activities of red pitaya. *Food Chemistry* 95 (2):319–27. doi: 10.1016/j.foodchem.2005.01.002.

Xiao, Z. B., Liu, J. H. Chen, F. Wang, L. Y. Niu, Y. W. Feng, T. Zhu. and J. C. 2015. Comparison of aroma-active volatiles and their sensory characteristics of mangosteen wines prepared by *Saccharomyces cerevisiae* with GC-olfactometry and principal component analysis. *Natural roduct esearch* 29 (7):656–62. doi: 10.1080/14786419.2014.981185.

Xie, C., Z. Xie, X. Xu, and D. Yang. 2015. Persimmon (*Diospyros kaki* L.) leaves: A review on traditional uses, phytochemistry and pharmacological properties. *Journal of thnopharmacology* 163:229–40. doi: 10.1016/j.jep.2015.01.007.

Xu, Y. X., M. Zhang, Z. X. Fang, J. C. Sun, and Y. Q. Wang. 2014. How to improve bayberry (*Myrica rubra* Sieb. et Zucc.) juice flavour quality: Effect of juice processing and storage on volatile compounds. *Food Chemistry* 151:40–6. doi: 10.1016/j.foodchem.2013.10.118.

Yahaya, A., M. Ali, F. I. EL-Hassan, and B. A. Jido. 2019. Antibacterial activity of guava (*Psidium Guajava* L.) Extracts on *Staphylococcus aureus* isolated from patients with urinary tract infections attending a tertiary-care hospital. *Science World Journal* 14 (1):2019.

Yang, D., H. Xie, B. Yang, and X. Wei. 2014. Two tetrahydroisoquinoline alkaloids from the fruit of *Averrhoa carambola*. *Phytochemistry Letters* 7:217–20. doi: 10.1016/j.phytol.2013.12.007.

Yang, H., Y.-C. Lee, K.-S. Han, H. Singh, M. Yoon, J.-H. Park, C.-W. Cho, and S. Cho. 2013. Green and gold kiwifruit peel ethanol extracts potentiate pentobarbital-induced sleep in mice via a GABAergic mechanism. *Food Chemistry* 136 (1):160–3. doi: 10.1016/j.foodchem.2012.07.111.

Yilmaztekin, M. 2014. Analysis of volatile components of cape gooseberry (*Physalis peruviana* L.) Grown in Turkey by HS-SPME and GC-MS. *The Scientific World Journal* 2014. 1–8. doi: 10.1155/2014/796097.

You, M.-K., M.-S. Kim, K.-S. Jeong, E. Kim, Y.-J. Kim, and H.-A. Kim. 2016. Loquat (Eriobotrya japonica) leaf extract inhibits the growth of MDA-MB-231 tumors in nude mouse xenografts and invasion of MDA-MB-231 cells. *Nutrition esearch and ractice* 10 (2):139–47. doi: 10.4162/nrp.2016.10.2.139.

Yuliani, N. N. 2018. Antihiperglicemic Activity Tests OF Tamarillo (Solanum Betaceum) on Aloksan's Diabetes Rats. *In: Proceeding 1st International Conference Health Polytechnic of Kupang. [lace nknown];* 373–83.

Yunsheng, W. 2021. A draft genome at chromosome level and metabolomes of leave, root and flowers provide insights into the molecular basis of medicinal ingredients of loquat (Eriobotrya japonica (Thunb.) Lindl). Research Square.

Yusuf Alkandahri, Patala, R., Indah Pratiwi, M. Setianingsih Agustina, L. Hari Kusumawati, A. Hidayah, H. S. Amal, and D. Frianto. 2021. Pharmacological studies of Durio zibethinus: A medicinal plant review. *Annals of the Romanian Society for Cell Biology*. 25:640–646. https://www.annalsofrscb.ro/index.php/journal/article/view/2497

Zar, P. P. K., A. Morishita, F. Hashimoto, K. Sakao, M. Fujii, K. Wada, and D.-X. Hou. 2014. Anti-inflammatory effects and molecular mechanisms of loquat (*Eriobotrya japonica*) tea. *Journal of Functional Foods* 6:523–33. doi: 10.1016/j.jff.2013.11.019.

Zhang, W., X. Zhao, C. Sun, X. Li, and K. Chen. 2015. Phenolic composition from different loquat (Eriobotrya japonica Lindl.) cultivars grown in China and their antioxidant properties. *Molecules (Basel, Switzerland)* 20 (1):542–55. doi: 10.3390/molecules20010542.

Zhang, X., S. Guo, C. T. Ho, and N. Bai. 2020. Phytochemical constituents and biological activities of longan (Dimocarpus longan Lour.) fruit: a review. *Food Science and Human Wellness* 9 (2):95–102. doi: 10.1016/j.fshw.2020.03.001.

Zhang, X., H. Huang, Q. Zhang, F. Fan, C. Xu, C. Sun, X. Li, and K Chen. 2015. Phytochemical Characterization of Chinese Bayberry (*Myrica rubra* Sieb. et Zucc.) of 17 Cultivars and Their Antioxidant Properties. *International Journal of Molecular Sciences* 16 (6):12467–81. doi: 10.3390/ijms160612467.

Zhang, X., H. Huang, X. Zhao, Q. Lv, C. Sun, X. Li, and K. Chen. 2015. Effects of flavonoids-rich Chinese bayberry (Myrica rubra Sieb. et Zucc.) pulp extracts on glucose consumption in human HepG2 cells. *Journal of Functional Foods* 14:144–53. doi: 10.1016/j.jff.2015.01.030.

Zhang, Y., J.-S. Wang, D.-D. Wei, Y.-C. Gu, X.-B. Wang, and L.-Y. Kong. 2013. Bioactive Terpenoids from the Fruits of *Aphanamixis grandifolia*. *Journal of Natural Products* 76 (6):1191–5. doi: 10.1021/np400126q.

Zhang, Y., X. Zhou, W. Tao, L. Li, C. Wei, J. Duan, S. Chen, and X. Ye. 2016. Antioxidant and antiproliferative activities of proanthocyanidins from Chinese bayberry (*Myrica rubra* Sieb. et Zucc.) leaves. *Journal of Functional Foods* 27:645–54. doi: 10.1016/j.jff.2016.10.004.

Zhao, C.-N., X. Meng, Y. Li, S. Li, Q. Liu, G.-Y. Tang, and H.-B. Li. 2017. Fruits for Prevention and Treatment of Cardiovascular Diseases. *Nutrients* 9 (6):598. doi: 10.3390/nu9060598.

Zhao, L., K. Wang, K. Wang, J. Zhu, and Z. Hu. 2020. Nutrient components, health benefits, and safety of litchi (Litchi chinensis Sonn.): A review. *Comprehensive Reviews in Food Science and Food Safety* 19 (4):2139–63. doi: 10.1111/1541-4337.12590.

Zhou, S., Z. Fang, Y. Lü, J. Chen, D. Liu, and X. Ye. 2009. Phenolics and antioxidant properties of bayberry (Myrica rubra Sieb. et Zucc.) pomace. *Food Chemistry* 112 (2):394–9. doi: 10.1016/j.foodchem.2008.05.104.

Zhou, Y. W. 2020. No Analysis of the co-dispersion structure of the health-related indicators of the main personTitle. 21 (1):1–9.

Zhu, Q., Y. Jiang, S. Lin, L. Wen, D. Wu, M. Zhao, F. Chen, Y. Jia, and B. Yang. 2013. Structural Identification of (1→6)-α- -Glucan, a Key Responsible for the Health Benefits of Longan, and Evaluation of Anticancer Activity. *Biomacromolecules* 14 (6):1999–2003. doi: 10.1021/bm400349y.

Zuraidah, M. A., B. A. John, and Y. Kamaruzzaman. 2017. Cytotoxicity On Mcf7 Cell Lines Exposed To An Extract Of The Jacalin From Jackfruit Seed. *Science Heritage Journal* 1 (2):16–8. doi: 10.26480/gws.02.2017.16.18.

Zwenger, S., and C. Basu. 2008. Plant terpenoids: Applications and future potentials. *Biotechnology and Molecular Biology Reviews* 3:1–7

JOURNAL OF CRITICAL REVIEWS

ISSN- 2394-5125 VOL 8, ISSUE 01, 2021

MODELING FOR THE ENERGY POTENTIAL OF BIOGAS POWER PLANTS IN NATIONAL CAPITAL TERRITORY

[a] Rohit Agrawal, [b] S.K. Singh

[a, b] Department of Environmental Engineering, Delhi Technological University, Delhi, India
Corresponding Author: [a] rohitagrawal_2k19ene04@dtu.ac.in, [b] sksinghdce@gmail.com

Abstract

Biogas is a renewable energy source which is being researched and widely developed as a future alternative energy source that is economical, sustainable, and environmentally friendly. Under the scheme for National Capital Territory, we used 150 cows for example where the dung from the cows is processed. Biogas production in every day which is 54 m^3 or equivalent to 54,000 liters. Biogas can be used as a generating system capable of producing energy of 540 kWh each day with a power of 540 kW. The generator system in this study divided into 2 parts, namely first, a simple generator system (Digester-biogas-Genset 30000W-electricity biogas) which is assumed to operate for 24 hours a day with the energy output from this biogas power plant is 613.8 kWh per day. Generating system, the second is a generator system using HOMER (Thermal-Boiler-Generator Bio 2 kW-Converter of 10 kW-electric load) with an energy output of 613.8 kWh per day. In realizing an efficient biogas-based generating system, so in this study use HOMER software to optimize generator size and value economic power plant with coverage in the form of net present cost (NPC) of Rs.2,50,000.00 and the cost of Energy (COE) of Rs. 1.57 per unit

Keywords: Anaerobic, Biogas, Digester, Energy, Homer

1. Introduction

Energy has a very important role in the activities of human life; the increasing use of energy has become the world's talk, especially in India. Some of the energy which is used by the Indian people today comes from hydro, solar, and fossil fuels, namely petroleum, coal, and gas. Based on India's Energy outlook, the national energy demand continues to increase along with economic growth, populations, energy costs, and governmental policies. An average Gross Domestic Product (GDP) growth rate of 4.14% per year and the population growth rate of 0.78% per year during 2016-2020, the growth rate for the final energy demand is approx. 2.3% per year as per International Energy Agency. "The total primary energy consumption from coal (452.2 Mtoe; 55.88%), crude oil (239.1 Mtoe; 29.55%), natural gas (49.9 Mtoe; 6.17%), nuclear energy (8.8 Mtoe; 1.09%), hydroelectricity (31.6 Mtoe; 3.91%) and renewable power (27.5 Mtoe; 3.40%) is 809.2 Mtoe (excluding traditional biomass use) in the calendar year 2018." As time goes by, fossil fuels because they are classified as non-renewable energy will sooner or later be depleted or their availability crisis; Based on statistical data on New Renewable Energy and Energy Conservation by International Energy Agency, India has a new and renewable energy source, namely bio-energy with a potential of 18,000 MW with an installed on-grid system capacity of 220.8 MW, of which only a small amount is still being utilized. As a South Asian country, India has abundant bio-energy as energy potential that can be used as renewable energy source to replace fossil energy which is still widely used today, as well as to maintain national energy security [1-2].

Delhi is the National Capital Territory in India that has installed electrical energy capacity from several power plants in several locations generates approx. 2,000 MW of electricity. The power plant used to supply electrical energy by Gas only. Whereas, 54MW of energy is generated from Bio-Waste from 5250 ton of per day waste; The need for electrical energy in Delhi in 2021 is 2,160.30 MW consisting of the government sector of 63.56 MW, the household sector of 1,330.85 MW, the industrial sector of 130.05 MW, the business sector of 508.15 MW, the social sector is 91.31 MW, the public lighting sector is 35.36 MW. With such a large energy demand, Delhi is still experiencing a deficit of 47.32 MW of electrical energy. The impact of the deficit in electrical energy is the occurrence of rotating blackouts in the National Capital Region of Delhi. Utilizing new and renewable energy to overcome the deficit in electrical energy in the Delhi is the best way. In addition to fulfilling energy needs, the use of new and renewable energy can also reduce environmental pollution caused by the use of fossil energy. There is still a lot of potential from biomass in the National Capital Region of Delhi that has not been utilized to overcome the problem of energy in electricity, one of the abundant biomass potentials that are still underutilized is solid waste or garbage [3]. The National Capital Region of Delhi has fertile soils and wild plants that are easily available. With this geographic condition, it is easy to develop the livestock sector. Based on data from Animal Husbandry Statistics Division, livestock in Delhi has a population consisting of 6 types of animals, namely cows, buffaloes, dairy cows, goats, sheep, and pigs approx. 16,00,000 heads, and continued to increase in 2021 to 16,34,128 heads. Of the livestock population, the cattle population has the highest number compared to other animals [4-5].

Previous research has examined the potential for cow dung to be used as a source of power generation, but this study is still a hypothesis, so the test is less accurate in actual conditions. The biogas production process using the anaerobic digestion method made from cow dung, it goes through several stages, each of which has erratic changes that can affect the production of biogas produced [6-7]. In this study, it has also analyzed the economic value that gets positive values so that the design is

ISSN- 2394-5125 VOL 8, ISSUE 01, 2021

feasible to be realized. The process of forming biogas has several factors that can affect the production of biogas, namely the temperature in the digester, the growth of microorganisms, inhibiting agents, etc. Previous research that examined cow dung as a raw material for power plants still used potential based calculations, without examining the factors that influence the production of biogas. So that the results obtained are not accurate. A study to calculate the factors that influence the formation of biogas is very necessary because in the process of a biogas power- plant the factors that influence it are very much taken into account in order to obtain optimal results [8-9]. Overcoming the shortcomings in calculations to predict biogas production in previous research has been done by making a mathematical model of each stage of biogas production as a differential and algebraic equation that is simulated in MATLAB software. Modeling is done to make it easier to optimize each process and to control each biogas formation process. In the simulation process, the performance of all stages of biogas that is being in production can be seen so that estimating the biogas production that will be produced from the whole process is more accurate and can optimize the results of biogas production without disturbing the ongoing anaerobic digestion process activities (trial and error).[10]

2. Literature Review

2.1 Related research

Before conducting this research, it is necessary to conduct a literature study which aims to find references and research relevant to the research to be carried out. These references are obtained from journals, books or papers related to this research. Research on the biogas power plant with a balloon type digester, this study analyzes the potential of cow dung to generate electricity using a prototype. The balloon type digester is used for the reason that it is simple to install, easy to assemble and assemble and the price is relatively cheap. The results obtained from the prototype are a mixture of cow dung and water with a 1: 1 ratio of 624 liters of gas can be produced from a plastic drum capable of turning on electricity for 35 minutes with a power capacity of 700 watts [11-13].

Research on the modeling of biogas production in batch type reactors using the Hamming predictor-corrector method, in this study analyzes a model of the biogas production process with a batch type digester. The amount of biogas which is produced from biogas production process was predicted using a model that is commonly used in the anerobic digestion process, namely Anaerobic Digestion Model No. 1 (ADM1) [14]. The ADM1 model is transformed into a system of differential equations and is solved using the Hamming predictor-corrector method. This method is a linear method from the previous points. The simulation of biogas production was carried out for 120 hours by defining the initial substrate concentration of 500 mgCOD / L. On the basis of simulation results, it is known that the maximum concentration of methane obtained at the end of the simulation is 417.48 mgCOD / L. In addition, the growth of microorganisms that digest glucose is faster than the growth of other microorganisms. The simulation results show II-3 that the initial concentration of glucose and microorganisms is very influential on the concentration of methane produced. [15] Research on the simulation of biogas from dairy cow dung, in this study analyzed a simulation model on Matlab for biogas production from cow dung on a dairy farm. Input in this study uses dairy cow dung which is diluted with 25% water after filtering with the output of high-quality fertilizer and biogas consisting of 70-73% methane that is produced from the diluted liquid fraction of dairy cow dung. The model in this study made several modifications based on the hill model to simulate the production of biogas methane in anaerobic digestion. The modified hill model is simulated in Matlab using the eulerian and ode solver methods to obtain changes in methane gas over time. And this study also uses the Matlab editor function block Simulink. The three simulators provide the same response curve with different simulation times [16,17].

Research on the modeling and anaerobic simulation of livestock manure into biogas, this study creates and analyzes a model of biogas production from livestock manure which aims to develop a method for testing the digestion of fertilizers and wastewater for biogas. The model made several additions from the basic anaerobic digestion model no 1 (ADM1), modeling was carried out using Matlab by implementing all the equations and parameters. guidelines to simulate biogas production in certain species [18]. Research on the modeling and simulation of biogas production based on anaerobic digestion of energy crops and manure, this study makes an anaerobic digestion model to improve the accuracy of predicting the dynamics of anaerobic digestion for plants and manure. The model is calibrated using an experimental dataset in a batch process which is mono-fermented corn amylases. Furthermore, the concept is being validated by experimental data in which corn silage has being digested and tested for twenty-eight days in a continuous pilot-scale biogas fermented at uninterrupted raw material loads. The resulting model accurately predicts the flow rate dynamics of CH_4 (methane) and the carboxylic acid concentration. After that, the II-4 calibration model was carried out using ADM1 (Anaerobic Digestion Model no 1) for silage grass and livestock manure. The calibrated model precisely predicts anaerobic digestion from subtract for biogas and methane flow rates, and volumetric concentration dynamics of biomass, carboxylic acid chains, inorganic carbon matter, organic matters, and the pH values. Process modeling in this research uses Matlab [19]. Based on several studies that have been carried out for the calculation of biogas production using mathematical equations based on its potential only and calculated manually; Several supporting studies have carried out the calculation of biogas production by adapting the actual conditions that are implemented in each biogas formation process into a differential equation that is solved using the Matlab simulator. However, this research still focuses on calculating biogas production. The author offers a modeling and simulation in producing biogas and the potential for electrical energy by utilizing cow dung waste. The simulation in this study not only examines the aspect of biogas production, but also involves the potential of electrical energy generated from biogas as well as analyzing the technical and economic aspects. By using modeling and simulation, the author can experiment in complex situations, save money, save time and focus on the important characteristics of the problem compared to the manual method

ISSN- 2394-5125 VOL 8, ISSUE 01, 2021

(trial-and-error) is less effective, and time consuming. Apart from that, modeling and simulation are also useful for analyzing system performance.

2.2 *Cow Manure*

2.2.1 Definition of Cow Manure

Cow manure is the result of digestion in the form of waste from cows which varies in color from green to black, depending on the food eaten by the cow. After exposure to air, the color of cow dung tends to darken. Cow manure is waste from the digestive process of cattle which is solid and in the process of its disposal it is often mixed with urine and gases, such as methane and ammonia. Nutrient content in cow dung varies depending on the state of the production level, type, amount of feed consumption, and individual livestock [9, 20, 21]; The composition of cow dung that has generally been studied can be seen in table 2.1.

Table 2.1: Composition of Cow Manure.

Compound	Percentage
Hemicelluloses	18.6%
Cellulose	25.20%
Lignin	20.20%
Protein	14.90%
Dust	13%

Specifications of cow dung produced from cows weighing 635 kg, the amount Total solids (TS) can generally also be estimated to be 10-15% of the initial impurity mass. Meanwhile, the number of volatile solids can be estimated at 8-10% of the mass of impurities early [22-24]. The specification of cow manure with a cow weight 636Kg can be seen in table 2.2.

Table 2.2: Cow Manure specifications with a total weight of 635 kg

Specifications	Cows with a weightofs635kg
Dirt	**S**50.8kg**s**
Manure	**S**51.1liter**s**
Total solids (total solid, ts)	**S**6.35kg**s**
Volatile solids (volatile solid, vs)	**S**5.4kg**s**

2.2.2 Potential for Cow Manure

Waste Cattle farming in India has enormous potential which is spread over several regions. Cattle breeding business requires ideal geographical conditions for the survival of cows. Weather in Delhi is good for cattle farming. Cow manure is a potential raw material for making biogas because it contains starch and lignocelluloses. Usually, cow dung is used as fertilizer and the rest is used to produce methane gas using anaerobic processes. Cow manure is a biomass that contains carbohydrates, protein and fat. Biomass that contains high carbohydrates will produce low methane gas and high CO_2, when compared to biomass that contains high amounts of protein and fat. In theory, the methane production resulting from carbohydrates, protein, and fat is 0.37; 1.0; 0.58 m^3 CH_4 per kg of organic dry matter. Cow manure contains the three elements of organic matter, so it is considered more effective to convert into methane gas. One way to determine the appropriate organic material to be used as an input for the biogas system is by knowing the ratio of carbon (C) and nitrogen (N) or what is called the C / N ratio. Several experiments that have been carried out by ISAT show that the activity of methanogenic bacteria will be best at a C / N ratio of around 8-20 [25-27]

2.2.3 Biogas

Biogas is a gas produced through anaerobic processes (without oxygen) where the molecules are complex carbon contained in organic matter degraded into molecules with simpler structures including CH_4 and CO_2. India mostly uses biogas for cooking or heating, whereas biogas which contains the main ingredient methane (CH_4) can be used as fuel in power plants because it has a fairly large heating value, which is 23,880 BTU / lbm [28]. Biogas is produced when microorganisms, especially bacteria, reduce levels of organic matter without air or anaerobic conditions. Compared

ISSN- 2394-5125 VOL 8, ISSUE 01, 2021

to air, biogas is about 20% lighter and has a flame temperature between 655° C to 750° C. Biogas is a gas that is odorless, has no color and burns with a blue embers color similar to liquid petroleum gas (LPG). Biogas burns with an efficiency of 60% in the conventional biogas furnace and a calorific value of 20 MJ / Nm^3. The volume of biogas is usually expressed in normal units of meters per cubic (Nm^3), namely the volume of gas at 0oC and atmospheric pressure. Biogas consists of 50% to 75% methane (CH_4), 20% to 44% carbon dioxide (CO_2) and small amounts of other substances. The biogas composition is as follows [29-33].

The composition of biogas can be seen in table 2.3.

Table 2.3: Compositional Biogas

Concentration	Formulas	Elements (Volume %)
Methane	CH_4	50-75
Carbon dioxide	$C0_2$	25-45
Water Vapor	H_20	2-7
Oxygen	O_2	<2
Nitrogen	N_2	<2
Hydrogen Fluid	H_2s	<2
Ammonia	Nh_3	<1
Hydrogen	H_2	<1

2.2.3 Biogas formation Process

The formation of biogas occurs based on chemical principles, namely the occurrence of fermentation of carbohydrates, fats and proteins by methane bacteria which are not mixed with air or what is called anaerobic digestion process. One gram of cellulosic material will produce 825 cm^3 of gas at atmospheric pressure. One gram of fat produces 1.25 liters of biogas at atmospheric pressure. The process of forming methane gas by anaerobic digestion involves a complex interaction of several different bacteria, protozoa, and fungi. Some of the bacteria that play a role are Bacteroides, clostridium butyrinum-coli and other intestinal bacteria. These two bacteria are the main bacteria producing methane and can live in anaerobic conditions. The fermentation process usually takes 7 to 10 days with an optimum temperature of 35°C and an optimum pH of 6.4-7.9. In general, the process of forming biogas is:

$$C_xH_yO_z + \left(x - \frac{1}{4}y - \frac{1}{2}\right)H_2O$$
$$\rightarrow \left(\frac{1}{2}x - \frac{1}{8}y + \frac{1}{4}z\right)CO_2 + \left(\frac{1}{2}x - \frac{1}{8}y + \frac{1}{4}z\right)CH_4 \quad \ldots\ldots (1)$$

In the formation of biogas, the process consists of the acid hydrolysis step (acidification), and the methanogenesis stage [33-39]. The different stages of biogas formations can be seen in figure 2.1.

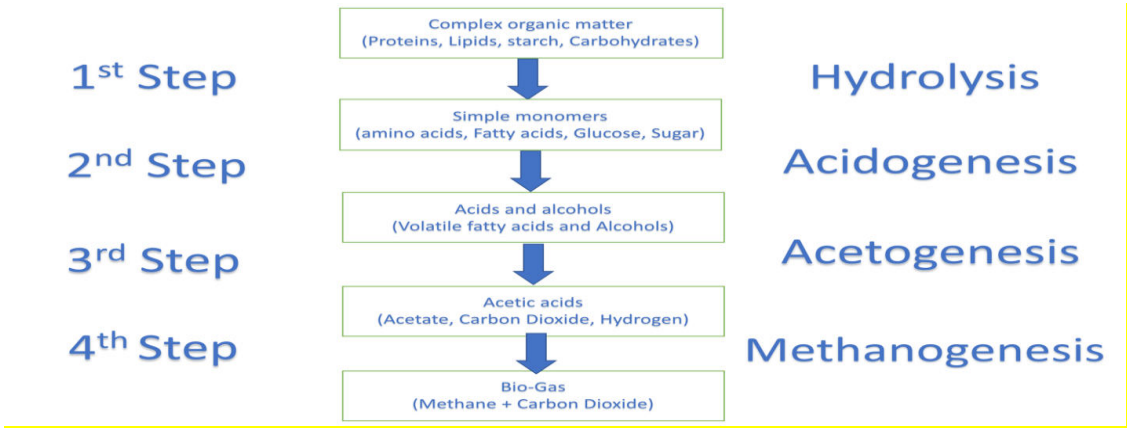


Figure 2.1: Biogas Formation Stages/Phases

ISSN- 2394-5125 VOL 8, ISSUE 01, 2021

2.2.3 Hydrolysis

At this stage of hydrolysis, it is the breakdown of complex organic materials being simple, changes the structure of the polymer to the monomeric form an insoluble compound with a lighter molecular weight. Lipids turn into acids long chain fat one and glycerin, polysaccharides into sugars (mono and disaccharides), protein into amino acids and nucleic acids, into purines and purimidines. Lipid conversion occurs slowly below 20°C. The hydrolysis process requires exo-enzyme mediation excretion by fermentative bacteria. Hydrolysis of molecules is catalyzed by an extra enzyme's cells such as celluloses, lipases, proteases, etc. [33-39].

$$\underset{\text{Cellulose}}{(C_6H_{10}O_5)n} + nH_20 \longrightarrow \underset{\text{Glucose}}{n(C_6H_{12}O_6)} \quad \ldots..(2)$$

2.2.4 Acidification

At this stage of acidification, the bacteria will change the polymer simply as a result hydrolysis to acetic acid (CH_3COOH), hydrogen (H_2), and carbon dioxide (CO_2). To converting into acetic acid, bacteria need oxygen and carbon contained in solution. This stage is carried out by obligate anaerobic bacteria and some of them are bacteria facultative anaerobes. These bacteria are anaerobic bacteria that can grow in acidic conditions namely pH 5.5-6.5 which works optimally at a temperature of about 30°C. Acetic acid very much needed which will then be used by microorganisms for formation methane gas. In addition, mixing is necessary for an even metabolism with a water concentration of > 60% [33-39].

$$\underset{\text{Glucose}}{(C_6H_{10}O_5)n} + nH_20 \longrightarrow \underset{\text{Lactic Acid}}{(CH_3CHOHCOOH)} \quad \ldots..(3)$$

$$\underset{\text{Glucose}}{(C_6H_{12}O_6)n} + nH_20 \rightarrow \underset{\text{Butyric Acid}}{(CH_3CH_2CH_2COOH)} + CO_2 + H_2 \quad \ldots..(4)$$

$$\underset{\text{Glucose}}{(C_6H_{12}O_6)n} + nH_20 \longrightarrow \underset{\text{Ethanol}}{(CH_3CH_2OH)} + CO_2 \quad \ldots..(5)$$

2.2.5 Acetogenesis

This acetogenesis stage is an advanced stage of the acidification stage, at this stage about 79% of COD is converted into acetic acid. The formation of acetate depends on the oxidation conditions of the organic matter which are usually accompanied by the formation of CO_2 and hydrogen. Ethanol, butyric acid and lactic acid are converted into acetic acid by acetogenetic bacteria. The reaction is as follows [33-39]:

$$4H_2 + C0_2 \longrightarrow 2H2O + CH4 \quad \ldots.. (6)$$
$$CH3CH2OH + C0_2 \longrightarrow CH3COOH + CH4$$
$$CH3COOH + C0_2 \longrightarrow C0_2 + CH4$$
$$CH3CH2COOH + 2H2 + CO_2 \longrightarrow CH3COOH + CH4$$

2.2.6 Methanogenesis

This stage of methanogenesis is the stage where methane and carbon are formed dioxide. Methane is produced from acetic acid or from the reduction of carbon dioxide by bacteria acetotropic and hydrogenotropic using hydrogen. Methane producing bacteria have appropriate atmospheric conditions due to the process of acid-producing bacteria. That acid the resulting acid-forming bacteria will be used for methane-producing bacteria. On at this stage low molecular weight compounds are decomposed by methanogenetic bacteria be a compound with a high molecular weight [33-39].

2.2.7 Biogas Formation Process Parameters

The factors that influence microorganisms are very important in determining speed of the biogas formation process, includes the temperature, pH, nutrition, concentration solid, volatile solid, substrate concentration, time of digestion, stirring of ingredients organic as well as pressure influences. The following is a discussion of these factors [33-39]:

1. Temperature

There are three conditions for anaerobic degasification based on the temperature of the digester, including:

i. Psychrophilic conditions: In these conditions, the digester temperature is between 10-18°C, and liquid organic waste digestified for 13-52 days.

ii. Mesophilic conditions: In these conditions, the temperature of the digester is between 20-45°C, and liquid organic waste digestified for 18-28 days. Compared to the digester in thermophilic condition, in mesophilic conditions, the operation is

ISSN- 2394-5125 VOL 8, ISSUE 01, 2021

easier, but the biogas produced less and the volume of the digester is larger.

iii. Thermophilic conditions: In this condition, the temperature of the digester is between 50-70°C, and liquid organic waste digestified for 11-17 days. In thermophilic conditions it produces a lot biogas, but the investment costs are high and the operation is complicated. The graph representative anaerobic digestions temperature can be seen in figure 2.2.

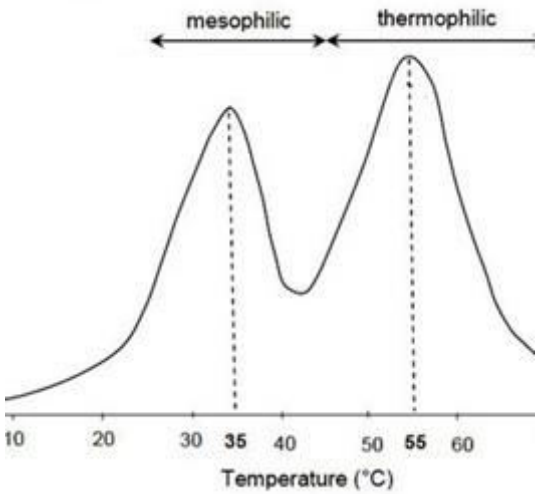


Figure 2.2: Graph Representative Anaerobic Digestion Temperature

The optimal temperature for anaerobic digestion is temperature 30-35° C. These temperature range combines the best situations for bacterial growth and production of methane gas in the digester for a long-time short process. At 35° C, it will digest the mass of the material same will be digested twice as fast as a temperature of 15° C and produces nearly 15 times as much gas at the same processing time. As with the biological process, the methane gas production increases for each increase in temperature of 11-15° C. In other words, the number the total amount of gas which is produced in a fixed amount of material increases with each other with increasing temperature [33-39].

iv. Degree of acidity (pH): In anaerobic decomposition, pH is a factor that affects microbes so that if the pH in the digester is not in accordance with the recommended pH range then the microbes cannot grow to the maximum. It can even cause microbial death which in turn will inhibit methane gas production. Anaerobic bacteria require an optimal pH between 6.2 - 7.6, but that is best1 is 6.6 - 7. At first the media has a pH of ± 6 then it rises up to 7.5. If the pH is smaller or greater, it will have toxic properties against methanogenic bacteria. When the anaerobic process is already on its way towards the formation of biogas, the pH ranges from 7-7.8. PH control is carried out naturally by the NH4 + and HCO3 - ions. These ions will play a role in determining the pH value [33-39].

v. Solids Concentration Factor (Total Solid Content / TS): Total solid content is the amount of solid material present in waste in organic material during the digester process occurs, which indicates the rate of destruction / decomposition of solid organic waste materials. Ideal concentration solids for producing biogas are 7-9% dry content, this condition can make the anaerobic digester process run well. It should be noted that TS concentrations should be kept at no more than 15% as it will inhibits metabolism. When introducing organic material into the biodigester must be added with a certain amount of water, the function of the water here is in addition to maintains TS <15%, also to simplify the mixing process, the process of flowing organic material into the biodigester and for facilitates1 that the gas stream formed at the bottom can flow to the passage over the biodigester [33-39].

vi. Volatile Solids (VS): VS or volatile solids is part of the TS solids that change into the gas phase at the acidification and methanogenesis stages as in the process fermentation of organic waste. In laboratory scale testing, the current weight is part the solid organic material is burnt out in the gasification process at a temperature of 538 °C called volatile solid. The following is a table of volatile solids (VS) components. The volatile solid components can be seen in table 2.4

Table 2.4 Volatile Solid Components

Component	TS%
Cellulose	31
Hemicelluloses	12.2
Lignin	12
Kanji	12.4
Protein	12.6

ISSN- 2394-5125 VOL 8, ISSUE 01, 2021

Ether	2,6
Ammonia	0.5
Acid	0.1
Total	**83.4**

It can be seen from the table above that the components of volatile solids (VS) generally consist of cellulose, hemicellulose, lignin, starch, protein, ether, ammonia and acids. The size of VS is about 83.4% TS. Taking into account that the TS from animal feces is not far from 10%, it is necessary to add some animal food waste in the biodigester, apart from containing high C / N it also has the potential for high biogas production because it contains high TS [33-39].

vii. Duration of the Digestion Process: The duration of the digestion process (Hydraulic Retention Time) or HRT is the amount of time (in days) the digestion process in the anaerobic tank counts from the entry of organic matter to the initial process of forming biogas in the anaerobic digester. From the biogas generation as a whole HRT covers 70-80% of the total time. The total time of HRT depends on the type of organic material and the treatment of organic matter before the digestion / digester process is carried out. If too much volume of material is inserted (overload) it results in the filling time being too short, the raw material will be pushed out while gas is still produced in small quantities.

viii. Carbon Nitrogen (C / N) Ratio Anaerobic processes will be optimal if given food ingredients containing carbon and nitrogen simultaneously. Carbon is needed to supply energy while nitrogen is needed to form the structure of bacterial cells. The C / N ratio shows the ratio of the sum of the two elements. For materials that have a carbon amount of 15 times the amount of nitrogen will have a C / N ratio of 15 to 1. The C / N ratio with a value of 30 (C / N = 30/1 or carbon 30 times the amount of nitrogen) is a digestion process at an optimum level, if other conditions also support. The process will run slowly if there is too much carbon, because nitrogen will run out first. Conversely, if there is too much nitrogen (low C / N ratio; for example, 30/15) then the carbon will run out first and the fermentation process will stop. One study showed that the metabolic activities of methanogenic bacteria would be optimal at the C / N ratio of 8-20 [40]. The following is a table showing the C / N ratio of some organic materials in common use:

ix. Volatile Solids (VS): VS or volatile solids is part of the TS solids that change into the gas phase at the acidification and methanogenesis stages as in the process fermentation of organic waste. In laboratory scale testing, the current weight is part the solid organic material is burnt out in the gasification process at a temperature of 538 °C called volatile solid. The following is a table of volatile solids (VS) components. The C/N ratio of organic materials can be seen in table 2.5.

Table 2.5 C/N Ratio of Organic Materials

RAWH MATERIAL	C/NH RATIO
Human Decoration	8
Goat Dung	121
Sheep Dung	191
Corn Waste	601
Wheat Waste	901
Duck Waste	8
Chicken Poop	101
Pig Dung	181
Cow Dung	241
Dirt Gajah	43
Rice Waste	7
Saw Dust	2

x. Stirring of Organic Materials: Stirring is very beneficial for the ingredients in the anaerobic digester, which provides the opportunity for the material to remain mixed with bacteria and to maintain an even temperature throughout the digester. With stirring, it will minimize the potential for material which is settling at the bottom of digester and the concentration is firmly distributed, and the potential for all materials to undergo an anaerobic fermentation process is greater. In large digesters the mixing system is very important. The purpose of stirring is to keep the solid material away from settling on the bottom of the digester. In addition, stirring can facilitate the release of gas produced by bacteria to the biogas reservoir [33-39]. Effect of Pressure has an important role, the higher the pressure in the digester, the lower the biogas production in the digester, especially in the hydrolysis and acidification processes. The pressure is maintained between 1.15-1.2 bar in the digester [33-39].

ISSN- 2394-5125 VOL 8, ISSUE 01, 2021

xi. Toxic and Inhibitor Compounds The anaerobic fermentation process of inhibiting compounds or inhibitors can be divided into 2 types, namely physical inhibitors and chemical inhibitors. Physical inhibitors are temperature and chemical inhibitors, also known as toxins, include heavy metals, antibiotics and volatile fatty acids (VFA) [33-39].

2.2.9 Equations for the Formation of Biogas

The following are some of the equations that determine the process of biogas formation from the fermentation of organic waste in anaerobic digester [34-36]. The theoretical decomposition time equation is the time the organic material is in the digester tank. When this process occurs, the growth of anaerobic bacteria decomposes, the process of decomposing organic matter, and stabilizes the formation of biogas to its optimum conditions. Overall, the hydraulic retention time or HRT covers 70% -80% of the total biogas formation time if the biogas formation cycle is idea, time the process of introducing organic matter directly obtains biogas as the final process without adding organic material again [33-39]. HRT can be formulated into the following equation:

$$\boldsymbol{HRT\ (days) = \frac{Volume\ Digester\ (m^3)}{Daily\ Organic\ Ingredient\ Addition\ Rate \frac{m^3}{day}}} \quad \text{…..(8)}$$

If the dry solid material is DM (Dry Material) or it is also called Total Solid (TS) ranges from 4-12%, so the optimum breakdown time (Optimum Retention Time) ranging from 10-151 days. If the Dry material value is greater than 1 the percentage value of material solids dries above, it means that the organic matter has a denser concentration so it takes a long-time breakdown time becomes specific, so that1 the length of time equation applies the following specific retention time or SRT:

$$\boldsymbol{SRT = \frac{Organic\ Solids\ in\ Anaerobic\ Digester\ (kg)}{Daily\ Organic\ Ingredient\ Addition\ Rate \frac{kg}{day}}} \quad \text{…..(9)}$$

For specific organic matter as above, the rate of addition of organic waste (Specific Loading Rate) or SLR can be seen as follows:

$$\boldsymbol{SLR = \frac{(kg\ ODM)}{m^3 - day} = \frac{Added\ Organic\ Ingredients (kg \frac{ODM}{day})}{Volume\ Digester\ (m^3)}} \quad \text{…..(10)}$$

The depth of the digester1 tank greatly affects the SLR value and when the parameters otherwise it can be maintained in ideal conditions, the maximum SLR values obtained range from 3-6 kg ODM / m^3-day.

- *Specific Biogas Production Equations*

Specific Biogas Production (SBP1) is a digester efficiency indicator value. Minimum conditions are 1.5 and the ideal target is 2.5.

$$\boldsymbol{SBP\ (day - 1) = \frac{Biogas\ Production\ (m^3/day)}{Volume\ Digester\ (m^3)}} \quad \text{…..(11)}$$

- ***Specific Methane Production Equations***

Methane Production Specific (Specific Methane Production) or SMP, relates to the total energy produced against that energy potential owned organic waste (feedstock). For organic waste from plants / seeds energy value between 0.3 - 0.4 (%) and for some types of animal waste can value up to 0.8%;

$$\boldsymbol{SMP\ (m^3\ CH_4/kg\ \ ODM(day - 1) = \frac{Volume\ Gas\ \left(\frac{m^3}{day}\right)}{Organic\ Material\ Addition\ Rate\ (kg\ ODM—day)}} \quad \text{…..(12)}$$

2.2.10 Equations for the Forming energy to power

The conversion of biogas energy for electric power generation can be done using several technologies, namely, gas turbines, microturbines and the Otto Cycle Engine. The need for biogas, such as gas concentration of methane and biogas pressure, load requirements and availability of available funds, are significantly affected by the choice of this technology. [41-50]. In the book Renewable energy conversion, transaction and storage by Bent Sorensen, that 1 kg of methane gas is equivalent to 6.13 x 10^7 J, while 1 kWh is equivalent with 3.6 x 10^7 Joule. For a gas density of 0.656 kg / m^3, so that is 1 m^3 methane gas produces 11.17 kWh of electricity. Then it can be assumed that the conversion potential biogas into electrical energy as follows:

ISSN- 2394-5125 VOL 8, ISSUE 01, 2021

$$W = CH_4 * 11,17\ kWh \quad \text{.....} \quad (13)$$

Where:
W = Electrical energy that can be produced (kWh)
CH_4 = Methane (M^3)
The Energy conversion from methane gas to electrical energy can be seen in table 2.6.

Table 2.6 Energy Conversion from Methane Gas to Electrical Energy

Energy Type	Energy Equivalent
1 kg of Methane Gas	$6.13 * 10^7$J
1 kWh	$3.6 * 10^6$J
1 m^3 of Density Methane Gas Methane gas is 0.656 Kg / m^3	$4.0213 * 10^7$J
1 m^3 of Methane Gas	11.17KWh

2.2.11 Equations for the Formation of Biogas

A biogas generator set or known as a biogas generator is a tool which has two main components, namely the engine and the generator that uses it biogas to produce electricity. This driving machine can be moved because of the combustion of gas fuel in it which is then used for generate mechanical energy. In the presence of mechanical energy which is coupled with generator, then there is a conversion of mechanical energy into electrical energy [51-57]. The following are the main components of a Biogas Generator:

1. Compressor is a mechanical power generator that functions to generate heat energy comes from the atmospheric air to meet the needs of the process combustion gas in the gas turbine combustion chamber. In the process of operation, the compressor is supported by tools, namely the intake air filter and the inlet gate fan.

2. Combustor is the combustion chamber which is the generator of heat energy from the process gas fuel. In the operation process, the combustor is supported by assistive tools namely gas station, control system, fuel nozzle, and igniter system (ignition system).

3. Gas Turbine is a mechanical energy generator from the heat energy conversion process into kinetic energy and further into capable mechanical energy drive the turbine shaft with mass gas burning fuel. In the operating process,

the gas turbine is supported by tools, namely a lubricating oil system, control oil system, turning motor, pony motor, starting motor, cooling water system, exhaust duck system, and turbine supervisory instrument.

3. Generator is a tool to convert mechanical energy from the turbine shaft into electrical energy.

The Biogas generator image can be seen on figure 2.3:



Figure 2.3: Biogas Generator

2.2.12 Economic Model

- *Total Net Present Cost (NPC)*

NPC is the value of all costing that are incurred during the lifetime, less the present value of all income earned over the lifetime. This Costs include capital costs, replacement costs, O&M costs, fuel costs, emission fines, and power purchase costs from the grid. Economic models for the HOMER simulation use the Net Present Cost (NPC) which is the total cost of installing and operating the system during the project lifetime [58-65]. Net Present Cost (NPC) itself can be calculated using the following equation:

$$\boldsymbol{NPC = Capital\ Cost + Replacement\ Cost + O\&M\ Cost + Fuel\ Cost\ + Salvage}$$

Where:
Capital Cost = Cost of capital components (Rs)
Replacement Cost = Cost of component replacement (Rs)
O&M Cost = Operational and maintenance costs (Rs)
Fuel Cost = Fuel cost (IDR)
Salvage = Cost remaining on components (Rs)

- *Cost of Energy (COE)*

The Cost of Energy (COE) is the costing that is being required to produce each 1 kWh of electrical energy, that is, the result of dividing the annual costs and energy production annual. The COE value of each scenario uses the following equation:

$$\boldsymbol{COE = \frac{TAC}{E_{tot,served}}} \qquad \textbf{….. (14)}$$

Where:
$\boldsymbol{E_{tot,served}}$ = Total annual energy used to serve the load(kWh)
$\boldsymbol{TAC}$ = Total Annualize Cost or total annual costs incurred for generating reserves. (Rs.)

3. Proposed Methodology

This research is a simulation research that aims to find a picture through a simple or small-scale system (modeling), in the model will be made changes to variable or control to see the effect. Research simulation aims to provide an overview of the application of a technique through process modeling so that the technique will not suffer unexpected losses prior to its application. This research was conducted using a mathematical model has been made in previous studies and continues the study of research previously, namely utilizing biogas into electrical energy. The conversion process to be done through a simulation to get a model that fits the case or the problem is there. In this research will also analyze technical aspects and economy, namely NPC (Net Present Cost) and COE (Cost of Energy). In this study, it was started from a literature study related to previous research to support the research that will be carried out. Furthermore, potential data collection raw materials for cow and buffalo dung in National Capital Region, then doing modeling and simulation of biogas production from cow dung using the anaerobic method digestion. Furthermore, modeling and simulating the conversion of electrical energy from biogas production that has been obtained from previous simulations. After that he will do it analysis of electrical and economic energy resulting from the modeling process that has been done. The stages to be carried out in this research are in accordance with figure in 3.1.1 and 3.1.2:

ISSN- 2394-5125 VOL 8, ISSUE 01, 2021

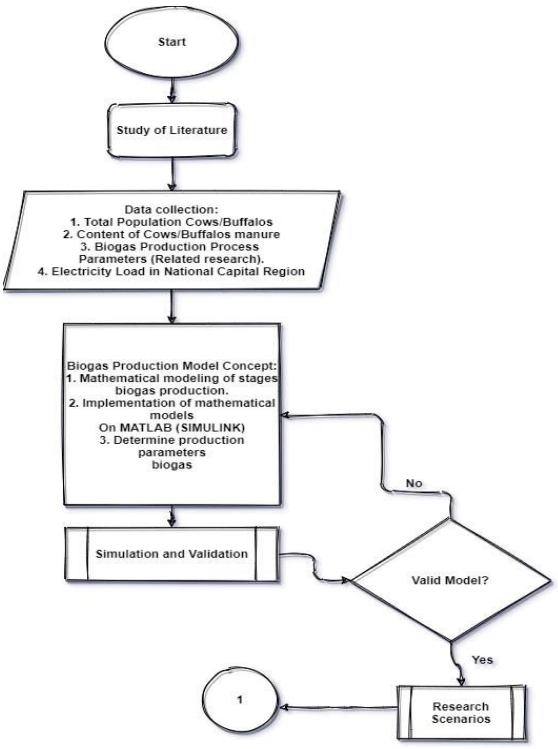


Figure 3.1.1: Research Flowchart

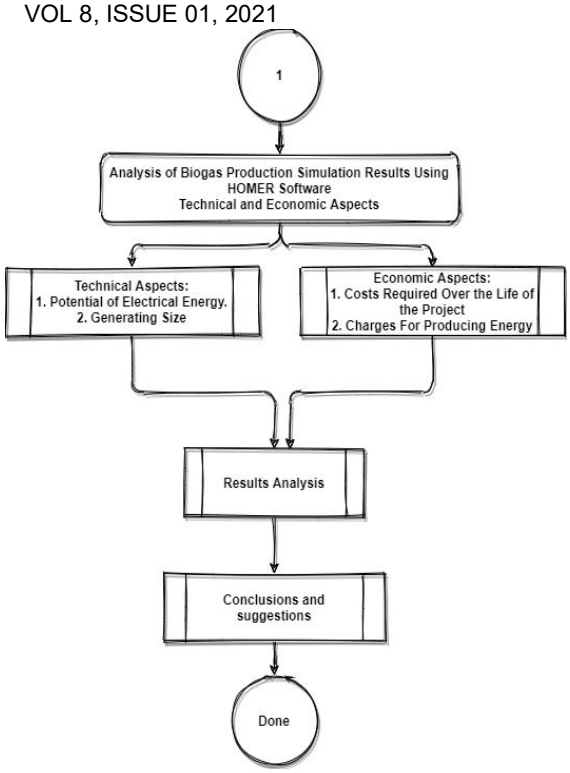


Figure 3.1.2: Research Flowchart continued

- **Literature Study**

This stage collects some of the research needed to be used references in this research, namely Final Project, Thesis, books and journals. On each Related research will be analyzed in the theory used, research methods and results. In the book you will find a theory that supports this research in better results.

- **Data Collection**

This research uses modeling and simulation methods with an approach literature using MATLAB software. Therefore, data is needed to support it this research. The data required consists of:

1. The originating statistics for the population of cattle cow and buffalo in National Capital Territory. This data is used to obtain potential cow & buffalo dung that will be produced.
2. Data on the content of cow & buffalo dung will be used as input parameters simulation of biogas production.
3. Anaerobic digestion process parameter data from related research (Experimental results and related journals)
4. National Capital Territory electricity load data which will be used to analyze technical aspects.

* Mathematical Modeling of Biogas Production Stages

This simulation research needs to determine the stages of the intermediate biogas production process other hydrolysis, acidogenesis, acetogenesis, and methanogenesis to be carried out on Matlab worksheet.

- **Hydrolysis Process Modeling**

The first stage of the anaerobic digestion process is the process of hydrolysis. The process can be interpreted as the rate of change during the anaerobic digestion process in the biodegradable concentration of volatile solids (BVS) in the reactor. This mechanism depends on the feed material type, the flow rate of the feed, the effective reactor volume and the reactor temperature. The following equation is the hydrolysis process:

Defines the portion of raw waste that can serve as a substrate:

$$Sb_{in} = B_o . Svs_{in} \quad \ldots\ldots (15)$$

Defines the portion of the biodegradable raw material which is originally in acidic form:

$$Sv_{in} = A_f . Sb_{in} \quad \ldots\ldots (16)$$

Mass balance of biodegradable volatile solids:

ISSN- 2394-5125 VOL 8, ISSUE 01, 2021

$$\frac{d(Sb)}{dt} = (Sb_{in} - Sb)\left(\frac{F_{feed}}{V}\right) + \frac{\mu_m . K_1 . X_{acid} . X_{meth}}{\frac{K_s}{S_b} + 1} \quad \ldots\ldots (17)$$

Where:

B_o= Biodegradability Constant $\left(\frac{kg\ BVS\ /\ m^3}{kg\ VS\ /\ m^3}\right)$

A_f = Acidity Constant $\left(\frac{kg\ VFA\ /\ m^3}{kg\ BVS\ /\ m^3}\right)$

Sb = biodegradable volatile solid concentrations in (kg / m^3)

Sb_{in} = The concentration of biodegradable volatile solids in the reactor feed (kg / m^3)

F_{feed}d = Feed flow rate (m^3 / day)

K_1 = Yield factor

K_s = Half Monod constant velocity for acidogens (kg / m^3)

X_{acid} = Concentration of acidogens (kg / m^3)

X_{meth} = Methanogens concentration (kg / m^3)

μ_m= Max. growth rate of acidogens (d^{-1})

V = Reactor volume (m^3)

The maximum growth rate for methanogens that can be expressed as a function of the temperature dependence of the reaction rate using the following empiric:

$$\mu_m T_{react} = \mu_{mc}.(T_{react}) = 0.013 . T_{react} - 0.129 \quad \ldots\ldots (18)$$

Where:

μ_{mc} : Maximum growth rate for methanogens (d^{-1})

T_{react} : Reactor temperature (° C).

- **Acidogenesis Process Modeling**

The acidogenesis stage is the rate of change in the concentration of volatile fatty acids during the fermentation process. This process depends on the total concentration of VFA in the reactor (type of feed material), feed flow rate, volume1effective reactor, and reactor temperature. The following equation is the acidogenesis process:

$$\frac{d(Sv)}{dt} = (Sv_{in} - Sv)\left(\frac{F_{feed}}{V}\right) + \frac{\mu_m . K_2 . X_{acid}}{\frac{K_s}{S_b} + 1} + \frac{\mu_{mc} . K_3 . X_{meth}}{\frac{K_{sc}}{S_v} + 1} \quad \ldots\ldots (19)$$

Where:

Sv = Total volatile fatty acid concentration in the reactor (kg / m^3)

Sv_{in} = The total volatile fatty acid concentration in the reactor feed (kg / m^3)

K_2 = Yield factor

K_3 = Yield factor related to methane gas growth rate

K_{sc} = Half Monod constant velocity for methanogenesis (kg / m^3).

- **Acetogenesis Process Modeling**

The 3rd stage of the AD process is the acetogenesis process. This process depends on the acidogens concentration, the type of feed ingredient, the feed flow rate, the effective reactor volume and the reactor temperature. The following equation is the process of acetogenesis:

$$\frac{d(X_{acid})}{dt} = \left[\frac{\mu_m}{\frac{K_s}{S_b} + 1} - K_d - \frac{F_{feed}/^b}{V}\right] . X_{acid} \quad \ldots\ldots (20)$$

Where:

ISSN- 2394-5125 VOL 8, ISSUE 01, 2021

b = Retention time factor estimated
K_d = Acidogens specific mortality rate (d^{-1}).

3.8 MODELING OF THE METHANOGENESIS PROCESS

The methanogenesis stage determines the concentration of methanogens which is used to produce methane. This process depends on retention time, the feed flow rate, the effective reactor volume and reactor temperature:

$$\frac{d(X_{meth})}{dt} = \left[\frac{\mu_m}{\frac{K_{sc}}{S_v} + 1} - K_{dc} - \frac{F_{feed}/^b}{V} \right] . X_{meth} \quad \ldots..(21)$$

Information:
K_{dc} = Specific mortality rate from methanogens (d^{-1})
$. X_{meth}$ = concentration of methanogens presents in (kg /m^3)
The equation for the amount of methane output is as follows:

$$F_{meth} = V . \frac{\mu_{mc}}{\frac{K_{sc}}{S_v} + 1} - K_4 . X_{meth}$$

Information:
K_4= Yield factor related to methane gas flow.

- Implementation of a Mathematical Model of Biogas Production Using Matlab (Simulink)

After all the data is obtained, anaerobic digestion system modeling simulation is performed at SIMULINK. This modeling is done based on existing mathematical modeling. Implementation of mathematical models in Matlab can use text code or SIMULINK. SIMULINK uses blocks contained in the SIMULINK library, these blocks function as mathematical functions, each block has a different function such as add, subtract, multiply, divide, integral etc. Biogas production parameters will be entered into each block according to the respective parameter values.

- **Reactor Modeling**

SIMULINK block shape shown in Figure 3.2 is a form of model based on combining all mathematical models of the biogas production process into a system.

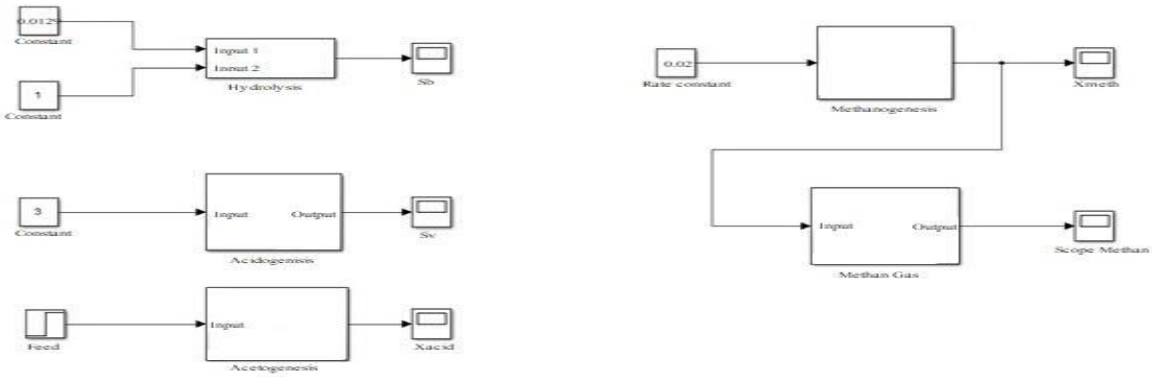


Figure 3.2: SIMULINK Reactor Model

- **DETERMINING BIOGAS PRODUCTION PARAMETERS**

The rate of the biogas formation process which is largely depend on the factors that affect microorganisms, including temperature, pH, nutrients, solids concentration, volatile solids, substrate concentration, digestion time, stirring of organic matter and the influence of pressure. The following are the parameters for each biogas production process:

- **Simulation and Validation**

After modeling, simulation testing of the system that has been modeled is carried out. Simulations were carried out using SIMULINK MATLAB R2014a. To run the simulation on Simulink by selecting the run button to run the created model. If, when running there is an error, a diagnostic viewer will appear which will explain the errors that occurred in the system. Then there will be a re-evaluation of the system model until there are no more errors. To see the results of the model, by selecting the Scope Fmeth block, a graph will appear which is the result of the model created. After obtaining the results from the system model that is made, verification is carried out. Whereas, validation is an action to prove a research is correct with a benchmark so as to achieve the desired results. The purpose of validation is to ensure the results of a study are close to real or maintain the credibility of proposed scheme.

In this study, validation was carried out using a mathematical equation from the study entitled "Simulation of a Biogas Reactor for Dairy Manure" then the initial step of modeling will use the same variables and parameters from the research above, then see the results of the model made whether it is in accordance with the results of the reference research or not, if appropriate, the research can be continued to the next stage. Verification aims to ascertain whether the model is suitable or not. The suitability refers to the standard theory of conversion of potential cow dung into biogas, namely 1 kg of cow dung (cattle dung) dung produces **0.023-0.04 m^3** of biogas. If, the results of the system model made are in accordance with the reference standard, then change the input parameters according to the case will be examined, the parameters that are changed are F_{feed} (input feed), T_{react} (temperature), and V (digester volume). If the results of the model made deviate too far from the reference standard, then re-evaluate the model. After the results are in accordance with the reference standard, you can proceed to the next stage.

4. Result and Simulation

- **Calculation of the Potential of Biogas in a Dairy Cattle**

In calculating a biogas power plant from cow dung, a farm location is required to obtain the basic model of the generator. This calculation uses a model in the dairy cows/buffalo's dung as an example of a potential case as proposed in section below. .

- **Potential hypothesis for the Biogas Plant**

The fixed dome type biogas reactor is designed for 10 cows (with 25 kg / day / head of cow dung and 45 days of retention time) with a reactor capacity of 18 m^3. Based on the results of the Matlab and Homer test of these activities and literature references as shown in the following table 4.1: -

Table 4.1 Sample performance of the biogas plant

Description	Referenced	Test Results and Analysis
1. Material Conditions (Cow Dung)		
• Total Solid, Kg/ Head / Day	4.8	4.2
• Volatile Solid, Kg / Head / Day	3.9	3.8
• Water Content, %	6.9 – 8.9	13.59
• C/N Ratio	1:20 1:30	1:17
• Cod, Mg/L**d**	-	19 800
• -BOD/COD	-	0.06
2. Conditions in The Reactor (Process)		
- Temperature, ^{O}C	35	25–27
- pH	7.0 - 8.01	7-8.61
3. Chemical Content of Biogas		
- CH_4, %	501-1601	76.131
- CO_2,%	301-1401	21.881
- H_2S, µg / m^3	<1%	1543.461
- NH_3, µg / m^3	-	40.121

4. Discharge sludge Condition from the Reactors (Effluent) - Cods - Bod/Cods - Nutrient content (Main), - % • Nitrogen • Phosphorus • Potassium	5001-12500	1 960
	0.51	0.37
	1.451	1.82
	1.101	0.73
	1.101	0.41
5. Performance • Lighting, m^3 / Hour	10.11 - 0.151 (Illumination Equivalent To 60 Watts of Bulbt≅T100 Candles power≅ 620tlumens). Pressure: 170-851 $Mmmh_2o1$	0.15-0.3 Pressure=30-60 mmh_2o
• Gas Stove, m^3 / Hour	0.2 - 0.45 0.3 m^3 / Person/Day Pressure: 75-901 $Mmmh_2o$	0.2-0.4 Pressure=60-85 mmh_2o

From the existing data, we try to calculate the biogas capacity generated from the existing potential, the percentage of Total Solid and Volatile Solid obtained is the sample of 20 kg / day cow dung as: -
%Total Solid = 14.2 kg / head / day: 120 kg / head / day = 121 %
%Total Volatile Solid = 13.8 kg / head / day: 120 kg / head / day = 119 %
So, for the example Delhi Capital Region, which produces (8-20 kg/head/day), taking 15 kg / head / day and considering data for 150 cattle as: -
Total Solid = 121% * 115 kg / head / day * 1501 = 472.51kg / day
Volatile Solid = 119%*1 15 kg / head / day * 1501 = 427.5 kg / day
Based on the potential mentioned above for biogas for cow dung as: -
Potential Biogas Volume = 0.04 m^3/kg *2,250 kg/ day = 90 m^3/ day
K = Volume of biogas production as: -
V_S = 190 m^3 / day:427.5 kg / day
K = 121% m^3/ kg ≈ 121%

- **Methane Production Calculation**

Energy production using biogas is proportional to the amount of methane gas production. With a known biogas production value (V_{BG}) of 90 m^3 / day and by using table 4.3 (depicted under); then it can be seen that the production of methane gas (V_{MG}) is, V_{MG} = 65.7% * V_{BG} = 65.7% x 90 m^3 / day =59.13 m^3 / day.

- **Electrical Energy Productions calculations:**

With the known volume of methane gas produced, namely 59.13 m^3 / day, and Conversion Factor (F_K) (m^3 of methane gas is equivalent to 11.17 kWh), so that the potential for electrical energy produced is, E = V_{MG} x F_K = 59.13 * 11.17 = 660.428 kWh / day. The power generated by the Biogas Power Plant is the energy generated per day divided by 24 hours, namely:
P = (E / 24) *time = (660.428 / 24) *24 = 660.428kW ≈ 0.660 MW So from the calculation of the available potential data, the following results are obtained: and presented in table 4.2: -
-

Table 4.2: Result of biogas capacity calculations

No.	Type of the Calculation involved in the Process	Calculated Results
1.	Potential of Cow Dung (Q)	15 Kg / Day

ISSN- 2394-5125 VOL 8, ISSUE 01, 2021

2.	Calculation of the sum Of Total Solids (Ts)	4.725 Kg / Day
3.	Calculation of The Amount of Volatile Solid (Vs)	4.275 Kg / Day
4.	Calculation of The Volume of Biogas Production (V_{bs})	90 m^3 / Day
5.	Calculation of The Volume of Methane Gas (V_{gm})	59.13 / Day
6.	Calculation of Potential Electrical Energy (E)	660.428 kWh / Day
7.	Power Generating from the Power Plant (Biogas Power)	660.428 Kw in a Day

- **Digester Design**

Digester Type and Dimension Design

From the available potential it is possible to design a digester for produce biogas. As explained in chapter II a design digester there are several considerations that must be considered. design digester with consideration of several aspects as follows: -

- Temperature

For countries such as India, an unheated digester is used for soil temperature conditions of 20 - 30 ^{o} C (Mesophilic - 20 – 40^{o} C).

- Degree of Acidity (pH)

Bacteria thrive in moderately acidic conditions (pH between 6.6 - 7.0) and pH should not be below 6.2. Therefore, the main key in the operational success of the biodigester is to keep the temperature constant (fixed) and the material input accordingly. Filling material C / N ratio - The ideal requirement for the digestion process is C / N = 20 - 30. Therefore, to obtain high biogas production, it is necessary to extract carbon (C) materials such as straw, or N (for example: urea) to achieve a C / N ratio = 20 - 30. Based on the data obtained, Cow dung has C / N = 24 so that it is sufficient for the process to obtain the required pH.

- Digester Design

As initial data, the potential for dairy cow dung is 2,250 kg / day. In simple terms, the sequence of biodigester facility design begins with the calculation of the volume of the biodigester which includes the potential of the raw materials present in producing methane gas, determining the biodigester model, designing storage tanks and ending with determining the location. The digester used in this plan uses the fixed dome type or fixed dump digester type. This model is the most popular model in Indonesia, where all digester installations are made in the ground with a permanent construction. Besides being able to save land space, making a digester in the soil is also useful for maintaining a stable digester temperature and supporting the growth of methanogenic bacteria. Digester of this type has advantages Low construction costs due to simple construction and long life. The digester uses a flow type, where the raw material flow is entered and the residue is removed at certain intervals. The length of time the raw material is in the digester reactor is called the retention time (RT). The construction parts in this type of digester include:

a. Gas storage room (gas collecting chamber).
b. Gas storage chamber.
c. Fermentation Chamber Volume.
d. Hydraulic Chamber Volume (hydraulic chamber).
e. Volume of the sludge layer.

Furthermore, the size and type of digester used will be designed based on the potency and available literature data.

Digester size planning is seen from the daily amount of cow dung, the ratio of the composition of the mixture of water and cow dung, digestion time and the volume of biogas produced. The daily amount of manure produced at Capital is approx. 2.25 tons or 2,250 kg while the composition of the mixture of water and organic waste is to obtain 8% solids, solids refer to the amount of Kg t_s (total solid). Based on the calculations above, the total solid produced is 472.5 Kg. To obtain water that is added to make biogas raw material, fresh cow dung is mixed with water in a ratio of 1: 1. So that the amount of water added = the potential amount of cow dung = 2,250 kg / day then; Q_t = 4,500 kg / day Based on available data storage time (HRT) of cow dung in the digester. Storage time depends on the ambient temperature and biodigester temperature. With tropical conditions like India, at a temperature of 25- 35 ° C, the digestion time is approximately 25-35 days, a short digestion time can reduce the volume of the digester and vice versa the digestion time length can increase the volume of the digester. By determining the digestification time is 30 days, then with equations given below, can be determined the working volume of the digester, where the working volume of the digester is the sum of the digestification room volume (V_{DR}) and the storage volume ($V_{Storage}$),

namely: -

The working volume of the digester = $V_{DR} + V_{Storage}$, where $V_{Storage} + V_{DR} = Q_t$ x HRT (digestion time), then:
$V_{DR} + V_{Storage} = Q_t$ x HRT
= 4,500 Kg / day x 30 days
= 1,35,500 Kg

Because approximately 80% of the total Q (raw material) is water, we assume the density Q (raw material) ≈ density of water (1000 kg / m^3)
Volume = m / ρ
$V_{DR} + V_{Storage}$ = 1,35,000 Kg / 1000 kg / m^3 = 135m^3 = V_1

Based on table 4.3 the assumption of geometrical equations for the size of the digester tank is obtained:
$V_{Storage} + V_{DR}$ = 80% V_1 or $V_1 = (V_{Storage} + V_{DR}) / 0.8$
V_1 = 135 / 0.8
V_1 = 168.75 m^3

If building a digester size of 168.75 m^3 apart from being impractical in maintenance it is also less possible due to limited land, so look for a much smaller size digester with more than 1 digester, making it possible for maintenance and if there is damage to one of the digester others are still able to produce biogas as fuel for their electricity generation. It is determined that the digester to be built is 50 m^3 in size so that the number of digester sizes that must be built is:
Number of digester =168.75 m^3/50 m^3 = 3.375≈ 4 digester pieces.
For the digester size (V) 50 m^3, by reviewing the geometric equation assumptions in Table 4.3 it is obtained:

$V_{Storage} + V_{DR}$ = 80% V
= 80% * 50
= 40 m^3

Volume of gas storage room (Vc) = 5% * V = 5% * 50 = 2.5 m^3
The volume of the sludge storage layer ($V_{Sludge\ storage}$) = 15% * V
= 15% * 50 = 7.5 m^3

Storage volume ($V_{Storage}$) = 0.5 ($V_{Storage} + V_{DR} + V_s$) C.
C is the rate of gas production per m^3 per day, based on the table the C value 3.4, for cow dung is 0.21, then:
$V_{storage}$ = 0.5 ($V_{storage} + V_{DR} + V_{sludge\ storage}$) K.
= 0.5 * (40 + 7.5) * 0.21 = 4.99 m^3

From the value of $V_{storage}$ = 4.99 m^3 so that it can be seen the value of V_{DR}, namely: $V_{storage} + V_{DR}$ = 40, V_{DR} = 40 - 4.99 = 35.01 m^3
From the geometric assumption it is also known that $V_{Storage} = V_H$ = 4.99 m^3, meaning that the biogas will occupy the entire gas storage space (fixed drump digester type) according to the volume of gas produced. So that the volume of each part of the digester is known, namely:
V ─ Total Digester volume = 50 m^3
V_c - Volume of the gas collecting chamber = 2.5 m^3
$V_{storage}$ - Volume of gas storage chamber = 4.99 m^3
V_{DR} - Volume of the fermentation chamber =35.01 m^3
V_H - Volume of the (Hydraulic chamber) = 4.99 m^3
$V_{sludge\ storage}$ - Volume of the sludge layer = 7.5 m^3

- **Process Hydrolysis Acidogenesis, Acetogenesis and Methanogenesis.**
  The anaerobic decomposition in biopolymers organic complexes into methane gas are carried out by combined activities microbes. In general, this decomposition can be classified into four reactions, namely: hydrolysis, acidogenesis, acetogenesis and methanogenesis.
- **Process Hydrolysis Modeling**
  The hydrolysis stages, the decomposition of the polymeric organic material into soluble monomers, such as carbohydrates (polysarides) are broken down into glucose: -

$$(C_6H_{10}O_5)n + nH_2O \rightarrow n(C_6H_{12}O_6) \quad \ldots\ldots(22)$$

Therefore, the hydrolysis stride was incorporated into the Anaerobic Digestion Model in which the degradable particulate organic substrate, X_c are partially disintegrated into carbohydrates (X_{CH}), proteins (X_{PR}) and lipids (X_{LI}) and is described by

ISSN- 2394-5125 VOL 8, ISSUE 01, 2021

Equation shown below. The hydrolysis of X_{CH}, X_{PR} and X_{LI} are defined as under: -

$$\frac{dXc}{dt} = -K_{dis}Xc + D_{in}\,(Xc_{in} - Xc) + k_{dec,x1}X1 + k_{dec,x2}X2 \quad \ldots..(23)$$

$$\frac{dXch}{dt} = -K_{hyd,ch}\,Xch + D_{in}\,(Xc_{in} - Xch) + f_{ch,xc} + k_{dis}\,Xc \quad \ldots..(24)$$

$$\frac{dXpr}{dt} = -K_{hyd,pr}\,Xpr + D_{in}\,(Xpr_{in} - Xpr) + f_{pr,xc} + k_{dis}\,Xc \quad \ldots..(25)$$

$$\frac{dXli}{dt} = -K_{hyd,li}\,Xli + D_{in}\,(Xli_{in} - Xli) + f_{li,xc} + k_{dis}\,Xc \quad \ldots..(26)$$

In where $\mathbf{k_{dis}}$ is the constraint for degeneration process; the macrobiotic substrate application, **S**1, incorporate the conditions interrelated to hydrolysis, as shown:

$$\frac{dSl}{dt} = D_{in}\,(Sl_{in} - Sl) - (k_1\mu_1 X1) + k_7\left(k_{dis}\,Xc - k_{dec,x1}X1 - k_{dec,x2}X2\right) + k_8\{\left(k_{hyd,ch}\,Xch - f_{ch,xc}k_{dis}Xc\right) + \left(k_{hyd,pr}\,Xpr - f_{pr,xc}k_{dis}Xc\right) + \left(k_{hyd,li}\,Xli - f_{li,xc}k_{dis}\right) \quad \ldots..(27)$$

In where $\mathbf{k_7}$ is the yield-coefficient of-substrate disintegration and $\mathbf{k_8}$ the yield-coefficient of hydrolysis of-carbohydrates, proteins and lipids however the simulation depicting the scenario using Matlab is as under that can be seen in figure 4.1, SIMULINK block shape shown in, is a form of model based on mathematical modeling in formula 17: -

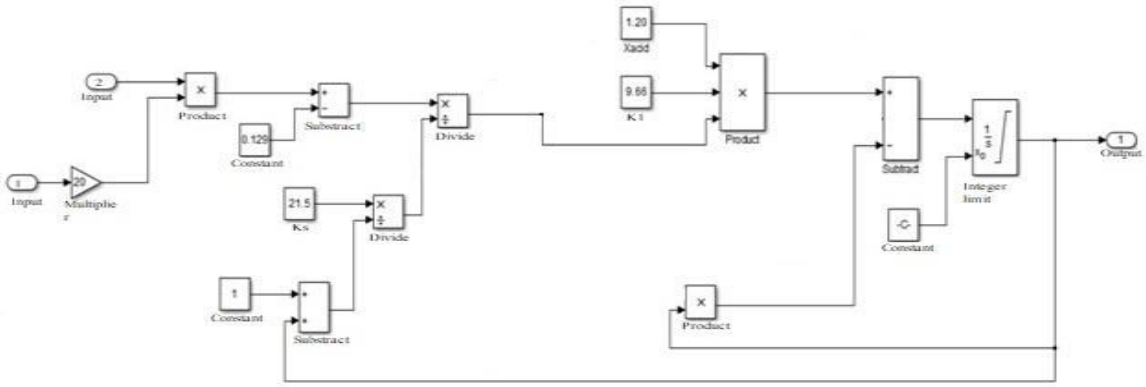


Figure 4.1: Process Hydrolysis Modeling

- **Process Acidogenesis**

In the acidogenesis stage, the bacteria generate acid and transform short-chain compounds into acetic acid, hydrogen and carbon dioxide formed in the hydrolysis stage. These bacteria are anaerobic bacteria that can grow and thrive in acidic conditions. To produce acetic acid these bacteria, require oxygen and carbon obtained from dissolved oxygen in solution, the formation of acid under anaerobic conditions is very important to form methane gas by microorganisms in the next process. In addition, these bacteria also turn alcohol, organic acids, amino acids, carbon dioxide, H_2S and a little methane gas into low molecular compounds. Acetic acid, propionic acid, butyric acid, H_2 and CO_2 are the most relevant compounds in the stage of acidogenesis. Furthermore, it contains small quantities of formic acid, lactic acid, valeric acid, methanol, ethanol, butadienol and acetone. Acid-forming bacteria can usually survive more abrupt conditions than methane-producing bacteria. These bacteria, if in anaerobic conditions, are able to produce staple food for producing methane gas and the resulting enzyme activity on proteins and amino acids will free amino salts which are the only source of nitrogen that can be accepted by methane-producing bacteria, therefore the simulation of below formulation is as under, SIMULINK block shape shown in Figure 4.2 is a form of model based on mathematical modeling in formula 19 and can be seen in figure 4.2.

$$K_1 S_1 \xrightarrow{r_1} X_1 + k_2 S_2 + k_4 CO_2 \quad \ldots..(28)$$

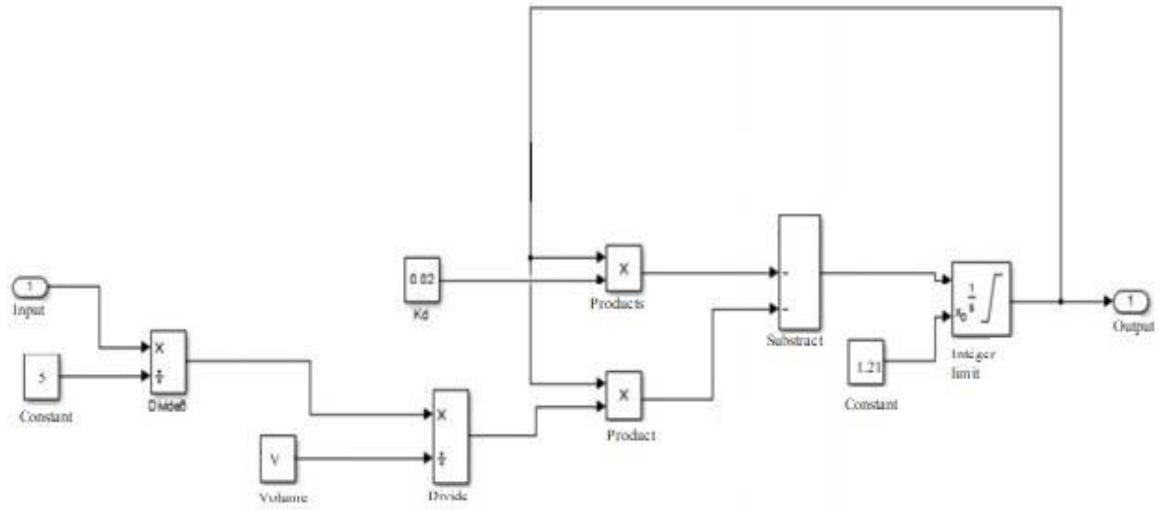


Figure 4.2: Process Acidogenesis Modeling

- **Process Acetogenesis**

Other results such as alcohol and Volatile Fatty Acid (VFA) from the process acidogenesis will be oxidized by acetogenic bacteria. On phase in this acetic acid and H_2 gas are produced which are used to form the gas methane. In the acidogenesis phase, about 20% acetic acid and 4% have been produced H_2 gas. In anaerobic environments, facultative microbes are able to break down acids long carbon chain fats such as propionic and butyric acids become acids acetate and H_2 gas. Therefore, at this stage, the acetogenic bacteria are producing hydrogen converting fatty acids and ethanol / alcohol to acetate, carbon dioxide and hydrogen. This advanced conversion is very important for success in biogas production, because methanogens cannot use fatty acid compounds and ethanol directly as: -

$$C_6H_{12}O_6 + 2H_2O \rightarrow 2CH_2COOH + 2CO_2 + 4H_2 \quad \ldots\ldots (29)$$

The Acetogenesis modeling can be seen in figure 4.3, SIMULINK block shape shown in Figure 4.3 is a form of model based on mathematical modeling in formula 20.

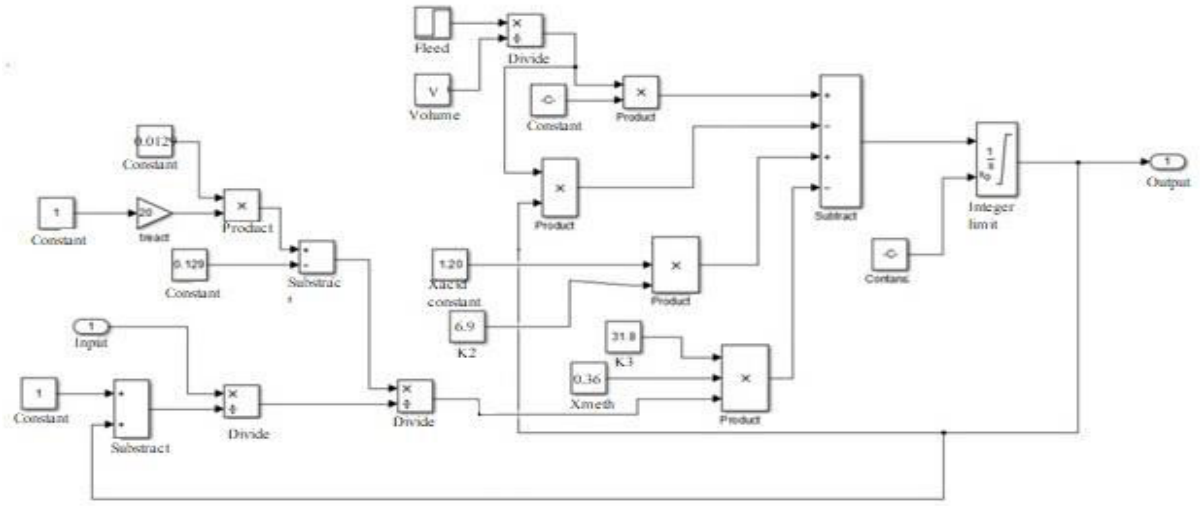


Figure 4.3: Process Acetogenesis Modeling

4.3.4 PROCESS METHANOGENESIS

Methanogenesis is the final stage of all conversion stages anaerobic organic matter into methane and carbon dioxide. On In the

ISSN- 2394-5125 VOL 8, ISSUE 01, 2021

early stages of growth, methanogenic bacteria depend on the availability of nitrogen in the form of ammonia and the amount of that substrate used. In the methanogenesis stage, methanogenic bacteria synthesize low molecular weight compounds become heavy compounds high molecule. For example, these bacteria use hydrogen, CO_2 and acetic acid to form methane and CO_2. Acid-producing bacteria and methane gas work together symbiosis. Acid-producing bacteria form a favorable environmental state ideal for methane producing bacteria. Meanwhile, gas-forming bacteria methane uses acids produced by acid-producing bacteria. Without this symbiotic process, it will create toxic conditions for acid-producing microorganisms as: -

a. Acetolactic methane bacteria break down acetic acid into:

$$CH_3COOH \rightarrow CH_4 + CO_2 \quad \text{.....(30)}$$

b. Methane bacteria synthesize hydrogen and carbon dioxide into:

$$2H_2 + CO_2 \rightarrow CH_4 + 2H_2O \quad \text{.....(31)}$$

Methanogenic bacteria are very sensitive to environmental changes. If the pH is below 6, the methanogenic bacteria cannot survive the Matlab simulation is depicted as under, SIMULINK block shape shown in Figure 4.4 is a form of model based on mathematical modeling in formula 21 and the methanogenesis process modeling can be seen in figure 4.4.

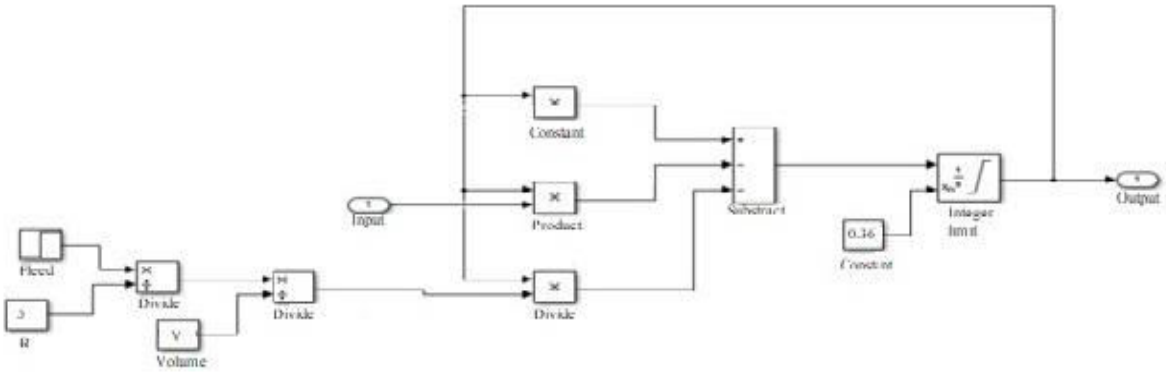


Figure 4.4: Process Methanogenesis Modeling

Therefore, using the above simulation modeling techniques, the amount of methane gas output is depicted as under and can be seen in figure 4.5: -

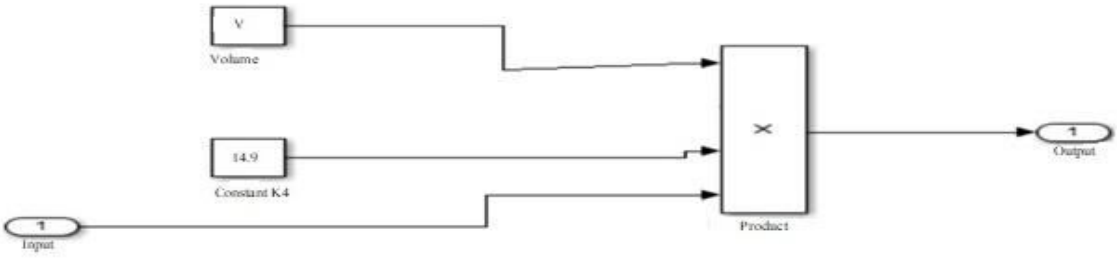


Figure 4.5: Modeling of the amount of methane gas output.

- **Gas Rector**

In terms of construction, generally biogas reactors can classify into three types, namely fixed dome, floating drum and reactor balloon. Fixed dome represents a reactor construction that has a fixed volume so that gas production will increase the pressure in the reactor. While floating drum means that there are parts in the reactor construction that can move to adjust to the increase

ISSN- 2394-5125 VOL 8, ISSUE 01, 2021

in reactor pressure. Movement of parts the reactor also marks the start of internal gas production biogas reactor. When viewed from the flow of raw materials (waste), a biogas reactor can also divide into two, namely the batch type (tub) and continuous (flow). In tub type, Reactor raw materials are placed in the container (specified space) from the start until the completion of the contamination process. This is only commonly used at stages experiments to determine the gas potential of a type of organic waste; whereas, in the flow type, there is a flow of raw materials in and out of residues at any given time. The length (time) the raw material is inside a biogas reactor is called the hydraulic retention time. The contact between raw materials and acid bacteria / methane, are two important factors that play a role in the biogas reactor. Schematic of fixed dome biogas reactor is inculcated in the solution the simulation depicted as under and can be seen in figure 4.6:

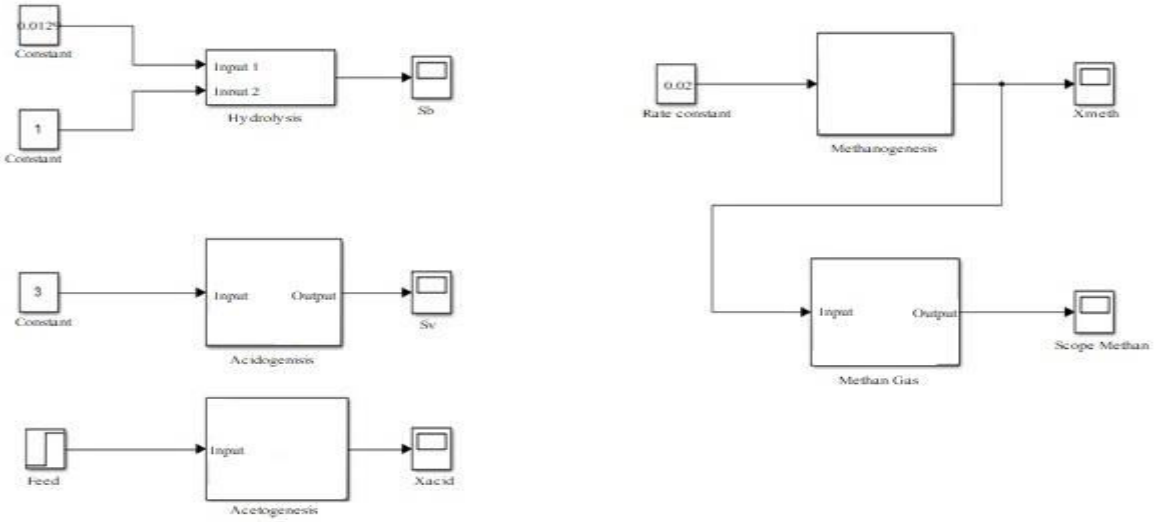


Figure 4.6: Reactor Model

- **Simulation Results**

The pressure in the reactor in the study, this is measured directly using Matlab so it can be seen that the process the reaction in the reactor for generate how much pressure that is generated as well as to know the increase that happens until the gas content is inside the material runs out. Based on the test preliminary, each repetition is carried out during the simulation to the point i.e., increase in methane gas production based on various temperatures. (Below simulated graphs shows X-Axis - time in days, while Y-axis consists of pressure in SI unit i.e., Pascal or N/m^2) and the result of simulations at temperature of 20°C,30°C,40°C, can be seen in figure 4.7,4.8,4.9 respectively.

- **Simulation results with scenario 20° C**

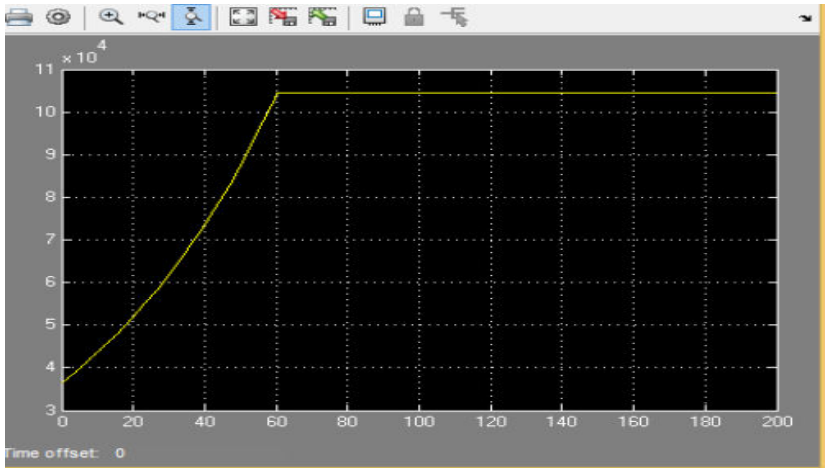


Figure: 4.7: Simulation Result of Converting Biogas Energy Scenario 20°C

ISSN- 2394-5125 VOL 8, ISSUE 01, 2021

- **Simulation results with scenario 30° C**

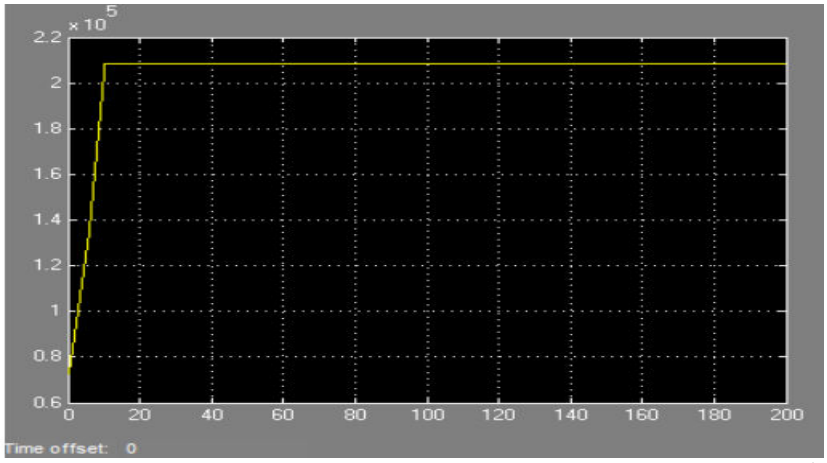


Figure: 4.8: Simulation Result of Converting Biogas Energy Scenario 30°C

- **Simulation results with scenario 40° C**

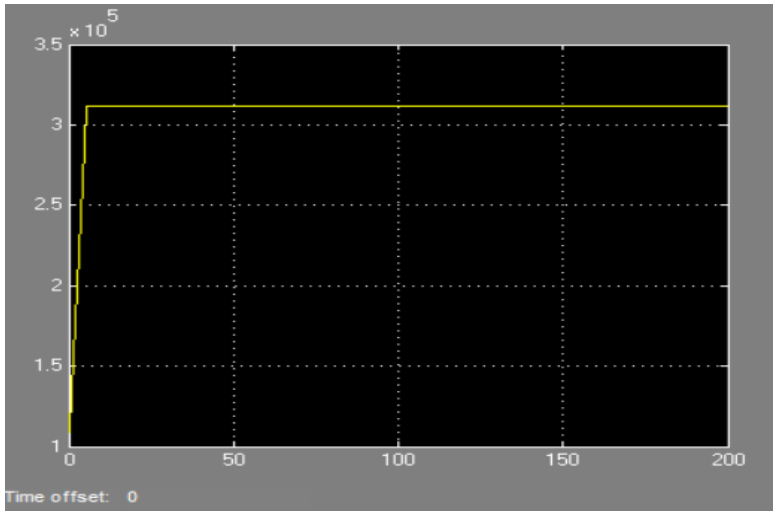


Figure: 4.9: Simulation Result of Converting Biogas Energy Scenario 40°C

- **Biogas Production**
  The biogas production process begins by diluting the manure with water with 1:1 ratio. Excessive water in the system can block the biogas channel, lowers the heat level of the fire, and makes the fire red. Stirring is possible at any given time to prevent solids from settling on the tank bottom. The manure that has been mixed with water is forwarded into the digester until it closes the channel enter and output, then wait for approximately 10-40 days. Then filling the digester can be done twice a day, namely morning and evening. The first gas produced must be discarded because it is dominated by CO_2 gas. Next, biogas production can be carried out normally so that CH_4 gas production will increase and CO_2 gas will decrease by a percentage of 54%: 27%. Furthermore, biogas can be obtained connected to a stove or electric generator. The gas produced is very good for combustion because it is able to generate a high enough heat, the fire is blue, no smelly, not smoky. The following is a schematic of the biogas production process.
- **Break Event Point**
  Break Even Point is a situation in which a company in a position does not experience gains or losses. This can happen if fixed costs and sales volume are used by the operation only to offset fixed costs and variable costs. The company suffers a loss if profits are only adequate to cover operating expenses and a portion of the fixed costs. In the meantime, the corporation will experience a profit if profits outweigh sales expenses and fixed costs. The components of the cost calculation at Break Even Point are as follows:
- **Fixed Costs**
  Fixed costs are the costings whose value tends to be stable without being influenced by the units produced. So, this one component is constant or appears during production or when production is not carried out by the company. Examples of fixed costs at companies are labor costs, machine depreciation costs, water costs, and so on.

ISSN- 2394-5125 VOL 8, ISSUE 01, 2021

- **Variable Cost**
  Variable costs are the costings whose value depends on the quantity of units or goods produced. So, this one component is its cost per unit does not remain or change according to the ongoing production action. So, for example, if production stops, variable costs decrease or don't exist and if production increases, variable costs will also increase. Some examples of variable costs are raw material costs, electricity costs, and so on.
- **Selling Price**
  The selling price is the selling price of electricity produced by the company. This selling price needs to be known because it is included in the Break Event Point calculation formula. The following is a formula for finding the Break Even Point value based on sales.

$$\boldsymbol{BEP = \frac{FC}{VC/P}}$$

  Where;
  FC is a Fixed Cost
  P is the Price per Unit
  VC is Variable Cost

- **Biogas Potential**
  As mentioned earlier cow can produce 8 kg to 20 kg of manure, of which one cows can produce biogas 0.36 m^3 / day, so if calculated, biogas produced from the cattle farm (having 150 cows) is 54 m^3 / day. It is known that 1 m^3 biogas can generate electric power of 11.17 kWh so that for 54 m^3 biogas can generate energy for:
  The amount of energy = volume of biogas * energy generated per m^3
  =2542$m^3$2*11.17 kWh
  = 603.18 kWh
  So, the theoretical amount of biogas energy in per cattle farm in National Capital Territory is 603.18 kWh with a power output of 603.18 KWh per day
- **Biogas Generator**
  The specifications of the biogas generator that will be used depicted in table 4.3 below: -

Table 4.3 Biogas Generator Set Specifications

Features	Double Cylinder
	4-stroke
	OHV
	Air-cooled
	Three phase AC
AC voltage-	220/230V
AC Outputs-	Running Power: 30KW
	Peak Power
Frequency	50/60Hz
Starting system	Recoil or Electric start
Fuel	Biogas
Weight	150Kg
Other	Min. Fuel Consumptions: 2m^3 /hour

Assuming the biogas generator will be operated 18 hours a day (in two shifts: morning and evening), and then the energy output from this biogas-based power plant is:
Energy = Power * Time
= 30 KW * 18 hours
= 540 KWh

The capacity of the digester with a power of 603.18 kwh and if you know the generator engine with a capacity of 540 kwh with the capability 603.18 kwh digester, then the digester can hold gas for 1.117 days. As for the biogas needed to turn on the generator for 18 hours based on minimum consumption of biogas stated in the generator specifications (2m^3 / hour) is = 18

hours * 2m^3 / hour = 36 m^3 / day. Meanwhile, the gas produced by 150 cows is 54 m^3 in 18 hours. So, the process of forming biogas to drive a generator is at least 36 m^3. Therefore, m^3 for 18 hours of use, it may take as long $\frac{36m^3}{54\ m^3} = 0.667\ days$ the length of time the generator set operates for a biogas volume of 54 m^3 can be determined by the following calculation:

$$\frac{\textbf{\textit{The volume of biogas production}}}{\textbf{\textit{Biogas for generator}}} = \frac{\mathbf{54}}{\mathbf{2}} = \mathbf{27\ \textit{hours}}$$

- **Homer Analysis**

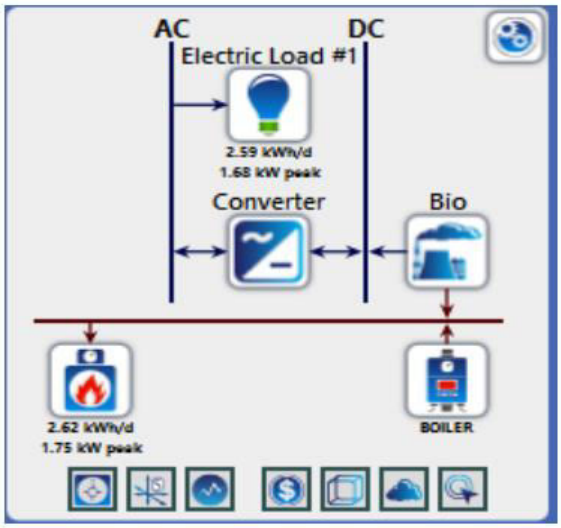


Figure 4.10 Schematic of the biogas power plant design

In Figure 4.10 there are several components including thermal loads, boilers, generators biogas, converters, and AC loads. The function of thermal load is as energy for heating water in the boiler. The function of the boiler in the circuit above is as a container where the process occurs heating water to produce hot steam. The function of the generator is as energy generator electricity. The converter function is to convert the DC current from the generator into the acceptable AC current used by AC loads. The following is a systematic process in Figure 4.13.

1- The thermal load heats the water in the boiler.
2- Water that has been heated in the boiler will produce hot steam.
3- The hot steam is directed to rotate the motor in the generator which then will generate electrical energy that is DC.
4- DC current from the generator flows to the converter to be converted into AC current.
5- AC current is applied to the load.

- Economic Analysis

The economic value of the biogas power plant is shown in Table- 4.4

Table 4.4 The Economical Value of the Biogas Power Generation System

Assessment Criteria	Score
Total energy production (KWh) Per Year	1,97,100
Net present cost Of Materials (Including Generator, Digestor, Tank, Pipeline and Other)	Rs-2,50,000
Cost of energy (RS/KWH) Per Year	1.268

The total energy production using the biogas power generation system generates power amounting to Rs. 1.268 per kWh / year. The result of the total energy produced can be seen in Table 4.5 and will be calculated using formulation as Energy = Volume of Biogas * Energy generated per m^3.

Table 4.5: Data on Total Energy Production per Year

Component	Output Production (KWh) In A Year
Generator (Operating 18 Hrs. A Day) R(540kwh*365days) in a year	1,97,100

$$\boldsymbol{E_{tot.prod}\ = 1,97,100\ kWh\ (197.10MWh) in\ a\ complete\ year}$$

ISSN- 2394-5125 VOL 8, ISSUE 01, 2021

The results of net present cost calculation using Homer software can be seen in table 4.6 below:

Table 4.6: Results of Net Present Cost Calculation for HOMER Software

Component	Capital	Replacement	O&M	Fuel	Salvage	Total
Generic biogas generator	200000	0	10	14,608.01	-152.581	2,14,455.43
Homer Load Following	10	10	10	10	0	10
System Converter	399.99	10	39.97	10	01	439.97
Other	50,000	10	45,249.7	10	0	95,249.71
System	2,50,999.98	0	45,289.68	14,608.01	-152.581	3,10,745.09

NPC = 2,50,999.98 +0 + 45,289.69 + 14,608.01 – 152.58
NPC = 3,10,745.09

Cost of Energy system Rs.3,10,745.09, total energy yield data serve loads and costs total per year used to calculate the Cost of Energy can be seen in Table 4.7 and calculated using equation $NPC = Capital\ Costs + Replacement\ costs + O\&M\ costs + Fuel\ Costs - Salvage$.

Table 4.7: Data on Total Energy Serving Expenses and Costs per Year

Assessment Criteria	Score
Total Energy Serving Load (kWh / year)	1,97,100 (Average Consumption)
Total Annual Fee (Rs)	3,10,745.09

$$COE = \frac{Rs.3,10,745.09}{1,97,100kWh} = 1.57 \text{Rs. / kWh in a year}$$

5. Conclusion and Suggestions

- **Conclusion**

From the research conducted it can be concluded that:

- National Capital Territory with a population of 150 heads (example) of cattle has the potential to produce 0.36 m^3 per cattle of biogas with the potential for electrical energy generated 603.18 kWh (***603.18 KW power***).
- Selection of a biogas generator set with a capacity of 30 kW suitable for use as an engine for converting biogas energy into electrical energy in a simple generator system with the HOMER generating system using a frequency of 50Hz.
- A simple generator system (Digester-biogas-Genset Biogas 30000 W-electricity) which is assumed to operate for 18 hours a day can generate energy of 540.00 kWh while the HOMER generator system for 24 hours can produce the 603.18 kWh electric energy).
- The remaining 63.18 m^3 can be utilized for cooking and boiling as fuel usages in ordinary course of business, livelihood and to counter any losses.
- Investment in the construction of a simple generator system (Digester-biogas-Genset Biogas 30 kW of power resulting 540.00 kWh) will be more easily realized as compared to the construction of a HOMER generating system (Thermal-Boiler-Generator Bio 30 kW-Converter 603.10 kWh electricity load) with consideration of a fairly the economical price of Rs.1.57 of per unit in a year. Consequently, which is much cheaper and more economical to existing electricity.
- By the use of cow dung which is Municipal solid waste (basically biodegradable organic waste), we can reduce the municipal solid waste generation and air pollution to some extent in Delhi.

- **Suggestions**

The suggestions in this study are:

- For the construction of a biogas-based power plant system in National Capital Region, it will be more efficient and economical with a simple generator system (Digester-biogas-Biogas Generator 30000 W-electricity) compared to the HOMER generating system (Thermal-Boiler-Generator Bio 30 kW -Converter 10 kW-electric load).
- It is necessary to hold further studies of course with different parameters regarding the biogas-based power plant system in National Capital Region so that the construction of the generator can be realized so that it can be distributed to the community.

- The bio-waste that is being generated during the production of biogas, can be used as manure for agriculture and farming which is much more effective and better than the harmful chemical compounds that is being used for agriculture and farming.

Declaration of Competing Interest

The authors declare no conflicts of interest concerning the research, authorship and publication of this article.

Funding

This research did not receive any specific grant from funding agencies in the public, commercial, or not-for-profit sectors.

References

[1] https://niti.gov.in/sites/default/files/2020-01/IEA-India%202020-In-depth-EnergyPolicy_0.pdf
[2] https://www.world-nuclear.org/information-library/energy-and-the-environment/renewable-energy-and-electricity.aspx
[3] http://delhiplanning.nic.in/sites/default/files/11%29%20Energy_0.pdf
[4] https://dahd.nic.in/about-us/divisions/cattle-and-dairy-development
[5] https://static.pib.gov.in/WriteReadData/userfiles/key%20results.pdf
[6] Khan, M E., Martin, A R. (2016) Review of biogas digester technology in rural Bangladesh. Renewable & sustainable energy reviews, 62: 247-259 http://dx.doi.org/10.1016/j.rser.2016.04.044
[7] https://www.eesi.org/papers/view/fact-sheet-biogasconverting-waste-to-energy
[8] Artanti, D & Saputro, Roy & Budiyono, B. (2012). Biogas Production from Cow Manure. International Journal of Renewable Energy Development (IJRED). 1. 61-64. 10.14710/ijred.1.2.61-64.
[9] Tallou, Anas & Haouas, Ayoub & Jamali, Mohammed Yasser & Atif, Khadija & Amir, Soumia & Aziz, Faissal. (2020). Review on Cow Manure as Renewable Energy. 10.1007/978-3-030-37794-6_17.
[10] Baredar, Prashant & Khare, Vikas & Nema, Savita. (2020). Biogas digester plant. 10.1016/B978-0-12-822718-3.00003-4.
[11] Caposciutti, Gianluca & Baccioli, Andrea & Ferrari, Lorenzo & Desideri, Umberto. (2020). Biogas from Anaerobic Digestion: Power Generation or Biomethane Production? Energies. 13. 743. 10.3390/en13030743.
[12] Jankowska, Ewelina & Zieliński, Marcin & Dębowski, Marcin & Oleskowicz-Popiel, Piotr. (2019). Anaerobic digestion of microalgae for biomethane production. 10.1016/B978-0-12-815162-4.00015-X.
[13] Li, Hailong & Mehmood, Daheem & Thorin, Eva & Yu, Zhixin. (2016). Biomethane production via anaerobic digestion and biomass gasification.
[14] Jeong, Hyeong-Seok & Suh, Changwon & Lim, Jae-Lim & Lee, Sang-Hyung & Shin, Hang-Sik. (2005). Analysis and application of ADM1 for anaerobic methane production. Bioprocess and biosystems engineering. 27. 81-9. 10.1007/s00449-004-0370-4.
[15] Assegaf, Ali & Umbara, Rian & Kurniawan, Isman. (2019). Pemodelan Produksi Biogas pada Reaktor Tipe Batch Menggunakan Metode Hamming Predictor-Corrector. Indonesian Journal on Computing (Indo-JC). 4. 1. 10.21108/INDOJC.2019.4.1.138.
[16] Saeed, Mohammed & Fawzy, Samaa & El-Saadawi, Magdi. (2018). Modeling and simulation of biogas-fueled power system. International Journal of Green Energy. 16. 1-27. 10.1080/15435075.2018.1549997.
[17] Pathmasiri, Kalpani & Haugen, Finn Aakre & Gunawardena, Sanja. (2013). Simulation of a Biogas Reactor for Dairy Manure. Annual Transactions of IESL. The Institution of Engineers, Sri Lanka. 394-398.
[18] Danielsson, Oskar. 2014. Modeling and Simulation of Anaerobic Manure Digestion into Biogas. Gothenburg, Sweden. Master's Thesis. Chalmers University of Technology.
[19] Antonio, Juan. 2018. Modeling and Simulation of Biogas Production Based on Anaerobic Digestion of Energy Crops and Manure. Chemical Engineering Dissertation. Technischen Universitat Berlin.
[20] Raj, Dr & Jhariya, Manoj & Toppo, Pratap. (2014). COW DUNG FOR ECOFRIENDLY AND SUSTAINABLE PRODUCTIVE FARMING. INTERNATIONAL JOURNAL OF SCIENTIFIC RESEARCH. 3. 201-202.
[21] Artanti, D & Saputro, Roy & Budiyono, B. (2012). Biogas Production from Cow Manure. International Journal of Renewable Energy Development (IJRED). 1. 61-64. 10.14710/ijred.1.2.61-64.
[22] Matos, Camila F., Paes, Juliana L., Pinheiro, Érika F. M., & Campos, David V. B. De. (2017). BIOGAS PRODUCTION FROM DAIRY CATTLE MANURE, UNDER ORGANIC AND CONVENTIONAL PRODUCTION SYSTEMS. Engenharia Agrícola, 37(6), 1081-1090. https://doi.org/10.1590/1809-4430-eng.agric.v37n6p1081-1090/2017
[23] Amanda D Cuéllar and Michael E Webberm, Cow power: the energy and emissions benefits of converting manure to biogas, 2008 Environ. Res. Lett. 3 034002 https://doi.org/10.1088/1748-9326/3/3/034002
[24] N O Abdullah and E S Pandebesie, The Influences of Stirring and Cow Manure Added on Biogas Production from Vegetable Waste Using Anaerobic Digester, 2018 IOP Conf. Ser.: Earth Environ. Sci. 135 012005 https://doi.org/10.1088/1755-1315/135/1/012005
[25] Abdallah, Mohamed & Shanableh, Am & Adghim, Mohamad & Ghenai, Chaouki & Saad, S.A... (2018). Biogas Production from Different Types of Cow Manure. 10.1109/ICASET.2018.8376791.
[26] Cuéllar, Amanda & Webber, Michael. (2008). Cow Power: The Energy and Emissions Benefits of Converting Manure to Biogas. Environ. Res. Lett. 3. 10.1088/1748-9326/3/3/034002.
[27] Drapcho. et al. 2008. Biofuel Engineering Process Technology. USA: The McGrawHill Companies, Inc

ISSN- 2394-5125 VOL 8, ISSUE 01, 2021

[28] Effendy, Sahrul. 2018. Biogas from Converting Cow Manure Waste as Material Generator Set To Generate Electrical Energy Capacity 0.3 kWA. National Seminar on Innovation and Technology Application in Industry. Polytechnic Sriwijaya. ISSN 2085-4218

[29] Sloby, C. (2020). biogas. 10.1002/9783527809080.cataz01953.

[30] Velivela, Asmitha & Barham, Husam & Bauer, John & Roschke, Jon & Daim, Tugrul & Meissner, Dirk. (2020). Biogas: Converting Waste to Energy. 10.1007/978-3-030-58301-9_18.

[31] Adisasmito, S.. (2020). Biogas Generation from Jakarta Municipal Waste. 10.1201/9781003078883-22.

[32] Khalil, Mohamed & Mansour, Hanaa. (2020). Biogas production. 10.13140/RG.2.2.30410.31680.

[33] Lamb, Jacob. (2020). Biogas and the Energy Sector. 10.48216/9788269203325CH1.

[34] http://www.fluid-biogas.com/?page_id=125&lang=en

[35] https://bigadan.com/p/biogas-technology/how-to-make-biogas

[36] https://vikaspedia.in/energy/energy-production/bio-energy/biogas

[37] Velmurugan, Sivasubramanian & Deepanraj, Balakrishnan & Jayaraj, Simon. (2014). Biogas Generation through Anaerobic Digetsion Process – An Overview. RESEARCH JOURNAL OF CHEMISTRY AND ENVIRONMENT. 18. 80-94.

[38] https://www.epa.gov/agstar/how-does-anaerobic-digestion-work

[39] Meisam Tabatabaei, Hossein Ghanavati, Biogas Fundamentals, Process, and Operation Series: Biofuel and Biorefinery Technologies https://www.springer.com/gp/book/9783319773346

[40] Danielsson, Oskar. 2014. Modeling and Simulation of Anaerobic Manure Digestion into Biogas. Gothenburg, Sweden. Master's Thesis. Chalmers University of Technology.

[41] https://energypedia.info/wiki/Electricity_Generation_from_Biogas

[42] https://www.britannica.com/technology/steam-engine

[43] https://www.sciencedirect.com/science/article/pii/S1876610217337840/pdf?md5=0cb79069294f4190dccdd47f7f449403&pid=1-s2.0-S1876610217337840-main.pdf

[44] http://www.bioenergyfarm.eu/de/klein-biogasanlagen-gulle-kleinanlagen/biogasnutzung/

[45] Taizhou Bison Machinery., Ltd

[46] https://eepafrica.org/about-us/success-stories/bio2watt/

[47] https://sistema.bio/success-stories/

[48] https://www.bmwgroup.com/en/responsibility/sustainable-value-report/popup/bio.html

[49] https://www.gree-energy.com/ground-breaking-of-hamparan-project/

[50] http://task37.ieabioenergy.com/files/daten-redaktion/download/Technical%20Brochures/Smart_Grids_Final_web.pdf

[51] https://blog.anaerobic-digestion.com/biogas-generator/

[52] https://www.researchgate.net/post/How_is_the_power_capacity_kW_or_MW_of_a_biogas_installation_determined

[53] https://www.biogasworld.com/

[54] https://www.biogas-info.co.uk/about/biogas/

[55] https://www.energy.gov/eere/bioenergy/biopower-basics

[56] Ogur, Eric. (2013). Design of a Biogas Generator. Concurrent Engineering Research and Applications. 3. 2248-9622.

[57] Price, Elizabeth & Cheremisinoff, Paul. (1985). METHODS OF BIOGAS GENERATION AND COMPARISONS.

[58] Motjoadi, Vinny & Adetunji, Kayode & Joseph, Prof. (2020). Planning of a sustainable microgrid system using HOMER software. 1-5. 10.1109/ICTAS47918.2020.233986.

[59] Djalilova, Nigora. (2021). Feasibility study of hybrid wind-solar stand-alone energy systems using HOMER software. 10.4324/9781003110071-6.

[60] Raveena, Battula & Rao, Bathina & Nadakuditi, Dr Gouthamkumar. (2018). Optimization of Hybrid off Grid Power System Using HOMER software. 696-700. 10.1109/RTEICT42901.2018.9012219.

[61] Kansara, B.U. & Parekh, B.R. (2011). Modelling and simulation of distributed generation system using HOMER software. 328-332. 10.1109/ICONRAEeCE.2011.6129804.

[62] Aly, Abdelmaged & Kassem, Ahmed & Sayed, Khairy & Aboelhassan, Ismail. (2019). Design of Microgrid with Flywheel Energy Storage System Using HOMER Software for Case Study. 485-491. 10.1109/ITCE.2019.8646441.

[63] Shahinzadeh, Hossein & Moazzami, Majid & Fathi, Shabnam & B. Gharehpetian, Gevork. (2016). Optimal sizing and energy management of a grid-connected microgrid using HOMER software. 1-6. 10.1109/SGC.2016.7882945.

[64] Noor, Md. Fahel & Mallick, Bijoy & Habib, Ahsan & Noor, Nahiyan. (2019). COMPARISON OF PERFORMANCE AND COST OF WIND AND SOLAR HYBRID SYSTEM FOR SAINT-MARTIN ISLAND USING HOMER SOFTWARE.

[65] S.K. Singh, M.kumar and S.Singh.(2020).PLASMA TECHNOLOGYAS WASTE TO ENERGY: A REVIEW.

List of figures

Figure 2.1: Biogas Formation Stages/Phase
Figure 2.2: Graph Representative Anaerobic Digestion Temperature
Figure 2.3: Biogas Generator
Figure 3.1.1: Research Flowchart
Figure 3.1.2: Research Flowchart continued
Figure 3.2: SIMULINK Reactor Model
Figure 4.1: Process Hydrolysis Modeling
Figure 4.2: Process Acidogenesis Modeling
Figure 4.3: Process Acetogenesis Modeling
Figure 4.4: Process Methanogenesis Modeling
Figure 4.5: Modeling of the amount of methane gas output
Figure 4.6: Reactor Model
Figure: 4.7: Simulation Result of Converting Biogas Energy Scenario 20^{o}C
Figure: 4.8: Simulation Result of Converting Biogas Energy Scenario 30^{o}C
Figure: 4.9: Simulation Result of Converting Biogas Energy Scenario 40^{o}C
Figure 4.10 Schematic of the biogas power plant design

List of Tables

Table 2.1: Composition of Cow Manure
Table 2.2: Cow Manure specifications with a total weight of 635 kg
Table 2.3: Compositional Biogas
Table 2.4 Volatile Solid Components
Table 2.5 C/N Ratio of Organic Materials
Table 2.6 Energy Conversion from Methane Gas to Electrical Energy
Table 4.1 Sample performance of the biogas plant
Table 4.2: Result of biogas capacity calculations
Table 4.3 Biogas Generator Set Specifications
Table 4.4 The Economical Value of the Biogas Power Generation System
Table 4.5: Data on Total Energy Production per Year
Table 4.6: Results of Net Present Cost Calculation for HOMER Software
Table 4.7: Data on Total Energy Serving Expenses and Costs per Year

Multimedia Tools and Applications
https://doi.org/10.1007/s11042-022-11958-5

Optimizable face detection and tracking model with occlusion resolution for high quality videos

Akshay Mool[1] · J. Panda[2] · Kapil Sharma[1]

Received: 9 July 2021 / Revised: 16 December 2021 / Accepted: 3 January 2022
© The Author(s), under exclusive licence to Springer Science+Business Media, LLC, part of Springer Nature 2022

Abstract
Recent state-of-the-art Face Detection algorithms in the field of Computer Vision focus greatly on real-time processing and results. The applications using these algorithms deal with low quality video feeds having less Pixels Per Inch (ppi) and/or low frame rate. The algorithms perform well with such video feeds, but their performance deteriorates towards high quality, high data-per-frame videos. Such video files mostly exist in offline mode, that could be used for post processing by the Computer Vision applications. This paper focuses on developing such an algorithm that gives faster results on high quality videos, at par with the algorithms working on live low quality video feeds. The proposed algorithm uses Convolutional-MTCNN as base algorithm, and speeds it up for high definition videos. This paper also presents a novel solution to the problem of occlusion and detecting partial or fully hidden faces in the videos. This is achieved by using probabilistic approaches, given that the face has been identified in first few frames, to give the algorithm an estimate of where the face should be in the occluded region.

Keywords Face detection · Feature tracking · Interpolation

1 Introduction

In this era of rapid modernisation, Computer Vision plays a very important role to act as a foundation for numerous digital applications and softwares that can analyse and process visual information [7] for various significant activities, which include Face detection and Face tracking. These are predominantly used in Real time processing applications like Automation, Surveillance, Machine Learning, Robotics, among other major fields.

Facial detection and face tracking is among one of the most worked-on fields these days, which in turn works as a prerequisite stage for more advanced processing applications.

✉ Akshay Mool
akshaymool_phd2k17@dtu.ac.in

[1] Department of Information Technology, Delhi Technological University, Shahbad Daulatpur, Main Bawana Road, Delhi, 110042, India

[2] Department of Electronics and Communications Engineering, Delhi Technological University, Shahbad Daulatpur, Main Bawana Road, Delhi, 110042, India

Published online: 15 February 2022

Even under facial detection and tracking, most work seems to be focused on processing of real-time videos to help with surveillance or identification, along-with other activities. Recent advances in algorithms in this field work really well and almost instantaneous with low quality, real-time videos. But when it comes to high definition, high quality videos in movies, or fields that require such videos, these algorithms become slow and less efficient. The processing time gets high, with computational speed getting low for them. Therefore, a new approach for developing an algorithm to attend to these high quality videos is needed, that could try to compete with the state-of-the-art existing algorithms for real-time videos.

Most traditional algorithms that are mainly categorized based on knowledge, feature-invariant, template matching, or appearance [21]. They have been proven to be very effective in both low and high quality videos, like Viola-Jones [20], Principle Component Analysis (PCA), Linear Discriminant Analysis (LDA) [4], Multi-view face detection [22] though their average performance still falls short compared to the next generation of algorithms. Pairo, Loncomilla and Solar [10] published a very efficient technique to utilize the real-time computationally expensive object detection and tracking algorithms, by using feature-tracking from KLT algorithm to discard non-facial regions in subsequent frames after object is detected in a previous frame. The paper identifies occlusion using KLT algorithm to track good features inside the object detection box over subsequent frames, and rejects the result if occlusion occurs. The newest algorithms that deal with machine learning, deep learning, neural networks get more complex than traditional algorithms, but give very fast and accurate results in real-time video feeds, like Histogram of Oriented Gradients (HoG) [3], You Only Look Once (YOLO) [9], among others [1, 11, 12]. There is very little work done on algorithms focused on high quality images and videos, so it has become a need of the hour to have good, flexible algorithms for them. There have been a few works that try to find high quality faces in images and videos, but not specifically faces in high quality videos.

This paper tackles the problem of lack of a good performing algorithm for detection and tracking of faces in high quality video feeds. This is done on three fronts: increasing the speed of a Cascaded Neural Network algorithm for detecting face in corresponding videos; using the detected face and its features to track it in further frames; and addressing the partial/total occlusion problems in such videos. Our paper, like [10], also uses KLT algorithm for tracking face across frames, but it tracks only the most essential features of a human face to track, i.e., the five landmark locations of a face. Those features are tracked only when the detected features of the KLT algorithm match with the five landmark locations, thereby eliminating the need to track other features inside the face detection box, decreasing the number of computations required. The referenced paper [10] uses the KLT algorithm for occlusion "detection" also, whereas our paper uses extrapolation techniques for occlusion "resolution", meaning the proposed model predicts the location of the previously detected face in subsequent occluded frames, instead of discarding the existence of face altogether.

2 Related work

2.1 Real-time AdaBoost cascade face tracker

Viola-Jones algorithm [23] is a benchmark face detection algorithm that was introduced in 2004. This algorithm achieved fast face detection speeds with decent accuracy of detected

faces. This algorithm is treated as a benchmark to compare the efficiency of newer techniques, and therefore has been used as a base standard to compare our proposed model against newer techniques.

Ranftl [13] tried to tackle the problem of implementing the main face detecting algorithm of Viola-Jones on each and every frame in a video by suggesting an optical flow based face tracker that used likelihood map to predict where the face would be in the next few frames, after it was detected in the previous frames. Viola-Jones algorithm is essentially a static algorithm that does not incorporate the temporal aspect of a detected face in a video; nor does it pay any significance to near-positive windows, i.e, those intermediate stage windows that pass a significant number of classification cascade levels. Ranftl tried to use the optical flow between frames for prediction of faces for the next frames. These optical flow calculations were then used to construct a likelihood map using interpolation techniques against time. The significance of the likelihood map was to determine the belonging-ness of a particular pixel as part of a face. It is constructed by taking care of how many stages of classification cascade a particular window has passed through, even if the resultant window is not a face at the end stage. This modified version of Viola-Jones would be called after every n frames, and uses likelihood map interpolated with optical flow calculations, for the frames in between. This algorithm was comparatively faster than traditional Viola-Jones algorithm, with decent accuracy. The likelihood map takes care of partial or total occlusions between frames, making use of the likelihood map and interpolation.

2.2 Joint face detection and alignment using multitask cascaded convolutional networks (MTCNN)

This algorithm is one of the modern face detecting algorithms [14, 24] that is more accurate than Viola-Jones, while also giving fast performance in real time. Zhang, Zhang and Li [25] developed this framework in 2016, and tried to tackle the challenges of pose variations, illumination variations and occlusion problems. They used a separate CNN (Convolutional Neural Network) for each of the three stages involved in the framework. The first stage results in various potential face windows in the whole frame using a shallow CNN, called Proposal Network (P-net). These various number of windows are treated with Non-Maximum Suppression (NMS) so that all the overlapping windows could be merged. The resultant candidate face windows are refined and reduced in the next stage using a complex CNN, called Refine Network (R-Net). It's job is to reject even more false candidate windows, to calibrate them using Bounding Box Regression, and to conduct NMS again. The final stage (O-net) uses more supervision to reduce and finalize the previous stage candidate windows into the optimal face windows, and outputs five locational landmarks in them: two eye markers, one nose marker, and two lips-ends markers.

2.3 Feature-points tracking using KLT algorithm

KLT algorithm [18] is named after the three researchers: Kanade-Lucas-Tomasi, who developed the method of tracking motion features across frames. The method first identifies important feature points to track. It identifies fixed-sized feature-point windows, and then tries to minimize the sum of squared intensity differences between consecutive frames, meaning the past frame and the current frame. A window is chosen over individual pixels to track because a single pixel cannot be tracked unless it's intensity has much difference with respect to it's neighboring pixels. Therefore, a window of pixels is chosen that has "sufficient texture" required for feature-point tracking reliably.

Essentially, for each point(s) in the previous frame, the point tracker attempts to find the corresponding point(s) in the current frame. Then the translation, rotation, and scale between the old points and the new points is estimated. This transformation is applied to the bounding box around the face.

2.4 Using Histogram of Oriented Gradients (HOG) and FaceNet face detection systems

Histogram of Oriented Gradients [17] is a face detection technique that works by dividing the face frame into dense grids and calculating normalized histograms of Oriented gradients in those grids. All the calculated HOG vectors then combine together to form feature expression for the whole face. This technique can be further extended to face recognition too. HOG technique is used here to compare our model's performance against it.

FaceNet [15] is a face detection that is trained to map faces in an image to Euclidean space. The significance of that Euclidean space is that distances inside it give a measure of similarity with faces. This technique can also be further extended to face recognition. FaceNet model is used for comparison because it's performance for high quality videos is the strongest among existing state-of-the-art techniques.

3 Proposed methodology

This section provides methodology for the proposed efficient face detector and tracker. The model is designed to use the face detection algorithm in an efficient manner for high definition videos, without compromising it's integrity, while maintaining it's speed at par with live, lower quality videos.

3.1 Overall framework

The proposed model comprises of three sub-frameworks, each having their own function, and work together with each other over a stream of images (videos) to detect and track the face. The flowchart for overall framework of proposed method is given in Fig. 1.

The working of the whole framework starts with input to the first sub-framework. It's input is the initial frame from the input video, on which the base face detecting algorithm of MTCNN is applied. The algorithm detects the faces in the frame, characterised by five feature points. The output of the algorithm is those five feature points marked on the frame, and a rectangular box around the detected face. The output of first sub-framework works as an input for the second sub-framework. The five feature points detected and marked by the first sub-framework and then fed into the KLT feature point tracking algorithm, which tracks those points for n subsequent frames, where n is the refresh rate, after which the MTCNN algorithm is called again for face detection. n is chosen appropriately according to the video, so that the overall framework works faster, but without compromising the accuracy of the detected framework. Now, whenever there is an occlusion problem in the frame, the third sub-framework is called, which tries to predict the location of the face in the occluded region, based on the positions of detected faces in the previous frames. This carries on for n subsequent frames, after which MTCNN is called again to check whether the face has appeared again or not.

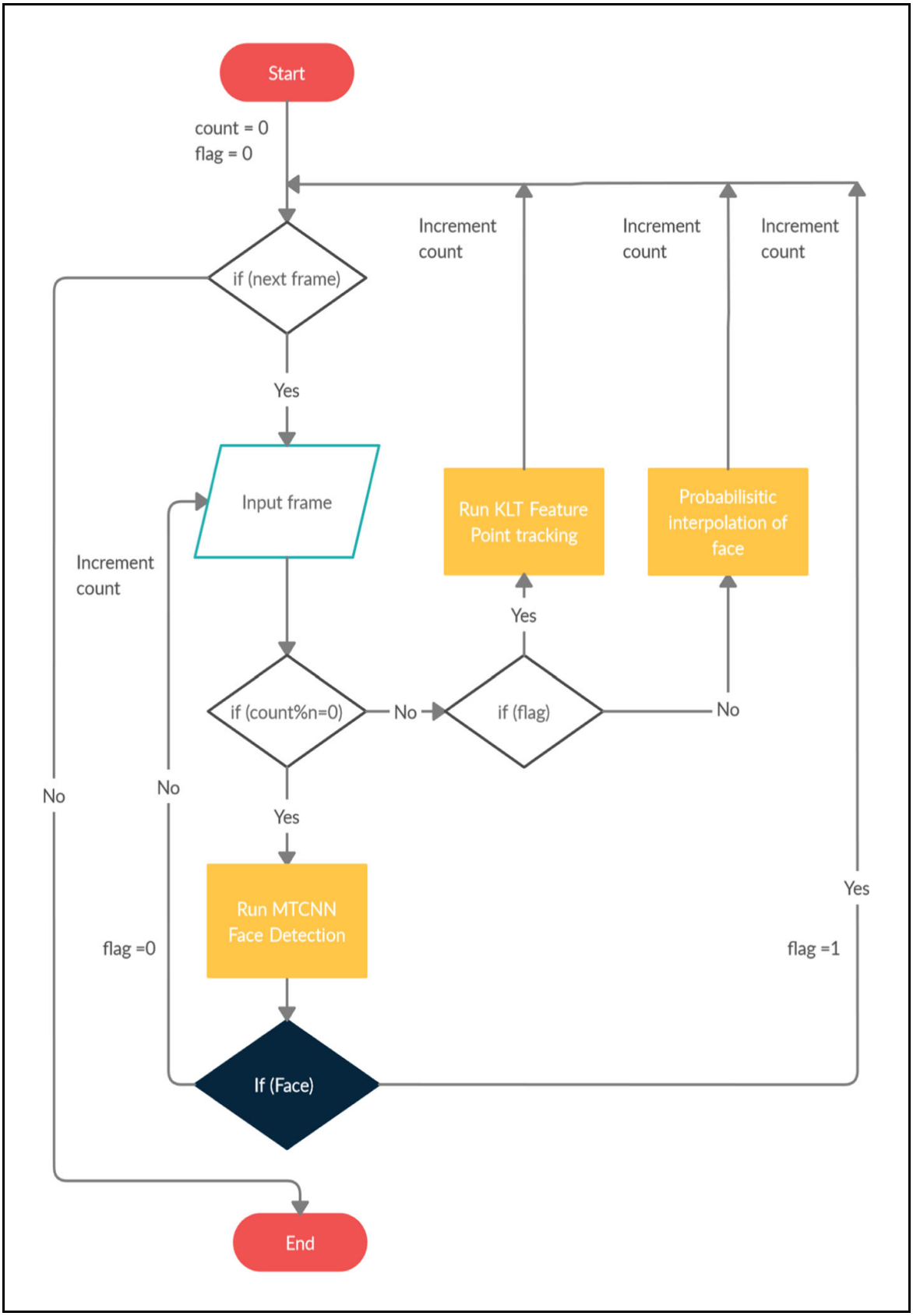


Fig. 1 Flowchart of the overall framework

3.2 Integrating face detecting with feature points tracking

As discussed earlier, experimental results show that recent modern algorithms like MTCNN algorithm achieve very accurate results with appreciable runtime performance for live video feeds, that are generally of lower quality. But they fail to perform at a par speed of execution when the quality of video feed increases. Numerous parameters, like frame rate, bitDepth, PixelAspectRatio, interlace, among many others, factor in the declined performance of these modern algorithms. So this paper tried to accelerate the speed of the algorithm while keeping it's high accuracy. The main output of the MTCNN face detection algorithm is the five location landmark points for the face, i.e, two eye points, one nose point, and two mouth end points. These points essentially identify the location of a face in a frame. Since MTCNN face detection is computationally quite heavy and time consuming for heavy frames, it is not feasible to run the algorithm for every frame in the video.

KLT feature-tracker is a fast and efficient algorithm to track good feature points across frames. It has been used in face tracking too, but it is not relied upon for it simply for the fact that there can be other things in a frame that might be identified as good features, and the algorithm will track all of them, thereby defeating the purpose of tracking only faces in a video feed. Therefore, that portion of the algorithm that identifies the good features to track is discarded, and instead only utilize the portion that tracks points from frame to frame. Since the face detection algorithm has already given out the most important feature points to track in a frame, those points are used input to the KLT feature tracker, and only those points are tracked across frames.

The main advantages of blending these two algorithms with each other are:

1. Output of the face detection algorithm acts as a direct input for the feature tracker algorithm.
2. As executing MTCNN algorithm is computationally expensive, using the feature tracker algorithm instead lowers the cost significantly, while maintaining the high accuracy of MTCNN.
3. Using a portion of feature tracker algorithm is also computationally less expensive than using it's whole algorithm, as identifying the good features in a frame is entirely skipped. The portion being used is also less expensive as the algorithm has to track only five feature points across frames, instead of numerous other feature points that the algorithm identifies.

A drawback of using the face detection algorithm just once during the initial phase is that KLT feature tracker cannot be relied on it's own over large number of frames, since properties of points and their corresponding windows might change over period, and actual face might be present at a different location than what the feature tracker gives as output. So accuracy suffers over time. Therefore, to tackle that problem, a frame variable n is introduced, that is defined by the programmer and acts as lever between accuracy and speed. The MTCNN algorithm is executed after every n frames, so that the face is accurately identified at that point, and then can be tracked by KLT feature tracker for n subsequent frames. n can be made to take values between programmer-defined range. Low value for n would result in higher accuracy for the framework, but speed of execution would be less, while large value of n would mean high speed of execution of the framework, but it's accuracy would be a compromised a little. Human eyes need a speed of more than 24 frames per second to register any incoming stream of images as a video. So, the ideal range of operation for n should

be >8. The higher limit can be set by the programmer in accordance with the frame rate of input video.

3.3 Extrapolation functions for occlusion resolution

The third sub-framework of the model tries to tackle the problem of occlusions among faces in a frame. This problem has existed ever since digital image processing got boost as a promising field, and researchers keep trying to find new ways of approaching this problem. This paper uses the simple mathematical concepts of interpolation and extrapolation to detect potential face position in occluded regions.

This paper compares the usage of three such interpolation/extrapolation functions in occlusion resolution by predicting approximate face regions. The functions used here are:

1. **Linear 1-D Interpolation/Extrapolation**: Here, it is assumed that the movement of the five landmark location points follows the path of a 1-D function. So first, a linear polynomial function is estimated that the path of the previous points' location follow closely, then the location of the points in the next frame is interpolated using that estimated function [8].
2. **Polynomial 1-D Interpolation/Extrapolation**: The same method as linear interpolation is followed here, except the estimate function assumed does not have to just be linear. It can be of any type of polynomial that closely resembles the path of previous frame points [5].
3. **Spline Interpolation/Extrapolation**: The Spline interpolation maps the points to a piece-wise polynomial called a spline. Interpolation is done between every pair of previous-current frame points with polynomials $y = p(i), i = 0, 1, 2....$ Then, the curvature k of the curve $y = f(x)$ is given by:

$$k = \frac{y''}{\left(1 + y'^2\right)^{\frac{3}{2}}} \tag{1}$$

To get y' and y'' continuous, it is mathematically required that

$$p_i'(x_i) = p_{i+1}'(x_i) \tag{2}$$

$$p_i''(x_i) = p_{i+1}''(x_i) \tag{3}$$

The above conditions are possible only in polynomials of degree 3 or above [6].

3.4 Experimental details

300 Videos in the Wild (300-VW) dataset is used to evaluate the proposed model's performance and compare it with other traditional and modern algorithms. The dataset contains 114 videos with various frontal head poses, expressions and illuminations. The videos have been recorded at 25–30 frames per second (fps). The video samples used from the dataset for speed and accuracy experimentation have resolutions of approximately 1280 pixels × 720 lines and 480 pixels × 360 lines respectively, and saved in uncompressed, *.avi* format. The video sample used for occulusion resolution experimentation has resolution of 1280 pixels × 720 lines, and saved in uncompressed, *.avi* format [2, 16, 19].

Table 1 Speed comparison of the model against other models, in Frames per Second FPS), for Video Sample 1

Model	Frame size	Speed (in FPS)
Viola-Jones	1280 × 720	9.002407 (i5-8300H)
MTCNN	1280 × 720	3.852317191 (i5-8300H)
HoG	1280 × 720	4.904332105 (i5-8300H)
FaceNet	1280 × 720	5.699034533 (i5-8300H)
Proposed	1280 × 720	12.12239514 (i5-8300H)

4 Experiments and results

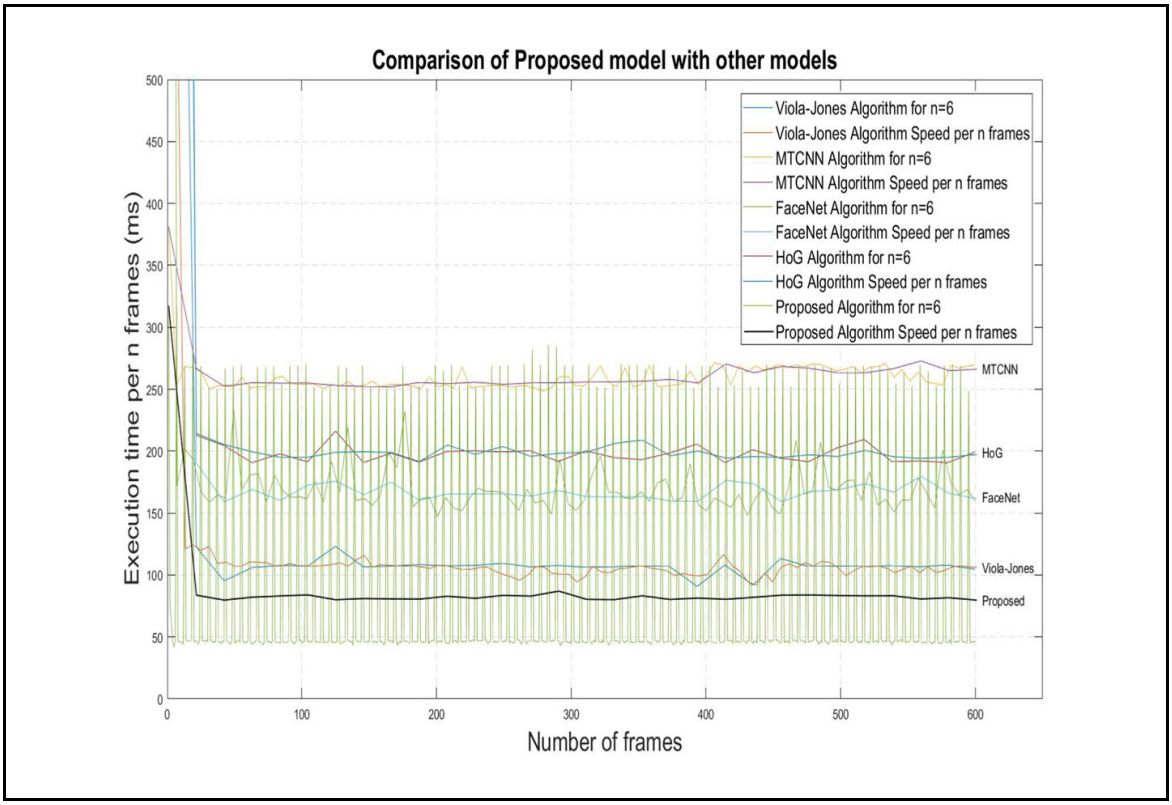
This section deals with evaluation of the proposed model on runtime efficiency, accuracy and occlusion resolution. 300 "Videos in the Wild" dataset is used to evaluate the model. Runtime efficiency and accuracy are evaluated on the videos with mostly frontal face/head pose, whereas occlusion resolution is evaluated on those videos having partial or fully occluded faces in some frames. Video Sample 1 contains more data with 1280 × 720 pixels resolution, while video sample 2 contains comparatively less data with 480 × 360 pixels resolution. We will see the difference of performance of models on both samples.

4.1 Evaluating runtime efficiency

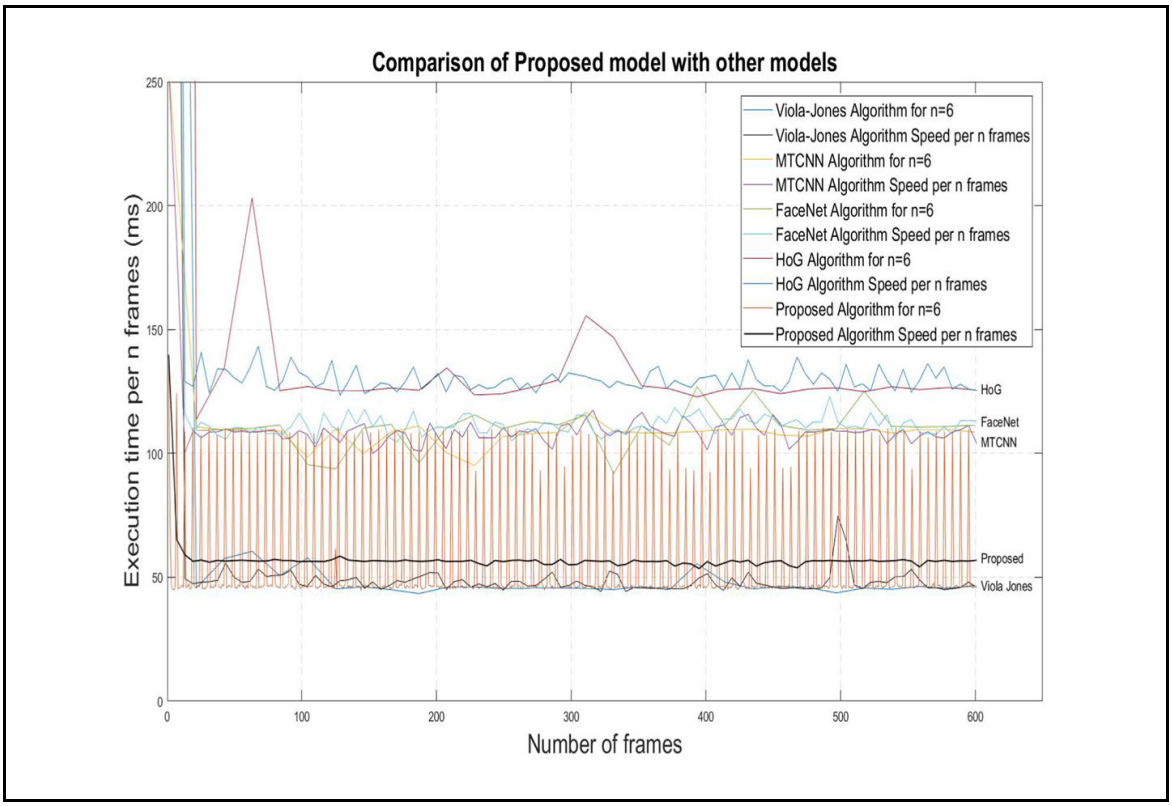
Tables 1 and 2 show the speed of the proposed model in comparison to other models for the taken video samples. It's clear from Table 1 that the proposed model is able to process more frames per second than other models for more data per frame. When we see Table 2, we notice that execution performance of all the models have increased, which is logically correct. But we see that Viola-Jones algorithm performs better than our proposed algorithm. We will see why this is not a concerning issue in the next section where we compare accuracy performances of all the models. Figure 2 shows the time that the processor takes to process each frame for a model. The Fig. 2a shows that over continuous frames, spikes appear at constant intervals (n) for our proposed model, which is dependent on the base face detection algorithm used (MTCNN here). But the time taken per n frames is the lowest for the proposed model, which implies that over a period of time, this model works averagely faster than other algorithms. This implication holds a high value in case of high quality videos, which have a lot of data stored per frame as compared to lower quality videos, and therefore each frame takes a lot of time to process by other models. We see in Fig. 2b that as video quality gets lower, better algorithms like MTCNN and the proposed model perform better and faster than other techniques, thereby confirming that state-of-the-art algorithms are dependent on the quality of the video being processed, and increase in quality results in decrease in execution speed.

Table 2 Speed comparison of the model against other models, in Frames per Second (FPS), for Video Sample 2

Model	Frame size	Speed (in FPS)
Viola-Jones	480 × 360	21.78955431 (i5-8300H)
MTCNN	480 × 360	9.619947924 (i5-8300H)
HoG	480 × 360	7.973284182 (i5-8300H)
FaceNet	480 × 360	8.852338567 (i5-8300H)
Proposed	480 × 360	17.57805462 (i5-8300H)

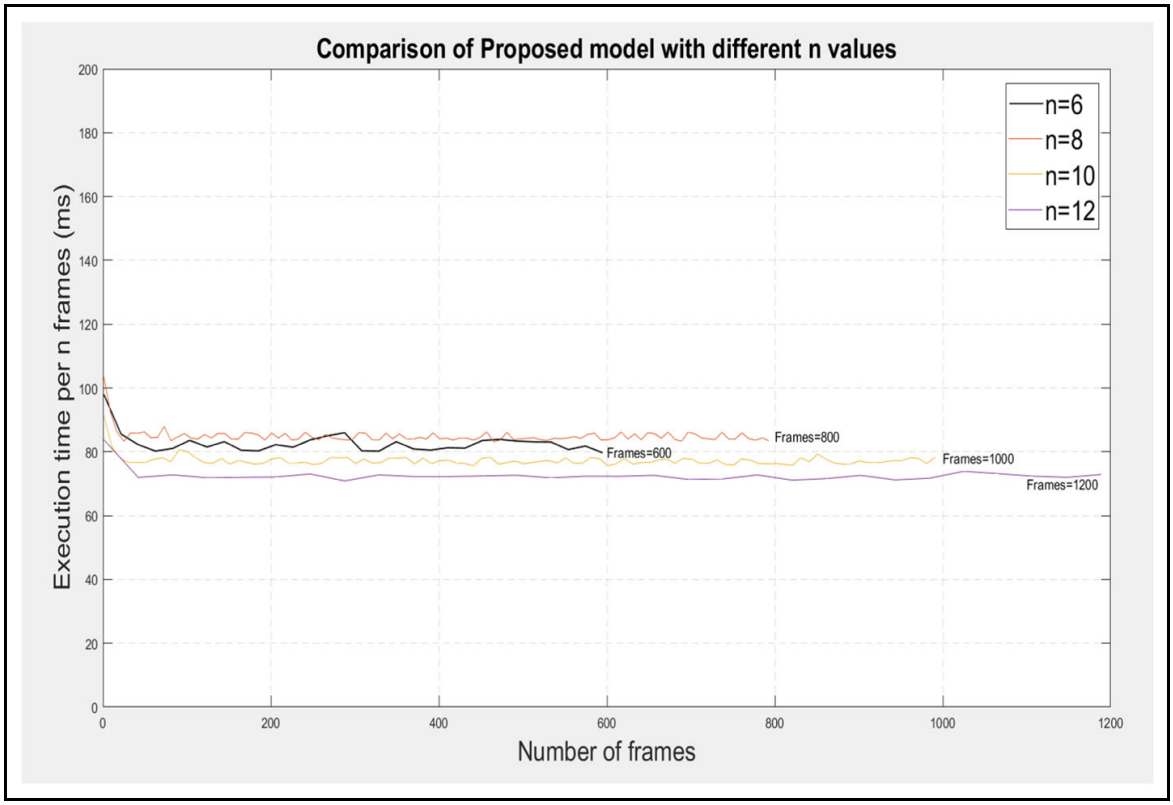


(a) Video Sample 1

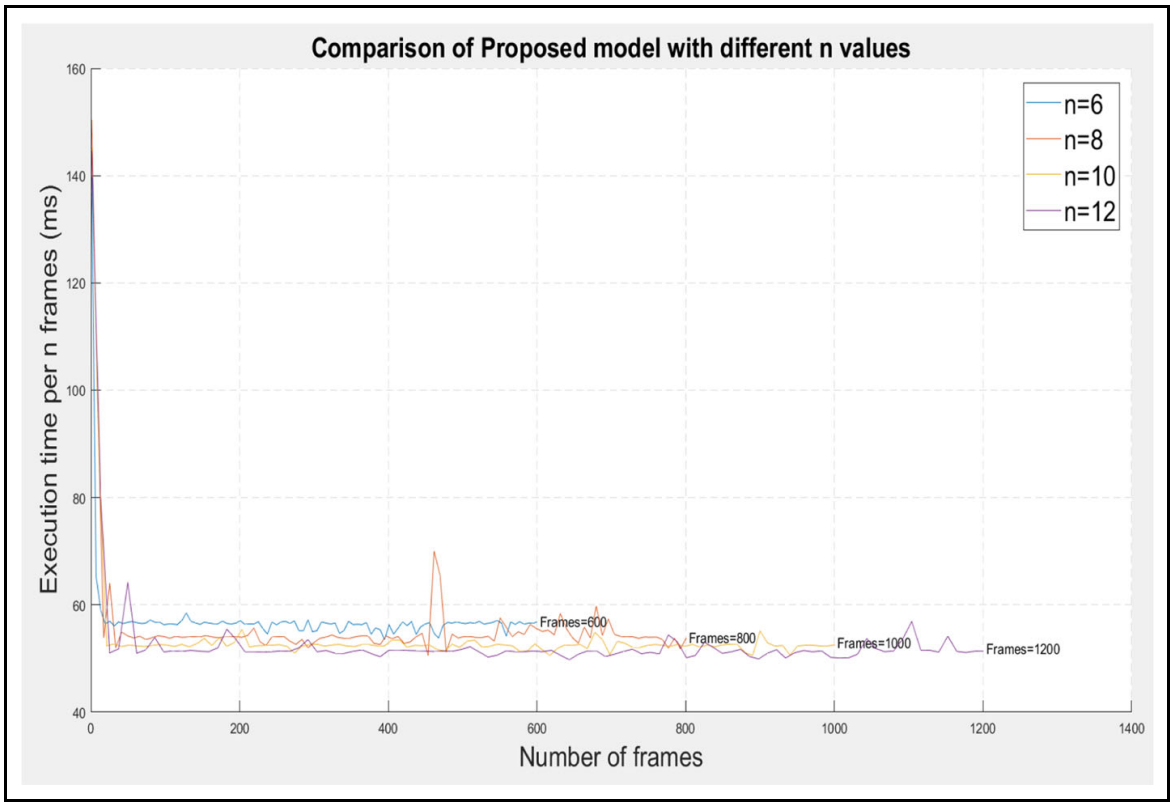


(b) Video Sample 2

Fig. 2 The Runtime performance of proposed model on 300-VW dataset compared against other models. It is seen that the proposed model is faster than other models for the given value of n; where n is the refresh rate of the Face Detection algorithm



(a) Video Sample 1



(b) Video Sample 2

Fig. 3 The Runtime performance of proposed model on 300-VW dataset for different values of n. It is seen that the proposed model gets faster as the value of n increases; where n is the refresh rate of the Face Detection algorithm

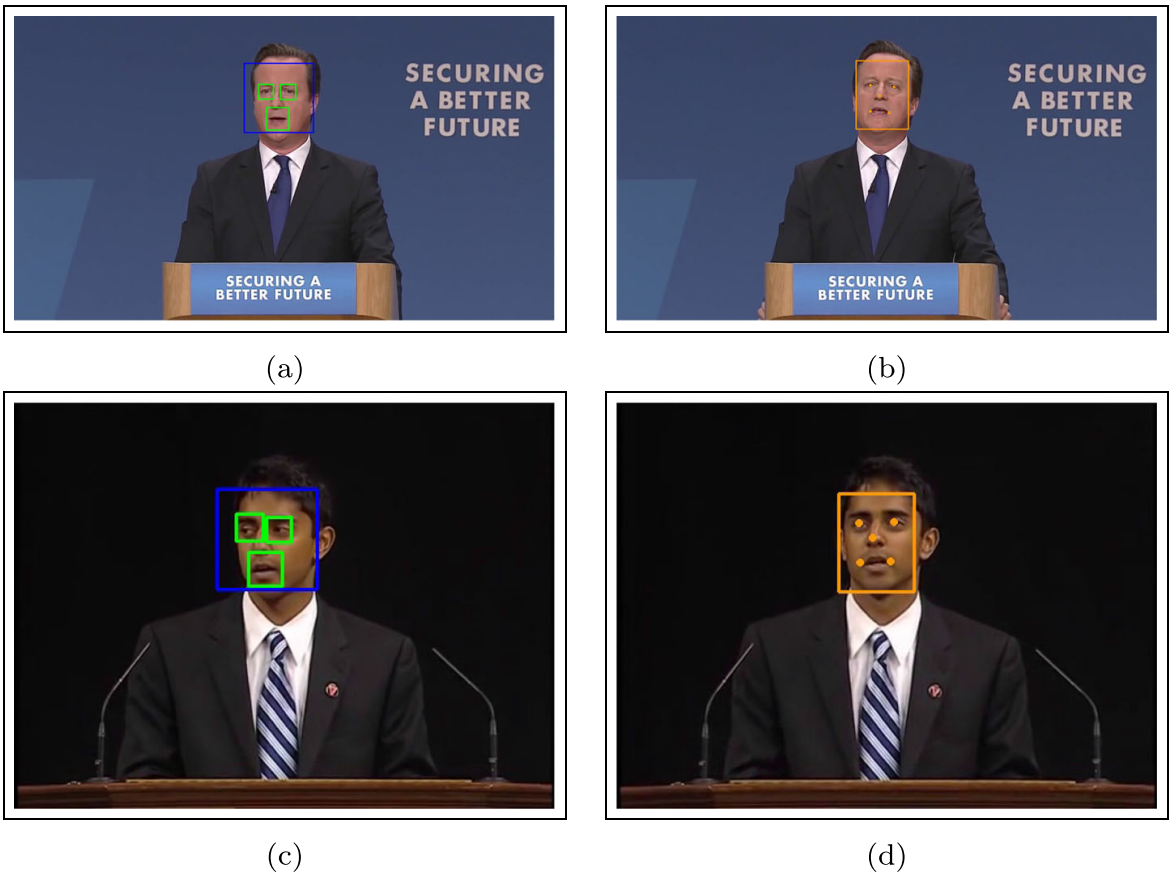


Fig. 4 Positive face frames

This improved speed of the proposed model can be attributed to the performance of the KLT feature tracking algorithm. Assuming the image intensities (brightness) of a particular region/window is denoted by *B(x,y,t)*. The pattern of motion from one frame to another is represented by:

$$B(x, y, t + t') = B(x - x', y - y', t) \tag{4}$$

The displacement from point *p=(x,y)* between time t and t' is denoted by $d = (x', y')$.

Let the local model of image to track the feature points is denoted by *R(p)*. So, initially, $R(p) = B(x, y, t + t')$. Then,

$$R(p) = B(p - d) + n(p) \tag{5}$$

where noise is denoted by n. Now, for the residue error to be minimized, the displacement vector is chosen appropriately using the following integral:

$$\epsilon = \int_r [B(p - d) - R(p)]^2 w dp \tag{6}$$

where r is the given displacement region, w is the assigned weight, and ϵ is the error to be minimized.

Here (Tables 1 and 2), the proposed model's runtime performance is compared against traditional algorithm of Viola-Jones face detection and HOG, as well as with modern algorithms of FaceNet and MTCNN face detection. The performance of Viola-Jones face detection algorithm is quite fast as compared to others, which is partly a reason why it is considered to be one of the benchmarks for other algorithms to compare their performances with. Even though the slower algorithm of MTCNN is chosen as the base algorithm for the

Table 3 Comparing the accuracy of the proposed model with other models for Video Sample 1

Model	No. of negative frames	Total no. of frames	% accuracy
Viola-Jones	343	600	57.166667
MTCNN	592	600	98.666667
HoG	558	600	93
FaceNet	550	600	91.666666
Proposed model for n = 6	555	600	92.5

proposed model, Fig. 2 shows us that averagely it performs even better than Viola-Jones algorithm over continuous bursts of frames.

Figure 3 shows the runtime performance of the proposed model for different refresh rates. Increase in refresh rate means the detected facial location landmarks are tracked over more number of frames, and therefore the speed of the proposed model increases with increase in the value of n. n cannot be too low because that would mean more frequency of calling expensive face detection algorithm, which would ultimately lead to slower overall runtime performance.

4.2 Evaluating accuracy of the proposed method

Tables 3 and 4 show the accuracy comparisons of the proposed model with other face detection models. It is seen from the tables that the accuracy of the proposed model is far greater than the traditional Viola-Jones algorithm. This is the reason why other modern algorithms like MTCNN face detection, are chosen over Viola-Jones in current times. The table shows MTCNN algorithm to have high accuracy of correctly detected faces than both the proposed model and Viola-Jones (Fig. 4). But the proposed model still has a comparative accuracy with MTCNN, which is actually the base algorithm in the proposed model. Table 4 also enforces the logical fact that experimentally, the accuracy of face detection models increases with decrease in video quality (Fig. 5).

The accuracy, α is calculated as follows:

$$\alpha = \frac{Number\ of\ negative\ frames}{Total\ number\ of\ frames\ with\ face} \tag{7}$$

Tables 5 and 6 shows that with increase in the value of n, the accuracy of the proposed model decreases. The implication made from this table is that to achieve higher accuracy, the value of n should be lower. Low n would mean that the detected facial location landmarks are refreshed more frequently, resulting in higher accuracy for the model. n cannot

Table 4 Comparing the accuracy of the proposed model with other models for Video Sample 2

Model	No. of negative frames	Total no. of frames	% accuracy
Viola-Jones	385	600	64.16666667
MTCNN	595	600	99.16666667
HoG	582	600	97
FaceNet	554	600	92.33333333
Proposed model for n = 6	571	600	95.16666667

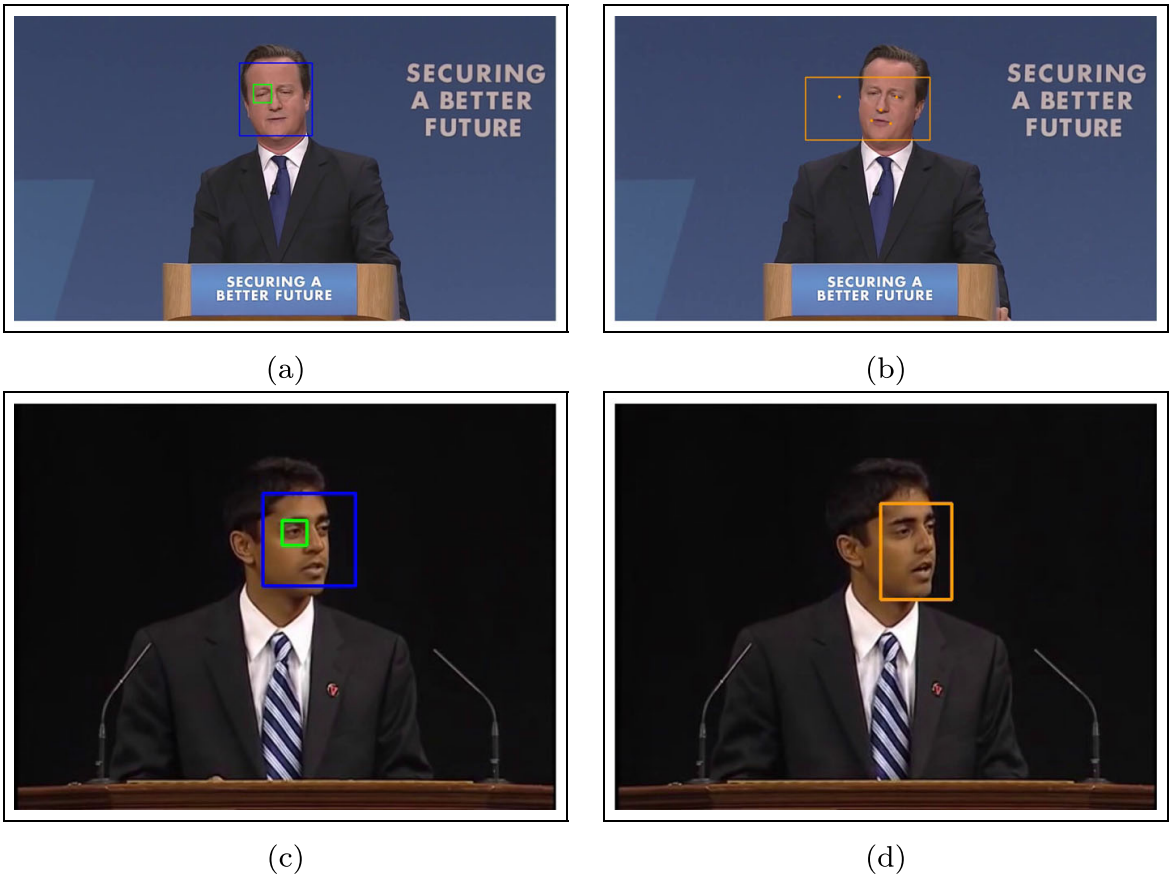


Fig. 5 Negative face frames

be too high as it would imply that too many number of frames have gone through without accurately detecting the facial landmark features, leading to lesser accuracy of the model.

Tables 7 and 8 show the efficiency and effectiveness of the proposed model. Even though some algorithms are faster than our model, while some are more accurate, no algorithm has both properties. Our model deals with this drawback and introduces a model to have faster and accurate face detection algorithms for high definition, high quality videos. The impact of n on optimizing the algorithm is shown in the tables, so that the model can be tweaked according to the requirement of the application needing more execution speed or accuracy.

4.3 Occlusion resolution by interpolation/extrapolation

Figure 6a, b and c show us how the method of interpolation/extrapolation helps in predicting the position of potential facial regions, where a face could be found. It is interesting to note that the three methods used here give us three different bounding boxes for the same facial region. So different interpolation/extrapolation techniques can be researched and used here so as to get the desired results.

Spline interpolation/extrapolation is better in most cases because the spline is tried to fit in the minimum oscillated function for corresponding data points (facial landmark positions here), which is why the spline is smoother. Other extrapolation techniques tend to oscillate a lot between data points, and therefore the predicted face window moves around sharply in their cases. It is also experimentally noted that these three methods give same bounding box for the same frame in special cases. This is because interpolation/extrapolation works on the principle of fitting preceding frame points to the closest type of function for a particular

Table 5 Comparing the effect of *n* on accuracy of the proposed model for Video Sample 1

Proposed model for	No. of negative frames	Total no. of frames	% accuracy
n = 6	555	600	92.5
n = 8	710	800	88.75
n = 10	870	1000	87
n = 12	1029	1200	85.75

Table 6 Comparing the effect of *n* on accuracy of the proposed model for Video Sample 2

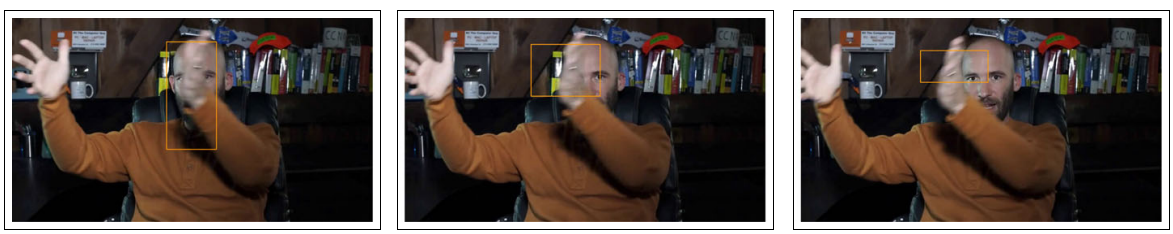
Proposed model for	No. of negative frames	Total no. of frames	% accuracy
n = 6	571	600	95.16666667
n = 8	750	800	93.75
n = 10	912	1000	91.2
n = 12	1068	1200	89

Table 7 Runtime and accuracy comparisons for different values of *n* for Video Sample 1

Proposed model for	Frame size	FPS speed	% accuracy
n = 6	1280 × 720	10.122395	92.5
n = 8	1280 × 720	11.772989	88.75
n = 10	1280 × 720	12.940982	87
n = 12	1280 × 720	13.80364	85.75

Table 8 Runtime and accuracy comparisons for different values of *n* for Video Sample 2

Proposed model for	Frame size	FPS speed	% accuracy
n = 6	480 × 360	17.72069687	95.16666667
n = 8	480 × 360	18.21308608	93.75
n = 10	480 × 360	18.93633601	91.2
n = 12	480 × 360	19.24842618	89



(a) Linear method (b) Polynomial method (c) Spline method

Fig. 6 Occlusion Resolution

method. Since the same frame points are present in all three methods, it is possible for all three methods to map them to the same function, thereby predicting the same facial window.

5 Contribution and significance of the model

This paper introduces a modified face detection and tracking technique for high quality, high data videos, so that a balance could be maintained between speed of the model with accuracy of the detected faces. This is introduced to approach towards solving the verified fact that most of the existing face detection techniques work quite well with respect to speed and accuracy for live feeds of low quality. When it comes to high definition and high quality videos, the performance of the same models decrease by a great extent. These algorithms fail to deliver fast results because data per frame is really high to be processed by the highly complex models. High accuracy at the cost of very slow speed does not do well in real-time conditions. Our proposed model speeds up the face detection process really fast while still maintaining above 90% accuracy, which makes the model usable for real-time processing.

6 Conclusion

This paper deals with three parameters of performance: runtime efficiency, accuracy of the detected faces, and occlusion resolution in between frames. Our model achieves optimal performance by trading-off between speed and accuracy. Even though the proposed model is a bit less accurate than it's base model algorithm, it compensates that with very high execution speed. Occlusion is resolved using three methods of interpolation/extrapolation, which achieve satisfactory results.

Pairo et al. [10] uses the delayed object detection to project it's detection box to the current frame and optimize it using the KLT algorithm. Our algorithm decreases the expensive computations of the face detection algorithm by using it only when required to get an accurate position of a face after n frames. Occlusion is also dealt differently by the proposed model, which predicts the existence of a face in occluded frames using the information of past frames where the face has been detected, whereas [10] rejects the existence of a detected object if any of the three types of discussed occlusions occur.

This model can be improved upon by choosing a more faster and accurate base face detection algorithm, since it's performance is still dependent on the initial face detecting algorithm chosen for the model. The refresh rate used with KLT algorithm can be substituted by some other point tracker that is faster and more accurate. Occlusion resolution can either be achieved by other techniques of extrapolation, that could predict the positions of facial landmarks locations in the current frame by utilizing previous frames' information more efficiently, or by suggesting some different predicting methods that could utilize inherent information.

Declarations

Competing interest The authors declare that they do not have any competing financial interests nor any personal relationships that could seem to have influenced the work presented by this paper.

Conflict of Interest Akshay Mool, J. Panda and Kapil Sharma declare that they have no conflict of interest.

References

1. Cao X, Wei Y, Wen F, Sun J (2012) Face alignment by explicit shape regression. In: IEEE conference on computer vision and pattern recognition, pp 2887–2894
2. Chrysos GG, Antonakos E, Zafeiriou S, Snape P (2015) Offline deformable face tracking in arbitrary videos. In: IEEE international conference on computer vision workshop (ICCVW), pp 954–962
3. Dalal N, Triggs B (2005) Histograms of oriented gradients for human detection. In: IEEE Computer society conference on computer vision and pattern recognition (CVPR'05), vol 1, pp 886–893
4. Ismail N, Sabri MIM (2009) Review of existing algorithms for face detection and recognition. In: World scientific and engineering academy and society (WSEAS), pp 30–39
5. Jia Y-B (2017) Polynomial interpolation. National Taiwan Ocean University Pub Scientific Computing
6. Li J, Song L, Liu C (2018) The cubic trigonometric automatic interpolation spline. IEEE/CAA J Autom Sin 5(6):1136–1141
7. Luo J, Liu J, Lin J, Wang Z (2020) A lightweight face detector by integrating the convolutional neural network with the image pyramid. Pattern Recogn Lett 133:180–187. [Online]. Available: http://www.sciencedirect.com/science/article/pii/S0167865520300805
8. Meijering E (2002) A chronology of interpolation: from ancient astronomy to modern signal and image processing. Proc IEEE 90(3):319–342
9. Nguyen DT, Nguyen TN, Kim H, Lee H (2019) A high-throughput and power-efficient fpga implementation of yolo cnn for object detection. IEEE Trans Very Large Scale Integr (VLSI) Syst 27(8):1861–1873
10. Pairo W, Loncomilla P, Ruiz-del Solar J (2019) A delay-free and robust object tracking approach for robotics applications. J Intell Robot Syst 95:07
11. Raja R, Sinha DT, Dubey R (2015) Recognition of human-face from side-view using progressive switching pattern and soft-computing technique. Adv Model Anal B 58:14–34, 01
12. Raja R, Sinha TS, Patra RK, Tiwari S (2018) Physiological trait-based biometrical authentication of human-face using lgxp and ann techniques. Int J Inf Comput Secur 10(2–3):303–320. [Online]. Available: https://www.inderscienceonline.com/doi/abs/10.1504/IJICS.2018.091468
13. Ranftl A, Alonso-Fernandez F, Karlsson S, Bigun J (2017) A real-time adaboost cascade face tracker based on likelihood map and optical flow. IET Biom 6:05
14. Ranjan R, Patel VM, Chellappa R (2019) Hyperface: a deep multi-task learning framework for face detection, landmark localization, pose estimation, and gender recognition. IEEE Trans Pattern Anal Mach Intell 41(1):121–135
15. Schroff F, Kalenichenko D, Philbin J (2015) Facenet: a unified embedding for face recognition and clustering. In: 2015 IEEE Conference on computer vision and pattern recognition (CVPR). [Online]. Available: https://doi.org/10.1109/CVPR.2015.7298682
16. Shen J, Zafeiriou S, Chrysos GG, Kossaifi J, Tzimiropoulos G, Pantic M (2015) The first facial landmark tracking in-the-wild challenge: Benchmark and results. In: IEEE international conference on computer vision workshop (ICCVW), pp 1003–1011
17. Singh S, Singh D, Yadav V (2020) Face recognition using hog feature extraction and svm classifier. 8:6437–6440, 09
18. Tomasi C, Kanade T (1991) Detection and tracking of point features. Int J Comput Vis
19. Tzimiropoulos G (2015) Project-out cascaded regression with an application to face alignment. In: IEEE conference on computer vision and pattern recognition (CVPR), pp 3659–3667
20. Viola P, Jones M (2004) Robust real-time face detection. Int J Comput Vis 57:137–154, 05
21. Yang M-H, Kriegman DJ, Ahuja N (2002) Detecting faces in images: a survey. IEEE Trans Pattern Anal Mac Intell 24(1):34–58
22. Yang B, Yan J, Lei Z, Li SZ (2014) Aggregate channel features for multi-view face detection. In: IEEE International joint conference on biometrics, pp 1–8
23. Yu B, Tao D (2019) Anchor cascade for efficient face detection. IEEE Trans Image Process 28(5):2490–2501
24. Zeng D, Zhao F, Ge S, Shen W (2019) Fast cascade face detection with pyramid network. Pattern Recogn Lett 119:180–186. [Online]. Available: http://www.sciencedirect.com/science/article/pii/S0167865518302125
25. Zhang K, Zhang Z, Li Z, Qiao Y (2016) Joint face detection and alignment using multitask cascaded convolutional networks. IEEE Signal Process Lett 23(10):1499–1503

Publisher's note Springer Nature remains neutral with regard to jurisdictional claims in published maps and institutional affiliations.

Biomass Conversion and Biorefinery
https://doi.org/10.1007/s13399-022-02444-x

ORIGINAL ARTICLE

Optimization of long-term storage stability of Kusum biodiesel using herbal anti-oxidant

Harveer Singh Pali[1] · Abhishek Sharma[2] · Naveen Kumar[3] · Yashvir Singh[4]

Received: 15 November 2021 / Revised: 27 January 2022 / Accepted: 6 February 2022
© The Author(s), under exclusive licence to Springer-Verlag GmbH Germany, part of Springer Nature 2022

Abstract

Currently, biodiesel is proclaimed as alternative fuel for compression ignition engines. However, poor oxidation stability of biodiesel is the major challenge for long-term storage of biodiesel. The oxidative nature of fuel degrades the viscosity, calorific value, acid value, and so on. Still, antioxidants provided satisfactory results. Ginger powder has good antioxidant properties. The present study explored the possibility to improve storage stability with the major characteristics of biodiesel fuel like calorific value, acid value, kinematic viscosity, and peroxide value. The response surface methodology (RSM) optimization has been employed and process parameters were taken as storage time, exposure temperature, and blending ratio and ginger antioxidant. For test fuels, oxidation stability results data was obtained by the EN14112 reference method Rancimat. The interaction plots have been shown in the present work and got 31.3% biodiesel blend, 676.7 ppm concentration of ginger, 120 °C exposure temperature, and 4.24 months storage time. After analysis, RSM optimizer results of calorific value, viscosity, acid value, and induction period were 42 MJ/kg, 3.3 cSt, 0.176 mgKOH/g, and 16 h respectively. Validation has been done through experimental trails and found satisfactory limits. So, ginger is explored as a novel antioxidant at variable concentration and found satisfactory for biodiesel fuel storage.

Keywords Ginger · Induction period · Natural antioxidant · Oxidation stability · RSM optimization

Nomenclature

BHA	Butylated hydroxyanisole
BHT	Hydroxyl toluene
TBHQ	Tert-butyl hydroquinone
PG	Propyl gallate
IP	Induction period
CCRD	Central composite rotating design
CC	Catalyst concentration
CI	Compression ignition
CFPP	Cold filter plugging point
cSt	Centistoke
CN	Cetane number
CV	Calorific value
g/kg	Gram per kilogram
g/cc	Gram per cubic centimeter
EN	European Standards
KME	Kusum biodiesel
D	Neat diesel
BSEC	Brake-specific energy consumption
BSFC	Brake-specific fuel consumption
BTE	Brake thermal efficiency
HCs	Hydrocarbons
Hr.	Hour
KOH	Potassium hydroxide
MR	Molar ratio
MJ/kg	Megajoule per kilogram
p-value	Probability value
RSM	Response surface methodology
RT	Reaction time
TBOs	Tree brone oils
% w/w	% Weight/weight
ASTM	American Society for Testing and Materials
CCRD	Central composit central design
FFA	Free fatty acid
PY	Tri-hydroxy benzene

✉ Yashvir Singh
yashvirkankara21@gmail.com

[1] Department of Mechanical Engineering, National Institute of Technology, Srinagar, India

[2] Department of Mechanical Engineering, G L Bajaj Institute of Technology and Management, Greater Noida, UP, India

[3] CASRAE, Delhi Technological University, Delhi, India

[4] Department of Mechanical Engineering, Graphic Era Deemed To Be University, Dehradun, Uttarakhand, India

Published online: 15 February 2022

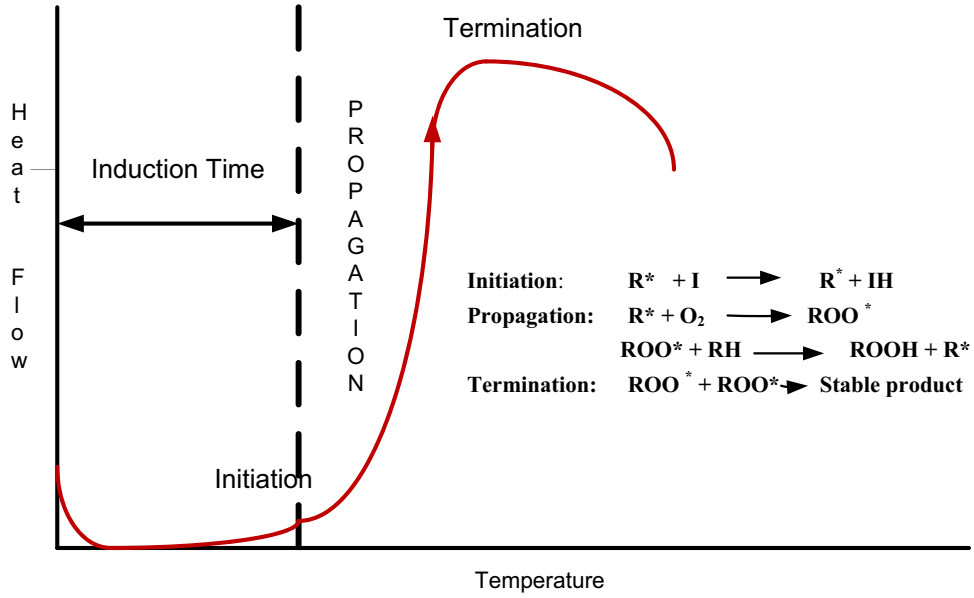


Fig. 1 Oxidation stages [16, 17]

1 Introduction

Biodiesel is a well-known alternative to diesel for an effective compression ignition (CI) engine due to its environment friendliness and its extraction from renewable sources. Biodiesel can be obtained from various feedstocks such as rapeseed oil [1], soybean oil [2], sunflower oil [3], palm oil [4], Jatropha [5], neem oil [6], and animal fat [7]. It is advantageous to use biodiesel in a CI engine as they are bio-degradable, non-toxic, and sulfur-free aromatic hydrocarbons [8]. The main problem with biodiesel is its cold flow behavior and oxidation stability which is primarily dependent upon its unsaturated content [9, 10]. After a long time has passed in storage, the esters in the biodiesel oxidize to form insoluble gums and deposits leading to filter plugging. The oxidation is accelerated when the biodiesel is exposed to sunlight and high-temperature conditions. The reaction leads to the formation of gums and darkening of the color of the fuel of biodiesel. Some parameters required to be studied for a better understanding of the evaluation of oxidation stability are iodine value, induction period, peroxide value, viscosity, oil stability index, acid value, fatty acid methyl ester content, density, etc. These parameters have a direct or indirect effect on the fatty acid composition of biodiesel [11–13]. Besides, the mechanism of oxidation is based on a fatty acid chain reaction [14].

The biodiesel oxidation is taking place under three steps viz. initiation, propagation, and termination. As the oxidation starts on its own, the reaction is called auto-oxidation. In the first step, the carbon atom present near the double bond gives its hydrogen atom resulting in the formation of carbon free radical (R^*). The radical reacts with the oxygen to form a peroxide free radical (ROO*). The peroxide radical can easily abstract the hydrogen atom from the carbon atom to form a hydroperoxide (ROOH) and a carbon free radical (R^*). The reaction propagates as the free radical formed reacts with oxygen. When two free radicals combine, the reaction is terminated and a stable compound is formed [15]. All three stages like initiation, propagation, and termination are shown in Fig. 1.

Oxidation stability of biodiesel is derived from different feed stocks evaluated by the induction period (in hour). After a certain length of time (induction period), the concentration of ROOH increases, thus implying that the oxidation process has started.

To increase the shelf life of biodiesel, antioxidants are added in small quantities to reduce its premature oxidation. The influence of vitamin E, BHA, TBHQ, BHT, and PG on the oxidation stability of used frying oil biodiesel was studied by Loh et al. [18]. The biodiesel was mixed with various concentrations of the antioxidants. As the antioxidant concentration increased, the oxidation stability increased. The oxidation stability decreased by 10–20% with vitamin E, 8–15% with BHT, 22–35% with TBHQ, 7–10% with BHA, and 3–15% with PG. The authors also observed that the biodiesel was stable and met the stability requirements after long-term storage when the antioxidants' concentration was above 500 ppm. The peroxide content and kinematic viscosity of mahua oil biodiesel stored for a period of 1 year in different storage conditions was studied by Bora et al. [19]. After a year of storage, the peroxide values for the samples that were open to air but inside the room and exposed to metal are high[26] indicating reduction in oxidation stability. The same samples also showed higher increase in viscosity.

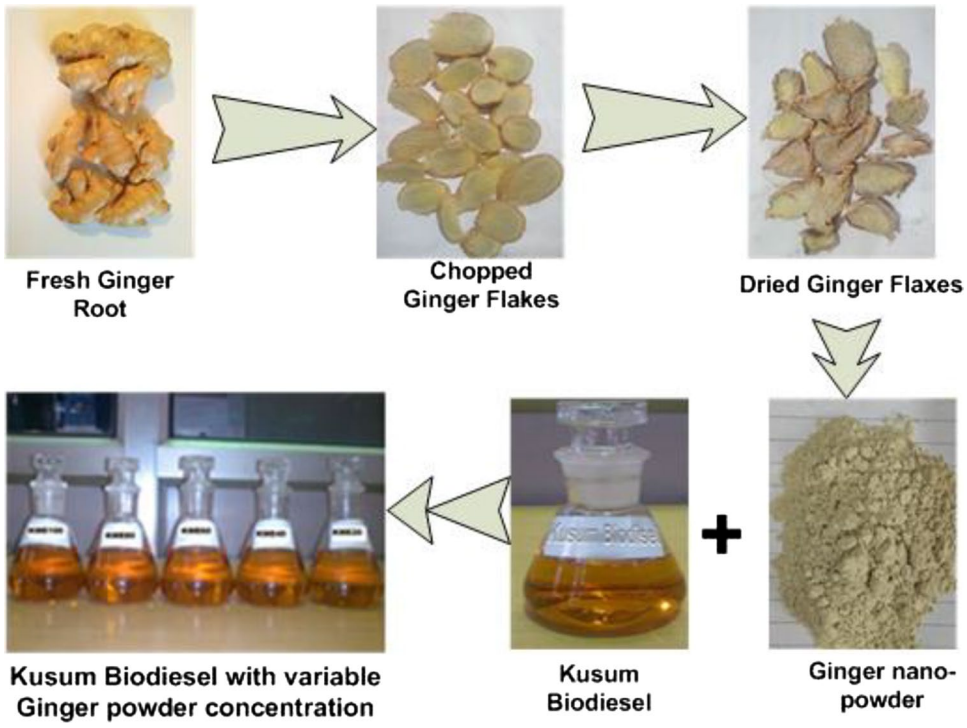


Fig. 2 Preparation of test fuels with variable concentration of ginger antioxidants

In another study, karanja oil was used [20] and the oxidants used were BHT, BHA, TBHQ, PG, and 1,2,3 tri-hydroxy benzene (PY). Initially, PY followed by PG was stable for a minimum period of 6 h. After 4 months, samples containing PY above 500 ppm and PG concentration above 700 ppm were stable. Biodiesel samples containing TBHQ, BHT, and BHA were not stable for longer durations. The authors conducted another study wherein the samples were exposed to different conditions. The induction period of samples exposed to air and sunlight reduced drastically in the first 10 days. However, the samples stored indoors maintained the oxidation stability even after 60 days. The samples that were stored in metal containers degraded faster than those that were not stored in metal containers, more so for copper containers as compared to steel containers.

Ryu [21] tested the oxidation stability of soybean biodiesel using a natural antioxidant alpha-tocopherol, and BHT, BHA, TBHQ, and PG at various concentrations. It was observed that 100 ppm of TBHQ and 300 ppm of PG passed the 6-h stability test. The authors also observed reduction in[42] brake-specific fuel consumption (BSFC) with antioxidants doping in comparison to neat biodiesel. However, the decrease in BSFC due to the variation in antioxidants' concentration does not follow a specific trend. Moreover, the antioxidants and their concentration have no effect on engine combustion and emissions.

Table 1 Main physico-chemical properties of Kusum biodiesel (KME)

Fuel property	Unit	Limits	Standard	Diesel	KME
Density at 15 °C	g/cm^3	0.85–0.89	D1298	0.8327	0.8967
Kinematic viscosity at 40 °C	mm^2/s (cSt)	1.9–6.0	D445	3.23	5.91
Calorific value	MJ/kg			44.7	39.11
Flash point	°C	130 (min.)	D93	65	148
Cloud point	°C		D 2500	− 16	2
Pour point	°C		D 97	− 20	0
CFPP	°C		D6371	− 15	− 1
Copper strip corrosion	Rating	No. 3 (min.)	D130	1a	1a
Oxidation stability at 110 °C	Hours	6 (min.)	EN 14,112	–	2.1
Acid value	mgKOH/g	0.5 (max.)	D664	–	0.13
Peroxide value	meq/kg			–	20.1
Ester content	% mass		EN14105	–	96.5

Varatharajan et al. [22] found reduced NOx emission and increased BSEC by using various antioxidants in different concentrations by weight. Similarly, the NOx emissions were reduced by Ashok et al. [23] using ethanox and butylated hydroxyl toluene mixed with *Calophyllum inophyllum* biodiesel in various concentrations. The oxides of nitrogen emission as compared to neat biodiesel reduced by 12.6% with ethanox at 1000 ppm concentration, whereas it reduced by 21% with butylated hydroxyl toluene at 500 ppm concentration. So unsaturated esters have relatively poor storage stability under pro-oxidizing condition and air exposure [13]. Some properties increased with time like acid value, peroxide value, caloric value, and viscosity. So additives, antioxidants, and stabilizers are frequently added to prevent fuel degradation and prolong storage life of fuels [4].

American standards (ASTM D6751), European biodiesel standards (EN 14,213 and EN 14,214)[27], and Indian standards biodiesel (IS 15607) use the Rancimat test method (EN 14,112) to evaluate oxidation stability of biodiesel [24]. In the Rancimat test method, peroxide values are measured in milliequivalents of peroxide per kilogram of sample for each sampling period. Many researchers found relative susceptibility ratio of oxidation instability of unsaturated fatty acids in the fuels [13, 25, 26]. As per Rizwanul et al., this ratio was 1:12:25 for oleic (C18:1), linoleic (C18:2), and linolenic (C18:3) acid methyl esters [27]. However, in another study, Hazrat et al. had found 1:41:98 for the same unsaturated fatty acids [16]. When biodiesel comes in contact with air or water, then unsaturated fatty acid and double-bond molecules react with oxygen. The primary products break up and react to form the secondary product. Primary products are unstable allylic hydroperoxides and secondary formed products are aldehydes, formic acid, short-chain fatty acid, format esters, and higher weight molecular material.

Additives are generally used in biodiesel to take benefit in different ways. Additives enhance properties of biodiesel by improving low-temperature flow characteristics, combustion performance, and emission [15]. These additives are metal-based, oxygenated, cetane number improver, antioxidants, cold flow improvers, lubricant, etc. Selection of additives among these is based on blending properties of biodiesel like viscosity, toxicity of blend fuel, and solubility of additives [28]. Most of the properties of biodiesel are quite similar to those of petroleum diesel apart from viscosity, cold flow property, and long-term storage stability or oxidation stability. Cold flow property and viscosity can mitigate through blending of alcohols and diesel. But long storage stability is the main challenge in the utilization and commercialization.

Table 2 Test fuel samples nomenclature

S. no	Nomenclature	Test fuel sample AxByCz (%Kusum biodiesel + %Diesel + antioxidant in ppm)
1	KME100B200	100% Kusum biodiesel + 200 ppm ginger nano-powder
2	KME80D20B200	80% Kusum biodiesel + 20% diesel + 200 ppm ginger nano-powder
3	KME60D40B200	60% Kusum biodiesel + 40% diesel + 200 ppm ginger nano-powder
4	KME40D60B200	40% Kusum biodiesel + 60% diesel + 200 ppm ginger nano-powder
5	KME20D80B200	20% Kusum biodiesel + 80% diesel + 200 ppm ginger nano-powder
6	KME100B400	100% Kusum biodiesel + 400 ppm ginger nano-powder
7	KME80D20B400	80% Kusum biodiesel + 20% diesel + 400 ppm ginger nano-powder
8	KME60D40B400	60% Kusum biodiesel + 40% diesel + 400 ppm ginger nano-powder
9	KME40D60B400	40% Kusum biodiesel + 60% diesel + 400 ppm ginger nano-powder
10	KME20D80B400	20% Kusum biodiesel + 80% diesel + 400 ppm ginger nano-powder
11	KME100B600	100% Kusum biodiesel + 600 ppm ginger nano-powder
12	KME80D20B600	80% Kusum biodiesel + 20% diesel + 600 ppm ginger nano-powder
13	KME60D40B600	60% Kusum biodiesel + 40% diesel + 600 ppm ginger nano-powder
14	KME40D60B600	40% Kusum biodiesel + 60% diesel + 600 ppm ginger nano-powder
15	KME20D80B600	20% Kusum biodiesel + 80% diesel + 600 ppm ginger nano-powder
16	KME100B800	100% Kusum biodiesel + 800 ppm ginger nano-powder
17	KME80D20B800	80% Kusum biodiesel + 20% diesel + 800 ppm ginger nano-powder
18	KME60D40B800	60% Kusum biodiesel + 40% diesel + 800 ppm ginger nano-powder
19	KME40D60B800	40% Kusum biodiesel + 60% diesel + 800 ppm ginger nano-powder
20	KME20D80B800	20% Kusum biodiesel + 80% diesel + 800 ppm ginger nano-powder
21	KME100B1000	100% Kusum biodiesel + 1000 ppm ginger nano-powder
22	KME80D20B1000	80% Kusum biodiesel + 20% diesel + 1000 ppm ginger nano-powder
23	KME60D40B1000	60% Kusum biodiesel + 40% diesel + 1000 ppm ginger nano-powder
24	KME40D60B1000	40% Kusum biodiesel + 60% diesel + 1000 ppm ginger nano-powder
25	KME20D80B1000	20% Kusum biodiesel + 80% diesel + 1000 ppm ginger nano-powder

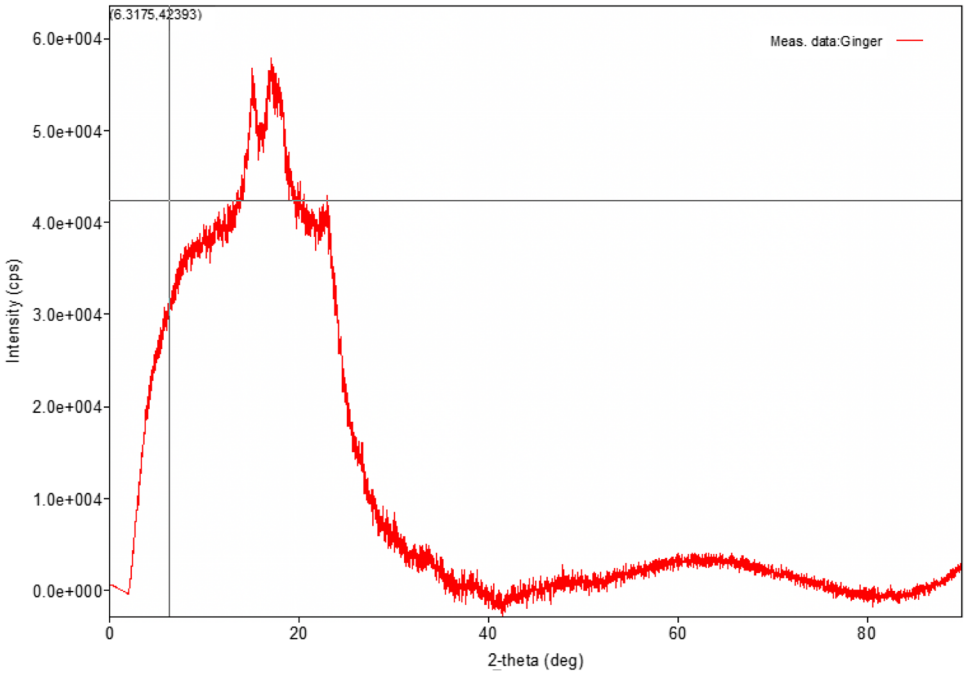
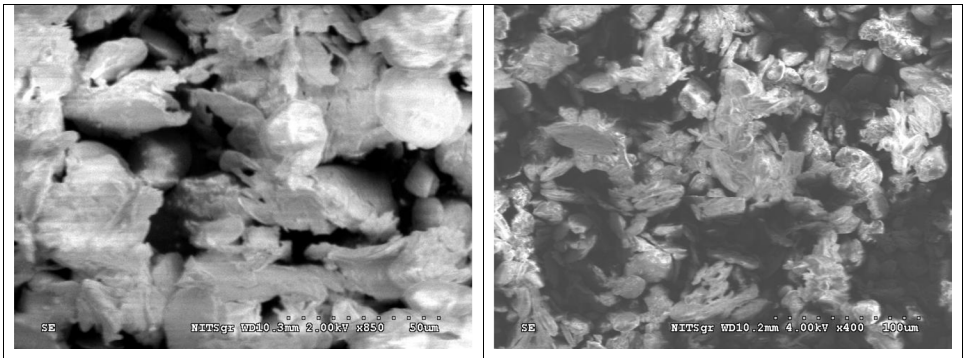


Fig. 3 XRD of ginger powder



SEM image of ginger powder at 50 µm | SEM image of ginger powder at 100 µm

Fig. 4 SEM images of ginger nano-powder

Table 3 Different coded stages

Biodiesel inputs	Coded stages				
	−2	−1	0	1	2
Blend (%)	20	40	60	80	100
Concentration (ppm)	200	400	600	800	1000
Exposure temperature (°C)	100	105	110	115	120
Storage time (months)	0	3	6	9	12

Table 4 Uncertainties associated with the measurements

Instruments	Accuracy	% Uncertainty
Temperature sensor	±1 °C	±0.2%
Rancimat instrument	±0.01 h	±0.5%
Weighing balance	±0.001 kg	±0.3%
Fuel burette	±1 ml	±1.0%
Watch	0.0002 h	±0.5%

However, saturated mono alkyl esters were found less susceptible to the unsaturated mono alkyl esters [29]. The composition and degree of unsaturation of oil are not altered even after transesterification into biodiesel. Hence, all biodiesels are prone to oxidation due to exposure with air, sunlight, and high temperature. Long-term storage is also a cause of oxidation. Literature review shows that long-term usability of biodiesel can be improved by antioxidants, metal oxides, free fatty acid (FFA), humidity, and storage temperature. Along with relations between governing fatty acid

Table 5 Experimental result after implementing CCRD

Exp. run	Blend (%)	Concentration ppm	Exposure temp (°C)	Storage time (in months)	IP (h)	AV (mgKOH/g)	Viscosity (cSt)	Calorific value (MJ/kg)
1	80	800	115	9	7.3	0.4	4.8	40.2
2	60	600	110	6	10.6	0.2	4.1	41.36
3	60	600	110	6	10.2	0.2	4.2	41.4
4	60	600	120	6	9.5	0.2	4.3	41.2
5	80	400	115	3	11.5	0.25	4.9	40.8
6	40	400	115	3	12.8	0.15	3.4	41.8
7	60	600	115	3	12.1	0.2	3.9	41.5
8	40	400	105	9	10.2	0.3	4.3	41.6
9	40	400	115	3	13.5	0.22	3.7	41.7
10	60	600	110	0	12.1	0.18	3.6	41.5
11	60	600	110	6	10.4	0.2	4.4	41.36
12	60	600	100	6	13.4	0.28	4.2	41.2
13	40	800	105	9	15.1	0.35	4.4	41.6
14	60	600	110	6	10.25	0.2	4.2	41.33
15	60	600	110	12	5.1	0.41	5.9	39.8
16	80	800	105	3	9.2	0.32	4.5	40.7
17	40	800	115	9	8.4	0.31	4.6	41.5
18	20	600	110	6	14.4	0.12	3.4	42.2
19	40	800	115	3	16.2	0.18	3.3	41.9
20	60	200	110	6	8.2	0.28	4.1	41.3
21	60	1000	110	6	18	0.31	4.4	41.4
22	40	400	115	9	12.4	0.29	4.7	41.7
23	60	600	120	6	10.36	0.2	4.3	41.28
24	60	600	120	6	10.38	0.2	4.2	41.3
25	80	400	105	9	9.4	0.44	4.9	40.5
26	80	800	105	9	15.1	0.48	5.1	40.6
27	80	400	115	9	11.2	0.41	5	40.4
28	40	800	105	3	10.4	0.32	4.8	41.9
29	60	600	120	6	10.3	0.2	4.4	41.34
30	80	400	105	3	12.5	0.34	4.7	40.6
31	100	600	110	6	7.8	0.42	5.1	39.6

constituents and its properties, the fuel storage characteristics are also expressed. Oxidation stability is crucial for biodiesel property in industrial applications. So, the quest of renewable nature-based and herbal antioxidant compounds is to enhance storage stability with desired specifications. However, commercially available synthetic and fossil-based feedstock increase the production cost. Along with some toxicological studies of synthetic compounds are carcinogenic effects. But synthetic antioxidants are restricted in some countries. So renewable and herbal antioxidants can be employed to overcome this challenge. The main objective of the present work was employed to design experiments and optimize the process parameters for good-quality storage of biodiesel using nature-based antioxidants like ginger.

2 Materials and methods

Since synthetic antioxidants are not good for engine health, it is essential for the biodiesel industry to explore non-toxic, renewable, and cost-effective antioxidants. In this context, extensively available herbal ginger root are employed as antioxidants for the current work. Ginger biomass contains a significant amount of phenolic compounds that have antioxidant properties. The chemical structures of biodiesels are the main issue to control the stability of the fuel. It is successfully employed to enhance the oxidation stability of biodiesel [30]. Ginger is an extensively available herbal root product in tropical countries like India. Its strong compounds include gingerols, shogaols, paradols, and zingerone [31].

The fresh ginger roots (*Zingiber officinale* Rosc.) were procured from the local market of Srinagar (J&K), India. Ginger was washed with water, and sliced and dried in a solar dryer 60 °C for 6 h. After that, ginger root nano-powder was produced by a ball mill. Analytical grade chemicals were bought from Sigma and Sons Delhi. The preparation of the test fuels with ginger antioxidant is presented as Fig. 2. Kusum biodiesel is produced through Kusum oil. Raw oil of Kusum was procured through a local vendor in Cuttack, Odisha (India). Kusum biodiesel was produced through transesterification process in a previous work reported by Pali et al. [32–34]. The quality of biodiesel is ensured by various standards like EN/ASTM as shown Table 1. Fatty acid profile of Kusum biodiesel has been investigated in previous work and it was found that 32.61% was saturated and 64.19% was unsaturated [32]. Oxidation stability is determined by Rancimat method (EN14112) and ASTM standards D-6751 at 110 °C with a minimum IP (induction period) of 6 h; however, it was found to be 2.1 h for the Kusum biodiesel and less than 1 h for 1-year-old Kusum biodiesel. Therefore, it was necessary to improve the IP of Kusum biodiesel. After the addition of nano-ginger powder, it was found that all characteristics were satisfactory and stable (Table 2).

After quality assurance of produced biodiesel, test fuel samples were prepared. Three types of constituents are present in the test fuels. It can be designated as A*x*B*y*C*z* (*x* means volume fraction Kusum biodiesel (KME), *y* means volume fraction of diesel (100-*x*), and *z* means ppm of aluminum oxide nanoparticles) which are developed for this experimental study. Nomenclature is shown in Table 1. To identify the antioxidant compounds of ginger, X-ray diffraction pattern has been carried out in nano-ginger powder as shown in Fig. 3. It presented three high peaks at 2 h value of around 18, 22, and 28 respectively. Some unassigned peaks were also observed in the area of the three high peaks in nano-ginger ginger powder. The present graph shows sharp Bragg peaks that confirmed some bioorganic compounds present in the nano-ginger powder.

To disclose the morphology of the ginger nano-powder, scanning electron microscopy (SEM) has been carried out. It gives clear indication of solid masses as shown in Fig. 4. The SEM image revealed irregular morphology and regular unidimensional pore system (Table 3).

2.1 Errors and uncertainty analysis

Uncertainties occur as a result of mistakes made while obtaining readings at various parameters like temperatures, humidity, time, and concentration. Generally, this happens due to poor instrument calibration and a variation of operating conditions. It is the gap between the observed value and the actual value. Error and uncertainty in the measurement system are based on several variables, including instrument calibration, apparatus selection, monitoring reading and execute test process and ambient conditions. Thus, the uncertainty of the equipment must be calculated to demonstrate the precision of the findings produced. Table 4 shows the average error estimates for various parameters. The measurement equipment uncertainty test was performed using the Holman standard technique. By applying the following equation, the total uncertainty analysis of the experiment has been found [35, 36]. Total percentage of uncertainty = ±2.13%, i.e., within the range.

$$\text{Overall uncertainty (\%)} = \text{Square root of } [(0.2)2 + (0.5)2 + 0.3)2 + (1)2 + (0.5)2 = \pm 1.276\%$$

3 Result and discussion

In the current research, biodiesel fuel blends, ginger antioxidant concentration, exposure temperature, and storage time were considered process parameters as shown Table 3. In conjunction with induction period, acid value, viscosity, and calorific value were taken as responses of optimization and experimental results are shown in design matrix Table 5.

3.1 Impact of process parameters on viscosity response

Viscosity is one of the most significant parameters of biodiesel quality and depends on the fatty acid composition of oil. It varies with chain length and the degree of saturation of fatty acids. Mainly, FFAs are responsible for enhancement of viscosity. An acceptable range was considered by ASTM D6751 using method D445 and prescribed limits 1.9 to 6 cSt, since oxidation processes start the formation of FFAs. Moreover, oxidation is directly coupled with storage time and concentration of biodiesel or percentage of blend in fuel. Figure 5a, c, and d depicted the effects of storage time in months. Storage time nonstop increases the viscosity of fuel due to the insoluble formation and contamination but addition of ginger antioxidant retracted these undesirable formations. Hence, the rate of deterioration is slow and remains in the acceptable range as shown in Fig. 5b and c. However, increase in concentration of ginger antioxidant attributed to decreased oxidation process, since higher oxidation process is a prime factor to enhance FFAs, isomerization of double bond (usually cis to trans). Surface plot of viscosity with respect to the storage time and biodiesel blend is shown in

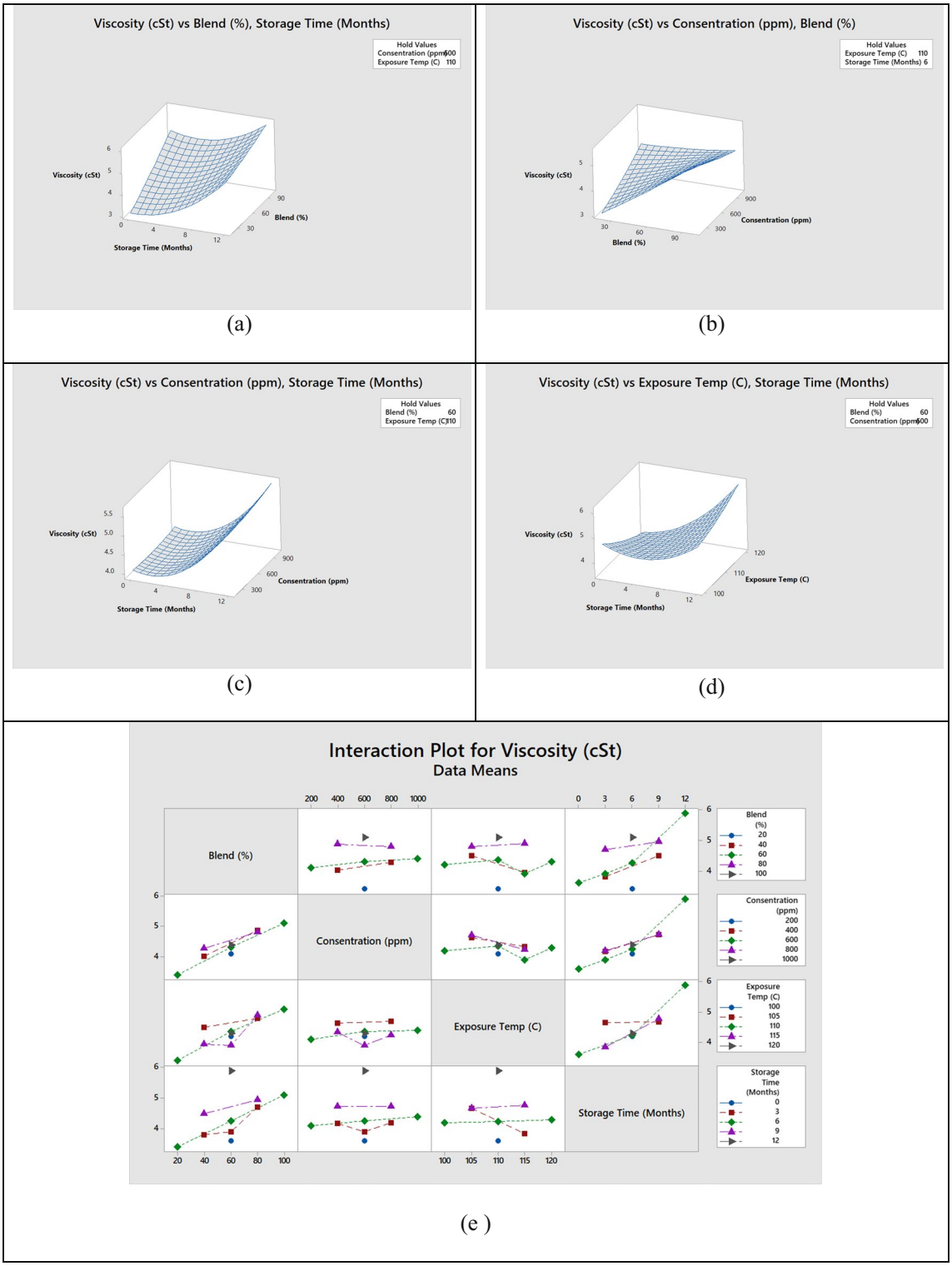


Fig. 5 **a-e** Effect of process parameters on viscosity

the Fig. 5a and interaction plot in Fig. 5e. It shows that viscosity increases with increase of storage time and blending ratio. However, the ginger powder retarders the viscosity as shown in Fig. 5b. Interaction plots show the significance of the process parameters on viscosity. Exposure temperature does not significantly affect viscosity as shown in Fig. 5e. Similar type findings were endorsed by a previous work [24].

3.2 Impact of production parameter on IP

Induction period is the time over and done until the secondary oxidation is identified. Oxidation stability of fuel is measured by induction period. It is an extremely important parameter for quality control and determined by the measurement of sudden increase of conductivity upon the development of volatile matters. It is expressed as the time required to reach the point at which the degree of oxidation increases considerably. It was evaluated as per the EN 14,112 Rancimat method. All the measurements of IP have been carried out by Metrohm 873 Biodiesel Rancimat instrument. IP was specified when the conductivity starts to surge. Parameters such as cetane number, density, and viscosity are affected by the peroxide value; for example, the cetane number increases with increase in peroxide value [37]. It was observed that the addition of ginger nano-powder exhibited good results and slowed down the oxidation of the biodiesels. Figure 6 shows the effect of phenolic content or ginger nano-powder with storage time, blending ratio, and exposure temperature. Phenolic content reacts with the peroxide radical and prevents the peroxide radical from forming the free radical, thus delaying the oxidation process [38]. Four experimental conditions are shown in Fig. 6. It is observed that storage time affects more than blending ratio. Effects of the blending ratio and storage time with induction period are illustrated in Fig. 6a. It is clearly depicted the decline in induction period with respect to blending % and storage time in months. The influence of exposure temperature on the induction period is significant and shown in Fig. 6d. Effect of ginger powder concentration with blending ratio and storage time is shown in Fig. 6b and c respectively. The interaction in which increase in concentration of ginger powder improves the IP is depicted. However, storage time declines the IP. Similar interactions of process parameters are confirmed by interaction plot Fig. 6e. It displays that all four process parameters are significant for the induction period. Similar results have been found in another natural antioxidant *Moringa oleifera* Lam by França et al. [39].

3.3 Impact of control factors on calorific value

Calorific value is an important property of fuel; however, it is generally lower in biodiesel than in diesel because of its higher oxygen content [40]. As storage time precedes, the calorific value decreases with time. Phenolic antioxidants like ginger are recognized as free radical terminators [27]. So the rate of decrease was found to be more with addition of ginger additive. Surface plots of calorific value with storage time, blend (%), ginger concentration, and exposure temperature are shown in Fig. 7. Calorific value depicted decline with storage time as shown in Fig. 7a and c. Similar trends were acquired for the increase of blending ratio as shown in Fig. 7b and d. In contrast, concentration of ginger powder and exposure temperature did not affect calorific value significantly as shown in Fig. 7b, c, and d. A similar effect has been established for the calorific value with respect process parameters as shown in Fig. 7e.

3.4 Impact of control factors on acid value

Acid number is a useful indicator to monitor the degradation of biodiesel with respect to storage time. The acid number increases significantly with increase in storage period for biodiesels without additive. The increase in acid number is due to the increase in formation of hydroperoxides which are further oxidized to acids. Presence of water also affects the acid number as it can hydrolyze the esters into alcohol and acids [13, 24]. Increase in the storage time and blending ratio directly adversely affected acid value as shown in Fig. 8a and c. But ginger concentrations prevent to change the acid value of the fuel as shown in Fig. 8b and c. At the same time, exposure temperature does not significantly disturb the acid value as shown in Fig. 8d. Interaction plot of acid value is shown in Fig. 8e. Similar trends and finding had been received by Leanne Silva de Sousa et al. [37]. It clearly shows the effect of storage time, ginger concentration, blending ratio, and exposure temperature. The incrase in acid value was possibly attributable to complex secondary reactions, wherein main oxidation hydroperoxide may undergoe complex reaction.

3.5 RSM optimization response

The response surface methodology (RSM) optimizer has been employed to optimize the process parameters of oxidation reaction. It is a multi-objective optimization tool. The main objective is to improve the shelf-life with desirable physico-chemical properties. The effects of the process parameters are shown in Fig. 9.

3.6 Validation test: confirmation and error

Using the estimated RSM values, experimental trials were conducted to authenticate the findings. The verification test was performed with optimal values of blend 31.31%, concentration of nano ginger powder 676.76 ppm, exposure temperature 120 °C, and storage time 4.24 months. Average value of three confirmation tests were carried out to validate the RSM predictions, and their mean is taken into account. Table 6 shows the detail of the experiments. Calorific value,

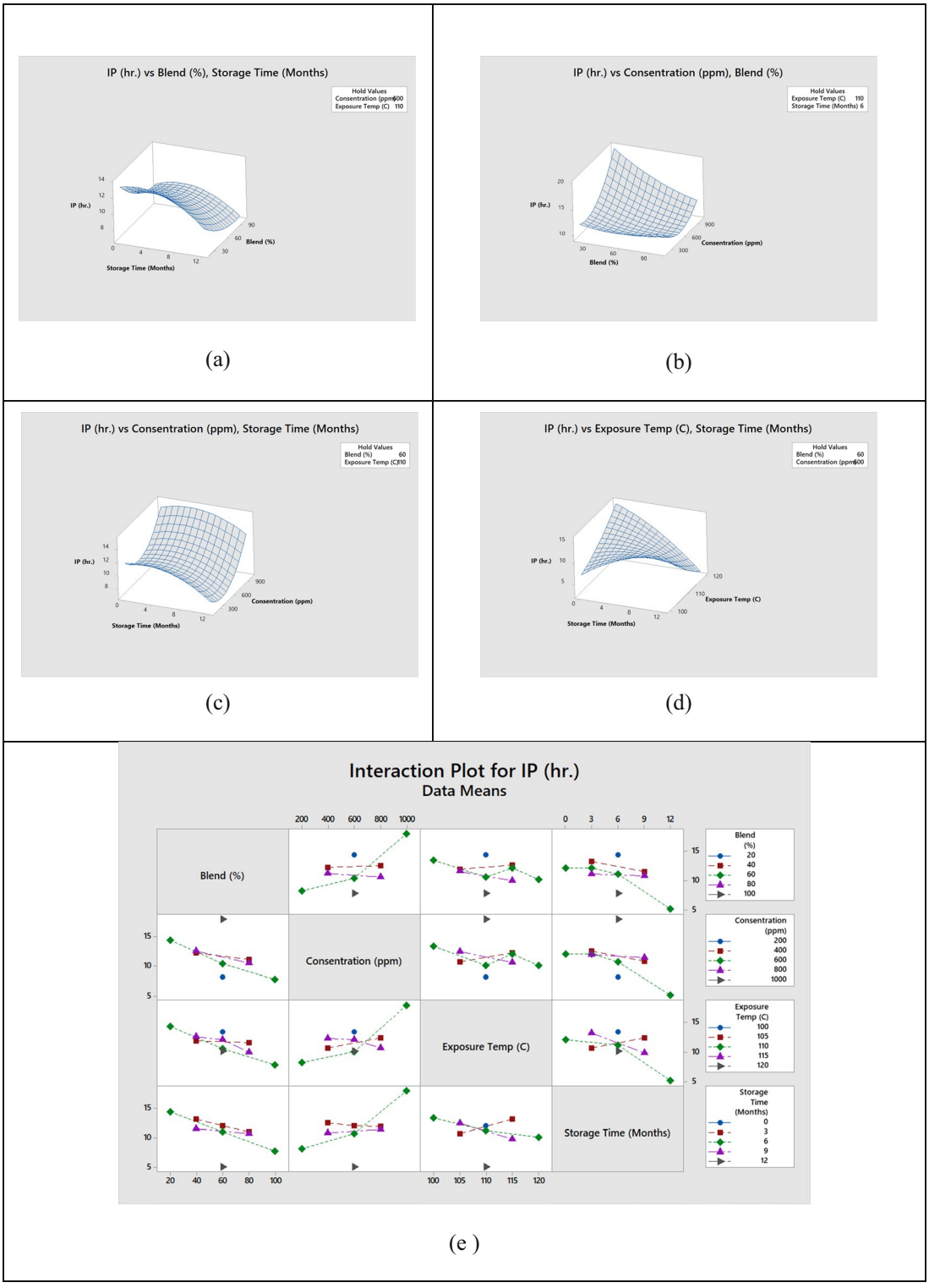


Fig. 6 **a-e** Effect of process parameters on IP

viscosity, acid value, and induction period were measured responses. These were compared and validated with experimental findings. The % error of these responses between predicted value and experimental values is shown in Table 6 and found satisfactory limits.

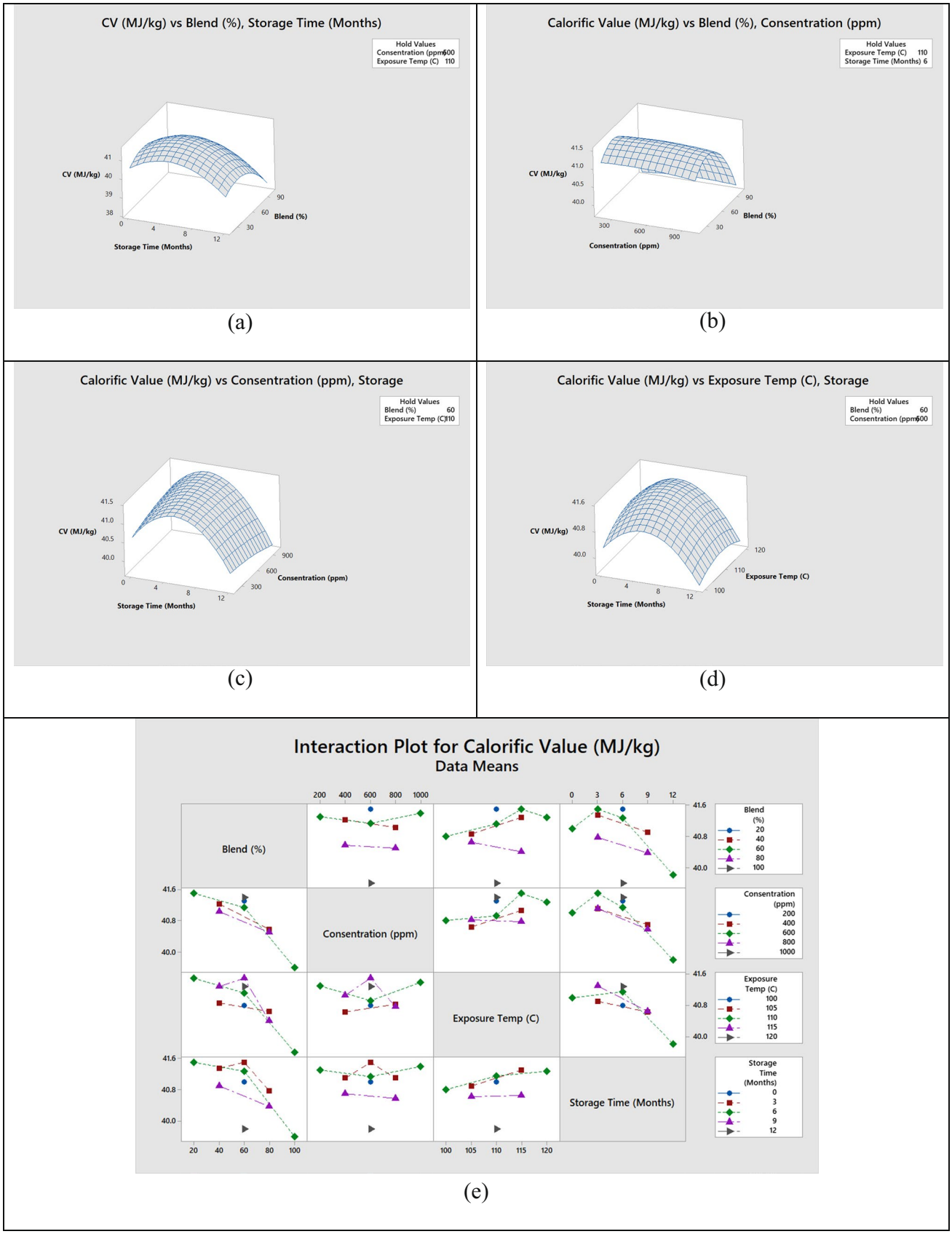


Fig. 7 **a-e** Effect of process parameters on CV

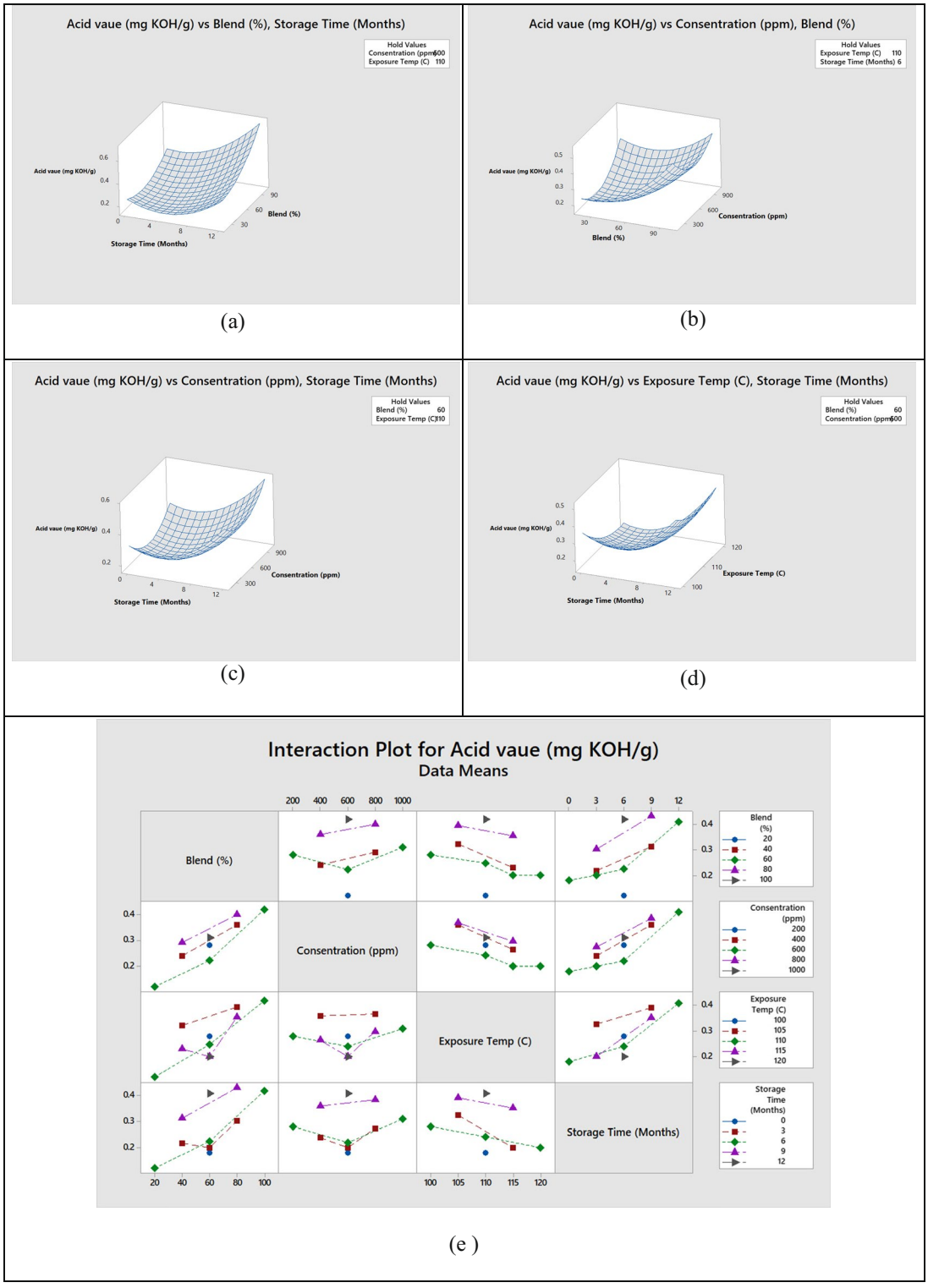


Fig. 8 **a-e** Effect of process parameters on acid value

4 Conclusion

Biodiesel's susceptibility to auto-oxidation is natural due to FFA content but oxidation can be delayed by using proper dosage of antioxidant. The present study shows that the problem associated with biodiesel that affects quality of biodiesel like viscosity, calorific value, acid value, and oxidation stability can be overcome by adding bio-additives

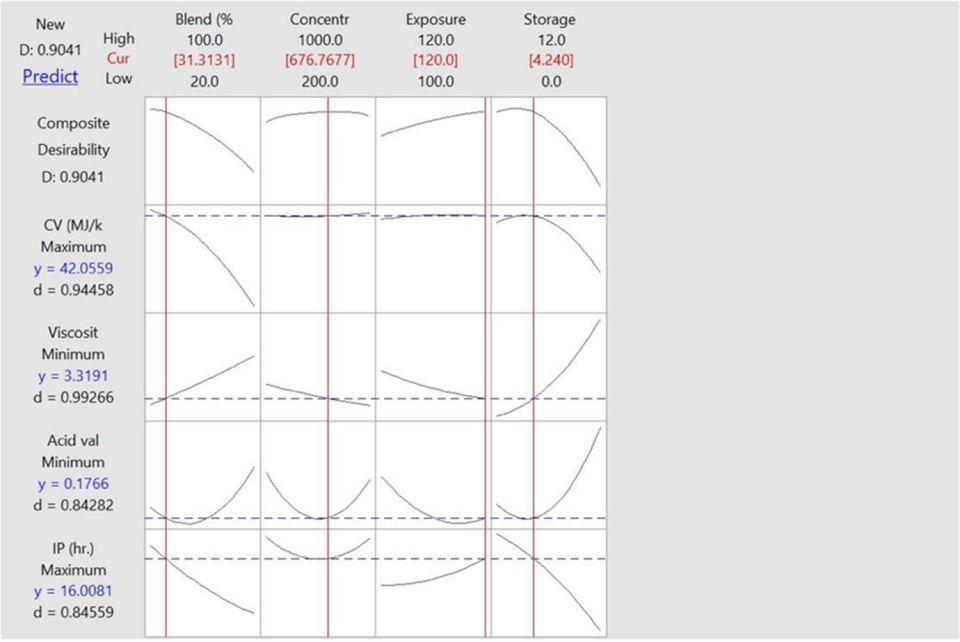


Fig. 9 Optimization plot: effect of process parameters on responses

Table 6 The verification output response

	Predicted value	Experimental value	Error (%)
Calorific Value (MJ/kg)	42.05	42.5	2.3
Viscosity (cSt)	3.3	3.5	5.7
Acid value (mgKOH/g)	0.176	0.18	2.2
IP (hour)	16.0	16.5	3.03

Blend 31.31%, ginger concentration 676.76 ppm, exposure temperature 120 °C, and storage time 4.24 months

in biodiesel. Bio-additives are one of the best solutions to improve oxidation stability. After applying of the RSM and selection of appropriate anti-oxidant with suitable process parameters, the following results were achieved:

- Ginger nano-powder was successfully employed as an antioxidant to enhance the oxidation stability of Kusum biodiesel.
- Blending ratio (20 to 100%), ginger anti-oxidant concentration (200 to 1000 ppm), storage time (0 to 12 months), and exposure temperature (100 to 120 °C) were the process parameters.
- RSM optimizer provided the optimal values of blending ratio which was 31.31%, concentration of nano ginger powder 676.76 ppm, exposure temperature 120 °C, and storage time 4.24 months.
- Optimized responses were received as calorific value (42.05 MJ/kg), viscosity (3.3cSt), acid value (0.176 mgKOH/g), and induction period (16 h).
- After experimental trails, responses were found satisfactory and % experimental errors were within satisfactory limits.

Usage of antioxidants delayed the auto-oxidation and improved the storage conditions; however, synthetic antioxidants affect engine performance and engine emission. So synthetic antioxidants are banned in some countries due to cancer-causing properties. Moreover, application of natural antioxidants like ginger powder is yet to be explored for engine parts and engine performance, emission, and combustion.

Declarations

Ethical statement This material is the authors' own original work, which has not been previously published elsewhere. The paper is not currently being considered for publication elsewhere. The paper reflects the authors' own research and analysis in a truthful and complete manner. The paper properly credits the meaningful contributions of co-authors and co-researchers. The results are appropriately placed in the context of prior and existing research. All authors have been personally and actively involved in substantial work leading to the paper, and will take public responsibility for its content.

Conflict of Interest The authors declare no competing interests.

References

1. Rakopoulos CD, Antonopoulos KA, Rakopoulos DC, Hountalas DT, Giakoumis EG (2006) Comparative performance and

emissions study of a direct injection diesel engine using blends of diesel fuel with vegetable oils or bio-diesels of various origins 47:3272–87. https://doi.org/10.1016/j.enconman.2006.01.006
2. Lin CY, Lin HA (2007) Engine performance and emission characteristics of a three phase emulsion of biodiesel produced by peroxidation. Fuel Process Technol 85:35–41
3. Lin BF, Huang JH, Huang DY (2009) Experimental study of the effects of vegetable oil methyl ester on DI diesel engine performance characteristics and pollutant emissions. Fuel 88:1779–1785
4. Igbokwe JO, Nwafor OMI (2016) Performance characteristics of palm kernel biodiesel and its blend in a CI engine. Int J Ambient Energy 37:103–106
5. Sahoo PK, Das LM (2009) Process optimization for biodiesel production from Jatropha. Karanja and Polanga oils Fuel 88:1588–1594. https://doi.org/10.1016/j.fuel.2009.02.016
6. Nabi MN, Akhter MS, Shahadat MMZ (2006) Improvement of engine emissions with conventional diesel fuel and diesel–biodiesel blends. Bioresour Technol 97:372–378
7. Varuvel EG, Mrad N, Tazerout M, Aloui F (2012) Assessment of liquid fuel (bio-oil) production from waste fish fat and utilization in diesel engine. Appl Energy 100:249–257
8. Usta N, Aydoğan B, On AH, Uğuzdŏan E, Özkal SG (2011) Properties and quality verification of biodiesel produced from tobacco seed oil. Energy Convers Manag 52:2031–2039. https://doi.org/10.1016/j.enconman.2010.12.021
9. Freire LM, José Filho R, Moura CV, Soledade LE, Stragevitch L, Cordeiro ÂM et al (2012) Evaluation of the oxidative stability and flow properties of quaternary mixtures of vegetable oils for biodiesel production. Fuel 95:126–130
10. Sarin A, Arora R, Singh NP, Sharma M, Malhotra RK (2009) Influence of metal contaminants on oxidation stability of Jatropha biodiesel. Energy 34:1271–1275. https://doi.org/10.1016/j.energy.2009.05.018
11. Das LM, Bora DK, Pradhan S, Naik MK, Naik SN (2009) Long-term storage stability of biodiesel produced from Karanja oil. Fuel 88:2315–2318. https://doi.org/10.1016/j.fuel.2009.05.005
12. Leung DYC, Koo BCP, Guo Y (2006) Degradation of biodiesel under different storage conditions. Bioresour Technol 97:250–256. https://doi.org/10.1016/j.biortech.2005.02.006
13. Bouaid A, Martinez M, Aracil J (2007) Long storage stability of biodiesel from vegetable and used frying oils. Fuel 86:2596–2602. https://doi.org/10.1016/j.fuel.2007.02.014
14. Dwivedi G, Sharma MP (2015) Effect of metal on stability and cold flow property of Pongamia biodiesel. Mater Today Proc 2:1421–1426. https://doi.org/10.1016/j.matpr.2015.07.062
15. Agarwal AK, Khurana D (2012) Long-term storage oxidation stability of Karanja biodiesel with the use of antioxidants initiation. Fuel Process Technol 106:447–457. https://doi.org/10.1016/j.fuproc.2012.09.011
16. Hazrat MA, Rasul MG, Khan MMK, Mofijur M, Ahmed SF, Ong HC et al (2021) Techniques to improve the stability of biodiesel: a review. Environ Chem Lett 19:2209–2236. https://doi.org/10.1007/s10311-020-01166-8
17. Pullen J, Saeed K (2014) Experimental study of the factors affecting the oxidation stability of biodiesel FAME fuels. Fuel Process Technol 125:223–235. https://doi.org/10.1016/j.fuproc.2014.03.032
18. Loh S, Chew S, Choo Y (2014) Oxidative stability and storage behavior of fatty acid methyl esters derived from used palm oil. J Am Oil Chem Soc 83:947–952. https://doi.org/10.1007/s11746-006-5051-9
19. Bora, D.K Das LM, Babu MKG (2009) Storage stability of mahua oil methyl ester. J Sci Ind Res 68:149–52
20. Agarwal AK, Khurana D (2013) Long-term storage oxidation stability of Karanja biodiesel with the use of antioxidants. Fuel Process Technol 106:447–452. https://doi.org/10.1016/j.fuproc.2012.09.011
21. Ryu K (2010) The characteristics of performance and exhaust emissions of a diesel engine using a biodiesel with antioxidants. Bioresour Technol 101:S78-82. https://doi.org/10.1016/j.biortech.2009.05.034
22. Varatharajan K, Cheralathan M, Velraj R (2011) Mitigation of NOx emissions from a jatropha biodiesel fuelled DI diesel engine using antioxidant additives. Fuel 90:2721–2725. https://doi.org/10.1016/j.fuel.2011.03.047
23. Ashok B, Nanthagopal K, Jeevanantham AK, Bhowmick P, Malhotra D, Agarwal P (2017) An assessment of calophyllum inophyllum biodiesel fuelled diesel engine characteristics using novel antioxidant additives. Energy Convers Manag 148:935–943. https://doi.org/10.1016/j.enconman.2017.06.049
24. Kumar N (2017) Oxidative stability of biodiesel: causes, effects and prevention. Fuel 190. https://doi.org/10.1016/j.fuel.2016.11.001
25. Kivevele TT, Mbarawa MM, Bereczky A, Laza T, Madarasz J (2011) Impact of antioxidant additives on the oxidation stability of biodiesel produced from Croton Megalocarpus oil. Fuel Process Technol 92:1244–1248. https://doi.org/10.1016/j.fuproc.2011.02.009
26. Jain S, Sharma MP (2012) Correlation development between the oxidation and thermal stability of biodiesel. FUEL 6–10. https://doi.org/10.1016/j.fuel.2012.06.110
27. Rizwanul Fattah IM, Masjuki HH, Kalam MA, Hazrat MA, Masum BM, Imtenan S et al (2014) Effect of antioxidants on oxidation stability of biodiesel derived from vegetable and animal based feedstocks. Renew Sustain Energy Rev 30:356–370. https://doi.org/10.1016/j.rser.2013.10.026
28. McCormick RL, Ratcliff M, Moens L, Lawrence R (2007) Several factors affecting the stability of biodiesel in standard accelerated tests. Fuel Process Technol 88:651–657. https://doi.org/10.1016/j.fuproc.2007.01.006
29. Ramos MJ, Fernández CM, Casas A, Rodríguez L, Pérez Á (2009) Influence of fatty acid composition of raw materials on biodiesel properties. Bioresour Technol 100:261–268. https://doi.org/10.1016/j.biortech.2008.06.039
30. Devi A, Das VK, Deka D (2017) Ginger extract as a nature based robust additive and its influence on the oxidation stability of biodiesel synthesized from non-edible oil. Fuel 187:306–314. https://doi.org/10.1016/j.fuel.2016.09.063
31. Jolad SD, Lantz RC, Solyom AM, Chen GJ, Bates RB, Timmermann BN (2004) Fresh organically grown ginger (Zingiber officinale): composition and effects on LPS-induced PGE2 production. Phytochemistry 65:1937–1954. https://doi.org/10.1016/j.phytochem.2004.06.008
32. Singh Pali H, Sharma A, Kumar N, Singh Y (2021) Biodiesel yield and properties optimization from Kusum oil by RSM. Fuel 291:120218. https://doi.org/10.1016/j.fuel.2021.120218
33. Pali HS, Sharma A, Kumar N, Singh Y (2020) Sustainable route for S. Oleosa biodiesel production using response surface methodology. Energy Sources, Part A Recover Util Environ Eff. https://doi.org/10.1080/15567036.2020.1837298
34. Pali HS, Kumar N, Mishra C (2014) Effect of blending of ethanol in kusum oil on performance and emission characteristics of a single cylinder diesel engine. SAE Tech Pap 1. https://doi.org/10.4271/2014-01-1396.
35. Holman JP (2012) Experimental methods for engineers. vol. s1-VIII. https://doi.org/10.1093/nq/s1-VIII.193.43-b
36. Rajak U, Verma TN (2018) Effect of emission from ethylic biodiesel of edible and non-edible vegetable oil, animal fats, waste oil

and alcohol in CI engine. Energy Convers Manag 166:704–718. https://doi.org/10.1016/j.enconman.2018.04.070
37. De Sousa LS, De Moura CVR, De Oliveira JE, De Moura EM (2014) Use of natural antioxidants in soybean biodiesel. Fuel 134:420–428. https://doi.org/10.1016/j.fuel.2014.06.007
38. Sarin A, Singh NP, Sarin R, Malhotra RK (2010) Natural and synthetic antioxidants: Influence on the oxidative stability of biodiesel synthesized from non-edible oil. Energy 35:4645–4648. https://doi.org/10.1016/j.energy.2010.09.044
39. França FRM, dos Santos FL, Ramos ALD, da Silva GF, Brandão ST (2017) Storage and oxidation stability of commercial biodiesel using Moringa oleifera Lam as an antioxidant additive. Fuel 203:627–632. https://doi.org/10.1016/j.fuel.2017.03.020
40. Krishnamoorthi M, Malayalamurthi R, He Z, Kandasamy S (2019) A review on low temperature combustion engines: performance, combustion and emission characteristics. Renew Sustain Energy Rev 116:109404. https://doi.org/10.1016/j.rser.2019.109404

Publisher's note Springer Nature remains neutral with regard to jurisdictional claims in published maps and institutional affiliations.

The current issue and full text archive of this journal is available on Emerald Insight at:
https://www.emerald.com/insight/0368-492X.htm

Positive reframing as a mediator between gratitude and technostress amongst Indian students during the COVID-19 pandemic

Received 3 December 2021
Revised 13 January 2022
Accepted 24 January 2022

Naval Garg and Shivangi Verma
University School of Management and Entrepreneurship, Delhi Technological University, Delhi, India, and
Jason Timothy Palframan
Faculty of Business and Hospitality, Technological University of the Shannon: Midlands Midwest, Athlone Campus, Athlone, Ireland

Abstract

Purpose – The aim of the current study was to examine the previously unexplored relationship between positive reframing as a mediator between gratitude and technostress in Indian students. By examining this relationship, the authors aim to expand the theoretical domain of gratitude research by examining its potential influence on technology-induced stress.

Design/methodology/approach – A cross-sectional survey was used to collect and analyze data from 552 Indian college students who participated in graduate and postgraduate programs across various educational institutions in India. Regression and mediation analyses were performed with both IBM SPSS 25 and AMOS.

Findings – This study's data suggest that positive reframing plays an important mediating role between gratitude and technostress. Gratitude also encourages positive reframing, which reduced technostress among the students. Taken together, our data showed that gratitude induces positive reframing, which in turn reduces techno-stress among Indian students in the current study.

Research limitations/implications – The sample size in this study is relatively small in relation to the student population in India. The current study relied primarily on quantitative data and analysis and further research could use a mixed-method approach to better understand the underlying mechanisms between positive reframing, gratitude and technostress. The results are derived under an extreme coronavirus disease 2019 (COVID-19) pandemic situation; therefore, the results cannot be generalized to normal times.

Practical implications – The paper includes implications for teachers, academic leaders, parents and civil society.

Originality/value – Overall, the relationship between positive reframing, gratitude and technostress has not been thoroughly explored. To the best of the authors' understanding, this is the first study to examine the influence of gratitude on technology-induced stress and the role of reframing.

Keywords Gratitude, Positive reframing, Students, Technostress, Mediation, Coping, COVID-19

Paper type Research paper

Introduction

The novel coronavirus disease 2019 (COVID-19) pandemic has impacted the world economically, financially, psychologically and socially. Country-by-country statistics on COVID-19 infections are largely disappointing for South Asian countries, particularly India. After the United States (USA), India is the second most affected country with a total of 33,174,954 cases of COVID-19 as at September 2021. Despite numerous government measures such as lockdowns, quarantine, social distancing, vaccination campaigns and rapid antigen

Kybernetes
© Emerald Publishing Limited
0368-492X
DOI 10.1108/K-12-2021-1250

tests, it has claimed a significant loss of life. It has challenged the ability of humankind to effectively address a public health crisis of global concern. On an individual level, the pandemic has created psychological pressure among people infected with COVID-19 and healthy people (Duan and Zhu, 2020). For example, people have reported high levels of stress, anxiety, depression and loneliness (Erren *et al.*, 2020; Zhou *et al.*, 2020). In addition, movement restrictions have reduced physical activity, disrupted sleep patterns, and increased high blood pressure, mortality and obesity (Majumdar *et al.*, 2020).

COVID-19 has also impacted the education system and students academically, financially, physically and psychologically (Kecojevic *et al.*, 2020). Psychologically, the shift has led to more stress, less interaction and more severe depressive symptoms in students (Crawford *et al.*, 2020; Klussman *et al.*, 2020; Mailizar *et al.*, 2021). Academically and physically, the move from the traditional physical classroom to online teaching and learning has resulted in a significant increase in acceptance and enrollment of online digital courses and distance learning as a viable option to fill the classroom void (Kaur *et al.*, 2020). India's digital online services include Diksha, e-Pathshala, SWAYAM, MOOCs and e-PG Pathshala (Jena, 2020). These services have emerged as a way for a developing country like India to move from a traditional education system to a digital India, increasing digital literacy and adoption of digital technologies.

Nonetheless, the shift towards the adoption of online learning and the increased reliance on various electronic and digital devices has resulted in students being constantly online. This longer screen time leads to decreased cognitive and academic performance (Majumdar *et al.*, 2020), discomfort, tension, digital burnout (Bozkurt and Sharma, 2020), obesity, high blood pressure, type 2 diabetes, depression, sleep disorders (Sultana *et al.*, 2021) and technology-induced stress, i.e. technostress. Recent studies have also reported the adverse effects of stress on the learning experience and mental health of students (Kecojevic *et al.*, 2020). With this abrupt change in the teaching and learning landscape, students are regularly exposed to an increased risk of technology stress (Sahu, 2020). Prior to the pandemic, students found technology beneficial for improving their academic performance and completing study-related tasks. However, technostress and fatigue created by excessive and invasive technology and information and communications technology (ICT) enabled devices have weakened students' mental resources to effectively complete learning activities (Aharony and Zion, 2018; Wang *et al.*, 2020). Overall, the quick transition to online learning was a challenge for most students.

The consequences of increased technostress and its impact on student performance need to be addressed. In general, students face many difficulties in their daily life, especially in the current pandemic; therefore, it is crucial to understand adaptive coping mechanisms that can be used to address the challenges of the pandemic. Studies on the assessment of stress in students during COVID-19 are primarily limited to the documenting and analysis of psychological and physiological sources and symptoms of technostress (Penado Abilleira *et al.*, 2021; Spagnoli *et al.*, 2020). In the current study, however, we examine the intervention of positive reframing along with expressing gratitude to alleviate the negative effects of technostress. The ability to reframe positively during the pandemic has been linked to less stress in adults (Shanahan *et al.*, 2020). Likewise, as a positive emotion, gratitude is incompatible with negative emotions (Garland *et al.*, 2010) and can help to buffer negative emotions such as fear and stress. Overall, the relationship between positive reframing, gratitude and technostress has not been thoroughly explored. Positive reframing and gratitude are associated with wellbeing and can act as useful resources against stressors such as technostress. In the present study, using the broaden-and-build theory (Fredrickson, 2004) as a theoretical premise, we examine positive reframing as a mediator between gratitude and technostress.

Theoretical framework

Gratitude

Gratitude has been conceptualized in a number of ways. It is defined as "an emotion, a virtue, a moral sentiment, a motive, a coping response, a skill, and an attitude" (Emmons and Crumpler, 2000, p. 56). More specifically, gratitude is evoked as an emotion when receiving costly, unexpected and deliberate benefits from others (Forster *et al.*, 2017). As an affective trait of the individual, gratitude is defined as a "generalized tendency to recognize and respond with grateful emotions to the roles of other people's benevolence in the positive experiences and outcomes that one obtains" (McCullough *et al.*, 2002, p. 112). As a virtue, gratitude is a tendency to acknowledge and respond to the benevolent behavior of others. As a skill, it is the ability to see positive things, even in a challenging situation (Allen, 2018). Gratitude has also been conceptualized through two paradigms: one worldly and one transcendent (Emmons and Stern, 2013). A worldly paradigm suggests gratuitous feelings arise out of beneficial interpersonal exchanges and is based on "benefit triggered" feelings. A transcendent paradigm suggests that a grateful person realizes that others are not the source of gifts; instead, they come through a deep connection with nature. Steindl-Rast (2004) portrays these two paradigms as two extreme ends of a continuum. At one end, worldly gratitude is expressed as a feeling of gratitude when receiving a gift from others. At the other end of the continuum, a transcendent paradigm understands that gratitude arises from an experience of cosmic oneness when one receives an undeserved gift or experiences a deep connection with nature. Steindl-Rast (2004) describes the first experience as personal and the second as transpersonal.

Based on these conceptualizations, previous researchers have described several ways that gratitude affects an individual's wellbeing. Grateful people report better physical health, and they are more likely to engage in physical activity (Hill *et al.*, 2013). The experience of gratitude leads to better sleep, less fatigue and less cellular inflammation (Mills *et al.*, 2015; Wood *et al.*, 2009). Individuals who show high levels of gratitude show more resilience and vitality (Garg and Sarkar, 2020). Gratitude is also positively associated with happiness (Mahipalan and Sheena, 2019; Watkins *et al.*, 2003), positive affect (Sun and Kong, 2013), less anxiety and depression (Bono *et al.*, 2020), being self-efficient (Sun *et al.*, 2020), trust and social intelligence (Garg *et al.*, 2020).

Positive reframing

Positive reframing refers to "construing a stressful transaction in positive terms" (Carver, 1997, p. 269). Positive reframing is a process of positively perceiving something that was previously viewed as unfavorable. For example, an employee loses their job but positively reframes the situation and then starts up their own small-scale business. Recent studies have shown that the use of positive reframing as a coping strategy in students has positive effects on satisfaction even after failure (Stoeber and Janssen, 2011). Students typically use active coping, planning and positive reframing as the most common coping strategies to buffer between different stressors that affect them (Abraham *et al.*, 2019). A recent study by Prasath *et al.* (2021) found the influence of positive reframing on predicting the wellbeing of individuals. They stated that such coping behaviors would be helpful in countering the negative wellbeing effects of the pandemic. Another study also characterized the role of positive reframing in improving physical health, managing adversity effectively and creating a more stable emotional response (Salman *et al.*, 2020).

Technostress

Technostress is understood as "a modern disease of adaptation caused by an inability to cope with new computer technologies in a healthy manner" (Brod, 1982, p. 16). It is a negative effect

that leads to disturbances in human thoughts, attitudes, behavior and psychology due to the direct or indirect consequences of exposure to technology (Brillhart, 2004). Technostress arises from an individual's inability to adapt to technology (Tarafdar *et al.*, 2007). Like other stressors, technostress induces tension, anxiety and depression (Galvin *et al.*, In press; Giorgi *et al.*, 2020). Tarafdar *et al.* (2007) discussed five components of technostress: techno-overload, techno-invasion, techno-complexity, techno-insecurity and techno-uncertainty. Techno-overload occurs when the use of ICT exceeds the optimum level and leads to negative results (Karr-Wisniewski and Lu, 2010). Techno-invasion refers to the impact of ICT on work and personal life and requires one to be easily accessible at all times. It leads to stress because the distinction between professional and personal life becomes blurred. Techno-complexity takes place when users do not have confidence working with computers. The users are forced to spend time and effort to learn the computer skills and required ICT tools. Techno-insecurity creates job loss fear among employees, believing that new technology could lead to automation or it could be replaced by people with better skills and abilities. Techno-uncertainty deals with the rapidly changing technical changes that make users uncertain about their work or job. Frequent changes in technology require users to keep upgrading and learning new ICT.

Gratitude and technostress

The proposed relationship between gratitude and technostress is theoretically premised in Fredrickson's (2004) broaden-and-build theory of positive emotion. The broaden-and-build theory holds that gratitude broadens the array of thoughts and actions of an individual. It encourages one to play and push limits. A grateful person indulges in creativity and innovation in dealing with others. This expansion of one's own thought-action repertoire builds psychological and social resources for a person. These resources can be relied on even in the most difficult phases of life (Fredrickson, 2004). Psychological resources include resilience, vitality, self-efficacy, hope, positive attitude and optimism. Social resources include social bonds, friendships, trustworthy and reliable friends, and colleagues. The broaden-and-build theory suggests different ways in which gratitude can reduce the technostress among students. First, gratitude provides technostressed students with psychological resources to help them cope with technology-induced stress. Stress is negatively associated with vitality (Satici, 2020), resilience (Petzold *et al.*, 2020) and self-efficacy (Freire *et al.*, 2020; Şahin and Çetin, 2017). Second, students with high levels of gratitude are more likely to have more trustworthy friends, teachers, relatives and family members. Such students can rely on these social resources to reduce technostress. For example, a student stressed out by the complexities of technologies can add new knowledge and skills with the help of seniors and friends.

Likewise, a student full of gratitude for the teachers will form a strong bond with them. In the case of techno-overload, such students can seek expert advice from their professionally trained teachers. Third, positive emotions like gratitude are incompatible with negative emotions (Garland *et al.*, 2010). They cancel out negative emotions like stress, anxiety and depression. Fourth, gratitude breeds innovation and creativity. In this way, a student who shows a high level of gratitude can find new ways to deal with technostressors. For example, students struggling to balance online classes, tests and household tasks may evenly distribute classes throughout the week with the help of recorded lectures and online tutorials. Thus, it is proposed that, like stress, gratitude may also counter technostress among students, and accordingly, the following three hypotheses are formulated:

H1. Gratitude is negatively associated with techno-overload.

H2. Gratitude is negatively associated with techno-invasion.

H3. Gratitude is negatively associated with techno-complexity.

The mediating effect of positive reframing

Several studies have stated that gratitude promotes positive reframing in at least three possible ways (Fredrickson *et al.*, 2000; Garg *et al.*, 2020). First, grateful people put their negative experiences on a more positive note. Second, they experience more positive emotions. Third, they tend to ignore negative emotions. In all three cases, gratitude reduces the frequency, intensity and density of negative emotions such as technostress.

A person who shows high levels of gratitude focuses on abundance and the fullness of life (Garg and Sarkar, 2020; Mahipalan and Sheena, 2019). Gratitude heralds a sense of abundance and negates a sense of deprivation. A grateful person could derive positivity even in the most testing times. Therefore, students who are overloaded with online courses during the COVID-19 pandemic may see a silver lining that they are some of the lucky ones who have the luxury of learning even during the pandemic. Additionally, that millions of other students were unable to take online courses for various reasons such as network connectivity and affordability. They may also realize that technostress will be the new normal of future professional organizations. Working from home will no doubt lead to techno-invasion and techno-complexity. Therefore, grateful students can view the current situation as training for their future professional life. They may also learn some techniques like meditation and breathing exercises to deal with technostress. Such focus on positivities is poised to lower the technostress level of students.

Students staying home due to COVID-19 can reframe the inevitable situation as an opportunity to hone and develop new skills or to try new things that they longed for but were unable to achieve due to work pressures or lack of time. Perceiving the positive aspects in such unpleasant and unfortunate events benefits the individual to discern a new path of exploration. Grateful people also have a strong sense of appreciation. A person who shows high levels of gratitude recognizes and appreciates most life events such as pleasant weather, their favorite meal and meeting an old friend (Lee *et al.*, 2019; Watkins *et al.*, 2003). They also appreciate others for their valuable contributions in their life. Such gratitude-induced positive reframing is poised to reduce technostress among students. Pirkkalainen *et al.* (2019) empirically validated that positive reframing shifts attention away from stressful situations, and users emphasize the positive, which reduces the negative consequences of technostress and enables higher productivity. Such gratitude-induced proactive coping, i.e. positive reframing, has contributed to foreseen challenges that lead to better outcomes in stressful situations (Vieselmeyer *et al.*, 2017). Positive reframing therefore leaves room for pause, reflection and reinterpretation by the individual in order to perceive technostress as a challenge rather than a threat. The current generation perceives ICT demanding situations as a positive challenge or as an opportunity for personal growth (Ioannou and Papazafeiropoulou, 2017; Reuman *et al.*, 2012).

Based on the previous discussion, the following three hypotheses are proposed which examine the mediating effect of positive reframing of the relationship between gratitude and technostress.

H4. Positive reframing mediates the relationship between gratitude and techno-overload.

H5. Positive reframing mediates the relationship between gratitude and techno-invasion.

H6. Positive reframing mediates the relationship between gratitude and techno-complexity.

In summary, the main purpose of our study is to examine the mediating effects of positive reframing on gratitude and technostress.

Research methodology

Sample and data collection

Using a cross-sectional survey strategy, we collected data from 552 Indian college students participating in graduate and postgraduate courses at various educational institutions in the Delhi-National Capital Region (NCR), India. The study is limited to the Delhi-NCR region for two reasons. First, almost all colleges, especially in this region, have quickly switched to online teaching and evaluation. Second, the area has good network connectivity and Internet coverage. Convenience sampling with some elements of snowball sampling was used in this study. The convenience sampling method was considered suitable and efficient for this study because of outside restrictions imposed and limited opportunity to physically interact with participants in Delhi-NCR due to the COVID-19 pandemic. Therefore, readily available students were contacted online to enable quick and efficient participation in this study. Online questionnaires were sent to the targeted sample of 600 college students. Of these 600 students, 560 returned the questionnaire, which corresponds to a response rate of 93%. In the data analysis, eight questionnaires were discarded due to incompleteness. Thus, a total of 552 participant questionnaires were processed.

The demographic description of the sample is shown in Table 1. The sample includes 51.8% females, 47.8% males and 0.4% third gender. The majority of the respondents were in the 17–20 age group (68.5%). Most of the respondents were pursuing a bachelors' degree (488 undergraduate students, i.e. 88.5%) and the remainder are either postgraduate (9.7%) or in 12th class (1.8%). 47.3% of students in the study reported that their ICT device usage time was less than 5 h, followed by 31.9% of students who used ICT devices for 5–6 h, and 20.8% of students use digital devices for more than 6 h.

Measures

Gratitude. We measured gratitude with 16 items from the gratitude, resentment and appreciation test (GRAT)(Watkins *et al.*, 2003). The GRAT consists of a 16-item measure of gratitude as a nine-point Likert scale (1 = *strongly disagree* to 9 = *strongly agree*). This measure assesses three different facets of grateful disposition: lack of sense of deprivation (LOSD), simple appreciation (SA) and appreciation for others (AO). Sample items include: "*Life has been good to me*", "*I think that it's important to pause often to count my blessings*" and "*I feel deeply appreciative for the things others have done for me in my life*".

Technostress. We measured technostress with 12 items using an adapted version of the technostress questionnaire developed by Westermann (2017). The items were rated on a five-point Likert scale (0 = *strongly disagree* to 4 = *strongly agree*). Since the present study comprises a sample of students, only three dimensions of technostress, i.e. techno-overload,

Table 1. Demographic description of the sample (N = 552)

Variable	Category	Frequency	Percent	Cumulative %
Gender	Male	263	47.8	47.8
	Female	286	51.8	99.6
	Third gender	3	0.4	100.0
Age groups	17–20 years	379	68.5	68.5
	21–25 years	173	31.5	100.0
Courses	10 + 2	10	1.8	1.8
	Undergraduate	488	88.5	90.3
	Postgraduate	54	9.7	100.0
ICT devices usage time (per day)	Less than 5 h	261	47.3	47.3
	5–6 h	176	31.9	79.2
	More than 6 h	115	20.8	100.0

Source(s): Primary data

techno-invasion and techno-complexity, were assessed in this study. The other two dimensions i.e. techno-insecurity and techno-uncertainty, were discarded because these techno-savvy students were well-equipped with information technology and its applications and are highly unlikely to experience techno-insecurity and techno-uncertainty. Moreover, post-millennial students have confidence in the use of technology, and are ready to learn new uses of technology (Upadhyaya and Vrinda, 2020). The sample items include "*I am forced to change my habits to adapt to new technologies,*" "*I have to be always available due to this technology*" and "*I need a long time to understand and use new technologies.*"

Positive reframing. We measured positive reframing with four items using the COPE Inventory developed by Carver *et al.* (1989). The items were rated on a four-point Likert scale (1 = *I usually do not do this at all to* 4 = *I usually do this a lot*) and were used to measure positive reframing. A sample item included "*I try to see it in a different light, to make it seem more positive.*"

Reliability, validity and common method bias

Reliability is assessed using Cronbach's alpha and composite reliability estimates (see Table 2). Cronbach's alpha values for gratitude, positive reframing, techno-invasion, techno-overload and techno-complexity are 0.754, 0.741, 0.716, 0.801 and 0.850, respectively. The composite reliability estimates for gratitude, positive reframing, techno-invasion, techno-overload and techno-complexity are 0.765, 0.743, 0.720, 0.789 and 0.862.

Both reliability estimates are greater than 0.70, which shows a satisfactory reliability (Fornell and Larcker, 1981). Convergent validity and discriminant validity are assessed using average variance extracted (AVE) values. The AVE estimates of all constructs are greater than 0.5 (see Table 2). These values explain the satisfactory convergent validity of the study variables. In addition, the square roots of the AVE values (diagonal cells in Table 3) are greater than the corresponding correlation coefficient between the

Variables	Mean	SD	CA	CR	AVE
Gratitude	5.645	0.708	0.754	0.765	0.569
Positive reframing	3.197	0.197	0.741	0.743	0.522
Techno-invasion	2.481	0.118	0.716	0.720	0.568
Techno-overload	2.125	0.083	0.801	0.789	0.586
Techno-complexity	2.113	0.154	0.850	0.862	0.557
Overall technostress	2.20	0.20	0.903	0.847	0.649

Note(s): SD-Standard Deviation, CA-Cronbach's alpha, CR-Composite reliability, AVE-Average Variance Extracted
Source(s): Primary data

Table 2. Descriptive statistics, reliability and validity estimates

Variables	1	2	3	4	5	6
Gratitude	0.754					
Positive reframing	0.526*	0.722				
Techno-invasion	−0.508	−0.372*	0.753			
Techno-overload	−0.498	−0.397*	0.678*	0.765		
Techno-complexity	−0.499*	−0.323*	0.596*	0.664*	0.746	
Overall technostress	−0.698*	−0.404*	0.723*	0.763*	0.731*	0.805

Note(s): * Sig. at 0.05, Highlighted values in the diagonal are square roots of the AVE and demonstrate existence of discriminant validity
Source(s): Primary data

Table 3. Correlation and discriminant validity

constructs, which demonstrates the existence of discriminant validity (Fornell and Larcker, 1981). The common method bias could seriously affect the results of the study; therefore, both procedural and quantitative methods should be used to deal with this (Podsakoff *et al.*, 2011). Two procedural remedies and a quantitative technique are used in this study. As per the suggestions of MacKenzie and Podsakoff (2012), measures with different scales are used e.g. gratitude–nine-point scale, technostress–five-point scale and positive reframing–four-point scale. Harman's one-factor method is also used to assess common method variance. All items in the study are subjected to a factor analysis. One single factor does not account for the majority of variation, negating the existence of common method bias.

Results

The data were analyzed using IBM SPSS 25 and AMOS. Table 2 shows the reliability, validity and descriptive statistics for each of the concerned variables used in this study. Reliability was rated using Cronbach's alpha, and all of the variables reported α value more than 0.70, which indicates a satisfactory, reliable scale (Schutte *et al.*, 2000). Few researchers have argued using composite reliability in place of Cronbach's alpha for a more robust understanding of reliability. Therefore, composite reliability (CR) values for all constructs are also greater than 0.70, suggesting good reliability (Hair *et al.*, 2010). For validity assessment, average variance extracted (AVE) values are reported to be greater than or equals to 0.50, suggesting an adequate level of convergent validity (Fornell and Larcker, 1981).

Table 3 highlights the correlation coefficients among variables of the study. There is a positive and significant correlation of 0.526 between gratitude and positive reframing. The correlation coefficient between gratitude and overall technostress is −0.698 and suggests that gratitude can reduce student technostress. A negative correlation ($r = -0.404$) between positive reframing and technostress is also reported.

The associative relationship between the predictor and outcome variables was established through regression analysis. Regression results are presented in Table 4. The results suggest that a significant variation in the dependent variables (techno-invasion, techno-overload, techno-complexity and overall technostress) could be explained by the independent variable (gratitude). R-square values showed 35.6% variation in techno-overload, 32.1% variation in techno-invasion, 31.7% variation in techno-complexity and 40.2% variation in overall technostress, are explained by gratitude. Our results suggest that gratitude significantly explains, techno-invasion, techno-overload, techno-complexity and overall technostress. The results support the assumption of the first three hypotheses, i.e. H1, H2 and H3.

The mediation results of each technostress component, i.e. techno-invasion, techno-overload and techno-complexity, are reported in Tables 5–7, respectively. The overall impact of gratitude on technostress with positive reframing is reported in Table 8. Table 5 shows

IV	DV	Unstandardized coefficient	Standard error	Standardized coefficient	*R*-square	Sig.
G	Techno-invasion	−0.263	0.011	−0.271	0.321	0.004*
	Techno-overload	−0.325	0.015	−0.278	0.356	0.013*
	Techno-complexity	−0.157	0.019	−0.299	0.317	0.003*
	Overall technostress	−0.597	0.039	−0.349	0.402	0.014*

Table 4. Regression results

Note(s): * Sig. at 0.05, G-Gratitude, IV-Independent Variable, DV-Dependent Variable
Source(s): Primary data

Relationships	Standardized	Unstandardized	*p*-value
Direct effect			
Gratitude → positive reframing	0.325	0.045	0.000*
Gratitude → techno-invasion	−0.220	−0.036	0.000*
Indirect effect			
Gratitude → PR → techno-invasion	−0.111	−0.018	0.001*
Total effect			
Gratitude on techno-invasion	−0.109	−0.017	0.004*

Note(s): * Sig. at 0.05
Source(s): Primary data

Table 5. Results of mediation analysis (DV–techno-invasion)

Relationships	Standardized	Unstandardized	*p*-value
Direct effect			
Gratitude → positive reframing	0.325	0.045	0.000*
Gratitude → techno-overload	−0.218	−0.048	0.001*
Indirect effect			
Gratitude → PR → techno-overload	−0.120	−0.026	0.001*
Total effect			
Gratitude on techno-overload	−0.098	−0.021	0.030*

Note(s): * Sig. at 0.05
Source(s): Primary data

Table 6. Results of mediation analysis (DV–techno-overload)

Relationships	Standardized	Unstandardized	*p*-value
Direct effect			
Gratitude → positive reframing	0.325	0.045	0.000*
Gratitude → techno-complexity	−0.304	−0.87	0.000*
Indirect effect			
Gratitude → PR → techno-complexity	−0.105	−0.030	0.000*
Total effect			
Gratitude on techno-complexity	−0.199	−0.057	0.002*

Note(s): * Sig. at 0.05
Source(s): Primary data

Table 7. Results of mediation analysis (DV–techno-complexity)

Relationships	Standardized	Unstandardized	*p*-value
Direct effect			
Gratitude → positive reframing	0.325	0.045	0.000*
Gratitude → technostress	−0.290	−0.171	0.000*
Indirect effect			
Gratitude → PR → technostress	−0.127	−0.075	0.000*
Total effect			
Gratitude on technostress	−0.163	−0.096	0.013*

Note(s): * Sig. at 0.05
Source(s): Primary data

Table 8. Results of mediation analysis (DV–technostress)

that the direct and indirect effects of gratitude on techno-invasion are significant. It is also noted that the effect of gratitude on techno-invasion increases from −0.220 to −0.111 with positive reframing (indirect effect). These results confirm the partial mediation effect of positive reframing and thus suggest the acceptance of H4. Similar results reported in Tables 6 and 7 also conclude the acceptance of H5 and H6. In parallel, Table 8 shows that positive reframing mediates the relationship between gratitude and overall technostress. The results show that gratitude induces positive reframing, which in turn reduces technostress among Indian students in the current study.

Discussion

The aim of the current study was to examine the previously unexplored relationship between positive reframing as a mediator between gratitude and technostress in Indian students. Our results suggest that positive reframing has a mediating effect between gratitude and technostress. In addition, we found a negative relationship between gratitude and three dimensions of technostress (techno-overload, techno-invasion and techno-complexity). Taken together, the results suggest that gratitude induces positive reframing, which in turn reduces technostress among Indian students in the current study. In the current study, students who show high levels of gratitude will positively reframe technology overload and possibly view the situation as an opportunity to learn various technologies, or as training for future roles. Such an optimistic interpretation will surely lessen the effects of the techno-overload stressor. Similarly, grateful students will try to learn different types of work–life balance while facing techno-invasion stressors.

Based on the broaden-and-build theory, previous researchers have reported empirical evidence for a negative relationship between gratitude and stress (Killen and Macaskill, 2015; Lee *et al.*, 2019; Leung and Tong, 2017; Sarkar and Garg, 2020; Vieselmeyer *et al.*, 2017). Likewise, using the same theoretical premise, this study confirms a negative relationship between gratitude and the three dimensions of technostress (techno-overload, techno-invasion and techno-complexity). To the best of the authors' understanding, this is the first study to examine the influence of gratitude on technology-induced stress.

Our results also confirm a positive relationship between gratitude and positive reframing. Grateful people are more likely to discover multiple ways to reinterpret negative events and reinforce the positive meanings behind them than to get bogged down without any endeavor (Frias *et al.*, 2011; Leon *et al.*, 2018). Gratitude benefits the individual indirectly in order to get out of a negative situation and at the same time promotes adaptive and flexible coping with a change of perspective (Lambert *et al.*, 2009, 2012; Sun *et al.*, 2020).

Theoretical implications

First, while the broaden-and-build theory is developed and used primarily in Western settings, it also shows applicability from an Eastern context. Generalizing a theory or phenomenon requires cross-cultural validation and application. Thus, empirical evidence for explaining the broaden-and-build theory among Indian students may encourage other researchers to investigate its usefulness in other non-Western countries. Second, this study is one of the few studies that examines the technostress among Indian students during COVID-19. We point out one of the hidden and indirect negative repercussions of the pandemic. While the whole world is intensely focused on rebuilding its health infrastructure, the present study also suggests some significant changes in education systems. Third, although previous studies have reported a negative association between gratitude and stress, this study extends the understanding of gratitude by concluding a negative association between gratitude and technostress. Finally, this study suggests another way that gratitude affects stress. It reports that gratitude develops positive reframing, which leads to less technostress in the students.

Practical implications

The results of the present study have some practical implications for teachers, academic leaders, parents and civil society. Although the study highlights the issue of technostress in difficult times of COVID-19, students are constantly exposed to technology-induced stress even in normal times too. The exponential growth of electronic devices, social media platforms and mobile apps is putting students under extreme pressure and increasing screen time, especially during the pandemic (Sultana *et al.*, 2021; Wong *et al.*, 2020). Together with lockdowns and restrictions on movement, as well as the sudden switch to online education, other stressors have been added. In addition, it has been suggested that online teaching and learning is the future of education. In summary, we suggest that college and school administrations organize seminars and workshops on how to apply gratitude in everyday life. These workshops could allow students to learn various gratitude interventions and practices, such as "count your blessings," "gratitude letter," "gratitude collages," "meditation," "self-introspection," "balancing blessings and wishes." Frequent interactions by in-house college teachers must follow these periodic exercises (Garg, 2020). The virtue of gratitude is contagion. Therefore, teachers, parents and the management of educational institutions are required to learn and express thankfulness more freely. It is also recommended to organize various short gratitude training programs for educators and parents.

As technostress is here to stay, we suggest integrating the concept of gratitude and its application into the curriculum. The University of Delhi and Delhi government schools have already introduced a "*Happiness course*" for their students. Similarly, Delhi Technological University has offered a course on gratitude for its management students. Other educational institutions could develop appropriate courses. Regulators like the University Grant Commission (UGC) and the All India Council of Technical Education (AICTE) could assist in the process. Similar to research ethics courses that are mandatory for doctoral students, we believe that courses on gratitude and happiness might be made mandatory for graduate or postgraduate students.

Limitations and future research directions

Several limitations of this study need to be acknowledged. First, the sample size in this study is relatively small in relation to the student population in India. In addition, the study is limited to the Delhi-NCR region only. Future research could examine a larger sample size with adequate representation from all over the country. Second, the current study relied primarily on quantitative data and analysis and further research could use a mixed-method approach to better understand the underlying mechanisms between positive reframing, gratitude and technostress. Third, the results are derived under an extreme COVID-19 pandemic situation; therefore, the results cannot be generalized to normal times. Follow-up studies could verify the results after the pandemic ends. Fourth, data on gratitude, positive reframing and technostress were collected from the same source and at the same time. This can lead to common method bias. Although appropriate remedies are used, future researchers may use longitudinal research design or double source data to negate common method bias.

In conclusion, the purpose of the current study was to examine the relationship between positive reframing as a mediator between gratitude and technostress. This study has shown that positive reframing has a mediating effect between gratitude and technostress. Moreover, we found a negative relationship between gratitude and three dimensions of technostress (techno-overload, techno-invasion and techno-complexity). Taken together, our data showed that gratitude induces positive reframing, which in turn reduces technostress among Indian students in the current study.

References

Abraham, J., Navya, C.J. and Joshy, V. (2019), "Perceived stress and coping strategies among post graduate students of a medical college in Thrissur, Kerala", *International Journal of Community Medicine and Public Health*, Vol. 6 No. 2, pp. 814-817.

Aharony, N. and Zion, A. (2018), "Effects of WhatsApp's use on working memory performance among youth", *Journal of Educational Computing Research*, Vol. 57 No. 1, pp. 226-245, doi: 10.1177/0735633117749431.

Allen, S. (2018), *The Science of Gratitude*, John Templeton Foundation, Conshohocken, PA.

Bono, G., Reil, K. and Hescox, J. (2020), "Stress and wellbeing in urban college students in the US during the COVID-19 pandemic: can grit and gratitude help?", *International Journal of Wellbeing*, Vol. 10 No. 3, pp. 39-57.

Bozkurt, A. and Sharma, R.C. (2020), "Education in normal, new normal, and next normal: observations from the past, insights from the present and projections for the future", *Asian Journal of Distance Education*, Vol. 15 No. 2, pp. i-x, doi: 10.5281/zenodo.4362664.

Brillhart, P.E. (2004), "Technostress in the workplace: managing stress in the electronic workplace", *Journal of American Academy of Business*, Cambridge, Vol. 5, pp. 302-307.

Brod, C. (1982), "Managing technostress: optimizing the use of computer technology", *The Personnel Journal*, Vol. 61 No. 10, pp. 753-757.

Carver, C.S. (1997), "You want to measure coping but your protocol is too long: consider the brief cope", *International Journal of Behavioral Medicine*, Vol. 4 No. 1, pp. 92-100.

Carver, C.S., Scheier, M.F. and Weintraub, J.K. (1989), "Assessing coping strategies: a theoretically based approach", *Journal of Personality and Social Psychology*, Vol. 56 No. 2, pp. 267-283, doi: 10.1037/0022-3514.56.2.267.

Crawford, J., Butler-Henderson, K., Rudolph, J., Malkawi, B., Glowatz, M., Burton, R., Magni, P. and Lam, S. (2020), "COVID-19: 20 countries' higher education intra-period digital pedagogy responses", *Journal of Applied Learning and Teaching*, Vol. 3 No. 1, pp. 1-20.

Duan, L. and Zhu, G. (2020), "Psychological interventions for people affected by the COVID-19 epidemic", *The Lancet Psychiatry*, Vol. 7 No. 4, pp. 300-302.

Emmons, R.A. and Crumpler, C.A. (2000), "Gratitude as a human strength: appraising the evidence", *Journal of Social and Clinical Psychology*, Vol. 19 No. 1, pp. 56-69, doi: 10.1521/jscp.2000.19.1.56.

Emmons, R.A. and Stern, R. (2013), "Gratitude as a psychotherapeutic intervention", *Journal of Clinical Psychology*, Vol. 69 No. 8, pp. 846-855.

Erren, T.C., Lewis, P. and Shaw, D.M. (2020), "COVID-19 and "natural" experiments arising from physical distancing: a hypothetical case study from chronobiology", *Chronobiology International*, Vol. 37 No. 7, pp. 1115-1117.

Fornell, C. and Larcker, D.F. (1981), "Evaluating structural equation models with unobservable variables and measurement error", *Journal of Marketing Research*, Vol. 18 No. 1, pp. 39-50, doi: 10.2307/3151312.

Forster, D.E., Pedersen, E.J., Smith, A., McCullough, M.E. and Lieberman, D. (2017), "Benefit valuation predicts gratitude", *Evolution and Human Behavior*, Vol. 38 No. 1, pp. 18-26.

Fredrickson, B.L. (2004), "The broaden-and-build theory of positive emotions", *Philosophical Transactions of the Royal Society B: Biological Sciences*, Vol. 359 No. 1449, pp. 1367-1377, doi: 10.1098/rstb.2004.1512.

Fredrickson, B.L., Mancuso, R.A., Branigan, C. and Tugade, M.M. (2000), "The undoing effect of positive emotions", *Motivation and Emotion*, Vol. 24 No. 4, pp. 237-258, doi: 10.1023/A:1010796329158.

Freire, C., Ferradásdel, M.M., Regueiro, B., Rodríguez, S., Valle, A. and Núñez, J.C. (2020), "Coping strategies and self-efficacy in University students: a person-centered approach", *Frontiers in Psychology*, Vol. 11, p. 841, doi: 10.3389/fpsyg.2020.00841.

Frias, A., Watkins, P.C., Webber, A.C. and Froh, J.J. (2011), "Death and gratitude: death reflection enhances gratitude", *Journal of Positive Psychology*, Vol. 6 No. 2, pp. 154-162, doi: 10.1080/17439760.2011.558848.

Galvin, J., Evans, M.S., Nelson, K., Richards, G., Mavritsaki, E., Giovazolias, T., Koutra, K., Mellor, B., Zurlo, M.C. and Smith, A.P. (In press), "Technostress, coping, and anxious and depressive symptomatology in university students during the COVID-19 pandemic", *Europe's Journal of Psychology*. doi: 10.23668/psycharchives.5108.

Garg, N. (2020), "Exploring role of gratitude in developing teacher leadership in Indian universities", *International Journal of Educational Management*, Vol. 34 No. 5, pp. 881-901, doi: 10.1108/ijem-07-2019-0253.

Garg, N. and Sarkar, A. (2020), "Vitality among university students: exploring the role of gratitude and resilience", *Journal of Organizational Effectiveness: People and Performance*, Vol. 7 No. 3, pp. 321-337.

Garg, N., Jain, A. and Punia, B.K. (2020), "Gratitude, social intelligence, and leadership among university teachers: mediation and moderation analysis", *International Journal of Organizational Analysis*, Vol. 29 No. 2, pp. 368-388.

Garland, E.L., Fredrickson, B., Kring, A.M., Johnson, D.P., Meyer, P.S. and Penn, D.L. (2010), "Upward spirals of positive emotions counter downward spirals of negativity: insights from the broaden-and-build theory and affective neuroscience on the treatment of emotion dysfunctions and deficits in psychopathology", *Clinical Psychology Review*, Vol. 30 No. 7, pp. 849-864.

Giorgi, G., Lecca, L.I., Alessio, F., Finstad, G.L., Bondanini, G., Lulli, L.G., Arcangeli, G. and Mucci, N. (2020), "COVID-19-related mental health effects in the workplace: a narrative review", *International Journal of Environmental Research and Public Health*, Vol. 17 No. 21, pp. 1-22, doi: 10.3390/ijerph17217857.

Hair, J.F., Anderson, R.E., Tatham, R.L., Black, W.C., Babin, B.J. and Anderson, R.E. (2010), *Multivariate Data Analysis: A Global Perspective*, 7th ed., Pearson Prentice Hall, New Jersey.

Hill, P.L., Allemand, M. and Roberts, B.W. (2013), "Examining the pathways between gratitude and self-rated physical health across adulthood", *Personality and Individual Differences*, Vol. 54 No. 1, pp. 92-96.

Ioannou, A. and Papazafeiropoulou, A. (2017), "Using IT mindfulness to mitigate the negative consequences of technostress", *AMCIS 2017 Proceedings*, available at: https://aisel.aisnet.org/amcis2017/AdoptionIT/Presentations/7/ (accessed 12 November 2021).

Jena, P.K. (2020), "Challenges and Opportunities created by Covid-19 for ODL: a case study of IGNOU", *International Journal for Innovative Research in Multidisciplinary Field (IJIRMF)*, Vol. 6 No. 5, pp. 217-222, doi: 10.31235/osf.io/jy2td.

Karr-Wisniewski, P. and Lu, Y. (2010), "When more is too much: operationalizing technology overload and exploring its impact on knowledge worker productivity", *Computers in Human Behavior*, Vol. 26 No. 5, pp. 1061-1072, doi: 10.1016/j.chb.2010.03.008.

Kaur, S., Sonali, S., Irawan, A.W., Dwisona, D., Lestari, M., Salman, M., Asif, N., Mustafa, Z.U., Khan, T.M., Shehzadi, N., Hussain, K., Tahir, H., Raza, M.H., Khan, M.T., Odriozola-González, P., Planchuelo-Gómez, Á., Irurtia, M.J., de Luis-García, R., Roy, A.A. and Panda, S. (2020), "Psychological impacts from COVID-19 among university students: risk factors across seven states in the United States", *International Journal of Environmental Research and Public Health*, Vol. 12 No. 1, pp. 1-14, doi: 10.31235/osf.io/2kasu.

Kecojevic, A., Basch, C.H., Sullivan, M. and Davi, N.K. (2020), "The impact of the COVID-19 epidemic on mental health of undergraduate students in New Jersey, cross-sectional study", *PLoS ONE*, Vol. 15 No. 9, pp. 1-16, doi: 10.1371/journal.pone.0239696.

Killen, A. and Macaskill, A. (2015), "Using a gratitude intervention to enhance well-being in older adults", *Journal of Happiness Studies*, Vol. 16 No. 4, pp. 947-964.

Klussman, K., Nichols, A.L., Langer, J. and Curtin, N. (2020), "Connection and disconnection as predictors of mental health and wellbeing", *International Journal of Wellbeing*, Vol. 10 No. 2, pp. 89-100.

Lambert, N.M., Graham, S.M., Fincham, F.D. and Stillman, T.F. (2009), "A changed perspective: how gratitude can affect sense of coherence through positive reframing", *Journal of Positive Psychology*, Vol. 4 No. 6, pp. 461-470, doi: 10.1080/17439760903157182.

Lambert, N.M., Fincham, F.D. and Stillman, T.F. (2012), "Gratitude and depressive symptoms: the role of positive reframing and positive emotion", *Cognition and Emotion*, Vol. 26 No. 4, pp. 615-633, doi: 10.1080/02699931.2011.595393.

Lee, H.W., Bradburn, J., Johnson, R.E., Lin, S.-H.J. and Chang, C.-H.D. (2019), "The benefits of receiving gratitude for helpers: a daily investigation of proactive and reactive helping at work", *Journal of Applied Psychology*, Vol. 104 No. 2, pp. 197-213.

Leon, E.D., Liang, Y., Lee, S., Kim, S.-A. and Kiang, L. (2018), "The development of gratitude in South Korean youth", *Cross-Cultural Research*, Vol. 52 No. 1, pp. 87-101.

Leung, C.C. and Tong, E.M.W. (2017), "Gratitude and drug misuse: role of coping as mediator", *Substance Use and Misuse*, Vol. 52 No. 14, pp. 1832-1839.

MacKenzie, S.B. and Podsakoff, P.M. (2012), "Common method bias in marketing: causes, mechanisms, and procedural remedies", *Journal of Retailing*, Vol. 88 No. 4, pp. 542-555.

Mahipalan, M. and Sheena, S. (2019), "Workplace spirituality and subjective happiness among high school teachers: gratitude as a moderator", *Explore*, Vol. 15 No. 2, pp. 107-114.

Mailizar, M., Burg, D. and Maulina, S. (2021), "Examining university students' behavioural intention to use e-learning during the COVID-19 pandemic: an extended TAM model", *Education and Information Technologies*, Vol. 26, pp. 7057-7077, doi: 10.1007/s10639-021-10557-5.

Majumdar, P., Biswas, A. and Sahu, S. (2020), "COVID-19 pandemic and lockdown: cause of sleep disruption, depression, somatic pain, and increased screen exposure of office workers and students of India", *Chronobiology International*, Vol. 37 No. 8, pp. 1191-1200, doi: 10.1080/07420528.2020.1786107.

McCullough, M.E., Emmons, R.A. and Tsang, J.A. (2002), "The grateful disposition: a conceptual and empirical topography", *Journal of Personality and Social Psychology*, Vol. 82 No. 1, pp. 112-127, doi: 10.1037/0022-3514.82.1.112.

Mills, P.J., Redwine, L., Wilson, K., Pung, M.A., Chinh, K., Greenberg, B.H., Lunde, O., Maisel, A., Raisinghani, A., Wood, A. and Chopra, D. (2015), "The role of gratitude in spiritual well-being in asymptomatic heart failure patients", *Spirituality in Clinical Practice*, Vol. 2 No. 1, pp. 5-17, doi: 10.1037/scp0000050.

Penado Abilleira, M., Rodicio-García, M.L., Ríos-de Deus, M.P. and Mosquera-González, M.J. (2021), "Technostress in Spanish university teachers during the COVID-19 pandemic", *Frontiers in Psychology*, Vol. 12, pp. 1-11, doi: 10.3389/fpsyg.2021.617650.

Petzold, M.B., Bendau, A., Plag, J., Pyrkosch, L., Mascarell Maricic, L., Betzler, F., Rogoll, J., Große, J. and Ströhle, A. (2020), "Risk, resilience, psychological distress, and anxiety at the beginning of the COVID-19 pandemic in Germany", *Brain and Behavior*, Vol. 10, e01745.

Pirkkalainen, H., Salo, M., Tarafdar, M. and Makkonen, M. (2019), "Deliberate or instinctive? Proactive and reactive coping for technostress", *Journal of Management Information Systems*, Vol. 36 No. 4, pp. 1179-1212, doi: 10.1080/07421222.2019.1661092.

Podsakoff, P.M., MacKenzie, S.B. and Podsakoff, N.P. (2011), "Sources of method bias in social science research and recommendations on how to control it", *Annual Review of Psychology*, Vol. 63 No. 1, pp. 539-569, doi: 10.1146/annurev-psych-120710-100452.

Prasath, P.R., Mather, P.C., Bhat, C.S. and James, J.K. (2021), "University student well-being during COVID-19: the role of psychological capital and coping strategies", *The Professional Counselor*, Vol. 11 No. 1, pp. 46-60, doi: 10.15241/prp.11.1.46.

Reuman, L.R., Mitamura, C. and Tugade, M.M. (2012), "Coping: an application of positive psychological constructs to disability", in Wehmeyer, M.L. (Ed.), *The Oxford Handbook of Positive Psychology and Disability*, Oxford University Press, New York, NY.

Şahin, F. and Çetin, F. (2017), "The mediating role of general self-efficacy in the relationship between the big five personality traits and perceived stress: a weekly assessment study", *Psychological Studies*, Vol. 62 No. 1, pp. 35-46.

Sahu, P. (2020), "Closure of universities due to coronavirus disease 2019 (COVID-19): impact on education and mental health of students and academic staff", *Cureus*, Vol. 2019 No. 4, pp. 4-9, doi: 10.7759/cureus.7541.

Salman, M., Asif, N., Mustafa, Z.U., Khan, T.M., Shehzadi, N., Tahir, H., Raza, M.H., Khan, M.T., Hussain, K., Khan, Y.H., Butt, M.H. and Mallhi, T.H. (2020), "Psychological impairment and coping strategies during the COVID-19 pandemic among students in Pakistan: a cross-sectional analysis", *Disaster Medicine and Public Health Preparedness*, pp. 1-7, doi: 10.1017/dmp.2020.397.

Sarkar, A. and Garg, N. (2020), "'Peaceful workplace' only a myth?", *International Journal of Conflict Management*, Vol. 31 No. 5, pp. 709-728, doi: 10.1108/IJCMA-11-2019-0217.

Satici, S.A. (2020), "Hope and loneliness mediate the association between stress and subjective vitality", *Journal of College Student Development*, Vol. 61 No. 2, pp. 225-239, doi: 10.1353/csd.2020.0019.

Schutte, N., Toppinen, S., Kalimo, R. and Schaufeli, W. (2000), "The factorial validity of the Maslach Burnout Inventory-General Survey (MBI-GS) across occupational groups and nations", *Journal of Occupational and Organizational Psychology*, Vol. 73 No. 1, pp. 53-66, doi: 10.1348/096317900166877.

Shanahan, L., Steinhoff, A., Bechtiger, L., Murray, A.L., Nivette, A., Hepp, U., Ribeaud, D. and Eisner, M. (2020), "Emotional distress in young adults during the COVID-19 pandemic: evidence of risk and resilience from a longitudinal cohort study", *Psychological Medicine*, pp. 1-10, doi: 10.1017/S003329172000241X.

Spagnoli, P., Molino, M., Molinaro, D., Giancaspro, M.L., Manuti, A. and Ghislieri, C. (2020), "Workaholism and technostress during the COVID-19 emergency: the crucial role of the leaders on remote working", *Frontiers in Psychology*, Vol. 11, 620310, doi: 10.3389/fpsyg.2020.620310.

Steindl-Rast, D. (2004), "Gratitude as thankfulness and as gratefulness", in Emmons, R.A. and McCullough, M.E. (Eds), *The Psychology of Gratitude*, Oxford University Press, Oxford, pp. 282-289, doi: 10.1093/acprof:oso/9780195150100.003.0014.

Stoeber, J. and Janssen, D.P. (2011), "Perfectionism and coping with daily failures: positive reframing helps achieve satisfaction at the end of the day", *Anxiety, Stress and Coping*, Vol. 24 No. 5, pp. 477-497.

Sultana, A., Tasnim, S., Hossain, M.M., Bhattacharya, S. and Purohit, N. (2021), "Digital screen time during the COVID-19 pandemic: a public health concern", *F1000Research*, Vol. 10 No. 81, p. 81.

Sun, P. and Kong, F. (2013), "Affective mediators of the influence of gratitude on life satisfaction in late adolescence", *Social Indicators Research*, Vol. 114 No. 3, pp. 1361-1369.

Sun, P., Sun, Y., Jiang, H., Jia, R. and Li, Z. (2020), "Gratitude as a protective factor against anxiety and depression among Chinese adolescents: the mediating role of coping flexibility", *Asian Journal of Social Psychology*, Vol. 23 No. 4, pp. 447-456.

Tarafdar, M., Tu, Q., Ragu-Nathan, B.S. and Ragu-Nathan, T.S. (2007), "The impact of technostress on role stress and productivity", *Journal of Management Information Systems*, Vol. 24 No. 1, pp. 301-328, doi: 10.2753/MIS0742-1222240109.

Upadhyaya, P. and Vrinda (2020), "Impact of technostress on academic productivity of university students", *Education and Information Technologies*, Vol. 26, pp. 1647-1664, doi: 10.1007/s10639-020-10319-9.

Vieselmeyer, J., Holguin, J. and Mezulis, A. (2017), "The role of resilience and gratitude in posttraumatic stress and growth following a campus shooting", *Psychological Trauma: Theory, Research, Practice, and Policy*, Vol. 9 No. 1, pp. 62-69.

Wang, X., Tan, S.C. and Li, L. (2020), "Technostress in university students' technology-enhanced learning: an investigation from multidimensional person-environment misfit", *Computers in Human Behavior*, Vol. 105, 106208.

Watkins, P.C., Woodward, K., Stone, T. and Kolts, R.L. (2003), "Gratitude and happiness: development of a measure of gratitude, and relationships with subjective well-being", *Social Behavior and Personality*, Vol. 31 No. 5, pp. 431-451, doi: 10.2224/sbp.2003.31.5.431.

Westermann, T. (2017), *User Acceptance of Mobile Notifications, T-labs Series in Telecommunication Services*, Springer, Singapore. doi: 10.1007/978-981-10-3851-8.

Wong, H.Y., Mo, H.Y., Potenza, M.N., Chan, M.N.M., Lau, W.M., Chui, T.K., Pakpour, A.H. and Lin, C.Y. (2020), "Relationships between severity of internet gaming disorder, severity of problematic social media use, sleep quality and psychological distress", *International Journal of Environmental Research and Public Health*, Vol. 17 No. 6, 1879.

Wood, A.M., Joseph, S., Lloyd, J. and Atkins, S. (2009), "Gratitude influences sleep through the mechanism of pre-sleep cognitions", *Journal of Psychosomatic Research*, Vol. 66 No. 1, pp. 43-48.

Zhou, X., Snoswell, C.L., Harding, L.E., Bambling, M., Edirippulige, S., Bai, X. and Smith, A.C. (2020), "The role of telehealth in reducing the mental health burden from COVID-19", *Telemedicine and E-Health*, Vol. 26 No. 4, pp. 377-379.

About the authors

Dr. Naval Garg is an assistant professor (HR and OB) at University School of Management and Entrepreneurship, Delhi Technological University, New Delhi. He holds four years of teaching and six years of industry experience. His research areas of interest are workplace spirituality, gratitude, techno-ethics and human–machine interactions. He has published more than forty papers in various national and international journals.

Shivangi Verma is a PhD research scholar at University School of Management and Entrepreneurship, Delhi Technological University, New Delhi. She holds an MBA degree from Dr. B.R. Ambedkar University Delhi, India, and an undergraduate degree in Psychology from University of Delhi, India. Her research interests include various aspects of organization behavior, human resource management, business ethics, technology, education and psychology.

Dr. Jason Timothy Palframan holds a PhD in Transpersonal Psychology and is lecturer in Human Resource Management and Social Psychology in the Department of Management Studies at Technological University of Shannon: Midlands and Midwest, Ireland. He is also a chartered psychologist with the British Psychological Society. His expertise lies in organisational behavior and social psychology, particularly in workplace spirituality and in sub-topics such as self-transformation, compassion and gratitude at work. His current research projects include workplace spirituality, thriving and trust; CSR and personal values orientations; and the value of work in a post-pandemic world. Jason Timothy Palframan is the corresponding author and can be contacted at: jason.palframan@tus.ie

For instructions on how to order reprints of this article, please visit our website:
www.emeraldgrouppublishing.com/licensing/reprints.htm
Or contact us for further details: **permissions@emeraldinsight.com**

J Mater Sci

Computational Materials Design

Realizing high thermoelectric performance in p-type $RbZn_4P_3$ Zintl compound: a first-principles investigation

Sangeeta[1], Ramesh Kumar[2], and Mukhtiyar Singh[1,*]

[1] *Department of Applied Physics, Delhi Technological University, Delhi 110042, India*
[2] *Department of Physics, Guru Jambheshwar University of Science and Technology, Hisar 124001, India*

Received: 30 November 2021
Accepted: 25 January 2022

© The Author(s), under exclusive licence to Springer Science+Business Media, LLC, part of Springer Nature 2022

ABSTRACT

This work presents structural, elastic, electronic, and thermoelectric properties of a tetragonal Zintl compound $RbZn_4P_3$, using the Density Functional Theory and Boltzmann transport equation. The computed structural parameters and bond lengths agree well with available experimental data. We use the density functional perturbation theory approach to obtain the Phonon dispersion curve to prove its dynamical stability. The charge density analysis confirms the coexistence of ionic and covalent bonding in the system. The calculated electronic structure shows the semiconducting nature of $RbZn_4P_3$ with a direct bandgap of 1.02 eV using the TB-mBJ approach. We analyze its thermoelectric properties for various hole doping concentrations at different temperatures (300 K-700 K). We obtained a high value of Seebeck coefficient (760.00 μVK^{-1}) at 700 K and (641.72 μVK^{-1}) at 300 K. The lattice thermal conductivity is estimated using Slack's equation to get the true value of total thermal conductivity. We obtain an ultra-low total thermal conductivity, which in conjunction with high power factor, results in enhanced thermoelectric efficiency or figure of merit (*ZT*). The maximum *ZT* value is found to be 0.78 for optimum hole doping concentration of 2×10^{20} cm^{-3} at 700 K. This study reveals that $RbZn_4P_3$ possesses excellent potential as thermoelectric energy harvesting material.

Introduction

A continuously increasing global energy demand resulted in an unprecedented consumption of fossil fuels, leading to harmful effects on the environment. To avoid the over usage of fossil fuels and safeguard the environment, clean and sustainable energy alternatives become the need of the hour. Various such options have been proposed in the recent past, such as piezoelectric, optoelectronics, thermoelectrics,

Handling Editor: M. Grant Norton.

Address correspondence to E-mail: mukhtiyarsingh@dtu.ac.in; msphysik09@gmail.com

https://doi.org/10.1007/s10853-022-06953-y

Published online: 09 February 2022

etc.[1–7]. Thermoelectric material that converts waste thermal energy into useable thermal energy and are utilized in thermoelectric power generation. The key property in this regard is known as the 'thermoelectric figure of merit (FOM)' often written as $ZT = S^2\sigma T/k_{total}$, where S, σ, T, and k_{total} are, respectively, the Seebeck coefficient, electrical conductivity, absolute temperature, and the total thermal conductivity [8–10]. A highly efficient TE has a high-Power Factor ($PF = S^2\sigma$) and low thermal conductivity ($k_{total} = k_e + k_l$) simultaneously, where k_e and k_l are electronic and lattice contributions, respectively, to k_{total}. However, these parameters are strongly dependent on each other and related to carrier concentration. Therefore, it becomes pretty challenging for material scientists to optimize them to achieve higher TE performance [11–13]. One can use several strategies to decouple these parameters, including enhancing PF by adjusting the carrier concentration through band engineering and reducing lattice thermal conductivity by nanostructuring [14, 15].

Currently, materials like Bi_2Te_3 [16], PbTe [17], SnSe [18], and Half-Heusler [19] are under quite intense research for TE application. Apart from these systems, Zintl compounds have been studied for the last few years to achieve high TE performance. These materials offer an excellent balance between large PF and low thermal conductivity, resulting in impressive TE performance [20, 21]. Furthermore, their chemical tunability, complex bonding patterns, low bandgap, and strong anharmonicity make them suitable TE hosts [22, 23]. In these compounds, electropositive cations such as alkali and alkaline earth metals donate their valence electrons to the anionic network, which further forms covalent bonding according to the Zintl-Klemm concept to satisfy valence requirement [24].

A broad class of Zintl compounds such as binary, ternary, and quaternary has been studied experimentally and theoretically [25–28]. Among these ternary compounds $M_2Zn_5As_4$ (M = K, Rb) [26], and Sr_3GaSb_3, [27] etc., exhibit good TE performance. A distinguishable characteristic of these TE materials is that they are natively p-type semiconductors having moderate to high hole concentrations due to self-doping [29]. It has been seen that As and Sb are used as major, and P is used as the minor substituting element [25, 26, 29]. Recent studies show that P-based Zintl compounds, such as NaSnP, $CaIn_2P_2$, $Ba_3Al_3P_5$ and $Ba_3Ga_3P_5$ have tuneable effective mass and carrier concentration with low lattice thermal conductivity and exhibits intriguing TE properties [30–32]. Experimentally synthesized p-type $RbZn_4As_3$ shows a high Seebeck Coefficient of about 800 μVK^{-1} and very high room temperature resistivity [33]. So, we envisaged that replacing As with P in $RbZn_4As_3$ can lead to better TE properties.

Thus, in this work, we studied the TE properties of ternary Zintl compound $RbZn_4P_3$, using first-principles calculations in conjunction with Boltzmann transport theory (BTE) under constant relaxation time and rigid band approximation. We have obtained phonon dispersion using the Density Functional perturbation theory (DFPT) approach to check the compounds' dynamical stability. To know the bonding character and charge transfer in the $RbZn_4P_3$, we analyze charge density behavior. In addition, we have also calculated elastic constants to obtain Debye temperature and thus lattice thermal conductivity using Slack's equation. Further to explore its TE performance, we have calculated Electronic Fitness Function (EFF), which determines the extent of decoupling between S and σ/τ. This study provides an efficient p-type Zintl phase with high potential as future TE energy harvesting material in a wide temperature range (300 K-700 K).

Computational methods

The structural, elastic, electronic, and TE properties of $RbZn_4P_3$ were carried out within the framework of Density Functional Theory (DFT) using Full potential linearized augmented plane wave as implemented in WIEN2K software [34]. The structural optimization was carried out by the generalized gradient approximation (GGA) of Perdew-Burke-Ernzerhof (PBE) [35]. We have used a $20 \times 20 \times 10$ k-point mesh which generates 393 k-points in the irreducible Brillouin zone (IBZ). The number of plane waves in the interstitial region and cut-off energy of core and valence states was set as $R_{MT} \times K_{max} = 7$ and -6 Ry, respectively. Kohn–Sham equation was solved self-consistently with an energy convergence of 0.0001 Ry. As in most cases, GGA underestimates the band gaps of semiconductors; therefore, we employed Tran Blaha modified Becke Johnson (TB-mBJ) approach to calculate the electronic band structure and transport properties [36]. The thermoelectric properties were calculated by solving the BTE under the constant

relaxation time approximation (CRTA) and rigid band approximation (RBA) as implemented in BoltzTraP code [37]. A denser k-point mesh (42 × 42 × 16) was used for this calculation. To analyze the extent of decoupling between S and σ/τ we have calculated EFF using transM code [38]. We have obtained the elastic constants of $RbZn_4P_3$ using the stress–strain relationship using VASP [39]. To check the dynamical stability, the DFPT approach was used to calculate the phonon dispersion of $RbZn_4P_3$ by building a 3 × 3 × 1 supercell and using a 9 × 9 × 5 k-point mesh employing the Phonopy code [40].

Results and discussion

Structural properties

$RbZn_4P_3$ Zintl compound crystallizes in the tetragonal structure having space group *P4/mmm* and has a framework of $[Zn_4P_3]^-$ layers with Rb^+ atoms between the layers. The unit cell of $RbZn_4P_3$ compound is shown in Fig. 1a. The Rb atom occupies the Wyckoff position 1*b* (0, 0, 1/2), Zn and P1, P2 atoms are located at 4*i* (0, 1/2, 0.1577) and 2 *h* (1/2, 1/2, 0.2864), 1*a* (0, 0, 0), respectively. Each unit cell is made up of four distinct ions due to the varied locations of the Phosphorus atoms. We have performed structural optimization of this compound and calculated its equilibrium lattice parameters. The optimized structural parameters and bond length are listed in Table 1, which are in good agreement with the available experimental results [33].

To check the stability of the compound, we have calculated the formation energy E_{for} using the following equation [41]:

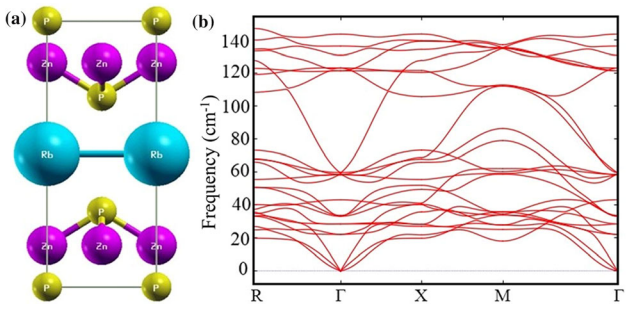


Figure 1 **a** Crystal Structure of the unit cell and **b** Phonon dispersion curve of $RbZn_4P_3$ compound.

$$E_{\text{for}} = \frac{[E_{RbZn_4P_3} - (E_{Rb} - 4E_{Zn} - 3E_P)]}{N} \quad (1)$$

where $E_{RbZn_4P_3}$ is the ground state energy of $RbZn_4P_3$, N is the *total* number of atoms in the unit cell and E_{Rb}, E_{Zn}, and E_P, respectively, are the total energy per atom for Rb, Zn, and P in bulk form. The calculated E_{for} is found to be -1.9108 eV/atom, indicating that this compound is thermodynamically stable.

Further to determine the dynamical stability, we have obtained the phonon dispersion along with R-Γ-X-M- Γ high symmetry direction in the Brillouin zone, which is presented in Fig. 1b using the DFPT approach [40]. Since there are eight atoms per unit cell in $RbZn_4P_3$, hence there are total 24 phonon branches in the phonon dispersion curve, out of which three are acoustic, and 21 are optical branches. The lower branches in the dispersion spectra correspond to acoustic branches and upper branches represent the optical branches with the corresponding frequency range (0–25 cm^{-1}), and (25–144 cm^{-1}), respectively. It can be seen that there are no negative frequencies, thereby confirming that tetragonal phase of $RbZn_4P_3$ compound is dynamically stable. Also, no phonon gap between optical and acoustic branches is observed, indicating a strong coupling of acoustic-optical phonon modes, which might provide a material with low lattice thermal conductivity [42]. The calculated total and projected phonon density of states is also shown in Fig. 2. It can be seen that projected phonon density of states in uppermost optical phonon density region is mainly contributed by the vibrational motion of P- atoms, while in the lower optical region, coupled vibrational motion of Rb- and Zn- atoms is dominated.

Elastic properties

The elastic constants of the tetragonal $RbZn_4P_3$ compound have been obtained by stress–strain relationship. Because of its tetragonal symmetry, this compound possesses six independent elastic constants: C_{11}, C_{12}, C_{13}, C_{33}, C_{44}, and C_{66}, as listed in Table 2. To check whether this compound is mechanically stable, we need to verify the Born stability criteria given as [43]:

$C_{11} > 0$, $C_{33} > 0$, $C_{44} > 0$, $C_{66} > 0$, $(C_{11}—C_{12}) > 0$, $(C_{11} + C_{33}—2C_{13}) > 0$ and $(2C_{11} + C_{33} + 2C_{12} + 4C_{13}) > 0$.

Table 1 Calculated structural parameters (a and c in Å and V in Å^3) and bond lengths (in Å) of $RbZn_4P_3$ in comparison with available experimental values

	Structural parameters			Bond lengths (Å)			
	a (Å)	c (Å)	V (Å^3)	Rb-Zn	Rb-P1	Zn-P1	Zn-P2
Present work	4.080	10.230	170.41	4.068	3.635	2.423	2.591
Expt. Work (Ref. 33)	4.059	10.069	165.92	3.999	3.586	2.408	2.577

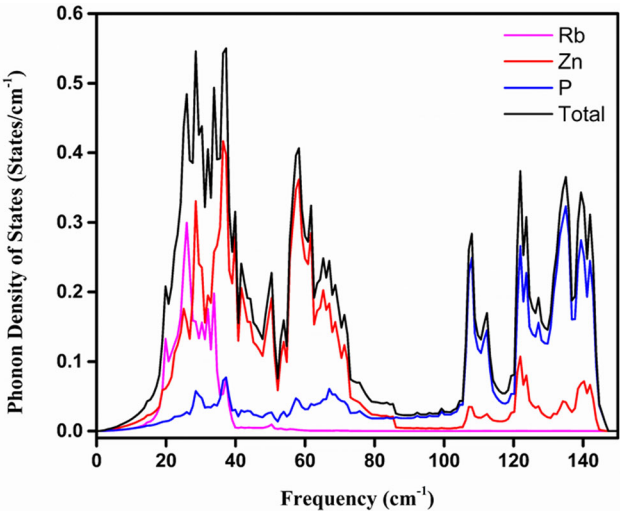


Figure 2 Total and Projected phonon density of state of $RbZn_4P_3$ compound.

All calculated elastic parameters completely satisfied the Born mechanical stability criteria for tetragonal structure, indicating the mechanical stability of the compound under ambient conditions. Further, we have calculated various mechanical properties such as bulk modulus (B), shear modulus (G), Young's modulus (Y), and Poisson ratio (v), using the elastic parameters in order to determine physical properties like stiffness, strength, hardness and ductile or brittleness behavior of $RbZn_4P_3$. These mechanical parameter values are also reported in Table 2, along with elastic constants. We have used Voigt-Reuss-hill approximation (VRH) to estimate B and G [44]. The mechanical stability is dominated by shear modulus as G is smaller than B. Young's modulus provides the degree of stiffness of a compound; the higher value of Y indicates that $RbZn_4P_3$ is stiffer. The value of Poisson's ratio is less than the threshold value ($v = 0.26$), which predicts the brittle nature of $RbZn_4P_3$ [45]. Apart from these, we have also determined Debye temperature (θ_D) an essential parameter for calculating lattice thermal conductivity. It linked to elastic constants via average sound velocity (v_m) as:

$$\theta_D = (h/k_B)\left[\left(\frac{3n}{4\pi}\right)(N_A\rho/M)\right]^{\frac{1}{3}}.v_m \tag{2}$$

where h is Planck's constant, k_B is Boltzmann's constant, N_A is Avogadro's number, n is the number of atoms in the unit cell, ρ is the density and M is the molecular weight of the compound. The average sound velocity is computed using transverse (v_t) and longitudinal sound velocity (v_l) using elastic constants as expressed by the following equations [46]:

$$v_m = \left[\frac{1}{3}\left(\frac{2}{v_t^3}+\frac{1}{v_l^3}\right)\right]^{\frac{-1}{3}} \tag{3}$$

$$v_l = \sqrt{\frac{G}{\rho}} \tag{4}$$

$$v_t = \sqrt{\frac{3B+4G}{\rho}} \tag{5}$$

The obtained values of v_l, v_t, v_m, and θ_D for $RbZn_4P_3$ are 7.30 kms^{-1}, 12.36 kms^{-1}, 8.09 kms^{-1}, and 870.03 K, respectively.

Electronic structure properties

The electronic band structure along with the density of states (DOS) of the compound is calculated using the TB-mBJ approach and shown in Fig. 3. Our calculations have predicted a direct bandgap of 1.02 eV

Table 2 Calculated elastic coefficients C_{ij} (i,j = 1–6), bulk modulus (B), shear modulus (G), Young's modulus (Y), all in units of GPa, and Poisson ratio (v)

Parameter	C_{11}	C_{12}	C_{13}	C_{33}	C_{44}	C_{66}	B	G	Y	v
$RbZn_4P_3$	1017.42	126.38	132.66	500.42	205.50	124.30	350.78	229.15	567.53	0.23

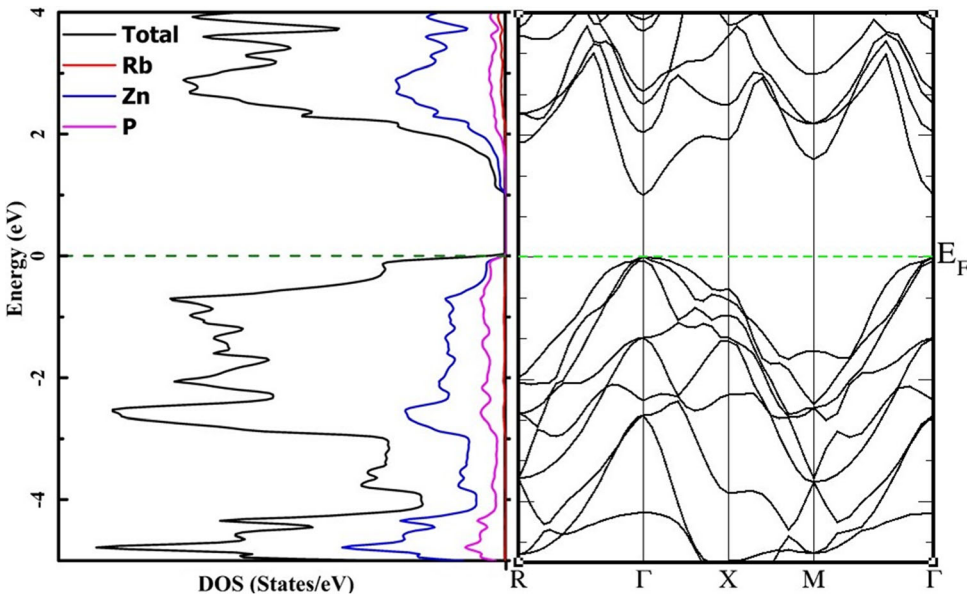


Figure 3 The electronic band structure and DOS of $RbZn_4P_3$ calculated within TB-mBJ approximation. The Fermi level is set to 0 eV.

at Γ-point. The Projected density of states (PDOS) shows that the P atom contributes the most to the valence band (VB), followed by a minor contribution from Zn atom and a very feeble contribution from Rb atom. In the conduction band (CB) *s*-orbitals of P atom are dominant from 1.5 eV–3.5 eV, and above this energy range, its *p*-orbital is prevalent over the Zn and Rb atoms as presented in Fig. 4. Therefore, we can see clearly from PDOS that the top of the VB is formed mainly by P-*p* and Zn-*p*, *s* orbitals, and the bottom of the conduction band is composed of P-*s* and Zn-*p* orbitals.

Next, we have calculated the charge density (in units of $eÅ^{-3}$) of $RbZn_4P_3$ in the *(010)* plane, which is shown in Fig. 5. The purple color shows the large accumulation of electrons in the region, while the red color shows the charge depleted region. The charge density analysis shows the transfer of electrons among Rb, Zn, and P, which is useful in determining the bonding properties of the compound [47]. The distribution of valence charge density around the Rb atom shows that it donates its valence electrons to the network $[Zn_4P_3]^-$, and indicates that balancing of valence charge is maintained as (Rb^+), (Zn^{2+}), (P^{3-}) within its configuration, which allows the separation of electron energy bands needed to form a bandgap. Both the VB maxima and CB minima are derived from hybridized P and Zn orbitals, which corresponds to the significant contribution of covalent Zn-P bonds. Therefore, covalent bonds are present in the polyanionic network, which interacts with the electropositive metal cations through ionic bonds. Covalent and ionic bonds coexist in the various Zintl

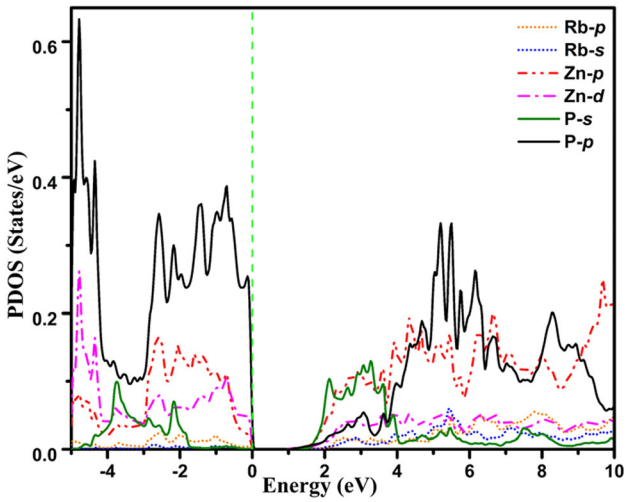


Figure 4 The calculated projected DOS of $RbZn_4P_3$ within TB-mBJ approximation. The Fermi level is set to 0 eV.

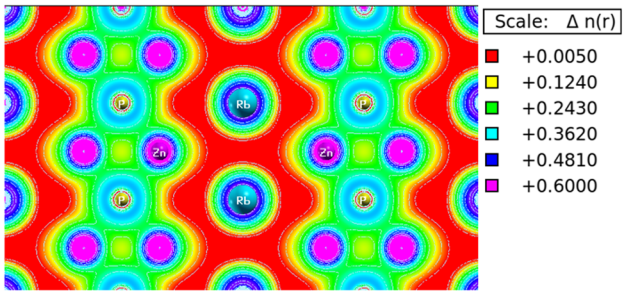


Figure 5 The computed charge density (in units of $eÅ^{-3}$) plot of $RbZn_4P_3$ in *(010)* plane.

phase compounds [26, 48], which is compatible with the bonding picture. As seen in the PDOS the major contribution of P and Zn atoms is also reflected in the charge density contour plot.

Thermoelectric properties

The TE parameters of $RbZn_4P_3$ have been calculated by solving BTE using BoltzTraP code. We have used CRTA, which means S is independent of scattering rate (τ), and RBA, which assumes that doping concentrations and temperature do not affect electronic band structure [37]. We have studied the effect of hole doping concentration and temperature on thermoelectric properties.

The Seebeck coefficient can be expressed as [49]:

$$S = \frac{8\pi^2 k_B^2}{3eh^2} m * T\left(\frac{\pi}{3n}\right)^{\frac{2}{3}} \quad (6)$$

where m^* is effective mass, n is the carrier concentration, T is the absolute temperature. As the doping concentration of hole (n) increases from 1×10^{18} cm^{-3} to 1×10^{21} cm^{-3}, S decreases as depicted in Fig. 6a at different temperatures from 300 to 700 K. It has been observed that the positive value of Seebeck coefficient sharply decreases with increase in the hole doping concentrations at fixed temperatures. The maximum observed value of S is 735.43 μVK^{-1} at 700 K, 725.75 μVK^{-1} at 600 K, 708.58 μVK^{-1} at 500 K, 683.41 μVK^{-1} at 400 K, and 641.72 μVK^{-1} at 300 K. It implies that for all doping concentrations, the Seebeck coefficient increases as the temperature increases. This shows that the material has p-type semiconducting nature. The calculated value of S for $RbZn_4P_3$ is comparable with the experimentally measured value of a similar Zintl compound [33]. The effective mass of electrons and holes is calculated along Γ-X direction, which is 0.14 m_e in the CB and 0.47 m_e (light hole), 1.31 m_e (heavy hole) in the VB. The high effective mass of holes leads to a high S value of $RbZn_4P_3$.

The calculated σ/τ increases with increase in hole doping concentration for the entire studied doping range (which as per the relation, $\sigma = ne\mu$) as shown in Fig. 6b. It remains almost constant up to 1×10^{19} cm^{-3} and then slightly increases up to 5×10^{19} cm^{-3}; after that, it abruptly increases and reaches a maximum value of 25.43×10^{18} Ω^{-1} m^{-1} s^{-1} at concentration 1×10^{21} cm^{-3}. The observed value of σ/τ versus hole concentration is nearly the same for all temperatures, indicating its weak dependence on T. The electronic contribution to thermal conductivity (k_e/τ) is shown in Fig. 6c. It has a similar behavior as σ/τ, as k_e and σ are interrelated by Wiedemann Franz law, $k_e = L\sigma T$ where L is Lorentz number [49], but highly temperature dependent.

The variation of PF for hole doping concentration at different temperatures is shown in Fig. 6d. As carrier concentration increases from 1×10^{18} cm^{-3} to 1×10^{19} cm^{-3}, PF increases slightly first and after that, it increases sharply for all temperatures and attains maximum value between 4×10^{20} cm^{-3} and 7×10^{20} cm^{-3}. The calculated highest values of PF are 5.57×10^{11} Wm^{-1} K^{-2} s^{-1} at 700 K, 4.89×10^{11} Wm^{-1} K^{-2} s^{-1} at 600 K, 4.19×10^{11} Wm^{-1} K^{-2} s^{-1} at 500 K, 3.46×10^{11} Wm^{-1} K^{-2} s^{-1} at 400 K, and 2.65×10^{11} Wm^{-1} K^{-2} s^{-1} at 300 K. It can be seen that the optimum carrier concentration for $RbZn_4P_3$ is of the order of 10^{20} cm^{-3}.

We have computed the electronic fitness function (EFF), using transM code [38], which is given by the formula $(S^2\sigma/\tau)(N/V)^{-2/3}$. Based on the complexity of electronic structure, EFF helps to detect high-performance TE material. As discussed above, S and σ/τ are correlated, and the degree of correlation is to be identified in order to manipulate these parameters independently [50, 51]. In Fig. 7, we have plotted EFF with hole doping concentration at different temperatures. The maximum observed value is 6.4×10^{-20} $W^{5/3}$ $ms^{-1/3}$ K^{-2} at 700 K for optimum doping concentration (1×10^{20} cm^{-3}), which indicates that there is a strong decoupling between S and σ/τ. The high value of EFF signifies the good TE behavior of a material.

In order to calculate the total thermal conductivity (k_{total}), we have determined the lattice thermal conductivity (k_l) of $RbZn_4P_3$ using Slack's equation [52]:

$$k_l = \frac{AM_a\delta n^{\frac{1}{3}}{\theta_D}^3}{\gamma^2 T} \quad (7)$$

where M_a denotes the average atomic mass of atoms in the unit cell, δ is the cube root of average volume of the unit cell, γ is Grüneisen parameter, θ_D is the.

Debye temperature and A is calculated using γ [53] as:

$$A = \frac{2.43 \times 10^{-8}}{1 - 0.514\gamma^{-1} + 0.228\gamma^{-2}} \quad (8)$$

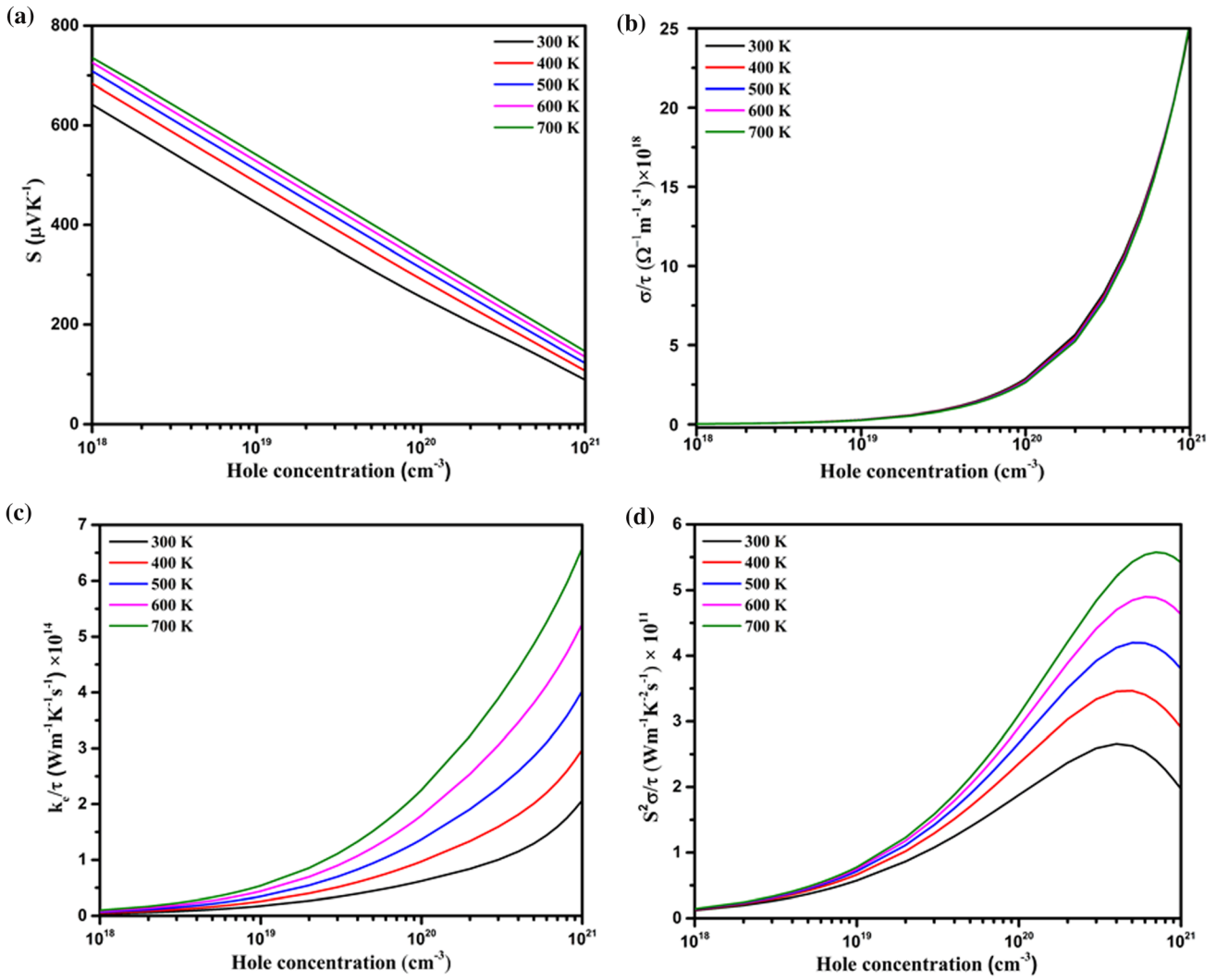


Figure 6 The variation of **a** S **b** σ/τ **c** k_e/τ and **d** $S^2\sigma/\tau$ with hole doping concentration for $RbZn_4P_3$ at different temperatures.

Further, we have calculated γ, which is related to Poisson's ratio as given by the following relation

$$\gamma = \frac{3}{2}\left(\frac{1+v}{2-3v}\right) \tag{9}$$

The Grüneisen parameter can partially address the issue of anharmonicity of phonon–phonon interaction [31, 54]. High Grüneisen parameter implies strong anharmonic phonon–phonon scattering. The calculated γ value (1.42) is comparable to that of Bi_2Te_3 [55]. Figure 8a, inset, shows the variation of lattice thermal conductivity with temperature. It is found that k_l decreases as temperature increases. The observed value of k_l at room temperature is estimated to be 1.32 $Wm^{-1}\,K^{-1}$, and it decreases to 0.56 $Wm^{-1}\,K^{-1}$ at temperature 700 K. This reduction in k_l is beneficial for yielding high thermoelectric conversion efficiency of the compound. Finally, k_{total} has been obtained using $k_e/\tau \times \tau$ ($\tau = 10^{-14}$ s) and k_l, as shown in Fig. 8a. The calculated value of k_{total} is 2.15 $Wm^{-1}\,K^{-1}$ at room temperature for optimum carrier concentration, 10^{20} cm^{-3}.

The variation of ZT with hole doping concentration at all temperatures ranging from 300 to 700 K is shown in Fig. 8b. At a fixed temperature, ZT increases with the increase in hole carrier concentration and reaches its maximum value at $\sim 2 \times 10^{20}$ cm^{-3}, then decreases significantly. Hence, we have obtained the enhanced FOM for our optimum hole doping concentration ($\sim 2 \times 10^{20}$ cm^{-3}). Moreover, at a fixed doping concentration, ZT increases as temperature increases from 300 to 700 K. The maximum observed ZT values at optimum hole doping concentration are 0.78, 0.72, 0.65, 0.52, and 0.33 at temperatures 700 K,

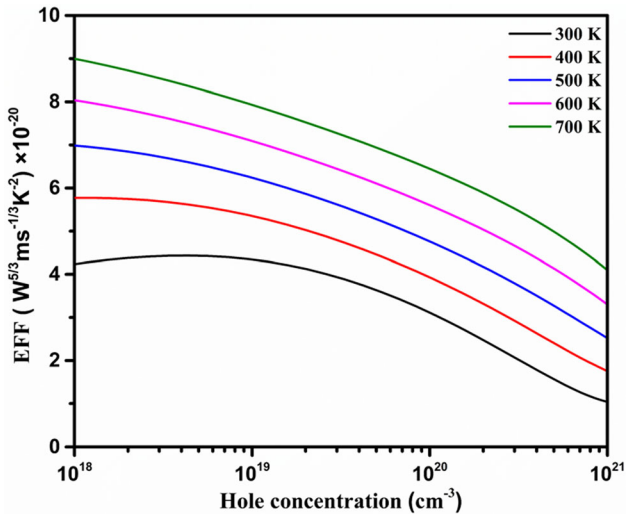


Figure 7 Computed Electronic Fitness Function with hole doping concentration at different temperatures.

600 K, 500 K, 400 K, and 300 K, respectively. This shows $RbZn_4P_3$ as a promising candidate for future thermoelectric applications. The observed high *ZT* of this compound is contributed by low k_{total} and high value of power factor.

Conclusion

In this study, we have explored the thermoelectric properties of $RbZn_4P_3$ Zintl compound at different hole doping concentrations using first-principles calculations in combination with Boltzmann transport theory. The obtained structural parameters and bond lengths are in good agreement with the experimentally measured values. The formation energy, phonon dispersion, and elastic properties have confirmed that $RbZn_4P_3$ is stable thermodynamically, dynamically, and mechanically, respectively. Charge density analysis shows the Rb atom completely transfers its valence electron to the covalently bonded cluster $[Zn_4P_3]^-$, thus confirming the coexistence of ionic and covalent bonding in $RbZn_4P_3$. The electronic band structure calculations reveal that $RbZn_4P_3$ is a moderate bandgap semiconductor. By solving Slack's equation, lattice thermal conductivity is found to be 0.56 $Wm^{-1}\,K^{-1}$ at 700 K temperature, and a peak *ZT* value (0.78) at 700 K for optimal hole doping concentration (2×10^{20} cm^{-3}) have been obtained. The high *ZT* values for a widely studied temperature range (300 K-700 K) make this compound quite promising for future TE material. Further efforts can be made to enhance thermoelectric performance by reducing lattice thermal conductivity by increasing the anharmonicity through the Grüneisen parameter and suppressing the average sound velocity by increasing density or decreasing stiffness. We believe that the present study would pave the way for future experimental thermoelectric energy harvesting studies on this material.

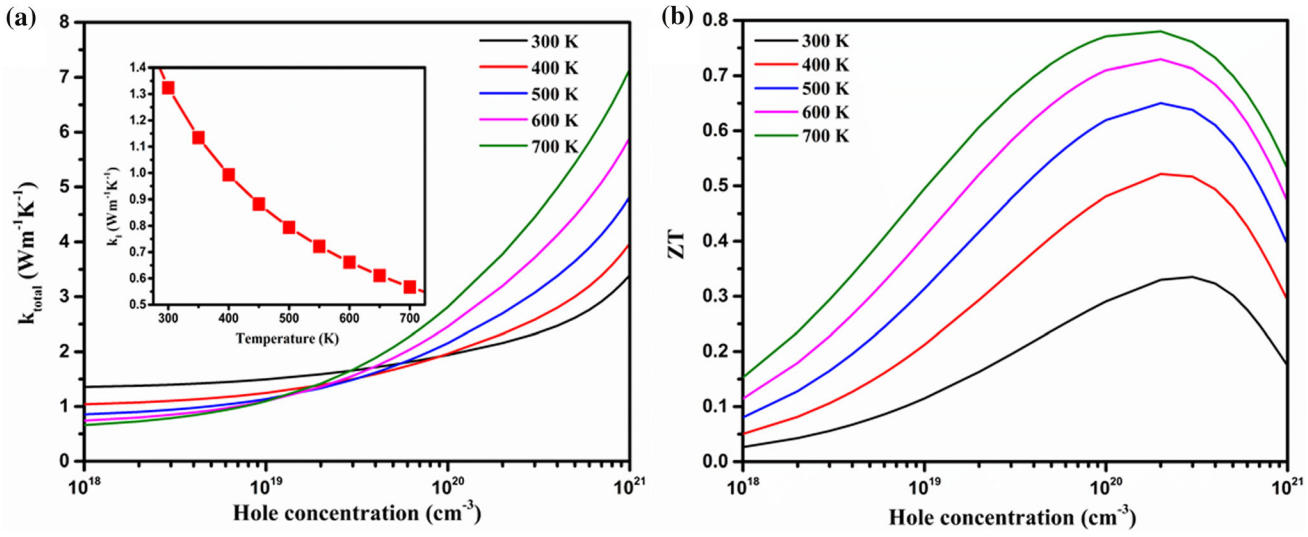


Figure 8 **a** The variation of total thermal conductivity (variation of lattice thermal conductivity with temperature is shown in inset) and **b** Figure of Merit *ZT* with hole doping concentration at various temperatures.

Acknowledgements

One of the authors (Sangeeta) wish to acknowledge the financial support provided by Delhi Technological University, Delhi for pursuing Ph.D.

Declarations

Conflict of interest The authors declare that they have no conflict of interest.

References

[1] Tong C (2019) Emerging materials for energy harvesting. Introduction to materials for advanced energy systems. Springer, Cham, pp 719–817

[2] Mori T, Priya S (2018) Materials for energy harvesting: At the forefront of a new wave. MRS Bull 43:176–180. https://doi.org/10.1557/mrs.2018.32

[3] Zareef F, Rashid M, Ahmadini AAH, Alshahrani T, Kattan NA, Laref A (2021) Optoelectronic and thermoelectrical and mechanical properties of CdLu2X4 (X = S, Se) using first-principles calculations for energy harvesting applications. Mater Sci Semicond Process 127:105695. https://doi.org/10.1016/j.mssp.2021.105695

[4] Cai Q, Zhu S (2022) The nexus between vibration-based energy harvesting and structural vibration control: a comprehensive review. Renew Sust Energ Rev 155:111920. https://doi.org/10.1016/j.rser.2021.111920

[5] Safaei M, Sodano HA, Anton SR (2019) A review of energy harvesting using piezoelectric materials: State-of-the-art a decade later (2008–2018). Smart Mater Struct 28:113001. https://doi.org/10.1088/1361-665X/ab36e4

[6] Roknuzzaman M, Ostrikov KK, Wang H, Du A, Tesfamichael T (2017) Towards lead-free perovskite photovoltaics and optoelectronics by ab-initio simulations. Sci Rep 7:1–8. https://doi.org/10.1038/s41598-017-13172-y

[7] Tritt TM, Subramanian MA (2020) Thermoelectric Materials. Phenom Appl A Bird's Eye View 31:188–197. https://doi.org/10.1557/mrs2006.44

[8] Tan G, Ohta M, Kanatzidis MG (2019) Thermoelectric power generation: From new materials to devices. Philos Trans R Soc A Math Phys Eng Sci 377:20180450. https://doi.org/10.1098/rsta.2018.0450

[9] Bell LE (2008) Cooling, heating, generating heat with and recovering waste thermoelectric. Science 321:1457–1461. https://doi.org/10.1126/science.1158899

[10] Pei Y, Lalonde AD, Heinz NA, Shi X, Iwanaga S, Wang H, Chen L, Snyder GJ (2011) Stabilizing the optimal carrier concentration for high thermoelectric efficiency. Adv Mater 23:5674–5678. https://doi.org/10.1002/adma.201103153

[11] Slack GA (1995) CRC Handbook of thermoelectrics—CRC Press Book. In: Handbook of thermoelectrics

[12] MehdizadehDehkordi A, Zebarjadi M, He J, Tritt TM (2015) Thermoelectric power factor: enhancement mechanisms and strategies for higher performance thermoelectric materials. Mater Sci Eng R Reports 97:1–22. https://doi.org/10.1016/j.mser.2015.08.001

[13] Yang J, Xi L, Qiu W et al (2016) On the tuning of electrical and thermal transport in thermoelectrics: An integrated theory-experiment perspective, npj Comput Mater 2:15015. Doi: https://doi.org/10.1038/npjcompumats.2015.15

[14] Pei Y, Wang H, Snyder GJ (2012) Band engineering of thermoelectric materials. Adv Mater 24:6125–6135. https://doi.org/10.1002/adma.201202919

[15] Rowe DM, Rosi FD (2006) CRC handbook of thermoelectrics: macro to nano

[16] Wright DA (1958) Thermoelectric properties of bismuth telluride and its alloys. Nature 181:834–834. https://doi.org/10.1038/181834a0

[17] Heremans JP, Thrush CM, Morelli DT (2004) Thermopower enhancement in lead telluride nanostructures. Phys Rev B Condens Matter Mater Phys 70:115334. https://doi.org/10.1103/PhysRevB.70.115334

[18] Chen ZG, Shi X, Zhao LD, Zou J (2018) High-performance SnSe thermoelectric materials: progress and future challenge. Prog Mater Sci 97:283–346. https://doi.org/10.1016/j.pmatsci.2018.04.005

[19] Poon SJ (2018) Recent advances in thermoelectric performance of half-heusler compounds. Metals (Basel) 8:989. https://doi.org/10.3390/met8120989

[20] Kauzlarich SM, Brown SR, Jeffrey Snyder G (2007) Zintl phases for thermoelectric devices. J Chem Soc Dalt Trans 21:2099–2107. https://doi.org/10.1039/b702266b

[21] Liu KF, Xia SQ (2019) Recent progresses on thermoelectric Zintl phases: Structures, materials and optimization. J Solid State Chem 270:252–264. https://doi.org/10.1016/j.jssc.2018.11.030

[22] Gascoin F, Ottensmann S, Stark D, Haile S, Snyder GJ (2005) Zintl phases as thermoelectric materials: tuned transport properties of the compounds CaxYb1-xZn2Sb2. Adv Funct Mater 15:1860–1864. https://doi.org/10.1002/adfm.200500043

[23] Chen C, Feng Z, Yao H et al (2021) Intrinsic nanostructure induced ultralow thermal conductivity yields enhanced thermoelectric performance in Zintl phase Eu2ZnSb2. Nat Commun 12:1–9. https://doi.org/10.1038/s41467-021-25483-w

[24] Nesper R (2014) The Zintl-Klemm concept—a historical survey. Zeitschrift fur Anorg und Allg Chemie 640:2639–2648. https://doi.org/10.1002/zaac.201400403

[25] Zhang J, Song L, Mamakhel A, Jorgensen MRV, Iversen BB (2017) High-performance low-cost n-type se-doped mg3sb2-based zintl compounds for thermoelectric application. Chem Mater 29:5371–5383. https://doi.org/10.1021/acs.chemmater.7b01746

[26] Yang G, Yang J, Yan Y, Wang Y (2014) The relationship between the electronic structure and thermoelectric properties of Zintl compounds M2Zn5As4 (M = K, Rb). Phys Chem Chem Phys 16:5661–5666. https://doi.org/10.1039/c3cp54545h

[27] Zevalkink A, Zeier WG, Pomrehn G, Schechtel E, Tremel W, Snyder GJ (2012) Thermoelectric properties of Sr3GaSb3—a chain-forming Zintl compound. Energy Environ Sci 5:9121–9128. https://doi.org/10.1039/c2ee22378c

[28] Azam S, Khan SA, Goumri-Said S (2015) Revealing the optoelectronic and thermoelectric properties of the Zintl quaternary arsenides ACdGeAs2 (A = K, Rb). Mater Res Bull 70:847–855. https://doi.org/10.1016/j.materresbull.2015.05.044

[29] Zheng L, Li W, Sun C, Shi X, Zhang X, Pei Y (2020) Ternary thermoelectric AB2C2 Zintls. J Alloys Compd 821:153497. https://doi.org/10.1016/j.jallcom.2019.153497

[30] Lin Z, Wang G, Le C, Zhao H, Liu n, Hu J, Guo L, Chen X, (2017) Thermal conductivities in NaSnAs, NaSnP, and NaSn2As2: Effect of double lone-pair electrons. Phys Rev B 95:1–7. https://doi.org/10.1103/PhysRevB.95.165201

[31] Guechi N, Bouhemadou A, Medkour Y, Al-Douri Y, Khenata R, Bin-Omran S (2020) Electronic and thermoelectric properties of the layered Zintl phase CaIn2P2: first-principles calculations. Philos Mag 100:3023–3039. https://doi.org/10.1080/14786435.2020.1799101

[32] Feng Z, Yang J, Wang Y, Yan Y, Yang G, Zhang X (2015) Origin of different thermoelectric properties between Zintl compounds Ba3Al3P5 and Ba3Ga3P5: a first-principles study. J Alloys Compd 636:387–394. https://doi.org/10.1016/j.jallcom.2015.02.133

[33] He H, Tyson C, Bobev S (2011) Eight-coordinated arsenic in the Zintl phases RbCd4As 3 and RbZn4As3: synthesis and structural characterization. Inorg Chem 50:8375–8383. https://doi.org/10.1021/ic2009418

[34] Schwarz K, Blaha P, Madsen GKH (2002) Electronic structure calculations of solids using the WIEN2k package for material sciences. Comput Phys Commun 147:71–76. https://doi.org/10.1016/S0010-4655(02)00206-0

[35] Perdew JP, Burke K, Ernzerhof M (1996) Generalized gradient approximation made simple. Phys Rev Lett 77:3865–3868. https://doi.org/10.1103/PhysRevLett.77.3865

[36] Tran F, Blaha P (2009) Accurate band gaps of semiconductors and insulators with a semilocal exchange-correlation potential. Phys Rev Lett 102:5–8. https://doi.org/10.1103/PhysRevLett.102.226401

[37] Madsen GKH, Singh DJ (2006) BoltzTraP. A code for calculating band-structure dependent quantities. Comput Phys Commun 175:67–71. https://doi.org/10.1016/j.cpc.2006.03.007

[38] Xing G, Sun J, Li Y, Fan X, Zheng W, Singh DJ (2017) Electronic fitness function for screening semiconductors as thermoelectric materials. Phys Rev Mater 1:1–13. https://doi.org/10.1103/PhysRevMaterials.1.065405

[39] Kresse G, Furthmüller J (1996) Efficient iterative schemes for ab initio total-energy calculations using a plane-wave basis set. Phys Rev B 54:11169–11186. https://doi.org/10.1103/PhysRevB.54.11169

[40] Togo A, Tanaka I (2015) First principles phonon calculations in materials science. Scr Mater 108:1–5. https://doi.org/10.1016/j.scriptamat.2015.07.021

[41] Mushtaq M, Sattar MA, Dar SA (2020) Phonon phase stability, structural, mechanical, electronic, and thermoelectric properties of two new semiconducting quaternary Heusler alloys CoCuZrZ (Z = Ge and Sn). Int J Energy Res 44:5936–5946. https://doi.org/10.1002/er.5373

[42] Lindsay L, Broido DA, Reinecke TL (2013) First-principles determination of ultrahigh thermal conductivity of boron arsenide: a competitor for diamond? Phys Rev Lett 111:1–5. https://doi.org/10.1103/PhysRevLett.111.025901

[43] Born M, Huang K (1956) Dynamical theory of crystal lattices. Acta Cryst 9:837–838. https://doi.org/10.1107/S0365110X56002370

[44] Hill R (1952) The elastic behaviour of a crystalline aggregate. Proc Phys Soc Sect A 65:349–354. https://doi.org/10.1088/0370-1298/65/5/307

[45] Parvin F, Hossain MA, Ahmed I, Aktr K, Islam AKMA (2021) First-principles calculations to investigate mechanical, optoelectronic and thermoelectric properties of half-Heusler p-type semiconductor BaAgP. Results Phys 23:104068. https://doi.org/10.1016/j.rinp.2021.104068

[46] Anderson OL (1963) A simplified method for calculating the debye temperature from elastic constants. J Phys Chem Solids 24:909–917. https://doi.org/10.1016/0022-3697(63)90067-2

[47] Chandran AK, Gudelli VK, Sreeparvathy PC, Kanchana V (2016) Structural and thermoelectric properties of zintl-phase CaLiPn (Pn=As, Sb, Bi). J Solid State Chem 243:198–206. https://doi.org/10.1016/j.jssc.2016.08.030

[48] Snyder GJ, Toberer ES (2010) Complex thermoelectric materials. Mater Sustain Energy A Collect Peer Rev Res Rev Artic from Nat Publ Gr 7:101–110. https://doi.org/10.1142/9789814317665_0016

[49] Dutta M, Ghosh T, Biswas K (2020) Electronic structure modulation strategies in high-performance thermoelectrics. APL Mater 8:040910. https://doi.org/10.1063/5.0002129

[50] Putatunda A, Xing G, Sun J, Li Y, Singh DJ (2018) Thermoelectric properties of layered NaSbSe 2. J Phys Condens Matter 30:225501. https://doi.org/10.1088/1361-648X/aabf5b

[51] Adebambo PO, Osafile OE, Laoye JA, Idowu MA, Adebayo GA (2021) Electronic fitness function, effective mass and thermoelectric properties of Rh-based (-ScTe; -TiSb; -VSn) alloys for thermoelectric generator applications. Comput Condens Matter 26:e00523. https://doi.org/10.1016/j.cocom.2020.e00523

[52] Slack GA (1979) The Thermal Conductivity of Nonmetallic Crystals. Solid State Phys Adv Res Appl 34:1–71. https://doi.org/10.1016/S0081-1947(08)60359-8

[53] Gupta Y, Sinha MM, Verma SS (2021) First-principles investigation on the electronic, mechanical and lattice dynamical properties of novel AlNiX (X = As and Sb) half-Heusler alloys. Mater Today Commun 26:101885. https://doi.org/10.1016/j.mtcomm.2020.101885

[54] Belomestnykh VN, Tesleva EP (2004) Interrelation between anharmonicity and lateral strain in quasi-isotropic polycrystalline solids. Tech Phys 49:1098–1100. https://doi.org/10.1134/1.1787679

[55] Bessas D, Sergueev I, Wille HC, Person J, Ebling D, Hermann RP (2012) Lattice dynamics in Bi2Te3 and Sb2Te3: Te and Sb density of phonon states. Phys Rev B Condens Matter 86:224301. https://doi.org/10.1103/PhysRevB.86.224301

Publisher's Note Springer Nature remains neutral with regard to jurisdictional claims in published maps and institutional affiliations.

ResearchGate

See discussions, stats, and author profiles for this publication at: https://www.researchgate.net/publication/358669638

Response of Tall Building with Different Side Ratiounder the Effect of Wind Load

Conference Paper · February 2022

CITATIONS
0

READS
40

3 authors, including:



Ritu Raj Ahirwar
Delhi Technological University
21 PUBLICATIONS **52** CITATIONS

SEE PROFILE



Rahul Kumar Meena
Delhi Technological University
6 PUBLICATIONS **6** CITATIONS

SEE PROFILE

Some of the authors of this publication are also working on these related projects:

Wind effects on tall buildings View project

All content following this page was uploaded by Rahul Kumar Meena on 17 February 2022.

The user has requested enhancement of the downloaded file.

ISBN: 978-93-5593-524-3

Response of Tall Building with Different Side Ratio under the Effect of Wind Load

PAYAL DEVI[1], RAHUL KUMAR MEENA[2], RITU RAJ[3]*

[1,2,3]Civil Engineering Department, Delhi Technological University, Delhi.
* Corresponding Author

***Abstract*— The intent of this research is to present a response study and investigate of the effect of side ratio for rectangular-shaped tall buildings under the action of wind loadings having the same plan area and height. High-rise buildings are cantilever structures that are subjected to significant lateral loads. In the design of such structures, occupant comfort, along with serviceability and structural safety, is the dominant criterion. The better understanding of the interface, between the building and the wind are necessary for the most efficient building. The present study focuses on tall buildings with different side ratios exposed to 0°, 30°, 60°, and 90° angles of attack. Response study is performed on the protype after evaluating the wind effects by CFD. In this study, various parameters such as axial force and deflections of storeys in X and Z were calculated for all the models under the action of wind load. To accomplish the objective of carrying out the wind response analysis, a rectangular-shaped model with different side ratios of 1, 1.44, 2.25, and 4 of height 90 m, having the same plan area, is made using STAAD Pro v8i. The prototype building comprises 30 stories, with each storey height of 3 metres being constituted of R.C.C. beams, slabs, and columns to construct building frames. The response of prototype buildings to different incidence angles, including deflections in X and Z directions, has been recorded to study the influence of wind loads.**

***Index Terms*—** *Wind Load; Tall Building; Cross sectional shapes; Storey Drift; STAAD Pro*

I. INTRODUCTION

In the design of tall buildings, wind force and their effects have a great influence on the structure. Design for wind load can be treated as static as well as dynamic in nature, and thus requires a substantial amount of knowledge to evaluate the responses of tall buildings under wind load action. Wind load response on a structure is determined by its shape, location, wind exposure, structure stiffness, and wind angle of attack. the 1960s, many researchers have concluded that much convenient information can be obtained using the traditional approach, assuming the wind pressure to act statically. Today's skyscrapers are the result of continuous innovation, experimentation, and discovery. In the 20th and 21st centuries, urbanization encouraged the construction of tall buildings, making them taller and taller with an increase in demand. As the building goes taller and taller, keeping in mind the demand of serviceability and functionality, cross sections should be selected very carefully as additional lateral forces are formed from unexpected deflections. Many studies demonstrates that mostly the focus has so far been solely on pressure and force coefficients of tall building models that will help in computation of wind load and responses. Various International Wind Standard codes [1–5] focused on few incidence angles and estimated the deign pressure coefficients for few conventional shapes only. These Codes provide guidelines on determining the action of wind on loading for confined research area and hence to deal with unconventional shapes and different angle of incidences wind attack responses, wind tunnel test is required to be carried. [6] Raj & Kumar Ahuja, 2013 carried an experimental wind tunnel study with varying cross-sectional shapes but having identical plan area and evaluated that the wind response is highly influenced due to model shape and with the angle of attack of wind.[7] Pal and Raj, 2021 evaluated the interference effect of wind on shape remodeled tall building in wind tunnel test on 1:300 length scale. [8] Kwok et al., 1988 have examined the impact of different edges configuration on the wind response for a tall rectangular-sectioned building using wind tunnel testing procedure.[9] Meena et al.,2020 discussed how the bracing system can influence the aerodynamic response in various types of multistoried steel buildings. [10] Amin & Ahuja, 2013 presented a study that shows the impact of side ratio change on pressure distribution and find out that side ratio change led to significant impact on the amplitude and pressure distribution on the leeward and sidewalls, but only a minor impact on the windward walls at wind incidence.[11] Nagar et al., 2020 experimentally studied on H shape building. [12] Pal et al., 2020 compared the result of wind induced effects for surrounding buildings on fish and square plan shaped tall building in wind tunnel test. [13] Raj et al., 2020 Numerically studied wind induced action on "H" plan shape tall building.[14] Gaur et al., 2021 numerical evaluated the interference effect on high rise

ISBN: 978-93-5593-524-3

structures. [15] Sanyal & Dalui, 2020 executed the effect of side ratio change on Y shaped tall building using CFD technique and evaluated the pressure coefficients at various faces. [16] Nagar et al., 2021 found proximity effects between two plus plans shaped high-rise buildings on mean and RMS pressure coefficients. [17] Pal et al., 2021 experimentally studied the interference effect on various shapes of tall buildings.[18] Kumar and Raj, 2021 studied in details the wind effects on tall building model having ovel shape. [19] Gaur and Raj, 2021 studied numerically mitigation by carrying out minor modifications (corner modification) on square model under wind loads using CFD and wind tunnel. [20] Raj et al., 2020 conducted a response study on plus shape tall building with different bracing system using Staad Pro V8i and obtained the response under wind loads for building with different bracing systems. Since, most of research work is based upon finding the pressure distribution and pressure coefficients; hence, it was observed that there is a need to investigate the response of tall buildings with different side ratio at different angle of attack under wind loads.

II. Numerical Modelling

A. Geometrical Model

In this study, rectangular-plan shaped buildings with different side ratios are analysed by using STAAD Pro v8i. All the models investigated have the same plan area of 900 m^2 and a height of 90 m. The prototype building model was designed as G+29, with each storey height of 3 m. The model considered in this study is depicted in Fig.1. It was designed as an RCC building with consideration of beam size of 450 mm x 500 mm and column size of 600 mm x 600 mm. The thickness of the floor slab is considered to be 225 mm.

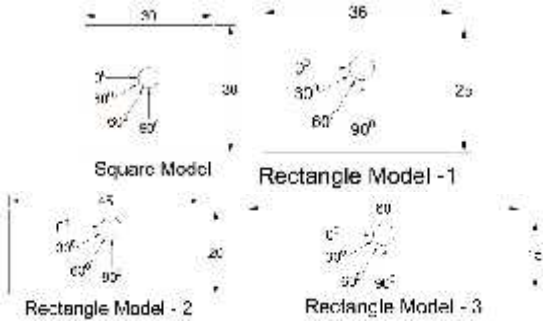


Fig 1 Plan Dimensions of Building Models

B. Basics of Numerical Modelling

Wind response coefficients are obtained by CFD analysis, which are directly used for computation of forces acting on the prototype. External pressure. The coefficient for various angles of incidence is taken from ANSYS data where Cpe is calculated for different faces using the CFD technique. Using these values of mean wind pressure coefficients and the tributary area, the nodal forces on the beam-column junctions are evaluated. These forces are then applied to the beam-column connections of the prototype principal building as wind loads. According to IS 875-part 3, 2015, the wind pressure at height z is calculated as eq. (1)

$$P_z = 0.6\,[V_z]^2 \quad (1)$$

And, the computation of wind loads is calculated in eq. (2).

$$F = (C_e - C_i) * A * P_d \quad (2)$$

Load Combination considered in this study are as follows:

1. Load Case 1 = 1.5 [D.L + L.L]
2. Load Case 2 = 1.2 [D.L + L.L + W.L]
3. Load Case 3 = 1.5 [D.L + L.L - W.L]
4. Load Case 4 = 1.5 [D.L + W.L]
5. Load Case 5 = 1.5 [D.L - W.L]

III. Details of Models

The building's plan area is 900 m^2. The floor height is 3 meters, and the number of floors in this research work is 30 (G+29). For all the shapes, Column A (windward column) is analyzed, and all the models are analyzed for wind incidence angles of 0°, 30°, 60°, and 90°. Axial force and deflection are observed, tabulated, and compared for column-A for change in side ratio, whereas only deflections are observed for column-B (middle column). Columns under consideration are also shown below in Fig 2 and Fig 3.

Table-1 Model Dimensions

Modal shape	Prototype Dimension(m)	Side Ratio	Height of Model (mm)
Square	30*30	1	900
Rectangle-1	36*25	1.44	
Rectangle-2	45*20	2.25	
Rectangle-3	60*15	4	

ISBN: 978-93-5593-524-3

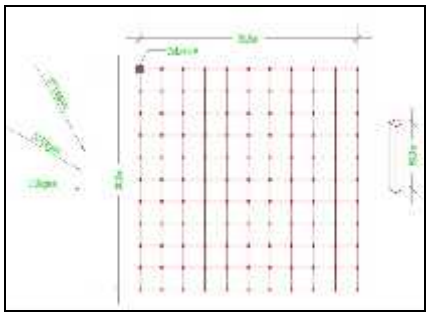


Fig 2 Position of Column-A in model 1

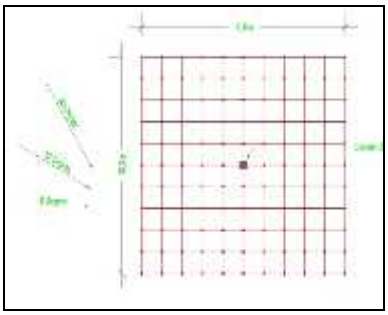


Fig 3 Position of Column-B in Model 1

The basis of modelling used in Staad Pro software modelling are as below:

Table-2 Modeling Parameters

S. No.	Details	Values
1.	Storey height	3 m
3.	Beam Size	450 mm x 500 mm
4.	Column Size	600 mm x 600 mm
5.	Thickness of floor slab	225 mm
6.	Grade of Concrete/Grade of steel	M40 / Fe415
7.	Dead Load	Self-weight assigned by software
8.	Live Load	4 KN/ m^2 (Assigned as Floor Load)

IV. CALCULATION OF WIND LOAD

In the present study, we have considered a basic wind speed of 47 m/s As per IS-875 Part 3, the Risk Coefficient (k1) is taken as 1 considering for all general structures and buildings. The Terrain Category Coefficient (k2) is evaluated by linear interpolation to calculate the factor as per the height of the building. The topography coefficient (k3) and the importance factor (k4) were also taken as 1. The wind directionality factor, area averaging factor, and combination factor considered for modelling are taken as 1, 0.90, and 0.90 respectively. The Plan View of the different models under analysis is as shown below in Fig 4.

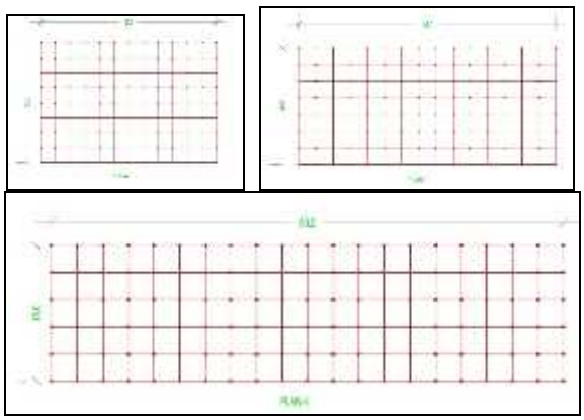


Fig 4 Plan View of Model 2, Model 3 and Model 4

V. RESULT AND DISCUSSION

A. *Model-1*

Deflection of Columns is obtained during the analysis, horizontal deflection at column-A and column-B at every floor level in the "X" direction and the "Z" direction at different wind incidence angles were obtained during the analysis. The results are plotted as line graphs, as shown in Fig. 5 and 6. Maximum deflection in Column-A is approximately 87.8mm at the top of the building at a wind incidence angle of 0^0 in the X-direction it is approximately 86.05 mm at the top of the building at 90^0 angle of wind incidence, the maximum X-direction deflection is roughly 92.38 mm, while at 90° angle of wind incidence, the maximum Z-direction deflection is almost 86.4 mm

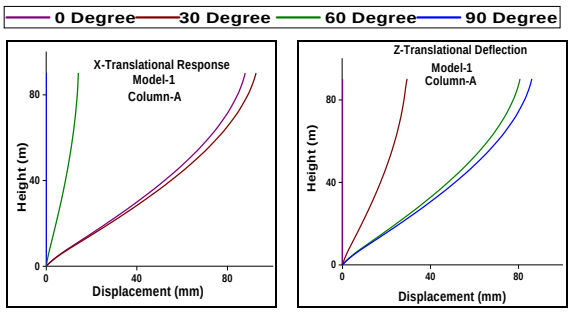


Fig 5 Numerical Response for Column A for Different AOA for Model

The study is performed into STAAD Pro and the results are presented in the form of deflection with respect to the height and displacement.

ISBN: 978-93-5593-524-3

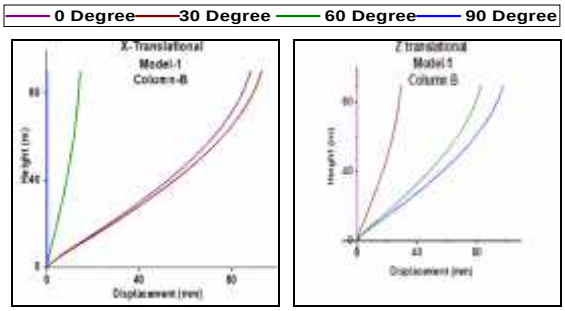


Fig 6 Numerical Response for Column B for Different AOA for Model 1

B. MODEL-2

Model-2 is a rectangular-shaped building with a side ratio of 1.44, having a plan area of 900 m^2 and a height of 90 m. Graphs are depicting the variation of deflection for column-A in the "X" direction and the "Z" direction for various angles of incidence are plotted as line graphs in Figures 7 and 8.Maximum deflection in Column-A is around 62.12 mm at the top of the building at a 0^0 wind incidence angle in the X-direction and maximum deflection in the Z-direction is around 97.495 mm at the top of the building at 90^0. Column-B at various angles of attack at an angle of incidence of 0° and 90°, respectively, the maximum horizontal deflection in the "X" direction and the "Z" direction is 62 mm and 98 mm respectively

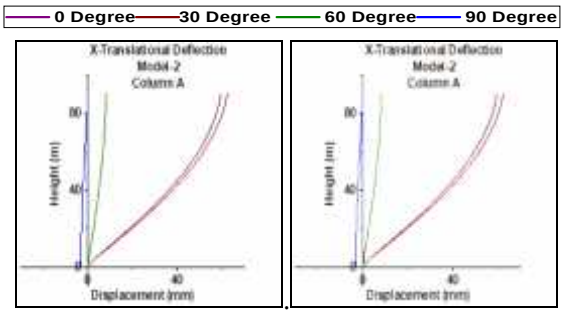


Fig 7 Numerical Response for Column A for Different AOA for Model 2

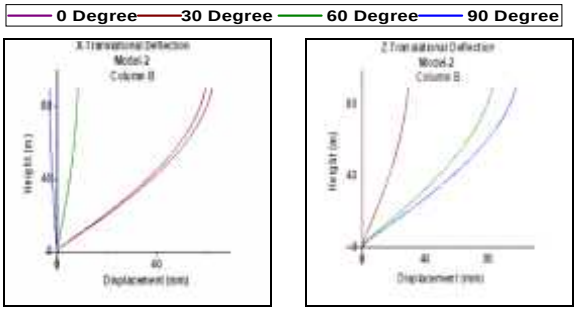


Fig 8 Numerical Response for Column B for Different AOA for Model 2

C. MODEL 3

Model 3 is a rectangular-shaped building with a side ratio of 2.25, having a plan area of 900 m^2 and a height of 90 m. Graphs depicting the variation of deflection for column A nodes in the "X" direction and the "Z" direction for various angles of incidence are plotted as line graphs in Figure 9 and 10.At the top of the building, maximum deflection in Column-A is around 38.84 mm in the X direction at 0° wind incidence angle, and maximum deflection in the Z-direction is around 126.42 mm at 90° wind incidence angle. At an angle of incidence of 0° and 90°, respectively, the maximum horizontal deflections in the "X" direction and the "Z" directions are 39.04 mm and 123.62 mm respectively in column-B.

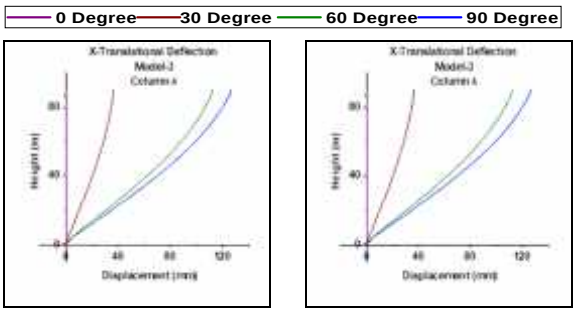


Fig 9 Numerical Response for Column A for Different AOA for Model 3

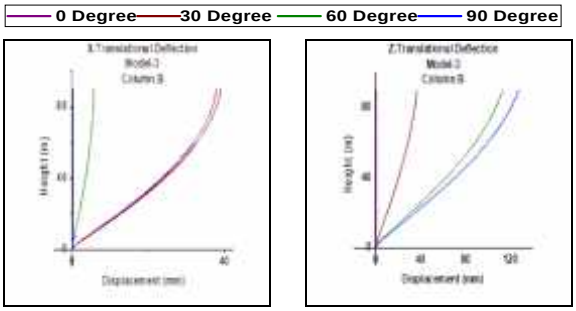


Fig 10 Numerical Response for Column B for Different AOA for Model 3

D. MODEL 4

Model 4 is a rectangular-shaped model with a side ratio of 4, having a plan area of 900 m^2 and a height of 90 m. Graphs depicting the variation of deflection for column A nodes in the "X" direction and the "Z" direction for various angles of incidence are plotted as line graphs in Figures 11 and 12. In the X direction, the maximum deflection in Column A is around 19.10 mm at the top of the building at a 30° wind incidence angle, and the maximum deflection in the Z direction is around 200.8 mm at the top of the building at a 90° wind incidence angle. At angles of incidence of 30° and 90°, respectively, the maximum horizontal deflection in the "X" direction and the "Z" direction is 17.84 mm and 201.8 mm respectively in column-B.

ISBN: 978-93-5593-524-3

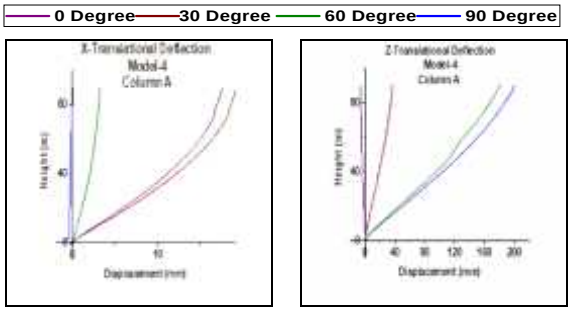


Fig 11 Numerical Response for Column A for Different AOA for Model 4

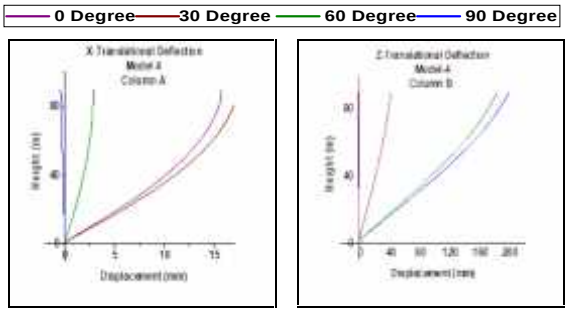


Fig 12 Numerical Response for Column B for Different AOA for Model 4

VI. CONCLUSION

The major conclusion from the present study is as follows:

- From the graphs obtained, it is clearly depicted that Deflection of columns increases with height and as the side ratio changes influence on deflection have been compared for models.
- Horizontal deflection at column A and B at every floor level in 'X' and 'Z' direction and in different wind incidence angle are obtained during the analysis.
- Deflection in X translational is found to be maximum when the angle of wind is 0^0 and as the angle of attack of wind changes the deflections also get reduced in X translational, however, deflection in Z translational is minimum for 0-degree angle of attack and increases as the angle of attack increases further.
- Max deflection in Z translational is noticed when the angle of attack is 90^0.
- Maximum deflection in X direction for Column-A and B is around 88 mm at top of the building at 0^0 wind incidence angle for Model-1 whereas maximum deflection in Z-direction is around 200 mm at 90^0 wind incidences for Model 4.

ACKNOWLEDGMENT

This study is funded by Delhi Technological University and resources to conduct this study are provided by Delhi Technological University.

REFERENCES

1. ASCE 7-10: Minimum Design Loads for Buildings and Other Structures.
2. BS 6399-2:1997 - Loading for buildings. Code of practice for wind loads (British Standard)
3. EN 1991-1-4: Eurocode 1: Actions on structures - Part 1-4: General actions - Wind actions. (2010)
4. AS/NZS 1170.2:2011 :: Standards New Zealand
5. IS 875.3: Code of Practice for Design Loads (Other than Earthquake) for Buildings and Structures - Part 3 : Wind Loads (IS 875 : Part 3) + Amendment 2016 : Bureau of Indian Standards : Free Download, Borrow, and Streaming : Internet Archive
6. Raj, R., Ahuja, A.K.: Wind Loads on Cross Shape Tall Buildings. Journal of Academia and Industrial Research (JAIR). 2, 111–113 (2013)
7. Pal, S., Raj, R.: Evaluation of Wind Induced Interference Effects on Shape Remodeled Tall Buildings. Arabian Journal for Science and Engineering. (2021). https://doi.org/10.1007/s13369-021-05923-x
8. Kwok, K.C.S., Wilhelm, P.A., Wilkie, B.G.: Effect of edge configuration on wind-induced response of tall buildings. Engineering Structures. 10, 135–140 (1988). https://doi.org/10.1016/0141-0296(88)90039-9
9. MEENA, R.K., Awadhiya, G.P., Paswan, A.P., Jayant, H.K.: Effects of Bracing System on Multistoryed Steel Building. (2018). https://doi.org/10.1088/1757-899X/1128/1/012017
10. Amin, J.A., Ahuja, A.K.: Effects of Side Ratio on Wind-Induced Pressure Distribution on Rectangular Buildings. Journal of Structures. 2013, 1–12 (2013). https://doi.org/10.1155/2013/176739
11. Nagar, S.K., Raj, R., Dev, N.: Experimental study of wind-induced pressures on tall buildings of different shapes. Wind and Structures, An International Journal. 31, 441–453 (2020). https://doi.org/10.12989/was.2020.31.5.431
12. Pal, S., Raj, R., Anbukumar, S.: Comparative study of wind induced mutual interference effects on square and fish-plan shape tall buildings. Sādhanā. 46, 86 (2021). https://doi.org/10.1007/s12046-021-01592-6
13. Raj, R., Rana, T., Anchalia, T., Khola, U.: Numerical study of wind excited action on H Plan-shaped tall building. International Journal on Emerging Technologies. 11, 591–605 (2020)
14. Gaur, N., Raj, R., Goyal, P.K.: Interference effect on corner - configured structures with variable

ISBN: 978-93-5593-524-3

geometry and blockage configurations under wind loads using CFD. Asian Journal of Civil Engineering. (2021). https://doi.org/10.1007/s42107-021-00400-0

15. Sanyal, P., Dalui, S.K.: Effects of side ratio for 'Y' plan shaped tall building under wind load. Building Simulation. (2020). https://doi.org/10.1007/s12273-020-0731-1
16. Nagar, S.K., Raj, R., Dev, N.: Proximity effects between two plus-plan shaped high-rise buildings on mean and RMS pressure coefficients. Scientia Iranica. 0–0 (2021). https://doi.org/10.24200/sci.2021.55928.4484
17. Pal, S., Raj, R., Anbukumar, S.: Bilateral interference of wind loads induced on duplicate building models of various shapes. Latin American Journal of Solids and Structures. 18, (2021). https://doi.org/10.1590/1679-78256595
18. Kumar, A., Raj, R.: Study of Pressure Distribution on an Irregular Octagonal Plan Oval-Shape Building Using CFD. Civil Engineering Journal. 7, 1787–1805 (2021). https://doi.org/10.28991/cej-2021-03091760
19. Gaur, N., Raj, R.: Aerodynamic mitigation by corner modification on square model under wind loads employing CFD and wind tunnel. Ain Shams Engineering Journal. 283 (2021). https://doi.org/https://doi.org/10.1016/j.asej.2021.06.007
20. Raj, R., Jha, S., Singh, S., Choudhary, S.: Response analysis of plus shaped tall building with different bracing systems under wind load. International Journal of Advanced Research in Engineering and Technology. 11, 371–380 (2020). https://doi.org/10.34218/IJARET.11.3.2020.032

View publication stats

ResearchGate

See discussions, stats, and author profiles for this publication at: https://www.researchgate.net/publication/342259648

Zymosan – an activator of macrophage

Conference Paper · November 2019

CITATIONS
0

READS
19

2 authors:



Mukesh Doble
Theevanam Additives & Neutraceuts p ltd(Indian Institute of Technology) Madras; …
512 PUBLICATIONS **12,142** CITATIONS
SEE PROFILE



Geetha Venkatachalam
Indian Institute of Technology Madras
22 PUBLICATIONS **233** CITATIONS
SEE PROFILE

Some of the authors of this publication are also working on these related projects:

Project ORGANIC View project

Project Pyridazine based metal complexes as anticancer agents View project

All content following this page was uploaded by Geetha Venkatachalam on 13 November 2021.

The user has requested enhancement of the downloaded file.

Samples from Radial, Ulnar and Dorsalis pedis arteries were collected from 50 cadavers, aged over 19 years and from them, the proximal, middle and distal segments were collected. Based on age, the samples were divided into the following groups; between 19 – 40 years into Group1, 41 – 60 years into Group 2, 61 years & above as Group 3, Hypertension Group into 'H' and Diabetic Group as 'D'. Arterial samples were processed for histological procedures then analysed for the histomorphometric changes.
The histomorphometric analysis of arterial wall confirmed noticeable changes with relation to age and disease. There was a significant decrease in the number of elastic laminae & smooth muscle layer and a significant change was observed in the tunica intima, luminal area, tunica intimal area, tunica medial area, tunica adventitial area, total cross-sectional area, TI/ TM ratio, internal and external elastic lamina.
This study revealed that aging affects the arterial wall and the changes were more noticeable in hypertension, and diabetes, especially in the proximal and distal segments. These changes could prove to be useful for surgeons and clinicians, taking into account the histomorphometric alterations before choosing an artery for graft selection.

Role of Bioactive Glass materials in Beyond Bone Regeneration

Deenan Santhiya

Department of Applied Chemistry, Delhi Technological University, Delhi-110042,
Email: deenan.santhiya@dce.ac.in

Bioactive glasses – a third generation biomaterials finds application in bone tissueengineering. Unlike conventional strategies, herein these materials are synthesized *via* bioinspired route at ambient condition using different organic surface directing agents namely, polyamido amine (PAMAM) dendrimer, cellulose and its derivatives as well as cetyltrimethyl ammonium bromide (CTAB). It is preferred as its synthesis comprises of fewsimple, cheaper and eco-friendly steps. Omission of high temperature sintering prevented thepossibility of material's fine architecture disintegration and mechanical rigidity loss.Interestingly, textural tunability has been observed in the nano bioactive glass materialaccording to the corresponding template. This in turn, affected the bioactive nature of thematerial i.e. its inherent nature to stimulate the biological response for osteogenesis. *In-vitro*bioactivity of the material has been evaluated in simulated body fluid at different interval oftime.
In the present study, first time an attempt has been made to explore the applications of thirdgeneration biomaterial i.e. bioactive glass beyond usual bone regeneration. The challenge liedin evaluating advanced applications of bioactive glass that has remained unexplored till date.According to the structural, morphological and textural characteristics of the varioustemplated bioactive glass materials, their applications in different field of gene and antibioticsdelivery as a nanocarrier have been studied. Initially, PAMAM dendrimer templatedbioactive glass has been synthesized and evaluated for its plasmid deoxyribonucleic acid (pDNA) compaction and transfection ability in CHO-K1 cell lines. This validated thecapability of bioactive glass as a non-viral gene cationic nanocarrier. Subsequently, anattempt has been made to design the CTAB templated bioactive glass material for the codelivery of two different antibiotics against osteomyelitis. This has been executed in search ofnew treatment development using existing antibiotics as the pathogen evolution currentlyoutruns novel drug development.

Zymosan – an activator of macrophage

Geetha Venkatachalam

Geetha Venkatachalam, Mukesh Doble
Bioengineering and Drug design Lab, Department of Biotechnology, IIT-Madras, Chennai-600036, India,
*Email: geegha@gmail.com ; *Email: mukeshd@iitm.ac.in*

β-1, 3- glucan also known as zymosan (ZM), is prepared from *saccharomyces cerevisiae*. β- 1, 3- glucans show various biological activities including immune responses and inflammatory reactions, and they have been used in cancer immunotherapy. Development of anti-inflammatory substances of cells was analyzed by ZM using it as model substance. In our study we have characterized ZM by FTIR, ^{1}H NMR, DSC, TGA and AFM. ZM

uptake by Raw 264.7 cells were analyzed by fluorescence microscopy. Particle size of ZM obtained by DLS, is 602.0 ± 0.004 nm and zeta potential 5.67 ± 0.001 mv, and they appeared oval shaped. FTIR of ZM shows the presence of two intense and broad bands at 3394 and 3399 cm^{-1} which indicates the presence of hydroxyl groups (OH) whereas the bands at 1042 and 1025 cm^{-1} could be attributed to stretching of CO. In ^{1}H NMR the chemical shift values at δ 4.0 to 5.0 are responsible for sugar residues of ZM. Initial weight loss of ZM was 9.174 % followed by 52.03 % and 33.64% in TGA and melting point temperature was observed at 134.08 °C. CHN analysis reveals the percentage of C, H and N to be 41.78, 6.69 and 2.54 respectively. Size of the particle measured in AFM is around 5.035 µm. Biocompatibility of ZM was determined by MTT assay and cells were viable upto 100µg ml^{-1}. ZM enters the cell through surface receptor Dectin -1 (which facilitates the entry of ZM into the cell). RNA was isolated from the cells (after ZM uptake) and expression of IL6 and IL β1 genes was quantified. Rhodamine tagged microparticles of ZM within the cell (Raw 264.7) appeared as red color under fluorescent microscopy. Our study reveals ZM is a potential candidate for different applications including macrophage targeted drug delivery, an adjuvent, and immune potentiator.

References

1. Venkatachalam, G., etal. (2012). Springer briefs in Microbiology, p - 90.
2. Ohno, N., etal. (2001).Carbohydrate polymers, 44, 339-349.
3. Underhill, D. M., etal. (1999). Nature 401, 811-815.

In vitro microenvironment study of 3D spheroid co-cultures: Colorectal cancer and Fibroblast cells on microstructure PDMS

Venkanagouda S. Goudar

Venkanagouda S. Goudar[1], Manohar Prasad Koduri[2], Ashish Kumar[1], Long-Seng Lu[3*], Fan-Gang Tseng[1, 2, 4, 5*]

[1]Engineering and System Sciences (ESS), National Tsing Hua University, Hsinchu, Taiwan, ROC.

[2]International Intercollegiate PhD program, National Tsing Hua University, Hsinchu, Taiwan, ROC.

[3]Graduate Institute of Biomedical Materials and Tissue Engineering, Taipei Medical University Hospital, Taipei, Taiwan ROC.

[4]Research Center for Applied Sciences, Academia Sinica, Taipei, Taiwan ROC.

*[5]Frontier Research Center on Fundamental and Applied Sciences of Matters, National Tsing Hua University, Taiwan ROC, [1]Email: venkatesh.gdr22@gmail.com; *Email: fangangtseng@gmail.com*

Colorectal cancer is one of the leading cause of cancer-related mortality. Importantly, the patient's prognosis and disease initiation are mainly relying on the interaction between tumor cells and their associated stromal cells. The collagen type I is the important building block of ECM in the tumor microenvironment, which increases drug resistance and metastasis in colorectal cancer. In-vitro microstructures on PDMS micro device closely mimics the in vivo cancer spheroid model in understanding of the tumor microenvironment.

In our study, we have developed a robust PDMS based co-culture device to culture 3D organoid. Colon cancer cells (HCT-8) (5.2×10^{6} cells/ml) and fibroblast cells (NIH3T3) (4.9×10^{6} cells/ml) were used on 16mm^2 PDMS micro well-structured chip.It is observed that after seeding of cells and during spheroid formation HCT-8 colon cancer cells were surrounded by fibroblast cells with internal networks and the spreading of HCT-8 cells across the tumor spheroid was observed from the 5day of culture as shown in figure 1(A). Collagen type-1 production is measured by immunostaining across the co-cultured spheroids (~315 spheroids) and is shown in figure 1 (B). Increased and complex network of collagen is observed on 9^{th} day as in figure 1 (B) in comparison to 5^{th} day. The 3-fold increase in production of collagen was observed from 5 days to 30 days' culture, which may cause stiffness and may inhibit penetration of chemotherapy drugs. In contrast, there is no any significant increase in collagen is observed when only Fibroblast were cultured from 5 days to 30 days. Further, we observed collagen production and spheroid circularity/solidity is directly proportional to the ratio of fibroblast cells used in co-culture against constant ratio of HCT-8 cells. With this, we understand that tumor cell and stromal cell interaction is very important in complex ECM production in tumor microenvironment and in formation of solid tumors. In preliminary drug testing, 4 Ayurvedic drugs were used to treat collagen. Out of all, 6-Shogaol (extract from ginger) were exhibited higher effectiveness (~83%) on collagen and least toxicity (figure 1(C)) on both the cells with its low concentration (10µM). The exact mechanism of action of 6-Shogaol on collagen is unknown and further investigation is ongoing.

View publication stats

The current issue and full text archive of this journal is available on Emerald Insight at:
https://www.emerald.com/insight/1355-2554.htm

Role of socioemotional wealth (SEW) in the internationalisation of family firms

Apoorva Jain and Sonal Thukral
Delhi School of Management, Delhi Technological University, Delhi, India, and
Justin Paul
Henley Business School, University of Reading, Whiteknights Campus, Reading, UK

Received 1 December 2021
Revised 12 January 2022
21 January 2022
Accepted 23 January 2022

Abstract

Purpose – Family firms' desire to preserve and uphold socioemotional wealth (SEW) makes their internationalisation a complex phenomenon. Despite the significance of SEW in guiding family firms' internationalisation decisions, the literature in the underlying research stream is still scant and inconclusive. Thus, the purpose of the study is to gain preliminary insights about various dimensions of SEW and its impact on family firms' degree of internationalisation.

Design/methodology/approach – The study employs the multi-case study research design. The multidimensional SEW scale developed by Berrone *et al.* (2012) is used to calculate the SEW scores for four prominent Indian family businesses through the content analysis of Chairman's Statements for a period of 13 years (2007–08 to 2019–20). Further, the study examines the relationship between SEW and family firms' degree of internationalisation through two non-parametric tests: Somers' D and Kendall-Theil regression.

Findings – The results reveal the prevalence of various dimensions of SEW in family businesses. They also indicate that different FIBER dimensions are prioritised differently in family businesses. Finally, the authors observe that there exists a negative relationship between SEW and internationalisation of family businesses, indicating that SEW hinders the internationalisation of family firms.

Research limitations/implications – The study lends to the readers, the understanding that SEW plays a significant role in the internationalisation of family firms; thus, some modification might be needed in the existing international business theories in order to explain the role of peculiar family characteristics in the internationalisation decisions of family firms. Further, since SEW hinders the internationalisation of family firms, it raises a question for researchers and family business leaders: Do family firms need to work on their socioemotional ties to avoid making suboptimal decisions?

Originality/value – The study is a response to the call by Cleary *et al. (2019)* to utilise the results of content analysis of SEW in determining its impact on the family firms' external events. Majority of the studies are still using univariate measures (e.g. percentage of family ownership) to capture SEW. However, this study attempts to calculate the SEW scores of the family firms along these FIBER dimensions through content analysis. This helps in scrupulously capturing the impact of SEW in the internationalisation of family firms.

Keywords Socioemotional wealth (SEW), Indian family firms, Internationalisation, Content analysis, Chairman's Statement, FIBER, Somers' D regression, Kendall-Theil regression

Paper type Research paper

1. Introduction

One of the factors that make internationalisation of family firms a complex phenomenon is the socioemotional wealth (SEW) that they accumulate over the years. The term SEW was first coined by Gómez-Mejía *et al.* (2007) in the family business literature and was defined as "non-financial aspects of the firm that meet the family's affective needs, such as identity, the

The paper was adjudged the best paper by the *International Conference on Rethinking New Work Order: A Policy Change Iniative*, organised by Ramanujan College, University of Delhi in collaboration with Phd Chamber of Commerce and Industry; Department Of Finance and Business Economics, University of Delhi; Shri Ram College of Commerce, University of Delhi; University Of Kerala and Delhi Management Association from 21-22 January 2022.

International Journal of Entrepreneurial Behavior & Research
© Emerald Publishing Limited
1355-2554
DOI 10.1108/IJEBR-12-2021-0961

ability to exercise family influence, and the perpetuation of the family dynasty". While undertaking strategic decisions, family firms confront unique socioemotional "trade-offs" by weighing their potential economic gains and losses against potential SEW gains and losses (Chrisman *et al.*, 2012; Kotlar and De Massis, 2013). SEW holds such supremacy in family firms that they are, in fact, willing to make decisions that are not driven by economic logic if at any point it threatens their socioemotional endowment (Berrone *et al.*, 2012).

Internationalisation often brings changes in the management policies and organisational structure in ways that downplay the historical foundations of the family firm (Patel and Chrisman, 2014). Internationalisation disturbs the status quo in family firms and the family's welfare, as a result of which the family managers may be discouraged to pursue a risky yet profitable internationalisation opportunity (Fernández and Nieto, 2006). Expanding internationally necessitates the need for raising additional external funding and employing managers outside their family networks, which poses a threat to SEW as it may result in the loss of family control (Jones *et al.*, 2008). This makes family firms believe that the risk to SEW from internationalisation is not worth the reward. While internationalisation may lead to SEW gains if successful, the loss of SEW is more certain due to dilution of family control and changes in the traditional business model (Alessandri *et al.*, 2018). Consequently, they refrain from taking risky decisions like internationalisation due to the dread of losing years of accumulated SEW (Liang *et al.*, 2014; Gomez-Mejia *et al.*, 2010; Tsao *et al.*, 2018).

The above arguments lend us the understanding that SEW is set as the primary reference point by family firms while undertaking any strategic decisions like internationalisation. Despite the significance of SEW in the family business decision-making process, the research on SEW is still in its nascent phase and has not taken a comprehensive shape. Although it has been more than a decade since the conceptualisation of SEW (Gómez-Mejía *et al.*, 2007), much of the empirical studies have used SEW as a theoretical lens or a latent explanatory construct without measuring it directly (e.g. Pongelli *et al.*, 2019; Ray *et al.*, 2018; Yamanoi and Asaba, 2018). Also, it has been nearly a decade since an exemplary work was undertaken by Berrone *et al.* (2012) in proposing the multidimensional SEW scale – FIBER – *F*amily Control and Influence (F), Family Members' *I*dentification with the Firm (I), *B*inding Social Ties (B), *E*motional Attachment (E) and *R*enewal of Family Bonds to the Firm through Dynastic Succession (R). Yet, the majority of studies are still using univariate measures (e.g. percentage of family ownership) to capture SEW. Given the significance of SEW in guiding the family firms' decision-making process, it is imperative that utmost care is taken while measuring SEW.

Therefore, as the first objective, the paper attempts to calculate the SEW scores using the multidimensional scale proposed by Berrone *et al.* (2012) for four prominent Indian family businesses, thus adopting the multi-case study research design. The SEW scores are calculated through the content analysis of Chairman's Statements for a period of 13 years (2007–08 to 2019–20). The intent is to gain preliminary insights about the prevalence of various SEW dimensions in emerging market family businesses and to understand if these dimensions vary across firms as well as time. The paper is thus a response to the call by Berrone *et al.* (2012) who, in their study, proposed, as a future research scope, to use content analysis for measuring SEW. They argued that since SEW is "anchored at a deep psychological level among family owners", the content analysis shall be an appropriate approach for measuring SEW.

Further, the second part of the study attempts to explore the role of SEW in the internationalisation decision of family firms from emerging economies like India. Albeit the inevitable need to enter the overseas markets as a response to global competition, family firms are reluctant to internationalise. This paradox can be explained by the need for preserving SEW in these firms. Since SEW is an important feature that distinguishes the internationalisation process of family firms from that of non-family firms (Berrone *et al.*,

2012), it becomes imperative to understand the role of SEW in the internationalisation of family firms. Consequently, as the second objective, we examine the relationship between SEW and family firms' degree of internationalisation through two non-parametric tests: Somers' D and Kendall-Theil regression. Thus, the study attempts to answer the following questions: (1) Does SEW exist in family firms from emerging economies like India? (2) Is SEW an important characteristic in affecting the internationalisation of family firms? If SEW emerges to play a significant role in the internationalisation of family firms, then it may imply that the existing international business theories need modification in order to take into account the role of peculiar family characteristics in the context of family firms.

We restrict our study to Indian family firms since it stands at the third position globally in terms of family-owned businesses, just after the US and China (Credit Suisse Research Institute, 2018) and the research on internationalisation of Indian family firms is still scant (Thukral and Jain, 2021). Since 82% of the top 500 firms listed on Bombay Stock Exchange (BSE) are recognised as family firms (authors' own compilation) and they contribute a total of 66% to the country's GDP (Tharawat Magazine, 2014), it becomes indispensable to understand the internationalisation behaviour of Indian family firms. Although some recent attempts have been made to study the internationalisation of Indian family firms (Manogna and Mishra, 2021; Rienda *et al.*, 2019; Ray *et al.*, 2018; Singh and Kota, 2017), to the best of our knowledge, none of these research studies have undertaken an in-depth analysis on the role of SEW in the internationalisation of Indian family firms. Further, except for Cleary *et al.* (2019), none of the previous studies have observed the various dimensions of SEW (FIBER) through the content analysis of corporate disclosures over a longitudinal time frame; hence, we take their study as a reference point for our research. However, the scope of their study (Cleary *et al.*, 2019) does not include the utilisation of the results of content analysis in determining its impact on the family firms' external events which, in fact, they proposed as a future research scope. This, consequently, becomes the basis for our research.

This study makes several contributions: First, the study contributes to the current body of literature by delving deeper into a relatively less explored yet important area in the family business literature – SEW – particularly in the context of Indian family firms. Since SEW is a psychological concept, it would not be appropriate to measure it through unidimensional measures, as done in the extant literature, but through content analysis which allows the study of beliefs and perceptions (D'Aveni and MacMillan, 1990). Second, by undertaking the case study analysis, our study provides a preliminary understanding about the prevalence of various dimensions of SEW, which we believe is imperative before testing the FIBER scale in the context of Indian family firms. Third, the study contributes to an emerging field of literature – internationalisation of family firms – by analysing the impact of SEW on the family firms' degree of internationalisation. Since there still exist inconclusive results with respect to the internationalisation of family firms, the study attempts to resolve this anomaly by giving a closer look at four prominent Indian family firms to understand the role of SEW in explaining their internationalisation behaviour.

2. Literature review

2.1 The conceptual nature of socioemotional wealth (SEW)

The introduction of SEW has provoked an intense discussion in the family business literature. SEW is the family members' social needs or various other non-economic benefits accruing beyond the financial rewards from running a business (Gomez-Mejia *et al.*, 2010). The SEW model is presented as a new "homegrown" theoretical formulation in the family business literature, which suggests that family firms are typically committed to the preservation of their SEW (Gomez-Mejia *et al.*, 2011). The identity of the family owners is inextricably tied to their organisation (Berrone *et al.*, 2010), and its preservation becomes an

end in itself. Consequently, the controlling family is likely to pursue these family-centred non-economic goals.

The broad conceptualisation of SEW lies in the fact that a family derives a stock of affect-related values from its controlling position in a firm (Berrone *et al.*, 2012). These affective values derived from family ownership influence the family firms' policy decisions and strategic choices. Family members' emotions, altruism and social capital affect the firms' decision-making, primarily because families seek to preserve SEW within the business (Gómez-Mejía *et al.*, 2007). Various decisions in a family business such as business venturing, firm strategies, stakeholder relationships, management processes and corporate governance are affected by SEW (Gomez-Mejia *et al.*, 2011). Thus, it is argued that SEW is set as the primary reference point while undertaking any strategic decision in a family firm (Gomez-Mejia *et al.*, 2011).

Berrone *et al.* (2012) pioneered in capturing the multidimensionality of the SEW construct by disentangling the five dimensions of SEW and collectively labelled it as FIBER. They argued that the secondary proxies (e.g. percentage of family ownership, family members' involvement in management or board) used in the prior research studies do not capture the full spectrum of the SEW construct. SEW encompasses the affective endowments of family owners, such as retaining strong family identity, desire to exercise family authority, the appointment of family members to the significant posts and continuing family dynasty (Gómez-Mejía *et al.*, 2007). Consequently, a univariate measure does not render us with the holistic understanding of the SEW construct. For instance, two family firms with the same level of family ownership may differ with respect to emotions, sentiments and relationships within the family (Berrone *et al.*, 2012). Thus, besides family ownership, there are other dimensions of SEW, which must be carefully examined.

Despite an exemplary and meticulous work undertaken by Berrone *et al.* (2012) in proposing the multidimensions of SEW, the majority of the studies are still using univariate measures to capture SEW. As argued in the previous section, SEW is the primary reference point while undertaking any strategic decision-making in the family firms; hence, utmost care needs to be taken while measuring SEW. We thus employ the multidimensional FIBER scale proposed by Berrone *et al.* (2012) to calculate SEW scores for four prominent Indian family businesses through the content analysis of the Chairman's Statements. We believe, before testing the FIBER scale in the context of Indian family firms, it is imperative to explore if these SEW dimensions are prevalent in Indian family businesses and to understand-

(1) if these dimensions vary among our case companies and

(2) if SEW and individual FIBER dimensions change over time

Hence, our study is an attempt to capture preliminary insights about the prevalence of various dimensions of SEW (FIBER) in Indian family firms, an important yet unexplored area in the context of Indian family firms. Thus, our first objective is:

> *Objective 1* – To explore if various dimensions of SEW are prevalent in family firms from emerging economies like India and if these dimensions vary across our case firms as well as time

The next section sheds light on the relationship between the family firms' SEW and their internationalisation decisions.

2.2 Role of socioemotional wealth in the internationalisation of family firms

SEW is set as the primary reference point while undertaking any strategic decision in a family firm (Gomez-Mejia *et al.*, 2011), one of them being internationalisation decisions. One potential explanation why internationalisation of family firms is a complex phenomenon is

due to their desire to prioritise SEW (Basco and Rodriguez, 2011). Preservation and enhancement of SEW is reflected in family firms' decision-making process (Berrone *et al.*, 2012). Thus, it becomes imperative to understand the role of SEW in the internationalisation of family firms.

Internationalisation is perceived as a potential threat to SEW since it entails substantial changes in the form of increased risk, uncertainty and threats to family control (Gomez-Mejia *et al.*, 2010; Arregle *et al.*, 2017). The "dark side" of SEW (Kellermanns *et al.*, 2012) often promotes self-serving behaviour in family firms wherein they put greater emphasis on family objectives and tend to fill employment positions based on family ties rather than competence (Kets de Vries, 1993). Non-family managers are believed to foster the internationalisation process of family firms (Liang *et al.*, 2014; Sciascia *et al.*, 2013); however, their employment may imply an immediate threat to SEW in the form of declining family control (Arregle *et al.*, 2012; Banalieva and Eddleston, 2011). When non-family managers have a say in a family business, family members' ability to behave altruistically towards each other is at stake (Lubatkin *et al.*, 2005; Schulze *et al.*, 2003). Hence, due to the fear of losing family control, family firms refrain themselves from entering international markets, and if at all they decide to expand internationally, they tend to opt for low commitment strategies (Claver *et al.*, 2007) and subsidiaries that are close to their home region (Banalieva and Eddleston, 2011).

However, contrary to this, there is a recent body of literature contending that SEW concerns are secondary while financial profitability comes first, since going global is no longer an option in the competitive global economy. They argue that long-term vision is of utmost importance to family firms which fosters the pursuit of financial success instead of myopic SEW concerns (Lohe *et al.*, 2021). Hence, insights on the role of SEW in the internationalisation of family firms remain inconclusive and scarce (Pukall and Calabrò, 2014; Lohe *et al.*, 2021). Such inconclusive results and the significance of SEW in determining family firms' internationalisation strategies make it imperative to delve deeper into the underlying research stream. Further, as already discussed, Cleary *et al.* (2019) proposed, as a future research scope, to utilise the results of SEW content analysis in determining its impact on the family firms' external events. This becomes the basis of our research, and, consequently, our second objective is:

> *Objective 2:* To analyse if SEW is an important characteristic in affecting the internationalisation of family firms

If SEW appears to play a significant role in the internationalisation of family firms, it may imply that the existing international business theories need to be revised in the context of family firms in order to take into account the role of peculiar family characteristics.

3. Data and methodology

Our study employed the multi-case study research design for its effectiveness in dealing with an under-researched phenomenon (Eisenhardt and Graebner, 2007; Yin, 1994). Table 1 presents the objective-wise summary of data and methodology. The detailed information about the selection of case firms, measurement of independent variable (SEW) and dependent variable (degree of internationalisation) and the methodology adopted is presented in the following subsections.

3.1 Selection of case firms

In order to select our case firms, the list of BSE 500 firms was extracted from the BSE website. BSE is the Asia's first stock exchange which was established in 1875. By providing an efficient capital-raising platform, BSE has facilitated the growth of the Indian corporate

Objective	Objective-wise data source	Objective-wise methodology
Case firms: Bajaj Auto limited, Godrej Consumer Products Limited, Cadila Healthcare Limited, SRF Limited		
To explore if various dimensions of SEW are prevalent in family firms from emerging economies like India and if these dimensions vary across our case firms as well time	• Data for SEW are collected from the Chairman's Message in the annual reports	• Content analysis of the Chairman's Message along FIBER dimensions • Kruskal–Wallis test to examine if FIBER dimensions are significantly different among case firms
To analyse if SEW is an important characteristic in affecting the internationalisation of family firms	• SEW (independent variable): Chairman's Message in the annual reports • Degree of internationalisation (dependent variable): Outward foreign direct investment (OFDI) data from Reserve Bank of India (RBI) monthly reports	• Somers' D test and Kendall-Theil non-parametric regression to examine the impact of SEW on family firms' degree of internationalisation

Table 1.
Objective-wise data and methodology

sector over the past 146 years. BSE is considered as the India's largest data repository with around 5,000 listed companies. It is the first listed stock exchange in India [1]. From BSE 500 firms, we first identified family firms using the dual criteria: (1) majority ownership (more than 51%) of the company must be in the hands of the family members and (2) at least three members of the family must be involved in firm's management or board. The family ownership, management and board data are extracted by the authors from BSE website, company websites and annual reports. The above-mentioned criteria fetched us with a total of 80 Indian family firms (after removing state-owned enterprises, Indian subsidiaries of foreign MNEs and financial service companies). These firms were then rank-ordered by their total assets in 2020–21. The total assets data were taken from *Prowess* database, an electronic database from the Centre for Monitoring the Indian Economy (CMIE). From the top 15 firms of this list, 11 family firms were dropped since (1) their OFDI data were not available for all the years in the RBI report or (2) Chairman's Message (used for measuring SEW through content analysis) in the annual report was not available or (3) the annual report was not available for the period before 2010 or (4) at least third generation of the family was not involved in running the family business (as it indicates that degree of family involvement is more). According to Family Business Institute, only 12% of the family businesses manage to keep their business functional till third generation. Thus, only those family businesses manage to survive till third generation who have strong business foundations and exhibit greater emotional attachment, strong sense of identification with the family firm and deep-rooted family values (Bhalla and Banerjee, 2019). Consequently, we believe that it is the appropriate criteria to select family businesses wherein at least third-generation family members are involved. Finally, the remaining four family firms – Bajaj Auto Limited, Godrej Consumer Products Limited, Cadila Healthcare Limited and SRF Limited – were then selected for the purpose of our analysis. The flowchart depicting the selection process of our case firms is represented in Figure 1.

The multiple criteria mentioned above ensure a meticulous selection of our case firms. Our criteria define family firms not only on the basis of family ownership and involvement in management but also on the basis of the number of generations involved in the family business. This makes it different from past research studies wherein family firms are defined either on the basis of family ownership only (Basly, 2007; Boellis *et al.*, 2016) or both

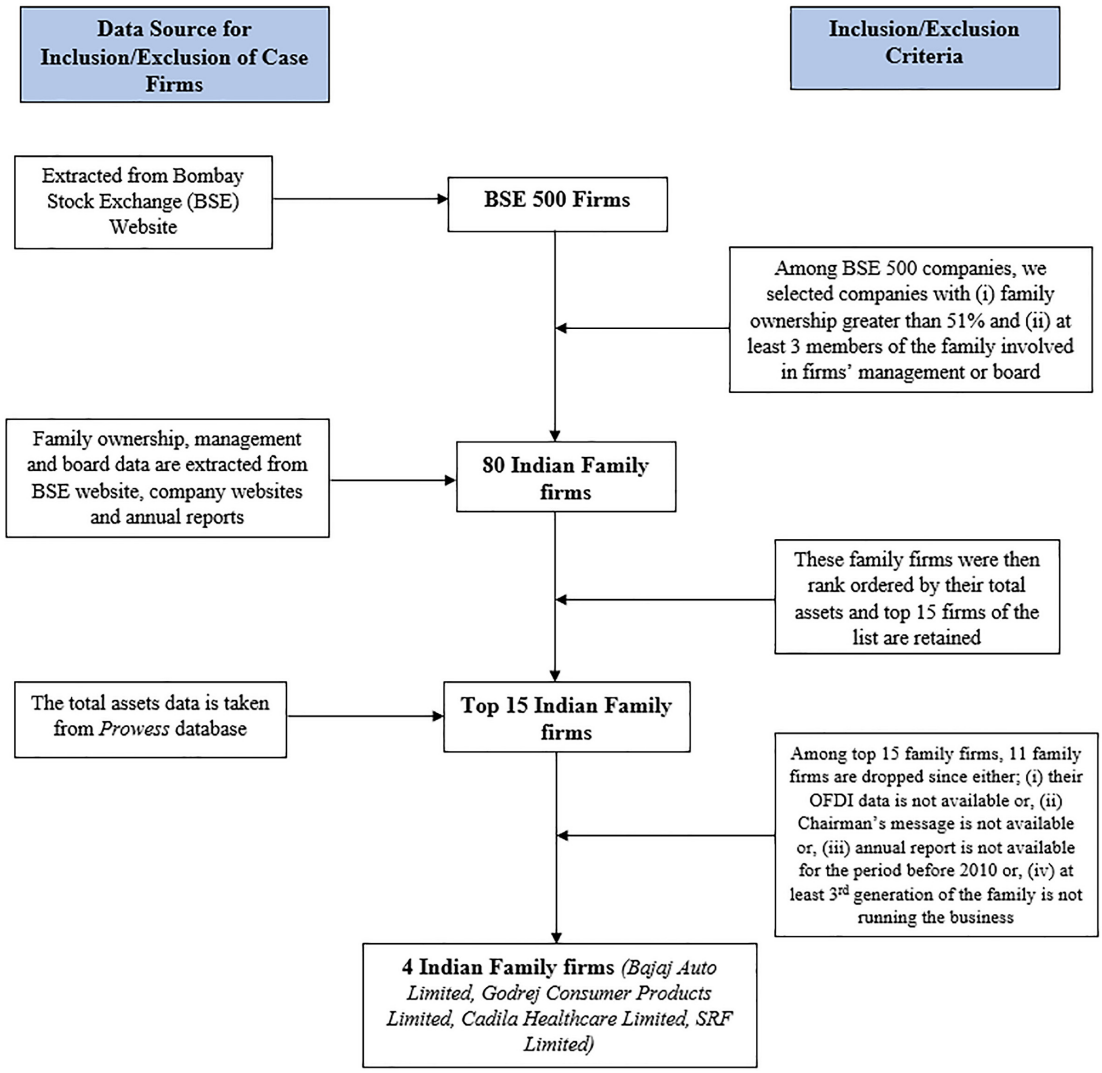


Figure 1.
Selection of case firms

ownership and involvement in management (D'Angelo *et al.*, 2016; Shi *et al.*, 2019; Ray *et al.*, 2018), while some others define it on the basis of the family generation involved in the business (Zahra, 2003). However, prior research studies do not employ the multiple criteria discussed above at once in defining the family businesses. Since the four selected family businesses are run by at least third-generation family members, it ensures that the family is actively involved in managing the businesses for a longer period of time and the family dynamics would have played a role in decision-making of the firm. Such multiple criteria for selection of sample/case firms will ensure that family control, family influence and family dynamics are adequately present in the firms' decision-making process, thus leading to better evaluation of the SEW construct (Table 2 highlights the characteristics of case companies, and detailed discussion about the case companies is done in Appendix 1).

3.2 Measurement of dependent variable – degree of internationalisation

The degree of internationalisation of our case firms, which is the dependent variable in our study, is measured by the level of their OFDI. OFDI as a measure of a firm's degree of internationalisation has been used in the past by various researchers (e.g. Ray *et al.*, 2018;

Tripathi and Thukral, 2018). The data for OFDI are collected from RBI's monthly reports on "Data on Overseas Investment" for a period of 13 years, from 2007–08 to 2019–20 (Table 3 highlights the internationalisation of case companies). We are bound to take data from 2007–08 onwards owing to the limited data availability in RBI database.

3.3 Measurement of independent variable – socioemotional wealth (SEW)

3.3.1 Measurement of SEW through content analysis. Berrone *et al.* (2012) in their paper on the exploration of SEW measurement scale (FIBER) suggested content analysis as a potential technique to capture the FIBER dimensions of SEW. Content analysis allows the study of beliefs and perceptions (D'Aveni and MacMillan, 1990) that are otherwise difficult to study by other means. As defined by Krippendorff (2004), content analysis is "a research technique for making replicable and valid inferences from texts (or other meaningful matter) to the contexts of their use". Since, SEW is "anchored at a deep psychological level among family owners" (Berrone *et al.*, 2010), the content analysis seems to be an appropriate approach for measuring SEW (Berrone *et al.*, 2012). For capturing managerial cognition, content analysis is considered to be a less obstructive technique than interviews (Phillips, 1994). Hence, it is believed to be a useful technique for collecting the otherwise unavailable data (Kabanoff *et al.*, 1995).

Table 2. Characteristics of case firms

Company	Family ownership (%)	Number of family members involved in management or board	Family generation currently ruling
Bajaj Auto Ltd	53.52%	6	4th generation
Godrej Consumer Products Ltd	63.25%	5	4th generation
Cadila Healthcare Ltd	74.78%	3	3rd generation
SRF Ltd	52.32%	3	4th generation

Table 3. Internationalisation of case firms

Company	Internationalisation
Bajaj Auto Ltd	1. Exports: 79+ countries 2. Foreign direct investment: a. Wholly owned subsidiaries: two wholly owned subsidiaries, one each in the Netherlands and Thailand b. Joint venture: one joint venture in Indonesia
Godrej Consumer Products Ltd	1. Exports: 90+ countries 2. Foreign direct investment: a. Wholly owned subsidiaries: nine foreign wholly owned subsidiaries – one in the Netherlands, four in Mauritius, one in Sri Lanka, one in Bangladesh, one in South Africa and one in the United States of America
Cadila Healthcare Ltd	1. Exports in the markets of the US, Europe, Latin America and South Africa 2. Foreign direct investment: a. Wholly owned subsidiaries: 26 foreign wholly owned subsidiaries – one in Ireland, one in Philippines, one in Sri Lanka, two in United Arab Emirates, three in South Africa, nine in the United States of America, one in France, three in the Netherlands, one in Brazil, one in Spain, one in Italy, two in Mexico
SRF Ltd	1. Exports: 75+ countries 2. Foreign direct investment: a. Wholly owned subsidiaries: five foreign wholly owned subsidiaries – one in the Netherlands, one in Thailand, two in South Africa and one in Hungary

One potential limitation of the survey method is that it collects data at a point in time, while we believe that the changes in SEW over time is an important dimension to be captured and explored. It is observed that at different stages of the firm's evolution, SEW considerations are prioritised differently (Breton–Miller and Miller, 2013). Thus, the longitudinal evaluation of SEW shall allow to analyse its impact on the family firms' degree of internationalisation over time, which is the prime objective of this paper. Hence, in order to undertake the longitudinal analysis, we believe that the content analysis is more appropriate than the survey method. Thus, content analysis method was adopted for the measurement of SEW variable.

We borrow from Cleary *et al.* (2019) and use the Chairman/Chairperson's Statement/ Message as the data source for measuring SEW. They advocated that in the case of family firms, Chairman's Statement is more likely to convey opinions of the family, and hence it is suitable to capture the FIBER dimensions of SEW from such statements. Chairman's Statement includes information with respect to the company's overall performance, its achievements, its future plans and strategies and notes to special events (Stittle, 2003). In a family business, it is often observed that the chairman is a family member only. Hence, in their message to stakeholders, they do mention about their family succession planning, the demise of a family member running the business, family legacy deeply rooted in the family business, their emotional ties and so forth. Hence, there are sufficient grounds to use the Chairman's Statement as the data source for capturing various dimensions of SEW (FIBER).

3.3.2 Content analysis method. As discussed in the previous section, we undertake the content analysis of the Chairman's Statements of four prominent Indian family businesses for measuring their SEW over a period of 13 years (2007–08 to 2019–20). The Chairman's Statements of our case firms were obtained from their annual reports, which are available on the company's website. Except for Godrej Consumer Products Limited where we observed the transition in the chairman/chairperson's position from Mr. Adi Godrej to Ms. Nisaba Godrej, in all the remaining three companies the chairman's position was held consistently by one person during our period of analysis. For all the companies, Chairman's Statements were available without any breaks; hence, we analysed 52 Chairman's Statements (13 for each company) for 2007–08 to 2019–20 period.

In our content analysis, the Chairman's Statement is the sampling unit and the individual paragraph is the unit of analysis (Krippendorff, 1980; Moreno and Cámara, 2014). While coding each paragraph, we adopted a deductive approach since we drew from the predetermined subject (Berg, 2001), that is, the FIBER dimensions of SEW proposed by Berrone *et al.* (2012). We coded each paragraph of the Chairman's Statement based on these dimensions (FIBER). We developed our coding scheme based on these FIBER dimensions since it captures the multidimensionality of the SEW construct and it is supported by extant literature (Cleary *et al.*, 2019; Swab *et al.*, 2020; Arzubiaga *et al.*, 2021). Each paragraph of the Chairman's Statements was coded along these FIBER dimensions from 1 to 5 *(respectively)*. The description of each of these FIBER dimensions is presented in Table 4.

Paragraphs highlighting "F (*F*amily Control and Influence)" dimension were coded as 1, paragraphs with "I (Family Members' *I*dentification with the Firm)" dimension were coded as 2, "B (*B*inding Social Ties)" as 3, "E (*E*motional Attachment)" as 4 and "R (*R*enewal of Family Bonds to the Firm through Dynastic Succession)" as 5. Paragraphs which did not relate to any of these FIBER dimensions were coded 0 and were excluded from our analysis. Also, multiple codes were assigned to the paragraphs if they referred to more than one dimension. Finally, for measuring SEW, we adopted quantitative content analysis technique wherein the analysis of the textual data is represented in the form of frequency expressed as a percentage or actual numbers of key categories (Krippendorff, 2004; Neuendorf, 2002). Thus, for calculating SEW for each of the four companies, the number of paragraphs coded was expressed as the percentage of the total number of paragraphs in the Chairman's Message.

Dimension	Description
F – *F*amily control and influence	The family members' direct and indirect control and influence over the affairs of the family firm
I – Family members' *I*dentification with the firm	Family members' sense of belongingness to the family business. The identity of the family members is tied in the family firm that usually carries the family's name
B – *B*inding social ties	The social relationships and kin ties among family members, with non-family employees and with community at large
E – *E*motional attachment of family members	The emotions and sentiments among the family members such as tenderness, warmth, consolation and disappointment, which affect the decision-making process in a family business
R – *R*enewal of family bonds to the firm through dynastic succession	The intention to pass the family business to the future generations in order to carry the family' heritage and tradition

Source(s): Berrone *et al.* (2012)

Table 4. Description of FIBER dimensions

In order to ensure the reliability of the coding procedure, the two authors independently pilot-tested five statements of each of the four companies and reported results based on the consensus achieved (Burnard, 1991; Graneheim and Lundman, 2004). Although we referred to the coding scheme adopted by Cleary *et al.* (2019) *(see Appendix 2)*, there were certain modifications done in some areas, particularly in the "R" and "E" dimensions based upon the results of pilot testing. Firstly, when the chairman referred to the long-term orientation of the family business, we coded it under the "R" dimension since family business continuation is an important item under the "R" dimension as proposed by (Berrone *et al.*, 2012). Next, when the chairman mentioned about the death of a family member, we coded it under the "E" dimension rather than "I" or "B" dimension which is done by Cleary *et al.* (2019), since it represents the emotional ties and bonds between the family members which is an important item of "E" dimension as proposed by Berrone et al.,(2012). After incorporating these measures, the two authors undertook the second round of independent test coding of five statements of each of the four companies, wherein the intercoder reliability between the two authors was found to be 90%, ensuring the reliability of the coding process. The authors then proceeded to code all the Chairman's Statements of each of the four companies in the 2007–08 to 2019–20 period.

3.4 Somers' D and Kendall-Theil non-parametric regression

In order to test the impact of SEW on family firms' degree of internationalisation, we performed two tests – Somers' D and Kendall-Theil non-parametric regression. Owing to the small sample size, non-parametric tests were used to analyse the relationship. Somers' D is a non-parametric test that measures the direction and strength of the relationship between ordinal independent and dependent variables. There are various studies in past which have employed Somers' D to test the impact of independent variable on the dependent variable (e.g. Baker *et al.*, 2009; Mitchell *et al.*, 2001; Klingbeil *et al.*, 2021; Balduck *et al.*, 2010). While there are other non-parametric tests to analyse the association between two variables such as chi-square test, Kendall's tau-b and Kendall's tau-c, these tests do not analyse the direction of relationship between the variables. Since the prime objective of the study is to analyse the impact of SEW on the internationalisation of family firms, Somers' D seems to be an appropriate non-parametric test. Thus, Somers' D helps in analysing the impact of independent variable on dependent variable which is not permitted in other non-parametric tests of association such as chi-square and Kendall's tau. Since Somers' D test can be performed on ordinal data only, we converted our SEW and OFDI variables into ordinal variables, ranking them into low, medium and high.

Further, for robustness, we performed the Kendall-Theil non-parametric regression to analyse the impact of SEW on the internationalisation of family firms using Kendall-Theil Robust Line (KTRLine – version 1.0) software (Granato, 2006). It is a robust nonparametric test of determining the regression coefficients between one continuous independent variable (SEW) and a continuous dependent variable (OFDI). The test is suitable for small samples to prevent the effects of outliers and non-normality in the residuals. Thus, the Kendall-Theil Robust Line (KTRL) is robust to the presence of outliers (Granato, 2006). Kendall-Theil regression estimates the slope of the line of best fit for the data which are not well suited for ordinary least square (OLS) regression. In OLS regression, the slope and the intercept are based on the means and sum of squares of the X and Y data sets, which, in turn, are substantially influenced by the outliers in the data (Helsel and Hirsch, 2002). However, in Kendall-Theil regression, the non-parametric slope is calculated as the median of all pairwise slopes. The Kendall-Theil slope is much more efficient than the OLS slope when residuals depart from normality (Granato, 2006). Hence, in our case, the test is appropriate in determining a robust regression line between SEW and OFDI.

4. Findings and discussion

As discussed above, the content analysis of the Chairman's Statement of our four case companies is done from 2007–08 to 2019–20. The descriptive results of the content analysis are reported in Tables 5 and 6. While Table 5 presents the results for overall SEW, Table 6 highlights the results for individual FIBER dimensions.

Table 5 shows the total number of paragraphs and the number of paragraphs coded in the Chairman's Statement for each of our case companies. There is not even a single year for which we did not code any paragraph for each of our case companies. Further, the table presents the calculation of SEW, that is, the number of paragraphs coded as the percentage of the total number of paragraphs. The SEW reported for Bajaj Auto Limited is maximum (i.e. 60.27%), indicating the strong reference to their family history, reference to the core values laid down by the founding generations and greater involvement of family members in managing the company. This is also evident from Table 6 wherein the "F" and "I" dimensions

	Bajaj Auto Ltd.		Godrej consumer Products Ltd.		Cadila Healthcare Ltd.		SRF Ltd.	
	n	%	*n*	%	*n*	%	*n*	%
Total number of paragraphs	146	100	188	100	195	100	161	100
Number of paragraphs coded *(equal to SEW)*	88	*60.27*	86	*45.74*	84	*43.07*	75	*46.58*

Note(s): The italic values indicates the value of SEW in case firms in percentage terms

Table 5. Case firms' SEW based on paragraph coding

	Bajaj Auto Ltd. (%)	Godrej Consumer Products Ltd. (%)	Cadila Healthcare Ltd. (%)	SRF Ltd. (%)
F	15.85	9.30	1.07	0.0
I	51.22	45.34	24.73	28.35
B	40.24	38.37	51.61	80.59
E	7.31	30.23	18.28	10.44
R	4.87	13.95	18.28	2.98

Table 6. Individual FIBER dimensions in case firms (as a percentage of total paragraphs coded)

appear to be high (amongst others) in Bajaj Auto Limited majorly due to the considerable involvement of the family in managing the business and greater reference to their family name in the Chairman's Statement. Also, two particular dimensions which appear to dominate in all our case firms are "I" and "B".

For *Objective 1,* our results indicate that various SEW dimensions are present in our case firms (as shown in Table 6). It is also observed that SEW and individual FIBER dimensions are not stable over time. The results for the dynamic nature of SEW are presented in Figure 2 which reports the overall SEW trend over the years and Figures 3–6 which highlight the trend of the individual FIBER dimensions for each of the case firms. As witnessed in Figure 1, the SEW trend in each of our case firms is dynamic throughout our analysis period. Also, in Figures 3–6, we observe that individual FIBER dimensions also change over time. Hence, we conclude that SEW concept is not stable over time. Relationships in family businesses are not stable over time since at different stages of the firm's evolution, SEW considerations are prioritised differently. As a family business grows and evolves over time, its relationship with the society, the emotional ties between the family members, their affective consideration and even the family members' involvement and control over the business ought to change throughout. Owing to the complex internal structures of the family businesses, it is observed that even extensive changes can happen over a short period.

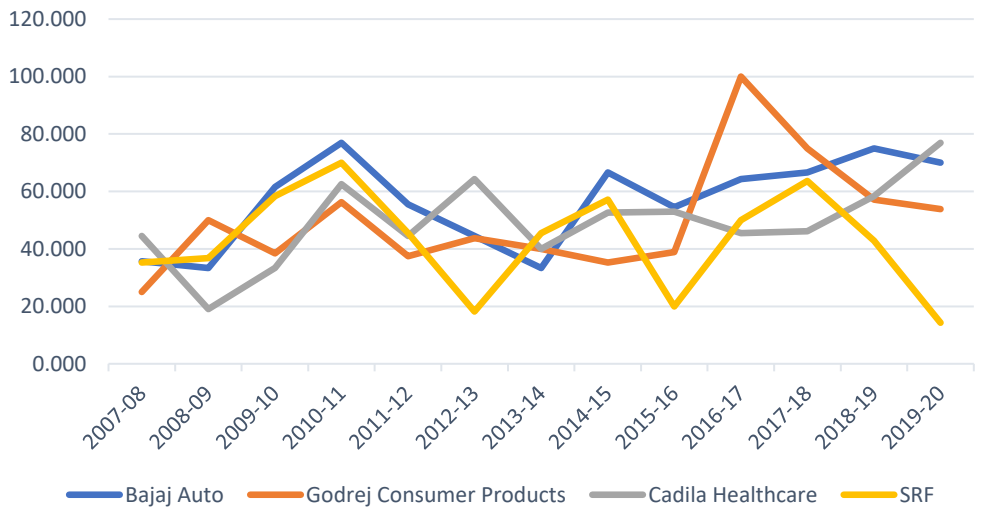


Figure 2.
SEW trend in case firms

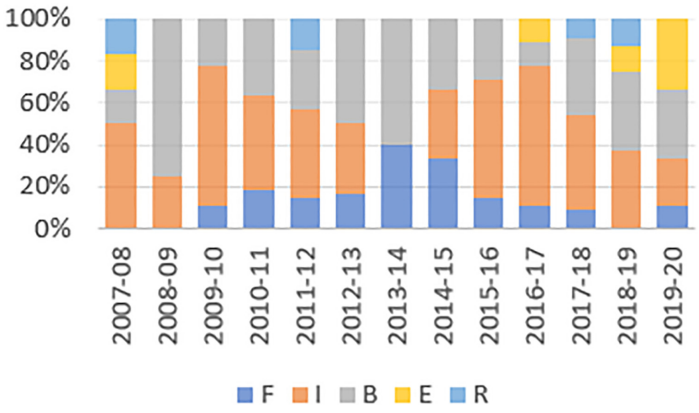


Figure 3.
FIBER trend – Bajaj Auto Limited

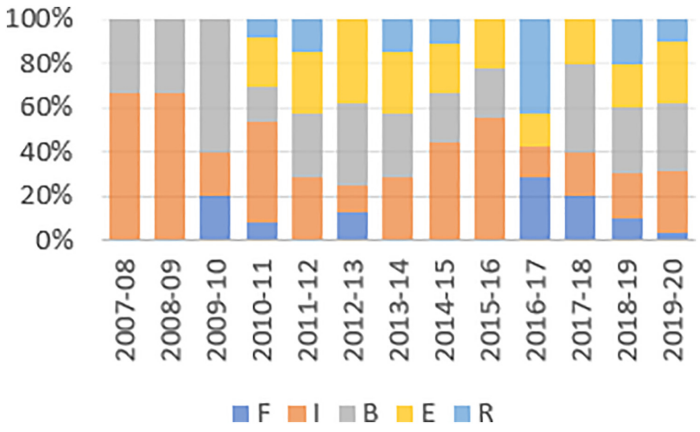


Figure 4.
FIBER trend – Godrej Consumer Products Limited

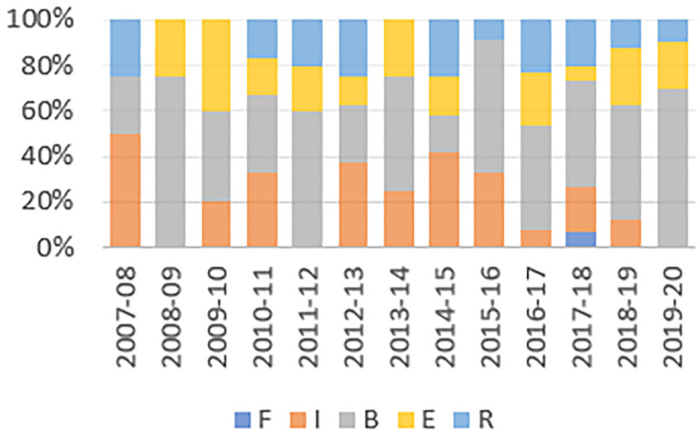


Figure 5.
FIBER trend – Cadila Healthcare Limited

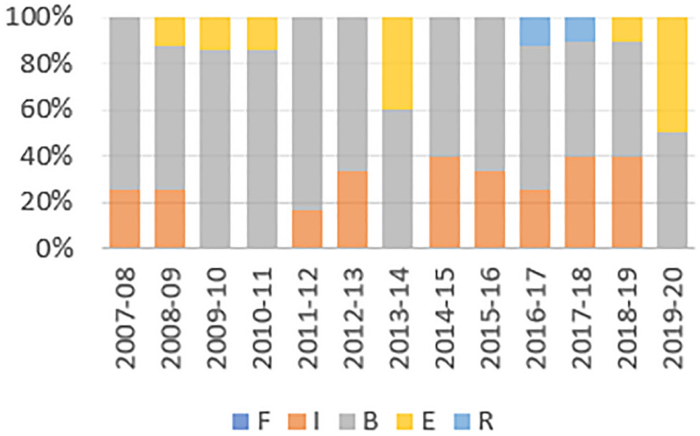


Figure 6.
FIBER trend – SRF Limited

Further, to analyse if these FIBER dimensions are significantly different among the four case companies, we conducted a nonparametric Kruskal–Wallis test. The test was run on each of the FIBER dimensions to know if they significantly differ from each other. The results of the Kruskal–Wallis test are depicted in Table 7.

The results indicate that F, I, E and R dimensions are significantly different among our case firms at 5% level of significance and dimension "B" is significantly different at 10% level

of significance. We believe that these FIBER dimensions are significantly different in family businesses due to the heterogeneity residing within them, with respect to the complex ties between family members, the degree of control in the hands of the family members, affective considerations and their emotional attachment with the family business.

As witnessed in Table 6, "F" dimension is dominant in Bajaj Auto Limited, not at all present in SRF Limited and is close to negligible in Cadila Healthcare Limited. This is because there were many instances in Bajaj Auto Limited wherein the chairman referred to "F" dimension in his message, such as decision-making by the family members, highlighting the management team been run by a family member, appointment/resignation of the family members or applauding the family members for successfully handling the key managerial positions. Some of these examples include the following:

The Chairman's Message in the years 2013–14 and 2014–15 *highlights that the family member running the position of Company's managing director leads a performance-driven team. The chairman expressed his trust and confidence that all the decisions taken by the family member (as Managing Director) are in the best interests of the company and will lead to more vigorous performance in future.*

Another instance is from the Chairman's Message in 2016–17 wherein *he announced that a family member is stepping down from the role of executive vice-chairman with effect from 1 April 2017 and will be continuing as the non-executive vice-chairman of the company. The chairman expressed his gratitude and sincere thanks to him for his role played in Bajaj Auto. He was delighted to share that his knowledge and years of experience will still be available to the family through his continued presence at the board.*

We observed that the first statement above was often highlighted by the chairman of Bajaj Auto Limited in his message. Hence, reference to family members holding key positions and making strategic decisions are quite prominent in the Chairman's Message of Bajaj Auto Limited. The company has always been spearheaded by the members of the Bajaj family; hence, such statements highlight the extent to which the Bajaj family influences the firm's operations. Six members of the Bajaj family are involved in the business and the family has successfully carried forward its legacy, wherein currently the fourth-generation family members (Mr. Rajiv Bajaj and Mr. Sanjiv Bajaj) are involved in the management of the company. Hence, such a strong presence of the family members in the business is the reason for the prominence of "F" dimension in Bajaj Auto Limited.

Moving to "I" dimension, we observe that it is also quite prominent in Bajaj Auto Limited and Godrej Consumer Products Limited. One reason for this is both of these companies belong to century-old family groups and hence their chairmen tend to refer to family history in their statements, which is one of the items of "I" dimension. Another reason is that since these companies belong to very old established groups, their family name is a source of self-identification and personal pride to them. As a result, they tend to sell a lot of products by their family name leading to the frequent mention of the family name in their Chairman's Statements. Reference to the family name in firms' products is also an important item of "I" dimension, as also argued by Cleary *et al.* (2019) who believed that such statements could reasonably be made without the mention of the family name/product name. Hence, if the family name is deeply rooted within the

Table 7. Kruskal–Wallis test results for individual FIBER dimensions for case firms

	F	I	B	E	R
Chi-square	23.151	8.448	7.462	13.192	13.077
Asymptomatic Sig	0.000*	0.038*	0.059**	0.004*	0.004*

Note(s): *$p < 0.05$; **$p < 0.10$

product name, it is reasonable to consider it as the "I" dimension. There were many instances in the Chairman's Statement of both Bajaj Auto Limited and Godrej Consumer Products Limited wherein they referred to family history, family name and so forth. Some examples include:

The chairman of Godrej Consumer Products Limited often highlighted that the Godrej Group has *left behind a legacy in India that is now over 100 years old and the company is very fortunate to be able to draw the values of trust, integrity and respect that have held the company for over a century now.*

Also, while referring to the current Covid-19 crisis, the chairman mentioned that *Godrej was founded in a crisis during India's Swadeshi Movement in 1897. In 1918, during the Spanish flu pandemic, the company made the first soap in the world to be made from vegetable oil and not from animal fat.*

Being part of an age-old family group ties them more to the family history, family legacy and the foundation laid down by the older generations. The functioning of these firms is deeply rooted in the core values set by the founding generations. Hence, family members in these firms appear to have a strong sense of belonging to the family firm. As a result, phrases like "Hamara Bajaj" or "Godrej Magic" are persistent in the Chairman's Statement of these companies, thus making the "I" dimension to appear more prominent.

Moving to the "E" dimension, we observe that it is relatively higher in Cadila Healthcare and Godrej Consumer Products in comparison to the other two family businesses. One particular reason for this is that family brand or family methods/ways of doing business were represented as being superior to that of competitors in these companies. The use of emotive language against the competitors indicates the emotional attachment of the family members to their business. In these companies, their affective considerations and emotional attachment to the family often come in the way of their business decision-making. For instance, in the case of Godrej Consumer Products Limited, all the decision-making in the company is guided by "The Godrej Way" which includes the core values laid down by the founding generation. Example:

The chairman of Godrej Consumer Products often mentioned that *their core values are determined by "The Godrej Way" and these are at the heart of all that they do. These values are the most powerful and differentiated asset of the company and they are reflected in all the actions of the company as it grows and evolves.*

Similarly, the chairman of Cadila Healthcare Limited frequently mentioned about their family foundation – *The Ramanbhai Patel Foundation through which the company is actively engaged in serving the community through initiatives in education, healthcare and research. The company focuses on touching the people's lives in different ways through the combination of core businesses and community responsibility.*

Also, as discussed in the methodology section, whenever the chairman mentioned about the death of a family member, we coded it under the "E" dimension rather than in the "I" or "B" dimension, which differs from what has been done by Cleary *et al.* (2019). This is because the chairman's mention about the death of a family member indicates the emotional ties and bonds among the family members which is an important item of "E" dimension as proposed by Berrone *et al.* (2012). Hence, the chairman of Bajaj Auto Limited mentioned about the *sudden demise of the family member and paid tribute for his committed service in the company*, which we coded as "E" dimension.

Moving on to the "R" dimension, we observe that this dimension is most prominent in Cadila Healthcare and somewhat in Godrej Consumer Products also. The dimension indicates the family members' intention to pass on the business to the successive generations, which was quite reflective in the case of these family businesses. Also, we made one modification in the coding scheme of "R" dimension, wherein, whenever the chairman referred to the long-term orientation of the family business, we coded it under "R" dimension since family

business continuation is an important item under "R" dimension as proposed by Berrone *et al.* (2012) which was not explicitly mentioned by Cleary *et al.* (2019). Accordingly, we observed that such statements relating to long-term orientation and business transfer to the next generation were most prominent in Cadila Healthcare and somewhat in Godrej Consumer Products. Example:

The chairman of the Cadila Healthcare Limited discussed about the *importance of* ***succession planning to ensure the continuity of the family business,*** *and in this light he announced the appointment of a family member as the Managing Director of the company in July 2017. The chairman expressed his confidence and trust in the newly appointed managing director mentioning that he is a young leader with a global perspective and has the strength in taking the enterprise to newer heights, spur innovation and build people to build our business.*

Similarly, the chairman of the Godrej Consumer Products Limited expressed *her gratitude to the board for giving her the opportunity to lead the company. She mentioned that the values of the founder, combined with his disciplined, results-driven and humble approach, will always be the core of the company's DNA.*

Finally, we move on to the "B" dimension where the differences are significant at 10% level. From Table 4, it is apparent that dimension "B" is dominant in SRF Limited amongst all the family businesses. The dimension majorly focuses upon the relationship that a family business develops with its society and its social standing in a community. One distinct feature about a family business is its commitment to serve the society in which it functions. They believe in developing binding ties with the society, thus leading to the enhancement of their brand image and reputation. Such commitment towards the society is found to be prominent in case of SRF Limited, since the first-generation family member, Sir Shri Ram, who, besides being an industrialist, was also an advocate of education and wanted their successive generations to carry forward that legacy. Hence, serving the society and carrying forward the family name is an important objective of SRF Limited. As a result, the company focuses on carrying forward the ideology of the founders through the CSR arm of the company, the SRF Foundation. The foundation is aimed at impacting the lives of poor students by implementing educational programmes, skill development workshops, among others. Example:

The Chairman's Message of SRF Limited repeatedly highlighted that the company *builds on the founder's legacy of social consciousness through SRF Foundation. The foundation is aimed at enriching the lives of thousands of poor students through its educational and skill development initiatives. SRF Foundation has expanded its outreach of positively impacting the lives of more than 10,000 students.*

Thus, our results confirm the prevalence of various dimensions of SEW in Indian family businesses. It is also observed that both SEW and individual FIBER dimensions are dynamic in nature. Finally, our results indicate that different FIBER dimensions are prioritised differently in family businesses, wherein "F" (15.85%) and "I" (51.22%) dimensions are dominant in Bajaj Auto Limited, "B" in SRF Limited (80.59%), "E" in Godrej Consumer Products Limited (30.23%) and "R" Cadila Healthcare Limited (18.28%). One FIBER dimension which may be dominant in one family business may not be prominent in the other.

We now move to our *objective 2* to explore the impact of SEW on the internationalisation of family firms over the longitudinal time frame. Thus, here our independent variable is the SEW measured through the content analysis of Chairman's Statements along FIBER dimensions, while our dependent variable is the internationalisation of family firms which is measured through OFDI. For this, we employ Somers' D test, and the results are presented in Table 8 which indicates the presence of a negative relationship between SEW and OFDI *(sig. 0.015)*.

Further, for robustness, we performed the Kendall-Theil non-parametric regression to analyse the relationship between two variables. The results for Kendall-Theil regression are

reported in Table 9, and KTRL is presented in Figure 7. This robust line does not depend upon the normality of the residuals, nor it is strongly affected by the extreme values, as in the case of OLS. The robust estimate of slope for the non-parametric fitted line is computed by comparing each pair of the data with others in a pair-wise manner. The median of all pair-wise slopes is taken as the robust estimate of the slope. Our results exhibit a slope of −1.284791, thus indicating that SEW negatively impacts the family firms' degree of internationalisation.

While the residual error in a linear model shall be normally distributed, a Kendall-Theil regression model is not bound to this assumption. In Kendall-Theil regression, the residual errors are depicted in the form of median deviation error (MDE) and root mean square error (RMSE). The median deviation error is defined as the median of the error values which is the location estimator for the population of residual errors. When MDE equals 0 or close to 0, then

Item	Value
Somers' D value	−0.692
Sig	0.015*
Asymptomatic Std. error	0.014

Note(s): *$p < 0.05$

Table 8. Somers' D test results for relationship between SEW and OFDI

Intercept	Slope	UCI[1]	LCI[2]	MDE[3]	RMSE[4]
3.677847	−1.284791	7.430325E-02	−3.723205	9.321487E-02	0.575753

Note(s): [1]Upper 95th percent confidence interval of slope
[2]Lower 95th percent confidence interval of slope
[3]Median deviation error
[4]Root mean square error

Table 9. Results for nonparametric regression using Kendall-Theil Robust Line (KTRL)

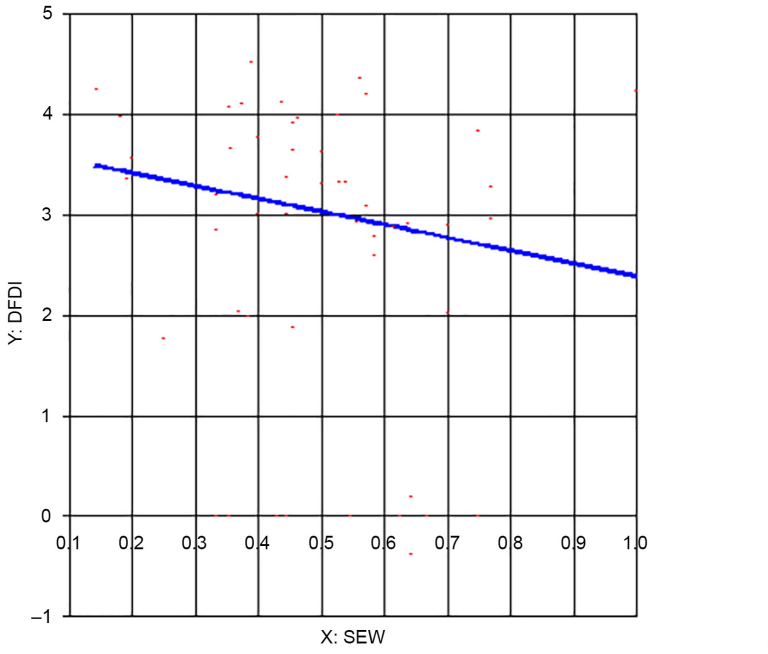


Figure 7. Kendall-Theil Robust Line (KTRL) between SEW and OFDI

the model is said to be a good fit (Granato, 2006). Our results exhibit the MDE of 9.321487E-02, thus indicating the goodness of fit of the model. Further, RMSE is defined as the standard deviation of the residuals and indicates the spread in the population of residual errors. Our results exhibit the RMSE of 0.575753, which is close to 0, again indicating the goodness of fit of the model.

Finally, Figure 7 presents the robust KTRL, indicating the negative impact of SEW on the internationalisation of family firms.

Our results corroborate with the prior studies that internationalisation is perceived as a potential threat to SEW since it entails substantial changes in the form of increased risk, uncertainty and threats to family control (Gomez-Mejia *et al.*, 2010; Arregle *et al.*, 2017). In our case companies, we observed that companies having low SEW appear to internationalise more through outward direct investments as compared to the ones having high SEW. For instance, Bajaj Auto Limited, which has the highest SEW amongst all the case companies (60.27%), has only three international subsidiaries, one each in the Netherlands, Thailand and Indonesia. Further, these subsidiaries are not material subsidiaries, that is, the income or net worth of these subsidiaries does not exceed 10% of the consolidated income or net worth of the listed entity. Also, the subsidiary located in Indonesia has been discontinued recently and the company is currently functioning with two international subsidiaries. In contrast, the case companies for which SEW is less than 50%, that is, Godrej Consumer Products Limited (45.74%), Cadila Healthcare Limited (43.07%) and SRF Limited (46.58%) have international subsidiaries in at least five countries. Cadila Healthcare has 26 subsidiaries outside India, Godrej Consumer Products has 9 foreign subsidiaries and SRF Limited has 5 foreign subsidiaries. Although Bajaj Auto is currently operating in nearly 79 countries, it is majorly through exports, which is a low commitment international market entry mode in comparison to wholly owned subsidiaries. Hence, the results also support the arguments put forward in the literature that if at all family firms decide to expand internationally, they tend to opt for low-commitment strategies due to the presence of SEW (Claver *et al.*, 2007). Bajaj Auto, although being the oldest among all, is currently functioning with the lowest number of foreign subsidiaries, mainly because family business is a source of self-identification, personal pride and satisfaction for the family members, and hence they exhibit loss aversion behaviour towards their non-economic endowments (SEW) while making strategic decisions. Hence, they are often hesitant in undertaking financially lucrative international expansion opportunities, if such expansion causes a reduction in their SEW endowments.

In sum, our results indicate that SEW hinders the degree of internationalisation of family firms; thus, we conclude that SEW may result in suboptimal decision-making in family firms.

5. Conclusion

As discussed, literature on internationalisation of family firms has gained traction in the recent past (Lohe *et al.*, 2021; Ray *et al.*, 2018). However, internationalisation of family firms is a complex phenomenon due to their desire to preserve and uphold SEW. The role of SEW in determining the internationalisation decisions of family firms is still unclear, potentially due to the inconclusiveness and difficulty in measuring SEW. Thus, the study employs multidimensional SEW scale proposed by Berrone *et al.* (2012) to calculate the SEW scores through the content analysis of the Chairman's Statements of four prominent Indian family businesses for a period of 13 years (2007–08 to 2019–20). Further, the study analyses the impact of SEW on the internationalisation of family firms. The objective is to gain preliminary insights about the prevalence of various dimensions of SEW in the context of Indian family firms and analyse its impact on their degree of internationalisation over a longitudinal time frame. The results indicate that various dimensions (FIBER) of SEW are

prioritised differently in different family firms. "F" (15.85%) and "I" (51.22%) dimensions are dominant in Bajaj Auto Limited, "B" in SRF Limited (80.59%), "E" in Godrej Consumer Products Limited (30.23%) and "R" in Cadila Healthcare Limited (18.28%). Also, by employing Somers' D and Kendall-Theil regression, the study finds that SEW significantly hinders Indian family firms' degree of internationalisation.

Our study has several limitations. First, since measuring SEW through content analysis is a new phenomenon in the underlying literature, there is a possibility of subjectivity. We, however, have tried to reduce this subjectivity by adopting the coding scheme proposed by Cleary *et al.* (2019) and further by undertaking coding by two researchers independently. Second, we had to restrict ourselves to take 13 years as our period of analysis due to the unavailability of the OFDI data before 2007 in the RBI database. Third, despite we studied four prominent cases (more than what Cleary *et al.* (2019) had worked on Irish firms), a larger sample of family firms (bifurcated into categories like Hindu Undivided Families (HUFs), sole proprietor firms, as in case of Indian firms) shall offer deeper insights into the role of SEW in affecting the internationalisation decision of family firms.

Although it might be difficult to generalise the results, our study provides some grounds in resolving the paradox on the internationalisation of family firms. The study contributes to the understanding that SEW leads to lower internationalisation in family firms. Consequently, it leads us to the conclusion that SEW may result in suboptimal decision-making in family firms. Thus, it is reasonable to say that some modification might be needed in the existing international business theories in order to explain the role of peculiar family characteristics in the internationalisation decisions of family firms. The study also provides sufficient grounds to believe that, besides internationalisation, other important decisions in family firms may also be taken sub-optimally due to the presence of SEW. Thus, the study raises some questions for future research scholars: Do family firms need to work on their socioemotional ties to avoid making suboptimal decisions? If this psychological wealth really leads to suboptimal decisions, is it really a wealth or is it a double-edged sword?

Note

1. https://www.bseindia.com/static/about/Company_Overview.html

References

Alessandri, T.M., Cerrato, D. and Eddleston, K.A. (2018), "The mixed gamble of internationalization in family and nonfamily firms: the moderating role of organizational slack", *Global Strategy Journal*, Vol. 8 No. 1, pp. 46-72.

Arregle, J.-L., Naldi, L., Nordqvist, M. and Hitt, M.A. (2012), "Internationalization of family-controlled firms: a study of the effects of external involvement in governance", *Entrepreneurship Theory Practice*, Vol. 36, pp. 1115-1143.

Arregle, J.L., Duran, P., Hitt, M.A. and Van Essen, M. (2017), "Why is family firms' internationalization unique? A meta-analysis", *Entrepreneurship Theory and Practice*, Vol. 41 No. 5, pp. 801-831.

Arzubiaga, U., Diaz-Moriana, V., Bauweraerts, J. and Escobar, O. (2021), "Big data in family firms: a socioemotional wealth perspective", *European Journal Management*, Vol. 39 No. 3, pp. 344-352.

Bain, D. (2011), "The family business vision of Adi Godrej", available at: Campden FB: https://www.campdenfb.com/article/family-business-vision-adi-godrej.

Baker, H.K., Hargrove, M.B. and Haslem, J.A. (2009), "An empirical analysis of the risk-return preferences of individual investors", *Journal of Financial and Quantitative Analysis*, Vol. 12 No. 3, pp. 377-389.

Balduck, A., Prinzie, A. and Buelens, M. (2010), "The effectiveness of coach turnover and the effect on home team advantage, team quality and team ranking", *Journal of Applied Statistics*, Vol. 37 No. 4, pp. 679-689.

Banalieva, R.E. and Eddleston, A.K. (2011), "Home-region focus and performance of family firms: the role of family vs non-family leaders", *Journal of International Business Studies*, Vol. 42, pp. 1060-1072.

Basco, R. and Rodriguez, M.J. (2011), "Ideal types of family business management: horizontal fit between family and business decisions and the relationship with family business performance", *Journal of Family Business Strategy*, Vol. 2 No. 3, pp. 151-165.

Basly, S. (2007), "The internationalization of family SME: an organizational learning and knowledge development perspective", *Baltic Journal of Management*, Vol. 2 No. 2, pp. 154-180.

Berg, B.L. (2001), *Qualitative Research Methods for the Social Sciences*, Allyn, Boston.

Berrone, P., Cruz, C., Gomez-Mejia, L. and Larraza-Kintana, M. (2010), "Socioemotional wealth and corporate responses to institutional pressures: do family-controlled firms pollute less?", *Administrative Science Quarterly*, Vol. 55, pp. 82-113.

Berrone, P., Cruz, C. and Gómez-Mejía, L.R. (2012), "Socioemotional wealth in family firms theoretical dimensions, assessment approaches, and agenda for future research", *Family Business Review*, Vol. 25 No. 3, pp. 258-279.

Bhalla, A. and Banerjee, A. (2019), "Life after 100? A leader's guide to resilient family businesses", available at: ISBINSIGHT: https://isbinsight.isb.edu/life-after-100-a-leaders-guide-to-resilient-family-businesses/.

Boellis, A., Mariotti, S., Minichilli, A. and Piscitello, L. (2016), "Family involvement and firms' establishment mode choice in foreign markets", *Journal of International Business Studies*, Vol. 47 No. 8, pp. 929-950.

Breton–Miller, I.L. and Miller, D. (2013), "Socioemotional wealth across the family firm life cycle: a commentary on "family business survival and the role of boards", *Entrepreneurship Theory and Practice*, Vol. 37 No. 6, pp. 1391-1397.

Burnard, P. (1991), "A method of analyzing interview transcripts in qualitative research", *Nurse Education Today*, Vol. 11, pp. 461-466.

Chrisman, J.J., Chua, J.H., Pearson, A.W. and Barnet, T. (2012), "Family involvement, family influence, and family-centered non-economic goals in small firms", *Entrepreneurship Theory and Practice*, Vol. 36 No. 2, pp. 267-293.

Claver, E., Rienda, L. and Quer, D. (2007), "The internationalisation process in family firms: choice of market entry strategies", *Journal of General Management*, Vol. 33, pp. 1-16.

Cleary, P., Quinn, M. and Moreno, A. (2019), "Socioemotional wealth in family firms: a longitudinal content analysis of corporate disclosures", *Journal of Family Business Strategy*, Vol. 10, pp. 119-132.

Credit Suisse Research Institute (2018), *The CS Family 1000 in 2018*, Credit Suisse AG, Zurich.

D'Angelo, A., Majocchi, A. and Buck, T. (2016), "External managers, family ownership and the scope of SME internationalization", *Journal of World Business*, Vol. 51 No. 4, pp. 534-547.

D'Aveni, R.A. and MacMillan, I.C. (1990), "Crisis and the content of managerial communications: a study of the focus of attention of top managers in surviving and failing firms", *Administrative Science Quarterly*, Vol. 35, pp. 634-657.

Eisenhardt, K.M. and Graebner, M.E. (2007), "Theory building from cases: opportunities and challenges", *Academy of Management Journal*, Vol. 50 No. 1, pp. 25-32.

Fernández, Z. and Nieto, M.J. (2006), "Impact of ownership on the international involvement of SMEs", *Journal of International Business Studies*, Vol. 37 No. 3, pp. 340-351.

Gómez-Mejía, L.R., Haynes, K.T., Núñez-Nickel, M., Jacobson, K.J. and Moyano-Fuentes, J. (2007), "Socioemotional wealth and business risks in family-controlled firms: evidence from Spanish olive oil mills", *Administrative Science Quarterly*, Vol. 52 No. 1, pp. 106-137.

Gomez-Mejia, L.R., Makri, M. and Kintana, M.L. (2010), "Diversification decisions in family-controlled firms", *Journal of Management Studies*, Vol. 47 No. 2, pp. 223-252.

Gomez-Mejia, L.R., Cruz, C., Berrone, P. and Castro, J.D. (2011), "The bind that ties: socioemotional wealth preservation in family firms", *The Academy of Management Annals*, Vol. 5 No. 1, pp. 653-707.

Granato, G.E. (2006), *Kendall-Theil Robust Line (KTRLine—Version 1.0)—A Visual Basic Program for Calculating and Graphing Robust Nonparametric Estimates of Linear-Regression Coefficients between Two Continuous Variables: Techniques and Methods 4-A7*, U.S. Geological Survey Publication, Virginia.

Graneheim, U.H. and Lundman, B. (2004), "Qualitative content analysis in nursing research: concepts, procedures and measure to achieve trustworthiness", *Nurse Education Today*, Vol. 24, pp. 105-112.

Helsel, D.R. and Hirsch, R.M. (2002), *Statistical Methods in Water Analysis*, Elsevier Science Publishers, Amsterdam.

Jones, C.D., Makri, M. and Gomez-Mejia, L.R. (2008), "Affiliate directors and perceived risk bearing in publicly traded, family-controlled firms: the case of diversification", *Entrepreneurship Theory and Practice*, Vol. 32 No. 6, pp. 1007-1026.

Kabanoff, B., Waldersee, R. and Cohen, M. (1995), "Espoused values and organizational change themes", *Academy of Management Journal*, Vol. 38, pp. 1075-1104.

Kellermanns, F.W., Eddleston, K.A. and Zellweger, T.M. (2012), "Extending the socioemotional wealth perspective: a look at the dark side", *Entrepreneurship Theory and Practice*, Vol. 36, pp. 1175-1182.

Kets de Vries, M.F. (1993), "The dynamics of family controlled firms: the good and the bad news", *Organizational Dynamics*, Vol. 21 No. 3, pp. 59-71.

Klingbeil, D.F., Osaili, T.M., Al-Nabulsi, A.A., Jemni, M. and Todd, E.C.D. (2021), "The public perception of food and non-food related risks of infection and trust in the risk communication during Covid-19 crisis: a study on selected countries from the Arab region", *Food Control*, Vol. 121, pp. 1-12, doi: 10.1016/j.foodcont.2020.107617.

Kotlar, J. and De Massis, A. (2013), "Goal setting in family firms: goal diversity, social interactions, and collective commitment to family-centered goals", *Entrepreneurship Theory and Practice*, Vol. 37 No. 6, pp. 1263-1288.

Krippendorff, K. (1980), *Content Analysis. An introduction to its Methodology*, Sage, Beverly Hills, CA.

Krippendorff, K. (2004), *Content Analysis: An introduction to its Methodology*, Sage Publications Inc, Thousand Oaks, California.

Liang, X., Wang, L. and Cui, Z. (2014), "Chinese private firms and internationalization: effects of family involvement in management and family ownership", *Family Business Review*, Vol. 27, pp. 126-141.

Lohe, F.W., Calabrò, A. and Torchia, M. (2021), "Disentangling the drivers of family firms internationalization through the lens of socioemotional wealth", *Journal of International Entrepreneurship*, Vol. 19, pp. 479-509, doi: 10.1007/s10843-021-00284-w.

Lubatkin, M.H., Schulze, W.S., Ling, Y. and Dino, R.N. (2005), "The effects of parental altruism on the governance of family-managed firms", *Journal of Organazational Behaviour*, Vol. 26, pp. 313-330.

Manogna, R.L. and Mishra, A.K. (2021), "Exploring the role of family ownership in internationalization: empirical investigation of Indian firms", *Review of International Business and Strategy*, Vol. 31 No. 1, pp. 1-15, doi: 10.1108/RIBS-05-2020-0058.

Mitchell, M.S., Lancia, R.A. and Gerwin, J.A. (2001), "Using landscape-level data to predict the disruption of birds on a managed forest: effects of scale", *Ecological Applications*, Vol. 11 No. 6, pp. 1692-1708.

Moreno, A. and Cámara, M. (2014), "Evolution of the information content from the in-situational perspective: El Alcázar brewery (1928-1993)", *Accounting History*, Vol. 19 No. 3, pp. 369-398.

Neuendorf, K. (2002), *The Content Analysis Guidebook*, Sage Publications, Thousand Oaks, California.

Patel, P.C. and Chrisman, J.J. (2014), "Risk abatement as a strategy for R&D investments in family firms", *Strategic Management Journal*, Vol. 35 No. 4, pp. 617-627.

Phillips, M.E. (1994), "Industry mindsets: exploring the cultures of two macro-organizational settings", *Organizational Science*, Vol. 5, pp. 384-402.

Pongelli, C., Calabro, A. and Basco, R. (2019), "Family firms' international make-or-buy decisions: captive offshoring, offshore outsourcing, and the role of home region focus", *Journal of Business Research*, Vol. 103, pp. 596-606.

Pukall, T.J. and Calabrò, A. (2014), "The internationalization of family firms: a critical review and integrative model", *Family Business Review*, Vol. 27, pp. 103-125.

Ray, S., Mondal, A. and Ramachandran, K. (2018), "How does family involvement affect a firm's internationalization? An investigation of Indian family firms", *Global Strategy Journal*, Vol. 8 No. 1, pp. 73-105.

Rienda, L., Claver, E., Quer, D. and Andreu, R. (2019), "Family businesses from emerging markets and choice of entry mode abroad: insights from Indian firms", *Asian Business and Management*, Vol. 18, pp. 6-30, doi: 10.1057/s41291-018-00053-z.

Schulze, W.S., Lubatkin, M.H. and Dino, R.N. (2003), "Toward a theory of agency and altruism in family firms", *Journal of Business Venturing*, Vol. 18, pp. 473-490.

Sciascia, S., Mazzola, P., Astrachan, J.H. and Pieper, T.M. (2013), "Family involvement in the board of directors: effects on sales internationalization", *Journal of Small Business Management*, Vol. 51, pp. 83-99.

Shi, H.X., Graves, C. and Barbera, F. (2019), "Intergenerational succession and internationalisation strategy of family SMEs: evidence from China", *Long Range Planning*, Vol. 52 No. 4, doi: 10.1016/j.lrp.2018.05.004.

Singh, R. and Kota, H.B. (2017), "A resource dependency framework for innovation and internationalization of family businesses: evidence from India", *Journal of Entrepreneurship in Emerging Economies*, Vol. 9 No. 2, pp. 207-231, doi: 10.1108/JEE.

Stittle, J. (2003), *Annual Reports: Delivering Your Corporate Message to Stakeholders*, Gower Publishing, Farnham.

Swab, R.G., Sherlock, C., Markin, E. and Dibrell, C. (2020), "SEW" What do we know and where do we go? A review of socioemotional wealth and a way forward", *Family Business Review*, Vol. 33 No. 4, pp. 424-445.

Tharawat Magazine (2014), "Economic impact of family businesses – a compilation of facts", available at: Tharawat Magazine: https://www.tharawat-magazine.com/economic-impact-family-businesses/economic-impact-family-businesses-2/.

Thukral, S. and Jain, A. (2021), "Unveiling contemporary dimensions in the internationalisation of family firms through bibliometric analysis and thematic analysis", *Review of International Business and Strategy*, Vol. 31 No. 4, pp. 507-539, doi: 10.1108/RIBS-09-2020-0121.

Tripathi, V. and Thukral, S. (2018), "Determinants of financing of outward foreign direct investment by Indian MNEs: a three-level analysis", *International Journal of Emerging Markets*, Vol. 13 No. 5, pp. 1154-1181.

Tsao, C.W., Wang, M.J., Lu, C.M., Chen, S.J. and Wang, Y.H. (2018), "Internationalization propensity in family-controlled public firms in emerging markets: the effects of family ownership,

governance, and top management team heterogeneity", *Journal of Small Business Strategy*, Vol. 28 No. 1, pp. 28-37.

Yamanoi, J. and Asaba, S. (2018), "The impact of family ownership on establishment and ownership modes in foreign direct investment: the moderating role of corruption in host countries", *Academy of Management Review*, Vol. 22, pp. 133-153.

Yin, R.K. (1994), *Case Study Research: Design and Methods*, Sage, London.

Zahra, S. (2003), "International expansion of U.S. manufacturing family businesses: the effect of ownership and involvement", *Journal of Business Venturing*, Vol. 18 No. 4, pp. 495-512.

Appendix 1
Discussion about the Case Companies

Bajaj Auto Limited

The journey of Bajaj family-owned and family-managed Bajaj Auto Limited began 76 years ago as part of one of the oldest and largest conglomerates in India, the Bajaj Group. It was founded in 1945 by Kamalnayan Bajaj and is currently headquartered in Maharashtra, India. Bajaj Auto, the flagship company of the Bajaj Group, is ranked as the world's fourth largest three- and two-wheeler manufacturer. Bajaj Group, founded in 1926 by Jamnalal Bajaj, today stands for its integrity, dedication and determination to succeed which are often traced back to its relentless devotion and involvement in India's independence movement. Mr. Rahul Bajaj, who has succeeded his grandfather Mr. Jamnalal Bajaj and his father Mr. Kamalnayan Bajaj, is the current chairman of Bajaj Auto and has been at the helm of the company since 1972. Under his leadership, the product portfolio of Bajaj Auto has expanded and the brand has entered the global marketplace. Not just this, the company's turnover has also increased from INR 72 million to INR 120 billion. With over two million unit sales to 79 countries in 2018–2019, Bajaj Auto Limited is India's largest exporter of motorcycles, three wheelers and quadricycles. During the financial year 2018–19, the company witnessed its highest ever total turnover of INR 319 billion (an increase by 18.5%) and total operating income of INR 305 billion (an increase by 20.1%). Following the words of the company's founder Mr. Kamalnayan Bajaj, *"Do what you think best, but be the best in what you do"*, the company has pioneered over the years in various areas by launching its scooter Chetak (also known as Hamara Bajaj) in 1970s which provided the first mass personal mobility to Indians or by launching the iconic Pulsar in 2001 or by making the presence in more than 79 countries around the world by significantly investing in innovation and technology. Due to its strong financial and industry leading metrics, Bajaj Auto is now recognised with a new and distinct brand image – *The World's Favourite Indian*.

The promoter family ownership in the company stands at 53.52% and six members of the family are either on board or holding key managerial positions. The Bajaj family has successfully carried forward its legacy, and currently the fourth-generation family members (Mr. Rajiv Bajaj and Mr. Sanjiv Bajaj) are involved in the management of the company. Since its inception, the reins of the company have been in the hands of family members only. In 1972, Mr. Rahul Bajaj took the reins of the company from his father Mr. Kamalnayan Bajaj and turned the company into a household name – Hamara Bajaj. Recently in May 2021, Mr. Rahul Bajaj stepped down as the chairman of the company after serving for nearly five decades and will now continue as Chairman Emeritus. His brother, Mr. Niraj Bajaj, will now be succeeding him as the chairman of the company with effect from 1 May 2021. Over a century ago, Mr. Jamnalal Bajaj decided to use his business to serve the society. His philosophy, "common good was more important than individual gain", is successfully taken forward by the successive generations of the family. The Bajaj family has dedicated themselves in creating a self-reliant nation over the years. The Bajaj family, up to the current generation, has naturally imbibed the values of nation service and ethical business practices. Each successive generation in the family has given greater importance to seeking knowledge and wisdom. The older generation family members have laid the foundations for the family's core values due to which the business group stands tall today.

Godrej Consumer Products Limited

Indian consumer goods company, Godrej Consumer Products limited, is part of the 123 years old Godrej Group. The company takes forward the proud legacy of the Godrej Group which is built on the strong values of integrity, trust and respect for others. Godrej Group, founded in 1897 by Ardeshir Godrej, has its roots in India's independence and Swadeshi Movement. The group today caters to 1.5 billion customers globally, with its footprints in more than 90 countries. The fourth generation scion, Ms. Nisaba Godrej, is the current chairperson of the Godrej Consumer Products Limited who took the reins of the company from her father Mr. Adi Godrej in 2017. The company has its presence in three categories – personal care, home care and hair care – and is spread across three emerging markets – Asia, Africa and Latin America. During the financial year 2018–19, the company had a turnover of INR 56.79 billion and a profit after tax of INR 17.54 billion. In emerging markets, the company is ranked amongst the largest hair care products and household insecticides. It is ranked as the top player in air fresheners in India and Indonesia and number two in soaps in India. Also, the company is ranked as the number one player in hair colour in India and sub-Saharan Africa. The company is aimed at solving real problems for its customers at low cost and broke barriers in various segments by launching the first one-rupee paper-based mosquito repellent, Goodknight Fast Card, to help people in rural areas, by launching a thirty-rupee hair colour sachet, Godrej expert rich crème or by rolling out the world's first powder to liquid hand wash, Mr. Magic, at just fifteen rupees. Due to their committed efforts in serving the nation, Godrej Consumer Products Limited has received immense recognition over the years – it was amongst the top 12 companies in India that cater environmental issues effectively, it has been awarded with the Porter Prize 2016 for creating shared value impact and enabling community development and it has also been awarded with "Women Empowerment" award at the 6th Asia Best CSR Practice Award.

The company is deeply rooted in the 123-year-old legacy of the Godrej group. Godrej was founded in a crisis during India's struggle for independence. Also, the group was the first in the world to manufacture a soap from vegetable oil during Spanish flu pandemic in 1918. Hence, the company believes the pandemic year of 2020 to set the "second beginning" for the glorious next 123 years of Godrej. Currently, the promoter family ownership in the company stands at 63.25%, and five members of the family are either on board or holding key managerial positions. The legacy of the Godrej family is successfully carried forward as the fourth-generation family members (Ms. Nisaba Godrej, Ms. Tanya Dubash and Mr. Pirojsha Godrej) are now involved in the management of the company. In fact, at such a young age, a woman family member, Ms. Nisaba Godrej, has been appointed as the chairperson of the company, which is quite rare in case of Indian family businesses. The family element in Godrej group has always remained paramount in running the business. The group believes that while maintaining the family control, they can grow at a very rapid pace – 10 times in 10 years (Bain, 2011). Since its inception, the Godrej group has been recognised as one of the successful close-knit family businesses. From its roots in India's independence and Swadeshi Movement to producing "Good and Green" products, all the members of the Godrej family have committed themselves in serving the nation. All the successive generations of the Godrej family take this legacy forward of doing the business in "The Godrej Way" – to never let go of its trust and being a good company.

Cadila Healthcare Limited

Cadila Healthcare Limited or Zydus Cadila is the global healthcare service provider which was founded in 1952 by Mr. Ramanbhai B. Patel, a first-generation entrepreneur. From wellness products to active pharmaceutical ingredients and animal healthcare products, the company has become a leader amongst India pharmaceutical companies for providing a wide range of healthcare solutions. The current chairman of Cadila Healthcare is Mr. Pankaj R. Patel who took the reins of the company from his father Mr. Ramanbhai B. Patel in 1995. Cadila Healthcare, run by Mr. Pankaj R. Patel along with his son Dr. Shravil P. Patel, has earned the title of the top generic drug manufacturer. In a short span of 15 years, the INR 200 crore group reached INR 3,700 crore, thus becoming India's fourth largest pharma group. The company serves 300 branded drugs and other healthcare products in more than 25 overseas markets. During the financial year 2019–20, the company's revenue stood at INR 142.5 billion and its net profit was INR 14.6 billion. Zydus Cadila has always been at the forefront of innovation-led growth by taking several pioneering initiatives – it launched world's first biosimilar of Adalimumab "Exemptia", launched world's second brand of typhoid conjugate vaccine "ZyVac TCV" and the company developed India's first quadrivalent influenza vaccine "Vaxiflu 4". Due to its dedication and commitment, the company has been conferred with several awards – Overall Indian Pharma Excellence Award from

Government of India, Award for Most Innovative Pharmaceutical Company by Thomson Reuters and it is declared as "Emerging Company of the Year" by *The Economic Times*.

The promoter ownership in the company stands at 74.78% and three members of the Patel family are involved in running the business. Currently, second-generation (Mr. Pankaj R. Patel) and third-generation family members (Dr. Shravil P. Patel) are managing the family business. The company takes the path of Mr. Ramanbhai Patel, the founder chairman, of creating happier and healthier communities by bridging the unmet healthcare needs. For Mr. Pankaj R. Patel, his father, Mr. Ramanbhai B. Patel, has always been the role model and he always wanted to take forward the legacy of his father – doing good towards the society, besides running the business. Each successive generation takes this legacy forward of doing good towards the society through Environment, Health and Safety (EHS) policy.

SRF Limited

SRF Limited was founded in 1970 as Shri Ram Fibres Limited by Dr. Bharat Ram who took forward the legacy of his father, Sir Shri Ram. The company began its operations as a textile company but later diversified into the chemicals business as well. Since its inception, the family members have committed themselves to improving the quality of life by serving people in more than 75 countries. Mr. Arun Bharat Ram is the current chairman of the company who took the reins of SRF Limited from his father Dr. Bharat Ram. Over the years, the company is recognised as the leader in its business – the company is the only manufacturer of ozone-friendly refrigerants in India, is one of the few manufacturers of Pharma grade HFA134a/P in the world, is the domestic market leader in the coated fabrics business for more than two decades and is recognised as the largest manufacturer of technical textiles in India. During the financial year 2019–20, the company earned a profit after tax of INR 9.16 billion (an increase of 55%) and revenue of INR 72.09 billion (an increase of 2%). Due to its strong business presence and the family members' dedication in serving the society, SRF Limited has achieved various recognition over the years – it was awarded with the *Family Business of the Year Award, 2019* by *The Economic Times*, was included in the Forbes' Best Under a Billion List in 2011, was also awarded with Deming Prize, 2012 for its chemical business and National CSR Award 2018, among others.

The promoter family ownership in the company stands at 52.32%, and three members of the Shri Ram family are involved in running the business. Sir Shri Ram, the first-generation family member, has been in the family business since 1909, and besides industrial business, he was also an advocate of education, who founded two prominent academic institutions in India – Shri Ram College of Commerce and Lady Shri Ram College for Women. Sir Shri Ram and his son Dr. Bharat Ram had the ideology of contributing towards the society through education and wanted their successive generations to carry forward that legacy. Today, SRF Limited is in the hands of third generation, Mr. Arun Bharat Ram (chairman) and fourth-generation family members, Mr. Ashish Bharat Ram (managing director) and Mr. Karthik Bharat Ram (deputy managing director); besides making SRF as global business leader, they are also carrying forward the ideology of the founders through the CSR arm of the company, the SRF Foundation.

Appendix 2

Table A2.
FIBER coding scheme adopted from Cleary *et al.* (2019) and certain modifications were made in "E" and "R" dimensions

FIBER dimension	Items
F – Family control and influence	• Reference to family member making decisions • References to family appointment/resignation from board • References to share issues to family/non-family • References to appointments/resignations to managerial positions for family
I – identification of family members with the firm	• Reference to family name in product name • Reference to family in daily operational terms • Reference to family history
B – Binding social ties	• Family donations, sponsorship, reference to social activities involving family • Reference to non-family manager/employee awards/recognition, retirements, bereavements • Reference to long-standing supplier relationships, business allies • Reference to business partners
E – emotional attachment of family members	• Use of emotive language against competitors/threats • References to family in decision-making alternatives, e.g. over economic considerations • References to superiority of family brand/methods • *Family bereavement* • *Emotions, values, trust, etc. guide the decision-making in the firm*
R – Renewal of family bond through dynastic succession	• Reference to business transfer to the next generation • Reference to transfer of board membership to family members • *Family firms indicating their intention to continue family legacy and tradition as well as evaluating their investment on long-term basis*

Corresponding author
Sonal Thukral can be contacted at: sthukral1@gmail.com; sonalthukral@dtu.ac.in

For instructions on how to order reprints of this article, please visit our website:
www.emeraldgrouppublishing.com/licensing/reprints.htm
Or contact us for further details: **permissions@emeraldinsight.com**

Journal of Electronic Materials
https://doi.org/10.1007/s11664-022-09466-1

ORIGINAL RESEARCH ARTICLE

Sensitivity Analysis of Biomolecule Nanocavity Immobilization in a Dielectric Modulated Triple-Hybrid Metal Gate-All-Around Junctionless NWFET Biosensor for Detecting Various Diseases

Mekonnen Getnet[1,2] · **Rishu Chaujar**[1]

Received: 22 July 2021 / Accepted: 21 January 2022
© The Minerals, Metals & Materials Society 2022

Abstract

In this paper, a novel biomolecule nanocavity immobilization in a dielectric modulated triple-hybrid metal gate-all-around (THM-GAA) junctionless (JL) NWFET has been proposed to improve sensitivity for detecting various diseases. A comparative analysis of the dielectric modulated triple-hybrid metal gate-all-around JL-NWFET biosensor has been carried out with unique and double-hybrid metal gate (DHM) transistors immobilizing different biomolecules (neutral) such as streptavidin, ChO_X, APTES, uricase, and biotin in the nanogap cavity region. The simulation results were analyzed using the Atlas-3D device simulation tool. The work shows that higher work-function and higher dielectric materials near the drain suppress/overcome short-channel effects and quantum mechanical tunneling caused by hot-carrier and electron scattering due to a high electric field and saturation velocity. The impact of neutral biomolecules on device output characteristics such as switching (I_{ON}/I_{OFF}) ratio, shifting threshold voltage (ΔV_{th}), intrinsic voltage gain $\left(g_m/g_d\right)$, drain off-current sensitivity $\left(S_{I_{OFF}}\right)$, subthreshold slope, transconductance $\left(g_m\right)$, output conductance $\left(g_d\right)$, surface potential and output resistance $\left(1/g_d\right)$ has been studied. Sensitivity of the proposed device for detecting a specific neutral biomolecule was examined using a drain off-current ratio, and the results were compared with available works. The result shows a higher sensitivity in a triple-hybrid metal gate transistor than a unique and double-hybrid metal gate transistor in addition to available works, as we have discussed under the results and discussion section. For example, drain off-current sensitivity ($S_{I_{OFF}}$) in a triple-hybrid metal gate when a biotin biomolecule is immobilized uniformly in the nanogap cavity was 217.6% and 46.43% higher than a unique and double-hybrid metal gate transistor, respectively. We found that the proposed device can detect a specific biomolecule to diagnose different biomarkers for diseases such as breast and lung cancer.

Keywords Atlas-3D · biomolecule immobilization · dielectric modulated · THM · GAA-JL-NWFET

Introduction

Recently, biomolecular species detection is considered significant research for detecting biological diseases such as cardiovascular disease,[1] Alzheimer's disease,[2] breast cancer,[3] ovarian cancer, viral infections, and Ebola.[4] However, detection of biomolecules such as uricase, APTES, streptavidin, ChO_X and biotin using a conventional method such as spectrometry, optical measurements, and surface plasmon resonance involve multi-stage processes and are unsuitable for online monitoring.[5,6] For instance, detecting the DNA sample complex using an optical microarray reader is very expensive and leads to superfluous DNA labels in a single region of a microarray.[4] Also, these label procedures make the sample preparation more time-consuming and complex. In addition to device fabrication complexity, there is a growing demand for launching conservative clinical laboratories in remote areas, military fields, and rural areas to detect biomolecules. To overcome these and other drawbacks, the newer FETs such as tunnel field-effect transistors,[7] gate-all-around junctionless transistors,[8] and FinFET[9] have emerged because of their low power consumption, easy scalability,

✉ Rishu Chaujar
chaujar.rishu@dtu.ac.in

Mekonnen Getnet
mekonnengetnet01@gmail.com

[1] Applied Physics Department, Delhi Technological University, Delhi, India

[2] Physics Department, Debre Tabor University, Debre Tabor, Ethiopia

Published online: 21 February 2022

and high packing density under small-scale node technology.[10] Detection using NWFET-based biosensors enables the integration of boosting and analyzing circuits on the same chip by minimizing both cost and space,[11] and as a result, NWFET-based biosensors have sparked a lot of attention in recent years. There is a huge demand for efficient technologies that can rapidly and effectively analyze biological constituents such as biomolecules and cells with quick, specific drug detection (label-free).[12] As the technology has grown, MOSFET size has decreased to an increase in the number of transistors in a single chip and boost transistor efficiency.[13] Thanks to today's microelectronic technology, miniaturized biosensors downsized to ultra-small-scale device size leads to a significant improvement of electrical sensor detection of NWFET-based biosensors to actually work at the cell scale[14] because the ability to measure a single cell represents a significant step forward in understanding numerous biological phenomena.[15] NWFET-based sensors can detect the molecules, which are of nanometer size.[16] For example, various biological species such as atoms (0.1 nm), DNA (1 nm), proteins (10 nm), and viruses (10 -100 nm) are found at nanometer scale.[17–20] The proposed device detecting site/nanocavity with 10-nm thickness can fit with those biological molecules such as DNA, atoms, and proteins. Previously, written works such as low-power silicon nanowire-based inversion mode MOSFETs have been demonstrated for the detection of DNA[1, 8] proteins[4, 5, 8, 21–23] and pH levels.[24, 25] But at present, fabricating conventional FET biosensors at ultra-small-scale device size has critical issues such as short-channel effect (SCEs), drain-induced barrier lowering (DIBL), hot-electron effect, threshold voltage instability, impact ionization effect, sub-threshold swing, and gate tunneling current.[5, 26–28] For instance, at small-scale device dimensions, it is problematic to maintain low drain off-current (I_{OFF}) at the same time maintaining a significant drain on-current (I_{ON}). This leads to a short-channel effect (SCEs) and quantum mechanical tunneling.[29, 30] At the nanoscale regime, problems related to an ultra-sharp doping profile due to a "diffusion of impurities between a *p*- or *n*-type drain/source (D/S) region and an *n*- or *p*-type substrate/body region [give] rise [to] an interface charge which develops parasitic gate resistance in the manufacture of ultra-small-scale devices".[31]

In recent years, multi-gate, junctionless device structures such as surrounding-gate-FET, Fin-FETs, and double-gate (DG)-FET have been proposed, which can control and alleviate SCEs and enhance electrostatic gate controllability.[32, 33] So, junctionless dielectric modulated multi-gate MOS field-effect transistors are the most hopeful candidate architecture in CMOS fabrication technology due to their protection from short-channel effects (SCEs) and random dopant profile effect (RDE).[23] When the thickness of MOSFET gate oxide (SiO_2) reaches an extremum limit (around 1 nm and below), a hot-electron effect arises leading to short-channel effects, consequently degrading device performance.[26, 28, 34] To overcome those problems related to gate oxide thickness in the case of small-scale device fabrication, silicon dioxide (SiO_2) gate insulator should be substituted with high-k dielectric gate oxide material such as hafnium oxide (HfO_2, $\varepsilon = 25$) using gate engineering device scaling, keeping adequate oxide thickness (EOT) as constant.[28, 31, 35, 36] The interface oxide (SiO_2) layer limits the fringing electric field across the channel.[37]

This paper examines the impact of different biomolecules on the proposed device's output electrical characteristics (sensitivity analysis of biomolecule nanocavity immobilization in a dielectric modulated triple-hybrid metal gate-all-around (THM-GAA) junctionless NWFET biosensor) using the Atlas-3D device simulation tool to analyze a specific biomolecule for the detection of various diseases.

Device Structure and Its Working Principle

The designed structure for the proposed device is illustrated in Fig. 1. Gate lengths of G_1, G_2 and G_3 are L_1(6 nm), L_2(8 nm), andL_3(6 nm), respectively, L_4 (10 nm) is the length of the nanogap cavity and silicon dioxide (SiO_2) which are near the drain and source ends, respectively, and L (20 nm) is the length of the high-k oxide (HfO_2) and the interface oxide layer (SiO_2). T_1 T_2, T_3, and T_4 are thicknesses of the metal gate, biomolecule cavity, hafnium oxide, and interface (SiO_2) oxides, respectively, and 2R is the thickness of silicon film. The work functions of each metal gate are described in Table I. A tunable work function has been used to reduce the ionization effect induced by a high electric field near the drain end,[38] threshold voltage fluctuation, parasitic gate resistance, and channel doping fluctuation[39] in modeling the THM-GAA-JL-NWFET biosensor. The target biomolecules are assumed to be immobilized and interact uniformly with the device in the nanogap cavity region. Biomolecules such as APTES ($\varepsilon = 3.57$)), Choli oxidase (ChO_x, $\varepsilon = 3.30$), streptavidin ($\varepsilon = 2.10$), biotin($\varepsilon = 2.63$), and uricase($\varepsilon = 1.54$) were simulated interchangeably by presenting their dielectric constant in the cavity region. The air cavity ($\varepsilon = 1.0$) was also considered by introducing its dielectric constant in the cavity[31] and does not react with SiO_2 and HfO_2 oxide materials[32] leading to production of a unique trace of binding event due to a change in electrical properties. This can be used as the recognition layer in the nanogap cavity.[8] Because of this, the proposed device can further be used to identify various diseases depending on the biomolecule under investigation. For instance, biomolecules such as uricase are responsible for detecting uric acid in human blood serum,[40] and APTES can detect cancer cells[1] and

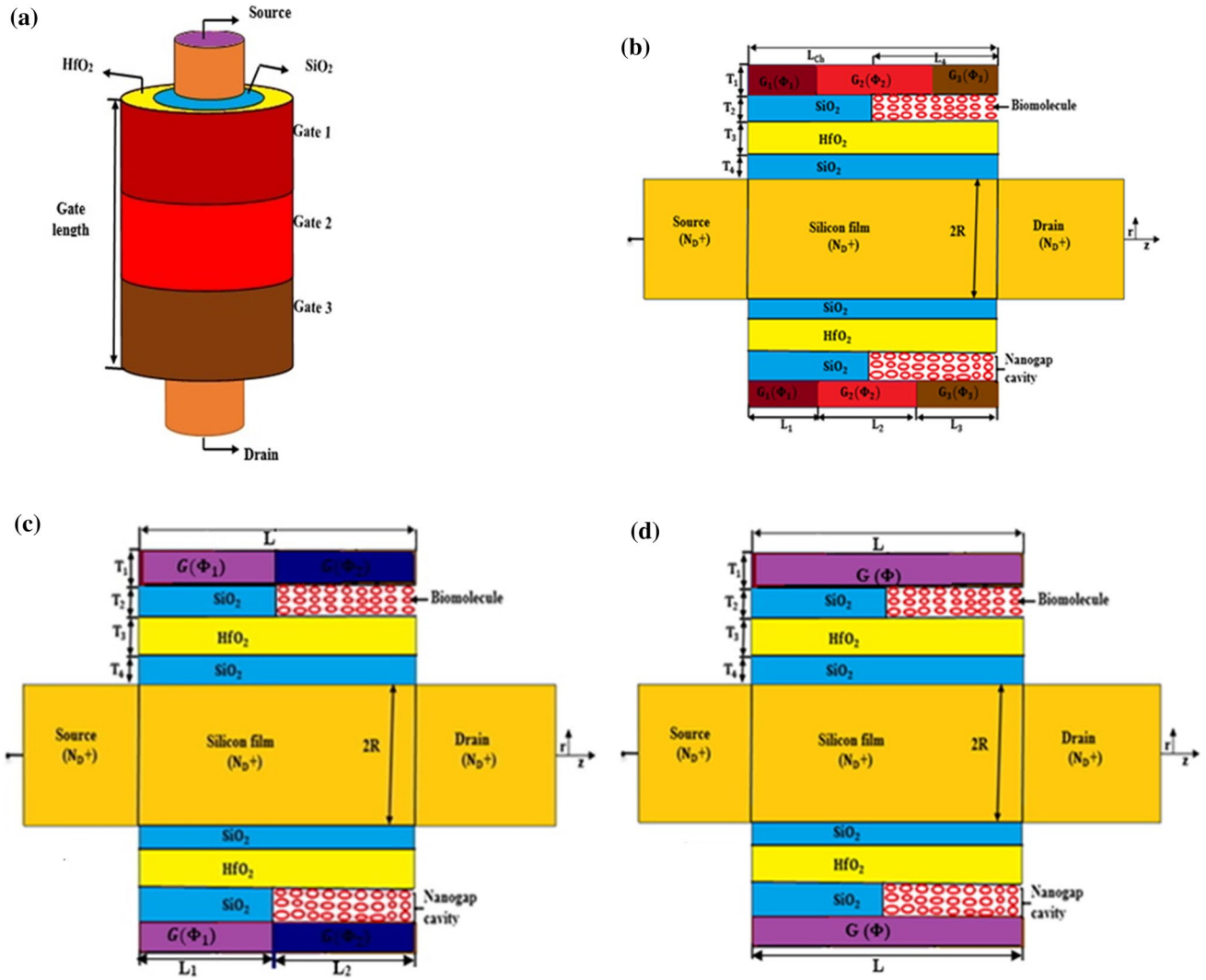


Fig. 1 (a) Illustrates the 3D schematic diagram. (b), (c), and (d) are 2D cross-sectional interpretations of n-type junctionless dielectric modulated unique, double-, and triple-hybrid metal gate-all-around NWFET biosensors, respectively.

Table I Designed parameters of double- and triple-hybrid metal GAA-JL-NWFET.

Physical device parameters	DHM-GAA-JL-NWFET		THM-GAA-JL-NWFET		
Channel length (nm)	20.0		20.0		
Oxide thickness,HfO_2 & SiO_2 (nm)	1.5 & 0.3		1.5 & 0.3		
Source oxide thickness SiO_2(nm)	1.0		1.0		
Source oxide length,SiO_2 (nm)	10.0		10.0		
Length of the cavity (nm)	10.0		10.0		
Length and thickness of source/drain (nm)	10.0		10.0		
Thickness of the cavity (nm)	1.0		1.0		
Thickness of siliconfilm (nm)	10.0		10.0		
Source/drain & channel doping (N_D+)	1×10^{19} cm^{-3}		1×10^{19} cm^{-3}		
HfO_2 and SiO_2 dielectric constants	25.0 & 3.9		25.0 & 3.9		
Metal gate work-function (eV)	4.50	4.894	4.50	4.86	4.96

thyroid diseases.[41] High doping concentration ($1\times10\ cm^{-3}$) has been applied uniformly during modeling of the THM-GAA-JL-NWFET biosensor through the channel from source to drain to have a tolerable threshold voltage variation and decreasing band gap separation.[42, 43]

Numerous simulations have been carried out using the materials listed in Table I and the Atlas-3D device simulator tool to study the impact of different biomolecules on electrical output characteristics in unique, double-, and triple-hybrid metal GAA-JL-NWFET.

Models incorporated in the simulations are carrier recombination and generation models for carrier mobility.[43] Doping versus mobility and high channel doping profile have been verified using the concentration-dependent mobility (CONMOB)[44] model along with the band gap narrowing (BGN) model. The carrier-carrier scattering (CCSMOB)[43] model has been used in the simulation is considered in our work due to the impact of high doping level, electron concentration, and hole concentration. Boltzman transport equations and Shockley–Read–Hall (SRH) were also used to account for the recombination of minority carriers under semiconductors without an impact ionization model.[44] The drift-diffusion model describes drain current as a function of drain voltage, including device surface potential that satisfies the model equations. The default values of the drift-diffusion model found in the ATLAS TCAD tool[43] are applied to describe the density of electron and hole change due to transport, generation, and recombination processes in the simulation,[45] and it is examined by Boltzmann transport approximation equations[46, 47] for accurate numerical simulation results.

The average time it takes an excess minority carrier to recombine is known as carrier lifetime and is determined by the SHR recombination lifetime model,[48, 49] and it can be used with the continuity equation to carry out carrier and recombination creation.[2] The statistics of recombination and creation of holes and electrons in semiconductors that occur via the trapping process are also described by the Shockley–Read–Hall (SRH) model.[50] The Concentration, Voltage, and Temperature (CVT) model has been applied in the simulation to study parallel and perpendicular field-dependent carrier and doping-dependent mobility.[44] Since the channel's radius is not less than 4 nm, quantum effect is not considered in our model.

Results and Discussion

Comparative Analysis on Dielectric Modulated Double- and Triple-Hybrid Metal GAA-JL-NWFET-Based Biosensors on Electrical Transfer Characteristics

The impact of biomolecules on subthreshold slope in both devices is illustrated in Fig. 2a. It is clear that, as the dielectric constant rises, subthreshold swing decreases because the biomolecule dielectric constant and metal work-function modulate electrostatic gate control by reducing threshold voltage roll-off through the channel such as with high-k materials, thereby improving gate control capacity.[51] In our study, for the APTES ($\varepsilon = 3.57$)

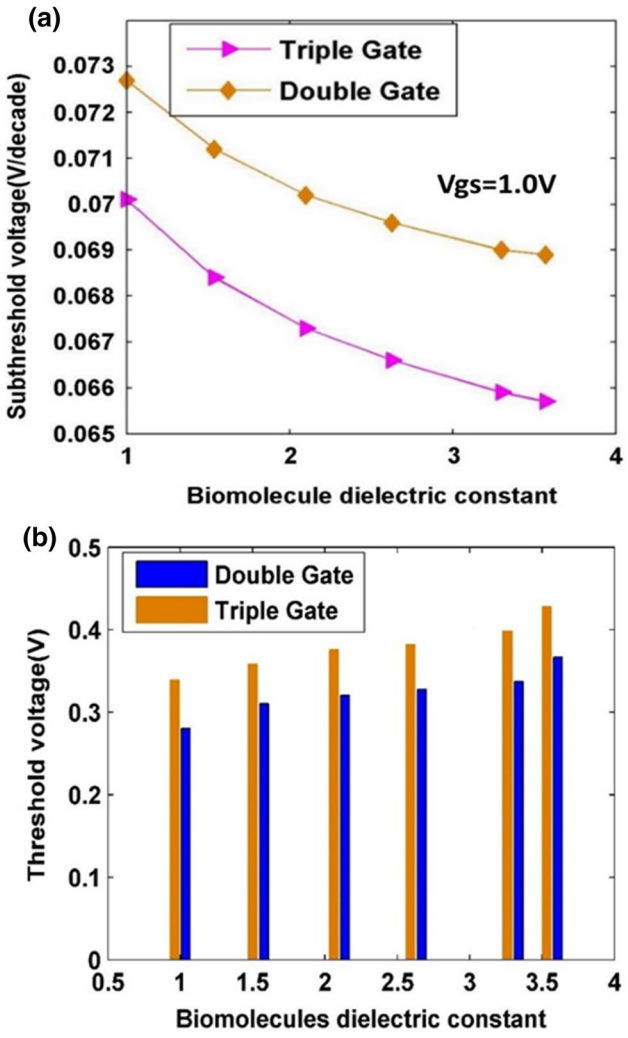


Fig. 2 Variation of (a) subthreshold slope (b) threshold voltage (V_{th}) versus biomolecules for n-type double- and triple-hybrid metal gate-all-around junctionless NWFET at a constant ($V_{DS} = 0.05$ V and $V_{GS} = 1.0$ V).

biomolecule, results of subthreshold slope in both devices are 6.90×10^{-2} V/decade and 6.50×10^{-2} V/decade for a double- and triple-hybrid metal gate transistor, respectively. Because of work-function (Φ_{G3}) suppression, there is a hot-electron effect and increase in carrier mobility through the silicon film.[52]

Figure 2b illustrates the impact of neutral biomolecules on the threshold voltage (V_{th}) for n-type double- and triple-hybrid metal gate-all-around junctionless NWFET. In both cases, as the dielectric constant rises, threshold voltage increases because threshold voltage roll-off is minimized by gate dielectric materials.[53] For instance, in the neutral APTES ($\varepsilon = 3.57$) biomolecule, the threshold voltage (V_{th}) in both devices are 0.33 V and 0.47 V for a double- and triple-hybrid metal gate, respectively, at $V_{GS} = 1.0$ V and $V_{DS} = 0.05$ V, which means there is 42.42% more improvement observed in the triple-hybrid than the double-hybrid metal gate. This threshold voltage variation (shift) indicates enhanced sensitivity in the triple-hybrid metal gate compared to the double-hybrid metal gate due to uniformity of carriers on the channel by the metal gate work-function.

Figure 3a demonstrates the effect of the neutral (APTES) biomolecule on drain current for unique, double-, and triple-hybrid metal gate-all-around junctionless NWFET. The tunneling current in the triple-metal gate is lower than a single- and double-metal gate because the gate work-function overpowers parasitic resistance and increases gate capacitive controllability.

Figure 3b illustrates impacts of neutral (air, uricase, streptavidin, biotin, ChO_X, and APTES) biomolecules to study their significant effect on leakage current in the case of double- and triple-hybrid metal gate devices, and the result shows that as the dielectric constant increases, leakage current decreases because the higher biomolecule dielectric constant increases gate electrostatic controllability by reducing electron tunneling from the gate and enhances gate control capacity.[51] This is because a higher gate dielectric oxide suppresses reverse tunneling current from the drain by creating a potential barrier in the channel region.[54] For instance, in the APTES ($\varepsilon = 3.57$) biomolecule, leakage current measurements in both devices are 2.32×10^{-12} A and 1.24×10^{-13} A for a double- and triple-metal gate, respectively. The work-function (Φ_{G2}) in the triple-metal gate forms barrier potential in the channel region, which enhances the driving current from source to drain lowering the high electric field and short-channel effect in the triple-metal gate compared to the double-metal gate device.[52]

Figure 4 demonstrates the effect of the biotin biomolecule on the output conductance and transconductance for unique, double-, and triple-hybrid metal gate-all-around junctionless NWFET. The output conductance (g_d) shown in Fig. 4a examines the first-order derivative of I_D, with

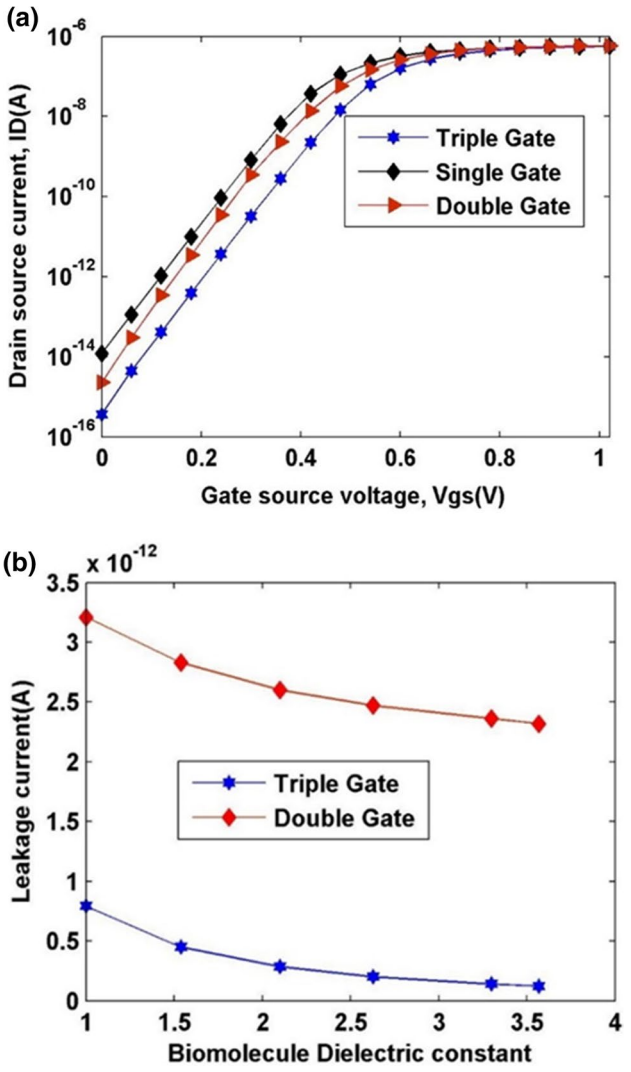


Fig. 3 (a) Drain current (I_D-V_G) and (b) leakage current comparison including different biomolecules for n-type unique, double-, and triple-hybrid metal gate-all-around JL-NWFET at ($V_{DS} = 0.05$ V and $V_{GS} = 1.0$ V).

respect to V_{DS} at constant $V_{GS} = 0.6$ V for all unique, double-, and triple-hybrid metal gate-all-around junctionless NWFET. It clearly shows that the triple-hybrid metal gate device shows lower output conductance (g_d) under a weak inversion region than the unique and double-hybrid gates due to lower drain-induced barrier lowering, short-channel effect, and parasitic resistance under the triple-hybrid metal gate device.[36, 55] The transconductance g_m described in Fig. 4b is the first-order derivative of I_D, with respect to gate-source voltage (V_{GS}) at constant $V_{DS} = 0.1$ V in the case of different gate engineering designs. At the cut-off region (gate-source bias voltage is equal to zero) and the weak inversion region (gate-source bias voltage is less than threshold voltage), higher transconductance in the case of unique and double-hybrid metal gates are recorded than

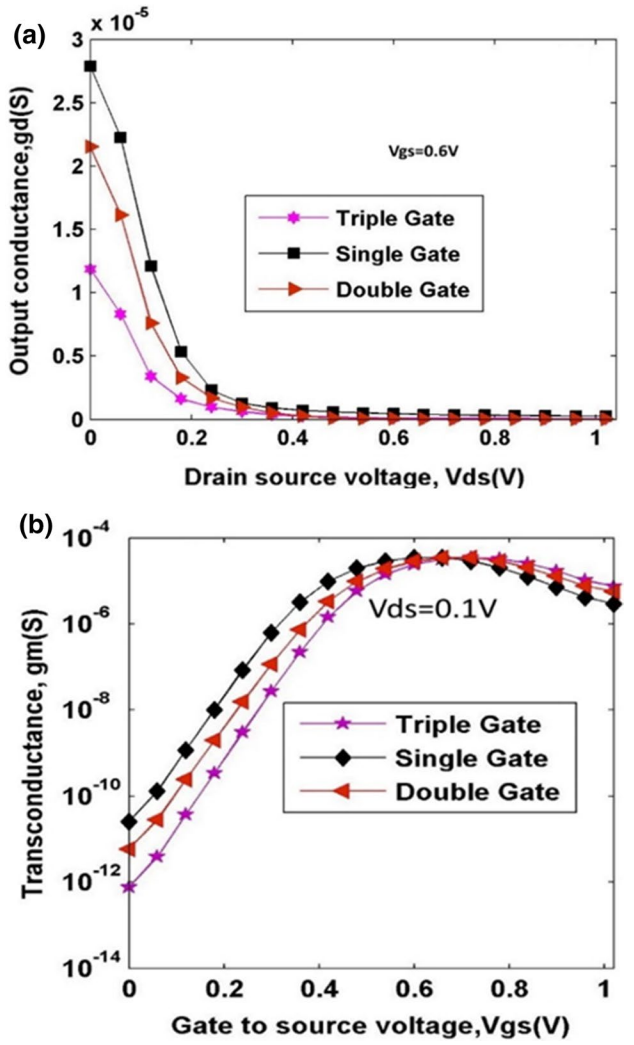


Fig. 4 Illustrates (a) the output conductance and (b) transconductance (g_m) comparisons for *n*-type unique, double-, and triple-hybrid metal gate-all-around JL-NWFET.

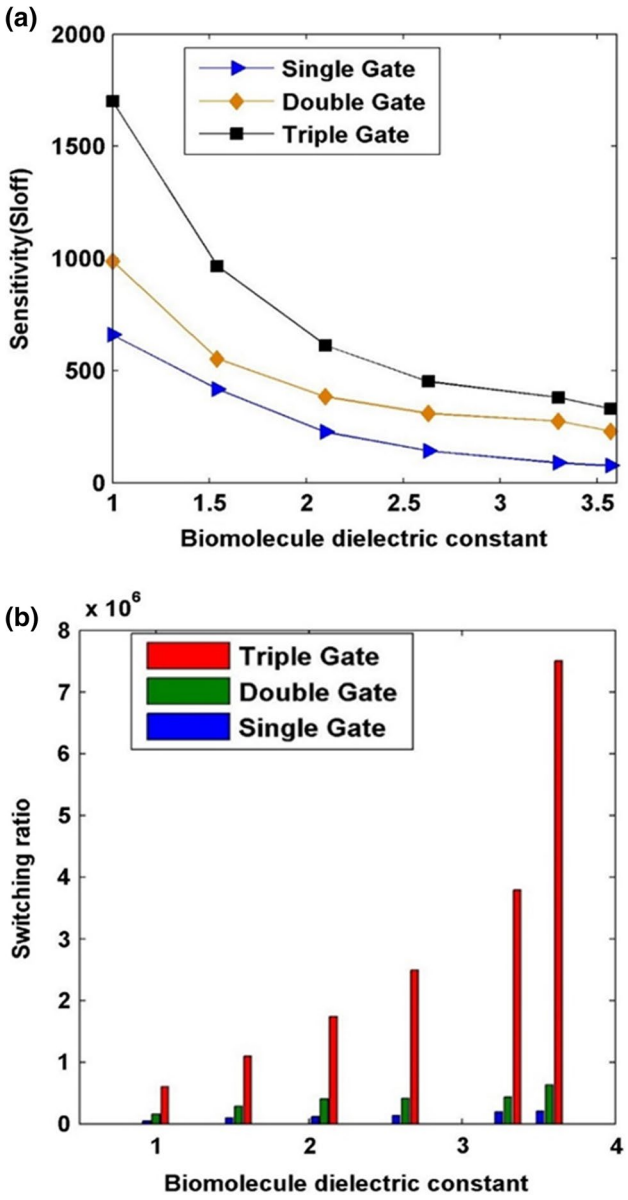


Fig. 5 Impact of biomolecules on (a) the sensitivity ($S_{I_{off}}$) and (b) switching ratio for n-type single-, double-, and triple-hybrid metal gate-all-around JL-NWFET at ($V_{DS} = 0.05$ V and $V_{GS} = 1.0$ V

triple-hybrid metal gate devices, while higher transconductance is recorded under the triple-hybrid metal gate device than unique and double-hybrid metal gate devices at the strong inversion region at $V_{GS} = 0.7$ V and $V_{DS} = 0.1$ V as shown in Fig. 4b. For instance, transconductance (g_m) measurements at constant $V_{GS} = 0.7$ V and $V_{DS} = 0.1$ are 2.34×10^{-5},2.63×10^{-5} and 2.72×10^{-5} siemens (S) in the case of unique, double-, and triple-hybrid metal gate devices, respectively. The percentage improvement of double and triple hybrid metal gates compared with unique metal gate devices are 12.39% and 16.24%, respectively. This is because the different gate work-function of THM-GAAJL-NWFET increases electrostatic coupling in the channel and improves carrier mobility, and surface potential across the channel proves the enhanced performance of the proposed device.[36]

Sensitivity Analysis and Switching Ratio Including Different Biomolecules

The impact of different biomolecules on drain off-current sensitivity ($S_{I_{off}}$) for unique, double-, and triple-hybrid metal gate-all-around JL-NWFET at $V_{DS} = 0.05$ V and $V_{GS} = 1.0$ V is illustrated in Fig. 5a. It clearly shows that the change in drain off-current sensitivity is higher for all devices at a lower dielectric constant due to lower electrostatic gate control and higher tunneling current. In contrast, as the dielectric constant of biomolecules increases, the change in drain off-current sensitivity

decreases due to impacts of higher dielectric constant modulating gate electrostatic control. For instance, drain off-current sensitivity using the triple-hybrid metal gate-all-around JL-NWFET for uricase ($\varepsilon = 1.54$) and APTES ($\varepsilon = 3.57$) biomolecules are 1.70×10^3 and 3.30×10^2 , respectively. This higher variation of drain off-current sensitivity in both cases indicates that tunneling current/leakage current controllability of thinner gate oxide increases for higher cavity dielectric material, as illustrated in Fig. 3b.

Figure 5b illustrates the impact of neutral biomolecules on switching ratio $\left(I_{ON}/I_{OFF}\right)$ for unique, double-, and triple-hybrid metal gate-all-around JL-NWFET at $V_{DS} = 0.05$ V and $V_{GS} = 1.0$ V. It clearly shows that the change in switching ratio $\left(I_{ON}/I_{OFF}\right)$ increases as the biomolecule's dielectric constant increases; therefore, the drain off-current ratio decreases since a higher biomolecule dielectric constant suppresses tunneling current and improves gate electrostatic controllability, and a higher gate work-function difference offers higher band bending near the source end, which increases the carrier mobility.[37] For instance, the switching ratio $\left(I_{ON}/I_{OFF}\right)$ is 6.26×10^5 and 7.50×10^6 for double- and triple-hybrid metal gate devices, respectively, when the APTES ($\varepsilon = 3.57$) biomolecule is immobilized in both nanocavity regions at the same condition. This higher switching ratio in the triple-hybrid metal gate is due to a potential barrier created in the channel region by gate work-function suppressing reverse tunneling from the drain [54] and indicates better device sensitivity when target biomolecules are immobilized uniformly in the targeted site. In addition to switching ratio, the new figure of merit used to determine device sensitivity under the weak inversion region is called drain off-current sensitivity $\left(S_{I_{OFF}}\right)$ is obtained using Eq. 1;[8]

$$S_{I_{OFF}} = \frac{I_{OFF[\text{with biomolecule}]}}{I_{OFF[\text{without biomolecule}]}}\Big|_{\text{at}\,V_{gs=0\text{ V}}} \tag{1}$$

Drain Off-Current Sensitivity ($S_{I_{off}}$) of the THM-GAA-JL-FET Biosensor for Different Biomolecules

Figure 6 depicts the comparison of drain off-current sensitivity $\left(S_{I_{off}}\right)$ of dielectric modulated triple hybrid metal gate GAA-JL-FET with available work's[8] when different biomolecules were immobilized in the nanogap cavity. It clearly, depicts higher sensitivity variation when various biomolecules were uniformly immobilized on the nanogap cavity biosensor devices. This higher drain off-current sensitivity $\left(S_{I_{off}}\right)$ of dielectric modulated THM-GAA-JL-FET is attributed to its higher electrostatic gate control capability than the available works,[8] along with increased metal work-function value $\left(G_{\Phi 3}\right)$ that allows uniform carrier mobility in the inversion/channel region.

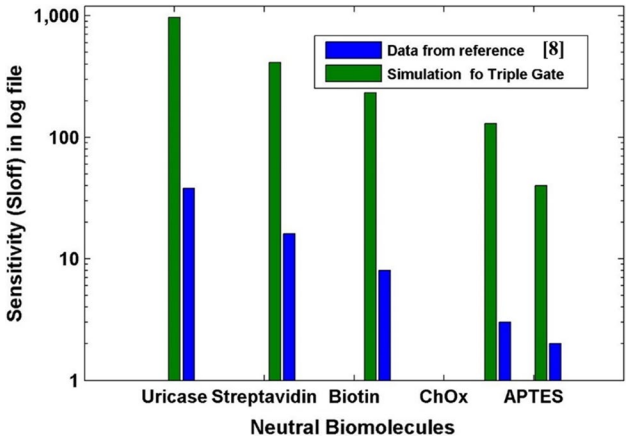


Fig. 6 Illustrates drain off-current sensitivity ($S_{I_{off}}$) comparison with available works[8] of n-type dielectric modulated triple hybrid metal-GAA-JL-FET, including different biomolecules.

Drain off-current sensitivity $\left(S_{I_{off}}\right)$ of the dielectric modulated triple-hybrid metal GAA-JL-FET,[8] switching ratio, and surface potential are improved over already available works,[8] due to new technologies incorporated in our device modeling such as device dimension, device structure, gate oxide material (high-k), and optimized gate electrode work-functions. Since our device has three oxide layers, namely, interface layer (SiO_2), high-k layer (HfO_2) and nanogap cavity layer, which is different from already available works, the new technology is more robust and controls tunneling current under 20-nm technology node and minimizes short-channel effects; this makes our work a better candidate for detecting various diseases caused by neutral biomolecules.

Effect of Nanogap Cavity Length on Device Sensitivity

Figure 7 depicts the effect of cavity length on the device transfer characteristics when different biomolecules were immobilized uniformly in the targeted site. The simulation results took place using 5-nm, 10-nm, and 15-nm cavity lengths, keeping gate length and nanogap cavity thickness constant. Figure 7a depicts the impact of different biomolecules on shifting threshold voltage at different cavity lengths. For instance, at 5-nm cavity length, shifting threshold voltage $\left(\Delta V_{th}\right)$ is lower than 10- and 15-nm cavity lengths due to a very small number of biomolecules embedded in the cavity region, contributing negligible significance to the change of the threshold voltage.[8] Higher threshold voltage variation is observed when nanogap cavity length increases, i.e., at half of the gate length, as shown in Fig. 7. Because the cavity length is determined based on the size of biomolecules to be detected (for instance, the size of

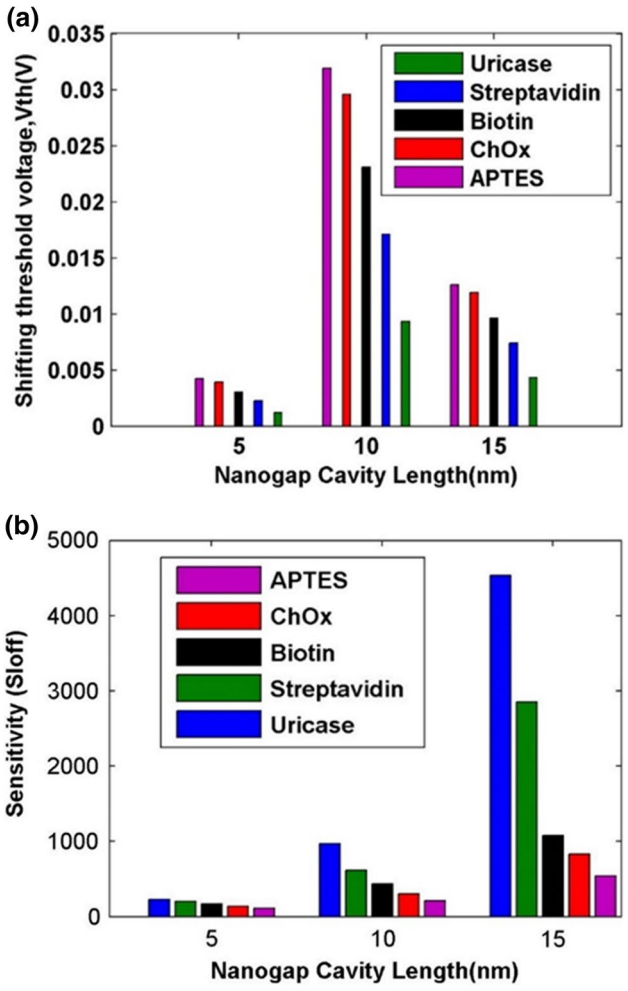


Fig. 7 Effect of cavity length on **(a)** shifting threshold voltage (ΔV_{th}), (b) drain off-current sensitivity ($S_{I_{off}}$) with different biomolecules for an n-type dielectric modulated triple-hybrid metal gate-all-around JL-NWFET at ($V_{DS} = 1.0$ V and $V_{DS} = 0.05$ V).

streptavidin and biotin are approximately 6-7 nm),[56] the sensitivity would have been high for biomolecules with dimensions approaching the cavity length. Therefore, it is also important to note that the gap in the nanoscale size significantly impacts the FET's electrical characteristics. I_{ON} reaches a maximum value/saturation when the gate length is almost fully covered by a higher dielectric biomolecule constant and threshold voltage roll-off (threshold voltage fluctuation) almost constant, leading to a decrease in threshold voltage due to small band bending amplitude in the case of higher biomolecule dielectric constant. Maximum drain current occurs because the channel gets "pinched off" at the drain end and leads to current saturation behavior in the case of higher gate dielectric biomolecules. Therefore, at $\frac{L_{gate}}{L_{nanogap}} > 0.5$, change in threshold voltage reaches saturation level, and a shift in threshold voltage is reduced. In this study, we have investigated higher threshold voltage variation (ΔV_{th}) observed at 10-nm cavity length compared to other cavity lengths obtained using Eq. 2[57] as described in Fig. 7a.

$$\Delta V_{th} = V_{th(\int_{bio}>1)} - V_{th(\int_{air}=1)} \tag{2}$$

where $(\varepsilon_{bio} > 1)$ represents the neutral biomolecule dielectric constant and $(\varepsilon_{air} = 1)$ is air or reference dielectric constant.

Figure 7b illustrates a higher drain off-current sensitivity ($S_{I_{off}}$) at higher cavity length and higher dielectric constant value because increasing biomolecules can increase gate electrostatic controllability, thereby lowering short-channel effects, reducing threshold voltage fluctuation and hot-electron effects. At smaller nanogap cavity length, the drain off-current sensitivity is almost the same among different biomolecules when nanogap cavity length is short, indicating that fewer biomolecules have no significant impact on the device performance.

Effect of Different Biomolecules on Device Surface Potential

An important output characteristic of FET-based biosensors is center/surface potential, which determines the threshold voltage variation, signifying the proposed device's sensitivity after biomolecules interact in the targeted cavity uniformly. Figure 8 clearly illustrates the effect of biomolecules on surface potential distribution along the channel for an *n*-type-triple hybrid metal GAA-JL-NWFET biosensor. The potential deforms under the cavity regions from lower to higher due to nanogap cavities present at the drain ends. Uniform surface potential emerges at the source end (as no nanogap cavity exists in that region), which indicates the impacts of dielectric constant. As the different biomolecules are immobilized in the cavity (near the drain end), channel region surface potential rises because the higher dielectric constant of the biomolecule impacts device operation for device performance modulation, as illustrated in Fig. 8. That means a higher inversion charge/channel was created, thus leading to an increased surface potential corresponding to the biomolecule dielectric constant even if input drain-source voltage (V_{SD}) is constant.

Figure 8 shows that the portion of the channel (drain side) over which different biomolecules were immobilized has lower to higher surface potential depending on the value of the dielectric constant interacting with the nanocavity region. In comparison, the uncovered gate portion of the device (source side) has lower and almost the same surface potential. So, we can conclude that the surface potential of the dielectric modulated THM-GAA-JL-NWFET varies

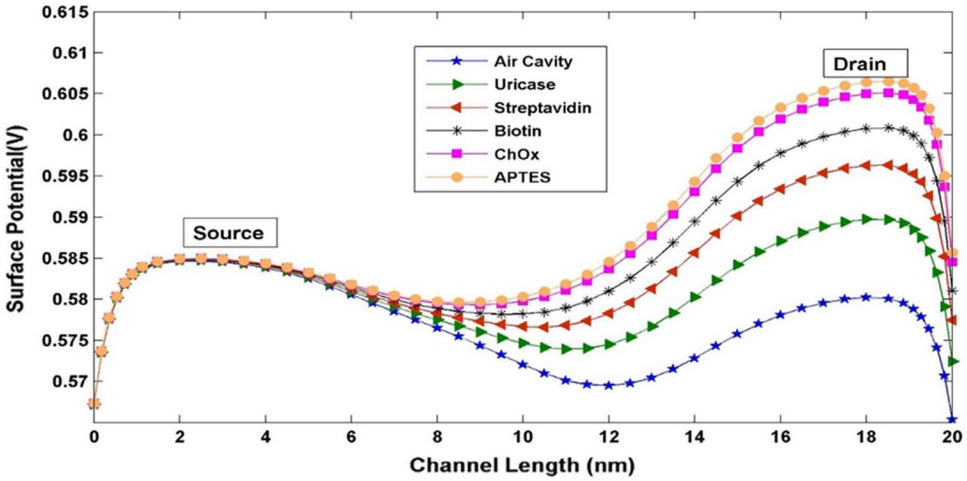


Fig. 8 Impact of different biomolecules on the surface potential for an n-type dielectric modulated triple-hybrid metal gate GAA-JL-NWFET at (V_{GS} = 1.0 V and V_{DS} = 0.0 5 V).

more with the nanogap cavity dielectric constant. It will be a better candidate for robust sensitivity of the device in the area of biomedical applications.

Effect of Biomolecules on Proposed Device Output Results Includes Transconductance, Output Conductance, Device Efficiency, Intrinsic Voltage Gain, and Output Resistance

In Fig. 9 both transconductance and output conductance are nonlinear parameters used to determine the analog performance of the proposed device. As illustrated in Fig. 9b, output conductance is higher under the weak inversion region than in the strong inversion region. This is because, in weak inversion regions, higher DIBL and SCEs affect carrier mobility along the channel, which affects the device performance and efficiency. As the dielectric constant of biomolecules (neutral) increases, voltage gain also increases at the strong inversion region due to inversion charge interaction on the channel as dielectric constant increases in this region and g_m increases while g_d decreases at a strong inversion region causing variation of intrinsic voltage gain $\left(\frac{g_m}{g_d}\right)$ as illustrated in Fig. 10a. The mathematical expression of intrinsic voltage gain (A_V) is given by Eq. 3, [58]

$$|A_V| = \frac{g_m}{g_d} \tag{3}$$

Figure 10b illustrates increased output resistance $\left(1/g_d\right)$ of the proposed device as the dielectric constant increases starting from a strong inversion region since higher dielectric constant increases carrier mobility through the channel and decreases the output conductance, thereby modulating gate controllability. So, it is possible to say that output resistance is an essential

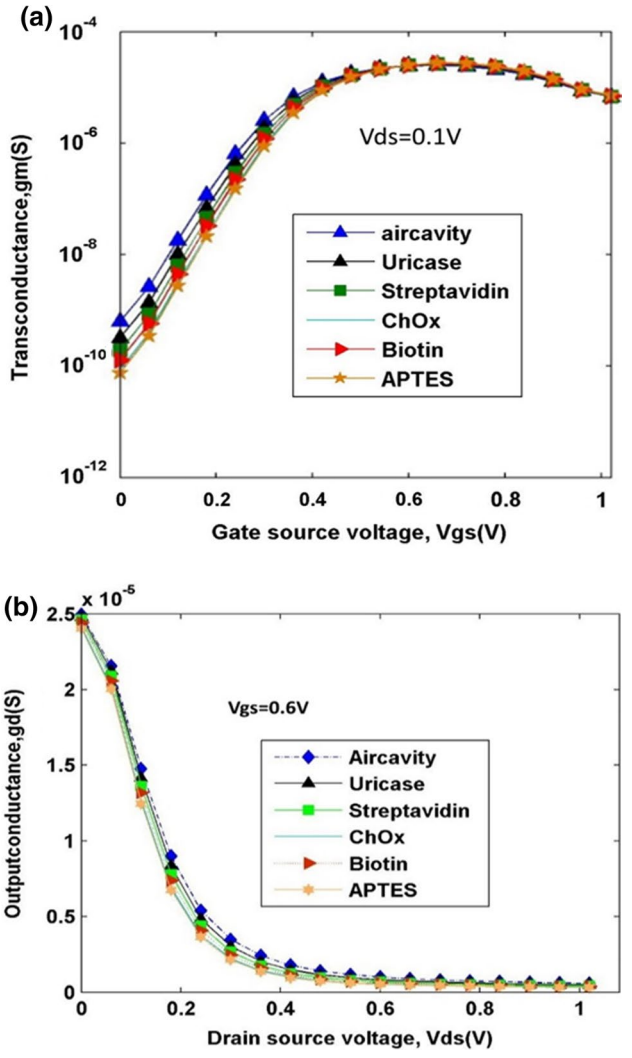


Fig. 9 Effect of biomolecules on (a) transconductance (g_m) log file and (b) output conductance (g_d) for an *n*-type triple hybrid metal GAA-JL-NWFET.

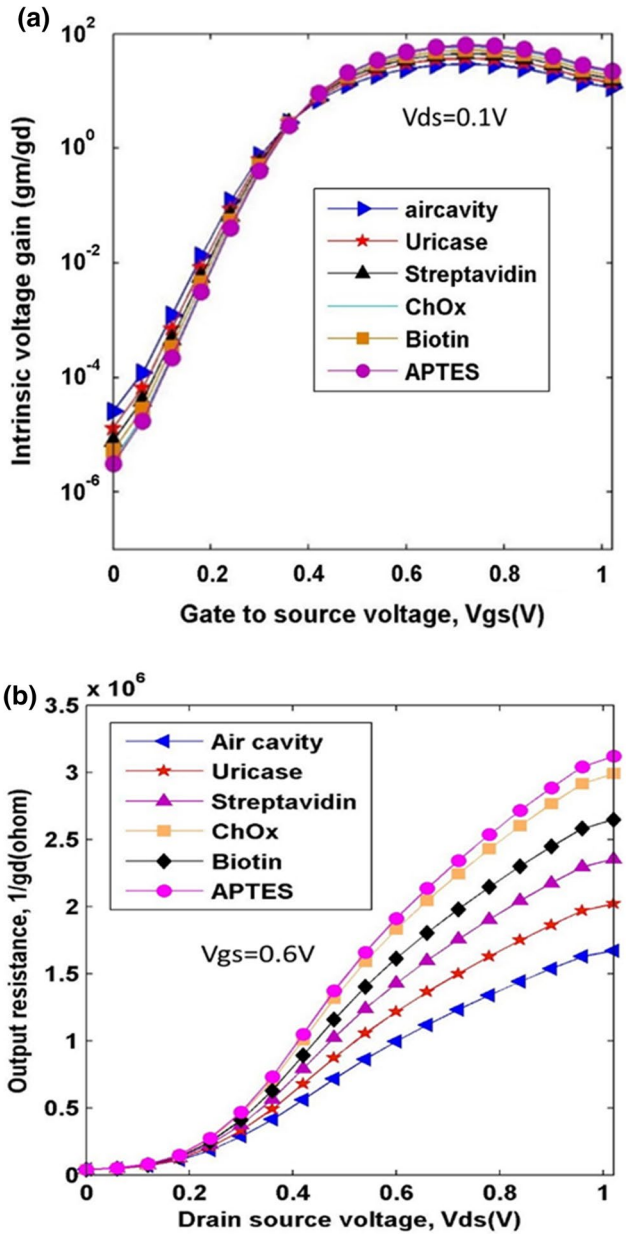


Fig. 10 Impact of different biomolecules on (a) intrinsic voltage gain $\left(\frac{g_m}{g_d}\right)$ log file and (b) output resistance $(1/g_d)$ for an *n*-type triple hybrid metal gate-all-around JL-NWFET.

characteristic of a transistor, in which its maximum R_{out} determines the maximum gain of the transistor. The output resistance $\left(R_{\text{out}}\right)$ of a transistor is given by Eq. 4.[59]

$$R_{\text{Out}} = \frac{1}{g_d} \tag{4}$$

Conclusion

In this work, the effect of an *n*-type dielectric modulated triple-hybrid metal gate-all-around junctionless nanowire transistor etched nanocavity to the immobilized biomolecule was presented and compared with unique and double-hybrid metal gate transistors to detect various diseases. The results were verified using the Atlas-3D device simulation tool. In both devices, electrical output characteristics, such as subthreshold slope, surface potential, drain off-current sensitivity $\left(S_{I_{\text{OFF}}}\right)$, switching ratio $\left(I_{\text{ON}}/I_{\text{OFF}}\right)$, transconductance $\left(g_m\right)$, output conductance $\left(g_m\right)$ and output resistance $\left(1/g_m\right)$, have been studied, including different biomolecules. We have observed lower leakage current and higher sensitivity results in a triple-hybrid metal gate than the available unique and double-hybrid metal GAA-JL-NWFET biosensor devices. For instance, leakage current using uricase biomolecule is 2.83×10^{-12}A for a double-hybrid metal gate and 4.50×10^{-13}A for triple-hybrid metal GAA-JL-NWFET. Another significant improvement of the triple-hybrid metal gate over the double-hybrid metal gate is device sensitivity, i.e., for the APTES biomolecule. Shifting the threshold voltage (ΔV_{th}) is 3.59×10^{-3} V for a double-hybrid metal gate and 3.19×10^{-2} V is for a triple-hybrid metal gate, so that 788.6% improvement was observed in the triple-metal gate compared with a double-hybrid metal gate. In addition to the biomolecule dielectric constant value, nanogap cavity length impacts the proposed device performance. The 10-nm cavity length has been investigated for better sensitivity, due to lower drain off-current and higher variation of threshold voltage shifting (ΔV_{th}) at this nanogap cavity length. Based on our investigations, we have concluded that the n-type triple-hybrid metal gate-all-around junctionless nanowire transistor with a 10-nm nanocavity length shows potential as a candidate for detection of neutral biomolecules (APTES, choli oxidase (ChO_x), streptavidin, biotin, and uricase) in the area of biomedical application. So, we can say our device can be used to diagnose and detect early, rapidly transmitted biomarkers of diseases such as breast and lung cancer (APTES) and uric acid in human blood serum (uricase).

Funding The study was funded by Ethiopia's Ministry of Higher Education and India's Delhi Technological University.

Conflict of interest The authors declare that they have no conflict of interest.

Reference

1. Y.-C. Syu, W.-E. Hsu, and C.-T. Lin, Review—field-effect transistor biosensing: devices and clinical applications. *ECS J. Solid State Sci. Technol.* 7, Q3196 (2018).
2. H.C. Lau, T.E. Bae, H.J. Jang, J.Y. Kwon, W.J. Cho, and J.O. Lim, Saliva-based screening approach for Alzheimer's disease via the cell-oriented ion-sensitive field-effect transistor. *Sens. Lett.* 12, 1096 (2014).
3. N. Lu, A. Gao, P. Dai, H. Mao, X. Zuo, C. Fan, Y. Wang, and T. Li, Ultrasensitive detection of dual cancer biomarkers with integrated CMOS-compatible nanowire arrays. *Anal. Chem.* 87, 11203 (2015).
4. V.M. Generalov, O.V. Naumova, B.I. Fomin, S.A. Pyankov, I.V. Khlistun, A.S. Safatov, B.N. Zaitsev, E.G. Zaitseva, and A.L. Aseev, Detection of ebola virus VP40 protein using a nanowire SOI biosensor. *Optoelectron. Instrum. Data Process.* 55, 618 (2019).
5. K.Y. Park, M.S. Kim, and S.Y. Choi, Fabrication and characteristics of MOSFET protein chip for detection of ribosomal protein. *Biosens. Bioelectron.* 20, 2111 (2015).
6. C. Gouvea, *Biosensors for health applications*, in *Open Access Peer-Reviewed Chapter*, edited by Pier Andrea Serra (IntechOpen, Universidade Federal de Alfenas, Brazil, n.d.).
7. D. Sarkar, and K. Banerjee, Proposal for tunnel-field-effect-transistor as ultra-sensitive and label-free biosensors. *Appl. Phys. Lett.* 100, 143108 (2012).
8. Y. Pratap, M. Kumar, S. Kabra, S. Haldar, R.S. Gupta, and M. Gupta, Analytical modeling of gate-all-around junctionless transistor based biosensors for detection of neutral biomolecule species. *J. Comput. Electron.* 17, 288 (2018).
9. B. Kumar, and R. Chaujar, TCAD temperature analysis of gate stack gate all around (GS-GAA) FinFET for improved RF and wireless performance. *Silicon* 13, 3741 (2021).
10. J.T. Qu, H.M. Zhang, X.B. Xu, and S.S. Qin, Study of drain induced barrier lowering(DIBL) effect for strained Si NMOSFET. *Procedia Eng.* 16, 298 (2011).
11. I. Sarangadharan, A.K. Pulikkathodi, C.-H. Chu, Y.-W. Chen, A. Regmi, P.-C. Chen, C.-P. Hsu, and Y.-L. Wang, Review—high field modulated FET biosensors for biomedical applications. *ECS J. Solid State Sci. Technol.* 7, Q3032 (2018).
12. T. Windbacher, V. Sverdlov, and S. Selberherr, Biotin-streptavidin sensitive BioFETs and their properties. *Commun. Comput. Inf. Sci.* 52, 85 (2010).
13. P. Ambhorkar, Z. Wang, H. Ko, S. Lee, K.I. Koo, K. Kim, and D.I.D. Cho, Nanowire-based biosensors: from growth to applications. *Micromachines* 9, 1 (2018).
14. V.P. Georgiev, M.M. Mirza, A.I. Dochioiu, F. Adamu-Lema, S.M. Amoroso, E. Towie, C. Riddet, D.A. Maclaren, A. Asenov, and D.J. Paul, Experimental and simulation study of silicon nanowire transistors using heavily doped channels. *IEEE Trans. Nanotechnol.* 16, 727 (2017).
15. J.-H. Lee, E.-J. Chae, S. Park, and J.-W. Choi, Label-free detection of γ-aminobutyric acid based on silicon nanowire biosensor. *Nano Converg.* 6, 6 (2019).
16. C. Vu, Field-effect transistor biosensors for biomedical applications: recent advances and future prospects. *Sensors* 19, 4214 (2019).
17. C. Buzea, Nanomaterials and nanoparticles : sources and toxicity. *Biointerphases* (2007).
18. S. Prasad, Nanobiosensors: the future for diagnosis of disease? *Nanobiosensors Dis. Diagnosis* 3, 1 (2014).
19. Y. He, C. Fan, and S.T. Lee, Silicon nanostructures for bioapplications. *Nano Today* 5, 282 (2010).
20. A.C.M. de Moraes, and L.T. Kubota, Recent trends in field-effect transistors-based immunosensors. *Chemosensors* 4, 20 (2016).
21. M.N. Omar, A.B. Salleh, H.N. Lim, and A. Ahmad Tajudin, Electrochemical detection of uric acid via uricase-immobilized graphene oxide. *Anal. Biochem.* 509, 135 (2016).
22. J. Y. Hung, Y. B. Manga, Y. J. Chen, H. M. Huang, W. L. Yang, and C. C. Wu, *P16 INK4a detection using an ultra-sensitive silicon nanowire field effect transistor*. In *Proc. - 2018 7th Int. Symp. Next-Generation Electron.* ISNE 2018 1 (2018).
23. S. Singh, B. Raj, and S.K. Vishvakarma, Analytical modeling of split-gate junction-less transistor for a biosensor application. *Sens. Bio-Sensing Res.* 18, 31 (2018).
24. B.M. Lowe, K. Sun, I. Zeimpekis, C.K. Skylaris, and N.G. Green, Field-Effect sensors-from PH sensing to biosensing: sensitivity enhancement using streptavidin-biotin as a model system. *Analyst* 142, 4173 (2017).
25. K. Kim, C. Park, T. Rim, M. Meyyappan, and J. S. Lee, *Electrical and PH sensing characteristics of si nanowire-based suspended FET biosensors*, In *14th IEEE Int. Conf. Nanotechnology, IEEE-NANO* 2014 **3**, 768 (2014).
26. A. Goel, S. Rewari, S. Verma, and R. S. Gupta, *Dielectric modulated triple metal gate all around MOSFET (TMGAA)for DNA bio-molecule detection*. In *2018 IEEE Electron Devices Kolkata Conf.* **1**, 337 (2019).
27. Y. Chen, R. Ren, H. Pu, X. Guo, J. Chang, G. Zhou, S. Mao, M. Kron, and J. Chen, Field-effect transistor biosensor for rapid detection of ebola antigen. *Sci. Rep.* 7, 4 (2017).
28. G. Dhiman, Investigation of junction - less double gate MOSFET with high - k gate - oxide and metal gate layers. *Int. J. Innov. Res. Sci. Eng. Technol.* 8, 289 (2019).
29. V. P. Georgiev, A. I. Dochioiu, F. A. Lema, S. Berada, M. M. Mirza, D. J. Paul, and A. Asenov, *Variability Study of High Current Junctionless Silicon Nanowire Transistors*, in *2017 IEEE 12th Nanotechnology Materials and Devices Conference, NMDC 2017*, Vol. 2018–Janua (2018), pp. 87–88.
30. A. Kumar, M.M. Tripathi, and R. Chaujar, Comprehensive analysis of sub-20 nm black phosphorus based junctionless-recessed channel mosfet for analog/RF applications. *Superlattices Microstruct.* 116, 171 (2018).
31. R. Narang, M. Saxena, and M. Gupta, Investigation of dielectric modulated (DM) double gate (DG) junctionless MOSFETs for application as a biosensors. *Superlatt. Microstruct.* 85, 557 (2015).
32. V. Kumar, R. Gupta, R. Preet, P. Singh, and R. Vaid, Performance analysis of double gate N-FinFET using high-k dielectric materials. *Int. J. Innov. Res. Sci. Eng. Technol.* 5, 13242 (2016).
33. B. Kumar, and R. Chaujar, Fin aspect ratio optimization of novel junctionless gate stack gate all around (GS-GAA) FinFET for analog/RF applications. *Microelectron. Circ. Syst. Lect. Not. Electr. Eng.* 755, 59 (2021).
34. L. Feilong, L. Yue-yang, L. Ling, Z. Guofu, J. Xiangwei, and L. Jun-wei, Three-dimensional mechanistic modeling of gate leakage current in high- κ MOSFETs. *Phys. Rev. Appl.* 10, 1 (2020).
35. M. W. Rony, P. Bhowmik, H. R. Myler, and P. Mondol, Short Channel Effects Suppression in a Dual-Gate Gate-All-around Si Nanowire Junctionless NMOSFET, in Proc. 9th Int. Conf. Electr. Comput. Eng. ICECE 2016 538 (2017).
36. N. Gupta, and R. Chaujar, Optimization of high-k and gate metal workfunction for improved analog and intermodulation performance of gate stack (GS)-GEWE-SiNW MOSFET. *Superlatt. Microstruct.* 97, 630 (2016).
37. B. Cheng, M. Cao, R. Rao, A. Inani, S. Member, P. Vande Voorde, W.M. Greene, J.M.C. Stork, Z. Yu, S. Member, P.M. Zeitzoff, S. Member, J.C.S. Woo, and S. Member, The impact of high- gate dielectrics and metal gate electrodes on sub-100 Nm MOSFET's. *IEEE Trans. ELECTRON DEVICES* 46, 1537 (1999).

38. O.A. Books, Work function setting in high-k metal gate devices. *INTECH* 32, 137–144 (2013).
39. G. James, S. Joseph, and V. Mathew, The influence of metal gate work function on short channel effects in atomic-layer doped DG MOSFETs. *J. Electron Dev.* 8, 310 (2010).
40. S. Piermarini, D. Migliorelli, G. Volpe, R. Massoud, A. Pierantozzi, C. Cortese, and G. Palleschi, Uricase biosensor based on a screen-printed electrode modified with prussian blue for detection of uric acid in human blood serum. *Sensors Actuators B Chem.* 179, 170 (2013).
41. N. Lu, P. Dai, A. Gao, J. Valiaho, P. Kallio, Y. Wang, and T. Li, Label-free and rapid electrical detection of HTSH with CMOS-compatible silicon nanowire transistor arrays. *ACS Appl. Mater. Interfaces* 6, 20378 (2014).
42. V. Narendar, R. Mishra, S. Rai, R.A. Mishra, and C. Engineering, Threshold voltage controlS chemes infinfets. *Int. J. VLSI Des. Commun. Syst.* 3, 175 (2012).
43. D. S. Software, *ATLAS User ' s Manual*, Vol. II (1998).
44. D. S. Software, *Atlas User ' s Manual* (2016).
45. J. Sarvas, and J. Spanier, A direct approach to solving the drift-diffusion model equations for use in certain MOSFET devices. *Math. Comput. Model.* 22, 17 (1995).
46. S. Selberherr, *Deterministic solvers for the boltzmann transport equation* (Springer, n.d.).
47. S. Scaldaferri, G. Curatola, and G. Iannaccone, Direct solution of the boltzmann transport equation and Poisson-Schrödinger equation for nanoscale MOSFETs. *IEEE Trans. Electron Devices* 54, 2901 (2007).
48. T. Ewert, *Advanced TCAD simulations and characterization of semiconductor devices* (2006).
49. L. Arivazhagan, D. Nirmal, A. Jarndal, H.F. Huq, S. Chander, S. Bhagyalakshmi, P. Kumar, J. Ajayan, and A. Varghese, Applicability of double channel technique in AlGaN / GaN HEMT for future biosensing applications. *Superlattices Microstruct.* 160, 107086 (2021).
50. T. Goudon, V. Miljanović, and C. Schmeiser, On the shockley-read-hall model: generation-recombination in semiconductors. *SIAM J. Appl. Math.* 67, 1183 (2007).
51. N. Thapa, and L. Maurya, Performance advancement of high-K dielectric MOSFET. *Int. J. Innov. Adv. Comput. Sci.* 3, 98 (2014).
52. N. Sachdeva, M. Vashishath, and P.K. Bansal, Effect of gate work-function on gate induced drain leakage of MOSFETs. *IJCEM Int. J. Comput. Eng. Manag.* 21, 11 (2018).
53. A. Kumar, D. Kaur, M. M. Tripathi, and R. Chaujar, Reliability of high-k gate stack on transparent gate recessed channel (TGRC) MOSFET, In 2017 International Confernce on Microelectronic Devices, Circuits Systems ICMDCS 2017 **2017–Janua**, 1 (2017).
54. N. Bagga, and S. Dasgupta, Surface potential and drain current analytical model of gate all around triple metal TFET. *IEEE Trans. Electron Dev.* 64, 606 (2017).
55. K.V. Cartwirght, Derivation of the exact transconductance of a FET without calculus. *Technol. Interface J.* 10, 7 (2009).
56. H. Im, X.J. Huang, B. Gu, and Y.K. Choi, A dielectric-modulated field-effect transistor for biosensing. *Nat. Nanotechnol.* 2, 430 (2007).
57. E. Rahman, A. Shadman, and Q.D.M. Khosru, Effect of biomolecule position and Fi Ll in factor on sensitivity of a dielectric modulated double gate junctionless MOSFET biosensor. *Sens. Bio-Sensing Res.* 13, 49 (2017).
58. W. F. Perina, J. A. Martino, S. Member, P. G. D. Agopian, and S. Member, Intrinsic voltage gain and unit-gain frequency of omega-gate nanowire SOI MOSFETs, in2019 34th *Symposium on Microelectronics Technology and Devices,* 1 (2019).
59. J.H. Huang, H. Liu, M.C. Jeng, and P.K. Ko, A physical model for MOSFET output resistance. *IEDM Tech. Dig* 569, 572 (1992).

Publisher's Note Springer Nature remains neutral with regard to jurisdictional claims in published maps and institutional affiliations.

This article has been accepted for publication in a future issue of this journal, but has not been fully edited. Content may change prior to final publication. Citation information: DOI 10.1109/TPWRD.2022.3149137, IEEE Transactions on Power Delivery

State and Parameter Estimation of Non-Uniform Transmission Line Using Kronecker Product Based Modeling

Amit Kumar Gautam, Sudipta Majumdar and Harish Parthasarthy

***Abstract*—The distributed parameters of a non-uniform transmission line (NTL) are assumed to depend on a finite set of unknown parameters, for example, their spatial Fourier series coefficients. The line equations are set up taking random voltage and current line loading into account with the random loading being assumed to be white Gaussian noise in the time and spatial variables. Bypassing over to the spatial Fourier series domain, these line stochastic differential equations (SDEs) are expressed as a truncated sequence of coupled stochastic differential equations for the spatial Fourier series components of the line voltage and current. The coefficients that appear in these stochastic differential equations are the spatial Fourier series coefficients of the distributed line parameters and these coefficients in turn are linear functions of the unknown parameters. By separating these complex stochastic differential equations into their real and imaginary part, the line equations become a finite set of SDEs for the extended state defined to be the real and imaginary components of the line voltage and current as well as the parameters on which the distributed parameters depend. The measurement model is assumed to be white Gaussian noise corrupted versions of the line voltage and current sampled at a discrete set of spatial points on the line and this measurement model can be expressed as a linear transformation of the state variables, i.e, of the spatial Fourier series components of the line voltage and current plus a white measurement noise vector. This work uses sparse matrix factorization using Kronecker product to implement the Fourier unitary transform. This work implements perturbation theory for non-uniform transmission line. The extended Kalman filter (EKF) equations are derived for this state and measurement model and our real timeline voltage and current and distributed parameter estimates show excellent agreement with the true values based on MATLAB simulations. The use of sparse matrix factorization using Kronecker product ease the mathematical complexity and provides compact representation.**

***Index Terms*—Extended Kalman filter, Fourier series expansion, Kronecker product, non-uniform transmission line, state space modeling.**

I. Introduction

INTEGRATION of renewals, power electronics technology and new regulation of market has increased the complexity of power systems. This requires the proper monitoring and control of power system. State and parameter estimation of such systems are helpful for these purpose. The power system substations and network parameters are input to these state estimations. In literature, various methods have been proposed for state estimation of power system. In [1], Ghiasi *et al*. proposed one node method for voltage and current estimation at the intermediate points of a lossy transmission line. It uses the Bergeron model of a transmission line. This method has the advantage of using parameters at one end of the transmission line which needs less computation time, less input data, and less memory than other methods. In [2], Fan *et al*. used an ensemble Kalman filter for fault location on transmission lines. The advantage of this method is its easy implementation. Also, the foreknowledge of fault type or fault location is not required. In [3], Rakpenthai *et al*. presented a nonlinear optimization based weighted least squares method that uses constrained nonlinear optimization. The method uses the bus voltage phasors and temperature of transmission line conductor for state estimation purpose. In [4], Malhara *et al*. proposed a least squares based state estimation for transmission line using various parameters to prevent malicious attacks. In [5], Liu *et al*. used dynamic state estimation for protection of series compensated transmission lines. The method used the dynamic model of protection zone. It has the advantage of faster detection of internal faults as compared to the legacy protection function. In [6], a least squares based state estimation of transmission line equation is proposed to estimate the conductor sag levels to generate the warning signal. In [7], Liu *et al*. proposed protection of mutually coupled transmission lines that uses dynamic state estimation based protection (EBP) algorithm and performed numerical experiments on various scenarios. In [8], Liu *et al*. proposed dynamic state estimation for fault location of transmission line that works on the sample values and uses the dynamic model. The method provides the higher accuracy than traditional methods. In [9], Liu *et al*. proposed the fault location of non-homogeneous transmission line using state estimation. The unconstraint weighted least square method is used for estimation by formulating the method of the non-homogeneous transmission line with fault. In [10], Yang *et al*. used unscented information filtering (UIF) method for state estimation of power networks. As the UIF is a nonlinear state estimation method, it achieves better accuracy than centralized UIF, maximum a posteriori (MAP) and the local UIF estimator. In [11], Li *et al*. proposed fully distributed state estimation using weighted least square method and graph theory for estimation of power system. The method has better performance than the traditional methods. In [12], Mohammed

A. K. Gautam and S. Majumdar are with the Department of Electronics and Communication Engineering, Delhi Technological University, Delhi, 110042, India. E-mail: amitgautam.cicdu@gmail.com, korsudipta@rediffmail.com.

H. Parthasarthy is with Electronics and Communication Engineering, Netaji Subhas University of Technology, New Delhi, 110078, India. E-mail: harisignal@yahoo.com.

(*Corresponding author: Sudipta Majumdar*)

0885-8977 (c) 2021 IEEE. Personal use is permitted, but republication/redistribution requires IEEE permission. See http://www.ieee.org/publications_standards/publications/rights/index.html for more information.
Authorized licensed use limited to: DELHI TECHNICAL UNIV. Downloaded on February 15,2022 at 10:03:33 UTC from IEEE Xplore. Restrictions apply.

This article has been accepted for publication in a future issue of this journal, but has not been fully edited. Content may change prior to final publication. Citation information: DOI 10.1109/TPWRD.2022.3149137, IEEE Transactions on Power Delivery

et al. used a modified re-iterated Kalman filter for state estimation of power system that can handle the lost and delayed measurements. In [13], Alhelou *et al*. used dynamic state estimation for decentralized load frequency control. The method has the advantage of high accuracy, efficiency and easy implementation. In [14], Dobakhshari *et al*. proposed closed-form and non-iterative solution for Supervisory Control And Data Acquisition (SCADA) based state estimation. The method has the advantage of fast implementation and low computation burden.

Various methods have been used in literature for parameter estimation of transmission lines. Ritzmann *et al*. [15] proposed the impedance estimation method for transmission line by assuming linearly changing parameters for short periods. The method presents better accuracy as compared to other methods. [16] presented a technique for estimation of electrical parameter of transmission line. The method uses synchronized sampled data. This method has the ability to obtain the steady state values of voltage and current of the transmission line as a function of time and line logic. Also, it has the ability to overcome practical obstacles during estimation. Tolic *et al*. [17] presented a method for determining the transmission losses in which, probability density estimation is done using the nonlinear least squares method. Yang *et al*. [18] proposed a method for conditional failure rate of transmission line. In [19], Asprou *et al*. proposed a method to estimate the erroneous transmission line parameters that are stored in database of power system control centre. The main advantage is that it needs only one phasor measurement units. In [20], Wang *et al*. presented least squares estimation based single line parameters estimation method to estimate the actual transmission line parameters. The method presents very small estimation errors. In [21], Sima *et al*. proposed an analytic method for estimating the lightning performance of transmission lines. This takes smaller computation time as compared to the traditional method. In [22], Sivanagaraju *et al*. proposed transmission line parameter estimation using hybrid measurements from phasor measurements and used for differential protection of the transmission lines. In [23], Halligan *et al*. presented a method to estimate the maximum crosstalk in transmission line. In [24], Ren *et al*. used state estimation and parameters tracking iteratively along with static parameter estimation to estimate the parameters of overhead transmission lines. The method is able to track the transmission line parameter for different conditions. They used state and parameter estimation of three phase untransposed transmission line. For this, they used weighted-least-square (WLS) method for static state estimation and Kalman filter (KF) method for parameter estimation. We used KF and EKF for state and parameter estimation of single phase transmission line.

This paper implements KF and EKF for state and parameter estimation of non-uniform transmission line. For this, state-space model of the NTL circuit has been derived. As the Telegrapher's equations used for modeling the NTL are a function of space and time, the Fourier series expansion of the voltage and current have been used to obtain the time-dependent equations. Further, Kronecker product has been used for representation of Fourier unitary transform. The measurements have been obtained by solving the eigenvector problem. The frequency-domain analysis is used to obtain the state-space equations. For this, the four distributed parameters of the line are expanded in Fourier series. Major contribution of the paper is as follows:- Nonlinearities in line voltage and current has been taken into account by implementing perturbation theory.

The paper is organized as follows. Section II introduces theory of SDEs. Section III gives a brief overview of KF and EKF algorithms. Section IV presents state-space modeling of NTL circuit. Section V describes the frequency domain analysis of NTL to obtain a measurement vector. Then, the state and parameters of NTL have been estimated in section VI. Section VII presents the simulation results. Finally, Section VIII concludes the paper.

II. Theory of Stochastic Differential Equations

In general, a continuous nonlinear stochastic differential equation [25] has been represented as

$$\frac{d}{dt}\mathbf{x}_t = \boldsymbol{f}(\mathbf{x}_t, \mathbf{w}_t, t);\ \ t \geq t_0 \tag{1}$$

where $\boldsymbol{f}(.)$ is a nonlinear function of time t. $\mathbf{w}_t$ is the random input function. Consider the initial condition $\mathbf{x}_{t_0}$. The integral of (1) is well defined when $\boldsymbol{f}$ and $\mathbf{w}_t$ are restricted. (1) can be written as

$$\mathbf{x}_t - \mathbf{x}_{t_0} = \int_{t_0} \boldsymbol{f}(\mathbf{x}_t, \mathbf{w}_t, t)dt \tag{2}$$

The SDE with an additive white Gaussian function is expressed as

$$\frac{d}{dt}\mathbf{x}_t = \boldsymbol{f}(\mathbf{x}_t, t) + \boldsymbol{G}(\mathbf{x}_t, t)\mathbf{w}_t;\ \ t \geq t_0 \tag{3}$$

$$d\mathbf{x}_t = \boldsymbol{f}(\mathbf{x}_t, t)dt + \boldsymbol{G}(\mathbf{x}_t, t)\mathbf{w}_t dt \tag{4}$$

where $\boldsymbol{G}(.)$ is matrix function and independent of $\mathbf{w}_t$. Integrating (4), we obtain

$$\mathbf{x}_t - \mathbf{x}_{t0} = \int_{t_0} \boldsymbol{f}(\mathbf{x}_t, t)dt + \int_{t_0} \boldsymbol{G}(\mathbf{x}_t, t)d\boldsymbol{B}(t) \tag{5}$$

where $\mathbf{w}_t = \frac{d\boldsymbol{B}(t)}{dt}$. $\boldsymbol{B}(t)$ is the Brownian motion process. Note that first integral in (5) is defined as the mean square Riemann integral. The second integral can be defined only in the mean square sense by $Itô$ because it has random component and known as $Itô$ stochastic differential equation. Let $i(t)$ and $v(t)$ denote line current and voltage Fourier series coefficient vector respectively with size $(2N+1)\times 1$ where the Fourier series truncation is from $-N$ to $+N$. Let $\boldsymbol{\theta}$ denotes the distributed parameter vector of Fourier series coefficients. It is assumed that by taking the real and imaginary parts, in the voltage, current and parameters Fourier series coefficients, the SDE becomes real. Then, $\left[v(t)^T, i(t)^T, \boldsymbol{\theta}(t)^T\right]^T = \boldsymbol{\eta}(t)$ becomes state vector and state equation has been formed as:

$$d\mathbf{x}(t) = \boldsymbol{f}(\boldsymbol{\theta}(t))\boldsymbol{\eta}(t)dt + \boldsymbol{G}(\boldsymbol{\theta}(t))\boldsymbol{B}(t) \tag{6}$$

where $\boldsymbol{B}(t)$ is a Brownian motion vector derived from the line loading. The measurement model involves measuring

0885-8977 (c) 2021 IEEE. Personal use is permitted, but republication/redistribution requires IEEE permission. See http://www.ieee.org/publications_standards/publications/rights/index.html for more information.
Authorized licensed use limited to: DELHI TECHNICAL UNIV. Downloaded on February 15,2022 at 10:03:33 UTC from IEEE Xplore. Restrictions apply.

This article has been accepted for publication in a future issue of this journal, but has not been fully edited. Content may change prior to final publication. Citation information: DOI 10.1109/TPWRD.2022.3149137, IEEE Transactions on Power Delivery

Table I
SUMMARY OF KF ALGORITHM

Step 1. Initialization: Initialize $\hat{\mathbf{x}}_0 = E[\mathbf{x}_0]$, $\boldsymbol{P}_0 = \Pi_0$, $\boldsymbol{Q}_0$ and $\boldsymbol{R}_0$.
Step 2. State prediction: **(i)** Compute predicted state:
$\hat{\mathbf{x}}_{n+1|n} = \boldsymbol{F}_n\hat{\mathbf{x}}_{n|n} + \boldsymbol{B}_n\mathbf{u}_n$
(ii) Compute covariance matrix of prediction error:
$\boldsymbol{P}_{n+1|n} = \boldsymbol{F}_n\boldsymbol{P}_{n|n}\boldsymbol{F}_n^T + \boldsymbol{Q}_n$
Step 3. Measurement update:
(i) Compute the Kalman gain: $\boldsymbol{K}_{n+1} = \boldsymbol{P}_{n+1|n}\boldsymbol{H}_n^T(S)^{-1}$
where $S = \boldsymbol{H}_n\boldsymbol{P}_{n+1|n}\boldsymbol{H}_n^T + \boldsymbol{R}_n$
(ii) Update the estimated state:
$\hat{\mathbf{x}}_{n+1|n+1} = \hat{\mathbf{x}}_{n+1|n} + \boldsymbol{K}_{n+1}(\mathbf{z}_n - \boldsymbol{H}_n(\hat{\mathbf{x}}_{n+1|n}))$
(iii) Compute covariance error matrix:
$\boldsymbol{P}_{n+1|n+1} = (\boldsymbol{I} - \boldsymbol{K}_{n+1}\boldsymbol{H}_n)\boldsymbol{P}_{n+1|n}$ and repeat step 2.
where $n+1|n$ and $n+1|n+1$ are a prior and a post estimate.

Table II
SUMMARY OF EKF ALGORITHM

Step 1. Initialization: Initialize $\hat{\mathbf{x}}_0 = E[\hat{\mathbf{x}}_0]$, $\boldsymbol{P}_0 = \Pi_0$, $\boldsymbol{Q}_0$ and $\boldsymbol{R}_0$.
Step 2. State prediction:
(i) Compute Jacobian matrix: $\boldsymbol{F}_n = \frac{\partial \boldsymbol{f}_n(\mathbf{x}_n,\mathbf{u}_n)}{\partial \mathbf{x}}|_{\mathbf{x}=\hat{\mathbf{x}}_{n|n}}$
(ii) Compute state: $\hat{\mathbf{x}}_{n+1|n} = \boldsymbol{f}_n(\hat{\mathbf{x}}_{n|n})$
(iii) Compute predicted covariance of error:
$\boldsymbol{P}_{n+1|n} = \boldsymbol{F}_n\boldsymbol{P}_{n|n}\boldsymbol{F}_n^T + \boldsymbol{Q}_n$
Step 3.Measurement update:
(i) Compute Jacobian matrix: $\boldsymbol{H}_n = \frac{\partial \boldsymbol{h}_n(\mathbf{x}_n,\mathbf{u}_n)}{\partial \mathbf{x}}|_{\mathbf{x}=\hat{\mathbf{x}}_{n|n}}$
(ii) Compute the Kalman gain: $\boldsymbol{K}_{n+1} = \boldsymbol{P}_{n+1|n}\boldsymbol{H}_n^T(S)^{-1}$
where $S = \boldsymbol{H}_n\boldsymbol{P}_{n+1|n}\boldsymbol{H}_n^T + \boldsymbol{R}_n$
(iii) Update the estimated state:
$\hat{\mathbf{x}}_{n+1|n+1} = \hat{\mathbf{x}}_{n+1|n} + \boldsymbol{K}_{n+1}(\mathbf{z}_n - \boldsymbol{h}_n(\hat{\mathbf{x}}_{n+1|n}))$
(iv) Compute covariance error matrix: $\boldsymbol{P}_{n+1|n+1} = (\boldsymbol{I} - \boldsymbol{K}_n\boldsymbol{H}_n)\boldsymbol{P}_{n+1|n}$

only a small subset of the voltage and current Fourier series coefficients. Thus the measurement model is of the form

$$d\mathbf{z}(t) = \boldsymbol{H}\boldsymbol{\eta}(t)dt + d\mathbf{v}(t) \tag{7}$$

where $\boldsymbol{H}$ is a sparse matrix of ones and zeroes. It should be kept in mind that measurement of a given Fourier component may not be possible. But, it is possible to measure the current and voltage vector at a finite set of spatial points along the line and express these spatio temporal measurements in terms of the spatial Fourier series coefficients. For example, $v(t,z)$ can be measured as

$$v(t,z) = \sum_{n\in z} v_n(t)e^{j2\pi nz/d} \tag{8}$$

and likewise for $i(t,z)$. The measured process $[v(t,z_1),...,v(t,z_n),i(t,z_1),...,i(t,z_n)]^T$ can then be expressed as a matrix of size $2n \times (2(2N+1))$ multiplied by the Fourier coefficient vector $[v_n(t); i_n(t) : -N \le n \le N]^R$. Thus $\boldsymbol{H}$ gets modified.

III. KALMAN FILTER AND EXTENDED KALMAN FILTER ALGORITHM

A. Kalman filter

A discrete time linear system is represented by the following equations:

$$\mathbf{x}_{n+1} = \boldsymbol{F}_n\mathbf{x}_n + \boldsymbol{B}_n\mathbf{u}_n + \boldsymbol{G}_n\mathbf{w}_n \tag{9}$$

$$\mathbf{z}_n = \boldsymbol{H}_n\mathbf{x}_n + \mathbf{v}_n \tag{10}$$

where $\mathbf{x}_n \in \mathbb{R}^k$ and $\mathbf{z}_n \in \mathbb{R}^m$ are state model and measurement model at time n respectively. $\boldsymbol{F}_n \in \mathbb{R}^{k\times k}$, $\boldsymbol{B}_n \in \mathbb{R}^{k\times l}$ and $\boldsymbol{H}_n \in \mathbb{R}^{m\times m}$ are the system transition matrix, input matrix and output matrix respectively. $\mathbf{u}_n$ is a known input vector. $\mathbf{w}_n \in \mathbb{R}^l$ and $\mathbf{v}_n \in \mathbb{R}^m$ are the system and measurement uncorrelated Gaussian noise with the following assumptions:
$\overline{\mathbf{w}}_n = 0$, $\overline{\mathbf{v}}_n = 0$, $\overline{\mathbf{w}_n\mathbf{w}_n^T} = \boldsymbol{Q}_n$, $\overline{\mathbf{v}_n\mathbf{v}_n^T} = \boldsymbol{R}_n$, $\overline{\mathbf{w}_n\mathbf{v}_j^T} = \mathbf{0}\ \forall\ n\&j$. Table I summarizes the KF steps.

B. Extended Kalman filter

A discrete time nonlinear system is represented as:

$$\mathbf{x}_{n+1} = \boldsymbol{f}_n(\mathbf{x}_n,\mathbf{u}_n) + \boldsymbol{G}_n\mathbf{w}_n \tag{11}$$

$$\mathbf{z}_n = \boldsymbol{h}_n(\mathbf{x}_n) + \mathbf{v}_n \tag{12}$$

where $\boldsymbol{f}_n(.) \in \mathbb{R}^k$ and $\boldsymbol{h}_n(.) \in \mathbb{R}^m$ denote the time variant nonlinear functions. EKF is a nonlinear version of Kalman filter and has been designed for nonlinear state estimation. It includes updation in time and measurement at time n after initialization. EKF linearizes the nonlinear function $\boldsymbol{f}_n(.)$ and $\boldsymbol{h}_n(.)$ using Taylor series. (13) and (14) has been approximated using Taylor series expansion as:

$$\mathbf{x}_{n+1} \cong \boldsymbol{f}_n(\hat{\mathbf{x}}_{n|n}) + \boldsymbol{F}_n\delta_n + \text{Higher order terms} \tag{13}$$

$$\mathbf{z}_n \cong \boldsymbol{h}_n(\boldsymbol{f}_n(\hat{\mathbf{x}}_{n|n})) + \boldsymbol{H}_n\delta_n + \text{Higher order terms} \tag{14}$$

where $\delta_n = \mathbf{x}_n - \hat{\mathbf{x}}_n$. δ_n denotes the priori estimated error. $\boldsymbol{P}_n$ denotes the covariance error at time n. Table II summarizes the EKF steps.

IV. STATE SPACE MODEL OF NON-UNIFORM TRANSMISSION LINE CIRCUIT

This section presents the state space analysis of non-uniform transmission line. An equivalent circuit of a transmission line has been shown in Fig. 1. The four fundamental parameters of the nonuniform distribution line are namely, resistance $R(z)$, inductance $L(z)$, capacitance $C(z)$ and conductance $G(z)$ per unit length d. The line voltage $v(t,z)$ and line current $i(t,z)$ at any point on the nonuniform transmission line is represented by both space and time dependent partial differential equations (Telegrapher's equation) as:

$$\frac{d}{dz}v(t,z) + R(z)i(t,z) + L(z)\frac{d}{dt}i(t,z) = w_v(t,z) \tag{15}$$

$$\frac{d}{dz}i(t,z) + G(z)v(t,z) + C(z)\frac{d}{dt}v(t,z) = w_i(t,z) \tag{16}$$

where $R(z) = R(z|\boldsymbol{\theta})$, $L(z) = L(z|\boldsymbol{\theta})$, $C(z) = C(z|\boldsymbol{\theta})$ and $G(z) = G(z|\boldsymbol{\theta})$ are non-uniform transmission line parameters.

0885-8977 (c) 2021 IEEE. Personal use is permitted, but republication/redistribution requires IEEE permission. See http://www.ieee.org/publications_standards/publications/rights/index.html for more information.
Authorized licensed use limited to: DELHI TECHNICAL UNIV. Downloaded on February 15,2022 at 10:03:33 UTC from IEEE Xplore. Restrictions apply.

This article has been accepted for publication in a future issue of this journal, but has not been fully edited. Content may change prior to final publication. Citation information: DOI 10.1109/TPWRD.2022.3149137, IEEE Transactions on Power Delivery

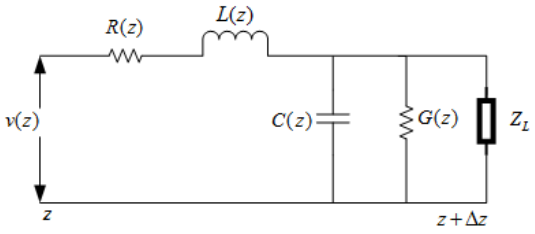


Figure 1. Circuit diagram of a nonuniform transmission line.

They can be assumed as:

$$R(z) = R(z|\boldsymbol{\theta}) = \sum_{m=1}^{p} \theta[m] R_m(z) \tag{17}$$

$$L(z) = L(z|\boldsymbol{\theta}) = \sum_{m=1}^{p} \theta[m] L_m(z) \tag{18}$$

$$C(z) = C(z|\boldsymbol{\theta}) = \sum_{m=1}^{p} \theta[m] C_m(z) \tag{19}$$

$$G(z) = G(z|\boldsymbol{\theta}) = \sum_{m=1}^{p} \theta[m] G_m(z) \tag{20}$$

$w_v(t,z)$ and $w_i(t,z)$ are zero mean exponential correlation process. Also, consider the voltage $v(t,z)$, current $i(t,z)$, $w_v(t,z)$ and $w_i(t,z)$ vectors of transmission line in terms of spatial Fourier series as:

$$v(t,z) = \sum_{n} v_n(t) exp\left(\frac{j2\pi nz}{d}\right) \tag{21}$$

$$i(t,z) = \sum_{n} i_n(t) exp\left(\frac{j2\pi nz}{d}\right) \tag{22}$$

$$w_v(t,z) = \sum_{n} w_{v,n}(t) exp\left(\frac{j2\pi nz}{d}\right) \tag{23}$$

$$w_i(t,z) = \sum_{n} w_{i,n}(t) exp\left(\frac{j2\pi nz}{d}\right) \tag{24}$$

where d is the total length of the transmission line. $v_n(t)$, $i_n(t)$, $w_{v,n}(t)$ and $w_{i,n}(t)$ are the Fourier coefficients with respect to time t. (21)-(24) can also be expressed in their matrix form as:

$$\boldsymbol{V}(z) = \sum_{N} v(n) {\boldsymbol{W}_N}^{nz} \tag{25}$$

$$\boldsymbol{I}(z) = \sum_{N} i(n) {\boldsymbol{W}_N}^{nz} \tag{26}$$

$$\boldsymbol{W}_v(z) = \sum_{N} w_v(n) {\boldsymbol{W}_N}^{nz} \tag{27}$$

$$\boldsymbol{W}_i(z) = \sum_{N} w_i(n) {\boldsymbol{W}_N}^{nz} \tag{28}$$

where $\boldsymbol{V}(z), \boldsymbol{I}(z), \boldsymbol{W}_v(z), \boldsymbol{W}_i(z)$ are N point DFT at $k = 0, ..., (N-1)$. Weight matrix ($\boldsymbol{W}_N$) is simply defined as:

$$\boldsymbol{W}_N = e^{j2\pi/N} = \begin{bmatrix} \boldsymbol{W}_N^0 & \boldsymbol{W}_N^0 & \boldsymbol{W}_N^0 & \dots & \boldsymbol{W}_N^0 \\ \boldsymbol{W}_N^0 & \boldsymbol{W}_N^1 & \boldsymbol{W}_N^2 & \dots & \boldsymbol{W}_N^{N-1} \\ \vdots & \vdots & \vdots & \dots & \vdots \\ \boldsymbol{W}_N^0 & \boldsymbol{W}_N^{N-1} & \boldsymbol{W}_N^{2N-1} & \dots & \boldsymbol{W}_N^{(N-1)^2} \end{bmatrix} \tag{29}$$

This Weight matrix ($\boldsymbol{W}_N$) can be represented by sparse matrix factorization using Kronecker product [26] as:

$$\boldsymbol{W}_N = \left\{\boldsymbol{B}\right\}_{N/2} \otimes \boldsymbol{W}_{N/2}, \boldsymbol{W}_1 = 1 \tag{30}$$

where N is a power of two, and $\left\{\boldsymbol{B}\right\}_{N/2}$ has $N/2$ matrices in the set, with the i^{th} matrix $i = 0$ to $(N/2-1)$ given by

$$\boldsymbol{B}_i = \begin{Bmatrix} \begin{bmatrix} 1 & 1 \\ 1 & j \end{bmatrix}, & i = 1 \\ \begin{bmatrix} 1 & 1 \\ 1 & -1 \end{bmatrix}, & \text{otherwise} \end{Bmatrix}$$

For example, if we choose $N = 8$, then $\boldsymbol{W}_8$ can be expressed as:

$$\boldsymbol{W}_8 = \left\{\boldsymbol{B}\right\}_4 \otimes \left\{\boldsymbol{B}\right\}_2 \otimes \boldsymbol{W}_2 \tag{31}$$

where

$$\left\{\boldsymbol{B}\right\}_4 = \begin{bmatrix} \begin{bmatrix} 1 & 1 \\ 1 & -1 \end{bmatrix} & & & \\ & \begin{bmatrix} 1 & -j \\ 1 & j \end{bmatrix} & & \\ & & \begin{bmatrix} 1 & 1 \\ 1 & -1 \end{bmatrix} & \\ & & & \begin{bmatrix} 1 & 1 \\ 1 & -1 \end{bmatrix} \end{bmatrix},$$

$$\left\{\mathbf{B}\right\}_2 = \begin{bmatrix} \boldsymbol{I}_2 \otimes \begin{bmatrix} 1 & 1 \\ 1 & -1 \end{bmatrix} & \\ & \boldsymbol{I}_2 \otimes \begin{bmatrix} 1 & -j \\ 1 & j \end{bmatrix} \end{bmatrix},$$

and $\boldsymbol{W}_2 = \boldsymbol{I}_4 \otimes \begin{bmatrix} 1 & 1 \\ 1 & -1 \end{bmatrix}$. Therfore, (25)-(28) are rearranged as:

$$\boldsymbol{V}(z) = \sum_{N} v(n) \times \left\{\boldsymbol{B}\right\}_{N/2} \otimes \boldsymbol{W}_{N/2} \tag{32}$$

$$\boldsymbol{I}(z) = \sum_{N} i(n) \times \left\{\boldsymbol{B}\right\}_{N/2} \otimes \boldsymbol{W}_{N/2} \tag{33}$$

$$\boldsymbol{W}_v(z) = \sum_{N} w_v(n) \times \left\{\boldsymbol{B}\right\}_{N/2} \otimes \boldsymbol{W}_{N/2} \tag{34}$$

$$\boldsymbol{W}_i(z) = \sum_{N} w_i(n) \times \left\{\boldsymbol{B}\right\}_{N/2} \otimes \boldsymbol{W}_{N/2} \tag{35}$$

From (17)-(20), the value of $R_m(z)$, $L_m(z)$, $C_m(z)$ and $G_m(z)$ can be expressed in terms of spatial Fourier series in z with period d as:

$$R_m(z) = \sum_{n} R_m[n] exp\left(\frac{j2\pi nz}{d}\right) \tag{36}$$

$$L_m(z) = \sum_{n} L_m[n] exp\left(\frac{j2\pi nz}{d}\right) \tag{37}$$

$$C_m(z) = \sum_{n} C_m[n] exp\left(\frac{j2\pi nz}{d}\right) \tag{38}$$

$$G_m(z) = \sum_{n} G_m[n] exp\left(\frac{j2\pi nz}{d}\right) \tag{39}$$

where the cofficients $R_m[n]$, $L_m[n]$, $C_m[n]$ and $G_m[n]$ are represented in finite form. (40)-(43) are truncated their Fourier

0885-8977 (c) 2021 IEEE. Personal use is permitted, but republication/redistribution requires IEEE permission. See http://www.ieee.org/publications_standards/publications/rights/index.html for more information.
Authorized licensed use limited to: DELHI TECHNICAL UNIV. Downloaded on February 15,2022 at 10:03:33 UTC from IEEE Xplore. Restrictions apply.

This article has been accepted for publication in a future issue of this journal, but has not been fully edited. Content may change prior to final publication. Citation information: DOI 10.1109/TPWRD.2022.3149137, IEEE Transactions on Power Delivery

series from $m=1$ to $m=P$ as

$$R[n|\theta]=R[n]=\sum_{m=1}^{p}\theta[m]R_m[n] \tag{40}$$

$$L[n|\theta]=L[n]=\sum_{m=1}^{p}\theta[m]L_m[n] \tag{41}$$

$$C[n|\theta]=C[n]=\sum_{m=1}^{p}\theta[m]C_m[n] \tag{42}$$

$$G[n|\theta]=G[n]=\sum_{m=1}^{p}\theta[m]G_m[n] \tag{43}$$

Substitute (17)-(24) along with (36)-(43) into (15)-(16) and equating both sides coefficients, we have

$$\sum_m R[n-m|\theta]i_m(t)+\sum_m L[n-m|\theta]i_m^{'}(t) + \frac{j2\pi n}{d}v_n(t)=w_{v,n}(t) \tag{44}$$

$$\sum_m G[n-m|\theta]v_m(t)+\sum_m C[n-m|\theta]v_m^{'}(t) + \frac{j2\pi n}{d}i_n(t)=w_{i,n}(t) \tag{45}$$

where $i_m^{'}(t)=\frac{d}{dt}i_m(t)$ and $v_m^{'}(t)=\frac{d}{dt}v_m(t)$. $v_n(t)$, $i_n(t)$, $w_{v,n}(t)$ and $w_{i,n}(t)$ are defined in their Fourier series vectors of samples size $2N+1$ as

$$\big(\big(v_{(n)}(t)\big)\big)_{-N}^{+N}=\ \mathbf{v}(t) \tag{46}$$

$$\big(\big(i_{(n)}(t)\big)\big)_{-N}^{+N}=\mathbf{i}(t) \tag{47}$$

$$\big(\big(w_{(v,n)}(t)\big)\big)_{-N}^{+N}=\mathbf{w}_v(t) \tag{48}$$

$$\big(\big(w_{(i,n)}(t)\big)\big)_{-N}^{+N}=\mathbf{w}_i(t) \tag{49}$$

Also, the line parameters are expressed in terms of Fourier series matrices as follows:

$$\big(\big(R[n-m|\boldsymbol{\theta}]\big)\big)_{-N\le n,l\le N}=\boldsymbol{R}(\boldsymbol{\theta})=\sum_{m=1}^{p}\theta[m]\boldsymbol{R}_m \tag{50}$$

$$\big(\big(L[n-m|\boldsymbol{\theta}]\big)\big)_{-N\le n,l\le N}=\boldsymbol{L}(\boldsymbol{\theta})=\sum_{m=1}^{p}\theta[m]\boldsymbol{L}_m \tag{51}$$

$$\big(\big(C[n-m|\boldsymbol{\theta}]\big)\big)_{-N\le n,l\le N}=\boldsymbol{C}(\boldsymbol{\theta})=\sum_{m=1}^{p}\theta[m]\boldsymbol{C}_m \tag{52}$$

$$\big(\big(G[n-m|\boldsymbol{\theta}]\big)\big)_{-N\le n,l\le N}=\boldsymbol{G}(\boldsymbol{\theta})=\sum_{m=1}^{p}\theta[m]\boldsymbol{G}_m \tag{53}$$

where

$$\boldsymbol{R}_m=\big(\big(R[n-l]\big)\big)_{-N\le n,l\le N},\boldsymbol{L}_m=\big(\big(L[n-l]\big)\big)_{-N\le n,l\le N}$$
$$\boldsymbol{C}_m=\big(\big(C[n-l]\big)\big)_{-N\le n,l\le N},\boldsymbol{G}_m=\big(\big(G[n-l]\big)\big)_{-N\le n,l\le N}$$

Substitute (46)-(49) along with (50)-(53) into (44)-(45), we get

$$\boldsymbol{R}[\boldsymbol{\theta}]\mathbf{i}(t)+\boldsymbol{L}[\boldsymbol{\theta}]\mathbf{i}^{'}(t)+j\boldsymbol{D}\,\mathbf{v}(t)=\mathbf{w}_v(t) \tag{54}$$

$$\boldsymbol{G}[\boldsymbol{\theta}]\mathbf{v}(t)+\boldsymbol{C}[\boldsymbol{\theta}]\mathbf{v}^{'}(t)+j\boldsymbol{D}\,\mathbf{i}(t)=\mathbf{w}_i(t) \tag{55}$$

where $\boldsymbol{D}=diag[\frac{2\pi n}{d};-N\le n\le N]$. Rearranging (54)-(55) to find their state space model, we get

$$\frac{d}{dt}\begin{bmatrix}\mathbf{v}(t)\\ \mathbf{i}(t)\end{bmatrix}=-\begin{bmatrix}\boldsymbol{C}[\boldsymbol{\theta}]^{-1}\boldsymbol{G}[\boldsymbol{\theta}] & j\boldsymbol{D}\\ j\boldsymbol{D} & \boldsymbol{L}[\boldsymbol{\theta}]^{-1}\boldsymbol{R}[\boldsymbol{\theta}]\end{bmatrix}\begin{bmatrix}\mathbf{v}(t)\\ \mathbf{i}(t)\end{bmatrix} + \begin{bmatrix}\boldsymbol{C}[\boldsymbol{\theta}]^{-1} & 0\\ 0 & \boldsymbol{L}[\boldsymbol{\theta}]^{-1}\end{bmatrix}\begin{bmatrix}\mathbf{w}_i(t)\\ \mathbf{w}_v(t)\end{bmatrix} \tag{56}$$

where state vector matrix denoted by $\boldsymbol{\xi}(t)$ is represented as

$$\begin{bmatrix}\mathbf{v}(t)\\ \mathbf{i}(t)\end{bmatrix}=\boldsymbol{\xi}(t)=\boldsymbol{\xi}_R(t)+j\boldsymbol{\xi}_I(t) \tag{57}$$

Here, $\boldsymbol{\xi}_R(t)$ and $\boldsymbol{\xi}_I(t)$ denote real and imaginary terms respectively.

State transition matrix $\boldsymbol{F}(\boldsymbol{\theta})$ obtained from (56) is defined in real and imaginary terms as

$$-\begin{bmatrix}\boldsymbol{C}[\boldsymbol{\theta}]^{-1}\,\boldsymbol{G}[\boldsymbol{\theta}] & j\,\boldsymbol{D}\\ j\,\boldsymbol{D} & \boldsymbol{L}[\boldsymbol{\theta}]^{-1}\,\boldsymbol{R}[\boldsymbol{\theta}]\end{bmatrix}=\ \boldsymbol{F}_R(\boldsymbol{\theta})+j\boldsymbol{F}_I(\boldsymbol{\theta}) \tag{58}$$

Also, processes noise matrix is

$$\begin{bmatrix}\boldsymbol{C}[\boldsymbol{\theta}]^{-1} & \mathbf{0}\\ \mathbf{0} & \boldsymbol{L}[\boldsymbol{\theta}]^{-1}\end{bmatrix}=\ \boldsymbol{P}_R(\boldsymbol{\theta})+j\ \boldsymbol{P}_I(\boldsymbol{\theta}) \tag{59}$$

$$\begin{bmatrix}\mathbf{w}_i(t)\\ \mathbf{w}_v(t)\end{bmatrix}=\mathbf{w}(t)=\mathbf{w}_R(t)+j\mathbf{w}_I(t) \tag{60}$$

Substitute (57)-(60) into (56), the line equation are

$$(\boldsymbol{\xi}_R^{'}(t)+j\boldsymbol{\xi}_I^{'}(t))=(\ \boldsymbol{F}_R(\boldsymbol{\theta})+j\ \boldsymbol{F}_I(\boldsymbol{\theta}))(\boldsymbol{\xi}_R(t)+j\boldsymbol{\xi}_I(t)) +(\ \boldsymbol{P}_R(\boldsymbol{\theta})+j\ \boldsymbol{P}_I(\boldsymbol{\theta}))(\mathbf{w}_R(t)+j\mathbf{w}_I(t)) \tag{61}$$

Seperate into real and imaginary parts, we get

$$\boldsymbol{\xi}_R^{'}(t)=\ \boldsymbol{F}_R(\boldsymbol{\theta})\boldsymbol{\xi}_R(t)-\ \boldsymbol{F}_I(\boldsymbol{\theta})\boldsymbol{\xi}_I(t)+\ \boldsymbol{P}_R(\boldsymbol{\theta})\mathbf{w}_R(t) -\ \boldsymbol{P}_I(\boldsymbol{\theta})\mathbf{w}_I(t) \tag{62}$$

$$\boldsymbol{\xi}_I^{'}(t)=\ \boldsymbol{F}_R(\boldsymbol{\theta})\boldsymbol{\xi}_I(t)+\ \boldsymbol{F}_I(\boldsymbol{\theta})\boldsymbol{\xi}_R(t)+\ \boldsymbol{P}_R(\boldsymbol{\theta})\mathbf{w}_I(t) +\ \boldsymbol{P}_I(\boldsymbol{\theta})\mathbf{w}_R(t) \tag{63}$$

Rearrange into matrix notation, we get

$$\frac{d}{dt}\begin{bmatrix}\boldsymbol{\xi}_R(t)\\ \boldsymbol{\xi}_I(t)\end{bmatrix}=\begin{bmatrix}\boldsymbol{F}_R[\boldsymbol{\theta}] & -\boldsymbol{F}_I[\boldsymbol{\theta}]\\ \boldsymbol{F}_I[\boldsymbol{\theta}] & \boldsymbol{F}_R[\boldsymbol{\theta}]\end{bmatrix}\begin{bmatrix}\boldsymbol{\xi}_R(t)\\ \boldsymbol{\xi}_I(t)\end{bmatrix} + \begin{bmatrix}\boldsymbol{P}_R[\boldsymbol{\theta}] & -\boldsymbol{P}_I[\boldsymbol{\theta}]\\ \boldsymbol{P}_I[\boldsymbol{\theta}] & \boldsymbol{P}_R[\boldsymbol{\theta}]\end{bmatrix}\begin{bmatrix}\mathbf{w}_R(t)\\ \mathbf{w}_I(t)\end{bmatrix} \tag{64}$$

where $\frac{d}{dt}\boldsymbol{\theta}(t)=\boldsymbol{\epsilon}_{\boldsymbol{\theta}(t)}$ The parameter vector to be estimated must are added in (57) to obtain the augmented matrix as:

$$\boldsymbol{\eta}(t)=\big[\boldsymbol{\xi}_R(t),\boldsymbol{\xi}_I(t),\boldsymbol{\theta}(t),\big]^T \tag{65}$$

Therefore, the combined augmented state space model is

$$\frac{d}{dt}\begin{bmatrix}\boldsymbol{\xi}_R(t)\\ \boldsymbol{\xi}_I(t)\\ \boldsymbol{\theta}(t)\end{bmatrix}=\begin{bmatrix}\boldsymbol{F}_R[\boldsymbol{\theta}] & -\boldsymbol{F}_I[\boldsymbol{\theta}] & \mathbf{0}\\ \boldsymbol{F}_I[\boldsymbol{\theta}] & \boldsymbol{F}_R[\boldsymbol{\theta}] & \mathbf{0}\\ \mathbf{0} & \mathbf{0} & \boldsymbol{I}\end{bmatrix}\begin{bmatrix}\boldsymbol{\xi}_R(t)\\ \boldsymbol{\xi}_I(t)\\ \boldsymbol{\theta}(t)\end{bmatrix} + \begin{bmatrix}\boldsymbol{P}_R[\boldsymbol{\theta}] & -\boldsymbol{P}_I[\boldsymbol{\theta}] & \mathbf{0}\\ \boldsymbol{P}_I[\boldsymbol{\theta}] & \boldsymbol{P}_R[\boldsymbol{\theta}] & \mathbf{0}\\ \mathbf{0} & \mathbf{0} & \boldsymbol{I}\end{bmatrix}\begin{bmatrix}\mathbf{w}_R(t)\\ \mathbf{w}_I(t)\\ \boldsymbol{\epsilon}_{\boldsymbol{\theta}(t)}\end{bmatrix} \tag{66}$$

where $\boldsymbol{I}$ is the unitary matix of sample size $2N+1$. It is noted that for EKF implementation in (66), we must calculate the

0885-8977 (c) 2021 IEEE. Personal use is permitted, but republication/redistribution requires IEEE permission. See http://www.ieee.org/publications_standards/publications/rights/index.html for more information.
Authorized licensed use limited to: DELHI TECHNICAL UNIV. Downloaded on February 15,2022 at 10:03:33 UTC from IEEE Xplore. Restrictions apply.

This article has been accepted for publication in a future issue of this journal, but has not been fully edited. Content may change prior to final publication. Citation information: DOI 10.1109/TPWRD.2022.3149137, IEEE Transactions on Power Delivery

Jacobian matrix for implementation the EKF. Therefore, we differentiate $\boldsymbol{F}_R(\boldsymbol{\theta})$, $\boldsymbol{F}_I(\boldsymbol{\theta})$, $\boldsymbol{P}_R(\boldsymbol{\theta})$, $\boldsymbol{P}_I(\boldsymbol{\theta})$ $w.r.t.$ $\boldsymbol{\theta}$. These expressions are derived as follows:

$$\frac{d}{d\boldsymbol{\theta}(m)}(\ \boldsymbol{F}_R(\boldsymbol{\theta}) + j\ \boldsymbol{F}_I(\boldsymbol{\theta})) = -\begin{bmatrix} \frac{d}{d\boldsymbol{\theta}(m)}\ \boldsymbol{C}[\boldsymbol{\theta}]^{-1}\ \boldsymbol{G}[\boldsymbol{\theta}] & \boldsymbol{0} \\ \boldsymbol{0} & \frac{d}{d\boldsymbol{\theta}(m)}\ \boldsymbol{L}[\boldsymbol{\theta}]^{-1}\ \boldsymbol{R}[\boldsymbol{\theta}] \end{bmatrix} \quad (67)$$

$$\frac{d}{d\boldsymbol{\theta}(m)}\ \boldsymbol{C}[\boldsymbol{\theta}]^{-1}\ \boldsymbol{G}[\boldsymbol{\theta}] = -\ \boldsymbol{C}[\boldsymbol{\theta}]^{-1}\frac{d}{d\boldsymbol{\theta}(m)}\ \boldsymbol{C}[\boldsymbol{\theta}]\ \boldsymbol{C}[\boldsymbol{\theta}]^{-1}\ \boldsymbol{G}[\boldsymbol{\theta}] + \ \boldsymbol{C}[\boldsymbol{\theta}]^{-1}\frac{d}{d\boldsymbol{\theta}(m)}\ \boldsymbol{G}[\boldsymbol{\theta}] \quad (68)$$

$$= -\ \boldsymbol{C}[\boldsymbol{\theta}]^{-1}\ \boldsymbol{C}_m\ \boldsymbol{C}[\boldsymbol{\theta}]^{-1}\ \boldsymbol{G}[\boldsymbol{\theta}] + \ \boldsymbol{C}[\boldsymbol{\theta}]^{-1}\ \boldsymbol{G}_m \quad (69)$$

similarly,

$$\frac{d}{d\boldsymbol{\theta}(m)}\ \boldsymbol{L}[\boldsymbol{\theta}]^{-1}\ \boldsymbol{R}[\boldsymbol{\theta}] = -\ \boldsymbol{L}[\boldsymbol{\theta}]^{-1}\frac{d}{d\boldsymbol{\theta}(m)}\ \boldsymbol{L}[\boldsymbol{\theta}]\ \boldsymbol{L}[\boldsymbol{\theta}]^{-1}\ \boldsymbol{R}[\boldsymbol{\theta}] + \ \boldsymbol{L}[\boldsymbol{\theta}]^{-1}\frac{d}{d\boldsymbol{\theta}(m)}\ \boldsymbol{R}[\boldsymbol{\theta}] \quad (70)$$

$$= -\ \boldsymbol{L}[\boldsymbol{\theta}]^{-1}\ \boldsymbol{L}_m\ \boldsymbol{L}[\boldsymbol{\theta}]^{-1}\ \boldsymbol{R}[\boldsymbol{\theta}] + \ \boldsymbol{L}[\boldsymbol{\theta}]^{-1}\ \boldsymbol{R}_m \quad (71)$$

Considering the equations of the form

$$d\boldsymbol{\xi}(t) = \boldsymbol{F}(t,\boldsymbol{\xi}(t),\boldsymbol{\theta}(t))dt + \ \boldsymbol{G}(t,\boldsymbol{\xi}(t),\boldsymbol{\theta}(t))d\boldsymbol{B}(t) \quad (72)$$

$$d\boldsymbol{\theta}(t) = d\boldsymbol{\epsilon}_{\boldsymbol{\theta}(t)} \quad (73)$$

and the measurement equation is of the form

$$d\mathbf{z}(t) = \ \boldsymbol{h}(t,\boldsymbol{\xi}(t))dt + d\mathbf{v}(t) \quad (74)$$

In fact, the state equations are linear in $\boldsymbol{\xi}(t)$ and hence can be expressed as

$$d\boldsymbol{\xi}(t) = \boldsymbol{F}(t,\boldsymbol{\theta}(t))\boldsymbol{\xi}(t)dt + \ \boldsymbol{G}(t,\boldsymbol{\theta}(t))d\boldsymbol{B}(t) \quad (75)$$

$$d\boldsymbol{\theta}(t) = d\boldsymbol{\epsilon}_{\boldsymbol{\theta}(t)} \quad (76)$$

and the measurement equations are also linear in $\boldsymbol{\xi}(t)$ and hence can be expressed as

$$d\mathbf{z}(t) = \ \boldsymbol{H}\boldsymbol{\xi}(t)dt + d\mathbf{v}(t) \quad (77)$$

Equivalently, in the discretized form,

$$\boldsymbol{\xi}_{n+1} = (\ \boldsymbol{I} + \Delta\ \boldsymbol{F}_n(\boldsymbol{\theta}_n))\boldsymbol{\xi}_n + \ \boldsymbol{G}_n(\boldsymbol{\theta}_n)\mathbf{w}_{n+1} \quad (78)$$

$$\boldsymbol{\theta}_{n+1} = \boldsymbol{\theta}_n + \boldsymbol{\epsilon}_{n+1} \quad (79)$$

$$\mathbf{z}_n = \boldsymbol{H}\boldsymbol{\xi}_n + \mathbf{v}_n \quad (80)$$

Thus if the parameter $\boldsymbol{\theta}_n = \boldsymbol{\theta}$ are known, we would require a simple KF to estimate the state as

$$\hat{\boldsymbol{\xi}}_{n|n} = \mathbb{E}(\boldsymbol{\xi}_n|\mathbf{z}_k, k \le n) \quad (81)$$

$$\hat{\boldsymbol{\xi}}_{n+1|n} = \mathbb{E}(\boldsymbol{\xi}_{n+1}|\mathbf{z}_k, k \le n) \quad (82)$$

If however, $\boldsymbol{\theta}$ is unknown, then we must use the EKF in the following form:

$$\begin{bmatrix} \hat{\boldsymbol{\xi}}_{n+1|n} \\ \hat{\boldsymbol{\theta}}_{n+1|n} \end{bmatrix} = \begin{bmatrix} (\ \boldsymbol{I} + \Delta\ \boldsymbol{F}_n(\hat{\boldsymbol{\theta}}_{n|n})\hat{\boldsymbol{\xi}}_{n|n} \\ \hat{\boldsymbol{\theta}}_{n|n} \end{bmatrix} \quad (83)$$

$$\begin{bmatrix} \hat{\boldsymbol{\xi}}_{n+1|n+1} \\ \hat{\boldsymbol{\theta}}_{n+1|n+1} \end{bmatrix} = \begin{bmatrix} \hat{\boldsymbol{\xi}}_{n+1|n} \\ \hat{\boldsymbol{\theta}}_{n+1|n} \end{bmatrix} + \ \boldsymbol{K}_{n+1}(\mathbf{z}_{n+1} - \ \boldsymbol{H}\hat{\boldsymbol{\xi}}_{n+1|n}) \quad (84)$$

$$\boldsymbol{P}_{\boldsymbol{n+1|n}} = \ \boldsymbol{A}\boldsymbol{P}_{\boldsymbol{n|n}}\boldsymbol{A}^{\boldsymbol{T}} + \ \boldsymbol{G}_{\boldsymbol{n}}(\hat{\boldsymbol{\theta}}_{\boldsymbol{n|n}})\boldsymbol{\Theta}\ \boldsymbol{G}_{\boldsymbol{n}}(\hat{\boldsymbol{\theta}}_{\boldsymbol{n|n}})^{\boldsymbol{T}} \quad (85)$$

$$\boldsymbol{P}_{n+1|n+1} = (\boldsymbol{I} - \boldsymbol{K}_{n+1}\boldsymbol{H})\boldsymbol{P}_{n+1|n}(\boldsymbol{I} - \boldsymbol{K}_{n+1}\boldsymbol{H})^T + \boldsymbol{K}_{n+1}\boldsymbol{R}_{\mathbf{v}}\boldsymbol{K}_{n+1}^T \quad (86)$$

where

$$\boldsymbol{K}_{n+1} = \ \boldsymbol{P}_{n+1|n}\ \boldsymbol{H}^T(\ \boldsymbol{R}_{\mathbf{v}} + \ \boldsymbol{H}\ \boldsymbol{P}_{n+1|n}\ \boldsymbol{H}^T)^{-1} \quad (87)$$

$$\boldsymbol{A} = \begin{bmatrix} \boldsymbol{I}_d + \Delta\ \boldsymbol{F}_n(\hat{\boldsymbol{\theta}}_{n|n}) & \Delta\boldsymbol{F}_n^{'}(\hat{\boldsymbol{\theta}}_{n|n})(\ \boldsymbol{I} \otimes \hat{\boldsymbol{\xi}}_{n|n}) \\ \boldsymbol{0} & \boldsymbol{I}_P \end{bmatrix} \quad (88)$$

The use of state estimation for measurement techniques in real system is as follows:- Suppose a transmission line is not operating satisfactorily owing to noise. For example, it may cause the voltage supply coming from the mains to fluctuate a great deal. Then we require to introduce control terms along the line. Since we do not have direct access to the line voltage/current but only to its real EKF estimate, we can design a feedback controller that computes the error between the desired state $\hat{\boldsymbol{\xi}}_d(t)$ ($i.e.$ the desire line voltage and current with $\hat{\boldsymbol{\xi}}(t)$) and its true EKF estimate $\hat{\boldsymbol{\xi}}(t)$ into the line dynamics. Such a feedback control will result in a modified state dynamics of the form

$$d\boldsymbol{\xi}(t) = \boldsymbol{F}(t,\boldsymbol{\theta}(t))\boldsymbol{\xi}(t)dt + \boldsymbol{G}(t,\boldsymbol{\theta}(t))d\boldsymbol{B}(t) + \boldsymbol{K}_c(\boldsymbol{\xi}_d(t) - \hat{\boldsymbol{\xi}}(t)) \quad (89)$$

or equivalent in the discrete time domain

$$\boldsymbol{\xi}_{n+1} = (\boldsymbol{I} + \Delta\boldsymbol{F}_n(\boldsymbol{\theta}))\boldsymbol{\xi}_n + \boldsymbol{G}_n(\boldsymbol{\theta}_n)\mathbf{w}_{n+1} + \boldsymbol{K}_c(n)(\boldsymbol{\xi}_{dn} - \hat{\boldsymbol{\xi}}_{n|n}) \quad (90)$$

The feedback control coefficient $\boldsymbol{K}_c(n)$ is adaptively or on a block processing basis controller to minimize $\mathbb{E}||\boldsymbol{\xi}_{d(n+1)} - \boldsymbol{\xi}_{n+1}||^2$. For example, the noiseless dynamics of $\boldsymbol{\xi}_{dn}$ is $\hat{\boldsymbol{\xi}}_{d(n+1)} = (\boldsymbol{I} + \Delta\boldsymbol{F}_n(\boldsymbol{\theta}))\boldsymbol{\xi}_{dn}$ and hence,

$$\boldsymbol{\xi}_{d(n+1)} - \boldsymbol{\xi}_{n+1} = (\boldsymbol{I} + \Delta\boldsymbol{F}_n(\boldsymbol{\theta}))(\boldsymbol{\xi}_{dn} - \boldsymbol{\xi}_n) - \boldsymbol{G}_n(\boldsymbol{\theta})\mathbf{w}_{n+1} - \boldsymbol{K}_c(n)(\boldsymbol{\xi}_{dn} - \hat{\boldsymbol{\xi}}_{n|n}) \quad (91)$$

where

$$\hat{\boldsymbol{\xi}}_{n+1|n+1} = (\boldsymbol{I} + \Delta\boldsymbol{F}_n(\boldsymbol{\theta}))\hat{\boldsymbol{\xi}}_{n|n} + \boldsymbol{K}(n+1)(\boldsymbol{H}\boldsymbol{\xi}_{n+1} + \mathbf{v}_{n+1} - \boldsymbol{H}(\boldsymbol{I} + \Delta\boldsymbol{F}_n(\boldsymbol{\theta}))\hat{\boldsymbol{\xi}}_{n|n}) \quad (92)$$

$$= (\boldsymbol{I} + \Delta\boldsymbol{F}_n(\boldsymbol{\theta}))\hat{\boldsymbol{\xi}}_{n|n} + \boldsymbol{K}(n+1)(\boldsymbol{H}((\boldsymbol{I} + \Delta\boldsymbol{F}_n(\boldsymbol{\theta}))\boldsymbol{\xi}_n + \boldsymbol{G}_n(\boldsymbol{\theta})\mathbf{w}_{n+1} + \mathbf{v}_{n+1} - \boldsymbol{H}(\boldsymbol{I} + \Delta\boldsymbol{F}_n(\boldsymbol{\theta}))\hat{\boldsymbol{\xi}}_{n|n}) \quad (93)$$

$$= (\boldsymbol{I} + \Delta\boldsymbol{F}_n(\boldsymbol{\theta}))\hat{\boldsymbol{\xi}}_{n|n} + \boldsymbol{K}(n+1)\boldsymbol{H}(\boldsymbol{I} + \Delta\boldsymbol{F}_n(\boldsymbol{\theta}))(\xi_n - \hat{\boldsymbol{\xi}}_{n|n}) + \boldsymbol{K}(n+1)\boldsymbol{G}_n(\boldsymbol{\theta})\mathbf{w}_{n+1} + \boldsymbol{K}(n+1)\mathbf{v}_{n+1} \quad (94)$$

Thus

$$\boldsymbol{\xi}_{d(n+1)} - \hat{\boldsymbol{\xi}}_{n+1|n+1} = (\boldsymbol{I} + \Delta\boldsymbol{F}_n(\boldsymbol{\theta}))(\boldsymbol{\xi}_{dn} - \hat{\boldsymbol{\xi}}_{n|n}) - \boldsymbol{K}(n+1)\boldsymbol{H}(\boldsymbol{I} + \Delta\boldsymbol{F}_n(\boldsymbol{\theta}))(\boldsymbol{\xi}_n - \hat{\boldsymbol{\xi}}_{n|n}) - \boldsymbol{K}(n+1)\boldsymbol{G}_n(\boldsymbol{\theta})\mathbf{w}_{n+1} - \boldsymbol{K}(n+1)\mathbf{v}_{n+1} \quad (95)$$

0885-8977 (c) 2021 IEEE. Personal use is permitted, but republication/redistribution requires IEEE permission. See http://www.ieee.org/publications_standards/publications/rights/index.html for more information.
Authorized licensed use limited to: DELHI TECHNICAL UNIV. Downloaded on February 15,2022 at 10:03:33 UTC from IEEE Xplore. Restrictions apply.

This article has been accepted for publication in a future issue of this journal, but has not been fully edited. Content may change prior to final publication. Citation information: DOI 10.1109/TPWRD.2022.3149137, IEEE Transactions on Power Delivery

From these two coupled linear stochastic difference equations for the two kind of error, trajectory tracker error $(\boldsymbol{\xi}_{dn} - \boldsymbol{\xi}_n)$ and state estimation error $(\boldsymbol{\xi}_{dn} - \hat{\boldsymbol{\xi}}_{n|n})$, we can in principle compute $\sum_n \mathbb{E}||(\boldsymbol{\xi}_{dn} - \boldsymbol{\xi}_n)||^2$ and $\sum_n \mathbb{E}||(\boldsymbol{\xi}_{dn} - \hat{\boldsymbol{\xi}}_{n|n})||^2$ and choose the feedback controller coefficient $\boldsymbol{K}_c(n)$ to minimize some weighted combination in these two error energies.

The measurement model consists of measuring the line voltage and current at the spatial points $z_1, ..., z_m$. so that this model becomes

$$d\boldsymbol{\xi}_{v,n}(t) = v(t, z_n)dt + dw_{v,n}(t), \quad n = 1, 2, ..., m \tag{96}$$

$$d\boldsymbol{\xi}_{i,n}(t) = i(t, z_n)dt + dw_{i,n}(t), \quad n = 1, 2, ..., m \tag{97}$$

Now noting that $v(t, z_n)$ and $i(t, z_n)$ can be expressed as linear combinations of the Fourier series components of the line voltage and current, i.e.

$$v(t, z_n) = \sum_n v_n(t) exp(j2\pi n z_n/d), \quad n = 1, 2, ..., m \tag{98}$$

$$i(t, z_n) = \sum_n i_n(t) exp(j2\pi n z_n/d), \quad n = 1, 2, ..., m \tag{99}$$

we can separate this into real and imaginary components and then express the measurement model in vector form as

$$d\mathbf{z}(t) = (\boldsymbol{H}_1\boldsymbol{\xi}_R(t) + \boldsymbol{H}_2\boldsymbol{\xi}_I(t))dt + \mathbf{v}(t) = \boldsymbol{H}\boldsymbol{\eta}(t)dt + d\mathbf{v}(t) \tag{100}$$

where $\mathbf{z}(t) = [\boldsymbol{\xi}_{v,1}(t), ..., \boldsymbol{\xi}_{v,m}(t), \boldsymbol{\xi}_{i,1}(t), ...\boldsymbol{\xi}_{i,m}(t)]^T$ is a $2m \times 1$ real vector.

$$\boldsymbol{H} = [\boldsymbol{H}_1, \boldsymbol{H}_2, \mathbf{0}] \tag{101}$$

where the non-zero matrix elements of $\boldsymbol{H}_1, \boldsymbol{H}_2$ are $cos(2\pi n\boldsymbol{\xi}_n/d), sin(2\pi n\boldsymbol{\xi}_n/d)$. Recall that $\boldsymbol{\eta}(t)$ is the extended state vector $[\boldsymbol{\xi}_R(t)^T, \boldsymbol{\xi}_I(t)^T, \boldsymbol{\theta}(t)^T]^T$ with $\boldsymbol{\xi}_R(t)$ being built out of the real parts of the Fourier series components $v_n(t), i_n(t)$ of the line voltage and current and $\boldsymbol{\xi}_I(t)$ being built out of their imaginary parts.

V. Modeling of NTL using frequency domain analysis

The line voltage $V(w, z)$ and current $I(w, z)$ are the Fourier transform of $v(t, z)$ and current $i(t, z)$ and can be expanded into an infinite set of spatial harmonics [27] as follows:

$$V(w, z) = \sum_n e^{-\gamma(w)z} \times V_n(w) \times e^{j2\pi nz/d} \tag{102}$$

$$I(w, z) = \sum_n e^{-\gamma(w)z} \times I_n(w) \times e^{j2\pi nz/d} \tag{103}$$

where $\gamma(w)$ is propagation constant as:

$$\gamma(w) = \sqrt{[R(w, z) + jwL(w, z)]\,[G(w, z) + jwC(w, z)]} \tag{104}$$

(15) and (16) can be expressed in frequency domain using Fourier transform as:

$$-\frac{d}{dz}V(w, z) = [R(z) + jwL(z)]\, I(w, z) + W_v(w, z) \tag{105}$$

$$-\frac{d}{dz}I(w, z) = [G(z) + jwC(z)]\, V(w, z) + W_i(w, z) \tag{106}$$

where

$$Z(z) = Z(z|\boldsymbol{\theta}) = R(z|\boldsymbol{\theta}) + jwL(z|\boldsymbol{\theta}) = \sum_n Z_n(w|\boldsymbol{\theta})e^{j2\pi nz/d}$$

$$Z_n(w|\boldsymbol{\theta}) = R_n(\boldsymbol{\theta}) + jwL_n(\boldsymbol{\theta}).$$

Similarly,

$$Y(z) = Y(z|\boldsymbol{\theta}) = G(z|\boldsymbol{\theta}) + jwC(z|\boldsymbol{\theta}) = \sum_n Y_n(w|\boldsymbol{\theta})e^{j2\pi nz/d}$$

$$Y_n(w|\boldsymbol{\theta}) = G_n(\boldsymbol{\theta}) + jwC_n(\boldsymbol{\theta}).$$

Substituting the Fourier series expansion of the distributed parameters (17)-(20) along with (102) and (103) into (105) and (106). By equating the coefficients of both sides, we get:

$$\left(\gamma(\omega) - j\frac{2\pi n}{d}\right) V_n(w) = \sum_k Z_{n-k}(w|\boldsymbol{\theta})I_k(w) + W_{v,n}(w) \tag{107}$$

$$\left(\gamma(\omega) - j\frac{2\pi n}{d}\right) I_n(w) = \sum_k Y_{n-k}(w|\boldsymbol{\theta})V_k(w) + W_{i,n}(w) \tag{108}$$

Here, $V_n(w)$, $I_n(w)$, $Z_{n-k}(w|\boldsymbol{\theta})$ and $Y_{n-k}(w|\boldsymbol{\theta})$ are periodic with total samples $2N + 1$. Now, perturbation theory is implemented to voltage $(V_n(w))$ and current $(I_n(w))$ to account the nonlinearity of the transmission line. Expanding the line voltage and current by adding σ as a perturbation parameter, we have:

$$V_n(w) = V_n^{(0)}(w) + \sigma V_n^{(1)}(w) + \sigma^2 V_n^{(2)}(w) + ... \tag{109}$$

$$I_n(w) = I_n^{(0)}(w) + \sigma I_n^{(1)}(w) + \sigma^2 I_n^{(2)}(w) + ... \tag{110}$$

where $V_n^{(0)}(w)$ and $I_n^{(0)}(w)$ are the line voltage and current with $\sigma = 0$ respectively, i.e. linear terms, whereas $\sigma V_n^{(1)}(w)$ and $\sigma I_n^{(1)}(w)$ respectively represent the perturbation of voltage and current caused by non-linearity. Substituting (109) and (110) into (107) and (108) and equating the coefficients of σ^0 and σ^1 terms, we have

$$(\gamma(w)\boldsymbol{I} - j\boldsymbol{D})\ \mathbf{V}^{(0)}(w) = \boldsymbol{Z}(w|\boldsymbol{\theta})\ \mathbf{I}^{(0)}(w) \tag{111}$$

$$(\gamma(w)\boldsymbol{I} - j\boldsymbol{D})\ \mathbf{I}^{(0)}(w) = \boldsymbol{Y}(w|\boldsymbol{\theta})\mathbf{V}^{(0)}(w) \tag{112}$$

Now, the voltage and current Fourier series vectors and the line impedance and admittance Fourier series matrices are defined

0885-8977 (c) 2021 IEEE. Personal use is permitted, but republication/redistribution requires IEEE permission. See http://www.ieee.org/publications_standards/publications/rights/index.html for more information.
Authorized licensed use limited to: DELHI TECHNICAL UNIV. Downloaded on February 15,2022 at 10:03:33 UTC from IEEE Xplore. Restrictions apply.

This article has been accepted for publication in a future issue of this journal, but has not been fully edited. Content may change prior to final publication. Citation information: DOI 10.1109/TPWRD.2022.3149137, IEEE Transactions on Power Delivery

as:

$$\mathbf{V}(w) = \big(\big(V(w)\big)\big)_{-N}^{+N} \tag{113}$$

$$\mathbf{I}(w) = \big(\big(I(w)\big)\big)_{-N}^{+N} \tag{114}$$

$$\boldsymbol{Z}(w|\boldsymbol{\theta}) = \big(\big(Z_{n-k}(w|\boldsymbol{\theta})\big)\big)_{-N}^{+N} \tag{115}$$

$$\boldsymbol{Y}(w|\boldsymbol{\theta}) = \big(\big(Y_{n-k}(w|\boldsymbol{\theta})\big)\big)_{-N}^{+N} \tag{116}$$

(111) and (112) can further be organized in the form of a matrix eigenvalue problem for the propagation constant $\gamma(w)$ (eigenvalue) and voltage-current Fourier series vector (eigenvector) which is used as measurement vector during the estimation process in KF and EKF method. In matrix form, these equations can be written as:

$$\begin{bmatrix} j\boldsymbol{D} - \gamma(\omega) & \boldsymbol{Z}(w|\boldsymbol{\theta}) \\ \boldsymbol{Y}(w|\boldsymbol{\theta}) & j\boldsymbol{D} - \gamma(\omega) \end{bmatrix} \otimes I_n \times \begin{bmatrix} \mathbf{V}(w) \\ \mathbf{I}(w) \end{bmatrix} = 0 \tag{117}$$

For simulations, measurements have been done using (117).

VI. State and Parameter Estimation for Transmission Line Circuit

To implement the state estimation technique for NTL, the state-space model in (56) needs to be discretized. The first-order exponential method is used to discretize the model. The discrete model of the NTL is given in (118) and (119).

$$\mathbf{x}_{n+1} = \boldsymbol{F}_n\mathbf{x}_n + \boldsymbol{B}_n\mathbf{u}_n + \boldsymbol{G}_n\mathbf{w}_n \tag{118}$$

$$\mathbf{z}_n = \boldsymbol{H}_n\mathbf{x}_n + \mathbf{v}_n \tag{119}$$

where

$$\boldsymbol{F}_n = \begin{bmatrix} 1 - T_s\boldsymbol{C}[\boldsymbol{\theta}]^{-1}\boldsymbol{G}[\boldsymbol{\theta}] & -jT_s\boldsymbol{D} \\ -jT_s\boldsymbol{D} & 1 - T_s\boldsymbol{L}[\boldsymbol{\theta}]^{-1}\boldsymbol{R}[\boldsymbol{\theta}] \end{bmatrix},$$
$$\boldsymbol{B}_n = \begin{bmatrix} 1, 1 \end{bmatrix}^T,$$
$$\boldsymbol{G}_n = \begin{bmatrix} \boldsymbol{C}[\boldsymbol{\theta}]^{-1} & \mathbf{0} \\ \mathbf{0} & \mathbf{L}[\boldsymbol{\theta}]^{-1} \end{bmatrix}, \boldsymbol{H}_n = \begin{bmatrix} 1 & 0 \\ 0 & 1 \end{bmatrix}.$$

$\mathbf{x}_n$ denote the state vector as $\mathbf{x}_n = \begin{bmatrix} V_n, I_n \end{bmatrix}^T$. Here $\mathbf{u}_n$ is the input vector. $\mathbf{w}_n$ and $\mathbf{v}_n$ are zero mean Gaussian noise in the state vector with covariance matrix $\boldsymbol{Q}_n$ and in the measurement vector with covariance matrix $\boldsymbol{R}_n$, respectively.

The state model is written as

$$\begin{bmatrix} \mathbf{V}_{n+1} \\ \mathbf{I}_{n+1} \end{bmatrix} = \begin{bmatrix} 1 - T_s\boldsymbol{C}[\boldsymbol{\theta}]^{-1}\boldsymbol{G}[\boldsymbol{\theta}] & -jT_s\mathbf{D} \\ -jT_s\boldsymbol{D} & 1 - T_s\mathbf{L}[\boldsymbol{\theta}]^{-1}\mathbf{R}[\boldsymbol{\theta}] \end{bmatrix} \begin{bmatrix} \mathbf{V}_n \\ \mathbf{I}_n \end{bmatrix} + \begin{bmatrix} \boldsymbol{C}[\boldsymbol{\theta}]^{-1} & \mathbf{0} \\ \mathbf{0} & \boldsymbol{L}[\boldsymbol{\theta}]^{-1} \end{bmatrix} \begin{bmatrix} \mathbf{w}_{i,n} \\ \mathbf{w}_{v,n} \end{bmatrix} \tag{120}$$

$$\mathbf{z}_n = \begin{bmatrix} 1 & 0 \\ 0 & 1 \end{bmatrix} \begin{bmatrix} \mathbf{V}_n \\ \mathbf{I}_n \end{bmatrix} + \begin{bmatrix} \mathbf{v}_{1n} \\ \mathbf{v}_{2n} \end{bmatrix} \tag{121}$$

where T_s is the sampling time. $\mathbf{v}_{1n}$ and $\mathbf{v}_{2n}$ are the measurement vector of line voltage and line current respectively. As the equation (120) is a linear estimation problem, KF has been used to estimate line voltage and line current. A fourth order parameter vector $\boldsymbol{\theta}_n = [R_n,\ L_n,\ C_n,\ G_n]^T$ is defined for parameter identification. The parameters to be estimated must are added in (120) to obtain the augmented matrix as:

$$\mathbf{x}_n^a = \begin{bmatrix} \mathbf{x}_n^T\ ,\ \boldsymbol{\theta}_n^T \end{bmatrix}^T \tag{122}$$

The augmented state model is:

$$\mathbf{x}_{n+1}^a = \boldsymbol{F}_n^a\mathbf{x}_n^a + \boldsymbol{B}_n^a\mathbf{u}_n + \boldsymbol{G}_n^a\mathbf{w}_n^a \tag{123}$$

$$\mathbf{z}_n^a = \boldsymbol{H}_n^a\mathbf{x}_n^a + \mathbf{v}_n^a \tag{124}$$

where

$$\mathbf{x}_n^a = \begin{bmatrix}\ V_n, I_n, R_n, L_n, C_n, G_n\ \end{bmatrix}^T,$$
$$\boldsymbol{B}_n^a = \begin{bmatrix}\ 1, 1, 0, 0, 0, 0\ \end{bmatrix}^T,$$
$$\boldsymbol{G}_n^a = \begin{bmatrix} \boldsymbol{C}[\boldsymbol{\theta}]^{-1} & \mathbf{0} & 0\ 0\ 0\ 0 \\ \mathbf{0} & \boldsymbol{L}[\boldsymbol{\theta}]^{-1} & 0\ 0\ 0\ 0 \\ 0 & 0 & 0\ 0\ 0\ 0 \\ 0 & 0 & 0\ 0\ 0\ 0 \\ 0 & 0 & 0\ 0\ 0\ 0 \\ 0 & 0 & 0\ 0\ 0\ 0 \end{bmatrix}, \mathbf{w}_n^a = \begin{bmatrix} \mathbf{w}_{\mathbf{x}}^T \\ \mathbf{w}_{\boldsymbol{\theta}}^T \end{bmatrix}.$$

Now, $\boldsymbol{F}_n^a$ is nonlinear function of $\mathbf{x}_n$ and $\boldsymbol{\theta}_n$. Therefore, EKF can be used to linearize $\boldsymbol{F}_n$ matrix using Jacobian transform as

$$\boldsymbol{F}_n^a = \begin{bmatrix} \frac{df_1}{d\mathbf{x}_1} & \frac{df_1}{d\mathbf{x}_2} & \frac{df_1}{d\boldsymbol{\theta}_1} & \frac{df_1}{d\boldsymbol{\theta}_2} & \frac{df_1}{d\boldsymbol{\theta}_3} & \frac{df_1}{d\boldsymbol{\theta}_4} \\ \frac{df_2}{d\mathbf{x}_1} & \frac{df_2}{d\mathbf{x}_2} & \frac{df_2}{d\boldsymbol{\theta}_1} & \frac{df_2}{d\boldsymbol{\theta}_2} & \frac{df_2}{d\boldsymbol{\theta}_3} & \frac{df_2}{d\boldsymbol{\theta}_4} \\ \frac{df_3}{d\mathbf{x}_1} & \frac{df_3}{d\mathbf{x}_2} & \frac{df_3}{d\boldsymbol{\theta}_1} & \frac{df_3}{d\boldsymbol{\theta}_2} & \frac{df_3}{d\boldsymbol{\theta}_3} & \frac{df_3}{d\boldsymbol{\theta}_4} \\ \frac{df_4}{d\mathbf{x}_1} & \frac{df_4}{d\mathbf{x}_2} & \frac{df_4}{d\boldsymbol{\theta}_1} & \frac{df_4}{d\boldsymbol{\theta}_2} & \frac{df_4}{d\boldsymbol{\theta}_3} & \frac{df_4}{d\boldsymbol{\theta}_4} \\ \frac{df_5}{d\mathbf{x}_1} & \frac{df_5}{d\mathbf{x}_2} & \frac{df_5}{d\boldsymbol{\theta}_1} & \frac{df_5}{d\boldsymbol{\theta}_2} & \frac{df_5}{d\boldsymbol{\theta}_3} & \frac{df_5}{d\boldsymbol{\theta}_4} \\ \frac{df_6}{d\mathbf{x}_1} & \frac{df_6}{d\mathbf{x}_2} & \frac{df_6}{d\boldsymbol{\theta}_1} & \frac{df_6}{d\boldsymbol{\theta}_2} & \frac{df_6}{d\boldsymbol{\theta}_3} & \frac{d\varphi_6}{d\boldsymbol{\theta}_4} \end{bmatrix} \tag{125}$$

$$\boldsymbol{F}_n^a = \begin{bmatrix} 1 + T_s(\boldsymbol{C}[\boldsymbol{\theta}]^{-1}\boldsymbol{G}_m - \boldsymbol{C}[\boldsymbol{\theta}]^{-1}\boldsymbol{C}_m\boldsymbol{C}[\boldsymbol{\theta}]^{-1}\boldsymbol{G}[\boldsymbol{\theta}]) & 0 & 0 & 0 & 0 & 0 \\ 0 & 1 + T_s(\boldsymbol{L}[\boldsymbol{\theta}]^{-1}\boldsymbol{R}_m - \boldsymbol{L}[\boldsymbol{\theta}]^{-1}\boldsymbol{L}_m\boldsymbol{L}[\boldsymbol{\theta}]^{-1}\boldsymbol{R}[\boldsymbol{\theta}]) & 0 & 0 & 0 & 0 \\ 0 & 0 & 1 & 0 & 0 & 0 \\ 0 & 0 & 0 & 1 & 0 & 0 \\ 0 & 0 & 0 & 0 & 1 & 0 \\ 0 & 0 & 0 & 0 & 0 & 1 \end{bmatrix} \tag{126}$$

$$\boldsymbol{H}_n^a = \begin{bmatrix} 1 & 0 & 0 & 0 & 0 & 0 \\ 0 & 1 & 0 & 0 & 0 & 0 \end{bmatrix} \tag{127}$$

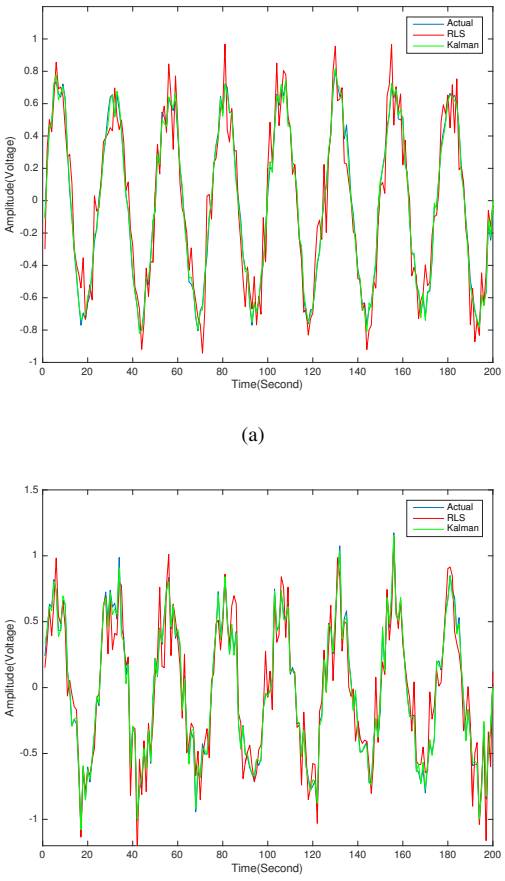
$$\mathbf{v}_n^a = \begin{bmatrix} \mathbf{v}_{\mathbf{x}}^T\ ,\ \mathbf{v}_{\boldsymbol{\theta}}^T \end{bmatrix}^T \tag{128}$$

VII. Simulation Results

MATLAB software has been used for simulation of derived equations. As compared to the other line losses, the power loss insulation resistance is small, so conductance G can be neglected. The objective is to estimate line resistance R, reactance X and susceptance B based on measurements up

0885-8977 (c) 2021 IEEE. Personal use is permitted, but republication/redistribution requires IEEE permission. See http://www.ieee.org/publications_standards/publications/rights/index.html for more information.
Authorized licensed use limited to: DELHI TECHNICAL UNIV. Downloaded on February 15,2022 at 10:03:33 UTC from IEEE Xplore. Restrictions apply.

This article has been accepted for publication in a future issue of this journal, but has not been fully edited. Content may change prior to final publication. Citation information: DOI 10.1109/TPWRD.2022.3149137, IEEE Transactions on Power Delivery



(a)

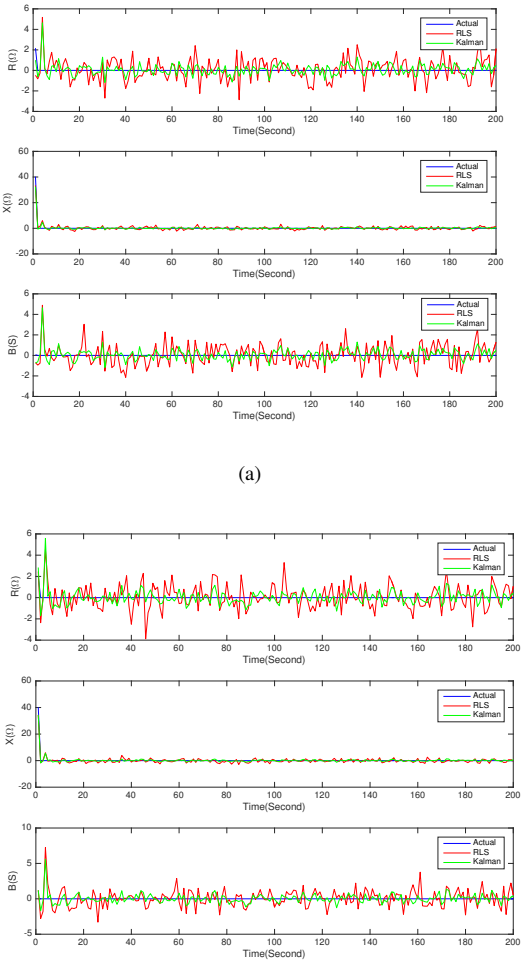
(b)

Figure 2. Voltage estimation using KF and RLS with Gaussian noise input, (a) μ=0, $\sigma^2 = 0.1$, (b) μ=0, $\sigma^2 = 0.5$.

to time n. The per unit (p.u.) parameters values used for simulations are: $R_0 = 1.92$ Ω/Km, $X_0 = 39.168$ Ω/Km, $B_0 = 1.65 \times 10^{-3} S$/Km and $d = 1000$. The line voltage of NTL is estimated using KF and recursive least squares (RLS) [28] methods for a 500 kV, 50 Hz transmission line. The white Gaussian noise of zero mean and different variances have been used for estimation. The process noise and measurement noise used are white Gaussian noise with zero mean and variances 0.001 and 0.1 respectively. The line voltages of NTL circuit have been estimated using KF and RLS methods for different noisy inputs are shown in Fig. 2. Estimated values have been compared with theoretical value obtained by solving the eigenvalue problem given in equation (117). Further, we estimate the distributed parameters of the line. Fig. 3 shows the estimation of different parameters.

Remarks

1) True EKF is only a suboptimal estimator based on second order truncated Taylor expression but when a very large number of random effects contribute to the dynamics, as for example a very large number of Browanian motions in different Fourier bins mode, then the signals by the central limit theorem are the



(a)

(b)

Figure 3. Parameters estimation using EKF and RLS methods with Gaussian noise input, (a) μ=0, $\sigma^2 = 0.1$, (b) μ=0, $\sigma^2 = 0.5$.

Table III
COMPARISION OF RMSE FOR R,X,B USING RLS AND EKF METHODS

S. No.	Gaussian noise at input source	Parameter	RMSE using RLS method	RMSE using EKF method
1	$\mu = 0$ $\sigma^2 = 0.0$	R(Ω)	0.5730	0.3775
		X(Ω)	0.6108	0.3803
		B(S)	0.5898	0.3780
2	$\mu = 0$ $\sigma^2 = 0.01$	R(Ω)	0.6031	0.3853
		X(Ω)	0.6347	0.3920
		B(S)	0.5970	0.3849
3	$\mu = 0$ $\sigma^2 = 0.1$	R(Ω)	0.6155	0.3902
		X(Ω)	0.6778	0.4052
		B(S)	0.6678	0.4602
4	$\mu = 0$ $\sigma^2 = 0.5$	R (Ω)	0.7166	0.4287
		X(Ω)	0.7058	0.4135
		B (S)	0.7785	0.5091

0885-8977 (c) 2021 IEEE. Personal use is permitted, but republication/redistribution requires IEEE permission. See http://www.ieee.org/publications_standards/publications/rights/index.html for more information.
Authorized licensed use limited to: DELHI TECHNICAL UNIV. Downloaded on February 15,2022 at 10:03:33 UTC from IEEE Xplore. Restrictions apply.

This article has been accepted for publication in a future issue of this journal, but has not been fully edited. Content may change prior to final publication. Citation information: DOI 10.1109/TPWRD.2022.3149137, IEEE Transactions on Power Delivery

Table IV
COMPARISION OF STANDARD DEVIATION OF PARAMETER ERRORS (σ_e) FOR R,X,B USING RLS AND EKF METHODS

S. No.	Gaussian noise at input source	Parameter	σ_e using RLS method	σ_e using EKF method
1	$\mu = 0$	R(Ω)	0.832	0.177
	$\sigma^2 = 0.0$	X(Ω)	0.041	0.013
		B(S)	0.788	0.178
2	$\mu = 0$	R(Ω)	1.102	0.255
	$\sigma^2 = 0.01$	X(Ω)	0.090	0.013
		B(S)	0.990	0.250
3	$\mu = 0$	R(Ω)	1.201	0.356
	$\sigma^2 = 0.1$	X(Ω)	0.803	0.045
		B(S)	1.102	0.530
4	$\mu = 0$	R (Ω)	1.504	0.482
	$\sigma^2 = 0.5$	X(Ω)	1.995	0.090
		B (S)	2.503	0.804

Table V
COMPARISION OF SNR (DB) AND RMSE FOR LINE VOLTAGE (v) ESTIMATION USING KF AND RLS METHODS

Gaussian noise at input source with μ=0	SNR using KF method	SNR using RLS method	RMSE using KF method	RMSE using RLS method
$\sigma^2 = 0$	41.080	36.975	0.6831	0.7259
$\sigma^2 = 0.1$	40.505	35.858	0.7239	0.9598
$\sigma^2 = 0.5$	37.508	35.192	0.8712	1.0128
$\sigma^2 = 1.0$	33.877	32.687	0.9549	1.2139

approximately Gaussian and further, when the noise variance is small and the signals are passed through nonlinearly then the output signals equal approximately non random quantity plus small Gaussian fluctuations $i.e.$

$$\boldsymbol{f}(x(t)) \ll \boldsymbol{f}(\mathbb{E}x(t)+\delta x(t)) \simeq \boldsymbol{f}(\mathbb{E}x(t))+\boldsymbol{f}^{'}(\mathbb{E}x(t))\delta x(t) \tag{129}$$

So that $\boldsymbol{f}(x(t))$ can be treated as being approximately Gaussian as the EKF represents a good approximation of the KF which has good convergence results.

2) State and measurement model equations are:-

$$\mathbf{x}_{n+1} = \boldsymbol{f}(\mathbf{x}_n) + \mathbf{w}_{n+1} \quad , \mathbf{x}_n \in \mathbb{R}^{d\times 1} \tag{130}$$

$$\mathbf{z}_n = \boldsymbol{h}(\mathbf{x}_n) + \mathbf{v}_n \tag{131}$$

Consider the EKF

$$\hat{\mathbf{x}}_{n+1|n} = \boldsymbol{f}(\hat{\mathbf{x}}_{n|n}) \tag{132}$$

$$\hat{\mathbf{x}}_{n+1|n+1} = \hat{\mathbf{x}}_{n+1|n} + \boldsymbol{K}_{n+1}(\mathbf{z}_{n+1} - \boldsymbol{h}(\hat{\mathbf{x}}_{n+1|n})) \tag{133}$$

$$= \boldsymbol{f}(\hat{\mathbf{x}}_{n|n}) + \boldsymbol{K}_{n+1}(\boldsymbol{h}(\mathbf{x}_{n+1}) - \boldsymbol{h}(\hat{\mathbf{x}}_{n+1|n}) + \mathbf{v}_{n+1}) \tag{134}$$

$$= \boldsymbol{f}(\hat{\mathbf{x}}_{n|n}) + \boldsymbol{K}_{n+1}(\boldsymbol{h}(\hat{\mathbf{x}}_{n+1|n} + \mathbf{e}_{n+1|n}) - \boldsymbol{h}(\hat{\mathbf{x}}_{n+1|n}) + \mathbf{v}_{n+1}) \tag{135}$$

$$\simeq \boldsymbol{f}(\hat{\mathbf{x}}_{n|n}) + \boldsymbol{K}_{n+1}(\boldsymbol{h}^{'}(\mathbf{x}_{n+1|n})\mathbf{e}_{n+1|n} + \mathbf{v}_{n+1}) \tag{136}$$

$$\mathbf{e}_{n+1|n} = \mathbf{x}_{n+1} - \hat{\mathbf{x}}_{n+1|n} \simeq \boldsymbol{f}(\mathbf{x}_n) + \mathbf{w}_{n+1} - \boldsymbol{f}(\hat{\mathbf{x}}_{n|n}) \tag{137}$$

So

$$\mathbf{e}_{n+1|n+1} = \mathbf{x}_{n+1} - \hat{\mathbf{x}}_{n+1|n+1} \tag{138}$$

$$= \boldsymbol{f}(\hat{\mathbf{x}}_{n|n} + \mathbf{e}_{n|n}) + \mathbf{w}_{n+1} - \hat{\mathbf{x}}_{n+1|n+1} \tag{139}$$

$$\simeq \boldsymbol{f}^{'}(\hat{\mathbf{x}}_{n|n})\mathbf{e}_{n|n} + \mathbf{w}_{n+1}$$

$$-\boldsymbol{K}_{n+1}(\boldsymbol{h}^{'}(\boldsymbol{f}(\hat{\mathbf{x}}_{n|n}))(\boldsymbol{f}^{'}(\hat{\mathbf{x}}_{n|n})\mathbf{e}_{n|n} + \mathbf{w}_{n+1}) + \mathbf{v}_{n+1}) \tag{140}$$

or

$$\mathbf{e}_{n+1|n+1} \approx \boldsymbol{f}^{'}(\hat{\mathbf{x}}_{n|n}) - \boldsymbol{K}_{n+1}\boldsymbol{h}'(\boldsymbol{f}(\hat{\mathbf{x}}_{n|n}))\boldsymbol{f}^{'}(\hat{\mathbf{x}}_{n|n})\mathbf{e}_{n|n}$$

$$+(\boldsymbol{I} - \boldsymbol{K}_{n+1}\boldsymbol{h}^{'}(\boldsymbol{f}(\hat{\mathbf{x}}_{n|n})))\mathbf{w}_{n+1} - \boldsymbol{K}_{n+1}\mathbf{v}_{n+1} \tag{141}$$

Suppose the nominal value of the state estimator $\hat{\mathbf{x}}_{n|n}$ is $\hat{\mathbf{x}}_0$ and the error covariance matrices $\boldsymbol{P}_{n+1|n}$ and $\boldsymbol{P}_{n|n}$ have converged to some constant values to the $\boldsymbol{K}_{n+1} \rightarrow \boldsymbol{K}_0$, Then the above recursion can be cast in the form (with $\mathbf{e}_n = \mathbf{e}_{n|n}$):-

$$\mathbf{e}_{n+1} \approx (\boldsymbol{I} - \boldsymbol{K}_0\boldsymbol{h}^{'}(\boldsymbol{f}(\hat{\mathbf{x}}_0)))\boldsymbol{f}^{'}(\hat{\mathbf{x}}_0)\mathbf{e}_n$$

$$+(\boldsymbol{I} - \boldsymbol{K}_0\boldsymbol{h}^{'}(\boldsymbol{f}(\hat{\mathbf{x}}_0)))\mathbf{w}_{n+1} - \boldsymbol{K}_0\mathbf{v}_{n+1} \tag{142}$$

It is clear that $\mathbf{e}_n \rightarrow 0$ approximately if the maximum magnitude eigenvalue of the matrix $(\boldsymbol{I} - \boldsymbol{K}_0\boldsymbol{h}^{'}(\boldsymbol{f}(\hat{\mathbf{x}}_0)))\boldsymbol{f}^{'}(\hat{\mathbf{x}}_0)$ is smaller than unity. We have ensured this during our simulations by taking nominal values of $\hat{\mathbf{x}}_0$. The maximum magnitude eigenvalue of a matrix $\boldsymbol{A}$ is also called its spectral radius and is given by $\rho(\boldsymbol{A}) = \lim_{n\rightarrow\infty} ||\boldsymbol{A}^n||^{1/n} \leq ||\boldsymbol{A}||$ where $||.||$ denotes spectral norm. Hence, we can ensure stability of the EKF by forcing $||(\boldsymbol{I} - \boldsymbol{K}_0\boldsymbol{h}^{'}(\boldsymbol{f}(\hat{\mathbf{x}}_0)))\boldsymbol{f}^{'}(\hat{\mathbf{x}}_0)|| < 1$. This can be achieved by changing the Kalman gain matrix $\boldsymbol{K}_0$ slightly. This may equivalently be achieved by estimating the error $\mathbf{e}_n$ (using a desire state) and giving a negative error feedback $(-\boldsymbol{K}_c\mathbf{e}_n)$ into the EKF so that the dynamics of $\mathbf{e}_n$ becomes (in the absence of noise):-

$$\mathbf{e}_{n+1} = (\boldsymbol{I} - \boldsymbol{K}_0\boldsymbol{h}^{'}(\boldsymbol{f}(\hat{\mathbf{x}}_0)))\boldsymbol{f}^{'}(\hat{\mathbf{x}}_0)\mathbf{e}_n - \boldsymbol{K}_c\mathbf{e}_n \tag{143}$$

with the feedback control matrix $\boldsymbol{K}_c$ being chosen so that $\rho((\boldsymbol{I} - \boldsymbol{K}_0\boldsymbol{h}^{'}(\boldsymbol{f}(\hat{\mathbf{x}}_0)))\boldsymbol{f}^{'}(\hat{\mathbf{x}}_0) - \boldsymbol{K}_c) < 1$. Further denoting

$$\boldsymbol{A} = (\boldsymbol{I} - \boldsymbol{K}_0\boldsymbol{h}^{'}(\boldsymbol{f}(\hat{\mathbf{x}}_0)))\boldsymbol{f}^{'}(\hat{\mathbf{x}}_0) - \boldsymbol{K}_c \tag{144}$$

$$\boldsymbol{B}_1 = \boldsymbol{I} - \boldsymbol{K}_0\boldsymbol{h}^{'}(\boldsymbol{f}(\hat{\mathbf{x}}_0)) \tag{145}$$

$$\boldsymbol{B}_2 = -\boldsymbol{K}_0 \tag{146}$$

We can write the estimation error evolution equation in the presence of noise as

$$\mathbf{e}_{n+1} = \boldsymbol{A}\mathbf{e}_n + \boldsymbol{B}_1\mathbf{w}_{n+1} + \boldsymbol{B}_2\mathbf{v}_{n+1} \tag{147}$$

which gives to noise contribution to $\mathbf{e}_n$ as

$$\mathbf{e}_n = \sum_{k=0}^{n-1} \boldsymbol{A}^{n-k-1}(\boldsymbol{B}_1\mathbf{w}_{k+1} + \boldsymbol{B}_2\mathbf{v}_{k+1}) \tag{148}$$

0885-8977 (c) 2021 IEEE. Personal use is permitted, but republication/redistribution requires IEEE permission. See http://www.ieee.org/publications_standards/publications/rights/index.html for more information.
Authorized licensed use limited to: DELHI TECHNICAL UNIV. Downloaded on February 15,2022 at 10:03:33 UTC from IEEE Xplore. Restrictions apply.

This article has been accepted for publication in a future issue of this journal, but has not been fully edited. Content may change prior to final publication. Citation information: DOI 10.1109/TPWRD.2022.3149137, IEEE Transactions on Power Delivery

which has variance of

$$\mathbb{E}[||\mathbf{e}_n||^2] = \sum_{k=0}^{n-1} T_r[\boldsymbol{A}^{n-k-1}(\boldsymbol{B}_1\boldsymbol{Q}\boldsymbol{B}_1^T + \boldsymbol{B}_2\boldsymbol{R}\boldsymbol{B}_2^T)\boldsymbol{A}^{T(n-k-1)}] \tag{149}$$

which is bounded above by

$$d\sum_{k=0}^{n-1} ||\boldsymbol{A}||^{2(n-k-1)}||\boldsymbol{B}_1\boldsymbol{Q}\boldsymbol{B}_1^T + \boldsymbol{B}_2\boldsymbol{R}\boldsymbol{B}_2^T||$$

$$= d\left[\frac{1-||\boldsymbol{A}||^{2n}}{1-||\boldsymbol{A}||}\right]||\boldsymbol{B}_1\boldsymbol{Q}\boldsymbol{B}_1^T + \boldsymbol{B}_2\boldsymbol{R}\boldsymbol{B}_2^T|| \tag{150}$$

are assuimg stablity so that $||\boldsymbol{A}|| < 1$, we get

$$\lim_{n\to\infty} \mathbb{E}[||\mathbf{e}_n||^2] \leq \frac{d}{1-||\boldsymbol{A}||}||\boldsymbol{B}_1\boldsymbol{Q}\boldsymbol{B}_1^T + \boldsymbol{B}_2\boldsymbol{R}\boldsymbol{B}_2^T|| \tag{151}$$

3) Our estimation show that the upper bound is very small as compared to $||\hat{\mathbf{x}}_{n|n}||^2$ so that noise does not significantly affect the convergence.
4) Inductance of the line is less prone to noise than the R, G values for the following reason. The line equation in the frequency domain are

$$\frac{d}{dz}V(w,z) = -(R+jwL)I(w,z) + W_v(w,z) \tag{152}$$

Owing to the factor of w in the numerator and w^2 in the denominator in the expression for $\hat{L}$, it is clear that if we operate at high frequencies, $\hat{L}$ will have a smaller variance related to L^2, as compared to that of $\hat{R}$ relative to R. Specially, substituting for $V^{'}(\omega,z)$ is the expression for $\hat{R}$, $\hat{L}$ gives

$$\hat{R} = \left[\frac{\sum \mathrm{Re}[\overline{I(w,z)}((R+jwL)I(w,z)+E_v(w,z))]}{\sum |I(w,z)|^2}\right] \tag{153}$$

$$= R + \left[\frac{\sum |I(w,z)|^2 \,\mathrm{Re}[\overline{I(w,z)}E_v(w,z)]}{\sum |I(w,z)|^2}\right] \tag{154}$$

$$\hat{L} = \left[\frac{\sum w\,\mathrm{Im}[\overline{I(w,z)}((R+jwL)I(w,z)+E_v(w,z))]}{\sum w^2|I(w,z)|^2}\right] \tag{155}$$

equivalently

$$\sum_{w,z} \mathrm{Re}[\overline{I(w,z)}V^{'}(w,z)] = \hat{R}\sum_{w,z}|I(w,z)|^2 \tag{156}$$

and

$$\sum_{w,z} w\,\mathrm{Im}[\overline{I(w,z)}V^{'}(w,z)] = \hat{L}\sum_{w,z} w^2|I(w,z)|^2 \tag{157}$$

$$\hat{R} = \left[\frac{\sum_{w,z} \mathrm{Re}[\overline{I(w,z)}V^{'}(w,z)]}{\sum_{w,z}|I(w,z)|^2}\right] \tag{158}$$

$$\hat{L} = \left[\frac{\sum_{w,z} w\,\mathrm{Im}[\overline{I(w,z)}V^{'}(w,z)]}{\sum_{w,z} w^2|I(w,z)|^2}\right] \tag{159}$$

$$= L + \left[\frac{\sum w\,\mathrm{Im}[\overline{I(w,z)}E_v(w,z)]}{\sum w^2|I(w,z)|^2}\right] \tag{160}$$

So,

$$Var(\hat{R}-R) \approx \sigma^2_{E_v}/\sum |I(w,z)|^2 \tag{161}$$

$$Var(\hat{L}-L) \approx \sigma^2_{E_v}/\sum w^2|I(w,z)|^2 \tag{162}$$

where $E_v(w,z)$ is white noise with

$$\mathbb{E}[E_v(w,z)\overline{E_v(w',z')}] = \sigma^2_{E_v}\delta_{ww'}\delta_{zz'} \tag{163}$$

Thus,

$$\frac{Var(\hat{R}-R)}{R^2} \ll \frac{Var(\hat{L}-L)}{L^2} \tag{164}$$

when w varies over high frequencies for which $wL \gg R$.

VIII. Conclusions

In this work, KF and EKF have been applied for state and parameter estimation of non-uniform transmission line. For this, stochastic based state equations are derived using Telegrapher's equation for transmission line. Measurement equation is formed and measurements for estimation purpose have been obtained by solving the eigenvalue problem. Sparse matrix factorization using Kronecker product for Fourier unitary transform ease the mathematical implementation by providing compact representation. The state and parameters estimated using KF and EKF have been compared with RLS method. As the process noise and measurement noise are taken into account by KF and EKF, they present better estimation than RLS.

References

[1] S. M. Ghiasi, M. Abedi and S. H. Hosseinian, "A new approach for the estimation of transient voltage profile along transmission line," *Canadian Journal of Electrical and Computer Engineering.*, vol. 40, no. 4, pp. 295-302, 2017.

[2] R. Fan, Y. Liu, R. Huang, R. Diao and S. Wang, "Precise fault location on transmission lines using ensemble Kalman filter," *IEEE Transactions on Power Delivery.*, vol. 33, no. 6, pp. 3252-3255, 2018.

[3] C. Rakpenthai and S. Uatrongjit, "Power system state and transmission line conductor temperature estimation," *IEEE Transactions on Power Systems.*, vol. 32, no. 3, pp. 1818-1827, 2017.

[4] S. Malhara and V. Vittal, "Mechanical state estimation of overhead transmission lines using tilt sensors," *IEEE Transactions on Power Systems.*, vol. 25, no. 3, pp. 1282-1290, 2010.

[5] Y. Liu, A. S. Meliopoulos, R. Fan, L. Sun and Z. Tan, "Dynamic state estimation based protection on series compensated transmission lines," *IEEE Transactions on Power Delivery*, vol. 32, no. 5, pp. 2199-2209, 2017.

[6] P. Ramachandran, V. Vittal and G. T. Heydt, "Mechanical state estimation for overhead transmission lines with level spans," *IEEE Transactions on Power Systems.*, vol. 23, no. 3, pp. 908-915, 2008.

[7] Y. Liu, A. P. Meliopoulos, L. Sun and R. Fan, "Dynamic state estimation based protection of mutually coupled transmission lines," *CSEE Journal of Power and Energy Systems.*, vol. 2, no. 4, pp. 6-14, 2016.

[8] Y. Liu, A. S. Meliopoulos, Z. Tan, L. Sun and R. Fan, "Dynamic state estimation-based fault locating on transmission lines," *IET Generation, Transmission and Distribution.*, vol. 11, no. 17, pp. 4184-4192, 2017.

[9] Y. Liu, B. Wang, X. Zheng, D. Lu, M. Fu and T. NengLing, "Fault Location Algorithm for Non-Homogeneous Transmission Lines Considering Line Asymmetry," *IEEE Transactions on Power Delivery.*, vol. 35, no. 5, pp. 2425-2437, 2020.

[10] J. Yang, W. A. Zhang and F. Guo, "Dynamic State Estimation for Power Networks by Distributed Unscented Information Filter," *IEEE Transactions on Smart Grid.*, vol. 11, no. 3, pp. 2162-2171, 2020.

0885-8977 (c) 2021 IEEE. Personal use is permitted, but republication/redistribution requires IEEE permission. See http://www.ieee.org/publications_standards/publications/rights/index.html for more information.
Authorized licensed use limited to: DELHI TECHNICAL UNIV. Downloaded on February 15,2022 at 10:03:33 UTC from IEEE Xplore. Restrictions apply.

This article has been accepted for publication in a future issue of this journal, but has not been fully edited. Content may change prior to final publication. Citation information: DOI 10.1109/TPWRD.2022.3149137, IEEE Transactions on Power Delivery

[11] Q. Li, L. Cheng, W. Gao and D. W. Gao, "Fully Distributed State Estimation for Power System with Information Propagation Algorithm," *Journal of Modern Power Systems and Clean Energy.*, vol. 8, no. 4, pp. 627-635, 2020.
[12] I. Mohammed, S. J. Geetha, S. S. Shinde, K. Rajawat and S. Chakrabarti, "Modified Re-Iterated Kalman Filter for Handling Delayed and Lost Measurements in Power System State Estimation," *IEEE Sensors Journal.*, vol. 20, no. 7, pp. 3946-3955, 2020.
[13] H. H. Alhelou, M. E. Golshan and N. D. Hatziargyriou, "Deterministic dynamic state estimation-based optimal LFC for interconnected power systems using unknown input observer," *IEEE Transactions on Smart Grid.* vol. 11, no. 2, pp. 1582-1592, 2020.
[14] A. S. Dobakhshari, S. Azizi, M. Paolone and V. Terzija, "Ultra fast linear state estimation utilizing SCADA measurements," *IEEE Transactions on Power Systems.*, vol. 34, no. 4, pp. 2622-2631, 2019.
[15] D. Ritzmann, P. S. Wright, W. Holderbaum, B. Potter, "A method for accurate transmission line impedance parameter estimation," *IEEE Transactions on instrumentation and measurement.*, vol. 65, no. 10, pp. 2204-2213, 2016.
[16] A. Bendjabeur, A. Kouadri and S. Mekhilef, "Novel technique for transmission line parameters estimation using synchronised sampled data," *IET Generation, Transmission and Distribution*, vol. 14, no. 3, pp. 506-515, 2020.
[17] I. Tolić, K. Miličević, N. Šuvak and I. Biondić, "Non-linear least squares and maximum likelihood estimation of probability density function of cross-border transmission losses," *IEEE Transactions on Power Systems.*, vol. 33, no. 2, pp. 2230-2238, 2018.
[18] M. Yang, J. Wang, H. Diao, J. Qi, X. Han, "Interval estimation for conditional failure rates of transmission lines with limited samples," *IEEE Transactions on Smart Grid.* vol. 9, no. 4, pp. 2752-2763, 2018.
[19] M. Asprou and E. Kyriakides, "Identification and estimation of erroneous transmission line parameters using PMU measurements," *IEEE transactions on power delivery.*, vol. 32, no. 6, pp. 2510-2519, 2018.
[20] C. Wang, V. A. Centeno, K. D. Jones and D. Yang, "Transmission lines positive sequence parameters estimation and instrument transformers calibration based on PMU measurement error model," *IEEE Access.*, vol. 7, pp. 145104-145117, 2019.
[21] W. Sima, Y. Li, V. A. Rakov, Q. Yang, T. Yuan and M. Yang, "An analytical method for estimation of lightning performance of transmission lines based on a leader progression model," *IEEE Transactions on Electromagnetic Compatibility*, vol. 56, no. 6, pp. 1530-1539, 2014.
[22] G. Sivanagaraju, S. Chakrabarti and S. C. Srivastava, "Uncertainty in transmission line parameters: Estimation and impact on line current differential protection," *IEEE Transactions on Instrumentation and Measurement.*, vol. 63, no. 6, pp. 1496-1504, 2014.
[23] M. S. Halligan and D. G. Beetner, "Maximum crosstalk estimation in weakly coupled transmission lines," *IEEE transactions on electromagnetic compatibility.*, vol. 56, no. 3, pp. 736-44, 2014.
[24] P. Ren, H. Lev-Ari and A. Abur, "Tracking three-phase untransposed transmission line parameters using synchronized measurements," *IEEE Transactions on Power Systems.*, vol. 33, no. 4, pp. 4155-63, 2018.
[25] A. H. Jazwinski, "Stochastic processes and filtering theory," *Courier Corporation*, 2007.
[26] P. A. Regalia and M. K. Sanjit, "Kronecker products, unitary matrices and signal processing applications," *SIAM review*, vol. 31, no. 4, pp. 586-613, 1989.
[27] L. Kumar, V. S. Pandey, H. Parthasarathy and V. Shrimali, "Hysteresis Effects on a Non-uniform Transmission Line with Induced Quantum Mechanical Atomic Transitions," *Journal of Superconductivity and Novel Magnetism*, vol. 31, no. 5, pp. 1587-1605, 2017.
[28] O. Nelles, "Nonlinear System Identification: From Classical Approaches to Neural Networks, Fuzzy Models, and Gaussian Processes," *Springer Nature*, pp. 60-66, 2020.

0885-8977 (c) 2021 IEEE. Personal use is permitted, but republication/redistribution requires IEEE permission. See http://www.ieee.org/publications_standards/publications/rights/index.html for more information.
Authorized licensed use limited to: DELHI TECHNICAL UNIV. Downloaded on February 15,2022 at 10:03:33 UTC from IEEE Xplore. Restrictions apply.

electronics

MDPI

Review

State-of-Art Review of Traffic Light Synchronization for Intelligent Vehicles: Current Status, Challenges, and Emerging Trends

Ishu Tomar *, Indu Sreedevi and Neeta Pandey

Electronics and Communication Engineering Department, Delhi Technological University, Delhi 110042, India; s.indu@dce.ac.in (I.S.); neetapandey@dce.ac.in (N.P.)
* Correspondence: ishutomar.611@gmail.com

Abstract: The effective control and management of traffic at intersections is a challenging issue in the transportation system. Various traffic signal management systems have been developed to improve the real-time traffic flow at junctions, but none of them have resulted in a smooth and continuous traffic flow for dealing with congestion at road intersections. Notwithstanding, the procedure of synchronizing traffic signals at nearby intersections is complicated due to numerous borders. In traditional systems, the direction of movement of vehicles, the variation in automobile traffic over time, accidents, the passing of emergency vehicles, and pedestrian crossings are not considered. Therefore, synchronizing the signals over the specific route cannot be addressed. This article explores the key role of real-time traffic signal control (TSC) technology in managing congestion at road junctions within smart cities. In addition, this article provides an insightful discussion on several traffic light synchronization research papers to highlight the practicability of networking of traffic signals of an area. It examines the benefits of synchronizing the traffic signals on various busy routes for the smooth flow of traffic at intersections.

Keywords: traffic lights; intersections; synchronization; traffic management and control

check for updates

Citation: Tomar, I.; Sreedevi, I.; Pandey, N. State-of-Art Review of Traffic Light Synchronization for Intelligent Vehicles: Current Status, Challenges, and Emerging Trends. *Electronics* **2022**, *11*, 465. https://doi.org/10.3390/electronics11030465

Academic Editor: José Santa

Received: 25 December 2021
Accepted: 26 January 2022
Published: 4 February 2022

Publisher's Note: MDPI stays neutral with regard to jurisdictional claims in published maps and institutional affiliations.

Copyright: © 2022 by the authors. Licensee MDPI, Basel, Switzerland. This article is an open access article distributed under the terms and conditions of the Creative Commons Attribution (CC BY) license (https://creativecommons.org/licenses/by/4.0/).

1. Introduction

For ensuring vehicular traffic safety and consistent flow of traffic, traffic signal control and management at road junctions is a challenging problem in the transportation system. Intersections are the points where two or more routes interact with each other. Intersections are where crossroads, pedestrians, vehicles, and bikes change their direction. Intersections act as an obstruction/barrier for smooth traffic flow within the urban areas because of the large number of vehicles traveling from one place to another. This leads to traffic interruption, congestion, and poor control and management of the traffic [1,2]. The intersection delay affects the signal control logic and the travel efficiency of road users [3]. According to a study, over 10% of the traffic delays all over the world are due to the fixed traffic signal delays. It was found that over 295 million traffic hours of delay was observed on major road intersections in the United States [4]. Therefore, precise estimates of time-dependent delays are needed at junctions on metropolitan roadways for traffic control and management.

Intelligent Transportation Systems (ITS) address the complex issue of effective control and management of traffic at junctions. There should be a balance in between safe and effective traffic control at the intersections in order to allow the maximum vehicles to move through while maintaining safety [5]. Nowadays, traffic-light signaling is used to regulate traffic at crucial junctions/crossings by distributing the same green light timings to all routes [6]. The complicated architecture of traffic systems does not coordinate/link the timings of traffic signals with the average daily road traffic, which leads to congestion at the intersections. Various metropolitan cities such as New Delhi, Bangalore, and Mumbai are going through this imbalanced/uneven traffic flow scenario in cities because the majority

of working people live in the neighboring areas. The traffic imbalance is generally seen during the peak hours (morning and evening) when people drive from their jobs and residency. Numerous traffic light management systems have been developed to improve the real-time traffic flow at junctions, but none of them have resulted in real-time traffic synchronization or networking. As a result, metropolitan cities require an updated traffic signal control mechanism/technique that updates traffic signal timing and synchronizes the traffic signals at the road intersections on the basis of real-time traffic information.

For large-scale TSC, synchronization provides a number of advantages. Synchronization is not reliant on any network design or set of rules. This is perfect for network traffic management. When the system's most comparable entities synchronize, it is called synchronization. When traffic signal timing and traffic conditions at nearby intersections are comparable or matching, adaptive and smooth traffic signal coordination can be achieved.

This article provides a comprehensive survey of the TSC strategies that have been developed so far. In addition, it provides a detailed analysis of the associated research study and technology advancement status by comparing the existing techniques used for congestion control at road intersections. This article offers an insightful discussion on several traffic light synchronization research papers to highlight the practicability of networking of traffic signals of an area. It emphasizes the gaps in research, open challenges, and provides potential directions for further research in this area.

This paper's key features and contributions are as follows:

- To explore the key role of real-time traffic signal control technology in managing congestion at road junctions within smart cities.
- To summarize the benefits and implementation status of traffic light synchronization and directions for future research for networking traffic lights at intersections of roads.

This article's layout is organized in the following manner. In the beginning, we provide a brief introduction about the history and development background of TSC technology and traffic tight synchronization for intelligent vehicles, and then, the technical benefits of the current traffic light systems are discussed. Then, we compare the existing techniques used for congestion control at road intersections with the help of related work. Afterwards, the synchronization of traffic light development status is summarized and directions for future research for networking traffic lights at road intersections are suggested. Then, typical applications of traffic light networking are discussed. Finally, we conclude the whole paper.

2. Background of Traffic Signal Synchronization for Intelligent Vehicles

The development of traffic signal synchronization for intelligent vehicles is derived from the traffic light control technology. To better understand the synchronization of traffic lights concept, this section outlines the traffic light control technology and analyzes the advantages of synchronization of traffic lights.

2.1. Overview of the Traffic Signal Control Technology

The design of an intelligent traffic light control system is an active research topic. Many researchers are working on the design and development of intelligent traffic signal control systems to solve this stressful issue. Traffic lights can be synchronized as part of regional traffic control methods to enhance the system performance at coordinated junctions. New methods and advanced systems based on artificial intelligence, fuzzy logic, swarm intelligence, evolutionary algorithms [7], image processing, neural network, data fusion, and linear programming etc. have been proposed by the researchers to solve this TSC problem. Table A2 shows the categorization of existing literature on techniques used for congestion control at road intersections. Figure 1 presents the year-by-year trend of the papers published in the area between 1990 and 2021.

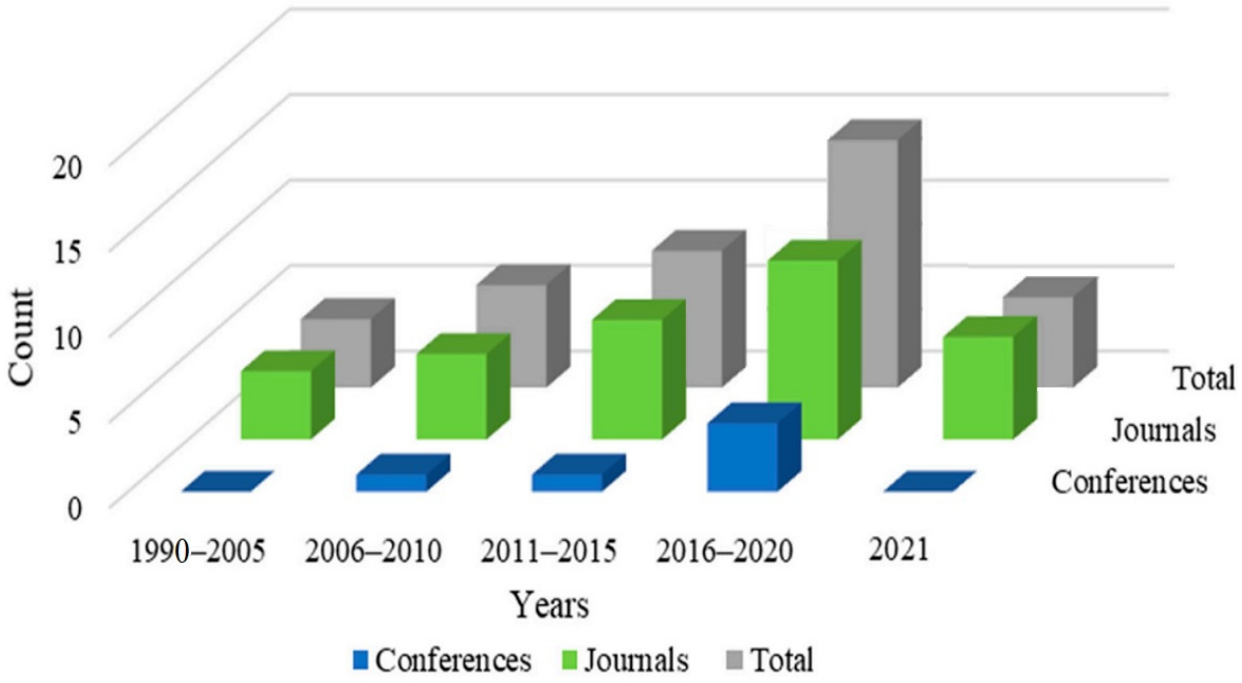


Figure 1. Number of papers published in TSC domain from 1990 to 2021.

Numerous traffic light management algorithms have been developed so far to improve the real-time traffic flow at junctions, but none of them have resulted in real-time traffic synchronization or networking. The rising trend reflects the increasing popularity in the subject and emphasizes the importance of current research. Figure 2 illustrates the taxonomy of the paper.

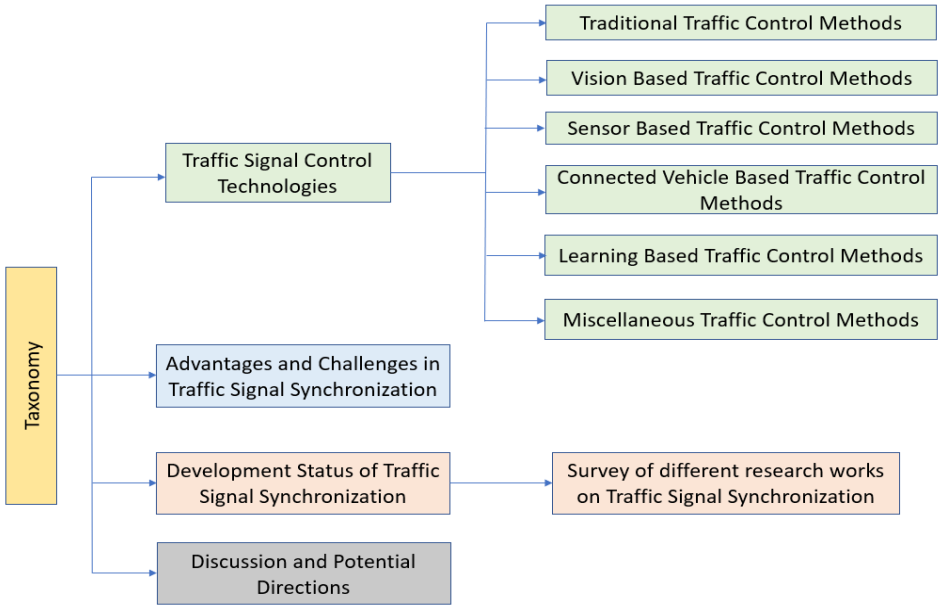


Figure 2. Taxonomy of the article.

2.1.1. Traditional Traffic Control Methods

Many researchers around the world are working in the field of ITS. It has been known for a long time that working on intelligent traffic monitoring and control systems gives various traffic-responsive management solutions that may reduce junction delays dramatically. SCOOT [8], SCATS [9], OPAC [10], RHODES [11], PRODYN [12], and MOTION [13]

are examples of adaptive traffic control systems that were designed and implemented in several cities in recent decades. SCOOT [8] and SCATS [9] are adaptive traffic control strategies. These systems use loop/magnetic detectors for gathering traffic data. However, the limitation in these methods is that they do not provide the vehicle's speed, heading, and position. While SCATS is a fully computer (microcomputer, regional computer, and central computer)-based system, it is very expensive to use. Unlike SCOOT and SCATS, PRODYN [12] is not based on cyclic settings. PRODYN addresses the global traffic problem using a two-level iterative computation structure after decomposing the enormous initial optimization problem into multiple smaller problems answered via Dynamic Programming.

These adaptive traffic systems generate a "green signal" for large vehicle flow by optimizing the network's traffic signal offset values according to the current traffic demand. Both real-time and predicted traffic arrivals are used in these systems to optimize the objective functions. These systems have significant drawbacks in terms of cost and functionality because they use cameras and loop/magnetic detectors to track vehicles. The initial implementation cost of the system is around $30,000/junction having a cost of $28,800 per mile/year [14]. Moreover, these systems need a large communication infrastructure that is capable of supporting a centralized control with a high data rate. As a result, many cities across the world have developed systems with high implementation cost.

The Webster procedure was used for fixed signal control at isolated junctions [15] for operation based on measured flows. In this method, the cycle length of every intersection is calculated using Webster's equation. The highest cycle length will act as the cycle length of the whole system. This modified demand-based strategy is viable for real-time undersaturated traffic conditions. In fact, the Traffic Response Urban Control (TUC) technique may be utilized to eliminate the predetermined static signal control sequence, which may lead to more successful outcomes than the original TUC approach. However, the issue is that this technique is quite complex.

2.1.2. Vision-Based Traffic Control Methods

A video camera was utilized to predict and monitor real-time traffic using a dynamic Bayesian networks technique in [16]. In this computationally light method, the distribution of spatial interest and spatiotemporal interest points is classified using the Gaussian mixture model (GMM), and then, the dynamic Bayesian approach is used.

Feature-based approaches [17] and neural networks [18] are also used to recognize and track vehicles coming toward an intersection. Feature-based methods track the features less sensitive to partial occlusion. This approach was ineffective for real-time TSC due to its low accuracy and large storage requirements. In these feature-based methods, binarization, rule-based logic, cameras, and road conditions are used to identify vehicles, which makes the process complex and tedious.

Indu et al. [19] proposed a simple but expensive adaptive traffic signaling system that uses video camera data to provide equal green light timings and then allocates enough time using a fair weight and optimal weight calculation algorithm.

Vehicle tracking and image segmentation algorithms become ineffective for real-time operations because of the computational complexity and longer execution time. However, some are not able to operate effectively at night or in variable weather conditions. Zheng et al. [20] use neural networks to predict the upcoming traffic volume from a 15-min daylight traffic flow on an expressway. As a result of the high complexity and memory needs, this approach is unsuitable for real-time systems.

2.1.3. Sensor-Based Traffic Control Methods

Sharma et al. [21] presented a method that assigns equal green signal duration and arrange fair lane departure at an intersection using the GPS data of the users.

Wang et al. [22] proposed a data fusion approach that collects the data on the speed, position, and direction of the vehicles approaching junctions with the help of GPS sensors

in vehicles. This method only improves the traffic flow on a road network; it does not control the traffic signal timing.

Other strategies such as detectors [23], on-board GPS, and big data technologies [24,25] are also used to monitor the arrival and departure of vehicles at a junction to reduce the congestion in urban areas. For monitoring the local traffic in a region, sensors and traffic servers are also used. Embedded technology [26] records the GPS data of vehicles and sends it to the traffic monitoring system through GSM/GPRS. This method has a very high implementation cost.

Coll et al. [27] introduced an adaptive system based on linear programming that controls the traffic lights and reduces the waiting time at intersections. This method uses the data gathered from the real-time sensors placed at every intersection.

TSC systems based on Wireless Sensor Network (WSN) have also been used at isolated intersections in [28,29]. Rida et al. [28] proposed a time-fragment based control mechanism that splits the time and calculates the percentage of green ratio. Yousef et al. [30] proposed a connected vehicle-based algorithm for isolated junctions that uses vehicle proximity for releasing vehicle platoons.

2.1.4. Connected Vehicle-Based Traffic Control Methods

Another technique to adaptive decision making is the Virtual Traffic Light (VTL) approach [31], which is a Vehicle-to-Vehicle (V2V) traffic control system with enormous potential, since it may increase traffic flow by more than 30% while eliminating the usage of expensive traffic signals. VTL makes use of V2V communication using the Signal Phase and Timing (SPaT) message and Basic Safety Message (BSM) from the Dedicated Short Range Communication (DSRC) radio for traffic management at intersections. The drawback of this approach is that it requires full penetration of DSRC technology in vehicles, which is not possible at the present time. Furthermore, V2V communications in VTL could come across non-LoS conditions, which makes rapid decision making extremely challenging [32].

A connected vehicle (CV) initiative [33,34] was established by the Virginia Department of Transportation (VDOT) to focus on different V2V and Vehicle-to-Infrastructure (V2I) applications. This program intends to lower the cost of infrastructure for roadside guidance signs and traffic lights by using DSRC technology. However, the complete penetration of the DSRC is required for the connected corridor setup.

Tonguz et al. [35] presented a DSRC-based traffic management method for road intersections. Roads with DSRC-equipped automobiles are given precedence under this system. Even if a small number of vehicles have DSRC technology, this strategy can be effective in reducing the average waiting time on each traffic light. When compared to alternative TSC systems that use detectors, sensors, and cameras, this technique provides a cost-effective solution for traffic management in urban areas by simply using DSRC Road-Side Units (RSUs).

Dresner et al. [36] describes autonomous intersection management (AIM) utilizing multiagent systems, in which drivers and junctions are considered as autonomous entities. Intersections employ a completely new reservation-based technique based on a detailed communication protocol in this mechanism.

2.1.5. Learning-Based Traffic Control Methods

Many studies have recommended using reinforcement learning (RL) to regulate traffic lights and reduce traffic congestion [37,38]. Unlike traditional TSC systems, which depend mainly on predefined models, RL may learn immediately from input as shown in Figure 3. Every junction in RL is portrayed as an agent that optimizes its input-based travel time from the surroundings when the action (i.e., the traffic lights) is set [39].

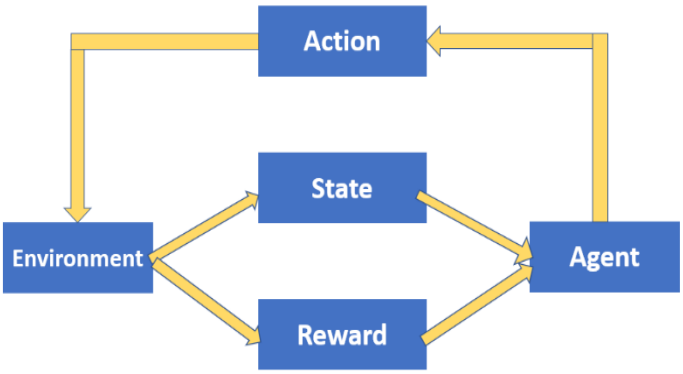


Figure 3. Reinforcement learning working procedure.

Zheng et al. [40] suggested a FRAP model based on phase competitive modeling, which achieves invariance in traffic flow flipping and rotation conditions. In complicated traffic situations and multi-junction configurations, this system discovers better solutions and delivers greater performance than prior learning methods.

To overcome the fixed traffic signal problem, ref. [41] proposes a novel MARL (Multi-agent Reinforcement Learning) approach called Co-DQL, which stands for co-operative double Q-learning. The overestimation problem that affects traditional independent Q-learning is avoided with Co-DQL. TSC simulators are used to test various traffic flow conditions. MARL provides a new reward allocation mechanism for boosting agent stability and resilience.

Joo et al. [42], WeiHua et al. [43], and Zhang et al. [44] investigated some recent improvements in RL techniques that may be applied to solve difficulties with traffic signal regulation. They describe the usage of PPO, A2C, and ACKTR algorithms to handle the problem of partial vehicle detection.

For TSC, Zhang et al. [45] proposes a deep Q-learning approach with partial vehicle identification using DSRC. This system has the benefit of being able to identify cars utilizing different detection technologies such as LTE/5G, BLE 5.0, and RFID.

2.1.6. Miscellaneous Traffic Control Methods

Dezani et al. [46,47] used genetic algorithm (GA) to optimize traffic signals in real time and determine the optimal paths for cars. With the use of a basic neighborhood algorithm, Sabar et al. [48] enhanced GA by using a local search strategy that lowers the average delay in traffic even more than feasible.

In a nine-junction network, Li and Sun [49] suggested a multifunctional GA for traffic optimization. However, this method did not use real-time traffic data.

For traffic light scheduling, refs. [50–52] employ a particle swarm optimization (PSO) technique to regulate traffic lights to minimize the waiting time at intersections so that vehicles can reach their destination in the minimum feasible time. Other swarm intelligence algorithms used for TSC include Ant Colony Optimization [53,54] and Harmony search [55,56].

Milanés et al. [57] presented a V2V communication-based method for reducing traffic congestion at intersections by utilizing the speed and location of autonomous vehicles.

Bi et al. [58,59] presented a type-2 FLC system to solve the coordination and complicated uncertainty issues in heavy but organized traffic. (based on fuzzy and Q learning). Firdous et al. [60,61] developed a real-time control system based on fuzzy logic to reduce vehicle waiting times at intersections.

3. Advantages of Synchronizing the Traffic Lights

The primary goals of TSC technology is to improve traffic safety and travel quality as well as lower the pollution caused by vehicles. However, due to the rapid growth of numerous issues such as the increase in the number of vehicles on the road, traffic jams,

and increased pollution over the last 20 years, even emerging countries have relied on the most basic traffic signal control technologies.

Traffic congestion has been a serious concern in metropolitan areas as vehicular traffic has increased. The problem is even worse at road intersections, where pre-timed traffic signals produce delays, increased vehicle activity costs, and air pollution. Time delays are least caused in roadways and rural areas; they are frequently observed in metropolitan cities. Consequently, metropolitan traffic shapes the concerned area of research on delays caused for vehicles and pedestrians. The basic objective of signalized junctions is to decrease the problems that are experienced more at unsignalized crossing points and rotaries and furthermore to give an equivalent chance to all vehicles to cross the intersection.

To address these concerns, traffic light synchronization is a technique in which a vehicle traveling along one side of the road at a specific speed can continue to the opposite end of the road indefinitely by obtaining the maximum number of green lights at the intersections.

4. Development Status of Synchronization of Traffic Lights

The synchronization of traffic signals across a city is supported by traffic light control frameworks. When automobiles pass through a junction network, these frameworks lower the amount of time they have to wait. Despite the previous research in this domain over the last five decades, improved traffic signal control framework administration is still required.

To enhance traffic flow efficiency at high-density junctions, Hu et al. [62] employed a long green and long red (LGLR) technique for synchronizing the traffic lights of an area. For smoothening the traffic flow across the city, ref. [63] employed a real-time system for the synchronization of traffic lights using multiagent fuzzy logic and the Q-learning approach.

Amogh et al. [64] presented a method for improving traffic synchronization efficiency by dynamically modifying timing settings. This system uses traffic cameras to obtain vehicle density at each intersection and then uses OpenCV to conduct operations on the pictures.

Khan et al. [65] proposes a self-organized TSC system based on sensors. It improves the efficiency of traffic flow and reduces the waiting time at intersections. In comparison to traditional traffic management systems, this technology gives more information and prioritizes the road with a large number of cars at an intersection first. However, this approach does not synchronize the traffic lights of all the intersections.

V2I connectivity was utilized in [66] for the networking of junctions and other road signs. It is used to transmit information on infrastructure such as speed restrictions, road alterations, and traffic light information to smart cars.

Sirikham et al. [67] presented a traffic light synchronization system that used two control boards, a sender and receiver. These control boards use the NodeMCU V.2 (2.4 GHz WiFi) to synchronize the control signals by ESP-NOW protocol, as shown in Figure 4. However, this system works only for single-lane traffic control.

Kumar et al. [68] proposed a synchronization method for two traffic signals using the Long Range (LoRa) module. It uses the time division algorithm to get the traffic information so that the rerouting of vehicles can be done during the peak hours. This concept helps the vehicles reach their destination in the shortest possible time by taking the fastest route.

A synchronization scheme for traffic light controllers based on an explicit finite state model (FSM) is presented in [69]. FSM is modeled using Verilog HDL, and the coding is done using Xilinx Spartan-6 XC6LX16-CS324 FPGA. The machine is merely simulated with six states, which are selected using the traffic control method. Each state provides the appropriate delay, and the requisite traffic signals are turned ON/OFF for that delay. For example, just two routes are picked, and a control algorithm controls the traffic lights on those roads. This study introduced a flexible architecture that uses a clock divider to give a delay in a certain state and discusses the difficulty of modeling the FSM. The topic of selecting a state-encoding technique was also discussed.

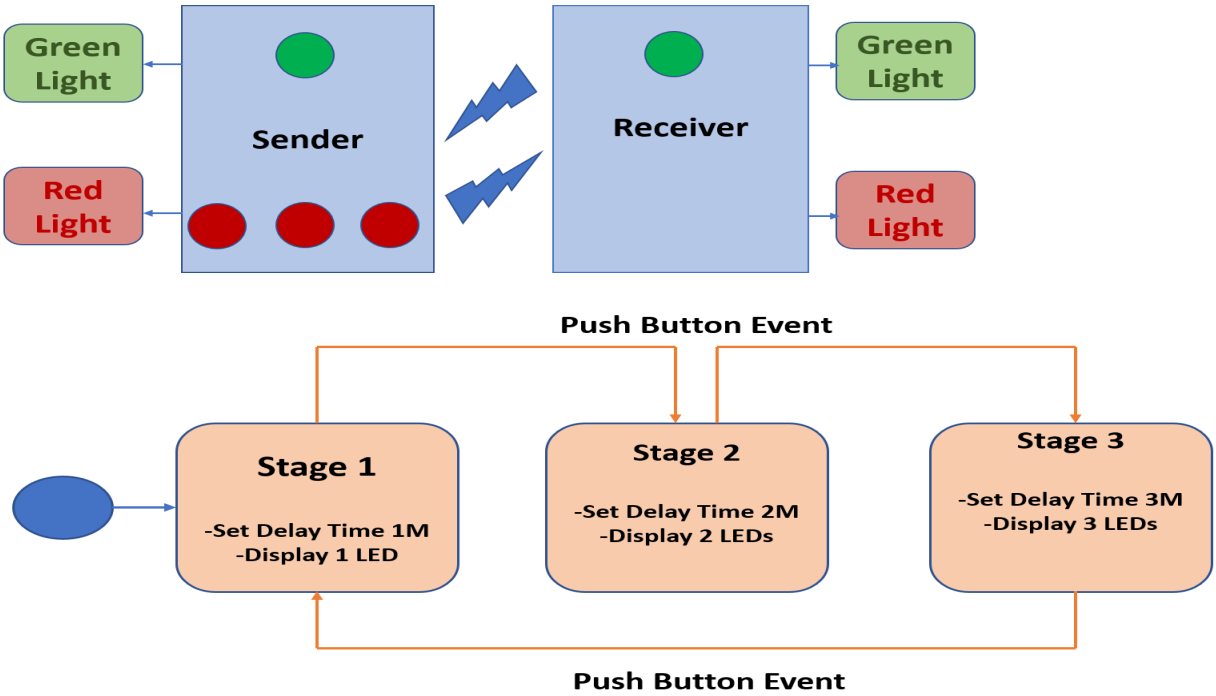


Figure 4. Overview of Single-lane traffic control using NodeMCU V.2 [67].

A self-synchronization mechanism for aerial vehicles and air traffic control (ATC) systems was introduced in [70] for avoiding collision. It assists in obtaining a unique path for each aircraft in order to reduce conflict, but if this is not possible, the system gives an optimum option to utilize other shared resources.

An adaptive, flexible, and robust distributed TSC method based on spontaneous synchronization was introduced in [71], which occurs when local interaction leads to a stable state. In this method, every junction is represented by a phase-oscillator model. The global coordination is achieved by synchronizing these phase oscillators to maintain the platoons flow.

Adacher et al. [72,73] proposed a distributed algorithm for solving the synchronization problem of urban traffic signals. They calculated the weighted sum of delays at signalized intersections by CTM-UT; i.e., (Cell Transmission Model for Urban Traffic) via simulation. A surrogate method (SM) based on an online and stochastic control scheme has been used to synchronize the traffic signals.

An IoT-based traffic signal synchronization method was proposed in [74] to reduce the traffic congestion at road intersections. This method allows the vehicles to travel a long distance by minimizing the number of STOP and GO occurrences by adapting the traffic light phases at the road intersections (Figure 5). This method reduces the average travel time up to 39% using traffic simulator SUMO in comparison to the other fixed time and non-synchronized traffic control strategies.

Nesmachnow et al. [75] introduced the synchronization of traffic lights using a parallel evolutionary algorithm for Bus Rapid Transit systems by considering various features such as real maps and mobility data and analyzing these features for optimization. This method improves the average speed of public transport up to 15.3% and other vehicles up to 24.8%. Using this method, different priorities can be assigned to buses and other vehicles using a multi-objective optimization analysis.

A model for synchronizing the traffic lights at road intersections is presented in [76]. This method uses a hybrid metaheuristic approach that combines variable neighborhood search and Tabu search into one algorithm. The method incorporates a memory structure into an iterative local search, allowing for a wider range of solutions. Certain changes such

as modification of a mixed integer linear model's constraints and the generalization of some bounds for integer variables were made to the MAXBAND in this algorithm.

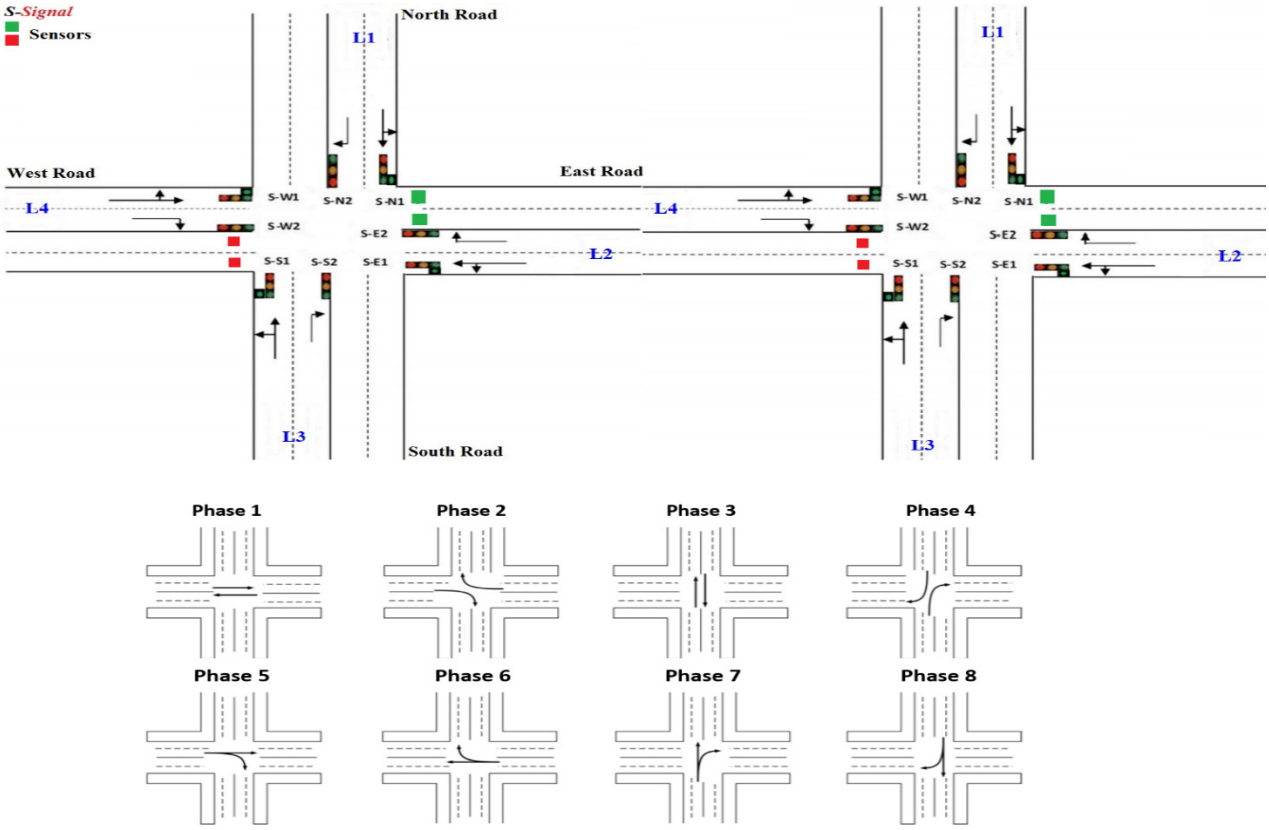


Figure 5. IoT-based mechanism for traffic signal synchronization using sensor deployment on adjacent junctions [74].

In [77], the decentralized spatial decomposition of a network has been used for the synchronization of traffic signals at the road junctions. This method uses the platoon model to calculate the weighted sum of delays induced by signalized crossings. To get a spatial breakdown of the network, distributed consensus approaches were utilized. Using the distributed communication architecture, each semaphore distributes information with its neighbors in a totally dispersed manner, hence removing the need for a central authority. A surrogate technique is used for synchronizing the traffic signals given the subnetwork.

A self-synchronization paradigm for connected vehicles in traffic networks has been used in [78] to solve the coordination problem at junctions. For safe spacing between cars moving on the same route, coordinating safe crossing at junctions with competing flows, a multilayer decentralized control method is utilized. The Kuramoto equation is used to synchronize the phase and frequency of the network's agents (vehicles). This approach considered the vehicles as oscillating agents instead of the traffic lights. This technique is classified as a decentralized approach since it is interconnected to achieve network-wide synchronization. It combines the advantages of coordinating vehicle crossings at particular crossroads with synchronizing flow from nearby junctions in this way.

In [79], floating car data (FCD) was used to synchronize the traffic signals at intersections. This approach used the penetration rate of "instrumented" vehicles to obtain synchronization in adaptive traffic light systems based on floating car data (FCDATS) in competition cooperation. This technology increases the traffic safety and energy efficiency of transportation systems.

Yang et al. [80] used cellular automaton for synchronizing traffic signals by building a network model of two intersections. By changing the signal duration and green time offset,

the synchronization of the signals is investigated, and results are obtained in MATLAB. An optimal signal scheme reduces the overall delay and increases the traffic flow at road junctions. Next, the network's essential features, such as fundamental and time–space diagrams, are addressed.

Li et al. [81] introduced a time synchronization method among VANET devices, claiming that On-Board Units (OBUs) can synchronize with other OBUs or RSUs on their own initiative. This technique lowers the synchronization error to less than 0.3 ms when there is no center node in the Basic Service Set, which fulfills the accuracy criterion of the VANET specification. In the Basic Safety System (BSS), a time-synchronization mechanism is introduced in which there is no central node, resulting in a more stable network. This method can achieve nanosecond precision while avoiding estimate errors. This method can correctly implement time synchronization in a BSS. In addition, there is a topology for the whole VANET in order to achieve time synchronization among RSUs. As a result, the amount of handoff done by OBUs can be drastically decreased. It can also greatly increase the system's stability.

A survey of the synchronization techniques is presented in [82], which addressed various situations and current cellular network generations while reviewing synchronization standards and approaches for V2V and Device-to-Device (D2D) enabled cellular networks. They looked at the major channels, entities, and signals that V2V and D2D enabled cellular networks employ for synchronization in various circumstances. Furthermore, to highlight current developments and give future perspectives, the focus is on the synchronization in V2V and Vehicle to Everything (V2X).

Du et al. [83] presented a rule-based algorithm for V2X speed synchronization at road junctions. Vehicles entering from separate lanes form a virtual platoon. When traffic is light, this system allows for fewer unnecessary stops, resulting in energy savings and an increase in average speed. As a result, speed synchronization is no longer effective, as the volume of traffic increases and cars must come to a halt. Virtual platooning is expanded here by introducing some principles that enable a virtual platoon to dynamically modify its whole behavior in response to traffic flow growth while maintaining safety. This technique is extremely efficient in boosting average speed while maintaining the intersection's high capacity.

The significance of nearby junctions has not been studied in the above cited research works. The categorization of existing literature on synchronization of traffic signals is shown in Table A1 (Appendix A). These works are restricted to one intersection only, which makes the problem appearance more complex and extensive in scope. More efforts should be made in order to obtain maximal modeling, control, and monitoring of several synchronized junctions.

5. Discussion and Potential Directions

The primary goals of TSC technology research were to improve traffic safety, improve trip quality, and minimize pollution emissions. Traffic congestion has been a serious concern in metropolitan areas as vehicular traffic has increased. The problem is even worse at road intersections, where pre-timed traffic signals produce delays, increased vehicle activity costs, and air pollution. Delay is caused by the status of one light at a crossroad, which impacts the flow of traffic at neighboring intersections also. Additionally, the traditional traffic system does not account for mishaps, road closures, or vehicle breakdowns, which contribute to travel delays. Furthermore, a major issue is the seamless movement of emergency vehicles with greater demands, such as emergency vehicles, ambulances, fire brigade, police, and VIPs, through crossing points. As a result, the regular traffic system must be upgraded in order to alleviate traffic congestion and minimize waiting times and travel time as well as maximize vehicle safety, efficiency, and economic benefits [84].

The majority of traffic monitoring technologies at junctions rely on high-cost cameras and sensors that are difficult to install and maintain. Computationally intensive traffic signal control technologies are utilized at road junctions. As a result, real-time signal

control tactics at road crossings must be enhanced in order to eliminate traffic congestion. A massive disadvantage is that the traditional methods do not synchronize the traffic signals of a region.

To address these concerns, traffic light synchronization is a technique in which a vehicle traveling along one side of the road at a specific speed can continue to the opposite end of the road indefinitely by obtaining the maximum number of green lights at all the intersections. Traffic signal synchronization is required so that the green light cycles for a series of junctions can be synchronized, enabling the greatest number of automobiles to pass through while avoiding waits and delays.

Synchronization can be done at different levels. Figure 6 shows traffic signal synchronization at level I and level II. We can define the levels of synchronization within an area. One will be the inner circle and another will be the outer circle, where the inner circle reflects peer junctions of level I and the outer circle reflects the peer junctions of level II. Level I consists of the nearest neighboring junctions, and level II consists of the junctions falling in the external area. The intelligence at level II also takes into consideration the density of the adjacent junctions. These levels of synchronization will help in reducing the congestion at neighboring intersections. In this way, the system will become smart when it is connected to the server.

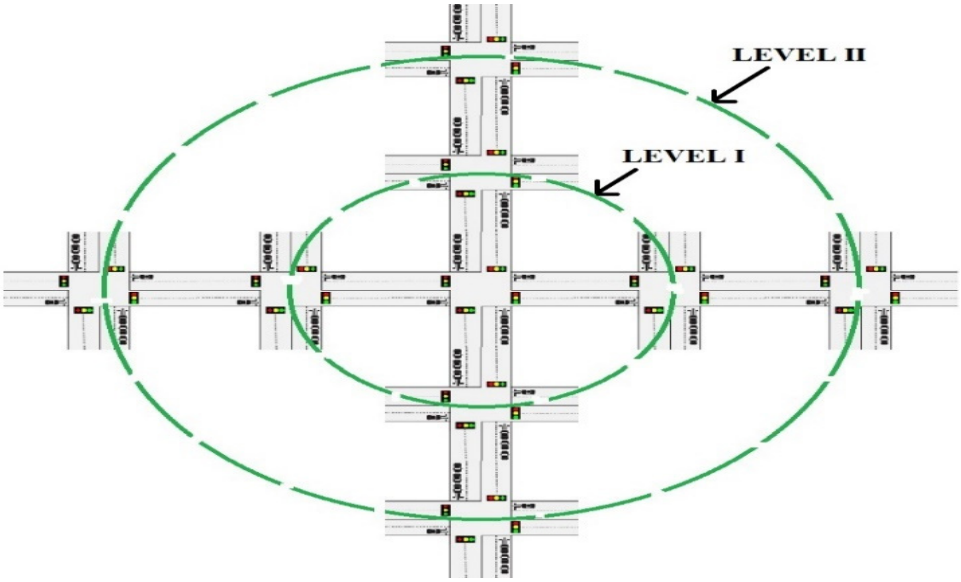


Figure 6. Levels of synchronization.

The designed traffic signal synchronization framework can work efficiently with any technology, whether it is DSRC, image processing, sensors, or any other technology that is used to collect traffic density at intersection. With minor changes to the current system, new junctions can also be incorporated for synchronization. In this way, it is possible to extend this system for covering all the intersections of a city or state, thus moving toward a well-coordinated and lucid method of traffic control.

6. Conclusions

Traffic signal synchronization for intelligent vehicles is a revolutionary innovative technology with exceptional potential in the intelligent transportation systems. Hence, this article provides a comprehensive survey on traffic light synchronization techniques for intelligent vehicles. First of all, we outline the different traffic light control technologies used for congestion control at intersections. Then, typical applications of synchronization of traffic signals are discussed. Next, we summarize the development status of synchronization of traffic signals for intelligent vehicles by surveying all the research works on traffic signal synchronization. In addition, we discuss many emerging and potential directions of

traffic light networking. This study will provide researchers with the basis for more understanding and investigation of the synchronization of traffic lights for intelligent vehicles.

Author Contributions: I.T.: Lead author of manuscript (Corresponding Author), Conceptualization and methodology, writing—original draft preparation, investigation, editing; I.S. and N.P.: Second author, research design, guidance, and reviewing. All authors have read and agreed to the published version of the manuscript.

Funding: This research received no external funding.

Data Availability Statement: Data sharing not applicable to this article as no datasets were generated or analyzed during the current study.

Acknowledgments: This work has been carried out under the supervision of Indu Sreedevi and Neeta Pandey, Department of ECE, Delhi Technological University, and I (Ishu Tomar) pay immense gratitude toward my guides for enlightening me through the process. In addition, I (Ishu Tomar) would like to acknowledge the financial assistantship provided by Delhi Technological University.

Conflicts of Interest: The authors declare that they have no conflict of interest.

Appendix A

Table A1. Categorization of existing literature on synchronization of traffic signals.

Reference Number	Objective	Strategies Used	Disadvantages	Comments
[62]	Traffic light synchronization strategy for saturated road networks	Long green and long red method for highly saturated road networks	Not suitable to the undersaturated HGRN	• Control the arrival and departure of queues • Increase the efficiency of traffic flows to the maximum level at signalized junctions
[63]	To synchronize traffic signals	Multiagent fuzzy logic and Q-learning		• Fully distributed multiagent architecture with no central supervising or synchronizing agent • Coordination between agents through communication of decision data
[64]	Traffic signal synchronization with dynamic timer value	Image processing and Raspberry Pi in synchronization with cloud	• Camera implementation cost is very high • System implemented on a small scale (in the laboratory, not in real-life scenarios) • Conflicts can arise when two emergency vehicles arrive on opposite sides of a junction at the same time	• Obtains the vehicle density using traffic cameras on every side of the junction using image processing on OpenCV • Provides priority to emergency vehicles • Increased efficiency in with dynamic change in timer value
[65]	Self-organized traffic light control based on sensors	• Pressure sensors to detect vehicles approaching the intersection • Microcontroller and Zigbee module to transfer the information to signal controller	No synchronization of traffic signals	Increases traffic flow efficiency and reduce the waiting time at intersections

Table A1. *Cont.*

Reference Number	Objective	Strategies Used	Disadvantages	Comments
[67]	Wireless traffic light synchronization system	• Uses two control boards (sender and receiver) • Control boards use NodeMCU V.2 (2.4GHz WiFi) for synchronization of control signals by ESP-NOW protocol	For single-lane traffic control only	• Uses wireless communication • Increased safety
[68]	Rerouting and synchronization of traffic	Using the Long Range (LoRa) module	Synchronization for two traffic signals only	• Congestion control at intersection by rerouting vehicles • Vehicles reach their destination in the shortest possible time by taking the fastest route
[69]	Synchronization scheme for traffic light controller	• Based on explicit finite state model (FSM) • FSM modeled using Verilog HDL and coding is done using Xilinx Spartan-6 XC6LX16- CS324 FPGA	Difficulty of modeling the FSM	Flexible architecture that uses a clock divider to give a delay in a certain state
[71]	Distributed traffic signal control method based on spontaneous synchronization	• Every junction is represented by a phase-oscillator model • These oscillators are synchronized to get the desired global coordination	Mathematical complexity	• Local interaction leads to a stable state • Maintain the platoons flow
[72,73]	Distributed approach for synchronizing traffic signals	CTM-UT i.e., (Cell Transmission Model for Urban Traffic) via simulation	Computational complexity	Surrogate method (SM), based on an online and stochastic control scheme, used for synchronizing the traffic signals
[74]	IoT-based traffic signal synchronization method	Uses magnetic sensors as the main IoT sensing technology	Not suitable for all kinds of road networks	Reduces the average travel time up to 39% using the road traffic simulator SUMO
[75]	Traffic signals synchronization for Bus Rapid Transit systems	Parallel evolutionary algorithm	In the context of Bus Rapid Transit systems	• Improves the average speed of public transport up to 15.3% and other vehicles up to 24.8% • Different priorities can be assigned to buses and other vehicles using a multi-objective optimization analysis
[76]	Model for synchronizing the traffic lights at road intersections	Hybrid metaheuristic approach that combines variable neighborhood search and Tabu search	Mathematical and computational complexity	Flexible and robust approach

Table A1. *Cont.*

Reference Number	Objective	Strategies Used	Disadvantages	Comments
[77]	Decentralized spatial decomposition of network for synchronization of traffic signals at the road junctions	Uses platoon model to calculate the weighted sum of delays induced by signalized crossings	More robust to failure	Distributed communication architecture for networking of traffic lights
[79]	To synchronize the traffic signals at intersections	Using floating car data (FCD)	Only a beginning step toward addressing the synchronization problem; need for more comprehensive optimization algorithms for general cases	Increases the traffic safety and energy efficiency of transportation systems
[80]	Traffic signal synchronization in a small urban road network	Cellular automation	Synchronization for two traffic signals only	Minimize total delay and maximize the flow
[82]	Survey of the synchronization techniques	Highlight current developments and give future perspectives on synchronization in V2V and V2X	Not Specified	Reviews synchronization standards and approaches for V2V and D2D-enabled cellular networks
[83]	Vehicle-to-Everything (V2X) speed synchronization at road junctions	Rule-based algorithm	Based on optimal scheduling	Improves the performance of cooperative intersection management

Table A2. Categorization of existing literature on techniques used for congestion control at road intersections.

Reference Number	Objective/Context	Intersection			Traffic Signal Control Strategies		Source of Data Collection			Comments
		Isolated	Single	Network	Real Time	Fixed Time	Sensors/Detectors	Field Cameras	GPS/DSRC	
[8]	Split Cycle Offset Optimization Technique (SCOOT)			✓	✓		Detectors			• Minimize stops and delays at intersections by synchronizing adjacent signals • Disadvantage: Increased overhead during heavy traffic in large complicated network
[9]	Sydney Cooperation Adaptive Traffic System (SCATS)			✓	✓		Sensors			• Monitors real-time traffic signals and a volume of traffic • Reduces average waiting time, travel time, and fuel consumption

Table A2. *Cont.*

Reference Number	Objective/Context	Intersection			Traffic Signal Control Strategies		Source of Data Collection			Comments
		Isolated	Single	Network	Real Time	Fixed Time	Sensors/Detectors	Field Cameras	GPS/DSRC	
[10]	Optimized Policies for Adaptive Control (OPAC)			✓	✓		✓			• Calculates signal timing by minimizing total delay and stops performance function • No special features for priority/pre-emption on the system level • No explicit features for pedestrians or oversaturation conditions
[11]	Real-Time Hierarchical Optimized Distributed Effective System (RHODES)			✓	✓		✓			Decomposition of traffic network by modules that individually deal with sub-problems
[15]	Traffic signal control of road networks in real time	✓				✓				Based on Webster procedure
[16]	Traffic monitoring and prediction on roads		✓		✓			✓		• Uses dynamic Bayesian networks approach • Real-time prediction and classification of the state of a road • Improvement of travel and transit information
[17,18]	Travel time prediction framework	Freeway			✓		Robust Travel Time framework			• Based on state-space neural network • Based on Bayesian combined neural network
[19]	To reduce waiting time of vehicles at road intersections		✓		✓			✓		A video-based adaptive traffic signaling system
[21]	Assign equal green signal durations and arrange fair lane departure at an intersection			✓	✓				GPS	Adaptive traffic signal timings and lane scheduling
[22]	To enhance the flow of traffic on current road network using a data fusion approach			✓	✓				GPS	• Using floating car data (FCD) • Improve traffic flows on roads
[23]	Traffic signal control system		✓		✓		✓			• Using two-stage fuzzy control system • Reduces the average vehicle delay
[27]	To minimize the waiting time at a crossroad			✓	✓		✓			• Using a linear programming model • Minimize the queue length of vehicles waiting at intersections

Table A2. *Cont.*

Reference Number	Objective/Context	Intersection			Traffic Signal Control Strategies		Source of Data Collection			Comments
		Isolated	Single	Network	Real Time	Fixed Time	Sensors/Detectors	Field Cameras	GPS/DSRC	
[28,29]	WSN-based traffic light control systems			✓	✓		✓			• Low-cost installation to existing traffic road infrastructure • Self-configurable, easy installation of new traffic sensor nodes
[30]	TSC at signalized intersections	✓			✓		V2V communication			• Using connected vehicle technology • Minimize average delay
[31]	V2V traffic control for traffic management at intersections		✓		✓				DSRC	Virtual Traffic Light phenomenon based on DSRC
[33,34]	Removal of intersection traffic signal infrastructures			✓	✓				DSRC	• Connected and autonomous vehicle program (CV) • V2V and V2I applications
[35]	Intersection traffic control scheme				✓				DSRC	Based on DSRC-Actuated Traffic Control
[36]	Autonomous intersection management (AIM)			✓	✓		Simulator			• Operate both human-driven and autonomous cars • Prioritizes emergency vehicles
[40]	Reinforcement Learning based traffic signal control			✓	✓		Mathematical Model			• FRAP (Flipping and Rotation and considers All Phase configurations) model • Gives priority to the road with high traffic density • Better performance in complicated traffic situations and multi-junction environment
[41]	Traffic signal control at a very large scale using Multiagent reinforcement learning (MARL) technique			✓	✓		Simulator			• Using cooperative double Q-learning (Co-DQL) • Stable and robust
[45]	Deep Q-learning algorithm based system for partially detected intelligent vehicles			✓	✓				DSRC	• Minimize the vehicles waiting time at junctions (even if the detection rate of vehicles in low) • Can be used with different detection technologies such as LTE/5G, BLE 5.0, and RFID

References

1. Nielsen, O.A.; Frederiksen, R.; Simonsen, N. Using Expert System Rules to Establish Data for Intersections and Turns in Road Networks. *Int. Trans. Oper. Res.* **1998**, *5*, 569–581. [CrossRef]
2. Sigua, R.G. *Fundamentals of Traffic Engineering*; University of the Philippines in Diliman: Quezon City, Philippines, 2008; p. 327. Available online: https://www.crcpress.com/Fundamentals-of-Picoscience/Sattler/p/book/9781466505094#googlePreviewContainer (accessed on 20 September 2021).
3. Heidemann, D. Queue length and delay distributions at traffic signals. *Transp. Res. Part B Methodol.* **1994**, *28*, 377–389. [CrossRef]
4. The National Traffic Signal Report Card. Available online: https://www.researchgate.net/publication/295961075_The_national_traffic_signal_report_card (accessed on 20 September 2021).
5. Chen, L.; Englund, C. Cooperative Intersection Management: A Survey. *IEEE Trans. Intell. Transp. Syst.* **2015**, *17*, 570–586. [CrossRef]
6. Zaghal, R.; Thabatah, K.; Salah, S. Towards a smart intersection using traffic load balancing algorithm. In Proceedings of the 2017 Computing Conference, London, UK, 18–20 July 2017.
7. Shaikh, P.W.; El-Abd, M.; Khanafer, M.; Gao, K. A Review on Swarm Intelligence and Evolutionary Algorithms for Solving the Traffic Signal Control Problem. *IEEE Trans. Intell. Transp. Syst.* **2020**, *23*, 48–63. [CrossRef]
8. Bing, B.; Carter, A.T. SCOOT: The World's Foremost Adaptive Traffic Control System. Traffic Technology International'95. 1995. Available online: https://trid.trb.org/view/415757 (accessed on 20 September 2021).
9. Sims, A.; Dobinson, K. The Sydney coordinated adaptive traffic (SCAT) system philosophy and benefits. *IEEE Trans. Veh. Technol.* **1980**, *29*, 130–137. [CrossRef]
10. Gartner, N.H. Demand-responsive traffic signal control research. *Transp. Res. Part A Gen.* **1985**, *19*, 369–373. [CrossRef]
11. Mirchandani, P.; Head, K.L. A real-time traffic signal control system: Architecture, algorithms, and analysis. *Transp. Res. Part C Emerg. Technol.* **2001**, *9*, 415–432. [CrossRef]
12. Henry, J.; Farges, J.; Tuffal, J. The Prodyn Real Time Traffic Algorithm. In Proceedings of the Control in Transportation Systems, Baden-Baden, Germany, 20–22 April 1983; Elsevier BV: Amsterdam, The Netherlands, 1984; pp. 305–310.
13. Brilon, W.; Wietholt, T. Experiences with Adaptive Signal Control in Germany. *Transp. Res. Rec. J. Transp. Res. Board* **2013**, *2366*, 9–16. [CrossRef]
14. Costs | U.S. Department of Transportation. Available online: https://www.itskrs.its.dot.gov/costs (accessed on 20 September 2021).
15. Kouvelas, A.; Aboudolas, K.; Papageorgiou, M.; Kosmatopoulos, E.B. A Hybrid Strategy for Real-Time Traffic Signal Control of Urban Road Networks. *IEEE Trans. Intell. Transp. Syst.* **2011**, *12*, 884–894. [CrossRef]
16. Chaudhary, S.; Indu, S.; Chaudhury, S. Video-based road traffic monitoring and prediction using dynamic Bayesian networks. *IET Intell. Transp. Syst.* **2018**, *12*, 169–176. [CrossRef]
17. Hadi, R.A.; Sulong, G.; George, L.E. Vehicle Detection and Tracking Techniques: A Concise Review. *Signal Image Process. Int. J.* **2014**, *5*, 1–12. [CrossRef]
18. van Lint, J.; Hoogendoorn, S.; van Zuylen, H. Accurate freeway travel time prediction with state-space neural networks under missing data. *Transp. Res. Part C Emerg. Technol.* **2005**, *13*, 347–369. [CrossRef]
19. Indu, S.; Nair, V.; Jain, S.; Chaudhury, S. Video based adaptive road traffic signaling. In Proceedings of the Seventh International Conference on Distributed Smart Cameras (ICDSC), Palm Springs, CA, USA, 29 October–1 November 2013.
20. Zheng, W.; Lee, D.-H.; Shi, Q. Short-Term Freeway Traffic Flow Prediction: Bayesian Combined Neural Network Approach. *J. Transp. Eng.* **2006**, *132*, 114–121. [CrossRef]
21. Sharma, K.K.; Indu, S. GPS Based Adaptive Traffic Light Timings and Lane Scheduling. In Proceedings of the 2019 IEEE Intelligent Transportation Systems Conference (ITSC), Auckland, New Zealand, 27–30 October 2019; pp. 4267–4274.
22. Tiedong, W.; Jingjing, H. Applying floating car data in traffic monitoring. In Proceedings of the 2014 IEEE International Conference on Control Science and Systems Engineering, Yantai, China, 29–30 December 2014; pp. 96–99.
23. Lin, Y. The Design and Simulation of Intelligent Traffic Signal Control System Based on Fuzzy Logic. In *Foundations of Intelligent Systems*; Springer: Berlin/Heidelberg, Germany, 2014; pp. 965–973. [CrossRef]
24. Tanwar, R.; Majumdar, R.; Sidhu, G.S.; Srivastava, A. Removing traffic congestion at traffic lights using GPS technology. In Proceedings of the 2016 6th International Conference—Cloud System and Big Data Engineering (Confluence), Noida, India, 14–15 January 2016; pp. 575–579.
25. Liu, Y. Big Data Technology and Its Analysis of Application in Urban Intelligent Transportation System. In Proceedings of the 2018 International Conference on Intelligent Transportation, Big Data & Smart City (ICITBS), Xiamen, China, 25–26 January 2018; pp. 17–19.
26. Liping, X.; Dangying, L. A Novel Embedded Vehicle Terminal for Intelligent Transportation. In Proceedings of the 2014 Fifth International Conference on Intelligent Systems Design and Engineering Applications, Hunan, China, 15–16 June 2014; pp. 52–54. [CrossRef]
27. Coll, P.; Factorovich, P.; Loiseau, I.; Gómez, R. A linear programming approach for adaptive synchronization of traffic signals. *Int. Trans. Oper. Res.* **2013**, *20*, 667–679. [CrossRef]
28. Rida, N.; Hasbi, A. Traffic Lights Control using Wireless Sensors Networks. In Proceedings of the 3rd International Conference on Smart City Applications, Tetouan, Morocco, 10–11 October 2018. [CrossRef]

29. Yousef, K.M.; Al-Karaki, J.N.; Shatnawi, A.M. Intelligent Traffic Light Flow Control System Using Wireless Sensors Networks. *J. Inf. Sci. Eng.* **2010**, *26*, 753–768.
30. Liang, X.; Guler, S.I.; Gayah, V.V. An equitable traffic signal control scheme at isolated signalized intersections using Connected Vehicle technology. *Transp. Res. Part C Emerg. Technol.* **2019**, *110*, 81–97. [CrossRef]
31. Zhang, R.; Schmutz, F.; Gerard, K.; Pomini, A.; Basseto, L.; Hassen, S.B.; Ishikawa, A.; Ozgunes, I.; Tonguz, O. Virtual Traffic Lights: System Design and Implementation. In Proceedings of the 2018 IEEE 88th Vehicular Technology Conference (VTC-Fall), Chicago, IL, USA, 27–30 August 2018; pp. 1–5. [CrossRef]
32. Tonguz, O.K. Red light, green light—No light: Tomorrow's communicative cars could take turns at intersections. *IEEE Spectr.* **2018**, *55*, 24–29. [CrossRef]
33. VDOT Launches Smarter Roads. Available online: https://augustafreepress.com/vdot-launches-smarterroads/ (accessed on 20 September 2021).
34. Virginia Connected Corridors | Virginia Tech Transportation Institute. Available online: https://www.vtti.vt.edu/facilities/vcc.html (accessed on 20 September 2021).
35. Tonguz, O.K.; Zhang, R. Harnessing Vehicular Broadcast Communications: DSRC-Actuated Traffic Control. *IEEE Trans. Intell. Transp. Syst.* **2019**, *21*, 509–520. [CrossRef]
36. Dresner, K.; Stone, P.A. Multiagent Approach to Autonomous Intersection Management. *J. Artif. Intell. Res.* **2008**, *31*, 591–656. [CrossRef]
37. Wei, H.; Zheng, G.; Gayah, V.; Li, Z. A Survey on Traffic Signal Control Methods, 2020. *Surv. Traffic Signal Control Methods* **2019**, *1*. [CrossRef]
38. Li, L.; Lv, Y.; Wang, F.Y. Traffic signal timing via deep reinforcement learning. *IEEE/CAA J. Autom. Sin.* **2016**, *3*, 247–254. Available online: https://www.academia.edu/28634266/Traffic_Signal_Timing_via_Deep_Reinforcement_Learning (accessed on 21 November 2021).
39. Mousavi, S.S.; Schukat, M.; Howley, E. Traffic light control using deep policy-gradient and value-function-based reinforcement learning. *IET Intell. Transp. Syst.* **2017**, *11*, 417–423. [CrossRef]
40. Zheng, G.; Xiong, Y.; Zang, X.; Feng, J.; Wei, H.; Zhang, H.; Li, Y.; Xu, K.; Li, Z. Learning Phase Competition for Traffic Signal Control. In Proceedings of the 28th ACM International Conference on Information and Knowledge Management, Beijing, China, 3–7 November 2019; pp. 1963–1972. [CrossRef]
41. Wang, X.; Ke, L.; Qiao, Z.; Chai, X. Large-Scale Traffic Signal Control Using a Novel Multiagent Reinforcement Learning. *IEEE Trans. Cybern.* **2021**, *51*, 174–187. [CrossRef] [PubMed]
42. Wei, H.; Zheng, G.; Gayah, V.; Li, Z. Recent Advances in Reinforcement Learning for Traffic Signal Control. *ACM SIGKDD Explor. Newsl.* **2021**, *22*, 12–18. [CrossRef]
43. Joo, H.; Ahmed, S.H.; Lim, Y. Traffic signal control for smart cities using reinforcement learning. *Comput. Commun.* **2020**, *154*, 324–330. [CrossRef]
44. Zhang, R.; Leteurtre, R.; Striner, B.; Alanazi, A.; Alghafis, A.; Tonguz, O.K. Partially Detected Intelligent Traffic Signal Control: Environmental Adaptation. In Proceedings of the 2019 18th IEEE International Conference on Machine Learning and Applications (ICMLA), Boca Raton, FL, USA, 16–19 December 2019; pp. 1956–1960. [CrossRef]
45. Zhang, R.; Ishikawa, A.; Wang, W.; Striner, B.; Tonguz, O.K. Using Reinforcement Learning With Partial Vehicle Detection for Intelligent Traffic Signal Control. *IEEE Trans. Intell. Transp. Syst.* **2021**, *22*, 404–415. [CrossRef]
46. Dezani, H.; Marranghello, N.; Damiani, F. Genetic algorithm-based traffic lights timing optimization and routes definition using Petri net model of urban traffic flow. *IFAC Proc. Vol.* **2014**, *47*, 11326–11331. [CrossRef]
47. Dezani, H.; Bassi, R.D.; Marranghello, N.; Gomes, L.; Damiani, F.; da Silva, I.N. Optimizing urban traffic flow using Genetic Algorithm with Petri net analysis as fitness function. *Neurocomputing* **2014**, *124*, 162–167. [CrossRef]
48. Sabar, N.R.; Kieu, L.M.; Chung, E.; Tsubota, T.; de Almeida, P.E.M. A memetic algorithm for real world multi-intersection traffic signal optimisation problems. *Eng. Appl. Artif. Intell.* **2017**, *63*, 45–53. [CrossRef]
49. Li, X.; Sun, J.-Q. Signal Multiobjective Optimization for Urban Traffic Network. *IEEE Trans. Intell. Transp. Syst.* **2018**, *19*, 3529–3537. [CrossRef]
50. García-Nieto, J.; Alba, E.; Carolina Olivera, A. Swarm intelligence for traffic light scheduling: Application to real urban areas. *Eng. Appl. Artif. Intell.* **2012**, *25*, 274–283. [CrossRef]
51. Zhang, Y.; Zhu, H.-B.; Liu, X.-Q.; Chen, X.-B. Optimal control for region of the city traffic signal base on Selective particle swarm optimization algorithm. In Proceedings of the 2017 36th Chinese Control Conference (CCC), Dalian, China, 26–28 July 2017; pp. 2723–2728.
52. Wijaya, I.G.P.S.; Uchimura, K.; Koutaki, G. Traffic light signal parameters optimization using particle swarm optimization. In Proceedings of the 2015 International Seminar on Intelligent Technology and Its Applications (ISITIA), Surabaya, Indonesia, 20–21 May 2015; pp. 11–16.
53. Baskan, O.; Haldenbilen, S. Ant Colony Optimization Approach for Optimizing Traffic Signal Timings. *Ant Colony Optim.—Methods Appl.* **2011**, *14*, 205–220. [CrossRef]
54. Renfrew, D.; Yu, X.-H. Traffic signal optimization using Ant Colony Algorithm. In Proceedings of the 2012 International Joint Conference on Neural Networks (IJCNN), Brisbane, Australia, 10–15 June 2012; pp. 1–7. [CrossRef]

55. Dell'Orco, M.; Baskan, O.; Marinelli, M. A Harmony Search Algorithm approach for optimizing traffic signal timings. *Promet—Traffic Transp.* **2013**, *25*, 349–358. [CrossRef]
56. Gao, K.; Zhang, Y.; Sadollah, A.; Su, R. Optimizing urban traffic light scheduling problem using harmony search with ensemble of local search. *Appl. Soft Comput.* **2016**, *48*, 359–372. [CrossRef]
57. Milanes, V.; Perez, J.; Onieva, E.; Gonzalez, C. Controller for Urban Intersections Based on Wireless Communications and Fuzzy Logic. *IEEE Trans. Intell. Transp. Syst.* **2009**, *11*, 243–248. [CrossRef]
58. Bi, Y.; Lu, X.; Sun, Z.; Srinivasan, D.; Sun, Z. Optimal Type-2 Fuzzy System For Arterial Traffic Signal Control. *IEEE Trans. Intell. Transp. Syst.* **2017**, *19*, 3009–3027. [CrossRef]
59. Moghaddam, M.J.; Hosseini, M.; Safabakhsh, R. Traffic light control based on fuzzy Q-leaming. In Proceedings of the 2015 International Symposium on Artificial Intelligence and Signal Processing (AISP), Mashhad, Iran, 3–5 March 2015; pp. 124–128.
60. Firdous, M.; Iqbal, F.U.D.; Ghafoor, N.; Qureshi, N.K.; Naseer, N. Traffic Light Control System for Four-Way Intersection and T-Crossing Using Fuzzy Logic. In Proceedings of the 2019 IEEE International Conference on Artificial Intelligence and Computer Applications (ICAICA), Dalian, China, 29–31 March 2019; pp. 178–182.
61. Hawi, R.; Okeyo, G.; Kimwele, M. Smart traffic light control using fuzzy logic and wireless sensor network. In Proceedings of the 2017 Computing Conference, London, UK, 18–20 July 2017; pp. 450–460. [CrossRef]
62. Hu, X.; Lu, J.; Wang, W.; Zhirui, Y. Traffic Signal Synchronization in the Saturated High-Density Grid Road Network. *Comput. Intell. Neurosci.* **2015**, *2015*, 1–11. [CrossRef]
63. Iyer, V.; Jadhav, R.; Mavchi, U.; Abraham, J. Intelligent traffic signal synchronization using fuzzy logic and Q-learning. In Proceedings of the 2016 International Conference on Computing, Analytics and Security Trends (CAST), Pune, India, 19–21 December 2016; pp. 156–161. [CrossRef]
64. Amogh, A.S.; Pujari, S.; Gowda, S.N.; Nyamati, V.M. Traffic timer synchronization based on congestion. In Proceedings of the 2016 International Conference on Computation System and Information Technology for Sustainable Solutions (CSITSS), Bengaluru, India, 6–8 October 2016; pp. 255–260. [CrossRef]
65. Khan, A.; Ullah, F.; Kaleem, Z.; Rahman, S.U.; Cho, Y.Z. Sensor-based self-organized traffic control at intersections. In Proceedings of the 2017 International Conference on Information and Communication Technology Convergence (ICTC), Jeju, Korea, 18–20 October 2017; pp. 634–638. [CrossRef]
66. Guler, S.I.; Menendez, M.; Meier, L. Using connected vehicle technology to improve the efficiency of intersections. *Transp. Res. Part C Emerg. Technol.* **2014**, *46*, 121–131. [CrossRef]
67. Sirikham, A. Development of a Wireless Stop Light Synchronization System for Single-lane Traffic Control. In Proceedings of the 2021 18th International Conference on Electrical Engineering/Electronics, Computer, Telecommunications and Information Technology (ECTI-CON), Chiang Mai, Thailand, 19–22 May 2021; pp. 1006–1009. [CrossRef]
68. Kumar, D.M.; Arthi, R.; Aravindhan, C.; Roch, A.A.; Priyadarsini, K.; Deny, J. Traffic Congestion Control Synchronizing and Rerouting Using LoRa. *Microprocess. Microsyst.* **2021**, 104048. [CrossRef]
69. Reddy, K.S.; Shabarinath, B. Timing and Synchronization for Explicit FSM Based Traffic Light Controller. In Proceedings of the 2017 IEEE 7th International Advance Computing Conference (IACC), Hyderabad, India, 5–7 January 2017; pp. 526–529.
70. Khedkar, A.; Kumar, V. Self synchronization based air traffic control and collision avoidance system. In Proceedings of the 2011 IEEE/AIAA 30th Digital Avionics Systems Conference, Seattle, WA, USA, 16–20 October 2011; pp. 1–8. [CrossRef]
71. Wu, J.; Yan, F.; Kuang, P. Distributed urban traffic signal control based on spontaneous synchronization. In Proceedings of the 17th International IEEE Conference on Intelligent Transportation Systems (ITSC), Qingdao, China, 8–11 October 2014; pp. 2202–2207. [CrossRef]
72. Adacher, L.; Tiriolo, M. A Distributed Approach for Traffic Signal Synchronization Problem. In Proceedings of the 2016 Third International Conference on Mathematics and Computers in Sciences and in Industry (MCSI), Chania, Greece, 27–29 August 2016; pp. 191–196.
73. Adacher, L. A Global Optimization Approach to Solve the Traffic Signal Synchronization Problem. *Procedia—Soc. Behav. Sci.* **2012**, *54*, 1270–1277. [CrossRef]
74. Aleko, D.R.; Djahel, S. An IoT Enabled Traffic Light Controllers Synchronization Method for Road Traffic Congestion Mitigation. In Proceedings of the 2019 IEEE International Smart Cities Conference (ISC2), Casablanca, Morocco, 14–17 October 2019; pp. 709–715.
75. Nesmachnow, S.; Massobrio, R.; Arreche, E.; Mumford, C.; Olivera, A.C.; Vidal, P.J.; Tchernykh, A. Traffic lights synchronization for Bus Rapid Transit using a parallel evolutionary algorithm. *Int. J. Transp. Sci. Technol.* **2019**, *8*, 53–67. [CrossRef]
76. Cabezas, X.; García, S.; Salas, S.D. A hybrid heuristic approach for traffic light synchronization based on the MAXBAND. *Soft Comput. Lett.* **2019**, *1*, 100001. [CrossRef]
77. Adacher, L.; Gemma, A.; Oliva, G. Decentralized Spatial Decomposition for Traffic Signal Synchronization. *Transp. Res. Procedia* **2014**, *3*, 992–1001. [CrossRef]
78. Rodriguez, M.; Fathy, H. Self-Synchronization of Connected Vehicles in Traffic Networks: What Happens When We Think of Vehicles as Waves? In Proceedings of the 2019 American Control Conference (ACC), Philadelphia, PA, USA, 10–12 July 2019; pp. 2651–2657. [CrossRef]

79. Astarita, V.; Festa, D.C.; Giofre, V.P. Cooperative-Competitive Paradigm in Traffic Signal Synchronization Based on Floating Car Data. In Proceedings of the 2018 IEEE International Conference on Environment and Electrical Engineering and 2018 IEEE Industrial and Commercial Power Systems Europe (EEEIC/I&CPS Europe), Palermo, Italy, 12–15 June 2018; pp. 1–6.
80. Yingxiang, Y.; Min, Y.; Lei, S.; Jian, S.; Yong, W. Traffic Signal Synchronization of a Small Urban Network Using Cellular Automaton. In Proceedings of the 2011 Third International Conference on Measuring Technology and Mechatronics Automation, Shanghai, China, 6–7 January 2011; Volume 3, pp. 1035–1039.
81. Li, Z.; Ding, Z.; Wang, Y.; Fu, Y. Time synchronization method among VANET devices. In Proceedings of the 2017 International Conference on Wireless Communications, Signal Processing and Networking (WiSPNET), Chennai, India, 22–24 March 2017; pp. 2096–2101.
82. Abbasi, M.; Shahraki, A.; Barzegar, H.R.; Pahl, C. Synchronization Techniques in "Device to Device- and Vehicle to Vehicle-Enabled" Cellular Networks: A survey. *Comput. Electr. Eng.* **2021**, *90*, 106955. [CrossRef]
83. Du, W.; Abbas-Turki, A.; Koukam, A.; Galland, S.; Gechter, F. On the V2X speed synchronization at intersections: Rule based System for extended virtual platooning. *Procedia Comput. Sci.* **2018**, *141*, 255–262. [CrossRef]
84. Tomar, I.; Indu, S.; Pandey, N. Traffic Signal Control Methods: Current Status, Challenges, and Emerging Trends. In *Proceedings of Data Analytics and Management*; Springer Science and Business Media LLC: Singapore, 2022; Volume 90, pp. 151–163.

ResearchGate

See discussions, stats, and author profiles for this publication at: https://www.researchgate.net/publication/351016621

State-of-the-Art Applications of Graph Convolutional Neural Networks

Chapter · April 2021

DOI: 10.1007/978-981-33-4501-0_11

CITATIONS
0

READS
51

3 authors, including:



Priyanka Meel
Delhi Technological University
35 PUBLICATIONS **166** CITATIONS

SEE PROFILE

Some of the authors of this publication are also working on these related projects:

Fake News and Rumour Detection View project

All content following this page was uploaded by Priyanka Meel on 14 January 2022.

The user has requested enhancement of the downloaded file.

Springer Link

State-of-the-Art Applications of Graph Convolutional Neural Networks

Proceedings of 6th International Conference on Recent Trends in Computing pp 107-115 | Cite as

- Rajat Singh (1) Email author (rajat.singh1084@gmail.com)
- Sanchit Bathla (1)
- Priyanka Meel (1)

1. Department of Information Technology, Delhi Technological University, , Delhi, India

Conference paper
First Online: 21 April 2021

- 57 Downloads

Part of the Lecture Notes in Networks and Systems book series (LNNS, volume 177)

Abstract

Graphs are practiced widely in various real-world applications because of their structure modelling capability. Currently, deep neural networks have been employed to produce excellent outcomes in tasks such as classification. A graph convolutional network (GCN) is a deep learning model that operates on the graphs. We offer the general architecture of a GCN and its utilization in semi-supervised learning. We also investigate the application and performance of GCN in the classification of fake news. Finally, we present different application areas of GCN and open challenges for future research.

Keywords

GCN CNN Graph Hidden layer Semi-supervised learning

This is a preview of subscription content, log in to check access.

References

1. Huang K-H (2019) A gentle introduction to graph neural networks (basics, DeepWalk, and GraphSage), 10 Feb 2019. [Online]. Available: https://towardsdatascience.com/a-gentle-introduction-to-graph-neural-network-basics-deepwalk-and-graphsage-db5d540d50b3 (https://towardsdatascience.com/a-gentle-introduction-to-graph-neural-network-basics-deepwalk-and-graphsage-db5d540d50b3)

2. Jepsen TS (2018) How to do deep learning on graphs with graph convolutional networks, 18 Sept 2018. [Online]. Available: https://towardsdatascience.com/how-to-do-deep-learning-on-graphs-with-graph-convolutional-networks-7d2250723780 (https://towardsdatascience.com/how-to-do-deep-learning-on-graphs-with-graph-convolutional-networks-7d2250723780)

3. Benamira A, Devillers B, Lesot E, Ray AK, Saadi M, Malliaros FD (2019) Semi-supervised learning and graph neural networks for fake news detection. In: IEEE/ACM International conference on advances in social networks analysis and mining, Chicago
Google Scholar (https://scholar.google.com/scholar?q=Benamira%20A%2C%20Devillers%20B%2C%20Lesot%20E%2C%20Ray%20AK%2C%20Saadi%20M%2C%20Malliaros%20FD%20%282019%29%20Semi-supervised%20learning%20and%20graph%20neural%20networks%20for%20fake%20news%20detection.%20In%3A%20IEEE%2FACM%20International%20conference%20on%20advances%20in%20social%20networks%20analysis%20and%20mining%2C%20Chicago)

4. Bian T, Xiao X, Xu T, Zhao P, Huang W, Rong Y, Huang J (2020) Rumor detection on social media with bi-directional graph convolutional networks. arXiv preprint arXiv:2001.06362 (http://arxiv.org/abs/2001.06362), Chicago

5. Dong M, Zheng B, Hung NQV, Su H, Li G (2019) Multiple rumor source detection with graph convolutional networks. In: 28th ACM International conference on information and knowledge management, Harvard
Google Scholar (https://scholar.google.com/scholar?q=Dong%20M%2C%20Zheng%20B%2C%20Hung%20NQV%2C%20Su%20H%2C%20Li%20G%20%282019%29%20Multiple%20rumor%20source%20detection%20with%20graph%20convolutional%20networks.%20In%3A%2028th%20ACM%20International%20conference%20on%20information%20and%20knowledge%20management%2C%20Harvard)

6. Li C, Goldwasser D (2019) Encoding social information with graph convolutional networks for political perspective detection in news media. In: 57th Annual meeting of the association for computational linguistics, Harvard
Google Scholar (https://scholar.google.com/scholar?q=Li%20C%2C%20Goldwasser%20D%20%282019%29%20Encoding%20social%20information%20with%20graph%20convolutional%20networks%20for%20political%20perspective%20detection%20in%20news%20media.%20In%3A%2057th%20Annual%20meeting%20of%20the%20association%20for%20computational%20linguistics%2C%20Harvard)

7. Wu Y, Lian D, Xu Y, Wu L, Chen E (2020) Graph convolutional networks with markov random field reasoning for social spammer detection
Google Scholar (https://scholar.google.com/scholar?q=Wu%20Y%2C%20Lian%20D%2C%20Xu%20Y%2C%20Wu%20L%2C%20Chen%20E%20%282020%29%20Graph%20convolutional%20networks%20with%20markov%20random%20field%20reasoning%20for%20social%20spammer%20detection)

8. Aljohani N, Fayoumi A, Hassan S (2020) Bot prediction on social networks of Twitter in altmetrics using deep graph convolutional networks. Soft Comput
Google Scholar (https://scholar.google.com/scholar?q=Aljohani%20N%2C%20Fayoumi%20A%2C%20Hassan%20S%20%282020%29%20Bot%20prediction%20on%20social%20networks%20of%20Twitter%20i

n%20altmetrics%20using%20deep%20graph%20convolutional%20networks.%20Soft%20Comput)

9. Ying R, He R, Chen K, Eksombatchai P, Hamilton WL, Leskovec J (2018) Graph convolutional neural networks for web-scale. In: 24th ACM SIGKDD international conference on knowledge discovery & data mining, Chicago, pp 974–983
Google Scholar (https://scholar.google.com/scholar?q=Ying%20R%2C%20He%20R%2C%20Chen%20K%2C%20Eksombatchai%20P%2C%20Hamilton%20WL%2C%20Leskovec%20J%20%282018%29%20Graph%20convolutional%20neural%20networks%20for%20web-scale.%20In%3A%2024th%20ACM%20SIGKDD%20international%20conference%20on%20knowledge%20discovery%20%26%20data%20mining%2C%20Chicago%2C%20pp%20974%E2%80%93983)

10. Yao L, Mao C, Luo Y (2019) Graph convolutional networks for text classification. In: AAAI Conference on artificial intelligence, Vancouver
Google Scholar (https://scholar.google.com/scholar?q=Yao%20L%2C%20Mao%20C%2C%20Luo%20Y%20%282019%29%20Graph%20convolutional%20networks%20for%20text%20classification.%20In%3A%20AAAI%20Conference%20on%20artificial%20intelligence%2C%20Vancouver)

11. Marcheggiani D, Titov I (2017) Encoding sentences with graph convolutional networks for semantic role labeling. arXiv preprint arXiv:1703.04826 (http://arxiv.org/abs/1703.04826), Harvard

12. Zhang S, Tong H, Xu J, Maciejewski R (2019) Graph convolutional networks: a comprehensive review, 10 Nov 2019. [Online]. Available: https://link.springer.com/article/10.1186/s40649-019-0069-y (https://link.springer.com/article/10.1186/s40649-019-0069-y)

13. Yang Z, Han S, Zhao J (2020) Poisson Kernel avoiding self-smoothing in graph convolutional networks. arXiv preprint arXiv:2002.02589 (http://arxiv.org/abs/2002.02589), 7 Feb 2020, Vancouver

Copyright information

© Springer Nature Singapore Pte Ltd. 2021

About this paper

Cite this paper as:

Singh R., Bathla S., Meel P. (2021) State-of-the-Art Applications of Graph Convolutional Neural Networks. In: Mahapatra R.P., Panigrahi B.K., Kaushik B.K., Roy S. (eds) Proceedings of 6th International Conference on Recent Trends in Computing. Lecture Notes in Networks and Systems, vol 177. Springer, Singapore. https://doi.org/10.1007/978-981-33-4501-0_11

- First Online 21 April 2021
- DOI https://doi.org/10.1007/978-981-33-4501-0_11
- Publisher Name Springer, Singapore
- Print ISBN 978-981-33-4500-3
- Online ISBN 978-981-33-4501-0
- eBook Packages Intelligent Technologies and Robotics Intelligent Technologies and Robotics (R0)

- Buy this book on publisher's site
- Reprints and Permissions

Personalised recommendations

SPRINGER NATURE

© 2020 Springer Nature Switzerland AG. Part of Springer Nature.

Not logged in Delhi Technological University (2000607895) - Convener, UGC-Infonet Digital Library Consortium (3000132959) - INDEST-AICTE-Level III (3000168247) - Information and Library Network (INFLIBNET) Centre (3994475188) 14.139.251.100

J Mater Sci: Mater Electron

Structural and color tunable properties in Sm^{3+}/Eu^{3+}-doped $Ca_3Bi(PO_4)_3$ phosphor for solar cell and w-LED applications

Mukesh K. Sahu[1] and M. Jayasimhadri[1,*]

[1] *Luminescent Materials Research Lab (LMRL), Department of Applied Physics, Delhi Technological University, Delhi 110 042, India*

Received: 13 September 2021
Accepted: 3 January 2022

© The Author(s), under exclusive licence to Springer Science+Business Media, LLC, part of Springer Nature 2022

ABSTRACT

Crystalline eulytite-type $Ca_3Bi(PO_4)_3$ (CBP) phosphors activated with Sm^{3+} and combination of Sm^{3+} & Eu^{3+} ions have been prepared by co-precipitation technique. Phase and crystal structure have been recognized using X-ray diffraction analysis and Rietveld refinement. The Sm^{3+}-doped CBP phosphor exhibits three emission peaks at 562, 598, and 644 nm under 400 nm excitation and the highest emission intensity has been observed for 5.0 mol% Sm^{3+}-doped CBP phosphor. The co-doping of Sm^{3+} and Eu^{3+} ions in CBP phosphor has expanded the excitation as well as emission spectra. The energy transfer (ET) between Sm^{3+} sensitizer ions to Eu^{3+} activator ions in CBP phosphor has been studied based on the photoluminescence (PL) and decay curves using Dexter ET formula and Reisfeld's theory. The PL quantum yield was obtained as high as 86.65%, indicating a potential red constituent in photonic devices. The CBP:Sm^{3+}/Eu^{3+} emission intensity was persisting to 81.27% at 150 °C in comparison to the emission intensity at room temperature, confirming the excellent thermal stability. Moreover, the color coordinates and decay curves have enhanced the suitability of CBP:Sm^{3+}, Eu^{3+} for accomplishing spectral conversion in solar cells, pc-w-LEDs, and other photonic devices.

1 Introduction

The worldwide energy demand and consumption have been rising rapidly due to the overgrowing population and people picking a lavish lifestyle [1, 2]. This energy demand and consumption can be resolved by opting two significant approaches: i.e., energy-saving strategy and employing green renewable energy. As a point of interest, phosphor-converted white light-emitting diodes (pc-w-LEDs) and solar cells have been considered within the two potential approaches [3, 4]. The solar spectrum is an abundant and valuable green renewable energy resource that is freely accessible in every part of the earth. It has the potential to fulfill the worldwide energy crises, which could possibly reduce the dependency on traditional fossil fuel-based power generation [5]. A solar cell has attracted much

Address correspondence to E-mail: jayaphysics@yahoo.com

https://doi.org/10.1007/s10854-022-07708-w
Published online: 03 February 2022

attention among researchers and industries as a favorable choice for green renewable energy generation without any harmful impact on the nature. Presently, silicon-based solar cells are leading the worldwide photovoltaic industries due to their easy availability in colossal quantity, zero toxicity, and high stability [6]. But the silicon-based solar cell operated with limited conversion efficiency because most of the spectrum was unexploited, i.e., spectral mismatch. Especially, the intensity of radiation in the solar spectrum within the range from 300 to 500 nm was not utilized by C-Si solar cell due to high reflection, surface recombination, and thermalization losses [7]. A number of scientists and researchers have continuously worked and devised numerous methods, which can enhance the solar cell energy conversion efficiency by utilizing the unused part of the solar spectrum [8–11]. One of the most important methods is the downshifting phosphor coating on top of the solar cell, which can enhance the conversion efficiency. To achieve this result, near-UV-pumped efficient green, orange, or red emitting phosphor material is required, which can directly be applied on the top of solar cell and enhance the spectral conversion efficiency. Also, the red emitting phosphor used in commercially available phosphor-converted white LEDs can conquer the shortcomings such as halo effect and color rendering index ($R_a < 65$–70) [12–15]. Thus, it is necessary to prepare effective visible red emitting phosphor having numerous eminent characteristics, for instance, highly efficient n-UV/blue excitation with intense emission and chemically stable and environmental friendly materials to use in solar cell and pc-w-LEDs [16–19].

In recent years, rare earth (RE)-induced downshifting phosphor materials had been synthesized for the utility in pc-w-LEDs [20]. RE-activated eulytite-type orthophosphate $A_3B(PO_4)_3$ (A = divalent ions and B = trivalent Pb, Bi or RE ion) has been reported as appropriate phosphor host material due to their excellent optical properties, high chemical, as well as thermal stability along with high luminous efficiency [21–24]. Among the eulytite-type orthophosphate hosts, $Ca_3Bi(PO_4)_3$ is a remarkable host for luminescent materials and possibly utilized in numerous lighting and display and sensing devices [25, 26].

The appropriate dopant of transition metal/ RE ions was essential in the phosphor host, which can effectively absorb UV/blue photons and emit in the red region [27, 28]. Among all the RE ions, Europium (Eu^{3+}/Eu^{2+})-activated phosphors are perfectly appropriate for downshifting phosphor, due to their numerous energy levels, as well as high luminescence efficiency and also emit in the red region upon excitation with the n-UV/blue wavelengths [29]. Adding a sensitizer to an activator will possibly expand the absorption profile and boost the emission intensity of the activator through the ET process. Among numerous RE ions, Sm^{3+} has been observed as the enormously suitable sensitizer for Eu^{3+} ions [30]. The inclusion of Sm^{3+} ions as the sensitizer enhanced the Eu^{3+} emission in different host matrices.

In the present study, single Sm^{3+}-doped and combination of Sm^{3+}, Eu^{3+} co-doped calcium bismuth phosphate [$Ca_3Bi(PO_4)_3$] phosphors have been prepared via co-precipitation technique. The crystallographic phase, structure, morphology, thermal behavior, and optical properties have been examined. Energy transfer mechanism was studied in detail via employing Dexter's ET formula and Reisfeld's approximation. Furthermore, temperature-dependent PL spectra, CIE coordinates, and lifetime curve analysis have been explored to enhance the quality of luminescence characteristics of CBP: xSm^{3+},yEu^{3+} phosphors for the utility in pc-w-LEDs, solar cell, and other photonic devices.

2 Experimental section

CBP doped with Sm^{3+} ion and co-doped with Sm^{3+}, Eu^{3+} ions samples were prepared via co-precipitation technique. In CBP:xSm^{3+} samples, doping concentration (Sm^{3+} ions) was varied as $x = 1.0$ to 8.0 mol%. In the case of co-doped CBP:xSm^{3+}, yEu^{3+} samples, Sm^{3+} ion concentration was fixed ($x = 5.0$ mol%) and varied with the Eu^{3+} ion concentration from $y = 1.0$ to 10.0 mol%. The highly pure $Ca(NO_3)_2{\cdot}4H_2O$ (99.00%), Bi_2O_3 (99.00%), H_3PO_4 (99.00%), $Sm(NO_3)_3{\cdot}6H_2O$ (99.99%), and $Eu(NO_3)_3{\cdot}5H_2O$ (99.99%) were used as precursor materials for the preparation of CBP:xSm^{3+} and CBP:xSm^{3+}, yEu^{3+} phosphors.

Initially, the stoichiometric amount of all metal nitrates was dissolved individually in the deionized water and Bi_2O_3 was dissolved in a minimum amount of HNO_3. The dissolved solutions were mixed together and thoroughly stirred for 1 h. Subsequently, H_3PO_4 was added dropwise in the

resultant solution, followed by adding 2 g of PEG-4000 and water solution. After certain period of time, the clear solution was acquired with pH ~ 1 and the pH value of the solution was adjusted to 7 via adding the dropwise ammonia solution, which was turned out into white precipitate. After subsequent aging for 2 h, the precipitate was separated by centrifuging process and several times washed with deionized water and ethanol to remove the residual chemicals. Finally, the powder was dried at 100 °C for 12 h and then was sintered at 1000 °C for 2 h to form the required material.

The crystalline structure was examined by X-ray diffraction (XRD) technique (Rigaku Ultima IV). The morphological analysis has been performed using SEM (EVO MA10, ZEISS). The PL excitation and emission spectra have been accomplished by a spectrofluorophotometer (RF-5301PC, Shimadzu). The decay curves were recorded using a spectrofluorometer (Horiba fluorolog-3) with a xenon flash lamp. The PL quantum yield calculation was accomplished with the help of spectrofluorophotometer (Horiba, Fluorolog-3) attached with $BaSO_4$-integrated sphere. The PL spectra variation by changing temperature was recorded by employing optics spectrometer (FLAME-S-XR1-ES, ocean with homemade heating sample assembly).

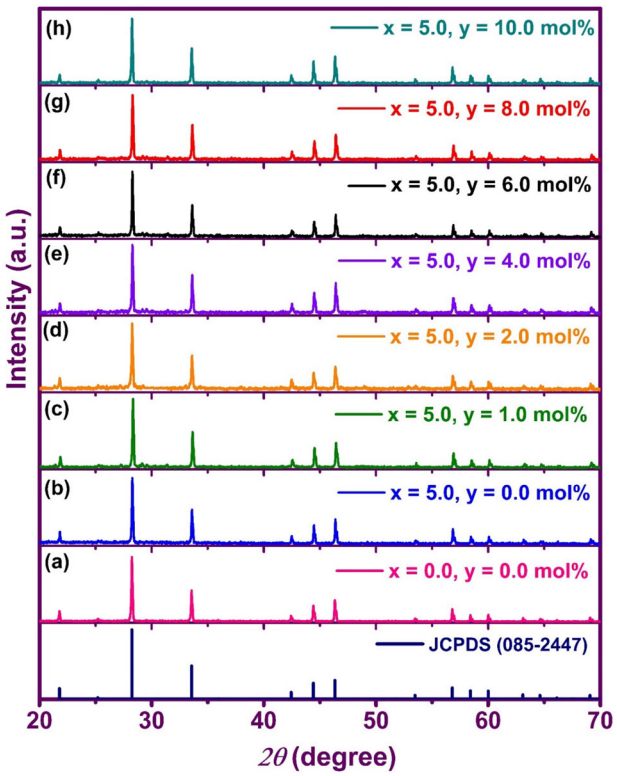


Fig. 1 XRD patterns for **a** undoped CBP powder, **b** CBP:xSm^{3+} (x = 5.0 mol%), and **c**–**h** co-doped CBP:xSm^{3+}, yEu^{3+} (x = 5.0 & y = 1.0 to 10.0 mol%) samples compared with standard JCPDS data

3 Results and discussion

3.1 X-ray diffraction studies

The crystalline phase and structure of undoped, doped, and co-doped CBP samples were investigated based on diffraction patterns as shown in Fig. 1. Several sharp and intense diffraction patterns indicate that the prepared samples are crystalline in nature. The diffraction patterns for the prepared samples were analogous and well indexed with standard patterns (JCPDS: 085–2447). All the prepared samples were crystallized in cubic structure with $I\bar{4}3d$ (220) space group. The diffraction patterns for Sm^{3+}-doped and Sm^{3+}/Eu^{3+} co-doped CBP samples did not disclose any anonymous peaks, intimating that the RE ions were efficiently assimilated into the CBP host lattice. The Debye Scherer formula $[D = K\lambda/\beta\cos\theta]$ has been used to estimate the average crystallite (D) size for the prepared samples [31]. Shape factor $(K \approx 0.91)$, X-ray wavelength for CuK_α radiation, $(\lambda \approx 1.5406\text{Å})$, full width at half maxima (β) of intense patterns at Braggs angles (2θ) of 28.2°, 33.5°, 46.3°, and 44.4° were used to estimate D value of samples. The average crystallite size for the prepared sample was tabulated in Table 1. The D value decreases with doping and co-doping of Sm^{3+} and Sm^{3+}/Eu^{3+} ions in CBP. Decrease in D values may be expected to the ionic radius discrepancy among Sm^{3+} (r = 0.95 Å for coordination number: CN = 6), Eu^{3+} (r = 0.94 Å for CN = 6), and Bi^{3+} (r = 1.03 Å for CN = 6) ions, which also recommends the successful incorporation of RE ions in CBP host. Also, the acceptable radii variation among doped and substituted ions was less than the limits of 30%.

The Rietveld refinement has been executed for the undoped CBP sample. Figure 2a represents the refinement pattern for the CBP sample. The refinement results of CBP have been endorsed by single cubic phase crystallization and the resulting lattice parameters $a = b = c$ = 9.893 Å and $\alpha = \beta = \gamma = 90°$. The goodness of fit (χ^2) was found to be 1.90, which indicates the superiority of refinement. Figure 2b

Table 1 Crystallite size of CBP:xSm^{3+}, yEu^{3+} powder sample assessed using Debye–Scherrer formula

Sample CBP:xSm^{3+}, yEu^{3+}	Crystallite size D (nm)
x = 0.0 & y = 0.0 mol%	72.95
x = 5.0 & y = 0.0 mol%	72.74
x = 5.0 & y = 1.0 mol%	71.47
x = 5.0 & y = 2.0 mol%	71.15
x = 5.0 & y = 4.0 mol%	71.02
x = 5.0 & y = 6.0 mol%	70.97
x = 5.0 & y = 8.0 mol%	70.02
x = 5.0 & y = 10.0 mol%	66.85

shows the unit cell structure of CBP prepared by executing the VESTA software. In CBP cubic structure, Ca, Bi, P, and O atoms were occupied at 16*c*, 16*c*, 12*a*, and 48*e* sites, respectively [25]. Atoms site and Wyckoff position are listed in Table 2. The occupation ratios of Bi and Ca ions in 16*c* site are 1/4 and 3/4, respectively, and bonded with eight O atoms to form octahedron as shown in Fig. 2c. The O atoms situated at two positions and four O atoms bonded with one P atom to form three-dimensional $[PO_4]^{3-}$ tetrahedron structure as displayed in Fig. 2d.

3.2 Morphological analysis

The morphology of the CBP particles examined using the SEM micrograph is displayed in Fig. 3a and b. The micrograph discloses that the sample consists of heterogenous structure with agglomeration of non-uniform particles. The CBP particle size was noticed in the range of around 1 μm.

3.3 Photoluminescence properties

Excitation spectra for Sm^{3+} ion (x = 1.0 to 8.0 mol%)-doped CBP phosphors were recorded with monitoring the emission at 598 nm wavelength. Excitation spectra is demonstrated in Fig. 4a, which exhibits a series of excitation peaks corresponding to $4f - 4f$ transitions in 300 to 500 nm range. Excitation peaks at 325 ($^6H_{5/2} \rightarrow {}^4P_{1/2}$), 341 ($^6H_{5/2} \rightarrow {}^4H_{9/2}$), 358 ($^6H_{5/2} \rightarrow {}^4D_{3/2}$), 372 ($^6H_{5/2} \rightarrow {}^4D_{1/2}$), 400 ($^6H_{5/2} \rightarrow {}^4F_{7/2}$), 413 ($^6H_{5/2} \rightarrow {}^4M_{19/2}$), 437 ($^6H_{5/2} \rightarrow {}^4G_{9/2}$), and 466 nm ($^6H_{5/2} \rightarrow {}^4I_{11/2} + {}^4I_{13/2} + {}^4M_{15/2}$) were attributed to the distinctive transitions of Sm^{3+} ions [32, 33]. The most populous peaks are noticed at 400 and 466 nm. Excitation intensity improved with the Sm^{3+} ion doping concentration up to x = 5.0 mol% and reduced afterward.

Emission spectra for CBP:xSm^{3+} were recorded under 400 nm excitation wavelengths as depicted in Fig. 4b. Three emission peaks are spotted at 562, 598, and 644 nm, which are evolving due to $^4G_{5/2} \rightarrow {}^6H_{5/2}$, $^4G_{5/2} \rightarrow {}^6H_{7/2}$, and $^4G_{5/2} \rightarrow {}^6H_{9/2}$ distinctive transitions of Sm^{3+} ion [34]. The first peak at 562 nm ($^4G_{5/2} \rightarrow {}^6H_{5/2}$) is purely magnetic dipole (MD) transition, which abides by the $\Delta J = 0, \pm 1$ selection rule and is unaffected from crystal field environment. The second peak at 598 nm ($^4G_{5/2} \rightarrow {}^6H_{7/2}$) is due to both partially MD and partially forced electric dipole (ED) transition, but only abide by $\Delta J = \pm 1$ selection rule, whereas the third peak at 644 nm ($^4G_{5/2} \rightarrow {}^6H_{9/2}$) is purely forced ED transition that follows the selection rule $\Delta J \leq 6$, which is hypersensitive in nature and strongly influenced by crystal field environment [32, 35]. The intensity fraction of ED with MD indicates symmetry of the local environment of dopant ions in the host lattice. In this phosphor, the ED transition is less intense than MD transition, which reveals the higher environmental symmetry of Sm^{3+} ions with an inversion center in CBP host lattice.

Emission intensity enhances with an increase in the Sm^{3+} ion doping concentration and reaches its highest intensity at the concentration of 5.0 mol%, after that the concentration quenching effect emerges. Inset image of Fig. 4b signifies the intensity variation concerning with Sm^{3+} ion doping concentration, which also confirms that the 5.0 mol% Sm^{3+}ion doped CBP phosphor gives the highest emission intensity under the 400 nm excitation wavelength. As a result, the optimized doping concentration of Sm^{3+} ion in CBP host is x = 5.0 mol%. The concentration quenching may be evolved due to a very less critical distance between doping ions and escalation in the possibility of non-radiative energy transfer among the nearest doping ions. The critical distance was evaluated and found to be 20.82 Å, as per the formula provided by Blasse [36]. Larger value (≥ 5 Å) of critical distance that discloses the quenching is attributed to the multipole interaction among the Sm^{3+} ions. Type of multipolar interaction was identified via Dexter's theory having modified formula as follows [37, 38]:

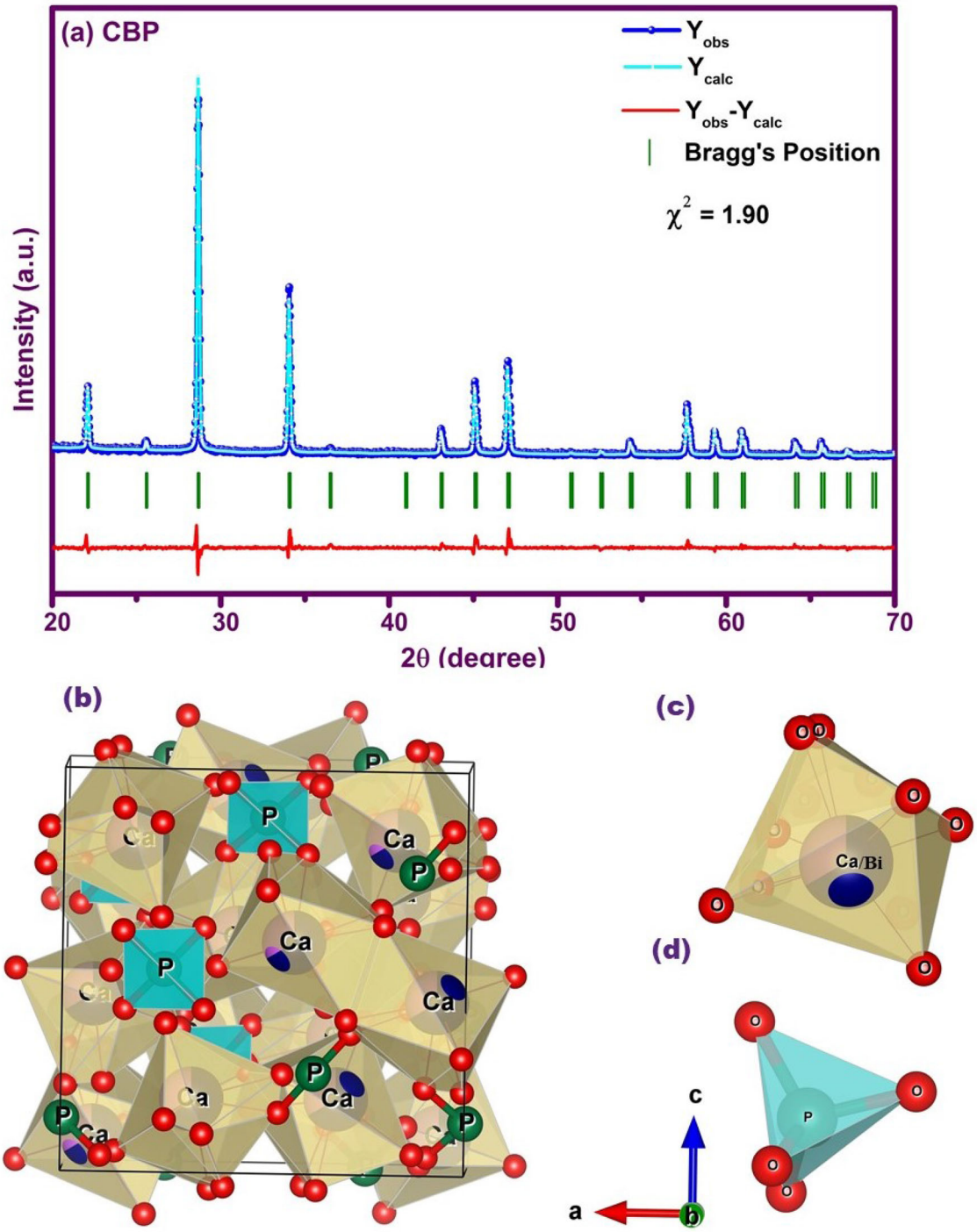


Fig. 2 **a** Reitveld refinement pattern, **b** unit cell structure of cubic CBP sample, **c** octahedron shape of Ca bonded with O atoms, and **d** tetrahedron shape of P bonded with O atoms

$$\log\left(\frac{I}{x}\right) = K' - \frac{Q\log(x)}{3}; (K' = \log k - \log\beta)$$

where I and x denotes the emission intensity and doping concentration, respectively. K' implies the constant and the Q value clarifies the type of interaction between Sm^{3+} ions. Figure 4c represents the Dexter's plot between $\log(I/x)$ and $\log(x)$ and the linear fitted slope is − 1.98. The Q value was retrieved to be 5.94, which is close to 6. Henceforth,

Table 2 Reitveld refinement results for cubic CBP sample

Atoms	Wyckoff site	*X*	*y*	*z*
Ca	16c	0.07435	0.07435	0.07435
Bi	16c	0.07435	0.07435	0.07435
P	12a	0.37500	0.00000	0.25000
O1	48e	0.49323	0.37926	0.71356
O2	48e	0.59125	0.38070	0.72700

the multipolar interaction in Sm^{3+}-doped CBP is dipole–dipole type.

To reveal the possibility to enhance emission profile and expand the excitation spectra of Sm^{3+} ions, co-dopant (Eu^{3+}) ion has been included to synthesize CBP phosphors with fixed Sm^{3+} ion concentration (i.e., optimized: x = 5.0 mol%) by varying the Eu^{3+} ion concentration (y = 0.0 to 10.0 mol%). Figure 5a shows the excitation spectra of CBP: yEu^{3+} (y = 1.0 mol%) and CBP: xSm^{3+}, yEu^{3+} (x = 5.0 mol% y = 1.0 mol%) with monitoring the emission at λ_{em} = 612 nm. Also, the excitation spectrum was recorded for CBP: xSm^{3+}, yEu^{3+} (x = 5.0 mol%, y = 1.0 mol%) with monitoring λ_{em} = 598 nm. Excitation spectrum of CBP: yEu^{3+} (y = 1.0 mol%) exhibits a series of peaks at 316, 359, 380, 391, 414, and 462 nm attributed to $f-f$ transitions of Eu^{3+} ions. Excitation spectrum for the CBP: xSm^{3+}, yEu^{3+} (x = 5.0 mol%, y = 1.0 mol%) monitoring with λ_{em} = 612 nm shows a number of peaks due to Eu^{3+} ions along with other several peaks due to Sm^{3+} ions, also the intensity got improved than the CBP: yEu^{3+} (y = 1.0 mol%). Excitation peaks were taking place at 341, 372, 400, and 441 and broad peak from 457 to 495 nm attributed to the $^6H_{5/2} \rightarrow {}^4H_{9/2}$, $^6H_{5/2} \rightarrow {}^4D_{1/2}$, $^6H_{5/2} \rightarrow {}^4F_{7/2}$, $^6H_{5/2} \rightarrow {}^4G_{9/2}$, and $^6H_{5/2} \rightarrow {}^4I_{11/2} + {}^4I_{13/2} + {}^4M_{15/2}$ transitions of Sm^{3+} ions, respectively. Excitation spectra of CBP: xSm^{3+}, yEu^{3+} (x = 5.0 mol%, y = 1.0 mol%) monitoring with λ_{em} = 598 nm which is similar with the excitation spectra of CBP: xSm^{3+} phosphor as presented in Fig. 4a.

In accordance with the excitation spectra, emission spectra for CBP:xSm^{3+}, yEu^{3+} phosphors were recorded under λ_{ex} = 400 and 466 nm excitation wavelengths as illustrated in Fig. 5b and c. The strongest emission peak observed at 598 nm ($^4G_{5/2} \rightarrow {}^6H_{7/2}$) is due to Sm^{3+} ions, when the Eu^{3+} concentration is low (i.e., y = 0.0 and 1.0 mol%). Further, the intensity related to $^4G_{5/2} \rightarrow {}^6H_{7/2}$ transition of Sm^{3+} ions is considerably dropped with the increasing Eu^{3+} concentration caused by the energy transfer from Sm^{3+} sensitizer to activator Eu^{3+} ions [30, 39]. However, the emission intensity related to Eu^{3+} ion improves with increasing the Eu^{3+} ion content from 1.0 to 10.0 mol% and at this concentration of Eu^{3+} ion quenching was not observed. In Fig. 5b and c, the analogous patterns were spotted for the emission spectra of CBP:xSm^{3+}, yEu^{3+} phosphor excited at 400 and 466 nm with slight intensity variation. The studied results suggest that the energy transfer was observed from the sensitizer Sm^{3+} ions to activator Eu^{3+} ions under λ_{ex} = 400 and 466 nm.

The exchange and multipolar interaction are the two ways of energy transfer between sensitizer and

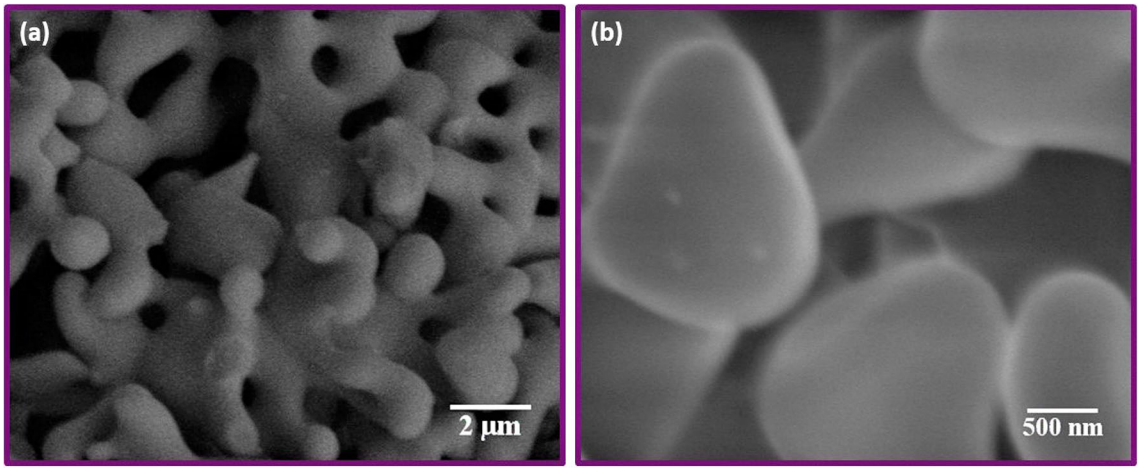


Fig. 3 SEM micrograph for undoped CBP powder sample at different magnification scales **a** 2 µm and **b** 500 nm

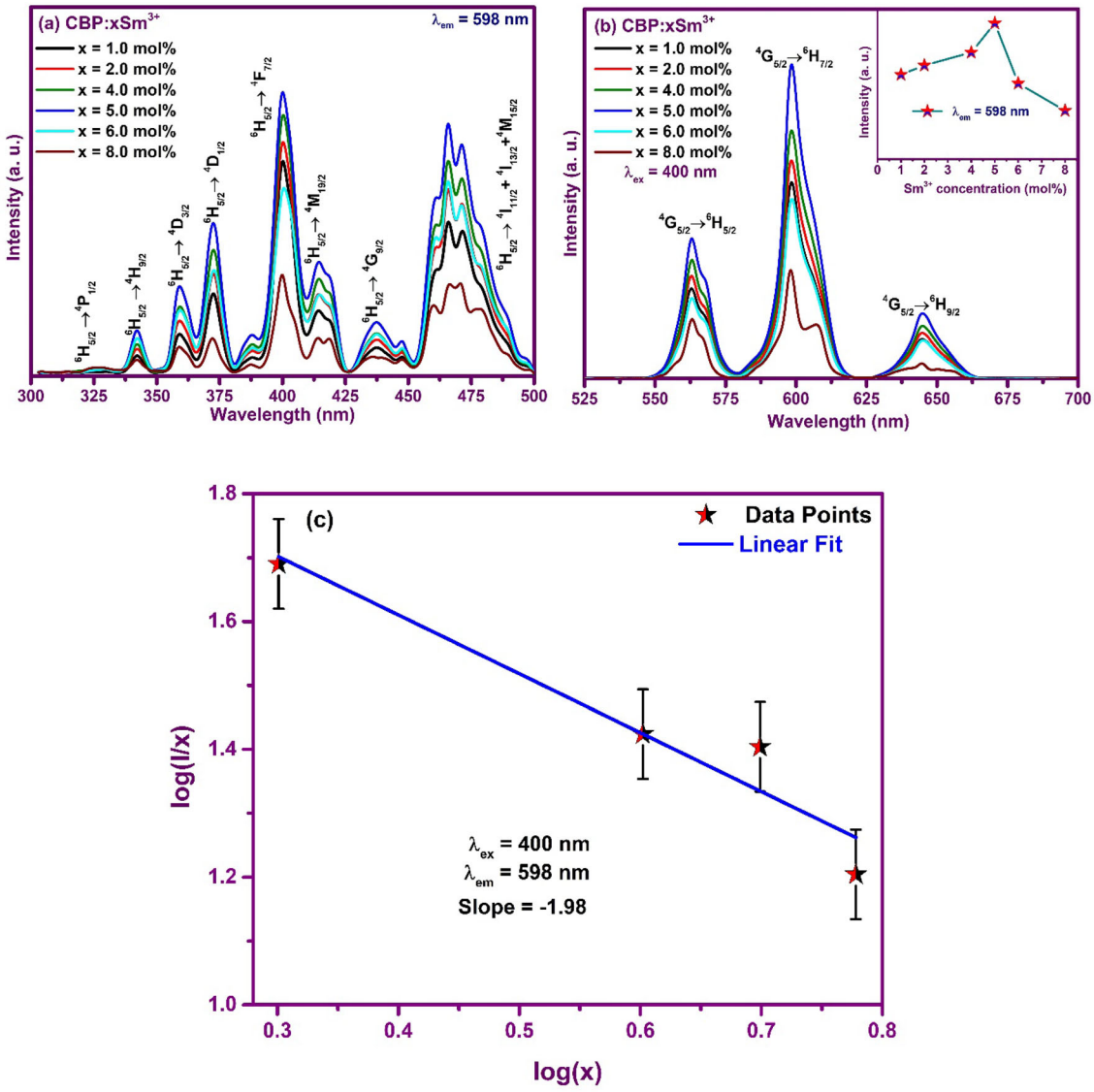


Fig. 4 **a** Excitation spectra measured at λ_{em} = 598 nm, **b** Emission spectra under λ_{ex} = 400 nm for CBP:xSm^{3+} (x = 1.0, 2.0, 4.0, 5.0, 6.0 and 8.0 mol%) phosphor, and **c** plot between log (I/x) and log(x)

activator ions. As per the expression given by Dexter's for multipolar interaction and Reitveld's estimation, the fraction of the sensitizer emission intensity without activator ion to emission intensity of sensitizer with activator ion can be acquired as follows[40]:

$$\frac{I_{SO}}{I_s} \propto C^{n/3}$$

where I_{SO} is the emission intensity of sensitizer Sm^{3+} ion only and I_S is the emission intensity of Sm^{3+} with activator Eu^{3+} ions. C denotes the sum of Sm^{3+} sensitizer and Eu^{3+} activator ions concentration in mol%. The parameter 'n' belongs to the type of multipolar interaction, having values of 10, 8, and 6 associated to (q–q) quadrupole–quadrupole, (d–q) dipole–quadrupole, and (d–d) dipole–dipole interactions, respectively [40]. Figure 5d shows the plot between I_{SO}/I_S and $C^{n/3}$ for d–d, d–q, and q–q interaction under the excitation wavelength of λ_{ex} = 400 nm. The best linear fit has been acquired for I_{SO}/I_S versus $C^{6/3}$ plot having n = 6, which recommends that the energy transfer from sensitizer Sm^{3+} ions to activator Eu^{3+} ion is owing to dipole–dipole in nature.

The partial energy-level diagram of Sm^{3+}, Eu^{3+} in CBP phosphor clarifies the ET process as presented in Fig. 6. The as-synthesized phosphor was effectively

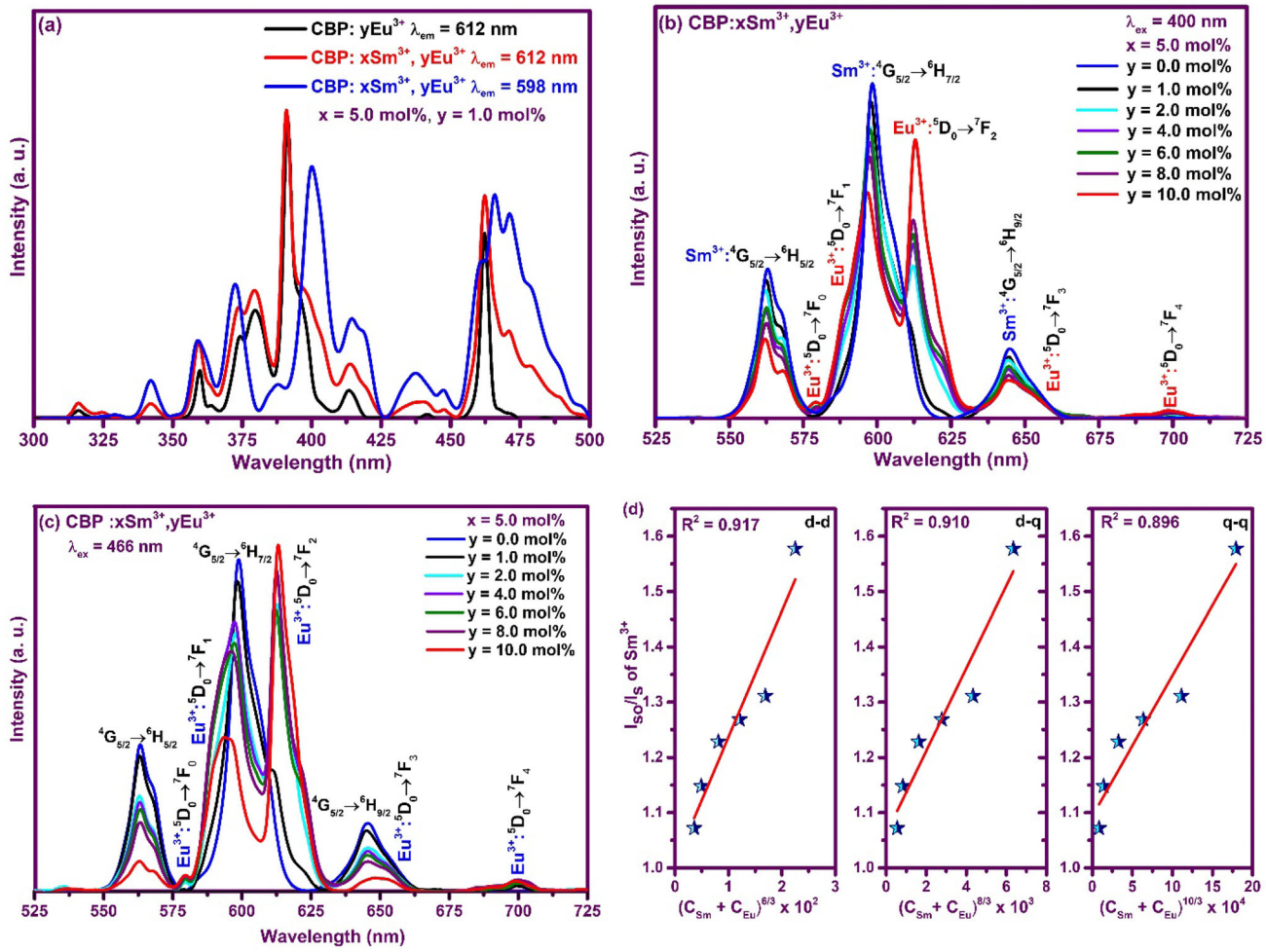


Fig. 5 **a** Black and red solid lines represent the excitation spectrum of CBP: yEu^{3+} phosphor (y = 1.0 mol%, λ_{em} = 612 nm) and CBP:xSm^{3+}, yEu^{3+} phosphor (x = 5.0 & y = 1.0 mol%, λ_{em} = 612 nm), respectively. Blue line show the excitation spectrum for CBP:xSm^{3+}, yEu^{3+} phosphor (x = 5.0 mol%, y = 1.0 mol%) with monitoring λ_{em} = 598 nm. Emission spectra under **b** λ_{ex} = 400 nm and **c** λ_{ex} = 466 for CBP:xSm^{3+}, yEu^{3+} (x = 5.0 & y = 0.0 to 10.0 mol%) **d** Dependence of I_{SO}/I_S of Sm^{3+} on $(C_{Sm+Eu})^{6/3}$, $(C_{Sm+Eu})^{8/3}$ and $(C_{Sm+Eu})^{10/3}$

excited by specific near-UV/blue radiation and excited atoms from ground level to different excited energy levels. Subsequently, some non-radiative transitions take place in between levels as mentioned by black-dotted lines and give radiative emission in the visible region as explained in earlier PL properties. The energy difference between lowest excited $^4G_{5/2}$ ($\sim$ 17,924 cm^{-1}) level of Sm^{3+} ion and $^5D_0$ ($\sim$ 17,286 cm^{-1}) levels of Eu^{3+} ion was found to be 638 cm^{-1} [35]. As the energy difference is very less, the part of energy from $^4G_{5/2}$ level of Sm^{3+} ion was migrated to $^5D_0$ level of Eu^{3+} ions. The result evidently specifies that Sm^{3+} act as an effective sensitizer for the Eu^{3+} activator ion in CBP phosphor.

PL quantum yield is one of the most important parameters of the phosphor for its practical utility in any optoelectronic devices. Hence, the PL quantum yield was evaluated for CBP:xSm^{3+}, yEu^{3+} (x = 5.0 mol% and y = 10.0 mol%) phosphor with the integrated sphere under λ_{ex} = 448 nm and λ_{em} = 612 nm [41]. The PL quantum yield is found to be 86.65%, which is higher than the commercial red phosphor Y_2O_3:Eu^{3+}, as well other reported phosphors [25, 42, 43]. The obtained PL characteristics of CBP:xSm^{3+}, yEu^{3+} phosphor with high value of PL quantum yield validate that the phosphor can be a potential red emitting component in pc-w-LEDs and other photonic devices.

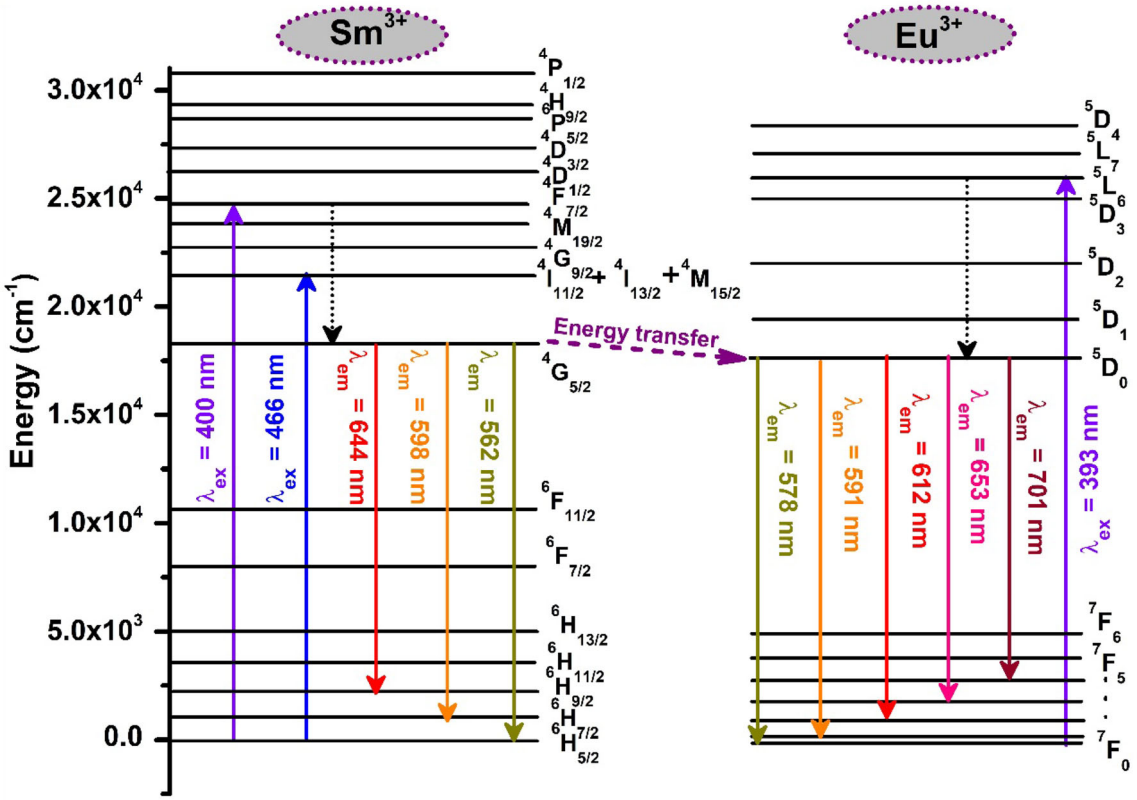


Fig. 6 Partial energy-level diagram presenting the energy transfer from sensitizer to activator in Sm^{3+}, Eu^{3+} co-doped CBP phosphor

3.4 Colorimetric properties

The Commission Internationale de l'Eclairage (CIE) color coordinates for the synthesized phosphors have been evaluated by utilizing the emission spectra at λ_{ex} = 400 nm, which are tabulated in Table 3. The CIE color coordinates for the as-prepared co-doped CBP: xSm^{3+}, y Eu^{3+} (x = 5.0 mol% & y = 0.0 to 10.0 mol%) phosphors can be seen from Fig. 7. The evaluated CIE color coordinates for CBP: xSm^{3+} (x = 5.0 mol%) phosphor were situated in orange region. The color coordinates were tuned toward red region with an increase in the Eu^{3+} ions concentration from 0.0 to 10.0 mol% in co-doped CBP phosphors. The inset of Fig. 7 depicts the variation in CIE coordinates from orange to red with an increase in the Eu^{3+} ion concentration from 0.0 to 10.0 mol% in the co-doped CBP phosphors. The aforementioned results reveal that the CBP: xSm^{3+}, yEu^{3+} phosphors have favorable characteristics for near-UV pumped tunable orange to red constituent to utilize in warm white LEDs and other photonic devices.

3.5 Decay time analysis

To examine the energy transfer mechanism from sensitizer to activator, the decay curves of $^4G_{5/2} \rightarrow {}^6H_{7/2}$ for the CBP:xSm^{3+}, yEu^{3+} (x = 5.0 mol% & y = 0.0 to 10.0 mol%) phosphors were recorded with the wavelength of λ_{em} = 598 nm and λ_{ex} = 400 nm. Figure 8a demonstrates that the decay profile rapidly reduces with an increase of Eu^{3+} activator ions content, which is a solid confirmation of a part of energy that migrates from Sm^{3+} to Eu^{3+} ions. The decay curve shows exponential nature and is best fitted with the bi-exponential equation as follows:

$$I(t) = I_o + A_1 exp\left(-\frac{t}{\tau_1}\right) + A_2 exp\left(-\frac{t}{\tau_2}\right)$$

where $I(t)$ and I_o signify the emission intensities CBP:xSm^{3+}, yEu^{3+} at time t and 0 s, respectively. τ_1 and τ_2 are the fast and slow lifetimes in ms. A_1 and A_2 indicate the two fitting constants. The average lifetime (τ_{avg}) has been determined by applying formula as follows [44, 45]:

Table 3 CIE color coordinates, lifetime, and ET efficiency of CBP:xSm^{3+}, yEu^{3+} (x = 5.0 & y = 0.0 to 10.0 mol%) phosphors at λ_{ex} = 400 and λ_{em} = 598 nm

CBP:xSm^{3+}, yEu^{3+} Phosphors (x = 5.0 mol%)	CIE color coordinates (x, y)	Lifetime (ms)	η_T (%)
y = 0.0 mol%	(0.572, 0.426)	2.453	–
y = 1.0 mol%	(0.576, 0.422)	2.365	3.58
y = 2.0 mol%	(0.584, 0.415)	2.193	10.59
y = 4.0 mol%	(0.592, 0.406)	1.978	19.36
y = 6.0 mol%	(0.593, 0.406)	1.946	20.64
y = 8.0 mol%	(0.596, 0.402)	1.754	28.49
y = 10.0 mol%	(0.607, 0.392)	1.368	44.20

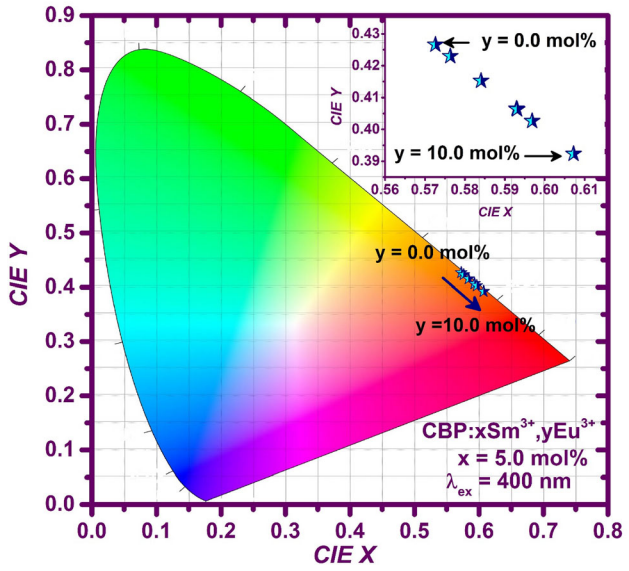


Fig. 7 CIE plot for CBP:xSm^{3+}, yEu^{3+} phosphor (x = 5.0 & y = 0.0 to 10.0 mol%) at λ_{ex} = 400. Inset plot reveals the color coordinate modulation with increasing Eu^{3+} concentration from 0.0 to 10.0 mol%

$$\tau_{avg} = \frac{A_1\tau_1^2 + A_2\tau_2^2}{A_1\tau_1 + A_2\tau_2}$$

The τ_{avg} (ms) values are tabulated in Table 3. It was noticed that the value of average lifetime for co-doped phosphors decreases with surge in the Eu^{3+} concentration as shown in Fig. 8b. The energy transfer (η_T) efficiency was calculated using τ_{avg} value in the following equation [46]:

$$\eta_T(\%) = \left(1 - \frac{\tau_d}{\tau_{d0}}\right) \times 100$$

where τ_{d0} and τ_d signify the average lifetime in ms of CBP: xSm^{3+},yEu^{3+} phosphor in the absence of Eu^{3+} ions (i.e., y = 0.0 mol%) and existence of the Eu^{3+} ions, respectively. The η_T values are presented in Table 3. A plot perceiving the variation in lifetime

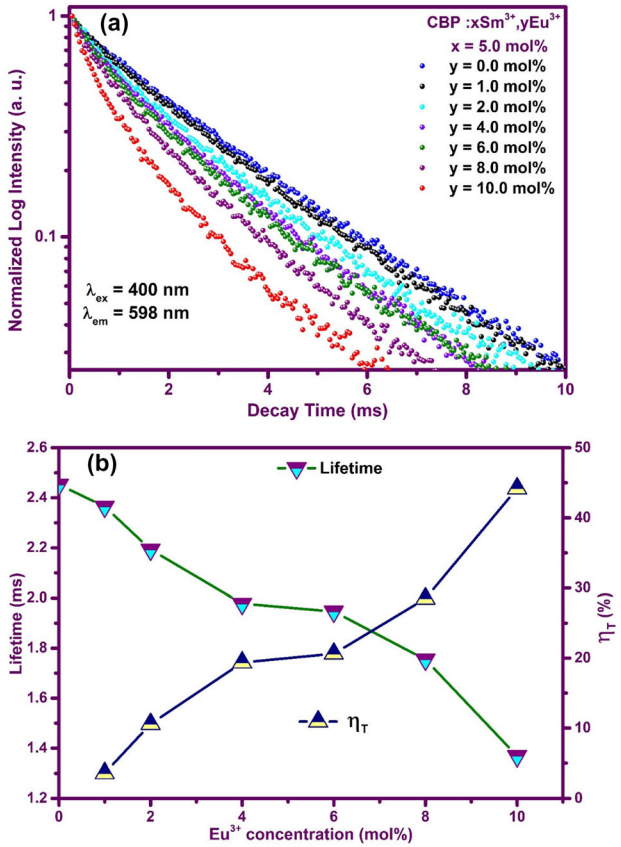


Fig. 8 (**a**) Decay curves of CBP:xSm^{3+}, yEu^{3+} phosphor with varying Eu^{3+} concentration (x = 5.0 & y = 0.0 to 10.0 mol%) at λ_{ex} = 400 and λ_{em} = 598 nm. (**b**) plots show the drop in lifetime value and enhancement in ET efficiency with increasing Eu^{3+} concentration from 0.0 to 10.0 mol%

and η_T values with increasing Eu^{3+} concentration is illustrated in Fig. 8b. It has been observed that η_T value improves with Eu^{3+} ion concentration, which implies a part of energy transfer from Sm^{3+} to Eu^{3+} ions. The η_T value in terms of percentage enhanced from 3.58 to 44.20% with the increase in Eu^{3+} ion concentration from 1.0 to 10.0 mol% in CBP: xSm^{3+}, yEu^{3+} phosphor. The enhancement in η_T value

signifies that with the surge in Eu^{3+} concentration, more and more energy is transferred from sensitizer Sm^{3+} to activator Eu^{3+} ion.

3.6 Thermal stability of CBP: xSm^{3+}, yEu^{3+} phosphor

Thermal stability is one of the important factors for phosphor to use as active component in many appliances. So the emission spectra were recorded with temperature rise from environmental temperature 32 to 200 °C with wavelength of λ_{ex} = 400 nm. The emission spectra for the CBP:xSm^{3+}, yEu^{3+} (x = 5.0 and y = 10.0 mol%) at different temperatures are exhibited in Fig. 9a. The intensity of the emission profile declines with increasing temperature. The emission intensity declined to 81.27% at 150 °C and 70.37% at 200 °C of initial intensity at 32 °C, which reveals that the as-prepared phosphor has higher thermal stability. In addition, the activation energy (ΔE) is calculated via formula expressed by Arrhenius equation [47]:

$$I_T = \frac{I_o}{1 + Cexp\left(-\frac{\Delta E}{K_B T}\right)}$$

where I_0 andI_T indicate the intensity of emission spectra at environmental temperature and T (K) temperature, respectively. C denotes an arbitrary constant and K_B is the Boltzmann constant having value $K_B = 8.617 \times 10^{-5}$ eV/K. The $ln((I_o/I_T)\text{-}1)$ versus $1/K_BT$ plot has been prepared and linearly fitted, which provides ΔE value and the resultant plot is shown in Fig. 9b. The ΔE value was noted as 0.217 eV for CBP:xSm^{3+}, yEu^{3+} (x = 5.0 & y = 10.0 mol%). The obtained activation energy was higher than the reported $Na_4CaSi_3O_9$:Sm^{3+}, Eu^{3+} (ΔE = 0.114 eV) and $Ca_9La(PO_4)_7$:Sm^{3+} (ΔE = 0.167 eV) and $Lu_2Ge_2O_7$:Bi^{3+},Sm^{3+} (ΔE = 0.114 eV) phosphors [48–50]. Hence the as-prepared phosphor has excellent thermal stability.

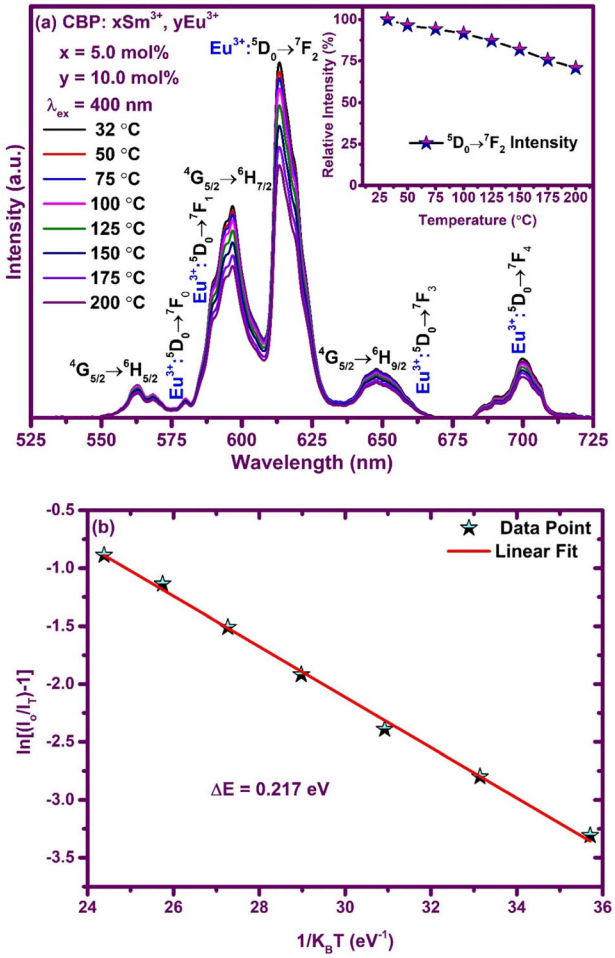


Fig. 9 **a** Emission intensity variation with temperature for CBP:xSm^{3+}, yEu^{3+} (x = 5.0 & y = 10.0 mol%) under λ_{ex} = 400 nm. The inset reveals the relative emission intensity variation with rise in temperature from 32 to 200 °C and **b** plot between $In[(I_o/I_T) - 1]$ versus $1/K_BT$

4 Conclusions

In summary, the tunable orange to red emitting CBP:Sm^{3+}, Eu^{3+} phosphors have been efficiently synthesized by employing co-precipitation technique. The XRD and refinement results reveal the pure and single phase of CBP crystallization in cubic structure. The CBP:Sm^{3+} phosphor is properly pumped by the near-UV and blue radiation and emits in the orange region. From the PL spectra of co-doped phosphors at λ_{ex} = 400 nm, it was found that the emission peak intensities of Sm^{3+} ions are reduced when increasing Eu^{3+} concentration, simultaneously enhancing the Eu^{3+} ions emission peak intensity. The lifetime values for CBP:Sm^{3+}, Eu^{3+} phosphors reduce with increase in the Eu^{3+} content under 400 nm excitation, which suggest ET between the Sm^{3+} to Eu^{3+} ions. The dipole–dipole nature of ET interaction takes place in CBP phosphors, which was verified by applying Dexter and Reisfeld's theory. The PL quantum yield for CBP:Sm^{3+}, Eu^{3+} phosphor has been found to be 86.65%, which is higher commercial phosphors, demonstrating that the as-prepared

phosphor can be a probable red emitting constituent in photonic devices. The CIE color coordinates modulate from orange to red region with Eu^{3+} ions under 400 nm excitation. The emission profile with varying temperature signifies excellent thermal stability of the as-synthesized CBP:Sm^{3+}, Eu^{3+} phosphor. The prominent results with optimum PL recommend that CBP phosphors will be useful for various fascinating applications in the field of displays, inorganic white LEDs, solar cells, and other photonic devices.

Acknowledgements

The author Mukesh K. Sahu sincerely acknowledges the Council of Scientific & Industrial Research (CSIR) for providing Senior Research Fellowship (File No. 08/133(0052)/2020 EMR-I).

Author contributions

MKS: Conceptualization, Formal analysis, Investigation, Methodology, Software, Writing—original draft; MJ: Supervision, Formal analysis, Methodology, Visualization, Validation, Writing—review and editing. All authors read and approved the final manuscript.

Data availability

The raw/processed data required to reproduce these findings cannot be shared at this time as the data also form part of an ongoing study.

Declarations

Conflict of interest The authors have no conflict of interest to declare.

References

1. B.M. Van Der Ende, L. Aarts, A. Meijerink, Phys. Chem. Chem. Phys. **11**, 11081 (2009)
2. P. Kumar, S. Singh, R. Lahon, A. Gundimeda, G. Gupta, B.K. Gupta, J. Lumin. **196**, 207 (2018)
3. K. Yoshikawa, H. Kawasaki, W. Yoshida, T. Irie, K. Konishi, K. Nakano, T. Uto, D. Adachi, M. Kanematsu, H. Uzu, K. Yamamoto, Nat. Energy **2**, 17032 (2017)
4. K. Li, R. Van Deun, A.C.S. Sustain, Chem. Eng. **7**, 16284 (2019)
5. R.V. Yadav, R.S. Yadav, A. Bahadur, A.K. Singh, S.B. Rai, Inorg. Chem. **55**, 10928 (2016)
6. J. Zheng, H. Mehrvarz, C. Liao, J. Bing, X. Cui, Y. Li, V.R. Gonçales, C.F.J. Lau, D.S. Lee, Y. Li, M. Zhang, J. Kim, Y. Cho, L.G. Caro, S. Tang, C. Chen, S. Huang, A.W.Y. Ho-Baillie, ACS Energy Lett. **4**, 2623 (2019)
7. J. Li, L. Chen, Z. Hao, X. Zhang, L. Zhang, Y. Luo, J. Zhang, Inorg. Chem. **54**, 4806 (2015)
8. H. Ahmed, J. Doran, S.J. McCormack, Sol. Energy **126**, 146 (2016)
9. G. Griffini, F. Bella, F. Nisic, C. Dragonetti, D. Roberto, M. Levi, R. Bongiovanni, S. Turri, Adv. Energy Mater. **5**, 1 (2015)
10. F. Bella, G. Griffini, M. Gerosa, S. Turri, R. Bongiovanni, J. Power Sources **283**, 195 (2015)
11. J.A. Luceño-Sánchez, A.M. Díez-Pascual, R.P. Capilla, Int. J. Mol. Sci. **20**, 976 (2019)
12. X. Li, J.D. Budai, F. Liu, J.Y. Howe, J. Zhang, X. Wang, Z. Gu, C. Sun, R.S. Meltzer, Z. Pan, Light Sci. Appl. **2**, e50 (2013)
13. Y. Gao, S. Murai, K. Shinozaki, J. Qiu, K. Tanaka, A.C.S. Appl, Electron. Mater. **1**, 961 (2019)
14. Z. Xia, Y. Zhang, M.S. Molokeev, V.V. Atuchin, J. Phys. Chem. C **117**, 20847 (2013)
15. F. Kang, Y. Zhang, M. Peng, Inorg. Chem. **54**, 1462 (2015)
16. G. Zhu, Z. Ci, Y. Shi, M. Que, Q. Wang, Y. Wang, J. Mater. Chem. C **1**, 5960 (2013)
17. V.R. Bandi, B.K. Grandhea, K. Jang, D.-S. Shin, S.-S. Yi, J.-H. Jeong, Mater. Chem. Phys. **140**, 453 (2013)
18. Y. Gao, B. Wang, L. Liu, K. Shinozaki, J. Lumin. **238**, 118235 (2021)
19. Y. Gao, J. Qiu, D. Zhou, J. Am. Ceram. Soc. **100**, 2901 (2017)
20. A. Mathur, P. Halappa, C. Shivakumara, J. Mater. Sci. Mater. Electron. **29**, 19951 (2018)
21. P.P. Sahoo, T.N. GuruRow, Inorg. Chem. **49**, 10013 (2010)
22. C. Zhang, H. Liang, S. Zhang, C. Liu, D. Hou, L. Zhou, G. Zhang, J. Shi, J. Phys. Chem. C **116**, 15932 (2012)
23. M.K. Sahu, M. Jayasimhadri, J. Lumin. **227**, 117570 (2020)
24. Z. Yang, D. Xu, J. Sun, Opt. Express **25**, A391 (2017)
25. M. Jiao, N. Guo, W. Lü, Y. Jia, W. Lv, Q. Zhao, B. Shao, H. You, Dalton Trans. **42**, 12395 (2013)
26. M.K. Sahu, J. Mula, J. Am. Ceram. Soc. **102**, 6087 (2019)
27. N. Chander, S.K. Sardana, P.K. Parashar, A.F. Khan, S. Chawla, V.K. Komarala, IEEE J. Photovolt. **5**, 1373 (2015)

28. B.P. Kore, A. Kumar, A. Pandey, R.E. Kroon, J.J. Terblans, S.J. Dhoble, H.C. Swart, Inorg. Chem. **56**, 4996 (2017)
29. S. Bishnoi, G. Swati, P. Singh, V.V. Jaiswal, M.K. Sahu, V. Gupta, N. Vijayan, D. Haranath, J. Appl. Crystallogr. **50**, 787 (2017)
30. X. Min, Z. Huang, M. Fang, Y. Liu, C. Tang, X. Wu, Inorg. Chem. **53**, 6060 (2014)
31. L. Alexander, H.P. Klug, J. Appl. Phys. **21**, 137 (1950)
32. L. Wang, H.M. Noh, B.K. Moon, S.H. Park, K.H. Kim, J. Shi, J.H. Jeong, J. Phys. Chem. C **119**, 15517 (2015)
33. S. Kaur, A.S. Rao, M. Jayasimhadri, Ceram. Int. **43**, 7401 (2017)
34. Y. Gao, S. Murai, K. Fujita, K. Tanaka, Opt. Mater. (Amst). **86**, 611 (2018)
35. K. Jha, M. Jayasimhadri, J. Lumin. **194**, 102 (2018)
36. G. Blasse, Philips Res. Rep. **24**, 131 (1969)
37. D.L. Dexter, J. Chem. Phys. **21**, 836 (1953)
38. Z. Yang, H. Dong, X. Liang, C. Hou, L. Liu, F. Lu, Dalton Trans. **43**, 11474 (2014)
39. M.K. Sahu, M. Jayasimhadri, K. Jha, B. Sivaiah, A.S. Rao, D. Haranath, J. Lumin. **202**, 475 (2018)
40. A. Huang, Z. Yang, C. Yu, Z. Chai, J. Qiu, Z. Song, J. Phys. Chem. C **121**, 5267 (2017)
41. S.G. Menon, A.K. Kunti, D.E. Motaung, H.C. Swart, New J. Chem. **43**, 17446 (2019)
42. G. Annadurai, B. Devakumar, H. Guo, R. Vijayakumar, B. Li, L. Sun, X. Huang, K. Wang, X.W. Sun, RSC Adv. **8**, 23323 (2018)
43. K. Li, H. Lian, R. Van Deun, Dalton Trans. **47**, 2501 (2018)
44. C.S. Kamal, T.K. Visweswara Rao, T. Samuel, P.V. Reddy, J.B. Jasinski, Y. Ramakrishna, M.C. Rao, K. Ramachandra Rao, RSC Adv. **7**, 44915 (2017)
45. P. Halappa, A. Mathur, D. Marie-Helene, C. Shivakumara, J. Alloys Compd. **740**, 1086 (2018)
46. R.A. Talewar, S. Mahamuda, K. Swapna, A.S. Rao, J. Alloys Compd. **771**, 980 (2019)
47. Z. Xia, S. Miao, M.S. Molokeev, M. Chen, Q. Liu, J. Mater. Chem. C **4**, 1336 (2016)
48. H. Tang, X. Zhang, L. Cheng, L. Jiang, X. Mi, Q. Liu, J. Xie, Y. Wang, J Lumin **214**, 116532 (2019)
49. B. Ma, X. Ma, T. Xu, K. Su, Q. Zhang, RSC Adv. **8**, 14164 (2018)
50. Q. Li, S. Zhang, W. Lin, W. Li, Y. Li, Z. Mu, F. Wu, Spectochim. Acta Part A Mol. Biomol. Spectrosc. **228**, 117755 (2020)

Publisher's Note Springer Nature remains neutral with regard to jurisdictional claims in published maps and institutional affiliations.

ResearchGate

See discussions, stats, and author profiles for this publication at: https://www.researchgate.net/publication/358524859

Sustainable supply chain risk mitigation: a mixed method approach

Article *in* International Journal of Intelligent Enterprise · February 2022

CITATIONS
0

READS
16

3 authors:



Madhukar Chhimwal
Delhi Technological University
8 PUBLICATIONS **8** CITATIONS
SEE PROFILE



Saurabh Agrawal
Delhi Technological University
36 PUBLICATIONS **840** CITATIONS
SEE PROFILE



G. Kumar
Delhi Technological University
56 PUBLICATIONS **271** CITATIONS
SEE PROFILE

Some of the authors of this publication are also working on these related projects:

Project Circular Economy Challenges View project

Project Circular Economy Risk View project

All content following this page was uploaded by Madhukar Chhimwal on 11 February 2022.

The user has requested enhancement of the downloaded file.

Sustainable supply chain risk mitigation: a mixed method approach

Madhukar Chhimwal*

Department of Mechanical and Automation Engineering,
Maharaja Agrasen Institute of Technology,
Delhi, India
Email: madhukar.chhimwal@gmail.com
*Corresponding author

Saurabh Agrawal and Girish Kumar

Department of Mechanical, Production and Industrial Engineering,
Delhi Technological University,
Delhi, India
Email: agrawals.iit@gmail.com
Email: girishkumar@dce.ac.in

Abstract: The objective of this research is to find a way to minimise risk in the supply chain by identifying the critical success factors and analysing the relationship between sundry critical success factors. The proposed study constructs a model of the critical success factors using the interpretive structural modelling approach and tests the model using regression analysis technique. Analysis of the results indicates that there are some critical success factors which have high driving power and low dependence that require utmost attention and are of great paramount while other cluster consists of those critical success factors which are highly dependent and need futuristic actions. In this work, only regression analysis technique is used to validate the model that is developed using interpretive structural modelling approach. This type of relegation will help the supply chain managers to distinguish between independent and dependent critical success factors and how the relationships among the critical success factors will efficaciously minimise the risk in a supply chain. This study can be considered as a base study for the practitioners and academicians who are working in the area of risk management for achieving sustainability in the supply chain.

Keywords: sustainable supply chain management; SSCM; interpretive structural modelling; ISM; regression analysis; risk mitigation.

Reference to this paper should be made as follows: Chhimwal, M., Agrawal, S. and Kumar, G. (2022) 'Sustainable supply chain risk mitigation: a mixed method approach', *Int. J. Intelligent Enterprise*, Vol. 9, No. 2, pp.142–162.

Biographical notes: Madhukar Chhimwal is an Assistant Professor in Mechanical and Automation Engineering Department at Maharaja Agrasen Institute of Technology, Delhi and he is pursuing his PhD in Mechanical Engineering from Delhi Technological University, Delhi, India. He obtained his Master's in Manufacturing Systems Engineering (MSE) with distinction

Copyright © 2022 Inderscience Enterprises Ltd.

from Sant Longowal Institute of Engineering and Technology (Deemed University, Estd. Govt. of India), Sangrur, Punjab, India. His focused areas of research are sustainability in supply chain, circular economy and risk management.

Saurabh Agrawal is an Assistant Professor in Mechanical, Production and Industrial Engineering Department at Delhi Technological University, Delhi, India. He has vast experience of academics, research and the industry both in India and in the USA. His research focus is in the areas of supply chain management, reverse logistics, sustainability, and e-waste management. He received his Master of Business Administration (MBA) from Oregon State University, USA, and Master in Technology (MTech) from Indian Institute of Technology (IIT), Delhi, India.

Girish Kumar is a faculty member in Mechanical Engineering Department at Delhi Technological University, Delhi, India. He has more than 20 years of experience in industry, teaching and research. His teaching and research areas include reliability engineering, maintenance management, quality engineering, stochastic modelling, etc. He holds a PhD degree in Reliability Engineering from Indian Institute of Technology Delhi, India. He has published 17 papers in international journals and conference proceedings. He also completed a visiting faculty assignment at AIT Bangkok in August-2017 semester.

1 Introduction

Sustainable business development has received much attention over the past decade owing to the significant attention given by governments and both profit and not-for-profit organisations to environmental, social and corporate responsibility. The emergence of a changing economic order has also made companies around the world seriously think about manufacturing and service sustainability (Ageron et al., 2012). Global markets and operations have prompted companies to revisit their corporate, business and functional strategies in addition to focusing on outsourcing, virtual enterprise and supply chain management.

Another term yet very familiar is green supply-chain management (GSCM) which is gaining increasing interest among researchers and practitioners of operations and supply chain management. The growing importance of GSCM is driven mainly by the escalating deterioration of the environment, e.g., diminishing raw material resources, overflowing waste sites and increasing levels of pollution. However, it is not just about being environment friendly; it is about good business sense and higher profits. In fact, it is a business value driver and not a cost centre (Srivastava, 2007).

Shrivastava (1995) provided a description of sustainability, which is directly related to risk. Sustainability means offering, "the potential for reducing long-term risks associated with resource depletion, fluctuations in energy costs, product liabilities, and pollution and waste management". Sustainability and Risk are evidently related. In the risk management literature, an existing gap is related to the absence of a clear differentiation between the concept of 'sustainable risk management' and the categorisation of 'risks in sustainable supply chain'.

"Risk is defined as how consumer's interpret skeptically and worst situations of procurement of product or service" (Chopra and Sodhi, 2004). Risks are unpredictable

and can occur at any level of supply chain. Risk management process involves examining the risks, and diminishing their effect by addressing. The risks can be minimised in the supply chains if companies focus on the CSFs having an impact on management of risk in the supply chains (Dowling and Staelin, 1994).

In this study, identification of 20 such critical success factors (CSFs) has been done through extensive literature review and after discussing with the experts from industry and academia. With the help of interpretive structural modelling (ISM) approach, relationship among these CSFs have been found out and a structural model has been developed which shows the level of importance of these factors. Thereafter CSFs are classified into various categories using MICMAC analysis based upon their driver and dependence power. With the help of ISM-based model and MICMAC analysis a conceptual framework is developed which shows relationship among different CSF's. Then a hypothesis testing is being done on the relationships using regression analysis technique and the results are validated using F-test.

The main objectives of this paper are:

- identify and ranking of the CSFs for risk mitigation in supply chains
- finding out the interaction among identified CSF's using ISM technique
- developing a hierarchal model of the CSF's depicting their various levels
- developing a conceptual framework stating the interrelationship between the various CSF's
- testing the hypothesis of the given conceptual framework using regression analysis technique.

Further the paper comprises of 'literature review' section stating contribution given by different authors in the field of sustainable supply chain management (SSCM) and risk management. CSFs are identified for successful implementation of sustainable supply chain risk management under the heading 'identification of CSFs'. These identified CSFs are then utilised to prepare a model using ISM approach under the section 'methodology'. Once the model has been developed the importance of each CSF is analysed using MICMAC analysis. Further a hypothesis is developed stating the relationship among different CSF's which is tested for its validity using regression analysis technique and the results of the test are tabulated under the section 'results'. On the basis of results obtained implications are made which concludes to our observation about the importance of CSF's and how these are related to each other under the section 'managerial implication'. At last conclusion is made and the scope for further research is provided under the heading 'conclusions and future scope'.

2 Literature review

Sustainability has become an imperative research agenda among the researchers/practitioners to achieve ecological, societal as well as financial benefits. At the moment, SSCM practices are at a very initial phase in developing countries like India due to existence of many hurdles (Luthra and Haleem, 2015). Fahimnia et al. (2015) conducted a systematic review of the analytical and quantitative models related to sustainable supply chain risk management. The authors during their review applied

bibliometric and network analysis tools to get insights into the topic which has not been covered during the past review.

However, available to date research on SSCM is still at the development stage. Gold et al. (2010) referred that "literature on SSCM is still limited, and literature reviews are scant", with only nine comprehensive literature review papers on SSCM are available today. Seuring and Müller (2008) have also concluded that SSCM "literature is still limited in quantity, and no major reviews of the field has been conducted". As part of their vast scan of 191 papers written in period of 1994–2007 on SSCM, only seven encompassing literature review articles were identified.

One of deficiencies of existing research in SSCM is inconsistency in understanding sustainability. Carter and Rogers (2008) have demonstrated the inconsistency of defining sustainability in vast scope of organisational, operational and supply chain management literature. According to their findings, substantial body of SSCM literature is restricted to specific environmental issues as green product development, logistics, waste treatment, human rights etc. and therefore provides narrow perspective on what SSCM represents. Different environmental issues are addressed "in a standalone fashion, without consideration of the potential interrelationships" between environmental, social and economic issues (Carter and Rogers, 2008). Seuring and Müller (2008) have also highlighted that research in SSCM is still dominated by green/environmental issues with a clear deficit in supply chain management and purchasing literature on the amalgamation of all three dimensions of sustainable development. Social issues and sustainability as integration of economic, environmental and social concerns are still rarely addressed. Interestingly, integration of three aspects of sustainability in academic literature has generally occurred since 2002 (Seuring and Müller, 2008).

In the popular, practitioner-oriented risk management literature (Goldberg et al., 1999), as well as among the managers interviewed, the uses of the term 'risk' can be confusing because it is perceived as a multidimensional construct (Zsidisin and Ellram, 2003). On the one hand, it is used to refer to uncertain internal or external, environmental variables that reduce outcome predictability. In this sense, 'risk' actually refers to a source of risk and uncertainty, such as 'political risks' and 'market risks' or, from a supply chain view, 'the volatility of customer demand'. On the other hand, the term risk is also used when referring to the consequences of risks, i.e., to the potential outcome indicators. In this sense, the terms 'operational risks', 'human risks' or 'risks to customer service levels' are consequences of risks becoming events.

In defining the concept of supply chain risk management for the purpose of this paper, we adopt the definition provided by March and Shapira (1987) and define 'risk' as "the variation in the distribution of possible supply chain outcomes, their likelihood, and their subjective values". From our supply chain perspective, these uncertain variations or disruptions affect the flows of information, materials or products across organisation borders.

In this paper, an effort has been made to identify and prioritise the CSFs for the effective implementation of risk management while adopting SSCM practices. Despite profound contributions by the academicians and practitioners of national and international repute on the topic of SSCM and risk management. The literature reviewed still has a wide range of gaps which are to be addressed in the upcoming years with focused dedication so as to enhance the concept of sustainable supply chain risk management. Some research gaps are removed by many researchers in the recent years

and have given good direction to their study. Some of the research gaps in this field of study are as mentioned below:-

- Many authors have discussed directly or indirectly about the different CSFs, but only few have discussed about the interdependence of one factor over the other which can help in effective implementation of risk mitigation. Discussion on the interdependence of CSF's will help future researchers in achieving sustainability in the supply chain.
- There are a few guidelines to maximise the effect of CSFs during the planning of risk minimisation in enhancing the sustainability in the supply chain.
- There is a need of preventive model which can predict the success of implementing effective risk mitigation in manufacturing organisation. Hence this research assumes importance in this context.

This study can be considered as a base study for the practitioners and academicians who are working in the area of risk management for achieving sustainable supply chain in the organisation.

3 Identification of CSFs

In this study, 20 such CSFs which will help in risk mitigation while implementing sustainability in the supply chain have been identified through extensive literature review and also through discussion with experts from industry and academia. The list of CSFs along with the definition and sources are discussed in Table 1.

Table 1 List of CSFs for mitigating the risk in supply chain

Critical success factors		*Definition*	*References*
1	Sharing of information	Communication done in an effective way may lead to better understanding between all the partners of supply chain.	Lee et al. (1997b), Hahn et al. (2000) and Lotfi et al. (2013)
2	Flexibility in the supply chain	Flexibility is defined as the facility to sustain yourself in a perpetually transmuting, capricious business environment. Flexibility can be also defined as the ability to mould yourself according to the demand of the market.	Prater (2001) and Kurien and Qureshi (2011)
3	Reliability among supply chain partners	Reliability build up through effective communication can have better outcomes which enhances overall customer service.	Sinha et al. (2004) and Luthra and Haleem, 2015 (2015)
4	Collaborative relationships among supply chain partners	Close relationships with key suppliers helps in risk management process in supply chain.	Giunipero and Eltantawy (2004)
5	Information security	Tampering of any kind of information that is passed through the supply chain partners may lead to miscommunication among them.	Finch (2004) and Tang and Musa (2011)

Table 1 List of CSFs for mitigating the risk in supply chain (continued)

Critical success factors		*Definition*	*References*
6	Organisational culture	Staff morale and commitment. Adaption to change and respect to external management consultants	Lee et al. (1997b) and Kurien and Qureshi (2011)
7	Corporate social responsibility	CSR is the responsibility of a company to take a stand for all its stakeholders for the operations and activities carried out.	Speckman and Davis (2004) and Grimm et al. (2014)
8	Resources availability	When resources are available in right quantity, at right time and at right place this may help in saving large amount of time.	Hahn et al. (2000) and Toke (2012)
9	Handling of external pressure	It illustrates how an organisation can handle market pressure. Everyday a new product with new features is launched in the market. Pressure can be handled easily if coordination among supply chain members is good.	Lee et al. (1997a) and Rozar et al. (2015)
10	Combining incentives and revenue sharing policies in a supply chain	A supply chain will function smoothly when the incentives provided to the member companies align with the policies of the organisation	Narayanan and Raman (2004) and Kanda and Deshmukh (2008)
11	Strategic risk planning	Identification and development of contingency plans is necessary to minimise various risks that exist internally and externally to the organisation	Lee (2002)
12	Sharing of risk in a supply chain	Sharing of both risks and rewards among the members of the supply chain not only sanctions them to fixate on their own risks but withal sanction them to fixate on risks with other members of supply chain.	Mentzer et al. (2001) and Xu et al. (2014)
13	Continuous improvement	Continuously striving for better ways to deliver a product or to provide best services that can enhance the performance of the supply chain	Scholten et al. (2014)
14	Effective utilisation of resources	Effective utilisation of man, machine, raw material and time can definitely put an organisation's supply chain into the front seat.	Chopra and Sodhi (2014)
15	Awareness about risks in a supply chain	Knowledge about various types of risk may lead to better understanding of risks in a supply chain that further helps in making good decisions.	Hallikas et al. (2004) and Scholten et al. (2014)
16	Continual risk analysis and assessment	Periodic assessment and analysis of various types of risk helps in better decision making and resolving problems that could create hindrance in future.	Shtub et al. (1994) and Heckmann et al. (2015)
17	Logistics synchronisation	Logistic synchronisation occurs when a flow-oriented coordination is present in the production-logistic process chain.	Badea et al. (2014)

Table 1 List of CSFs for mitigating the risk in supply chain (continued)

Critical success factors		*Definition*	*References*
18	Use of modern technologies	The use of modern technologies in manufacturing, freight transportation, information sharing etc. reduces the chances of risk significantly.	Lee et al. (1997b), Giannakis and Louis (2011)
19	Forecasting of demand on point of sale (POS)	Collaborative decision making by supply chain members results in better forecasting of demand, trust between the supply chain members, and flow of information. Availability of point of sales (POS) data is important for a responsive supply chain.	Stadtler (2015) and Nachtmann et al. (2010)
20	Long-term vision for survival and growth	Company long term vision for survival and growth can help them in facing forthcoming risk in supply chain and will also reduce the occurrence of risks in future.	Ganesan et al. (1994) and Kumar et al. (2015)

4 Methodology

ISM is a methodology which indentifies relationship among particular CSFs, which have connections with the defined problem (Warfield, 1974; Sage, 1977). ISM is interpretive because the relationship among the CSFs is established depending on the judgment of selected group of experts. Gopal and Thakkar (2016) analysed 25 CSFs behind the successful implementation of sustainable supply chain practices in Indian automobile industry and proposed a solution through a structural model built using the ISM technique. Further, the importance of CSFs had been determined based on their driving and dependence power using MICMAC analysis. Dubey et al. (2015) contributed to the literature on green supply chain management (GSCM) enablers by arguing for the use of mixed methods for theory building. ISM, MICMAC analysis, and confirmatory factor analysis (CFA) were used to illustrate the application of mixed methods in GSCM by testing a model on the enablers of GSCM. Kumar et al. (2015) identified 13 CSFs for implementation of SCM in SMEs and studied their impact on performance of Indian SMEs. Top management commitment, long term vision, focus on core strengths, devoted resources for supply chain, and development of effective SCM strategy emerged as the most pertinent CSFs. Jayant and Azhar (2014) determined the relationship among the GSCM barriers and identified the most influential barriers from the recommended barrier list with the help of ISM technique. Khurana et al. (2014) used the qualitative research technique to study the critical factors which affect the integration of sustainability with innovation taking into account Indian manufacturing SMEs. ISM approach was applied to establish the interrelationship between the various CSFs.

ISM and MICMAC approach is utilised in this research because this technique is structural in its kind and a complete structure can be extracted from the intricate set of CSFs depending on the kind of relationship among them. It is a modelling technique too because relationships among the CSFs and the overall structure of the system is displayed in a digraph model. As compared to other rating techniques like AHP, ANP, DEMATEL, VIKOR, TOPSIS etc this technique provides a contextual relationship among the CSFs

based on the driving potential and the dependency while defining the levels of each and every CSF. ISM generally has following steps (Faisal et al., 2006):

Step 1 Identification of CSFs is done that affect the system.

Step 2 A one to one relationship is established among CSF's with veneration to which dyads of CSF would be examined.

Step 3 A structural self-interaction matrix (SSIM) is prepared using CSF, which establishes pair wise relationships among CSF's of the system.

Step 4 Reachability matrix is extracted from the SSIM and the matrix is checked for transitivity. The transitivity of the contextual cognation among the CSF's states that if a CSF A is cognate to B and B is cognate to C, then A is obligatorily cognate to C.

Step 5 The reachability matrix obtained in the previous step is divided into different levels.

Step 6 Predicated on the relationships build in the reachability matrix, a directed graph is drawn and the transitive links are abstracted.

4.1 Structural self-interaction matrix

To analyse the CSF's of the risk mitigation, a contextual relationship is established. This denotes that one CSF avails to achieve another CSF. Predicated on this, contextual relationship between the CSFs is developed. Considering the contextual relationship for each CSF, the subsistence of a cognation between any two CSF's (i and j) and the associated direction of the cognation is tenacious. Four types of symbols are habituated to show the direction of relationship between the CSF's (i and j):

V CSF i will avail to achieve CSF j

A CSF j will be achieved utilising CSF i

X CSF i and j both avail in achieving each other

O CSFs i and j are unrelated.

Table 2 would expound the utilisation of the symbols V, A, X, and O in Structural Self Interaction Matrix.

4.2 Initial reachability matrix

In this step, the reachability matrix is extracted from SSIM. The SSIM format is transmuted into an initial reachability matrix format by transforming the information of each cell of SSIM into binary digits (i.e., ones or zeros) in the initial reachability matrix by superseding V,A,X,O by 1 or 0 applying complying with rules.

- if the (x, y) ingress in the SSIM is V, then the (x, y) ingress in the reachability matrix becomes 1 and the (y, x) ingress becomes 0
- if the (x, y) ingression in the SSIM is A, then the (x, y) ingression in the reachability matrix becomes 0 and the (y, x) ingression becomes 1

- if the (x, y) ingression in the SSIM is X, then the (x, y) ingress in the reachability matrix becomes 1 and the (y, x) ingress withal becomes 1
- if the (x, y) ingress in the SSIM is O, then the (x, y) ingress in the reachability matrix becomes 0 and the (y, x) ingression withal becomes 0.

Following the above rules the initial reachability matrix is shown in Table 3.

Table 2 Structural self interaction matrix

CSFs	*20*	*19*	*18*	*17*	*16*	*15*	*14*	*13*	*12*	*11*	*10*	*9*	*8*	*7*	*6*	*5*	*4*	*3*	*2*	*1*
1	V	V	V	A	V	V	V	V	V	V	V	V	V	V	O	V	X	X	V	
2	V	A	A	V	O	O	V	A	A	A	A	A	A	O	A	A	A	A		
3	V	V	O	V	V	O	V	V	V	V	V	V	O	V	V	V	X			
4	V	V	O	V	V	O	V	V	V	V	V	V	O	V	A	V				
5	V	V	A	V	O	A	V	O	O	A	A	O	O	A	V					
6	V	O	O	V	O	O	V	V	A	O	V	V	O	V						
7	V	O	O	O	V	A	O	O	V	O	X	X	O							
8	V	O	O	V	O	O	A	A	O	A	O	V								
9	X	V	A	A	A	A	V	V	A	A	O									
10	O	O	O	V	V	A	O	V	V	V										
11	A	V	X	A	V	A	V	V	V											
12	O	V	O	V	V	A	V	V												
13	A	V	A	A	A	A	A													
14	A	O	A	A	O	O														
15	V	V	O	O	V															
16	A	V	O	X																
17	A	V	A																	
18	A	O																		
19	V																			
20																				

4.3 Final reachability matrix

Initial reachability matrix is extracted from the SSIM and transitivity of the matrix is examined. The transitivity of the contextual cognation states that if a CSF A is cognate to B and B is cognate to C, then A is obligatorily cognate to C. Complying with these rules and after incorporating the transitivity the final reachability matrix is shown in Table 4.

4.4 Level partition

In the final reachability matrix, for each CSF the reachability and antecedent set are found. The reachability set comprises of the variable itself and the other variables which may be affected from it, whereas on the other side antecedent set comprises of the variable itself and the other variables which may impact it. Thereafter, the intersection of both the sets is derived for all the CSFs. The CSFs for which the reachability and the

intersection sets are the same are then placed at the top most level in the ISM hierarchy. The top most elements would not help achieve any other element above its own level. Once the top-level element are identified, these are disunited out from the other elements. Then, the same process is reiterated to ascertain the elements in the next level. This process is perpetuated until the level of each element is found.

Table 3 Initial reachability matrix

CSFs	*1*	*2*	*3*	*4*	*5*	*6*	*7*	*8*	*9*	*10*	*11*	*12*	*13*	*14*	*15*	*16*	*17*	*18*	*19*	*20*
1	1	1	1	1	1	0*	1	1	1	1	1	1	1	1	1	1	0*	1	1	1
2	0*	1	0	0	0	0	0	0	0	0	0	0	0	1	0	0	1	0	0	1
3	1	1	1	1	1	1	1	0*	1	1	1	1	1	1	0*	1	1	0*	1	1
4	1	1	1	1	1	0*	1	0*	1	1	1	1	1	1	0*	1	1	0*	1	1
5	0*	1	0	0	1	1	0	0	0	0	0	0	0	1	0	0	1	0	1	1
6	0*	1	0*	1	0*	1	1	0*	1	1	0*	0*	1	1	0	0*	1	0	0*	1
7	0	0*	0	0	1	0*	1	0	1	1	0	1	0*	0*	0	1	0*	0	0*	1
8	0	1	0	0	0	0	0	1	1	0	0	0	0	0*	0	0	1	0	0	1
9	0	1	0	0	0*	0	1	0	1	0*	0	0	1	1	0	0*	0*	0	1	1
10	0	1	0	0	1	0*	1	0	0*	1	1	1	1	0*	0	1	1	0	0	0
11	0	1	0	0	1	0*	0	1	1	0	1	1	1	1	0	1	0*	1	1	0*
12	0	1	0	0	0	1	0	0	1	0	0	1	1	1	0	1	1	0	1	0
13	0	1	0	0	0	0	0	1	0*	0	0*	0	1	0*	0	0	0*	0	1	0*
14	0	0*	0	0	0	0	0	1	0*	0	0*	0	1	1	0	0	0*	0	0	0*
15	0	0*	0	0	1	0*	1	0	1	1	1	1	1	0*	1	1	0*	0	1	1
16	0	0*	0	0	0	0	0*	0	1	0	0	0	1	0*	0	1	1	0	1	0*
17	1	0*	0*	0*	0*	0	0*	0*	1	0*	1	0*	1	1	0*	0*	1	0*	1	0*
18	0	1	0	0	1	0	0	0	1	0	1	0	1	1	0	0	1	1	0	0*
19	0	1	0	0	0	0	0	0	0	0	0	0	0	0*	0	0	0*	0	1	1
20	0	0*	0	0	0	0	0	0	1	0	1	0	1	1	0	1	1	1	0*	1

Note: *Denotes rule of transitivity is applicable.

Table 4 Final reachability matrix after applying transitivity

CSF's	*1*	*2*	*3*	*4*	*5*	*6*	*7*	*8*	*9*	*10*	*11*	*12*	*13*	*14*	*15*	*16*	*17*	*18*	*19*	*20*	*Driver*
1	1	1	1	1	1	1	1	1	1	1	1	1	1	1	1	1	1	1	1	1	20
2	1	1	0	0	0	0	0	0	0	0	0	0	0	1	0	0	1	0	0	1	5
3	1	1	1	1	1	1	1	1	1	1	1	1	1	1	1	1	1	1	1	1	20
4	1	1	1	1	1	1	1	1	1	1	1	1	1	1	1	1	1	1	1	1	20
5	1	1	0	0	1	1	0	0	0	0	0	0	0	1	0	0	1	0	1	1	8
6	1	1	1	1	1	1	1	1	1	1	1	1	1	1	0	1	1	0	1	1	18
7	0	1	0	0	1	1	1	0	1	1	0	1	1	1	0	1	1	0	1	1	13
8	0	1	0	0	0	0	0	1	1	0	0	0	0	1	0	0	1	0	0	1	7
9	0	1	0	0	1	0	1	0	1	1	0	0	1	1	0	1	1	0	1	1	11

Table 4 Final reachability matrix after applying transitivity (continued)

CSF's	*1*	*2*	*3*	*4*	*5*	*6*	*7*	*8*	*9*	*10*	*11*	*12*	*13*	*14*	*15*	*16*	*17*	*18*	*19*	*20*	*Driver*
10	0	1	0	0	1	1	1	0	1	1	1	1	1	1	0	1	1	0	0	0	12
11	0	1	0	0	1	1	0	1	1	0	1	1	1	1	0	1	1	1	1	1	14
12	0	1	0	0	0	1	0	0	1	0	0	1	1	1	0	1	1	0	1	1	10
13	0	1	0	0	0	0	0	1	1	0	1	0	1	1	0	0	1	0	1	1	9
14	0	1	0	0	0	0	0	1	1	0	1	0	1	1	0	0	1	0	0	1	8
15	0	1	0	0	1	1	1	0	1	1	1	1	1	1	1	1	1	0	1	1	15
16	0	1	0	0	0	0	1	0	1	0	0	0	1	1	0	1	1	0	1	1	9
17	1	1	1	1	1	0	1	1	1	1	1	1	1	1	1	1	1	1	1	1	19
18	0	1	0	0	1	0	0	0	1	0	1	0	1	1	0	0	1	1	0	1	9
19	0	1	0	0	0	0	0	0	0	0	0	0	0	1	0	0	1	0	1	1	5
20	0	1	0	0	0	0	0	0	1	0	1	0	1	1	0	1	1	1	1	1	10
Dependence	7	20	5	5	12	10	10	9	17	9	13	10	16	20	5	13	20	7	15	19	

Table 5 Iteration i

CSF	*Reachability set*	*Antecedent set*	*Intersection set*	*Level*
1	1, 2, 3, 4, 5, 6, 7, 8, 9, 10, 11, 12, 13, 14, 15, 16, 17, 18, 19, 20	1, 2, 3, 4, 5, 6, 17	1, 2, 3, 4, 5, 6, 17	
2	1, 2, 14, 17, 20	1, 2, 3, 4, 5, 6, 7, 8, 9, 10, 11, 12, 13, 14, 15, 16, 17, 18, 19, 20	1, 2, 14, 17, 20	I
3	1, 2, 3, 4, 5, 6, 7, 8, 9, 10, 11, 12, 13, 14, 15, 16, 17, 18, 19, 20	1, 3, 4, 6, 17	1, 3, 4, 6, 17	
4	1, 2, 3, 4, 5, 6, 7, 8, 9, 10, 11, 12, 13, 14, 15, 16, 17, 18, 19, 20	1, 3, 4, 6, 17	1, 3, 4, 6, 17	
5	1, 2, 5, 6, 14, 17, 19, 20	1, 3, 4, 5, 6, 7, 9, 10, 11, 15, 17, 18	1, 5, 6, 17	
6	1, 2, 3, 4, 5, 6, 7, 8, 9, 10, 11, 12, 13, 14, 16, 17, 19, 20	1, 3, 4, 5, 6, 7, 10, 11, 12, 15	1, 3, 4, 5, 6, 7, 10, 11	
7	2, 5, 6, 7, 9, 10, 12, 13, 14, 16, 17, 19, 20	1, 3, 4, 6, 7, 9, 10, 15, 16, 17	6, 7, 9, 10	
8	2, 8, 9, 11, 14, 17, 20	1, 3, 4, 6, 8, 11, 13, 14, 17	8, 14, 17	
9	2, 5, 7, 9, 10, 13, 14, 16, 17, 19, 20	1, 3, 4, 6, 7, 8, 9, 10, 11, 12, 13, 14, 15, 16, 17, 18, 20	7, 9, 10, 13, 14, 16, 17, 20	
10	2, 5, 6, 7, 9, 10, 11, 12, 13, 14, 16, 17	1, 3, 4, 6, 7, 9, 10, 15, 17	6, 7, 9, 10, 17	
11	2, 5, 6, 8, 9, 11, 12, 13, 14, 16, 17, 18, 19, 20	1, 3, 4, 6, 8, 10, 11, 13, 14, 15, 17, 18, 20	6, 11, 13, 14, 17, 18, 20	
12	2, 6, 9, 12, 13, 14, 16, 17, 19	1, 3, 4, 6, 7, 10, 11, 12, 15, 17, 20	12, 17	

Table 5 Iteration I (continued)

CSF	*Reachability set*	*Antecedent set*	*Intersection set*	*Level*
13	2, 8, 9, 11, 13, 14, 17, 19, 20	1, 3, 4, 6, 7, 9, 10, 11, 12, 13, 14, 15, 16, 17, 18, 20	9, 11, 13, 14, 17, 20	
14	2, 8, 9, 11, 13, 14, 17, 20	1, 2, 3, 4, 5, 6, 7, 8, 9, 10, 11, 12, 13, 14, 15, 16, 17, 18, 19, 20	2, 8, 9, 11, 13, 14, 17, 20	I
15	2, 5, 6, 7, 9, 10, 11, 12, 13, 14, 15, 16, 17, 19, 20	1, 3, 4, 15, 16, 17	15, 17	
16	2, 7, 9, 13, 14, 15, 16, 17, 19, 20	1, 3, 4, 6, 7, 9, 10, 11, 12, 15, 16, 17, 20	7, 9, 16, 17, 20	
17	1, 2, 3, 4, 5, 7, 8, 9, 10, 11, 12, 13, 14, 15, 16, 17, 18, 19, 20	1, 2, 3, 4, 5, 6, 7, 8, 9, 10, 11, 12, 13, 14, 15, 16, 17, 18, 19, 20	1, 2, 3, 4, 5, 7, 8, 9, 10, 11, 12, 13, 14, 15, 16, 17, 18, 19, 20	I
18	2, 5, 9, 11, 13, 14, 17, 18, 20	1, 3, 4, 11, 17, 18, 20	11, 17, 18, 20	
19	2, 14, 17, 19, 20	1, 3, 4, 5, 6, 7, 9, 11, 12, 13, 15, 16, 17, 19, 20	17, 19, 20	
20	2, 9, 11, 13, 14, 16, 17, 18, 19, 20	1, 2, 3, 4, 5, 6, 7, 8, 9, 11, 13, 14, 15, 16, 17, 18, 19, 20	2, 9, 11, 13, 14, 16, 17, 18, 19, 20	I

Table 6 Iteration ii-v

Iteration	*CSF*	*Reachability set*	*Antecedent set*	*Intersection set*	*Level*
ii	19	19	1, 3, 4, 5, 6, 7, 9, 11, 12, 13, 15, 16, 19	19	II
ii	5	1, 5, 6	1, 3, 4, 5, 6, 7, 9, 10, 11, 15, 18	1, 5, 6	II
ii	9	7, 9, 10, 13, 16	1, 3, 4, 6, 7, 8, 9, 10, 11, 12, 13, 15, 16, 18	7, 9, 10, 13, 16	II
ii	13	8, 11, 13	1, 3, 4, 6, 7, 8, 10, 11, 12, 13, 15, 16	8, 11, 13	II
iii	18	11, 18	1, 3, 4, 11, 18	11, 18	III
iii	16	7, 15, 16	1, 3, 4, 6, 7, 10, 11, 12, 15, 16	7, 15, 16	III
iii	8	8, 11	1, 3, 4, 6, 8, 11	8, 11	III
iii	6	1, 3, 4, 6, 7, 10, 11, 12	1, 3, 4, 6, 7, 10, 11, 12, 15	1, 3, 4, 6, 7, 10, 11, 12	III
iv	12	12	1, 3, 4, 7, 10, 11, 12, 15	12	IV
iv	11	11	1, 3, 4, 10, 11, 15	11	IV
iv	7	7, 10	1, 3, 4, 7, 10, 15	7, 10	IV
iv	10	10	1, 3, 4, 10, 15	10	IV
v	15	15	1, 3, 4, 15	15	V
v	1	1, 3, 4	1, 3, 4	1, 3, 4	V
v	3	3, 4	3, 4	3, 4	V
v	4	4	4	4	V

Figure 1 ISM-based model for risk mitigation in supply chain

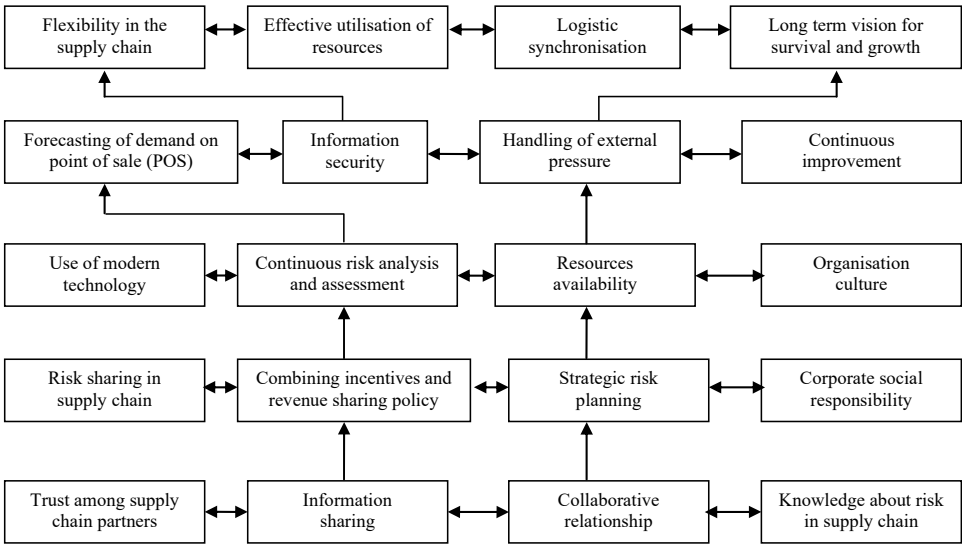
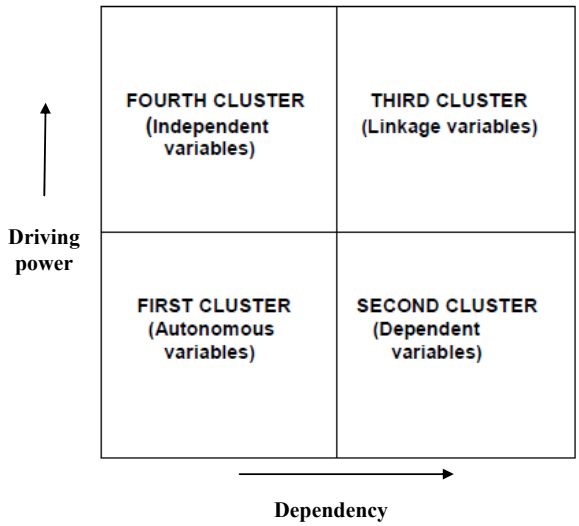


Figure 2 Digraph

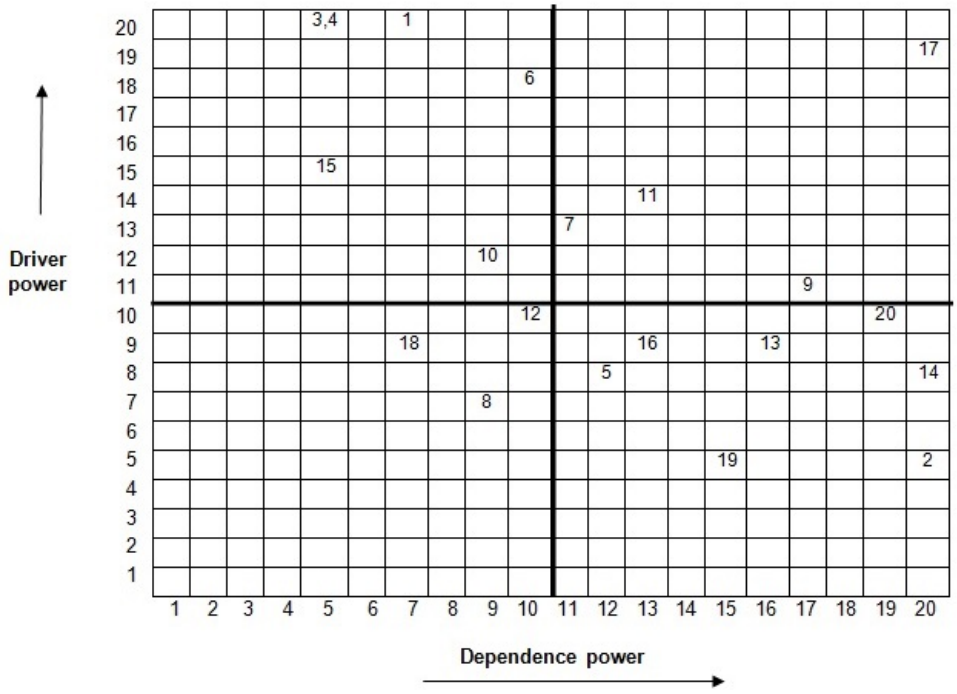


4.5 MICMAC analysis

The purpose of the matriced' impacts croise's multiplication appliquée a un classement (MICMAC) analysis is to analyse the driver power and the dependence power of the CSFs. The CSFs are relegated into four categories. The first category consists of the 'autonomous CSFs' that have impuissant driver power and impuissant dependence. These CSFs are not well connected with the system, with which they have only few links, which may be vigorous. Second category consists of the dependent CSFs that have impuissant driver power but vigorous dependence. Third category has the linkage CSFs that have

vigorous driving power and additionally vigorous dependence. These CSFs are unstable because any action on these CSFs will have an effect on others and with a feedback on themselves. Fourth category includes the independent CSFs having strong driving power but weak dependence. It is observed that a CSF with a strong driving power called the key CSFs, falls into the category of independent or linkage CSFs. Figure 2 represents the digraph which classifies the factors into four categories depending upon the driving power and dependency.

Figure 3 Driver and dependence power diagram

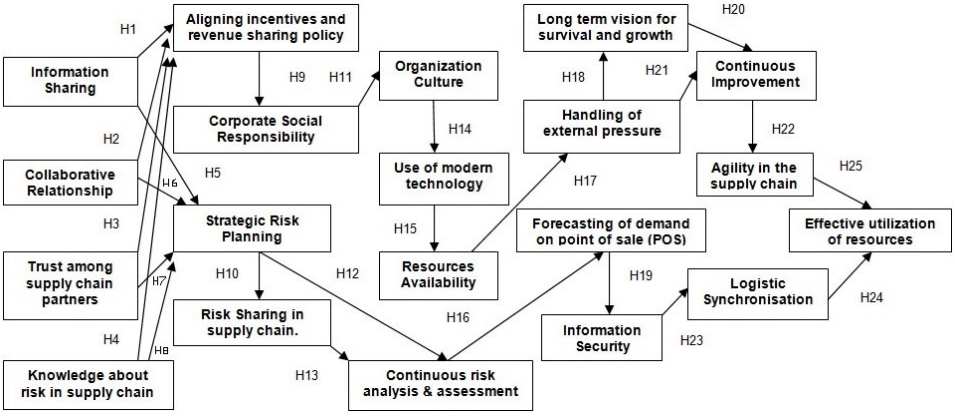


4.6 Conceptual framework

In the previous section an ISM model was used to present the hierarchical relationships among CSFs using a level matrix (see Table 5 and Table 6). The CSF's were further classified into four categories based on driving power and dependency (see Figure 3). We attempted further to extend the existing literature by synthesising the outcome of two independent analyses to build a conceptual framework. The conceptual framework depicts causality that was missing in the existing literature of ISM which defines the polarity or direction of relationship between driving and dependence variable (Sushil, 2018). The CSF's (information sharing, trust among supply chain partners, knowledge about risk in supply chain and collaborative relationship or partnership) possess high driving power and low dependence power. Hence, we can consider these CSF's as independent CSFs in our conceptual framework. The CSFs (combining incentives and revenue sharing policies, corporate social responsibility, risk sharing in supply chain, continual risk analysis and assessment, information security, use of modern technology,

resource availability, organisational culture, handling of external pressure, continuous improvement, forecasting of demand on point of sale and strategic risk planning) have medium driving power and medium dependence power. Hence, we argue that these 12 building blocks will represent mediating CSFs of our conceptual framework and remaining CSFs (effective utilisation of resources, logistic synchronisation, long term vision for survival and growth and Flexibility in the supply chain) have strong dependence power and weak driving power. Subsequently, we argue that these four CSFs will be regarded as dependent CSFs of our conceptual framework. In the next section we test this framework deriving our research hypotheses from ISM and MICMAC output.

Figure 4 Conceptual framework



5 Research hypothesis

The research hypothesis for each linkage of the conceptual framework developed in this chapter using ISM and MICMAC analysis is stated as shown in Table 7.

Table 7 Research hypothesis

Linkage	*Type of relationships*
H1 (IS → AIRSP)	There is a positive relationship between information sharing and Combining incentives and revenue sharing policy.
H2 (CRP→AIRSP)	There is a positive relationship between collaborative relationship or partnership and Combining incentives and revenue sharing policy.
H3 (TASP→ AIRSP)	There is a positive relationship between trust among supply chain partners and Combining incentives and revenue sharing policy.
H4 (KAVTRSC→AIRSP)	There is a positive relationship between knowledge about various types of risk in supply chain and Combining incentives and revenue sharing policy.
H5 (IS → SRP)	There is a positive relationship between information sharing and strategic risk planning
H6 (CRP → SRP)	There is a positive relationship between collaborative relationship or partnership and strategic risk planning

Table 7 Research hypothesis (continued)

Linkage	*Type of relationships*
H7 (TASCP → SRP)	There is a positive relationship between trust among supply chain partners and strategic risk planning.
H8 (KAVTRS → SRP)	There is a positive relationship between knowledge about various types of risk in supply chain and strategic risk planning.
H9 (AIRSP→CSR)	There is a positive relationship between Combining incentives and revenue sharing policy and corporate social responsibility
H10 (SRP→ RSSC)	There is a positive relationship between strategic risk planning and risk sharing in supply chain
H11 (CSR → OC)	There is a positive relationship between corporate social responsibility and organisational culture
H12 (SRP→ CRAA)	There is a positive relationship between strategic risk planning and continuous risk analysis and assessment.
H13 (RSSC → CRAA)	There is a positive relationship between risk sharing in supply chain and continuous risk analysis and assessment.
H14 (OC → UMT)	There is a positive relationship between organisational culture and use of modern technology.
H15 (UMT → RA)	There is a positive relationship between use of modern technology and resources availability.
H16 (CRAA → FDPOS)	There is a positive relationship between continuous risk analysis and assessment and forecasting of demand at point of sale.
H17 (RA → HEP)	There is a positive relationship between resources availability and handling of external pressure.
H18 (HEP → LTVSG)	There is a positive relationship between handling of external pressure and long term vision for survival and growth.
H19 (FDPOS → IS)	There is a positive relationship between forecasting of demand at point of sale and information security.
H20 (LTVSG → CI)	There is a positive relationship between long term vision for survival and growth and continuous improvement
H21 (HEP → CI)	There is a positive relationship between handling of external pressure and continuous improvement.
H22 (CI → AISC)	There is a positive relationship between continuous improvement and Flexibility in the supply chain.
H23 (IS → LS)	There is a positive relationship between information security and logistics synchronisation.
H24 (LS → EUR)	There is a positive relationship between logistics synchronisation and effective utilisation of resources.
H25 (AISC → EUR)	There is a positive relationship between Flexibility in the supply chain and effective utilisation of resources.

6 Results of hypothesis testing

Table 8 Results of hypothesis testing

Hypothesis	*R*	R^2	*F(df1, df2)*	β	*p-value*	*Durbin-Watson statistics*	*Hypothesis supported or not supported*
H1	0.9880	0.9763	123.49	0.3795	0.002	2.5341	Supported
H2	0.9924	0.9850	197.09	0.5486	0.001	1.41571	Supported
H3	0.9898	0.9799	146.22	0.5411	0.001	2.3574	Supported
H4	0.9929	0.9860	211.96	0.4243	0.001	2.7767	Supported
H5	0.9898	0.9799	145.89	0.4718	0.001	1.13161	Supported
H6	0.9920	0.9841	186.11	0.3468	0.001	2.00125	Supported
H7	0.9917	0.9835	178.63	0.3484	0.001	3.1020	Supported
H8	0.9905	0.9812	156.46	0.503	0.001	1.48663	Supported
H9	0.9906	0.9814	158.53	0.3377	0.001	1.07038	Supported
H10	0.9907	0.9816	160.02	0.2305	0.001	2.8247	Supported
H11	0.9950	0.9912	338.37	0.2108	0.000	3.13038	Supported
H12	0.9941	0.9884	256.65	0.2897	0.001	2.1976	Supported
H13	0.9877	0.9756	119.83	0.4174	0.002	1.1219	Supported
H14	0.9896	0.9794	142.51	0.4386	0.001	1.45262	Supported
H15	0.9860	0.9723	105.25	0.4630	0.002	3.3176	Supported
H16	0.9907	0.9816	160.39	0.2803	0.001	2.7480	Supported
H17	0.9922	0.9845	190.21	0.3660	0.001	2.47338	Supported
H18	0.9914	0.9829	171.93	0.3951	0.001	2.5593	Supported
H19	0.9938	0.9878	242.55	0.4773	0.001	3.398	Supported
H20	0.9991	0.9984	1,923.88	0.1183	0.000	2.57288	Supported
H21	0.9955	0.9912	337.90	0.3073	0.000	1.870	Supported
H22	0.9898	0.9798	145.52	0.6774	0.001	2.4934	Supported
H23	0.9981	0.9964	835.30	0.2948	0.000	3.0076	Supported
H24	0.9956	0.9913	341.49	0.3704	0.000	2.253	Supported
H25	0.9888	0.9779	132.93	0.4893	0.001	2.8514	Supported

7 Managerial implications

In present paper, CSF's for the effective implementation of risk management in achieving sustainability in supply chain have been identified and analysed. Models developed attempts to suggest how the CSF's for the successful implementation of risk management towards sustainability are interrelated along with their levels. Strategic importance of CSF's are also analysed.

The objective of this research was to build a hierarchy of CSFs and check their interdependencies that would avail to mitigate risks in the supply chain of an industry.

These CSFs postulates consequentiality because individual organisations are not competing rather it is the supply chains and consequently it is the responsibility of the individual members of the supply chain to manage risk.

Twenty such CSFs have been finalised through brainstorming sessions with different experts from industries and academia. These CSF's are utilised to develop a hierarchal model utilising ISM predicated approach. These CSF's are then checked for their interdependency and a hypothesised relationship is verbally expressed for each of the pair of interconnected CSF. These relationships are then tested for supremacy by using F-test and the model is validated utilising regression analysis technique.

8 Discussion and conclusions

The diagraph avails to categorise sundry CSFs of risk mitigation. There are three CSFs in the autonomous category viz. resource availability, risk sharing in supply chain, utilisation of modern technology. These CSFs have impuissant driver power and impotent dependence power and are not well connected with the system, with which they have only few links, which may be vigorous. In the next category we have dependent CSFs like Flexibility in the supply chain, efficacious utilisation of resources, long term vision for survival and magnification which are having high dependence power and low driver power and are placed at the top level in the ISM hierarchy. These CSFs are the result of efficacious risk mitigation in a supply chain. Since these have vigorous dependence power it denotes that they require all the other CSFs to enable them counter jeopardises. The next category of CSFs are termed as linkage CSFs and include strategic risk orchestrating, corporate convivial responsibility, handling of external pressure and logistics synchronisation which is influenced by lower calibre CSFs and in turn impacts other CSFs in the model. The last category includes independent CSFs like information sharing, trust among supply chain partners, collaborative relationship among supply chain partners and cognisance about risk in supply chain which have high driving power but little dependence. These CSFs play a key role to contravene risks in a supply chain.

In the present work hypothesis testing has been done using regression analysis. The regression analysis outputs are presented in Table 8. From the table, it is concluded that all stated hypothesis are supported. It can be clearly seen that the R^2 value of each linkage is quite high and the beta coefficients of each path of the conceptual framework are found to be positive and statistically significant at $p < 0.003$. The Durbin-Watson statistics of each linkage are found to be between 0 and 4. In this case it can be seen that the Durbin-Watson statistics are well within range, suggesting no auto correlation effect. The upper limit of the confidence interval for each linkage is 10.13. In this case it is found that the value of F-statistic is well above 10.13 for each linkage. Overall it is concluded that the constructs and the measures of the theoretical model, derived using the ISM technique and MICMAC analysis based on expert's opinion, are found to be valid and each linkage was supported and found to be statistically significant.

In this work only regression analysis technique is used to validate the model that is developed using ISM and MICMAC approach. Other structural equation modelling (SEM) techniques like CFA approach, path analysis etc. can also be used to validate these type of models. This study can be considered as a base study for the practitioners and academicians who are working in the area of risk management for achieving sustainable supply chain in the organisation.

References

Ageron, B., Gunasekaran, A. and Spalanzani, A., (2012) 'Sustainable supply management: an empirical study', *International Journal of Production Economics*, Vol. 140, No. 1, pp.168–182.

Badea, A., Prostean, G., Goncalves, G. and Allaoui, H., (2014) 'Assessing risk factors in collaborative supply chain with the analytic hierarchy process (AHP)', *Procedia – Social and Behavioral Sciences*, Vol. 124, pp.114–123.

Carter, C.R. and Rogers, D.S. (2008) 'A framework of sustainable supply chain management: moving toward new theory', *International Journal of Physical Distribution & Logistics Management*, Vol. 38, No. 5, pp.360–387.

Chopra, S. and Sodhi, M.S. (2014) 'Reducing the risk of supply chain disruptions', *MIT Sloan Management Review*, Vol. 55, No. 3, p.73.

Chopra, S. and Sodhi, M.S. (2004) 'Managing risk to avoid supply chain breakdown', *Sloan Management Review*, Fall, Vol. 46, No. 1, pp.53–61.

Dowling, G. and Staelin, R., (1994) 'A model of perceived risk and intended risk-handling activity', *Journal of Consumer Research*, Vol. 21, No. 1, pp.119–34.

Dubey, R., Gunasekaran, A., Papadopoulos, T. and Childe, S.J. (2015) 'Green supply chain management enablers: mixed methods research', *Sustainable Production and Consumption*, Vol. 4, pp.72–88.

Fahimnia, B., Tang, C.S., Davarzani, H. and Sarkis, J. (2015) 'Quantitative models for managing supply chain risks: a review', *European Journal of Operational Research*, Vol. 247, No. 1, pp.1–15.

Faisal, M., Banwet, D.K. and Shankar, R. (2006) 'Supply chain risk mitigation: modeling the CSFs', *Business Process Management Journal*, Vol. 12, No. 4, pp.535–552.

Finch, P. (2004) 'Supply chain risk management', *Supply Chain Management: An International Journal*, Vol. 9, No. 2, pp.183–196.

Ganesan, S. (1994) 'Determinants of long-term orientation in buyer-seller relationships', *Journal of Marketing*, Vol. 58, No. 2, pp.1–19.

Giannakis, M. and Louis, M. (2011) 'A multi-agent based framework for supply chain risk management', *Journal of Purchasing and Supply Management*, Vol. 17, No. 1, pp.23–31.

Giunipero, L.C. and Eltantawy, R.A. (2004) 'Securing the upstream supply chain: a risk management approach', *International Journal of Physical Distribution & Logistics Management*, Vol. 34, No. 9, pp.698–713.

Gold, S., Seuring, S. and Beske, P. (2010) 'The constructs of sustainable supply chain management – a content analysis based on published case studies', *Progress in Industrial Ecology, An International Journal*, Vol. 7, No. 2, pp.114–137.

Goldberg, S., Davis, S. and Pegalis, A., (1999) *Y2k Risk Management*, Wiley, New York.

Gopal, P.R.C. and Thakkar, J., (2016) 'Analysing critical success factors to implement sustainable supply chain practices in Indian automobile industry: a case study', *Production Planning & Control*, Vol. 27, No. 12, pp.1005–1018.

Grimm, J.H., Hofstetter, J.S. and Sarkis, J. (2014) 'Critical factors for sub-supplier management: a sustainable food supply chains perspective', *International Journal of Production Economics*, Vol. 152, pp.159–173.

Hahn, C.K., Duplaga, E.A. and Hartley, J.L. (2000) 'Supply chain synchronization: lessons from Hyundai Motor Company', *Interfaces*, Vol. 30, No. 4, pp.32–45.

Hallikas, J., Karvonen, I., Pulkkinen, U., Virolainen, V.M. and Tuominen, M. (2004) 'Risk management processes in supplier networks', *International Journal of Production Economics*, Vol. 90, No. 1, pp.47–58.

Heckmann, I., Comes, T. and Nickel, S., (2015) 'A critical review on supply chain risk – definition, measure and modeling', *Omega*, Vol. 52, pp.119–132.

Jayant, A. and Azhar, M. (2014) 'Analysis of the barriers for implementing green supply chain management (GSCM) practices: an interpretive structural modeling (ISM) approach', *Procedia Engineering*, Vol. 97, pp.2157–2166, DOI: 10.1016/j.proeng.2014.12.459.

Kanda, A. and Deshmukh, S.G. (2008) 'Supply chain coordination: perspectives, empirical studies and research directions', *International Journal of Production Economics*, Vol. 115, No. 2, pp.316–335.

Khurana, S., Mannan, B. and Haleem, A. (2014) 'Integrating innovation with sustainability: a study of practices/status for Indian manufacturing industries (SMEs)', in *AGBA 11th World Congress Conference*, IIT, Delhi.

Kumar, R, Singh, R.K. and Shankar, R. (2015) 'Critical success factors for implementation of supply chain management in Indian small and medium enterprises and their impact on performance', *IIMB Management Review*, Vol. 27, No. 2, pp.92–104.

Kurien, G.P. and Qureshi, M.N. (2011) 'Study of performance measurement practices in supply chain management', *International Journal of Business, Management and Social Sciences*, Vol. 2, No. 4, pp.19–34.

Lee, H.L. (2002) 'Aligning supply chain strategies with product uncertainties', *California Management Review*, Vol. 44, No. 3, pp.105–119.

Lee, H.L., Padmanabham, V. and Whang, S., (1997a) 'The bullwhip effect in supply chains', *Sloan Management Review*, Vol. 38, No. 3, pp.93–102.

Lee, H.L., Padmanabhan, P. and Whang, S., (1997b) 'Information distortion in a supply chain: the bullwhip effect', *Management Science*, Vol. 43, No. 4, pp.546–558.

Lotfi, Z., Mukhtar, M., Sahran, S. and Zadeh, A.T. (2013) 'Information sharing in supply chain management', *Procedia Technology*, Vol. 11, pp.298–304.

Luthra, S. and Haleem, A., (2015) 'Hurdles in implementing sustainable supply chain management: an analysis of Indian automobile sector', *Procedia – Social and Behavioral Sciences*, Vol. 189, pp.175–183.

March, J.G. and Shapira, Z. (1987) 'Managerial perspectives on risk and risk taking', *Management Science*, Vol. 33, No. 11, pp.1404–1418.

Mentzer, J.T., Foggin, J.H. and Golicic, S.G. (2000) 'Supply chain collaboration: CSFs, impediments, and benefit', *Supply Chain Management Review*, Vol. 4, No. 4, pp.52–58.

Nachtmann, H., Waller, M.A. and Rieske, D.W. (2010) 'The impact of point-of-sale data inaccuracy and inventory record data errors', *Journal of Business Logistics*, Vol. 31, No. 1, pp.149–158.

Narayanan, V.G. and Raman, A. (2004) 'Combining incentives in supply chains', *Harvard Business Review*, Vol. 82, No. 11, pp.94–103.

Prater, E., Biehl, M. and Smith, M.A. (2001) 'International supply chain flexibility – tradeoffs between flexibility and uncertainty', *International Journal of Operations & Production Management*, Vol. 21, Nos. 5/6, pp.823–839.

Rozar, N.M., Mahmood, W., Hasrulnizzam, W., Ibrahim, A. and Razik, M.A. (2015) 'A study of success factors in green supply chain management in manufacturing industries in Malaysia', *Journal of Economics, Business and Management*, Vol. 3, No. 2, pp.287–291.

Sage, A. (1977) *Interpretive Structural Modeling: Methodology for Large scale Systems*, pp.91–164, McGraw-Hill, New York.

Scholten, K., Sharkey Scott, P. and Fynes, B. (2014) 'Mitigation processes-antecedents for building supply chain resilience', *Supply Chain Management: An International Journal*, Vol. 19, No. 2, pp.211–228.

Seuring, S. and Müller, M. (2008) 'From a literature review to a conceptual framework for sustainable supply chain management', *Journal of Cleaner Production*, Vol. 16, No. 15, pp.1699–1710.

Shrivastava, P. (1995) 'Environmental technologies and competitive advantage', *Strategic Management Journal*, Vol. 16, No. S1, pp.183–200.

Shtub, A., Bard, J.F. and Globerson, S. (1994) *Project Management: Engineering, Technology and Implementation*, Prentice-Hall, Englewood Cliffs, NJ.

Sinha, P.R., Whitman, L.E. and Malzahn, D. (2004) 'Methodology to mitigate supplier risk in an aerospace supply chain', *Supply Chain Management: An International Journal*, Vol. 9, No. 2, pp.154–168.

Speckman, R.E. and Davis, E.W. (2004) 'Risky business: expanding the discussion on risk and the extended enterprise', *International Journal of Physical Distribution & Logistics Management*, Vol. 34, No. 5, pp.414–33.

Srivastava, S.K. (2007) 'Green supply-chain management: a state-of-the-art literature review', *International Journal of Management Reviews*, Vol. 9, No. 1, pp.53–80.

Stadtler, H. (2015) 'Supply chain management: an overview', *Supply Chain Management and Advanced Planning*, pp.3–28, Springer Berlin, Heidelberg.

Sushil (2018) 'Incorporating polarity of relationships in ISM and TISM for theory building in information and organization management', *International Journal of Information Management*, Vol. 43, pp.38–51.

Tang, O. and Musa, S. N. (2011) 'Identifying risk issues and research advancements in supply chain risk management', *International Journal of Production Economics*, Vol. 133, No. 1, pp.25–34.

Toke, L.K., Gupta, R.C. and Dandekar, M. (2012) 'An empirical study of green supply chain management in Indian perspective', *International Journal of Applied Science and Engineering Research*, Vol. 1, No. 2, pp.372–383.

Warfield, J.W. (1974) 'Developing interconnected matrices in structural modeling', *IEEE Transcript on Systems, Men and Cybernetics*, Vol. 4, No. 1, pp.51–81.

Xu, G., Dan, B., Zhang, X., and Liu, C. (2014) 'Coordinating a dual-channel supply chain with risk-averse under a two-way revenue sharing contract', *International Journal of Production Economics*, Vol. 147, pp.171–179.

Zsidisin, G.A. and Ellram, L.M. (2003) 'An agency theory investigation of supply risk management', *Journal of Supply Chain Management*, Vol. 39, No. 2, pp.15–27.

View publication stats

ResearchGate

See discussions, stats, and author profiles for this publication at: https://www.researchgate.net/publication/357757143

Therapeutic applications of mesenchymal cells derived from human placenta: A comprehensive meta-review

Article · December 2021

DOI: 10.37881/1.637

CITATIONS
0

READS
50

3 authors, including:



Ritika Luthra
Delhi Technological University
7 PUBLICATIONS **18** CITATIONS

SEE PROFILE

Some of the authors of this publication are also working on these related projects:

Evaluation of phytocompounds against JAB1 View project

All content following this page was uploaded by Ritika Luthra on 21 January 2022.

The user has requested enhancement of the downloaded file.

NEUROPHARMAC JOURNAL 6 (2021) 277-294

NeuroPharmac Journal
Journal Homepage: https://www.neuropharmac.com

Review

Therapeutic applications of mesenchymal cells derived from human placenta A comprehensive meta-review

Ritika Luthra[1], Saanya Yadav[1], Smita Rastogi Verma[1]*
[1]Department of Biotechnology, Delhi Technological University, Delhi

ARTICLE INFO

Article history
Received 11 November 2021,
Revised 29 November 2021,
Accepted 8 December 2021,
Published online
30 December 2021

Keywords
Placental mesenchymal stem cell (PMSC), cell therapy, clinical trials, regenerative medicine, multipotent.

ABSTRACT

There has been an increase in the incidence of diseases and injuries which has encouraged the advancements in treatments that could repair tissues as well as minimize the dependence on organ transplantation and tissue loss. Regenerative medicine based on stem cells is a newer integrative domain that has the potential to facilitate the regeneration of diseased and damaged tissues and organs. Stem cells can be effectively exploited for medical purposes with no severe challenges, according to a wide range of literature as well as long-term human and animal studies conducted on them. Amongst several types of stem cells, placenta-derived mesenchymal stem cells possess unique immunomodulatory characteristics as well as the potential to differentiate into various cell types, which make them suitable candidates for cellular therapies for many chronic diseases including cancers, heart and liver disorders, ulcers, bone damage, and neurological diseases, etc. The present study thus aims at providing a comprehensive overview of placenta-derived mesenchymal stem cells, their types, and potentially therapeutic for various chronic and non-chronic diseases. Recent pre-clinical and clinical studies conducted on them have also been incorporated.

Introduction

In recent times, modern science and medicine have seen an appreciable rise in stem cell research which has garnered recognition globally attributed to its enormous therapeutic potential in the field of regenerative medicine.[1] This is a result of the regenerative capability as well as the pliability possessed by the stem cells. These stem cells manifesting therapeutic potential originate and develop from embryonic as well as adult tissues. Nonetheless, ethical concerns along with the challenges in procuring them and tumorigenicity limit the clinical usage of embryonic stem cells. The adult stem cells have been discovered in various tissues and organs, such as bone marrow[2], brain, placenta[3], skin, adipose tissue le, umbilical cord[4], etc. However, the amount of stem cells obtained from adult tissues is limited. There are numerous risks involved in isolating them and these cells possess a minimal range of differentiation and proliferation after their extraction from the body. As a result, it is burdensome to obtain large quantities

*Corresponding author at: Department of Biotechnology, Delhi Technical University, Delhi-110042, India
E-mail address: smitar@dtu.ac.in
https://orcid.org/0000-0002-3812-5314
https://doi.org/10.37881/1.637

of stem cells from them. On the other hand, a good source of mesenchymal stem cells (MSCs) in the human placenta, a vital part of the body found at the time of pregnancy for assisting fetal development. It is a multicellular immunoregulatory organ where both maternal, as well as fetal cells, exist side-by-side. It performs several functions including exchange of metabolites and regulation of the secretion of hormones between the mother and fetus along with the maintenance of immune tolerance between the two.[5] Placenta is also an abundant reservoir of stem cells in comparison to other sources like bone marrow, adipose tissue, etc. where there is a decline in the recuperation of cells with benefactor's age.[6] MSCs procured from the placenta reveal various features making them a better alternative for cellular therapy in comparison to their counterparts from adult tissues. The placenta is contemplated to be a medical waste having no ethical issues in its utilization as seen in the case of embryonic stem cells.[3] It is voluntarily removed at the time of birth without the requirement of any encroaching procedures unlike those needed in other adult stem cell sources. Because of their primordial origin, placental cells possess great ambidexterity as well as the ability to differentiate.[7] Stem cells procured from the placenta present a distinctive range of mesenchymal markers,[8,9] along with the potential to differentiate into neurogenic and glial cells[10], insulin-producing cells[11] as well as liver cells.[12] MSCs acquired from the placenta have been employed for treating a wide range of diseases, including cancer, cardiovascular, neurological, and liver diseases, ulcers, as well as bone and cartilage diseases. These MSCs are of comparatively recent types, exhibiting particular immunomodulatory functions with undetermined mechanisms. Certain soluble factors secreted by placental MSCs appear to be the primary cause for therapeutic effects. This shows that placenta-derived MSCs possess paracrine effects.[13] Contrastingly, because of their migration capabilities and tropism for wounded regions, placental MSCs can also act as mobile carriers for drugs.

Recently, there has been immense progress in the field of nanotechnology for curing damaged tissues or organs. Owing to the unique features manifested by placental MSCs, these cells together with nanotechnology will turn out to be a considerable and reassuring domain that may bestow remarkable contributions in the field of stem cell therapy in subsequent times. Therefore, this review seeks to incorporate the formation of placenta-derived mesenchymal stem cells and gives a comprehensive overview of their potential therapeutic applications. Furthermore, the prospects have also been discussed.

Sources of mesenchymal stem cells

MSCs may be extracted from a variety of tissues, including bone marrow, adipose tissue, and synovium, as well as human umbilical cord blood, and bone marrow is one of the most important sources of MSCs.[14] The human body contains adipose tissue (AT) in numerous places, including visceral and subcutaneous fat pads, as well as the pelvic region. AT-derived MSCs, also known as Adipose Stem Cells (ASCs), have comparable properties to Bone marrow-MSCs but, unlike Bone marrow mesenchymal stem cells (BM-MSCs), are easier to isolate in large quantities and have a larger expansile property. The physician must consider the difficulties of obtaining the samples as well as the potential negative consequences of harvesting the cells on the donor while choosing an appropriate cell source. Collecting MSCs from BM-MSCs, for example, might cause pain, hemorrhage, or infection, making it more difficult than harvesting cells from peripheral blood or surgical leftovers like AT or birth-derived tissues.[15] MSCs from peripheral blood cells can be obtained by density gradient centrifugation and a large volume of MSCs can be extracted as compared to bone marrow.[16] However, placental mesenchymal stem cells are harvested with minimal invasiveness thereby being the best candidate for therapeutics.[17]

Different forms of placental mesenchymal stem cells based on origin

Mesenchymal stem cells are derived from mesoderm.[18] Specifically, placental mesenchymal stem cells can be derived from amniotic membrane, amniotic fluid, chorionic plate as well as chorionic villus.[19]

The amniotic membrane is a placental component that develops in extra-embryonic tissue and provides additional nutrition to the fetus throughout pregnancy.[20] Cells derived from amniotic membranes are called amniotic membrane-derived MSCs (AMe-MSC). They are pluripotent. AMe-MSCs have been shown to reduce inflammation and improve immunomodulation. They induce remyelination, increase angiogenesis, reduce oxidative stress, and control matrix metalloproteinases.[21] Amniotic fluid-derived mesenchymal stem cells (AF-MSCs) are made up of differentiated and undifferentiated progenitor cells generated from fetal tissue. AF-MSCs are more pluripotent and less differentiated than BM-MSCs, having a longer replicative lifetime and proliferative capacity. In AF-MSCs, cytokines and chemokines stimulate vasculogenesis, angiogenesis, and osteogenesis due to their paracrine nature. *In vivo*, AF-MSCs do not produce teratoma.[22] Because of the ease of their acquisition, multipotency, low immune response, reduced donor damage, and acceptable ethical issue, AM-MSCs and AF-MSCs have been reported as a better new prospective field of regenerative medicine when compared to other MSC sources like chorionic, Wharton's jelly, etc.[23]

The amnion, extra-amniotic mesenchymal stem cells, cytotrophoblast, and syncytiotrophoblast make up the chorionic plate. Chorionic plate-derived MSCs (CP-MSCs) are extracted from chorionic placental plates. Compared to other placental stem cells, CP-MSCs have a greater ability to suppress T-cell proliferation and have a stronger angiogenic potential. Higher genes for differentiation into adipogenic, osteogenic, and hepatogenic lineages are expressed in them.[24] Chorionic villus cells, which are made up of stromal fibroblasts, endothelial cells, and macrophages, have characteristics similar to MSCs.[25] Chorionic villous-derived MSCs (CV-MSCs) are more pluripotent and have a slower aging phenotype than bone marrow-derived stem cells.[26]

Placenta and Stem Cell Therapy

Stem cell therapy, also known as regenerative medicine, emphasizes the repair and rejuvenation of injured tissues and organs which may occur due to age, disease, or any physical damage. Such approaches turn out to be beneficial in cases where biological processes are incompetent for responding during the emergence of acute as well as chronic disorders. They may necessitate the transplantation of stem cells which will restore the injured tissues, instigate body functions for repairing of tissues, or work as mobile carriers for delivering remedial agents such as genes, medications, or cytokines. Stem cells are considered exceptional in regenerative medicine because of their ability to restore as well as to differentiate to various specialized cells. Advancements in the field of regenerative medicine have drawn attention to the complex characteristics and heterogeneity of stem cells procured from distinct sources. In the past few years, researchers have traversed various properties of adult MSCs suggesting them to be advantageous in regenerative medicine.[27] Hence, MSCs obtained from several sources have displayed enormous prospects in damaged tissues as well as organ repairing and restoration. Being an immune-privileged organ, placental cells exhibit low immunogenicity *in vitro*[28]as well as *in vivo*[29] when xenotransplanted in animals displaying a normal immune response. Researchers have illustrated the viability of placenta-derived cells for allogeneic transplantations.[30]

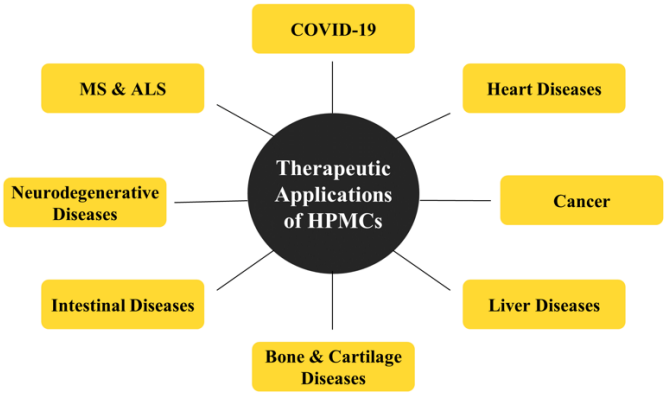
In stem cell therapy, along with tissue repairing, the short-lived paracrine actions are also affected by stem cells. The factors generated and released by stem cells induce these paracrine actions. These factors are responsible for controlling injuries, modulating the immune responses as well as promoting self-restoration in damaged tissues which are still alive.[31] Concerning modulation of the immune system, stem

cells obtained from the placenta possess an auxiliary advantage over those derived from other sources. This can be well explained by the primary role of the placenta in fetomaternal immune tolerance.[13] During pregnancy, fetal and, particularly, the tissues of the placenta are responsible for maternal tolerance. They provide immune-privileged conditions and regulate the immune system. MHC class II antigens which generally arbitrate transplant rejection are absent in placental cells.[32] Placental cells express fewer amounts of extremely diverse types of antigens belonging to MHC class I as well as the unconventional type HLA-G (histocompatibility antigen class I, G) which can be responsible for suppressing body defenses along with contributing to immune tolerance during pregnancy.[33,34] Additionally, placenta-derived cells diverge the maternal immune response towards immune tolerance via the secretion of soluble forms of MHC antigens, hormones, and cytokines.[35,36] Furthermore, B-cells as well as most of the T-cells vanish leaving behind regulatory T-cells, also called Tregs, as the larger population of T-cells that possess immunosuppressive as well as anti-inflammatory effects.[37]

Therapeutic applications of placenta-derived mesenchymal stem cells

Regenerative medicine is anticipated to bestow considerable advantages to individuals affected by a broad array of pathologies. Placenta-derived mesenchymal stem cells exhibit flexibility and pleiotropic characteristics which incorporate immune system modulation and control of inflammation. Some of the properties like angiogenesis, neuroprotective and anti-apoptotic are the properties that have been broadly assessed at preclinical levels.[7,38,39] Owing to these properties, HPMCs possess huge potential as therapeutics against several diseases, which are illustrated in Figure 1 and have been discussed in detail in further sections.

Figure 1: Therapeutic applications of human placenta-derived mesenchymal stem cells against various diseases



COVID-19

SARS-CoV-2 is classified as a novel coronavirus that belongs to the β–coronavirus family. After Middle East Respiratory Syndrome (MERS) and Severe Acute Respiratory Syndrome (SARS), COVID-19 has emerged as the third zoonotic illness-based pandemic produced by viruses belonging to this family.[40] The genome of the COVID-19 virus is 26-32 kilobase pairs in length with crown-like projections on surfaces called spike proteins. The spike protein mainly interacts with the ACE-2 (angiotensin-converting enzyme) on alveolar epithelial cells and performs interspecies transmission of the genome.[41] This attachment leads to an elevated expression of ACE-2 which injures alveolar cells causing lesions. These lesions can cause serious systemic responses and eventually death if not treated on time. From affecting the lungs, these lesions can cause dysfunction of numerous organs.[42,43] An immune destruction in the form of cytokine

storm occurs in the body, in which pro-inflammatory cytokines, for example, interferons (INFs), interleukins (IL-1, 6, 12, 8, 33), tumor necrosis factors (TNFs), tumor growth factors (TGFs), accumulate in abundance.[44]

MSC treatment can inhibit the immune system from releasing a flood of cytokines and boost endogenous healing about the stem cell's reparative abilities. P-MSCs inhibit further infection of pulmonary alveolar cells by acting on the ACE-2 receptor and TMPRSS-2 (endothelial cell surface protein) receptor.[22] Placental MSC cells, when injected into the body, get entrapped in the lungs to restrict the systemic infusion of the virus. Thereafter, these MSCs have the potential to restore the required pulmonary environment, preserve alveolar epithelial cells, prevent pulmonary fibrosis, and treat lung dysfunction and COVID-19 pneumonia.[45] P-MSCs reduce the severity of cytokine storm caused by the virus, change the microenvironment to an anti-inflammatory state, and then further limit mononuclear cell entrance into the infected/damaged alveolar epithelium cells. In injured alveolar cells, P-MSCs increase immunomodulatory and anti-inflammatory properties. Thereby accelerating the repair mechanism of damaged alveolar cells.[22] Patients treated with MSC showed increased levels of peripheral lymphocytes and a decline in the amount of cytokine-secreting immune cells including CXCR3+ CD4+ T cells, CXCR3+ CD8+ T cells, and NK CXCR3+ cells compared with patients treated with conventional therapy.[45]

Myocardial Infarction

Cardiovascular disorders are a major cause of morbidity and death globally, with myocardial infarction (MI) being the most frequent cardiovascular disorder.[46] MI happens as a result of intervention in the circulation of blood to heart muscles which are accompanied by myocardial ischemia. This is influenced by the capability as well as the timing of the restoration of blood flow, and therefore, may or may not be reversible.[47] The impaired cardiac muscle is substituted by scar tissue as the restoration of the myocardium is practically not present, thereby limiting the functioning of the heart. Transplantation of placenta-derived mesenchymal stem cells acts as a promising approach for restoring heart function as well as lessening cardiac fibrosis because of the angiogenic and immunomodulatory characteristics possessed by them. These cells can potentially transform into myocardiocytes along with exhibiting voluntary movements *in vitro* environments indicating their therapeutic application in the process of heart repair.[7,48,49] Various researchers have inspected the influence of placenta-derived mesenchymal stem cells after transplanting them in animal models of MI. These stem cells when administered in the heart of rats after inducing MI exhibited incorporation into heart tissues and *in vivo* lineage programming to form myocardiocytes.[48] The prime route for arbitrating the relocation of mesenchymal stem cells in the vicinity of damaged tissues is the axis of chemokine receptor type 4 (CXCR4), and its ligand i.e., stromal cell-derived factor (SDF-1) forming CXCR4-SDF1. As observed, due to hypoxia, CXCR4 is instigated at a high extent in placental mesenchymal stem cells. Therefore, a huge chemotactic reaction is anticipated by the placental mesenchymal stem cells to the ischemic microenvironment of the damaged portion of the heart.[50] Injecting these stem cells intravenously in an infarcted rat manifested an upraised heart function after around 32 weeks from infarction.[51] Provisioning these stem cells with a novel ester of hyaluronan linked to butyric as well as retinoic acid (HBR) reinforces their restorative capability. Transplanting these provisioned stem cells in pigs generated a notable lowering in the extent of scar, more myocardial transmigration and glucose absorption, elevated density of capillaries, as well as a decline of fibrous tissues.[52] Researchers have also assessed the angiogenic paracrine effect of the conditioned medium of placental mesenchymal stem cells. In a rat model of reperfusion injury, injecting the conditioned medium of these stem cells reduced the size of infarction as well as myocardiocyte apoptosis, whilst encouraging the capillary density in the borderline of infarction.[53]

Intracoronary injection of umbilical cord mesenchymal stem cells in people suffering from MI led to a healthy and markedly increased myocardial tolerance and circulation in the infarcted area. Enhancements in certain factors, like increased left ventricular ejection fraction as well as decreased end-diastolic volumes and LV end-systolic volumes, have been reported up until 18 months after therapy.[54] A phase I/II clinical study named RIMECARD showed the security and effectiveness of these stem cells which were injected intravenously in people suffering from chronic heart failure. There was also a decreased fraction ejection. Advancements in left ventricular activity, cognitive function, and life expectancy have been identified in treated groups.[55] The capacities of first trimester placental chorionic mesenchymal stem cells (FCMSCs) and third trimester placental chorionic mesenchymal stem cells (TCMSCs) have also been studied. FCMSCs had a better capacity to produce EC differentiation, as shown by improved *in vitro* morphology, angiogenic ability, *in vivo* cardiac function, and higher levels of pro-angiogenesis gene expression than TCMSCs.[56]

Critical Limb Ischemia

Critical limb ischemia is the most dangerous and advanced phase of peripheral artery disease which results from the thickening of walls of arteries due to the formation of plaque and brings scarcity in the blood perfusion, incorporating acute limb ischemia, gangrene, and even ulcers.[57,58] It is accompanied by accelerating stenosis, and eventually leads to blockage of peripheral arteries. The risks of developing peripheral artery disease increase with advancing age, high lipid content such as cholesterol (hyperlipidemia), high blood pressure, and predominantly diabetes. The hostile tissue environment generated by diabetes and ischemia can impair the functioning of a patient's cell products for autologous and allogeneic related therapies.[59] Angiogenic cells can contribute directly to the creation of new arteries while also providing endogenous growth factors, encouraging vascular expansion in a paracrine manner. Angiogenic treatment includes the use of angiogenic growth factors (HIF-1α, VEGF, FGF1, etc.), gene transfer techniques utilizing viral or non-viral vectors to transport a gene coding for a therapeutic protein to target tissues, or the use of angiogenic stem cells.[60] However, in several instances, amputation is the sole alternative possible for treating critical limb ischemia. This is because the blood capillaries cannot be rectified, and recompression of vessels is generated. It has been outlined in the preclinical trials that cell therapy exhibits several benefits in neovascularization in numerous mice suffering from hindlimb ischemia. Placental mesenchymal stem cells have illustrated pro-angiogenic properties, when introduced into the ischemic area of the infected limb via intramuscular injections, thereby enhancing the blood circulation as well as encouraging the development of new vessels.[24,61,62] PMSCs can be administered with insulin (from external sources) and even without insulin. Upon administration, the efficacy of PMSC was calculated. The results were promising as there were newly formed capillaries, a higher number of arterioles, and even high secretion of different proangiogenic factors.[63] Furthermore, conditioned medium from placental mesenchymal stem cells also possessed pro-angiogenic effects in a mouse model having hindlimb ischemia, equivalent to the transplanted placental stem cells in the same research, disclosing that action of placental mesenchymal stem cell led fundamentally from the paracrine effect of the angiogenic elements secreted from these stem cells.[24] Nonetheless, in one more examination, cells were more effective in comparison to the cell lysate in liberating blood circulation, presumably stipulating the significance of elongated paracrine action for optimal blood flow restoration.[63]

Stroke

Ischemic stroke, also called a cerebrovascular accident, is acute damage in the central nervous system caused due to compromised vasculature or brain perfusion, incorporating cerebral infarction, cerebral

bleed, and subarachnoid hemorrhage. It predominantly causes disability globally, and about 85% of strokes appear to be ischemic.[64] The frequently utilized curative technique for this condition is thrombolysis; however, many patients avoid out of window visits which is necessary for efficacious treatment. It has been outlined via experimental facts that regenerative medicine can lessen the degeneration of neurons as well as boost functional outcomes. Placental mesenchymal stem cells exhibit neuroprotective effects, which have been illustrated in stroke rat models. Administering these stem cells intravenously leads to a noteworthy enhancement of functional outcomes along with a considerable reduction in the mass of lesions, after 4 hours in the injury. This can be correlated with an escalation in the amounts of vascular endothelial and hepatocyte growth factors, as well as a brain-derived neurotrophic factor in the ischemic brain in comparison with the controls.[65] Similarly, stem cells can limit the injury caused by stroke. For the first time, Barzegar et al, (2021)[66] discovered that intravenous injection of placental MSCs administered at the moment of reperfusion dramatically reduced ischemia damage in the ipsilateral hemisphere. This protection is linked to a substantial return of normal blood flow to the brain following MCAO (middle cerebral artery occlusion).

Cancer

Over the years, our understanding and ability to deal with cancer have improved significantly. Despite the accelerated progress in the oncology domain, cancer remains a major lethality affecting both developing and developed parts of the world. The conventional treatment of cancer including surgical removal of the tumor, radiotherapy, and chemotherapy, have proven to be effective, however, severe side effects and drug resistance highlight the need to find an alternate therapy that could minimize the toxicity and still be efficient in treating the tumor cells.[67]

Placenta-derived mesenchymal stem cells offer a novel approach to cancer treatment. Placenta-derived MSCs have an intrinsic nature to migrate to the sites in the body which shows any kind of wear and tear. This property of PMSCs is majorly exploited in cancer treatment. Cancer and tumor sites behave as an unhealed wounded environment which sends a signal through paracrine signaling to PMSCs to migrate to the site of action. Inflammation is another factor that contributes to the movement of the cells.[68,69] This migration property was first observed in a xenograft mouse model.[70] PMSCs can be used as cellular Trojan horses as well for the targeted drug delivery. Nanoparticles are a novel approach for drug delivery but being foreign particles, nanoparticles are prone to high immunogenic response and have a high rate of failure as well due to inefficient dissemination in tumors. All these can be overcome by using stem cells as their delivery system.[71,72] This compound system of drug delivery has proven to be quite efficient in tumor apoptosis. MSC cell membrane coated with doxorubicin enclosed in porous silica nanoparticles is a fine example.[73] Furthermore, PMSCs can also be programmed genetically to produce certain antitumor compounds and peptides. Generally, PMSCs are modified with viral particles for the expression of certain cytokines like interferon-β (INF-β). A study conducted by Shen et al. showed induced apoptosis in breast cancer cells when umbilical cord MSCs were subjected to adenovirus particles expressing INF-β.[74] They can also be modified for producing particular enzymes as evident in the case of cytosine deaminase-producing MSCs when injected into the brain hindered the growth of glioblastoma.[70] Endostatin, a neurovascular and anti-angiogenesis inhibitor, has been successfully administered using hPMSCs, which works as a gene vector in the treatment of ovarian cancer.[75] Along with acting as an accessory to other forms of therapies, PMSCs as their own also have anti-tumorigenic responses. Studies have demonstrated MSCs secreting cytotoxic peptides, mediating pro-apoptotic pathways, and inducing an anti-cancer immune response. Growth of breast cancer was attenuated by the placental MSCs through inhibiting ERK1/2 and activating the AKT pathway, leading to apoptosis.[76] TNF-related apoptosis-inducing ligand

(TRAIL) is another cytotoxic agent released by MSCs inducing apoptotic pathways, all leading to inhibiting the growth of several types of carcinomas.[77] Combining PMSCs with drugs to improve restrictions in treatment is also considered. Therapeutic medicines combining anti-angiogenic treatment and chemotherapy can be utilized with decidua-derived MSCs. The decidua mesenchymal stem cells were used to carry out a combination of endostatin transfection and doxorubicin-nanoparticle loading.[78]

Parkinson's Disease

In Parkinson's disease (PD) a gradual impairment of motor skills can be observed. This happens when neurons in the brain controlling the locomotive functions become functionally inactive or die. It is characterized by the loss of dopamine-releasing neurons and thereby, decreased levels of dopamine in the striatum. There is no cure available for the full-fledged treatment of the disease, however, few medicines and therapies have been employed to target the symptoms. Anticholinergics, dopamine agonists, and neuroprotective (drug therapy) are the most common treatments for PD to date.[14,79] When talking to stem cells, the main objective becomes to re-establish the dopaminergic neurons and related transmission signals. Neural progenitors produced by the differentiation of PMSCs were transplanted into a rat with PD. The results showed alleviation of the PD symptoms and the neural progenitors transformed into dopaminergic differentiation.[80] In a study on mice, MSCs can lower the amount of α-synuclein, block microglia cell polarization, and increase neuron survival.[81] It is believed and being studied that treatment with PMSCs can also help in symptoms unrelated to the motor like constipation and hyposmia through the secretion of anti-apoptotic and anti-inflammatory factors.

Alzheimer's Disease

Alzheimer's disease (AD) is yet another progressive disease that is characterized by dementia i.e., memory loss with aging. It is a result of abnormal accumulation of amyloid peptides and tau tangles all over the brain causing loss of neural activity.[79] Structurally, it usually starts with the hippocampus and entorhinal cortex, parts primarily responsible for memory response. With time, shrinkage in other parts of the brain is also visible. AD mice models injected with PMSCs demonstrated higher levels of amyloid breaking enzymes and also lower levels of pro-inflammatory peptides. PMSCs showed a strong immunomodulatory effect by increasing the levels of anti-inflammatory cytokines like IL-10 and TGF-β. Moreover, enhanced memory response was also observed.[82] MSCs generated from the placental amniotic membrane can help AD model mice enhance their spatial learning and memory. The number of amyloid plaques was also decreased, suggesting that MSC therapy generated from the human placental amniotic membrane might ameliorate AD pathogenesis and cognitive performance by regulating oxidative stress.[83]

Amyotrophic Lateral Sclerosis

Another neurological disease is amyotrophic lateral sclerosis (ALS), which is characterized by symptoms like muscle weakness, paralysis, respiratory problems ultimately leading to death. These symptoms are caused by the degeneration of neurons in the brain and spinal cord. Although no conclusive therapies are available for ALS, the stem cells put forward an approach that leads to extended lifespan. ALS mice models injected with PMSCs demonstrated delayed degeneration of motor neurons by shielding them from inflammatory peptides.[84] MSCs have been found to migrate to the spinal cord of mice and inhibit microglial activation and tissue glial proliferation, increasing the number of motor neurons, suggesting that MSCs may have neuroprotective properties. Experiments have demonstrated that exosomes produced from ASC can protect motor neuron-like NSC-34 cells from oxidative damage and improve cell viability.[14]

Multiple Sclerosis

The pathogenicity of multiple sclerosis (MS) can be divided into two sections; inflammatory immune response and the degenerative process. The main characteristic of MS is the demyelinated portion in the central nervous system. The demyelination is healed by the formation of a glial scar. MS is also an auto-immune disorder mediated by the T-cells, attacking the myelin sheath peptides leading to loss of neurons and dendrocytes. Therapies available and in the study mostly target the immune system. PMSCs provide a unique approach to the treatment of MS patients by regulating both the immune response and facilitating the regeneration of the neural cells. Many studies have been conducted which use PMSCs on autoimmune encephalomyelitis (EAE) mouse models. The symptoms of EAE closely resemble MS symptoms. An immune response is triggered by the injection of myelin antigen and transplantation of PMSCs at 5th day and 14th day from immunization was concluded to reduce disease lethality and extended survival.[85] Injection of PMSCs is the EAE mice models were also an effective approach as these delayed the motor symptoms, modulated immune response by inhibiting the T cell proliferation and reducing inflammatory reactions, preventing neural network loss, and decreasing the seriousness of MS.[86,87]

The therapeutic efficacy of transplanting these stem cells in patients suffering from MS has been tested in various trials. Injecting umbilical cord-derived mesenchymal stem cells intravenously comes out to be feasible and safe in such patients. Additionally, the overall effects on treatment groups were observed to be stable or increased in comparison to the standard group.[88] In another research, patients having relapsing-remitting MS or secondary progressive MS were spontaneously administered with placental stem cells (PDA-001, a preparation of hPMSCs) and several individuals who were treated had steady or declining expanded disability status scale ratings (EDSS), which showed potential reparative influence on the patients.[89]

Liver diseases

Cirrhosis is the final stage of many liver injuries like viral infections, metabolic disorders, alcoholism, and even acute liver failure resulting from various processes. The typical functioning of the liver is disturbed due to the formation of the scar by the extracellular matrix. It further leads to necroinflammation and fibrogenesis.[90,91] Liver cirrhosis is an irrevocable condition that can be deadly, and the sole option for curing the disease is liver transplantation. However, the lesser availability of donors along with the constant requirement of immunosuppressants restrict liver transplantation and this is why cell transplantation emerges to be an appropriate alternative. Besides fetal and adult hepatocytes, stem cells are also taken into consideration for cell transplantations. It has been outlined that PMSCs can potentially be beneficent because of their ability to transform to hepatic-like cells, thereby forming functioning 3D structures.[92] AF-MSCs can engraft in the injured liver and produce Annexin-A1 and other helpful cytokines to successfully reduce the degree of liver damage and promote liver repair and regeneration.[93] Vascular cell adhesion molecule-1 and very late antigen-4 adhesion molecules help PMSCs to concentrate in injured areas. Through cell-cell interactions and the production of growth factors including hepatocyte growth factor (HGF) and vascular endothelial growth factor (VEGF), PMSCs help to heal the injured liver.[94,95] These stem cells have been shown to induce a notable decrease in fibrosis and also in the serum amounts of transaminases. An enhancement in liver regeneration has been suggested due to initiation in the mechanism of autophagy[96], a decline in apoptosis, repression in the activation of stellate cells[97], and incitement in liver cell proliferation.[98] They are also shown to limit hepatocyte inflammation as well as prevent apoptosis by suppression of TNF-α and IFN-γ. This causes the rejuvenation of hepatocytes and release of HGF, VEGF, IL-6, and PAF (Platelet-activating factor).[75,99] No indications regarding the formation of hepatocytes from cell transplants have been revealed in the rat model exhibiting CC14-

induced fibrosis[98], however, engraftment of PMSCs along with human albumin and α-fetoprotein expression has been outlined.[97,100,101]

Bone and Cartilage Diseases

Although bones have a physiological capability of regeneration and remodeling as evident from the healing of bones in case of any damage, there are some physiological scenarios when the physical regeneration of bone is compromised and insufficient. Osteoporosis is one of the conditions where compromised regeneration is seen. Deployment of PMSCs as a therapy for bone disorders exploits their multipotency. PMSCs possess the potential to differentiate and transform into osteocytes. They are *in vivo* potential of forming bones have been acknowledged by many studies thereby making the therapy an interesting candidate to facilitate bone repair. In a study, PMSCs injected in mice models with femur defects were able to fully recover the damage without any signs of fibrosis. They were injected in combination with nano biphasic calcium phosphate ceramics.[102] Another study used hydroxyapatite/tricalcium phosphate particles to form bones at the implants in a severe immune deficiency (SCID) mice model.[103] The multipotency and ability to differentiate into musculoskeletal lineages makes PMSC an alternative and interesting option for osteoarthritis (OA), a degenerative disease of cartilages in the joints. Many studies have been conducted supporting the regenerative hypothesis using PMSCs. Rat models with osteochondral defects in the knee were found to form hyaline cartilage when administered with the PMSCs grown on silk fibroin.[104] In a study, for covering the femoral defects, PMSCs infused in collagen I gel were subjected to a diseased rat model. Upon testing, the soft-grown tissue was positive for toluidine blue which indicated the differentiation of transplanted cells.[105] Proliferative and osteogenic effects of andrographolide (AP) on human-PMSCs have also been studied. It also improved osteogenic differentiation by increasing the expression of osteoblast-specific mRNA. Furthermore, it can aid bone development by increasing the amount of the bone structural protein osteocalcin in osteoblastic cells.[106]

Intestinal Diseases

Crohn's disease, as well as ulcerative colitis, are chronic illnesses triggered due to prolonged swelling of the epithelial cells in the intestinal tract leading to tissue damage all over the gastrointestinal system. These conditions are thought to be a consequence of an aberrant immunological response to intra-luminal antigens among susceptible individuals. Many other specific gene mutations of the nucleotide-binding oligomerization domain 2 (NOD2) are involved in the progression of this disorder.[107] These two illnesses have significant effects on well-being and presently no cure is available. In addition, most sufferers are not receptive to early detection and treatment. Injecting a conditioned medium of PMSCs intraperitoneally improved clinical characteristics in a mouse paradigm suffering from colitis instigated by dextran sulfate sodium.[108] These stem cells when injected intraperitoneally also inhibited tissue necrosis and reduced mouse fatalities. These positive effects seemed to be significantly higher while using NOD2-activated stem cells.[82]

A study showed the safety of intravenous infusion of these stem cells (PDA001) in individuals suffering from intermediate to serious level Crohn’s disorder, and subsequently, certain recovery rates of the illness were also noted.[109] Similarly, in another monitored clinical experiment, the patient’s situation enhanced dramatically on intravenously injecting these stem cells. This led to a considerable decrease in steroid concentrations. Furthermore, many patients having anal fistula exhibited significant progress.[110]

Clinical trials of placenta-derived mesenchymal stem cells for treating various diseases

Clinical trials are human research studies that are used to assess the effectiveness of pharmacological, surgical, or cognitive interventions. PMSCs have also undergone clinical trials for the treatment of certain diseases. For instance, a Phase 1 study has been conducted for determining the safety of intramuscular dosage of PLX-PAD (placenta-derived MSC) for treating critical limb ischemia. Similarly, recently another phase 1 and 2 clinical trials are being conducted for assessing the potential of cryopreserved PMSCs against deadly SARS-COV-2. Many such registered clinical levels are mentioned in Table 1.

Table 1: List of registered clinical trials of placenta-derived mesenchymal stem cells for treating various diseases.[111]

NCT Number	Purpose of Study	Disease	Phase
NCT00919958 (YOS-2009)	Determining the safety of PLX-PAD (placenta-derived MSC) single dose, intramuscular injection for the treatment of CLI	Critical limb ischemia	Phase 1
NCT04464213 (YOS-2020)	Evaluate the efficacy and safety of human PMSCs on diabetic foot ulcer	Diabetic foot ulcer	Phase 1
NCT04464213 (YOS- 2020)	Study the pharmacokinetics and tolerance of hPMSC on diabetic foot ulcer	Diabetic foot ulcer	Phase 1
NCT01420432 (YOS-2011)	Safety and efficacy study of umbilical cord/PMSCs to treat ankylosing spondylitis	Ankylosing spondylitis (inflammatory arthritis)	Phase 1
NCT01413035 (2011)	Evaluate the safety and efficacy of hPMSCs at a dose of 1.0E+6 MSC/kg for type 2 diabetes	Type 2 diabetes	Phase 1 and 2
NCT01413035 (2011)	Evaluate the safety and efficacy of MSCs derived from the human placenta at a dose of 1.0E+6 MSC/kg for type 2 diabetes	Type 2 diabetes	Phase 1 and 2
NCT04652908 (2020)	Study the efficacy of treatment of human placenta-derived MSCs seeded on a commercially available dural graft extracellular matrix against myelomeningocele	Myelomeningocele	Phase 1 and 2 (ongoing)
NCT04461925 (2020)	Assessing infusions of cryopreserved allogeneic multipotent mesenchymal stem cells of the placenta and umbilical cord for COVID-19 patients with acute respiratory distress syndrome	SARS-CoV-2	Phase 1 and 2 (ongoing)
NCT01129739 (2010)	Evaluate safety and efficacy of hPMSCs at a dose of 1.0E+6 MSC/kg on subjects for refractory anemia (RA) and refractory anemia with ring sideroblast (RARS) of myelodysplastic syndromes (MDS)	Myelodysplastic syndromes (a type of cancer)	Phase 2

Future Prospects and Concluding Remarks

Placenta derived mesenchymal stem cells serve as potential sources for use in stem cell therapy in humans. Cell therapy employing these stem cells is primarily based on three essential properties they possess, i.e., their innate remedial ability or the release of paracrine factors, their ability to homing and engraftment and immune regulation capacity. Conversely, the medical utilization of PMSCs is still in its infant stages and many trials are still under research. Many trails involving cell therapy have been conducted using autologous stem cells. However, there are many drawbacks to using a patient's own cells. Firstly, there is a time constraint, as the growth and quality control of autologous cells can take some months. In addition, cells may exhibit lesser efficacy owing to inherent elderly factors, and these PMSCs pose some attributes which can make autologous gene therapy virtually impossible, as observed in the case of older patients as well as those with particular systemic chronic conditions such as diabetes. Allogeneic mesenchymal stem cells, on the other hand, have the ability to be produced in high yields quickly so that they can be easily accessible and delivered instantly. They can be procured under more systematic and explicitly tested parameters and are likely to minimize costs. Till now, published reports on the efficacy of therapy using PMSCs suggest that these cells are safe and thus they are already 'off-the-shelf' products. While many clinical studies are underway or provide no published findings, there are a few positive reports on effectiveness of this treatment. Regenerative nanomedicine is indeed a propitious field which has provided very satisfactory outcomes at pre-clinical levels. Therapies of many illnesses can profit with the utilization of scaffolds, which provide a three-dimensional framework to facilitate cells, promote its adherence and development, thereby improve engraftment and subsequently the therapeutic outcomes. Apart from the use of cells as transporters of nanomaterials to transport medications within the wounded tissue and, even more, the prospect of stimulus-controlled secretion of medicines appears to be exhilarating. Along the way, further research is required on these stem cells which can potentially give promising results in the field of regenerative medicine.

Acknowledgments

The authors are grateful to the Delhi Technological University, New Delhi, India for providing the opportunity and support to conduct this study.

Conflicts of Interest

The author declares that there are no conflicts of interest relevant to this article.

References

1. Hipp J, Atala A. Sources of Stem Cells for Regenerative Medicine. Stem Cell Rev. 2008 Mar 20;4(1):3–11.
2. Quartu M, Serra MP, Boi M, Ibba V, Melis T, Del Fiacco M. Polysialylated-neural cell adhesion molecule (PSA-NCAM) in the human trigeminal ganglion and brainstem at prenatal and adult ages. BMC Neurosci. 2008 Dec 6;9(1):108.
3. Yen BL, Huang H-I, Chien C-C, Jui H-Y, Ko B-S, Yao M, et al. Isolation of Multipotent Cells from Human Term Placenta. Stem Cells. 2005 Jan;23(1):3–9.
4. Lee OK, Kuo TK, Chen W-M, Lee K-D, Hsieh S-L, Chen T-H. Isolation of multipotent mesenchymal stem cells from umbilical cord blood. Blood. 2004 Mar 1;103(5):1669–75.
5. Napso T, Yong HEJ, Lopez-Tello J, Sferruzzi-Perri AN. The Role of Placental Hormones in Mediating Maternal Adaptations to Support Pregnancy and Lactation. Front Physiol. 2018 Aug 17;9.
6. Zakrzewski W, Dobrzyński M, Szymonowicz M, Rybak Z. Stem cells: past, present, and future. Stem Cell Res Ther. 2019 Dec 26;10(1):68.

7. Macias MI, Grande J, Moreno A, Domínguez I, Bornstein R, Flores AI. Isolation and characterization of true mesenchymal stem cells derived from human term decidua capable of multilineage differentiation into all 3 embryonic layers. Am J Obstet Gynecol. 2010 Nov;203(5):495.e9-495.e23.
8. Anker PS, Scherjon SA, Kleijburg-van der Keur C, de Groot-Swings GMJS, Claas FHJ, Fibbe WE, et al. Isolation of Mesenchymal Stem Cells of Fetal or Maternal Origin from Human Placenta. Stem Cells. 2004 Dec;22(7):1338–45.
9. Fukuchi Y, Nakajima H, Sugiyama D, Hirose I, Kitamura T, Tsuji K. Human Placenta-Derived Cells Have Mesenchymal Stem/Progenitor Cell Potential. Stem Cells. 2004 Sep;22(5):649–58.
10. Yen BL, Chien C-C, Chen Y-C, Chen J-T, Huang J-S, Lee F-K, et al. Placenta-Derived Multipotent Cells Differentiate into Neuronal and Glial Cells In Vitro. Tissue Eng Part A. 2008 Jan;14(1):9–17.
11. Chang C-M, Kao C-L, Chang Y-L, Yang M-J, Chen Y-C, Sung B-L, et al. Placenta-derived multipotent stem cells induced to differentiate into insulin-positive cells. Biochem Biophys Res Commun. 2007 Jun;357(2):414–20.
12. Chien C-C, Yen BL, Lee F-K, Lai T-H, Chen Y-C, Chan S-H, et al. In Vitro Differentiation of Human Placenta-Derived Multipotent Cells into Hepatocyte-Like Cells. Stem Cells. 2006 Jul;24(7):1759–68.
13. Lee JM, Jung J, Lee H-J, Jeong SJ, Cho KJ, Hwang S-G, et al. Comparison of immunomodulatory effects of placenta mesenchymal stem cells with bone marrow and adipose mesenchymal stem cells. Int Immunopharmacol. 2012 Jun;13(2):219–24.
14. Yao P, Zhou L, Zhu L, Zhou B, Yu Q. Mesenchymal Stem Cells: A Potential Therapeutic Strategy for Neurodegenerative Diseases. Eur Neurol. 2020;83(3):235–41.
15. Ns S, Na A. Sources of Mesenchymal Stromal Cells : An Overview. Am Jorunal Pharmacol. 2018;1(1):1–7.
16. Yun Cheng H. The Impact of Mesenchymal Stem Cell Source on Proliferation, Differentiation, Immunomodulation and Therapeutic Efficacy. J Stem Cell Res Ther. 2014;04(10).
17. Pipino C, Shangaris P, Resca E, Zia S, Deprest J, Sebire NJ, et al. Placenta as a reservoir of stem cells: an underutilized resource? Br Med Bull. 2013 Mar 1;105(1):43–68.
18. Kim EY, Lee K-B, Kim MK. The potential of mesenchymal stem cells derived from amniotic membrane and amniotic fluid for neuronal regenerative therapy. BMB Rep. 2014 Mar 31;47(3):135–40.
19. Siddesh SE, Gowda DM, Jain R, Gulati A, Patil GS, Anudeep TC, et al. Placenta-derived mesenchymal stem cells (P-MSCs) for COVID-19 pneumonia-a regenerative dogma. Stem Cell Investig. 2021 Feb;8:3–3.
20. Woods L, Perez-Garcia V, Hemberger M. Regulation of Placental Development and Its Impact on Fetal Growth—New Insights From Mouse Models. Front Endocrinol (Lausanne). 2018 Sep 27;9.
21. Abbasi-Kangevari M, Ghamari S-H, Safaeinejad F, Bahrami S, Niknejad H. Potential Therapeutic Features of Human Amniotic Mesenchymal Stem Cells in Multiple Sclerosis: Immunomodulation, Inflammation Suppression, Angiogenesis Promotion, Oxidative Stress Inhibition, Neurogenesis Induction, MMPs Regulation, and Remyelination Stim. Front Immunol. 2019 Feb 20;10.
22. Siddesh SE, Gowda DM, Jain R, Gulati A, Patil GS, Anudeep TC, et al. Placenta-derived mesenchymal stem cells (P-MSCs) for COVID-19 pneumonia-a regenerative dogma. Stem Cell Investig. 2021 Jul 9;8.
23. Toda A, Okabe M, Yoshida T, Nikaido T. The Potential of Amniotic Membrane/Amnion-Derived Cells for Regeneration of Various Tissues. J Pharmacol Sci. 2007;105(3):215–28.
24. Ambrósio CE, Orlandin JR, Oliveira VC, Motta LCB, Pinto PAF, Pereira VM, et al. Potential application of aminiotic stem cells in veterinary medicine. Anim Reprod. 2020 May 22;16(1):24–30.
25. Portmann-Lanz CB, Schoeberlein A, Huber A, Sager R, Malek A, Holzgreve W, et al. Placental mesenchymal stem cells as potential autologous graft for pre- and perinatal neuroregeneration. Am J Obstet Gynecol. 2006 Mar;194(3):664–73.
26. Ventura Ferreira MS, Bienert M, Müller K, Rath B, Goecke T, Opländer C, et al. Comprehensive characterization of chorionic villi-derived mesenchymal stromal cells from human placenta. Stem Cell Res Ther. 2018 Dec 5;9(1):28.
27. L. PK, Kandoi S, Misra R, S. V, K. R, Verma RS. The mesenchymal stem cell secretome: A new paradigm towards cell-free therapeutic mode in regenerative medicine. Cytokine Growth Factor Rev. 2019

Apr;46:1–9.
28. Bailo M, Soncini M, Vertua E, Signoroni PB, Sanzone S, Lombardi G, et al. Engraftment Potential of Human Amnion and Chorion Cells Derived from Term Placenta. Transplantation. 2004 Nov 27;78(10):1439–48.
29. Vegh I, Grau M, Gracia M, Grande J, de la Torre P, Flores AI. Decidua mesenchymal stem cells migrated toward mammary tumors in vitro and in vivo affecting tumor growth and tumor development. Cancer Gene Ther. 2013 Jan 5;20(1):8–16.
30. Pogozhykh O, Prokopyuk V, Figueiredo C, Pogozhykh D. Placenta and Placental Derivatives in Regenerative Therapies: Experimental Studies, History, and Prospects. Stem Cells Int. 2018;2018:1–14.
31. Gnecchi M, Zhang Z, Ni A, Dzau VJ. Paracrine Mechanisms in Adult Stem Cell Signaling and Therapy. Circ Res. 2008 Nov 21;103(11):1204–19.
32. Taglauer ES, Adams Waldorf KM, Petroff MG. The hidden maternal-fetal interface: events involving the lymphoid organs in maternal-fetal tolerance. Int J Dev Biol. 2010;54(2–3):421–30.
33. Blaschitz A, Hutter H, Dohr G. HLA Class I protein expression in the human placenta. Early Pregnancy. 2001 Jan;5(1):67–9.
34. Xu X, Zhou Y, Wei H. Roles of HLA-G in the Maternal-Fetal Immune Microenvironment. Front Immunol. 2020 Oct 22;11.
35. Bowen JM, Chamley L, Mitchell MD, Keelan JA. Cytokines of the placenta and extra-placental membranes: biosynthesis, secretion and roles in establishment of pregnancy in women. Placenta. 2002 Apr;23(4):239–56.
36. McCracken SA, Hadfield K, Rahimi Z, Gallery ED, Morris JM. NF-κB-regulated suppression of T-bet in T cells represses Th1 immune responses in pregnancy. Eur J Immunol. 2007 May;37(5):1386–96.
37. Heikkinen J, Möttönen M, Alanen A, Lassila O. Phenotypic characterization of regulatory T cells in the human decidua. Clin Exp Immunol. 2004 May;136(2):373–8.
38. Abumaree MH, Al Jumah MA, Kalionis B, Jawdat D, Al Khaldi A, Abomaray FM, et al. Human Placental Mesenchymal Stem Cells (pMSCs) Play a Role as Immune Suppressive Cells by Shifting Macrophage Differentiation from Inflammatory M1 to Anti-inflammatory M2 Macrophages. Stem Cell Rev Reports. 2013 Oct 28;9(5):620–41.
39. Yust-Katz S, Fisher-Shoval Y, Barhum Y, Ben-Zur T, Barzilay R, Lev N, et al. Placental mesenchymal stromal cells induced into neurotrophic factor-producing cells protect neuronal cells from hypoxia and oxidative stress. Cytotherapy. 2012 Jan;14(1):45–55.
40. Li Q, Guan X, Wu P, Wang X, Zhou L, Tong Y, et al. Early Transmission Dynamics in Wuhan, China, of Novel Coronavirus–Infected Pneumonia. N Engl J Med. 2020 Mar 26 [cited 2021 Jul 4];382(13):1199–207.
41. Madabhavi I, Sarkar M, Kadakol N. COVID-19. A review. Monaldi Arch Chest Dis. 2020 May 14;90(2).
42. Sun P, Lu X, Xu C, Sun W, Pan B. Understanding of COVID-19 based on current evidence. J Med Virol. 2020 Jun 5;92(6):548–51.
43. Luthra R, Kaur S, Bhandari K. Applications of CRISPR as a potential therapeutic. Life Sci. 2021 Nov;284:119908.
44. Iwata-Yoshikawa N, Okamura T, Shimizu Y, Hasegawa H, Takeda M, Nagata N. TMPRSS2 Contributes to Virus Spread and Immunopathology in the Airways of Murine Models after Coronavirus Infection. Gallagher T, editor. J Virol. 2019 Mar 15;93(6).
45. Leng Z, Zhu R, Hou W, Feng Y, Yang Y, Han Q, Shan G, Meng F, Du D, Wang S, Fan J, Wang W, Deng L, Shi H, Li H, Hu Z, Zhang F, Gao J, Liu H, Li X, Zhao Y, Yin K, He X, Gao Z, Wang Y, Yang B, Jin R, Stambler I, Lim LW, Su H, Moskalev A, Cano A, Chakrabarti S, Min KJ, Ellison-Hughes G, Caruso C, Jin K, Zhao RC. Transplantation of ACE2- Mesenchymal Stem Cells Improves the Outcome of Patients with COVID-19 Pneumonia. Aging Dis. 2020 Mar 9;11(2):216-228.
46. Finegold JA, Asaria P, Francis DP. Mortality from ischaemic heart disease by country, region, and age: Statistics from World Health Organisation and United Nations. Int J Cardiol. 2013 Sep;168(2):934–45.
47. Faiella W, Atoui R. Therapeutic use of stem cells for cardiovascular disease. Clin Transl Med. 2016 Dec 18;5(1).

48. Zhao P, Ise H, Hongo M, Ota M, Konishi I, Nikaido T. Human Amniotic Mesenchymal Cells Have Some Characteristics of Cardiomyocytes. Transplantation. 2005 Mar 15;79(5):528–35.
49. Okamoto K, Miyoshi S, Toyoda M, Hida N, Ikegami Y, Makino H, et al. 'Working' cardiomyocytes exhibiting plateau action potentials from human placenta-derived extraembryonic mesodermal cells. Exp Cell Res. 2007 Jul;313(12):2550–62.
50. Li L, Jaiswal PK, Makhoul G, Jurakhan R, Selvasandran K, Ridwan K, et al. Hypoxia modulates cell migration and proliferation in placenta-derived mesenchymal stem cells. J Thorac Cardiovasc Surg. 2017 Aug;154(2):543-552.e3.
51. Lpez Y, Lutjemeier B, Seshareddy K, M. Trevino E, Sue Hageman K, I. Musch T, et al. Wharton's Jelly or Bone Marrow Mesenchymal Stromal Cells Improve Cardiac Function Following Myocardial Infarction for More Than 32 Weeks in a Rat Model: A Preliminary Report. Curr Stem Cell Res Ther. 2013 Feb 1;8(1):46–59.
52. Simioniuc A, Campan M, Lionetti V, Marinelli M, Aquaro GD, Cavallini C, et al. Placental stem cells pre-treated with a hyaluronan mixed ester of butyric and retinoic acid to cure infarcted pig hearts: a multimodal study. Cardiovasc Res. 2011 Jun 1;90(3):546–56.
53. Danieli P, Malpasso G, Ciuffreda MC, Cervio E, Calvillo L, Copes F, et al. Conditioned Medium From Human Amniotic Mesenchymal Stromal Cells Limits Infarct Size and Enhances Angiogenesis. Stem Cells Transl Med. 2015 May;4(5):448–58.
54. Gao LR, Chen Y, Zhang NK, Yang XL, Liu HL, Wang ZG, et al. Intracoronary infusion of Wharton's jelly-derived mesenchymal stem cells in acute myocardial infarction: double-blind, randomized controlled trial. BMC Med. 2015 Dec 10;13(1):162.
55. Bartolucci J, Verdugo FJ, González PL, Larrea RE, Abarzua E, Goset C, et al. Safety and Efficacy of the Intravenous Infusion of Umbilical Cord Mesenchymal Stem Cells in Patients With Heart Failure. Circ Res. 2017 Oct 27;121(10):1192–204.
56. Yu S, You X, Liang H, Li Y, Fu Y, Zhang X, Hu X, An J, Xu Y, Li F. First trimester placental mesenchymal stem cells improve cardiac function of rat after myocardial infarction via enhanced neovascularization. Heliyon. 2021 Feb 1;7(1):e06120.
57. Sprengers RW, Teraa M, Moll FL, de Wit GA, van der Graaf Y, Verhaar MC. Quality of life in patients with no-option critical limb ischemia underlines the need for new effective treatment. J Vasc Surg. 2010 Oct;52(4):843-849.e1.
58. Xie B, Luo H, Zhang Y, Wang Q, Zhou C, Xu D. Autologous Stem Cell Therapy in Critical Limb Ischemia: A Meta-Analysis of Randomized Controlled Trials. Stem Cells Int. 2018;2018:1–12.
59. Gu Y, Rampin A, Alvino V V., Spinetti G, Madeddu P. Cell Therapy for Critical Limb Ischemia: Advantages, Limitations, and New Perspectives for Treatment of Patients with Critical Diabetic Vasculopathy. Curr Diab Rep. 2021 Mar 2;21(3):11.
60. Beltrán-Camacho L, Rojas-Torres M, Durán-Ruiz MC. Current Status of Angiogenic Cell Therapy and Related Strategies Applied in Critical Limb Ischemia. Int J Mol Sci. 2021 Feb 26;22(5):2335.
61. Prather WR, Toren A, Meiron M, Ofir R, Tschope C, Horwitz EM. The role of placental-derived adherent stromal cell (PLX-PAD) in the treatment of critical limb ischemia. Cytotherapy. 2009 Jan;11(4):427–34.
62. Xie N, Li Z, Adesanya TM, Guo W, Liu Y, Fu M, et al. Transplantation of placenta-derived mesenchymal stem cells enhances angiogenesis after ischemic limb injury in mice. J Cell Mol Med. 2016 Jan 18;20(1):29–37.
63. Liang L, Li Z, Ma T, Han Z, Du W, Geng J, et al. Transplantation of Human Placenta-Derived Mesenchymal Stem Cells Alleviates Critical Limb Ischemia in Diabetic Nude Rats. Cell Transplant. 2017 Jan 1;26(1):45–61.
64. Mozaffarian D, Benjamin EJ, Go AS, Arnett DK, Blaha MJ, Cushman M, et al. Heart Disease and Stroke Statistics-2016 Update. Circulation. 2016 Jan 26;133(4).
65. Zahavi-Goldstein E, Blumenfeld M, Fuchs-Telem D, Pinzur L, Rubin S, Aberman Z, et al. Placenta-derived PLX-PAD mesenchymal-like stromal cells are efficacious in rescuing blood flow in hind limb ischemia

mouse model by a dose- and site-dependent mechanism of action. Cytotherapy. 2017 Dec;19(12):1438–46.

66. Barzegar M, Wang Y, Eshaq RS, Yun JW, Boyer CJ, Cananzi SG, et al. Human placental mesenchymal stem cells improve stroke outcomes via extracellular vesicles-mediated preservation of cerebral blood flow. EBioMedicine. 2021 Jan;63:103161.
67. Luthra R, Datta S, Roy A. Role of Different Peptides for Cancer Immunotherapy. Int J Pept Res Ther. 2021 Sep 23.
68. Moodley Y, Vaghjiani V, Chan J, Baltic S, Ryan M, Tchongue J, et al. Anti-Inflammatory Effects of Adult Stem Cells in Sustained Lung Injury: A Comparative Study. Mezey E, editor. PLoS One. 2013 Aug 1;8(8):e69299.
69. Spaeth E, Klopp A, Dembinski J, Andreeff M, Marini F. Inflammation and tumor microenvironments: defining the migratory itinerary of mesenchymal stem cells. Gene Ther. 2008 May 10;15(10):730–8.
70. Aboody KS, Brown A, Rainov NG, Bower KA, Liu S, Yang W, et al. Neural stem cells display extensive tropism for pathology in adult brain: Evidence from intracranial gliomas. Proc Natl Acad Sci. 2000 Nov 7;97(23):12846–51.
71. Auffinger B, Morshed R, Tobias A, Cheng Y, Ahmed AU, Lesniak MS. Drug-Loaded Nanoparticle Systems And Adult Stem Cells: A Potential Marriage For The Treatment Of Malignant Glioma? Oncotarget. 2013 Mar 31;4(3):378–96.
72. Mooney R, Roma L, Zhao D, Van Haute D, Garcia E, Kim SU, et al. Neural Stem Cell-Mediated Intratumoral Delivery of Gold Nanorods Improves Photothermal Therapy. ACS Nano. 2014 Dec 23;8(12):12450–60.
73. Li L, Guan Y, Liu H, Hao N, Liu T, Meng X, et al. Silica Nanorattle–Doxorubicin-Anchored Mesenchymal Stem Cells for Tumor-Tropic Therapy. ACS Nano. 2011 Sep 27;5(9):7462–70.
74. Shen C-J, Chan T-F, Chen C-C, Hsu Y-C, Long C-Y, Lai C-S. Human umbilical cord matrix-derived stem cells expressing interferon-β gene inhibit breast cancer cells via apoptosis. Oncotarget. 2016 Jun 7;7(23):34172-9.
75. Zhang G-Z, Sun H-C, Zheng L-B, Guo J-B, Zhang X-L. In vivo hepatic differentiation potential of human umbilical cord-derived mesenchymal stem cells: Therapeutic effect on liver fibrosis/cirrhosis. World J Gastroenterol. 2017 Dec 14;23(46):8152–68.
76. Ganta C, Chiyo D, Ayuzawa R, Rachakatla R, Pyle M, Andrews G, et al. Rat Umbilical Cord Stem Cells Completely Abolish Rat Mammary Carcinomas with No Evidence of Metastasis or Recurrence 100 Days Post–Tumor Cell Inoculation. Cancer Res. 2009 Mar 1;69(5):1815–20.
77. Stuckey DW, Shah K. TRAIL on trial: preclinical advances in cancer therapy. Trends Mol Med. 2013 Nov;19(11):685–94.
78. De la Torre P, Paris JL, Fernández-de la Torre M, Vallet-Regí M, Flores AI. Endostatin Genetically Engineered Placental Mesenchymal Stromal Cells Carrying Doxorubicin-Loaded Mesoporous Silica Nanoparticles for Combined Chemo- and Antiangiogenic Therapy. Pharmaceutics. 2021 Feb 10;13(2):244.
79. Luthra R, Roy A. Role of medicinal plants against neurodegenerative diseases. Curr Pharm Biotechnol. 2021 Feb 12;22.
80. Park S, Kim E, Koh S-E, Maeng S, Lee W, Lim J, et al. Dopaminergic differentiation of neural progenitors derived from placental mesenchymal stem cells in the brains of Parkinson's disease model rats and alleviation of asymmetric rotational behavior. Brain Res. 2012 Jul;1466:158–66.
81. Shin JY, Lee PH. Mesenchymal stem cells modulate misfolded α-synuclein in parkinsonian disorders: A multitarget disease-modifying strategy. Stem Cell Res. 2020 Aug;47:101908.
82. Kim H, Shin T, Lee B, Yu K, Seo Y, Lee S, et al. Human Umbilical Cord Blood Mesenchymal Stem Cells Reduce Colitis in Mice by Activating NOD2 Signaling to COX2. Gastroenterology. 2013 Dec;145(6):1392-1403.e8.
83. Jiao H, Shi K, Zhang W, Yang L, Yang L, Guan F, et al. Therapeutic potential of human amniotic membrane-derived mesenchymal stem cells in APP transgenic mice. Oncol Lett. 2016 Sep;12(3):1877–83.

84. Garbuzova-Davis S, Rodrigues MCO, Mirtyl S, Turner S, Mitha S, Sodhi J, et al. Multiple Intravenous Administrations of Human Umbilical Cord Blood Cells Benefit in a Mouse Model of ALS. Mosley RL, editor. PLoS One. 2012 Feb 3;7(2):e31254.
85. Fisher-Shoval Y, Barhum Y, Sadan O, Yust-Katz S, Ben-Zur T, Lev N, et al. Transplantation of Placenta-Derived Mesenchymal Stem Cells in the EAE Mouse Model of MS. J Mol Neurosci. 2012 Sep 26;48(1):176–84.
86. Bravo B, Gallego MI, Flores AI, Bornstein R, Puente-Bedia A, Hernández J, et al. Restrained Th17 response and myeloid cell infiltration into the central nervous system by human decidua-derived mesenchymal stem cells during experimental autoimmune encephalomyelitis. Stem Cell Res Ther. 2016 Dec 17;7(1):43.
87. Jiang H, Zhang Y, Tian K, Wang B, Han S. Amelioration of experimental autoimmune encephalomyelitis through transplantation of placental derived mesenchymal stem cells. Sci Rep. 2017 Mar 10;7(1):41837.
88. Li J-F, Zhang D-J, Geng T, Chen L, Huang H, Yin H-L, et al. The Potential of Human Umbilical Cord-Derived Mesenchymal Stem Cells as a Novel Cellular Therapy for Multiple Sclerosis. Cell Transplant. 2014 Jan 1;23(1_suppl):113–22.
89. Lublin FD, Bowen JD, Huddlestone J, Kremenchutzky M, Carpenter A, Corboy JR, et al. Human placenta-derived cells (PDA-001) for the treatment of adults with multiple sclerosis: A randomized, placebo-controlled, multiple-dose study. Mult Scler Relat Disord. 2014 Nov;3(6):696–704.
90. Schuppan D, Afdhal NH. Liver cirrhosis. Lancet. 2008 Mar;371(9615):838–51.
91. Williams R. Sherlock's disease of the liver and biliary systems. Clin Med (Northfield Il). 2011 Oct 1;11(5):506–506.
92. Bornstein R, Macias MI, de la Torre P, Grande J, Flores AI. Human decidua-derived mesenchymal stromal cells differentiate into hepatic-like cells and form functional three-dimensional structures. Cytotherapy. 2012 Sep;14(10):1182–92.
93. Zagoura D, Trohatou O, Makridakis M, Kollia A, Kokla N, Mokou M, et al. Functional secretome analysis reveals Annexin-A1 as important paracrine factor derived from fetal mesenchymal stem cells in hepatic regeneration. EBioMedicine. 2019 Jul;45:542–52.
94. Eom YW, Shim KY, Baik SK. Mesenchymal stem cell therapy for liver fibrosis. Korean J Intern Med. 2015 Aug 27;30(5):580–9.
95. Luan Y, Kong X, Feng Y. Mesenchymal stem cells therapy for acute liver failure: Recent advances and future perspectives. Liver Res. 2021 Jun;5(2):53–61.
96. Jung J, Choi JH, Lee Y, Park J-W, Oh I-H, Hwang S-G, et al. Human Placenta-Derived Mesenchymal Stem Cells Promote Hepatic Regeneration in CCl 4 -Injured Rat Liver Model via Increased Autophagic Mechanism. Stem Cells. 2013 Aug;31(8):1584–96.
97. Zhang D, Jiang M, Miao D. Transplanted Human Amniotic Membrane-Derived Mesenchymal Stem Cells Ameliorate Carbon Tetrachloride-Induced Liver Cirrhosis in Mouse. Aziz S, editor. PLoS One. 2011 Feb 4;6(2):e16789.
98. Tsai P-C, Fu T-W, Chen Y-MA, Ko T-L, Chen T-H, Shih Y-H, et al. The therapeutic potential of human umbilical mesenchymal stem cells from Wharton's jelly in the treatment of rat liver fibrosis. Liver Transplant. 2009 May;15(5):484–95.
99. Fiore EJ, Bayo JM, Garcia MG, Malvicini M, Lloyd R, Piccioni F, et al. Mesenchymal Stromal Cells Engineered to Produce IGF-I by Recombinant Adenovirus Ameliorate Liver Fibrosis in Mice. Stem Cells Dev. 2015 Mar 15;24(6):791–801.
100. Cao H, Yang J, Yu J, Pan Q, Li J, Zhou P, et al. Therapeutic potential of transplanted placental mesenchymal stem cells in treating Chinese miniature pigs with acute liver failure. BMC Med. 2012 Dec 6;10(1):56.
101. Yu J, Hao G, Wang D, Liu J, Dong X, Sun Y, et al. Therapeutic Effect and Location of GFP-Labeled Placental Mesenchymal Stem Cells on Hepatic Fibrosis in Rats. Stem Cells Int. 2017;2017:1–11.
102. Reddy S, Wasnik S, Guha A, Kumar JM, Sinha A, Singh S. Evaluation of nano-biphasic calcium phosphate ceramics for bone tissue engineering applications: In vitro and preliminary in vivo studies. J Biomater Appl. 2013 Jan 27;27(5):565–75.

103. Kusuma GD, Menicanin D, Gronthos S, Manuelpillai U, Abumaree MH, Pertile MD, et al. Ectopic Bone Formation by Mesenchymal Stem Cells Derived from Human Term Placenta and the Decidua. Matsusaki M, editor. PLoS One. 2015 Oct 20;10(10):e0141246.
104. Li F, Chen Y-Z, Miao Z-N, Zheng S, Jin J. Human Placenta-Derived Mesenchymal Stem Cells with Silk Fibroin Biomaterial in the Repair of Articular Cartilage Defects. Cell Reprogram. 2012 Aug;14(4):334–41.
105. Wei JP, Nawata M, Wakitani S, Kametani K, Ota M, Toda A, et al. Human Amniotic Mesenchymal Cells Differentiate into Chondrocytes. Cloning Stem Cells. 2009 Mar;11(1):19–26.
106. Phunikom N, Boonmuen N, Kheolamai P, Suksen K, Manochantr S, Tantrawatpan C, et al. Andrographolide promotes proliferative and osteogenic potentials of human placenta-derived mesenchymal stem cells through the activation of Wnt/β-catenin signaling. Stem Cell Res Ther. 2021 Dec 14;12(1):241.
107. Hugot J-P, Chamaillard M, Zouali H, Lesage S, Cézard J-P, Belaiche J, et al. Association of NOD2 leucine-rich repeat variants with susceptibility to Crohn's disease. Nature. 2001 May;411(6837):599–603.
108. Song J, Kang HJ, Hong JS, Kim CJ, Shim J-Y, Lee CW, et al. Umbilical cord-derived mesenchymal stem cell extracts reduce colitis in mice by re-polarizing intestinal macrophages. Sci Rep. 2017 Dec 25;7(1):9412.
109. Mayer L, Pandak WM, Melmed GY, Hanauer SB, Johnson K, Payne D, et al. Safety and Tolerability of Human Placenta-Derived Cells (PDA001) in Treatment-Resistant Crohn's Disease. Inflamm Bowel Dis. 2013 Mar;19(4):754–60.
110. Zhang J, Lv S, Liu X, Song B, Shi L. Umbilical Cord Mesenchymal Stem Cell Treatment for Crohn's Disease: A Randomized Controlled Clinical Trial. Gut Liver. 2018 Jan 15;12(1):73–8.
111. What Are Clinical Trials and Studies? National Institute on Aging. https://www.nia.nih.gov/health/what-are-clinical-trials-and-studies. Accessed on 5 October 2021.

Cite this article

Luthra R. Yadav S. Verma S. Therapeutic applications of mesenchymal cells derived from human placenta: A comprehensive meta-review**.** NeuroPharmac J. 2021; 6(3): 277-294.
DOI: 10.37881/1.637

Copyright

© 2021 NeuroPharmac J. This is an open-access journal, and articles are distributed under the terms of the Creative Commons Attribution-NonCommercial-ShareAlike 4.0 License.

View publication stats

Sādhanā (2022)47:36
https://doi.org/10.1007/s12046-021-01791-1

© Indian Academy of Sciences

Thermodynamic analysis of sensible heat storage based double pass hybrid solar air heater with and without reflector

OM PRAKASH[1,*], ANIL KUMAR[2,3,*] and VINOD LAGURI[4]

[1]Department of Mechanical Engineering, Birla Institute of Technology, Mesra, Ranchi, India
[2]Department of Mechanical Engineering, Delhi Technological University, Delhi, India
[3]Centre for Energy and Environment, Delhi Technological University, Delhi, India
[4]Department of Mechanical Engineering, Indian Institute of Science (IISc), Bangalore, India
e-mail: 16omprakash@gmail.com; anilkumar76@dtu.ac.in; vinodlaguri@iisc.ac.in

MS received 1 June 2021; revised 29 November 2021; accepted 8 December 2021

Abstract. Solar air heater or solar heating system is a very useful solar thermal product used for multiple purposes such as drying, space heating, desalination, and various industrial applications for low temperature. In this communication, a comprehensive study on the energy-exergy analysis of sensible heat storage based on double pass solar air heater with and without the reflector. System is manufactured with locally available materials. Heat storage material (Metco material and aluminium scrap mixture) was used under the bottom layer. Three cases of experiments were planned, namely natural mode (case 1), double pass solar heater (case 2) and double pass solar air heater with reflector (case 3). Case 3 shows the superior thermal performance as compared to case 1 and 2. The outlet temperature varies from 36 to 60°C; 35 to 58.20°C and 38.5° to 73.2°C in Cases 1, 2 and 3, respectively. This was mainly due to the application of the reflector. It provided additional input energy to the solar air heater.

Keywords. Double pass; solar air heater; reflector; sensible thermal storage.

1. Introduction

Solar air heater is a multipurpose device used in various applications such as drying and space heating. This work is based on the greenhouse effect and utilizes solar radiation's heat to heat the flowing air [1, 2]. Its conversion efficiency is higher than solar photovoltaic panels. There are three major parts for the solar air heater or solar air heating system: close box with inlet and outlet holes, top transparent glass, and absorber plate [3]. Intense research work is happening in the field of solar air heaters to improve the performance and reduce cost by modification in its design, change of material for absorber plate and structure [4].

Initially, the system was developed as Single Pass Solar Air Heater (SPSAH). Inlet air comes from the downward side, which gets heated up due to greenhouse effect and exhaust is through outlet vent. The system can be operated in both active and passive modes [5]. For higher mass flow rate, researchers prefer to use active mode based system. To take full advantage of the available heat, Double Pass Solar Air Heater (DPSAH) is being first developed by Satcunanathan and Deonarine [6]. In this concept, top loss from transparent glass to surrounding is being minimized greatly. The system can be operated in both active and passive however for better performance active mode is preferred.

In comparison with performance of DPSAH with SPSAH, the outlet temperature is much higher in SPSAH. Here the secret of success is due to contact of flowing inside air to the top and bottom of the absorber plate. However, in the SPSAH, the flow air contact only on the top of the absorber plate. The curved type DPSAH is studied by Kumar *et al* [7]. Various designs of this system are being investigated in this study. Asymmetric semi-circular ribs in the system have the highest thermo-hydraulic performance compared to other types of DPSAH. It is also suggested that absorber plate of the DPSAH should be kept at the middle of the inlet and outlet duct. It was also found that asymmetric semi-circular ribs show better efficiency than symmetric circular ribs. A study had been carried out by Yeh *et al* [8] on innovative DPSAH. In this system, fins are attached on both sides of the absorber plate. There is a significant increase in the overall efficiency of the proposed system as compared to the SPSAH.

An innovative solar DPSAH is being investigated by Ho *et al* [9]. In this system, baffles and fins are attached to the DPSAH. Due to this, more heat exchange happens between the absorber plates to the flowing air. This leads to significant improvement in the overall thermal efficiency of the system as compared to the SPSAH.

*For correspondence
Published online: 12 February 2022

A DPSAH with mixed thermal heat storage (paraffin wax with foam aluminium) had been studied experimentally by Baig and Ali [10]. The experiment is conducted in four different conditions. In first condition, there is no storage concept applied in the DPSAH; however, in the second condition, aluminium and paraffin wax were kept inside the two cooper tubes, in third condition, same as second condition except for four storage based copper tube and in fourth condition, same as third case except no induced fan is used. Study shows that in the fourth condition, system works 2. 5 hours more after off sunshine hour, which is highest in all the cases.

Vijayan *et al* [11] studied the sensible thermal storage concept based on solar heating systems or solar air heaters. In the system, absorber plate is of corrugated shape and storage materials applied on it. Energy efficiency of the storage bed varies from 20.35% to 50.92.% and exergy efficiency vary from +3.97% to −2.81% when air mass flow rates vary from 0.0141 kg/s to 0.0872 kg/s. Energy efficiency of the proposed system is 3-8% higher than without storage system operating under the same condition. The outlet air temperature from system varies from 45°C to 60°C, which is appropriate for various applications such as drying and space heating.

Kalaiarasi *et al* [12] studied the comparative study of solar heating systems with and without sensible thermal storage material. Therminol-55 material is used as storage material for this system. Proposed system is operated in three different quantities namely 0.017, 0.02 and 0.028 kg/s. The maximum outlet air temperature (97°C) is obtained at 0.017 kg/s and minimum outlet temperature at 0.028 kg/s. The efficiency of the storage based system has higher thermal efficiency as compared to the without storage system.

After intense literature review, some research work was found in the field of double pass solar air heater assisted with the thermal storage material. However, there is no literature on the thermodynamic analysis of DPSAH with sensible thermal storage assisted stainless steel reflector.

Hence, main objective of present work is to compare the performance of DPSAH with sensible storage material between with and without reflector. To achieve the desired objective, cost effective proposed system is designed and developed with locally available material. In the first section of the article, the experimentation of the proposed system is being conducted in three different cases; namely, natural mode, induced forced mode and induced forced mode coupled with reflector. Uncertainty analysis of the experimental data has been done. Second section deals with the energy and exergy analysis of the experimental data. Lastly, thermal efficiency was being compared with previously published literature, and results of the proposed system were found to be superior compared to other systems. The conclusions are provided at the end.

2. Material and method

2.1 *Experiment setup*

The experimental setup was used in this study is shown in figures 1, 2 and 3. This study had three different sets of experiments conducted on three different consecutive days. On Day 1 (case 1) study conducted under natural mode of DPSAH (figure 1). Day 2 (case 2) study had been conducted under induced mode of DPSAH as shown figure 2 and Day 3 (case 3) study had been conducted under induced mode of DPSAH with reflector as shown in figure 3. In all three cases, dimension and materials of DPSAH remain same. In case 2, one induced fan was provided additional to case 1 and case 3, one additional reflector is provided compared to case 2. The external structure of the entire solar heating system was made up of 05 mm thick polycarbonate sheet. Polycarbonate sheet was selected due to its high durability and light weight. Two vents of square type (15×15 cm^2) were provided in the system for the incoming and outgoing air. The absorber plate was located in the middle of two vents. Copper sheet of 02 mm thick was used as absorber plate and it was coated with Aluminium silicon-boron nitride powder. This coating material was selected due to higher heat absorbent capacity. The entire system was well insulated with the help of glass wool so that minimum heat loss happens in side, bottom and edges of the system and top surface of the system was made up of 03 mm thick transparent toughen glass. Toughen glass was used in the place of normal glass due to its enhanced strength. Absorber plate was kept at a distance of 05 mm below the toughen glass. Sensible thermal storage concept was applied beneath the bottom layer of the air heater. Aluminium scrap painted with aluminium silicon boron nitride was used as storage material. Thickness of the storage material is 50 mm and weights 20 kg. This makes it uniform below the bottom layer of the air heater. The thickness of the storage material is selected as per recommendation by Aboul-Enein *et al* [13]. Emissivity and absorptivity of the coated material is higher than conventional black paint. Emissivity and absorptivity for conventional black paint were found to be 0.85 and 0.95; however, for coated material in the proposed study (aluminium silicon-boron nitride) found to be 0.80 and 0.97 as per Duffie and Beckman [14]. Due to this, heat absorption capacity of the absorber plate gets enhanced.

Solar air heating system was kept on the iron frame in the inclined position. The inclination angle which was the latitude angle of Ranchi, India which is 23°. At this inclination, optimum solar radiation is received round the year [11]. Square shaped polished steel of size 0.5×0.5 m^2 was used as reflector. Position of the reflector fixed in the frame can be adjusted according to movement of the sun. Hence, enhancement in the received solar radiation on the proposed system takes place.

The direction of air flow within the system in Case 1 (natural mode) was from top to bottom i.e. comes in the top vent and moves above the absorber plate and flows out under the absorber plate. It comes out from the lower vent. In Case 2 and Case 3, the direction of air flow is just reverse as compared to Case 1. Inlet air comes through the lower vent and gets out through the upper vent. In both cases, exhaust fan is being applied at the outlet vent. DC Fan (18 W) is powered by 40 W polycrystalline solar cell assisted with solar charge controller cum rechargeable battery.

Locally available materials had been used to fabricate in the proposed system in which Polycarbonate sheets hold 15.60 kg. Table 1 represents different components used with their weight in the manufacturing of the proposed system. Contribution of various materials used is presented in figure 4. Embodied energy of various components is used in the proposed system is given in Table 2 and their contribution presented in figure 5, in which Metco material holds highest percentage of 38%. Embodied energy in Case 1 is 681.484 KW/h, in Case 2 is 751.5809 kW/h and in Case 3 is 841.8309 kW/h.

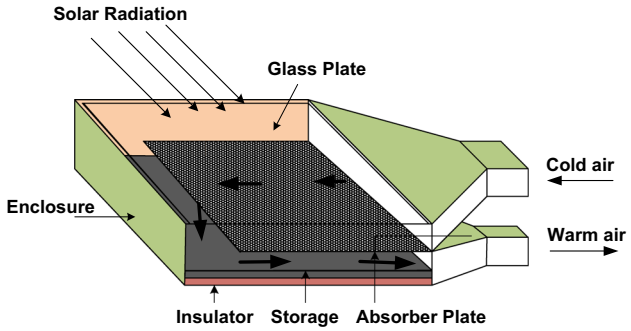


Figure 1. Schematic diagram under natural mode.

Various measuring instruments used in this experiment are given in Table 3 with their specification. Least count of different devices is mentioned in figure 6. In which moist evaporation has the highest least count 0.5 and voltage, current and wind velocity together holding a least count of 0.01 and the values of each is mentioned in Table 4.

2.2 *Methodology*

A. Energy analysis

Energy analysis of the proposed system was conducted with the help of experimental data (figure 6). This analysis is based on the conservation of energy principle. For the present system, the following energy balance equations are used:

$$Q_A = Q_u + Q_{loss} + Q_{st} \tag{1}$$

Now each term can be expressed in the following ways:

The Q_u is expressed as the total amount of heat utilized and which is mathematically expressed as follows (Nidhul *et al* [15]):

$$Q_u = \dot{m}\, C_p(T_{out} - T_{inlet}) \tag{2}$$

Where, m is the MFR of the air inside the system. This can be evaluated by the following expression (Nidhul *et al* [15]):

$$\dot{m} = \rho V_{ai} S \tag{3}$$

In this system, the primary source of energy is solar radiation. The net solar radiation absorbed by the absorber plate is denoted by Q_A which is evaluated by the following expression (Nidhul *et al* [15]):

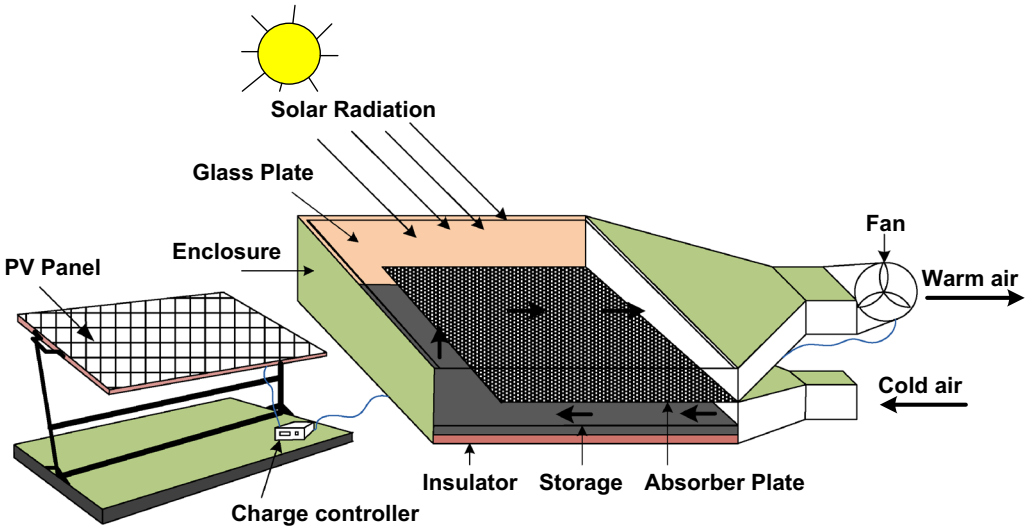


Figure 2. Schematic diagram under induced mode.

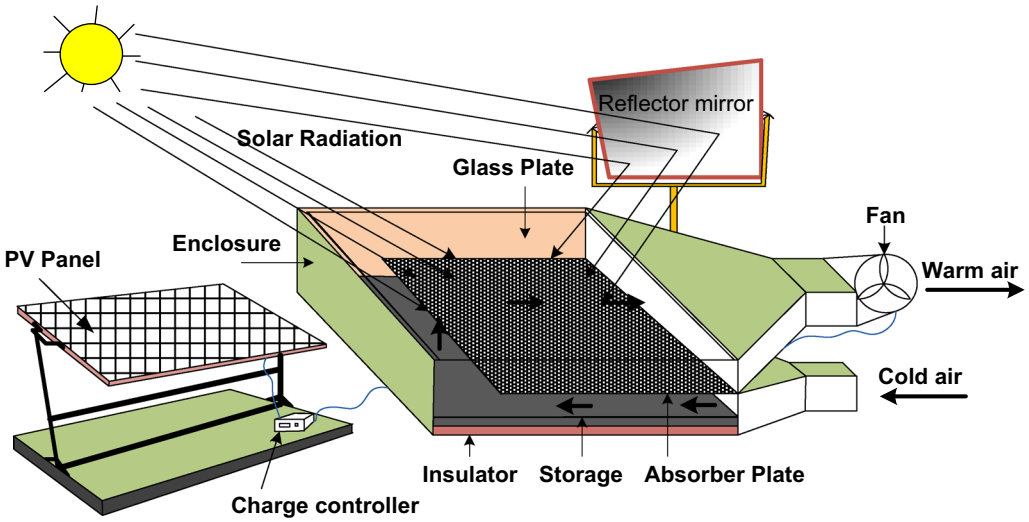


Figure 3. Schematic diagram of the double pass solar air heater with reflector.

$$Q_A = A_{plate}(\alpha\tau)I_i \tag{4}$$

In the solar collector, some heat loss occurs on the bottom side and top surface of the system. Therefore, the total amount of heat loss is calculated by the following expression (Nidhul *et al* [15]):

$$Q_{loss} = U_{loss}A_{plate}(T_{plate} - T_{ambient}) \tag{5}$$

U_{loss} is total heat losses coefficient which include losses from the top (U_{top}), bottom (U_{bot}) and side (U_{side}). Mathematically it is expressed as follows:

$$U_{loss} = U_{side} + U_{bot} + U_{top} \tag{6}$$

Where the parameters are evaluated as Esen [16]:

$$U_{top} = \left[1/(h_{r,Pg} + h_{c,Pg}) + 1/(h_{r,ga} + h_w)\right]^{-1} \tag{7}$$

$$U_{bot} = \lambda_i/\delta_{bot} \tag{8}$$

$$U_{side} = ((L_1 + L_2)L_3\lambda_i)/(L_1L_2\delta_e) \tag{9}$$

The unknown parameters can be evaluated as follow [17–21]:

$$h_{c,pg} = Nu(\lambda/t) \tag{10}$$

$$Nu = 0.68 + \frac{(0.67 \times Ra^{1/4})}{(1 + (0.492/\mathrm{Pr})^{9/16})^{4/9}} \quad [Ra \le 10^9] \tag{11}$$

$$h_{r,Pg} = \left(\frac{\sigma(T_{ground}^2 + T_{Plate}^2)(T_{ground} + T_{plate})}{\left(\frac{1}{\varepsilon_{plate}} + \frac{1}{\varepsilon_{plate}} - 1\right)}\right) \tag{12}$$

$$h_w = 3.86V_{air} + 5.67 \tag{13}$$

Table 1. Mass of various component used for fabrication of the SAH.

Sl. No	Material	Quantity
1	Glass	5.40 kg
2	Polycarbonate sheet	15.60 kg
3	Black coating	0.75 m^2
4	Copper Sheet	0.30kg
5	Metco Material	12.00 kg
6	Aluminium Scrap	8.00 kg
7	Ceramic Wool	1.00 kg
8	DC fan	
	(I)Plastic	0.120
	(II) Copper wire	0.050
9	Polycrystalline solar cell	0.059 m^2
10	Battery	
11	Solar charge controller	
12	Stainless steel	1 kg
13	Iron	05 kg

$$h_{r,ga} = \varepsilon_g\sigma(T_{ground}^2 + T_{sky}^2)(T_{ground} + T_{sky}) \tag{14}$$

$$T_{sky} = 0.0552T_{ambient}^{1.5} \tag{15}$$

According to the first law of thermodynamics, the thermal efficiency of the SAH is the ratio between the useful energy (Q_u) and the solar radiation received on the collector. Thermal efficiency can be calculated by the Eq. (16) [22, 23]:

$$\eta_{Thermal} = Q_u/I_iA_{plate} \tag{16}$$

The dimensionless parameters referred above are given by Eqs. (17), (18) and (19) [24]

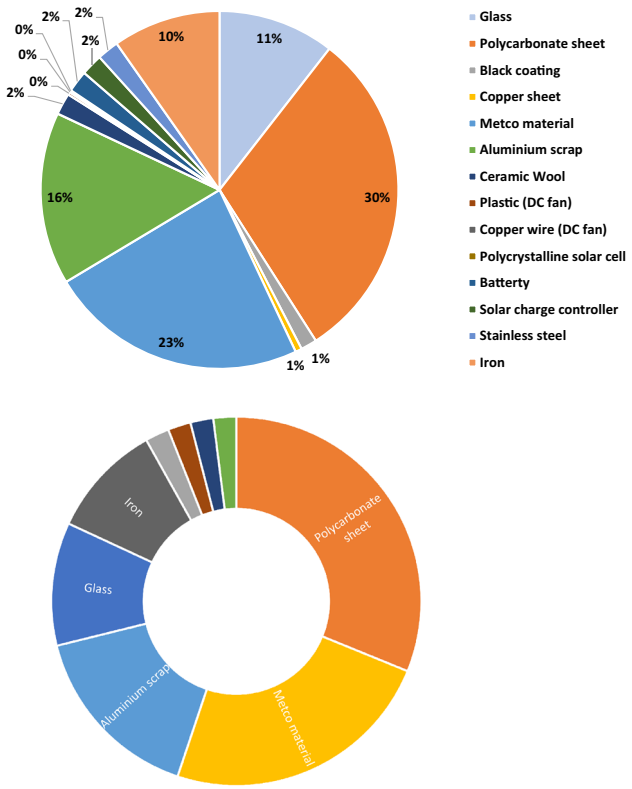


Figure 4. Distribution of different material in construction of solar heating system.

$$Ra = \frac{g\beta\Delta TL^3}{\alpha v} \tag{17}$$

$$\Pr = \frac{v}{\alpha} \tag{18}$$

$$\mathrm{Re} = \frac{V_{air}D_h}{v} \tag{19}$$

B. Exergy analysis of the SAH

Exergy analysis of the proposed system was evaluated based on experimental data. Few assumptions were taken to do the analysis:

a. System is in thermodynamic equilibrium.
b. Inside air flow is of steady-state with constant physical properties along with very small amount of relative humidity.

Exergy balance equation is being developed based on second law of thermodynamics. Exergy at the inlet of the SAH is given as Eq. (20).

$$Ex_{inlet} = Ex_{dest} + Ex_{outlet} + Ex_{stored} + Ex_{lost} \tag{20}$$

Where

Ex_{inlet},$Ex_{dest}Ex_{outlet}Ex_{stored}$ and Ex_{lost} are the various exergy for the inlet flowing air, destroyed, outlet point, stored and lost exergy.

Exergy for inlet airflow is calculated by Eq. (21) [25]:

$$\begin{aligned} &Ex_{inlet}(flowing\ air) \\ &= \dot{m}\,C_P\left(T_{inlet} - T_{ambient}\left(1 + \ln\left(\frac{T_{inlet}}{T_{ambient}}\right)\right)\right) \\ &\quad + \dot{m}\,RT_{ambient}\ln\left(\frac{P_{inlet}}{P_{amb}}\right) \end{aligned} \tag{21}$$

And the exergy at outlet air flow is expressed as Eq. (22) [26]:

$$\begin{aligned} &Ex_{outlet}(flowing\ air) \\ &= -\dot{m}C_P\left(T_{out} - T_{ambient}\left(1 + \ln\left(\frac{T_{out}}{T_{ambient}}\right)\right)\right) \\ &\quad - \dot{m}RT_{ambient}\ln\left(\frac{P_{out}}{P_{amb}}\right) \end{aligned} \tag{22}$$

Table 2. Embodied energy analysis for fabrication of SAH.

Sl. No	Material	Embodied Energy Coefficient	Case 1	Case 2	Case 3
1	Glass	7.28 (KWh/kg)	39.312	39.312	39.312
2	Polycarbonate sheet	10.20 (KWh/kg)	159.12	159.12	159.12
3	Black coating	0.28 (KWh/m^2)	0.21	0.21	0.21
4	Copper Sheet	19.44 (KWh/kg)	5.832	5.832	5.832
5	Metco Material	26.76 (KWh/kg)	321.12	321.12	321.12
6	Aluminium Scrap	18.98 (KWh/kg)	151.84	151.84	151.84
7	Ceramic Wool	4.05 (KWh/kg)	4.05	4.05	4.05
8	DC fan				
	(I)Plastic	19.44 (KWh/kg)	–	2.332	2.332
	(II) Copper wire	19.61 (KWh/kg)	–	0.9805	0.9805
9	Polycrystalline solar cell	1130.60 (KWh/m^2)	–	66.7054	66.7054
10	Battery		–	0.046	0.046
11	Solar charge controller		–	0.033	0.033
12	Stainless steel	55.55 (KWh/m^2)	–	–	55.55
13	Iron	6.94 (KWh/m^2)	–	–	34.70
		Total Embodied Energy (KWh)	681.484	751.5809	841.8309

Exergy for absorbed solar radiation can be calculated as Eq. (23) [27]:

$$Ex_{inlet}(solar\ radiation) = I_i\left[1-\frac{4}{3}\left(\frac{T_{ambient}}{T_{sky}}\right)+\left(\frac{T_{ambient}}{T_{sky}}\right)^4\right] \quad (23)$$

where T_{sky}= 5777 K.

The lost exergy, Ex $_{lost}$ can be indicated as Eq. (24) [28, 29]:

$$Ex_{lost} = -U_{lost}A_{col}[(T_{Plate}-T_{ambient})-(T_{ambient}+273)ln\frac{(T_{Plate}+273)}{(T_{ambient}+273)}] \quad (24)$$

The exergy destruction Ex_{dest} is dependent on three different terms [29]

i. Temperature difference between the absorber plate and sun (shown in Eq. (25)).
ii. Pressure drop at duct as shown in Eq. (26).
iii. Heat transfer to the flowing air from absorber plate to the surface as shown in Eq. (27).

$$Ex_{dest(p-s)} = -\eta_0 I_i A_{col} T_{ambient}\left(\left(\frac{1}{T_{plate}}\right)-\left(\frac{1}{T_{sky}}\right)\right) \quad (25)$$

$$Ex_{dest(\Delta P)} = -(\Delta P T_{ambient}/\rho)\left(_{ambient}\ln\left(\frac{T_{out}}{T_{ambient}}\right)\right)(T)/(T_{out}-T_{inlet}) \quad (26)$$

$$Ex_{dest(p-f)} = -\dot{m}\,C_p T_{ambient}\left(\ln\left(\frac{T_{out}}{T_{inlet}}\right)-\left(\frac{T_{out}-T_{inlet}}{T_{plate}}\right)\right) \quad (27)$$

The daily exergy efficiency of the SAH can be calculated as Eq. (28) [30]

$$\eta_{Exergy} = \left(\int Ex_{out}/\int Ex_{inlet}\right)\times 100\% \quad (28)$$

2.3 *Uncertainty analysis*

Every measuring instrument has limitations; none of the measuring devices is 100% accurate. Uncertainty analysis is intended to indicate the possible error in measurement by the instruments. The uncertainty analysis is being calculated with the help of Eqs. 29–33. Table 2 shows the external Uncertainty Percentage Error.

$$W_Y = \sqrt{\left(\frac{\partial Y}{\partial y_1}W_1\right)^2+\left(\frac{\partial Y}{\partial y_2}W_2\right)^2+\left(\frac{\partial Y}{\partial y_3}W_3\right)^2+\cdots+\left(\frac{\partial Y}{\partial y_n}W_n\right)^2} \quad (29)$$

$$W_{Temp} = \sqrt{(W_{thermometer})^2+(W_{reading})^2} \quad (30)$$

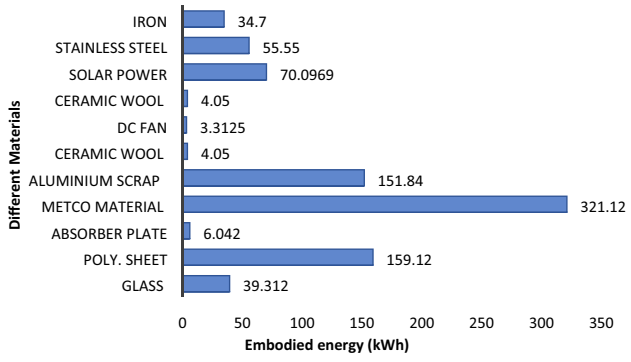


Figure 5. Distribution of embodied energy of different materials.

Table 4. External Uncertainty Percentage Error.

Sl. No	Measurement Error	Value
1	Absorber temperature	0.10
2	Air temperature	0.10
3	Relative humidity	0.10
4	Moisture evaporation	0.50
5	Voltage	0.01
6	Current	0.01
7	Wind velocity	0.01
8	Plate Temperature	0.10
	Total Percent External Uncertainty	0.93

Table 3. Technical instruments and measurement device.

Device	Quantity	Model/Producer	Range	Accuracy
Anemometer	1	Lutron/AM4202	0.4-30 m/s	± 0.1 ms^{-1}
Solar Power Meter	1	CEM/LA-1017	0e1999 W/m^2	±10W/m^2
Thermocouples	8	K-type/ Jain Automation	− 200–1200°C	±0.5°C

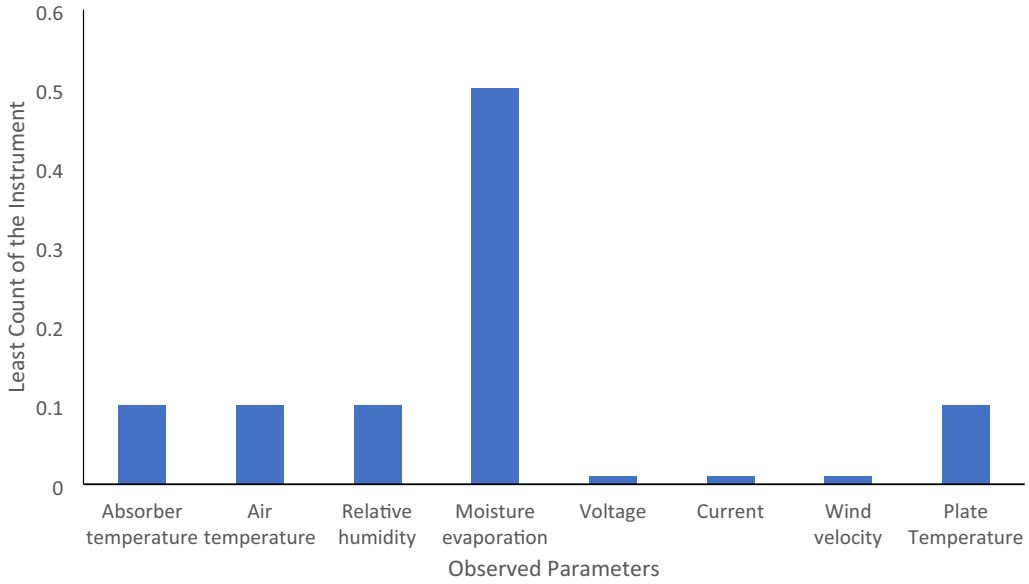


Figure 6. Least count of instruments to major parameters.

$$W_{Wind}=\sqrt{(W_{anemometer})^2+(W_{reading})^2} \quad (31)$$

$$W_{Radiation}=\sqrt{(W_{Pyranometer})^2+(W_{reading})^2} \quad (32)$$

$$W_{Exp}=\sqrt{(W_{Wind})^2+(W_{Temp})^2+ \ +(W_{Radiation})^2} \quad (33)$$

By solving all these equations Eqs. (30)–(33) with the help of Table 3, total uncertainty is found to be ±0.2004% which is in actable range.

3. Result and discussion

In this section, the discussion on the experimental results and energy-exergy analysis is presented.

3.1 *Experimental results*

The proposed system is being experimented on three consecutive days in three different modes. In case 1 system is in natural mode, case 2 system is in induced mode and case 3 system is induced with reflector mode. In all three cases, ambient parameters were very similar with little variation due to clear sky conditions. Hence comparison of the thermal performance becomes appropriate in the atmospheric condition.

The variation of ambient wind speed in case 1 is 0.22–0.70 m/s; 0.27–0.65 m/s in case 2 and 0.28–0.71 m/s in case 3 as presented in figure 7. Hence average variation in wind speed is less than 10% among all three cases of experimentation.

Various temperature at important location is also measured to evaluate thermal performance of the proposed system. These temperatures are the top glass temperature, absorber plate temperature and outlet temperature in all three cases.

The variation of all the different temperatures (ambient temperature, glass temperature, outlet temperature and plate temperature) depends on solar radiation. The variation of all different temperatures and solar radiation during experimentation in all three cases is shown in figure 8. Experiment was conducted from 9.00 AM to 5.00 PM in all three cases on 10–12 April 2020. The variation of solar radiation on case 1 is 360–950 W/m^2; 355–945 W/m^2 on case 2 and 350–940 W/m^2 on case 3, as presented in figure 8. In all three cases, the maximum solar radiation comes out at 1.00 PM and minimum at 5.00 PM. Hence average variation in global radiation is less than 1% among all three cases of experimentation. The variation of ambient temperature on case 1 is 30°–35.80°C; 26°–40.40°C on case 2 and 25.20°–37.80°C on case 3 as presented in figures 8 and 9. The maximum ambient temperature for case 1 is at 2.00 PM, case 2 is at 2.00 PM, and case 3 is at 1.00 PM. Hence average variation in ambient temperature is less than 10% among all three cases of experimentation.

The variation of top glass temperature on case 1 is 34°–58°C; 31°–45°C on case 2 and 29.5°–65°C on case 3 as presented. The average top glass temperature was found to be lowest in case 2 i.e., 39.33oC; however,in case 3, it was found 54.28°C.

The variation of absorber plate temperature on case 1 is 40°–81°C; 34.5°–70°C on case 2 and 55°–89 ° C on case 3 as presented in figure 8. The average top glass temperature

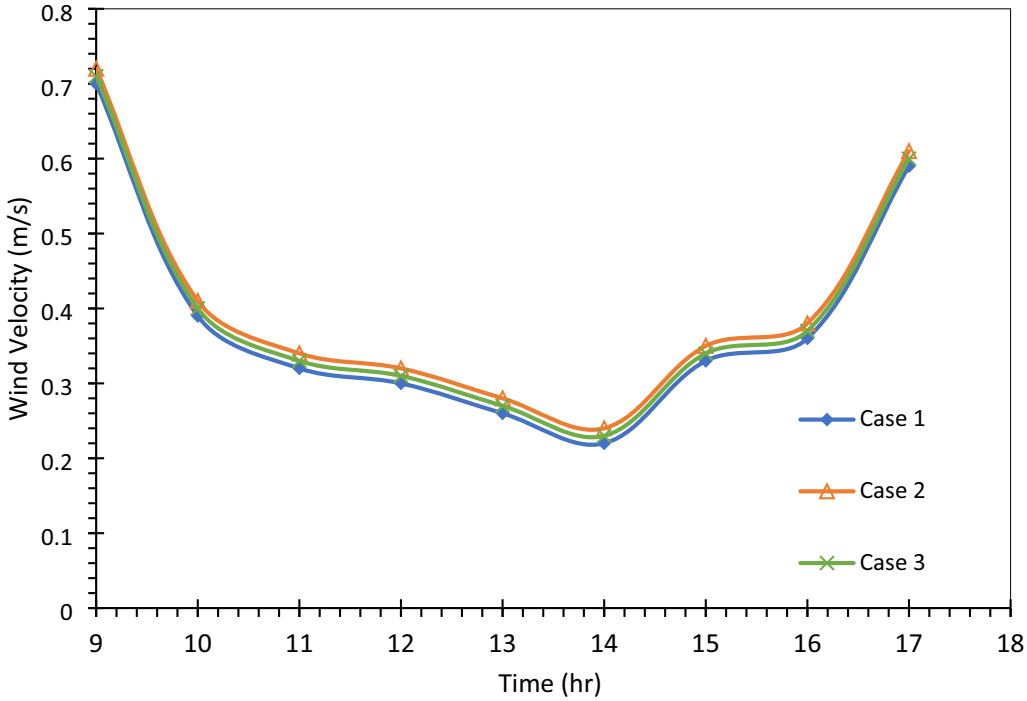


Figure 7. Wind velocity during experimentation.

was found to be lowest in case 2 i.e., 59.28°C; however, in Case 3, it was found 70.11°C.

The variation of outlet temperature on case 1 is 36°–60°C; 35°–58.20°C on case 2 and 38.5°–73.2°C on case 3 as presented in figure 8. The average outlet temperature was found to be lowest in case 2 i.e., 48.23°C; however, in case 3. It was found that 55.36°C. Case 3 shows superior performance due to the application of the reflector because it provides additional input energy to the solar air heater.

Thermal efficiency and exergy efficiency depend on global solar radiation. The variation of global solar radiation, thermal efficiency and exergy efficiency during experimentation in all three cases is shown in figure 9. Experiment was conducted from 9.00 AM to 5.00 PM in all three cases on 10–12 April 2020. The variation of solar radiation on case 1 is 360–950 W/m^2; 355–945 W/m^2 on case 2 and 350–940 W/m^2 on case 3 as presented. In all three cases, the maximum solar radiation comes out at 1.00 PM and minimum at 5.00 PM. Hence average variation in global radiation is less than 1% among all three cases of experimentation.

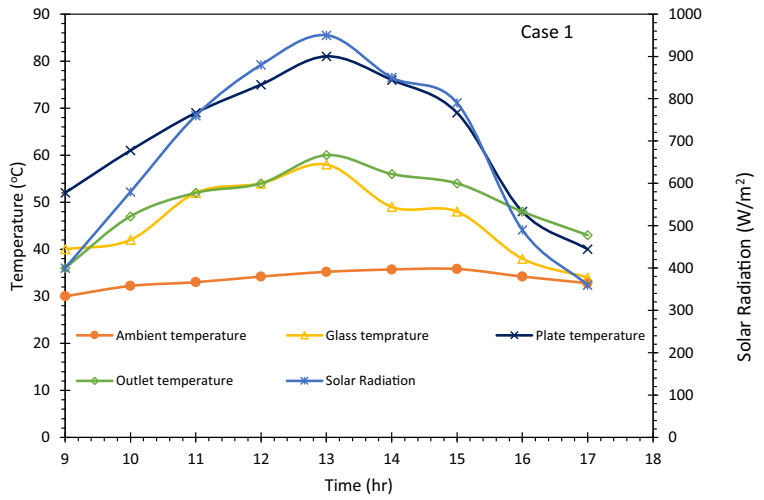
Based on experimental results, thermal energy and exergy efficiencies are evaluated.

The variation of thermal efficiency on case 1 is 7.16–19.67 %; 43.2–66.13 % on case 2 and 54.08–75.92 % on case 3 as presented in figure 9. Average thermal efficiency was found to be lowest in case 1 i.e., 14.21 %; however,in case 3, it was found that 65.05%.

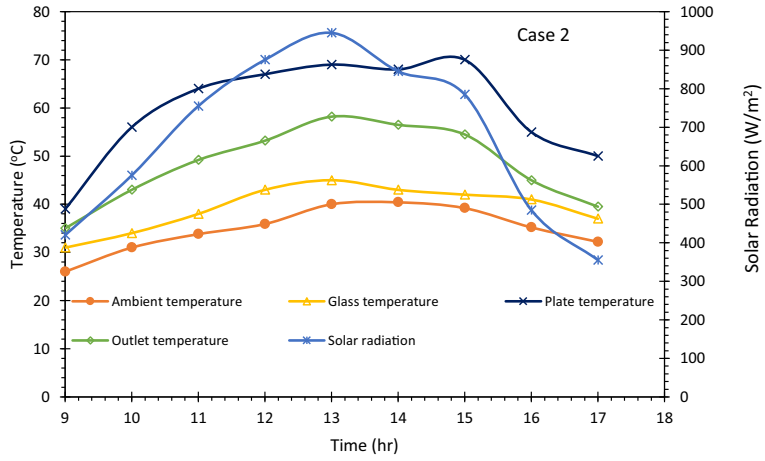
The variation of exergy efficiency on case 1 is 1.15–3.57%; 6.97–12.48% on case 2 and 10.28–21.83 % on case 3, as presented in figure 9. The average exergy efficiency was found to be lowest in the case 1 i.e., 2.2 %; however, in case 3, it was found to be 17.61 %. Case 3 shows superior performance due to the application of the reflector because it provides additional input energy to the solar air heater.

3.2 *Validation*

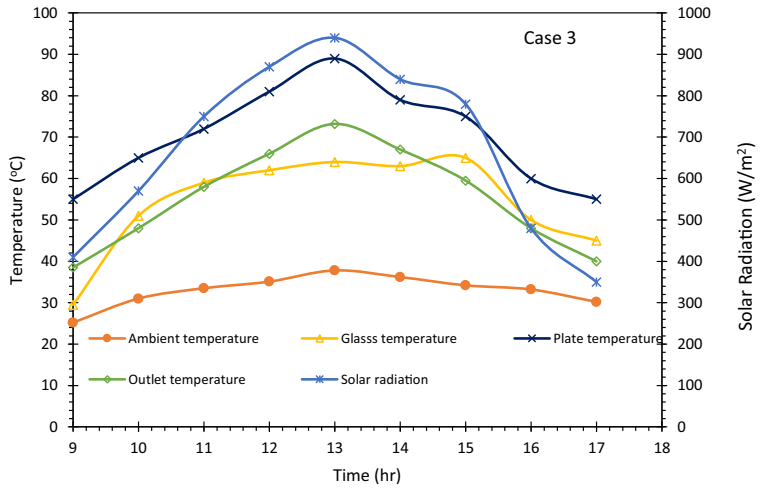
Esen *et al* [16] studied the double pass solar heater. The absorber plate of the system was made of aluminium cane. The maximum solar radiation was found to be 1003 W/m^2. Proposed system with reflector, the maximum solar radiation was found to be 940 W/m^2. All other parameters are dependent on solar radiation. Both ambient conditions were almost similar, with less than 10% increase or decrease. The peak outlet temperature of the referred system is 68°C; however, for the proposed system, the peak temperature is 73.5°C under same mass flow rate (0.025 kg/s). The peak temperature of the referred system was found to be 37.1°C and 37.18°C for the proposed system. Both systems had same dimension and absorber plate area. The peak thermal efficiency of the referred system was found to be 59.65% at 1.00 PM. However, 65.05 % was found for the proposed system. Hence the proposed system shows higher thermal performance than the other types of double pass solar air



(**a**) Case 1

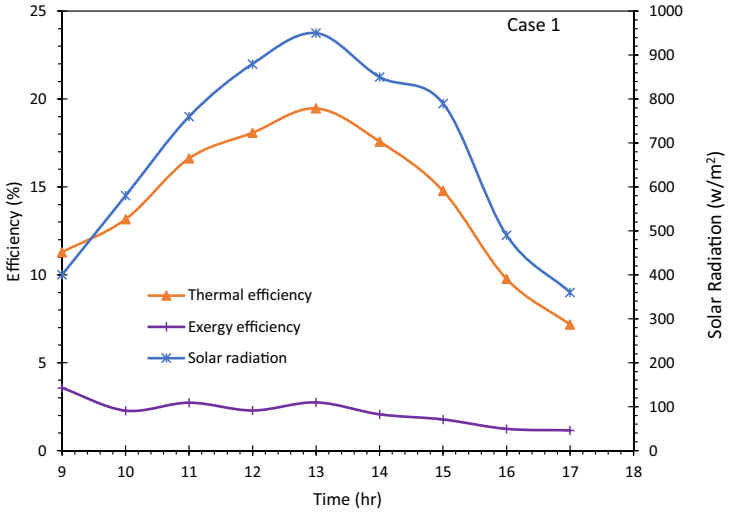


(**b**) Case 2

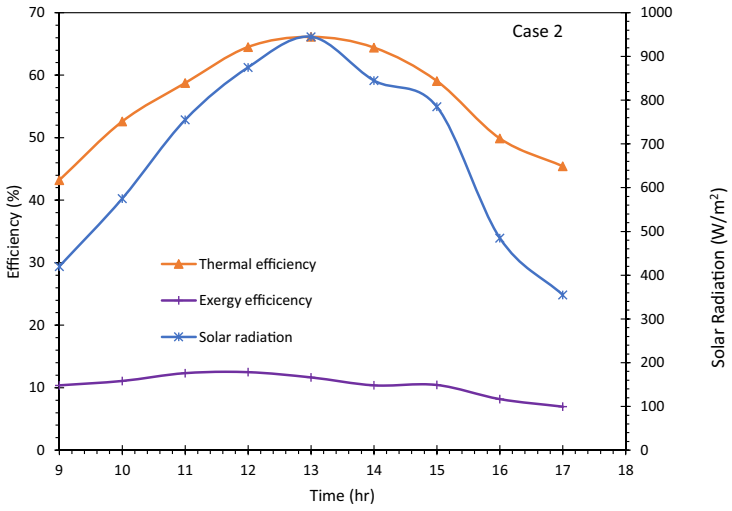


(**c**) Case 3

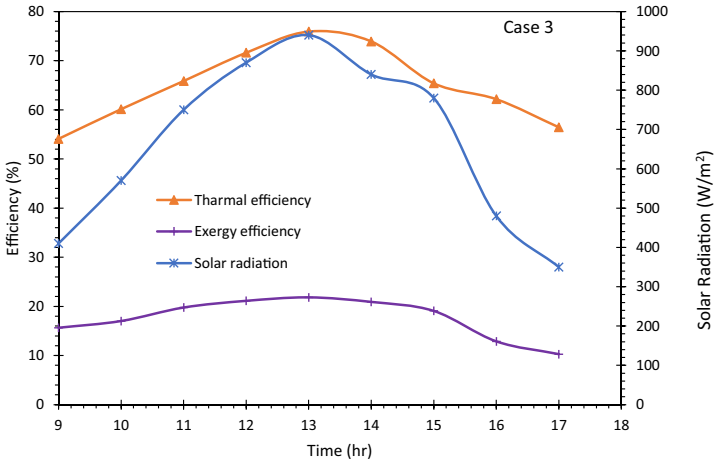
Figure 8. Temperature and Solar radiation during experimentation in all cases.



(a) Case 1



(b) Case 2



(c) Case 3

Figure 9. Efficiency and Solar radiation during experimentation in all cases.

heater. This is mainly due to reflector and thermal storage material.

4. Conclusion

A sensible heat storage based double pass hybrid solar air heater with and without reflector was experimentally investigated. Following conclusions could be drawn from this study.

1. The system is designed to have double pass type. Here black coated aluminum sheet is used as absorber sheet and Metco material and aluminum scrap mixture is used as sensible heat storage material which is applied under the bottom layer. Steel reflector is applied in the solar air heater to provide additional input energy.
2. Global solar radiation is the most important ambient parameters. In all three cases have almost similar variation. The variation of solar radiation on case 1 is 360–950 W/m^2; 355–945 W/m^{2}on case 2 and 350–940 W/m^{2}on case 3.
3. The outlet temperature of the system in case 1 shown highest temperature as compared to case 1 and 2. All three cases were experimented under almost similar atmospheric conditions. Air mass flow rate for case 2 and 3 was 0.025 kg/s. The outlet temperature varies from in case 3 was 38.5°–73.2°C and average temperature was 55.36°C.
4. The variation of thermal efficiency on case 1 is 7.16–19.67 %; 43.2–66.13 % on case 2 and 54.08–75.92 % on case 3. The average thermal efficiency was found to be lowest in case 1 i.e., 14.21 %; however, in case 3, it was found that 65.05 % on case 3. This was mainly due to application of the reflector. It provided additional input energy to the solar air heater.
5. The variation of exergy efficiency on case 1 is 1.15–3.57 %; 6.97–12.48 % on case 2 and 10.28–21.83 % on case 3. Average exergy efficiency was found to be lowest in case 1 i.e., 2.2%; however, in case 3, it was found that 17.61 % on case 3.
6. This was mainly due to application of the reflector. It provided additional input energy to the solar air heater.

The proposed solar air heater can be effectively used for industrial and domestic applications such as drying, space heating, desalination, etc.

List of symbols

Q_A	Total heat (W)
Q_u	Heat utilized (W)
Q_{loss}	Heat loss (W)
Q_{st}	Incident heat energy stored in the heater area (W)
$\dot{m}$	Mass flow rate (MFR), kg/s
C_p	Specific Heat in constant pressure (J/kg.K)
T_{out}	Outlet Temperature (^{o}C)
T_{inlet}	Inlet Temperature (^{o}C)
V_{air}	Velocity of air (m/s)
S	Area of the duct (m^2)
A_{plate}	Area of Absorber Plate (m^2)
I_i	Solar radiation (W/m^2)
U_{loss}	Overall heat loss coefficient [W/(m^{2}K)]
T_{plate}	Absorber plate temperature (^{o}C)
$T_{ambient}$	Ambient Temperature (^{o}C)
U_{side}	Side heat loss coefficient [W/(m^{2}K)]
U_{bot}	Bottom heat loss coefficient [W/(m^{2}K)]
U_{top}	Top heat loss coefficient [W/(m^{2}K)]
$h_{r,Pg}$	Radiative heat transfer coefficient (Wm^{-2}K^{-1})
$h_{c,Pg}$	Convective heat transfer coefficient (Wm^{-2}K^{-1})
$h_{r,ga}$	Radiative heat transfer coefficient due to wind velocity (Wm^{-2}K^{-1})
h_w	External radiative and convective heat transfer coefficient due to velocity of wind (Wm^{-2}K^{-1})
Nu	Nusselt Number
Ra	Reynolds number
Pr	Prandtl number
t	Temperature (^{o}C)
T_{ground}	Temperature of glass plate (^{o}C)
$T_{ambient}$	Ambient Temperature (^{o}C)
ε_{plate}	Emissivity of the plate
T_{sky}	Temperature of the external air at the surrounding (^{o}C)
L_1	Length of Solar air heater(m)
L_2	Width of solar air heater (m)
L_3	Height of the solar air heater(m)
g	Gravitation constant (m^3 kg^{-1} s^{-2})
ΔT	Temperature difference of air, (^{o}C)
L	Length of the solar air heater (m)
v	Kinematic viscosity of air (J)
D_h	Characteristic distance (m)
Ex_{inlet}	Exergy at entrance (J)
Ex_{dest}	Exergy destroyed (J)
Ex_{outlet}	Exergy at outlet(J)
Ex_{stored}	Exergy stored (J)
Ex_{lost}	Exergy lost(J)
P_{inlet}	Air Pressure inside solar air heater[kg/(mS^2)]
P_{amb}	Atmospheric Pressure [kg/(mS^2)])
T_s	Mean temperature of the absorber plate (^{o}C)
r	Distribution of solar radiation
A_{col}	Area of the collector (m^2)
$Ex_{dest(p-s)}$	Exergy destroyed due to pressure drop (J)
$\eta_{thermal}$	Thermal Efficiency
η_{exergy}	Exergy Efficiency
$Ex_{dest(\Delta P)}$	Exergy destroyed from absorber plate to surrounding (J)

ΔP	Pressure drop [kg/(mS^2)]
$Ex_{dest(p-f)}$	Exergy destroyed from absorber plate surface to flowing air (J)
W_Y	Uncertainty analysis due to anomalous system
$W_{Temperature}$	Uncertainty analysis due to temperature measuring instrument
$W_{thermometer}$	Error due to thermometer
$W_{reading}$	Reading error
W_{Wind}	Temperature error due to wind speed
$W_{anemometer}$	Error due to wind speed and pressure
W_{SR}	System deformities error
$W_{Pyranometer}$	Error in solar irradiance on a planar surface
$W_{Experimental}$	Experimental error

Greek symbols

α	Absorptivity
ρ	Density of air (kg/m^3)
ε_g	Emissivity of glass surface
λ	Insulation thermal conductivity (W/mK)
λ_e	Insulation thermal conductivity at the side (W/mK)
δ_{bot}	Insulation thickness at the bottom(mm)
δ_e	Insulation thickness at the side (mm)
σ	Stefan–Boltzmann Constant (W/m^2 K^4)
τ	Transmissivity
μ	Air viscosity (Ns/m^2)
β	Thermal expansion coefficient

References

[1] Ahmad A, Prakash O, Kumar A and Pandey A 2020 A Review of Solar Air Heater. *Low Carbon Energy Supply Technologies and Systems*. 1:1-10

[2] Benli H 2013 Experimentally derived efficiency and exergy analysis of a new solar air heater having different surface shapes. *Renew. Energy* 50: 58–67

[3] Abo-Elfadl S, Hassan H and El-Dosoky M F 2020 Study of the performance of double pass solar air heater of a new designed absorber: an experimental work. *Sol. Energy* 198: 479–489

[4] Abo-Elfadl Saleh, Yousef Mohamed S and Hassan Hamdy 2021 Energy, exergy, and enviroeconomic assessment of double and single pass solar air heaters having a new design absorber. *Process Saf. Environ. Protect.* 149: 451–464

[5] Bensaci C E, Moummi A, Sanchez de la Flor F J, Rodriguez Jara E A, RinconCasado A and Ruiz-Pardo A 2020 Numerical and experimental study of the heat transfer and hydraulic performance of solar air heaters with different baffle positions. *Renew. Energy* 155: 1231–1244

[6] Satcunanathan S and Deonarine S 1973 A two-pass solar air heater. *Sol. Energy* 15(1): 41–49

[7] Kumar A, Singh A P and Singh O P 2020 Efficient designs of double-pass curved solar air heaters. *Renew. Energy* 160: 1105–1118

[8] Yeh H M, Ho C D and Hou J Z 2002 Collector efficiency of double-flow solar air heaters with fins attached. *Energy* 27(8): 715–727

[9] Ho C, Chang H, Wang R and Lin C 2012 Performance improvement of a double-pass solar air heater with fins and baffles under recycling operation. *Appl. Energy* 100: 155–163

[10] Baig W and Ali H M 2019 An experimental investigation of performance of a double pass solar air heater with foam aluminum thermal storage medium. *Case Stud. Thermal Eng.* 14: 100440

[11] Vijayan S, Arjunan T V, Kumar A and Matheswaran M M 2020 Experimental and thermal performance investigations on sensible storage based solar air heater. *J. Energy Storage* 31: 101620

[12] Kalaiarasi G, Velraj R, Vanjeswaran M N and Pandian N G 2020 Experimental analysis and comparison of flat plate solar air heater with and without integrated sensible heat storage. *Renew. Energy* 150: 255–265

[13] Aboul-Enein S, El-Sebaii A A, Ramadan M R I and El-Gohary H G 2000 Parametric study of a solar air heater with and without thermal storage for solar drying applications. *Renew. Energy* 21(3–4): 505–522

[14] Duffie J A, Beckman W A and Blair N 2020 Solar engineering of thermal processes, photovoltaics and wind. John Wiley & Sons

[15] Nidhul K, Yadav A K, Anish S and Arunachala U C 2020 Efficient design of an artificially roughened solar air heater with semi-cylindrical side walls: CFD and exergy analysis. *Sol. Energy* 207: 289–304

[16] Esen H 2008 Experimental energy and exergy analysis of a double-flow solar air heater having different obstacles on absorber plates. *Build. Environ.* 43(6): 1046–1054

[17] Rhee S J and Edwards D K 1981 Laminar entrance flow in a flat plate duct with asymmetric suction and heating. *Numer. Heat Transfer* 4(1): 85–100

[18] Bouadila S, Lazaar M, Skouri S, Kooli S and Farhat A 2014 Energy and exergy analysis of a new solar air heater with latent storage energy. *Int. J. Hydrog. Energy* 39(27): 15266–15274

[19] Kurtbas I and Durmuş A 2004 Efficiency and exergy analysis of a new solar air heater. *Renew. Energy* 29(9): 1489–1501

[20] Abuşka M 2018 Energy and exergy analysis of solar air heater having new design absorber plate with conical surface. *Appl. Thermal Eng.* 131: 115–124

[21] Acır A, Canlı M E, Ata İ and Sakıroğlu R 2017 Parametric optimization of energy and exergy analyses of a novel solar air heater with grey relational analysis. *App. Thermal Eng.* 122: 330–338

[22] Matheswaran M M, Arjunan T V and Somasundaram D 2018 Analytical investigation of solar air heater with jet impingement using energy and exergy analysis. *Sol. Energy* 161: 25–37

[23] Alta D, Bilgili E, Ertekin C and Yaldiz O 2010 Experimental investigation of three different solar air heaters: energy and exergy analysis. *Appl. Energy* 87(10): 2953–2973

[24] Ghaderian J, Azwadi C N and Mohammed H 2015 Modelling of energy and exergy analysis for a double-pass solar air heater system. *J. Adv. Res. Fluid Mech. Thermal Sci.* 16: 15–32

[25] Koroneos C, Nanaki E and Xydis G 2010 Solar air conditioning systems and their applicability—an exergy approach. *Resour. Conserv. Recycl.* 55(1): 74–82

[26] Kumar A, Saini R P and Saini J S 2014 A review of thermohydraulic performance of artificially roughened solar air heaters. *Renew. Sustain. Energy Rev.* 37: 100–122

[27] Prakash O and Kumar A 2017 Solar drying technology: concept, design, testing, modeling, economics, and environment. Springer

[28] Menni Y, Azzi A and Chamkha A 2019 The solar air channels: comparative analysis, introduction of arc-shaped fins to improve the thermal transfer. *J. Appl. Comput. Mech.* 5(4): 616–626

[29] Öztürk H H 2005 Experimental evaluation of energy and exergy efficiency of a seasonal latent heat storage system for greenhouse heating. *Energy Convers. Manag.* 46(9–10): 1523–1542

[30] Phu N M and Luan N T 2020 A review of energy and exergy analyses of a roughened solar air heater. *J. Adv. Res. Fluid Mech. Thermal Sci.* 77(2): 160–175

Computational and Theoretical Chemistry 1209 (2022) 113631

Contents lists available at ScienceDirect

Computational and Theoretical Chemistry

journal homepage: www.elsevier.com/locate/comptc

Uncovering the geometrical aspects of intramolecular hydrogen bond in *meta*-benziporphodimethenes through molecular tailoring approach

Deepali Ahluwalia [a], Anil Kumar [a,*], Sudhir G. Warkar [a], Milind M. Deshmukh [b,*], Arijit Bag [c]

[a] Department of Applied Chemistry, Delhi Technological University, Delhi, India
[b] Department of Chemistry, Dr. Harisingh Gour Vishwavidyalaya (A Central University) Sagar, India
[c] Applied Sciences Department, Maulana Abul Kalam Azad University of Technology, Nadia, West Bengal, India

ARTICLE INFO

Keywords:
Meta-benziporphodimethene
Non-covalent interactions
Reduced density gradient
Intramolecular hydrogen bond
Molecular tailoring approach
Substitution effects
MESP

ABSTRACT

meta-Benziporphodimethene (*m*-BPDM), a newly synthesized analogue of porphyrin, has drawn our attention owing to its distinct applications. A variety of factors are responsible for the stability of *m*-BPDM molecules. One of the major factors is the N—H•••N intramolecular hydrogen bonds (IHBs) and the planarity of inner core ring. In the present work, we illustrate 15 different analogues of free-base *m*-BPDM with varying the substituents at C3-position (R") and sp^3 *meso* positions (R'). The non-covalent interactions analysis has been conducted on the B3LYP/6-311G(d,p) optimized structures. The isosurfaces and reduced gradient of density graphs are plotted to visualize the long range forces like H-bond, van der Waal and steric effect. The strength of N—H•••N IHBs are estimated using molecular tailoring approach employing B3LYP-D3/6–311++G(d,p) level. The estimated N—H•••N IHB energies are found in the range of 4.6 to 16.0 kcal/mol. The molecular electrostatic surface potentials are also seen to check the electron density distribution for additional confirmation of these outcomes.

1. Introduction

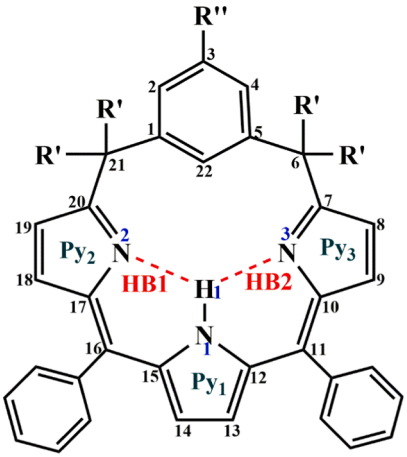
The new porphyrin analogue- *meta*-benziporphodimethene (m-BPDM) has recently gathered the interest of researchers owing to its remarkable toxic metal-ion sensing property [1–6]. The synthesis of *m*-BPDM involves a condensation reaction between α,α-dihydroxy-1, 3-substituted benzene (diol), pyrrole, and benzaldehyde in the ratio 1:3:2, in the presence of Lewis acids and oxidants [7]. The *m*-BPDM and its derivatives produced by incorporating substituted benzaldehydes possessing electron-withdrawing (EWG) and electron-donating (EDG) groups have been synthesized and studied computationally [2,7–11]. In the recent past, various research groups have reported different applications of this moiety such as metal-ion sensing [1,2], breast cancer detector [3], UV turn-on behavior for toxic metals [2] and lately, an application in hydrogels [4–6] has also been reported. Despite so many applications, the molecule did not find appropriate notability. This is due to the low yield and rapid oxidizing tendency of free base *m*-BPDMs. We recently reported some conformational analysis of this prosthetic molecule, studying the effect of various substitutions in the molecules at different sites [9,10].

Kumar et. al. found that the incorporation of another heteroatom in place pyrrolic nitrogen renders a change in planarity of the inner core [9]. For example, when unprotonated sulphur atom is present at the middle pyrrole ring (Py_1 in Fig. 1) of m-BPDM, the molecule appeared to be more symmetrical and stable compared to its O- and N- analogue. In a similar fashion, various isomers were studied by either inverting one of the three pyrrole rings or placing the N atom close to the benzene ring (*N*-up conformer) or otherwise (*N*-down conformer). The hydrogen bond strength for the O-up and O-down conformers has also been determined in their work [9]. Furthermore, Ahluwalia et. al. proved that these substitutions play a key role in stabilizing the free base m-BPDM [10]. In terms of stability, the placement of electron withdrawing groups at *meso*- positions (C11- and C16-) dominated over the electron releasing groups (Fig. 1). Also, it has been reported that the placement of a bulkier group (phenyl > methyl) at C6- and C21- *meso* carbon have influenced the geometry and stability of the systems constructively [10].

Subsequently, we wished to explore all the factors that may or may not hamper the stability of free base m-BPDM, thus this time we have placed different groups at C3-position alongside increasing the bulkiness at C6 and C21- positions. The basic characteristics of the substituents at C3-position invoked our interest to study its impact on the conventional (HB1 and HB2). For this purpose, the non-covalent interactions (NCI) analysis was done using Multiwfn [12]. The isosurfaces and reduced density gradient (RDG) plots helped to visualize the presence of weak

* Corresponding authors.
E-mail addresses: anil_kumar@dce.ac.in (A. Kumar), milind.deshmukh@gmail.com, mdeshmukh@dhsgsu.edu.in (M.M. Deshmukh).

https://doi.org/10.1016/j.comptc.2022.113631
Received 21 September 2021; Received in revised form 24 January 2022; Accepted 3 February 2022
Available online 5 February 2022
2210-271X/© 2022 Elsevier B.V. All rights reserved.



where,
1. R'= H
2. R'= CH_3
3. R'= Ph
(a) R''= $N(CH_3)_2$
(b) R''= OCH_3
(c) R''= CF_3
(d) R''= Cl
(e) R''= H

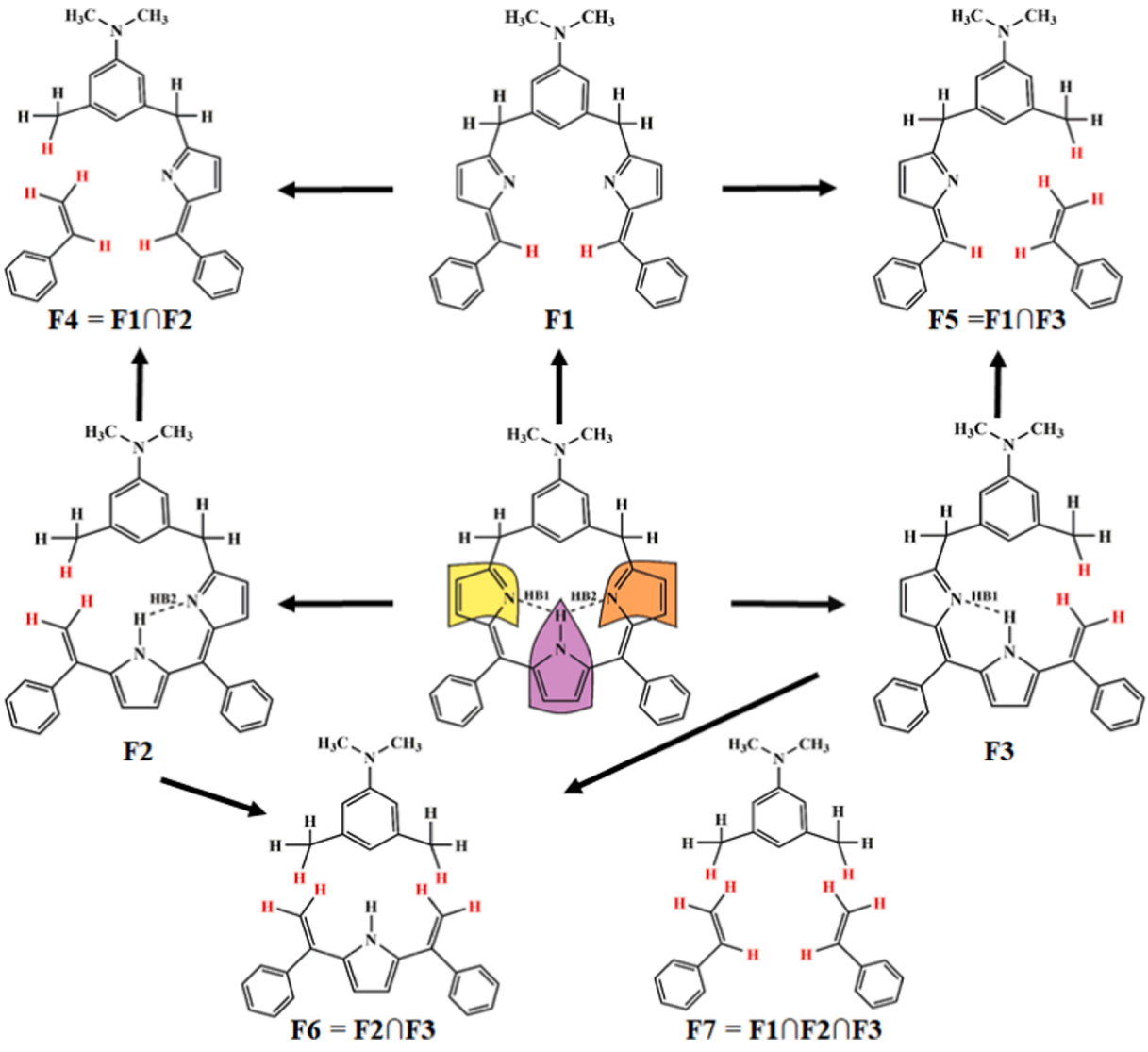
Fig. 1. *meta*-benziporphodimethene structures under study.

interactions at the inner core of these molecules. Further, the energies of these H-bonds was determined by molecular tailoring approach (MTA)-based approach. The optimized structures were also subjected to map molecular electrostatic potential surfaces, to understand the distribution of electron density throughout the system. To the best of our knowledge, no such work has been reported to understand the effect of substitution at C3-position on the IHB in m-BPDM. The results of this report would give the readers a clearer picture of the factors that could enhance the stability of m-BPDM molecules, in order to further explore its applications.

2. Methodology

2.1. Computational details

Geometries of all the molecules studied in this work were optimized under C1 symmetry by the density functional theory (DFT) method employing B3LYP functional [13–15]. Two kinds of basis sets BS-I and BS-II i.e., 6-311G(d, p) and 6–311++G (d, p), respectively, are employed in the present work. Geometry and relative stability of these molecules were established using the B3LYP/BS-I level of theory. The NCI analysis have been performed on these optimized systems using Multiwfn 3.8 software [12]. The isosurfaces were generated using VMD 1.9.4a51 program. [16] In order to plot the colored 2D RDG graphs, gnuplot 5.4 software have been used [17]. The intramolecular hydrogen bond (IHB) energy were evaluated at B3LYP-D3/BS-II level using molecular tailoring approach (MTA) based method developed by Deshmukh and



Scheme 1. Fragmentation scheme for the estimation of N—H…N hydrogen bonds **HB1** and **HB2** in parent molecule **1a**; see Fig. 1 and text for details.

Table 1
Non-bonded angles in degrees for structures in Fig. 1.*

Structure	17/C_6[a]	17/sp^3[b]	P_o[c]	P_{core}[d]	C_6/N_3[e]	$Py_1/17$[f]	$Py_2/17$[g]	$Py_3/17$[h]
1a	32.10	56.52	40.70	0.13	16.66	10.40	28.83	28.56
1b	32.53	56.76	41.28	0.13	18.12	10.40	28.69	28.08
1c	32.09	56.81	39.70	0.09	17.43	10.50	27.88	28.20
1d	31.65	56.70	41.44	0.00	16.12	10.48	28.22	28.21
1e	30.61	57.94	38.70	2.01	18.93	11.71	21.44	31.59
2a	36.19	51.47	45.07	0.21	17.93	10.96	32.92	31.91
2b	36.23	51.51	45.12	0.17	18.11	11.06	33.39	31.03
2c	35.88	51.80	46.16	0.09	18.31	11.18	31.74	31.62
2d	35.90	51.77	46.16	0.00	18.19	11.12	31.83	31.83
2e	35.72	52.13	45.01	2.61	18.96	13.41	24.73	37.09
3a	35.21	53.82	43.18	0.00	21.21	12.39	28.17	28.17
3b	35.14	54.47	42.59	0.48	22.01	12.37	26.92	28.17
3c	35.37	53.98	45.54	0.16	22.01	12.70	27.43	28.25
3d	35.25	53.96	45.52	0.00	21.76	12.65	27.89	27.89
3e	34.82	54.93	44.94	1.98	22.11	13.69	32.32	21.56

[a] Angle between the 17 tripyrrin atoms mean plane and phenylene ring plane.
[b] Angle between the 17 tripyrrin atoms mean plane and a vector through sp^3 *meso* carbon
[c] Dihedral angle between four *meso* carbon atoms C6-C11-C16-C21.
[d] Dihedral angle between the inner core atoms C22-N3-N1-N2.
[e] Angle between the phenylene ring plane and inner N atom core (N3-N1-N2).
[f,g,h] Angle between the Pyrrole Py_i (i = 0,1,2) ring plane and 17 tripyrrin atoms mean plane.
* Visuals of the planes and vectors across structure 1d have been displayed in Chart S1.

Gadre [18–24]. All the calculations were performed with the Gaussian 09 program package [25]. All the molecular structures were generated using the Chemcraft program package [26].

2.2. Fragmentation method for estimation of N—H•••N hydrogen bond energy

The IHB energy in *m*-BPDM molecules were calculated using molecular tailoring approach (MTA). The general fragmentation procedure is depicted in Scheme 1 for the estimation of **HB1** and **HB2** in parent molecule **1a**. As seen in Fig. 1, **HB1** corresponds to the N1-H1•••N2 H-bond between the Py_1 and Py_2 pyrrole rings and **HB2** corresponds to the N1-H1•••N3 H-bond between Py_1 and Py_3 pyrrole rings; See Fig. 1 for atomic numbering. In Scheme 1, the parent molecule **1a** is fragmented in three primary fragments, F1, F2 and F3. The fragment F1 was obtained by removing the Py_1 pyrrole ring. The fragments, F2 and F3 were similarly generated by cutting the portions of Py_2 and Py_3 rings, respectively. Here, the complete Py_2 and Py_3 rings were not cut in order to keep the hybridization of carbon atoms intact in these fragments as in the parent molecule **1a**.

The cut regions for all the three primary fragments are shown by appropriate colored portions. The valencies of cut regions (carbon atoms) were satisfied by adding the H-atoms at 1.0 Å along the cut C—C bonds. The added H-atoms in these fragments are shown in the red color. The secondary fragments were obtained by taking the appropriate intersections of these primary fragments. Here, intersection means a common structural part apart from added dummy H-atoms. For example, F4 is the intersection of two primary fragments F1 and F2 i.e. F4 = F1 ∩ F2. Similarly, F5 = F1 ∩ F3 and F6 = F2 ∩ F3 were obtained. The fragment F7 is the ternary overlap of three primary fragments i.e. F7 = F1 ∩ F2 ∩ F3. The fragmented geometries were not optimized in order to prevent the conformational changes in them. The single point energy calculation at B3LYP-D3/BS-II level of theory was carried out on all the seven fragments. Using these fragment energies, $E_{\mathbf{HB1}}$ in the parent molecule **1a** is calculated as $E_{\mathbf{HB1}} = (E_{F1} + E_{F2} - E_{F4}) - E_{parent}) =$ (-1401.444889 + (-1440.812301) – (-1232.924996)) – (-1609.344132)) = 0.01193793 a.u. = 7.49 kcal/mol. In a similar fashion, the IHB energies $E_{\mathbf{HB1}}$ and $E_{\mathbf{HB2}}$ were estimated in the substituted and unsubstituted *m*-BPDM molecules studied in the present work.

We wish to emphasize here that this E_{HB1} is estimated in the presence of hydrogen bond HB2. For instance, for the estimation of E_{HB1}, the energies of fragments F1, F2 and F4 were utilized along with energy of parent **1a**. It should be noted here that in the fragment F2, the hydrogen bond HB2 is intact. Thus, calculated E_{HB1} includes the cooperativity networking effect of other hydrogen bond (HB2). Similarly, fragment F3 utilized for the estimation of E_{HB2}, ensures the cooperativity contribution of HB1 towards HB2. If the E_{HB1} is estimated in the absence of cooperative networking of HB2, this E_{HB1} would be different than that discussed above. The difference in the energy of HB1 in the presence of HB2 and with its absence is the cooperativity contribution of HB2 towards HB1. For details of the evaluation of cooperativity contributions in a multiple H-bonded system [27–31].

3. Results and discussion

As discussed above, in this work, 15 different analogues of free-base *m*-BPDM with varying the substituents at C3-position (R") and sp^3 *meso* positions (R') are considered. The functional groups at C3-position considered here are: $N(CH_3)_2$ (**a**), OCH_3 (**b**), CF_3 (**c**), Cl (**d**) and H (**e**). The prefix **1**, **2** and **3** in Fig. 1 signifies the molecules with R' = H, CH_3 and Ph groups, respectively at C6 and C21 positions. Herein, we have only studied the effect of substitutions at C3-positions and not *C*2– and C4-positions (Fig. 1) on *m*-BPDM because the synthesis of the precursor diol (for *C*2 and C4-positions) is not possible owing to the steric factor caused by the groups present at 1, 3-position of the diol.

3.1. Geometries of meta-benziporphodimethene structures

The structures optimized under B3LYP/BS-I levels displaying N2-H1 (HB1), N3-H1 (HB2) (Fig. 1), hydrogen bond distance is shown in Chart S2, S3 and S4 for H atom, methyl and phenyl group, respectively placed at C6 and C21 positions. Refer to Table S1 in supporting information (SI) for Cartesian coordinates and energies of these structures. In order to study the inner geometry and core cavity of these structures, we have incorporated the study of non-bonded angles by passing the planes through various atoms in the molecules and calculating angles between them (refer to Chart S1 for visual depiction of these non-bonded angles). For instance, $Py_1/17$ depicts the angle between the plane through middle pyrrole ring i.e., the plane involving C12, C13, C14, C15, N1 atoms to the plane passing through tripyrrin atoms (involving all three pyrrole rings and 2 sp^2 *meso* carbon atoms) i.e., plane involving 17 atoms- C7, C8, C9, C10, N3, C11, C12, C13, C14, C15, N1, C16, C17, C18, C19, C20, N2 [9,10]. Likewise, $Py_i/17$ (i = 2, 3) represents the angle between the pyrrole ring consisting N2 and N3 atoms,

Table 2
Intramolecular Hydrogen Bond energy (in kcal mol^{-1}) and distances (in Å). See Chart S2-S4 for corresponding geometries of these molecules

	Bond Energy (kcal/mol)		Bond distance (NH•••N; Å)		*N*-H[c](Å)	φ[d]	φ[e]
	HB1[a]	HB2[b]	HB1[a]	HB2[b]			
1a	7.49	7.63	2.27	2.23	1.014	115.25	113.13
1b	8.01	7.35	2.22	2.28	1.014	115.90	112.63
1c	7.78	7.67	2.23	2.27	1.014	115.51	113.36
1d	7.71	7.71	2.25	2.25	1.013	114.49	114.49
1e	5.92	10.05	2.39	2.13	1.016	107.45	121.27
2a	7.47	7.35	2.21	2.23	1.013	113.28	114.75
2b	7.21	6.70	2.19	2.24	1.013	115.46	112.65
2c	7.06	7.05	2.21	2.21	1.012	114.39	114.32
2d	7.05	7.05	2.22	2.22	1.012	114.28	114.28
2e	4.62	10.11	2.42	2.05	1.016	123.94	103.77
3a	8.12	8.12	2.21	2.21	1.015	115.32	115.32
3b	7.94	8.34	2.20	2.22	1.015	115.82	114.99
3c	16.03	15.97	2.21	2.20	1.014	115.38	115.76
3d	8.08	8.08	2.20	2.20	1.015	115.51	115.51
3e	6.33	10.05	2.34	2.10	1.017	122.22	108.79

[a] HB1 corresponds to N2-H1 bond.
[b] HB2 corresponds to N3-H1 bond.
[c] Bond distance of N1-H1.
[d] Angle between N1-H1-N2 in degrees.
[e] Angle between N1-H1-N3 in degrees.

respectively, with the tripyrrin plane or say, the mean plane of *meta*-benziporphodimethene structures. Other non-bonded angles like 17/C6 represents the angle between the mean plane and the benzene ring of the molecule i.e., plane passing through C1, C2, C3, C4, C5, C22 atoms; 17/sp^3 depicts the angle between tripyrrin plane and a vector passing through the two sp^3 *meso* carbon atoms C6 and C21, etc. have also been calculated and reported in Table 1.

As seen in Table 1, the calculated Py_2/17 and Py_3/17 angles are nearly similar in molecules **1d**, **2a**, **2d**, **3a** and **3d**. These nearly similar Py_2/17 and Py_3/17 angles suggests that the two pyrrole rings Py_2 and Py_3 are coplanar to each other with respect to the mean trypyrrin plane. The difference in the Py_2/17 and Py_3/17 angles for structures **1b**, **2b**, **3b** and **3c** were observed to be only moderately larger compared to the former discussed molecules, ranging from ± 0.61° to 2.36°. These two angles are distinctly different (±10.15° to 12.36°) in the geometries of **1e**, **2e** and **3e**. Note that **1e**, **2e** and **3e** are the molecules without any substitutents at C3-position; see Fig. 1. These results suggests that the substitution at the C3-position enforces the planarity (or symmetry) to the core of C3-substituted m-BPDMs. Indeed, as seen in Table 1, the P_{core} angles are very small (in between 0.00 and 0.48°) in all the C3-substituted *m*-BPDMs. On the other hand, when no substitutent is present at the C3-position (R''), the Py_2 and Py_3 rings are majorly deviated from the mean plane. Also, the P_{core} angles are distinctly larger (in between 1.98° to 2.61°) when no substituent is present at C3-position. These results suggest that the substitution affects the core structure which in turn may have affect on the strength on the N—H•••N IHBs energies. The position of two pyrrole rings seems to be affecting the N—H•••N IHB angles (**φ^d** and **φ^e**, Figure S1). As can be seen in Table 2, these two angles are distinctly different from each other when no substituent is present at C3-position. On the other hand, in case of C3-substituted *m*-BPDMs, these two H-bond angles have nearly similar values to each other. We shall discuss the energies of these H-bonds in the subsequent sections.

3.2. Non-covalent interactions

It is important to know the type of interactions present at the inner core of m-BPDM systems under consideration. Thus, herein the study of long-range interactions has been incorporated, which requires only the information about the molecular geometry. The prime feature of density functional theory (DFT) method is the determination of quantum–mechanical electron density (ρ), which is further utilized to study all the possible chemical properties of a system [32–34]. Reduced gradient of density (RDG) on the other hand, is the density and its first derivative which is a dimensionless quantity that represents the divergence from homogeneous electronic distribution. The NCI index is a 2D plot based on the reduced density gradient, s and the electron density ρ, having a relation as shown in equation (1):

$$s = \frac{1}{(2(3\pi^2)^{1/3})}\frac{|\nabla\rho|}{\rho^{4/3}} \quad (1)$$

The plot not only determines the presence of long-range interactions but also enables us to find out the type of the weak interaction present in a certain system. The kind of interaction is further determined by the Laplacian of density, $\nabla^2\rho$. The Laplacian is the sum of three eigenvalue components λ_i of the electron density Hessian (second derivative) matrix, that is represented as $\nabla^2\rho = \lambda_1 + \lambda_2 + \lambda_3$. In a molecule, λ_3 varies along the internuclear direction, whereas the λ_1 and λ_2 describes the variation of density in the plane normal to that of λ_3 eigenvector. The value of the second eigenvector (λ_2) differs in accordance to the type of interactions. For bonding interactions, such as H-bond, the value of λ_2 less than 0, while for non-bonding interactions λ_2 is greater than zero. The value of λ_2 is nearly zero for weak van der Waals interactions [35–37].

In our study, the isosurfaces and RDG plots for all the 15 molecules were visualized. This analysis has been performed for a specific region between N2 and N3 atoms in Multiwfn software [12]. To visualize this phenomenon, colored 2D plots and isosurfaces were drawn with the help of softwares like gnuplots [17] and VMD [16], respectively. The results have been compiled in Chart S5 to S7. All the RDG plots revealed the presence of hydrogen bond in all the systems. The presence of steric effect was also visualized by these plots. There is no van der Waals interactions present in these systems as per our results. Though the presence of H-bond has been visualized using RDG maps, it now becomes important to study the energy of these H-bonds present in these systems. Hence, we now apply molecular tailoring based approach to estimate HB1 and HB2 energies.

3.3. Effect of bulkiness at sp^3 meso-positions

The N—H•••N bond energy (HB1 and HB2) is greatly dependent upon the placement of N2 and N3 pyrrole rings i.e., Py_2 and Py_3 rings, respectively (Fig. 1). Table 2 summarizes the HB1 and HB2 bond energies, bond distances, N1-H1 bond length and N—H•••N bond angles (Figure S1).

The estimated **HB1** and **HB2** for **1e**, **2e** and **3e** are merely for recognizing the difference when there is no substituents present at C3–position and sp^3 *meso* carbon atoms. The bond distance HB1 and HB2 differ more as compared to values for other molecules. This may suggest that the pyrrole rings are not at equal distance from H1 atom (Table 1 and 2). It was further indicated by the deviation in N—H•••N angle for this class (**e**) of molecules (Table 2,). Henceforth, the deviation in the HB1 and HB2 bond energies is observed for (**e**) class of *m*-BPDM under study. Subsequently, shifting the focus to HB1 and HB2 bond lengths and energies of classes (**a**), (**b**), (**c**) and (**d**) of **1**, **2** and **3** type of m-BPDM, some interesting results were observed.

It is well reported in literature that the delocalization of electrons in *m*-BPDM is obstructed due to the presence of two sp^3 *meso* carbon atoms at C6- and C21- position [7,11]. Hence, the increment in bulkiness at C6- and C21- positions may be held responsible for the positioning of Py_2 and Py_3 rings and thereby causing deviations in this N—H•••N IHB for their respective classes (Fig. 1). The general observation made amongst (**b**), (**c**) and (**d**) sub-classes is such that upon increasing the bulkiness at C6- and C21- position, the IHB energy increased. For instance, **HB1** and **HB2** for R''=OCH_3, CF_3 and Cl have the same order viz. Ph > H > CH_3

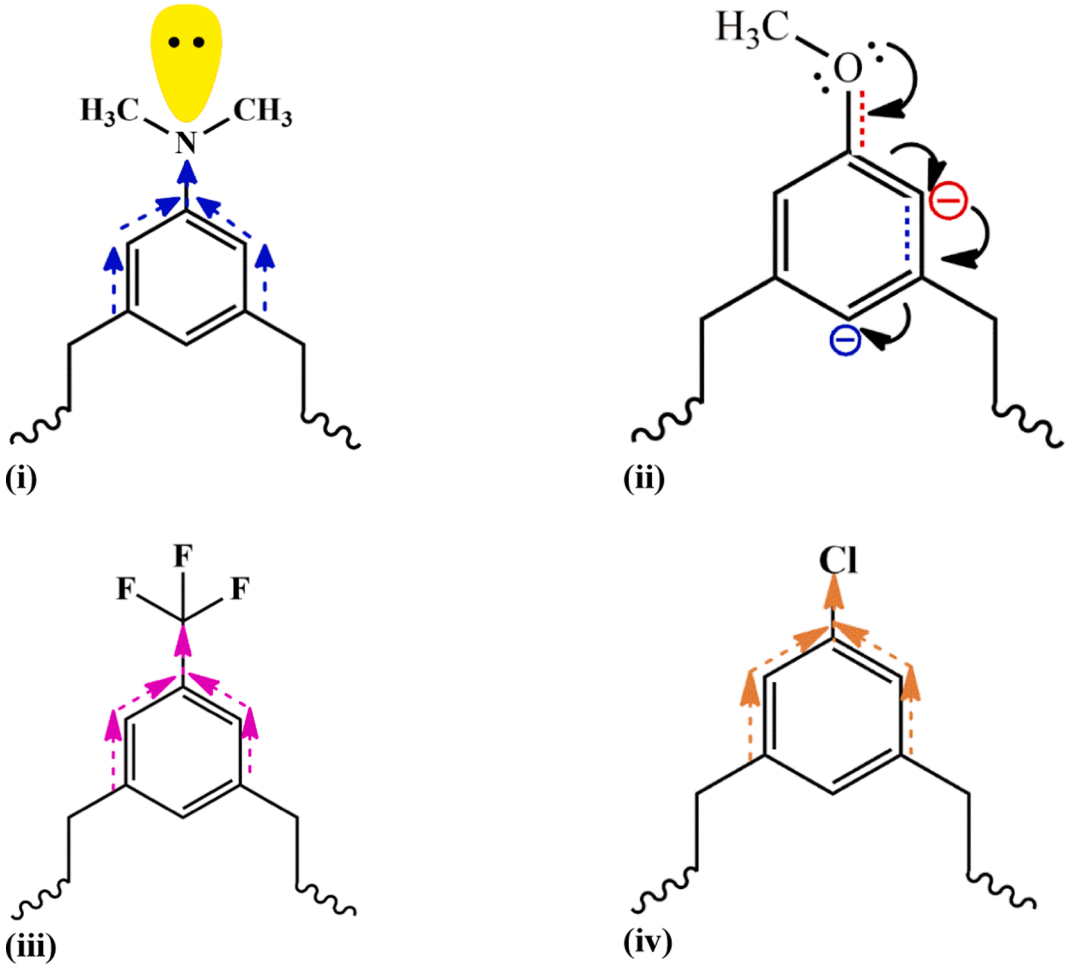


Fig. 2. Effect of substituents at C3-position on the phenylene ring.

(Fig. 1, Table 2). Although, the estimated IHB energy value of HB1 and HB2 for **2b** is less than **1b**, but the $Py_i/17$ (i = 2, 3) angles for R'= CH_3 are less deviated compared to R'= H.

The order for energy of **HB1** when R'=H (1) is such that, **1b > 1c > 1a > 1d**, while for **HB2** of this class, it is **1c = 1a > 1d > 1b**, though the variation amongst **HB1** and **HB2** is not as much. The dissimilarity in the pattern of **HB1** and **HB2** may have aroused due to the difference in φ^d and φ^e angles. It is noteworthy that φ^d and φ^e for **1d** is same, and hence the bond energies **HB1** and **HB2** are equal for **1d.** Likewise, for 2d and 3d, **HB1** and **HB2** are equal owing to equal φ^d and φ^e angles. As observed in Table 1, $Py_i/17$ (i = 2, 3) values for **1d**, **2d** and **3d** are also equal. It is thus worthy highlighting here, that the presence of -Cl group at C3-position of m-BPDM may be responsible for this planarity in these structures, irrespective of the bulky groups present at C6- and C21-positions. The details of these substituents shall be covered in the next section in this article.

The order of energy for **HB1** and **HB2** when R'= CH_3 (**2**) is **2a > 2b > 2c ≥ 2d** and **2a > 2c = 2d > 2b**, respectively. It has been observed that the estimated energy of **HB1**, **HB2** for **2c** and **2d** are nearly the same i.e., (7.06 kcal/mol) and (7.05 kcal/mol), respectively and so is their φ^d and φ^e angles. **2a** and **2b** showed deviation in φ^d and φ^e angles, and thus the IHBs for their respective geometries varied. Although, the range of the IHB energies for R'= CH_3 (**2**) lies between (7.05 to 7.47 kcal/mol) for **HB1** and (6.70 to 7.35 kcal/mol) for **HB2**, which implied for subclasses **a**, **b**, **c** and **d**, the **HB1** and **HB2** did not show much divergence. The IHB energies were quite contrasting in case of R'= Ph (3). The order of energy for **HB1** and **HB2** for this class is **3c > 3a > 3d > 3b** for **HB1** and **3c > 3b > 3a > 3d** for **HB2**. Exceptionally high IHB energies is observed for **3c** molecule. It must not be ruled out that the IHB energies of **3a**, **3b**, **3c** and **3d** are on the higher side compared to all the other geometries under study. This may be attributed to the presence of bulky phenyl groups at C6- and C21- positions. The molecular electrostatic potential surface of **3c** (Fig. 3), discussed in later section of this article, also showed electron deficiency at H1 atom (displayed via blue region). The φ^d and φ^e angles for **3a**, **3b**, **3c** and **3d** were also found to be in a close proximity each other in their respective systems, suggesting the two pyrrole rings i.e., Py_2 and Py_3 lied nearly in the same plane to each other and are equidistance from H1 atom. The trend of these systems invoked our interest to study the effect of substituents at C3-position upon the geometry and inner- core strength of m-BPDM molecules.

3.4. *Effect of substitutions at C3-positions*

As expected by the substituent placed at C3– position of the phenyl ring of m-BPDM, change in the electron density may occur due to their presence. In order to understand this distribution of electron density, molecular electrostatic potential (MESP) surfaces were studied (Chart S8, S9 and S10). The MESP surfaces depicts the dimension and overall charge distribution of a molecule with respect to the negative, positive and neutral electrostatic charge, in the form of electron density represented by different colors. It thus gives the insights to chemically reactive sites of the molecule. The nucleophilic sites or electron rich regions are denoted by red while blue color displayed electron deficient centers and neutral sites were shown by other colors on the scale (Chart S8, S9, and S10). [38–41] The region around N1-H1 indicated blue color, thus a good H-bond donor capacity is contemplated from this site and thus it

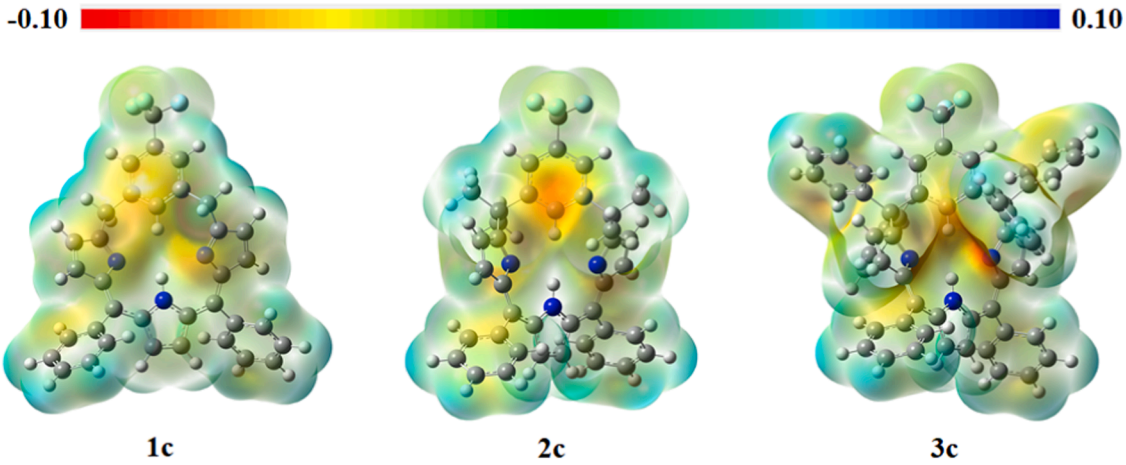


Fig. 3. MESP surfaces of *m*-BPDM molecules when R'= H (1), CH3 (2) and Ph (**3**) and R''= CF_3. The electron density isosurface of value 0.001 a.u. was chosen.

may foreshow typically strong IHB energy.

The substituent R''= N $(CH_3)_2$, is expected to behave as an electron-withdrawing group, due to the electronegativity of N atom. The lone pair on N atom may not participate in the delocalization of electrons with the phenylene ring of m-BPDM, owing to the steric inhibition of resonance (SIR) effect, which may lead to shifting of the lone pair out of the resonating plane. Thus, this group can only exhibit negative inductive effect (-I). But, the –I effect is operative up to 3 adjacent carbons only (Fig. 2 (i)). For R''= OCH_3, the methoxy group is expected to show positive mesomeric effect, making the *ortho* and *para*- groups electronically rich centers as shown in Fig. 2(ii). When R''= CF_3, exceptionally high **HB1** and **HB2** energy values were observed for **3c** molecule. It may be attributed to the presence of the strong electron- withdrawing nature, (-I) effect of CF_3 group. The 2p-2p orbital interaction occurring in this molecule, summed up with the bulkiness of -Ph group placed at C6- and C21-position may have played a major role in this (Fig. 2 (iii)). The N1-H1 bond in Fig. 3 (3c) is in blue region, hence it also gives significant idea about the electron deficiency at this H atom and the electron richness at N2 and N3 is also visual (red region). Another unusual characteristic observed in this particular structure (3c) is that, the C3-subsituted phenyl ring showcased blue color while for all the other structures under consideration, nucleophilicity has been visualized on this ring. This suggested that the electron density is majorly pulled by the $–CF_3$ group. Additionally, the two bulky –Ph (R') groups further cancel out the distortion that could have been there, had the molecule been unsubstituted (like **3e**), thus nearly same φ^d and φ^e were observed (Table 2). Therefore, we may interpret this occurrence of high **HB1**, **HB2** value for this particular molecule. Another interesting fact noticed in conventional IHB is that for R''=Cl (**d**), the values of **HB1**, **HB2** as well as φ^d, φ^e angles (Figure S1) viz, (7.71 kcal/mol; 114.49°), (7.05 kcal/mol; 114.28°) and (8.08 kcal/mol; 115.51°) for classes **1**, **2** and **3**, respectively, are the same (Table 2). Thus, we may infer that -Cl group is providing some kind of planarity to m-BPDM molecules through is negative inductive effect (Fig. 3 (iv)). Also, chloro-group can facilitate the smooth interaction of 2p-Cl orbital with the π-cloud system of the macrocycle (weak 2p- 3p interactions). This may be responsible for imparting this planarity to **1d**, **2d** and **3d** molecules.

4. Concluding remarks

In this work, we investigated the intramolecular non-covalent interaction viz. N—H•••N hydrogen bonding in substituted m-BPDM analogues. Initially, non-covalent interactions (NCI) plots revealed the presence of H-bond, steric factor and no vdW forces. The 2D RDG plots and isosurfaces are visualized that go well with our expectations about the presence of H-bond in the inner core region. Furthermore, molecular tailoring approach is used to investigate the numerical value of these IHB energies (**HB1** and **HB2**). The investigation of N—H•••N intramolecular IHBs energies leads us to a new way of exploring the synthetic routes of m-BPDM molecules. The N—H•••N IHB falls under the range 4.6 to 16.0 kcal/mol, which is actually the moderate to strong type of intramolecular hydrogen bond. Interesting results were observed while calculating IHB, as the molecule **3c** exhibiting comparatively higher HB1 and HB2 values. The estimated values were then checked and went well in agreement with the MESP surfaces. This discovery of a distinguished substitution at C3-position of phenylene ring of m-BPDM also inferred that the substitution of -Cl group irrespective of bulkiness at C6- and C21- position provides a planarity in the molecule as observed in **1d**, **2d** and **3d**. The metalation of these molecule shall be easier compared to those having distorted geometry and we may expect a higher yield in these cases.

CRediT authorship contribution statement

Deepali Ahluwalia: Writing – original draft, Methodology. **Anil Kumar:** Conceptualization, Methodology. **Sudhir G. Warkar:** Conceptualization. **Milind M. Deshmukh:** Conceptualization, Methodology. **Arijit Bag:** Conceptualization, Methodology.

Declaration of Competing Interest

The authors declare that they have no known competing financial interests or personal relationships that could have appeared to influence the work reported in this paper.

Acknowledgements

The authors thank Delhi Technological University for infrastructural facilities. DA also thank UGC for financial aid. MMD is thankful to the University Grant Commission (UGC), New Delhi for the initial Start-up Grant (No. F.30-56/2014/BSR).

Appendix A. Supplementary material

Supplementary data to this article can be found online at https://doi.org/10.1016/j.comptc.2022.113631.

References

[1] C.H. Hung, G.F. Chang, A. Kumar, G.F. Lin, L.Y. Luo, W.M. Ching, E. Wei-Guang Diau, m-Benziporphodimethene: A new porphyrin analogue fluorescence zinc(II) sensor, Chem. Commun. (2008) 978–980, https://doi.org/10.1039/b714412a.

[2] R.K. Sharma, L.K. Gajanan, M.S. Mehata, F. Hussain, A. Kumar, Synthesis, characterization and fluorescence turn-on behavior of new porphyrin analogue: meta-benziporphodimethenes, Spectrochim. Acta - Part A Mol. Biomol. Spectrosc. 169 (2016) 58–65, https://doi.org/10.1016/j.saa.2016.06.020.

[3] R.K. Sharma, A. Maurya, P. Rajamani, M.S. Mehata, A. Kumar, meta -Benziporphodimethenes: New Cell-Imaging Porphyrin Analogue Molecules, ChemistrySelect. 1 (2016) 3502–3509, https://doi.org/10.1002/slct.201600812.

[4] D. Chauhan, A. Kumar, S.G. Warkar, An efficient adsorbent for the removal of Zn^{2+} Cd^{2+} and Hg^{2+} from the real industrial effluents, Int. J. Environ. Sci. Technol. (2021), https://doi.org/10.1007/s13762-021-03615-5.

[5] D. Chauhan, A. Kumar, S. G. Warkar, Modified polymeric hydrogels for the detection of Zn2+ in E.coli bacterial cells and Zn2+, Cd2+ and Hg2+ in industrial effluents (2021) Environmental Technology, DOI: 10.1080/09593330.2021.1928294.

[6] D. Chauhan, A. Kumar, S.G. Warkar, Synthesis, characterization and metal ions sensing applications of meta-benziporphodimethene-embedded polyacrylamide/carboxymethyl guargum polymeric hydrogels in water, Environ. Tech. (2020), https://doi.org/10.1080/09593330.2020.1812730.

[7] M. Stępień, L. Latos-Grazyński, L. Szterenberg, J. Panek, Z. Latajka, Cadmium(II) and Nickel(II) Complexes of Benziporphyrins. A Study of Weak Intramolecular Metal-Arene Interactions, J. Am. Chem. Soc. 126 (2004) 4566–4580. 10.1021/ja039384u.

[8] G.F. Chang, C.H. Wang, H.C. Lu, L.S. Kan, I. Chao, W.H. Chen, A. Kumar, L. Lo, M. A.C. Dela Rosa, C.H. Hung, Factors that regulate the conformation of m-benziporphodimethene complexes: Agostic metal-arene interaction, hydrogen bonding, and Î· 2, π coordination, Chem. A Eur. J. 17 (2011) 11332–11343, https://doi.org/10.1002/chem.201100780.

[9] A. Kumar, C.H. Hung, S. Rana, M.M. Deshmukh, Study on the structure, stability and tautomerisms of meta-benziporphodimethene and N-Confused isomers containing γ–lactam ring, J. Mol. Struct. 1187 (2019) 138–150, https://doi.org/10.1016/j.molstruc.2019.03.064.

[10] D. Ahluwalia, A. Kumar, S.G. Warkar, M.M. Deshmukh, Effect of substitutions on the geometry and intramolecular hydrogen bond strength in meta-benziporphodimethenes: A new porphyrin analogue, J. Mol. Struct. 1220 (2020) 128773–128783, https://doi.org/10.1016/j.molstruc.2020.128773.

[11] D. Ahluwalia, A. Kumar, S.G. Warkar, Recent developments in meta-benziporphodimethene: A new porphyrin analogue, J. Mol. Struct. 1228 (2021) 129672, https://doi.org/10.1016/j.molstruc.2020.129672.

[12] T. Lu, F. Chen, Multiwfn: A multifunctional wavefunction analyzer, J. Comput. Chem. 33 (2012) 580–592, https://doi.org/10.1002/jcc.22885.

[13] A.D. Becke, Density-functional exchange-energy approximation with correct asymptotic behavior, Phys. Rev. A 38 (6) (1988) 3098–3100, https://doi.org/10.1103/PhysRevA.38.3098.

[14] A.D. Becke, Density-functional thermochemistry. III. The role of exact exchange, J. Chem. Phys. 98 (7) (1993) 5648–5652, https://doi.org/10.1063/1.464913.

[15] C. Lee, W. Yang, R.G. Parr, Development of the colic-salvetti correlation energy formula into a functional of the electron density, Phys. Rev. B 37 (1988) 785–789, https://doi.org/10.1103/PhysRevB.37.785.

[16] W. Humphrey, A. Dalke, K. Schulten, VMD: Visual molecular dynamics, J. Mol. Graph. 14 (1) (1996) 33–38, https://doi.org/10.1016/0263-7855(96)00018-5.

[17] T. Williams, C. Kelly, gnuplot 5.4 An Interactive Plotting Program. http://sourceforge.net/projects/gnuplot.

[18] M.M. Deshmukh, S.R. Gadre, Molecular Tailoring Approach for the Estimation of Intramolecular Hydrogen Bond Energy, Molecules 26 (2021) 2928, https://doi.org/10.3390/molecules26102928.

[19] V. Singh, I. Ibnusaud, S.R. Gadre, M.M. Deshmukh, Fragmentation Method Reveals a Wide Spectrum of Intramolecular Hydrogen Bond Energies in Antioxidant Natural Products, New J. Chem. 44 (15) (2020) 5841–5849, https://doi.org/10.1039/D0NJ00304B.

[20] M.B. Ahirwar, S.R. Gadre, M.M. Deshmukh, Direct and Reliable Method for Estimating the Hydrogen Bond Energies and Cooperativity in Water Clusters Wn, n = 3 to 8, J. Phys. Chem. A 124 (33) (2020) 6699–6706, https://doi.org/10.1021/acs.jpca.0c05631.

[21] D. Patkar, M.B. Ahirwar, S.P. Shrivastava, M.M. Deshmukh, Assessment of hydrogen bond strengths and cooperativity in self- and cross-associating cyclic (HF)m(H2O)n (m + n = 2 to 8) clusters, New J. Chem. 46 (5) (2022) 2368–2379, https://doi.org/10.1039/D1NJ05431G.

[22] D. Patkar, M.B. Ahirwar, S.R. Gadre, M.M. Deshmukh, Unusually Large Hydrogen-Bond Cooperativity in Hydrogen Fluoride Clusters, (HF)n, n = 3 to 8, Revealed by the Molecular Tailoring Approach, J. Phys. Chem. A 125 (2021) 8836–8845, https://doi.org/10.1021/acs.jpca.1c06478.

[23] M.B. Ahirwar, N.D. Gurav, S.R. Gadre, M.M. Deshmukh, Molecular Tailoring Approach for Estimating Individual Intermolecular Interaction Energies in Benzene Clusters, J. Phys. Chem. A 125 (28) (2021) 6131–6140, https://doi.org/10.1021/acs.jpca.1c03907.

[24] M.B. Ahirwar, D. Patkar, I. Yadav, M.M. Deshmukh, Appraisal of individual hydrogen bond strengths and cooperativity in ammonia clusters via a molecular tailoring approach, Phys. Chem. Chem. Phys. 23 (32) (2021) 17224–17231, https://doi.org/10.1039/D1CP02839A.

[25] M.J. Frisch, G.W. Trucks, H.B. Schlegel, G.E. Scuseria, G.A.P. J.R. Cheeseman, G. Scalmani, V. Barone, B. Mennucci, J.B. H. Nakatsuji, M. Caricato, X. Li, H.P. Hratchian, A.F. Izmaylov, R.F. G. Zheng, J.L. Sonnenberg, M. Hada, M. Ehara, K. Toyota, T.V. J. Hasegawa, M. Ishida, T. Nakajima, Y. Honda, O. Kitao, H. Nakai, E. B. J.A. Montgomery Jr., J.E. Peralta, F. Ogliaro, M. Bearpark, J.J. Heyd, J.N. K.N. Kudin, V.N. Staroverov, T. Keith, R. Kobayashi, M.C. K. Raghavachari, A. Rendell, J.C. Burant, S.S. Iyengar, J. Tomasi, C.A. N. Rega, J.M. Millam, M. Klene, J.E. Knox, J.B. Cross, V. Bakken, R.C. J. Jaramillo, R. Gomperts, R.E. Stratmann, O. Yazyev, A. J. Austin, V.G.Z. C. Pomelli, J.W. Ochterski, R.L. Martin, K. Morokuma, O.F. G.A. Voth, P. Salvador, J.J. Dannenberg, S. Dapprich, A.D. Daniels, D.J.F. J.B. Foresman, J.V. Ortiz, J. Cioslowski, Gaussian 09 Suites, (2016). https://gaussian.com/g09citation.

[26] Chemcraft graphical software for visualization of quantum chemistry computations. https://www.chemcraftprog.com.

[27] M.M. Deshmukh, S.R. Gadre, L.J. Bartolotti, Estimation of Intramolecular Hydrogen Bond Energy via Molecular Tailoring Approach, J. Phys. Chem. A. 110 (45) (2006) 12519–12523, https://doi.org/10.1021/jp065836o10.1021/jp065836o.s001.

[28] M.M. Deshmukh, C.H. Suresh, S.R. Gadre, Intramolecular Hydrogen Bond Energy in Polyhydroxy Systems: A Critical Comparison of Molecular Tailoring and Isodesmic Approaches, J. Phys. Chem. A. 111 (2007) 6472–6480, https://doi.org/10.1021/jp071337r.

[29] M.M. Deshmukh, L.J. Bartolotti, S.R. Gadre, Intramolecular Hydrogen Bonding and Cooperative Interactions in Carbohydrates via the Molecular Tailoring Approach, J. Phys. Chem. A. 112 (2) (2008) 312–321, https://doi.org/10.1021/jp076316b10.1021/jp076316b.s001.

[30] M.M. Deshmukh, S.R. Gadre, Estimation of N-H···O=C Intramolecular Hydrogen Bond Energy in Polypeptides, J. Phys. Chem. A. 113 (27) (2009) 7927–7932, https://doi.org/10.1021/jp9031207.

[31] M.M. Deshmukh, L.J. Bartolotti, S.R. Gadre, Intramolecular Hydrogen Bond Energy and Cooperative Interactions in α-, β-, and γ-cyclodextrin Conformers, J. Comput. Chem. 32 (14) (2011) 2996–3004, https://doi.org/10.1002/jcc.21881.

[32] G. Friesecke, The Multiconfiguration Equations for Atoms and Molecules: Charge Quantization and Existence of Solutions, Arch. Rational Mech. Anal. 169 (1) (2003) 35–71, https://doi.org/10.1007/s00205-003-0252-y.

[33] A.D. Becke, D.R. Yarkony, "Modern electronic structure theory." (1995), Ed.; World Scientific: River Edge, NJ, 1995; pp 1022–1046.

[34] A. J. Cohen, P. Mori-Sánchez, W. Yang, Insights into Current Limitations of Density Functional Theory, Science, 321 (2008), 792–794. Doi: 10.1126/science.1158722.

[35] C. Lefebvre, G. Rubez, H. Khartabil, J.-C. Boisson, J. Contreras-García, E. Hénon, Accurately extracting the signature of intermolecular interactions present in the NCI plot of the reduced density gradient versus electron density, Phys. Chem. Chem. Phys. 19 (27) (2017) 17928–17936, https://doi.org/10.1039/C7CP02110K.

[36] E. R. Johnson, S. Keinan, P. Mori-Sánchez, J. Contreras- García, A. J. Cohen and W. Yang, J. Am. Chem. Soc. 132 (2010), 6498–6506. 10.1107/S2056989019001129.

[37] E.R. Johnson, S. Keinan, P. Mori-Sánchez, J. Contreras-García, A.J. Cohen, W. Yang, Revealing noncovalent interactions, J. Am. Chem. Soc. 132 (18) (2010) 6498–6506, https://doi.org/10.1021/ja100936w.

[38] C.H. Suresh, S.R. Gadre, A Novel Electrostatic Approach to Substituent Constants: Doubly Substituted Benzenes, J. Am. Chem. Soc. 120 (1998) 7049–7055, https://doi.org/10.1021/ja973105j.

[39] A. Kumar, S.R. Gadre, N. Mohan, C.H. Suresh, Lone Pairs: An Electrostatic Viewpoint, J. Phys. Chem. A 118 (2014) 526–532, https://doi.org/10.1021/jp4117003.

[40] M.M. Deshmukh, S.R. Gadre, R. Tonner, G. Frenking, Molecular electrostatic potentials of divalent carbon(0) compounds, Phys. Chem. Chem. Phys. 10 (2008) 2298–2301, https://doi.org/10.1039/B803068E.

[41] S.R. Gadre, M.M. Deshmukh, T. Chakraborty, Electrostatics-guided ab initio studies on weakly bonded complexes of substituted naphthalenes, Chem. Phys. Let. 384 (2004) 350–356, https://doi.org/10.1016/j.cplett.2003.11.099.